Proceedings of the 10th European Review Meeting on Severe Accidents Research (ERMSAR2022)

Severe Accident Research Eleven Years after the Fukushima Accident

in memory of Martin Kissane

Karlsruhe, Germany

May 16-19, 2022

Karlsruhe Institute of Technology

NUGENIA TA2 Severe Accidents
Nuclear Generation II&III Alliance

SNETP
Sustainable Nuclear Energy Technology Platform

FOREWORD

The 10th edition of the ERMSAR (European Review Meeting on Severe Accident Research) Conference, in memory of Martin Kissane, was held from 16 to 19 May 2022 in Karlsruhe, hosted and locally organized by KIT, after 3 years for the previous edition in Prague. For the fourth time, it has been organized in the frame of the Technical Area 2 of the NUclear GENeration II and III pillar (NUGENIA TA2) of SNETP Association, and for the first time in collaboration with IAEA and OECD/NEA. The Technical Programme Committee involved 18 researchers from diverse organizations (BT, CEA, CIEMAT, ENEA, Framatome GmbH, GRS, IAEA, INRN, IRSN, JSI, KIT, KTH, NEA and University of Pisa).

ERMSAR 2022 gathered 118 participants from nearly 50 organizations settled in 21 countries worldwide (EU, USA, Republic of Korea, Brazil, Japan, India), which highlights ERMSAR as the reference international conference on Severe Accidents. Sixty papers were orally presented and 9 more were exhibited in the posters stand. The conference was focused on the latest progress of international knowledge on severe accidents and has been mainly an opportunity for researchers to discuss about future R&D priorities in this field. The Conference topics are highlighted in the following technical session list.

1. In-vessel corium and debris coolability
2. Severe accident scenarios
3. Ex-vessel corium interactions and coolability
4. Severe accidents scenarios in innovative systems
5. Source term
6. Severe Accident Modeling and Code Development
7. Hydrogen and Containment Related issues

In addition, the technical programme included three plenary sessions, in addition to a specific presentation on NUGENIA/TA2 latest activities and status:

- International programmes on severe accident research.
- Fukushima, from the understanding to accident management and decommissioning.
- Round table on new elements in the SA research domain.

As major conclusions from ERMSAR 2022 it is also possible to highlight:

- A good part of R&D will continue investigating on SA mitigation, in particular on feasibility/development of “new” mitigation measures.
- An increased investigation is on the floor about very near-term deployment systems, like PW-SMRs, with a major take on “safety demonstration” and current analytical tools drawbacks for “very innovative” systems and the potential ways to overcome some of these limits.
- Efforts should be also oriented to widen the range of applicability of the SA codes both to Gen-IV technologies and to improve further the modelling of specific components in deployed systems.

Next edition ERMSAR2024 will be organized in the frame of the SEAKNOT project by KTH in Stockholm on the week of May 17th 2024.

Editors: Fabrizio Gabrielli, Luis E. Herranz and Sandro Paci

In memory of Martin Kissane (by Luis E. Herranz)



Back in the early years of the 80's last century, Martin Kissane got his BSc on Mathematics and Theoretical Physics from the University of Exeter; four years later he got his PhD. On Mechanical Engineer from the University of Sheffield. It was 1986.

From that time on, his running track (he was a runner, at least I met him when he was) took him to organizations as important in the nuclear world as UK Atomic Energy Authority (SRD), IRSN, and OECD/NEA. This journey made him become an expert on several reactor technologies (Light-, Sodium- and gas-cooled reactors). When doing research, he was always involved in the understanding and modeling of physico-chemical phenomena of nuclear safety and, particularly, of severe accidents. LOFT, ICHEMM, LPP, PHEBUS-FP, PHEBEN, RAPHAEL, CP-ESFR, JASMIN, were just some of the projects he was involved in. And when doing research management at OECD/NEA, he became responsible for the NEA's portfolio of joint safety research projects. And this, along with the fact that he was a man more than 190 cm tall, made him be a big person in our field. Someone who deserves being remembered.

When talking to people of the three organizations he served in, they gave away words that I want to share with you.

On the professional side

- Rigorous physicist and modeler
- Excellent and conscientious researcher

- Knowledgeable expert on fission product chemistry
- Valuable asset of the Organization
- Responsible and capable administrator of research projects
- Steady leader
- Naturally team-worker
- Able to make good judgements and take quick decisions (technical acumen)
- Genuine internationalist (“ambassador”), with a strong European feeling and an unquestionable British touch
- Believer in the international networking
- Constant concern to progress in the acquisition of knowledge (Intnl. Network)

Personal words

- Reliable on his integrity and honesty.
- Excellent inter-personal skills
- Vegan
- Truly generous and warm human being
- Lovely man
- Kind person

Wherever he is, he will stay with us for long because much of his legacy remains in our work and it is in our list of references at the end of our papers or reports or just because of this belief of ours in the international networking as an efficient way to enhance nuclear safety.

Probably you deserve better, but at least take this conference as our humble tribute to the “Big man” you’ve always been.

Martin, thank you!

List of Participants

Name	Institution	Country
Agnello, G.	Università degli Studi di Palermo	Italy
Ahn, Kwang-Il	KAERI	Republic of Korea
Angelucci, M.	University of Pisa	Italy
At Khen, K	EDF	France
Bakouta, N.	EDF	France
Bechta, S.	KTH	Sweden
Bentaib, A.	IRSN	France
Bigot, B.	CEA	France
Bittan, J.	EDF	France
Bocanegra, R.	CIEMAT	Spain
Bouyer, V.	CEA	France
Brumm, S.	European Commission	Netherlands
Campbell, S.	U.S. NRC	USA
Chailan, L.	IRSN	France
Chatelard, P.	IRSN	France
Clark, G.	Jacobs	United Kingdom
Coindreau, O.	IRSN	France
Cormack, M.	National Nuclear Laboratory	United Kingdom
De Malmazet, E.	EDF	France
Dejardin, P.	Tractebel	Belgium
Dittmer, S.	Ringhals AB, Vattenfall	Sweden
Dovizio, D.	NRG	Netherlands
Esmaili, H.	U.S. NRC	USA
Espegren, F.	Paul Scherrer Institut	Switzerland
Farhat, M.	IRSN	France
Fischer, M.	Framatome GmbH	Germany
Fontaine, P.	TechnicAtome	France
Fontanet, J.	CIEMAT	Spain
Freitag, M.	Becker Technologies GmbH	Germany
Gabrielli, F.	KIT	Germany
Gaus-Liu, Y.	KIT	Germany
Girault, N.	IRSN	France
Golakoti, S.	Office for Nuclear Regulation	United Kingdom
Gupta, S.	Becker Technologies GmbH	Germany
Hansson Concilio, R.	Forsmark	Sweden
Herranz, L.-E.	CIEMAT	Spain
Hudson, R.	EDF	United Kingdom
Hupp, M.	Framatome GmbH	Germany
Ingremeau, J.-J.	IRSN	France
Iorizzo, A.	European Commission	Belgium
Jacquemain, D.	OECD Nuclear Energy Agency	France
Journeau, C.	CEA	France
Kaliatka, T.	Lithuanian Energy Institute	Lithuania
Keim, T.	Framatome GmbH	Germany
Khatib-Rahbar, M.	Energy Research, Inc.	USA

Kim, S.	KAERI	Republic of Korea
Kljenak, I.	Jožef Stefan Institute	Slovenia
Kotouc, M.	UJV Rez	Czech Republic
Krieger, J.	Ruhr-Universität Bochum	Germany
Krist, F.	Ruhr-Universität Bochum	Germany
Krpan, R.	Jožef Stefan Institute	Slovenia
Kumagai, Y.	OECD Nuclear Energy Agency	France
Kuznetsov, M.	KIT	Germany
Laffolley, H.	CEA	France
Lamont, I.	Jacobs	United Kingdom
Le Fessant, E.	IRSN	France
Le Tellier, R.	CEA	France
Lecomte, M.	Framatome	France
Leskovar, M.	Jožef Stefan Institute	Slovenia
Lind, T.	Paul Scherrer Institute	Switzerland
Lovasz, L.	GRS	Germany
Luxat, D.	Sandia National Laboratories	USA
Maas, L.	IRSN	France
Maccari, P.	ENEA	Italy
Maciel Neto, U.	University of Sao Paulo	Brazil
Malicki, M.	PSI	Switzerland
Marchand, O.	IRSN	France
Markova, T.	State Office for Nuclear Safety	Czech Republic
Martinez-Delcayrou, A.	Framatome	Germany
Mascari, F.	ENEA	Italy
Massara, S.	International Atomic Energy Agency	Austria
Mathé, G.	TechnicAtome	France
May, R.	National Nuclear Laboratory	United Kingdom
Meignen, R.	IRSN	France
Mercan, A.K.	KIT	Germany
Miassoedov, A.	International Atomic Energy Agency	Österreich
Mizokami, M.	Tokyo Electric Power Company Holdings, Inc.	Japan
Mizokami, S.	TEPCO HD	Japan
Modak, M.	Seoul National University	Republic of Korea
Morreale, A.	CNL	Canada
Müer, M.	Ruhr-Universität Bochum	Germany
Murat, O.	KIT	Germany
Murdock, I.	National Nuclear Laboratory	United Kingdom
Nerisson, P.	IRSN	France
Nguyen-Sadassivame, J.	IRSN	France
Nukatsuka, S.	MHI NS Enginnering Co., Ltd.	Japan
Nunes Araujo, N.	University of Sao Paulo	Germany
Okamoto, K.	JAEA/University of Tokyo	Japan
Paci, S.	University of Pisa	Italy
Park, R.-J.	KAERI	Republic of Korea
Park, S.	Lee & Ko	Republic of Korea
Pasi, A.-E.	Chalmers Tekniska Högskolan	Sweden

Pauli, E.-M.	Framatome GmbH	Germany
Perez-Martin, S.	KIT	Germany
Piluso, P.	CEA	France
Pontillon, Y.	CEA	France
Raskob, W.	KIT	Germany
Rehman, Haseeb ur	International Atomic Energy Agency	Österreich
Rehrmann, J.	Ruhr Universität Bochum	Germany
Rocchi, F.	ENEA	Italy
Rodriguez Gual, M.	University of Sao Paulo	Brazil
Sanchez Espinoza, V.-H.	KIT	Germany
Sandén, F.	Chalmers University of Technology	Sweden
Nobrega, G.	IRSN	France
Sercombe, J.	CEA	France
Sil, S.	NPCIL	India
Sim, Suk Ku	en2t	Republic of Korea
Spengler, C.	GRS	Germany
Stakhanova, A.	Karlsruhe Institute of Technology	Germany
Steinbrück, M.	KIT	Germany
Stuckert, J.	KIT	Germany
Tromm, W.	KIT	Germany
Uršic, M.	JSI	Slovenia
Whang, S.	Seoul National University	Republic of Korea
Yatabe, S.	Japan Electric Power Information Center	France

10th European Review Meeting on Severe Accidents Research

Severe Accident Research Eleven Years after the Fukushima Accident

May 16-19, 2022, GenoHotel, Karlsruhe, Germany

Conference Program

MONDAY, MAY 16th, 2022

PLENARY SESSION: WELCOME AND INTRODUCTORY

Chairs: R. Stieglitz (KIT), F. Gabrielli (KIT)

Welcome
W. Tromm (KIT)
In Memory of Martin Kissane
L. E. Herranz (CIEMAT/NUGENIA TA2)
Opening
W. Tromm (KIT)
Overview of the NUGENIA TA2 Status
L. E. Herranz (CIEMAT/NUGENIA TA2)

PLENARY SESSION: INTERNATIONAL PROGRAMS

Chairs: L.E. Herranz (CIEMAT), A. Bentaib (IRSN)

Euratom Projects on Severe accidents
A. Iorizzo (European Commission)
OECD/NEA Projects & WGAMA Activities On Severe Accidents
D. Jacquemain (OECD/NEA)
Recent IAEA Activities Related to Severe Accidents
A. Miassoedov (IAEA)

Technical Session 1-1: In-vessel Corium and debris coolability

Chairs: T. Hollands (GRS), F. Gabrielli (KIT)

ID265	**The IAEA Coordinated Research Project on Developing a Phenomena Identification and Ranking Table and a Validation Matrix, and Performing a Benchmark for In-Vessel Melt Retention** A. Miassoedov (IAEA), S. Massara (IAEA)	**Paper Presentation**
ID319	**Iron and zirconium oxidation at liquid state under Ar-O2 and Ar-H2O gas mixtures in Severe Accident conditions** P. Piluso (CEA)	**Paper Presentation**
ID336	**In-vessel debris melting experiments performed in LIVE3D test facility** X. Gaus-Liu (KIT)	**Paper Presentation**

ID259	**Integral modelling of continuous/dispersed phases mass transfer during in-vessel corium stratification transients** R. Le Tellier (CEA)	**Paper Presentation**

Technical Session 2-1: Severe Accident Scenarios

Chairs: S. Brumm (JRC), S. Paci (University of Pisa)

ID287	**Source term estimation and dispersion analysis of VVER-1000 reactor in case of LBLOCA along with SBO** A. K. Mercan (KIT)	**Paper Presentation**
ID311	**Prediction of the Radiological Consequences of a Severe Accident Scenario in a Generic KONVOI Nuclear Power Plant** E.-M. Pauli (Framatome)	**Paper Presentation**
ID261	**CCFL Model Effect of Pressurizer Surge Line Flow on Severe Accident Progression in TMI-2 using CINEMA** R.-J. Park (KAERI)	**Paper Presentation**
ID318	**Analysis of LOCA accident for BWR-4 under DEC-A conditions using ASTEC code** T. Kaliatka (LEI)	**Paper Presentation**

TUESDAY, MAY 17th, 2022

PLENARY SESSION: FUKUSHIMA: 10 (+1) YEARS AFTER

Chairs: A. Bentaib (IRSN), L.E. Herranz (CIEMAT)

NEA Fukushima Activities
Y. Kumagai (OECD/NEA)
Current situation of the site -Facts & Future of Fukushima Daiichi NPS-
S. Mizokami (TEPCO)
Accident management & nuclear decommissioning
K. Okamoto (JAEA/CLADS)

Technical Session 1-2: In-vessel Corium and debris coolability

Chairs: S. Massara (IAEA), F. Gabrielli (KIT)

ID300	**Characterization of prototypic corium sample simulating Fukushima Daiichi unit 2 lower head composition** C. Journeau (CEA)	**Paper Presentation**
ID309	**Modelling of premixed layer in stratified fuel–coolant configuration** M. Uršič (IJS)	**Paper Presentation**
ID322	**Analysis of RANS Turbulence Models of Natural Convection of Corium Pool for In-Vessel Retention** D. Dovizio (NRG)	**Paper Presentation**
ID277	**Assessment of a dynamic global-coefficient subgrid-scale model for turbulent natural convection in a confined cavity** S. Whang (SNU)	**Presentation**

Technical Session 2-2: Uncertainties in Severe Accident Scenarios

Chairs: F. Mascari (ENEA), S. Paci (University of Pisa)

ID278	**Status of the Uncertainty Quantification for Severe Accident Sequences of Different NPP Designs in the Frame of the H-2020 Project MUSA** S. Brumm (JRC)	**Paper Presentation**
ID314	**Overview of IAEA CRP I31033 "Advancing the state-of-practice in uncertainty and sensitivity methodologies for severe accident analysis in water cooled reactors"** H. U. Rehman (IAEA)	**Paper Presentation**
ID264	**The APR1400 SOARCA Study: Insights into the Severe Accident Progression and Source Term Analysis Results** K. Ahn (KAERI)	**Paper Presentation**
ID275	**Uncertainty Quantification for a Severe Accident Sequence in a SFP in the Frame of the H2020 Project MUSA: First Outcomes** O. Coindreau (IRSN)	**Paper Presentation**

Technical Session 3-1: Ex-vessel Corium interactions and coolability

Chairs: S. Bechta (KTH), P. Piluso (CEA)

ID331	**PIRT Development for the Corium Coolability and MCCI Phenomena during Postulated Severe Accidents in the Reactor Cavity** S.K. Sim (EN2T)	**Paper Presentation**
ID270	**Enhancing Ex-Vessel Corium Coolability for Installed Base Nuclear Power Plants** M. Hupp (Framatome)	**Paper Presentation**
ID279	**Quenching Phenomena in High Temperature Cylindrical Particle Bed-MONET Tests** M. Modak (SNU)	**Paper Presentation**
ID299	**Thermodynamics of aerosols during a molten core-concrete interaction at Fukushima Daiichi unit 2 conditions** H. Laffolley (CEA)	**Paper Presentation**

Technical Session 2-3: Uncertainties in Severe Accident Scenarios

Chairs: O. Coindreau (IRSN), S. Paci (University of Pisa)

ID327	**Preliminary Uncertainty and Sensitivity Analysis of the ASTEC simulations results of a MBLOCA scenario at a Generic KONVOI Plant using FSTC tool** A. Stakhanova (KIT)	**Paper Presentation**
ID324	**CIEMAT's outcomes from the PHEBUS-FPT1 uncertainty analysis in the framework of the EU-MUSA project** R. Bocanegra (CIEMAT)	**Paper Presentation**
ID274	**Parametric analysis of FPT-1 MELCOR 2.2 input deck as a preparation for uncertainty quantification study** M. Malicki (PSI)	**Paper Presentation**

Technical Session 3-2: Ex-vessel Corium interactions and coolability

Chairs: A. Miassoedov (IAEA), P. Piluso (CEA)

ID271	**Super Absorbing Polymers as a Means to Suppress Steam Explosions and Improve Melt Jet Fragmentation** M. Fischer (Framatome)	**Paper** **Presentation**
ID317	**Assessment of Ex-Vessel Corium Coolability of the VVER-1000 Reactor as a Measure of Severe Accident Mitigation** M. Kotouc (UJV)	**Paper** **Presentation**
ID337	**Experiment and Numerical Simulations on SFR Core-Catcher Analysis After Relocation of Corium** B. Bigot (CEA)	**Paper** **Presentation**

Technical Session 4-1: Severe Accident Scenarios in Innovative Systems

Chairs: H. U. Rehman (IAEA), F. Rocchi (ENEA)

ID338	**Analysis of BDBA sequences in a generic IRIS reactor using ASTEC code** P. Maccari (ENEA)	**Paper** **Presentation**
ID276	**Severe Accident Analysis Research at CNL for Small Modular and Advanced Reactor Designs** A. Morreale (CNL)	**Paper** **Presentation**
ID304	**MELCOR Integrated Severe Accident Code Scoping Uncertainty Study of Heat Pipe Reactor Accident Progression** D. Luxat (SNL)	**Presentation**
ID305	**MELCOR Integrated Severe Accident Code Demonstration Uncertainty Study of High-Temperature Gas-cooled Reactor Accident Progression** D. Luxat (SNL)	**Presentation**

WEDNESDAY, MAY 18th, 2022

Technical Session 5-1: Source Term

Chairs: N. Girault (IRSN), S. Gupta (Becker Techn.)

ID328	**Research needs on Source Term: a CSNI/WGAMA perspective** L. E. Herranz (CIEMAT)	**Paper** **Presentation**
ID292	**Fission Product Behaviour in Severe Accident Condition: Focus on Information gained from VERCORS/VERDON Analytical Programs** Y. Pontillon (CEA)	**Paper** **Presentation**
ID268	**Experimental study of CsI revaporization behavior in RCS condition after a SA** E. Le Fessant (IRSN)	**Paper** **Presentation**
ID269	**Experimental study on the feasibility for noble gases (Xe, Kr) trapping using Metal-Organic Framework** J. Nguyen-Sadassivame (IRSN)	**Paper** **Presentation**

Technical Session 7-1: Hydrogen and Containment Related issues

Chairs: M. Hupp (Framatome GmbH), I. Kljenak (IJS)

ID340	**Results of metallographic analysis of the QUENCH-20 bundle with B4C absorber** J. Stuckert (KIT)	**Paper** **Presentation**
ID315	**Status of Modeling of FeCrAl Claddings in Severe Accident Codes and Application on the QUENCH-19 Experiment** T. Hollands (GRS)	**Paper** **Presentation**
ID284	**Current understanding of high-temperature oxidation phenomena during air ingress scenarios** S. Park (Lee & Co)	**Paper** **Presentation**
ID356	**THAI Experiments on Iodine Behavior in a Room Chain Representing Flow Conditions in Large Containments** M. Freitag (Becker Technologies)	**Paper** **Presentation**

Poster Session

ID267	**Organic Iodides trapping using silver-exchanged zeolites in conditions representative of a French pressurized water reactor severe accident** C. Le Gall (CEA)	**Paper** **Poster**
ID283	**THE EVOLUTION OF SEVERE ACCIDENT RESEARCH AT CHALMERS UNIVERSITY OF TECHNOLOGY – STATE-OF-THE-ART** A.-E. Pasi (Chalmers University)	**Paper** **Poster**
ID288	**Extending Capabilities of the ASTEC Severe Accident Code to Simulate Accident Sequences of Generic BWR4 Mark1** O. Murat (KIT)	**Paper** **Poster**
ID345	**IVMR system. Analytical justification results for VVER-440/V-213** O. Mazurok (ES Group)	**Paper** **Poster**
ID357	**The NewPLINIUS project: France future prototypic corium experimental platform for severe accident R&D** C. Journeau (CEA)	**Paper** **Poster**
ID358	**Evaluation of Long-Term Containment Cooling System (LTCCS) concepts for reactor facility VVER-1000/V-320** V. Ivanov (ES Group)	**Poster**
ID360	**TOP FLOODING TESTS OF PROTOTYPIC CORIUM ON MERELAVA FACILITY** V. Bouyer (CEA)	**Paper** **Poster**
ID362	**FAN COOLER IMPACT UNDER A TLOFW ACCIDENT IN A NEW SMR IN DESIGN PHASE** M. R. Gual (University of São Paulo)	**Paper** **Poster**
ID386	**Development of CFD Code for Prediction and Improvement of Core-Catcher Performance** Sangmin Kim (KAERI)	**Paper** **Poster**

Technical Session 5-2: Source Term

Chairs: T. Lind (PSI), S. Gupta (Becker Techn.)

ID294	**Pool scrubbing in Unit 1 of Fukushima Daiichi** L. E. Herranz (CIEMAT)	**Paper Presentation**
ID298	**Bubbles dynamics under pool scrubbing conditions for iodine compounds trapping applications** M. Farhat (IRSN)	**Paper Presentation**
ID329	**New pool scrubbing correlations based on reliable data** L. E. Herranz (CIEMAT)	**Paper Presentation**
ID332	**The R2CA project for a better evaluation of radiological consequences under Design Basis Accidents and Design Extension Conditions in LWRs : Motivation and first results** N. Girault (IRSN)	**Paper Presentation**

Technical Session 6-1: Severe Accident Modeling and Code Development

Chairs: E.-M. Pauli (Framatome), F. Gabrielli (KIT)

ID302	**Synthesis of the ASTEC V2.2 code validation vs. experimental data** P. Chatelard (IRSN)	**Paper Presentation**
ID266	**Development of Severe Accident Code CORVES for Analysing In-Vessel Degradation Phase of Severe Accident in VVER-1000 Reactor** S. Sil (NPCIL)	**Paper Presentation**
ID303	**Modeling of Fission Product Release during Severe Accidents: Overview of Recent Developments in the Fuel Performance Code Alcyone** J. Sercombe (CEA)	**Paper Presentation**
ID313	**A Simplified Core Catcher Model for the Containment Code AC2/COCOSYS** C. Spengler (GRS)	**Paper Presentation**

PLENARY SESSION: NEW ELEMENTS IN THE SA RESEARCH DOMAIN

Chairs: H. U. Rehman (IAEA), I. Kljenak (IJS)

Phenomena Identification Ranking Tables for Near Term Accident Tolerant Fuels (ATF) Applicable to Severe Accident Conditions
M. Khatib-Rahbar (Energy Research, Inc.)
SMR impact on SA research and community
P. Dejardin (TRACTEBEL)
Advanced decision support system: JRODOS Application for Ukraine
W. Raskob (KIT)
Innovation in Modeling
L. Chailan (IRSN)

Technical Session 7-2: Hydrogen and Containment Related issues

Chairs: M. Freitag (Becker Techn.), I. Kljenak (IJS)

ID339	**High combustion risk sequences: Identification and characterization** L. E. Herranz (CIEMAT)	**Paper Presentation**
ID312	**Dynamically Prescribed Turbulent Numbers in Containment Atmosphere Mixing Simulations** R. Krpan (IJS)	**Paper Presentation**
ID334	**An Analysis of Combustion Regimes for Hydrogen/CO/Air Mixtures in Different Geometries** M. Kuznetsov (KIT)	**Paper Presentation**

Technical Session 4-2: Severe Accident Scenarios in Innovative Systems

Chairs: C. Journeau (CEA), F. Rocchi (ENEA)

ID306	**MELCOR Integrated Severe Accident Code Scoping Uncertainty Study of Fluoride-salt-cooled High-Temperature Reactor Accident Progression** D. Luxat (SNL)	**Presentation**
ID272	**MSR Simulation with cGEMS: Fission product release** T. Lind (PSI)	**Paper Presentation**
ID323	**Modelling FPs Release from Sodium Pools under DBDA Conditions** L. E. Herranz (CIEMAT)	**Paper Presentation**
ID333	**On the Pursuing of Safety Enhancements in Sodium Fast Reactors** S. Perez-Martin (KIT)	**Paper Presentation**

THURSDAY, MAY 19th, 2022

Technical Session 7-3: Containment Behavior - Recombination

Chairs: A. Bentaib (IRSN), I. Kljenak (IJS)

ID301	**Experimental Investigation on the Effect of Carbon Monoxide on Platinum- and Palladium-based Catalysts for Passive Auto-catalytic Recombiners** G. Nobrega (IRSN)	**Paper Presentation**
ID286	**Enhancement of Recombination Rate Correlations for PARs in Oxygen-Lean Conditions** J. Fontanet (CIEMAT)	**Paper Presentation**
ID330	**Effectiveness of Hydrogen Recombination by AgX and AgR Zeolites** F. Espegren (PSI)	**Paper Presentation**

Technical Session 6-2: Severe Accident Modeling and Code Development

Chairs: L. Chailan (IRSN), F. Rocchi (ENEA)

ID320	**Sensitivity Analyses on MELCOR Accumulators Modelling** G. Agnello (ENEA)	**Paper** **Presentation**
ID316	**Experiment Investigation of QUENCH-20 and Simulation with AC2/ATHLET-CD** T. Hollands (GRS)	**Paper** **Presentation**
ID335	**Detection of radionuclides in northern Europe in June 2020: investigations on possible source term location and origin** J.J. Ingremeau (IRSN)	**Paper** **Presentation**
ID293	**RCCS-2021 OECD specialist workshop on "Reactor core and containment cooling systems – long term management and reliability workshop" -Overview on the main outcomes** A. Bentaib (IRSN)	**Paper** **Presentation**

PLENARY SESSION: CLOSING

Chairs: L.E. Herranz (CIEMAT), F. Gabrielli (KIT)

Summary and conclusion of the Session Chairs
Session Chairs
Concluding Remarks and Introduction of ERMSAR2024
A. Bentaib (IRSN), L. E. Herranz (CIEMAT)
Closing Remarks
L. E. Herranz (CIEMAT), F. Gabrielli (KIT)

The 10th European Review Meeting on Severe Accidents Research

Severe Accident Research Eleven Years after the Fukushima Accident

May 16-19, 2022, Karlsruhe, Germany

PLENARY SESSION: WELCOME AND INTRODUCTORY

Chairs: R. Stieglitz (KIT), F. Gabrielli (KIT)

Welcome
W. Tromm (KIT)

In Memory of Martin Kissane
L. E. Herranz (CIEMAT/NUGENIA TA2)

Opening
W. Tromm (KIT)

Overview of the NUGENIA TA2 Status
L. E. Herranz (CIEMAT/NUGENIA TA2)

Karlsruhe Institute of Technology

Welcome Address:
10th European Review Meeting on Severe Accidents Research
May 16-19, 2022, AkademieHotel, Karlsruhe, Germany

Outlook Programme NUSAFE at KIT and Helmholtz Association

Th. Walter Tromm, Programme Nuclear Waste Management, Safety and Radiation Research




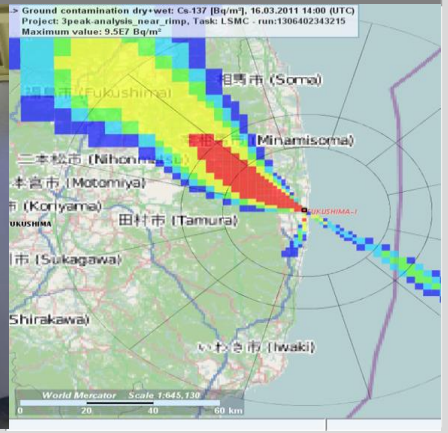






Spitalmasse

KIT – Part of the Helmholtz Association



Helmholtz research centers

KIT	**Karlsruhe Institute of Technology**
DLR	German Aerospace Center
FZJ	Forschungszentrum Jülich
DESY	Deutsches Elektronen-Synchrotron
DKFZ	German Cancer Research Center
IPP	Max-Planck-Institute for Plasma Physics
HMGU	Helmholtz-Zentrum München
GSI	Helmholtz Center for Heavy Ion Research
HZB	Helmholtz-Zentrum Berlin für Materialien und Energie
AWI	Alfred-Wegener-Institute for Polar and Marine Research
HZDR	Helmholtz Center Dresden Rossendorf
UFZ	Helmholtz Center for Environmental Research
GKSS	Helmholtz-Zentrum Geesthacht – Center for Materials and Coastal Research
GFZ	Helmholtz-Zentrum Potsdam – German Research Center for Geosciences
MDC	Max-Delbrück-Center for Molecular Medicine
GEOMAR	Helmholtz Centre for Ocean Research Kiel
HZI	Helmholtz Center for Infection Research
DZNE	German Center for Neurodegenerative Diseases

Nuclear Waste Management, Safety and Radiation Research

Participating Helmholtz - Centres

Forschungszentrum Jülich GmbH (FZJ)

Helmholtz – Zentrum Dresden – Rossendorf (HZDR)

Karlsruher Institut für Technologie (KIT)









Research - Teaching - Innovation

≈ 9,780 employees, including
≈ 385 professors
> 3,100 doctoral researchers
> 2,000 postdoctoral researchers and staff scientists
≈ 22,500 students

1.090,7 Mio. € budget

(Status 2021)

The Research University in the Helmholtz Association

- **University of Karlsruhe (1825)**
- **Research Center Karlsruhe (1956)**

→ **merger to**
Karlsruhe Institute of Technology KIT (2009)

→ **Institutional change as part of our DNA**
→ an excellent staff-student ratio

KIT stands for vision and tradition



Ferdinand Braun

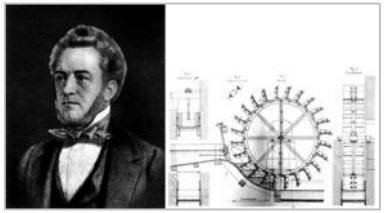

Ferdinand Redtenbacher

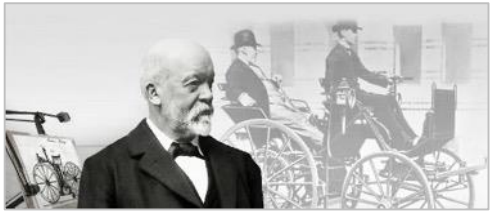

Carl Benz

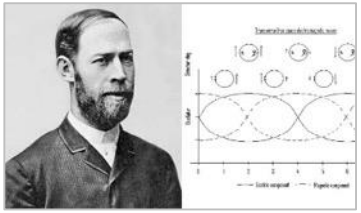

Heinrich Hertz



The first department for computer sciences in Germany

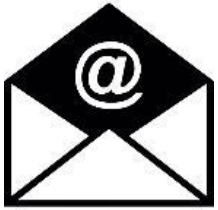

Receipt of the first e-mail in Germany



One of the largest energy research centers in Europe







Robotics/ Artificial Intelligence

Highlights in Research



KIT coordinates projects for energy transition



high-performance computer (Hochleistungsrechner) Karlsruhe – HoreKa

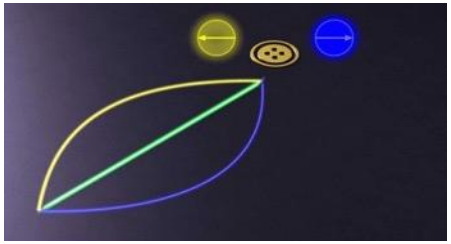

One step to the quantum computer



GridKa – Grid Computing Centre Karlsruhe

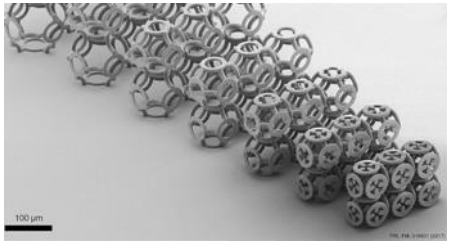

Materials from the 3D printer



Batteries beyond lithium

KIT – Research, teaching and innovation at several locations



Campus Nord



Campus Süd



Campus Ost



Campus West



Campus Alpine



Helmholtz Institut Ulm

Thank you for your attention



Th. Walter Tromm
Karlsruhe Institute of Technology
Programme Nuclear Safety Research

walter.tromm@kit.edu

In memory of Martin Kissane (by Luis E. Herranz)



Back in the early years of the 80's last century, Martin Kissane got his BSc on Mathematics and Theoretical Physics from the University of Exeter; four years later he got his PhD. On Mechanical Engineer from the University of Sheffield. It was 1986.

From that time on, his running track (he was a runner, at least I met him when he was) took him to organizations as important in the nuclear world as UK Atomic Energy Authority (SRD), IRSN, and OECD/NEA. This journey made him become an expert on several reactor technologies (Light-, Sodium- and gas-cooled reactors). When doing research, he was always involved in the understanding and modeling of physico-chemical phenomena of nuclear safety and, particularly, of severe accidents. LOFT, ICHEMM, LPP, PHEBUS-FP, PHEBEN, RAPHAEL, CP-ESFR, JASMIN, were

just some of the projects he was involved in. And when doing research management at OECD/NEA, he became responsible for the NEA's portfolio of joint safety research projects. And this, along with the fact that he was a man more than 190 cm tall, made him be a big person in our field. Someone who deserves being remembered.

When talking to people of the three organizations he served in, they gave away words that I want to share with you.

On the professional side

- Rigorous physicist and modeler
- Excellent and conscientious researcher
- Knowledgeable expert on fission product chemistry
- Valuable asset of the Organization
- Responsible and capable administrator of research projects
- Steady leader
- Naturally team-worker
- Able to make good judgements and take quick decisions (technical acumen)
- Genuine internationalist ("ambassador"), with a strong European feeling and an unquestionable British touch
- Believer in the international networking
- Constant concern to progress in the acquisition of knowledge (Intnl. Network)

Personal words

- Reliable on his integrity and honesty.
- Excellent inter-personal skills

- Vegan
- Truly generous and warm human being
- Lovely man
- Kind person

Wherever he is, he will stay with us for long because much of his legacy remains in our work and it is in our list of references at the end of our papers or reports or just because of this belief of ours in the international networking as an efficient way to enhance nuclear safety.

Probably you deserve better, but at least take this conference as our humble tribute to the “Big man” you’ve always been.

Martin, thank you!

Karlsruhe Institute of Technology

Welcome Address:
10th European Review Meeting on Severe Accidents Research
May 16-19, 2022, AkademieHotel, Karlsruhe, Germany

Outlook Programme NUSAFE at KIT and Helmholtz Association

Th. Walter Tromm, Programme Nuclear Waste Management, Safety and Radiation Research




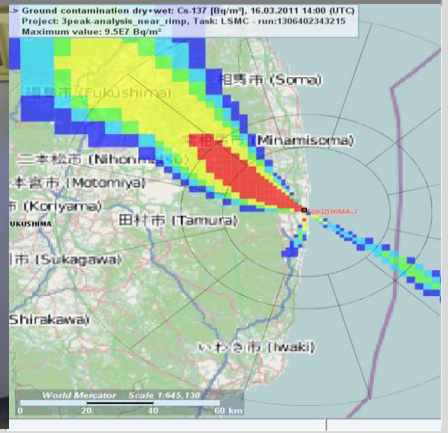

Nuclear Energy in Germany





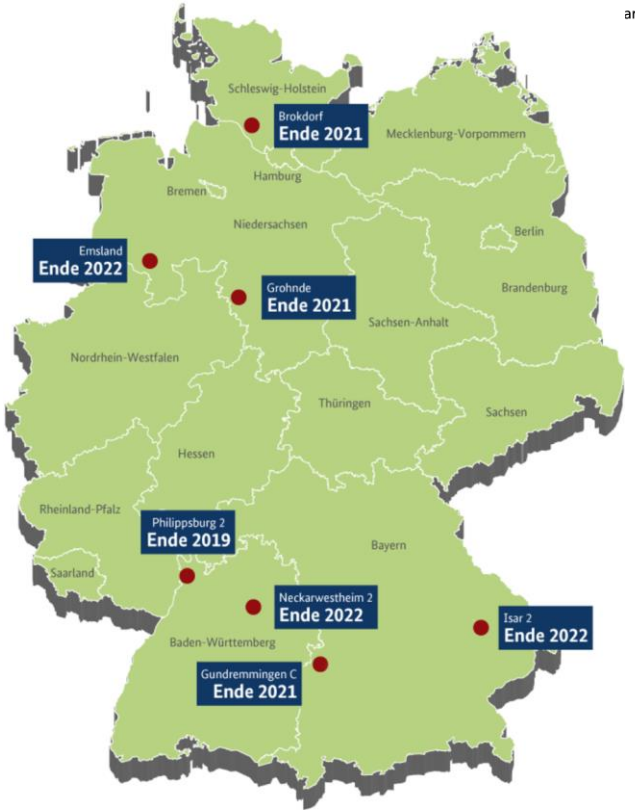

Grand Challenges in Energy Research and Beyond

- Nuclear energy **phase out** in 2022
- Coal power plant **phase out** in 2038
- Reduction of greenhouse gases to **zero** in **2045**
- Share of renewables up to **100%** in 2050
- Feasibility of commercial **nuclear fusion**
- **NEW: Independence from Russian fossil fuels and raw materials**

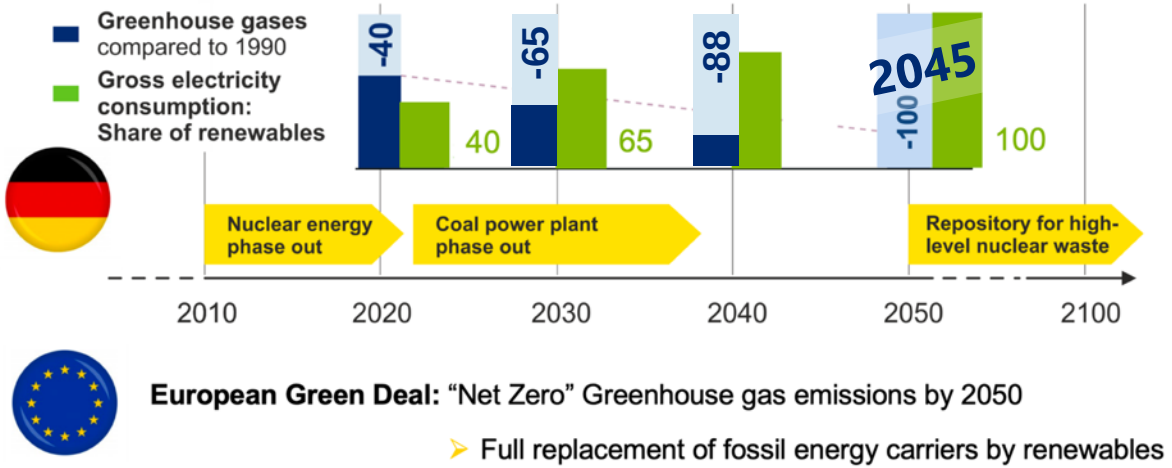

KIT Mission in Energy Research

KIT - The Research University in the Helmholtz Association

- We support the **transformation** of the energy system in Germany.
- We focus on **holistic and systemic approaches**, which include all relevant energy conversion paths.
- We are one of the **largest energy research centers** in Europe.
- We cross the lines between **disciplines** and combine **fundamental and applied research**.
- We develop **energy technology solutions** and provide **advice** to politics, business, and society.
- We operate **unique research infrastructure** and **simulation tools** to describe a multi-modal, multi-scale energy system.
- We educate and train the **next generation** to solve the global energy challenge.

Strategic Scientific Goals at KIT

- Emphasizing the **systems perspective**: from technologies to integrated systems
- Provide energy storage technologies addressing **sector coupling**
- **Risk and security research** (resilience) for dependable energy systems
- **Efficient process chains** for renewable energy sources and sustainable raw materials
- **Final disposal** of nuclear waste and reactor safety research as a national responsibility
- **Fusion energy** as a long-term option







Research Field Energy
Programs in POF IV at KIT 2021 – 2027

Helmholtz Energy Transition Roadmap (HETR)
- Science driven
- Research-strategy tool
- Advice to politics and society

Energy System Design
- Energy System Transformation
- Digitalization and System Technology

Fusion
- Stellerator Research
- Tokamak Physics
- Fusion Technologies and Materials
- Plasma-Wall Interactions



Materials and Technologies for the Energy Transition
- Photovoltaics and Wind Energy
- Electrochemical Energy Storage
- Chemical Energy Carriers
- High-Temperature Thermal Technologies
- Resource and Energy Efficiency

Nuclear Waste Management, Safety and Radiation Research
- Nuclear Waste Management
- Reactor Safety

Topic 2 Reactor Safety

- Development of advanced safety analysis tools for Small Modular reactors (SMR)
  - Assessment of established Light Water Reactor tools for SMR conditions
  - Adaptation and validation of Helmholtz tools for the specifics of SMR
- Radiation tolerance of advanced structural materials
  - Application of ion irradiation to simulate neutron irradiation effects
  - Nanostructure-informed modelling of radiation hardening
- KALLA: Experimental liquid metal heat transfer investigations of rod bundles with blockages within the EU-project PATRICIA
- Helmholtz QUENCH Test Facility: Conduction of experiments on accident tolerant fuels (ATF) cladding materials as OECD/NEA Joint Undertaking
- Open source CFD code containmentFOAM: Implementation of advanced models for thermal radiation, fog and aerosol transport, sensitivity/uncertainty quantification

Nuclear Waste Management, Safety and Radiation Research

Topic 2

- McSAFER (High-Performance Advanced Methods and Experimental Investigations for the Safety Evaluation of Generic Small Modular Reactors)
- Development of advanced safety analysis tools for Small Modular reactors (SMR)
- Advanced neutronic (MC and transport) and thermal hydraulics (two-phase, porous-media) for the core and plant behavior of SMR
- Two series of experiments to investigate the thermal hydraulics in different SMR concepts
    - Investigation of flow boiling up to the critical heat flux under reactor typical conditions

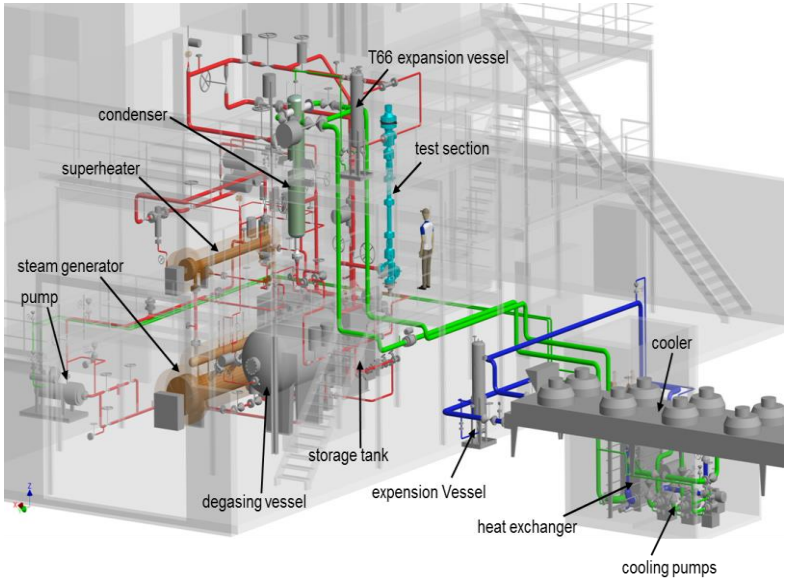

Nuclear Waste Management, Safety and Radiation Research

Topic 2

Assessment of the radiological consequences of severe accidents in NPP

- Supporting emergency management in abnormal events
- Innovative calculation platform for **realistic** evaluations of fission products dispersion in the environment during severe accidents in NPPs, i.e. PWR, VVER-1000, BWR and SMR
- Database of the ASTEC source terms results → quantification of the uncertainty and prediction
- **Outlook:** Employment of artificial intelligence algorithms to improve the performance of the ASTEC code and of source term predictions

European Reference ASTEC code

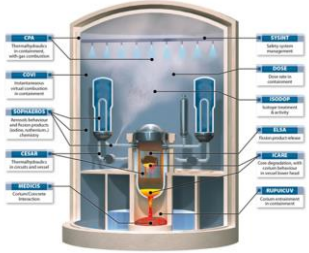

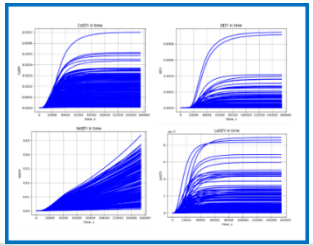

JRODOS

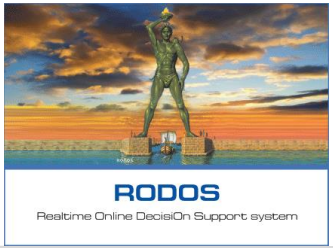

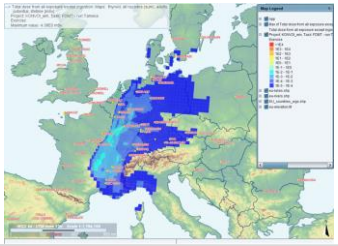

QUENCH-ATF Joint Undertaking

- Three bundle experiments with ATF cladding in the QUENCH facility (Cladding tubes provided by WEC (and others?))
- Time frame: 2021-2024
- Costs: 1.5 M€ (approx. 500 000 €/test) + NEA fee
  - 50% covered by KIT/Germany, 50% covered by collaborators



NUSAFE Topic 2, EU-projects

- In the Euratom Call NFRP-2021-2022 in October 2021 overall 10 proposals with participation of KIT submitted, 1 coordinated by KIT.
- Evaluation results in February 2022: 9 of 10 proposals funded, as well the KIT coordinated: 90% success rate
- Funding for KIT: about 2,9 Mio Euro for 4 years

Acronym	*EC funding for KIT*	*Full title*
bewilligt:		
ANSELMUS	68.719,00	Advanced Nuclear Safety Evaluation of Liquid Metal Using Systems
ASSAS	358.313,00	Artificial intelligence for the Simulation of Severe AccidentS
ENEN2plus	105.000,00	Building European Nuclear Competence through continuous Advanced and Structured Education and Training Actions
ESFR-SIMPLE	578.774,00	European Sodium Fast Reactor - Safety by Innovative Monitoring, Power Level flexibility and Experimental research
INNUMAT (Koord.: KIT)	1.021.986,00	Innovative Structural Materials for Fission and Fusion
OFFERR	42.500,00	eurOpean platForm For accEssing nucleaR R&d facilities
SASPAM-SA	247.032,00	Safety Analysis of SMR with PAssive Mitigation strategies - Severe Accident
SCORPION	249.930,00	SiC composite claddings: LWR performance optimization for nominal and accident conditions
SEAKNOT	192.047,00	SEvere Accident research and KNOwledge managemenT for LWRs
bewillgte Summe	***2.864.301,00***	
nicht bewilligt:		
ARMSTRONG		Advanced Robust Multiphysics Simulation Tools for Reactors Of New Generation

Recommendations of Strategic Advisory Board 2021 NUSAFE Topic 2 Reactor Safety

- The NUSAFE programme on reactor safety **with the major experimental projects Quench-ATF and KALLA as well as the multi-physics simulation, e.g project McSafer**, is attractive and ensures highest-level reactor safety research. Hence, these projects are strongly supported by the SAB.
- **The projects will help to attract young talents and by this contribute to know-how transfer and knowledge developing**, strongly contributing to the programme of BMBF/BMWi/BMU on “Kompetenz- und Nachwuchsentwicklung für die nukleare Sicherheit”. **The SAB recommends to foster competence keeping and development (especially of young scientists, also female).**
- **International cooperation with many countries is well developed by KIT. This also will help to keep competence in the relevant research fields and to contribute to specific questions pertaining to international nuclear safety.**

Goal of nuclear generating 25% of electricity before 2050

To meet the goal, need to build 1000 GWe of new nuclear capacity by 2050. The average build rate required is:

- 25 GWe per year between 2021 and 2025.
- 33 GWe per year between 2026 and 2050

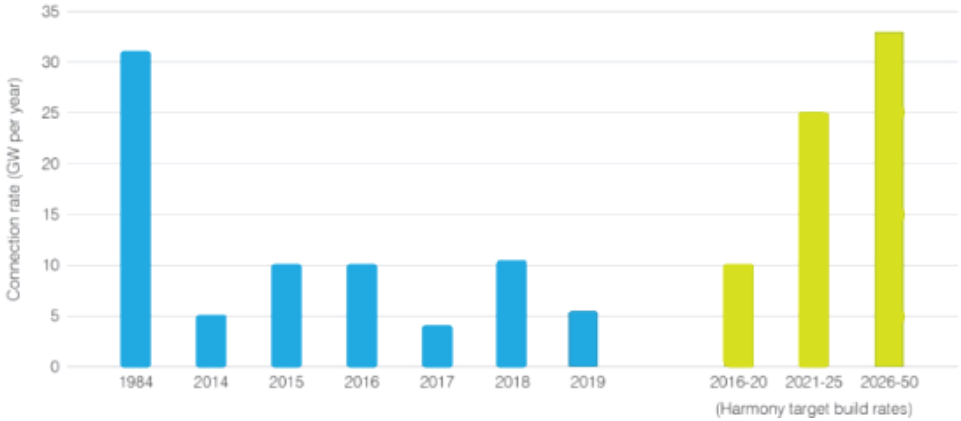

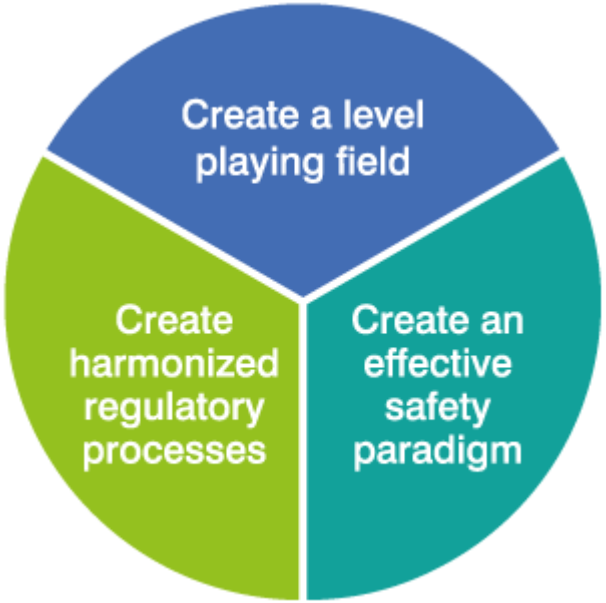

Today, with the experience and knowledge it has gained, the nuclear energy industry is in a strong position to deliver on the goal of generating 25% of electricity before 2050. This is an ambitious target, but the rate at which new reactors will have to be built is no higher than what has been historically achieved.

The European Commission's vision outlines seven main strategic building blocks:

- maximise the benefits of energy efficiency, including zero emission buildings;
- maximise the deployment of renewables and the use of electricity to fully decarbonise Europe's energy supply;
- embrace clean, safe and connected mobility;
- a competitive EU industry and the circular economy as a key enabler to reduce GHG emissions;
- develop an adequate smart network infrastructure and interconnections;
- reap the full benefits of bioeconomy and create essential carbon sinks;
- tackle remaining CO2 emissions with Carbon Capture and Storage (CCS)



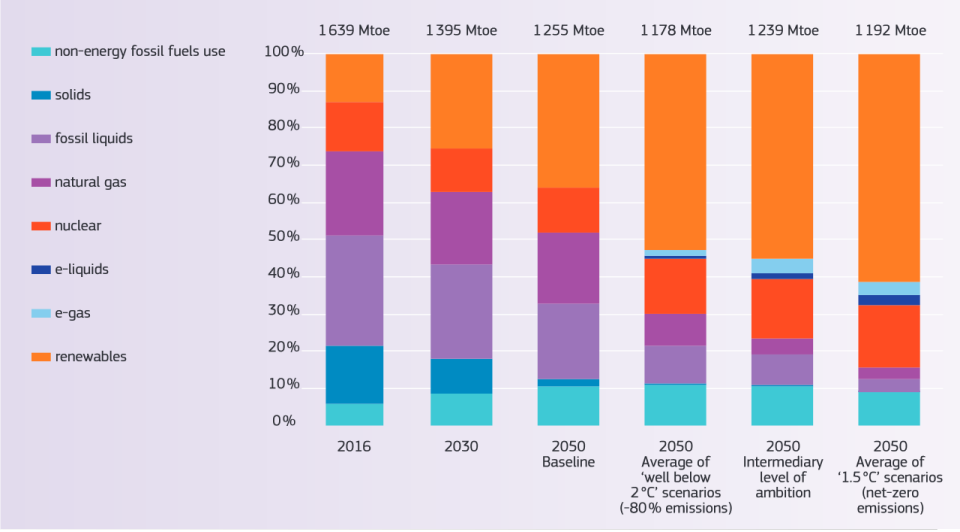

Thank you for your attention



Th. Walter Tromm
Karlsruhe Institute of Technology
Programme Nuclear Safety Research

walter.tromm@kit.edu

Current Status & Major Ongoing Activities of NUGENIA/TA2

L.E. Herranz (CIEMAT), A. Bentaib (IRSN), F. Gabrielli (KIT),
S. Gupta (B-T), I. Kljenak(JSI), S. Paci (Univ. of Pisa),
P. Piluso (CEA), F. Rocchi (ENEA)

10th European Review Meeting on Severe Accident Research
May 16th-19th, 2022

OUTLINE

- INTRODUCTION
- TA2 BIG PICTURE
- SUB-TECHNICAL AREAS
- BEYOND SUB-TAs
- FINAL REMARKS

INTRODUCTION

SARNET

- **The SARNET network (Severe Accident Research NETwork of excellence) was co-funded by EC from 2004 to 2013 in FP6-FP7 and then integrated in NUGENIA.**
- **The main network activities are continuing in the NUGENIA Technical Area (TA) N°2:**
  - Research projects (EC-funded & in-kind projects).
  - Dissemination of knowledge
    - Textbook on SA.
    - **ERMSAR conferences.**
    - SAP courses.
    - Ranking research priorities.

NUGENIA

- **NUGENIA is one of the pillars of SNETP.**
  - NUGENIA keeps its "technical identity" and management.
- **Overall objectives:**
  - Bringing together top scientists in SA research **to build a world leadership position.**
  - **Integration of efforts of European R&D** organisations in definition of research priorities and common research programmes.
  - **Capitalization of the knowledge** (SOARs, codes & databases).
  - **Dissemination of knowledge to students, young researchers and new nuclear countries** through E&T programmes and papers.
- **Extension to EP&R and SA impact on environment.**

SNETP Association

- Three pillars / Eight Committees



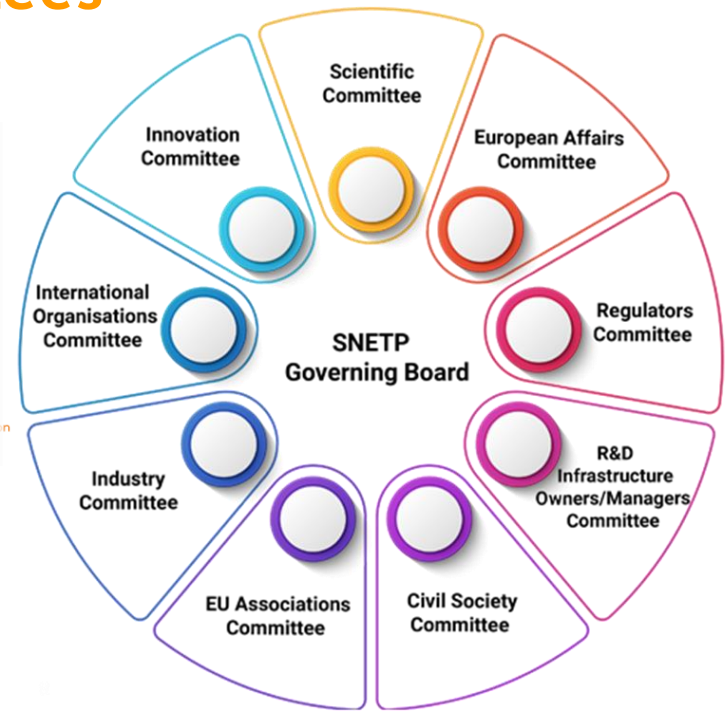

- More than 110 members:
  - Research & Academia (51%)
  - Industry & SMEs (30%)
  - Others (19%)

TA2 BIG PICTURE

Structure

- **Coordination:** CIEMAT (IRSN, Deputy)
- **Sub-TA and leaders:**
  - 2.1 In-vessel corium/debris coolability (KIT)
  - 2.2 Ex-vessel corium interactions-coolability (CEA)
  - 2.3 Containment behaviour, incl. combustion risk (JSI)
  - 2.4 Source term to the environment (BT)
  - 2.5 Environmental impact & emergency management (ENEA)
  - 2.6 Severe accident scenarios (UNIPI)
- **Dissemination of knowledge (coordination):** UNIPI

Projects Portfolio

Acronym	Sub-TA	Coordinator	Funding
SAMHYCO-Net	2.3 (H2 risk)	IRSN	In-kind
ASCOM	2.6 (SA Modeling)	IRSN	In-kind
IPRESCA	2.4 (Pool scrubbing)	BT	In-kind
MUSA	**2.6 (SA Modeling)**	**CIEMAT**	**H2020**
R2CA	**2.6 (SA Modeling)**	**IRSN**	**H2020**
AMHYCO	**2.3 (H2&CO risk)**	**UPM**	**H2020**
SEAKNOT	**2.x (Cross-cutting)**	**CIEMAT**	**HEUROPE**
ASSAS	**2.6 (SA Modeling)**	**IRSN**	**HEUROPE**
SASPAM-SA	**2.6 (SA Modeling)**	**ENEA**	**HEUROPE**

- TA2 organizations collaborate in other international activities, mostly under **NEA and IAEA frameworks**.

SUB-TECHNICAL AREAS

TA2.1: In-vessel Corium/debris coolability (F. Gabrielli, KIT)

- **Four subtopics**
  - Reflooding and coolability of a degraded core
  - Remelting of debris, melt pool formation and coolability
  - Bringing research results into reactor application
  - Spent fuel pool analysis
- **Joint TA2.1/TA2.2 annual review meetings** (2014 – 2019)
- **Running and "starting" (2022) projects**
  - ASCOM; MUSA; ASSAS, SASPAM-SA, SEAKNOT
  - (IAEA/IVMR; NEA/QUENCH-ATF)

TA2.2: Ex-vessel Corium interactions / coolability (P. Piluso, CEA)

- **Five subtopics**
  - Fuel Coolant Interaction
  - Spreading and Molten Corium Concrete Interaction
  - Debris Cooling
  - Corium properties and ATF
  - Fukushima ex-vessel activities
- **Joint TA2.1/TA2.2 annual review meetings**
- **Running and "starting" (2022) projects**
  - ASCOM; MUSA; ASSAS, SASPAM-SA, SEAKNOT
  - (IAEA/Expert meeting; NEA/ROSAU – TA2 EoI!)

TA2.3: Containment Behaviour & H2/CO Risk (I. Kljenak, JSI)

- **Three subtopics**
  - Containment atmosphere mixing
  - Mitigation of combustion risk
  - H2 & CO combustion
- **Running and "starting (2022) projects**
  - **SAMHYCO-Net; AMHYCO**
  - ASCOM; MUSA; ASSAS, SASPAM-SA, SEAKNOT
  - (NEA/HYMERES-Followup; NEA/THEMIS)

TA2.3: Containment Behaviour & H2/CO Risk (I. Kljenak, JSI)

- **Atmosphere mixing** (flammable mixtures) - Slowdown
  - **Experimental activities**: no explicit EC or OECD projects
  - **Theoretical activities**:
    - CFD codes
    - System codes (AMHYCO project)
    - ContainmentFoam (development)
- **Mitigation of combustion risk** (PARs) - Intense
  - **Experimental activities:**
    - REKO facility
    - THAI facility (BT)
  - **Theoretical activities:**
    - Simulations with CFD codes
    - Develop. of correlations (system codes)
- **Combustion** - Slowdown
  - **Experimental activities:**
    - Spherical vessels
    - In tubes & large vessels
  - **Theoretical activities:** Simulations with CFD codes

TA2.4: Source Term (S. Gupta, BT)

- **Four subtopics**
  - FP-water interaction (scrubbing & reentrainment)
  - FP interaction with safety systems (FCVS; PARs; sprays; …)
  - Remobilization of FP – Delayed releases
  - "Uncertainty quantification".
- **Running and "starting" (2022) projects**
  - **IPRESCA; MUSA**
  - ASSAS, SASPAM-SA, SEAKNOT
  - (NEA/WGAMA-BCAPFIS; NEA/THEMIS; NEA/ESTER)

TA 2.5 Environmental impact & emergency management (F. Rocchi, ENEA)

- **Four subtopics**
  - Insights from long term land contamination
  - Optimization of mitigation strategies from RCs
  - Inverse ATM as complementary validation of SA codes
  - "Interfacing" SA & ATM codes.
- **Running and "starting" (2022) projects**
  - MUSA; R2CA; SASPAM-SA; LW-SMR EPZ
  - Forthcoming cooperation with MENA Platforms (NERIS)

TA 2.6 Severe accident sequences (S. Paci, UNIPI)

- **Four subtopics**
  - Analysis of Large LWR severe accident sequences (R & SFP)
  - BEPU application to SA analysis
  - SA codes application to SMRs
  - SA codes application to other technologies (fusion).
- **Running and "starting" (2022) projects**
  - **ASCOM; MUSA; R2CA; AMHYCO; SASPAM-SA; ASSAS**
  - SEAKNOT
  - (IAEA/CRP on UASA to SA analysis)

BEYOND SUB-TECHNICAL AREAS

Dissemination

Objectives

- To efficiently and extensively articulate the **transfer of projects outcomes to stakeholders.**
- To foster the **communication to the public** of the continuous enhancement of nuclear safety.
- To facilitate the **knowledge/knowhow transfer in SA to YG.**
- To strengthen the collaboration with ENEN in the area of SA.

- SEAKNOT: a singular project!

Latest Communications

- **Nuclear España:** 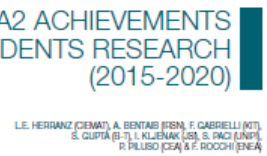

https://www.revistanuclear.es/seguridad/nugenia-ta2-achievements-in-severe-accidents-research-2015-2020

- **Paper 59 to the Specialist Meeting on Thermal-hydraulics (NEA/CSNI/WGAMA).**

  "Overview of Key Thermalhydraulic phenomena in Severe Accident Unfolding: Current knowledge and further needs"

- **Presentation at CSNI/WGAMA annual meeting (Sept., 2020) and ETSON/ERG meeting (May 2020).**
- **Contribution to the NUGENIA Vision document and to the NUGENIA charter.**

Dissemination Activities

- **Severe Accident Phenomenology (SAP) Course**

  - Ten editions of the SAP Course (> 850 attendees).
  - Discount fees for students
  - 3 ECTS recognized
  - 10th SAP hosted online by ENEA (Oct., 2021)
  - Next SAP: planned in Madrid, June 2023 (SEAKNOT)

    - Focus on SA phenomena.
    - Extended to: SA accidents & uncertainties.
    - On-codes and on-Gen III sections updated.
    - More changes likely coming

Dissemination Activities

- **ERMSAR European Review Meeting on SA Research**
  - Ten editions since 2005 – A forum just focused on SA research.
  - Biennial periodicity: previous 9th ERMSAR organized by ÚJV Řež (Prague) (163 participants from 23 countries and 73 organizations).
    Free download of Proceedings (snetp.eu/technical-area-2-severe-accidents)
    Special ANUCENE issue
  - ERMSAR2022 – Collaboration with NEA & IAEA
  - **Next ERMSAR already planned in 2024 (SEAKNOT Project)**

Dissemination Activities

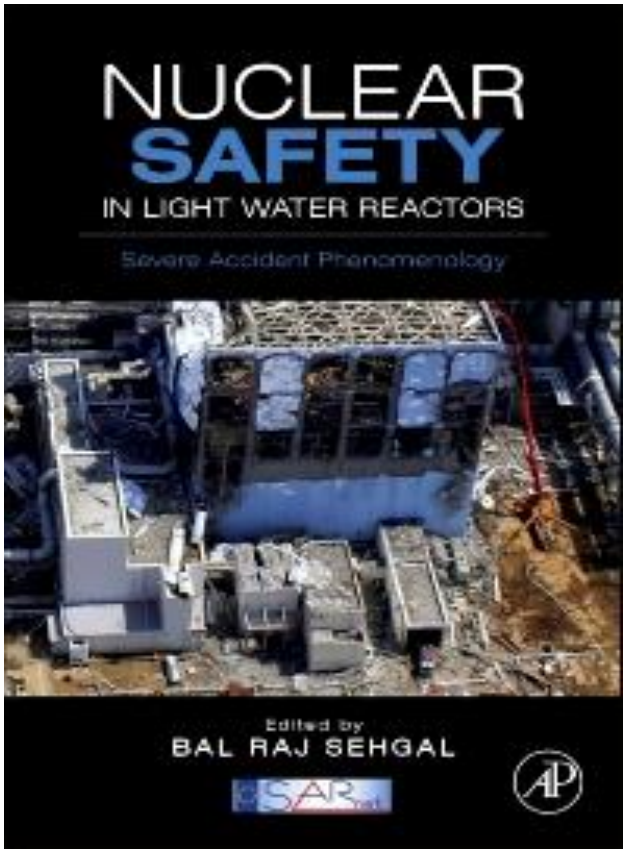

Update of the 2012 Severe Accident Textbook (SEAKNOT Project)

Final Remarks

Networking more fundamental than ever for SAR!

- Doing through projects
- Strengthening dissemination
  - ERMSAR-2024 (Stokholm)
  - Next SAP course in June 2023 (Madrid)
  - SA Textbook
- Pursuing colaboration with IAEA, NEA, ETSON, …

Deep & sound SARP (research priorities) necessary

- Research map towards cross-cutting projects
- Innovation on modeling/simulation approach
- Innovation in nuclear technology (ATF; SMR)
- SA … beyond SA (long term; consequences)

SNETP
Sustainable Nuclear Energy Technology Platform

Thank you for your attention!

NUGENIA TA2 Severe Accidents
Nuclear Generation II&III Alliance

The 10th European Review Meeting on Severe Accidents Research

Severe Accident Research Eleven Years after the Fukushima Accident

May 16-19, 2022, Karlsruhe, Germany

PLENARY SESSION: INTERNATIONAL PROGRAMS

Chairs: L.E. Herranz (CIEMAT), A. Bentaib (IRSN)

Euratom Projects on Severe accidents
A. Iorizzo (European Commission)

OECD/NEA Projects & WGAMA Activities On Severe Accidents
D. Jacquemain (OECD/NEA)

Recent IAEA Activities Related to Severe Accidents
A. Miassoedov (IAEA)

European Commission

European Review Meeting on Severe Accidents Research
ERMSAR2022
May 16-19, 2022, Karlsruhe, Germany

Euratom Research funded Projects on Severe Accidents

Angelgiorgio IORIZZO

Unit C.4–Euratom Research
DG Research & Innovation
European Commission

Outline

- Horizon Europe and the Euratom R&T
- Euratom Programme financial envelope 2021-2025
- Selection procedure for the Euratom funded Projects
- Eutatom Research Projects currently-recently funded on Severe Accidents - H2020
- Euratom Research incoming Projects on Severe Accidents - Horizon Europe

Horizon Europe and Euratom R&T

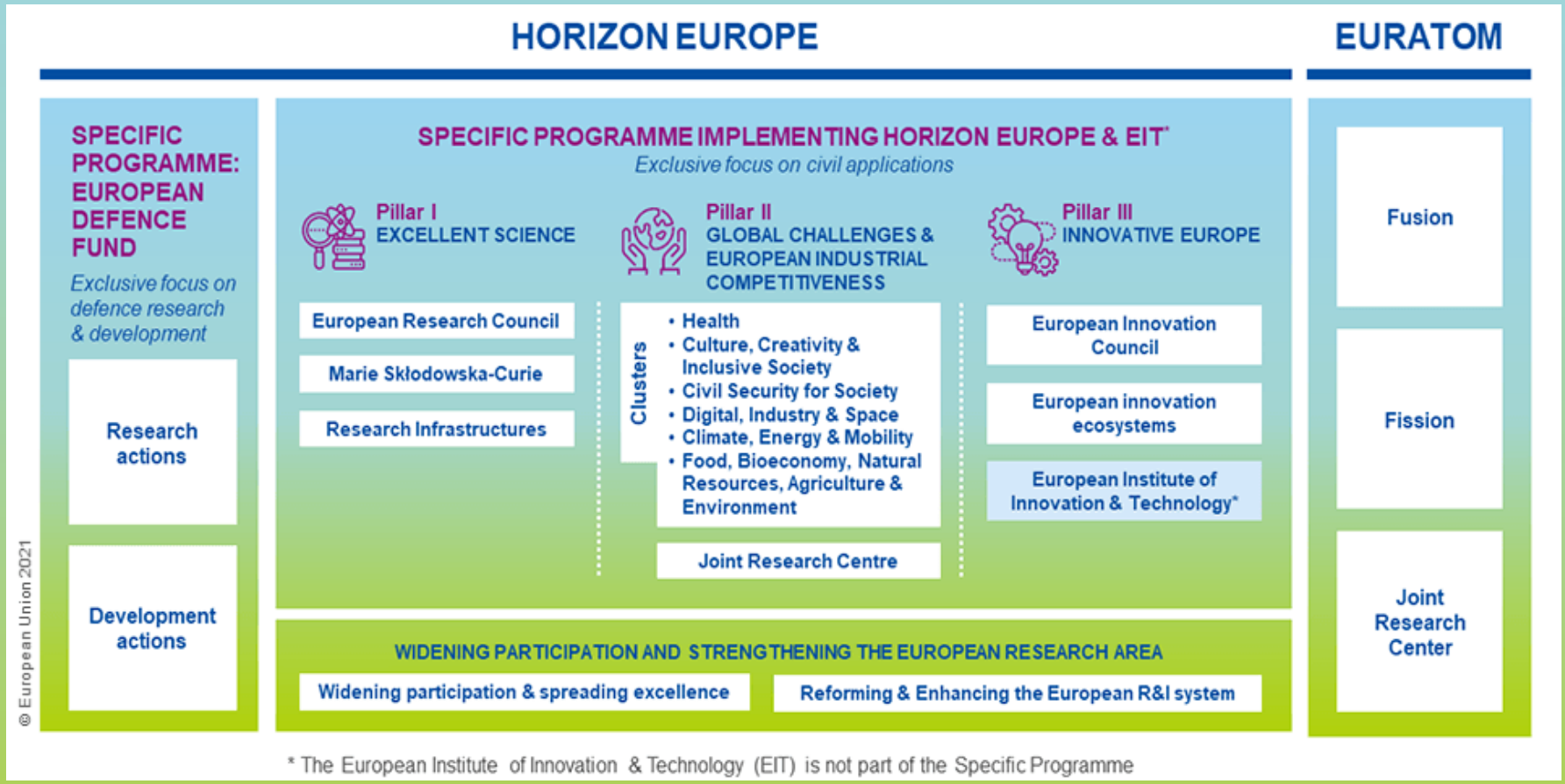

European Commission

Euratom Programme financial envelope 2021-2025



The financial envelope for the implementation of the ~~new~~ Euratom Programme 2021-2025 shall be **€1.382 billion in current prices.**

€583 million for indirect actions in fusion research and development

€266 million for indirect actions in nuclear fission, safety and radiation protection

€532 million for direct actions undertaken by the Joint Research Centre

European Commission

Selection procedure for the Euratom Euratom funded Projects

The Euratom funded Research Projects are selected via a competitive process:

- The EC publishes calls for proposal
  (last one for 2021-2022;
  new one planned for 2023-2025, under discussion with Member States)
- Potential beneficiaries apply proposing research Projects
- Research projects are selected **for funding** by independent Experts panels

Euratom Research Projects currently-recently funded on Severe Accidents - H2020 (2014-2020)

• NARSIS	II-III PSA (closed)	1.09.2017-28.02.2022	Total cost:~ 5.5 m. Euros
• MUSA	II-III SA Uncertainties Severe Accidents	1.06.2019-31.05.2023	Total cost:~ 5.9 m. Euros
• PIACE	II-III SA Passive Isolation Condenser	1.06.2019-31.05.2022	Total cost:~ 3.2 m. Euros
• R2CA	II-III PSA Design Basis / Ext. Accident	1.09.2019-31.08.2023	Total cost:~ 4.2 m. Euros
• sCO2-4-NPP	II-III SA SCO2 Heat removal	1.09.2019-31.08.2022	Total cost:~ 2.8 m. Euros
• BESEP	II-III PSA Benchmark	1.09.2022-29.02.2024	Total cost:~ 2.8 m. Euros
• AMHYCO	II-III SA H2 Accident Management	1.10.2022-30.09.2024	Total cost:~ 4 m. Euros

TOTAL= 28.4 m. €

NARSIS NFRP-2016-2017-1

New **A**pproach to **R**eactor **S**afety **I**mprovement**S**

Closed project

Start date-End date:	1 September 2017-28 February 2022 (closed)
Total cost:	€ 5 493 096,35
EU contribution:	€ 4 965 472,14
Number of participants:	21
Coordinated by:	COMMISSARIAT A L ENERGIE ATOMIQUE ET AUX ENERGIES ALTERNATIVES (France)

- Probabilistic Safety Assessment (PSA) procedures allow to better understand and estimate the likelihood of the most causes prone to initiate nuclear accidents and to identify the most critical elements of the systems.
- However, despite of the remarkable reliability of current procedures, the 2011 Fukushima Daiichi accident highlighted a number of challenging issues with respect to their application and to the validity of their results.
- From this nuclear disaster the upgrading of the current methodological framework appeared to be necessary in areas such as cascading/conjunct events characterization, fragility analyses and uncertainties treatment. New developments in those areas would even enable the extension of their use in accident management.

NARSIS NFRP-2016-2017-1

New **A**pproach to **R**eactor **S**afety **I**mprovement**S**

- Based on recent theoretical progresses, the NARSIS project aimed at making significant scientific updates of some elements required for the PSA, focusing on external natural events (earthquake, tsunami, flooding, high speed winds).
- These improvements mainly concern:
  - Natural hazards characterization, considering concomitant external (simultaneous-yet-independent or cascading) events, and the correlation in intra-event intensity parameters
  - Fragility and functionality assessment of main critical NPPs' elements, accounting for conjunct effects (including ageing effects) and interdependencies under single or multiple external aggressions
  - Risk integration combined with uncertainty characterization and quantification, to allow efficient risks comparison and account for all possible interactions and cascade effects
  - Better processing/integration of expert-based information within PSA, through modern uncertainty theories both to represent in flexible manner experts' judgments and to aggregate them to be used in a comprehensive manner.
  - The proposed improvements was tested and validated on simplified and real NPP case studies. Demonstration supporting tools for operational & severe accident management will be also provided.

MUSA NFRP-2018

Management and **U**ncertanties of **S**evere **A**ccidents

Start date-End date:	1 June 2019-31 May 2023
Total cost:	€ 5 929 652,50
EU contribution:	€ 3 186 503,05
Number of participants:	29
Coordinated by:	CENTRO DE INVESTIGACIONES ENERGETICAS, MEDIOAMBIENTALES Y TECNOLOGICAS-CIEMAT (Spain)

Detecting uncertainties in severe accident management

- The continuous efforts to raise nuclear safety to the highest standards possible has pointed the need to assess the methodologies used in severe accident simulation.
- The overall objective of the MUSA project is to assess the capability of severe accident codes when modelling reactor and SFP (Spent Fuel Pool) accident scenarios of Gen II and Gen III reactor designs.
- To do so UQ (Uncertainty Quantification) methodologies are to be used, with emphasis on the effect of already-set and innovative accident management measures on accident unfolding, particularly those related to ST (Source Term) mitigation.
- Therefore, ST related FOM (Figures Of Merit) are to be used in the UQ application.
- Given the focus of FOM on source term, the project will identify variables governing ST uncertainties that would be worth investigating further.

PIACE NFRP-2018

Passive **I**sol**a**tion **C**ond**e**nser

Start date-End date:	1 June 2019-31 May 2022
Total cost:	€ 3 210 439,81
EU contribution:	€ 2 247 229,76
Number of participants:	11
Coordinated by:	AGENZIA NAZIONALE PER LE NUOVE TECNOLOGIE, L'ENERGIA E LO SVILUPPO ECONOMICO SOSTENIBILE (Italy)

- The main objective is to support the technology transfer from the research to industry in the area of safety of nuclear installations.
- An Innovative Decay Heat Removal System for nuclear reactors, presently under technology validation in relevant environment (SIRIO facility), will be scaled-up to achieve a system prototype demonstration in operational environment, relevant for LFRs/ADSs and LWRs.

R2CA NFRP-2018

Reduction of **R**adilogical **C**onsequences of design basis and design extension **A**ccidents

Start date-End date:	1 September 2019-31 August 2023
Total cost:	€ 4 156 896,25
EU contribution:	€ 3 184 940,82
Number of participants:	16
Coordinated by:	INSTITUT DE RADIOPROTECTION ET DE SURETE NUCLEAIRE (France)

Updating European nuclear safety methodologies in light of new risks

- Nuclear power plants can produce cost-effective and emission-free electricity around the clock.
- About a quarter of all electricity and half of the low-carbon electricity in the EU is currently generated with nuclear energy.
- Nuclear safety is an EU priority, and the EU-funded R2CA project is supporting this with an eye on both operating and future nuclear power plants.
- The focus is on developing methods to reassess safety margins considering new risks that may have arisen from the original designs or extensions to them.
- Based on evaluations, the team is also identifying new accident management measures and technologies to reduce the radiological consequences of emergency situations.

sCO2-4-NPP NFRP-2018

Innovative **sCO2**-based heat removal technology **for** an increased level of safety of **N**uclear **P**ower Plants

Start date-End date:	1 September 2019-31 August 2022
Total cost:	€ 2 786 971,25
EU contribution:	€ 2 352 452,01
Number of participants:	10
Coordinated by:	ELECTRICITE DE FRANCE (France)

Heat removing in nuclear power plants

- Removing heat from nuclear reactors is an essential step in energy generation.
- The effectiveness of that process depends on many factors including the cooling agents used.
- The main aim of the EU-funded project sCO2-4-NPP is to introduce and commercialize innovative technology for heat removal in nuclear power plants.
- Technology used in the sCO2-4-NPP initiative will provide a backup cooling system, attached to the principal steam-based cooling system, which considerably delays or eliminates the need for human intervention in the case of accidents.
- Its compact size and the modularity of the system, allows the innovative technology to be fitted into existing nuclear power plants. It can also be included in nuclear power plants under development.

BESEP NFRP-2019-2020

Benchmark **E**xercise on **S**afety **E**ngineering **P**ractices

Start date-End date:	1 September 2020-29 February 2024
Total cost:	€ 2 759 701,25
EU contribution:	€ 2 759 701,25
Number of participants:	6
Coordinated by:	TEKNOLOGIAN TUTKIMUSKESKUS VTT OY (Finland)

Developing best practices to keep nuclear stations running

- In the EU, most operational nuclear power plants were built in the 1970s and 1980s and they were designed to last around 40 years.
- Preparing nuclear power plants for old age is a top priority to keep them longer and safer.
- The BESEP project will develop best practices for safety requirements' verification against external hazards.
- It will use an efficient and integrated set of safety engineering practices and probabilistic safety assessment.
- The project aims to provide clear guidance on the closer connection of deterministic and probabilistic safety analysis and human factors engineering for the determination and realistic quantification of safety margins.
- The findings will provide guidance for more sophisticated safety analysis methods, such as upgrades of simulation tools.

AMHYCO NFRP-2019-2020

Towards an henanced **A**ccidnt **M**anagement of the **HY**drogen/**CO** combustion risk

Start date-End date:	1 October 2020-30 September 2024
Total cost:	€ 4 071 051,25
EU contribution:	€ 3 974 402,50
Number of participants:	12
Coordinated by:	UNIVERSIDAD POLITECNICA DE MADRID (Spain)

Updating safety guidelines for nuclear power plants

- Nuclear power plants are designed to minimize the risk of radiological releases. In addition, severe accident management guidelines (SAMGs) have been developed and implemented to provide operators with a systematic guidance on mitigatory actions.
- Building on these guidelines, the EU-funded AMHYCO project considers practical issues to further reduce (as much as possible) the threat posed by combustion of gases generated during accidents on containment integrity.
- It will improve the SAMGs for both in-vessel and ex-vessel phases using numerical and experimental results.
- It will also experimentally study the phenomena that are difficult to predict numerically (such as H2/CO/H20 distribution and combustion).
- A third goal will be to improve the predictability of the numerical tools used for explosion hazard evaluation.

Euratom Research incoming Projects on Severe Accidents - Horizon Europe (2021-2027)

- SEAKNOT II-III SA Knowledge Management 1.10.2022 - 48 months Total cost:~ 2.8 m. Euros
- SASPAM-SA II-III SA SMR Emergency Management 1.10.2022 - 48 months Total cost:~ 3.8m. Euros
- ASSAS II-III SA Simulator PWR 1.11.2022 - 48 months Total cost:~ 3.7 m. Euros

TOTAL= 10.3 m. €

SEAKNOT HE-2021-NRT-01

SEvere **A**ccident research and **KNO**wledge managemen**T** for LWR

Duration:	48
Fixed start date:	1 October 2022
Total budget:	€ 2,726,993.75
Total requested EC contribution:	€ 2,158,778.00
Number of participants:	17
Coordinator:	CENTRO DE INVESTIGACIONES ENERGETICAS, MEDIOAMBIENTALES Y TECNOLOGICAS-CIEMAT (Spain)

Keywords

Severe Accidents, Phenomena Identification Ranking Table, Experimental Infrastructures, Knowledge and know-how transfer

SEAKNOT HE-2021-NRT-01

SEvere **A**ccident research and **KNO**wledge managemen**T** for LWR

- Severe Accidents (SA) are known to dominate the risk associated with the commercial production of nuclear energy and a vast amount of research has been done for decades in order to practically eliminate SAs with the potential for large early releases.
- At present time, when some of the knowledge acquired is at risk of being lost (as many specialists have already retired or are retiring) and new approaches for the SA assessment are being explored, it seems appropriate timing to deeply review and document the sound existing background and project it into the future, including an update on experimental research on SA mitigation tools.
- By putting in place the best resources possible to conduct any needed additional research and by articulating the most efficient ways possible to bring the young generation on board to face near- and mid-term research challenges, the best use of the current SA background with guarantees to target those issues bearing most uncertainties nowadays might be ensured.

SEAKNOT HE-2021-NRT-01

SEvere **A**ccident resercah and **KNO**wledge managemen**T** for LWR

- Therefore, it is of utmost relevance to conduct a firm assessment of the current State-of-the-Art and to pass this onto the generation who are inheriting such legacy. Management, exploitation, and assessment of this knowledge, are the main objectives of the SEAKNOT project.
- In addition, new emerging research needs, as those concerning Small Modular Light Water Reactors (SMLWR) and Accident Tolerant Fuels (ATF), will be considered.
- Meeting SEAKNOT objectives requires entails carrying out a deep, critical assessment of the current state of the art of the experimental infrastructure and analytical tools that would be necessary to efficiently tackle the challenges posed.
- The main expected outcomes will be: a sound and critical analysis of the current knowledge on SA.
- An update of the experimental research needs remaining;
- A strengthening of background and skills of young generations in the field.

SASPAM-SA HE-2021-NRT-01

Safety **A**nalysis of SMR with **PA**ssive **M**itigation strategies - **S**evere **A**ccident

Duration:	48 months
Fixed start date:	1 October 2022
Total budget:	€ 3,816,038.75
Total requested EC contribution	€ 2,991,694.00
Number of participants:	22
Coordinator:	AGENZIA NAZIONALE PER LE NUOVE TECNOLOGIE, L'ENERGIA E LO SVILUPPO ECONOMICO SOSTENIBILE - ENEA (Italy)

Keywords

SMR, iPWR, Severe accident, IVMR, Containment Integrity, Source Term, Emergency planning zone

SASPAM-SA HE-2021-NRT-01

Safety **A**nalysis of SMR with **PA**ssive **M**itigation strategies - **S**evere **A**ccident

- Small Modular Reactors (SMR) are one of the key options for the near-term deployment of new nuclear reactors.
- Currently in Europe there is a growing interest towards the deployment of SMRs, and several activities are underway in many countries preparing for possible licensing needs.
- In particular, Integral Pressurized Water Reactor (iPWR) are ready to be licensed as new builds because they start from the well-proven and established large Light Water Reactor (LWR) technology, incorporate their operational plant experience/feedback, and include moderate evolutionary design modifications to increase the inherent safety of the plant.
- However, despite the reinforcement of the first three levels of the Defence-in-Depth (DiD), e.g., with the adoption of passive safety systems, a sound demonstration of iPWR ability to address Severe Accidents (SA) should be carried out (DiD levels 4-5).
- The main objectives of the project will be to transfer and adapt such knowledge and know-how to iPWR, in view of the European SA and Emergency Planning Zone (EPZ) analyses.

SASPAM-SA HE-2021-NRT-01

Safety **A**nalysis of SMR with **PA**ssive **M**itigation strategies - **S**evere **A**ccident

- The main elements considered are:
  I. the identification of plausible SA scenarios for iPWRs with the related conditions in the vessel and in the containment,
  II. the study of the applicability of the existing experimental databases to iPWR and identify new experimental needs,
  III. the assessment of the capability of internationally recognized European and Non-European computational tools (largely used in Europe) to describe the behavior of the most promising iPWR designs during SA scenarios, and
  IV. the prediction of the resulting radiological impact on- and off-site, taking into account special SA mitigation/management strategies.
- The expected outcomes of the project will help speeding up the licensing of iPWRs in Europe, as well as the siting processes of these reactors in light of their possible use near densely populated areas.

ASSAS HE-2021-NRT-01

Artificial intelligence for the **S**imulation of **S**evere **A**ccident**S**

Duration:	48 months
Fixed start date:	1 November 2022
Total budget:	€ 3,700,350.00
Total requested EC contribution:	€ 3,008,132.00
Number of participants:	14
Coordinator:	INSTITUT DE RADIOPROTECTION ET DE SURETE NUCLEAIRE (France)

Keywords

Artificial Intelligence, severe accident, simulator, knowledge transfer, surrogate models, human-machine interface, digital twin, accident mitigation systems

ASSAS HE-2021-NRT-01

Artificial intelligence for the **S**imulation of **S**evere **A**ccident**S**

- The ASSAS project aims at developing a proof-of-concept SA (severe accident) simulator based on ASTEC (Accident Source Term Evaluation Code).
- The prototype basic-principle simulator will model a simplified generic Western-type pressurized light water reactor (PWR).
- It will have a graphical user interface to control the simulation and visualize the results.
- It will run in real-time and even much faster for some phases of the accident.
- The prototype will be able to show the main phenomena occurring during a SA, including in-vessel and ex-vessel phases.
- It is meant to train students, nuclear energy professionals and non-specialists.
- In addition to its direct use, the prototype will demonstrate the feasibility of developing different types of fast-running SA simulators, while keeping the accuracy of the underlying physical models.
- Thus, different computational solutions will be explored in parallel.
- Code optimization and parallelization will be implemented.

ASSAS HE-2021-NRT-01

Artificial intelligence for the **S**imulation of **S**evere **A**ccident**S**

- Beside these reliable techniques, different machine-learning methods will be tested to develop fast surrogate models.
- This alternate path is riskier, but it could drastically enhance the performances of the code.
- A comprehensive review of ASTEC's structure and available algorithms will be performed to define the most relevant modelling strategies, which may include the replacement of specific calculations steps, entire modules of ASTEC or more global surrogate models.
- Solutions will be explored to extend the models developed for the PWR simulator to other reactor types and SA codes.
- The training data-base of SA sequences used for machine-learning will be made openly available.
- Developing an enhanced version of ASTEC and interfacing it with a commercial simulation environment will make it possible for the industry to develop engineering and full-scale simulators in the future.
- These can be used to design SA management guidelines, to develop new safety systems and to train operators to use them.

European Commission



Thank you for your attention!

IAEA
International Atomic Energy Agency
Atoms for Peace and Development

Recent IAEA Activities Related to Severe Accidents

Presented by A. Miassoedov

The 10th European Review Meeting on Severe Accident Research (ERMSAR2022)
Akademiehotel, Karlsruhe, Germany
May 16-19, 2022

Outline

- IAEA short information
- Technical meetings
- Coordinated Research Projects
- Publications, education and training

International Atomic Energy Agency

IAEA is the UN's scientific forum for cooperation in the nuclear field





The IAEA's motto is Atoms for Peace and Development.

Transferring nuclear technology to developing countries, working to prevent the spread of nuclear weapons, and serving as a global platform for nuclear safety and nuclear security, are core Agency business and most important areas of our work

IAEA Main Work Areas

The IAEA is the world's centre for cooperation in the nuclear field and seeks to promote the safe, secure and peaceful use of nuclear technologies

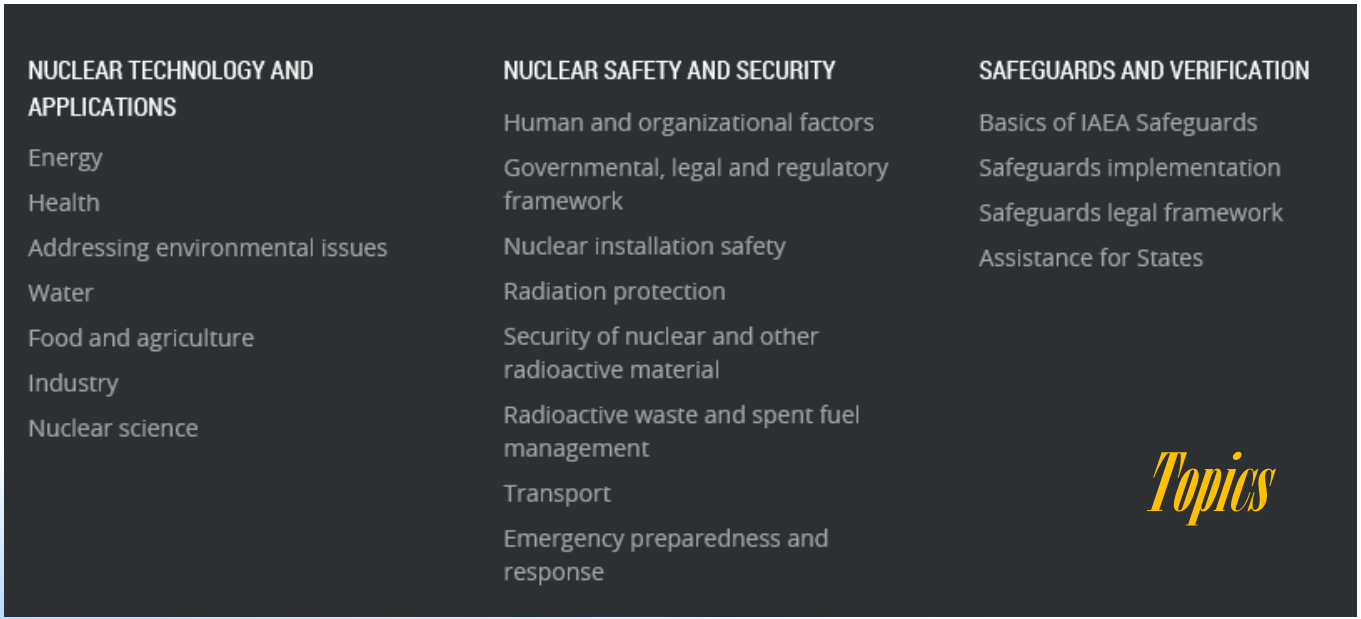

Nuclear Power Technology Development Section / Division of Nuclear Power
Department of Nuclear Energy

IAEA: 6 Departments

ORGANIZATIONAL STRUCTURE

Offices Reporting to the Director General

- Management
- Technical Cooperation
- Nuclear Energy
- Nuclear Safety and Security
- Nuclear Sciences and Applications
- Safeguards

- Fosters sustainable nuclear energy development by supporting existing and new nuclear programmes around the world.
- Provides technical support on the nuclear fuel cycle and the life cycle of nuclear facilities, and builds indigenous capability in energy planning, analysis, and nuclear information and knowledge management.





Division of Nuclear Power

The Division supports countries with operating nuclear power plants in enhancing the performance and safe long-term plant operation and the effectiveness of engineering processes for new builds, and helps increase capacity in Member States to use advanced management and human resource development methods for nuclear power programmes. It also assists Member States embarking on nuclear power programmes in planning and building their national nuclear infrastructures. Read more →



Division of Nuclear Fuel Cycle and Waste Technology

The Division formulates and implements the IAEA's activities regarding the nuclear fuel cycle, waste management and research reactors. It focuses on safe, secure, environmentally sound and cost-effective activities that support nuclear power, including the fuel cycle, waste management, decommissioning c nuclear installations and environmental remediation; access to and operation of research reactors; and waste management strategies and technologies covering all activities that generate radioactive waste, including disused sealed radioactive sources.



Division of Planning, Information and Knowledge Management

The Division provides support in the field of nuclear economics and energy system planning, sustainable development issues related to the environment, information management and information dissemination, and nuclear knowledge management.

Nuclear Power Technology Development Section
Division of Nuclear Power
Department of Nuclear Energy





Nuclear Power Engineering Section

The Section supports countries operating nuclear power plants or expanding their existing programmes to improve engineering, performance, management systems, human resource management, stakeholder involvement and technical infrastructure. It shares best engineering practices and innovations consistent with the global objectives of nuclear safety, security and non-proliferation. Read more →



Nuclear Power Technology Development Section

Fostering information exchange and collaborative research and development for advanced nuclear reactor technologies, this Section provides information to the IAEA's Member States on technology status and development trends for advanced reactor systems and their applications. Read more →



Nuclear Infrastructure Development Section

This Section is responsible for coordinating IAEA assistance to Member States considering or embarking on nuclear power programmes. It supports capacity-building, conducts review missions and offers guidelines, standards and workshops on developing the infrastructure for a safe, secure and sustainable nuclear power programme. Read more →



International Project on Innovative Nuclear Reactors and Fuel Cycles Section

The Section coordinates the activities of the membership-based International Project on Innovative Nuclear Reactors and Fuel Cycles (INPRO) to increase international cooperation on global nuclear energy sustainability, long term strategies and institutional and technical innovations for nuclear energy development and deployment. Read more →

Department of Nuclear Safety and Security (NS)

- The protection of people, society and the environment from the harmful effects of ionizing radiation is at the heart of the Department for Nuclear Safety and Security's work
- Whether the cause is an unsafe act or a security breach, it aims at providing a strong, sustainable and visible global nuclear safety and security framework



Incident and Emergency Preparedness and Response



Nuclear Security



Management of Radioactive Waste



Safety of Nuclear Installations



Radiation and Transport Safety



Division of Nuclear Installation Safety

The Division of Nuclear Installation Safety supports Member States in establishing the appropriate safety infrastructure and in continuously improving the safety of nuclear installations during site evaluation, design, construction and operation. The Division contributes to the development of safety standards for nuclear installations and provides safety reviews and advisory services to support their effective application.

Division of Nuclear Installation Safety (NSNI)
Mission



- To support Member States
  - in establishing the appropriate safety infrastructure
  - to continuously improve the safety of nuclear installations
    - site evaluation
    - design
    - construction
    - operation
  - through the development of up-to-date safety standards and providing for their effective application

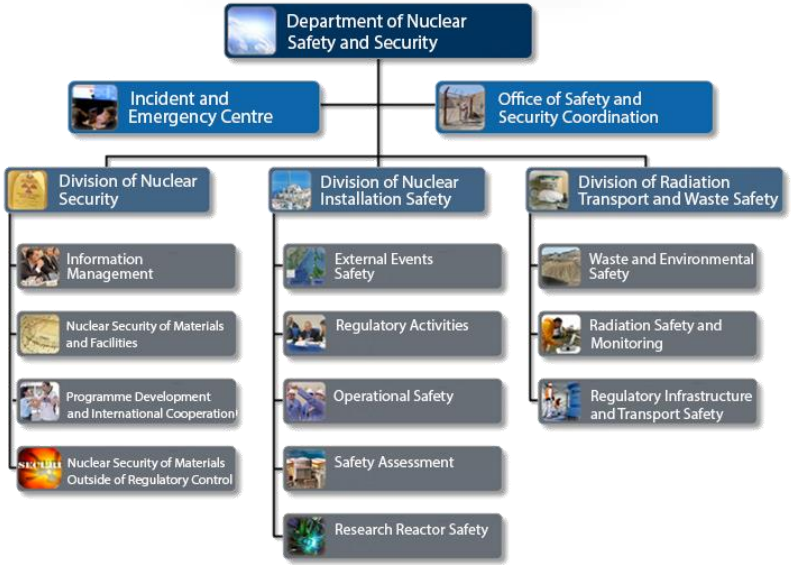

Outline

- IAEA short information
- Technical meetings
- Coordinated Research Projects
- Publications, education and training

Technical Meeting on the Phenomenology, Simulation and Modelling of Accidents in Spent Fuel Pools

- 2-5 September 2019, IAEA Headquarters, Vienna, Austria
- Exchange information on the codes dedicated to SFPs severe accident analysis, their capabilities and validation status
- Discuss the current gaps and the prospects for future R&D dedicated to SFPs accident analysis
- Discuss and review possible preventive or mitigative measures
- Technical papers from Member States on topics included in the meeting special topical areas
- TECDOC, proceedings of the meeting, summary of meeting outcomes

Technical Meeting on Ex-Vessel Molten Corium Behaviour and Coolability

- Virtual event, 14-17 June 2022, IAEA, Vienna
- Overview of ex-vessel phenomena
- Regulatory activities in the ex-vessel strategy
- Current practices in ex-vessel corium stabilisation in different designs
- Lessons learned, ex-vessel corium behaviour in Chernobyl and Fukushima accidents
- Current practices in modelling and analysis of ex-vessel corium behaviour
- Discuss current gaps and the prospects for future R&D
- Nomination deadline: 20 May 2022 (late submissions may be also considered)

Technical Meeting on Advanced Technologies and Systems for Containment Preservation in Design Basis Accidents and Design Extension Conditions with Core Melting

- In-person event, 11-14 October 2022, IAEA, Vienna
- To present and discuss recent advances in technological solutions, active and passive systems applied to preserve containment integrity during DBA and DEC with core melting
- Advanced technological solutions that could protect containment integrity and reduce radionuclide releases
- To harmonising international understanding and identifying major issues, recent achievements and future directions for R&D for advanced active and passive systems used for containment preservation.
- Official announcement will be sent out end of May 2022

Outline

- IAEA short information
- Technical meetings
- Coordinated Research Projects
- Publications, education and training

IAEA Coordinated Research Activities

- Provide opportunities to engineers and scientists in developing and developed Member States to collaborate on research topics of common interest

- Results of research activities supported by the Agency are disseminated to all Member States through national, international and IAEA scientific and technical publications, and other communications media

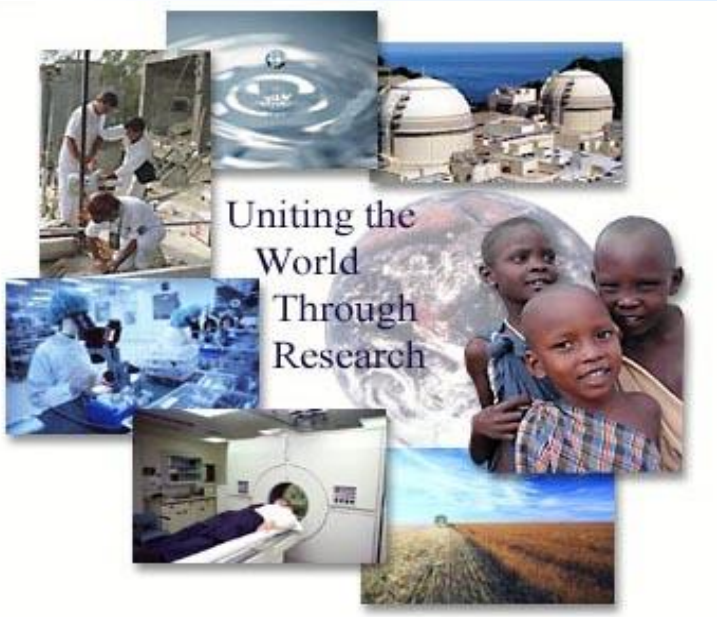

http://cra.iaea.org/cra/index.html



- IAEA plans and coordinates research to be carried out by selected organizations
- CRPs are networks of research institutes in developing and developed IAEA Member States concentrating on thematic topics for research and its application or a set of tools, or to test a set of technologies to solve specific problems of interest to Member States
  - CRPs are developed to solve well-defined research topics in which an appropriate number of institutes are invited to collaborate
  - CRPs have proven to be an effective means of bringing together researchers from both developing and industrialised countries to solve a problem of common interest

Advancing the State-of-Practice in Uncertainty and Sensitivity Methodologies for Severe Accident Analysis in Water Cooled Reactors (2019 – 2024)
18 organizations from 10 Member States

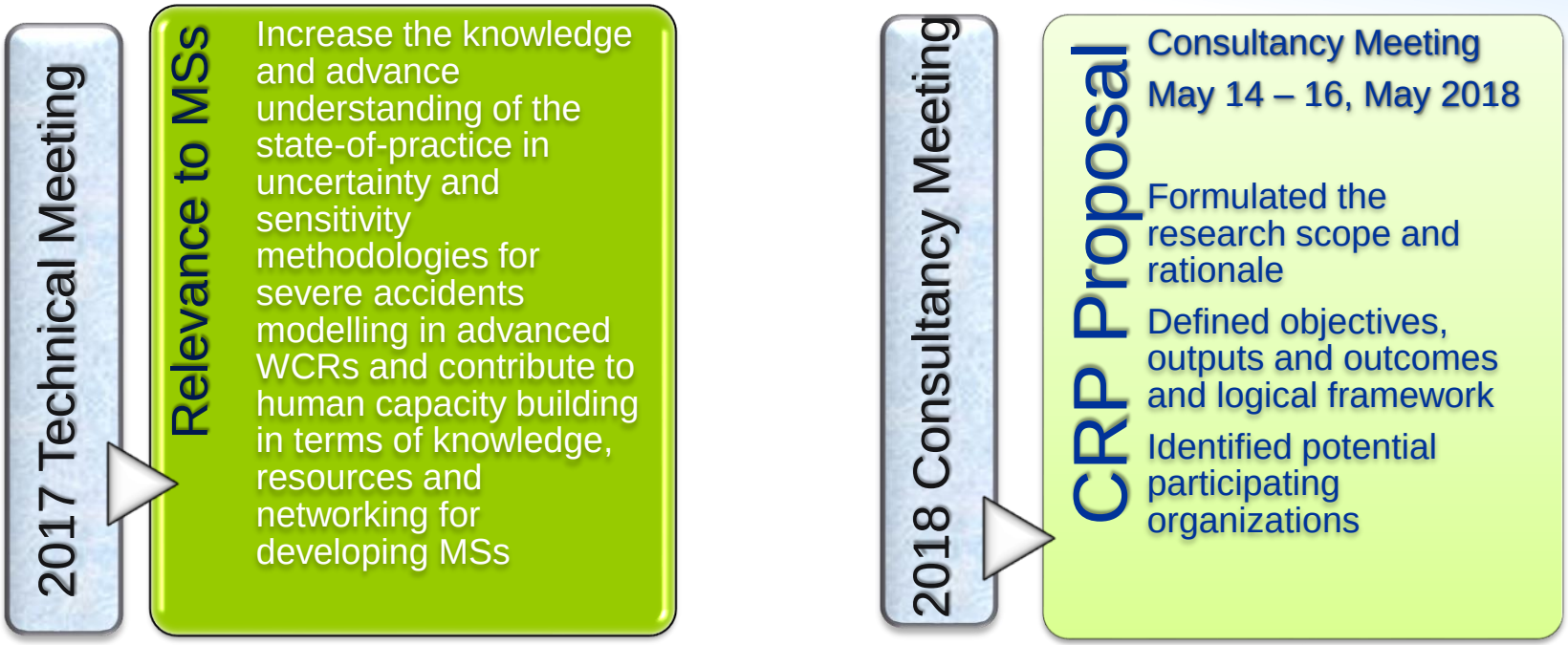

The objective is to advance the understanding and characterization of sources of uncertainty and their effect on the **key figure-of-merit** (FOM) in prediction of uncertainty in severe accident codes for WCRs

Developing a Phenomena Identification and Ranking Table (PIRT) and a Validation Matrix, and Performing a Benchmark for In-Vessel Melt Retention (2020 – 2024)

- Where does the CRP originate from?
  - IAEA International Experts Meeting (IEM8) on strengthening research and development effectiveness, VIC, Feb. 2015
  - IAEA TM on “Post-Fukushima R&D Strategies and Priorities”, VIC, May 2015
  - IAEA TM on “Phenomenology and Technologies Relevant to In-Vessel Melt Retention and Ex-Vessel Corium Cooling”, Shanghai, Oct. 2016
    - IAEA TECDOC-1906 In-vessel Melt Retention and Ex-vessel Corium Cooling



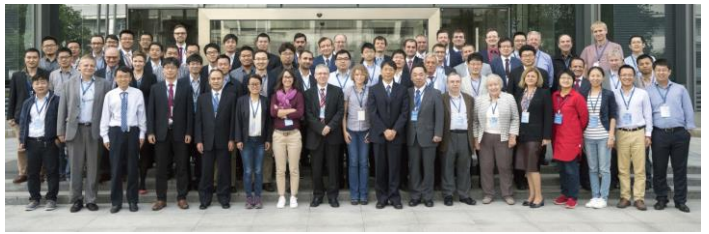

- Other related activities
  - EURATOM H2020 Project IVMR (2014 – 2020)
  - OECD/NEA/CSNI CAPS: “RPV Integrity Assessment during IVMR with ERVC” (update will be provide at this RCM-1)

CRP objectives and tasks

The general objective of the CRP is to harmonize the international understanding of scientific and technological bases underpinning crucial parts of the safety demonstration of IVMR, including for (but not limited to) high-power reactors

1. To develop a PIRT for IVMR
2. To develop a validation matrix for IVMR and to identify relevant high-quality experimental data requested for the validation of computer codes for IVMR simulation
3. Benchmark involving code-code comparison and comparison with experimental data on individual phenomena
4. To carry out an analytical benchmark on an IVMR comprehensive scenario exercise

23 participating organizations
14 Member States and one International Organization



Outline

- IAEA short information
- Technical meetings
- Coordinated Research Projects
- Publications, education and training

Related IAEA publications

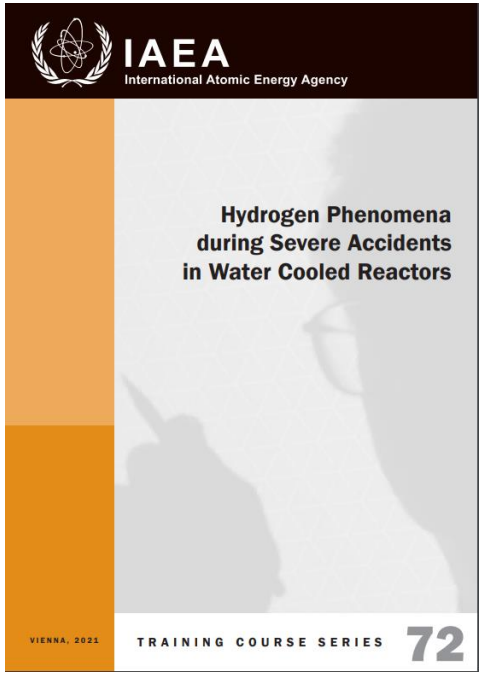

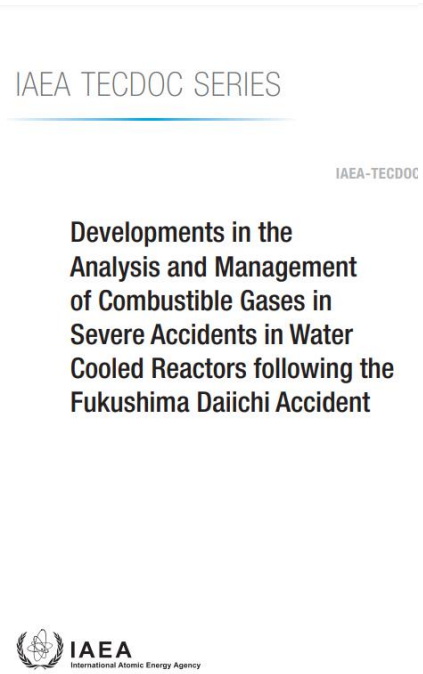

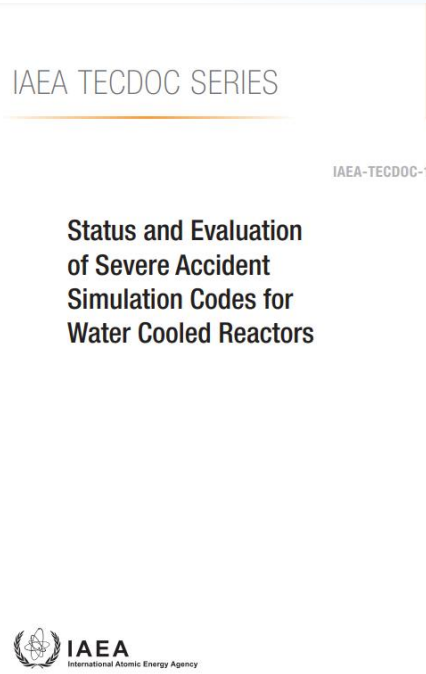

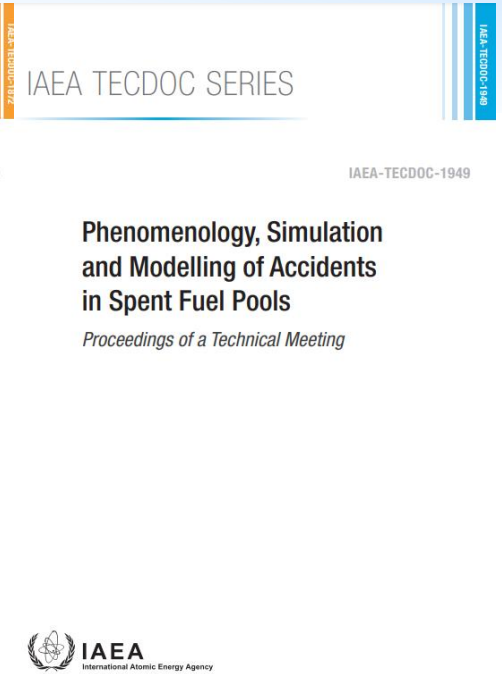

Related IAEA publications

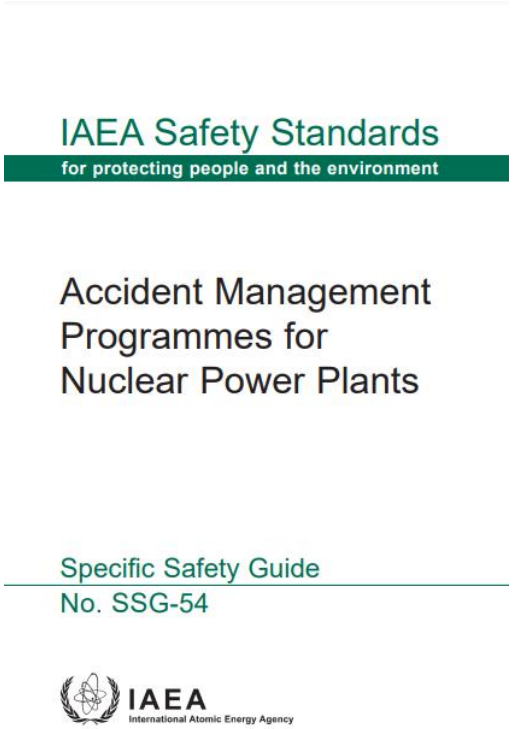

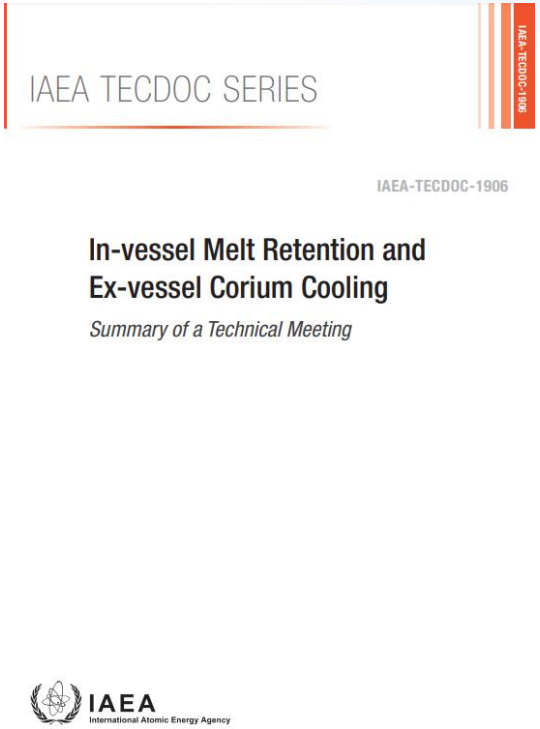

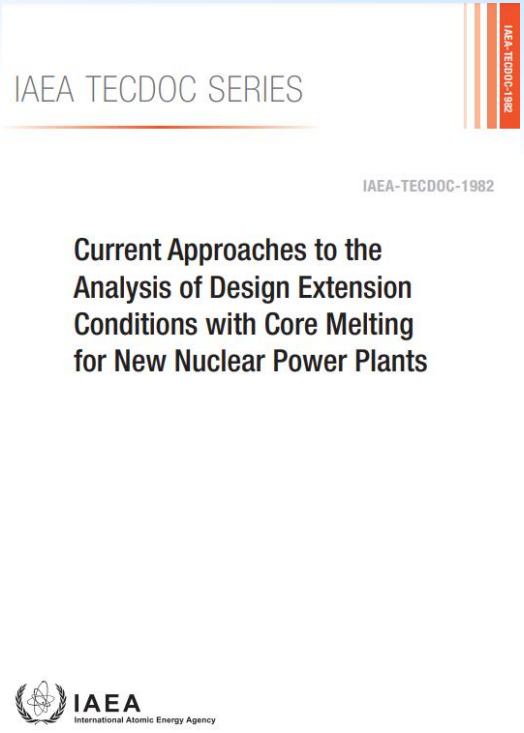

Planned publications

Experience in Modelling and Simulation of severe accidents for Water-Cooled Reactors with Accident Tolerant Fuels

- **Technical Meeting in 2023-Q1, prepared through Consultancy Meetings in 2022**
- **Objective:**
  - To review MSs progress in expanding the capabilities of current severe accident codes to address Accident Tolerant Fuels under development, including:
    i. Cr-coated Zr-alloys, doped-UO_2, FeCrAl
    ii. SiC, high density fuels
  - To provide a platform for reviewing results already available, and to judge whether longer-term activities (e.g. benchmarking, PIRT, possibly addressed in new CRP?) could be initiated at the IAEA
- **Outcome:** TECDOC
- **Technical Officers:** A. Miassoedov (NE/NPTDS), S. Massara (NS/SAS)

Planned publications

Modelling and simulation of severe accidents/CDA for Liquid Metal-cooled Fast Reactors: status of knowledge and challenges

- **Technical Meeting in 2023-Q1, prepared through Consultancy Meetings in Jul-2022 and Dec-2022**
  - To review the status of development and validation of numerical codes for modelling and simulation of severe accidents for LMFR
  - To identify ongoing trends towards the development of more mechanistic models in replacement of empirical legacy models and to identify major challenges anticipated for the verification process
  - To collect examples of applications, including towards the goal of supporting the development of specific design measures allowing to mitigate the consequences of a severe accident/CDA
  - If appropriate, to identify areas where increased cooperation among MSs would be beneficial (e.g. to support experimental validation, benchmarking)
- **Outcome:** TECDOC
- **Technical Officers:** S. Massara (NS/SAS), V. Kriventsev (NE/NPTDS)

SAMG-D toolkit updated



OVERVIEW OF THE SAMG-D TOOLKIT



The Tool to Enhance Severe Accident Management

The SAMG-D describes the elements necessary to develop a set of Severe Accident Management Guidelines (SAMG), which serve to achieve the main goals of severe accident management at a Nuclear Power Plant (NPP). Severe accident management is a subset of accident management as follows:

Accident management is taking of a set of actions during the evolution of an accident:
(a) To prevent escalation to a severe accident;
(b) To mitigate the consequences of a severe accident;
(c) To achieve a long term safe stable state.

The second aspect of accident management (to mitigate the consequences of a severe accident) is also termed **severe accident management**. It includes measures to: Read more →
(1) Terminate the progress of core damage once it has started;
(2) Maintain the integrity of the containment as long as possible;
(3) Minimize releases of radioactive material.

See *Accident Management*, *Anticipated Operational Occurrence*, *Beyond Design Basis Accident*, *Design Extension Condition*, *Design Basis Accident*, *Operational states*, *Severe Accident*, and *Severe Accident Management*.

Guidelines that have been developed for the operating staff for managing severe accidents are called Severe Accident Management Guidelines (SAMG).

The SAMG-D is also an education and training tool to help plant staff understand the severe accidents phenomenology and mitigation strategy and the associated procedures and guidelines. The SAMG-D describes the elements that a set of SAMG should encompass to achieve the goals of severe accident management. It constitutes a useful input for utilities which are in the process of selecting proper SAMG products from the various vendors and implementing those at their plants. The SAMG-D is designed for use with LWRs and PHWRs. **The SAMG-D is not designed to independently construct a full SAMG package.**

The IAEA Nuclear Power Technology Development Section (NPTDS) developed the SAMG-D as part of its contributions to the IAEA Action Plan on Nuclear Safety. The current updated version was developed in 2020 jointly with the IAEA Safety Assessment Section (SAS).

Please, before starting the use of SAMG-D have a look at the *DISCLAIMER* and the information provided in About.

IAEA SAMG-D structure

SAMG-D

Severe Accident Management Guideline Development toolkit

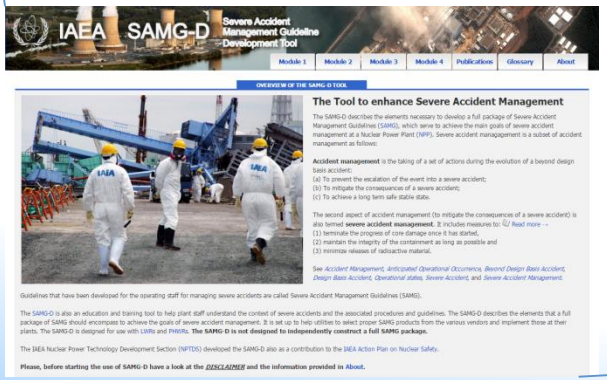

Module 1

Fundamentals of reactor safety

Module 2

Severe accident challenges and mitigation strategies

Module 3

Severe accident management guidelines

Module 4

Implementation, requirements and infrastructure

Major activities related to the SAMGs toolkit

Five Training Workshops

Toolkit revision in 2019-2020

- Review the toolkit ensuring coherency with IAEA Specific Safety Guide SSG 54
- Review and update the toolkit with information for BWRs, including practical examples of SAMG for BWRs
- Include additions or changes regarding CANDU reactors
- Review and update the sections focusing on computer codes used for the accident analysis
- Update the toolkit based on advances in the state-of-the-art (mainly the phenomenology of severe accidents, Module 2), revision of the list of references

Seventh training workshop: 5-9 December 2022, Vienna (in-person)

Joint ICTP-IAEA Course on Scientific Novelties in the Phenomenology of Severe Accidents in Water Cooled Reactors

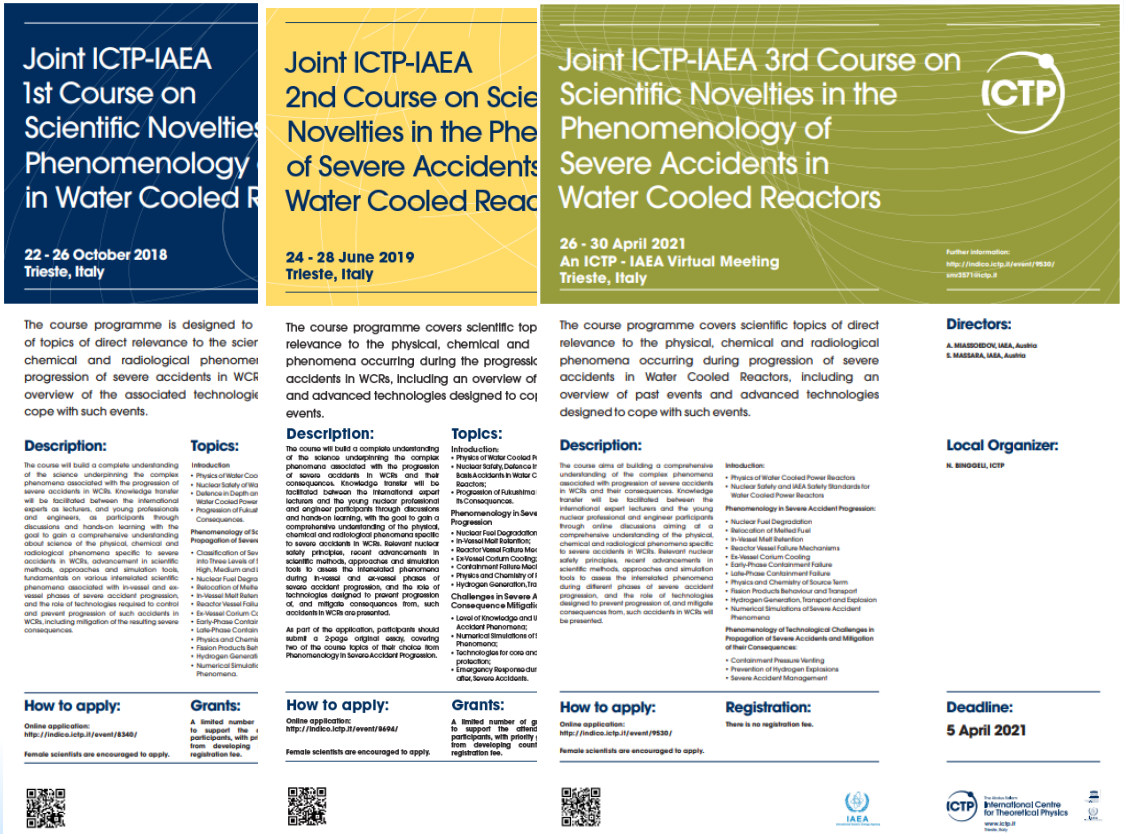

- Scientific topics of direct relevance to the physical, chemical and radiological phenomena occurring during the progression of severe accidents in WCRs
- Knowledge transfer between the international expert lecturers and the young nuclear professionals through discussions and hands-on learning
- **2023 course in planning**

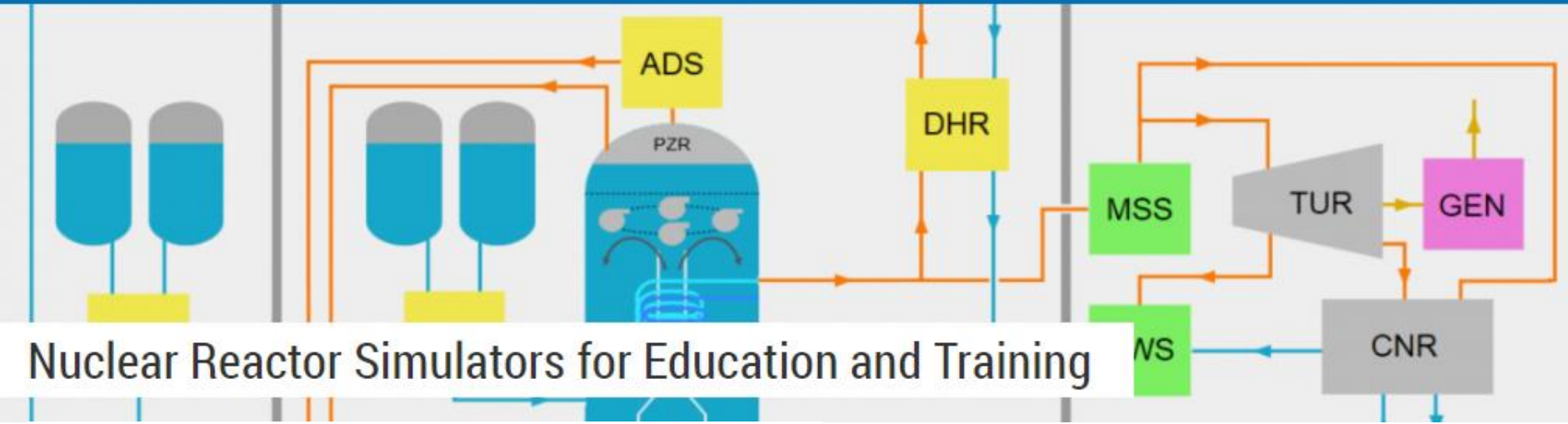

Nuclear Reactor Simulators for Education and Training

Pressurized Water Reactor (PWR) Simulators

- Advanced PWR: Two-Loop Large PWR (Korean-OPR 1000)
- Russian-type PWR (VVER-1000)
- Advanced Passive PWR (AP-600)
- Integral Pressurized Water Reactor (SMR)

Boiling Water Reactor (BWRs) Simulators

- Conventional Boiling Water Reactor with Active Safety Systems (BWR)
- Advanced BWR with Passive Safety Systems (ESBWR)

Pressurized Heavy Water Reactor (PHWR)

- Conventional Pressurized Heavy Water Reactor (PHWR)
- Advanced PHWR (ACR-700)

Part-Task Simulator

- Micro-Physics Nuclear Reactor Simulator

Under Development

- High Temperature Gas Cooled Reactor (HTGR)
- Sodium Cooled Fast Reactor (SFR)

The IAEA sponsors training courses and workshops on a regular basis, and would also be willing to support additional training events on this topic at the request of Member States. If you/your organization are interested in hosting a training session, educational course or workshop in your country, please contact the IAEA to further discuss the proposal.

Simulation of LOCA accident in OPR-1000

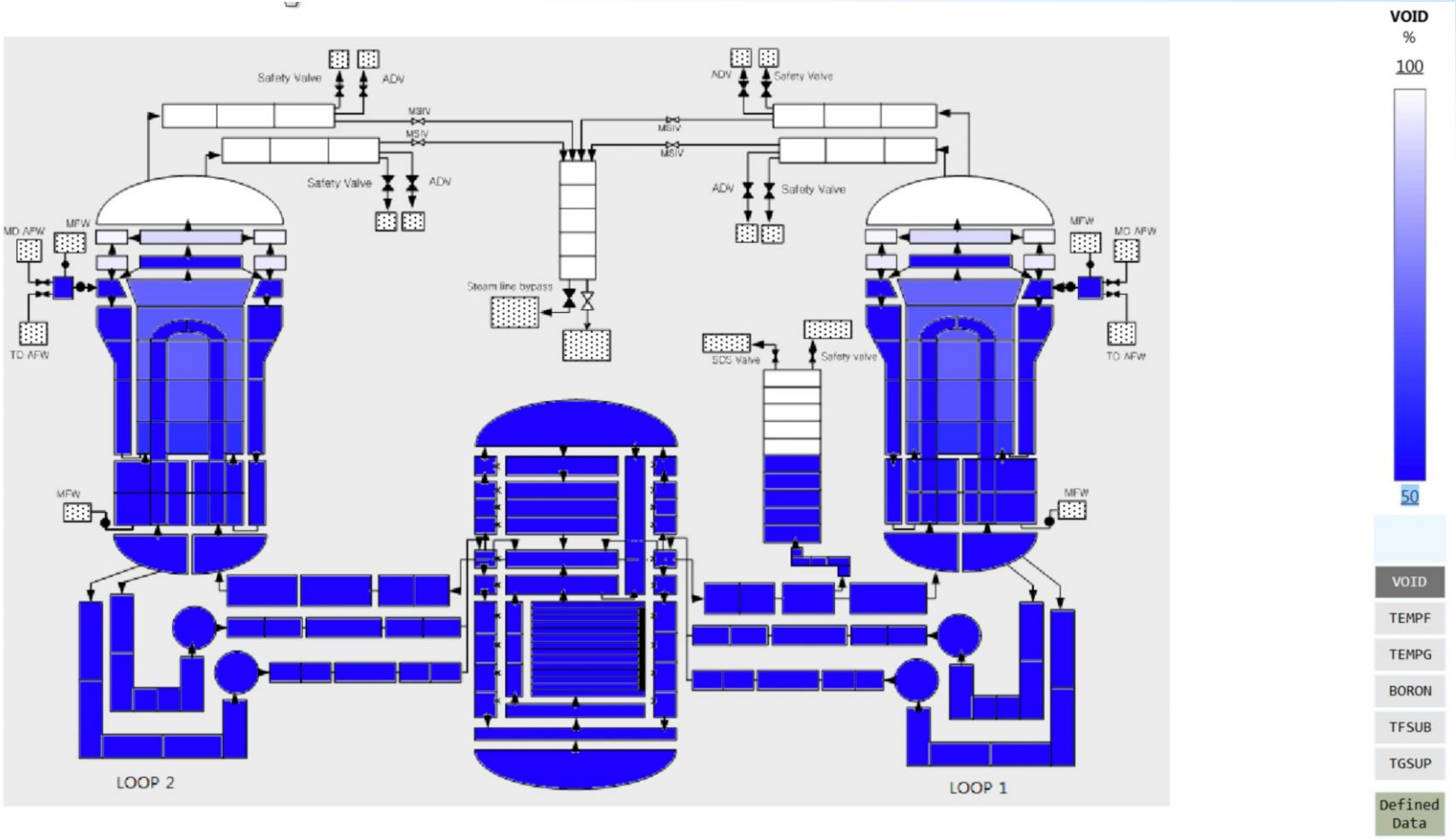



Topic 1. Applying safety approaches and standards for evolutionary and innovative reactor technologies

Topic 2. Enhancing safety by innovative design features

Topic 3. Supporting integrated decision making through safety/risk analyse

Topic 4. Accelerating innovations for safety assessment through the advanced simulation and modelling, and experimental programmes

Acknowledgments

IAEA activities on severe accidents are carried out in a close cooperation between the Department of Nuclear Energy and the Department of Nuclear Safety and Security.

The help of Colleagues in preparing this presentation is greatly appreciated.

IAEA
International Atomic Energy Agency
Atoms for Peace and Development

Thank you!



The 10th European Review Meeting on Severe Accidents Research

Severe Accident Research Eleven Years after the Fukushima Accident

May 16-19, 2022, Karlsruhe, Germany

Technical Session 1-1: In-vessel Corium and debris coolability

Chairs: T. Hollands (GRS), F. Gabrielli (KIT)

ID265	**The IAEA Coordinated Research Project on Developing a Phenomena Identification and Ranking Table and a Validation Matrix, and Performing a Benchmark for In-Vessel Melt Retention** A. Miassoedov (IAEA), S. Massara (IAEA)	**Paper** **Presentation**
ID319	**Iron and zirconium oxidation at liquid state under Ar-O2 and Ar-H2O gas mixtures in Severe Accident conditions** P. Piluso (CEA)	**Paper** **Presentation**
ID336	**In-vessel debris melting experiments performed in LIVE3D test facility** X. Gaus-Liu (KIT)	**Paper** **Presentation**
ID259	**Integral modelling of continuous/dispersed phases mass transfer during in-vessel corium stratification transients** R. Le Tellier (CEA)	**Paper** **Presentation**

10TH CONFERENCE ON SEVERE ACCIDENTS RESEARCH
May 16-19, 2022 – Karlsruhe, Germany
ERMSAR 2022

THE IAEA COORDINATED RESEARCH PROJECT ON DEVELOPING A PHENOMENA IDENTIFICATION AND RANKING TABLE AND A VALIDATION MATRIX, AND PERFORMING A BENCHMARK FOR IN-VESSEL MELT RETENTION

L. Carénini[1], W. Ma[2], P. Matejovic[3], P. Pandazis[4], S. Massara[5], A. Miassoedov[5]

[1]Institut de Radioprotection et de Sûreté Nucléaire, B.P. 3 - 13115 St Paul lez Durance, France, laure.carenini@irsn.fr
[2]Royal Institute of Technology (KTH), Roslagstullsbacken 21, 10691 Stockholm, Sweden, weimin@kth.se
[3]Inzinierska Vypoctova Spolocnost (IVS), Jana Holleho 5, 917 01 Trnava, Slovakia, ivstt@ivstt.sk
[4]Gesellschaft für Anlagen- und Reaktorsicherheit, Schwertnergasse 1, 50667 Köln, Germany, Peter.Pandazis@grs.de
[5]International Atomic Energy Agency, PO Box 100, 1400 Vienna, Austria S.Massara@iaea.org, A.Miassoedov@iaea.org

ABSTRACT

In-Vessel Melt Retention (IVMR) is a severe accident mitigation strategy for nuclear power plants (NPP) consisting of cooling the melted reactor core material from outside the reactor vessel in order to avoid reactor vessel failure and retain the corium in the reactor vessel. The safety demonstration of IVMR aims at proving that this strategy effectively retains the corium inside the reactor vessel, hence providing conditions for ensuring the containment integrity and confinement of radioactive materials. In 2020 the IAEA started the 4-year Coordinated Research Project (CRP) on IVMR with the main objective to harmonize the international understanding of the scientific and technological bases underpinning crucial parts of the safety demonstration of IVMR. Specific research objectives include the following activities.

Developing a phenomena identification and ranking table (PIRT) for IVMR to support the activities during the CRP. The PIRT is created on the basis of PIRTS developed in past projects, extended with new results and addresses different reactor designs. Moreover, two further PIRTs are being developed to address the safety demonstration of IVMR and reactor pressure vessel (RPV) penetration failure during IVMR. All PIRTs share the same methodology and a common pool of phenomena.

Development of a validation matrix including identification of representative experiments which can be used to validate the models and computer codes applied in the IVMR analysis, achieved in two steps: (1) establishment of a cross-reference table based on the phenomena identified in the available IVMR PIRT; and (2) update of the cross-reference table using the extended PIRT developed within the CRP.

Based on the outcomes of the PIRT and the validation matrix, several benchmarks on individual phenomena are being carried out. These benchmarks involve code-to-code comparison as well as comparison with experimental data. Attention has been paid especially to in-vessel corium behavior and external reactor vessel cooling phenomena. These benchmark exercises aim at characterizing the state-of-the-art of modelling and simulation capabilities of individual phenomena.

Analytical benchmarks on a full IVMR exercise representative of a comprehensive reactor scenario will be performed for 3 different reactor designs: a generic 1000 MWe PWR design, the Russian VVER-1000 design and the Chinese CAP1400 design. Attention will be paid to the transient evolution with time-dependent addition of corium and steel, up to steady-state and evaluating the profile of RPV wall ablation.

The paper describes in detail the content and activities of the CRP and discusses the expected outputs.

KEYWORDS
Severe accidents, safety, corium, coolability, melt retention

1. INTRODUCTION

Following the Accident at the Fukushima Daiichi Nuclear Power Plant, the IAEA has held various meetings to strengthen research and development strategies and priorities regarding severe accidents. The IAEA International Experts Meeting on Strengthening Research and Development Effectiveness in the Light of the Accident at the Fukushima Daiichi Nuclear Power Plant, held in Vienna in 2015, prepared a list of recommendations for research and development (R&D) activities to be promoted by the IAEA. This comprehensive list represents compiled experts' views on the needs for further R&D activities and international cooperative efforts. It was further refined at the Technical Meeting on Post-Fukushima Research and Development Strategies and Priorities held in December 2015 [1]. During these meetings, in-vessel melt retention (IVMR) was confirmed to be one of the highest research and development priority areas which represents a possible mitigative measure (at defence in depth level 4) of the consequences of severe accidents at a NPP. The safety demonstration of IVMR aims at proving with the necessary robustness that this strategy effectively retains the corium inside the RPV, hence ensuring the containment integrity and confinement of radioactive materials.

Despite an effort spanning over three decades which has requested considerable methodological developments (based on both deterministic and probabilistic approaches), as well as experimental and numerical simulation works, aiming at building a large and robust scientific base underpinning the safety demonstration of IVMR effectiveness, previous IAEA meetings on this topic and state-of-the-art knowledge conclude that further work would be necessary on various aspects including the following topics, which are particularly relevant when incorporating IVMR into high-power reactors:

- Experimental data needed for validating individual models are often considered limited in covering relevant phenomena (e.g. focusing effect, influence of layer inversion on the heat flux towards the vessel wall), insufficient quality (e.g. contradictory CHF experimental data) and quantity (e.g. data for material behavior of RPV steel, hampering the performance of structural integrity analyses);
- The quality of numerical simulations, through the improvement of models for the simulation of lower plenum phenomena, identified as those responsible of most of the deviation with respect to experimental data, i.e. on the heat flux on the outer vessel wall;
- Related to the previous item, the limitation of a purely steady-state approach is also widely recognized, pushing for a methodological improvement towards a more comprehensive consideration of transient effects (all kinetic effects since the beginning of the transient should be taken into consideration, including possible heat flux spikes, to address the effect on the RPV wall and to assess its possible failure);
- The identification of most pertinent acceptance criteria to be considered in the safety demonstration. However, it is recognized that these are design dependent and that the minimum vessel thickness appears to be one of the most critical for the RPV failure (probably more relevant than the critical

heat flux as it includes all kinetic effects since the beginning of the transient, including possible heat flux spikes).

In 2020 the IAEA started the 4-year CRP on IVMR with 23 organizations from 14 IAEA Member States (Bulgaria, Canada, China, Czech Republic, Finland, France, Germany, Lithuania, Republic of Korea, Pakistan, Russian Federation, Slovakia, Sweden and Ukraine) and one international organization (the European Commission's DG Joint Research Centre). The CRP aims at providing a platform facilitating interactions with the objective of tackling the abovementioned topics. The main objective of the CRP is to harmonize the international understanding of the scientific and technological bases underpinning crucial parts of the safety demonstration of IVMR. To achieve these goals, the implementation of the CRP will be carried out through four tasks described in the following sections.

2. TASK 1: DEVELOPMENT OF A PHENOMENA IDENTIFICATION AND RANKING TABLE

The main objectives of the PIRT which will be developed during the CRP are to summarize the current knowledge level about IVMR, provide a common technological basis for the further tasks such as development of the validation matrix and performing benchmark exercises, support the safety demonstration of the IVMR strategy as well as identify further research needs. Within the CRP 19 organizations are contributing to the task 1 PIRT development, with various technical background (scientific as well as industrial) and specific interest (e.g. different reactor designs). Generally, the success of a PIRT exercise is dependent on the specification of the objective and on a common understanding for the successful teamwork. Therefore, the first steps were to collect ideas and reach a consensus between the participants.

To provide a basis for the common work, first the critical assessment of existing selected PIRT exercises has been done. Several related PIRT exercises have been carried out in previous projects, partially with active contribution of the participant organizations of the present CRP. Three of those have been selected for the assessment:

1. the IVMR PIRT, developed within the European H2020 project IVMR [2];
2. the Chinese PIRT jointly developed by NSC, SNERDI and CNPRI;
3. the CANDU PIRT developed by AECL and CNL.

Within the recently completed H2020 IVMR project a PIRT was developed to identify and rank IVMR relevant phenomena to support the IVMR modelling and the development of computer codes. The PIRT was not developed for a specific reactor design, it considered modelling capabilities of dedicated system codes. The outcomes highlight the needs for the code development and recommend complementary sensitivity studies to reduce remaining uncertainties. Furthermore, it concluded that the consideration of a specific reactor design may have an impact on the ranking of phenomena. The objective of the Chinese IVMR PIRT is the identification of further research needs and the support of code development. For identification and ranking the IVMR relevant phenomena a Large Break Loss Of Coolant Accident (LB-LOCA) scenario in Pressurized Water Reactor (PWR) without reflooding has been investigated. The PIRT developed in Canada by AECL and CNL in 2008 was dedicated to severe accident phenomena in CANDU reactors with focus on IVMR. As a basis of the PIRT a station blackout scenario (SBO) has been selected.

The assessment of these PIRTs has been achieved along two parameters: phenomena definition and PIRT methodology. All three PIRTs provide very valuable contribution for the safety demonstration of the IVMR strategy, however because of the different scope and specific objectives a direct comparison of the outcomes is not reliable. The assessment showed that while the collected phenomena in all of the three PIRT describe correctly the entire problem, however several differences exist in the definition of the phenomena. In some cases, the phenomena definition was made on different detail level or was reactor design-specific. For this reason, a common list of phenomena was developed for the planned PIRT with a homogeneous level of details. The list has been developed on the basis of the IVMR PIRT phenomena list considering the

phenomena list of the Chinese and the CANDU PIRTs to enhance the applicability of previous outcomes. Moreover, after a critical review performed by the task 1 participants, such list was extended with the inclusion of additional phenomena, considering the objectives of the CRP. The introduced new phenomena list includes the description of about 85 phenomena and material properties and provide a solid basis for the common work within organizations involved in the task 1. Beside of the description, it is continuously filled up with references and will be evaluated regarding of the relevance of different reactor designs and further tasks of the CRP.

The common phenomena list also supports the investigation of the existing uncertainties and sensitivity analyses which results strongly support the justification of the phenomena ranking. The goal of the IAEA PIRT is to reduce existing uncertainties by avoiding as much as possible expert judgments and include more recent sensitivity calculations. Therefore, the available analyses are being collected and organized among the common list of phenomena.

The main objective of the IAEA PIRT is to support the development of the validation matrix and the benchmark exercises. The identified and ranked phenomena will be used as a direct input for the development of the validation matrix performed in the task 2. During the CRP preparatory phase four different reactor designs have been selected for the investigations. These are the CANDU, CAP-1400, VVER-1000 and the Nordic BWR type. In order to achieve more valuable results, the participants agreed to perform separate PIRTs for each reactor design instead of a common one. The basis of the separate PIRTs is provided from the developed common phenomena list to ensure a comparison of the outcomes and support the evaluation process. The separate PIRTs will be developed on the same basis and with the same methodology from different dedicated working group of experts.

To support the work with different reactor designs, a brief, formalized reactor data sheet has been developed with all the main IVMR relevant data of the specific design of the VVER-1000/320 reactor. Data sheets of the further investigated reactor designs are currently under development.

Two further topics have been identified during the discussions, corresponding to additional individual sub-PIRTs, which will be developed to complement the abovementioned PIRTs:

1. The first one is to extend the scope of the PIRT towards safety demonstration. The scope of this planned sub-PIRT includes the relevant safety systems of a specific power plant, and the parameters and uncertainty comes not necessarily from severe accident codes. This PIRT is intended to address more broadly the phenomena related to the success of IVMR (and its justification for licensing purposes), well beyond the scope of previous PIRTs which mainly focus on the status of knowledge for the validation of numerical codes used for modeling and simulation.
2. The second planned sub-PIRT is dedicated to the RPV lower head penetration failure under external cooling. Also, here the scope is different as it is focused on the specific phenomena related to the lower head penetrations.

Both these two sub-PIRTs are related to the main IAEA PIRT, however, because of the different scope they will not necessarily share the same phenomena list and methodology.

With the development of a common phenomena list and the specification of the objectives a common basis has been established, as the first step to perform the planned PIRT exercises. The next step is the agreement on the methodology, with reference to those applied for previous PIRTs. Once the methodology and the common phenomena list will be defined, the design-specific PIRTs will be developed, and the results will benefit other CRP tasks.

3. TASK 2: DEVELOPMENT OF A VALIDATION MATRIX

In parallel with the development of a PIRT for IVMR in the task 1, a validation matrix will be developed in the task 2 where experiments are identified in order to validate physical models and computer codes which simulate the important phenomena in the PIRT. The experiments include separate-effect tests, integral tests, qualitative tests, etc. The validation matrix can be used for the benchmarks of physical models and computer codes in task 3 and task 4.

Table I: Cross-reference table against the PIRT developed within the EC H2020 IVMR Project [2]

Phenomena/Parameters	Impact on heat flux (%)	Uncertainty	Experiment program for validation	Selected tests	Comments
Molten pool formation	52	High			
Transient establishment of heat transfer	52	High			
Oxide and metal phases composition	48	Low			
Kinetics of stratification	43	High			
Correlations of heat transfer in upper metal layer	38	High			
Chemical interactions between metal and oxide crusts	34	High			
Progressive ablation of vessel wall	32	Low			
Crust mechanical resistance	32	High			
Debris bed heat-up and melting	31	Medium			
Oxidation during degradation in the core	29	Medium			
Ratio UO_2/steal (mass)	29	Low			
Progressive ablation of lower core plate	28	Medium			
Metal properties	28	High			
Progressive ablation of lower plenum internals	28	Low			
Corium pool / vessel structures failure	26	High			
Radiative heat transfer modelling	25	Medium			

Partition of FP between metal and oxide	24	Low
Correlation of heat transfers on oxide pool	24	Low
Heat transfer with top water	22	Medium
Crust thermal conductivity	22	Medium
Emissivity of metal layer	20	High
Oxidation during relocation of corium, and interaction with water in the lower head	19	Medium
Formation of debris bed	19	Medium
Correlation of heat transfer in heavy metal layer	15	Medium
Oxidation after corium relocation due to steam above the corium pool	14	Medium
Oxide properties	14	Medium
Residual power evolution after scram	11	Low
Release of FP	10	Low

The approach for developing the validation matrix involves the following steps:

- To specify the phenomena involved in IVMR (typically an output from the task 1) as the basis for common evaluations of experimental data;
- To identify test facilities and specific experiments related to specified phenomena and are suitable for validation of corresponding models and computer codes;
- To establish criteria for quality requirements and completeness of data that are finally used for the validation of models and computer codes employed in the assessment of IVMR strategies.

The first step will leverage on the PIRT developed in task 2. But before the completion of the PIRT to be developed in task 1, task 2 will start from existing PIRTs [2-4]. In fact, a preliminary cross-reference table as shown in Table I was established based on the phenomena identified in the PIRT of the EC H2020 IVMR project [2]. When the PIRT developed within the CRP task 1 will be ready, the cross-reference table will be updated accordingly, resulting in the final validation matrix. There were 68 phenomena/parameters (associated with models) and physical properties defined in the PIRT of EC H2020 IVMR project, and Table I shows the phenomena whose overall impact on excessive heat flux in stabilized or in transient situations is above 10% [2]. The information in the currently empty last three columns will be discussed and defined by the task 2 participants in 2022.

The preliminary cross-reference table was developed based on the information from experiment programs and specific tests currently available, with the information and rationale of selected experiments, as well as their sources/accessibility (publications, data sets, etc., as specific as possible). The next step of task 2 is the

compilation of the preliminary cross-reference tables filled by the participants of the task. The compiled cross-reference table will be reviewed by all participants in the CRP, and a synthesis of the cross-reference table accommodating the feedbacks and comments of the participants will form the first version of validation matrix. The path forward is to update the validation matrix according to the PIRT from the CRP, and associated experiments which are useful for validation purposes.

4. TASK 3: BENCHMARK INVOLVING CODE-CODE COMPARISON AND COMPARISON WITH EXPERIMENTAL DATA ON INDIVIDUAL PHENOMENA

Several benchmarks on individual phenomena will be carried out within the task 3. These benchmark exercises aim at characterizing the state-of-the-art of modelling and simulation capabilities of individual phenomena, while also providing useful inputs for further code improvements of individual models and uncertainty reduction. During the first year of the CRP these benchmarks were selected based on their relevance for IVMR (outcome of the PIRT, section 2) and the validation matrix, section 3). Furthermore, the benchmark leaders have almost completed the specifications of benchmarks and working groups were created. These benchmarks involve code-to-code comparison as well as comparison with experimental data. Experimental data on related experiments will be made available for benchmark participants within the next stage of the CRP. From the physical point of view, the task 3 individual phenomena benchmarks can be split into three categories:

- In-vessel corium behaviour;
- Structural response of the RPV;
- External reactor vessel cooling (ERVC).

In the absence of relevant experiments dedicated to structural response of RPV subjected to steep temperature gradient through its wall, it was finally decided to perform such kind of benchmark as a complex code-to-code comparison for a specific reactor design (VVER-1000) within the task 4. Thus, within the task 3 the attention is paid especially to the in-vessel corium behavior and ERVC phenomena.

Regarding the in-vessel corium behaviour, benchmarks with prototypic and simulant materials are considered within the task 3. Topics for individual benchmarks include corium properties, thermochemistry, phase separation and stratification and heat transfer in heat generated stratified corium pool in reactor lower head. The following benchmarks will be performed:

1. The MASCA-CORDEB 2 benchmark was prepared and will be led jointly by France (CEA and IRSN). This benchmark will be devoted to oxide/metal pool thermochemistry phenomena associated to the liquid miscibility gap of such a system. It will be a three-step benchmark with code-to-experiment comparisons for:

    i. Two-layer stationary (under chemical equilibrium conditions) pool configurations using oxide/metal phases' composition and relative position info taken from the MASCA-MA tests series (6 tests). Here, in particular, different approaches (e.g. surface response, tabulation/ interpolation from CALPHAD thermodynamic database) for modelling the liquid miscibility gap of the U-O-Zr-steel thermodynamic system in SA codes will be compared and assessed;
    ii. Heavy metal layer formation kinetics considering the last phase of the MASCA-RCW experiment and associated post-mortem ingot information. This second task can be of interest for both integral intra-layer mass-transfer models of SA codes and distributed parameter models (e.g. phase-field model) for CFD simulations. A semi-quantitative comparison with experimental results (in terms of metal phase spatial distribution and composition) will be carried out;
    iii. Transient evolution of stratified corium pool in a three-layer pool configuration in presence of a mechanically stable crust at the top oxide surface, considering the results of CORDEB2 CP7-02

test on the stratification kinetics. In this experiment, the thermal gradient expected in reactor configuration leading to crust formation between the oxide and the top metal layer is considered.

MASCA-MA tests were performed in the RASPLAV-3 facility at NITI (Russia) in the frame of the OECD MASCA-2 project in the mid-2000s. These prototypical tests involved ~2 kg of corium in a 7 cm diameter cold crucible.

The RCW-100 test was carried out at the RRC Kurchatov Institute (Russia) in 2002 in the frame of the OECD MASCA-1 project. It studied the interaction between 45.3 kg of sub-oxidized corium with 4.6 kg of steel in a ~18 cm diameter crucible; the experiment was stopped after 18 minutes of interaction in such a way that the ingot post-mortem analysis gives information about the transient formation of a heavy metal layer below the oxide pool.

The CORDEB2 CP7-02 test was performed in the RASPLAV-3 facility at NITI (Russia) in 2019 in the frame of the EU IVMR project (proposed and co-founded by IRSN, CEA, EDF and Framatome). It studied the interaction of a two-layer pool, characterized by a heavy metal layer below the oxide (formed from the interaction of 2.15 kg of sub-oxidized corium and 0.43 kg of steel) and crust at the oxide surface, with 0.33 kg of steel added above the crust. The test facility uses a 7 cm diameter cold crucible.

2. The second BALI-Metal corium related benchmark was prepared and will be led by France (CEA). The benchmark is devoted to light metal layer thermal-hydraulics. The main safety issue in relation to this study is the focusing effect associated with a thin light metal layer on top of a stratified pool under transient conditions. The benchmark will be performed in 3 successive steps of increasing complexity:

   i. In the first step code-to-experiment comparisons based on the BALI-Metal results will be performed. To start with a common simple base case before complexing it, it is proposed to simulate (with different CFD solvers) a low-height BALI test involving water as simulant fluid. The first proposed studied experimental BALI-Metal test for solver validation is the 5 cm high test BALI 7U with a uniform bottom heating. This test ensured a thermal-hydraulic laminar regime simplifying the flow behaviour. Sensibility to boundary conditions (upper plate emissivity, environmental temperature, lateral boundary condition, imposed bottom heat flux) could be proposed and discussed between participants;
   ii. In the next step, on the strength of previous solver confrontations on the laminar test case, a turbulent test case (the 40 cm high test BALI 8U) will be used where more complex models will be involved. Sensibility study to turbulence models will be proposed.
   iii. The third step is proposed for this 40 cm high test BALI 8U configuration but considering prototypic material. Moreover, depending on the participants interest, sensitivity to the lateral boundary condition could also be envisaged, simulating the presence of a pre-existing refractory crust, which would have resulted from oxide/metal stratification inversion of the pool. Thus, the light metal layer could be in partial contact with both the vessel wall and this refractory crust.

3. Another benchmark, related to CANDU reactors, is under preparation by Canada (CNL). This benchmark is devoted to convection and exiting heat flux distribution in a shallow corium pool with a lower volumetric decay heat than in a typical LWR. The focus of this effort is a series of experiments performed at CNL, simulating corium convection using a simulant material (nitrate salt mixture). These experiments were performed using a 1:5 linear scale apparatus, with a stepped-cylinder geometry representative of the CANDU calandria vessel. Based on the current understanding of CANDU corium miscibility, the experiments involve a single-layer corium pool.

Regarding the ERVC experiments, these are typically performed for specific reactor design. Two kinds of PWR designs are considered: Korean APR1400 and advanced generation of Chinese PWRs.

1. The HERMES ERVC benchmark is devoted to Korean APR1400 reactor design. Both the comparison of code-to-experimental data using the HERMES-HALF experimental results or HERMES-1D experimental results, as well as code-to-code comparison, will be made within this benchmark. The HERMES is focused on hydraulic evaluations of reactor vessel cooling mechanisms by external self-induced flow. An analysis of coolant circulation flow between the outer reactor vessel wall and the vessel insulation in the reactor cavity under ERVC condition should be performed within this benchmark. The main comparison parameter is the coolant circulation mass flow rate as a function of experimental parameters, such as heat flux from corium pool to the outer reactor vessel wall, water level in the reactor cavity, water inlet area and configuration, and water out area and position. Other comparison parameters are the local pressure and local void fraction. If CFD computer code will be used, the flow pattern will be observed as well. The HERMES-HALF tests using a half-height and half-sector model of the APR1400 was performed to observe and evaluate the two-phase natural circulation phenomena through the annulus gap between the outer reactor vessel wall and the vessel insulation material, and finally to propose enhanced designs for the coolant inlets and upper steam venting slots in the reactor vessel insulator of the APR1400. Since the heating method is very difficult and expensive for a large scale and three-dimensional spherical test section, the non-heating method of an air injection was used in this test. The natural circulation flow according to ERVC design factors, such as inlet and outlet areas, wall heat flux (air injection rate), water level, and outlet height was estimated. The HERMES-1D tests was performed to compare the non-heating with heating experimental results, to observe the sub-cooling (condensable gas) effect and steam bubble behavior, to evaluate natural circulation flow instability, and to compare the 3D results of the HERMES-HALF with the HERMES-1D results.

2. Regarding the new advanced generation of Chinese PWRs (e.g. CAP1400) two experimental facilities are under consideration for possible benchmarks in this task: the TWINS and REVECT (Reactor Vessel External Cooling Test) facilities. These electrically-heated 2-D facilities with a full-height circulation loop (slice geometry) were designed and constructed to study the influencing factors which determine the CHF distribution along the outer surface of the RPV and natural circulation induced by heat transfer in the riser part of the ERVC loop. Both facilities are capable to generate high heat flux values on the outer surface of RPV.

5. TASK 4: ANALYTICAL BENCHMARK

Task 4 is dedicated to analytical benchmarks, with the aim of testing codes capabilities based on an IVMR exercise representative of a comprehensive scenario. This activity takes benefit of the achievements of previous benchmarks on IVMR performed within the European H2020 IVMR project [5]. To extend the scope of IVMR configurations covered and to consider design specific issues, three different reactor designs were chosen to be studied in this task: a generic PWR design of 1000 MWe, the Russian VVER-1000/320 design and the Chinese CAP1400 design. For all these designs, a Lower Plenum (LP) benchmark has been defined, which means that it starts from the situation where the corium has been relocated to the LP. In this case the calculation domain represents only the lower part of the reactor. Possible later relocation of material from the core part of the reactor is prescribed to have consistent initial and boundary conditions for all codes. For the VVER-1000/320 reactor design, a deeper analysis will be performed thanks to the consideration of two other complementary benchmarks:

- An integral benchmark, i.e., simulation of the whole scenario with core degradation and melt relocation to the LP;

- A mechanical benchmark to assess more precisely the mechanical resistance of the ablated vessel wall using finite element calculations.

An overview of these five different benchmarks defined in this task 4 of the CRP is presented in Fig. 1, showing the different reactor designs and type of benchmarks covered.

In the following sections, each benchmark is shortly described with the objective of highlighting its main purposes and complementarities with other benchmarks.

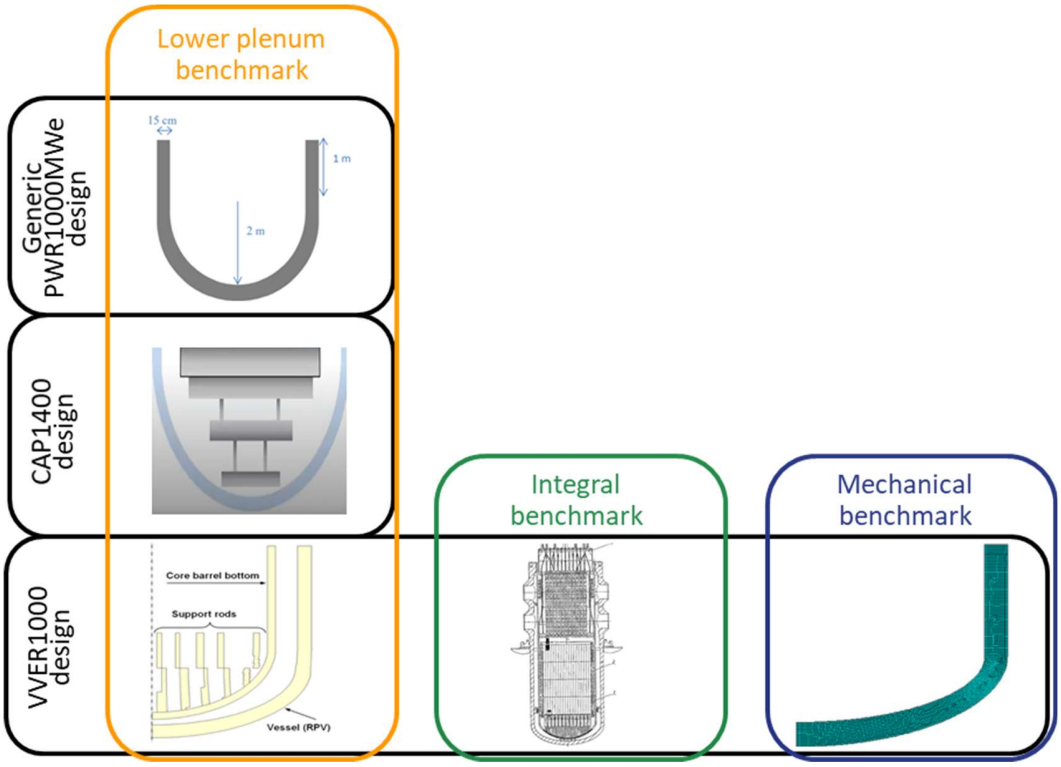

Figure 1. Overview of five different benchmarks defined in the scope of the CRP task 4.

5.1. Generic PWR1000 MWe Reactor LP Benchmark

This benchmark was initially set-up in the framework of the H2020 IVMR project to allow detailed comparison of models based on prescribed and simplified configurations. It does not intend to represent a specific reactor design and scenario but to cover generic configurations to be simulated by capable codes. The methodology used was to first begin with simple steady-state configurations and then progressively increase the complexity to finally simulate a comprehensive configuration with the effect of transient evolutions and thermochemistry. A specific configuration with stratification inversion during the transient was also considered. Complementary results for these configurations are expected during the CRP, thanks to new partners and possible improvements of codes. Moreover, it was proposed to extend this generic PWR1000 MWe LP benchmark to study the impact of molten pool formation on ablated vessel profile.

Initially, the attention was paid to transient effects during vessel wall ablation, progressive molten steel incorporation and possible stratification inversion, considering the corium as already molten in the LP. In this second part of the benchmark, the focus will be on models dealing with the molten pool formation.

Indeed, directly considering the molten pool in the lower head with conservative assumptions is often used when studying IVMR. However, the justification of such assumptions and of their conservatisms is not straightforward. In particular, the assumption regarding the initial mass of molten steel in the molten pool is tricky and conservative assumption cannot be defined due to focusing effect. In addition, there is a link between the mass of corium relocated in the LP and the one of molten steel. Therefore, it may be necessary to calculate the molten pool formation to evaluate the mass of molten steel which will be incorporated with time and associated uncertainties. To benchmark the models implemented in the codes for this phase, new configurations have been specified to study the two following key processes:

- The melting of the debris. Indeed, solid particles are expected in the LP at corium relocation, either due to fragmentation of molten corium jet in the water or due to collapse of debris formed in the core part of the vessel;
- The kinetics of corium arrival in the lower head. The effect of the variability of the mass of corium relocated in the LP on the vessel wall ablation will be studied.

5.2. CAP1400 Reactor LP Benchmark

In this benchmark the geometry of the LP and especially the one of the internal structures in the CAP1400 design are considered. The internal structures below the core are composed of the lower support plate which is lowered in the hemispherical part of the LP, the flow plate and the second support structure (Fig. 1). The melting of these structures will impact the transient formation of the molten pool in the LP and corresponding maximum heat flux. A challenged scenario, the LB LOCA without core flooding sequence, is chosen as it provides fast core melting and large decay heat (for CAP1400 this corresponds more precisely to the scenario of Automatic Depressurization System stage 4 (ADS4) spurious opening because the valves are 18 in (457 mm) diameter and equipped above the containment flooding elevation). A steady-state two-layer configuration is proposed to be a simple benchmark case for the molten pool heat flux profile comparison. Then, the transient relocation of the molten materials from the core to the LP is prescribed (the prediction of the core melting progress and the corium interaction and relocation is done referring to previous integral calculation with MAAP code) and the corium evolution in the LP up to the steady-state is studied.

5.3. VVER 1000/320 Reactor LP Benchmark

As for the CAP1400 design, in this benchmark the attention will be paid to the impact of melt arrival and melt-structures interactions on the ablated vessel profile. These two LP benchmarks will allow comparing the impact of design specificities. Indeed, in the VVER 1000/320 the LP contains several internal structures such as the support rods and the core barrel bottom which forms a double wall with the vessel (Fig. 1). Consistency with the corresponding integral benchmark will be achieved by means of using the same data for reactor structure and taking in the LP benchmark the results for core melt relocation obtained in integral calculations. However, the influence of initial/boundary conditions on the benchmark results is planned on a final stage of the calculations. In the first stage, the data will be simplified for more straightforward comparisons of the individual results.

For the three LP benchmarks described hereabove, either integral codes or codes dedicated to the LP simulations will be compared. A total of seven codes is planned to be used including commercial codes and in-house codes.

5.4. VVER-1000/320 Integral Reactor Benchmark

The challenge with integral benchmark lies on the researched elimination of differences in input decks, so to allow identifying discrepancies in results caused by models and variables or approaches used to model

core degradation and IVMR phenomena. Specifications regarding the primary and secondary circuits, the core, the LP and the containment design have been proposed, as well as for the material properties and the initial state of the reactor. The LB LOCA with simultaneous station blackout is considered as an initiating event of the accident. Main circulation pipeline break is happening immediately with a diameter of 300 mm on the cold leg of the pressurizer loop. Four different integral SA codes will be used: AC2 (ATHLET-CD), ASTEC, MELCOR and SOCRAT. The use of the same code by different partners will allow consideration of the user effect.

5.5. VVER-1000/320 Mechanical Resistance of the Vessel Wall Benchmark

The justification of the mechanical resistance of the significantly ablated vessel wall in the IVMR configuration requires accurate thermo-mechanical analyses, especially for situations when internal pressure may increase. Benchmarking current finite elements codes used to assess the RPV mechanical behavior under the IVMR conditions is then highly important. This benchmark will consider inputs from the VVER-1000/320 integral benchmark for the definition of the initial and boundary conditions. Exchanges are also planned with the parallel activity on RPV integrity during IVMR performed at the OECD/NEA dedicated to the preparation of a status report on RPV integrity.

This benchmark activity may benefit from other tasks of the CRP, especially from the individual benchmarks of the task 3 (section 4), which may lead to modifications in the models and to code improvements. Inversely, it is also planned in these analytical benchmarks to perform uncertainties analyses, to obtain more consolidated results and give feedback to the task 1 on PIRT development (section 2) with a more quantitative evaluation of the impact of the different parameters or phenomena.

6. CONCLUSIONS

To harmonize the international understanding of the scientific and technological bases underpinning crucial parts of the safety demonstration of IVMR, the IAEA started in 2020 the 4-year CRP with 23 organizations from 14 IAEA Member States. The CRP aims to progress the understanding and modelling and simulation of major physical phenomena occurring in the strategy of In-Vessel Melt Retention, which may be adopted for mitigating the consequences of a severe accident with core melting. It focuses at harmonizing the international understanding of scientific and technological bases underpinning crucial parts of the safety demonstration of the IVMR strategy. Participants are expected first to develop a Phenomena Identification and Ranking Table and then a validation matrix for IVMR. Subsequently, the CRP will organize a series of benchmarks, include comparison of modelling and simulation results with experimental data representative of medium, as well as high-power reactors implementing IVMR, to mainly address the following: corium properties and stratification in the lower plenum of the reactor pressure vessel, heat transfer in stratified corium pools; external reactor vessel cooling and mechanical resistance of ablated wall. Significant progress has already been achieved during the first year of the project: PIRTs for different reactor designs have been defined in the task 1; the first version of cross-reference table containing IVMR relevant phenomena has been proposed and is being discussed by the task 2 partners; the specifications of benchmarks on individual phenomena (code-to-code comparison and comparison with experimental data) were defined and working groups were created in the task 3; reactor designs and accident scenarios for integral benchmarks have been selected in the task 4. The output of the CRP will be disseminated in the form of an IAEA workshop, IAEA publications and conference papers.

REFERENCES

1. INTERNATIONAL ATOMIC ENERGY AGENCY, In-vessel Melt Retention and Ex-vessel Corium Cooling, IAEA-TECDOC-1906, TECDOC Series (2020).

2. F. Fichot, et al., "Elaboration of a Phenomena Identification Ranking Table (PIRT) for the modelling of In-Vessel Retention," *Annals of Nuclear Energy* **146**. 107617. 10.1016/j.anucene.2020.107617 (2020).
3. D. Magallon, et al., "European expert network for the reduction of uncertainties in severe accident safety issues (EURSAFE)," *Nuclear Engineering and Design* **235**, 309–346 (2005).
4. W. Klein-Heßling, et al., "Conclusions on severe accident research priorities," *Annals of Nuclear Energy* **74**, 4–11–346 (2014).
5. L. Carénini, F. Fichot, N. Bakouta, A. Filippov, R. Le Tellier, L. Viot, I. Melnikov, P. Pandazis, "Main outcomes from the IVR code benchmark performed in the European IVMR project," *Annals of Nuclear Energy,* **146** (2020), https://doi.org/10.1016/j.anucene.2020.107612.

IAEA
International Atomic Energy Agency
Atoms for Peace and Development

The IAEA Coordinated Research Project on Developing a Phenomena Identification and Ranking Table and a Validation Matrix, and Performing a Benchmark for In-Vessel Melt Retention

L. Carénini (IRSN), W. Ma (KTH), P. Matejovic (IVS), P. Pandazis (GRS), S. Massara (IAEA), A. Miassoedov (IAEA)

The 10th European Review Meeting on Severe Accident Research (ERMSAR2022)
Akademiehotel, Karlsruhe, Germany
May 16-19, 2022

IAEA Coordinated Research Activities

- Provide opportunities to engineers and scientists in developing and developed Member States to collaborate on research topics of common interest

- Results of research activities supported by the Agency are disseminated to all Member States through national, international and IAEA scientific and technical publications, and other communications media

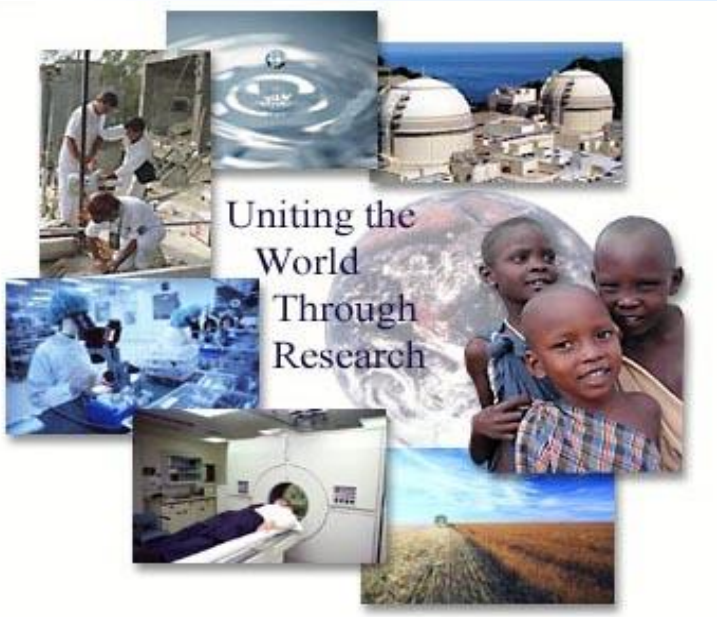

http://cra.iaea.org/cra/index.html

Background

- Where does the CRP originate from?
  - IAEA International Experts Meeting (IEM8) on strengthening research and development effectiveness, VIC, Feb. 2015
  - IAEA TM on “Post-Fukushima R&D Strategies and Priorities”, VIC, May 2015
  - IAEA TM on “Phenomenology and Technologies Relevant to In-Vessel Melt Retention and Ex-Vessel Corium Cooling”, Shanghai, Oct. 2016
    - IAEA TECDOC-1906 In-vessel Melt Retention and Ex-vessel Corium Cooling



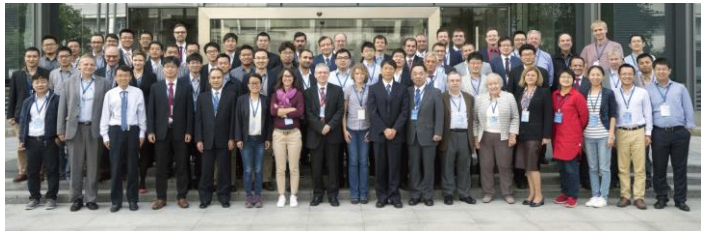

- Other related activities
  - EURATOM H2020 Project IVMR (2014 – 2020)
  - OECD/NEA/CSNI CAPS: “RPV Integrity Assessment during IVMR with ERVC” (update will be provide at this RCM-1)

Challenges related to IVMR

Despite a 3+ decades effort, which has requested methodological developments, experimental and numerical simulation works, previous IAEA meetings on this topic and state-of-the-art knowledge conclude that further work would be necessary including on:

- Experimental data needed for validating individual models are often considered limited in covering relevant phenomena (e.g. focusing effect, influence of layer inversion on the heat flux towards the vessel wall), insufficient quality (e.g. contradictory CHF experimental data) and quantity (e.g. data for material behaviour of RPV steel, hampering the performance of structural integrity analyses);
- The quality of numerical simulations, through the improvement of models for the simulation of lower plenum phenomena, identified as those responsible of most of the deviation with respect to experimental data, i.e. on the heat flux on the outer vessel wall;
- Related to the previous item, the limitation of a purely steady-state approach is also widely recognized, pushing for a methodological improvement towards a more comprehensive consideration of transient effects (all kinetic effects since the beginning of the transient should be taken into consideration, including possible heat flux spikes, to address the effect on the RPV wall and to assess its possible failure);
- The identification of most pertinent acceptance criteria to be considered in the safety demonstration. However, it is recognized that these are design dependent and that the minimum vessel thickness appears to be one of the most critical for the RPV failure

CRP Scope

- The CRP will aim at providing a platform facilitating interactions among IAEA Member States with the objective of tackling the abovementioned challenges related to IVMR
- The general objective of the CRP is to harmonize the international understanding of scientific and technological bases underpinning crucial parts of the safety demonstration of IVMR, including for (but not limited to) high-power reactors

CRP Tasks

1. To develop a PIRT for IVMR
2. To develop a validation matrix for IVMR and to identify relevant high-quality experimental data requested for the validation of computer codes for IVMR simulation
3. Benchmark involving code-code comparison and comparison with experimental data on individual phenomena
4. To carry out an analytical benchmark on an IVMR comprehensive scenario exercise

23 participating organizations
14 Member States and one International Organization



Nuclear Power Technology Development Section
Division of Nuclear Power
Department of Nuclear Energy





Nuclear Power Engineering Section

The Section supports countries operating nuclear power plants or expanding their existing programmes to improve engineering, performance, management systems, human resource management, stakeholder involvement and technical infrastructure. It shares best engineering practices and innovations consistent with the global objectives of nuclear safety, security and non-proliferation. Read more →



Nuclear Power Technology Development Section

Fostering information exchange and collaborative research and development for advanced nuclear reactor technologies, this Section provides information to the IAEA's Member States on technology status and development trends for advanced reactor systems and their applications. Read more →



Nuclear Infrastructure Development Section

This Section is responsible for coordinating IAEA assistance to Member States considering or embarking on nuclear power programmes. It supports capacity-building, conducts review missions and offers guidelines, standards and workshops on developing the infrastructure for a safe, secure and sustainable nuclear power programme. Read more →



International Project on Innovative Nuclear Reactors and Fuel Cycles Section

The Section coordinates the activities of the membership-based International Project on Innovative Nuclear Reactors and Fuel Cycles (INPRO) to increase international cooperation on global nuclear energy sustainability, long term strategies and institutional and technical innovations for nuclear energy development and deployment. Read more →

Department of Nuclear Safety and Security (NS)

- The protection of people, society and the environment from the harmful effects of ionizing radiation is at the heart of the Department for Nuclear Safety and Security's work
- Whether the cause is an unsafe act or a security breach, it aims at providing a strong, sustainable and visible global nuclear safety and security framework



Incident and Emergency Preparedness and Response



Nuclear Security



Management of Radioactive Waste



Safety of Nuclear Installations



Radiation and Transport Safety



Division of Nuclear Installation Safety

The Division of Nuclear Installation Safety supports Member States in establishing the appropriate safety infrastructure and in continuously improving the safety of nuclear installations during site evaluation, design, construction and operation. The Division contributes to the development of safety standards for nuclear installations and provides safety reviews and advisory services to support their effective application.

CRP activities since 2019

- Jul to Oct-2019: IAEA development/approval of CRP proposal
- Nov-2019: Consultancy Meeting to further develop the CRP proposal and start identifying potential participants **(VIC)**
- Feb to Apr-2020: Submission of proposals
- Jul-2020: CRP start
- 17-19 November 2020: Kick-off Consultancy Meeting **(virtual)**
- 27-28 January 2021: Task 1 (PIRT) meeting (methodology adopted in the H2020 EU IVMR project), **(virtual)**
- 13-15 March 2021: Progress Consultancy Meeting **(virtual)**
- 1st and 6th July 2021: Task 1 (PIRT) meetings (RPV lower head penetrations; PIRT supporting safety demonstration of IVMR), **(virtual)**
- 13-17 December 2021: RCM-1 **(hybrid)**
- 5-6 April 2022: Task 4 (full-scale benchmarks) progress meeting **(virtual)**

Task 1 objectives

Development of a PIRT to identify and describe the involved phenomena in IVMR in details as the basis for a common evaluation and assessment, identifying of uncertainties and importance of the phenomena.

- 19 organization
- Summarize the current knowledge level about IVR
- Avoiding expert judgments
  - Experiments, sensitivity studies & uncertainty calculations
- **Support of further Tasks in the CRP:**
  - Validation matrix development (Task 2)
  - Benchmark calculations (Task 3 & 4)
- **Addressing different reactor designs**
  - CANDU, CAP-1400, VVER-1000, Nordic BWR
- Assessment of existing IVMR-related PIRTs
- Enhance common understanding

Assessment of existing PIRTs

Three recent PIRT has been investigated and assessed:

- **H2020 IVMR PIRT** (IRSN et al.)
  - *Objective: Identification of relevant and essential models for IVR evaluation*
  - developed for PWR and BWR, without accident specification but IVR scenario
  - introducing third abstract layer (macro variables) between risk and phenomena (traditional PIRT methodology)
- **Joint Chinese IVR PIRT** (NSC, SNERDI, CNPRI)
  - *Objective: support code development and definition of further research areas.*
  - developed for PWR, LB-LOCA wo reflooding
- **CANDU IVR PIRT** (AECL, CNL): severe accident phenomena in CANDU reactors with focus on IVMR
- to achieve a basis for a common work, focus of assessment on phenomena definition and methodology
- all three PIRTs describe good the entire problem, differences identified in methodology and definition of the phenomena (detail level)

Additional PIRTs planned in the CRP

Development on the basis of the CRP PIRT (PIRT 1) as much as possible:

- use/extend the CRP IVR phenomena pool
- comparable methodology
- parameters and uncertainty comes not necessary from SA codes

1. **Extension of scope towards safety demonstration (PIRT 2)**
   - Objective: support the safety assessment of IVR
   - Complementary to IVR PIRT but (re)introducing new topics:
     - Depressurization, primary pressure, safety systems, cavity flooding
     - Reactor design specific issues
   - Evaluation of the reliability of safety systems (uncertainty)
   - Core group mainly operators, regulators, TSO
2. **PIRT on RPV lower head penetration failure under external cooling condition (PIRT 3)**
   - Objective: phenomena & modelling of LH penetration failure
   - Relevant designs: PWR, CANDU, BWR

Task 1 activities for 2022

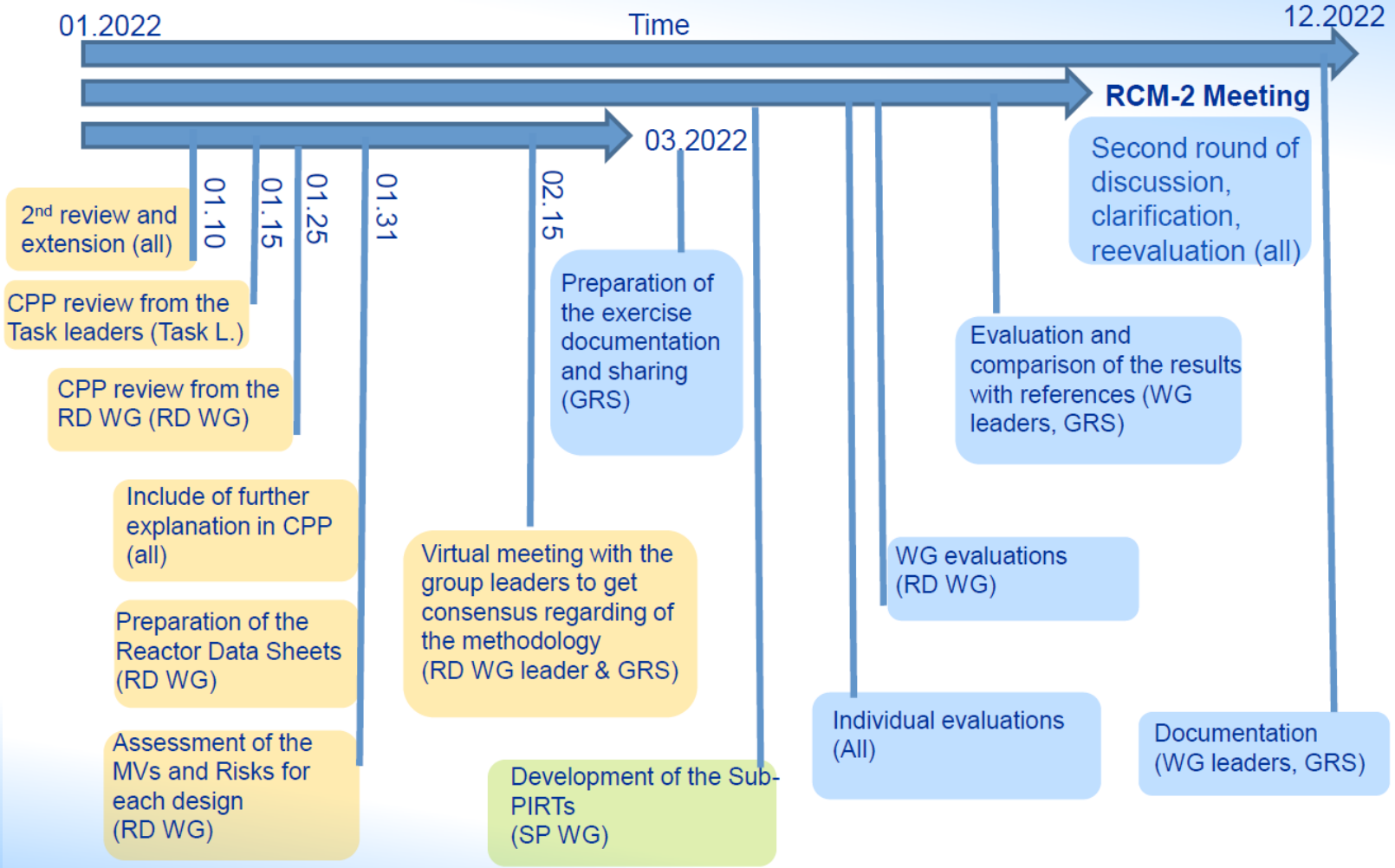

Task 2 objectives

- To identify **experiments** which can be used for the validation of computer codes applied in the IVMR analysis
  - separate-effect tests
  - integral tests
  - qualitative tests, etc.
- Two stages are foreseen to develop the validation matrix:
  - In the first stage, the validation matrix will be developed based on the phenomena identified in the EC H2020 IVMR PIRT (Fichot et al. 2020), i.e. to construct a cross-reference table (Important phenomena from the EC H2020 IVMR PIRT vs. available experimental facilities/tests)
  - In the second stage, the validation matrix is updated using the PIRT developed within the CRP

Identification of experiments

- Organizations participating in Task 2 provide information on their experimental facilities and the specific data which could be available to the CRP: data reports are expected
- Important experiments identified but not owned by participating organizations:
  - Digest of open sources (e.g. publications): data reports are expected
  - If no open sources, initiating possible actions to get access to the data

Example of a cross-reference table

Phenomena/Parameters \ Micro-variables		Residual power	Characteristics			Presence of crusts	Top cooling conditions		CHF profile	Overall impact (%) on Risks 2&3	Uncertainty	Experiment program for validation of models and codes	Selected tests	Comments
			Top metal	Oxide	Bottom metal		radiative	boiling						
Lower head molten pool behaviour	1.1.1 Failure of corium pool/core supprting structures		15.32	4.81	6.24					26	High	TMI2 ?		
	1.2.1.1 Oxidation during degradation in the core		16.85	5.02	7.24					29	Medium			
	1.2.1.2 Oxidation during corium relocation and interaction with water in the lower head		10.72	3.98	4.74					19	Medium			
	1.2.1.3 Oxidation after corium relocation due to steam above the corium pool		8.17	2.93	3					14	Medium	CORDEB (NITI, Russia)		https://doi.org/10.1016/j.nucengdes.2017.11.030
	1.2.2 Metal mass fraction (in total inventory)		18.38	2.93	7.49					29	Low			
	1.2.3.1 Residual power evolution after scram	11.12	0	0	0					11	Low			
	1.2.3.2 Release of FP	9.89	0	0	0					10	Low			
	2.1 Formation of debris bed		10.21	4.18	4.25					19	Medium	DEFOR (KTH, Sweden)		
	2.2 Debris bed heat-up and melting		11.74	3.77	5.49		5.83	4.59		31	Medium	SIMECO-2 (KTH, Sweden)		
	2.3 Molten pool formation		14.30	4.81	5.74	14.08	8.74	4.21		52	High	PHEBUS-FP (IRSN), ACRR-MP (SNL)	FPT4, MP2	
	2.4.1.1 Oxide and metal phases composition		14.3	5.65	6.49	9.8	6.99	4.59		48	Low	MASCA (NRC-KI, Russia)	All STFM-FE tests All MA tests	
	2.4.1.2 Partition of FP between metal and oxide		9.19	3.98	5.24	1.84	2.33	1.15		24	Low	MASCA (NRC-KI, Russia)	All STFM-FP tests	
	Oxide properties		2.30	5.61	0.71	4.82	0.66	0.43		14	Medium			
	Metal properties		11.87	1.26	5.42	3.90	4.59	1.59		28	High			

(Fichot et al, 2020)

Task 3 objectives

The aim of Task 3 benchmarks is characterizing the state-of-the-art of modelling and simulation capabilities for the individual phenomena

- Set of benchmark exercises was selected based on the outcomes of the PIRT (Task 1) and the validation matrix (Task 2)
- For each of the benchmark proposed within Task 3 there is allocated a leading person from the proposing organisation
- These benchmarks involve code-to-code comparison as well as comparison with experimental data
- Focus on in vessel corium and external reactor vessel cooling (ERVC) phenomena

Task 3 benchmarks

5 benchmarks have been defined based on participants interests

MASCA – CORDEB2
Leader: Laure CARENINI (IRSN) and Romain LE TELLIER (CEA)

Organization	*Code*
CEA	PROCOR
IRSN	ASTEC
XJTU	CH-NS coupled models
IBRAE	HEFEST_URAN package
INRNE (?)	ASTEC
NRC-KI	HEFEST-ULR code

BALI – metal
Leaders : Nathalie SEILER (CEA)

Organization	*Code*
CEA	Trio CFD
UJV	Fluent CFD
SSTS NRS	ANSYS CFX
PAEC (?)	ANSYS CFX
Gidropress	ANSYS CFX

CANDU – related benchmark
Leader : Justin SPENCER (CNL)

Organization	*Code*
CNL	LES and RANS technique
McMU	LES and RANS technique
CEA	Trio CFD

HERMES – half
Leader : Rae- Joon PARK (KAERI)

Organization	*Code*
KAERI	RELAP-5/mod3
LEI	AC 2

IVR Twins
Leader : Han WANG (NCEPU)

Organization	*Code*
NCEPU	
GRS	AC 2
IVS	ASTEC

Task 3 benchmark illustration

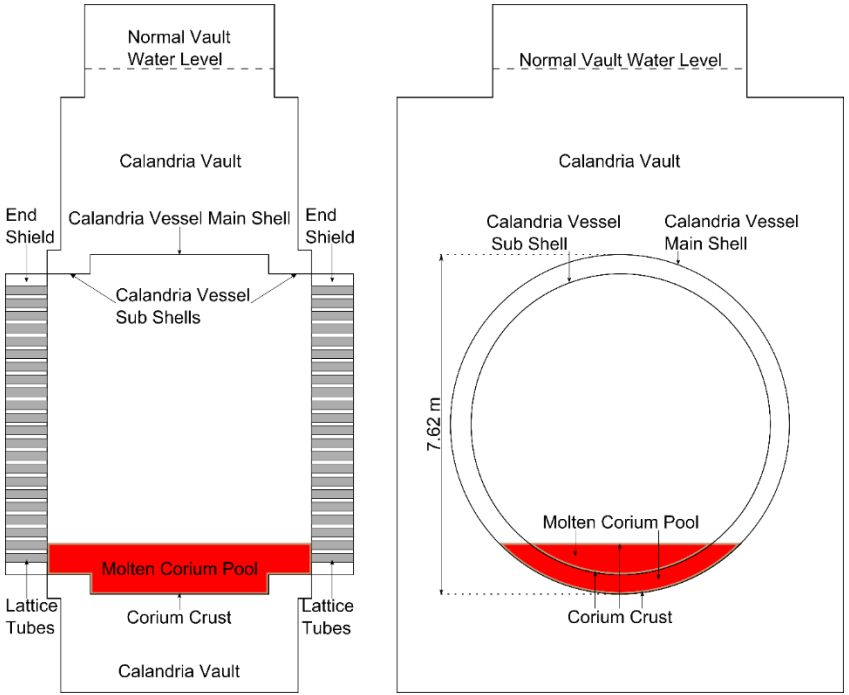

CANDU shallow corium pool benchmark

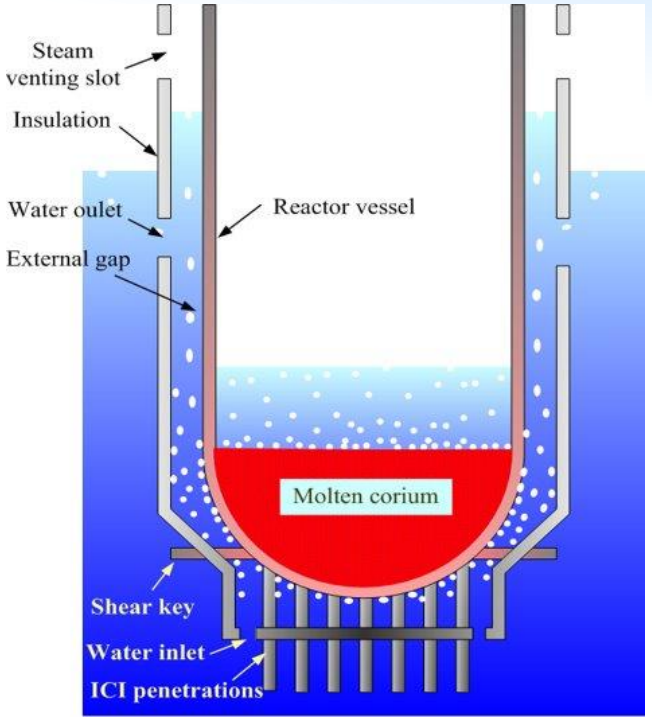

HERMES half non-heated ERVC benchmark

Oxide/metal corium pool thermochemistry and stratification

- Benchmark coordinators: Romain Le Tellier (romain.le-tellier@cea.fr) and Laure Carénini (laure.carenini@irsn.fr)
- Benchmark participants: Yapei Zhang (XJTU), I. Melnikov (NRC KI), P. Groudev (INRNE), A. Filippov (IBRAE)
- Three-step benchmark constructed by "merging" initial CEA proposal (MASCA) and IRSN proposal (CORDEB2), expression of interest from XJTU and NRC-KI

Addressing in a progressive manner, a high-uncertainty, high-impact "phenomenon" (*cf.* PIRT)

- Step 1: Code-to-experiment comparisons using small scale prototypic experiments of the MASCA projects: MA 6-test series
  - Species partitioning in a two-layer pool under chemical equilibrium conditions
  - modelling the liquid miscibility gap of the U-O-Zr-steel thermodynamic system in both SA codes/CFD simulations
- Step 2: Code-to-experiment comparisons using medium scale prototypic experiment MASCA RCW-100 test
  - kinetics of interfacial mass transfer (wo crust) + Rayleigh-Taylor instabilities + droplet relocation
  - Stratification models in SA codes - Tentative modelling and simulation at mesoscopic scale (CFD) e.g. phase-field approach



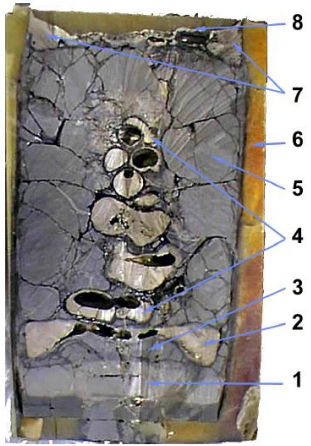

Oxide/metal corium pool thermochemistry and stratification

- Step 3: Code-to-experiment comparisons using small scale prototypic experiment CORDEB2 CP7-02 test
  - Stratification kinetics in presence of a mechanically stable crust at the top oxide surface
  - Stratification models in SA codes (inter-layer mass transfer model + liquid miscibility gap model) - Tentative modelling of chemical interactions between molten metal and oxide crusts



Provisional schedule

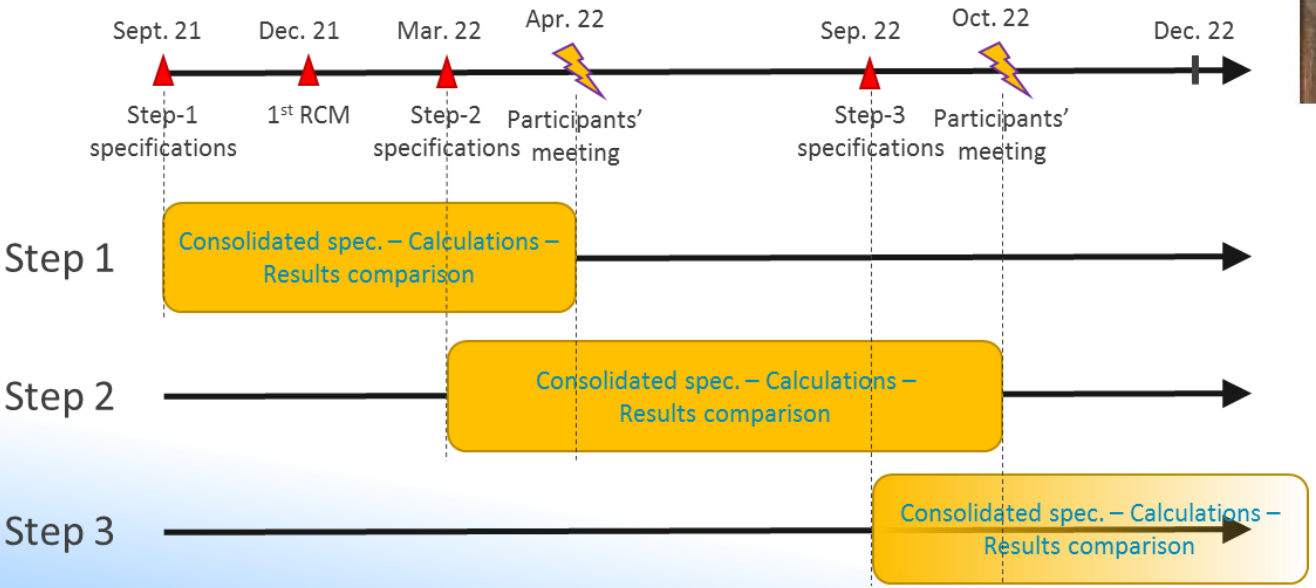

Light metal layer thermalhydraulics

- Benchmark coordinator: Nathalie Seiler-Marie (nathalie.marie@cea.fr)
- Benchmark participants: Ladislav Vyskocil (UJV), Oleg Zhabin (SSTC NRS), Walter Villanueva (KTH)
- **To pursue the CFD simulation effort on the light metal layer thermalhydraulics** behaviour started in the frame of the H2020 IVMR project (WP2.3)
- Two-step benchmark
- Step 1: Code-to-experiment comparisons using the BALI-Metal simulant experiments

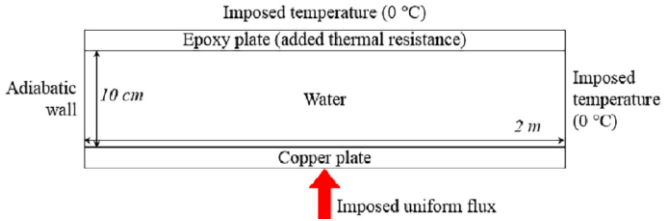

- parallelipedic geometry, water as simulant material (N.B. Representativeness limitation: Pr~7 for water)
- different layer heights
- carried out at CEA, France in the late 90s (cofunded by EDF and FRAMATOME)

- Partial overlap with H2020 IVMR project
- A different focus: going into more details in the code-experiment comparison using information about local temperatures and flow patterns

Name	Run n°	Height	Power	Heating condition
1U	1	20 cm	2 kW	Uniform heating
2N	2	20 cm	2 kW	Non uniform heating
3U	3	10 cm	2 kW	Uniform heating
4U	4	10 cm	2 kW	Uniform heating
5N	5	10 cm	2 kW	Non uniform heating
6U	6	5 cm	2 kW	Uniform heating
7U	7	5 cm	2 kW	Uniform heating
8U	8	40 cm	2 kW	Uniform heating
9N	9	40 cm	2 kW	Non uniform heating

Light metal layer thermalhydraulics

- Step 2: Code-to-experiment comparisons using the BALI-Metal simulant experiments
  - Starting from a common simple base case: a low height BALI test involving water as simulant fluid (laminar regime): 5-cm height test BALI 7U - uniform bottom heating
    - Sensitivity to boundary conditions
  - Then, a turbulent test case: 40-cm height test BALI 8U - uniform bottom heating
    - Sensitivity to turbulence modelling
- Step 3: Code-to-code comparisons for the reactor case application
  - 40-cm height test BALI 8U geometry
  - with prototypic material (steel): in particular, a much lower Pr number that water: 7 → 0.1

Provisional schedule

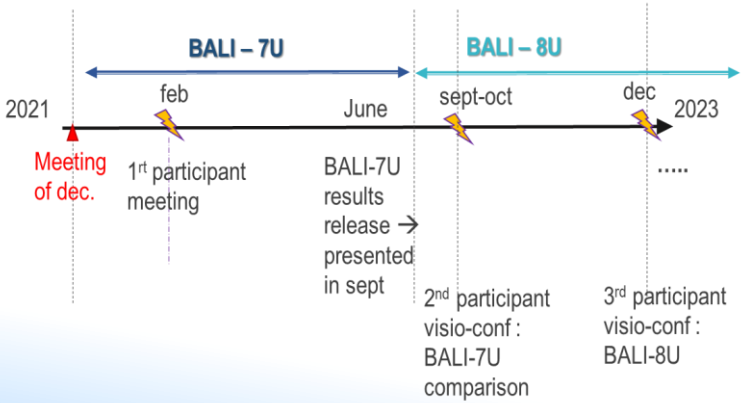

Task 4 objectives

The aim of the analytical benchmark is to test codes capabilities on the basis of an IVMR exercise representative of a comprehensive scenario

- Consider as a basis the IVR code benchmark performed in the H2020 IVMR project and to adapt it to this task, possibly by considering **different designs and scenarios** to be agreed by the participants
- Two runs **before and after** the implementation of the modifications in the models and methodology resulting from other tasks
- Encourage calculations starting from the situation where the molten material has been relocated to the lower plenum of the RPV in order to have **consistent initial and boundary conditions** for all the codes
- **Mechanical calculations** may be also considered if code allows (and synergies with parallel OECD/NEA activity on RPV integrity during IVR)

Task 4 benchmarks

- 3 different designs studied
- Deeper analysis of VVER1000 case
  - → interactions between the 3 benchmarks
- Various configurations covered to challenge IVR models in codes
- Uncertainty analyses will also be performed

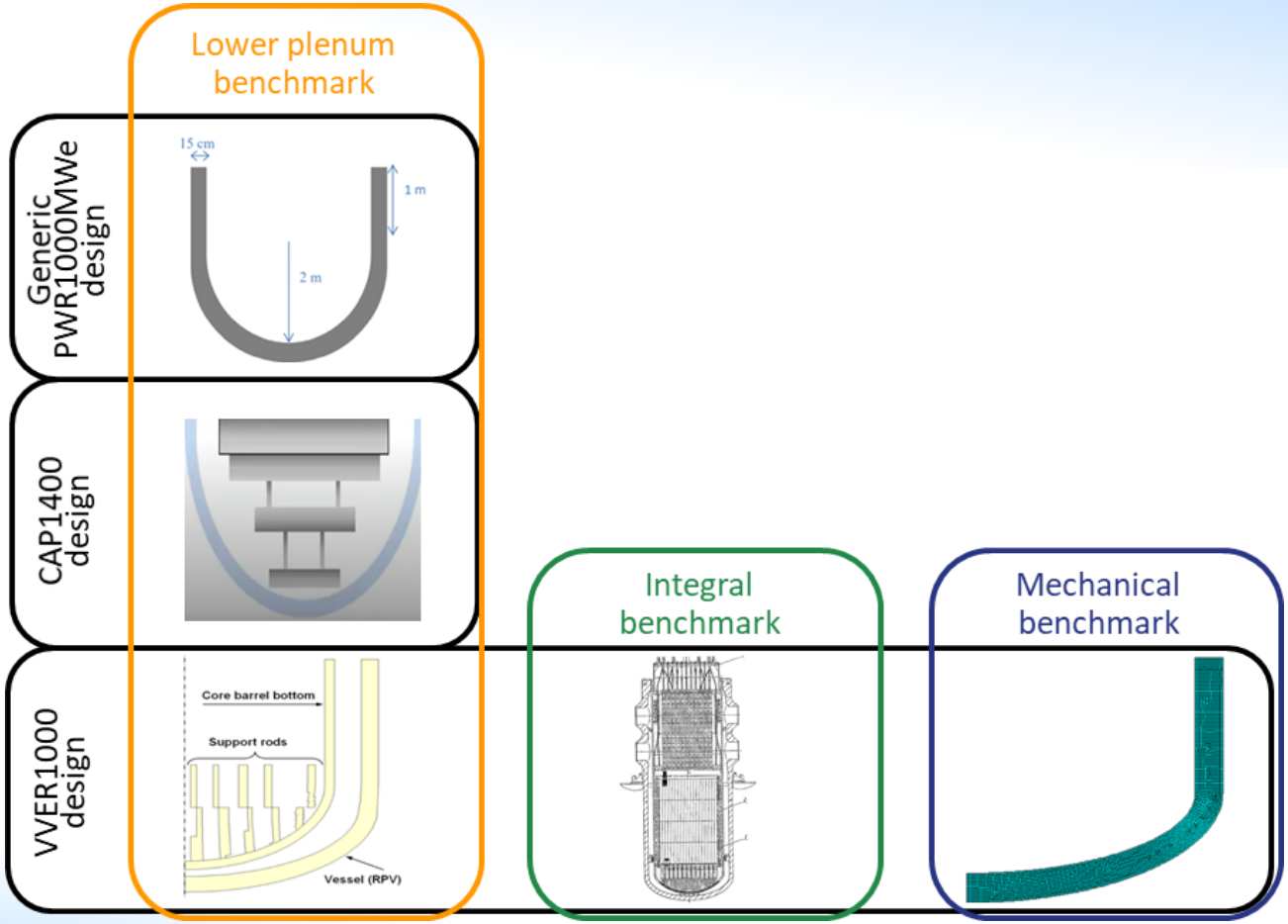

Task 4 benchmarks

5 benchmarks have been defined based on participants interests:

Generic PWR – Lower plenum
Leader: Laure CARENINI (IRSN)

Organization	*Code*
CEA	PROCOR
CNPRI	ASTEC
GRS	AC² (ATHLET-CD)
IBRAE	HEFEST_URAN package
IRSN	ASTEC
JRC	ASTEC
LEI	AC² (ATHLET-CD)
NRC-KI	HEFEST-ULR code
NSC	MELCOR and ASTEC
PAEC	DCMR(2.0)
SNERDI	MAAP
XJTU	MIDAC

CAP1400 – Lower plenum
Leaders : Zhiyi YANG (NSC)
Jiayun WANG (SNERDI)

Organization	*Code*
CEA	PROCOR
CNPRI	ASTEC
GRS	AC² (ATHLET-CD)
IRSN	ASTEC
NSC	MELCOR and ASTEC
PAEC	DCMR(2.0)
XJTU	MIDAC

VVER1000 – Lower plenum
Leader : Aleksandr FILIPPOV (IBRAE)

Organization	*Code*
GRS	AC² (ATHLET-CD)
IBRAE	HEFEST_URAN package
INRNE	ASTEC
IVS	ASTEC
LEI	AC² (ATHLET-CD)

VVER1000 – Integral
Leader : Ivan MELNIKOV (NRC-KI)

Organization	*Code*
GRS	AC² (ATHLET-CD)
Gidropress	SOCRAT/B3 code
IVS	ASTEC
NRC-KI	SOCRAT/B1 code
SSTC NRS	MELCOR

VVER1000 - Mechanical FEA
Leader : Walter VILLANUEVA (KTH)

Organization	*Code*
CNPRI	ANSYS
GRS	ANSYS
IBRAE	HEFEST_URAN package
JRC	ABAQUS
KINS	ANSYS
KTH	ANSYS

Task 4 benchmark specifications

Generic PWR lower plenum:

- Cases 1 to 5 (H2020 IVMR benchmark): transient corium stratification → updated results and new codes
- Cases 6 to 8: consideration of molten pool formation in the lower plenum (solid debris, progressive relocation)

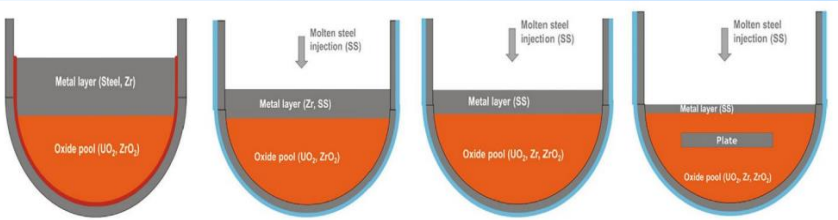

Cases n°1 and 2 | Case n°3 | Case n°4 | Case n°5

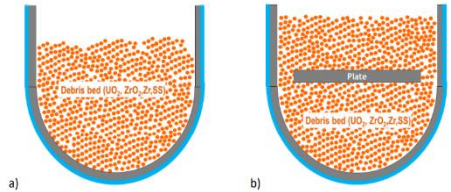

Case n°6 (a and b)

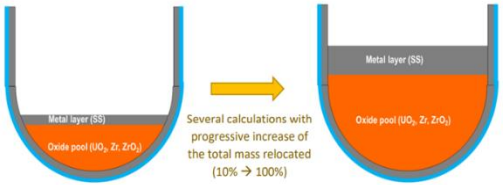

Case n°7

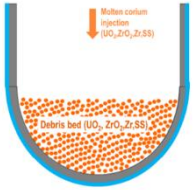

Case n°8

CAP1400 lower plenum:

- 1 steady state configuration with 2 corium layers
- 1 transient configuration with corium relocation in two steps and consideration of lower plenum structures: impact of massive steel structures

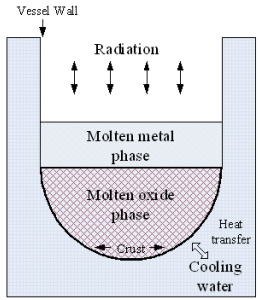

Case n°1

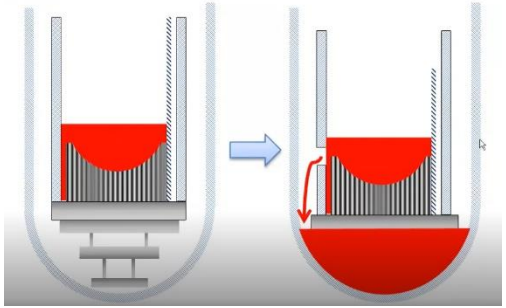

Case n°2

Task 4 benchmark specifications

- VVER1000 lower plenum:
  - Several stages with increasing complexities
  - Specific attention to melt arrival and lower plenum structures

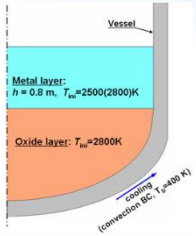

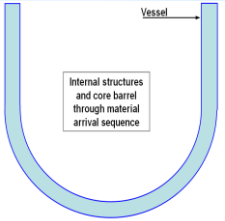

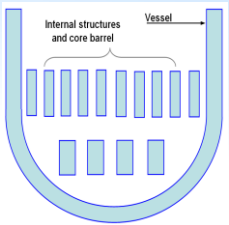

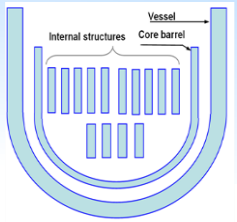

- VVER1000 integral:
  - Numerical simulation of LB LOCA DN300 on VVER-1000/B320

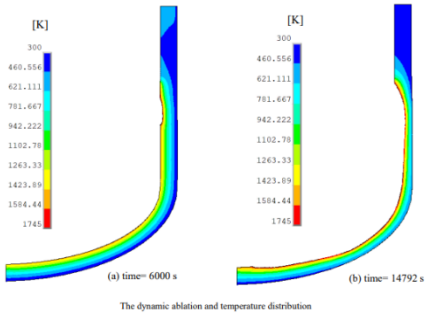

The dynamic ablation and temperature distribution

- VVER1000 mechanical resistance:
  - Transient boundary conditions from the integral calculation
  - Material properties and models

→ Exchanges between the three benchmarks for harmonization of boundary conditions

Task 4 activities

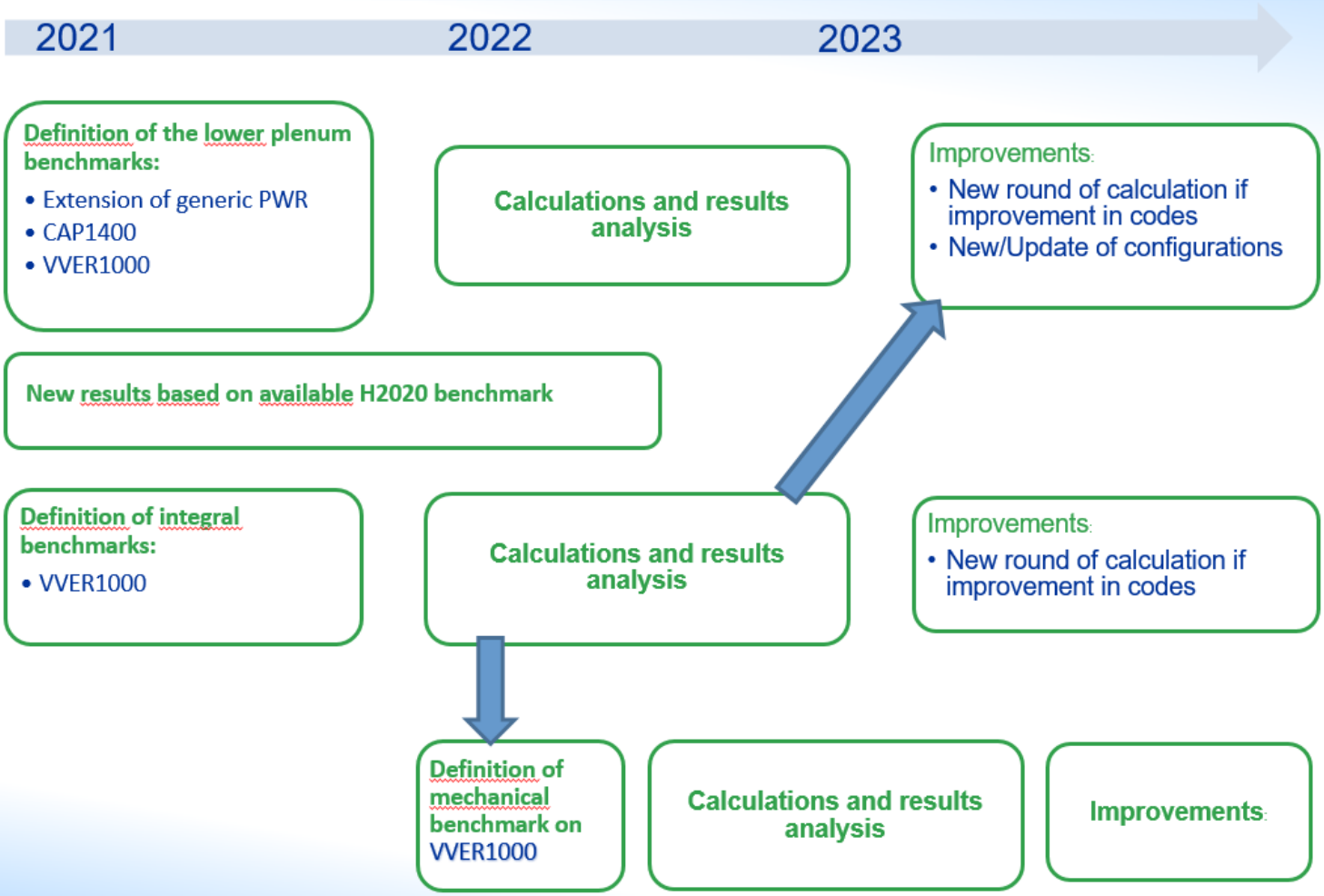

Conclusion

- The IAEA started the CRP in 2020 with 23 organizations from 14 IAEA Member States and 1 International Organization aiming at harmonizing the international understanding of the scientific and technological bases underpinning crucial parts of the safety demonstration of IVMR
- Progress in the 4 tasks will be discussed at the 2nd Research Coordination Meeting (RCM-2), planned for **7-11 November 2022 in Vienna**
- CRP outputs
  - 2024: publication of an IAEA TECDOC summarizing technical achievements
  - 2024-Q4: a final WS will be organized by the IAEA (participation open to all interested Member States), aiming at:
    - ❖ Sharing CRP achievements
    - ❖ Collect feedback & facilitate interactions with designers, licensees and regulators/TSOs with experience in IVMR
    - ❖ Evaluate the state-of-play and envisage possible future activities in the field

IAEA
International Atomic Energy Agency
Atoms for Peace and Development

Thank you!



IRON AND ZIRCONIUM OXIDATION AT LIQUID STATE UNDER AR-O_2 AND AR-H_2O GAS MIXTURES IN SEVERE ACCIDENT CONDITIONS

Sarah Thilliez, Pascal Piluso, and Jules Delacroix
CEA, DES, IRESNE, DTN, SMTA, LEAG.
Cadarache F-13108 Saint-Paul-Lez-Durance, France.
sarah.thilliez@cea.fr; pascal.piluso@cea.fr; jules.delacroix@cea.fr

Emmanuel de Bilbao and Jacques Poirier
CNRS, CEMHTI UPR3079
Univ. Orléans, F-45071 Orléans, France
emmanuel.debilbao@univ-orleans.fr; jacques.poirier@univ-orleans.fr

ABSTRACT

In case of severe accident in nuclear reactor, corium will be formed at high temperature and will be composed of nuclear fuel UO_2, Zircaloy -based zirconium- claddings, and the stainless steel of the surrounding structures.
Throughout the accident, the oxidizing gaseous atmosphere of steam water and dioxygen can interact with the corium. The oxidation phenomenon can influence the corium properties (i.e. liquid-solid transition, density, surface tension) thus impacting severe accident scenarios. There is a lack of knowledge (data and mechanisms) about the corium oxidation kinetics at liquid state because the available literature is often based on integral experiments, assuming specific scenario, with limited instrumentation.
For this purpose, several tests on the oxidation of liquid corium at high temperature have been conducted recently on the oxidation key phenomena on the VITI facility of the PLINIUS Severe Accident Platform at CEA Cadarache. The VITI facility allows to conduct tests at high temperature through induction heating and to measure the oxygen consumption by the sample all along the test with "on-line" oxygen gas analysis. A mass-spectrometer is also used to measure the amount of H_2 generated during the interaction between the sample and the steam all along the tests. In a first approach, the oxidation of the main corium components (i.e. Fe, Zr and U) at liquid state under oxygen and steam atmosphere are separately studied. Here, the focus is put on the oxidation of the iron and zirconium at liquid state by two gas mixtures: 95% mol.Ar-5% mol.O_2 and 90% mol.Ar-10% mol.H_2O. The liquid iron tests were conducted at 1893 K during 10, 15, 20 or 30 minutes. The liquid zirconium experiments were carried out at 2173 K during 1, 5, 10, 20 minutes. After the experiments in the VITI facility, post-test analysis of oxidized samples were carried out with Scanning Electron Microscopy (SEM) coupled with Energy Dispersive Spectroscopy (EDS). The metallographic analyses have showed the presence of metallic Fe and wüstite ($Fe_{1-x}O$) in the oxidized iron samples, and the presence of solid solutions Zr(O) and zirconia ZrO_2 in the oxidized zirconium samples. With the experimental data provided by the oxidation tests under Ar-O_2, oxidation kinetic models have been developed to describe the key mechanisms of iron and zirconium oxidation at liquid state and calculate the oxidation rate constants. The effect of the steam on the kinetics and mechanisms of oxidation of iron and zirconium at liquid state is also studied.

KEYWORDS
Severe Accident, steam oxidation, liquid state, iron, zirconium

1. INTRODUCTION

One key point for Severe Accident Management (SAM) strategies for LWRs (Generation 2, 3, 3+) is to preserve containment integrity in order to avoid release of fission products to the environment as it occurred at Chernobyl in 1986 and at Fukushima in 2011 [1]. The main mitigation tool to stop the severe accident progression in the reactor pressure vessel or in the reactor pit is the ability to cool the hot corium (T>2000 K) with water injection, meaning that there will be several possible configurations of interactions between hot materials, especially at liquid state, and steam/water mixture.

For the early in-vessel stages, previous studies have been mainly focused on interaction between degraded zircalloy and steam [2] and stainless steel (RPV internal structure) and steam [3], both at solid state. For the late in-vessel stages, corium is formed at high temperature (T>2000 K) at liquid state with variable iron and zirconium contents. In-Vessel Melt Retention (IVMR) strategy [4] implies stratification phenomena and a multi-layer corium configuration at liquid state, the lightest layer mainly composed of steel-zirconium alloy [5]. In this configuration, interaction between metallic alloy at liquid state and steam can last from a few minutes to a few tenth minutes. During corium re-localization at liquid state, Fuel Coolant Interaction (FCI) and Steam Explosion (SE) can occur in the vessel or in the reactor pit in case of vessel failure [6]. In this configuration, interaction between metallic alloy at liquid state and steam can last from a few milliseconds to a few seconds. Ex-Vessel Melt Retention (EVMR) implies Molten Corium Concrete Interaction (MCCI) with formation of metallic and oxide immiscible liquids and stratification [7]. Injection of water on the free surface promotes interaction between hot metallic melts and steam.

Whatever the severe accident configuration, interaction between steam and metallic alloys at liquid state will play an important role for severe accident mitigation whereas very few analytical studies have been devoted to this high domain of temperature, especially because high technological challenges. Furthermore, several phenomena will occur simultaneously at the interface between steam and metallic alloys: *oxidation, hydrogen production, solidification, liquefaction.*

In order to understand and to model these phenomena, several analytical experimental tests have been conducted at the VITI facility of the PLINIUS Severe Accident Platform at CEA Cadarache. Separate tests have been performed on iron and zirconium at liquid state with oxidizing gases: oxygen and steam. In this approach, oxidation kinetics at liquid state of iron and zirconium by oxygen and steam will be described. The effect of the steam on the kinetics and mechanisms of iron and zirconium will be discussed.

2. OXIDATION PHENOMENA OF METALLIC ALLOYS

2.1. Oxidation at solid state: stainless steel and zircalloy

Oxidation phenomena for metallic alloys under severe accident conditions have been mainly studied at solid state. We remind here briefly the main empirical laws used in the severe accident codes to model oxidation kinetics of solids, hydrogen production, the range of temperature (below melting point).

- *Zircalloy oxidation mechanisms*

Steam zircalloy oxidation mechanisms are following classical Arrhenius-type laws. Two temperature ranges have been distinguished for severe accident conditions [2]:

- Between 1500 K and 1800 K: *a «slow» process* of external oxidation of zircalloy. Below 1800 K, it is rather the Leistikov-Schanz law which is recommended to simulate the zircalloy oxidation and therefore the kinetics of hydrogen production [8].
- Above 1800 K: *a «fast» process* of external oxidation with a phenomenon of “thermal runaway” for oxidation of the zircalloy cladding with a parabolic law.

$$W = K_T \sqrt{t} \quad (1)$$

- ✓ W: weight gain (kg/m^2)
- ✓ t: time (s)
- ✓ K_T= parabolic constant (kg/m^2/s$^{0.5}$)

For this domain at high temperature, the laws proposed by the two authors do not evolve in the same way: they don't have the same parabolic constant Kt. Above 1800 K, it is rather Prater–Courtright law that is often used to simulate the oxidation of zircalloy cladding and thus the kinetics of hydrogen production in the current severe accident codes [2], but there are no justifications for the extrapolation till high temperature and above liquidus temperature of zircalloy alloy. Furthermore, the experimental conditions to control the steam flow are not so well described whereas they play an important role in the oxidation processes.

- *Stainless steel oxidation mechanism*

Stainless steel oxidation by steam can be described for T>1000 K following successive mechanisms:

- Formation of a Cr_2O_3protective layer : linear kinetic

$$W = K_L t \quad (2)$$

- ✓ W: weight gain (kg/m^2.)
- ✓ t: time (s)
- ✓ K_L= linear constant (kg/m^2/s$^{0.5}$)

- Breakaway of Cr_2O_3protective layer
- Formation of a non-protective layer based on iron oxides: parabolic kinetics (*i.e*. equation 1).

White [3] has proposed stainless steel oxidation kinetics laws in 1965. Again, experimental conditions (temperature measurement, steam injection) are not so well described and the extrapolation to higher temperature till liquidus temperature is not justified.

It has to be stressed that these laws are used in severe accident codes to describe the oxidation phenomena and the hydrogen production on the full range interesting the severe accident, i.e. from 1500 K till 3000 K, whereas these laws have been experimentally established at low temperature. For these reasons, it seems justified to study more specifically steam oxidation process at high temperature for metal phase at liquid state.

2.2. Oxidation at liquid state

Oxidation studies at liquid state need local approach in order to model reliably the key-mechanism, as it has been done in the past for stainless oxidation at low temperature (T<1000 K) under different gas and temperature conditions for metallurgical application. Another challenge concerns the identification of the slowest process, which will impose the full oxidation kinetics of the system. At last, it is important to take into account the evolution of the different interfaces during oxidation process: gas/liquid, gas/solid, liquid/liquid, liquid/solid.

Taking into account this approach [9], it is possible to describe on elementary mechanisms the oxidation process of a liquid metal by oxygen or steam (Fig. 1):

①: Transport of the oxidant gas (dioxygen or steam) till the free External Interface. To perform reliable experiments, qualification of starvation conditions will play an important role in order to have an "infinite" source of oxidation condition (no limiting mechanism).

②: Adsorption and dissociation of the oxidant gas (dioxygen or steam) on the free External Interface: $O_2+2s \rightarrow 2\ O\text{-}s$; $H_2O+1s \rightarrow H_2+O\text{-}s$ where s is a specific site.

③: Steam cracking: $H_2O \rightarrow H_2 + 0.5\ O_2$

④: Hydrogen release (steam conditions)

⑤: Oxidation reaction:

- External Interface: $xMe + y\ H_2O \rightarrow Me_xO_y + yH_2$
  $xMe + y\ O_2 \rightarrow Me_xO_y$
- Internal Interface: $xMe + y\ O_2 \rightarrow Me_xO_y$

⑥ Diffusion of O^{2-} or Me^{z+} through the oxide layer

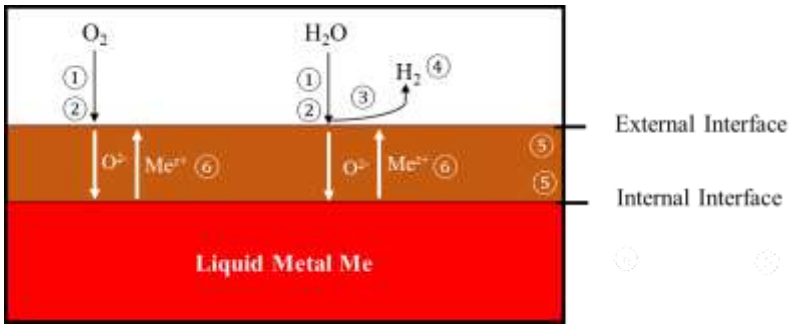

Figure 1. Oxidation mechanism of liquid metal alloys (brown: oxide layer (liquid or solid) and red: liquid metal).

The four first elementary mechanisms will not play a key role for the oxidation phenomena of a metal at liquid state. By the contrary, mechanism 5 will be very specific for this kind of configuration because the oxide formed phase can be a *solid or a liquid*. Mechanism 6 will have also a major impact on the kinetics oxidation process, stressing that in case of formation of a liquid oxide layer, other species such as Me_xO_y could be able also to diffuse in the layer. Thermophysical properties such as surface tension between oxide liquid/metallic liquid will play also an important role in these conditions. In order to separate the oxidation effects, *i.e. oxidation, hydrogen production, solidification, liquefaction*, two pure elements -iron and zirconium-, main corium constituents, have been chosen to be studied individually.

3. EXPERIENCES

3.1. VITOX experimental facility

The iron and zirconium oxidation experiments at liquid state have been carried out in the VITI facility located in the PLINIUS Severe Accident Platform at CEA Cadarache.

The VITI experimental facility is a furnace with an induction heating system that allows reaching high temperature till 3000 K. The VITOX (VITI-Oxidation) configuration has been especially develop in order to perform analytical oxidation experiments on iron and zirconium at liquid state with oxygen or steam

(Fig. 2). Components 1 to 4 represented on Figure 2 are ceramic refractory materials such as alumina (Al_2O_3) or stabilized zirconia (ZrO_2).

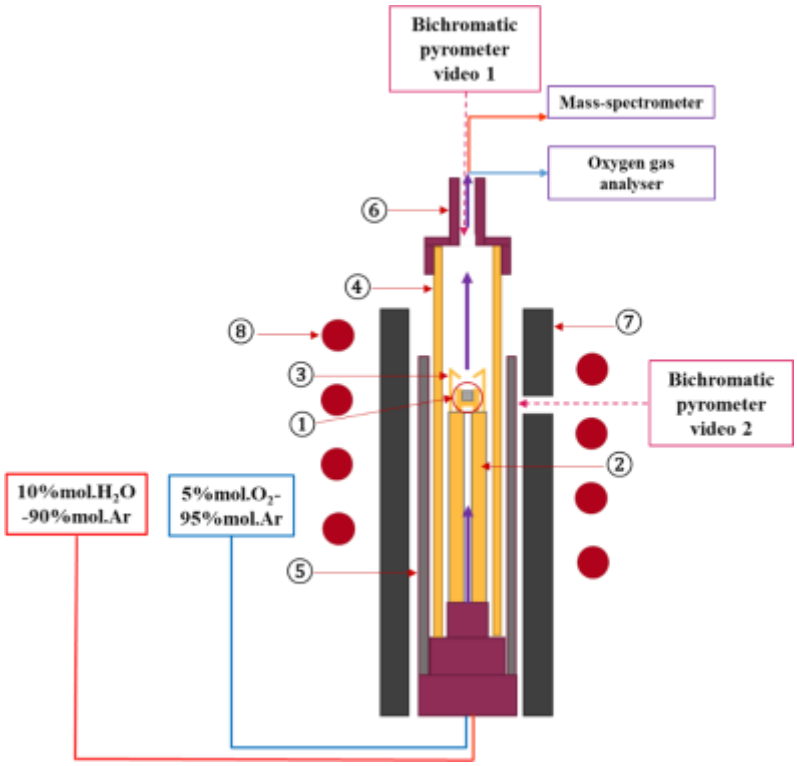

Figure 2. VITOX set-up: ① crucible and sample ② support ③ crucible lid ④ separating tube ⑤ susceptor ⑥ tube lid ⑦ thermal shield ⑧ inductor.

The oxidation tests are performed at high temperature by induction heating and coupling with a susceptor in tungsten. Two bichromatic pyrometers, *video 1 and 2*, measure respectively the surface temperature of the metallic sample and the tungsten susceptor during the experiment.
Two types of oxidant gases have been used to simulate Severe Accident Conditions: Ar-O_2 or an Ar-H_2O. Oxidant gases are injected in a separate canal. The Ar-O_2 oxidant gas is generated and controlled with two flow-meters connected to an oxygen and an argon tank.
For the oxidant Ar-H_2O gas mixture, a water flow and an argon flow are mixed together in a controlled evaporator mixer at 393 K. Then, the oxidant gases are injected in the separating tube of the VITOX set-up. A specific qualification of VITOX to ensure the value of the steam flow rate at the interface of the liquid metal has been performed.
The experiments with Ar-O_2 are carried out with an oximeter in order to measure the oxygen concentration all along the oxidation experiment.
For the oxidation tests with steam, a mass spectrometer is used to measure the dihydrogen release.

3.2. Experimental protocol

Before the temperature raise, the VITI facility is placed under vaccum by pumping and argon is injected at the end of the pumping in order to avoid any residual oxygen traces in the VITI tank. The temperature raise is carried out under argon atmosphere with a heating rate of 20 K/min. Experimental temperature has been chosen above the melting point of each element with a small overheating in order to ensure liquid state. When the experimental temperature is reached, a thermal plateau is applied in order to obtain isothermal stationary conditions. Then, the oxidant atmosphere Ar-H_2O or Ar-O_2 is supplied during the time oxidation plateau. At the end, the injection of the oxidant gaseous mixture is stopped and the cooling down is carried out under argon atmosphere with a cooling rate about 20 K/min.
Each sample is precisely weighted before oxidation (m_0) and after oxidation (m(t)) in order to measure weight gain during oxidation process. On-line measurement of oxygen consumption and hydrogen production can also give dynamic measurement and verification of the final weight gain. At last, Post-Test materials analyse can be performed in order to characterize the nature of the formed oxide phase.

The time evolution of the a metallic melt oxidation can be written as an oxidation rate α(t) (%) [11] defined by:

$$\alpha(t) = \frac{m_0 - m(t)}{m_0 - m_\infty} \quad (3)$$

- ✓ m_0: sample mass before the oxidation:
- ✓ m(t): sample mass after the oxidation
- ✓ m_∞: maximal sample mass experimentally determine(full oxidation: 100% oxide)

The α(t) parameter is really representative of the oxidation process because it takes into account the final real state of oxidation for given conditions (temperature, pressure, gas flow, nature of gas). In the next sections, the oxidation rate α(t) will be used as main parameter to follow oxidation process.

3.3. Experimental grid

In order to determine oxidation kinetics under Ar-O_2 and Ar-H_2O gas of iron and zirconium at liquid state mixture, several interaction time representative of severe accident conditions have been chosen.
Two oxidant gas compositions, 5%O_2-95%Ar and 10%H_2O-90% and a flow-rate of the oxidant gases of 2,6 Nl/min. have been chosen to avoid starvation regime.
The composition of the oxygen gas mixture allow monitoring closely the oxygen consumption by the sample with the oximeter and preventing the oxidant starvation state during the oxidation test.
To determine the impact of steam on the oxidation phenomena of iron and zirconium at liquid state, the same atomic oxygen rate as in oxygen experiments has been used.
For pure iron oxidation tests, the oxidation temperature plateau has been chosen at 1893K (overheating of 82K).
For pure zirconium oxidation tests, the oxidation temperature plateau has been chosen at 2173 K (overheating of 45 K).
The experimental grid of the oxidation tests for liquid iron or zirconium in presence of oxygen or steam are shown from Table I to Table IV.

Table I. Experimental grid for iron oxidation tests with steam.

	Sample mass (g)	Interaction time (s)
Fe-H_2O-t10	0,618	600
Fe-H_2O-t15	0,627	900
Fe-H_2O-t20	0,628	1200
Fe-H_2O-t30	0,625	1800
Fe-H_2O-t40	0,628	2400

Table II. Experimental grid for iron oxidation tests with oxygen.

	Sample mass (g)	Interaction time (s)
Fe-O_2-t1	0,626	60
Fe-O_2-t10	0,626	600
Fe-O_2-t15	0,616	900
Fe-O_2-t20	0,624	1200
Fe-O_2-t30	0,628	1800

Table III. Experimental grid for zirconium oxidation tests with steam.

	Sample mass (g)	Interaction time (s)
Zr-H2O-t1	0,872	60
Zr-H2O-t5	0,874	300
Zr-H2O-t10	0,875	600
Zr-H2O-t20	0,877	1200

Table IV. Experimental grid for zirconium oxidation tests with oxygen.

	Sample mass (g)	Interaction time (s)
Zr-O_2-t1	0,877	60
Zr-O_2-t5	0,872	300
Zr-O_2-t10	0,878	600
Zr-O_2-t15	0,871	900
Zr-O_2-t20	0,868	1200

4. Results and discussion

4.1. Iron oxidation

Experimental results on iron oxidation by oxygen and steam at 1893K are shown in Fig. 3. Iron oxidation mechanisms by oxygen or steam show same behaviour with a general *sigmoid curve* but with a shift on time for steam conditions.

In a first stage, a slow process of oxidation occur for both configuration with oxygen or steam.
In a second stage, a same acceleration of oxidation rate is observed but with a shift: for oxygen, the acceleration occurred at t=600 seconds whereas for steam acceleration occurred at t= 1000 seconds. The results will be a more rapid full oxidation in oxygen at t= 1000 seconds whereas the full oxidation is observed at t =1800 seconds for steam conditions.
For iron oxidation system, the formed first oxide on surface and then in volume is *liquid*, meaning that it is necessary to take into account different kind of interface in the oxidation phenomena modeling: gas/liquid (FeO_x) at external interface and liquid/liquid (FeO_x/Fe) at internal interface. This kind of configuration for oxidation is very specific: it is assumed that the surface tension between the two liquids (FeO_x/Fe) will play a major role for oxidation process.

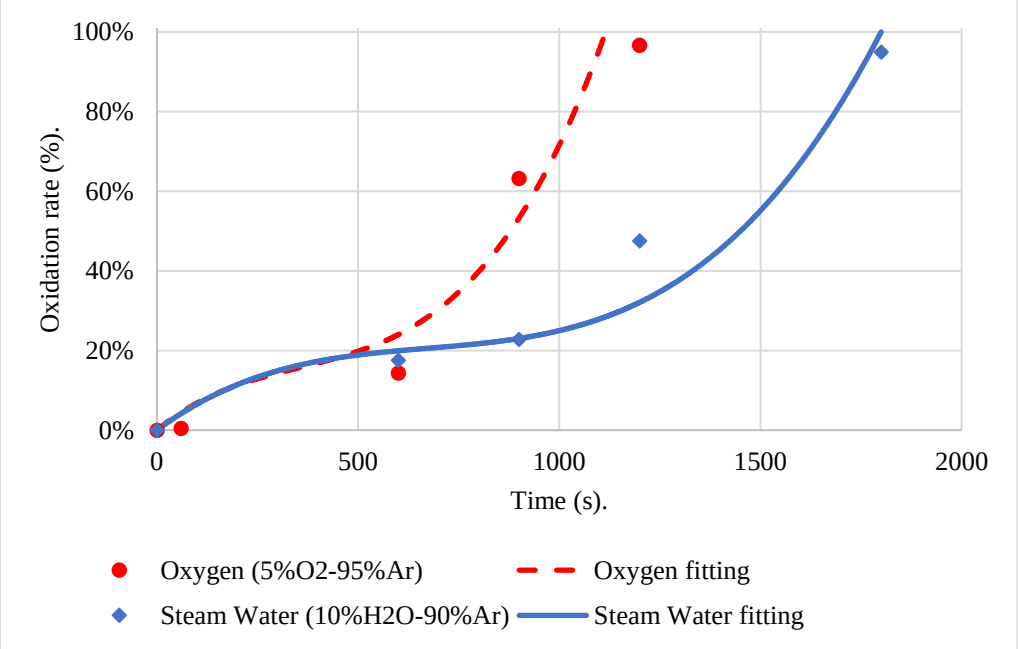

Figure 3. Oxidation rate for iron at liquid state (T=1893 K) under oxygen and steam.

Dynamic data make it possible to propose powers law to follow oxidation phenomena of iron at liquid state at 1600°C for oxygen (equation 4) and for steam (equation 5):

$$\alpha(t)=1{,}50\times10^{-9}t^3-1{,}61\times10^{-6}t^2+8{,}26\times10^{-4}t \quad (4)$$

$$\alpha(t)=4{,}70\times10^{-10}t^3-1{,}00\times10^{-6}t^2+8{,}20\times10^{-4}t \quad (5)$$

- ✓ t: time (s)

Dihydrogen release for iron-steam oxidation conditions can be also assessed assuming that the oxidation reaction at the external interface (see Fig. 1) is the main mechanism of hydrogen release. In addition, it is considered that one mole of reacted oxygen will produce, one mole of dihydrogen release.
Fig. 4 shows the evolution of dihydrogen production in mass per initial iron in mass.

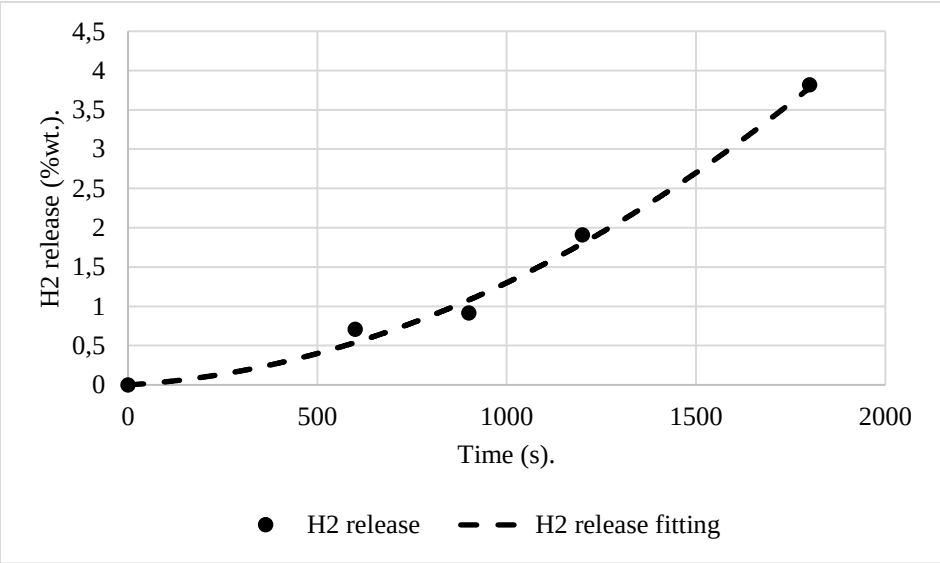

Figure 4. H_2 release for iron oxidation at liquid state (T=1893 K).

A dihydrogen production by steam oxidation at 1893K of iron is proposed in equation 6:

$$H_2(\%wt) = 1\times10^{-6}t^2 + 3\times10^{-4}t \quad (6)$$

4.2. Zirconium oxidation

Experimental results on zirconium oxidation by oxygen and steam at 2123 K are shown in Figure 5. zirconium oxidation mechanisms shows different behaviour under oxygen or steam conditions.

- For oxygen conditions, two stages are identified: in a first stage, a rapid linear process of oxidation occurred until 350 seconds. This process can be explained by interfacial reactions controlling the full process of oxidation. A second slower stage shows a parabolic behaviour from 350 seconds. For this second stage, it is well known that diffusion processes at solid state (Zr^{4+} or O^{2-}) will control the full process of oxidation trough the oxide layer.

- For steam conditions, only one stage is identified: a parabolic behaviour from the very beginning is observed, cancelling the rapid first stage observed under oxygen. It can be explained by the more rapid formation of an oxide layer having the ability to control by diffusion processes at solid state (Zr^{4+} or O^{2-}) the full process of oxidation (formation of vacancy)

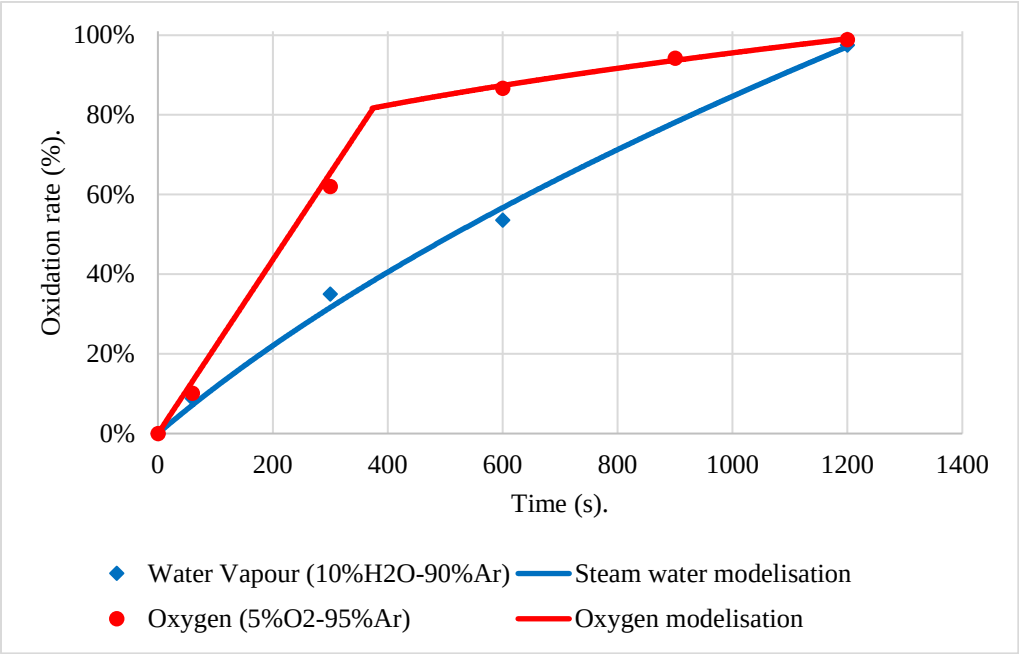

Figure 5. Oxidation for zirconium at liquid state (T=2173 K) under oxygen and steam.

Dynamic data make it possible to propose linear and parabolic laws to follow oxidation phenomena of zirconium at liquid state at 2173 K for oxygen (equation 7 and 8) [12] and for steam (equation 9):

$$\alpha(t) = 2{,}18\times10^{-3}t, \ [0\text{-}373\ s] \tag{7}$$

$$\alpha(t) = \sqrt{(t+128)\ 1{,}54\times10^{-4}} + 53{,}92 \ \ [373\text{-}1200\ s] \tag{8}$$

$$\alpha(t) = \sqrt{(t+373)\ 2{,}28\times10^{-3}} - 92{,}21 \tag{9}$$

The kinetic of dihydrogen release due to liquid zirconium oxidation has been also assessed applying the same method as those in the previous section (Fig.6).

$$H_2(\%wt.) = -1\times10^{-6}t^2 + 4{,}8\times10^{-3}t \tag{10}$$

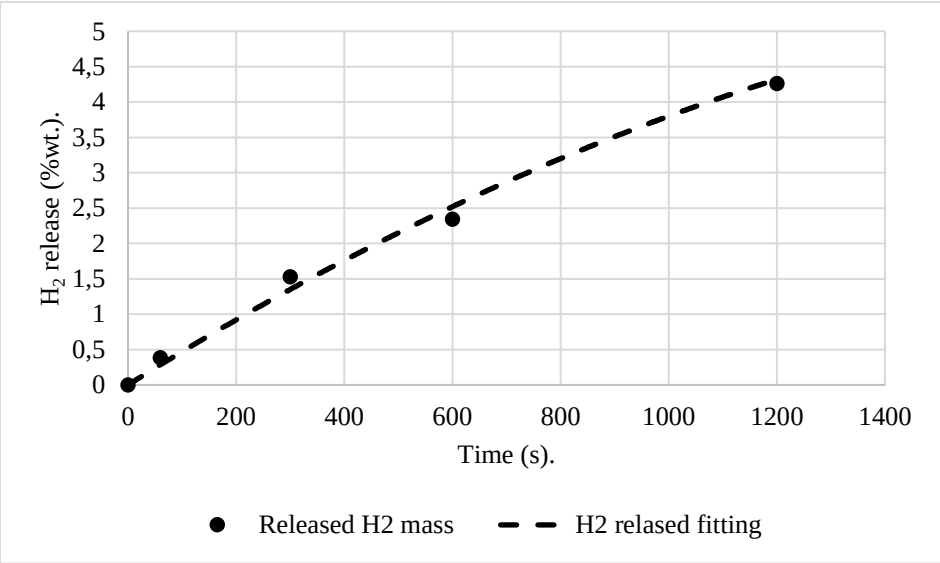

Figure 6. H_2 release for zirconium oxidation at liquid state (T=2173 K).

5. CONCLUSION

In the frame of severe accidents management for LWRs, an important mitigation tool concerns the ability to cool the corium and its constituents, mainly injecting water. Metallic mixture at liquid state, elements of the corium will be in contact with water during the full progression of the severe accident from a few milliseconds until a few tenth minutes. During this time delay, interaction at the interface between the metallic alloys at liquid state and the steam will occur, promoting important oxidation phenomena involving elementary mechanisms such as oxidation reaction, hydrogen production, solidification, liquefaction. Up to now, the studies have been mainly focused on solid state behavior of stainless steel and zircalloy cladding, representative of the early phase of the accident (T<1800 K), but not at higher temperature and for liquid state conditions.

This paper has shown the ability to perform studies on oxidation by oxygen and steam with separate effect tests in the VITI facility of the PLINIUS severe accidents platform. Two metallic elements, iron and zirconium, have been chosen, being main constituents of corium. Oxidation studies under oxidation and steam conditions, respectively at 1873 K and 2173 K, have shown specific behavior. For iron, a sigmoid behavior has been observed whereas for zirconium a linear, then parabolic behavior has been found. For both systems, it has been possible to establish oxidation and hydrogen production laws. These laws could be useful for severe accident codes. It is planned as perspectives to study steam oxidation at 2273 K of metallic mixture of zircaloy-stainless steel uranium.

REFERENCES

1. B. R. Sehgal et al., *Nuclear Safety in Light Water Reactors: Severe Accident Phenomenology*, p57, Elsevier, 225 Wyman Street, Waltham, MA 02451, USA, (2012).
2. G. Schanz, B. Adroguer, A. Volchek **;** 2004 ; "Advanced treatment of zircaloy cladding high-temperature oxidation in severe accident code calculations: Part I. Experimental database and basic modeling", *Nuclear Engineering and Design*, **vol 232**, (2004).
3. E. F. Juenke and J. F. White, "Physico-chemical studies of clad UO_2 under reactor accident conditions," General Electric Company, Report GEMP-731, (1970).

4. F. Fichot, L. Carénini, M. Sangiorgi, S. Hermsmeyer, A. Miassoedov, S. Bechta, J. Zdarek, D. Guenadou,," " Some considerations to improve the methodology to assess In-Vessel Retention strategy for high-power reactors" *Annals of Nuclear Energy*, **vol 119**, pp 36-45, (2018).
5. Almjashev V.I., Granovsky V.S., Khabensky V.B., Kotova S.Yu., Krushinov E.V., Sulatsky A.A., Vitola S.A. Gusarov V.V., Fichot F., Michel B., Piluso P., Le Tellier R., Fischer M., Le Guennic C., Bakouta N., "Experimental study of transient phenomena in the three-liquid oxidicmetallic corium pool", *Nuclear Engineering and Design* **332**, pp 31–37, (2018).
6. P. Piluso et al., "*Steam Explosion Resolution for Nuclear Applications*"-Phase 2, OECD/NEA-NEA/CSNI/R15 (2014).
7. M. Sanchez-Brusset, "*Mécanismes d'oxydation de l'acier liquide lors de l'Interaction Corium Béton à haute température en cas d'accident grave de réacteur nucléaire*", Ph-D thesis, Université de Perpignan Via Domitia, France, (2015).
8. K K Polunin, A A Urusov, S S Bazyuk, D S Kiselev and Yu A Kuzma-Kichta, "Study of High-Temperature Oxidation of the Claddings of Tolerant Fuel Elements of VVER-type Reactor", *Journal of Physics:* Conference Series **1370 012050** (2019).
9. J. Delacroix, P. Piluso, R. LeTellier, "Oxygen diffusion in liquid (over)stoichiometric corium", Nuclear Engineering and Design 337 148–160,149 (2018).
10. S. Glasstone and W.H. Jordan, *Nuclear Power and Its Environmental Effects*, pp. 50, American Nuclear Society, La Grange Park, Illinois, USA (1980).
11. A. Khawam and D. Flanagan, "Solid-State Kinetic Models: Basics and Mathematical Fundamentals," *The Journal of Physical Chemistry B*, **vol. 110**, n°135, pp. 17315-17328, 2006.
12. D. Monceau and B. Pieraggi, "Determination of Parabolic Rate Constants from a Local Analysis of Mass-Gain Curves," *Oxidation of Metals*, **vol. 50**, n°5-6, pp. 477-493, 1998.

IRON AND ZIRCONIUM OXIDATION AT LIQUID STATE UNDER Ar-O_2 AND Ar-H_2O GAS MIXTURES IN SEVERE ACCIDENT CONDITIONS

FROM RESEARCH TO INDUSTRY

ERMSAR-2022

Sarah Thilliez, Pascal Piluso, Jules Delacroix, Emmanuel de Bilbao and Jacques Poirier**

16/05/2022

IRESNE** | **DTN** | **SMTA** | **LEAG

Research Institute for Nuclear Systems for Low Carbon Energy Production

* CNRS, CEMHTI UPR3079, Univ. Orléans, F-45071 Orléans, France.

Outlines

- General laws of steam oxidation used for Severe Accident code applications
- Limitations of Zircalloy-4 and stainless steel (304L) steam oxidation kinetics laws at high temperature (solid state)
- Oxidation simple modelling at high temperature (liquid state)
- VITOX facility: an efficicient and reliable tool for steam oxidation studies
- Separate studies: iron oxidation at liquid state, zirconium oxidation at liquid state
- Conclusion

Document owned by the CEA - Reproduction and distribution outside the CEA subject to the issuer's authorization

Severe Accident and oxidation phenomena by water/steam

- ✓ In case of Severe Accident for a PWR, what ever the scenario, main mitigation tool:
  - **Water** (+steam) in order to cool and extract heat from corium at liquid state, multiphase (oxidic or metallic), multi-elements (U,Zr,Fe,Ni,O…)
- ✓ 2 main configurations for in or ex-vessel strategies using water:
  - Corium jet into water (1 and 3: **FCI/SE**)
  - Reflooding of corium (2 and 4: **Reflooding/MCCI/Spreading under water**)
- ✓ Coupling of phenomena involved during corium-water interaction (non-linear):
  - **Physico-chemistry**:
    - ➢ **Oxidation (mechanisms, kinetics)**
    - ➢ **Hydrogen production (mechanisms, kinetics)**
    - ➢ Water cracking
    - ➢ Solidification (crust/bulk)
  - **Thermal :**
    - ➢ Heat transfer from corium to the water/steam
    - ➢ Modification of gaseous interface : mixture $H_2/O_2/H_2O$

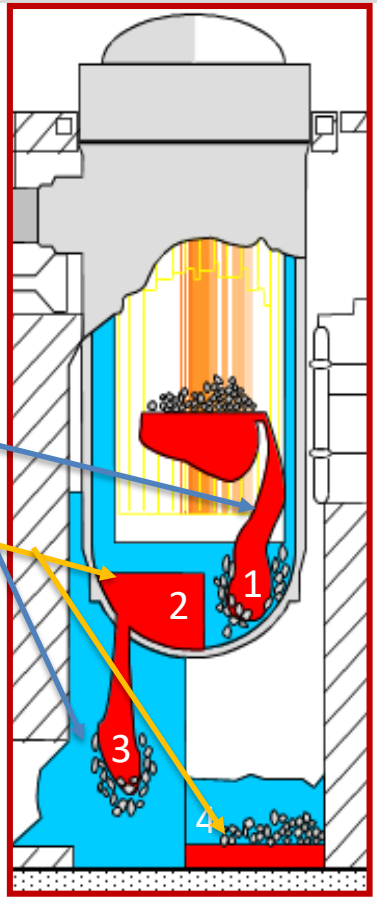

Document owned by the CEA - Reproduction and distribution outside the CEA subject to the issuer's authorization

General laws for oxidation phenomena : Severe Accident applications

✓ **Linear kinetics** : k_l : mg/(cm^2 s)

$$\frac{\Delta m}{S} = k_l . t$$

✓ **Parabolic kinetics:** k_p : mg^2 /(cm^4 s)

$$\left(\frac{\Delta m}{S}\right)^2 = k_p . t$$

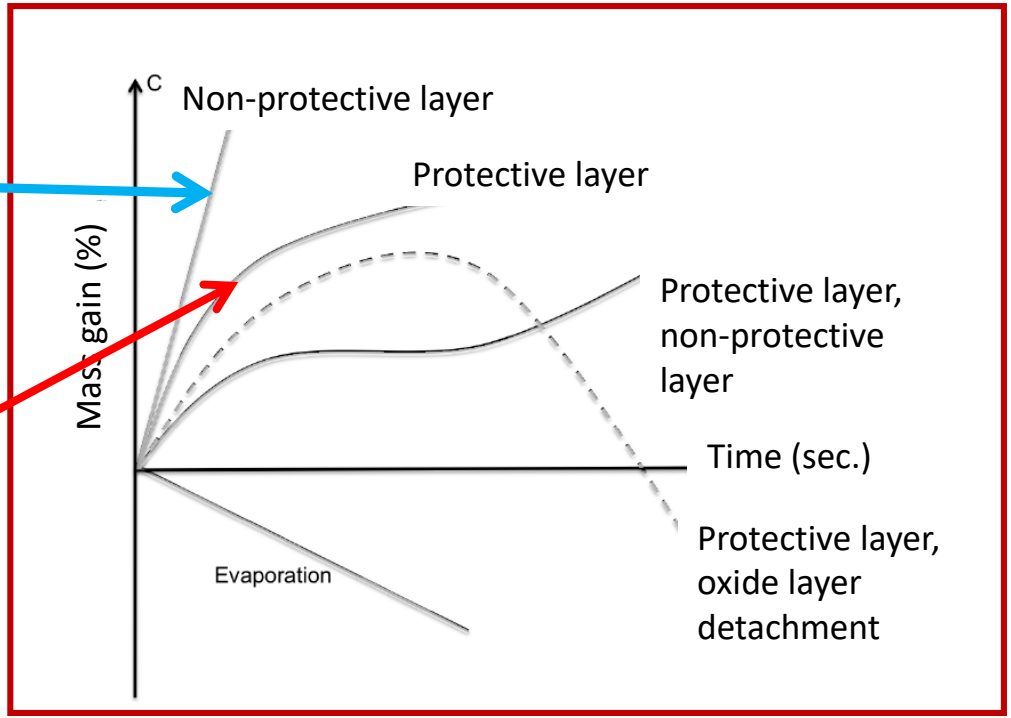

✓ **"Simplified" laws**

✓ **Usually, "normalization" to an initial surface, but the surface evolves continuously during oxidation process**

Document owned by the CEA - Reproduction and distribution outside the CEA subject to the issuer's authorization

Oxidation laws at solid state for zircalloy used in Severe Accident Codes*

- ✓ Few experimental points at high temperature between 1200°C and 1900°C (parabolic)
- ✓ Impact of elements of zircalloy alloys: Zircalloy-4, M5, other ?
- ✓ For steam studies: importance of calibration of the exact steam flow rate at the interface between the surface and the steam
- ✓ Temperature measurement and Post-test Analyses
- ✓ **Disagreement for extrapolation at high temperature (solid state)**
- ✓ **Only one experiment in 1987 above melting point with few information on tests results (liquid state)**
- ✓ **E-ATF (External Cr protective layer): key point to improve robustness to SA conditions****

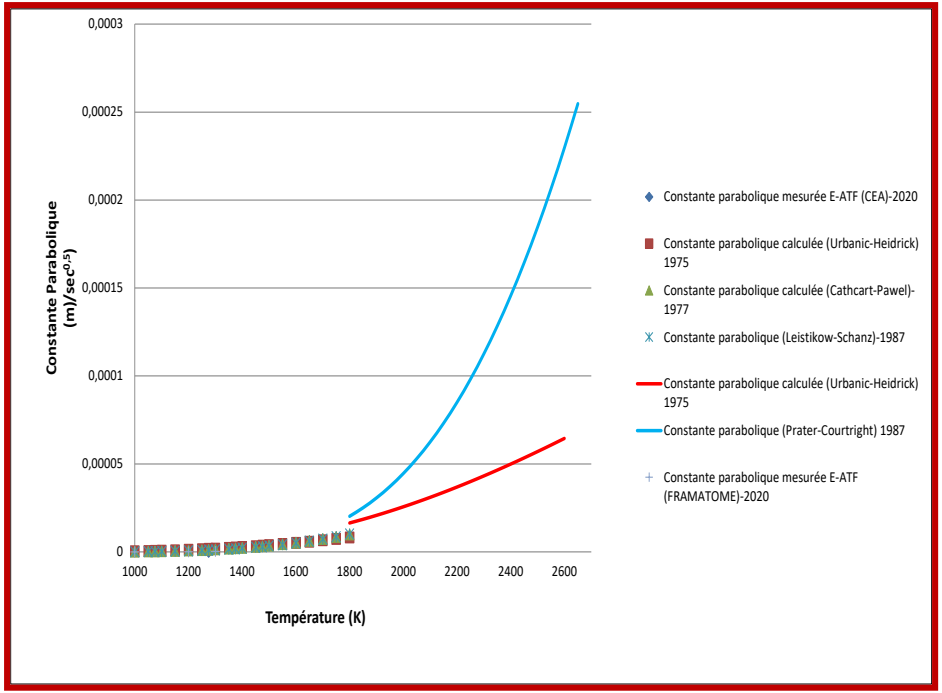

*: *G. Schanz, B. Adroguer, A. Volchek ; 2004 ; Advanced treatment of zircaloy cladding high-temperature oxidation in severe accident code calculations: Part I. Experimental database and basic modeling Nuclear Engineering and Design, 232* ***(2004)****.*

*: *J.-C. Brachet, et al., « High temperature steam oxidation of chromium-coated zirconium-based alloys: Kinetics and process », Corrosion Science 167 108537, (2020).*

Document owned by the CEA - Reproduction and distribution outside the CEA subject to the issuer's authorization

Oxidation laws at solid state for for Stainless Steel (304L) used in Severe Accident Codes*

- ✓ Few experimental points at high temperature below 1350°C (linear and parabolic)
- ✓ Impact of elements of stainless steel alloys: 304L, 316, austenitic
- ✓ For steam studies: importance of calibration of the exact steam flow rate at the interface between the surface and the steam
- ✓ Temperature measurement and Post-test Analyses :
  - $Fe_{0,94}O$
  - Fe_2O_3
  - Fe_3O_4
  - Spinel
- ✓ **Extrapolation at high temperature (solid state)**
- ✓ **No results above melting point (liquid state)**

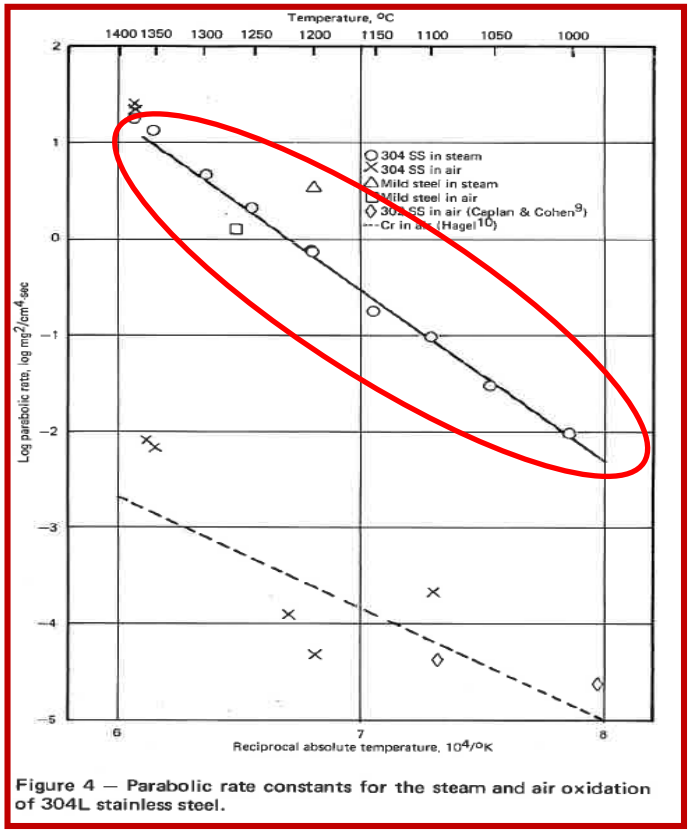

Figure 4 — Parabolic rate constants for the steam and air oxidation of 304L stainless steel.

*: J.T. Bittel, L.H. Sjodahl, J.F. White, Corros. NACE 125 **(1969) 7–14**.

Document owned by the CEA - Reproduction and distribution outside the CEA subject to the issuer's authorization

Key phenomena in oxidation process and dihydrogen production

✓ **6 steps for oxidation process and dihydrogen production at solid/liquid state**

① Steam or oxygen transport till metal (or oxide) liquid interface

② Steam or oxygen adsorption at the liquid interface

③ Dissociation of molecular oxygen or steam water

④ Di-hydrogen desorption

⑤ Oxidation reaction at internal or external interfaces

- $xMe_{(L)} + yO_{ad.} \rightarrow Me_xO_{y_{(L\ or\ S)}}$
- $xMe_{(L)} + yH_2O_{ad.} \rightarrow Me_xO_{y_{(L\ or\ S)}} + yH_{2_{(g)}}$

⑥ Oxygen diffusion through the oxide layer: O diffusion, Me diffusion

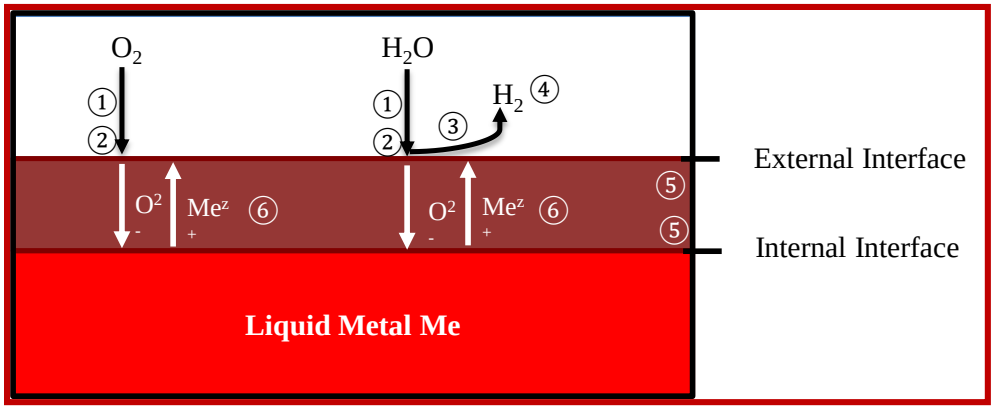

Document owned by the CEA - Reproduction and distribution outside the CEA subject to the issuer's authorization

VITOX – General experimental issues (1/2)

✓Principles

Induction Radiation

- Inductor Susceptor → ST + sample

=

indirect induction (T_{max}= 3000°C)

- **Severe accident conditions: HT + steam→ confinement & technological development (innovative ceramics)**
- On-line data: Video-Pyrometer (by the top)
- Spectrometer
- Oximeter
- Post-test analysis : cold trap (condensed water), SEM (µ-structure, composition gradients), EDS (oxidation front), EBSD (crystallography, stoichiometry)

➢ **Reliable measurements of oxidation and dihydrogen process at HT**

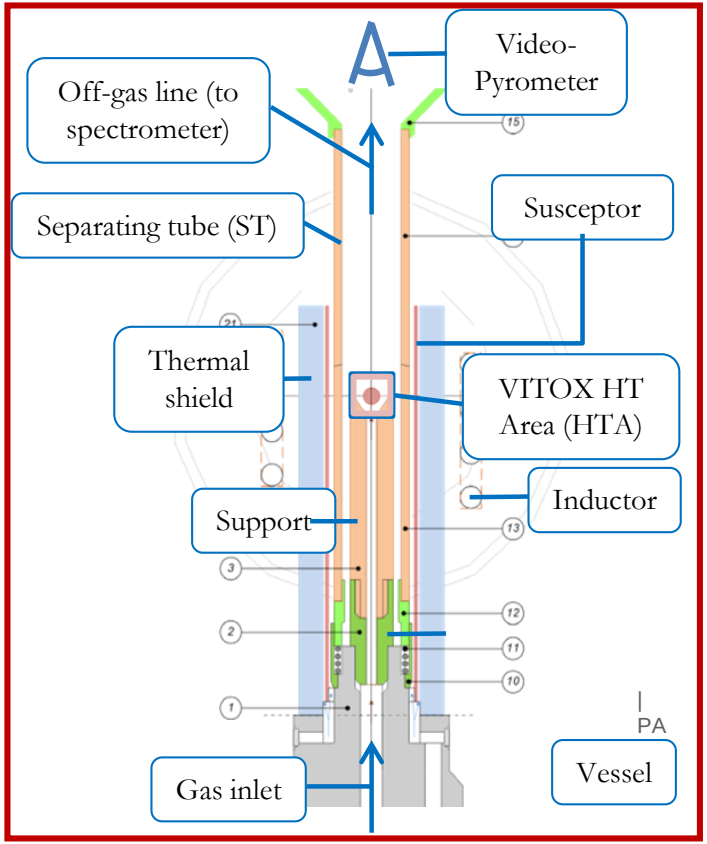

Schematic view of VITOX

Document owned by the CEA - Reproduction and distribution outside the CEA subject to the issuer's authorization

VITOX – General experimental issues (2/2)

- ✓ Gas circuit oxidation is governed both by oxidant supply to the interface ($\dot{m}_{H_2O}$, system-dependant)
- ✓ Controlled supply with CEM, overheated lines, Δp regulation, gas analysis.
- ✓ Mixture analysis with mass spectrometer→ $\dot{m}_i = \frac{M_i}{M_{Ar}} . \frac{C_i}{C_{Ar}} . \dot{m}_{Ar}$
- ✓ O_2 analysis with oximeter
- ✓ Cold traps for H_2O calibration and inventory

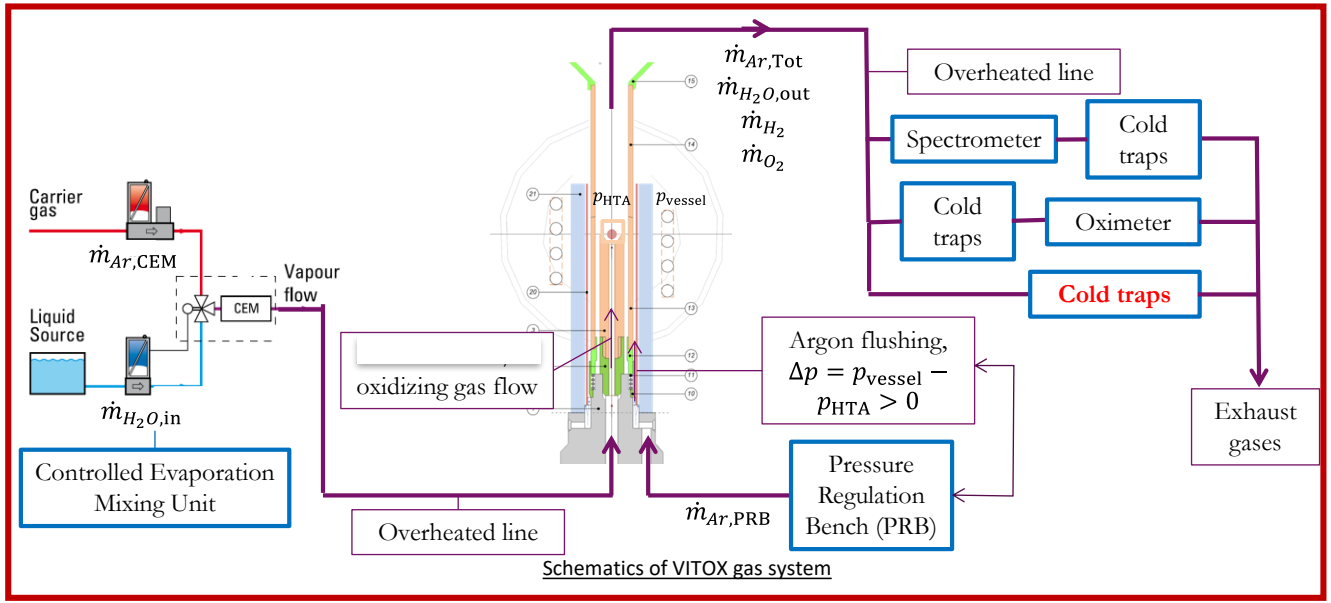

Schematics of VITOX gas system

Document owned by the CEA - Reproduction and distribution outside the CEA subject to the issuer's authorization

VITOX experimental protocol

✓ Oxidation rate α(t) (%)

$$\alpha(t) = \frac{m_0 - m(t)}{m_0 - m_\infty}$$

- m_0: sample mass before the oxidation:
- m(t): sample mass <u>after</u> the oxidation –time t
- m_∞: maximal sample mass (full oxidation: α(t) =100%)

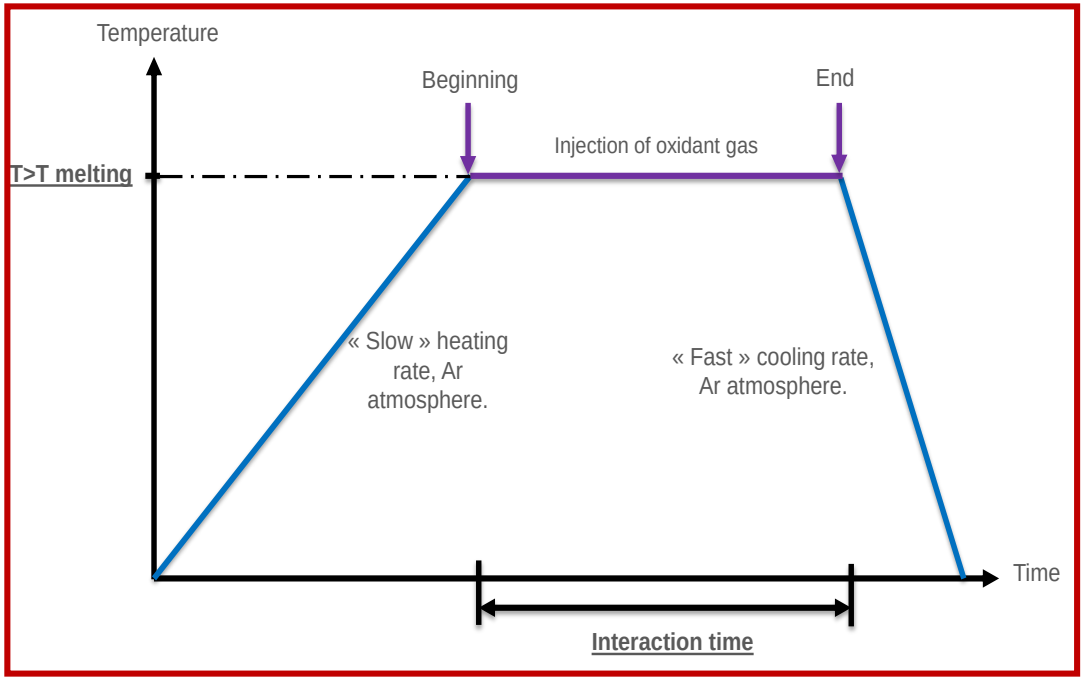

Document owned by the CEA - Reproduction and distribution outside the CEA subject to the issuer's authorization

Importance for steam flow rate control at the interface between oxidant gas and metallic surface (1/3)

Example of a “non-controlled” flow rate of oxidant gas on zirconium at liquid state: what should not be done !

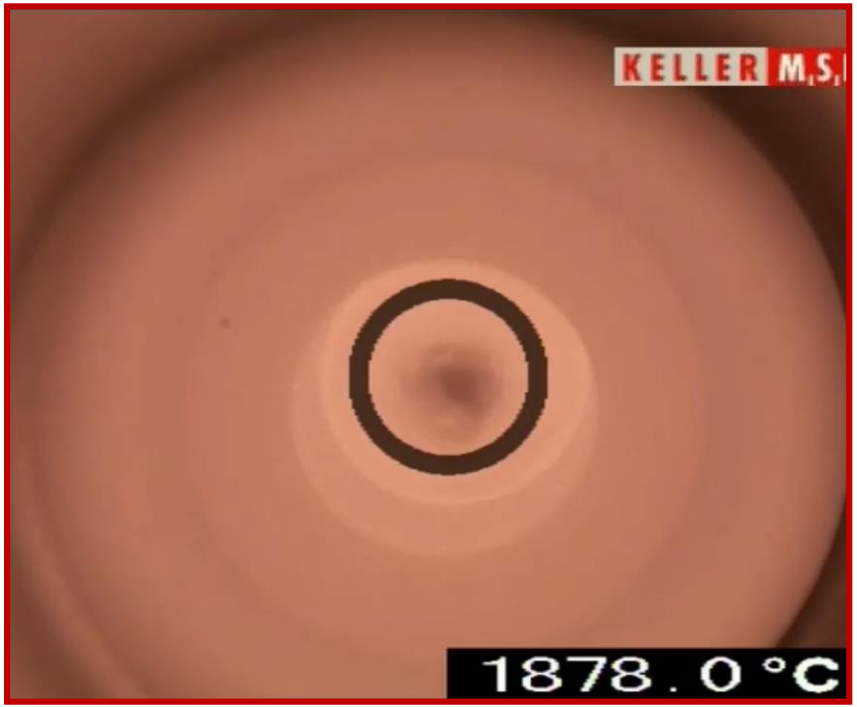

✓ **Importance of visual view of the interface to follow on-line process of oxidation**

Document owned by the CEA - Reproduction and distribution outside the CEA subject to the issuer's authorization

Importance for steam flow rate control at the interface between oxidant gas and metallic surface (2/3)

COMSOL modelling of oxidant speed gas , injection gas condition and geometry of test section

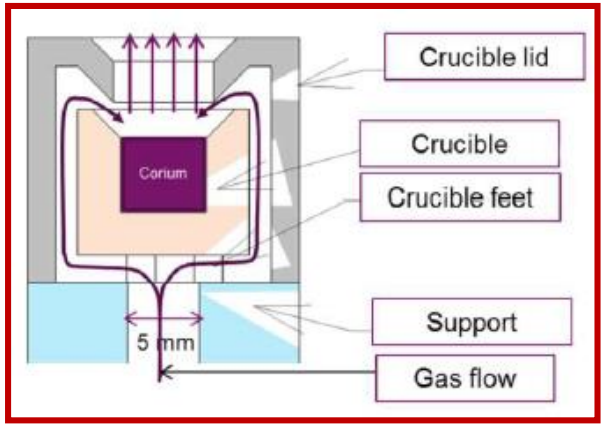

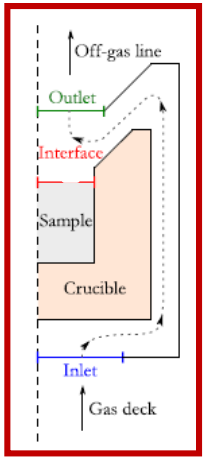

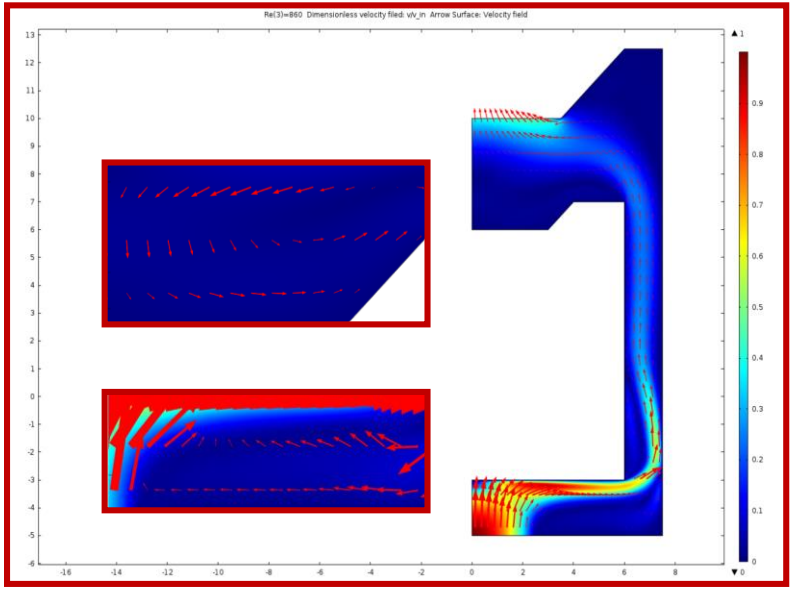

- ✓ **Design of tube/crucible/entrance oxidant gaz flow rate**
- ✓ **Exemple : 5%O_2-95%Ar and 10%H_2O-90%**

Document owned by the CEA - Reproduction and distribution outside the CEA subject to the issuer's authorization

Importance for steam flow rate control at the interface between oxidant gas and metallic surface (3/3)

Example of a controlled flow rate of oxidant gas on iron at liquid state: what should be done !

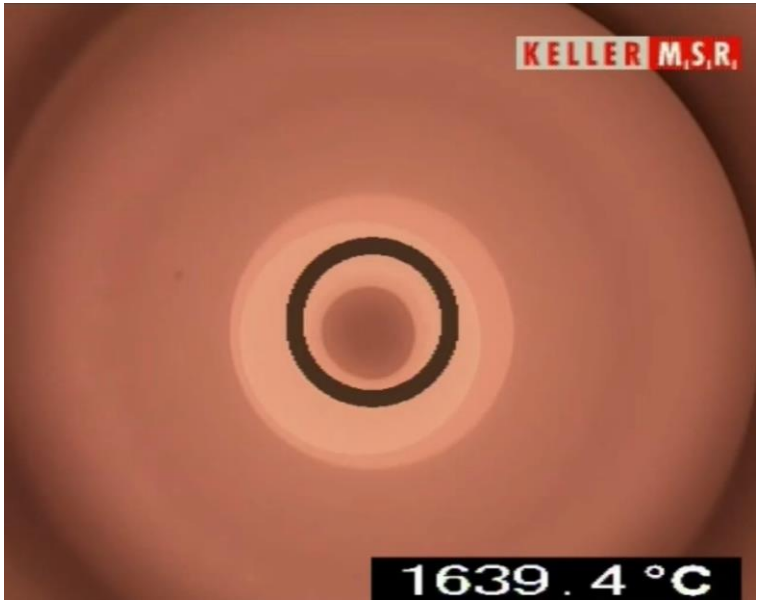

✓ **Even for iron oxidation, consequent exothermic release can be measured**

Document owned by the CEA - Reproduction and distribution outside the CEA subject to the issuer's authorization

VITOX experimental grid

- ✓ **Experimental grid for iron oxidation tests with steam and oxygen at 1620°C (+85°C/melting point)**
  - Exothermic heat release

	Sample mass (g)	Interaction time (s)
Fe-H_2O-t10	0,618	600
Fe-H_2O-t15	0,627	900
Fe-H_2O-t20	0,628	1200
Fe-H_2O-t30	0,625	1800
Fe-H_2O-t40	0,628	2400
	Sample mass (g)	**Interaction time (s)**
Fe-O_2-t1	0,626	60
Fe-O_2-t10	0,626	600
Fe-O_2-t15	0,616	900
Fe-O_2-t20	0,624	1200
Fe-O_2-t30	0,628	1800

- ✓ **Experimental grid for zirconium oxidation tests with steam and oxygen at 1900°C (+45°C/melting point)**
  - Exothermic heat release: : oxidized upper surface at **2024°C**

	Sample mass (g)	Interaction time (s)
Zr-H2O-t1	0,872	60
Zr-H2O-t5	0,874	300
Zr-H2O-t10	0,875	600
Zr-H2O-t20	0,877	1200
	Sample mass (g)	**Interaction time (s)**
Zr-O_2-t1	0,877	60
Zr-O_2-t5	0,872	300
Zr-O_2-t10	0,878	600
Zr-O_2-t15	0,871	900
Zr-O_2-t20	0,868	1200

Document owned by the CEA - Reproduction and distribution outside the CEA subject to the issuer's authorization

Oxidation of iron at liquid state (1/2)

- ✓ Oxidation of iron at liquid state is very specific (same phenomena for stainless steel): the formed oxide ($Fe_{0,94}O_x$) is **liquid below the melting point of iron !**
- ✓ System of oxidation is unique and has been never studied: **liquid oxide on liquid metal**
- ✓ **Necessity to develop new approach and modelling**
- ✓ **Direct impact on hydrogen release**

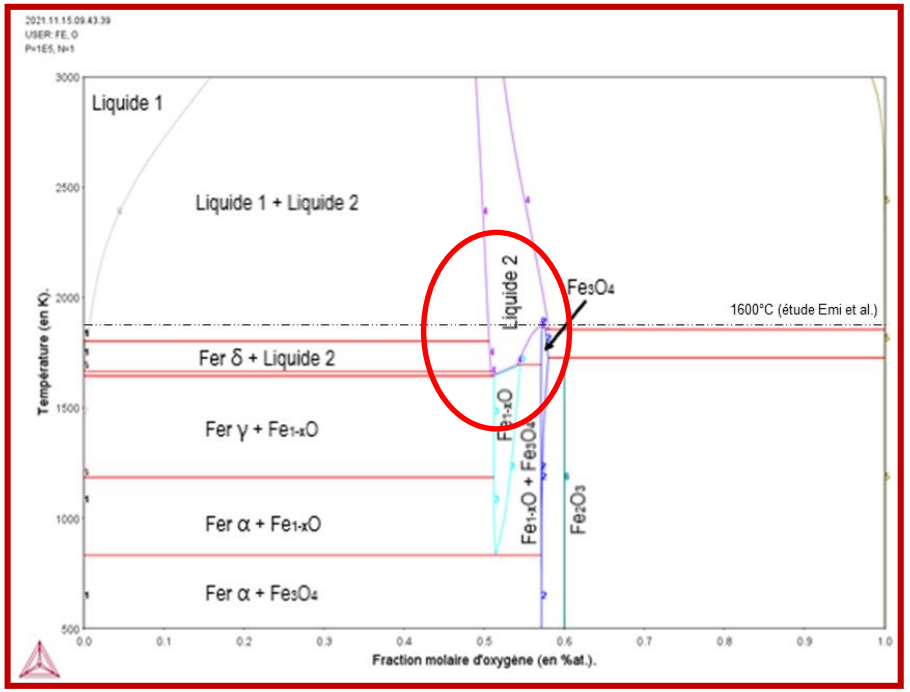

Document owned by the CEA - Reproduction and distribution outside the CEA subject to the issuer's authorization

Oxidation of iron at liquid state (2/2)

- ✓ Kinetics oxidation of iron: power law

$$\alpha(t)=1{,}50\times10^{-9}t^3-1{,}61\times10^{-6}t^2+8{,}26\times10^{-4}t \qquad \textit{oxygen}$$

$$\alpha(t)=4{,}70\times10^{-10}t^3-1{,}00\times10^{-6}t^2+8{,}20\times10^{-4}t \qquad \textit{steam}$$

- ✓ Oxidation phenomena are governed by exchanges at the interface between two liquids: one metallic, one oxidic, driving mode: surface tension
- ✓ Oxidation process is slower for steam than for oxygen
- ✓ **Hydrogen production** (one mole of reacted oxygen produce one mole of dihydrogen)

$$H_2(\%wt)=1\times10^{-6}t^2+3\times10^{-4}t$$

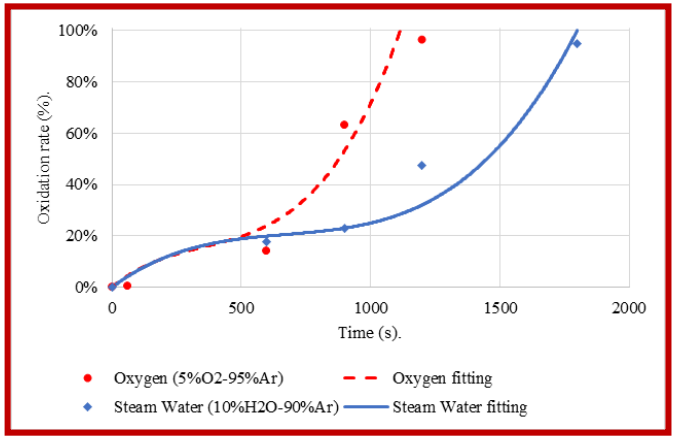

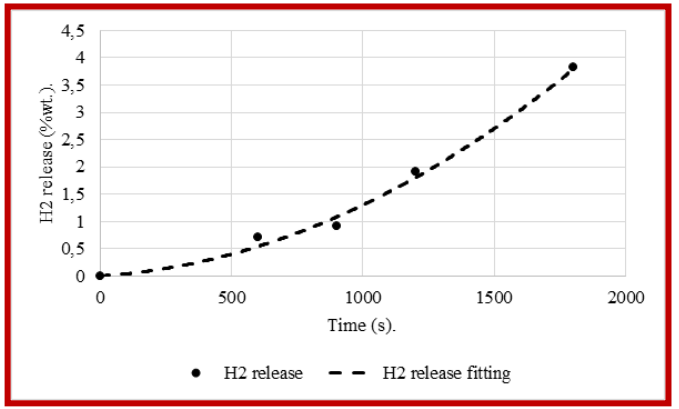

Document owned by the CEA - Reproduction and distribution outside the CEA subject to the issuer's authorization

Oxidation of zirconium at liquid state (1/2)

✓ For oxygen conditions, two stages

- in a first stage, **a rapid linear process** of oxidation occurred **until 350 seconds**. This process can be explained by interfacial reactions controlling the full process of oxidation
- a second stage, **a parabolic behaviour from 350** seconds. For this second stage, diffusion processes at solid state (Zr^{4+} or O^{2-}) will control the full process of oxidation trough the oxide layer.

✓ For steam conditions, only one stage

- a **parabolic behaviour** from the very beginning

Document owned by the CEA - Reproduction and distribution outside the CEA subject to the issuer's authorization

Oxidation of zirconium at liquid state (2/2)

- ✓ Kinetics oxidation of zirconium

$$\alpha(t) = 2{,}18\times10^{-3}t, \quad [0\text{-}373\ s] \qquad \textit{oxygen}$$

$$\alpha(t) = \sqrt{(t+128)\ 1{,}54\times10^{-4}} + 53{,}92 \quad [373\text{-}1200\ s]$$

$$\alpha(t) = \sqrt{(t+373)\ 2{,}28\times10^{-3}} - 92{,}21 \qquad \textit{steam}$$

- ✓ Formation of α Zr-O and ZrO_2
- ✓ Oxidation process is slower for steam than for oxygen
- ✓ **Hydrogen production** (one mole of reacted oxygen produce one mole of dihydrogen)

$$H_2(\%wt.) = -1\times10^{-6}t^2 + 4{,}8\times10^{-3}t$$

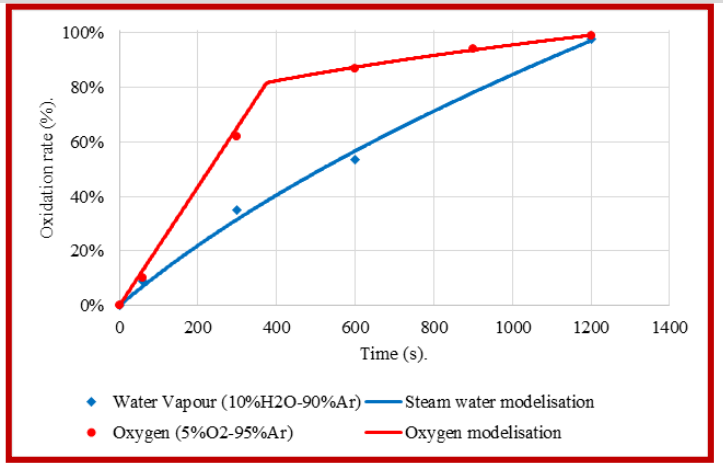

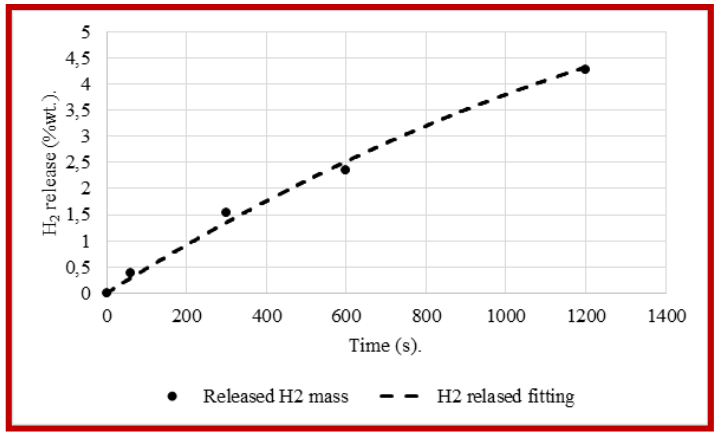

Document owned by the CEA - Reproduction and distribution outside the CEA subject to the issuer's authorization

Conclusion

- ✓ **Water cooling**: main mitigation tool for severe accidents management of PWRs
- ✓ For both in or ex-vessel configuration, metallic alloys zirconium or iron based
- ✓ Interaction between steam/water and hot metallic melts: from few seconds till few tenth minutes at reactor scale
- ✓ Oxidation phenomena with strong consequences: **heat release, hydrogen production**
- ✓ Kinetics will play an important role, but laws used by Severe Accident codes:
  - Range of temperature: not the full range till melting point
  - Reliability
- ✓ **VITOX:** a reliable and qualified facility to study steam oxidation till melting points of metallic alloys
- ✓ **New oxidation and hydrogen kinetics laws supported by mechanistic approach for iron and zirconium**
- ✓ **Perspectives: oxidation of metallic alloy representative of PWRs (stainless steel +zircalloy cladding+ uranium), for in-vessel melt retention and focusing effect application**

Document owned by the CEA - Reproduction and distribution outside the CEA subject to the issuer's authorization



FROM RESEARCH TO INDUSTRY

Thank you for your attention
Any questions ?

IRESNE I DTN I SMTA I LEAG

Research Institute for Nuclear Systems for Low Carbon Energy Production

Zirconium oxidation

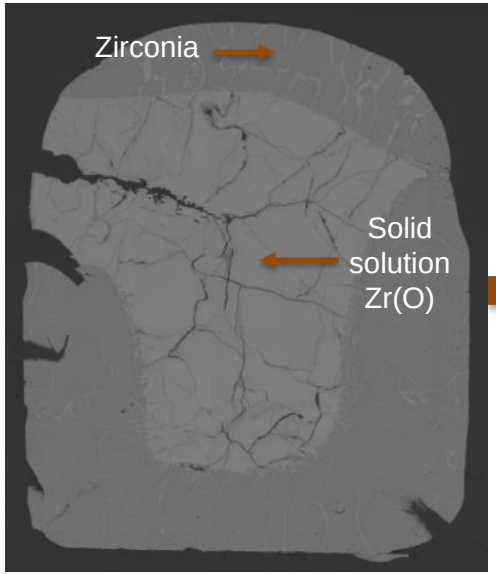

Zirconium sample oxidized 5 min.



Zirconium sample oxidized 10 min.



Zirconium sample oxidized 20 min.

- Surface oxidation then bulk oxidation
- Formation of a solid solution Zr(O) and ZrO_2

Document owned by the CEA - Reproduction and distribution outside the CEA subject to the issuer's authorization

Liquid iron oxidation

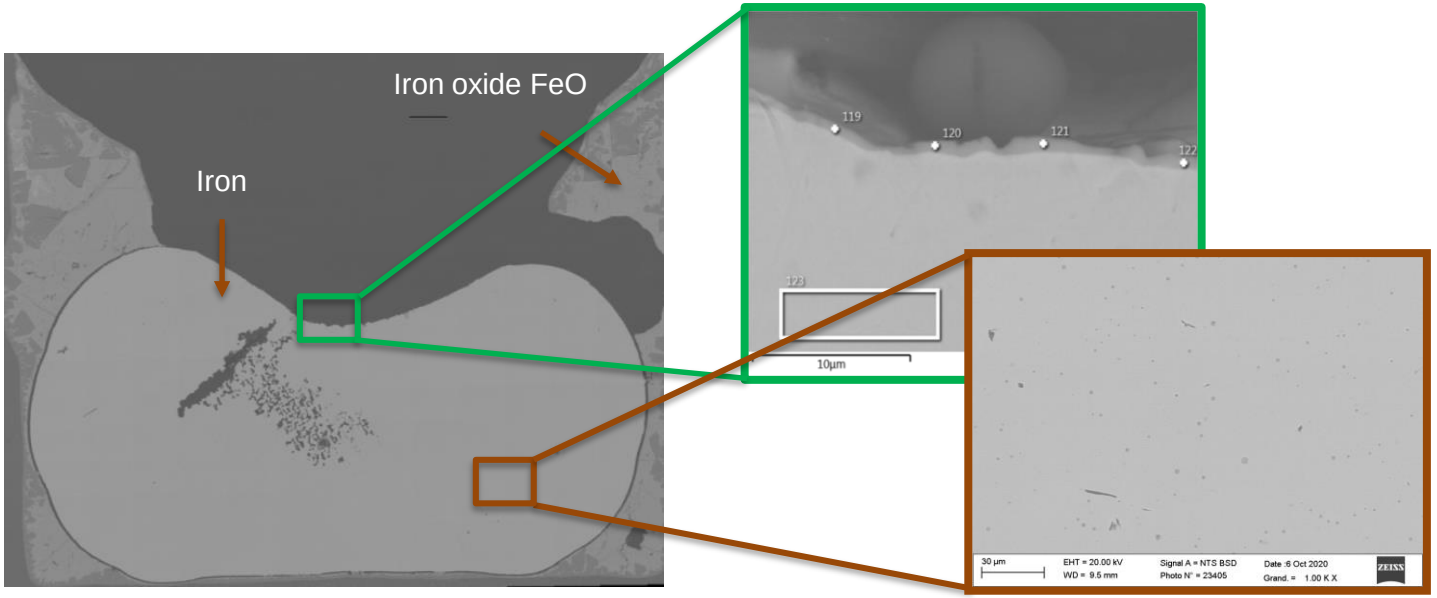

Iron sample oxidized
10 min.

- Surface and bulk oxidation.
- Formation of wustite.

Document owned by the CEA - Reproduction and distribution outside the CEA subject to the issuer's authorization

EXPERIMENTAL STUDY ON HEAT TRANSFER OF POST-DRYOUT DEBRIS/MELT MIXTURE IN THE LOWER HEAD OF REACTOR PRESSURE VESSEL

Xiaoyang Gaus-Liu
Karlsruhe Institute of Technology
Hermann-von-Helmholtz-Platz 1, 76344 Eggenstein
Xiaoyang.gaus-liu@kit.edu

ABSTRACT

The heat transfer of a post-dryout solid debris bed filled with molten melt in Light Water Reactor (LWR) lower head was experimentally studied in LIVE3D facility. The experiment simulated the transient stage between water-cooled debris and a fully developed molten pool during the late phase in-vessel accident. A series of test phases were carried out from the solid debris without melt, the solid debris with several melt fill stands and finally under the operation of external water cooling. The general heat transfer rate, the 2D temperature distributions and local heat flux on the vessel wall can be determined. The heat transfer indicates that heat conduction is the dominant heat transfer mechanism, which is different to the convective heat transport of a fully developed melt pool. The change of effective thermal conductivity in the local debris region is observed by varying the fill stand of molten melt, which leads to the migration of hotspot in the debris and the peak heat flux.

KEYWORDS
Heterogeneous debris, effective thermal conductivity, post dryout, In-vessel melt retention, LIVE3D

1. INTRODUCTION

The in-vessel retention strategy during the course of a core-meltdown severe accident in a Reactor Pressure Vessel (PRV) of LWR is to retain the molten/solid core material inside the lower head of the reactor by removing the decay heat in the core debris and therefore to depress the vessel thermal load under its designed value. The cooling concepts of the relocated core material could be e.g. flooding the vessel externally, or when possible, water injection inside the vessel, or spray cooling on the vessel outer surface for boiling water reactor (BWR). The external cooling is the mostly favorable concept for the pressure water reactor (PWR) which, however, is effective only if the heat transfer of the decay heat through a large area of the vessel wall. This is the case of cooling a fully developed melt pool with turbulent nature convection.

The progression of the late-phase accident inside the reactor vessel starts with the melt/debris relocation from core region to the lower head, fragmentation and solidification of liquid melt in residue water, dry-out of debris by evaporation of the residue water, melting of debris after dry-out, and finally the formation of a fully developed melt pool. Viewing this chain of process, the transition stage from the dry-out of debris till the formation of a whole melt pool becomes very critical caused by the low heat transfer efficiency inside the debris. Due to the poor thermal conductivity of solid debris, the temperature of the debris in the center region increases rapidly to the melting point, where the initial melting of debris begins. The high-temperature local melt, with no efficient thermal conduction to its surrounding downwards and upward, can expand its

way toward the vessel wall, results a local heat flux, which could beyond the critical heat flux of the external cooling medium.

The heat transport inside the debris is a series of transient under the continuous change in debris configuration. The particulate debris in the lower head is initially non-uniform in composition, which is a result of the accident development before and during the relocation [1, 2]. When melt is released from the core, it interacts with the residual water in the lower head. The intensity of the interaction and the resulting configuration of corium debris depends on several parameters. There are mainly the height of the residual water level, the conditions of the melt (superheat, composition) and especially the mode of the melt relocation from the core to the lower head. One very possible scenario is that the melt is released from the molten pool in the core through breaches in the supporting crust, it will enter the lower head in the form of one or several melt jets with typically 5-10 cm diameter. The small stream of jet facilitate the fragmentation of melt and leads to the formation of particulate debris composed of a mixture of oxide fuel fragment and partially oxidized metallic particles. With a still high decay power in the debris, dryout region in debris appears even before the residue water is completely evaporated. Depending on the particle size and the form of the debris bed, the dryout heat flux is up from 200 kW/m² [3, 4]. Without effective water cooling, the temperature in dryout region increases rapidly and the onset of melting of low-temperature components occurs consequently. The liquid melt fills in the pores among still solid particles and leads to a higher thermal conductivity in the debris/melt region than in the debris/gas region. This process is accompanied by the simultaneous shrinkage of the debris bed volume and change of the debris bed form. Another realistic scenario is that the subsequent relocation of liquid melt from the core area during the dryout period. Depending on the mass of low-melt-point component in debris, and the occurrence of the subsequent melt relocation, the post-dryout debris bed endures a long period of the coexistence of dry and molten regimes, where the boundary between the two regions continuously changes. The heat conduction is considered to be the main heat transport mechanism in the porous medium due to the minor contribution of radiation and convective [5]. However, the heat conductivity keeps changing in the debris bed, this arises a keen interest on the view of its heat flux on the vessel wall.

Since the uncertainties in debris bed composition and the ever-changing configuration during the post-dryout stage, few theoretical and experimental studies have been performed. The lack of exiting knowledge on this topic is especially apparent comparing to the large database on the heat transfer of water cooled debris and of a fully developed melt pool.

Several single-effect post-dryout experiments have been carried out in the LIVE3D facility at Karlsruhe Institute of Technology, exploring the heat transfer characteristics of different debris configurations. LIVE- L8A and L8B experiments address the melt pool progression after subsequent melt pour in a solid debris bed with homogeneous debris composition [6]. LIVE-L8C test describes the deformation of a two-component debris bed during the meltdown of the low-melting component and the critical high heat flux on the vessel wall. LIVE-BWR experiment studies the transient debris heat-up of a high power debris bed with and without the influence of cooling of the in-vessel penetration tubes [7], and LIVE-J1 test mimics debris meltdown process of the FUKISHIMA-DAICHI Unit 2 during the accident [8]. This paper presents the result of LIVE-L8D test, which stresses the heat transport of a co-existing solid-liquid and solid-gas regimes with varying melt levels and the effect of the external cooling. The experiment highlights the main heat transfer process. The results can be validated by CFD programs with the aim of the extended applicability for prototypical debris material.

2. LIVE 3D FACILITY

The LIVE3D test facility consists of a hemispherical test vessel with external and top cooling system, a volumetric heating system and a separate heating furnace for the preparation of liquid simulant melt, Figure 1. The inner diameter of the test vessel is 1 m. The material of the test vessel is stainless steel and the wall thickness is ~25 cm. The test vessel is enclosed by a cooling vessel to enable external cooling. The cooling water flows in at the bottom and flows out through one outlet at the top of the cooling vessel. The flow rate of the external cooling water and its inlet and outlet temperatures were measured.

The decay heat of the core melt is simulated by 8 horizontally-oriented electrical heating coils. Their power inputs can be controlled individually to generate the power homogenously in the melt pool. The maximum homogeneous heat generation is 29 kW. The liquid melt for the subsequent melt pour was prepared in the external heating furnace, which can tilt and pour the liquid melt into the test vessel via a heated pouring spout either centrally or near the vessel wall.

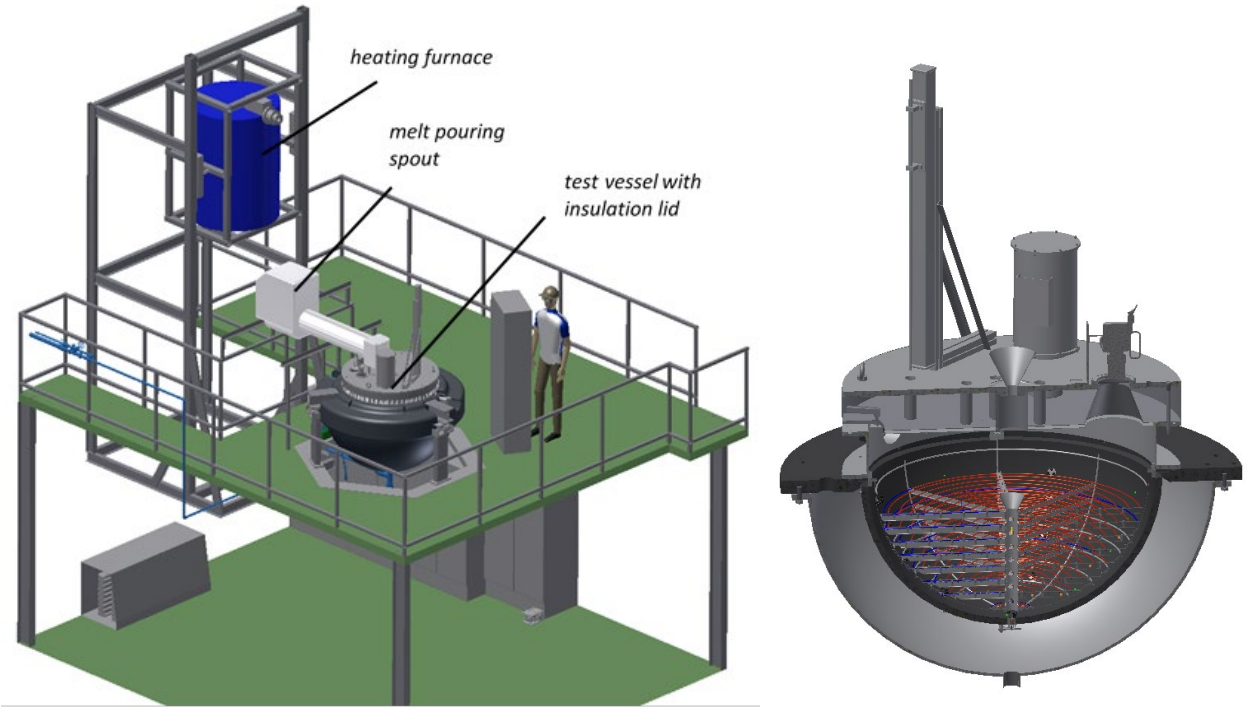

Figure 1. Right: Sketch of LIVE3D test facility system; left: LIVE3D test vessel with the upper insulation and external cooling vessel.

The LIVE3D test vessel is equipped with a multitude of T-type thermocouples. 3D melt temperature distribution and 3D heat flux distribution can be determined with 80 thermocouples (MTs) in the bulk melt, 26 pairs of thermocouples at the inner (ITs) and outer (OTs) surface of the test vessel wall and 7 arrays of thermocouples (CTs) perpendicular to the wall in the pool boundary area, as shown in Figure 2. With the help of the thermocouples in the bulk and the boundary regions, a rough 2D temperature distribution of debris bed can be generated. Also the heat flux through the vessel wall can be determined upon the IT-OT temperature difference on the vessel wall. In case of external cooling, the heat removal rate of cooling water can be determined by the flow rate and inlet-outlet temperature difference.

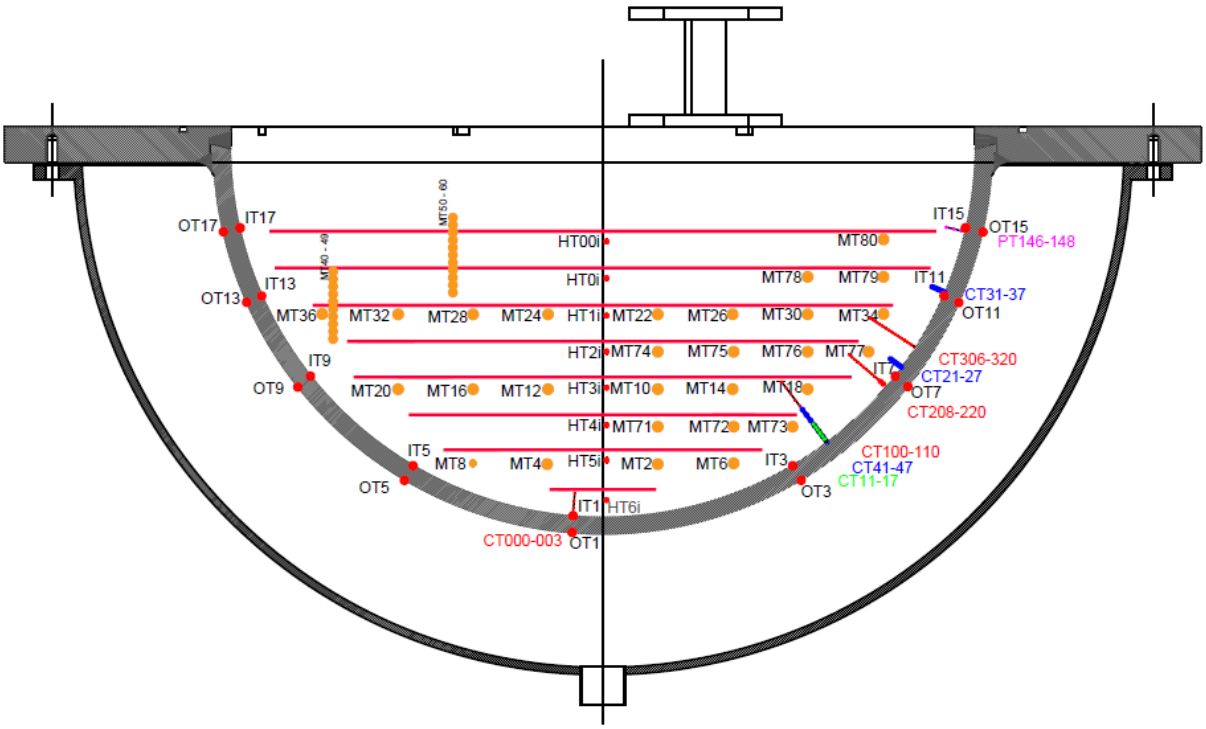

Figure 2. 2D sketch of thermocouple positions.

The simulant of debris bed is sintered ZrO_2 - SiO_2 spherical particles with diameter of 2.5 to 2.8 mm bearing the commercial name "RIMAX". The composition of the patrticle is 58 wt.% ZrO_2, 37 wt.% SiO_2 and 5 % other oxides. Its density is 4000 kg/m^3. The bulk density is 2400 kg/m^3 and the porosity of the debris bed is 0.4. The temperature-stable particles remain their solid state and properties during all test phases. More physical properties at different temperatures delivered from the producer are presented in Table I. The liquid melt simulant is a binary nitrate non-eutectic composed of 80 mol. % KNO_3 - 20 mol. % $NaNO_3$. The properties are given in Table 2. The value or equations in Table 2 are derived from the data given in [9].

Table I. Thermal physical properties of pure substance of RIMAX

Debris: (RIMAX)	**25 °C**	**250 °C**	**500 °C**
Thermal diffusivity, [mm^2/s]	2.9	1.9	1.4
Heat capacity, [J/gK]	0.74	1.01	1.28
Thermal conductivity, [W/(mK)]	8.8	7.7	7.2

Table II. Thermal physical properties of nitrate melt [9]

Melt: 80% KNO_3- 20 % $NaNO_3$	Value or f(T)
Density, [10³ · kg/m³]	$2.2992 - 7.0038 \cdot 10^{-4} \cdot T(K)$
Thermal expansion coefficient, [1/K]	3.81×10^{-4}
Thermal conductivity, [W/(mK)]	0.439 at 573 K
Dynamic viscosity, [mPa·S]	$0.074755 \cdot e^{17878 / RT}$
Kinetic viscosity, [m²/s]	$1.75 \cdot 10^{-6}$ at 573 K, $1.07 \cdot 10^{-6}$ at 673 K
Thermal diffusivity, [m²/s]	$1.69 \cdot 10^{-7}$
Prandtl number, -	7
Liquidus temperature, [K]	558
Solidus temperature, [K]	497

3. PERFORMANCE

The whole test starts with the volumetric heating of a preload debris bed in 303 mm height. A top insulation lid was mounted on the top of the vessel, resulting a hot gas layer above the debris bed. The whole test can be divided in 6 phases. Each phase reached its steady state before the next phases began. The duration of the phases and the performance are given in Table 3 and were illustrated in Figure 3. During the first four phases, three melt pools were performed subsequently after a preheating phase of debris. The melt level after the 1st, the 2nd and the 3rd pours were 260 mm, 363 mm and 453 mm respectively. Without external cooling in the first four phases, the internal heating rate was limited to low level to avoid the overheat of debris/melt (< 400 °C). During the Phase 5 and the Phase 6, external cooling with water flow rate of 150 ml/s was in operation, and thus considerable higher power level could be realized. In Phase 5 only the 6 lower heating planes were in operation which generated a heated zone between 0- 303 mm height, whereas in Phase 6 the volumetric heating of the whole 453 mm height pool was realized by the 8 heating planes.

Table III. Heating phases in L8D test

Phase	duration	action	Liquid melt pool height, mm	Total heating power,	External cooling
Phase 1	0 - 265890s	preheating	0	1.4kW	no
Phase 2	265891-348142s	1.Melt pour	260	2kW: 265891-278134s 3KW: 278135-348142	no
Phase 3	348143-433901s	2. Melt pour	363	3kW: 348143-363649s 4kW: 363650-433901	no
Phase 4	433902-520347s	3. Melt pour	453	4kW	no
Phase 5	520348-604829s	External cooling begin	453	18kW heating zone 0-303 mm height in pool height,	yes
Phase 6	604830-626398s	Change of power distribution	453	18 kW, heating zone: whole pool height.	yes

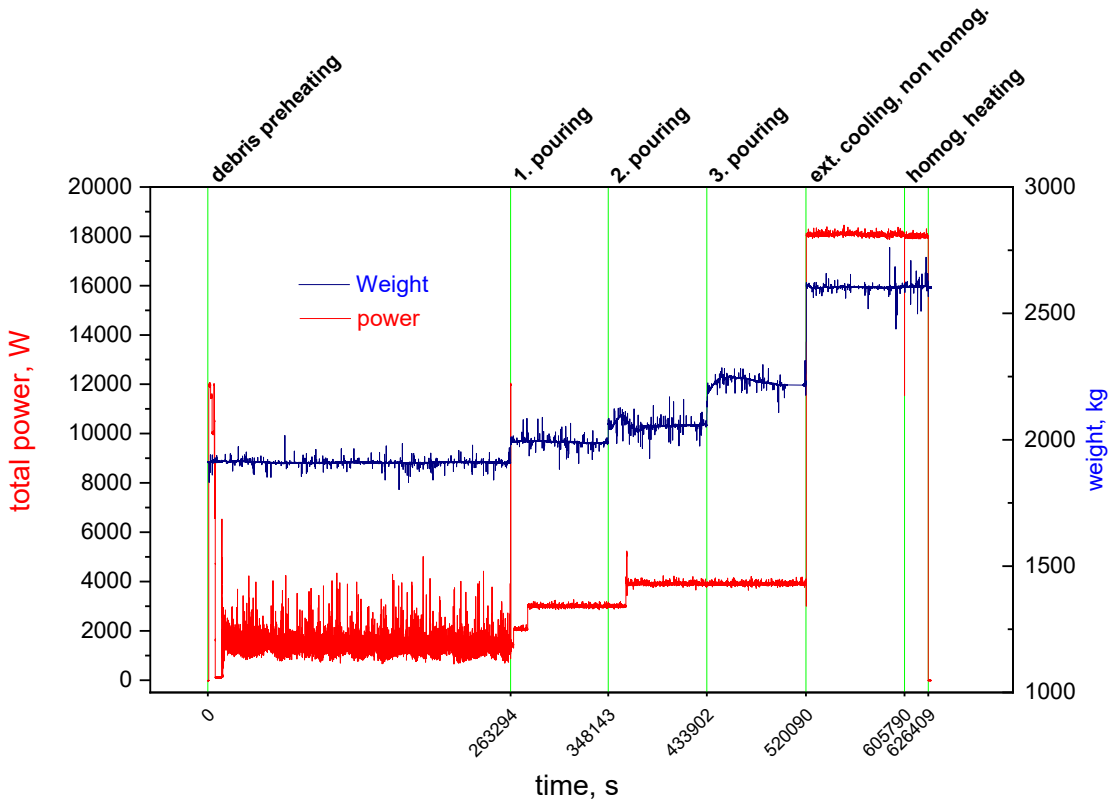

Figure 3. The course of heating power and melt pour during LIVE-L8D test.

3.1. Heat balance

The heating power dissipated in the debris was transferred through its boundaries at the top and at the vessel wall. The external cooling water, if it is available, removed the heat from the vessel outer surface. The heating power and the heat transfer rate through the vessel sidewall and by the cooling water are illustrated in Figure 4. The heat transfer rate through the vessel wall is the integral value of local heat flux and its controlled area, whereas the heat flux is calculation based on the measured values of IT and OT thermocouples. Water inlet/outlet temperatures and its flow rate determine the heat transfer of cooling water. The heat transfer rates through the wall during Phase 1 to Phase 4 were almost zero. The test vessel and empty cooling vessel were gradually heated up. Due to the heat conduction inside the vessel wall, the vessel outer surface temperatures were even higher than the IT temperatures during Phase 2 to Phase 4, resulting negative heat fluxes. After the initiation of external cooling, the test vessel and the cooling vessel were rapidly cooled down, so that the total heat transfer rate of the cooling water transport includes both the ongoing heating power from the debris and the heat stored in the vessel constructions during the previous phases.

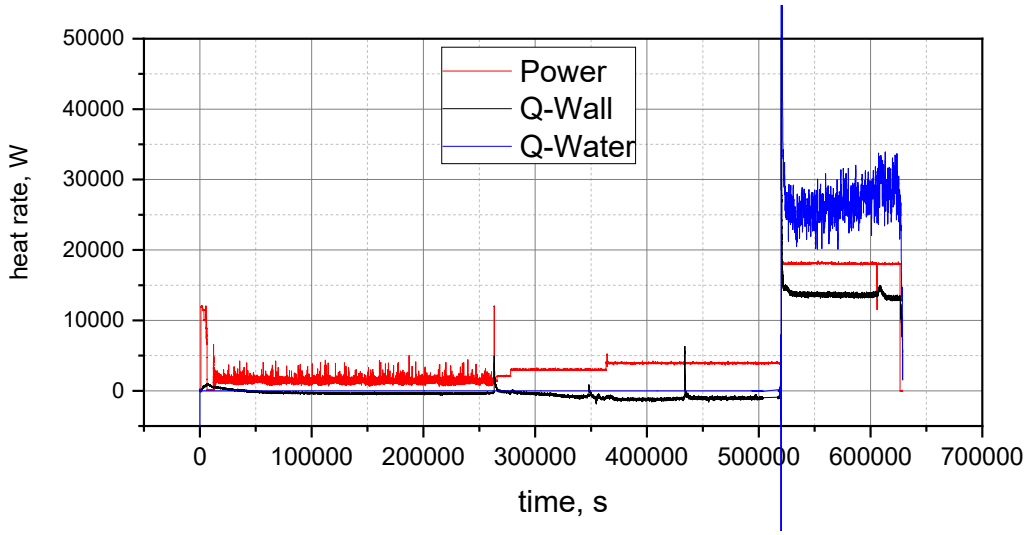

Figure 4. Heating power, heat transfer rate through wall (W-Wall) and heat transfer rate of external cooling water (Q-Water).

3.2. Melt temperature

Melt temperature distributions during the 6 test phases were illustrated roughly in 2D temperature plateaus, as shown in Figure 5. The region with the temperature above 284°C is in liquid melt phase. During the preheating phase, the very poor thermal conductivity of the porous debris bed led to large and uniform temperature gradient from the debris center to all its boundaries. After the first pour, that the melt fill level reached to 260 mm, the heat transport inside the liquid region is improved and the hot region in the debris migrated toward the surface of the liquid melt, where the thermal resistance toward the top surface is lower than other directions. After the 2nd pour and the 3rd pour, the temperature plateaus inside the debris were furtherly flatten, and the highest temperature zone remained in the upper melt region. External cooling changed the heat transport pattern in the debris extensively that heat sink at the wall surface promotes the buildup of a temperature boundary layer on the vessel wall and a continuously crust layer forms. Since the melt level in Phase 5 and Phase 6 were higher than the debris bed, the heat transport are characterized with a combined conduction of porous medium inside the debris and one-phase convection above the debris bed. The higher heating density inside the debris in Phase 5 than in Phase 6 led to the result that the highest temperature was located inside the debris bed in Phase 5.

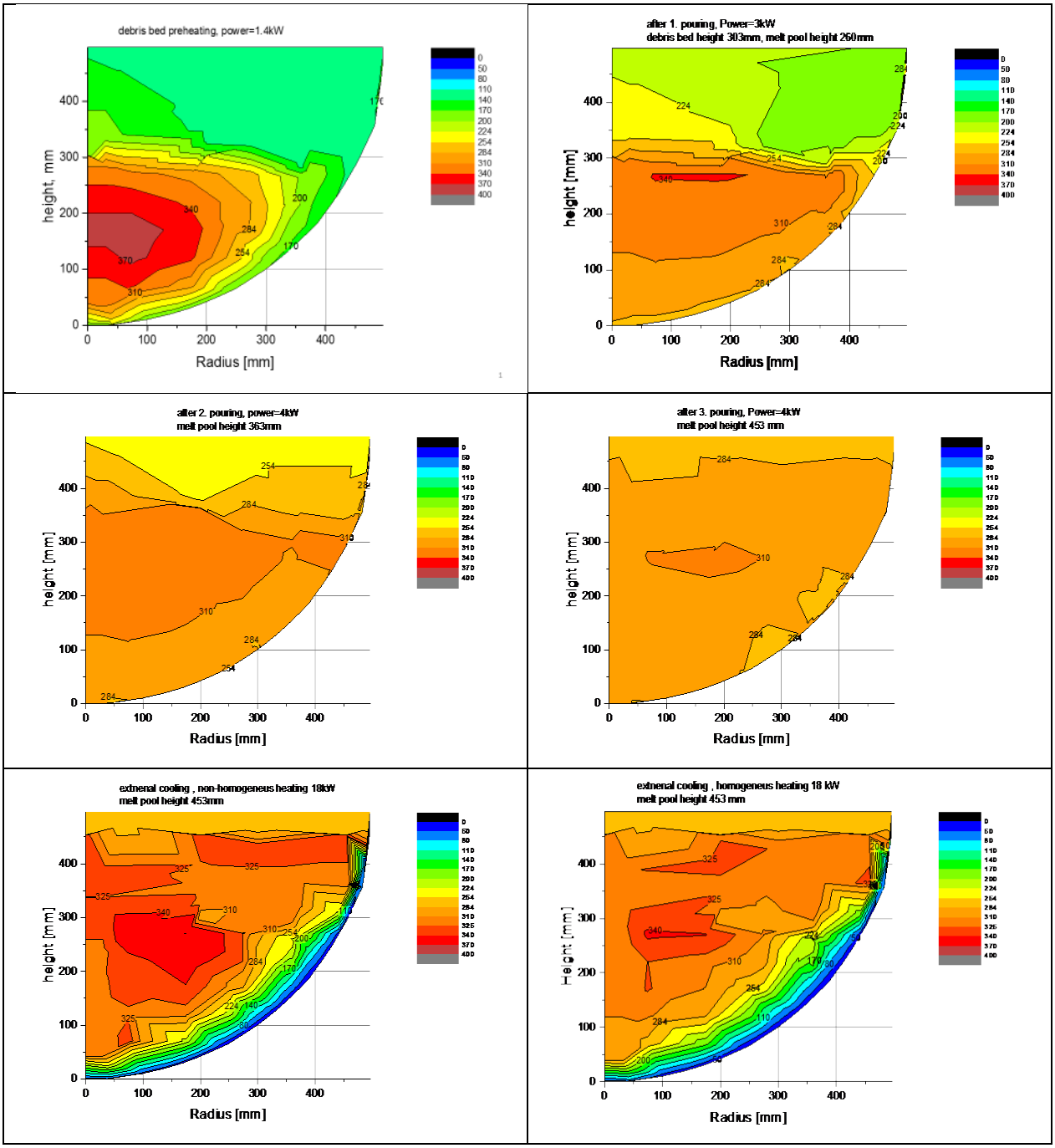

Figure 5. 2D melt temperature distributions during the steady states of L8D test phases. Top-left: Phase 1; top-right: Phase 2, 3 kW; middle left: Phase 3, 4 kW; middle right: Phase 4, 4 kW; bottom-left: Phase 5; bottom right: Phase 6.

3.3. Heat flux

The local heat fluxes at one latitude and of four azimuth angles are averaged and the vertical heat flux profiles from the bottom to the upper range of the debris/melt are shown in Figure 6. During the preheating of debris in Phase 1, the heat flux through the vessel wall was very low and was uniformly distributed. After each melt pour during Phase 2 and Phase 4, the heat fluxes increased moderately firstly from vessel bottom upwards and were in conjunction with a sharp peak near the melt upper surface. External cooling changed the heat flux profiles extensively in

two ways: a) the moderate improvement of the heat transfer at the lower vessel area, and b) the 3 - 4 times improvement of the highest heat flux near the melt surface. It is necessary to note that the high heat flux at the bottom came from two facts: a stronger local convection at the bottom and local overheating by the lowest heater. Since the lowest heater with very high area power density could not dissipate its power homogeneously into its controlled volume.

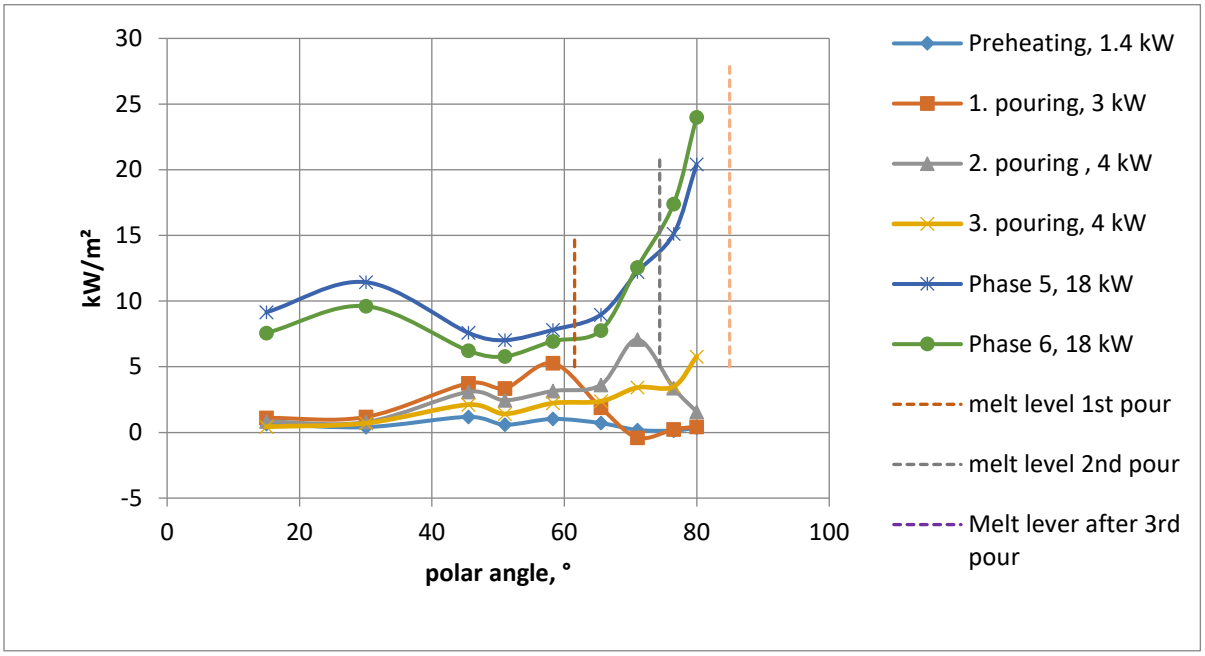

Figure 6. Heat flux profiles along the polar angle of the vessel wall.

4. DISCUSSION

The heat transfer in solid debris, either filled with air or filled with a liquid melt, is dominated by heat conduction in case that the porous bed is filled with low conductive fluid, such as gases. An improvement of the heat transfer could be the laminar flow of a low Pr liquid in the porous melt. Unlike the natural convection that the heat transport is always upwards, the heat conduction takes place in all directions from hot region toward cold region, e.g. upwards, sidewards and downwards. To describe the heat conductivity in a saturated porous medium, an effective thermal conductivity, k_e, is defined in the ratio $\eta = k_e / k_f$, and η is a function of porosity ϕ and the solid-fluid conductivity ratio κ, as described in Eq (1) [10].

$$\eta = f(\phi, \kappa), \quad \kappa = k_s / k_f \tag{1}$$

Where, k_s and k_f are the thermal conductivity of solid and of fluid respectively in the porous medium. There is high uncertainty of η. If the solid-liquid conductivity ratio is small ($\kappa < 10$), the effective conductivity is linearly related to κ and is insensitive to the morphology of the solid / fluid interface. For a higher κ, e.g. $\kappa > 10^3$, the geometry of the solid-fluid interface, e.g. the morphology affects η increasingly. Applying the equation provided by [10], here as Eq. (2), and with the porosity of 0.38, the effective conductivity of RIMAX/ air, RIMAX/nitrate liquid and RIMAX/liquid steel are calculated.

RIMAX/air configuration relates to the Phase 1 configuration, RIMAX/nitrate relates to the melt-filled debris region of Phase 2 to Phase 6. RIMAX/liquid steel predicts approximately the prototypical porous bed, which is composed of solid oxide debris and liquid iron. Comparing

to the solid/air configuration, the nitrate melt as fluid in the porous medium improves the effective conductivity to about 7-8 times. If the fluid melt is liquid iron, the effective conductivity will be improved more than 50 times comparing to a solid/air porous medium. Therefore it can be principally predicted that with the presence of a low Pr fluid in the debris bed, the effective conductivity will be improved enormously, which leads to a more uniform temperature distribution cross the debris bed and high heat conduction rate to the colder boundary area. Detailed prediction of various solid-fluid combinations can be performed with CFD calculation, which is out of the scope of this study.

$$\eta = \frac{2\phi + \kappa(3-2\phi)}{3-\phi+\kappa\phi} \quad (2)$$

Table IV. Effective thermal conductivities and their functional parameters

Conductivity, W/ (mK)	RIMAX (573K): 7.6	Nitrate (573K): 0.439	Liquid steel {Harding, 1989 #146}(1810K): 25.7
κ: (k_s/k_f)	RIMAX / air: 173.1	RIMAX / nitrate: 17.3	RIMAX / steel: 0.296
η in Eq 2	RIMAX/air: 5.68	RIMAX/nitrate: 4.3	RIMAX/steel: 0.52
Eff. Conductivity, k_e W/(mK)	RIMAX / air: 0.25	RIMAX / nitrate: 1.89	RIMAX / steel: 13.38

5. CONCLUSION

L8D test simulates co-existence of solid oxide debris in the LWR reactor lower head with changing fill level of liquid melt. Thermal conduction dominates the heat transfer in a solid debris bed without liquid melt. Due to the very poor thermal conductivity, the core of the debris undergoes rapid heatup and onsite of melting. Liquid melt in the solid debris bed can improve the effective thermal conductivity about 7-8 folds, leading to a flatter temperature distribution across the debris. Laminar flow of the liquid melt seems to play a role on the temperature distribution that the highest temperature is always near the melt upper surface level. Without external cooling, the heat transfer through the vessel wall is very limited, and the heat flux tapers consequently just below the melt level. External cooling demonstrates its high effectivity to remove the heat from the debris bed, which creates a temperature boundary layer, and harmonizes the debris bulk temperature. The experimental results are conservative regarding the high Pr of the nitrate melt. For the prototypical debris material constituted of such as oxide debris and metallic melt, the effective thermal conductivity of the debris bed could be largely improved.

6. REFERENCES

1. M.,Buck, *Modeling of the late phase of core degradation in Light Water Reactors,* PhD thesis, University of Stuttgart (2007).
2. K.Y. Suh, R. E. Henry, "*Debris interactions in reactor vessel lower plena during a accident I. Predictive model".* Nuclear Engineering and Design, **166**: p. 147-163 (1996).
3. I., Lindholm, et al., "Dryout heat flux experiments with deep heterogeneous particle bed", *Nuclear Engineering and Design*, **236**: p. 2060-2074 (2006).

4. W. Ma, "Predicton of dryout heat flux of volumetrically heated particulate beds packed with multi-size particles*"*, *The 14th International Topical Meeting on Nuclear Reactor Thermal Hydraulics (NURETH-14)*. Toronto, Canada. p. Nr. 199 (2011).
5. Lipinski, *A Model for boiling and dryout in Particle beds*. Sandra National Laboratories (1982).
6. Gaus-Liu, X., et al., "The experimental results of LIVE-L8B-debris melting process in a simulated PWR lower head*"*, in *5th European Review Meeting on Severe Accident Research (ERMSAR 2012), Köln, March 21-23,* (2012).
7. B. Fluhrer,, et al., "LIVE-BWR experiments to study the effecct on CRGT cooling on in-vessel melt retention strategy", *Nureth-19*. Online. p. 35414 (2022).
8. H. Madokoro, et al., "LIVE-J1 experiment on debris melting behavior toward understanding late in-vessel accident progression of the Fukushima Daiichin Nuclear Power Station*"*, *NURETH-19*. online. p. 36023 (2022).
9. G.J., Janz, et al., *Physical properties data complications relevant to Energy storage II. Molten salts, Data on single and mulit component salt systems*, in *NSRDS-NBS 61, Part II*. (1979). National Bureau of Standards, U.S. Department of Commerce: New Work.
10. H.T. Aichlmayr, and F.A. Kulacki, "On the effective thermal conductivity of saturated porous media", *ASME Summer Heat Transfer Conference*. p. HT2005-72144 (2005).
11. J.H. Harding, D.G. Martin, P.E. Potter, T*hermalphysical and thermalchemical properties of reactor material*, EUR 12402 EN, ISSN 92-826-0829-8 (1989)

Karlsruhe Institute of Technology

EXPERIMENTAL STUDY ON HEAT TRANSFER OF POST-DRYOUT DEBRIS/MELT MIXTURE IN THE LOWER HEAD OF REACTOR PRESSURE VESSEL

Xiaoyang Gaus-Liu, KIT
Xiaoyang.gaus-liu@kit.edu

Institute for Nuclear and Energy Technologies





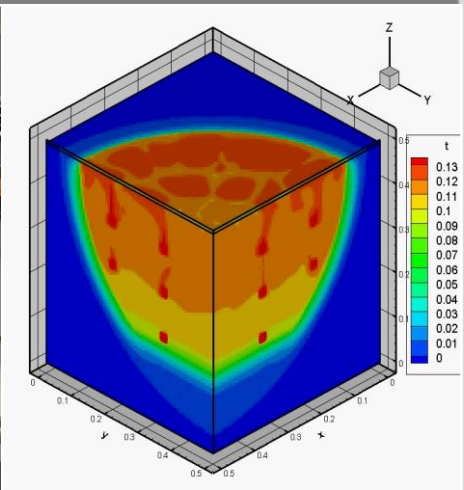

Outline

- Accident scenario
- Experimental setup
- Performance of experiment
- Results
  - Melt temperature distribution
  - Heat flux
- Discussion on heat transfer characteristics
- Summary

Debris dryout in reactor case

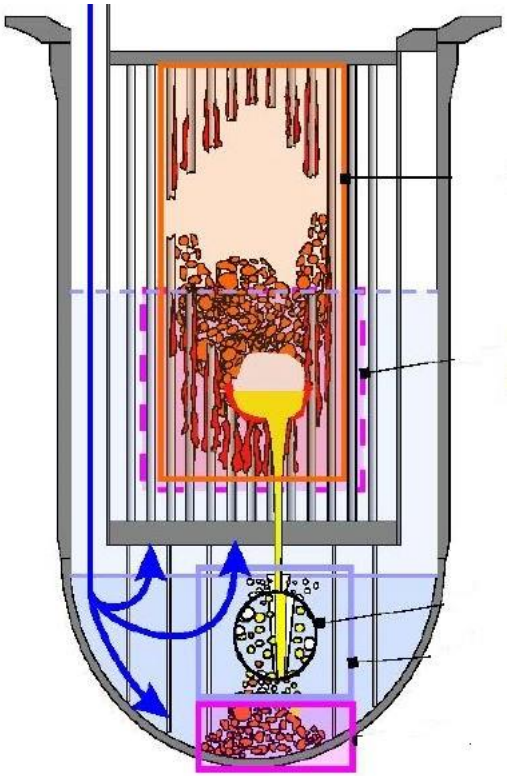

Before dryout

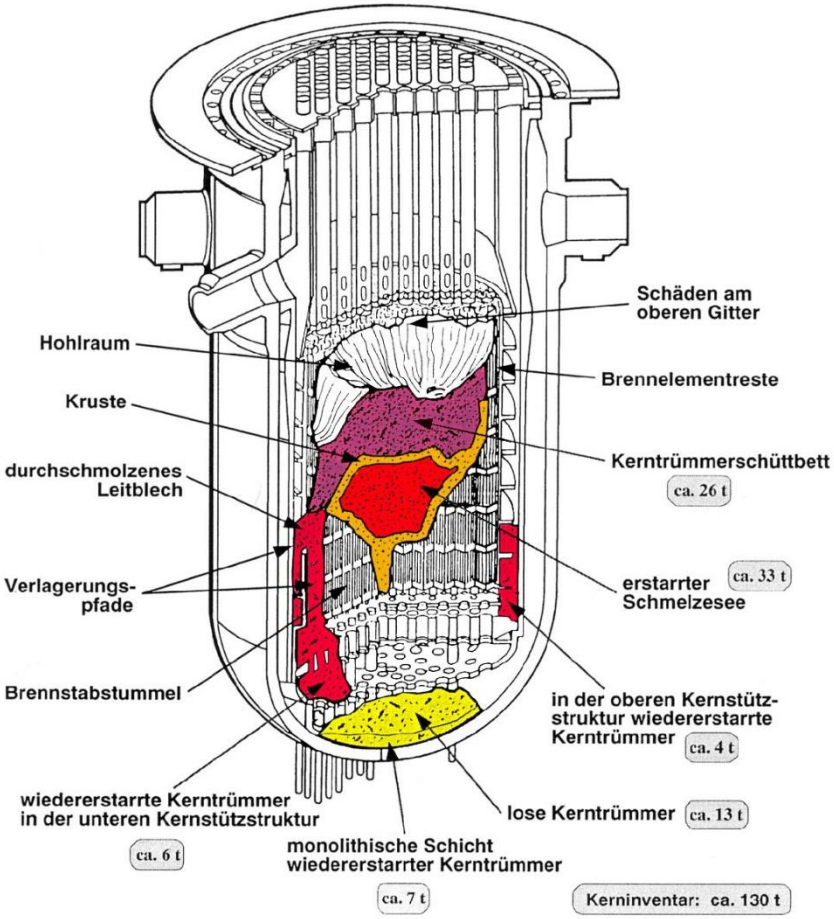

P. Schäfer, PHD Thesis, Universität Stuttgart, 2005

Debris melting experiments in LIVE facility

L8A and L8B: debris melting process after subsequent relocation of melt

Gaus-Liu, X., et al. (2012). The experimental results of LIVE-L8B-debris melting process in a simulated PWR lower head. 5th European Review Meeting on Severe Accident Research (ERMSAR 2012), Köln, March 21-23, 2012

L8C: melting of low-temperature debris in a non-homogenous debris bed

Miassoedov, A., et al. (2016). Heat Transfer in Homogeneous and Stratified Melt Pools in the Lower Head of a Reactor Pressure Vessel. Technical Meeting on Phenomenology and Technologies Relevant to In-Vessel Melt Retention and Ex-Vessel Corium Cooling, Shanghai, CHN, October 17-21, 2016.

LIVE-JAEA: Melting of non-homogenous debris in Fukushima reactor scenario

Madokoro, H., et al. (2022). LIVE-J1 experiment on debris melting behavior toward understanding late in-vessel accident progression of the Fukushima Daiichi Nuclear Power Station. NURETH-19. online: 36023.

LIVE-BWR: Cooling of debris in BWR lower head with additional cooling of CRGT

Fluhrer, B., et al. (2022). LIVE-BWR experiments to study the effect on CRGT cooling on in-vessel melt retention strategy. Nureth-19. Online**:** 35414.

Accident Scenario in LIVE-L8D experiment

- Dryout of in-vessel debris bed → formation of a melt pool
- Two phase heat transfer: Oxide phase in solid state, and metallic phase in liquid state
- No external cooling during the initial stage

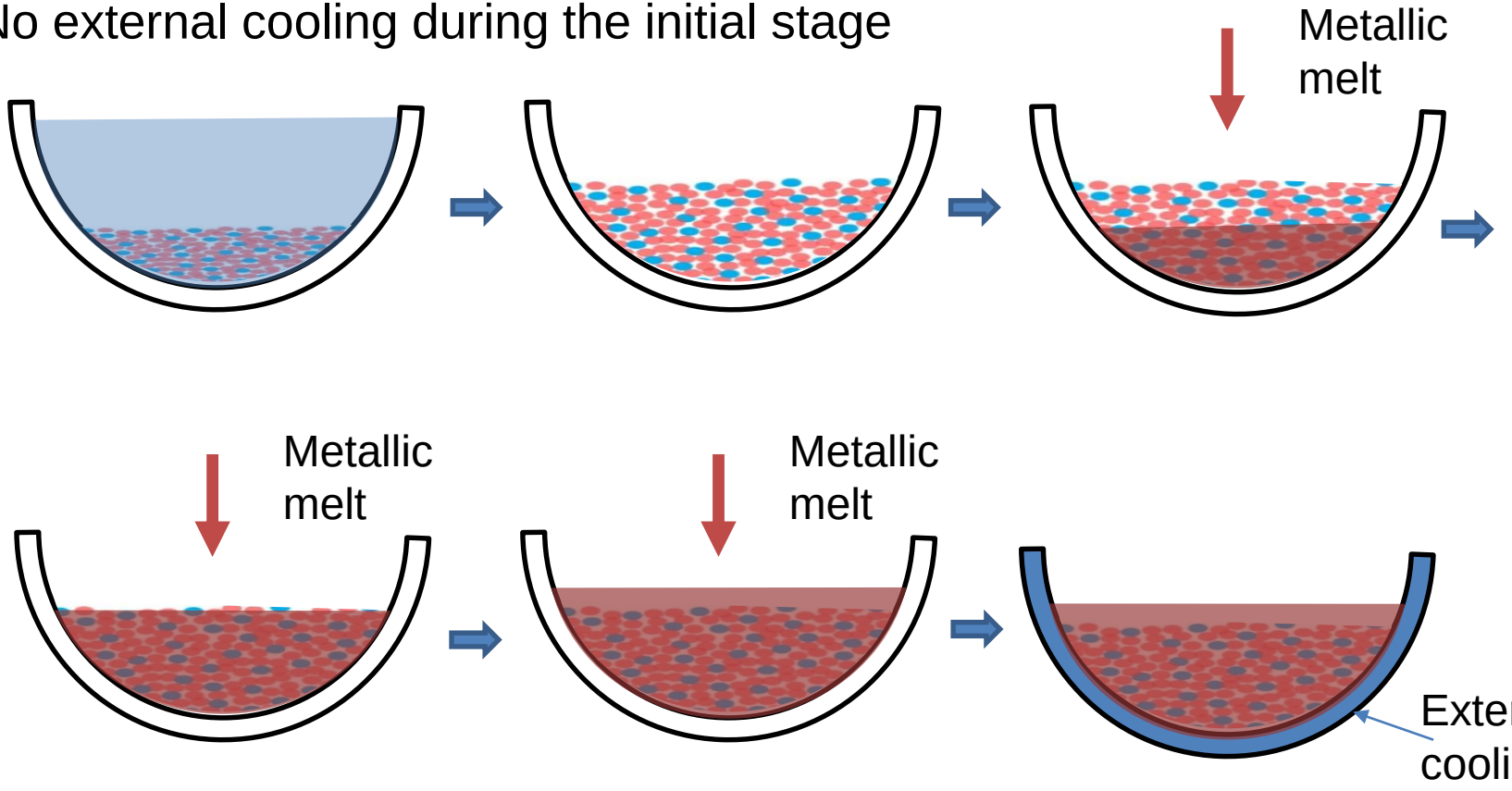

LIVE3D facility

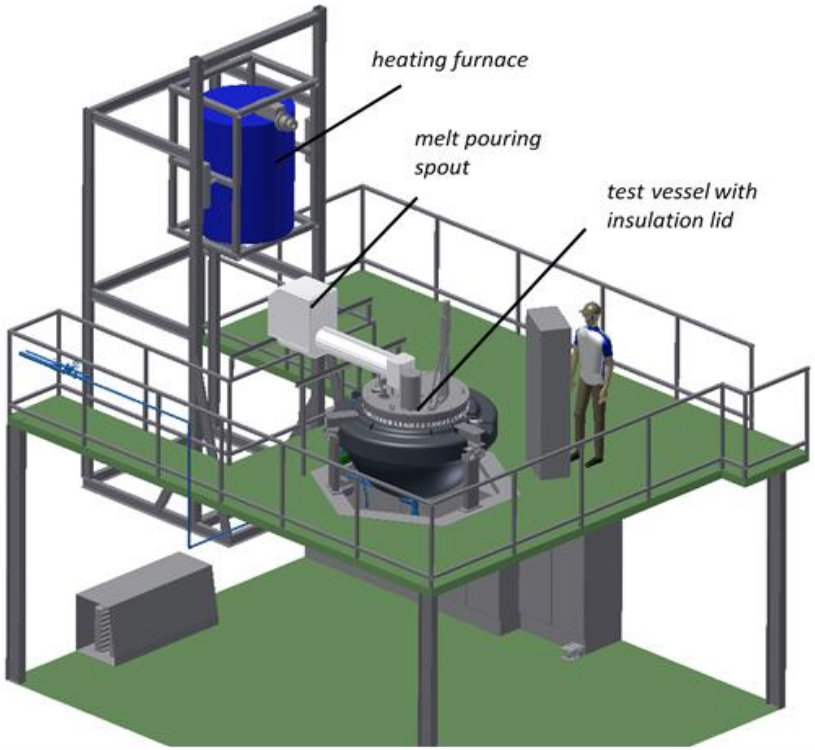

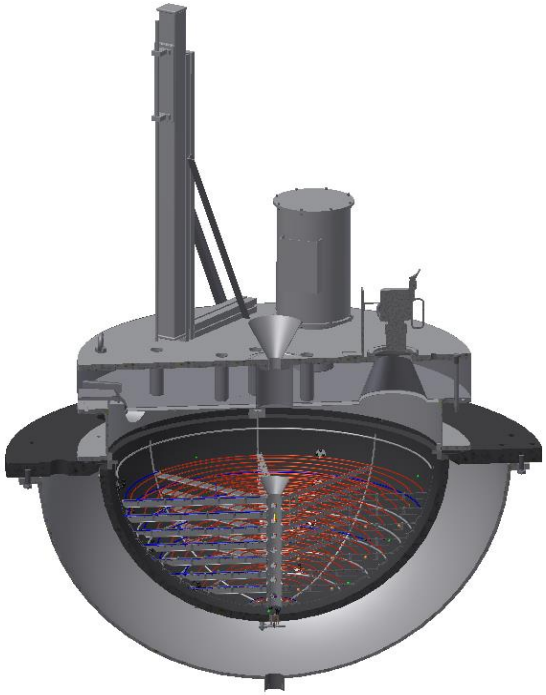

- 1:5 scaled LWR lower head
- simulant material: water, nitrate salt mixture (220°C-400°C)
- transient scenarios of melt/debris relocation/melting
- volumetric heating system with electrical wires
- external and top water cooling system

LIVE3D heating and Instrumentation

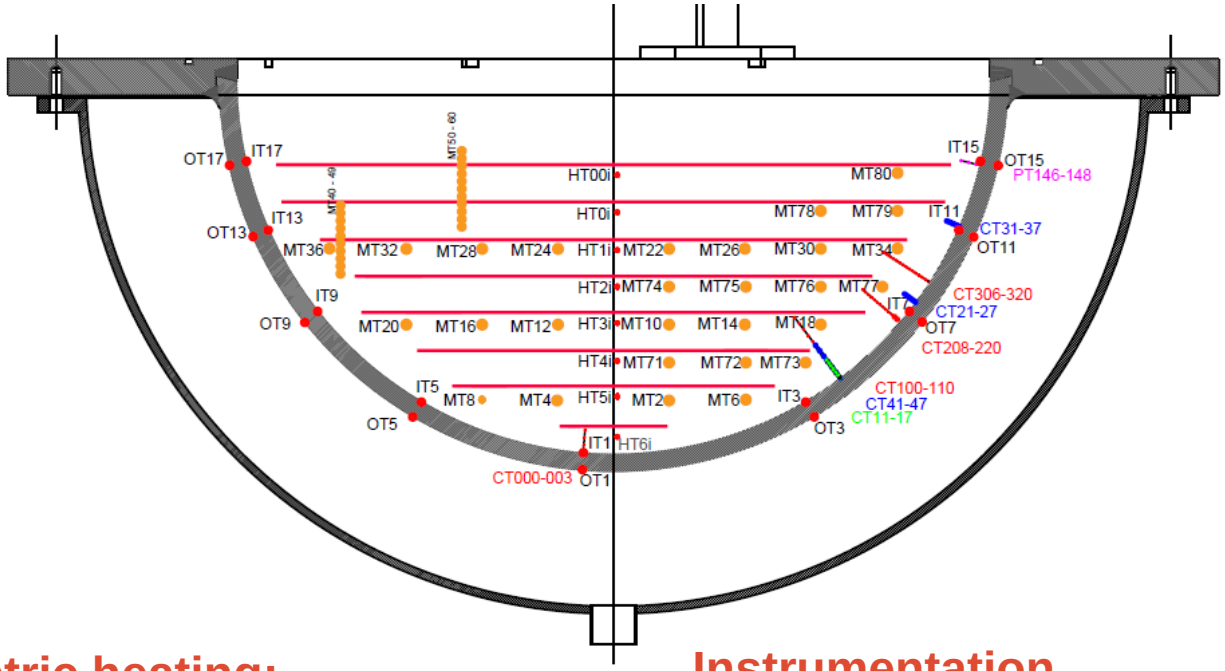

Volumetric heating:

- 8 individual heating planes
- Total heating rate: 28 kW

Instrumentation

- Bulk melt: 80 TCs
- Vessel wall: 26 pairs of TCs at wall surface
- Boundary: 7 TC trees
- Weight of vessel

➢ 3D Heat flux, 2D melt temperature, heat balance

Simulation materials

- Solid Oxide: Rimax ceramic
  - ZrO_2-SiO_2 spherical particles
  - Φ: 2.5 – 2.8 mm
  - ρ: 2400 kg/m³
  - C_p: 1.01 J/gk at 250 °C
  - k: 7.7 W/(mK)

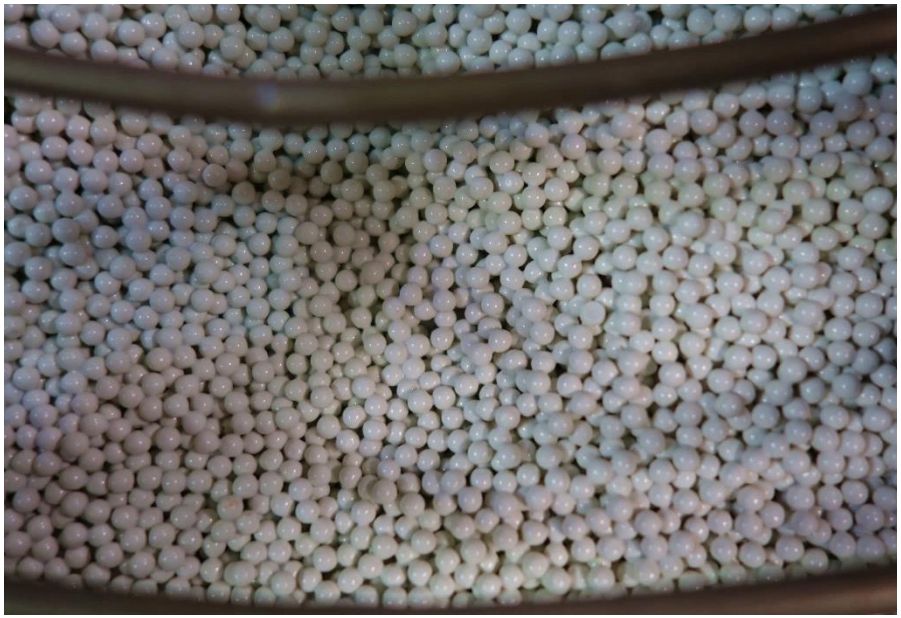

- Metallic melt: 80% KNO_3- 20 % $NaNO_3$
  - ρ: 2000 kg/m³
  - C_p: 1.46 J/(gK)
  - k: 0.439 W/(mK)
  - ν: $1.75 \cdot 10^{-6}$ m²/s at 300°C
  - T_{sol}: 220°C
  - T_{liq}: 285°C

Performance of LIVE-L8D test

Phase	Duration	Action	Height of liquid melt, mm	Total heating power,	External cooling
Phase 1	0 - 265890s	Preheating Debris bed at 303mm	0	1.4kW	no
Phase 2	265891-348142s	1.Melt pour	260	2kW: → 3KW	no
Phase 3	348143-433901s	2. Melt pour	363	3kW→ 4kW	no
Phase 4	433902-520347s	3. Melt pour	453	4kW	no
Phase 5	520348-604829s	External cooling Power increase	453	18kW in 0-303 mm height	yes
Phase 6	604830-626398s	Change of power distribution	453	18 kW in whole pool height.	yes

Chronology of performance

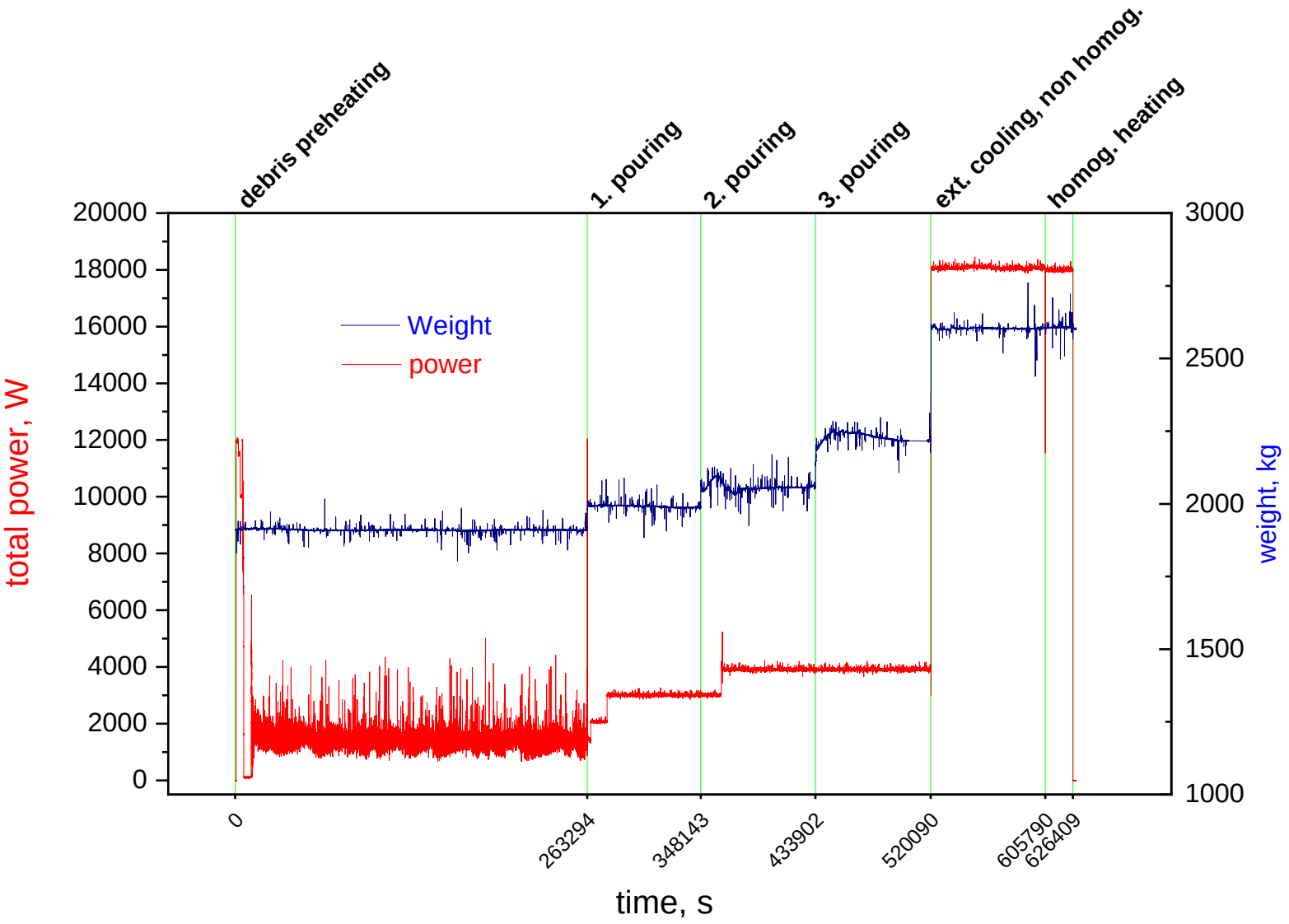

2D Melt Temperature Distribution

P1: No liquid melt, 1.4kW

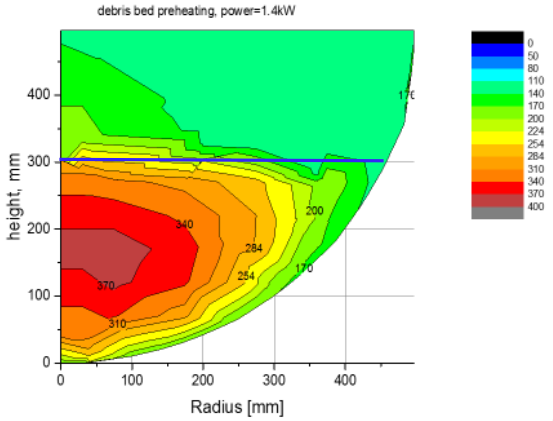

P2: liquid melt 260mm, 3kW

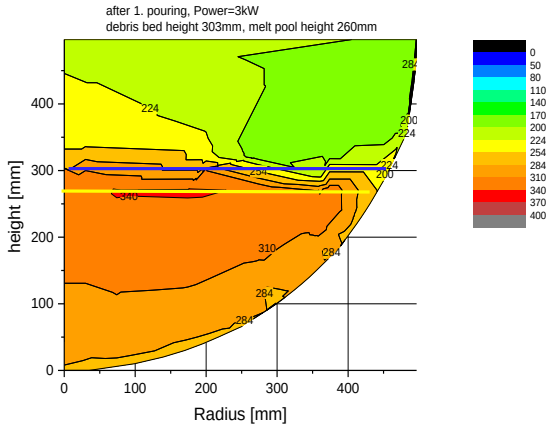

P5: liquid melt 453mm, 18kW

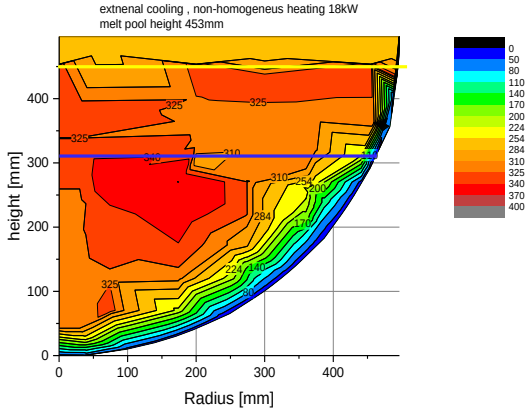

P3: liquid melt 363mm, 4kW

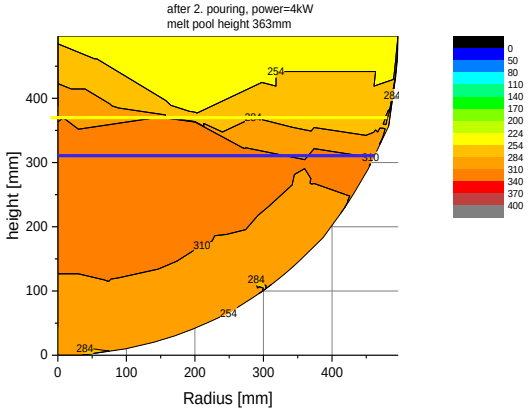

P4: liquid melt 453mm, 4kW

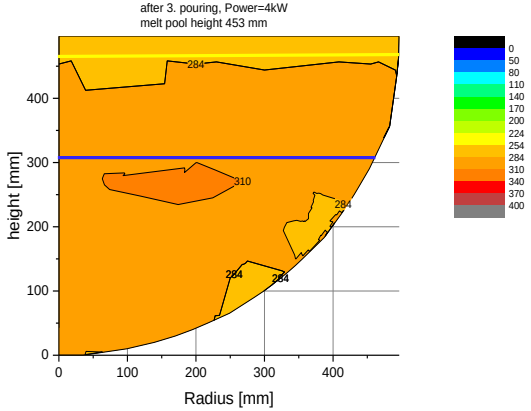

Surface of debris

Surface of liquid melt

Heat flux along vessel wall

From preheating to 3rd pour, no external heating

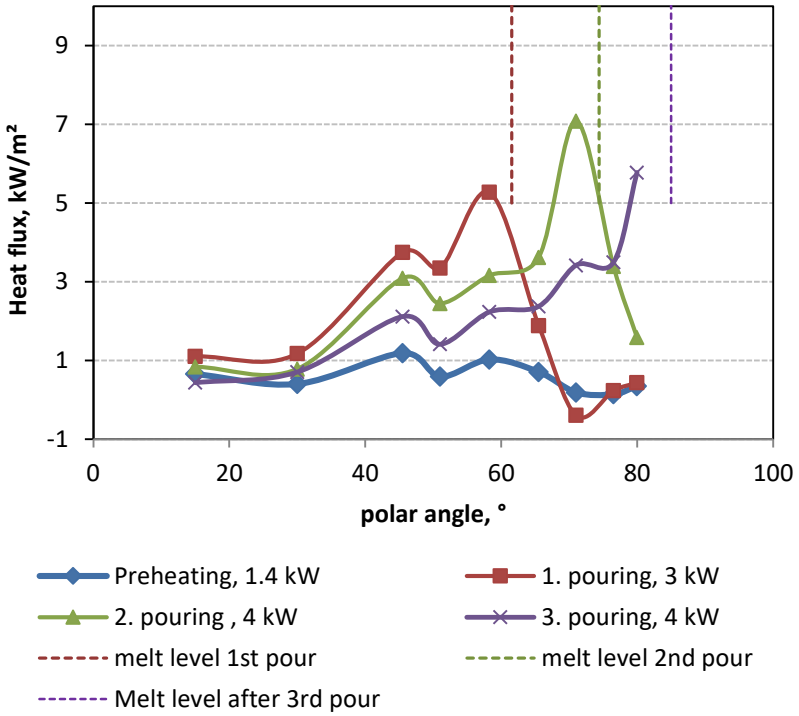

Phase 5 and Phase 6, with external heating, 18kW

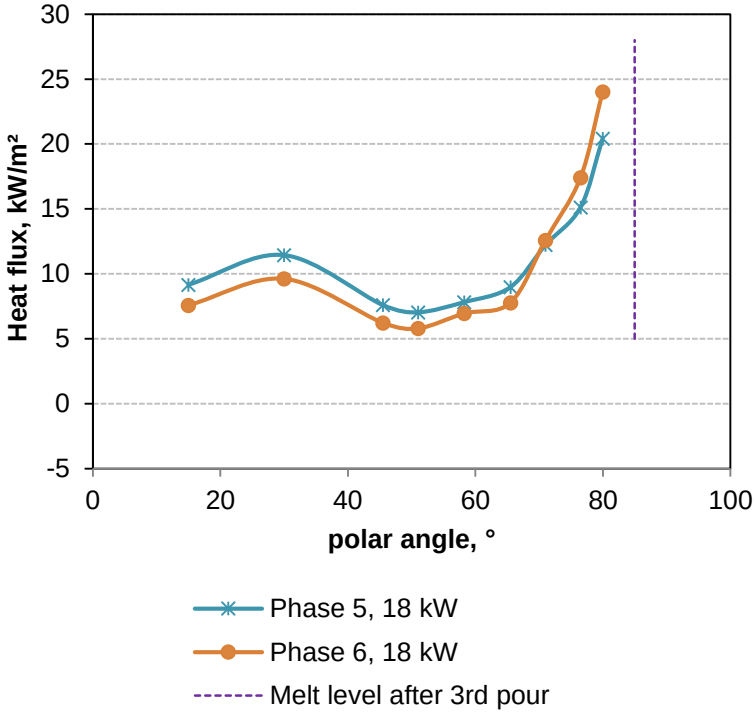

Discussion on heat transfer in porous medium

- Solid debris pile without liquid melt
  - Porous medium of solid particle / gas
  - Very low heat conductivity in pile leads to fast heat-up inside the pile
  - Not critical to vessel wall, but it is a short transient.
- Liquid melt below the pile surface
  - Porous medium of solid particle / liquid melt
  - Improved heat conductivity in pile leads to high temperature at wall below liquid melt
- Liquid melt above the pile surface

  Slight relief of the thermal load due to the larger heat transfer area below the liquid melt
- External cooling: decisive measure to protect the vessel
  - High heat removal rate
  - Cool-down of vessel wall

Effective thermal conductivity of a porous medium

k_e: effective conductivity in a particle bed

$$k_e = \eta k_f,\ \eta = \frac{2\phi + \kappa(3-2\phi)}{3-\phi+\kappa\phi},\quad \kappa = \frac{k_s}{k_f}$$

Φ: porosity, f: fluid, s: solid

H.T. Aichlmayr, and F.A. Kulacki, "On the effective thermal conductivity of saturated porous media", ASME Summer Heat Transfer Conference. p. HT2005-72144 (2005).

Conductivity, W/ (mK)	RIMAX (573K): 7.6	Nitrate (573K): 0.439	Liquid steel (1810K): 80
	RIMAX / air	RIMAX / nitrate	RIMAX / steel
κ: (k_s/k_f)	173.1	17.3	0.095
η	5.68	4.3	0.37
Eff. Conductivity, k_e W/(mK)	0.25	1.89	29.30

Conclusion

- Transient phase of debris heat up after the dryout of rest water in LWR is simulated in LIVE experiments.
- The very low heat conductivity in a debris bed without liquid melt leads to rapid heat up in the central core.
- Liquid melt filling in the solid bed transports the decay heat to the vessel wall and results in high thermal load.
- Without external cooling, the configuration of a low-level liquid melt leads to the most critical situation.
- External cooling improves the heat transfer decisively and simultaneously cools down the vessel wall.
- Thermal conductivity plays an important role in the heat transfer inside the pile. The effective thermal conductivity is induced to the heat transfer of the two-phase porous medium.

INTEGRAL MODELLING OF CONTINUOUS/DISPERSED PHASES MASS TRANSFER DURING IN-VESSEL CORIUM STRATIFICATION TRANSIENTS

R. Le Tellier
CEA, DES, IRESNE, DTN, Cadarache
F-13108 Saint Paul-lez-Durance, France
romain.le-tellier@cea.fr

ABSTRACT

In the frame of in-vessel corium modeling, the miscibility gap in the $U-O-Zr-steel$ thermodynamic system induces complex liquid phases stratification transients in the pool that play a major role on the boundary heat flux distribution. Key parameters that drive the pool stratification are the molten steel relocation into the pool and the mass transfer among the pool phases. The present work is related to such phenomena.
The molten steel relocation "path" to the pool is largely uncertain, in particular for the ablated vessel wall where it depends on the refractory crust behaviour. When considering a permeable crust, some molten steel will be directly relocated into the oxidic melt and a simple homogeneous treatment of a "zone" comprising both oxidic corium and molten steel is not adequate from the thermodynamic point of view.
Following a recent work where the mass transfer between a mono-dispersed molten steel phase into an oxide phase was modelled, this paper presents an integral stratification model that takes into account such dispersed metal phases. These droplets can either come from a direct molten steel relocation or be detached by Rayleigh-Taylor instabilities at the interface between the heavy or light metal layer and the oxide layer of the stratified pool. At all interfaces between metal and oxide phases, a same consistent local equilibrium assumption (based on a same simplified thermodynamic representation of the liquid miscibility gap) is made.
A limited parametric analysis is reported. It highlights the possible impact of direct molten steel relocation into the oxide phase in comparison with a relocation on the top of the pool. Indeed, the U,Zr enrichment of the metal droplets during their residence time in the oxide phase significantly affects the remainder of the stratification transients in all cases. The parameters that affect this mass transfer are shown to have a significant impact on the overall stratification kinetics. These results also highlight an important qualitative difference between the two kinds of stratification transients: heavy metal phase formation or stratification inversion. In the latter, the heavy metal phase average composition always stays close to its interface composition equilibrium with the oxide and, accordingly, when the density criterion associated with the Rayleigh-Taylor instability is met, the heavy metal layer is, in most cases, completely relocated at the top of the pool. During the heavy metal phase formation, the situation is drastically different as the light metal layer is not initially close to equilibrium with the oxide in such a way that several intermittent droplets detachment are predicted.
These different trends are reported taking into account the model underlying hypotheses and the path to move forward and increase knowledge about stratification kinetics is discussed.

KEYWORDS

in-vessel corium, stratification, local equilibrium, mass transfer, droplets

1. INTRODUCTION

In the frame of the analysis of severe accidents (SA) in light water reactors, this work is related to the corium behaviour in the vessel lower head. Indeed, when considering an in-vessel retention strategy [1, 2], such an analysis requires the transient simulation of the vessel wall ablation due to the heat flux imposed by the corium pool. The multiphase multicomponent corium pool behaviour depends on the coupling between thermalhydraulics (natural convection in the liquids and conduction in the solid) and thermochemistry (phase segregation).
In particular, the miscibility gap in the U-O-Zr-steel thermodynamic system induces complex liquid phases stratification transients in the pool that play a major role on the boundary heat flux distribution. As discussed in [3], key parameters that drive the pool stratification are the molten steel relocation into the pool (associated with internal structures and vessel wall ablation) and the mass transfer among the pool phases. The present work is related to such phenomena.
The molten steel relocation "path" to the pool is largely uncertain, in particular for the ablated vessel wall where it depends on the refractory crust behaviour (formation, possible dissolution by molten metal, mechanical stability). Accordingly, as discussed in [4], the different SA codes that simulate lower head transients exhibit differences in this matter: no actual modelling of the molten steel migration is used but different hypotheses are made. When considering a permeable crust, some molten steel will be directly relocated into the oxidic melt. In the frame of lumped parameter thermal models, in [5], it was shown that a simple homogeneous treatment of a "zone" comprising both oxidic corium and molten steel is not adequate from the point of view of thermodynamic closures (enthalpy-temperature-composition relationships).
Accordingly, a first-of-a-kind analysis was performed in [6] for a system composed of a mono-dispersed molten steel phase into an infinite oxide phase. "First-order" simplifying hypotheses were considered so that a rather "simple" isothermal model, suitable for order of magnitudes and trends analyses, was proposed. In particular, it is based on a representative elementary volume comprising a single metallic droplet into oxide corium. Inter-phase mass transfer is taken into account through a two-zone integral model with a simplified thermodynamic representation of the U-O-Zr-steel system and it is coupled with a 1D momentum conservation equation for droplets dynamics. This model has been developed as a stand-alone model in the frame of the PROCOR software platform [7]. It was used in a limited parametric analysis, in particular, w.r.t. to the model parameters associated with mass transfer and the droplet size. Within the model scope, it was shown that mass transfer can play a significant role in case of "small" (millimetric) droplets so that, depending on the composition related parameters, the droplets U,Zr enrichment can be such that droplets will be relocated at the bottom of the pool. For larger (centimetric) droplets, a faster relocation to the top of the pool can be expected, albeit with a composition significantly different from pure molten steel. It was also concluded that the "mixing" of the metallic dispersed phase in the oxide can only be stable for a very limited composition range near the density inversion threshold. The main limitation of this analysis is that it was uncoupled from the mass transfer between the oxide phase and the continuous metal phases at the top and the bottom of a stratified pool.
Under the same "first-order" simplifying hypotheses as [6], the present work proposes an integral stratification model that takes into account dispersed metal phases into the continuous oxide phase. These droplets can either come from a direct molten steel relocation or be detached by Rayleigh-Taylor instabilities at the interface between the bottom or light metal layer and the oxide layer of the stratified pool. At all interfaces between metal and oxide phases, a same consistent local equilibrium assumption (based on a same simplified thermodynamic representation of the U-O-Zr-steel system) is made. This is a clear *a priori* improvement when compared with the treatment of the equilibrium conditions in PROCOR legacy model [8] (where the transient model takes the form of a relaxation model whose steady state is evaluated by a global equilibrium calculation) or other models of the literature [9] (where interface equilibrium conditions are approximated by a global equilibrium evaluated considering the inventory of the oxide layer and, either the light, or heavy

metal layer depending on the interface under consideration).
With this stratification model, the "first-order" study initiated in [6] about the impact of the molten steel relocation path on the overall pool stratification transients can be completed and this is the main objective of this document. The model itself is presented in Section 2 while the results of limited parametric analysis are discussed in Section 3. Finally, Section 4 is devoted to conclusions and perspectives.

2. MODELLING

The model described in this section for a stratified pool is a direct extension of the model thoroughly discussed in [6] for the case of a dispersed metal phase into an oxide one. The same simplifying hypotheses are considered as follows:

- **H1** The dispersed metallic phases are considered to be mono-dispersed and the interactions between droplets are neglected *i.e.* they can be considered as isolated
- **H2** The convection in the continuous oxidic phase does not affect the droplets dynamics *i.e.* the oxidic phase is treated as stagnant
- **H3** Inter-phase mass transfer conservation equations are decoupled from inter-phase heat transfer
- **H4** Local chemical equilibrium at the liquid/liquid interfaces is supposed to be maintained at all time
- **H5** The U/Zr molar ratio $R_{U/Zr}$ is assumed to be uniform over all the phases [10, 11]
- **H6** No steel component (resp. oxygen) is present in the oxide phase (resp. metallic phases) [11]

In particular, with H5 and H6, the pseudo-quaternary system $\{O,U,Zr,steel\}$ is reduced to two pseudo-binary systems: $(U,Zr)+O$ for the oxide phase and $(U,Zr)+steel$ for the metal phases.[1] The reader is referred to [6] for more details.
In this multiphase model, in addition to a continuous oxide phase (denoted *oxy*), different metal phases are distinguished:

- n different mono-dispersed metal phases denoted $(met_i)_{i\in[\![1,n]\!]}$; for each such phase, the associated dependent variables are its mass m_i, steel mass fraction w_i^{steel}, droplet equivalent radius r_i, axial position z_i and velocity $v_{z,i}$;
- two continuous ones: met_{n+1}, alternatively denoted $met_\uparrow$, (resp. met_{n+2}, alternatively denoted $met_\downarrow$) for the light (resp. heavy) metal phase on top (resp. at the bottom) of the oxide phase; the associated dependent variables are its mass m_i and steel mass fraction w_i^{steel}.

Consistently with neglecting droplet interactions (*cf.* H1), droplet coalescence and fragmentation are ignored in such a way that only the interfaces between the different metal phases and the oxide one are to be considered. Γ_i denotes the interface with met_i and the same subscripting convention is used for all phase-related quantities (see the complete nomenclature at the end of the paper). The axial position of Γ_i, $i\in[\![n+1,n+2]\!]$, is denoted z_i.
Figure 1 presents a schematics that summarises the different inter-phase mass transfers at play in this model that will be detailed in the forthcoming sections. Note that the set of dispersed phases is time-dependent: a "new" phase is created when droplets are formed at Γ_{n+1} or Γ_{n+2} by Rayleigh-Taylor instabilities while a dispersed phase "disappears" when it coalesces into one of the continuous metal phases at Γ_{n+1} or Γ_{n+2} by hydrodynamic movement. Such changes in the metallic phase set are associated with discrete time events that introduce discontinuities in the system behaviour. Conservation equations will be presented for a fixed set of phases in Section 2.1 while dispersed phase associated discrete events will be discussed afterwards when discussing mass transfer between continuous and dispersed metallic phases (Section 2.2) and the numerical integration scheme (Section 2.3).

[1] Steel is considered as a pseudo-component here.

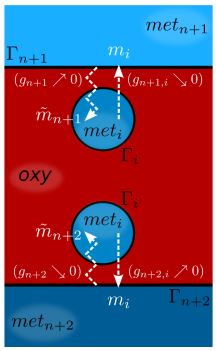

- continuous transfer between met_i and oxy phases through interface Γ_i
- discontinuous transfer when a dispersed phase met_i ($i \in [\![1,n]\!]$) coalesces into (resp. detaches from) met_{n+1} or met_{n+2} (straight - resp. zigzag - arrows) as described by switching function $g_{n+1,i}$ and $g_{n+2,i}$ (resp. g_{n+1} and g_{n+2}) that describe discrete time events (see Section 2.2 for their definition); $\tilde{m}_{n+1}$ and $\tilde{m}_{n+1}$ represent the mass of the detached droplets (see Eq. 17)

Figure 1. Schematic view of inter-phase mass transfers described in this model.

2.1. Conservation equations

The different conservation equations and their closures are discussed in the following sections.

2.1.1. Mass conservation equations

Mass conservation for the oxide phase and the different metal phases can be written as:

$$\frac{dm_{oxy}}{dt} = -\sum_{j=1}^{n+2} \dot{m}_{\Gamma_j} \tag{1}$$

$$\frac{dm_i}{dt} = \dot{m}_{\Gamma_i} \quad \forall i \in [\![1,n+2]\!] \tag{2}$$

where, $\forall i \in [\![1,n+2]\!]$, $\dot{m}_{\Gamma_i}$ is the interfacial mass flow rate at interface Γ_i between oxy and met_i.
Under H5 and H6, equations associated with oxygen mass conservation in the oxide phase and steel mass conservation in the different metal phases are:

$$\frac{d}{dt}\left(w^O_{oxy} m_{oxy}\right) = 0 \tag{3}$$

$$\frac{d}{dt}\left(w^{steel}_i m_i\right) = 0 \quad \forall i \in [\![1,n+2]\!] \tag{4}$$

Accordingly, at the different interfaces $\{\Gamma_i\}_{i\in[\![1,n+2]\!]}$, jump conditions can be simplified as:

$$w^O_{oxy,\Gamma_i}\dot{m}_{\Gamma_i} + J^O_{oxy,\Gamma_i} S_{\Gamma_i} = 0 \tag{5}$$

$$-w^{steel}_{i,\Gamma_i}\dot{m}_{\Gamma_i} + J^{steel}_{i,\Gamma_i} S_{\Gamma_i} = 0 \tag{6}$$

where the mass fluxes are expressed as:

$$J^O_{oxy,\Gamma_i} = -\rho_{oxy,\Gamma_i} h^O_{oxy,\Gamma_i}\left(w^O_{oxy,\Gamma_i} - w^O_{oxy}\right) \tag{7}$$

$$J^{steel}_{i,\Gamma_i} = -\rho_{i,\Gamma_i} h^{steel}_{i,\Gamma_i}\left(w^{steel}_{i,\Gamma_i} - w^{steel}_i\right) \tag{8}$$

in terms of the interfacial oxygen (resp. steel) mass fraction w^O_{oxy,Γ_i} (resp. w^{steel}_{i,Γ_i}) along with the effective mass transfer coefficients h^O_{oxy,Γ_i} and h^{steel}_{i,Γ_i}.

2.1.2. Interface local equilibrium closure

The closure of the simplified interface jump conditions Eqs. 5 and 6 obtained under H5 and H6 requires an hypothesis that relates the mass fractions on both sides of the interface.
Under the hypothesis of local equilibrium at the interface (H4), w^{steel}_{i,Γ_i} and w^O_{oxy,Γ_i} are linked together as they should belong to a same tie-line. With H5 and H6, the possible equilibrium conditions, as detailed in [6],

can be characterised by a function $f : w^O_{oxy,eq} \mapsto w^{steel}_{met,eq} = f\left(w^O_{oxy,eq}\right)$ constructed from a thermodynamic database.
Combining Eqs. 5 and 6, the interface conditions are then associated with the following non-linear root-finding problem:

$$\text{find } w^O_{oxy,\Gamma_i} \text{ such that } \left\{ \begin{array}{rcl} \rho_{oxy,\Gamma_i} h^O_{oxy,\Gamma_i} \left(w^O_{oxy,\Gamma_i} - w^O_{oxy}\right) f\left(w^O_{oxy,\Gamma_i}\right) & + & \\ \rho_{i,\Gamma_i} h^{steel}_{i,\Gamma_i} \left(f\left(w^O_{oxy,\Gamma_i}\right) - w^{steel}_i\right) w^O_{oxy,\Gamma_i} & = & 0 \end{array} \right. \tag{9}$$

2.1.3. Mass transfer coefficients

Eqs. 7 and 8 or Eq. 9 require the evaluation of effective coefficients associated with the mass transfer between *oxy* and met_i for $i \in [\![1, n+2]\!]$. In the frame of this integral model, it is considered that h^O_{oxy,Γ_i} (resp. h^{steel}_{i,Γ_i}) is to be obtained from the following Sherwood number $Sh_{oxy,\Gamma_i} = \dfrac{h^O_{oxy,\Gamma_i} L_{oxy,\Gamma_i}}{D_{oxy}}$ (resp. $Sh_{i,\Gamma_i} = \dfrac{h^{steel}_{i,\Gamma_i} L_{i,\Gamma_i}}{D_i}$) where L_{oxy,Γ_i} and L_{i,Γ_i} are characteristic lengths and D_{oxy} (resp. D_i), an effective diffusion for O in the oxide phase (resp. for steel in the metallic phase).
For $n+1$ and $n+2$ *i.e* the interface between the oxide and light and heavy metal phases respectively, an analogy between heat and mass transfers is considered to evaluate the Sherwood numbers. Note that this is the same approach as in the PROCOR legacy stratification kinetics model [8]. More precisely, such an analogy takes the form of a correlation that relates *Sh* to the Nusselt number *Nu*:

$$\frac{Sh}{Nu} = Pr^a Sc^b Gr^c \tag{10}$$

where the dimensionless numbers are the Prandlt number $Pr = \frac{\nu}{\alpha}$, the Schmidt number $Sc = \frac{\nu}{D}$ and the Grashof number $Gr = \frac{g\beta L^3 \Delta T}{\nu^2}$ (related to a temperature difference ΔT); a, b, c are exponents that depends on the flow regime (laminar or turbulent natural convection) and $Pr \lesseqgtr 1$. The characteristic length is the layer height in this case. The reader is referred to [12] for more details and the actual exponents values. Note that *Nu* and *Gr* are associated with the intra-layer heat transfer. In practice (see numerical tests of Section 3), they are evaluated by the PROCOR stratified pool thermal model.
For $i \in [\![1, n]\!]$ and the mass transfer between the oxide phase and the metallic droplets, the same closures as in [6] are considered:

- without further knowledge about the "internal" heat (or mass) transfer in the oxide phase, an order of magnitude of 10^4 (consistent with *Sh* value at the oxide pool boundary evaluated through Eq. 10) is considered for Sh_{i,Γ_i} in such a way that the overall mass transfer between *oxy* and met_i is always limited by the droplet internal mass transfer;
- for the dispersed metallic phase, two different correlations for Sh_{i,Γ_i} are considered with d_i, the droplet (equivalent) diameter, as characteristic length. The first one, denoted `Juncu2010`, is based on Direct Numerical Simulations from [13] valid for spherical droplets in the following ranges of Reynolds and Peclet numbers: $0 \leq Re_i = \frac{v_i d_i}{\nu_i} \leq 10^2$, $1 \leq Pe_i = \frac{v_i d_i}{D_i} \leq 10^4$ (and for viscosity and density ratios equal to 1). The second one, `Wegener2014`, is a variant of the Kumar & Hartland correlation [14] based on various experimental data and discussed in [15]. Such a correlation has been established for a wider range of Reynolds number in such a way that mass transfer regimes where the droplet is deformed are covered albeit for an narrow range of interfacial tension that is probably not consistent with our application.

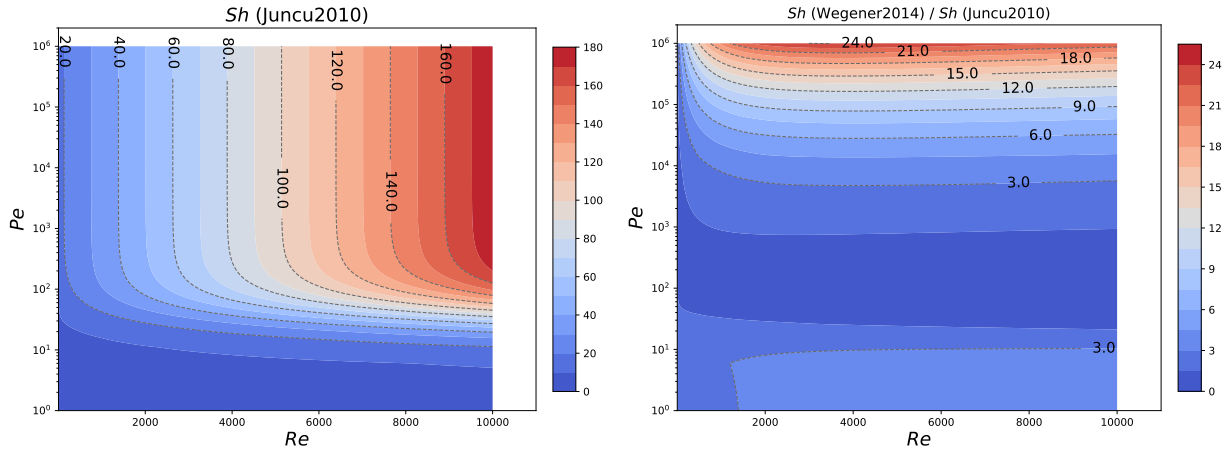

(a) `Juncu2010` **correlation.**

(b) ratio between `Wegener2014` **and** `Juncu2010` **correlations.**

Figure 2. Sherwood number as evaluated from `Juncu2010` **and** `Wegener2014` **correlations for** $0 \leq Re \leq 10^4$**,** $1 \leq Pe \leq 10^6$**.**

None of these two correlations is to be considered as strictly valid for the present application but, based on the results obtained in [6], they are retained in this subsequent analysis to cover a large range for Sh_{i,Γ_i} in a parametric study. As depicted in Figure 2, while both correlations give close results in the $10^2 \leq Pe_i \leq 10^3$ range they differ by one order of magnitude for large Re_i.

2.1.4. Droplet dynamics

For $i \in [\![1,n]\!]$, mass transfer (through Sh_{i,Γ_i} correlation) is dependent on the droplet (rising or falling) velocity with respect to the oxide phase. Assuming a stagnant oxide liquid (see H2), considering a metallic droplet of volume V_i, the 1D momentum equation for $v_{z,i}$ velocity can be written as:

$$\frac{d}{dt}\left[\left(\rho_i + C_M \rho_{oxy}\right) V_i v_{z,i}\right] = V_i \left(\rho_{oxy} - \rho_i\right) g - \text{sign}\left(v_{z,i}\right) \frac{1}{2} C_D S_\perp \rho_i v_{z,i}^2 \tag{11}$$

where C_M is the virtual mass coefficient, C_D is the drag coefficient and $S_\perp = \frac{\pi d^2}{4}$.
The same semi-empirical closure laws as in [6] are considered for C_M and C_D. For a rigid sphere in a fluid, $C_M = \frac{1}{2}$. For C_D, the general correlation proposed in [16], under the form introduced in [17], is used:

$$C_D = \max\left\{\min\left[\max\left(\frac{16}{\frac{v_i}{v_{oxy}}Re_i}, \frac{13.6}{\left(\frac{v_i}{v_{oxy}}Re_i\right)^{4/5}}\right), \frac{48}{\frac{v_i}{v_{oxy}}Re_i}\right], \min\left[\frac{Eo_i}{3}, 0.47 Eo^{1/4} We^{1/2}, \frac{8}{3}\right]\right\} \tag{12}$$

with $Eo_i = \frac{|\rho_{oxy} - \rho_i| g d^2}{\sigma}$, the Eötvös number (ratio between gravitational force and interfacial tension).
Accordingly, the time-dependent position of droplets i, $z_i(t)$ can be obtained from $z_i(t) = \int_{t^0}^{t} v_{z,i}(t)dt + z_i(t^0)$.

2.2. Mass transfers between metallic phases

So far, in Section 2.1, only continuous inter-phase mass transfer have been considered. In addition, discrete time events have to be considered in order to take into account the "appearance" (resp. "disappearance") of a dispersed metal phase by Rayleigh-Taylor instabilities (resp. coalescence by hydrodynamic movement into one of the continuous metal phases) at Γ_{n+1} or Γ_{n+2}.

2.2.1. Droplets relocation into a continuous phase

The different events associated with droplet coalescence into one of the continuous metal phases are defined in terms of the following set of "switching functions" $\left\{g_{j,i}\right\}_{j\in[\![n+1,n+2]\!],i\in[\![1,n]\!]}$ where:

$$g_{j,i}(t) = z_j(t) - z_i(t) \tag{13}$$

i.e. the coalescence of phase met_j into met_{n+1} is assumed to occur when $g_{j,n+1}$ decreases (resp. $g_{j,n+2}$ increases) and reaches zero ($z_i = z_j$). As discussed in Section 2.3, the numerical integration scheme uses, through a root-finding algorithm (see Section 6.3 in [18] for instance for more details), these functions to adapt the time-step and correctly detect the associated instantaneous inter-phase mass transfer.

2.2.2. Rayleigh-Taylor induced droplets formation

The Rayleigh-Taylor instability induced by interfacial mass transfer at Γ_{n+1} or Γ_{n+2} is a complex phenomenon and its description in the frame of an integral model can only be parametric in nature. Here, as in many SA codes (see [4]), the occurrence of such instabilities is to be evaluated through a simple density-based criterion that depends on the continuous phase under consideration. Formally, two switching functions can be defined as:

$$g_{n+1}(t) = \rho_{n+1,\Gamma_{n+1}} - \rho_{oxy} - \Delta\rho^{+} \tag{14}$$

$$g_{n+2}(t) = \rho_{n+2,\Gamma_{n+2}} - \rho_{oxy} + \Delta\rho^{-} \tag{15}$$

where $\Delta\rho^{+}$ and $\Delta\rho^{-}$ are model parameters. Then, droplets formation at interface Γ_{n+1} (resp. Γ_{n+2}) occurs when g_{n+1} increases up to zero (resp. g_{n+2} decreases down to zero).
One has then to estimate the amount of phase met_{n+1} or met_{n+2} that is associated with droplets formation. To do so, as illustrated in Figure 3, a simple piecewise constant steel mass fraction profile is considered in the continuous metal phase in contact with the continuous oxide phase. More precisely, $\forall i \in [\![n+1, n+2]\!]$, an interfacial region (in contact with the oxide) of uniform mass fraction equal to the interface equilibrium value w_{i,Γ_i}^{steel} is distinguished from the bulk characterised by a steel mass fraction denoted $w_{i,\infty}^{steel}$ that is not affected by the interfacial mass transfer. Such a simple approach is qualitatively consistent with the stratification phenomenology in the sense that inter-layer mass transfer is slower than metal relocation through Rayleigh-Taylor instability as discussed in more details in [19, 8] based on the MASCA-RCW experiment analysis [20].

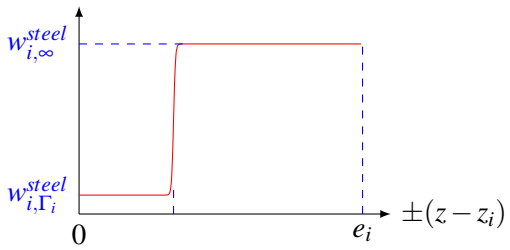

Figure 3. Schematic 1D molar fraction profile in the met_i continuous metal phase – the axis is $(z-z_i)$ (resp. (z_i-z)) for $i=n+1$ (resp. $i=n+2$) and e_i is the metal layer thickness.

Denoting $\tilde{m}_i$, the mass of the boundary region, mass conservation in this phase can be summarised as

$$\tilde{m}_i w_{i,\Gamma_i}^{steel} + (m_i - \tilde{m}_i)\, w_{i,\infty}^{steel} = m_i w_i^{steel} \tag{16}$$

in such a way that the interfacial region mass is simply

$$\tilde{m}_i = \left(\frac{w_i^{steel} - w_{i,\infty}^{steel}}{w_{i,\Gamma_i}^{steel} - w_{i,\infty}^{steel}} \right) m_i \tag{17}$$

It is this boundary region mass $\tilde{m}_i$ that is supposed to "detach" and form a new dispersed metallic phase when g_i reaches zero. The "initial" radius r^{RT} of the new dispersed phase is a model parameter.
The mass fraction $w_{i,\infty}^{steel}$, initially set at w_i^{steel}, is supposed to remain constant during the continuous integration of the conservation equations. When a discrete event associated with one of the $g_{i,j}$ switching function occurs, $w_{i,\infty}^{steel}$ is reset to w_i^{steel} *i.e.* when a dispersed metallic phase met_j coalesces into the continuous met_i, we assume that it makes the mass fractions in met_i spatially uniform. For the light metal layer, it is also the case when molten steel is added to the system.

2.3. Model discretization and implementation

As in [6], this model has been developed as a stand-alone model in the PROCOR platform [7].
Species mixture physical properties (at liquid state) are mostly obtained from the laws proposed in the CORPRO database [21] and available in PROCOR through an interface with the TOLBIAC-ICB code [22]. The interfacial tension between both liquid phases was taken constant equal to 360 $\mathrm{mN.m^{-1}}$ as in [6]. For the effective diffusion coefficients, D_{oxy} is taken equal to $5 \cdot 10^{-9} \mathrm{m^2.s^{-1}}$. This order of magnitude is consistent with U and O self-diffusion coefficients in molten UO_2 as evaluated by molecular dynamics simulations in [23] and close to the optimal value for the effective uranium diffusion coefficient in the oxide phase to be used when comparing PROCOR stratification model to MASCA-RCW experiment, see [7]. Without further information about the diffusion in the metallic phase, the same value is considered for D_{met}.
Thermodynamic equilibrium in the U-O-Zr-steel system is evaluated from the NUCLEA database [24, 25] version 17.1 with the OpenCalphad code [26] as interfaced in PROCOR [27]. For given $R_{U/Zr}$ and C_{Zr}, such equilibrium calculations are performed varying x_{steel} in order to construct f as detailed in [6].
Regarding the time integration of this model, as a trade-off between accuracy and computational complexity, a three-level semi-explicit scheme has been used in order to take into account the three following different time scales: a first one associated with the "slow" inter-layer mass transfer for $i \in [\![n+1, n+2]\!]$ (with an associated macro timestep Δt), a second intermediate one for the mass transfer at interfaces Γ_i, $\forall i \in [\![1, n]\!]$ (with a time step δt) and a last one for the "fast" droplet dynamics (integrated with a five-step Adams-Moulton implicit scheme considering an adaptive time step). A limited convergence analysis of the time discretization was performed and typical values for the time steps Δt and δt used in Section 3 are 10s, 10^{-3}s respectively. While this scheme is explicit, Δt is adjusted when needed to adequately capture any pool layer disappearance (and avoid any negative mass).

3. NUMERICAL RESULTS AND ANALYSIS

In order to assess the model behaviour, two different transients have been considered for a single oxide composition given by $R^{U/Zr} = 1.2$ and $C_{Zr} = 0.5$. The first one, presented in Figure 4 and denoted `HM transient`, is a transient where, starting from an homogeneous oxide pool, molten steel ($x_{steel} = 0.1$) is progressively added during 600s in such a way that the system will evolve toward a two-layer pool with an heavy metal layer at the bottom. This steel mass flow rate of $10\mathrm{kg.s^{-1}}$ is consistent with the order of magnitude observed in reactor applications. In the second one (`LM transient`, see Figure 5), starting from the final state of the previous one, molten steel ($x_{steel} = 0.1$) is further added during 600s and a stratification inversion is expected in such a way that the metal layer is lighter than the oxide one at steady-state. In both cases, metal addition is considered either on top of the pool (`on top`) or as a dispersed phase relocated into the oxide one (`in oxide`) in such a way that the impact of molten steel relocation to the pool can be studied. The initial mass of oxide is $m_{oxy}(0) = 60$t in such a way that 6t of molten steel is added in both `HM`

`transient` and `LM transient` cases. The geometry consists in a 2m−radius hemispherical vessel.

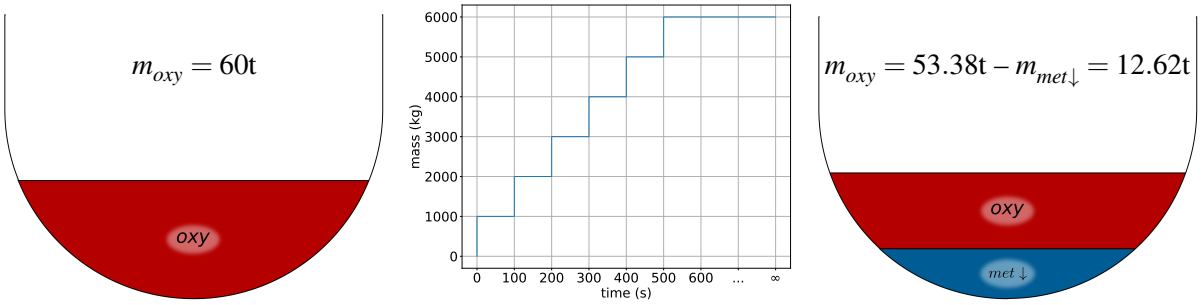

(a) Initial state. **(b) Accumulated mass of molten steel added to the pool as a function of time.** **(c) Expected steady-state.**

Figure 4. Description of the heavy metal formation transient test case (`HM transient`).

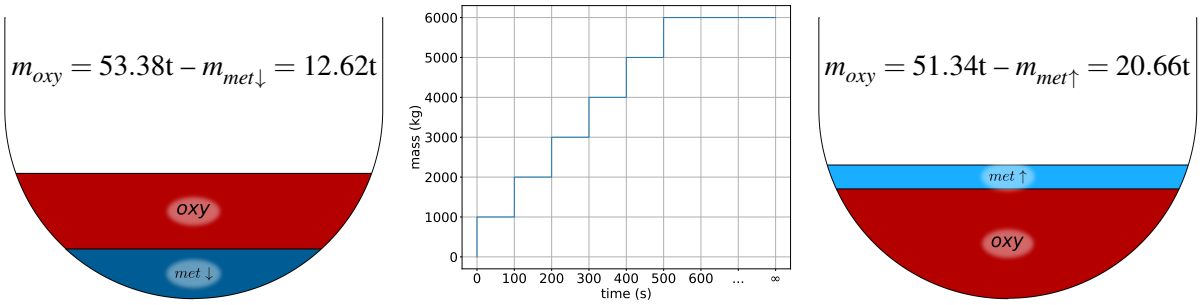

(a) Initial state. **(b) Accumulated mass of molten steel added to the pool as a function of time.** **(c) Expected steady-state.**

Figure 5. Description of the stratification inversion transient test case (`LM transient`).

In all these transients, a same mass density threshold for triggering the Rayleigh-Taylor instabilities $\Delta\rho = \Delta\rho^+ = \Delta\rho^-$ has been considered for both interfaces $\Gamma_{met\uparrow}$ and $\Gamma_{met\downarrow}$. In the `in oxide` cases, two additional parameters regarding the metal addition into the oxide have been defined: r^{in}, the radius of these droplets, and $\tilde{z}^{in}$, the relative axial position of this mass injection (0 – resp. 1 – corresponds to the bottom – resp. top – of the oxide layer). A limited one-at-a-time parametric study has been performed considering the following parameters:

- $\Delta\rho = \Delta\rho^+ = \Delta\rho^- \in \{1, 10, 100\}$kg.m^{-3}, the mass density threshold for triggering Rayleigh-Taylor instabilities;
- $r^{RT} \in \{10^{-3}, 10^{-2}, 5\cdot10^{-2}\}$m, the "initial" radius of droplets detached by Rayleigh-Taylor instabilities;
- Sh_{i,Γ_i} ($\forall i \in [\![1,n]\!]$) with `Juncu2010` or `Wegener2014`, the droplet internal mass transfer correlation.

In the `in oxide` cases, two more parameters have been varied regarding the metal addition into the oxide:

- $r^{in} \in \{10^{-3}, 10^{-2}\}$m, the radius of these droplets;
- $\tilde{z}^{in} \in \{0.1, 0.5, 0.9\}$, the relative axial position of this mass injection: 0 (resp. 1) corresponds to the bottom (resp. top) of the oxide layer.

For these simulations, the Grashof and Nusselt numbers associated with the inter-layer heat transfer are evaluated by the PROCOR stratified pool thermal model; they are updated every 100s (consistently with the usual time step used in the PROCOR-FDC application) or when the pool layer configuration is modified. In the present study, pseudo-stationary Grashof and Nusselt numbers are considered *i.e.* for given masses of the different layers, the steady-state thermal balance is evaluated by the transient PROCOR stratified pool thermal model using a large time step (typically 5000s).
For the sake of comparison, calculations with the legacy stratification model of the PROCOR platform [7] have also been performed when metal is relocated on top of the pool. With this model, the kinetics is controlled by an effective diffusion coefficient for uranium in the oxide phase and it has been set to $10^{-8}\mathrm{m}^2.\mathrm{s}^{-1}$.
For the sake of conciseness, the general trends are presented in the case where $\Delta\rho = 10\mathrm{kg.m}^{-3}$, $r^{RT} = 10^{-2}\mathrm{m}$, `Wegener2014` correlation for Sh_{i,Γ_i}, $r^{in} = 10^{-2}\mathrm{m}$ and $\tilde{z}^{in} = 0.5$ in Section 3.1 while Section 3.2 will provide a synthesis of the impact of the model parameters. These results partially complete the "first-order" study initiated in [6] about the impact of the molten steel relocation path on the overall pool stratification.

3.1. General trends

In order to discuss the general trends exhibited by this model, results are presented in terms of phase masses (Figures 6a and 6b) and steel mass fractions in the metallic phases (Figures 7a and 7b) for the `HM transient` and `LM transient` respectively. Note that, as expected, the steady-state reached by this model is, in any case, consistent with the associated thermodynamic equilibrium conditions. More precisely, the relative difference in the heavy or light metal (resp. oxide) mass is limited to about -1.4% (resp. 0.3 %).
In addition to the continuous phase masses (m_{oxy}, $m_{met\downarrow}$, $m_{met\uparrow}$), the mass of falling (resp. rising) droplets $m_{drop\downarrow}$ (resp. $m_{drop\uparrow}$) is depicted for the `HM transient` (resp. `LM transient`) cases along with the heavy metal (resp. light metal) layer mass as calculated by the PROCOR legacy model denoted $m^{legacy}_{met\downarrow}$ (resp. $m^{legacy}_{met\uparrow}$).
Contrarily to the PROCOR legacy model, this model captures the discontinuous nature of the stratification transient with intermittent droplets detached from the light metal (resp. heavy metal) phase in the `HM transient` (resp. `LM transient`). The frequency of these detachments and the overall kinetics are largely dependent on the transient that is considered and the steel relocation path. The associated trends will now be discussed.
First of all, in the case of the stratification inversion transient (`LM transient`), in both `on top` and `in oxide` cases, the inversion occurs "en bloc" while in the `HM transient`, several droplets detachments can be distinguished. This difference comes from the fact that, contrarily to the light metal layer, the heavy metal layer is formed from a metal under equilibrium conditions with the oxide phase. Then, heat and mass transfer at the bottom of the oxide layer is less effective than through its top surface (associated Nusselt numbers typically differ by one order of magnitude) in such a way that the interfacial mass transfer at $\Gamma_{met\uparrow}$ is faster than at interface $\Gamma_{met\downarrow}$ (as clearly exhibited in Figure 7b). As a consequence, with such a slower mass transfer, at any time, in any transient, the heavy metal average composition follows very closely (in a quasi-static way), the interfacial composition as clearly highlighted in Figures 7a and 7b. Accordingly, the "boundary" metal mass $\tilde{m}_{met\downarrow}$ is close to $m_{met\downarrow}$ (see Eq. 17) *i.e.* the metal layer composition is almost uniform and equal to the interfacial composition. Accordingly, when the density criterion for droplet detachment is met, the heavy metal layer is completely relocated. Note that this trend regarding the heavy metal layer would be the same if another monotonous composition profile (e.g. linear) had been selected.
Then, regarding the influence of the molten steel relocation path, for both `HM transient` and `LM transient`, large differences can be observed, depending if steel is relocated on top (`on top` case) or in the oxide phase as droplets (`in oxide` case). Indeed, the light metal layer that is formed at the beginning of both transients

(associated with the 600s-mass injection, see Figures 4b and 5b) is significantly affected:

- in the `on top` case, pure molten steel directly forms the light metal layer and the U,Zr enrichment of this phase is only associated with the mass transfer through the $\Gamma_{met\uparrow}$ interface, during this 600s-initial period; as such, around 600s, its steel mass fraction is about 0.8 (resp. 0.9) in `HM transient` (resp. `LM transient`);
- in the `in oxide` case, the light metal layer is formed from molten steel droplets rising through the oxide phase in such a way that its composition is significantly affected by the mass transfer between the oxide phase and the droplets; as consequence, around 600s, the steel mass fraction in the light metal layer is about 0.6 (resp. 0.68) in `HM transient` (resp. `LM transient`).

In the `HM transient`, after this initial phase of molten steel injection, this higher U,Zr enrichment in the `in oxide` case is such that the density criterion for triggering the Rayleigh-Taylor instability is met sooner (around 800s). Accordingly, when this criterion is met, the difference in composition between the interface and the bulk light metal is noticeably less important in the `in oxide` in such away that $\tilde{m}_{met\downarrow}/m_{met\downarrow}$ is smaller. As consequence, the mass of relocated droplets is less important. In brief, in the `in oxide` case, droplet detachment occurs more often while in the `on top` case, more droplets are detached at a time. On the overall, the characteristic time associated with the complete heavy metal phase formation is increased by more than 50% in the `on top` case in comparison with the `in oxide` case.
In the `LM transient`, one can notice in Figure 7b that this difference in the light metal layer composition at the beginning of the transient has an indirect impact on the heavy metal layer during the first 600s: indeed, the U,Zr depletion of this layer is much faster in the `in oxide` case during this initial part of the transient. Because of the U,Zr-enrichment of the molten steel droplets, the U,Zr mass transfer from the heavy metal layer to the oxide phase is intensified. As a consequence of this initial "fast" variation of the heavy metal layer composition, the density criterion for phase inversion is met much earlier in the `in oxide` case in comparison with the `on top` case.

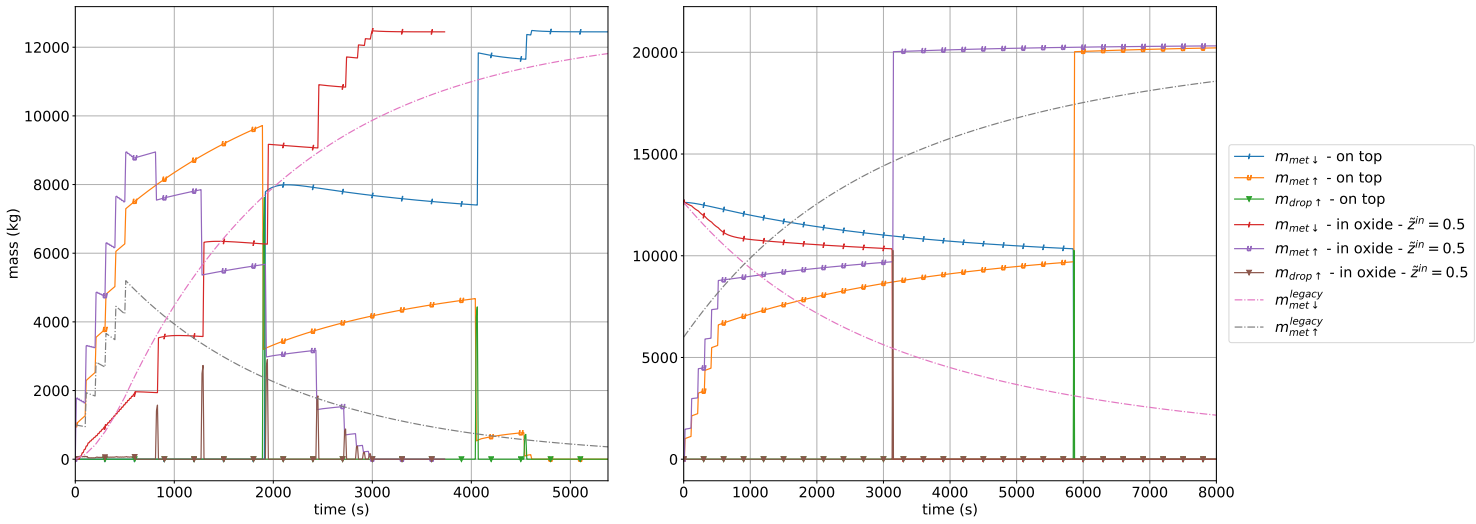

(a) `HM transient`. **(b)** `LM transient`.

Figure 6. Evolution of the phase masses for both `on top` and `in oxide` ($r^{in} = 10^{-2}$m and $\tilde{z}^{in} = 0.5$) cases – $\Delta\rho = 10$kg.m^{-3}, $r^{RT} = 10^{-2}$m, `Wegener2014`.

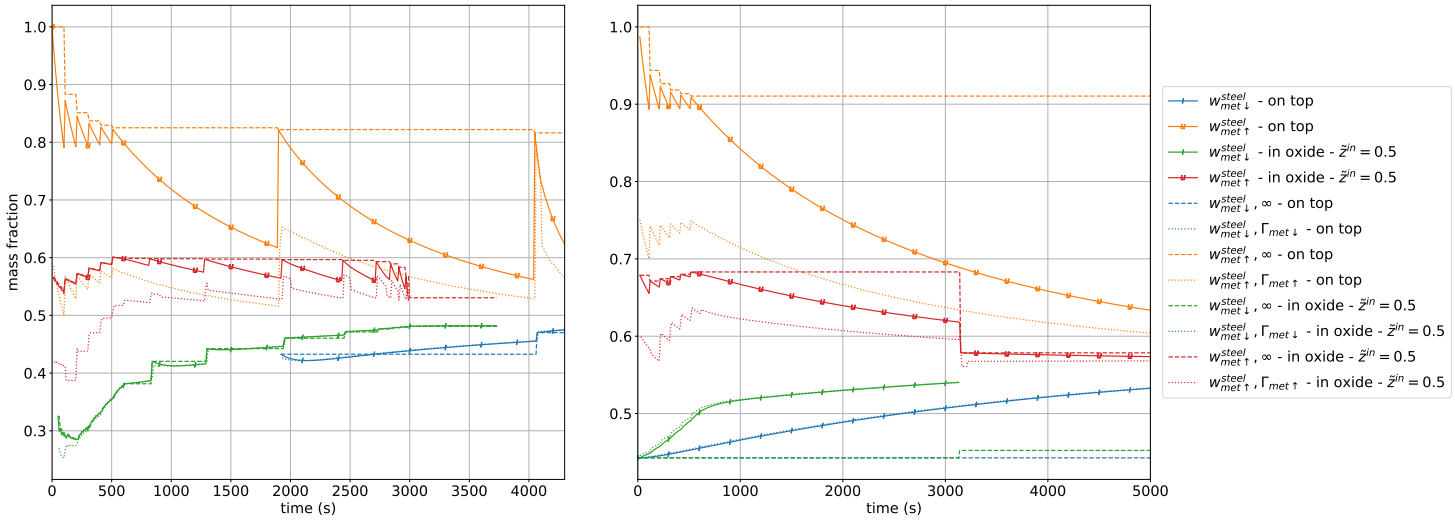

(a) `HM transient`**.** **(b)** `LM transient`**.**

Figure 7. Evolution of the steel mass fractions for both `on top` and `in oxide` ($r^{in} = 10^{-2}$m and $\tilde{z}^{in} = 0.5$) cases – $\Delta\rho = 10$kg.m^{-3}, $r^{RT} = 10^{-2}$m, `Wegener2014`.

3.2. Limited parametric analysis

Only the conclusions of this limited study are reported here for the sake of conciseness.

3.2.1. Effect of $\Delta\rho$

In the `HM transient`, varying $\Delta\rho$ does not affect qualitatively the evolution of the phase masses in both `on top` and `in oxide` cases respectively. However, as expected, it has a strong quantitative impact on the falling droplets detachments sequence: the lower $\Delta\rho$ is, the sooner the associated density criterion is met. When $\Delta\rho$ is increased from 10kg.m^{-3} to 100kg.m^{-3}, the transient characteristic time is increased by about 15% (resp. 30%) in the `on top` (resp. `in oxide`) case.
The only peculiarity that should be noted concerns the `on top` case when $\Delta\rho = 1$kg.m^{-3}. Indeed, in this case, this density criterion is first met during the initial transient phase when molten steel is added in such a way that a limited amount of heavy metal phase is formed around 100s. As a consequence, the subsequent droplet detachment is significantly delayed and the overall transient for $\Delta\rho = 1$kg.m^{-3} is actually slightly longer than the one for $\Delta\rho = 10$kg.m^{-3}.
When considering the `LM transient`, the effect of $\Delta\rho$ is the same: the higher $\Delta\rho$ is, the later, the "en bloc" inversion occurs. While this effect is limited when increasing $\Delta\rho$ from 1kg.m^{-3} to 10kg.m^{-3}, when it is further increased to 100kg.m^{-3}, the inversion time is multiplied by about 2 (resp. 3) in the `on top` (resp. `in oxide`) case.

3.2.2. Effect of r^{RT}

In the `LM transient`, in both `on top` and `in oxide` cases, the impact of the initial droplets radius is very limited and, as expected, can only be seen on the evolution of the light metal layer after stratification inversion has been triggered. Smaller droplets ($r^{RT} = 10^{-3}$m) tend to stay slightly longer in the oxide phase before reaching its top surface and form the light metal layer in such a way that the associated U,Zr-depletion (in comparison with the heavy metal layer) is more important.
In the `HM transient`, for both `on top` and `in oxide` cases, the impact on the overall transient is also

limited *i.e.* the sequence in time of droplets detachments and relocations is only slightly affected (at the most, a time shift of about 200s is observed). However, a qualitative difference can be observed. As discussed before, when the droplets size decreases, they stay longer in the oxide phase in such a way that, in this transient, their U,Zr-enrichment is more important when they coalesce to form the heavy metal phase and, actually, goes above the equilibrium U,Zr-enrichment of the heavy metal phase. Accordingly, between the droplets detachment events, the mass of the heavy metal layer decreases for $r^{RT} = 10^{-3}$m while it increases for $r^{RT} = 10^{-2}$m or $r^{RT} = 5 \cdot 10^{-2}$m.

3.2.3. Effect of Sh_{i,Γ_i}

Parameter Sh_{i,Γ_i} affects the mass transfer between the oxide phase and the dispersed metal phases: the `Wegener2014` correlation leads to a higher mass transfer than the `Juncu2010` correlation.
When considering the `on top` case for both `HM transient` and `LM transient`, the effect of this parameter is limited (and almost zero in the `LM transient`) as it only plays a role on the droplets detached by Rayleigh-Taylor instability. Actually, it is similar as the effect of r^{RT} discussed in the previous section.
In the `in oxide` case, this parameter has also an impact on the droplets from the molten steel relocation into the oxide phase during the first 600s of the transient. With the `Juncu2010` correlation, the U,Zr-enrichment of these droplets is less important in such a way that the light metal layer has initially a larger steel mass fraction. From there, as expected when following the same line of reasoning as in Section 3.1 (when comparing the `in oxide` and `on top` cases), the overall transient characteristic time is significantly larger with the `Juncu2010` correlation in both `HM transient` and `LM transient`.

3.2.4. Effect of r^{in}

As expected from the results in [6], this parameter, that corresponds to the initial size of the droplets injected into the oxide phase in the `in oxide` cases, can have a very strong impact on the phase masses evolution.
Indeed, when considering "small enough" droplets in the `HM transient` (it is the case for $r^{in} = 10^{-3}$m), the kinetics of their U,Zr enrichment is such that their density becomes larger than the oxide phase one before the droplets reaches the top oxide surface. As a consequence, a heavy metal phase is directly formed without any light metal layer during the transient. As such the transient time is largely reduced.
In the `LM transient`, the same effect is observed during the first 200s of the transient with a heavy metal phase mass that increases (by about 30%) when $r^{in} = 10^{-3}$m droplets are considered without formation of a light metal layer. After 200s, the light metal layer starts to appear. In terms of composition, this initial mass flow contains significantly less heavy metal elements in such a way that the average steel mass fraction of the heavy metal phase rapidly increases at the beginning of the transient. It has a large impact on the remainder of the transient as the density inversion threshold is reached at about 600s (in comparison with 3200s for $r^{in} = 10^{-2}$m) with an incomplete mass transfer from the heavy metal layer (a second droplets detachment occurs at about 1200s). In this parametric analysis, this is the only reported `LM transient` simulation where the stratification inversion does not occur "en bloc".

3.2.5. Effect of $\tilde{z}^{in}$

As expected, in both `HM transient` and `LM transient` transients, the closer to the top of the oxide pool this steel injection is, the closer to the `on top` result the `in oxide` simulation is. However, the effect of this parameter is strongly non-linear as it is directly related to the droplets residence time in the oxide phase (and their associated level of U,Zr enrichment as discussed previously for other parameters). In the `HM transient` (resp. `LM transient`), the complete disappearance of the light (resp. heavy) metal is delayed by about 100s (resp. 1100s) in the `on top` case in comparison with the `in oxide` case with $\tilde{z}^{in} = 0.9$.

4. CONCLUSIONS AND PERSPECTIVES

An enhanced integral model dedicated to in-vessel corium stratification has been proposed and implemented as a "mock-up" model in the PROCOR platform. In particular, it takes into account dispersed metal phases into the continuous oxide phase, either from a direct molten steel relocation into the oxide, or from droplets detached from the interface between a continuous metal metal layer and the oxide layer because of Rayleigh-Taylor instabilities. In this work, the PROCOR platform is used for model development and parametric analysis independently of any PROCOR application. As such, this model was compared with the PROCOR legacy stratification kinetics model but has not been introduced into the PROCOR-FDC application; this is a clear perspective of this work so that the overall impact on the heat distribution at the pool boundary can be assessed.

A limited parametric analysis has been reported. It has confirmed (and even reinforced) the conclusions of [6] regarding the possible impact of molten steel direct relocation into the oxide phase in comparison with a relocation on the top of the pool. Indeed, the U,Zr enrichment of the metal droplets during their residence time in the oxide phase significantly affects the remainder of the stratification transients in all cases. Consistently with [6], the parameters that affect this mass transfer are shown to have a significant impact on the overall stratification kinetics.

In comparison with [6], additional model parameters had to be introduced in the present model regarding Rayleigh-Taylor instabilities. Among them, this study suggests that the most important one is the associated density threshold. Further work is required for making recommendation regarding a value range for this parameter. As a starting point, a more detailed analysis based on the simulation of the MASCA-RCW test with the present model is recommended to go further in this model parametrization. CFD simulations (typically, the phase-field modelling under study for stratification kinetics [28]) could also be very useful for this matter.

These results have also highlighted an important qualitative difference between the two kinds of stratification transients: heavy metal phase formation or stratification inversion. In the latter, the heavy metal phase average composition always stays close to its interface composition equilibrium with the oxide and, accordingly, when the density criterion associated with the Rayleigh-Taylor instability is met, the heavy metal layer is, in most cases, completely relocated at the top of the pool. During the heavy metal phase formation, the situation is drastically different as the light metal layer is not initially close to equilibrium with the oxide in such a way that several intermittent droplets detachment are observed. This qualitative difference regarding these two transient types is an important finding of this work that requires further confirmation (through CFD simulations and, in a longer term, by experimental results).

The high sensitivity of the stratification transients to the molten steel relocation "path" that this model highlights shows that it is necessary to go further and gain knowledge about the molten steel relocation "path" through the crust to the oxidic pool. Thermochemistry (dissolution [29]) and thermomechanics phenomena need to be considered; while the former is an "active" research theme, the latter remains to be explored.

One should also recall that some of the hypotheses introduced in [6] and used in the present work may affect the quantitative predictive capability of the present model. First, the simplification of the thermodynamic system $\{O,U,Zr,steel\}$ could be improved by lifting the hypothesis of a uniform and constant U/Zr molar ratio. Then, the oxidic phase is not stagnant and, as discussed in [6], even if the droplet velocity is larger than the oxide one, convection in the oxide phase probably plays a role in the recirculating zone along the lateral boundary of the pool and will modify the droplets residence time in the oxide phase. Once again, more detailed simulations at a finer scale using CFD would be very valuable to further quantify these effects.

NOMENCLATURE

Greek letters

α	thermal diffusivity	$m^2.s^{-1}$
β	thermal expansion coefficient	K^{-1}
Γ_i	interface between spatial domains Ω_{oxy} and Ω_{met_i}	
μ	dynamic viscosity	Pa.s
ν	kinematic viscosity $\nu = \frac{\mu}{\rho}$	$m^2.s^{-1}$
$\Omega_\star$	spatial domain $\star$	
ρ	mass density	$kg.m^{-3}$
σ	interfacial tension	$N.m^{-1}$

Subscripts and superscripts

in	initial state of the molten steel droplets relocated into the oxide phase
met_i or i	metal phase, either continuous on top ($i = n+1$) or at the bottom ($i = n+2$) of the pool, or discontinuous ($\forall i \in [\![1,n]\!]$)
n	time-dependent number of discontinuous metal phases
oxy	continuous oxide phase
$\star$	met_i ($\forall i \in [\![1,n+2]\!]$) or *oxy*

Latin letters

C_{Zr}	Zr molar oxidation index	
D	mass diffusion coefficient	$m^2.s^{-1}$
d (resp. r)	droplet (equivalent) diameter (resp. radius)	m
e	layer thickness	m
g	gravitational acceleration	$m.s^{-2}$
$h^c_{\star,\Gamma}$	effective mass transfer coefficient relative to component c at interface Γ for phase $\star$	$m.s^{-1}$
J^j	component j mass flux	$kg.m^{-2}.s^{-1}$
$L_{\star,\Gamma}$	characteristic length associated with phase $\star$ for mass transfer at interface Γ	m
$m_\star$	mass of $\Omega_\star$	kg
$\dot{m}_{\star,\Gamma}$	total mass flow rate through Γ (counted positive when leaving from $\Omega_\star$)	$kg.s^{-1}$
$R_{U/Zr}$	U/Zr molar ratio	
S	area	m^2
V	volume	m^3
v	velocity norm	$m.s^{-1}$
v_z	axial velocity component	$m.s^{-1}$
w^j	component j mass fraction	
x_{steel}	global initial mass ratio between steel and oxide	
z	axial position	m
$\tilde{z}$	normalized axial position in the oxide layer	

ACKNOWLEDGMENTS

This work was funded in the framework of the PROCOR platform development by CEA, EDF and Framatome.

REFERENCES

[1] R. E. Henry and H. K. Fauske, "External cooling of a reactor vessel under severe accident conditions," *Nuclear Engineering and Design*, vol. 139, no. 1, pp. 31 – 43, 1993.

[2] H. Tuomisto and T. Theofanous, "A consistent approach to severe accident management," *Nuclear Engineering and Design*, vol. 148, no. 2, pp. 171 – 183, 1994.

[3] F. Fichot, L. Carénini, R. Le Tellier, L. Viot, N. Bakouta, and A. Filippov, "Identification and evaluation of the remaining uncertainties for transient situations," in *Proc. of International Seminar "In-vessel retention: outcomes of IVMR project"*, Juan-les-Pins, France, January 2020.

[4] R. Le Tellier, L. Viot, L. Carénini, F. Fichot, N. Bakouta, and A. Filippov, "Transient stratified corium pool modelling for in-vessel retention analysis," in *Proc. of International Seminar "In-vessel retention: outcomes of IVMR project"*, Juan-les-Pins, France, January 2020.

[5] R. Le Tellier, B. Habert, V. Tiwari, and N. Bakouta, "Consistent use of CALPHAD data for in-vessel corium pool modeling: some analytical and practical considerations," in *Proc. of the 9th European Review Meeting on Severe Accident Research ERMSAR2019*, Prague, Czech Republic, 2019.

[6] R. Le Tellier, "Mass transfer between a continuous oxide phase (U-O-Zr) and a steel droplet at liquid state: Potential impact on corium pool behaviour during in-vessel melt retention," *Nuclear Engineering and Design*, vol. 385, p. 111525, Dec. 2021.

[7] R. Le Tellier, L. Saas, and F. Payot, "Phenomenological analyses of corium propagation in LWRs: the PROCOR software platform," in *Proc. of the 7th European Review Meeting on Severe Accident Research ERMSAR-2015*, Marseille, France, 2015.

[8] R. Le Tellier, L. Saas, and S. Bajard, "Transient stratification modelling of a corium pool in a LWR vessel lower head," *Nuclear Engineering and Design*, vol. 287, pp. 68–77, 2015.

[9] L. Carénini and F. Fichot, "Evaluation of the kinetics of molten pool stratification in case of in-vessel melt retention strategy," in *Proc. of 26th International Conference on Nuclear Engineering ICONE 26*, London, England, 2018.

[10] M. Salay and F. Fichot, "Modelling of metal-oxide corium stratification in the lower plenum of a reactor vessel," in *Proc. of Int. Topical Meeting on Nuclear Thermal-Hydraulics (NURETH-11)*, Avignon, France, 2005.

[11] S. Nandan, F. Fichot, and B. Piar, "A simplified model for the quaternary U-Zr-Fe-O system in the miscibility gap," *Nuclear Engineering and Design*, vol. 364, p. 110608, 2020.

[12] J. M. Seiler, K. Froment, and J. P. Garandet, "Equations for solidification of corium without sparging gas - scaling criteria," in *Proc. of OECD Workshop on Ex-Vessel Debris Coolability*. Karlsruhe, Germany: OECD, 1999.

[13] G. Juncu, "A numerical study of the unsteady heat/mass transfer inside a circulating sphere," *International Journal of Heat and Mass Transfer*, vol. 53, pp. 3006–3012, 2010.

[14] A. Kumar and S. Hartland, "Correlations for prediction of mass transfer coefficients in single drop systems and liquid-liquid extraction columns," *Transactions IChemE*, vol. 77, no. A, pp. 372–384, 1999.

[15] M. Wegener, N. Paul, and M. Kraume, "Fluid dynamics and mass transfer at single droplet in liquid/liquid systems," *International Journal of Heat and Mass Transfer*, vol. 71, pp. 475–495, 2014.

[16] G. B. Wallis, "The terminal speed of single drops or bubble in an infinite medium," *International Journal of Multiphase Flow*, vol. 1, pp. 491–511, 1974.

[17] P. Di Marco, W. Grassi, and G. Memoli, "Experimental study of rising velocity of nitrogen bubble in FC-72," *International Journal of Thermal Sciences*, vol. 42, pp. 435–446, 2003.

[18] G. K. Gupta, R. Sacks-Davis, and P. E. Tischer, "A review of recent developments in solving ODEs," *Computing Surveys*, vol. 17, no. 1, pp. 5–47, 1985.

[19] G. Ratel, F. Deffort, K. Froment, B. Tourniaire, and J. M. Seiler, "Considerations on mass transfer kinetics for layer inversion and layer oxidation: from MASCA program to the reactor situation," in *Proc. of MASCA-2 Seminar*, Cadarache, France, 2007.

[20] V. G. Asmolov, S. S. Abalin, Y. A. Veselkin, V. Y. Vishnevsky, V. V. Vlasov, B. L. Gershman, Y. G. Degaltsev, Y. K. Dyakov, J. F. Isaev, A. N. Kiselev, N. P. Kiselev, A. M. Kovalev, A. G. Ol'khovsky, K. V. Pechalin, L. M. Semenov, V. F. Strizhov, T. V. Trushkina, V. S. Uglov, Y. M. Utkin, V. V. Chudanov, A. E. Aksenova, V. A. Pervichko, and L. M. Khazanivich, "RCW post-test analysis results," Russian Research Centre Kurchatov Institute, Technical Report MP-TR-11, 2003.

[21] C. Journeau, P. Piluso, and K. N. Frolov, "Corium physical properties for severe accident r&d," in *Proc. of the 2004 international congress on advances in nuclear power plants - ICAPP'04*, 2004.

[22] B. Spindler, B. Tourniaire, and J. M. Seiler, "Simulation of MCCI with the TOLBIAC-ICB code based on the phase segregation model," *Nuclear Engineering and Design*, vol. 236, pp. 2264–2270, 2006.

[23] A. Y. Kupryazhkin, A. N. Zhiganov, D. V. Risovany, K. A. Nekrassov, V. D. Risovany, and V. N. Golovanov, "Simulation of diffusion of oxygen and uranium in uranium dioxide nanocrystals," *Journal of Nuclear Materials*, vol. 372, pp. 233–238, Jan. 2008.

[24] B. Cheynet, P. Chevalier, and E. Fischer, "Thermosuite," *Calphad*, vol. 26, no. 2, pp. 167–174, 2002.

[25] S. Bakardjieva, M. Barrachin, S. Bechta, D. Bottomley, L. Brissoneau, B. Cheynet, E. Fischer, C. Journeau, M. Kiselova, L. Mezentseva, P. Piluso, and T. Wiss, "Improvement of the european thermodynamic database NUCLEA," *Progress in Nuclear Energy*, vol. 52, no. 1, pp. 84–96, 2010.

[26] B. Sundman, U. R. Kattner, M. Palumbo, and S. G. Fries, "OpenCalphad - a free thermodynamic software," *Integrating Materials and Manufacturing Innovation*, vol. 4, no. 1, 2015.

[27] B. Sundman, U. R. Kattner, C. Sigli, M. Stratmann, R. Le Tellier, M. Palumbo, and S. G. Fries, "The OpenCalphad thermodynamic software interface," *Computational Materials Science*, vol. 125, pp. 188–196, 2016.

[28] R. Zanella, R. L. Tellier, M. Plapp, G. Tegze, and H. Henry, "Three-dimensional numerical simulation of droplet formation by Rayleigh–Taylor instability in multiphase corium," *Nuclear Engineering and Design*, vol. 379, p. 111177, Aug. 2021.

[29] A. Pivano, P. Piluso, N. Chikhi, P. Fouquart, J. Delacroix, and R. Le Tellier, "Experiments on interactions of molten steel with suboxidized corium crust for in-vessel melt retention," *Nuclear Engineering and Design*, vol. 355, p. 110271, 2019.

Integral modelling of continuous/dispersed phases mass transfer during in-vessel corium stratification transients

DE LA RECHERCHE À L'INDUSTRIE

ERMSAR 2022

The 10th European Review Meeting on Severe Accident Research

May 16, 2022

Romain Le Tellier

IRESNE/DTN/SMTA/LMAG

Institut de recherche sur les systèmes pour la production d'énergie bas carbone

Context

- *In-Vessel Melt Retention* $\rightarrow$ corium pool behaviour in the vessel lower head
- U-O-Zr-steel liquid miscibility gap $\Longrightarrow$ complex *stratification transients*
  $\rightarrow$ a major role on the boundary heat flux distribution

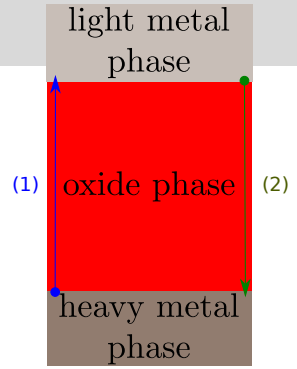

Context

- *In-Vessel Melt Retention* → corium pool behaviour in the vessel lower head
- U-O-Zr-steel liquid miscibility gap ⟹ complex *stratification transients*
  → a major role on the boundary heat flux distribution
- *Key phenomena* that drive the pool stratification [Fichot et al., 2020]:

  1. the *molten steel relocation* into the pool (internal structures and vessel wall ablation)
  2. the *mass transfer* among the pool phases

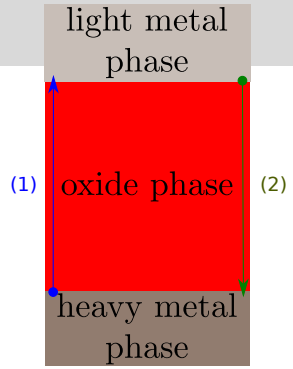

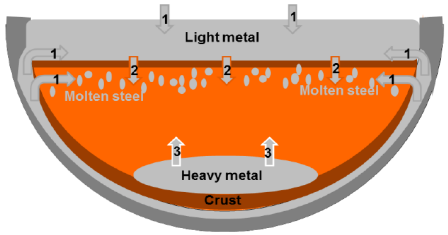

Context

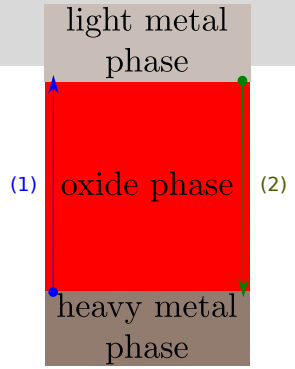

- *In-Vessel Melt Retention* → corium pool behaviour in the vessel lower head
- U-O-Zr-steel liquid miscibility gap ⟹ complex *stratification transients*
  → a major role on the boundary heat flux distribution
- *Key phenomena* that drive the pool stratification [Fichot et al., 2020]:

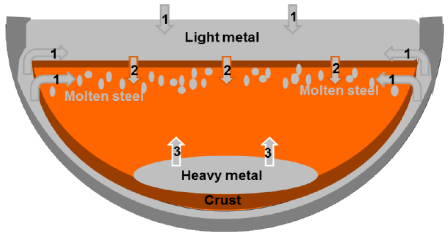

1. the *molten steel relocation* into the pool (internal structures and vessel wall ablation)
2. the *mass transfer* among the pool phases

- Both phenomena come with a *large uncertainty*:

1. relocation of steel from the *vessel wall ablation*
   - depends on the *refractory crust behaviour* (formation, possible dissolution by molten metal, mechanical stability)
   - in SA codes: no modelling, different hypotheses [Le Tellier et al., 2020]

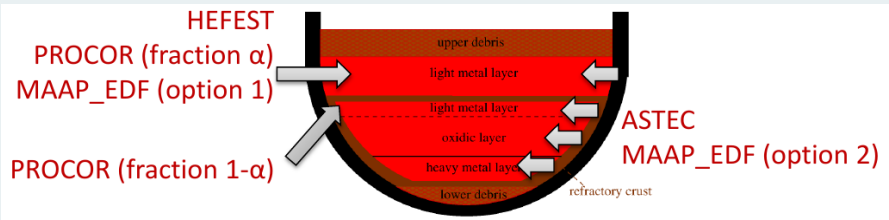

2. very incomplete knowledge about *mass transfer kinetics*
   - limited experimental data
   - *only simplified integral models* in SA codes in need for validation/parameter calibration

This work

To go ahead: modelling of the *dispersed metal phase in the oxide*

1. assuming *permeable crust*: steel droplets into the oxide (homogeneous treatment inadequate [Le Tellier et al., 2019])
2. impact of the *metal droplets - oxide mass transfer* on stratification transients

This work

To go ahead: modelling of the *dispersed metal phase in the oxide*

1. assuming *permeable crust*: steel droplets into the oxide (homogeneous treatment inadequate [Le Tellier et al., 2019])
2. impact of the *metal droplets - oxide mass transfer* on stratification transients

Previous work: mono-dispersed molten steel phase into infinite oxide phase [Le Tellier, 2021]

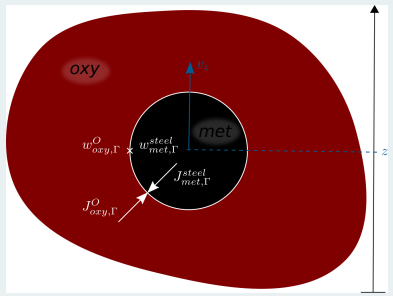

- *"first-order" simplifying hypotheses*
- two-zone integral isothermal model for mass transfer coupled with 1D momentum conservation equation for droplets dynamics
- main conclusions of limited parametric study:
  - *"mixed" dispersed phase* only stable for *very limited composition* range near inversion threshold
  - *droplets short residence time* (few seconds) in the oxide but *significant U, Zr enrichment*

→ *impact on the overall stratification transients?*

This work

To go ahead: modelling of the *dispersed metal phase in the oxide*

1. assuming *permeable crust*: steel droplets into the oxide (homogeneous treatment inadequate [Le Tellier et al., 2019])
2. impact of the *metal droplets - oxide mass transfer* on stratification transients

Previous work: mono-dispersed molten steel phase into infinite oxide phase [Le Tellier, 2021]

- *"first-order" simplifying hypotheses*
- two-zone integral isothermal model for mass transfer coupled with 1D momentum conservation equation for droplets dynamics
- main conclusions of limited parametric study:
  - *"mixed" dispersed phase* only stable for *very limited composition* range near inversion threshold
  - *droplets short residence time* (few seconds) in the oxide but *significant U, Zr enrichment*

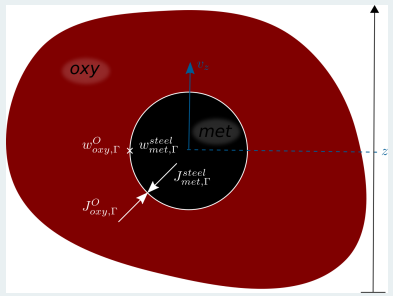

→ *impact on the overall stratification transients?*

Present work: integral *stratification model* taking into account *dispersed metal phases in the oxide*

- molten steel "direct" relocation
- droplets detached by Rayleigh-Taylor (RT) instabilities

Contents

- Modelling
- Numerical discretization and implementation
- Numerical results
- Summary and perspectives

Modelling - Hypotheses - Mass conservation equations

- Same *"first-order" hypotheses* as [Le Tellier, 2021]

  - mono-dispersed droplets – no droplets interaction
  - stagnant oxide phase for droplet dynamics
  - decoupling between inter-phase mass transfer and heat transfer
  - simplified U-O-Zr-steel system: uniform $R_{U/Zr}$, steel in metal, O in oxide [Nandan et al., 2020]
    $\rightarrow$ two pseudo-binary systems: $(U, Zr) + O$ and $(U, Zr) + steel$
    $\rightarrow$ construction of $f : w^{O}_{oxy,eq} \mapsto w^{steel}_{met,eq}$ from NUCLEA database
  - local chemical equilibrium at the interfaces (jump conditions closed with f)

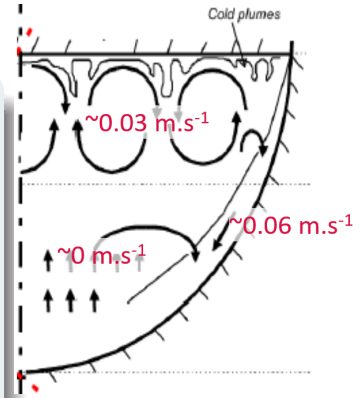

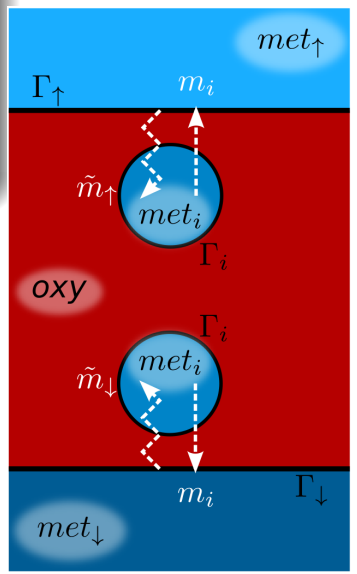

Modelling - Hypotheses - Mass conservation equations

- Same *"first-order" hypotheses* as [Le Tellier, 2021]

  - mono-dispersed droplets – no droplets interaction
  - stagnant oxide phase for droplet dynamics
  - decoupling between inter-phase mass transfer and heat transfer
  - simplified U-O-Zr-steel system: uniform $R_{U/Zr}$, steel in metal, O in oxide [Nandan et al., 2020]
    $\rightarrow$ two pseudo-binary systems: $(U, Zr) + O$ and $(U, Zr) + steel$
    $\rightarrow$ construction of $f : w^O_{oxy,eq} \mapsto w^{steel}_{met,eq}$ from NUCLEA database
  - local chemical equilibrium at the interfaces (jump conditions closed with f)

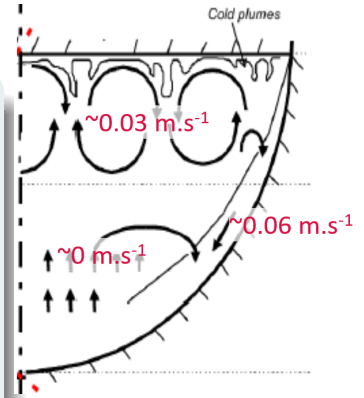

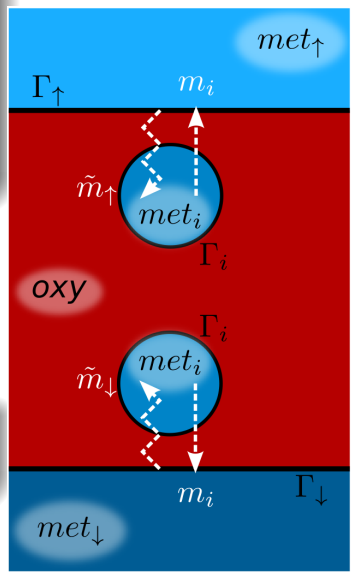

- *Mass conservation equations* incl. continuous transfer between $met_\star$ and *oxy*

  - in terms of *interfacial O/steel mass fluxes*

$$J^O_{oxy,\Gamma_\star} = -\rho_{oxy,\Gamma_\star} h^O_{oxy,\Gamma_\star} \left(w^O_{oxy,\Gamma_\star} - w^O_{oxy} \right) \quad \text{and} \quad J^{steel}_{met,\Gamma_\star} = \dots$$

  - with *interface conditions* reduced to

$$\text{find } w^O_{oxy,\Gamma_\star} \text{ such that } \left\{ \begin{array}{rcl} \rho_{oxy,\Gamma_\star} h^O_{oxy,\Gamma_\star} \left(w^O_{oxy,\Gamma_\star} - w^O_{oxy} \right) f\left(w^O_{oxy,\Gamma_\star} \right) & + & \\ \rho_{met,\Gamma_\star} h^{steel}_{met,\Gamma_\star} \left(f\left(w^O_{oxy,\Gamma_\star} \right) - w^{steel}_{met_\star} \right) w^O_{oxy,\Gamma_\star} & = & 0 \end{array} \right.$$

Modelling - Mass transfer coefficient closures

- $h^{O/steel}_{oxy/met_\star,\Gamma_\star}$ from *Sherwood number* with $D^O_{oxy} = D^{steel}_{met_\star} \sim 5 \cdot 10^{-9} \mathrm{m}^2.\mathrm{s}^{-1}$

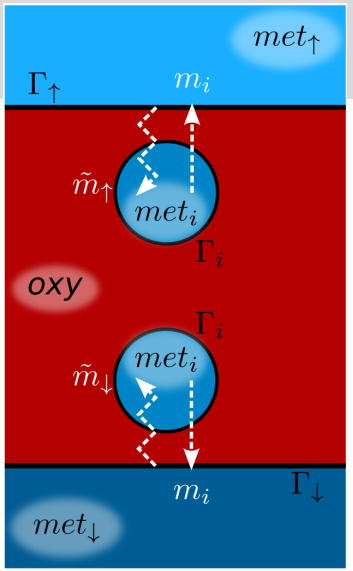

Modelling - Mass transfer coefficient closures

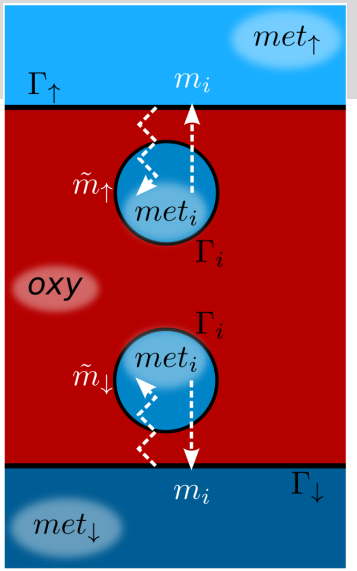

- $h^{O/steel}_{oxy/met_\star,\Gamma_\star}$ from *Sherwood number* with $D^O_{oxy} = D^{steel}_{met_\star} \sim 5 \cdot 10^{-9} \mathrm{m}^2.\mathrm{s}^{-1}$
- For *continuous metal phase interfaces* $\Gamma_\uparrow$ and $\Gamma_\downarrow$:
  - *heat/mass transfer analogy* $\frac{Sh}{Nu} = Pr^a Sc^b Gr^c$ [Seiler et al., 1999]
  - *Nu* for *intra-layer heat transfer* $\rightarrow$ evaluated by the stratified pool integral thermal model using $Nu = f(Ra, Pr, \dots)$ correlations

Modelling - Mass transfer coefficient closures

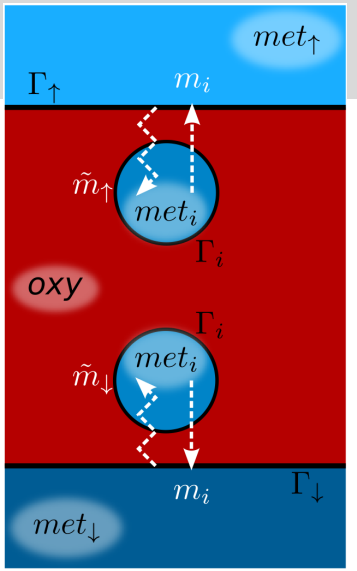

- $h^{O/steel}_{oxy/met_\star,\Gamma_\star}$ from *Sherwood number* with $D^O_{oxy} = D^{steel}_{met_\star} \sim 5 \cdot 10^{-9} \mathrm{m}^2.\mathrm{s}^{-1}$
- For *continuous metal phase interfaces* $\Gamma_\uparrow$ and $\Gamma_\downarrow$:
  - *heat/mass transfer analogy* $\frac{Sh}{Nu} = Pr^a Sc^b Gr^c$ [Seiler et al., 1999]
  - *Nu* for *intra-layer heat transfer* $\rightarrow$ evaluated by the stratified pool integral thermal model using $Nu = f(Ra, Pr, \dots)$ correlations
- For *dispersed metal interfaces* Γ_i (as [Le Tellier, 2021]):
  - Sh_{oxy} *considered to be high* (10^4) $\rightarrow$ mass transfer limited by droplet internal mass transfer
  - $Sh_{met_i} = f(Re_{met_i}, Pe_{met_i}, \dots)$ by `Juncu2010` and `Wegener2014` correlations

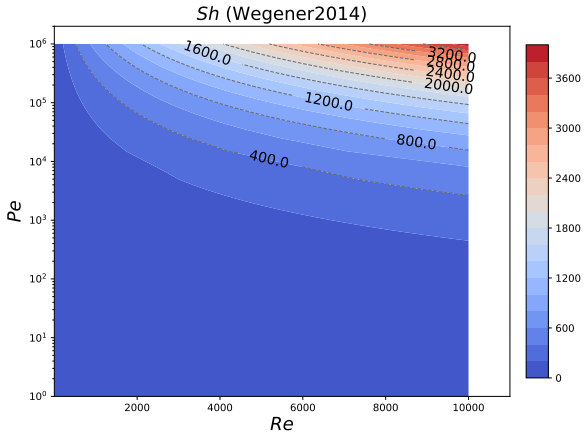

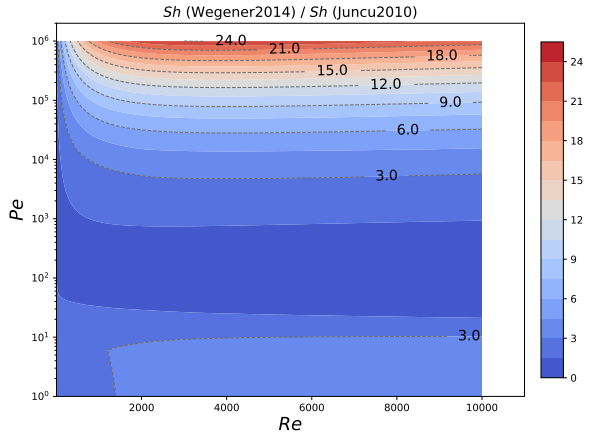

- None is to be considered as strictly valid for the present application
- Cover a large range for Sh_{i,Γ_i} (close for $10^2 \leq Pe_i \leq 10^3$, one order of magnitude difference for large Pe_i) $\rightarrow$ *parametric study*

- *Droplet dynamics*: 1D momentum eq. for velocity $v_{z,i}$ of dispersed met_i phase:

$$\frac{d}{dt}\left[(\rho_i + \underbrace{C_M \rho_{oxy}) V_i}_{\text{virtual mass}} v_{z,i}\right] = V_i \left(\rho_{oxy} - \rho_i\right) g - \underbrace{\text{sign}\left(v_{z,i}\right) \frac{1}{2} C_D S_\perp \rho_i v_{z,i}^2}_{\text{drag force}}$$

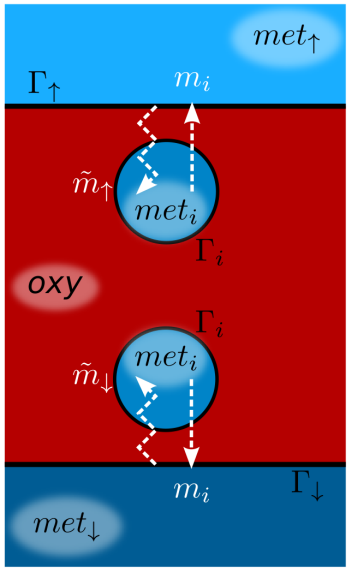

Modelling - Droplet dynamics - Metal phases transfers

- *Droplet dynamics*: 1D momentum eq. for velocity $v_{z,i}$ of dispersed met_i phase:

$$\frac{d}{dt}\left[\left(\rho_i + \underbrace{C_M \rho_{oxy}}_{\text{virtual mass}}\right) V_i \, v_{z,i}\right] = V_i \left(\rho_{oxy} - \rho_i\right) g - \underbrace{\text{sign}\left(v_{z,i}\right) \frac{1}{2} C_D S_\perp \rho_i v_{z,i}^2}_{\text{drag force}}$$

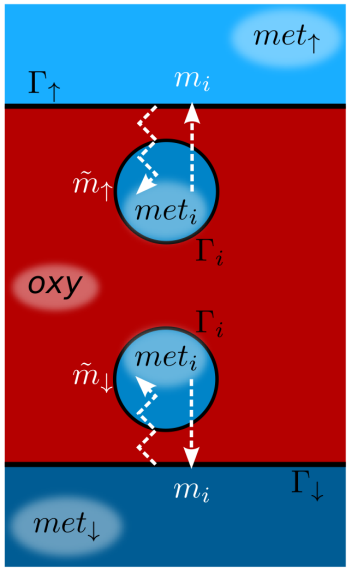

- *Discrete events* for discontinuous *mass transfer between metal phases*
  - *droplets* $\rightarrow$ *continuous phase*
  - *Rayleigh-Taylor* (RT) induced droplets formation
    - simple density difference threshold criteria for RT triggering

$$\rho_{met,\Gamma_\uparrow} - \rho_{oxy} > \Delta\rho^+ \qquad \rho_{met,\Gamma_\downarrow} - \rho_{oxy} < -\Delta\rho^-$$

    - when criterion met (t_{RT}), droplets (radius r^{RT}) detachment from continuous $met_\star$ phase:

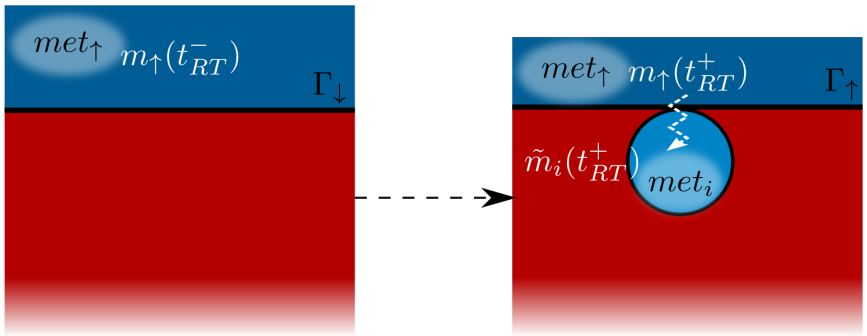

(assuming stepwise intra-layer composition profile)

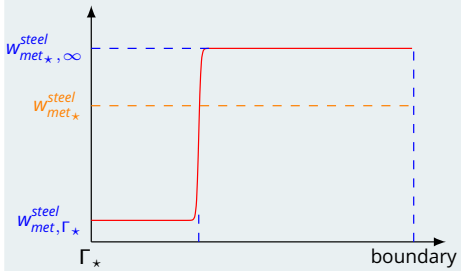

$$\frac{\tilde{m}_\star(t_{RT}^+)}{m_\star(t_{RT}^-)} = \left(\frac{w^{steel}_{met_\star} - w^{steel}_{met_\star,\infty}}{w^{steel}_{met,\Gamma_\star} - w^{steel}_{met_\star,\infty}}\right)$$

Numerical discretization and implementation

Time discretization: *Three-level semi-explicit scheme*

Associated with the following time scales:

- *"slow" inter-layer mass transfer* ($\sim$ 1000s) $\rightarrow$ macro time step Δt ($\sim$ 10s)
- *"intermediate" mass transfer at droplets interfaces* ($\sim$ 10s) $\rightarrow$ time step δt ($\sim 10^{-2}$s)
- *"fast" droplets dynamics* ($\sim$ 1s) $\rightarrow$ time step $< 0.1\delta t$ (adaptive Adams-Moulton implicit scheme)

N.B. Explicit scheme but Δt adjusted to adequately capture any pool layer disappearance

Numerical discretization and implementation

Time discretization: *Three-level semi-explicit scheme*

Associated with the following time scales:

- *"slow" inter-layer mass transfer* ($\sim$ 1000s) $\rightarrow$ macro time step Δt ($\sim$ 10s)
- *"intermediate" mass transfer at droplets interfaces* ($\sim$ 10s) $\rightarrow$ time step δt ($\sim 10^{-2}$s)
- *"fast" droplets dynamics* ($\sim$ 1s) $\rightarrow$ time step $< 0.1\delta t$ (adaptive Adams-Moulton implicit scheme)

N.B. Explicit scheme but Δt adjusted to adequately capture any pool layer disappearance

Implementation: a model *in the PROCOR platform* [Le Tellier et al., 2015]

- *Nu*, *Gr* for intra-layer heat transfer: evaluated using the PROCOR stratified pool thermal model
- comparison with the legacy PROCOR stratification model [Le Tellier et al., 2015]

Numerical results – Setup

Two *"idealized" transients* representative of *PWR IVR conditions*

2m−radius hemispherical vessel – $R^{U/Zr} = 1.2$, $C_{Zr} = 0.5$

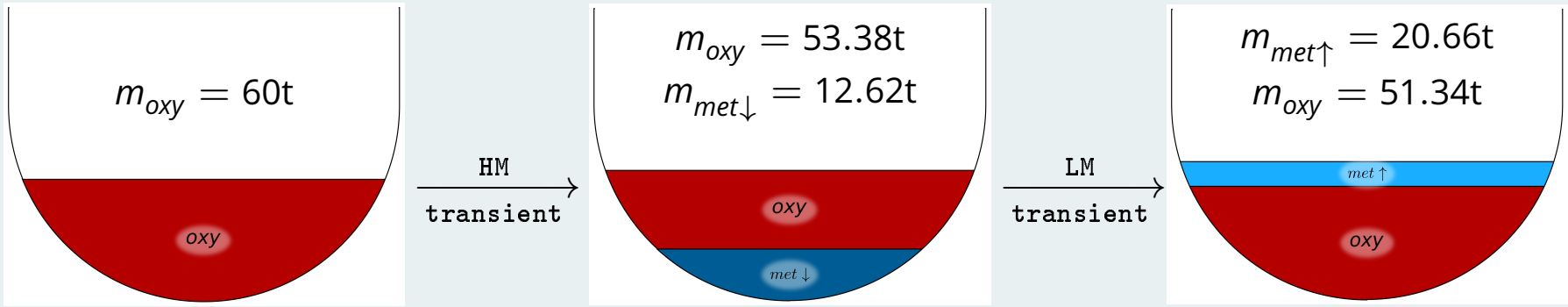

$x_{steel} = 0$ $x_{steel} = 0.1$ $x_{steel} = 0.2$

Steel injection (6t in 500s) *on top* of the pool (`on top`) or *into the oxide* as droplets (`in oxide`)

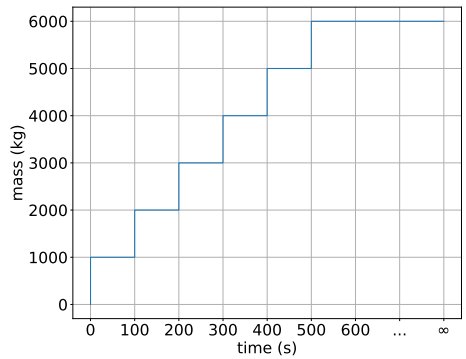

Numerical results – Setup

Two *"idealized" transients* representative of *PWR IVR conditions*

2m−radius hemispherical vessel – $R^{U/Zr} = 1.2$, $C_{Zr} = 0.5$

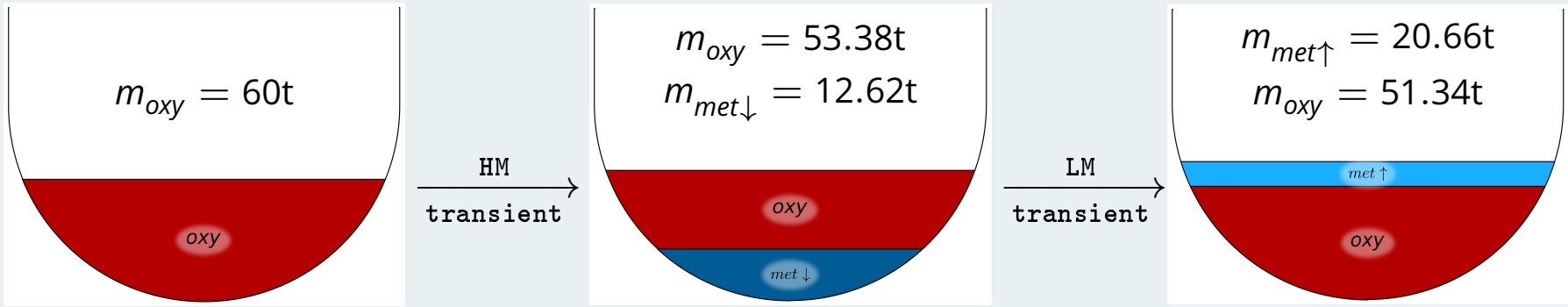

$x_{steel} = 0$ $x_{steel} = 0.1$ $x_{steel} = 0.2$

Steel injection (6t in 500s) *on top* of the pool (`on top`) or *into the oxide* as droplets (`in oxide`)

- *Full paper*: limited one-at-a-time *parametric study*
  - $\Delta\rho = \Delta\rho^+ = \Delta\rho^- \in \{1, 10, 100\}$kg.m^{-3} mass density threshold (RT instabilities)
  - $r^{RT} \in \{10^{-3}, 10^{-2}, 5 \cdot 10^{-2}\}$m "initial" droplets radius (RT instabilities)
  - $Sh_{i,\Gamma_\star} \in \{$`Juncu2010`, `Wegener2014`$\}$ droplet internal mass transfer correlation

  And, for `in oxide` transients:
  - $r^{in} \in \{10^{-3}, 10^{-2}\}$m steel droplets' radius
  - $\tilde{z}^{in} \in \{0.1, 0.5, 0.9\}$ relative axial position (0: bottom, 1: top)

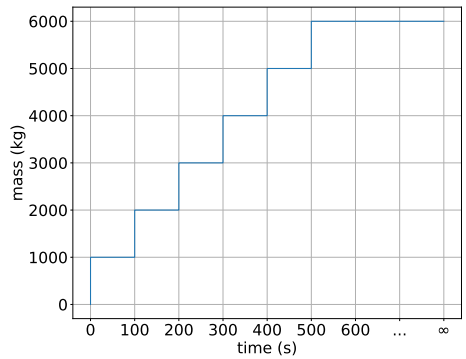

- *This presentation*: *general trends* illustrated with the case where: $\Delta\rho = 10$kg.m^{-3}, $r^{RT} = 10^{-2}$m, $Sh_{i,\Gamma_\star} =$ `Wegener2014`, $r^{in} = 10^{-2}$m and $\tilde{z}^{in} = 0.5$

Numerical results – HM transient – on top

HM transient

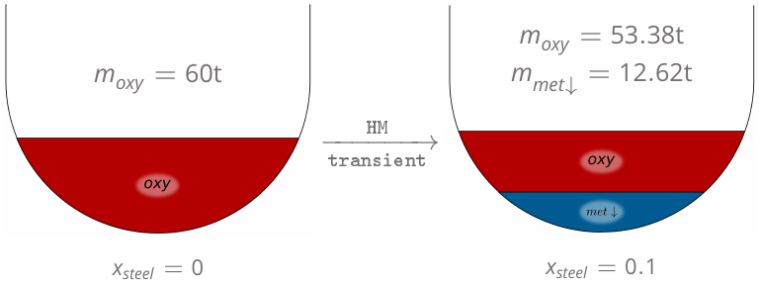

Transient overview

metal layer masses

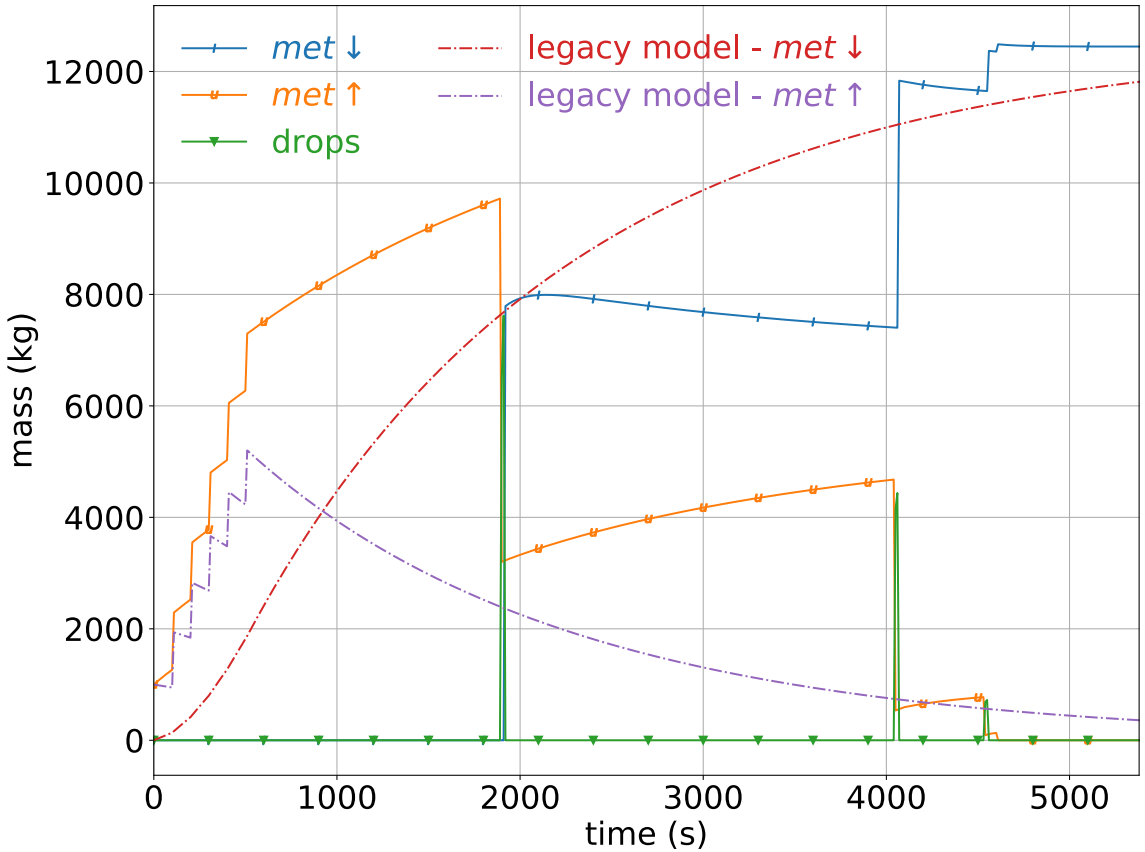

Numerical results – HM transient – on top

HM transient

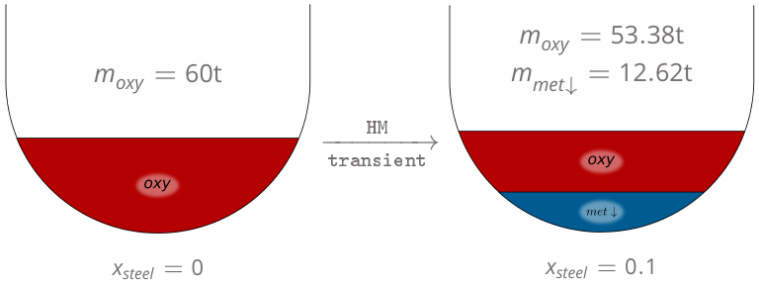

Transient overview

- steel injection

metal layer masses

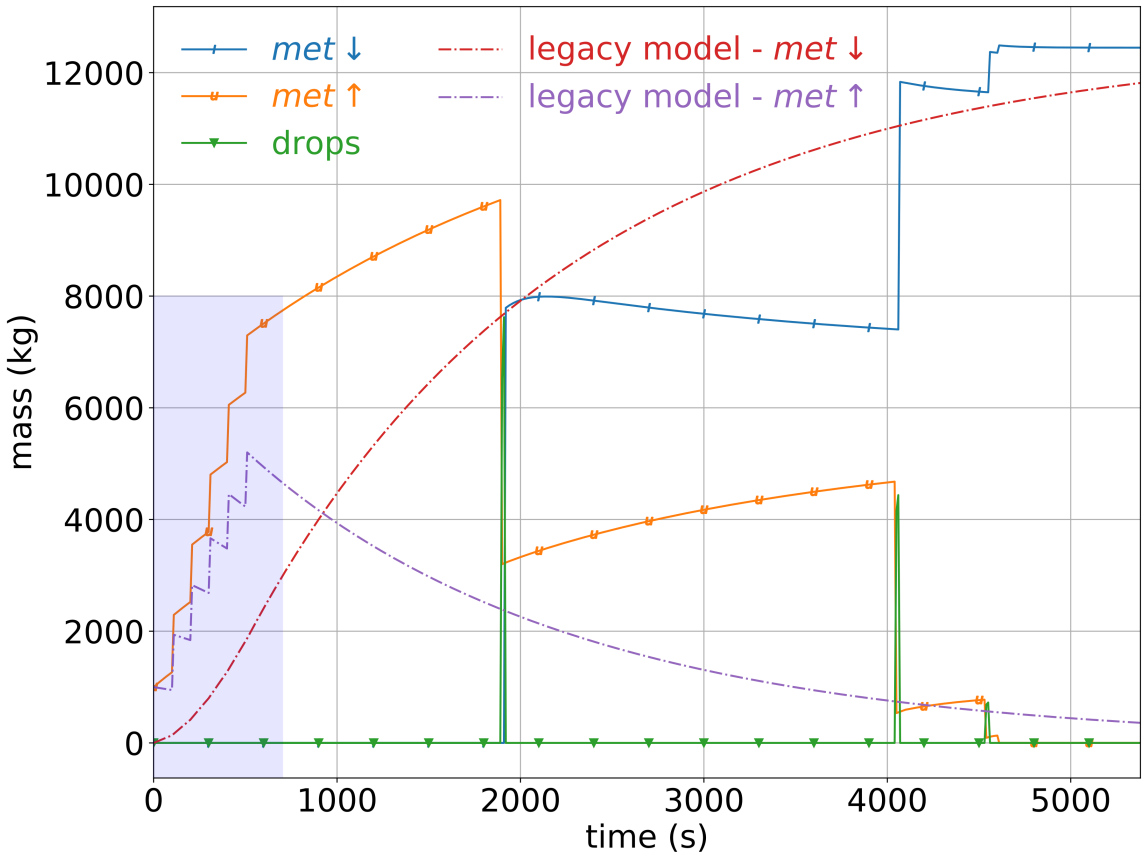

Numerical results – HM transient – on top

HM transient

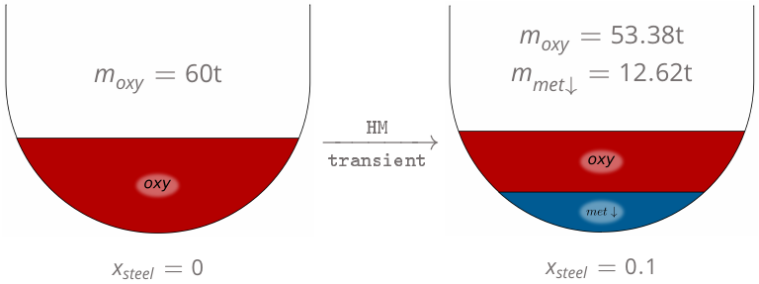

Transient overview

- droplets detachment and downward relocation

metal layer masses

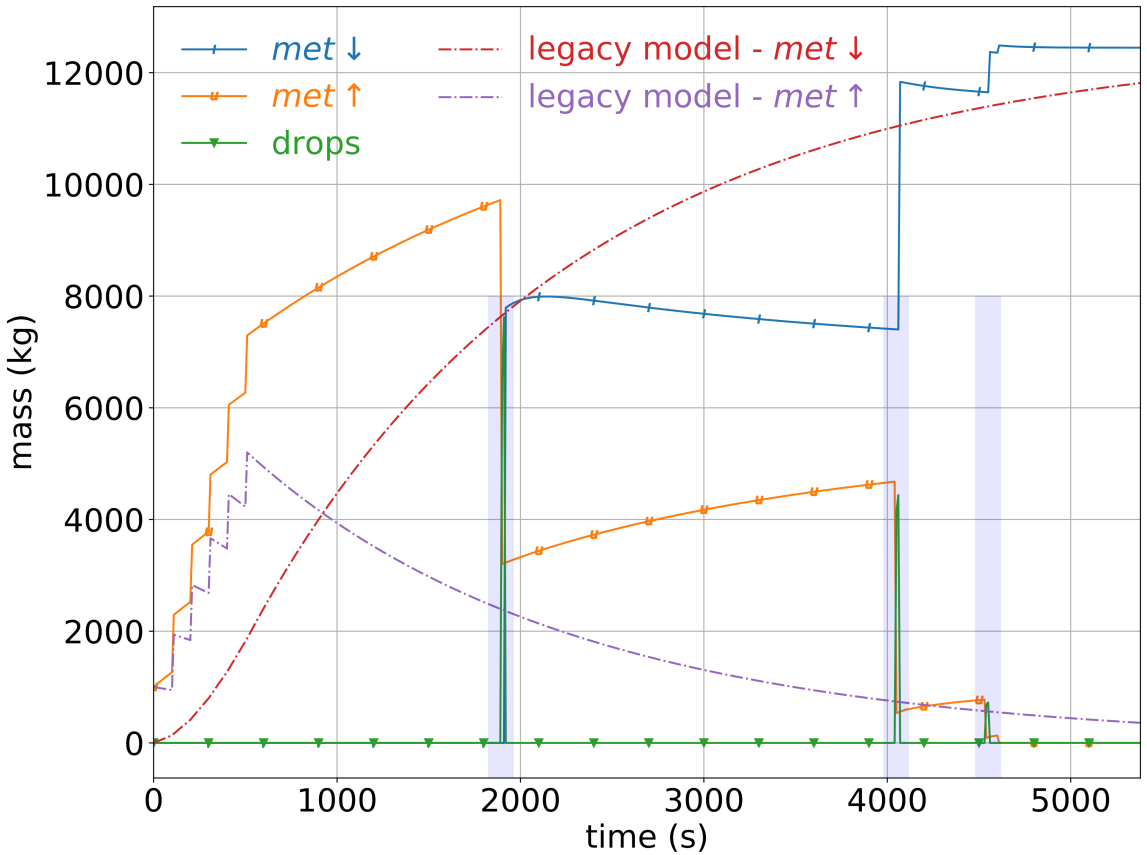

Numerical results – HM transient – on top

HM transient

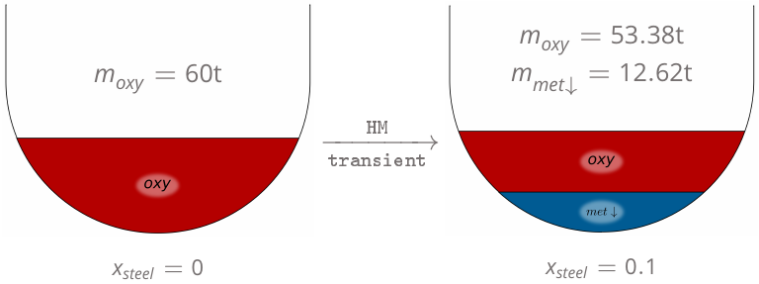

General trends analysis

steel mass fraction in the metal layers

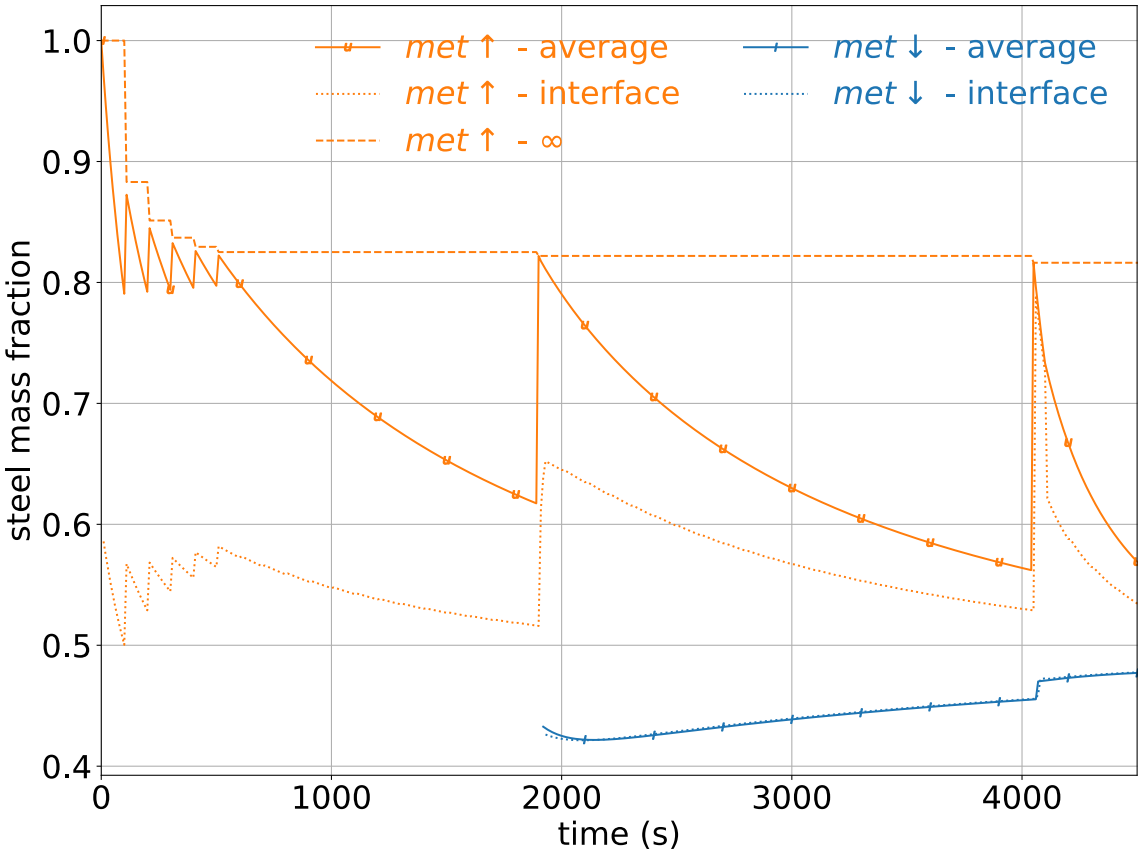

Numerical results – HM transient – on top

HM transient

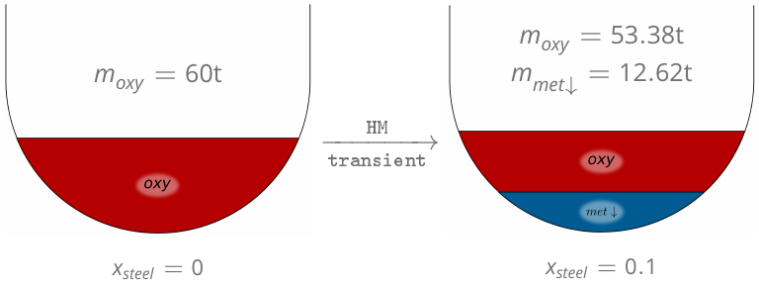

General trends analysis

- (*met* ↑) "competition" between steel injection and *U*, *Zr* interfacial transfer

steel mass fraction in the metal layers

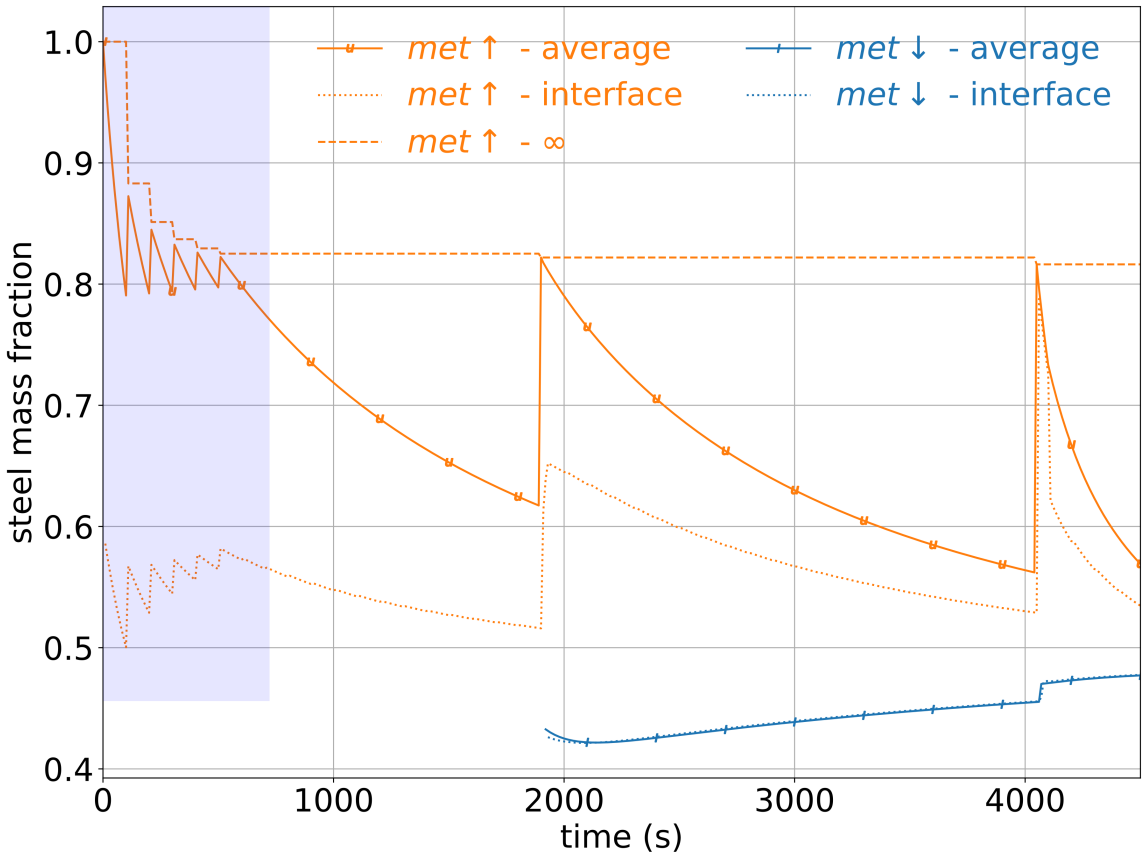

Numerical results – HM transient – on top

HM transient

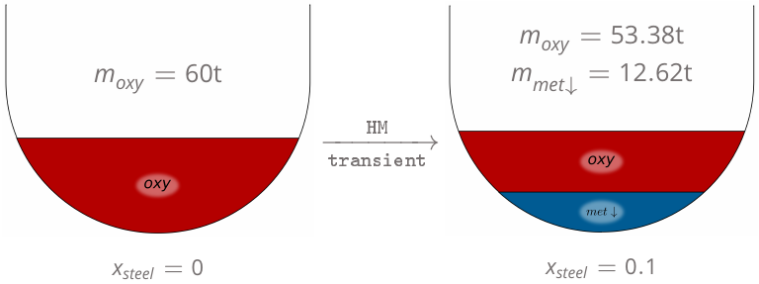

General trends analysis

- (*met* ↑) *U*, *Zr*-enrichment ↗
- (*met* ↑) interfacial region ↗
- (*met* ↑) interfacial mass density ↗ up to RT threshold

steel mass fraction in the metal layers

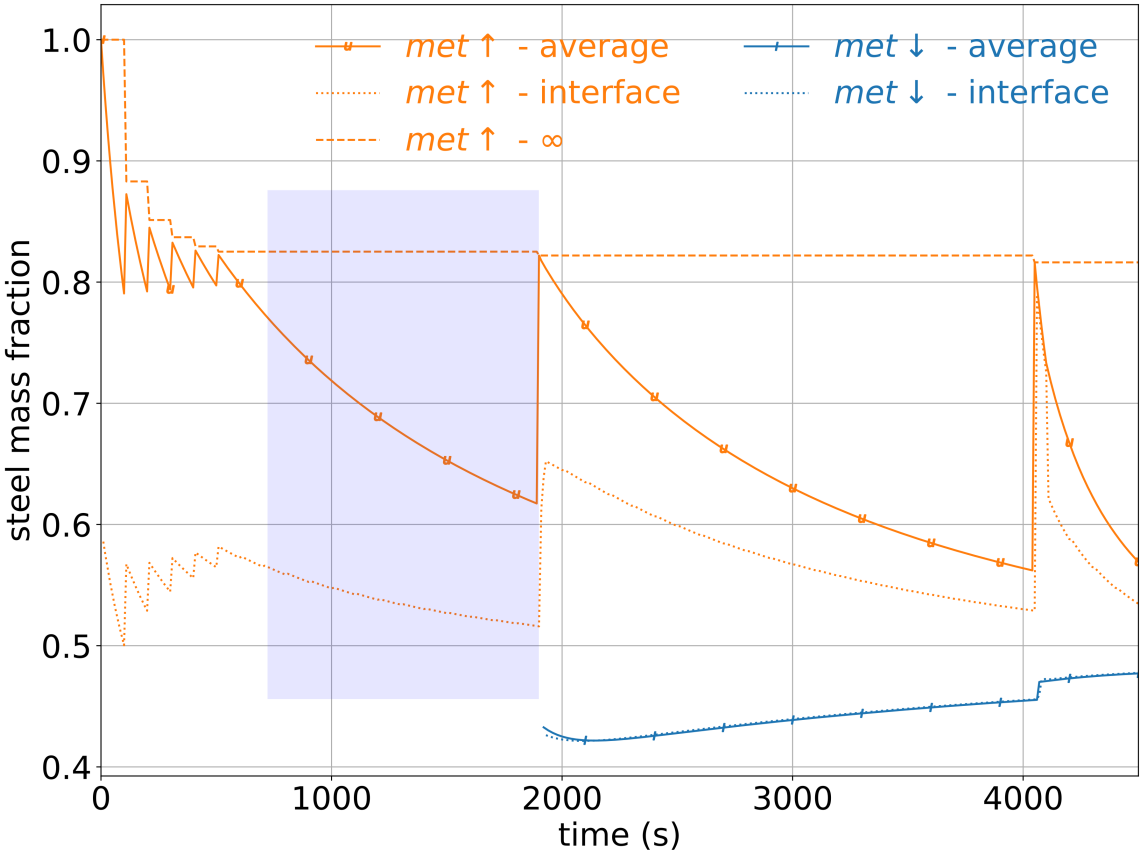

Numerical results – HM transient – on top

HM transient

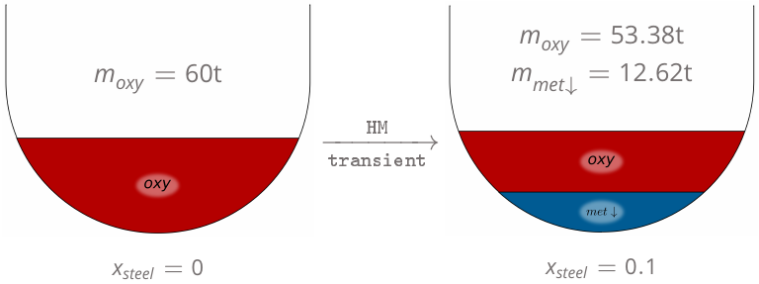

General trends analysis

- $(met \downarrow)$ U, Zr-enrichment ↗ up to the point where interface and bulk w^{steel} are equal

steel mass fraction in the metal layers

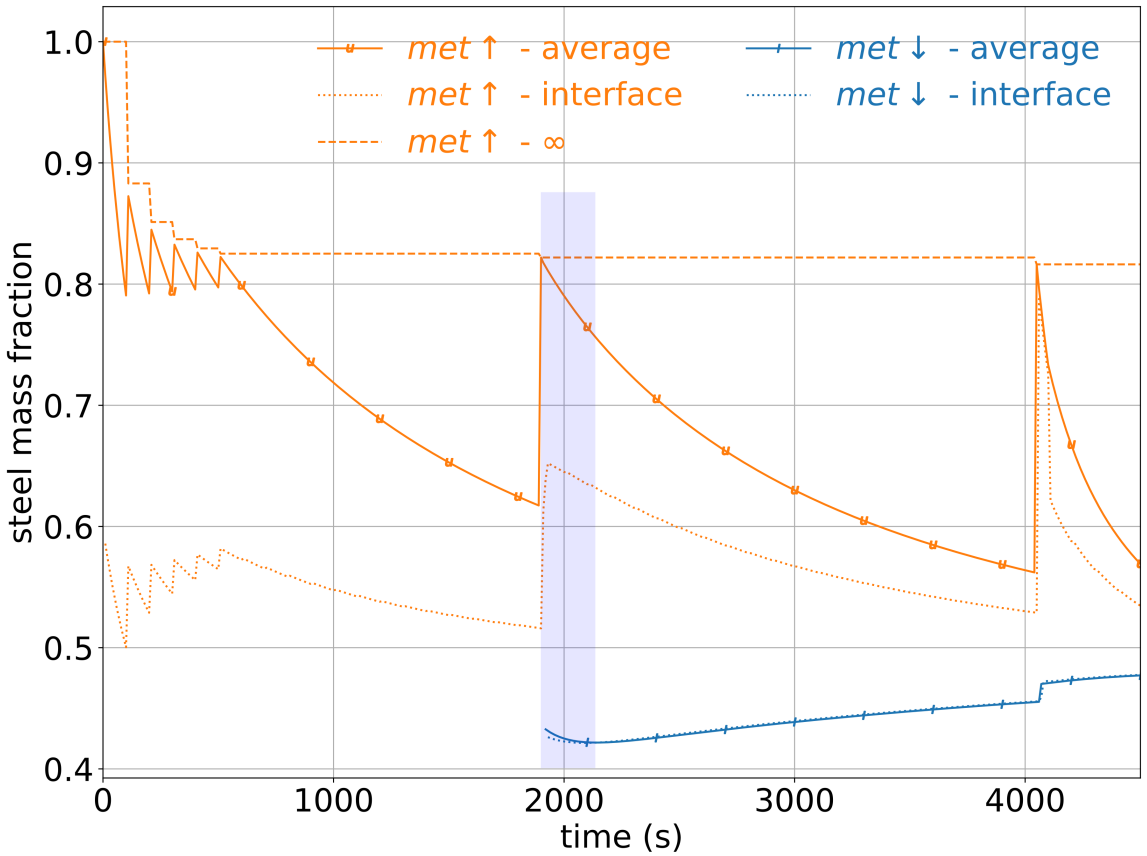

Numerical results – HM transient – on top

HM transient

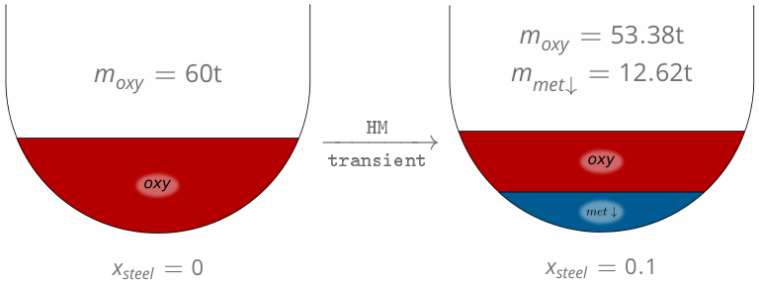

General trends analysis

- (*met* ↓) *U*, *Zr*-enrichment ↘

steel mass fraction in the metal layers

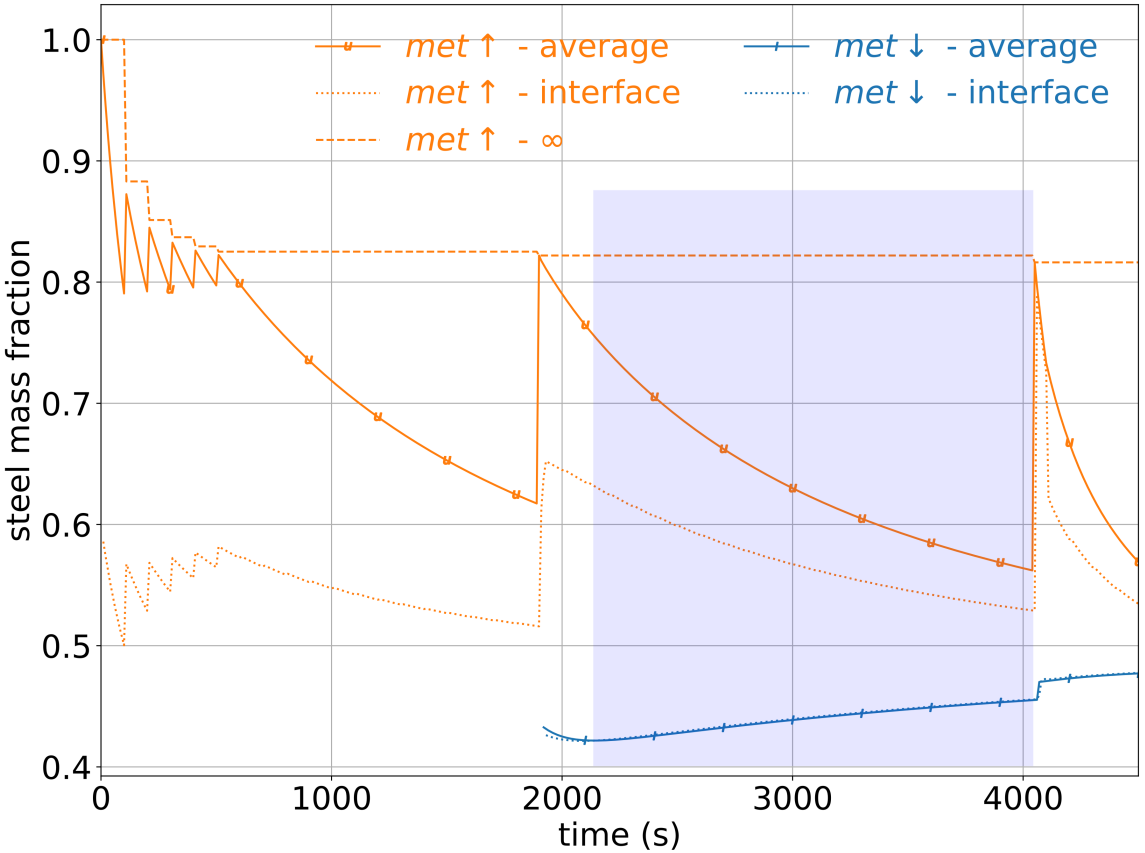

Numerical results – HM transient – on top vs. in oxide

HM transient

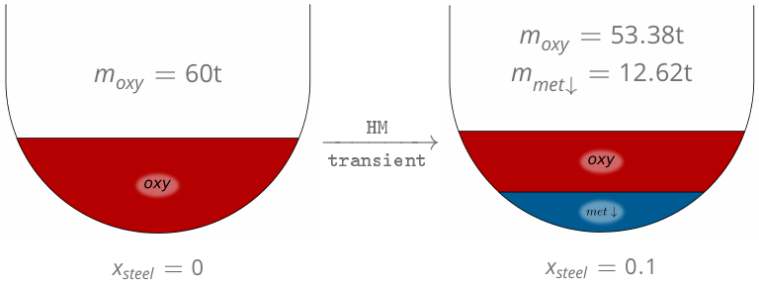

light metal layer mass

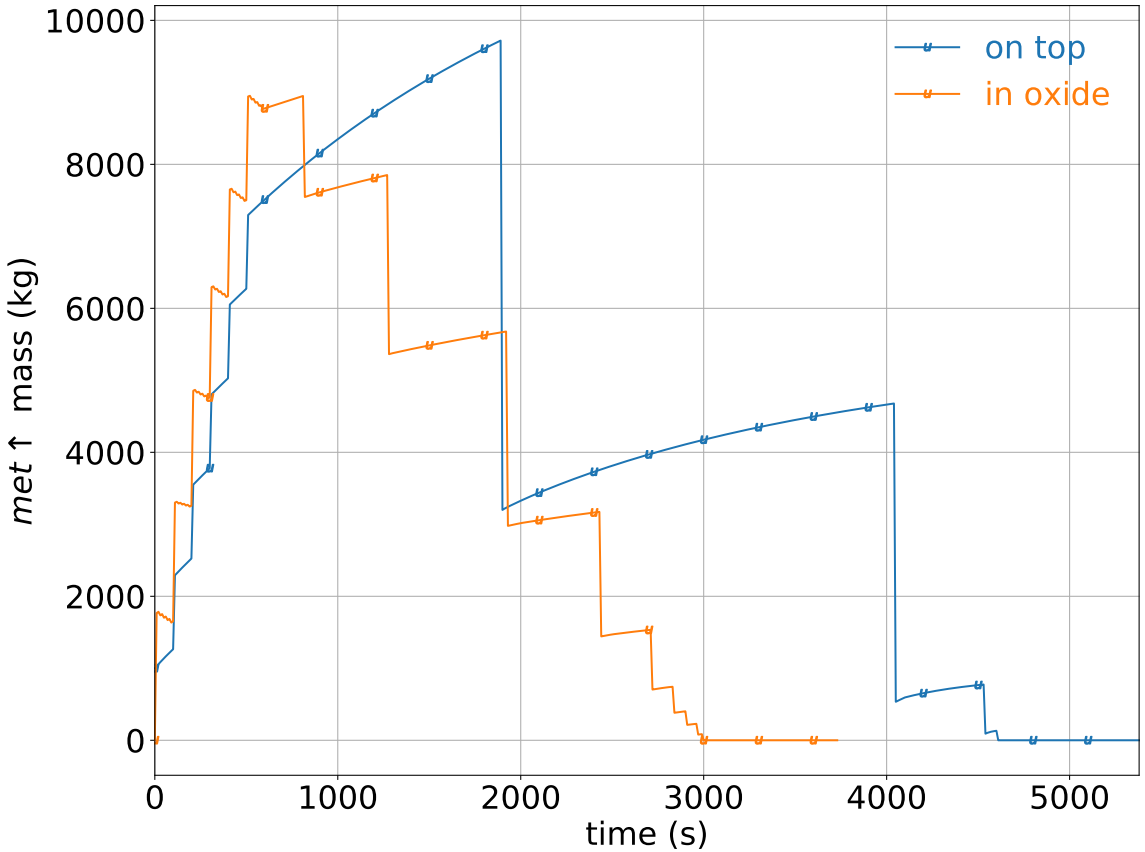

Impact of steel injection mode

- `in oxide`: droplet detachment occurs more often
- `on top`: more droplets are detached at a time

- `on top` → `in oxide`: more than 50% increase in transient time

Numerical results – HM transient – on top vs. in oxide

HM transient

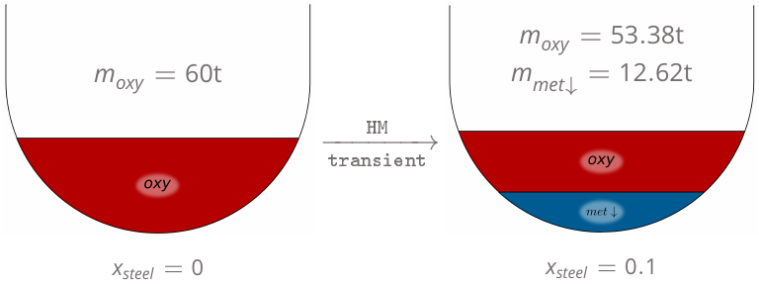

Impact of steel injection mode

steel mass fraction in the upper metal layer

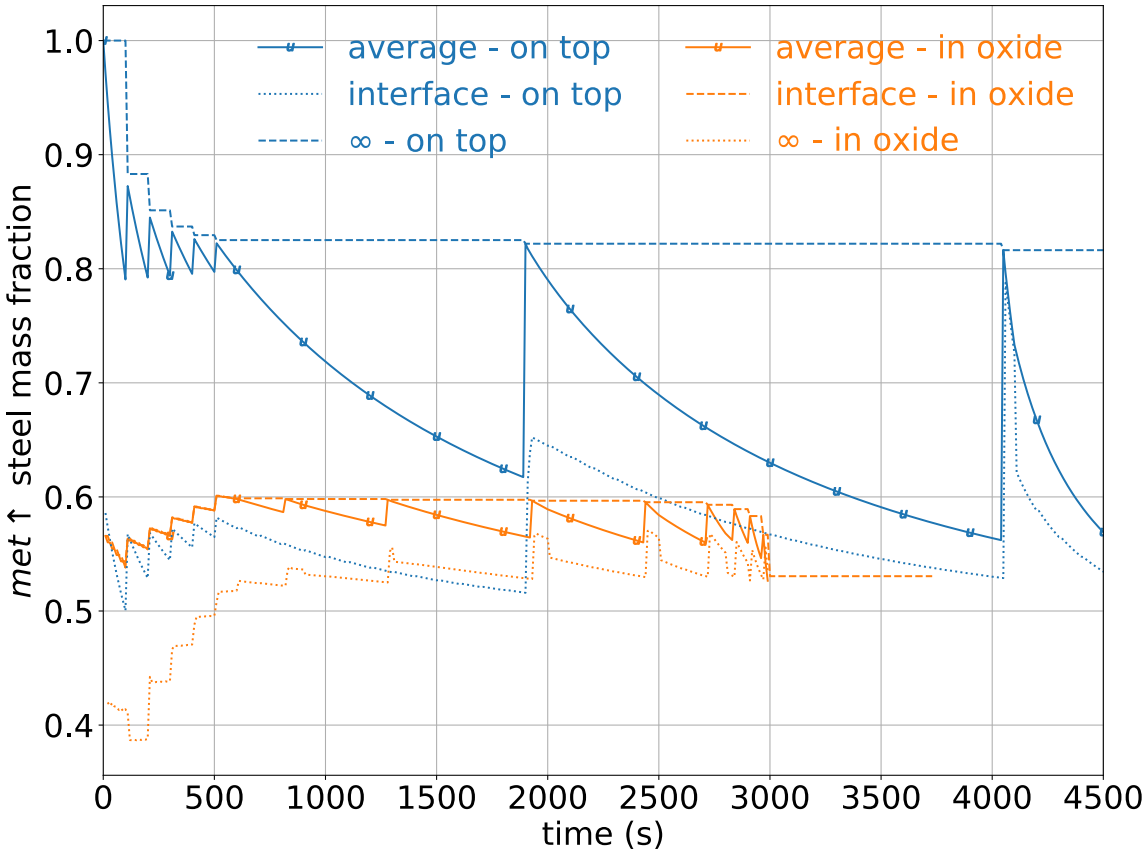

Numerical results – HM transient – on top vs. in oxide

HM transient

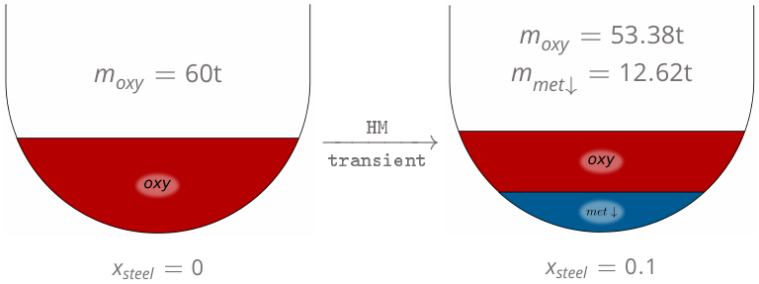

Impact of steel injection mode

- `on top`: direct steel addition
- `in oxide`: *U*, *Zr*-enriched droplets coalescence

steel mass fraction in the upper metal layer

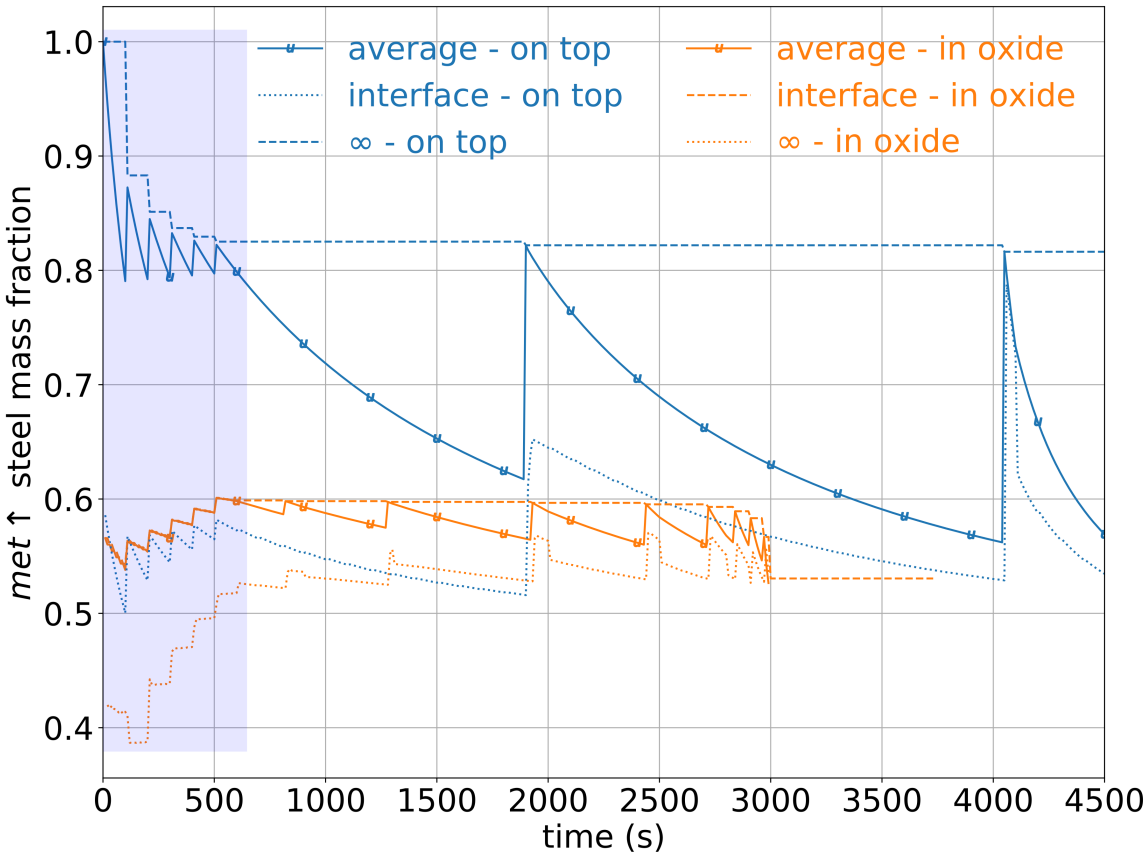

Numerical results – HM transient – on top vs. in oxide

HM transient

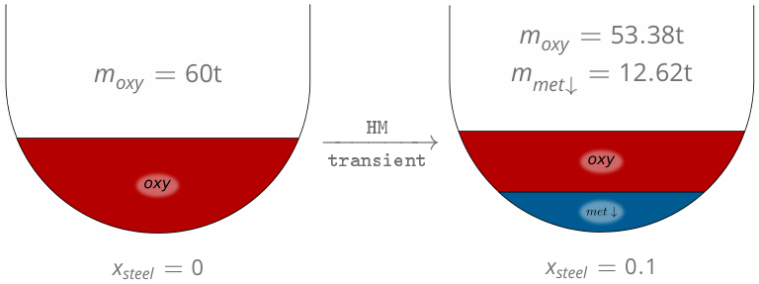

Impact of steel injection mode

- `on top` → `in oxide`: at 600s, $w^{steel} \approx 0.8 \rightarrow 0.6$
- RT threshold met sooner
- when RT threshold is met, interfacial region much smaller → less droplets detached at a time

steel mass fraction in the upper metal layer

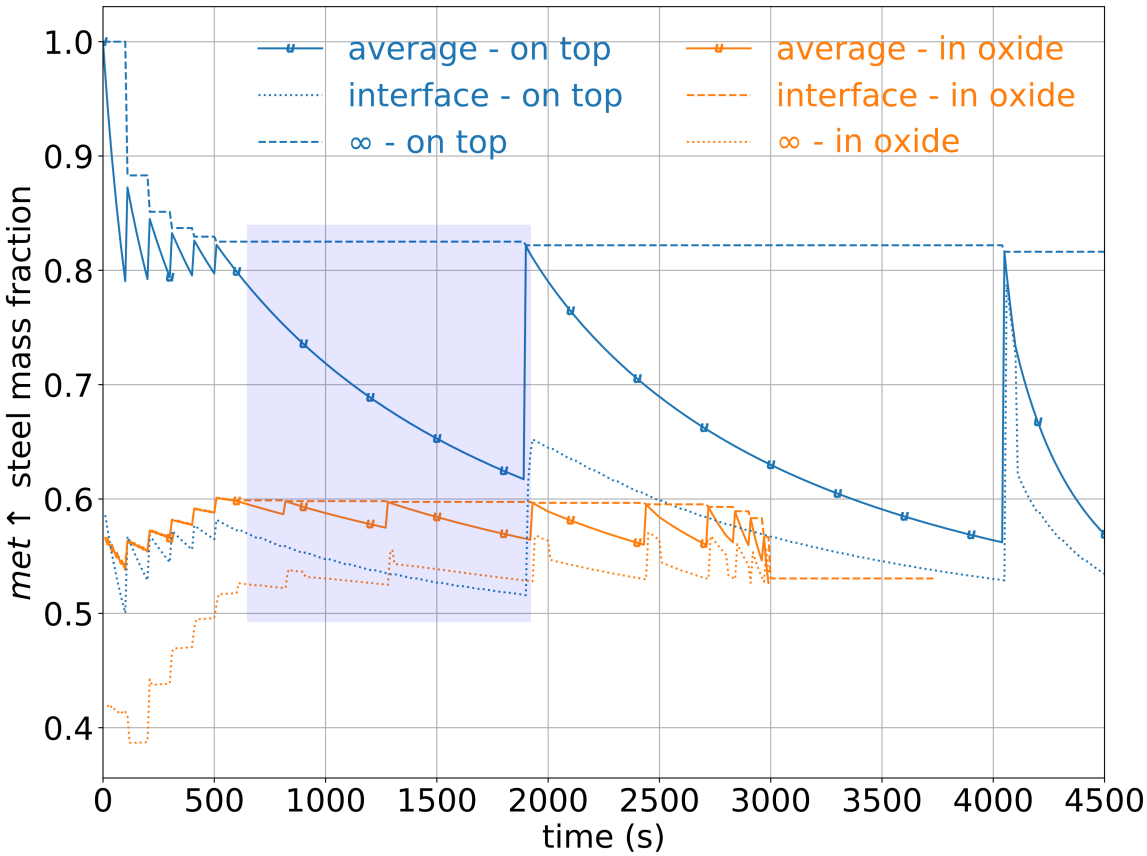

Numerical results – LM transient – on top

LM transient

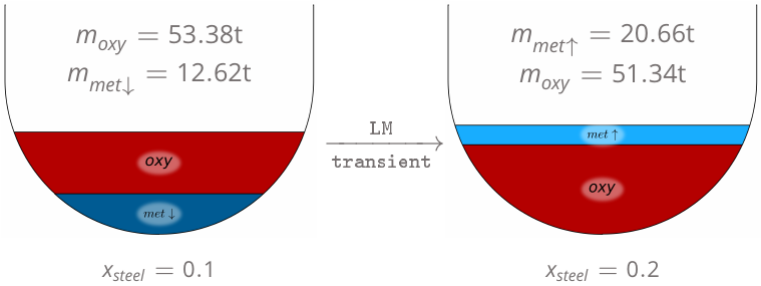

Transient overview

metal layer masses

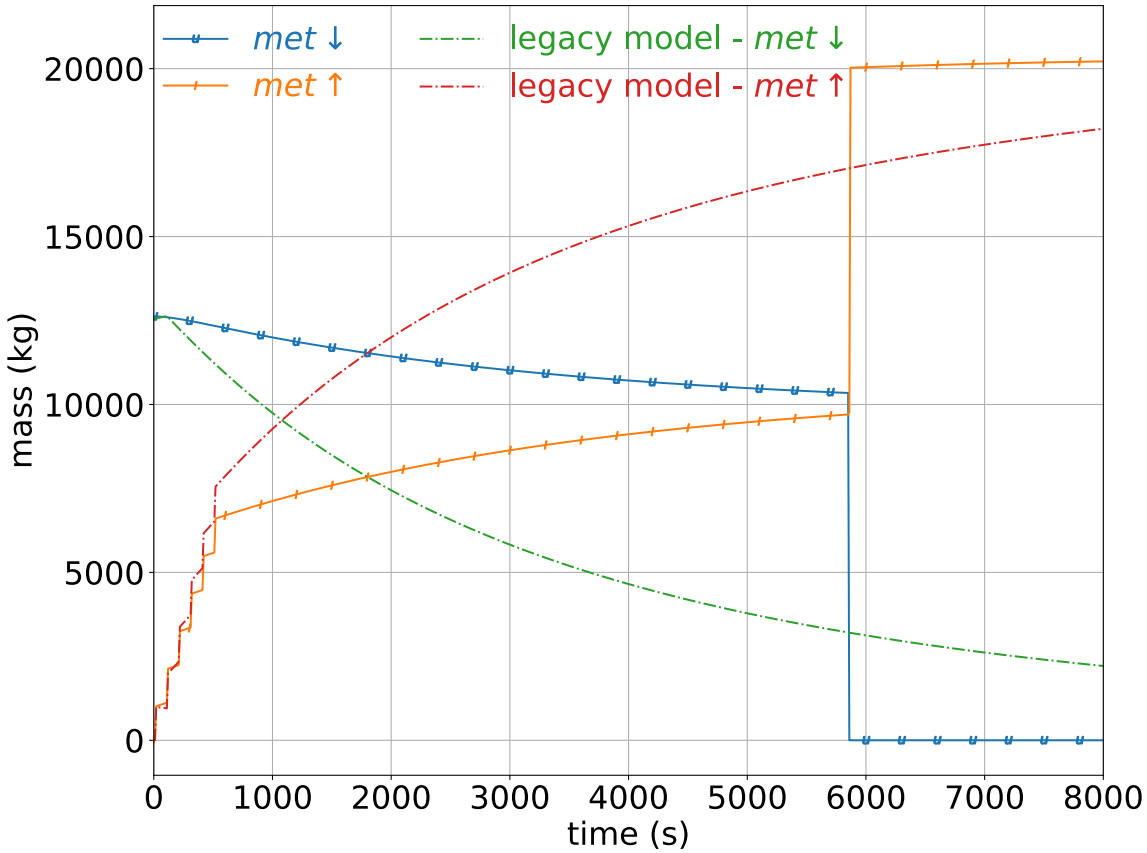

Numerical results – LM transient – on top

LM transient

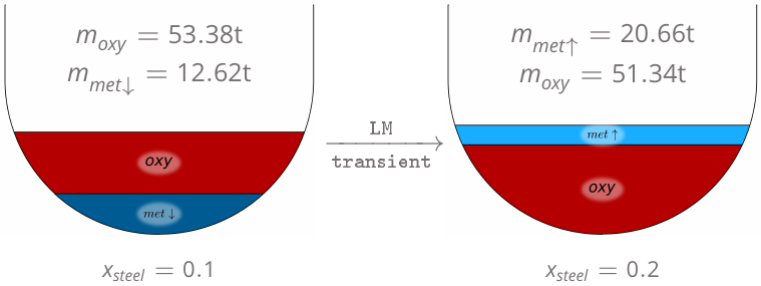

Transient overview

- steel injection

metal layer masses

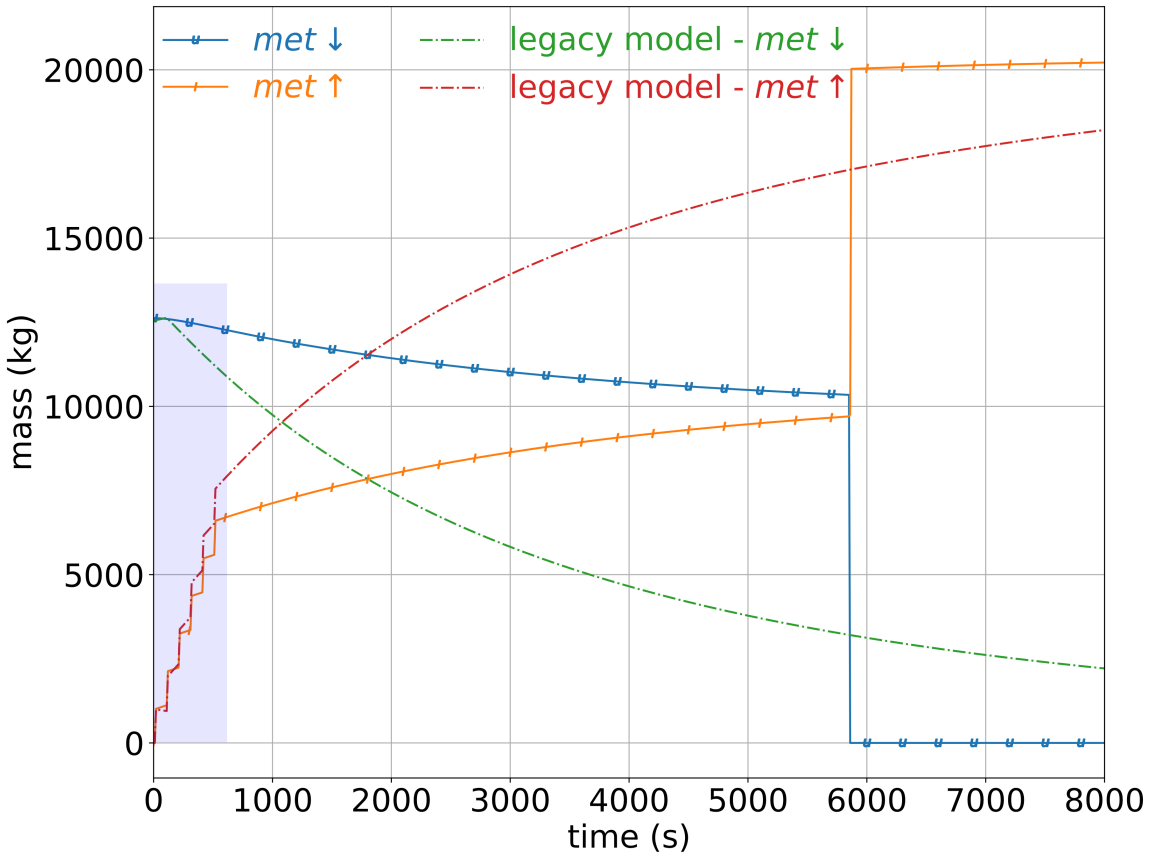

Numerical results – LM transient – on top

LM transient

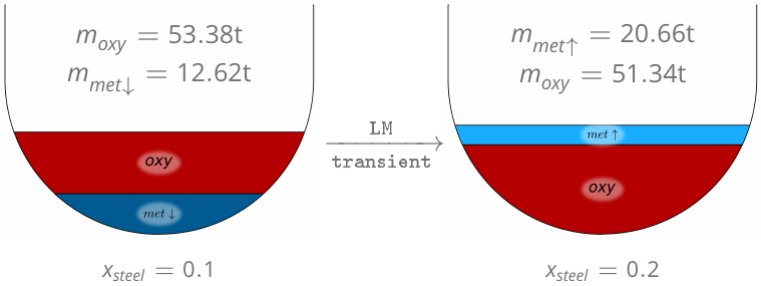

Transient overview

- "en bloc" inversion

metal layer masses

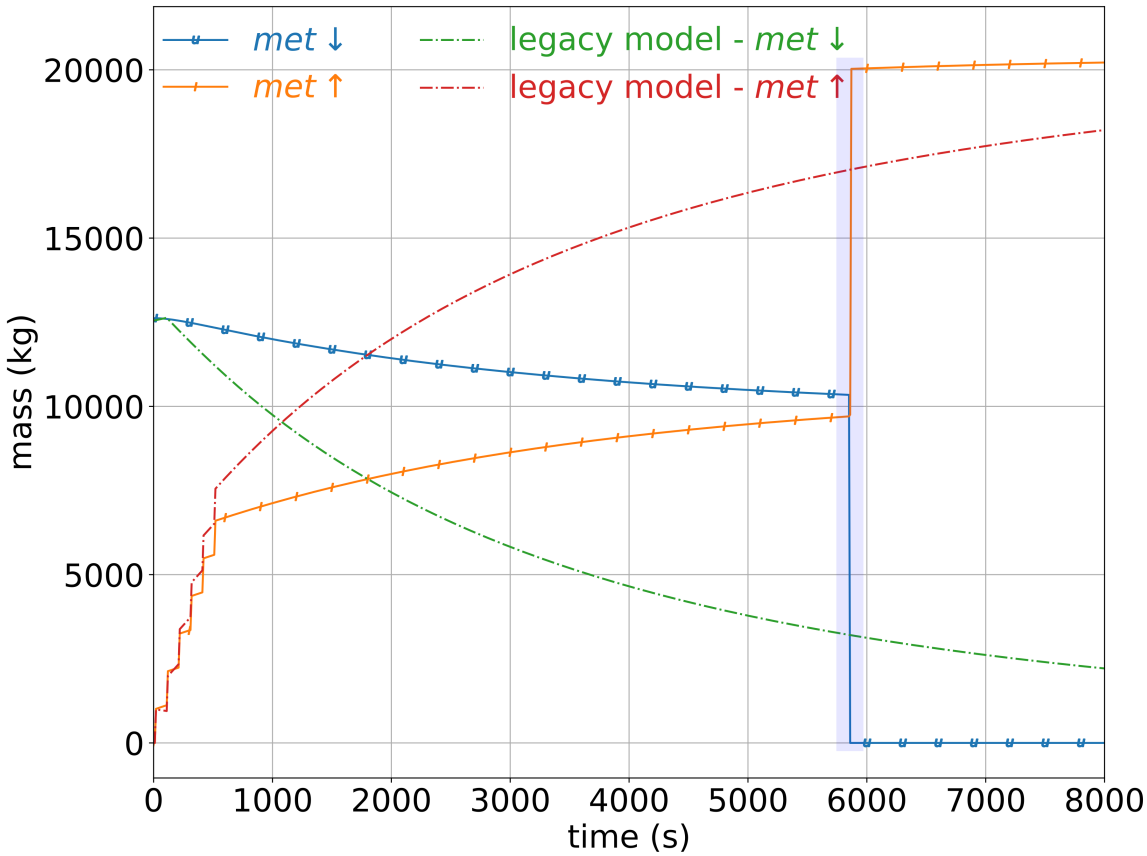

Numerical results – LM transient – on top

LM transient

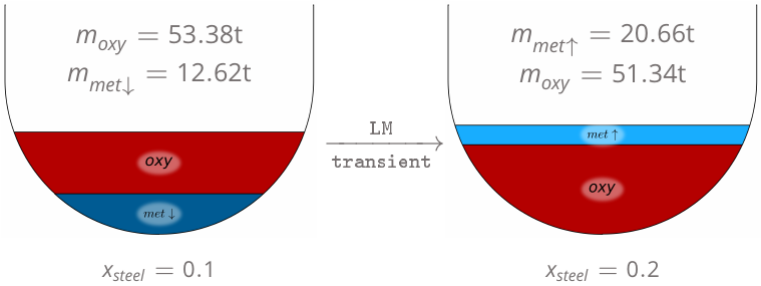

General trends analysis

- at $t = 0$, heavy metal layer under equilibrium conditions with oxide
- interfacial mass transfer slower at $\Gamma_{\downarrow}$ than at $\Gamma_{\uparrow}$

steel mass fraction in the metal layers

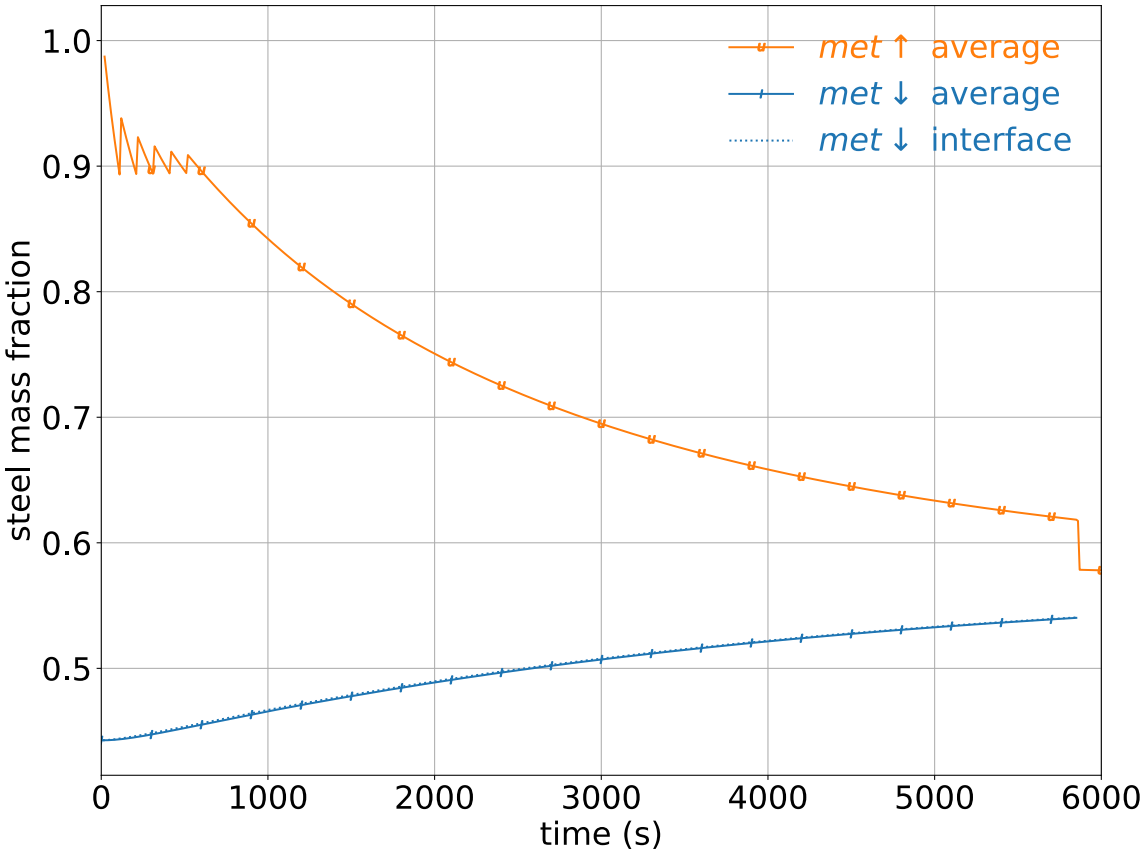

Numerical results – LM transient – on top

LM transient

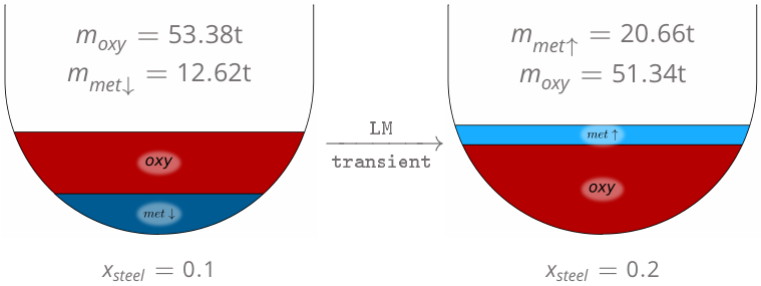

steel mass fraction in the metal layers

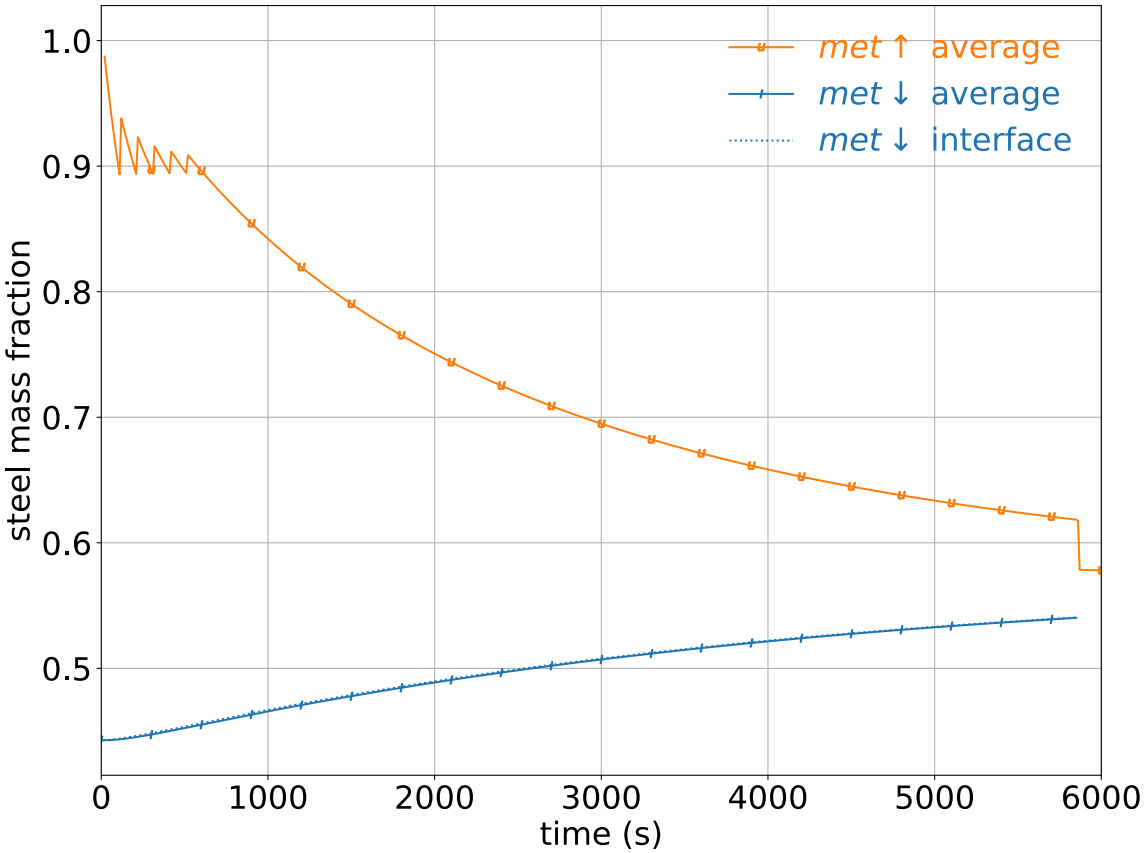

General trends analysis

- at $t = 0$, heavy metal layer under equilibrium conditions with oxide
- interfacial mass transfer slower at $\Gamma_{\downarrow}$ than at $\Gamma_{\uparrow}$

- quasi-static evolution of heavy metal *met* ↓ average composition vs. interfacial composition
- almost homogeneous composition → when RT threshold is met, “en bloc” inversion

Numerical results – `LM transient` – `on top` vs. `in oxide`

`LM transient`

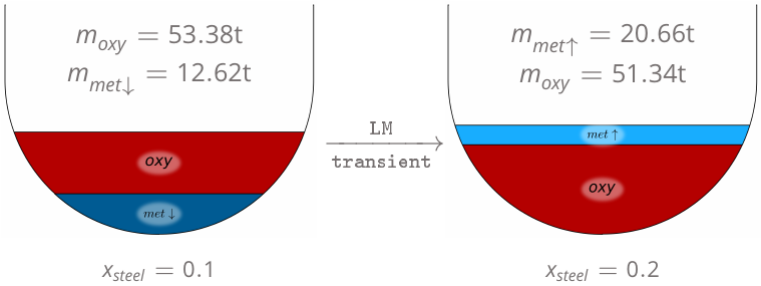

metal layer masses

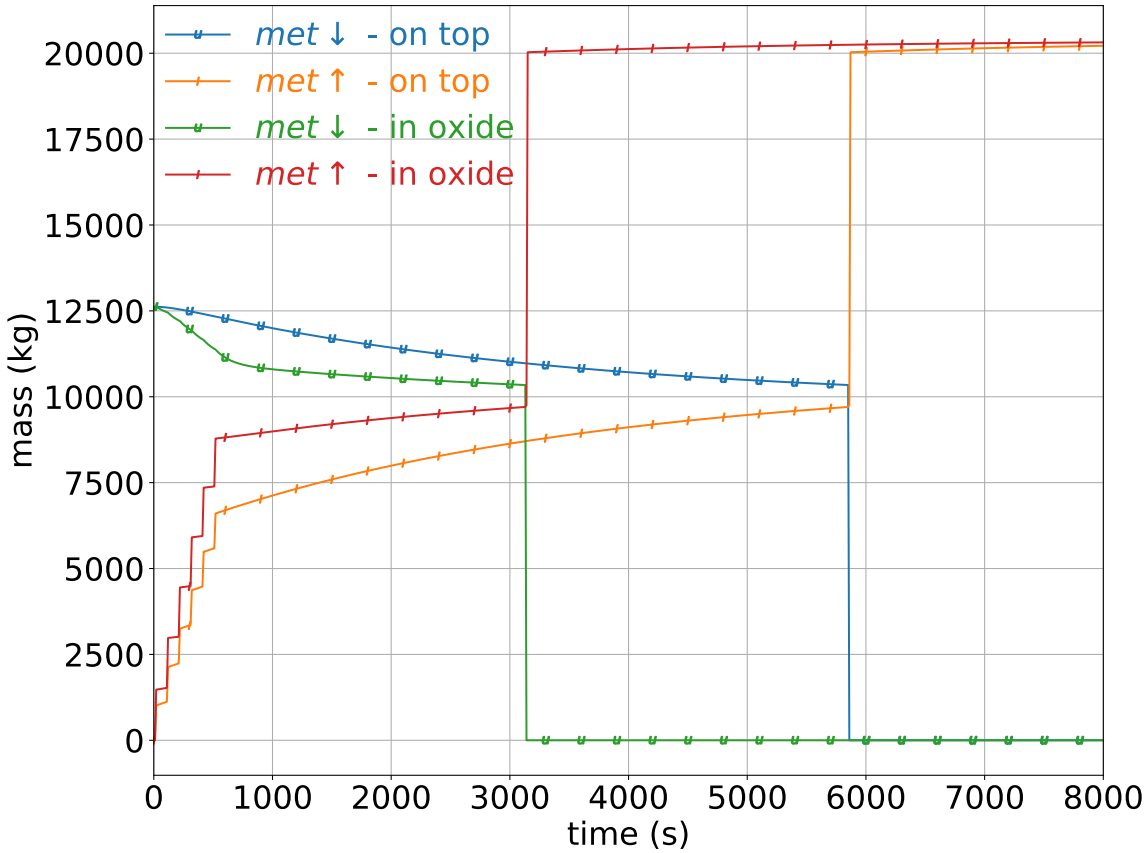

Impact of steel injection mode

- same qualitative behaviour: “en bloc” inversion
- `on top` → `in oxide`, inversion time almost divided by 2

Numerical results – `LM transient` – `on top` vs. `in oxide`

`LM transient`

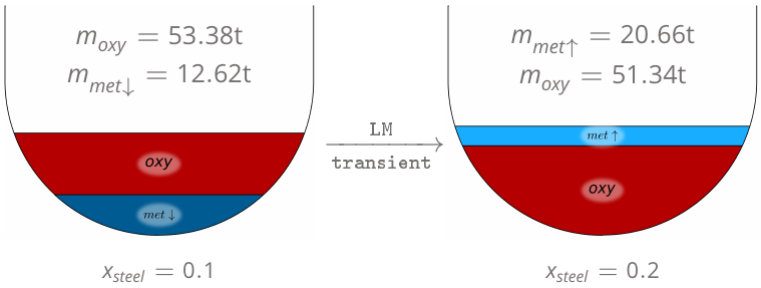

steel mass fraction in the metal layers

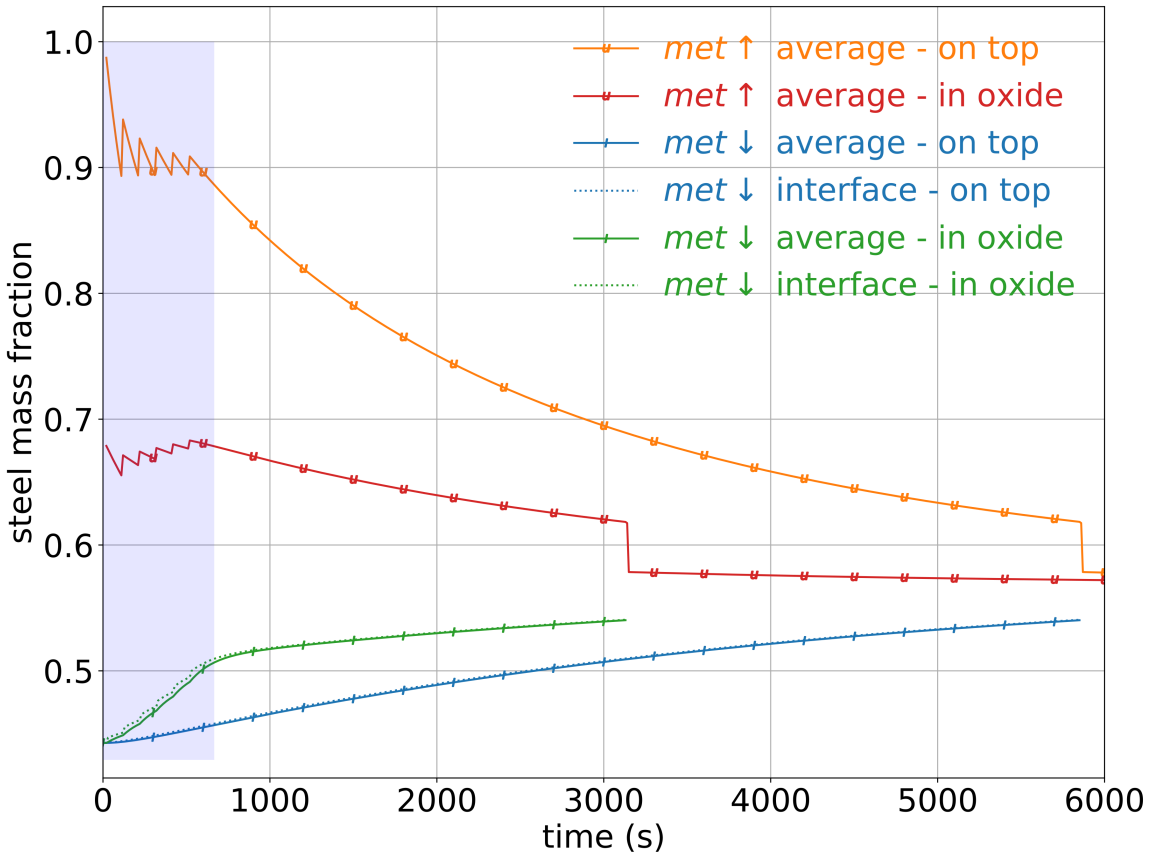

Impact of steel injection mode

- `in oxide`: *U*, *Zr*-enrichment of the injected molten steel droplets
  $\rightarrow$ much faster *U*, *Zr* mass transfer from the heavy metal layer to the oxide
- `on top` $\rightarrow$ `in oxide`: at 600s, heavy metal $w^{steel} \approx 0.3 \rightarrow 0.5$

- even if *met* $\downarrow$ subsequent evolution slower in `in oxide` case, RT criterion met much earlier

Summary and perspectives

Summary

- An *enhanced pool stratification model* to "explore" the effects of mass transfer between dispersed metal phase and oxide phase
- Main trends of *limited parametric study*:
  - *impact of metal droplets U, Zr enrichment* during residence time in oxide $\rightarrow$ *high sensitivity* of the stratification transients to the *molten steel relocation mode*
  - *qualitative difference* between *heavy metal phase formation* or *stratification inversion* transients: several droplet detachments vs. "en bloc" relocation

Summary and perspectives

Summary

- An *enhanced pool stratification model* to "explore" the effects of mass transfer between dispersed metal phase and oxide phase
- Main trends of *limited parametric study*:
  - *impact of metal droplets U, Zr enrichment* during residence time in oxide $\rightarrow$ *high sensitivity* of the stratification transients to the *molten steel relocation mode*
  - *qualitative difference* between *heavy metal phase formation* or *stratification inversion* transients: several droplet detachments vs. "en bloc" relocation

Perspectives

- Raising the *uniform and constant $R_{U/Zr}$ hypothesis* $\rightarrow$ reactor applications
- Towards more "quantitative" simulations: a *groundwork on model closures*:
  - *model validation/calibration* in the frame of the MASCA-CORDEB2 benchmark in *Task 3 of IAEA CRP on IVMR* (see A. Miassoedov's presentation)
  - *"Computational Fluid Dynamics" simulations* (e.g. phase-field based modelling [Zanella et al., 2021]) and new *experiments* (e.g. NEW PLINIUS platform)
- Knowledge to be gained about the *molten steel relocation through the crust* incl. thermochemistry (dissolution [Pivano et al., 2019]) and thermomechanics (yet to be explored)



Thank you for your attention

Acknowledgements: this work has been carried out within the framework of the PROCOR platform development funded by CEA, EDF and Framatome.

References



Fichot, F., Carénini, L., Le Tellier, R., Viot, L., Bakouta, N., and Filippov, A. (2020).

Identification and evaluation of the remaining uncertainties for transient situations.
In *Proc. of International Seminar "In-vessel retention: outcomes of IVMR project"*, Juan-les-Pins, France.



Le Tellier, R. (2021).

Mass transfer between a continuous oxide phase (U-O-Zr) and a steel droplet at liquid state: Potential impact on corium pool behaviour during in-vessel melt retention.
Nuclear Engineering and Design, 385:111525.



Le Tellier, R., Habert, B., Tiwari, V., and Bakouta, N. (2019).

Consistent use of CALPHAD data for in-vessel corium pool modeling: some analytical and practical considerations.
In *Proc. of the 9th European Review Meeting on Severe Accident Research ERMSAR2019*, Prague, Czech Republic.



Le Tellier, R., Saas, L., and Payot, F. (2015).

Phenomenological analyses of corium propagation in LWRs: the PROCOR software platform.
In *Proc. of the 7th European Review Meeting on Severe Accident Research ERMSAR-2015*, Marseille, France.



Le Tellier, R., Viot, L., Carénini, L., Fichot, F., Bakouta, N., and Filippov, A. (2020).

Transient stratified corium pool modelling for in-vessel retention analysis.
In *Proc. of International Seminar "In-vessel retention: outcomes of IVMR project"*, Juan-les-Pins, France.



Nandan, S., Fichot, F., and Piar, B. (2020).

A simplified model for the quaternary U-Zr-Fe-O system in the miscibility gap.
Nuclear Engineering and Design, 364:110608.



Pivano, A., Piluso, P., Chikhi, N., Fouquart, P., Delacroix, J., and Le Tellier, R. (2019).

Experiments on interactions of molten steel with suboxidized corium crust for in-vessel melt retention.
Nuclear Engineering and Design, 355:110271.

References



Seiler, J. M., Froment, K., and Garandet, J. P. (1999).

Equations for solidification of corium without sparging gas - scaling criteria.
In *Proc. of OECD Workshop on Ex-Vessel Debris Coolability*, Karlsruhe, Germany. OECD.



Zanella, R., Tellier, R. L., Plapp, M., Tegze, G., and Henry, H. (2021).

Three-dimensional numerical simulation of droplet formation by Rayleigh–Taylor instability in multiphase corium.
Nuclear Engineering and Design, 379:111177.

The 10th European Review Meeting on Severe Accidents Research

Severe Accident Research Eleven Years after the Fukushima Accident

May 16-19, 2022, Karlsruhe, Germany

Technical Session 2-1: Severe Accident Scenarios

Chairs: S. Brumm (JRC), S. Paci (University of Pisa)

ID287	**Source term estimation and dispersion analysis of VVER-1000 reactor in case of LBLOCA along with SBO** A. K. Mercan (KIT)	**Paper** **Presentation**
ID311	**Prediction of the Radiological Consequences of a Severe Accident Scenario in a Generic KONVOI Nuclear Power Plant** E.-M. Pauli (Framatome)	**Paper** **Presentation**
ID261	**CCFL Model Effect of Pressurizer Surge Line Flow on Severe Accident Progression in TMI-2 using CINEMA** R.-J. Park (KAERI)	**Paper** **Presentation**
ID318	**Analysis of LOCA accident for BWR-4 under DEC-A conditions using ASTEC code** T. Kaliatka (LEI)	**Paper** **Presentation**

10TH CONFERENCE ON SEVERE ACCIDENTS RESEARCH
May 16-19, 2022 – Karlsruhe, Germany
ERMSAR 2022

SOURCE TERM ESTIMATION AND DISPERSION ANALYSIS OF VVER-1000 REACTOR IN CASE OF LBLOCA ALONG WITH SBO

Ahmet Kağan Mercan*, Fabrizio Gabrielli, Victor Hugo Sanchez-Espinoza
Karlsruher Institute of Technology
Hermann-von-Helmholtzplatz, 1

D - 76344 Eggenstein-Leopoldshafen
Karlsruhe, Germany
ahmet.mercan@partner.kit.edu; fabrizio.gabrielli@kit.edu; victor.sanchez@kit.edu

ABSTRACT

Concept of defense-in-depth is developed to protect public health and environment for nuclear plants. This concept establishes provisions to maintain integrity of the cladding, vessel, and the containment respectively. Estimation of the impact of possible release of radioactive materials to the environment as severe accident analysis is required to develop accident management plans and preventative measure planning. The Accident Source Term Evaluation Code (ASTEC) is commonly applied for nuclear power plant under selected severe accident sequences which based on the probabilistic risk analysis, and atmospheric dispersion models are used to calculate dispersion. In the frame of this work, severe accident investigations of VVER-reactors with the goal of the quantification of the radiological source term for a subsequent JRODOS-simulation and calculating possible dispersion of selected radioactive materials. The first step of calculation is estimating inventory of a generic VVER-1000 plant at the end of cycle with burn-up data and cladding material by using in-house KORIGEN tool to predict Fission Product (FP) inventory. The generated inventory is applied to the ASTEC model of VVER plant to estimate transport and release of source material to the environment for the case of LBLOCA along with SBO accident. Finally, JRODOS calculation is performed for a selected location and a selected time frame to assess the dispersion of source material to the environment by including the weather conditions such as wind speed, wind direction, precipitation, and geographical landmarks like mountains, rivers, population, and urbanization. Additionally, preventative measures such as sheltering, thyroid treatment according to regulatory body will be performed to estimate effect on environment and habitat in long and short period by using the release data from ASTEC.

KEYWORDS
ASTEC, JRODOS, KORIGEN, Source term, VVER

1. INTRODUCTION

Nuclear accidents show the requirement of enhancing Defence-in-depth (DiD) concept in nuclear power plants (NPP) to mitigate impact of severe accident [1]. Thus, investigations on severe accidents have been established by the regulators to maintain public health and enhance the capabilities for keeping safety barriers. Indeed, many countries created emergency action plans and measures in case of a severe accidents [2] [3] [4].
KORIGEN tool has been developed by KIT from Oak Ridge Isotope Generation and Depletion Code (ORIGEN) to predict molar concentrations, radioactivities, heat release for nuclides and elements by using fuel burn-up studies and material composition with pre-generated nuclear data libraries [5]
The European Accident Source Term Evaluation Code (ASTEC) has been developed to simulate severe accidents from the initiator event to the release of radioactive material to the environment [6]. Numerous

validation and verification studies on different test and reactor cases have been established and enhancement of the capabilities of ASTEC has been upgraded with state-of-the-art experiments.
Java based Real-Time On-Line Decision Support (JRODOS) code is actively used to support decision making organizations in case of radiological or nuclear event, and emergency plan preparation and exercise anywhere in Europe [7]. JRODOS system allows users to model radiological dispersion and impact to a certain area by including meteorological information and geopotential data.
This study focused on radiological impact of the released Source Term (ST) from the containment in case of hypothetical severe accident case in a generic VVER-1000. With this aim, ASTEC-JRODOS coupling has been established to estimate the consequences from the initiating event to the radiological dispersion. Additionally, the KORIGEN tool was employed for the end of cycle to predict realistic Fission Product (FP) inventory in the reactor. The predicted FP inventory was applied to the ASTEC code with the modelling of vessel, primary and secondary systems and the containment. As a transient, Large Break Loss of Coolant Accident (LBLOCA) with Station Black-Out (SBO) was demonstrated until the basemat rupture in the cavity, and sequence of events was estimated and FP transport and release to the environment during the selected transient. Finally, the radiological dispersion of the released inventory was performed by JRODOS for the selected area, and deposition of radioisotopes, contamination due to deposition, and impact on different organ groups for short and long term was calculated. The chain of the calculation can support regulators to predict radiological consequences accurately and efficiently for different severe accident scenarios. Furthermore, it allows users to test Severe Accident Management (SAM) measures and develop further strategies on reactor safety and emergency preparedness.

2. SHORT DESCRIPTION OF THE VVER-1000 REACTOR

Although VVER type reactor is water-cooled water-moderated as the other pressurized water reactors (PWRs), it has characterizing highlights such as horizontal steam generators, larger coolant inventory and hexagonal fuel assemblies. The typical VVER-1000 reactor consists of 163 hexagonal fuel assemblies with 312 fuel pins which the enrichment is 4.4-wt % U^{235} [8]. The fuel rod dimensions of the VVER-1000 plant described at Table 1. The clad type, namely E-110, includes approximately 1% Nb. The material composition of the cladding is given at Table 2.

Parameter	Value (cm)
Central hole diameter	0.23
Fuel pellet diameter	0.755
Inner clad diameter	0.772
Clad thichness	0.0722
Lattice pitch	1.275
Active height	355

Table 1: Fuel rod dimensions [8]

Element	Weight %
Zr	94.21849
Nb	0.95199
Hf	0.02856
Fe	3.35491
Ni	0.50410
Cr	0.88818
Ti	0.04801
C	0.00576

Table 2: Material composition of cladding [8]

The scheme of the reactor is described on Figure 1. The core region has 163 fuel assemblies with 312 fuel rods. The vessel also includes 163 support column and a support plate inside of the lower plenum (LP).

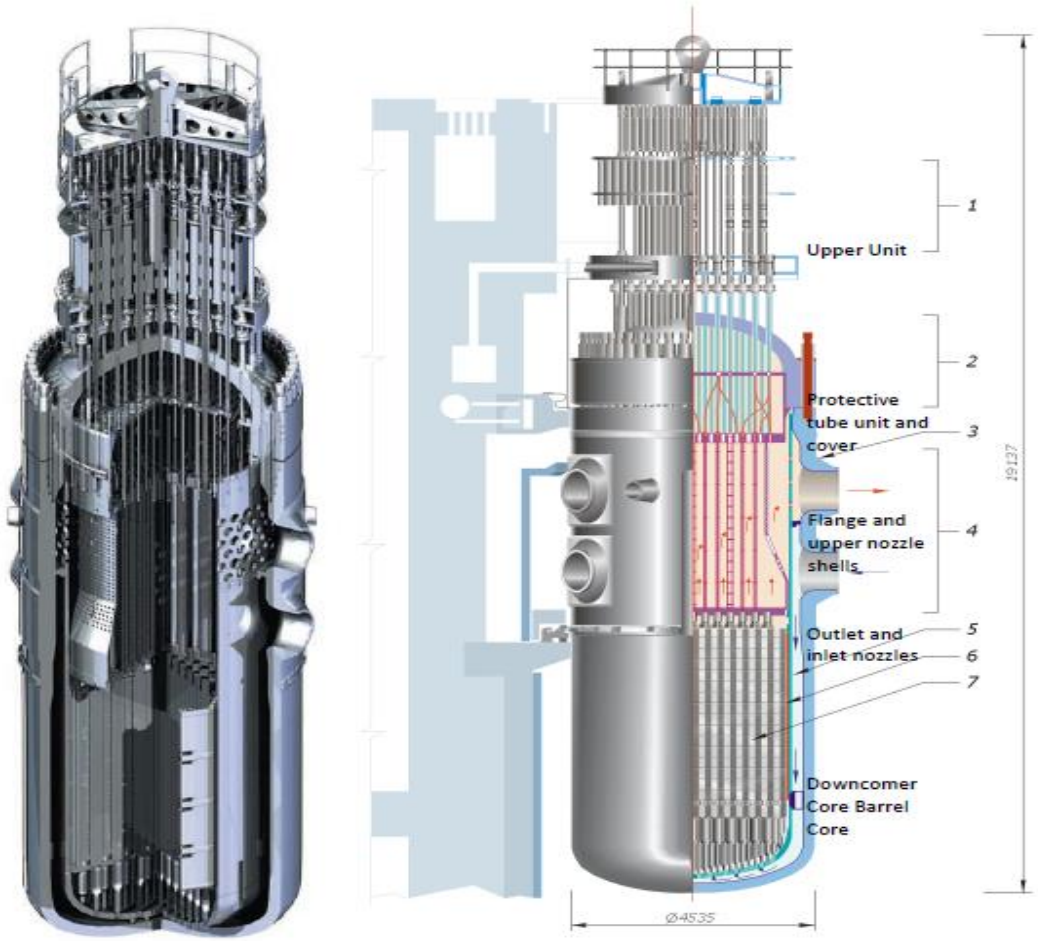

Figure 1: VVER-1000 scheme [9]

The steam generator has 2 head which 11000 tubes connect them. The secondary side of the steam generator is 4 m. with 2.55 m. is filled with liquid water.

The steady-state parameters of generic VVER-1000 reactor are described in Table 3.

Parameter	Value
Core power (MW)	3000
Operating pressure (MPa)	15.7
Core inlet temperature(K)	560.15
Core exit temperature(K)	592.05
Coolant flow rate (kg/s)	17600
SG pressure (MPa)	6.27
SG steam temperature (℃)	278.2
Feedwater flow (kg/s)	409
Feedwater temperature (℃)	220
SG level	2.55
Pressurizer liquid water volume (m^3)	55

Table 3: Steady-state conditions of VVER-1000

3. SOURCE TERM ESTIMATION AND DISPERSION ANALYSIS

There are three main steps of the calculation. These are FP inventory estimation by KORIGEN, ASTEC modelling of VVER-1000 and LBLOCA with SBO transient analysis, and radiological impact estimation with JRODOS.

3.1. VVER-1000 KORIGEN Model

The KORIGEN model of VVER-1000 plant was developed to estimate initial FP inventory for the transient and decay heat power during the accident. As the irradiation history, the Balakova plant data with 45 MWd/t burn-up is selected. The cycle lengths with downtime and burn-up values are given in Table 4.

Cycle number	Cycle length (d)	Downtime (d)	Cumulative Burn-up (MW/t HM)
1	297	94	11.373
2	350	78	28.541
3	413	-	45.600

Table 4: Irradiation history [8]

3.2. VVER-1000 ASTEC Model

The VVER-1000 input deck to estimate in-vessel and ex-vessel phenomena was developed from starting the generic input deck released at 2017. Initially, new steam generator model and containment model including cavity has been modelled in order to reach steady-state conditions which was not achieved in generic input deck. The latest models of the physical phenomena such as heat exchanges between structures and lower plenum, relocation of materials inside of the core and lower plenum (LP) and interactions inside the LP were activated. Finally, the VVER-1000 ASTEC model was extended with the ex-vessel modules to estimate molten core-concrete interaction (MCCI), gas generation and distribution inside of the containment and molten material ejection to the cavity.

Parameter	Reference Data [10]	ASTEC
Core Power [MW]	3000	3000
System Pressure [MPa]	15.7	15.762
Coolant Flow Rate [kg/s]	17760	17760
Core Inlet Temperature [K]	560.15	561.71
Core Exit Temperature [K]	592.05	592.02
SG Exit Pressure [MPa]	6.27	6.27
SG Temperature [℃]	278.5	278.2
Feedwater Flow [kg/s]	409	409
Feedwater Temperature [℃]	220	220
SG Water Level [m]	2.55	2.55

Table 5: Steady-state parameter comparison

After the steady-state conditions were fulfilled, LBLOCA along with the SBO transient was modelled until the basemat rupture. Following assumptions were selected for the transient. The general view of ASTEC VVER-1000 model and break location is given in Fig. 2.

- 850 mm break between cold leg and downcomer was active at time=0 s.
- SCRAM signal and pump coast-down was given at time=0 s.
- Main coolant pumps (MCPs) coasted down at time=0 s.
- Turbine was trip at time=1.6 s.
- Feedwater flow connections was closed at time=5 s.
- Hydroaccumulators activated after the pressure was below 5.9 MPa.
- BRU-A valves released steam when the pressure of secondary side was over
- Steam, hydrogen, xenon and krypton were modelled as the carrier fluid for FPs
- When the RPV fails, molten materials ejected to the cavity.

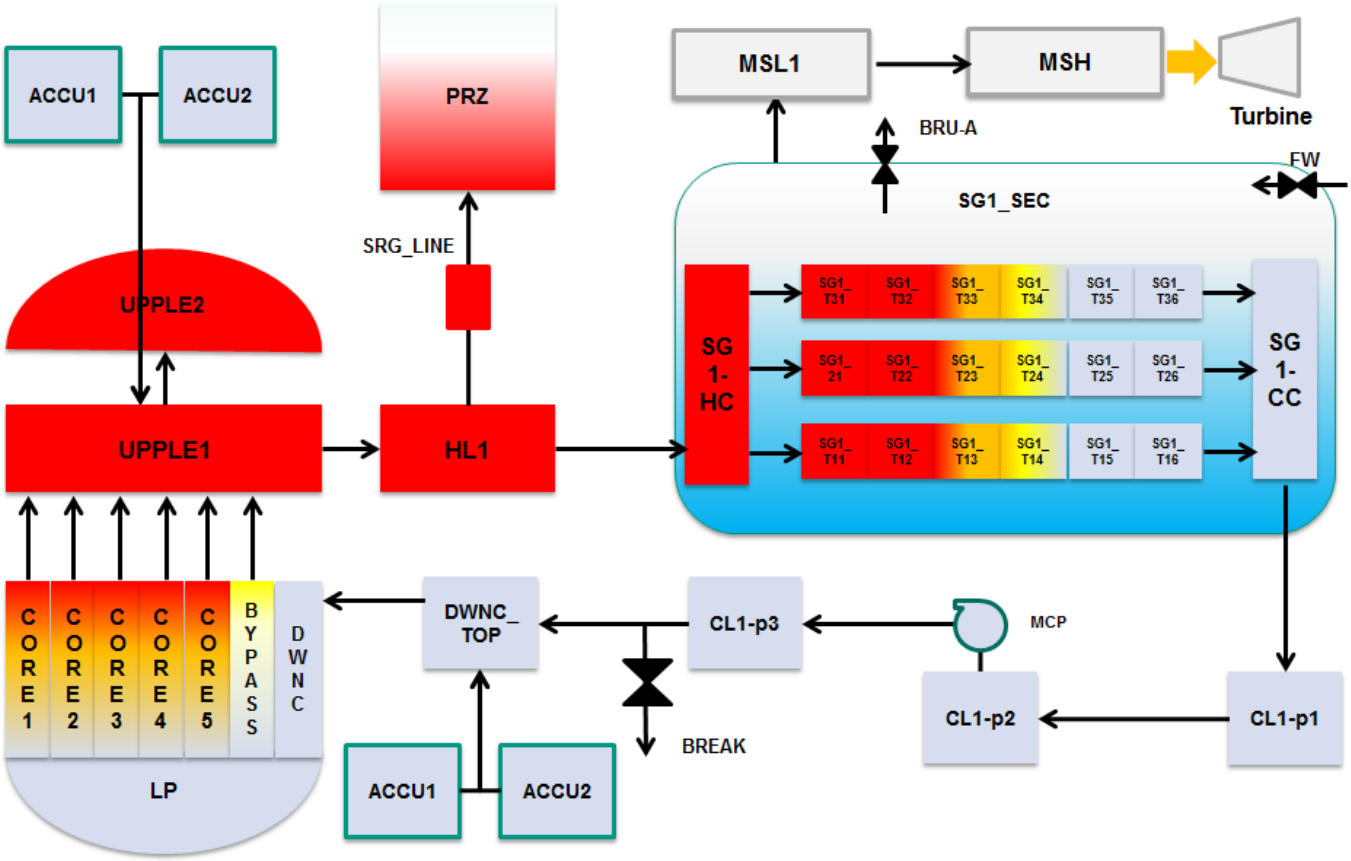

Figure 2: VVER-1000 ASTEC Model

As expected from the nature of LBLOCA case, the pressure inside of the primary system declined as it can be seen at Fig. 3. Additionally, the containment, Fig.4, pressure increased critically to the 4.75 bar for a small period which is above the design limit of 4.1 bar [11].

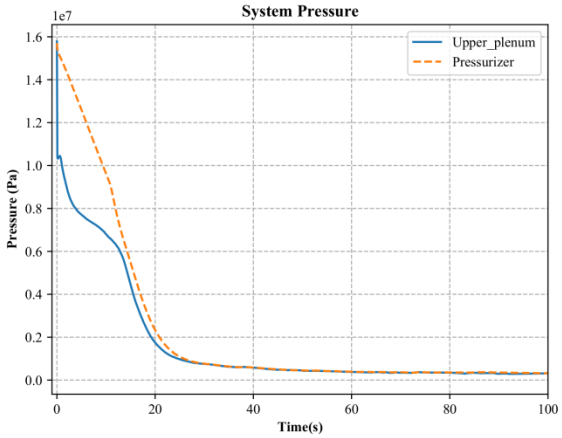

Figure 3: Primary system pressure

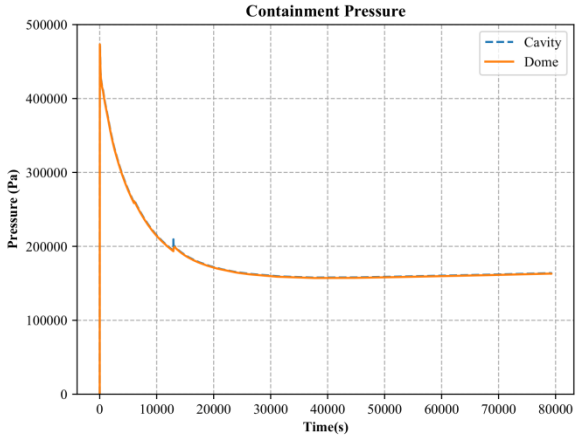

Figure 4: Containment pressure

The accumulators activated due to pressure and ejected 50 ton from upper plenum and downcomer, and the core water inventory sustained. However, the inventory was not enough to support decay heat and core uncovered at 3904 seconds. The FP release started at 1276 s because of cracking of the fuel and cladding. After the meltdown of materials, relocation to the lower parts of the core and the lower plenum initiated. The lower plenum lost the integrity due to temperature criteria as seen from Fig. 5 and ejection of molten materials to the cavity started after RPV failure. Eventually, the cavity erosed horizontally and radially as can be observed at Fig. 6 and basemat rupture observed at 79252 s. which is approximately 22 hours after the initiation of transient. The sequence of events listed in Table 6.

Event	Time (s)
Openning of a break (850 mm)	0
Reactor Scram	0
MCPs stopped	0
Turbines trip	1.6
Start of accumulators	12.9
Accumulator depletion	97.78
Start of FP release	1276.82
First slump of corium in LP	1285.88
First slump of corium in LP with FPs	1285.88
Start of structural material release	1287.69
Core uncovery (until the fuel bottom)	3904.13
BRU-A release from SG2	5974.51
Dryout of vessel	6212.51
BRU-A release from SG1	9790.06
RPV failure	12918.10
Basemat rupture	79252.7

Table 6: Sequence of events

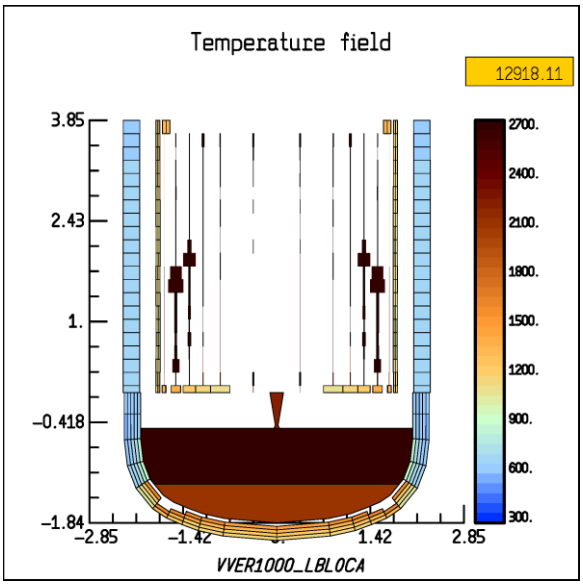

Figure 5: Vessel representation of ASTEC at the end of in-vessel phase

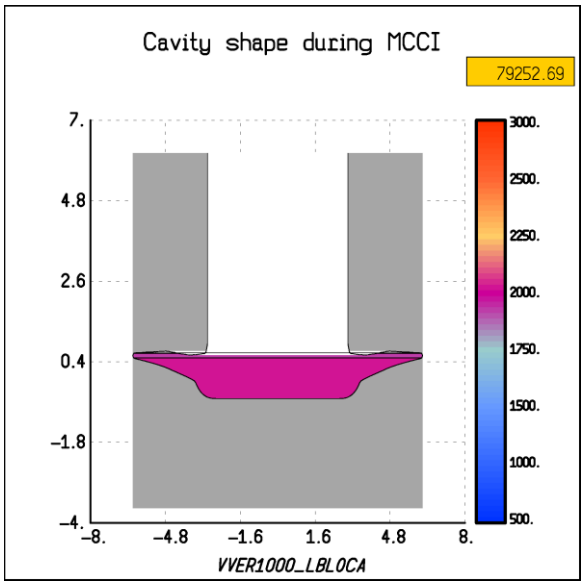

Figure 6: Cavity representation of ASTEC at the end of the calculation

Fig. 7 represented the hydrogen generation profiles during in-vessel stage and total generated hydrogen showed in Fig. 8. 224 kg of hydrogen generated at the end of the in-vessel phase. In the beginning of the transient, Zr oxidation was dominant. However, uncovery of molten materials inside of the LP accelerated the oxidation of these materials and generated more hydrogen until the RPV failure. The Molten Material-Concrete Interaction (MCCI) happens after the RPV failure and creates gases such as hydrogen and CO inside of the containment. Eventually, these gases can deflagrate or explode inside of the containment and create pressure peaks at the walls of the containment. During ex-vessel phase, the amount of the hydrogen generation was 790 kg which was triple of in-vessel stage. Totally, 1015 kg hydrogen generated for the LBLOCA along with SBO accident case. Also, the suitable environment for the hydrogen deflagration has been reached about 20000 seconds inside of the containment and the pressure reached 10.1 bars virtually at the end of the calculation.

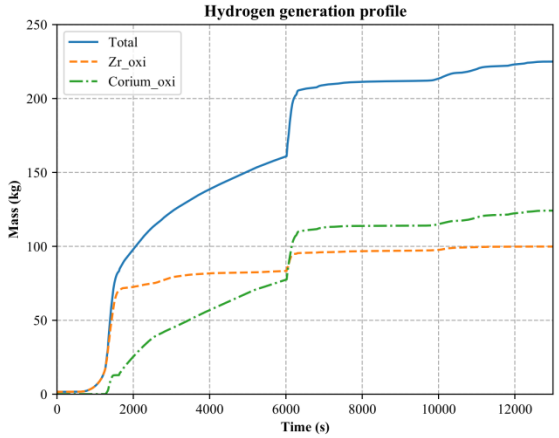

Figure 7: Hydrogen generation profile during in-vessel phase

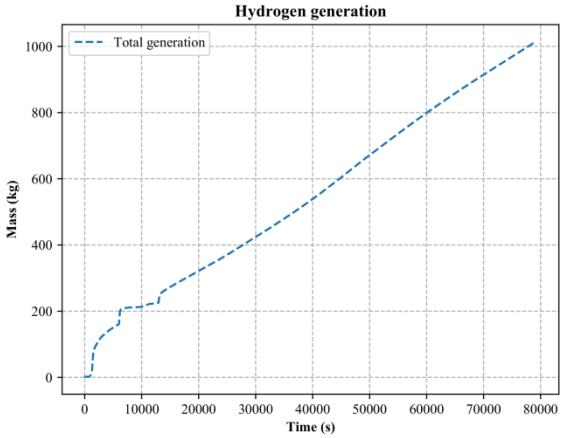

Figure 8: Generated hydrogen at the end of the calculation

After FP release from the fuels initiated, transport of these materials to the primary circuit and the containment by hydrogen, steam, Kr and Xe also started. However, most of FPs retended on the walls of the primary circuit, especially steam generators, and very low percentage of FPs transported to the containment which can be seen at Fig 9. Additional retention was involved on the walls of the containment and small amount of the FPs released to the environment. Despite the high retention inside of the primary circuit and the containment walls, noble gases and volatile isotopes leaked to the environment. The leaked activity from iodine isotopes, high volatile isotopes and noble gases are showed on Fig. 10 to Fig. 12 in log scale respectively. Iodine isotope activity reached 1E9 Bq and noble gases reached 1E13 Bq even though some of them started to decay and the activity decreased. Cs-137 activity was about 1E15 Bq which has long half-life that might affect the environment and people for long periods

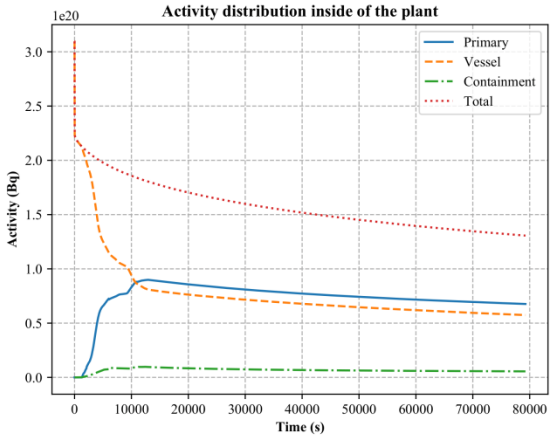

Figure 9: Total activity distribution during the transient

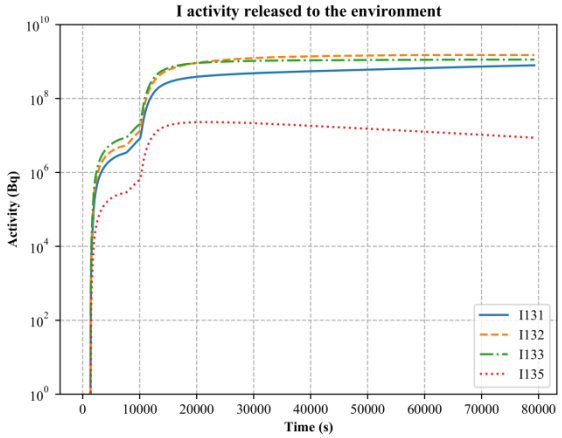

Figure 10: Leaked iodine isotopes activity

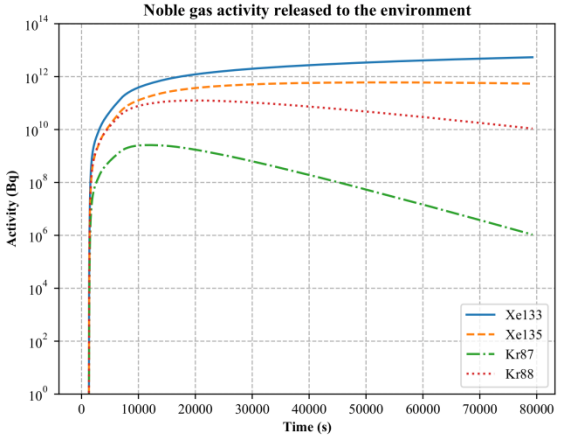

Figure 11: Leaked volatile isotope activity

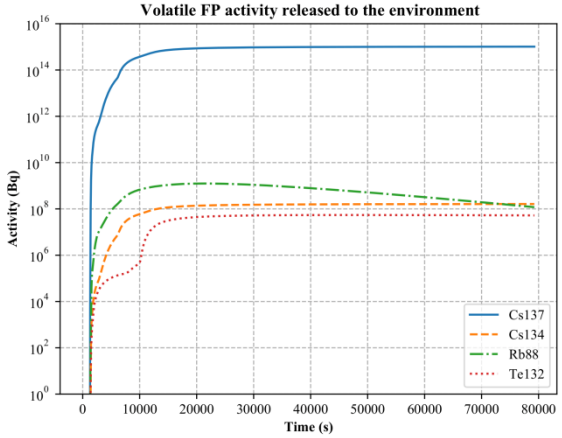

Figure 12: Leaked noble gas isotope activity

3.3. VVER-1000 JRODOS Model

After the leaked isotope inventory had been acquired, the data was transferred to the JRODOS in order to estimate dispersion to the environment. The assumptions of the calculations have been listed below.

- Summer season weather data (15/07/21-25/07/21) was used.
- Kozloduy plant location was selected.
- 160 isotope data was used.
- 800 km range was selected for dispersion.
- Emergency preparedness plan was not activated.

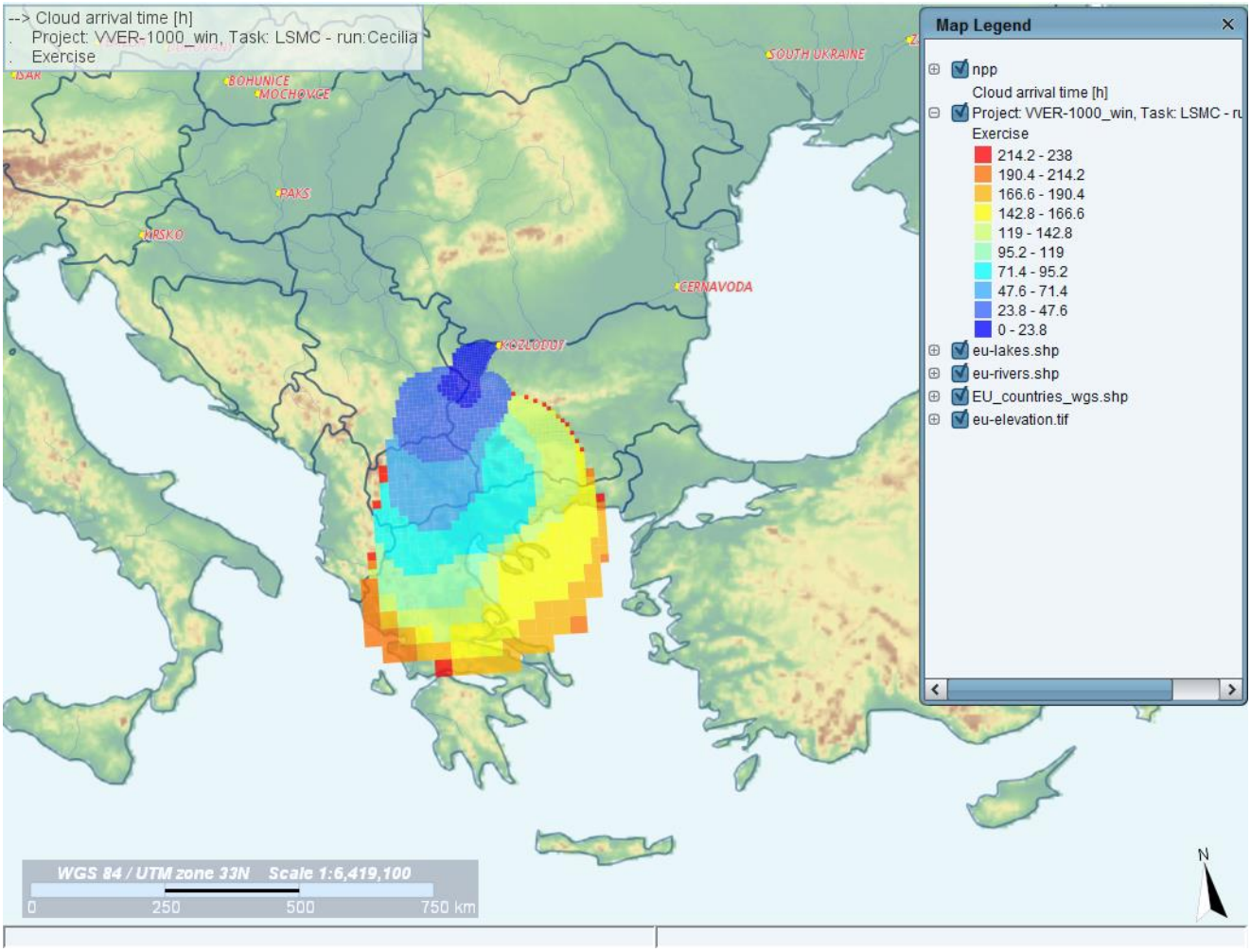

Figure 13: Cloud direction in 10 days

Fig. 13 shows the direction of the clouds in 10 days. The clouds took south-west direction in first 24 hours and evenly distributed over Macedonia and Greece in next 9 days. Following the trajectory, the contamination mostly concentrated over these region and made important impact especially first 3 days. Cs-137 was selected in the calculations since it has relatively high half-life (30.17 y), and the deposition reached almost 95% of the total inventory. The maximum value of the contamination due to Cs-137 reached to the 1.31 MBq/m^2 at the south-western direction due to instant cloud movement as seen on Fig. 14.

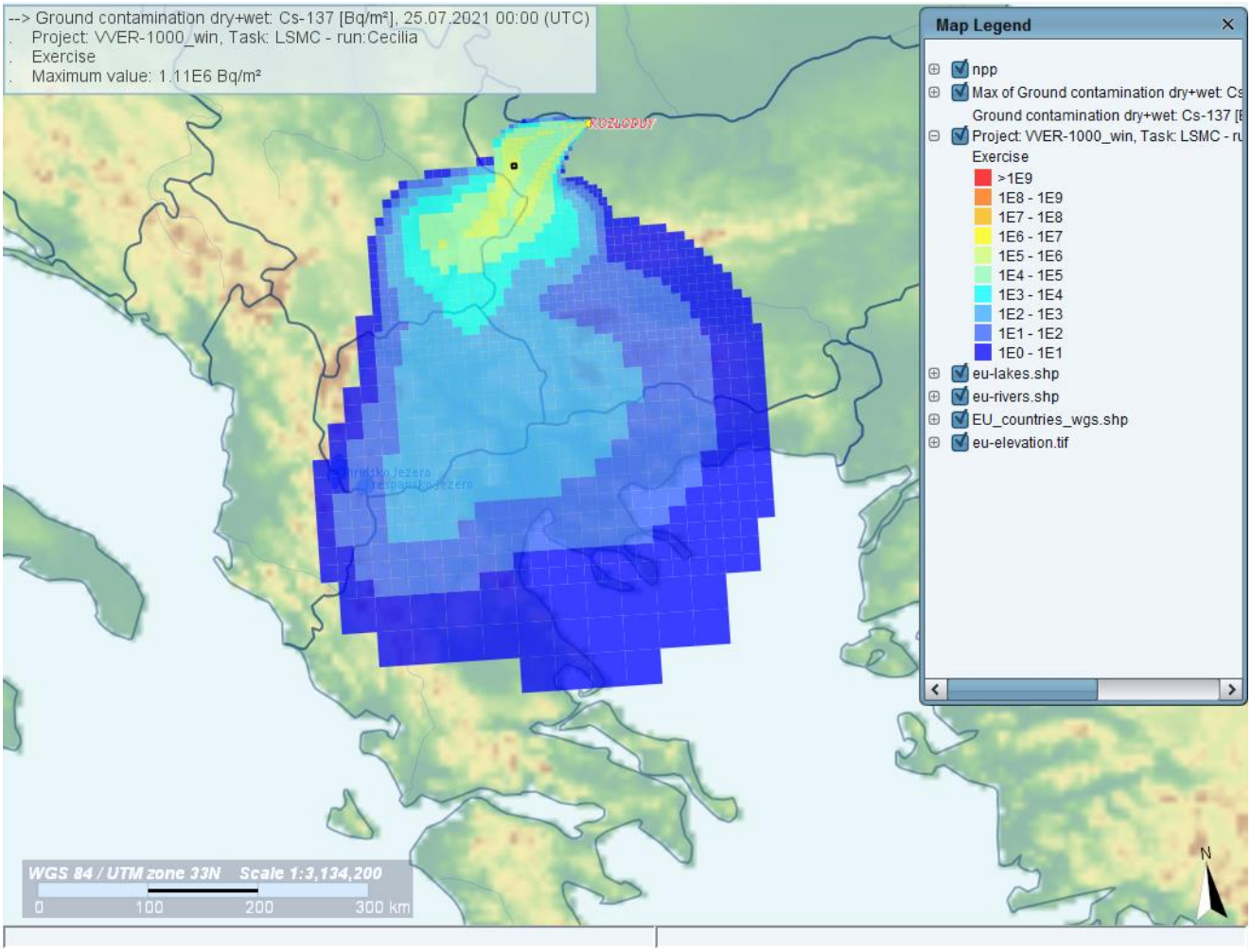

Figure 14: Dry and wet contamination due to Cs-137

When the potential dose was investigated, it can be observed that the total effective dose reached to 1.27 mSv and the thyroid dose reached 1.24 mSv at maximum. As seen from Fig. 15 and Fig. 16, the affected area followed the trajectory of the cloud movement and distributed over the 800 km range. When the recommended ICRP dose limits considered, the potential dose rate is over annual dose limit of 1 msV for the public exposure [12].

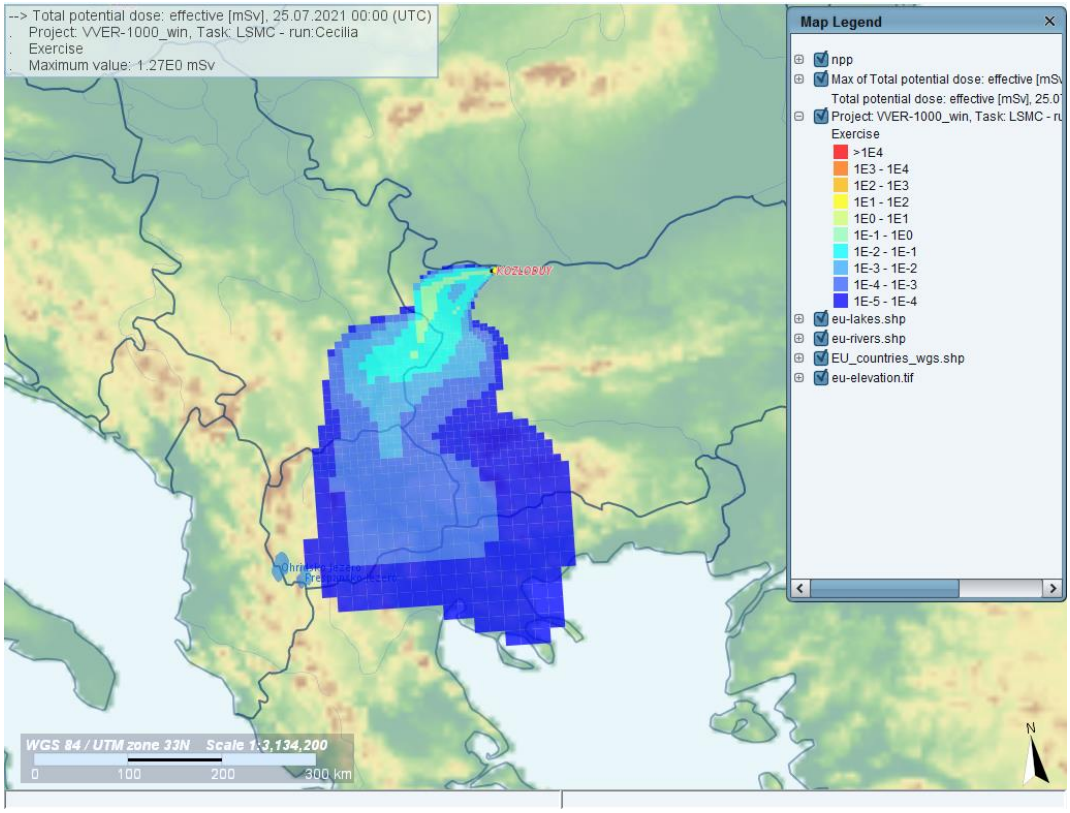

Figure 15: Total potential effective dose in 10 days

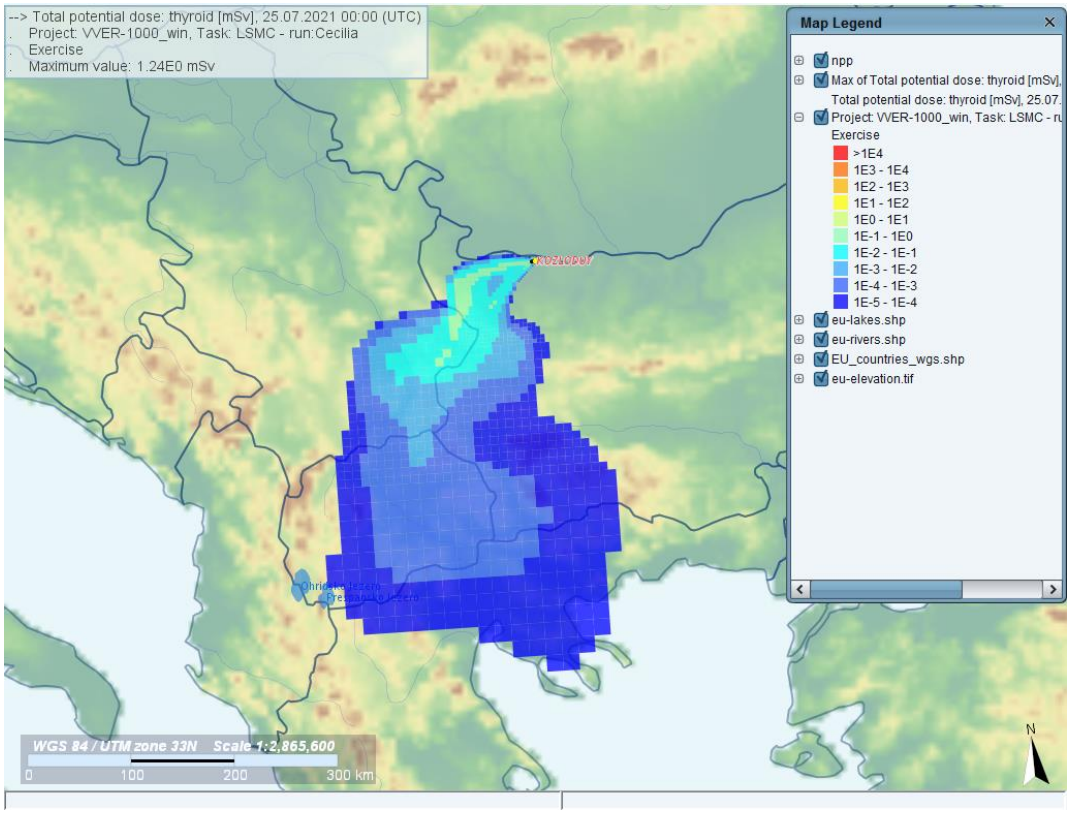

Figure 16: Total potential thyroid dose in 10 days

4. CONCLUSIONS

In summary, the radiological impact analysis was established for a generic VVER-1000 plant by starting from the estimation of the Fission Product inventory by KORIGEN, following with estimation of Source Term and accident progression by ASTEC and finalized with the radiological dispersion. The KORIGEN is used first time with ASTEC to obtain accurate estimations over radiological consequences due to a severe accident. Accurate prediction of Fission products is essential to estimate possible source term in case of a severe accident. Also, estimation of the generation of hydrogen during a severe accident gains importance since it is one of the carriers of source term to the containment and environment. More than 1000 kg of hydrogen generated during the calculation which the MCCI process was the dominant for generation.
Additionally, the first time joint usage of the ASTEC and JRODOS is achieved which allows estimating both Level 2 and Level 3 accidents and possible outcomes. The exposed dose rate reached over the limits of ICRP in the calculation. However, the best results can be obtained by activating emergency preparedness activities. Next steps of this study will be estimating dose estimations for a person and for a child in different conditions and dose change of feedstuff and foodstuff in following years.

ACKNOWLEDGMENTS
The corresponding author is funded by Republic of Turkey Ministry of National Education during his Ph.D. studies. The authors would like to thank JRODOS team under IKET/KIT for enlightening specific points.

REFERENCES

[1] OECD/NEA, "The Fukushima Daiichi Nuclear Power Plant Accident OECD/NEA Nuclear Safety Response and Lessons Learnt," OECD, 2013.

[2] BMUB, "German Action Plan for the implemantation of measures after Fukushima Daiichi reactor accident," 2012.

[3] BMUB, "Updated German Action Plan for the implementation of measures after Fukushima reactor accident," 2014.

[4] O. Kymäläinen, H. Tuomisto and T. Theofanous, "In-vessel retention of corium at the Loviiase plant," *Nuclear Engineering and Design,* vol. 169, pp. 109-130, 1997.

[5] H. Wiese, "Development and application of KORIGEN," in *Brennelementtechnik, Kernauslegung, Reaktorbetrieb : Fachtagung der KTG-Fachgruppen 'Brennelemente' und 'Reaktorphysik und Berechnungsmethoden'*, Karlsruhe, 1998.

[6] P. Chatelard and N. Reinka, "Overview of the integral code ASTEC V2.0," IRSN, 2009.

[7] W. Raskob, D. Trybushnyi, I. Ievdin and M. Zheleznyak, "JRODOS: Platform for improved long term countermeasures modelling and management," *Radioprotection,* vol. 46, no. 6, pp. 731-736, 2012.

[8] B. Murphy, Kravchenko J., L. A., P. A., S. V. and C. A., "Simulation of Low-Enriched Uranium (LEU) Burnup in Russian VVER Reactors with the HELIOS Code Package," Oak Ridge National Laboratory, Tennessee, 2000.

[9] JRC, "In-Vessel Melt Retention (IVMR) Analysis of a VVER-1000 NPP," EU Publication Office, EUR 27951 EN; doi 10.2790/ 62596, 2016.

[10] K. Ivanov, B. Ivanov, P. Groudev, M. Pavlova and V. Hadjiev, "VVER-1000 Coolant Transient Benchmark-Phase 1 (V1000CT-1) Volume I: Final Specifications," NEA , 2004.

[11] O. Noori-Kalkhoran, A. Minuchehr, M. Rahgoshay and A. S. Shirani, "Shot-term and long term analysis of WWER-1000 containment parameters in a large break LOCA," *Progress in Nuclear Energy*, vol. 74, no. ISSN 0149-1970, pp. 201-212, 2014.

[12] ICRP, "The 2007 Recommendations of the International Commission on Radiological Protection," ICRP Publication 103. Ann. ICRP 37 (2-4)., Paris, 2007.

Karlsruhe Institute of Technology

SOURCE TERM ESTIMATION AND DISPERSION ANALYSIS OF VVER-1000 REACTOR IN CASE OF LBLOCA ALONG WITH SBO

Ahmet Kağan Mercan, Fabrizio Gabrielli, Victor Hugo Sanchez-Espinoza

Hermann-von-Helmholtzplatz, 1

D - 76344 Eggenstein-Leopoldshafen

Karlsruhe, Germany

Institute for Neutron Physics and Reactor Technology



Content

- **Motivation**
- **KORIGEN: FP Inventory Analysis**
- **ASTEC: LBLOCA with SBO Severe Accident Analysis**
- **JRODOS: Radiological Impact Analysis on VVER-1000**
- **Summary & Outlook**

Motivation

- Accidents especially Fukushima demonstrated the importance of Severe Accidents and requirement to improve “Numerical Tools”;
  - To predict radiological source term,
  - To estimate radiological impact,
  - To quantify the uncertainties of the code’s models,
  - To test the influence of SAM-measures on the release and timing of fission products into the environment

- The importance of supporting emergency team with reliable, best-possible and fast information regarding of ST and dispersion.

- The aim of this work is prediction of the ST that can be released to the environment in the event of an hypotetical severe accident on VVER-1000 plant and estimation of the radiological impact to the environment and the population.

KORIGEN: FP Inventory Analysis

KORIGEN: FP Inventory Analysis / VVER-1000 Fuel

KORIGEN was developed at KIT-CN from the Oak Ridge Isotope Generation and Depletion code ORIGEN.

Studies shown that accurate FP inventory is essential to predict ST (Talk 311 and Talk 327)

Parameter	Value
Enrichment	4.4% wt
Lattice pitch	1.275 cm
Active height	355 cm
Fuel mass	80.44 t
Clad mass	22.5 t

Fuel rod parameters for Balakova NPP

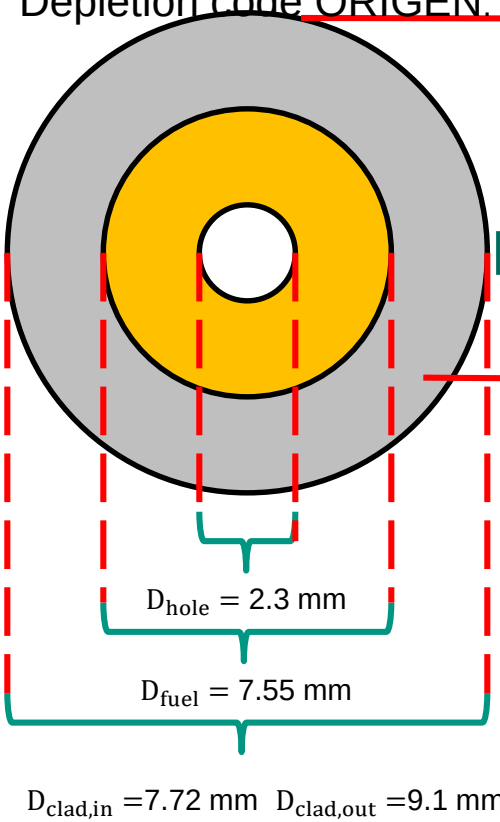

x312 fuel rods



x163 fuel assemblies

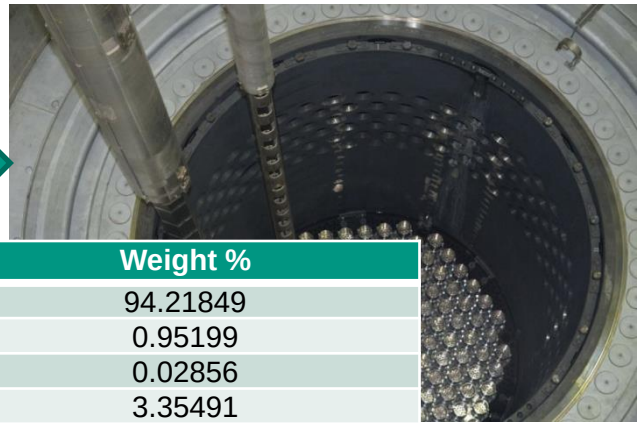

Element	Weight %
Zr	94.21849
Nb	0.95199
Hf	0.02856
Fe	3.35491
Ni	0.50410
Cr	0.88818
Ti	0.04801
C	0.00576

Cladding material composition for Balakova NPP

KORIGEN: FP Inventory Analysis / Irradiation, FP Inventory and Decay Heat Estimation

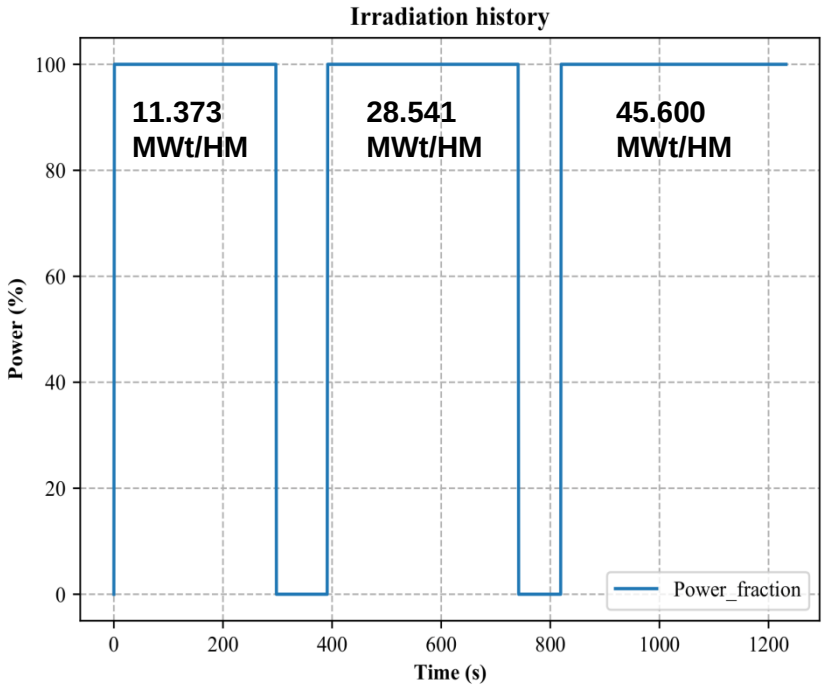

Irradiation time with downtimes

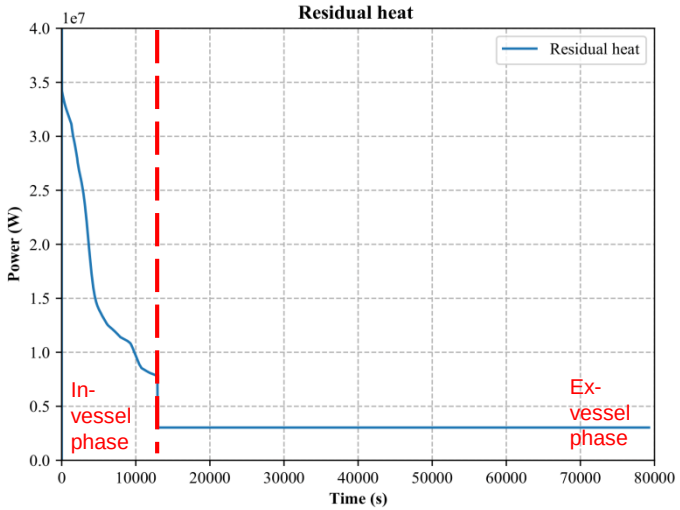

Decay heat during the simulation

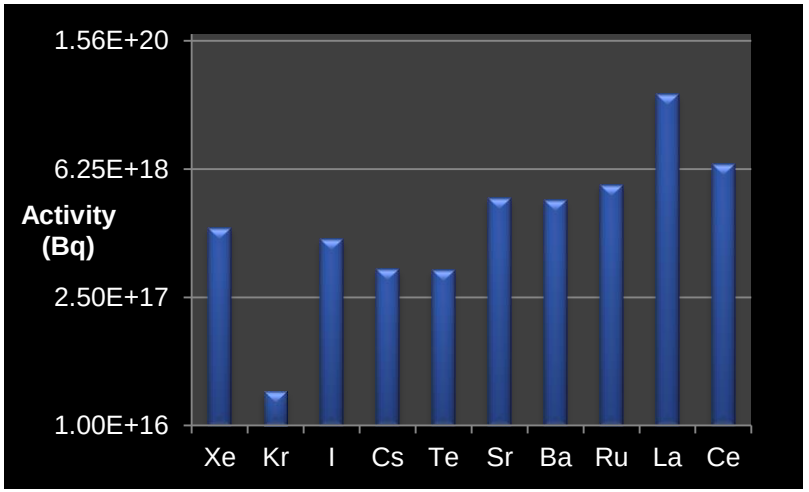

Activity levels for 1 t HM at the beginning of the transient

Remarks:

- With given material information and irradiation history, 45 MWt/HM burn-up was reached with KORIGEN.
- The FP inventory and decay heat due to this inventory has been calculated.
- This FP inventory have been implemented to the ASTEC.

ASTEC: LBLOCA with SBO Severe Accident Analysis

ASTEC: LBLOCA with SBO Severe Accident Analysis/ Primary Circuit Representation

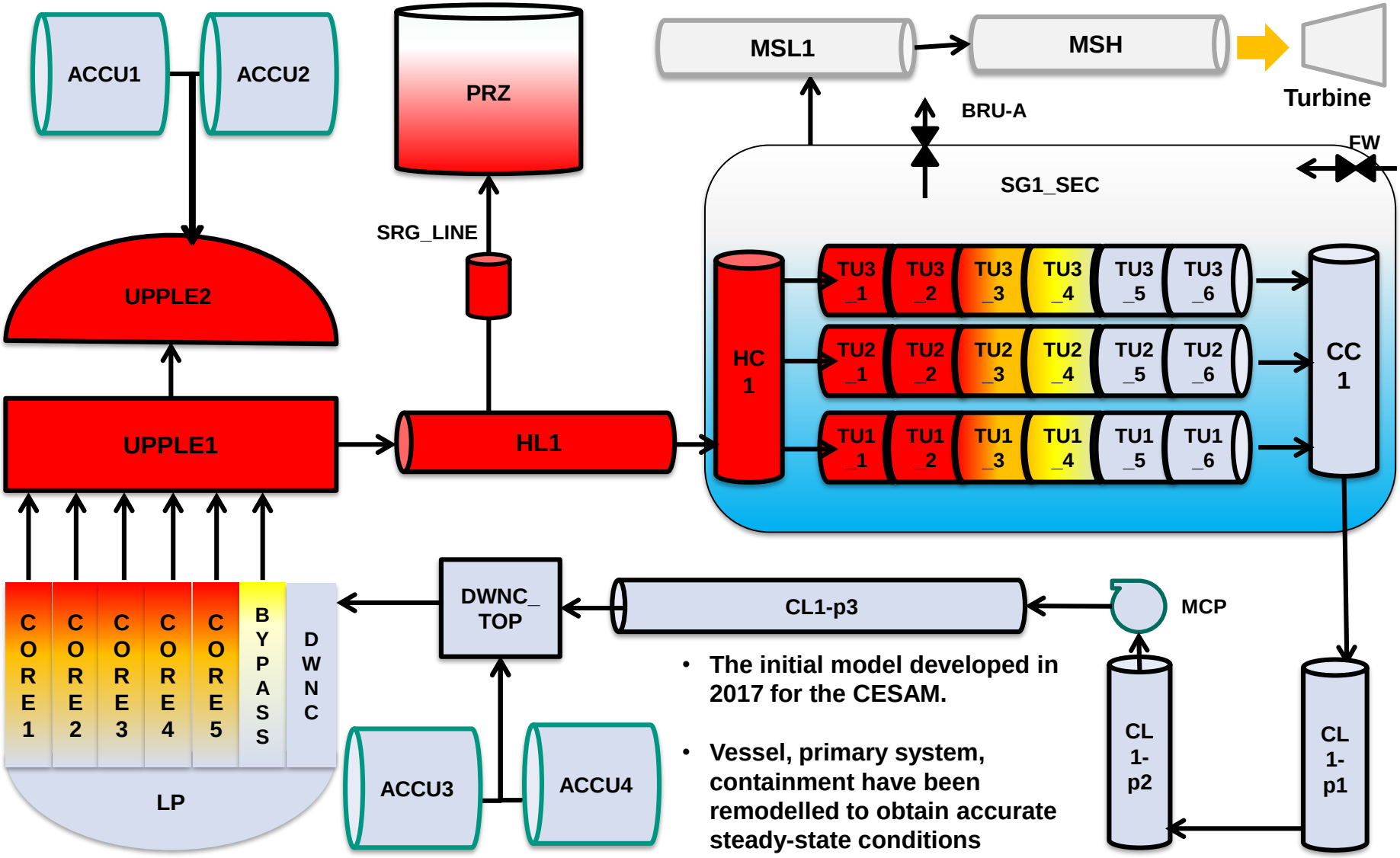

- The initial model developed in 2017 for the CESAM.
- Vessel, primary system, containment have been remodelled to obtain accurate steady-state conditions

ASTEC: LBLOCA with SBO Severe Accident Analysis/ Containment and Cavity Representation

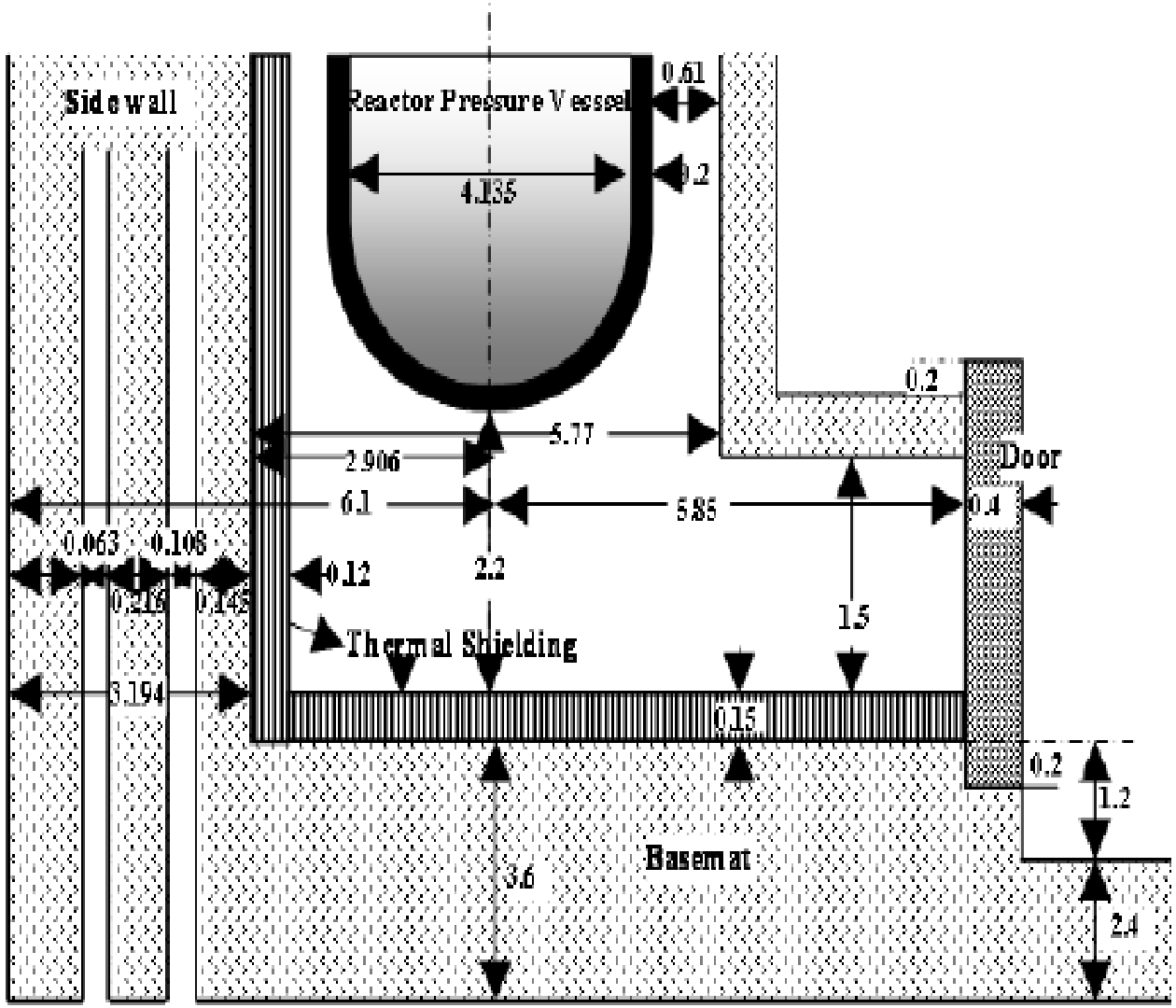

Model includes;

- 27 zones
- 60 junctions
- Natural leakage to the environment

Cavity has silicous type of concrete with low gas and water content but higher iron fraction.

ASTEC: LBLOCA with SBO Severe Accident Analysis/ Checking the Model Predictions

Parameter	Real Plant Data	ASTEC model	Relative Error
Core power [MW]	3000	3000	%0
Lower plenum pressure [MPa]	15.842	15.868	%1
Pressure above the core [Mpa]	15.7±0.3	15.762	%1
Core inlet temperature Loop 1 [K]	560.15	561.71	%1
Core inlet 2 temperature Loop 2 [K]	560.15	561.71	%1
Core exit 1 temperature Loop 1 [K]	592.05	592.02	>%1
Core exit 2 temperature Loop 2 [K]	592.05	592.02	>%1
Coolant heat up over the reactor [K]	31.9	30.31	%5
SG1 outlet pressure [Mpa]	6.27	6.27	%0
SG1 outlet steam temperature [°C]	278.5	278.2	>%1
SG2 outlet pressure [Mpa]	6.27	6.27	%0
SG2 outlet steam temperature [°C]	278.5	278.2	>%1
Feedwater flow [kg/s]	409	409	%0
Feedwater temperature [°C]	220	220	%0
SG1 level [m]	2.55	2.55	%0
SG2 level [m]	2.55	2.55	%0

Results are in great coherence with real plant data

ASTEC: LBLOCA with SBO Severe Accident Analysis/ Modelling Assumptions

- Scenario:
  - Large break (850 mm) on cold leg between pump and downcomer
  - Assumption:
    - Coincident SBO:
      - i.e. no active ECCS available: LPIS, HPIS
    - Passive accumulators available when the pressure is below 5.9 MPa.
      - 2 group of accumulator injects to the upper plenum
      - Other 2 group of accumulator injects to the downcomer
    - SCRAM and pump coast-down is given at time=0 s
    - BRU-A valves are activated to pressure release from steam generator secondary side to the atmopsphere.
    - Steam, hydrogen, xenon and kripton have been modelled as carrier fluid for FPs.
    - Natural leakage between the containment and the environment.
    - All ASTEC modules have been activated.
- Simulation approach:
  - Stead state simulation
  - Transient simulation

ASTEC: LBLOCA with SBO Severe Accident Analysis/ Sequence of Events

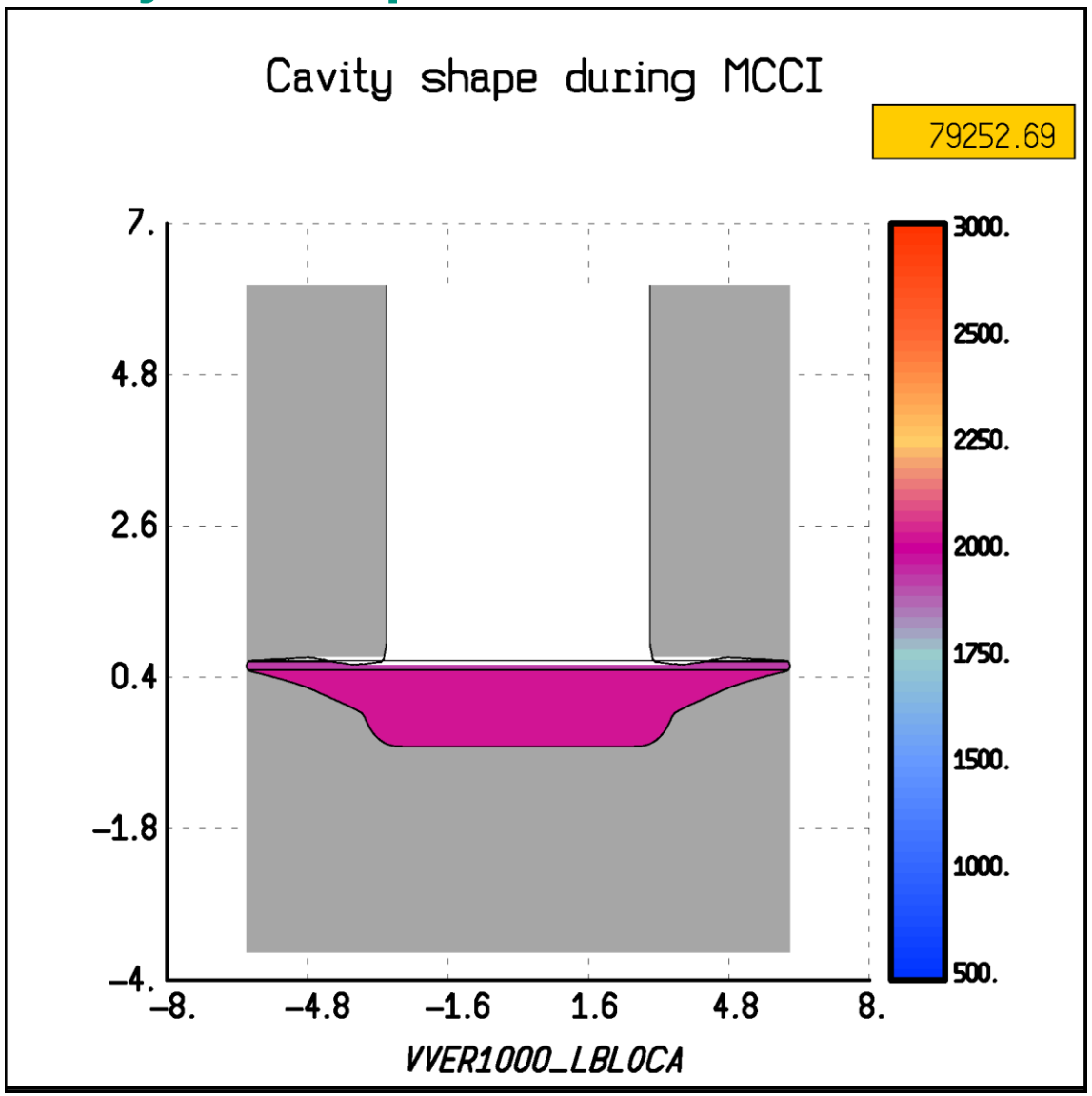

- Start of accumulators @ t=13 s.
- End of accumulators @ t=97 s.
- FP release start @ t=1276 s.
- First slumps in LP @ t=1285 s.
- Uncovered core @ t=3904 s.
- Dryout of vessel @ t=6212 s.
- RPV failure @ t=12918 s.
- Injection of corium @ t=12919 s.
- Cavity failure @ t=79252 s.

ASTEC: LBLOCA with SBO Severe Accident Analysis/ Global Parameters

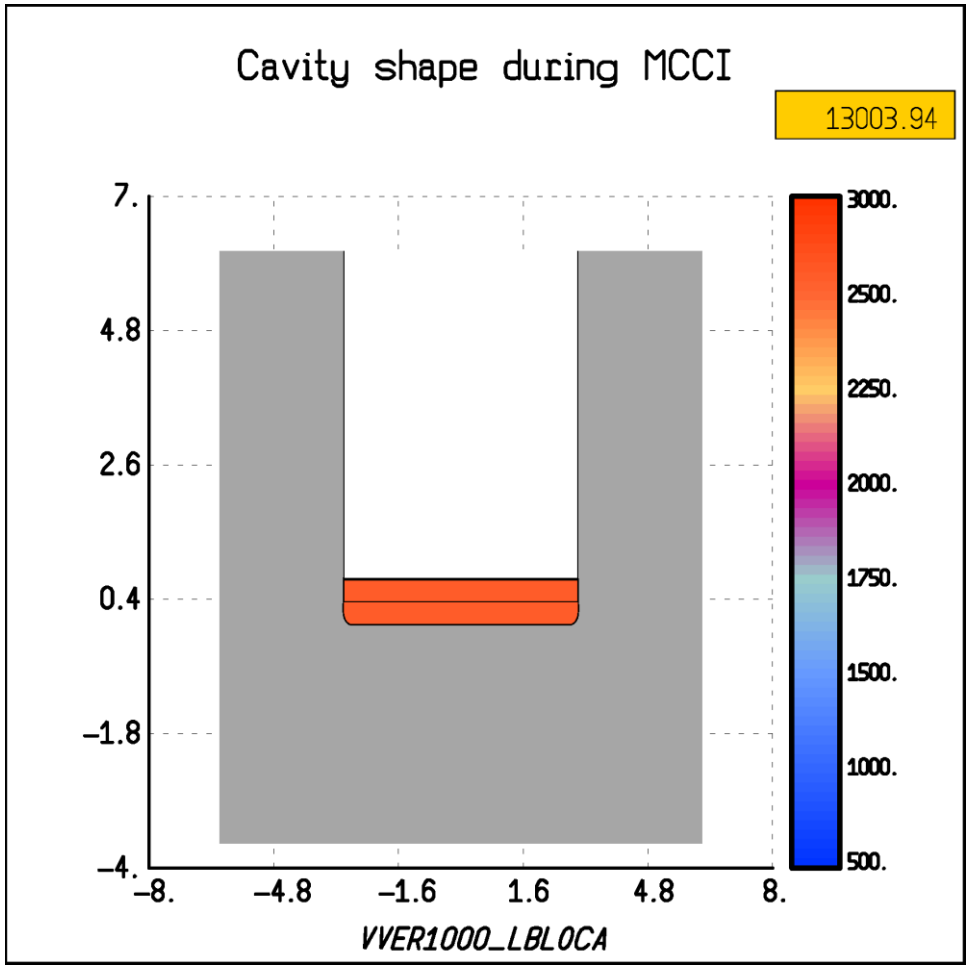

ASTEC representation of sequence of events

Remarks:

- At the end of the phase, 224,1013 kg of hydrogen generated in ASTEC, effective thermal to 6600 kg oxidation.

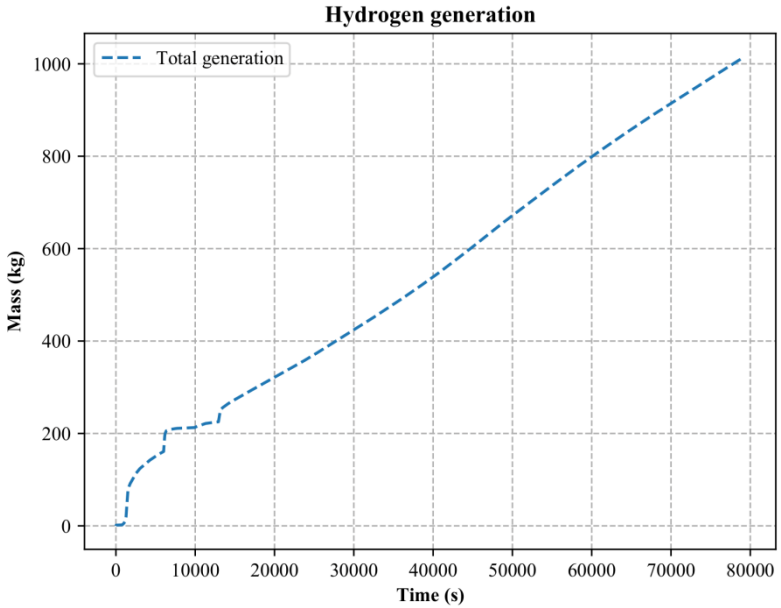

ASTEC: LBLOCA with SBO Severe Accident Analysis/ FP Transport and Release

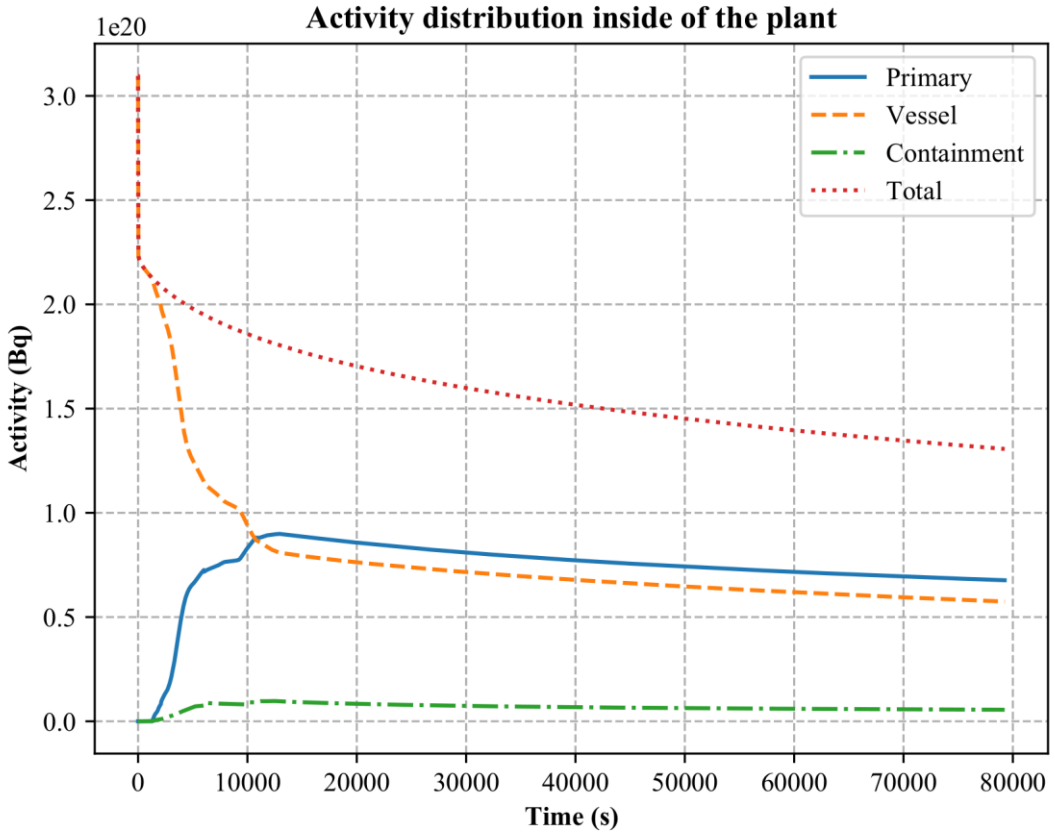

Activity change in the plant during the transient

Despite the high retention, the activity in the containment reached 5.55E18 Bq, the leaked activity was 6.17E15 Bq

JRODOS: Radiological Impact Analysis on VVER-1000

JRODOS: Radiological Impact Analysis on VVER-1000 /Calculation Steps

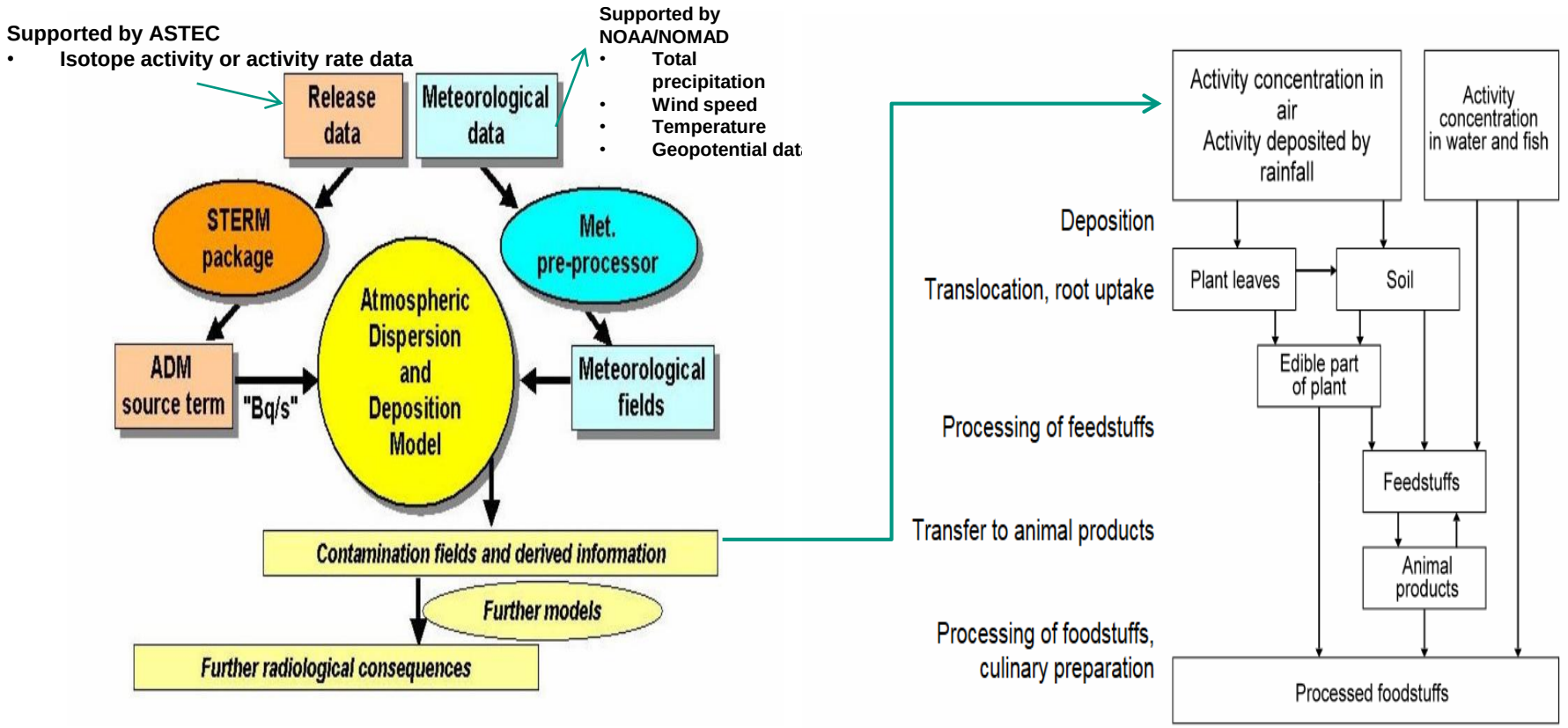

Remarks:

- **JRODOS supports location data which include urbanization, population and vegetation data.**
- **By including release and meteorological data, the code calculate the contamination with various pathways.**
- **Additionally, code support countermeasure variants across world according to their regulations**

JRODOS: Radiological Impact Analysis on VVER-1000 /Modelling Assumptions

- Scenario:
  - Radiological dispersion analysis during LBLOCA with SBO simulation (until cavity rupture)
  - Assumption:
    - Summer season weather data
      - Between 15/07/21-25/07/21
      - Data acquired from National Oceanic and Atmospheric Administration (NOAA) for 6 hour interval with the resolutions between 25 km to 100 km
    - Kozloduy-6 plant location
      - Same type of VVER plant (V320) with ASTEC model
      - 60 m was assumed for release height
    - Gaussian Plume based RIMPUFF (Risø-Mesoscale-Puff)
    - 800 km range for dispersion calculations
    - Activity level at different time points for 160 isotope
      - ASTEC was arranged to give activity of each isotope for each time step
      - These activities were implemented manually but connection between these codes is possible by python.
- Result approach:
  - Contamination over the area by Cs-137
  - Total potential doses and lifetime doses
  - Activity over foodstuff and feedstuff

JRODOS: Radiological Impact Analysis on VVER-1000 /Contamination over the Area by Cs-137

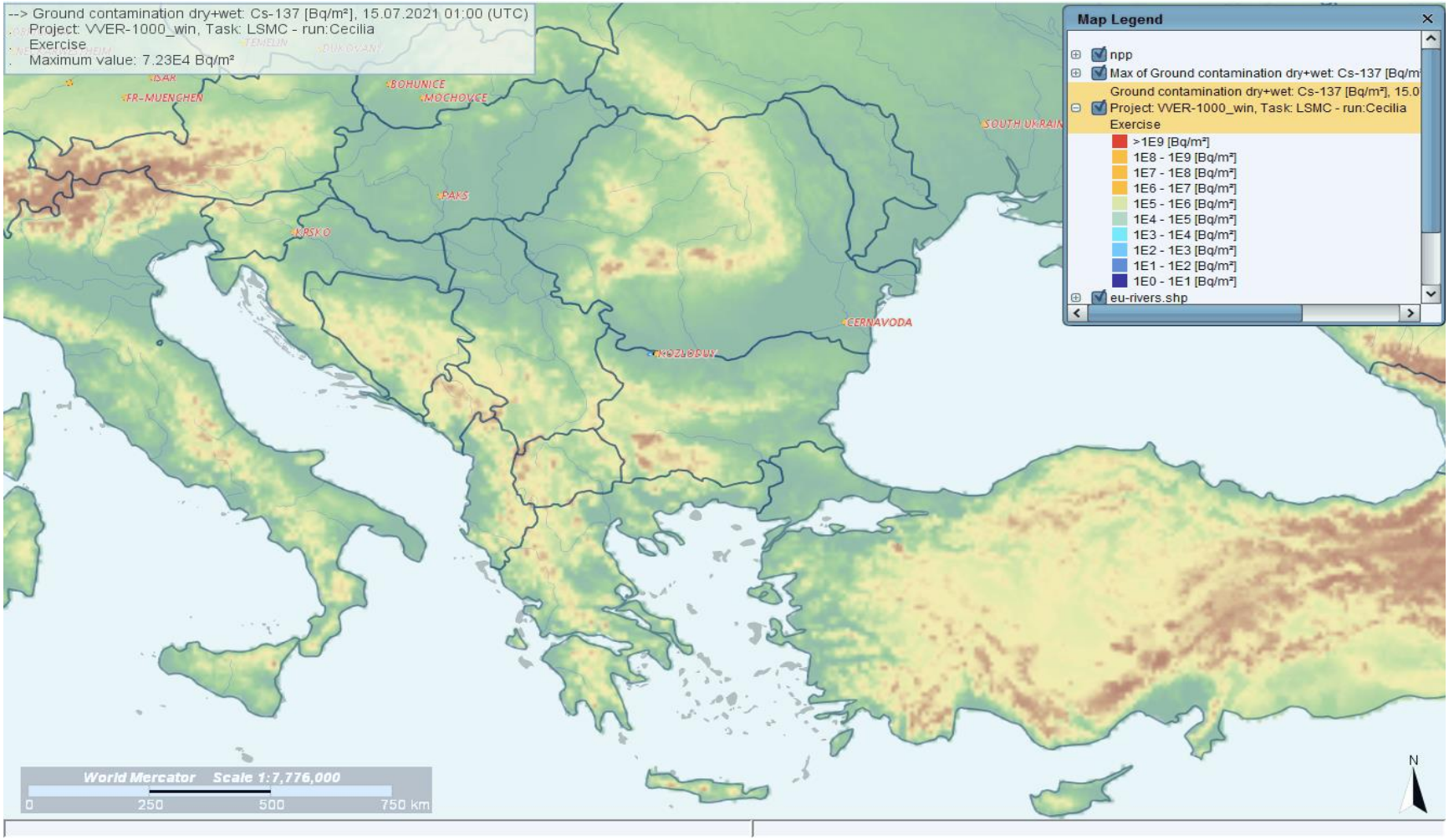

Remarks:

- Maximum contamination reached 1.1 MBq/m^2
- The maximum distance that contamination was 520 km away from the source

JRODOS: Radiological Impact Analysis on VVER-1000 /Total Potential Doses & Lifetime Doses

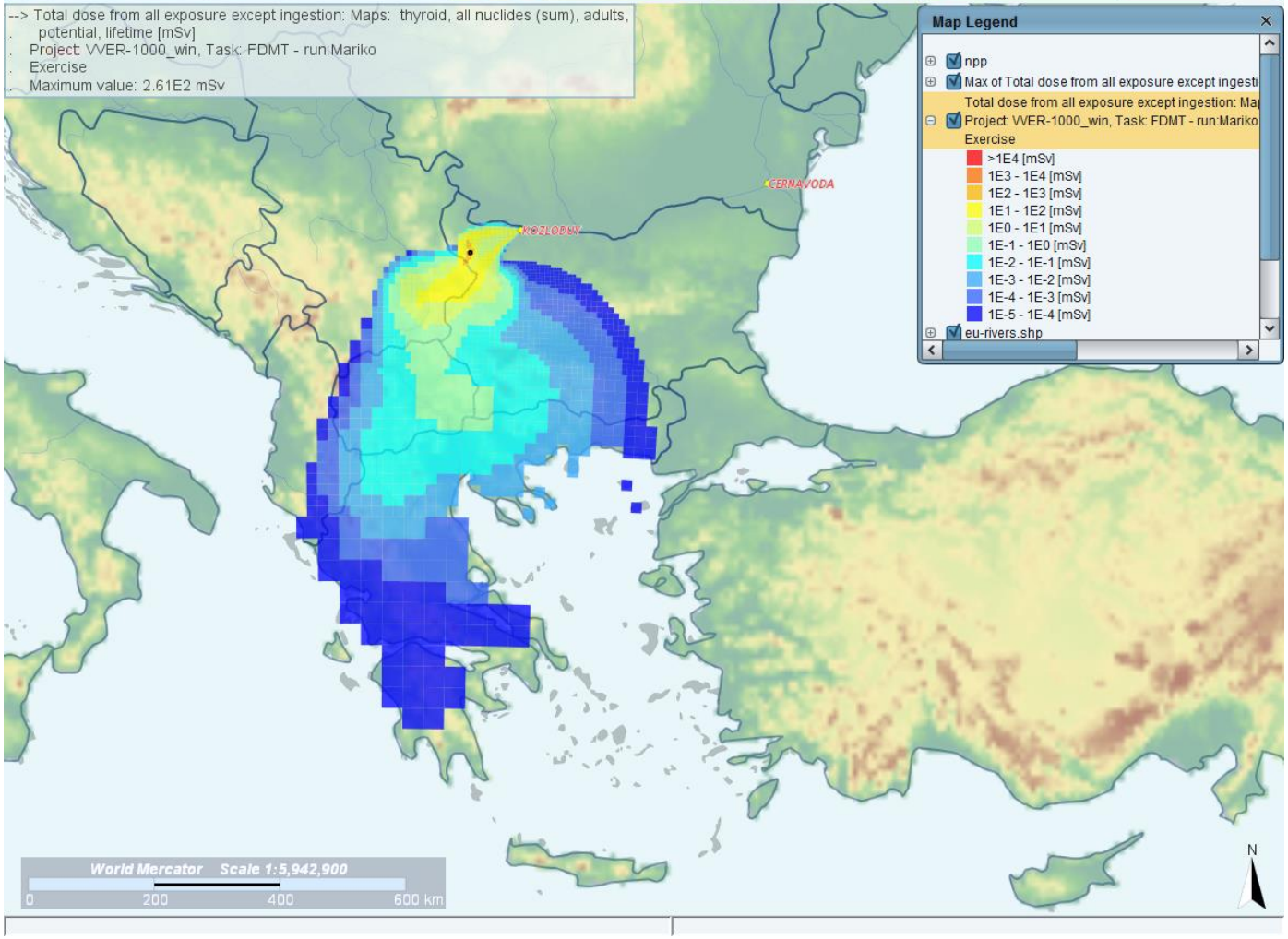

Total thyroid potential dose from all exposure except ingestion for an adult in lifetime

Total acute doses are higher than ICRP limit of 1 mSv for every organ group.

One adult might encounter more than 250 mSv in lifetime.

JRODOS: Radiological Impact Analysis on VVER-1000 /Activity over Foodstuff and Feedstuff

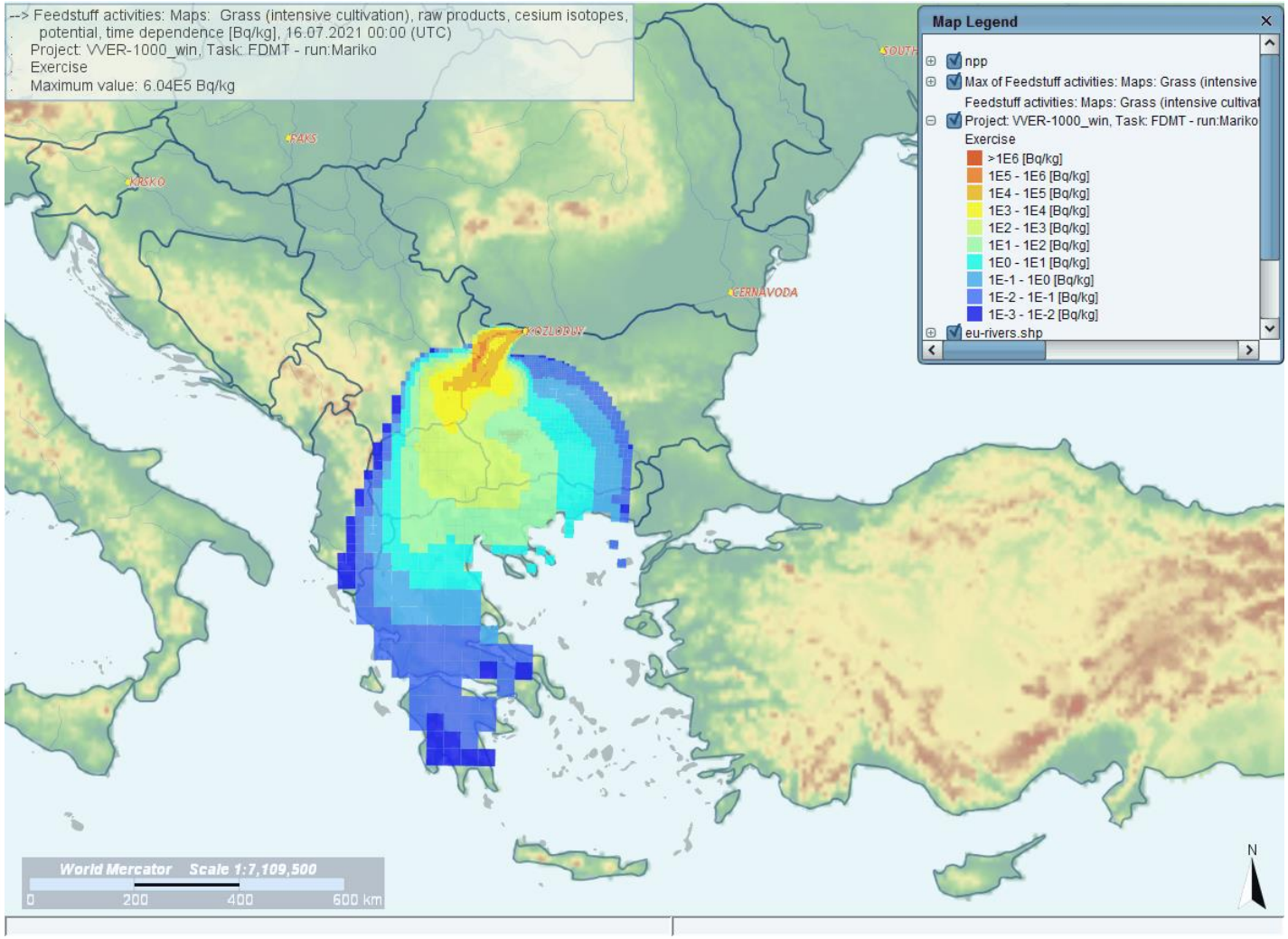

Activity change over the grass in time

Potential dose from cesium isotopes for grass became 604 MBq/kg after one day of the event.

Doses decayed 0.88 MBq/kg after one year for grass.

39.3 MBq/kg for cow milk and 691 MBq/kg for leafy vegetables.

Summary & Outlook

Summary & Outlook

SUMMARY:

- First-of-a-kind application of in-house, European code KORIGEN with ASTEC in order to estimate FP inventory to be used as decay heat and FP transport.

- VVER-1000 ASTEC model has been constructed with all modules. LBLOCA along with SBO accident on VVER-1000 has been simulated ASTEC code.

- First-of-a-kind application of JRODOS with ASTEC to predict radiological dispersion and impact analysis.

- Establishment of reliable, fast and efficient information chain with real plant data to be used by regulators and emergency management that can be applied for any reactor type, any severe accident scenario and any location.

OUTLOOK:

- Emergency preparedness applications on JRODOS

- U&S studies with in-house FSTC tool

Back-up Slides

ASTEC: LBLOCA with SBO Severe Accident Analysis/ ASTEC Integral Code

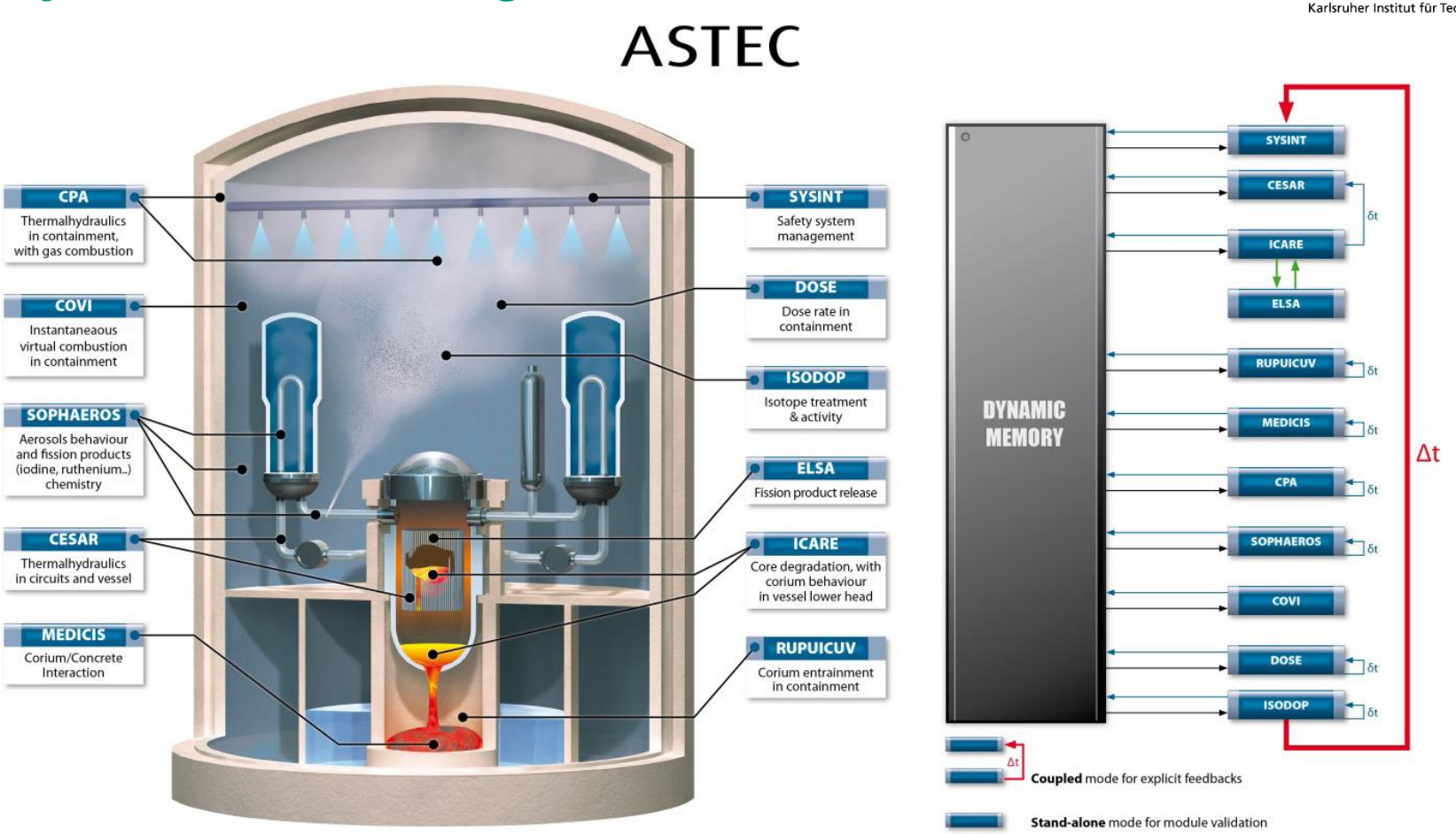

Structure of the ASTEC software and main modules

The ASTEC, developed by IRSN, (Accident Source Term Evaluation Code) software system makes it possible to simulate all phenomena that take place during a water-cooled reactor meltdown accident, from the initiating event to the discharge of radioactive materials (called the "source term") out from the containment

ASTEC: LBLOCA with SBO Severe Accident Analysis/ Physical Limits

Chemical kinetics model	Involved components	Correlation
Zircaloy oxidation by steam	Clad, control rods, guide tubes, grid spacers	BEST-FIT
UO_2 and Zirconia dissolution by molten Zircaloy	Fuel elements	KIM-CONV
Steel oxidation by steam	Control rod cladding, lower grid plates	MATPRO (J.F. White)

Physical models

Integrity Criteria	Involved components	Limit
Zr oxidation start	Zircaloy rod, spacer grids, control rod cladding	T > 600 K
Fuel rod cladding integrity	Zircaloy rod	T > 2400 K and thickness< 250 µm or T > 2550 K
Spacer grid melting	Spacer grids	T > 1730 K
Relocation of control rod cladding, plates	Control rods and plates	T > 1730 K
Vessel bottom head failure	Lower head	Tmax > 1473 K or Pmax > 150 MPa

Physical criteria

ASTEC: LBLOCA with SBO Severe Accident Analysis/ FP Transport and Release

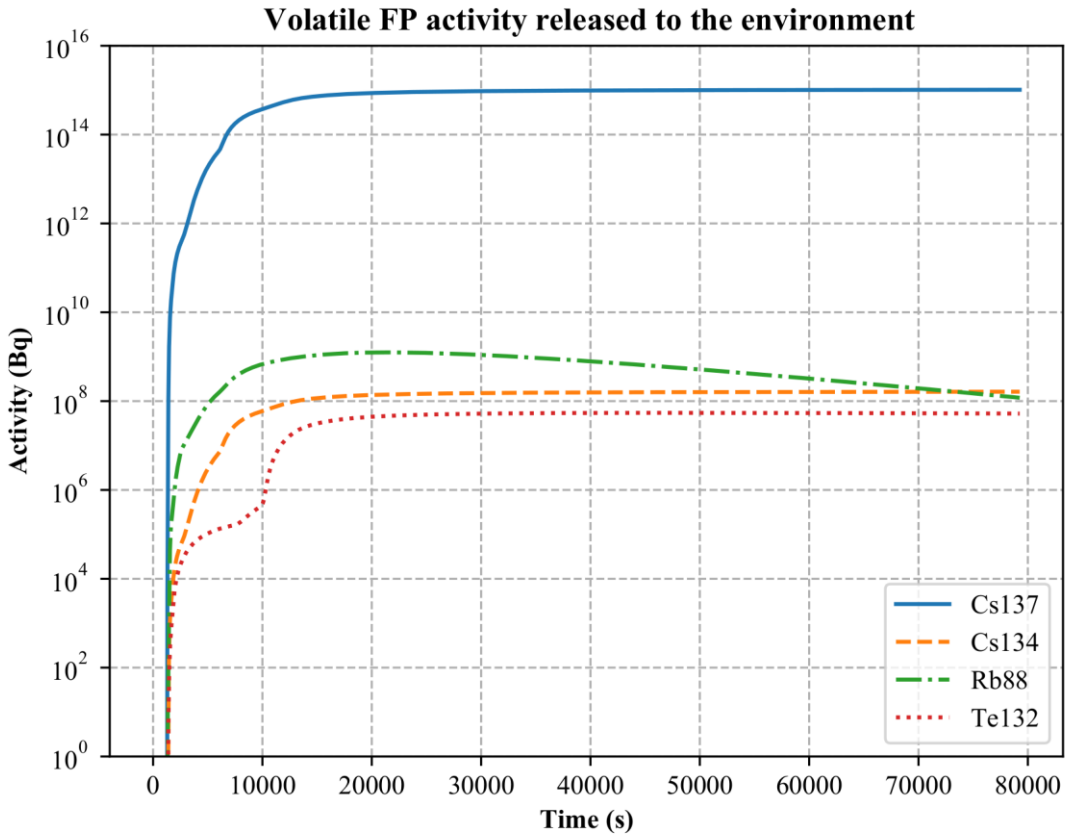

- After 1276 s., FPs started to be transported to the primary circuit by H_2, steam, Xe and Kr. Until the core uncovered, this transport was faster due to steamy environment.
- Most of the FPs went under retention inside of the primary circuit walls. Noble gas elemnest like Xe and Kr were transported without retention and volatile isotopes such as Rb, Cs and I were transported with lower retention levels.
- Despite the high retention, the activity in the containment reached 5.55E18 Bq, the leaked activity was 6.17E15 Bq
- The released activity for Xe-133 and Xe-135 were about 6E12 Bq and 5E11. Kr isotopes started to decay after 10000 s. due to their half-time, but they still were in the level that can affect people with inhalation.
- The iodine isotopes‘ activity reached to 1E9 Bq levels which can affect thyroid.
- Activity of Cs-137 was about 1E15 Bq and it is hazardous for long years.

JRODOS: Radiological Impact Analysis on VVER-1000 /Cloud Movement

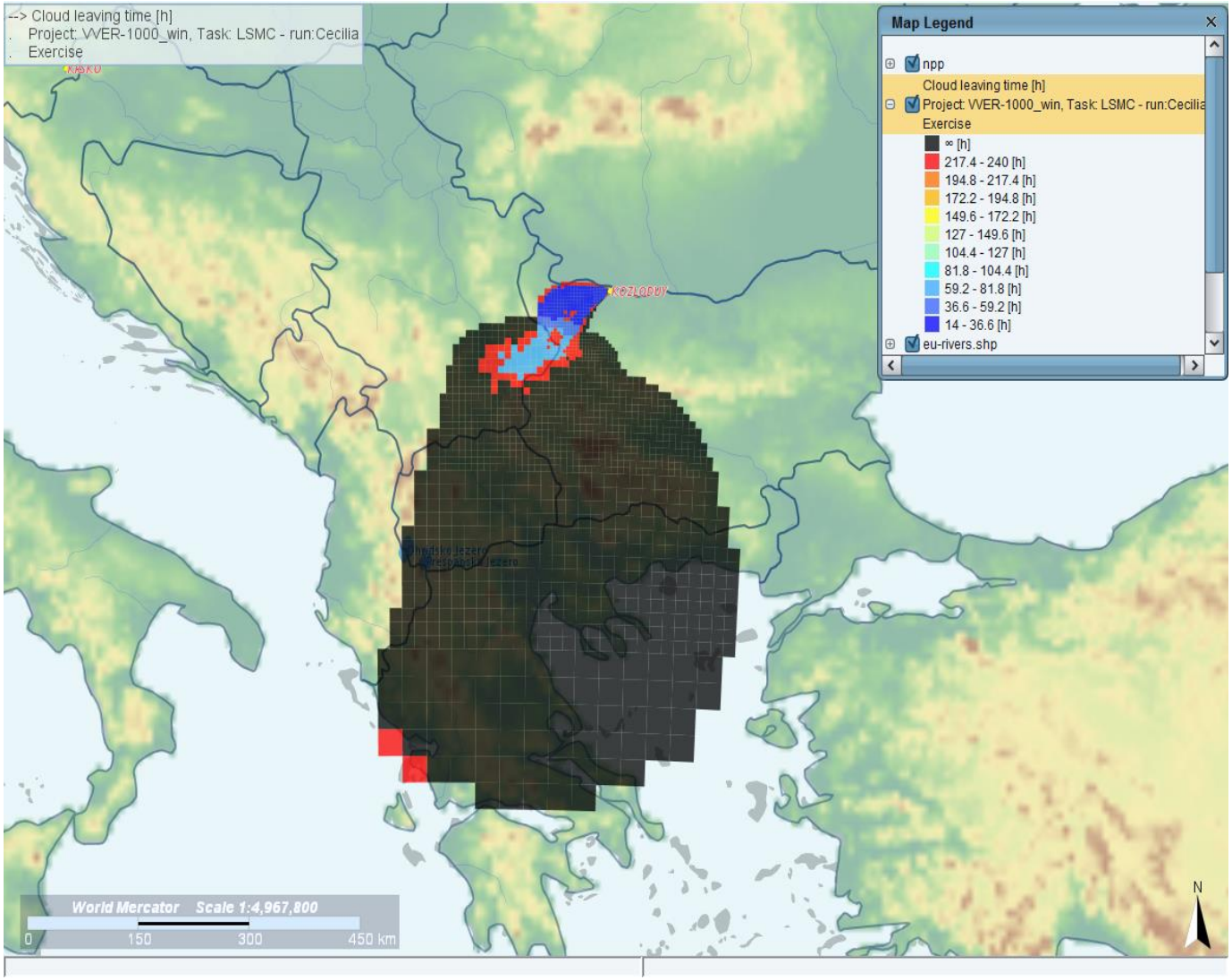

Cloud arrival time

Remarks:

- The clouds started to move south-west direction at the beginning.
- Within 48 h., clouds traveled 250 km. In the next 192 h., these clouds dispersed over the selected area.
- In the first 100 h., clouds left the range of 155 km.
- However clouds remained on the area which led to long deposition over this area.

JRODOS: Radiological Impact Analysis on VVER-1000 /Total Potential Doses & Lifetime Doses

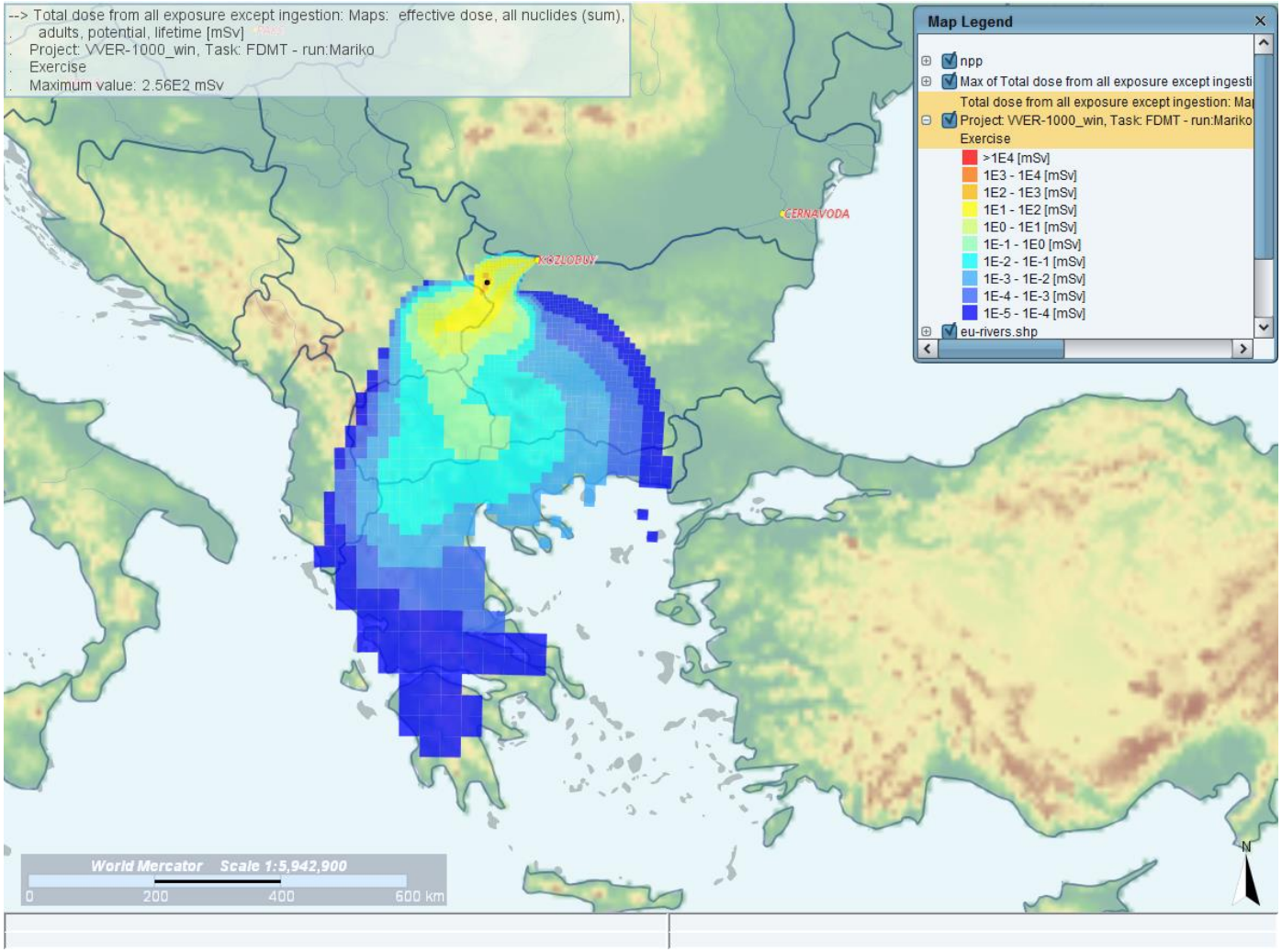

Total thyroid dose from all exposure except ingestion for an adult in lifetime

Remarks:

- Total potential thyroid dose reached 1.24 mSv as maximum.
- The dose reached 400 km away from the source.
- The maximum total potential doses for bone marrow, effective, lung and uterus were 1.21 mSv, 1.27 mSv, 1.21 mSv and 1.32 mSv respectively.
- This dose levels are greater than the ICRP limits of acute 1 mSv.
- Total thyroid dose from all exposure for an adult can be 262 mSv
- Total effective dose from all exposure except ingestion for an adult can reach 256 mSv

PREDICTION OF THE RADIOLOGICAL CONSEQUENCES OF A SEVERE ACCIDENT SCENARIO IN A GENERIC KONVOI NUCLEAR POWER PLANT

E. Pauli*
Framatome GmbH
Paul Gossen Straße 100, 91052 Erlangen, Germany
eva-maria.pauli@framatome.com

A. Hoefer
Framatome GmbH
Seligenstädter Straße 100, 63791 Karlstein am Main, Germany
axel.hoefer@framatome.com

F. Gabrielli, A Stakhanova, V.H. Sanchez-Espinoza
Karlsruhe Institute of Technology (KIT)
Hermann-von-Helmholtz-Platz 1, Eggenstein-Leopoldshafen, Germany
fabrizio.gabrielli@kit.edu; anastasia.stakhanova@kit.edu; victor.sanchez@kit.edu

ABSTRACT

We present selected results obtained within the WAME project, performed in cooperation between Karlsruhe Institute of Technology (KIT) and Framatome GmbH. This project is devoted to developing and testing a methodology for real-time source term prediction for accidents at nuclear power plants. To achieve that goal, a time series prediction algorithm is used, which is based on the MOCABA data assimilation framework developed by Framatome. This prediction algorithm has been implemented in the form of Fortran code by Framatome and in the form of Python code within KIT's Fast Source Term Calculation (FSTC) tool for uncertainty and sensitivity analysis.

To investigate the suitability of the MOCABA prediction algorithm for predicting the course of an accident at a nuclear power plant based on measured plant data, it is applied to the prediction of the radioactive release (source term) from a generic Konvoi nuclear power plant following a medium break loss of coolant accident with core melt. The training database for the algorithm is generated by performing a large number of severe accident simulations with the Accident Source Term Evaluation Code (ASTEC), developed by IRSN, for Monte-Carlo-sampled input parameters.

The results of this analysis demonstrate that the trained MOCABA prediction algorithm is capable of predicting relevant accident variables like radioactive source terms and dose rates. We discuss what conditions must be fulfilled to obtain reasonable predictions of the to-be-predicted accident variables. Under these conditions, the MOCABA prediction algorithm is suitable to be applied within emergency preparedness tools like Framatome's Central Radiological Computer System (CRCS).

Severe Accident, Radiological Consequences, U&S Analysis, Machine Learning, ASTEC, MOCABA

1. INTRODUCTION

In radiological emergencies, nuclear power plant operators require tools to assess and minimize the radiological risk to the public and potential radiation dose to workers and emergency response personnel. Radiological tools for emergency preparedness and emergency response must provide answers in real time and must be versatile and easy-to-use.

This paper is devoted to the prediction of the radiological consequences for severe accidents at nuclear power plants using a time series prediction algorithm based on Framatome's MOCABA data assimilation framework [1]. The presented results have been obtained within the WAME project, a joint project between KIT and Framatome GmbH, which is financed by the German Federal Ministry of Economic Affairs and Climate Action (BMWi). The main objective of the WAME project is to find a methodology to perform improved source term predictions for severe accidents based on available measurements from plant detectors.

As an example application, we consider the prediction of the radioactive release (source term) from a generic Konvoi nuclear power plant (NPP) following a medium break loss of coolant accident (MBLOCA) with core melt [2]. For this application case, the model parameters of the MOCABA prediction algorithm are estimated from a training database obtained from a large number of severe accident simulations with the Accident Source Term Evaluation Code (ASTEC) [3] for randomly sampled input parameters. This training database is generated with KIT's Fast Source Term Calculation (FSTC) tool for uncertainty and sensitivity (U&S) analysis. For more details about the ASTEC simulations and selected results from the related U&S analysis we refer to [4].

The paper is organized in the following way:

- Chapter 2: Mathematical framework of MOCABA prediction algorithm
- Chapter 3: Software implementation of U&S analysis and MOCABA algorithm
- Chapter 4: Input data from ASTEC simulations
- Chapter 5: Application of MOCABA prediction algorithm to MBLOCA scenario
- Chapter 6: Conclusions

2. MATHEMATICAL FRAMEWORK OF MOCABA PREDICTION ALGORITHM

The MOCABA prediction algorithm for time series applications is based on the mathematical framework presented in [1]. Its purpose is to translate Monte Carlo (MC) simulation data for a set of correlated time-dependent variables and corresponding time-dependent measurements into future predictions of a set of to-be-predicted variables.

Within the considered prediction model, the to-be-predicted variables are represented by a discrete function $y_A(i_A, i_t)$ and the to-be-measured variables by a discrete function $y_B(i_B, i_t)$ ($i_A = 1, \dots, n_A$, $i_B = 1, \dots, n_B$, $i_t = 1, \dots, n_t$). Here, i_A is an indicator of the to-be-predicted variable (n_A = number of to-be-predicted variables), and i_B is an indicator of the to-be-measured variable (n_B = number of to-be-measured variables). The indicator i_t defines the time grid $t(i_t)$ ($i_t = 1, \dots, n_t$) covering the relevant time interval of the considered accident scenario.

Performing accident simulations for MC-sampled input parameters leads to n_{MC} accident sequences (n_{MC} being the number of MC samples) with different values of $y_A(i_A, i_t)$ and $y_B(i_B, i_t)$. The values of $y_A(i_A, i_t)$ and $y_B(i_B, i_t)$ obtained from the different MC simulations ($i_{MC} = 1, \dots, n_{MC}$) are represented by the discrete functions $y_A^{MC}(i_A, i_t, i_{MC})$ and $y_B^{MC}(i_B, i_t, i_{MC})$, respectively. They represent the training data used to estimate the model parameters of the MOCABA prediction model. These model parameters are here given

by the $(n_A + n_B)$-dimensional prior mean vectors $\boldsymbol{y}_{0p}^{(i_t)}$ (each representing for a given time step i_t the prior best estimate values of $y_A(i_A, i_t)$ and $y_B(i_B, i_t)$) and the corresponding covariance matrices $\boldsymbol{\Sigma}_{0p}^{(i_t)}$, as well as the n_t-dimensional mean vectors $\boldsymbol{y}_{0t}^{(i_p)}$ (each representing for a given – to-be-predicted or to-be-measured – variable, indicated by i_p, the best estimate values at the different time steps) and the corresponding covariance matrices $\boldsymbol{\Sigma}_{0t}^{(i_p)}$. The measurements of the to-be-measured variables at the different time steps i_t are represented by the n_B-dimensional measurement vectors $\boldsymbol{v}^{(i_t)}$, and the corresponding measurement uncertainties are represented by the measurement covariance matrices $\boldsymbol{\Sigma}_V^{(i_t)}$.

The objective of the MOCABA prediction algorithm is to predict, at a given time step k_t, the values of $y_A(i_A, i_t)$ and $y_B(i_B, i_t)$ for the future time steps $i_t > k_t$ when taking into account the currently available measurement information represented by $\boldsymbol{v}^{(j_t)}$ and $\boldsymbol{\Sigma}_V^{(j_t)}$ $(j_t \leq k_t)$. Applying the MOCABA prediction algorithm yields the $(n_A + n_B)$-dimensional posterior mean vectors $\boldsymbol{y}_p^{(i_t,k_t)*}$ (each representing the posterior prediction values of $y_A(i_A, i_t)$ and $y_B(i_B, i_t)$ at a given time step $i_t > k_t$ when taking into account the currently available measurements) and the corresponding standard deviation vectors $\boldsymbol{\sigma}_p^{(i_t,k_t)*}$, containing the standard deviations of the posterior predictions of the different variables.

In the following, the different computational steps are sketched that lead us from the Monte Carlo data to the prior model parameters and from the trained prediction model to the posterior predictions when taking into account the measurement information:

- Monte Carlo (MC) input:
  - MC data for to-be-predicted variables $y_A^{MC}(i_A, i_t, i_{MC})$
  - MC data for to-be-measured variables $y_B^{MC}(i_B, i_t, i_{MC})$
    - $i_A = 1, \dots, n_A$ (n_A = number to-be-predicted variables)
    - $i_B = 1, \dots, n_B$ (n_B = number of to-be-measured variables)
    - $i_t = 1, \dots, n_t$ (n_t = number of time steps $t(i_t)$)
    - $i_{MC} = 1, \dots, n_{MC}$ (n_{MC} = number of MC samples)
  - Definitions:
    - $n_p := n_A + n_B$
    - $y^{MC}(i_p, i_t, i_{MC}) := \begin{cases} y_A^{MC}(i_p, i_t, i_{MC}) & , \quad 1 \leq i_p \leq n_A \\ y_B^{MC}(i_p - n_A, i_t, i_{MC}) & , \quad n_A + 1 \leq i_p \leq n_p \end{cases}$
    - $\boldsymbol{y}_p^{MC}(i_t, i_{MC}) := \left(y^{MC}(1, i_t, i_{MC}), \dots, y^{MC}(n_p, i_t, i_{MC})\right)^T$
    - $\boldsymbol{y}_t^{MC}(i_p, i_{MC}) := \left(y^{MC}(i_p, 1, i_{MC}), \dots, y^{MC}(i_p, n_t, i_{MC})\right)^T$
- Estimation of prior model parameters:
  - Mean values and covariances between different variables $i_p = 1, \dots, n_p$ for each time step $i_t = 1, \dots, n_t$, respectively:
    - Prior mean vector for time step i_t:

$$\boldsymbol{y}_{0p}^{(i_t)} = \frac{1}{n_{MC}} \sum_{i_{MC}=1}^{n_{MC}} \boldsymbol{y}_p^{MC}(i_t, i_{MC}) = \left(y_{0p}(1, i_t), \dots, y_{0p}(n_p, i_t)\right)^T = \left(\boldsymbol{y}_{0A}^{(i_t)^T}, \boldsymbol{y}_{0B}^{(i_t)^T}\right)^T$$

- Prior covariance matrix for time step i_t:

$$\boldsymbol{\Sigma}_{0p}^{(i_t)} = \frac{1}{n_{MC}-1}\sum_{i_{MC}=1}^{n_{MC}}\left(\boldsymbol{y}_p^{MC}(i_t,i_{MC}) - \boldsymbol{y}_{0p}^{(i_t)}\right)\left(\boldsymbol{y}_p^{MC}(i_t,i_{MC}) - \boldsymbol{y}_{0p}^{(i_t)}\right)^{\boldsymbol{T}}$$
$$= \begin{pmatrix} \Sigma_{0p,1,1}^{(i_t)} & \cdots & \Sigma_{0p,1,n_p}^{(i_t)} \\ \vdots & \ddots & \vdots \\ \Sigma_{0p,1,n_p}^{(i_t)} & \cdots & \Sigma_{0p,n_p,n_p}^{(i_t)} \end{pmatrix} = \begin{pmatrix} \boldsymbol{\Sigma}_{0A}^{(i_t)} & \boldsymbol{\Sigma}_{0AB}^{(i_t)} \\ \boldsymbol{\Sigma}_{0AB}^{(i_t)^T} & \boldsymbol{\Sigma}_{0B}^{(i_t)} \end{pmatrix}$$

  - Mean values and covariances between different time steps $i_t = 1, \dots, n_t$ for each variable $i_p = 1, \dots, n_p$, respectively:
    - Prior mean vector for variable i_p:

$$\boldsymbol{y}_{0t}^{(i_p)} = \frac{1}{n_{MC}}\sum_{i_{MC}=1}^{n_{MC}}\boldsymbol{y}_t^{MC}(i_p,i_{MC}) = \left(y_{0t}(i_p,1), \dots, y_{0t}(i_p,n_t)\right)^T$$

    - Prior covariance matrix for variable i_p:

$$\boldsymbol{\Sigma}_{0t}^{(i_p)} = \frac{1}{n_{MC}-1}\sum_{i_{MC}=1}^{n_{MC}}\left(\boldsymbol{y}_t^{MC}(i_p,i_{MC}) - \boldsymbol{y}_{0t}^{(i_p)}\right)\left(\boldsymbol{y}_t^{MC}(i_p,i_{MC}) - \boldsymbol{y}_{0t}^{(i_p)}\right)^{\boldsymbol{T}}$$
$$= \begin{pmatrix} \Sigma_{0t,1,1}^{(i_p)} & \cdots & \Sigma_{0t,1,n_t}^{(i_p)} \\ \vdots & \ddots & \vdots \\ \Sigma_{0t,1,n_t}^{(i_p)} & \cdots & \Sigma_{0t,n_t,n_t}^{(i_p)} \end{pmatrix}$$

- Measurement information for benchmark variables $i_B = 1, \dots, n_B$ at time steps $i_t = 1, \dots, k_t$ (with $k_t \leq n_t$)
  - Measurements

$$v(i_B, i_t)$$

  - Measurement standard deviations

$$\sigma_V(i_B, i_t)$$

    - Measurement vector

$$\boldsymbol{v}^{(i_t)} = \left(v(1,i_t), \dots, v(n_B,i_t)\right)^T$$

    - Measurement covariance matrix (assuming independence of measurements):

$$\boldsymbol{\Sigma}_V^{(i_t)} = \begin{pmatrix} \sigma_V^2(1,i_t) & \cdots & 0 \\ \vdots & \ddots & \vdots \\ 0 & \cdots & \sigma_V^2(n_B,i_t) \end{pmatrix}$$

- 1st updating step: calculation of posterior model parameters for observed time steps $i_t = 1, \dots, k_t$:
  - $\boldsymbol{y}_p^{(i_t)*} = \left(y^*(1,i_t), \dots, y^*(n_p,i_t)\right)^T = \left(\boldsymbol{y}_A^{(i_t)*^T}, \boldsymbol{y}_B^{(i_t)*^T}\right)^T$,
  - $\boldsymbol{\Sigma}_p^{(i_t)*} = \begin{pmatrix} \Sigma_{p,1,1}^{(i_t)*} & \cdots & \Sigma_{p,1,n_p}^{(i_t)*} \\ \vdots & \ddots & \vdots \\ \Sigma_{p,1,n_p}^{(i_t)*} & \cdots & \Sigma_{p,n_p,n_p}^{(i_t)*} \end{pmatrix} = \begin{pmatrix} \boldsymbol{\Sigma}_A^{(i_t)*} & \boldsymbol{\Sigma}_{AB}^{(i_t)*} \\ \boldsymbol{\Sigma}_{AB}^{(i_t)*^T} & \boldsymbol{\Sigma}_B^{(i_t)*} \end{pmatrix}$,
  - $\boldsymbol{y}_A^{(i_t)*} = \boldsymbol{y}_{0A}^{(i_t)} + \boldsymbol{\Sigma}_{0AB}^{(i_t)}\left(\boldsymbol{\Sigma}_{0B}^{(i_t)} + \boldsymbol{\Sigma}_V^{(i_t)}\right)^{-1}\left(\boldsymbol{v}^{(i_t)} - \boldsymbol{y}_{0B}^{(i_t)}\right)$,
  - $\boldsymbol{y}_B^{(i_t)*} = \boldsymbol{y}_{0B}^{(i_t)} + \boldsymbol{\Sigma}_{0B}^{(i_t)}\left(\boldsymbol{\Sigma}_{0B}^{(i_t)} + \boldsymbol{\Sigma}_V^{(i_t)}\right)^{-1}\left(\boldsymbol{v}^{(i_t)} - \boldsymbol{y}_{0B}^{(i_t)}\right)$,
  - $\boldsymbol{\Sigma}_A^{(i_t)*} = \boldsymbol{\Sigma}_{0A}^{(i_t)} - \boldsymbol{\Sigma}_{0AB}^{(i_t)}\left(\boldsymbol{\Sigma}_{0B}^{(i_t)} + \boldsymbol{\Sigma}_V^{(i_t)}\right)^{-1}\boldsymbol{\Sigma}_{0AB}^{(i_t)^T}$,

- $\boldsymbol{\Sigma}_B^{(i_t)*} = \boldsymbol{\Sigma}_{0B}^{(i_t)} - \boldsymbol{\Sigma}_{0B}^{(i_t)} \left(\boldsymbol{\Sigma}_{0B}^{(i_t)} + \boldsymbol{\Sigma}_V^{(i_t)}\right)^{-1} \boldsymbol{\Sigma}_{0B}^{(i_t)^T}$,
- $\boldsymbol{\Sigma}_{AB}^{(i_t)*} = \boldsymbol{\Sigma}_{0AB}^{(i_t)} - \boldsymbol{\Sigma}_{0AB}^{(i_t)} \left(\boldsymbol{\Sigma}_{0B}^{(i_t)} + \boldsymbol{\Sigma}_V^{(i_t)}\right)^{-1} \boldsymbol{\Sigma}_{0B}^{(i_t)^T}$.

- 2nd updating step: future predictions for time steps $i_t = k_t + 1, \dots, n_t$:
  - Initialization: identification of posterior model parameters of 1st updating step with measurements for 2nd updating step:
    - $\boldsymbol{v}_t^{(i_p)} = \left(v_t(i_p, 1), \dots, v_t(i_p, k_t)\right)^T := \left(y^*(i_p, 1), \dots, y^*(i_p, k_t)\right)^T$
    - $\boldsymbol{\Sigma}_{Vt}^{(i_p)} = \begin{pmatrix} \Sigma_{Vt,1,1}^{(i_p)} & \dots & \Sigma_{Vt,1,k_t}^{(i_p)} \\ \vdots & \ddots & \vdots \\ \Sigma_{Vt,1,k_t}^{(i_p)} & \dots & \Sigma_{Vt,k_t,k_t}^{(i_p)} \end{pmatrix} = \begin{pmatrix} \sigma_{Vt}^2(i_p, 1) & \dots & 0 \\ \vdots & \ddots & \vdots \\ 0 & \dots & \sigma_{Vt}^2(i_p, k_t) \end{pmatrix} := \begin{pmatrix} \Sigma_{p,i_p,i_p}^{(1)*} & \dots & 0 \\ \vdots & \ddots & \vdots \\ 0 & \dots & \Sigma_{p,i_p,i_p}^{(k_t)*} \end{pmatrix}$
  - Choose number of past time steps to be taken into account per updating step: Δ_t^-
  - Choose number of future time steps to be predicted per updating step: $\Delta_t^+ \leq \Delta_t^-$
  - Select prior model parameters covering past and future time steps to be considered in updating step:
    - $\boldsymbol{y}_{0t}^{(i_p,k_t)} = \left(\boldsymbol{y}_{0t,+}^{(i_p,k_t)^T}, \boldsymbol{y}_{0t,-}^{(i_p,k_t)^T}\right)^T$
    - $\boldsymbol{y}_{0t,+}^{(i_p,k_t)} = \left(y_{0t}(i_p, k_t + 1), \dots, y_{0t}(i_p, k_t + \Delta_t^+)\right)^T$
    - $\boldsymbol{y}_{0t,-}^{(i_p,k_t)} = \left(y_{0t}(i_p, k_t - \Delta_t^- + 1), \dots, y_{0t}(i_p, k_t)\right)^T$
    - $\boldsymbol{\Sigma}_{0t}^{(i_p,k_t)} = \begin{pmatrix} \boldsymbol{\Sigma}_{0t,++}^{(i_p,k_t)} & \boldsymbol{\Sigma}_{0t,+-}^{(i_p,k_t)} \\ \boldsymbol{\Sigma}_{0t,+-}^{(i_p,k_t)^T} & \boldsymbol{\Sigma}_{0t,--}^{(i_p,k_t)} \end{pmatrix}$
    - $\boldsymbol{\Sigma}_{0t,++}^{(i_p,k_t)} = \begin{pmatrix} \Sigma_{0t,k_t+1,k_t+1}^{(i_p)} & \dots & \Sigma_{0t,k_t+1,k_t+\Delta_t^+}^{(i_p)} \\ \vdots & \ddots & \vdots \\ \Sigma_{0t,k_t+1,k_t+\Delta_t^+}^{(i_p)} & \dots & \Sigma_{0t,k_t+\Delta_t^+,k_t+\Delta_t^+}^{(i_p)} \end{pmatrix}$
    - $\boldsymbol{\Sigma}_{0t,--}^{(i_p,k_t)} = \begin{pmatrix} \Sigma_{0t,k_t-\Delta_t^-+1,k_t-\Delta_t^-+1}^{(i_p)} & \dots & \Sigma_{0t,k_t-\Delta_t^-+1,k_t}^{(i_p)} \\ \vdots & \ddots & \vdots \\ \Sigma_{0t,k_t-\Delta_t^-+1,k_t}^{(i_p)} & \dots & \Sigma_{0t,k_t,k_t}^{(i_p)} \end{pmatrix}$
    - $\boldsymbol{\Sigma}_{0t,+-}^{(i_p,k_t)} = \begin{pmatrix} \Sigma_{0t,k_t+1,k_t-\Delta_t^-+1}^{(i_p)} & \dots & \Sigma_{0t,k_t+1,k_t}^{(i_p)} \\ \vdots & \ddots & \vdots \\ \Sigma_{0t,k_t+\Delta_t^+,k_t-\Delta_t^-+1}^{(i_p)} & \dots & \Sigma_{0t,k_t+\Delta_t^+,k_t}^{(i_p)} \end{pmatrix}$
  - Select measurements covering past time steps to be considered in updating step:
    - $\boldsymbol{v}_t^{(i_p,k_t)} = \left(v_t(i_p, k_t - \Delta_t^- + 1), \dots, v_t(i_p, k_t)\right)^T$

- $\boldsymbol{\Sigma}_{Vt}^{(i_p,k_t)} = \begin{pmatrix} \Sigma_{Vt,k_t-\Delta_t^-+1,k_t-\Delta_t^-+1}^{(i_p)} & \cdots & \Sigma_{Vt,k_t-\Delta_t^-+1,k_t}^{(i_p)} \\ \vdots & \ddots & \vdots \\ \Sigma_{Vt,k_t-\Delta_t^-+1,k_t}^{(i_p)} & \cdots & \Sigma_{Vt,k_t,k_t}^{(i_p)} \end{pmatrix}$

- MOCABA updating ➔ posterior predictions for updating step:
  - $\boldsymbol{y}_t^{(i_p,k_t)*} = \left(\boldsymbol{y}_{t,+}^{(i_p,k_t)*^T}, \boldsymbol{y}_{t,-}^{(i_p,k_t)*^T}\right)^T$,
  - $\boldsymbol{\Sigma}_t^{(i_p,k_t)*} = \begin{pmatrix} \boldsymbol{\Sigma}_{t,++}^{(i_p,k_t)*} & \boldsymbol{\Sigma}_{t,+-}^{(i_p,k_t)*} \\ \boldsymbol{\Sigma}_{t,+-}^{(i_p,k_t)*^T} & \boldsymbol{\Sigma}_{t,--}^{(i_p,k_t)*} \end{pmatrix}$,
  - $\boldsymbol{y}_{t,+}^{(i_p,k_t)*} = \boldsymbol{y}_{0t,+}^{(i_p,k_t)} + \boldsymbol{\Sigma}_{0t,+-}^{(i_p,k_t)} \left(\boldsymbol{\Sigma}_{0t,--}^{(i_p,k_t)} + \boldsymbol{\Sigma}_{Vt}^{(i_p,k_t)}\right)^{-1} \left(\boldsymbol{v}_t^{(i_p,k_t)} - \boldsymbol{y}_{0t,-}^{(i_p,k_t)}\right)$,
  - $\boldsymbol{y}_{t,-}^{(i_p,k_t)*} = \boldsymbol{y}_{0t,-}^{(i_p,k_t)} + \boldsymbol{\Sigma}_{0t,--}^{(i_p,k_t)} \left(\boldsymbol{\Sigma}_{0t,--}^{(i_p,k_t)} + \boldsymbol{\Sigma}_{Vt}^{(i_p,k_t)}\right)^{-1} \left(\boldsymbol{v}_t^{(i_p,k_t)} - \boldsymbol{y}_{0t,-}^{(i_p,k_t)}\right)$,
  - $\boldsymbol{\Sigma}_{t,++}^{(i_p,k_t)*} = \boldsymbol{\Sigma}_{0t,++}^{(i_p,k_t)} - \boldsymbol{\Sigma}_{0t,+-}^{(i_p,k_t)} \left(\boldsymbol{\Sigma}_{0t,--}^{(i_p,k_t)} + \boldsymbol{\Sigma}_{Vt}^{(i_p,k_t)}\right)^{-1} \boldsymbol{\Sigma}_{0t,+-}^{(i_p,k_t)^T}$,
  - $\boldsymbol{\Sigma}_{t,--}^{(i_p,k_t)*} = \boldsymbol{\Sigma}_{0t,++}^{(i_p,k_t)} - \boldsymbol{\Sigma}_{0t,--}^{(i_p,k_t)} \left(\boldsymbol{\Sigma}_{0t,--}^{(i_p,k_t)} + \boldsymbol{\Sigma}_{Vt}^{(i_p,k_t)}\right)^{-1} \boldsymbol{\Sigma}_{0t,--}^{(i_p,k_t)^T}$,
  - $\boldsymbol{\Sigma}_{t,+-}^{(i_p,k_t)*} = \boldsymbol{\Sigma}_{0t,+-}^{(i_p,k_t)} - \boldsymbol{\Sigma}_{0t,+-}^{(i_p,k_t)} \left(\boldsymbol{\Sigma}_{0t,--}^{(i_p,k_t)} + \boldsymbol{\Sigma}_{Vt}^{(i_p,k_t)}\right)^{-1} \boldsymbol{\Sigma}_{0t,--}^{(i_p,k_t)^T}$.
- Identify posterior results for predictions with measurements of next updating step ($k_t \rightarrow k_t + \Delta_t^+$):
  - If $\Delta_t^+ = \Delta_t^-$
    - $\boldsymbol{v}_t^{(i_p,k_t+\Delta_t^+)} = \boldsymbol{y}_{t,+}^{(i_p,k_t)*}$
    - $\boldsymbol{\Sigma}_{Vt}^{(i_p,k_t+\Delta_t^+)} = \boldsymbol{\Sigma}_{t,++}^{(i_p,k_t)*}$
  - If $\Delta_t^+ < \Delta_t^-$
    - $\boldsymbol{v}_t^{(i_p,k_t+\Delta_t^+)} = \left(v_t\left(i_p, k_t + \Delta_t^+ - \Delta_t^- + 1\right), \ldots, v_t\left(i_p, k_t + \Delta_t^+\right)\right)^T = \left(v_t\left(i_p, k_t + \Delta_t^+ - \Delta_t^- + 1\right), \ldots, v_t\left(i_p, k_t\right), \boldsymbol{y}_{t,+}^{(i_p,k_t)*^T}\right)^T$
    - $\boldsymbol{\Sigma}_{Vt}^{(i_p,k_t+\Delta_t^+)} = \begin{pmatrix} \Sigma_{Vt,k_t+\Delta_t^+-\Delta_t^-+1,k_t+\Delta_t^+-\Delta_t^-+1}^{(i_p)} & \cdots & \Sigma_{Vt,k_t+\Delta_t^+-\Delta_t^-+1,k_t+\Delta_t^+}^{(i_p)} \\ \vdots & \ddots & \vdots \\ \Sigma_{Vt,k_t+\Delta_t^+-\Delta_t^-+1,k_t+\Delta_t^+}^{(i_p)} & \cdots & \Sigma_{Vt,k_t+\Delta_t^+,k_t+\Delta_t^+}^{(i_p)} \end{pmatrix} =$

$$\begin{pmatrix} \Sigma_{Vt,k_t+\Delta_t^+-\Delta_t^-+1,k_t+\Delta_t^+-\Delta_t^-+1}^{(i_p)} & \cdots & \Sigma_{Vt,k_t+\Delta_t^+-\Delta_t^-+1,k_t}^{(i_p)} & \\ \vdots & \ddots & \vdots & \boldsymbol{\Sigma}_{t,+-}^{(i_p,k_t)*} \\ \Sigma_{Vt,k_t+\Delta_t^+-\Delta_t^-+1,k_t}^{(i_p)} & \cdots & \Sigma_{Vt,k_t,k_t}^{(i_p)} & \\ & \boldsymbol{\Sigma}_{t,+-}^{(i_p,k_t)*^T} & & \boldsymbol{\Sigma}_{t,++}^{(i_p,k_t)*} \end{pmatrix}$$

- Perform updating for updating step $k_t + \Delta_t^+$
- Repeat procedure until n_t is reached ➔ posterior predictions for all time steps.

The posterior prediction values for $i_t = k_t + 1, \dots, n_t$, obtained for the different variables i_p, and their standard deviations, obtained from the corresponding posterior covariance matrices, are then identified with the components of the n_p-dimensional posterior vectors $\boldsymbol{y}_p^{(i_t,k_t)*}$ and the components of the corresponding posterior standard deviation vectors $\boldsymbol{\sigma}_p^{(i_t,k_t)*}$, respectively. The vectors $\boldsymbol{y}_p^{(i_t,k_t)*}$ and $\boldsymbol{\sigma}_p^{(i_t,k_t)*}$ then represent the posterior predictions for $i_t > k_t$ of the considered variables when taking into account the available measurements up to time step k_t.

3. SOFTWARE IMPLEMENTATION OF U&S ANALYSIS AND MOCABA ALGORITHM

To be able to apply the MOCABA prediction algorithm described in section 2, a set of different computer codes is needed. Such codes have been implemented within KIT's FSCT tool [4]. The computational sequence of the FSCT tool is presented in Figure 1 [5] and consists of the following 6 parts:

1. **Part 1**: The *Sampling* part uses the uncertainty information about the input parameters, their uncertainty ranges and related probability density functions. This code generates random samples, writes the results of the sampling into a database, and creates plots with sampling characteristics. The Latin Hypercube Sampling (LHS) method is used for the random sampling.

2. **Part 2**: The *Running Multiple Simulations* part uses the results of Part 1 as input data to create n_{MC} input files for the ASTEC code and after that runs n_{MC} simulations in parallel.

3. **Part 3**: The *Collecting Results of Multiple Runs* part collects values of all output parameters of interest from the ASTEC results files. All results are stored in a database, which will be used later in Part 4, 5 and 6.

4. **Part 4**: The *Statistics and Sensitivity Analysis* part uses data collected in the database provided by Part 3 for calculating simple statistics and Pearson and Spearman correlation coefficients.

5. **Part 5**: The *Training* part uses the data provided by Part 3 to calculate the prior model parameters of the MOCABA prediction algorithm according to the description in section 2 and writes this prior information into output files.

6. **Part 6**: The *MOCABA Data Assimilation* part uses the prediction algorithm described in section 2 to calculate the posterior values of the considered variables by applying the trained MOCABA prediction model (Part 5) to the measurements of the to-be-measured variables. Posterior values (mean values and standard deviations) are generated for each variable and each measurement time step, taking into account the measurements for each times step included in the measurement files. Furthermore, posterior prediction data (mean values and standard deviations) are generated for all future time steps and all considered variables.

Part 5 and 6, which are devoted to the MOCABA data assimilation procedure, are also implemented in Framatome's in-house Fortran codes. The calculation results presented in this paper are based on training data provided by the FSCT tool (Part 1 – 3) and MOCABA calculations (Part 5 and 6) performed with Framatome's Fortran codes.

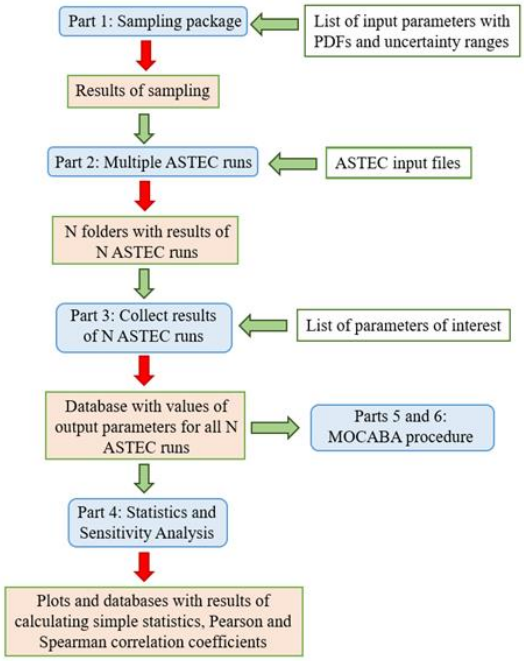

Figure 1. Computational Sequence Implemented in FSCT Tool [5]

4. INPUT DATA FROM ASTEC SIMULATIONS

The ASTEC model of a generic KONVOI NPP used in this paper is based on the input deck developed within the EU CESAM project [6]. The original input deck has been further extended during the WAME project.

The training database for the MOCABA prediction model has been generated by applying the FSCT tool to ASTEC simulations of the considered MBLOCA scenario at a generic KONVOI NPP. 16 input parameters have been considered for uncertainty propagation. They include parameters modeling the release of fission products from the fuel, parameters related to the integrity criteria of the fuel cladding, and parameters related to the modeling of the aerosol behavior in the primary system and the containment. Furthermore, there is a parameter which reflects the uncertainty of the leakage rate from the containment to the annulus and a parameter which refers the uncertainties on the fuel burn-up, namely the number of effective full power days. The probability density functions of the selected ASTEC parameters are based on the information derived from the literature and on engineering judgment. To better represent the actual physics of the process, correlations between physically related uncertain input parameters have also been taken into account. Further details can be found in [4].

The ASTEC simulations start at time $t = 0$ when the break occurs in the cold leg. After that, a SCRAM is initiated, and the admission to the turbine and main feed water pumps is closed. The Emergency Core Cooling System is activated, the main coolant pumps are coasted down, and the pressure regulation in the pressurizer is switched off. The Emergency Feed Water System is activated when the water level in one of the steam generators is below 4.5 m. The High and Low Pressure Injection Systems are activated when the gas temperature in the primary system exceeds 650 ºC. Water injection continues until the water tanks are empty. After that, the core starts to melt. Finally, cavity flooding occurs when the horizontal erosion reaches 0.5 m. Further details can be found in [2].

5. APPLICATION OF MOCABA PREDICTION ALGORITHM TO MBLOCA SCENARIO

To verify if the MOCABA prediction method described in section 2 is suitable to perform real-time predictions of accidents at nuclear power plants based on measured plant data, this method is applied to the source term prediction for the considered MBLOCA scenario. The results of the ASTEC MC simulations are used as training database. Since real measurement data of the considered accident scenario are not available, we use simulated data from selected MC runs as measurements.

For each Monte Carlo simulation, the time-dependent dose rates in the containment and the annulus and the time-dependent cumulative release of xenon into the environment (source term) are calculated. Identifying Monte Carlo sample #150 with the "true" accident scenario, the corresponding measured dose rate values in the containment and the annulus are used as predictors of the future xenon source term through application of the MOCABA prediction method. The predicted source term values are then compared to the "true" source term values from MC sample #150. For this analysis, the parameters Δ_t^- and Δ_t^+ (see section 2) are set to $\Delta_t^- = \Delta_t^+ = 1$.

The ASTEC Monte Carlo simulation results for the annulus and containment dose rate and the xenon source term are shown in Figure 2, Figure 3 and Figure 4. Figure 5 shows the Pearson correlation between the xenon source term and the annulus and containment dose rate. This leads us to the following observations:

- The ASTEC results for the dose rate in the containment and the annulus for the different Monte Carlo samples (Figure 2 and Figure 3) are fairly noisy after $t \simeq 7000\,s$. Here the curves show significantly different shapes and many crossings. This means that after $7000\,s$ the information content of the Monte Carlo ASTEC data base w.r.t. future predictions of the considered accident parameters is fairly low. Consequently, just considering the ASTEC Monte Carlo data, we may expect a limited prediction quality for $t > 7000\,s$.

- The Pearson correlation between the annulus dose rate and the xenon source term is very high during accident progression (see Figure 5). This means that the measured annulus dose rate can be expected to be a good predictor of the xenon source term in time regions where the noisiness of the training data is sufficiently low, i.e. for $t < 7000\,s$. The correlation between the containment dose rate and the xenon source term, on the other hand, is much lower, especially for $t > 7000\,s$. Hence, the measured containment dose rate is not a good predictor of the xenon source term.

The prediction results illustrated in Figure 6 through Figure 8 generally confirm the above expectations:

- The prediction quality is good in time regions where the noisiness of the training data is sufficiently low but can become worse at later times where the training data are very noisy (see, e.g., Figure 6).

- Measurements of the annulus dose rate significantly improve the prediction of the xenon source term (see Figure 7), but measurements of the containment dose rate do not (see Figure 8).

- Taking into account both measurements of the annulus dose rate and the containment dose rate leads to very similar results as taking into account just the measurements of the annulus dose rate (see Figure 6 and Figure 7), which reflects the fact that the dose rate measurements in the containment do not provide significant additional information w.r.t. the xenon source term prediction.

Finally, we would like to mention that in case of noisy training data it is generally recommended to choose low values of the parameters Δ_t^- and Δ_t^+ (see section 2). $\Delta_t^- = \Delta_t^+ = 1$ can be regarded as a good default choice. For less noisy training data, the values of Δ_t^- and Δ_t^+ may be increased in order to improve the performance of the prediction algorithm.

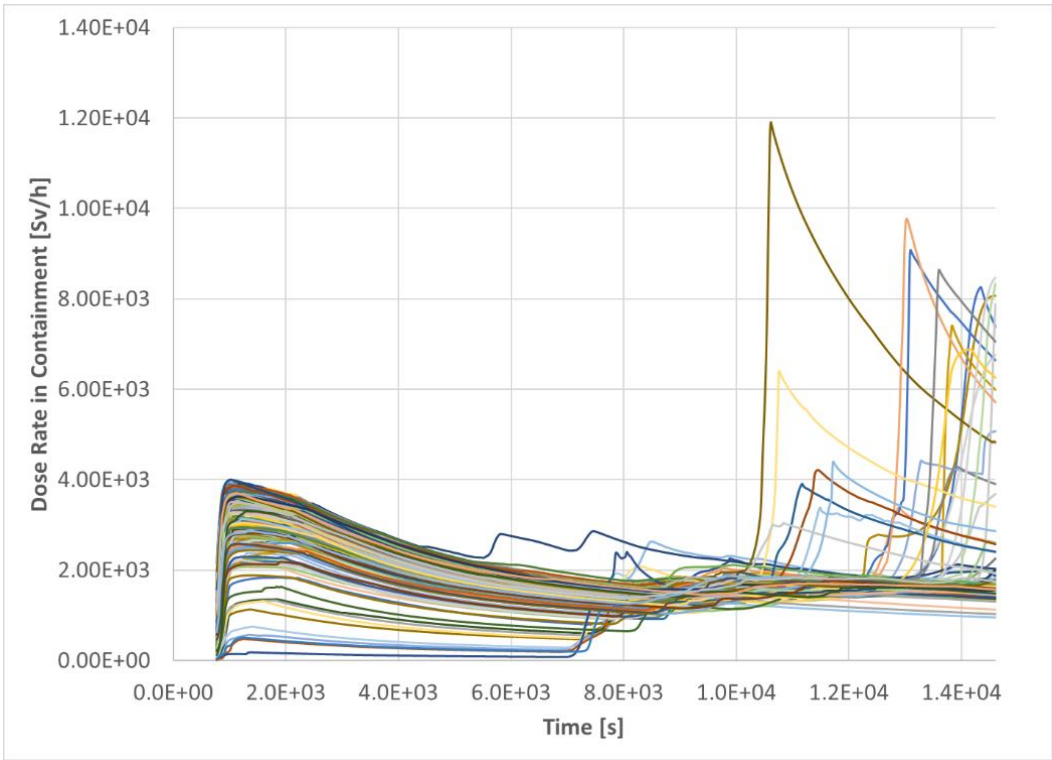

Figure 2. Dose Rate in Containment for different Monte Carlo Samples

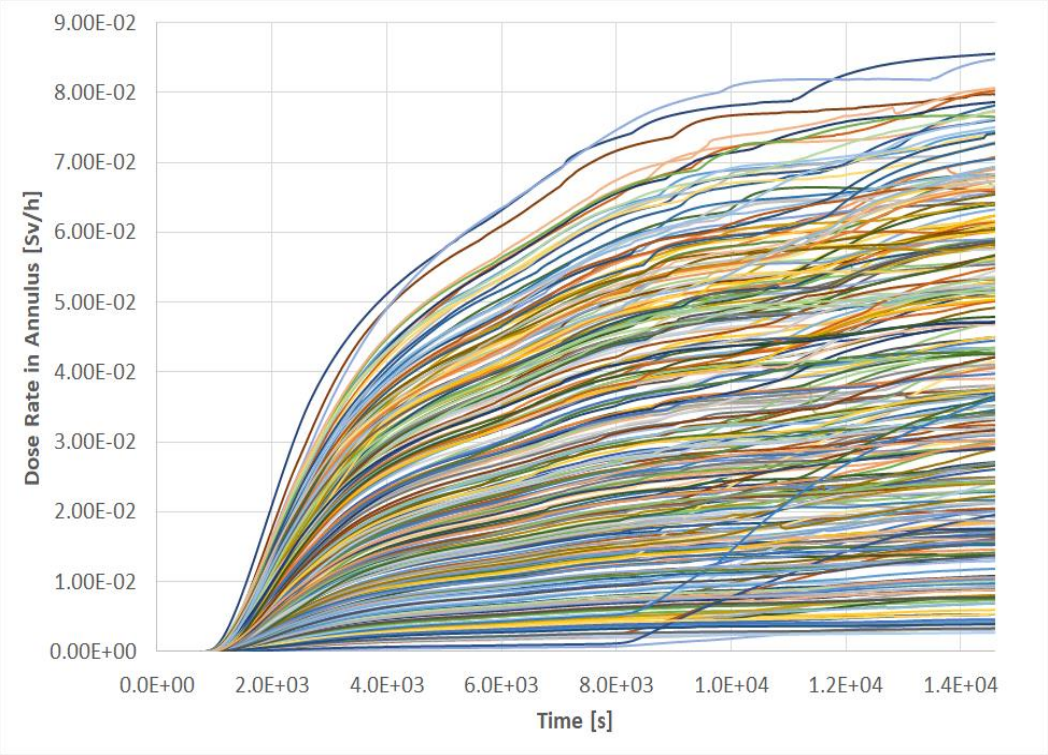

Figure 3. Dose Rate in Annulus for different Monte Carlo Samples

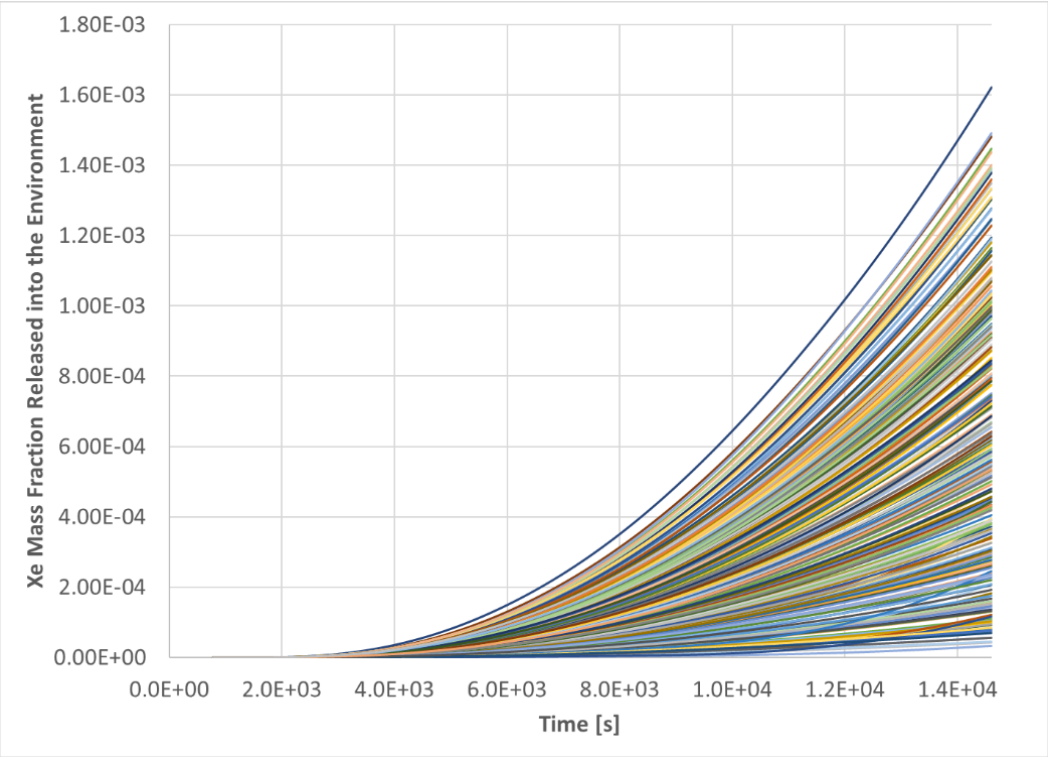

Figure 4. Xenon Release to the Environment for different Monte Carlo Samples

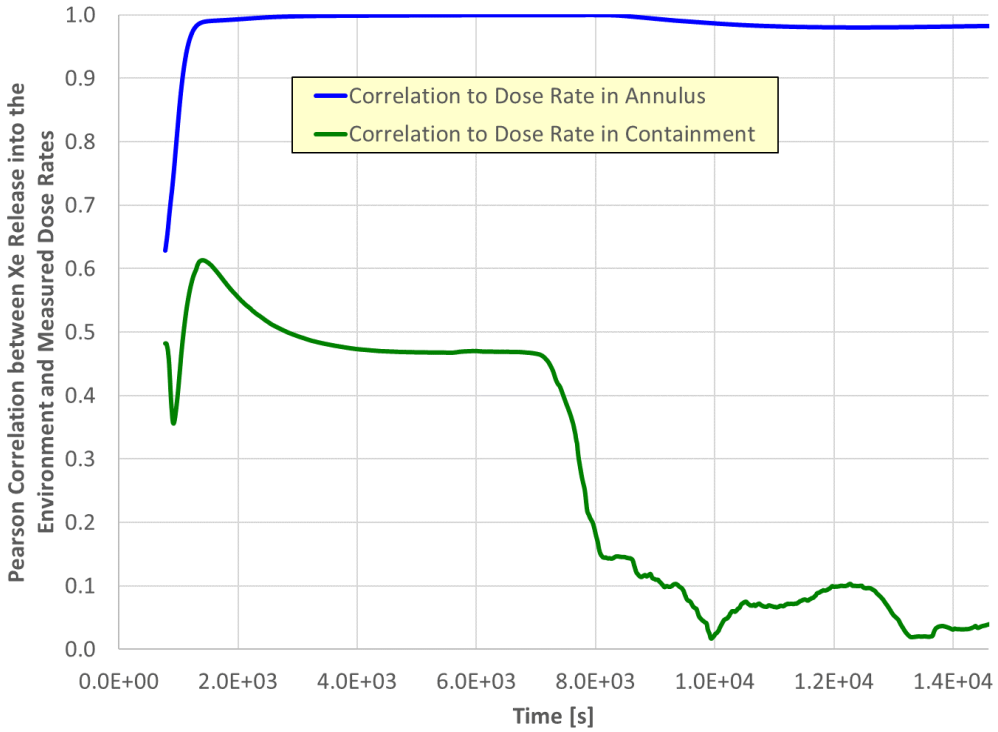

Figure 5. Pearson Correlations between the Xenon Release into the Environment and the Dose Rates in the Annulus and the Containment

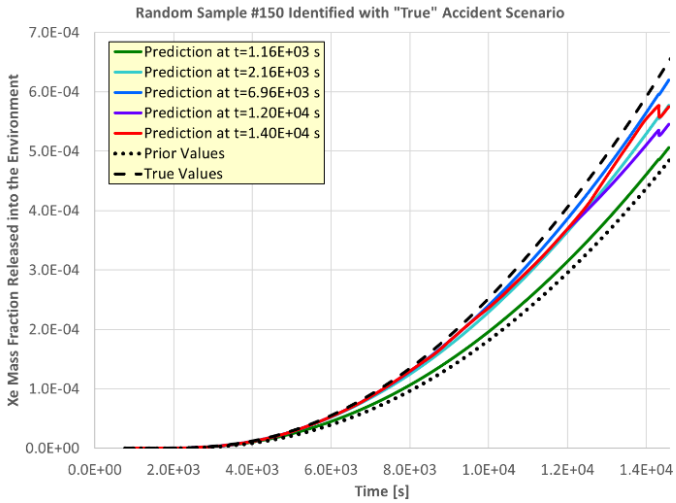

Figure 6. Sample #150 Identified with "True" Accident Scenario: Future Prediction of Xenon Source Term Based on Previous Dose Rate Measurements in Annulus and Containment

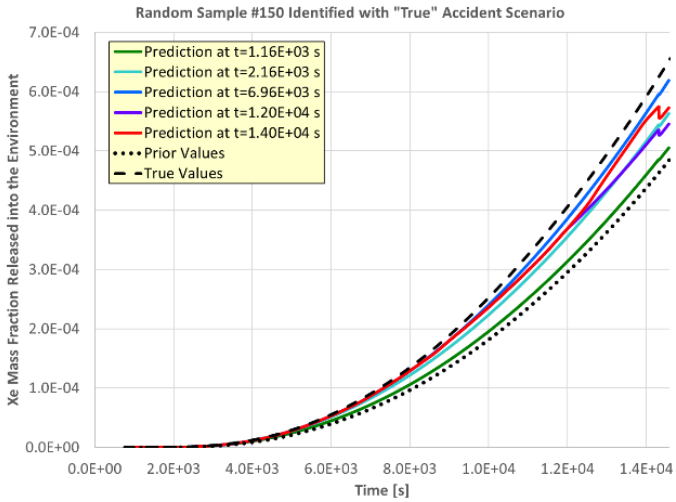

Figure 7. Sample #150 Identified with "True" Accident Scenario: Future Prediction of Xenon Source Term Based on Previous Dose Rate Measurements in Annulus

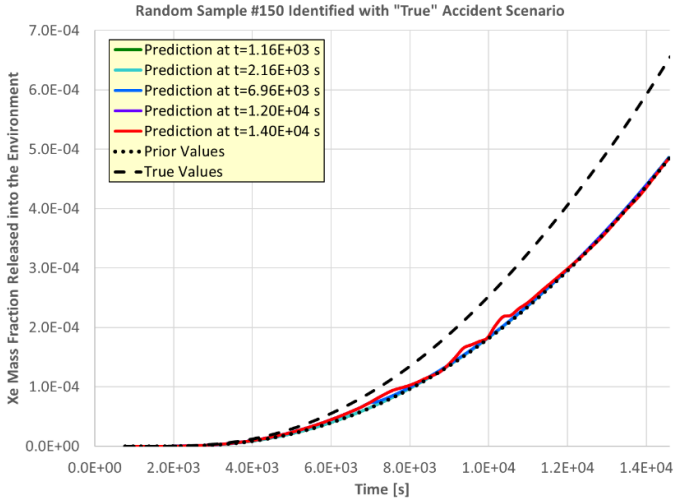

Figure 8. Sample #150 Identified with "True" Accident Scenario: Future Prediction of Xenon Source Term Based on Previous Dose Rate Measurements in Containment

6. CONCLUSIONS

A time series prediction algorithm has been introduced based on the MOCABA data assimilation framework.

To investigate the suitability of this algorithm for predicting accidents at NPPs, this algorithm has been applied to the prediction of the xenon release from a generic Konvoi NPP following a MBLOCA with core melt. Here, the measurements of the dose rates in the containment and annulus have been used to improve the prediction of the xenon source term.

The presented results demonstrate that the developed MOCABA method is generally suitable to perform predictions of accidents at nuclear power plants based on measured plant data. However, the main challenge is to provide high quality (not too noisy) Monte Carlo input data, which is a general pre-condition for obtaining reasonable predictions.

Since the computer codes written by Framatome and KIT involve fast matrix algorithms, prediction results based on current measurements are typically provided within a few seconds. This makes it possible to use these programs as real-time accident predictor modules within software packages such as Framatome's Central Radiological Computer System (CRCS) [7].

ACKNOWLEDGMENTS

The project was funded by the German Federal Ministry of Economic Affairs and Energy, funding code FZK 1501582 (WAME project).

REFERENCES

1. A. Hoefer, O. Buss, M. Hennebach, M. Schmid, M., D. Porsch, "MOCABA: A General Monte Carlo-Bayes Procedure for Improved Predictions of Integral Functions of Nuclear Data," *Annals of Nuclear Energy*, **Volume 77**, pp. 514-521 (2015).
2. F. Gabrielli, V.H. Sánchez-Espinoza, A. Stakhanova, A. Hoefer, E. Pauli, H. Feldmann, "Source Term Evaluation Following MBLOCA and SBLOCA Scenarios in a Generic KONVOI-1300 NPP by Means of the ASTEC Code," *Eurosafe 2021*, Paris, November 22-23 (2021).
3. P. Chatelard et al., "ASTEC V2 Severe Accident Integral Code Main Features, Current V2.0 Modelling Status, Perspectives," *Nuclear Engineering and Design*, **Volume 272**, pp.119-135 (2014).
4. A. Stakhanova, F. Gabrielli, V. Sánchez-Espinoza, E. Pauli, A. Hoefer, "Preliminary Uncertainty and Sensitivity Analysis of the ASTEC Simulation Results of a MBLOCA Scenario in a Generic Konvoi Plant by Using the FSTC tool", *The 10th European Review Meeting on Severe Accident Research (ERMSAR2022)*, Karlsruhe, May 16-19 (2022).
5. A. Stakhanova, F. Gabrielli, V.H. Sanchez-Espinoza, A. Hoefer, E. Pauli, "Uncertainty and sensitivity analysis of the QUENCH-08 experiment using the FSTC tool", *Annals of Nuclear Energy*, **Volume 169** (2022)
6. EC. "D40 .42 – 1st set of reference NPP ASTEC input decks", CESAM FP7-GA-323264, (2015).
7. S. Torchiani, O. Buss, S. Haussler, O. Ludwik, A. Hoefer, "AREVA computer codes for radiological consequence analysis," *International Experts Meeting on Assessment and Prognosis in Response to a Nuclear or Radiological Emergency*, IAEA, Vienna, Austria, April 20 – 24 (2015) https://www-pub.iaea.org/iaeameetings/IEM9p/Session2/6Torchiani.pdf.

framatome

Karlsruher Institut für Technologie

Prediction of the Radiological Consequences of a Severe Accident Scenario in a Generic KONVOI Nuclear Power Plant

Eva-Maria Pauli, Axel Hoefer (Framatome GmbH)
Fabrizio Gabrielli, Anastasia Stakhanova, Victor Sanchez-Espinoza (KIT)

Karlsruhe 2022/05/16

AL: N ECCN: N

Confidentiality

[X] **This document contains Framatome's know-how**

EXPORT CONTROL

AL = N	ECCN =

Goods labeled with "AL not equal to N" are subject to European or German export authorization when being exported within or out of the EU.
Goods labeled with "ECCN not equal to N or EAR99" are subject to U.S. reexport authorization. Even without a label, or with label: "AL:N" or "ECCN:N" or "ECCN:EAR99," authorization may be required due to the final whereabouts and purpose for which the goods are to be used.

FRAMATOME'S INFORMATION PROTECTION RULES

[X] **C1** -This document and any and all information contained therein and/or disclosed in discussions supported by this document are **restricted**.

[ ] **C2** : This document and any and all information contained therein and/or disclosed in discussions supported by this document are sensitive and **Framatome confidential,** such as its disclosure, alteration or loss are detrimental with a significant-to-high impact for Framatome.

The document, if disclosed, and any information it contains are intended for the sole attendees. The disclosure or reference to such information or document shall be made only on a proper judgment basis and by mentioning expressly "this information shall not be disclosed / transferred without prior consent".

[ ] **C3** –This document and any and all information contained therein and/or disclosed in discussions supported by this document are classified **Framatome Secret**.

Each one must commit to keep secret any written or oral information disclosed during the meeting. It is forbidden to disclose it to any legal entity and any individual (including within Framatome) without prior consent of the meeting chairman.

This document and any and all information contained therein and/or disclosed in discussions supported by this document, are confidential, protected by applicable intellectual property regulations and contain data subject to trade secrets regulations. Any reproduction, alteration, disclosure to any third party and/or publication in whole or in part of this document and/or its content is strictly prohibited without prior written express approval of Framatome. This document and any information it contains shall not be used for any other purpose than the one for which they were provided. Legal and disciplinary actions may be taken against any infringer and/or any person breaching the aforementioned obligations.
© Framatome – All rights reserved

CONTENT

01 . Motivation

02 . MOCABA Algorithm

03 . ASTEC Results

04 . MOCABA Prediction Results

© Framatome - All rights reserved

C1 –Framatome Restricted / Framatome know-how / Export Control - AL: N ECCN: N /

1. Motivation

 © Framatome - All rights reserved
C1 –Framatome Restricted / Framatome know-how / Export Control - AL: N ECCN: N /

Motivation

- In 2019 KIT and Framatome launched GERMAN WAME project in the framework of the activity ‘Maintaining Competence in Nuclear Technology’ of the Federal Ministry of Economics and Technology (BMWi).
- **Goal:** support emergency preparedness teams during Severe Accident (SA) events by developing methodology for real-time Source Term (ST) predictions based on plant measurements and pre-calculated learning database from integral code calculations
- Learning database consists of a large number of ASTEC calculations with Monte-Carlo sampled input parameters as part of uncertainty and sensitivity (U&S) analysis
- Application of Framatome’s data assimilation framework MOCABA which is also implemented in KIT’s FSTC tool

© Framatome - All rights reserved
C1 –Framatome Restricted / Framatome know-how / Export Control - AL: N ECCN: N

2. MOCABA Algorithm

 © Framatome - All rights reserved
C1 –Framatome Restricted / Framatome know-how / Export Control - AL: N ECCN: N /

The MOCABA Algorithm

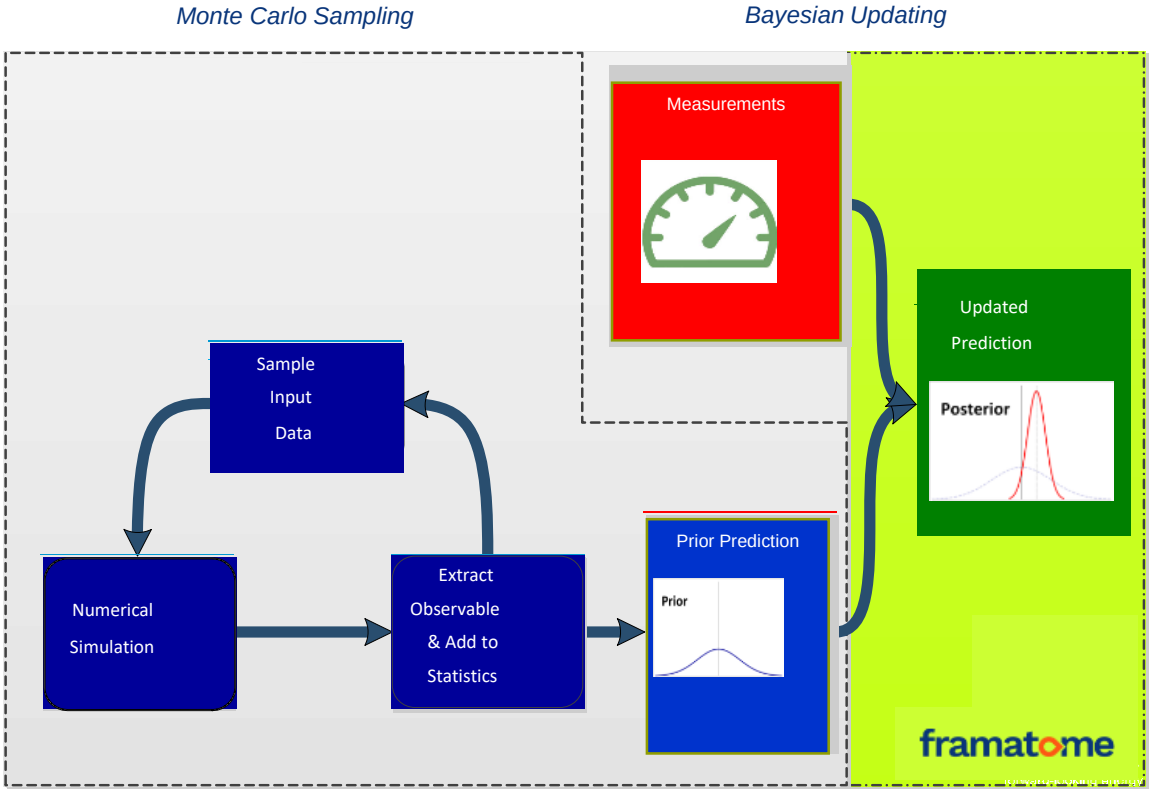

 © Framatome - All rights reserved
C1 –Framatome Restricted / Framatome know-how / Export Control - AL: N ECCN: N /

The MOCABA Algorithm

MOCABA Prediction algorithm for time series involves 2 parts

- Prior Part: results of N Monte Carlo simulations for the to-be-predicted variables and the to-be-measured variables are used as training data. Mean values, covariances between different variables for each time step and covariances between different time steps for each variable are calculated
- Posterior Part: Measurement information for the to-be-measured variables is taken into account by applying Bayesian updating to the prior model parameters.

 © Framatome - All rights reserved
C1 –Framatome Restricted / Framatome know-how / Export Control - AL: N ECCN: N /

The MOCABA Algorithm

MOCABA Prediction algorithm for time series involves 2 parts

- 1. Posterior model parameters are calculated for all observed time steps until current point in time
- 2. Posterior values $\mathbf{Y}_{-}^{*}$ corresponding to current time step and to a certain number of previous time steps are identified with measurements to calculate posterior variables $\mathbf{Y}_{+}^{*}$ for future time steps taking into account prior cross covariances $\mathbf{Cov}_{+-}$ between $\mathbf{Y}_{-}^{*}$ and $\mathbf{Y}_{+}^{*}$, repeat identifying latest $\mathbf{Y}_{+}^{*}$ value with new current time step

Figures from Paper Stakhanova et al.: „Application of MOCABA algorithm and FSTC tool for source term prediction“, to be submitted to Ann. Nucl. Energy

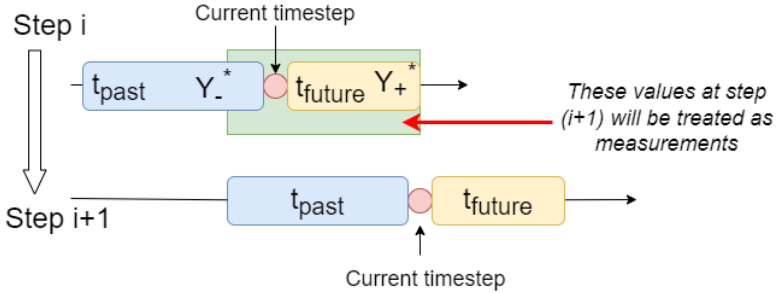

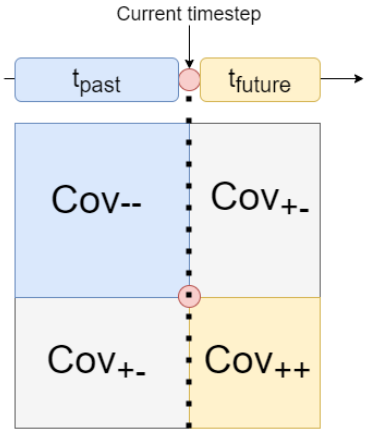

 © Framatome - All rights reserved
C1 –Framatome Restricted / Framatome know-how / Export Control - AL: N ECCN: N /

MOCABA Publications

MOCABA Prediction algorithm for time series involves 2 parts

- Basic MOCABA framework
  - Hoefer et al., Ann. Nucl. Energy 77, pp. 514 - 521, 2015.
- Extension 1: MOCABA framework with linear Contraints
  - Hoefer et al., Nucl. Technology 205 (12), pp. 1578 - 1587, 2019.
- Extension 2: Generalized MOCABA framework
  - Hoefer et al., Nucl. Technology 162,108490, 2021.

© Framatome - All rights reserved
C1 –Framatome Restricted / Framatome know-how / Export Control - AL: N ECCN: N /

Software Implementation of U&S Analysis and MOCABA

All Implemented in KIT's FSTC tool

MOCABA part also in Framatome's in-house tool

Figure adopted from Paper Stakhanova et al.:

„Uncertainty and sensitivity analysis of the QUENCH-08 experiment using the FSTC tool"

Ann. Nucl. Energy 169 (2022)

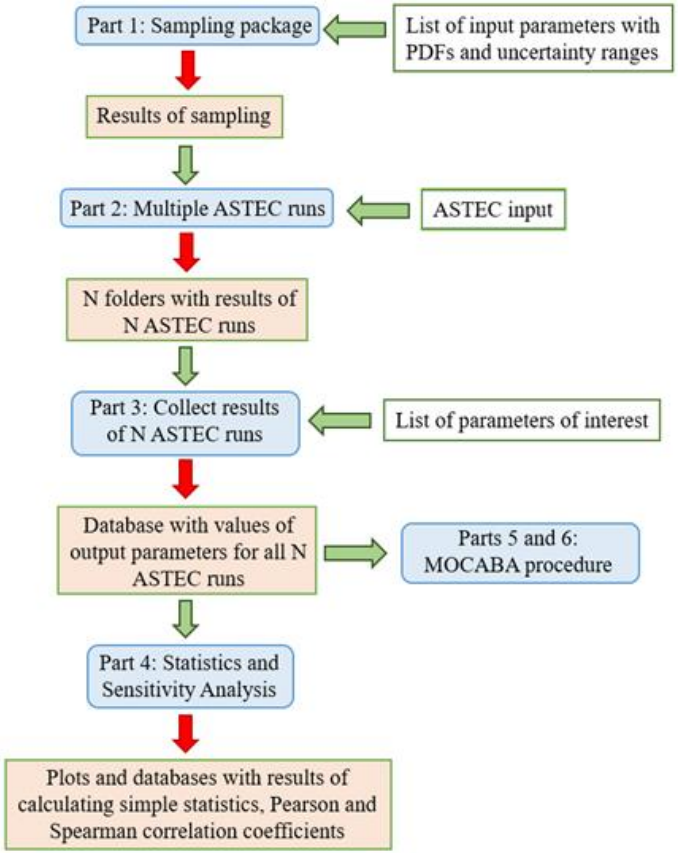

 © Framatome - All rights reserved
C1 –Framatome Restricted / Framatome know-how / Export Control - AL: N ECCN: N /

3. ASTEC Results

 © Framatome - All rights reserved
C1 –Framatome Restricted / Framatome know-how / Export Control - AL: N ECCN: N /

Input Data from ASTEC Simulations

- ASTEC Model of a generic KONVOI NPP
- Simulation of a Medium Break loss of coolant accident (MBLOCA)
- Monte Carlo simulations varying 16 input parameters related to
  - fuel burnup
  - release of fission products from the fuel
  - integrity criteria of fuel cladding
  - aerosol behaviour in primary system and containment
  - leakage rate from containment to analysis

Details can be found in ERMSAR talk 327 „Preliminary Uncertainty and Sensitivity Analysis of the ASTEC simulation results of a MBLOCA scenario at a Generic KONVOI Plant using FSTC tool“

© Framatome - All rights reserved
C1 –Framatome Restricted / Framatome know-how / Export Control - AL: N ECCN: N /

ASTEC U&S Results

Dose Rate in Containment for different Monte Carlo Samples

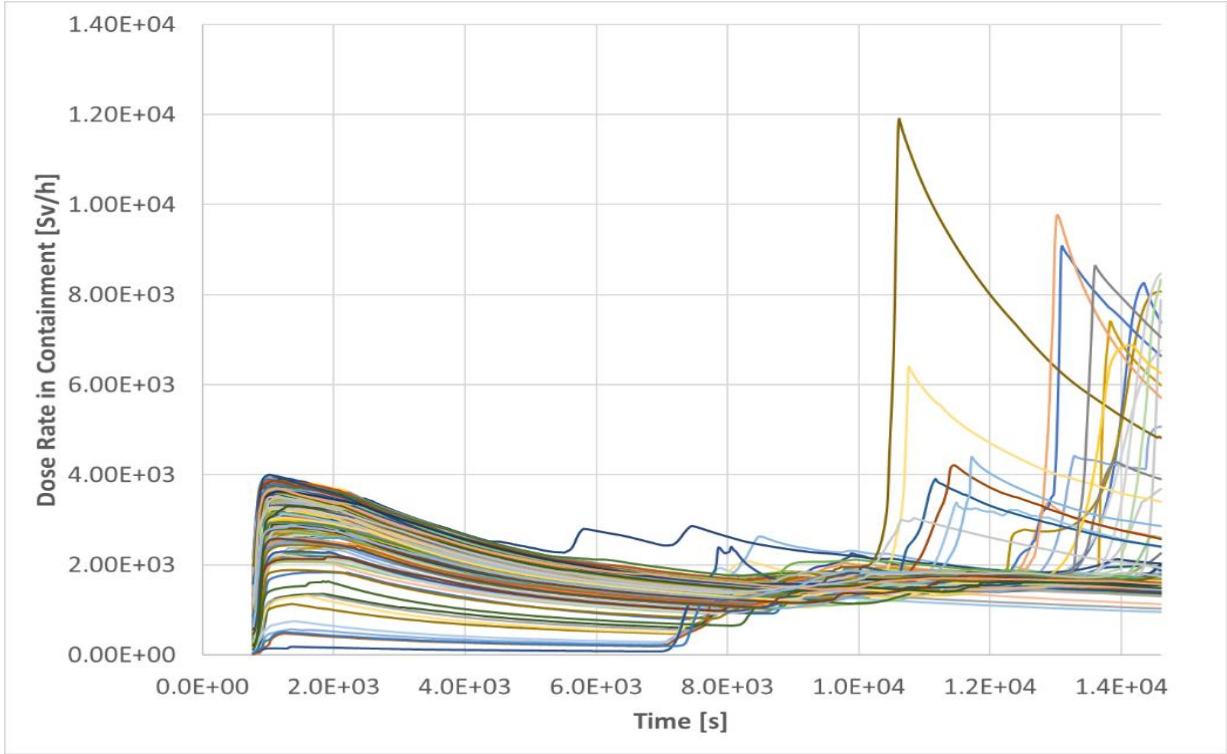

 © Framatome - All rights reserved
C1 –Framatome Restricted / Framatome know-how / Export Control - AL: N ECCN: N /

ASTEC U&S Results

Dose Rate in Annulus for different Monte Carlo Samples

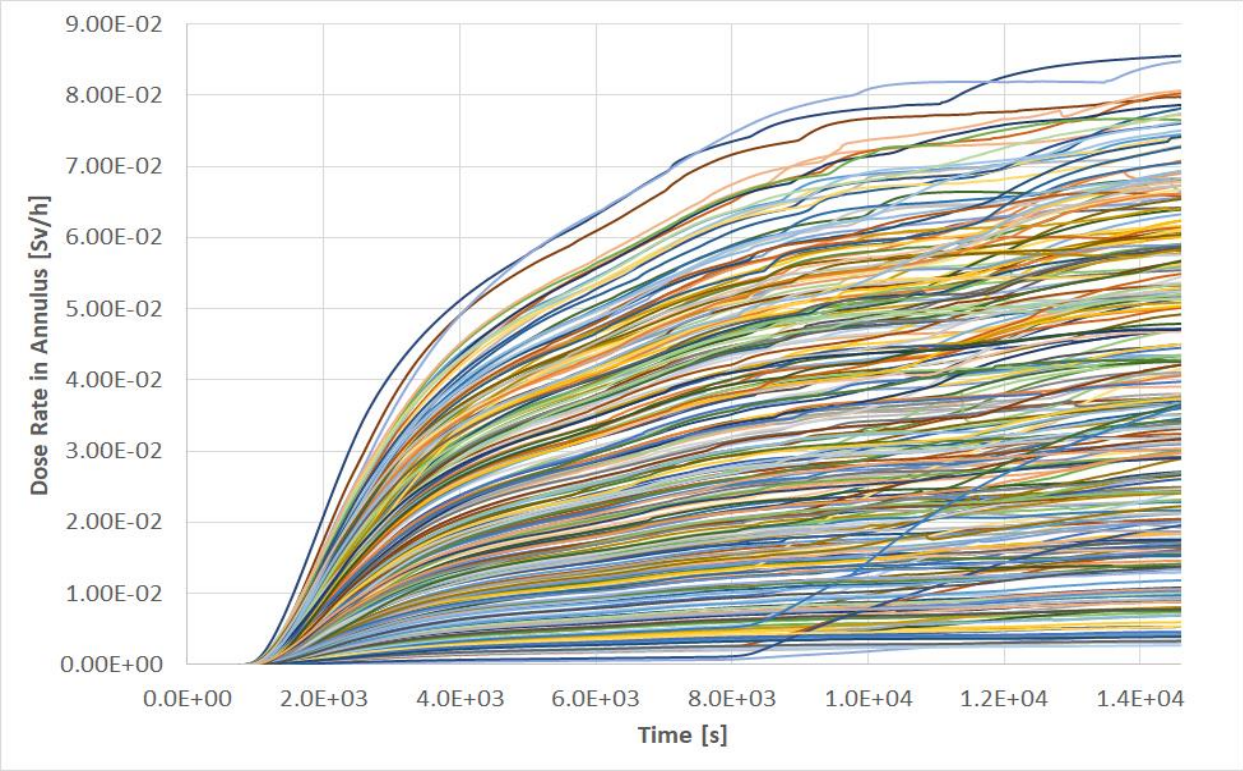

 © Framatome - All rights reserved
C1 –Framatome Restricted / Framatome know-how / Export Control - AL: N ECCN: N /

ASTEC U&S Results

Xenon Release to the Environment for different Monte Carlo Samples

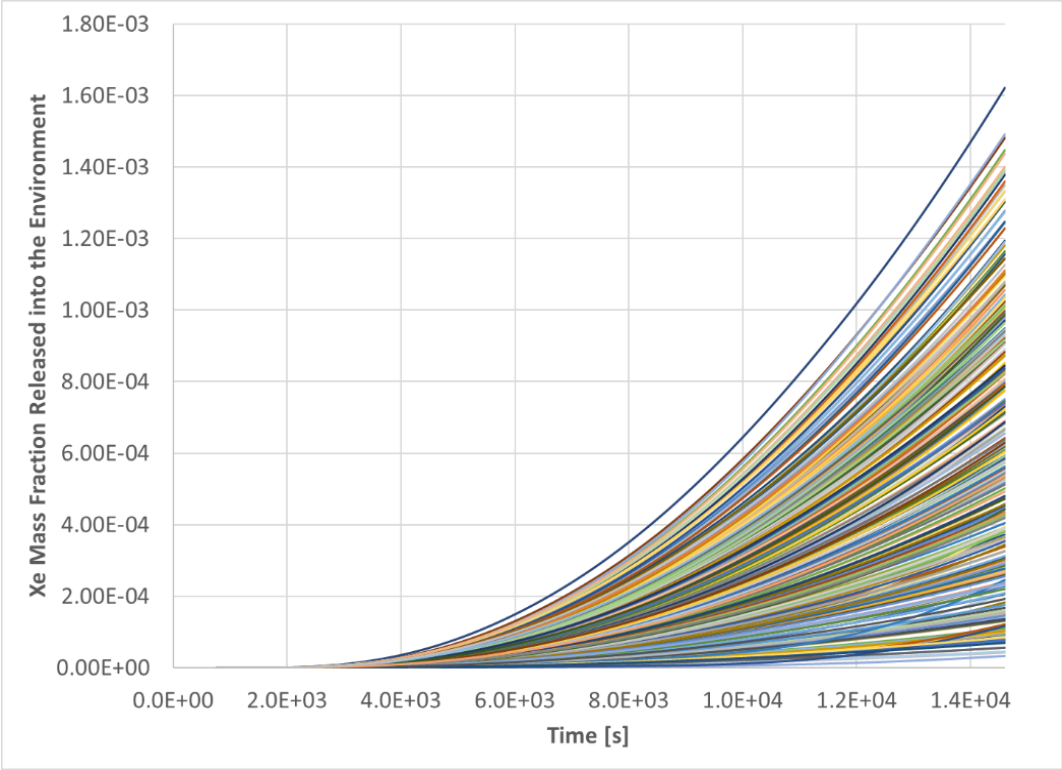

 © Framatome - All rights reserved
C1 –Framatome Restricted / Framatome know-how / Export Control - AL: N ECCN: N /

ASTEC U&S Results

Pearson Correlations between Xe Release to the Environment and Dose Rates in Annulus and Containment

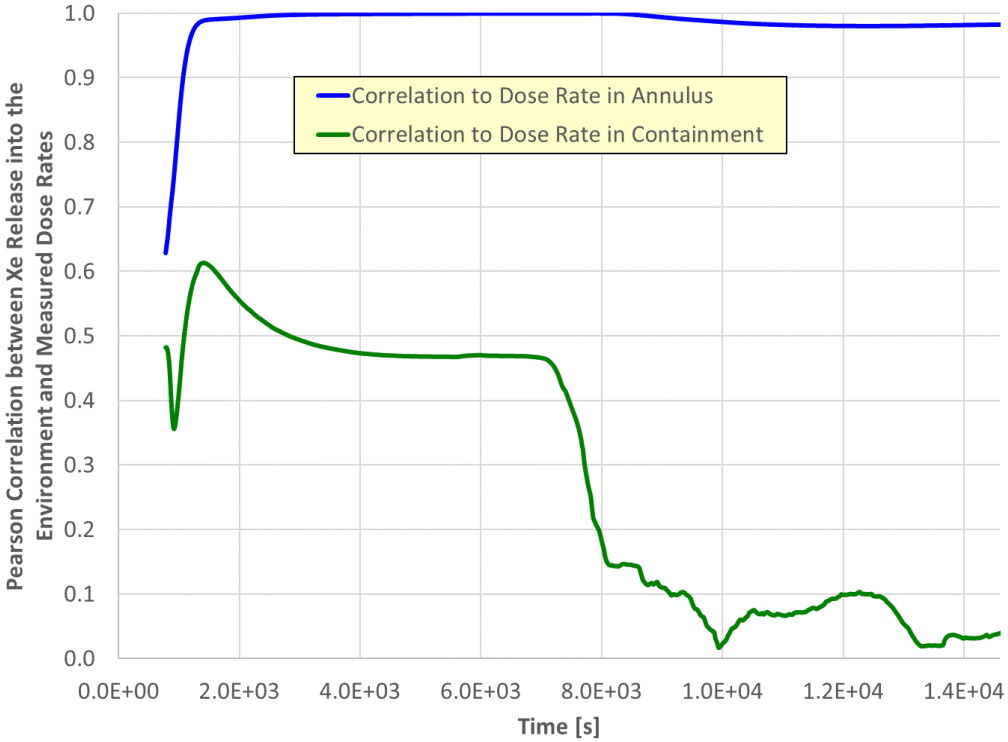

 © Framatome - All rights reserved
C1 –Framatome Restricted / Framatome know-how / Export Control - AL: N ECCN: N

4. MOCABA Prediction Results

 © Framatome - All rights reserved
C1 –Framatome Restricted / Framatome know-how / Export Control - AL: N ECCN: N /

MOCABA Prediction Results

Future Prediction of Xe Source Term based on previous Dose Rate Measurements in Annulus

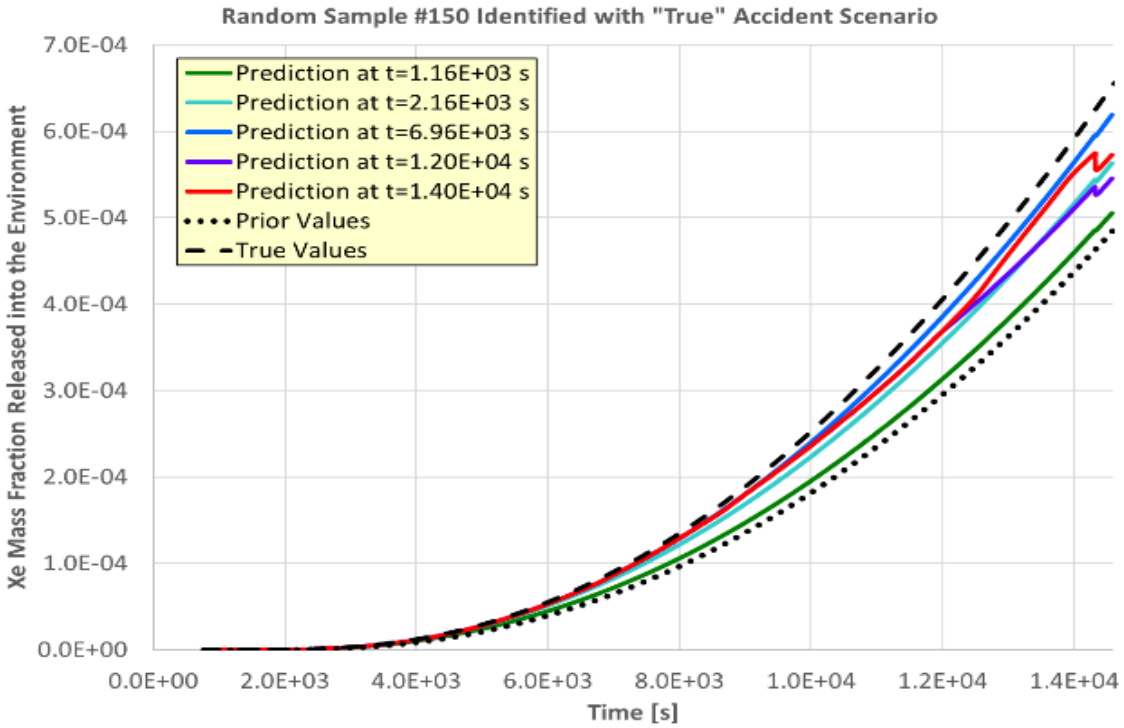

 © Framatome - All rights reserved
C1 –Framatome Restricted / Framatome know-how / Export Control - AL: N ECCN: N /

MOCABA Prediction Results

Future Prediction of Xe Source Term based on previous Dose Rate Measurements in Containment

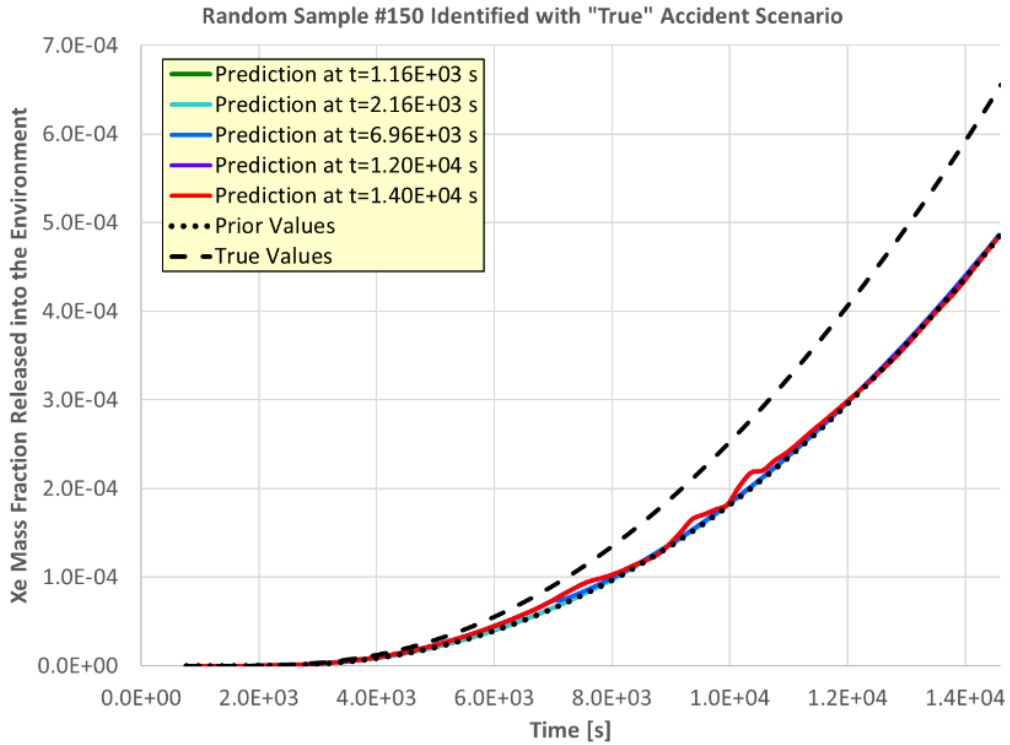

 © Framatome - All rights reserved
C1 –Framatome Restricted / Framatome know-how / Export Control - AL: N ECCN: N /

MOCABA Prediction Results

- Good prediction using dose rate in annulus because of high Pearson correlation between annulus dose rate and xenon source term
- Containment dose rate not suitable for good prediction because of low Pearson correlation between containment dose rate and xenon source term (curve stays at prior curve)

- Good prediction quality when noisiness of training data is sufficiently low

© Framatome - All rights reserved
C1 –Framatome Restricted / Framatome know-how / Export Control - AL: N ECCN: N /

Conclusions

- A time series prediction algorithm has been introduced based on MOCABA data assimilation framework
- It has been demonstrated that MOCABA method is suitable for source term predictions

- It can be used in real-time accident predictor modules within software packages such as Framatome‘s Central Radiological Computer System (CRCS)

 © Framatome - All rights reserved
C1 –Framatome Restricted / Framatome know-how / Export Control - AL: N ECCN: N /

Acknowledgements

The project was funded by the German Federal Ministry of Economic Affairs and Energy, funding code FZK 1501582 (WAME project).

 © Framatome - All rights reserved
C1 –Framatome Restricted / Framatome know-how / Export Control - AL: N ECCN: N /

framatome

Thank you for your attention!



To discover more about how we can help, visit us at
www.framatome.com/solutions-portfolio

Legal Notice

Editor and Copyright 2022: Framatome GmbH – Paul-Gossen-Straße 100 – 91052 Erlangen, Germany. It is forbidden to reproduce the present publication entirely or partially without prior consent in whatever form. Legal action may be taken against any infringer and/or any person breaching the aforementioned conditions.

Subject to change and error without notice. Illustrations may differ from the original. The contained statements and information are for advertising purposes only and do not constitute an offer of contract. They shall neither be construed as a guarantee of quality or durability, nor as warranties of merchantability or fitness for a particular purpose. These statements, even if they are future-oriented, are based on information that was available to us at the date of publication. Type, quantity and characteristics of goods and services are subject to formal individual formal contracts.

 © Framatome - All rights reserved

C1 –Framatome Restricted / Framatome know-how / Export Control - AL: N ECCN: N

CCFL MODEL EFFECT OF PRESSURIZER SURGE LINE FLOW ON SEVERE ACCIDENT PROGRESSION IN TMI-2 USING CINEMA

Rae-Joon Park, Dong Gun Son, Jun Ho Bae, Sung Won Bae, Kwang Soon Ha
Korea Atomic Energy Research Institute
1045 Daedeok-daero, Yuseong-Gu, Daejeon, Korea
rjpark@kaeri.re.kr; donggunson@kaeri.re.kr; bjh@kaeri.re.kr; bswon@kaeri.re.kr; tomo@kaeri.re.kr

Bub-Dong Chung
FNC Technology Co., 593 Daedeok-daero, Yuseong-Gu, Daejeon, Korea
bdchung@fnctech.com

ABSTRACT

As a part of a validation of the CINEMA computer code, the TMI (Three Mile Island Unit)-2 severe accident has been analyzed. This analysis has been performed to estimate the efficiency of the CINEMA and the predictive qualities of its models from an initiating event to a corium relocation into the lower plenum of the reactor vessel. In the TMI-2 severe accident, the break location was the PORV (Pilot Operated Relief Valve), which was located top of the pressurizer. A flow path through the surge line between the hot leg and the pressurizer was generated and the water level of the pressurizer was very high, which resulted in the melt progression of the core. The surge line modeling effect on the core melt progression in the TMI-2 severe accident was analyzed using the CINEMA computer code. More accurate representations of the surge line flow and pressurizer might eliminate some of the problems encountered in primary TMI-2 analyses. The junction connecting the surge line to the hot leg A should be oriented horizontally rather than vertically (to reflect its true alignment) and the CCFL (Counter Current Flow Limitation) model should be activated at the junction connecting the surge line to the pressurizer. The CCFL input parameters affect the pressurizer water drain to the core. For this problem in the first analysis, the SPACE input model on the CCFL was modified as strong as possible in the second analysis, which resulted in the small water drain to the core. The CINEMA result in strong CCFL input model in the modified SPACE input of the secondary case is very similar to the TMI-2 data in general.

KEYWORDS
TMI-2 Severe Accident, Core Melt Progression, Surge Line Flow, Counter Current Flow Limitation, CINEMA Computer Code

1. INTRODUCTION

As an integrated severe accident computer code development in Korea, CINEMA (Code for INtegrated severe accidEnt Management Analysis) has been developing for a severe accident sequence analysis from an initiation event to a containment failure. The basic goal of this code development is to design a severe accident analysis code package by exploiting the existing domestic DBA (Design Basis Analysis) code system for the severe accident analysis. The CINEMA computer code [1] are composed of CSPACE [2], SACAP (Severe Accident Containment Analysis Package) [3], and SIRIUS (SImulation of Radioactive nuclide Interaction Under Severe accident) [4], which are capable of core melt progression with thermal

hydraulic analysis of the RCS (Reactor Coolant System), severe accident analysis of the containment, and fission product analysis, respectively.

The CSPACE is the result of merging the COMPASS (COre Meltdown Progression Accident Simulation Software) [5, 6] and SPACE (Safety and Performance Analysis CodE for nuclear power plants) models, which is designed to calculate the severe accident situations of an overall RCS thermal-hydraulic response in SPACE modules [7, 8] and a core damage progression in COMPASS modules. As a part of a validation of the CINEMA computer code, the TMI (Three Mile Island) unit 2 severe accident has been analyzed. This analysis has been performed to estimate the efficiency of the CINEMA computer code and the predictive qualities of its models from an initiating event to a corium relocation into the lower plenum of the reactor vessel.

On March 28, 1979, the TMI-2 pressurized water reactor underwent a prolonged, a total loss of feed water with a SBLOCA (Small Break Loss Of Coolant Accident) that resulted in a significant cladding oxidation, a partial melting of the core material, and a significant release of fission products from the fuel [9]. The progression of the TMI-2 accident was mitigated by an injection of the emergency cooling water. In the TMI-2 severe accident, the break location was the PORV (Pilot Operated Relief Valve), which was located top of the pressurizer. For this reason, a flow path through the surge line between the hot leg and the pressurizer was generated and the water level of the pressurizer was very high, which resulted in the melt progression the core. In this study, the surge line modeling effect on the core melt progression in the TMI-2 severe accident was analyzed using the CINEMA computer code.

2. DETAILED DESCRIPTION OF TMI-2 SEVERE ACCIDENT

The TMI-2 severe accident scenario can be divided into four phases, beginning with a reactor scram, as follows:

- Phase 1: From 0 to 6,000s. This represents the part of the accident where some or all of the main coolant pumps were operating, forcing convective two phase coolant through the core.
- Phase 2: From 6,000 to 10,440s. During this time span, all the main pumps were shut down, and a boiling off of the water in the reactor vessel resulted in a progressive uncovering of the core, causing major and very severe core damage.
- Phase 3: From 10,440 to 12,000s. This represents the first recovering and major quenching of the core by a short operation of the main coolant pump at 10,440s and a continued core heat up and damage, even when the core is recovered again by an operation of the high pressure safety injection system after 12,000s.
- Phase 4: From 12,000 to 18,000s. This represents the initiation of the HPI (High Pressure Injection). The central region of the partially molten core material was not coolable by HPI even through the water level reached the level of the hot legs by 12,420s, because the corium pool was generated in the core. Between 13,440s and 13,560s, the crust encasing and supporting the molten core region is believed to have failed, allowing molten material to relocate to the lower plenum. However, the molten material was quenched by coolant in the reactor vessel at this phase.

Table I shows detailed main events in the TMI-2 severe accident. Turbine and main feedwater pump were tripped by a total loss of feed water at 0 seconds, which resulted in the opening of the pressurizer PORV

valve by a high pressure opening set point of 15.5 MPa. The reactor was tripped by a high pressurizer pressure signal. The pressurizer PORV valve was not closed when the pressurizer pressure was reached 15.2 MPa, which was the closed set point. This resulted in the SBLOCA. The 1 (of 3) makeup pump 1B was operated at 441s The HPI was operated by high pressurizer pressure signal at 122s.

Table I. Detailed main events in the TMI-2 severe accident

Time (second)	Main Events
0	Turbine and main feedwater pump trip (Total Loss of Feed Water)
3	Pressurizer PORV valve opening (15.5 MPa)
8	Reactor scram on high pressure signal
13	No Pressurizer PORV valve closing (15.2 MPa) (SBLOCA)
41	Operation of 1 (of 3) makeup pump 1B
222	HPI operation
278	Stop of HPI
480	Auxiliary feedwater startup
552	Core boiling begins
4,440	Shutdown B-loop RCP (end of phase 1)
6,000	Shutdown A-loop RCP
6,184	Core uncovery
7,742	Cladding oxidation begins (T= 1,000K)
7,719	Cladding failure (T=1,117K)
8,340	Close of the PORV line block valve
9,014	Fuel melting
10,440	Restart one B-loop RCP (end of phase 2)
11,580	Shutdown of the B-loop RCP
12,000	Start of primary system feed and bleed
13,440	Core material slumping (end of phase 3)
18,000	General emergency declared (end of phase 4)

However, this pump was stopped by the operator, because of a misreading of the high level of the pressurizer. The auxiliary feedwater was startup at 480s. Boiling was occurred in the core at 552s (second). The B-loop and A-loop RCPs were stopped at 4,440s and 6,000s, respectively. The core was uncovered at 6,184s, which resulted in an increase of the fuel cladding temperature. The fuel cladding oxidation begun at 7,442s. The cladding was failed by overstrain at 7,719s. The operator closed the PORV line block valve at 8,340s, which meant the close of the SBLOCA. However, the fuel was melted at 9,014s. One B-loop RCP was operated to supply the coolant into the core at 10,440s. This pump was stopped at 11,580s. The feed and bleed operation of the primary system was started to cooldown the core at 12,000s. However, the melted core material was relocated to the lower plenum at 13,440s, because of the molten pool formation in the core. The general emergency declared at 18,000s.

Fig. 1 shows the end state of TMI-2 severe accident. During the TMI-2 severe accident, approximately 62 tons of core material was melted in the core and 19 tons of the melted material was relocated to the lower plenum of the reactor vessel. However, the reactor vessel did not fail.

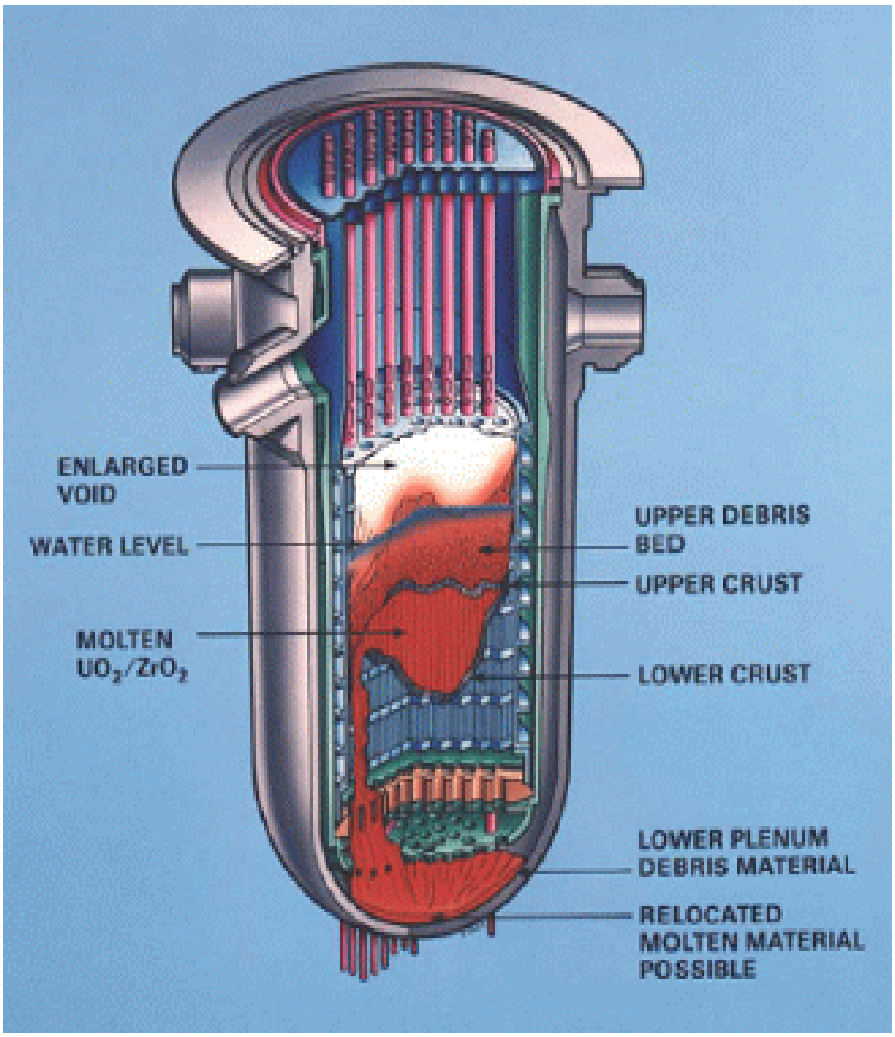

Figure 1. End state of TMI-2 severe accident.

3. CINEMA INPUT MODEL

TMI-2 was designed and manufactured by Babcock & Wilcox, Inc. The core contained 177 fuel assemblies. The RCS (Reactor Coolant System) consisted of the reactor vessel, two vertical one-through steam generators, four reactor coolant pumps, an electrically heated pressurizer, and interconnecting piping. The system was arranged with two heat transport loops, each with two RCPs and one steam generator. Fig. 2 shows an input nodalization of the CINEMA computer code for the TMI-2.

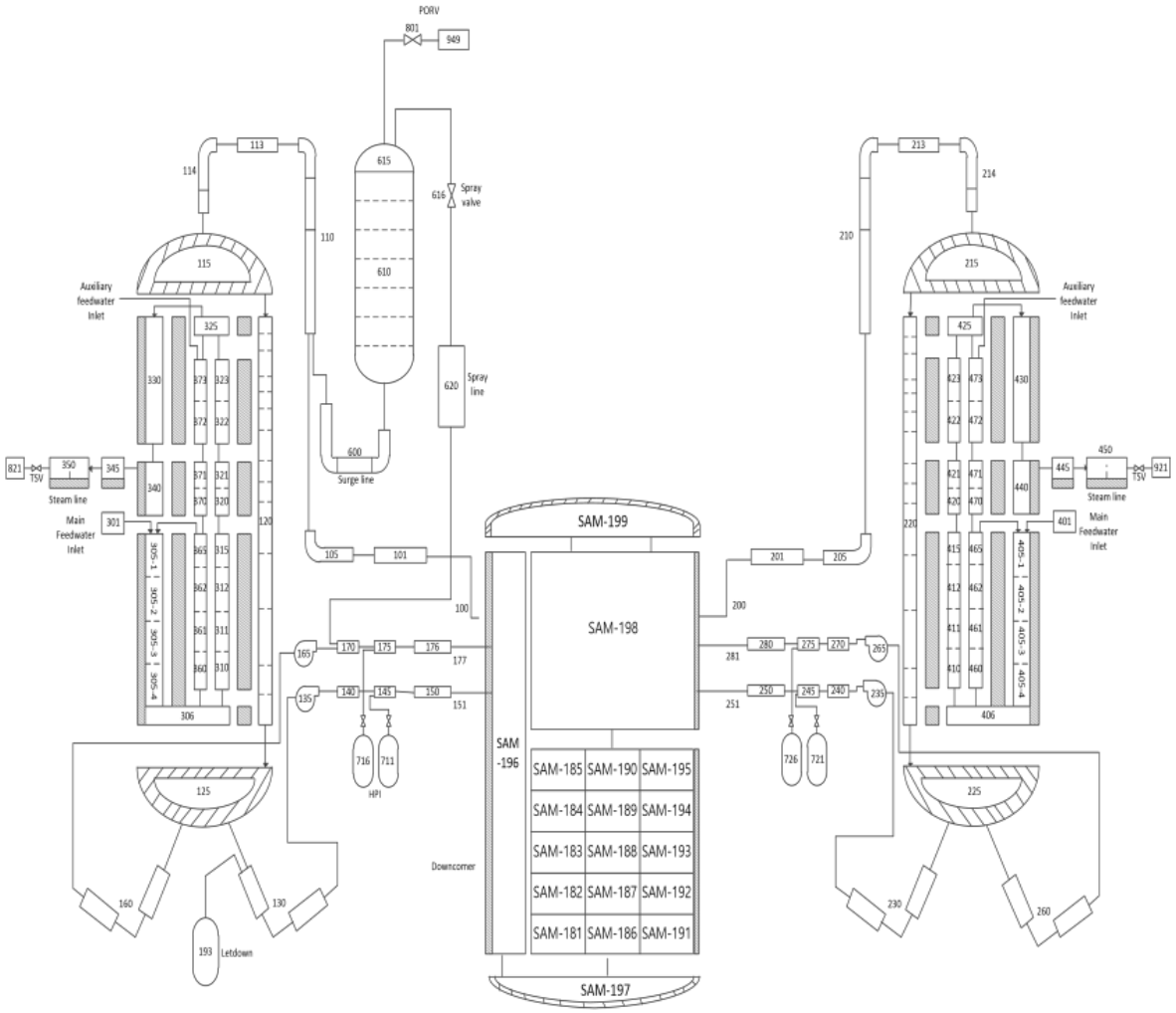

Figure 2. CINEMA nodalization for TMI-2.

All primary and main secondary systems are modeled including the pressurizer, PORV, and safety injections. In core input model, 3 radial and 5 axial nodes are used. Fuel and control rod are connected to the fluid volumes in the core.

4. CINEMA RESULTS AND DISCUSSION

A steady state calculation was performed to verify the input nodalization of CINEMA for TMI-2 severe accident. The steady state conditions obtained from the simulation were used as initial conditions for the transient calculation.

Fig. 3, 4, and 5 shows the CINEMA results on liquid level in the pressurizer, pressurizer pressure, and fuel cladding surface temperature, respectively, to compare with the measured data and SCDAP/RELAP5 results. The SCDAP/RELAP5 computer code [10], which is the result of merging the RELAP5/MOD3 and severe core damage analysis package (SCDAP) models, is designed to calculate the severe accident situations of the overall RCS thermal-hydraulic response, core damage progression, reactor vessel heat-up and damage, and fission product release and transport. The code was developed at the Idaho National Laboratory (INL) under the sponsorship of the U.S. Nuclear Regulatory Commission (USNRC).

In Fig. 5, position of nodes 1, 2, 3, 4, 5 are 0.36 m, 1.09 m, 1.82m, 2.55 m, 3.28 m from the bottom of the fuel rod, respectively. Fuel cladding mass of only one fuel rod is in this Figure. In the first calculation, the pressurizer water drained completely after the PORV block valve was closed at 8,340s, which effectively affected core heat up, as shown in Fig. 5. More accurate representations of the surge line flow and pressurizer might eliminate some of the problems encountered in the first TMI-2 analyses. For example, the junction connecting the surge line to the hot leg A should be oriented horizontally rather than vertically (to reflect its true alignment) and the CCFL (Counter Current Flow Limitation) model should be activated at the junction connecting the surge line to the pressurizer, rather than at the hot leg junction. For this reason, the CCFL input parameters affect the pressurizer water drain into the core.

For this problem in the first analysis, the SPACE input model on the CCFL was modified as strong as possible in the second analysis [10], which resulted in the small water drain to the core as shown in Fig. 3. As shown in Fig. 4, the CINEMA result in strong CCFL input model in the modified SPACE input of the second case is very similar to the TMI-2 data in general.

A reduction feed water to the steam generator caused the coolant to expand and initially increased the RCS pressure. The pressurizer PORV opened when the pressure reached 15.7 MPa. The PORV failed to close as the RCS pressure decreased, which resulted in initiating the SBLOCA. Emergency core cooling was reduced by operators who thought that the pressurizer liquid level indicated a nearly full RCS, while coolant continued to be lost from the PORV. After an initial decrease in the RCS pressure, the pressurizer pressure remained at approximately 7MPa. After a pump termination at 10,000s, the liquid level in the reactor vessel decreased, which resulted in a core uncovery. Continued core degradation with a coolant boiling caused the pressurizer pressure to increase.

As shown in Fig. 5, the fuel cladding was quenched rapidly by water injection into the core at 10,440s, which was occurred by RCP operation in the secondary case. This results is not agree with TMI-2 data. For this reason, it is necessary to modify the CINEMA computer code on the quench model of the melted core material.

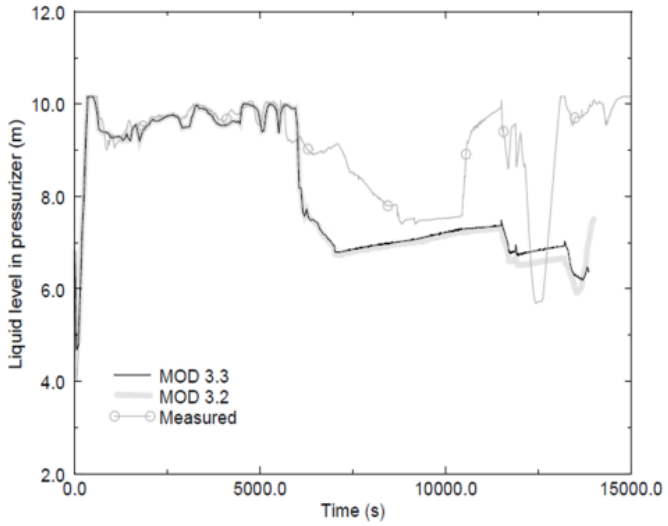

(Measured Data and SCDAP/RELAP5 Results)

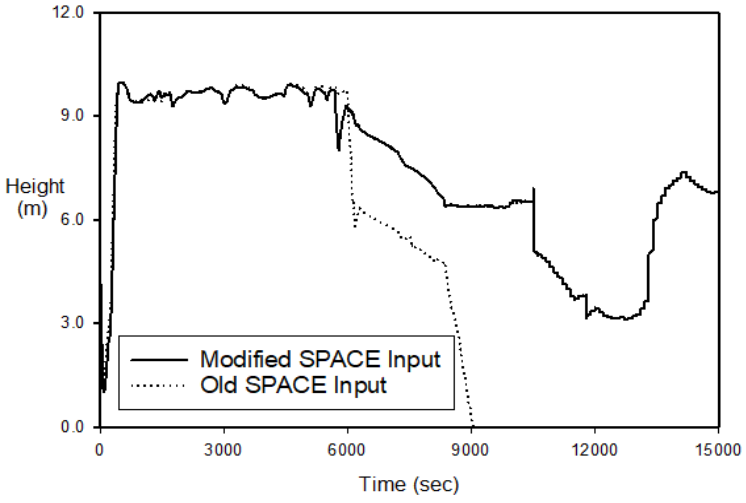

(CINEMA Results)

Figure 3. CINEMA results on pressurizer liquid level in TMI-2 severe accident.

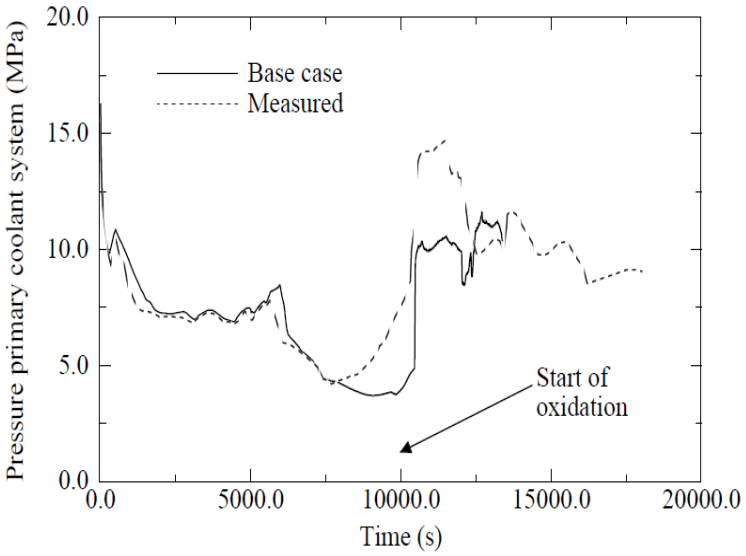

(Measured Data and SCDAP/RELAP5 results)

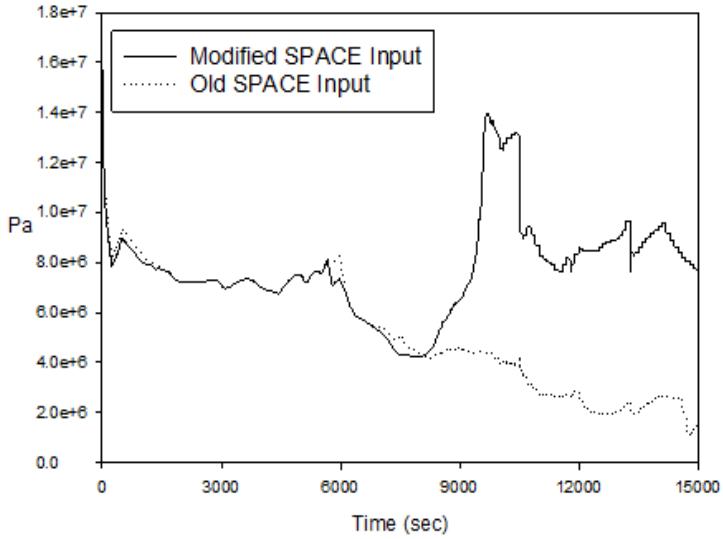

(CINEMA Results)

Figure 4. Pressurizer pressure history in TMI-2 severe accident.

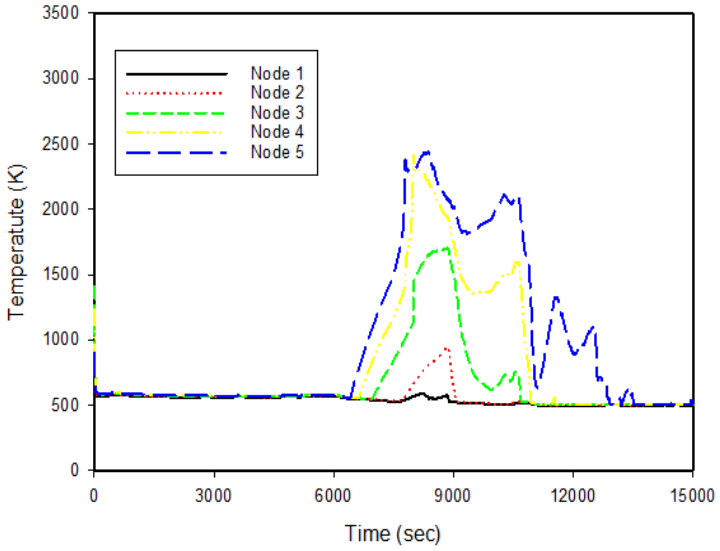

(Old SPACE Input)

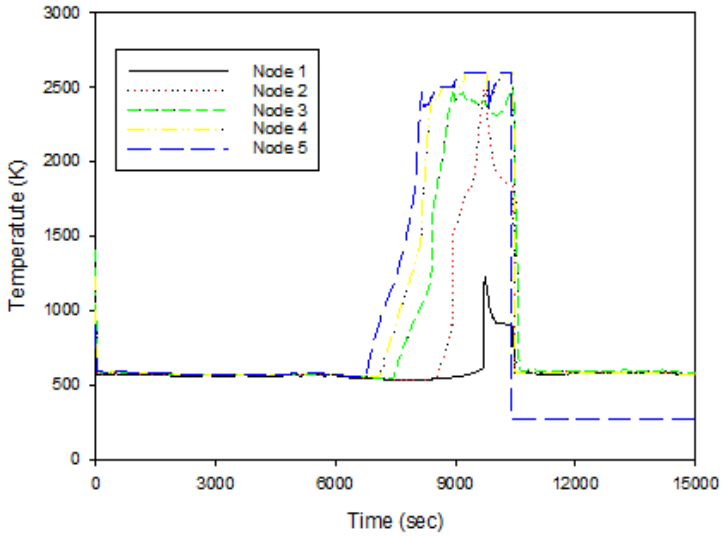

(Modified SPACE Input)

Figure 5. CINEMA results on fuel cladding surface temperature in TMI-2 severe accident.

5. CONCLUSIONS

The surge line flow modeling effect on the core melt progression in the TMI-2 severe accident was analyzed using the CINEMA computer code. The CCFL input parameters in CINEMA affect the pressurizer water drain to the core through the pressurizer surge line. The fuel cladding mass is not changed by no melting and relocation with no increase of the fuel cladding temperature in the general CCFL model case. However, the fuel cladding mass in the strong CCFL model case is changed by melting and relocation of the fuel cladding, which is very similar to the TMI-2 data in general. More CINEMA analysis for a melted fuel relocation and quenching process in the core and lower plenum are necessary to simulate the TMI-2 severe accident.

ACKNOWLEDGMENTS

This work was supported by the Korea Institute of Energy Technology Evaluation and Planning (KETEP) grant funded by the Korean government (Ministry of Trade, Industry, & Energy, Republic of Korea) (No. KETEP-20193110100050).

REFERENCES

1. KHNP, KAERI, FNC, KEPCO E&C, “CINEMA User Manual”, S11NJ16-2-E-TR-7.4, Rev. 0 (2018).
2. J.H. Song, D.G. Son, J.H. Bae, S. W. Bae, K.S. Ha, B.D. Chung, Y.J. Choi, “CSPACE for a Simulation of Core Damage Progression during Severe Accidents,” *Nuclear Engineering and Technology* **53**, (2021).
3. FNC, “SACAP User Manual”, S11NJ16-2-E-TR-7.4, Rev. 0 (2017).
4. K.S. Ha, I.S. Kim, H.S. Kang, D.H. Kim, “SIRIUS: a Code on Fission Product Behavior under Severe Accident,” *Transactions of the Korean Nuclear Society Spring Meeting*, Jeju, Korea (2017).
5. M. Z. Podowski, R. M. Podowski, H.D. Kim, J.H. Bae, G.D. Son, “Compass - New Modeling and Simulation Approach to PWR In vessel Accident Progression,” *Nuclear Engineering and Technology* **51** (2019).
6. J.H. Bae, G.D. Son, H.D. Kim, “Core Degradation Simulation of the PHEBUS FPT3 Experiment using COMPASS Code,” *Nuclear Engineering and Dessin* **320**, (2017).
7. KHNP, KEPCO E&C, KAERI, “SPACE User Manual”, S 06NX08-K-1-TR-36, Rev. 0 (2017).
8. S.J. Ha, “Development of the SPACE Code for Nuclear Power Plants,” *Nuclear Engineering and Technology* **43** (2011).
9. J.M. Broughton, P. Kuan, D.A. Petti, E.L. Tolman, et al., “A Scenario of the Three Mile Island Unit 2 Accident,” *Nuclear Technology* **87** (1989).
10. Siefken L. J. et al. (2001). “SCDAP/RELAP5/MOD3.3 Code Manual, Vol. I-V,” NUREG/CR-6150.

ERMSAR2022
Karlsruhe, Germany, May 16-19, 2022



CCFL Model Effect of Pressurizer Surge Line Flow on Severe Accident Progression in TMI-2 Using CINEMA

Rae-Joon Park, Bub-Dong Chung, Donggun Son, Jun Ho Bae, Sung Won Bae, Kwang Soon Ha



Content

- Introduction
  - TMI-2 Plant Data
  - TMI-2 Severe Accident
  - CINEMA Computer Code
- CINEMA Input Model & S.S. Calculation
- CINEMA Results and Discussion
- Conclusions

Introduction

❑ TMI-2 Severe Accident

	TMI-2
Reactor Location	Pennsylvania in U.S.A.
Reactor Type	PWR
Manufacturer Company	Babcock & Wilcox
Reactor Power	906 MWe
Operation Beginning Time	1978.12.30
Accident Occurrence Time	1979.3.28
Main Accident Reason	Equipment Fault and Human Error
Dead People Number	No
Main Accident Events	Core Melting, No Reactor vessel and Containment Failure

TMI-2 Plant

PWR with one-through SG

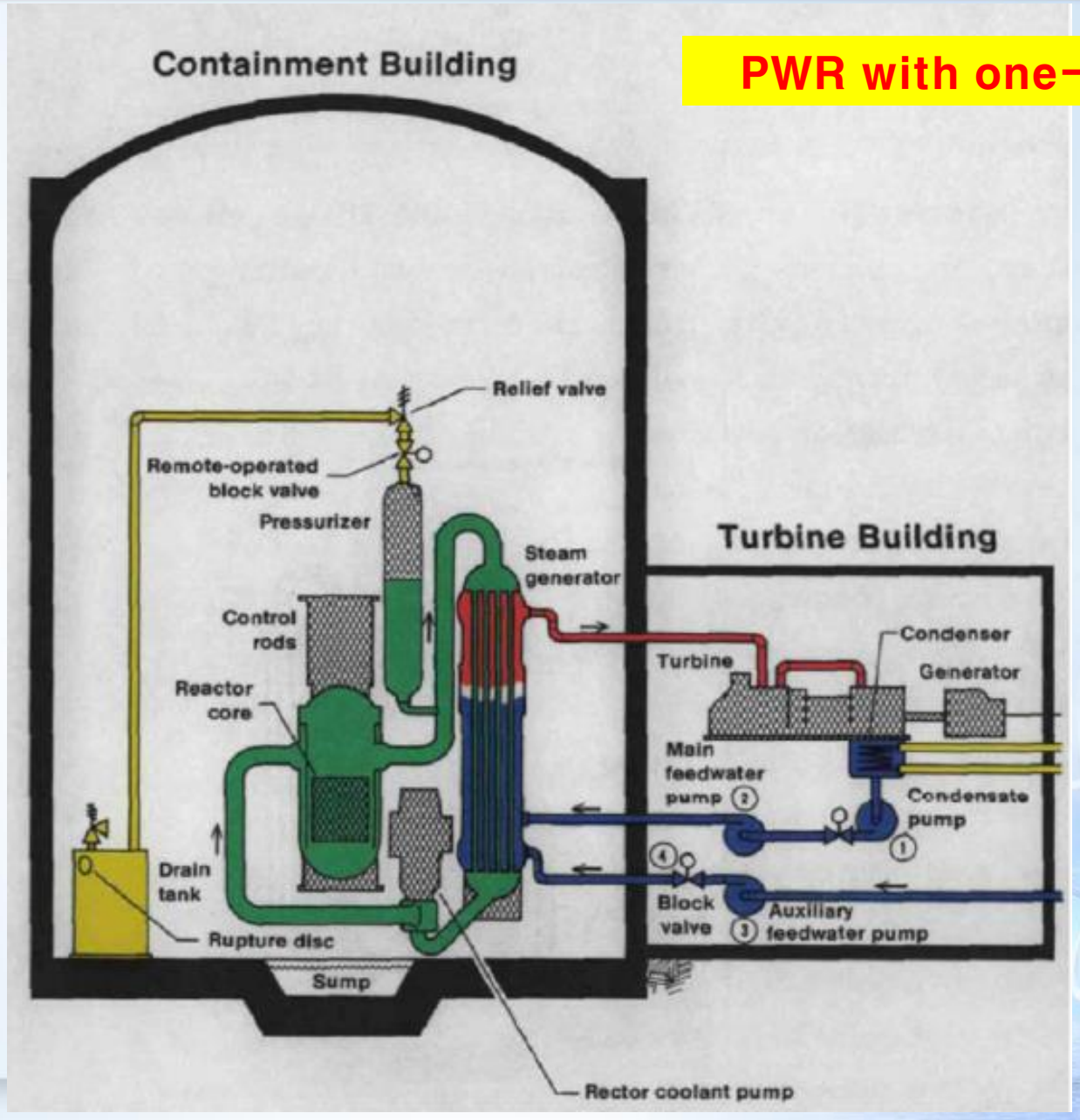

Plant Data of TMI-2

Reactor	Data	Core & Fuel Assemblies	Number
Design Heat Output	2,272 MWt	Fuel Assemblies	177
Vessel Coolant Inlet Temperature	292 ˚C	Fuel Rods per Fuel Assemblies	208
Vessel Coolant Outlet Temperature	320 ˚C		
Core Coolant Outlet Temperature	321 ˚C	Control Rod Guide Tubes per Assembly	16
Average Core Fuel Temperature	649 ˚C		
Core Operating Pressure	15 MPa		

Detailed TMI-2 Main Events

Time (s)	Main Events
0	Turbine and main feedwater pump trip (Total Loss of Feed Water)
3	Pressurizer PORV opening (15.5 MPa)
8	Reactor scram on high pressure signal
13	No Pressurizer PORV closing (15.2 MPa) (SBLOCA)
41	Operation of 1 (of 3) makeup pump 1B
122	HPI operation
278	Stop of HPI
480	Auxiliary feedwater startup
552	Core boiling begins
4,440	Shutdown B-loop RCP (end of phase 1)
6,000	Shutdown A-loop RCP
6,184	Core uncovery
7,742	Cladding oxidation begins (T= 1,000K)
7,719	Cladding failure (T=1,117K)
8,340	Close of the PORV line block valve
9,014	Fuel melting
10,440	Restart one B-loop RCP (end of phase 2)
11,580	Shutdown of the B-loop RCP
12,000	Start of primary system feed and bleed
13,440	Core material slumping (end of phase 3)
18,000	General emergency declared (end of phase 4)

End State in TMI-2

- Approx. 45 %(62 tons) of Core Material Melting
- Molten Pool Formation with Crust in middle Part of Core
- Approx. 19 tons of Corium Relocation to the Lower Plenum
- No Reactor Vessel Failure

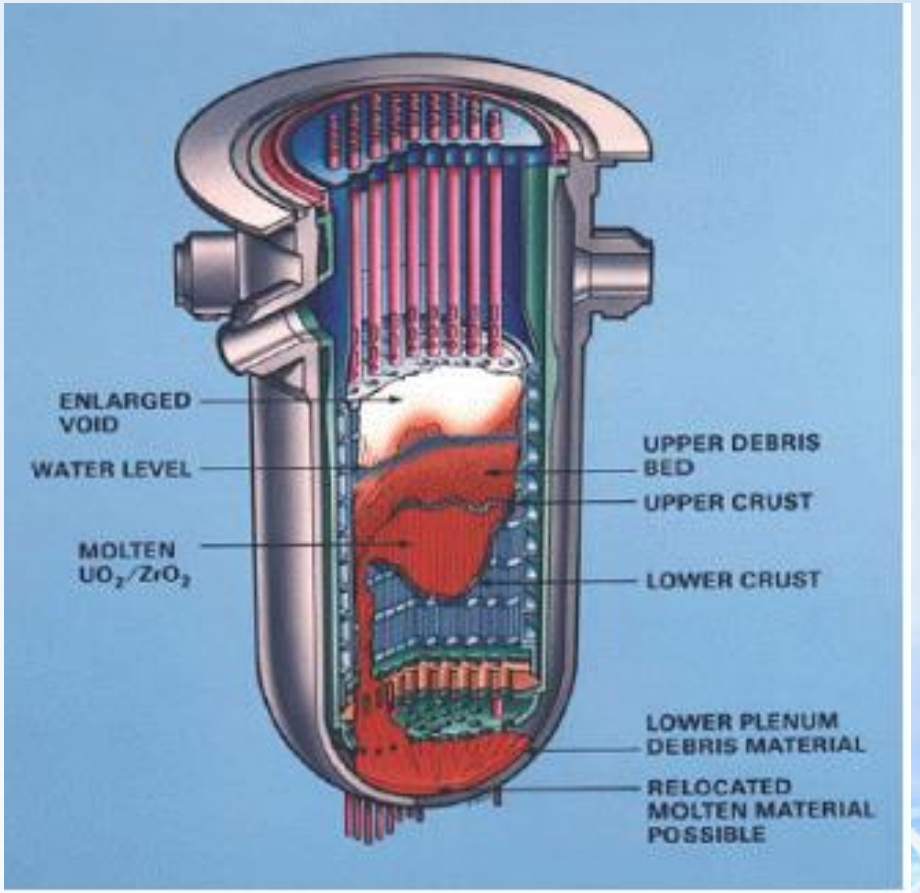

End State Configuration of TMI-2 Severe Accident

Research Needs & Objective

- The surge In the TMI-2 severe accident, the break location was the PORV (Pilot Oprated Relief Valve), which was located top of the pressurizer.

- A flow path through the the surge line between the hot leg and the pressurizaer was generated and the water level of pressurizer was very high, which resulted in the melt progression in the core.

- The surge line modeling effect on the core melt progression in the TMI-2 severe accident was analyzed using the CINEMA computer code.

CINEMA Development in Korea

- An integrated severe accident analysis computer code (CINEMA) has been developing by the collaboration in Korea.

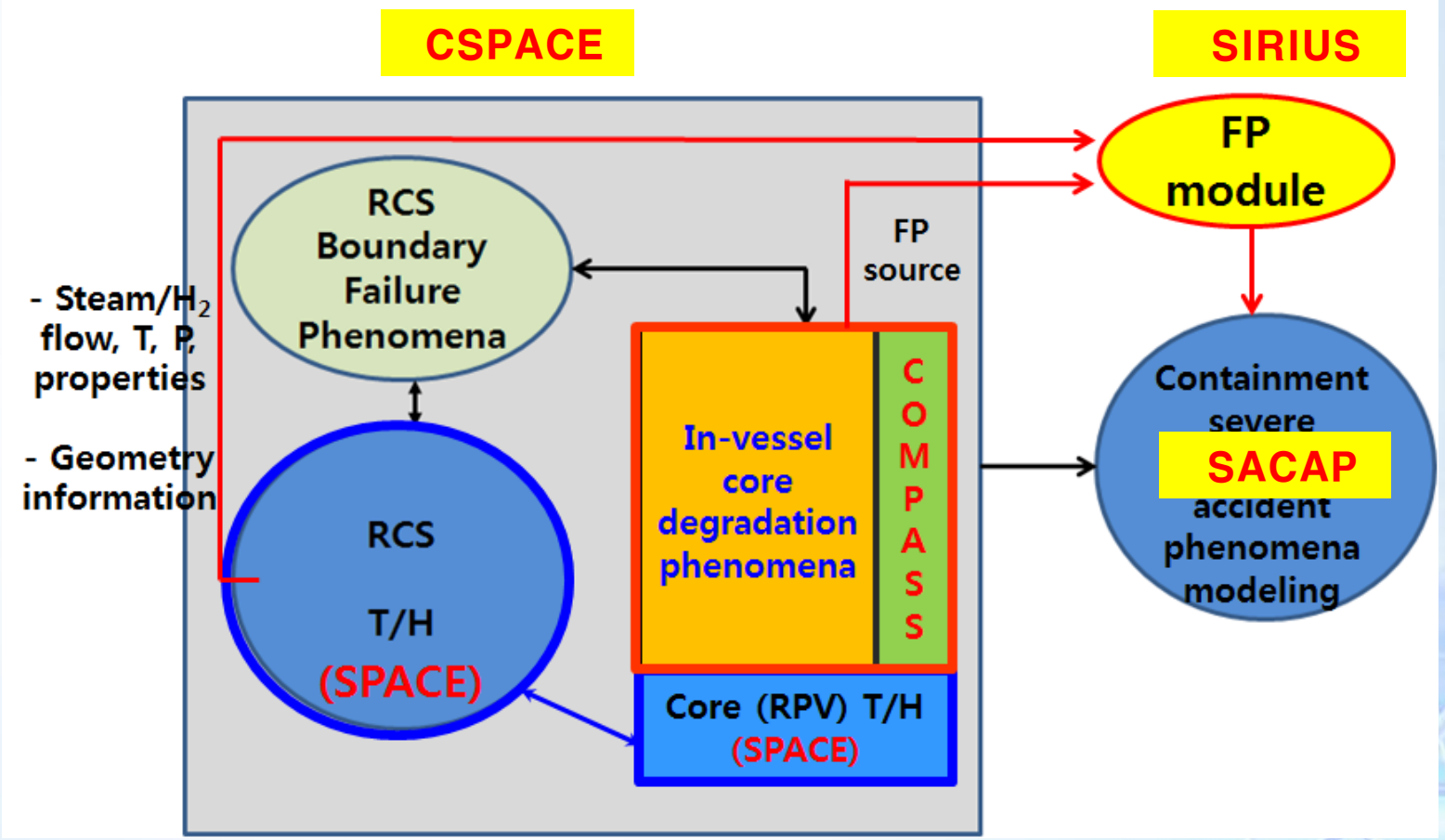

- **CINEMA: Code for INtegrated severe accidEnt Management Analysis**

CSPACE Coupling

- RCS SA simulation: COMPASS: fuel & RPV solid structure behavior
  SPACE: RCS & RPV T/H, components, neutronics, control & trip
- Data transfer: COMPASS → SPACE: heat flux, H_2 generation, geometry change
  SPACE → COMPASS: RPV T/H solution, reactor power

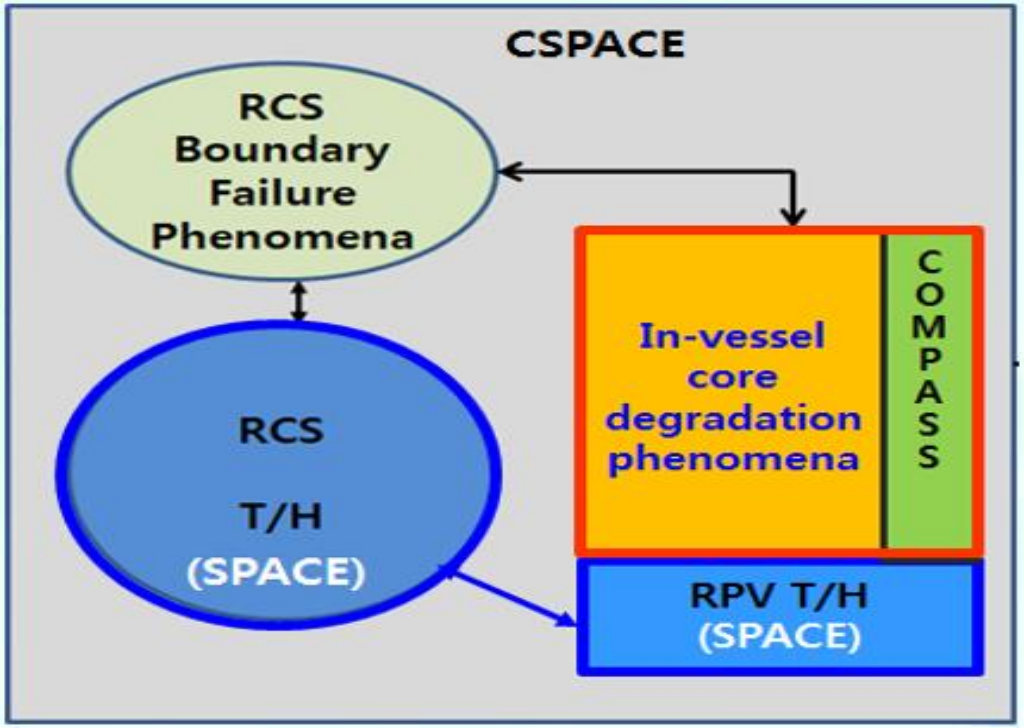

CSPACE Structure

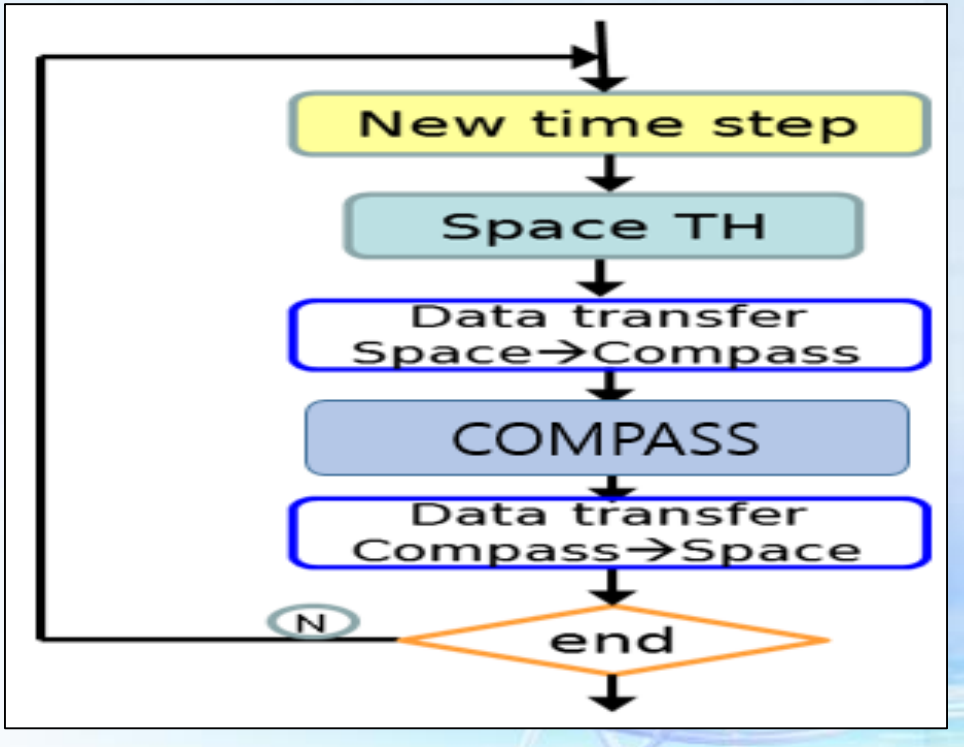

CSPACE Numerical Scheme

CINEMA Nodalization for TMI-2

- Using TMI-2 Design Data
- Based on SCDAP/RELAP5 Input

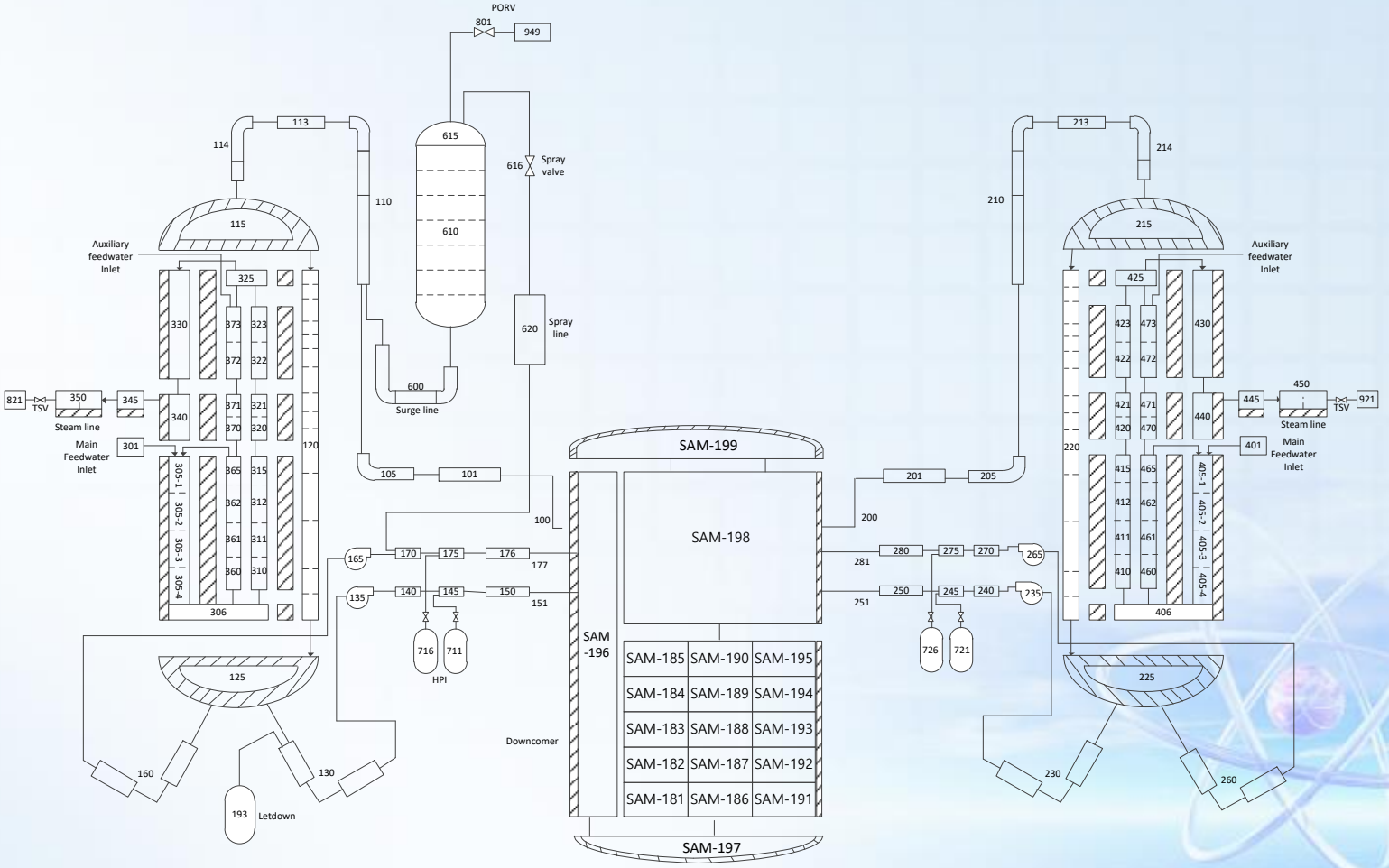

CINEMA-CSPACE Nodalization

Steady State Results

Parameter	Plant Operating Condition	CINEMA Results
Reactor Power (MW)	2700.0	2700
Primary System Pressure (MPa)	15.2	15.3
Cold Leg Temperature 1A (K)	561.0	571.0
Cold Leg Temperature 2A (K)	548.0	571.0
Hot Leg Temperature Loop A (K)	592.0	598.0
Hot Leg Temperature Loop B (K)	592.0	598.0
Feedwater Temperature (K)	513.0	513.0
SG A Pressure (MPa)	7.31	5.85
SG B Pressure (MPa)	7.24	5.85
SG A Steam Temperature (K)	586.0	578.0
SG B Steam Temperature (K)	585.0	579.0

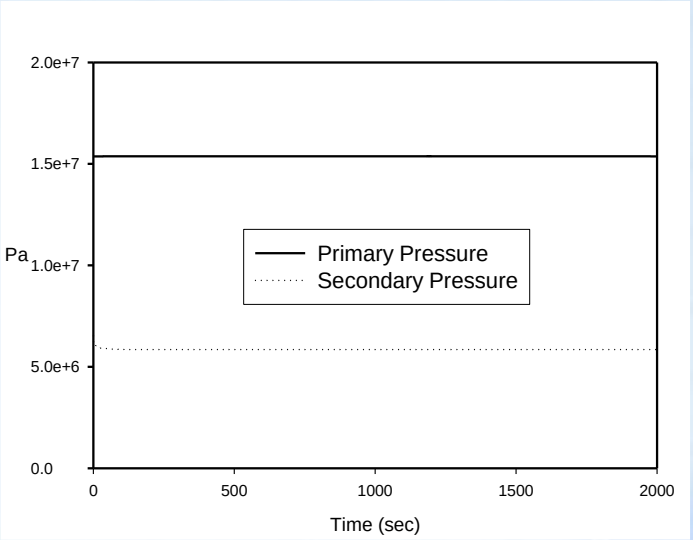

CINEMA Nodalization for TMI-2

❖ **Modified SPACE Input: Strong CCFL in Pressurizer Surge Line**

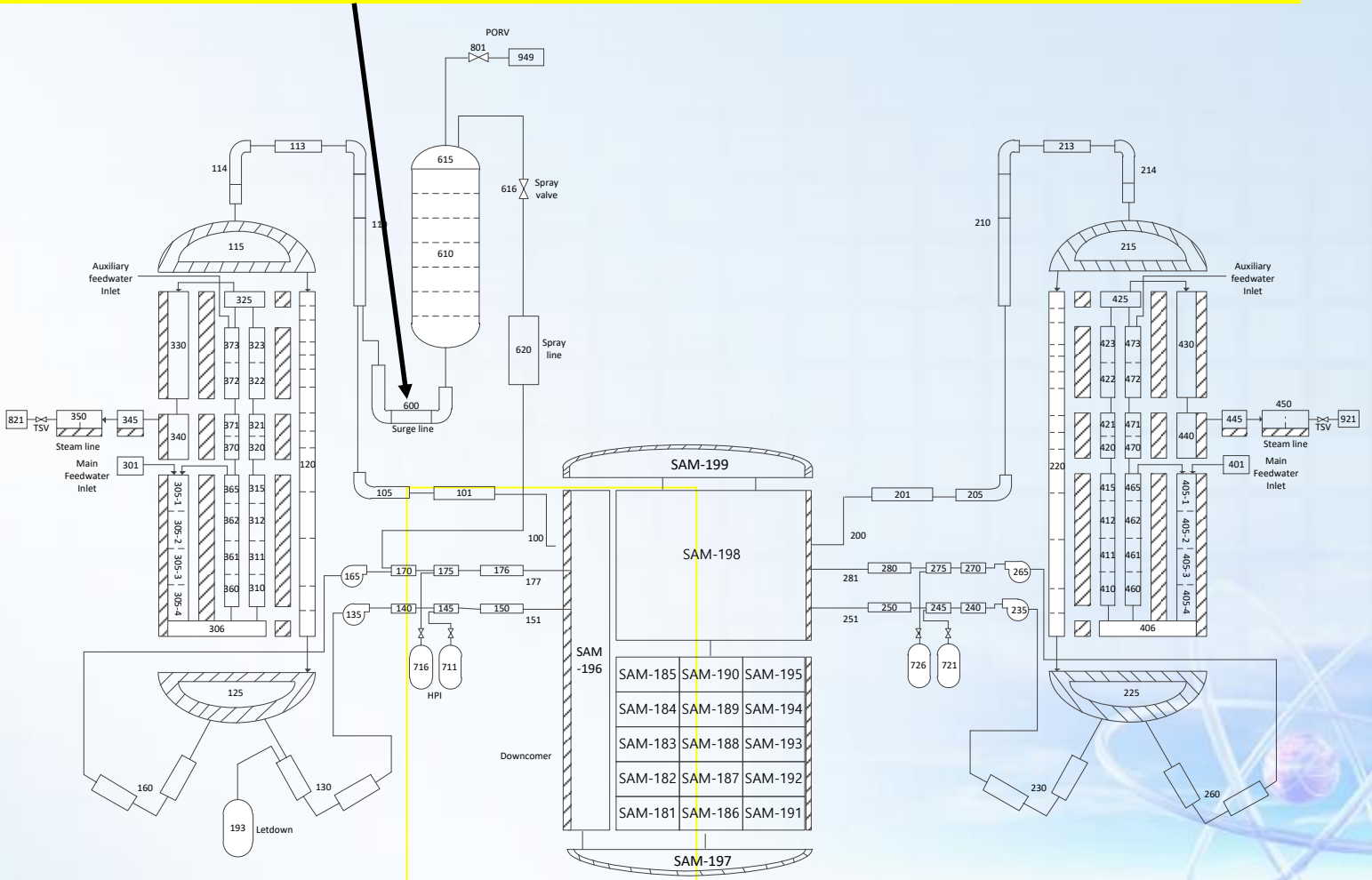

CINEMA-CSPACE Nodalization

Pressurizer Water Level

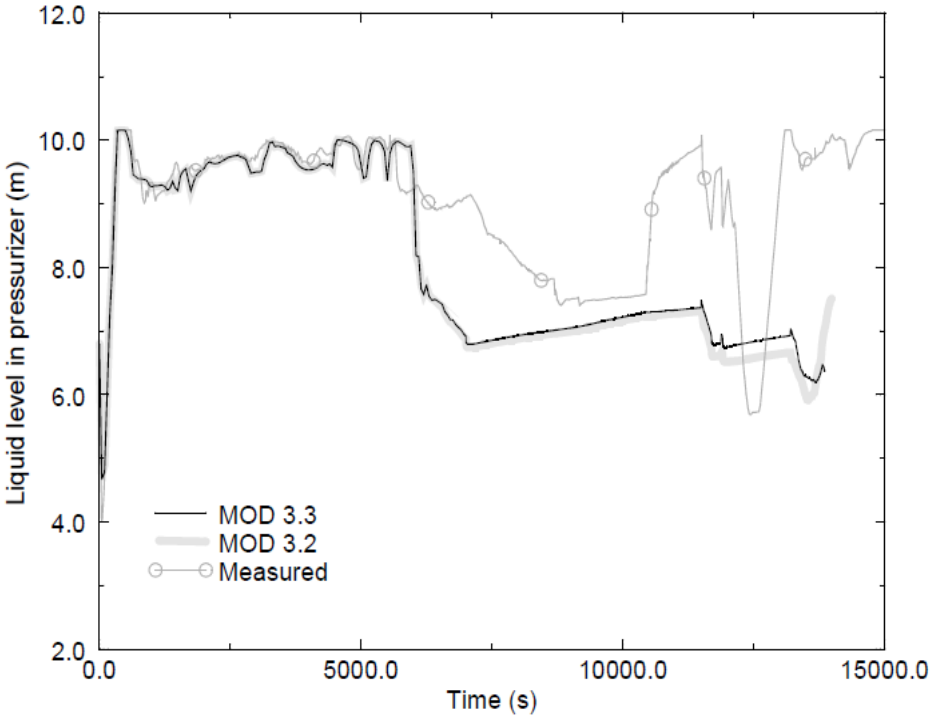

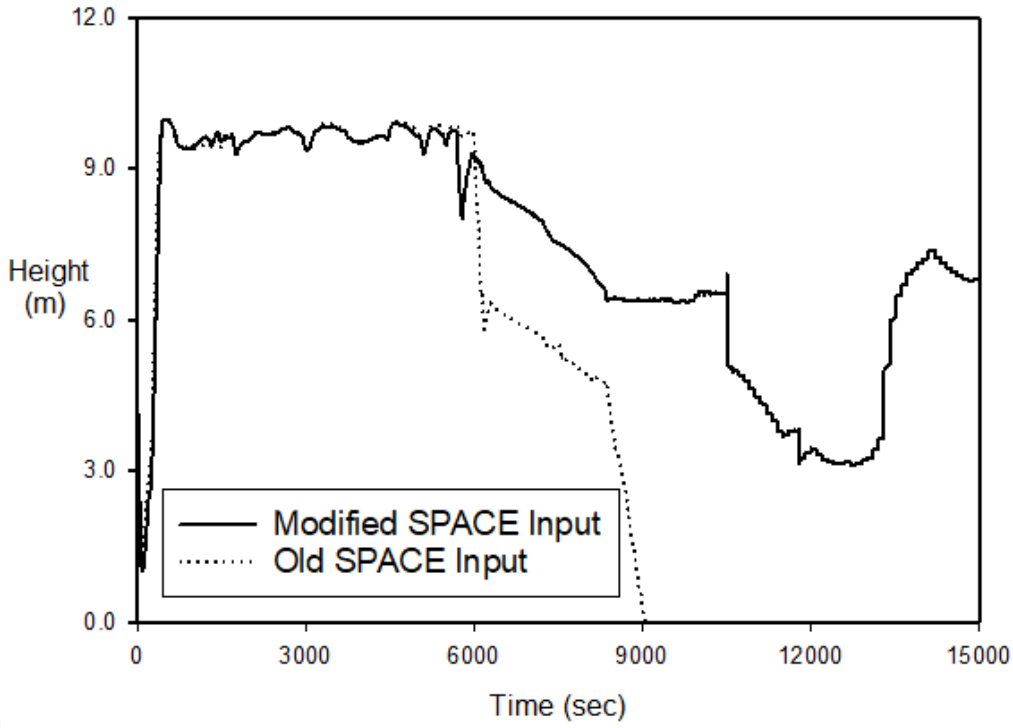

Measured Data and SCDAP/RELAP5 Results

CINEMA Results

Pressurizer Pressure

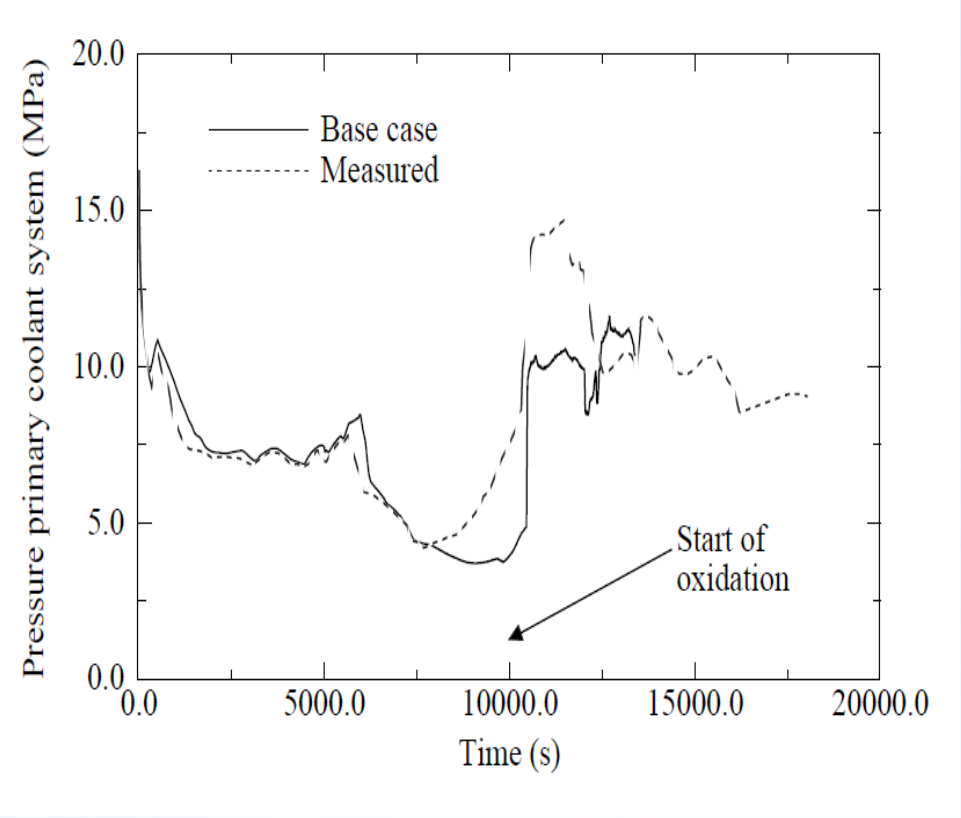

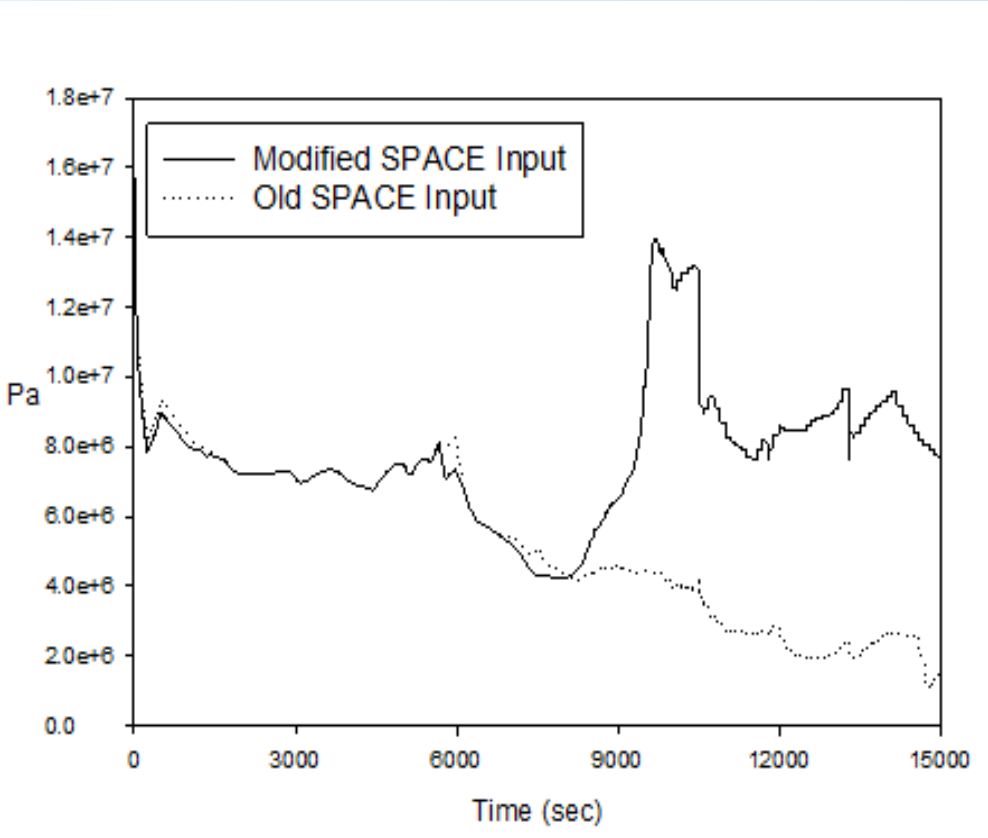

Measured Data and SCDAP/RELAP5 Results

CINEMA Results

Fuel Cladding Temperature

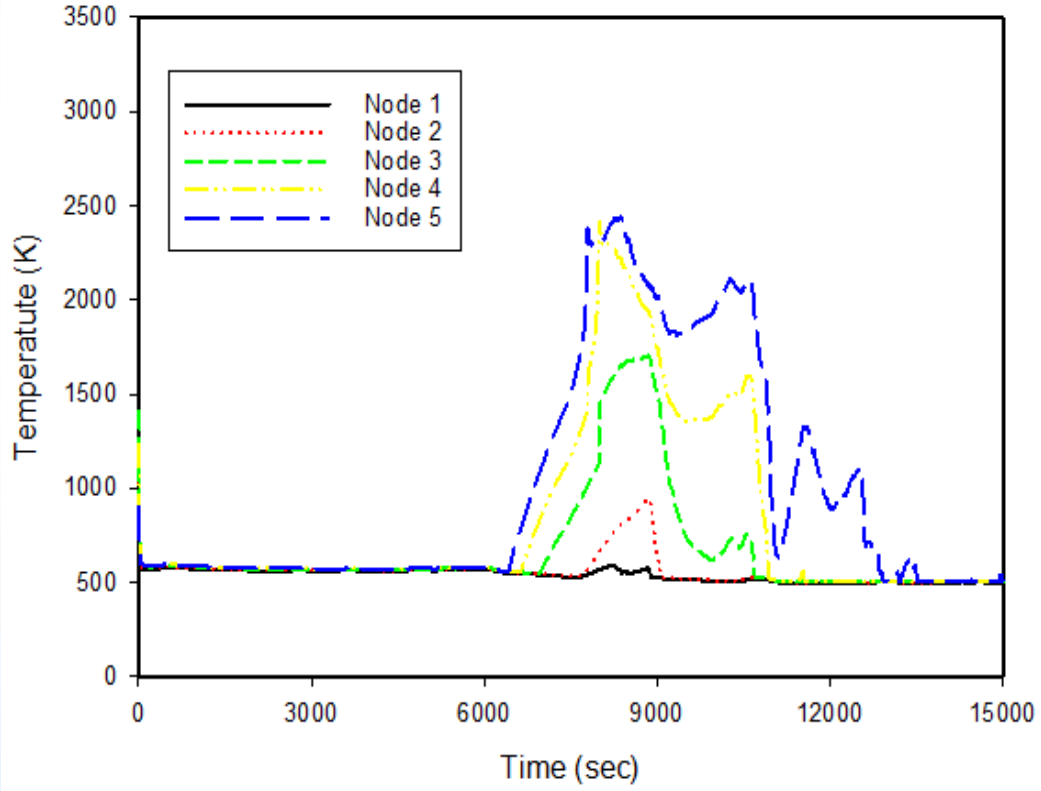

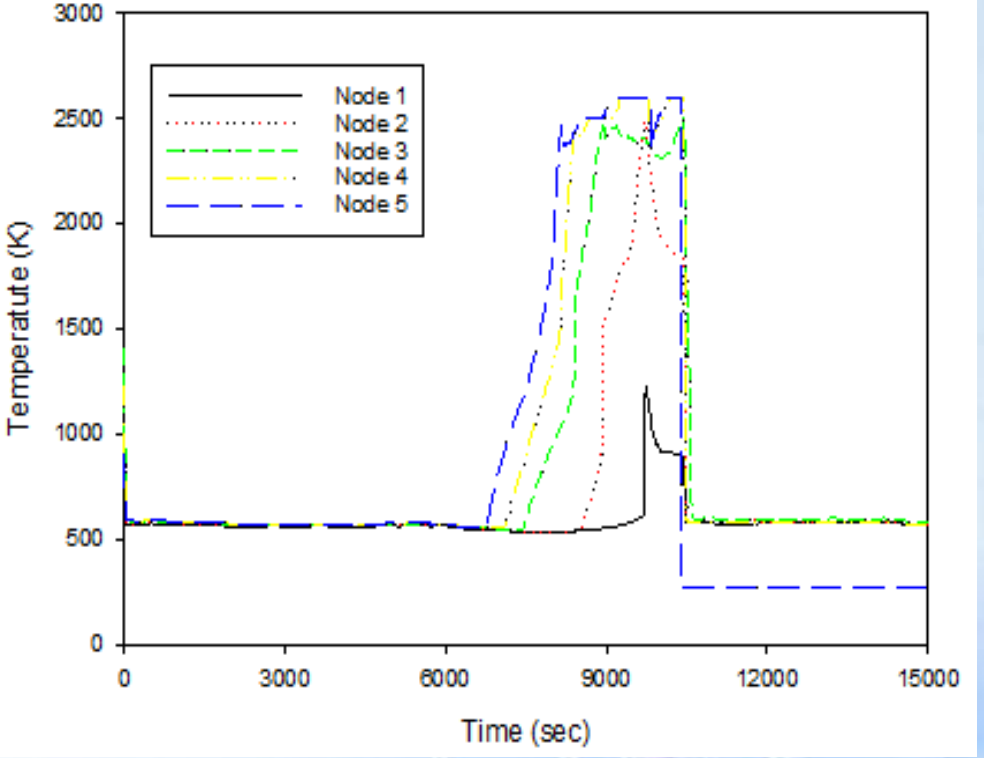

CINEMA Results on Weak CCFL in Pressurizer Surge Line

CINEMA Results on Strong CCFL in Pressurizer Surge Line

Fuel Cladding Mass Distribution

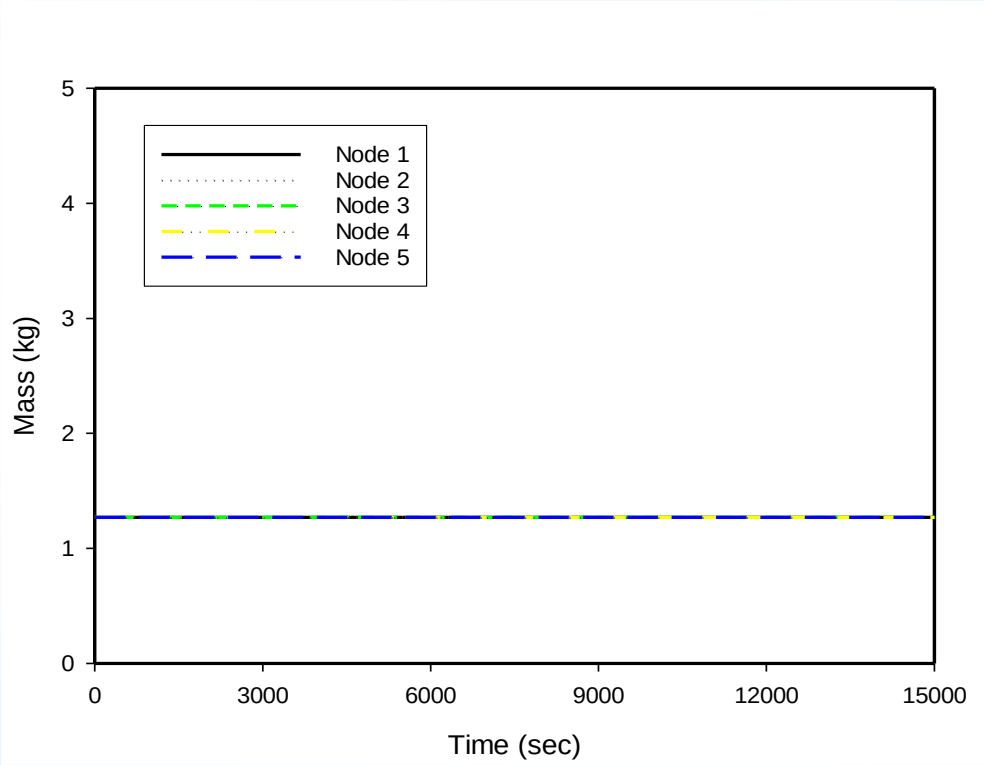

CINEMA Results on Weak CCFL in Pressurizer Surge Line

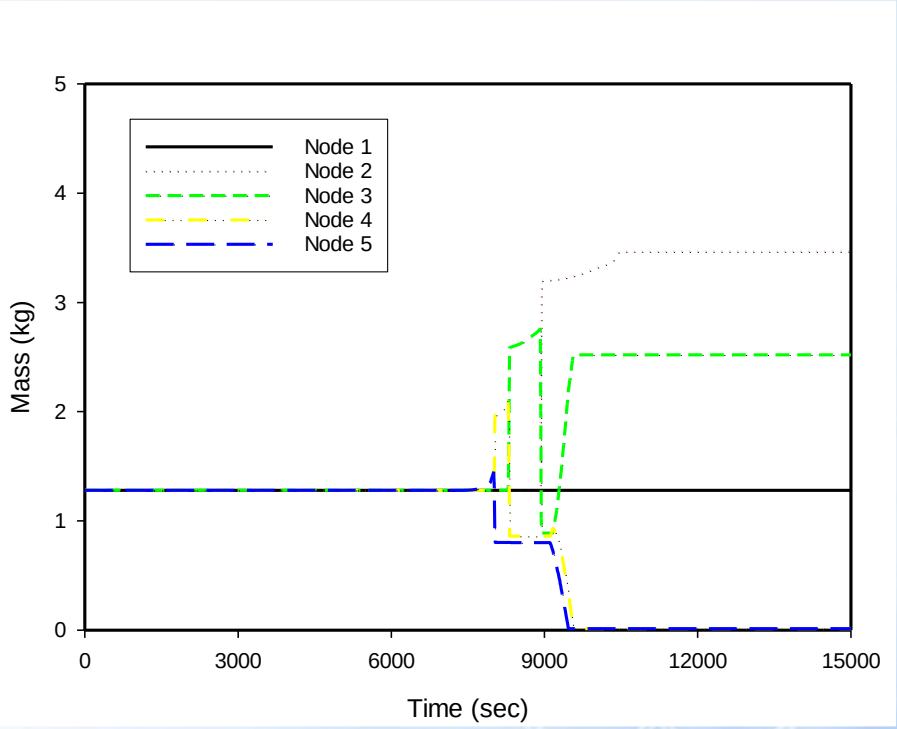

CINEMA Results on Strong CCFL in Pressurizer Surge Line

Comparison of CINEMA Results with TMI-2 Data

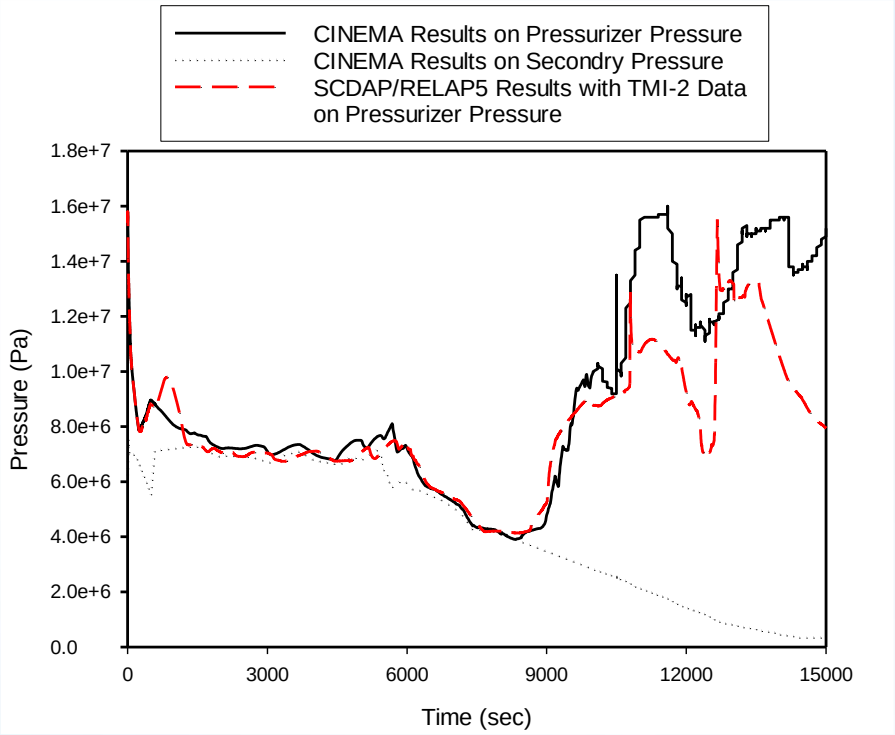

Pressure History

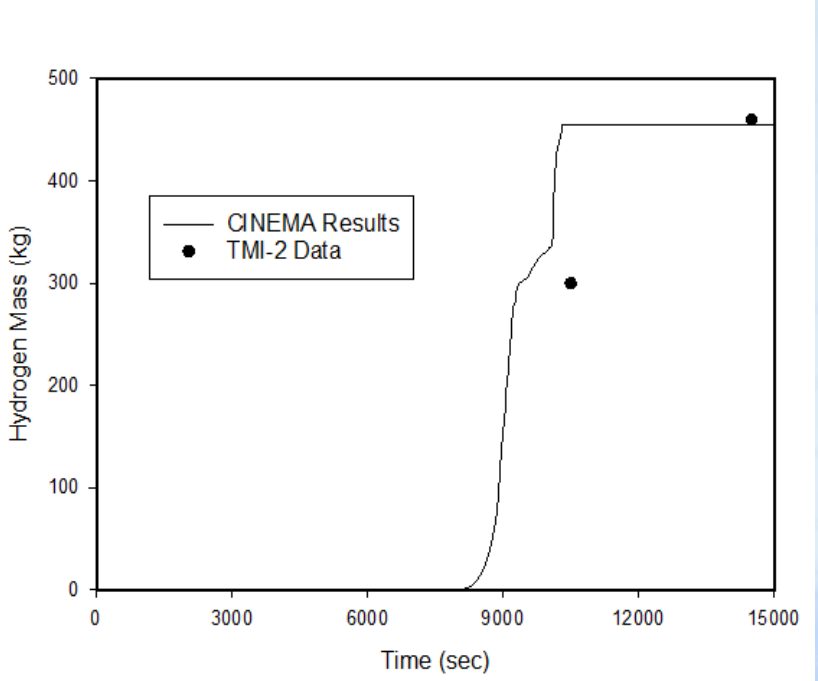

Hydrogen Generation Mass

Conclusions

- The surge line flow modeling effect on the core melt progression in the TMI-2 severe accident was analyzed using the CINEMA.
- The CCFL input parameters in CINEMA affect the pressurizer water drain to the core through the pressurizer surge line.
- The CINEMA results on strong CCFL model are very similar to the TMI-2 data in general.
- More CINEMA analysis for a melted fuel relocation and quenching process in the core and lower plenum are necessary to simulate the late phase of the TMI-2 severe accident.



Thank You!

KAERI 중대사고 · 중수로안전연구부
SEVERE ACCIDENT AND PHWR SAFETY RESEARCH DIVISION



ANALYSIS OF LOCA ACCIDENT FOR BWR-4 UNDER DEC-A CONDITIONS USING ASTEC CODE

Tadas Kaliatka, Tomas Kacegavicius, Mantas Povilaitis and Algirdas Kaliatka
Lithuanian Energy Institute
Breslaujos st. 3, LT-44403 Kaunas
Tadas.Kaliatka@lei.lt; Tomas.Kacegavicius@lei.lt; Mantas.Povilaitis@lei.lt;
Algirdas.Kaliatka@lei.lt

ABSTRACT

Significant research and development efforts have been paid in the last 3 decades on the analysis of the initiating events (especially with the loss of coolant (LOCA)) leading to the release of fission products to the environment. The experience shows that the most important factor for the analysis is determination of the source term. In 2019, the EU launched the "Reduction of Radiological Consequences of design basis and extension Accidents" (R2CA) project. The Lithuanian Energy Institute is taking part in this project as well.
In this article, simulation results (as the part of R2CA project) of the LOCA accident in a BWR-4 type reactor under Design Extended Conditions without significant fuel degradation (DEC-A) are presented. The DEC-A conditions and scenario were agreed upon with the R2CA partners. For this scenario, only Low Pressure Coolant Injection and Containment Spray System were available for the mitigation of the accident. In this accident scenario, the core was fully uncovered and the maximal temperature of the fuel rod claddings reached 1100 K. This caused damage of the fuel rod claddings, ~55% of the total core fuel rods were damaged. Fission products were released from the gaps (between pellet and cladding) of the damaged fuel rods to the cooling circuit and then to the containment. The analysis of results indicates that the containment integrity was preserved. The fission product release to the environment only due to the containment design leakages was evaluated. Calculation results showed a slow, but constant increase of the activity in the environment, depending on pressure evolution inside the containment.
Additionally, it was decided to make a parametric analysis of the ASTEC code oxidation parameters: zirconium oxidation physical laws (Cathcart, Urbanic, Prater), the start of oxidation temperature, maximal hoop creep allowed before burst and axial extension of the cracking after the clad burst. This was done to investigate parameters that influence the cladding burst time, total hydrogen generation and fission product release. The analyzed parameters showed a small effect on the cladding burst time (time difference less than 10 s). However, it showed significant influence by increasing hydrogen generation and the fission product release.

KEYWORDS
ASTEC, DEC-A, BWR-4, LOCA, fission product release

1. INTRODUCTION

The behaviour of nuclear power plants during Beyond Design Basic Accidents (BDBA), have been widely studied all over the world for several decades. Numerous experimental campaigns were provided to investigate the main physical phenomenon occurring in the case of the BDBA. Together with provided experiments, the simulation tools have been developed to consider the complexity of BDBA including thermal-hydraulics, thermo-mechanical and chemical processes as well as the possibility of evaluating the fission product releases and transport in the reactor cooling circuit, containment and potentially to the

environment. Simulation tools were validated against the provided experimental data. These simulation tools have been currently used for safety analyses, to check the compliance of the safety features of a power plant with the safety requirements and increase the predictability of BDBA progression.
The R2CA (Reduction of Radiological Consequences of design basis and design extension Accidents) launched in 2019 is a four-year HORIZON-2020 project. The reduction of the real radiological source term of the main Design Basic Accident (DBA) as well as for BDBA has not been fully studied. There is a clear need to propose new accident management strategies and evolutions of reactor designs to reduce radiological source term in DBA and Design Extended Conditions without significant fuel degradation (DEC-A) conditions. The ambition of the project is to provide knowledge and numerical tools that will allow a less conservative evaluation of safety margins and provide recommendations for a reduction of radiological consequences of DBA and DEC-A situations. R2CA project consists of several stages. The first stages are dedicated to the review of the existing methodologies, simulation tools and database. Also, during the first part of the project, the reactor case simulations with existing simulation tools and best practice methodologies are provided. Results of these simulations identify foreseen improvements in modelling approaches and models implemented in the simulation tools. During the next project steps, it is planned to realise these improvements and perform reactor case simulations again in order to compare obtained results.
Lithuanian Energy Institute (LEI) is taking part in R2CA project as well. At this stage of the project, LEI provided reactor case simulations (presented in this article). Continuing project work LEI will improve the ASTEC modelling approaches and perform more detailed fuel rod analysis with TRANSURANUS code to obtain a more realistic status of the fuel and more precise evaluation of possible radiological consequences.
LEI has performed the simulation of the Loss Of Coolant Accident (LOCA) in a generic BWR-4 reactor under the DEC-A conditions using integral DBA and BDBA code ASTEC (Section 2). In this analysis, LEI assumed the guillotine break of the main recirculation pipe for BWR-4 with delayed (due to the shortage of electricity and some delay start of diesel generators) activation of Emergency Core Cooling System (ECCS). An additional assumption was made for the simulation that only Low Pressure Cooling Injection (LPCI) system is available from all ECCS. The containment spray system was also available in this selected scenario. These DEC-A conditions and scenario were agreed upon with the R2CA partners.
The calculation results received by LEI of this accident scenario are presented in Section 3. Additionally, it was decided to make a parametric sensitivity analysis of this simulation (Section 4). In this analysis, the zirconium oxidation physical laws (CATHCART, URBANIC, PRATER), the start of oxidation temperature, maximal hoop creep allowed before burst and axial extension of the cracking after clad burst were evaluated for the first 1000 s of transient calculation. This was done to investigate parameters that influence the cladding burst time, total hydrogen generation and fission product release.

2. MAIN BWR-4 MODELLING ASSUMPTIONS AND MODEL FOR ASTEC CODE

The considered reactor is a generic Boiling Water Reactor (BWR) of class 4. The analyzed reactor has Mark I containment. This type of reactor and containment was constructed in Fukushima Daiichi NPP. This reactor has two recirculation loops. The thermal power of the reactor is 2381 MW. It was assumed that before the accident reactor was operated at full power.
To identify the initial inventory of the fuel, it was decided to make calculations with SCALE program. Average values of the average burnup (26 MWdays/tonUO2) were extracted from BWR fuel bundle (ATRIUM-10). ATRIUM-10 is the modern 10×10 BWR design fuel assembly, with a large internal water channel. The numerical model of the assembly was compiled by using data from a Nuclear Energy Agency BWR-MOX benchmark [4].
Decay heat power is a very important parameter, especially for thermal-hydraulic simulations. For the performed calculations it was decided to use ANS-5.1 decay heat curve [5].
Fuel assemblies load pattern and power history of each region were assumed according to the reference 6. According to that information relative horizontal distribution for the quarter of reactor have been simulated (Figure 1 a)). The axial power distribution was selected according to the literature [6] (**Error! Reference source not found.**) and was applied for all concentric rings (Figure 1 b)).

Due to the peculiarities of modelling, the reactor zone had to be divided into several concentric rings. In this calculation it was decided to use 4 concentric rings, containing 4, 80, 224 and 240 fuel assemblies respectively. Different rings of fuel assemblies are presented with different colours in Figure 1 a. According to this information the radial power distribution was calculated and presented in Table I.

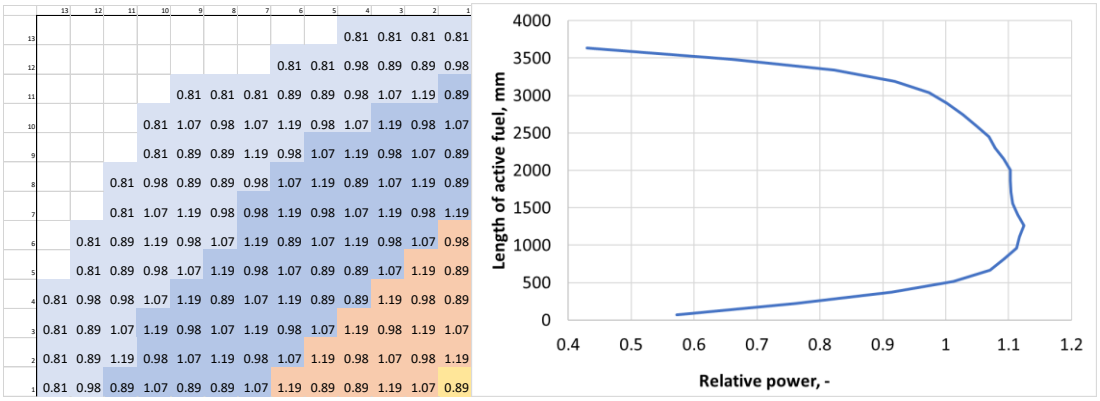

a) b)

Figure 1. Relative power distribution: a) horizontal (quarter of reactor zone) b) vertical (axial)

Table I. Radial power distribution through the rings

Ring	Number of fuel assemblies	Number of control rods	WEIGHT FACTOR
1	4	1	0.890
2	80	20	1.066
3	224	56	1.043
4	240	60	0.943

According to the selected LOCA scenario, only LPCI system is available. Moreover, system triggering points are different compared to the normal system operation. Due to the assumed Loss Of Off-site Power (LOOP) accident LPCI system started at t=100 s after the accident. LPCI injection was switched off when the water level in the core downcomer reached aboveTop of Active Fuel (TAF) ≥ 5.24 m or pressure in the steam separator component ≤ (6.9 x10^5 Pa).

The LPCI system injects emergency core cooling water into the recirculation loop discharge piping between the discharge valve and reactor vessel. The recirculation system suction and discharge valves are motor-operated valves used to isolate the recirculation pumps for maintenance. Each valve is individually controlled from the control room by a hand switch. In the simulations, an assumption was made that power plant operators do not take any actions, so the suction and discharge valves during the accident stay open. However, both recirculation loop discharge valves receive an automatic close signal upon the LPCI initiation and low reactor pressure to ensure water introduction into the core.

Injected water flow rate from the LPCI system to the reactor pressure vessel strongly depends on the pressure in Reactor Pressure Vessel (RPV) [7], when the pressure in the RPV is decreasing the flow rate is increasing. However, in the calculation, it was assumed a constant 300kg/s mass flow rate.

The integral code ASTEC (Accident Source Term Evaluation Code) version V2.1.1.6 was used for the simulations. ASTEC is an integral code for light water reactors capable to analyse a wide range of processes and physical phenomena, from the initiating event until radioactive release out of the containment [1]. The main physical phenomena are validated in more than 20 applications on experiments (validation test-cases), in more than 26 operational test-cases and 16 plant application test-cases. ASTEC code consists of several modules, which are developed for the analysis of separate tasks.

The ASTEC model of the generic BWR-4 type reactor with MARK I containment developed in the frame of the CESAM project [2] was selected as a basis for the LOCA analysis. However, to perform the analysis of the LOCA scenario corresponding to DEC-A conditions several changes had to be implemented in the

model (for example reactor recirculation loop, containment design leakages, different LPCI system activation logic, etc.).
The following ASTEC modules were activated in the performed simulations: CESAR, ICARE, MEDICIS, RUPUICUV, CORIUM, CPA, ISODOP, DOSE, SOPHAEROS, SYSINT.
The reactor pressure vessel section defined in the ASTEC module ICARE input consists of two parts, a cylindrical part containing the core, downcomer and jet pump and a hemispherical part simulating the lower plenum Figure 2. The upper plenum with the steam separator is defined in the CESAR module.
The reactor core, downcomer and jet pump are modelled using ICARE module. The reactor core is divided into 4 rings, and 12 meshes in the axial direction, plus a separate volume of the lower plenum.
The Nodalization scheme of the primary and secondary loops are shown in Figure 3. The two recirculation loops (volumes JET_L11, JET_L11A, JET_L12, JET_L13, JET_L21, JET_L22, JET_L23), junctions between these volumes, and separator, upper head, main steam lines, feedwater lines and downcomer top are modelled with CESAR module. Two pumps RCP_1 and RCP_2 providing water flow in the recirculation lines are modelled (see Figure 3). For the modelling of the main circulation pipe, guillotine break two connections LOCA and LOCA1 between recirculation loops and containment (zone Drywell) were added (see Figure 3).
BWR containment is modelled using CPA module by 15 zones, heat structures connected to the zones, atmospheric and liquid junctions between them, and valves and pumps. For the modelling of design leakage from the containment to the environment, an additional connection "DRENV" was added, see Figure 4. Sprays systems of the drywell and wetwell zones are activated by logic considering temperature and pressure in drywell and wetwell.

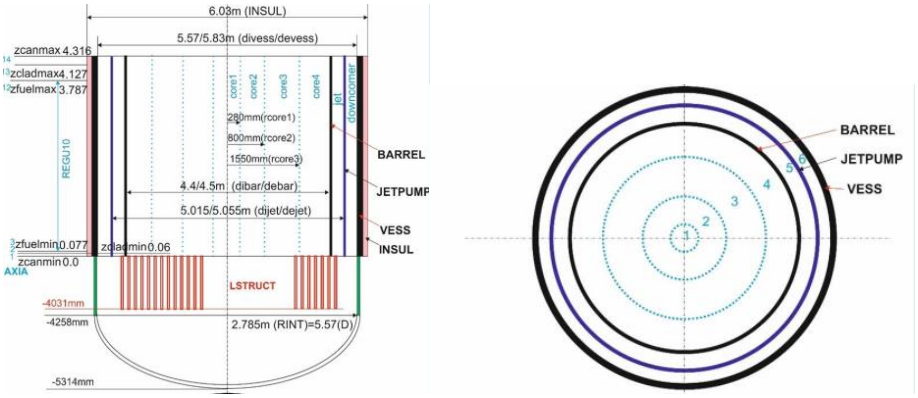

Figure 2. Sketch of the pressure vessel (top and side view) [1].

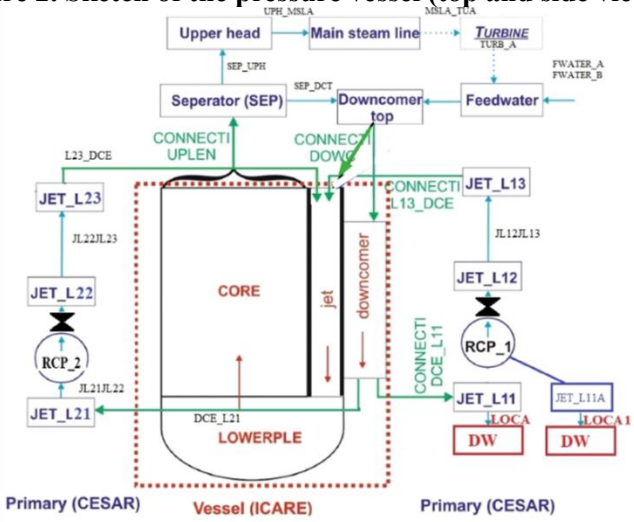

Figure 3. ASTEC nodalization scheme of the primary and secondary circuits

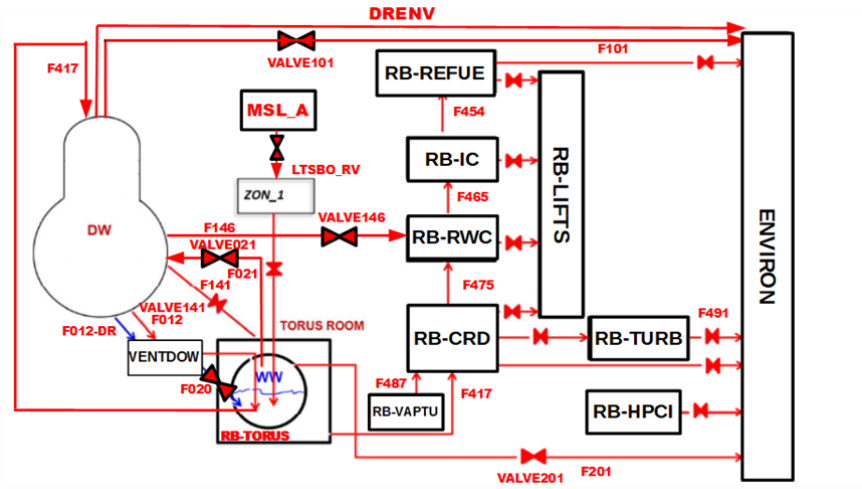

Figure 4. ASTEC nodalization scheme of the BWR4-Mark I containment

3. CALCULATION RESULTS OF LOCA SCENARIO

For the LOCA it was considered that a guillotine break at the main circulation pipe takes place close to the suction side of the pump at t=0 s. This event is combined with LOOP. Feedwater injection was terminated 5s after the start of the accident. Within 1 sec from the power outage, auxiliary batteries and compressed air supplies are starting the Emergency Diesel Generators. Electrical power is restored after 25 s.
Additionally, in the analysis it was assumed that all ECCS systems except LPCI system are not available. Water from LPCI system to the core zone was injected through the intact recirculation loop at 100 s. Drywell and wetwell sprays started 20 s after the power was restored, 45 s after the accident. Chronology of the main events of the LOCA transient calculation is given in Table II.

Table II. Main events of the LOCA transient

Time, s	Event
T= 0	Large break (guillotine break of the main circulation pipe) take place close to the suction side of the pump. Loss of offsite power. SCRAM signal initiated.
T=1	Auxiliary batteries and compressed air supplies are starting the emergency diesel generators. RCIC, HPCI systems failed to start.
T=5	Feedwater injection to the reactor stopped. Main steam lines closed. Junction changes: Closed: “Downcomer Top” to “Downcomer” Opened: “Downcomer Top” to “Jet”
T=25	Insite electrical power is restored
T=45	Activation of wetwell and drywell spray
T=82	Dry out of fuel assemblies
T=100	LPCI system starts injecting water to the core zone through the intact recirculation loop.

Time, s	Event
	According to the LPCI procedure the discharge valves close as part of the automatic initiation sequence for the (LPCI) mode of the RHR system to provide an emergency core cooling water flow path to the reactor vessel. Junction changes: Opened: "Downcomer Top" to "Downcomer"
T=280	Junction changes: Opened: "Downcomer Top" to "Jet_L11" Closed: "Downcomer Top" to "Downcomer"
T=338	Maximal temperature (1100 K) reached in fuel bundles
T=348	Water injected by LPCI system reaches the lower part of the active fuel.
T=358	Rupture of the first group of fuel assemblies (ring 2, 80 FA)
T=419	Rupture of the second group of fuel assemblies (ring 3, 224 FA)
T= 550	The water level in the RPV restored

The mass flow rate through the main recirculation pipe break is presented in Figure 5. During the first seconds after the accident mass flow rate reaches ~16000 kg/s, but it sharply decreases and after 120 s mass flow is close to 0 kg/s. This situation occurs due to the sudden pressure decrease in the recirculation loop and sudden pressure increase in the containment Figure 6 a), and water inventory decrease caused by the break (Figure 6). The water level in the core region and void fraction in the lower plenum (Figure 6 b) and c)) give the impression of the reactor water inventory loss. According to the received results only ~40% of water is left in the lower plenum in 100 s after the accident. At this time LPCI system is activated and this, together with decreased pressure, stops the further increase of the void fraction in the lower plenum. The activated LPCI system is injecting a constant 300 kg/s flow rate until the core region is filled. Further LPCI system work is restricted to maintain the water level in the core region.
Mass flow through the break increased again when the water injected by LPCI system reached the lower part of the active fuel (Figure 5, Figure 6 b), c)). Cold injected water contacts with hot surfaces in the bottom of the core region – steam is generated and released from the break, this also slightly increases pressure in the recirculation loop (Figure 6 a)).

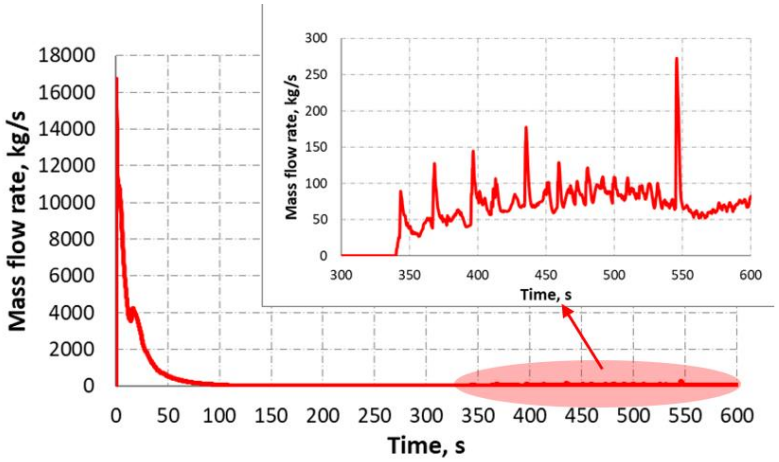

Figure 5. The mass flow rate through the break

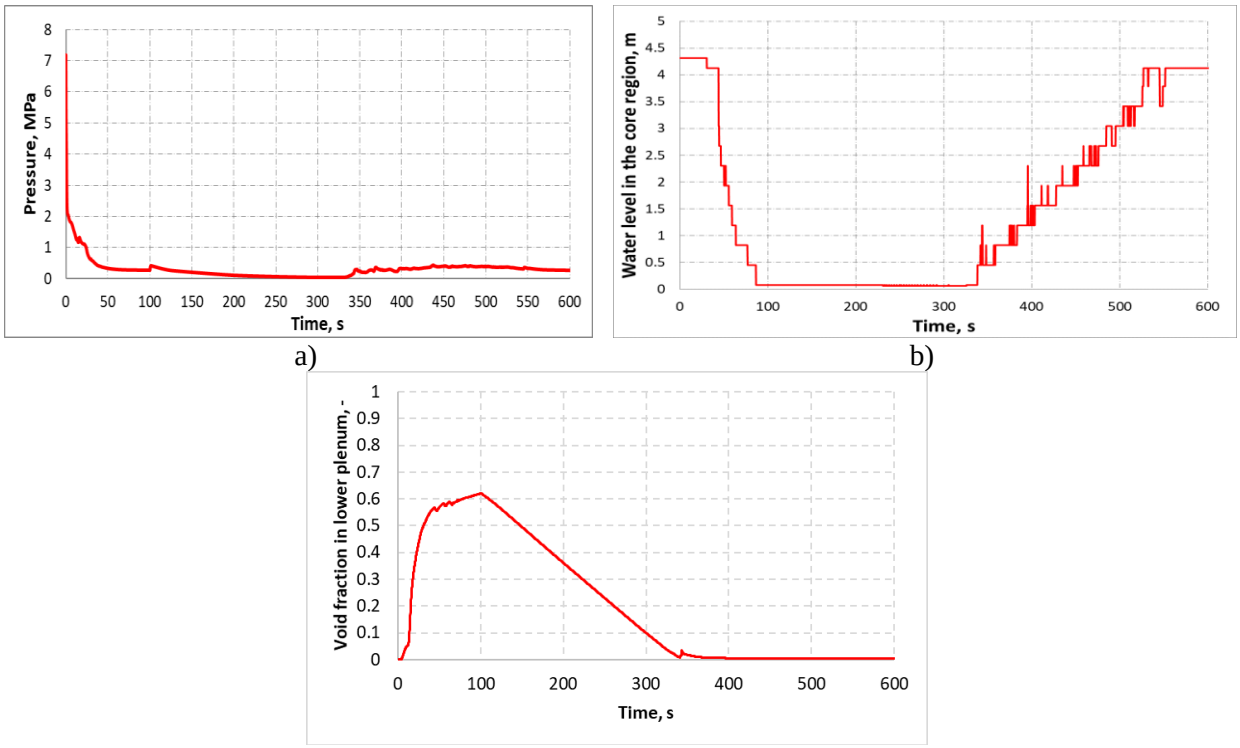

a) b)

c)

Figure 6. Calculation results: a) Pressure in the broken recirculation loop; b) Water level in the core region, from the bottom; c) Void fraction in the lower plenum

During the first seconds of the accident, the pressure in the containment is increasing up to 0.3 MPa. The containment spray system activates 45 s after the break and it helps to decrease the pressure to slightly higher than atmospheric (Figure 7 a)). However, when the core re-fill due to injection of the LPCI system - the steam and hydrogen is generated, pressure in the containment increases again and only after 1000 s stabilizes to ~0.15 MPa pressure. Containment design leakage is 0.5% of vol/day. However, with an increase of pressure in the containment, the mass flow rate from the containment to the environment is also increasing (Figure 7 b)). The maximum obtained flow rate from the containment to the environment is 0.0006 kg/s, after the stabilization of the pressure in containment (1000 s) flow rate stabilizes at ~0.00025 kg/s.

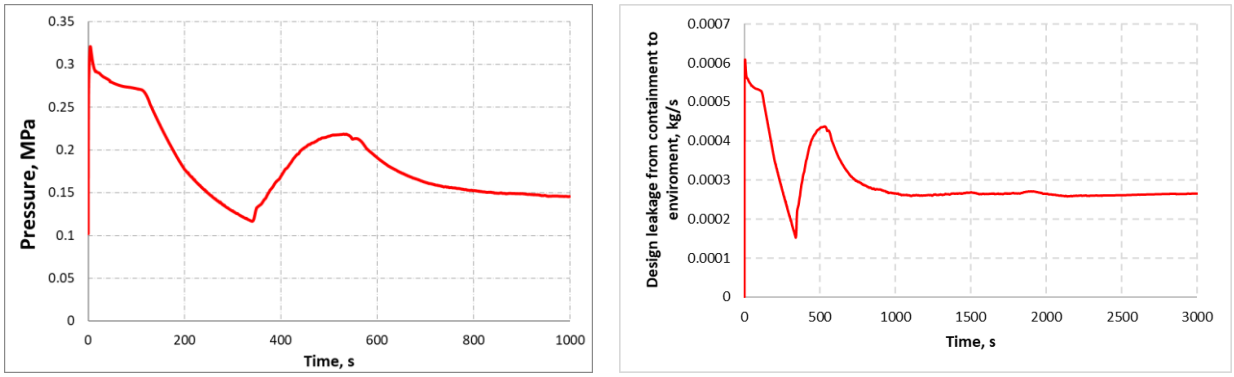

a) b)

Figure 7. Calculation results: a) pressure in the containment; b) flow rate from the containment to environment

Number of failed fuel rods, time and elevation of failure is presented in Table III. As it was mentioned before, the whole active zone is modelled using 4 concentric rings. The first failure of fuel rods cladding due to the ballooning occurs in the second ring with 80 fuel assemblies, second failure in the third ring with 240 fuel assemblies. Other rings do not fail. In total, ~55% of all active zone failed in the simulated scenario.

Table III. Number of failed fuel rods, time, and elevation of failure

	Number of the failed fuel assemblies	Cladding failure time, s	Cladding failure elevation from the bottom of active fuel, m
Failure of the 2nd ring	80	358 s	Between 1.932 ÷ 2.303
Failure of the 3rd ring	240	419 s	Between 1.932 ÷ 2.303
Total:	320		

Peak cladding temperature in 4 concentric rings of the core is presented in Figure 8. Maximum temperature ~1100 K is reached in the second ring, very similar temperatures are observed also in the third ring. The temperature in all rings starts to decrease when injected water from the LPCI system reaches the core zone (~350 s after the transient).

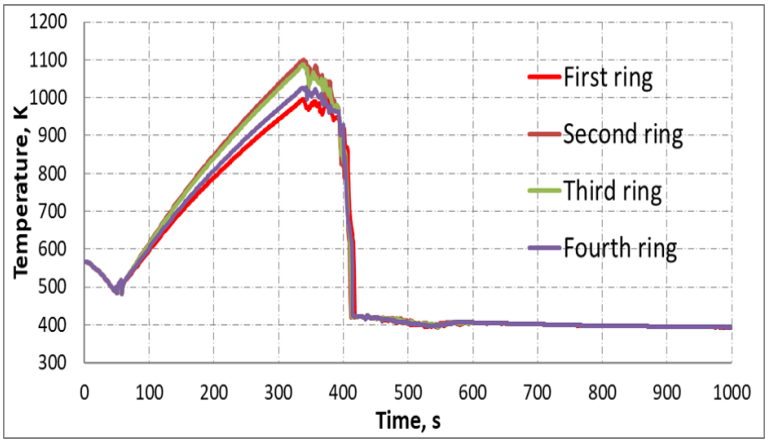

Figure 8. Peak cladding temperature in 4 concentric rings

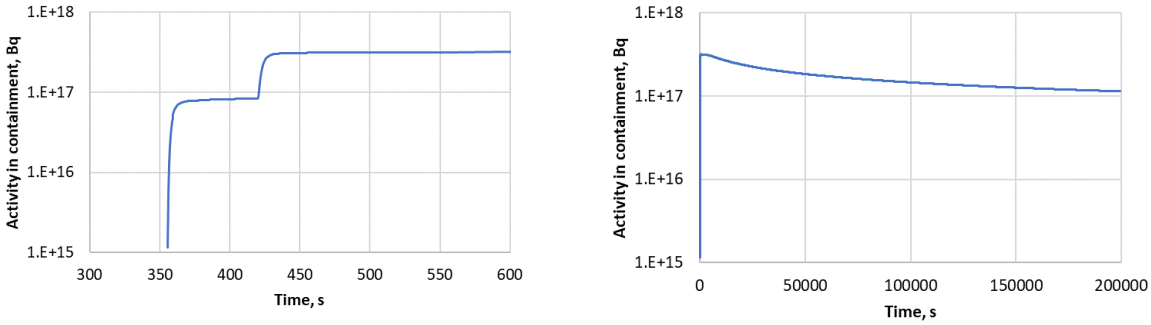

(a) (b)

Figure 9. Activity in containment

According to the analysis, the ruptures of the second and third concentric rings start at 358 and 419 s respectively. Fission products from the gap between the pellets and claddings of the ruptured assemblies are spread in the RPV and through the break reach containment. Some of the fission products are retained in the broken cooling circuit and RPV. Activity in the containment is presented in Figure 9. Figure 9 a) shows

two peaks of activity increase which are related to the burst of the claddings in the second and third concentric rings of fuel rods. Fuel melting situation was not achieved, due to the activation of the LPCI system the fuel temperatures decreased. At time ~550 s the water level in the RPV was restored. This stopped discharge of fission products and activity in the containment did not increase further. Due to the containment design leakage small fraction of fission products leaked from the containment to the environment. This caused an activity decrease in the containment and an increase in the environment (Figure 10). 200000 s after the accident it was decided to stop calculation because the flow rate through the design leakages to the environment is stable and it gives linear activity increase in the environment.

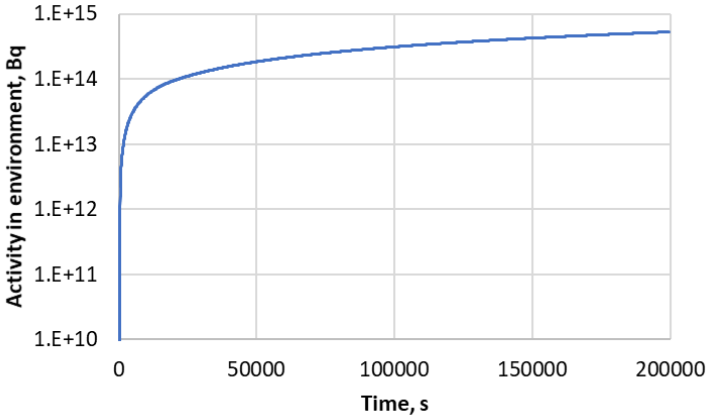

Figure 10. Activity in environment

4. SENSITIVITY ANALYSIS

The sensitivity analysis was performed to evaluate several ASTEC parameters (related to oxidation and burst of the claddings) impact on fuel rod failure time, hydrogen generation, and then on source term prediction. In total 6 calculations were provided. In each calculation case only one parameter was changed (Table IV). Sensitivity was studied for: zirconium oxidation physical laws (Cathcart, Urbanic, Prater), the minimum temperature to start the reaction of oxidation, maximal hoop creep allowed before burst and axial extension of the cracking after the clad burst.

Table IV. Different parameters for the sensitivity analysis

Case 0	Basic	Zirconium oxidation physical law – BEST-FIT TBEG (minimum temperature to start the reaction of oxidation) – 700 K Burst parameters: EPMX 0.25; CRAC 0.50.
Case 1	CATHCART	Zirconium oxidation physical law – CATHCART
Case 2	URBANIC	Zirconium oxidation physical law – URBANIC
Case 3	PRATER	Zirconium oxidation physical law – PRATER
Case 4	TBEG	TBEG (minimum temperature to start the reaction of oxidation) – 600 K
Case 5	EPMX	EPMX (maximal hoop creep allowed before burst – 0.4 (standard value according to manual)
Case 6	CRAC	CRAC (axial extension of the cracking after the clad burst) – 0.0 (standard value according to manual)

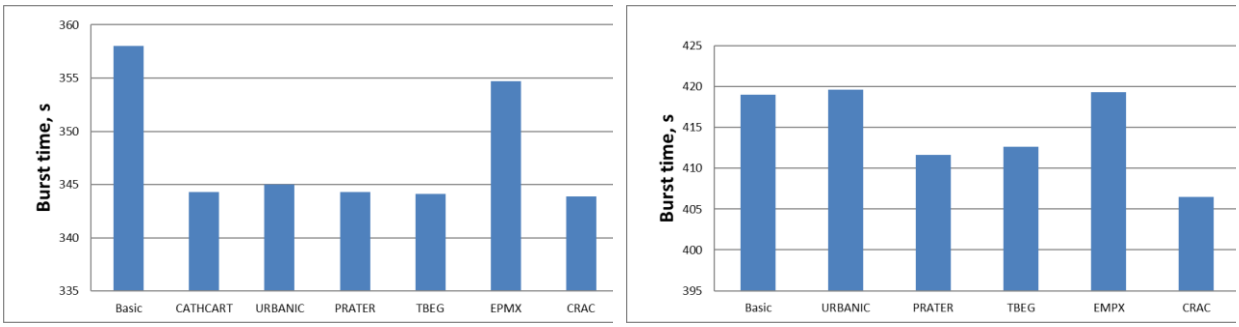

(a) (b)

Figure 11. Cladding burst time: a) the second ring, b) the third ring

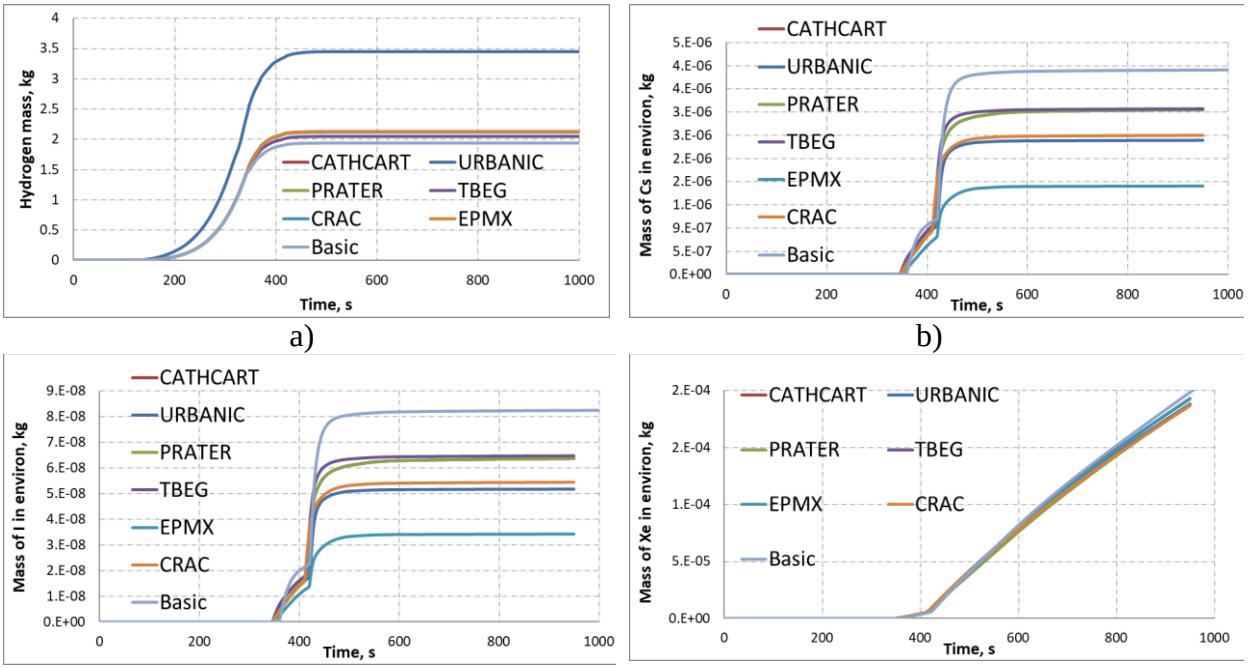

a) b)

c) d)

Figure 12. Calculation results: a) hydrogen generation, b) Cs mass released to the environment, c) I mass released to the environment, d) Xe mass release to the environment

The result of provided sensitivity analysis showed that parameters have a small effect on the cladding burst time (Figure 11). Time differences are less than 10 s. The latest burst time was achieved using a standard value according to the manual for the EPMX parameter. However, analyzing hydrogen generation and the fission product release, a significant influence was observed (Figure 12 a)). Using URBANIC zirconium oxidation physical law the highest amount of total hydrogen was calculated. The result was ~60% higher compared to other calculation results. Using PRATER zirconium oxidation physical law and changing TBEG a higher fission product release in the environment was achieved (Figure 12 b), c) d)). However, for the gaseous fission products the difference is minimal (Figure 12 d)).

5. CONCLUSIONS

In this article the LOCA event at DEC-A conditions for generic BWR-4 type reactor was analysed using ASTEC code. Analysis results showed:

- During the initial phase of LOCA the fuel temperature is increasing, but later decreasing due to activation of core cooling systems. Core uncover was reached 90 s after beginning of the accident and maximal temperature of the fuel rod claddings reached 1100 K at t = 330 s.

- The cladding of fuel rods in second and third concentric rings burst at t = 358 s and 419 s respectably. This corresponds to ~55% of the total core fuel claddings.
- Fission products were released from the gap (between pellet and cladding) of the burst fuel claddings to the cooling circuit and then transported to the containment and through containment design leakages to environment.
- The total activity in the environment at the end of calculation (200000 s after beginning of the accident) reached ~8e+14 Bq.

The sensitivity analysis of ASTEC parameters related to oxidation and burst of the claddings were evaluated:

- All nalysed parameters have an insignificant effect on the cladding burst time (difference <10 s).
- Using URBANIC zirconium oxidation physical law the highest amount (~60% higher compared to other results) of total generated hydrogen was calculated.
- Parameter indicating the minimum temperature to start the reaction of oxidation (TBEG) have a significant influence on fission product release calculations, especially for Zs and I. However, for the gaseous fission products (for example Xe) the difference is minimal.

In this article presented work is related to the R2CA project taks dedicated to reactor case simulations. Futher step is to verify ASTEC calculation results using specific analysis tool like TRANSURANUS and to evaluate more precisely possible cladding burst during analyced LOCA scenario. At the last step of R2CA project the another calculation using ASTEC for the same scenario will be provided taken in to account received experience (results of sensitivity analysis, sepific analysis tool, ect.).

ACKNOWLEDGMENTS

This project has received funding from the Euratom research and training programme 2014-2018 under grant agreement No 847656.

REFERENCES

1. P. Chatelard, N. Reinke, S. Arndt, S. Belon, L. Cantrel, L. Carenini, et al., ASTEC V2 severe accident integral code main features, current V2.0 modelling status, perspectives, Nucl. Eng. Des. 272, 2014, pp. 119-135.
2. M. Vela-Garcia, V. Matuzas, D. Krönung, R. Iglesias, V. Vileiniskis, A. Nieminen, S. Hermsmeyer, N. Reinke, H. Nowack, J. Fontanet, L. Herranz, "Documentation for BWR ASTEC generic input deck" CESAM FP7-GA 323264, 24/02/2017
3. S. Wang, H. Muscher, ASTEC-Team at KIT., “Preliminary Analysis of a BWR SBO SA-Sequence with ASTEC2.1rev3”. 8th ASTEC Users Club meeting, Aix-en-Provence, F, October 8-11, 2018
4. OECD/NEA (2003), Physics of Plutonium Recycling: Volume VII: BWR MOX Benchmark - Specification and Results, Nuclear Science, OECD Publishing, Paris, https://doi.org/10.1787/9789264299054-en.
5. ANS, 1973. ANS-5.1 1973 Decay Energy Release Rates Following Shutdown of Uranium-Fueled Thermal Reactors, Draft ANS-5.1 / N18.6, October 1973
6. Keisuke OKUMURA, Kensuke KOJIMA, Tsutomu OKAMOTO, Hiroyuki HAGURA, Kenya SUYAM, “Nuclear Data for Severe Accident Analysis and Decommissioning of Nuclear Power Plant”, Proceedings of the 2012 Symposium on Nuclear Data, November 15-16, 2012, Research Reactor Institute, Kyoto University, Kumatori, Japan.
7. NUREG-1230 R4, Compendium of ECCS Research for Realistic LOCA Analysis, final report, 1988

LITHUANIAN ENERGY INSTITUTE

ANALYSIS OF LOCA ACCIDENT FOR BWR-4 UNDER DEC-A CONDITIONS USING ASTEC CODE

Tadas Kaliatka, Tomas Kacegavicius, Mantas Povilaitis, Algirdas Kaliatka

ERMSAR2022, Karlsruhe, Germany, May 16-19, 2022

Content

- Introduction
- Main Modelling Assumptions
- LOCA Scenario
- ASTEC nodalization schemes
- Calculation results
- Sensitivity analysis
- Conclusions

Introduction

- Work is done in the frame of the R2CA (Reduction of Radiological Consequences of design basis and design extension Accidents) project.
- This work is related to the R2CA project task dedicated for reactor case simulations. Lithuanian Energy Institute (LEI) performed the simulation of the Loss Of Coolant Accident (LOCA) in a generic BWR-4 reactor under the DEC-A conditions using ASTEC code.
- Also, it was decided to make a parametric sensitivity analysis of this simulation. The zirconium oxidation physical laws (CATHCART, URBANIC, PRATER), the start of oxidation temperature, maximal hoop creep allowed before burst and axial extension of the cracking after clad burst were evaluated. This was done to investigate parameters that influence the cladding burst time, total hydrogen generation and fission product release.



Main Modelling Assumptions for BWR-4

- Initial inventory calculated with SCALE
- ATRIUM-10 (10×10) BWR design fuel assembly
- Average burnup 26MWdays/tonUO_2
- Decay heat power according to ANS-5.1 curve

	13	12	11	10	9	8	7	6	5	4	3	2	1
13										0.81	0.81	0.81	0.81
12								0.81	0.81	0.98	0.89	0.89	0.98
11					0.81	0.81	0.81	0.89	0.89	0.98	1.07	1.19	0.89
10				0.81	1.07	0.98	1.07	1.19	0.98	1.07	1.19	0.98	1.07
9				0.81	0.89	0.89	1.19	0.98	1.07	1.19	0.98	1.07	0.89
8			0.81	0.98	0.89	0.89	0.98	1.07	1.19	0.89	1.07	1.19	0.89
7			0.81	1.07	1.19	0.98	0.98	1.19	0.98	1.07	1.19	0.98	1.19
6		0.81	0.89	1.19	0.98	1.07	1.19	0.89	1.07	1.19	0.98	1.07	0.98
5		0.81	0.89	0.98	1.07	1.19	0.98	1.07	0.89	0.89	1.07	1.19	0.89
4	0.81	0.98	0.98	1.07	1.19	0.89	1.07	1.19	0.89	0.89	1.19	0.98	0.89
3	0.81	0.89	1.07	1.19	0.98	1.07	1.19	0.98	1.07	1.19	0.98	1.19	1.07
2	0.81	0.89	1.19	0.98	1.07	1.19	0.98	1.07	1.19	0.98	1.07	0.98	1.19
1	0.81	0.98	0.89	1.07	0.89	0.89	1.07	1.19	0.89	0.89	1.19	1.07	0.89

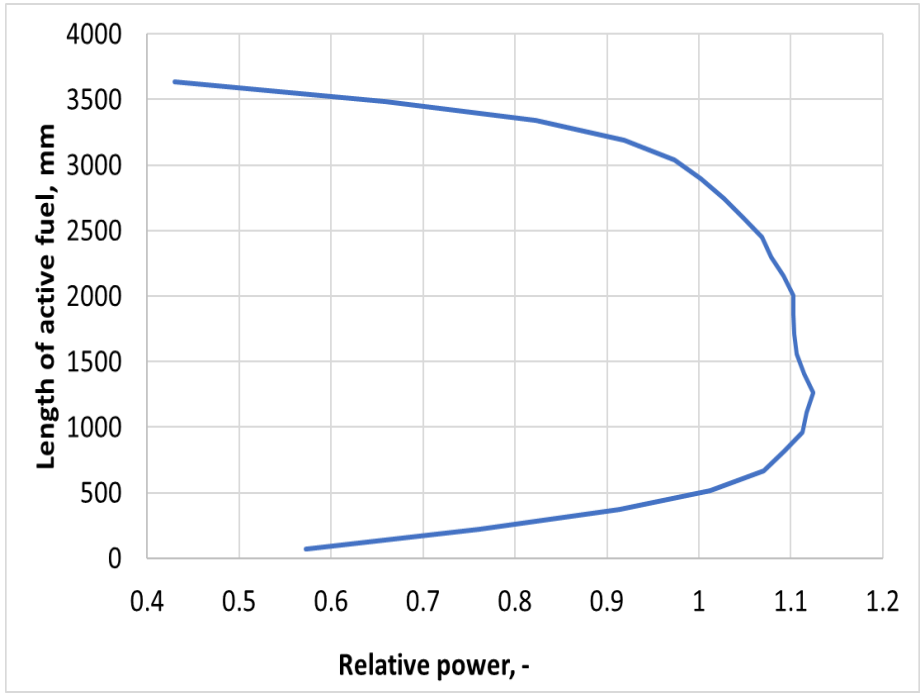

Relative power distribution

Ring	Number of fuel assemblies	Number of control rods	WEIGHT FACTOR
1	4	1	0.890
2	80	20	1.066
3	224	56	1.043
4	240	60	0.943

LOCA Scenario

- Guillotine break of the main recirculation pipe for BWR-4 with delayed (due to the shortage of electricity and some delay start of diesel generators) activation of Emergency Core Cooling System (ECCS).
- Only Low Pressure Cooling Injection (LPCI) system is available from all ECCS. LPCI system started at t=100 s after the accident. LPCI injection was switched off when the water level in the core downcomer reached above Top of Active Fuel ≥ 5.24 m or pressure in the steam separator component ≤ (6.9×10^5 Pa).
- Injected water flow rate from the LPCI system to the Reactor Pressure Vessel (RPV) strongly depends on the pressure in RPV, when the pressure in the RPV is decreasing the flow rate is increasing. In the calculation, it was assumed a constant 300 kg/s mass flow rate.
- The containment spray system was available in this selected scenario.
- Plant operators do not take any actions, so the suction and discharge valves during the accident stay open. However, both recirculation loop discharge valves receive an automatic close signal upon the LPCI initiation and low reactor pressure to ensure water introduction into the core.

ASTEC nodalization schemes

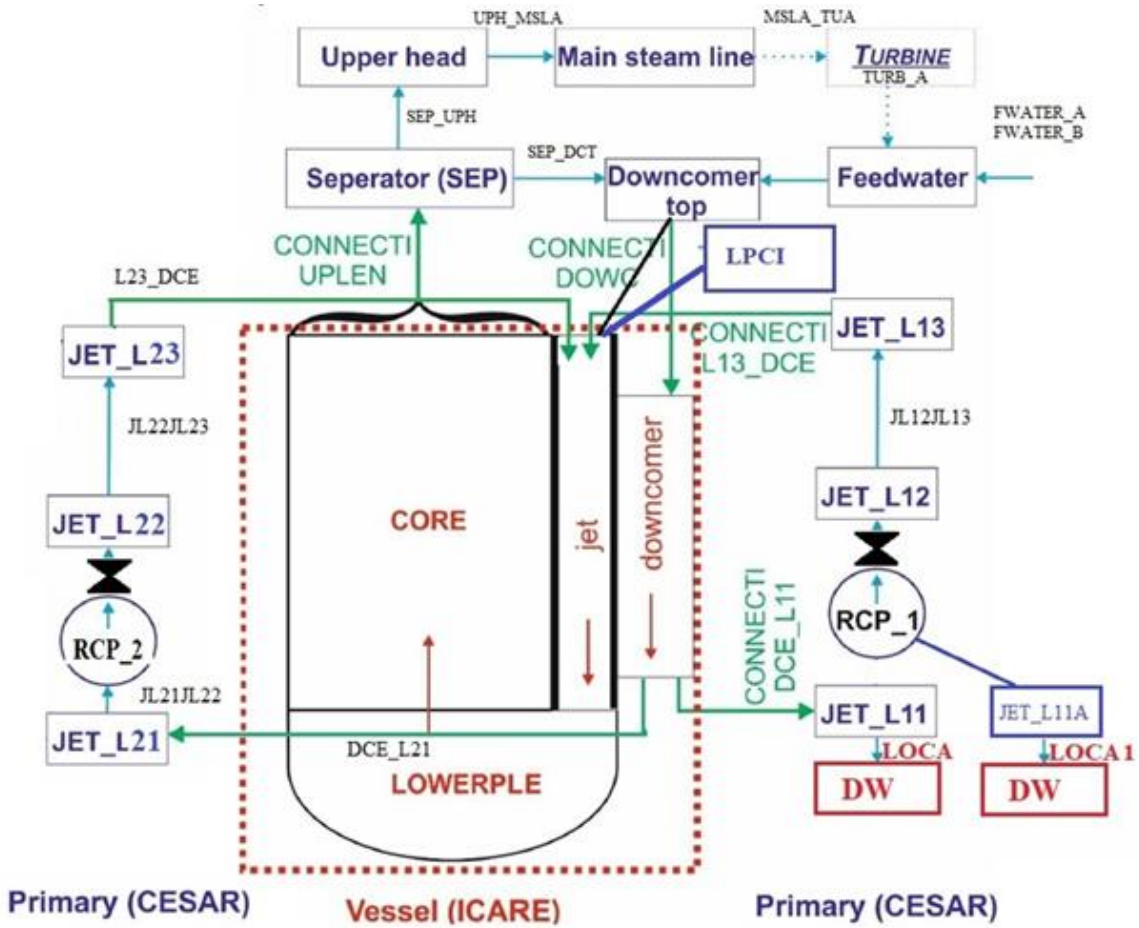

Nodalization scheme of the recirculation circuit

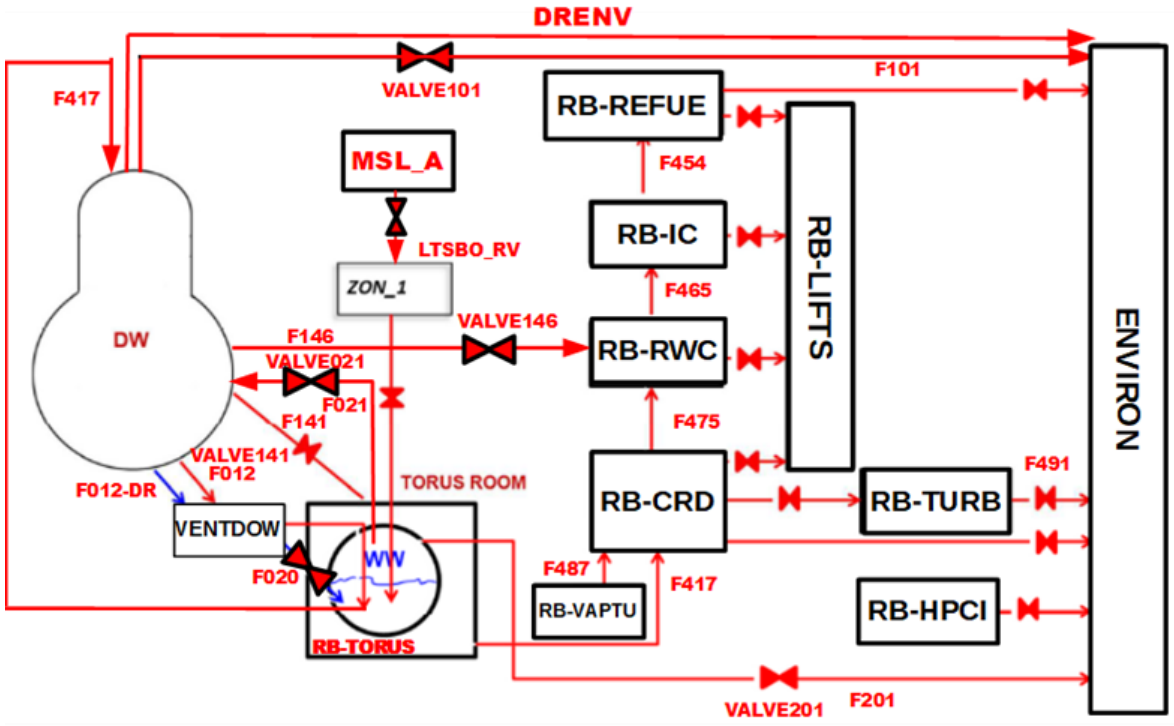

CPA model

Nodalization scheme of the BWR4-Mark I containment

Main events of the LOCA transient

Time, s	Event
T= 0	Large break (guillotine break of the main circulation pipe) take place close to the suction side of the pump. Loss of offsite power. SCRAM signal initiated.
T=1	Auxiliary batteries and compressed air supplies are starting the emergency diesel generators. RCIC, HPCI systems failed to start.
T=5	Feedwater injection to the reactor stopped. Main steam lines closed.
T=25	Insite electrical power is restored
T=45	Activation of wetwell and drywell spray
T=90	Dry out of fuel assemblies
T=100	LPCI system starts injecting water.
T=330	Maximal temperature (~1100 K) reached in fuel bundles
T=348	Water injected by LPCI system reaches the lower part of the active fuel.
T=358	Rupture of the first group of fuel assemblies (ring 2, 80 FA)
T=419	Rupture of the second group of fuel assemblies (ring 3, 224 FA)
T= 550	The water level in the RPV restored

ASTEC calculation results (1)

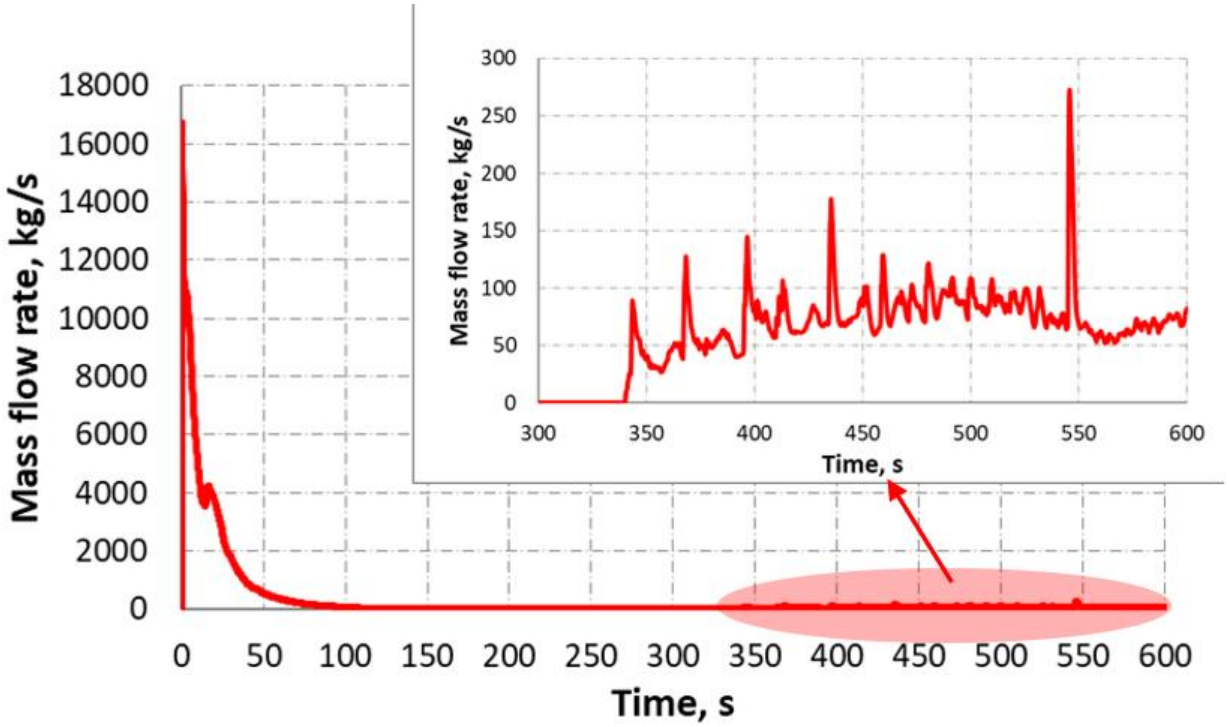

The mass flow rate through the break

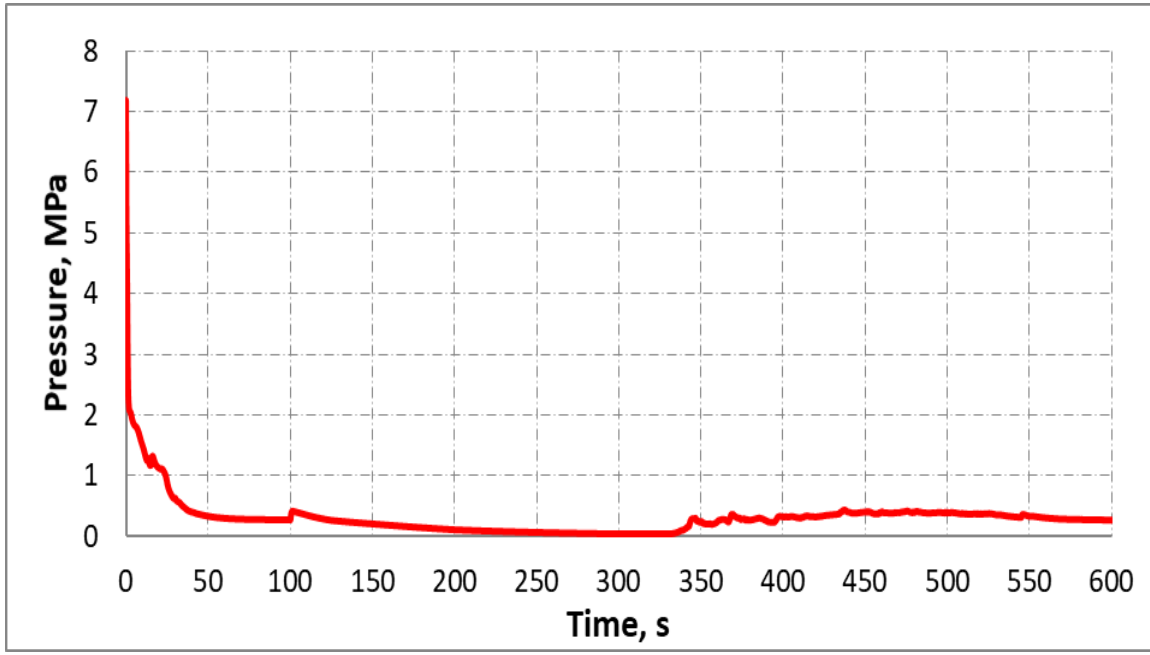

Pressure in the broken recirculation loop

ASTEC calculation results (2)

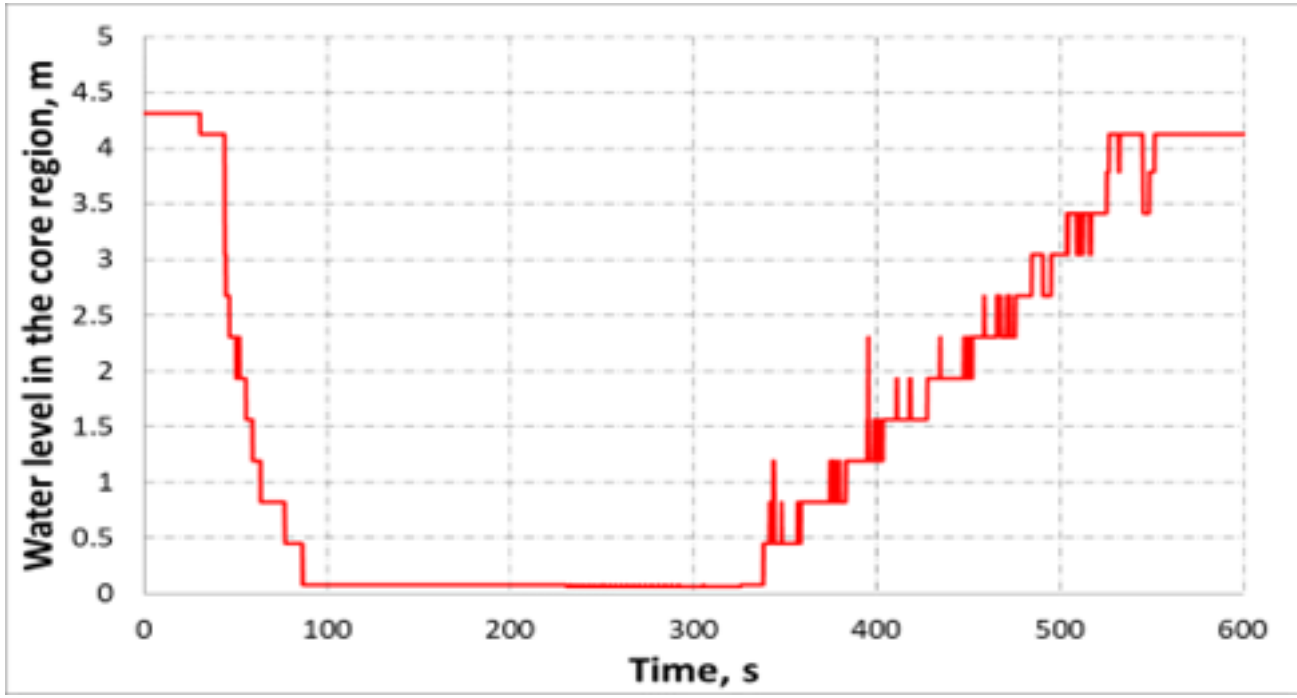

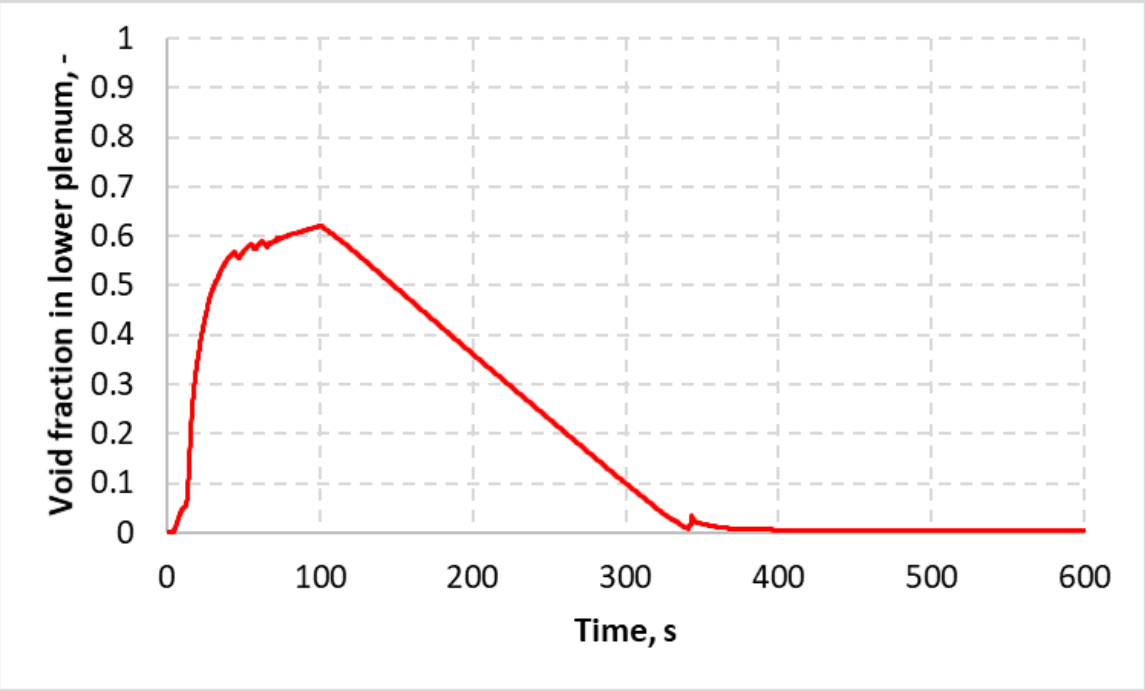

Water level in the core region, from the bottom

Void fraction in the lower plenum

ASTEC calculation results (3)

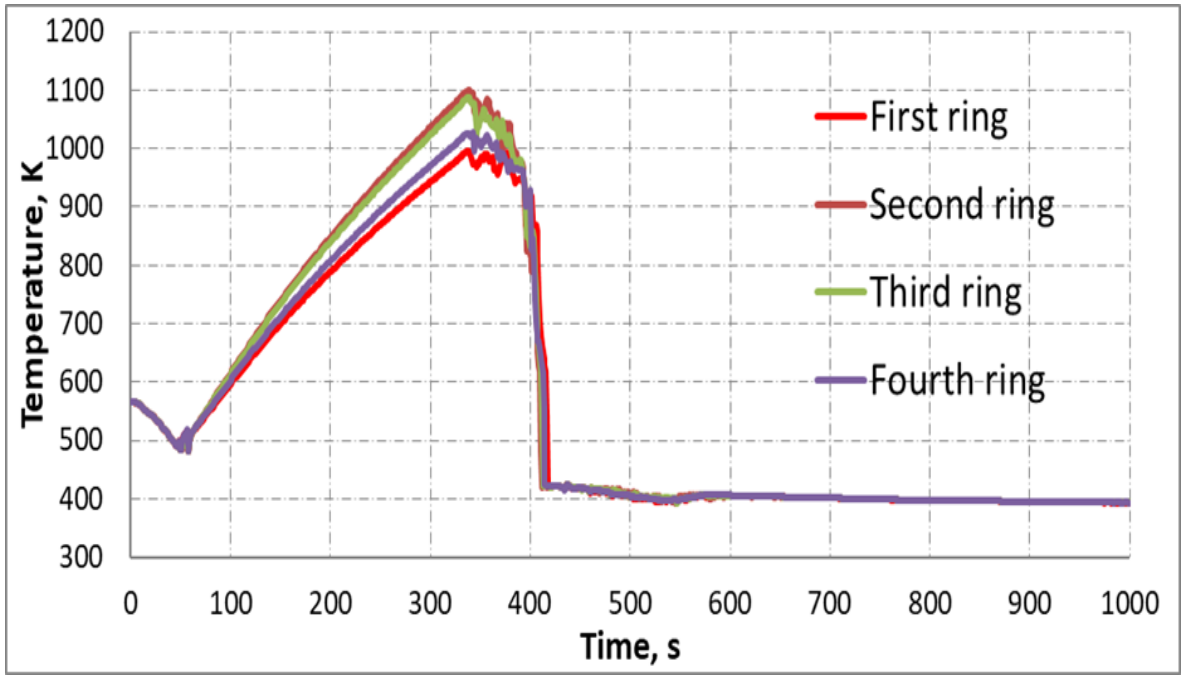

Peak cladding temperature in different rings of fuel assemblies

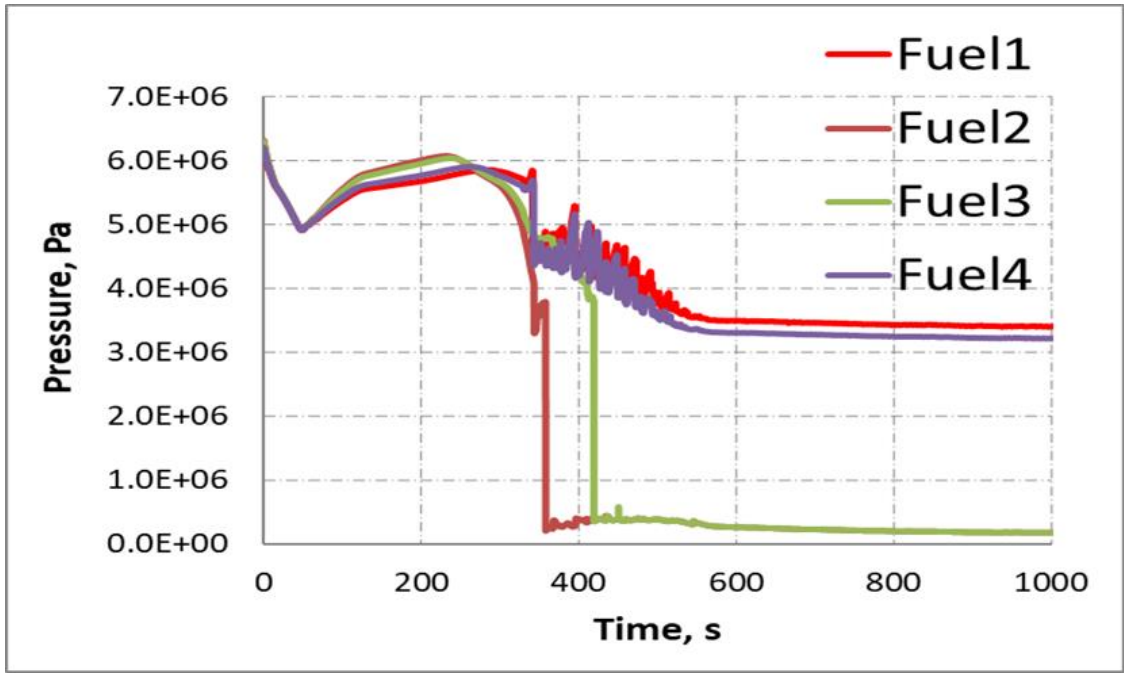

Pressure in the fuel rods

ASTEC calculation results (4)

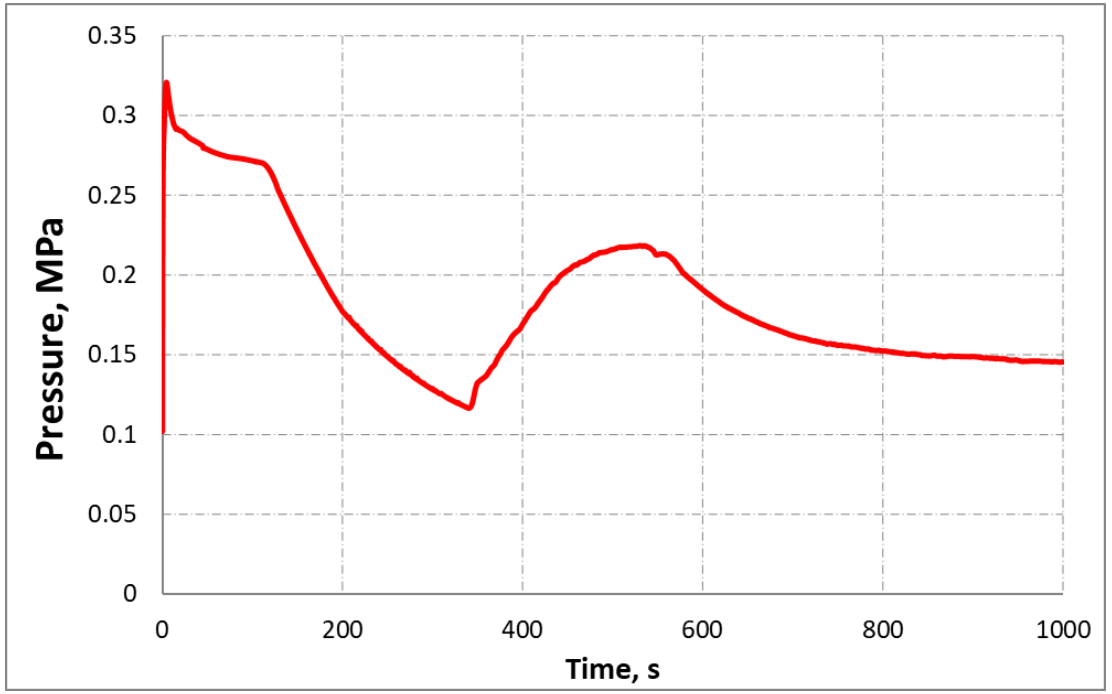

Pressure in the containment

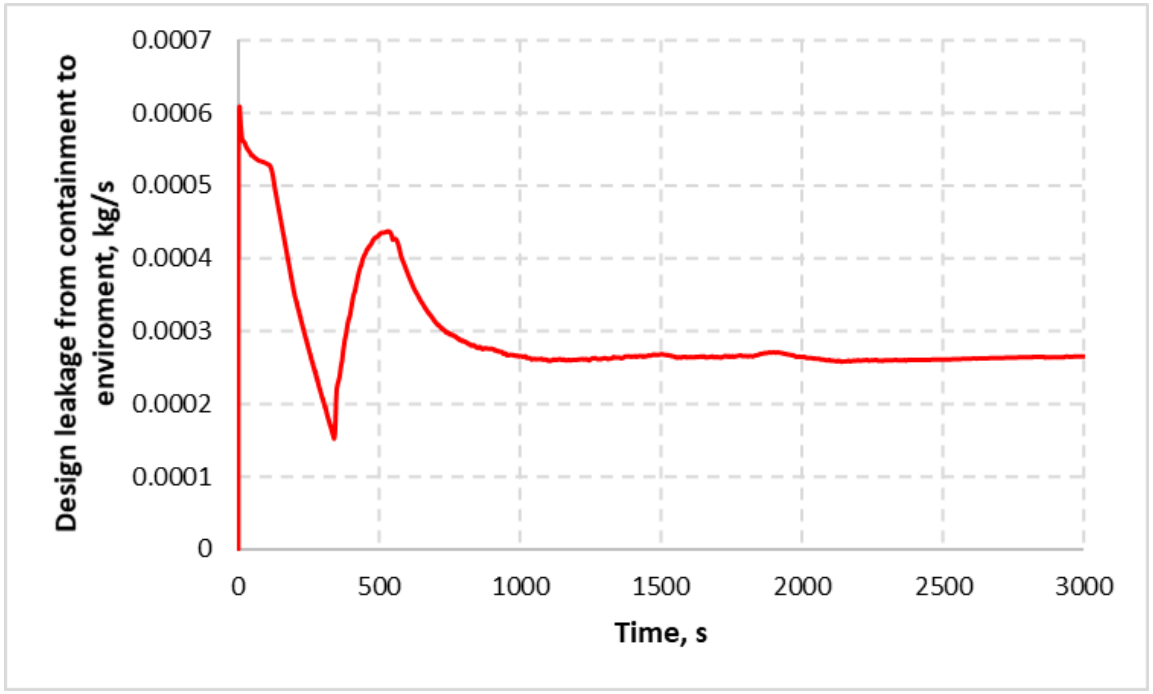

Flow rate from the containment to environment

ASTEC calculation results (5)

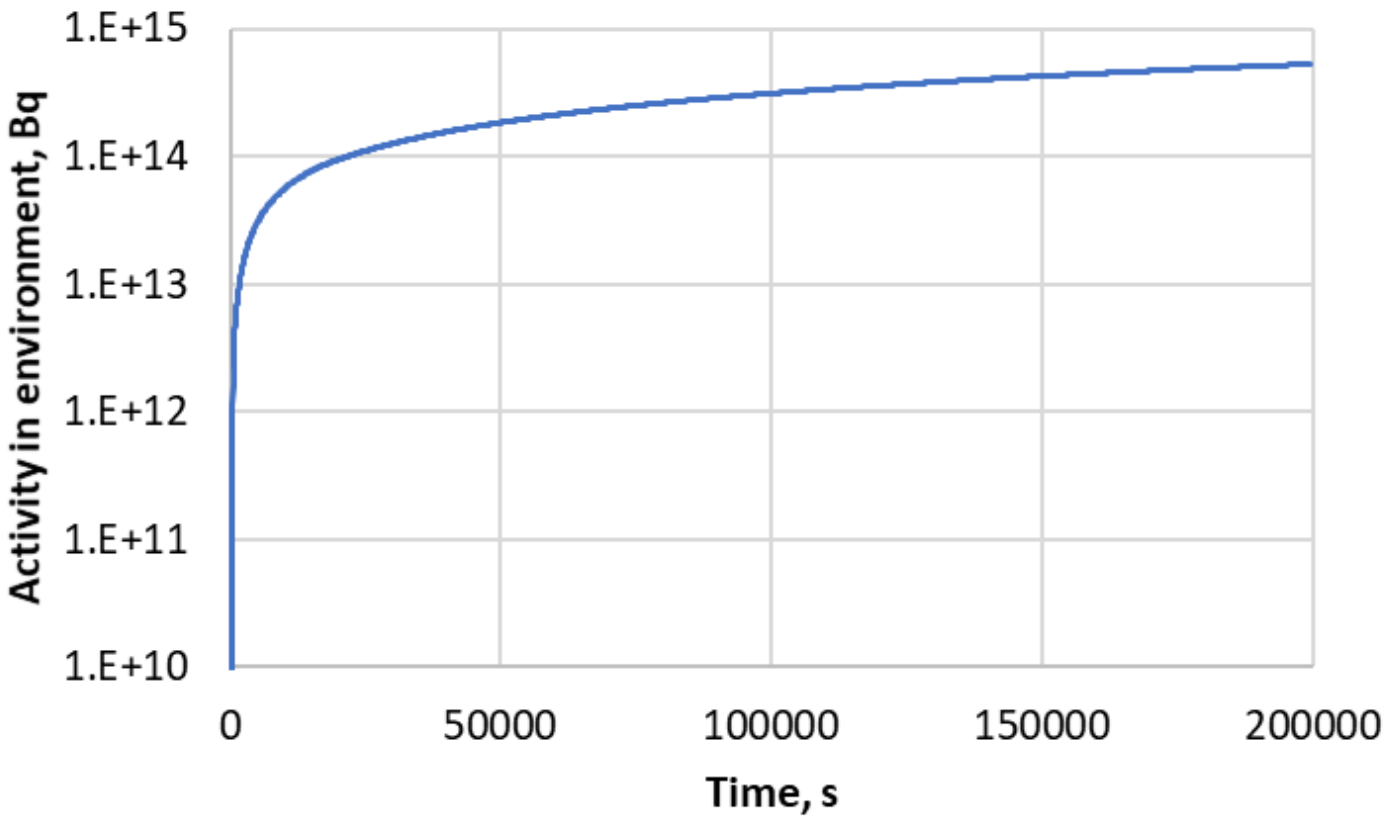

Activity in environment

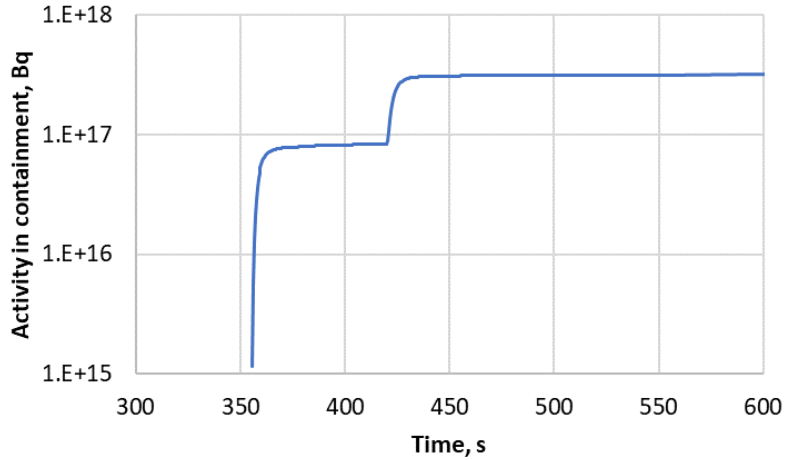

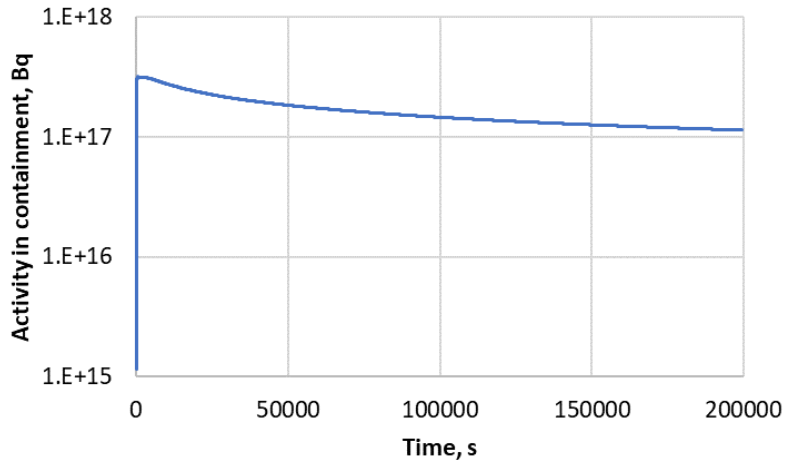

Activity in containment

Sensitivity analysis

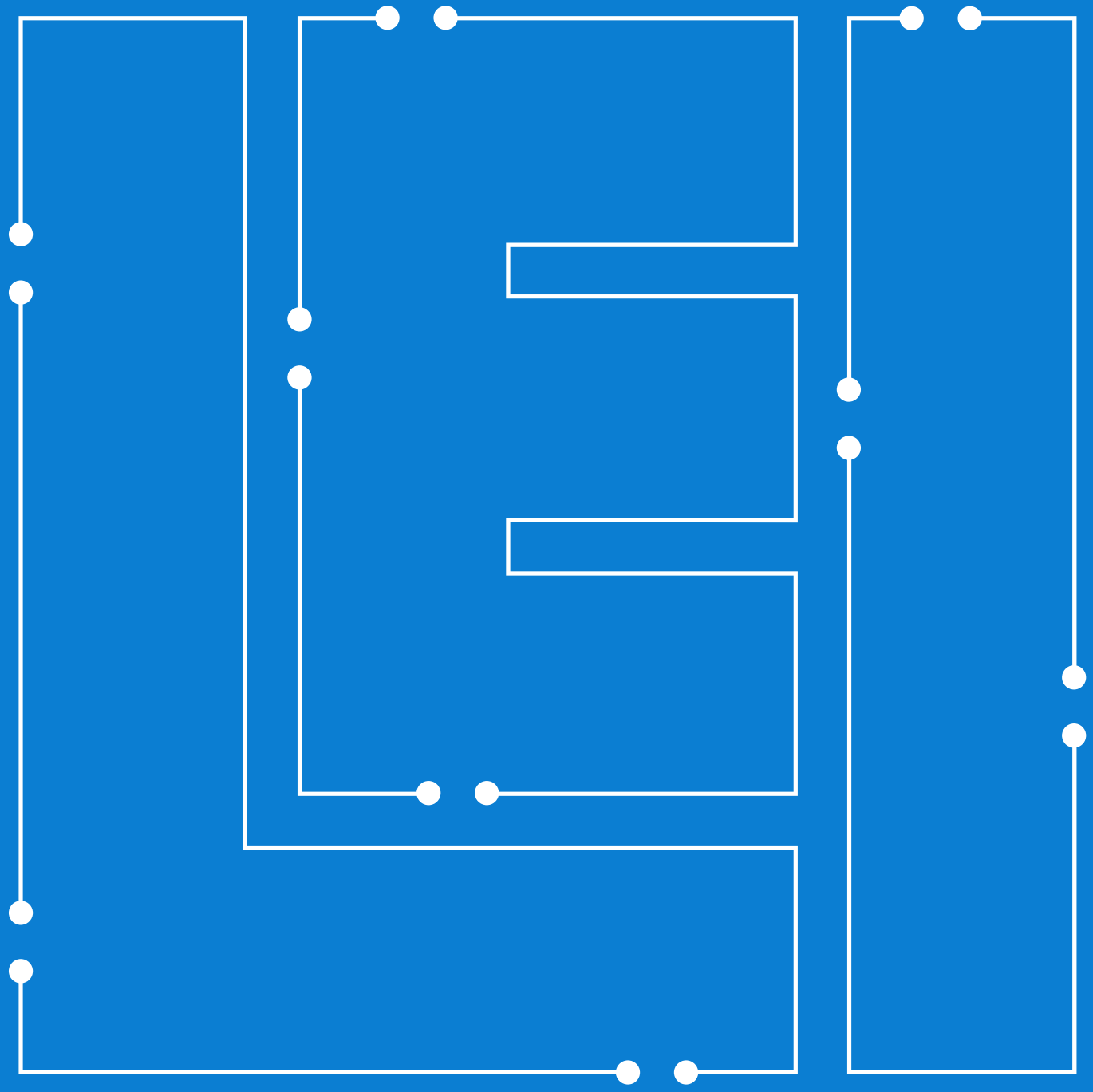

SENSITIVITY ANALYSIS

Case 0	**Basic**	**Zirconium oxidation physical law – BEST-FIT TBEG (minimum temperature to start the reaction of oxidation) – 700 K Burst parameters: EPMX 0.25; CRAC 0.50.**
Case 1	CATHCART	Zirconium oxidation physical law – CATHCART
Case 2	URBANIC	Zirconium oxidation physical law – URBANIC
Case 3	PRATER	Zirconium oxidation physical law – PRATER
Case 4	TBEG	TBEG (minimum temperature to start the reaction of oxidation) – 600 K
Case 5	EPMX	EPMX (maximal hoop creep allowed before burst – 0.4 (standard value according to manual)
Case 6	CRAC	CRAC (axial extension of the cracking after the clad burst) – 0.0 (standard value according to manual)

Sensitivity results for burst time and H_2 generation

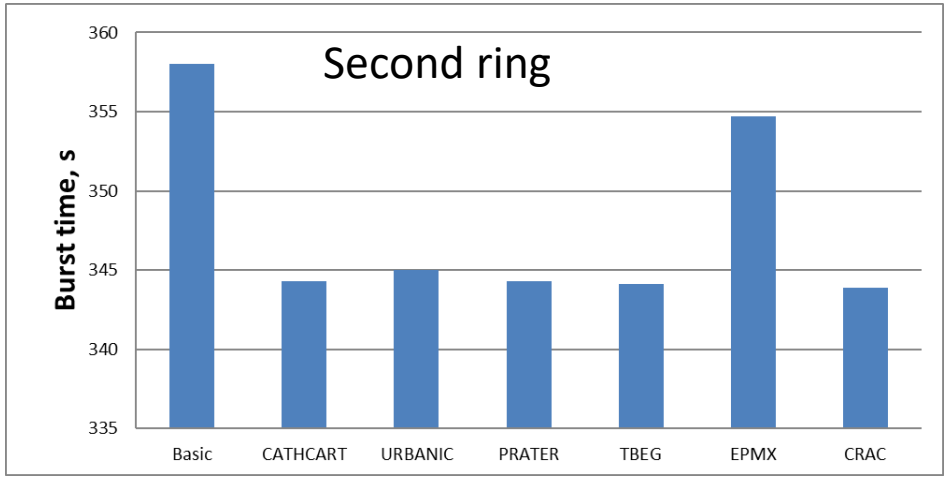

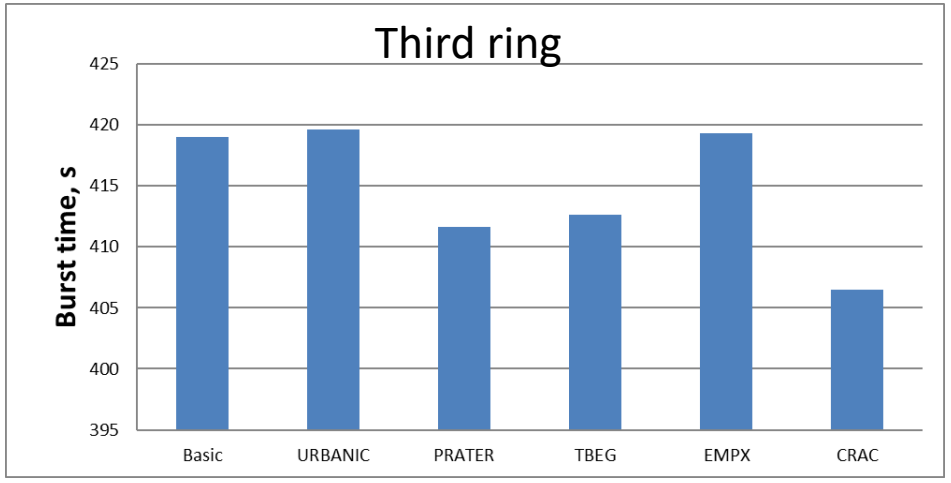

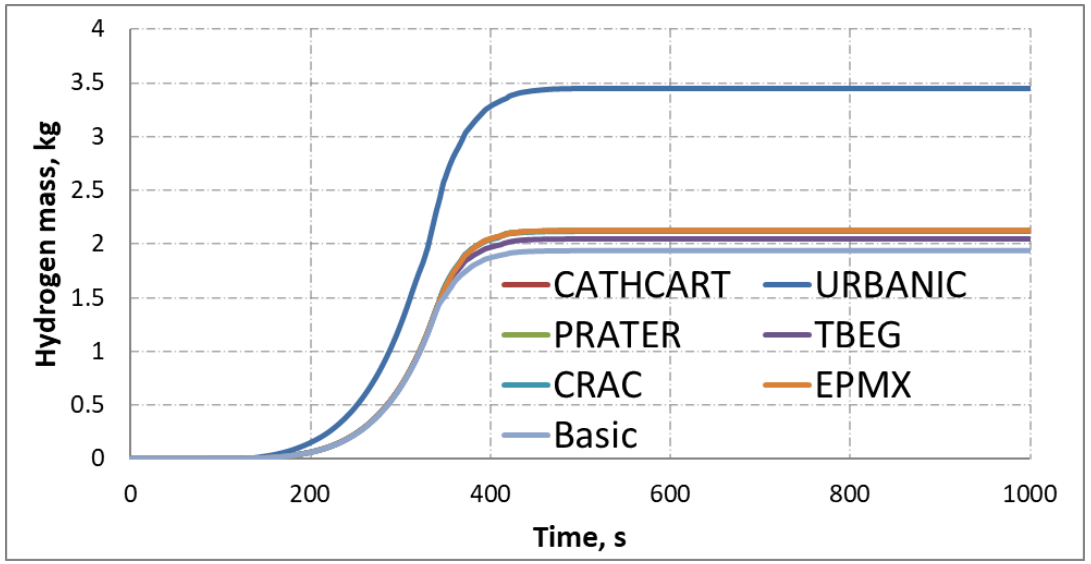

Sensitivity results for FP mass release to environment

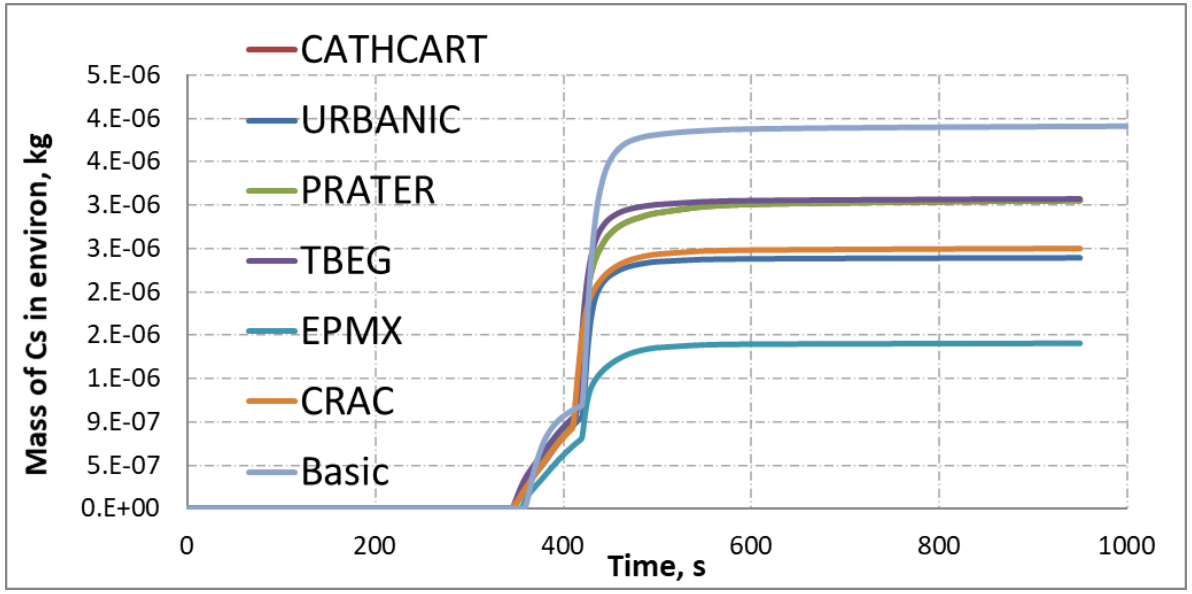

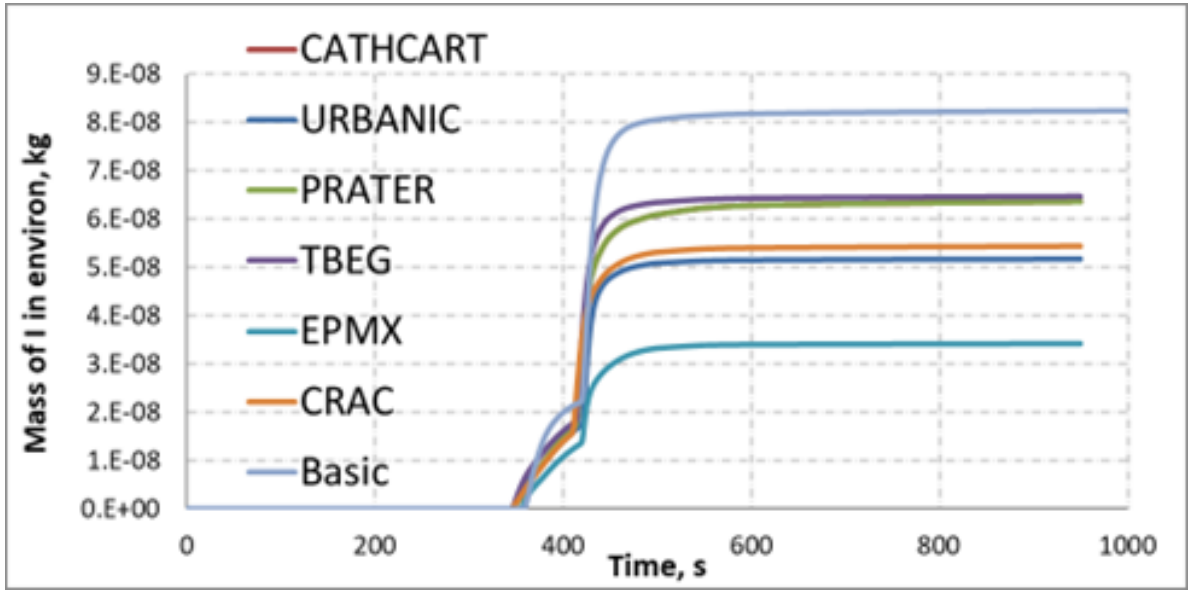

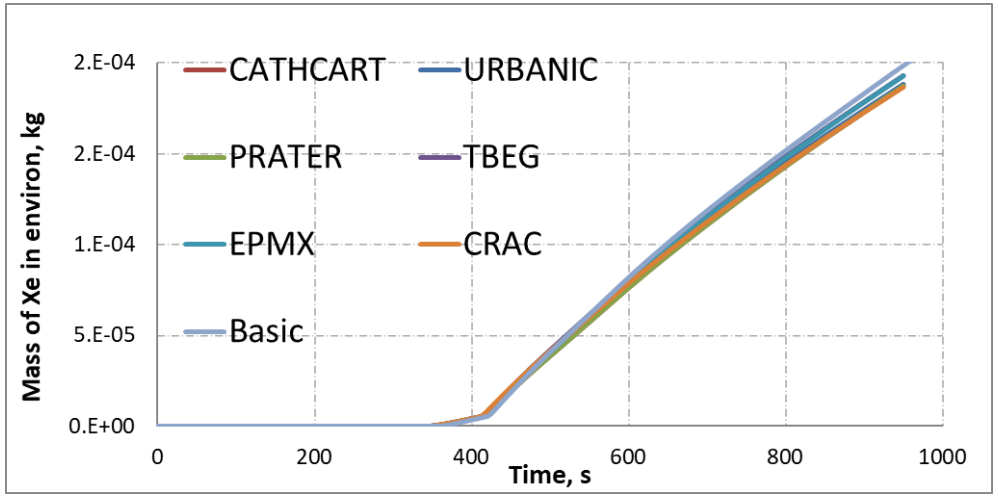

Conclusions (1)

- The LOCA event at DEC-A conditions for generic BWR-4 type reactor was analyzed using ASTEC code. Analysis results showed:
  - Core uncover was reached 90 s after beginning of the accident and maximal temperature of the fuel rod claddings reached 1100 K at t = 330 s.
  - The cladding of fuel rods in second and third concentric rings burst at t = 358 s and 419 s respectably. This corresponds to ~55% of the total core fuel claddings.
  - Fission products were released from the gap (between pellet and cladding) of the burst fuel claddings to the cooling circuit and then transported to the containment and through containment design leakages to environment. The total activity in the environment at the end of calculation (200000 s after beginning of the accident) reached ~8e+14 Bq.

Conclusions (2)

- The sensitivity analysis of ASTEC parameters related to oxidation and burst of the claddings were evaluated:
- All analyzed parameters have an insignificant effect on the cladding burst time (difference ~10 s).
- Using URBANIC zirconium oxidation physical law gives highest amount (~60% higher compared to other results) of total generated hydrogen.
- Parameters indicating the minimum temperature to start the reaction of oxidation (TBEG) and maximal hoop creep allowed before burst (EPMX) have a significant influence on fission product release calculations.

Future fork

- Work is related to the R2CA project task dedicated to reactor case simulations.
- Further step is to verify ASTEC calculation results using specific analysis tool like TRANSURANUS and to evaluate more precisely possible cladding burst during analyzed LOCA scenario.
- At the last step of R2CA project the another calculation using ASTEC for the same scenario will be provided considered received experience.

Acknowledgments



This project has received funding from the Euratom research and training programme 2014-2018 under grant agreement No 847656.

LITHUANIAN ENERGY INSTITUTE

Thank you for your attention!

Tadas Kaliatka, Tadas.Kaliatka@lei.lt

ERMSAR2022, Karlsruhe, Germany, May 16-19, 2022

The 10th European Review Meeting on Severe Accidents Research

Severe Accident Research Eleven Years after the Fukushima Accident

May 16-19, 2022, Karlsruhe, Germany

PLENARY SESSION: FUKUSHIMA: 10 (+1) YEARS AFTER

Chairs: A. Bentaib (IRSN), L.E. Herranz (CIEMAT)

NEA Fukushima Activities
Y. Kumagai (OECD/NEA)

Current situation of the site -Facts & Future of Fukushima Daiichi NPS-
S. Mizokami (TEPCO)

Accident management & nuclear decommissioning
K. Okamoto (JAEA/CLADS)



FUKUSHIMA: 10 (+1) YEARS AFTER

Current situation of the site

-Facts & Future of Fukushima Daiichi NPS-

TEPCO

10th EUROPEAN REVIEW MEETING
ON SEVERE ACCIDENTS RESEARCH
MAY 16-19, 2022 – KARLSRUHE, GERMANY

2022/05/17

TEPCO HD
Shinya MIZOKAMI

1.1 Introduction

TEPCO

- On March 11, 2011, Great East Japan Earthquake(GEJE) and successive Tsunami hit the Fukushima Daiichi NPS(1F). These caused the total Station Blackout, loss of AC/DC power. Then, unit 1 to 3 lost all cooling functions and fell into severe accident.
- Just after the accident, nobody could explain the accident progressions correctly. One of the reason is that the consequence of accident was different from knowledge accumulated before 2011.
- Now, 10+1 years past since the accident. Researchers in the nuclear field made massive efforts to understand the 1F accident by data analysis, code calculation, robot investigation, etc.. Therefore, we know the accident progression and debris distribution for each plant better than before.
- Activities related to Decontamination and Decommissioning are on-going. Debris retrieval will be started within this year. Spent fuel in the pool in unit 3 and 4 was removed from each R/B. The policy of GoJ on treated water was fixed in April 2021.

1.2 Time series towards RPV failure in unit 1 to 3

time			unit 1	unit 2	unit 3
3/11	0h	day 1	Earthquake		
			LOPA	LOPA	LOPA
	1h		Tsunami		
			SBO(AC/DC)	SBO(AC/DC)	SBO(AC)
	4h		core damage		
3/12	15h		RPV breach		
	21h				RCIC trip
	30h	day 2			SBO(AC/DC)
3/13	36h				HPCI shutdown
	38h				core damage
3/14	64h	day 3			RPV breach
	66h			RCIC trip	
	76h	day 4		RPV depressurization	
	77h			Fire truck AWI	
	78h			core damage	
3/15	9xh			RPV breach	

w/ core cooling

w/o core cooling, RPV water level decreasing phase

w/o core cooling, core exposure, heat up phase

1.1 Introduction

- On March 11, 2011, Great East Japan Earthquake(GEJE) and successive Tsunami hit the Fukushima Daiichi NPS(1F). These caused the total Station Blackout, loss of AC/DC power. Then, unit 1 to 3 lost all cooling functions and fell into severe accident.
- Just after the accident, nobody could explain the accident progressions correctly. One of the reason is that the consequence of accident was different from knowledge accumulated before 2011.
- Now, 10+1 years past since the accident. Researchers in the nuclear field made massive efforts to understand the 1F accident by data analysis, code calculation, robot investigation, etc..
  Therefore, we know the accident progression and debris distribution for each plant better than before.
- Activities related to Decontamination and Decommissioning are on-going. Debris retrieval will be started within this year. Spent fuel in the pool in unit 3 and 4 was removed from each R/Bs. The basic policy of GoJ on treated water was fixed in April 2021.

2.1 PCV investigation done in unit 2 and 3

TEPCO

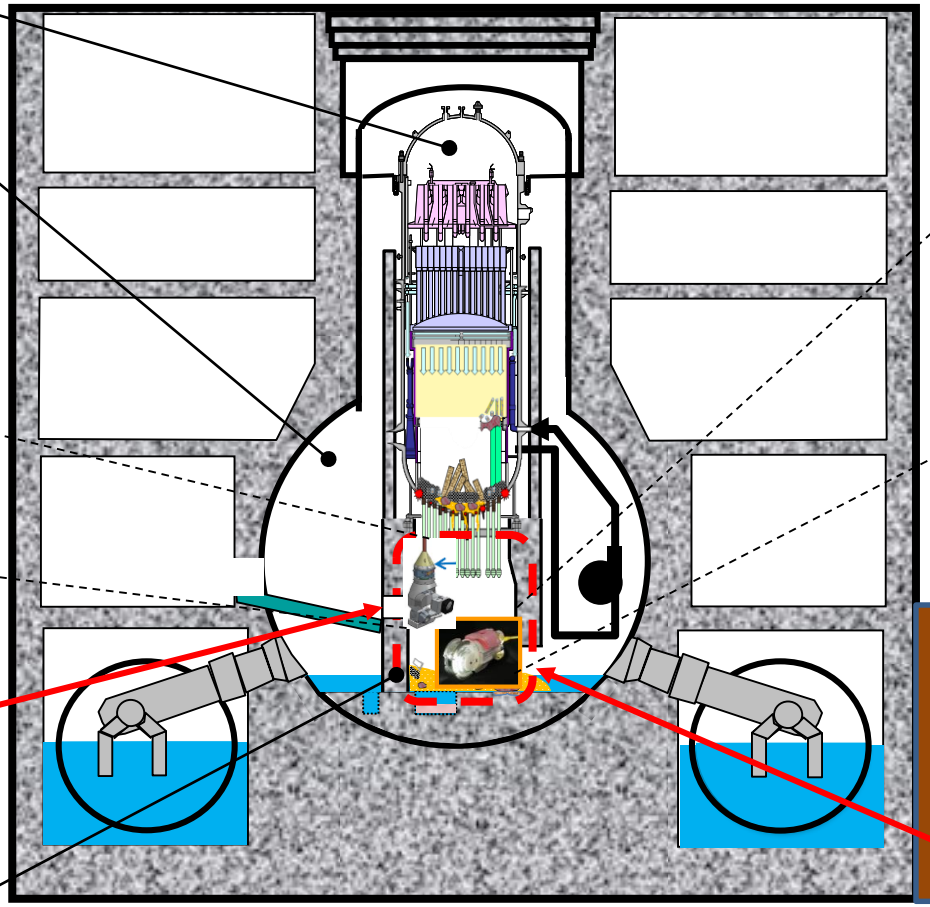

(ref) Inside Unit 5 PCV pedestal (on platform)



(ref) Inside Unit 5 PCV pedestal (pedestal floor)

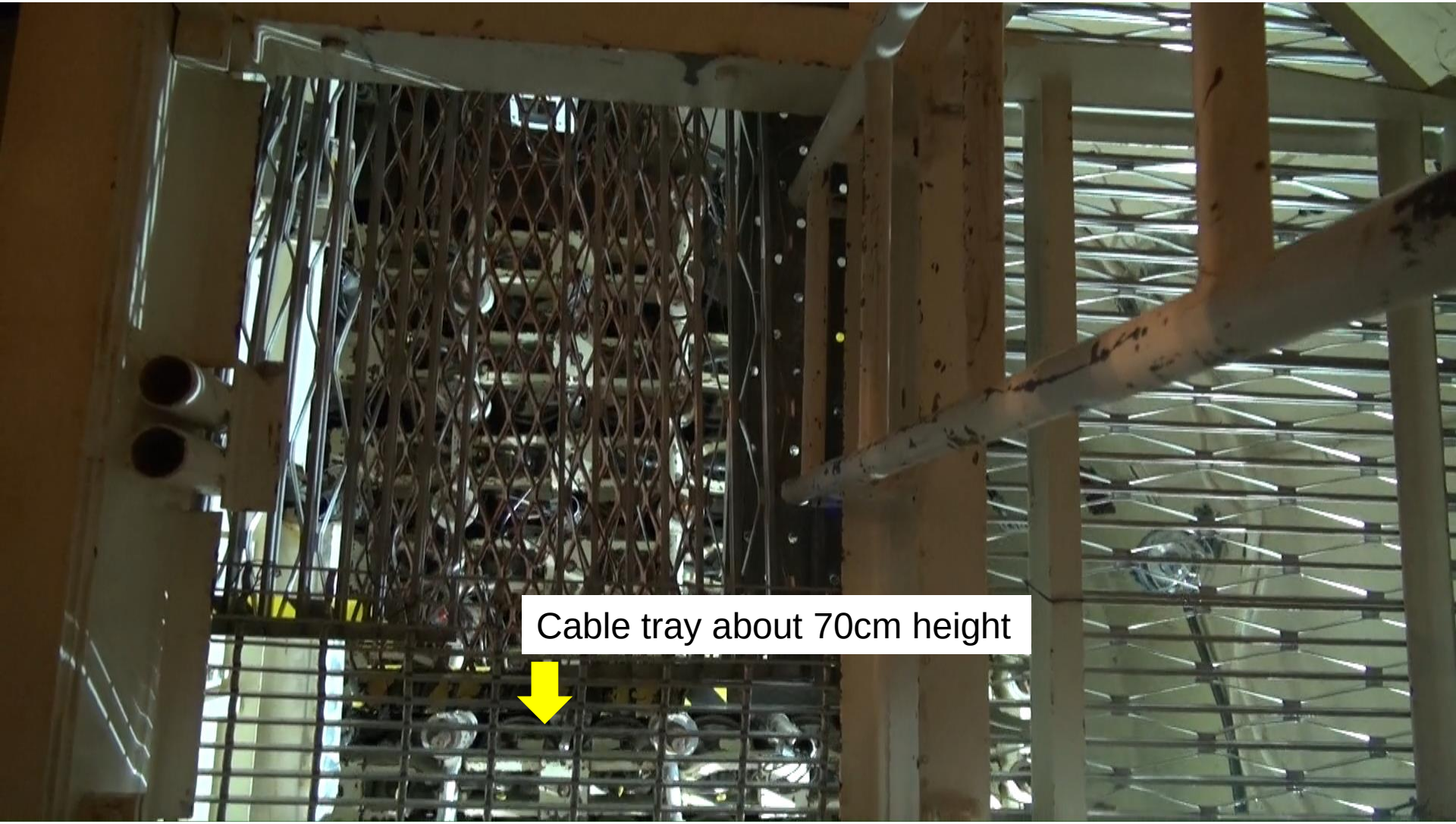

2.2 Images inside pedestal in unit 2

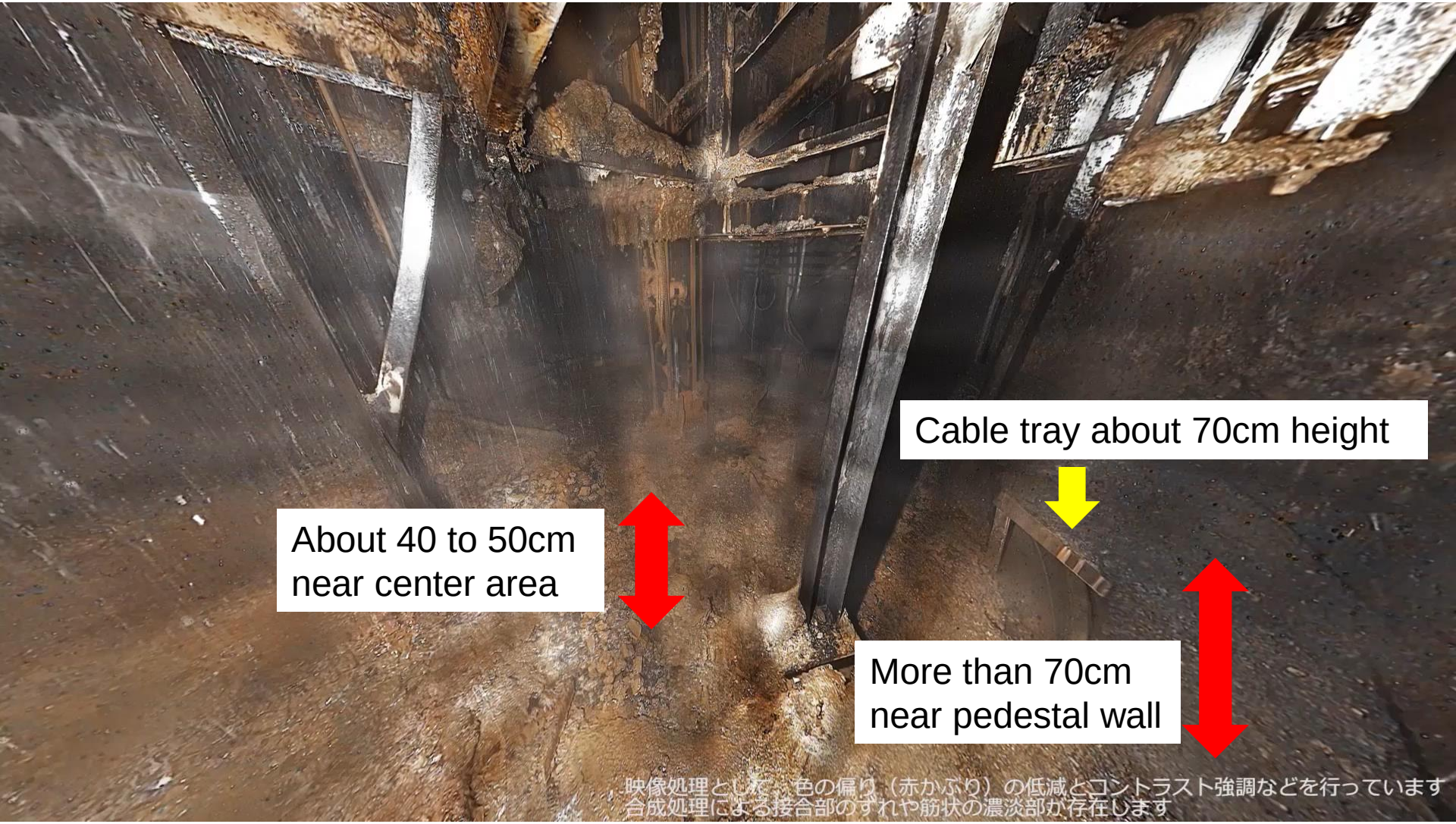

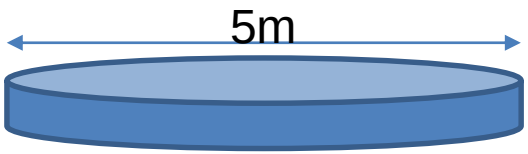

More than $10m^3$

2.3 Trial to grab the pebble like deposits



2.4 Images inside pedestal in unit 3

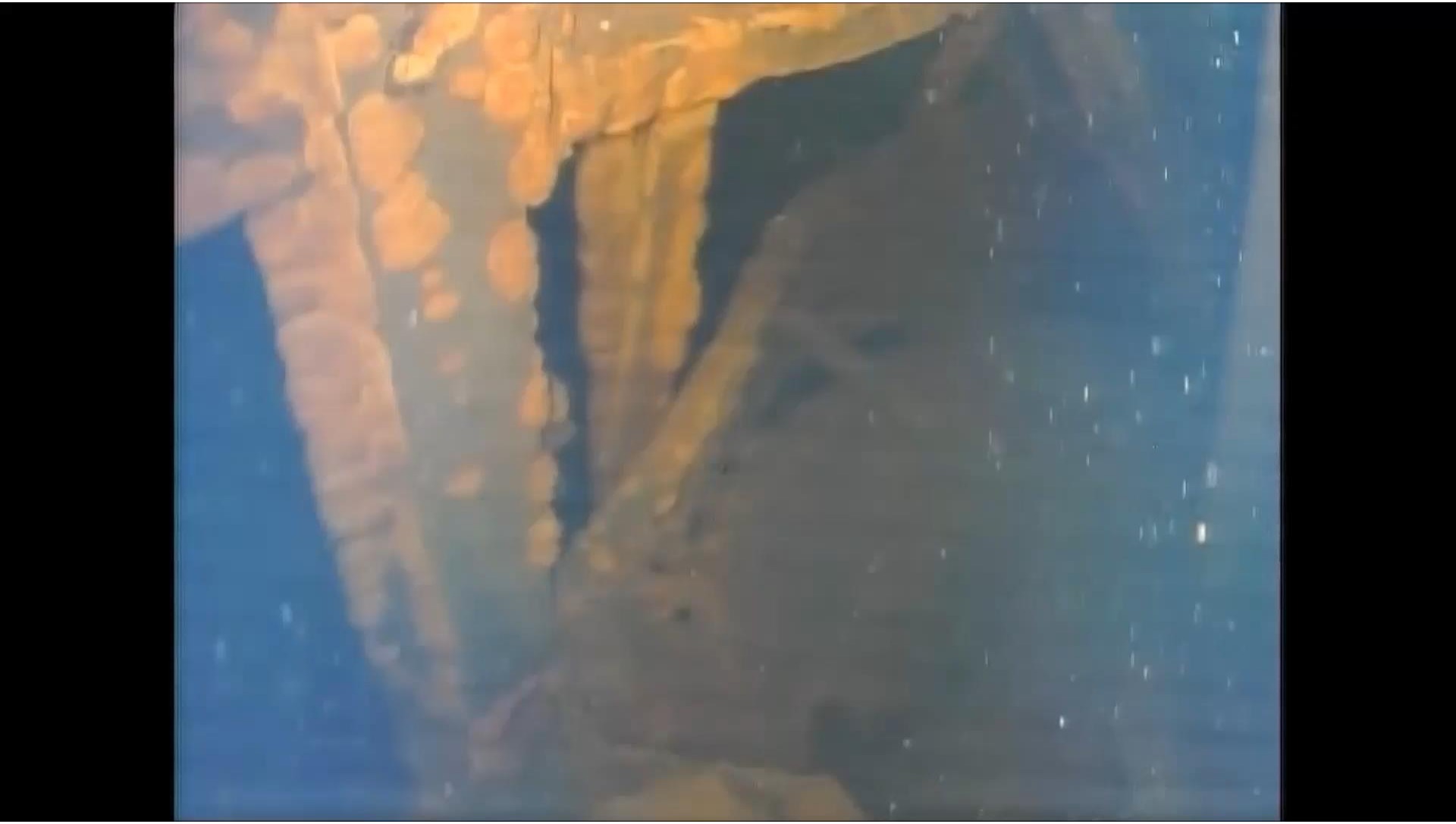

2.5 3D reconstruction image inside pedestal

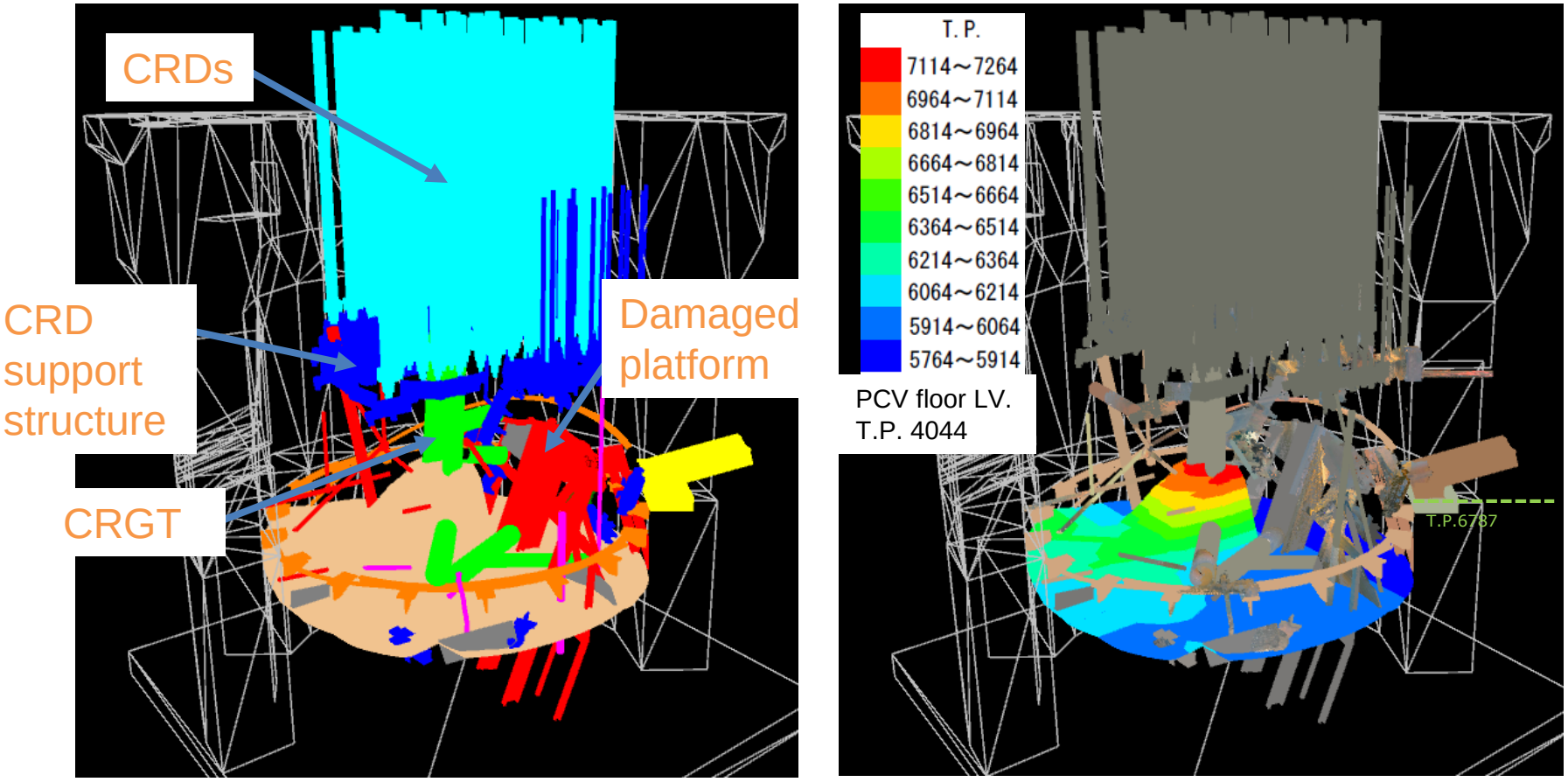

The height of debris like deposits is about 2m to 3m. (unit 2: less than 1m)
CRDs were confirmed but part of CRD support structure disappeared.
Platform was no longer standing.
CRGTs, which are core internals, were slumping down to pedestal.

2.6 3D reconstruction image inside pedestal

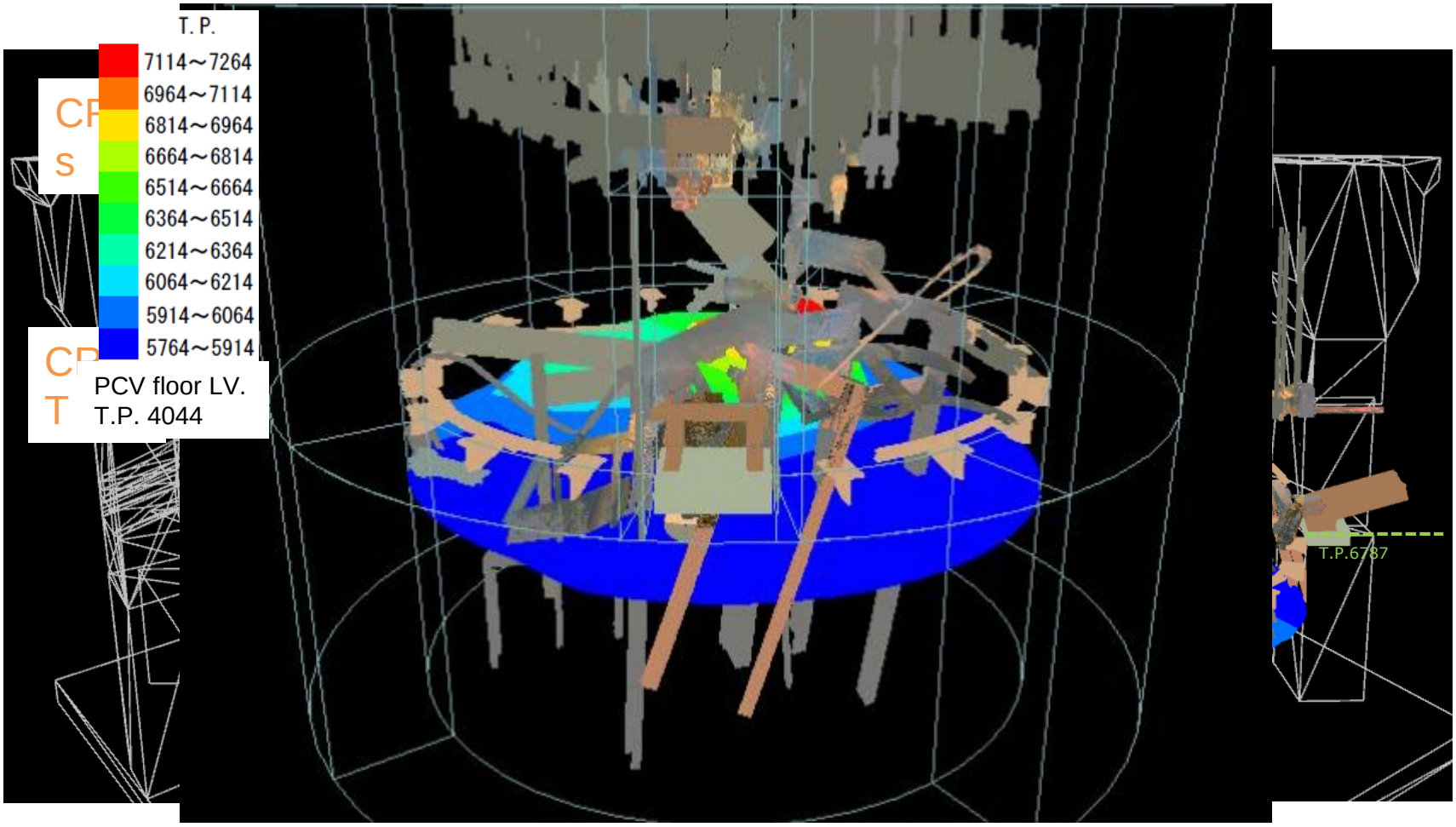

CRDs were confirmed but part of CRD support structure disappeared.
Platform was no longer standing.
CRGTs, which are core internals, were slumping down to pedestal.
The height of debris like deposits is about 2m to 3m. (unit 2: less than 1m)

3.1 PCV investigation done in unit 1

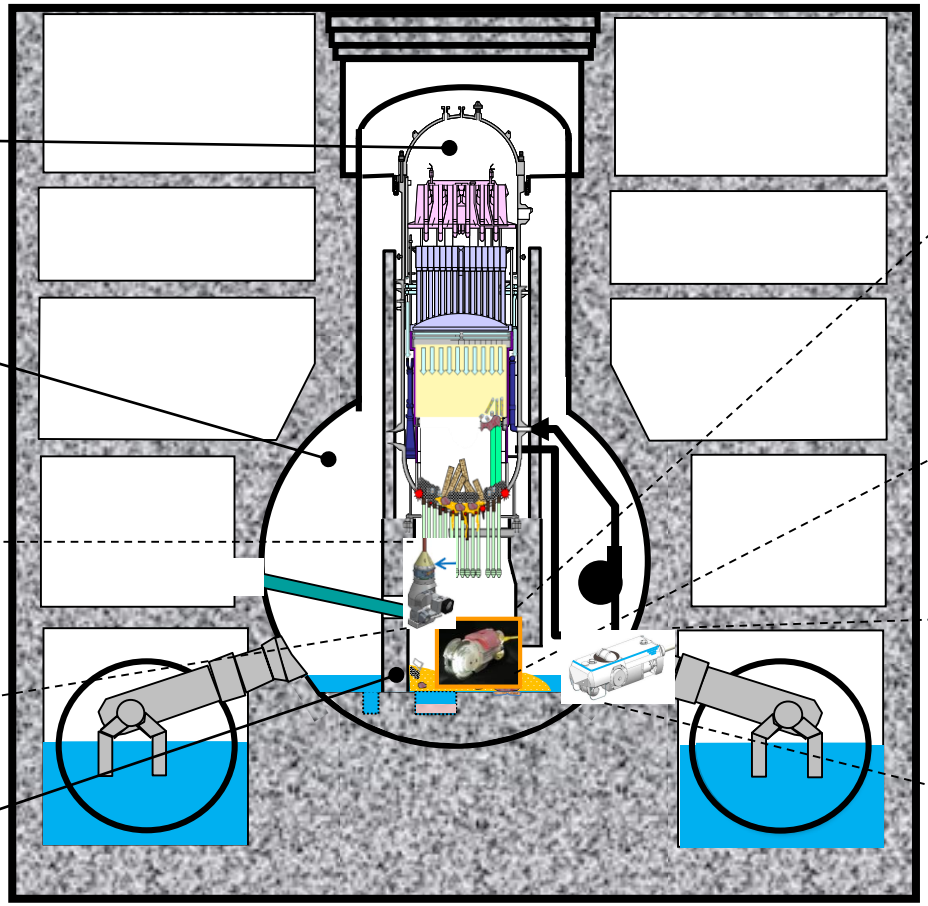

Camera robot investigation unit 2 2018.1



Pedestal area
(slumped debris from RPV)

Submarine robot investigation unit 3 2017.7



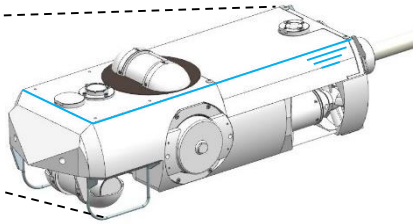

Boat robot investigation unit 1 2022.2～

(ref) 3D model of lower part of PCV

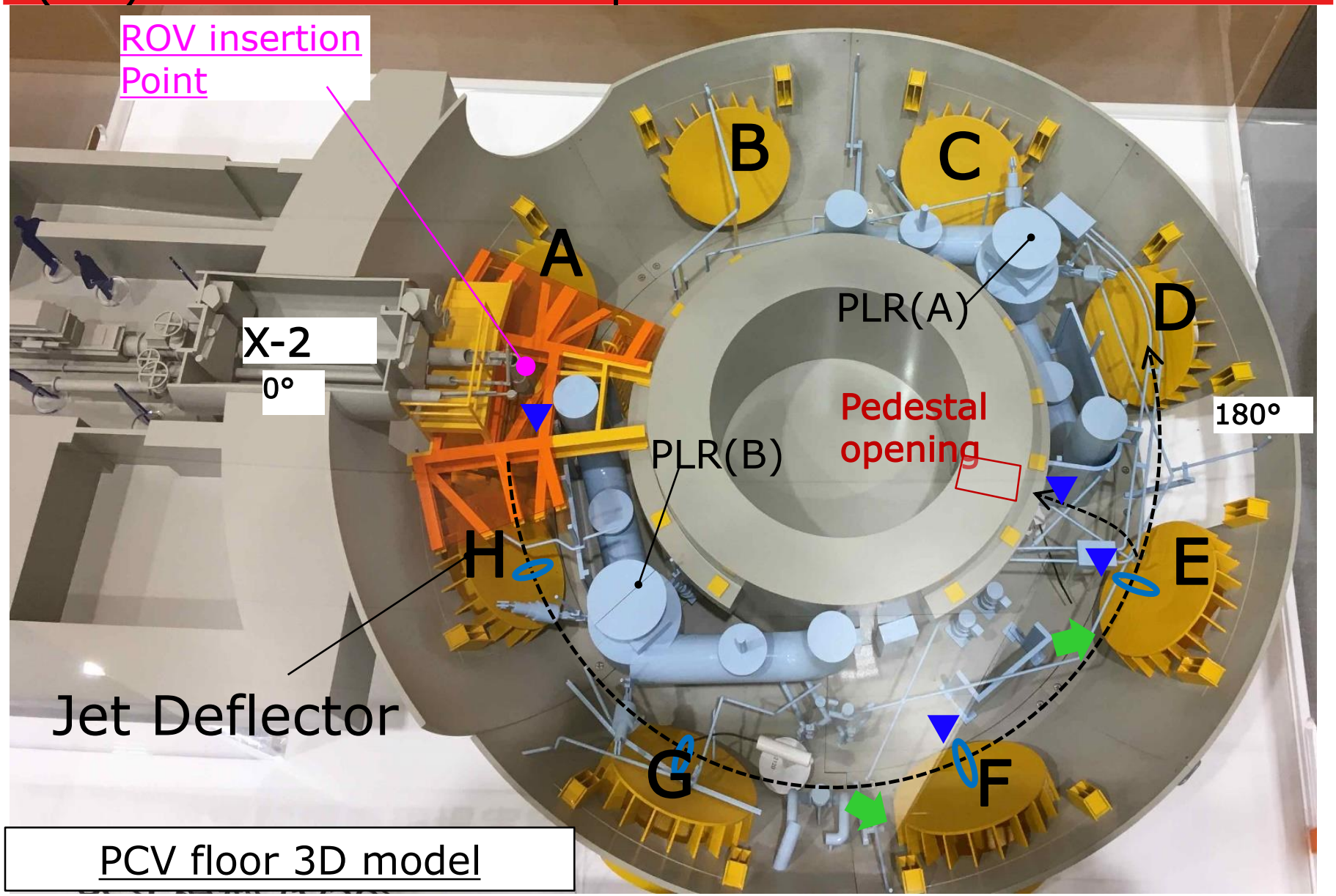

PCV floor 3D model

(ref) Unit 5 PCV floor outside of pedestal



(ref) picture around pedestal opening before accident



Photo: taken in 2001

3.2 Unit 1 investigation by ROV-A2

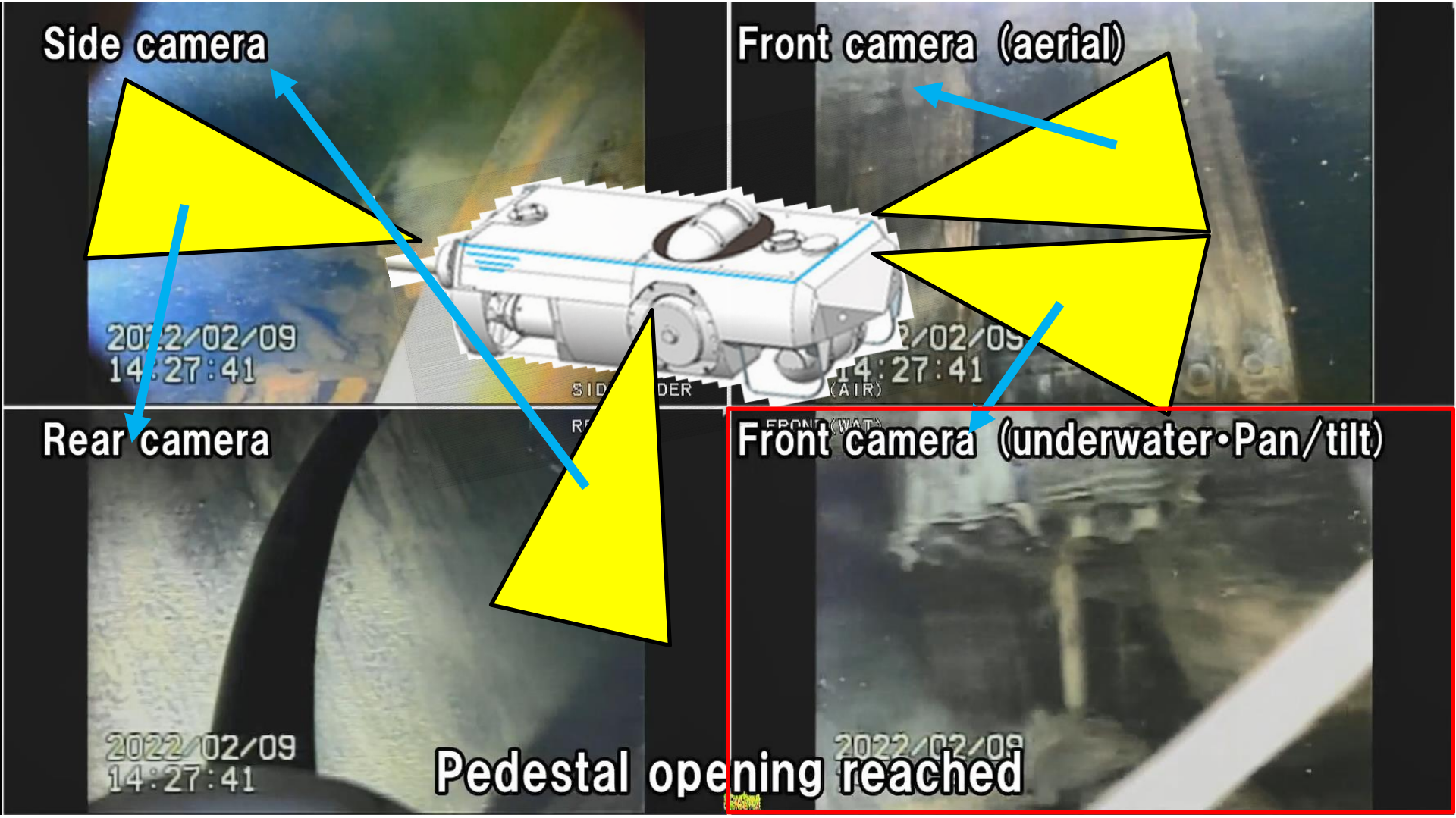

2022/02/08 :You can confirm the clearness of water in upper left view.
2022/02/09 :Bottom right is the most important view!!

3.3 Unit 1 investigation results

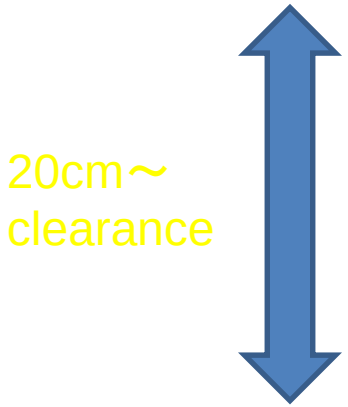

3.4 images around pedestal opening

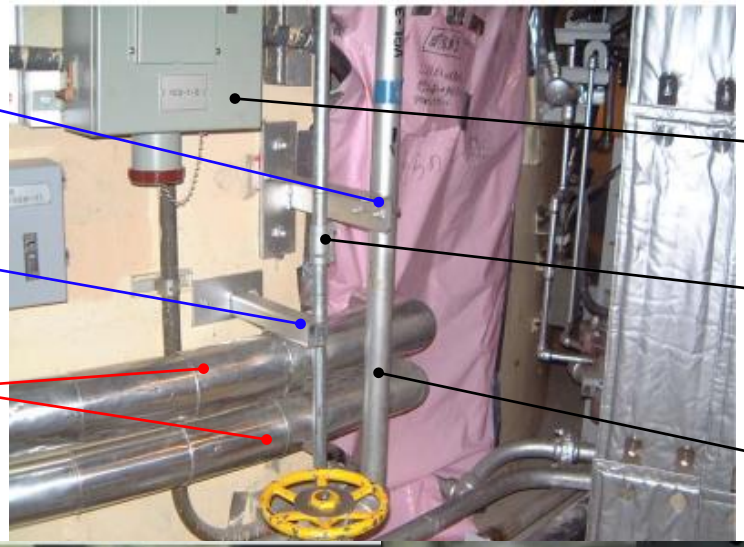



3.5 Images jet deflector and PLR piping





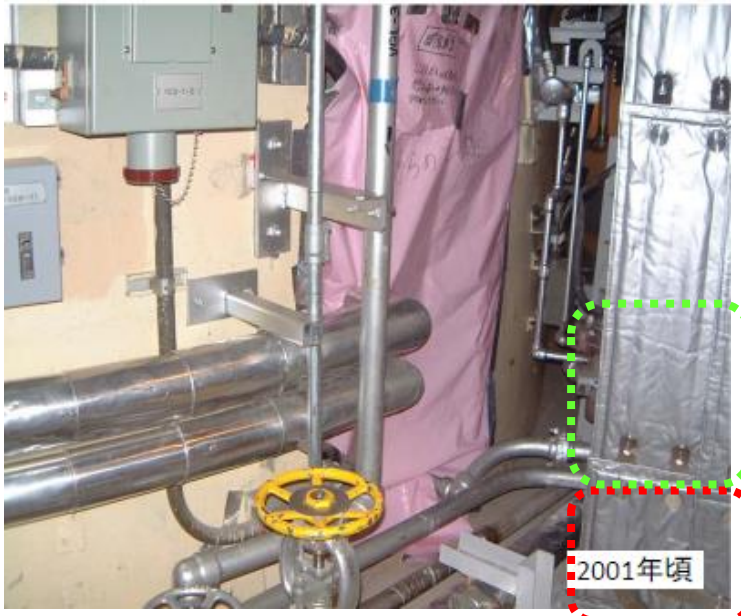



4.1 debris distribution diagram for unit 1 to

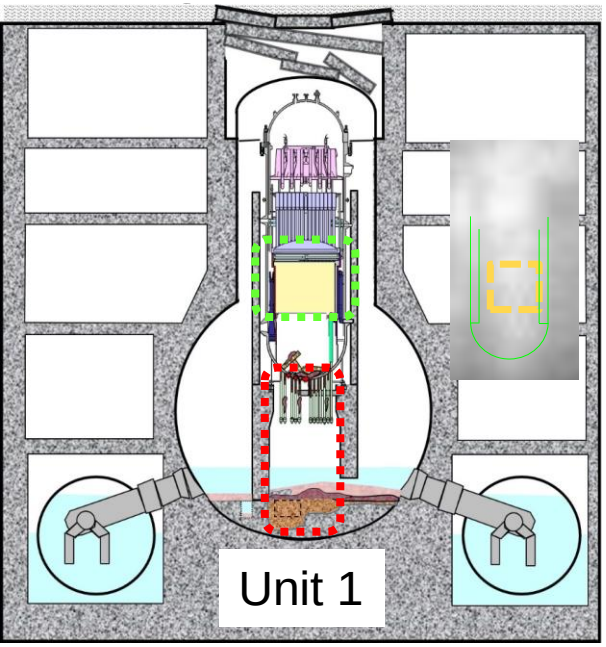

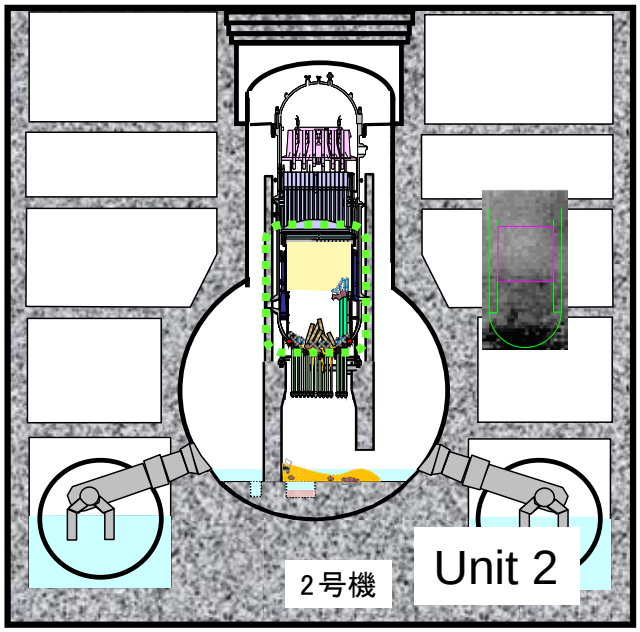

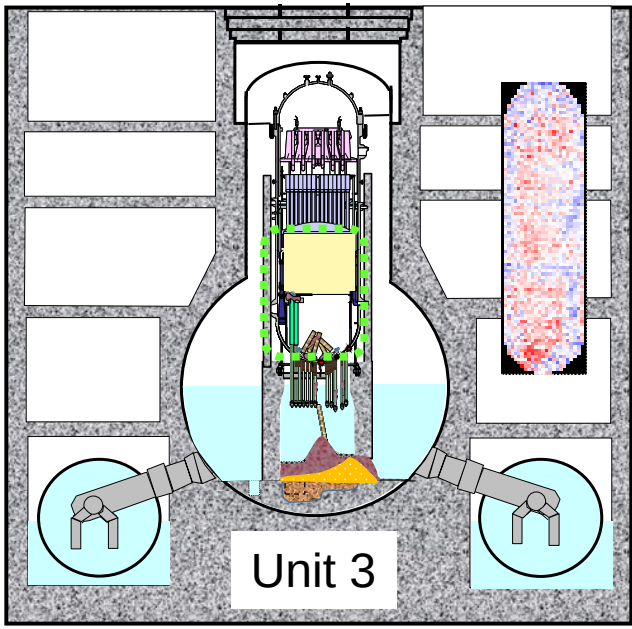

- ROV investigation in unit 1 will bring us the information of debris accumulation on pedestal floor. Maybe, debris height should be modified higher.
- The situation in RPVs were confirmed by using muon tomography.
  Unit 1: no debris Unit 2: debris remains in RPV bottom Unit 3: a few in RPV bottom
  The results of muon tomography have large uncertainty, but, the results are qualitatively consistent with other investigation in PCV.
- This Japanese fiscal year is the starting year of debris retrieval in unit 2 by using robot arm developed in UK and real debris analysis is also planned.
- And we started the preparation for RPV internal investigation.

4.2 Current situation of spent fuel removal

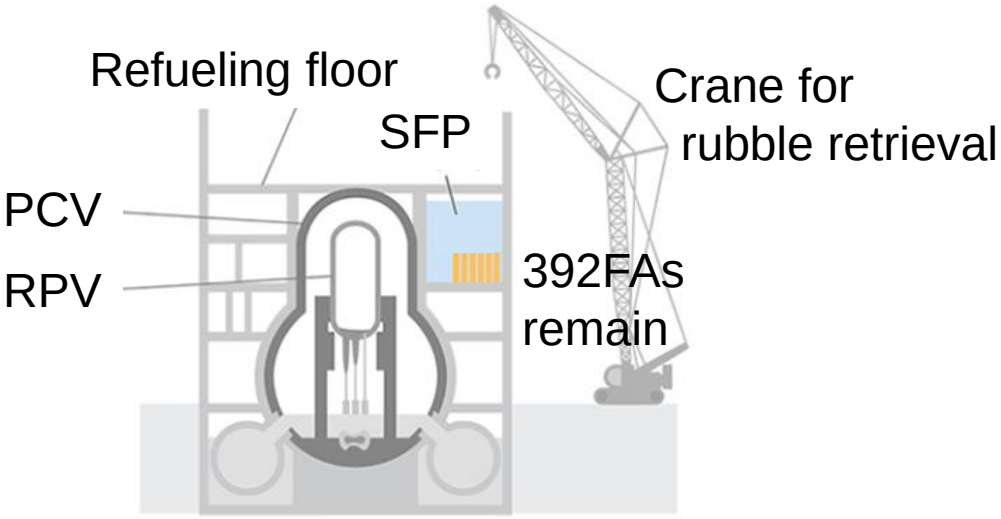

Unit 1

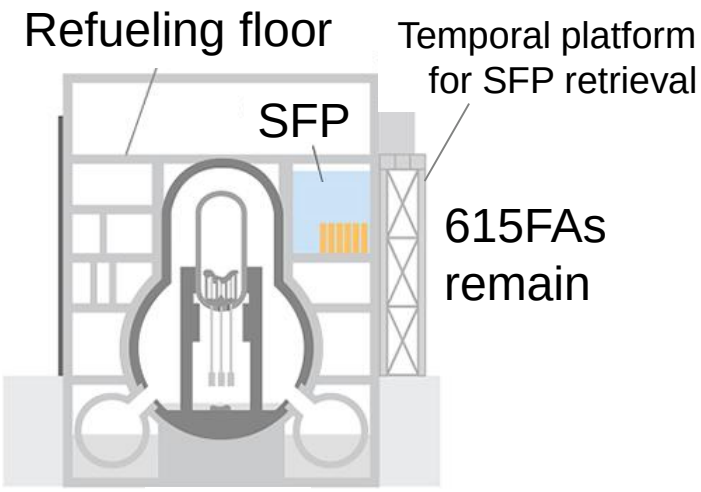

Unit 2

566/566 FAs removed (2021/2/28)

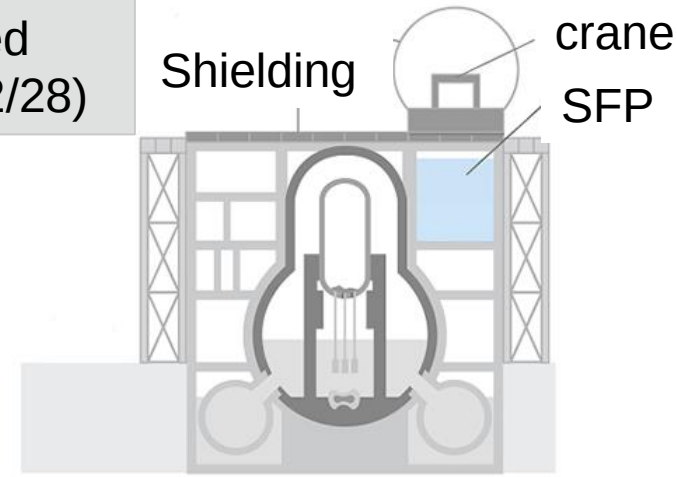

Unit 3

1535/1535 FAs removed (2014/12/22)

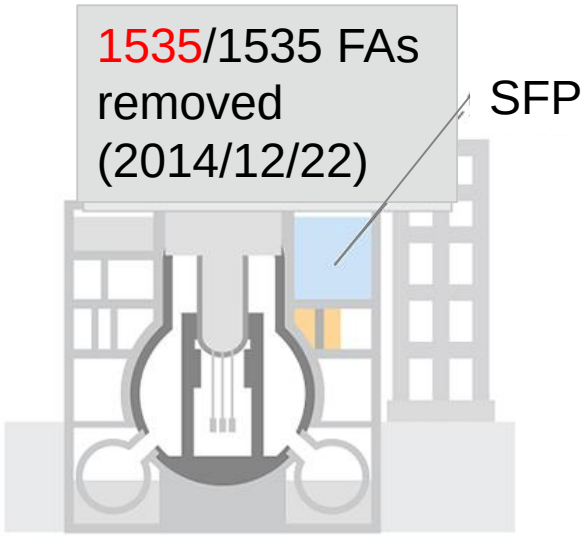

Unit 4

4.3 Facility overview for ALPS Treated Water

Contaminated water as a mixture of underground water and FPs was decontaminated by ALPS etc.. We are in preparation process to discharge treated water about 1.3Mm^3.

Secondary treatment facility (new RO equipment)

Secondarily treats treated water to be purified whose sum of ratios of legally required concentrations of nuclides, with the exception of tritium, is 1 to 10.

Secondary treatment facility (ALPS)

Secondarily treats treated water to be purified whose sum of ratios of legally required concentrations of nuclides, with the exception of tritium, is 1 or higher.

Measurement/confirmation facilities

Consists of three groups, each of which is responsible for receiving, measurement/confirmation, and discharge. In the measurement/confirmation process, water is circulated and stirred to become homogenized, and then sampled for analysis. (Approx. 10,000 m^3 × 3 groups)

ALPS treated water transfer pump

Seawall

Installed mainly around emergency isolation valves and transfer piping.

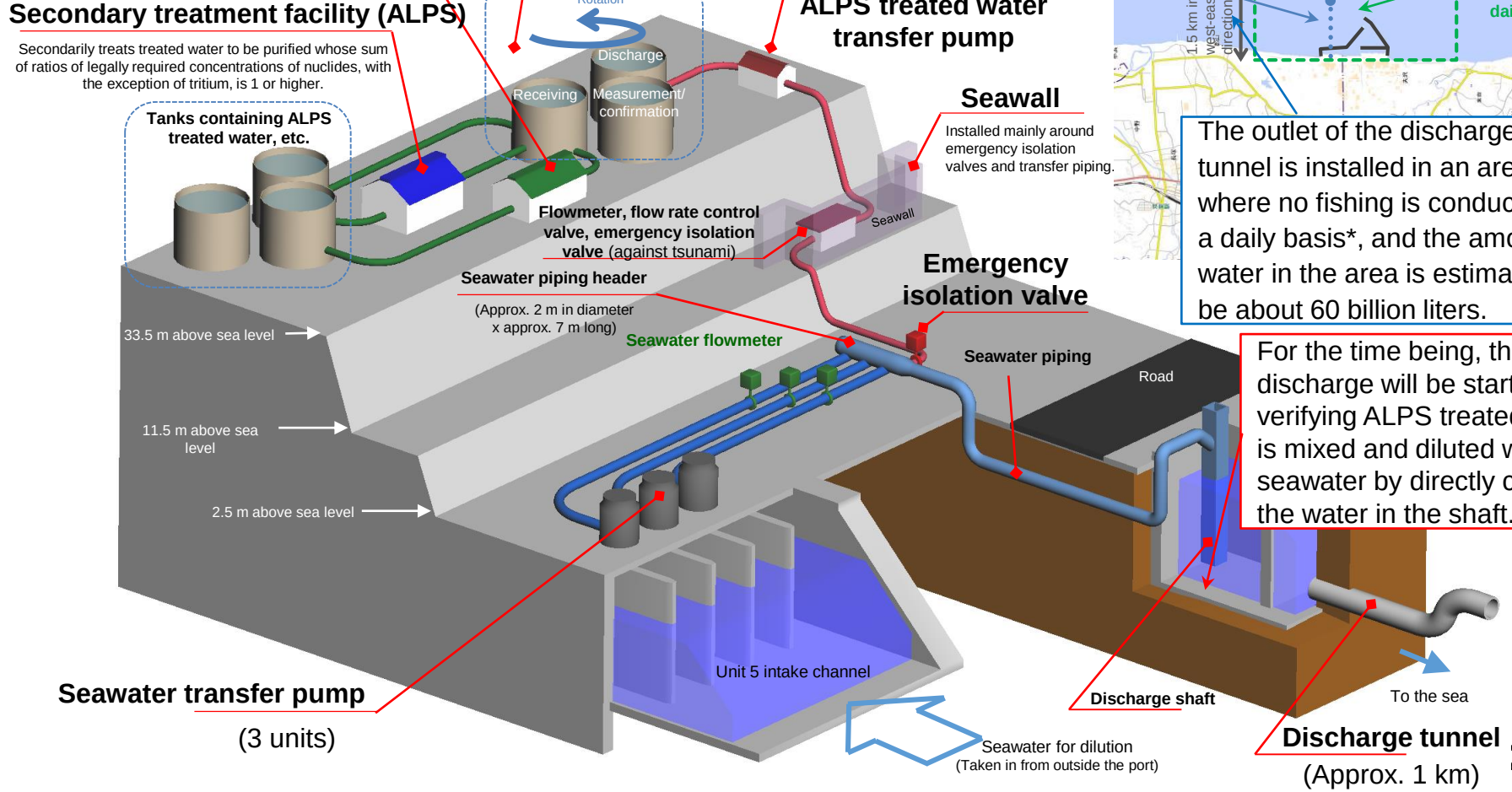

Source: Prepared by Tokyo Electric Power Company Holdings, Inc. based on the map published by the Geospatial Information Authority of Japan (Electronic National Land Website)
https://maps.gsi.go.jp/#13/37.422730/141.044970/&base=std&ls=std&disp=1&vs=c1j0h0k0l0u0t0z0r0s0m0f1

The outlet of the discharge tunnel is installed in an area where no fishing is conducted on a daily basis*, and the amount of water in the area is estimated to be about 60 billion liters.

For the time being, the discharge will be started after verifying ALPS treated water is mixed and diluted with seawater by directly checking the water in the shaft.

*Area where common fishery rights are not set.

5.Conclusion

- In this talk, debris distribution and interaction between molten core and pedestal were focused on, because those are crucial for decommission.
- Depending on the accident progressions in each plants, the current status inside PCV are very different each other.
- Owing to the progress of PCV internal investigation, the conditions of accumulated debris inside pedestal were figured out except for unit 1.
- TEPCO’s Investigation team are now inserting the ROV to PCV outside of pedestal in unit 1. And it will enter inside pedestal within this JFY 2022.

- Other D&D activities are also on-going, such as spent fuel removal from SFP, treated water disposal.
- Thank you for the IAEA and international experts’ support!!

- It is expected that lessons learned from this accident will contribute to the enhancement of future nuclear safety to prevent the accident like Fukushima Daiichi.

Thank you for your kind attention.

3．ROV-A2調査概要と調査実績

■ 調査範囲はPCV地下階の0°から215°（ペデスタル開口部含む）とし，カメラによる目視調査を計画

＜主な調査箇所＞

- 既設構造物の状態確認及び堆積物の広がり状況･高さ･傾斜確認
- ペデスタル開口部付近の状況及び開口部近傍のコンクリート壁状況（★箇所）
- ジェットデフレクター付近の堆積物状況（⬇ 箇所）
- 堆積物上の中性子束測定（▼箇所）

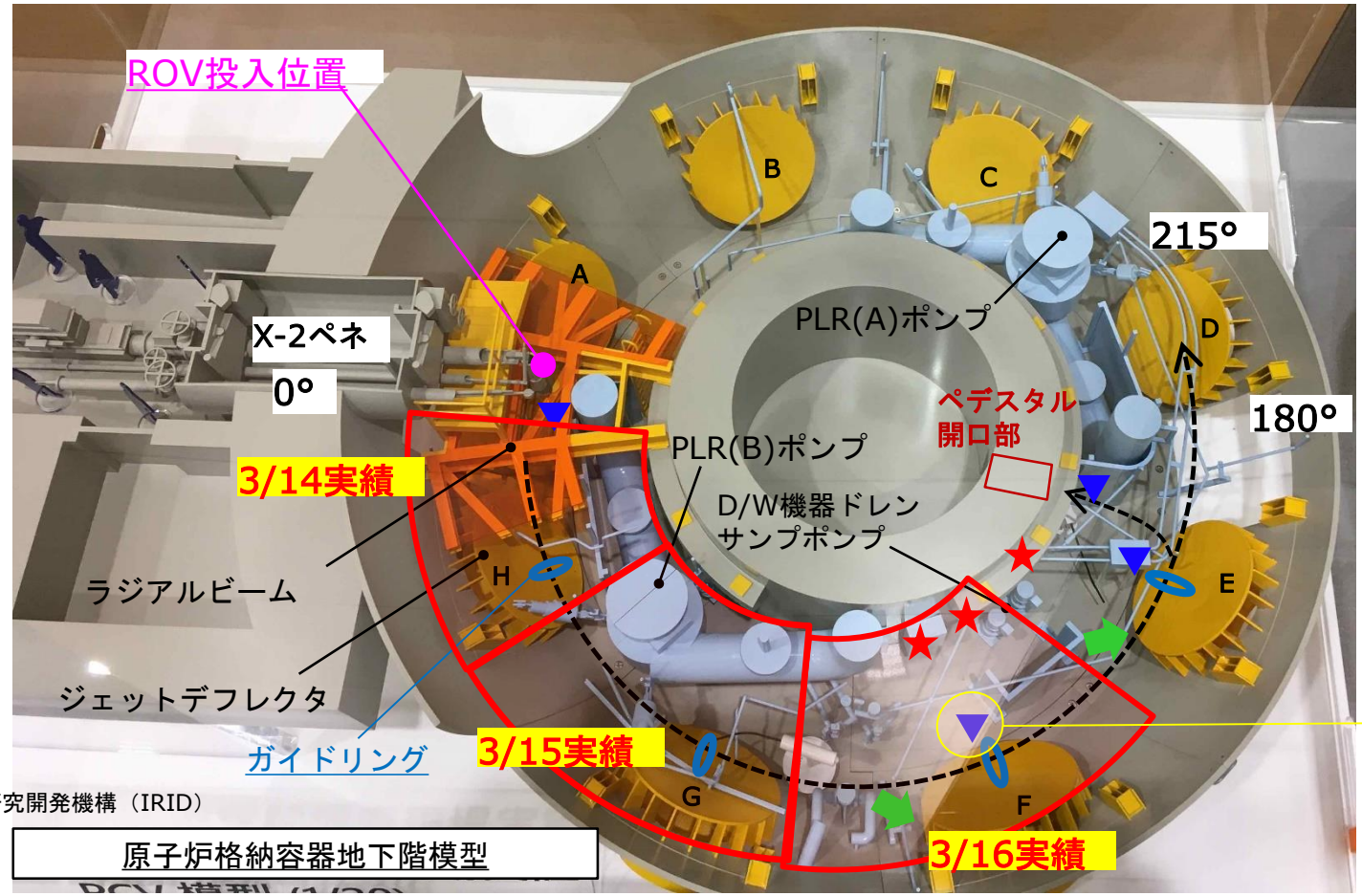

資料提供：
国際廃炉研究開発機構（IRID）

原子炉格納容器地下階模型

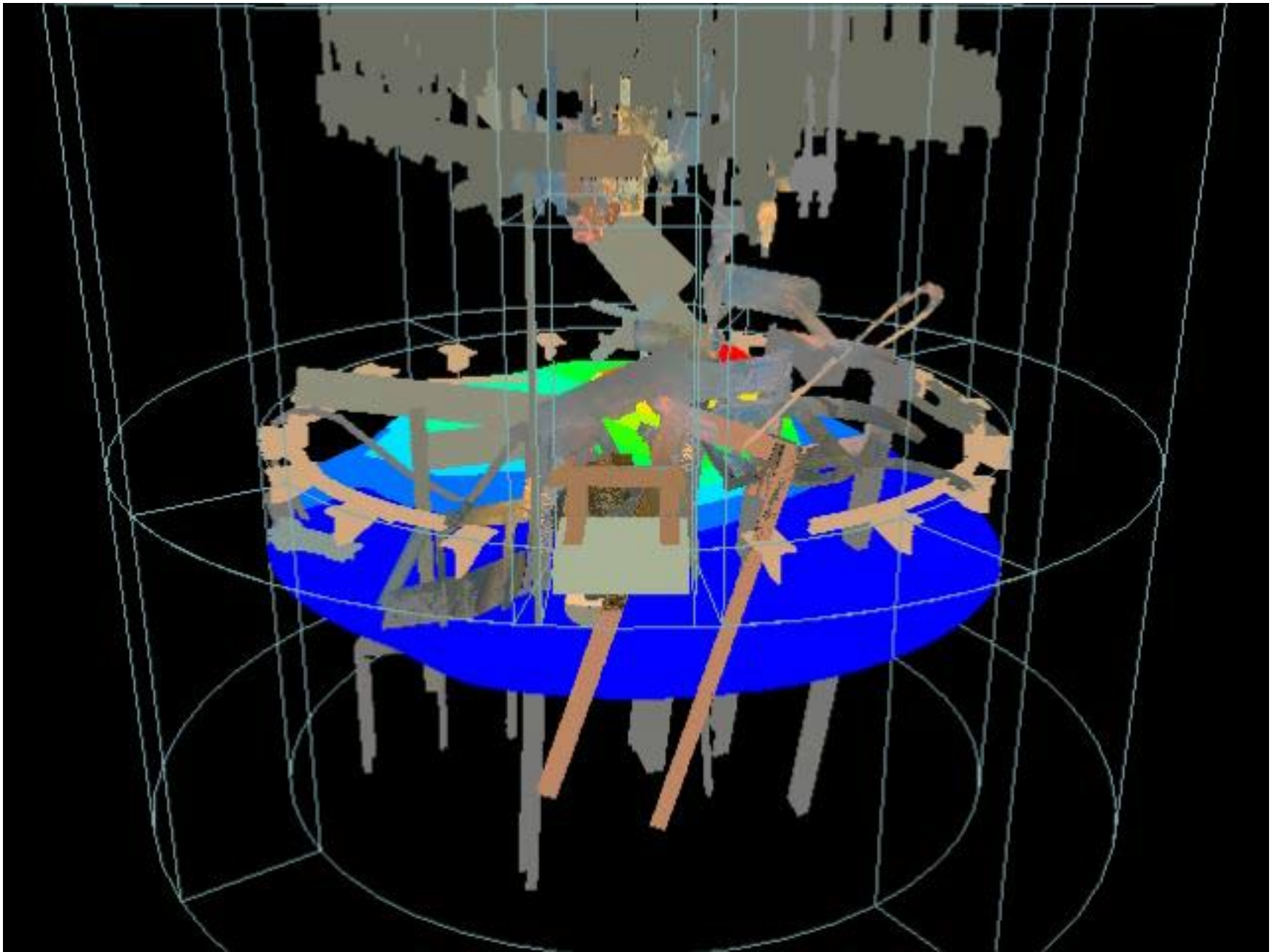

TEPCO

5. Investigation result and 3D map in the

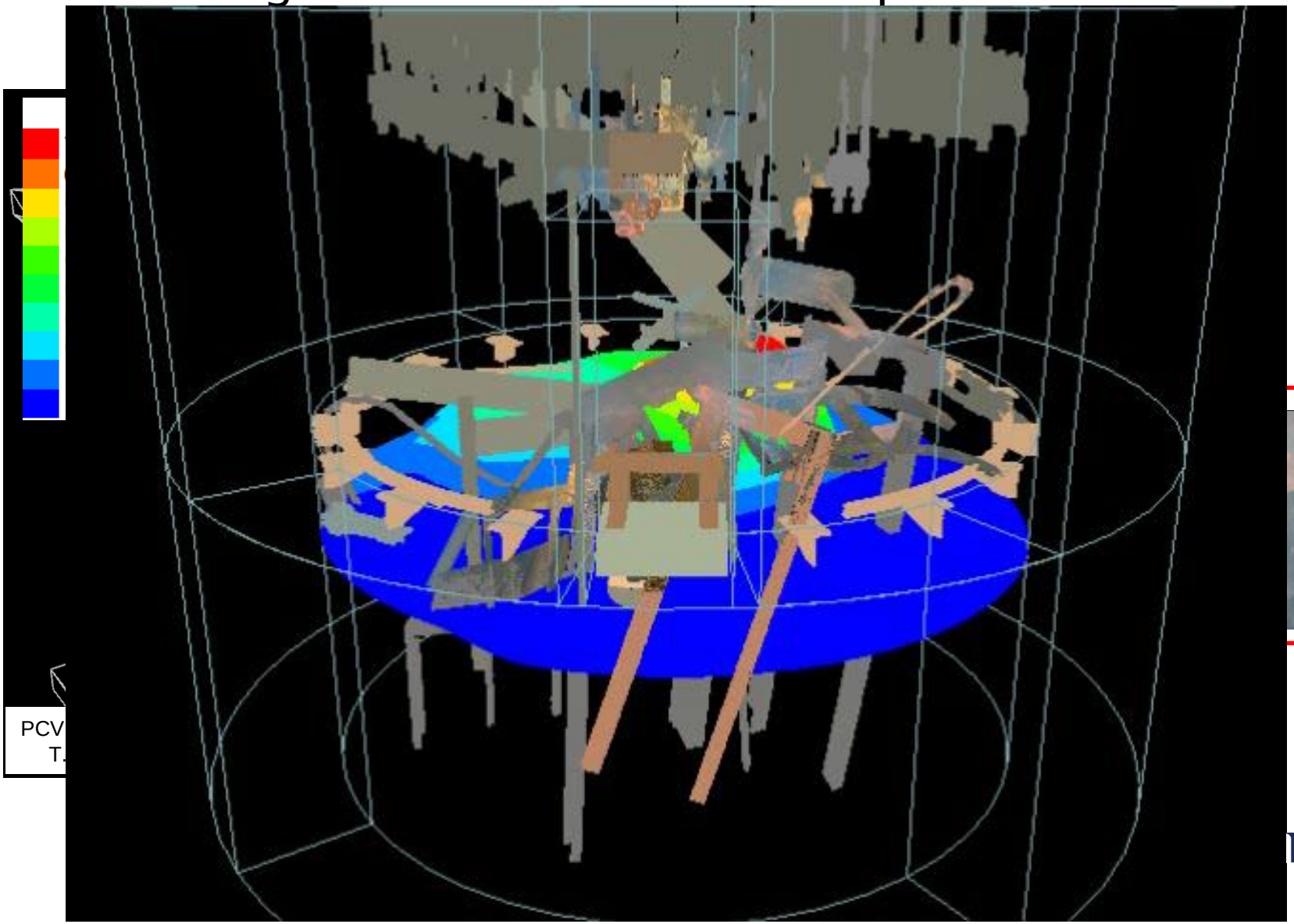

IRID

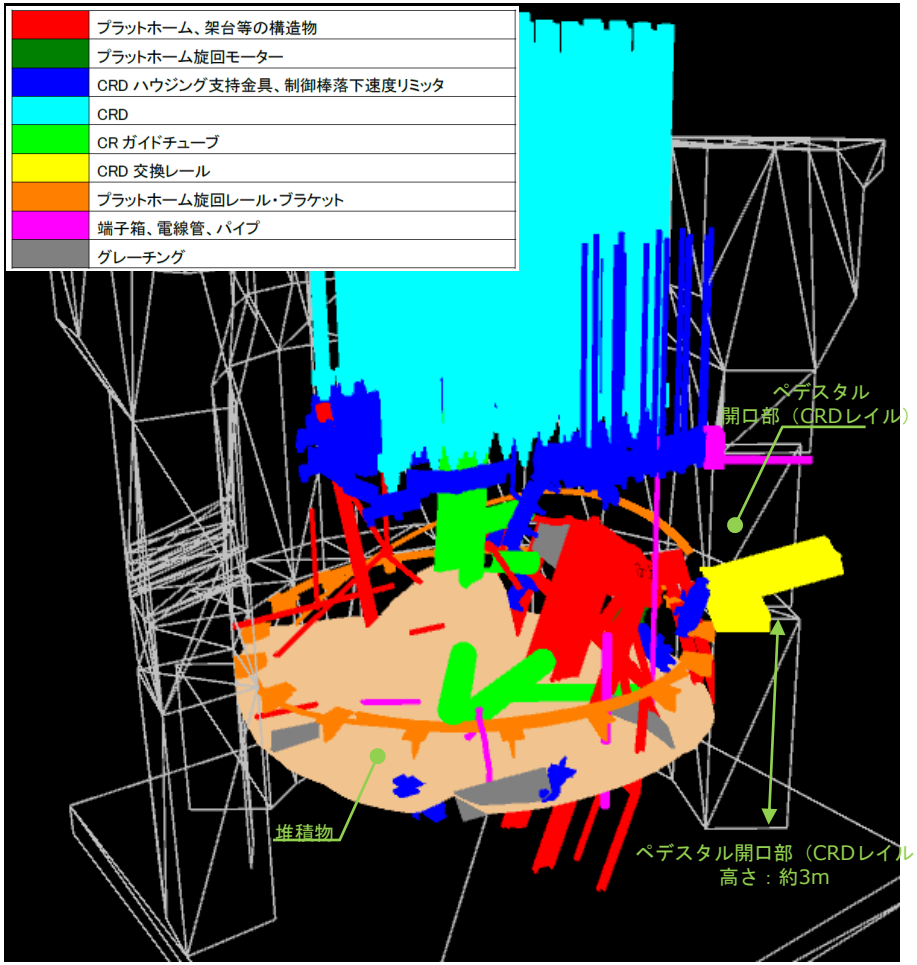
プラットホーム、架台等の構造物
プラットホーム旋回モーター
CRD ハウジング支持金具、制御棒落下速度リミッタ
CRD
CR ガイドチューブ
CRD 交換レール
プラットホーム旋回レール・ブラケット
端子箱、電線管、パイプ
グレーチング
ペデスタル
開口部（CRDレイル）
堆積物
ペデスタル開口部（CRDレイル）
高さ：約3m

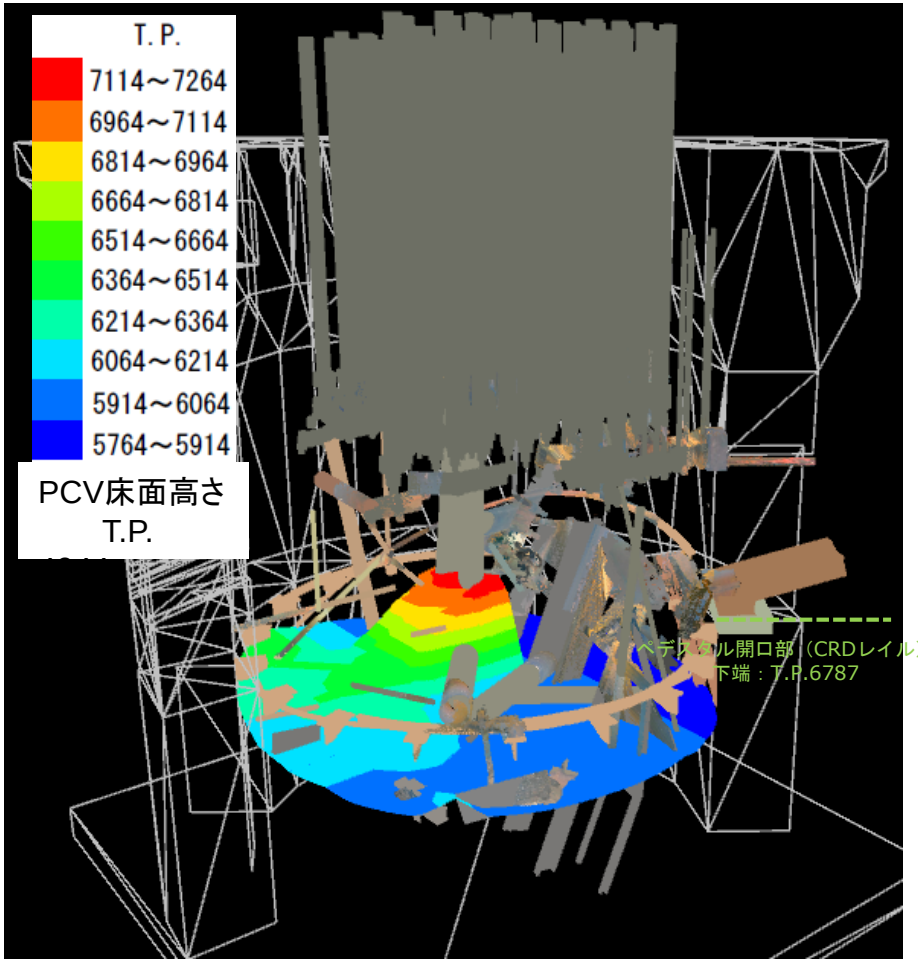
T. P.
7114～7264
6964～7114
6814～6964
6664～6814
6514～6664
6364～6514
6214～6364
6064～6214
5914～6064
5764～5914
PCV床面高さ
T.P.
ペデスタル開口部（CRDレイル）
下端：T.P.6787

（参考）調査装置概要

水中ROVは6種類（A/A2/B/C/D/E）を準備し、調査を行う5種類(A2/B/C/D/E)とケーブル引掛りの事前対策用のROV-Aがある

㋐ROV-A（ガイドリング取付用）

・有線型水中ロボットの遊泳機能（スラスタによる推進/旋回/潜航）を阻害する要因は自身の動力・通信ケーブルの構造物等への引掛りが支配的である。
・ケーブルがPCV地下階で自由に動いて構造物などに引っ掛からないように、ガイドリング（輪っか）をROVが通過することでケーブルの自由度を制限する。
・ROV-Aはガイドリングをジェットデフに取付ける水中ROVである。

直径25cm×長さ111cm

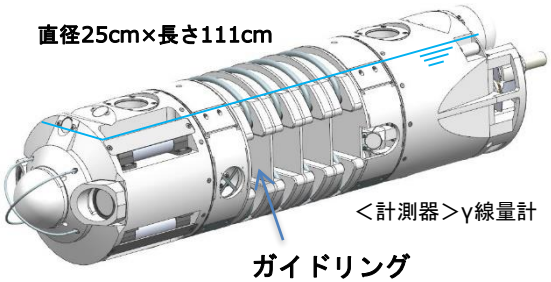

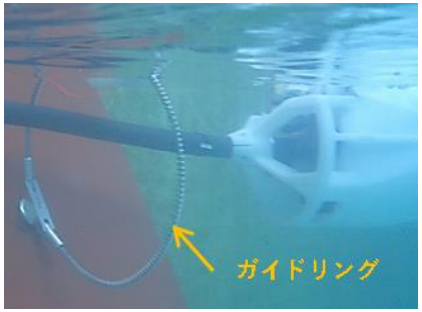

㋑ROV-A2（詳細目視調査用）

・カメラにより映像を取得
・6種類のROVの中で唯一ペデスタル内部に侵入するROV
・ペデスタル開口部の侵入スペースが不明であるため、極力小型化した設計としている

縦17.5cm×横20cm×長さ45cm

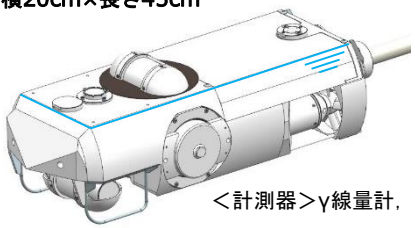

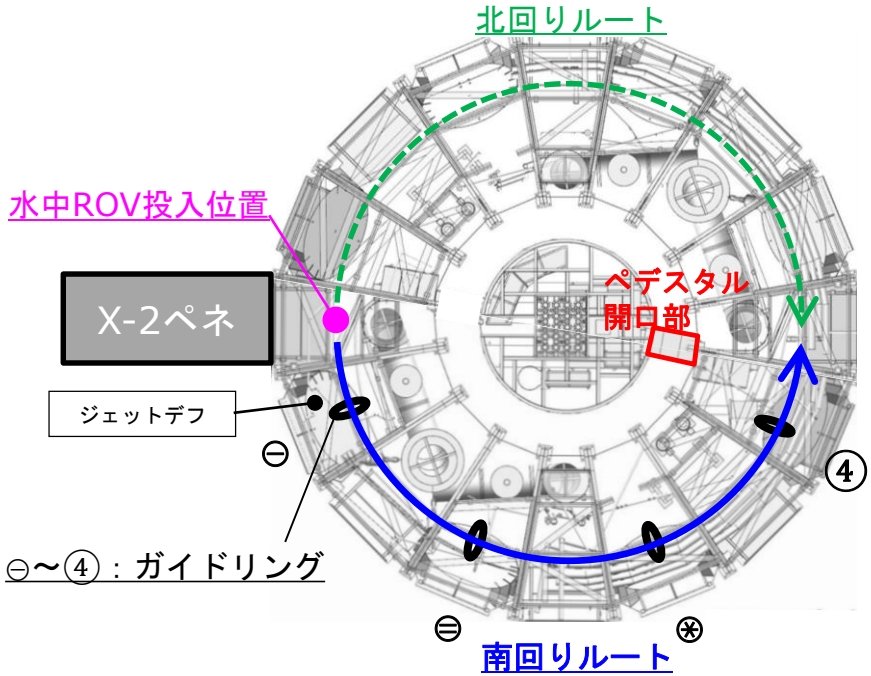

㋒ROV-B/C/D/E（各調査用）

・ROV腹部に各調査用センサ類を搭載したROV

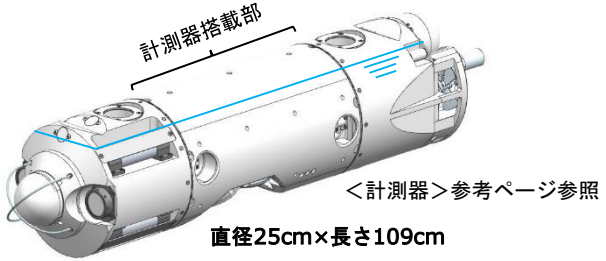

ROV	項目	計測方法
B	堆積物3Dマッピング	走査型超音波距離計
C	堆積物厚さ測定	高出力超音波
D	燃料デブリ検知	核種分析/中性子束測定
E	堆積物サンプリング	吸引式サンプリング

資料提供：国際廃炉研究開発機構（IRID）

3.4 RCIC turbine system

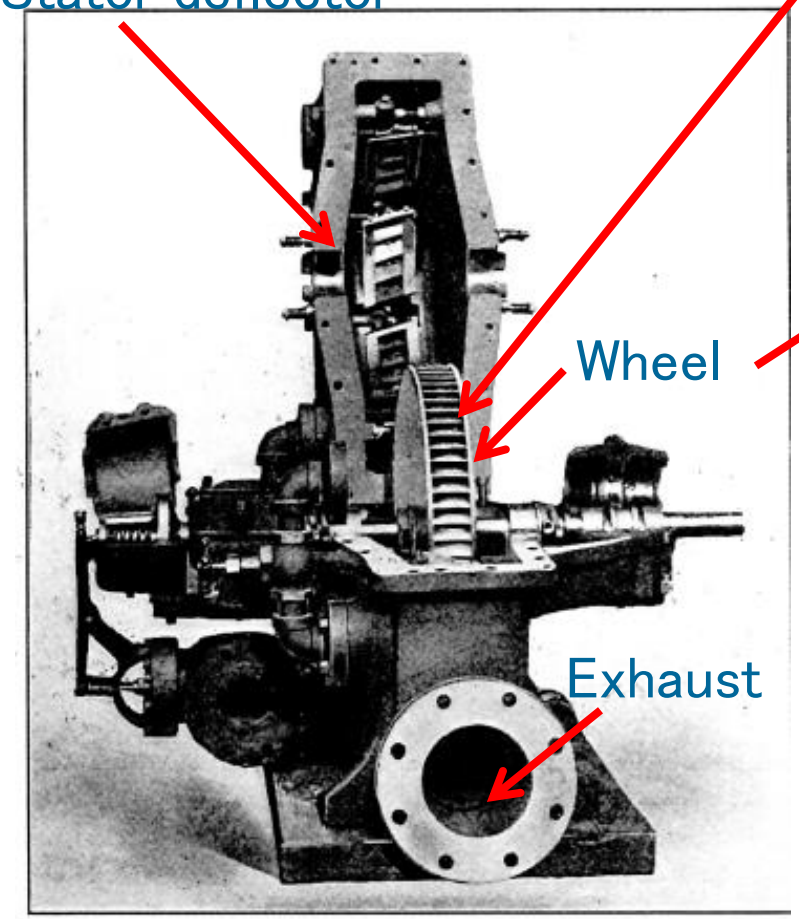

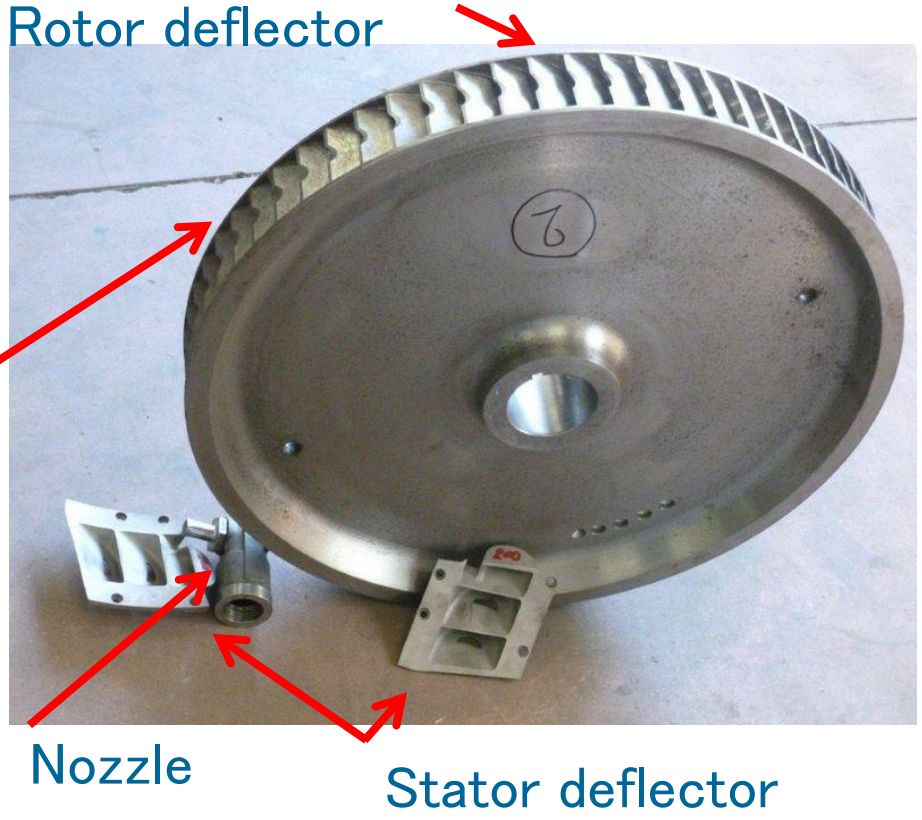

This simple system can continue operation even by water rich steam.
There is a possibility to enhance nuclear safety by using this knowledge.
Of course, it is required to develop the CET database outside of Tech. Spec..

[Reference] Overview of discharge tunnel design

- Design overview
  - As the discharge tunnel is designed to pass through the bedrock layer, the leakage risk is small, and the seismic resistance is excellent. The design also considers the impact of typhoons (high waves) and storm surges (sea level rise).
  - This time, a shield method is adopted, and double-layer seals are installed on the tunnel wall-facing materials made of reinforced concrete (segments) to ensure water cut-off performance.

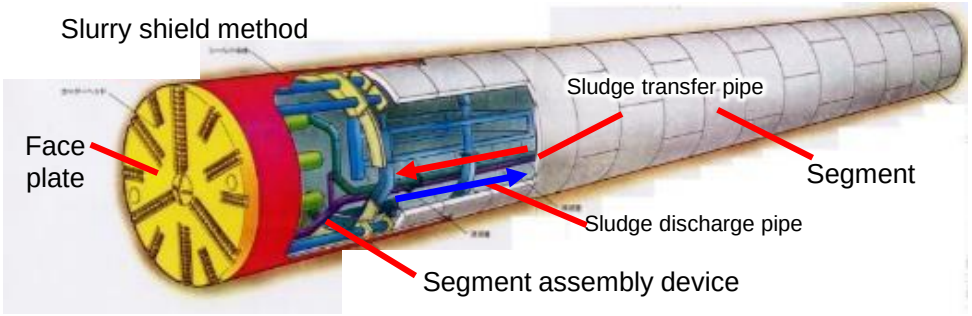

Schematic diagram of a shield machine

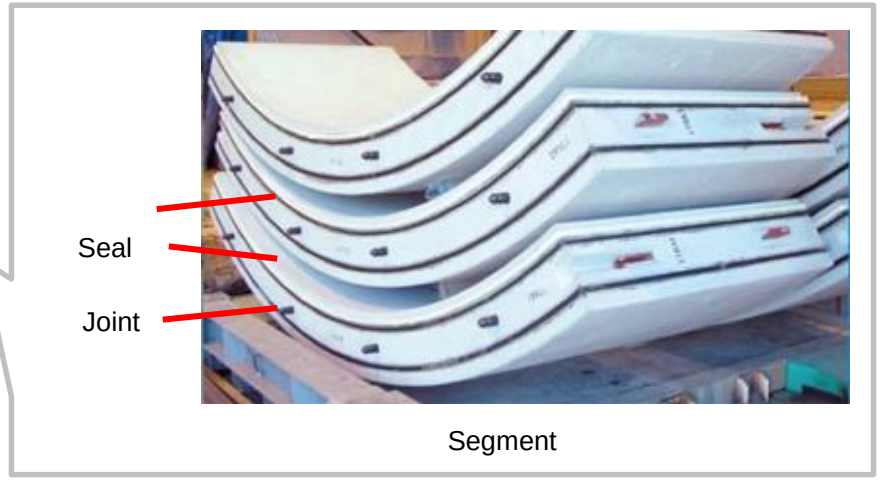

Segment

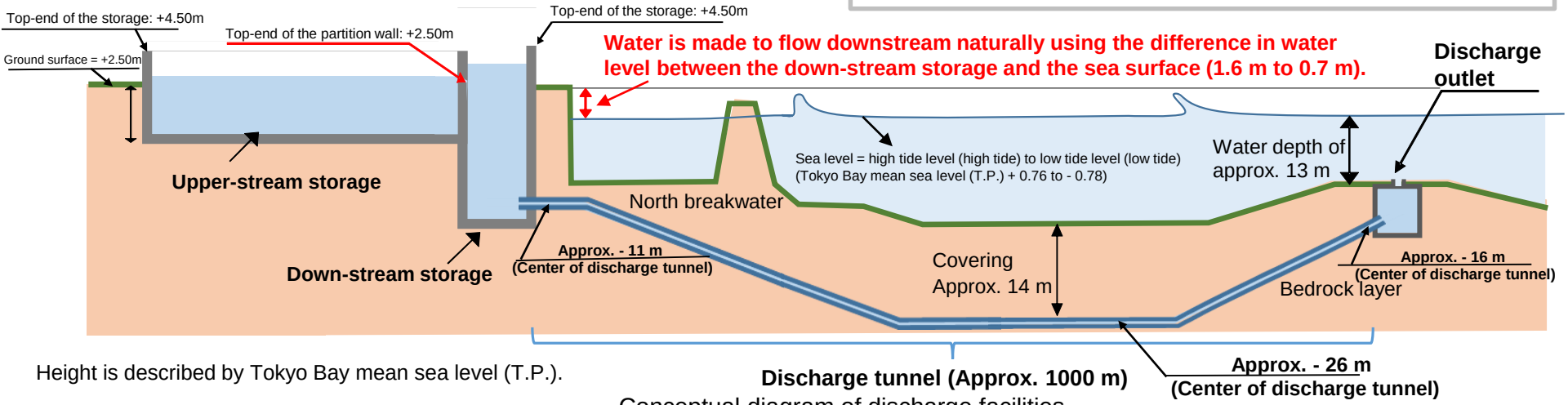

Height is described by Tokyo Bay mean sea level (T.P.).

Conceptual diagram of discharge facilities

The 10th European Review Meeting on Severe Accidents Research

Severe Accident Research Eleven Years after the Fukushima Accident

May 16-19, 2022, Karlsruhe, Germany

Technical Session 1-2: In-vessel Corium and debris coolability

Chairs: S. Massara (IAEA), F. Gabrielli (KIT)

ID300	**Characterization of prototypic corium sample simulating Fukushima Daiichi unit 2 lower head composition** C. Journeau (CEA)	**Paper** **Presentation**
ID309	**Modelling of premixed layer in stratified fuel–coolant configuration** M. Uršič (IJS)	**Paper** **Presentation**
ID322	**Analysis of RANS Turbulence Models of Natural Convection of Corium Pool for In-Vessel Retention** D. Dovizio (NRG)	**Paper** **Presentation**
ID277	**Assessment of a dynamic global-coefficient subgrid-scale model for turbulent natural convection in a confined cavity** S. Whang (SNU)	**Presentation**

10TH CONFERENCE ON SEVERE ACCIDENTS RESEARCH
May 16-19, 2022 – Karlsruhe, Germany
ERMSAR 2022

CHARACTERIZATION OF PROTOTYPIC CORIUM SAMPLE SIMULATING FUKUSHIMA DAIICHI UNIT 2 LOWER HEAD COMPOSITION

Christophe Journeau, Diego Molina*
CEA, DES, IRESNE
DTN, SMTA, Severe Accident Experimental Laboratory, Cadarache,
F 13108 Saint-Paul-lez-Durance, France
christophe.journeau@cea.fr, diego.molina@cea.fr

Renaud Domenger, Emmanuelle Brackx, Célia Guevar, Véronique Testud
CEA, DES, ISEC,
DMRC, SASP, Material chemical analyses and characterization Laboratory,
Marcoule, F 30207 Bagnols-sur-Cèze, France
renaud.domenger@cea.fr, emmanuelle.brackx@cea.fr,
celia.guevar@cea.fr, veronique.testud@cea.fr

Atsushi Ikeda-Ohno
International Research Institute for Nuclear Decommissioning (IRID) / Japan Atomic Energy Agency (JAEA), Collaborative Laboratories for Advanced Decommissioning Science (CLADS),
2-4 Shirakata, Tokai-mura, Naka-gun, Ibaraki 319-1194, Japan
ikeda.atsushi16@jaea.go.jp

ABSTRACT

Prototypic fuel debris samples have been fabricated to represent the lower head corium composition estimated in Fukushima Daiichi Unit 2. The average from BSAF benchmark calculations have been considered. It corresponds to a zirconium oxidation ratio of about 25%. In this test, depleted uranium oxide has been used, fission products have been represented by their natural isotopic composition and cerium has been used as surrogate for transuranium elements. The load, made from 19 different raw materials, has been melted by induction heating in the VULCANO facility under a nitrogen flow representative of BWR containment atmosphere. 11 kg of in-vessel prototypic fuel debris blocks have been fabricated.
Scanning Electron Micrography of samples from these fuel debris prototypes has been carried out in conjunction with Energy Dispersive Spectrometry and X-Ray Diffraction. Quantitative phase analysis were realized with Rietveld method. This provides insights on the composition of these debris and the large number of phases (Uranium-zirconium oxides, uranium-zirconium oxynitrides, zirconium boride, metallic phases …) present in them.

KEYWORDS
Fukushima Daiichi, fuel debris, prototypic corium, SEM-EDS, XRD

* Current affiliation: CEA, DES, IRESNE, DTN, STCP, Sodium Technological Test Laboratory, Cadarache, F 13108 Saint-Paul-lez-Durance, France

1. INTRODUCTION

One of the important challenges for the decommissioning of the damaged reactors of the Fukushima Daiichi Nuclear Power Station (1F) is the fuel debris cutting and retrieval. Therefore, the Technical Strategic Plan 2020 for Decommissioning of the Fukushima Daiichi Nuclear Power Station [1] indicates that "*an optimum combination of retrieval methods should be selected depending on the location where fuel debris exists for each reactor unit*" and that "*it is important to proceed with research and development toward a future scale expansion*" from the small scale retrieval of loose debris. To carry out necessary experimental R&D on debris cutting issues, it is necessary to have simulants of 1F fuel debris [2]. Due to the expected heterogeneity of fuel debris, industrial materials such as ceramic and/or metallic pieces [2, 3] are not suitable for a complete validation. Fuel debris simulants have thus been fabricated with non-radioactive simulants [4, 5] but uranium chemistry cannot well be simulated so that there is interest in carrying out experiments with uranium-containing prototypic fuel debris [2].

Within the URASOL project carried out for IRID/JAEA by a French consortium (CEA, IRSN, ONET) [6], uranium-containing fuel debris prototypes have been fabricated at VULCANO facility in CEA Cadarache site in order to estimate the dust production during thermal or mechanical cutting. This paper concentrates on an in-vessel fuel debris prototype. In a first part, the fabrication process will be described. Then, material analyses of samples from this prototype blocks will be presented.

2. FUEL DEBRIS PROTOTYPE FABRICATION

2.1. Fuel Debris Prototype Composition

The composition of the in-vessel prototypic fuel debris has been determined from the average of the Fukushima Daiichi Unit 2 lower head debris composition computed by CIEMAT (Spain), CRIEPI (Japan), IAE (Japan) and IBRAE (Russia) within the OECD/BSAF project [7] with the fission product inventory 10 years after the accident [8]. This corresponds to the non-radioactive simulant materials that had previously been fabricated with hafnium dioxide as surrogate for uranium dioxide [9]. Table I presents the obtained composition. In this composition, depleted uranium oxide is used. Only 24% of zirconium is oxidized in this composition. The fission products representing more than 0.014 wt% (except technetium) have been replaced by their natural isotopic composition.

Table I. Load composition for test VF-U2 (wt%).

UO_2	35.7%	$CsOH.H_2O$	0.06%
Zr	34.5%	BaO	0.04%
ZrO_2	18.8%	La_2O_3	0.032%
CeO_2	0.2%	PdO	0.030%
SnO2	0.9%	Pr_2O_3	0.030%
B4C	1.0%	Sm_2O_3	0.015%
Stainless steel 304L	8.4%	SrO	0.022%
RuO_2	0.06%	Y_2O_3	0.014%
Nd_2O_3	0.11%	TeO_2	0.029%
MoO_2	0.09%		

Capriotti et al. [10] have shown that "*many similarities exist between the system Pu-O and the system Ce-O, even in the very high temperature behavior*" and that "*CeO_2 displays … a melting behaviour which has been recently proven to be typical of other similar metal-oxygen systems such as Ca-O, Np-O and Pu-O*", Also, Raraz et al. [11] concluded that "*the prominent similarities [between Ce and Pu] include the electronic structure, specific heat, standard electrode potential, electrical resistivity […], and volume expansion upon solidification. Melting and boiling points [Ce boils at 3446°C and plutonium at 3560°C], thermal conductivity, density, viscosity, atomic weight, heat of fusion and coefficient of thermal expansion are the prominent dissimilarities*". Claparede et al. [12] justify the use of cerium as plutonium surrogate on the similarities of ionic radii (0.96 Å for Pu^{4+} vs. 0.97 Å for Pu^{4+}; unit cell parameters of 5.395 Å for fluorite-PuO_2 vs. 4.4104 for fluorite-CeO_2). Stockdale et al. [13] considering vaporization of metallic and oxidic compounds recommends the use of natural cerium as a surrogate of plutonium. Cerium has thus been used in this work as surrogate of plutonium and by extension of the other transuranians. Overall, more than 94% of the radioactivity in the inventory is represented in this composition.

2.2. Fabrication in VULCANO facility

Firstly, non-radioactive powders have been mixed. Then, depleted uranium oxide has been mixed with the other powders in a controlled area. Finally, the powders have been transferred to VULCANO facility [15] and loaded in the crucible which is surrounded by induction coils. Figure 1 presents a scheme of the layout of this experimental set-up in the VULCANO cell. The initially planned Faraday cage (displayed in the sketch) has been removed since it had been verified during the simulant material heating tests that it was not necessary. The 304L stainless steel has been inserted inside the powders.

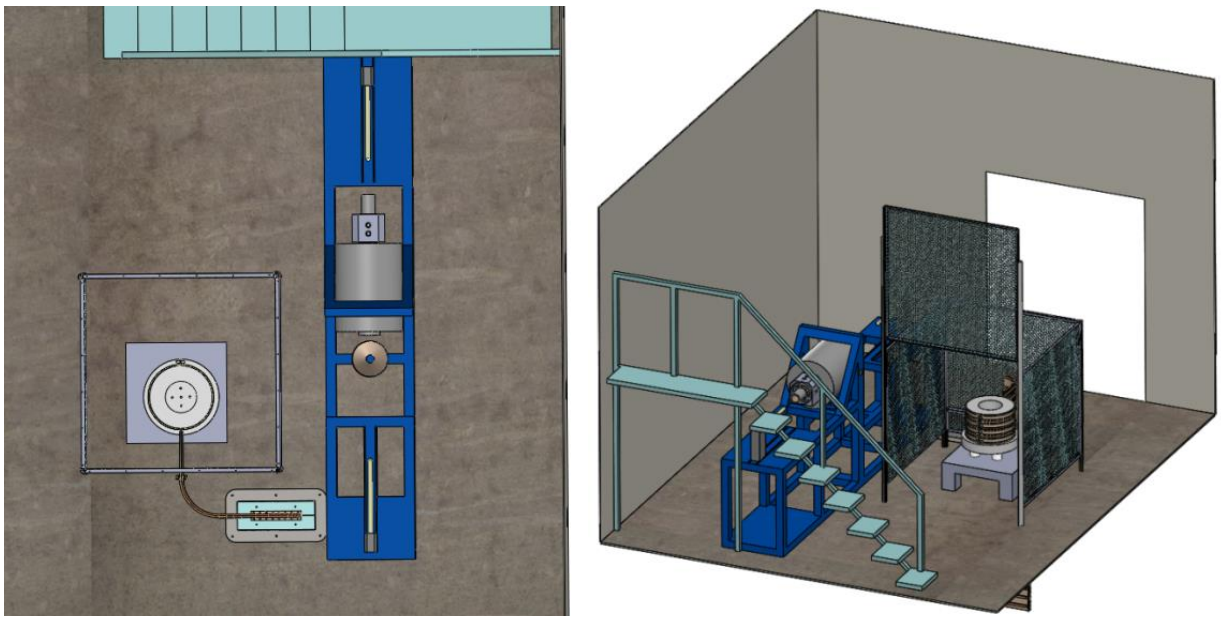

Figure 1. Sketch of experimental set-up in VULCANO cell for VF-U2 test.

Most of the steel is inserted as cylindrical pellets, but a small mass - lower to that of one pellet – has been inserted as 304L stainless steel balls. Finally, the exact required mass is achieved by adding 304L steel powder. Figure 2 left presents a photograph of the load in the crucible before induction heating is started. Nitrogen gas is flown over the crucible to reproduce Primary Containment Vessel atmosphere and to prevent excessive oxidation.



Figure 2. Test VF-U2 at successive stages of process
Left: Before heating; Center: Beginning of heating;
Right: Later in heating phase with visible aerosols.

Induction heating has been applied for 17 minutes, the steel cylinders and balls acting as susceptor until the other loads became conducing. Figure 2 center and right presents some views of the crucible during heating and melting phase. Some aerosol releases were observed as fumes (Figure 2 right). After cooling, the crucible has been disassembled. The solidified melt has broken into pieces, possibly because of thermal stresses. Figure 3 presents the photographs of four of these blocks. Out of the 18 kg of load, 11 kg of prototypic fuel debris have been melted. A golden aspect was locally observed on the surface of some blocks. It is assumed that this correspond to the formation of nitrides in reaction between the prototypic corium and nitrogen, similarly to what had been observed in the simulant blocks.



Figure 3. Some in-vessel prototypic fuel debris blocks from VF-U2 (weighing from 400 to 650 g).

3. MATERIAL ANALYSIS

3.1 Methods

Samples have been taken from the VF-U2 blocks and sent for analysis to LMAT laboratory at CEA Marcoule. In particular, X-ray diffraction is carried out to determine the existing phases. These analyses are complemented by Scanning Electron Microscopy (MERLIN from Carl Zeiss) with Energy Dispersive X-ray spectrometry (SEM/EDS) using an X max detector from Oxford Instruments. From an international round robin on EDS analyses of corium samples [16], uncertainties of about $1/10^{th}$ of the measured values can be considered, except for light elements like oxygen. A systematic error (bias) of $1/4^{th}$ of the oxygen fraction shall be taken into account.
X-Ray Diffraction (XRD) was carried out by a D8 ADVANCE diffractometer from BRUCKER AXS equipped with a copper cathode tube. The tube power was set at 40 kV with 40 mA. 2θ angular scanning

between 20 and 100° with a step of 0.01° and an acquisition time of 1s by step was selected. Samples were crushed into powder before measurement using a sample holder with reflecting mirror.
Diffraction line indexing was performed with DiffracEva software from Bruker AXS with the 2020 Powder Diffraction Files (PDF) international database. The X-ray diffraction patterns have been analyzed by Rietveld refinement with Le Bail pattern matching using the DIFFRAC.TOPAS v6 software distributed by BRUKER. The profile parameters (cell dimensions; peak shape, background, sample displacement correction and asymmetry) were refined. The peak shape was described by a pseudo-Voigt function with the formulation of Caglioti. TOPAS is built around a general non-linear least squares system written specifically to integrate various types of Bragg diffraction for minimizes the resultant, i.e. the difference between the computed and experimental points at all angles.

3.2 Samples

Four samples have been taken from VF-U2 prototypic in-vessel fuel debris. The first three samples are chunks of a few centimeters while sample VF-U2d is a powdery material made of millimeter-sized grains. There is some golden material (likely nitride) on several sample surfaces. Figure 4 presents photographs of these 4 samples.

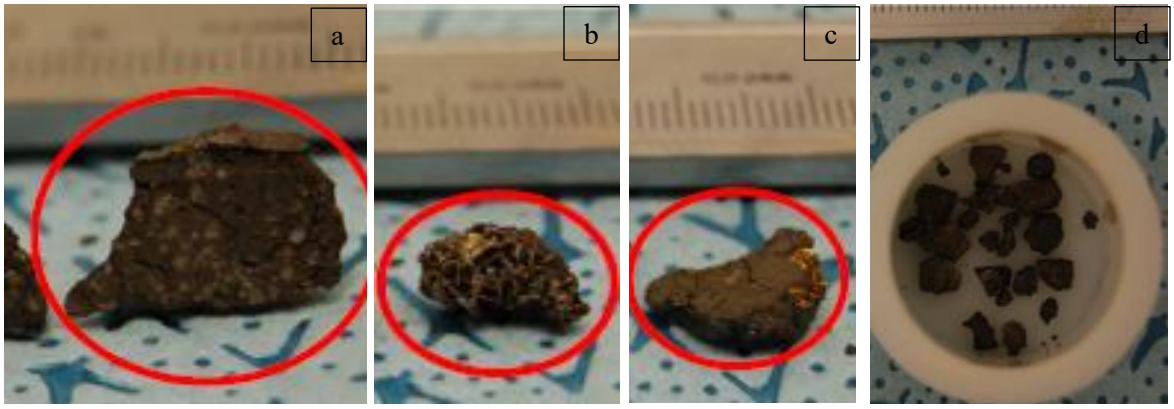

Figure 4. Samples VF-U2a, VF-U2b, VF-U2c, VF-U2d (from left to right).

3.3 SEM-EDX Analysis

Sample VF-U2a surface is presenting less golden aspect than samples VF-U2b or VF-U2c. After cutting, large heterogeneities appears on the visible light macrograph (Figure 5 left) with several whitish areas. The composite SEM micrograph of the same surface (Figure 5 right) also presents some heterogeneous aggregates. A darker aggregate is for instance visible in site 1 and site 2 of Figure 5 right.

Figure 6 presents elemental mapping by EDS of a micrograph at the boundary between the two main areas of site 1. At the bottom of the micrograph, there is a uranium-zirconium oxide. In the top, there is an alternation of metallic zirconium (in purple) and iron-chromium-nickel-uranium alloy (in yellow-green). In between, there is a transition zone.

VF-U2 original materials such as uranium dioxide powder, zirconium grains, stainless steel balls, have all interacted and transformed into this complex microstructure.

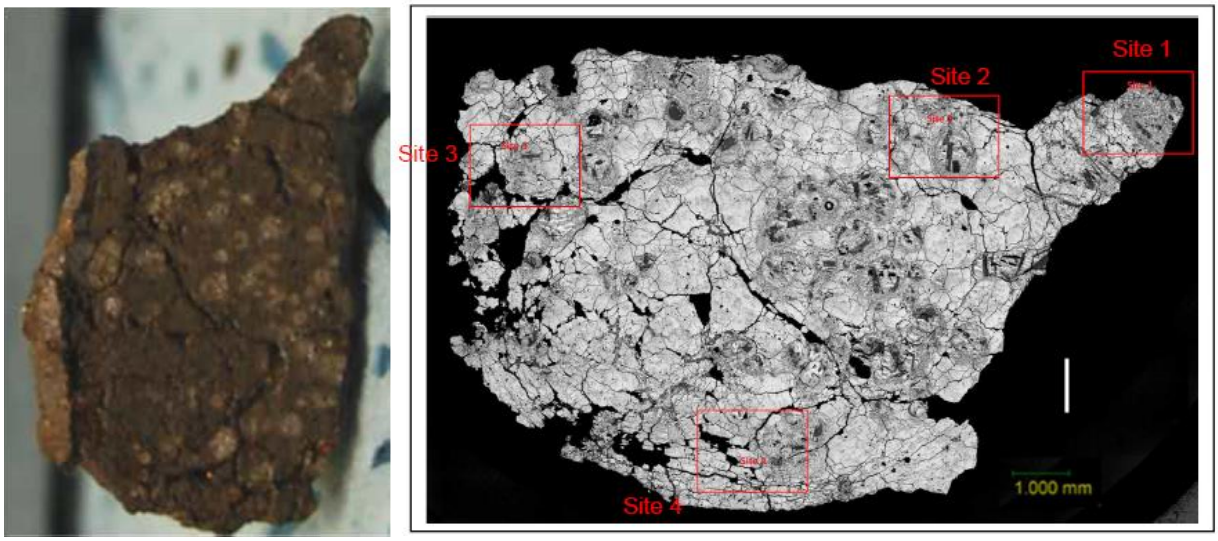

Figure 5. Macrograph (left) and composite micrograph (right) of VF-U2a.

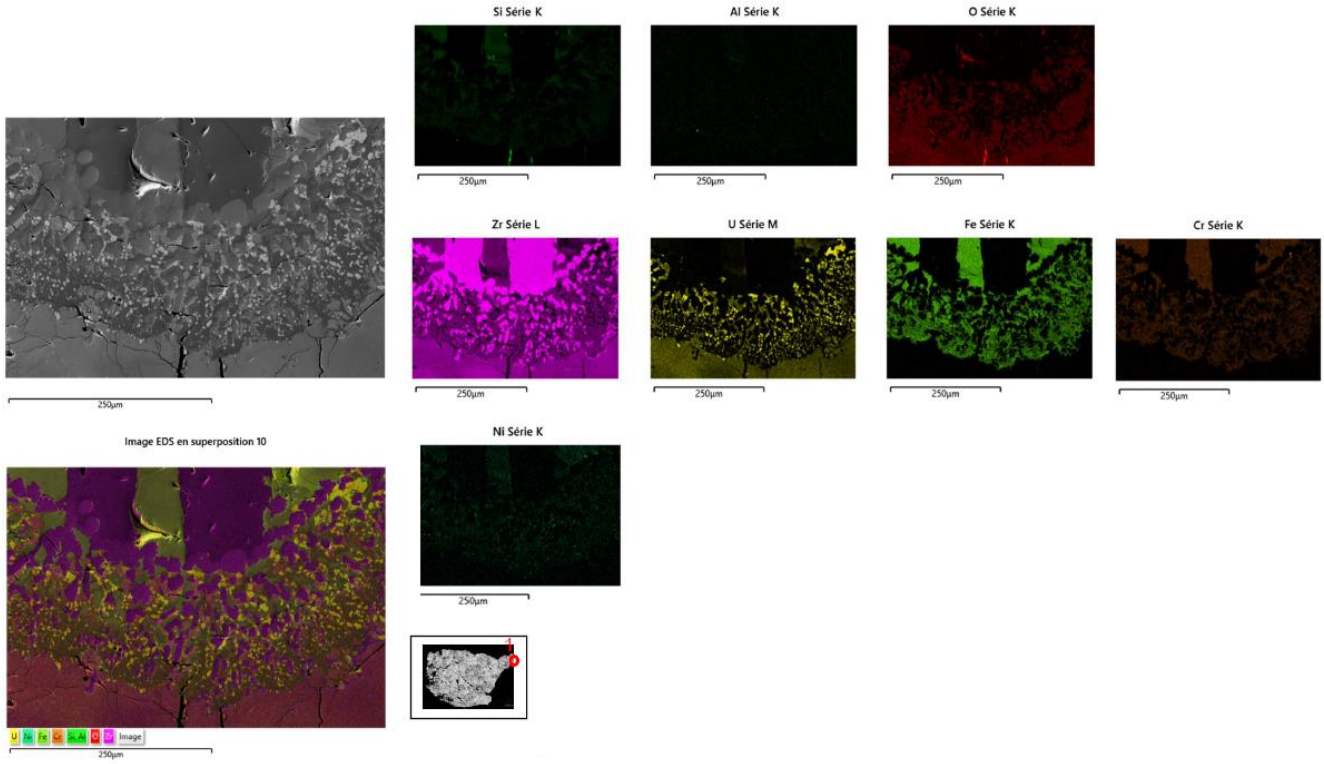

Figure 6. EDS elemental mapping of an area of VF-U2a site 1.

Figure 7 shows 3 micrographs with VF-U2a SEM-EDS analyses. Several uranium-zirconium oxide phases are detected: Point 128 (34 at% U, 3% Zr, 1% Fe, 62% O) and 140 (36 at%U, 2% Zr, 1% Fe, 61% O) are close to $U_{0.9}Zr_{0.1}O_{2-x}$ with some iron solid solution. Point 132 (27 at%U, 6% Zr, 67% O) is close to

$U_{0.8}Zr_{0.2}O_2$. Point 139 is a uranium rich oxide with a large solution of iron, close to $U_{0.6}Fe_{0.3}Zr_{0.1}O_{2-x}$ (24 at% U, 10% Fe, 4% Zr, 3% Cr, 2% Ni, 1% Si, 56% O). Zirconium-rich oxides have also been observed as $Zr_{0.8}U_{0.2}O_{2\pm x}$ (point 131: 32 at% Zr, 7% U, 61% O; point 142: 28 at% Zr, 7% U, 65% O) or more complex solid solutions as point 134 (33 at% Zr, 6% Fe, 2% Cr, 2% Al, 1% Si, 1% U, 55% O). $U_{0.7}Zr_{0.3}O_{2\pm x}$ and $Zr_{0.7}U_{0.3}O_{2-x}$ have also observed, in other micrographs from this test.

Mixed U,Zr sub-oxidized phase have also been found in other samples (e.g. 29 at% Zr, 23% U, 10 % Ni, 9% Sn, 5% Fe, 2% Si, 1% Cu, 1% Cr, 20% O) and are likely close to α–Zr(O) phase with dissolved uranium. It is remarked that the uranium solution in these α–Zr(O) phases is much smaller than that of hafnium in α–Zr(O) phases analyzed in the surrogate samples simulating the same composition. Other point compositions (e.g. 29 at% Fe, 22% Zr, 6% Cr, 3% Si, 3% Ni, 1% Sn, 1% U, 35% O) could be seen either as a solution of Zr in FeO or as a solution of iron-chromium in α–Zr(O) [23].

Metallic phases such as point 121 (45 at% Fe, 29% Zr, 10% Cr, 9% Si, 4% Ni, 1% Al, 1% U, 1% Sn), 127 (47 at% Fe, 20% Zr, 8% Cr, 8% Ni, 6% U, 5% Sn, 4% Si, 1% Al), 135 (44 at% Fe, 22% Zr, 11% Cr, 7% Ni, 6% U, 5% Si, 3% Sn, 1% Al, 1% Mn) and 136 (44 at% Fe, 27% Zr, 11% Cr, 7% Si, 5% Ni, 2% U, 2% Sn, 1% Al) are alloys of steel with zirconium and uranium, characteristic of in-vessel pools [17] with various compositions. Of all the analyzed alloy compositions, almost all were richer in zirconium than in uranium. Three of the introduced fission product simulants (palladium, molybdenum and ruthenium) have been concentrated enough (around 1 at% for Pd and Mo, around 0.25 at% for Ru) to be detected by EDX in a few iron-rich metallic phases from other samples. The other minor elements (including Ce, the surrogate for Pu) have not been detected and must be quite evenly spread as traces in some of the observed phases, which is a positive point with respect to criticality issues.

Some compositions include neither uranium nor zirconium such as points 130 (53 at% Fe, 42% Cr, 2% Al, 1% Si, 1% Ni, 1% Mo). Point 125 is a tin-zirconium- nickel alloy (34 at% Sn, 32% Zr, 31% Ni, 1% Pd, 1% Fe, 1% U). Palladium is a fission product introduced in the load as monoxide that has been found in this tin-zirconium-nickel alloy. Point 138 is close to Zr_2Fe intermetallic (66 at% Zr, 22% Fe, 6% Cr, 3% Si, 2% Ni, 1% U). A phase close to Zr_5Sn_3 intermetallic [24] (63 at% Zr, 36% Sn, 1% Fe) has been also observed that has a much larger tin fraction than Zircalloy.

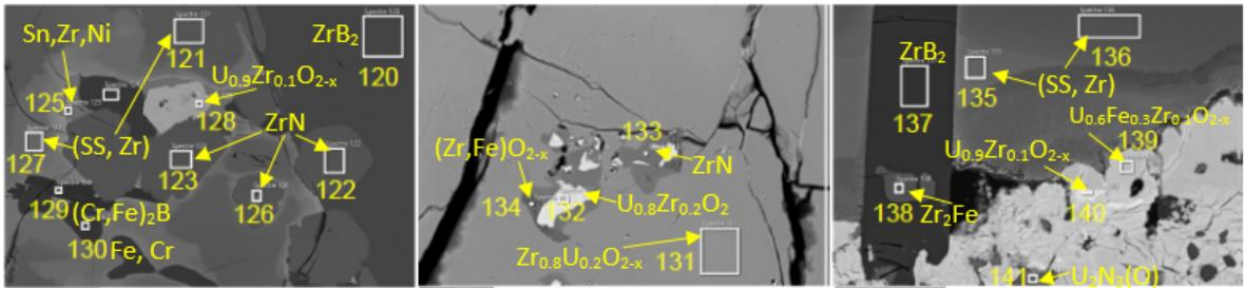

Figure 7: Some EDS analyses of VF-U2a sample micrographs
Left and center micrographs come from site 1, right micrograph from site 2.
Scale is 10 µm long, except for left micrograph (25 µm).

Nitrides are also present (due to the nitrogen flow during the test, representing the PCV nitrogen atmosphere): point 122 is close to slightly oxidized ZrN (54 at% Zr, 39 % N, 7% O, traces U) as points 123 (51 at% Zr, 41% N, 7% O, traces U), 126 (49 at% Zr, 1% Fe, 1% U, 38% N, 12% O) and 133 (42 at% Zr, 54% N, 4% O, traces of U). It must be recalled that ZrN has a reflectance spectrum close to that of gold [18]

and thus a golden aspect. Point 141 is an oxidized uranium nitride (20 at% U, 2 % Zr, 1% Fe, 18 % O, 59% N) that is close to an UO_2 solid solution in U_2N_3 [19]. Some intermediate composition between uranium-zirconium oxide and nitride have also been found in other micrographs (with typical measured composition of e.g. 17 at% U, 7% Zr, 58 % O, 18% N). They could be analogues to (U,Zr) mixtures to the O solubility in U_2N_3 and N solubility in UO_2 observed by Ribeiro Costa et al. during the interaction of UN and UO_2 [20].

Area 120 is rich in boron. As it is a light element, it is quite difficult to quantitatively estimate boron in close vicinity of heavier elements like zirconium and uranium. The estimated composition (23 at% Zr, 2% O, 76% B) is likely to be a slightly oxidized zirconium diboride (ZrB_2, as the only borides in the Zr-B phase diagram are ZrB_2 and ZrB_{12} [21]). It is also found in areas 137 (23 at% Zr, 2% O, 75% B). Contrary to what has been observed in micrographic analyses the simulant in which Table I composition has been simulated by replacing each mole of uranium dioxide by a mole of hafnium dioxide, uranium is not significantly present in these borides. A chromium-iron boride is present at point 129 (52 % Cr, 11% Fe, 36% B, traces of vanadium and sulfur that come from the stainless steel) and is likely $(Cr,Fe)_2B$ [22].

3.4. X-ray Diffraction

Figure 8 presents the X-ray diffraction pattern of powders ground from VF-U2a. The following lines have been detected: zirconium-uranium oxide $U_{0.18}Zr_{0.82}O_2$, zirconium boro-nitride $ZrB_{0.4}N_{0.6}$, overstoichiometric uranium oxide $UO_{2.11}$, and zirconium diboride ZrB_2. Comparing with the EDS analyses, boro-nitride has not been observed. It is assumed that the pattern of zirconium-uranium oxynitride (which may be absent of the database) may be close to that of the boronitride. Likely, the lattice parameter attributed to an 11 at% oxygen overstoichiometry in uranium oxide, could be caused by the presence of 4% of zirconium in solution in cubic UO_2, according to Vegard's law proposed by Trillon et al. [25].

It must be noted that no metallic phase has been detected. This may be due to the large composition variability in the EDS analyses of the metallic phases which leaves each of them below the XRD detection threshold.

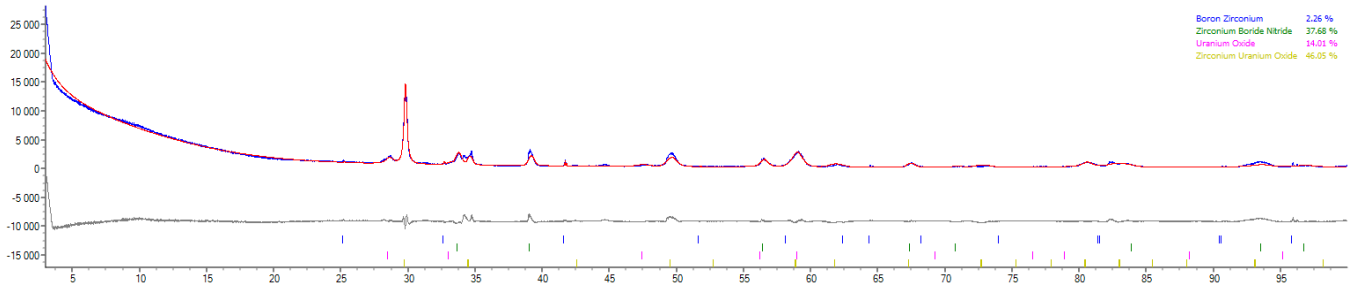

Figure 8: Rietveld refinement of X ray diffraction diagram of sample VF-U2a with X ray Cu *Kα* radiation: Sample VF-U2a (in red), Rietveld best-fit (in blue) and residue (in grey). Lines for zirconium diboride (ZrB_2 in blue), zirconium boro-nitride ($ZrB_{0.4}N_{0.6}$ in green), uranium oxide ($UO_{2.11}$ in purple) and zirconium-uranium oxide ($U_{0.18}Zr_{0.82}O_2$ in yellow) are indicated below the pattern.

Rietveld refinement has been carried out and its results are shown in Figure 8. The phase compositions obtained by Rietveld refinement from the 4 samples are reported on Table II. It appears that VF-U2a and VF-U2b (average value 46 wt% $U_{0.18}Zr_{0.82}O_2$, 38 % zirconium boro-[or oxy]nitride, 14% $UO_{2.11}$, 3% ZrB_2) are close and that there is a second composition representative of samples VF-U2c and VF-U2d compositions (average value 65 wt% $U_{0.18}Zr_{0.82}O_2$, 27 % zirconium boro-(or oxy)nitride, 6% $UO_{2.11}$, 1%

ZrB_2, 1.5% UN_2). This shows the presence of heterogeneity at a macroscopic scale in addition to the microscale heterogeneity seen in the micrographs.

Table II. Comparison of Rietveld best-fit compositions from XRD patterns of the 4 VF-U2 samples.

Phases (wt%)	VF-U2a	VF-U2b	VF-U2c	VF-U2d
zirconium diboride (ZrB_2)	2.3	2.8	0.01	
zirconium boro-nitride ($ZrB_{0.4}N_{0.6}$)	38	39	26	28
uranium oxide ($UO_{2.11}$)	14	13	7	6
zirconium-uranium oxide ($U_{0.18}Zr_{0.82}O_2$)	46	45	66	64
Uranium nitride (UN_2)			1	2

3.5 Chemical Analyses

Although no chemical analyses of this sample have been carried out, those of in-vessel fuel debris simulant samples in which uranium was replaced by hafnium are presented here as they can provide some insights, in particular for the minor elements that have not been detected by EDS. After breaking the sample into pieces, two types of pieces have been separated and analyzed separately as the repartition between these two types was not constant from place to place. They have been determined to represent an oxidic and a metallic part of the sample that are assumed to have solidified from immiscible liquid phases.

Both types have been dissolved and analyzed with ICP-MS (Inductively Couples Plasma Mass Spectrometer) or ICP/AES (Inductively Coupled Plasma Atomic Emission Spectroscopy) depending on the analyzed elements. Table III presents the analyzed compositions. The so-called "metal" type is richer in iron (21.7% vs. 3.5%) and chromium (2.3 vs. 0.7 %). There is a large fraction of zirconium in both types (37-44 %) while the content of hafnium (surrogate for uranium) is much lower in the "metal" (5 vs 32 %). Boron, lanthanum, molybdenum, neodymium, palladium, samarium, tin, strontium and yttrium are largely present in the oxidic debris. Nickel and, to a lesser extent, magnesium and praseodymium have mainly been found in the metallic parts of the debris.

The fact that some elements (like Sn) have been found to be almost 100 times more present in one sample (the oxide) than in the other (the metal) is a good indicator of the quality of the separation that has been done in the sampling phase.

Table III. Composition (wt%) of oxide and metal samples normalized to 100% without oxygen and nitrogen.

Sample	Al	B	Ba	Ca	Ce	Cr	Fe	Hf	La	Mg
Metal	*0.07%*	*0.09%*	*0.007%*	*0.05%*	*0.04%*	*3.42%*	*32.11%*	*7.42%*	*0.01%*	*0.08%*
Oxide	0.11%	1.68%	0.007%	0.05%	0.20%	0.80%	4.18%	38.28%	0.04%	0.04%
	Mo	**Nd**	**Ni**	**Pd**	**Pr**	**Sm**	**Sn**	**Sr**	**Y**	**Zr**
Metal	*0.02%*	*0.06%*	*1.25%*	*0.00%*	*0.05%*	*0.009%*	*0.02%*	*0.00%*	*0.01%*	*55.27%*
Oxide	0.14%	0.16%	0.26%	0.08%	0.03%	0.022%	1.59%	0.02%	0.03%	52.26%

From the knowledge of the initial composition and of the elements released during the fabrication phase, it is possible to propose the following scheme that would explain the measured compositions. A good fit is

obtained when assuming that 81 wt% of the mass contributes to the oxidic phase, 14 wt% to the metallic phase and 5 wt% is volatilized. For each element, a fraction of oxide and volatiles has been attributed (the remainder being metal phase) in order to fit the measured data within uncertainties. For instance, 80% of zirconium is attributed to the oxides, about 5% to volatiles and 15% to metal. For iron, on the opposite, 48% is considered oxidized, 1% volatilized and 51% in metal phase. It appears that almost all cesium and tellurium have been volatilized (as these elements were not detected in the solid samples, even though some Cs and Te have been observed in the aerosols released from the laser cutting of these in-vessel simulant fuel debris [9] indicating the presence of some traces of these volatiles in the blocks), as well as 68% of nickel, 38% of chromium, 1% of cerium (surrogate for plutonium and transuranians), tin and hafnium (surrogate for uranium). In the absence of direct analyses, the released fraction during fabrication, which can somewhat reproduce the releases during severe accident, could be, in first approximation, transposed from this simulant to the uranium-containing prototype, especially for the elements with large volatilities.

4. CONCLUSIONS

An in-vessel fuel debris prototype has been defined from calculations of Fukushima Daiichi Unit 2 scenario. From a load of powders, including depleted uranium dioxide, stainless steel and 15 other elements, 11 kg of in-vessel fuel debris blocks have been fabricated in the VULCANO facility by induction heating.

In this test, no gravitational segregation of metallic and oxidic phases has been observed as it was the case for ex-vessel (Molten Core Concrete Interaction) compositions [2] for which the density of the oxidic layer is much smaller than that of the metal layer. Nevertheless, the obtained blocks presented both macroscopic segregation (with some samples richer in boride and nitride and other richer in oxides) and microscopic segregation: more than 10 different types of phases (uranium-zirconium oxides of various U/Zr ratios, oxidized α–zirconium, iron-rich alloys, intermetallics, oxidized nitrides, borides) have been observed. This complex structure is a challenge for fuel debris cutting, especially for mechanical cutting since these phases have very different mechanical properties [5]. Indeed, during cutting tests of these blocks in CEA FUJISAN facility [6], some positions were quite hard to cut.

In a next phase, the aerosols collected during core boring of these blocks shall be compared to the observed microstructures in order to interpret the phenomena linked to aerosol generation during this type of cutting process. It would also be interesting to compare these analyses with the results of chemical thermodynamic calculations.

ACKNOWLEDGMENTS

Most of this work is part of tasks by ONET/CEA/IRSN consortium contributing to the Japanese governmental subsidy program “Project of Decommissioning and Contaminated Water Management (Development of Analysis and Estimation Technology for Characterization of Fuel Debris)”. This work was performed for this Japanese project organized by International Research Institute for Nuclear Decommissioning (IRID).

Section 3.5 results have been achieved within the R&D actions related to the advancement of fundamental technologies for retrieval of fuel debris remote controlled laser cutting and dust gathering that have been awarded by the Management Office for the Project of Decommissioning and Contaminated Water management (MRI) to COMEX NUCLEAIRE.

REFERENCES

1. Nuclear Damage Compensation and Decommissioning Facilitation Corporation (NDF), Technical Strategic Plan 2020 for Decommissioning of the Fukushima Daiichi Nuclear Power Station of Tokyo Electric Power Company Holdings, Inc. NDF report (2020). https://www.dd.ndf.go.jp/files/user/pdf/en/strategic-plan/book/20201214_SP2020eFT.pdf
2. C. Journeau, D. Roulet, E. Porcheron, P. Piluso, C. Chagnot, Fukushima Daiichi fuel debris simulant materials for the development of cutting and collection technologies, *J. Nucl. Sci. Technol.* **55**(9), pp. 985-995 (2018).
3. K. Nomura, K. Shiihara, I. Chida, W. Kono, J. Suzuki "Evaluation of removal technologies of fuel debris using the laser processing", *Proc. 20th national symposium on power and energy systems (SPES 2015), .* Tokyo, Japan (June 2015).
4. C. Journeau, J. Monneris, B. Tormos, L. Brissonneau, E. Excoiffier, V. Testud, C. Chagnot, D. Roulet, "Fabricating Fukushima Daiichi in-vessel and ex-vessel fuel debris simulants for the development and qualification of laser cutting technique", *Proc. ERMSAR-2017 (Eur. Rev. Mtg Sev. Accident Res.)*, May 16-18 2017. Warsaw, Poland (2017).
5. M. Takano, T. Nishi, N. Shirasu, "Characterization of solidified melt among materials of UO2 fuel and B4C control blade", *J. Nucl. Sci. Technol.* **51**(7-8) pp. 859-875 (2014).
6. E. Porcheron, Y. Leblois, A. Bouland, C. Journeau, C. Suteau, J. Delacroix, D. Molina, R. Berlemont, Y. Lallot, D. Roulet, Y. Tsubota, A. Ikeda-Ohno, "Particle Generation Test Using Simulated Uranium Containing Debris: The URASOL project in the framework of Fukushima Daiichi dismantling", *Proc. DEM 2021 – International Conference on Decommissioning Challenges: Industrial Reality, Lessons learned and Prospects*, Avignon, France, 13-15/9/2021 (2021).
7. M. Pellegrini, K. Dolganov, L. Herranz Puebla, H. Bonneville, M. Sonnekalb, D. Luxat, J. Ishikawa, J.-H. Song, R.O. Gauntt, L. Fernandez Moguel, F. Payot, Y. Nishi, Y., "Benchmark Study of the Accident at the Fukushima Daiichi NPS Best Estimate Case Comparison", *Proc. NURETH-16*, Chicago, IL(2015).
8. K. Nishihara, H. Iwamoto, K. Suyama, *Estimation of Fuel Compositions in Fukushima-Daiichi Nuclear Power Plant*, JAEA Report JAEA-Data/Code 2012-018 (2012).
9. C. Dazon, E. Porcheron, C. Journeau, C. Suteau, C. Chagnot, I. Doyen, E. Excoffier, D. Roulet, "Characterization of chemical composition and particle size distribution of aerosols released during laser cutting of fuel debris simulants", *J. Environ. Chem. Eng.* **8**(4), 103872 (2020).
10. L. Capriotti, A. Quaini, R. Böhler, K. Boboridis, L. Luzzi, D. Manara, "A laser heating study of CeO2 solid/liquid transition: challenges related to a refractory compound with a very high oxygen pressure", *High Temperatures - High Pressures*, **44**, pp. 69-82 (2014).
11. A. Raraz, B. Mishra, W.A. Averill, "Application of surrogate materials in process study of actinides", *Proc. Annual meeting of The Metallurgical Society*, Denver, CO (United States), 21-25 Feb (1993).
12. L. Claparede, N. Clavier, N. Dacheux, P. Moisy, R. Podor, J. Ravaux, "Influence of Crystallization State and Microstructure on the Chemical Durability of Cerium-Neodymium Mixed Oxides", *Inorg. Chem.* **50**, pp. 9059-9072 (2011).
13. J.A.D. Stockdale, W.D. Bostick, D. Poffmann, H.T. Lee, *Surrogate formulations for thermal treatment of low-level mixed waste. Part 1: Radiological surrogates*, Oak Ridge K-25 site Report DOE/MWIP-15 (1994).
14. M. Cholet, R.C. Belin, J.-C. Richaud, M. Reynaud, F. Adenot, High-Temperature X-ray Diffraction Study of Uranium-Neptunium Mixed Oxides, *Inorg. Chem.* **52**, pp. 2519-2525 (2013)
15. C. Journeau, V. Bouyer, F. Charollais, N. Chikhi, J. Delacroix, C. Mattassoglio, D. Molina, P. Piluso, P. Sauvecane, S. Thilliez, B. Turquais, C. Suteau, "Upgrading The PLINIUS Platform Toward Smarter Prototypic-Corium Experimental R&D", *Proc. International Topical Meeting on Advances in Thermalhydraulics (ATH'20)*, Saclay, France, pp. 294-307 (2020).
16. L. Brissonneau, C. Journeau, P. Piluso, M. Kiselova, S. Bakardjieva, T. Wiss, D. Bottomley, H. Thiele, "Prototypic corium analysis : a round robin for SEM and EDS characterization", *Proc. EMAS 2011, IOP Conf. Ser.: Mater. Sci. Eng.* **32**, 012005 (2012).

17. S.V. Bechta, V.S. Granovsky, V.B. Khabensky, V.V. Gusarov, V.I. Almiashev, L.P. Mezentseva, E.V. Krushinov, S.Yu. Kotova, R.A. Kosarevsky, M. Barrachin, D. Bottomley, F. Fichot, M. Fischer, "Corium phase equilibria based on MASCA, METCOR and CORPHAD results", *Nucl. Eng. Des.,* **238**, pp. 2761-2771 (2008).
18. B. Zega, "Hard decorative coatings by reactive physical vapor deposition: 12 years of development", *Surf. Coatings Technol.* **39/40**, pp. 507-520 (1989).
19. J.M. Martin, *Contribution à l'étude du système Uranium-Oxygène-Azote*, Dr-Ing Thesis, University of Grenoble, CEA report CEA-R-3801 (1969).
20. D. Ribeiro Costa, M. Hedberg, S.C. Middleburgh, J. Wallenius, P. Olsson, D. Adorno Lopes, "UN microspheres embedded in UO2 matrix: An innovative Accident Tolerant Fuel", *J. Nucl. Mater.* **540**, 152355 (2020).
21. P. Rogl, P. E. Potter, "A critical review and thermodynamic calculation of the binary system: Zirconium-boron", *CALPHAD*, **12**(2), pp. 191-204 (1988).
22. Z. Lu, H. Fu, J. Xing, S. Ma, Y. Hu, "Microstructure and crystallography of borides and mechanical properties of Fe–B–C–Cr–Al alloys", *J. Alloys Comp.* **662**, pp.54-62 (2016)
23. E. Forlerer de Svarch, C. Rodriguez, "On the influence of iron on the Zr-α (hcp) self-diffusion", *J. Nucl. Mater.* **185**, pp. 167-173 (1991).
24. Y-U Kwon, J.D. Corbett, "The zirconium-tin system, with particular attention to the Zr_5Sn_3-Zr_5Sn_4 region and Zr_4Sn", *Chem. Mater.* **2**, pp. 27-33 (1990).
25. G. Trillon, P. Piluso, C. Journeau, "The UO2–ZrO2 system at high temperature (T > 2000 K): importance of the meta-stable phases under severe accident conditions", *J. Nucl. Mater.* **344**, pp. 259-264 (2005).

ERMSAR 2022

MAY 16-19, 2022 — KARLSRUHE, GERMANY

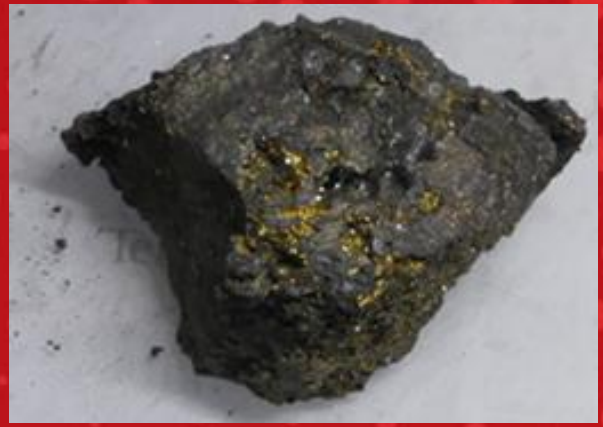

DE LA RECHERCHE À L'INDUSTRIE

CHARACTERIZATION OF PROTOTYPIC CORIUM SAMPLE SIMULATING FUKUSHIMA DAIICHI UNIT 2 LOWER HEAD COMPOSITION

Christophe Journeau, Diego Molina, Renaud Domenger, Emmanuelle Brackx, Célia Guevar, Véronique Testud, Atsushi Ikeda-Ohno

ERMSAR Karlsruhe, May 17th, 2022

IRESNE | DTN/SMTA/LEAG

Research Institute for Nuclear Systems for Low Carbon Energy Production

R&D in support of Fukushima Daiichi Fuel Debris Retrieval

- Technical Strategic Plan 2020 for Decommissioning of the Fukushima Daiichi Nuclear Power Station :
  - “an optimum combination of retrieval methods should be selected depending on the location where fuel debris exists for each reactor unit”
  - “it is important to proceed with research and development toward a future scale expansion” from the small scale retrieval of loose debris.
- Needs for simulants of fuel debris to carry out this R&D
  - Due to fuel debris heterogeneity, industrial ceramics/metal pieces not suitable
    - Dedicated non-radioactive simulants have been fabricated (among others at CEA)
  - Due to uranium peculiar chemistry, difficulties to simulate uranium oxides
    - URASOL Project has been launched between JAEA, CEA, IRSN and ONET Technologies with uranium-containing fuel debris prototypes to study aerosols generated during their cutting or heating,

Document is property of CEA – Reproduction and external diffusion submitted to authorization by emitter

Outline of Presentation

- Choice of fuel debris compositions
- In-vessel Fuel Debris prototype fabrication
- Material Characterization
  - Samples
  - SEM-EDX
  - X-Ray Diffraction
  - Chemical Analyses
- Synthesis and Conclusions

Document is property of CEA – Reproduction and external diffusion submitted to authorization by emitter

Choice of a typical Lower Head composition

- **OECD/BSAF Benchmark compositions for unit 2 at Lower Head**
  - Only 24% of Zr is oxidized (C24)
- **FP composition estimated 10 years after accident (Nishihara et al. 2012)**
  - FP representing more than 0.014 wt% (except technetium) have been replaced by their natural isotopic composition.
  - Ce surrogate for Pu and minor actinides
  - Overall, more than 94% of the radioactivity in the inventory is represented in this composition.

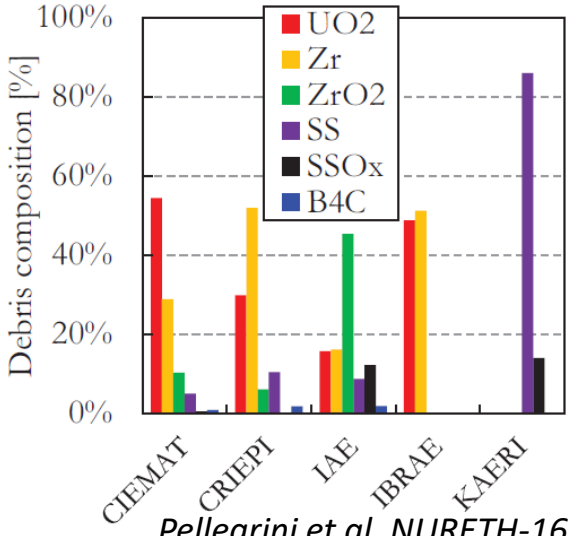

Pellegrini et al, NURETH-16, 2015

UO_2	35.7%	$CsOH.H_2O$	0.06%
Zr	34.5%	BaO	0.04%
ZrO_2	18.8%	La_2O_3	0.032%
CeO_2	0.2%	PdO	0.030%
SnO2	0.9%	Pr_2O_3	0.030%
B4C	1.0%	Sm_2O_3	0.015%
Stainless steel 304L	8.4%	SrO	0.022%
RuO_2	0.06%	Y_2O_3	0.014%
Nd_2O_3	0.11%	TeO_2	0.029%
MoO_2	0.09%		

Document is property of CEA – Reproduction and external diffusion submitted to authorization by emitter



Fuel debris prototype fabrication

IRESNE | DTN/SMTA/LEAG

Research Institute for Nuclear Systems for Low Carbon Energy Production

Fabrication in the VULCANO facility

- **18 kg of load has been prepared and installed in a zirconia crucible**
  - ❑Powders and grains of raw materials
  - ❑Stainless Steel bars and balls used as susceptors for the initiation of melting
- **Induction heating has been applied for 17 minutes**
  - ❑Electromagnetic coupling preferentially heats molten oxides
  - ❑Nitrogen flow over test section
- **11 kg of prototypic fuel debris have been melted then solidified.**

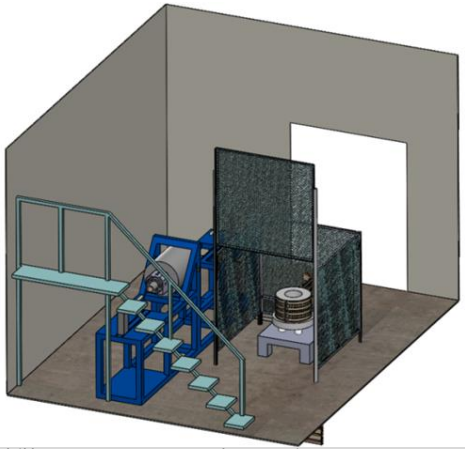

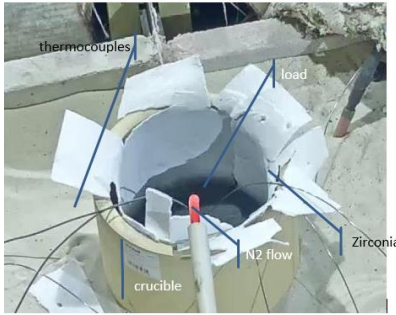





Document is property of CEA – Reproduction and external diffusion submitted to authorization by emitter

Some of the Fuel Debris Prototyopes

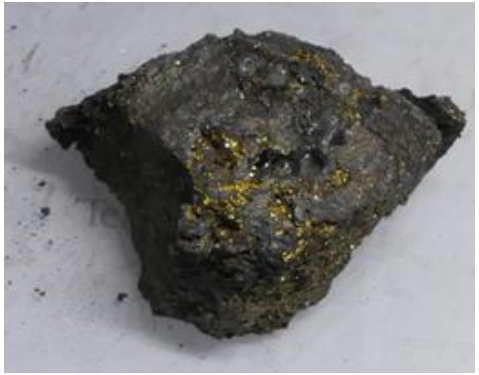




View of 4 prototypic blocks (top) *golden surface attributed to nitrides*

4 samples have been taken for material analyses







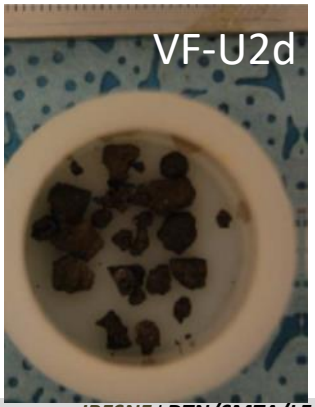

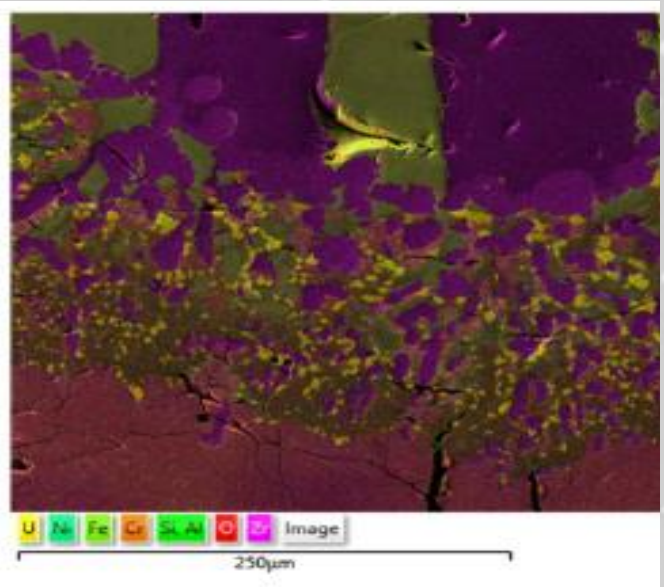

Material characterization

IRESNE | DTN/SMTA/LEAG

Research Institute for Nuclear Systems for Low Carbon Energy Production

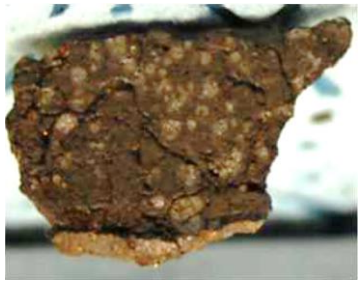



After VF-U2a sample cutting, large heterogeneities appears on the visible light macrograph with several whitish areas (in macrograph) and darker areas (in micrograph)

Next slide: zoom on transition between 2 zones of Site 1

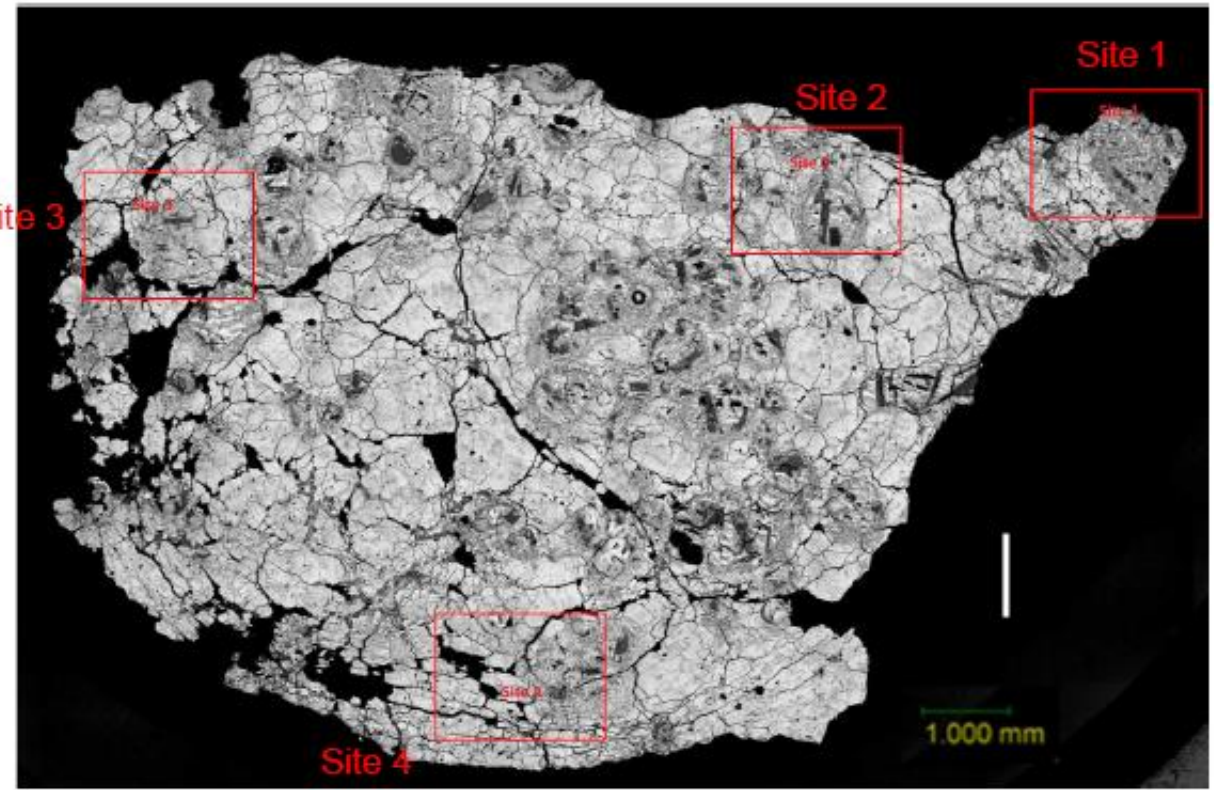

Document is property of CEA – Reproduction and external diffusion submitted to authorization by emitter

SEM-EDX Elemental mapping of a zone of site 1



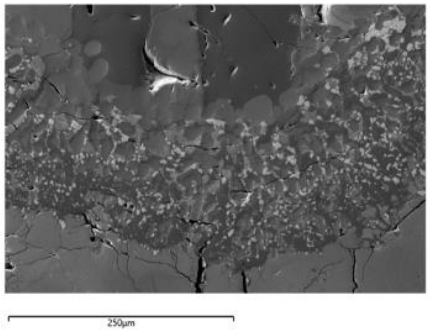

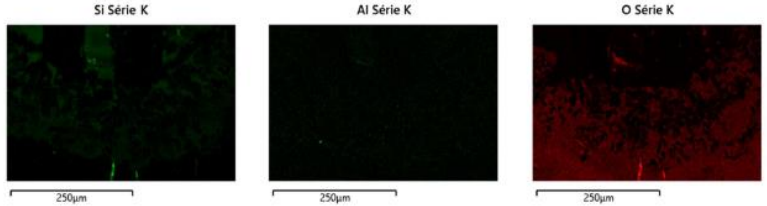

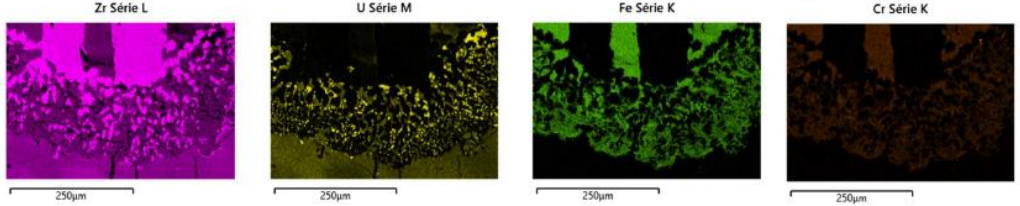

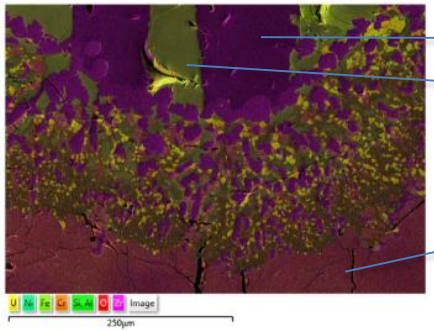

Zirconium oxide

iron-chromium-nickel-uranium alloy

Uranium- Zirconium oxide

Document is property of CEA – Reproduction and external diffusion submitted to authorization by emitter

Many different phases are present:

- **Uranium-zirconium oxides with various U/Zr:**
  $U_{0.9}Zr_{0.1}O_{2-x}$, $U_{0.8}Zr_{0.2}O_2$, $U_{0.6}Fe_{0.3}Zr_{0.1}O_{2-x}$, $Zr_{0.8}U_{0.2}O_{2\pm x}$
- **Mixed U,Zr sub-oxidized phase close to α-Zr(O) phase with dissolved uranium**
- **Alloys of steel with zirconium and to a lesser extend uranium and tin (from Zry)**
  - Ex: Point 121: 45 at% Fe, 29% Zr, 10% Cr, 9% Si, 4% Ni, 1% Al, 1% U, 1% Sn

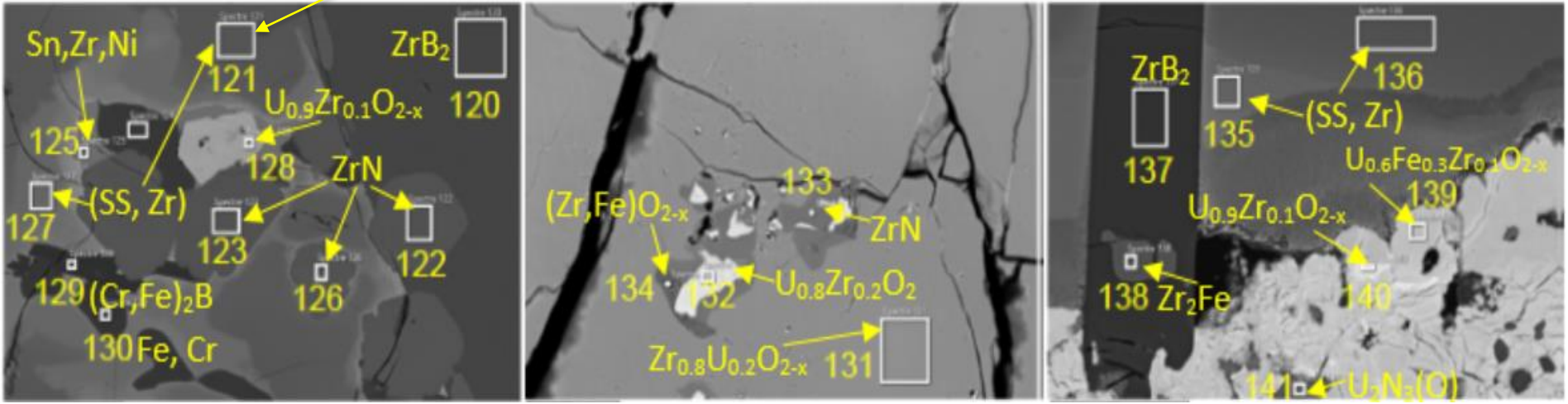

SEM EDX analyses (2/2)

- **Alloys without (U,Zr): e.g. point 130: 53 at% Fe, 42% Cr, 2% Al, 1% Si, 1% Ni, 1% Mo**
- **Tin-zirconium-nickel alloy (point 125)**
- **Zr_2Fe and Zr_5Sn_3 intermetallics**
- **Nitrides close to ZrN with traces U and/or Fe (e.g. points 126, 133)**
  - Also oxidized uranium nitrides close to UO_2 solution in U_2N_3 (point 141)
- **Borides: slightly oxidized ZrB_2, chromium-iron borides $(Cr,Fe)B_2$**

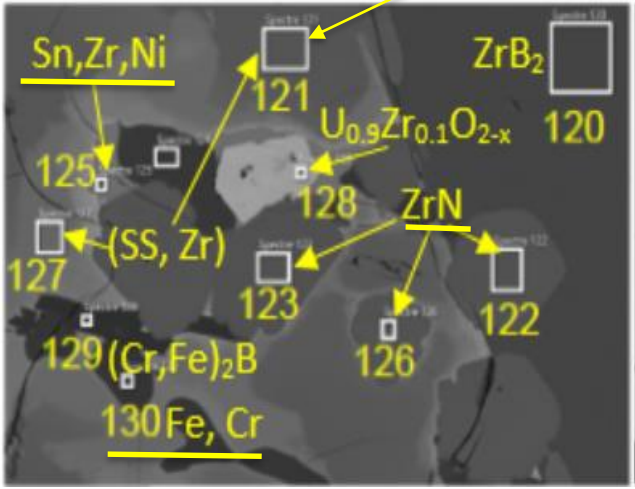

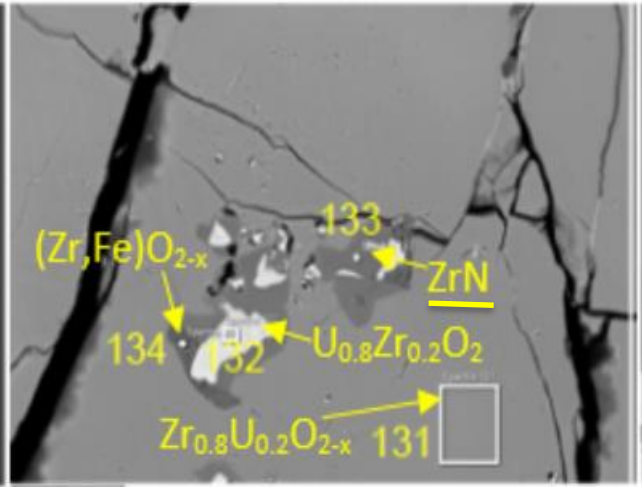

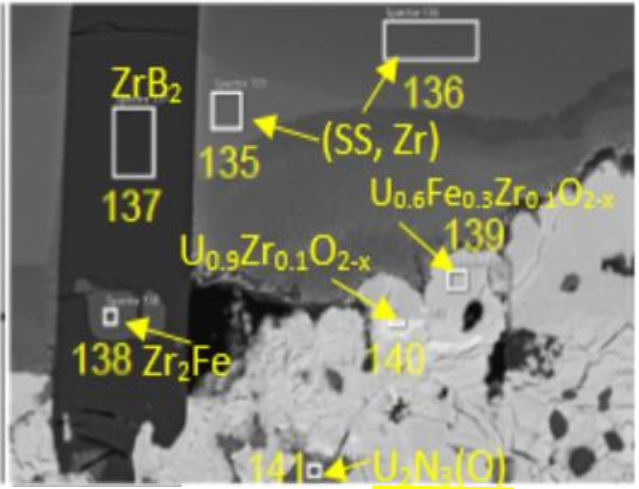

Document is property of CEA – Reproduction and external diffusion submitted to authorization by emitter

X-ray Diffraction

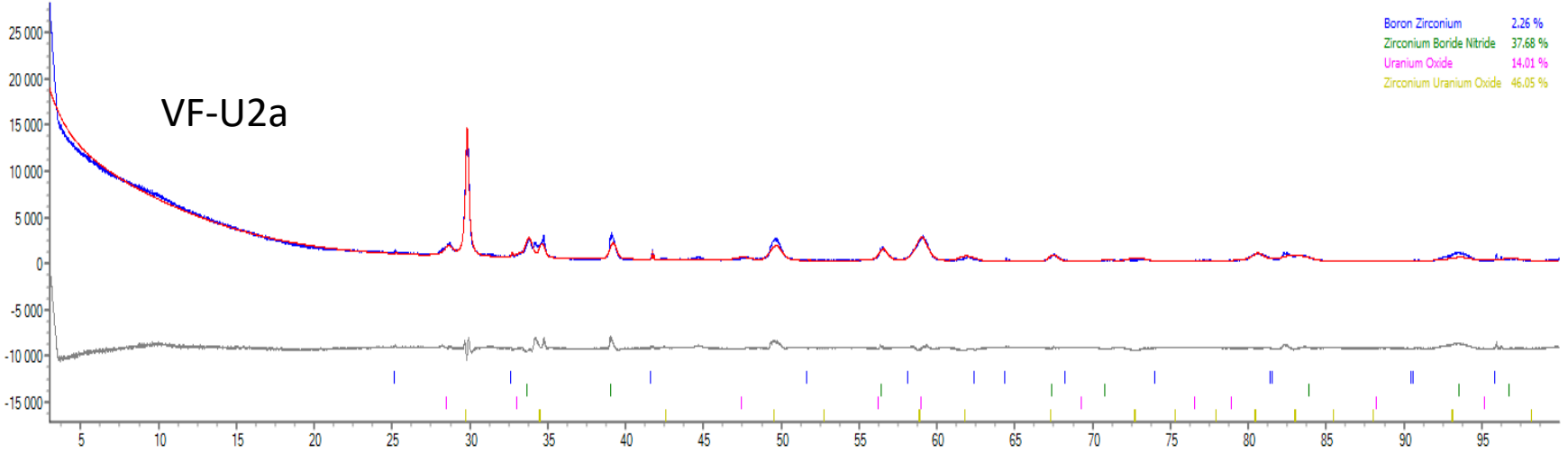

Macro-heterogeneities (a-b vs. c-d) in addition to microscale heterogeneities
Boro-nitride likely to represent oxynitrides as it has not been observed with SEM-EDX.
No metallic phase detected
(too heterogeneous ?)

Phases (wt%)	VF-U2a	VF-U2b	VF-U2c	VF-U2d
zirconium diboride (ZrB_2)	2.3	2.8	0.01	
zirconium boro-nitride ($ZrB_{0.4}N_{0.6}$)	38	39	26	28
uranium oxide ($UO_{2.11}$)	14	13	7	6
zirconium-uranium oxide ($U_{0.18}Zr_{0.82}O_2$)	46	45	66	64
Uranium nitride (UN_2)			1	2

Document is property of CEA – Reproduction and external diffusion submitted to authorization by emitter

Chemical analyses

No chemical analyses have been carried out on these samples. Nevertheless, previous analyses on simulant – Hf replacing U mole by mole – are reported

- Separation of crushed samples into metallic-looking and oxidic-looking parts
- ICP-MS and ICP-AES has been conducted
- “metal” type is richer in Fe (21.7% vs. 3.5%) and Cr (2.3 vs. 0.7 %).
- There is a large fraction of Zr in both types (37-44 %) while the content of Hf (surrogate for uranium) is much lower in the “metal” (5 vs 32 %).
- B, La, Mo, Nd, Pd, Sm, Sn(100 x more), Sr, Y are largely present in the oxidic debris.
- Ni (and to lesser extend Mg, Pr) are more found in metal
- Ru had not been inserted for chemical safety issue.

81 wt% of the mass contributes to the oxidic phase, 14 wt% to the metallic phase and 5 wt% has been volatilized during fabrication (most of Cs, 68% Ni, 38% Cr, 1% Ce).

Document is property of CEA – Reproduction and external diffusion submitted to authorization by emitter

Conclusions

- **An in-vessel fuel debris prototype has been defined from calculations of Fukushima Daiichi Unit 2 scenario.**
- **From a load of powders, including depleted UO_2, stainless steel and 15 other elements, 11 kg of in-vessel fuel debris blocks have been fabricated in the VULCANO facility by induction heating.**
- **No gravitational segregation of metallic and oxidic phases has been observed as it was the case for ex-vessel (Molten Core Concrete Interaction) compositions**
- **Nevertheless, the obtained blocks presented both macroscopic segregation (with some samples richer in boride and nitride and other richer in oxides) and microscopic segregation:**
  - ❑ More than 10 different types of phases
- **This complex structure is a challenge for fuel debris cutting, especially for mechanical cutting since these phases have very different mechanical properties .**
  During cutting tests of these blocks in CEA FUJISAN facility, some positions were indeed quite hard to cut.

Document is property of CEA – Reproduction and external diffusion submitted to authorization by emitter

ERMSAR 2022

MAY 16-19, 2022 — KARLSRUHE, GERMANY

Thank you for your attention!
Any questions?

DE LA RECHERCHE À L'INDUSTRIE

Most of this work is part of tasks by ONET/CEA/IRSN consortium contributing to the Japanese governmental subsidy program "Project of Decommissioning and Contaminated Water Management (Development of Analysis and Estimation Technology for Characterization of Fuel Debris)".
This work was performed for this Japanese project organized by International Research Institute for Nuclear Decommissioning (IRID).

Chemical analyses have been achieved within the R&D actions related to the advancement of fundamental technologies for retrieval of fuel debris remote controlled laser cutting and dust gathering that have been awarded by the Management Office for the Project of Decommissioning and Contaminated Water management (MRI) to COMEX NUCLEAIRE.

IRESNE | DTN/SMTA/LEAG

Research Institute for Nuclear Systems for Low Carbon Energy Production

MODELLING OF PREMIXED LAYER IN STRATIFIED FUEL–COOLANT CONFIGURATION

Janez Kokalj, Mitja Uršič, Matjaž Leskovar
Jožef Stefan Institute (JSI),
Jamova cesta 39, 1000 Ljubljana, Slovenia
janez.kokalj@ijs.si, mitja.ursic@ijs.si, matjaz.leskovar@ijs.si

Renaud Meignen
Institut de Radioprotection et de Sûreté Nucléaire (IRSN),
Cadarache Nuclear Center, BP 3, 13115 Saint-Paul-lez-Durance, France
renaud.meignen@irsn.fr

ABSTRACT

A hypothetical severe accident in a nuclear power plant can lead to significant core damage, including melting of the core. The interaction between the molten core and the coolant water is known as a fuel-coolant interaction. One of the consequences can be a rapid transfer of a significant part of the molten corium thermal energy to the coolant in a time scale smaller than the characteristic time of the pressure relief of the created and expanding vapour. Such a phenomenon is known as a vapour explosion. Given possibly large amount of thermal energy, initially stored in the liquid corium melt at about 3000 K, and pressure peaks of the order of 100 MPa, vapour explosion can be a credible threat to the structures, systems and components inside the reactor containment. It can also threaten the integrity of the reactor containment itself, which would lead to release of radioactive material into the environment and threaten the general public safety. In analyses of severe accidents in nuclear power plants, a fuel-coolant interaction was mostly addressed in a geometry of a melt jet poured into a coolant pool. Based on some experimental and analytical work from the past a geometry with a continuous layer of melt under a layer of water, called stratified configuration, was believed to be incapable of producing energetic fuel-coolant interaction. However, the results from recent experiments performed at the PULiMS and SES facilities (KTH, Sweden) with corium simulants materials contradict this hypothesis. In some of the tests, a premixing layer of ejected melt drops in water was clearly visible and was followed by strong spontaneous vapour explosions.

The purpose of our research is to improve the knowledge, understanding and modelling of the fuel-coolant interaction and vapour explosion in stratified configuration. Based on the past experimental and analytical research, mechanisms for the premixed layer formation are identified and model for the melt-coolant premixed layer formation in stratified configuration is presented. The analyses on the PULiMS and SES experimental results demonstrate the model's capability to describe the premixed layer formation.

KEYWORDS
severe accident, fuel-coolant interaction, vapour explosion, stratified configuration, premixed layer

1. INTRODUCTION

During a hypothetical severe accident in a light water nuclear power plant, the molten reactor core may come in contact with the coolant water [1]. The consequence can be a rapid transfer of a significant part of

the molten corium thermal energy to the coolant in a time scale smaller than the characteristic time of the pressure relief of the created and expanding vapour. Such a phenomenon is known as a steam explosion. Behind the shock wave front, the relative difference between the melt and surrounding coolant enhances further melt drops fine fragmentation, which causes a significant increase of the interface area and consequently an increase of the heat transfer between both liquids. An important condition for the possible energetic steam explosion and the self-sustained process of the shock wave propagation is the existence of a premixture of fragmented melt and coolant. Given the amount of thermal energy, initially stored in the liquid corium melt at about 3000 K, the steam explosion can be a credible threat to the systems and components inside the reactor containment. It can also threaten the integrity of the reactor containment itself, which would lead to release of radioactive material into the environment and threaten the general public safety.

In analyses of severe accidents in nuclear power plants, a fuel-coolant interaction is mostly addressed in a configuration of a melt jet poured into a coolant pool [2]. Based on some experimental and analytical work from the past, a geometry with a continuous layer of melt under a layer of water, called stratified configuration, was believed to be incapable of producing energetic fuel-coolant interaction [3]. However, the results from recent experiments performed at the PULiMS and SES facilities (KTH, Sweden) with corium simulants materials [3, 4] and research work at AREVA [5] contradict this hypothesis. In some of the tests, a premixed layer of ejected melt drops in water was clearly visible and was followed by strong spontaneous vapour explosions. It is then believed that a major task for modelling such type of interaction is to provide a description of this premixed layer, in contrast with previous models assuming flat interfaces and a vapor film separating the melt and the coolant [6].

The purpose of this research work is to improve the knowledge, understanding and modelling of the fuel-coolant interaction and vapour explosion in stratified configuration. In the paper, short overview of the previously performed experimental and analytical research is given at first and the mechanisms for the premixed layer formation are identified and evaluated. Further, our developed model [7] for the melt-coolant premixed layer formation in stratified configuration, developed based on the visual observations and some available mechanisms from the literature, is presented. Finally, the model validation on available PULiMS and SES experimental results is discussed. The presented analysis demonstrates the model's capability to describe the premixed layer formation in agreement with the experimental data.

2. PAST EXPERIMENTAL AND ANALYTICAL RESEARCH

Some of the experiments providing valuable information about the vapour explosions in stratified configuration were not primarily devoted to the investigation of this phenomenon [4, 8]. Therefore, one of the difficulties is a lack of measurements and visual observations, which would further enlighten the phenomenon.

Some of the performed experiments resulted in an explosive interaction between the hot and the cold liquid. This interaction can be spontaneous, when two liquids come in contact and energetic interaction occurs between them without additional triggering [9, 10], or triggered, e.g. with external pressure pulse, tapping or in case of high impact velocity of the liquids. It seems that for an explosive interaction the temperature of the hot liquid has to be higher than the spontaneous nucleation temperature of the cold liquid [11] and the cold liquid has to be sufficiently subcooled. In case of the cold liquid being slightly subcooled, no strong interaction has been observed and this may be due to a larger vapour film separated both liquids [10]. The explosion is not necessarily an instant event. Sometimes it took couple of seconds to occur [4, 12]. Prior to the explosion, some milder melt-coolant interaction, such as smaller melt eruptions [12, 13], mixing [11], or even stronger interaction such as larger eruptions of water and melt [12] could be observed. In some cases, the observed interface instabilities were marked as undesirable and suppressed [14] though the installation of a plate separating the two fluids. In some cases the increased waviness of the fluids enabled

the interaction propagation to be self-sustained [15]. It seems that sometimes the first interaction (usually triggered) deformed the vapour film and the liquid interface and caused some mixing of the liquids. Therefore, in some cases, after the first explosion, more secondary explosions followed [9, 16]. The propagation of the interaction was self-sustained if the inertial confinement (e.g. by the layer of the cold liquid on top) was sufficient. Increasing the confinement through the cold liquid height increased the impulse [16]. The propagation velocity of the interaction was from about 5 m/s up to 250 m/s, but usually of the order of 50 m/s. With an increase of the propagation velocity, the pressure peak also increased. In some small-scale experiments, similarities of the vapour explosions in stratified configuration with experiments, where the cold liquid is injected into the hot one, were observed. This is suggesting that the phenomenon of trapping coolant in the melt takes place also in the stratified geometry. In case of supplying water through a porous concrete layer below the melt layer, only mild interaction occurred [17], but the amount of water available for energetic event was limited in that case. Sometimes, the interaction between the flowing melt and the coolant resulted in a porous layer in the debris bed. Porosity there was too large to be only due to the melt shrinkage on cooling [8]. In case of pouring melt onto the concrete basemat in the reactor cavity, the interaction between the molten core and the concrete can produce large amount of gases and drive out bound and unbound water. Gas sparging from the molten core-concrete interaction was simulated in some experiments. With added gas in the stratified geometry, the explosions were suppressed. It was also found that premixing could be suppressed by a high viscosity of the hot liquid (e.g. glycerine) [4].

Some of the experiments in a stratified-like configuration did not result in a vapour explosion. When adding the cold liquid on top of the hot one slowly (e.g. spraying), a crust was formed which prevented further energetic melt-coolant interaction [12, 13]. However, some solidified tower-like structures were observed after the end of the experiments, indicating melt eruptions and freezing during the eruption [10].

Similar experiments, studies and observations related to the stratified vapour explosions were performed also in other research fields, such as volcanic eruptions, where lava can be in contact with water, and in case of a liquefied natural gas spillage.

In the recently performed PULiMS and SES experiments (KTH, Sweden), a superheated high melting temperature eutectic simulant of corium melt was poured as a jet into a shallow pool of subcooled water. In the PULiMS experiments, underwater melt spreading observation was the primary aim. However, unexpectedly strong spontaneous vapour explosions occurred and premixed layer was clearly observed [3, 4]. At the early stage of the melt propagation, bubble growth and collapse in subcooled water was seen. When the amount of melt increased and the melt spread further away from the jet impingement, more violent interaction was observed. Splashes of melt reached up to 10 cm in height. Similar phenomena were observed also in the SES experiments [18]. On the contrary, the DEFOR experiments (KTH), using the same materials and similar temperatures but deeper water pool, which resulted in complete jet breakup, did not result in spontaneous vapour explosion [10].

For the vapour explosion in stratified configuration, few models were developed in the past [19, 20]. They describe the initiation of the interaction, its propagation and mixing right in front or just behind the vapour film collapse. However, none of the models above describes the premixed layer formation as observed in some of the experiments (e.g. PULiMS and SES) or any other mixing before the initiation of the explosion.

Interestingly, it seems that the existing models, not describing any mixing before the explosion, actually affected the experimental work. For example, any possible premixed layer in the experiments was not followed or not well documented, as it was not expected. Even if any interface instabilities before the explosion were observed, they were usually marked as undesirable. Sometimes, measures were performed to minimize the instabilities [14, 16].

In the frame of this research, we try to fill this gap in modelling and describe the premixed layer formation. In our research, we will not assess existing models, but rather complement them. The results of our model could serve as initial conditions for any explosion model based on a pre-existing premixing in stratified configuration.

3. MECHANISMS FOR PREMIXED LAYER FORMATION

From the analysed experimental results, it can be observed, that one of the most common plausible mechanism for the premixed layer formation is the growth, expansion and collapse of vapour bubbles. The melt is usually hot enough for boiling of the coolant and if the coolant is subcooled and the coolant layer high enough, the bubbles collapse. Indeed, the mechanism of growth, expansion and collapse of the vapour bubbles was mentioned in many experiment discussions [6, 9, 16]. Also in the recent PULiMS experiments, in the early stage of the melt propagation, vapour bubble formation, growth and collapse in the subcooled water was clearly observed by a high speed camera [10]. A bubble collapse can be a very energetic process. At a certain frequency of the bubble collapse event, sufficient momentum flux can be transferred to the melt to sustain the premixed layer [21].

Other mechanisms also seem plausible for some experiments. For the evaporation of coolant entrapped in the melt or under the melt, the most favourable geometry is the pouring of melt in a pool of coolant. This geometry was used only in few experiments, e.g. PULiMS, SES (both KTH, Sweden) [3, 22], Board and Hall experiment (BNL, USA) [9].

In case of pouring the coolant on the melt, e.g. Greene et al. experiment (BNL, USA) [11], Bang and Corradini experiment (University of Wisconsin, USA) [14], Sainson et al. experiment (Gaz de France, France and Gas Research Institute, USA) [15], some smaller amount of coolant can become entrapped in the melt. In this case the phenomena are local, but can disturb the melt surface and cause some melt ejection.

For the mechanism of release of gases from the interaction of a melt with a concrete, the necessary condition is the presence of concrete, which is not the case in most of the experiments. Experiments with the concrete were e.g. S3E (KTH, Sweden) [8], KATS (FZK, Germany) [8]. However, in some cases, e.g. Meeks et al. experiment (University of Wisconsin, USA) [23], the MCCI was simulated with a gas injection through the bottom plate. In the experiments, the bubbles of gases cause instability of the melt surface and they can push the melt to the overlying coolant. Due to the vaporization of water in the concrete and related vapour pressure, small pieces of the concrete also broke off, which resulted in significant disturbance of the spreading melt and small amount of melt was splashed outside. The gas injection can be considered also as the simulation of the release of non-condensable gases during the melt cooling. However, it seems unlikely for cooling or any other process (e.g. oxidation) to produce enough gases to cause any substantial instabilities.

In the mechanism of jet breakup, impingement and splattering, different contributions are covered. The melt jet breakup, most known from the classical melt jet – coolant pool geometry, is greatly dependent on the coolant pool depth. In the case of deeper coolant pool, its contribution should be more pronounced. In the case of jet geometry, e.g. PULiMS, SES (both KTH, Sweden) [3, 22], Board and Hall experiment (BNL, USA) [9], the momentum of the melt jet falling onto the melt surface can cause instabilities. However, the jet geometry was not present in all the experiments where the premixed layer was observed (e.g. Meeks et. al experiment [23], SES S1 experimental test [22]). In addition, the melt jet breakup and impingement on the melt free surface are not very sensitive to the coolant subcooling. Therefore the effect of the coolant subcooling should be minor on the premixed layer formation phenomena which is contradictory to the comparison of the SES-E3 and other tests [21].

Apart the jet of melt, the jet of coolant was also considered, e.g. Greene et al. experiment (BNL, USA) [11], Bang and Corradini experiment (University of Wisconsin, USA) [14], Sainson et al. experiment (Gaz de France, France and Gas Research Institute, USA) [15]. In fact, this configuration was more often in the experiments, but should be emphasised that the melt instabilities in this case would be localized. From the experiments, it can be noted that the jet geometry can cause instabilities but the premixed layer is formed also after the jet pouring stopped.

The formation, growth and collapse of vapour bubbles seems to be the most plausible amongst the described mechanisms [24]. Thus, our developed models for the premixed layer formation in stratified melt-coolant configuration are based on it. However, as stressed above, besides the bubble formation, growth and collapse, other mechanisms, relevant for the individual experimental geometry (e.g. jet break-up), could serve as an additional source of the melt instabilities. Additionally, a contribution to the amount of melt-coolant mixture, which could participate in the vapour explosion, can be a consequence of mixing during the explosion itself.

4. MODEL FOR PREMIXED LAYER FORMATION

It was concluded that one of the most common plausible mechanisms for the premixed layer formation is the boiling of the coolant. Due to the Rayleigh-Taylor instabilities, the bubbles arise from the vapour film. In subcooled water, bubbles condense and collapse. During the bubble collapse, water at the bubble interface accelerates towards the melt surface, creating a so-called coolant micro-jet [25]. The coolant micro-jet impacts on the melt surface and can produce the melt surface instabilities and fragmentation of the melt.

Our model describes the premixed layer formation with three key characteristics, i.e. size of ejected melt drops, their initial velocity and the fragmentation rate of the continuous melt phase.

The modelling values depend on the scale of the instabilities, given by the value of the most dangerous wavelength on the surface, i.e. for which the instability growth rate is the highest – in our case this is the distance between the formed bubbles [26]:

$$\Lambda = 2\pi \sqrt{\frac{3\sigma_L}{g(\rho_L - \rho_G)}}\,, \tag{1}$$

where σ_L is the liquid coolant surface tension at saturation temperature, g the gravity acceleration and ρ_L and ρ_G density of liquid and gaseous phase of the coolant, respectively.

The melt surface instabilities can result in fragmentation of the melt. The size of the ejected melt drops in our model is related to the instability wavelength. The hypothesis by Leclerc and Berthoud [27] for the thermal fragmentation of single melt drop is adopted, where the melt drop diameter is defined as one quarter of the instability wavelength. Based on the performed analysis [7], the melt drop diameter in our model is multiplied with the factor C_d, being 1.25:

$$d = C_d \cdot 0.25 \cdot \Lambda\,. \tag{2}$$

The fragmentation rate of the melt layer can be established from the size of the ejected melt drops and the frequency of their ejections per melt area. The size of the melt drop is defined in Eq. 2. The single melt drop ejects from the surface area that is defined with the wavelength as given in Eq. 1. It should be emphasized that in this area we have node and antinode, therefore the effective surface area is $\frac{1}{2}\Lambda^2$. Based on the performed analysis [7], the fragmentation rate in our model is multiplied with the factor C_f, being 0.5:

$$\Gamma = C_f \cdot \frac{\pi d^3 F}{3\Lambda^2}\ , \tag{3}$$

The frequency of the melt ejections F is proportional to the frequency of the bubble formations and collapses. It can be derived from the relation by Berenson [26] for the bubble detachments for a horizontal surface film-boiling heat transfer, considering the Rayleigh-Taylor instabilities. With some simplifications due to the large differences in the liquid and vapour density, the following equation is obtained:

$$F = \frac{1}{2\pi}\sqrt{\frac{\rho_G v_{vf}^2 n}{\rho_L a} + gn - \frac{\sigma_L n^3}{\rho_L}}, \tag{4}$$

where n is wavenumber and v_{vf} and a vapour velocity and vapour film thickness:

$$v_{vf} = 0.45\frac{\lambda_{vf}\Delta T}{\rho_{vf}\Delta H a^2 n}\ , \tag{5}$$

$$a = 2.35 \cdot \frac{\sigma_L^{\frac{1}{8}}}{(g\rho_L)^{\frac{3}{8}}} \cdot \left(\frac{\mu_{vf}\lambda_{vf}\Delta T}{\Delta H \rho_{vf}}\right)^{\frac{1}{4}}. \tag{6}$$

where index vf stands for the vapour film, ΔT is temperature difference between the melt and the coolant and ΔH is average enthalpy difference between vapour and liquid coolant. The constant factors of Berenson [26] are used in correlations.

The initial velocity of the ejected melt drops is calculated from the available energy. As shown in experiments by Caldarola and Kastenberg [25], the available energy (and consequently velocity) lies between the transmitted (energy due to the shock wave from a hemispherical source to the surrounding medium) and the acoustic (energy of the elastic wave traveling in the fuel) energy limits. Thus, the velocity as calculated from the acoustic energy (lower limit) is in our model multiplied with a free factor C_v. Based on the performed analysis [7], C_v was assessed to 6:

$$v = C_v\sqrt{C_{v1} \cdot C_{v2} \cdot \frac{(p_{max} - p_0)^2 \Delta T_{sub}^2}{\Lambda^{0.8}\sqrt{\Delta p}}}\ . \tag{7}$$

where p_0 is the ambient pressure, p_{max} is the pressure of coolant micro jets acting on the melt, ΔT_{sub} is the water subcooling, Δp is the pressure difference between inside and outside of the bubble, C_{v1} is a constant, related to the dimension of the formed coolant micro-jet generated after the bubble collapse and its value is around 0.01. C_{v2} is related to the material properties:

$$C_{v2} = \frac{(\rho_M - \rho_L)\rho_L^{1.9}}{(\rho_M + \rho_L)\rho_M^2 \rho_G^2} \cdot \frac{\lambda_L^{\frac{4}{3}} c_p^{\frac{2}{3}}}{c g^{0.2} L^2 \sigma_L^{0.2} \mu_L^{\frac{8}{15}}}\ . \tag{8}$$

where index M stands for melt, λ is thermal conductivity, c_p is specific heat, c is sound velocity, L is latent heat and μ is dynamic viscosity.

Our model, reduced to the three equations for the melt drops diameter (Eq. 2), fragmentation rate (Eq. 3) and ejected melt drop initial velocity (Eq. 7), can be implemented into the fuel-coolant interaction codes to mathematically describe the phenomenon of the premixed layer formation in stratified configuration.

5. APPLICATION TO EXPERIMENTS

The complex phenomena of premixed layer formation as described by our model was assessed on the experimental results by simulating the SES S1 and PULiMS E6 experimental tests. On these tests, some previous simulation analysis were performed, but without modelling the premixed layer formation [28].

The developed model for premixed layer formation was implemented as a patch in the computational multi-fluid dynamic code MC3D V3.9.0.p1, which is being developed at IRSN (France) with fuel-coolant interactions in mind. MC3D is one of the leading codes in the field of fuel-coolant interactions and it is suitable for the planned purpose, because it covers both the premixing phase and the explosion phase of the fuel-coolant interaction. The premixing phase module [29] deals with the initial mixing of the melt and the coolant and this module was upgraded with the premixed layer formation model, developed in the frame of our research work. To compute the explosion phase, the results from the premixing phase module serve as an input for the explosion phase module. The explosion phase module concerns the fine fragmentation of the melt during the explosion and the heat transfer between the created fine fragments and the coolant. It is not modified in our modelling.

5.1. SES S1 Experimental Test

The SES experiments were performed at KTH (Sweden). The test section consisted of a square tank of the size of 1 m^2, filled with water to the height of 25 cm. The melt was released in the water through the funnel, which ended in the water, 25 mm above the melt spreading surface. The initial melt temperature was 1303 K, which corresponds to 160 K of superheating. Water was at 348 K. During the release of the melt under water, a spontaneous vapour explosion occurred after 0.6 s. A more detailed description is given in [22].

The 3D calculation domain contains half of the experimental tank applying symmetry boundary conditions at the symmetry plane. The melt pouring and spreading is not modelled. Therefore, initially all the continuous melt is described as a 5 mm high melt pool with diameter of around 25 cm. The analyses are based on the best case [7], parameters C_v, C_d and C_f being 6, 1.25 and 0.5.

Firstly, the premixed layer formation phase was simulated. After the initial transient of first melt drops being ejected, quasi-stationary conditions are developed. The melt drops are constantly being ejected from the continuous melt and coalescing back. In Figure 1, the formed premixed layer is shown. The largest melt fraction is at the bottom, as a shallow pool of continuous melt remains there. The ejected melt drop volume fraction increases towards the top of the premixed layer because numerically the velocity of the melt drops decreases and all the melt drops reach approximately the same height. The phenomenon of the premixed layer formation is not completely homogeneous, which indicates the complexity of the feedback loops. Namely, heating of the coolant water, vaporization and flow currents of the vapour, water and melt affect the height of the premixed layer and the melt fraction distribution. Nevertheless, the simulation results where the maximum reached height of melt drops is around 10 cm seem to be close to the experimental observation.

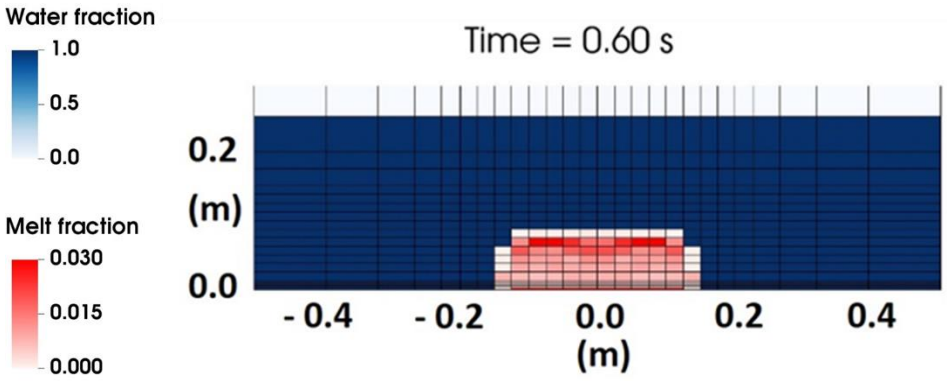

Figure 1: Simulated premixed layer for the SES S1 experimental test after 0.6 s. Melt fraction is shown where its volume fraction exceeds 0.001.

Because of the lack of more detailed experimental data regarding the premixed layer, further analyses and comparison of our model with the experiments are made regarding the explosion phase, as seen in Figure 2. The force signal on the bottom of the test section and the total gained impulse are compared. The total gained impulse is in the simulation around 20 % lower, compared to the experimental one. Initially, the simulation's impulse is almost identical to the experimental one. The difference is made in the second half of the explosion, when the explosion in the simulation decays earlier.

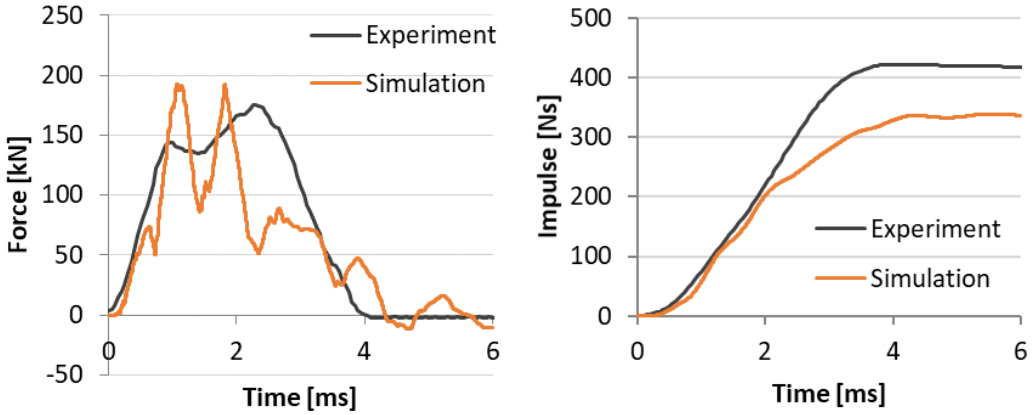

Figure 2: Comparison of the force and total gained impulse on the bottom plate for SES S1 simulation and experiment.

For the simulation case, the force signal is more fluctuating compared to the experimental one, although in the experimental results two force peaks can be also observed. In the simulation, the pressure shock waves are reflected and when meeting, a local increase in fine fragmentation increases pressure and a maximum in the force signal can be observed. The force signal in the simulation decreases more gradually compared to the experiment.

The simulation results for the SES S1 experimental test seem to be, considering the uncertainty in simulating the vapour explosions, in relatively good agreement with the experimental findings. The height of the developed premixed layer seems to be similar to the experimental one and the total impulse of simulation is around 80% of the experimental one. The difference in impulse is made towards the end of the explosion. This might indicate additional contribution to the strength of the explosion from the coarse mixing between

melt and coolant during the explosion. The so-produced melt drops would also undergo fine fragmentation and contribute to the explosion strength.

5.2. PULiMS E6 Experimental Test

The PULiMS experiment was simulated in addition. The PULiMS experiment was performed at KTH (Sweden). Main experimental conditions and results are summarized here, while more detailed description is given in [3, 10]. The test section consisted of a rectangular tank of the size of 2 m × 1 m, filled with water to the height of 20 cm. The melt was released through the funnel, which ended 20 cm above the water surface. The initial melt temperature was 1322 K, which corresponds to 179 K of superheating. Water was at 348 K. During the release of the melt, a spontaneous vapour explosion occurred after around 7 s.

The 3D calculation domain contains half of the experimental tank applying symmetry boundary conditions at the symmetry plane. The continuous melt is described as a 25 mm high melt pool with diameter of around 40 cm. The analyses are based on the best case [7] with the same parameters as in the SES case - C_v, C_d and C_f being 6, 1.25 and 0.5.

For the PULiMS E6 case, the simulated premixed layer also seems to be close to the experimental observations. However, the explosion for the PULiMS E6 case is underpredicted to around one third of the experimental impulse in the simulation analysis (Figure 3). Although the impulse of the explosion is underpredicted in the simulations, the force signal is initially almost identical to the experimental one, indicating similar initial development of the explosion.

Overall, it seems the simulation does not describe the explosion phenomena as good as for the SES S1 case. Similar to the SES S1 case, additional contribution to the amount of melt, participating in the explosion, can be a consequence of mixing during the explosion itself. However, additional observed underestimation of the explosion strength in simulation might indicate possible additional contributions from the other mechanisms related to the melt-coolant mixing, premixed layer formation and vapour explosion. In the PULiMS E6 experimental test, contrary to the SES S1 experimental test, the melt jet falls through 20 cm of water. This geometry presents potential for some amount of mixing between the melt and the coolant as a consequence of the melt jet breakup.

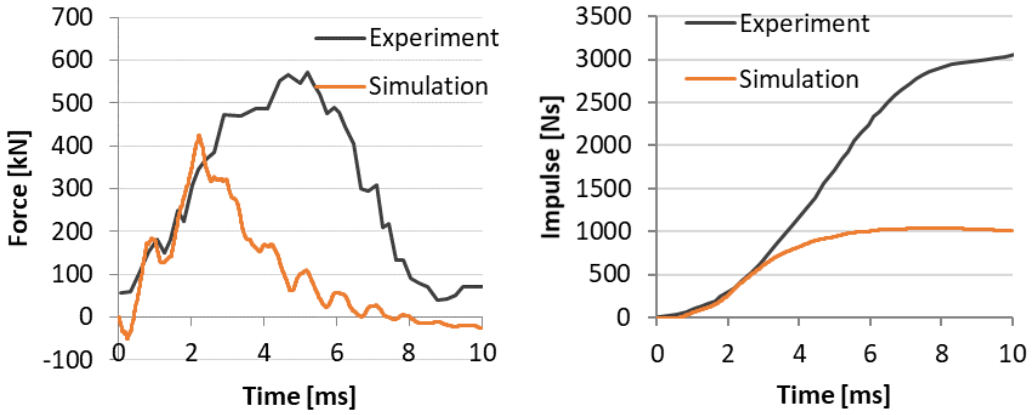

Figure 3: Comparison of the force and total gained impulse on the bottom plate for PULiMS E6 simulation and experiment.

6. CONCLUSIONS

The recent experimental results from the PULiMS and SES (KTH, Sweden) experimental facilities with spontaneous vapour explosions again raised interest in vapour explosions in the stratified configuration. During the experiments, an extensive premixed layer was observed prior to the explosion. From the perspective of nuclear safety studies, it is important to be able to simulate potential energetic fuel-coolant interactions in stratified configurations with the preceded premixed layer of ejected melt drops in the coolant layer.

Short overview of the experimental and analytical research is given. Based on the experiments, possible mechanisms for the premixed layer formation are given and assessed. Developed model for the premixed layer formation, based on the bubble formation and collapse mechanism is presented in the paper. The model was implemented into the Eulerian fuel-coolant interaction code MC3D (IRSN, France) and validated against the SES S1 and the PULiMS E6 experimental results. The simulation results are in agreement with the experimental results regarding the expected premixed layer. For the explosion phase, it seems that the simulations accurately describe the initial phase of the vapour explosion in both aspects – force and impulse, but underestimate the explosion strength of the second part.

The observed underestimation of the explosion strength in simulations might indicate possible additional contributions from the other mechanisms related to the melt-coolant mixing, premixed layer formation and vapour explosion. Some amount of mixing between the melt and the coolant could be a consequence of the melt jet breakup, especially in the PULiMS case, where in the experiment the melt jet falls through 20 cm of water. Additional contribution to the amount of melt, participating in the explosion in both cases, can be a consequence of mixing during the explosion itself.

In-line with this assessment, the simulation results with our model, considering only the bubble formation, growth and collapse mechanism, underestimate the experimental results. This indicates some other plausible contributions, for research of which the future experimental and analytical work would be of great help. With improved experimental observations, more detailed comparison of the premixed layer characteristic would also be possible.

Overall, the proposed premixed layer formation model enables more reliable assessment of the stratified vapour explosions risk in nuclear power plants and in other industries.

ACKNOWLEDGMENTS

The authors acknowledge the financial support of the Slovenian Research Agency within the research program Reactor engineering (P2-0026) and the project Understanding stratified steam explosions in reactor conditions (L2-1828).

REFERENCES

1. Seghal, B.R., *Nuclear Safety in Light Water Reactors: Severe Accident Phenomenology*. 2012: Elsevier Inc.
2. Berthoud, G., *Vapor explosions.* Annual Review of Fluid Mechanics, 2000. **32**(1): p. 573-611.
3. Kudinov, P., et al., *Premixing and steam explosion phenomena in the tests with stratified melt-coolant configuration and binary oxidic melt simulant materials.* Nuclear Engineering and Design, 2017. **314**: p. 182-197.

4. Grishchenko, D., et al. *Insight into steam explosion in stratified melt-coolant configuration*. in *15th International Topical Meeting on Nuclear Reactor Thermal Hydraulics*. 2013. Pisa, Italy.
5. Fischer, M. and T. Keim, *Retrofitting of ex-vessel core catchers into operating nuclear power plants at the example of a Mark-I BWR.* Annals of Nuclear Energy, 2020. **146**: p. 107646.
6. Corradini, M.L., B.J. Kim, and M.D. Oh, *Vapor explosions in light water reactors: a review of theory and modeling.* Progress in Nuclear Energy, 1988. **22**(1): p. 1-117.
7. Kokalj, J., M. Uršič, and M. Leskovar, *Modelling of premixed layer formation in stratified fuel–coolant configuration.* Nuclear Engineering and Design, 2021. **378**: p. 111261-111277.
8. Dinh, T.N., M.J. Konovalikhin, and B.R. Sehgal, *Core melt spreading on a reactor containment floor.* Progress in Nuclear Energy, 2000. **36**(4): p. 405-468.
9. Board, S.J. and R.W. Hall. *Propagation in thermal explosions*. in *2nd Specialist Meeting On Sodium Interaction In Fast Reactors*. 1974. Ispra, Italy.
10. Konovalenko, A., A. Karbojian, and P. Kudinov. *Experimental results on pouring and underwater liquid melt spreading and energetic melt-coolant interaction*. in *The 9th International Topical Meeting on Nuclear Thermal-Hydraulics, Operation and Safety*. 2012. Kaohsiung, Taiwan: American Nuclear Society.
11. Greene, G.A., et al., *Some observations on simulated molten debris-coolant layer dynamics*. 1983, Brookhaven National Laboratory, Upton, New York, USA. p. 15.
12. Yamano, N., et al., *Phenomenological studies on melt-coolant interactions in the ALPHA program.* Nuclear Engineering and Design, 1995. **155**(1): p. 369-389.
13. Farmer, M.T., D.J. Kilsdonk, and R.W. Aeschlimann, *Corium coolability under ex-vessel accident conditions for LWRs.* Nuclear Engineering and Technology, 2009. **41**(5): p. 575-602.
14. Bang, K.H. and M.L. Corradini, *Stratified vapor explosion experiments.* Chemical Engineering Communications, 1989. **86**(1): p. 31-42.
15. Sainson, J., M. Gabillard, and T. Williams. *Propagation of vapor explosion in a stratified geometry experiments with liquid nitrogen and water*. in *CSNI Specialists Meeting on Fuel-Coolant Interactions*. 1993. Santa Barbara, California, USA.
16. Frost, D.L., B. Bruckert, and G. Ciccarelli, *Effect of boundary conditions on the propagation of a vapor explosion in stratified molten tin/water systems.* Nuclear Engineering and Design, 1995. **155**(1): p. 311-333.
17. Alsmeyer, H. and W. Tromm, *The COMET concept for cooling core melts: Evaluation of the experimental studies and use in the EPR*. 1999, Institut für Kern und Energietechnik, Forschungszentrum Karlsruhe, Germany. p. 94.
18. Kudinov, P., et al., *Investigation of steam explosion in stratified melt-coolant configuration*, in *2nd NUGENIA Review Meeting TA2.2*. 2015: Jandía, Spain. p. 37.
19. Harlow, F.H. and H.M. Ruppel, *Propagation of a liquid-liquid explosion*. 1981, Los Alamos National Lab., USA. p. 13.
20. Bang, K.H. and M.L. Corradini, *Vapor explosions in a stratified geometry.* Nuclear Science and Engineering, 1991. **108**(1): p. 88-108.
21. Kudinov, P., et al., *Investigation of steam explosion in stratified melt-coolant configuration*, in *The 10th International Topical Meeting on Nuclear Thermal-Hydraulics, Operation and Safety*. 2014: Okinawa, Japan. p. 16.

22. De Malmazet, E., et al. *Stratified Steam Explosion Phenomena: SAFEST SES-S1 test results and preliminary analysis*. in *The 8th European Review Meeting on Severe Accident Research, ERMSAR-2017, Warsaw, Poland*. 2017.
23. Meeks, M.K., et al., *Suppression of stratified explosive interactions*, in *OECD/CSNI Specialist Meeting on Fuel-Coolant Interactions*. 1997: Tokai, Japan. p. 624-638.
24. Kokalj, J., M. Leskovar, and M. Uršič. *Premixed layer formation modelling in stratified melt-coolant geometry*. in *18th International Topical Meeting on Nuclear Reactor Thermal Hydraulics*. 2019. Portland, USA: ANS.
25. Caldarola, L. and W.E. Kastenberg, *Mechanism of fragmentation during molten fuel/coolant thermal interactions*, in *Fast reactor safety meeting*. 1974: Beverly Hills, California, USA. p. 937-954.
26. Berenson, P.J., *Film-boiling heat transfer from a horizontal surface.* Journal of Heat Transfer, 1961. **83**(3): p. 351-356.
27. Leclerc, E. and G.J. Berthoud, *Modeling of Melt Droplet Fragmentation Following Vapor Film Destabilization by a Trigger Pulse.* Nuclear Technology, 2003. **144**(2): p. 158-174.
28. Leskovar, M., et al., *Investigation of steam explosion duration in stratified configuration.* Nuclear Engineering and Design, 2019. **353**: p. 110233.
29. Meignen, R., et al., *The challenge of modeling fuel–coolant interaction: Part I – Premixing.* Nuclear Engineering and Design, 2014. **280**: p. 511-527.



Jožef Stefan
Institute

R4

Reactor
Engineering
Division

Modelling of Premixed Layer in Stratified Fuel–coolant Configuration

Janez Kokalj[1], Mitja Uršič[1], Matjaž Leskovar[1], Renaud Meignen[2]

[1]Jožef Stefan Institute (JSI), Slovenia
[2]Institut de Radioprotection et de Sûreté Nucléaire (IRSN), France

The 10th European Review Meeting on Severe Accident Research (ERMSAR2022)
Akademiehotel, Karlsruhe, Germany, May 16-19, 2022

Overview

- Fuel coolant interaction in stratified configuration
- Premixed layer formation
- Identification of mechanisms for premixed layer formation
- Development of model for premixed layer formation
- Implementation of model in MC3D (IRSN, France)
- Model validation

- Goal: To develop, present and discuss an original model for the **premixed layer formation** and to demonstrate its capabilities.

Vapour explosion in stratified configuration

- Stratified configuration was believed to be incapable of generating strong explosion due to the lack of premixing, based on some hypothesis and experiments with low temperature melt.

- Hypothesis proposed by Harlow and Ruppel remained the state-of-the-art view since 1981:

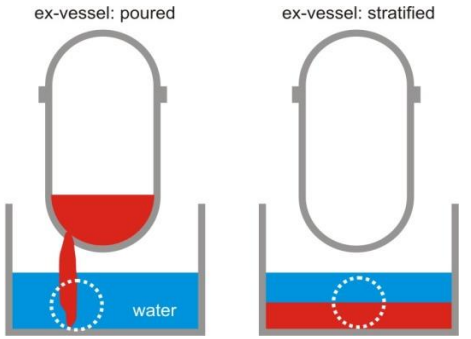

Possible configuration of FCI.

» as for the stratified mode of contact, there is no premixing phase, but it is believed that the propagation of the pressure wave is responsible for the mixing and fragmentation of the two liquids «

- In recent experiments in stratified configuration, strong spontaneous vapour explosions occurred and premixed layer was observed, which again raised the interest in stratified vapour explosions.



Premixed layer during melt spreading in PULiMS experiment (KTH, Sweden).

Premixed layer formation

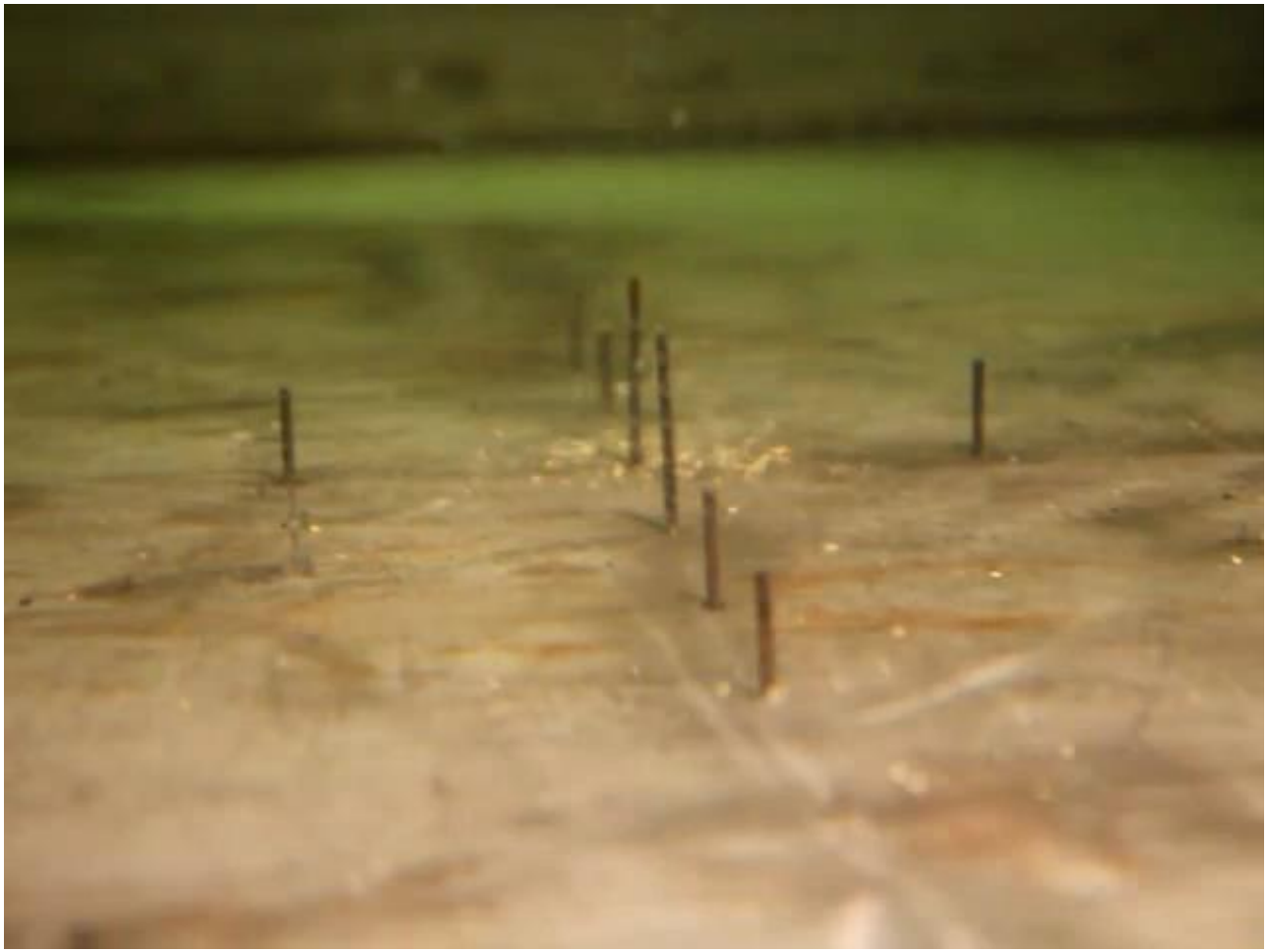

Underwater melt spreading and premixed layer formation in PULiMS experiment. Video: KTH

Why is it important?

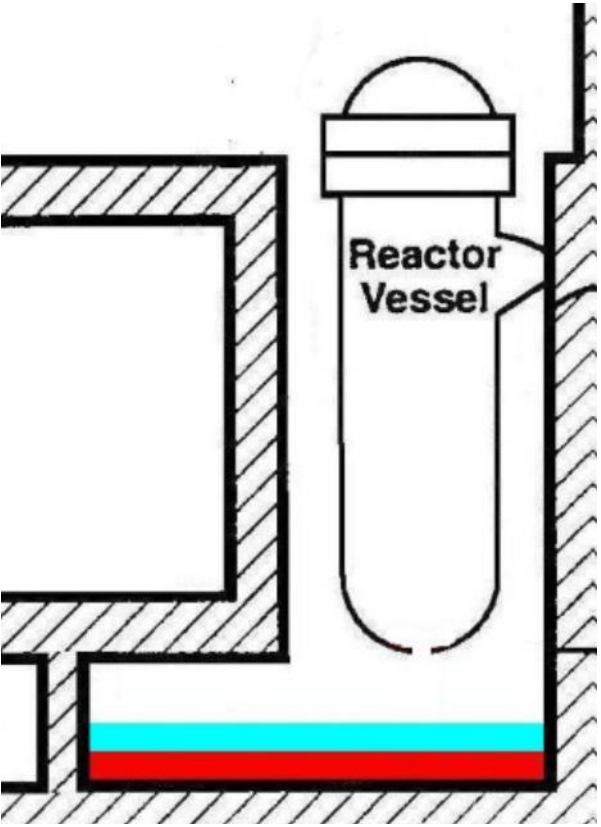



PULiMS experiment

Video: KTH

Possible mechanisms for premixed layer formation

- Growth, expansion and collapse of vapour bubble
- Evaporation of coolant entrapped in melt or under melt
- Release of gases from interaction of melt with concrete
- Release of non-condensable gases during melt cooling
- Jet breakup, impingement and splattering

Our model for premixed layer formation

- Two developed modelling approaches:
  - Pressure perturbation model
  - Water entrapment model

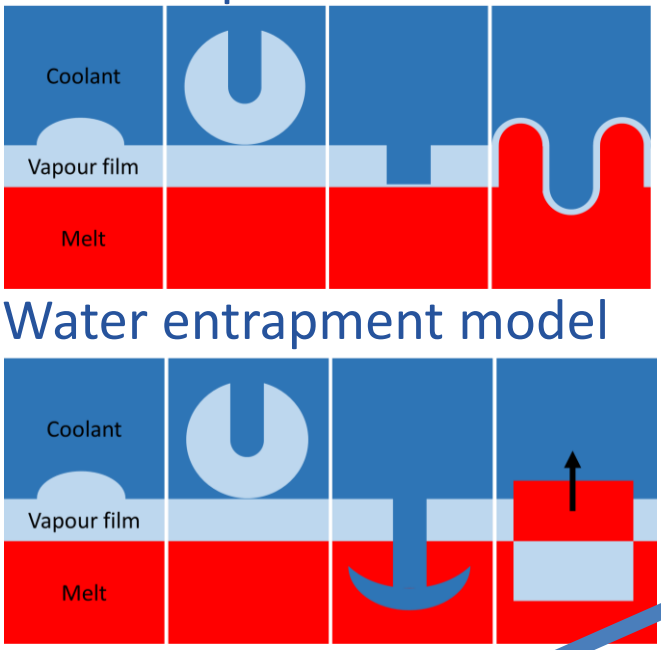

- **Melt drop size**
- **Fragmentation rate**
  - **Spatial distribution of melt ejections**
  - **Frequency of melt ejections**
- **Melt drop initial velocity**

in consensus

implementation

- In MC3D code (IRSN, France)

Melt drop diameter



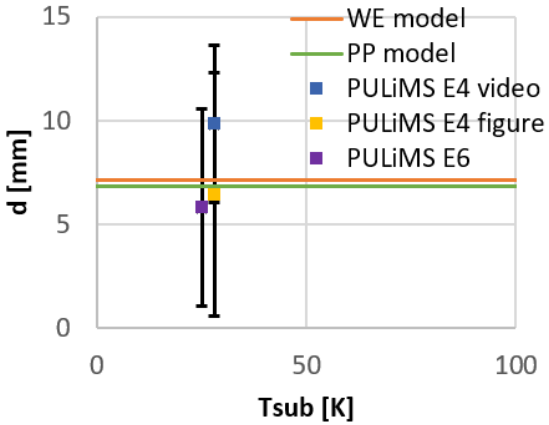

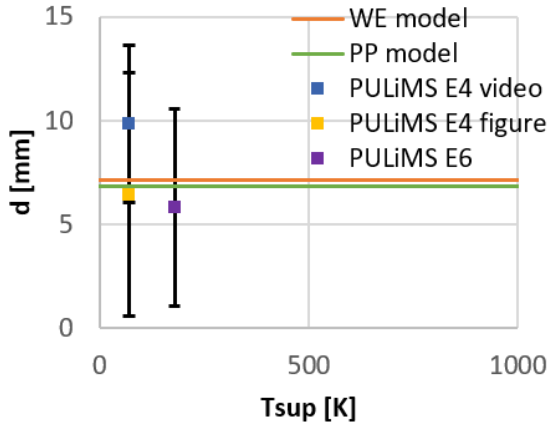

$$d = C_{OMd} \cdot \frac{1}{4} \cdot \Lambda$$

$$\Lambda = most\ dangerous\ wavelength$$

Spatial distribution of melt ejections

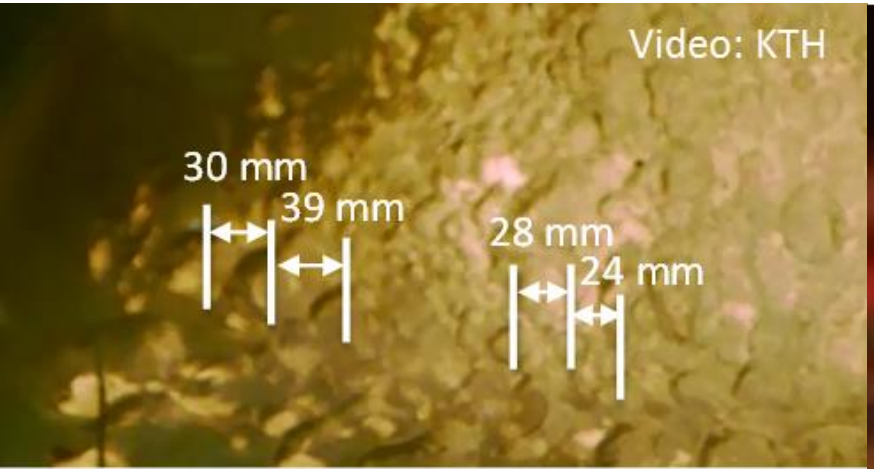

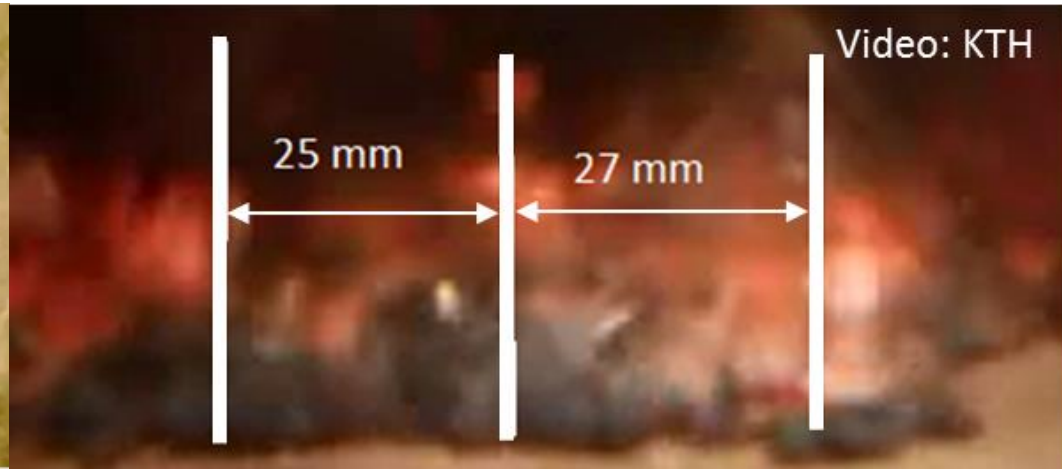

$$S_1 = C_{OMs} \cdot \frac{1}{2} \Lambda^2$$

$$\Lambda = 2\pi \sqrt{\frac{3\sigma_L}{g(\rho_L - \rho_G)}}$$

- For water as coolant: Λ = 27 mm

Frequency of melt ejections

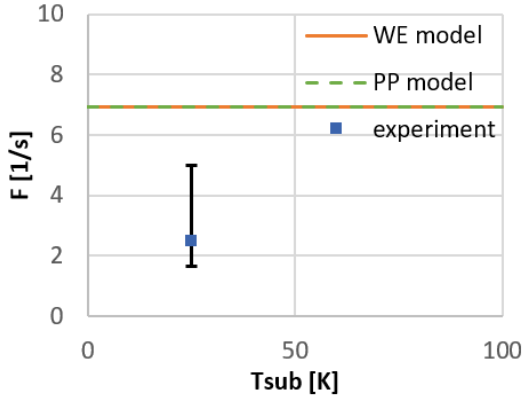

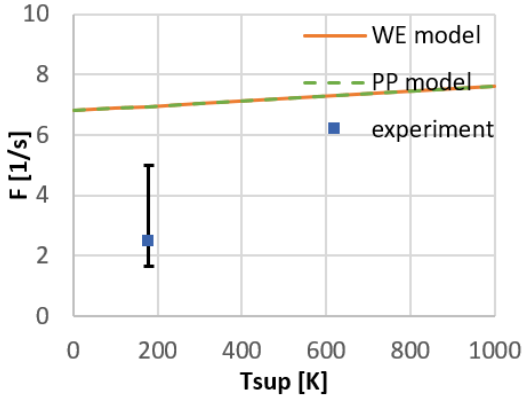

Berenson (1961) studied the film-boiling heat transfer from a horizontal surface. Considering the Rayleigh-Taylor instability, he derived the frequency of the instability growth.

$$F = C_{OMfreq} \cdot \frac{1}{2\pi}\sqrt{\frac{\rho_G v_{vf}^2 n}{\rho_L a} + gn - \frac{\sigma_L n^3}{\rho_L}}$$

$$v_{vf} = 0.45\frac{\lambda_{vf}\Delta T}{\rho_{vf}\Delta H a^2 n}$$

$$a = 2.35 \cdot \frac{\sigma_L^{\frac{1}{8}}}{(g\rho_L)^{\frac{3}{8}}} \cdot \left(\frac{\mu_{vf}\lambda_{vf}\Delta T}{\Delta H \rho_{vf}}\right)^{\frac{1}{4}}$$

$$\Gamma = \frac{dV}{Sdt} = \frac{\pi d^3 F}{6S_1} = C_{OMf}\frac{\pi^2}{96}\sqrt{\frac{3\sigma_L}{g(\rho_L - \rho_G)}} \cdot F$$

$$C_{OMf} = C_{OMs} \cdot C_{OMfreq}$$

Melt drop initial velocity

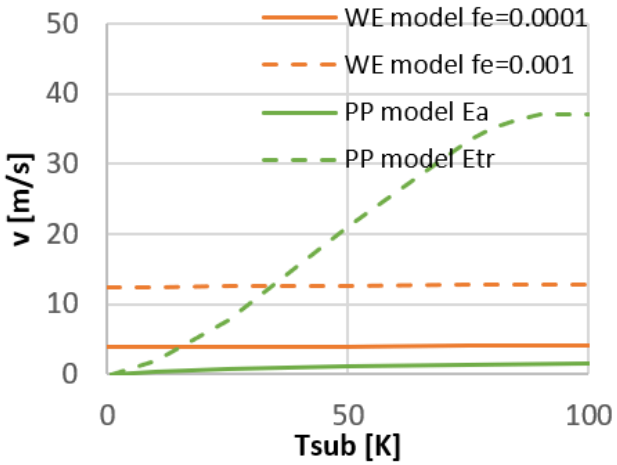

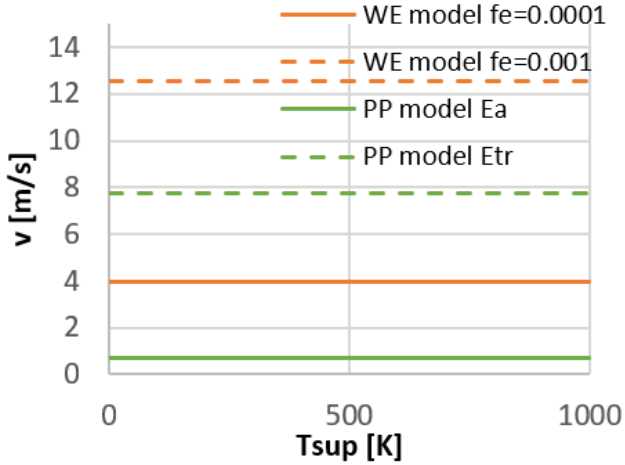

E_{tr} – energy due to the shock wave from a hemispherical source to the surrounding medium

E_a – energy of the elastic wave traveling in the fuel

$$v = C_{OMv}\sqrt{C_{PPv1}\cdot C_{PPv2}\cdot\frac{(p_{max}-p_0)^2\Delta T_{sub}^2}{\Lambda^{0.8}\sqrt{\Delta p}}}$$

$$C_{PPv1} = 0.0191\frac{d_c^2 l_c f_b^{2.2}}{C_{PPd}^3} \approx \frac{0.00015}{C_{PPd}^3}$$

$$C_{PPv2} = \frac{(\rho_M-\rho_L)\rho_L^{1.9}}{(\rho_M+\rho_L)\rho_M^2\rho_G^2}\cdot\frac{\lambda_L^{\frac{4}{3}}c_p^{\frac{2}{3}}}{cg^{0.2}L^2\sigma_L^{0.2}\mu_L^{\frac{8}{15}}}$$

Implementation

- MC3D (IRSN, France) is an Eulerian code
- Two-melt-drop-group approach:

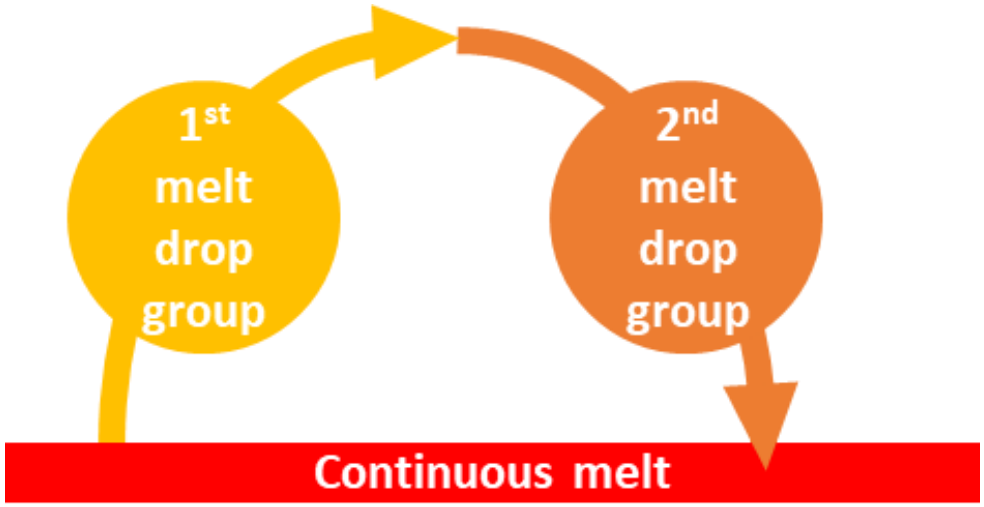

Validation on experimental results PULiMS E6

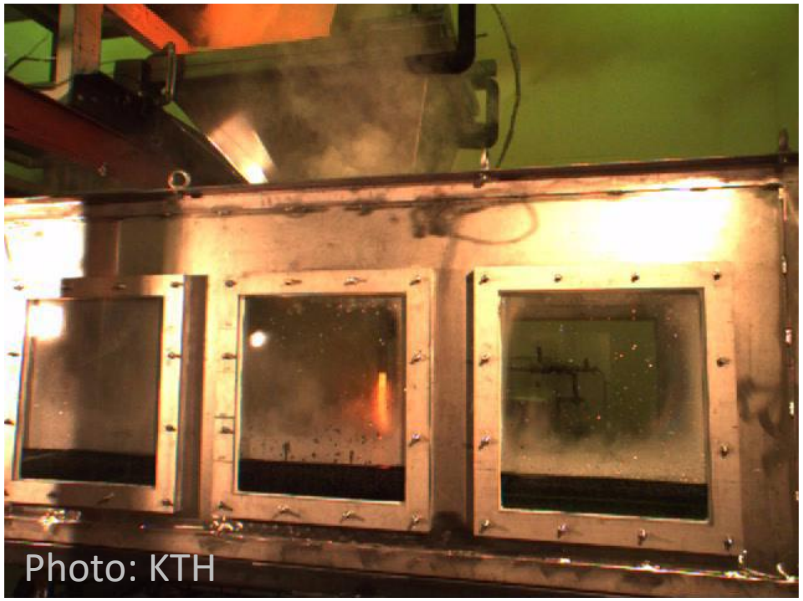

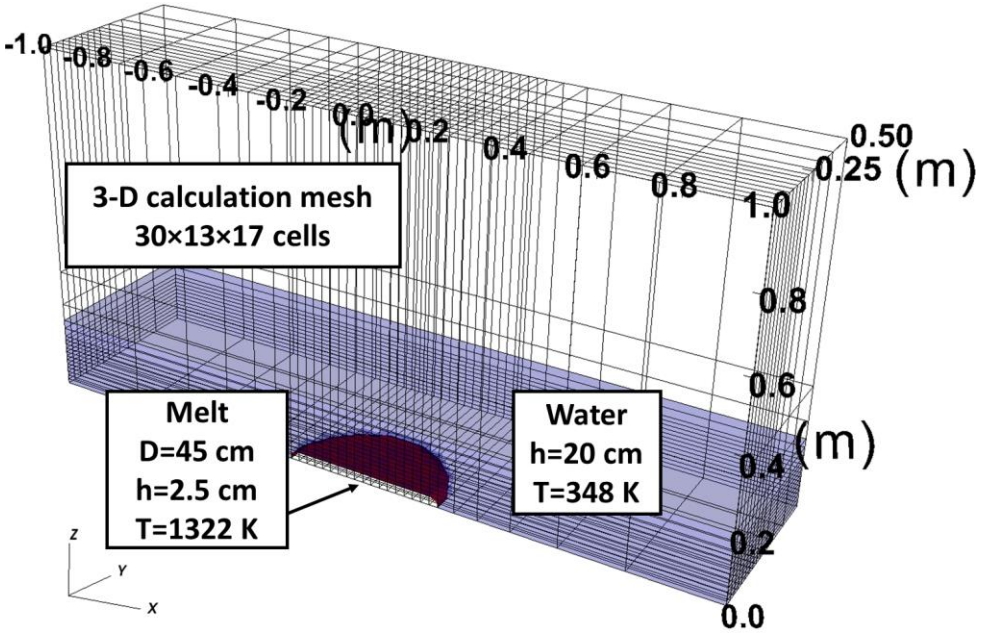

Premixing phase

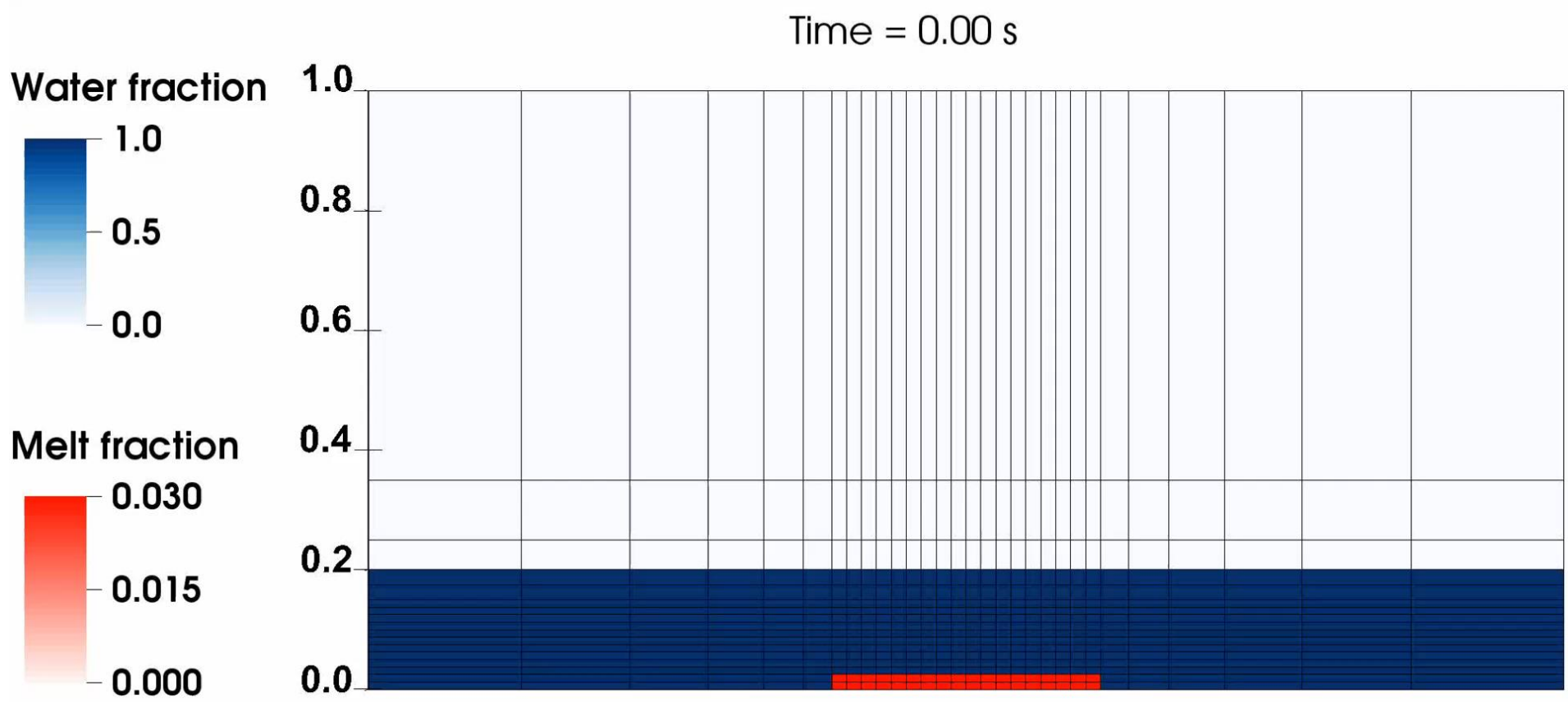

Explosion phase

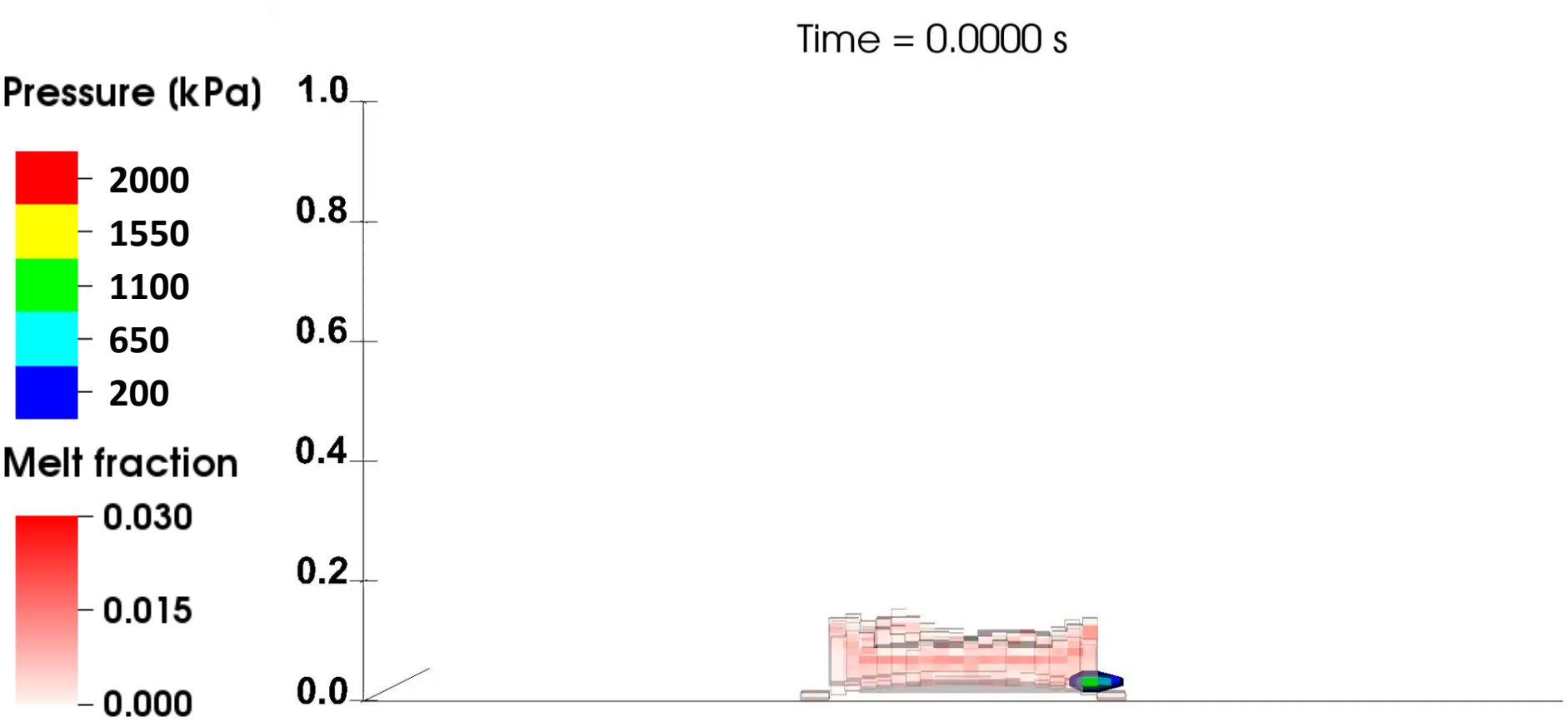

Analysis

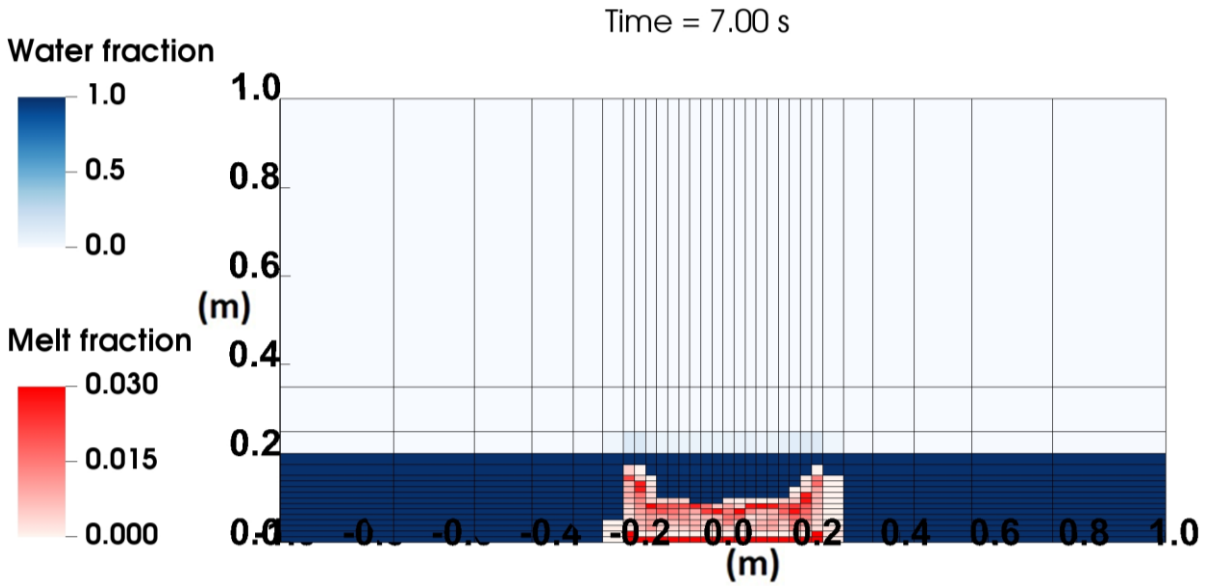

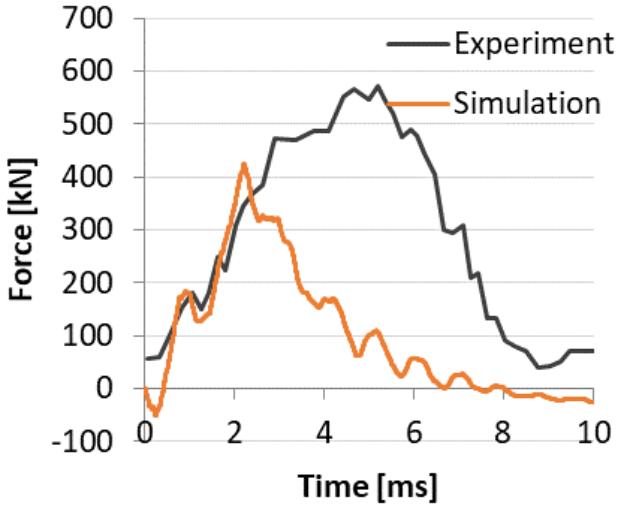

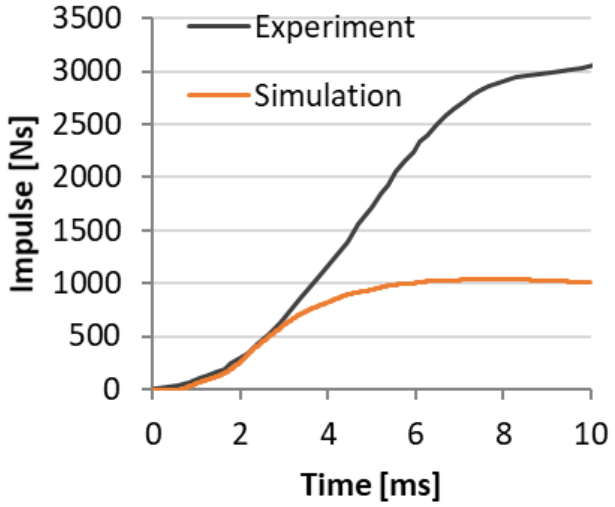

The analyses are established on the optimal parameters C_{OMv}=6, C_{OMf}=0.5 and C_{OMd}=1.25.

Validation on experimental results SES S1



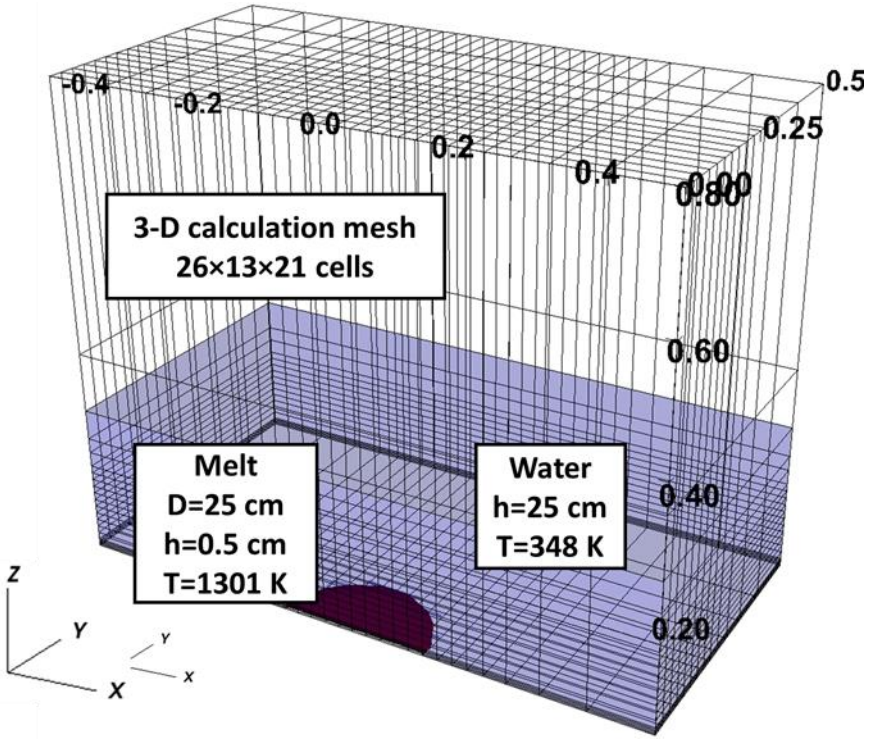

Analysis

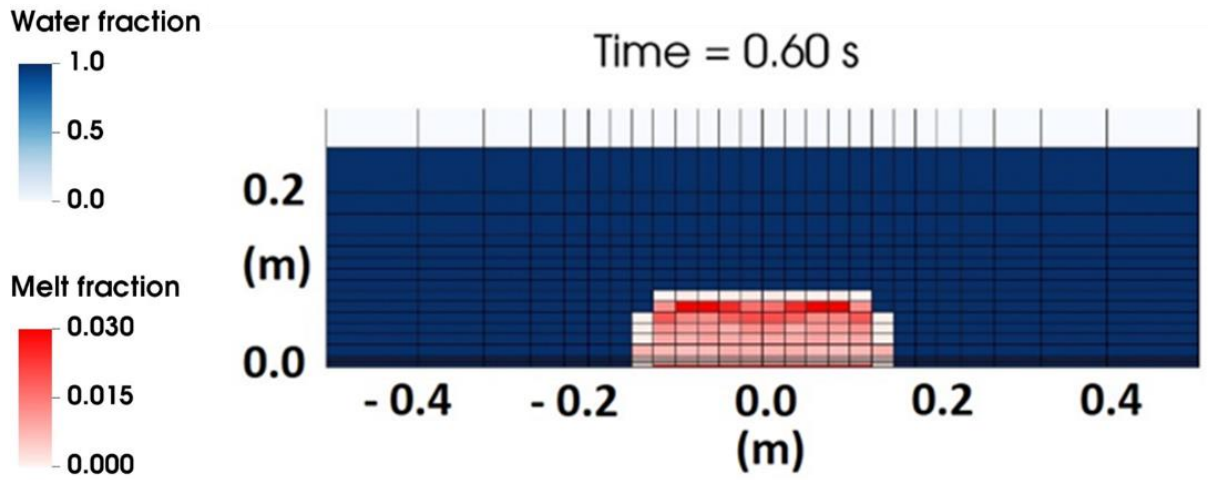

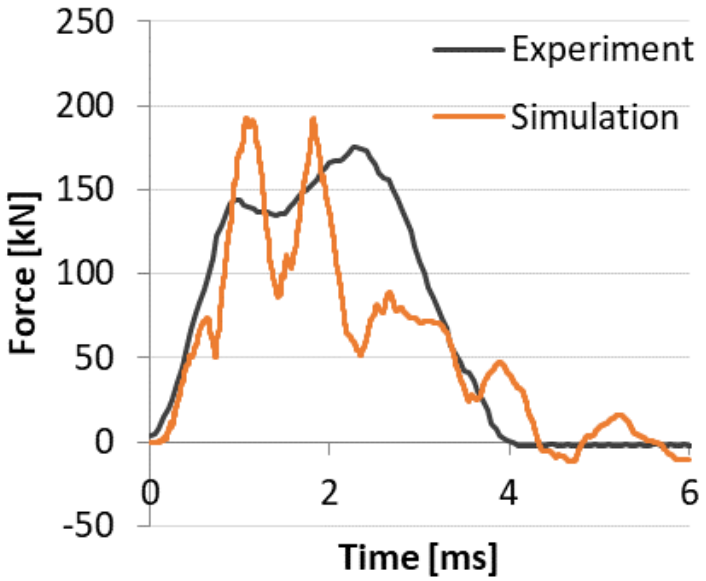

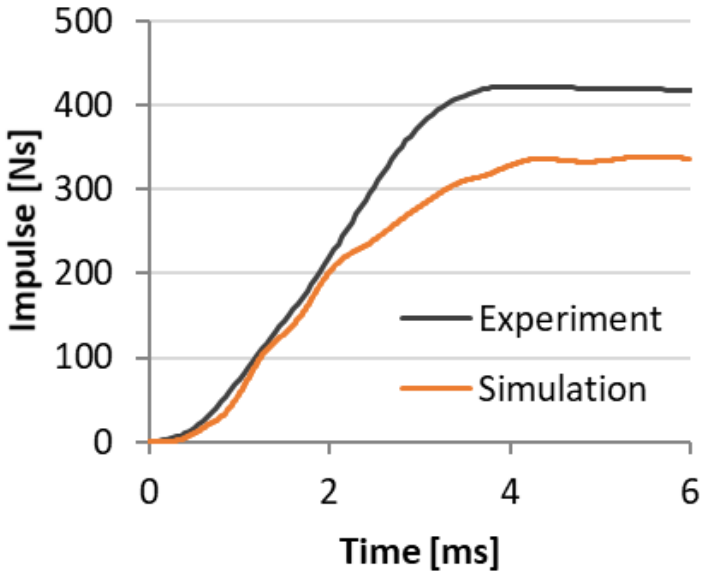

- The analyses are based on the best case with parameters C_{OMv}=6, C_{OMf}=0.5 and C_{OMd}=1.25.

Conclusions 1/2

- The stratified configuration was usually of secondary importance in the nuclear safety analyses. The available experimental information is scarce.
- Unexpected strong vapour explosions in stratified configuration with premixed layer (PULiMS & SES, KTH, Sweden) were observed, for which no model existed yet.
- For the vapour explosion in stratified configuration, few models were developed in the past. They describe the initiation of the interaction, its propagation and mixing right in front or just behind the vapour film collapse. However, none of the models describes the premixed layer formation.
- Based on comprehensive overview of experiments, growth, expansion and collapse of vapour bubble was determined to be most common plausible mechanism.

Conclusions 2/2

- Two modelling approaches were developed: pressure perturbation model and water entrapment model.
- Both models were combined into our model for premixed layer formation, simultaneously satisfying description of experimental phenomena.
- Our model was implemented in MC3D code (IRSN, France) via developed two-melt-drop-group approach.
- Validation (simulations) on experiments shows qualitatively and quantitatively reasonable agreement.
- It seems that beside premixed layer, important contributions to explosion strength are also melt jet fragmentation and melt layer mixing with water during explosion.



Jožef Stefan
Institute

R4

Reactor
Engineering
Division

ANALYSIS OF RANS TURBULENCE MODELS OF NATURAL CONVECTION OF A CORIUM POOL FOR IN-VESSEL RETENTION

D. Dovizio*[1], B. Bian[2], W. Villanueva[2], E.M.J. Komen[1]
[1]: Nuclear Research and Consultancy Group (NRG), Netherlands
Westerduinweg 3, 1755 LE Petten, Nederland
dovizio@nrg.eu; komen@nrg.eu

[2]: Division of Nuclear Power Safety, Royal Institute of Technology (KTH), Sweden
Royal Institute of Technology (KTH)
SE-100 44 Stockholm, Sweden boshen@kth.se; walterv@kth.se

ABSTRACT

In-Vessel Retention (IVR) is a severe accident mitigation strategy that has been shown to work for low-to-intermediate power reactors. For this reason, several efforts have been put forward to make this strategy feasible for high power reactors. In this context, the European H2020 IVMR project was launched in 2015 with the objective to evaluate and improve current modelling strategies, such as the use of CFD codes for the prediction of mass and heat transfer in a homogenous corium pool. However, the validation was mainly performed against an available water-based experimental data, rather than a corium mixture. Recent high fidelity numerical calculations, in the form of DNS, have been performed and used here as a reference for the validation purpose of the RANS approach. In this work, RANS numerical simulations of a three-dimensional hemispherical configuration are performed using the STAR-CCM+ code. The Boussinesq assumption is used to characterize the natural convection problem. The flow conditions correspond to a Rayleigh number of 10^{11} and a Prandtl number of 0.8. Several turbulence models available in STAR-CCM+ are compared and evaluated against the DNS results, in terms of velocity, temperature, buoyancy production of the turbulent kinetic energy and heat flux. Overall, most models are capable of predicting the main qualitative features of the flow configuration, such as thermal stratification, fast descending flow on the curved sides and high turbulence at the top of the domain. The main divergence between RANS and DNS is observed in the bulk region, where all the RANS computations present strong recirculation, while an extended nearly stagnant zone is predicted by DNS calculations. Quantitative analysis is performed and shows the behavior of the different approaches in detail. Advantages and limitations of such models are described, as well as potential future improvements.

KEYWORDS
In-Vessel Retention, Severe Accident, Internally Heated Natural Convection, RANS, DNS

1. INTRODUCTION

During a hypothetical Severe Accident (SA) scenario in a light water reactor, the molten core may relocate and accumulate in the lower plenum of the reactor pressure vessel (RPV). The decay heating in the core melt, generally referred to as corium, may cause the formation of a molten core pool. As a result, an

* dovizio@nrg.eu

internally heated natural convection flow regime is established and the heat generated from the corium and its corresponding weight impose a thermo-mechanical load on the vessel wall, which can threaten the structural integrity of the RPV. The In-vessel Retention (IVR) by external cooling with water is a Severe Accident Management (SAM) strategy that has been established and implemented for low- and medium-power reactors and looks to be promising for higher power reactors as well. For example, IVR is adopted by the AP600, AP1000 and APR1400 reactor [1], by means of natural convection on the external vessel wall, which is achieved by flooding the compartment that houses the vessel and subsequently establishing a natural circulation regime.

The safety evaluation for such an accident scenario has been performed historically using lumped parameter methods [2, 3], characterized by a zero-dimensional approach, which might not be adequate for natural circulation problems, due to the presence of three-dimensional and multi-scale flow structures.

Moreover, the feasibility of IVMR and consequent safety margins [4] have been assessed for relatively low-power reactors (below 600 MWe), while higher power plants (> 1000 MWe) present lower safety margin and the integrity of the vessel is no longer certified [5]. Furthermore, one additional reason for which these high power plants tend to have low safety margins consists of the so-called 'focusing effect', which significantly increases local heat fluxes from molten pool to the vessel in the location of the top layer [6, 7].

One of the key requirements for the success of the IVR is that the transient heat fluxes from the corium do not exceed the given Critical Heat Flux (CHF) of the external vessel cooling by water. For this reason, it is crucial to investigate the thermo-fluid behavior of the corium to predict the heat flux distribution on the vessel, which is a direct consequence of the turbulent natural convection in the corium pool.

A number of experimental studies on natural convection heat transfer in corium pools have been performed under different conditions in different geometrical facilities. A detailed review of these experimental studies can be found in [8]. Overall, two main limitations can be identified in the experimental campaigns, namely 1) the geometry does not often resemble the real scenario (experiments with hemispherical pools could directly present the natural convection heat transfer in prototypical geometry, avoiding the uncertainties from the extrapolation from 2D to 3D) and 2) the use of alternative material instead of corium (although, the use of prototypical conditions is necessary to better simulate the transient effects and evaluate their impact on the heat flux along the vessel wall [9]).

Moreover, since large scale experiments are difficult to reproduce, numerical analysis of the transient phenomena are performed with stationary models along with probabilistic approaches to evaluate the IVR strategy. These limitations become evident for high power reactors, for which less conservative models are needed in order to correctly evaluate the strategy [9, 10]. One way to overcome such limitations and to avoid costly and complex experimental studies, is to perform complementary high fidelity calculations in the form of Direct Numerical Simulations (DNS), for which no modelling strategies are applied. DNS data is highly valuable for validation purposes and provide data complementary to experiments to gain insights into the complex phenomena of corium pool natural convection.

Recently, DNS was conducted on a homogeneous oxidic molten pool in a hemispherical configuration for a Rayleigh number equal to 10^{11} [11], which is the highest value reached for such a configuration, according to the authors' knowledge. This high fidelity calculation can be used for validating low order models such as Reynolds-Averaged Navier-Stokes (RANS), which have been extensively used for their capability of resolving more detailed phenomena, when compared to system codes, and which are not so extremely costly as DNS.

In this context, Shams [12] performed the assessment of several turbulence models for two BALI test cases, as part of the European IVMR project. These turbulence models include a linear $k-\varepsilon$ model, a non-linear Reynolds stress model and an advanced turbulent heat flux model known as the Algebraic Heat Flux Model (AHFM). RANS numerical calculations were performed with the CFD software STAR-CCM+. It was found that all the models show poor predictions for such high Rayleigh number regimes. Consequently, a new version of the turbulent heat flux model, called AHFM-NRG+, was proposed and provided improvements in the numerical predictions. Similarly, by Whang et al. [13] implemented the Algebraic Flux Model (AFM) in OpenFOAM in combination of the $k-\omega$ SST turbulence model, obtaining good predictions in terms of temperature and wall heat flux of the BALI experiments.

In the present work, RANS calculations are validated against the recent DNS database obtained by Bian et al. [11], following the strategy adopted in [12]. Compared to previous experimental work, the advantages of the DNS calculations reside in the fact that hemispherical configuration is adopted and, more importantly, no limitations are encountered in the access to the data, i.e., theoretically all the quantity of interest (such as velocity, temperature, heat flux, turbulent quantities) are accessible at every point of the domain. In this way, a thorough validation of the RANS approach can be performed, as presented in this work.

2. NUMERICAL MODELLING OF THE OXIDE POOL

The numerical modelling follows the assumptions made in the DNS campaign, namely single phase flow conditions are adopted, without considering other complex phenomena such as crust formation, and mushy zone or metallic layer formation. Furthermore, the Boussinesq approximation is adopted to reproduce the turbulent natural convection regime, while the decay heat is modelled with a constant volumetrically heat source. As a result, an internally heated natural convection flow regime is established, which is mainly controlled by two parameters, namely the internal Rayleigh number (Ra) and the Prandtl number (Pr). In the current case, fixed values of these are adopted, consistent with the DNS calculations: $Ra = 10^{11}$ and $Pr = 0.8$. The hemispherical pool has a depth of 2 m and full three-dimensional conditions are adopted.. Convective terms are discretized with a second-order upwind scheme, following previous work [12]. The pressure-velocity coupling is addressed through the Rhie-Chow type combined with a Semi-Implicit Method for Pressure Linked Equations (SIMPLE) type algorithm.

2.1. Mesh Generation

Consistent with previous work [12], the 3D mesh of the oxide pool is generated with the commercially available software STAR-CCM+, version 12.02. More specifically, the mesh consists of structured prism layers close to the wall region, in order to capture the strong gradients, and an unstructured polyhedral mesh in the bulk region, where mesh resolution is less stringent. Mesh sensitivity is performed with three different meshes, for which both the base size and the number of prism layers have been changed, as summarized in Table I, along with the resulting mesh size (in cell count) and the maximum value of the Wall y+ (defined as $y \cdot u\tau/\nu$, where y is the vertical height of the first grid point and $u\tau$ the friction velocity). It is worth mentioning that, following what was previously done in [12], the maximum value of the Wall y+ is kept below unity even for the coarsest mesh (MESH1), in order to have an appropriate resolution near the wall and to use, among the different turbulence models, the low-Re formulation. Finally, the thickness of the prism layers is kept constant for the three meshes and equal to 60mm in order to include the thermal boundary layer (which is estimated to be between 3.22mm and 7.98mm, according to the Niemela [14] and the Kulacki and Nagle [15] correlations, respectively). Fig. 1 presents a cross section of the generated computational domain. For brevity, only MESH 2 is shown.

Table I. Meshing parameters adopted for the mesh independence study

MESH	Cells	Base Size	Prism Layers	Max Wall y^+
1	271K	60 mm	10	0.88
2	2.1M	30 mm	20	0.13
3	7.2M	20 mm	30	0.02

2.2. Flow and Boundary Conditions

A three-dimensional hemispherical configuration is adopted with a radius equal to 2 m, corresponding to a prototypic size of the reactor pressure vessel. The top and curved surfaces are represented by wall boundary

conditions. More specifically, the liquidus temperature of the oxidic melt is adopted as isothermal boundary conditions at the wall, while no slip conditions are used for the velocity components.
Material properties of the oxidic melt are taken from [16] and summarized in Table II.



Figure 1. Cross-section of the CFD Mesh 2

Table II. Material properties of the oxidic melt [16]

	$\boldsymbol{\rho}$	$\boldsymbol{\mu}$	$\boldsymbol{cp}$	$\boldsymbol{\lambda}$	$\boldsymbol{\beta}$	**Pr**	$\boldsymbol{\alpha}$	**Ra**
Value	7588.4	0.0044	540	3	6.71×10^{-5}	0.8	7.3×10^{-7}	1×10^{11}
Units	$\frac{kg}{m^3}$	$Pa \cdot s$	$\frac{J}{kg \cdot K}$	$\frac{W}{m \cdot K}$	$\frac{1}{K}$	[−]	$\frac{m^2}{s}$	[−]

The value of the decay heat is derived by the assigned Ra and corresponds to Q_{vol} = 6.11 W/m , while isothermal boundary conditions are used for the top and lateral surface: T_w = 2623.15 K. The calculations are started with the flow at rest and uniform temperature of T = 2623.15 K. Since the difference in the density due to the temperature increase is 0.00017%, the use of the Boussinesq approximation is justified.

3. RANS RESULTS

In the validation procedure of RANS calculations, four different turbulence models that are commonly used in natural convection regimes are adopted, namely the Low-Reynolds k − ε with Yap correction, the k − ω SST, the realizable k − ε Two-Layer with the Xu buoyancy driven correction [17] and the second-moment Elliptic Blending Reynolds-Stress turbulence Model (EB-RSM). Such models are already implemented in STAR-CCM+ and no modifications are applied here. In particular, it is worth mentioning that k − ω SST , contrary to the other models, does not assume buoyancy contribution terms in Turbulent Kinetic Energy (TKE).
The results presented here are mesh independent, since a preliminary sensitivity study on the adopted computational mesh was performed but not shown here for brevity. More specifically, mesh independence was reached for MESH 2 of Table I, hence numerical results obtained with MESH 2 will be taken into considerations hereafter.

3.1. Assessment of Different Turbulence Models

Assessment of the four turbulence model mentioned above is presented here, in terms of relevant quantities such as velocity, temperature, buoyancy production and heat flux. Due to the unsteadiness of the natural circulation, the numerical simulations do not reach a converged steady-state solution, but rather a pseudo steady-state condition, which numerically can be observed by oscillations of temporal profiles of quantities such as volumetrically averaged temperature or surface averaged heat flux, not shown here for brevity. For this reason, temporal averaging is applied after this pseudo steady-state configuration is reached (which is dependent on the specific turbulence model) and the resulting averaged fields are considered here. Such a strategy is consistent with the DNS calculations [11].

3.1.1. Qualitative analysis

The mean flow fields obtained by RANS and DNS are displayed in Figure 3.

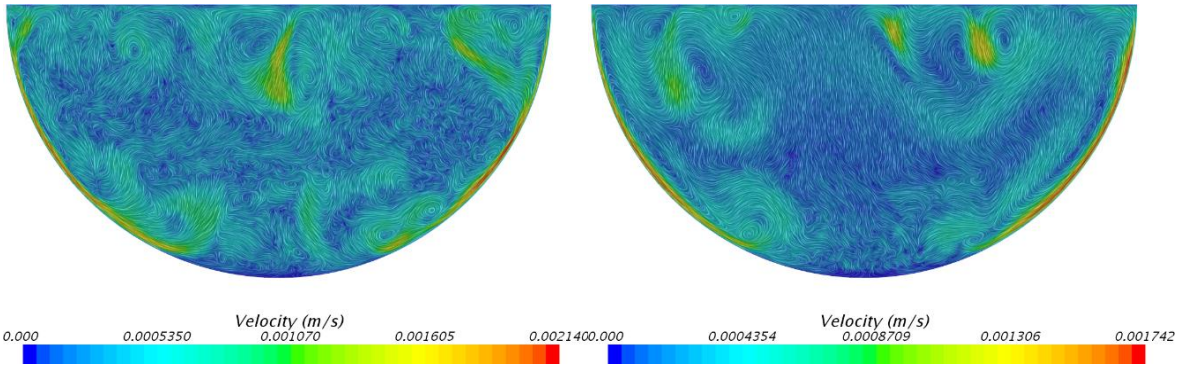

(a) Low-Reynolds $k-\varepsilon$ (b) $k-\omega$ SST

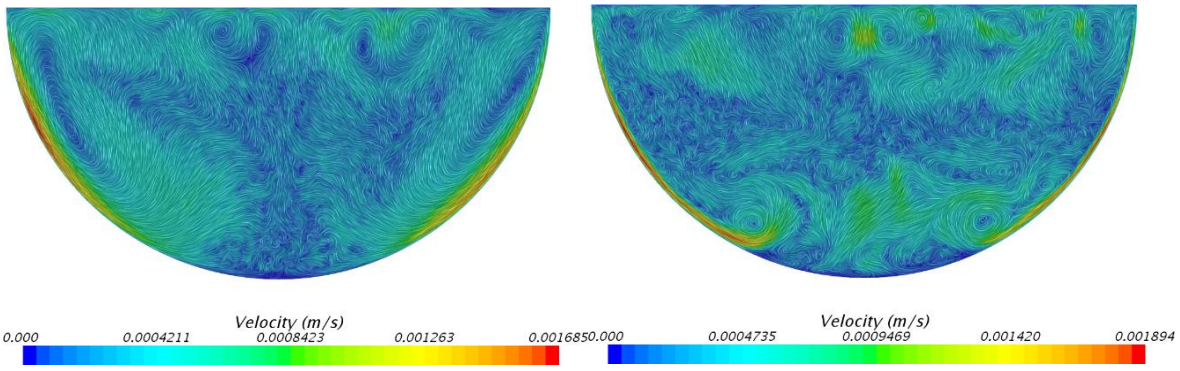

(c) Realizable $k-\varepsilon$ (d) EB-RSM

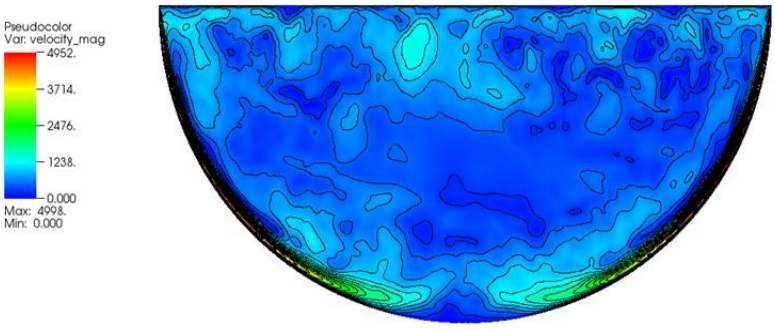

(e) DNS

Figure 3. Integrated line convolution contours for Low-Reynolds $k-\varepsilon$ (a), $k-\omega$ SST (b), Realizable $k-\varepsilon$ (c) and EB-RSM (d). Velocity magnitude iso-contours of the DNS data (e) [11].

In particular, the RANS results are presented in terms of a line integration convolution (LIC) technique colored with velocity magnitude, in order to better visualize the vector fields, while velocity magnitude iso-contours are used for of the DNS.
Looking at the DNS results, it can be seen that the three major zones observed in [18] can be identified here as well: 1) an unstable zone in the upper region, characterized by vigorous eddies and uniform temperature (see also Figure 4(e) for the thermal field), 2) a descending flow region along the cooled curved walls, characterized by the maximum velocity values, and 3) a thermally stratified zone with low ascending velocities in the lower stable zone. It is also interesting to note that the descending flows along the walls interact at the bottom, due to the symmetry of the domain, by creating a sort of "fountain" effect. From the qualitative comparison presented in Fig. 3, it is evident that all the RANS models tend to present these different features. In particular, the presence of the big vortices in the upper part is observed in all models, as well as the high velocity descending along the curved walls. Thermal stratification is well predicted by Low-Re k – ε and the k − ω SST, while at the bottom only the RSM-EB models seems to correctly reproduce the "fountain" effect, while it is quite limited in the Low-Re k – ε and the k − ω SST models, while the realizable k − ε fail to predict these vortices the pool.

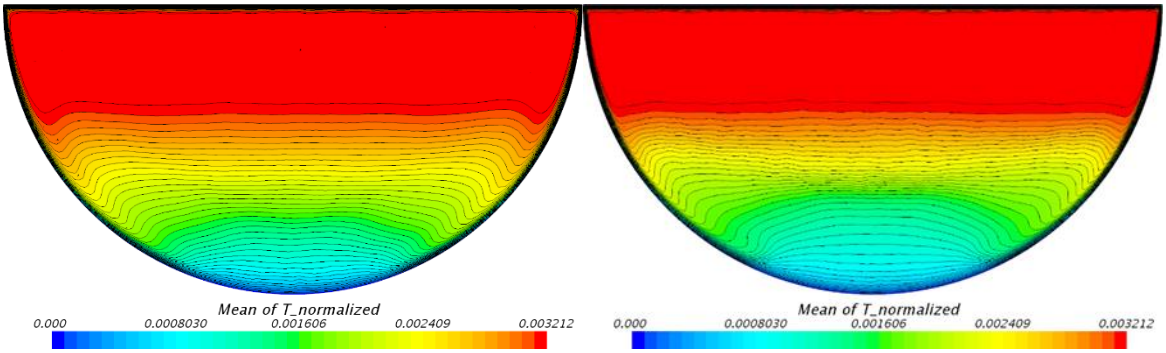

(a) Low-Reynolds $k-\varepsilon$ (b) $k-\omega$ SST

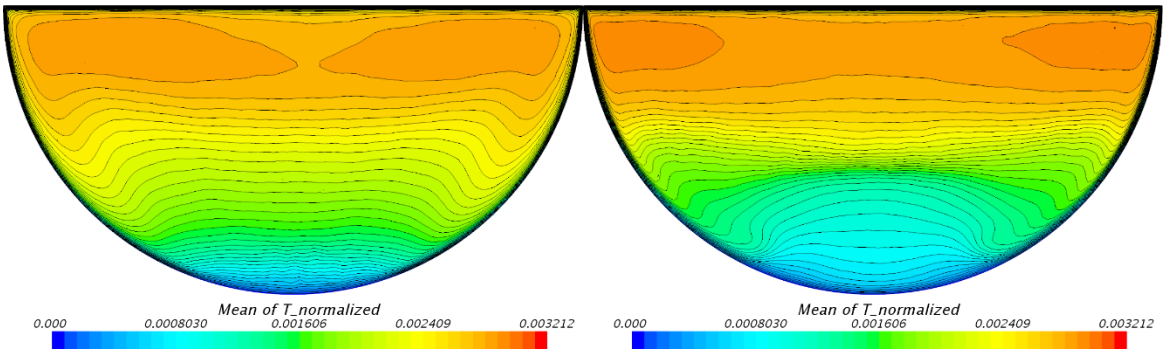

(c) Realizable $k-\varepsilon$ (d) EB-RSM

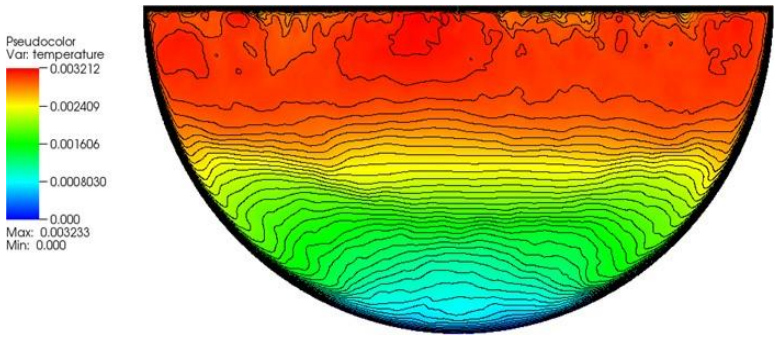

(e) DNS

Figure 4. Temperature iso-contours for Low-Reynolds $k-\varepsilon$ (a), $k-\omega$ SST (b), Realizable $k-\varepsilon$ (c), EB-RSM (d) and DNS (e) [11.

Finally, the main divergence between RANS and DNS is observed in the bulk region, where all the RANS computations present strong recirculation, while an extended nearly stagnant zone is predicted by DNS calculations (dark blue color in Fig. 3(e)). The explanation of this over-prediction of the velocity field in RANS could be attributed to the limitations of this approach when dealing with regimes characterized by low velocity and re-laminarization, such as the one under consideration.

Figure 4 shows the iso-contours of the thermal field for the different turbulence models. The range of the legend is taken the same as the DNS results, in order to obtain a straightforward comparison for the different cases and non-dimensional quantities are used, consistent with the DNS data. In particular, the non-dimensional temperature T^* is used and given by

$$T^* = (T - T_w)(g\beta H^3)/(\alpha\nu \mathrm{Ra}) \quad , \tag{1}$$

where α is the thermal diffusivity, ν the kinematic viscosity, β the thermal expansion coefficient, g the gravity acceleration and H the length scale.

The different zones observed in the DNS (stagnant cold zone in the bottom, strong thermal stratification in the middle and uniform high temperature at the top) are quite well predicted by the RANS computations. However, k − ω SST and realizable k − ε are not able to predict the distortion of the isolines in the bulk, but show a rather uniform stratification. Furthermore, the temperature field is over-predicted at the top of the domain by Low-Re k − ε and k − ω SST, while under-predicted by realizable k − ε and EB-RSM. This latter can be seen as a clear consequence of the over-prediction of the flow field described above. In particular, a stronger mixing is observed in these two RANS models, favoring the thermal mixing between the hot top region with the cold bottom region, resulting in a lower temperature at the top. This has direct implication in the overall assessment of IVR in 2-layer configuration as the heat flux to the upper metal layer (which in turn is responsible for the focusing effect) is underpredicted by RANS.

By definition, the RANS turbulence models solve transport equations for both the turbulent kinetic energy and its dissipation rate in order to provide a closure for the turbulent stresses. Hence, the turbulent kinetic energy is an important quantity in the validation process of a RANS turbulence model. In natural circulation problems, one specific term of the turbulent kinetic energy plays an important role, namely the buoyancy production, which is given by

$$P_b = -\beta g \overline{w'T'} \quad , \tag{2}$$

where $\overline{w'T'}$ is the component of the turbulent heat flux acting along the gravity vector. Unfortunately, experimental data present notorious limitations in the determination of turbulence quantities, such as the turbulent kinetic energy budget. Therefore, it is interesting to analyze P_b coming directly from the DNS database, which has never been done for such a hemispherical configuration to the authors' knowledge.

In RANS, the Simple Gradient Diffusion Hypothesis (SGDH) is adopted, i.e.

$$\overline{w'T'} = -\frac{\overline{\nu_T}}{Pr_T}\nabla\bar{T} \quad , \tag{3}$$

where ν_T is the turbulent viscosity and Pr_T is the turbulent Prandtl number, leading to:

$$P_b = \beta \frac{\overline{\nu_T}}{Pr_T} (\nabla \overline{T} \cdot \boldsymbol{g}) \quad . \tag{4}$$

Figure 5 shows the P_b field, obtained with Eq. (1), for the different turbulence models along with the one obtained in the DNS computations. Consistent with the velocity contours displayed in Fig. 3, P_b in the DNS calculations present three major zones: high level of P_b at the top (associated to the turbulent convective motion) and along the lateral walls, while smaller values in the bulk.

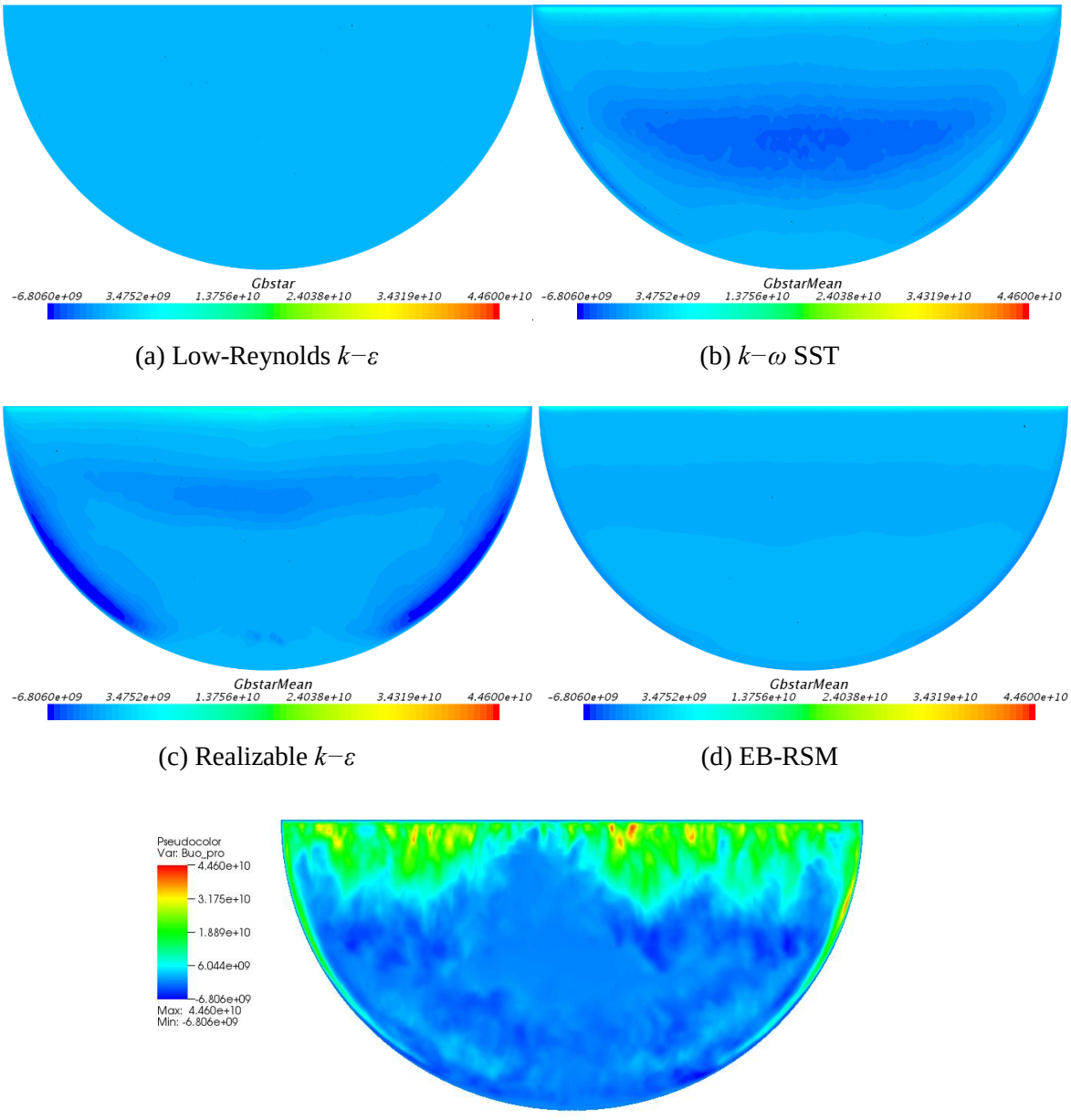

(a) Low-Reynolds $k-\varepsilon$ (b) $k-\omega$ SST

(c) Realizable $k-\varepsilon$ (d) EB-RSM

(e) DNS

Figure 5. Buoyancy production term P_b for Low-Reynolds $k-\varepsilon$ (a), $k-\omega$ SST (b), Realizable $k-\varepsilon$ (c), EB-RSM (d) and DNS (e) [11].

These three zones are not well identified in the RANS calculations, since P_b is under-predicted in the top part and null values are obtained along the curved walls (dark blue color), while large values are observed in the DNS results. It is worth mentioning that the Low-Reynolds k − ε model is too dissipative and results in a null P_b field (light blue color in Fig. 5 (a)), while RSM-EB seems to be the one better reproducing the bulk region, i.e. not showing negative values like the other two turbulence models.

3.1.2. Quantitative analysis

A more detailed analysis can be obtained by performing a quantitative comparison of the RANS computations with the DNS data. The same quantities introduced in the qualitative analysis are used here. In particular, a vertical line, positioned in the center of the pool, is used for the estimation of the velocity magnitude, temperature and P_b. The corresponding profiles are presented in Fig. 6.

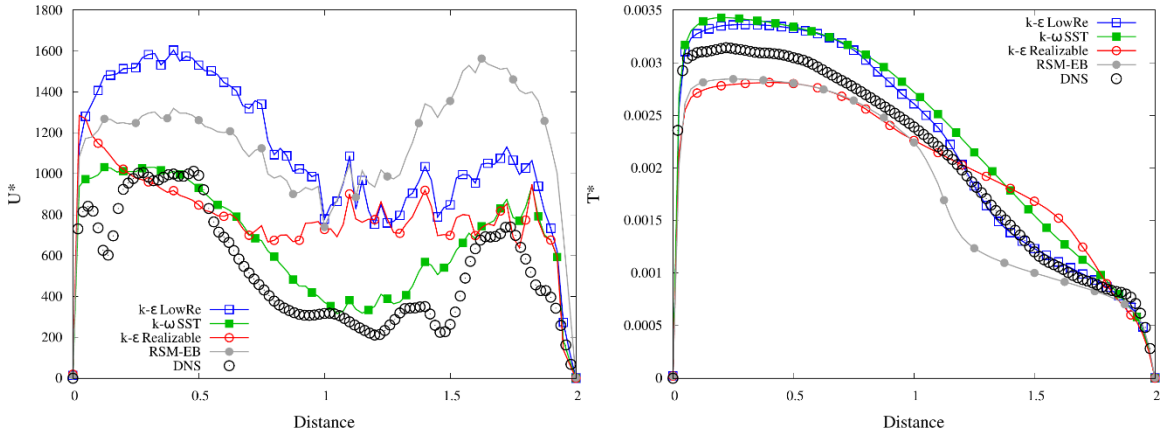

(a) Velocity magnitude (b) Temperature

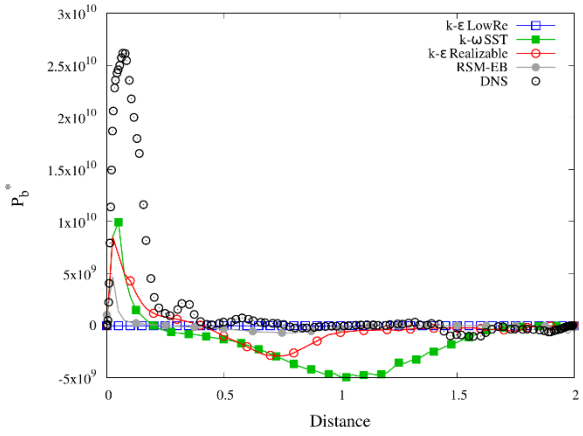

(c) P_b

Figure 6. Velocity magnitude (a), temperature (b) and P_b (c) profiles along the vertical central line for different RANS turbulence models and DNS [11].

The over-prediction of the velocity field by the RANS approaches is evident in Fig. 6a, since all models provide values of the velocity field higher than the DNS predictions. In particular, two peaks are observed in the DNS, the first one at the top, corresponding to the high convective zone, and the second one at a

vertical distance of 1.7 m from the top, corresponding to the recirculation region from the descending flows along the walls (referred before as the "fountain" effect). However, the second peak is smaller in intensity with respect to the first peak. In the RANS calculations, on the other hand, different trends are observed for the different models. In particular, the Low-Re k − ε does not predict a second peak, but rather high velocity values extending from the bulk to the bottom of the domain, highlighting its limitations for this natural convection scenario. The Realizable k − ε does not predict two peaks either, but rather a relatively uniform level of the velocity magnitude through the domain. The EB-RSM shows two distinct peaks, but the second peak is higher than the first one, in disagreement with the DNS data. Only the k − ω SST presents a descending trend towards the bulk and this can be attributed to the capacity of the model in predicting somehow the re-laminarization better than the other models, rather than the capability in predicting natural circulation phenomena, which is common to all the models considered here to some extent. The large over-estimation of the velocity field by the Low-Re k − ε appears not to affect excessively the thermal field, as shown in Fig. 6b, where the temperature over-prediction is similar to the one of the k − ω SST model. The Realizable k − ε and the EB-RSM, on the other hand, show a similar under-prediction of the temperature field at the top of the domain, while an opposite behavior is observed in the bulk. It is also worth noticing that, as evident by the isolines of the qualitative comparison (Fig. 4d), the EB-RSM is the only model capable of reproducing the particular behavior of the thermal field close to the bottom of the pool, namely the less uniform thermal stratification associated to the stretching of the isolines, resulting in a change of the steepness of the vertical temperature profile.

Finally, the P_b profiles along the same vertical line are displayed in Fig. 6c. The DNS data show a peak of P_b at the top of the domain and null values for the rest of the domain. The RANS limitations are evident here, since none of the models can correctly reproduce the DNS trend. In particular, the Low-Re k – ε provides null results, as already mentioned in the qualitative analysis. The k − ω SST and Realizable k – ε models present an under-predicted peak at the top (roughly 0.4 times the DNS value), along with large negative values in the bulk (especially for k − ω SST). EB-RSM severely under-predict the peak at the top, but does not provide negative values in the bulk, similar to the DNS case.

It is evident that SGDH shows concrete limitations in correctly predicting P_b suggesting the need of improved approaches to be considered in the future.

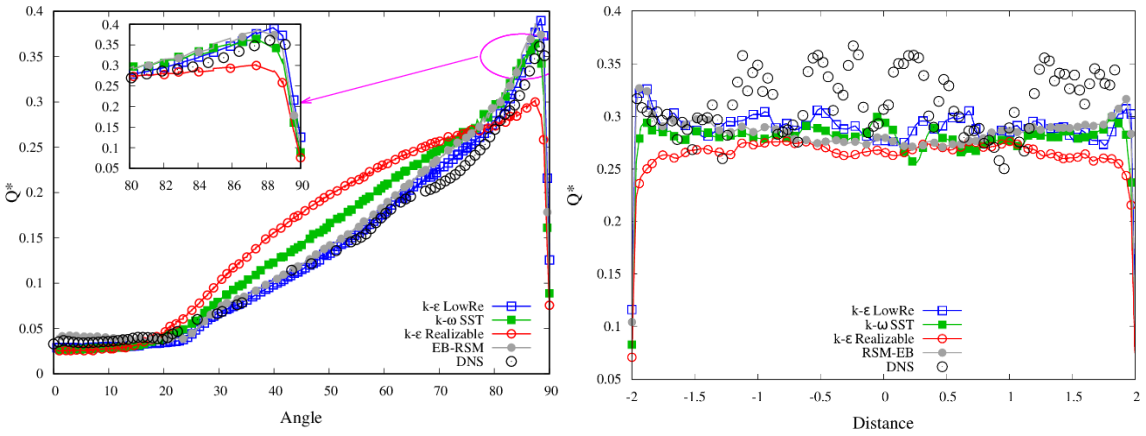

(a) Heat flux along the curved surface (b) Heat flux along the top surface

Figure 7. Heat flux along the curved surface (a) and heat flux along the top surface (b) profiles for different RANS turbulence models and DNS [11].

As mentioned above, the accurate determination of the surface heat flux, especially in relation of the CHF, is fundamental in the analysis of the IVR strategy. Values of the heat flux along the external surface line with x = 0m and ranging from $-2 \leq z \leq 2$m is adopted for the estimation of the wall heat flux. For brevity,

only half of the line is considered, i.e. the angle ranging from 0° (at the top surface) to 90° (at the extreme bottom). Furthermore, an additional probe crossing the diameter on the top surface is adopted for the evaluation of the heat flux of the top surface. The resulting plots for the different turbulence models are introduced in Fig. 7.
Remarkable agreement is observed for the RANS models in terms of heat flux along the curved surface as shown in Fig. 7a, with the exception of the Realizable k – ε model, which under-predicts the peak heat flux along the curved surface (Fig. 7a) and over-predicts the heat flux in the middle (for the angle between 30° and 75°). Similar behavior can be observed for the heat flux on the top surface (Fig. 7b), where all the models provide reasonable results, with the exception of the Realizable k – ε model, consistent with the heat flux along the curved surface. It is worth noticing the high fluctuations observed in the DNS are less evident in the RANS results. Nevertheless, it can be concluded that all models are quite reliable in predicting the surface heat flux, despite the less accurate prediction of the thermal field.

4. CONCLUSIONS

RANS calculations of a homogeneous oxidic molten pool in a hemispherical configuration for a Rayleigh number equal to 10^{11} are performed with the commercial CFD code STAR-CCM+ v12.02. The decay heat acts as in internal heat source, leading to the so-called internally heated convection regime. Numerical predictions are compared to recent high fidelity calculations, generated by Bian et al. [11]. The Boussinesq assumption is used to characterize the natural convection problem. Four different turbulence models, which are currently available in STAR-CCM+ and are commonly used in natural convection regimes, are investigated, namely the Low-Reynolds k − ε with Yap correction, the k − ω SST, the realizable k − ε Two-Layer with the Xu buoyancy driven correction [17] and the second-moment Elliptic Blending Reynolds-Stress turbulence Model (EB-RSM). Both qualitative and quantitative analysis are performed, in terms of relevant quantities such as velocity magnitude, temperature and buoyancy production of the turbulent kinetic energy. Overall, the flow field features of such a regime are well reproduced by the RANS calculations, even though the so-called "fountain effect" at the bottom is reproduced only by EB-RSM. The main divergence between RANS and DNS is observed in the bulk region, where all the RANS computations present strong recirculation, while an extended nearly stagnant zone is predicted by DNS calculations. Thermal stratification resembles quite accurately the high fidelity data. However, two models (Low-Reynolds k – ε and k − ω SST) over-predict the maximum temperature, while the other two models under-predict it. Finally, analysis of the buoyancy production shows the limitations of the RANS models, especially in terms of the turbulent heat flux, which is calculated through the common SGDH approach.
Overall, the wall heat flux is well predicted, with the exception of the Realizable k – ε model, thanks to the adequate resolution of the computational grid in proximity of the wall.
The under-estimation of the turbulent kinetic energy for Low-Reynolds k – ε will be the focus of future work. In particular, a modified k − ε model utilizing damping functions to reduce the turbulent kinetic energy in regions characterized by low velocity and re-laminarization can be investigated. Furthermore, the AHFM model is only available in combination to the Low-Reynolds k − ε in STAR-CCM+, making its use very limited. Based on the current study, it appears that it will be beneficial if AHFM will be implemented in more advanced turbulence models, such as the EB-RSM, which proved to be more superior than the Low-Reynolds k − ε for the present work. Finally, it is worth mentioning that limitations of the RANS models for higher Ra might be less severe, hence investigations of higher Ra are planned.

ACKNOWLEDGMENTS

The work described in this paper is funded by the Dutch Ministry of Economic Affairs. The DNS calculations were performed on the PDC Center for High Performance Computing at KTH, Sweden.

REFERENCES

1. W. Ma, Y. Yuan, and B. R. Sehgal, "In-Vessel Melt Retention of Pressurized Water Reactors: Historical Review and Future Research Needs," *Engineering*, **2** (1), pp. 103–111 (2016).
2. M. Valinˇcius, T. Kaliatka, A. Kaliatka, and E. Uˇspuras, "Modelling of Severe Accident and In-Vessel Melt Retention Possibilities in BWR Type Reactor," *Science and Technology of Nuclear Installations*, Article ID **7162387** (2018).
3. Q. Hu, X. Yan, S. Huang, and J. Yu, "The comprehensive analysis of coolability limits of passive external reactor vessel cooling under in-vessel retention," *Annals of Nuclear Energy*, **120**, pp. 296–303 (2018).
4. T. G. Theofanous et al., "In-vessel coolability and retention of core melt," *Nuclear Engineering and Design*, **169** (1-3), pp. 1–48 (1997).
5. F. Fichot et al., "Some considerations to improve the methodology to assess In-Vessel Retention strategy for high-power reactors," *Annals of Nuclear Energy*, 119, pp. 26–45 (2018).
6. J. L. Rempe, D. L. Knudson, M. Cebull, and C. L. Atwood, "In-vessel retention strategy for high power reactors," INEEL/EXT-04-02561, Idaho National Engineering and Environmental Laboratory (2005).
7. S. Whang et al., "Uncertainty analysis of in-vessel retention in a high power reactor during severe accident," *Nuclear Engineering and Design*, **319** (1-3), pp. 1–11 (2017).
8. L. Zhang, Y. Z. Y. Zhang, W. Tian, S. Qiu, and G. Su, "Natural convection heat transfer in corium pools: A review work of experimental studies," *Progress in Nuclear Energy*, **79**, pp. 167–181 (2015).
9. F. Fichot et al., "Elaboration of a Phenomena Identification Ranking Table (PIRT) for the modelling of In-Vessel Retention," *Annals of Nuclear Energy*, **146**, pp. 107617 (2020).
10. R. L. Tellier, L. Saas, and S. Bajard, "Transient stratification modelling of a corium pool in a LWR vessel lower head," *Nuclear Engineering and Design*, **287**, pp. 68–77 (2015).
11. B. Bian, W. Villanueva, and D. Dovizio, "Direct Numerical Simulation of Molten Pool Natural Convection in a Hemispherical configuration," *Proc. The 19th International Topical Meeting on Nuclear Reactor Thermal Hydraulics (NURETH-19)*, Brussels, Belgium, (2022).
12. A. Shams, "Towards the accurate numerical prediction of thermal hydraulic phenomena in corium pools," *Annals of Nuclear Energy*, **117**, pp. 234–246 (2018).
13. S. Whang, H. S. Parka, K. Lim, and Y. J. Cho, "Prandtl number effect on thermal behavior in volumetrically heated pool in the high Rayleigh number region," *Nuclear Engineering and Design*, **351**, pp. 72–79 (2019).
14. J. J. Niemela, L. Skrbek, K. R. Sreenivasan, and R. J. Donnelly, "Turbulent convection at very high Rayleigh numbers," *Nature*, **404**, pp. 837–840 (2000).
15. F. A. Kulacki and M. Z. Nagle, "Natural convection in a horizontal fluid layer with volumetric energy sources," *Journal of Heat Transfer*, **97**, pp. 204–211 (1975).
16. S. A. Smirnov et al., "Direct numerical simulation of molten corium pool inductively heated in the cold crucible," *Proc. of the MASCA-2 Seminar*, Cadarache, France, (2007).
17. Xu, Q. Chen, and F. T. M. Nieuwstadt, "A new turbulence model for near-wall natural convection," *International Journal of Heat and Mass Transfer*, **41**, pp. 3161–3176 (1998).
18. 26. J. M. Bonnet, "Thermal hydraulic phenomena in corium pools: the BALI experiment," *Proc. Workshop on Severe Accident Research (SARJ-98)*, Tokyo, Japan, (1999).

RANS Validation of a Corium Pool in a Hemispherical Configuration for In-Vessel Retention

Daniele Dovizio (NRG)
Boshen Bian (KTH)
Walter Villanueva (KTH)
Ed Komen (NRG)

ERMSAR 2022, 16-19 May, 2022

EU DuC = N 26127/23.4307

NRG

Nuclear. For life.

KTH VETENSKAP OCH KONST

ROYAL INSTITUTE OF TECHNOLOGY

Introduction

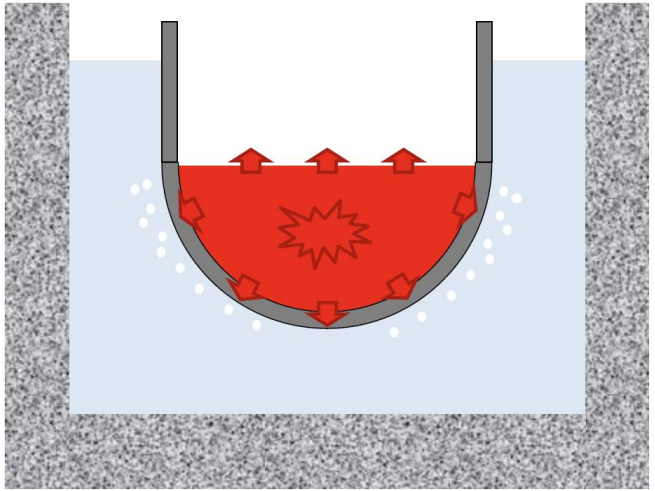

- The In-Vessel Retention through External Reactor Vessel Cooling (IVR)-ERVC strategy is designed to prevent or mitigate passively the progression of the melting of the nuclear reactor core, by safely keeping the melted material inside the reactor vessel.
- The thermal loading in the vessel, as a consequence of the turbulent natural convection in the corium pool, needs to be very well estimated, as it defines the safety margin for the vessel integrity.
- For high power reactors safety margins are expected to be lower → more detailed safety analysis needed.

Objectives

- One way to overcome these issues and to avoid costly and complex experimental studies, consists of performing high fidelity calculations in the form of Direct Numerical Simulations (DNS), for which no modelling strategies are applied.

- Recently, DNS simulation was conducted on a homogeneous oxidic molten pool in a hemispherical configuration for a Rayleigh number equal to 10^{11}.

- RANS calculations are validated against the recent DNS database.

Numerical Modelling of the Oxide Pool

Consistent to the DNS calculations:

- Single phase conditions are adopted.
- The turbulent natural convection regime is reproduced with the Boussinesq approximation.
- The decay heat acts as in internal heat source, leading to the so-called internally heated convection regime.

This kind of natural convection is mainly controlled by the internal Rayleigh number (Ra_{int}) and the Prandtl number (Pr).

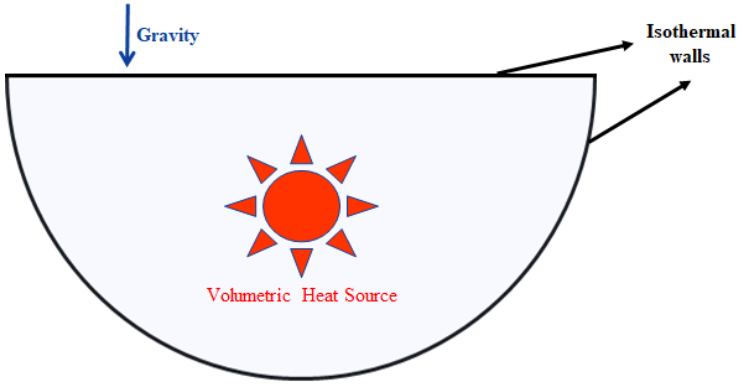

Boundary	Condition
Top Surface	$T_w = 2623.15\ K$
Lateral Surface	$T_w = 2623.15\ K$
Internal Field	$Q_{vol} = 6.11\ W/m^3$

$$\mathrm{Ra}_{int} = \frac{g\beta\dot{Q}H^5}{k\alpha\nu}$$

Fluid properties

From Smirnov [1] (T=2623.15 K): $\beta = 6.71 \cdot 10^{-5}\,\frac{1}{K}$ $\rho = 7588.4\,\frac{kg}{m^3}$ $c_p = 540\,\frac{J}{kg\,K}$ $\lambda = 3\,\frac{W}{m\,K}$

$$Pr = \frac{\nu}{\alpha} = \frac{\nu\,\lambda c_p}{\rho} \rightarrow \nu = Pr\,\alpha \qquad Ra_{int} = \frac{g\beta Q_{vol} H^5}{k\alpha\nu} \rightarrow Q_{vol} = \frac{k\alpha\nu}{g\beta H^5} Ra_{int}$$

	ρ	μ	c_p	λ	β	Pr	α	Ra	Q_{vol}
Value	7588.4	0.0044	540	3	$6.71 \cdot 10^{-5}$	0.8	$7.3 \cdot 10^{-7}$	$1 \cdot 10^{11}$	6.11
Units	$\frac{kg}{m^3}$	$Pa \cdot s$	$\frac{J}{kg \cdot K}$	$\frac{W}{m \cdot K}$	$\frac{1}{K}$	[ ]	$\frac{m^2}{s}$	[ ]	$\frac{W}{m^3}$

[1] S. A. Smirnov et al., "Direct numerical simulation of molten corium pool inductively heated in the cold crucible," Proc. of the MASCA-2 Seminar, Cadarache, France, (2007).

MESH GENERATION

- 3D mesh (Radius = 2 m)
- Advancing layer mesher: prismatic cell layers next to wall boundaries and polyhedral mesh elsewhere.
- Thickness of the prism layer large enough to include the thermal boundary layer



MESH	Cells	Base Size	Prism Layers	Max Wall y^+
1	271K	60 mm	10	0.88
2	2.1M	30 mm	20	0.13
3	7.2M	20 mm	30	0.02

Meshes generated in STAR-CCM+

Mesh sensitivity

Velocity

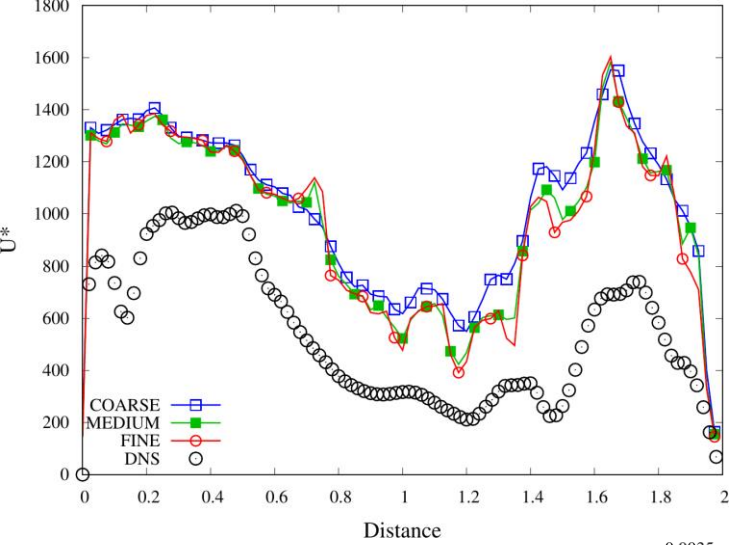

TKE

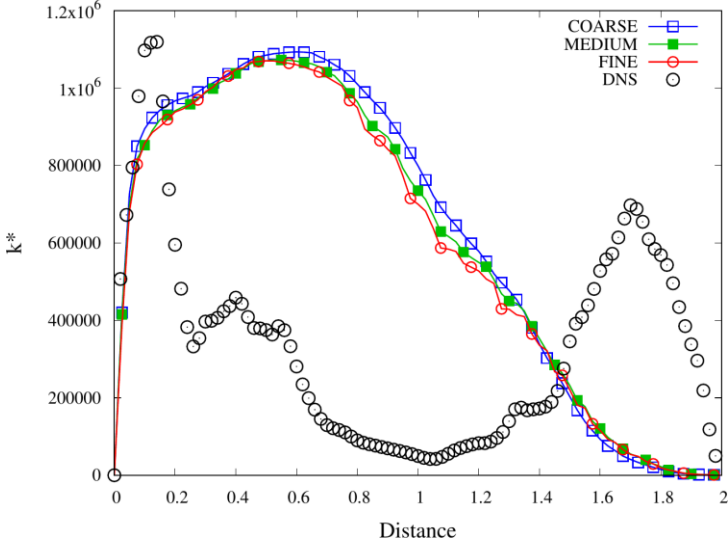

Temperature

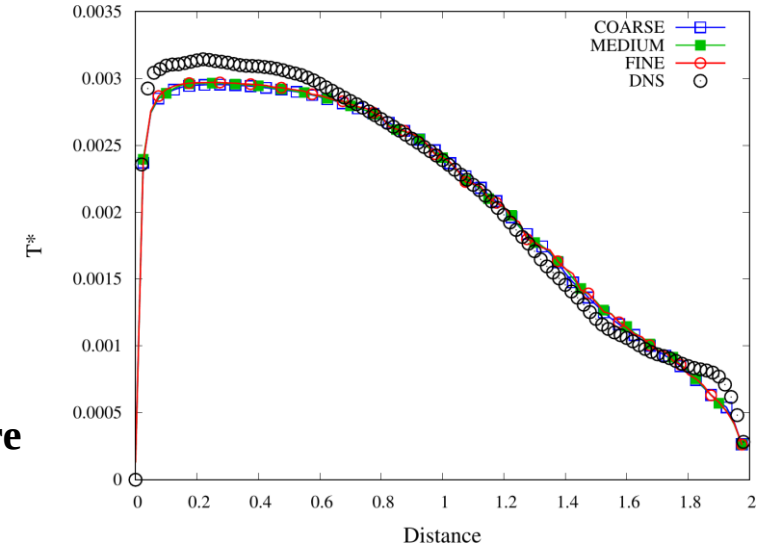

CFD Parameters

CFD code	STAR-CCM+
Solver	3-Dimensional, Rhie-Chow type combined with a SIMPLE-type algorithm, steady, 2nd order in space
Fluid properties	Constant, corresponding to $T_w = 2623.15\ K$
Mesh	2.1 M Prismatic cell layers + polyhedral
Turbulence model	k-ε Low-Re, k-ω SST, Realizable k-ε with Xu buoyancy driven correction, RSM-EB
Radiation	Not included
Buoyancy	Boussinesq approximation

RANS Results
Qualitative Analysis

NRG
Nuclear. For life.

Mean Velocity

DNS

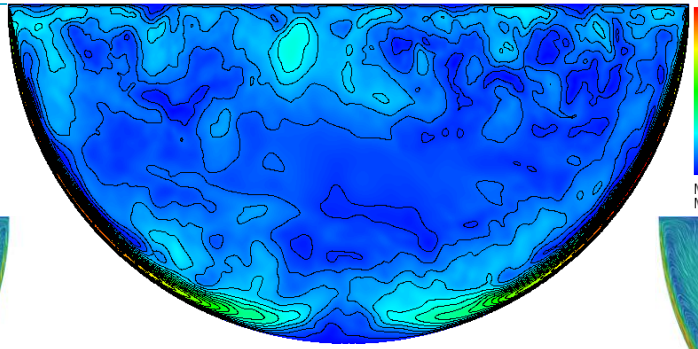

k-ε Low_Re

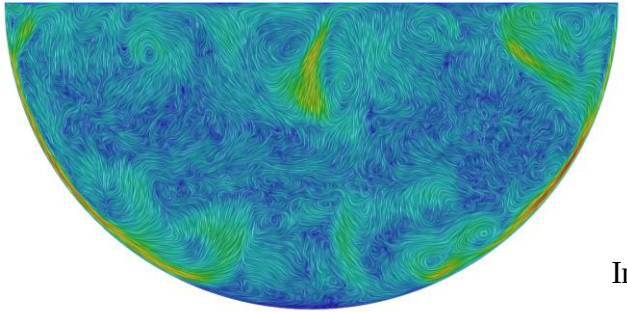

k-ω SST

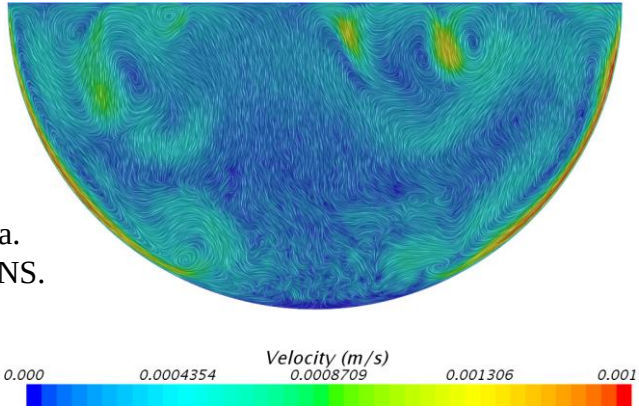

Velocity magnitude iso-contours of the DNS data.
Integrated line convolution contours (LIC) for RANS.

Realizable k-ε

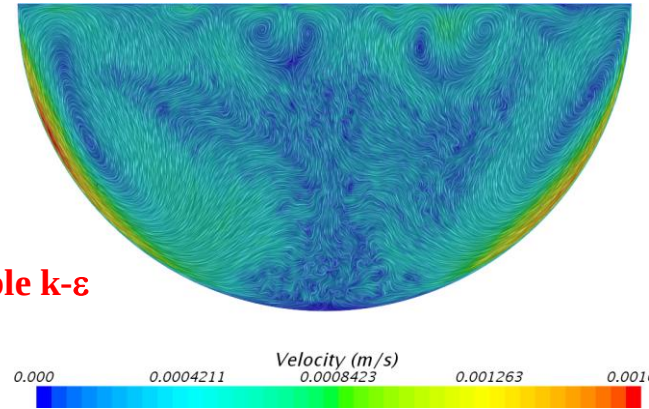

RSM-EB

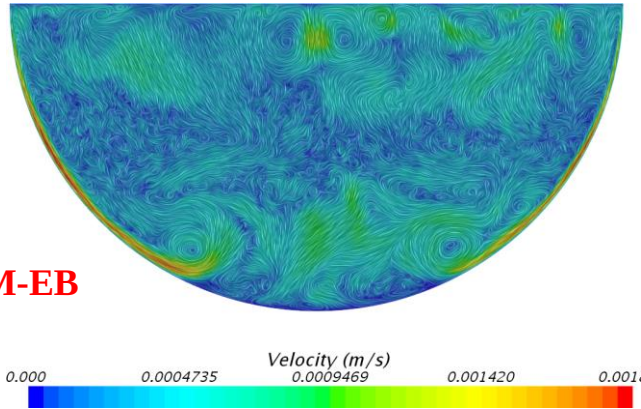

Mean Temperature

DNS

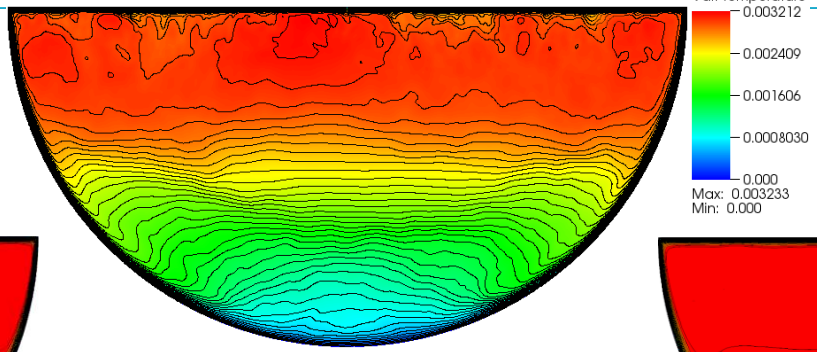

k-ε Low_Re

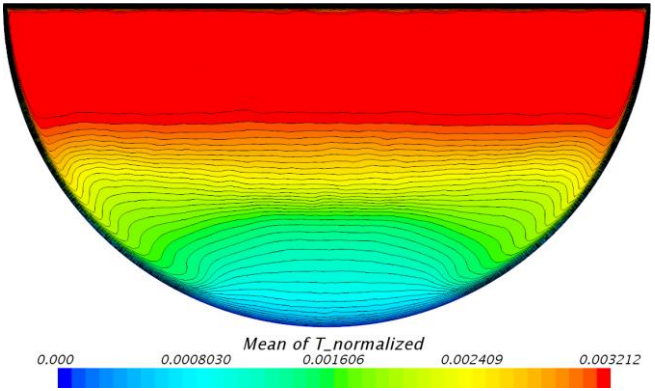

k-ω SST

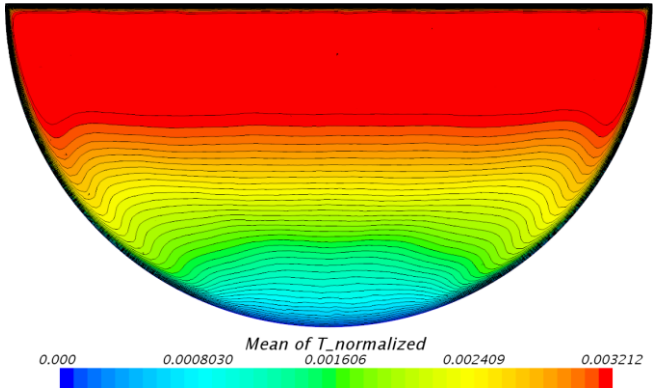

Realizable k-ε

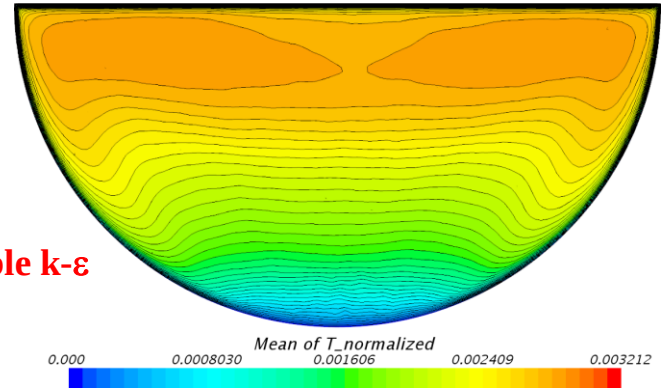

RSM-EB

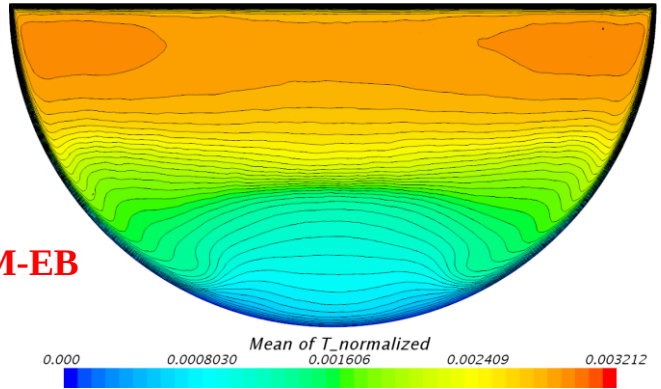

Mean TKE

DNS

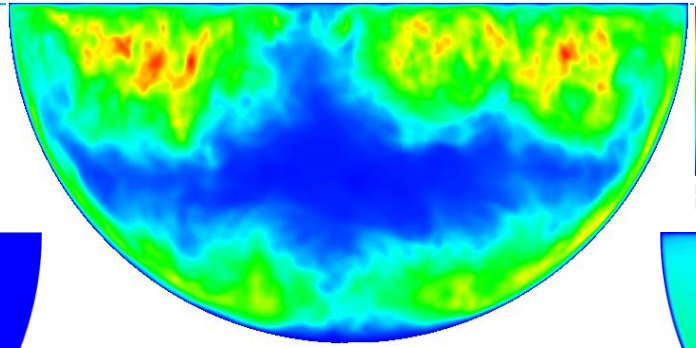

k-ε Low_Re

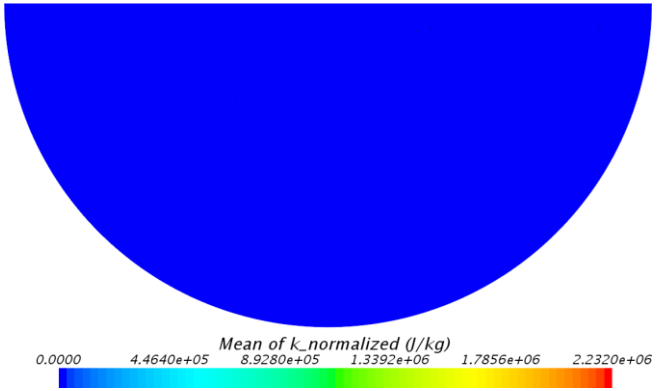

k-ω SST

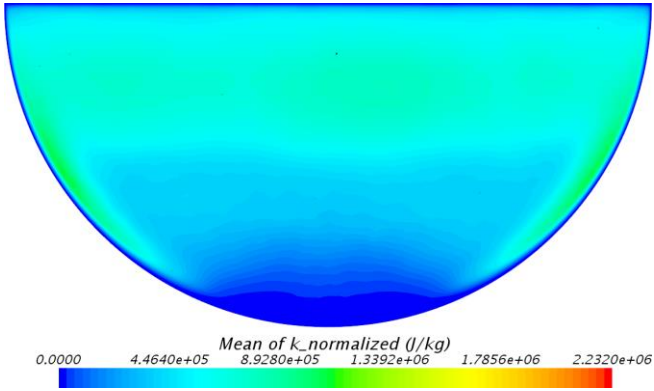

Realizable k-ε

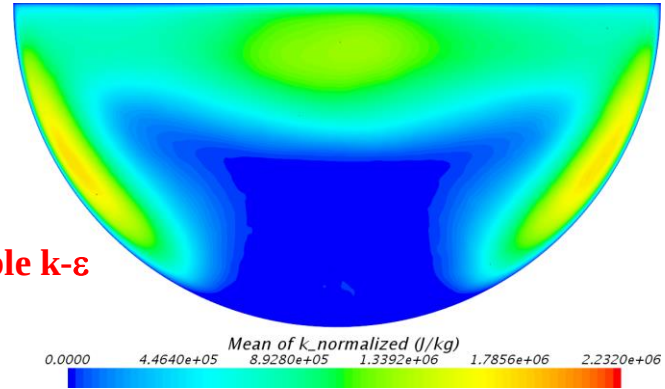

RSM

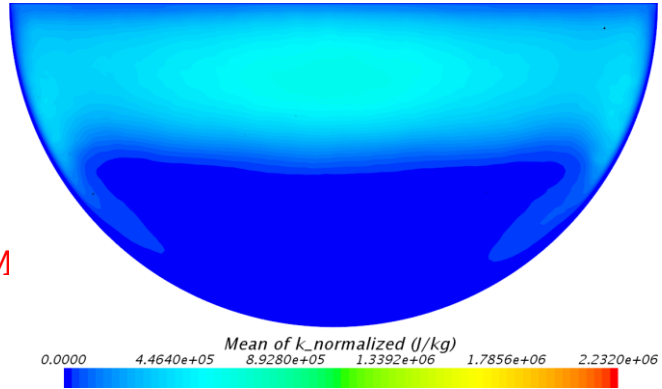

Buoyancy Production

$$P_b = -\beta g \overline{w'T'}$$

DNS

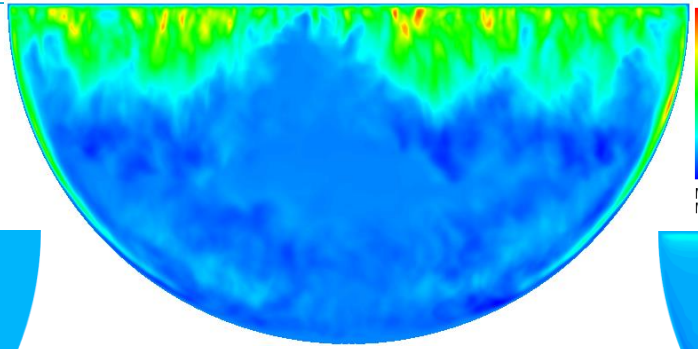

k-ε Low_Re

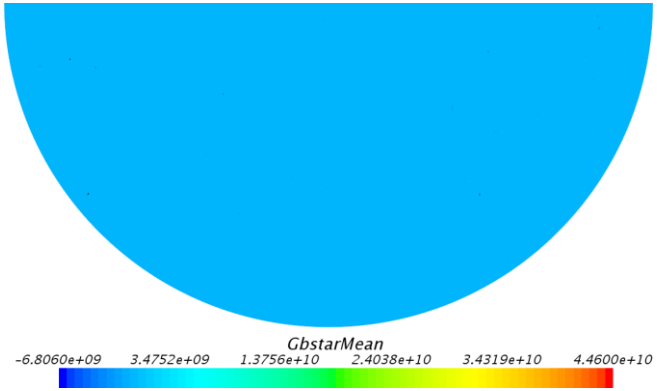

k-ω SST

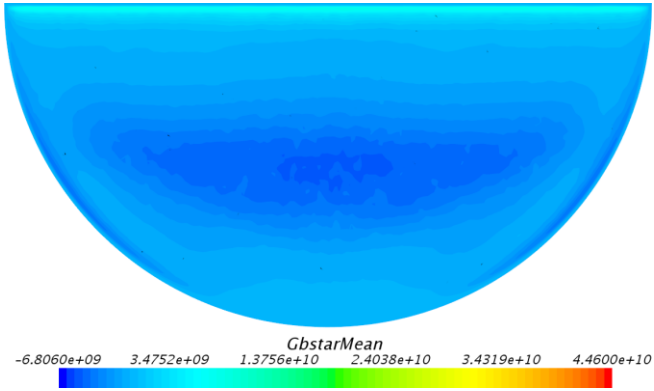

In RANS, SGDH adopted:

$$\overline{w'T'} = -\frac{\overline{\nu_T}}{Pr_T}\nabla\bar{T} \rightarrow P_b = \beta\frac{\overline{\nu_T}}{Pr_T}(\nabla\bar{T}\cdot\boldsymbol{g})$$

Realizable k-ε

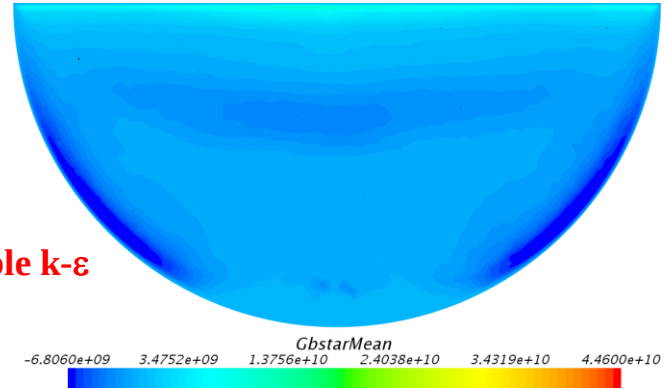

RSM-EB

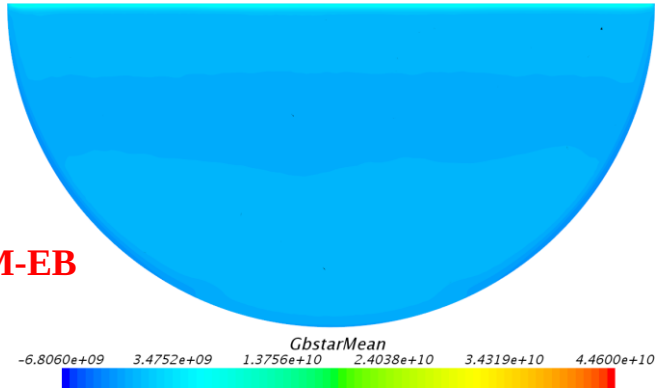

RANS Results
Quantitative Analysis

NRG
Nuclear. For life.

Probes

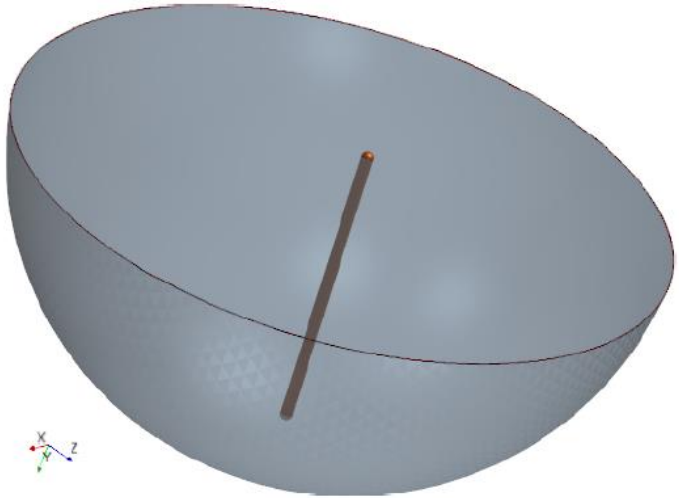

(a) Central vertical probe

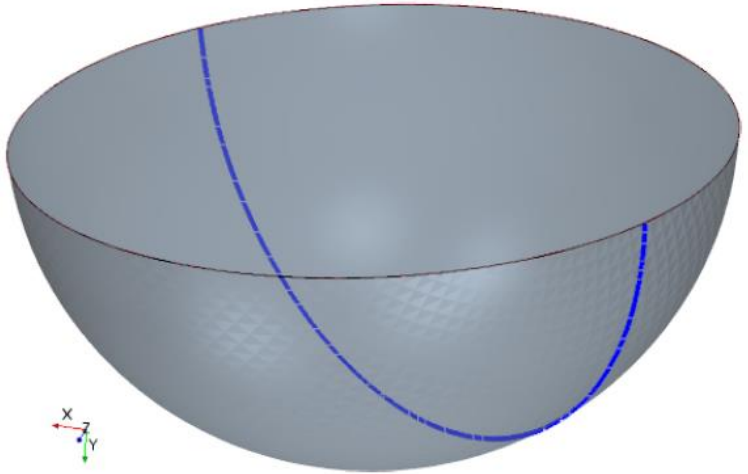

(b) External surface probe

Turbulence models sensitivity

Velocity

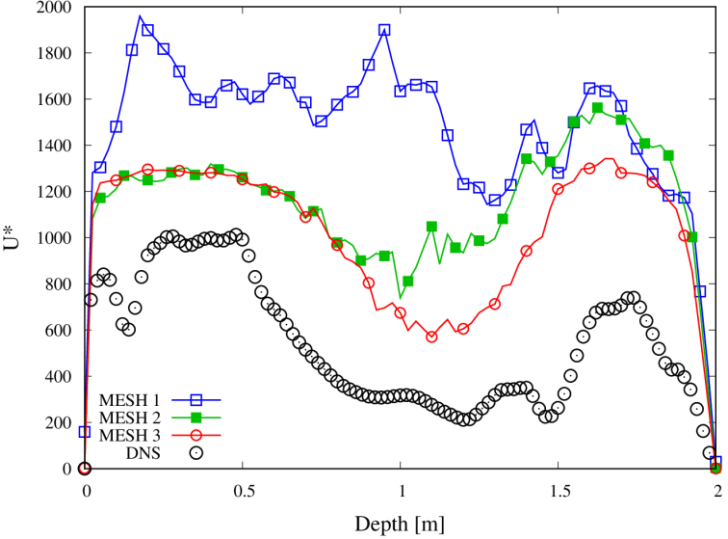

TKE

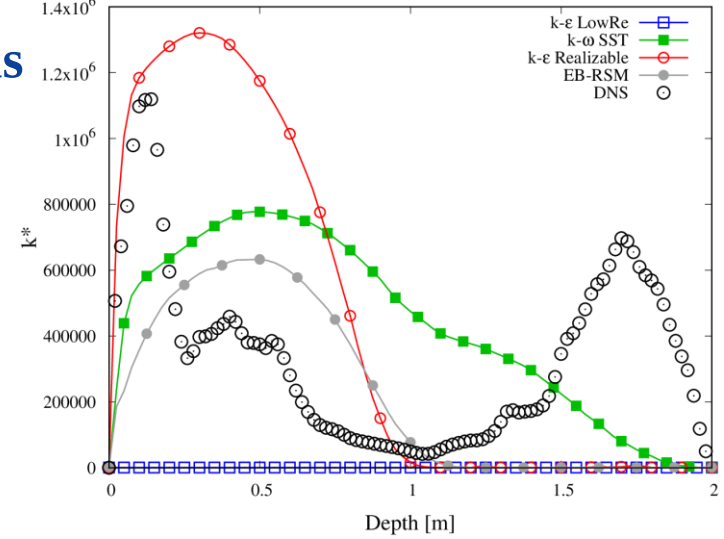

Temperature

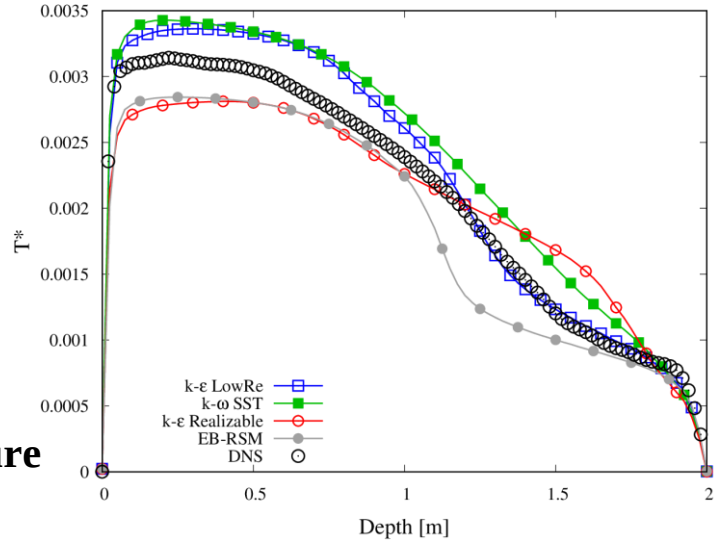

P_b

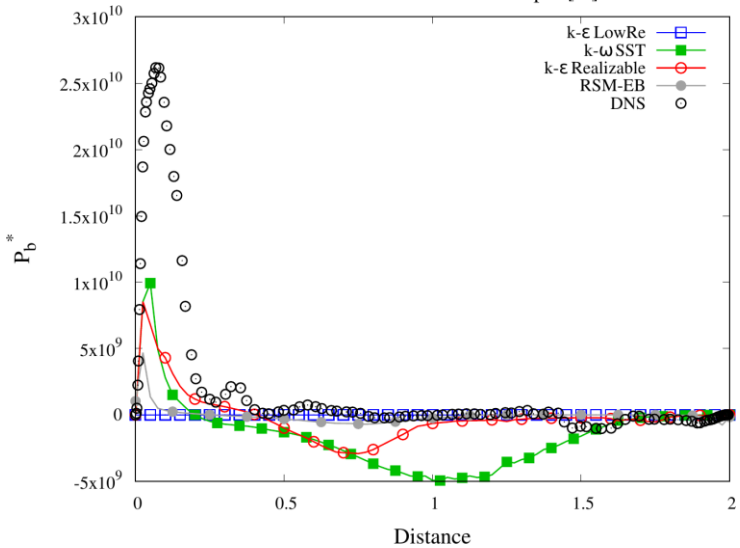

Turbulence models sensitivity

Heat Flux along curved wall

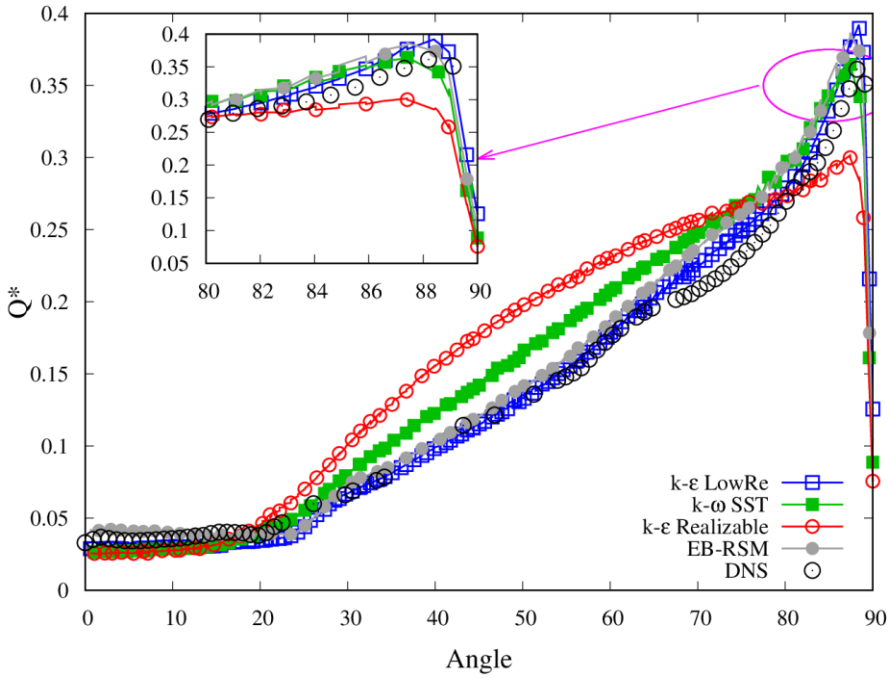

Heat Flux on top wall

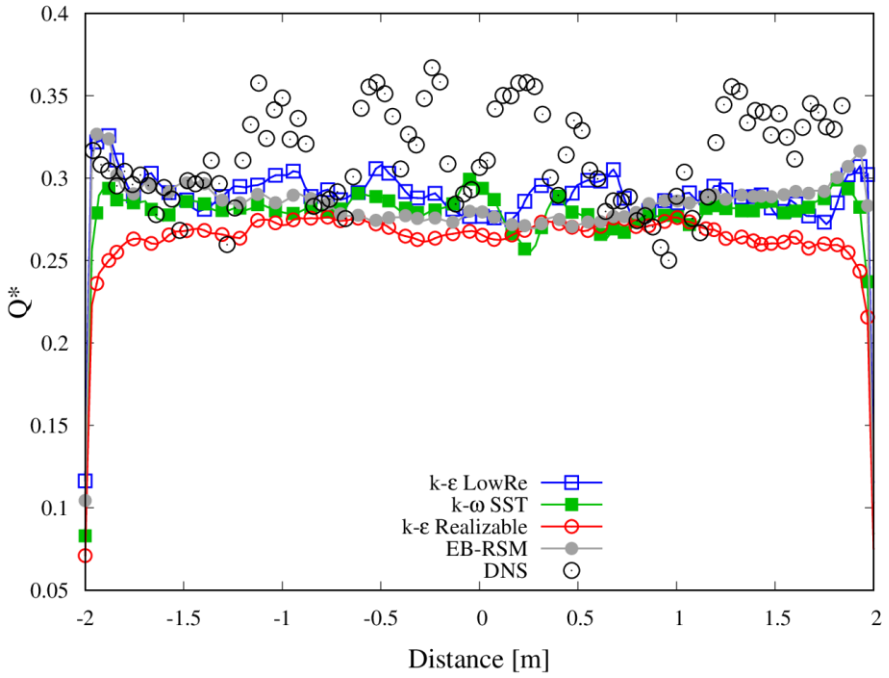

Conclusions

- RANS calculations of a homogeneous oxidic molten pool in a hemispherical configuration for a Ra = 10^{11} are performed with the commercial CFD code STARCCM+.
- Four different turbulence models, which are currently available in STARCCM+ and are commonly used in natural convection regimes, are investigated.
- Thermal stratification resembles quite accurately the high fidelity data. However, the stagnant region in the bulk is not well reproduced.
- Analysis of the buoyancy production shows the limitations of the RANS models, especially in terms of the turbulent heat flux, which is calculated through the common SGDH approach.
- Overall, the wall heat flux is well predicted, thanks to the adequate resolution of the computational grid in proximity of the wall.

Future efforts

- Future work includes

i. The implementation of a model to improve the predictions in regions characterized by low velocity and re-laminarization.

ii. The AHFM model, only available in combination to the Low-Reynolds k-ε in STARCCM+, should be associated to more advanced turbulence models, such as the EB-RSM.

iii. Limitations of the RANS models for higher Ra might be less severe, hence investigations of higher Ra are planned.

THANKS FOR YOUR ATTENTION!

dovizio@nrg.eu



Disclaimer

EU DuC = N

Goods labeled with an EU DuC (European Dual-use Codification) not equal to ‘N’ are subject to European and national export authorization when exported from the EU and may be subject to national export authorization when exported to another EU country as well. Even without an EU DuC, or with EU DuC ‘N’, authorization may be required due to the final destination and purpose for which the goods are to be used. No rights may be derived from the specified EU DuC or absence of an EU DuC.

Thermal boundary layer

$Ra = 10^{11}$

$$\delta_{th} = \frac{H}{2Nu}$$

NEW: Advancing Layer mesher

Grötzbach estimates [3]

Niemela correlation [1] $Nu = 0.124\, Ra^{0.309} = 311$ $\delta_{th} = 3.22\, mm$

Kulacki and Nagle [2] $Nu = 0.389\, Ra^{0.228} = 125$ $\delta_{th} = 7.98\, mm$

	CELLS	Prism layer	# layers	Base size
MESH IVMR	9.4M	15 mm	30	15 mm
MESH COARSE	271K	60 mm	10	60 mm
MESH MEDIUM	2.1M	60 mm	20	30 mm
MESH FINE	7.2M	60 mm	30	20 mm

[1] J.J. Niemela, L. Skrbek, K.R. Sreenivasan, and R.J Donnelly. Turbulent convection at very high Rayleigh numbers. Nature, 404, 2000.
[2] Kulacki, F.A., Nagle, M.Z., 1975. Natural convection in a horizontal fluid layer with volumetric energy sources. ASME, J. Heat Transfer 97, 204–211.
[3] G. Grötzbach. Spatial resolution requirements for direct numerical simulation of the Rayleigh-Bérnard convection. *Journ comput phys*, 49:241–264, 1983

Assessment of a Dynamic Global-coefficient Subgrid-scale Model for Turbulent Natural Convection in a Confined Cavity

Seokwon Whang [a]

Dasol Joo [b], **Hyun Sun Park** [a], **Donghyun You** [b]

[a] **SNU** Nuclear Research Institute for Future Technology and Policy

[b] **POSTECH** Department of Mechanical Engineering

May 17, 2022

Contents

I. Introduction

II. Numerical Method

III. Results

VI. Conclusion

I. Introduction

IVR-ERVC In-Vessel Retention by External Reactor Vessel Cooling

- **Safety evaluation** : **Thermal failure** criterion (Internal heat flux vs. CHF)
  - **Major phenomena** to determine **thermal behavior** of molten pool
    : **Natural convection**, Decay heat, Crust formation, Mushy zone etc.
    - **Rayleigh number** of oxide layer up to 10^{17}, meaning **strong turbulence**

$$\mathrm{Ra} = \frac{g\beta H^3 \Delta T}{\alpha \upsilon} \qquad \mathrm{Ra}' = \frac{g\beta Q''' H^5}{\alpha \upsilon k}$$

    - **Turbulent natural convection** (TNC)
      - Complex flow: Different flow characteristics over the entire domain
        - (Un)stable layer, thermal plume, transition
      - Boundary layer: Highly anisotropic behavior adjacent to the wall

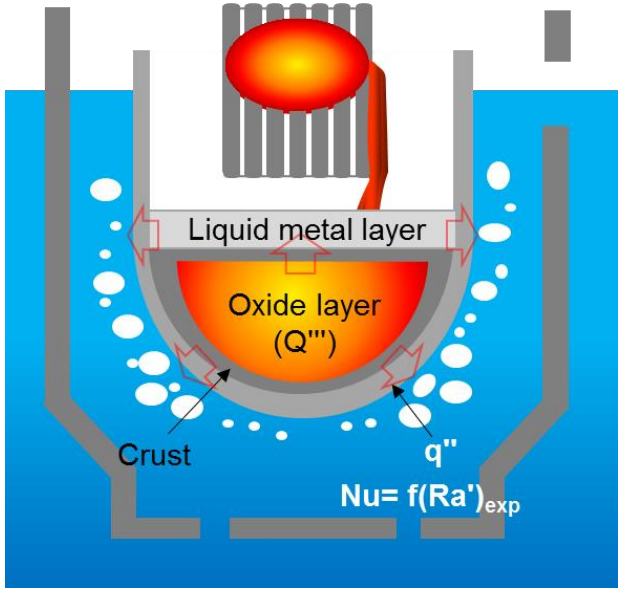

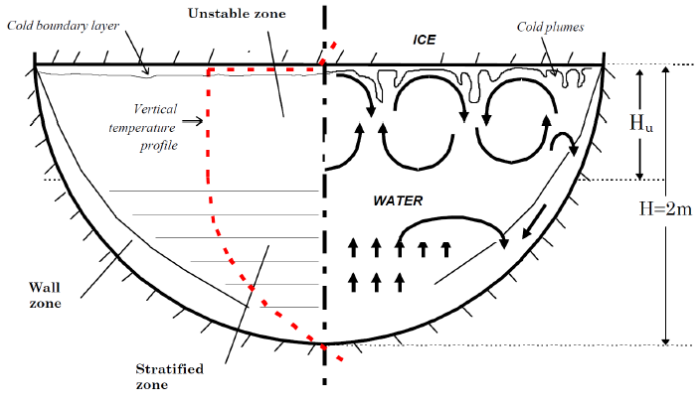

General flow observations of oxide layer [1]

[1] Bonnet, J.M. and Seiler, J.M., Thermal Hydraulic Phenomena in Corium Pools : the Bali Experiment ., in: 7th ICONE. Tokyo, pp. 1–10, 1999.

I. Introduction

Experimental Researches for Estimating Thermal Load of the Oxide pool

- **Lack of Experimental Data**: Turbulent natural convection, geometry, corium (property)

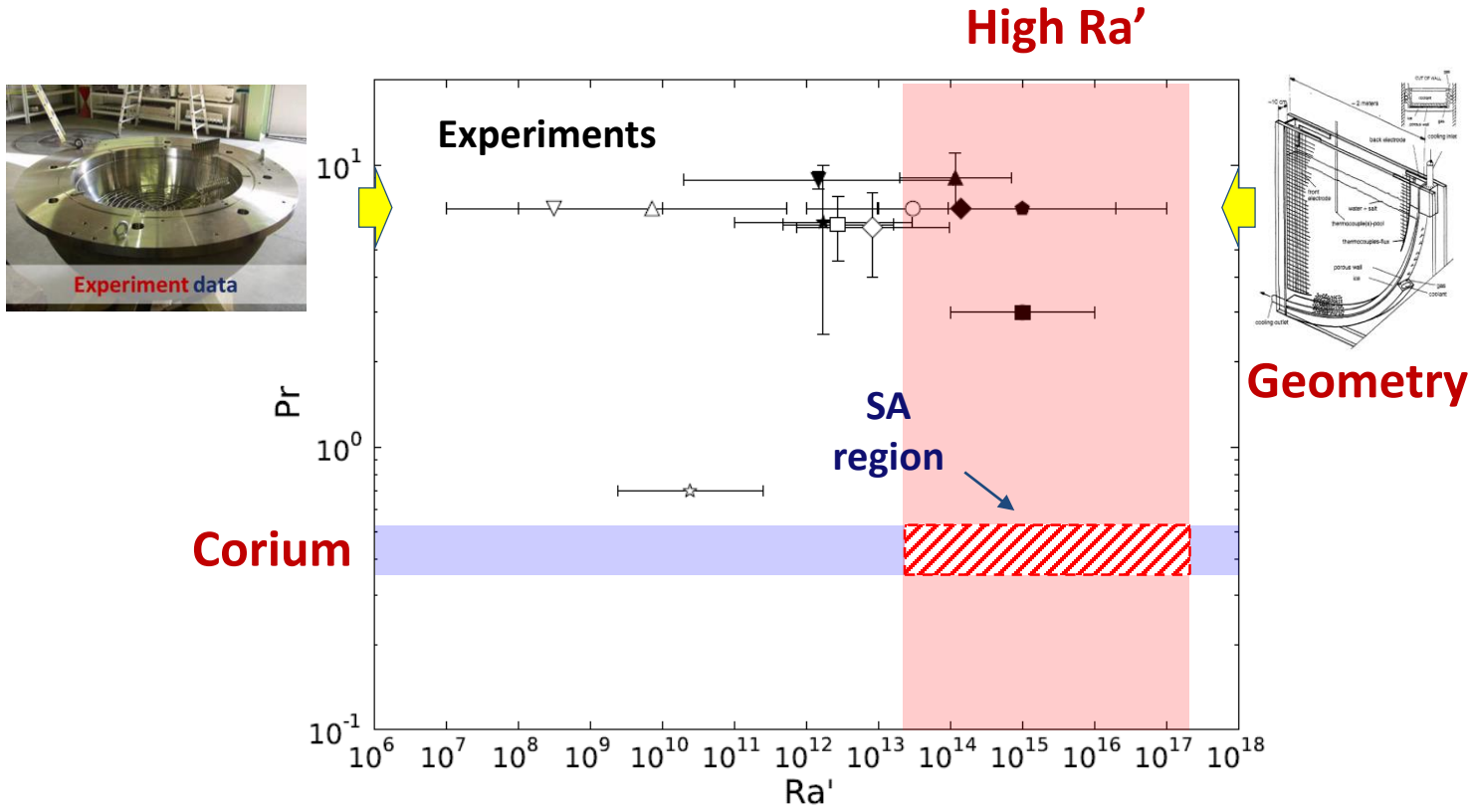

I. Introduction - IVMR Project Summary

- **Key issues from the results of WP2.3 - Use of CFD (Oxide pool) [1]**
  1. **RANS model (NRG, Tractebel)**
  2. **Property (ENEA, POSTECH)**
  3. **Geometry (UJV)**

NRG - Turb. model

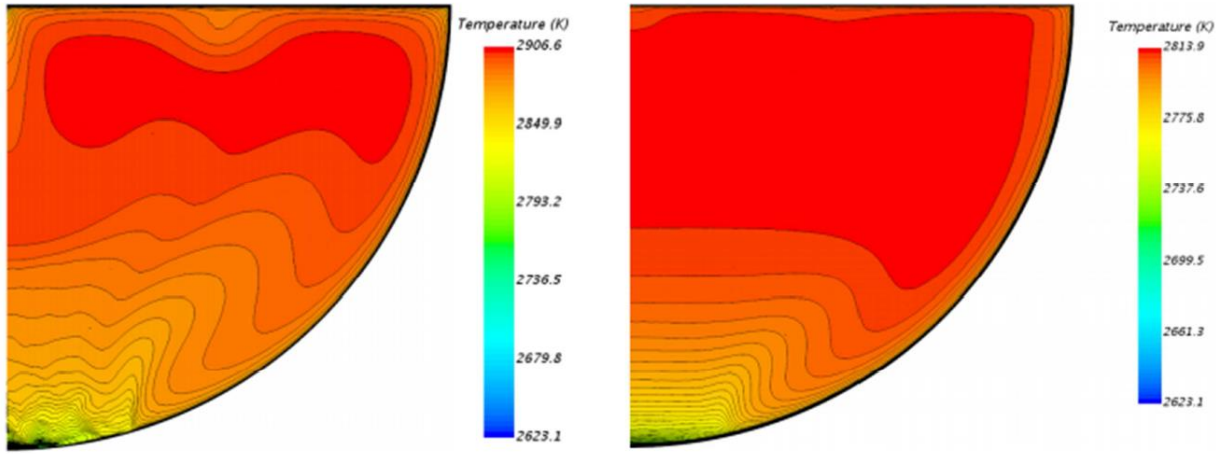

Temperature contour

Tractebel - Pr_t (Turb. model)

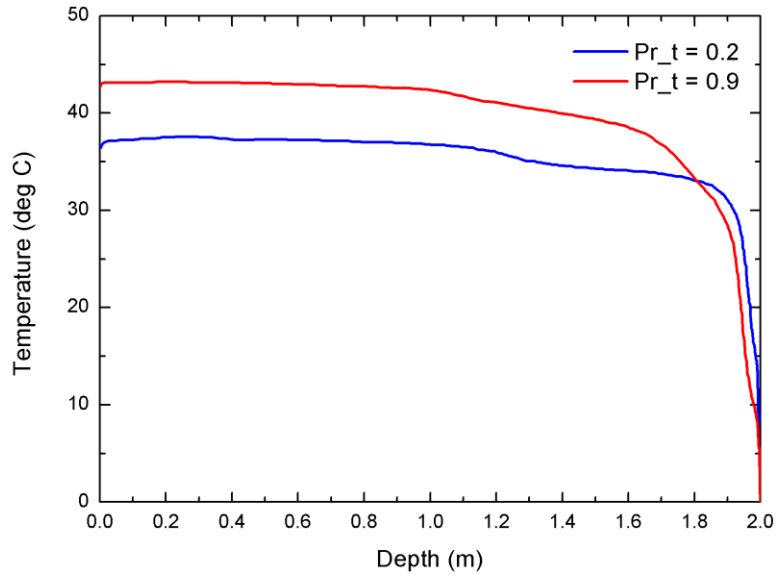

Temperature distribution

[1] IVMR annual report, 2018, 2019

I. Introduction - IVMR Project Summary

- **Key issues from the results of WP2.3 - Use of CFD (Oxide pool) [1]**

1. **Turbulence model (NRG, Tractebel)**
2. **Property (ENEA, POSTECH)**
3. **Geometry (UJV)**

ENEA - Property

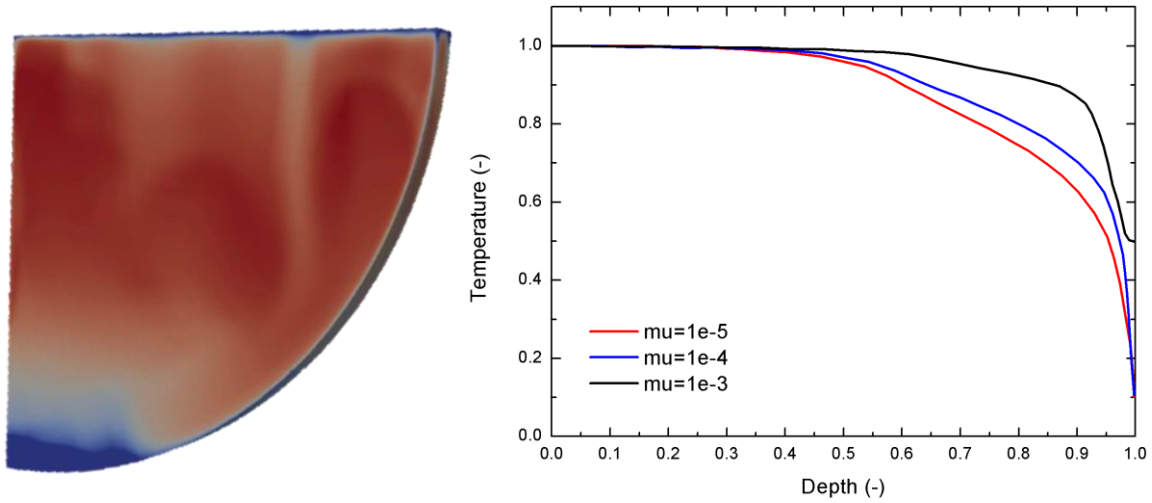

Temperature contour (left), distribution (right)

UJV - Geometry

Geometry	P_{top}/P_{total}
2D Slice	49.4 %
3D Prototypical	38.9 %

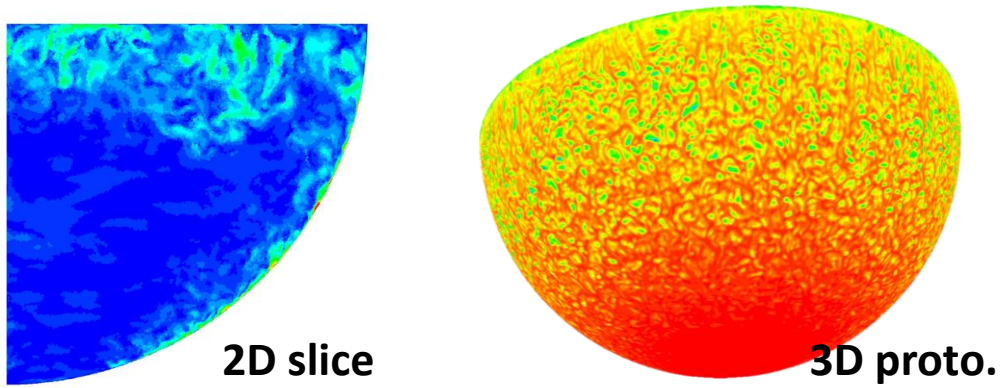

Velocity contour(left), heat flux (right)

[1] IVMR annual report, 2018, 2019

I. Introduction

▪ CFD Method for Simulating the Oxide Pool

- **DNS:** Navier-Stokes eqn. -> **Computing Power Limit**
- **RANS:** RANS eqn. + Turbulence Model -> **Model Limit**
- **LES:** filtered N-S eqns. + Subgrid scale (SGS) Model
  - Resolve large eddies (grid scale: energy-containing)
  - Model small eddies (subgrid scale: isotropic, universal)

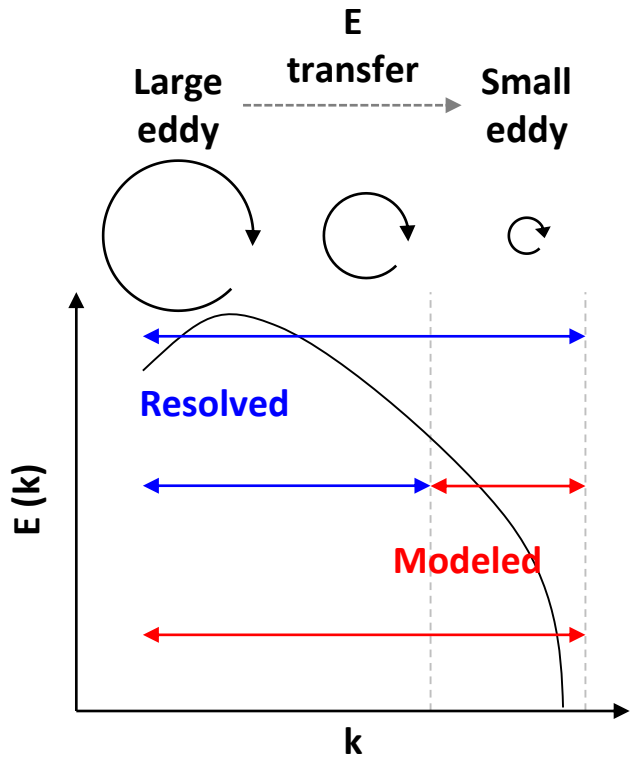

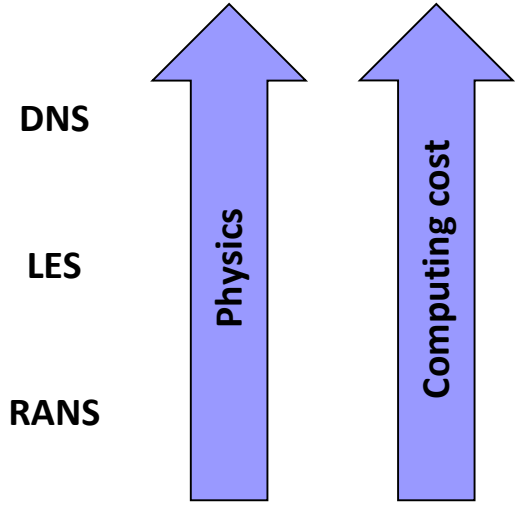

I. Introduction - Our Perspective to Resolve the Highly Turbulent Oxide Pool Issues

- **To Resolve the Oxide Pool Issue (in terms of turbulent flows)**
  - **Numerical Database** through the **high-fidelity simulation (LES)**
    - **Advanced turbulence model (RANS)**
    - **Better understanding** of oxide pool behavior
    - **Database** of **representative scenarios** for **Integral Analysis** of **IVR**

Main issues

- Model
- Property
- Geometry

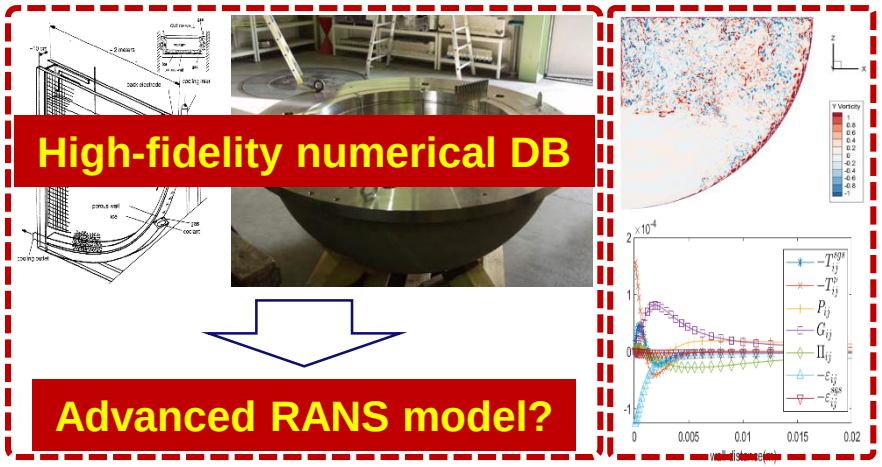

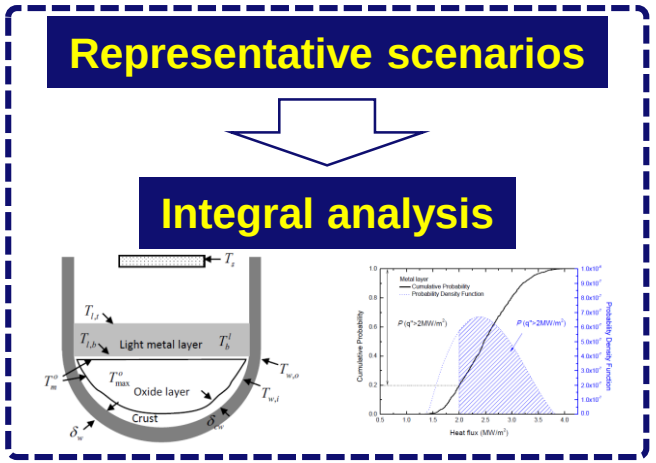

- **Objective**: validate the **LES models** with the experiments, and generate the **high-fidelity numerical DB for oxide pool**

II. Numerical method

Large Eddy Simulation

- **Filtered Navier-Stokes Equations**

$$\frac{\partial \overline{u_i}}{\partial x_i} = 0$$

$$\frac{\partial \overline{u_i}}{\partial t} + \frac{\partial \overline{u_i}\,\overline{u_j}}{\partial x_j} = -\frac{1}{\rho}\frac{\partial \overline{p}}{\partial x_i} + \nu \frac{\partial^2 \overline{u_i}}{\partial x_j \partial x_j} - \frac{\partial \tau_{ij}}{\partial x_j}$$

$$\frac{\partial \overline{T}}{\partial t} + \frac{\partial \overline{T}\,\overline{u_j}}{\partial x_j} = \alpha \frac{\partial^2 \overline{T}}{\partial x_j} - \frac{\partial q_j}{\partial x_j}$$

- **Subgrid-scale (SGS) Model**

$$\tau_{ij} = \overline{u_i u_j} - \overline{u_i}\,\overline{u_j}$$

$$\Rightarrow \quad \tau_{ij} - \frac{1}{3}\tau_{kk}\delta_{ij} = -2\nu_T \overline{S_{ij}}$$

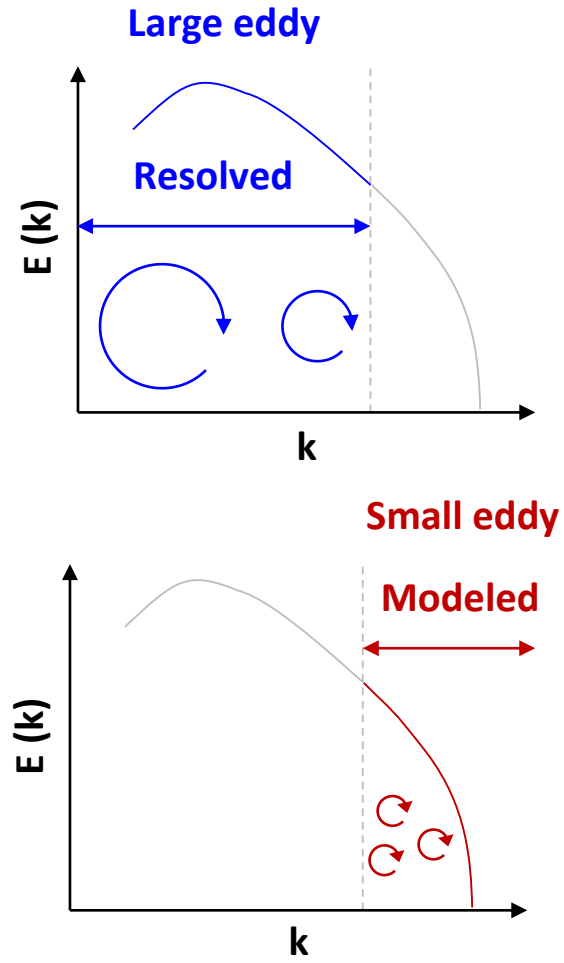

II. Numerical method

Large Eddy Simulation

- **Subgrid-scale (SGS) Model**

$$\tau_{ij} = \overline{u_i u_j} - \overline{u_i}\,\overline{u_j} \quad \Rightarrow \quad \tau_{ij} - \frac{1}{3}\tau_{kk}\delta_{ij} = -2\nu_T \overline{S_{ij}}$$

$$\nu_T^g = C_v \prod^g$$

C_v: Model constant

Π^g: Kernel

Smagorinsky kernel (SM): $\boldsymbol{\Pi^g = \sqrt{S_{ij}S_{ij}}}$

Vreman kernel (VM): $\boldsymbol{\Pi^g = \sqrt{\frac{B_\beta^g}{\bar{\alpha}_{kl}\bar{\alpha}_{kl}}}}$

$$q_j = -\frac{\nu_T^g}{D_T}\frac{\partial \overline{T}}{\partial x_j},$$

D_T: Model constant

- **Smagorinsky** (SM), Dynamic **Smagorinsky** (DSM), **Vreman** (VM), Dynamic **Vreman** (DVM) [1]

Model		SM	DSM	VM	DVM
$\boldsymbol{\nu_T}$	Π^g	SM		VM	
	C_v	const. (0.094)	dyn.	const. (0.07)	dyn.
$\boldsymbol{q_j}$	D_T	const. (0.9)			dyn.

[1] You, D., Moin, P., 2009. A dynamic global-coefficient subgrid-scale model for large-eddy simulation of turbulent scalar transport in complex geometries. Phys. Fluids.

II. Numerical method

Flow configuration and **Boundary conditions**

- **Differentially heated cavity** (DHC): Turbulent natural convection
  - Aspect ratio (H/W) = 5, Spanwise (S) = 0.2 m [1]
  - Boundary conditions
    - Top, bottom & side: Wall
    - Spanwise direction: Periodic condition

Parameters	Value
T_{hot}-T_{cold}	45.8 K
Ra	5×10^{10}
Pr	0.7 (air)
Grid (y^+)	200 x 400 x 40 (< 0.6)
Courant #	< 0.5

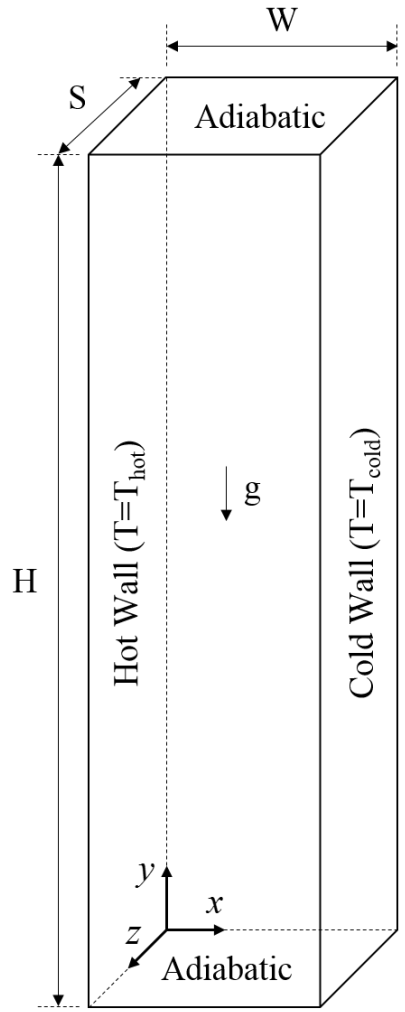

[1] Barhaghi, D.G., Davidson, L., 2007. Natural convection boundary layer in a 5:1 cavity. Phys. Fluids 19, 1–15.

II. Numerical method

Flow configuration and **Boundary conditions**

- **BALI** experiment [1]: Turbulent natural convection with internal heat generation
  - 1/4 Circular slice shape (R = 2m)
  - Ra': ~10^{16}
  - Boundary conditions
    - Top & Side: Fixed temperature
    - Center, Front & Back: Adiabatic

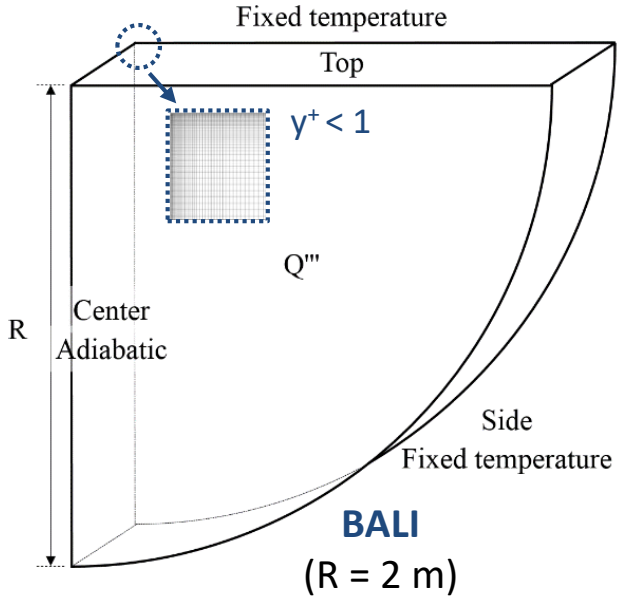

Grid parameters	Value
Number of grid	2.8M
Near wall grid size	~ 0.05 mm
Bulk grid size	~ 8 mm
y+	<0.39 (water), <1.18 (Corium)

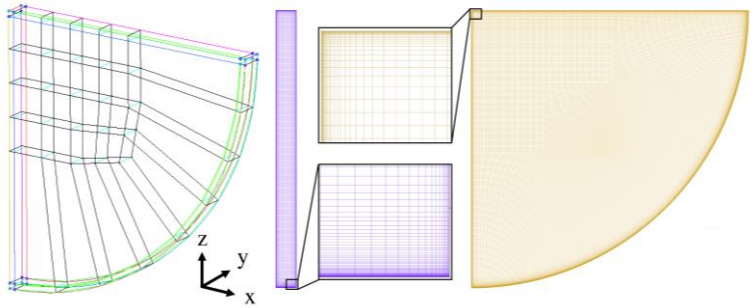

Grid system for the simulation

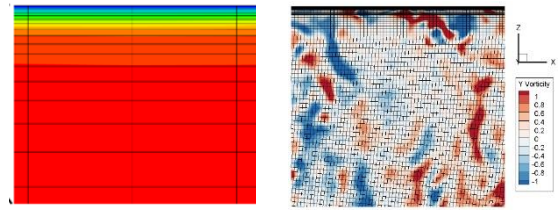

Near wall behavior:
(left) Temperature, (right) vorticity

[1] Bonnet, J.M. and Seiler, J.M., Thermal Hydraulic Phenomena in Corium Pools : the Bali Experiment ., 7th ICONE. Tokyo, pp. 1–10, 1999.

III. Results

Differentially heated cavity

- **Velocity & Temperature**

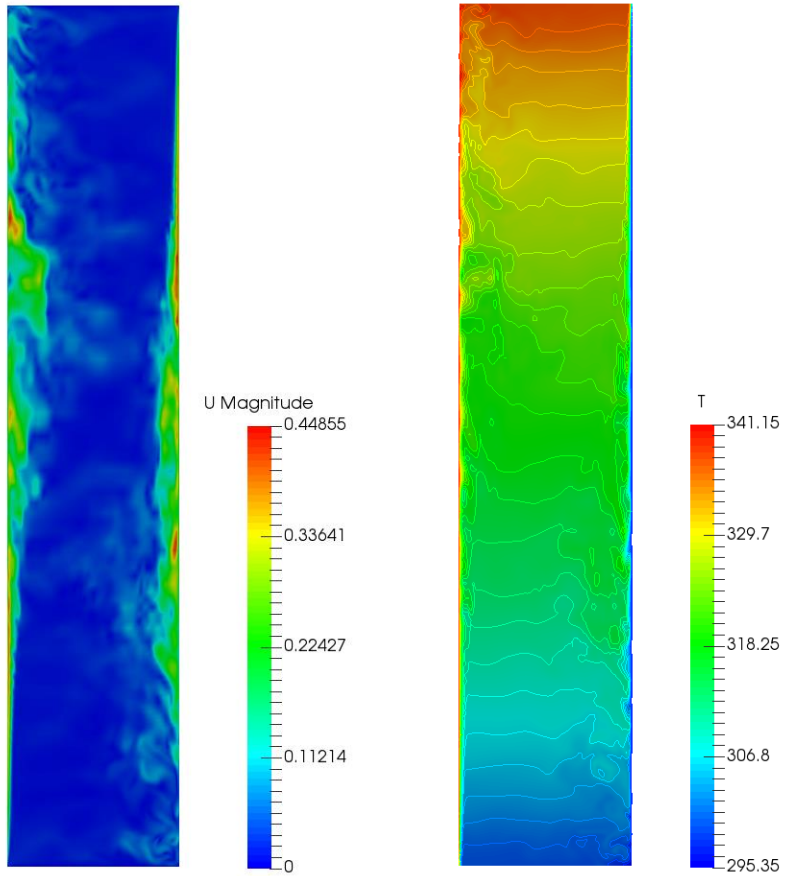

Velocity **Temperature**

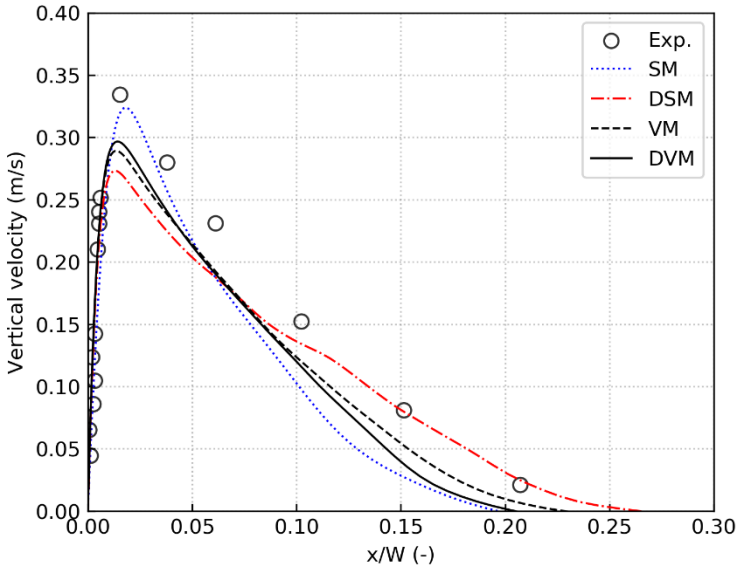

Mean vertical velocity

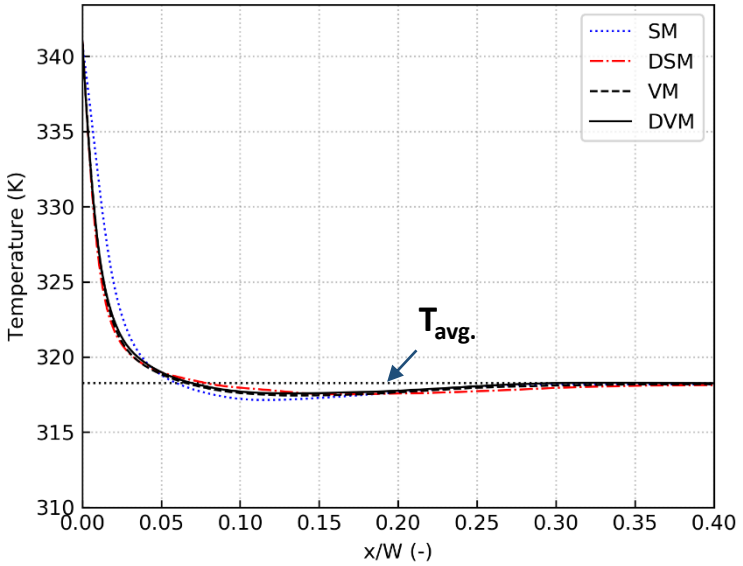

Mean Temperature



III. Results

Differentially heated cavity

- **Turbulent momentum/heat flux**

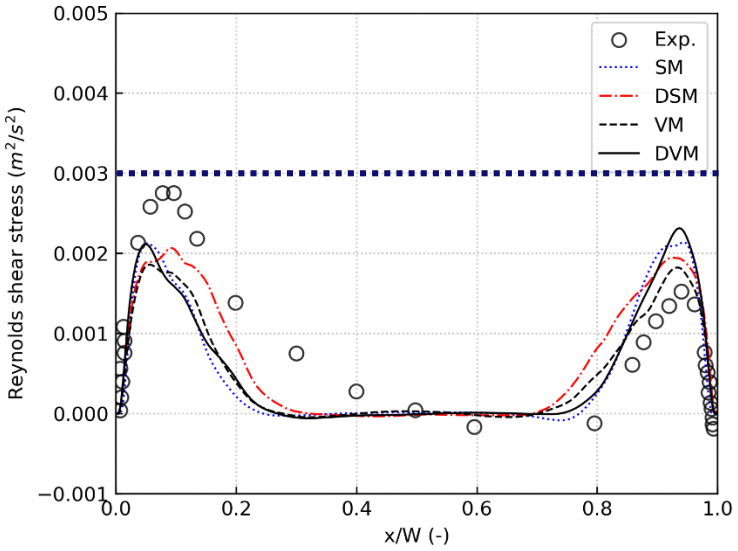

Reynolds shear stress

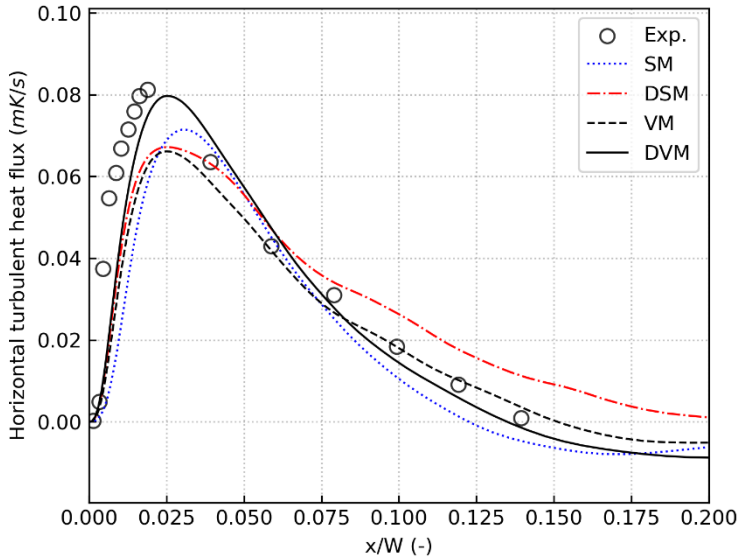

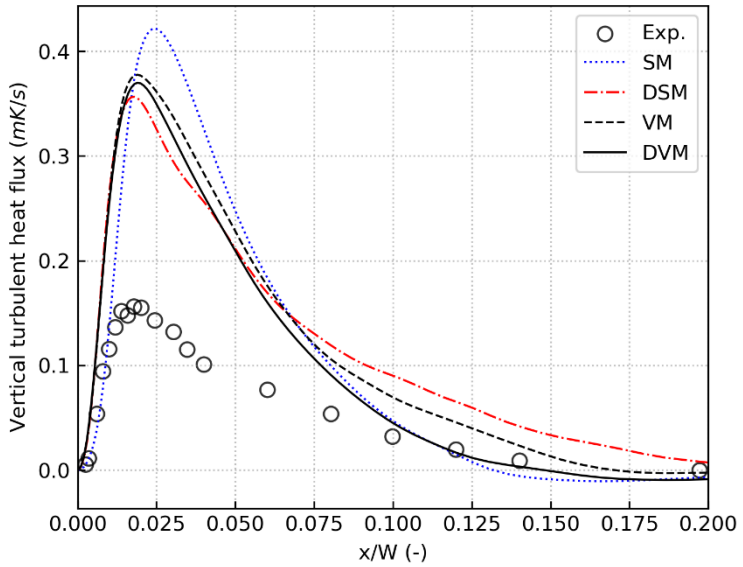

Turbulent heat flux



III. Results

Differentially heated cavity

- **Nusselt number**

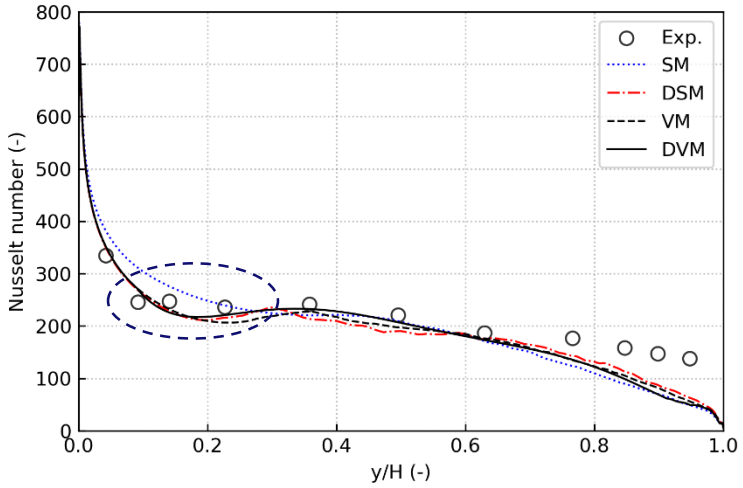

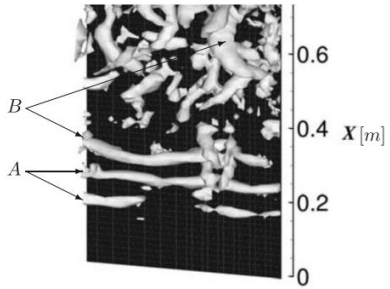

(Air case, LES) [1]
Transition location indication:
vorticity iso-surfaces
A: straight, B: hairpin vortices

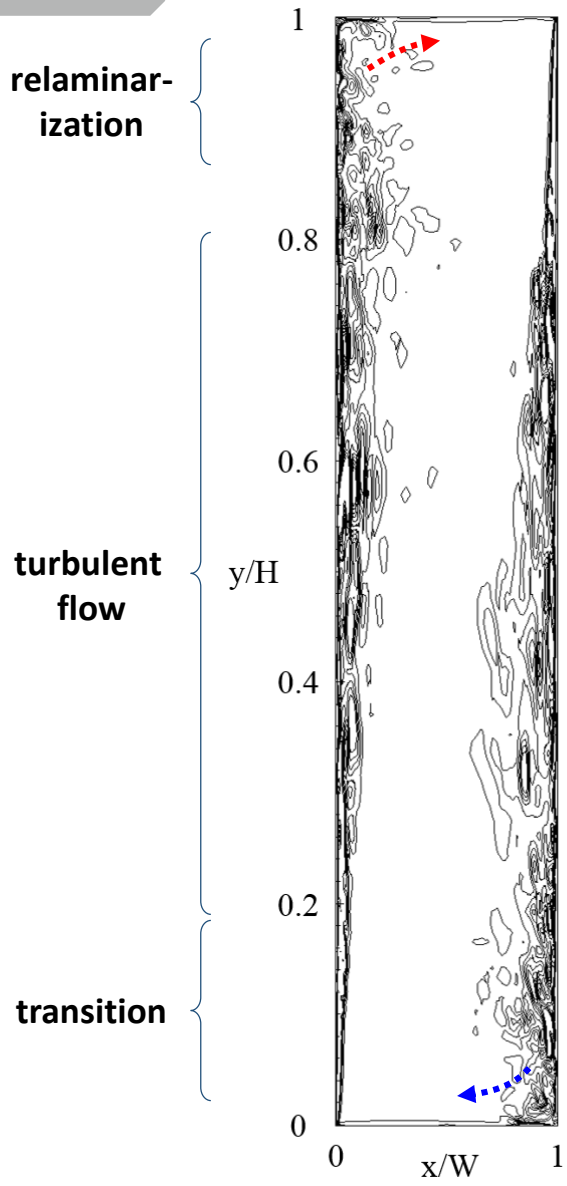

Spanwise vorticity
(-10~10)

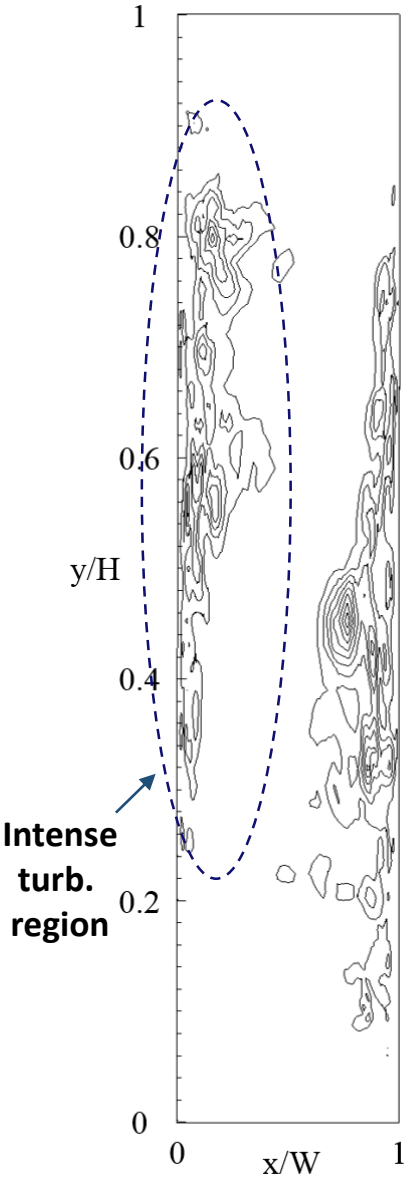

Ratio of viscosity, ν_T/ν
(0.5~2.9)

[1] Barhaghi, D.G., Davidson, L., 2007. Natural convection boundary layer in a 5:1 cavity. Phys. Fluids 19, 1–15.

III. Results

Differentially heated cavity

- **Model coefficients** of dynamic Vreman model
  - Proposed value: C_V (0.07 for channel flow) [1] & D_T (0.4 for TNC) [2]

$$\nu_T = C_V \Pi^g$$

$$q_j = -\frac{\nu_T}{D_T}\frac{\partial \overline{T}}{\partial x_j}$$

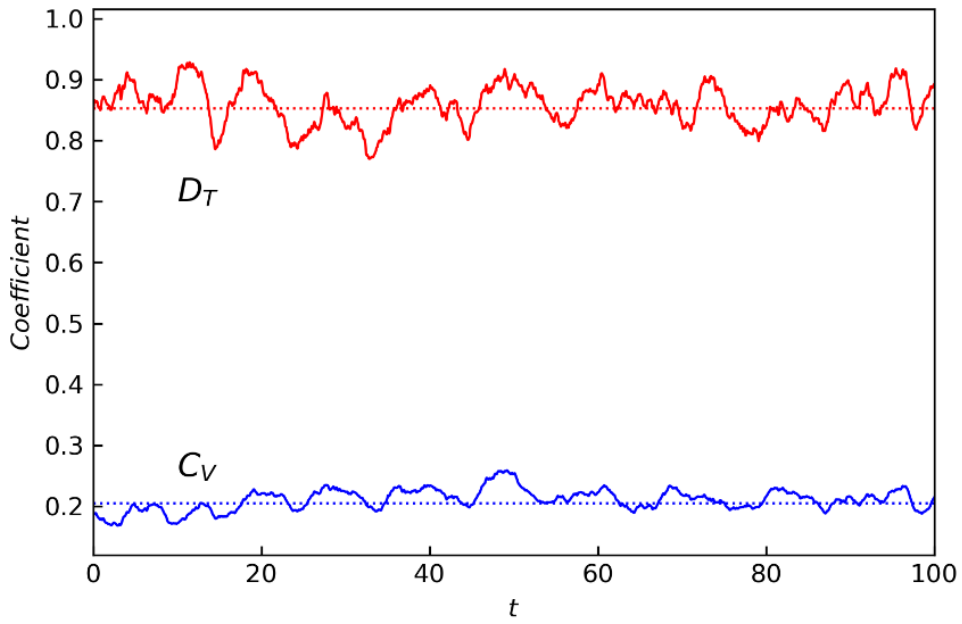

D_T: ~0.85

C_V: ~0.2

[1] Vreman, A.W., 2004. An eddy-viscosity subgrid-scale model for turbulent shear flow: Algebraic theory and applications. Phys. Fluids.
[2] Barhaghi, D.G., Davidson, L., 2007. Natural convection boundary layer in a 5:1 cavity. Phys. Fluids 19, 1–15.

III. Results

BALI

- **Overall behavior**: Velocity and temperature

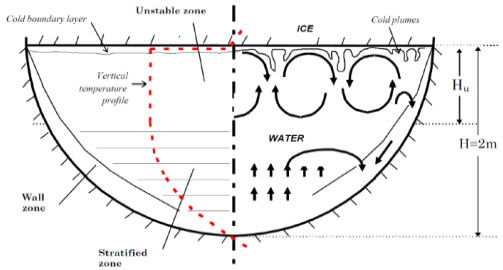

General observation

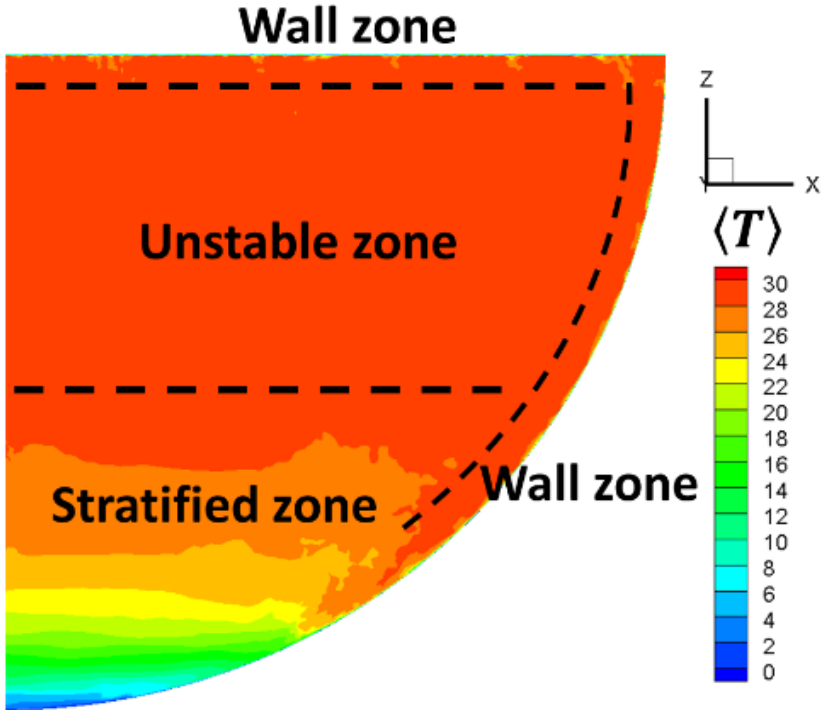

Instantaneous temperature

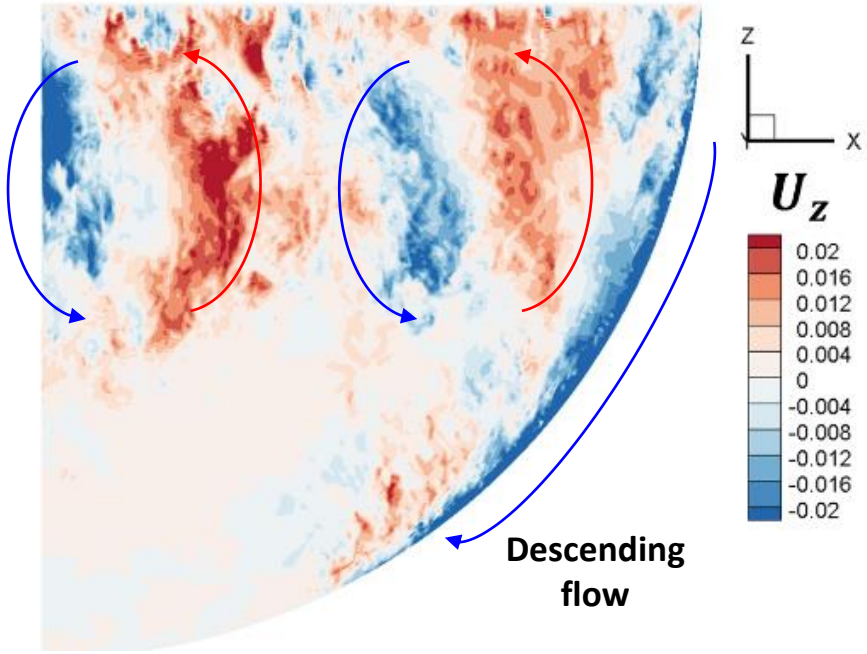

Instantaneous velocity

III. Results

BALI

- **Overall behavior**: Turbulent characteristics

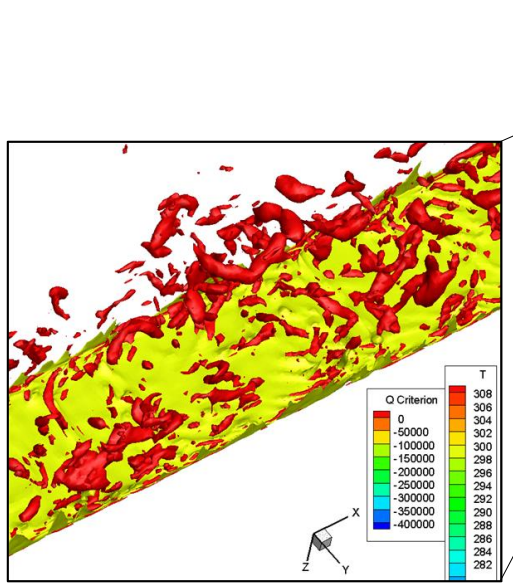

Q-criterion near wall

Highly turbulent region

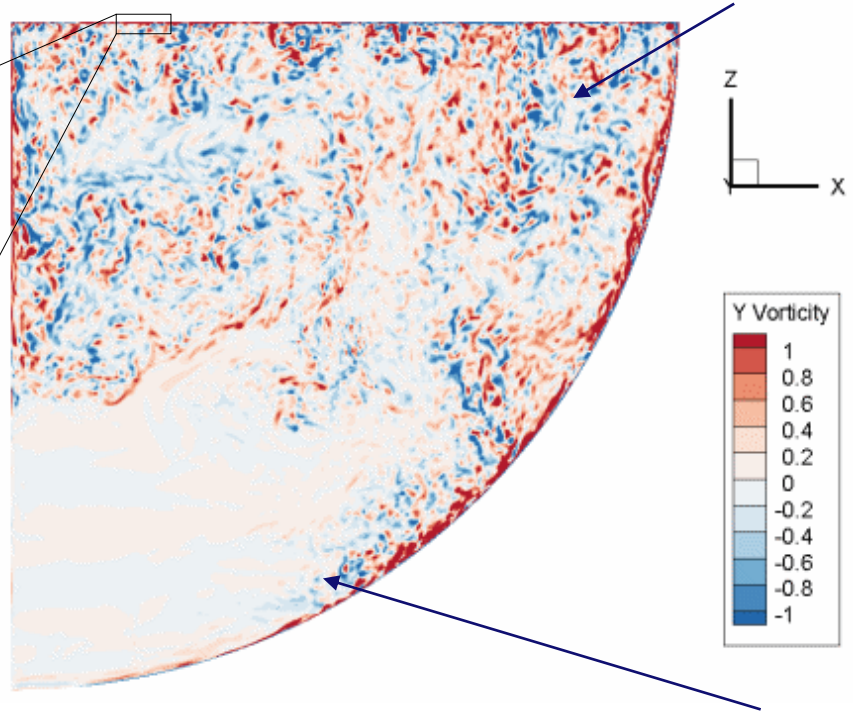

Stable region

Vorticity

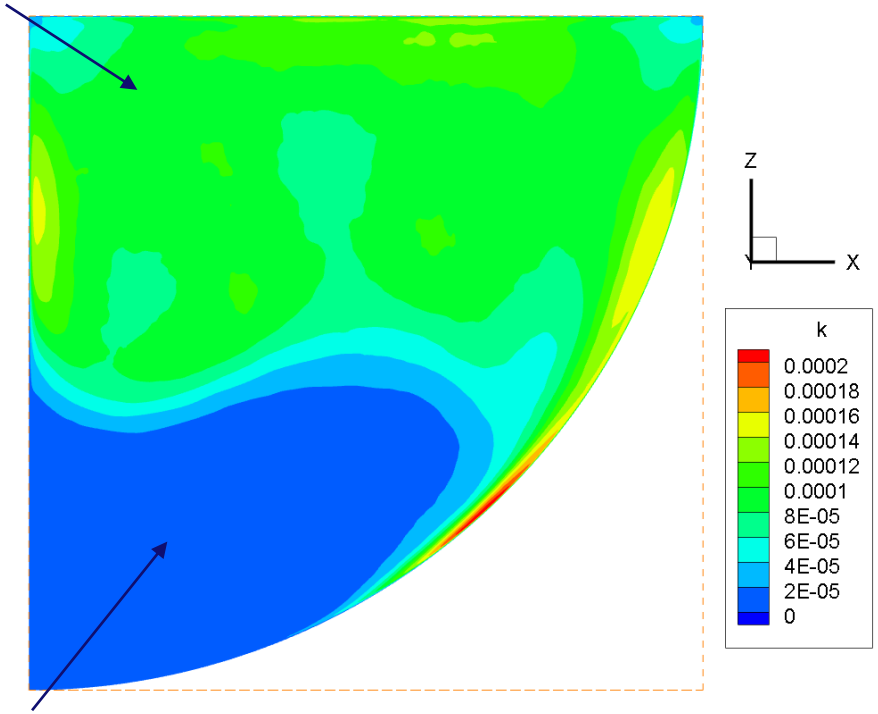

Turbulent kinetic energy

III. Results

BALI

- **Validation**: Nusselt numbers

	Exp.	LES	Error (%)
ΔT	25.46	25.22	5.1
Nu_{up}	2031	2072	2.5
Nu_{down}	1150	1135	1.7

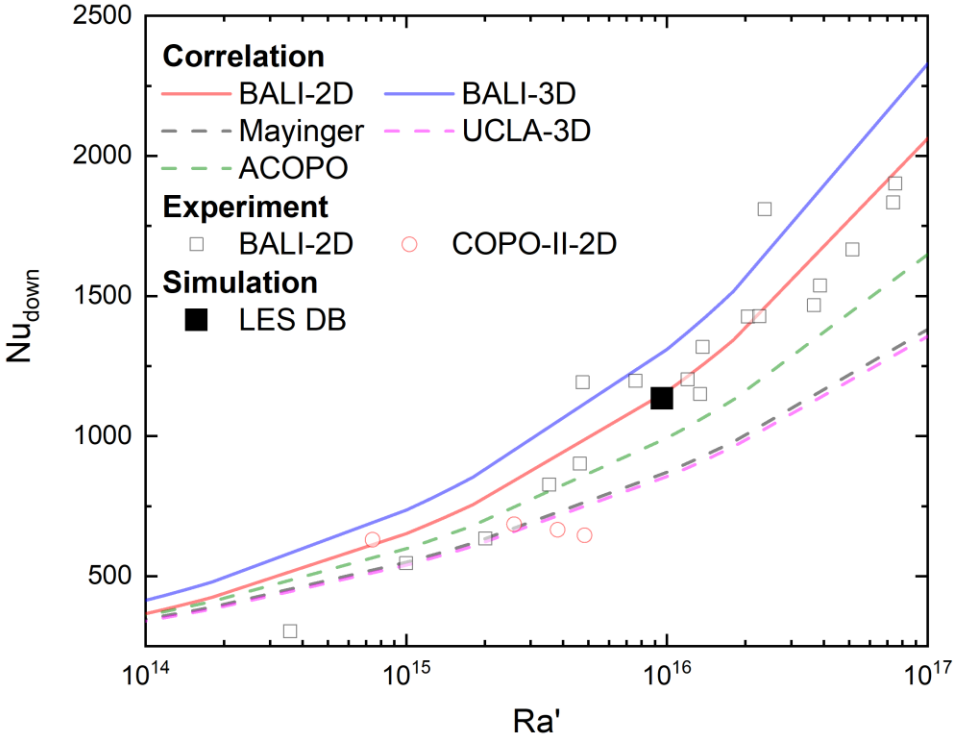

Downward Nusselt number

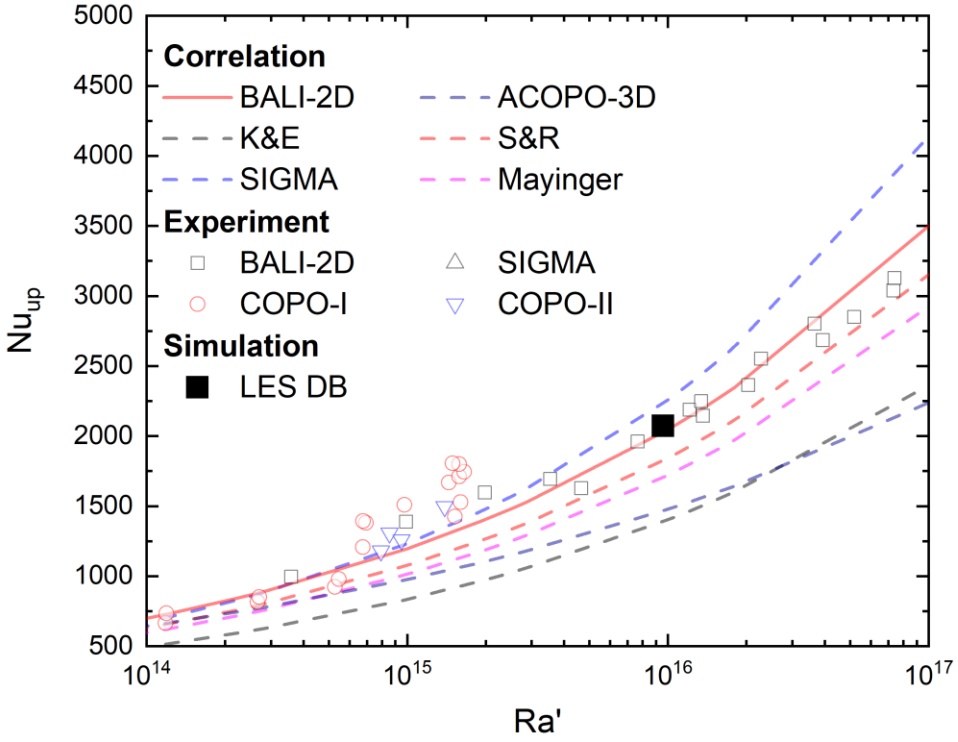

Upward Nusselt number

III. Results

BALI+

- (Preliminary) **Corium case** in the same geometry (slice-type) and Ra'

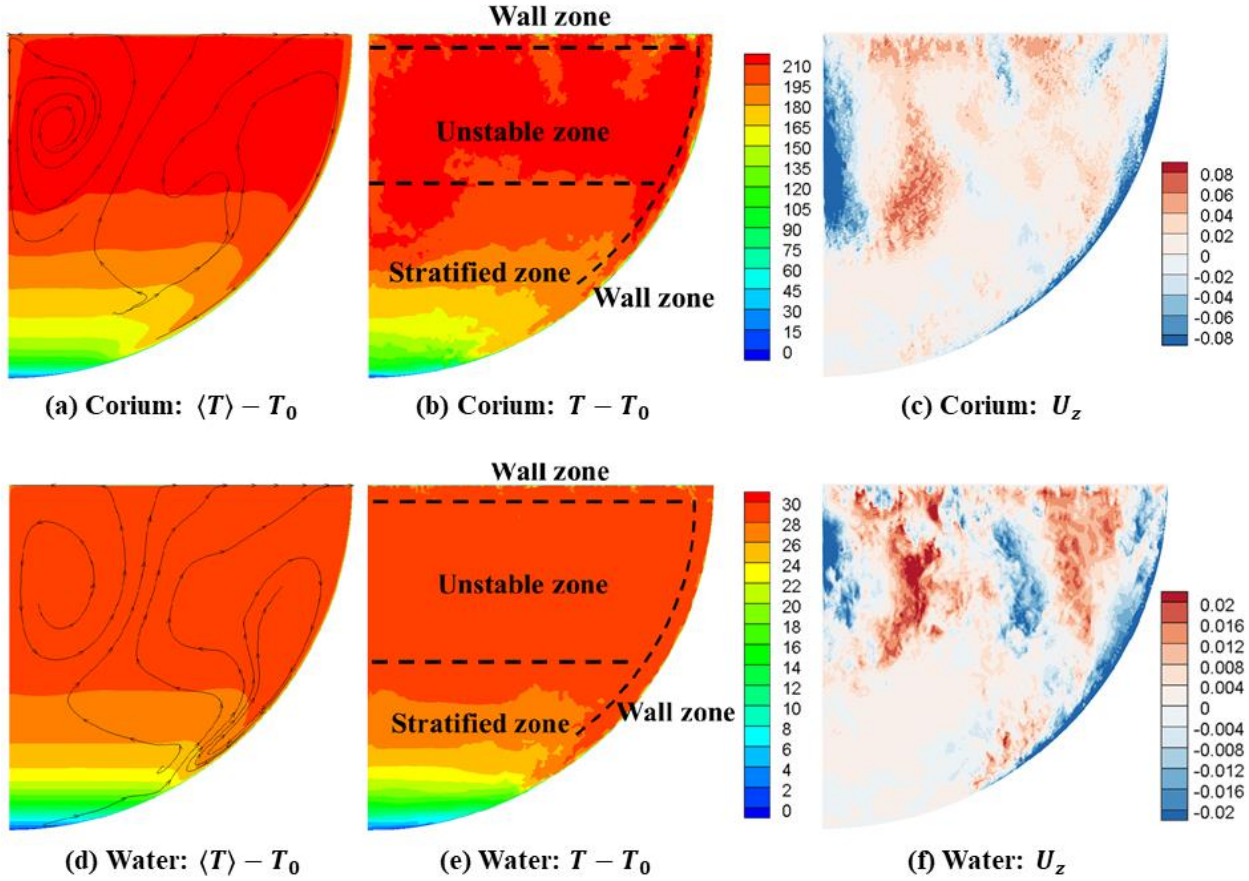

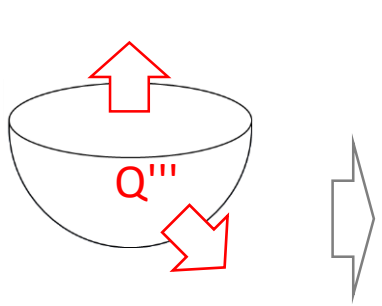

Power split ratio
(P_{up}/P_{total})

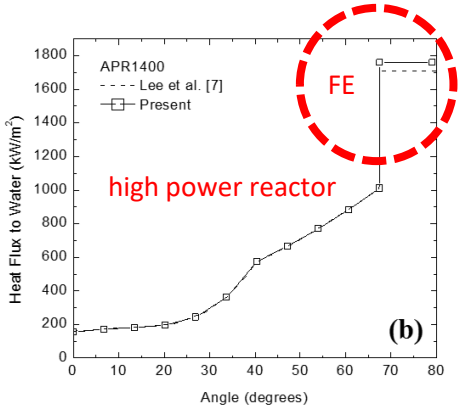

Heat flux distribution

	Water	Corium
Pr	5	0.5
PSR	56.8	57.9

IV. Conclusion

- **Turbulent natural convection** should be resolved to understand **thermal behavior** of the **oxide layer**

- **In this study,**
  - **Applicability of the high-fidelity method (LES)** has been examined by testing **SGS models** in simple flow **(DHC)**
  - **High-fidelity numerical DB** has been generated in **BALI geometry (2D slice)** with **corium properties**

- **Future work,**
  - Expanding the range of numerical DB (ongoing)
    - Rayleigh number
    - Geometry (3D hemisphere, multi-layer system)

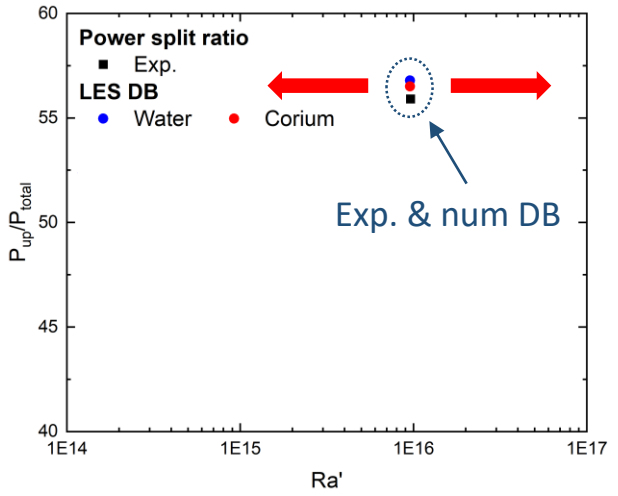

Need to expand LES DB

"in preliminary study"

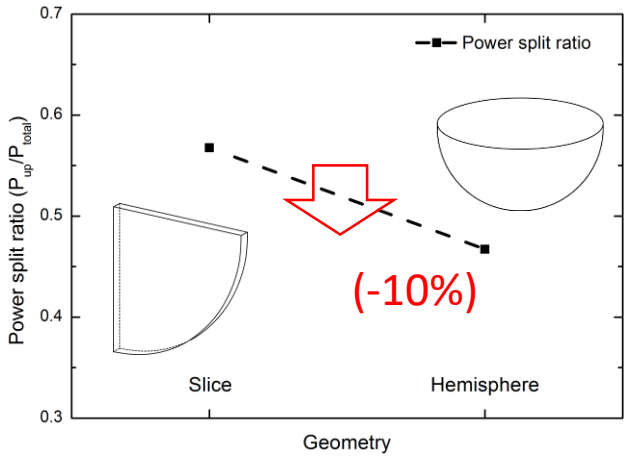

Power split ratio

Thanks for your attention

s.whang@snu.ac.kr
ARTS Lab. (https://anergz.com/)

This work was supported by KOREA HYDRO & NUCLEAR POWER CO., LTD
(2019-Tech-05, "High-Fidelity Numerical Analysis of Highly Turbulent Corium Pool for In-Vessel Retention (IVR) Strategy Feasibility Assessment")

The 10th European Review Meeting on Severe Accidents Research

Severe Accident Research Eleven Years after the Fukushima Accident

May 16-19, 2022, Karlsruhe, Germany

Technical Session 2-2: Uncertainties in Severe Accident Scenarios

Chairs: F. Mascari (ENEA), S. Paci (University of Pisa)

ID278	**Status of the Uncertainty Quantification for Severe Accident Sequences of Different NPP Designs in the Frame of the H-2020 Project MUSA** S. Brumm (JRC)	**Paper** **Presentation**
ID314	**Overview of IAEA CRP I31033 "Advancing the state-of-practice in uncertainty and sensitivity methodologies for severe accident analysis in water cooled reactors"** H. U. Rehman (IAEA)	**Paper** **Presentation**
ID264	**The APR1400 SOARCA Study: Insights into the Severe Accident Progression and Source Term Analysis Results** K. Ahn (KAERI)	**Paper** **Presentation**
ID275	**Uncertainty Quantification for a Severe Accident Sequence in a SFP in the Frame of the H2020 Project MUSA: First Outcomes** O. Coindreau (IRSN)	**Paper** **Presentation**

STATUS OF THE UNCERTAINTY QUANTIFICATION FOR SEVERE ACCIDENT SEQUENCES OF DIFFERENT NPP-DESIGNS IN THE FRAME OF THE H-2020 PROJECT MUSA

S. Brumm
European Commission, Joint Research Centre (JRC)
Westerduinweg 3, 1755 LE Petten, The Netherlands
stephan.brumm@ec.europa.eu

F. Gabrielli, V. Sanchez-Espinoza
Karlsruhe Institute of Technology (KIT)
Hermann-von-Helmholtzplatz, 1, 76344 Eggenstein-Leopoldshafen, Germany
fabrizio.gabrielli@kit.edu; victor.sanchez@kit.edu

P. Groudev
Institute for Nuclear Research and Nuclear Energy, Bulgarian Academy of Sciences (INRNE-BAS)
Tzarigradsko Chaussee 72, 1784 Sofia, Bulgaria
pavlinpg@inrne.bas.bg

P. Ou, W. Zhang
CNPRI
21/F, Science and Technology Building, Shangbuzhong Road, Futian District, Shenzhen, China
oupingwen@cgnpc.com.cn; zhangwencheng@cgnpc.com.cn

A. Malkhasyan
BEL-V
Rue Walcourt 148, 1070, Anderlecht, Belgium
albert.malkhasyan@belv.be

R. Bocanegra, L.E. Herranz
Nuclear Safety Research Unit, Department of Energy, CIEMAT
Avda. Complutense 40 Edificio 12-P0-13) 28040 Madrid, Spain
rafael.bocanegra@ciemat.es, luisen.herranz@ciemat.es

M. Berdaï
CNSC
280 Slater Street, Ottawa, ON K1P 5S9 Canada
mounia.berdai@cnsc-ccsn.gc.ca

F. Mascari, G. Agnello
ENEA
Via Martiri di Monte Sole 4, Bologna, 40129, Italy
fulvio.mascari@enea.it

O. Cherednichenko
Energorisk LLC
off. 141, 7 Simii Steshenkiv Str., Kyiv, 03148, Ukraine
e.risk@ukr.net

M. Nudi
EPRI
1300 West WT Harris Blvd, Charlotte, NC 28262, United States
mnudi@epri.com

A. Hoefer, E.-M. Pauli
Framatome GmbH
Paul-Gossen-Str. 100, 91052 Erlangen, Germany
Axel.Hoefer@framatome.com; Eva-Maria.PAULI@framatome.com

S. Beck, L. Tiborcz
Gesellschaft für Anlagen- und Reaktorsicherheit (GRS) gGmbH
Schwertnergasse 1, 50667 Köln, Germany
sara.beck@grs.de; livia.tiborcz@grs.de

O. Coindreau
IRSN
Centre de Cadarache, B.P. 3 – 13115 Saint-Paul-lez-Durance Cedex, France
olivia.coindreau@irsn.fr

G. Clark, I. Lamont
Jacobs
305 Bridgewater Place, Birchwood Park, Warrington WA3 6XF, United Kingdom
graeme.clark@jacobs.com; iain.lamont2@jacobs.com

X. Zheng, K. Kubo
Japan Atomic Energy Agency (JAEA)
2-4, Shirakata Shirane, Tokai, Naka, Ibaraki, 319-1195, Japan
zheng.xiaoyu@jaea.go.jp; kubo.kotaro@jaea.go.jp

B. Lee
Korea Atomic Energy Research Institute (KAERI)
Daedeokdaero 989-111, Yuseong, Daejeon, 34057, Korea
leebh@kaeri.re.kr

M. Valincius
Lithuanian Energy Institute (LEI)
Breslaujos str. 3, 44403 Kaunas, Lithuania
mindaugas.valincius@lei.lt

W. Giannotti
NINE S.R.L.
Via della Chiesa XXXII 759, Lucca 55100, Italy
w.giannotti@nineeng.com

M. Malicki
Paul Scherrer Institut (PSI)
Forschungsstrasse 111, CH-5232 Villigen PSI, Switzerland
mateusz.malicki@psi.ch

S. Gao
SNERDI
No.29 Hongcao Road, Shanghai, 200233, China
gaoshengqin@snerdi.com.cn

Y. Vorobyov
SSTC NRS
03142, 35-37 V.Stusa Street, Kyiv, Ukraine
yy_vorobyov@sstc.ua

M. Di Giuli
Tractebel ENGIE, Severe Accident Group,
Avenue S. Bolivar 34-36, Brussels, Belgium
mirco.digiuli@tractebel.engie.com

I. Ivanov
Technical University of Sofia (TUS)
1000 Sofia, 8, St. Kliment Ohridski Blvd., Bl. 12, Bulgaria
ivec@tu-sofia.bg

M. D'Onorio, F. Giannetti
Sapienza University of Rome
DIAEE Corso Vittorio Emanuele II 244, 000186 Rome, Italy
matteo.donorio@uniroma1.it; fabio.giannetti@uniroma1.it

M. Salay
U.S. Nuclear Regulatory Commission
Washingon, D.C. 20555, U.S.A.
michael.salay@nrc.gov

T. Sevon
VTT Technical Research Centre of Finland
Kivimiehentie 3, Espoo, Finland
tuomo.sevon@vtt.fi

ABSTRACT

The current HORIZON-2020 project on "Management and Uncertainties of Severe Accidents (MUSA)" aims at applying Uncertainty Quantification (UQ) in the modelling of Severe Accidents (SA), particularly in predicting the radiological source term of mitigated and unmitigated accident scenarios. Within its application part, the project is devoted to the uncertainty quantification of different severe accident codes when predicting the radiological source term of selected severe accident sequences of different nuclear power plant designs e.g. PWR, VVER, and BWR.
Key steps for this investigation are: a) the selection of severe accident sequences for each reactor design; b) the development of a reference input model for the specific design and SA-code; c) the selection of a list of uncertain model parameters to be investigated; d) the choice of an UQ-tool e.g. DAKOTA, SUSA, URANIE, etc.; e) the definition of the figures of merit for the UQ-analysis; f) the performance of the simulations with the SA-codes; and, g) the statistical evaluation of the results using the capabilities, i.e. methods and tools offered by the UQ-tools.
This paper describes the project status of the UQ of different SA codes for the selected SA sequences, and the technical challenges and lessons learnt from the preparatory and exploratory investigations performed.

KEYWORDS
Severe accident, modelling, uncertainty quantification, MUSA, source term

1. INTRODUCTION

Recalling the maturity of Severe Accident (SA) codes in terms of phenomena addressed and extensive validation conducted, the H-2020 4-year-project MUSA has been set up to explore uncertainty quantification in the SA domain including accident management (AM) actions [1]. In [2], an Uncertainty Quantification (UQ) approach is compared to conservative methods for the prediction of potential radiological off-site consequences after SAs in different reactor types. [3] introduces uncertainty propagation in the SA context, applying it to thermal-hydraulic phenomena in Reactor Cooling System (RCS) and containment.
The expectable gains from UQ are manifold: in addition to reducing conservatism and getting an idea of uncertainty bands of estimates (Figures of Merit, FoM), it allows the identification of most relevant parameters (input, models, initial and boundary conditions) impacting the prediction of the FoM of interest in a systematic manner. Moreover, the impact of SA Management (SAM) actions (e.g., time of initiation, location, delays, injection rates, pressure set-points) on uncertainty bands and FoM can be quantified.
The overall goal of MUSA is to quantify the uncertainty and sensitivities embedded in different SA codes when predicting the radiological Source Term (ST) for the SA sequences of different NPP designs using various UQ tools. The fact that almost half of the partners are from non-EU countries underlines the large interest in cooperating in this field. The technical work in the project is structured into (i) two preparatory Work Packages (WP) addressing the quantification of uncertainty sources (WP2) and reviewing uncertainty methodology (WP3), and (ii) three application WPs featuring an integral experiment, Phebus FPT1 [4, 5] (WP4), different reactor designs selected by the partners (WP5), and a Spent Fuel Pool (WP6).
This paper describes the status of work in the reactor applications WP, at 30 months into the project. It starts off by describing the organisation of the WP, the choices made by partners for their contributions, and how analyses in the first phase have been set up. It then discusses the results of the first "preliminary" phase of the analyses, i.e. the most important challenges that have been encountered during the setting up and running of the first UQ applications. This is the foundation for progressing to the project stage that is described in the outlook.

2. DESCRIPTION, AND STATUS, OF WORK ON REACTOR APPLICATIONS

WP5 is the largest WP in MUSA, taking contributions from 27 partner organisations and about 30% of the total human resources. It is built on output from MUSA WP2 and WP3, and is greatly supported by

experience gained in WP4. Given this interrelation, WP5 started later than these three WPs. Towards the end of MUSA, it is foreseen that experience gained in WP5 will be fed back to WPs 2 and 3.

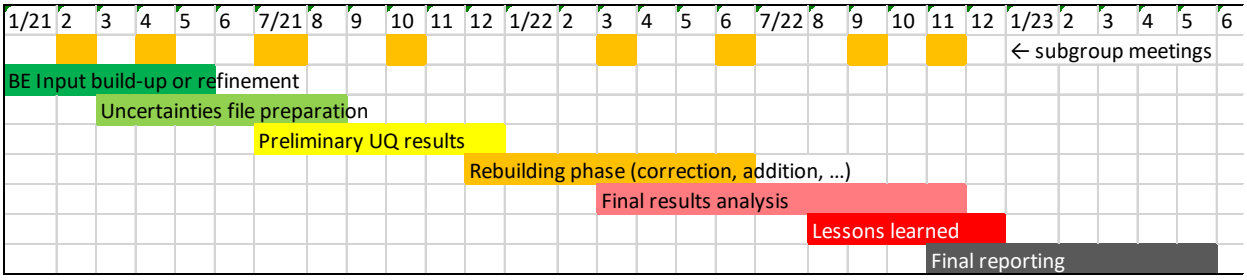

Figure 1 WP5 work phases from January 2021 to the end of MUSA [months].

For a better exchange, partners in WP5 are divided into 4 subgroups according to the reactor type they are investigating: PWR Gen. III (5 partners), PWR Gen. II (10), VVER plus CANDU (6), and BWR (6). **Table II** shows the group make-up in detail.
Figure 1 indicates that 4 subgroup meetings are organised per year where partners present their work and discuss within the group. One of the meetings in 2021 was organised as a plenum meeting with presentations of WP2, 3 and 4 outputs and of US-American ST studies and the state of the art [2].
Figure 1 also highlights the phases that have been proposed for partners' work. Knowing that many partners had to build up their capability for Uncertainty Analysis (UA) in SA modelling, work was initially focussed on a best-estimate base case. The second phase, "uncertainties file preparation", concerns coupling SA codes and Uncertainty Tools (UTs) and creating all files required for the UQ. This step benefitted greatly from work done in WP4, where 21 of the partner organisations have been involved. The third and still ongoing phase, is the running of preliminary cases as proof of concept. The sections below report from the work in these 3 phases.
The year 2022 is foreseen for running the full analyses, and for evaluating and interpreting the results.
It has to be recalled that working together and achieving the common objectives of WP5 is a challenging endeavour. The variation among partners' work is huge owing to differences in reactor types; the codes applied; the power of computing hardware used; previous experience with UQ; and, finally, the research interest selected. The effort to harmonise the outcome rests on several requirements: that ST analyses are to be carried out and ST nuclides to be used as FoM; that risk-dominant scenarios are analysed, i.e. SBO, LOCA and in some cases SGTR; that Uncertain Parameters (UPs) as defined in WP2 are to be used; and, that a best practice for results evaluation will be sought.

2.1. Selection of SA sequences

Any modelling of a SA relies on a large number of choices – e.g. initial conditions, available safety systems, mitigation measures – to reflect the situation in the damaged reactor and to demonstrate how the accident sequence is impacted. In the reactor applications WP of MUSA participants have been able to make these choices according to the reactor type they are investigating, their previous experience, their research interest, etc. However, they have also been committed to common guidelines expressed in the project definition and in recommendations made by the project's End User Group:

- MUSA is oriented towards exploring uncertainties in the ST estimate, implying that any accident sequence considered needs to lead to core damage and the release of Fission Products;
- MUSA aims at analysing risk-dominant and thus highly relevant accident sequences;
- it has been proposed not to feature completely unmitigated scenarios, but rather consider SAM actions with an impact on the ST. Examples for mitigation are late core flooding and, during the ex-vessel phase, water injection into the cavity or filtered containment venting.

It is important to note that the effort for investigating sequences prolonged by mitigating actions tends to be significant. This has been a concern for many partners, in particular where the runtime requirements of the SA code are high and where High Performance Computing (HPC) is not available for the project.

Table I Scenario choices made by the contributors to WP5 for the preliminary analyses

Organisation	Reactor	SA scenario	SAM action
CNPRI	HPR1000	LLOCA	
NPIC	HPR1000	LOCA, SBO	
SNERDI	CAP1400	SGTR, LLOCA, SLOCA	
KAERI	APR1400	SBO leading to SGTR	UA for triggering ADV
CNPE	HPR1000	LB-LOCA	
KIT	KONVOI	MB-LOCA plus SBO	
BelV	PWR-1000	LB-LOCA	
ENEA	PWR-900	SBO	
CIEMAT	PWR (Surry)	SBO	
PSI	PWR-1100	SBO plus SGTR	Fixed-time SG re-flooding
GRS	KONVOI		
IRSN	PWR-900	SBO plus loss of aux. FW	Fixed-time sump flooding, CFVS
EPRI	PWR (Surry)	ELAP w/o+ w/ mitigation	Un-mitigated vs. AC restored at RPV failure
TRACTEBEL	PWR-1000	SBO	UA for triggering CSS, DCIS, PPORV, CFVS
USNRC	PWR (Surry)		
FRAMATOME	KONVOI	MB-LOCA plus SBO	
INRNE	VVER-1000	LB-LOCA plus SBO	Core quenching at SAMG criterion
CNSC	CANDU	LB-LOCA; SBO	
NINE	VVER-1000	LB-LOCA plus SBO	
TUS	VVER-1000	LB-LOCA plus SBO	
SSTC	VVER-1000	SBO	UA for Pressurizer PORVs
Energorisk	VVER-1000	LB-LOCA plus SBO	
LEI	BWR5-LIKE	LB-LOCA plus SBO	
JAEA	BWR4 Mark1	SBO	UA for CFVS, DC water injection
VTT	BWR4 Mark1	SBO	Fixed-time wet-well venting
SAPIENZA	BWR4 Mark1	SBO	Pressure-based wet-well venting
JACOBS	ABWR-LIKE	SBO	UA for triggering/flow rate of High-Pressure Core Flooder

Table I shows the reactor type and the scenario choices made by the contributors to WP5. The SAM actions described have been explored during the preliminary analyses and may still be adapted during the full analyses. Please notice the distinction between SAM actions subject to uncertainty (mostly the timing in initiating the action) and other "hardwired" actions (fixed time, or based on a key parameter reaching a threshold). Please note also that all accident scenarios in the table make assumptions on the availability of a reactor's safety systems like passive hydro-accumulators or safety relief valves. These assumptions are made by the partners and are not coordinated by the project; they will be important when discussing results, at a later stage of the project.

2.2. Development of a reference input model for the specific reactor design and SA code

One of the first steps taken in WP5 was to invite all partners to complete a functioning input deck, demonstrated by a best-estimate reference case simulation leading to a radioactive release. Technical meetings have shown the effort that has had to be invested in adapting input decks to the UQ exercise.

Table II Hardware/software choices and WP5 subgroup split

Organisation	WP subgroup	SA code	Uncertainty Tool	Computer hardware
CNPRI	PWR Gen. III	ASTEC	SUNSET	no info
NPIC		MELCOR	DAKOTA	no info
SNERDI		MAAP 4.0.7	DAKOTA	PC, 4GB RAM
KAERI		MELCOR 2.2	DAKOTA	HPC, 128GB RAM
CNPE		MELCOR	DAKOTA	no info
KIT	PWR Gen. II	ASTEC	Python-based FTSC	HPC
BelV		MELCOR	URANIE	PC, 8GB RAM
ENEA		MELCOR	DAKOTA	PC, 32GB RAM
CIEMAT		MELCOR	DAKOTA	PC, 8GB RAM
PSI		MELCOR	DAKOTA, Python	PC, 16GB RAM
GRS		AC^2	SUSA	no info
IRSN		ASTEC	SUNSET, Python	HPC, 125GB RAM
EPRI		MAAP 5.05	Python scripts	HPC
TRACTEBEL		MELCOR	Python scripts	HPC, 32GB RAM
USNRC		MELCOR	Python scripts	no info
FRAMATOME		other	Genpara, MOCABA	no info
INRNE	VVER / CANDU	ASTEC	SUNSET	PC, 8GB RAM
CNSC		MAAP	Python scripts	PC, 8GB RAM
NINE		MELCOR	NEMM method	no info
TUS		ASTEC	SUNSET	PC, 4GB RAM
SSTC		MELCOR	SUSA	PC, 32GB RAM
Energorisk		MELCOR	DAKOTA	PC, 128GB RAM
JRC	BWR	-	-	-
LEI		RELAP/SCDAPSIM	SUSA	PC, 16GB RAM
JAEA		MELCOR	RAVEN	HPC, 192GB RAM
VTT		MELCOR	DAKOTA	PC, 8GB RAM
SAPIENZA		MELCOR	RAVEN	PC, 16GB RAM
JACOBS		MELCOR	DAKOTA, Python	HPC

Modifications are required for all partners to automate setting the values of the UPs in the input deck. For their individual reference case scenario, partners were asked to

1. Run the case and show the credibility of the results in terms of characteristic parameters like primary and containment pressure. These transients are well known from previous studies or from literature;
2. Show the evolution of some Fission Products in the ST; and,
3. Record key metadata of the simulation, like (i) scenario duration; (ii) hardware used; and, (iii) runtime required.

At the end of October 2021, 24 of 27 partners have completed the reference case and have established basic data characterising the effort posed by one simulation.
The results confirm that most SA codes require a computing time similar to the simulated time on a local scientific PC; only the fast-running code MAAP is an exception. Depending on their IT boundary conditions, partners favour different approaches to the task of running multiple simulations for uncertainty propagation:

A. For MAAP, large numbers of cases can run with acceptable effort[1], moving the challenge of managing the amount of data created into the foreground.
B. Partners who have access to HPC rely on the parallel execution of multiple runs of the SA code (the software licence permitting).
C. Partners who are limited to local PCs need to economise, and plan to do this in terms of
    - Reduction of the complexity of the reactor description, i.e. input deck simplification;
    - Selection of a less complex SA-scenario;
    - Reduction of the duration of the accident scenario. This can be related to the choice of mitigation action that prolongs the accident scenario, but it also touches on the criterion for the termination of the simulation.

Table II shows SA codes, UQ tools and computing hardware used by the different partners.

2.3. Setting up preliminary uncertainty analysis cases

The UA work in MUSA is organized as a two-staged approach of (i) first setting up all necessary models and tools and demonstrating their functioning; and, (ii) the full-scale analyses according to their individual scientific interest in terms of scenario and mitigation actions. This approach takes account of the fact that few partners have previously carried out UA in the SA context, and of the complexity of setting up the necessary constituents of the analysis described hereafter. The uncertainty application in MUSA's WP4 has been part of developing the collective capabilities and has been very effective in all points discussed below.

The problem definition itself builds on the input deck and the scenario selection that have been described above, and on the definition of ST FoM. Within the early work reported here, partners have experimented with FoM ranging from

- the FP groups provided as output by the SA codes; to
- inventories in the zones of the reactor or releases from them, i.e. RCS and containment; to
- non-ST quantities, e.g. hydrogen in the containment; to also
- time instances of events during the accident sequence, e.g. the creep rupture of hot leg, surge line and SG tubes.

For the full analysis, and considering the overall goal of MUSA, it is foreseen that the FoM will include the total release of radioactive Noble Gases, Caesium and Iodine to the environment.

The choice of the set of UP to investigate is typically driven by the search for the parameters with the highest impact on the FoM during the accident progression (in-vessel, ex-vessel, containment, etc). It also reflects the focus of the investigation, like: (i) the physical models in the SA code that partners want to investigate; (ii) phases of the accident (in-/ex-vessel, containment) of special interest; (iii) SA management and mitigation considerations. For the preliminary analyses partners selected a minimum number of UP, their Probability Density Function (PDF), and their maximum/minimum values. At this stage, the need for justifying assumptions on the PDF (an important aspect in WP2) has been relaxed.

Further steps to be carried out in the context of running a preliminary analysis are:

[1] It is stressed that this paper is not comparing the modelling approach of different SA codes. The accuracy of the MAAP results in this study is the same as in any other application of the MAAP code.

- The choice and implementation of a UP sampling method. Most partners chose Latin Hypercube Sampling (LHS) which promises the minimum number of runs for a given confidence interval. Even so, a few partners chose the less efficient Monte Carlo (MC) random sampling to avoid making the strong assumptions of parameter independence in LHS. KIT found that taking account of pre-correlations among the selected UP governing the same phenomenon increased the related correlation coefficients between such parameters and the FoMs (up to a factor of four).
- Automation of the analysis: uncertainty propagation requires the SA code to run with a large number of sampled UP sets. Automating the creation of these input deck variations is not only a question of economy; it also helps avoiding typographical errors from manual input. Ideally, the selected UT would already have an interface to the selected SA code that provides this automation and initiates the execution of all simulations. In MUSA, this held only for a few partners; most faced situations like: (i) the interface of SA code and UT needed to be created, or errors corrected; (ii) the interface was reinforced by additional code to meet the requirements of the partner; and, (iii) some partners opted for a self-programmed solution altogether, providing flexibility e.g. with regard to the IT platform and taking advantage of programming languages like Python and statistics software packages.
- Post-processing of the results from the uncertainty propagation runs. Goals reach from checking plausibility of single runs to generating ensemble data that display graphically key messages of the UQ.

2.4. Status of preliminary uncertainty analysis

At the end of October 2021, and thus 29 months into the project, 15 of the partners have achieved a proof of concept for the set-up of their UA. Most others are in the process of solving technical issues related mainly to coupling of SA codes and UT and to frequent code failures.

Many partners have already gone beyond these preliminary analyses by selecting larger numbers of FoM and UP, running a hundred or more simulations, and beginning to perform a critical review of the obtained results in view of MUSA's objectives. A brief overview of these activities will be given in Section 3.

The phase of preliminary UA together with experience gained in WP4 has been very useful in highlighting the challenges met during the UA, and in showing partners' ideas on how to address them:

- The crashing of the SA code during the execution, for some of the UP sets. This is a reminder of codes' sensitivity to the choice of parameter values in the physical models and correlations. The discussion of partners' results in MUSA subgroup meetings provided some interesting insights, e.g.
    a. Code crashes were observed much less when carrying out a pre-correlation analysis of UP – and by this avoiding physically meaningless random combinations of correlated UP
    b. Fewer code crashes seemed to be also observed when sampling with MC rather than LHS method.
    c. One partner observed random code crashes for small variations in the UP. This could mean that a parameter set causing a code crash could be replaced by a set changed by random noise, with a chance of not thrashing. Analyses on the bias this might cause are on-going.
- The overall hardware requirements of the preliminary runs also give an indication of how much time would be required for the full-scale UQ analysis.

3. MAIN RESULTS FROM PRELIMINARY ANALYSES

3.1. Examples of results from Uncertainty Analyses

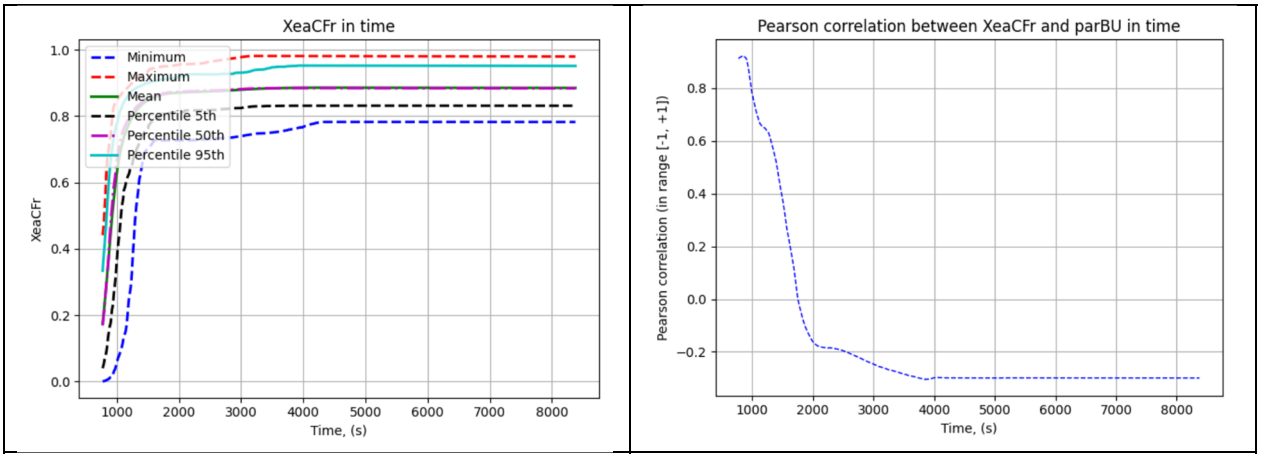

Figure 2 Xe release XeaCFr to containment (left) and correlation of XeaCFr with fuel burn-up (KIT)

During the setting up of their analyses, partners have explored ways of presenting their results. Next to the type of plots in **Figure 2** they have looked at (i) FoM evolution in time, plotted for all simulated cases and thus giving a picture of the FoM ensemble; (ii) values of correlation coefficients for all UP in bar charts or color-coded matrices to highlight dominating uncertainties; (iii) FoM PDF assembled from all simulations and plotted for a given time instant to look for patterns in the statistics of the result; etc. Post-processing will become relevant for the full-sized final analyses.

Figure 2 displays uncertainty bands of a ST FoM, and its sensitivity towards one of the uncertain parameters; see ***Table I*** : KIT for more details on the case. The correlation coefficient as a function of time underlines that the fuel burn-up has a significant impact at the beginning of the scenario and is weakening with time.

3.2. Computational set-up and cost

In MUSA, the computational effort poses the most severe limit to the reactor application of UQ. There is a range of factors that determine the cost of the analyses, with the most influential (i) the complexity of the reactor model; (ii) the complexity and length of the simulated accident scenario; (iii) the runtime requirement of the SA code used; (iv) the complexity/size of the UQ; and, (v) the available hardware to run the analyses. Moreover, the handling and post-processing of huge amounts of data should not be underestimated.

A poll of the computing hardware to be used shows that, out of 20 respondents, 6 are using HPC that run many simulations in parallel and are allowing demanding analyses within, say, a couple of weeks to a couple of months, even for codes that are not fast-running. The remaining 14 partners run PC systems of varying computing power. In terms of runtime requirements for the base case, partners have quoted between 20 minutes and 120 hours – this longest value reflecting a case terminated only after 10 days of problem time. Limits in hardware power lead to a situation where many partners need to make trade-offs between points (i), (ii) and (iv) described above. Even so, computing power is not a pre-condition for making sensible contributions to the methodological questions addressed by MUSA. See **Table II** for details on the hardware.

3.3. SA-codes behaviour during the UQ

Setting up the computational framework for the preliminary UA, see the description in section 3.3, is in itself a process of tracing and correcting faults before the system works well. However, the failure of some SA codes when running with an instance of the set of varied UP is a more complex challenge that may have different root sources, e.g. the selected PDF, the value ranges assigned to each UP (narrow/wide range), the combination of UP for each run, or the numerical stability of the SA-code.
The experiences of partners, for the different SA codes, can be summarised like this:

1. For MAAP, almost no code failure is observed, meaning that the code set-up is resilient towards the variation of selected UP. For MAAP-CANDU, CNSC experienced some problems with UP outliers and proposed using bounded PDF as a fix.
2. For MELCOR, the situation is more varied, judging by the reports of 11 partners:
    a. Two partners report no code failure. One of them (KAERI) was not simulating core slump or RPV failure during the preliminary phase, while the other (Energorisk) was looking at a very short and very severe sequence. All others acknowledge that a small number of code failures is to be expected.
    b. The quality of the model seems to have an impact: SSTC could reduce the number of code failures significantly by changing the resolution of the core model. This point is echoed by other partners who adapted/simplified an existing input deck and who know from experience the need to look for model optimisation.
    c. Several partners report schemes for reducing the minimum time step and restarting simulations. This led to fewer code failures, at the price of increasingly long simulation duration. For code failures after time step reductions, SSTC reports making small changes (1% of the variation range) to some of the parameters related to the core model – which in their case had been identified as the origin for code failure.
    d. Jacobs has performed a study of biases that may result from the absence of failed calculations from the output distribution. A method was developed to automatically rerun failed calculations with reduced time steps around the time of failure, which greatly improved the percentage of successfully completed runs. It was observed the initial failures were unevenly distributed in key output quantities, suggesting bias would have been introduced by omitting calculations that initially failed.
    e. Finally, some partners have included the timing of SAM actions as UP and have shown a large impact on code performance. Jacobs did this for core re-flooding and reports up to 55% of code failures when a narrow band of initiation times was considered during core degradation.
3. Experiences of partners using ASTEC showed few code failures. INRNE reports less than 4% of their simulations, while KIT reported 2 code failures from 300 runs. It is worth mentioning that KIT used pre-correlated UP to minimize unphysical parameter combinations.

3.4. Sampling of uncertain parameters

Practically all partners use the Wilks formula [6] to establish the minimum number of simulations required for achieving FoM estimates with a 95% confidence interval for the 95% probability content. Most of them combine, or intend to combine, this with LHS of the UP, which promises the most efficient coverage of parameters' uncertainty ranges.
First experiences with sampling can be characterised like this:

- Due to code failures, many partners need to run additional cases to arrive at the minimum number of simulations required by Wilks, e.g. by increasing Wilks' minimum number of UP variations with the estimated number of code failures when sampling UP space.

- Just dropping failed runs can injure the mathematical assumptions of the UA and bias the results. Partners have analysed sets of UP in failed cases to detect a causal link for the failure. So far, few cases have been reported where such a link could be detected.
- Dropping cases from a LHS scheme can also lead to an uneven representation of UP. Ways of addressing this problem have been:
    - To re-run failed cases with some parameters in the UP set changed by small systematic or random perturbations. Analyses of potential bias in this case are on-going.
    - To use MC sampling and run significantly more cases than required by the Wilks formula, to make sure that the parameter uncertainty space is well covered
- There are concerns that correlations of UP exist and could be ignored, potentially leading to un-physical choices of parameter combinations. KIT reported positive results for taking into account such pre-correlations.

Finally, it is noted that partners running large numbers of cases typically use MC random sampling and achieve confidences higher than 95%.

3.5. Accident Management and Mitigation

It is an important goal of MUSA to include AM actions in the UA. Such actions are fundamentally different from parameters in the phenomenological models of the SA code: they represent sequence-specific uncertainties. UP in SAM actions are often the time instant of activating a system, e.g. cavity flooding or CFV, but they can also include other parameters of an activated system, such as a flow rate. During the preliminary phase five partners included uncertainty in SAM actions in their analyses, see Table I.
Four partners have analysed SAM action: all for SBO scenario, where 3 have looked at the uncertainty in triggering the depressurization of the RCS and one at high-pressure re-flooding. While these are preliminary results and will not be discussed in detail, there are some observations made to guide other partners in analysing SA actions:

- Triggering the SAM actions does not in itself imply more code failures, but the simulation can indeed react sensitively to the choice of uncertainty interval – in Jacobs' case early core re-flooding starting between 8,000s and 12,000s into the SBO led to significantly more code failures than for later times;
- The SAM triggering time was selected within a larger set of uncertain model parameters and did not upset the uncertainty propagation. Tractebel found a triggering delay strongly correlated with one FoM (CsMb) and weakly correlated with another (CsI), while JAEA and SSTC found such a delay weakly / not correlated with their FoM of choice.

Having made these two points, it should still be clear that any SAM action changing drastically the scenario, e.g. mitigating vessel failure, is likely to have a big impact on FoM.

4. CONCLUSIONS

The paper has given a view of the extent of work to be carried out under WP5 of MUSA, highlighting the large number of partners; the variety of reactor types, scenarios, codes and hardware; and, the organisation of the work.
The reactor applications WP has seen most of the partners concluding the setting up of their analyses with 18 months to the end of the project. In this, the level of progress is wide-ranging, with some partners already running large uncertainty propagation and addressing key questions of applying UA to SA modelling.
Challenges shared by the partners when setting up their UA have been described. The issues identified as a result of this learning process may be regarded as preliminary lessons learnt. They will remain issues during the full-sized analyses in WP5: computational aspects, like effort and code performance; the selection, definition and sampling of uncertain parameters; and particularities of SAM actions. MUSA will support its participants to manage these issues according to their capacity and scientific interest.

Two examples of the results that will be achieved with the uncertainty analyses – uncertainty bands of the FoM and correlation coefficients for UP and FoM – have been shown. Details of these analyses go beyond the scope of this paper and will be addressed in more technical contributions in the future.

ACKNOWLEDGEMENTS

The MUSA project has received funding from the Euratom research and training program 2014 – 2018 under grant agreement No. 847441.

REFERENCES

1. L.E. Herranz, S. Beck, V.H. Sánchez-Espinoza, F. Mascari, S. Brumm, O. Coindreau and S. Paci, "The EC MUSA Project on Management and Uncertainty of Severe Accidents: Main Pillars and Status", *Energies*, **14** (4473), pp. 1-11 (2021).
2. S.T. Ghosh, H. Esmaili, A.G. Hathaway III, D.M. Osborn, N.E. Bixler, D. Brooks, K.W. Ross and K.C. Wagner, "State-Of-the-Art Reactor Consequence Analyses project: Uncertainty Analyses for Station Blackout Scenarios", *Nucl. Technol.*, **207**, pp. 441–451 (2021).
3. H. Glaeser, "GRS Method for Uncertainty and Sensitivity Evaluation of Code Results and Applications", *Science and Technology of Nuclear Installations*, **2008**, 7 pages, doi:10.1155/2008/798901 (2008).
4. D. Jacquemain, S. Bourdon, A. de Braemaeker, M. Barrachin, "FPT1 Final Report (Final version)", IPSN/DRS/SEA/PEPF report SEA1/00, IP/00/479 (2000).
5. F. Mascari et al., "First outcomes from the PHEBUS FPT1 uncertainty application done in the EU MUSA project", Proceedings of the 19th International Topical Meeting on Nuclear Reactor Thermal Hydraulics (NURETH-19), Brussels, Belgium (2022).
6. S.S. Wilks, "Determination of Sample Sizes for Setting Tolerance Limits", *Ann. Math. Stat.,* **12**, pp. 91–96 (1941).

Status of the Uncertainty Quantification for Severe Accident sequences of different NPP-designs in the frame of the H-2020 project MUSA

S. Brumm, EC Joint Research Centre (JRC)

MUSA has received funding from the Euratom research and training programme 2014-2018 under grant agreement No 847441.

Related ERMSAR-2022 paper

#278

Status of the Uncertainty Quantification for Severe Accident sequences of different NPP-designs in the frame of the H-2020 project MUSA

S. Brumm, F. Gabrielli, V. Sanchez-Espinoza, P. Groudev, P. Ou, W. Zhang, A. Malkhasyan, R. Bocanegra, L.E. Herranz, M. Berdaï, F. Mascari, G. Agnello, O. Cherednichenko, M. Nudi, A. Hoefer, E.-M. Pauli, S. Beck, L. Tiborcz, O. Coindreau, G. Clark, I. Lamont, X. Zheng, K. Kubo, B. Lee, M. Valincius, W. Giannotti, M. Malicki, S. Gao, Y. Vorobyov, M. Di Giuli, I. Ivanov, M. D'Onorio, F. Giannetti, M. Salay, T. Sevon

Table of Contents

- ‘Management and Uncertainties of Severe Accidents’ (MUSA)
  - Objective
  - Project structure
- Organisation of WP5
  - Objective
  - Schedule
- Preliminary Uncertainty Analysis
  - Set-up
  - Lessons learned
- Conclusions on WP5 status

MUSA Consortium Members





































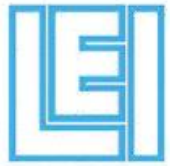









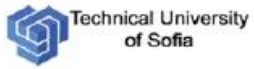











MUSA objectives and scope

- Objectives: To assess the capability of SA codes when modelling accident scenarios
  - Identification and characterization of input & models uncertainties
  - Assessment of available UaSA methodologies
  - Adaptation of available UaSA methodologies
  - Application to postulated NPP scenarios
- Scope:
  - Gen II, Gen III & Gen III+
  - Reactor & SFP
  - Focused on Source Term
  - SA measures (existing & innovative)

Technical Work Packages in MUSA

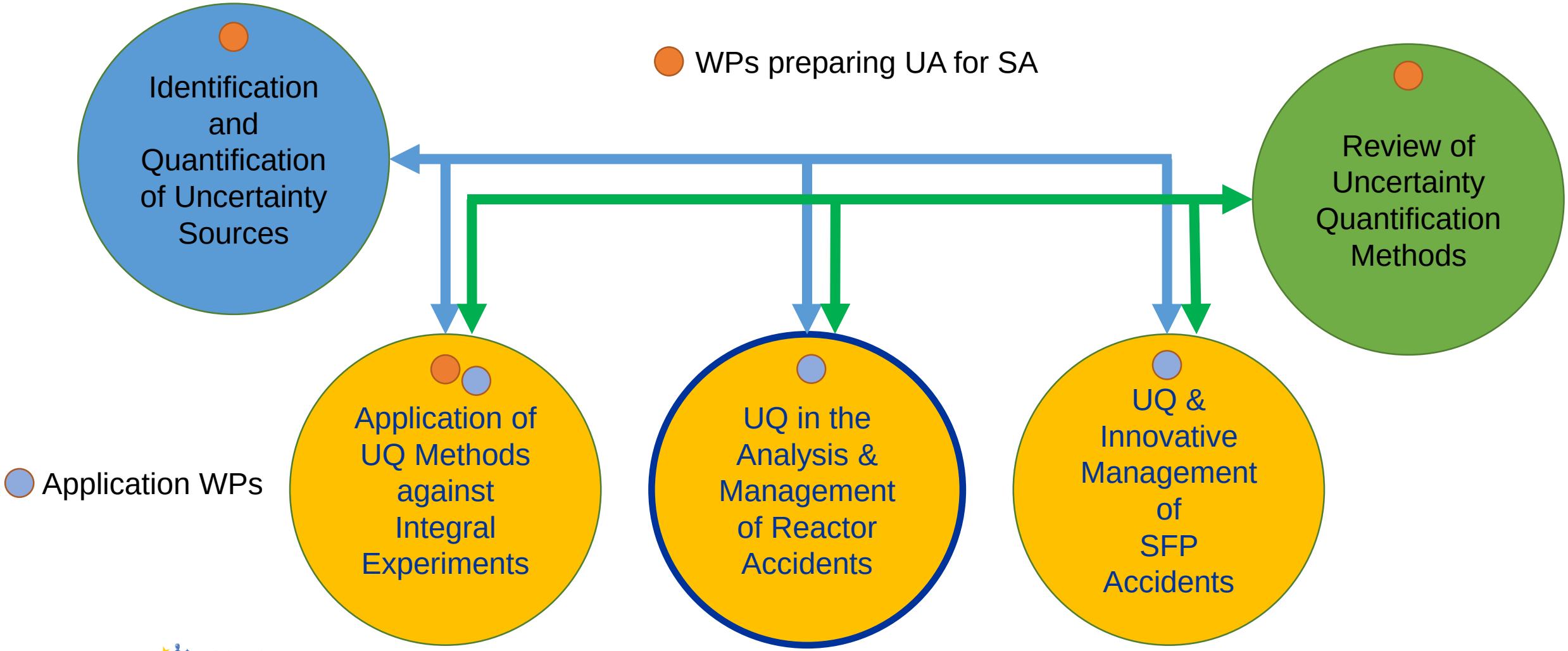

Objectives of reactor applications WP5

- Demonstrate the applicability and the level of readiness of uncertainty assessment

  in the broad range of set-ups presented by different NPPs and different tools investigated by the partners.
- Pursue an agreed best practice
- Provide results for analyses and dissemination
- Identify areas where further research is needed to effectively reduce uncertainties affecting ST estimates.

Organisation of WP5

- 28 partners contributing
- Large no. of partners brings a broad range of reactor types, SA scenarios, SA codes, expert knowledge, experience
- 4 subgroups have been formed for sharing and discussing work and progress: PWR Gen III, VVER, PWR Gen II, BWR
- 3 deliverables to be compiled on (i) results, (ii) best practice, (iii) gaps and recommendations

Schedule for work in WP 5

- Subgroup meetings

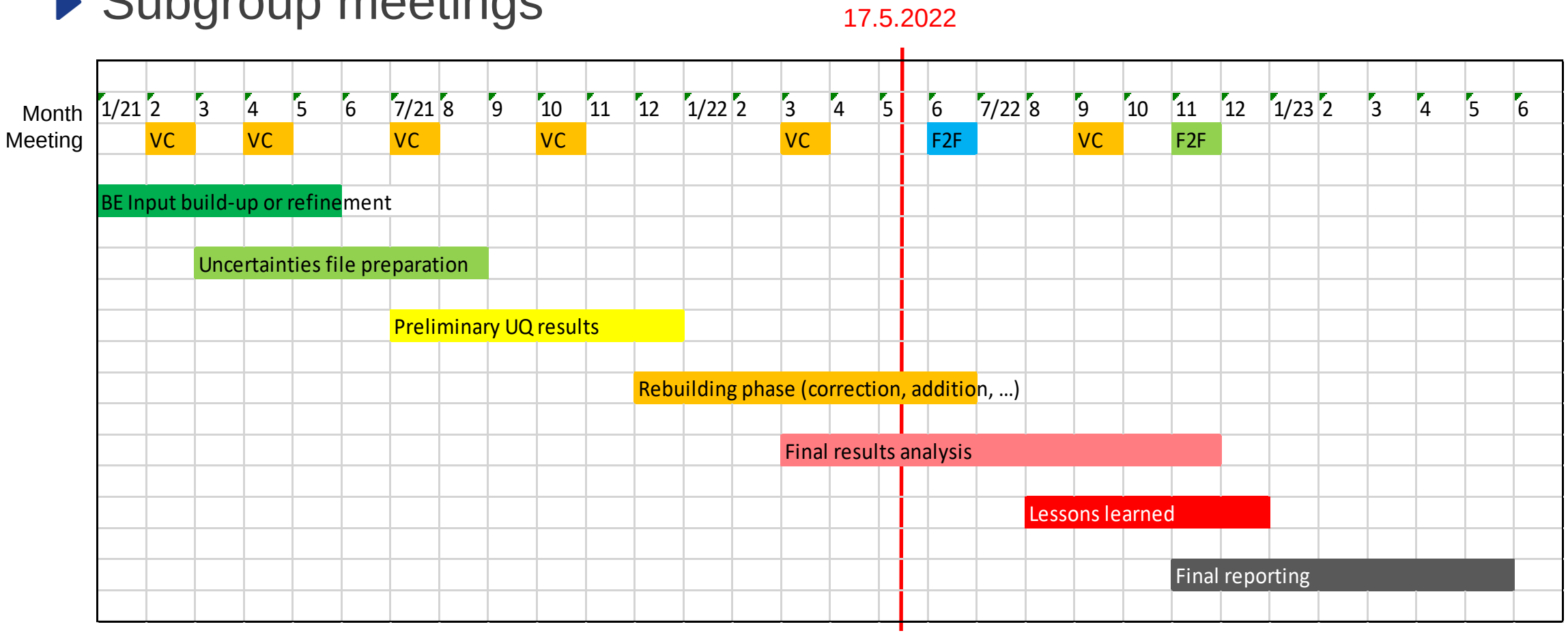

Pre-liminary uncertainty analysis

- Objective: give partners the time and feedback to set up UA
- Try to bridge the large experience gap between partners
- Collect and discuss experiences made
- Address challenges and help partners find solutions
- Develop best practices and share them

Setting up SA Uncertainty Analysis

Select parameters that are expected to be relevant for part of or entire scenario (↔ WP2)

Risk-dominant SA scenario
e.g. SBO, LOCA, SGTR
+ aggravating failures
+ SAM actions

FP: NG, I, CS, aerosols
Other FP, non-FP like H_2
Control volume: environment, containment
(↔ WP2)

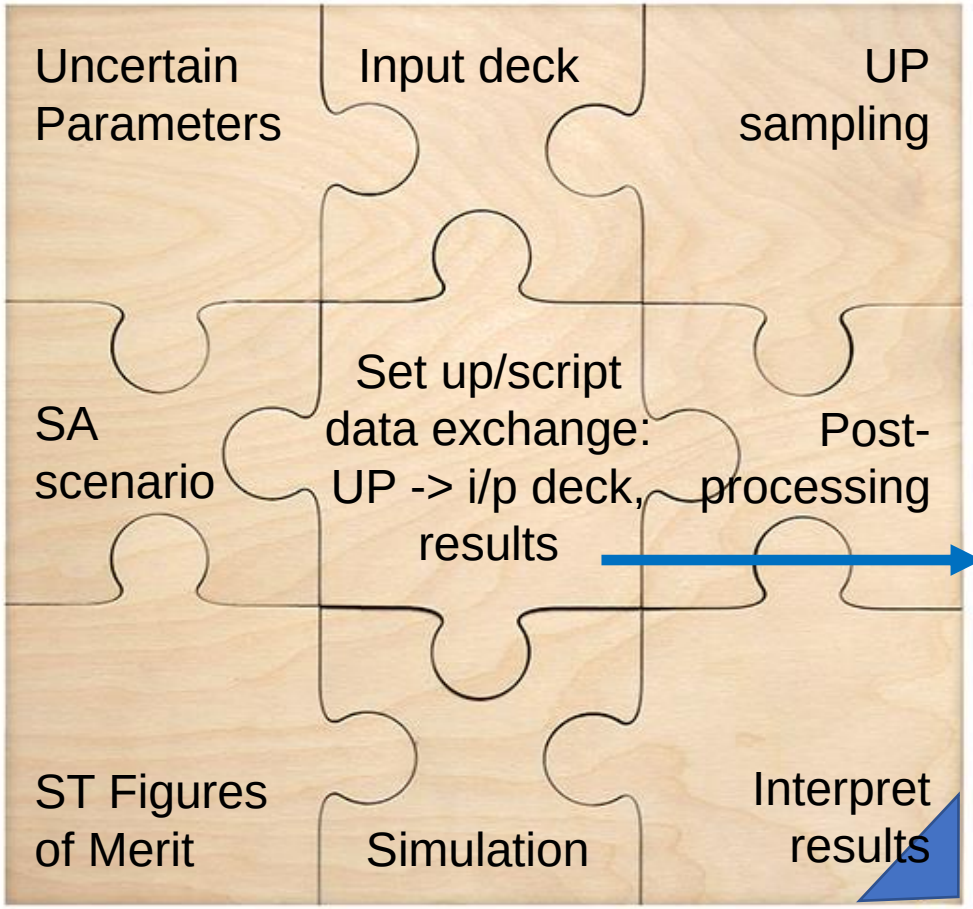

Choose confidence interval (Wilks), sampling method (LHS, MC)
(↔ WP3)

Correlation coefficients; variance explained
(↔ WP3)

Use options provided by the UQ tool or write scripts e.g. in Python
(↔ WP3)

Preliminary analyses look at plausibility of results

Scenario duration; no. of runs; available computer hardware; code thrashing

MUSA

KIT/Framatome

Example of an UA result

ASTEC V2.1

HPC

300 simulations

Simulations stop 6000s after RPV rupture

Python-based FSTC

KONVOI

16 UP (extra slide)

MBLOCA + SBO

Xe release XeaCFr to containment (left) and correlation of XeaCFr with fuel burn-up (KIT/Framatome)

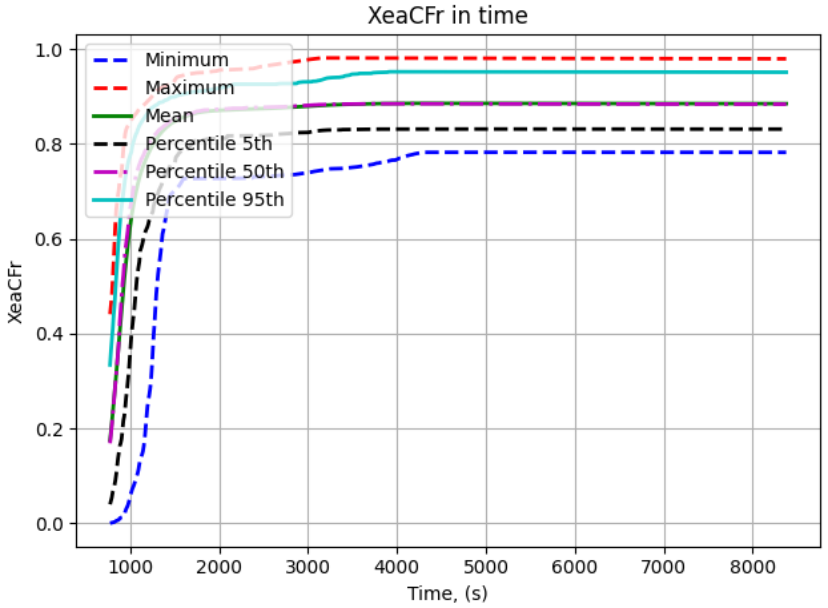

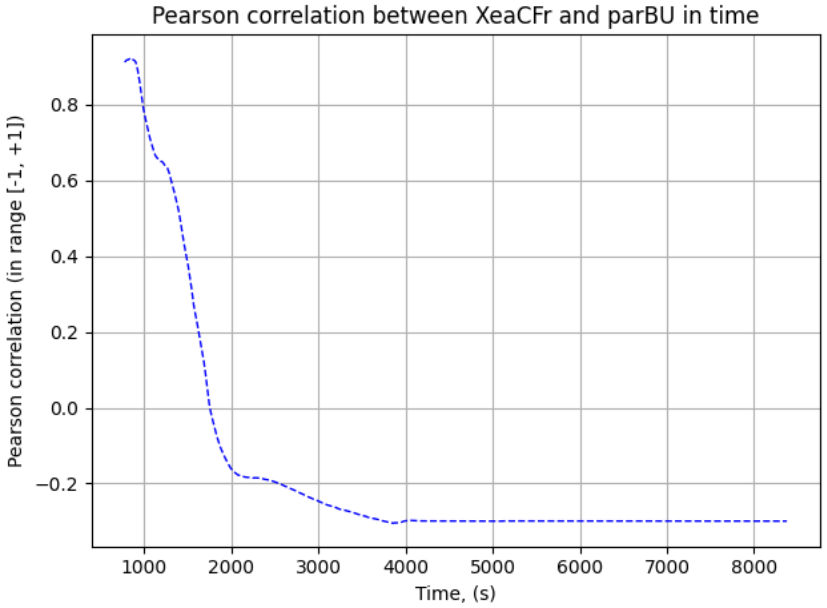

Uncertain parameters in KIT/Framatome example

par#	Modelling Phenomena	ASTEC Keyword - Description	
par1	ELSA Model: FP release from the fuel	FSONV_ST - Correction factor for the ratio S/V of the fuel pellets due to roughness	
par2		FSONV_AX - Correction factor for the ratio S/V of the fuel pellets for the limited steam access	
par5		DGRA - Geometrical diameter of the grain	
par5a		SIGM - Sigma of geometrical diameter distribution	
par14	INTE: Vessel Integrity Criteria	Threshold Temperature of the cladding Dislocation [K]	
par15		Threshold Temperature of the oxide layer Dislocation [K]	
par16		Threshold thickness of the oxide layer [mm]	
par31	Aerosols	lambda - Particle mean thermal conductivity (J/m/K)	
par32		Speacheat - Average specific heat (J/kg K) of the aerosol	
par33		rho - Particle mean density (kg/m3)	
par34	Aerosols Size	R_min - Particle minimum geometrical radius (m)	
par35		R_max - Particle maximum geometrical radius (m)	
par36	Aerosols Shape	coagulat - Shape factor relative to particle coagulation	
par37		v_Stokes- Shape factor relative to Stokes velocity	
par41		Coefficient applied to the containment leakage flow rate	
parBU		Effective full power days	

Preliminary UA: Lessons learned 1

- Computing effort requires economical choices and computing power
  - Minimise complexity of i/p deck, scenario, uncertainty quantification
  - Maximise computing power
  - Fast-running code saves time, at the price of less complex modelling
- SA-codes behave differently during uncertainty propagation
  - most codes exhibit a percentage of thrashed runs (mostly, the minimum time step limit is reached at some point in the transient)
  - for MELCOR it was shown that small perturbations (“noise”) added to the UP set affected the simulation result and cause a small percentage of thrashing
  - accounting for UP correlation minimizes unphysical parameter combinations

Preliminary UA: Lessons learned 2

- Efforts to counter bias imposed by thrashed simulations
  - explore pattern in UP that lead to code thrashing → fix UP space
  - fix thrashed simulations e.g. by smaller time step around code crash
  - add small perturbations to a thrashing UP set and hope that the modified case will not thrash
  - account for UP correlation to minimise unphysical parameter combinations
  - run more simulations than required to account for “lost” cases

Preliminary UA: Lessons learned 3

- Assumptions on SAM actions have a direct impact on the accident scenario and on the Source Term
- Code trashing can be sensitive to the timing of SAM actions (example: re-flooding)
- Not in all cases investigated have SAM actions been the dominant uncertainty for ST FoM
- SAM investigation during the pre-liminary UA phase has been limited and is continued

Conclusions

- MUSA WP5 is coordinating the reactor applications carried out by 28 partners
- 6 series of subgroup meetings have been held until now to support partners develop their application case
- During 2022, partners are running and concluding their final Uncertainty Analysis
- Setting up preliminary UA has been an important effort in itself and has provided lessons needed for progressing to full Uncertainty Analyses

Thank you
for your attention!

OVERVIEW OF IAEA CRP I31033 "ADVANCING THE STATE-OF-PRACTICE IN UNCERTAINTY AND SENSITIVITY METHODOLOGIES FOR SEVERE ACCIDENT ANALYSIS IN WATER COOLED REACTORS"

Fulvio Mascari, Andrea Bersano
FSN-SICNUC
ENEA C.R. Bologna
Via Martiri di Monte Sole 4, 40129, Bologna, Italy
fulvio.mascari@enea.it, andrea.bersano@enea.it

Fabrizio Gabrielli
Karlsruhe Institute of Technology (KIT)
Hermann-von-Helmholtz-Platz 1, 76344 Eggenstein-Leopoldshafen, Germany
fabrizio.gabrielli@kit.edu

David Luxat, Lucas Albright
Sandia National Laboratory
Sandia National Laboratories, 1515 Eubank SE, Albuquerque, New Mexico, 87123, United States
dlluxat@sandia.gov, lialbri@sandia.gov

Tatjana Jevremovic, Haseeb Ur Rehman
IAEA
Vienna International Centre, 1400 Vienna, Austria
T.Jevremovic@iaea.org, H.u.Rehman@iaea.org

Javier Ortiz-Villafuerte
ININ
Carretera México – Toluca s/n, Ocoyoacac, Estado de México, CP 52750, México.
javier.ortiz@inin.gob.mx

Kwang-II Ahn
Korea Atomic Energy Research Institute (KAERI)
989-111, Daedeok-daero, Yuseong-gu, Daejeon 34057, Republic of Korea
kiahn@kaeri.re.kr

Nikolai Ryzhov
IBRAE RAN
52, Bolshaya Tulskaya Street, Moscow, 115191, Russia
rni@ibrae.ac.ru

Juan Matias Garcia
CNEA
Bustillo 9500, Bariloche, Argentina.
garciam@cab.cnea.gov.ar

Sergei M. Petoukhov
CNL
Chalk River, ON K0J 1J0, Canada
sergei.petoukhov@cnl.ca

ABSTRACT

Considering the complexity and mutual different interacting and interrelated phenomena/processes along a Severe Accident (SA) transient progression, a key role is played by the state-of-the-art SA integral codes that can be considered the key tool to design a suitable accident management strategy. However, providing the result of a best estimate calculation alone may be not sufficient and the evaluation of the uncertainty on the results is required. Therefore, considering the need to reduce and/or evaluate some uncertainties still present and the reached level of development and maturity of SA codes, the discussion and application of SA progression analyses with uncertainty estimation is currently a key topic in the Best Estimate Plus Uncertainty (BEPU) framework. For this reason, IAEA launched the Cooperative Research Program (CRP) I31033 aimed at improving the state of practice in SA analyses by examining and characterizing the impact of uncertainty and variability on SA analyses. The CRP has a duration of 5 years and involves 22 organizations from 18 countries. The CRP is structured into four main tasks and the main objectives are to: i) achieve significant improvement in sophistication and quality of SA analyses performed by the participants from Member States with well-developed knowledge, adequate simulation capabilities (both software and hardware) and long years of relevant practice; ii) foster national excellence and international cooperation through an exercise to elevate the ability and sophistication of global SA code users and participation in benchmark calculations; iii) share the research results relevant to evaluation of uncertainties in SA various codes to contribute to capacity building in developing countries. The aim of this paper is to present the CRP objectives, structure and the current status of the activity.

KEYWORDS
Uncertainty analysis, IAEA, CRP, water cooled reactors, Severe accident

1. INTRODUCTION

The uncertainty quantification of a computational tool is a topic of current interest in the adoption of the Best Estimate Plus Uncertainty (BEPU) approach. In fact, despite the maturity level of best estimate codes adopted to perform deterministic safety analysis, sources of uncertainty are still present [1]. In nuclear thermal-hydraulics the development of Uncertainty Analysis (UA) methodologies and their application received a particular attention in the last two decades; some examples of international projects are reported in [2,3]. In the last years there has been a growing interest towards the application of BEPU also in Severe Accident (SA) analysis. This is emphasized by the start of two international projects on this topic: IAEA CRP I31033 [4] and EC MUSA Project [5].

After a technical meeting held in 2017 and a consultancy meeting in 2018, IAEA CRP I31033 entitled “Advancing the State-of-Practice in Uncertainty and Sensitivity Methodologies for Severe Accident Analysis in Water-Cooled Reactors” started in 2019. The CRP is aimed at improving the state of practice in SA analyses by examining and characterizing the impact of uncertainty on SA analyses. The main focus of the CRP is on Water-Cooled Reactors (WCR) and the expected duration is 5 years. 22 Organizations from 18 countries participate to the CRP. The aim of this paper is to present the CRP objectives, outcomes and outputs, to describe the CRP structure and to show the current status of the activity.

2. CRP OBJECTIVES, OUTCOMES AND OUTPUTS

During the 2018 consultancy meeting the CRP objectives, outcomes and outputs have been identified. The CRP objectives are [6]:

- Achieve significant improvement in sophistication and quality of SA analyses performed by the participants from Member States with well-developed knowledge, adequate simulation capabilities (both software and hardware) and long years of relevant practice;
- Foster national excellence and international cooperation through an exercise to elevate the ability and sophistication of global SA code users and participation in benchmark calculations;
- Share the research results relevant to evaluation of uncertainties in SA various codes to contribute to capacity building in developing countries.

Starting from the objectives set, the expected CRP outcomes are:

- Improve capabilities and expertise in Member States to perform state-of-the-art Uncertainty and Sensitivity (U&S) analysis with SA codes;
- More defensible application of SA codes;
- Establish best practices for U&S analyses in the realm of SA analysis;
- Increase depth and breadth of SA and U&S analysis using integral SA codes by Member States;
- Elevate ability and sophistication of global SA code users with improved characterization of the effect of various sources of uncertainty and variability in the predictive output of relevant codes for advanced WCRs;
- Foster a common understanding of U&S methodologies and tools among Member States.

The outputs that are expected to be produced within the CRP are:

- IAEA Nuclear Energy Series (NES) on state of practice with lessons learned on best practices in U&S methodologies for the SA analyses in WCRs;
- IAEA TECDOCs on uncertainty methods and tools for SA codes with relevant benchmark results;
- Relevant training workshops and courses and supporting lecture materials to be published as the IAEA Training Series Documentations;
- Publications in conference proceedings and peer reviewed journals;
- PhD training programme to strengthen promotion of research on SA simulation and modelling in developing Member States through pair building between agreement holders and contract holders institutes.

3. CRP STRUCTURE

To fulfill the identified objectives, outcomes and outputs, the CRP has been structured in 4 tasks described afterwards, and shown in Figure 1, together with the leading organizations and participants:

- Task 1 (lead by KIT): Quench 6 test application uncertainty exercise;
- Task 2 (lead by ENEA): Plant application uncertainty exercise:
    - Task 2.1 (lead by SNL): BWR Mark I;
    - Task 2.2 (lead by ININ): BWR Mark II;
    - Task 2.3 (lead by KAERI): PWR;
    - Task 2.4 (lead by IBRAE): VVER;
    - Task 2.5 (lead by CNEA): SMR;
    - Task 2.6 (lead by CNL): CANDU 6.
- Task 3: Develop reports on uncertainty and sensitivity in SA analysis
    - Task 3.1: TECDOCs;
    - Task 3.2: Nuclear Energy Series;
- Task 4: Development of PhD training programme (lead by SNL).

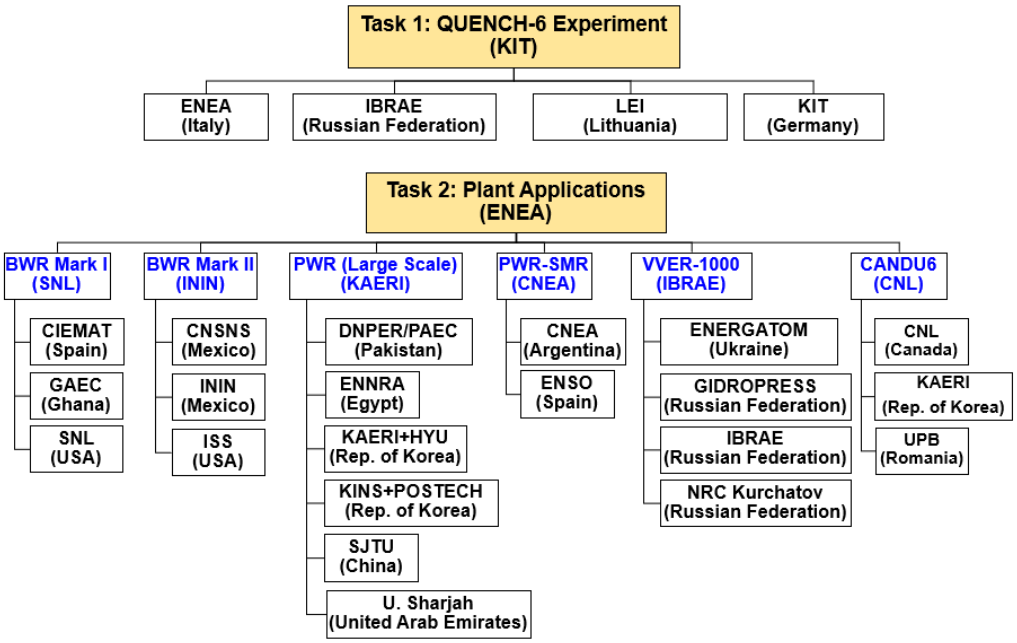

Figure 1. Participants in CRP Task 1 and 2.

ENEA, KIT and SNL serve as a technical chairs supporting IAEA chairs. ENEA coordinates the entire technical activity stimulating discussions, information exchange between the partners, proposing the annual Integrated Research Plan, interacting directly with the IAEA chairs, organizing internal review meetings, etc. ENEA also coordinates the whole plant application exercise. KIT and SNL support ENEA in the CRP coordination and coordinate respectively the Quench exercise and the PhD training program.

3.1. Task 1: QUENCH-6 experiment

The UA of the of the QUENCH-06 experiment [7] by means of SA codes and Uncertainty Tools (UT) has been performed to test relevant calculation platforms in view of their applications to plant analyses. Four institutions participated to the QUENCH-06 test exercise employing the SA/UT codes platforms shown in Table I. The goal of the QUENCH-06 test, performed in 2000 at the Forschungszentrum Karlsruhe (former KIT), was the investigation of the thermal-mechanical behavior of a pre-oxidized LWR rod bundle quenched with water as well as the determination of the resulting hydrogen source term. Because of the amount of available qualified experimental data, the test has been being of special importance in the validation phase of SA codes and it was as OECD International Standard Problem (ISP) no. 45 [7]. The test consists of four main phases: heatup, pre-oxidation, transient, and quenching. The hydrogen accumulated mass and generation rate, temperature of the central rod at 950 mm height, and axial profile of the oxide scale of the heated and corner rods are the Figures Of Merit (FOMs) selected for the exercise. 23 parameters employed by the SA codes for the modeling the test section and the test conduct have been selected and the Probability Distribution Functions (PDFs) of the corresponding uncertainties have been assessed for the UA. The uncertain input parameters refer to: the geometrical modeling of the test section (6 in total); the boundary conditions of the test (8 in total); the heat transfer modeling (5 in total); the clad integrity criteria model (4 in total). The corresponding uncertainties have been evaluated based on QUENCH KIT reports, past studies and literature review. The parameters related to the geometrical modeling are assumed to be affected by 1% uncertainty, uniform PDFs being employed. Concerning the uncertainties of boundary conditions of the test, normal PDFs are employed, the mean being the nominal value from the experimental data with an uncertainty range of 2%. Finally, uniform PDFs are employed to describe the behavior of the uncertainty of the other parameters. The mean of such PDFs are the reference values of the corresponding input parameters employed in each SA code, the uncertainties ranging from 5% to 10%.

Table I. CRP participants, plant and transient analyzed and SA code and UT employed.

Institution	Plant/transient	SA code	UT
Task 1			
ENEA	QUENCH-06 test	ASTEC	RAVEN
IBRAE RAN	QUENCH-06 test	SOCRAT	ELENA
KIT	QUENCH-06 test	ASTEC	URANIE and FSTC
LEI	QUENCH-06 test	RELAP/SCDAPSIM	SUSA
Task 2.1			
CIEMAT	BWR Mark I / SBO (In-vessel)	MELCOR	DAKOTA
SNL	BWR Mark I / SBO (In-vessel)	MELCOR	in-house python-based tools
GAEC	BWR Mark I / SBO (In-vessel)	MELCOR	DAKOTA
Task 2.2			
CNSNS	BWR/5, MARK-II / SBO with RCIC injection; ADS actuation.	MELCOR 2.1	DAKOTA
ININ	BWR/5, MARK-II / Unmitigated high pressure SBO	MAAP 5.03	AZTUSIA via Python scripts
Task 2.3			
DNPER	ACP1000 (K-2) / SBO (In/Ex-vessel)	MELCOR 1.8.6	MATLAB-based DST
ENRRA	KWU-PWR1300 / LBLOCA (In-vessel, early phase)	ATHLET & SCALE 6.3	Python
KAERI	OPR1000 / STSBO (In-/Ex-vessel)	MELCOR 2.2 & MAAP5	DAKOTA & MOSAIQUE
KINS	APR1400 / SBO (In-vessel & Reactor cavity)	MELCOR 2.2 & COOLAP2	DAKOTA
SJTU	CPR600 / SBO (In-/Ex-vessel)	MELCOR 1.8.5	MATLAB
U. SHARJAH	APR1400 / SBO (In-vessel, early phase)	RELAP5/ NESTLE-based 3Keymaster	DAKOTA + ROMUSE
Task 2.4			
NNEGC ENERGOATOM	VVER-1000 South-Ukrainian NPP / SBO	MELCOR 1.8.5	In-house
OKB GIDROPRESS	VVER-1000 / SBO with opening of 3 PORVs	SOCRAT	In-house
IBRAE RAN	VVER-1000 / LB LOCA (cold leg rupture) with unmitigated SBO	SOCRAT	In-house
KURCHATOV INSTITUTE	VVER-1000 / LB LOCA (pressurizer surge line rupture) with SBO	SOCRAT	In-house
Task 2.5			
CNEA	iPWR / SB-LOCA	MELCOR 1.8.6	DAKOTA
ENSO	iPWR / SBO	RELAP/SCDAPSIM MOD3.5	IUA (Integrated Uncertainty Package)
Task 2.6			
CNL	CANDU 6 / SBO	MAAP-CANDU	SUSA
KAERI	CANDU 6 / SBO	CAISER	MOSAIQUE
UPB	CANDU 6 / SBO	RELAP/SCDAPSIM	IUA (Integrated Uncertainty Package)

To evaluate their effect on the FOMs, the uncertainty of the parameters are propagated in the SA/UT codes platforms assessed by ENEA, KIT, IBRAE and LEI [8] by using the Monte Carlo or the Latin Hypercube sampling methods. As example of UA results, the sampling results (ASTEC/RAVEN) and the Pearson correlations (ASTEC/FSTC) for the hydrogen mass production are shown in Figure 2, left and right respectively. Furthermore, the dash lines in Figure 2 indicate the different phases of the test. The results in Figure 2 (left) show a fast increase of the uncertainty band at the onset of the oxidation acceleration. The results of the sensitivity analysis in Figure 2 (right), showing only the parameters with the largest correlation, reveals that the uncertainties on the steam flow rate and the electric power mainly affect the hydrogen mass production during the whole test. In particular, the results show a rather strong direct correlation of the electric power (+0.8 to +0.9) as well as a quite large anti-correlation of the steam flow rate (-0.5 to -0.4) with the FOM. The other parameters are characterized by lower correlations, the maximum ranging from 0.2 to 0.8, in the heat-up phase only. In general, the codes platforms employed by the participants to the exercise provide similar insights. The results of the QUENCH-06 test exercise showed that the SA/UT codes platforms developed by Task 1 participants are well characterized by high performance in terms of computational time and accuracy. Task 1 allowed to provide meaningful insights with respect to the QUENCH-06 experiment and to show the capabilities of SA code/UT platforms to be employed in the preparation phase of SA-related experiments. Furthermore, the outcome of the QUENCH-06 test exercise represents a solid basis of understanding in view of UA for SA analyses in the plant application.

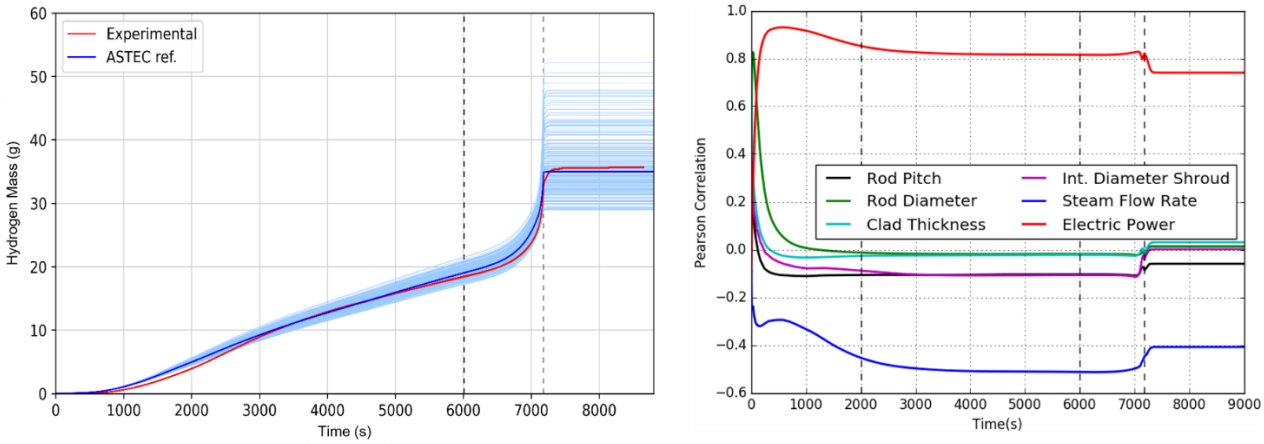

Figure 2. Hydrogen accumulated mass: samples (left) and Pearson correlations (right).

3.2. Task 2: Plant application

3.2.1 BWR Mark I

The BWR Mark I design group is made up by participants from Centro de Investigaciones Energéticas, Medioambientales y Tecnológicas (CIEMAT, Spain), Ghana Atomic Energy Commission (GAEC, Ghana), and Sandia National Laboratories (SNL, USA). Participating institutes have selected a common scenario and are using the MELCOR code for their respective analyses. Additionally, each of the participants has chosen to focus on the in-vessel phase of a Station Blackout (SBO) styled after the events that took place at Fukushima Daiichi Unit 1. Participants from both CIEMAT and GAEC are using the DAKOTA UT to perform their analyses, and the participants from SNL are using in-house Python-based tools. While similarities exist between participant analyses, the BWR Mark I design group participant efforts represent range of SA analysis applications including (1) safety significant accident features such as hydrogen generation or fission product release, (2) SA progression, (3) Severe Accident Management Guidelines (SAMG) development, and (4) SA model development. Each of the BWR Mark I models employed by the participants represents a full scale BWR Mark I nuclear reactor. Modeled systems include a nodalized reactor core with associated support and upper vessel structures, the reactor pressure vessel, primary circuit

piping including main steam lines, recirculation pumps, jet pumps, and feedwater systems. Mark I containment structures are also included in participant models including both the suppression chamber (wetwell) and drywell regions.

The approach to the application of UA methods to SA analysis employed by the participants varies significantly by institution. Deviations arise in part, because of the diverse intended applications. An example of such differences includes input parameter distribution selection. In one approach targeting safety significant plant responses, “best-estimate” distributions have been applied to input parameters with the intent of obtaining a “best-estimate” distribution of the accident response. In a separate approach that targeting model form differences, uniform distributions have been applied to promote coverage of the entire uncertainty space. In addition to these differences the range of methods applied in the BWR Mark I design group has encouraged discourse on the applicability of standard statistical techniques such as Wilk’s formula to SA analysis. These ongoing efforts by the BWR Mark I design group add to the collective value of this CRP. Key contributions by this group include fostering a common understanding of U&S methodologies and their application to SA analysis and improving the sophistication of SA analyses.

3.2.2 BWR Mark II

U&S analysis applied to transient and accident scenarios in BWR is performed consistently in Mexico. The Comisión Nacional de Seguridad Nuclear y Salvaguardias (CNSNS) and the Instituto Nacional de Investigaciones Nucleares (ININ) have carried out collaborative efforts to set the basis of a more comprehensive study of SA scenarios in BWRs, including U&S. In this work, the reactor design under study is a mid-size BWR/5 with MARK-II primary containment, starting from nominal initial operating conditions: 100% power (2317 MWth), 100% core flow, and rated pressure under nominal operating conditions. A SBO is the base case scenario for both ININ and CNSNS, but there is a notable difference in the simulation of the accident evolution. CNSNS allows depressurization of the reactor pressure vessel and actuation of the RCIC, while ININ simulated an unmitigated SBO, that is, the scenario is at high pressure and without any emergency coolant injection. The scope of the analysis is also different, CNSNS´s main FOM is the time of primary containment failure, so that SA ex-vessel phenomena need to be addressed, while ININ´s study reaches only to the time of the reactor pressure vessel breach time, thus its FOMs are all related to SA in-vessel phenomena. The U&S analysis results are expected to support the technical basis on regulation issues and the review of SAMGs, since modelling SA phenomena is still an ongoing research and development process, and there exists areas with significant uncertainty. A summary of the U&S analysis application is shown in Table I.

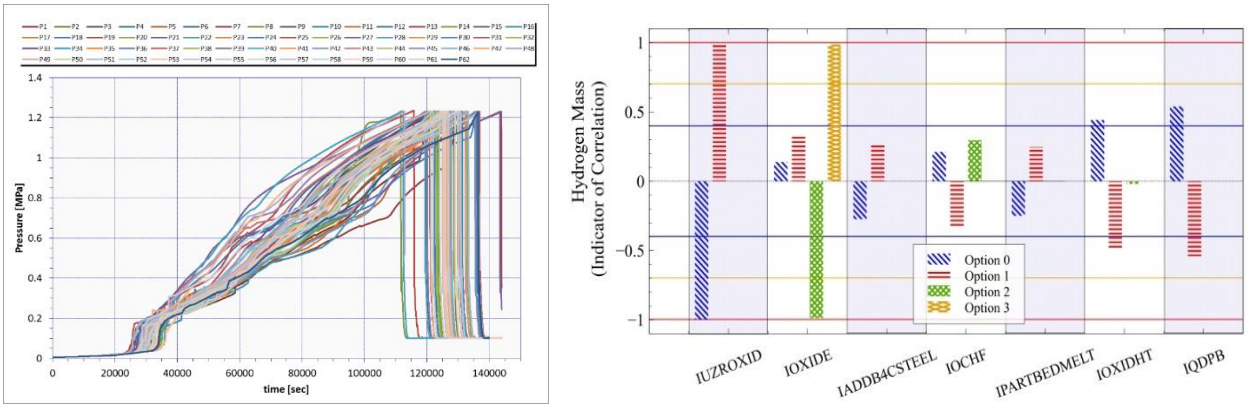

Figure 3. CNSNS´s uncertainty band for the FOM Primary Containment Failure Time due to overpressure (left) ININ´s MCF Indicator of Correlation results for qualitative uncertain input variables related to hydrogen mass generation in core, for each of their available option (right).

As example of results obtained so far, Figure 3 (left) shows the uncertainty band obtained by CNSNS for the FOM *primary containment failure time*, and Figure 3 (right) shows the sensitivity analysis results of the FOM *hydrogen mass generated in core*, by applying the Monte Carlo Filtering (MCF) Indicator of Correlation to the 7 proposed qualitative uncertain input variables, that is, the different options that MAAP5 offers to choose from to the analyst. Future work includes a deeper statistical analysis of the FOMs, and studying possible correlations between the uncertain input variables. The present work has shown that the application of an integral U&S analysis to SA studies depends significantly on the accident simulation tool, because some codes offer many input variables to choose different physical models that impact simulation results, while others require more detailed nodalization.

3.2.3 PWR

In relation to the CRP Task 2.3 (PWR), six institutions in five Member States participated in the project, as shown in Figure 1, and the summary of the U&S analyses proposed by each institution is shown in Table I. The PWR task group utilized five types of reactors, four SA simulation codes, especially with three different versions in the case of MELCOR, three reference scenarios (SBO, LBLOCA, and STSBO), and two accident phases (in-vessel only and both in-/ex-vessel).

Key input parameters affecting the defined FOMs were identified after the screening-out process per each participant: (a) 30 parameters in DNPER, (b) 1 parameter (reactivities at different coolant densities subject to 14 multivariate Gaussian PDFs) in ENRRA, (c) 26 parameters for MELCOR and 29 parameters for MAAP5 in KAERI, (d) 13 parameters in KINS, (e) 18 parameters in SJTU, and (f) 44 groups SCALE covariance library for the cross-sections affecting on the fuel early phase fuel temperature in U. of Sharjah. The corresponding PDFs and ranges were assigned based on the relevant code manuals, literature survey, engineering judgment, and parametric sensitivity analysis wherever necessary. Relating to the regression and correlation analysis between uncertain inputs and relevant FOMs, each institution selectively employed (a) three correlation-based approaches (Pearson, Spearman, and Kendall correlation coefficients), three regression-based coefficients (partial correlation coefficient, partial rank correlation coefficient and standardized rank correlation coefficient), and deterministic method based on a generalized perturbation theory (ENNRA). The foregoing situation indicates that the conventional benchmark study, which has been focused on a single target plant and reference scenario, but different predictions from the different SA tools, was not feasible in this task group. Accordingly, all member institutions employed their own U&S analysis framework for this CRP task.

The planed tasks proposed by each participant (nodalization of plant model, simulation of the reference case, calculation of the U&S through a coupling the SA code with of the corresponding UT, and estimation of FOMs' range) were almost completed and, as a result, a general conclusion was made for the corresponding task.

As implemented by participants, who employed the Monte Carlo sampling approach for U&S analyses, a deeper understanding of several aspects is still required in order to assess the applicability of the utilized approaches in the context of SA analyses and to advance the current framework for U&S analyses, e.g., (a) the impact of the relatively high failure rate of SA code, (b) the impact of different sample sizes on each relevant FOM in terms of how many samples should be performed to ensure sufficient confidence in the analysis results, (c) the impact of different PDFs for given input parameters on each relevant FOM, (d) the impact of pseudo-correlations between model input parameters, which would be generated in the sampling process, (e) the possibility of outliers in the estimated FOMs and, if exist, their underlying causes, and (f) the limitation of typical correlation and/or regression-based sensitivity/importance measures, which have been widely utilized in the context of SA analysis, and applicability of the other non-linear regression approaches as the possible alternative.

3.2.4 VVER

The VVER group consists of four members: NNEGC "ENERGOATOM" (Ukraine), OKB GIDROPRESS, IBRAE RAN, and NRC "KURCHATOV INSTITUTE" (Russian Federation). To demonstrate the approaches used to analyze the uncertainties of SA calculations, the group members have considered an in-vessel stage of SA scenarios at a VVER-1000 reactor [9]. ENERGOATOM performs UA to determine the code parameters that affect at the most the FOM and to improve the usage of the MELCOR 1.8.5 code [6]. The activity of Russian organizations is directed to follow the requirements of Federal Rules and Regulations in the Area of Atomic Energy ("General Provisions for Nuclear Power Plant Safety Assurance", NP-001-15). In paragraph 1.2.9 of NP-001-15, it is stated that *safety analyses shall be accompanied with assessment of errors and uncertainties for the obtained results*. Russian members use the SA code SOCRAT [6]. Members paid attention to the justification of PDFs of uncertain input parameters giving preference to literary sources rather than expert judgment. For demonstration of the result of UA methodology implementation, the members have considered different accident scenarios.

NNEGC "ENERGOATOM" simulates a SBO at the first unit of South-Ukrainian NPP. Monte Carlo method with Latin Hypercube Sampling is used to propagate input uncertainties of the parameters that can affect the hydrogen release. A list of input parameters for UA consists of 11 parameters related to the MELCOR code models. ENERGOATOM uses Pearson's correlation and Spearman's rank correlation to estimate a relation between uncertain inputs and FOMs. Sensitivity analysis showed that six input parameters are the most important for the uncertainty of a total hydrogen mass generated at in-vessel stage.

OKB GIDROPRESS investigates a SBO scenario at VVER-1000 with account for accident management actions consisting in the opening of 3 PORVs 2 h since the initiating event. The mass of hydrogen released into containment together with some reactor and containment parameters have been addressed in UA using SRS, with the aim of comparing the results with design limits. SRS was used to propagate input uncertainties. A full list of uncertain input parameters consists of 42 items. Parameters of PDFs are based on VVER design documentation. Sensitivity analysis using Pearson's, Spearman's, and Kendall's rank correlation coefficients have shown that the following input parameters have the greatest impact on the predicted FOMs: decay heat power, coolant temperature in ECCS HA, BRU-A opening delay, setpoint pressure of BRU-A opening, setpoint pressure of pressurizer PORV opening.

IBRAE RAN has opted for LBLOCA (cold leg rupture) that happens simultaneously with unmitigated SBO. The proposed methodology for UA of SA calculations is based on the validation approach used for the SOCRAT code. The SOCRAT code is validated according to the ASME V&V20 standard [10]. The main idea, considered to be productive for deterministic calculations of SA using both a realistic approach and a realistic code. is the assumption of the existence of the "true" but unknown value of the measured parameter. The result of the UA of SA is the interval for the "true" value of the parameter under consideration, that takes validation results into account. IBRAE considers one FOM – a mass of hydrogen released into a break. A list of uncertain input parameters consists of eight items. The Monte Carlo method with SRS was used to propagate input uncertainties to estimate the best estimate value of the FOM and the associated uncertainty. Preliminary results demonstrated that the mass of hydrogen has a negative correlation with decay heat power using Spearman's rank correlation coefficient.

NRC "KURCHATOV INSTITUTE" investigates LBLOCA (rupture of the pressurizer surge line) with simultaneous SBO. A list of FOMs includes a mass of hydrogen released into the break and 15 other reactor and containment output parameters that include the timings of important events. The list of input parameters for UA includes 50 parameters related to plant normal operation, geometric characteristics of reactor equipment, and some model parameters. The Monte Carlo method with SRS was used to propagate input uncertainties. Kendall's rank correlation coefficients have shown that the mass of hydrogen inversely correlates only with the decay heat power.

3.2.5 SMR

The Small Modular Reactor (SMR) group comprises two organizations from two different countries: CNEA and ENSO (Figure 1). The reference plant for the analyses is in both cases an integral PWR SMR (CAREM-like), where all the major components of a typical primary system are located inside the reactor pressure vessel, the power is removed by natural circulation and passive safety systems are implemented by design. CRP analyses are expected to contribute providing a knowledge basis associated to SAMG development and possible implementation, as well as to provide insights on best practices related to U&S calculations with SA codes, which in turn leads to a significant improvement in the quality of the SA analysis. A brief description of the U&S analyses proposed by each participant organization is presented in Table I. Key parameters affecting the defined FOMs were identified after a careful selection process. A total number of 11 parameters were considered by CNEA which were grouped into the categories of accident management, physical models, integrity criteria and relocation models. A group of 20 parameters was selected by ENSO, including boundary and initial conditions, material properties and code correlations. It is important to remark that extensive experience on SA modelling and analysis together with engineering judgment are required aspects for the identification and selection of relevant parameters and for the definition of the corresponding PDF and ranges. It is suggested to complement this with an exhaustive literature review.

Plant model nodalizations were developed and the reference case simulations were performed. After preparation of the uncertainty model with the corresponding coupling to the SA plant code, U&S calculations were conducted. As a result, FOM's range were estimated using Wilks formula with a 95% probability level and 95% confidence level, and relevant correlation coefficients were calculated. CNEA has also performed a parametric sensitivity analysis using the most relevant parameters found. As a general conclusion the U&S methodology proposed has been successfully applied using different SA and UT by both organizations. FOM's range were estimated and the most impacting parameters were identified. Nevertheless, deeper understanding of several aspects is still required to assess the applicability of the methodology and to evaluate the implementation of possible improvements. Among this, the impact of the relatively high failure rate of SA runs, the impact of different assumed parameters PDF, the applicability and interpretation of typical correlation coefficients in the context of SA analysis and the use of possible alternative UA methodologies have to be investigated in more detailed.

3.2.6 CANDU 6

The SA progression for a generic CANDU 6 plant undergoing a postulated SBO SA scenario as well as a plant design are briefly described in reference [11]. This type of CANDU plant with the associated design input data as well as accident scenario is nearly identical in analyses performed by all Task 2.6 participants. The output computed by SA integrated codes includes important FOM evaluated in this analysis, such as: (i) hydrogen releases (in-vessel and ex-vessel), (ii) fission product releases (in-vessel, ex-vessel, and to environment), and (iii) outputs that detail the accident progression and consequences such as significant event timings. As shown in Figure 1, there are 3 participants in the CANDU-related Task 2.6: CNL (Canada) [12], KAERI (South Korea), and UPB (Romania). The summary of the analyses is reported in Table I. The uncertain input parameters (the actual number of these parameters is different for every partner, and varies from 12 to 30) are selected based on each partner's SA phenomenological models, and they are not identical for each partner. The uncertain input parameters cover (but not limited to) the following SA phenomena: Core heat-up, Debris formation, Core collapse, Fission Product releases.

CANDU 6 SBO SA scenario was simulated by all three Task 2.6 partners, and it was concluded that the simulation results such as major event timings are relatively close among the partners. A preliminary selection and set-up of PDFs for the uncertain input parameters was performed, and the input decks for each integral code were generated, simulations were executed, and results are being analyzed now. It is planned to refine the uncertain input parameter PDFs, and to perform a final set of simulations. Based on this updated

simulation results, U&S analyses will be conducted by each Task 2.6 partner for the identified FOMs, and analyses outcomes will be evaluated/compared among all participants. In the development of Task 2.6 the following difficulties have been encountered:

- It is very common to have multiple simulation crashes, when a new set of input data (including new values of uncertain input parameters), is implemented. It is required for the analyst to investigate the crashes, update the input data, and to re-submit for execution the new simulations;
- It often takes significant computational resources to execute the simulations as some SA integral codes require ~ 24 hours or more to complete one run;
- It is not a trivial task to correctly set up the PDFs for the uncertain input parameters due to the complexity of physical/chemical phenomena involved. However, assessments show that the PDF are very important for the final analysis outcome(s).

3.3. Task 3: Develop reports on uncertainty and sensitivity in severe accident analysis

Task 3 is related to the development of reports on U&S analysis in SA. Currently 5 TECDOCs are planned describing the applications carried out in the CRP grouped by technology (QUENCH, BWR, PWR+SMR, VVER, CANDU 6). A Nuclear Energy Series document will then collect the main findings, lessons learned and best practices identified in the CRP framework.

3.4. Task 4: Development of PhD training programme

From its start, this CRP has emphasized development of the next generation of SA experts. In its original conception, this CRP included the PhD training programme, which envisioned pairings between agreement holders and contract holders institutes, which would strengthen promotion of research on SA simulation and modelling in developing Member States. Unfortunately, due to the impact of the COVID-19 pandemic on international research activities and exchanges, the PhD training programme required adaptation. Thus, to meet the originally outlined goals of the PhD training programme, the Virtual Graduate Student Experience was developed. The Virtual Graduate Student Experience is comprised of three parts: (I) presentation on graduate (PhD or MS) research and how it relates to the CRP objectives and scopes; (II) virtual exchange between student pairs to share knowledge and experiences; (III) preparation and submission of a joint report. Part I presents an opportunity for students to present their graduate student research within the IAEA CRP I31033 framework. Student presentations are given during an annual "Consultancy Meeting on Graduate Student Programme within the IAEA CRP I31033," or "Virtual Graduate Student Conference". Part II affords students the opportunity to participate in a "Virtual Exchange". The virtual exchange is an opportunity for students to spend a virtual day with a partner student to discuss their respective research and also to work on a common topic. During the exchange, students are asked to discuss research presentations given at the consultancy meeting on graduate student programme, and to work on a common topic, identified by the students during their exchange. A joint report summarizing the virtual exchange, written by both students, will be submitted to the IAEA (Part III). Each student prepares a summary of their graduate student research which they presented at the consultancy meeting. Student pairs are invited to highlight how their research overlaps, differs, and could be improved considering the concepts/approaches of their partner's research. Student efforts have demonstrated the value of this CRP from fostering the next generation of professionals to providing students the opportunity to interact and collaborate with topical experts. To date this effort has included two groups of graduate students that have presented at consultancy meetings. Participants represent a diverse set of backgrounds, research topics, and nations; thus far representing six separate institutions from six different Member States.

4. CONCLUSIONS

In the framework of IAEA CRP I31033, 22 organizations from 18 countries are applying U&S analysis methodologies to SA analysis. QUENCH 06 experiment and six plant applications are being carried out to

improve the capabilities and expertise in Member States to perform state-of-the-art U&S analysis with SA codes. The present paper summarized the CRP objectives, outcomes and outputs, described the CRP structure and showed the current status of the activity. The complete description of the CRP results will be collected in a series of TECDOCs for the various technologies and in a Nuclear Energy Series document. A series of consultancy meetings (topical meetings) have been already also organized and are planned on specific topics to disseminate the CRP results and to share lessons learned and best practices.

NOMENCLATURE

BEPU: Best-Estimate Plus Uncertainty; CRP: Coordinated Research Project; FOM: Figure Of Merit; IAEA: International Atomic Energy Agency; LBLOCA: Large Break Loss Of Coolant Accident; PDF: Probability Distribution Function; PORV: Pilot Operated Relief Valve; SA: Severe Accident; SAMG: Severe Accident Management Guidelines; SBO: Station Blackout; SRS: Simple Random Sampling; STSBO: Short-term Station Blackout; UA: Uncertainty Analysis; U&S: Uncertainty and Sensitivity; UT: Uncertainty Tool; WCR: Water-Cooled Reactors.

ACKNOWLEDGMENTS

This research is supported by the International Atomic Energy Agency under the Coordinated Research Project award I31033 on Advancing the State-of-Practice in Uncertainty and Sensitivity Methodologies for Severe Accident Analysis in Water Cooled Reactors, launched in 2019.

REFERENCES

1. IAEA, “Best Estimate Safety Analysis for Nuclear Power Plants: Uncertainty Evaluation,” *Safety Reports Series No. 52* (2008).
2. OECD/NEA/CSNI, “BEMUSE Phase IV Report: Simulation of a LB-LOCA in ZION Nuclear Power Plant,” NEA/CSNI/R(2008)6/VOL1 (2008).
3. OECD/NEA/CSNI, “Post-BEMUSE Reflood Model Input Uncertainty Methods (PREMIUM) Benchmark,” NEA/CSNI/R(2016)18 (2017).
4. IAEA, “CRP I31033,” https://www.iaea.org/projects/crp/i31033 (2021).
5. L.E. Herranz, et al., “The EC MUSA Project on Management and Uncertainty of Severe Accidents: Main Pillars and Status,” *Energies*, **14**(15), 4473 (2021).
6. IAEA, TECDOC-1872, “Status and Evaluation of Severe Accident Simulation Codes for Water Cooled Reactors,” (2019)
7. L. Sepold, et al., “Experimental and Computational Results of the QUENCH-06 Test (OECD ISP-45),” Report FZKA-6664, Forschungszentrum Karlsruhe (2004)
8. T. Kaliatka, et al., "Uncertainty Quantification of QUENCH-6 Experiment using Severe Accident Code RELAP/SCDAPSIM and Statistical Tool SUSA,” *Proc. of NURETH-19*, Brussels, Belgium, March 6 - 11, 2022.
9. B. Ivanov, et al., “VVER-1000 Coolant Transient Benchmark. PHASE 1 (V1000CT-1) Vol. I: Main Coolant Pump (MCP) switching On – Final Specifications,” NEA/NSC/DOC(2002)6, 2002.
10. Standard for verification and validation in computational fluid dynamics and heat transfer. ASME V&V20–2009. New York: ASME, (2009).
11. IAEA, TECDOC-1727, "Benchmarking Severe Accident Computer Codes for Heavy Water Reactor Applications", (2013).
12. S.M. Petoukhov, et al., “An Assessment of Uncertainties and Sensitivities in Severe Accident Progression Simulation for a Generic CANDU 6 Plant”, *40th Annual Conference of the Canadian Nuclear Society and 45th Annual CNS/CNA Student Conference*, Canada, June 6-9, 2021.

IAEA
International Atomic Energy Agency
Atoms for Peace and Development

OVERVIEW OF THE CURRENT STATUS OF THE CRP: ADVANCING THE STATE-OF-PRACTICE IN UNCERTAINTY AND SENSITIVITY METHODOLOGIES FOR SEVERE ACCIDENT ANALYSIS IN WATER COOLED REACTORS (I31033)

Haseeb ur Rehman and Tatjana Jevremovic

Nuclear Power Technology Development Section (NPTDS), IAEA

Presented at

The 10th European Review Meeting on Severe Accident Research (ERMSAR), May 16–19 2022

IAEA
International Atomic Energy Agency
Atoms for Peace and Development

OUTLINE

1. INTRODUCTION
2. TASK 1 – QUENCH-06 Experiment
3. PLANT APPLICATION RESULTS TEMPLATE
4. DEVELOP REPORTS ON U&S IN SA ANALYSIS
5. STUDENT PROGRAM
6. INTERNAL REVIEW MEETINGS AND TOPICAL MEETINGS
7. CONCLUSIONS

1. INTRODUCTION: IAEA CRP INITIATION AND PROPOSAL

- *CRP INITIATION: 2017 IAEA Technical Meeting :*
  - *Common observations from 2017 Technical Meeting led to the CRP rationale*
    - *Severe accident codes embody complex multi discipline physics spanning wide range of phenomena often outside user range of experience and competency;*
    - *Code users are often unsure about correctness or accuracy of their plant accident analyses;*
    - *Code users are often not aware of importance or impact of uncertainty and variability in predicted code results.*
  - *Therefore:*
    - *This CRP is aimed at improving the state of practice in severe accident analyses by examining and characterizing the impact of uncertainty and variability on severe accident analyses*
  - *Detail information about the TM "Technical Meeting on the Status and Evaluation of Severe Accident Simulation Codes for Water Cooled Reactors IAEA Headquarters Vienna, Austria, 9–12 October 2017" can be found in IAEA TECDOC 1872: Status and Evaluation of Severe Accident Simulation Codes for Water Cooled Reactors: https://www-pub.iaea.org/MTCD/Publications/PDF/TE-1872web.pdf*

- *CRP PROPOSAL: 2018 Consultancy Meeting*
  - *Formulate the research scope and rationale;*
  - *Define objective, output and outcomes and logical framework;*
  - *Identified potential participating organizations.*

1. INTRODUCTION: CRP MAIN INFORMATION

❑**IAEA CRP TITLED:**

- Advancing the State-of-Practice in Uncertainty and Sensitivity Methodologies for Severe Accident Analysis in Water Cooled Reactors

❑**Website:**

- https://www.iaea.org/newscenter/news/new-crp-advancing-the-state-of-practice-in-uncertainty-and-sensitivity-methodologies-for-severe-accident-analysis-in-water-cooled-reactors-i31033

❑ **Duration:**

- 5 years

❑ **CRP participants:**

- *Argentina : National Atomic Energy Commission (CNEA);*
- *Canada: Canadian Nuclear Laboratory (CNL);*
- *China : Shangai Jiao Tong University (SJTU);*
- *Egypt: Egyptian Nuclear and Radiological Regulatory Authority (ENRRA);*
- *Germany: Karlsuhe Institute of Technology (KIT); Institute for Neutron Physics and Reactor Technology (IKIT- NR);*
- *Ghana: Ghana Atomic Energy Commission (GAEC);*
- *Italy: Italian Agency for New Technology, Energy and Sustainable Economic Development (ENEA);*
- *Lithuania: Lithuanian Energy Institute (LEI);*
- *Malaysia:* Malaysian Nuclear Agency (*MNA- joined after the start of the CRP);*
- *Mexico: National Institute for Nuclear Studies (Instituto Nacional de Investigaciones Nucleares) (*ININ);
- *Pakistan: Pakistan Atomic Energy Commission (PAEC);*
- *Republic of Korea: Korea Atomic Energy Research Institute (KAERI),*
- *Romania: Politechnica University of Bucharest;*
- *Russian Federation: Nuclear Safety Institute of the Russian Academy of Science (IBRAE), OKB "Gidropress", NRC "Kurchatov Institute";*
- *Spain:* Centro de Investigaciones Energéticas, Medioambientales y Tecnológicas (*CIEMAT),* Energy Software SLP (*ENSO) (joined after the start of the CRP);*
- *Ukraine: Scientific and technical Center of SE NNEGC Energoatom;*
- *United Arab Emirates: University of Sharjah (join after the start of the CRP);*
- *USA: Sandia National Laboratory (SNL) ,* Innovative Systems Software (ISS, *joined after the start of the CRP).*

1. INTRODUCTION: CRP OBJECTIVES AND OUTPUTS

- **CRP Objectives**
  - Achieve significant improvement in sophistication and quality of severe accident analyses performed by the participants from Member States with well developed knowledge, adequate simulation capabilities (both software and hardware) and long years of relevant practice;
  - Foster national excellence and international cooperation through an exercise to elevate the ability and sophistication of global severe accident code users and participation in benchmark calculations;
  - Share the research results relevant to evaluation of uncertainties in severe accident various codes to contribute to capacity building in developing countries.

- **CRP Outputs**
  - IAEA NES on state of practice with lessons learned on best practices in uncertainty and sensitivity methodologies for the severe accidents analyses in WCRs;
  - IAEA TECDOCs on uncertainty methods and tools for severe accidents codes with relevant benchmark results
  - Relevant training workshops and courses and supporting lecture materials to be published as the IAEA Training Series Documentations
  - Publications in conference proceedings and peer reviewed journals
  - PhD training programme to strengthen promotion of research on severe accidents simulation and modelling in developing Member States through pair building between agreement holders and contract holders institutes.

1. INTRODUCTION: CRP OUTCOMES

❑ CRP Outcomes:

- Improve capabilities and expertise in Member States to perform state-of-the-art uncertainty and sensitivity analysis with severe accident codes;
- More defensible application of severe accident codes;
- Establish best practise for uncertainty and sensitivity analyses in the realm of severe accident analysis;
- Increase depth and breadth of severe accident analysis and uncertainty/sensitivity analysis using integral severe accident codes by Member States;
- Elevate ability and sophistication of global severe accident code users with improved characterization of the effect of various sources of uncertainty and variability in the predictive output of relevant codes for advanced WCRs;
- Foster a common understanding of uncertainty and sensitivity methodologies and tools among Member States.

1. INTRODUCTION: CRP CHAIRS

- **IAEA CRP Chairs (**NENP/NPTDS)
  - Tatjana Jevremovic
  - Haseeb ur Rehman

- **CRP Chairs**
  - Considering that the IAEA CRP is co-ordinated with another parallel international activity, MUSA, to avoid, as much as possible, duplications and provide synergies betwen the two activities, the IAEA Chairs asked. along the 1° RCM, that the IAEA-CRP chairs should be also selected from Partner involved in MUSA.

  - F. Gabrielli and F. Mascari agree to serve as a chair of the CRP;

  - CRP Chair group:
    - Gabrielli Fabrizio (KIT);
    - Mascari Fulvio (ENEA);
    - Luxat David (SNL).

1. Introduction: CRP Tasks

❑ **TASK PLAN OF ENTIRE CRP (Participants are involved in task 1 or 2 but generally not both):**

- TASK 1: Quench 6 test application uncertainty exercise; - LEAD-KIT

- TASK 2: Plant application uncertainty exercise: - LEAD-ENEA
  - BWR Mark I; - LEAD SNL
  - BWR Mark II; - LEAD ININ
  - PWR; - LEAD KAERI
  - VVER; - LEAD IBRAE
  - SMR; - LEAD CNEA
  - CANDU - LEAD CNL

- TASK 3: Develop reports on uncertainty and sensitivity in severe accident analysis
  - TASK 3.1:

  TECDOC: Application of Uncertainty and Sensitivity Methodologies to Severe Accident Analysis in Water Cooled Reactors — Final Report of a Coordinated Research Project
  - TASK 3.2:

  NES: Best Practice for Uncertainty and Sensitivity Assessment in the Realm of Severe Accident Analysis

- TASK 4: Development of PhD training programme: It will be developed and implemented for students from countries embarking on nuclear power, in which PhD candidates will be supported by organizations in experienced Member States.

1. Introduction: CRP participants

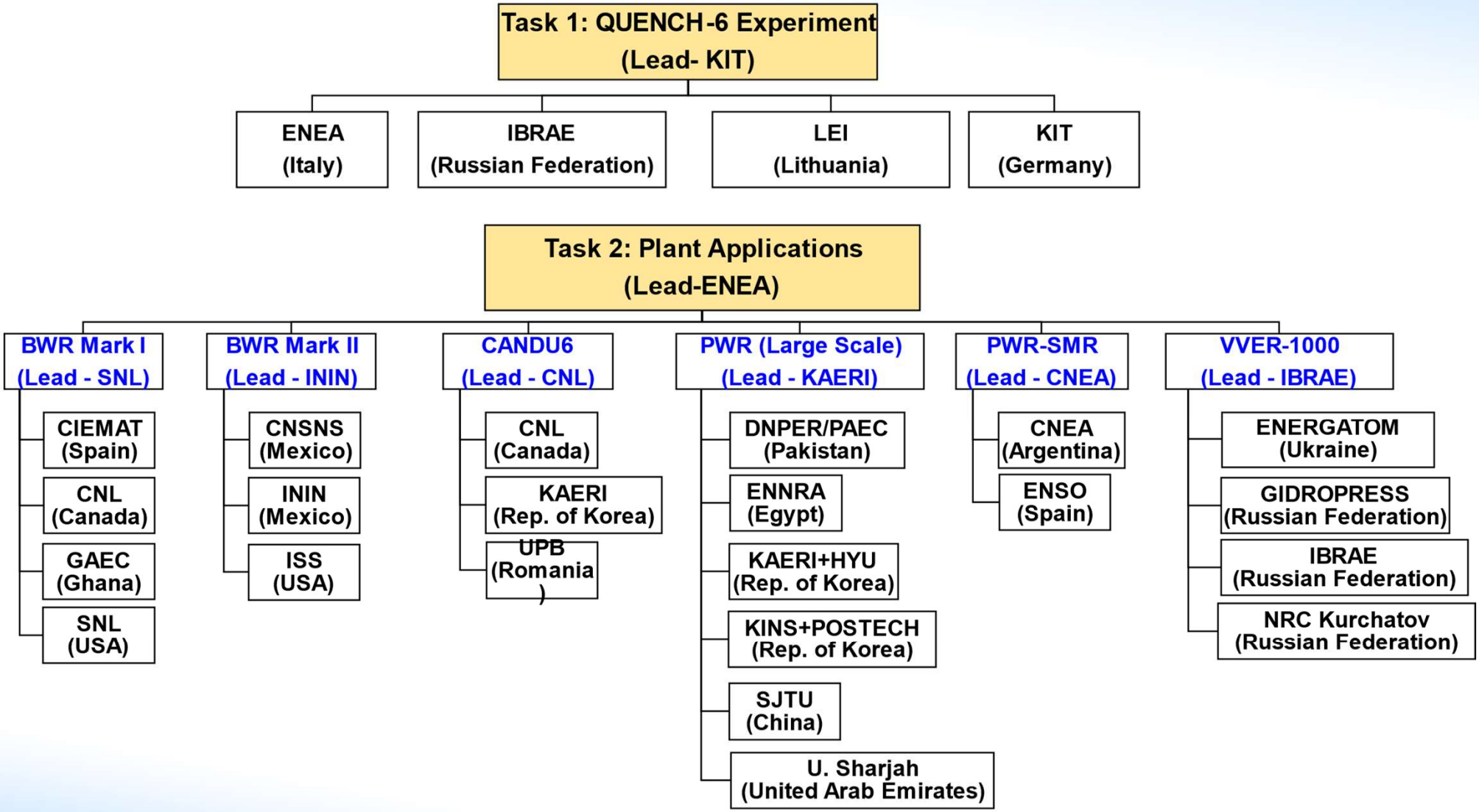

2. Task 1 – QUENCH-6 Experiment

- The UA of the QUENCH-06 experiment by means of SA codes and UT has been performed.
- Figure of Merits for exercise: *i)* hydrogen accumulated mass and generation rate; *ii)* temperature of the central rod at 950 mm height; *iii)* axial profile of the oxide scale of the heated and corner rods.
- 23 parameters have been employed by the SA codes for the modeling of the test section and test conduct have been selected and PDFs of the corresponding uncertainties have been assessed for UA.

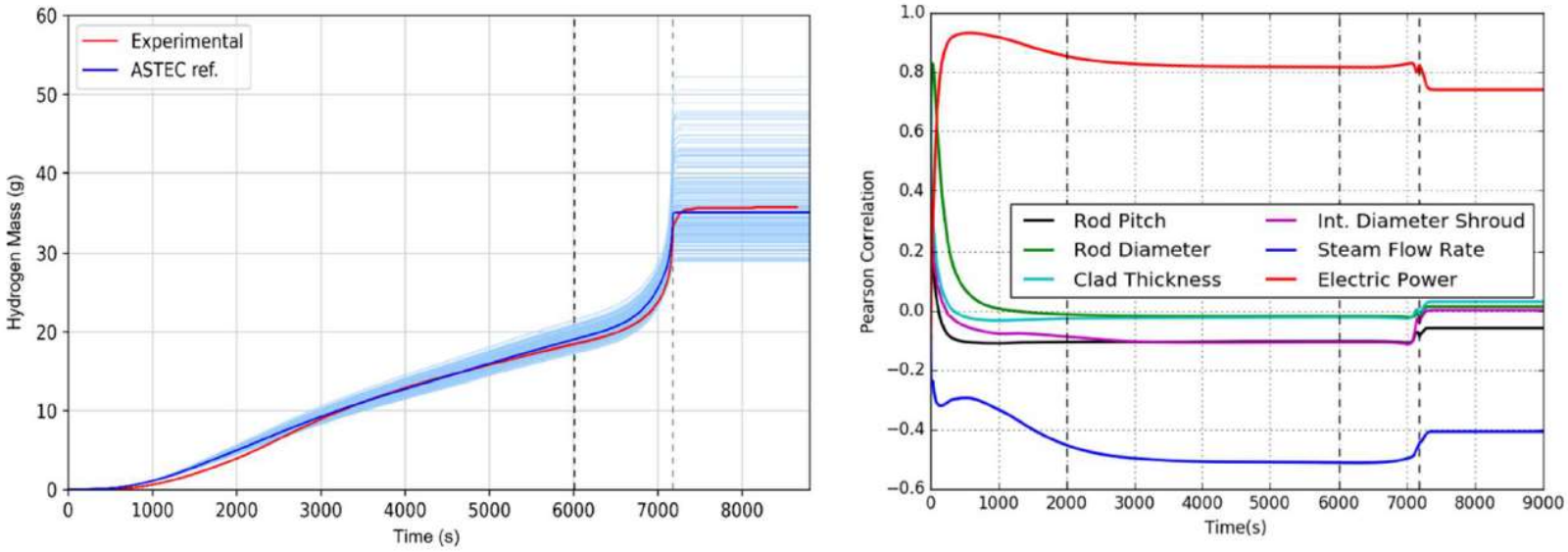

Figure 2. Hydrogen accumulated mass: samples (left) and Pearson correlations (right).

QUENCH-06 – investigation of the thermal-mechanical behavior of pre-oxidized LWR rod bundle quenched with water as well as the determination of resulting hydrogen source term.

3. PLANT TYPES

- For the plant application uncertainty exercise (TASK 2 of the CRP) 6 reactor types have been selected:
  - BWR (Mark I)
  - BWR (Mark II)
  - PWR (Large scale)
  - VVER1000
  - Integral type PWR-SMR
  - CANDU6

- 19 Institutions are involved in the plant application uncertainty exercise.

IAEA
International Atomic Energy Agency
Atoms for Peace and Development

Task 2.1

Task 2.1 BWR5 Mark I leader: Lucas ALBRIGHT

Participant Institutions:
CIEMAT (Spain)
CNL (Canada)
GAEC (Ghana)
SNL (USA)

Analyses and Scope of Accident Scenarios

Institution	Transient	Framework of The Analyses (e.g. Design, regulation, etc)	Question That We Need to Answer with The Uncertainty Analyses	In-Vessel or EX-vessel	SA code	UT code
CIEMAT	SBO	External uncertainties affecting Source Term (i.e. uncertainties other than intrinsic ST ones). SAMGs	How uncertainties in core degradation affect FP release from fuel rods	In-vessel	MELCOR	DAKOTA
SNL	SBO	SA Model development	How can uncertainties in core degradation inform model development	In-vessel	MELCOR	In-house
GAEC	SBO unmittigated	In support of SAMGs development	Provide insight to code users on the effect of uncertainty in selected input parameters on the key FOM.	In-vessel	MELCOR	DAKOTA
CNL	SBO	Support for SA management activities and understanding SA source term	To evaluate the influence of various model input parameters on FOM and to derive the input parameters that contribute the most to the key FOMs	In-vessel + ex-vessel	MELCOR	TBD

Modelled systems include a nodalized reactor core with associated support and upper vessel structures, reactor pressure vessel, primary circuit piping including main steam lines, recirculation pumps, jet pumps, and feedwater systems. Containment structure are also included in models.

Main points

- The approach of the application of UA methods to SA analysis employed by the participants varies significantly by institutions. Deviation arise in part, because of the diverse intended applications.
  - Best-estimate distribution have been applied to input parameters with an intent of obtaining best estimate distribution of accident response.
  - Uniform distribution have been applied to get coverage of entire uncertainty space.
- Despite the differences in the range of models applied, group has encouraged discourse on the applicability of the standard statistical technique such as Wilk's formula for SA analysis which add collective value to this CRP.

IAEA
International Atomic Energy Agency
Atoms for Peace and Development

Task 2.2

Task 2.2 BWR5 Mark II leader: Javier ORTIZ-VILLAFUERTE

Participant Institutions:
ININ / CNSNS (Mexico) in a single project: IAEA RA 23467/R0
ISS (USA)

Analysis and Scope of Accident Scenarios

Analyses Scope and Accident Scenarios						
Institution	**Transient**	**Framework of the analyses**	**Question that we need to answer with the uncertainty analyses**	**In-Vessel or Ex-Vessel**	**SA code**	**UT**
CNSNS	SBO with RCIC injection; ADS actuation.	Support technical basis on regulation issues	To determine the propagation of uncertainties in models due to key parameters	In- and ex-Vessel phenomena	MELCOR 2.1.	DAKOTA
ININ	Unmitigated high pressure SBO	Support development and review of technical basis of SAMGs	To investigate the range of valid application of the different physical models	Only In-Vessel phenomena	MAAP5.03	AZTUSIA via Python Scripts

Figures of Merit Definition			
Institution	**Main FOMs**	**Uncertain Variables**	**PDFs**
CNSNS	1. Hydrogen mass 2. Fission product mass generation 3. Time until core damaged criterion 4. Debris mass in lower head 5. Reactor Pressure Vessel breach time 6. Containment failure time	11 for in-vessel + 6 for ex-vessel	Already set. No change.
ININ	1. Hydrogen mass 2. Fission product mass fractions 3. Time to core damage criterion 4. Core support plate failure 5. Debris mass in lower head 6. Reactor Pressure Vessel breach time	28	Already set. No change.

Main Results

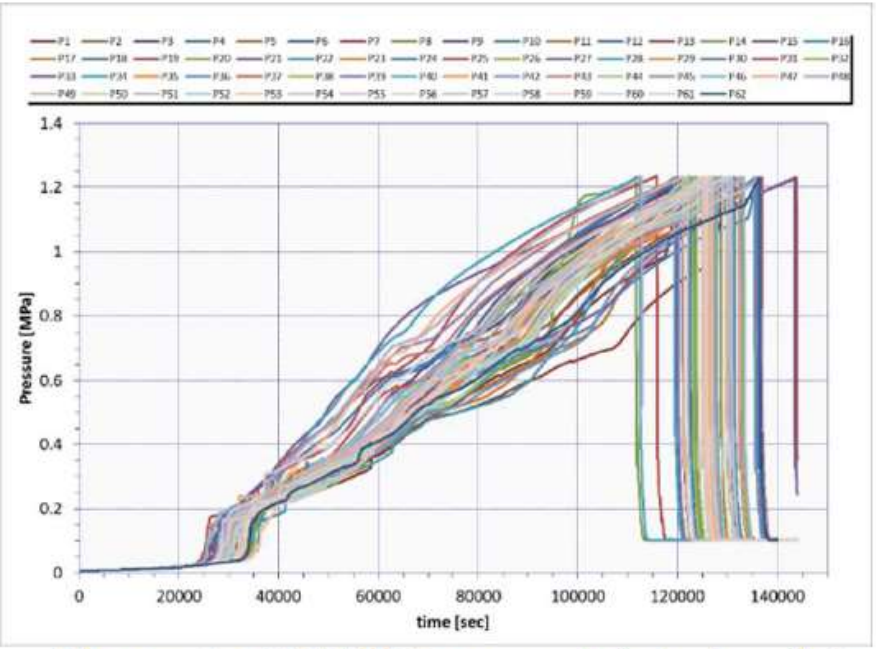

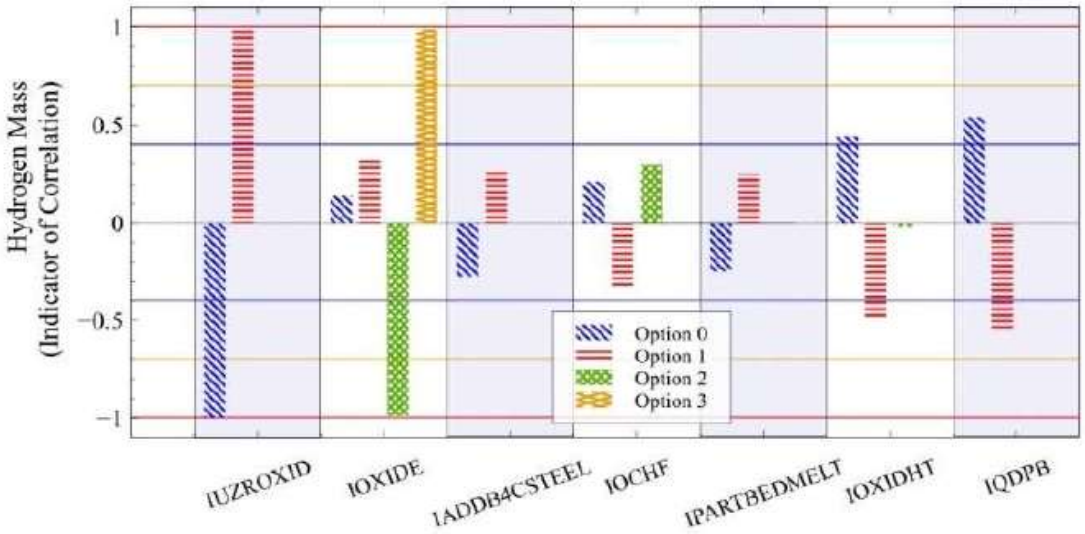

Figure 3. CNSNS´s uncertainty band for the FOM Primary Containment Failure Time due to overpressure (left) ININ´s MCF Indicator of Correlation results for qualitative uncertain input variables related to hydrogen mass generation in core, for each of their available option (right).

IAEA
International Atomic Energy Agency
Atoms for Peace and Development

Task 2.3

Task 2.3 PWR (large scale) leader: Kwang Il Ahn

Participant Institutions:

KAERI (S. Korea)

ENRRA (Egypt)

SJTU (China)

DNPER/PAEC (Pakistan)

KINS (S. Korea)

U. Sharjah (UAE)

Analyses and Scope of Work

Institution	Reactor type	Scenario/Scope	SA Tool		UQ Tool
KAERI+HYU	OPR1000 (Korea)	STSBO (In-/Ex-vessel)	MELCOR 2.2 (SNL)	MAAP5.05 (EPRI)	DAKOTA (MELCOR) / MOSAIQUE (MAAP5, In-house)
ENRRA	KWU-PWR 1300 (Germany)	LBLOCA w/o SCRAM (In-vessel, early phase PCT)	ATHLET (GRS, DBA/BDBA w/o core degradation) & SCALE6.3 (ORNL)		PYTHON (In-house)
SJTU	CPR600 (China)	SBO (In-/Ex-vessel)	MELCOR1.8.5 (SNL)		MATLAB (In-house)
DNPER/PAEC	ACP1000 (K-2)	SBO (In-/Ex-vessel)	MELCOR1.8.6 (SNL)		DST (MATLAB-based DNPER statistical tool, In-house)
KINS+Postech	APR1400 (Korea)	SBO (In-vessel & Reactor cavity)	MELCOR2.2 (SNL) & COOLAP2 (SNU)		DAKOTA + In-house
U. Sharjah	APR1400 (UAE)	SBO (In-vessel, early phase PCT)	RELAP5/NESTLE-based 3KEYMASTER simulator (using SCALE6.1)		DAKOTA + ROMUSE (In-house)

Main points of discussion and Group actions

The PWR Group is carrying out the benchmark exercises using

- **Different reactor types:** 5 reactor types (OPR1000, CPR600, ACP1000, KWU-PWR1300, APR1400)
- **Different analysis scopes (including different uncertain inputs & relevant PDFs):** In-vessel, In-/Ex-vessel, FP releases, and all accident phases
- **Different SA simulation codes:** MELCOR (version 2.2, 1.8.6, 1.8.5), MELCOR2.2/COOLAP2, MAAP5, ATHLET/SCALE6
- **Different UQ methods and Inputs:** Statistical approach (SRS, LHS, Wilks' formula), Statistical & deterministic approach (SVD/UT)
- **Different calculation schemes for UA:** MELCOR (DAKOTA, ROMUSE, MATLAB), MAAP5 (MOSAIQUE), ATHLET/SCALE6 (PYTHON script for SVD/UT)

Current Status of the PWR Group

- **A consolidation of uncertain inputs is not easy and the conventional benchmark study (using a singe target Plant, but different SA tools) is not feasible to implement.**
- **Each partner applied their own UA framework & relevant inputs for the planned CRP task.**

IAEA
International Atomic Energy Agency
Atoms for Peace and Development

Task 2.4

Task 2.4 VVER leader: N. Ryzhov

Participant Institutions:
ENERGATOM (Ukraine)
GIDROPRESS (Russian Federation)
KURCHATOV (Russian Federation)
IBRAE (Russian Federation)

Analyses and Scope of Work

Institution	Transient	Question That We Need to Answer with The Uncertainty Analyses	In-Vessel or EX-vessel	SA code	UT
IBRAE RAN, RUSSIA	LB LOCA with unmitigated SBO	Influence of reactor model input parameters (user input parameters like nominal power, geometry, fuel porosity etc.) on FOM calculations.	In-vessel	SOCRAT	Inhouse
ENERGOATOM, UKRAINE	SBO	to evaluate the objectivity and the accuracy of the calculations	In-vessel	MELCOR	Inhouse
KURCHATOV, RUSSIA	PRZ SL rupture with SBO	The main purpose of the proposed analysis is the evaluation of the influence of input-deck data uncertainties, which includes uncertainty of the plant operating parameters, geometric uncertainties of computational domain, unfrozen model options and uncertainties of thermophysical properties of substances, on calculated representative values of nuclear safety (figures of merit).	In-vessel	SOCRAT	Inhouse
GIDROPRESS, RUSSIA	SBO	• Stability of the computational model and code we use; • Absents/presence of cliff edge effects in the scenario; • Influence of reactor model input parameters (user input parameters like nominal power, geometry, fuel porosity etc.) on FOM calculations. As the result of uncertainty analysis we should determine minimal, maximal and the most probable values of FOMs.	In-vessel	SOCRAT	Inhouse

IAEA
International Atomic Energy Agency
Atoms for Peace and Development

Task 2.5

Task 2.5 SMR leader: J. M. Garcia

Participant Institutions:
CNEA (Argentina)
ENSO (Spain)

Analyses and Scope of the Work

Institution	Transient	Framework of The Analyses	Question That We Need to Answer with The Uncertainty Analyses	In-Vessel or EX-vessel	SA code
CNEA	SB-LOCA	Support SAMG	Time available for human recovery actions and SAMG system	In-vessel	MELCOR 1.8.6
ENSO	SBO	Support SAMG	Evaluation of safety margin in comparison with BE evaluation Mitigation strategies	In-vessel	RELAP/SCDAPSIM/MOD3.5

Institution	Calculation scheme
CNEA	MELCOR + DAKOTA + In-house developed scripts
ENSO	RELAP/SCDAPSIM + IUA

Main points of discussion and Group actions

- **Improvement of SA model and UA tool**
  - Plant model improvements based on findings from the first application of the uncertainty analysis methodology.
  - Uncertainty model improvements in order to enhance model capabilities and robustness.
- **New applications of UA methodology**
  - Verification of models improvements.
  - Possible new calculations taking into consideration the experience from other CRP Partners.
- **Results analysis, conclusions and recommendations**

IAEA
International Atomic Energy Agency
Atoms for Peace and Development

Task 2.6

Task 2.6 CANDU leader: S. Petoukhov

Participant Institutions:
CNL (Canada)
KAERI (S. Korea)
UPB (Romania)

Task 2.6 brief overview

- Case study: a generic CANDU 6 plant; an SBO scenario;
- Participants:
- Romania: University POLITEHNICA of Bucharest: UPB (Daniel Dupleac, Roxanna Nistor-Vlad); RELAP-SCDAP-SIM + Integrated Uncertainty Analysis package in RELAP/SCDAP-SIM
- Korea: Korea Atomic Energy Research Institute: KAERI (Jun-Ho BAE and Kwang-Il AHN); CAISER (severe accident analysis code) + MOSAIQUE (uncertainty analysis engine);
- Canada: Canadian Nuclear Laboratories: CNL (Sergei M. Petoukhov and Andrew Morreale); MAAP-CANDU + SUSA

Task 2.6 brief overview (cont'd)

- It was decided to adhere to the previous work under IAEA guidance:

  TECDOC No. 1727 (issued in 2013): "Benchmarking Severe Accident Computer Codes for Heavy Water Reactor Applications".

- The same (or very close) input data and failure criteria as defined in TECDOC-1727 were adopted for use by all CANDU CRP (Task 2.6) Partners.

Future Steps

- Expand analysis to cover other important FOM (FP releases, event timings, etc.);
- Identification and quantification of possible dependencies (correlations) between input parameters and ensuring statistical independence between the random samples for each pair of uncertain input parameters;
- Refining the PDF types and boundary values, for the uncertain input parameters and assigning the updated PDFs to the uncertain input;
- Inclusion of model flags into the set of uncertain input parameters;
- Continue writing the IAEA TECDOC/NES documents;
- Task 2.6 (CANDU) information exchange/technical meetings.

4. Task 3: Develop reports on uncertainty and sensitivity in severe accident analysis

- Task 3 is related to the development of reports on U&S analysis in SA. Currently 5 TECDOCs are planned describing the applications carried out in the CRP grouped by technology (QUENCH, BWR, PWR+SMR, VVER, CANDU 6). A Nuclear Energy Series document will then collect the main findings, lessons learned and best practices identified in the CRP framework.

5. STUDENT PROGRAM

- Along the first year of the CRP a PhD program has been launched but it was delayed due to the COVID-19 issues and currently a Virtual Graduate Students Experience is being conducted.

- **CRP FRAMEWORK FOR VIRTUAL GRADUATE STUDENTS EXPERIENCE**: is based on the graduate students' pair building between CRP institutes. Graduate students are asked to select one day in a semester to spend time together virtually, and to prepare a brief report to IAEA. Their virtual experience should include the following:
  - Virtual breakfast to get to know each other; time to discuss and a brief virtual tour of the offices, views through your office windows, or corridors in the buildings; take some pictures for your report to IAEA;
  - Present with well-developed slides the graduate (PhD or MS) research and how it relates to the CRP objectives and scopes;
  - Spend virtual afternoon working on a common topic;
  - Write jointly the report and submit to IAEA Chairs.
- A consultancy meeting on the graduate student program was held on September 8th-9th, 2021

6. CONCLUSIONS

- In the 1st year of activity for the plant application, the Partners have provided information regarding the analyzed transient, framework of the analysis, SA code, UA tool, uncertainty methodology adopted, calculation scheme, sampling method, uncertainty band definition, statistical analysis, possible adoption of correlation coefficients.
- The collection of information is almost complete.
- It should be also underlined a huge effort from the Partners in the selection of the uncertain input parameters (with proper range and PDF).
- Missing information (e.g. calculation scheme, coefficient used, Uncertainty Analysis method used, uncertain input parameters and PDF, etc.), should be provided as soon as possible.
- In relation to the Quench exercise the main facility information and experimental data has been distributed together with the input uncertainty parameters and figure of merit of the analyses; each participant performed the reference calculation.
- Interesting topics are being addressed in the CRP, and these topics can be discussed with more in detail; during topical meetings within the CRP, in order to share knowledge and for discussing with more detail selected topics.

IAEA
International Atomic Energy Agency
Atoms for Peace and Development

Thank you!

THE APR1400 SOARCA STUDY: INSIGHTS INTO THE SEVERE ACCIDENT PROGRESSION AND SOURCE TERM ANALYSIS RESULTS

Kwang-Il Ahn
Korea Atomic Energy Research Institute (KAERI)
989-111, Daedeok-daero, Yuseong-gu, Daejeon 34057, Republic of Korea
kiahn@kaeri.re.kr

Keo-hyoung Lee
FNC Technology Co., Ltd.
32 Fl., 13 Heungdeok 1-ro, Giheung-gu, Yongin-si, Gyeonggi-do Republic of Korea
khlee@fnctech.com

Seok-Won Hwang
KHNP Central Research Institute
1312-gil, Yuseong-daero, Yuseong-gu, Daejeon 34101, Republic of Korea
swhwang1221@khnp.co.kr

ABSTRACT

The Korean utility, KHNP (Korea Hydro and Nuclear Power Co.), carried out a three-year research study in July 2016 (named the K-SOARCA), which is similar with the United State (US) SOARCA (State-of-the-Art Reactor Consequence Analysis) study. One of the two reference reactors designated for the study was APR1400 (Advanced Power Reactor 1400 MWe). To consider the integral response of the reactor, steam generators (SGs), and containment to severe accidents initiated by the representative accident scenarios screened out from the plant-specific probabilistic safety assessment (PSA) results, dedicated modeling was performed for a broad spectrum of plant safety/mitigation systems and relevant phenomena influencing the evolution of the accident. The influence of dedicated accident mitigation strategies on the evolution of accident progression and fission product (FP) source terms was also investigated to assess their effectiveness in coping with relevant severe accident scenarios. Especially, relating to the APR1400 SOARCA, the latest versions of two severe accident analysis codes, MELCOR 2.2 and MAAP5.04, were used to compare the analysis results of interest. This paper presents best-practice analysis results for the evolution of key accidents and plant response including the environmental release of FP Cs (cesium), as implemented through the APR1400 SOARCA study, and relevant insights.

KEYWORDS
SOARCA, APR1400, Severe accident, FP source term (Cs), Best-practice analysis

1. INTRODUCTION

In the wake of the Fukushima nuclear disaster in March 2011, the Korean Nuclear Safety and Security Commission (NSSC) has required that nuclear power plants in Korea evaluate their ability to cope with potential severe accidents. In response to this requirement, the Korean utility, the Korea Hydro and Nuclear Power Co. (KHNP), launched a three-year research study in July 2016 (named the K-SOARCA), which is similar with the United State (US) State-of-the-Art Reactor Consequence Analysis (SOARCA) study [1, 2].

The goal of the K-SOARCA study [3, 4], which was carried out under a collaboration with the Korea Atomic Energy Research Institute (KAERI), is to (a) establish severe accident coping strategies and evaluate their effectiveness through a best-practice analysis of Level 2 probabilistic safety assessment (PSA) accident progression and fission product (FP) source terms, (b) reduce a possibility of containment bypass events such as steam generator tube rupture (SGTR) and interfacing system loss of coolant accident (ISLOCA), and (c) secure the state-of-the art Level 2 & 3 PSA technologies for diverse application to Korean reactors. Two types of nuclear reactors have been designated for the study: one for a pressurized water reactor (PWR: APR1400) and one for a pressurized heavy water reactor (PHWR: CANDU6): one for pressurized water reactors (PWR: APR1400) [5, 6] and one for pressurized heavy water reactors (PHWR: CANDU-6) [7]. Dominant accident scenarios including long-term/short-term station blackouts (SBOs) have been screened out based on the specified core damage frequency (CDF) criteria. Otherwise, two containment bypass events leading to a severe accident, ISLOCA and spontaneous SGTR (S-SGTR), have been additionally considered in the study for their importance to off-site consequence.

For each accident scenario, plant-specific accident progression and FP source term analyses were carried out, using the latest versions of relevant severe accident analysis codes, e.g., MELCOR2.2 [8] and MAAP5.04 [9] for APR1400; MAAP-ISAAC [10] for CANDU6, and the site-specific offsite consequences, based on a computer code for the Level 3 PSA (WinMACCS) [11]. The influence of dedicated mitigation strategies on the results of interest was also investigated to assess their effectiveness in coping with relevant severe accident scenarios. Relating to the APR1400, the reason why both MELCOR and MAAP5 are employed is because while both codes predict similarly general trends of accident progression and source term, prediction capability might be a greater or lesser different for specific phenomena, thanks to different modelling schemes and basis employed by these codes [12].

Among them, this paper presents best-practice analysis results for the evolution of key accidents and plant response including the environmental release of FP Cs (cesium), as implemented through the APR1400 SOARCA study, and relevant insights. For reference, the amount of Cs-137 release into the environment and its frequency are currently being used as one of the probabilistic risk criteria to guarantee the safety of NPP in terms of environment risk [13. 14].

2. PLANT AND PHENOMENA MODELING

2.1. Design features of the APR1400

The reference PWR, APR1400 (Advanced Power Reactor 1400 MWe) [5, 6], is a generation III reactor with two primary coolant loops, with each loop having one SG and two reactor coolant pumps (RCPs) attached in one hot leg (HL) and two cold legs (CLs) arrangement, which is capable of generating an electricity of 1400 MWe (a rated thermal power of 4000 MW_{th}). As part of post-Fukushima countermeasures, the APR1400 employed additional accident mitigation means [15] and Shin Kori units 3&4 [16] are the first generation of plants employing the APR1400 design.

2.2. Dedicated accident coping strategies

As a coping strategy considering the multiple defense concept, the KHNP has also introduced a strategy called MACST (multi-barrier accident coping strategy) [17], which is based on a general understanding of US FLEX [18]. Then, the MACST utilizes all available resources in plant including pre-staged and mobile equipment to maintain and restore the plant's key safety functions in a beyond design basis accident (BDBA). Similar to the NEI 12-06 approach [19], it’s operation is basically divided into three phases [20]: phase 1 using pre-staged/installed plant safety equipment (available until 8 h after the accident), phase 2 shifting from the installed safety equipment to on-site mobile equipment (available until 72 h after the accident), and phase 3 using all available on-site and off-site equipment until when power, water, and coolant injection

systems are restored or commissioned (available after 72 h). Among them, the majority of the accident mitigation strategies, which help to prevent the occurrence of core damage or the failure of containment integrity as well as to reduce possible FP release to the environment, are typically implemented in phase 2 or 3 when the evolving accident cannot be properly coped with by the use of the installed equipment alone.

2.3. Screening-out of reference scenarios

Based on the APR1400 PSA results, eight accident sequences were selected for the Level 2 accident progression and source term analysis, as shown in Table I. Two different CDF criteria were applied to screen out these accident sequences: $1.0x10^{-7}$/ry for general events (such as SBO, SLOOP, and SLOCA) and $1.0x10^{-8}$/ry for bypass events (ISLOCA and S-SGTR). The bypass events were selected to reflect a direct and large release aspect of radioactive material to the environment. The foregoing criteria are lower by one order of magnitude than the corresponding US SOARCA criteria, thanks to several advanced safety features employed by the APR1400 by which the estimated plant CDF is lower than $1.0x10^{-5}$/ry. The last column of Table I dedicated accident mitigation means employed in the APR1400.

Table I. Eight reference scenarios considered for the APR1400 SOARCA study

No	Base scenarios (w/o AM actions)	CDF (/ry)	Mitigated scenarios (Base + dedicated AM actions)
1	SBO-025 [LTSBO (long-term SBO), internal initiating event)	$6.36x10^{-7}$	Mobile EDG + TD-AFWP + EWI to the SG using mobile pump (after the AFWST dried out)
2	SSBO-001 (STSBO, seismic-induced SBO)	$3.43x10^{-7}$	Mobile EDG + EWI to the SG and RCS using mobile pump + CFS + ECSBS
3	SLOOP-004 (Seismic-induced LOOP + a failure of CHR)	$2.83x10^{-7}$	EWI into the RCS using mobile pump
4	SLOOP-005 (Seismic-induced LOOP + a failure of F&B operation)	$1.03x10^{-7}$	EWI into the RCS using mobile pump + ECSBS
5	SLOCA-020 (Small LOCA, internal initiating event)	$1.40x10^{-7}$	EWI into the RCS using mobile pump + ECSBS
6	ISLOCA-001 (Aux. Building A region-SCP suction pipe 4 inch break)	$2.80x10^{-8}$	CFS + ECSBS
7	Spontaneous SGTR-032 (with a failure of safety injection and an isolation of the faulted SG, internal initiating event)	$1.42x10^{-8}$	EWI into the RCS using mobile pump + ECSBS
8	Spontaneous SGTR-010 (with a failure of SG isolation and an isolation failure of the faulted SG, internal initiating event)	$1.22x10^{-8}$	Auxiliary feed-water injection into the faulted SG using MD-AFWP

[Note] AM: accident management/mitigation; CFS: cavity flooding system; CHR: containment heat removal; ECSBS: emergency containment spray backup system; EWI: emergency water injection; F&B: feed and bleed; LOCA: loss of coolant accident; LOOP: loss of offsite power; LTSBO: long-term SBO; SCP: shutdown cooling pump; MD-AFWP: motor-driven auxiliary feedwater pump; RCS: reactor coolant system; STSBO: short-term SBO; TD-AFWP: turbine-driven auxiliary feedwater pump.

2.4. Key modeling and assumptions

The followings summarize key plant modeling and relevant assumptions used for the present MELCOR and MAAP5 analyses, which are either embedded in the relevant code as models with input control parameters or assumed for the analysis. For reference, many portions for the present plant modeling and relevant assumptions are also given in the authors' previous papers [21-23].

2.4.1. Base models

(1) Plant modeling and nodalization [21-23]:

<table>
<tr><th>Code</th><th>Reactor core</th><th>RPV (core region)</th><th>RPV LH wall</th><th>Reactor building</th><th>Auxiliary building</th><th>Relevant scenarios</th></tr>
<tr><td>MELCOR</td><td rowspan="2">five radial rings and 13 axial-levels</td><td>30 CVs</td><td rowspan="2">10 radial segments</td><td rowspan="3">18 compartments and 52 FLs between compartments</td><td rowspan="3">19 CV nodes</td><td>SBO/SGTR</td></tr>
<tr><td>one CV</td><td>ISLOCA</td></tr>
<tr><td>MAAP5</td><td colspan="3">MAAP5 standard model (fixed)</td><td rowspan="2">All</td></tr>
<tr><td></td><td>seven radial rings and 13 axial-levels</td><td>one CV</td><td>25 axial nodes and 5 radial nodes</td><td></td><td></td></tr>
<tr><td colspan="7">[Note] CV: (hydrodynamic) control volum; FL: flow path</td></tr>
</table>

(2) Initial inventory of FPs and decay heat:
- For the three fuel cycle stages (EOC: end of cycle, MOC: middle of cycle, and BOC: beginning of cycle), the ORIGEN (Oak Ridge Isotope GENeration) code [24] was used to estimate the initial inventories of the FPs. Among them, EOC was applied for the present analysis. The decay heat with time was evaluated using the American Nuclear Society (ANS) decay heat model [25].

(3) Release of FPs through the fuel-cladding gap [8, 9]:

MELCOR	Modified ORNL-Booth model (best-practice according to the US SOARCA)
MAAP5	ORNL-Booth model adjusted by a scale factor to obtain a similar trend with the modified ORNL-Booth model.

(4) Decay heat of FPs inside the RCS:

MELCOR	Similar to the US SOARCA [2], the decay heat was assumed to be distributed over the primary system and piping as follows: 25% and 74.38% of the decay heat from the FPs inside the HL pipe are allocated into the vapor inside the piping and to the pipe walls, respectively, with the remaining 0.62% is transferred to the outside of the piping.
MAAP5	Simulates the decay heat of the FPs within the RCS through the corresponding heat structure models employed in the code.

(5) Modeling of two layers concrete materials to simulate the molten-core concrete interaction (MCCI) in the dry reactor cavity (MAAP5 only). Such a configuration was not simulated in the MELCOR analysis, while it can be indirectly simulated through the MELCOR FDI package. For reference, in the APR14000, the limestone concrete is placed below the cavity, and basaltic concrete is embedded between the limestone concrete layer and the containment liner plate.

(6) RPV lower head (LH) failure mechanisms according to the relocation of molten corium into the RPV lower plenum [8, 9]:

MELCOR	According to the best-practice experience from the US SOARCA [1, 2], the Larson-Miller (LM) creep rupture model was used, assuming an initial rupture of 0.01 m^2.
MAAP5	The MAAP5 default model (parametric LH tube failure model) was utilized, assuming a melting temperature of the welding material of 1273.15 K and an initial rupture of 0.1 m diameter.

(7) Reactor/containment building damage/rupture: Based on the APR1400 design and relevant PSA results [5, 15], the following containment leakage and failures modes were defined in the present analysis:
- Design leakage of 0.1% volume/day (6.23E-03 kg/s) at the pressure (P_{design} = 60 psig = 0.515 MPa);
- Initiation of the overpressure leakage at a containment pressure ($P = 1.56P_{design}$), leading to a leakage of 13% mass/day (1.16 kg/s) at a pressure ($P = 1.99P_{design}$);
- Leak failure at a containment pressure ($P_{leak} = 2.3P_{design}$), corresponding to the 5th percentile of the ultimate pressure capacity (UPC) of the containment;
- Rupture failure at a containment pressure ($P_{rupt} = 3.6P_{design}$), corresponding to the 1% displacement of

containment tendon [leading to the containment leakage of 62% mass/day (9.57 kg/s)];
- The above leakage and failures modes were simulated assuming an opening of 1ft^2 (0.01 m^2) in the upper compartment of the containment.

2.4.2. Scenario-specific modeling

(1) Natural circulation through the HL and SG and induced creep rupture in high pressure accident scenarios like SBO [23]:
- In the case of MELCOR, the nodalization scheme in Fig.1 was employed to simulate the natural circulation between HL and SG. Differently from MELCOR, the standard MAAP5 nodalization simulates the HL as a single node without splitting it into upper and lower sides, and the SG inlet plenum is also modeled as a single node, consequently assuming that the natural circulation fluids coming from the HL and the SG U-tubes are completely mixed in the SG inlet plenum.

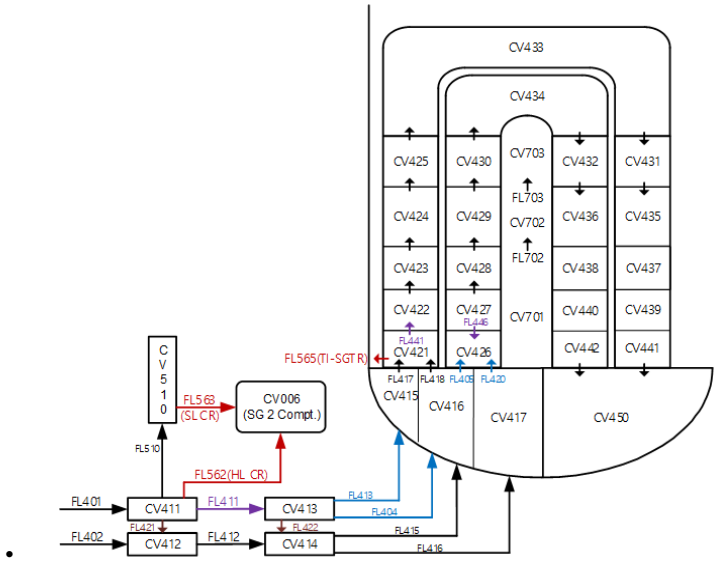

Figure 1. HL/SG nodalization for the natural circulation analysis (MELCOR).

- The followings are additional conditions applied to simulate the natural circulation in both codes:

MELCOR	・ According to the best-practice experience from the US SOARCA [1, 2], the counter-current natural circulation starts when the void fraction of the HL exceeds 0.95 and the degree of superheat in the HL exceeds 10 K. The heat transfer coefficient in the RPV outlet nozzle conservatively increased 1.5 times, taking into account a temperature gradient between the RPV outlet nozzle and the SG inlet nozzle [26]. ・ MELCOR does not implicitly model the mixing of fluids in the RCS loop, but instead employs relevant predetermined mixing and flow parameters [27]. The foregoing physical parameters associated were determined based on the Computational Fluid Dynamics (CFD) analysis [28].
MAAP5	・ According to the standard MAAP5 model [9], the counter-current natural circulation starts when the void fraction in the SG outlet plenum approaches 1.0 and the temperature of the RPV upper plenum is greater than that of the SG inlet plenum. ・ All hot and cold fluid is mixed in the inlet plenum of the SG (mixing fraction is 1.0) and the SG natural circulation flow rate is calculated by the code, based on the density gradient and the pressure drop through the SG U-tubes. ・ Hottest temperature of SG U-tubes is not considered and temperature of the RPV outlet nozzle is simulated based on the temperature gradient in the HL

Both	The natural circulation stops when the RCS loop seal is cleared or the RCS boundary is opened due to a failure of the HL or a stuck open of the POSRV [23].

- Natural circulation induced-creep rupture of the RCS pressure boundary (such as induced hot-leg pipe and nozzle break, induced pressurizer surge line break, and induced SGTR) was estimated based on the Larson-Miller creep model built-in the both codes [8, 9].

(2) Retention of FP aerosol (ISLOCA) [21]: (a) turbulent deposition & re-vaporization during transport through the ISLOCA piping network, (b) deposition inside the auxiliary building (including ventilation systems), and (c) pool scrubbing through the submerged pipe break within the auxiliary building:

MELCOR	· Turbulent deposition in the straight pipe: Wood model (MELCOR RN2 package); Impaction in pipe bent: INL model (RN2 package) · Pool scrubbing in the submerged pipe: SPARC-90 model or mechanistic pool scrubbing model [29, 20]
MAAP5	· Turbulent deposition in the straight pipe and Impaction in pipe bent: MAAP5 containment hard pipe vent junction model · Pool scrubbing in the submerged pipe: SUPRA code model [31, 32]

(3) Retention of FP aerosol in the faulted SG (SGTR) [22]:

MELCOR	ARTIST (Aerosol Trapping In a Steam Generator) experimental data [33, 34]: ARTIST Phase 1 for U-tube internal; Phase II for U-tube bundles for the flooded SG; Phase VII for U-tube bundles for the dried SG
MAAP5	Multiplier adjusted by the ARTIST test results to the SUPRA bare pool model, in order to consider the effect of a flooded U-tube bundle or retention inside the faulted SG U-tube or in the dry SG secondary side.

2.4.3. Additional modeling assumptions

(1) Four passive safety injection tanks (SITs) are always available to cool the reactor core, but the pre-staged containment spray systems (CSSs) are assumed to be unavailable in order to investigate the impact of the dedicated accident mitigation strategy.
(2) The rate of EWI into the SG or RCS, which uses dedicated mobile pumps and external water sources is calculated from the system pressure referred in the utility document [16]. For reference, the injection of emergency cooling water is taken only for the intact SG.
(3) All PARs (passive auto-catalytic recombiners) of 20 are available to remove hydrogen released to the containment from the RCS, but 10 hydrogen ignitors of active design are not triggered during the operation of the PARs.
(4) The SAMG (Severe Accident Management Guidance) entry condition starts when the core exit temperature (CET) exceeds 649 ℃ (923.15 K)].
(5) SBO: A stuck-open failure of the main steam safety valve (MSSV), which could influence on the creep rupture of the RCS pressure boundary in high pressure sequences like the SBO, was not considered in the reference scenarios, since there is no currently available data to define it in the case of the APR1400. The RCP seal leakage was also not included in the reference scenarios.
(6) SGTR: The break size of the faulted SG U-tube is assumed as an open area corresponding to the inner cross-section area of a single U-tube (1.692×10^{-2} m in inner diameter), i.e., a guillotine break, and the break location is 0.25 m above the U-tube tube sheet.
(7) ISLOCA: A rupture of 0.006 m^2 takes place in the SCP suction line of the auxiliary building, corresponding to an internal area of the HL safety injection pipe of 4 inch (0.102 m) diameter and almost equivalent to that of a large break LOCA.

3. RESULTS AND FINDINGS

For the reference scenarios selected for the APR1400 SOARCA (i.e., 8 base/unmitigated scenarios and corresponding mitigated scenarios), the MELCOR and MAAP5 code simulations were run until 72 (mission time of the Level 2 PSA) to 200 h after the accident, taking into account the scenario-specific plant responses. Fig. 2 and Fig. 3 show the environmental release fractions of a radiological Cs, as predicted at various time points after the accident, and time trends for the Cs release fraction in various locations of the accident sequences of interest, respectively. Table II summarizes the timings of the key events for all the base and mitigated scenarios, as predicted by both codes. The followings summarize the analysis results of interest and key findings.

(1) For most scenarios, both codes similarly predicted the general trend of the evolution of the severe accident and plant responses, but the environmental release of the FP Cs as well as the late phase of core degradation and subsequent containment behavior significantly differed for most scenarios.
(2) Relating to the environmental release of Cs, the primary reason of the foregoing results was due to the difference of modeling schemes employed to deal with the behavior of FPs in each code, more specifically (a) inevitable differences in defining the initial core inventory of FPs, (b) different release characteristics of FPs from the fuel-cladding gap in the early phase of core damage, and (c) different modeling schemes for the transport and deposition of FPs in the RCS, SG, reactor/containment building, and ISLOCA piping network and auxiliary building. The second reason was due to the failure time of reactor/containment building: the earlier the reactor building/containment fails, the more environmental release of Cs is made until the end of calculation (72 h).
(3) Relating to the dedicated mitigation strategies, most of mitigated scenarios employed in the present study greatly decreased the environmental release of FP Cs, except for SLOOP-004, which led to a failure of the containment before the core damage and RPV LH failure, and took the dedicated mitigation action (i.e., injection of the emergency water into the RCS at around 4 h after reaching the SAMG entrance condition). The foregoing result indicates that when the containment fails to isolate before the core damage like SLOOP-004, the operator action time for mitigation could be a critical factor to minimize the influence of relevant accident.
(4) Relating to the behavior of the RCS pressure boundary, which is one of main concerns in high pressure sequences like SBO, the analysis result shows that either the HL nozzle (LTSBO) or the RPV LH (STSBO) was first predicted to fail by creep rupture in the reference scenarios, but the SG U-tubes maintained their integrity
(5) Relating to the prediction capability of MELCOR and MAAP5, Table III summarizes additional findings identified through the present study.

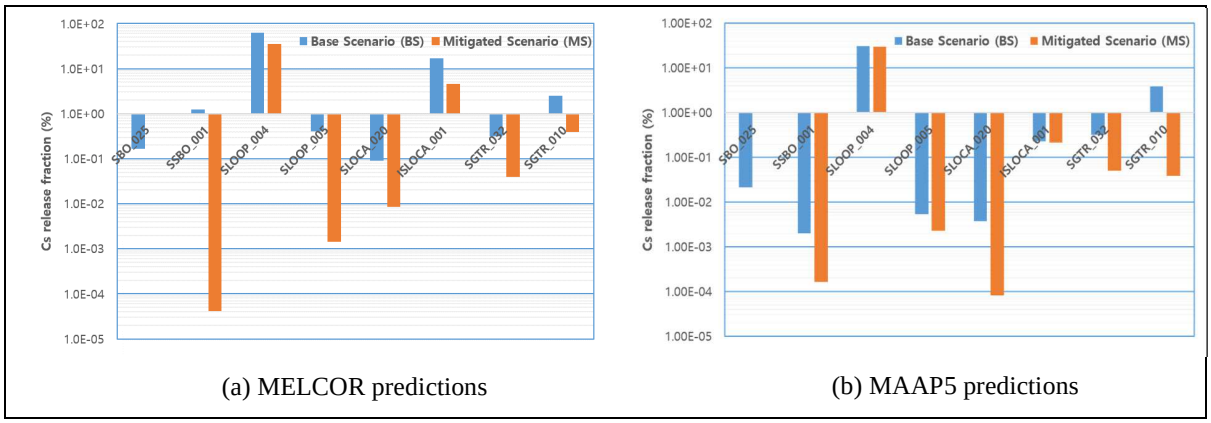

(a) MELCOR predictions (b) MAAP5 predictions

[Note] SGTR-032 (BS): SGTR + Cont. failure; SGTR-032 (MS) and SGTR-010: SGTR only.

Figure 2. Environmental release fractions of Cs at 72 h after accident (EOC)

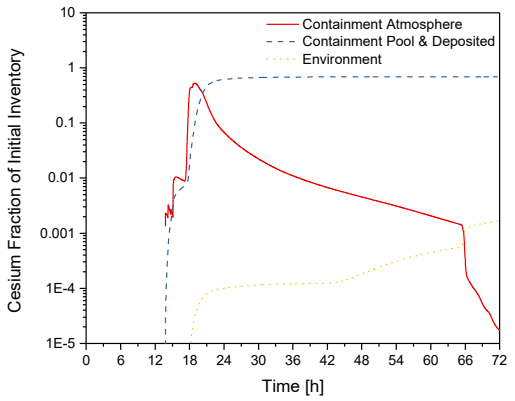

(a) SBO-025 (MELCOR, BS)

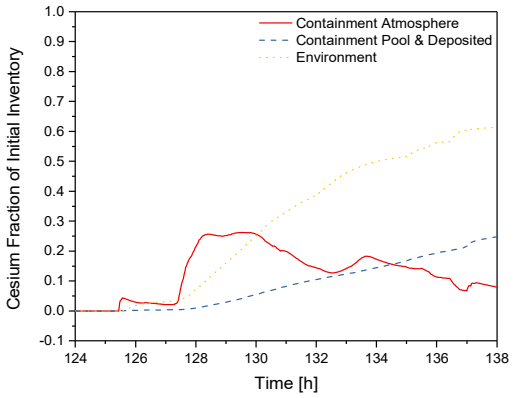

(b) SLOOP-004 (MELCOR, BS)

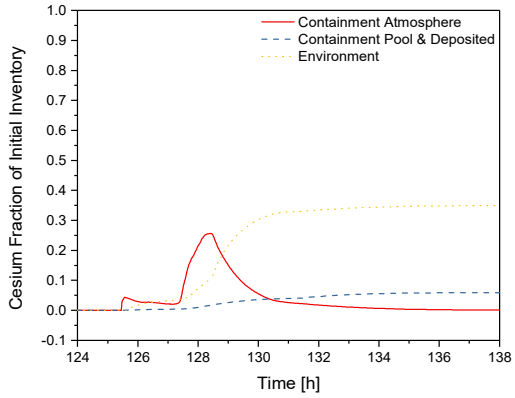

(c) SLOOP-004 (MELCOR, MS)

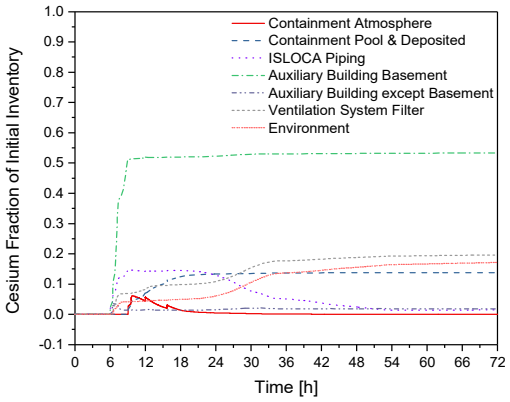

(d) ISLOCA-001 (MELCOR, BS)

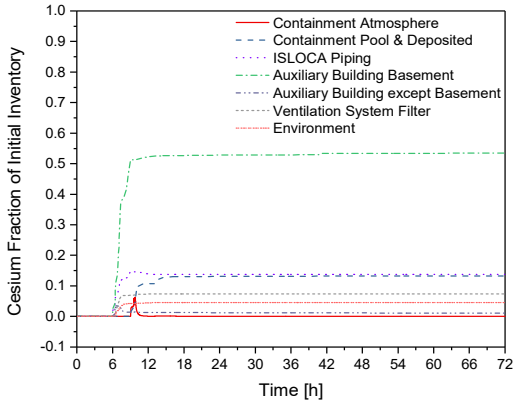

(e) ISLOCA-001 (MELCOR, MS)

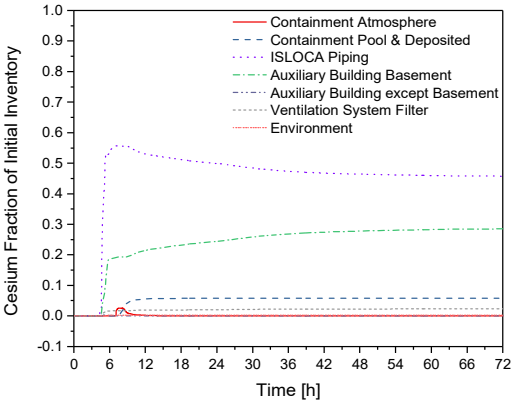

(f) ISLOCA-001 (MAAP5, BS)

Fig. 7. Time trends of the Cs fraction in various locations (1/2).

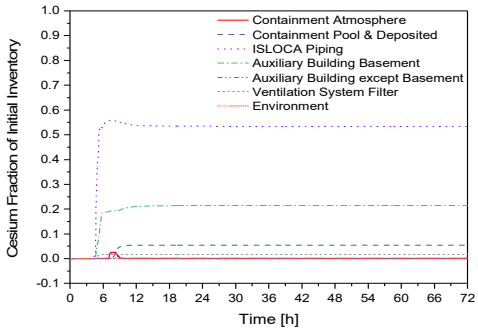

(g) ISLOCA-001 (MAAP5, MS)

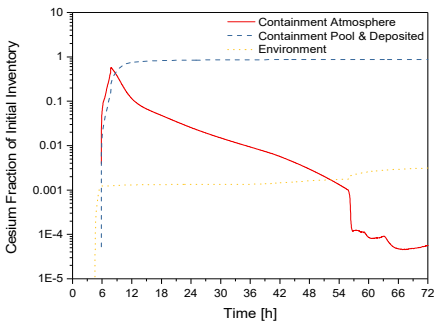

(h) SGTR-032 (MELCOR, BS)

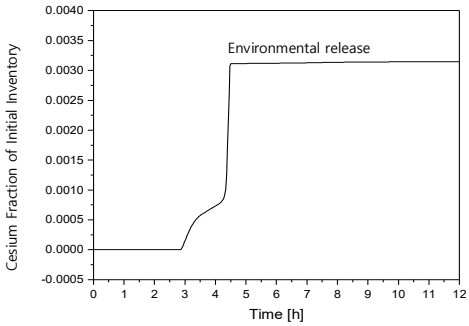

(i) SGTR-032 (MAAP5, BS)

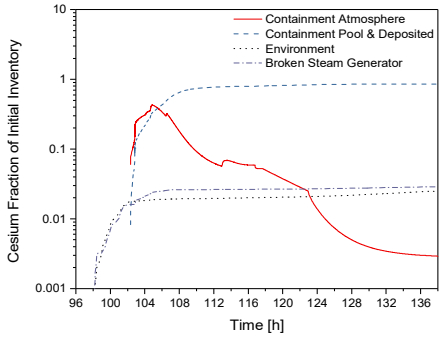

(j) SGTR-010 (MELCOR, BS)

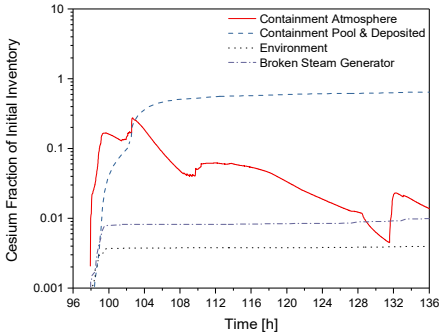

(k) SGTR-010 (MELCOR, MS)

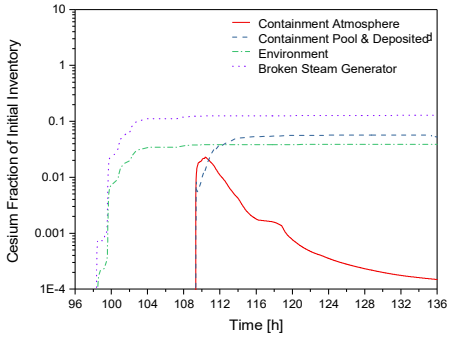

(l) SGTR-010 (MAAP5, BS)

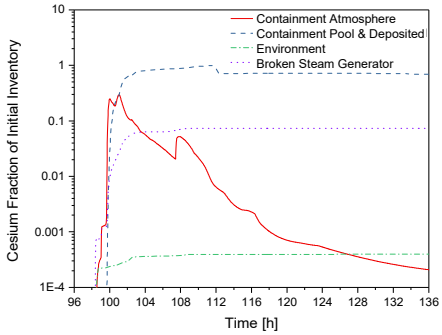

(m) SGTR-010 (MAAP5, MS)

Fig. 7. Time trends of the Cs fraction in various locations (2/2).

Table II. Key event timings predicted by MELCOR and MAAP5 (h)

	MELCOR predictions															
Scenarios	SBO-025		SSBO-001		SLOOP-004		SLOOP-005		SLOCA-020		ISLOCA-001		SGTR-032		SGTR-010	
Events/Cases	BS[1]	MS[2]	BS	MS	BS	MS	BS	MS	BS	MS	BS	MS	BS	MS	BS	MS
Reactor trip	0.0								0.009		0.018		0.14			
SG-2 dryout	2.0		1.6		–								2.4		–	
SG-1 dryout[3]	10.3	–	1.7										3.6		90.7	
Core uncovery	11.9		2.8		122.1		37.0		0.7		5.2		3.53		94.6	
SAMG entrance (CET > 923.15 K)	12.9		3.4		124.4		38.0		4.9		5.8		4.3		97.2	
HL creep rupture	15.1								–							
Corium relocation into the RPV LP	19.1	–	5.5	–	135.5	–	41.5		8.0	18.0	7.8		5.1	–	101.1	101.5
RPV LH failure	19.7		5.8		135.8		46.5	–	9.1	–	9.0		5.8		102.3	102.2
Cont. leak failure	42.4		35.3		94.0		82.3		38.7		–		36.0		–	
Cont. rupture failure	65.5		57.7		120.9[4]		117.6		61.0				55.9			
Reactor cavity liner plate failure (MCCI)	–		–		190	–	–									
	MAAP5 predictions															
Events/Cases	BS	MS	BS	MS	BS	MS	BS	MS	BS	MS	BS	MS	BS	MS	BS	MS
Reactor trip	0.0								0.001				0.2			
SG-2 dryout[3]	1.8		1.2		–								1.2		–	
SG-1 dryout	10.3	–													86.9	
Core uncovery	11.8		2.1		148.0		37.0		1.1		3.9		2.4		93.1	
SAMG entrance (CET > 923.15 K)	12.5		2.5		151.9		37.6		1.3		4.3		2.8		98.1	
HL creep rupture	14.2				–								4.5	–	–	
Corium relocation into the RPV LP	17.0		4.7	4.2	159.8	–	42.8	–	4.5	–	5.7		7.4	–	103.8	102.2
RPV LH failure	18.1		4.8	-	161.4		45.0		7.7		7.1		8.2		109.3	107.4
Cont. leak failure	48.3		30.5		108.7		105.1		31.7		–		36.0		–	
Cont. rupture failure	102.1		63.1		146.8[4]		198.6		76.3				82.1			
Reactor cavity liner plate failure (MCCI)	–		–		192	–	–									

Note superscript: [1] Base (unmitigated) scenario; [2] Mitigated scenario; [3] Faulted SG in the SGTR sequences; [4] Failure of the containment before core damage & RPV LH failure.

Table III. Cross-comparison of the MELCOR and MAAP5 models employed in the present study

Events/Phenomena		MELCOR modeling	MAAP5 modeling	Results & findings
Induced HL/SG creep rupture (SBO)	HL natural circulation flow rate	Calculated by the density difference between the upper & lower regions of the HL	Calculated by the density difference between the RPV upper plenum and the SG inlet plenum	Both codes lead similar calculation results.
	SG natural circulation flow rate	Determined by users based on the CFD analysis	Calculated by the code based on the density gradient and the pressure drop through the SG U-tubes	MAAP5 does not reflect the geometrical information of the SG inlet plenum, which affects the creep damage of the RCS pressure boundary.
	Mixing fraction in the SG inlet plenum		All hot and cold fluid are completely mixed in the SG inlet plenum.	The temperature of the gas entering the U-tubes relatively underestimates in the case of MAAP5.
	Hottest temperature of SG U-tubes		Not considered	The possibility of creep rupture of the SG U-tubes is relatively low, compared to MAAP5.
	Pressurizer surge line creep rupture	Simulated based on the fluid behavior	Simulated based on the Larson-Miller (LM) creep damage fraction	The event for the creep rupture of the pressurizer surge line is set to be always false in the case of MAAP5.
	Temperature of the RPV outlet nozzle	Simulated using 1.5 times heat transfer coefficient	Simulated based on the temperature gradient in the HL	Both methodologies applied to MELCOR and MAAP5 could distort actual phenomena.
	Characteristic curve of MSSVs	Simulated based on the plant specific data	Simulated relatively simply	The opening and closing times of MSSVs could be distorted in the case of MAAP5.
RPV LH	Dominant failure mechanisms	LM creep rupture model was used, instead of the ejection of instrument penetration tubes (US SOARCA)	Always, the RPV LH is failed by an ejection of instrument penetration tube before its creep damage fraction exceeds 1.0.	MELCOR relatively delays the failure time of the reactor vessel, compared to MAAP5.
MCCI in the reactor cavity	Melt eruption and water ingress phenomena	Not simulated due to the lack of verification	Simulated based on both validation & verification results	MELCOR conservatively simulates the concrete erosion by MCCI, compared to MAAP5.
	Two-layered concrete modelling of basaltic & limestone	Not simulated, but it can be indirectly simulated through FDI package.	Simulated	The concrete erosion and the amount of the non-condensable gas can be distorted in the case of MELCOR.
Fission Products (FPs)	Initial inventory including Cs, I, and Mo	Calculated by users	Calculated by the code	There are inevitable differences in the initial core inventory between MELCOR and MAAP5.
	Release from the fuel-cladding gap	Modified ORNL-Booth model	ORNL-BOOTH model adjusted by relevant scale factor to each group	MELCOR and MAAP5 simulate different FP release characteristics early in core damage.
		Simulated individually for all FP classes		
	Retention (ISLOCA)	· Turbulent deposition in the straight pipe : Wood model (RN2 package); Impaction in pipe bent: INL model (RN2 package) · Pool scrubbing in the submerged pipe: SPARC-90 model or mechanistic pool scrubbing model	· Turbulent deposition in the straight pipe & Impaction in pipe bent: cont. hard pipe & vent junction model · Pool scrubbing in the submerged pipe: SUPRA code model	There is a significant difference in results between MELCOR and MAAP5.
	Retention (SGTR)	Calculated based on the ARTIST project test results (PSI)	Applied multipliers derived from the ARTIST project test results (PSI) to the SUPRA bare pool model	Both codes led a similar result for the base/unmitigated scenario in terms of the environmental release of Cs, but somewhat difference for the mitigated scenario.

4. CONCLUSIONS

In this paper, best-practice analysis results for the evolution of key accidents and plant response including the environmental release of radiological FP Cs, based on the eight reference scenarios selected for the APR1400 SOARCA study. The influence of dedicated mitigation strategies on the results of interest was also investigated to assess their effectiveness in coping with relevant severe accident scenarios. The latest versions of the MELCOR and MAAP5 codes, MELCOR 2.2 and MAAP5.04, were utilized to compare the results of interest. As implemented through the APR1400 SOARCA study, relevant insights are summarized as follows.

(1) For most scenarios employed in the present study, both codes similarly predicted the general trend of the evolution of the severe accident and plant responses, but the environmental release of the radiological FP Cs as well as the late phase of core degradation and subsequent containment behavior significantly differed.

(2) Most mitigation strategies employed in the present study greatly decreased the environmental release of radiological Cs, except for SLOOP-004 which led to a failure of the containment isolation before the core damage and RPV LH failure. The code predictions for SLOOP-004 showed that the operator action time is very much important in mitigating the adverse effect of relevant accident.

(3) Additional findings identified through the present study shows that the following points need to be further studied in order to obtain more indepth insights for the results of interest:
- More realistic estimation of the initial inventory of Cs compounds (CsI, CsOH, and Cs_2MoO_4) affecting the amount and timing of the Cs release to the environment (e.g., during its late phase revalorization);
- Influence of a two-layer concrete model on the MCCI-induced generation of combustible gases (such as H_2 and CO) in the dry reactor cavity (MELCOR);
- Influence of the RCP seal leakage on the induced RCS pressure boundary creep rupture (high pressure accident sequences like SBO);
- Influence of relevant uncertainty in model input parameters and different modelling options, which may highly influence on the evolution of severe accidents and FP source terms.

NOMENCLATURE

APR	Advanced Power Reactor
CET	Core Exit Temperature
Cs	Cesium
EWI	Emergency (External) Water Injection
FDI	Fuel Dispersion Interactions
FP	Fission Product
ISLOCA	Interfacing System Loss of Coolant Accident
KHNP	Korea Hydro & Nuclear Power Co., Ltd.
LTSBO	Long-Term Station Blackout
MAAP	Modular Accident Analysis Program
PSA	Probabilistic Safety Assessment
SAMG	Severe Accident Management Guidance
SSBO	Seismic-induced Station Blackout (SBO)
SGTR	Steam Generator Tube Rupture
SLOOP	Seismic-induced Loss of Offsite Power
SOARCA	State-of-the-Art Reactor Consequence Analyses

STSBO Short-Term Station Blackout
TI-SGTR Thermally-induced Steam Generator Tube Rupture

ACKNOWLEDGMENTS

This work was carried out as part of the 'Development of the Level 2&3 PSA Technologies based on the State-of-the-Art Technology (L16S059000)' project funded by the Central Research Institute (CRI) of the Korea Hydro & Nuclear Power (KHNP) Co., Ltd. This work was also partially supported by the National Research Foundation of Korea (NRF) grant funded by the Korean government (MSIT: Ministry of Science and ICT).

REFERENCES

1. USNRC, "State-of-the-Art Reactor Consequence Analyses Report," NUREG-1935, U.S. Nuclear Regulatory Commission, Washington, DC, USA (2012).
2. USNRC, "State-of-the-Art Reactor Consequence Analyses Project, Volume 2: Surry Integrated Analysis," NUREG/CR-7110, Vol. 2, Rev.1, Prepared for U.S. Nuclear Regulatory Commission, Sadia National Laboratories, Albuquerque, NM, USA (2013).
3. K.I. Ahn and S.W. Hwang, "The KHNP SOARCA Project: Development Strategy," KHNP Severe Accident and SOARCA Workshop, Sadia National Laboratories, Albuquerque, NM, USA, April 17 (2017).
4. KHNP, "Development of State-of-the-Art Technology for Level 2&3 PSA: Final Report." KHNP-2019-50003339, Korea Hydro & Nuclear Power Company, Korea (2019).
5. KHNP, "Standard Safety Analysis Report for APR1400," Korea Hydro & Nuclear Power Company, Korea (2002).
6. H.G. Kim, "The Design Characteristics of Advanced Power Reactor 1400," IAEA-CN- 164-3S09, Vienna, Austria (2017).
7. KHNP, "At-Power Internal Events Level 1 PSA for Wolsong Unit 1: Vol. 7. Quantification," Korea Hydro & Nuclear Power Company, Korea (2015).
8. SNL, "MELCOR Computer Code Manuals (Vol.1): Primer and Users' Guide," Version 2.2.9541. SAND2017-0455, Sadia National Laboratories, Albuquerque, NM, USA (2017).
9. EPRI, "Modular Accident Analysis Program (MAAP5.04): Vol. 1-4," Electric Power Research Institute, USA (2016).
10. KAERI, "MAAP-ISAAC (Modular Accident Analysis Program-Integrated Severe Accident Analysis Code for CANDU plants) Computer Code User's Manual," KAERI/TR-3645/2008, Korea Atomic Energy Research Institute, Daejeon, Korea (2008).
11. USNRC, "MACCS Best Practices as Applied in the State-of-the-Art Reactor Consequence Analyses (SOARCA) Project," NUREG/CR-7009, Prepared for U.S. Nuclear Regulatory Commission, Sadia National Laboratories, Albuquerque, NM, USA (2014).
12. EPRI, "Modular Accident Analysis Program (MAAP)-MELCOR Crosswalk: Phase 1 Study," Technical Report 3002004449, Electric Power Research Institute, USA (2014).
13. OECD, "Use and development of probabilistic safety assessments at nuclear facilities," NEA/CSNI/R(2019)10, OECD/NEA, Paris, France, September (2020).
14. K.T. Kim, "Recent changes of safety regulation in Korea," *IAEA Technical Meeting on Novel Design and Safety Principles*, Vienna, Austria (2016).
15. KHNP, "Extreme Events Coping Strategy for APR1400. A16IP39-29.2, Rev. 0," Korea Hydro & Nuclear Power Co. (KHNP), Korea (2017).
16. KHNP, "Probabilistic Safety Assessment for the SKN Units 3&4," Korea Hydro & Nuclear Power Company, Korea (2011).

17. S.W. Jang, S.W. Lee, H.C. Oh, "Improvement of Diagnostic Flow Chart in Severe Accident Management Guidance for Nuclear Power Plants in Korea," *Transactions of the Korean Nuclear Society Autumn Meeting*, Gyeongju, Korea, Oct. 27-28 (2016).
18. NEI, "Diverse and Flexible Coping Strategies (FLEX) Implementation Guide. NEI 12-06 (Rev 4)," Nuclear Energy Institute, USA (2016).
19. NEI, "Crediting Mitigating Strategies in Risk-Informed Decision Making. NEI 16-06 (Rev 0)," Nuclear Energy Institute, USA (2016).
20. H.S. Ryu, J.I. Park, H.K. Lim, "Consideration about developing human reliability analysis method applicable to external events with a focus on seismic of domestic nuclear power plants," *Asian Symposium on Risk Assessment and Management (ASRAM2019)*, Gyeongju, Korea, Sept. 30 - Oct. 2 (2019).
21. K.I. Ahn, K.H. Lee, S.W. Lee, S.W. Hwang, H.G. Lee, "Estimation of fission product source terms for the ISLOCA of a reference PWR plant using MELCOR and MAAP5," *Nuclear Engineering and Design*, **370**(110932) (2020).
22. K.I. Ahn, K.H. Lee, S.W. Lee, G. Choi, S.W. Hwang, "Estimation of fission product source terms for the SGTR accident of a reference PWR plant using MELCOR and MAAP5," *Nuclear Engineering and Design*, **371**(110967) (2021).
23. G. Choi, K.I. Ahn, K.H. Lee, S.W. Lee, S.W. Hwang, "Plant-specific assessment of the natural circulation-induced creep rupture characteristics in the RCS pressure boundary during the SBO accident," *Progress in Nuclear Energy*, **139**(103871) (2021).
24. J.C. Ryman, "ORIGEN-S Data Libraries (SCALE 6 Code Manual)," NUREG/CR-0200, Vol.3, Rev. 6, Vol. 3. M6, U.S. Nuclear Regulatory Commission, Washington, DC, USA (2000).
25. ANS, "Decay Heat Power in Light Water Reactors," ANSI/ANS-5.1-2014, American Nuclear Society, USA (2014).
26. USNRC, "Consequential SGTR Analysis for Westinghouse and Combustion Engineering Plants with Thermally Treated Alloy 600 and 690 Steam Generator Tubes," Draft, NUREG-2195, U.S. Nuclear Regulatory Commission, Washington, DC (2016).
27. USNRC, "Computational Fluid Dynamics Analysis of Natural Circulation Flows in a Pressurized-Water Reactor Loop under Severe Accident Conditions," NUREG-1922, U.S. Nuclear Regulatory Commission, Washington, DC, USA (2010).
28. W.T. Kim and K.I. Ahn, "Computational Fluid Dynamics Analysis for the Improvement of the KHNP-SOARCA model," Technical Report for KHNP-SOARCA, RETech Co., Ltd., Yong-in, Korea (2019).
29. P. Owczarski and K. Burk, "SPARC-90: A code for calculating fission product capture in suppression pools," NUREG/CR-5765, PNL-7723, USA (1991).
30. K.H. Lee, K.I. Ahn, S.W. Hwang, "Analyses of Fission Product Retention under ISLOCA using MELCOR for APR1400," *Transactions of the Korean Nuclear Society 2019 Autumn Meeting*, Jeju, Korea, May 23-24 (2019).
31. A.T. Wassel, J.L. Farr, M.S. Hoseyni, "SUPRA: A Code for Simulating Removal of Radionuclides by Water Pools Under Severe Accident Conditions," EPRI/NP-3886-CCMP, Electric Power Research Institute, USA (1985).
32. P. McMinn, C.Y. Paik, K.I. Ahn, S.Y. Park, K.H. Lee, S.W. Hwang, "Source Term Analysis for PWR ISLOCA Using MAAP5," *16th International Topical Meeting on Probabilistic Safety Assessment and Analysis (PSA 2019)*, Charleston, South Carolina, USA, April 28 - May 4 (2019).
33. A. Rýdl, T. Lind, J. Birchley, "Integral analyses of fission product retention at mitigated thermally-induced SGTR using ARTIST experimental data," *Nuclear Engineering and Design*, 297, pp. 175-187 (2016).
34. K.H. Lee, K.I. Ahn, S.W. Hwang, "Analyses of aerosol retention under SGTR accident based on ARTIST experimental data," *Transactions of the Korean Nuclear Society 2018 Autumn Meeting*, Yeosu, Korea, October 25-26 (2018).

Log Number: 264

The APR1400 SOARCA Study: Insights into the Severe Accident Progression and Source Term Analysis Results

Kwang-Il Ahn* (KAERI)

K.H. Lee (FNC), **S.W. Hwang** (KHNP-CRI)

OUTLINE

- Korean SOARCA?
- APR1400 SOARCA
  - Scope and objectives
  - Underlying strategies & approaches
  - Results of interest including the environmental release of FP Cs
  - Relevant finding and insights
- Concluding Remarks

1. The K-SOARCA: Summary

❑ Project Title

Development of the State-of-the Art Level 2&3 PSA Technologies

❑ Motivation

- Resolve the regulatory requirement & safety issues raised from the CANDU reactor stress test after the Fukushima accident: risk-informed assessment for the SA coping strategies/means and (b) two bypass events (SGTR/ISLOCA)
- Secure core technologies for more realistic analysis of the accident progression and off-site consequence following SA: best-practice/estimate SA modeling and relevant computational tools (such as MELCOR 2.2/MAAP5/MAAP-ISAAC, WinMACCS)
- Explore the state-of-the art Level 2&3 PSA technologies for diverse applications to the emerging safety issues (such as newly-established AMP in legal framework and relevant safety goals (CDF/LERF, Cs-137 requirement) in legal framework, Multi-unit Risk)

❑ Pilot/Reference Plants

- **SKN 3&4 (APR1400 series): APR1400 SOARCA**
- **WS-1 (CANDU-6 Type): CANDU-6 SOARCA**

❑ **Principal Investigating Organization: KHNP (Korean Utility)**

❑ **Technical Supporting Organization: KAERI** [collaboration with FNC & ACT (Domestic SME), **SNL** & **F&A (US)**]

❑ **Project Period**: 2016.07 - 2019.06 (36 Months)

1. The K-SOARCA: Strategy

Reference Plants: SKN 3&4 (APR1400) and WS-1 (CANDU)

SKN3&4 / WS-1: 8 / 9 ASs

Level 2 PSA

APR1400: MELCOR2.2 & MAAP5.04

Representative Accident Sequences (ASs)

① Long-term SBO (LTSBO)
② Short-term SBO (STSBO)
③ Bypass sequences:
ISLOCA and S-SGTR
④ Other contributors (SLOOP, SLOCA)

Modeling of Mitigation Measures (SAM)

① Mitigation Measures:
PARs, Portable EDG & Pumps, External Water Injection, ECSBS, CFS
② Mitigation Strategy (SAMG)

Modeling of Accident Progressions

①The latest SA Codes:
- PWR: MELCOR2.2 / MAAP5
- CANDU: MAAP-ISAAC

②Best-estimates & best-practices

Modeling of Source Term Behaviors

① Core inventory (60 nuclides)
② Release fractions (for 9 radioactive nuclides group)
③ Time & duration of releases
④ Release of tritium (CANDU)

US SOARCA

(NUREG/CR-7110, PWR/BWR, NRC/SNL)

PSA-based four AS	Relevant Codes
Internal Events • **ISLOCA**: 7E-7/ry • **SGTR**: 3E-7 to 5E-7/ry **External Events (Seismic)** • **LTSBO**: 1E-5 to 2E-5/ry • **STSBO**: 1E-6 to 2E-6/ry	• **SA/ST** (incl. **Mitigation**): **MELCOR 1.8.6 & 2.2** • **Consequence** (incl. **EP&R**): **MACCS2** (WinMACCS 3.6)

Level 3 PSA

- Domestic Food Chain Model (FCM)
- Meteorological Data
- Site Information (topography, agro & livestock products)
- Population Distribution
- Risk Conversion Factors
- Emergency Response Model

Offsite Consequence Analysis (WinMACCS)

① Individual/Population Dose
② Prompt & Latent Fatality (including their CCDF)
③ Sensitivity Analysis
④ Cost-benefit Analysis (CBA)

2. The APR1400 SOARCA

❑ Scope and Objectives

- Performing the **best practice modeling of the accident progression and relevant FP source** terms expected for the representative accident sequences: **MELCOR (Audit tool for regulation) & MAAP5 (Utility tool for PSA & SA analysis)**
- Investigating the **influence of dedicated accident mitigation actions (SAM, SAMG)** on the results of interest through the established best-practice modelings [such as the evolution of key plant events and environmental release of the FP 'cesium' (Cs)];
- Identifying **potential gaps between the two different codes (MELCOR & MAAP)** on the analysis results of interest to support the regulatory aspects.

❑ APR1400 (Advanced Power Reactor 1400 MWe)

- **Gen-III reactor** with two primary coolant loops, and each loop has one SG and two RCPs in one HL and two CLs arrangement;
- Incorporated several engineering improvements and operational experience from the earlier OPR1000 design to enhance safety;
- **SKN units 3&4 are the FOAK** employed the APR1400 design.

2. The APR1400 SOARCA: Mitigation Measures

KHNP-MACST for the plant's key safety functions during BDBA

- **Phase 1:** using on-site installed plant safety equipment (until 8 h after the accident)
- **Phase 2:** shifting from the installed safety equipment to on-site mobile equipment (until 72 h)
- **Phase 3:** using all available on-/off-site equipment (after 72 h)

MACST Equipment	Relevance with SAMG/SAG	Phase
Mobile EDG of 1 MW	· EOG (supply AC power during SBO)	· Phase 2
Low-/Medium-pressure mobile pumps	· SAG-02 (inject water into the SGs) · SAG-03 (maintain the RCS inventory and core cooling)	· Phase 2
POSRVs (Pilot-operated Safety Relief Valves)	· SAG-01 (depressurize the RCS)	· Phase 1
TD-AFWP (Turbine-driven Auxiliary Feedwater pump) using a DC battery (lasting for 8 h)	· SAG-02 (inject water into the broken SGs) to mitigate a release of FPs to the environment during an SGTR	· Phase 1
ECSBS (Emergency Containment Backup System) with dedicated pumps	· SAG-04 (inject water into the reactor cavity) · SAG-05 (control FP release) · SAG-06 (control containment conditions for long-term cooling)	· Phase 2 (when the CSS is not available)
PARs, POSRV three-way valves & Hydrogen-ignitors (active)	· SAG-07 (control hydrogen in the reactor/containment building)	· Phase 1 or 2
CFS (Cavity Flooding System)	· SAG-04 (inject water into the reactor cavity to cool down the RPV, core debris released to the reactor cavity, and scrub FPs in the cavity during a severe accident)	· Phase 2

MACST: multi-barrier accident coping strategy; **EOG**: emergency operating guideline; **SAG**: severe accident guideline; **CSS**: Cont. Spray System

2. The APR1400 SOARCA: Accident Sequences

- **Five general sequences** screened out based on **the specified CDF criterion (1.0E-07/ry)**
- Three bypass events (**S-SGTR** and **ISLOCA), one-order less than the general event (1.0E-08/ry)**

No	Accident Sequences	CDF (/ry)	Dedicated AM Strategies
1	**SBO_025** (**LTSBO**, internal initiating event): **Potential TI-SGTR**	6.36E-07	Mobile EDG + TD-AFWP + EWI to the SG using mobile pump (after the AFWST dried out)
2	**SSBO_001** (**STSBO**, Seismic-induced SBO): **Potential TI-SGTR**	3.43E-07	Mobile EDG + EWI to the SG and RCS using mobile pump + CFS + ECSBS
3	SLOOP_004 (Seismic-induced LOOP and a failure of CHR operation)	2.83E-07	EWI into the RCS (using mobile pump)
4	SLOOP_005 (Seismic-induced LOOP and a failure of F&B operation)	1.03E-07	EWI into the RCS (using mobile pump) + ECSBS
5	SLOCA_020 (Small LOCA, internal initiating event)	1.40E-07	EWI into the RCS (using mobile pump) + ECSBS
6	**ISLOCA**_001 (Aux. Building A Region-SCP suction pipe 4” break)	2.80E-08	CFS + ECSBS
7	**SGTR**_032 (with a failure of safety injection and an isolation of the faulted SG, internal initiating event)	1.42E-08	EWI into the RCS (using mobile pump) + ECSBS
8	**SGTR**_010 (with a failure of SG isolation and an isolation failure of the faulted SG, internal initiating event)	1.22E-08	Aux. feed-water injection into the faulted SG (using MD-AFWP)

[Note] **TI-SGTR**: Thermally-induced SGTR; **EWI**: Emergency/External Water Injection); AM: accident mitigation; CHR: containment heat removal; F&B: feed and bleed; LOOP: loss of offsite power.

2. The APR1400 SOARCA: Plant/Code Modeling

❑ Fundamental plant modeling

- **Detailed hydrodynamic nodalizations and core models** (RCS loop, RPV/reactor core, and containment)
- **FP initial inventory** (ORIGEN 2), **ANS decay heat model**, **FP gap release** (modified ORNL-Booth model for MELCOR; ORNL-Booth model adjusted by scale factor for MAAP5), and **FP deposition & scrubbing in various structures/locations**
- **Two-layered concrete for the reactor cavity (MCCI):** limestone – basaltic – containment liner plate
- **RPV failure mechanisms:** penetration tube failure and/or L-M creep-rupture model for the lower head
- **Containment leakage: design leakage (**0.1 vol%/day at 0.515 Mpa), **leak failure (**$P_{leak} = 2.3P_{design}$), **rupture failure (**$P_{rupt} = 3.6P_{design}$)

<table>
<tr><th>Code</th><th>Reactor core</th><th>RPV (core region)</th><th>RPV-LH wall</th><th>Reactor building (R/B)</th><th>Auxiliary building</th><th>Relevant scenarios</th></tr>
<tr><td rowspan="2">MELCOR</td><td rowspan="2">Five radial rings and 13 axial-levels</td><td>30 CVs</td><td rowspan="2">10 radial segments</td><td rowspan="4">18 compartments and 52 FLs between compartments</td><td rowspan="4">19 CV nodes</td><td>SBO/SGTR</td></tr>
<tr><td>one CV</td><td>ISLOCA</td></tr>
<tr><td rowspan="2">MAAP5</td><td colspan="3">MAAP5 standard model (fixed)</td><td></td></tr>
<tr><td colspan="2">seven radial rings and 13 axial-levels</td><td>one CV</td><td>25 axial nodes and five radial nodes</td><td>All</td></tr>
<tr><td colspan="7">CV: (hydrodynamic) control volum; FL: flow path</td></tr>
</table>

2. The APR1400 SOARCA: Plant/Code Modeling

Plant Nodalization for Both Codes

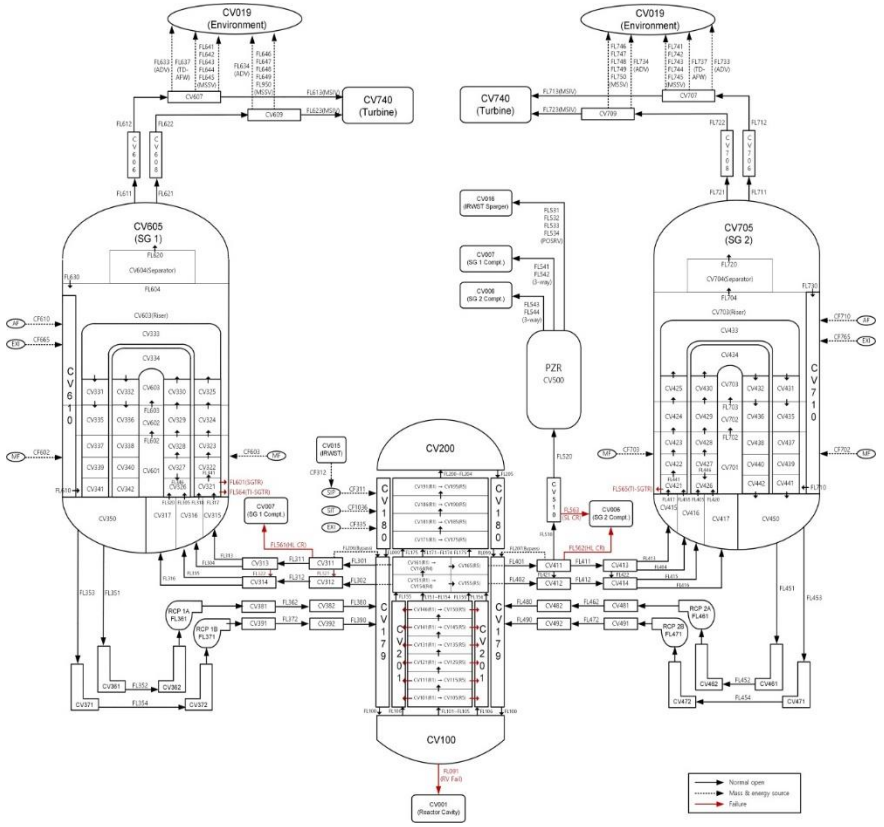

RCS loop and RPV (MELCOR)

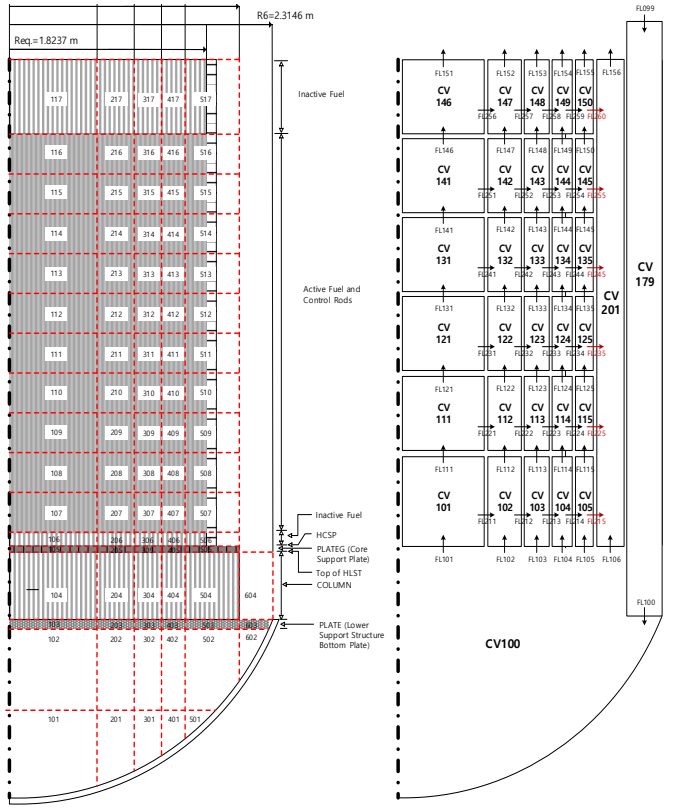

Reactor core and RPV lower head (MELCOR)

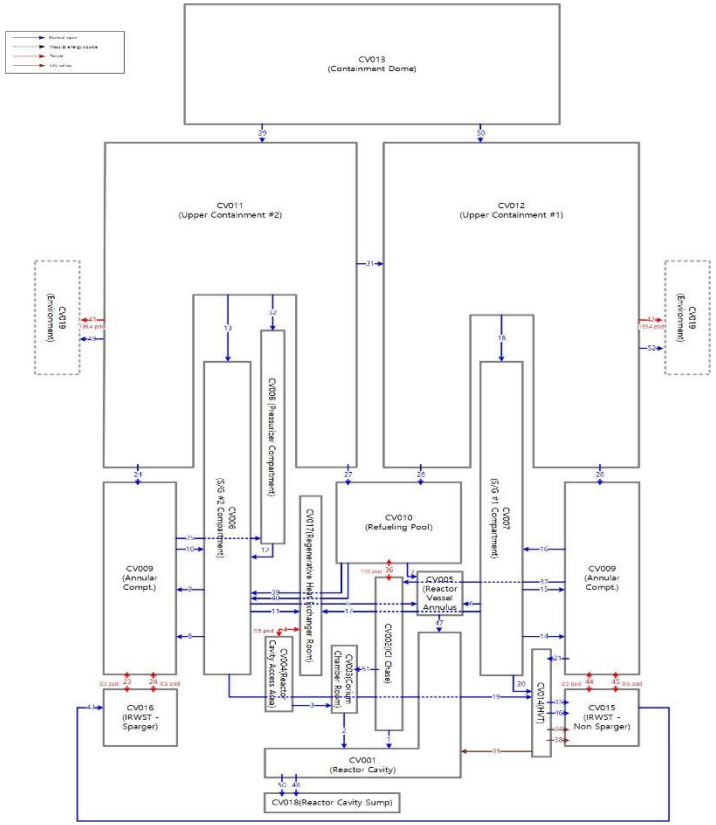

Reactor/containment building (MELCOR/MAAP5)

2. The APR1400 SOARCA: Plant/Code Modeling

❑ Sequence-specific modeling

- **LTSBO/STSBO**:
  - Stuck-open of the primary (POSRV) & secondary side (MSSV) pressure relief valves
  - **Counter-current natural circulation between HL and SG (coupled with the CFD analysis) and induced creep rupture**
- **ISLOCA**:
  - **ISLOCA piping network and auxiliary building models** (including ventilation systems)
  - **Turbulent deposition & re-vaporization of FPs inside the ISLOCA piping, FP pool scrubbing in the auxiliary building**, filtration of FPs through the auxiliary building ventilation system
- **SGTR**: **Deposition & decontamination of FPs in the faulted SG** (ARTIST Phase 1 for U-tube internal; Phase II for U-tube bundles for the flooded SG; Phase VII for U-tube bundles for the dried SG)

Auxiliary building & ventilation system

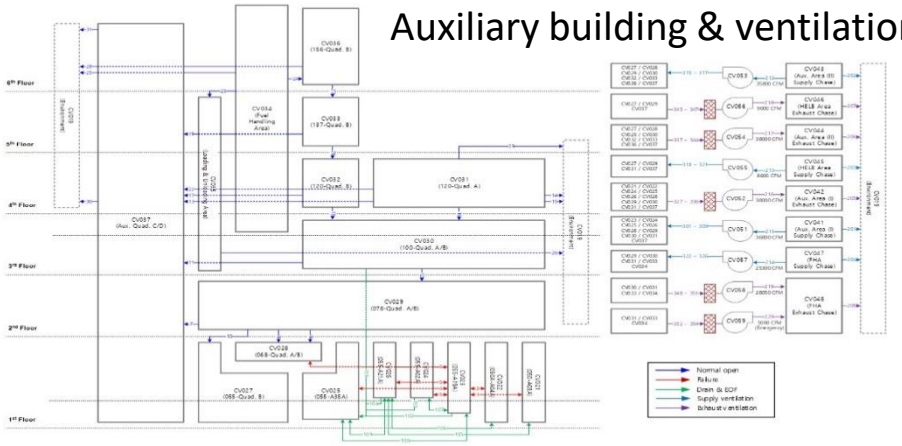

Piping network between HL and SCP

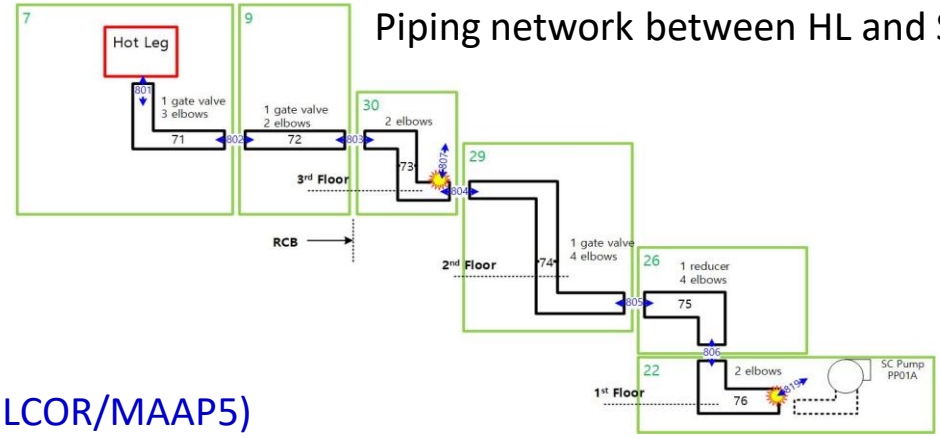

(ISLOCA, MELCOR/MAAP5)

2. The APR1400 SOARCA: Plant/Code Modeling

CFD analysis for PWRs subject to different geometries of the HL and pressurizer surge line

Symbol	Description	NUREG-1922 (WH, Side)	NUREG-1922 (WH, Top)	NUREG-2195 (CE, Top)	APR1400 (Top)
C_d	Discharge Coefficient	0.12	0.11	0.13 ~ 0.14	0.11
f	Mixing Fraction	0.96	over 1.0 -> 1.0	0.65 ~ 0.75	over 1.0 -> 1.0
r	Recirculation Ratio	2.4	2.6	1.05 ~ 1.10	3.5
F	Hot Tube Fraction	0.41	0.44	0.2 ~ 0.25	0.49
T_n	Normalized Temperature	0.6 ~ 0.65	0.50 ~ 0.55	0.95 ~ 0.99	0.44

PWRs subject to the top mounted pressurizer surge line

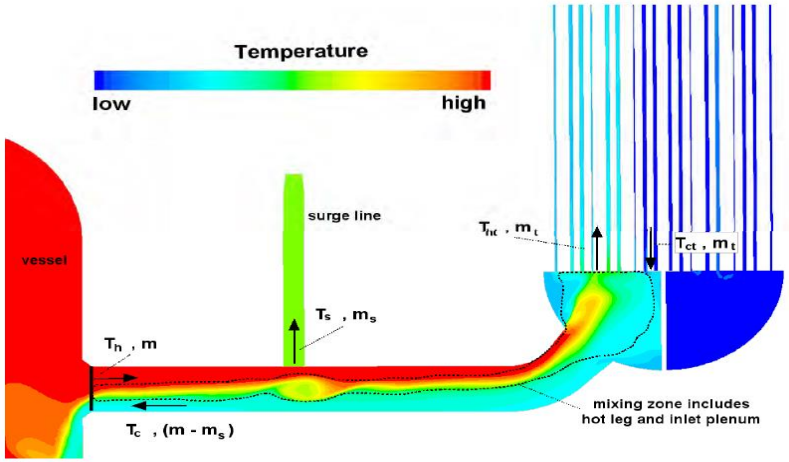

[NUREG-1922, WH, 2010]

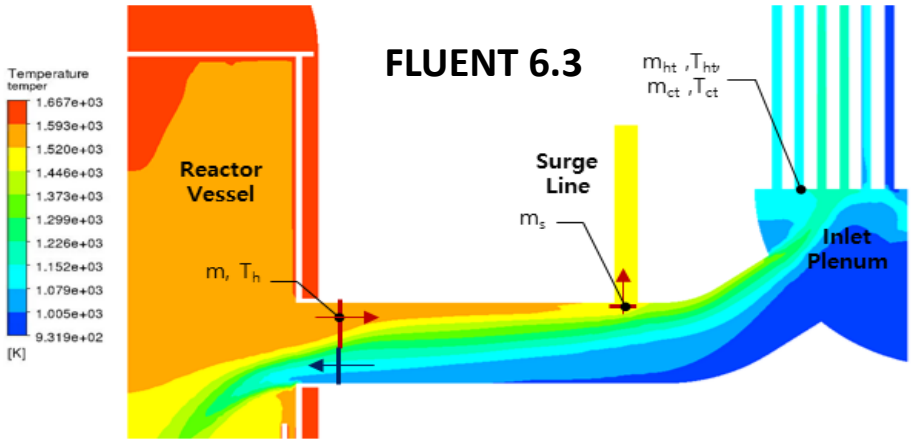

[APR1400 SOARCA, 2019]

2. The APR1400 SOARCA: Plant/Code Modeling

Coupling of MELCOR and MAAP5 with the CFD analysis results

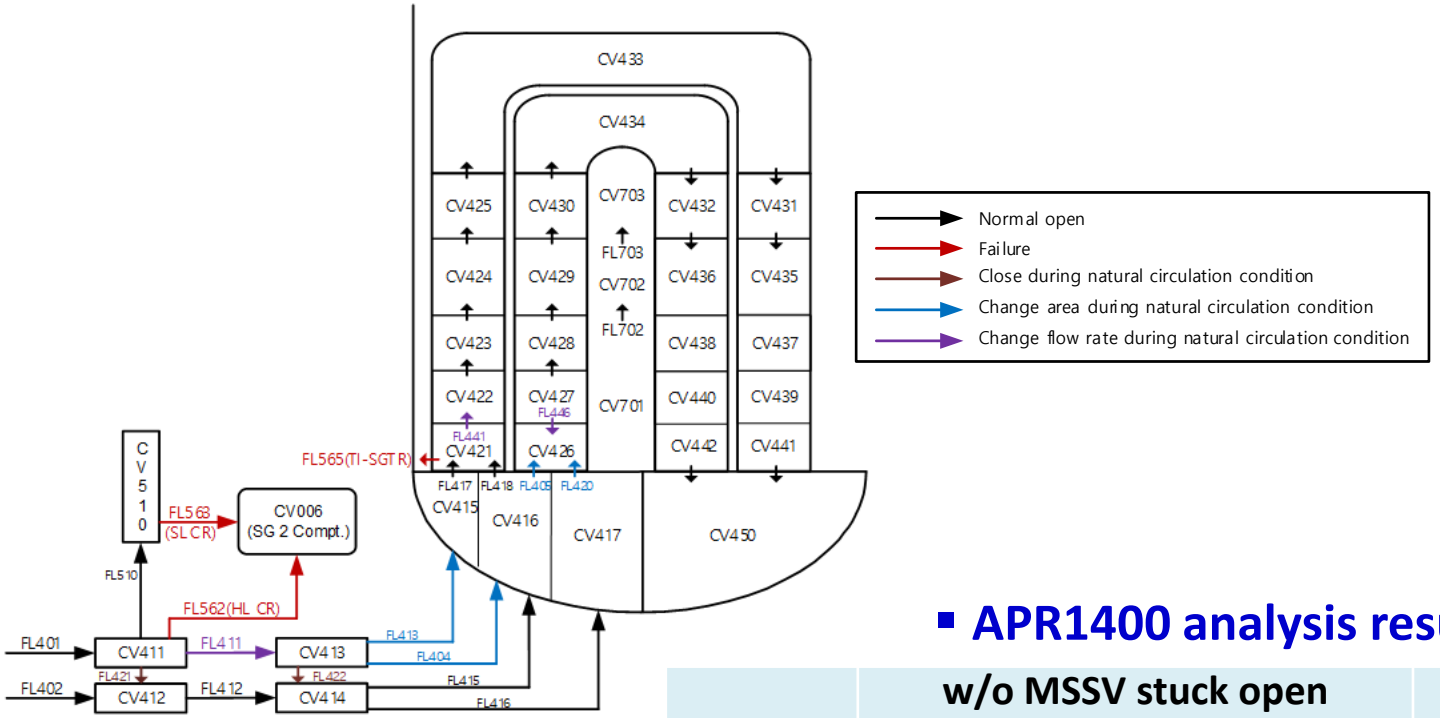

- **APR1400 analysis results (Base Scenario)**

	w/o MSSV stuck open		with MSSV stuck open	
	MELCOR	**MAAP5**	**MELCOR** (13.6 h)	**MAAP5**
LTSBO	HL creep rupture at 15.1 h	HL creep rupture at 14.2 h	TI-SGTR at 14.8 h and HL nozzle rupture at 15.2 h	TI-SGTR at a similar time with MELCOR
STSBO	RPV LH failure only, but no RCS creep rupture and TI-SGTR			

2. The APR1400 SOARCA: Sensitivity Analysis

Accident sequence	Sensitivity Parameters
• **SBO (LTSBO, TI-SGTR)**	• **MSSV Stuck open** (forced for TI-SGTR) • **SG U-tube stress** (multiplier 1.5 & 2.0) • SG U-tube material (Inconel 600, 690) • **SG Hottest tube temperature** (CFD analysis) • **Core inventory of FPs** (EOC, MOC, BOC)
• **SSBO (STSBO)**	• **Core inventory of FPs** (EOC, MOC, BOC)
• **SLOOP**	• **Maintaining safety injection after containment failure** (SAM strategy)
• **ISLOCA**	• **Pool scrubbing** (Down-comer model, Mechanistic pool scrubbing model) - MAAP5 only • **Turbulent deposition model** - MELCOR only (VICTORIA) • **Break elevation of SCS** (shutdown cooling system) and SIS (safety injection system) pipes (No pool scrubbing) • **Failure of auxiliary building venting system itself** • Functional degradation of auxiliary building venting system filters
• **SGTR**	• **DF (Decontamination factor) in SG 2ndry side** (ARTIST, Mechanistic pool scrubbing model) - MAAP5 only

Core inventory of FPs

(EOC, MOC, BOC)

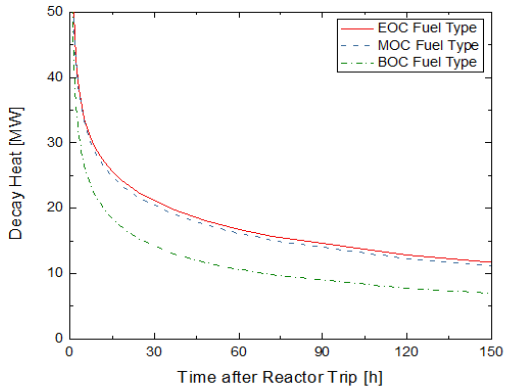

3. The APR1400 SOARCA: Results of interest (1/4)

Key plant responses predicted by MELCOR and MAAP5 (h)

	MELCOR predictions															
Scenarios	**SBO-025**		**SSBO-001**		**SLOOP-004**		**SLOOP-005**		**SLOCA-020**		**ISLOCA-001**		**SGTR-032**		**SGTR-010**	
Events/Cases	**BS**[1]	**MS**[2]	**BS**	**MS**	**BS**	**MS**	**BS**	**MS**	**BS**	**MS**	**BS**	**MS**	**BS**	**MS**	**BS**	**MS**
Core uncovery	11.9	–	2.8		122.1		37.0		0.7		5.2		3.53		94.6	
SAMG entrance (CET > 923.15 K)	12.9		3.4		124.4		38.0		4.9		5.8		4.3		97.2	
HL creep rupture	15.1		–													
RPV LH failure	19.7		5.8	–	135.8	–	46.5	–	9.1	–	9.0	5.8	–		102.3	102.2
Cont. leak failure	42.4		35.3		94.0		82.3		38.7		–	36.0			–	
Cont. rupture failure	65.5		57.7		120.9[4]		117.6		61.0			55.9				
	MAAP5 predictions															
Events/Cases	BS	MS	BS	MS	BS	MS	BS	MS	BS	MS	BS	MS	BS	MS	BS	MS
Core uncovery	11.8	–	2.1	148.0		37.0		1.1			3.9		2.4		93.1	
SAMG entrance (CET > 923.15 K)	12.5		2.5	151.9		37.6		1.3			4.3		2.8		98.1	
HL creep rupture	14.2		–										4.5	–	–	
RPV LH failure	18.1		4.8	–	161.4	–	45.0	–	7.7	–	7.1		8.2		109.3	107
Cont. leak failure	48.3		30.5		108.7		105.1		31.7		–		36.0		–	
Cont. rupture failure	102.1		63.1		146.8[3]		198.6		76.3				82.1			

[1] Base (unmitigated) scenario; [2] Mitigated scenario; [3] Failure of the containment before core damage & RPV LH failure.

3. The APR1400 SOARCA: Results of interest (2/4)

Environmental release fractions of Cs at maximum 72 h (EOC)

Accident scenarios	Fraction (%) with respect to its initial inventory [1]			
	MELCOR		MAAP5	
	BS[2]	MS[3]	BS	MS
SBO-025	0.168 (72 h)	0 (72 h) (no core damage)	0.021 (140 h)	0 (140 h) (no core damage)
SSBO-001	1.241 (72 h)	4.13×10^{-5} (72 h) (< cont. design leakage)	2.01×10^{-3} (96 h)	1.65×10^{-4} (96 h)
SLOOP-004	63.8 (200 h)	35.0 (200 h)	30.4 (200 h)	30.2 (200 h)
SLOOP-005	0.407 (120 h)	1.45×10^{-3} (120 h) (< cont. design leakage)	5.37×10^{-3} (200 h)	2.27×10^{-3} (200 h)
SLOCA-020	0.091 (72 h)	8.68×10^{-3} (72 h) (< cont. design leakage)	3.72×10^{-3} (96 h)	8.29×10^{-5} (96 h) (< cont. design leakage)
ISLOCA-001[4]	17.2 (72 h)	4.56 (72 h)	0.228 (72 h)	0.213 (72 h)
SGTR-032	0.314 (72 h)[5]	0.041 (72 h)[4]	0.315 (96 h)[5]	0.051 (96 h)[4]
SGTR-010[4]	2.532 (140 h)	0.398 (140 h)	3.904 (140 h)	0.0395 (140 h)

[1]4.8378E5 TBq; [2]Base (unmitigated) scenario; [3]Mitigated scenarios; [4]Bypass only; [5]Bypass & overpressure failure.

3. The APR1400 SOARCA: Results of interest (3/4)

Environmental release fractions of Cs at maximum 72 h (EOC)

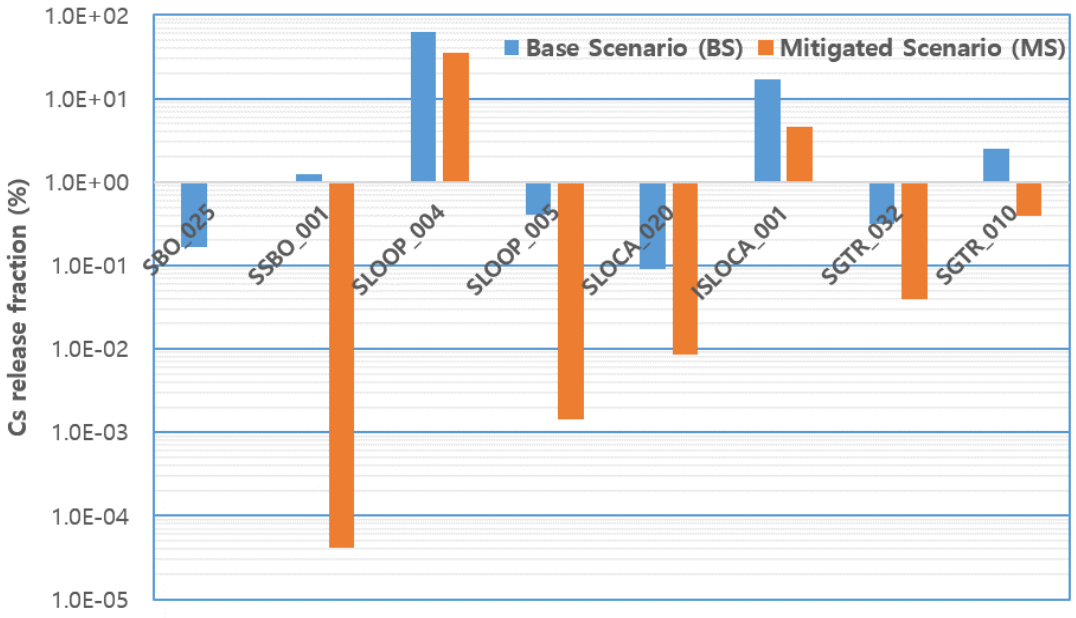

(a) MELCOR predictions

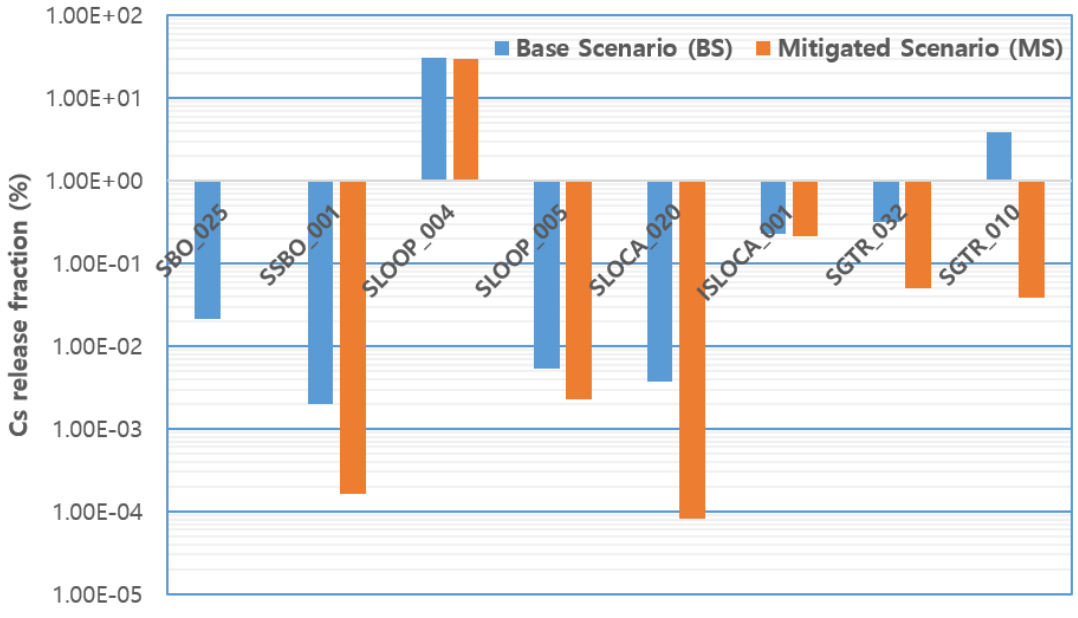

(b) MAAP5 predictions

[Note] SGTR-032 (BS): SGTR + Cont. failure; SGTR-032 (MS) and SGTR-010: SGTR only

3. The APR1400 SOARCA: Results of interest (4/4)

Time trends of the fractions of Cs at various locations (EOC) : SGTR and ISLOCA

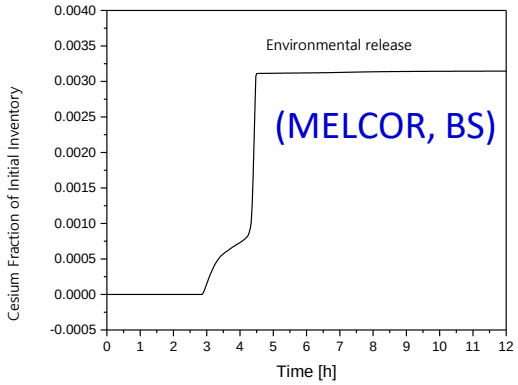

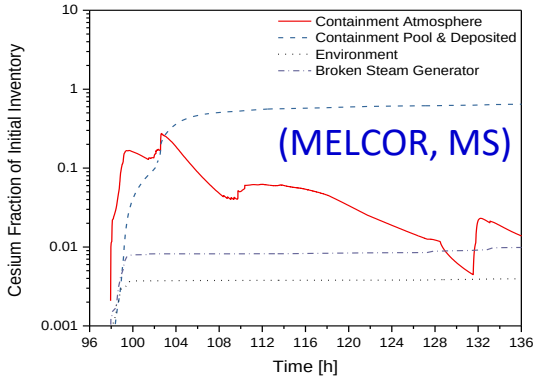

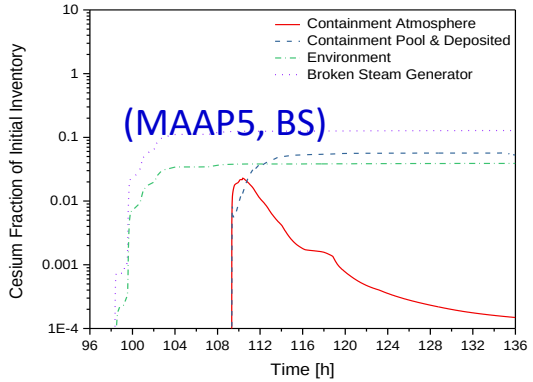

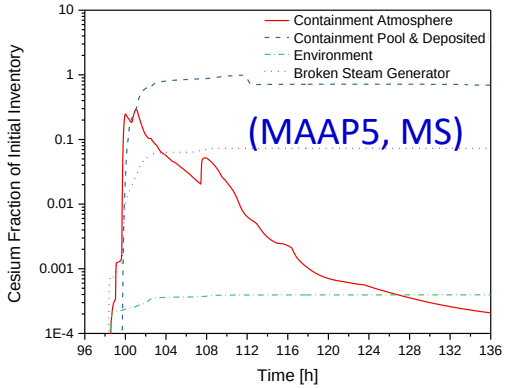

SGTR-010

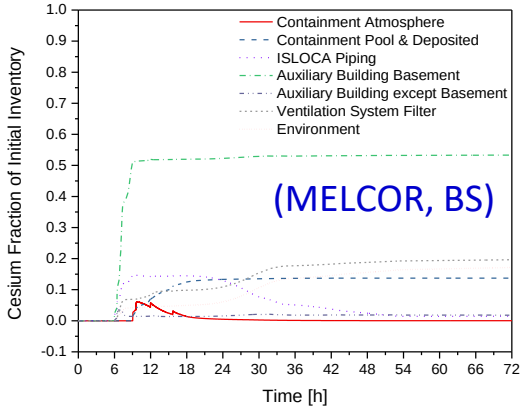

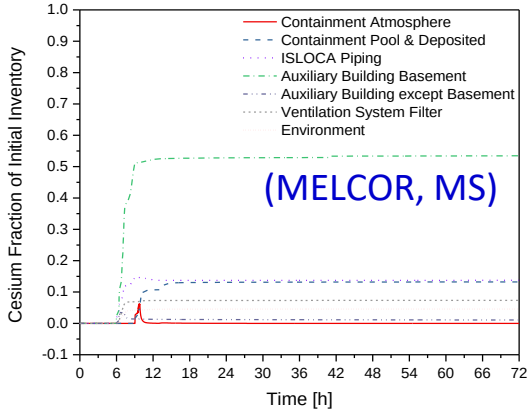

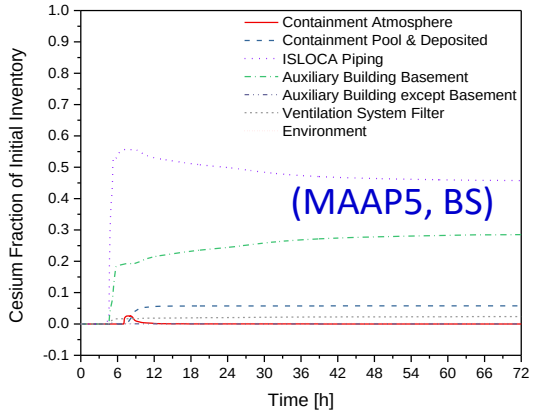

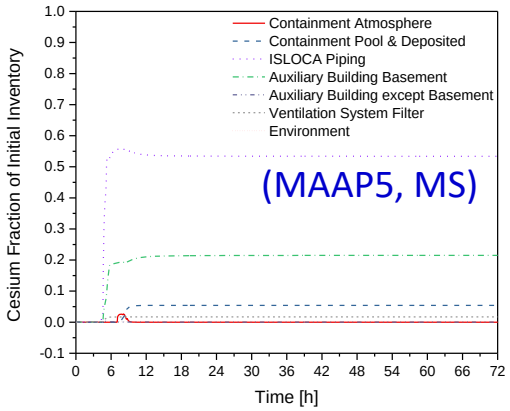

ISLOCA-001

4. The APR1400 SOARCA: Finding & Insights (1/3)

Events/Phenomena		MELCOR modeling	MAAP5 modeling	Results & insights
CCNC in HL/SG and induced creep rupture (SBO)	**Counter-current natural circulation flow rate in HL**	Calculated by the density difference between upper & lower regions of the HL	Calculated by the density difference between the RPV upper plenum and the SG inlet plenum	Both codes lead similar calculation results.
	Natural circulation flow rate in SG	Determined by users based on the CFD analysis	Calculated by the code based on the density gradient and the pressure drop through the SG U-tubes	MAAP5 does not reflect the geometrical information of SG inlet plenum, which affects the induced RCS creep damage.
	Mixing fraction in the SG inlet plenum		All hot and cold fluid are completely mixed in the SG inlet plenum.	MAAP5 relatively underestimates the temperature of the gas entering the U-tubes.
	Hottest temperature of SG U-tubes		Not considered	MELCOR relatively underestimates the possibility of creep rupture of the SG U-tubes than MAAP5.
	Pressurizer surge line creep rupture	Simulated based on the fluid behavior	Simulated based on the Larson-Miller (LM) creep damage fraction	The event for the creep rupture of the pressurizer surge line is set to be always false in MAAP5.
	RPV outlet nozzle temperature	Simulated using 1.5 times heat transfer coefficient	Simulated based on the temperature gradient in the HL	Methodologies applied to both codes could distort actual phenomena.
	Characteristic curve of MSSVs	Simulated based on the plant specific data	Simulated relatively simply	The opening and closing times of MSSVs could be distorted in MAAP5.

In the APR1400, the pressurizer surge line is mounted on the HL upper side, directing only the hot fluid of the HL upper side into it.

4. The APR1400 SOARCA: Finding & Insights (2/3)

Events/Phenomena		MELCOR modeling	MAAP5 modeling	Results & insights
RPV LH	**Dominant failure mechanisms**	LM creep rupture model was used, instead of the ejection of instrument penetration tubes (US SOARCA)	Always, the RPV LH is failed by an ejection of instrument penetration tube before its creep damage fraction exceeds 1.0.	MELCOR relatively delays the failure time of the reactor vessel, compared to MAAP5.
MCCI in the reactor cavity	**Melt eruption and water ingress phenomena**	Not simulated due to the lack of verification	Simulated based on both validation & verification results	MELCOR conservatively simulates the concrete erosion by MCCI, compared to MAAP5.
	Two-layered concrete of basaltic & limestone	Not simulated, but it can be indirectly simulated through FDI package.	Simulated	The concrete erosion and the amount of the non-condensable gas can be distorted in MELCOR.

4. The APR1400 SOARCA: Finding & Insights (3/3)

Events/Phenomena		MELCOR modeling	MAAP5 modeling	Results & insights
Fission Products (FPs)	**Initial inventory including Cs, I, and Mo**	Calculated by users	Calculated by the code	There are inevitable differences in the initial core inventory between MELCOR and MAAP5.
	Release from the fuel-cladding gap	Modified ORNL-Booth model	ORNL-BOOTH model adjusted by relevant scale factor to each group	Both codes simulate different FP release characteristics early in core damage.
		Simulated individually for all FP classes		
	Retention (ISLOCA)	• Turbulent deposition in the straight pipe : Wood model (RN2 package); Impaction in pipe bent: INL model (RN2 package) • Pool scrubbing in the submerged pipe: SPARC-90 model or mechanistic pool scrubbing model	• Turbulent deposition in the straight pipe & Impaction in pipe bent: cont. hard pipe & vent junction model • Pool scrubbing in the submerged pipe: SUPRA code model	There is a significant difference in results between both codes.
	Retention (SGTR)	Calculated based on the ARTIST project test results (PSI)	Applied multipliers derived f rom the ARTIST project test results (PSI) to the SUPRA b are pool model	Both codes led a similar environmental Cs release for the base/unmitigated cases, but somewhat difference for the mitigated scenario.

5. Concluding Remarks

❑ General Conclusions

- **The APR SOARCA study demonstrated that the best-practice SA modeling** has the potential to greatly decrease the environmental release of FPs, and **the dedicated mitigation strategies play an ultimate role in reducing** them.
- For most sequences tested, **both codes** similarly predict the evolution of SAs and plant responses, but **inevitable differences arise from how the initial core inventory of the FPs is defined in each code. For example, MAAP5 simulates different FP release characteristics in the fuel-cladding gap and early phase of core damage** when compared with MELCOR.

❑ The remaining issues for further clarification

- **The initial inventory of Cs compounds** (CsI, CsOH, and Cs_2MoO_4) affecting the amount and timing of the Cs release to the environment (e.g., during its late phase revalorization);
- **FP retention & decontamination mechanisms** and relevant models reflecting state-of-the-art information (ISLOCA & SGTR);
- **Influence of the MCCI phenomenon** affecting the temperature of the steam-gas mixture passing the RCS loop and/or ISLOCA piping network, and generation of combustible gases (H2 and CO);
- **Consequently accounting for uncertainties addressed in model input parameters and different modelling options**, which may influence on the behaviour of FP source terms

Thank you for your attention

UNCERTAINTY QUANTIFICATION FOR A SEVERE ACCIDENT SEQUENCE IN A SFP IN THE FRAME OF THE H-2020 PROJECT MUSA: FIRST OUTCOMES

O. Coindreau
IRSN
Centre de Cadarache, B.P. 3 – 13115 Saint-Paul-lez-Durance Cedex, France
olivia.coindreau@irsn.fr

L.E. Herranz, R. Bocanegra
Nuclear Safety Research Unit, Department of Energy, CIEMAT
Avda. Complutense 40 Edificio 12-P0-13, 28040 Madrid, Spain
luisen.herranz@ciemat.es, rafael.bocanegra@ciemat.es

S. Ederli, P. Maccari, F. Mascari
ENEA
Lungotevere Thaon di Revel 76, 00196 Roma, Italy
stefano.ederli@enea.it, pietro.maccari@enea.it, fulvio.mascari@enea.it

O. Cherednichenko, A. Iskra
Energorisk LLC
off. 141, 7 Simii Steshenkiv Str., Kyiv, 03148, Ukraine
e.risk@ukr.net, andriy.iskra@ukr.net

P. Groudev, P. Vryashkova, P. Petrova
Institute for Nuclear Research and Nuclear Energy,
Bulgarian Academy of Sciences (INRNE-BAS)
Tzarigradsko Chaussee 72, 1784 Sofia, Bulgaria
pavlinpg@inrne.bas.bg, pivryashkova@inrne.bas.bg, petia@inrne.bas.bg

A. Kaliatka, V. Vileiniškis
Lithuanian Energy Institute (LEI)
Breslaujos str. 3, 44403 Kaunas, Lithuania
algirdas.kaliatka@lei.lt, virginijus.vileiniskis@lei.lt

M. Malicki, T. Lind
Paul Scherrer Institut (PSI)
Forschungsstrasse 111, CH-5232 Villigen PSI, Switzerland
mateusz.malicki@psi.ch, terttaliisa.lind@psi.ch

O. Kotsuba
SSTC NRS
03142, 35-37 V.Stusa Street, Kyiv, Ukraine
ol_kotsuba@sstc.ua

I. Ivanov
Technical University of Sofia (TUS)
1000 Sofia, 8, St. Kliment Ohridski Blvd., Bl. 12, Bulgaria
ivec@tu-sofia.bg

F. Giannetti, M. D'Onorio
Sapienza University of Rome
DIAEE Corso Vittorio Emanuele II 244, 000186 Rome, Italy
fabio.giannetti@uniroma1.it, matteo.donorio@uniroma1.it

P. Ou, L. Feiye,
CNPRI
21/F, Science and Technology Building, Shangbuzhong Road, Futian District, Shenzhen, China
oupingwen@cgnpc.com.cn, liaofeiye@cgnpc.com.cn

P. Piluso, Y. Pontillon
CEA
Cadarache F-13108 Saint-Paul-Lez-Durance, France
pascal.piluso@cea.fr, yves.pontillon@cea.fr

M. Nudi
EPRI
1300 West WT Harris Blvd, Charlotte, NC 28262, United States
mnudi@epri.com

ABSTRACT

The Management and Uncertainties of Severe Accidents (MUSA) project, funded in HORIZON 2020 and coordinated by CIEMAT (Spain), aims at consolidating a harmonized approach for the analysis of uncertainties and sensitivities associated with Severe Accidents (SAs) focusing on Source Term (ST). In this framework, the objectives of the Innovative Management of Spent Fuel Pool Accidents (IMSFP – WP6), led by IRSN (France), are to quantify and rank the uncertainties affecting accident analyses in a Spent Fuel Pool (SFP), to review existing and contemplated SA management measures and systems and to assess their possible benefits in terms of reduction of radiological consequences.
To quantify the propagation of the uncertainties of the input parameters to the output uncertainties of severe accident codes (ASTEC, MELCOR, RELAP/SCDAP), a diverse set of uncertainty quantification (UQ) tools (DAKOTA, RAVEN, SUNSET, SUSA) are used. The statistical framework used by the different UQ-tools is similar e.g. pure random (Monte Carlo) and Latin hypercube sampling (LHS).
Fourteen partners from three different world regions are involved in the WP6 activities. The target of this paper is to describe the achievements during the first two years of the project. In a first part, a description is given of the SFP accidental scenario, of the key target variables and radionuclides chosen as ST Figure of Merits (FoM) and of the identified uncertainty sources in models and input parameters. A key element when defining the SFP scenario has been the consideration (or not) of the reactor building, as it is expected to significantly affect analyses. In a second part, the first insights coming out from the calculation phase of the project are presented. The review of existing SA management measures is also exposed, as well as systems whose benefits will be assessed in the second phase of the project. Finally, challenges that arise from such

an exercise are discussed, as well as major difficulties found when applying UQ methodologies to SFP scenarios and solutions adopted.

KEYWORDS
SFP, source term, uncertainty quantification, SA codes

1. INTRODUCTION

The community of Severe Accidents (SA) does not rely anymore entirely on the use of a conservative approach, since it showed its limitation in a number of situations. Because the phenomenology is complex and represents a hopefully closed system, being conservative in one aspect may result in being dramatically optimistic in another aspect [1]. Consequently, a more realistic called "best-estimate approach" is followed worldwide and requires quantifying the embedded uncertainty of the codes used for safety assessment. This safety assessment approach is named Best Estimate Plus Uncertainty (BEPU).
The uncertainties of numerical codes can be quantified taking into account the latest developments in methods and algorithms as well as the availability of computing resources. Mathematical tools for quantification of code uncertainties and sensitivities have been under development for many years, with a huge accumulated experience in performing Uncertainty Quantifications (UQ) with numerical tools applied for the analysis of events of the safety level 1 to 3 [2]. So far, this is not the case for SA codes and only a few investigations have focused on SA and UQ [3, 4]. To address this gap, the Management and Uncertainties of Severe Accidents (MUSA) project was founded in HORIZON 2020 EURATOM NFRP-2018 call on "*Safety assessments to improve accident management strategies for generation II and III reactor*" [5, 6]. MUSA project aims at establishing a harmonized approach for the analysis of uncertainties and sensitivities associated with SA analysis among EU and non-EU entities. It is coordinated by CIEMAT (Spain) and 28 Organizations from 16 Countries are involved. In this framework, the goal of MUSA-WP6, coordinated by IRSN, is to quantify uncertainties affecting accident analyses in a Spent Fuel Pool (SFP), to review existing and contemplated SA management measures and systems and to assess their possible benefits in terms of reduction of radiological consequences. WP6 is one of the applicative WPs of MUSA, with 14 partner organisations involved and about 20% of the total human resources.
To quantify the propagation of the uncertainties of the input parameters to the output uncertainties of SA codes, the statistical framework used by the MUSA partners is the sampling of a vector of input parameters characterized by a range of variations and a Probability Density Function (PDF), then performing the corresponding calculations, and getting a vector of output of the same size as the sample. These different steps will be detailed in this paper. In section 2, a description will be given of the SFP accidental scenario studied, of the key target variables and radionuclides chosen as Source Term (ST) Figure of Merits (FoM) and of the identified uncertainty sources in models and input parameters. In section 3, the results of the best estimate computations and the first insights coming out from the UQ phase will be presented. The review of existing SA management measures will be exposed, as well as systems whose benefits will be assessed in the second phase of the project. Finally, challenges that arise from such an exercise are summarized, as well as major difficulties found when applying UQ methodologies to SFP scenarios and solutions adopted.

2. ASSESSING THE EFFECT OF UNCERTAINTIES IN A SFP ACCIDENTAL SCENARIO

To assess the effect of uncertainties, it is necessary to (i) select a scenario, (ii) chose a set of uncertain parameters and define key variables as FoM, (iii) carry out the Uncertainty and Sensitivity Analysis (UaSA). These different steps are described hereafter.

2.1. Description of the SFP accidental scenario

Due to the fact that accidents in SFP that lead to large Fission Product (FP) releases are practically eliminated since they are very unlikely with a high degree of confidence, the participants to MUSA-WP6 agreed to study an accidental scenario that leads to FP releases that are not too important and for which mitigation measures make sense. Consequently, the scenario computed has been chosen to fulfil these criteria and benefit from experience gained during the AIR-SFP NUGENIA+ project [7].
The geometry for MUSA-WP6 calculations is similar to that of the Unit 4 of the Fukushima Dai-ichi NPP set in the AIR-SFP NUGENIA+ project [7]. The SFP is 12.2 m long and 9.9 m wide. The total number of fuel assemblies (FA's) in the pool is 1535 with the average assembly decay heat pattern as displayed in Fig.1a. For this study, the fuel loading is simplified and FA's are divided into three groups: recently unloaded (548 FA's named “hot” FA's), longer stored (783 FA's named “cold” FA's) and fresh fuels (204 FA's). The FP inventory for low and high decay heat has been provided to the participants, assuming a cooling time for hot (resp. cold) FA’s of 3.7 months (resp. 3.15 years), a burnup of about 21 MWd/kg (resp. 42 MWd/kg) with a remaining enrichment of about 2.03 % (resp. 0.77 %). This corresponds to a total decay power of 1.9 MW for recently unloaded FA's and 0.5 MW for longer stored FA's. For the calculations, only one type of fuel assembly is used (9x9-9 assembly with a central squared water channel called STEP3B, see Fig. 1c. Each FA is surrounded by a steel rack cell and the spent fuel assemblies are stored in 3x10 spent fuel racks (see Fig. 1b), with 53 racks placed in the SFP. The steel walls of the racks are double walls with some space for water in between. Each participant can chose to model only the pool or to include the building in the spatial modelling. Indeed, even if the modelling of the building is more representative of the real situation, it requires time and resources that partners might not have. In case the SFP building is taken into account in the modelling, the SFP is considered to be located in the secondary containment of type Mark-I, on the top floor of the refueling bay. The building above the SFP is 46 m length, 34.2 m width and 16.4 m height. It is assumed a 10 m^2 opening of the fuel pool area outwards in order to avoid pressurization.

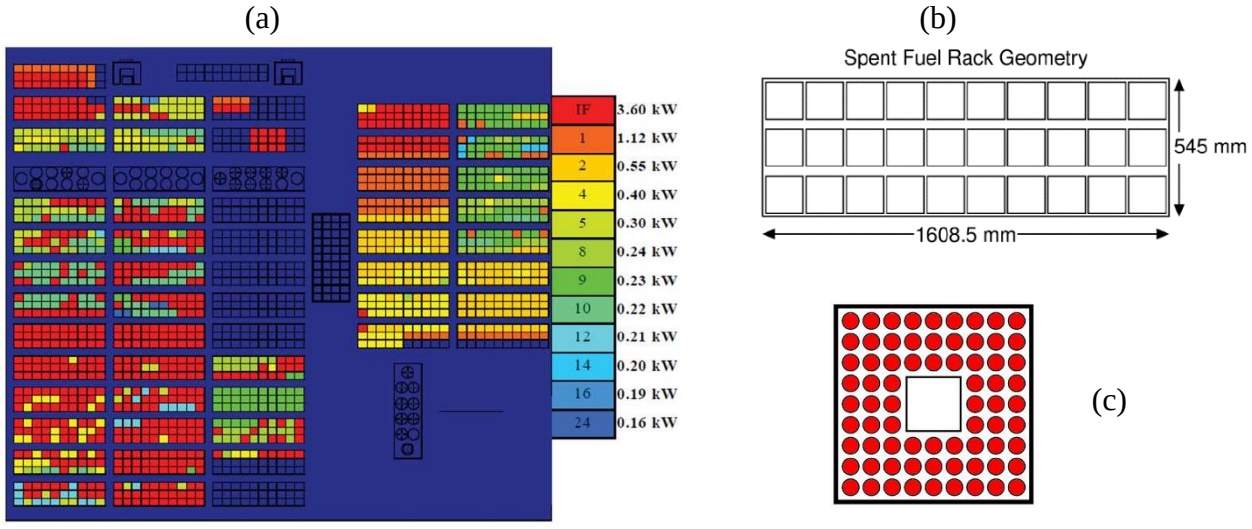

Figure 1. Layout of Fukushima unit 4 SFP (a), scheme of a spent fuel rack (b) and of a STEP3B fuel assembly (c)

The accidental scenario is a loss-of-cooling scenario with a computation starting at the onset of fuel uncovery and ending when the amount of fuel matter lost from initially intact components and transferred to degraded components reaches 1 or 3%. It must be emphasized that the criterion to end the computation strongly depends on the code modelling. To determine if the criterion is reached, the amount of still intact fuel is computed at each time step and compared to the initial mass of UO_2. Initial conditions are a pressure in the SFP building of 1 bar, a water temperature of 100°C and an atmosphere temperature of 80°C with 100% relative humidity.

2.2. Identified uncertainty sources and key target variables

The identification of uncertainty sources and the definition of key target variables as FoMs were carried out during the 1st phase of the MUSA project in the framework of WP2.
A list of phenomena affecting the ST in SFP was proposed, divided in 5 categories: 1) Modelling uncertainties; 2) Initial conditions; 3) Boundary conditions (scenario); 4) Boundary conditions (systems/SAM); 5) Mesh, numerics.
In MUSA-WP6, the SFP design and the accidental scenario to be addressed have been set as described in paragraph 2.1. Initial and boundary conditions, i.e. categories 2) and 3), are consequently excluded. It has also been decided that mesh and numerics should not come onboard the UQ exercise, but are investigated separately. Finally, the impact of systems will be addressed in the second phase of the project. The uncertainty sources investigated in this paper consequently belongs to the first category. Based on [8], a table of phenomena was established, closely linked to the models developed in most SA codes. This table is divided in 7 groups:

1. Thermal-hydraulic in the pool
2. Power generation
3. Heat transfer
4. Fuel assemblies behavior and degradation
5. FP release and transport
6. Thermal-hydraulic in the SFP building
7. Material properties

The table has been filled with a list of uncertain parameters, characterized by their probability density function. For the first version of the UaSA, the number of input uncertain parameters considered by each participant is indicated in Table I, as well as the category they belong to. Most uncertain parameters are in categories 3, 4 and 5. The lack of uncertain parameters investigated in other categories can be due to the fact that only a few are available to the user (especially for thermal-hydraulic), that they have not been considered as having a high impact on the ST or that they are usually not investigated and are consequently missing. On this last point, it is planned to do a review to determine if important uncertain parameters are missing and should be added in the table.

Since the MUSA project is ST driven, only variables linked to FP release into the environment have been considered as FoMs. Radionuclides with greatest radiological impact have been determined based on the inventory in the SFP, release rates of the elements and dose coefficients of the isotopes for three different modes of exposition (inhalation, groundshine and cloudshine). It was found that most contributing isotopes are Sr90, Cs137, Cs134, Ru106, Ce144, Sr89, Ba137m and Ru103. Taking into account this result, the list of FoMs are:

- Total release of Cs, Ru and Sr from fuel. Unit is mass fraction of the initial inventory.
- Onset time of FP release from fuel. Unit is h.
- Total release into environment from SFP building of Cs, Ru and Sr (only if the SFP building is modelled). Unit is mass fraction of the initial inventory.

- Total Ruthenium release in gaseous form to environment (only if Ruthenium chemistry in the building is investigated). Unit is mass fraction of the initial inventory.
- Dose due to isotopes with the greatest radiological impact (i.e. Sr90, Cs137, Cs134, Ru106, Ce144, Sr89, Ba137m, Ru103) relative to that of total release of Cs137. Unit is fraction.

Additional variables are needed to describe and analyze the SA scenario and are worth keeping track on, like the FoMs. These additional variables are used to analyze the reference computation (see paragraph 3.1) but they should not be considered in the sensitivity analysis.

2.3. Uncertainty analysis applications methodology and tools used

The UaSA is carried out in the MUSA project by the probabilistic propagation of input uncertainties [3] which is particularly suitable for code simulation applications. The method is based on the random sampling of different selected input uncertain parameters values, see Fig. 2. All UQ-tools used in MUSA have the capability for pure random (Monte Carlo) and Latin hypercube sampling (LHS). The set of sampled values is used for running several code calculations, in which all the input uncertain parameters are sampled based on their own PDF. After the numerous simulations are performed with the SA code, the data of interest are extracted from the result files and written in files in the format required by the UQ-tool to be statistically post-processed. Statistics indicators (e.g. minimum, maximum values, mean, standard deviation, cumulative density function, probability density functions, quantiles) and sensitivity functionalities (correlation coefficients, standard regression coefficients, coefficients of determination, scatter plots) are then provided by the UQ-tools.
The UQ-tools used in MUSA-WP6 are listed in Table I as well as the SA codes. The coupling between the UQ-tool and the SA code as described in Table I was considered as functional at the beginning of the MUSA project since it had already been used. However, uncertainty applications carried out in MUSA-WP4 on the PHEBUS FPT1 test have put in light major challenges [9]: 1) Identification and characterization of the input uncertain parameters; 2) SA code and UQ-tool coupling in a powerful and flexible way (e.g. coupling by scripting instead of the Graphical User Interface); 3) Managing of the failed calculations and debugging; 4) Extraction of the data for the post-processing; 5) Eventual implementation in the cluster of the SA code and UQ-tool.

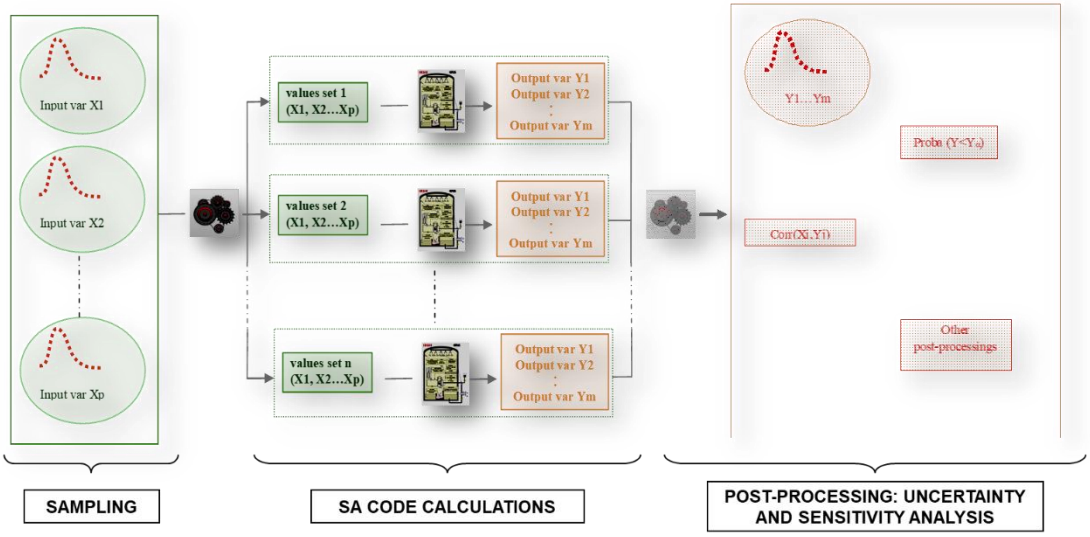

Figure 2. Probabilistic propagation of input uncertainties applied in MUSA to perform the uncertainty analysis

Some of these issues have been solved in the framework of WP4 (for instance 2, 4, 5) and the experience gained was consequently extremely useful for WP6. Other issues are still open and point of discussion.

Table I. List of participants, SA codes and UQ-tools used and characteristics of the simulations: modelling (or not) of the SFP building, number of uncertain parameters investigated and category they belong to

Organisation	SA code	UQ-tool	Building modeled	Nb of input u.p.	1.	2.	3.	4.	5.	6.	7.
CIEMAT	MELCOR	DAKOTA	No	n.a.							
ENEA	ASTEC	RAVEN + Python script	Yes	15	*			*	*		
Energorisk	MELCOR	DAKOTA	Yes	8			*	*			
INRNE	ASTEC	SUNSET	Yes	5				*	*		
IRSN	ASTEC	R + Python script	Yes	13				*	*		
LEI-ASTEC	ASTEC	SUNSET	Yes	12			*	*	*		
LEI-SCDAP	RELAP/SCDAP	SUSA	No	25		*	*	*			*
PSI	MELCOR	DAKOTA	No	19			*	*			
SSTC	MELCOR	SUSA	Yes	24	*		*	*	*		
TUS	ASTEC	SUNSET	Yes	5				*	*		
UNIRM1	MELCOR	RAVEN	Yes	25				*	*		
CNPRI	ASTEC	SUNSET	Yes	n.a.							

3. RESULTS FROM PRELIMINARY ANALYSES

3.1. Reference computation

All participants were asked to fill a table to retrieve the main outputs of the reference computation (see Table II). It must be emphasized that this study is not a benchmark, but it is essential to check the consistency of the input data deck before performing the UaSA. This comparison has enabled the participants to improve their input data deck, to correct some mistakes and to share procedures to retrieve the results, especially the FoMs.

In lack of cooling, and due to decay heat, the pool water, which is at saturation temperature, evaporates and the amount of water progressively decreases. The temperature of the uncovered part of the fuel assemblies increases regularly in a first time, and then more rapidly when oxidation comes into play. First FP release occurs when the cladding of hot fuel assemblies bursts (more than 80 h after the beginning of the transient). Depending on the criterion chosen to stop the computation, and on the modelling options, the simulation ends between 100 and 185 h.

The analysis of the reference case has put in evidence that the thermal-hydraulics in the SFP and in the building are strongly influenced in ASTEC computations by the use of the 5 or 6 equations modelling for diphasic thermal-hydraulics [10]. It was found that the evaporation flow rate increases unexpectedly due to downward flow of the steam in the bypass channel. In MELCOR computations, it was observed that the way of setting the specified decay heat is not straightforward and can lead to differences between the computations carried out with different decay heat modelling. These results are discussed with the development teams of the SA codes and should result in improvement in the models or to recommendations for the input data deck. In the meantime, the UaSA has started with the most consistent input data decks and latest versions of the SA codes. During the interpretation of the results, it is essential to keep in mind the

limitations that the analysis of the reference computation have put in evidence. It is also worth mentioning that once operational, all the tools developed to carry out the UaSA can be used to re-evaluate the uncertainties of the results and the sensitivity of input parameters with a new version of the code and/or of the input data deck.

Table II. Results of the reference computations

	Maximum cladding T° at (h)				1% reloc. fuel (h)	Mass of water in the SFP at (h)				
	500 K	1000 K	1500 K	2000 K	end of the sim.	400 t	300 t	200 t	100 t	50 t
ENEA	32	90.2	121.1	122	123.3	15.3	44.3	85.3	-	-
Energorisk	61.8	92.9	99.9	101.1	101.9	15.9	43.6	74.9	111.9	131.3
INRNE	61	82	101	110	161	20	44	73	114	143
IRSN	29.2	96.5	130.9	131.6	132.6	15.3	43.7	81.2	-	-
LEI-ASTEC	33.2	103.17	123.6	125.34	126.2	15.5	43.3	75.7	122.7	-
LEI-SCDAP	37.2	88.4	95.9	116.2	184.2	20.8	46.3	64.1	82.0	100.0
PSI	62	102.9	118.5	121	122.2	31.5	58.8	92.3	123.3	128.1
SSTC	59.9	85.3	105.2	106.3	152.2	15.2	41.7	70.85	106.9	125.6
TUS	60	85	97	101	117	21	46	65	102	-
UNIRM1	36.6	85.8	97.9	110.7	160.	16.7	43.47	73.4	122.4	153.8

	Start of (h)			At the end of the simulation		
Organisation	**H2 Prod°**	**Gap release**	**Mass relocation**	**Collapsed water level (m)**	**Amount of H2 generated (kg)**	**Amount of magma and/or debris (kg)**
ENEA	51.7	78.7	121.9	1.324	352.5	18538
Energorisk	98.1	98.5	101.9	0	1716	531589
INRNE	89	81	99	0.3	3500	97000
IRSN	52.1	87.3	132.6	1.04	322.1	12843
LEI-ASTEC	57.6	100.95	124.5	0.841	1078	18456
LEI-SCDAP	88.4	86.5	161.9	0.18	1012	n.a.
PSI	116.8	118.8	120.8	1.255	978.4	60623
SSTC	93.3	94.5	152.2	0.105	1307	n.a.
TUS	89	81	104	0.70	1544	60100
UNIRM1	40.9	91.9	139.1	0.35	1042	30299

3.2. First Results of Uncertainty and Sensitivity Analyses

For the UaSA phase, it was decided that each partner should consider a unique ending simulation time. This ending simulation time is the computation time of the reference computation that ends upon the criterion described in paragraph 2.1. This makes the hypothetical assumption that the accidental scenario ends at a given time (i.e. the computation time of the reference computation).
To carry out the UQ, the partners adopted the Wilks formula [11, 12] to evaluate the minimum number of code runs for a selected probability and confidence level. For a two-sided tolerance interval, a probability content and a confidence set to 95% and 95% (values generally taken by the participants), the minimum number of code runs is approximately 100.
First results of the uncertainty analysis were presented as dispersion plots, quantiles and Cumulative Distribution Function (CDF). In Fig. 3a, a dispersion plot enables the visualization of the spreading of the amount of Cs released into the environment. In these simulations, the spreading starts to be significant after ≈120 h and the final amount of Cs released ranges between 37 and 47% of the initial inventory. Another post-processing approach is the determination of quantiles. In Fig. 3b, the amount of Cs released into the environment is plotted for various percentiles. Another post-processing approach proposed by the partners is to visualize the PDF or the CDF of the FoMs. This has been done at a particular instant in Fig. 3c for the released mass of Cs.

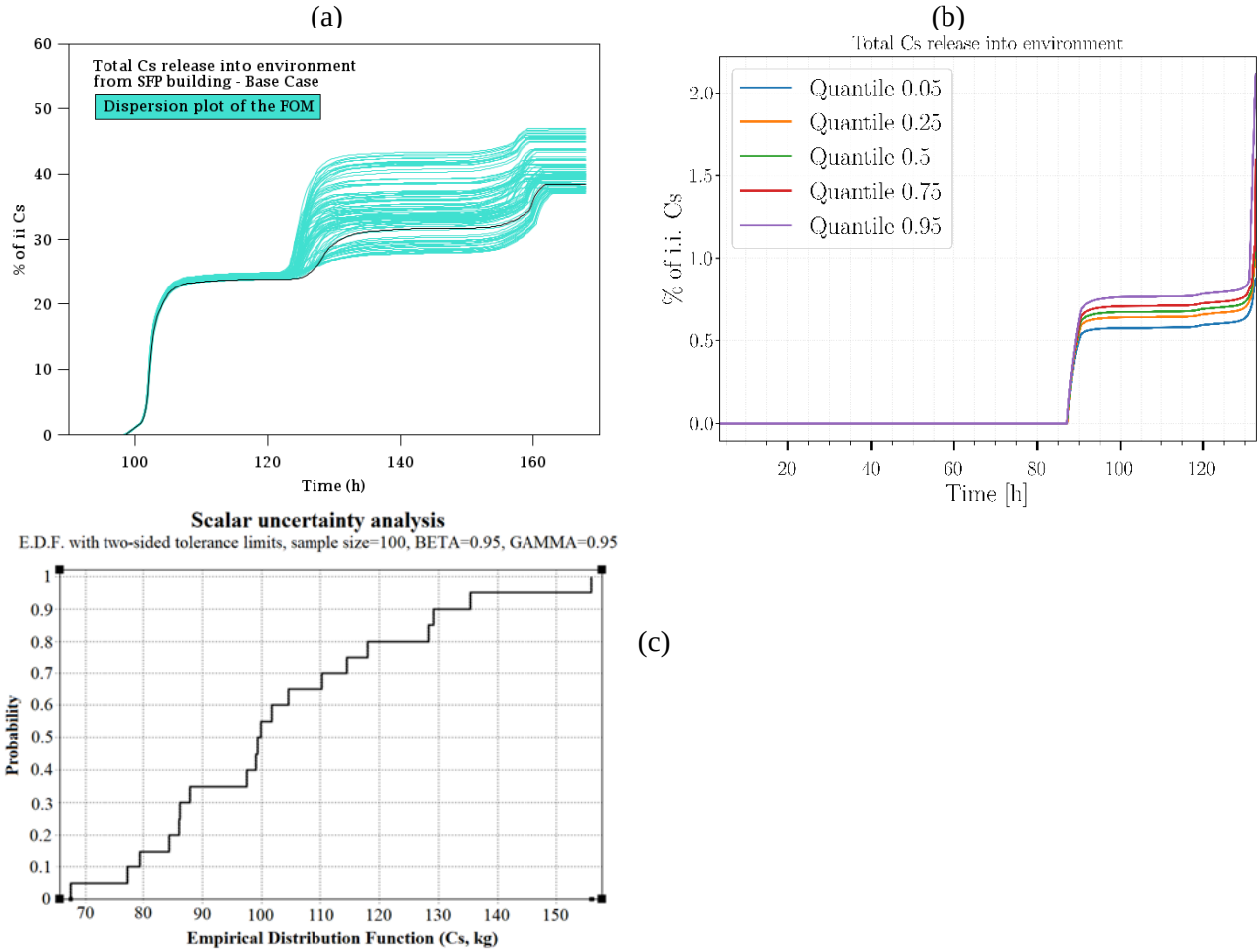

Figure 3. (a) Time dependent dispersion plot of % of the initial inventory (i.i.) of Cs released into environment, (b) Percentiles for % of the initial inventory (i.i.) of Cs released into environment, (c) CDF, named here Empirical Distribution Function (EDF), for the released mass of Cs

For the sensitivity analysis, the post-processing approaches presented by the partners are the characterization of the statistical correlation between the uncertain input parameters and the FoMs through Pearson and Spearman correlation coefficients. The correlation coefficients are scale-free measures of linear association between the uncertain input parameters and the FoMs, either based on the values (Pearson coefficient) or on the ranks of the values (Spearman coefficient). A correlation coefficient close to 1 (resp. -1) indicates a positive (resp. negative) linear dependence. It must be highlighted that, for a given sample size, the Bravais-Pearson confidence threshold matches the correlation coefficient to a level of confidence. For instance, for a sample size of 100, the confidence threshold is ≈ 0.2 for a confidence level of 95%.
The statistical and correlation analysis has been done on a single selected time value, see Fig. 4a, or time dependent value, see Fig. 4b. In Fig. 4a, the bar plot shows in an easy way that Cs release into environment is positively correlated to Vsto and negatively correlated to Coag and Rho. These three parameters are linked to aerosol deposition in the building. Vsto is the particle shape factor relative to Stokes velocity. Since the sedimentation velocity is a decreasing function of Vsto, an increase of Vsto leads to a decrease of the amount of aerosols that settle down in the SFP building and consequently to an increase of Cs release into environment. Coag is the particle shape factor relative to coagulation and Rho the particle mean density. An increase of Coag (resp. Rho) leads to an increase of the mass of a single particle due to an increase of its diameter (resp. its density) and consequently to an increase of the amount of aerosols that settle down in the SFP building and a decrease of Cs release into environment. The correlation coefficients for other input parameters are not high enough to be considered as significant. The evolution through time of these correlation coefficients is shown in Fig 4b. It puts in evidence that the correlation of an input parameter can be significant only at a given time or during a phase of the transient. 120 calculations were carried out to perform this statistical analysis.

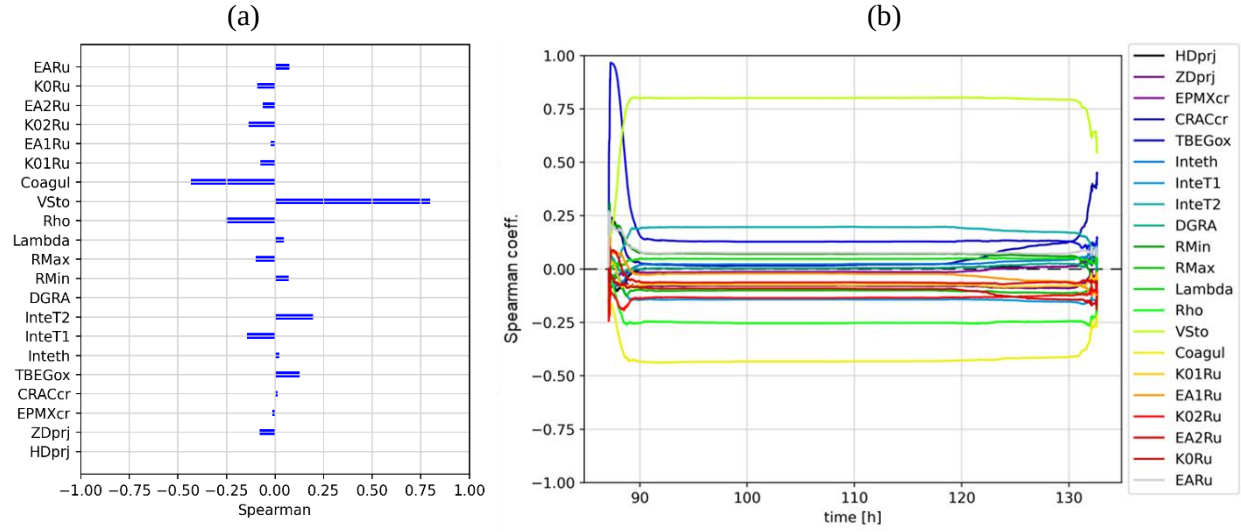

Figure 4. Correlation coefficient between the mass of Cs137 in environment and input uncertain parameters (a) at a given time (100 h), (b) variation through time

At this stage, the UaSA has not been carried out in detail. Only the feasibility has been checked, with first runs performed and post-processing done. The results presented in this section should consequently not be considered as quantitatively but only as first outcomes of MUSA-WP6. In particular, it must be reminded that simulations differ from one participant to another one by: 1) the modelling domain (i.e. the consideration, or not, of the reactor building, 2) the criterion to end the computations, 3) the uncertain parameters considered for the UQ phase. A detailed analysis of the results is consequently ongoing to quantify and rank the uncertainties affecting the SFP accident and will be presented in a further publication.

3.3. Review of existing SA management measures

A review of existing and innovative SAM measures in the partner countries was carried out. For this, the MUSA partners from 10 countries provided information about the accident management measures and related safety systems employed in the nuclear power plants in their countries. The review showed that a large number of systems are in place and used to prevent and mitigate accidents in SFPs both for pools in- and outside of the containment. The most common systems used to monitor the SFPs and their status are temperature and water level measurements, monitoring of the activity and dose rate in the SFPs and buildings, as well as measurement of pressure and flow of the coolant, ventilation flow rate, and concentration of combustible gases. Safety systems are redundant and focused on ensuring and if needed, restoring cooling of the SFP by different means, and when necessary locating and isolating a leak in the pool. In many countries, the monitoring and safety systems were reviewed and upgraded after 2011.
The criteria to enter accident management in SFPs were mainly related to the water level in the pool, e.g., loss of water, decrease in the water level, and an exceptionally fast water level decrease in the pool. Similarly, most of the accident management measures had the aim of restoring the water injection by different water sources. In some cases, opening the fuel pool area outwards was done to avoid pressurization. In some cases, the irradiated fuel bay atmosphere was vented by using fans and filters to manage combustible gases and to maintain active areas at a negative pressure. Absorber injection was also considered in some SFPs. No country has reported to plan any major new accident management measures specific to SFPs to be implemented in the near future. Several countries reported that further analytical activities will be carried out to validate the SFP accident management measures.
A review was also made of the work that has been carried out to analyze the accidents in SFPs with the focus on international activities and on accident management measures specific to SFPs. Reports of source term assessment from postulated SFP accidents were found to be scarce. Several reports emphasized the challenge of calculating the ST from SFPs using current severe accidents codes which have been developed for reactor accidents. Several other challenges and recommendations for analyzing SFP accidents were also identified. It was agreed that the benefits of systems that have been installed to prevent SA in a SFP, like water injection by spray systems, will be assessed in the second phase of the project.

4. CONCLUSIONS

The paper has given a view of the extent of work carried out by the fourteen partners involved in MUSA-WP6 and described main achievements during the first two years of the project. The first steps required to carry out the UaSA have been completed: selection of an accidental scenario, creation of an input deck and check of its consistency, determination of uncertainty sources in models, choice of key target variables as ST FoMs. In the meantime, a review of SAM measures and systems in SFP has been done. The partners agreed to assess, in the second phase of the project, the benefits of spray systems. Then, the uncertainty analysis phase has started with the use of UQ-tools to propagate input uncertainties. To achieve this task, WP6 participants have benefited from the experience gained in WP4. In particular, the coupling by scripting between the SA code and UQ-tool and the automation of data extraction for the post-processing were very useful. The implementation in the cluster of the SA code and UQ-tool for those who have access to such a system has required some time but issues have been handled (for instance by adding libraries in the cluster).
The UaSA is ongoing, and the participants aim at elaborating a harmonized approach. In particular, arguments for the selection of uncertain parameters, criteria for the determination of the number of runs and the significance threshold of correlation coefficients should be provided. A template will be distributed to the participants in order to get the results with the same units, to have common standard for post-processing and make the analysis more easily comparable from one participant to another one.
Major challenges have been found when applying UQ methodologies to SFP scenarios and difficulties are addressed by the participants:

- Computational aspects with large CPUs (from a few hours to 4 days for one computation). The use of multi-core processor or PC cluster seems necessary to perform the UQ with more than 100 runs.
- Code crashes. Some partners decided to perform a number of runs larger than the minimum required number according to Wilks' formula in order to be sure to have enough computations with a normal end. But this raises questions about the statistical treatment of failed calculations.
- Identification and characterization of the input uncertain parameters. A review is ongoing to identify if input parameters are lacking. But the input uncertainty quantification, which has been identified as an important step in the UQ phase [13], is a long task which is out of the scope this project.

ACKNOWLEDGEMENTS

The MUSA project has received funding from the Euratom research and training program 2014–2018 under grant agreement No. 847441.



REFERENCES

1. R. Cozeret, J. Chambarel, S. Phoudiah, D. Corbin and S. Pignet, "Improvement on 900 MWe NPPs in the occasion of the 4th 10-year periodic safety review on severe accidents", *Proceedings of EUROSAFE 2019*, Cologne, Germany, November 4-5, 2019, pp. 43-51.
2. "PREMIUM: A Benchmark on the Quantification of the Uncertainty of the Physical Models in the System Thermal-Hydraulic Codes - Methodologies and Data review", NEA/CSNI/R(2016)9 (2016).
3. S.T. Ghosh, H. Esmaili, A.G. Hathaway III, D.M. Osborn, N.E. Bixler, D. Brooks, K.W. Ross and K.C. Wagner, "State-Of-the-Art Reactor Consequence Analyses project: Uncertainty Analyses for Station Blackout Scenarios", *Nucl. Technol.*, **207**, pp. 441–451 (2021).
4. K. Chevalier-Jabet, F. Cousin, L. Cantrel and C. Séropian, "Source term assessment with ASTEC and associated uncertainty analysis using SUNSET tool", *Nucl. Eng. Des.*, **272**, pp. 207-218 (2014).
5. L.E. Herranz, S. Beck, V.H. Sánchez-Espinoza, F. Mascari, S. Brumm, O. Coindreau and S. Paci, "The EC MUSA Project on Management and Uncertainty of Severe Accidents: Main Pillars and Status", *Energies*, **14** (4473), pp. 1-11 (2021).
6. F. Mascari, "Application of Uncertainty Quantification Methods against Integral Experiments (AUQMIE) in the EU-MUSA project", ETSON news, March 2021
7. O. Coindreau et al., "Severe accident code-to-code comparison for two accident scenarios in a spent fuel pool", *Ann. Nucl. Energy*, **120**, pp. 880-887 (2018).
8. "Phenomena Identification and Ranking Table. R&D Priorities for Loss-of-Cooling and Loss-of-Coolant Accidents in Spent Nuclear Fuel Pools", NEA/CSNI/R(2017)18, http://www.oecd-nea.org/nsd/pubs/2018/7443-pheno_id_rank_table.pdf (2018).
9. F. Mascari et al, "First outcomes from the PHEBUS FFT1 uncertainty application done in the EU-MUSA project", *Proceedings of 19th International Topical Meeting on Nuclear Reactor Thermal Hydraulics (NURETH-19)*, Brussels, Belgium, March 6 - 11, 2022.
10. T. Glantz, T. Taurines, O. de Luze, S. Belon, G. Guillard and F. Jacq, "DRACCAR: A multi-physics code for computational analysis of multi-rod ballooning, coolability and fuel relocation during LOCA transients Part one: General modelling description", *Nucl. Eng. Des.*, **339**, pp. 269-285 (2018).
11. S.S. Wilks, "Determination of sample sizes for setting tolerance limits," *Ann. Math. Stat.*, **12**(1), pp. 91–96 (1941).
12. S.S. Wilks, "Statistical prediction with special reference to the problem of tolerance limits," *Ann. Math. Stat.*, **13**(4), pp. 400–409 (1942).
13. "SAPIUM: Development of a Systematic APproach for Input Uncertainty quantification of the physical Models in thermal-hydraulic codes", NEA/CSNI/R(2020)16 (2020).

ERMSAR 2022

MAY 16-19, 2022 — KARLSRUHE, GERMANY

IRSN
INSTITUT DE RADIOPROTECTION
ET DE SÛRETÉ NUCLÉAIRE

Uncertainty quantification for a severe accident sequence in a SFP in the frame of the H-2020 project MUSA: first outcomes

Olivia Coindreau (IRSN), L.E. Herranz, R. Bocanegra, S. Ederli, P. Maccari, F. Mascari, O. Cherednichenko, A. Iskra, P. Groudev, P. Vryashkova, P. Petrova, A. Kaliatka, V. Vileiniškis, M. Malicki, T. Lind, O. Kotsuba, I. Ivanov, F. Giannetti, M. D'Onorio, P. Ou, L. Feiye, P. Piluso, Y. Pontillon, M. Nudi

MUSA

MUSA has received funding from the Euratom research and training programme 2014-2018 under grant agreement No 847441.

- Context
- Methodology used to assess the uncertainties in a SFP accidental scenario
- First results and preliminary analyses
- Conclusions and perspectives

Context

- **Spent fuel pools (SFPs): large structures equipped with storage racks designed to temporarily store irradiated nuclear fuel removed from the reactor**
- **Vulnerability of nuclear fuels stored in SFPs in case of prolonged loss of cooling accidents**
- **As conservative approach showed its limitation, use of Best Estimate Plus Uncertainty (BEPU) approach for safety assessment**



Underwater conditions in the SFP4,
(Image from video courtesy TEPCO)

WP6 of the MUSA H-2020 project [July 2019 - July 2023]

Methodology

- **Selection of a scenario**
- **Choice of a set of uncertain parameters**
- **Definition of key variables as Figure of Merit (FOM)**
- **Propagation of the uncertainties of the input parameters to the output parameters**
- **Uncertainty and Sensitivity Analysis (UaSA)**

Methodology

- **Selection of a scenario**
- Choice of a set of uncertain parameters
- Definition of key variables as Figure of Merit (FOM)
- Propagation of the uncertainties of the input parameters to the output parameters
- Uncertainty and Sensitivity Analysis (UaSA)

Methodology – Scenario (1/2)

Geometry identical to the unit 4 of Fukushima Daiichi with simplifications*

Dimensions: 12.2 m × 9.9 m

Heat load: 2.4 MW

1535 FA: 548 hot (3,47 kW/FA), 783 cold (0,507 kW/FA), 204 non irradiated

Loss-of-cooling scenario with a computation starting at the onset of fuel uncovery and ending at the onset of fuel melting. The criterion to stop the computation is a fraction of relocated (liquefied or debris) greater than 1 %

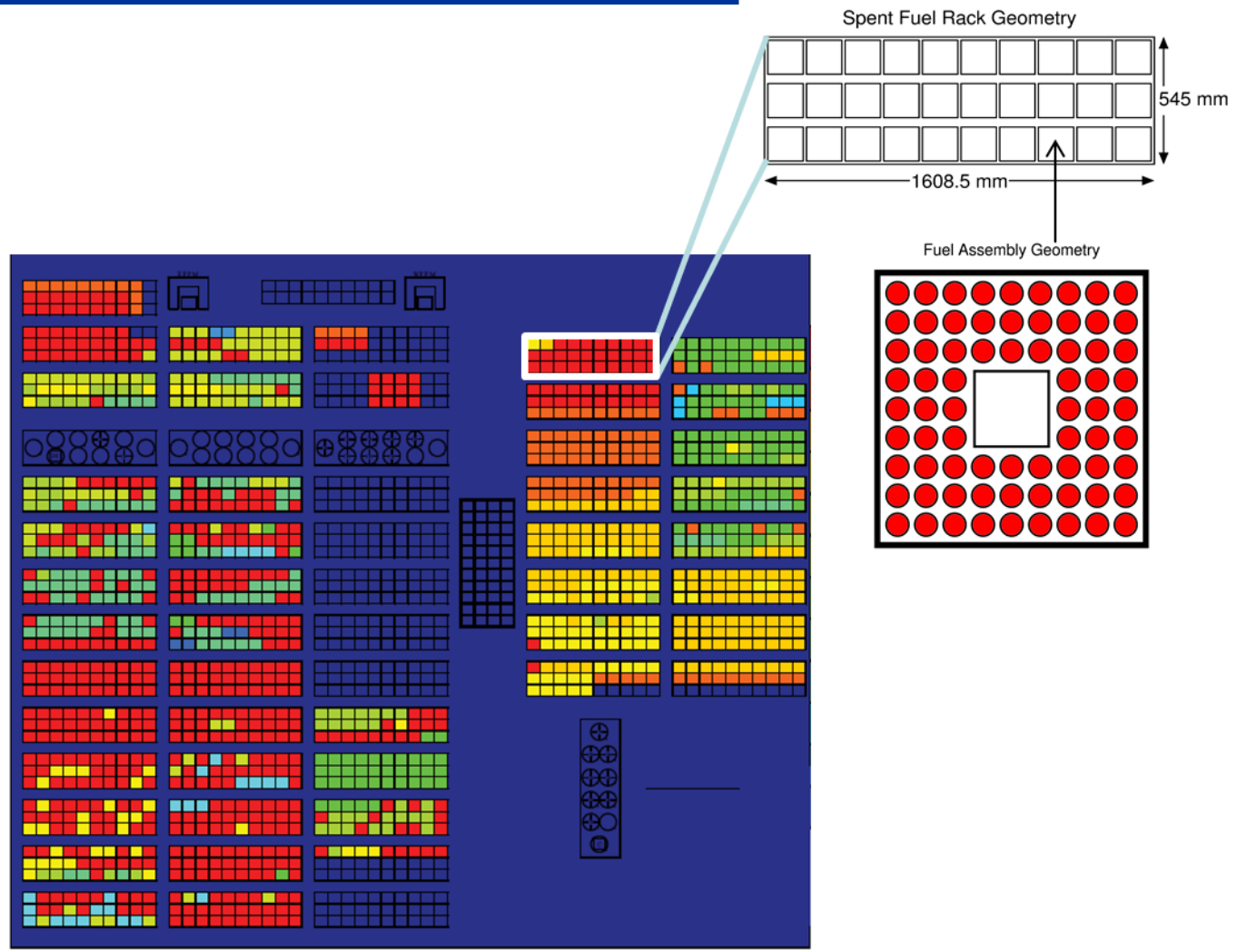

* See NUGENIA+ AIR-SFP project [May 2015-Sept 2016]

Methodology – Scenario (2/2)

FP inventory: provided to the participants, assuming a cooling time for hot (resp. cold) FA's of 3.7 months (resp. 3.15 years), a burnup of about 21 MWd/kg (resp. 42 MWd/kg) with a remaining enrichment of about 2.03 % (resp. 0.77 %)

Modelling domain: only the pool or the pool and the building above the SFP (46 m length, 34.2 m width and 16.4 m height and a 10 m^2 opening of the fuel pool area outwards in order to avoid pressurization)

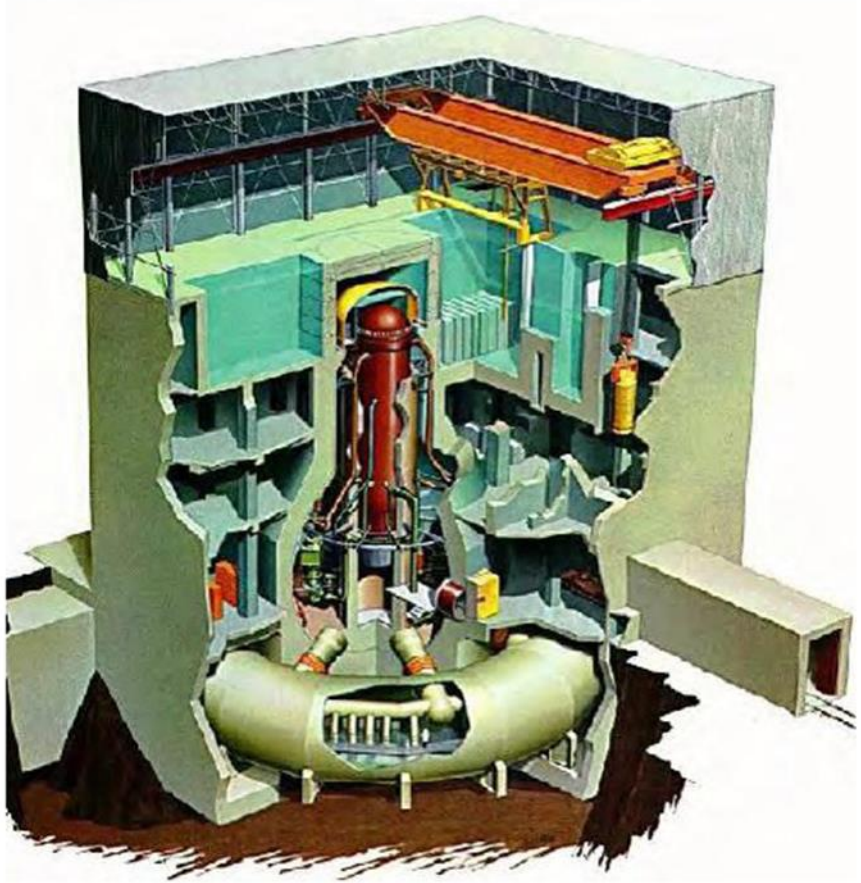

Methodology

- Selection of a scenario
- **Choice of a set of uncertain parameters**
- Definition of key variables as Figure of Merit (FOM)
- Propagation of the uncertainties of the input parameters to the output parameters
- Uncertainty and Sensitivity Analysis (UaSA)

Methodology – u.p. (1/2)

Uncertainty sources divided in 5 categories*:

1) **Modelling uncertainties**
2) **Initial conditions**
3) **Boundary conditions (scenario)**

SFP design and accidental scenario set as previously described

4) **Boundary conditions (systems/SAM)** → impact of systems will be addressed in the second phase of the project
5) **Mesh, numerics** → mesh and numerics investigated separately

***** See MUSA/WP2

Methodology – u.p. (2/2)

Table of phenomena, closely linked to the models developed in most SA codes, divided in 7 groups*:

1. **Thermal-hydraulic in the pool**
2. **Power generation**
3. **Heat transfer**
4. **Fuel assemblies behavior and degradation**
5. **FP release and transport**
6. **Thermal-hydraulic in the SFP building**
7. **Material properties**

***** See MUSA/WP2

5. FP release and transport				
	SA code	u.p.	Ref. value	Pdf
5.1 FP release	ASTEC	DGRA: Average fuel grain diameter	12 µm	Uniform distribution LB: ref - 2 µm UB: ref + 2 µm
	MELCOR	RN1_GAP00, CLFAIL: Gap release temperature	1173 K	Uniform distribution LB: ref – 100 K UB: ref + 100 K
5.2 FP aerosol transport and deposition in the pool	ASTEC	lambda: Particle mean thermal conductivity	3.5 J/m/K	Normal distribution LB: ref -10% UB: ref +10% 95% between LB/UP
	ASTEC	rho: Particle mean density	3.10^3 kg/m^3	Normal distribution LB: ref -10% UB: ref +10% 95% between LB/UP
	MELCOR	RHONOM: Aerosol density		Uniform distribution LB:1000 kg/m^3 UB: 4120 kg/m^3
	MELCOR	RN, CHI: Dynamic shape factor		Uniform distribution LB:1.0 UB: 2.0

Small extract from the table of u.p.

Methodology

- Selection of a scenario
- Choice of a set of uncertain parameters
- **Definition of key variables as Figure of Merit (FOM)**
- Propagation of the uncertainties of the input parameters to the output parameters
- Uncertainty and Sensitivity Analysis (UaSA)

Methodology – FOM

Criteria to chose the FOM (output variables)*:

- **ST driven ⇒ only variables linked to FP release into the environment have been selected**
- **Simple evaluation of radionuclides with greatest radiological impact ⇒ most contributing isotopes are Sr90, Cs137, Cs134, Ru106, Ce144, Sr89, Ba137m and Ru103**

List of FOM:

1. **Total release of Cs, Ru and Sr from fuel [mass fraction of the i.i.]**
2. **Onset time of FP release from fuel [h]**
3. **Total release into environment from SFP building of Cs, Ru and Sr** [mass fraction of the i.i.]**
4. **Total Ruthenium release in gaseous form to environment** [mass fraction of the i.i.]**
5. **Dose due to isotopes with the greatest radiological impact relative to that of total release of Cs137 [fraction]**

* See MUSA/WP2
** If relevant

Methodology

- Selection of a scenario
- Choice of a set of uncertain parameters
- Definition of key variables as Figure of Merit (FOM)
- **Propagation of the uncertainties of the input parameters to the output parameters**
- Uncertainty and Sensitivity Analysis (UaSA)

Methodology – Tools (1/2)

⇒ **Probabilistic propagation of input uncertainties***

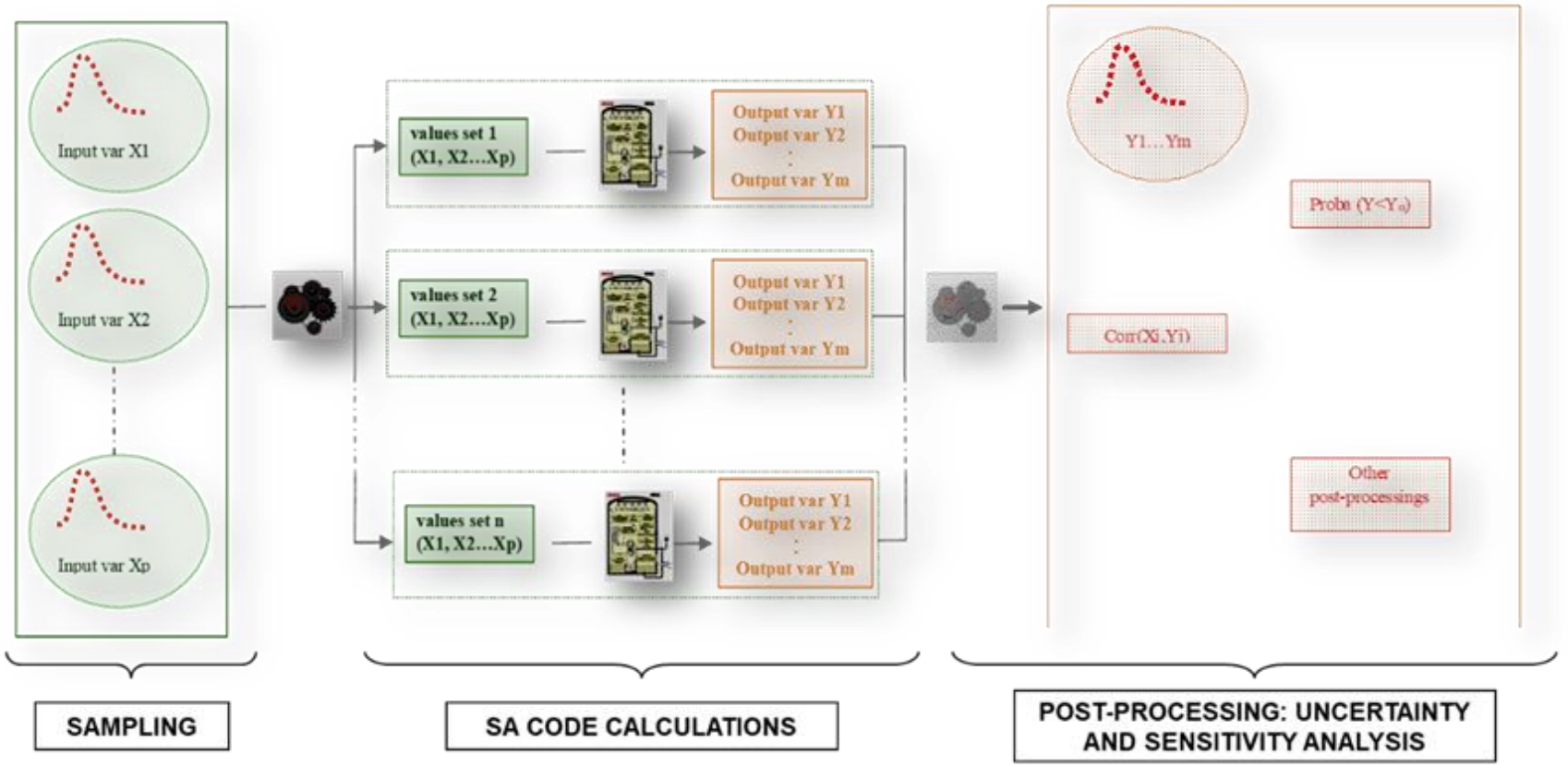

* See MUSA/WP3

Methodology – Tools (2/2)

Organisation	SA code	UQ-tool	Building modeled	Nb of input u.p.	Group the u.p. belong to						
					1. TH pool	2. Power	3. Heat tr.	4. Degrad	5. FP	6. TH build.	7 . Mat.
CIEMAT	MELCOR	DAKOTA	No	n.a.							
ENEA	ASTEC	RAVEN + Python script	Yes	21	*			*	*		
Energorisk	MELCOR	DAKOTA	Yes	8			*	*			
INRNE	ASTEC	SUNSET	Yes	5				*	*		
IRSN	ASTEC	R + Python script	Yes	13				*	*		
LEI-ASTEC	ASTEC	SUNSET	Yes	12			*	*	*		
LEI-SCDAP	RELAP/SCDAP	SUSA	No	25		*	*	*			*
PSI	MELCOR	DAKOTA	No	19			*	*			
SSTC	MELCOR	SUSA	Yes	24	*		*	*	*		
TUS	ASTEC	SUNSET	Yes	5				*	*		
UNIRM1	MELCOR	RAVEN	Yes	25				*	*		
CNPRI	ASTEC	SUNSET	Yes	n.a.							

Methodology

- Selection of a scenario
- Choice of a set of uncertain parameters
- Definition of key variables as Figure of Merit (FOM)
- Propagation of the uncertainties of the input parameters to the output parameters
- **Uncertainty and Sensitivity Analysis (UaSA)**

Results – Reference case (1/2)

Comparison of main outputs of the reference computation:

Maximum cladding T° at (h)				1% reloc. fuel (h)	Mass of water in the SFP at (h)				
500 K	1000 K	1500 K	2000 K	end of the simulation	400 t	300 t	200 t	100 t	50 t

Start of (h)			At the end of the simulation		
H2 Production	Gap release	Mass relocation	Collapsed water level (m)	Amount of H2 generated (kg)	Amount of magma and/or debris (kg)

- **Check the consistency of the input data deck before performing the UaSA, improve the input data decks, correct some mistakes**
- **Have a good understanding of the physical phenomena occurring during the accidental scenario**
- **Limitations of SA codes to be kept in mind:** simplified geometry, a single inventory
- **Some unconsistencies also put in evidence:** unexpected increase of the evaporation flow rate in ASTEC computations due to downward flow of the steam in the bypass channel, difficulties in setting the specified decay heat in MELCOR computations…

Results – Reference case (2/2)

- In lack of cooling, and due to decay heat, the pool water evaporates and the amount of water progressively decreases.
- T° of the uncovered part of the FAs increases regularly, and then more rapidly when oxidation comes into play.
- First FP release occurs when the cladding of hot fuel assemblies bursts (more than 80 h after the beginning of the transient).
- Depending on the criterion chosen to stop the computation, and on the modelling options, the simulation ends between 100 and 185 h.

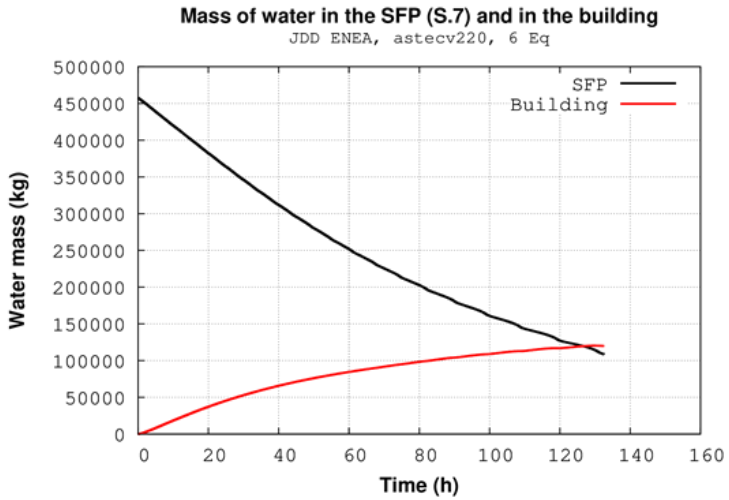

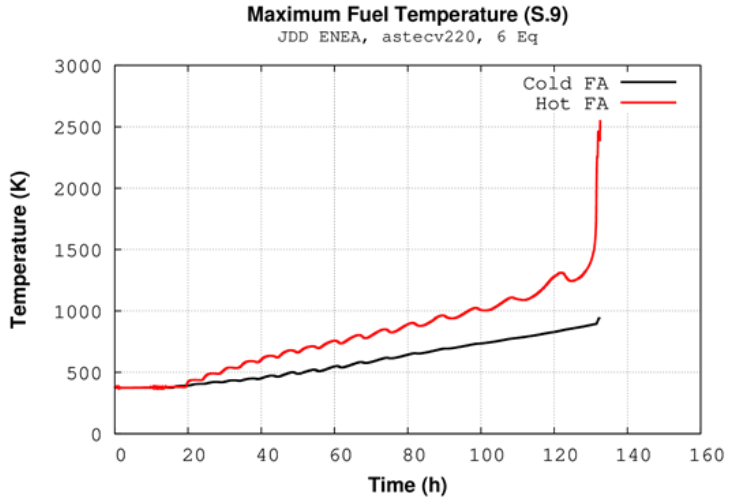

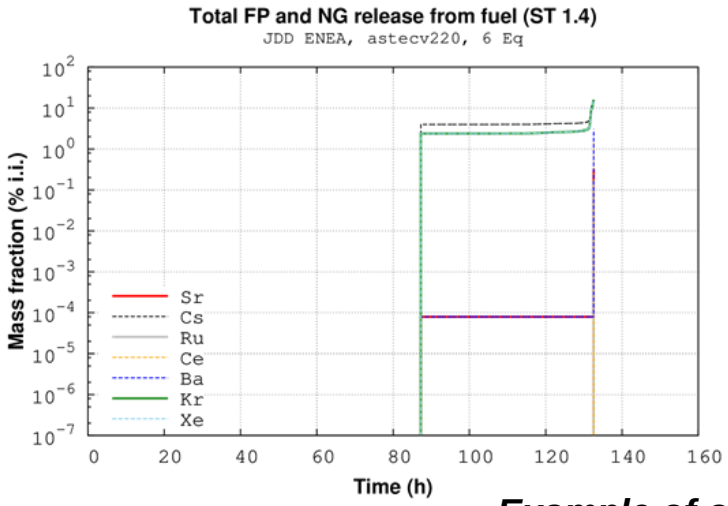

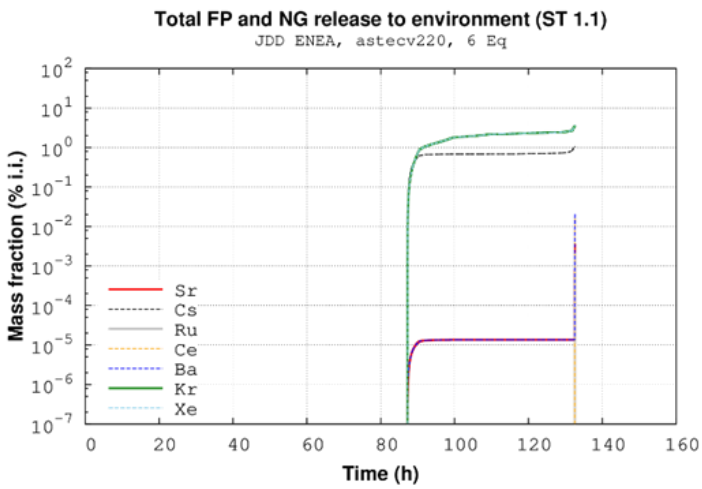

Example of one of the reference calculations [IRSN]

Results – Uncertainty analysis (1/2)

- **Each partner has considered a unique ending simulation time (the computation time of the reference computation) ⇒ hypothetical assumption that the accidental scenario ends at a given time**
- **Run of N computations with fluctuating input ⇒ sample $\{y_1, y_2, \ldots y_N\}$ of the random variable y, where y is one of the FOMs**
- **Dispersion plot: enables the visualization of the spreading of the results**

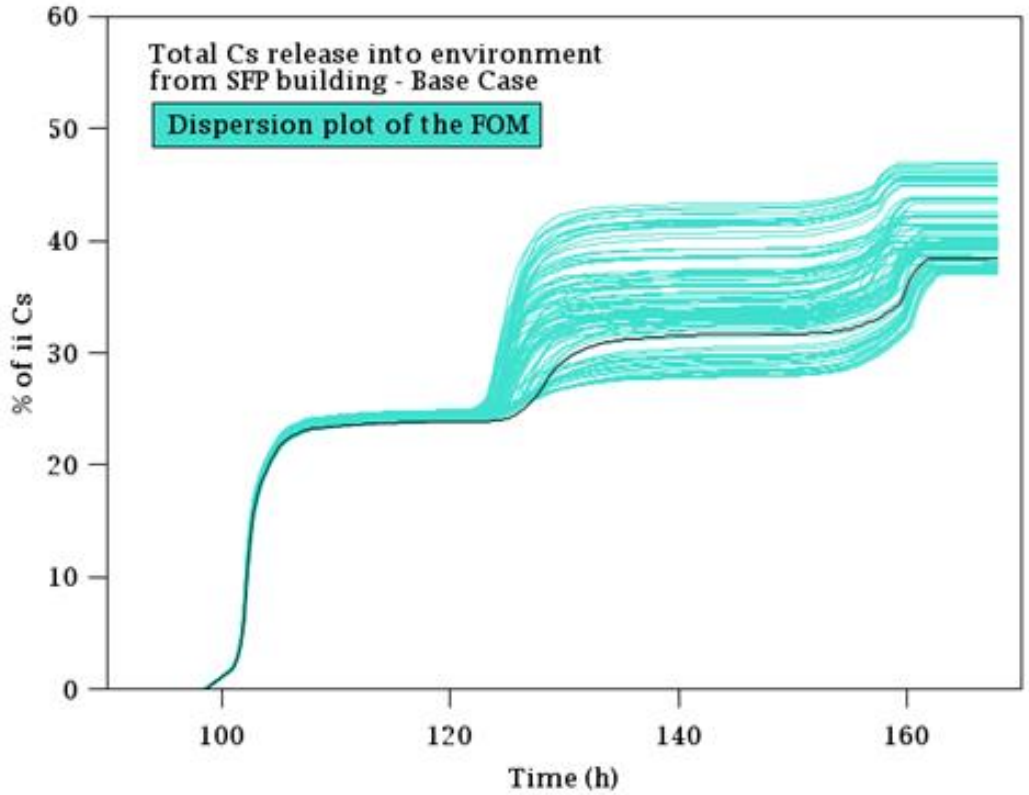

Time dependent dispersion plot of % of the initial inventory (i.i.) of Cs released into environment [ENERGORISK]

Results – Uncertainty analysis (2/2)

- **Statistics indicators: minimum, maximum values, mean, standard deviation, cumulative density function, probability density functions, fractiles…**

- **Wilks formula: considering the number N of runs performed, we have the probability β (confidence level) that more than a fraction γ (probability content) lies between the min – max values ⇒ For a two-sided tolerance interval, a probability content and a confidence set to 95% and 95% (values generally taken by the participants), the minimum number of code runs is approximately 100.**

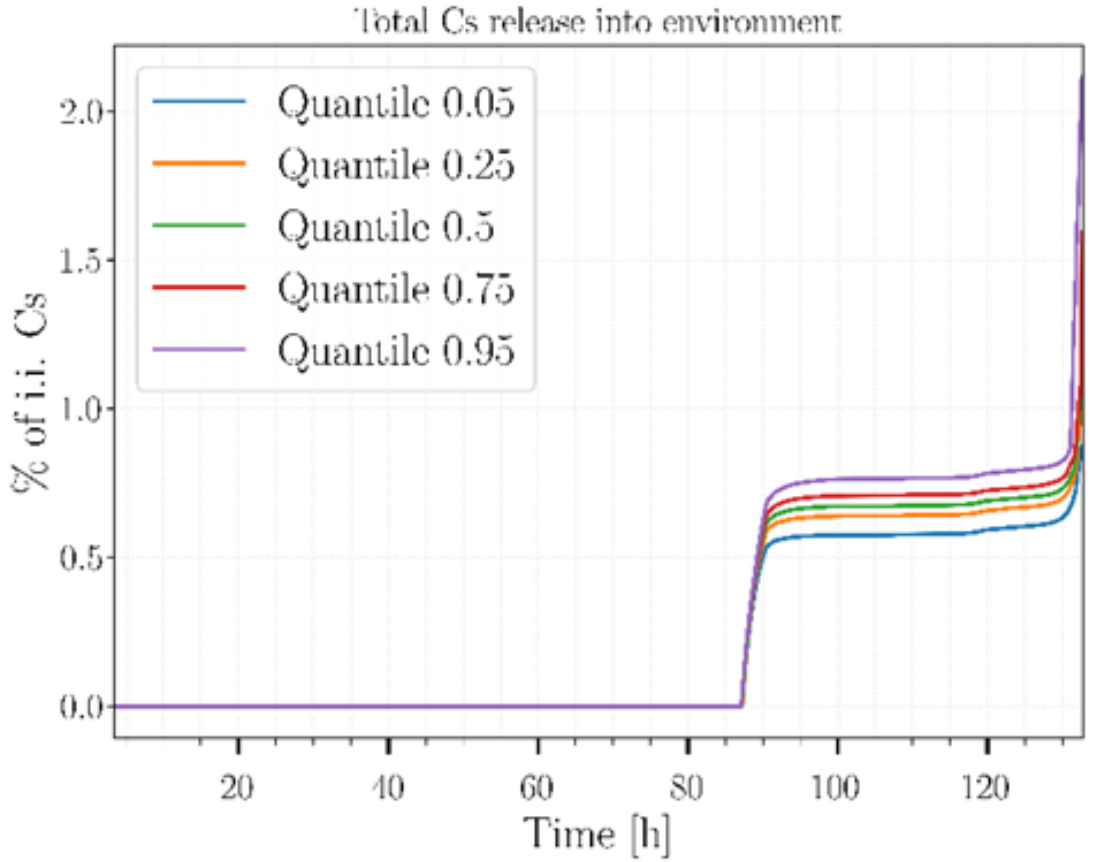

Time dependent Percentiles for % of the initial inventory (i.i.) of Cs released into environment [IRSN]

Results – Sensitivity analysis (1/2)

- **Characterization of the statistical correlation between the uncertain input parameters and the FoMs through Pearson and Spearman correlation coefficients: a correlation coefficient close to 1 (resp. -1) indicates a positive (resp. negative) linear dependence.**

- **For a given sample size, the Bravais-Pearson confidence threshold matches the correlation coefficient to a level of confidence. For instance, for a sample size of 100, the confidence threshold is ≈ 0.2 for a confidence level of 95%.**

- **More sophisticated regression methods are available but have not been used yet.**

Results – Sensitivity analysis (2/2)

Spearman correlation coefficient at 100 h [ENEA]

Cs release into environment :

- positively correlated to Vsto (particle shape factor relative to Stokes velocity)
- negatively correlated to Coag (particle shape factor relative to coagulation) and Rho (particle mean density)

⇒ **Most significant parameters linked to aerosol deposition**

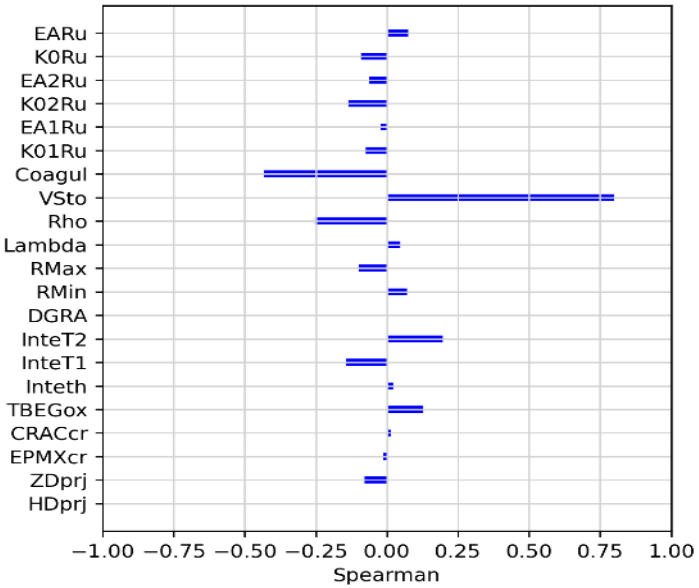

Evolution with time of Spearman correlation coefficient [ENEA]

The correlation of an input parameter can be significant only at a given time or during a phase of the transient

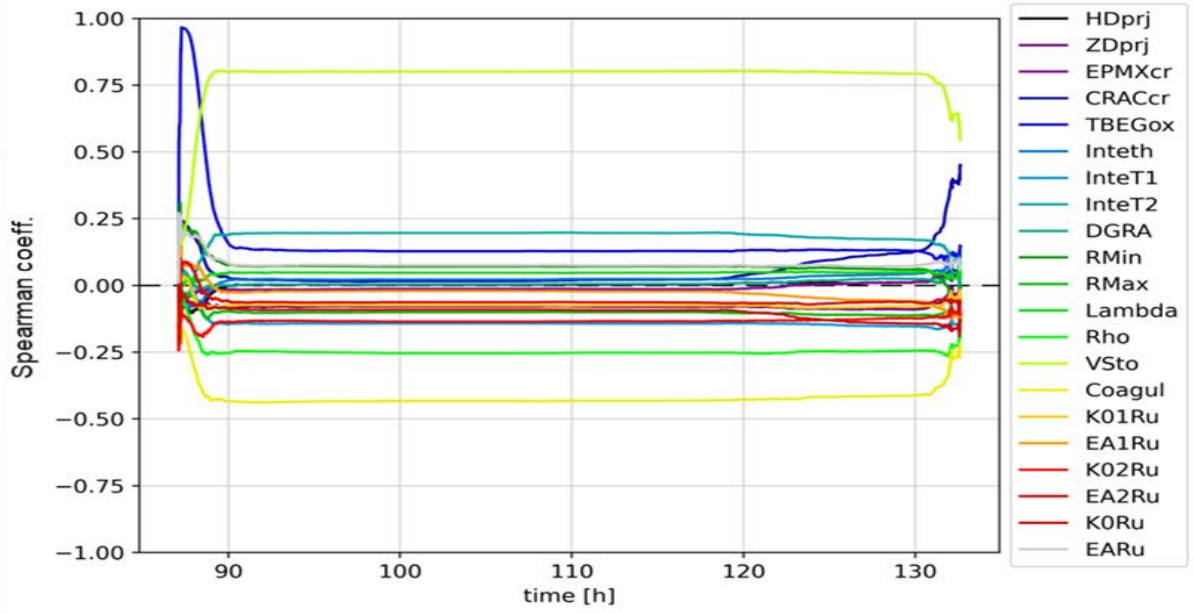

Conclusions

- **The first steps required to carry out the UaSA have been completed:**
  - selection of an accidental scenario
  - creation of an input deck and check of its consistency
  - share of procedures to retrieve the results, especially the FoMs
  - determination of uncertainty sources in models
  - choice of key target variables as ST FoMs
  - start of the uncertainty analysis phase with the use of UQ-tools to propagate input uncertainties

- **Participants have benefited from the experience gained in other WPs in MUSA:** coupling by scripting between the SA code and UQ-tool, automation of data extraction for the post-processing, implementation in a cluster of the SA code and UQ-tool…

- **Major challenges have been found when applying UQ methodologies to SFP scenarios:** large CPUs (from a few hours to 4 days for one computation), code crashes (questions about the statistical treatment of failed calculations), identification and characterization of the input uncertain parameters...

Perspectives

1. Continuation of the UaSA:

- Elaboration of common standard for post-processing to make the analysis more easily comparable from one participant to another one
- Taking RC into account (coupling with a dedicated tool)
- Analysis of single realizations to understand some unexpected dependencies
- Determination of governing uncertainties
- Elaboration of a harmonized approach: selection of uncertain parameters? criteria for the determination of the number of runs? significance threshold of correlation coefficients?...

2. Assessment of the benefits of spray systems (uncertainty sources of 4th category) following the review of SAM measures and systems in SFP

ACKNOWLEDGEMENTS

The MUSA project has received funding from the Euratom research and training program 2014–2018 under grant agreement No. 847441



The 10th European Review Meeting on Severe Accidents Research

Severe Accident Research Eleven Years after the Fukushima Accident

May 16-19, 2022, Karlsruhe, Germany

Technical Session 3-1: Ex-vessel Corium interactions and coolability

Chairs: S. Bechta (KTH), P. Piluso (CEA)

ID331	**PIRT Development for the Corium Coolability and MCCI Phenomena during Postulated Severe Accidents in the Reactor Cavity** S.K. Sim (EN2T)	**Paper** **Presentation**
ID270	**Enhancing Ex-Vessel Corium Coolability for Installed Base Nuclear Power Plants** M. Hupp (Framatome)	**Paper** **Presentation**
ID279	**Quenching Phenomena in High Temperature Cylindrical Particle Bed-MONET Tests** M. Modak (SNU)	**Paper** **Presentation**
ID299	**Thermodynamics of aerosols during a molten core-concrete interaction at Fukushima Daiichi unit 2 conditions** H. Laffolley (CEA)	**Paper** **Presentation**

10TH CONFERENCE ON SEVERE ACCIDENTS RESEARCH
May 16-19, 2022 – Karlsruhe, Germany
ERMSAR 2022

PIRT Development for the Corium Coolability and MCCI Phenomena during Postulated Severe Accidents in the Reactor Cavity

Y. S. Kim*, Y. K. Kwack, N. H. Hoang, J. H. Kim, S. K. Sim
Environment & Energy Technology, Inc.
yskim@en2t.com

ABSTRACT

Following revised nuclear regulatory guides in 2016 due to Fukushima accident by the Korea Nuclear Safety and Security Council, Korea Hydro and Nuclear Power utility company submitted Accident Management Plan in June 2019 for all the operating reactors as well as reactors under construction in Korea. Currently, twelve units of OPR1000 are operating in Korea and the OPR1000 AMP is based on the pre-flooding of the reactor cavity for the case of severe accident in the reactor cavity due to postulated lower head vessel failures. Environment & Energy Technology is currently developing a stand-alone best estimate severe accident analysis code, CASTLE, for the severe accidents in the reactor cavity due to lower head vessel failures with Korea Atomic Energy Research Institute and Sejong University. During the postulated severe accident in the reactor cavity, molten corium is assumed to be discharged from the lower plenum of the reactor vessel into the pre-flooded reactor cavity according to the OPR1000 Accident Management Plan. In this postulated severe accident scenario, the coolability of the discharged corium and the molten corium and concrete interaction are the major phenomena of the severe accident in the reactor cavity. In this study, phenomena identification ranking table and test matrix were developed to prioritize the development and validation of the phenomenological models for the CASTLE code.
The final PIRT also accommodated the results of international expert's review for the developed PIRT of the core debris coolability and molten corium and concrete interaction phenomena during the postulated severe accident in the reactor cavity due to lower head vessel failures.

KEYWORDS
Severe Accident, Debris Coolability, MCCI, PIRT, CASTLE

1. INTRODUCTION

Due to the strengthened regulatory guides on the severe accident by the Korea Nuclear Safety and Security Council (NSSC), Korea Hydro and Nuclear Power (KHNP) utility company is required to submit Accident Management Plan (AMP) to NSSC for the operating reactors as well as the reactors under construction in Korea. Especially, for the OPR1000 operating reactors, KHNP submitted AMP to the NSSC based on the pre-flooding strategy for mitigating severe accidents in the reactor cavity [1]. However, currently, there is no licensed detailed severe accident analysis code for the sequences specific in the reactor cavity due to Lower Head Vessel Failures (LHVFs). Korean nuclear industry identified a need for development of a stand-alone and best estimate severe accident analysis code to simulate the phenomena in the reactor cavity due to LHVFs. Currently, Environment & Energy Technology (en^2t), Korea Atomic Energy Research Institute (KAERI) and SeJong University (SJU) are cooperatively developing a stand-alone best estimate CASTLE (reactor Cavity Severe accidenT reaListic Evaluation) code to analyze the phenomena and sequences in the reactor cavity during postulated severe accidents with LHVFs. Thus, the PIRT (Phenomena Identification Ranking Table) and experimental test data are necessary to develop phenomenological models and validation of the CASTLE code.
The objective of the PIRT development is to identify the debris coolability and Molten Corium and Concrete

Interaction (MCCI) phenomena and thus prioritize the phenomenological models for the development of the CASTLE code during postulated severe accidents in the reactor cavity due to LHVFs. During the PIRT development, test matrix is also developed for the validation of the phenomenological models and the CASTLE code using available experimental test data as well as the severe accident analysis results of the major integrated severe accident analysis codes.

2. PIRT DEVELOPMENT

2.1. Reference Plant

OPR1000 was selected as a reference plant for the PIRT development of the CASTLE code due to the fact that the AMP of the severe accident in the reactor cavity is based on the pre-flooding strategy of the reactor cavity [1].
Major OPR1000 design parameters are shown in Table 1 [2]. Reactor cavity geometry [1] and In-Core Instrumentation (ICI) cables [3] of the OPR1000 are also shown in Figures 1(a) and 1(b), respectively.
Available resources of the pre-flooding water for the OPR1000 reactor cavity during the severe accident are Reactor Coolant System (RCS) through pressurizer safety valves or safety depressurization systems, safety injection tanks and refueling water tank through containment spray pumps. However, even though the total water inventory resources for the pre-flooding water is sufficient for the OPR1000 to fill the reactor cavity up to the top of the lower head vessel, the amount of water to fill the cavity is quite dependent on the accident scenario. Figure 2 shows the reactor cavity pre-flooding injection flow paths of the OPR1000 [1].

Table 1. Design Parameters of OPR1000 [2]

Major Design Parameter	Design value
Core thermal power (MWt)	2,815
RCS pressure (MPa)	15.5
Core inlet temperature (K)	569
Core outlet temperature (K)	600
Primary flow rate (kg/sec)	15,306
Secondary side pressure (MPa)	7.37
SG steam temperature (K)	562.6
Steam flow rate per SG (kg/sec)	800

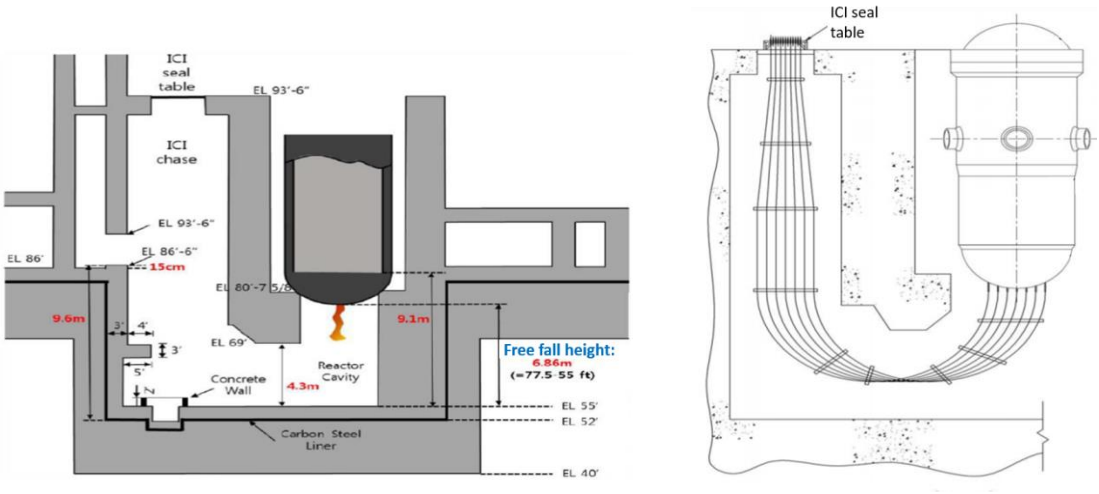

(a) Reactor Cavity Geometry of OPR1000 [1] **(b) ICI Instrumentation Cables [3]**

Figure 1. OPR1000 Reactor Cavity Geometry and In-Core Instrumentation System

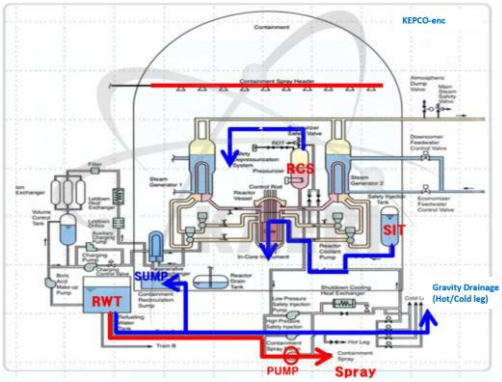

Figure 2. Reactor Cavity Pre-flooding Injection Flow Paths of OPR1000 [1]

2.2. PIRT Development Process

2.2.1. Safety Parameters and Safety Criteria

For the PIRT development process, phenomena ranking are determined by the relative importance of the phenomena during postulated severe accident in the reactor cavity due to LHVFs considering following major safety parameters and the safety criteria to determine the relative importance;

- Corium Temperature
- Reactor Cavity Pressure
- Integrity of the Concrete Wall and Basemat
- Integrity of the Containment
- Release of Radiological Sources

Also, major components and subsystem equipment related to the postulated severe accident in the reactor cavity due to LHVF are assumed as follows with the major parameters;

- Reactor Cavity: Temperature, Pressure
- Corium Jet: Corium Composition, Initial Corium Discharge Conditions
- Cavity Water: Mixture Water Level, Temperature, Pressure
- Corium Melt : Temperature, Fragmentation, Relocation
- Cavity Concrete Side Wall and Downward Basemat

2.2.2. Transient Phases of the Accident Scenario

In this study, it is assumed that the LHVF during the severe accident is initiated from multiple or sequential failures of the ICI cables in the reactor cavity of the OPR1000 reference plant [1]. The accident scenario after multiple or sequential failures of the ICI cables in the reactor cavity is summarized in Table 2 below. The ranking of the phenomena during the postulated severe accident in the cavity should be determined by the importance of the phenomena during each phase of the severe accident in regard to the accident scenario. To determine the ranking of the phenomena. Therefore, 5 transient phases of the postulated severe accident scenario in the reactor cavity are categorized based on the physical sequences of the accident scenario of Table 2 as follows;

Table 2. Accident Scenario of the Severe Accident in the Reactor Cavity

Phase	Accident Scenario	Initiating Phenomena	Results
Corium Discharge	Existence of Cavity Water	Cavity Water depending on the Accident Management Strategy and Accident Sequence before the Occurrence of LHVF	Pre-Flooding or Post-Flooding
	Corium Jet Discharge to Reactor Cavity	Multiple or Sequential Failures of the ICI Cables	Corium in the Lower Plenum is discharged into the Reactor Cavity by Initial Conditions
FCI	Fuel Melt and Coolant Interaction	Discharged Corium and Coolant Interaction in the Cavity	Corium Jet Breakup, Steam Explosion and Fragmentation
	Corium Fragmentation	Jet Breakup and Particle Fragmentations	Particular Debris Sedimentation and Solidification
Debris Bed Formation and Cooling	Debris Bed Formation	Debris Particle Sedimentation	Separation of Debris Bed and Melt Pool
Melt Pool Formation and Cooling	Crust Formation	Interaction of Corium Sediment with Coolant through Heat Transfer	Crust Separation
	Separation of Metal and Oxide Layers	Separation of Upper Metal and Lower Oxide Layers	Concrete Ablation through Temperature Increase of Oxide Layer due to Decay Heat of Oxide Layer

MCCI	MCCI	Concrete Temperature increases to Concrete Decomposition Temperature due to Sedimentation of Oxide and Metal Layers	Corium Cooling or Basemat Melt-Through (BMT) causing Radiation Release to Environment due to Failure of Containment Integrity

2.2.3. Validation Matrix

The PIRT will be used for the development of the phenomenological models of the stand-alone best estimate CASTLE code during postulated severe accidents in the reactor cavity. Firstly, the phenomenological models implemented in the CASTLE code should be verified and validated through Separate Effect Tests (SETs). Secondly, CASTLE code should be verified and validated its predictions through Integral Effect Tests (IETs) or comparisons with other integrated severe accident analysis computer codes such as CINEMA [4], MELCOR [5], and MAAP5 [6]. Table 3 shows the test matrix of the specific phenomena as well as the experimental and analysis database for the corium coolability, MCCI and corium cooling facility of Core-Catcher. The database in the test matrix will be used for the verification and validation of the CASTLE code.

Table 3. Test Matrix for the Validation of the CASTLE Models

Major Phenomena and Models		Experimental and Analysis Database	Remark
Lower Head Vessel Failure		IVMR	KAERI
Corium Melt Fragmentation		TROI	
		FARO	JRC-ISPRA
		KROTOS	
		3D CFD Analysis	SJU
Corium Relocation	Thermal-hydraulic Model	DEFCON	KAERI
	Debris Formation Model	DEFCON	KAERI
		3D CFD Analysis	SJU
	DHF Model	DEFCON	KAERI
	MCCI Phenomena	MACE & CCI	ANL
		OECD/MCCI	OECD/ANL
		OECD/ROSAU	
		BETA COMET-L MOCKA	KfK KIT/Karlsruhe
		ECOKATS2	FZK/Karlsruhe
	Corium Coolability and MCCI Analysis	COOLAP-MELCOR Analysis	POSTECH
		MAAP5 Analysis	KEPCO E&C
Core Catcher Cooling Performance	Corium Coolability	CE-PECS	KHNP/KAERI
		VESTA	KAERI
Data	Corium Material Property	TCOFF	OECD/NEA
		PreADES	

2.3. PIRT Prioritization Methodology

The priority of developing models for the severe accident in the reactor cavity due to LHVFs should be determined according to the objective of the PIRT. In order to prioritize importance of the characteristic phenomena occurring during severe accidents in the reactor cavity, current status of phenomenological model development and current knowledge level are selected as the basic prioritization standards. Each prioritization standard has three steps as was used in the USNRC next generation nuclear plant PIRT [7]. In addition, the priority ranking of the current status of the model development and the current knowledge level of each phenomenon was determined for each severe accident scenario phase as shown in Table 2. In this study, the PIRT development methodology is derived by the following prioritization methods;

- **Status of the Model Development**
  Status of the phenomenological model development is categorized in High (H), Medium (M) and Low (L) in three steps based on the current model of the specific phenomenon involved. Each step is defined the priority ranking of importance as shown in Table 4 considering model development, experimental validation and uncertainty.

- **Status of Knowledge Level**
  Status of knowledge level is categorized in Level 1, Level 2 and Level 3 in three steps considering current knowledge level for the thermal hydraulic phenomena and existence of the experimental database on the characteristic phenomena. Each step is defined the priority ranking of knowledge level as shown in Table 5.

Table 4. Definition of Ranking for Current Model Development

Step	Definition
H	**High Importance: High Impact on Model Development**
	Status of Model Development Phenomenological model is available with high accuracy.
	Experimental Tests and Validation Experimental tests are available with scaling analysis as well as validation of the phenomenological model.
	Uncertainty Quantification Uncertainty is quantified and accurate uncertainty evaluation of the phenomenological model is available.
M	**Medium Importance : Medium Impact on Model Development**
	Status of Model Development Phenomenological model is available with appropriate feasibility analysis.
	Experimental Tests and Validation Experimental tests are partially available with partial scaling analysis of the test and partial validation of the phenomenological model using experimental test data.
	Uncertainty Quantification Uncertainty quantification is partially available with appropriate feasibility analysis.
L	**Low Importance: Low Impact on Model Development**
	Status of Model Development

	Phenomenological model is not available but can be substituted by other methods.
	Experimental Tests and Validation Experimental test and thus validation is not available but can be substituted by other methods.
	Uncertainty Quantification Uncertainty quantification is necessary and recommended but not must.

Table 5. Definition of Ranking for Current Knowledge Level

Step	Definition
Level 1	Phenomenon is well studied with many test data and the uncertainty is well quantified.
Level 2	Phenomenon is generally understood and phenomenological model is available with limited understanding and large uncertainty, and thus further model validation and uncertainty quantification are necessary using experimental test data.
Level 3	Phenomenon is partially understood and phenomenological model is very limited and validation of the phenomenological model is not done due to lack of test data and thus uncertainty analysis is not available, thus needed further R&D.

2.4 Corium Coolability and MCCI PIRT for the Severe Accident in the Reactor Cavity

The corium coolability and MCCI phenomenological models of the CASTLE code, which is currently under development for the severe accident in the reactor cavity, are presented in Table 6 comparing with the phenomenological models of the internationally used integrated severe accident analysis codes. As shown in Table 6, CASTLE is planning to develop all major phenomenological models such as cavity water level, corium jet fragmentation, relocation, sedimentation, corium coolability, MCCI phenomena and their interfacial feedbacks. CASTLE code will trace the atomic elements but not the forms of the fission products for the fission product behavior.

The PIRT for the severe accident in the reactor cavity was developed by the PIRT development criteria described above; i.e., status of the phenomenological model development and status of the knowledge level. In addition, current severe accident analysis code modeling capability as well as the relative importance of each phenomenon for severe accident mitigation was also used to determine the PIRT.

Initial PIRT for the postulated severe accident in the reactor cavity due to LHVFs has been developed through discussions and reviews by the CASTLE code development participants considering major models for developing the CASTLE code. The initial PIRT has been reviewed by the international experts of this specific field as listed in Appendix A. Final PIRT has been developed accommodating the review of the international expert group as shown in Table 7 [8]. AS shown in Table 7, the steam explosion is ranked High for the impact on the model development, but Low knowledge level. Thus, the CASTLE code will use simple steam explosion model as user option due to low frequency of the steam explosion for the OPR1000 pre-flooding strategy.

The authors will incorporate further comments and reviews from the international expert community of the severe accidents to develop a final PIRT for the development of the CASTLE code. International cooperation on the experimental tests for the validation of the phenomenological models is also needed.

Table 6. Comparison of Corium Coolability and MCCI Models in the Severe Accident Analysis Codes

Major Phenomena		MAAP5	ASTEC	MELCOR	CINEMA	CASTLE
Fragmentation	Jet Breakup	○	×	○	○	○
	Particle Size and Distribution	△	×	×	×	○
	Debris Particle Sedimentation	○	×	△	○	○
Corium Melt Relocation	Debris Particle Coolability	○	×	△	○	○
	Debris Bed Formation	×	×	×	×	○
	Evaporation Heat Transfer	○	○	○	○	○
Corium Coolability and MCCI Interface Phenomena	Corium Configurations	×	×	×	×	○
	Debris Particle Coolability	×	×	×	×	○
	Debris Bed Coolability	×	×	×	×	○
	Melt Pool Coolability	○	○	○	○	○
	Multi-Layer Modeling (Debris Bed, Crust, Pool)	×	×	×	×	○
MCCI Phenomena	Chemical Reaction	○	○	○	○	○
	Concrete Ablation	○	○	○	○	○
	Fission Product Behavior	○	△	○	○	△
	Gas Generation Behavior	○	○	○	○	○

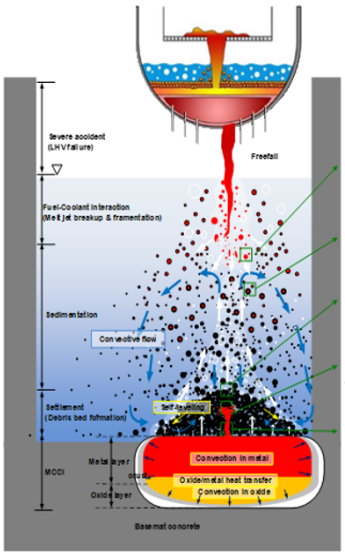

○ – Modeled, × - not modeled, △ – partially modeled

Table 7. PIRT of the Corium Coolability and MCCI during Postulated Severe Accident in the Reactor Cavity

	Major Phenomena					Rank by Impact on Model Development					Rank by Current Knowledge Level					Validation Test
	Severe Accident Phase (Physical Sequence of Scenario)					Severe Accident Phase					Severe Accident Phase					
	1	2	3	4	5	1	2	3	4	5	1	2	3	4	5	
Components	Corium Discharge	FCI	Debris Bed Formation and Cooling	Melt Pool Formation and Cooling	MCCI											
Corium Jet	Corium Properties Initial Conditions					H	H	H			L2	L1	L1			
	Decay Heat					H			H	H	L1			L2	L2	
Cavity Water	Cavity Mixture Level	Jet Break-up	Evaporation	Bubble Rise	Gas Rise	M	H	H	H	H	L2	L2	L2	L3	L3	
		Corium-Water Interface Heat Transfer				M	H	H	H	H	L1	L2	L2	L2	L2	
Corium Melt	Jet Mass/Velocity					H					L2					IVMR
		Cavity Water					H	H	H	H		L1	L1	L1	L1	
		Steam Explosion					H	H				L2	L3			TROI FARO KROTOS CFD(SJU)
		Rapid Steaming and Reactor Cavity Pressurization					M	M	M			L2	L2	L2		
		Oxidation of Unreacted Zirconium in Particles					L	L				L2	L2			
		Jet Breakup Length					H	H				L2	L2			
		Particle Size					H	H				L2	L2			
		Debris Particle Shape					M	M				L3	L3			
		Debris Particle Spreading/ Distribution					M	M				L3	L3			
		Debris Particle Sedimentation					H	H				L2	L2			
Corium Melt/ Concrete Ablation			Debris Particle Cooling				H	H	H			L2	L2	L2		DEFCON CFD(SJU)
			Debris Bed Formation				H	H	H	H		L3	L3	L2	L2	DEFCON
			Debris Bed Cooling				H	H	H	H		L3	L2	L2	L2	FARO OECD/ROSAU
				Oxide Layer Formation and Cooling					H	H				L2	L2	CCI/ANL ECOKARS-2/ FzK(Karlsruhe)
				Crust Formation					M	M				L2	L2	CCI/ANL ECOKATS-2/ FzK(Karlsruhe)
				Crust Formation And Cooling					M	M				L2	L2	
				Crust Breach, Water Ingression And Melt Eruption					H	M				L3	L3	MASCA
				Metal Layer Formation and Cooling					H	H				L2	L2	
				Stratification of Oxide and Metal					H	H				L3	L3	
				Melt Pool Height					H	H				L2	L2	
				Oxide and Metal Layer Heating					H	H				L2	L2	
					Oxide and Melt Configuration				H	H				L2	L2	
					Chemical Reaction Heat				H	H				L2	L2	MACE OECD/MCCI BETA/COMET-L MOCKA (KfK/KIT Karlsurhe) OECD/ROSAU
					Convective Heat Transfer	M	M	M	H	H	L1	L1	L1	L2	L2	
					Melt Eruption					H					L2	
					Radiation Heat Transfer	M	M	ML	ML	L2	L2	L2	L2	L2	L2	
					Concrete Slag Formation				M	M				L3	L3	
					Gas Release				H	H				L2	L2	
					Concrete Decomposition					H					L2	
					Conduction Heat Transfer between Melt and Concrete					H					L1	ACE
					Oxide and Concrete Melt Properties				H	H				L2	L2	
					Concrete Slag Heat Transfer				M	M				L3	L3	
					Fission Product Behavior	L	M	M	M	M	L3	L3	L3	L3	L3	

3. CONCLUSIONS

The PIRT of the corium coolability and MCCI phenomena during postulated severe accident in the reactor cavity has been developed to prioritize corium coolability and MCCI phenomenological model development and to verify and validate the stand-alone best estimate CASTLE code. The validation test matrix is also developed using the experimental test data as well as the analysis results of the specific phenomena for the validation of the phenomenological models and the CASTLE code.
The PIRT has been initially developed by the CASTLE code development participants of en^{2}t, KAERI and SJU and then it was reviewed by the international expert review group. The final PIRT will be used to develop the CASTLE code as well as to develop experimental test program for the validation of the debris coolability and MCCI phenomenological models during severe accidents in the reactor cavity due to LHVFs.
The PIRT developed in this report will contribute to enhance understanding of the debris coolability and MCCI phenomena during postulated severe accidents in the reactor cavity due to LHVFs and thus prevent and mitigate severe accidents. The PIRT and the CASTLE code can be used to strengthen the reactor safety in conjunction with the pre-flooding strategy for the OPR1000 AMP during postulated severe accident in the reactor cavity due to LHVFs.

ACKNOWLEDGMENTS

This study has been funded and supported by Korea Institute of Energy Technology Evaluation and Planning (KETEP) and Ministry of Trade, Industry and Energy (MOTIE).
The authors of this report appreciate the support from the participants of the CASTLE development project at KAERI and SJU. The authors also appreciate the international expert review group for the independent review and valuable comments for the PIRT development.

REFERENCES

1. Preliminary Evaluation of Accident Management for Ex-vessel Debris Coolability, KAERI/TR-7401/2018, Korea Atomic Energy Research Institute (2018).
2. Final Safety Analysis Report, Shin-Kori Units-1/2, Korea Hydro and Nuclear Power, (2008).
3. A Mechanical Characteristic of the In-core Instrument assembly for Pressurized Water Reactor, KAERI/TR-3613/2008, Korea Atomic Energy Research Institute (2008).
4. D.H. Kim, J.H. Song, B.C. Lee, J.H. Na, H.T. Kim, Development of an Integrated Severe Accident Analysis Computer Program Package in Korea, The 8th ERMSAR-2017 Conference, Warsaw, Poland (2017).
5. MELCOR, Computer Code Manuals Vol. 1: Primer and Users' Guide, Version 1.8.6, NUREG/CR-6119, Vol. 1, Rev. 3, USNRC Report, Sandia National Laboratories (2005).
6. MAAP5 (Modular Accident Analysis Program 5), User's Manual Rev. 0, Fauske & Associates (2008).
7. Next generation Nuclear Plant Phenomena Identification ranking Tables (PIRTs), Vol. 2, Accident and Thermal Fluids Analysis PIRTs, NUREG/CR-6944, Vol. 2, USNRC (2008).
8. PIRT Development for the Integrated Realistic Severe Accident Analysis CASTLE Code for the Postulated Severe Accident in the Reactor Cavity, en2t-NBTR-20-001, Environment & Energy Technology, Inc., (2020).

APPENDIX A

International Independent PIRT Review Group

Name	Organization	Title
Dr. Chang Hwan Park	FNC, Ltd.	Director of NPP Accident Management
Dr. Hyun Sun Park	Seoul National University	Research Professor
Dr. Kiyofumi Moriyama	MasakiTech LLC	President
Dr. Mitchell T. Farmer	Argonne National Laboratory	Program Manager of LWR
Dr. Jerzy Jan Foit	KIT	Consultant
Dr. Sung Jin Lee	FAI, LLC	Senior Consulting Engineer

ERMSAR 2022

PIRT Development for the Corium Coolability and MCCI Phenomena during Postulated Severe Accidents in the Reactor Cavity

May 17, 2022

www.en2t.com

Y. S. Kim, Y. K. Kwack, H. H. Hoang, J. H. Kim and S. K. Sim
sksim@en2t.com

(주)이엔이티
Environment & Energy Technology, Inc.

Karlsruhe Institute of Technology

Contents

I Introduction

II Reference Plant

III PIRT Development Process

IV PIRT Prioritization Methodology

V PIRT for the Severe Accidents in the Cavity

VI CASTLE Code Development

VII Summary and Conclusions

epilogue

Strengthened Nuclear Safety Regulatory Guide in Korea

❖ NSSC : Post-Fukushima Nuclear Safety Regulatory Guide for Prevention and Mitigation of the Severe Accidents

- Stress Tests : Evaluation of Safety Margin for All the Operating Reactors in Korea
  - ✓ SBO and Loss of RHRS due to Earthquake and Flooding
  - ✓ Loss of Core Cooling, SFP Cooling and Containment Integrity
- Increased Site Emergency Power
  - ✓ Emergency Diesel Generators : Two 7,000 Kw EDGs per Unit
  - ✓ Alternative AC DG : One 7,000 Kw AAC DG per 4 Units
  - ✓ Movable DG : One 3,200 Kw MDG per Site
- Accident Management Plan : SAR Ch. 19 for all the Operating and Developing Reactors

❖ Technology Development for Prevention and Mitigation of the Severe Accidents

- Integrated Severe Accident Analysis Code : COMPASS, SIMPLE, CAP, CINEMA, CASTLE
- Pre-Flooding Strategy of the Reactor Cavity
- Core Catcher Development and Performance Evaluation

Need for Nuclear Safety Enhancement

❖ Post-Fukushima Accident Regulatory Measures

- USNRC : Strengthened Post-Fukushima Regulatory Guide
  - ✓ Enhance Core Cooling
  - ✓ Enhance Spent Fuel Pool Cooling : Special SFP Inspection
  - ✓ 10CFR 50.155 : “Mitigation of BDBEs”

❖ OECD/NEA MCCI Status Report

- Need for Model Improvement for Corium Coolability and MCCI Phenomena

❖ OECD/BSAF International Joint Research

- Need for Improvement of models for the integrated severe accident analysis codes

❖ Improvement of the conservative models in integrates Severe Accident analysis codes using recent Experimental tests on Severe accidents

- USNRC : MELCOR
- EPRI : MAAP5

Experimental Research on the Severe Accident Phenomena

❖ Ex-core Severe Accident Tests using Prototype Corium Material

- US ANL : MCCI Tests
  - ✓ 1989~2015년 : MACE, OECD/CCI 1~9
  - ✓ 2019~2024년 : OECD/ROSAU (International Joint Research)
- Italy JRC-ISPRA
  - ✓ FARO, KROTOS
- Japan JAEA
  - ✓ COTELS
- KAERI
  - ✓ TROI : Steam Explosion
  - ✓ DEFCON : Corium Debris Formation

❖ Severe Accident Database Management Platform

- KAERI : In-core Severe Accident DB Management Platform
- en^{2}t : In-core and Ex-core Severe Accident DB Management Platform

OPR1000 : 12 Units are operating in Korea

❖ Design Parameters

Major Design Parameter	Design Value
Core thermal power (MWt)	2,815
RCS pressure (MPa)	15.5
Core inlet temperature (K)	569
Core outlet temperature (K)	600
Primary flow rate (kg/sec)	15,306
Secondary side pressure (MPa)	7.37
SG steam temperature (K)	562.6
Steam flow rate per SG (kg/sec)	800

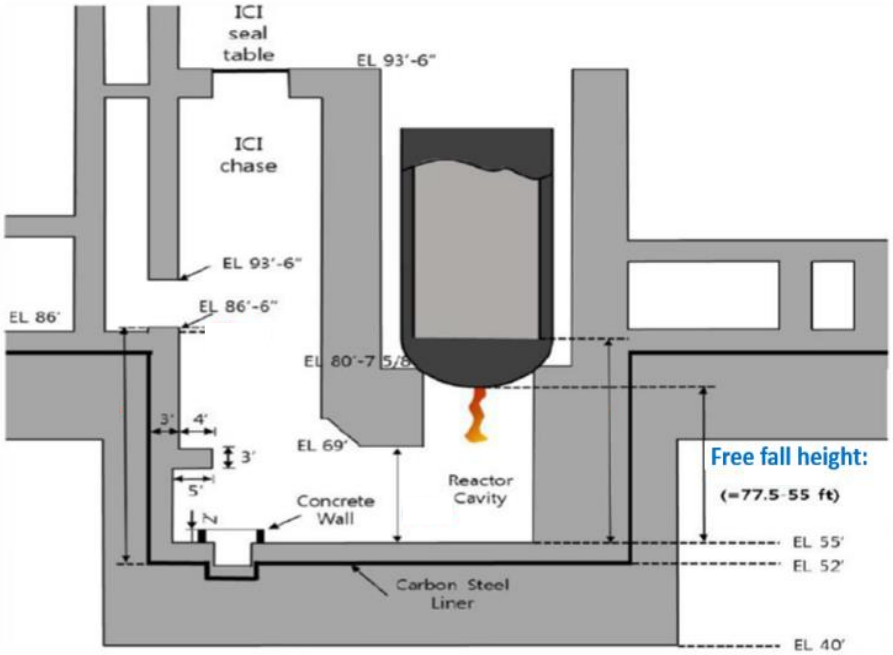

Reactor Cavity Geometry of OPR1000

OPR1000 : Optimized Power Reactor 1000 Mwe

- 12 OPR1000 Units are operating in Korea
- OPR1000 AMP : Based on the Pre-flooding Strategy of the Reactor Cavity
- Pre-flooding Injection Flow Paths
  - Pressurizer Safety Valves
  - Safety Depressurization Systems
  - Safety Injection Tanks
  - Containment Spray Pumps : RWT
- Postulated LHVF
  - Multiple ICI Cable Failures
  - Assumed based on PRA on LHVFs

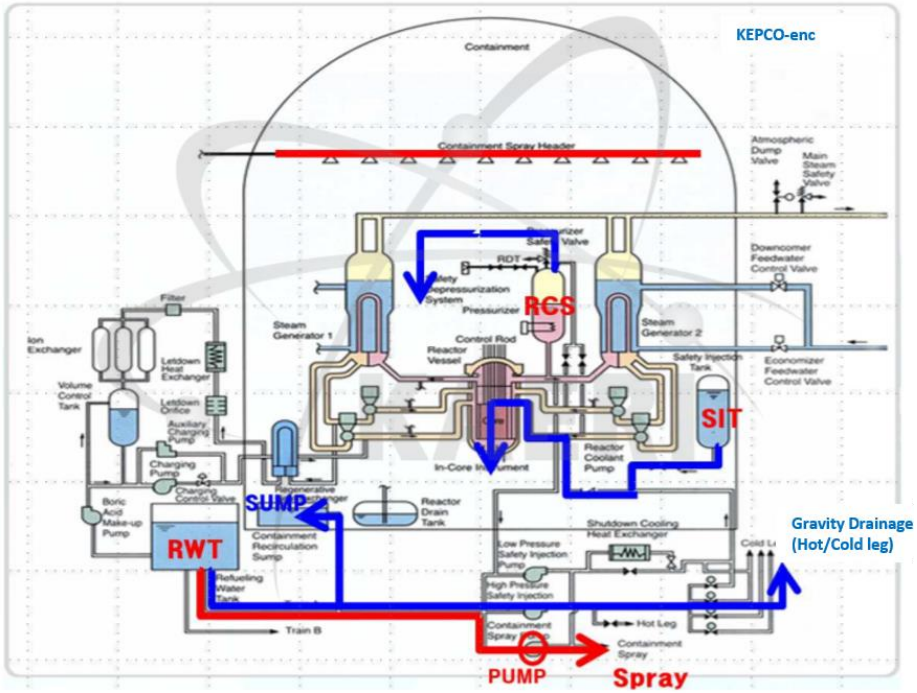

Pre-flooding Injection Flow Paths
OPR1000 Reactor Cavity

PIRT Development Process

Safety Parameters and Safety Criteria to determine Relative Importance

- Corium Temperature
- Reactor Cavity Pressure
- Integrity of the Concrete Wall and Basemat
- Integrity of the Containment
- Release of Radiological Sources

Major Components and Subsystem Equipment

- Reactor Cavity : Temperature, Pressure
- Corium Jet : Corium Composition, Initial Corium Discharge Conditions
- Cavity Water : Mixture Water Level, Temperature, Pressure
- Corium Melt : Temperature, Fragmentation, Relocation
- Cavity Concrete Side Wall and Basemat : Composition and Temperature

Transient Phases of the Accident Scenario

Phase	Accident Scenario	Initiating Phenomena	Results
Corium Discharge	Existence of Cavity Water	Cavity Water depending on the Accident Management Strategy and Accident Sequence before the Occurrence of LHVF	Pre-Flooding or Post-Flooding
	Corium Jet Discharge to Reactor Cavity	Multiple or Sequential Failures of the ICI Cables	Corium in the Lower Plenum is discharged into the Reactor Cavity by Initial Conditions
FCI	Fuel Melt and Coolant Interaction	Discharged Corium and Coolant Interaction in the Cavity	Corium Jet Breakup, Steam Explosion and Fragmentation
	Corium Fragmentation	Jet Breakup and Particle Fragmentations	Particular Debris Sedimentation and Solidification
Debris Bed Formation and Cooling	Debris Bed Formation	Debris Particle Sedimentation	Separation of Debris Bed and Melt Pool
Melt Pool Formation and Cooling	Crust Formation	Interaction of Corium Sediment with Coolant through Heat Transfer	Crust Separation
	Separation of Metal and Oxide Layers	Separation of Upper Metal and Lower Oxide Layers	Concrete Ablation through Temperature Increase of Oxide Layer due to Decay Heat of Oxide Layer
MCCI	MCCI	Concrete Temp increases to Decomps. Temp due to Sediment. of Oxide and Metal Layers	Corium Cooling or Basemat Melt-Through causing Radiation Release to Environment due to Failure of Containment Integrity

Validation Matrix of the CASTLE Models and Code

Major Phenomena and Models		Experimental and Analysis Database	Remark
Lower Head Vessel Failure		IVMR	KAERI
Corium Melt Fragmentation		TROI	
		FARO	JRC-ISPRA
		KROTOS	
		3D CFD Analysis	SJU
Corium Relocation	Thermal-hydraulic Model	DEFCON	KAERI
	Debris Formation Model	DEFCON	KAERI
		3D CFD Analysis	SJU
	DHF Model	DEFCON	KAERI
	MCCI Phenomena	MACE & CCI	ANL
		OECD/MCCI	OECD/ANL
		OECD/ROSAU	
		BETA COMET-L MOCKA	KfK KIT/Karlsruhe
		ECOKATS2	FZK/Karlsruhe
	Corium Coolability and MCCI Analysis	COOLAP-MELCOR Analysis	POSTECH
		MAAP5 Analysis	KEPCO E&C
Core Catcher Cooling Performance	Corium Coolability	CE-PECS	KHNP/KAERI
		VESTA	KAERI
Data	Corium Material Property	TCOFF	OECD/NEA
		PreADES	

✓ Status of the Model Development

Step	Definition
H	High Importance: High Impact on Model Development
	Status of Model Development Phenomenological model is available with high accuracy.
	Experimental Tests and Validation Experimental tests are available with scaling analysis as well as validation of the phenomenological model.
	Uncertainty Quantification Uncertainty is quantified and accurate uncertainty evaluation of the phenomenological model is available.
M	Medium Importance : Medium Impact on Model Development
	Status of Model Development Phenomenological model is available with appropriate feasibility analysis.
	Experimental Tests and Validation Experimental tests are partially available with partial scaling analysis of the test and partial validation of the phenomenological model using experimental test data.
	Uncertainty Quantification Uncertainty quantification is partially available with appropriate feasibility analysis.
L	Low Importance: Low Impact on Model Development
	Status of Model Development Phenomenological model is not available but can be substituted by other methods.
	Experimental Tests and Validation Experimental test and thus validation is not available but can be substituted by other methods.
	Uncertainty Quantification Uncertainty quantification is necessary and recommended but not must.

PIRT Prioritization Methodology

✓ Status of the Knowledge Level

Step	Definition
Level 1	Phenomenon is well studied with many test data and the uncertainty is well quantified.
Level 2	Phenomenon is generally understood and phenomenological model is available with limited understanding and large uncertainty, and thus further model validation and uncertainty quantification are necessary using experimental test data.
Level 3	Phenomenon is partially understood and phenomenological model is very limited and validation of the phenomenological model is not done due to lack of test data and thus uncertainty analysis is not available, thus needed further R&D.

PIRT for the Corium Coolability and MCCI during Postulated Severe Accident in the Reactor Cavity

PIRT Development and Review

- PIRT Development
- CASTLE Developer's Internal Review : en2t, KAERI and SJU
- International Expert Review : FNC, SNU, MasakiTech, KIT, FAI
- Need Further Comments from International Expert Community

Name	Organization	Title
Dr. Chang Hwan Park	FNC, Ltd.	Director of NPP Accident Management
Dr. Hyun Sun Park	Seoul National University	Research Professor
Dr. Kiyofumi Moriyama	MasakiTech LLC	President
Dr. Mitchell T. Farmer	Argonne National Laboratory	Program Manager of LWR
Dr. Jerzy Jan Foit	KIT	Consultant
Dr. Sung Jin Lee	FAI, LLC	Senior Consulting Engineer

PIRT for the Severe Accidents in the Cavity

PIRT for the Corium Coolability and MCCI during Postulated Severe Accident in the Reactor Cavity (1/3)

	Major Phenomena					Rank by Impact on Model Development					Rank by Current Knowledge Level					Validation Test
	Severe Accident Phase (Physical Sequence of Scenario)					Severe Accident Phase					Severe Accident Phase					
Components	1	2	3	4	5	1	2	3	4	5	1	2	3	4	5	
	Corium Discharge	FCI	Debris Bed Formation and Cooling	Melt Pool Formation and Cooling	MCCI											
Corium Jet	Corium Properties Initial Conditions					H	H	H			L2	L1	L1			
	Decay Heat					H			H	H	L1			L2	L2	
Cavity Water	Cavity Mixture Level	Jet Break-up	Evaporation	Bubble Rise	Gas Rise	M	H	H	H	H	L2	L2	L2	L3	L3	
		Corium-Water Interface Heat Transfer				M	H	H	H	H	L1	L2	L2	L2	L2	
Corium Melt	Jet Mass/Velocity					H					L2					IVMR
		Cavity Water					H	H	H	H		L1	L1	L1	L1	
		Steam Explosion					H	H				L2	L3			TROI FARO KROTOS CFD(SJU)
		Rapid Steaming and Reactor Cavity Pressurization					M	M	M			L2	L2	L2		
		Oxidation of Unreacted Zirconium in Particles					L	L				L2	L2			
		Jet Breakup Length					H	H				L2	L2			
		Particle Size					H	H				L2	L2			
		Debris Particle Shape					M	M				L3	L3			
		Debris Particle Spreading/ Distribution					M	M				L3	L3			
		Debris Particle Sedimentation					H	H				L2	L2			

PIRT for the Corium Coolability and MCCI during Postulated Severe Accident in the Reactor Cavity (2/3)

	Major Phenomena					Rank by Impact on Model Development					Rank by Current Knowledge Level					Validation Test
	Severe Accident Phase (Physical Sequence of Scenario)					Severe Accident Phase					Severe Accident Phase					
	1	2	3	4	5	1	2	3	4	5	1	2	3	4	5	
Components	Corium Discharge	FCI	Debris Bed Formation and Cooling	Melt Pool Formation and Cooling	MCCI											
Corium Melt/ Concrete Ablation			Debris Particle Cooling				H	H	H			L2	L2	L2		DEFCON CFD(SJU)
			Debris Bed Formation				H	H	H	H		L3	L3	L2	L2	DEFCON
			Debris Bed Cooling				H	H	H	H		L3	L2	L2	L2	FARO OECD/ROSAU
				Oxide Layer Formation and Cooling					H	H				L2	L2	CCI/ANL ECOKARS-2/ FzK(Karlsruhe)
				Crust Formation					M	M				L2	L2	CCI/ANL ECOKATS-2/ FzK(Karlsruhe)
				Crust Formation And Cooling					M	M				L2	L2	
				Crust Breach, Water Ingression And Melt Eruption					H	M				L3	L3	MASCA
				Metal Layer Formation and Cooling					H	H				L2	L2	
				Stratification of Oxide and Metal					H	H				L3	L3	
				Melt Pool Height					H	H				L2	L2	
				Oxide and Metal Layer Heating					H	H				L2	L2	

PIRT for the Severe Accidents in the Cavity

PIRT for the Corium Coolability and MCCI during Postulated Severe Accident in the Reactor Cavity (3/3)

	Major Phenomena					Rank by Impact on Model Development					Rank by Current Knowledge Level					Validation Test
	Severe Accident Phase (Physical Sequence of Scenario)					Severe Accident Phase					Severe Accident Phase					
	1	2	3	4	5	1	2	3	4	5	1	2	3	4	5	
Components	Corium Discharge	FCI	Debris Bed Formation and Cooling	Melt Pool Formation and Cooling	MCCI											
Corium Melt/ Concrete Ablation					Oxide and Melt Configuration				H	H				L2	L2	
					Chemical Reaction Heat				H	H				L2	L2	MACE OECD/MCCI BETA/COMET-L MOCKA (KfK/KIT Karlsurhe) OECD /ROSAU
					Convective Heat Transfer	M	M	M	H	H	L1	L1	L1	L2	L2	
					Melt Eruption					H					L2	
					Radiation Heat Transfer	M	M	ML	ML	L2	L2	L2	L2	L2	L2	
					Concrete Slag Formation				M	M				L3	L3	ACE
					Gas Release				H	H				L2	L2	
					Concrete Decomposition					H					L2	
					Conduction Heat Transfer between Melt and Concrete					H					L1	
					Oxide and Concrete Melt Properties				H	H				L2	L2	
					Concrete Slag Heat Transfer				M	M				L3	L3	
					Fission Product Behavior	L	M	M	M	M	L3	L3	L3	L3	L3	

CASTLE Code Development

Severe Accident Analysis Codes

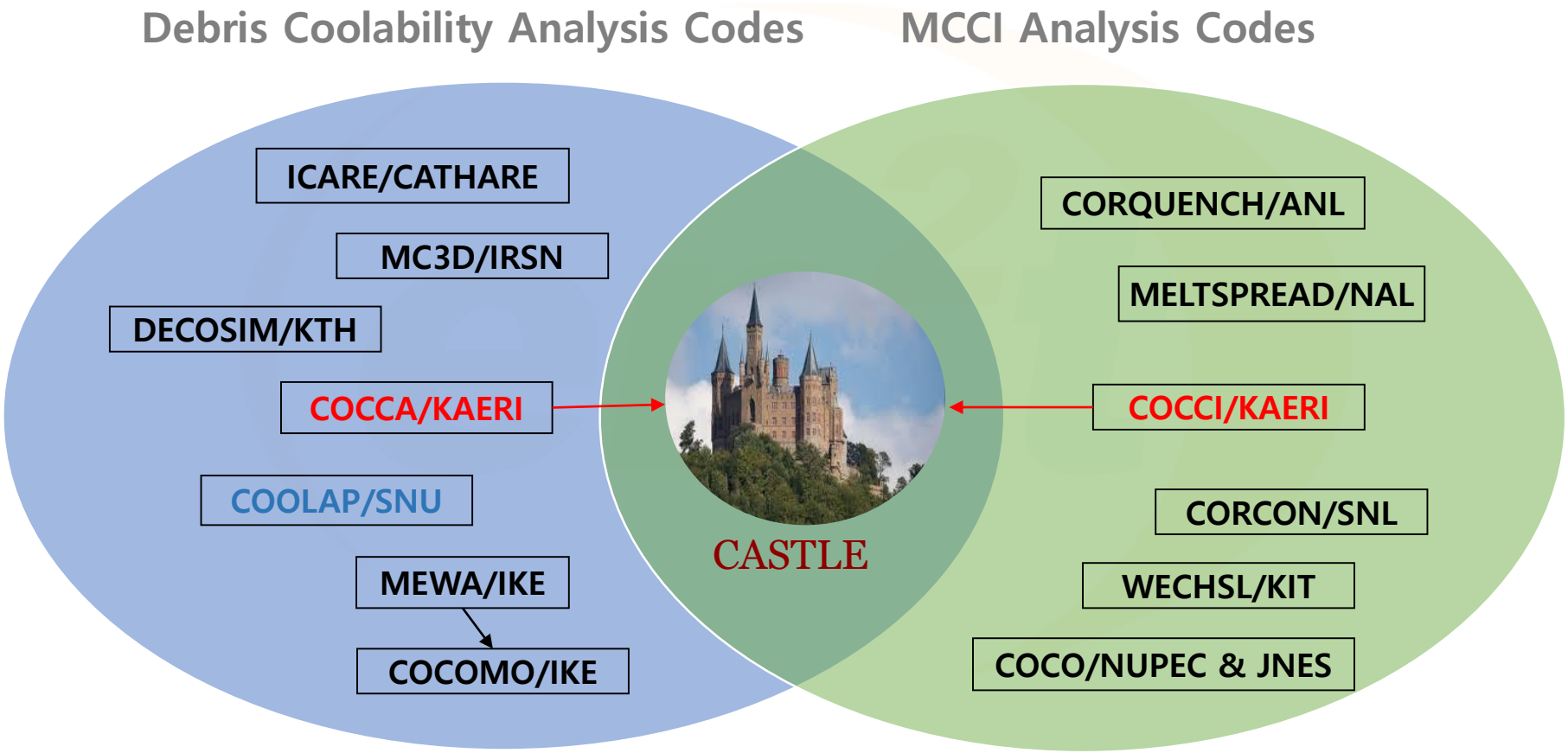

CASTLE : reactor CAvity Severe accidenT reaListic Evaluation

CASTLE Code Model Development

CASTLE Code Model Development Goal

Major Phenomena		MAAP5	ASTEC	MELCOR	CINEMA	CASTLE
Fragmentation	Jet Breakup	○	×	○	○	○
	Particle Size and Distribution	△	×	×	×	○
	Debris Particle Sedimentation	○	×	△	○	○
Corium Melt Relocation	Debris Particle Coolability	○	×	△	○	○
	Debris Bed Formation	×	×	×	×	○
	Evaporation Heat Transfer	○	○	○	○	○
Corium Coolability and MCCI Interface Phenomena	Corium Configurations	×	×	×	×	○
	Debris Particle Coolability	×	×	×	×	○
	Debris Bed Coolability	×	×	×	×	○
	Melt Pool Coolability	○	○	○	○	○
	Multi-Layer Modeling (Debris Bed, Crust, Pool)	×	×	×	×	○
MCCI Phenomena	Chemical Reaction	○	○	○	○	○
	Concrete Ablation	○	○	○	○	○
	Fission Product Behavior	○	△	○	○	△
	Gas Generation Behavior	○	○	○	○	○

○ – Modeled, × - not modeled, △ – partially modeled

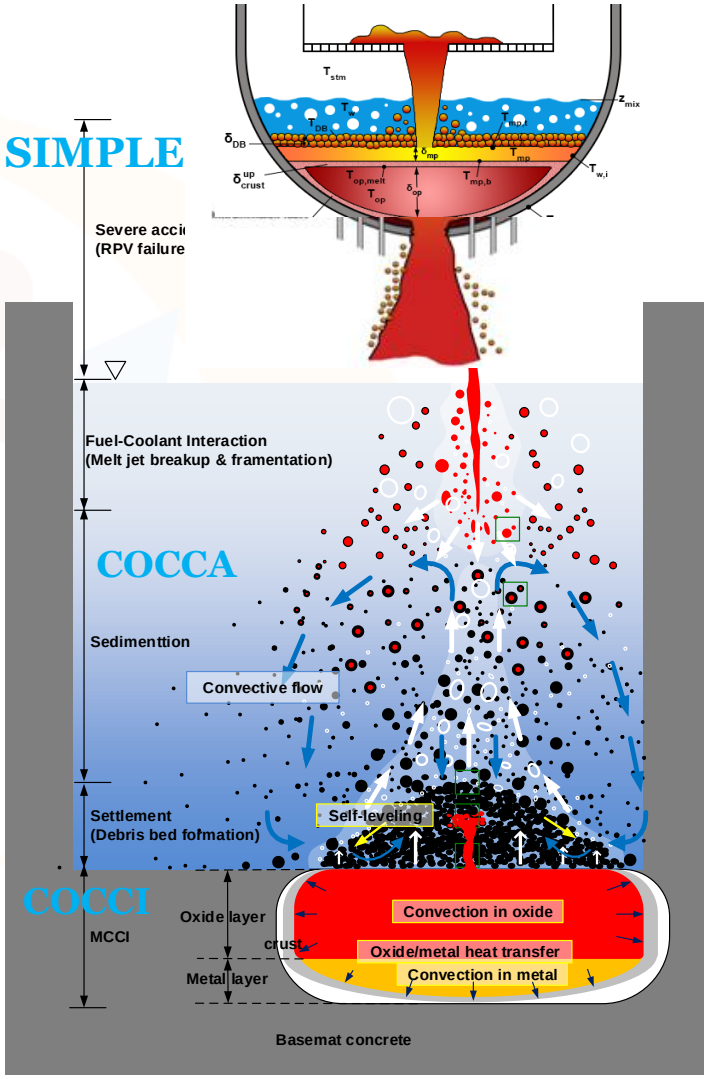

Summary and Conclusions

Prevention and Mitigation of the Severe Accident in the Reactor Cavity

❖ PIRT Development for the Corium Coolability and MCCI Phenomena

- Identify Corium Coolability & MCCI Phenomena during Postulated SAs in the Reactor Cavity
- PIRT Development for the Best Estimate Stand-alone CASTLE Code Model Development
- Detailed Analysis of the Severe Accidents in the Cavity due to LHVFs
- Need Further PIRT Review from the International Expert Community
- Develop International Experimental Test Program for the V&V of the Corium Coolability & MCCI Models and SA Analysis Codes

❖ Further Applications

- Development and Validation of the OPR1000 Reactor Cavity Pre-flooding Strategy
- International Joint Experimental Program for the Corium Coolability and MCCI Phenomena
- Prevention and Mitigation of the Severe Accidents in the Reactor Cavity
- Independent Review and Validation of the integrated Severe Accident Analysis Codes
- Methodology Development to strengthen Severe Accident Management in the Rector Cavity and thus Nuclear Safety

Human being has never been perfect.

But we became the only species on this earth to create and control our own evolution through dreaming for the future with incredible creativity.

Nuclear energy will be safe and clean, and become our sustainable and circular renewable energy source overcoming its safety and radioactive wastes by our incredible creativity, wisdom and communication.

Build Sustainable Future together!

THANK YOU!

Acknowledgement

This study has been funded and supported by Korea Institute of Energy Technology Evaluation and Planning (KETEP) and Ministry of Trade, Industry and Energy (MOTIE). The authors of this report appreciate the support from the participants of the CASTLE development project at KAERI and SJU. The authors also appreciate the international expert review group for the independent review and valuable comments for the PIRT development.

ENHANCING EX-VESSEL CORIUM COOLABILITY FOR INSTALLED-BASE NUCLEAR POWER PLANTS

Torsten Keim, Manfred Fischer, Markus Hupp
Framatome GmbH
Paul-Gossen-Str. 100, 91052 Erlangen, Germany
torsten.keim@framatome.com; manfred.fischer.ext@framatome.com;
markus.hupp@framatome.com

ABSTRACT

Framatome is currently developing a new technology for core melt stabilization based on the use of super absorbing polymers (SAPs). It can significantly improve the situation in severe accident scenarios with reactor pressure vessel (RPV) melt-through in cases where the reactor cavity is flooded. While Gen-III and later plant designs typically feature fully integrated core catcher solutions, the broad range of Gen-II reactors – by far the larger number of nuclear power reactors in operation today – is yet struggling to find viable options for core melt stabilization. Back-fitting of a core catcher is either technically challenging or economically ruled out and the common strategy of flooding the reactor cavity before or after failure of the RPV involves risks from insufficient melt coolability and steam explosions. Even in cases where, based on the extensive research and development works in the past decades, these risks can be argued to be acceptable for Gen-II reactors, further improvements are nevertheless a highly important ambition with regard to long-term operation and life-time extensions of these reactors. The intention behind the SAP technology is to address this ambition by directly targeting the relevant risks. Despite allowing substantial safety improvements the SAP technology is easy to implement and maintain (both as strategy and system) and can be realized economically.

The paper gives an overview of the features of the solution and the characteristics and properties of the proposed material. Furthermore, it summarizes the results of ongoing experiments which demonstrate the capability of SAP to enhance corium fragmentation and suppress steam explosions. A more detailed discussion of these experiments and the obtained results is provided in a separate paper.

KEYWORDS
super absorber, core melt, stabilization, fragmentation, steam explosion

1. INTRODUCTION

The main target of severe accident mitigation is to preserve the integrity of the containment as the last remaining fission product barrier against the environment. Achieving this target requires the re-stabilization of the molten core to limit or avoid molten core-concrete interaction (MCCI) which can ultimately lead to liner penetration or long-term overpressure failure of the containment. Melt stabilization can be achieved either inside the reactor pressure vessel (in-vessel) or after the melt is released through its bottom into the lower containment (ex-vessel). Based on the assessment of various concepts in [1] the most effective ex-vessel strategy is the implementation of a so-called "core catcher", which can contain, cool, and separate the melt from the concrete basemat. However, as their back-fitting into operational nuclear power plants (NPPs) is extremely challenging, core catchers are mainly a solution for new Gen-III designs. As compared to this, Gen-II plants typically rely on simpler solutions, such as quenching and fragmenting the melt based on flooding of the space below the reactor pressure vessel (RPV) before or after melt release. As compared to the latter case, where fragmentation takes place only during the MCCI, a preexisting water pool below the RPV can additionally disperse the melt jet before its arrival at the concrete floor. Unfortunately, this involves a high potential risk of energetic steam explosions, both inside the water pool and during the later melt spreading at the concrete floor. Whenever the containment of a certain reactor type is not capable to withstand the resulting pressure loads the steam explosion risk can be a significant obstacle for the acceptance of severe accident mitigation (SAM) strategies based on cavity flooding.

With focus on this issue, Framatome is currently developing a technology that can lower the steam explosion risk under the described conditions. It is based on the reduction of the amount of free water below the RPV by addition of water-absorbing particles. Besides suppressing steam explosions, these particles also enhance coolability because their mechanical resistance will disperse the melt jet more effectively than water alone. The key features of this SAP-based technology, the related requirements, and exemplary practical applications are described in the following paragraphs. In addition, an overview of the results of the performed validation experiments is given.

2. CHARACTERISTICS OF THE WATER-ABSORBING MATERIAL

2.1. Requirements

Materials suitable for the intended application were screened based on the following criteria:

- Compatibility with the operational conditions inside a NPP, high water uptake rate
- Low costs, high availability, easy handling
- Mechanical and thermal stability during melt contact

Among the groups of materials investigated certain organic materials namely super absorbing polymers (SAPs), e.g. poly-acrylic acid and its salts, were found best-suited and capable to absorb the highest amount of water relative to their own weight. SAPs come in various forms and their properties can be customized to fulfill a wide range of specific requirements.

2.2. Physical and Mechanical Structure

For the investigations reported in this paper, generic poly-acrylic acid-based SAP material was used. Because there was no prior optimization, the quantitative data given in the following shall be seen as preliminary. An adaptation of the properties of the SAP material for its intended use in SAM concepts is foreseen in future stages of the project.

In particulate form, SAPs typically have a two-layer structure [2]: an inner bulk part of lightly cross-linked hydrogel surrounded by an outer, highly cross-linked layer created by chemical surface reactions, as depicted in Fig. 1a. Depending on their intended application the sizes of the dry particles range from a few tenth of a mm to several mm. The particles applied here had an average density of about 2000 kg/m^3 (solid material) and were in the range of 1-3 mm diameters.

When submerged, the diameter of these particles increases to more than 1 cm. During the water absorption process the inner region and the outer shell inflate proportionally. Though the shell limits the extent of water uptake, it increases the stability and mechanical properties (elasticity) of the particles. In addition, the high water content and high resulting heat capacity of the shell give the particles strength to resist the initial thermal impact of the hot melt.

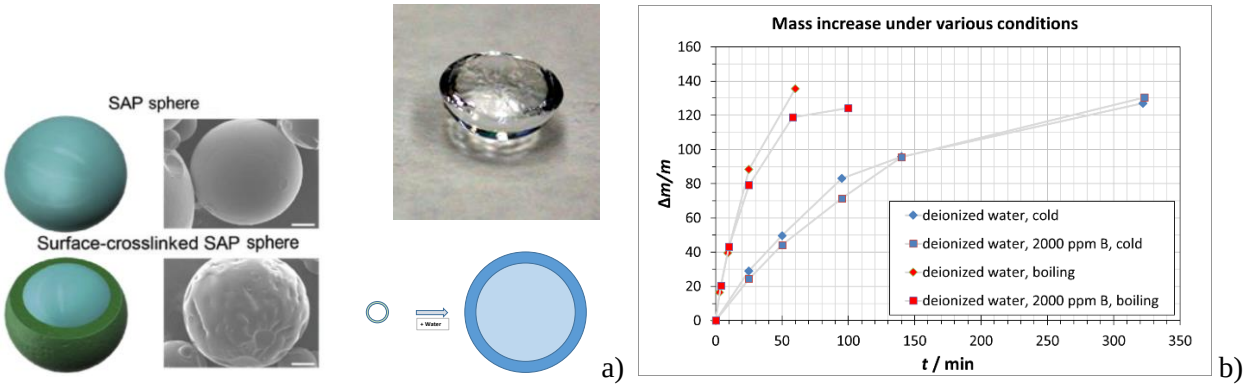

Figure 1. SAP particle, structure and cut, from [2] (a), water uptake (b)

The rate at which the particles can absorb water depends on the permeability of the outer skin and on the velocity at which the water can migrate within the uncured bulk part, which both depend on concentration differences. Therefore, the absorption rate decreases in time and also depends on the water's temperature and chemical properties. Experiments performed in the labs of Framatome in Erlangen have shown that:

- the final mass of absorbed water was ~130 times the initial particles mass.
- the particle volume increased even more, by a factor of up to ~200.
- in subcooled water, the uptake velocity significantly increases with temperature, while the final size and mass of the particles remain the same
- in boiling water, the absorbed mass is ~10 % lower than under subcooled conditions.

Tests on the impact of the boron concentration showed that, at lower temperatures, the presence of boron (2000 ppm B, added as H_3BO_3) has only negligible effect, but that there is a measurable impact on both, the uptake rate and the final water content, at temperatures close to saturation, see Fig. 1b.

Because, in a severe accident, the water applied to the particles will be contaminated, also the impact of fission products was investigated. For this, a standard set of fission products, which included Ba, Cs, La, Li, Mo, Sr, and Zr, was dissolved in water and then acidified with HNO_3 (pH values 6.6). In accordance with theoretical predictions, the dissolved metal ions reduce the final water uptake. The measured reduction was up to 20 % and became stronger with decreasing pH-values.

2.3. SAP-Water Pool Properties

When dry SAP particles are added to a water pool they take up water, ultimately until a saturated state is reached. Denoting the total water mass contained in all these water-saturated particles as $m_{w\text{-}sat}$, and the masses of particles and water provided as m_{SAP} and m_w, the following final states of the pool are possible:

$m_w >> m_{w\text{-}sat}$:
All particles can reach the water-saturated state and the remaining water can completely fill the interstices between them. Considering that the density of the dry SAP is twice that of water and that the inflation factor is >100, the density of a water-saturated particle is only a few percent higher than that of the surrounding water. Therefore, the upper part of the pool does not impose a major pressure on the lower part and the particles also near the bottom remain close to spherical and tend to arrange in a way that the resulting porosity ε_{pool} is lowest. In this paper, such a pool configuration is denoted as a **"wet" pool**. The minimum theoretical porosity for tightly packed, equal-sized spheres is ε_{theo}= 0.26. In practice, the porosity and hence the water content in the pool can either be higher or lower, depending on the size distribution and shapes of the provided particles. If m_w exceeds $(1+ \varepsilon_{pool})*m_{w\text{-}sat}$, a water layer free of SAP particles will exist at the top of the pool.

$(1+ \varepsilon_{pool})*m_{w\text{-}sat} > m_w >= m_{w\text{-}sat}$:
All particles can still become water-saturated but not all of the them will float. Therefore, the particles in the lower part of the pool must support part of the weight of the "non-floating" particles in the upper part. The resulting pressure increases with depth and leads to: (i) a deformation of the elastic particles, (ii) less free water between them and thus, (iii) in a higher packaging density in the lower region of the pool. Evidently, the compactness will be highest if m_w approaches $m_{w\text{-}sat}$. In the following, this configuration is denoted as a **"dry"** pool. The height-dependent porosity inside a "dry" pool and hence the max. free water content were found to decrease to ~0.1 already at a depth of 1 m.

$m_w < m_{w\text{-}sat}$:
In this case there is not enough water to saturate all particles, which leads to a "dry" pool with smaller particles and finer "pores". Evidently, such a pool is very compact and shows the highest mechanical resistance against melt ingress.

2.4. Stability

Sufficient stability of the SAP particles is an important issue for the intended application. During normal plant operation the particles have to tolerate the ambient conditions (temperature, humidity, radiation) inside the containment without showing a significant reduction in their ability to absorb water. In addition, they must fulfill their intended function even under the harsh conditions during a severe accident.

2.4.1. Thermal Stability

The thermal stability of the dry particles was investigated by thermo-gravimetrical analysis. Two minor decomposition points at about 50 °C and 80 °C and three major decomposition points at about 214 °C, 410 °C, and 562 °C were identified, see Fig. 2a. The figure shows that already at temperatures of >200 °C a significant mass loss occurs. When submerged in water, saturated particles remain stable independent of the applied pressure and temperature (in the range of values relevant during a severe accident). However, once these particles are exposed to air, the water starts to evaporate, see Fig. 2b. Like for other wet substances, the dry-out rates mainly depend on the ambient humidity. At very high heating rates, water evaporation at the surface is no longer effective in limiting the temperature inside the particles. In this case the bulk temperature will exceed the water saturation temperature and the related increase in internal steam pressure will rupture the outer skin and release the contained amorphous gel.

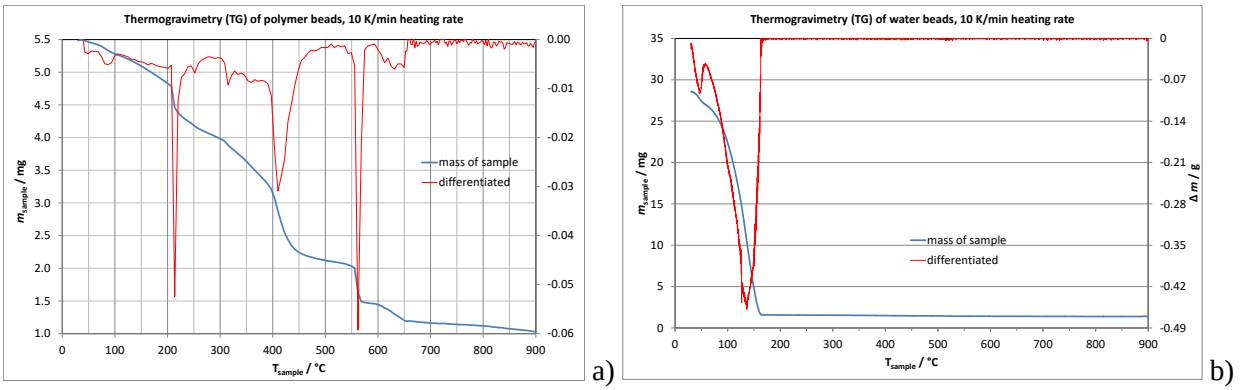

Figure 2. Results of thermo-gravimetric tests for dry (a) and wet (b) particles

2.4.2. Chemical Stability

Chemically, the applied SAP material is a co-polymer mainly consisting of acrylic acid, sodium acrylate $(C_3H_3NaO_2)_n$, and additional network-formers. When heated, first the absorbed water is released. After that, the now dry material will chemically decompose into various organic and non-organic substances, incl. ketones, carbon and its oxides, as well as sodium carbonate, in accordance with Fig. 2a. Depending on the ambient conditions, these substances can react further, eventually forming CO_2 and Na_2O.

2.4.3. Irradiation Stability

To investigate the response of the material to γ–radiation, dry SAP particles were exposed to a dose rate of about 1.3 MGy (60Co irradiation, 984 Gy/h for 1.369 h, which is equivalent to an assumed exposure at the storage location with a conservatively high dose rate of 30 Gy/h over a time period of 5 years. The exposed particles showed various changes in their color from nearly colorless to dark-yellow or orange; some became translucent, some remained transparent, all of which indicates that the irradiation had caused changes in the molecular structure. After irradiation, some particles were then put into borated water of 2000 ppm B at room temperature and left there overnight to absorb water. The resulting average diameter was 5.8±0.5 mm. Compared with the average diameter of non-radiated particles after water uptake in borated water of about ~9 mm this demonstrates a significant negative effect of high irradiation levels. Therefore, avoiding high doses by: (i) shielding the storage area, (ii) selecting a low-dose location, or (iii) customizing the SAPs in a way that they become more tolerant against irradiation, is highly recommendable. After entering severe accident conditions, an immediate and intense contact between the cooling water and the SAPs shall be realized by design measures to quickly initiate the absorption process and to avoid a long exposure time of the dry SAP material.

3. EXPERIMENTAL RESULTS

A number of experiments on the interaction of metallic, oxidic, and mixed melt jets with both “dry” and “wet” SAP pools were performed to investigate the impact on melt fragmentation and the likelihood of steam explosions. The tests were performed at KTH Stockholm, Sweden and at the Framatome test site Karlstein, Germany. While the KTH tests used either molten tin (at temperatures 400-600 °C) or a close-to-eutectic mixture of molten Bi_2O_3 and WO_3 (at temperatures close to 1000°°C), all Framatome experiments were performed with Al/iron-oxide-thermite melt (temperature ~2100 °C). With respect to the main subject of the investigations – the suppression of steam explosions – both fractions of the thermite melt are conservative substitutes for the metallic and oxidic corium released from the RPV: the steel due to

its higher superheat and the alumina due to its high tendency to engage in energetic interactions with water. Furthermore, and similar to Zr-containing molten corium, the superheated liquid iron can chemically reduce steam which leads to the formation of hydrogen. Hydrogen, as a non-condensable gas, enhances the mixing inside the SAP pool and impacts the quenching and distribution of the melt as well as its interaction with water and the containment atmosphere.

An overview of the performed tests and their results is given in [3] (with focus on melt fragmentation) and [4] (with focus on steam explosion suppression). An updated summary, which includes also some later results, is provided in [5] and, in short form, in the following chapter.

3.1. Melt Discharge into "Dry" SAP-Water Pools

Both the KTH and Framatome test series started with "dry" pools, due to their low content of free water. These first experiments not only confirmed the absence of dynamic events, but also revealed an unexpected favorable characteristic of dry pools, namely the ability to effectively disperse and fragment the melt jet. Thanks to this ability, which is likely caused by the high mechanical resistance and form-stability of the compacted particle bed, the melt jets completely solidified inside the SAP-water volume if only the pool depth was sufficiently high. The created filigree structures were surrounded by and filled with intact SAP particles. As shown in Fig. 3 the structures preserve the shapes of the interstices in which they were formed.

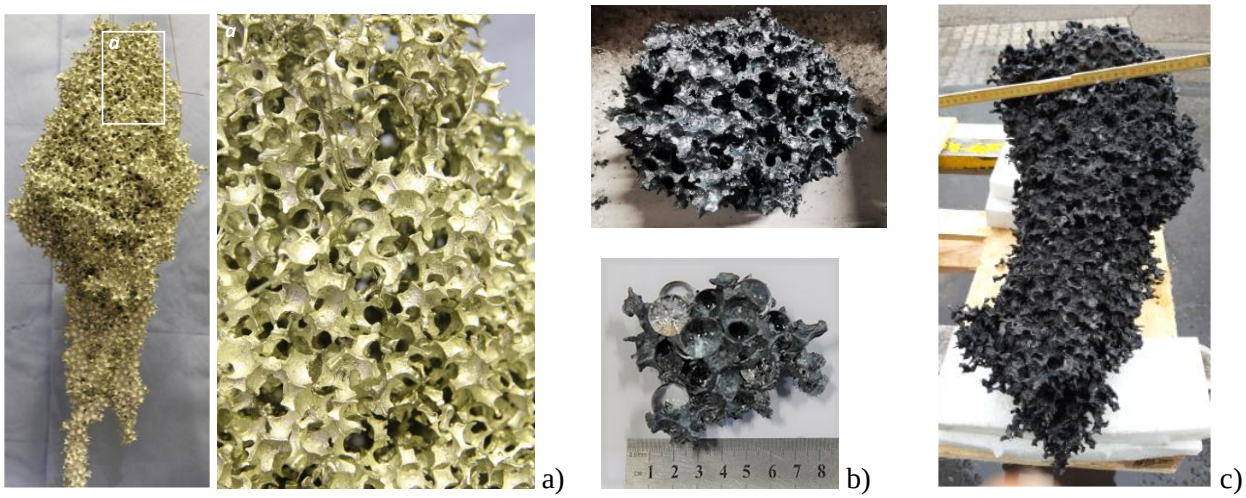

a) b) c)

Figure 3. Solidified melt in KTH tests with molten tin (a), molten oxide (b), and the oxide-filled iron structure obtained in one of the Framatome experiments (c)

To complement the metal melt tests, comparable tests with oxide melt were also performed at KTH. Despite the similar melt density, the measured penetration depth into the pool and the spatial extent of the solid structure were both lower compared to the metal melt tests. Also, a much larger fraction of small particles not connected to the bulk part was found distributed inside the volume with sizes ranging from several mm to a few cm. Despite the observed differences, which can be explained by lower thermal conductivity and the resulting faster freezing at the surfaces of the oxidic flow, the debris structures found in all tests – independent of whether they were performed with metal, oxide and mixed melts – are characterized by a high degree of porosity and a high surface-to-volume ratio, which are preconditions for long-term coolability.

3.2. Melt Discharge into "Wet" SAP-Water Pools

The "wet" pool configuration maximizes the water volume between the SAP particles. Hence, their mobility is very high and it is easy to spatially displace them. Because of this the presence of SAP particles was expected to have a much lower impact on the interaction between the melt jet and the water in a wet pool than in a dry pool. To check this prediction, some of the dry Framatome tests were repeated under wet conditions applying the same mass flow rate (~2 kg/s) and pool depth. In further tests the jet's impact velocity was increased from 3 m/s to 6.5 m/s, see Fig. 4a, and the totally released mass from 24 kg to 48 kg, see Fig. 4b. Surprisingly, these variations did not result in corresponding increases in the jet penetration depth as in all cases the jet was completely dispersed and immobilized within a distance of about 1.2 m.

The most obvious difference to the preceding "dry" tests is the complete absence of large coherent structures. The solid debris now entirely consisted of individual pieces most of them in the diameter range between 1 cm and 10 cm, see Fig. 4c, and hence significantly larger than the particles typically found after thermite melt jet fragmentation in pure water. Many of the larger pieces consisted of agglomerated metallic (Fe) and oxidic (alumina) fractions, so their average particle densities were between 2500 kg/m^3 and 6000 kg/m^3. Due to their small dimensions these particles could not remain suspended inside the SAP-water pool but settled near the bottom.

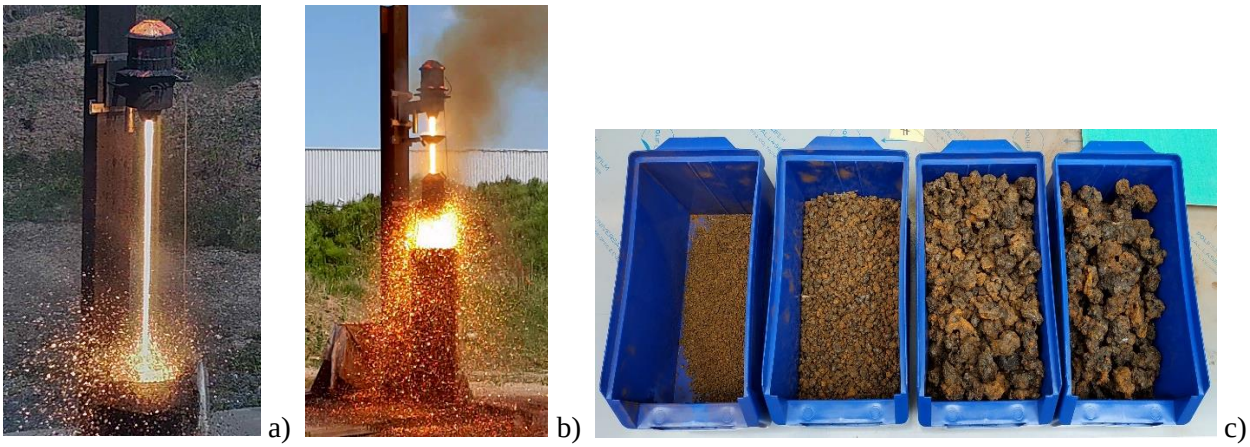
a) b) c)

Figure 4. Wet pool Framatome tests with a higher jet impact velocity (a) and melt mass (b) and typical debris size distribution (c)

The performed tests indicate that, despite their higher water contents, also "wet" SAP pools can effectively disperse melt jets. In the range of the applied flow rates and jet dimensions, the underlying fragmentation processes took place without any signs of energetic melt water interactions: not only in case of oxidic, but also for highly superheated metallic jets. However, steam explosions can also occur while the melt spreads on the floor of the cavity after passing the pool. Such stratified explosions are known from the PULiMS tests at KTH, Stockholm and earlier tests with thermite melt performed by Framatome in the 1990s.
The interesting question is whether the addition of SAPs to the water pool can also have a suppressive effect on this kind of energetic events, either due to a more effective dispersal (and cool-down) of the molten material inside the pool, or due to changes in the interface conditions at the surface of the spreading melt. Evidently, both effects would be the stronger the higher the SAP density in the pool is. Therefore, if the suppressive effect of the added SAPs could be demonstrated for "wet" pools it would automatically apply also for "dry" pools.

As a first step towards a corresponding experimental demonstration, the PULiMS-E6 test [6], in which a self-triggered steam explosion had occurred during the early phase of underwater spreading, was repeated but now with SAPs added to the water. The created "wet" pool covers all other possible SAP-water configurations due to its highest possible content of free water. The experimental conditions were practically identical to the PULiMS-E6 test, except for a reduction in melt mass to about 26 kg. The aim of this reduction was to prevent the spreading melt from contacting the walls of the test section as this may act as an unintended trigger. Considering that, in the PULiMS-E6 test, the melt mass released into the water before the explosion was only ~19 kg and that, in all other "explosive" tests of the PULiMS-E series, this mass was even lower, the related reduction in mass was considered acceptable.

As Fig. 5 shows, the repeated test resulted in a rather symmetric distribution of the discharged melt on the provided surface. Different from the PULiMS-E6 test there were no recorded energetic interactions, neither at a local nor global scale. Further tests are planned to check the ability of the SAP's to also mitigate stratified explosions in situation when the melt spreads on concrete.



Figure 5. Melt jet entering the SAP-water pool (a) and solidified debris (b)

3.3. Preliminary Conclusions

The results of the performed experiments suggest that the addition of the SAP material leads to a significant increase in the efficiency of the fragmentation process compared to the case of pure water. This effect which is likely caused by the mechanical resistance of the particles is the stronger the denser the packaging and hence, the lower the free water content is. The enhanced dispersal and cool-down of the melt jet was found to either result in extended porous structures and/or highly fragmented particle beds. Quenching and debris formation were especially effective for oxidic melts, the surface of which cools down much faster than in case of liquid metal, leading to an early formation of a stable surface crust and a resulting fast immobilization of the particles inside the volume of the SAP-water pool. In combination, these effects are deemed to significantly improve the coolability of the created debris. Besides leading to enhanced fragmentation the presence of the SAP particles also seems capable to suppress energetic interactions between melt and water, either while the jet penetrates the pool or during melt spreading at the floor, in cases when the melt was capable to penetrate the pool as a liquid jet. This was experimentally confirmed for both metallic and oxidic melts of various levels of superheat for melt masses < 50 kg, and jet flow rates of <4 kg/s. The impact of the SAPs on fragmentation and steam explosion suppression is especially strong for SAP pools with only limited amount of free water, incl. the here-investigated "dry" pools.

4. APPLICATION OF SAP IN SEVERE ACCIDENT MANAGEMENT

As the aim of the proposed addition of SAP material to the coolant water in the reactor cavity is to reduce the risk of energetic steam explosions and enhance coolability via fragmentation the applicability and function of this solution must be demonstrated for the following conditions.

4.1. During Normal Plant Operation

Based on the stability assessment in Section 2.4, the related environmental conditions with the highest negative impact on the SAP function are humidity and radiation. As compared to these, an increase in temperature and pressure (within the limits expectable during normal operation) are of minor relevance. Any resulting limitations have to be considered when selecting a suitable storage location. Due to the intended easy application, the SAP material containers will likely be located close to the RPV, which means either inside the cavity (if accessibility and sufficient space are ensured) or in compartments adjacent to it.

4.2. After Entry into the Severe Accident

The addition of the SAP material can be activated either passively, by the incoming water, or actively by the operator. In any case, activation must be early enough to ensure a sufficiently long period of water uptake. The measured data indicate that, even for non-optimized SAP material and accident scenarios with early RPV failure, the water uptake rates are compatible with the related SAM timing requirements. The total amount of SAP particles (bulk density ~1500 kg/m³ for sphere packing) that will have to be added to the water mainly depends on the volume of the cavity. Based on a volume increase during saturation by a factor of 200, each m^3 of SAP-water mixture requires a SAP particle volume (mass) between ~7 l (10 kg) for a "dry" configuration and ~5 l (7 kg) for a "wet" configuration, following the definition in Section 2.3.

The mass of SAPs added in the cavity is further influenced by the predictions for the efficiency of the melt fragmentation process and the porosity of the created solid debris. For example: for a melt volume and intended average porosity of the debris in the SAP-water region of 20 m^3 and 80 %, respectively, a water volume of >80 m^3 (considering some evaporation during quenching) and a volume and mass of added SAP material (for a "wet" pool) of about 0.4 m^3 and 600 kg, respectively, are needed. Such small SAP volume can be easily stored at appropriate locations. What must be also kept in mind is the transient character of the SAP-water pool during the fill-up period. If the water inflow rate is low (e.g. due to limitations in the water supply during the severe accident) and the velocity of water uptake by the SAP particles is high (as intended), the SAP pool will only slowly approach the condition of a "dry" or "wet" pool. This is because, during the initial period, not all particles will equally come in contact with water as most of the added water will be absorbed in lower regions. Liquid water will only fill the gaps between the particles in later phases when the entire pool approaches saturation. As a consequence, the free water content will not increase uniformly and not equally at all levels. Only after the water reaches or exceeds the upper level of the SAP particle bed, homogeneous saturated conditions will be achieved. Alternatively, it may be seen advantageous if – during the initial period – only the lower part of the particle bed becomes "wet", while the upper part remains "dry", as in this case the pool might be able to disperse the melt and suppress steam explosions more effectively.

4.3. After the Start of Melt Release from the RPV

In this period the SAP pool has to fulfill the following objectives:

- Fragmentation of the liquid jet
  The performed experiments have shown that the SAP pool can effectively disperse an incoming melt jet, under conditions comparable to those realized in the tests. This holds true, independent of whether the melt is oxidic or metallic and whether the pool is "wet" or "dry". Some of the incoming

melt will (temporarily) remain suspended in the volume where it solidifies and later relocates towards the bottom. Alternatively, for high release rates and shallow SAP-water pools, a part of the dispersed liquid material or even the jet itself may reach the floor. Jet progression and dispersal as well as the generation of steam and gas were observed to induce global convective motions inside the SAP pool which carry fresh, cold SAP material to the jet inflow region. As a result, also longer lasting or repeated jets will not change the described sequence.

- Quenching of the fragmented liquid melt
  The energy released during melt solidification must be absorbed by the water in the SAP pool (contained either inside the particles or as liquid in the interstices between them). Due to the high heat capacity of water and the effective mixing inside the SAP pool the required cooling capacity is easily achievable, given an adequate size of the cavity.
- Reduction of the steam explosion risk
  Steam explosions are stochastic processes, which can occur while liquid melt penetrates the water pool below the RPV or later while it spreads on the concrete floor. Unfortunately, the underlying phenomena are not sufficiently well understood. In addition, there is a generally low predictability of the initial and boundary conditions during melt release into the reactor cavity. Therefore, it will not be possible to fully exclude steam explosions neither by analyses nor by any, necessarily limited, number of experiments. What can be demonstrated though is that certain physical conditions established by the SAP pool, e.g. the limitation of the fraction of free water in contact with liquid melt, significantly reduce the risk of steam explosions. Here a “dry”, or even an only partially saturated SAP-water pool certainly has the highest potential. It may further be possible to demonstrate that the characteristics of the SAP pool (which can still be optimized) have an inhibiting effect on processes that are essential for energetic interactions, like fine-fragmentation during jet entry, or pressure wave progression.

4.4. After debris bed formation

Once the melt release and fragmentation processes are complete, most of the solid debris will become deposited in the lower region of the SAP pool, near the floor of the cavity. At this time the porosity between the debris particles will be filled either with disintegrated SAP particles (watery slurry) or liquid water. For the large mean diameters of the debris and high porosity values observed in the performed experiments, long term cooling is not a problematic issue if there will be an adequate permanent water supply to the cavity (which is required for long term cooling in any case).
A topic that requires discussion is the local blockage of the coolant flow by SAP particles trapped inside the debris matrix. If this causes insufficient cooling, the local debris temperatures will increase which, in turn, results in local dry-out, shrinkage, and ultimately the chemical decomposition of the SAP particles. These processes are expected to successively clear the way for water to re-enter the corresponding region. In parallel, a disintegration of the particle will also occur as a result of the high radiation levels in the fragmented debris. Due to the low mass of added SAP material, the maximum amount of non-condensable gas, slurry, or other residuals created by these processes is negligibly small. A potential positive side-effect may be that the SAP material can absorb and retain fission products and hence limit their release into the containment atmosphere. In addition, if specific measures against re-criticality would be necessary, neutron-absorbing chemicals could also be added to the matrix of the SAP material.

5. COMPATIBILITY WITH EXISTING REACTOR TYPES AND SAM STRATEGIES

Generally, the application of SAP material is intended as a back-fitting measure in operating nuclear power plants. However, there are also reactors under construction or new-build projects where: (i) the selected reactor design is based on Gen-II state (for whatever reason e.g., long interruption of construction, political constraints, etc.), or (ii) the severe accident mitigation measures are not clear or finally concluded, respectively, for the target markets.

Also in these cases, the SAPs can provide a solution to strengthen and improve existing severe accident mitigation concepts. In general, the application of SAP requires a certain space i.e. free volume in the region to which corium will relocate after failure of the RPV, which is typically the space directly below the vessel. This is fulfilled for a wide range of different reactor types and plant designs. In addition, a certain pool height is necessary to achieve effective fragmentation and quenching of the released molten material. Furthermore, this space has to be able (or needs to be enabled) to receive and contain within reasonable boundaries both SAP material and water. Plants that already decided on the flooding of the space beneath the reactor prior to vessel failure have all respective measures in place. Most other plants have at least implemented the necessary provisions for injecting water while the measures required to enable the formation of a deep pool underneath the reactor pressure vessel still need to be added (e.g. the water tight closure of penetrations, etc.).

5.1. Exemplary Plant Application

The potential integration of SAP into existing or future severe accident management strategies largely depends on the individual overall melt stabilization concept. Plants that have already decided on flooding the reactor cavity prior to vessel failure could implement SAP in a straight-forward manner to take benefit from enhanced corium coolability and to reduce the risk of energetic steam explosions. A SAP storage and delivery system consisting of a hermetically sealed container and an active or passive release / injection mechanism can provide the SAP material to the reactor cavity.
The timing for the injection of both water and SAP material during accident progression will be an important element in the management strategy. Flooding needs to be initiated in a timely manner such that a sufficient water level can be realized before vessel failure to avoid melt relocation into a shallow pool. However, as the time of vessel failure depends on the type and progression of the accident, its prediction is only possible with large uncertainties. Therefore, water injection is typically initialized based on the earliest expected RPV failure time. With respect to this topic the additional use of SAPs does not introduce new restrictions and requirements, as the timescale of water addition to the cavity is well compatible with the required water uptake time of the SAP material.
Hence, cavity flooding and the provision of SAP to the cavity may be triggered as a common action. Firstly, this ensures that sufficient time is available for the SAP material to absorb water, expand in volume and form a SAP-water pool with the desired characteristics. Secondly, no additional decision criterion, or even action, needs to be implemented to the procedures as the trigger of flooding will also become the trigger of SAP release. Finally, the water injection rate and the rate at which the SAP material is added are independent of each other. A transient surplus of either water or SAP material does not impact of the final state of the pool. The only relevant consideration has to be that the desired pool formation is sufficiently complete at the expected earliest time of vessel failure. An established SAP pool beneath the RPV at the time of RPV failure can significantly improve the situation with respect to melt fragmentation and steam explosion suppression, which can be considered a significant safety enhancement, especially for installed base reactors without other dedicated core melt stabilization measures.
Depending on the plant type, long-term debris heat removal can be realized in the same way as originally planned without SAP material addition. Steam from the melt pool can be condensed by suppression pools, by cooling the containment form the outside, by containment cooling condensers, or even by active recirculation-cooling of the pool / sump water. Among those, recirculation-cooling may be unfavorable due to the fact that contaminated water is routed outside the containment. In combination with SAPs the additional issue of a potential impact of degraded material on suction filters and pumps may have to be addressed even though the total mass and volume of potentially generated non-gaseous material is very low. Besides for Gen-II plant back-fitting SAP may also have benefits for other concepts. However, due to the higher complexity of the related issues, alternative applications of SAP, e.g. in IVMR pools are currently not part of the investigations and developments at Framatome.

6. SUMMARY AND OUTLOOK

This paper presents a new technology applicable for core melt stabilization which is currently being developed at Framatome and based on the use of super absorbing polymers (SAPs). The main driver for this development is to provide a solution for existing plants to improve the situation in core melt scenarios with RPV failure in combination with flooded cavities. While Gen-III plant designs and later developments feature integrated core catcher solutions, the broad range of Gen-II reactors – by far the larger number of nuclear power reactors today – are yet struggling to find viable options to improve core melt stabilization. For them back-fitting of core catcher solutions is either technically challenging or economically ruled-out e.g. by alternative options at the preventive level. Hence, the SAM solution typically chosen is the flooding of the reactor cavity before or after RPV melt-through. Especially the first one involves a trade-off between the risk of insufficient melt coolability and the risk of steam explosions.
Acknowledging that, based on extensive research and development works in the past decades, these risks can be argued to be acceptable for Gen-II reactors, improving the situation is a highly important ambition with regard to long term operation and life-time extensions of these reactors. The target of the SAP technology is to address this ambition by offering a solution which directly addresses the relevant risks and provides substantial safety improvements. This technology is easy to implement and maintain (both as system and as strategy) and economically feasible to be realized for many reactors.

The paper introduces the main envisaged characteristics of the proposed technology and the respective SAP material. It further summarizes the results of the performed dedicated experiments and gives an introduction how the proposed technology can be implemented in the SAM strategies of existing nuclear power plants. A parallel paper addresses, in more technical detail, the aspects of melt fragmentation and steam explosion suppression as well as the related performed experiments. Further development is ongoing and the experimental validation will be continued by further tests. In particular, these tests will include experiments to identify the range and potential limits for the application of the SAP technology. Furthermore, the development of a prototype system concept for its implementation in existing and new severe accident management strategy of an operating NPP is foreseen.

REFERENCES

1. M. Fischer, S. V. Bechta, V. V. Bezlepkin, R. Hamazaki, A. Miassoedov, “Core melt stabilization concepts for existing and future LWRs and associated R&D needs”, 16th International Topical Meeting on Nuclear Reactor Thermal Hydraulics (NURETH-16), Chicago, IL U.S.A., Aug 30 – Sep 4, 2015, #14141.
2. S. Chang, et. al. “Multi-scale characterization of surface-crosslinked superabsorbent polymer hydrogel spheres”, Polymer. 145 (2018) 174-183.
3. T. Keim, M. Fischer, M. Hupp, “Super Absorbing Polymers as a Means to Enhance Melt Fragmentation in Water During the Ex-Vessel Phase of a Severe Accident”, 19th International Topical Meeting on Nuclear Reactor Thermal Hydraulics (NURETH-19), Brussels, Belgium, March 6-11, 2022, #35511.
4. T. Keim, M. Fischer, M. Hupp, “Suppression of Ex-Vessel Steam Explosions by Super Absorbing Polymers Added to the Cooling Water”, 19th International Topical Meeting on Nuclear Reactor Thermal Hydraulics (NURETH-19), Brussels, Belgium, March 6-11, 2022, #35512.
5. T. Keim, M. Fischer, M. Hupp, “Super Absorbing Polymers as a Means to Suppress Steam Explosions and Improve Melt Jet Fragmentation”, 10th European Review Meeting on Severe Accident Research (ERMSAR2022), Karlsruhe, Germany, May 16-19, 2022, #271.
6. D. Grishchenko, A. Konovalenko, A. Karbojian, V. Kudinova, S. Bechta, P. Kudinov, “Insight into steam explosion in stratified melt-coolant configurations”, 15th International Topical Meeting on Nuclear Reactor Thermal Hydraulics (NURETH-15), Pisa, Italy, May 12-17, 2013, #599.

framatome

Enhancing Ex-Vessel Corium Coolability for Installed-Base Nuclear Power Plants

Markus Hupp, Torsten Keim, Manfred Fischer

ERMSAR 2022 - 17.05.2022

C1 - Framatome Restricted - Framatome know-how

Export Control - AL : N / ECCN : N



framatome

Enhancing Ex-Vessel Corium Coolability for Installed-Base Nuclear Power Plants

Markus Hupp,
Torsten Keim, Manfred Fischer

ERMSAR 2022 - 17.05.2022

C1 - Framatome Restricted - Framatome know-how

Export Control - AL : N / ECCN : N

Confidentiality

☒ **This document contains Framatome's know-how**

EXPORT CONTROL

AL = N	ECCN = N

Goods labeled with "AL not equal to N" are subject to European or German export authorization when being exported within or out of the EU.
Goods labeled with "ECCN not equal to N or EAR99" are subject to U.S. reexport authorization. Even without a label, or with label: "AL:N" or "ECCN:N" or "ECCN:EAR99," authorization may be required due to the final whereabouts and purpose for which the goods are to be used.

FRAMATOME'S INFORMATION PROTECTION RULES

☒ C1 -This document and any and all information contained therein and/or disclosed in discussions supported by this document are **restricted**.

☐ C2 : This document and any and all information contained therein and/or disclosed in discussions supported by this document are sensitive and **Framatome confidential,** such as its disclosure, alteration or loss are detrimental with a significant-to-high impact for Framatome.

The document, if disclosed, and any information it contains are intended for the sole attendees. The disclosure or reference to such information or document shall be made only on a proper judgment basis and by mentioning expressly "this information shall not be disclosed / transferred without prior consent".

☐ C3 –This document and any and all information contained therein and/or disclosed in discussions supported by this document are classified **Framatome Secret**.

Each one must commit to keep secret any written or oral information disclosed during the meeting. It is forbidden to disclose it to any legal entity and any individual (including within Framatome) without prior consent of the meeting chairman.

This document and any and all information contained therein and/or disclosed in discussions supported by this document, are confidential, protected by applicable intellectual property regulations and contain data subject to trade secrets regulations. Any reproduction, alteration, disclosure to any third party and/or publication in whole or in part of this document and/or its content is strictly prohibited without prior written express approval of Framatome. This document and any information it contains shall not be used for any other purpose than the one for which they were provided. Legal and disciplinary actions may be taken against any infringer and/or any person breaching the aforementioned obligations.
© Framatome – All rights reserved

CONTENT

01 . Motivation

02 . New solution

03 . Experiments

04 . Application to NPPs

 © Framatome - All rights reserved

C1 - Framatome Restricted / Framatome know-how / Export Control - AL : N ECCN : N

Motivation

- Modern Gen III/III+ plants feature **Core Catcher** technology to mitigate ex-vessel core melt scenarios
- **Gen II plants** – today, by far more numerous – have to rely on (use in SAMG)
  - flooding the space below the reactor (reactor pit) before reactor pressure vessel failure
    - ➔ **risk of highly energetic fuel-coolant interactions**
  - top flooding of corium after melt release into cavity is complete
    - ➔ **risk of insufficient fragmentation and cooling (& complicated timing)**
- Severe accidents with ex-vessel core melt scenarios are beyond design base conditions
  - Back-fitting a Core Catcher is rather challenging (technically & commercially)
- **Prolonged Gen II operation / life-time extensions**
  - **Goal:** Provide viable option to significantly **improve Gen II safety**

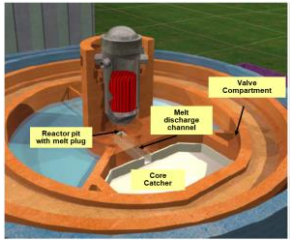

EPR Core Catcher


VVER-TOI Core Catcher

 © Framatome - All rights reserved
C1 - Framatome Restricted / Framatome know-how / Export Control - AL : N ECCN : N

New solution

Framatome is currently developing a new technology for easy back-fitting of Gen II plants to significantly improve mitigation of ex-vessel core melt scenarios

- **Super Absorbing Polymers (SAP)** are used for "**coolant conditioning**"
  - ➔ reduce risk of steam explosions
  - ➔ enhance corium fragmentation and coolability
  - ➔ retain long-term cooling function

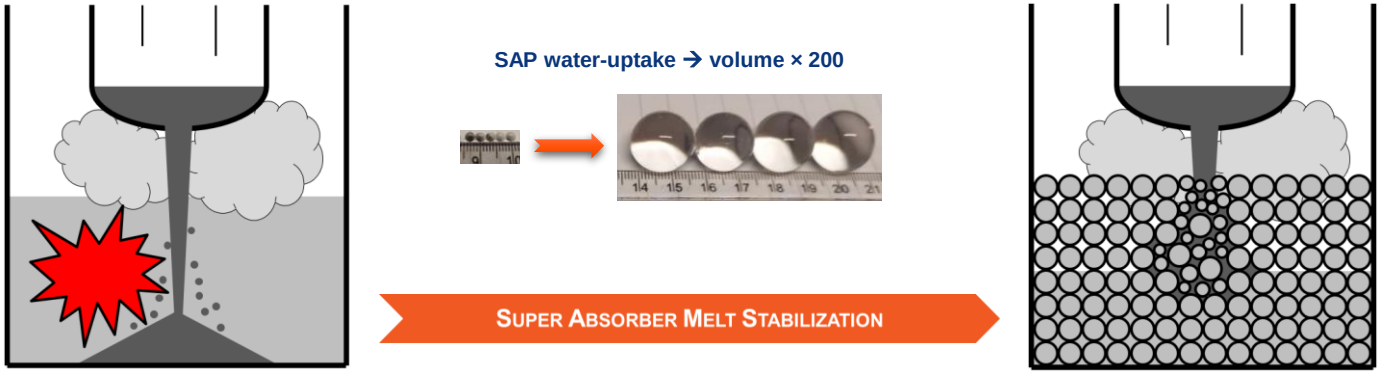

 © Framatome - All rights reserved

New solution

- **Proposed solution:**
  - Store container with particles of **SAPs in reactor pit/lower containment** or nearby (dry: < 3 mm diameter each, very small storage space)
  - In contact to water, **SAP particles increase their volume by factor ~200**
    - **5 l / 7 kg SAP_{dry} ➔ 1 m³ "wet" pool**
    - **7 l / 10 kg SAP_{dry} ➔ 1 m³ "dry" pool**

    } **(m_{SAP} ≤ 1%)**

- SAPs are foreseen **in addition to the water in the cavity**

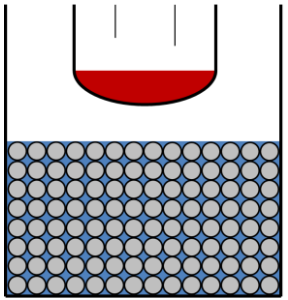

- **Pit:** Ø = 6 m, h = 2.8 m, V ~ 80 m³
- **SAP:**
  - 80 m³ SAP conditioned pool
  - 0.4 m³ dry SAP material in storage

 © Framatome - All rights reserved

Experiments

Increasing overall complexity of experimental setup

Increasing energy content toward realistic conditions

Variation of SAP pool conditions

Melt mass & pool depth

reduction of risk of steam explosions
melt fragmentation / porosity / cooling

Lab experiments

- basic material tests (mechanics, absorption, …)
- physico-chemical properties
- irradiation tests

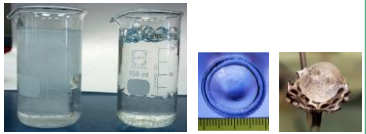

Thermal properties

- melt temperature
- melt superheat

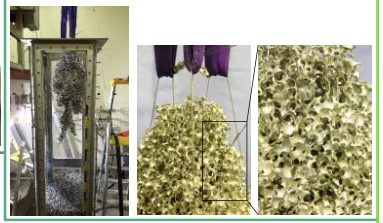

“Dry” / “Wet” SAP pool

- not free water present
- surplus of liquid water



Further variations

- melt mass
- metallic / oxidic melts
- free fall / impact velocity
- pool depth
- bottom spreading



- Please note further specific ERMSAR2022 contribution
  - Super Absorbing Polymers as a Means to Suppress Steam Explosions and Improve Melt Jet Fragmentation

framatome

 © Framatome - All rights reserved
C1 - Framatome Restricted / Framatome know-how / Export Control - AL : N ECCN : N

Super Absorbing Polymers melt stabilization



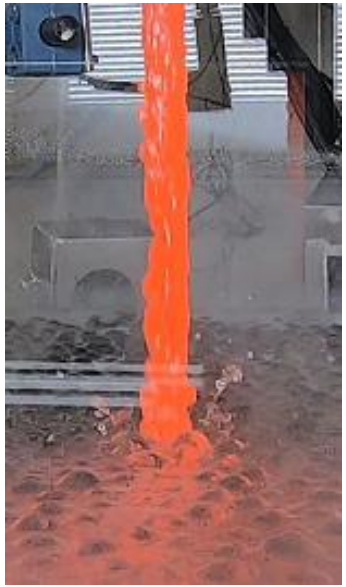


- Suppression of steam explosions during fuel-coolant interaction
- Enhanced corium fragmentation and porosity for more efficient cooling

 © Framatome - All rights reserved

C1 - Framatome Restricted / Framatome know-how / Export Control - AL : N ECCN : N

Application to NPPs

Application of Super Absorbing Polymers in reactor pit

- **Normal operation / design base conditions**
  - conditions:
    - ⚠ humidity, radiation
    - 👍 pressure, temperature
  - storage:
    - close to RPV / reactor cavity
    - sealed & shielded

  ➔ no interference / no negative feedback

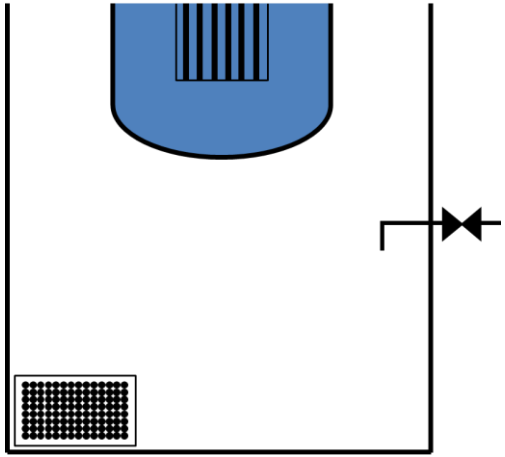

 © Framatome - All rights reserved

C1 - Framatome Restricted / Framatome know-how / Export Control - AL : N ECCN : N

Application to NPPs

Entry into Severe Accident conditions

- **Core outlet temperature 650°C**
  - initiation:
    - active or passive SAP release
    - flexible according to requirements
  - conditioning:
    - fast water uptake
    - time for flooding ~ time for absorption
  - pool formation:
    - 80 m³ water ~ 0.4 m³ SAP material
    - easy storage

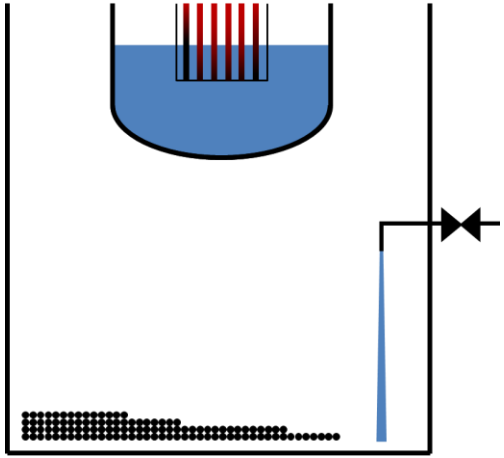

 © Framatome - All rights reserved

C1 - Framatome Restricted / Framatome know-how / Export Control - AL : N ECCN : N

Application to NPPs

Melt relocation, fragmentation and cooling

- **SAP pool to stabilize molten core**
  - fragmentation of liquid jet
    - dispersion and (temporary) suspension of corium
    - global convective motion of SAP material
  - quenching of fragmented liquid melt
    - energy absorption by water inside SAP or interstices
    - principle of high-heat capacity water cooling
  - reduction of steam explosion risk
    - physical conditions in SAP pool reduce risk
    - limitation of free water
    - inhibition of energetic interactions and pressure wave progression

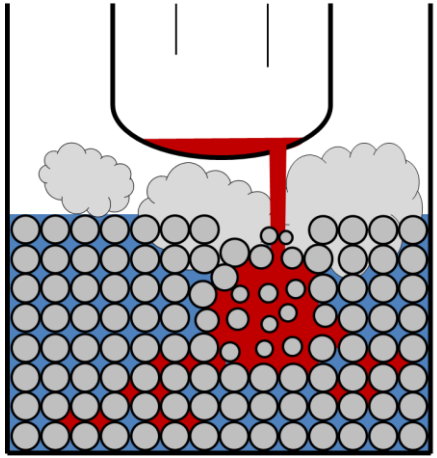

 © Framatome - All rights reserved

C1 - Framatome Restricted / Framatome know-how / Export Control - AL : N ECCN : N

Application to NPPs

Highly fragmented and easily coolable end state

- **Long-term melt stabilization and cooling**
  - water in SAPs and interstices to provide efficient cooling
  - at hotspots SAP material will shrink (eventually disintegrate) and give way for free water to enter for cooling
  - long-term debris heat removal via plant systems (e.g. steam condensation and pool cooling, containment cooling, re-circulation cooling)

- **Potential issues**
  - limit localization of SAP material to room beneath reactor
  - although small SAP mass, prevent system interferences

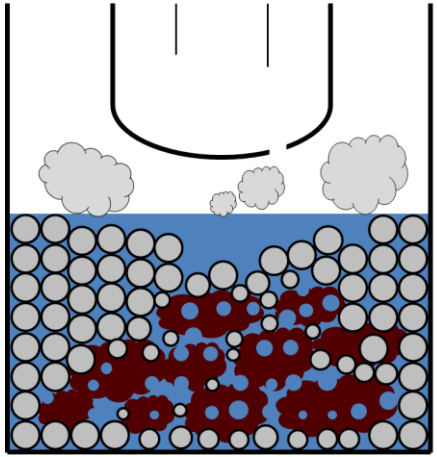

 © Framatome - All rights reserved

C1 - Framatome Restricted / Framatome know-how / Export Control - AL : N ECCN : N

Conclusions

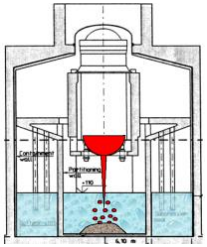

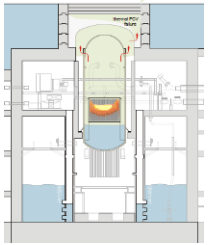

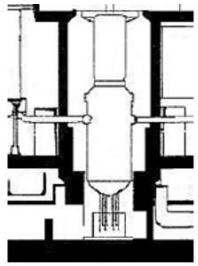

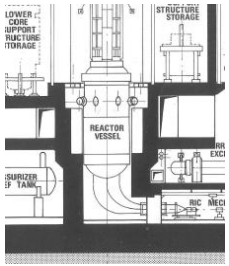

- **Introduction** of **new solution** to address the need of **Gen II plants** to enhance their **resilience** against beyond design base accidents resulting in ex-vessel core melt scenarios
  - Second ERMSAR2022 paper/presentation: details on the experiments on **melt fragmentation** and **suppression of steam explosions**
- SAP technology can be **easily implemented** in various plant designs
- **Systematic** evaluation and testing performed
- Tests show **excellent fragmentation** and high level of porosity of stabilized melts
- No **steam explosions** during melt progression inside wet and dry SAP pools
- Further experiments and **prototype** systems are being developed

- Patent (DE 102019126049 B3), PCT (PCT/EP2020/076521)
- Contact: markus.hupp@framatome.com

 © Framatome - All rights reserved

Legal Notice

Editor and Copyright 2022: Framatome GmbH – Paul-Gossen-Straße 100 – 91052 Erlangen, Germany. It is forbidden to reproduce the present publication entirely or partially without prior consent in whatever form. Legal action may be taken against any infringer and/or any person breaching the aforementioned conditions.

Subject to change and error without notice. Illustrations may differ from the original. The contained statements and information are for advertising purposes only and do not constitute an offer of contract. They shall neither be construed as a guarantee of quality or durability, nor as warranties of merchantability or fitness for a particular purpose. These statements, even if they are future-oriented, are based on information that was available to us at the date of publication. Type, quantity and characteristics of goods and services are subject to formal individual formal contracts.

framatome

Thank you for your attention!



To discover more about how we can help, visit us at
www.framatome.com/solutions-portfolio

Quenching Phenomena in High Temperature Cylindrical Debris Bed: MONET Tests

Mayank Modak, Vishal Nirgude, Hyun Sun Park*
Department of Nuclear Engineering, Seoul National University, Gwanak-ro, Gwanak-gu, 08826, Seoul, Republic of Korea
mayankmodak@snu.ac.kr; vishal@snu.ac.kr; hejsunny@snu.ac.kr*

ABSTRACT

Severe accidents (SA) in Light Water Reactors (LWRs) consist of a sequence of thermal-hydraulic events which leads to situations that progress beyond design-based accidents (DBAs), and involve significant core degradation which threatens the integrity of the containment. As witnessed in the Fukushima accidents, corium was released into containment when the reactor vessel failed. In such a case the cooling of the relocated corium will determine the accident progression, its termination, and the mitigation of accidental results. In a flooded cavity, a porous corium debris bed is expected to develop on the bottom of the cavity pool due to the melt jet breakup and fragmentation. The debris bed needs to be quenched via top or bottom flooding until continuous cooling is established. If it is not quenched, this mass will begin to re-melt due to decay heat and leads to Molten Corium Concreate Interaction (MCCI). To investigate the quenching behavior of the debris bed by means of experiments, a test facility MCCI-mitigatiON through passive cooling Effect Test (MONET) apparatus is setup. To enhance the understanding of multidimensional particle bed coolability, here the objective is to understand the mechanism of heat transfer inside the cylindrical heated debris bed with varied particle sizes (Ø 3 - 10 mm alumina) during quenching by cooling water supplied from the bottom of the bed. This paper reports the preliminary findings from quenching tests performed using the test facility MCCI-mitigatiON through passive cooling Effect Test (MONET) established to investigate the quenching behavior of the cylindrical debris bed through experiments.

KEYWORDS
quenching, porous debris bed, severe accidents, light water reactors

1. INTRODUCTION

Severe accidents (SA) in Light Water Reactors (LWRs) consist of a sequence of thermal-hydraulic events which leads to situations that progress beyond design-based accidents (DBAs), and involve significant core degradation (severe accidents) which threatens the integrity of the containment. As witnessed in the Fukushima accidents, corium was released into containment when the reactor vessel failed. In such a case the cooling of the relocated corium will determine the accident progression, its termination, and the mitigation of accidental results. Hence, flooding of the reactor cavity with coolant water may be essential to cool the relocated corium in the cavity floor and keep the integrity of the containment building against the Molten Core Concrete Interaction (MCCI) [1]. In the wet cavity strategy, it is estimated that when the corium melt with a moderate release rate falls in the deep water pool, the corium jet will break up into small debris particles and create porous debris beds on the bottom of the water pool in the reactor cavity [2].

In contrast to the long-term coolability analysis, the quenching of porous debris bed will be characterized by the localized thermal non-equilibrium between the solid particles and fluid (water and vapor). The complex flow patterns and heat transfer mechanisms during quenching process makes it difficult for experimental measurement and modeling. Tutu et al. [3] studied the quenching of porous debris bed by the saturated water injected from the bottom with constant flow rates. Author reported that

the quench front of a homogeneous bed during bottom flooding usually proceeds with a uniform one dimensional rate, while the flooding from the top is much more complex, characterized by a multi-dimensional progression. One of the most important conclusions from the DEFOR-E experiment (Karbojian et al. [4]), the temperature of the debris bed resulted from the melt coolant interaction still remained higher than the saturation temperature of surrounding water for more than 100 seconds after settling down, which is far behind the melt-coolant-interaction time of 10 seconds. In a realistic situation, such "dry zone" in a debris bed which is hardly accessible by coolant is subject to a high risk of re-melting, as it continues to be heated up by the decay heat. Therefore, the successful quench of a hot debris bed is critical since it is the prerequisite for achieving the long-term coolability.

From the survey of literature, it was established that many studies have been conducted on debris bed coolability but majority of these were primarily focused on one-dimensional homogeneous debris beds with top-flooding condition of coolant, under which the dryout heat flux (DHF) is determined by Counter-Current Flow Limit (CCFL). However, in a realistic severe accident scenario, the geometry and configuration of the formed porous debris bed will be multi-dimensional and heterogeneous (Karbojian et al. [4] ;Ma and Dinh [5]). The most possible shape of a debris bed is heap-like (conical) or mound-like (truncated conical) bed, which favors lateral ingression of coolant.

In order to understand the coolability of debris beds with such multi-dimensional characteristics, earlier using the COOLOCE facility at VTT (Takasuo et al. [6-8]) and POMECO-HT facility at KTH (Thakre et al., [9]) conducted a series of experiments to investigate the dryout phenomena of conical beds and stratified beds, respectively. Multi-dimensional flow of coolant was found to increase heat removal capacity (coolability enhancement) compared to one-dimensional flow of coolant. A downcomer was also employed in the POMECO-HT to enable bottom flooding of the particulate beds, which also enhances coolability. In case of multi-dimensional debris beds, the model and correlations developed based on one-dimensional assumptions for predicting the dry-out heat flux are no longer applicable. For enhancing the understanding of two-phase flow and boiling heat transfer in porous media, numerical simulation is necessary to solve the problem. For this purpose, the COCOMO code (MEWA, Bürger et al. [10]) and the DECOSIM code (Yakush et al. [11]) were developed by IKE-Stuttgart University and Royal Institute of Technology (KTH), respectively. These codes simulate the transient boiling or quenching behaviors of debris beds, which thus can be used for the evaluation of debris bed coolability. So far only limited validations of the codes have been accomplished due to lack of experimental data. Also, limited information is available on the effect of multi-dimensional debris bed on the quench front propagation which is important to provide accurate boundary conditions for the numerical simulations.

Earlier, Rahman et al. [12] presented the dryout heat flux under bottom water in flow condition. However a previous attempt [13] on predicting dryout power for multi-dimensional particle bed supports reported that Rahman's model tended to over-estimate dryout power. In view of this, efforts have been made earlier from our research team (Lee et al. [14-17]) for the development of two-phase flow model for predicting dryout heat flux in particle packed bed. At the validation process, the proposed model [17] showed great agreement to the measured two-phase flow data in literature including boiling condition. In addition to this, applying proposed model into DHF prediction was able to predict measured DHF values in literature within 15 % of error, regardless of its flooding condition including top, forced injection from bottom, natural circulated in flow from bottom and lateral water ingression.

To enhance the understanding of multidimensional particle bed coolability, here the objective is to understand the mechanism of heat transfer inside the cylindrical heated debris bed with varied particle sizes (Ø 3 - 10 mm alumina) during quenching by cooling water supplied from the bottom of the bed. This paper reports the description of the test facility MCCI-mitigatiON through passive cooling Effect Test (MONET) apparatus established to investigate the quenching behavior of the cylindrical debris bed by means of experiments. Initial findings from the tests are also discussed here.

2. MONET Tests Facility

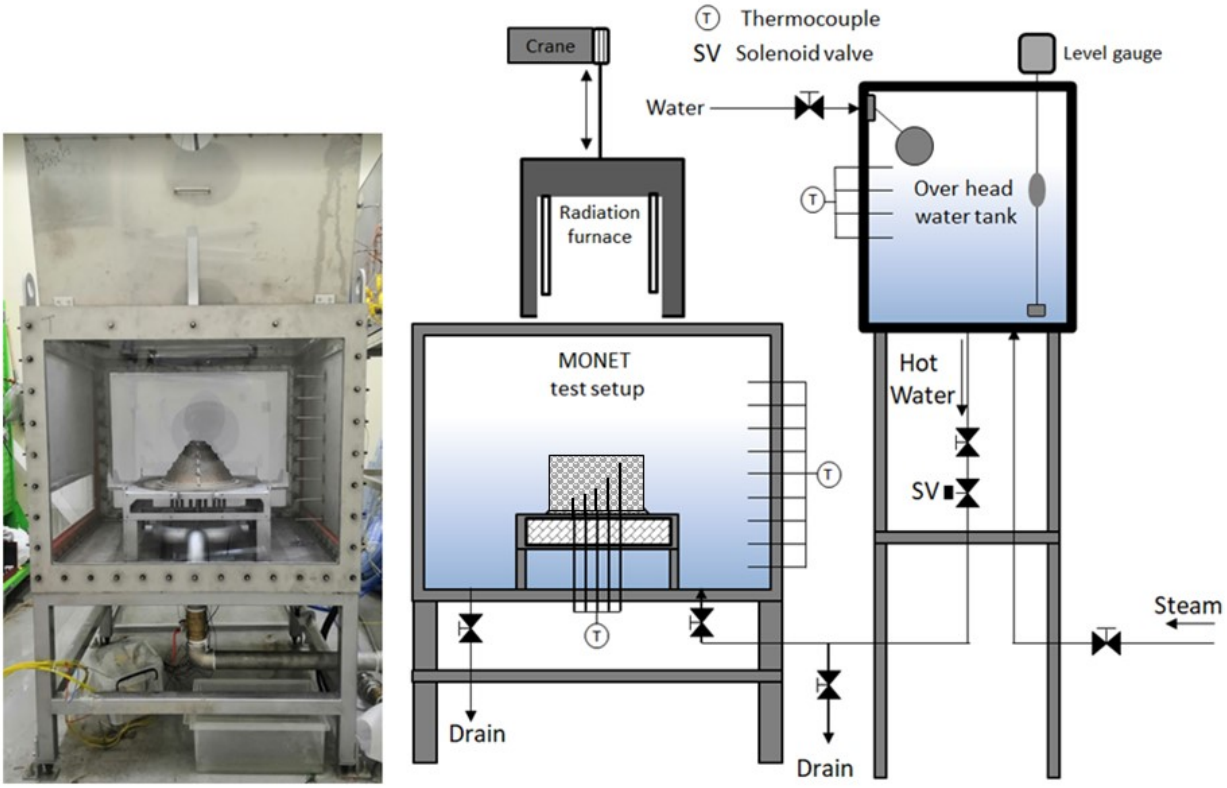

Fig. 1: Monet test setup

Fig. 1 shows photographic and schematic view of the MONET test facility, which was designed to simulate the particulate debris bed quenching performance. The MONET test facility consists of three major components; testing tank, particle (debris) bed bottom support (DBS) and cylindrical particle (Debris) bed (CDB). Additionally a separate storage water tank was fabricated to heat the water to saturated level. A radiation furnace was used to heat the particle bed to superheated temperature. The testing tank of dimensions 800 x 1000 x 1000 mm is made of SS 304 material. Two sides of the testing tank have a solid SS 304 wall which comprises of various ports for thermocouple connections along the vertical direction. While, the other two sides are made from the polycarbonate window of 10 mm thickness to allow visualization. The bottom of the tank has provision for water input and drainage.

The Particle bed (debris) bottom support (DBS) is made from SS 304 and high temperature cement to withstand high temperatures during tests as depicted in Fig. 2). The DBS frame is of 520 x 520 x 100 mm in dimensions and supported by 150 mm high SS 304 legs. Bed (DBS) has 17 openings allowing a passage for TC's to particle bed from bottom of the testing tank. The particle bed is heated to required test temperature using a radiation furnace (15.6 kW) which is maneuvered by an overhead crane.

Cylindrical particle (Debris) Bed (CDB) has a height of 145 mm and 290 mm and made of SS 304 as shown in Fig. 3. The outer frame will be enclosed by 2 mm thick SS mesh from all sides using M5 bolt. The particle bed consist of 20 shielded thermocouples (OD 1/8 inch, Type K), of which 16 are located in 4 concentric circles (4 TC's in each circle, C1; r = 30 mm, C2; r = 65 mm, C3; r = 85 mm, & C4; r = 105 mm from center line of the particle bed) and one at center (CM; r = 0) as shown in Fig. 4. The thermocouples measure the temperature in the voids between the particles, which are filled by liquid, vapor or a mixture of both. The test beds were filled with spherical beads (SS 304 or Alumina), used as the debris simulant material as depicted in Fig. 5 (a-b). The size of the beads was measured by vernier calipers for a sample of 100 particles for each type.

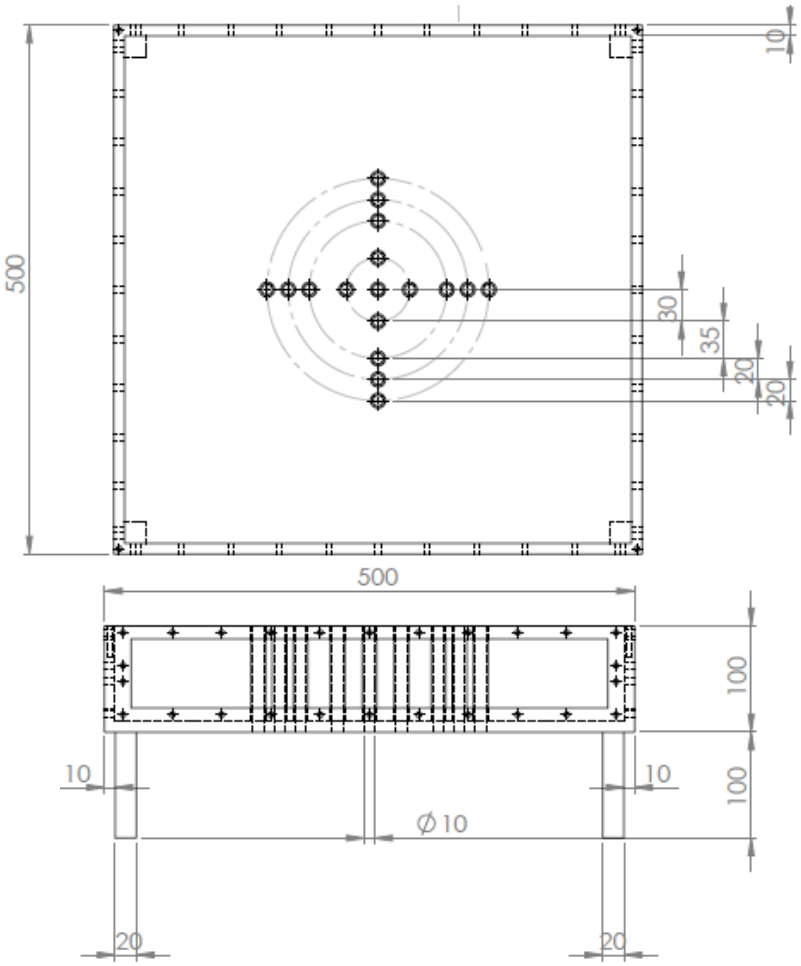

Fig. 2: Particle bed (debris) bottom support (DBS)

A custom made radiation furnace is employed for heating the debris particle bed as shown in Fig. 6 (a-b). The furnace has a power rating of 15.6 kW which can raise the temperature of 900°C in 20 mins. The furnace is guided over the cylindrical particle bed using an electric crane and placed over the top of the DBS supporting frame. The furnace outer surface is insulated with glass wool and ceramic housing, which are then enclosed by a steel cover.

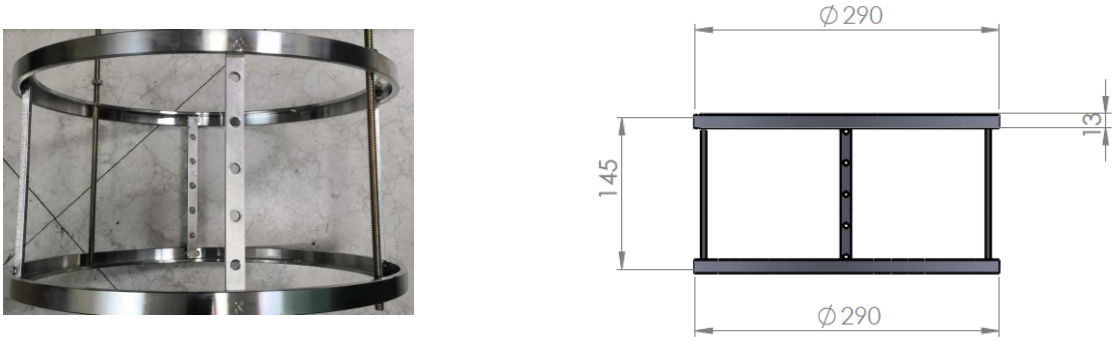

Fig. 3: Particle bed (debris) bottom support (DBS)



(a) Photographic view of TC's in the bed

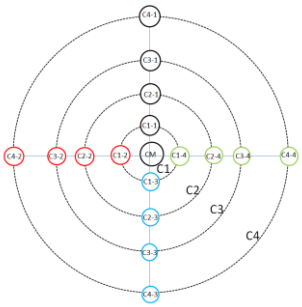

(b) total TC's spread

Fig. 4: Thermocouples location (r,z) inside the cylindrical debris bed (CDB)



(a) SS 304



(b) Alumina

Fig. 5: Photographs simulant particles for debris bed

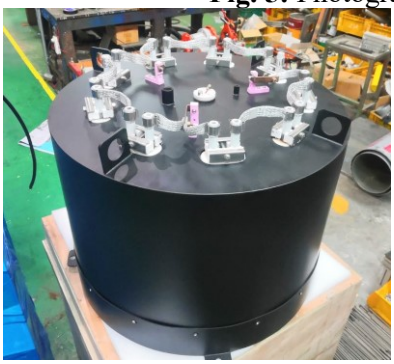

(a) Outer furnace housing

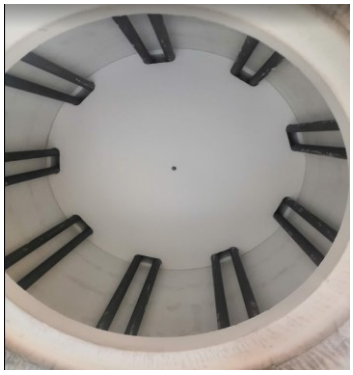

(b) Inside heating element

Fig. 6: Radiation furnace (15 kW) employed for heating the debris particle bed

Table 1: Test matrix for MONET experiments

Test Case	Particle (Dia.; Type)	Debris bed weight	Porosity	Initial bed temp. range	Water temp.
Identification tests					
MONET-CL-1	3 mm; Alumina	23.16 kg	0.421	700°C-400°C	95°C-99°C
MONET-CL-2	3 mm; SS304	46.16 kg	0.423	700°C-400°C	95°C-99°C
MONET-CL-3	5 mm; Alumina	22.32 kg	0.442	700°C-400°C	95°C-99°C
MONET-CL-4	5 mm; SS304	43.44 kg	0.457	700°C-400°C	95°C-99°C

*Currently only MONET-CL-1 is reported in the following paper.

The saturated water for the experiments was produced in a separate storage water tank of dimensions 1500 x 600 x 800 mm as shown in Fig. 7. The tank is connected to 90 kW steam generator to heat the water to saturation level. Temperature was measured at 9 different locations (1/8 inch, K type) and their average was considered for experiments. The heated tank is connected to the testing tank by 2 inch SS pipe which is insulated with fiber glass wool to reduce temperature drop during flooding. A solenoid valve is provided in the input water line to control the water flooding.

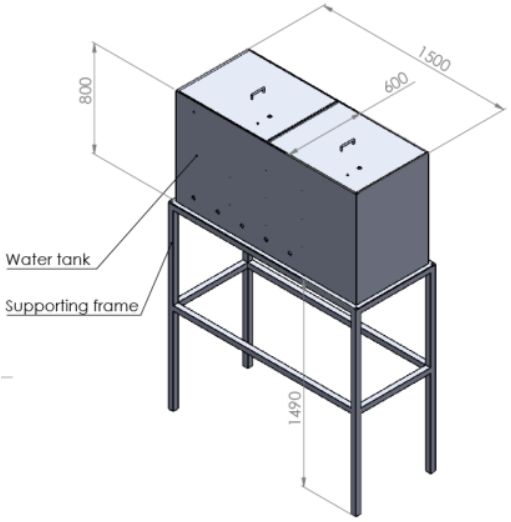

Fig. 7: Schematic of overhead tank for water heating

3. Test Procedure

Preparation for the tests began with the installation of the DBS module at the bottom of the testing tank water pool. After assembling the test pool, the cylindrical particle (Debris) bed (CDB) was arranged at the position where the centerlines of radiation furnace and CDB can be vertically aligned. Then, the CDB was filled step wise with spherical beads to the predetermined level. On each step, the weight of the spherical beads was measured to evaluate the total weight of the cylindrical debris bed in order to determine the bed porosity.

Once the debris bed is ready, the visualization window was closed using M8 bolts. A general O-ring is used for sealing against water leakages. The radiation furnace is maneuvered using the crane at center of DBS above cylindrical particle (Debris) bed (CDB). The test runs are started with heating the debris bed using the radiation furnace. As the radiation furnace and the particle bed (debris) bottom support (DBS) is not completely sealed, after a certain period of time the rise in the temperature of the particle bed becomes almost stagnant. Thus the heat-up sequence consists of stepwise increases of heating power until temperature rise of the particle bed at each location becomes less than ~ 0.5^{o}C/min. The water in the storage tank was heated using the steam from the steam generator (Make: Pyeong HWA; Model: HA-90) till the saturated conditions are reached. Due to the condensation of steam, the water level in the storage tank rises and it was monitored continuously using level gauge (Make: Omega; Model: LVR500-Series). Saturated temperature conditions of the tank was maintained using the immersion heater (Make: Omega; Model: ARTM-1500TH/240V). Each experimental scenario was observed visually and recorded using two digital video cameras (Make: Sony, Model: ILCE-7M3, 120 fps and Make: View Works, Model: VC-12MX-C180, 345 fps). The heat up sequence approximately takes 6 hrs. to reach the specified bed temperature for each test case. When the required temperature conditions in the bed and the water is reached, the test facility is ready for quenching tests. The radiation furnace was switched off and removed from top of the DBS and placed in the side of the testing tank on a furnace mounting which seals the bottom of the furnace from steam generated during quenching. A data acquisition system (DAQ) (Make:

Keysight; Model: 973DAQ) is employed to monitor and record the temperature transients of different location in particle bed, testing tank and inside the water storage tank during the heating up sequence and quenching process.

To initiate the quenching tests, the solenoid valve was opened and saturated water was allowed to flow into the testing tank. At the same time, both the high-speed camera started recording the flooding and quenching process. When the water level reaches the top of the testing tank, the solenoid valve was closed. The major physical variables for current tests are as follows:

- Temperature of the particle bed (thermocouples at different elevations and radial positions: center, mid radius and periphery),
- Quench front propagation inside the particle bed,
- Visualization of quenching process of debris bed.

The experimental parameters studied in present tests are reported in Table 1. Initially preliminary (Identification) flooding tests were carried out on both types of particles at atmospheric pressure. A number of experimental parameters were established in these pre-tests runs which include the particle bed heat up rate at different elevations and radial positions, temperature uniformity at same elevations and radial positions, total particle bed heating up sequence time period, water flooding mass flow rate, variation in particle packing (porosity) due to self levelling after quenching experiments and, total particle mass to be filled in particle bed for each particle type and size. The pre-test also demonstrated the feasibility of flooding experiments up to 700◦C, with variation of mass flow rate due to gravimetric injection. Once all the required experimental parameters were attained from the pre-test runs, the actual quenching experiments were initiated with MONET - CB test cases. Here, the studies were made with two different particles types (Ø 3 mm; SS 304 and alumina) and bed type (closed and open bottom wall).

4. Results And Discussion

The tests on the quenching behaviour of the cylindrical bed with closed bottom wall boundary conditions during bottom flooding were performed and described. Here the water ingression into the particle bed can only occur from lateral and from top direction, because the particle bed is placed over a flat surface (DBS) made of high temperature cement. The ports for the TC's are sealed with high temperature sealant to avoid any water ingression from bottom. The bed is heated by radiation furnace to specified temperatures ranging from 400°C up to 700°C depending upon the location. Earlier it was reported that the quenching observed in the bottom flooding experiments is relatively simple and one-dimensional compared to the top-flooding experiments [18, 19]. However due to the differences in heating method in current tests and water ingression pattern, bed temperature profile will exhibit very distinct behavior during heating up sequence and quenching.

The typical temperature evolution can be divided in three parts. First, the bed is dry and its temperature increases due to the radiation furnace heating. Second, the bed reached the required test temperature and heating is stopped and water is released into the testing tank. In this part, the quench front approaches different thermocouple positions and the bed is cooled down by a steam-water flow to the saturation temperature within a few seconds. Various modes of boiling heat transfer can be observed depending upon the location in the bed. Finally, the bed remains at the saturation temperature for a long period of time, and then very slowly bed temperature decreases to water pool temperature by single-phase cooling. It is assumed that the quench front has reached a thermocouple position when its temperature drops by hundreds of degrees Celsius within a few seconds. A single test run may last for more than 4 hrs from heating to completion of quenching. Therefore, it is difficult to provide an analysis using the complete temperature time history. However, from the analysis of the temperature transients, it was observed that the quenching of the debris bed completes in ≈ 80 sec after the quench front has touched the bottom sides walls of the CDB. Thus, a 200 sec time scan window was selected manually from the complete temperature time curve which can exhibit the temperature transients for all the TC's after the initiation of

quenching. This procedure provides a better demonstration of temperature transients of different TC's during quenching.

Fig. 8 (a-d) depicts the normalized temperature transients for different radial locations for tests case Monet-CL-1 (Ø 3 mm; Alumina). The temperature data are normalized by introducing T/T_{max} for mapping the temperature profile. By doing such a procedure, the temperature slopes of different TC locations can be compared in a similar time frame and provide ease of analyzing the temperature profiles. The top and outer locations of the cylindrical particle bed have higher temperature compared to inner location because of closer proximity from the heaters of radiation furnace. The maximum temperature ranging between T_{CM} = 690-700°C is at the top center of the bed which is near to the center of the radiation furnace. The quenching first occurs at the bottom boundary locations (T_{C4-4}, T_{C4-3}) and then the quench front propagates to the bottom center of the bed (T_{C1-4}) and then further proceeds to top (T_{C1-3}, T_{C1-2}) like that of a homogenous flooding. Also the time period for quenching at same radial and elevation level was found relatively similar. The temperature variation in outer most circle C4 (r = 105 mm) is ranging between 550°C to 590°C for T_{C4-4} (z = 20 mm) to T_{C4-1} (z = 50 mm), respectively (Fig. 8 (d)). While the temperature variations in the inner most circle C1 (r = 30 mm; Fig. 8 (a)) is between 400°C to 690°C for T_{C1-4} (z = 20 mm) to T_{C1-1} (z = 120 mm), respectively. The variation in temperature is higher in the inner most circle compared to outer-most circle because of the increased difference in TC's heights (See Fig. 4a).

Fig. 8 (a) shows normalized temperature transients for TC locations in circle C1 (r = 30 mm). For this case, the quench front will be moving *from* T_{C1-4} (r = 30, z = 20) which is lowest in the particle bed to T_{C1-1} (r = 30, z = 120) which is highest in the particle bed for circle C1. However, one can observe that the T_{C1-4} (r = 30, z = 20) is have a significant variation in temperature time slope compared to other TC's. Such behavior is called as quench delay which was previously observed by Karbojian et al. [4] from DEFOR-E experiment and Cho and Bova [20] suggesting the formation of dry-zone inside the heated particle bed during quenching. Fig. 8 (b) shows normalized temperature transients for TC locations in circle C2 (r = 65). For this case, the quench front will be moving from T_{C2-4} (r = 65, z = 20) which is lowest in the particle bed to T_{C2-1} (r = 65, z = 120) which is highest in the particle bed for circle C2. Similar to earlier observation, quenching delay for temperature curve was observed for T_{C2-4} (r = 65, z = 20) for which the quenching finished after T_{C2-3} (r = 65, z = 80) which is at much higher height in the particle bed. Fig. 8 (c) and Fig. 8 (d) depicts the normalized temperature transients for circles C3 (r = 85) and C4 (r = 105), respectively. It can be observed from the temperature trends at these radial locations (r ≥ 85) that the quenching delays are negligible. Thus the quenching delays are higher for TC's at inner radial locations (r ≤ 65; C1 and C2) and reduce for distance away from the center (r ≥ 85; C3 and C4). By observing the trends of temperature curve for T_{C1-4} in circle C1 and T_{C2-4} in circle C2, it can be postulated that the initial cooling at these locations ($r \leq 65$, $z \leq 45$; bottom center of particle bed) will progress by film boiling mode of heat transfer for both types of particles. The vapor blanket formed at these locations has sustained even after the quench front has cooled the location higher in the particle bed. This quenching delay suggests formation of dry zone inside the particle bed which blocks the water ingression thus preventing effective cooling of the particles in these locations. In previous studies by Tutu et al. [3] also reported that the wall region quenches much faster than the central region. This is due to the wall effect the peripheral locations of the bed has higher porosity compared to inner locations which assist faster quench front movement. While the findings from the current test cases (Monet-CL-1), such dry zones existed in these locations ($r \leq 65$, $z \leq 45$; bottom center of particle bed) for 20 - 30 sec after the quench front has passed the TC's location and eventually losses its strength due to decreasing particle superheats and increasing water pressure.

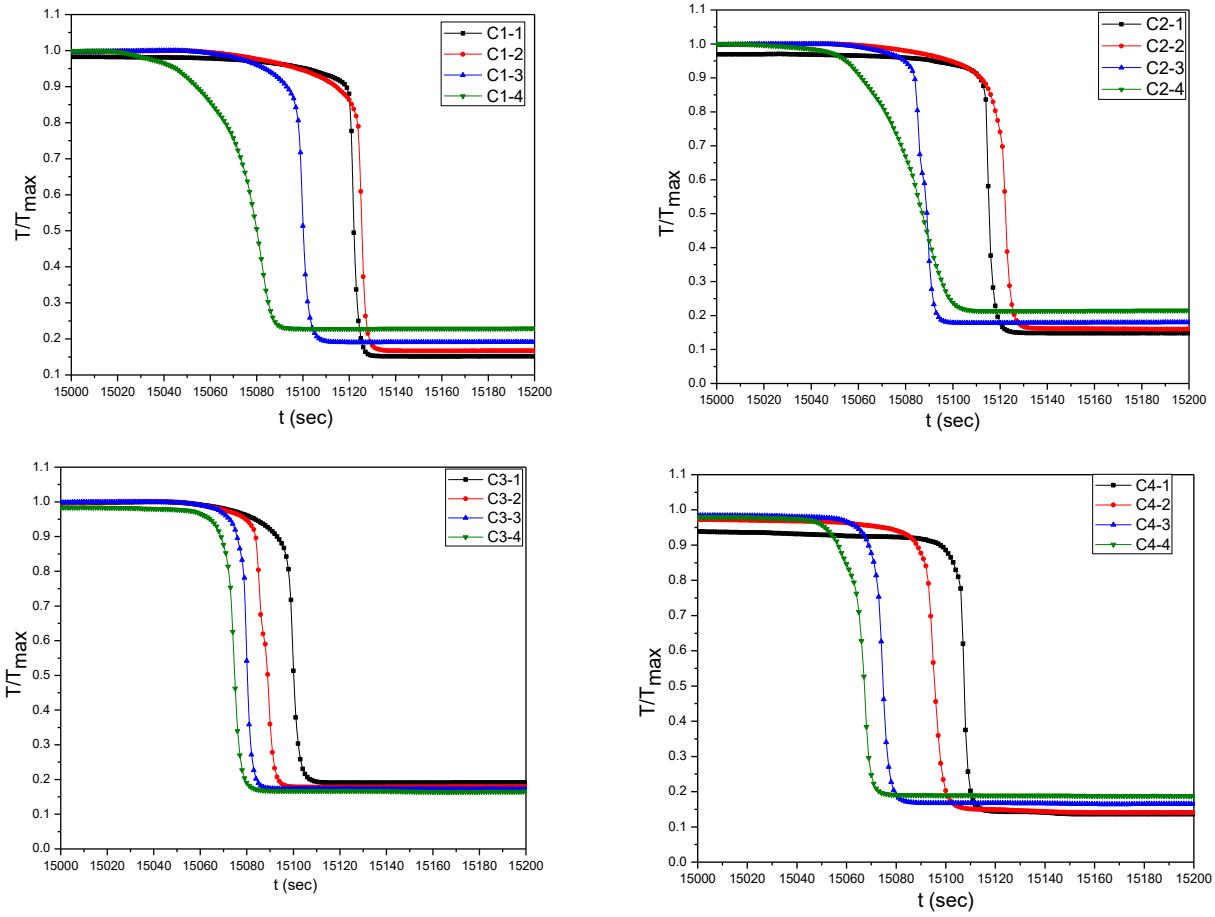

Fig. 8: Temperature transients for different radial TC's locations at the bottom of particle bed (TC1-4, TC2-4, TC3-4 and, TC4-4)

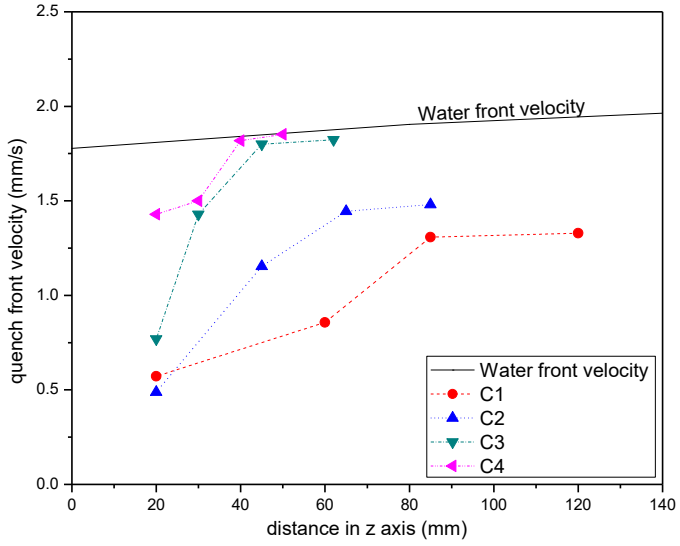

Fig. 9: Quench front movement for different radial TC's locations at the bottom of particle bed

Fig. 9 depicts the quench front propagation trends for different TC locations as a function of particle bed height (z). To calculate experimental quench front velocity from thermocouple reading, one requires to find out the time gap taken by quench front to propagate between two consecutive thermocouples. The following procedure was used to find the experimental quench front velocity. Two tangents were drawn on the quenching curve before and after the quenching and an intersection point was found. A horizontal line was drawn passing through the intersection point, and it cuts the quenching curve at a point, which is the rewetting point. Horizontal and vertical lines passing through the rewetting point give us rewetting temperature (contact of quench front) and rewetting time, respectively. The formula used for experimental quench front velocity is:

$$U_e = \frac{L_e}{\Delta t_e} \tag{1}$$

Where U_e is the experimental quench front velocity, L_e is the distance between two consecutive thermocouples, and Δt_e is the time difference between two consecutive thermocouples:

$$\frac{\partial U_e}{U_e} = \sqrt{\left(\frac{\partial L_e}{L_e}\right)^2 + \left(\frac{\partial \Delta t_e}{\Delta t_e}\right)^2} \tag{2}$$

Eq. 2 provides the uncertainty in the value of quench front velocity for different cases. It can be observed that the quench front velocity increases with increasing bed height in most radial location inside the particle bed. As the bed height increases, the distance of vapor to escapes from the side wall of the particle bed decreases. In case of Monet-CL-1, the quench front velocities for outer TC's circles of C3 (r = 85) and C4 (r = 105) are closer to the water front velocity outside the particle bed and vary from 0.75-1.76 mm/s (C3) and 1.4-1.8 mm/s (C4), respectively. As for these radial locations, the water enters from the lateral direction and quenches the outer locations initially and then progress towards the center of the bed. In case of inner TC circle locations of C1 and C2 ($r \leq 65$) in the bed, the quench front velocity remains very low (~0.5 mm/s) at lower bed height ($z \leq 65$ mm) for both type of particles.

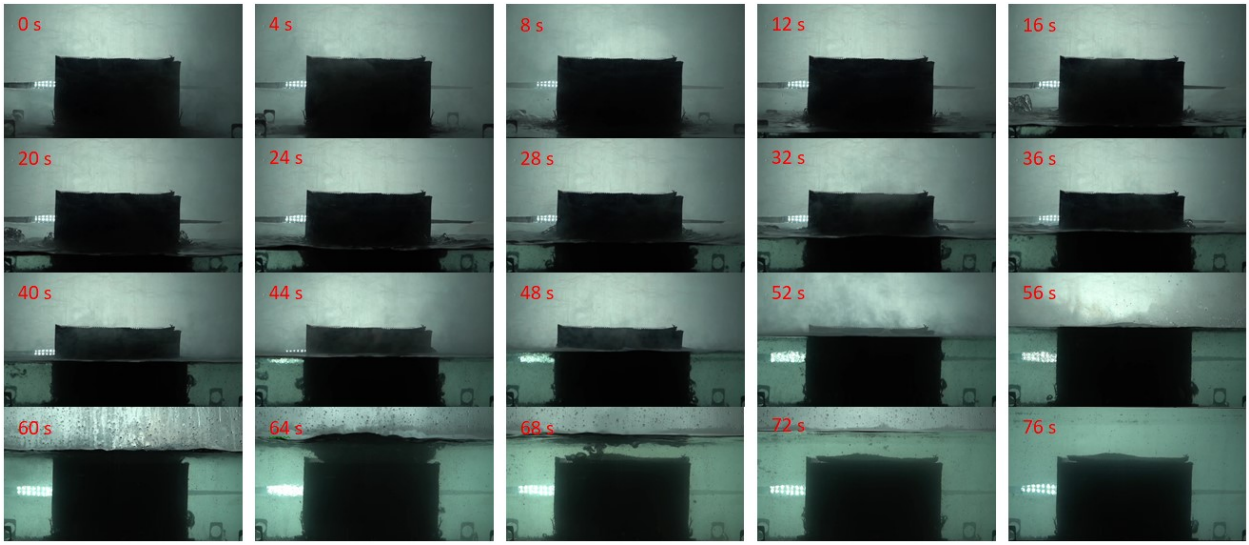

Fig. 10: Visualization of cylindrical particle bed quenching

Earlier, the movement of quench front was tracked based on temperature transient data from TC's at varied locations inside the particle bed. Visualization of quenching of particle bed is discussed below. Quenching front movement plays important role in cooling the particle bed during flooding process. In the propagation of the quench front, the particle bed experiences dry region, transition region, nucleate region, and forced convection region at different sections of the bed. Fig. 10 shows the snapshots of quenching

process for Monet-CL-1 tests case. The water front takes almost 60 sec to move from bottom of the particle bed to the top. For this case the water will enter the particle bed from the lateral direction (at t ≈ 5 sec). As the water front comes in contact with the particle bed, it wets the particles, but soon vapor film formation occurs over it in the peripheral locations. The ejection of liquid drops at the interface of quenching front, also called sputtering, favors precursory cooling of the superheated solid particles ahead of the quenching front. Such sputtering phenomenon is visible near the borders of the particle bed as the water front moves towards the top of the bed (z ≈ 0 mm →100mm; at t ≈ 5 sec →35 sec). As the water front reaches near the top of particle bed (z ≥ 100 mm), ejection of liquid can be seen from the center top of particle bed (*similar to eruption*) due to sputtering of liquid inside the particle bed (at t ≈ 45 sec→65 sec). When the water front has passed the top of the particle bed (at t > 65 sec), vapor bubbles can be seen escaping the bed from the top center of the bed. The visual water front velocity has been calculated using IMAGEJ software.

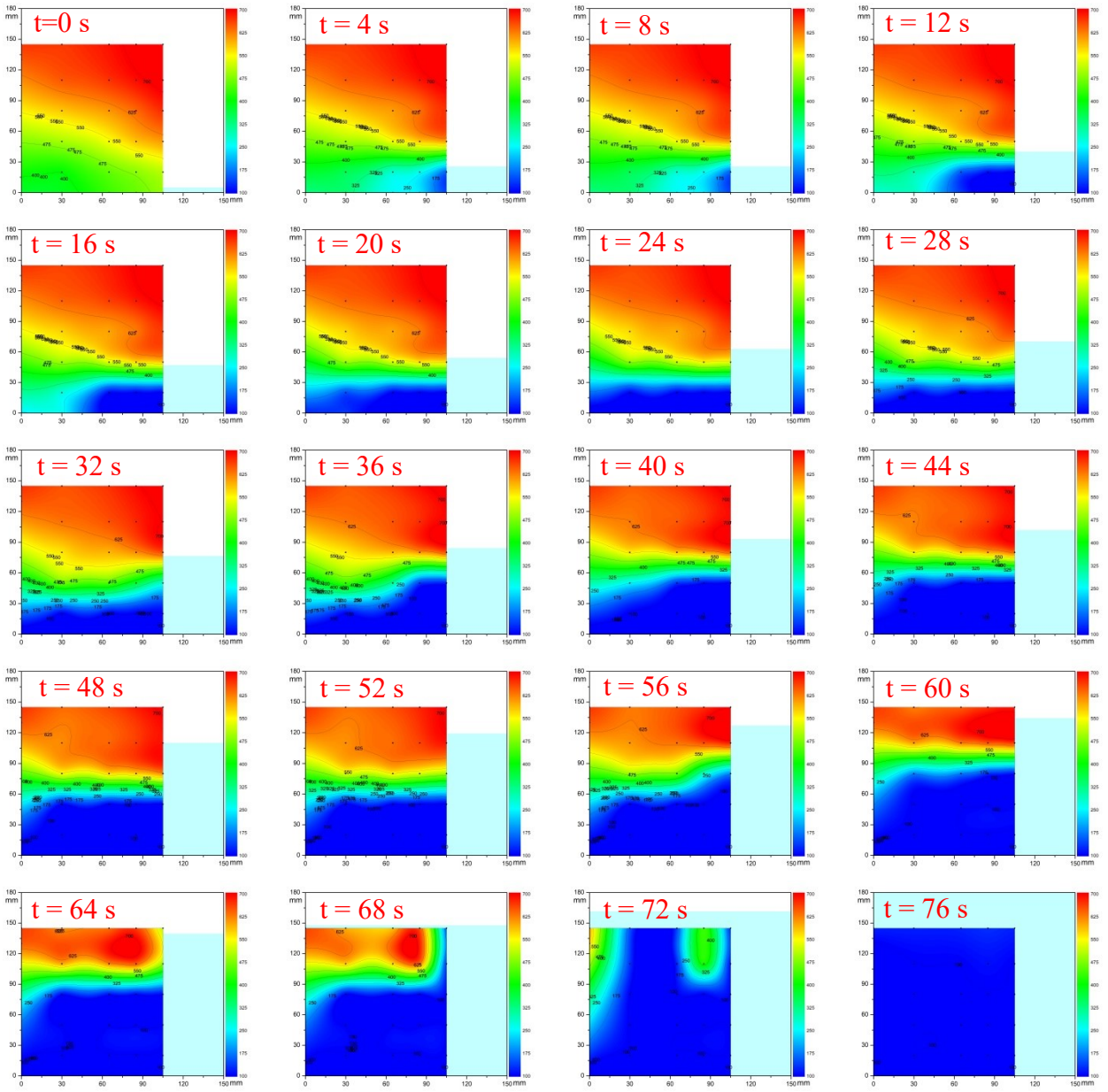

Fig. 11: Contour mapping for quench front flow during cylindrical debris bed quenching

Using the temperature transients presented above, 2D temperature-time contours were plotted using the Origin 2018 to illustrate the behavior of debris particle bed during quenching. For these curves, the coordinates of the TC's were used to define the geometry of the CDB. While the temperature transient data sets were used to determine the color map. From the analysis of the temperature transient, it was observed that the quenching of the debris bed completes within 80 sec after the quench front has been detected at the first location (C4-4) till the completion of quenching at the last location (CM) of the CDB. Here in order to demonstrate the quench front propagation, the temperature-time contours were plotted for each individual time step in that 80 sec time scan window. Fig. 11 depicts the temperature maps as a function of time demonstrating the quench front movement inside the heated particle bed. The top and outer locations of the cylindrical particle bed have higher temperatures compared to the inner location because of closer proximity from the heaters of the radiation furnace. Temperatures are lower at the center bottom of the bed due to heat losses. In Monet-CL-1 test case, when the water reaches the bottom of the debris bed, the quenching is observed for all the radial location near the periphery at t12. Then the quench front propagates upwards and inside the bed at t12 to t24. One can observe that the outer radial locations of the bed were cooled at a faster rate. Due to the shape of the particle bed, the exit path for vapor to release from the sides is shorter which facilitates the ingression of fresh coolant. In the lower locations of the bed, quench front progressed in a unidirectional upwardly directed manner. As the quench front move towards top, it ca be seen forming an arc shape due to the hindrance caused by the movement of vapor. A dry zone can be observed at location near the center between r = 0 to 30 mm for t = 68 -72 s. This may be due to the vapor movement from the center of the bed blocking the movement of fresh coolant and subsequent quenching.

5. Conclusions

A new test facility MONET (MCCI-mitigatiON through passive cooling Effect Test) has been designed for investigations of quenching behavior in porous particle beds of different geometries. The issue is of importance in the severe accident management of nuclear power reactors since debris beds may be formed of solidified corium. The main objective of the experiments to be performed with the new experimental set-up is to compare the quenching in a cylindrical particle bed with varied bed porosity. This is done in order to increase knowledge on the coolability of particle beds that have complex geometries and to produce data for code validation purpose. Initial findings from the tests suggest, significant variation is quenching performance with radial and elevations inside the particle bed. This is due to the non-uniform movement of quench front inside the superheated particle bed during quenching. Such observation is different from the findings of Rashid et al. [18, 19] and Chikhi et al. [21], which reported a one-dimensional configuration with flat quenching and cooling fronts and very low thermal gradients in the z-direction. These findings can significantly improve the understanding of current knowledge on quench front movement inside the superheated particle bed. Further tests are being performed in variety of particle and bed boundary conditions.

ACKNOWLEDGMENTS

The authors would like to acknowledge the support from the Nuclear Safety Research Program through the Korea Foundation Of Nuclear Safety (KoFONS) using the financial resource granted by the Nuclear Safety and Security Commission (NSSC) of the Republic of Korea. (Grant No. 1805001-0522-CG100).

REFERENCES

[1] D. Magallon, I. Huhtiniemi, H. Hohmann, Lessons learnt from FARO/TERMOS corium melt quenching experiments. *Nucl. Eng. Des*. **189**, pp. 223–238, (1999).

[2] P. Kudinov, A. Karbojian, C.T. Tran, W. Villanueva, Agglomeration and size distribution of debris in DEFOR-A experiments with Bi2O3–WO3 corium simulant melt, *Nucl. Eng. Des.*, **263** pp. 284-295, (2013),.

[3] N. Tutu, T. Ginsberg, J. Klein, C. Schwarz, J. Klages, Transient quenching of superheated debris beds during bottom reflood. *Brookhaven National Lab*., Upton, USA. (1984).

[4] A. Karbojian, W.M. Ma, P. Kudinov, T.N. Dinh, A scoping study of debris bed formation in the DEFOR test facility. *Nucl. Eng. Des.* **239,** pp. 1653-1659, (2009).

[5] W.M. Ma, T.N. Dinh, The effects of debris bed's prototypical characteristics on corium coolability in a LWR severe accident. *Nucl. Eng. Des.*, **240**, pp. 598–608, (2010).

[6] E. Takasuo, S. Holmström, T. Kinnunen, The effect of lateral flooding on the coolability of irregular core debris beds. *Nucl. Eng. Des*. **241**, 1196–1205, (2011).

[7] E. Takasuo, S. Holmström, T. Kinnunen, P.H. Pankakoski, The COOLOCE experiments investigating the dryout power in debris beds of heap-like and cylindrical geometries. *Nucl. Eng. Des*. **250**, pp. 687–700, (2012).

[8] E. Takasuo, An experimental study of the coolability of debris beds with geometry variations. *Ann. Nucl. Energy,* **92**, pp. 251–261, 2016.

[9] S. Thakre, L.X. Li, W.M. Ma, An experimental study on coolability of a particulate bed with radial stratification or triangular shape, *Nucl. Eng. Des.* **276**, pp. 54–63, (2014).

[10] M. Bürger, M. Buck, W. Schmidt, Validation and application of the WABE code: Investigations of constitutive laws and 2D effects on debris coolability. *Nucl. Eng. Des*. **236**, 2164–2188, (2006).

[11] S.E. Yakush, P. Kudinov, T.N. Dinh, Multiscale simulations of self-organization phenomena in the formation and coolability of corium debris bed. In: *13th Int. Top. Meet. Nucl. React. Therm. Hydraul*., **N13P1143**, (2009).

[12] S. Rahman. Coolability of corium debris under severe accident conditions in light water reactors. *PhD thesis*, *Universitat Stuttgart*, (2013).

[13] E. Takasuo, V. Taivassalo, and V. Hovi. A study on the coolability of debris bed geometry variations using 2d and 3d models. *Technical report*, *VTT Technical Research Centre of Finland*; (2014).

[14] J. H. Park, H. S. Park, M. Lee, and K. Moriyama. Modeling of pressure drop in two-phase flow of mono-sized spherical particle beds. *Int. J. Heat and Mass Transf.*, **127,** pp. 986-995, (2018).

[15] M. Lee, J. H. Park, H. S. Park, K. Moriyama and M. H. Kim, Modified Two-Phase Friction Model for Porous Media to Better Predict Dryout Heat Flux, *Tran. of the Korean Nucl. Society Spring Meeting*, Jeju, Korea, May, pp. 17-19, (2017).

[16] M. Lee, J. H. Park, H. S. Park, K. Moriyama and M. H. Kim, Validation of New Friction Model for Dryout Heat Flux in Ex-Vessel Porous Debris Bed in the Multi-Dimensional Congurations, *Tran. of the Korean Nuclear Society Autumn Meeting*, Gyeongju, Korea, October, pp. 25-37, (2017).

[17] M. Lee, Development of two-phase flow model for predicting dryout heat flux in particle packed bed, *PhD Thesis*, POSTECH, (2019).

[18] Rashid, M., Kulenovic, R., Laurien, E., 2011. Experimental results on the coolability of a debris bed with multidimensional cooling effects. *Nucl. Eng. Des*. 241 (11), 4357–4543.

[19] Rashid, M., Kulenovic, R., Laurien, E., 2012. Experimental results on the coolability of a debris bed with down comer configurations. *Nucl. Eng. Des*. 249, 104–110.

[20] Cho, D.H., Bova, L., 1983. Formation of dry pockets during water penetration into a hot particle bed. Trans. ANS 41, 418-419.

[21] Chikhi, N., Fichot F., 2017, Experimental and theoretical study of large scale debris bed reflood inthe PEARL facility, Nuclear Engineering and Design, 312, 48-58.

ERMSAR Log Number: 279

The 10th European Review Meeting on Severe Accident Research (ERMSAR2022)
Akademie hotel, Karlsruhe, Germany, May 16-19, 2022

Quenching Phenomena in High Temperature Cylindrical Debris Bed: MONET Tests

Presented by
MAYANK MODAK
Senior Researcher
Nuclear Research Institute for Future Technology and Policy
Department of Nuclear Engineering
Seoul National University
Email: mayankmodak@snu.ac.kr
16 – 19 May, 2022

Co-authors
Prof. Hyun Sun Park, Seoul National University
Dr. Vishal V. Nirgude, Seoul National University

ARTS Laboratory
(*Advances in Risk Tolerance Safety*)

Contents

01. Introduction and Contents of R & D

02. Test Facility and data acquisition

03. Experimental findings from Quenching tests

04. Results and Discussion

05. Conclusion

01 Introduction

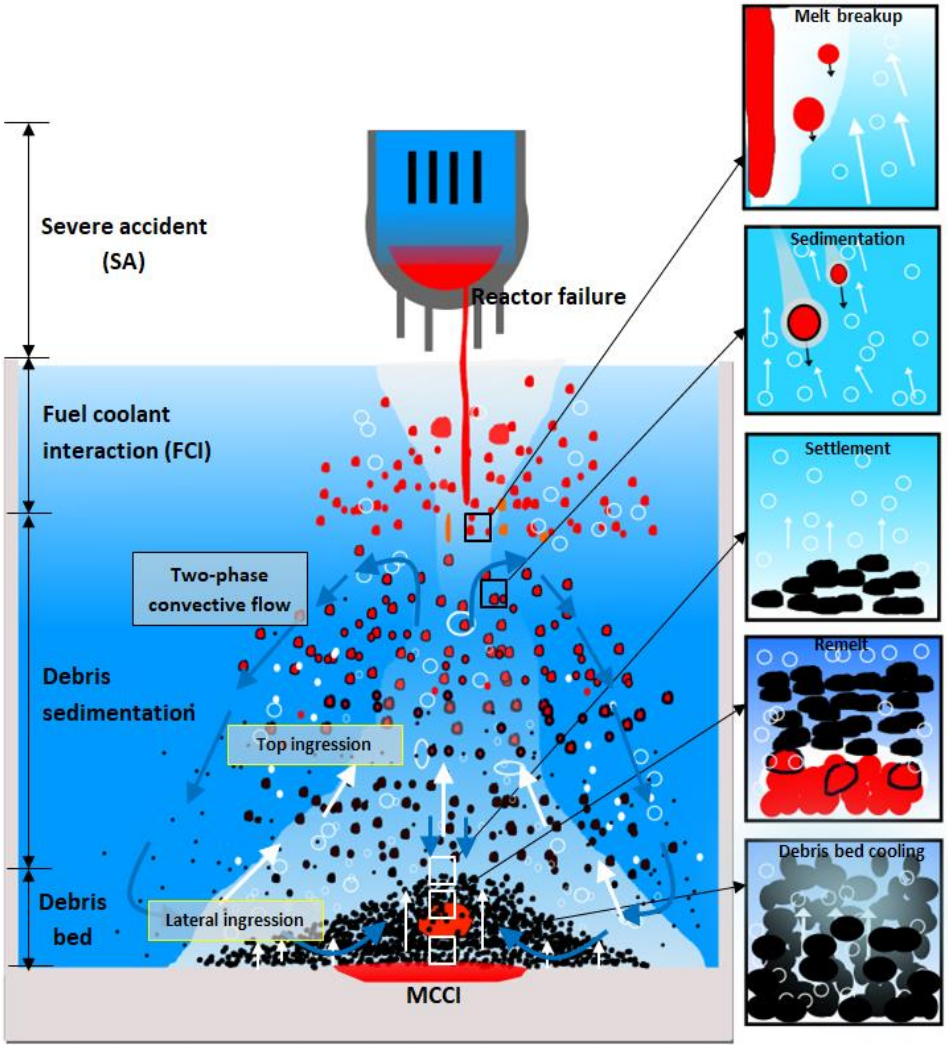

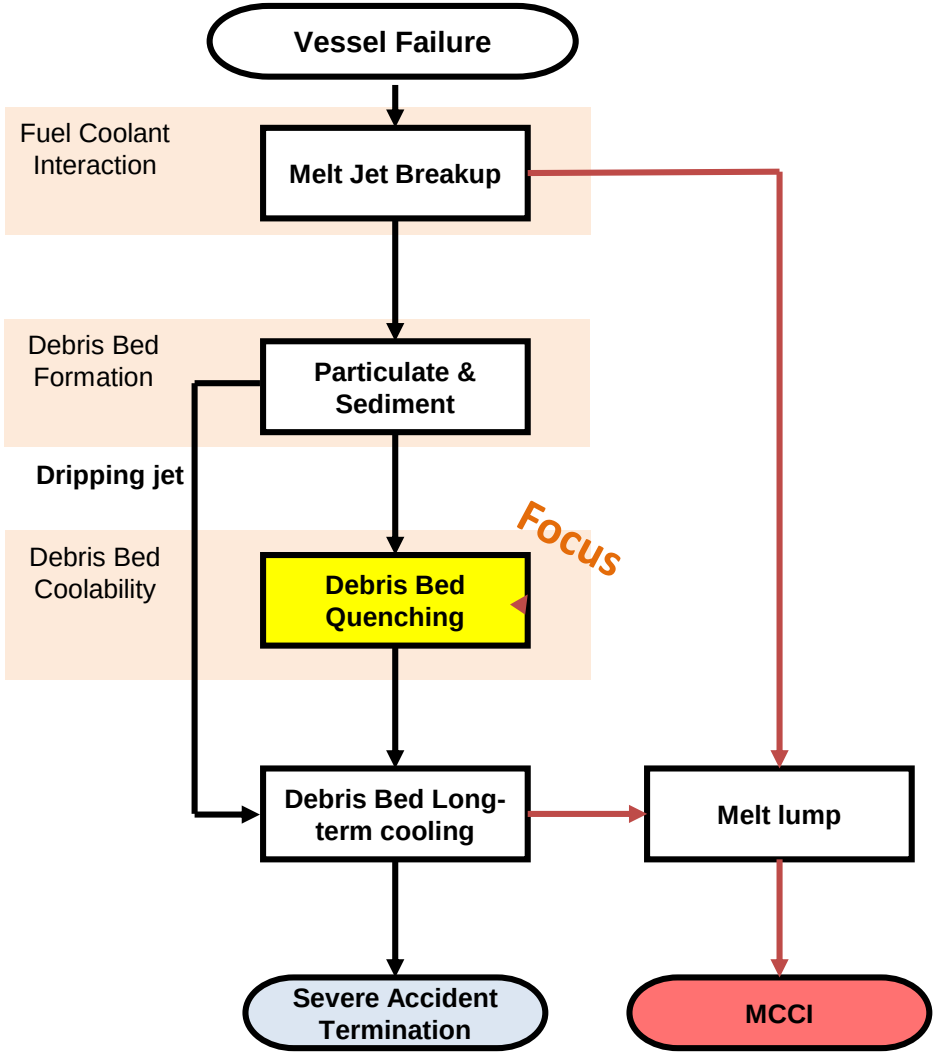

Understanding of development of ex-vessel debris bed is important to achieve the accurate assessment of coolability

E. Kim et al (2016), Nucl. Eng. Des 298, 240-254.

02 Objective

Research Objective: Quenching Phenomena in High Temperature Cylindrical Debris Bed: MONET Tests

- ✓ To enhance the understanding of coolant ingression in the heated multidimensional particle bed coolability.
- ✓ Understand the mechanism of heat transfer inside the cylindrical heated debris bed.
- ✓ Different bed configuration were studied to provide insight to the quench front movement inside the heated particle bed.
- ✓ Particle sizes were varied from Ø 3 - 10 mm alumina
- ✓ Comparison of the present data from cylindrical bed quenching with the data from conical bed quenching

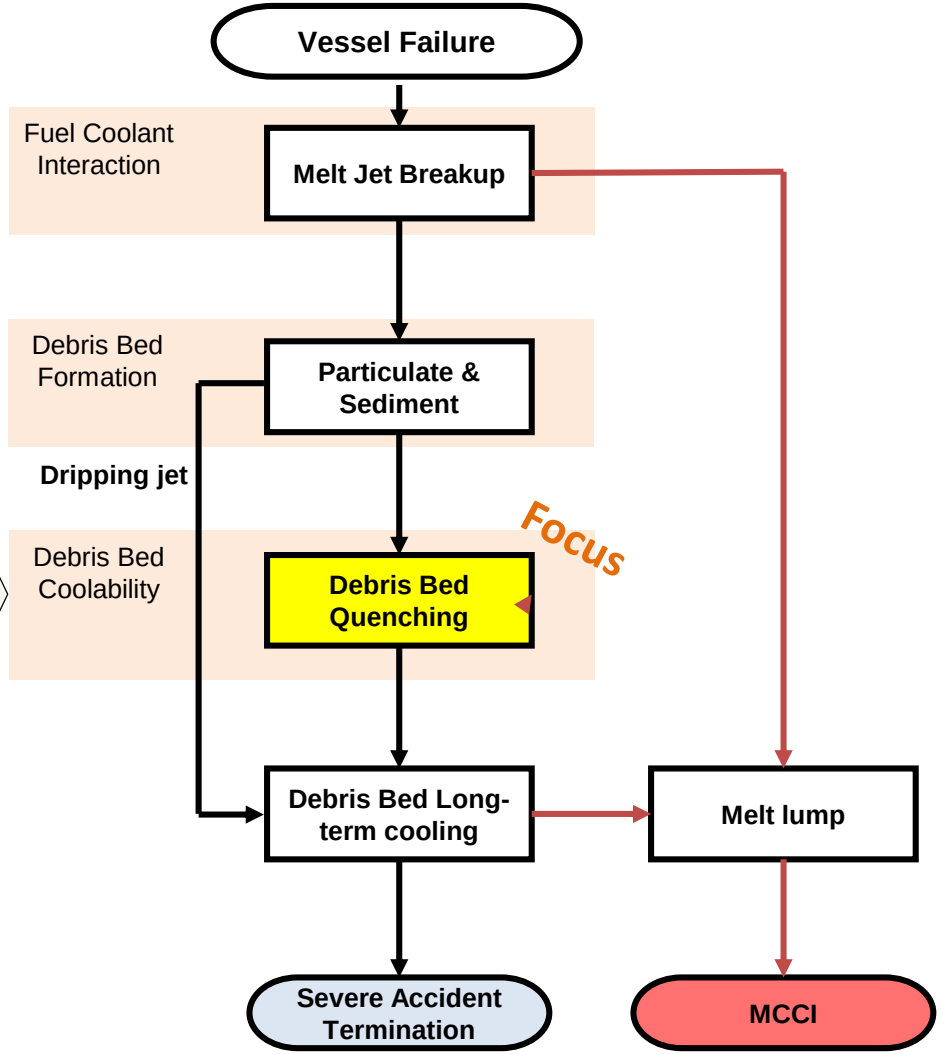

Understanding of development of ex-vessel debris bed is important to achieve the accurate assessment of coolability

E. Kim et al (2016), Nucl. Eng. Des 298, 240-254.

03 MONET Test Setup

Research Objective: Quenching Phenomena in High Temperature Cylindrical Debris Bed: MONET Tests



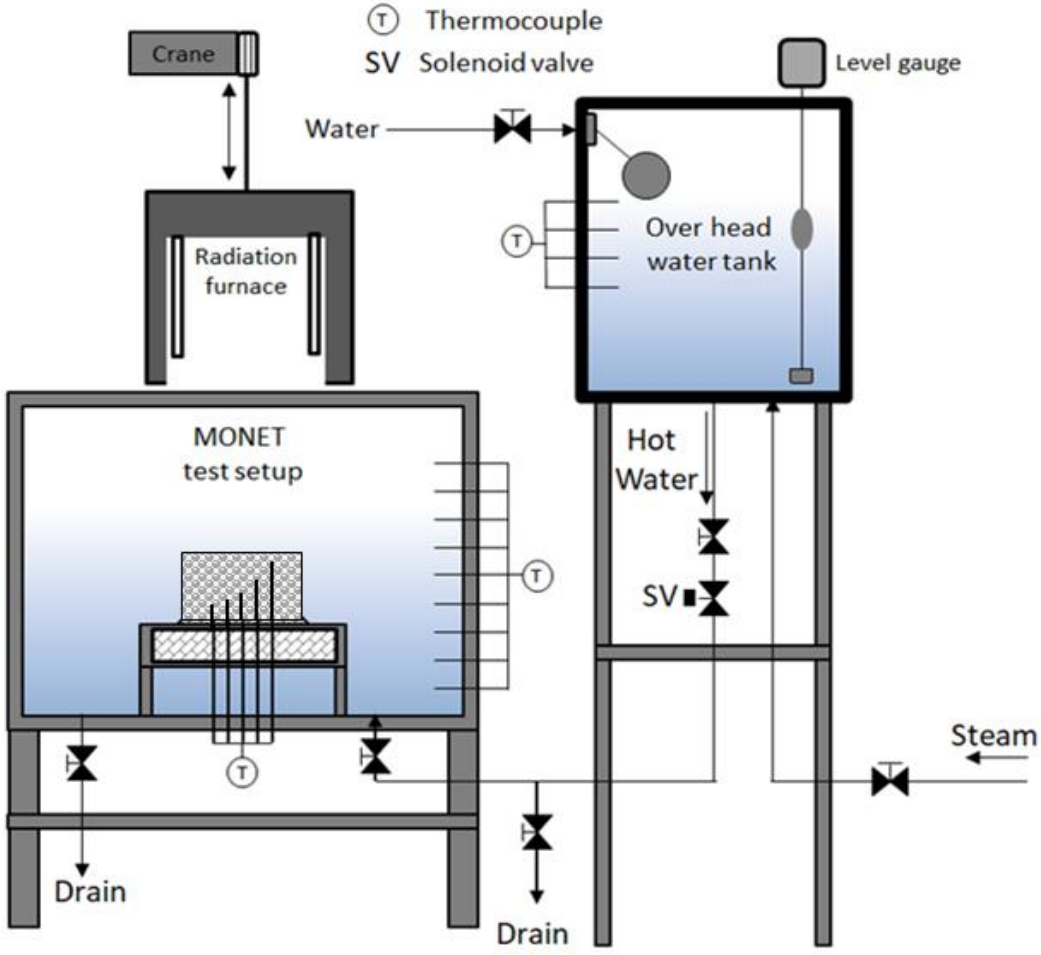

03 Test Setup

Research Objective: Quenching Phenomena in High Temperature Cylindrical Debris Bed: MONET Tests

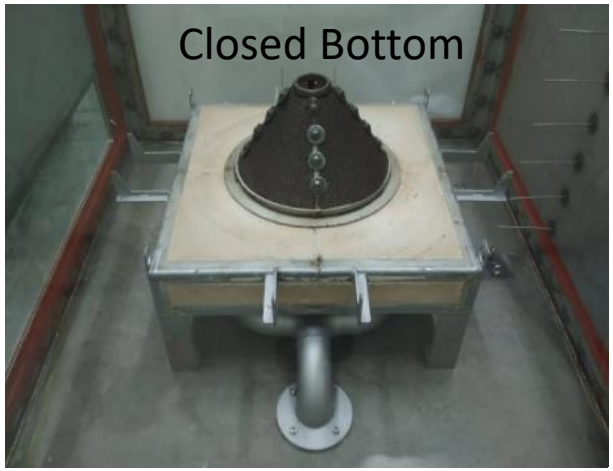

Cylindrical Debris bed (CDB)

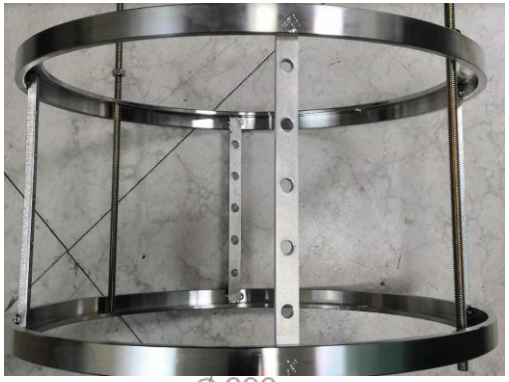

Conical Debris bed (CDB)

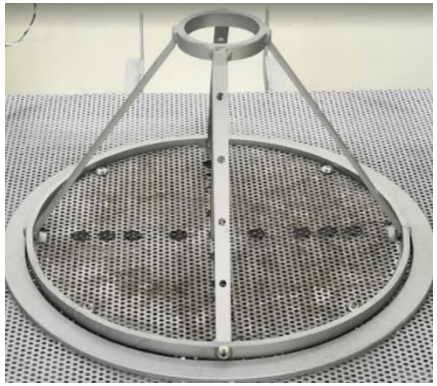



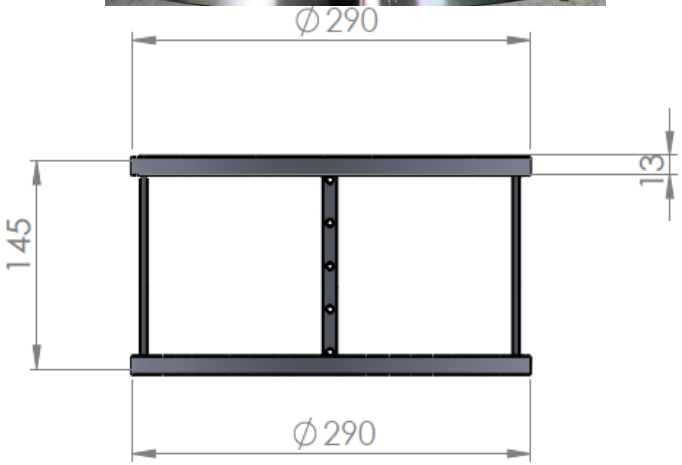



03 Test Setup

Research Objective: Quenching Phenomena in High Temperature Cylindrical Debris Bed: MONET Tests

TC's locations

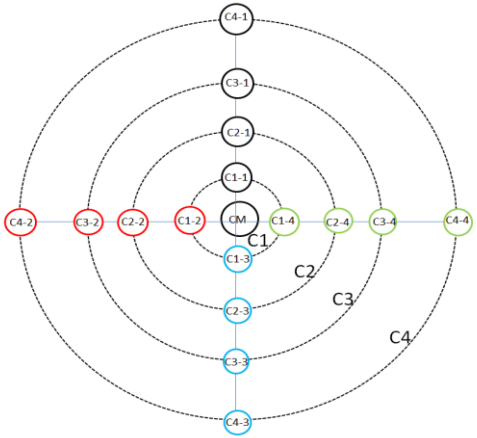



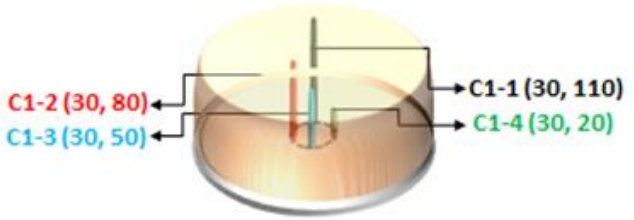

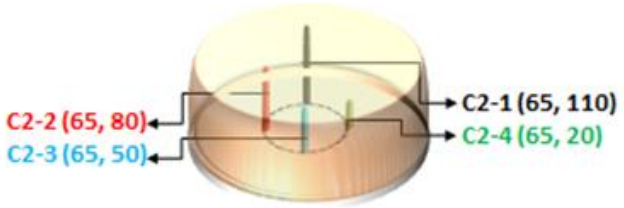

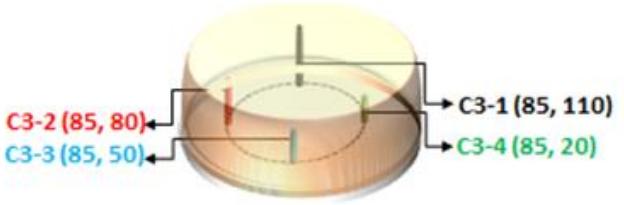

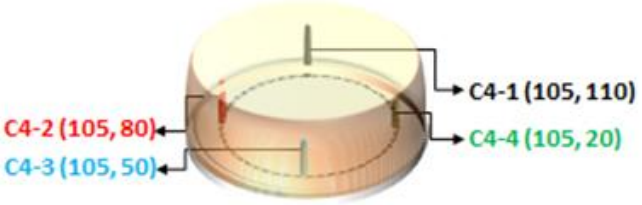

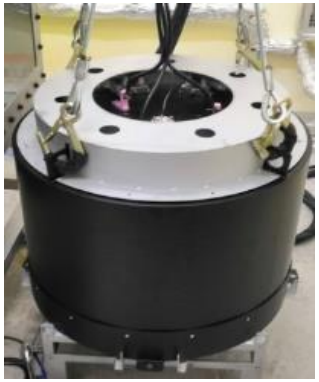

Radiation Furnace

Simulant particles

SS 304, 3-5 mm



Aluminium, 3-5 mm



03 Test Matrix

Research Objective: Quenching Phenomena in High Temperature Cylindrical Debris Bed: MONET Tests

Tests matrix

Test case	Bed type	Particle	Particle size	Porosity	Furnace Temperature	Particle bed temperature range	Water Temperature
#MONET Phase 1							
MONET-CO-1	Closed bottom	Alumina	3 mm	0.421	700°C-800°C	700°C-500°C	~99°C
MONET-CO-2	Open bottom	Alumina	3 mm	0.425	700°C-800°C	700°C-500°C	~99°C
MONET-CO-2	Open bottom	Alumina	3 mm	0.436	700°C-800°C	700°C-500°C	~99°C
#MONET Phase 2							
MONET-CL-1	Closed bottom	Alumina	3 mm	0.422	700°C-800°C	700°C-500°C	~99°C
MONET-CL-2	Closed top & bottom	Alumina	3 mm	0.424	700°C-800°C	700°C-500°C	~99°C
MONET-CL-3	Stratified bed	Al & SS	2 - 3.5 mm	0.442	700°C-800°C	700°C-500°C	~97°C
MONET-CL-4	Closed Side	Alumina	3 mm	0.423	700°C-800°C	700°C-500°C	~97°C
MONET-CL-5	Stratified bed	Al & SS	2 - 3.5 mm	0.445	700°C-800°C	700°C-500°C	~97°C

MONET Phase 1 MONET Phase 2

Bed boundary conditions

a) Bottom insulated

b) Side ingression top closed

c) Stratified bed



d) Side closed
Planned

04 Results

Research Objective: Quenching Phenomena in High Temperature Cylindrical Debris Bed: MONET Tests

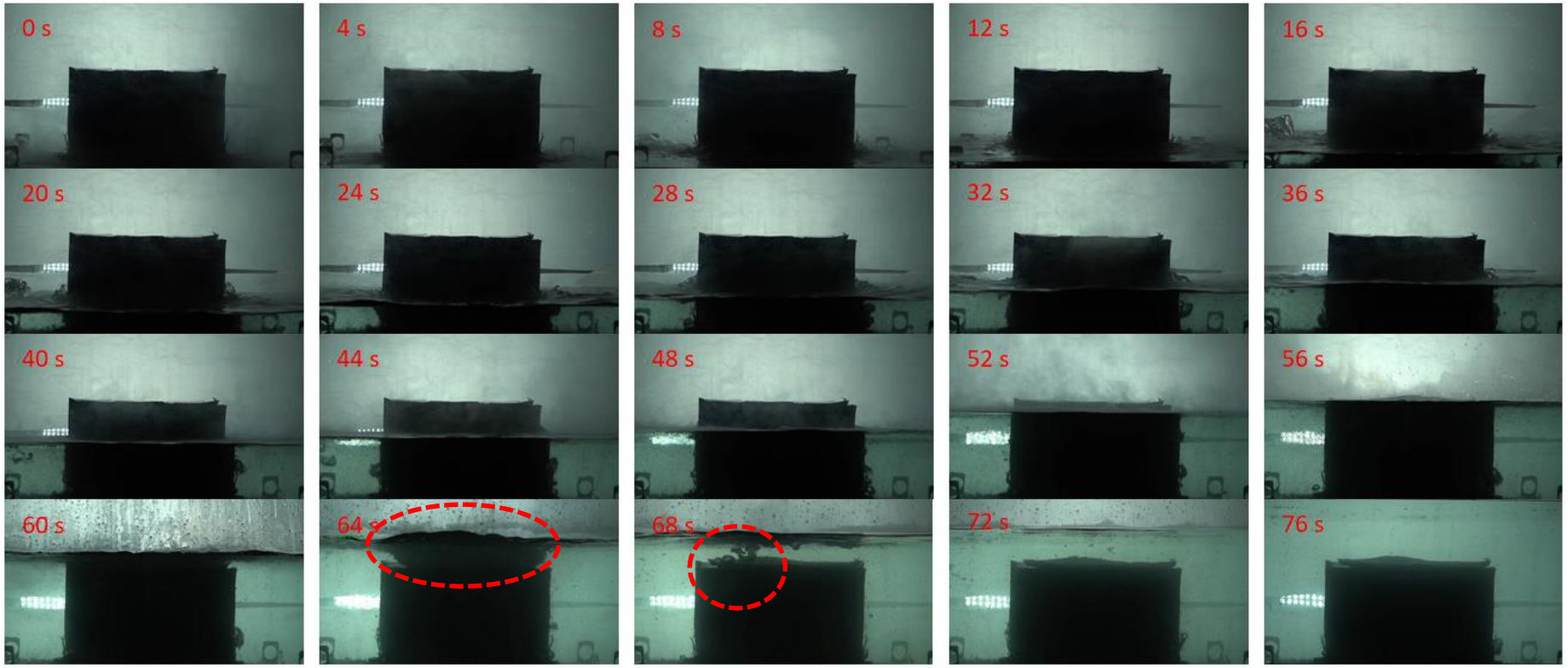

Vapor bubbles largely can be seen ejecting from the center the cylindrical particle bed

04 Results

Research Objective: Quenching Phenomena in High Temperature Cylindrical Debris Bed: MONET Tests

Development of "dry zones" can be seen in the contour curve for the case of MONET-CL in the center top locations

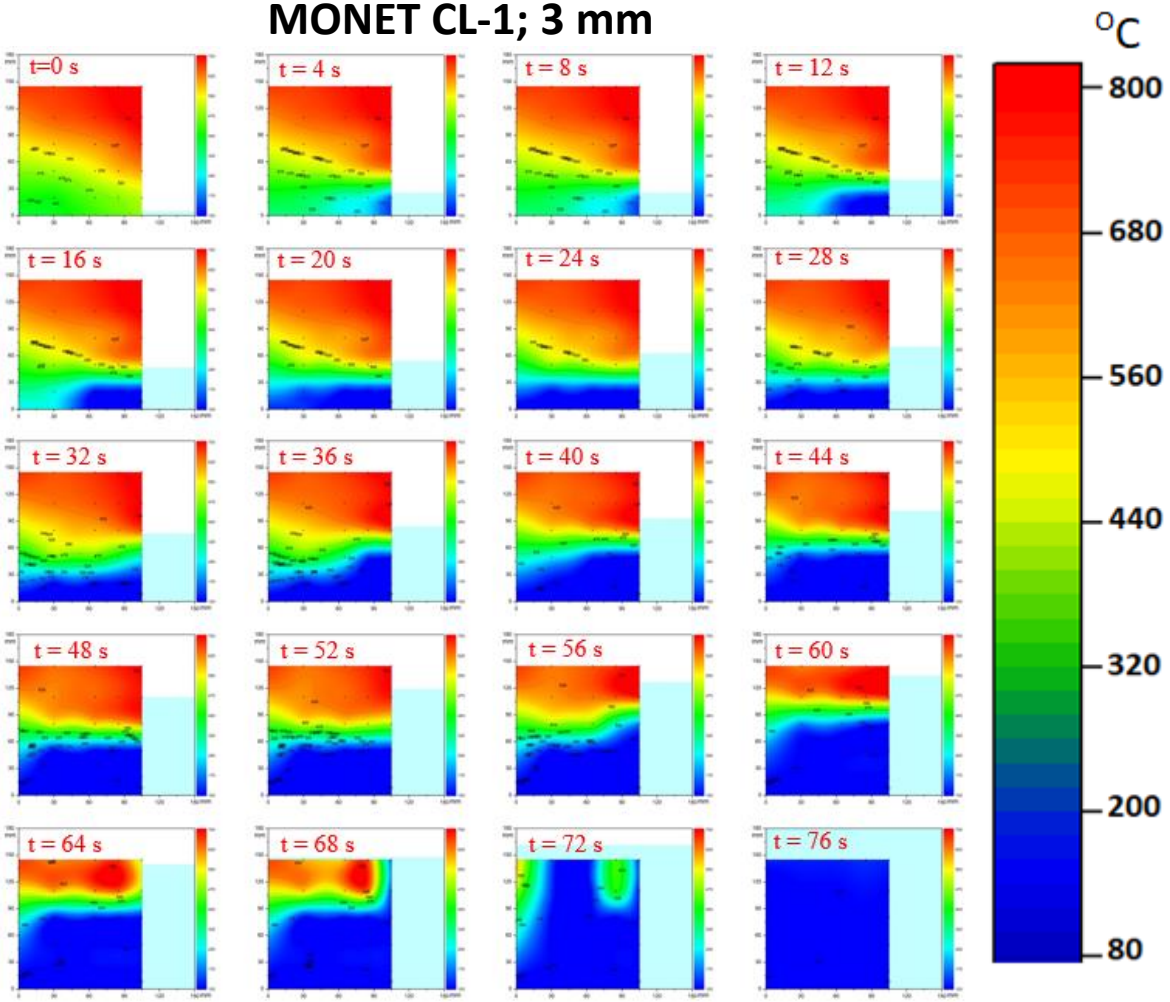

04 Results

Research Objective: Quenching Phenomena in High Temperature Conical Debris Bed: MONET Tests

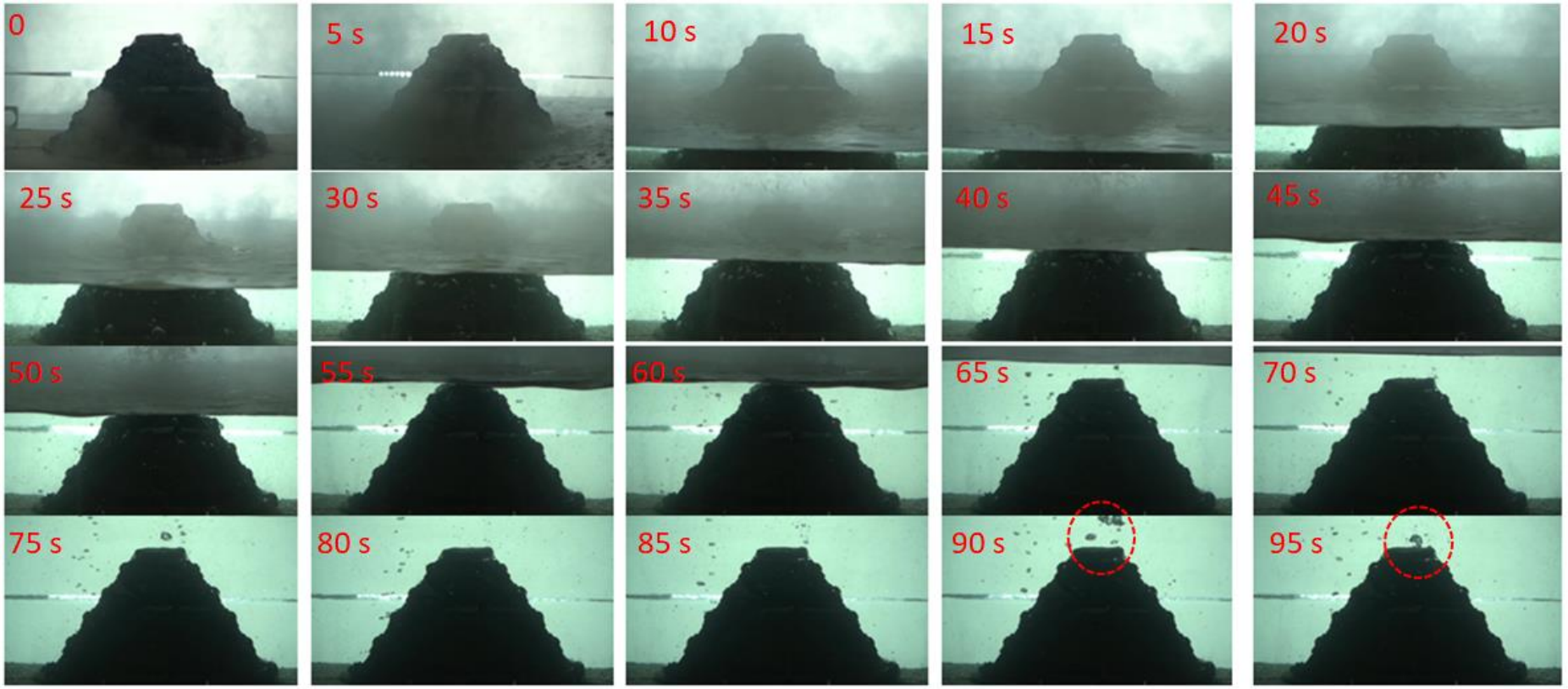

Vapor bubbles can be seen ejecting from the center and top of the conical bed

04 Results

Research Objective: Quenching Phenomena in High Temperature Conical Debris Bed: MONET Tests

Development of "dry zones" can be seen in the contour curve for the case pf MONET-CO near the bottom center locations

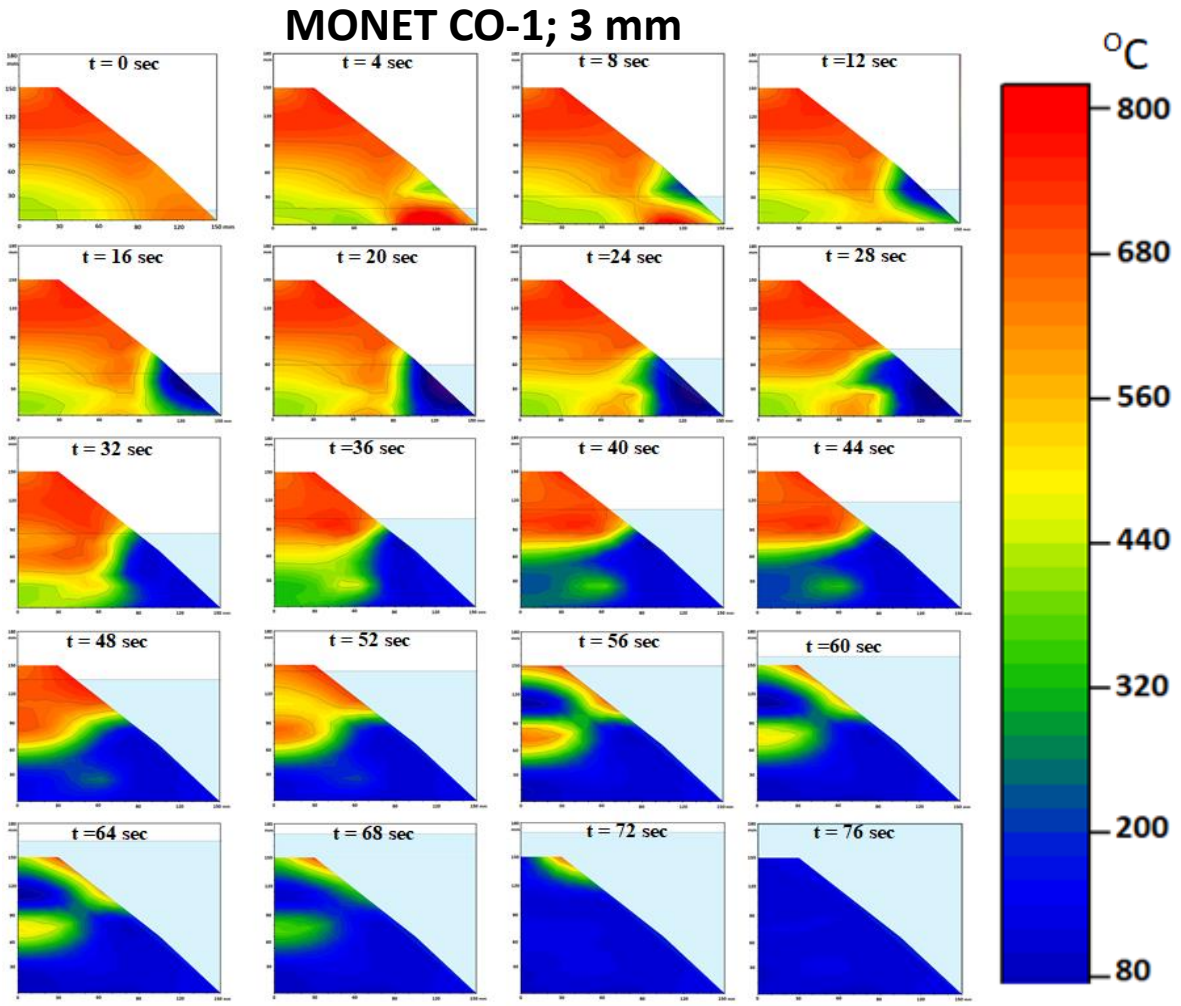

04 Results

Research Objective: Quenching Phenomena in High Temperature Cylindrical Debris Bed: MONET Tests

MONET-CL-1, (Alumina, ~3 mm)



Bottom closed

MONET-CL-2, (Alumina, ~3 mm)

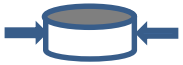

Top & Bottom closed

MONET-CL-3, (Al & SS, ~2 - 3.5 mm)

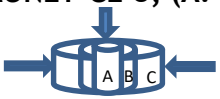

Bottom closed

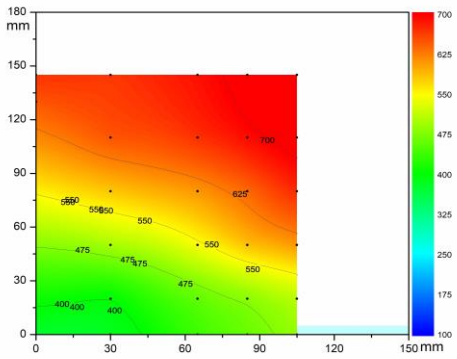



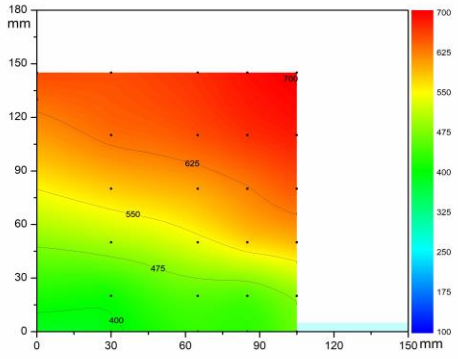



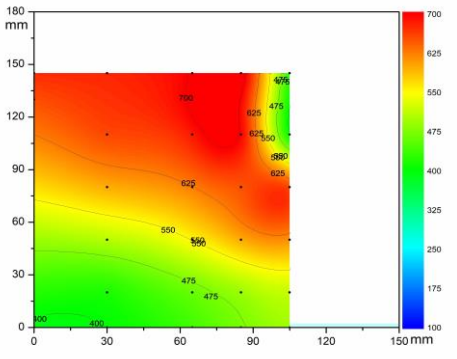



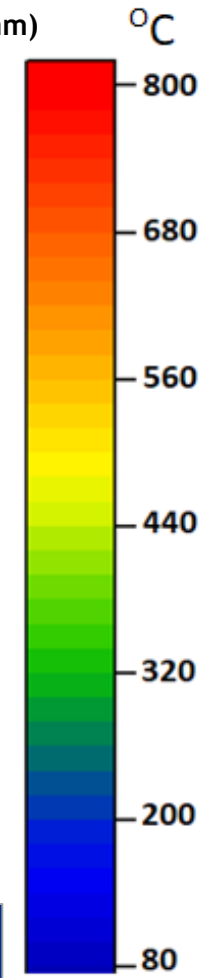

Development of "dry zones" can be seen in the contour curve for the case of MONET-CL in the center top locations

05 Conclusion

Research Objective: Quenching Phenomena in High Temperature Cylindrical Debris Bed: MONET Tests

- ✓ Significant variation in the quenching behaviour of porous bed can be observed with different bed configurations
- ✓ Cooling rates were higher for MONET-CO in higher bed positions compared to MONET-CL because of higher water ingression rates for conical bed.
- ✓ "**Dry zones**" development can be noticed in the lower bed region for MONET-CO tests.
- ✓ While the "**Dry zones**" can be noticed in the top center locations in case of MONET-CL tests.
- ✓ "Pre-liminary" tests suggests that bed internal configuration have greater effect in bed coolability compared to boundary configurations



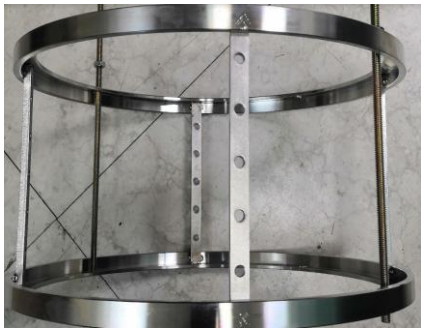

"Internal bed configuration" can significantly affect the quenching behavior of debris bed

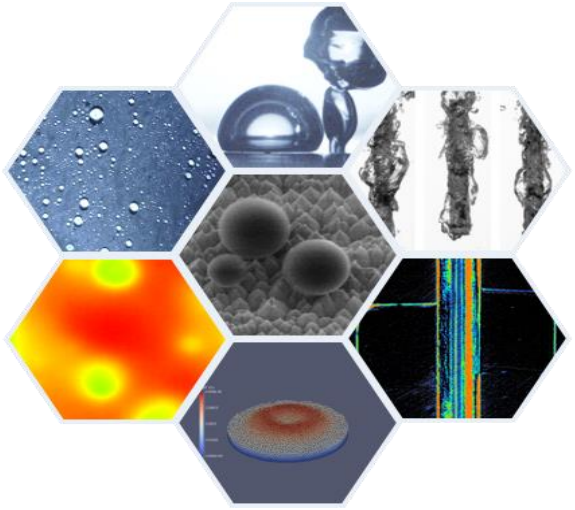

Thank you

THERMODYNAMICS OF AEROSOLS DURING A MOLTEN CORE-CONCRETE INTERACTION AT FUKUSHIMA DAIICHI UNIT 2 ESTIMATED CONDITIONS

Hugo LAFFOLLEY[1,2], Christophe JOURNEAU[1], Sarah THILLIEZ[1], Bernd GRAMBOW[2]
[1]: CEA, DES, IRESNE, DTN, Severe Accident Experimental Laboratory, Cadarache F-13108 St-Paul-lez-Durance, France
[2]: SUBATECH (IMT Atlantique, CNRS-IN2P3, University of Nantes) 44307 Nantes, France

hugo.laffolley@cea.fr
christophe.journeau@cea.fr
sarah.thilliez@cea.fr
grambow@subatech.in2p3.fr

ABSTRACT

Several radioactive releases from Containment Vessel took place during all the events that led to Fukushima Daiichi end state. Depending on the unit involved in the venting and on the progress of the accident, radionuclides released into the environment can differ in their composition or chemical form. These differences may result from the path of the radionuclides from the core to the environment (e.g. through suppression pool water) and from the chemico-physical properties inside the reactor core and containment.

On March 14th and 15th 2011, spherical glassy Cs-bearing microparticles (type-A CsMP) were collected for the first time. These microparticles might result from a Molten Core-Concrete Interaction (MCCI) inside unit 2, when the zircaloy from the fuel cladding interacted with the SiO_2 of the concrete pedestal at high temperature. In other words, a phenomenon of vaporization-condensation might be responsible for the CsMP generation.

Calculations using ThermoCalc with OECD/NEA's database TAF-ID version 11 have been carried out on the thermodynamics of vaporization during an MCCI to find correlations between the chemico-physical properties of the atmosphere of the reactor and the chemical composition of type-A CsMP. Data from ORIGEN2 and MELCOR calculations have been used to estimate the composition of the core melt and of the atmosphere at the supposed time when RPV failure occurred.

The vapour temperature from which type-A CsMP may have condensed in the containment has been evaluated. Using Fe/Si, U/Si and Cs/Si as tracers, it suggests that type-A CsMP might result from condensation of vapours around 2000-2200°C from a low oxidised composition of corium, rich in zirconium and poor in stainless steel.

KEYWORDS
Molten core-concrete interaction, Aerosol, CsMP, TAF-ID

1. INTRODUCTION

In March 2011, the Fukushima Daiichi Nuclear Power Station (FDNPS) experienced severe accidents triggered by a magnitude 9.0 earthquake followed by a tsunami, causing airborne radioactive releases on Japanese lands and in the Pacific Ocean [1]. Airborne monitoring of the air dose rate and soil contamination survey have been carried out following the accident to investigate the scope of the releases.
Cs^{134} and Cs^{137} (half-life of 2.2 years and 30 years respectively [2]) are among the most volatile and abundant fission products of a reactor core [3] and are commonly used as tracers for radionuclide releases. It has been estimated that the total release of Cs^{137} caused by the FDNPS is in the range of 20.1 to 53.1 PBq [4]. Chemical forms and properties of radionuclides can differ according to their source or their path from the fuel pellet to the atmosphere and may have a significant impact on their behaviour in the environment.

In the days following the initiating events (i.e. earthquake and tsunami), a research team located in Tsukuba city, Ibaraki prefecture (Japan) at 170 km south-west from the FDNPS discovered a new kind of radioactive particles collected on an atmospheric filter [5]. The study reports Si-rich spherical particles with a size around 2µm and containing radiocesium. Further analysis confirmed the amorphous SiO_2 matrix of these Cs-bearing microparticles (CsMP) in addition with the presence of other major elements (Cs, K, Rb, Fe, Zn, etc.) [6] and a very recent work reports also a high content in C [7] or the presence of segregated phases of U [8]. Due to this silica matrix, CsMP have a very low solubility that confers to them an unalike behaviour (compared to cesium salts for instance) in the environment (low impact of weathering [9]) or in the respiratory system [10, 11]. Analysis of surface soil samples estimate that CsMP may represent 30% of the radioactive fraction under the trajectory of major plumes and even more that 40% of the radioactive fraction in some specific sample spots [12].

As a major concern for the environment and health, research on CsMP has been actively conducted to evaluate their composition, their solubility, their abundance, etc. [6]. However, the physicochemical phenomenon that lead to their formation is still subject to lots of uncertainties. In the perspective of improving the knowledge on their generation process, this paper reports thermodynamics calculations using composition and results of the Benchmark Study of the Accident at Fukushima Daiichi Nuclear Power Station (BSAF) project [13] and chemical analysis of collected CsMP.

2. HYPOTHESIS AND DATA INPUT PARAMETERS

2.1. Database and Calculation Software

2.1.1. Database

Calculations are carried out using the Thermodynamics of Advanced Fuels – International Database (TAF-ID) version 11 developed by OECD/NEA. The TAF-ID has been established with the Calphad method and is designed for calculations on nuclear fuels. Fission products (FP) and structural materials are also taken in count to provide results under normal operation and accidental conditions of a reactor core [14]. In total, 43 elements are available in the TAF-ID.

For this study, the TAF-ID has been chosen for its larger number of elements and especially the availability of nitrogen and cesium.

2.1.2. Calculation software

The software chosen for the thermodynamics calculations is Thermo-Calc (versions 2017b and 2019a). Thermo-Calc is a calculation software based on the Calphad method compatible with the TAF-ID [14].

2.2. Hypothesis

2.2.1. Generation process

The knowledge on the generation process of CsMP is still hazy but three major hypothesis have been made. The silica matrix implies that the generation process must include an abundant source of silicon. It could be: stainless steel from the Reactor Pressure Vessel (RPV) and from the structural materials [15], insulating materials from the primary loop [16] or concrete from the pedestal after Lower Head Failure (LHF) [9], [17].

This work focuses on the concrete as the source of silicon via Molten Core-Concrete Interaction (MCCI). When non-oxidised zirconium from the fuel rod cladding hits the concrete pedestal, a highly exothermic chemical reaction takes place [18].

$$Zr + SiO_2 \rightarrow Si + ZrO_2 + 2.1\ MJ/kg\ of\ Zr \quad (1)$$

This reaction occurs simultaneously with an incomplete reaction forming $SiO_{(g)}$ instead of Si as the temperature increases [19].

$$Zr + 2 \cdot SiO_2 \rightarrow 2 \cdot SiO_{(g)} + ZrO_2 \quad (2)$$

With a sufficient partial pressure of oxygen, the oxidation of silicon can then be complete and form silica. Once gaseous silicon species are generated from a hot spot, their migration through convection to a colder spot of the Primary Containment Vessel (PCV) causes condensation to form microparticles of amorphous silica. At the same time, other volatile species such as Cs (maybe as CsOH) or Fe (maybe as an oxide) may be trapped inside the growing particles. This whole process is referred as a reaction of evaporation-condensation.

2.2.2. Unit of origin

During the FDNPS accident, units 1 (1F1), 2 (1F2) and 3 (1F3) underwent a loss of coolant in the primary loop, resulting in a partial or total melting of the reactor core [1]. Through the burn up ratio of each fuel assembly, the ORIGEN2 code gives analytical results on the amount of radionuclides inside every reactor core and spent fuel pools [20]. Nuclear fuels of a reactor core are never renewed entirely at each reloading, but rather partly as well as relocalised to optimise the energy recover from the fuel. Thus, radionuclides amount varies significantly depending on subassembly history. In the case of a partly molten core, it is therefore imprecise to conclude on the local amount of radionuclides from a global point of view. However, analytical results from the ORIGEN2 code show that on the 11th of March, the $^{134}Cs/^{137}Cs$ activity ratios for 1F1, 1F2 and 1F3 were 0.941, 1.08 and 1.05 respectively [20]. Therefore, the so-called Type-A CsMP (i.e. those with a diameter under 10 µm and a high specific radioactivity [6]) have been associated to 1F2 or 1F3 due to their $^{134}Cs/^{137}Cs$ activity ratio generally higher than 1.0 even though heterogeneities exist in each of the three reactor cores. It is currently uncertain if Type-A CsMP come from 1F2, 1F3 or both of them. A TEPCO report yet refers to a glassy particle that can be identified as a Type-A CsMP, found on the operating floor of the unit 2 reactor building [21]. In this study, 1F2 is therefore considered as the hypothetical unit of origin of CsMP for calculation.

2.2.3. Choice of elemental tracers

Quantitative or semi-quantitative chemical analysis of major species in CsMP have been reported in references [7, 22, 23]. The chemical composition of CsMP may be considered as an indicator of the chemical conditions existing in the reactor at the time they were formed. Thus, thermodynamic calculations on the gas phase could be used as a forensic tool to determine physicochemical conditions inside the reactor.

Si, Fe, U, and Cs are used as chemical tracers and have been chosen according to their availability in the TAF-ID, their availability in the literature on CsMP compositions and the capacity to quantify the initial content of this element in the melt pool involved in the MCCI.

From the chemical analysis conducted on 37 type-A particles, Table I has been established [7].

Table I. Minimum, median and maximum values for the chosen tracers.

Element	Minimum	Median (spherical)	Median (non-spherical)	Maximum
Fe/Si	0.10	0.23	0.19	0.33
U/Si	-	0.0015	0.0021	0.014
Cs/Si	0.019	0.069	0.077	0.23

2.3. Data Input Parameters

2.3.1. Reactive atmosphere composition and physical properties

During the first years after the accident, it was unclear if unit 2 RPV went through a Lower Head Failure (LHF) and if the fuel had totally or partially relocated on the concrete pedestal [24]. Later on, camera inspections of the unit 2 PCV reported fuel debris on the concrete pedestal and confirmed the RPV failure [25]. There are still a lot of uncertainties on the time LHF occurred, some institutes of the BSAF project estimate that it happened between 83h and 129h after scram but the first isolated CsMP have been collected between 78h and 90h after scram.

During the period of time in which CsMP could have been generated, the PCV pressure may have varied from 1 bar(abs.) to 7 bar(abs.) and the atmosphere composition may have changed, mainly due to water vaporisation, dihydrogen production by zirconium oxidation by water and volatile FP release. MELCOR code calculations by Sandia National Laboratories* report that in the 10 hours before LHF, the atmosphere could have been composed of a few percent of dihydrogen, a few percent (or tenth of percent) of dioxygen and 40% to almost 100% of water vapour (while the balance is made by nitrogen and FP). The following calculations only consider N_2 and H_2O for the atmosphere composition due to a negligible impact of a few percent of H_2 and O_2 on thermodynamic equilibria. This assumption is supported by calculations made using a few percents of H_2 and/or O_2 to check the evolution of the system. Initially, with an atmosphere composed of H_2O and N_2, the gas phase naturally contains a significant fraction of H_2 (high content of H in the system due to H_2O) and a negligible fraction of O_2. Hence, adding O_2 in the composition only affects the H_2O fraction as the O_2 immediately combines to H_2 to form H_2O. Adding H_2 to the system increase the already high H_2 fraction increasing the reducing potential.

2.3.2. Corium composition

For the assumed chemical reactions (1) and (2), a large quantity of Si and Zr needs to be available, meaning that the corium cannot be fully oxidised when contacting concrete. Table II and Table III list in-vessel and ex-vessel composition from the BSAF project. KAERI composition will not be used as it is only composed of stainless steel and its oxides [13].

2.3.3. Concrete composition

The concrete used for the FDNPS building is a basaltic concrete. Its composition has been estimated from analytical results of samples collected on 1F1 reactor building : SiO_2 = 59.6%wt., Al_2O_3 = 14.7%, CaO = 12.2%, H_2O = 7.8% et Fe_2O_3 = 5.7% [26].

* Results provided by David L. Luxat from Sandia National Laboratories from MELCOR code calculations.

Table II. Unit 2 in-vessel corium composition (data from chart [13]).

	Institutes					Average	
Species (%.wt)	**CIEMAT**	**CRIEPI**	**IAE**	**IBRAE**	**KAERI**	**All institutes (Ci1)**	**Except IBRAE & KAERI (Ci2)**
UO_2	55	30	16	49	0	30	34
Zr	29	52	16	51	0	30	32
ZrO_2	10	6	45	0	0	12	20
SS†	5	10	9	0	86	22	8
SS Oxides	0	0	12	0	14	5	4
B_4C	1	2	2	0	0	1	2

Table III. Unit 2 ex-vessel corium composition (data from chart [13]).

	Institutes			Average	Initial Inv. (Ce2)
Species (%.wt)	**IBRAE**	**IRSN**	**JAEA**	**All institutes (Ce1)**	
UO_2	40	53	48	47	52
Zr	9	6	6	7	17
ZrO_2	10	24	19	18	0
SS	41	17	27	28	31

3. RESULTS

3.1. Sensibility Analysis

CIEMAT composition is used as a reference composition for the sensibility analysis for its intermediate behaviour among the others. The sensibility analysis concentrates on the variation of the Fe/Si molar rate as a function of temperature, depending on three parameters described in the following paragraph.

Except the corium composition and the MCCI progression rate, three uncertain parameters have been identified as possibly influential on the results: the system pressure (i.e. PCV pressure), the atmosphere composition (i.e. H_2O vapour fraction in nitrogen) and the mass ratio between the corium and the atmosphere in interaction with the corium. The sensibility is evaluated by determining the condition for which a Fe/Si ratio of 0.30 called hereafter the Reference Value (RV) is achieved. This ratio is close to the upper value of the Fe/Si ratio valid range for environmental CsMP (Table I).

3.1.1. System pressure

The system pressure variation does not seem to have a significant influence on the RV in the range 1-7 bar(abs.). The RV temperature varies between 1898°C and 1895°C, corresponding to a variation of 0.1% on the average temperature. The pressure variation is consequently considered as a negligible effect on the temperature at which the Fe/Si ratio meets the optimum composition for CsMP generation (Figure 1).

† Stainless steel (type 304)

3.1.2. Atmosphere composition

The analysis shows that the composition of the PCV atmosphere needs to have a H_2O content higher than 15% for the calculation to converge in our scope of study. From 15% to 100% of H_2O, the RV temperature varies of 0.6% on the average temperature. Hence, calculations need to be done with more than 15% of H_2O, which seems conceivable with the accident scenario and the variations above 15% of H_2O are considered negligible (Figure 1).

3.1.3. Mass ratio between corium and atmosphere in the control volume

The quantity of atmosphere considered in our control volume is the mass of atmosphere being in equilibrium with our chemical reaction as an approximation of kinetic effects in the real case MCCI. The analysis on the mass ratio between corium and atmosphere is conducted for a ratio greater than 0.25 because either calculations do not converge for lower ratios or they provide inconsistent results in terms of temperature (Figure 1).

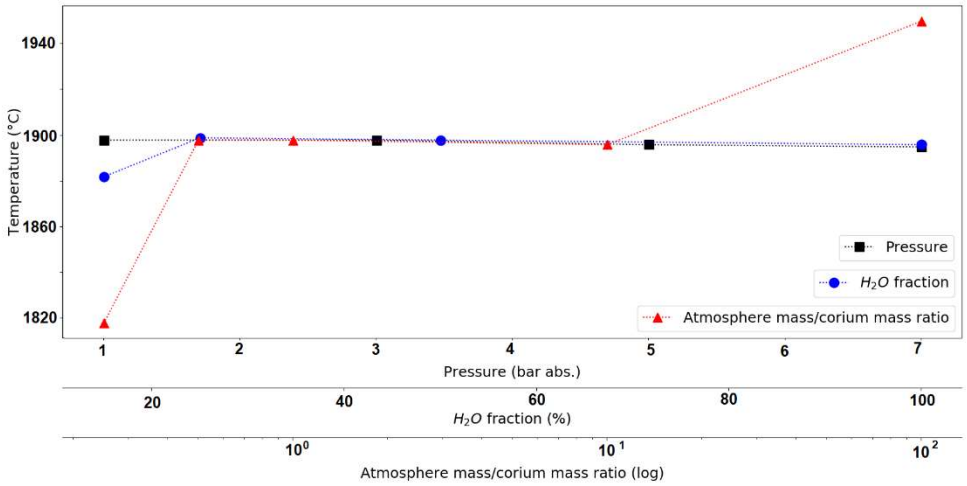

Figure 1. Sensibility analysis on three parameters considering a fixed Fe/Si ratio of 0.30.

3.1.4. Forms of Si, Fe, U and Cs in the gas phase

The assumption of using Fe/Si, U/Si and Cs/Si as tracers suggest that all forms of Si, Fe, U and Cs contribute to the generation process of CsMP. To support this hypothesis, calculations on the CIEMAT composition have been conducted to study gas species and their proportions (species below 0.01% of the gas phase where ignored).

The major Si species in the gas phase are SiO and SiO_2. They are considered to entirely take part in the generation process of the silica matrix composing the CsMP. The major Fe species in the gas phase are Fe and FeO. It has been analysed that Fe mainly exists as a divalent cation in CsMP (except on the surface layer, maybe due to weathering in the environment) as in its oxidation state in the FeO molecule [27]. The metallic Fe is subject to a probable oxidation in the humid atmosphere as well as SiO, leading to form iron oxide also. The major U species in the gas phase are UO_2 and UO_3, these oxides are likely to directly participate in the low fraction included in CsMP. In the gas, calculations implies that Cs only exists significantly as its atomic form. Literature reports the existence of CsOH in a humid atmosphere but as the temperature increases, CsOH tends to dissociate (around 1800°C-2200°C), especially if the atmosphere is rather reducing [28]. In association with other elements not taken into account in our calculations, Cs can usually also form other species such as CsI, $Cs_xMo_yO_z$, $Cs_xB_yO_z$, $Cs_xRu_yO_z$, etc. [29]. CsI is a major concern as I is also an significant FP, but experiments showed that in steam atmosphere, only 10% of Cs would form CsI against 90% CsOH [30].

3.2. Evaluation of CsMP's Temperature of Generation without FP

While MCCI occurs, at a given moment, only a fraction of corium, of concrete and of gas take part in the reaction. Even though these calculations are made at the thermodynamic equilibrium, by considering the right fraction of each component of the system, an approximation on the kinetic effect can be achieved. The following calculations consider three cases according to the fraction of concrete in the system, representing a local corium-concrete interface condition.

3.2.1. Corium rich system

A corium rich system is simulated by a Si/Zr molar ratio of 0.10 (3.2%wt. of concrete for CIEMAT composition). For every corium composition (cf. Table II & Table III), this early phase MCCI simulation does not reach any satisfying criteria for Fe/Si and U/Si. This case may not provide a sufficient amount of volatile Si species as equation (1) and (2) show a needed molar ratio between 1 and 2 to be in stoichiometric conditions.

3.2.2. Si-Zr equimolar system

This case is simulated by a Si/Zr molar ratio of 1 (25% to 50%wt. of concrete for all of the in-vessel compositions except IAE and KAERI).

Fe is a satisfying tracer as it is found as a major element in CsMP. Moreover, Fe benefits from a consequent feedback on its thermodynamic behaviour since it has been a major concern for industry development. Figure 2a shows that in the scope of this study, only four compositions reach the Fe/Si target range. These corium compositions are only in-vessel compositions, hence with a lower content in stainless steel (except KAERI) than ex-vessel compositions, implying that the initial stainless steel content influences directly the Fe/Si ratio in the gas and has to be moderate to satisfy the criteria. Except for the IBRAE composition, the Fe/Si molar ratio in the gas phase seems to remain in the target range from its entry temperature to the end of the calculation range. It should be noted that IBRAE composition is a simplified composition since it is only composed of uranium oxide and non-oxidised zirconium, thus essential components taking part in the chemical reactions such as stainless steel, stainless steel oxides, zirconia and boron carbide are missing. Ci2 and CRIEPI compositions have a Zr content significantly different but show a pretty similar behaviour between 1900°C and 2600°C, meaning that the stainless steel content is more likely to be the only parameter driving the Fe/Si ratio value, without influence of the silicon aerosols generation. At these conditions, it seems that CsMP may have been generated at a temperature above 1800-1900°C. Also, these results do not seem to show a clear temperature upper limit, but MCCI may occur at lower temperature than fuel melting temperature since concrete ablation can generally exist below 1500°C [18]. The temperature is hugely dependent on the heat dissipation and production rate. These parameters are especially influenced by the debris physical configuration, the cooling efficiency (in case of cooling system operating), the time elapsed from reactor scram, the exothermic oxidation reactions rate, etc.

Uranium is also a tracer of choice since its origin is clearly identified from a single source. However, unlike Fe, U is a minor element in CsMP requiring highly precise instruments to be quantified or even detected in some particles. U, as well as Fe and Zn, might also exists as segregated phases in some particles due to the capture of more minute particles in suspension in the atmosphere during CsMP growth. Figure 2b shows that no composition reach the maximum content of CsMP. One or several parameters in the composition yet have a significant influence on the U/Si ratio since its value varies significantly depending on the corium composition. The initial U content does not seem to have a substantial influence since CRIEPI, Ci1 and Ci2 compositions contain almost the same amount of U but have a different behaviour. The environment is more likely to drive these variations since the corium oxidation rate seems to significantly influence U/Si ratio : among these five corium compositions, the highest the Zr/ZrO_2 mass ratio in the composition is, the lowest the U/Si ratio in the gas phase is, with the only exception of IAE composition which have the lowest Zr/ZrO_2 mass ratio. This exception is justified by the fact that IAE composition is the only one that contains stainless

steel oxides while the others contain only metallic stainless steel. This result agrees with the binary diagram U-O that suggest that the vaporisation temperature of uranium oxides decreases with the rate of oxygen increasing in the system [31]. Even if target U/Si ratio values are not reached for any composition, the CRIEPI composition flirt with the upper value around 2200°C.

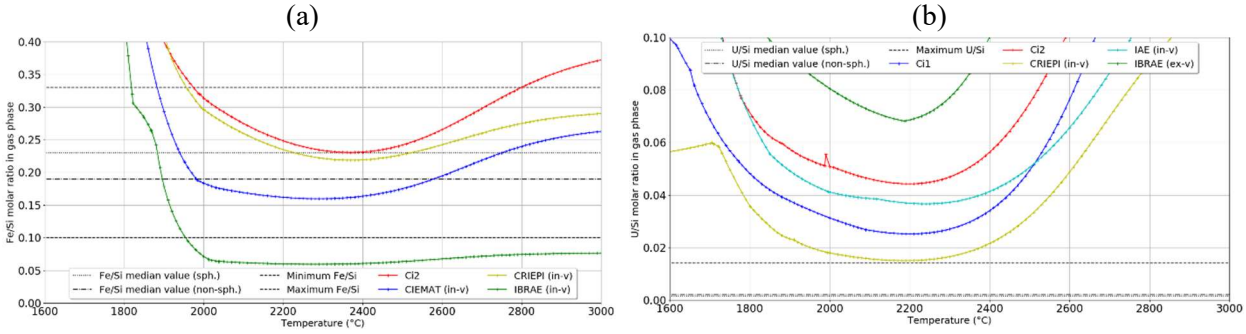

Figure 2. Temperature dependence of Fe/Si (a) and U/Si (b) molar ratio in the gas phase at Si/Zr=1 for different corium composition.

3.2.3. Concrete rich system

The concrete rich system is simulated by a Si/Zr ratio of 10, which represents more than 75%wt. of concrete for most compositions (66%wt. for IAE composition). It may represent local composition near the corium-concrete interface.

In this configuration, the different compositions seems to have a more similar behaviour (explained by the dilution of corium in concrete) with a smaller range of temperature for the same Fe/Si ratio value (Figure 3a). All the in-vessel compositions enter the target range between 1900°C and 2100°C and most of them remain in the Fe/Si ratio valid range (Table I) until 3000°C. Except IAE and Ci1 compositions, the median values are reached in the range 2000-2200°C.

A higher content in concrete also has the effect of lowering the U fraction in the gas phase. Figure 3b shows that the temperature range for a valid U/Si ratio (Table I) value starts at higher temperature. Most of the in-vessel compositions are close to the U/Si ratio median values around 2500-2600°C.

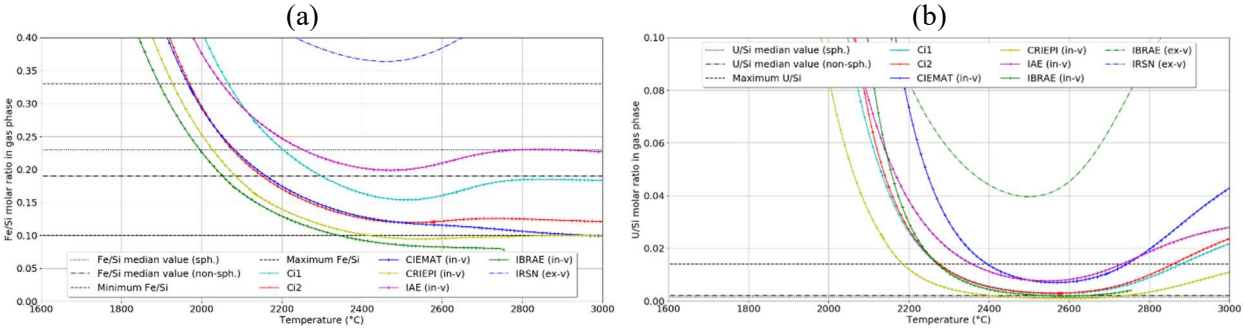

Figure 3. Temperature dependence of Fe/Si (a) and U/Si (b) molar ratio in the gas phase at Si/Zr=10 for different corium composition.

3.3. Adding Cs

The inventory of Cs in the reactor core of unit 2 (3 days after scram) has been calculated around 1.9×10^{2} kg (all Cs isotopes included), which represents 2.1×10^{-3} % of the total mass of U in the core [20]. Considering the BSAF conclusions on unit 2, it has been estimated for most of the institutes that the mass fraction of the

total Cs inventory does not exceeds 3% in the dry well and 10% in the water of the suppression chamber [32].

For further calculations, CIEMAT in-vessel composition has been chosen as the reference composition as a compromise for its intermediate behaviour in Fe/Si analysis among all the other satisfying compositions. The true content of Cs participating in the generation process of CsMP is hardly definable, in particular since there may be Cs aerosol deposited on the concrete prior to corium relocation on it. Thus two cases are considered in the Figure 4: 100% and 1% of the total Cs inventory of the reactor core (3 days after scram). These two cases are extreme values of Cs content ; the real situation is supposedly between these two cases. Consequently, the temperature range that corresponds to an acceptable Cs/Si ratio is 1650°C-2300°C and more specifically 1750°C-2150°C with median values.

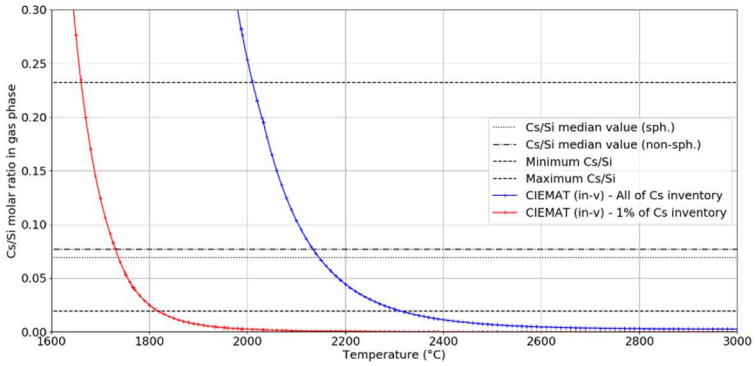

Figure 4. Temperature dependence of Cs/Si molar ratio in the gas phase at Si/Zr=1 for CIEMAT composition.

4. DISCUSSION

In the case of a Si-Zr equimolar composition, the gas phase seems too rich in U species and no composition reach the target range. The heterogeneity of corium could cause a phenomenon where a part richer in zirconium and impoverished in uranium oxide is more likely to form CsMP, and thus, providing less or no U in the growing process of the droplet. This assumption is supported by the CRIEPI composition calculations (highest Zr/UO_2 ratio) which shows the lowest U/Si.

Temperatures with a U/Si ratio value in the target range (Figure 3b) match with upper temperatures for Fe/Si ratio (Figure 2a and Figure 3a). It has been a few decades since numerous MCCI experiments have been conducted aiming to study interactions and temperatures of interaction. An early phase MCCI can have a melt temperature close to 2500°C due to the high decay heat of FP and the exothermic oxidation reactions. At the interface, the temperature is usually lower than the calculated conditions for CsMP generation. However, Zr oxidation could locally provide a high temperature due to the exothermicity of the reaction and also provide the suboxidised Zr needed to react with the silica. Then, gas generation could create enough convection to maintain the generation process until the oxidation rate of Zr and the concrete fraction in the melt are too high to keep the temperature sufficiently high and the reaction between silica and Zr going on.

Calculations also show that stainless steel content influences directly Fe/Si ratio. Ex-vessel compositions usually contain a high amount of stainless steel, as the internals have been molten. In order to have a limited amount of stainless steel in the interaction composition, two possibilities are suitable : the low amount of debris could be justified by a limited ablation of the internals, resulting in a low amount of stainless steel in the melt ; or, the melt could undergo heterogeneities creating a region impoverished in stainless steel and rich in suboxidised zirconium in favour of this behaviour.

Calculations on aluminium have also been carried out but do not appear in the results as the Al/Si molar ratio was constantly 10 times lower than the median values of the literature at best. This suggests that the source of Al could be underestimated (more in concrete or omission of another source) or that Al interactions modelling needs to be improved.

5. CONCLUSION

As stated by Miura et al. [33], type-A CsMP are very likely to result from condensation of SiO vapours, especially due to their spherical shape. However, the authors conclude that the silicon of type-A CsMP comes from the eluting of the suppression chamber paint (Si < 5%wt.). Calculations reported in this present work show that a rather Si rich system would be more suitable for CsMP mass production along with a corresponding chemical composition. This statement goes in the same direction of an IRID report assuring that the SiO_2/K_2O ratio from the paint is significantly different from the average composition ratio of CsMP, concluding that the paint could not be the only source of silicon for CsMP generation [34].

MCCI is likely to be responsible for the generation process of CsMP. If the chemical composition of CsMP can be considered as an indicator of the atmosphere at the time they were formed, the corium composition that resulted in their formation may be closer to an in-vessel corium with a low oxidisation rate. The calculations also suggest that the temperature was around 2000-2200°C, higher than the interface temperature of an MCCI, possibly in a heavy metal zone, close to the concrete, rich in zirconium and relatively poor in stainless steel.

It should be noted that all these calculations were achieved at the thermodynamic equilibrium. However, high temperatures are generally in favour of thermodynamics as temperature is a kinetic factor, hence these calculations may provide a good estimation.

This paper is also a preliminary work for a set of trials carried out on the experimental facility VITI on the PLINIUS platform at the CEA Cadarache [35]. These calculations will help to set the initial experimental parameters with the aim of generate CsMP through MCCI.

ACKNOWLEDGMENTS

We acknowledge the helpful contribution of David L. Luxat from the Sandia National Laboratories for kindly providing us results calculated on the MELCOR code about the atmosphere inside the unit 2 PCV.

REFERENCES

[1] IAEA, Ed., *The Fukushima Daiichi accident*. Vienna: International Atomic Energy Agency, 2015.
[2] H. L. Finston and M. T. Kinsley, 'The radiochemistry of cesium', NAS-NS--3035, 4003916, Feb. 1961. doi: 10.2172/4003916.
[3] Y. Pontillon, G. Ducros, and P. P. Malgouyres, 'Behaviour of fission products under severe PWR accident conditions VERCORS experimental programme—Part 1: General description of the programme', *Nuclear Engineering and Design*, vol. 240, no. 7, pp. 1843–1852, Jul. 2010, doi: 10.1016/j.nucengdes.2009.06.028.
[4] A. Stohl *et al.*, 'Xenon-133 and caesium-137 releases into the atmosphere from the Fukushima Dai-ichi nuclear power plant: determination of the source term, atmospheric dispersion, and deposition', *Atmospheric Chemistry and Physics*, vol. 12, no. 5, pp. 2313–2343, Mar. 2012, doi: 10.5194/acp-12-2313-2012.
[5] K. Adachi, M. Kajino, Y. Zaizen, and Y. Igarashi, 'Emission of spherical cesium-bearing particles from an early stage of the Fukushima nuclear accident', *Sci Rep*, vol. 3, no. 1, p. 2554, Dec. 2013, doi: 10.1038/srep02554.
[6] Y. Igarashi *et al.*, 'A review of Cs-bearing microparticles in the environment emitted by the Fukushima Dai-ichi Nuclear Power Plant accident', *Journal of Environmental Radioactivity*, vol. 205–206, pp. 101–118, Sep. 2019, doi: 10.1016/j.jenvrad.2019.04.011.

[7] H. Hagiwara, H. Funaki, N. Shiribiki, M. Kanno, and Y. Sanada, 'Characterization of radiocesium-bearing microparticles with different morphologies in soil around the Fukushima Daiichi nuclear power plant', *Journal of Radioanalytical and Nuclear Chemistry*, Oct. 2021, doi: 10.1007/s10967-021-08061-8.
[8] E. Kurihara *et al.*, 'Particulate plutonium released from the Fukushima Daiichi meltdowns', *Science of The Total Environment*, vol. 743, p. 140539, Nov. 2020, doi: 10.1016/j.scitotenv.2020.140539.
[9] T. Ohnuki, Y. Satou, and S. Utsunomiya, 'Formation of radioactive cesium microparticles originating from the Fukushima Daiichi Nuclear Power Plant accident: characteristics and perspectives', *Journal of Nuclear Science and Technology*, vol. 56, no. 9–10, pp. 790–800, Oct. 2019, doi: 10.1080/00223131.2019.1595767.
[10] T. Okumura, N. Yamaguchi, T. Dohi, K. Iijima, and T. Kogure, 'Dissolution behaviour of radiocaesium-bearing microparticles released from the Fukushima nuclear plant', *Sci Rep*, vol. 9, no. 1, p. 3520, Dec. 2019, doi: 10.1038/s41598-019-40423-x.
[11] M. Suetake *et al.*, 'Dissolution of radioactive, cesium-rich microparticles released from the Fukushima Daiichi Nuclear Power Plant in simulated lung fluid, pure-water, and seawater', *Chemosphere*, vol. 233, pp. 633–644, Oct. 2019, doi: 10.1016/j.chemosphere.2019.05.248.
[12] R. Ikehara *et al.*, 'Abundance and distribution of radioactive cesium-rich microparticles released from the Fukushima Daiichi Nuclear Power Plant into the environment', *Chemosphere*, vol. 241, p. 125019, Feb. 2020, doi: 10.1016/j.chemosphere.2019.125019.
[13] M. Pellegrini *et al.*, 'Main Findings, Remaining Uncertainties and Lessons Learned from the OECD/NEA BSAF Project', *Nuclear Technology*, pp. 1–15, Apr. 2020, doi: 10.1080/00295450.2020.1724731.
[14] C. Guéneau *et al.*, 'TAF-ID: An international thermodynamic database for nuclear fuels applications', *Calphad*, vol. 72, p. 102212, Mar. 2021, doi: 10.1016/j.calphad.2020.102212.
[15] L. Zheng, B. Yan, B. Peng, H. Li, Z. Jiang, and S. Ueda, 'A proposed formation mechanism of the Type-A radiocaesium-bearing microparticles released from Units 2/3 during the Fukushima Daiichi Nuclear Power Plant accident', *Journal of Nuclear Materials*, vol. 563, p. 153623, May 2022, doi: 10.1016/j.jnucmat.2022.153623.
[16] M. Rizaal, K. Nakajima, T. Saito, M. Osaka, and K. Okamoto, 'Investigation of high-temperature chemical interaction of calcium silicate insulation and cesium hydroxide', *Journal of Nuclear Science and Technology*, vol. 57, no. 9, pp. 1062–1073, Sep. 2020, doi: 10.1080/00223131.2020.1755733.
[17] N. Fujita, K. Ninomiya, Z. Zhang, A. Shinohara, and T. Yoshimura, 'Production simulation experiments of the insoluble Cs-concentrated particles released by the FDNPP accident and their imaging on a filter', *Proceedings of the 18th Workshop on Environmental Radioactivity*, 2017.
[18] OECD/NEA, 'State-of-the-Art Report on Molten Corium Concrete Interaction and Ex-Vessel Molten Core Coolability', no. NEA/CSNI/R(2016)15, p. 365, 2017.
[19] H. Alsmeyer *et al.*, 'Molten corium/concrete interaction and corium coolability: a state of the art report', *EUR(Luxembourg)*, 1995.
[20] K. Nishihara, H. Iwamoto, and K. Suyama, 'Estimation of fuel compositions in Fukushima-Daiichi nuclear power plant', Japan, 2012. [Online]. Available: http://inis.iaea.org/search/search.aspx?orig_q=RN:44087069
[21] TEPCO, 'Analyses of samples related to inside survey of primary containment vessel of Unit 1-3, FDNPP.', 2018. [Online]. Available: http://irid.or.jp/wpcontent/ uploads/2018/07/20180726_02.pdf
[22] T. Kogure *et al.*, 'Constituent elements and their distribution in the radioactive Cs-bearing silicate glass microparticles released from Fukushima nuclear plant', *Microscopy (Tokyo)*, vol. 65, no. 5, pp. 451–459, Oct. 2016, doi: 10.1093/jmicro/dfw030.
[23] N. Yamaguchi, M. Mitome, A.-H. Kotone, M. Asano, K. Adachi, and T. Kogure, 'Internal structure of cesium-bearing radioactive microparticles released from Fukushima nuclear power plant', *Scientific Reports*, vol. 6, no. 1, Apr. 2016, doi: 10.1038/srep20548.

[24] M. Pellegrini *et al.*, 'Benchmark Study of the Accident at the Fukushima Daiichi Nuclear Power Plant (BSAF Project) - Phase I Summary Report', p. 53, Feb. 2016.
[25] D. Peko, S. Kraft, and J. Rempe, 'Working together to enhance nuclear reactor safety', p. 7.
[26] V. Bouyer *et al.*, 'Large scale Vulcano molten core-concrete interaction test considering Fukushima Daiichi condition', no. 107, p. 13, 2019.
[27] T. Okumura, N. Yamaguchi, H. Suga, Y. Takahashi, H. Segawa, and T. Kogure, 'Reactor environment during the Fukushima nuclear accident inferred from radiocaesium-bearing microparticles', *Sci Rep*, vol. 10, no. 1, p. 1352, Dec. 2020, doi: 10.1038/s41598-020-58464-y.
[28] L. Devell and K. Johansson, 'Specific features of cesium chemistry and physics affecting reactor accident source term predictions', OECD/NEA and SKI, SKI Report 94:29, Aug. 1994.
[29] M. Osaka, M. Gouëllo, and K. Nakajima, 'Cesium Chemistry in the LWR severe accident and towards the decommissioning of Fukushima Daiichi Nuclear Power Station', *Journal of Nuclear Science and Technology*, pp. 1–14, Dec. 2021, doi: 10.1080/00223131.2021.1997664.
[30] M. F. Osborne and R. A. Lorenz, 'ORNL studies of fission product release under LWR severe accident conditions', *nuclear safety*, vol. 33, no. 3, pp. 344–365, 1992.
[31] C. Guéneau *et al.*, 'Thermodynamic modelling of advanced oxide and carbide nuclear fuels: Description of the U–Pu–O–C systems', *Journal of Nuclear Materials*, vol. 419, no. 1–3, pp. 145–167, Dec. 2011, doi: 10.1016/j.jnucmat.2011.07.033.
[32] M. Sonnenkalb *et al.*, 'Overview and outcomes of the OECD/NEA benchmark study of the accident at the Fukushima Daiichi NPS (BSAF), phase 2 – Results of severe accident analyses for unit 2', *Nuclear Engineering and Design*, vol. 369, p. 110840, Dec. 2020, doi: 10.1016/j.nucengdes.2020.110840.
[33] H. Miura *et al.*, 'Characterization of two types of cesium-bearing microparticles emitted from the Fukushima accident via multiple synchrotron radiation analyses', *Scientific Reports*, vol. 10, no. 1, Dec. 2020, doi: 10.1038/s41598-020-68318-2.
[34] IRID, 'Decommissioning / contaminated water countermeasure project cost subsidy (advancement of comprehensive understanding of the situation inside the reactor) (Japanese translation) - International Research Institute for Nuclear decommissioning', 2018. Accessed: Jun. 23, 2020. [Online]. Available: https ://irid.or.jp/_pdf/20170 000_01.pdf
[35] C. Journeau *et al.*, 'Upgrading the PLINIUS platform toward smarter prototypic-corium experimental R&D', *Nuclear Engineering and Design*, vol. 386, p. 111511, Jan. 2022, doi: 10.1016/j.nucengdes.2021.111511.

ERMSAR 2022 - 10th European Review Meeting On Severe Accidents Research

Severe Accident Research Eleven Years after the Fukushima Accident

May 16-19, 2022 – Karlsruhe, Germany

FROM RESEARCH TO INDUSTRY

Thermodynamics of aerosols during molten core-concrete interaction at Fukushima Daiichi Unit 2 estimated conditions

Hugo LAFFOLLEY[1,2], Christophe JOURNEAU[1], Sarah THILLIEZ[1], Bernd GRAMBOW[2]

[1]: CEA, DES, IRESNE, DTN, Severe Accident Experimental Laboratory, Cadarache F-13108 St-Paul-lez-Durance, France

[2]: SUBATECH (IMT Atlantique, CNRS-IN2P3, University of Nantes) 44307 Nantes, France

IRESNE I DTN I SMTA I LEAG

Research Institute for Nuclear Systems for Low Carbon Energy Production

17/05/2022

Context

IRESNE | DTN | SMTA | LEAG

Research Institute for Nuclear Systems for Low Carbon Energy Production

Context

- Type-A Cs-bearing MicroParticles (CsMP)

  - Glassy matrix (amourphous silica)
  - Radiocesium
  - Micrometer (type-A)
  - Large diversity of elements
  - From **1F2** or 1F3 ($^{134}Cs/^{137}Cs$ ratio)

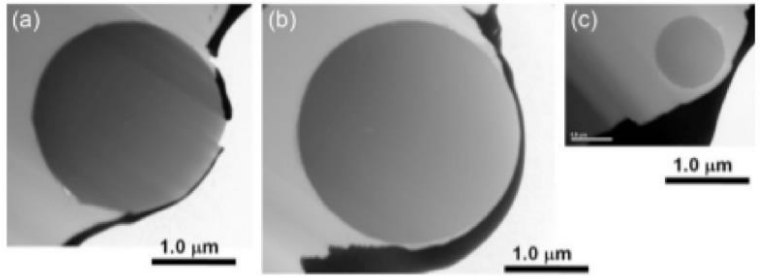

- Hypothetical generation processes (major)

Silicon source →
- Structural stainless steel
- Primary loop insulation materials
- Molten core-concrete interaction

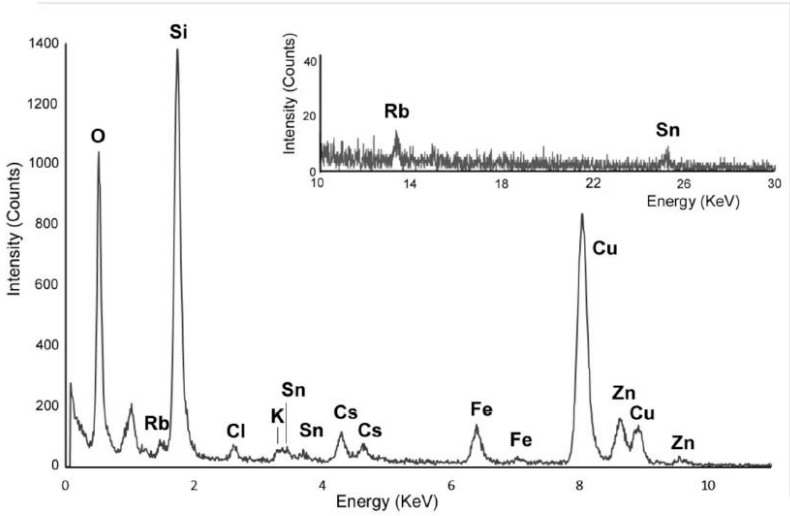

T. Kogure *et al.*, 'Constituent elements and their distribution in the radioactive Cs-bearing silicate glass microparticles released from Fukushima nuclear plant', *Microscopy (Tokyo)*, vol. 65, no. 5, pp. 451–459, Oct. 2016, doi: 10.1093/jmicro/dfw030.
N. Yamaguchi, M. Mitome, A.-H. Kotone, M. Asano, K. Adachi, and T. Kogure, 'Internal structure of cesium-bearing radioactive microparticles released from Fukushima nuclear power plant', *Scientific Reports*, vol. 6, no. 1, Apr. 2016, doi: 10.1038/srep20548.

Document owned by the CEA - Reproduction and distribution outside the CEA subject to the issuer's authorization

Context

Lots of uncertainties on the generation process
Si source, temperature, composition



Attempting to estimate generation conditions using thermodynamic calculations
(OECD/NEA TAF-ID v11 – ThermoCalc Software)

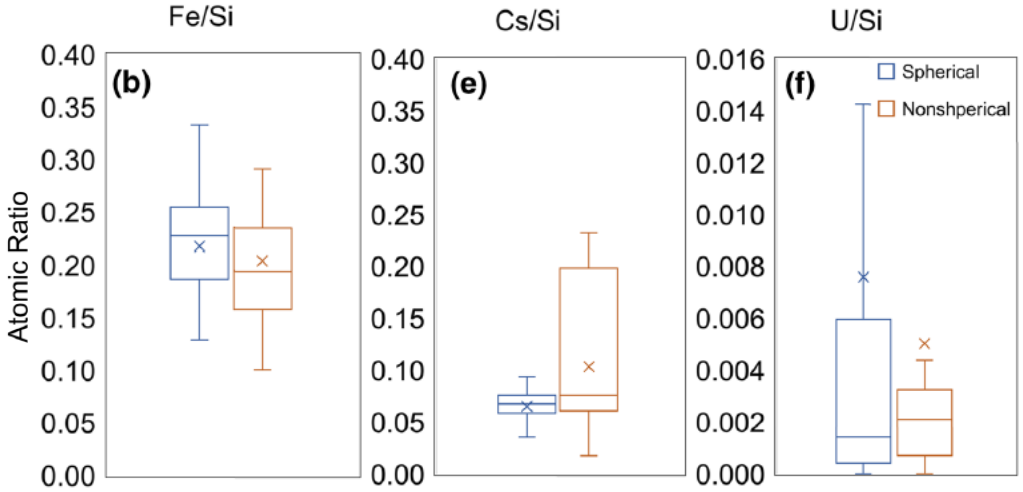

CsMP composition as indicator of vapour phase composition

H. Hagiwara, H. Funaki, N. Shiribiki, M. Kanno, and Y. Sanada, 'Characterization of radiocesium-bearing microparticles with different morphologies in soil around the Fukushima Daiichi nuclear power plant', *Journal of Radioanalytical and Nuclear Chemistry*, Oct. 2021, doi: 10.1007/s10967-021-08061-8.

Document owned by the CEA - Reproduction and distribution outside the CEA subject to the issuer's authorization

Molten core-concrete interaction (MCCI) parameters

- Generation process through MCCI

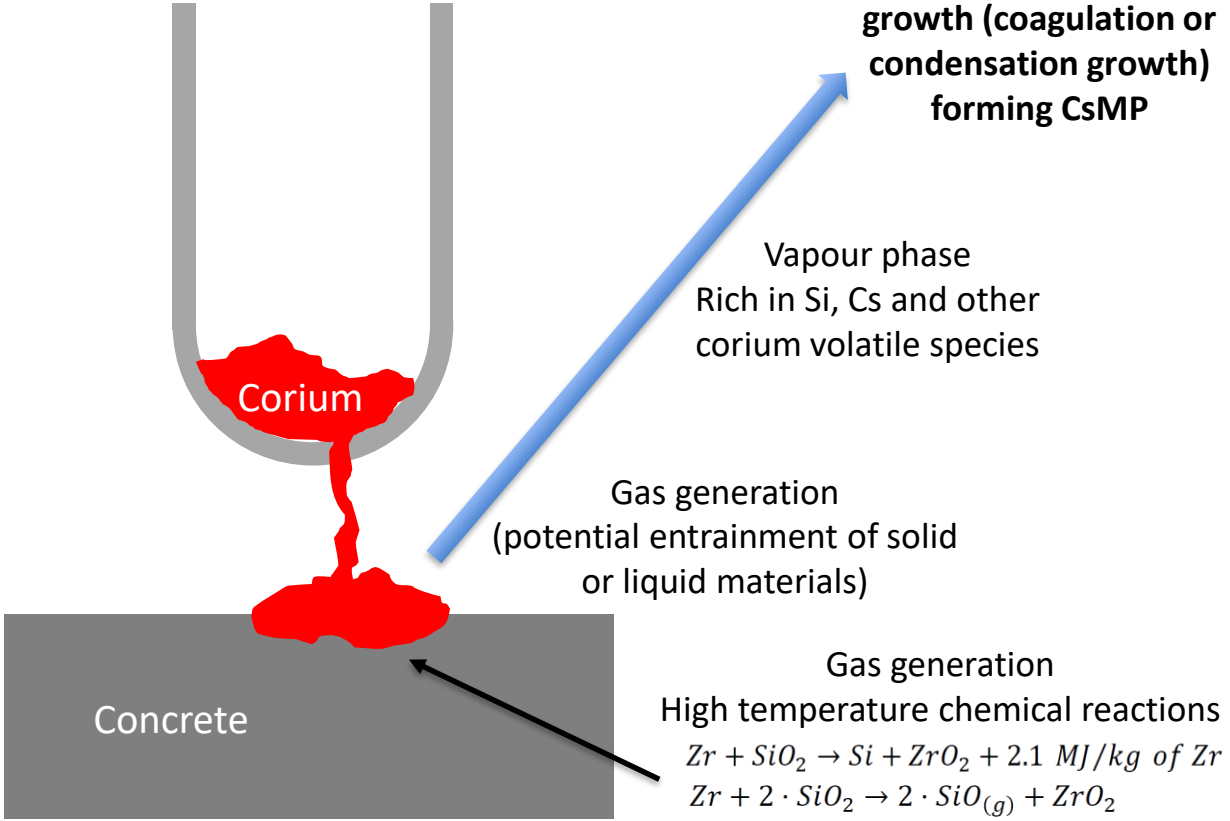

Nucleation and particle growth (coagulation or condensation growth) forming CsMP

Vapour phase
Rich in Si, Cs and other corium volatile species

Gas generation
(potential entrainment of solid or liquid materials)

Gas generation
High temperature chemical reactions

$$Zr + SiO_2 \rightarrow Si + ZrO_2 + 2.1\ MJ/kg\ of\ Zr$$
$$Zr + 2 \cdot SiO_2 \rightarrow 2 \cdot SiO_{(g)} + ZrO_2$$

- Composition input

→ OECD/NEA BSAF project data

	Concrete	+	Corium
-	SiO_2	-	UO_2
-	Al_2O_3	-	Zr
-	CaO	-	ZrO_2
-	H_2O	-	304 SS
-	Fe_2O_3	-	SS oxides
		-	B_4C

Atmosphere

- N_2
- H_2O

Document owned by the CEA - Reproduction and distribution outside the CEA subject to the issuer's authorization

Approach

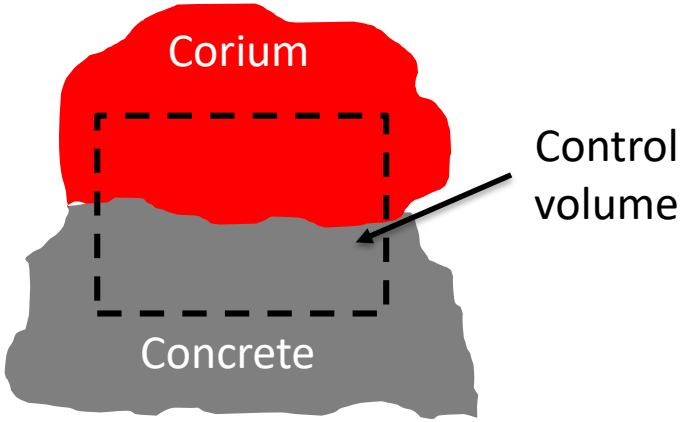

Thermodynamic calculations at the interface on the control volume

1) Defining input parameters (corium composition, corium/concrete ratio, pressure, amount of atmosphere in equilibrium, etc.)
2) Calculate the vapour phase elemental composition on a specific temperature range (typically 500-3000°C)
3) Extract data and post-process to get elemental ratios on silicon (e.g. Fe/Si)
4) Compare results with the literature on real CsMP compositions to adjust input parameters and best fit.

Document owned by the CEA - Reproduction and distribution outside the CEA subject to the issuer's authorization

Results

Forms of Si, Fe, U and Cs in the vapour phase

Si → SiO and SiO_2

Fe → Fe and FeO

U → UO_2 and UO_3

Cs → Cs

All these species could be incorporated in CsMP as they are or after further oxidation

2 approaches (without Cs) - Temperature evolution study of Fe/Si and U/Si ratios in the vapour phase :

- ~~Corium-rich system/low concrete concentration (atomic Si/Zr~~ = 0,1)
- Si-Zr equimolar system
- Concrete-rich system/low corium concentration (atomic Si/Zr = 10)

Document owned by the CEA - Reproduction and distribution outside the CEA subject to the issuer's authorization

Equimolar system results (without Cs)

In-vessel

Species (%.wt)	Institutes: CIEMAT	CRIEPI	IAE	IBRAE	KAERI	Average: All institutes (Ci1)	Except IBRAE & KAERI (Ci2)
UO_2	55	30	16	49	0	30	34
Zr	29	52	16	51	0	30	32
ZrO_2	10	6	45	0	0	12	20
SS	5	10	9	0	86	22	8
SS Oxides	0	0	12	0	14	5	4
B_4C	1	2	2	0	0	1	2

Ex-vessel

Species (%.wt)	Institutes: IBRAE	IRSN	JAEA	Average: All institutes (Ce1)	Initial Inv. (Ce2)
UO_2	40	53	48	47	52
Zr	9	6	6	7	17
ZrO_2	10	24	19	18	0
SS	41	17	27	28	31

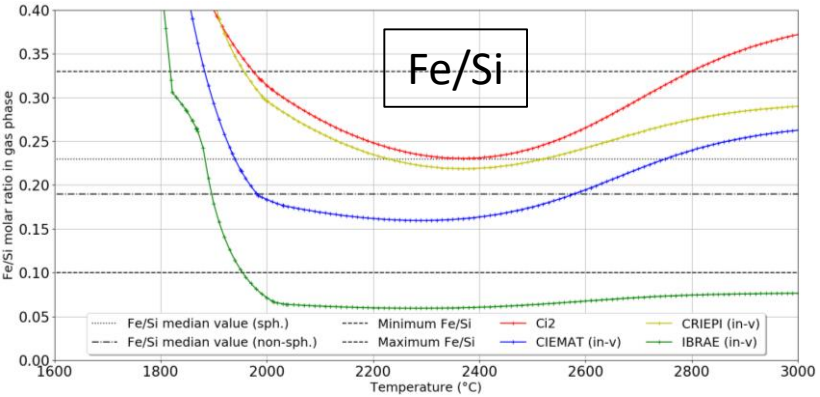

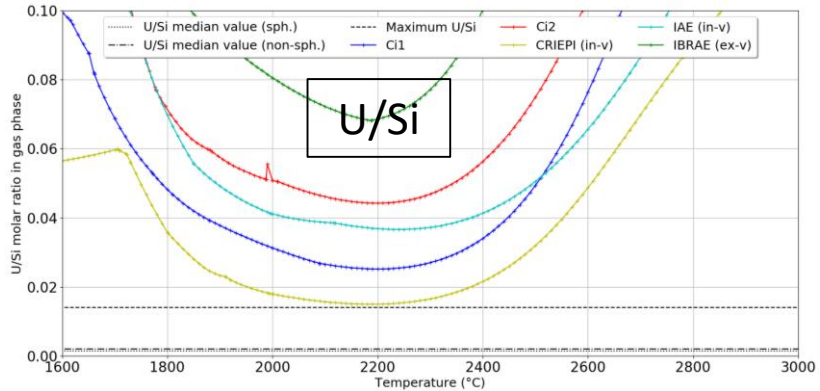

- **Fe :**
- Only « in-vessel » compositions in our target range
- Steel initial concentration influences directly Fe/Si
- Target range reached between 1900°C and 2000°C
- Conditions still valid for 2 compositions at 3000°C
- **U :**
- UO_2 initial concentration does not seem affect U/Si radically
- In average, U/Si is lower when Zr/ZrO_2 is higher, meaning that suboxidised melt tends to increase U concentration in the vapour phase (consistent with U-O binary)
- No compositions reach the target range

M. Pellegrini *et al.*, 'Main Findings, Remaining Uncertainties and Lessons Learned from the OECD/NEA BSAF Project', *Nuclear Technology*, pp. 1–15, Apr. 2020, doi: 10.1080/00295450.2020.1724731.
C. Guéneau *et al.*, 'Thermodynamic modelling of advanced oxide and carbide nuclear fuels: Description of the U–Pu–O–C systems', *Journal of Nuclear Materials*, vol. 419, no. 1–3, pp. 145–167, Dec. 2011, doi: 10.1016/j.jnucmat.2011.07.033.

Document owned by the CEA - Reproduction and distribution outside the CEA subject to the issuer's authorization

Concrete-rich system (without Cs)

In-vessel

Species (%.wt)	Institutes: CIEMAT	CRIEPI	IAE	IBRAE	KAERI	Average: All institutes (Ci1)	Except IBRAE & KAERI (Ci2)
UO_2	55	30	16	49	0	30	34
Zr	29	52	16	51	0	30	32
ZrO_2	10	6	45	0	0	12	20
SS	5	10	9	0	86	22	8
SS Oxides	0	0	12	0	14	5	4
B_4C	1	2	2	0	0	1	2

Ex-vessel

Species (%.wt)	Institutes: IBRAE	IRSN	JAEA	Average: All institutes (Ce1)	Initial Inv. (Ce2)
UO_2	40	53	48	47	52
Zr	9	6	6	7	17
ZrO_2	10	24	19	18	0
SS	41	17	27	28	31

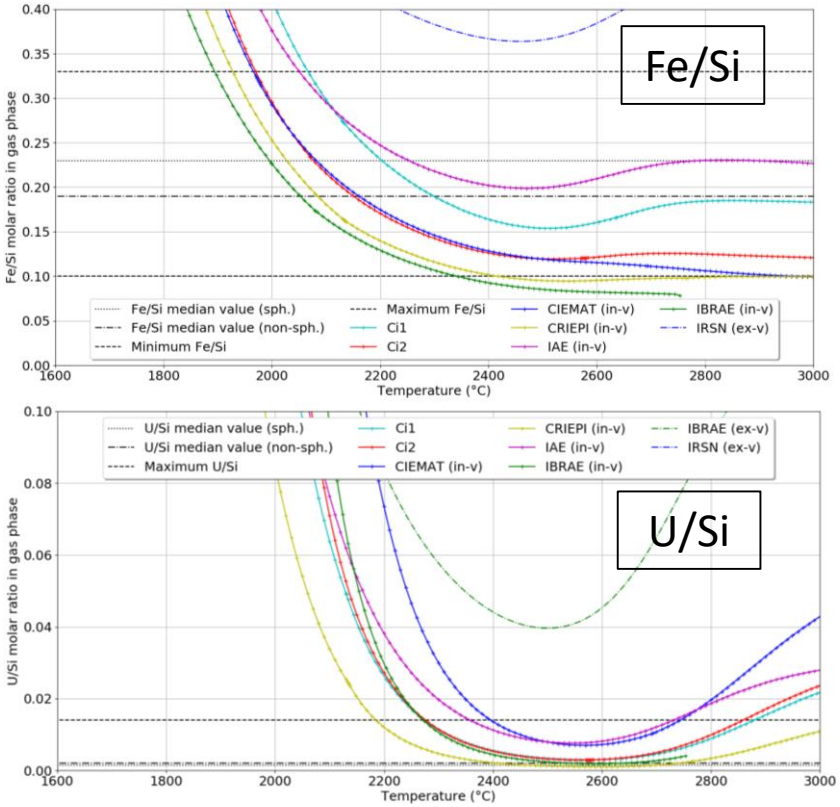

- **Fe :**
  - Every « in-vessel » composition's behaviour tends to be the same (dilution in concrete)
  - Fe/Si target range reached around 1900-2100°C
  - Median value around 2000-2200°C
  - Most of « in-vessel » compositions stay in the target range
- **U :**
  - U/Si ratio reach the targe range
  - As stated before, high Zr/ZrO_2 ratio tend to lower U/Si ratio
  - Target range is reached between 2150 and 2400°C

M. Pellegrini *et al.*, 'Main Findings, Remaining Uncertainties and Lessons Learned from the OECD/NEA BSAF Project', *Nuclear Technology*, pp. 1–15, Apr. 2020, doi: 10.1080/00295450.2020.1724731.

Document owned by the CEA - Reproduction and distribution outside the CEA subject to the issuer's authorization

With Cs in the composition

Species (%.wt)	CIEMAT
UO_2	55
Zr	29
ZrO_2	10
SS	5
SS Oxides	0
B_4C	1

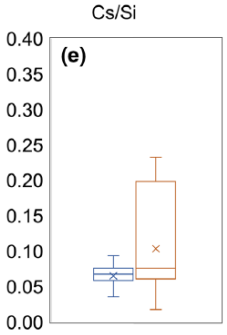

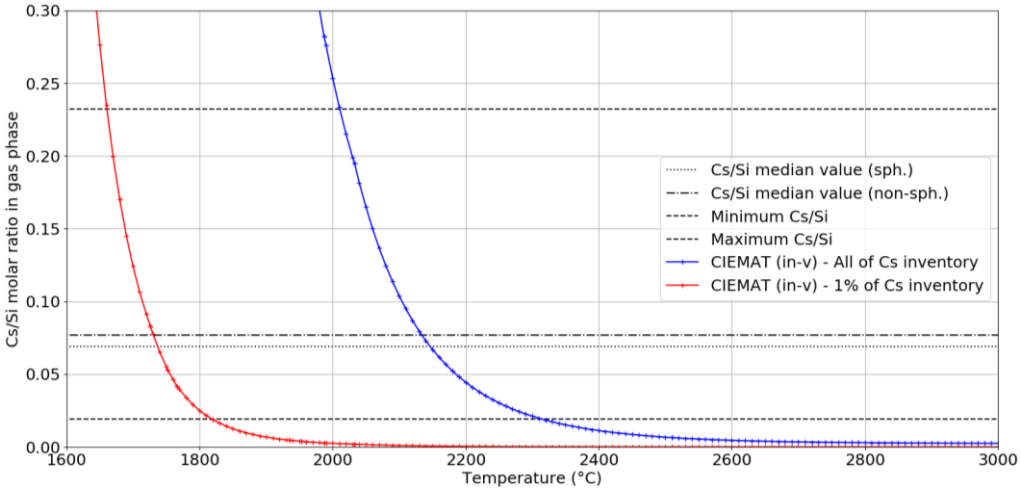

Cs inventory
(3 days after scram)

→ If 1% participates

→ If 100% participate

Median value → 1750 to 2150°C
Min → 1700°C and max → 2300°C

Document owned by the CEA - Reproduction and distribution outside the CEA subject to the issuer's authorization

Conclusions/Perspectives

IRESNE | DTN | SMTA | LEAG

Research Institute for Nuclear Systems for Low Carbon Energy Production

Conclusions

⚠ Very low Al concentration in the vapour phase ≠ CsMP composition → It could be modelling artefact

⚠ Diversity of composition in the literature (limited semi-quantitative study)

If MCCI is responsible for CsMP generation :

- Corium must be sub-oxidised, rich in Zr but with a moderate content in steel and UO_2. Cs concentration must be close to the total inventory.

- Concrete (SiO2) must be the excess reagent to provide favourable conditions for U/Si ratio but at higher temperature.

- Temperature around 2200°C is the best compromise.

Document owned by the CEA - Reproduction and distribution outside the CEA subject to the issuer's authorization

Following experimental work

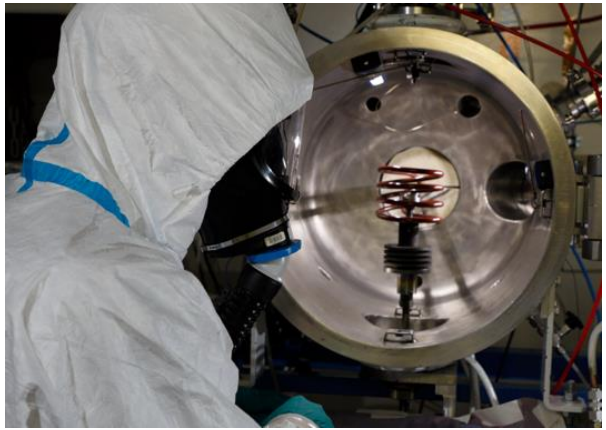



VITI furnace of the PLINIUS experimental platform
CEA, Cadarache site

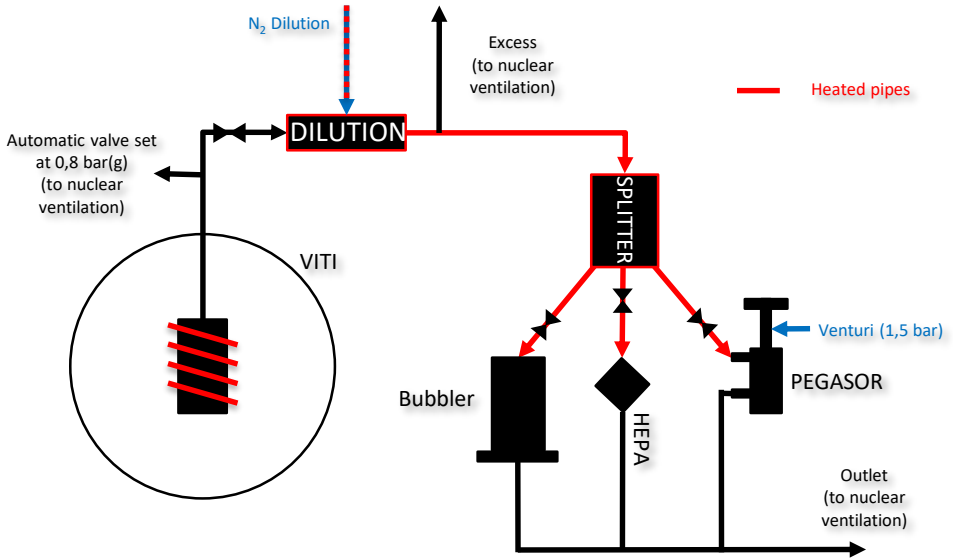

VITAE configuration (aerosol generation and collection)

Document owned by the CEA - Reproduction and distribution outside the CEA subject to the issuer's authorization

Following experimental work

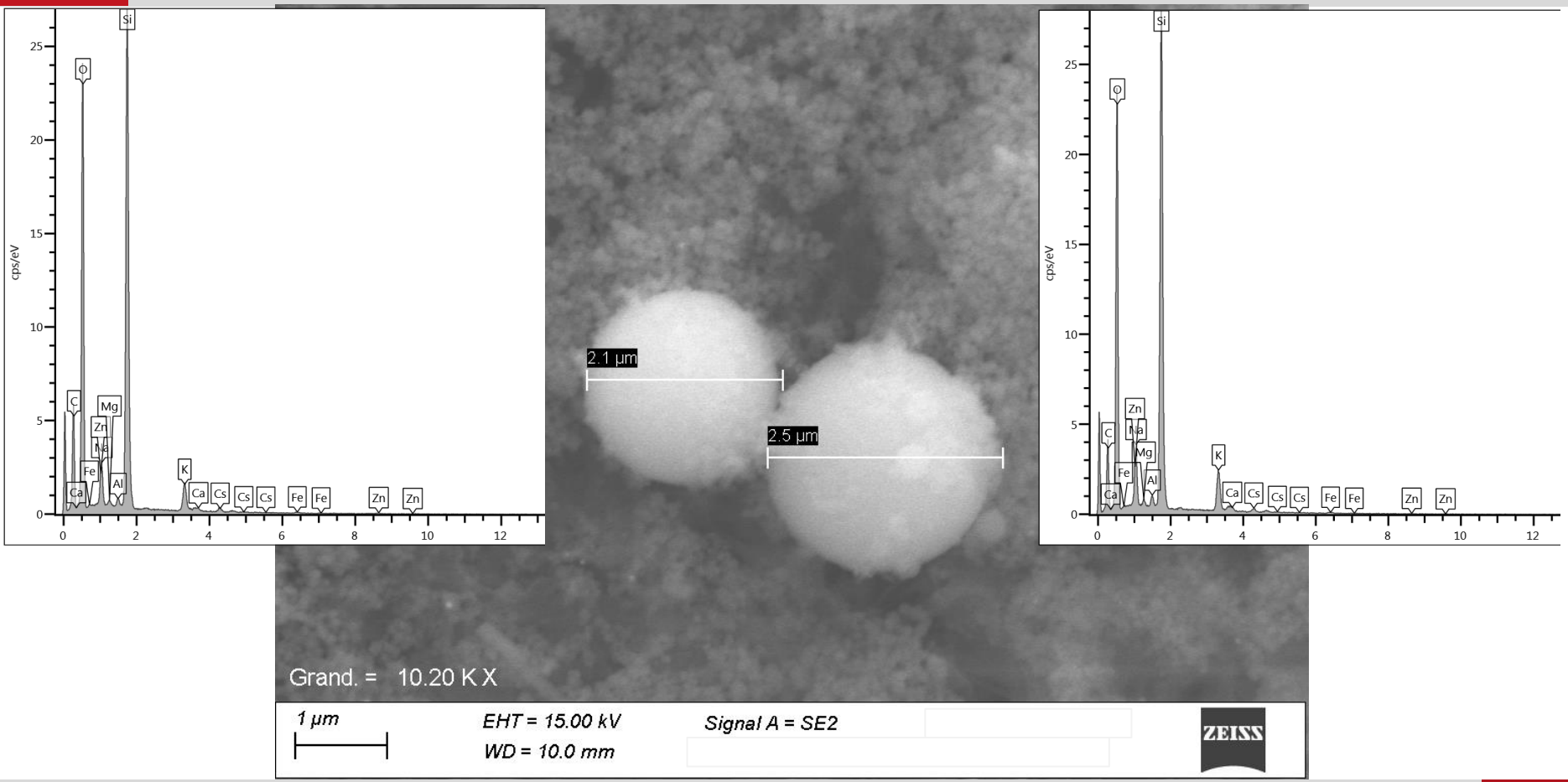

Document owned by the CEA - Reproduction and distribution outside the CEA subject to the issuer's authorization

Thank you for your attention



17/05/2022

FROM RESEARCH TO INDUSTRY

IRESNE I DTN I SMTA I LEAG

Research Institute for Nuclear Systems for Low Carbon Energy Production



FROM RESEARCH TO INDUSTRY

Appendix

IRESNE I DTN I SMTA I LEAG

Research Institute for Nuclear Systems for Low Carbon Energy Production

Sensibility analysis

3 parameters :
- Pressure
- H_2O vapour fraction
- Atmosphere mass/corium mass ratio (in equilibrium)

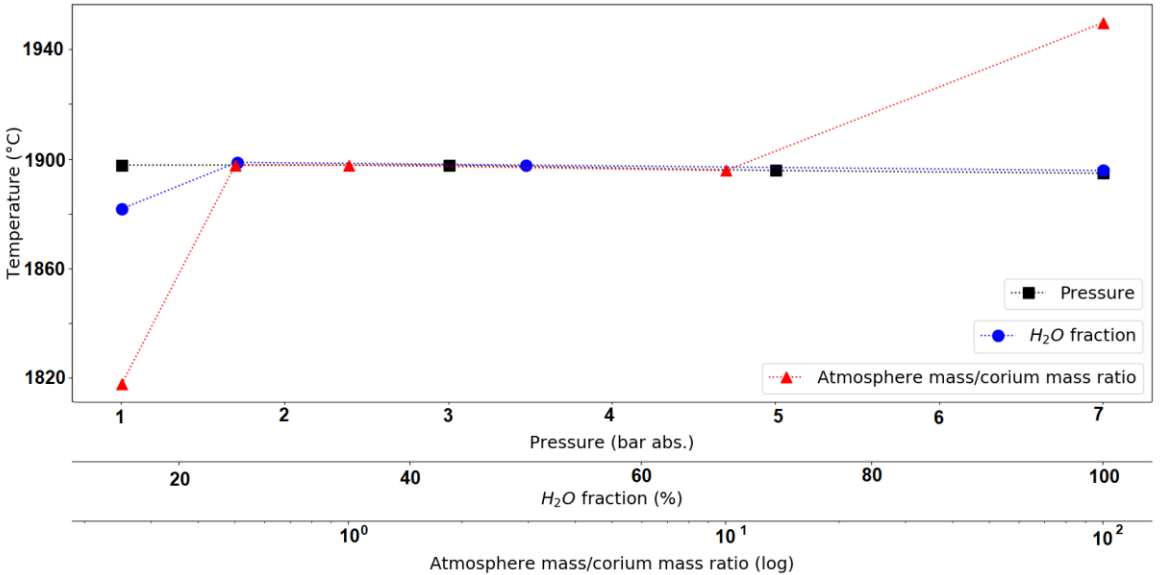

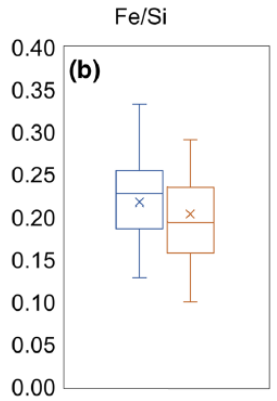

- Negligible effect of pressure change between 1 to 7 bar(abs.)
- Negligible effect of H_2O fraction change over 15%
- Atmosphere mass in equilibrium should be at least 0,25 times the mass of the melt to have a negligible effect on calculations

Document owned by the CEA - Reproduction and distribution outside the CEA subject to the issuer's authorization

U-O binary diagram

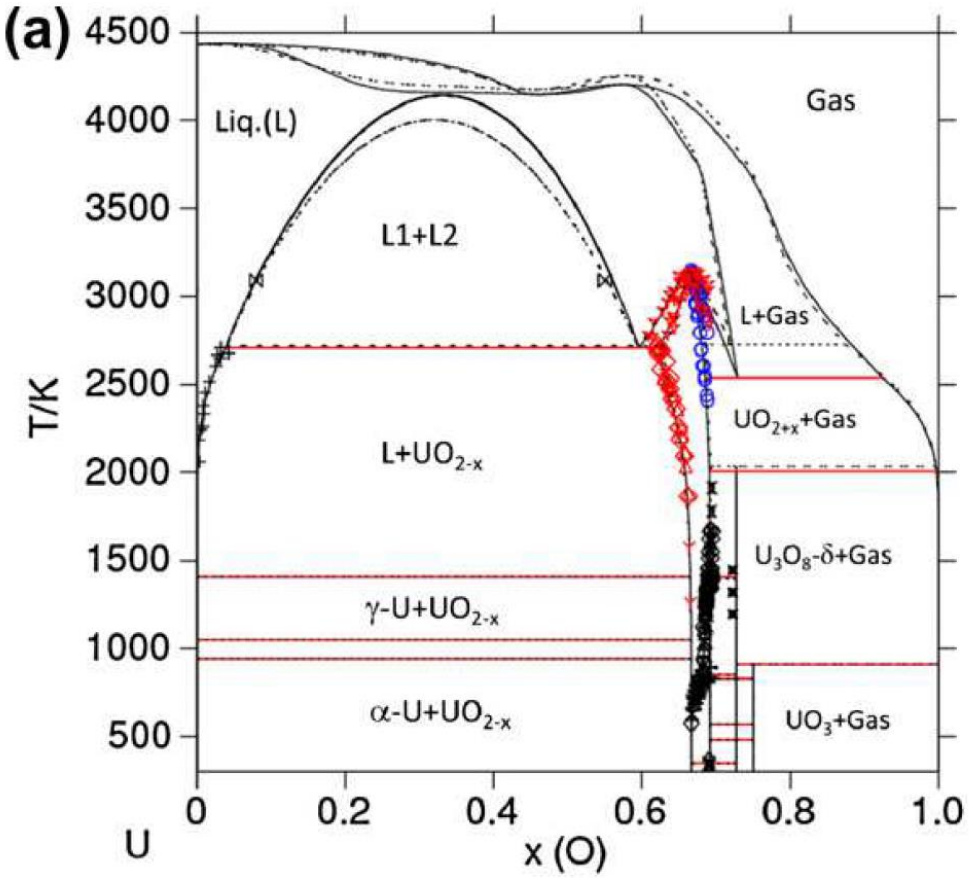

C. Guéneau *et al.*, 'Thermodynamic modelling of advanced oxide and carbide nuclear fuels: Description of the U–Pu–O–C systems', *Journal of Nuclear Materials*, vol. 419, no. 1–3, pp. 145–167, Dec. 2011, doi: 10.1016/j.jnucmat.2011.07.033.

Document owned by the CEA - Reproduction and distribution outside the CEA subject to the issuer's authorization

The 10th European Review Meeting on Severe Accidents Research

Severe Accident Research Eleven Years after the Fukushima Accident

May 16-19, 2022, Karlsruhe, Germany

Technical Session 2-3: Uncertainties in Severe Accident Scenarios

Chairs: O. Coindreau (IRSN), S. Paci (University of Pisa)

ID327	**Preliminary Uncertainty and Sensitivity Analysis of the ASTEC simulations results of a MBLOCA scenario at a Generic KONVOI Plant using FSTC tool** A. Stakhanova (KIT)	**Paper** **Presentation**
ID324	**CIEMAT's outcomes from the PHEBUS-FPT1 uncertainty analysis in the framework of the EU-MUSA project** R. Bocanegra (CIEMAT)	**Paper** **Presentation**
ID274	**Parametric analysis of FPT-1 MELCOR 2.2 input deck as a preparation for uncertainty quantification study** M. Malicki (PSI)	**Paper** **Presentation**

UNCERTAINTY AND SENSITIVITY ANALYSIS OF THE ASTEC SIMULATIONS RESULTS OF A MBLOCA SCENARIO IN A GENERIC KONVOI PLANT USING THE FSTC TOOL

A Stakhanova*, F. Gabrielli, V.H. Sanchez-Espinoza
Karlsruhe Institute of Technology (KIT)
Hermann-von-Helmholtz-Platz 1, Eggenstein-Leopoldshafen, Germany
anastasia.stakhanova@kit.edu; fabrizio.gabrielli@kit.edu; victor.sanchez@kit.edu

E. Pauli
Framatome GmbH
Paul Gossen Straße 100, 91052 Erlangen, Germany
eva-maria.pauli@framatome.com

A. Hoefer
Framatome GmbH
Seligenstädter Straße 100, 63791 Karlstein am Main, Germany
axel.hoefer@framatome.com

ABSTRACT

This paper presents the uncertainty and sensitivity (U&S) quantification of the ASTEC code [1] in predicting the radiological source term (ST) in case of a severe Medium Break Loss-of-Coolant accident (MBLOCA) in a KONVOI nuclear power plant (NPP) performed with the in-house Python-based Fast Source Term Calculation (FSTC) tool [2]. This tool was developed in the frame of the German WAME project. First, a set of uncertain ASTEC input parameters have been selected with their corresponding probability density functions (PDFs) and multi-ASTEC simulations were performed with varied values of such uncertain input parameters, using the Latin hypercube sampling (LHS) [3]. These investigations allow identifying the uncertain parameters with major influence on the ST prediction. The obtained results show that FSTC tool is very much appropriate to perform uncertainty quantification of ASTEC simulations and to find out the most influencing parameters regarding the figure of merit (FoM) thanks to the implemented statistic models for the determination of the sensitivities (e.g. Spearman, Pearson). The paper discusses the uncertainty bands of the FoMs in the containment and environment and the results of the sensitivity analysis.

ASTEC, FSTC, KONVOI, MBLOCA, U&S analysis

* Corresponding author.

1. INTRODUCTION

The uncertainty quantification of the severe accident (SA) codes predictions of the radiological source term – as main FoM – is a recent research topic in Europe and worldwide. Within the H2020 program, the MUSA-project is fully devoted to this research topic [4], where many severe accident sequences of different reactor types are being analyzed by different institutions using different severe accident codes (ASTEC, MAAP, MELCOR, etc.) and U&S analysis tools such as DAKOTA, URANIE, SUSA, SUNSET, etc.

KIT is participating together with FRAMATOME both on MUSA and on German project, named WAME, financed by German Federal Ministry of Economic Affairs and Climate Action (BMWi) [5]. The main goal of WAME project is to develop a fast running tool for the prediction of the radiological ST in case of a SA in a NPP by using dose rate measurements from plant detectors and a mathematical approach – Monte-Carlo Bayes procedure (MOCABA), developed by Framatome [6].

A key element of this approach is the generation of a database consisting of the results of the radiological ST evaluations by means of reference SA codes. For this purpose, a Python-based FSTC tool, was developed at KIT and coupled with the European reference Accident Source Term Evaluation Code (ASTEC), developed by IRSN. Tool consists of two main parts: one part is devoted to U&S analysis with similar capabilities than the well know tools (SUSA, URANIE, etc.) and another part devoted to the Bayesian inference method that is a Python based replica of MOCABA-approach.

In the frame of the WAME project, the FSTC/ASTEC coupling was extensively applied to the different SA scenarios in a generic KONVOI NPP. Before, the performance of the FSTC/ASTEC coupling was successfully tested [2] by performing the U&S analysis of QUENCH-08 experiment [7] ASTEC simulations. A key step in performing U&S analysis is the identification of a set of uncertain parameters, with the final goal to perform a sensitivity analysis by employing different correlations that allows the identification of most important parameters influencing the ST prediction.

This paper presents and discusses the application of the FSTC tool to quantify the uncertainties and sensitivities of ASTEC code predicting the radiological ST of a MBLOCA SA in a generic KONVOI NPP. The SA sequence is analyzed form the early phase to the basemat rupture. The investigations presented here greatly contributed to improve the expertise and understanding of the complexity of U&S analysis with large benefits for the joint KIT/Framatome participation to H2020 MUSA-project.

Furthermore, the present work also describes the assessment of FSTC/ASTEC training database for the preliminary evaluations of the ST predictions for MBLOCA scenario in the generic ASTEC KONVOI NPP, which are performed in [8, 9].

The Chapter 2 introduces the key features of the FSTC tool, while the Chapter 3 briefly describes the ASTEC model of the pressurized water reactor (PWR) KONVOI plant for the prediction of the radiological ST. Chapter 4 gives a list of the selected uncertain parameters and describes how the numerous ASTEC simulations are performed. The SA scenario MBLOCA is presented in Chapter 5 with some details. The Chapter 6 discusses the main results of the U&S analysis regarding the FoM. Finally, the Chapter 7 summarizes the main conclusions and provides an outlook.

2. FSTC TOOL

The FSTC tool was developed by KIT in the framework of the WAME project to address the project's needs. This tool can be, for the purpose of discussion, divided into two parts – one part allows to perform

U&S analysis, and the other part contains the MOCABA implementation. This paper focuses on the first part.

The FSTC tool is written in the programming language Python and has a modular structure – each module can be run independently with its own set of input data. The tool can be run both on Windows and Linux, thanks to the fact that Python is a cross-platform programming language. Currently, the FSTC tool is coupled only with the ASTEC code and does not have a graphical user interface (GUI) – coupling with other codes and adding a GUI are planned for the future.

Performing an U&S analysis involves the following steps:

1. Identify the list of uncertain input parameters and their probability density functions (PDFs) and use this information as input for the sampling algorithm. Currently, two options are available in the FSTC tool – Simple Random Sampling (SRS) and LHS [3]. Input parameters can be correlated (see Chapter 4 of this paper);
2. The results of step 1 are used as input data for running multiple simulations. Each simulation has its own input deck with a specific set of values of uncertain input parameters. Simulations can be run in parallel;
3. In principle, some simulations from step 2 could fail, due to problems with convergence, for example, and, therefore, the correctness of the finished code runs will be checked. Failed runs will be excluded from the further analysis. Another task, which is specific to ASTEC simulations of severe accidents, is performed at this step. ASTEC code generates the *quicklook* file, where the timing of the main events occurring during the accident progression is stored. That data is also extracted and used in U&S analysis;
4. The user specifies the list of parameters of interest, which shall be extracted from the ASTEC output *.plt* files. The code detects where the values of the given output parameters are stored in the output files and extracts these values for each time step;
5. Different values of uncertain input parameters lead to different accident progressions, and therefore, the main events (like start of fission product (FP) release, lower head vessel failure (LHVF), etc.) occur at different times, which makes the further analysis trickier. Hence, the user can specify two specific time points or names of the two main events, between which the data should be extracted;
6. At this last step, finally, all data is ready for U&S analysis. Using data from steps 1, 3, and 5, the following statistics is calculated for each parameter of interest:
   - Simple statistics (minimum, mean, maximum, 5th, 50th and 95th percentiles values);
   - Time-dependent Pearson and Spearman correlation coefficients for all *output* – *input* parameters pairs.

The steps described above are presented schematically in Figure 1. In the next chapter the ASTEC model of a generic KONVOI NPP will be described briefly.

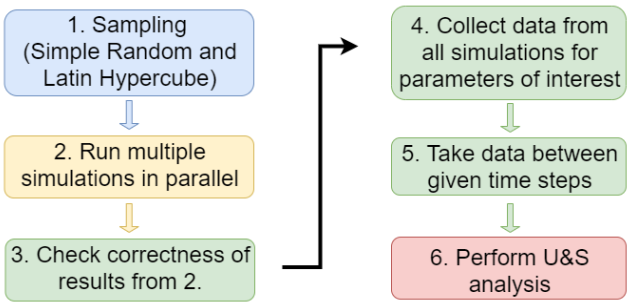

Figure 1. Scheme of U&S analysis task steps

3. ASTEC MODEL OF KONVOI NPP

The ASTEC model of a generic KONVOI NPP used in this paper is based on the input deck developed in the frame of the EU CESAM project [10]. A detailed description of the KONVOI ASTEC simulations earlier performed at KIT and the KONVOI model nodalization can be found in [11].

The original input deck has been further extended during the WAME project. In particular, attention has been devoted to:

1. The activation of all the ASTEC calculation modules to consider the main in-vessel and ex-vessel phenomena occurring during the severe accident scenarios;
2. Fine nodalization of the reactor coolant system (RCS) in order to improve the analysis of the fission product transport from the RCS to the containment;
3. The employment of fuel inventories from realistic depletion calculations;
4. The improvement of the model for the containment leakage to the annulus, by employing more detailed plant data like annulus leakage;
5. Compared with the original input deck, no filtering has been modelled.

4. UNCERTAIN INPUT PARAMETERS

The U&S simulations have been performed with the ASTEC (v2.2_b) code for a MBLOCA scenario. 16 input parameters have been considered for uncertainty propagation (Table I). The parameters *par1 – par5a* allow for modeling the release of FPs from the fuel, simulated by the ASTEC ELSA model [12]. The parameters *par14 – par16* are related to the integrity criteria of the fuel cladding and, therefore, influence the degradation process in the reactor core. The subsequent seven parameters are related to the modeling of the aerosol behavior in the primary system and in the containment, which is simulated by the ASTEC SOPHAEROS and CPA calculation models. Parameter *par41* refers to the uncertainty of the leakage rate from containment to annulus. Finally, parameter *parBU* refers to the uncertainties on the fuel burn-up, namely the number of effective full power days. Having this in mind, realistic fuel inventories for an equilibrium cycle with 328 effective full power days have been computed by Framatome for the core loaded with 193 Fuel Assemblies (48 U FAs, 6 batches; 81 U-Gd FAs, 6 batches; 64 MOX FAs, 4 batches). For the depletion calculations, the ORIGEN-ARP tool has been used, employing the ORIGEN reactor libraries for an 18x18 FA design embedded in SCALE 6.2.3 [13].

The choice of the uncertain input parameters is not an easy task and to a certain degree is always based on engineering judgement. A good understanding of the physical processes occurring during the accident progression is required, which can help to focus on a particular set of the code models. The PDFs of the selected ASTEC parameters in the current paper are based on information derived from the literature, i.e [12, 14, 15] and on engineering judgment. Significant effort has been spent on reviewing reference papers and reports based on experimental results used to validate the physical models employed in ASTEC for governing the fission product transport behavior as well as recommendations from code user guides. All references are presented in Table I.

To represent the actual physics of the process as well as possible, correlations between selected uncertain input parameters were introduced. The correlation values are presented in Figure 2. For example, the PDFs of the uncertainty of the input parameters *par1* and *par2* are set based on the results of the Phebus tests [14], which have been extensively used to validate the ELSA and SOPHAEROS ASTEC models [15]. The mean values for *par1* and *par2* are set to the values recommended in the ASTEC manuals, the standard deviations were increased from 20% (estimated error bar in Phebus-FPT1 test [15]) to 30%. Increasing the standard deviations allows us to better study the effect of these parameters on the output parameters in the U&S analysis. The correlation between *par1* and *par2* is set to 1 (see Figure 2), based on the suggestion that increasing the roughness of the fuel pellet surface will make the access of oxygen to its surface more

difficult. Namely, the employment of correlations between uncertain input parameters, allows a more reliable representation of the physics of different processes during SA.

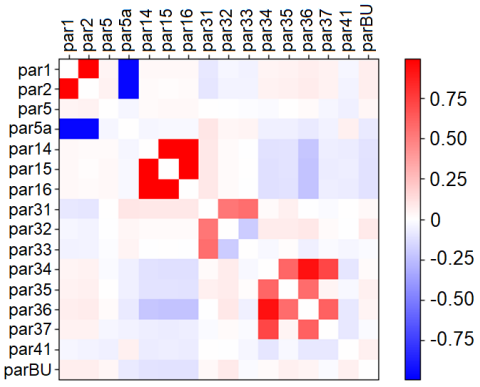

Figure 2. Correlations between uncertain input parameters

5. ACCIDENT SCENARIO DESCRIPTION

The simulation of the MBLOCA scenario starts at time t = 0 s, when the break (size – 440 cm^2) occurs in the cold leg. After that (at t =1 s) the SCRAM happens, and the admission to the turbine and main feed water pumps is closed. The Emergency Core Cooling System (ECCS) is activated, when conditions are fulfilled – at 2.8 s and 6 s, and then the main coolant pumps (MCPs) are coasted down, and the pressure regulation in the pressurizer is switched off. The Emergency Feed Water System (EFWS) is activated when the water level in one of the steam generators drops below 4.5 m. The High and Low Pressure Injection Systems (HPIS/LPIS) are activated when the gas temperature in the primary system exceeds 650 ºC. Water injection continues until the tanks are empty. After that core melt starts. The cavity is flooded when the horizontal erosion reaches 0.5 m.

6. RESULTS OF U&S ANALYSIS

In the current chapter, the results of the U&S analysis are shown, focusing only on some main elements – Xe, Cs, I, Mo and Ba. It is investigated how the uncertain input parameters influence the amount of these elements released into the containment and environment. For the presented analysis, 200 ASTEC simulations were run, 10 of them failed due to convergence problems and other issues and were excluded from the further analysis.

First, to illustrate how the accident progression varies significantly depending on the uncertain input parameters values, the time of start of FP release is shown in Figure 3 for all non-failed simulations. The start of FP release varies from ~440 s up to ~750 s – see left part of the Figure 3; the end of the process (in our simulations it is the basemat rupture) – between ~$1.5 \cdot 10^5$ up to ~$2.8 \cdot 10^5$ (see the right part of Figure 3).

To take into account all simulations with different progressions in time together in the U&S analysis, the following procedure was carried out:

1) Choose *'start'* and *'final'* events – between these events data will be extracted and analyzed;
2) From all samples, find the maximum time value when the *'start'* event happens and the minimum time value when the *'final'* event happens
3) Extract data between the points in time defined in 2)

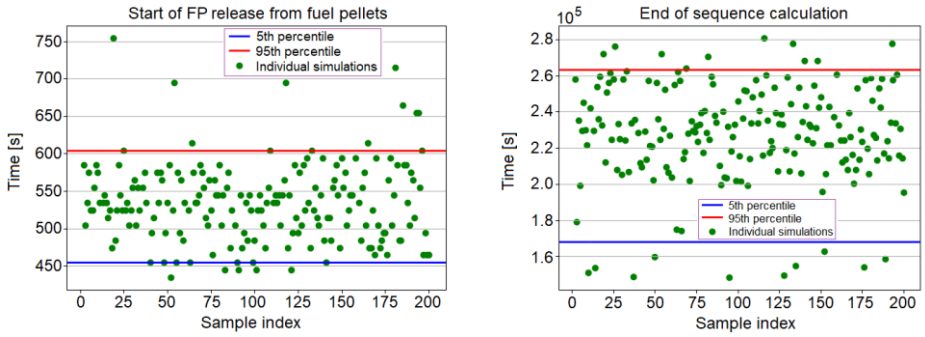

Figure 3. Time of start of FP release and end of calculation

The total amount of Xe, Cs, I, Ba and Mo released into the containment and into the environment during the accident is presented (in logarithmic scale for both axes) in Figure 4. The results are provided as fraction of the initial mass in the core. One can see that release into the containment reaches its final plateau quite fast – in the first $2 \cdot 10^4$ - $3 \cdot 10^4$ s, which corresponds to the instant of LHVF and the end of corium slump. The first plateau of release into the containment is located around $1 \cdot 10^3$ s for all elements except for Cs (for Cs this plateau is located around $3 \cdot 10^3$ s). The second increase of the amount of FPs released into the containment happens around the time of first slump of the corium into the lower plenum. The release to the environment continues during the whole course of the accident, but the fastest release rate can be observed at the beginning of the process – in the first $1 \cdot 10^4$ s, when the active degradation of the core takes place. After that time, the release is very slow.

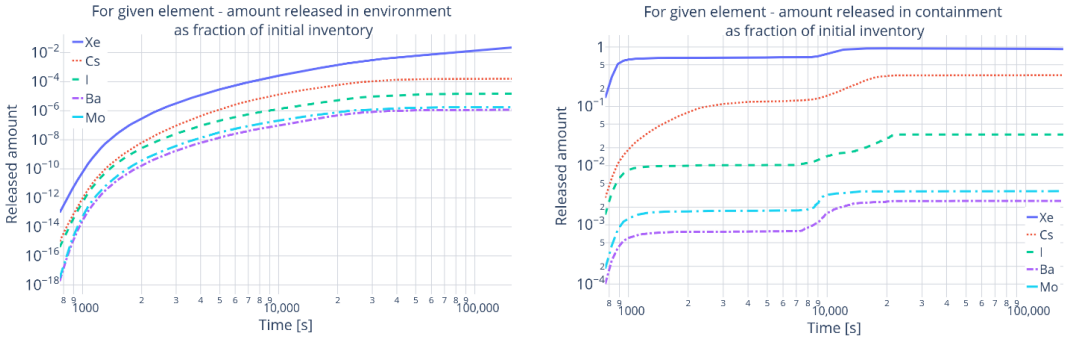

Figure 4. Amount of Xe, Cs, I, Ba and Mo released in environment (left) and containment (right) as fraction of initial inventory

The Pearson and Spearman correlations for those uncertain input parameters with the highest influence on the release to the environment are presented on the Figure 5 (for both left and right parts of the figure, the x axis if limited to $8 \cdot 10^4$ s, because after that point in time the Pearson correlations remain constant for the rest of the accident). As was expected, the most important parameters for the release into environment are *par41*, governing the leakage from the containment and *parBU*, governing the inventory itself, which obviously affects the release. The influence of *parBU* on the release is high at the very beginning of the process, around the time of start of FP release and start of core degradation. After that, its influence decreases very fast and reach a plateau around $4 \cdot 10^4$ -$5 \cdot 10^4$ s when the release to the environment also reaches a plateau. Parameter *par41* has a high Pearson correlation value for the whole process of the accident, which is expected also from a physical point of view. The remaining uncertain parameters have practically no impact on the release to the environment for all considered elements, and the Pearson (or Spearman) correlation values are mostly lying the range [-0.1; 0.1]. From Figure 5 one can see the difference between Pearson and Spearman correlation coefficients – it becomes especially large for the correlation between the release of

iodine into the environment and *par41* after about 10^4 s. The reason of this difference is that for a few samples the release values at the given point in time differ significantly from the rest of the samples. These *'outliers'* are disrupting the linear (or close to the linear, at least) relationship between the output and uncertain input parameters, especially at later times, see Figure 6. Therefore, the different correlation coefficients probably should be calculated to provide a clearer picture of the influence of the uncertain input parameters on the output.

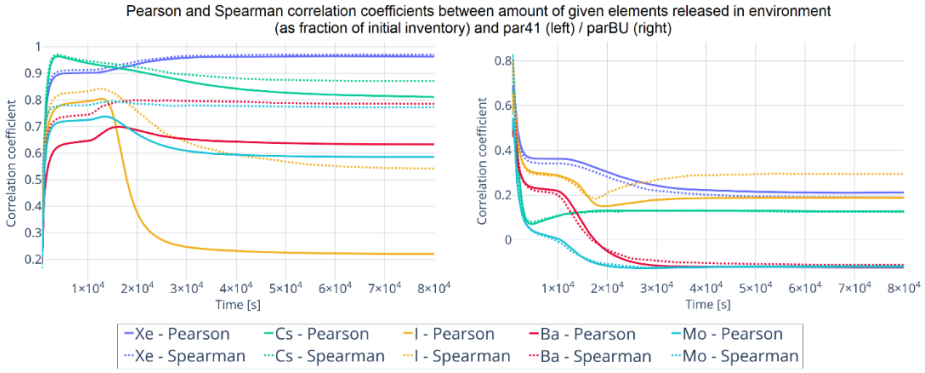

Figure 5. Pearson and Spearman correlation coefficients between amount of given element released into the environment and *par41* (left) / *parBU* (right)

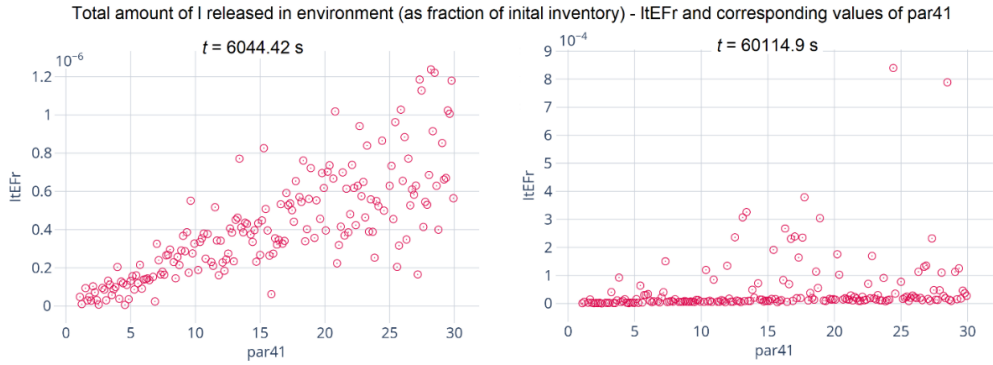

Figure 6. Amount of I released into the environment (*ItEFr*) at *t*=6044.42 s (left) / *t*=60114.9 s (right) and corresponding values of *par41*

The uncertain input parameter which mostly influences the release into the containment is *parBU* – see the Figure 7 (as in Figure 5, the x-axis is limited, because after some point in time the correlation coefficients remain practically constant). In that case, also no big difference between Pearson and Spearman correlation coefficients was observed, as it was for release into the environment (Figure 6 (right)). Other parameters could play a role, but mostly lying again in the range [-0.1; 0.1] as for the release into environment. In some cases (for example, for low volatile FPs like Mo) absolute value of Pearson correlation coefficient between release and parameters related to release from fuel pellets and integrity criteria could reach ~ 0.25 at the beginning of the accident, but Spearman correlation values will be slightly lower – see the right part of Figure 8.

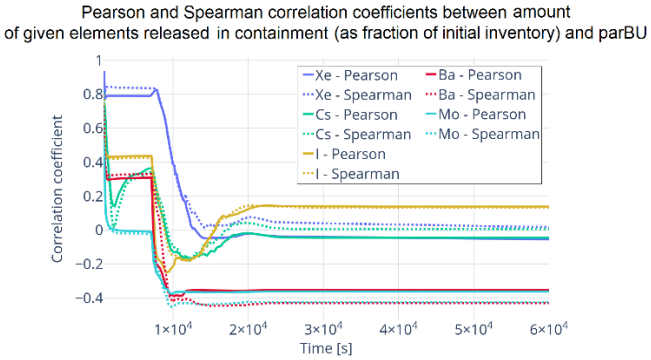

Figure 7. Pearson and Spearman correlation coefficients between amount of given element released into the containment and *parBU* (left)

The effect from uncertain input parameters related to the modelling of aerosol behavior can be seen, when considering the amount of aerosol in the containment. For amount of Cs and I aerosols in the containment are shown on the left-hand side of Figure 8. Pearson and Spearman correlation coefficients for *par32* and *par37* are shown on at the right-hand side of Figure 8. The correlation values stay high in the late phase of the accident, when the slump of the corium to the lower plenum is finished and LHVF occurred. The correlations are comparable to the previous results for *parBU* at the beginning of the process. These results reveal the necessity to perform U&S analysis of ASTEC results for the full scenario (up to the rupture of the basemat), since some aerosol-related phenomena may occur much later than vessel rupture.

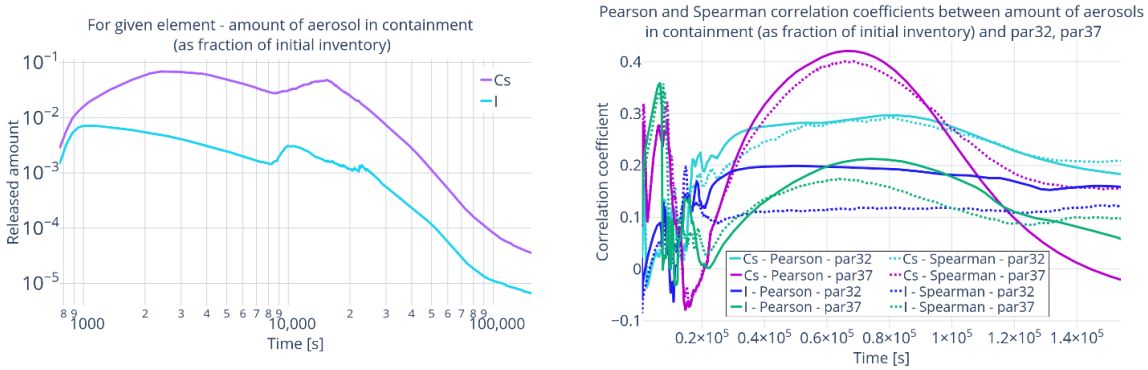

Figure 8. Amount of aerosol in containment (as fraction of initial inventory) – left; Pearson and Spearman correlation coefficients between amount of aerosol in containment and *par32*, *par37*

7. CONCLUSIONS AND OUTLOOK

U&S analysis results were presented, which were obtained from MBLOCA accident simulations (up to basemat rupture) at a KONVOI NPP performed with the ASTEC SA code and the FSTC tool. This work was performed in the framework of the WAME project, which focuses on developing a methodology for predicting ST for SA at NPPs. The U&S plays an important role in the WAME project and helps to prepare the training database for the ST predictions with MOCABA.

In this work, 16 input parameters have been selected for uncertainty propagation. Their PDFs have been assessed based on literature review and engineering judgement. These parameters refer both to the ASTEC

physical models for key phenomena related to the fission product transport behavior and to relevant plant modeling.

Simple statistics, Pearson and Spearman correlation coefficients were shown for the releases of the following elements: Xe, Cs, I, Mo, Ba. For the release into the environment, the parameters with the highest influence are *par41* and *parBU*, governing the containment leakage and the fuel burnup, respectively. Parameters governing the aerosol behavior are playing a significant role when degradation of the core is finished, and this effect is observed for the Cs and I aerosols in the containment when the MBLOCA scenario is simulated up to basemat rupture.

The observed differences between Pearson and Spearman correlation values are significant in some cases, but this is related to time regions with low correlations and related to data with seemly random relationship between input and response parameter. Therefore, to make conclusions about the influence of the release values from the different input parameters, further investigations should be made using re-sampling of the input parameters.

ACKNOWLEDGMENTS

The project was funded by the German Federal Ministry of Economic Affairs and Energy, funding code FZK 1501582 (WAME project).

REFERENCES

1. P. Chatelard, et al., “ASTEC V2 severe accident integral code main features, current V2.0 modelling status, perspectives”, *Nuclear Engineering and Design*, **Volume 272**, pp.119-135 (2014).
2. A. Stakhanova, et al., “Uncertainty and sensitivity analysis of the QUENCH-08 experiment using the FSTC tool”, accepted in *Annals of Nuclear Energy* (2022).
3. M. D. McKay, R. J. Beckman and W. J. Conover, “A Comparison of Three Methods for Selecting Values of Input Variables in the Analysis of Output from a Computer Code”, *Technometrics*, **Volume 21**, pp. 239-245 (1979).
4. MUSA – Management and Uncertainties of Severe Accidents. European H2020 project. https://musa-h2020.eu/ (Accessed 31.01.22).
5. “Strategy for Competence Building and the Development of Future Talent for Nuclear Safety,” https://www.bmwi.de/Redaktion/EN/Publikationen/Energie/strategy-for-competence-building-and-the-development-of-future-talent-for-nuclear-safety.pdf (2020).
6. A. Hoefer, et al., "MOCABA: A general Monte Carlo-Bayes procedure for improved predictions of integral functions of nuclear data", *Annals of Nuclear Energy*, **Volume 77**, pp. 514-521 (2015).
7. J. Stuckert, A. V. Boldyrev and A. Miassoedov, 2005. *Experimental and computational results of the QUENCH-08 experiment (reference to QUENCH-07)* (No. FZKA--6970). Forschungszentrum Karlsruhe GmbH Technik und Umwelt (Germany). Inst. fuer Materialforschung.
8. E. Pauli, et. al., “Prediction of the radiological consequences of a severe accident scenario in a generic KONVOI nuclear power plant,” *Proceedings of 10th European Review Meeting on Severe Accident Research (ERMSAR-2022)*, Karlsruhe, Germany, 16-19 May, 2022.
9. F. Gabrielli, et. al., “Source Term Evaluation Following MBLOCA and SBLOCA Scenarios in a Generic KONVOI-1300 NPP by Means of the ASTEC Code,” *Eurosafe 2021*, Paris, November 22-23 (2021).
10. EC. “D40 .42 – 1st set of reference NPP ASTEC input decks”, CESAM FP7-GA-323264, (2015).
11. I. Gómez-García-Toraño, “Further development of Severe Accident Management Strategies for a German PWR Konvoi Plant based on the European Severe Accident Code ASTEC”, PhD Thesis, KIT, Germany, (2017).

12. G. Brillant, C. Marchetto, and W. Plumecocq, "Fission product release from nuclear fuel I. Physical modelling in the ASTEC code", Annals of Nuclear Energy, **Volume 61**, pp. 88–95 (2013).
13. "SCALE: A Comprehensive Modeling and Simulation Suite for Nuclear Safety Analysis and Design," ORNL/TM-2005/39, Version 6.2.3, March 2018.
14. M. Schwarz, G. Hache and P. von der Hardt, "Phebus FP: a severe accident research programme for current and advanced light water reactors," Nuclear Engineering and Design, **Volume 187** (1), pp. 47-69 (1999).
15. G. Brillant, C. Marchetto and W. Plumecocq, "Fission product release from nuclear fuel II. Validation of ASTEC/ELSA on analytical and large scale experiments," *Annals of Nuclear Energy*, **Volume 61**, pp. 96–101 (2013).
16. T. Ikeda, et al., "Analysis of core degradation and fission products release in Phebus FPT1 Testat IRSN by detailed severe accidents analysis code, IMPACT/ SAMPSON", *Journal of Nuclear Science and Technology*, **Volume 40** (8), pp. 591–603 (2003).
17. G. Pastore, et al., "Uncertainty and Sensitivity Analysis of Fission Gas Behavior in Engineering-Scale Fuel Modeling," Journal of Nuclear Materials, **Volume 456**, pp. 398-408 (2015).
18. Kun Woo Song, et. al., "Sintering of mixed UO_2 and U_3O_8 powder compacts", *Journal of Nuclear Materials*, **Volume 277** (2-3), pp. 123-129 (2000).
19. D. Osborn, et al., "State-of-the-Art Reactor Consequence Analysis (SOARCA) Project Sequoyah Integrated Deterministic and Uncertainty Analyses", NUREG/CR-Draft, U.S. Nuclear Regulatory Commission, Washington, DC, (2017).
20. Y. Pontillon, et al., "Lessons learnt from VERCORS tests: Study of the active role played by UO_2-ZrO_2-FP interactions on irradiated fuel collapse temperature", *Journal of Nuclear Materials*, **Volume 344** (1-3), pp. 265–273 (2005).
21. P. Hofmann, et al., "ZrO2 Dissolution by Molten Zircaloy and Cladding Oxide Shell Failure. New Experimental Results and Modelling," FZKA 6383, INV-CIT(98)-P-026, Forschungszentrum Karlsruhe (1999).
22. P. D. Mattie, et al., "State-of-the-Art Reactor Consequence Analyses Project Uncertainty Analysis of the Unmitigated Long-Term Station Blackout of the Peach Bottom Atomic Power Station", U.S. Nuclear Regulatory Commission, NUREG/CR-7155, Washington, DC, 2015.
23. J. C. Helton, et al., "Uncertainty and sensitivity analysis of a model for multicomponent aerosol dynamics", *Nuclear technology*, **Volume *73***(3), pp. 320-342 (1986).

Table I. Uncertain input parameters for MBLOCA scenario simulation

Parameter name	Probability density function (PDF)	PDF parameters	Parameter meaning and corresponding ASTEC model	Source
par1	Normal	$\mu = 5.0$; $\sigma = 30\%$	Correction factor for the ratio S/V of the fuel pellets due to roughness	[12, 15, 16]
par2	Normal	$\mu = 0.03$; $\sigma = 30\%$	Correction factor for the ratio S/V of the fuel pellets for the limited steam access	[12, 15, 16]
par5	Normal	$\mu = 1.2E-5$; $\sigma = 30\%$	Geometrical diameter of the grain	[17, 18]
par5a	Triangular	mode = 2.0E-6; min = 1.6E-6; max = 3.4E-6	Standard deviation of geometrical diameter of the grain	[17, 18]
par14	Normal	$\mu = 2500.0$; $\sigma = 10\%$	Threshold Temperature of the cladding Dislocation [K]	[19, 20]
par15	Normal	$\mu = 2300.0$; $\sigma = 10\%$	Threshold Temperature of the oxide layer Dislocation [K]	[21]
par16	Normal	$\mu = 250.0E-4$; $\sigma = 20\%$	Threshold thickness of the oxide layer [mm]	[21]
par31	Uniform	min = 2.975; max = 4.025	Particle mean thermal conductivity (J/m/K)	Engineering judgement
par32	Uniform	min = 714.0; max = 966.0	Average specific heat (J/kg K) of the aerosol	Engineering judgement
par33	Triangular	mode = 3000.0; min = 2610.0; max = 10000.0	Particle mean density (kg/m3)	[22]
par34	Triangular	mode = 1.1E-8; min = 1.0E-8; max = 2.0E-07	Particle minimum geometrical radius (m)	[23]
par35	Triangular	mode = 1.99E-5; min = 5.0E-6; max = 2.0E-5	Particle maximum geometrical radius (m)	[23]
par36	Triangular	mode = 1.0; min = 0.9, max = 1.0	Shape factor relative to particle coagulation	[22]
par37	Beta	$\alpha = 1.0$; $\beta = 5.0$, min = 1.0; max = 3.0	Shape factor relative to Stokes velocity	[19]
par41	Uniform	min = 1.0; max = 30.0	Coefficient for the leakage rate between containment and annulus	Engineering judgement
parBU	Uniform	min = 10.0; max = 328.0	Effective full power days	Engineering judgement

The 10th European Review Meeting on Severe Accident Research (ERMSAR2022), Akademiehotel, Karlsruhe, Germany, May 16-19, 2022

Karlsruhe Institute of Technology

framatome

ERMSAR Talk 327

Uncertainty and Sensitivity Analysis of the ASTEC simulations results of a MBLOCA scenario at a Generic KONVOI Plant using FSTC tool

Stakhanova A, Gabrielli F, Sanchez-Espinoza V. H - Karlsruhe Institute of Technology (KIT)
Pauli E, Hoefer A - Framatome GmbH

Institute for Neutron Physics and Reactor Technology





framatome

Karlsruhe Institute of Technology

Table of content

- Introduction
- Fast Source Term Calculation (FSTC) tool
- ASTEC model of a generic KONVOI NPP
- Uncertain input parameters
- Results of U&S analysis
- Conclusions and outlook

Introduction

- Work is made in cooperation with Framatome GmbH in the frame of the German WAME project (2019-2022) financed by the Federal Ministry of Economics Affairs and Climate Action (BMWi) in the frame of activity 'Maintaining Competence in Nuclear Technology'
- Solid basis for the KIT/Framatome joint contribution to the H2020 Management and Uncertainties Of Severe Accidents (MUSA) project (2019-2023) (see talk 278, S. Brumm)

Main goal of the WAME project: develop methodology and the tool for fast source term prediction in case of severe accident to support emergency team

The Monte Carlo-based Bayesian inference model MOCABA [1, 2] developed by Framatome is used for source term predictions during severe accident scenarios (details in the talk 311, E.M. Pauli).

This talk is focused on U&S analysis of severe accident simulations aiming at assessing the training database for the prediction algorithm

- SA code: ASTEC 2.2b
- Generic KONVOI NPP
- MBLOCA scenario up to basemat rupture
- Tool for U&S analysis – in-house Fast Source Term Calculation (FSTC)

FSTC tool

- Fast Source Term Calculation (FSTC) [3] tool developed at KIT in the frame of WAME project.
- Could be used separately for performing U&S analysis or fast source term predictions.
- FSTC has been coupled with the ASTEC code
- MOCABA is a proprietary Framatome code. Like-named approach is implemented in FSTC.

FSTC tool info:

- Python language
- Modular structure
- Sampling – SRS, LHS
- Option of correlated uncertain input parameters
- Pearson, Spearman, and other correlation coefficients

FSTC tool

- Scheme of FSTC tool in frame of performing source term prediction

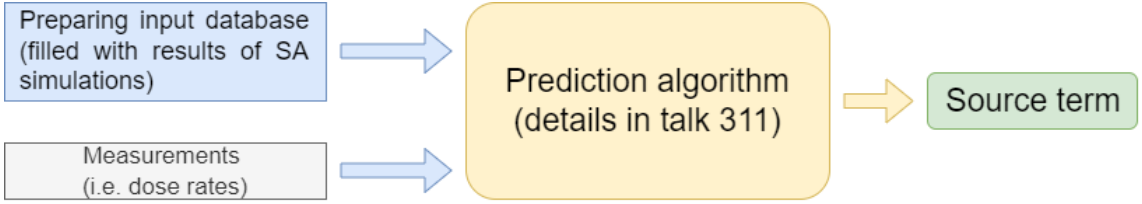

- Scheme of the part of FSTC tool in frame of U&S analysis

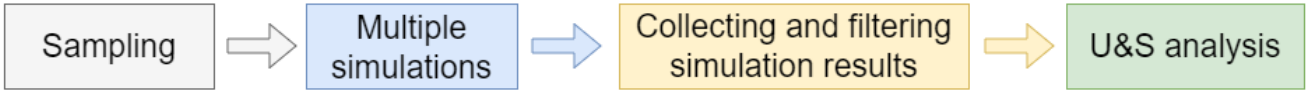

KONVOI NPP ASTEC model

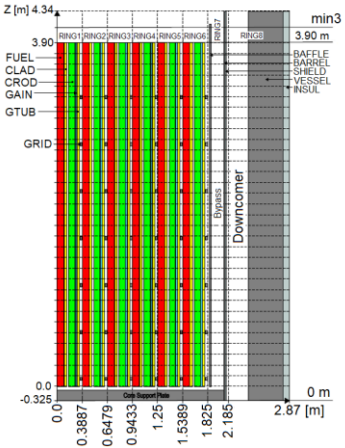

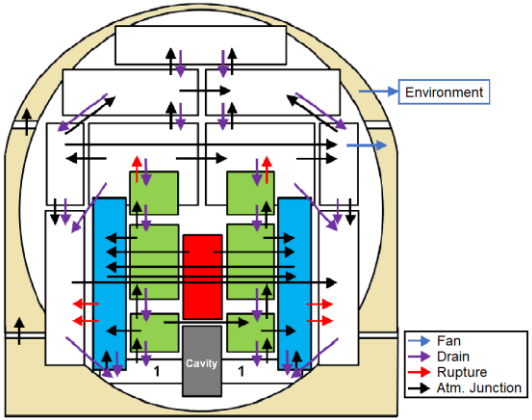

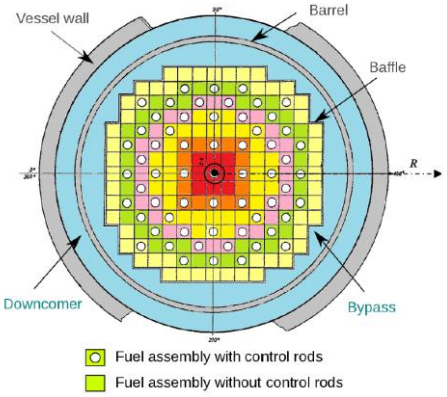

- ASTEC 2.2b is used
- All ASTEC modules are activated
- Extension and improvement of the generic input deck developed during the EU CESAM project [6]
- Fuel inventories calculated with ORIGEN-ARP code
- Containment leakage to the annulus
- No filtering
- Simulation up to basemat rupture

Figures are from [4] – left, [5] - right

Uncertain input parameters

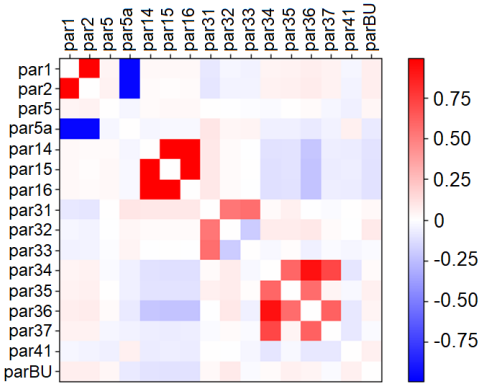

Iman-Conover method is used to correlate input parameters

Distributions: normal distribution – 6 parameters; Triangular – 5; Uniform – 4; Beta - 1

PDFs and PDFs parameters accessed based on literature, code manuals, and engineering judgement

Par-r	Phenomenon	Meaning
par1	Fission Product release from the fuel	Correction factor for the ratio S/V of the fuel pellets due to roughness
par2		Correction factor for the ratio S/V of the fuel pellets for the limited steam access
par5		Geometrical diameter of the grain
par5a		Standard deviation of geometrical diameter of the grain
par14	Cladding integrity criteria	Threshold Temperature of the cladding Dislocation [K]
par15		Threshold Temperature of the oxide layer Dislocation [K]
par16		Threshold thickness of the oxide layer [mm]
par31	Aerosols behavior in the RCS	Particle mean thermal conductivity (J/m/K)
par32		Average specific heat (J/kg K) of the aerosol
par33		Particle mean density (kg/m3)
par34		Particle minimum geometrical radius (m)
par35		Particle maximum geometrical radius (m)
par36		Shape factor relative to particle coagulation
par37		Shape factor relative to Stokes velocity
par41	Containment leakage	Flow rate (m3/s)
parBU	Fuel burn-up	Effective full power days

U&S analysis

- FSTC tool is preparing the database for prediction algorithm & calculate source term prediction
- This database should cover broad range of possible variants of SA scenario progression
- Input parameters potentially influencing the source term are selected
- U&S analysis performed to identify the most important uncertain parameters
- FoMs are - release of different FPs in vessel, primary circuit, containment, and environment
- For release values, simple statistics and correlation coefficients are calculated

framatome

U&S analysis

Karlsruhe Institute of Technology

[Time of start of FP release and basemat rupture for 200 simulations]

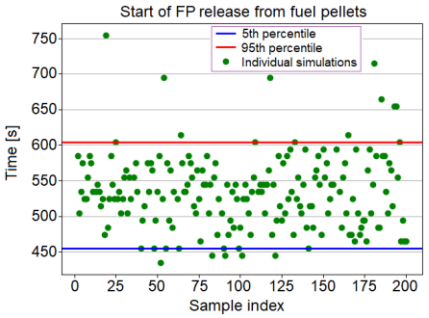

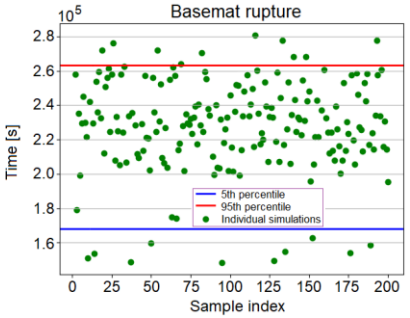

[Example of simple statistics]

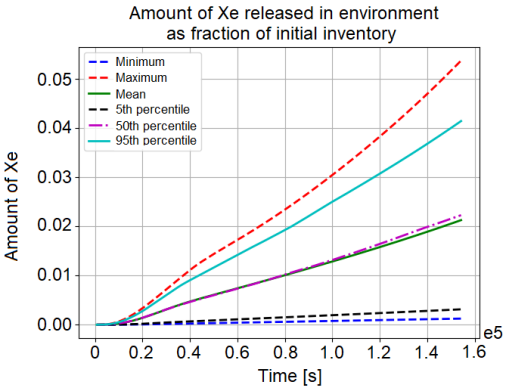

[Median amount for 5 elements released in environment and containment]

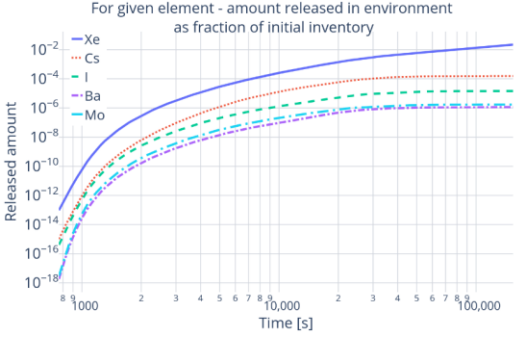

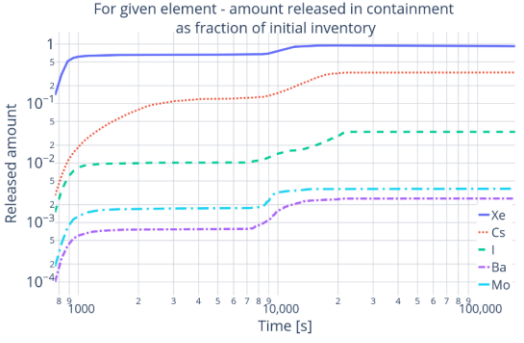

U&S analysis

Effect on the release to the environment from the containment leakage par-r

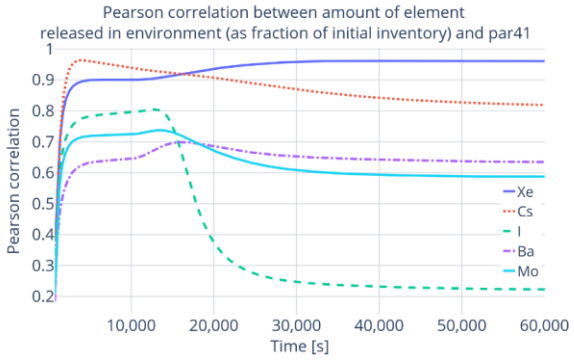

Effect on the release to the environment from the fuel inventory

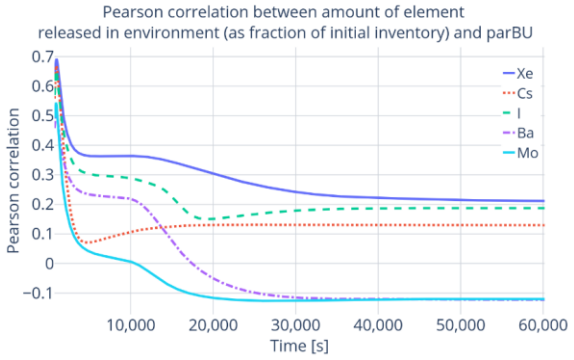

Effect on the release to the environment from the containment leakage par-r and the fuel inventory

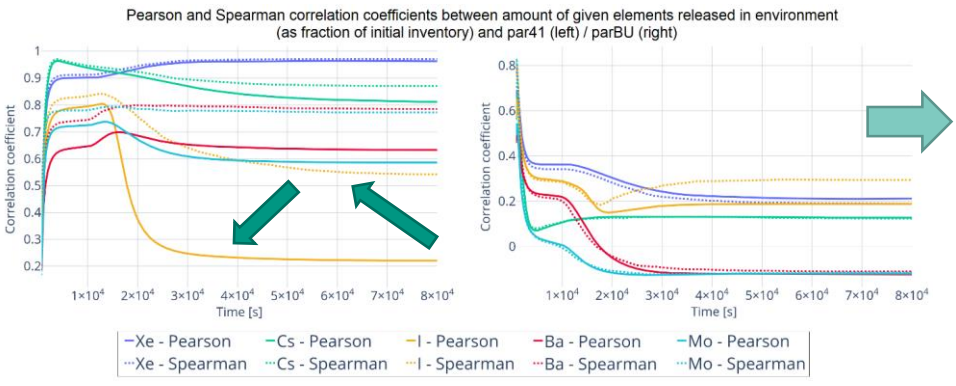

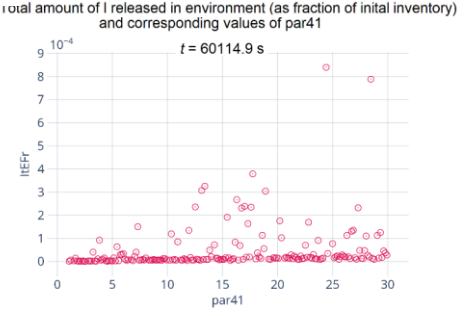

U&S analysis

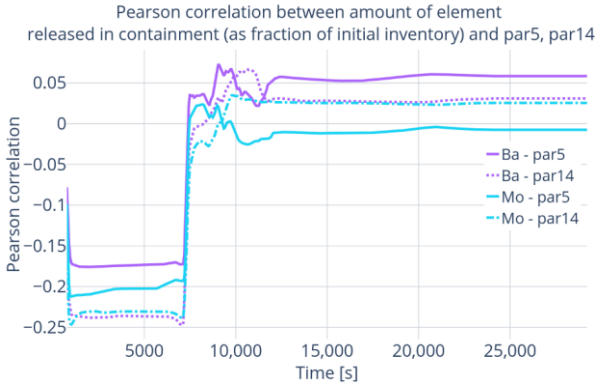

- For most of the uncertain input parameters Pearson and Spearman correlations are lying in the range [-0.1; 0.1] both for release in containment and environment

- Effect of some input parameters observed on the release of low-volatile fission products into the containment up to the rupture of the vessel:
  - Par 5: Std. dev. of geometrical diameter of the fuel grain
  - Par 14: Threshold Temperature of the cladding dislocation

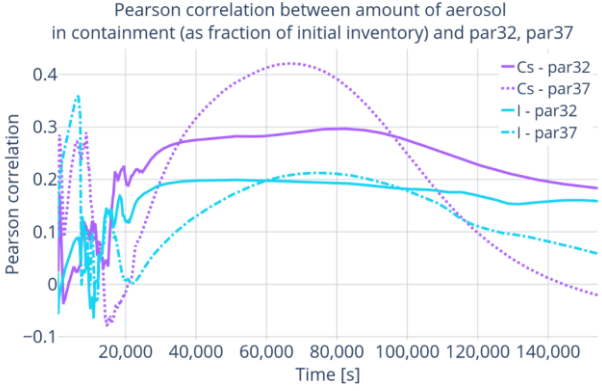

- The sensitivity of the amount of Cs and I aerosols in the containment to the physical models may significantly change during the accident progression:
  - Par 32: Average specific heat of the aerosol
  - Par 27: Shape factor relative to Stokes velocity

- Analysis of scenarios up to several hours after the vessel rupture provide a more general and reliable picture

U&S analysis

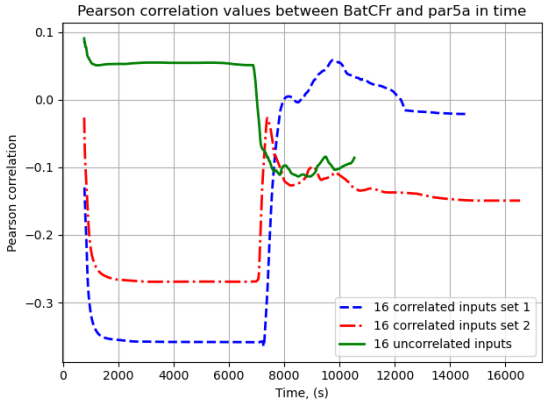

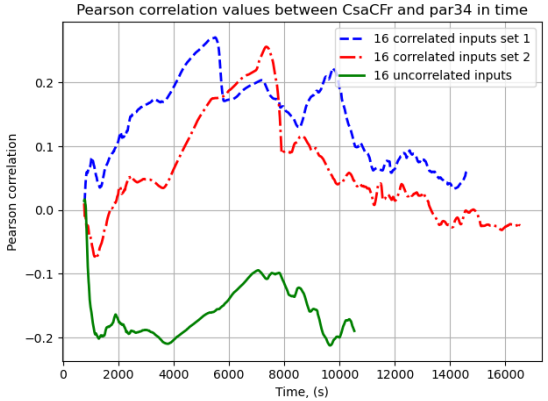

Effect of pre-correlating the uncertain input parameters

Three sets of simulations of MBLOCA scenario (stopped at 6000 s after lower head vessel failure). Each set – 300 simulations

Example of the Pearson correlation between:

- the amount of Ba aerosols in the containment and the std. dev. of geometrical diameter of the fuel grain (par 5)
- the amount of Cs aerosols in the containment and minimum geometrical radius of the particles (par 34)

Large deviations observed among the U&S results coming from ASTEC databases assessed by pre-correlating and not-correlating the uncertainties of the input parameters

Deviation observed on both:

- Values of the correlation coefficients
- Time-dependent behavior of the correlation coefficients

framatome

Conclusions & outlook

Karlsruhe Institute of Technology

- ✓ Fast Source Term Calculation (FSTC) tool developed at KIT and coupled to ASTEC for purposes of U&S analysis and fast source term prediction of SA scenario analyses
- ✓ For source term predictions the Monte Carlo-based Bayesian inference model based on MOCABA was implemented
- ✓ U&S analysis of source term during a MBLOCA scenario on KONVOI NPP performed using FSTC tool and ASTEC SA code
- ✓ Uncertainty of containment leakage and fuel burn-up significantly affects the fission product release to the environment and containment
- ✓ Significant effect of the uncertainty of the parameters governing the aerosol behavior observed on Cs and I release to the containment
- ✓ Need of analyzing the full scenario up to the basemat rupture identified
- ✓ Large effect of employing pre-correlated uncertain parameters on the UQ of the source term observed

- UQ of the source term for MBLOCA+SBO scenario is going on in the frame of the H2020 MUSA project
- U&S analyses for additional scenarios are going on in view of the assessment of a database of ASTEC source term results

framatome

Karlsruhe Institute of Technology

Thank you for your attention!

Acknowledgements

The project was funded by the Federal Ministry of Economics Affairs and Climate Action (BMWi), funding code FZK 1501582 (WAME project).

Contacts: KIT, INR; Stakhanova Anastasia, anastasia.stakhanova@kit.edu

References

1. Hoefer, A., Buss, O., Hennebach, M., Schmid, M. and Porsch, D., 2015. MOCABA: A general Monte Carlo–Bayes procedure for improved predictions of integral functions of nuclear data. *Annals of Nuclear Energy*, *77*, pp.514-521.
2. Castro, E., Ahnert, C., Buss, O., Garcia-Herranz, N., Hoefer, A. and Porsch, D., 2016. Improving PWR core simulations by Monte Carlo uncertainty analysis and Bayesian inference. *Annals of Nuclear Energy*, *95*, pp.148-156.
3. Stakhanova, A., Gabrielli, F., Sanchez-Espinoza, V.H., Hoefer, A. and Pauli, E., 2022. Uncertainty and sensitivity analysis of the QUENCH-08 experiment using the FSTC tool. *Annals of Nuclear Energy*, *169*, p.108968. Link to the QUNECH-08 FSTC paper
4. Gabrielli F., Stakhanova A., Sanchez-Espinoza V.H., Pauli E., Hoefer A., Feldmann H., "Impact of realistic fuel inventories on the radiological consequences of a severe accident scenario in a generic KONVOI plant by means of the ASTEC code", Kerntechnik 2022, 21. - 22. Juni 2022, Hyperion Hotel, Leipzig, Germany
5. Gómez-García-Toraño, I., 2017. Further development of Severe Accident Management Strategies for a German PWR Konvoi plant based on the European Severe Accident Code ASTEC (PhD Thesis). Fakultät für Maschinenbau, Karlsruhe Institute für Technologie, Karlsruhe, Germany.]
6. EC. “D40 .42 – 1st set of reference NPP ASTEC input decks”, CESAM FP7-GA-323264, (2015).

CIEMAT's outcomes from the PHEBUS-FPT1 uncertainty analysis in the framework of the EU-MUSA project

Rafael Bocanegra, Luis E. Herranz
CIEMAT
Avenida Complutense 40, 28040 Madrid, Spain
rafael.bocanegra@ciemat.es, luisen.herranz@ciemat.es

ABSTRACT

In 2019, the first European project fully focused on uncertainty quantification in severe accident analysis was launched. Referred as "Management and Uncertainties of Severe Accidents (MUSA)" and led by CIEMAT, the project foresees testing uncertainty quantification methods in a simplified but still representative scenario of a severe accident: the PHEBUS-FPT1 experiment. This study synthesizes the results got by CIEMAT when using the MELCOR 2.2 code and the DAKOTA statistical software for such a purpose. A BEPU analysis has been performed including all the input variables considered uncertain which affect the fission product release and transport phenomena. The uncertainties have been propagated applying the Monte Carlo method and the uncertainty region has been obtained according to the Wilk's method. A subsequent regression analysis, based on the Pearson's and Spearman's coefficients, has been also performed to identify the most influential parameters on the main figures of merits, being these the cesium and iodine release, and airborne mass transport to the containment. The results have indicated that the uncertainty band is broader than an order of magnitude in the case of FP transport and determined not just by particle shape but also by some thermal-hydraulic variables.

KEYWORDS

Uncertainty Quantification, Severe Accident, Source Term, PHEBUS-FPT1, MELCOR

1. INTRODUCTION

Numerical simulation tools are widely used in the nuclear community to assess the behavior of Nuclear Power Plants (NPPs) during postulated accidents, including Severe Accidents (SAs). They are a central element of the safety demonstration where the compliance of the main safety features of a NPP is assessed against safety requirements. In addition, the development and optimization of Accident Management (AM) measures, aiming at preventing and mitigating the consequences of SA, heavily rely on numerical simulations with codes such as ASTEC, AC2, MAAP, or MELCOR. Among the key parameters to predict are the time of failure of safety barriers and the potential radiological Source Term (ST) to the environment.

The EU project Management and Uncertainties Of Severe Accidents (MUSA) was founded in the HORIZON 2020 EURATOM NFRP-2018 call on "Safety assessments to improve accident management strategies for generation II and III reactors". It is coordinated by CIEMAT with the participation of 28 Organizations from 16 Countries [1]. The project aims to establish a harmonized approach for the Uncertainty Quantification (UQ) associated with Severe Accident (SA), with the main objective of assessing the capability of SA codes for estimating the uncertainty range in ST in GEN II and III Nuclear Power Plants (NPPs), as well as for Spent Fuel Pool (SFPs) accident scenarios. To do so and going beyond the State-Of-the-Art in terms of predictive capability, SA analysis codes are to be coupled with the best available or improved UQ methods and tools.

In this context, the Work Package 4 (WP4, Application of UQ Methods against Integral Experiments) is aimed at applying and testing UQ methodologies against the PHEBUS FPT1 test [2]. This paper summarizes

the CIEMAT's UQ methodology (section 2) to simulate the PHEBUS FPT1 UQ scenario (section 3). The main insights coming out from these calculations are then outlined (section 4) and finally synthesized in some final remarks and conclusions (section 5).

2. CIEMAT's UQ Methodology

The Best Estimate (BE) approach has been gaining momentum in the nuclear safety community as a means to achieve more realistic calculations than the original conservative approach applied for decades. However, a single BE calculation is not enough when safety is concerned; it needs to be complemented by assessing the precision of the calculation through considering the scattering effect on estimates caused by input and code uncertainties; CIEMAT's approach to do so is based on the BEPU-CSA methodology [3] which relies on the input-driven uncertainty propagation. Calculations are performed with the MELCOR 2.2 code [4] for the Severe Accident (SA) phenomenology complemented with the DAKOTA tool [5] for the statistical analysis. The goal of the statistical analysis is the estimation of the tolerance interval of the selected FOMs, which is achieved by means of the Wilks' order statistic method [6]. In addition, a regression analysis is also performed in order to highlight the input uncertainties influence, being this focused on Pearson's and Spearman's Correlation Coefficients (CCs).

MELCOR is a fully integrated, engineering-level computer code that models the progression of severe accidents [4]. It includes a broad spectrum of phenomena, from core degradation to source term to the environment; just to mention a few: thermal-hydraulic response in the reactor coolant system, reactor cavity, containment, and confinement buildings; core heat-up, degradation, and relocation; core-concrete attack; hydrogen production, transport and combustion; fission product release, transport and behavior.

The statistical tool DAKOTA [5] was originally conceived to more readily interface simulation codes and optimization algorithms. However, latest versions include other iterative analysis methods such as UQ. Dakota is able to perform forward uncertainty propagation in which probability information for input parameters is mapped to probability information for output response functions. CIEMAT used the DAKOTA tool in "stand-alone" mode, which required developing several python scripts to compute the Monte Carlo (MC) sequence and perform the pairing process of input parameters. The whole process is governed by another python script; whose task is just to follow the flow chart shown in Figure 1.

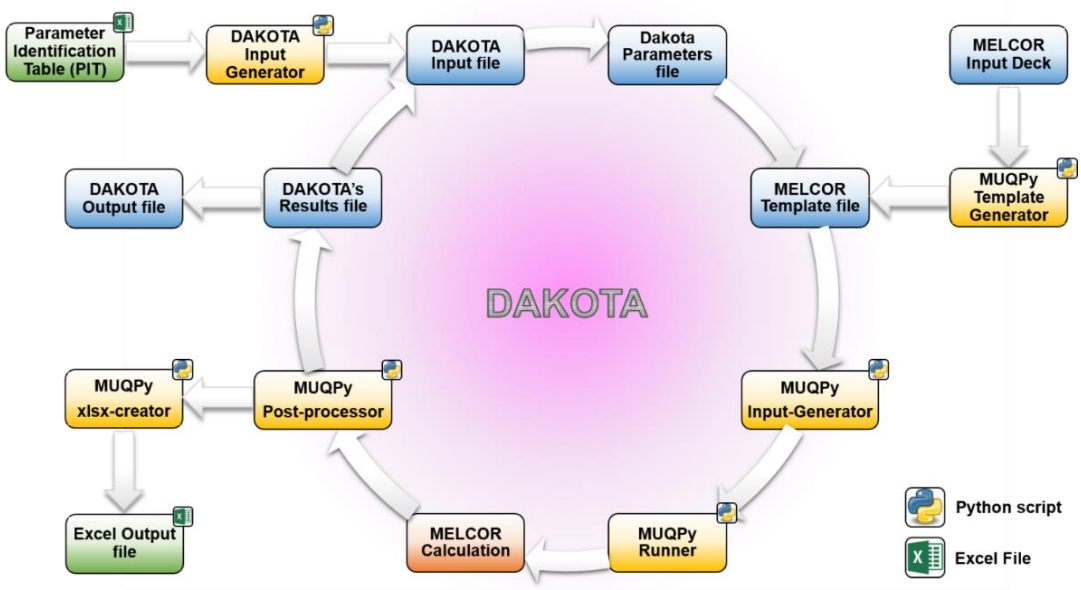

Figure 1: MELCOR-DAKOTA coupling scheme

When the UQ is conducted, it is necessary to adapt the MELCOR output to the DAKOTA format. The method employed by CIEMAT consist in define the FOMs variables with Control Functions (CFs) and write them into an External Data File (EDF) with the correct format. Then, this file is used by the DAKOTA iteration algorithm to include it in the statistical analysis. In addition, a python script is also employed to perform a parallel post-processing for the statistical analysis and also to plot all the FOMs in an Excel file.

One aspect to be accounted is that the sensitivity analysis has been performed using a relatively small sample size. This should not have any effect in parameters highly correlated with FOMs, but for robustness, it is convenient to realize a significance test. That means that the probability value (p-value) obtained for the CCs in a hypothesis test should fall below a significance level (α). The α-value is defined as $\alpha=1-\beta$, being β the confidence level desired. Therefore, for a 95% confidence $\alpha=0.05$. Since the FOM analyzed is an integral magnitude, the test is performed for values resulted at the end of the transient, that is at 20000 s.

3. MUSA-WP4: PHEBUS FPT1 Exercise

As said above, the WP4 was built to test the UQ methodologies against the PHEBUS FPT1 test. The FPT1 test involved the degradation to melting of a 1 m long fuel bundle, made of 18 irradiated fuel rods (about 24 GWd/tU), two fresh fuel rods and a silver-indium-cadmium control rod. The fuel bundle was re-irradiated in situ in order to build up a close-enough inventory in short-lived Fission Products (FPs). The degradation of the fuel was carried out by a progressive increase of the driver-core power, up to the formation of a molten pool in the lower part of the bundle. The test comprises several phases: fuel degradation-, aerosol transport, containment washing, and a chemistry-phase. However, only the first two of them were decided to be faced in WP4. More information about the PHEBUS-FPT1 test can be found in [2]. The Figures Of Merit (FOMs) are collected in Table 1.

Table 1: CIEMAT's 1st calculation Figures of Merit for the PHEBUS-FPT1 exercise

Parameter
Release of iodine from the fuel bundle [% of i.i.]
Release of cesium from the fuel bundle [% of i.i.]
Cesium retention in the circuit [% of cesium released]
Iodine airborne in the containment's atmosphere [mg]
Deposited iodine in the containment [mg]

A database has been built in MUSA WP2 (Identification and Quantification of Uncertainty Sources). Nonetheless, CIEMAT built an own database with more than 700 input MELCOR parameters, of which only those related to core degradation, FP release and aerosol dynamic processes have been included in this analysis (Table 2); a total of 56 input parameters considered. The characterization of input parameters uncertainty was done through a literature survey, as shown in the table; note that there is diversity of sources for some parameters, while no information was found for others. When several sources were found for a specific parameter, a combination was applied by selecting the minimum, maximum and expected values from the data available (note that the expected value could be the mean value or the mode). As for the probability distribution, if more than one distribution is proposed, a triangular one was used. In the case that no data were found, engineering judgement was put in place.

Table 2: CIEMAT's 1st calculation Figures of Merit for the PHEBUS-FPT1 exercise

Description	Parameter id.	Range		Exp. Val. / B.Est.	Distribution	Reference
Aerosol Resuspension Fraction [a.u.]	fractResuspend	1.00%	100.00%	100.0%	Uniform	Expert Judgment
Fission Power [W]	oprpow	89.00%	111.00%	100.0%	Uniform	[1, p. 1]

Rod spacing [m]	pitch	5.00E-03	1.50E-02	1.26E-3	Uniform	Expert Judgment (Range) / [1, p. 0] (Best Estimate value)
Laminar Nusselt Number in fully developed flow in a rod bundle with constant heat flux	C1212_2	4.36	17.81	4.36	Uniform	[2], [3]
Temperature above which conduction enhancement is employed for molten components [K]	C1250_1	2800	3200	2800	Uniform	[3], [4]
Oxidation rate constant Low Temperature (H_2O)	C1001_1_1	27.82	32.56	29.6	Uniform	[5], [6]
Oxidation rate constant High Temperature (H_2O)	C1001_3_1	79.11	93.17	87.90	Uniform	[5], [6]
Oxidation rate: Upper temperature boundary for low temperature range [K] (H_2O Oxidation)	C1001_5_1	1825.00	1875.00	1850.00	Normal	[3], [7]
Oxidation rate: Lower temperature boundary for high temperature range [K] (H_2O Oxidation)	C1001_6_1	1845.00	1895.00	1870.00	Normal	[3], [7]
Minimum oxidation temperature [K]	C1004_1	933.15	1348.16	1323.16	Normal	[3], [7]
Eutectic reaction temperature [K] (Zircaloy-Steel)	C1011_2	1200	1400	1400	Triangular	[3]
Cladding failure (FP release)	clfail	973.00	1673.00	1073.00	Lognormal	[5], [6], [8]–[10]
Fuel failure time vs. Clad temperature (TF Scale factor affecting failure time)	tfscal_23	45.0%	200.0%	100.0%	Uniform	[11]
Initial FP mass (x11 RN Classes)	rinp1_cor_	87.0%	113.0%	100.0%	Uniform	[1]
I2 in cladding gap	rinp1_clad_	0.01	0.10	0.05	Uniform	Expert Judgment
Aerosol density [kg/m^3]	rhonom	870.00	4500.00	2000.00	Triangular	[11]
Dynamic Shape Factor [a.u.]	chi	0.50	15.00	1.00	Triangular	[12] & Expert Judgment
Agglomeration Shape Factor [a.u.]	gamma	1.00	10.00	1.75	Triangular	[12] & Expert Judgment
Slip factor [a.u.]	fslip	1.01	1.51	1.26	Triangular	Expert Judgment
Condensation coefficient [a.u.]	stick	0.20	1.00	1.00	Triangular	[13]

Thermal accomodation coefficient [a.u.]	ftherm	1.00	3.00	2.25	Triangular	[14], [15].
Turbulent dissipation [m^2/s^3]	turbds	7.50E-04	3.00E-02	1.00E-03	Triangular	[14]
Gas thermal conductivity / Particle thermal conductivity [a.u.]	tkgop	6.00E-03	1.00E+00	5.00E-02	Triangular	[14]
Diffusion boundary layer thickness [m]	deldif	5.00E-06	8.00E-03	1.00E-05	Triangular	[3], [14]
ZR Specific Heat [J/kgK]	tfscal_102	80.00%	120.00%	100.0%	Uniform	Expert Judgment
ZIRCONIA Specific Heat [J/kgK]	tfscal_130	88.00%	112.00%	100.0%	Uniform	[1]
CS Specific Heat [J/kgK]	tfscal_138	80.00%	120.00%	100.0%	Uniform	Expert Judgment
SS Specific Heat [J/kgK]	tfscal_142	80.00%	120.00%	100.0%	Uniform	Expert Judgment
AGINC Specific Heat [J/kgK]	tfscal_158	80.00%	120.00%	100.0%	Uniform	Expert Judgment
Spray Coating [J/kgK]	tfscal_166	94.00%	106.00%	100.0%	Uniform	[1]
Thoria [J/kgK]	tfscal_162	95.00%	105.00%	100.0%	Uniform	[1]
ZR Thermal Conductivity [W/mK]	tfscal_103	80.00%	120.00%	100.0%	Uniform	Expert Judgment
ZIRCONIA Thermal Conductivity [W/mK]	tfscal_131	55.00%	145.00%	100.0%	Uniform	[1]
CS Thermal Conductivity [W/mK]	tfscal_139	80.00%	120.00%	100.0%	Uniform	Expert Judgment
SS Thermal Conductivity [W/mK]	tfscal_143	80.00%	120.00%	100.0%	Uniform	Expert Judgment
AGINC Thermal Conductivity [W/mK]	tfscal_159	80.00%	120.00%	100.0%	Uniform	Expert Judgment
Spray Coating [W/mK]	tfscal_167	80.00%	120.00%	100.0%	Uniform	[1]
Thoria [W/mK]	tfscal_163	65.00%	135.00%	100.0%	Uniform	[1]
ZR Density [kg/m^3]	tfscal_104	90.00%	110.00%	100.0%	Uniform	Expert Judgment
ZIRCONIA Density [kg/m^3]	tfscal_132	97.50%	102.50%	100.0%	Uniform	IPSN/DRS/SEA/PEPF, 2000)
CS Density [kg/m^3]	tfscal_140	90.00%	110.00%	100.0%	Uniform	Expert Judgment
SS Density [kg/m^3]	tfscal_144	90.00%	110.00%	100.0%	Uniform	Expert Judgment
AGINC Density [kg/m^3]	tfscal_160	90.00%	110.00%	100.0%	Uniform	Expert Judgment
Spray Coating [kg/m^3]	tfscal_168	95.00%	105.00%	100.0%	Uniform	IPSN/DRS/SEA/PEPF, 2000)
Thoria [kg/m^3]	tfscal_164	96.50%	103.50%	100.0%	Uniform	IPSN/DRS/SEA/PEPF, 2000)

The MELCOR Evaluation Model (EM) of the PHEBUS apparatus has been modeled as shown in Figure 2. The bundle is discretized into 11 axial nodes and 2 radial rings, with 2 thermal hydraulic flow channels. The circuit is divided into 18 additional nodes, this being the minimum considered necessary for an adequate calculation of deposition [2]. The containment has been modeled with a single node for the main volume and another one for the sump, taking advantage of the well-mixed conditions.

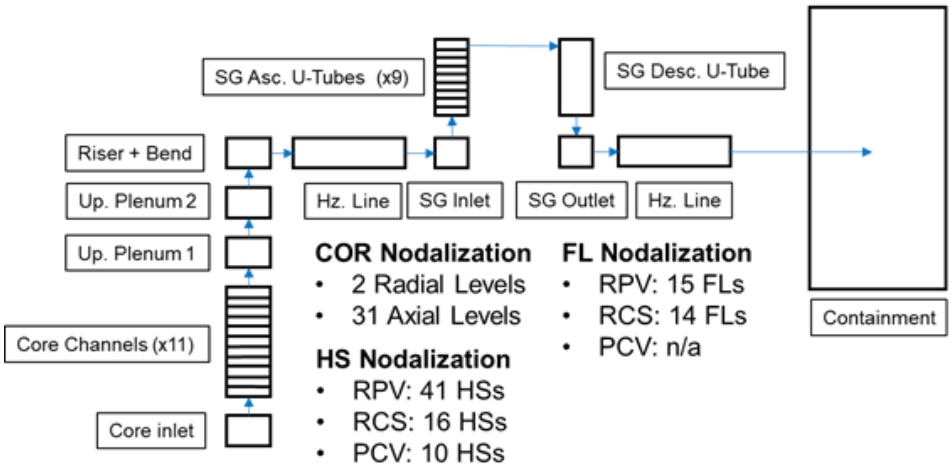

Figure 2: PHEBUS-FPT1 MELCOR nodalization

4. Results & Discussion

Results are shown in the following figures. Experimental results are not included to focus on identifying the challenges showed up by applying the above methodology to the experimental scenario. More importantly, the MELCOR evaluation model developed for the FPT1 has been thought for predictive analysis in the same way a NPP analysis would be performed. Therefore, no model calibration has been done. In addition, the experimental uncertainties, which are non-depreciable, has not been accounted. Out of the whole set of runs (93), 14 did not reach the targeted sample time (20000 s) and were considered failed. However, the analysis assumed that the entire set of calculations launched were successful; as a result, the focus has been set on trends rather than numerical results.

Cesium release from fuel is shown in Figure 3. The blue curve represents the base case result, and the red ones the upper and lower uncertainty bounds, respectively. The released mass differs in both, magnitude and timing, but what it is of interest for obtaining the tolerance interval is the quantity at the end of the transient. Therefore, the cesium released from the fuel at 20000 s ranges between 70-82 % of the initial cesium inventory in the fuel if a 95/95 criterion is applied in the analysis. Interestingly, one of the failed cases (at around 16500 seconds) shows a tendency that indicates that it would be the highest value obtained at the end of the sequence. This is of major importance when the Wilks' approach is employed, because "crash runs" might play a role, and a strategy should be figured out to deal with them.

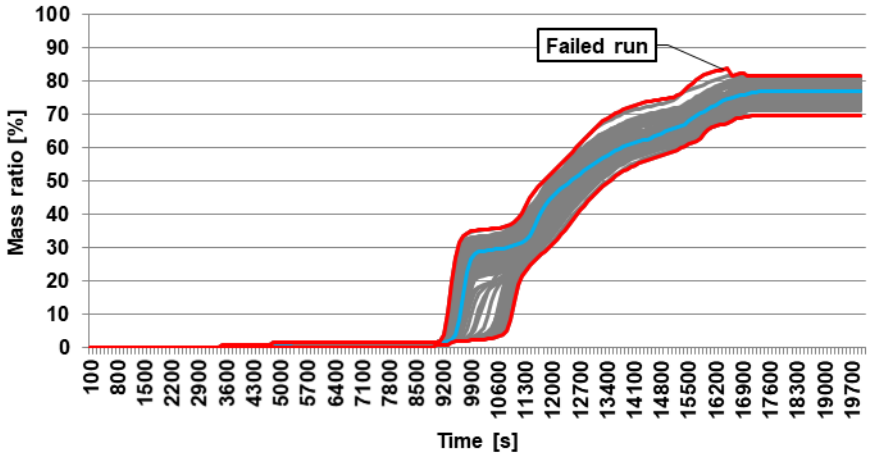

Figure 3: Released Cesium from the fuel

The Pearson correlation coefficients as a function of time can be seen in Figure 4. The first observation to make is that influence of some input parameters notably change along the transient. For instance, the red curve that reaches the value of around -0.9 corresponds to the "clfail" input variable, which represents the cladding failure temperature. If it is analyzed along with the cesium released ratio (Figure 3), it can be realized that this parameter is the dominant between 3500-9000 seconds, even though the released quantity is still small at this time. At this stage, the FP release rate is dependent on the number of failed rods, which is mainly controlled in MELCOR by the failure temperature set in the input deck. The nodalization in the COR package is also responsible for the number of failed rods along the time (the finer the mesh, the more progressive the number of leaking rods). The second period (9000-20000 s) looks dominated by the "C1212_2" and "tfscal_131" input parameters, which represents the laminar Nusselt number in fully developed flow in a rod bundle with constant heat flux, and the zirconia thermal conductivity, respectively. Both parameters are closely related with the temperature evolution in the fuel bundle, and since the released model employed (CORSOR-M) is dependent on the COR cell temperature, they both play a noticeable role during this period.

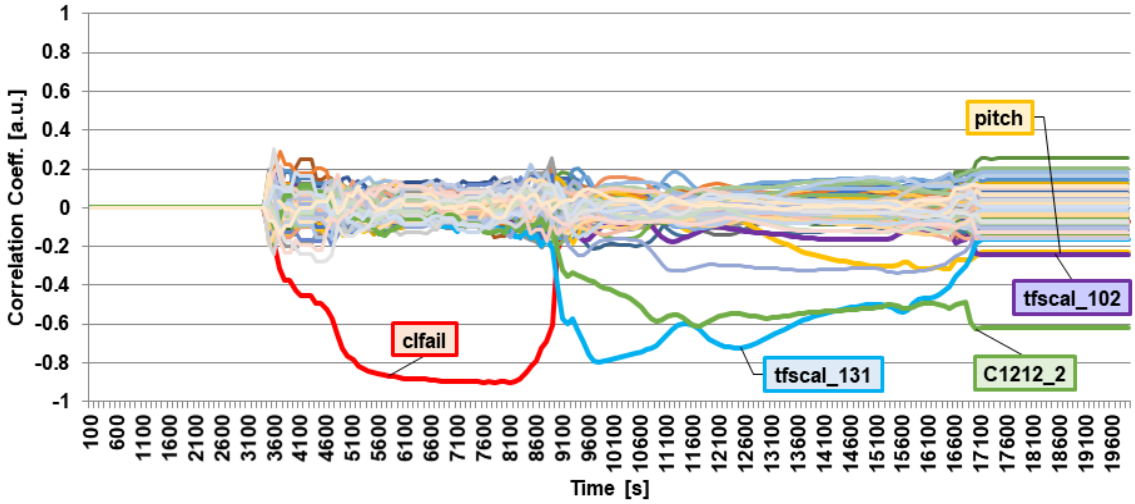

Figure 4: Pearson's correlation coefficients for the released cesium

Only the "pitch", "tfscal_102", and "C1212_2" input variables met the so called significance test. Namely, they should be the only ones considered correlated with the cesium released ratio: the pitch value (distance between fuel rods), the zirconium specific heat, and the already cited laminar Nusselt number in fully developed flow in a rod bundle with constant heat flux. Two CCs have been computed, the Pearson's and Spearman's CC (Figure 5). Both of them resulted similar in magnitude, indicating that the parameters are negatively, linearly, and monotonically descendent correlated.

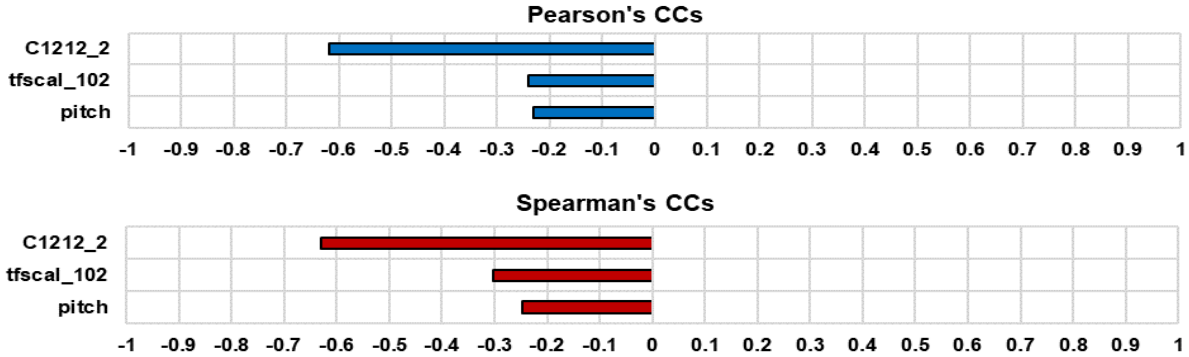

Figure 5: Released cesium correlation coefficients

Such as modeled, FP release occurs in two stages; firstly, FP located in the gap of failed fuel rods at the moment of cladding failure; secondly, FP from the pellets of the failed rods when according to temperature escalation. Another meaningful insight from the uncertainty analysis is that the release onset is rather uncertain, between 3500-9000 s, but the Cs release fraction in this period predicted in the calculation was negligible when compared to the total one. In short, uncertainty of Cs release from fuel is tightly bonded to fuel rod failure criterion, nodalization and thermal hydraulics during the first phase of an accident.

Something similar to the released cesium happens with the iodine (Figure 6), which ranges between 70-80 % of the initial iodine inventory. For this FOM, the scattering in the onset time is even more noticeable than for Cs, given that the fraction of I defined in the gap is higher.

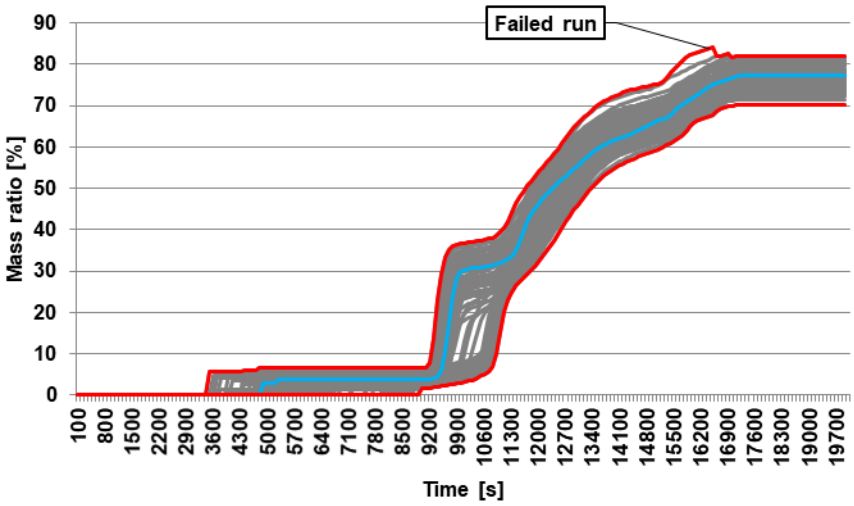

Figure 6: Released Iodine from the fuel

The correlation coefficients are shown in Figure 7. During the first stage (3500-9000 s), two parameters stand out above the rest, the “rinp1_clad_I2” and the “clfail”, referred to the proportion of iodine into the cladding gap and the cladding failure temperature, respectively. The difference with respect to cesium stems from the fact that, although both nuclides are released from the fuel according to an Arrhenius equation (i.e., temperature dependent) and get out from fuel rods at a specific clad temperature (as set in the input deck), a significant fraction of iodine inventory is initially located in the fuel rod gap. For the second release stage, the most correlated parameters resulted in the “tfscal_139” and “C1212.2”, being the “tfscal_139” referred to the carbon steel thermal conductivity.

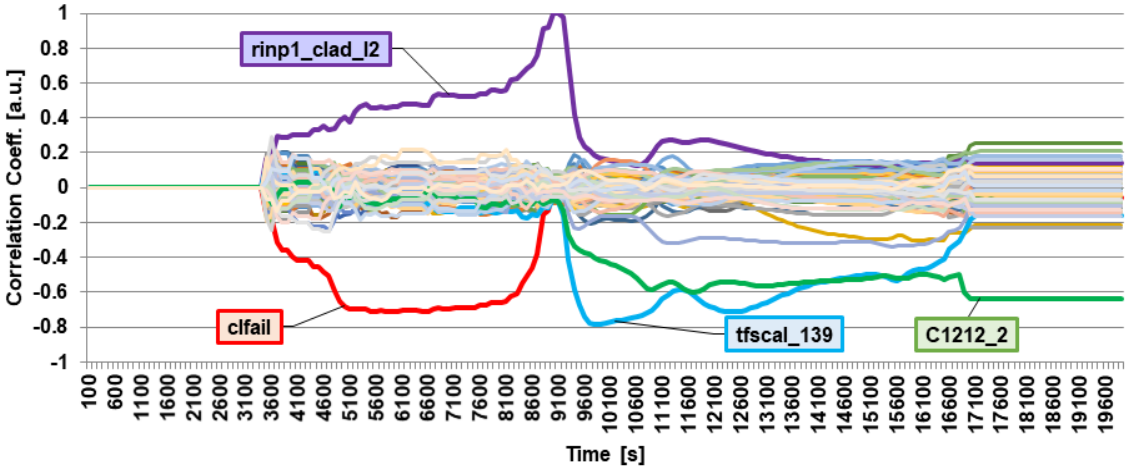

Figure 7: Pearson's CCs for the released iodine

The significance test is also performed for values at the end of the sequence (20000 s). It is not surprising that three of the four parameter CCs with statistical significance are the same than that for the cesium release (see Figure 8). Both, the cesium and iodine, are volatile FPs, thus it is expected to be governed by the same release equation. In MELCOR, the FP release is only estimated for the cesium class. For obtaining the release rate for all the other classes, a proportional multiplier is applied to the cesium release rate. The last remaining parameter included in Figure 8, the "tfscal_139", is positive and weak (~22%). Both its absolute contribution and its positive sign may be hardly supported on physical grounds, so that it might be considered a casualty due to the small sample employed in the sensitivity analysis.

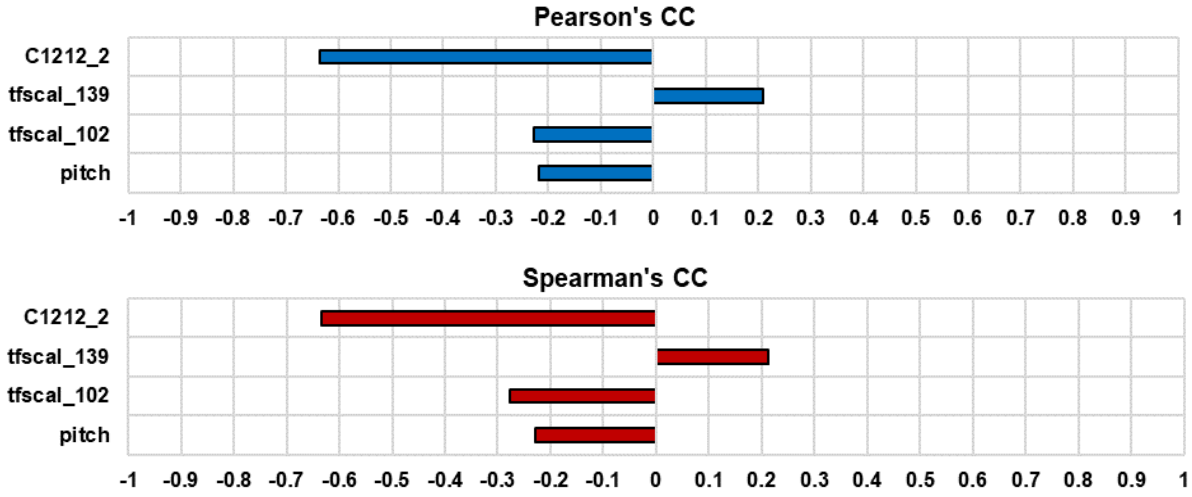

Figure 8: Released iodine correlation coefficients

The cesium deposits in the circuit in relation to that released from fuel are shown in Figure 9 as a function of time. However, the study interest is focused on the final cesium deposits (at the end of the transient), and it resulted in a range between 6-63 %.

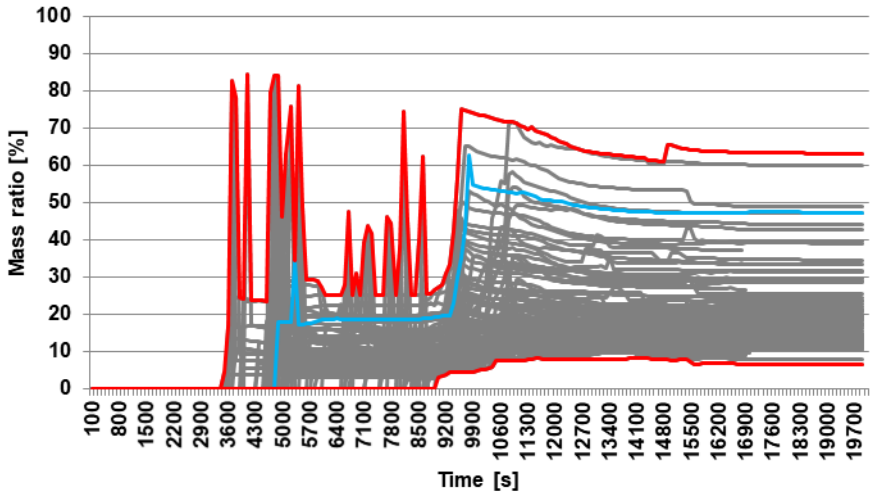

Figure 9: Cesium deposited in the circuit

This phenomenon is characterized to produce peaks between roughly 3000 and 9000 s, which are related with the cladding failure rate according to the clad failure criterion discussed above. Anyway, the quantitative impact of these peaks is negligible when the amount released is noted (see Figure 3 and Figure 6). Then, the deposition is mainly governed by the aerosol dynamics, and this can be confirmed looking at the correlation coefficients computed (see Figure 10). Only 2 out of the 86 input parameters included in the analysis could be considered correlated after the significant test, and both of them, "ftherm" and "chi", are parameters related with the calculation of the aerosol transport phenomena. The parameter "ftherm" represent the thermal accommodation coefficient and "chi" the aerosol dynamic shape factor. "Both the "chi" Spearman's CC (~99%) and the Pearson's CC (~76%) show very high values. This finding is consistent with the effect of inertial removal mechanisms on the overall deposition process. On the other hand, "ftherm" is also correlated for both CCs, although to a noticeable less extent.

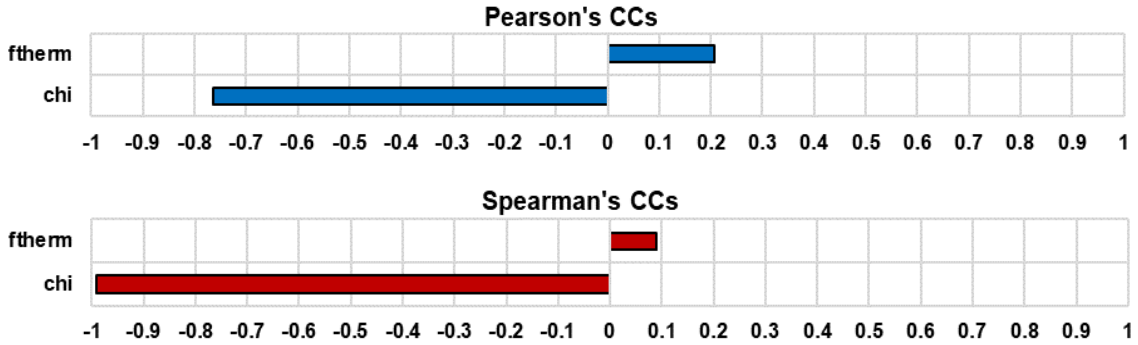

Figure 10: Cesium retained in circuit correlation coefficients

The mass of particulate iodine in containment is shown in Figure 11. The magnitude at the end of the transient ranges between 177-477 g, increasing the results dispersion along the transient.

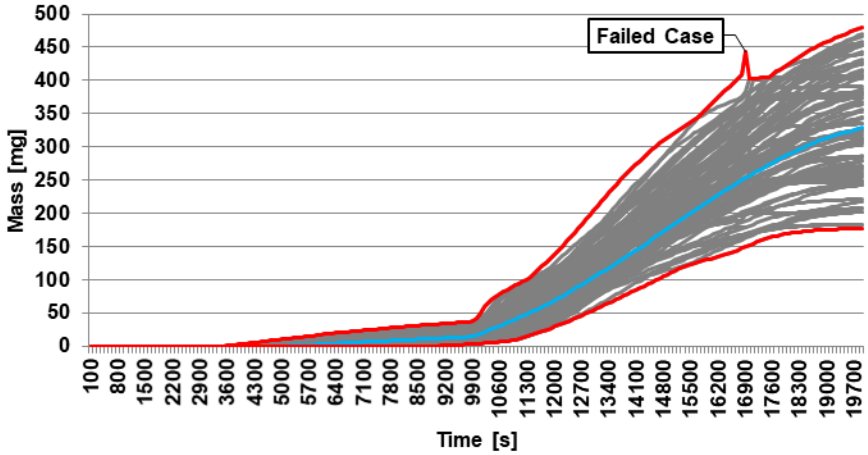

Figure 11: Iodine aerosol mass in containment

The Pearson's CCs are shown in Figure 12. As observed, uncertainties are heavily correlated with those of the release, which highlights the fact that transport to containment is, to a good extent, transparent in "uncertainty" terms ("clfail", "rinp1_cor_I2", "tfscal_131"). Then, once in the containment, uncertainties affecting other parameters governing aerosol dynamics, like "chi" or "gamma", also become visible. In other words, this FOM inherits uncertainties occurring in previous processes affecting the transport to and in containment.

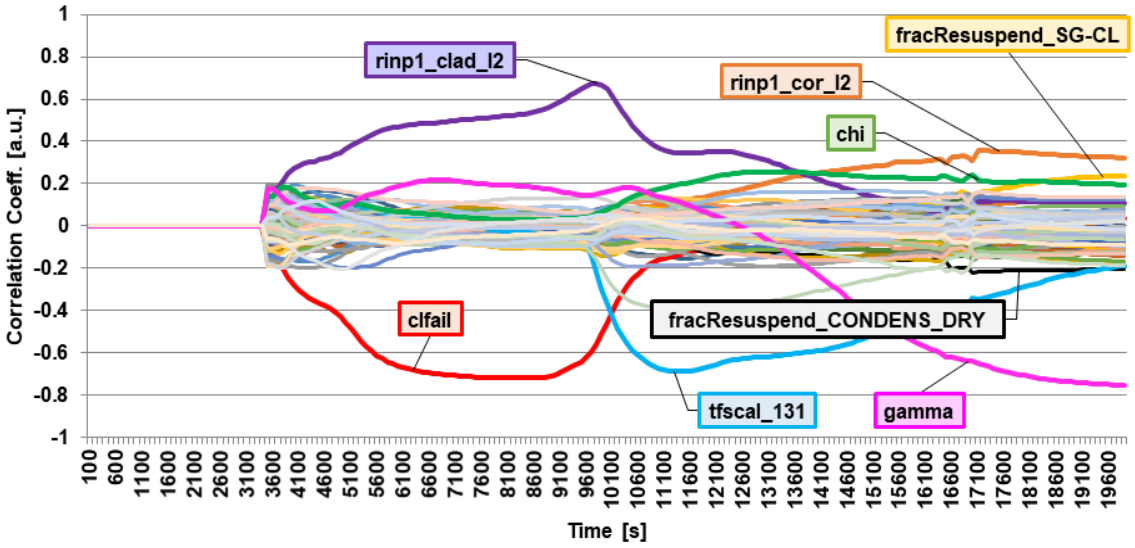

Figure 12: Pearson's CCs for the iodine aerosol mass in containment

From all the parameters analyzed, those whose CC present a statistical significance at the end of the transient (t=20000 s) are the "fractResuspend_SG-CL", "fractResuspend_CONDENS_DRY", "rinp1_cor_I2", "gamma", and "turbds", which represent the resuspension fraction of aerosols into the steam generator tube, the resuspension fraction of aerosols over the containment condenser (dry part), the initial inventory of iodine within the fuel, the agglomeration shape factor and the turbulent dissipation respectively. Their resultant CCs for both, Pearson's and Spearman's, are shown in Figure 13. As can be seen, the parameters correlated are those involved in the quantity of iodine available in the system and those related to the transport of aerosols from the fuel bundle to the containment, being the most influencing the gamma factor, with a negative CC of almost -0.8. This is again physically consistent: the bigger the iodine particles are (i.e., higher average agglomeration rate), the less the probability of remaining airborne in containment.

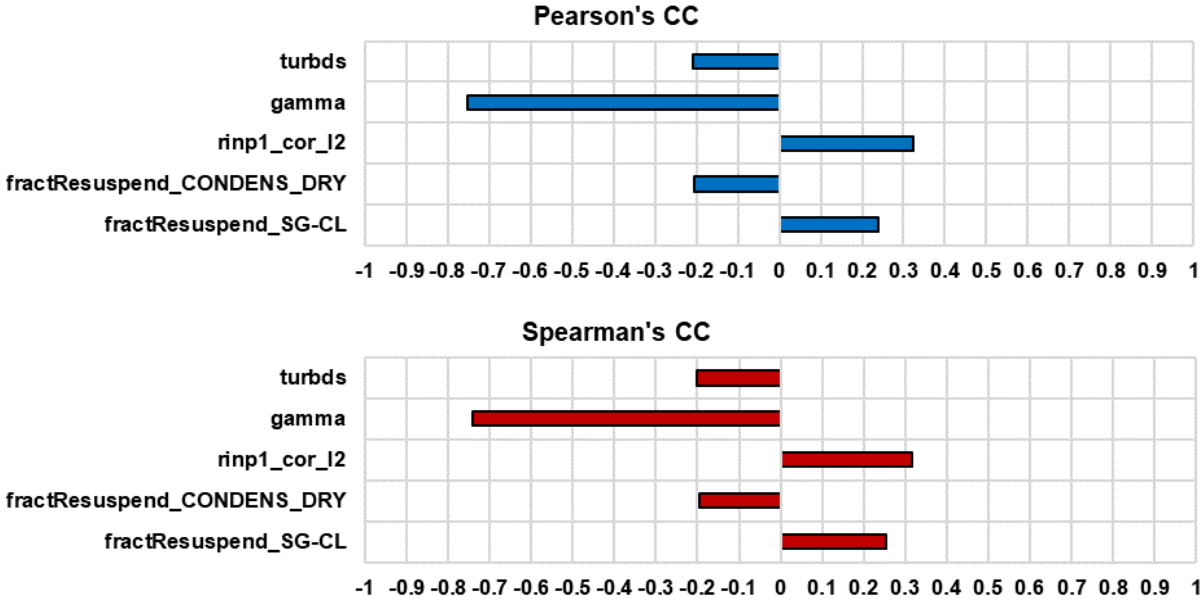

Figure 13: Total iodine aerosol in containment correlation coefficients

The last FOM analyzed is the iodine deposited in containment, which is shown in Figure 14. The total mass deposited at the end of the transient ranges from 311 to 800 mg. However, this interval "does not tell the entire story" as several cases crashed and some of them might have become bounding cases. The uncertainty in the deposited iodine in containment increases while the FPs are released into the system and transported through it to the containment; the profile closely follows the one in Fig. 11 (in-containment airborne iodine). The main factors governing uncertainties till 9000 s are the iodine inventory available, and those parameters noted in the analysis of release rate computation (Figure 15).

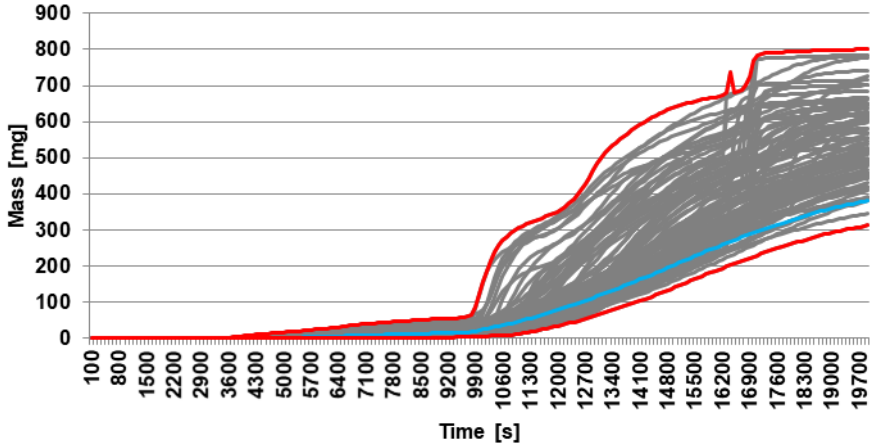

Figure 14: Iodine deposited in containment

The CCs with statistical significance at the end of the transient are shown in Figure 16. As expected, "rin1_cor_I2", "tfscal_131", "chi" and "gamma" are the parameters that can be said with a 95% confident that are correlated with the quantity of iodine deposited into the containment. The "chi" parameter corresponds to dynamic shape factor involved in the computation of the aerosol dynamics, particularly in sedimentation (dominating removal mechanism in containment). The other has already been discussed above.

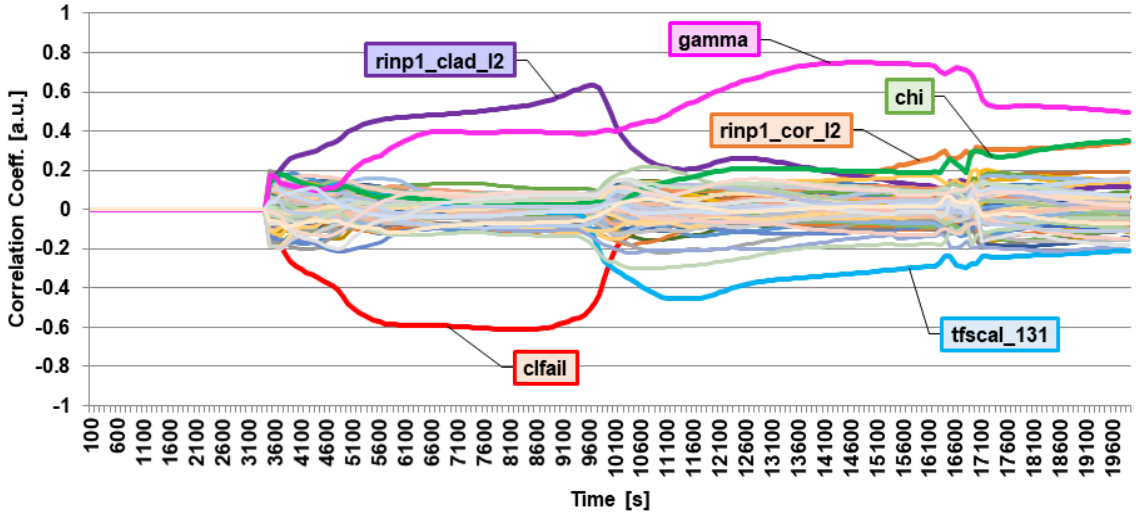

Figure 15: Pearson's CCs for the deposited iodine mass in containment

Both CCs, Pearson's and Spearman's, are almost identical indicating that the correlation is highly linear and increasing monotonically, except for the "tfscal_131" which is negative. The agglomeration shape factor

"gamma" resulted the most influencing (~50%), followed by the dynamic and iodine inventory in the fuel (~35%).

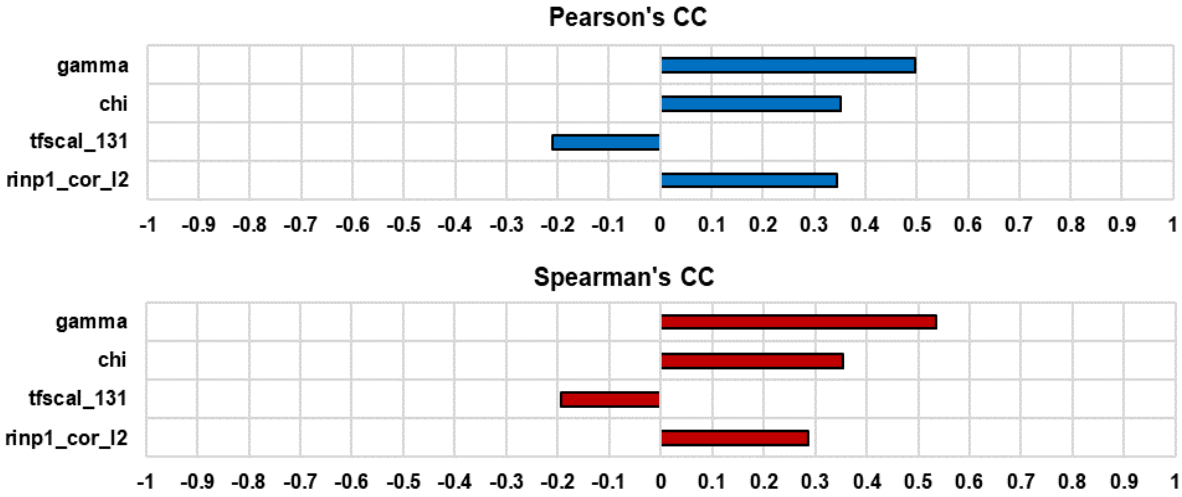

Figure 16: Iodine deposited in containment correlation coefficient

5. Final Remarks

Under the framework of the EU-MUSA project, focused on the application of the BEPU approach to severe accident analyses, the CIEMAT's methodology for uncertainty quantification has been tested against the scenario setup in the FPT1 experiment of the PHEBUS program. Two aspects have been given the utmost interest: on a practical side, the MELCOR-DAKOTA coupling through python scripts; on a conceptual one, how to manage the calculation database to gain deep and sound insights into the scenario predictability. Given the scope of MUSA and the FPT1 setup, FOMs concerning fission products release from fuel and transported through the facility were chosen.

From the work done, some generic observations have been settled:

- The extreme and intrinsic complexity of severe accident scenarios. The number of phenomena involved in severe accidents is huge and entails different disciplines, from thermal-hydraulics to aerosol physics, chemistry, structural mechanics and many others. This and the close interlink of many of them make particularly complicated to conduct a thorough identification and characterization of input deck parameters whose uncertainties should be propagated through the calculation. In the case of FPT1, with the specific focus already mentioned, more than 700 parameters have been identified in MELCOR 2.2; in the root of this large set is the close link of source term phenomena and thermal-hydraulics.
- Even when the number of parameters are drastically reduced (56) to make the trial applications more manageable, the adoption of the Wilk's method to limit the number of runs needed (93 for a 95% probability and 95% confidence) turns code crashes into a non-negligible matter. Replacing them by alternate ones might lead to an ill-coverage of the sampling domain, which would handicap the robustness of the calculation database. The more acceptable option seems to conduct a deep study of the crashes to identify the reasons underneath and make them work. Some authors (NEA/CSNI, 2017) suggest increasing the Wilks' order to allow discarding higher FOM's values, but this implicitly assume that the failed cases are those corresponding to the higher FOM's magnitudes.
- Sensitivity analysis might be a powerful tool to exploit the calculation database, but further work is necessary to find a suitable way of carrying it out. On one side, the regression techniques used in this work have been limited to the traditional Pearson and Spearman coefficients and further data analysis techniques should be explored to find out their potential. On the other, it is highly recommended to

conduct the so called significance test to identify parameters with a relevant role in the FOM's uncertainties; however, it should be expected that other variables than those accomplishing the significance test might be also correlated, as the size of the calculations database is limited. This said, by crossing the statistical information with the physical understanding of the scenario provides sound arguments supporting the identification through the significance test.

Additionally, some lessons from this exercise might be also drawn concerning Source Term FOMs:

- In-containment FOMs inherit uncertainties involved in fission product release and transport. Namely, those input parameters visibly influencing release and transport do also affect containment variables. What is interesting is that some of those variables, particularly those related to the time onset, are structural variables which setting are closely related to thermal-hydraulics.
- Uncertainties affecting in-containment FOMs grow with time, as expected, and at the end-of-transient their scatter does not exceed a factor of 2.0 with respect the baseline calculation. What might be of interest, though, is that uncertainties in fission product release onset might extend in a range of hours. This sort of observations might be of high relevance for practical implementation of accident management actions, if confirmed.
- Particles shape uncertainties do directly affect their transport and deposition mechanisms and, consequently, do have an observable impact in related source term FOMs other than release from the fuel. If confirmed when modeling NPP severe accidents, this might be a worth-to-investigate issue.

The natural steps of this work are: its extension to a larger set of input deck uncertain parameters and noticing the major discrepancies, if any, with the study here presented; application of the CIEMAT's approach to NPP severe accident analysis, both in reactor (MUSA/WP5) and in SFP (MUSA/WP6).

REFERENCES

1. IPSN/DRS/SEA/PEPF, «PHEBUS FPT1 Final Report», Cadarache, France, 2000.
2. T. L. Bergman y F. P. Incropera, Eds., *Fundamentals of heat and mass transfer*, 7th ed. Hoboken, NJ: Wiley, 2011.
3. Sandia National Laboratories, *MELCOR 2.2 Code Manuals*. Albuquerque, New Mexico: Sandia National Laboratories, 2019.
4. Sandia National Laboratories, «State-of-the-Art Reactor Consequence Analyses Project. MELCOR Best Modeling Practices», Sandia National Laboratories, Albuquerque, New Mexico, NUREG NUREG/CR-7008, 2010.
5. F. Sanchez-Saez, A. I. Sánchez, J. F. Villanueva, S. Carlos, y S. Martorell, «Uncertainty analysis of a large break loss of coolant accident in a pressurized water reactor using non-parametric methods», *Reliability Engineering & System Safety*, vol. 174, pp. 19-28, 2018, doi: 10.1016/j.ress.2018.02.005.
6. E. Zugazagoitia *et al.*, «Uncertainty and sensitivity analysis of a PWR LOCA sequence using parametric and non-parametric methods», *Reliability Engineering & System Safety*, vol. 193, p. 106607, 2020, doi: 10.1016/j.ress.2019.106607.
7. V. F. Urbanic y T. R. Heidrick, «HIGH-TEMPERATURE OXIDATION OF ZlRCALOY-2 AND ZIRCALOY-4 IN STEAM», *Journal of Nuclear Materials*, vol. 75, pp. 251-261, 1978.
8. NRC, «Cladding Swelling and Rupture Models for LOCA Analysis», NRC, NUREG-0630, 1980. [En línea]. Disponible en: https://www.nrc.gov/docs/ML0534/ML053490337.pdf
9. D. Y. Oh, J. Lee, Y. S. Bang, y C. Yang, «Uncertainty Evaluation considering Burnup Effect during LBLOCA», p. 12, 2017.

10. G. Schanz, S. Hagen, P. Hofmann, G. Schumacher, y L. Sepold, «Information on the evolution of severe LWR fuel element damage obtained in the CORA program», *Journal of Nuclear Materials*, vol. 188, pp. 131-145, 1992, doi: https://doi.org/10.1016/0022-3115(92)90462-T.

11. US NRC, «SOARCA Uncertainty Analysis of the Unmitigated Long-Term Station Blackout of the Peach Bottom Atomic Power Station», US NRC, NUREG/CR-7155, 2016. Accedido: 30 de enero de 2020. [En línea]. Disponible en: https://www.nrc.gov/docs/ML1318/ML13189A145.pdf

12. S. Y. Park y K. I. Ahn, «Uncertainty Analysis of the Fission Product Behaviors during Severe Accidents for a Typical PWR», *Progress in Nuclear Science and Technology*, vol. 1, n.º 0, Art. n.º 0, 2011, doi: 10.15669/pnst.1.448.

13. M. Mozurkewich, «Aerosol Growth and the Condensation Coefficient for Water: A Review», *Aerosol Science and Technology*, vol. 5, n.º 2, Art. n.º 2, 1986, doi: 10.1080/02786828608959089.

14. J. C. Helton, R. L. Iman, J. D. Johnson, y C. D. Leigh, «Uncertainty and Sensitivity Analysis of a Model for Multicomponent Aerosol Dynamics», *Nuclear Technology*, vol. 73, n.º 3, Art. n.º 3, 1986, doi: 10.13182/NT86-A16075.

15. L. Talbot, R. K. Cheng, R. W. Schefer, y D. R. Willis, «Thermophoresis of particles in a heated boundary layer», *J. Fluid Mech.*, vol. 101, n.º 4, Art. n.º 4, 1980, doi: 10.1017/S0022112080001905.

CIEMAT's outcomes from the PHEBUS-FPT1 uncertainty analysis in the framework of the EU-MUSA project

Rafael Bocanegra & Luis E. Herranz

Unit of Nuclear Safety Research
CIEMAT (Spain)

MUSA Horizon 2020 (contract number 847441)

Structure

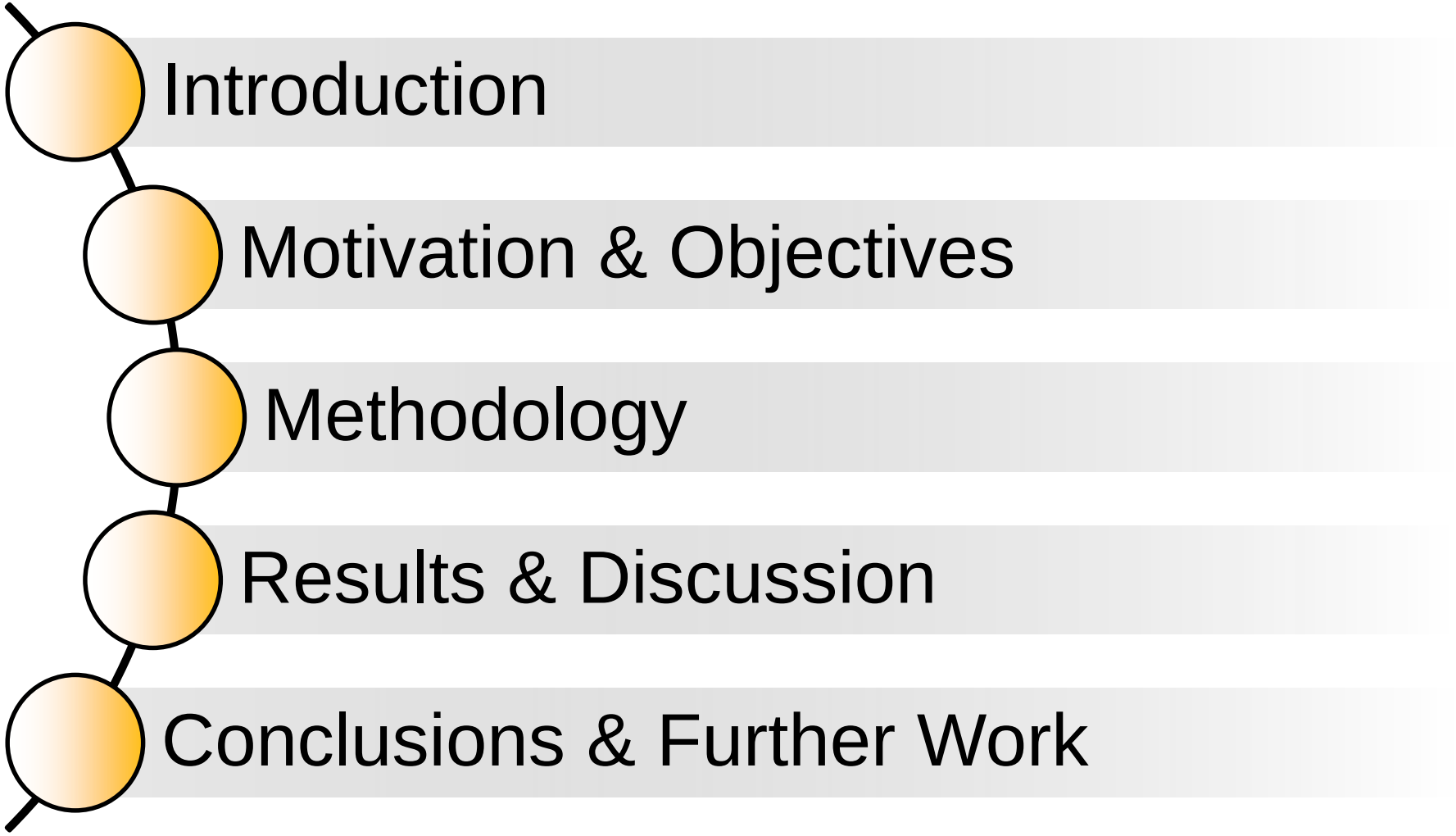
Introduction
Motivation & Objectives
Methodology
Results & Discussion
Conclusions & Further Work

MUSA – Management and Uncertainties of Severe Accidents

The Horizon 2020 MUSA project aims to establish **a harmonized approach for the analysis of uncertainties and sensitivities associated with severe accident (SA) analysis** among EU and non-EU entities.



MUSA kick-off meeting in Madrid, Spain
July 10-12, 2019

MUSA Structure

- **WP1:** Coordination & project management
- **WP2:** Identification & quantification of uncertainty sources
- **WP3:** Review of Uncertainty Quantification Methodologies
- **WP4: Application of UQ methods against integral experiments**
- **WP5:** Uncertainty Quantification in Analysis & Management of Reactor Accidents
- **WP6:** Innovative Management of SFP Accidents
- **WP7:** Communication & Results Dissemination

Motivation & Objectives

MUSA-WP4: PHEBUS FPT1 uncertainty analysis

- Test the Uncertainty Quantification Methodology in Severe Accident contexts
- Test the calculation scheme between the severe accident code and the statistical tool
- Identify the main challenges to deal with in a full-scaled plant uncertainty analysis
- Improve the methodology and/or the calculation scheme

Figures of Merit (FOMs)
Release of iodine from the fuel bundle [% of i.i.]
Release of cesium from the fuel bundle [% of i.i.]
Cesium retention in the circuit [% of cesium released]
Iodine airborne in the containment's atmosphere [mg]
Deposited iodine in the containment [mg]

Methodology

- **Input-driven** methodology ➔ Simple Random Sampling + Monte-Carlo
- **Wilks**' approach for obtaining 95/95 tolerance intervals ➔ sample size = 93
- Sensitivity analysis based on **Pearson**'s and **Spearman**'s correlation coefficients

Uncertainties considered:

- **Aerosol dynamics**
- **Aerosol resuspension**
- **Core THs**
- **Oxidation**
- **Cladding failure**
- **Initial FP inventory**
- **Material properties**

56 input parameters ➔

Severe accident code:

MELCOR 2.2

Statistical tool:

DAKOTA 6.12

MELCOR-DAKOTA Coupling Scheme

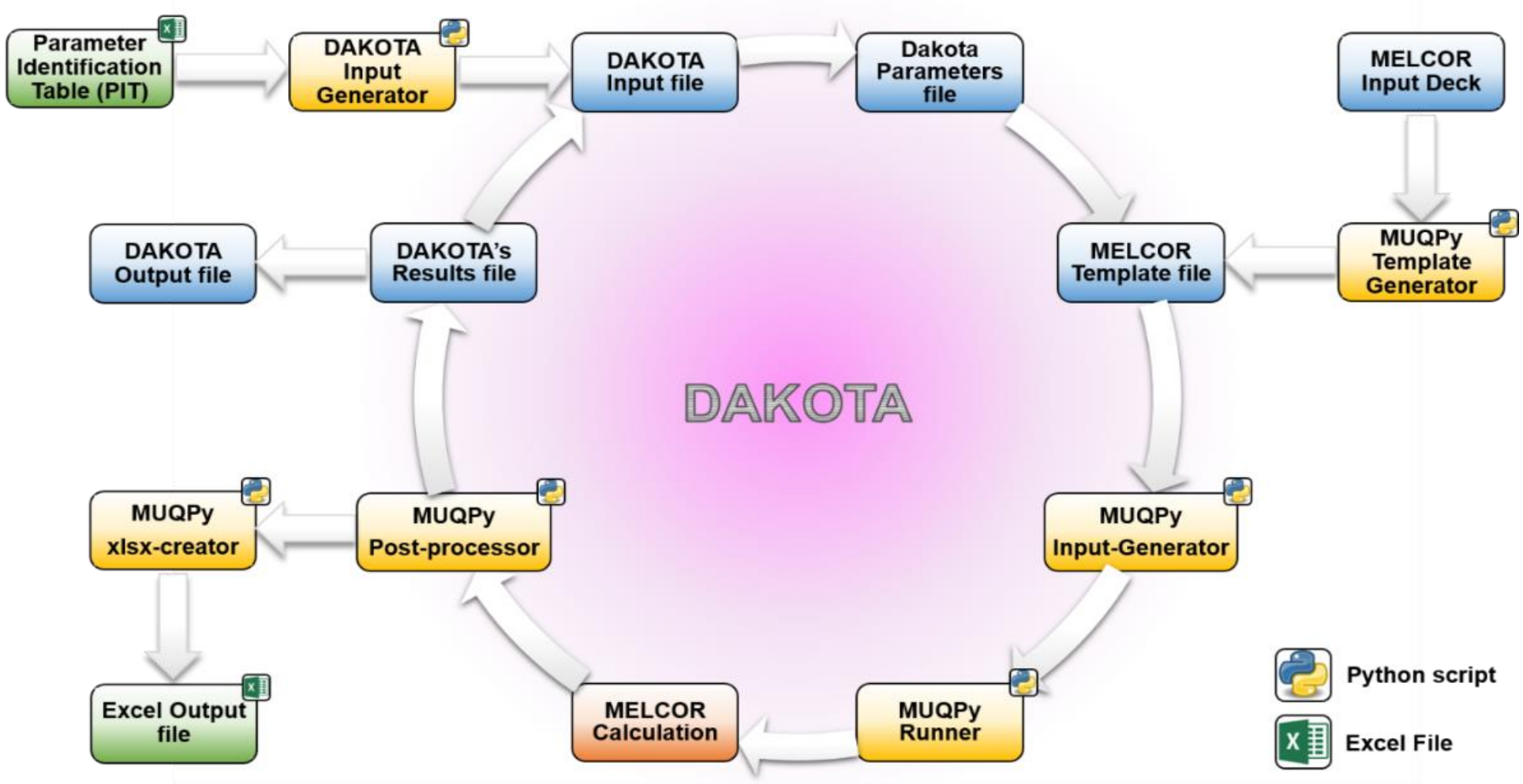

MELCOR Evaluation Model

PHEBUS Scheme

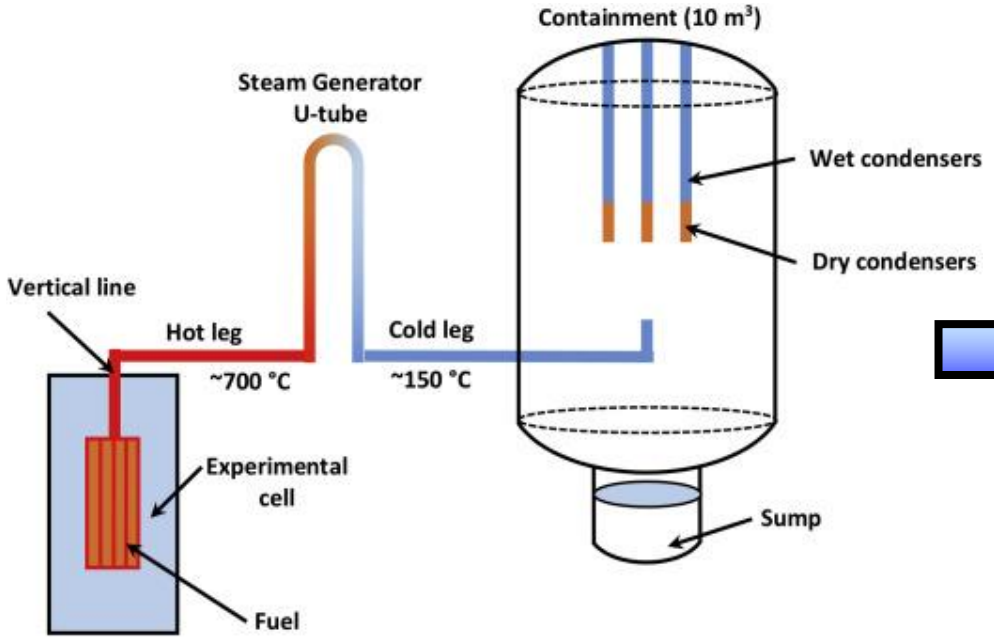

MELCOR Nodalization

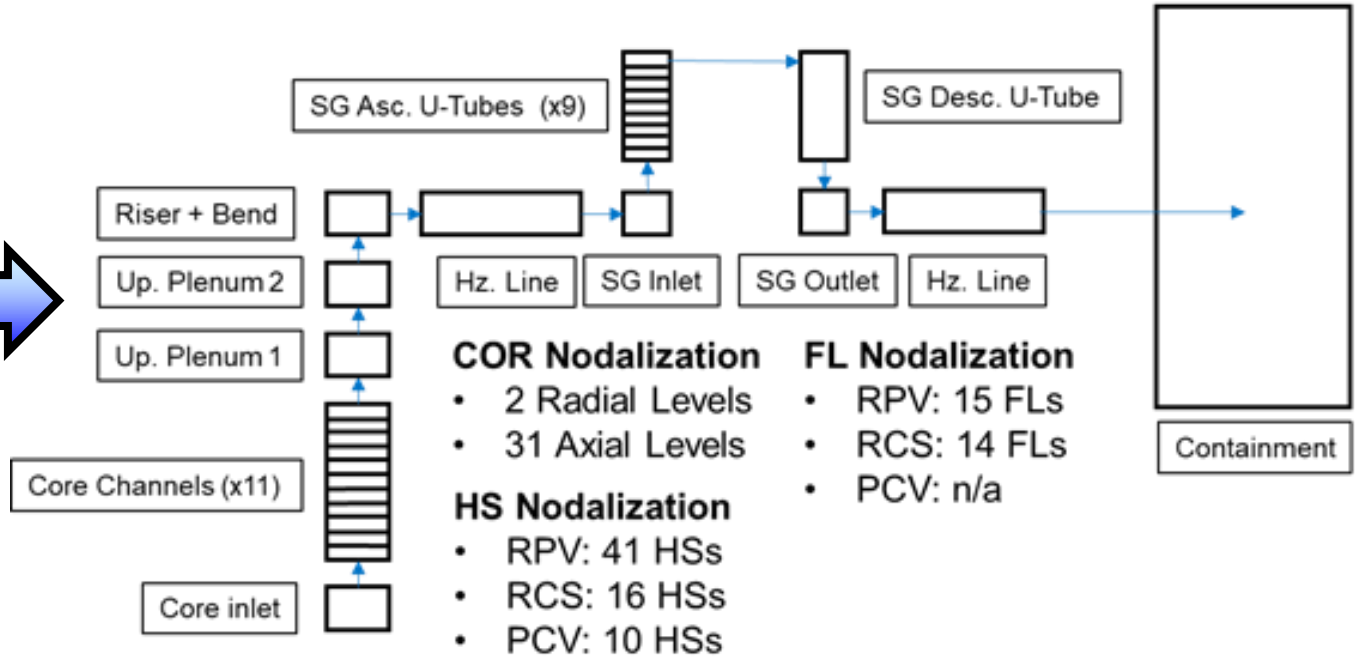

COR Nodalization
- 2 Radial Levels
- 31 Axial Levels

HS Nodalization
- RPV: 41 HSs
- RCS: 16 HSs
- PCV: 10 HSs

FL Nodalization
- RPV: 15 FLs
- RCS: 14 FLs
- PCV: n/a

Cesium Released

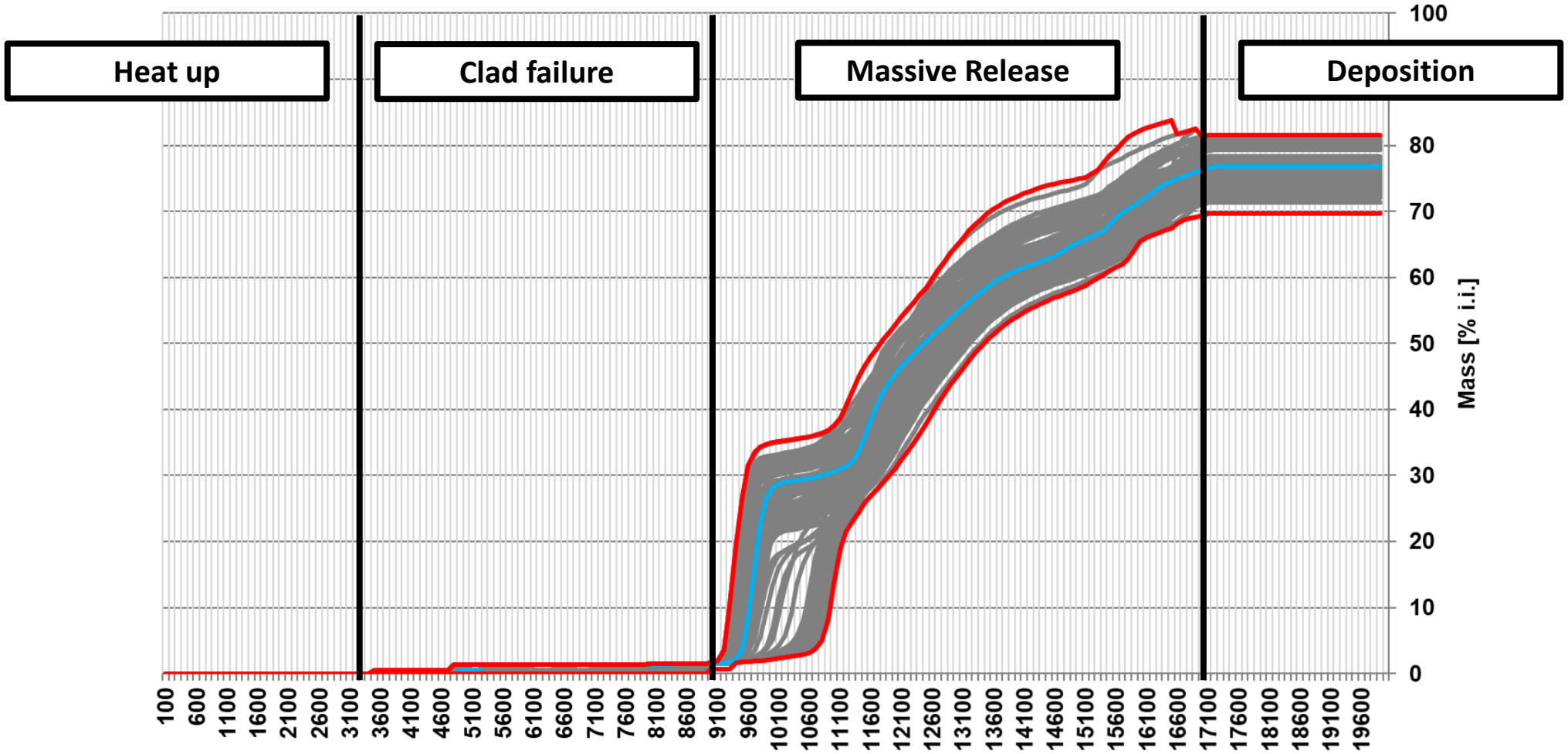

Cesium Released

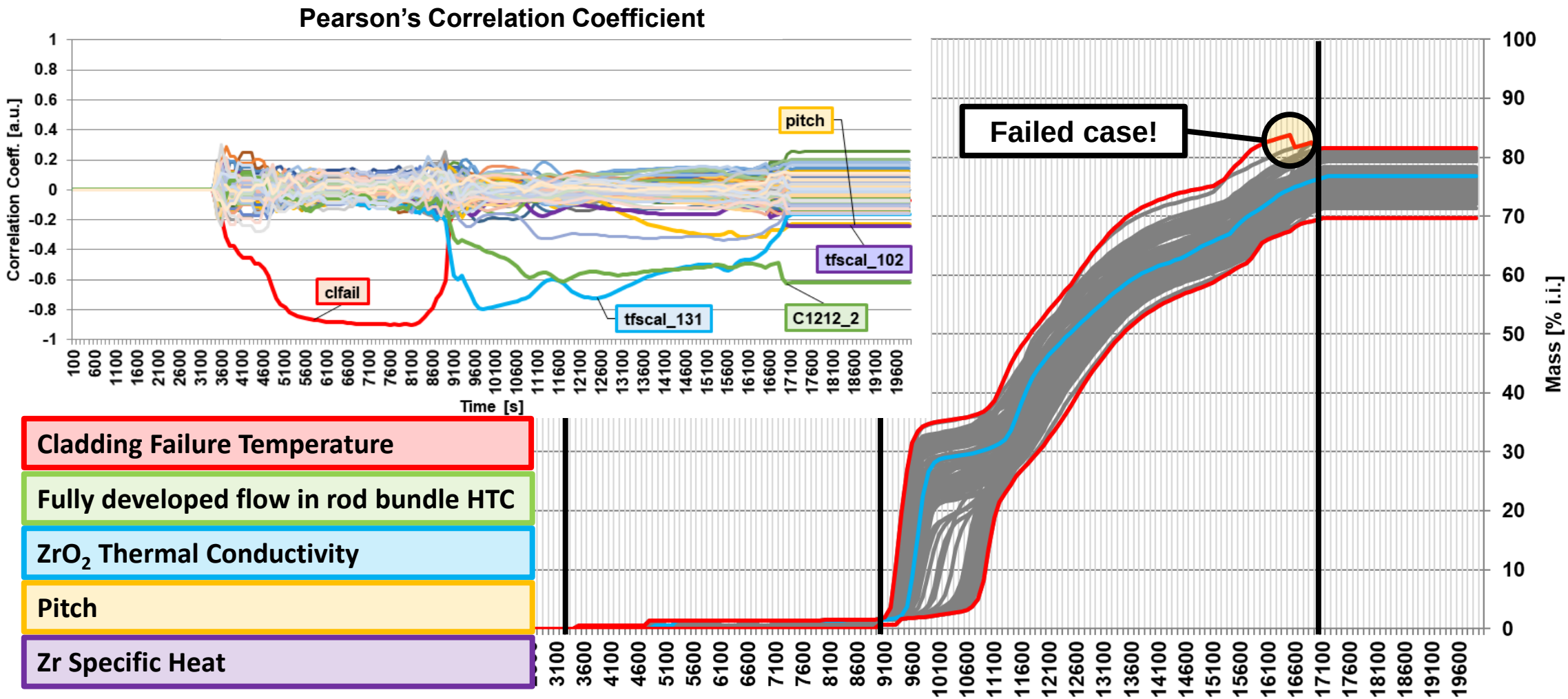

Cesium Released

CCs with p-value < 0.05 at time = 20,000 s

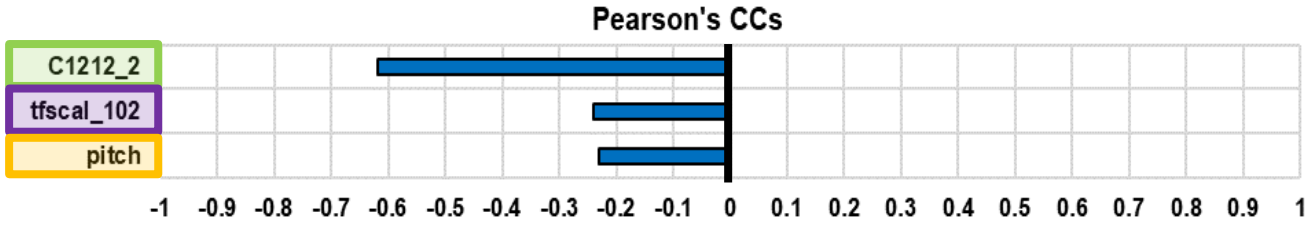

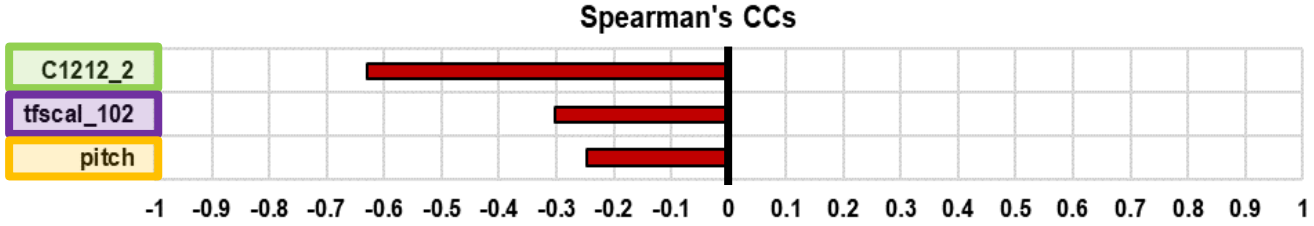

Fully developed flow in rod bundle HTC

Zr Specific Heat

Pitch

Iodine Released

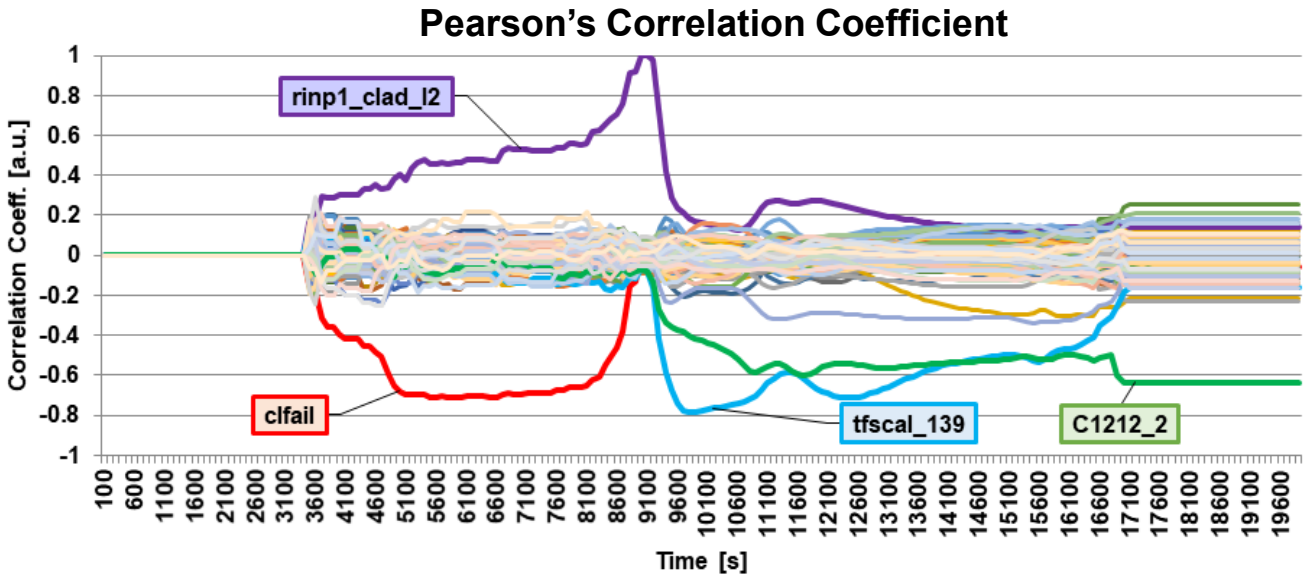

- Cladding Failure Temperature
- Initial I_2 mass in gap
- Fully developed flow in rod bundle HTC
- C. Steel Thermal Conductivity

Iodine Released

CCs with p-value < 0.05 at time = 20,000 s

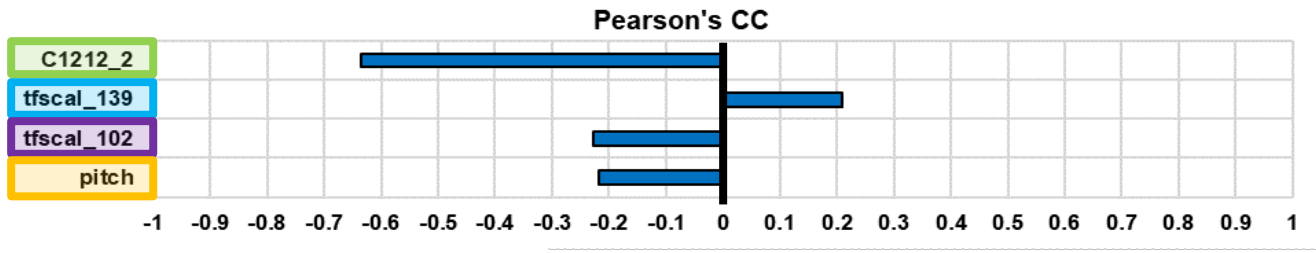

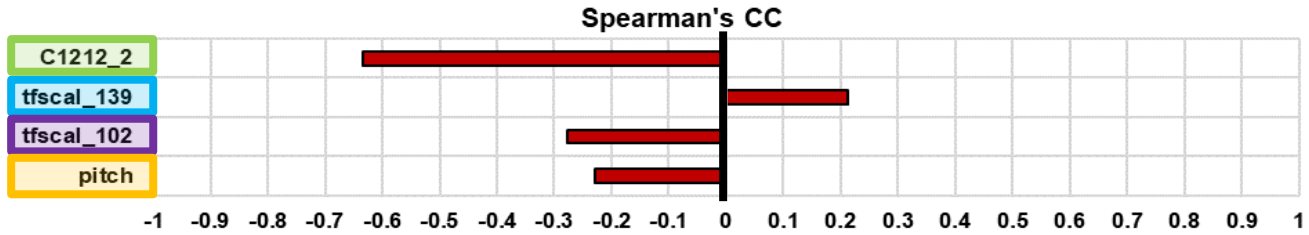

Fully developed flow in rod bundle HTC

C. Steel Thermal Conductivity

Zr Specific Heat

Pitch

Cesium Deposited in Circuit

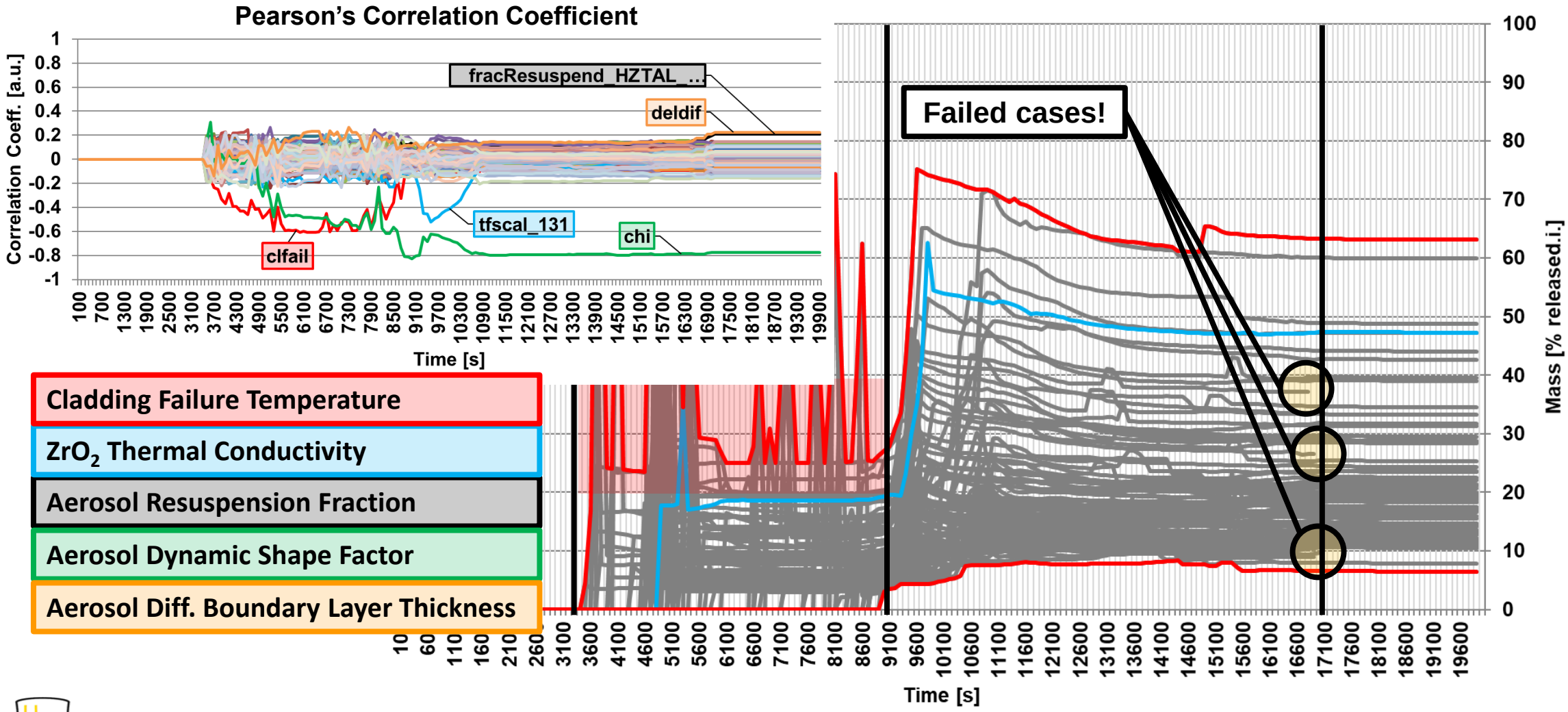

Cesium Deposited in Circuit

CCs with p-value < 0.05 at time = 20,000 s

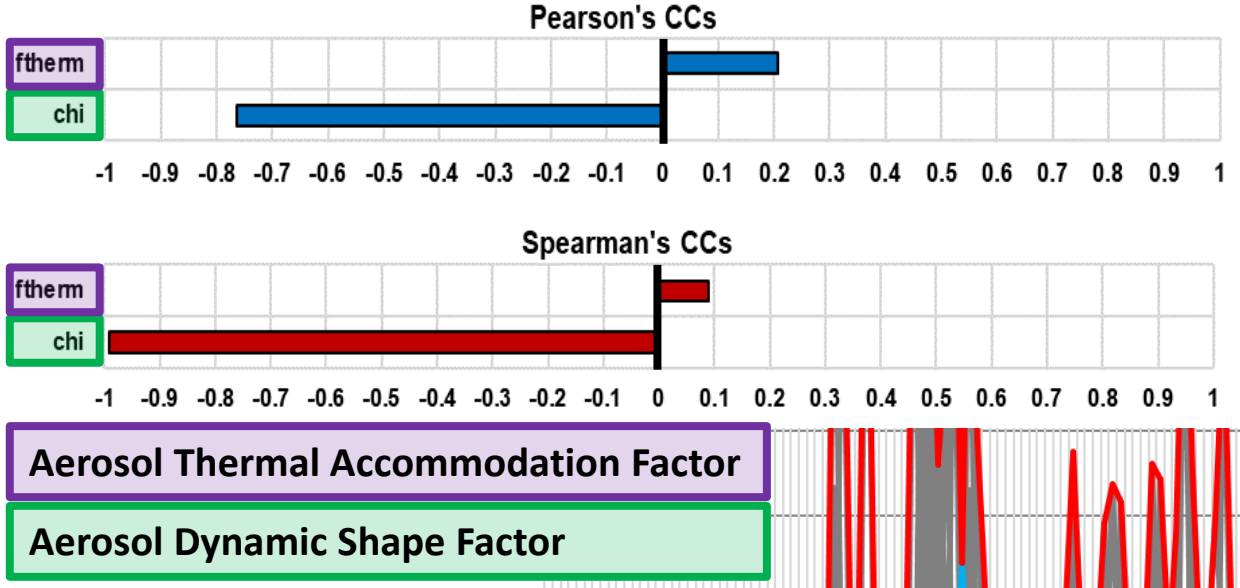

Aerosol Thermal Accommodation Factor

Aerosol Dynamic Shape Factor

Iodine Aerosol in Containment

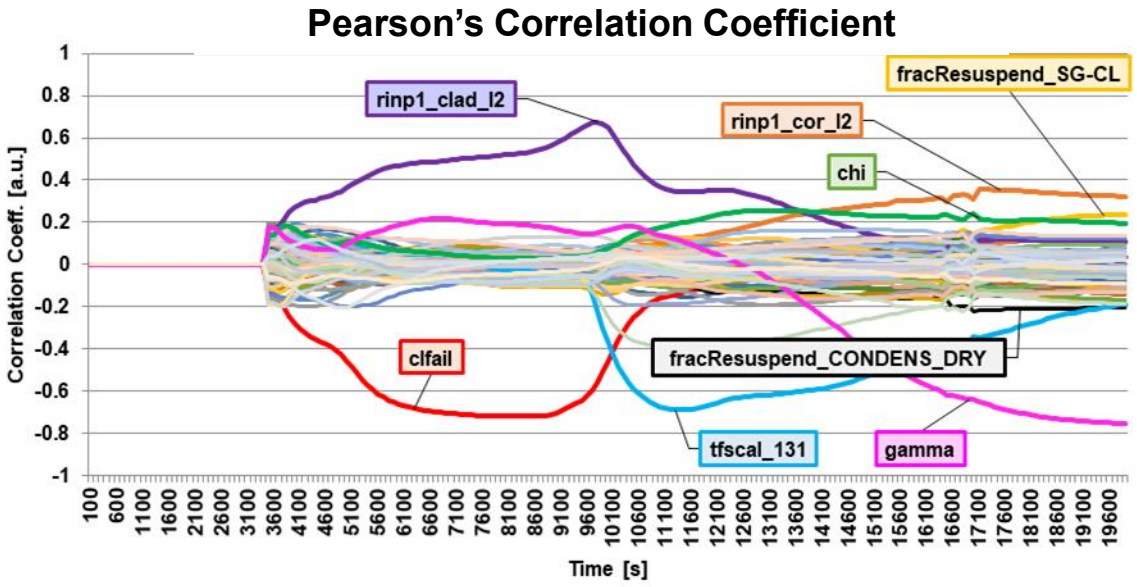

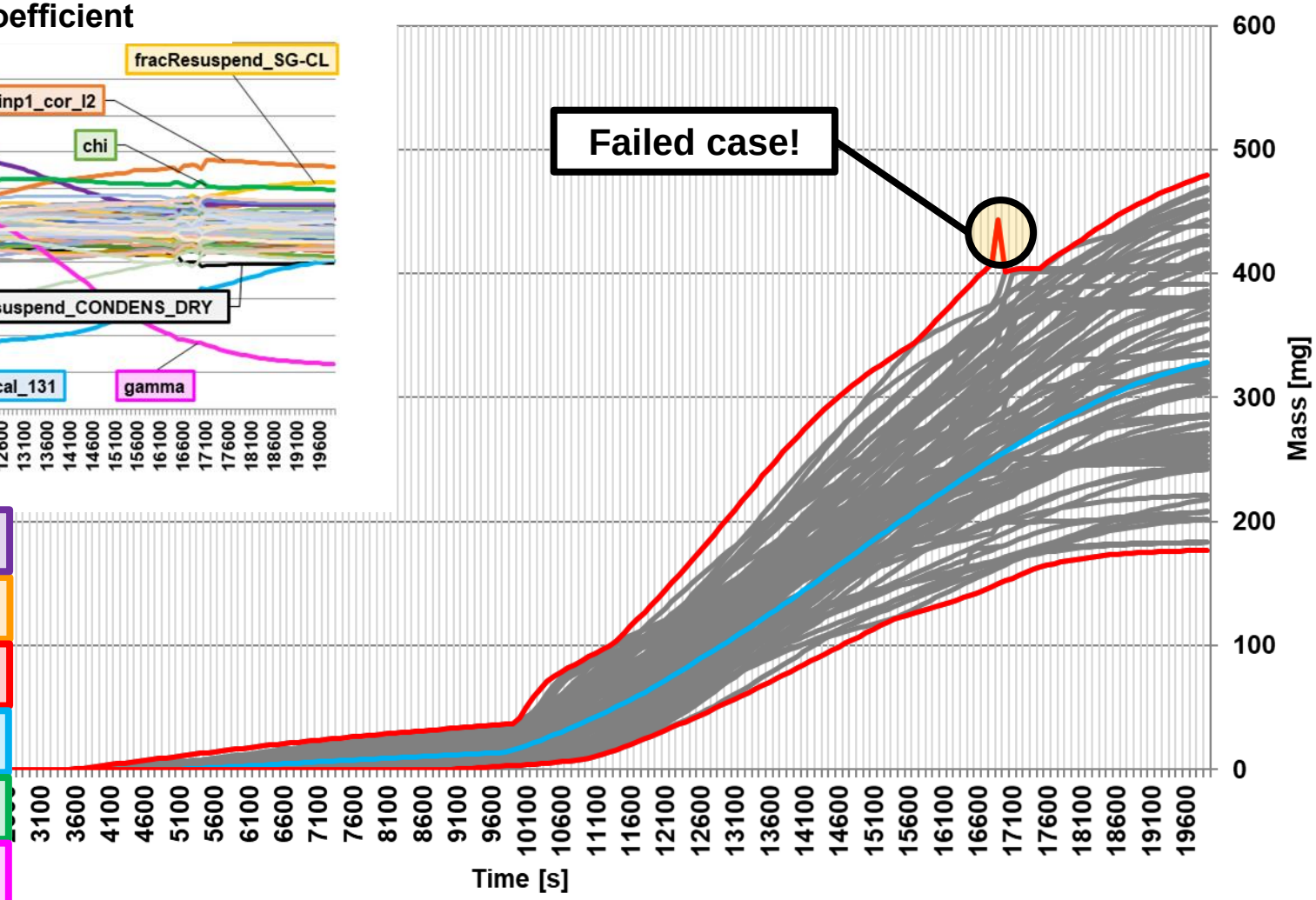

- Initial I_2 mass in gap
- Initial I_2 mass in fuel
- Cladding Failure Temperature
- ZrO_2 Thermal Conductivity
- Aerosol Dynamic Shape Factor
- Aerosol Agglomeration Factor
- Aerosol Resuspension Fraction

Iodine Aerosol in Containment

CCs with p-value < 0.05 at time = 20,000 s

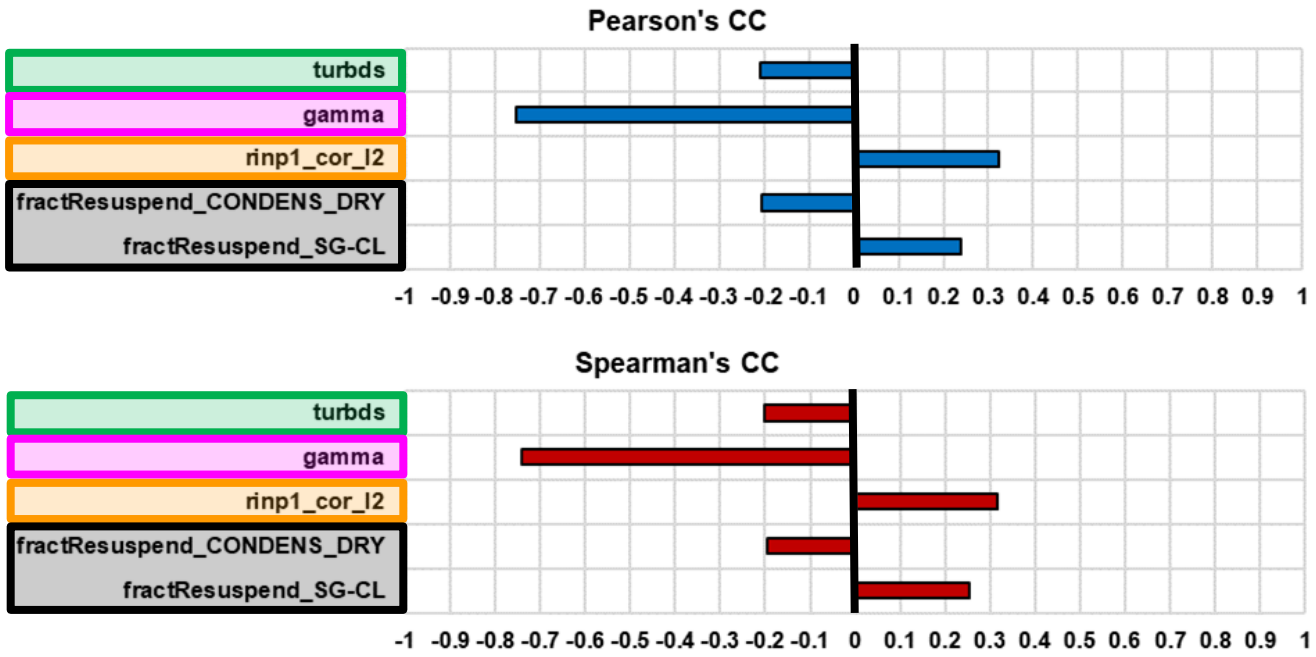

- Aerosol Turbulent Dissipation
- Aerosol Agglomeration Factor
- Initial I_2 mass in fuel
- Aerosol Resuspension Fraction

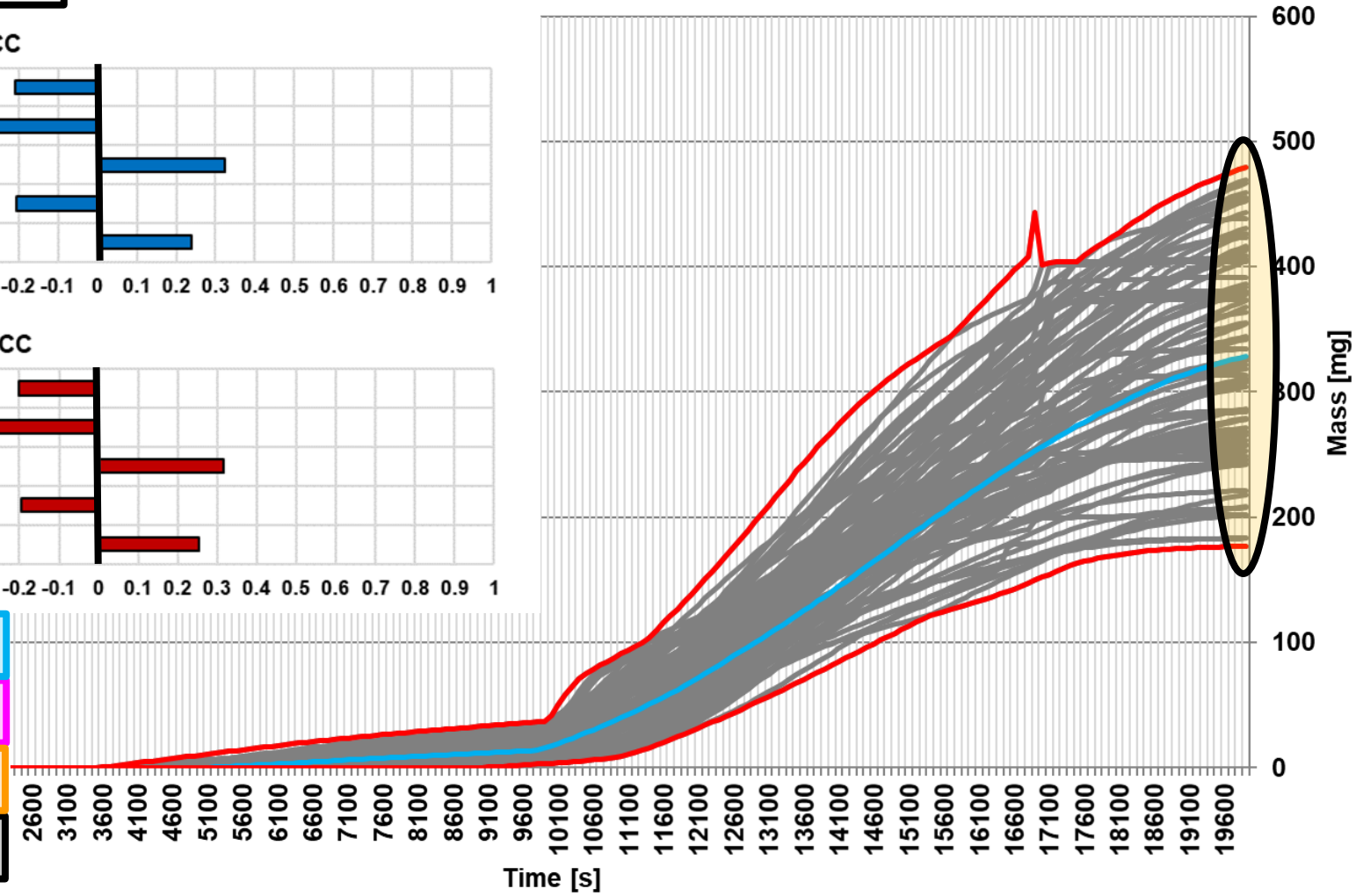

Iodine Deposited in Containment

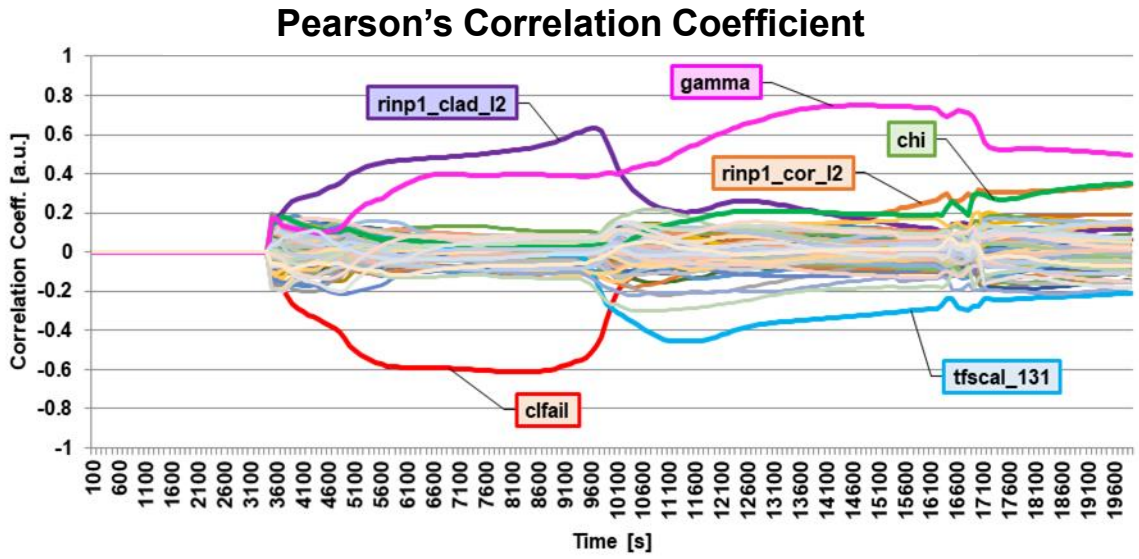

- Initial I_2 mass in gap
- Initial I_2 mass in fuel
- Cladding Failure Temperature
- ZrO_2 Thermal Conductivity
- Aerosol Dynamic Shape Factor
- Aerosol Agglomeration Factor

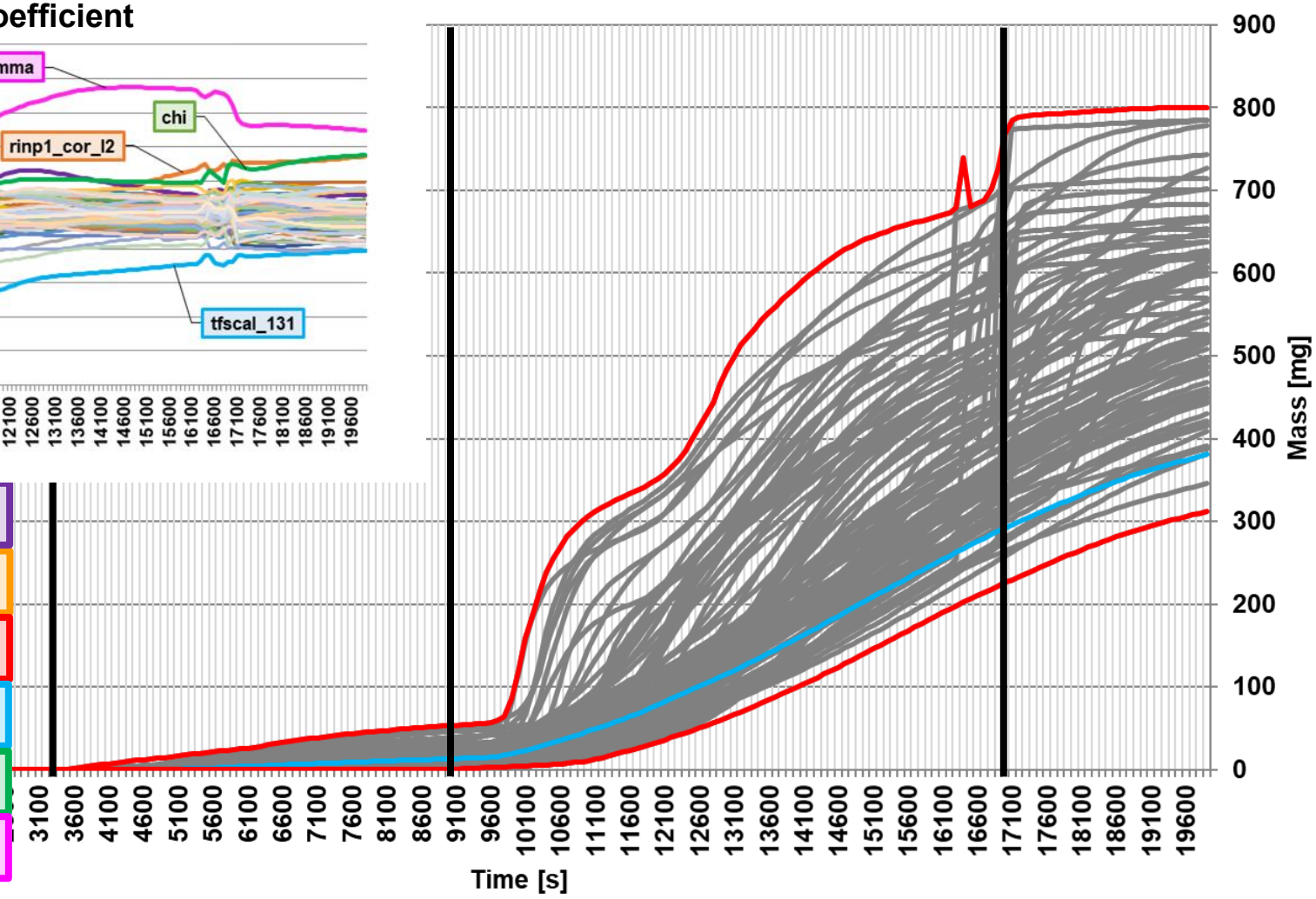

Iodine Deposited in Containment

CCs with p-value < 0.05 at time = 20,000 s

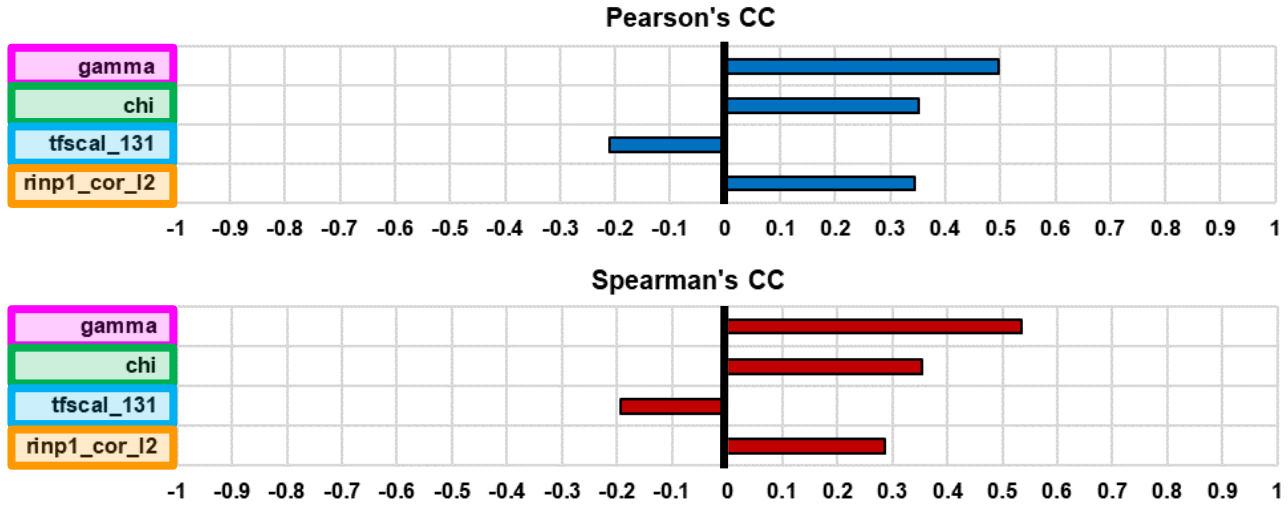

- Initial I_2 mass in fuel
- ZrO_2 Thermal Conductivity
- Aerosol Dynamic Shape Factor
- Aerosol Agglomeration Factor

Final Remarks

- **Main challenges in applying the BEPU approach to Severe Accident:**
  - Deal with a huge number of phenomena involved.
  - Identify and characterize all the uncertain parameters.
  - Manage the statistics with failed runs.
- **Even though several cases have failed, some conclusions can be drawn from this analysis:**
  - **FP release**: these FOMs mainly governed by the thermal-hydraulics.
  - **FP transport and deposition**: resulted more dependent on the aerosol dynamics, with influence of core thermal-hydraulics.
  - Containment FOMs are dependent on **variables non-directly related** to the containment phenomena
  - **Definition of the FOM(s)**: Governing uncertainties may vary depending on how the FOM is defined.
  - **Larger samples** are needed to obtain more information from the sensitivity analysis.

Thank you for your attention!!!



THE PARAMETRIC SENSITIVITY ANALYSIS OF FPT-1 MELCOR 2.2 INPUT DECK AS A PREPARATION FOR UNCERTAINTY QUANTIFICATION STUDY

M. Malicki, T. Lind, J. Kalilainen[1]
Paul Scherrer Institute
Forschungsstrasse 111, 5232 Villigen, PSI, Switzerland
mateusz.malicki@psi.ch, terttaliisa.lind@psi.ch, jarmo.kalilainen@gmail.com

ABSTRACT

The Phébus test FPT-1 investigated fission product release from irradiated fuel followed by transport in the reactor coolant system and into the simulated containment during a severe accident. The test was divided into three phases: i) core degradation, ii) aerosol transport, and iii) iodine chemistry phase. In this work, we revisit the analysis of fission product release from the fuel and the transport in the reactor coolant system during the first two phases of the test. The analyses are carried out using the integral severe accident code MELCOR2.2 as preparation for further uncertainty quantification study of mentioned input deck.

Earlier analyses have shown that the cumulative fission product transport through the reactor coolant system was relatively well predicted [1], but the relative deposition of fission products on the hot surfaces in the upper parts of the bundle and on the steam generator surfaces was not properly reproduced. In this work, we assess the effect of fission product speciation and MELCOR fission product release models on the release from fuel and transport in the reactor coolant system. The Cs speciation affects mostly Cs distribution among Cs classes and their masses at the end of the transient. The release models influence mainly the quantity of the total aerosol mass in the containment.

KEYWORDS
Fission products, source term, severe accident, MELCOR

1. INTRODUCTION

The Phébus experiments provided crucial data used to improve modelling and code development. The MUSA project in which this study was done focuses on management and uncertainties of severe accidents (SA) [2]. The aim of the project is to increase the accuracy of the SA analysis by decreasing the uncertainty of the simulation results. Nowadays, the SA uncertainty issue has become more and more essential, and it is investigated internationally by leading institutions like U.S. NRC[3] and IAEA[4]. The FPT-1 experiment was chosen as a base case to test and develop a methodology to carry out uncertainty quantification (UQ) analysis in the MUSA project and as a precursor which let participants establish a common path for further project evolution. The project's primary goal is to develop a severe accident UQ methodology. A few factors, such as tools, approach to uncertain parameters implementation, statistical analysis, and correct definition of the input deck, were notified as crucial and investigated in the project. The presented sensitivity study is the first approach of the UQ analysis in Work Package 4 (WP4) of the MUSA project, in which the authors assess the influence of the Cs speciation on the final results. As a

[1] Affiliation ended in June 2021

computation tool, MELCOR2.2 has been chosen with DAKOTA for statistical analysis. Coupling MELCOR and DAKOTA is done within the SNAP environment, allowing the user to efficiently manage the whole UQ process and generate reports with the main results.

The MUSA project focus on the source term phenomenology, and therefore, the FPT-1 test was chosen as the first subject to investigate within WP4 - Application of UQ Methods against Integral Experiments. The test was performed in 1996. The test set-up was composed of 18 irradiated and 2 fresh pressurized water reactor (PWR) fuel rods with high burn up (~23 GWd/tU). Control rods material was Ag-In-Cd (AIC). The simulated scenario was a LOCA in the low-pressure steam environment [5].

Phébus experiments are widely used for model evaluation, development, and code validation, including severe accident codes like MELCOR. Numerous publications confirm their importance and usefulness in showing the impact of the new models or testing different approaches [6],[7],[8]. One of the phenomena revealed from the FPT experiments was the importance of chemical forms of the fission products and the impact of the poison material on the final source term [1],[9].

In this study, the authors evaluate the FPT-1 input deck and perform sensitivity analysis to help understand the uncertainties of the models and the input deck. As a first step, MELCOR 1.8.6 FPT-1 input deck was converted in the SNAP environment to the MELCOR 2.2 and cross-checked with available experimental data to ensure representation of expected behavior. As the MUSA is not a benchmark, the focus was on the impact of the sensitivity cases on the investigated parameters, i.e., aerosol concentration in the containment and deposition in the reactor coolant system (RCS). However, it was observed that the base case results were in acceptable agreement with the experimental results.

Based on the Phébus experiment results and following investigations [1],[9], Cesium (Cs) speciation significantly impacts the Cs release from the fuel and subsequent transport. This paper aims to investigate the impact of Cs speciation on the fission product release to the containment and retention in the RCS. The same Figures Of Merits (FOMs) will later be used for the UQ study:

- Aerosol amount in the containment atmosphere.
- Cesium retention in the circuit [as % of Cs released from the core].

In addition, the effect of different fuel release models on Cs release and transport will be assessed.

2. METHOD

2.1 Input deck description

The input deck used in this work is based Sandia National Laboratories (SNL) MELCOR 1.8.6 input deck [7] converted to MELCOR2.2 using SNAP and modified to ensure best practice and use the latest models in MELCOR. A precise description of the FPT-1 experiment based on which input deck and scenario sequence was developed is possible to find in FPT1 final reports [10].

The visualization and the templates were developed in the SNAP environment. The nodalization of the input deck is shown in Figure 1. Input deck contains 281 Control Functions (CF), 31 Control Volumes Hydrodynamics (CVH), 72 Heat Structures (HS), and 29 Flow Paths (FL). The core is divided axially into 31 levels and radially into two rings. Each of the core axial levels is connected with a separate HS, the rest of CVHs are arranged similarly. The uranium and zircaloy are proportionally distributed in both core rings. Control rods material is placed only in the 1st ring. The supporting steel and zircaloy are located at the bottom of the core.

In the radionuclide package (RN) the CORSOR-Booth for high burn-up fuel is used as a base release model. Default values for MELCOR 2.2 were used to define the CORSOR-Booth class scaling factors except Class 7 (Mo) which was set up to 0.2 based on [11]. Calculations were done with the chemisorption model activated.

One of the FPT1 experiment outcomes was that the control rod material releases significantly affect the airborne aerosol mass in the containment. Further, it was observed that values decisively different from the MELCOR default values were needed for the AIC release parameters to match the experimental results with the calculations. Therefore, it was decided to address the release of control rod materials and corresponding model parameters as part of the study.

In MELCOR, control rod materials are implemented in the COR package and thereby not available for release as aerosols or vapors. In order to model the release of the control rod materials to the gas phase, the user needs to define additional radionuclide classes with corresponding parameters for the control rod materials. The authors added three new classes for the control rod materials: AG-CR, IN-CR, and CD-CR. An additional goal of this study is to understand better the impact of the AIC releases on the Source Term (ST) and possibly consider related parameters as uncertain parameters in further studies.

To achieve the experimentally observed release of the AIC, adding Ag, In and Cd radionuclide classes to the radionuclide (RN) package was necessary. For this purpose, the following sensitivity coefficients (SC) needed to be defined for AIC classes:

- 7103 – Class Scaling Factors,
- 7110 – Vapor Pressure,
- 7111 – Vapor Diffusivity Constants,
- 7120 – Class Molecular Weights.

The values for the necessary sensitivity coefficients along with RN class mapping were defined based on data published in [9].

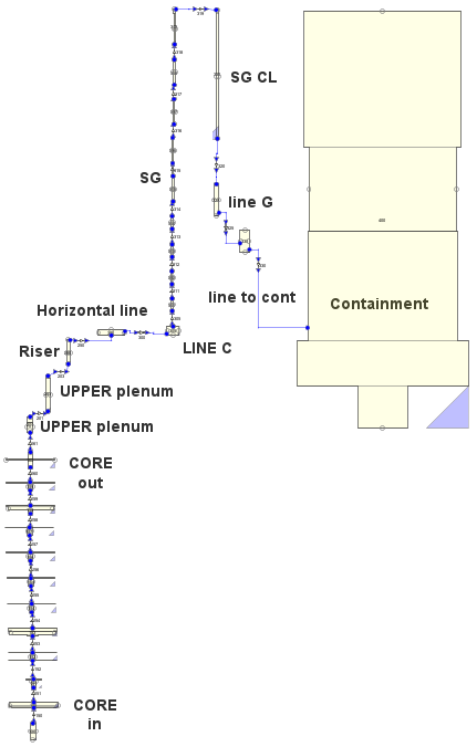

Figure 1 FPT1 MELCOR input nodalization.

2.2. CPU time consumption with and without Control Rods releases model

Because the presented work is a part of the UQ project, MUSA, it is crucial to control CPU time consumption when implementing additional features into the input deck. In the UQ, many calculations need to be performed, which increases CPU time significance.

Figure 2 shows CPU consumption for various MELCOR packages. Overall, implementing the AIC release model increases computational time; however, not significantly and the biggest difference is noted for COR package. This relatively small difference lets us use it in the base case calculation and the further UQ study without increasing the needed CPU time.

- Without AIC: Time= 3.038008E+04 s, total CPU time= 1.772402E+04
- With AIC: Time= 3.038008E+04 s, total CPU time= 1.803917E+04

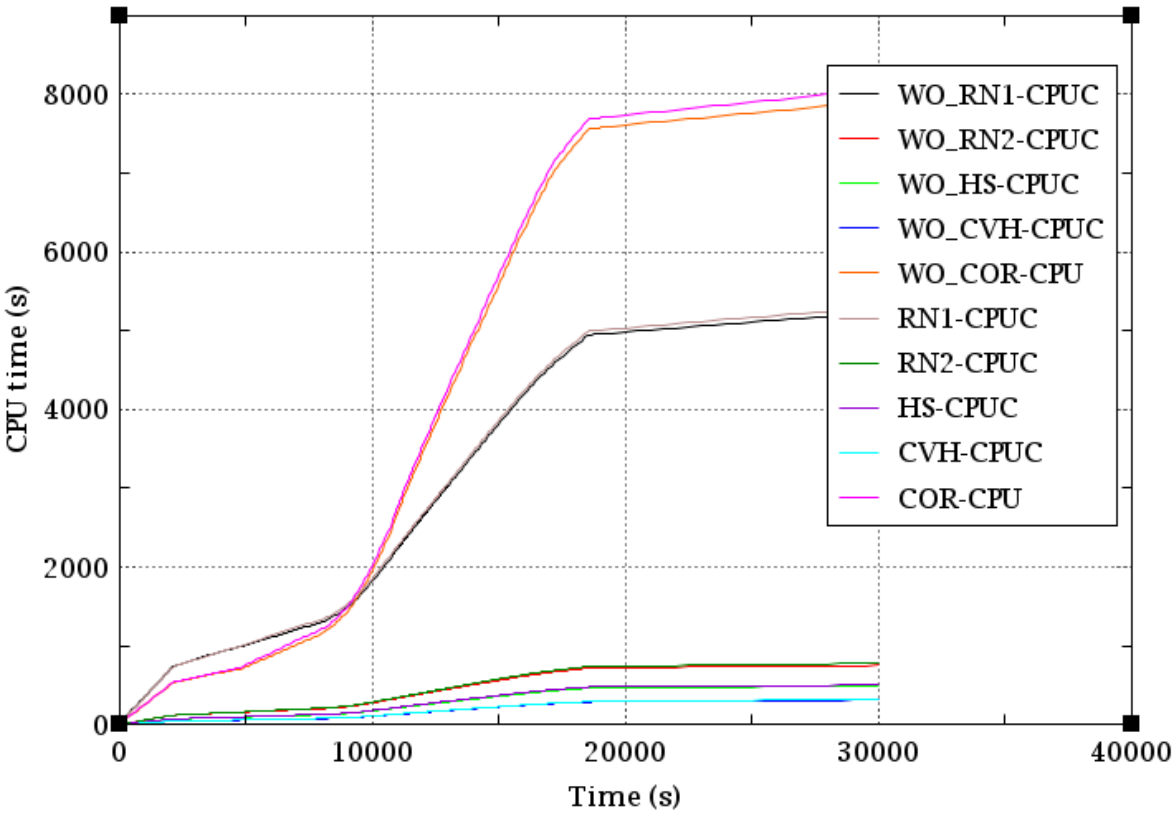

Figure 2 Comparison of CPU time consumption by different MELCOR packages in case with and without AIC releases model. WO-without AIC release model, RN radionuclide, HS-Heat Structures, CVH-Control Volume, COR-Core

2.3. Sensitivity of Cs speciation and release model

The main goal of this study was to investigate the impact of differently modelled Cs speciation on the results in light of the uncertainty quantification of severe accident analysis with a focus on source term assessment. MELCOR gives a few possibilities to implement Cs speciation. In the MELCOR "Best practices" [12], Cs is divided into three different species: CsOH, CsI, and Cs_2MoO_4, with CsOH representing the gap inventory, CsI the whole iodine inventory and Cs_2MoO_4 being the rest of Cs in the

fuel. The user can also include additional Cs species as needed. In this work, we used the existing Cs species available in MELCOR and distributed Cs in the available species in three different ways.

Additionally, the impact of the different release models was studied by performing the same Cs speciation calculations with two different release options. In total, six sensitivity calculations were performed and analyzed, see Table 1 and Table 2.

Release models have a potentially strong influence on the source term calculation. Two of them were chosen for this study to evaluate their impact on previously mentioned FOMs.

- CORSOR-Booth model for high burn-up fuel (model activation flag in MELCOR: -5). This model is based on the Booth diffusion model, and it calculates total mass release rate as a combination of diffusion and gas-phase mass transport (evaporation) rates (eq.1). The total mass released ($\dot{m}_{tot,k}$) by gas transport ($\dot{m}_{k,gas}$), and diffusion release rate ($DIFF_k$) for class k:

$$\dot{m}_{tot,k} = \left[\frac{1}{DIFF_k} + \frac{1}{\dot{m}_{k,gas}}\right]^{-1} \quad (eq.1)$$

Where

$$\dot{m}_{k,gas} = Nu\frac{D_k}{d}A\frac{P_k}{RT} \quad (eq.2)$$

D_k- diffusion coefficient calculated for Cs

$$D_{Cs} = D_0 e^{-\frac{Q}{RT}} \quad (eq.3)$$

d - fuel pellet diameter, A - surface area of the fuel rod, Nu – Nusselt number, P_k - the vapor pressure of the class, R - universal gas constant, T - temperature, Q - activation energy, D_0 – pre-exponential factor which is a function of the fuel burn-up

$$DIFF_{Cs} = \left[\frac{1}{ReleaseRate_{Cs}} - \frac{1}{\dot{m}_{Cs,gas}}\right]^{-1} \quad (eq.4)$$

$$DIFF_k = DIFF_{Cs} \cdot S_k \quad (eq.5)$$

$$ReleaseRate_{Cs} = \frac{[(f\sum D'\,\Delta t) - (f\sum D'\,\Delta t)_t]V\rho}{(1-f)\Delta t} \quad (eq.6)$$

S_k –MELCOR release scaling factor, ρ - molar density of UO2 in the fuel, V -fuel volume, D'-temperature dependent diffusion coefficient calculated for Cs.

The diffusion release rate is calculated for Cs (eq.4), while for the rest of the RN classes it is evaluated by multiplying the Cs diffusion release rate by pre-defined scaling factors (eq.5) [13],[14]. This modelling approach bound all the releases with Cs release, which simplifies the calculation but at the same time could increase uncertainty.

- Revised CORSOR-Booth (model activation flag in MELCOR: ORNL or -7) for high burn-up fuel. The class release rates are no longer bound to the Cs release in this model. Instead, scaling of the diffusion release rate as it presented in eq.5 the diffusion coefficient is scaled (eq.7). Thus this

solution allow independent releases for all RN classes (eq.7) as it is done for Cs class described above [13],[14].

$$D_{Class} = S_{Class} D_0 e^{-\frac{Q}{RT}} \quad \text{(eq.7)}$$

Detailed description of the models is available in MELCOR workshop materials [13] and in MELCOR reference manual [15].

Cs speciation sensitivity was investigated by defining Cs speciation by three options:

- Inventory (INV): Pre-definition of the initial inventory masses. The user can manually calculate and implement the CsI and CsM masses. It means that according to the available initial mass of the Cs, I, and Mo in the RN classes, users can compose inventory for each one and manually implement it as a new initial speciation of the inventory. This solution requires more actions from the user; however, it also gives more flexibility. In this option, the initial inventory is extended by artificially implementing masses of the CsM and the CsI classes via modifying the RN1_FPN card. In the presented study, the authors decided to use all available mass of the Cs and I as a substrate for CsI and CsM classes; thus, the initial mass of the Cs, I, and Mo classes were decreased accordingly.

- CARD: The class combination at release time[15]. MELCOR combines the classes defined by the user proportion based on the molecular weights. The limitation is the mass availability of the source classes at a given time step. The combination is done automatically by MELCOR, and the user needs to define only stoichiometric proportions of the elements in the formed compounds. In presented calculations, the Cs and the I class will be stoichiometrically combined into CsI instantaneously upon release in proportion 1 to 0.5 because I in MELCOR RN class is represented as I_2. The Cs with Mo are combined in proportion 2 to 1. The class combination is implemented by the RN1_CLS card, where the CsM and CsI are determined.

- Only_Cs: In this option, all the Cs is in the Cs class as CsOH

3. RESULTS AND DISCUSSION

3.1. Cs release from fuel

The first investigated parameter is the Cs release. The presented results are calculated for the end state of the transient (30000s).

Table 1, Table 2, Table 3 and Table 4 show a comparison of the Cs releases and retention in the RCS between investigated sensitivity cases. In the "Inventory" and the "Card" case, the Cs was divided into above mentioned three classes, Cs (CsOH), CsI (CsI), CsM (Cs_2MoO_4). Moreover, the results are presented as Cs element and percentage of the initial mass. The element mass is calculated based on the mass proportion of the elements in the mentioned compounds. Used percentages for the Cs element mass calculations are 88.655%, 62.434% and 51.155% respectively for CsOH, Cs_2MoO_4 and CsI. Table 1 and Table 3 correspond to the standard CORSOR-BOOTH model, and Table 2 and Table 4 to the revised CORSOR-BOOTH model. All values in the Tables 1-4 are based on MELCOR radioactive masses. In the “Only_Cs” option, there is no release of CsI and CsM as Cs is only present as CsOH.

It was seen that the selected speciation of Cs made a difference in the mass of released Cs, Table 1. The largest mass of Cs was released from the fuel when all Cs was assumed as CsOH. This is to be expected due to the high vapor pressure of CsOH at temperatures during fission product release. In the option “Inventory”, a large fraction of Cs is released as Cs_2MoO_4, and the rest as CsI with a small amount of

CsOH. In the option "Card", the Cs release is the lowest of the selected options. This low value can be explained by the higher fraction of CsI, which has been shown to have a lower vapor pressure than Cs_2MoO_4 under oxidizing conditions [16]. It should be noted that selected Cs speciation options were chosen to get three decisively different representations of Cs speciation during release from the fuel.

The difference in the Cs releases between the CORSOR-BOOTH, Table 1, and the revised CORSOR-BOOTH, Table 2, is not significant compared to the Cs speciation impact. The percentage of the Cs inventory released in the experiment was about 84% [17],[18]. The calculated release percentage of the initial inventory is comparable with the experimental results. The calculations show that the "only Cs" and "Inventory" options agreed relatively well with the experimental data, giving 85-88% release. The "Card" case calculates around 10% lower release than the other two cases. Presented results show that Cs speciation affects the composition and the overall mass of the Cs releases. Differently implemented Cs speciation could affect the ratio of the releases between Cs classes and consequently the final mass of releases. The impact of the two investigated release models is negligible for the overall results of Cs release; however, the CsOH in the "Card" option varies from other results.

Table 1 Comparison of Cs releases of investigated options (CORSOR-BOOTH)

	Cs element [g]				Cs release % i.i.			
	CsOH	CsI	CsM	Total	CsOH	CsI	CsM	sum
Inv	1.90	0.85	11.06	13.80	11.9	5.3	69.7	87.0
Card	0.82	1.57	9.68	12.07	5.2	9.9	61.1	76.1
Only Cs	14.03	0.00	0.00	14.03	88.5	0.0	0.0	88.5

Table 2 Comparison Cs releases of investigated options (revised CORSOR-BOOTH)

	Cs element [g]				Cs release % i.i.			
	CsOH	CsI	CsM	Total	CsOH	CsI	CsM	sum
Inv	1.89	0.87	10.83	13.59	11.9	5.5	68.3	85.7
Card	0.20	1.62	10.25	12.07	1.3	10.2	64.6	76.1
Only Cs	13.74	0.00	0.00	13.74	86.6	0.0	0.0	86.6

3.2. Cs retention in the RCS

The following evaluated parameter is related to the second FOM considered for UQ analysis, namely Cs retention in the RCS. In MELCOR, the parameter defined as a total radioactive mass of Cs classes, including the mass deposited on heat structures, was used for the analysis. All control volumes were considered, excluding the containment. To extract the mass of the retained Cs element from the total mass of the Cs classes, the Cs mass ratios mentioned previously were used.

Table 3 and Table 4 show the Cs retention results in the RCS, respectively, for the CORSOR-BOOTH and revised CORSOR-BOOTH release models. The retained masses of the Cs vary between investigated options; however, they are consistent with the releases. The highest Cs retention occurs in the "Inventory" option followed by "Only_Cs" and "Card", which is expected taking into account molecular mass of related compounds and the differences in the release from fuel. In the "Inventory" the high fraction of released Cs_2MoO_4 leads to the highest retention fraction. However, the difference between the "Inventory" and the "Card" cases is negligible. The "Card" option gives the lowest retention in agreement with the lowest releases calculated with this option. The proportion between released and retained masses among

Cs classes does not change. The "Card" option, with both release models, gives the lowest values of the initial Cs inventory retention, around 37%. In contrast, the other two cases calculate approximately 41% of Cs inventory retention while the experiment noted about 48% [17],[19]. In the case of the retained percentage of the released Cs mass, all the calculations give relatively similar results. Namely, retained percentage of the released cesium is between 46.63% and 48.66%, which gives around a 2% difference between all cases. Based on that 2% discrepancy, it could be assumed that there is no direct impact of the Cs speciation or release model on the Cs retention.

The presented analysis of the Cs retention aligns with the above-discussed observations concerning releases. Thus, the Cs speciation affects the proportion of the Cs distribution among the RN classes and consequently the related compound's mass, having only an indirect impact on the retention by causing the differences in the released mass. However, it should be highlighted that presented results concern only the end state of the calculation.

Table 3 Comparison of Cs retention of investigated options (CORSOR-BOOTH)

	Cs element [g]				Cs retained % i.i.				retention % of the Cs release
	CsOH	CsI	CsM	Total	CsOH	CsI	CsM	retained [% i.i.]	retained [%]
Inv	0.91	0.46	5.28	6.65	5.74	2.90	33.28	41.92	48.11
Card	0.38	0.83	4.66	5.87	2.41	5.23	29.36	37.01	48.66
Only Cs	6.60	0.00	0.00	6.60	41.64	0.00	0.00	41.64	47.18

Table 4 Comparison of Cs retention of investigated options (revised CORSOR-BOOTH)

	Cs element [g]				Cs retained % i.i.				retention % of the Cs release
	CsOH	CsI	CsM	Total	CsOH	CsI	CsM	retained [% i.i.]	retained [%]
Inv	0.90	0.46	5.19	6.55	5.66	2.91	32.75	41.32	47.49
Card	0.09	0.85	4.87	5.81	0.55	5.38	30.71	36.65	48.14
Only Cs	6.54	0.00	0.00	6.54	41.25	0.00	0.00	41.25	46.63

3.3. Aerosol mass in the containment

Aerosol mass in the containment at the end of the transient is the next investigated parameter. The radioactive aerosol mass evolution in the containment was used as a parameter to study above-mentioned FOM. The data that compares the investigated cases are presented in Figure 3 and Figure 4.

The effect of Cs speciation and the CORSOR-BOOTH model on the aerosol mass in the containment is shown in Figure 3. The first phase of the test was core degradation, during which aerosols were released to the containment. This phase lasted approximately 18000s, which is the time of the highest aerosol concentration in the containment, Figure 3. After the core degradation phase, the containment was isolated from the reactor coolant circuit, and the airborne aerosol concentration in the containment started to decrease. During this so-called "Aerosol phase", the Cs speciation has only a minor effect on the total aerosol depletion as expected. Some differences in airborne aerosol concentration are seen during the core degradation phase. Especially once larger aerosol release was started at around 12000 s, the three speciation options show slightly different aerosol release dynamics. The "Inventory" option calculates the highest aerosol release in the both, core degradation and aerosol phase. The end state shows the highest deposition for the "Inventory" followed by "Only_Cs". The "Card" calculates the lowest deposition in the aerosol phase.
The results obtained by revised CORSOR-BOOTH results follow the described above behavior during the core degradation phase, Figure 4. However, on average, the revised release model calculates higher values

and the aerosol mass at the end of the calculations differs less than in the case with standard CORSOR-BOOTH. Still, the deposition calculated with the "Card" option is similarly low to the previously discussed case. Also, the difference in the highest aerosol concentration was noticed. In the aerosol phase, the "Only_Cs" and "Card" option shows the highest aerosol mass, opposite to the calculations performed with standard CORSOR-BOOT. The increase of aerosol mass for "Card" and "Only_Cs" is mainly related to enlarged releases of U for these two options when the revised release model is used, discussed in the next sub-chapter.

The different aerosol dynamics in the containment presented in Figure 3 and Figure 4 shows the impact of Cs speciation and confirm its importance for such studies. Indeed, it strongly depends on the particular study demands. The observed behavior suggests that uncertainty and related discrepancies should be investigated in a time-dependent manner. It was shown that if only the results at 30000s were considered, the total mass of aerosols in the containment (proposed FOM) would not be significantly affected by Cs speciation, which could be the case for the degradation phase.

Figure 5 and Figure 6 show respectively the radioactive mass of the Cs speciation aerosols in the containment and the mass of the Cs element in the containment aerosols at the end of the analysis. The values presented in the above figures show that the release model has a limited impact on the release of Cs into the containment. The most visible difference is that the revised release model with "Card" option calculates lower values and the Cs class is significantly lower. Still, it is consistent with its low release. The Cs mass variation relates mainly with the Cs speciation; however, it needs to be highlighted that the presented data represents the final stage of the calculations. The high values given by "Card" are consistent with discussed previously lower deposition fraction. Figure 3 and Figure 4 show how aerosol masses changed among cases; thus, more detailed time-dependent analyses should be performed to fully understand the impact of the Cs speciation on the containment aerosols.

The difference in the peak value of aerosol concentration in the containment with the different Cs speciation options is only partly explained by the Cs speciation. It is seen in Figure 7 and Figure 8 that the aerosol mass in the containment consists to a large extent of U and Ag. Their concentration in the containment depends mostly on the selected fuel release model and, to a smaller extent, on Cs speciation.

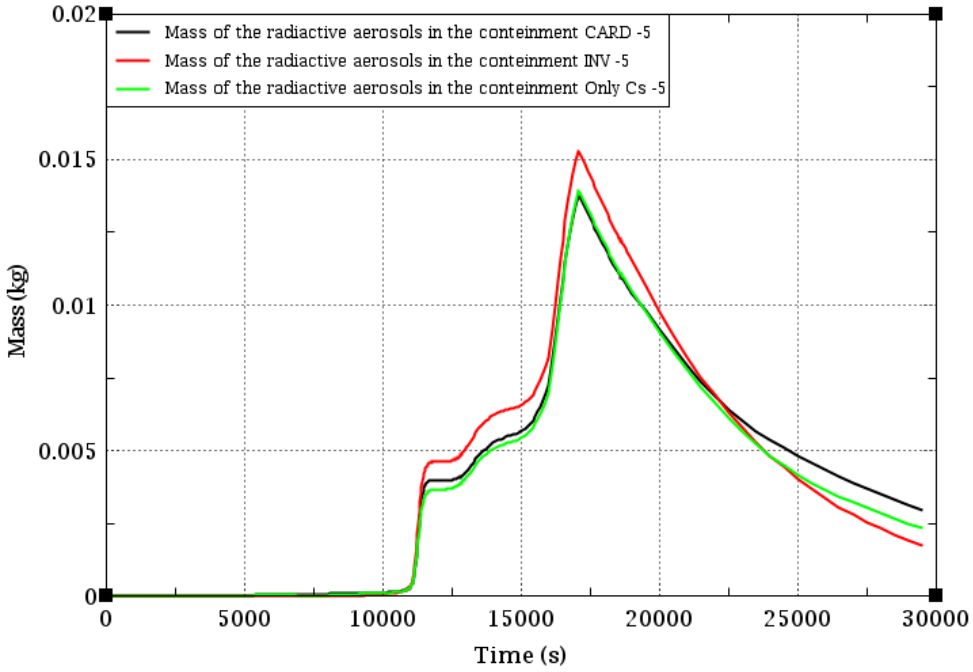

Figure 3 Total airborne aerosol mass comparison of investigated Cs speciation options in the containment CVH, using CORSOR-BOOTH.

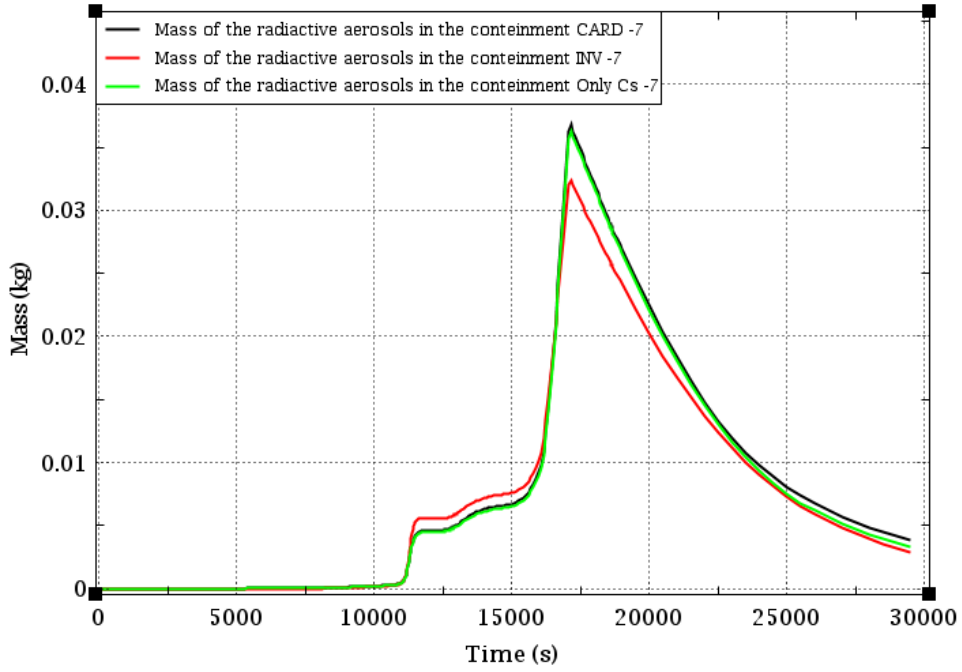

Figure 4 Total airborne aerosol mass comparison of investigated Cs speciation options in the containment CVH, using revised CORSOR-BOOTH.

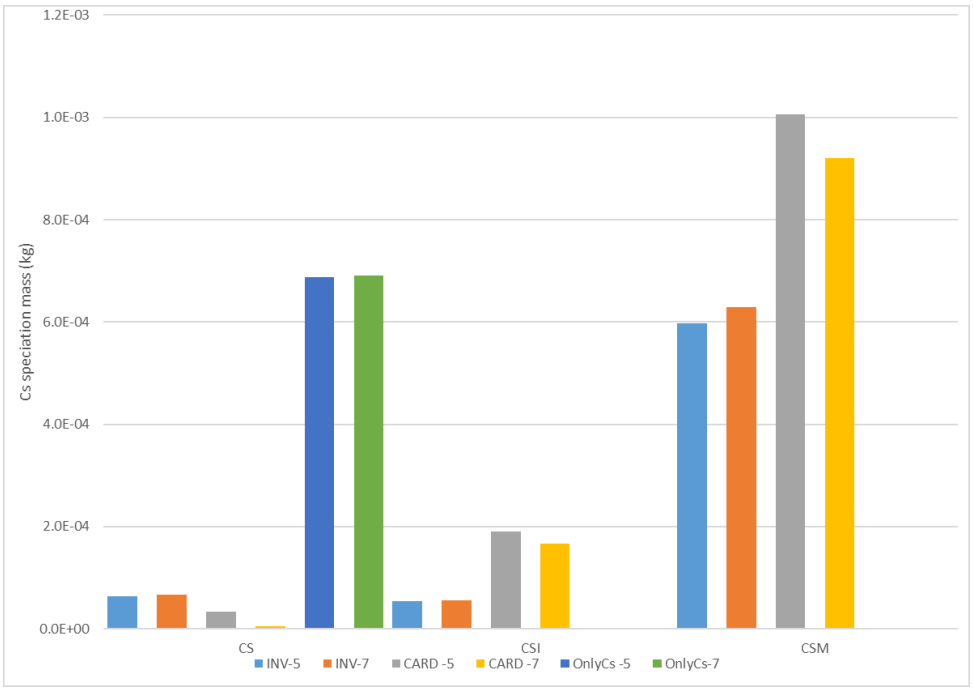

Figure 5 The mass of radioactive airborne Cs classes aerosols in the containment at the end of the transient.

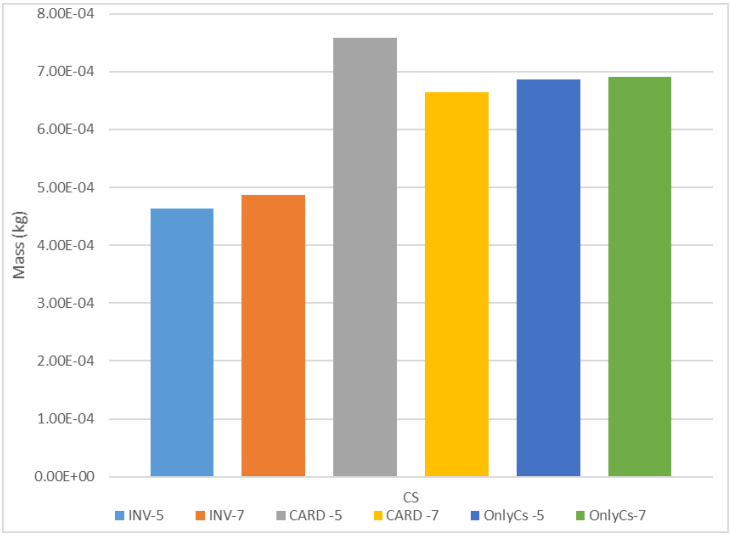

Figure 6 Cs element mass related to the airborne aerosols in the containment at the end of the transient.

Figure 7 shows calculated radioactive mass and Figure 8 total mass of chosen RN classes in the airborne aerosols at the end of the transient. As expected, Cs and related Mo masses vary among cases caused directly by implementing Cs speciation. However, U and AIC classes show significant discrepancies as well. The U and Mo releases in the CORSOR-BOOTH model are much lower than when the revised releases model is used. This discrepancy is expected as the revised model allows releases independently from Cs releases. The release model affects less the Cs and Te than AIC classes, which shows the highest variations between all cases. Especially high discrepancies in AIC related aerosols were noticed when the "Card" and the "Inventory" were used. The FPT1 results show that a large fraction of the aerosol composition consists of Ag, followed by Cd, U and Cs [14], confirming the importance of the AIC materials, which are responsible for more than 60% of the total aerosols in the containment. The obtained

discrepancies of the control rods material releases and theirs influence on the overall results confirm the importance of the AIC related uncertainty study.

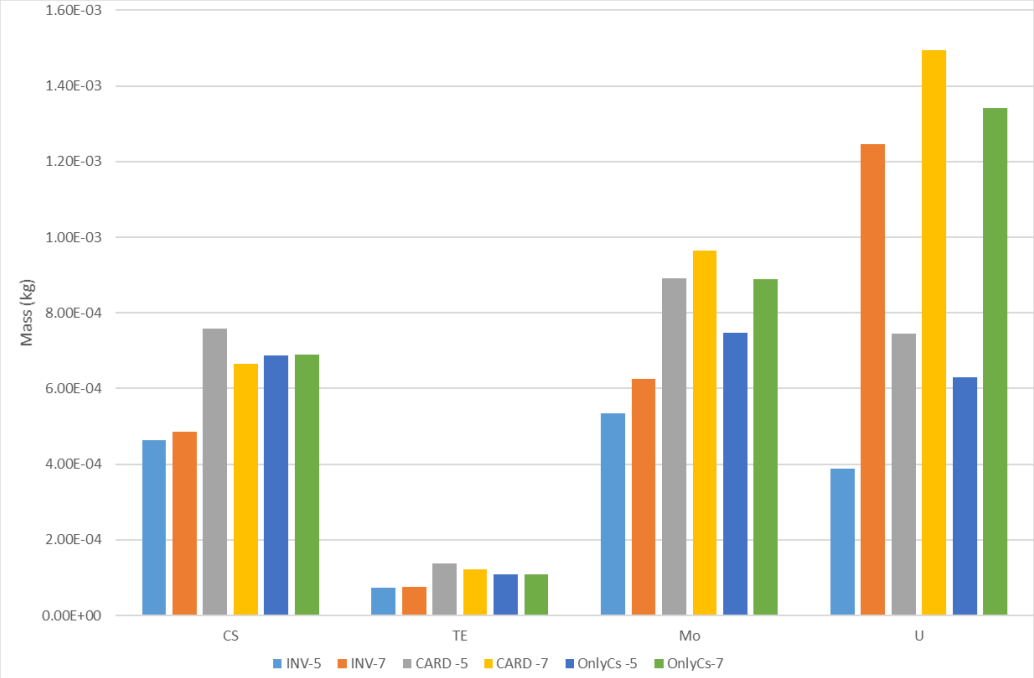

Figure 7 Radioactive mass of the selected airborne aerosols in the containment at the end of the calculation at 30000 s.

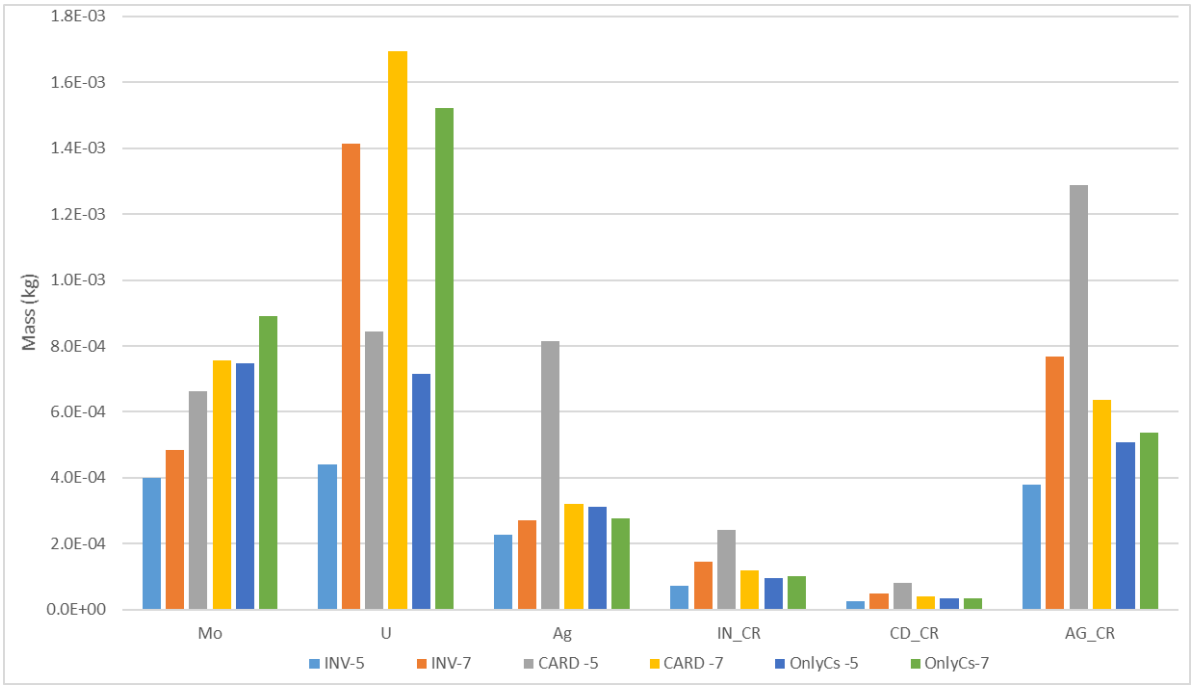

Figure 8 Total mass of the selected airborne aerosols in the containment at the end of the calculation at 30000 s.

4. FINAL REMARKS

The presented study focuses on the impact of Cs speciation and fuel release models on fission product release and aerosol transport in the Phébus FPT-1 test. The work has been conducted using MELCOR sensitivity calculations in the frame of the EU MUSA project. The main task was the preparation of the input deck for the foreseen UQ analysis and gathering the knowledge about MELCOR release models and Cs speciation. The project concentrates on the uncertainties of severe accident analysis, focusing on the source term. The main goal is to develop a dedicated methodology for uncertainty analysis of the nuclear severe accidents. As preparation for UQ analysis, the authors performed a sensitivity study on the MELCOR release models and the different methods of Cs speciation implementation. In this work, the authors analyzed the above-mentioned sensitivity's impact on potential FOMs, namely aerosol composition in the containment and the Cs retention in the RCS. In total, six sensitivity calculations were performed using two release models: CORSOR-BOOTH, revised CORSOR-BOOTH and three Cs speciation configurations: initial inventory implementation, class combination card and Cs present only as CsOH. The authors focus on the sensitivity impact to the Cs releases and retention in the RCS along with aerosol mass in the containment.

The results show that the Cs speciation impacts the Cs release from the fuel, and consequently, it affects the Cs retention in the RCS. Representation of the Cs speciation in the calculation has only a small effect on the containment aerosol concentration, which is more sensitive to the fuel release modelling. Applying the revised CORSOR BOOTH model over the standard CORSOR-BOOTH model more than doubled the concentration of certain elements in the containment at the end of the calculation. Thus it needs to emphasize that the selection of the release model has a major effect on the released masses, thereby it could have a significant effect on overall aerosol behavior in the accident analysis.

Of the Cs speciation options, the "Inventory" and the "Only_Cs" options calculate the highest Cs release varying between 85-88% of the initial Cs inventory when the "Card" gives 76%. Moreover, the way of implementing the Cs speciation affects the distribution of the Cs element amongst the Cs related classes. The "Inventory" calculates higher CsOH and Cs_2MoO_4 when the "Card" gives higher releases of CsI class accordingly.

The Cs retention results follow the calculated releases. Namely, the "Inventory" and the "Only_Cs" calculate Cs retention around 41% and the "Card" around 37% of the initial Cs inventory mass. The results show that the Cs speciation indirect affect the retention due to the different compound mass.

The sensitivity analysis of the aerosol composition in the containment shows differences also in the transition phase, which is not visible at the end of the simulation. It emphasizes the need for time-dependent sensitivity and uncertainty analysis in transient simulations. Additionally, the transient comparison shows the impact of the Cs speciation on the containment aerosol mass in the core degradation phase. The cases where the Cs_2MoO_4 or CsI were a significant part of the releases show an earlier increase in the containment aerosol mass. The most impacted classes are related to Cs, U and AIC materials. Thus, the obtained results differ mainly for the AIC and U classes when the Cs, Mo, and Te show less variation between the calculated sensitivity cases. It could suggest that AIC release and related parameters should be further investigated in the UQ analysis.

CREDIT AUTHORSHIP CONTRIBUTION STATEMENT

M. Malicki: Methodology, Calculations, Data curation, Writing - original draft, Visualization, Validation. T. Lind: Supervision, Writing - review & editing. J. Kalilainen: results consultation & review.

DECLARATION OF COMPETING INTEREST

The authors declare that they have no known competing financial interests or personal relationships that could have appeared to influence the work reported in this paper.

ACKNOWLEDGMENTS



The MUSA project has received funding from the Euratom research and training program 2014–2018 under grant agreement No. 847441.

REFERENCES

[1] Kissane, M., Drosik, I., "Interpretation of fission-product transport behaviour in the Phébus FPT0 and FPT1 tests", *Nuclear Engineering and Design,* **Volume 236**, Issue 11, Pages 1210-1223, (June 2006)
[2] The MUSA project objectives https://musa-h2020.eu/about-musa/
[3] U.S. NRC, State-of-the-Art Reactor Consequence Analyses Project Uncertainty Analysis of the Unmitigated Long-Term Station Blackout of the Peach Bottom Atomic Power Station, (2016)
[4] IAEA CRP project: Advancing the State-of-Practice in Uncertainty and Sensitivity Methodologies for Severe Accident Analysis in Water Cooled Reactors (I31033) https://www.iaea.org/newscenter/news/new-crp-advancing-the-state-of-practice-in-uncertainty-and-sensitivity-methodologies-for-severe-accident-analysis-in-water-cooled-reactors-i31033
[5] B.Clément et al. "Thematic network for a Phebus FPT1 international standard problem (THENPHEBISP)", *Nuclear Engineering and Design*, **Volume 235**, (2005)
[6] Noura Elsalamouny, Tadas Kaliatka, (2021), Uncertainty Quantification of the PHEBUS FPT-1 Test Modelling Results, Energies 14(21):7320, https://doi.org/10.3390/en14217320
[7] L. L. Humphries, D. L.Y. Louie, V. G. Figueroa, M. F. Young, S. Weber, K. Ross, J. Phillips, R. J. Jun MELCOR Computer Code Manuals Vol. 3: MELCOR Assessment Problems Sandia National Laboratories, (2015)
[8] J. Birchley, Assessment of the MELCOR Code Against PHEBUS Experiment FPT-1 Performed in the Frame of ISP-46, *ICONE12-49267*, pp. 551-560, https://doi.org/10.1115/ICONE12-49267
[9] P. Darnowski, M. Włostowski, M. Stępień, G, Niewiński, "Study of the material release during PHÉBUS FPT-1 bundle phase with MELCOR 2.2", *Annals of Nuclear Energy*, **Volume 148,** (2020)
[10] IRSN Institut de radioprotection et de sûreté nucléaire, "FPT-1 final report", (2000)
[11] Randall O. Gauntt, Synthesis of VERCORS and Phebus Data in Severe Accident Codes and Applications, SAND2010-1633, (2010)
[12] K. Ross, J. Phillips, R. O. Gaunt, K. C. Wagner, MELCOR Best Practices as Applied in the State-of-the-Art Reactor Consequence Analyses (SOARCA) Project Sandia National Laboratories, (2014)
[13] L.L. Humphries. FP Release Modeling - EMUG 2018 Workshop presentation, https://www.psi.ch/sites/default/files/import/emug/WS2018EN/WS_2018_03.pdf , (2018)
[14] L.L. Humphries, B.A. Beeny, F. Gelbard, D.L. Louie, J. Phillips, "MELCOR Computer – Code Manuals", Vol 1: User Manual, Version 2.2.14959, (October 2019)
[15] L.L. Humphries, B.A. Beeny, F. Gelbard, D.L. Louie, J. Phillips, "MELCOR Computer – Code Manuals", Vol 2: Reference Manual, Version 2.2.14959, (October 2019)
[16] S. Nichenko, J. Kalilainen, L. Fernandez Moguel. T. Lind "Modelling of fission products release in VERDON-1 experiment with cGEMS: Coupling of severe accident code MELCOR with GEMS thermodynamic modelling package", *Annals of Nuclear Energy*, **Volume 152**, (2021)
[17] T. Haste, F. Payot, P.D.W. Bottomley, "Transport and deposition in the Phébus FP circuit", *Annals of Nuclear Energy*, **Volume 61**, (2013)
[18] R. Dubourg, H. Faure-Geors, G. Nicaise, M. Barrachin, "Fission product release in the first two PHEBUS tests FPT0 and FPT1", *Nuclear Engineering and Design*, **Volume 235**, (2005)
[19] B. Clément et al., "Thematic network for a Phebus FPT1 international standard problem (THENPHEBISP)", *Nuclear Engineering and Design*, **Volume 235,** (2005)

PAUL SCHERRER INSTITUT

PSI



Mateusz MALICKI, Terttaliisa LIND, Jarmo KALILAINEN :: Paul Scherrer Institut

Parametric analysis of FPT-1 MELCOR 2.2 input deck as a preparation for uncertainty quantification study

The 10th European Review Meeting on Severe Accident Research (ERMSAR2022),
AkademieHotel, Karlsruhe, Germany, May 16-19, 2022,

Laboratory for
Reactor Physics and Thermal-Hydraulics

Content

- **Introduction to** →
  - UQ
  - MUSA project - WP4
- **Methodology** →
  - Transient definition
  - Sensitivity cases
- **Results** →
  - Cs release from fuel
  - Cs retention in the RCS
  - Aerosol mass in the containment
- **Final remarks**

Uncertainty Quantification –tool which is helping to determine uncertainty related to the obtained outcomes if not all data are known.

Not well defined.

UQ study:

- Define UQ methodology
- Figure Of Merit (FOMs)
- Uncertain Parameters, their ranges and distributions
- Run multiple calculations
- Analyze the obtained results

Many parameters are uncertain due to lack of experiments and experience.

Mostly only general ranges are known.

Codes are unstable and crashes during calculations.

Often lack of clear guidance for calculation failure management.

Preliminary study to develop methodology – MUSA

- **WP4 -**Application of UQ Methods against Integral
- In this work we focus on the **aerosol phenomenology**
- One of the phenomena revealed from the FPT experiments was the importance of chemical forms of the fission products and the impact of the poison material on the final source term.
- Our FOMs:
  - **Aerosol in the containment atmosphere**.
  - **Cesium retention** in the circuit [as % of Cs released from the core].

Transient specification of FPT-1:

- LOCA in a low-pressure steam environment
- Calculation time 30 000 s (two first phases of the test):
  - core degradation until 18 000 s
  - aerosol phase between 18 000 s and 30 000 s

Performed sensitivity cases

Calc nb.	Release model	Cs speciation
1	CORSOR-BOOTH (-5)	INV
2		CARD
3		Only Cs
4	Revised CORSOR-BOOTH (-7)	INV
5		CARD
6		INV

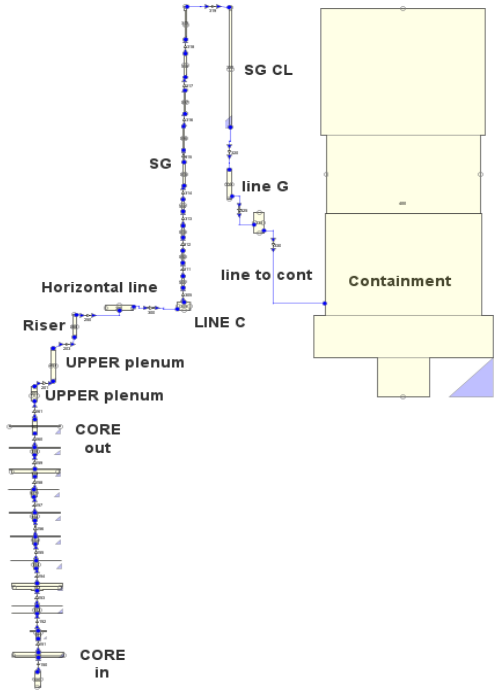

FPT1 experiment facility – MELCOR nodalization

MELCOR Cs speciation:

- **Only Cs**: In this option, Cs is represented only as CsOH in Cs class.
- **Inventory (INV)**: Pre-definition of the initial inventory by implementing masses of the CsM (Cs_2MoO_4) and the CsI classes via RN1_FPN card. Thus, Cs speciation are introduced already in the initial inventory as CsOH (Cs class), CsI (CsI class) and Cs_2MoO_4 (CsM class).
- **CARD**: The class combination at release time. The Cs speciation are created from Cs, I and Mo RN classes by the MELCOR model as defined in RN1_CLS card.

MELCOR releases models:

- CORSOR-Booth model for high burn-up fuel (model activation flag in MELCOR: -5). Releases bounded with Cs releases.
- Revised CORSOR-Booth (model activation flag in MELCOR: ORNL or -7). Releases independent for all RN classes.

Cs speciation:

- The largest mass of Cs was released when all Cs was assumed as CsOH (high vapor pressure of CsOH).
- Introducing Cs speciation in initial inventory gives highest releases of Cs_2MoO_4 and CsOH.
- The Cs release is the lowest in case when Cs speciation were combined after releases by MELCOR CLS card. This low value can be explained by the higher fraction of CsI, which has been shown to have a lower vapor pressure than Cs_2MoO_4 under oxidizing conditions.

Comparison of Cs releases of investigated options (CORSOR-BOOTH -5)

	Cs element [g]				Cs release % i.i.			
	CsOH	CsI	CsM	Total	CsOH	CsI	CsM	sum
Inv	1.90	0.85	11.06	13.80	11.9	5.3	69.7	87.0
Card	0.82	1.57	9.68	12.07	5.2	9.9	61.1	76.1
Only Cs	14.03	0.00	0.00	14.03	88.5	0.0	0.0	88.5

Comparison Cs releases of investigated options (revised CORSOR-BOOTH -7)

	Cs element [g]				Cs release % i.i.			
	CsOH	CsI	CsM	Total	CsOH	CsI	CsM	sum
Inv	1.89	0.87	10.83	13.59	11.9	5.5	68.3	85.7
Card	0.20	1.62	10.25	12.07	1.3	10.2	64.6	76.1
Only Cs	13.74	0.00	0.00	13.74	86.6	0.0	0.0	86.6

Release model:

- Impact of the release model is not significant compared to the Cs speciation.
- The calculated release percentage of the initial inventory is comparable with the experimental results (84%).
- The case where only CsOH is assumed agreed relatively well with the experimental data, giving 85-88% release similar to the one where Cs speciation were introduced as initial inventory. Class combination case calculates around 10% lower release than the other two cases.

Comparison of Cs releases of investigated options (CORSOR-BOOTH -5)

	Cs element [g]				Cs release % i.i.			
	CsOH	CsI	CsM	Total	CsOH	CsI	CsM	sum
Inv	1.90	0.85	11.06	13.80	11.9	5.3	69.7	87.0
Card	0.82	1.57	9.68	12.07	5.2	9.9	61.1	76.1
Only Cs	14.03	0.00	0.00	14.03	88.5	0.0	0.0	88.5

Comparison Cs releases of investigated options (revised CORSOR-BOOTH -7)

	Cs element [g]				Cs release % i.i.			
	CsOH	CsI	CsM	Total	CsOH	CsI	CsM	sum
Inv	1.89	0.87	10.83	13.59	11.9	5.5	68.3	85.7
Card	0.20	1.62	10.25	12.07	1.3	10.2	64.6	76.1
Only Cs	13.74	0.00	0.00	13.74	86.6	0.0	0.0	86.6

Cs retention in the RCS

- The highest Cs retention occurs in when Cs speciation were implement as initial inventory, however the results are similar among all investigated cases.
- The Cs speciation affects the proportion of the Cs distribution among the RN classes.
- The highest differences are seen when Cs speciation were combined by MELCOR models after releases.

Comparison of Cs retention of investigated options (CORSOR-BOOTH -5)

	Cs element [g]				Cs retained % i.i.				retention % of the Cs release
	CsOH	CsI	CsM	Total	CsOH	CsI	CsM	retained [% i.i.]	retained [%]
Inv	0.91	0.46	5.28	6.65	5.74	2.90	33.28	41.92	48.11
Card	0.38	0.83	4.66	5.87	2.41	5.23	29.36	37.01	48.66
Only Cs	6.60	0.00	0.00	6.60	41.64	0.00	0.00	41.64	47.18

Comparison Cs retention of investigated options (revised CORSOR-BOOTH -7)

	Cs element [g]				Cs retained % i.i.				retention % of the Cs release
	CsOH	CsI	CsM	Total	CsOH	CsI	CsM	retained [% i.i.]	retained [%]
Inv	0.90	0.46	5.19	6.55	5.66	2.91	32.75	41.32	47.49
Card	0.09	0.85	4.87	5.81	0.55	5.38	30.71	36.65	48.14
Only Cs	6.54	0.00	0.00	6.54	41.25	0.00	0.00	41.25	46.63

Aerosol mass in the containment

CORSOR-BOOTH

- Differences are seen during the core degradation phase (especially once larger aerosol release was started 12 000 s)
- The modified initial inventory calculates the highest aerosol release in the both, core degradation and aerosol phase.
- The end state shows the highest deposition as well for the case in which Cs speciation were introduced in initial inventory followed by the cases with only CsOH and Cs combined after releases.

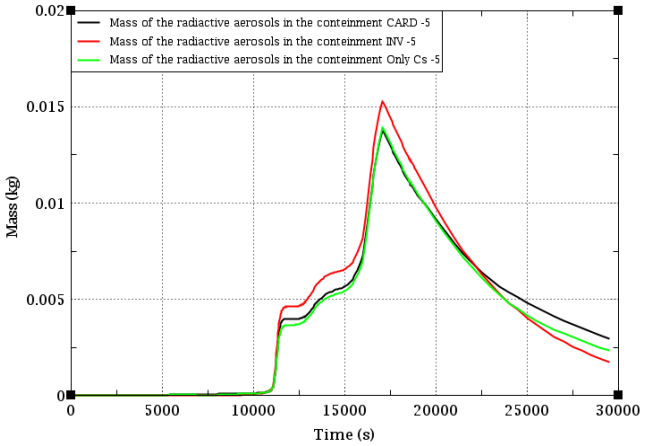

Total airborne aerosol mass comparison of investigated Cs speciation options in the containment CVH, using CORSOR-BOOTH.

Revised CORSOR-BOOTH

- The results follow the described above behavior during the core degradation phase.
- However, on average, the revised release model calculates higher values and the aerosol mass at the end of the calculations differs less.
- In the aerosol phase, the cases where Cs were implemented as initial inventory shows the lowest aerosol mass, opposite to the calculations performed with standard CORSOR-BOOT.

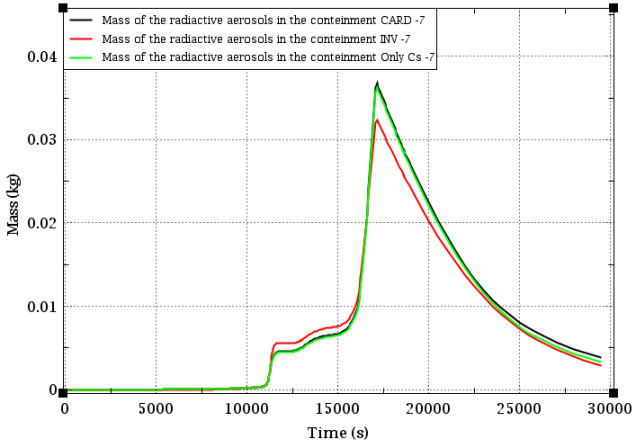

Total airborne aerosol mass comparison of investigated Cs speciation options in the containment CVH, using revised CORSOR-BOOTH.

Aerosol mass in the containment

In general, the presented sensitivity analysis results show the impact of Cs speciation and release models on aerosol dynamics and confirm its importance for understanding uncertainties related to severe accident numerical analysis.

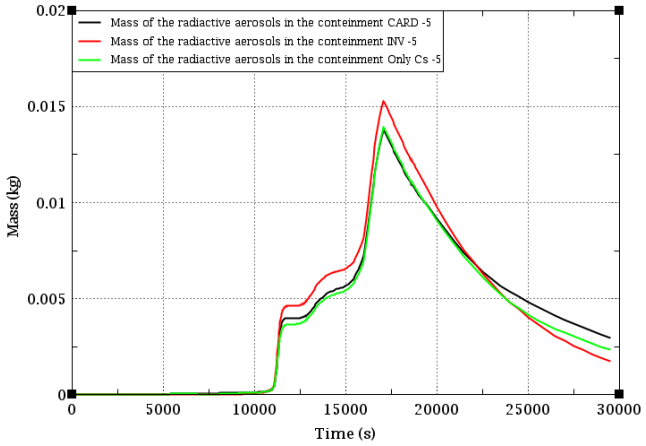

Total airborne aerosol mass comparison of investigated Cs speciation options in the containment CVH, using CORSOR-BOOTH.

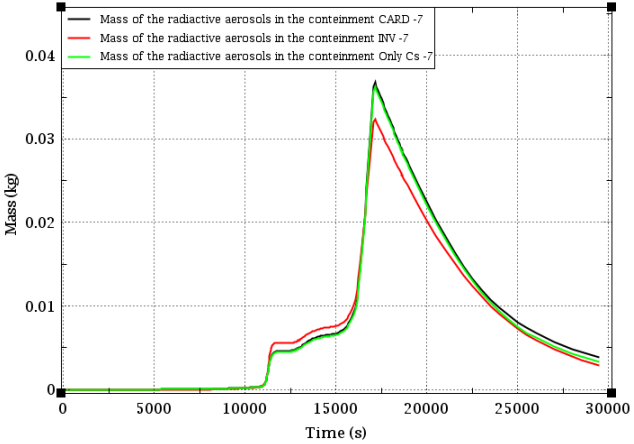

Total airborne aerosol mass comparison of investigated Cs speciation options in the containment CVH, using revised CORSOR-BOOTH.

Aerosol mass in the containment

- The values presented in the below figures show that the release model has a limited impact on the release of Cs into the containment.
- The Cs mass variation relates mainly with the Cs speciation; however, it needs to be highlighted that the presented data represents the final stage of the calculations.

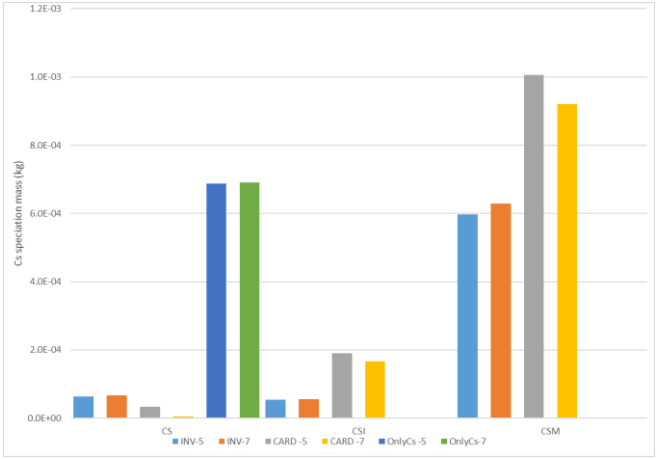

The mass of radioactive airborne Cs classes aerosols in the containment at the end of the transient.

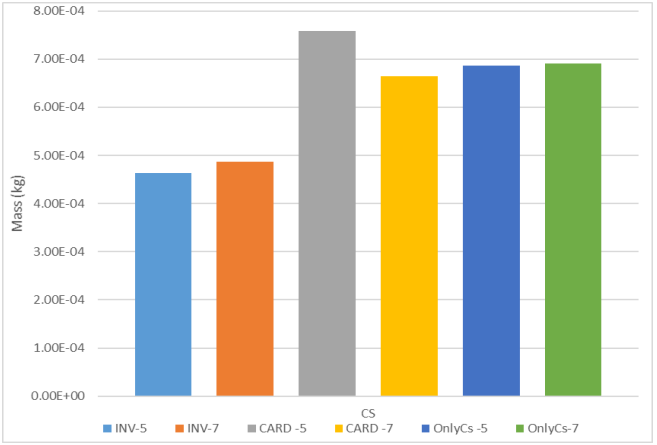

Cs element mass related to the airborne aerosols in the containment at the end of the transient.

Aerosol mass in the containment

- Cs and Mo masses vary among cases caused directly by implementing Cs speciation.
- However, U and AIC classes show significant discrepancies as well. The U and Mo releases in the CORSOR-BOOTH model are much lower than when the revised release model is used.

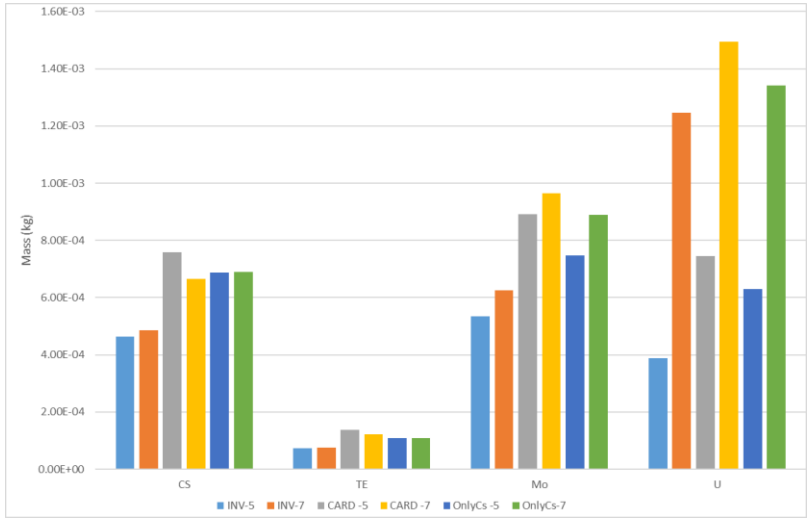

Radioactive mass of the selected airborne aerosols in the containment at the end of the calculation at 30000 s.

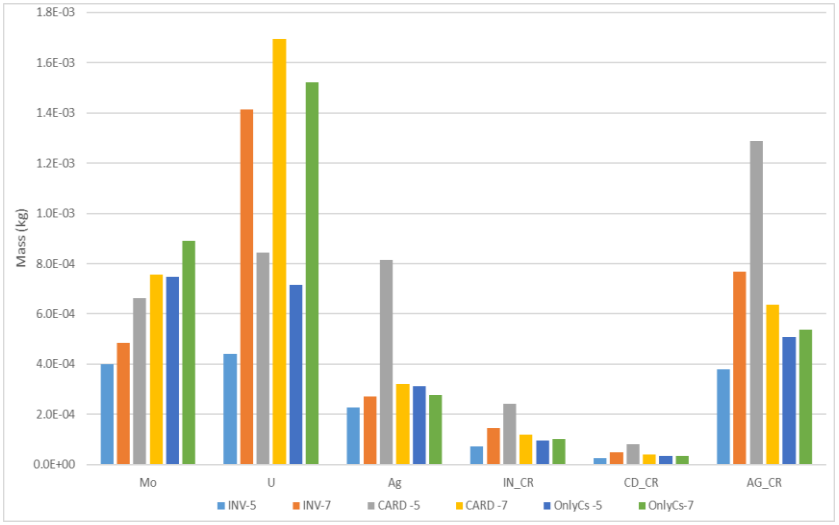

Total mass of the selected airborne aerosols in the containment at the end of the calculation at 30000 s.

Aerosol mass in the containment

- This discrepancy is expected as the revised model allows releases independently from Cs releases.
- The release model affects less the Cs and Te than AIC classes. Especially high discrepancies were noticed in the cases which include Cs speciation (INV and CARD).

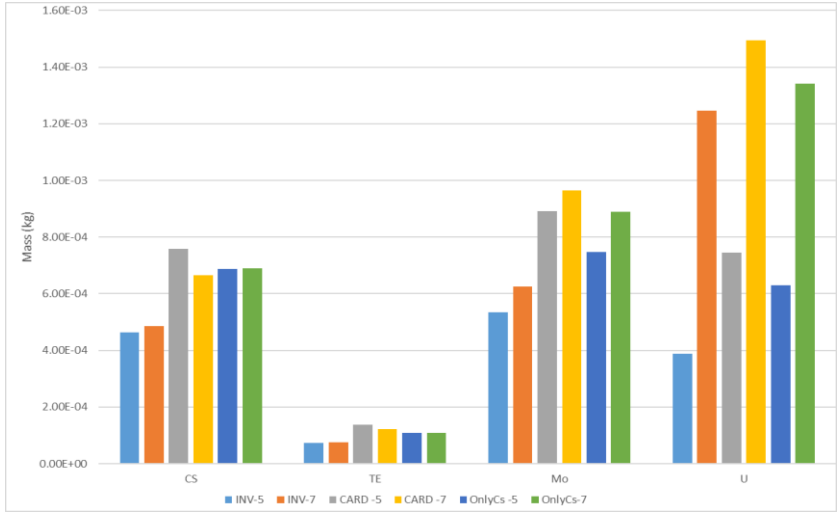

Radioactive mass of the selected airborne aerosols in the containment at the end of the calculation at 30000 s.

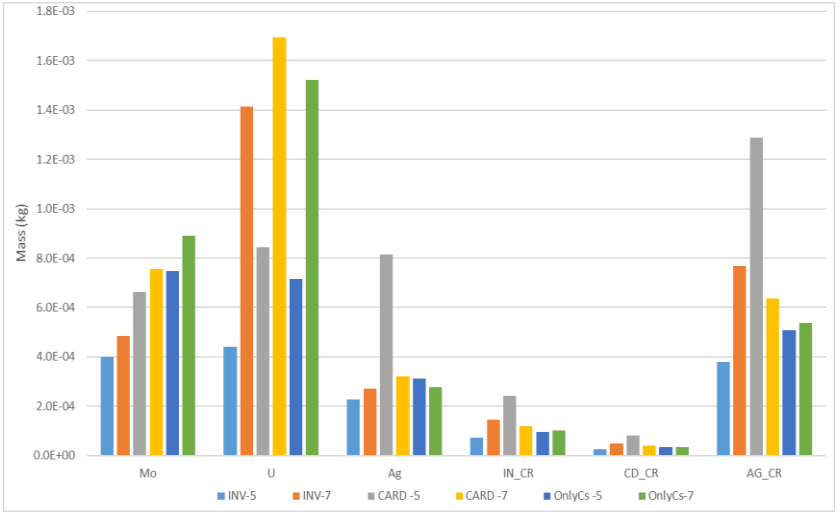

Total mass of the selected airborne aerosols in the containment at the end of the calculation at 30000 s.

Final remarks

Releases:

- Differently implemented Cs speciation could affect the ratio of the releases between Cs classes and consequently the final mass of releases. The impact of the two investigated release models is negligible for the overall results of Cs release; however, the CsOH in the “Card” option varies visibly from other results.

Retention:

- The Cs speciation affects the proportion of the Cs distribution among the RN classes (Cs, CsI, CsM) and consequently the related compound’s mass, having only an indirect impact on the retention by causing the differences in the released mass. However, it should be highlighted that presented results concern only the end state of the calculation.

Final remarks

Aerosol mass in the containment:

- It was shown that if only the results at 30000s were considered, the total mass of aerosols in the containment (proposed FOM) would not be significantly affected by Cs speciation, which could be the case for the degradation phase.
- The values presented in the study show that the release model has a limited impact on the release of Cs into the containment. The most visible difference is that the revised release model where Cs speciation were combined after releases by MELCOR model.
- The obtained discrepancies of the control rods material releases and theirs influence on the overall results confirm the importance of the AIC related uncertainty study.

Acknowledgements

The MUSA project has received funding from the Euratom research and training program 2014–2018 under grant agreement No.847441.

We thank Sandia National Laboratories for providing a generic input deck that was used as a base in this work, it was updated and adapted to fit project purposes.



Thank you for your attention !



ETHZ-EPFL MSc in Nuclear Engineering

- Swiss joint MSc program between ETHZ and EPFL
- Established in 2008, more than 100 students
- Two-year program, 120 ECTS credits
- Students attend two top-ranked universities:
  - ETH Zurich #9
  - EPF Lausanne #14 (based on QS)
- Scientific support and research at the Paul Scherrer Institute
- Grants and scholarships available









The 10th European Review Meeting on Severe Accidents Research

Severe Accident Research Eleven Years after the Fukushima Accident

May 16-19, 2022, Karlsruhe, Germany

Technical Session 3-2: Ex-vessel Corium interactions and coolability

Chairs: A. Miassoedov (IAEA), P. Piluso (CEA)

ID271	**Super Absorbing Polymers as a Means to Suppress Steam Explosions and Improve Melt Jet Fragmentation** M. Fischer (Framatome)	**Paper** **Presentation**
ID317	**Assessment of Ex-Vessel Corium Coolability of the VVER-1000 Reactor as a Measure of Severe Accident Mitigation** M. Kotouc (UJV)	**Paper** **Presentation**
ID337	**Experiment and Numerical Simulations on SFR Core-Catcher Analysis After Relocation of Corium** B. Bigot (CEA)	**Paper** **Presentation**

SUPER ABSORBING POLYMERS AS A MEANS TO SUPPRESS STEAM EXPLOSIONS AND IMPROVE MELT JET FRAGMENTATION

Torsten Keim, Manfred Fischer, Markus Hupp
Framatome GmbH
Paul-Gossen-Str. 100, 91052 Erlangen, Germany
torsten.keim@framatome.com, manfred.fischer.ext@framatome.com,
markus.hupp@framatome.com

ABSTRACT

Framatome is currently developing a technology for enhancing ex-vessel melt coolability based on the addition of super absorbing polymers (SAP) to the coolant water in the cavity. When submerged, this material quickly expands in volume by orders of magnitude creating pools that consist of water and water-saturated SAP particles. Melt jets discharged into these pools were effectively fragmented, resulting in debris configurations of high porosity. In addition, the added SAP material was found capable to suppress energetic interactions between melt and water.
In corresponding experiments oxidic, metallic and mixed melts with masses and temperatures of up to 50 kg and 2100 °C, respectively, were discharged into SAP pools of various depth and particle densities (water fractions). In pools with low water fraction, the melt jets solidified into filigree coherent structures that remained suspended inside the pool's volume. The degree of spatial dispersion and the coherency of the formed structures was significantly higher for metallic than for oxidic melts. In pools with high water fraction, no coherent structures were formed for both metallic and oxidic melt jets. Instead, the melt was completely dispersed into coarse debris with high average particle diameters.
If the SAP pools were shallow, the jets penetrated to the bottom and spread on the floor independent of the applied water fraction. In all performed experiments, no energetic interactions between the jet and the surrounding SAP pool were observed.
The paper gives an overview of the performed experiments and the mechanisms that may be responsible for the enhanced fragmentation and the observed steam explosion-inhibiting effect. An overview of the SAP-based mitigation concept is given in a separate paper.

KEYWORDS
super absorber, core melt, stabilization, fragmentation, coolability

1. INTRODUCTION

The main target of severe accident mitigation is to preserve the integrity of the containment as the last remaining barrier against fission product release into the environment. A necessary precondition for achieving this target is the re-stabilization of the molten core. Re-stabilization can be achieved either inside the reactor pressure vessel (in-vessel) or after the melt is released into the lower containment (ex-vessel). Following the assessment of various related concepts in [1], the most effective way to achieve ex-vessel melt stabilization is a so-called "core catcher", a dedicated structure that is capable to contain the melt and ensure its long-term cooling. However, the back-fitting of a core catcher into operational nuclear power plants (NPPs) can be extremely challenging, which makes them an option mainly for new Gen-III designs. Compared to this, Gen-II plants typically rely on simpler solutions, e.g. the flooding of the space below the reactor pressure vessel (RPV) before or after RPV melt-through, with the aim to achieve fragmentation either while the melt penetrates the water, or during the interaction with concrete. Evidently, the efficiency of the first method will increase with the depth of the provided water pool, but so does the risk of energetic steam explosions. Whenever the containment of a certain reactor type is not capable to withstand the related pressure loads, this can be a significant obstacle for the acceptance of the corresponding severe accident mitigation (SAM) strategy. In addressing this issue, Framatome currently develops a technology aimed at lowering the steam explosion risk in such situations. The main idea is to reduce the amount of free water in the pool by the addition of particles consisting of super-absorbing polymers (SAPs). The characteristics of the SAP material, its stability against various severe accident load conditions and the possible use of the proposed technology in SAM strategies are described in [2].
To confirm their predicted ability to suppress steam explosions, a number of experiments have been performed in which melt jets of various type were released into SAP pools of various depth and water content. In all these tests no steam explosions occurred. In addition, the mechanical resistance of the added particles improved the dispersion of the melt jet which can significantly enhance the coolability of the created debris bed.

2. CHARACTERISTICS OF SAP-WATER POOLS

2.1. Physical and Mechanical Properties

Several candidate materials for the intended application in the reactor cavity were screened based on how they fulfill the following criteria:

- Compatibility with the operational conditions inside a NPP, high water uptake rate
- Low costs, high availability, easy handling
- Mechanical and thermal stability during melt contact

Among the investigated material, super absorbing polymers (SAPs) were selected as most suitable because they fulfill all above requirements and are capable of absorbing the highest amount of water relative to their own weight. Typical applications are the removal of humidity/undesired liquids or the long-term provision of the stored water for agriculture in arid regions.

While the properties of SAPs can be customized to fulfill a wide range of specific requirements, generic poly-acrylic acid-based material was used in all experiments reported in this paper. Therefore, the quantitative results given in the following chapters must be seen as preliminary. A further optimization of the SAP properties is foreseen in future stages of the project. In their here-applied particulate form, SAPs typically have a two-layer structure [3]: an inner bulk part of lightly cross-linked hydrogel surrounded by an outer, highly cross-linked layer created by chemical surface reactions, as depicted in Fig. 1a.

The average density of the dry material is ~2000 kg/m^3 and the diameters of the particles are in the range of 1-3 mm. When submerged, their diameter increases to more than 1 cm. During water absorption both the inner region and the outer shell inflate. The shell limits the extent of water uptake but increases the stability and mechanical properties (elasticity) of the particles. In addition, the high heat capacity of the contained water gives the shell strength to resist the initial thermal impact of the hot melt.

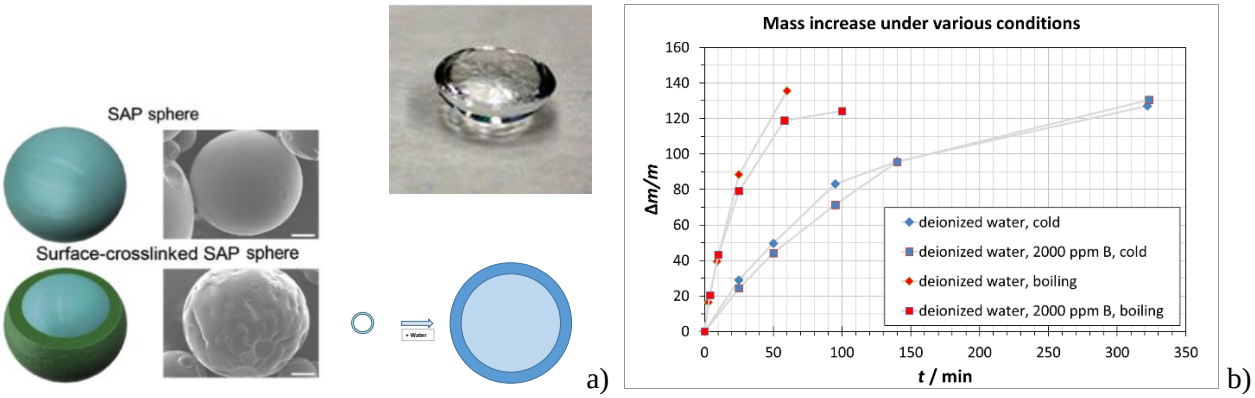

Figure 1. SAP particle, structure and cut, from [3] (a), water uptake (b)

The rate at which the particles can absorb water decreases in time and also depends on the water's temperature and chemical properties. Experiments performed in the labs of Framatome in Erlangen have shown that:

- the final mass of absorbed water was ~130 times the initial particles mass.
- the particle volume increased even more, by a factor of up to ~200.
- in subcooled water, the uptake velocity significantly increases with temperature, but the final size and mass of the particles remain the same
- in boiling water the absorbed mass is ~10 % lower than under subcooled conditions.

Tests on the impact of the boron concentration showed that, at lower temperatures, the presence of boron (2000 ppm B, added as H_3BO_3) has only negligible effect, but that there is a measurable impact on both, the uptake rate and the final water content, at temperatures close to saturation, see Fig. 1b. More details on the properties of the SAP material used in the experiments presented here are given in [2].

2.2. SAP-Water Pool Properties

When dry SAP particles are added to a water pool they take up water, ultimately until a saturated state is reached. Denoting the total water mass contained in all these water-saturated particles as $\mathbf{m_{w\text{-}sat}}$, and the masses of particles and water provided as $\mathbf{m_{SAP}}$ and $\mathbf{m_w}$, the following final states of the pool are possible:

$\mathbf{m_w >> m_{w\text{-}sat}}$: All particles can reach the water-saturated state and the remaining water can completely fill the interstices between them. Considering that the density of the dry SAP is twice that of water and that the inflation factor is >100, the density of a water-saturated particle is only a few percent higher than that of the surrounding water. Therefore, the upper part of the pool does not impose a major pressure on the lower part and the particles also near the bottom remain close to spherical and tend to arrange in a way that the resulting porosity ε_{pool} is lowest. In this paper, such a pool configuration is denoted as a "wet" pool. The minimum theoretical porosity for tightly packed, equal-sized spheres is ε_{theo}= 0.26. In practice, the porosity and water

content in the pool can either be higher or lower, depending on the size distribution and shapes of the particles. If m_w exceeds $(1+ \varepsilon_{pool})*m_{w\text{-}sat}$, a water layer free of SAP particles will exist at the top of the pool.

$(1+ \varepsilon_{pool})*m_{w\text{-}sat} > m_w >= m_{w\text{-}sat}$: All particles can still become water-saturated but not all of the them will float. Then, the particles in the lower part of the pool must support the weight of the "non-floating" particles in the upper part. The resulting pressure increases with depth and leads to: (i) a deformation of the elastic particles, (ii) less free water between them and thus, (iii) in a higher packaging density in the lower region of the pool. Evidently, the compactness will be highest if m_w approaches $m_{w\text{-}sat}$. In the following, this configuration is denoted as a "dry" pool. The height-dependent porosity inside a "dry" pool and hence the max. free water content were found to decrease to ~0.1 already at a depth of 1 m.

$m_w < m_{w\text{-}sat}$: In this case there is not enough water to saturate all particles, which leads to a "dry" pool with smaller particles and finer "pores". Evidently, such a pool can be very compact and show the highest mechanical resistance against melt ingress.

3. OVERVIEW OF PERFORMED EXPERIMENTS

In a number of dedicated experiments, various aspects of the interaction between melt jet and both "dry" and "wet" SAP pools were investigated. Two main test series have been conducted, the first at KTH Stockholm, Sweden, and the second at the Framatome test site in Karlstein, Germany.

3.1. SAP-DEFOR Tests

A sketch of the apparatus used in these tests is shown in Fig. 2a. The furnace allows to generate metallic and oxidic melts with temperatures up to 1500 °C. The applied procedure for melt generation is practically identical to that used in earlier DEFOR experiments. The test section below which contains the SAP pool, see Fig. 2b, has large windows through which the interaction process can be observed and recorded.

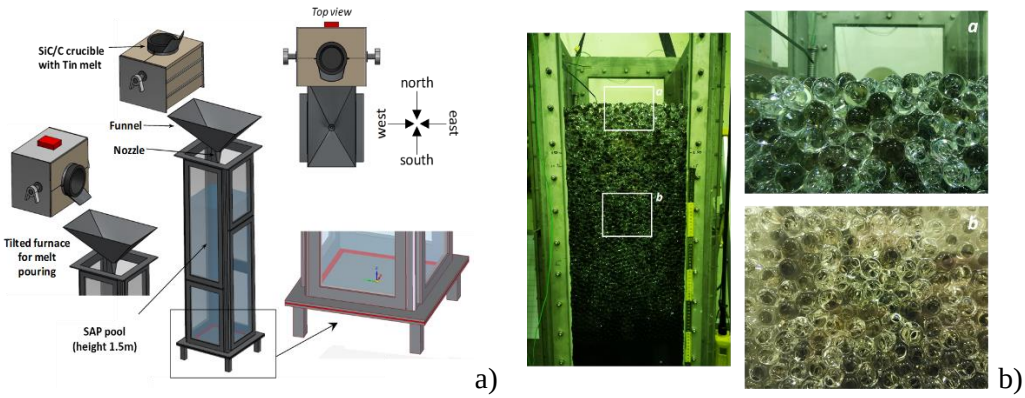

Figure 2. Main elements of the DEFOR facility (a) and pictures showing the "dry" SAP pool (b)

The simulant material in the SAP-DEFOR01/02 tests was molten tin (density: ~6800 kg/m^3, melting temperature: 232 °C), while in the SAP-DEFOR03 test an oxidic powder mixture composed of ~42 wt% Bi_2O_3 and 58 wt% WO_3 (close to eutectic composition) was applied yielding a melt with a density of ~6700 kg/m^3 and a liquidus temperature of ~900 °C. The melt is generated in an inductively heated, inclinable furnace from where it is discharged into a funnel and released through a vertical nozzle into the

test section below, see Fig. 2a. The nozzle consists of two parts: an upper conical section and a straight pipe with an inner diameter of 20 mm. The measured melt delivery conditions for the three performed tests, SAP-DEFOR01/02/03, are summarized in Table A.

Table A. SAP-DEFOR experiments, melt release conditions

SAP -	DEFOR01	DEFOR02	DEFOR03
Melt temperature in the funnel, °C	455	625	1073
Melt superheat in the funnel, °C	223	393	173
Discharged melt volume, liter	4.3	4.4	3.2
Duration of melt release, s	6.8	6.9	6.5
Averaged melt flow rate, kg/s	4.35	4.32	3.3
Averaged melt flow rate, liter/s	0.634	0.639	0.493
Estimated jet impact velocity, m/s	3.33	3.33	3.07

The SAP pool had a depth of 1.5 m and a quadratic cross section of 0.5*0.5 m^2. The test section, shown in Fig. 3a, was instrumented with three lines of vertically arranged thermocouples (TCs), one in the center and two at radial distances of 62.5 mm and 125 mm, respectively. In preparation of the tests, the SAP particles were saturated with water for two days at an ambient temperature of ~20°C. Before the experiment the water was drained from the test section to create the intended "dry" pool configuration, see Fig. 3b. In the SAP-DEFOR02/03 tests colored SAP particles were deposited at the top of the pool to obtain information about the mixing during melt inflow.


a)
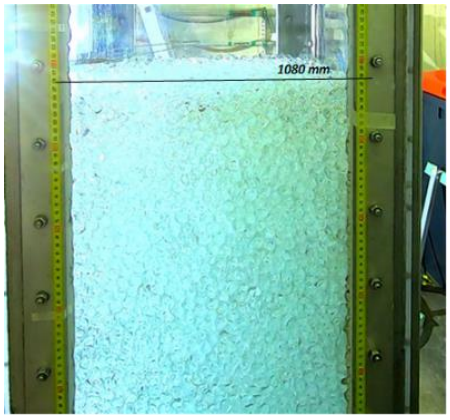

b)

Figure 3. SAP-DEFOR02, test section with TCs (a), SAP pool after drainage (b)

3.2. SAP-FRA Tests

In a second set of about 10 experiments (incl. pretests) performed at the Framatome test site Karlstein commercially available thermite melt generators and standard aluminum/iron-oxide welding mixtures were used. The temperatures of the generated liquid iron and alumina were ~2100 °C and hence significantly higher than the temperatures realizable in the DEFOR facility. In addition, molten steel is highly prototypic as it is also part of the molten corium and, like the Zr in real corium, can chemically reduce steam leading to the formation of iron oxide and hydrogen. Further, with respect to the steam explosions issue, not only

the steel (due to its high superheat) but also the alumina (due to its known high tendency to engage in energetic interactions with water) are conservative substitutes for metallic and oxidic corium [4],[5],[6].
In the performed tests, either one or two thermite generators were used, which allowed melt masses from 17 kg to 50 kg. Two crucibles were combined by mounting them one on top of the other with their common axis above the center of the SAP pool. The ignition times for the crucibles were synchronized to achieve continuous releases of first the metallic and then oxidic phase. The fraction of iron/steel in the thermite mixture, as determined in a pretest, was ~80 wt%, which – for the tests with two crucibles – resulted in about 40 kg of iron and 10 kg of aluminum oxide.

To limit the impact of potential steam explosions, the outer wall of the test section was realized as a 1 cm-thick steel pipe, see Fig. 4a, which housed a removable, cylindrical insert with an inner diameter of ~48 cm. It was made from perforated sheet metal and contained the SAP pool, see Fig. 4b. The TC arrays for the "wet" tests, see Fig. 4c, were mounted against these inserts, while the pressure sensors could be placed inside the completely flooded outer steel cylinder.

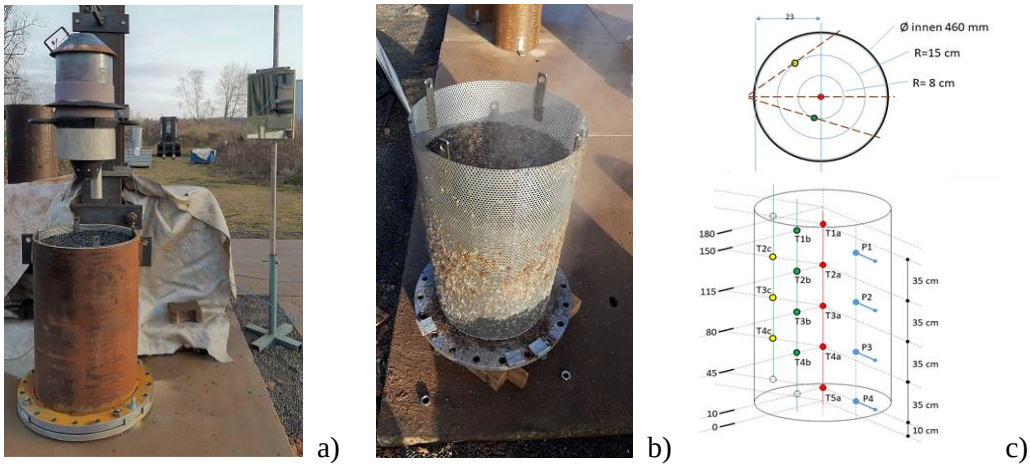

a) b) c)

Figure 4. Thermite generator and test section before (a) and after (b) the SAP-FRA01 test, TC array arrangement used in the SAP-FRA06 test (c)

Two series of experiments (with 3 tests each) were performed in the FRA-facility, the first one with "dry" SAP pools and the second with "wet" pools following the prediction that "dry" pools have a lower potential for energetic events than "wet" ones. In all "wet" tests the water level was chosen equal to the level of the SAP particle bed (no excess water on top). The height of the test sections varied between 0.8 m and 1.80 m. An overview of the FRA tests is given in Table B.

Table B. SAP-FRA experiments, test conditions

Test	FRA01	FRA02	FRA03	FRA04	FRA05	FRA06
Thermite mass, kg	24	17	50	24	24	48
Melt release period, s	14	12	19/13	14	13	17/12
Impact velocity)*, m/s	3.02	2.93	3.18	3.02	6.49	3.15
SAP pool height, m	0.77	0.86	1.53	1.50	1.50	1.70
SAP pool type	dry	dry	dry	wet	wet	wet

)* - averaged during the period of metal discharge

4. OBTAINED EXPERIMENTAL RESULTS

4.1. Tests with "Dry" SAP Pools

Corresponding tests were conducted by both, KTH and Framatome. The KTH metal tests (SAP-DEFOR01 and 02) resulted in solid coherent structures consisting of an upper, cup-shaped section (the "arms" in Fig. 5a), and a cone-like middle part with one or two extrusions ("legs") at the bottom. All parts are very porous which is very favorable for water ingress and coolability. The sizes of the interconnected pores correspond to the sizes of the water-saturated SAP particles (Figs. 5b and 5c).

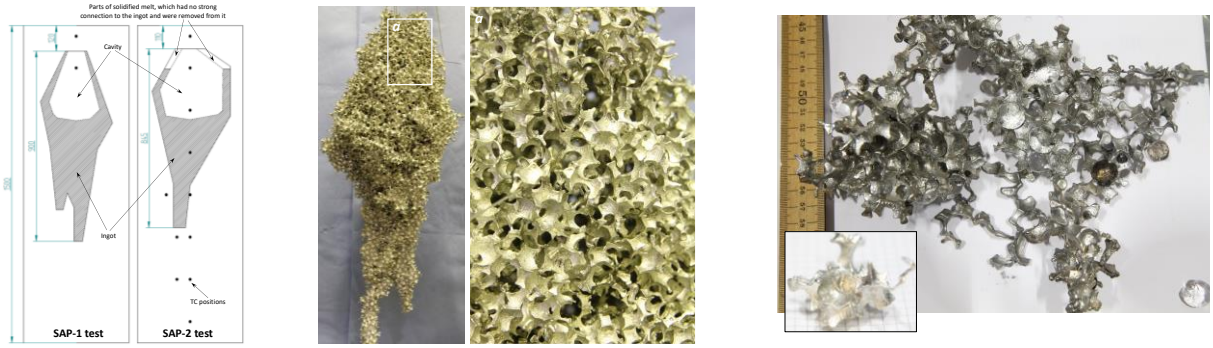

a) b) c)

Figure 5. Debris position in the SAP-DEFOR test section (a), post-test view of SAP-DEFOR01 debris cleaned of SAP particles (b) and SAP-DEFOR02 debris with captured SAP particles (c)

The recorded videos reveal an initially strong lateral dispersal of the jet followed by an extension in axial direction. Hence, the "arm"-like structures at the top of the ingot, see Fig. 5a, were created by the first-arriving melt which shows that, already at a relatively low penetration depth, the SAP pool was able to effectively deflect the incoming melt jet. During its progression in radial direction the contact area between the liquid material and the wet particles progressively increased, which led to solidification within a well-defined radial distance. Most of this solid material remained interconnected, see Fig. 5b, so only a small amount of separated fragments/particles were recovered, see Fig. 5c. All fragments preserve the shapes of the interstices between SAP particles in which they were formed.

The non-deflected part of the jet kept penetrating into the SAP pool; the deeper, the more heat is transferred and the more agitated the inner part of the pool becomes. During this process, the ratio of radial vs. axial penetration steadily increases, which formed the lower bulk part of the structures shown in Fig. 5. The high spatial concentration of melt in this region results in less cooling, so the melt remains liquid over a longer time period. This is the likely reason for the late downward spreading events observed after the end of the jet inflow which formed the "legs" at the bottom. Further interesting observations are: (i) that the created filigree metallic structure remained suspended inside the pool, and (ii) that the inside of these structure incl. pores was filled with still intact SAP particles. Only a small fraction of the added particles became damaged. The later performed test with oxidic melt SAP-DEFOR03 yielded similar results with a few differences: (i) a lower penetration depth, (ii) a more compact bulk region, and (iii) the absence of extensions ("legs") at the bottom. This indicates that all material became immobilized once it had reached the bulk's positions.

The first two Framatome tests SAP-FRA01/02 were also performed with "dry" pools and 17 kg / 24 kg of thermite melt. As the depth of the SAP pool in these tests was only ~90 cm, a part of the jet reached the bottom of the test section and spread on its steel base.

In the third test, the melt mass and pool depth were increased to 50 kg and 1.5 m (to better approach the conditions as in the DEFOR tests), which again resulted in a complete solidification within the pool's volume. This shows that, in the range of mass flow rates between 1 kg/s (min. Framatome) and 4 kg/s (max. DEFOR), the penetration depth into a "dry" pool is determined mainly by its depth and not by the jet's duration, flow rate and temperature.
In all thermite tests steam and burnable gases were generated, the latter by iron-steam reaction and/or the thermal decomposition of the SAP material in contact with hot melt. Steam and gas escaped the SAP pool not only through the top surface, were they caused periodic uplifts see Fig. 6a, but also in radial direction through the perforated inner test section. In later stages of the test, intense flames were observed. These flames were particularly intense in test SAP-FRA03, performed with 50 kg of thermite, see Fig. 6b.

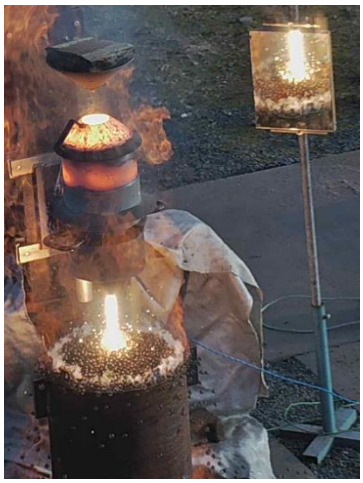
.a)

b)

c)

Figure 6. SAP-FRA01, pool surface during melt impact (a), SAP-FRA03, jet inflow (b) and solidified melt (c)

The solidified melt in the SAP-FRA03 test was located half a meter below the pool's initial surface. After removal of the surrounding, mostly intact SAP particles the structure shown in Fig. 6c was recovered. With respect to outer shape and porosity this structure resembles the ones in the SAP-DEFOR01/02 tests, with the main difference that now the inside of the metallic structure is filled with the later-released oxidic melt. The "cup"-shaped upper part of the metallic structure enclosed the oxidic debris and limited its further spatial progression. The black color of the metal was likely caused by oxidation (FeO), or by carbon-containing decomposition products of the SAP material.

All "dry" SAP tests showed enhanced fragmentation but no signs of energetic interactions. Instead, the inflow of the jet was very smoothly without any major ejections of SAP material.

4.2. Tests with "Wet" SAP Pools

After the "dry" pool tests, a second series of jet fragmentation experiments – now in "wet" pools – was conducted in the Framatome facility, see Table B. Following the definition in Section 2.2, the term "wet" pool refers to conditions where the free water level is equal to the level of the SAP particles. In such a pool, the water content in the particle region is at its maximum. Hence, with respect to the steam explosion risk, tests with "wet" pools are conservative and bounding for all other pool configurations.

The first "wet" test SAP-FRA04 was performed successful showing no signs of energetic interactions. The test was therefore used as a reference for later variations in the jet parameters, namely: the impact velocity (SAP-FRA05) and thermite mass (SAP-FRA06), see Table B.
Surprisingly, the >100% increase in the jet's impact velocity had only limited effect. While the axial progression of the jet to the position of TC1a (at -20 cm, relative to the SAP pool surface) was still significantly faster, the time needed to reach TC2a (at -60 cm) was only ~20% shorter than in the SAP-FRA04 test. The TCs at all deeper locations showed a rather erratic and stochastic response. While, in test SAP-FRA04, the thermocouple TC3a (at -100 cm) failed already ~3.2 s after TC2a, the TC at the same position survived ~8 s longer in test SAP-FRA05, despite the now much higher jet impact velocity.

The increase in melt mass to 48 kg in the final test of the series, SAP-FRA06, resulted in a longer release period and higher melt fractions in the center of the pool, which led to more steam generation and a higher void. Likely because of this, the jet could now penetrate deeper but still did not reach the bottom of the pool. A comparison of the images recorded during SAP-FRA06 with those from the corresponding "dry" test SAP_FRA03 indicates that less burnable gas was generated under "wet" conditions. This can be explained by a now faster cool-down of the metallic melt, as a consequence of enhanced heat transfer to the free water, and the resulting shorter period in which the metal is hot enough to chemically react with steam. The same effect may have limited the extent of the thermal decomposition of the SAP particles.

The main difference to the preceding "dry" tests, however, was the absence of coherent debris structures. Instead, the quenched melt formed individual pieces, see Fig. 7a, which ultimately settled to the bottom of the pool. The sizes of the particles are mostly between 1 cm and 10 cm and thus larger than in comparable experiments with oxidic melt and pure water, where the particle sizes are typically <1 cm. The debris from test SAP-FRA06 has been separated by dimension in four boxes, see Fig. 7b, which contain the particles that are (from left to right):

- smaller than 5 mm: 3.3 wt%,
- between 5 mm and 10 mm: 23.3 wt%,
- between 10 mm and 25 mm: 45.1 wt%,
- larger than 25 mm: 28.4 wt%.

Many of the collected large pieces still enclosed intact SAP particles. The pieces often consisted of metallic and oxidic fractions, so their average densities ranged from 2500 kg/m^3 to 6000 kg/m^3.


a)


b)

Figure 7. Debris retrieved after test SAP-FRA06

Due to the high deposited melt mass in the SAP-FRA06 test, the pool temperatures locally exceeded 100°C over an extended period of time. As a consequence, the steam pressure inside the SAP particles exceeded the ambient pressure so the outer shells of the SAP particles broke and their amorphous content was released which resulted a mixture of intact spheres and slurry-like material.

Tests SAP-FRA04/05/06 had shown that deep SAP-water pools are capable to stabilize the melt without causing energetic events. However, in shallow configurations the melt jet may penetrate the pool without being fully quenched. As, in such cases, still liquid material will spread across the cavity floor it is of interest whether an overlying SAP-water pool can also suppress stratified steam explosions.

The issue of underwater melt spreading had formerly been addressed in the PULiMS project, where several of the experiments, e.g. the PULiMS-E6 test [7], resulted in self-triggered stratified explosions after melt was released and distributed in a 20 cm deep water pool. To check the effect of SAPs on the occurrence of such events, test PULiMS-E6 has been repeated, now with a "wet" SAP-pool instead of water. All other experimental conditions were kept the same, except for the total generated melt mass, which was reduced from 76 kg to 26 kg to prevent the melt from contacting the sidewalls of the test section, as this may have acted as an unintended trigger. Considering that, in the PULiMS-E6 test, the actual melt mass released into the water before the explosion, was only ~19 kg and that this mass was even lower in all other "explosive" PULiMS-E tests, this reduction was seen acceptable.

As Fig. 8 shows, the repeated test, denoted as SAP-MS01, resulted in a quite symmetric distribution of the discharged melt across the provided steel plate. No energetic interactions, neither at global nor local scale, were recorded during the outflow and spreading process despite the high level of achieved fragmentation.

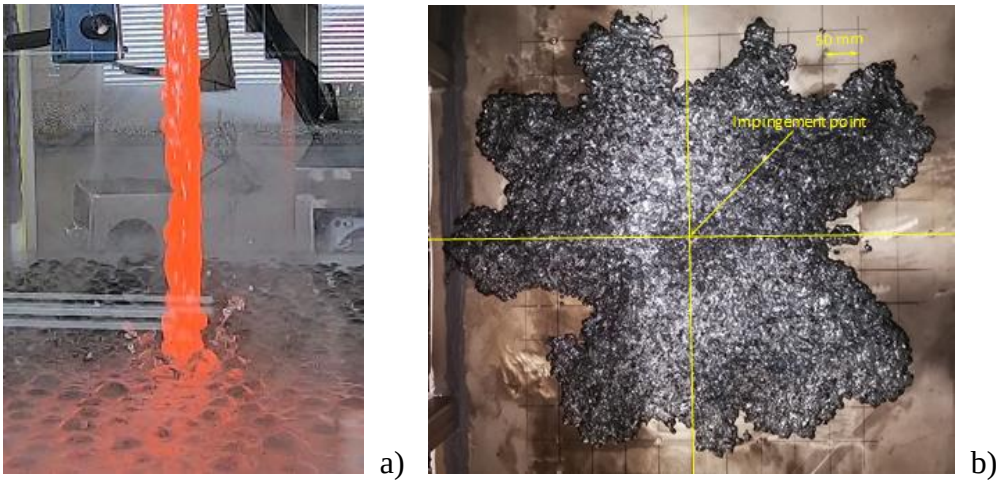

a) b)

Figure 8. SAP-MS01: Melt jet entering the SAP pool (a) and solidified spread melt (b)

Further tests are planned to check the ability of the SAP's to also mitigate stratified explosions in situations when the melt spreads on concrete.

5. SUMMARY AND PRELIMINARY INTERPRETATION

5.1. Melt Fragmentation

The results of the performed experiments demonstrate a significant increase in the efficiency of the fragmentation process when SAP material is added to the water. This effect, which is likely caused by the mechanical resistance of the particles, is the stronger the denser the packaging and hence the lower the free water content is. The enhanced dispersal and cool-down of the melt jet led to either extended porous structures (in "dry" pools) or highly fragmented particle beds (in "wet" pools). Quenching and debris formation were especially effective for oxidic melts, as their surface can cool down much faster than that of

liquid metal, which leads to an early formation of a stable surface crust and faster immobilization of the particles within the SAP-water pool. In combination, these effects are deemed to significantly improve the coolability of created debris beds.

5.2. Steam Explosions

The presence of the SAP particles seems capable to also suppress energetic events between melt and water while the jet penetrates the pool and/or during melt spreading at the floor. This effect was experimentally confirmed for metallic, oxidic and mixed melts with various superheats for released masses < 50 kg, and jet flow rates <4 kg/s. The impact of SAPs on fragmentation and steam explosion suppression seems especially strong for pools with only limited amount of free water, e.g. the here-investigated "dry" pools.

Using SAP particles as a means to suppress steam explosions or mitigate their consequences is a new topic, so applicable experimental data and information are rare. Based on the principle differences between water and SAP-water mixtures, the following hypotheses with respect to the mechanisms that caused the observed suppression effect can be formulated.

The SAP particles can attenuate the breakup of the melt jet

This effect could be justified based on the following rational. In water, the jet breakup is marked by strong upwards flow of steam, leading to effective melt fragmentation caused by high relative velocities at the interface. Such strong velocities will not develop in a SAP-water pool due to the restricted mobility of the coolant with the likely consequence of: less fine-fragmentation and larger coarse droplets and agglomerates, in consistence with the experimental findings in Section 4.
Beyond this, the extent of lateral melt spreading in SAP mixtures should be reduced compared to water, due to the enhanced friction which suppresses large-scale motion of the coolant. As a result, the spatial extension of the premixing region (where liquid coarse melt droplets and coolant coexist) should be smaller.

Water depletion/voiding is enhanced in SAP-water pools

Due to the coarser pre-fragmentation of the melt, an attenuation of the steam production can be expected. As a result of the exacerbated transport of heat inside the SAP particles, there will be changes in the partitioning of the heat flux from the melt to the coolant leading to a larger fraction going into the superheat of the steam instead of evaporation. Nevertheless, because of the adverse effect of an impeded release of steam out of the mixing zone, caused by the restricted mobility in combination with the concentration of the melt into a smaller volume, it is expected that water depletion/voiding is more pronounced in SAP-water pools than in pure water. This yields a tendency towards weaker steam explosions, due to the effects of higher compressibility and a potential prevention of direct melt-water contact.

Triggering is less likely in SAP-water pools than in water

Besides for the fact that the experiments performed with SAP-water pools did, so far, not show explosive events, in spite of the well-known tendencies of alumina and iron [4],[5],[6] to result in such events, the following theoretical arguments can be provided to support this hypothesis. Due to the expected larger void content in the mixing zone and the limited access of water to the melt, as discussed above, there is a lower probability for a direct contact of melt droplets with liquid coolant (and thus for thermal fragmentation). In addition, the potential for spontaneous interactions caused by the destabilization of isolating vapor films around droplets is reduced by the lower relative velocities between water and melt. Last but not least, it can be expected that stronger trigger events will be needed to overcome the damping effect of the high void and the enhanced friction in the SAP-water mixture and to cause an escalation to strong explosion waves.

Pressure wave propagation is attenuated in SAP-water pools

Even if a sufficiently strong trigger might occur during premixing in a SAP-water pool, the escalation potential of the trigger will likely be impeded by a number of effects:

- The high void, which limits the direct contact between melt and coolant, which in turn suppresses fine fragmentation and thus withdraws the explosion its driving power source
- The reduction in the interfacial area for fine fragmentation, due to the larger size of the melt droplets, which hampers the required fast heat transfer from fine debris to coolant
- The limitations in the heat transfer. Due to the lowered mobility of the SAP-water mixture and the inefficient heat transport inside the SAP particles, the heat transfer from fine debris to the coolant will only affect a small fraction of the pool. Although this may result in higher local pressure peaks, the pressure forces at surrounding structure will be lower.
- Further, it is expected that the propagation of pressure waves inside a SAP-water-steam mixture will be damped more than in a pure water-steam pool due to friction and deflection at SAP particles.

Hence, in comparison to the above-discussed large number of effects that negatively impact a steam explosion, or mitigate its potential consequences, only one effect was found that potentially acts in the opposite direction, namely the lower solidification rate of the melt which could allow more melt to actively participate in an explosive interaction and thus increase its strength. The relevance of above argumentation will have to be checked and verified by future more detailed work.

6. OUTLOOK

In successively approaching the conditions in the much larger reactor cavity, further tests with an increased size of the SAP pool and higher melt/pool mass ratios are currently under preparation. These tests will apply metallic and oxidic melts with masses of up to several tons together with a larger diameter of the jet. In addition, further underwater melt spreading tests are planned.

REFERENCES

1. M. Fischer, S. V. Bechta, V. V. Bezlepkin, R. Hamazaki, A. Miassoedov, “Core melt stabilization concepts for existing and future LWRs and associated R&D needs”, 16th International Topical Meeting on Nuclear Reactor Thermal Hydraulics (NURETH-16), Chicago, IL U.S.A., Aug 30 – Sep 4, 2015, #14141.
2. T. Keim, M. Fischer, M. Hupp, “Enhancing Ex-Vessel Corium Coolability for Installed-Base Nuclear Power Plants”, 10th European Review Meeting on Severe Accident Research (ERMSAR2022), Karlsruhe, Germany, May 16-19, 2022, #270.
3. S. Chang, et. al. “Multi-scale characterization of surface-crosslinked superabsorbent polymer hydrogel spheres”, Polymer. 145 (2018) 174-183.
4. I. Huhtiniemi , D. Magallon, H. Hohmann, “Results of recent KROTOS FCI tests: alumina versus corium melts”, Nuclear Engineering and Design 189 (1999) 379–389.
5. W. Cherdron, F. Huber, A. Kaiser, W. Schütz, „Eco steam explosion experiments. Documentation and evaluation of experimental data“, Wissenschaftliche Berichte, FZKA-7011 (December 2005).
6. A. Kaiser, W. Schütz, H. Will, “Melt water interaction tests. (PREMIX tests PM10 and PM11)”, Proc.of the OECD/CSNI Specialists Meeting on Fuel-Coolant Interactions (FCI), Tokai-Mura, Japan, May 19-21, 1997, JAERI-Conf 97-011 (Part II) (January 98) NEA/CSNI/R(97)26.
7. D. Grishchenko, A. Konovalenko, A. Karbojian, V. Kudinova, S. Bechta, P. Kudinov, “Insight into steam explosion in stratified melt-coolant configurations”, 15th International Topical Meeting on Nuclear Reactor Thermal Hydraulics (NURETH-15), Pisa, Italy, May 12-17, 2013, #599.

framatome

Super Absorbing Polymers as a Means to Suppress Steam Explosions and Improve Melt Jet Fragmentation

Manfred Fischer, Torsten Keim, Markus Hupp

ERMSAR 2022 - 17.05.2022

C1 - Framatome Restricted - Framatome know-how

Export Control - AL : N / ECCN : N



framatome

Super Absorbing Polymers as a Means to Suppress Steam Explosions and Improve Melt Jet Fragmentation

Manfred Fischer,
Torsten Keim, Markus Hupp

ERMSAR 2022 - 17.05.2022

C1 - Framatome Restricted - Framatome know-how

Export Control - AL : N / ECCN : N

Confidentiality

X **This document contains Framatome's know-how**

EXPORT CONTROL

AL = N	ECCN = N

Goods labeled with "AL not equal to N" are subject to European or German export authorization when being exported within or out of the EU.
Goods labeled with "ECCN not equal to N or EAR99" are subject to U.S. reexport authorization. Even without a label, or with label: "AL:N" or "ECCN:N" or "ECCN:EAR99," authorization may be required due to the final whereabouts and purpose for which the goods are to be used.

FRAMATOME'S INFORMATION PROTECTION RULES

X **C1** -This document and any and all information contained therein and/or disclosed in discussions supported by this document are **restricted**.

☐ **C2** : This document and any and all information contained therein and/or disclosed in discussions supported by this document are sensitive and **Framatome confidential,** such as its disclosure, alteration or loss are detrimental with a significant-to-high impact for Framatome.

The document, if disclosed, and any information it contains are intended for the sole attendees. The disclosure or reference to such information or document shall be made only on a proper judgment basis and by mentioning expressly "this information shall not be disclosed / transferred without prior consent".

☐ **C3** –This document and any and all information contained therein and/or disclosed in discussions supported by this document are classified **Framatome Secret**.

Each one must commit to keep secret any written or oral information disclosed during the meeting. It is forbidden to disclose it to any legal entity and any individual (including within Framatome) without prior consent of the meeting chairman.

This document and any and all information contained therein and/or disclosed in discussions supported by this document, are confidential, protected by applicable intellectual property regulations and contain data subject to trade secrets regulations. Any reproduction, alteration, disclosure to any third party and/or publication in whole or in part of this document and/or its content is strictly prohibited without prior written express approval of Framatome. This document and any information it contains shall not be used for any other purpose than the one for which they were provided. Legal and disciplinary actions may be taken against any infringer and/or any person breaching the aforementioned obligations.
© Framatome – All rights reserved

CONTENT

01 . Background

02 . SAP Material Characteristics

03 . SAP Pool Characteristics

04 . Performed Experiments

05 . Summary and Outlook

© Framatome - All rights reserved

C1 - Framatome Restricted / Framatome know-how / Export Control - AL : N ECCN : N

Background

In ERMSAR-2021 paper #270 “Enhancing Ex-Vessel Corium Coolability for Installed-Base Nuclear Power Plants” Framatome presented a new technology for improving the resilience of NPPs during ex-vessel core melt scenarios when the related SAM procedure includes the preflooding of the space below the RPV. The solution is based on the addition of Super Absorbing Polymers (SAP) to the water, which “conditions” it in a way that:

- **Steam explosions are suppressed**
- **Corium fragmentation and coolability is enhanced**

both, without hampering the water’s ability to quench and long-term cool the molten debris.



 © Framatome - All rights reserved

SAP Material Characteristics (1)

Properties of SAP particles:

- Material: polyacrylic acid and its salts (various forms)
- Application form used: Surface cross-linked spheres (elastic shell, filled with amorphous material)
- During water uptake, the mass/volume increases by a factor of 130/200
- Density: dry: ~2000 kg/m^3 (dry) , wet: slightly higher than water
- Water uptake velocity increases with temperature, but the final size is about the same (~10% lower in boiling water)
- Impact of Boron is insignificant, but high radiation doses were found to degrade the structure and water absorption capability

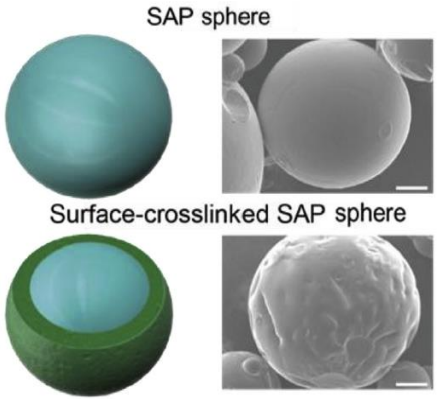



 © Framatome - All rights reserved

SAP Material Characteristics (2)

Properties of the Individual Particles

- **Thermal stability:**
  - "Dry SAPs: decomposition occurs in several stages with releases of volatile products (organic volatile compounds, carbon dioxide and sodium oxide)
  - Saturated SAPs (slow heating): water release (shrinking), dry decomposition/burning (in air)
  - Saturated SAPs (fast heating): shell burst (by internal steam pressure) and outflow of gel content

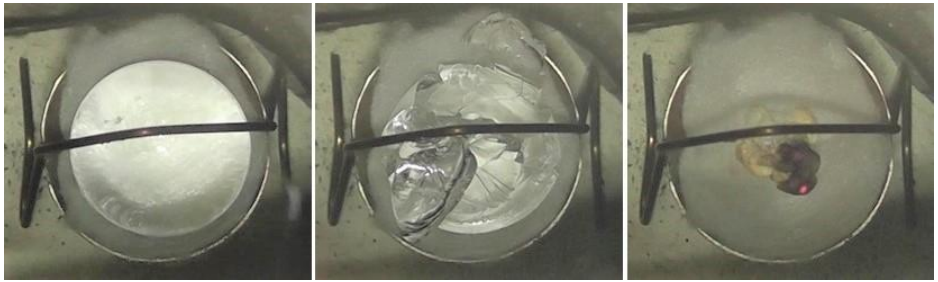

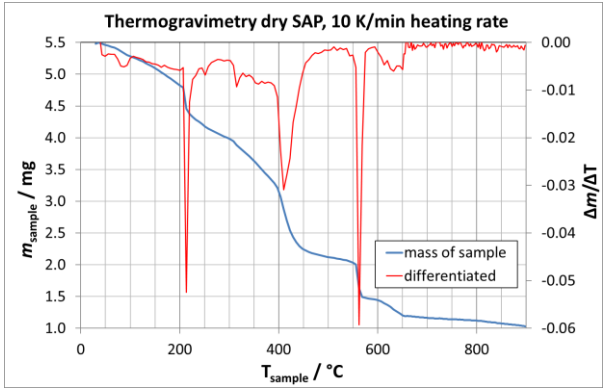

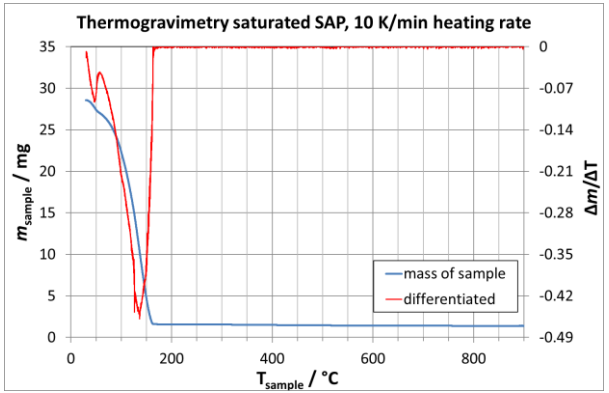

 © Framatome - All rights reserved
C1 - Framatome Restricted / Framatome know-how / Export Control - AL : N ECCN : N

SAP Pool Characteristics (1)

Water Uptake, “Dry” and “Wet” Pools

- Given enough time (< 1h) and water, SAP particles inflate until saturation is reached.
- Consumption of all water leads to a **“Dry” pool (a)**:
  - Particles saturated, no water in the interstices
  - Pool porosity decreases from top to bottom, with deformation of the (elastic) particles
- If more water is available, the interstices between particles are filled from bottom up. The state when the water reaches the surface is denoted as **“Wet” pool (b)**:
  - Particles saturated, all interstices filled with water
  - Also near the bottom particles are ~ spherical
  - Highest possible porosity, excess water will accumulate above



(a)

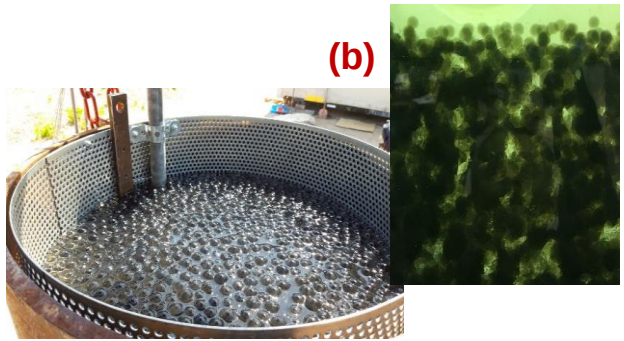

(b)

SAP Pool Characteristics (2)

Predicted Impact on Steam Explosion

In a **"Dry" SAP Pool** there is little free water

Steam explosions can be excluded, if the particles remain intact during liquid melt contact (no large scale destruction leading to melt-gel interaction)

In a **"Wet" SAP Pool,** free water do exist in the interstices between SAP particles

Steam explosions during jet dispersal

- **Low mass ratio between water and melt**
- **SAP particles result in more coarse and less fine fragmentation**
- **Enhanced voiding and water depletion in mixing zone, lower probability of steam film collapse**
- **Spatial dispersion of pressure waves at particles**
- **… but lower solidification rate → more liquid melt theoretically available for interactions**

Steam explosions during underwater spreading

- **SAP particles limit mixing of melt and water at the interface**
- **Suppression of pressure waves traveling along the surface**

→ **To be demonstrated by experiments**

SAPs-Pool Characteristics (3)

Predicted Impact on Melt Fragmentation

“Dry” Pools provide the highest mechanical resistance against incoming melt jets, due to the narrow gaps between particles and the resulting form-stability of the SAP array

The a high spatially distribution and fragmentation of the impacting melt is expected. The described effect is likely supported by the fact that the compactness of the SAP pool increases with depth (and hydrostatic pressure) and by the high specific heat capacity provided by the water in their shell of the individual particles.

“Wet” Pools have less impact on melt jet propagation, as SAP particles are less constrained by their neighbors. In addition, gaps are wider (up to the bottom)

Nevertheless, better fragmentation than in pure water is expected due to the jet deflection at particles

→ **To be demonstrated by experiments**

 © Framatome - All rights reserved

C1 - Framatome Restricted / Framatome know-how / Export Control - AL : N ECCN : N

SAPs-Pool Characteristics (4)

Predicted Impact on Long-term Cooling

"Dry" and "Wet" Pools contain about the same amount of water. Given an adequate size of the cavity, both ensure adequate melt quenching. Long-term cooling requires sustained re-supply of water.

Associated Issue:

- **Trapped SAP particles may inhibit cooling**

  Local dryout automatically leads to shrinkage and decomposition of the particles, which gives way for the water to re-enter. Decomposed material will be carried away by the water/steam flow. Thermal decomposition is accompanied by the expected decay of the organic SAP material at very high radiation levels.

- **Potential impact of decomposed organic material**

  Total mass of the solid SAP material is very low:

  - **5 /7 l and 7/10 kg SAP yield ➔ 1 m³ of "wet"/"dry" pool**

  This naturally limits the effect on the containment and the severe accident cooling chain. Further (plant specific) investigations are needed.

 © Framatome - All rights reserved

Performed Experiments (1)

Objective

- **“Dry” SAP pools**
  - Demonstrate the functional efficiency of the solution with respect to steam explosion suppression and fragmentation.
  - Confirm that SAP particles remain intact during melt contact as a precondition to avoid large-scale melt interaction with the water/gel contained inside them
- **“Wet” SAP pools**
  - Check the efficiency of the underlying physical mechanisms, identify applicability limits
- Test Conditions
  - **Melts with representative/conservative properties used (incl. thermite)**
    - Superheated metal (steel) is prototypic and has a higher thermal impact on SAP particles and shows lower tendency to fragment than oxide melts
    - Molten aluminia engages in steam explosions more easily than real corium
  - **Water conditions bounding for the reactor case (low temperature and pool depth)**
  - **Non-optimized SAP material (commertially available, mono-disperse)**

Performed Experiments (2)

“Dry” Pools, SAP-DEFOR (KTH Stockholm): 01/02: tin, 03: Bi_2O_3-WO_3

- Instrumented test section (a)
- DEFOR01, ingot cleaned of SAP particles (b)
- DEFOR01, solidified ingot morphology (c)
- DEFOR02, solidified ingot in particle bed (d)
- DEFOR01/02, ingot positions (e)
- DEFOR01/02, fragments of solidified metal (f)
- DEFOR03, pour of oxidic melt (g)
- DEFOR03, bulk part and fragmented debris (h)

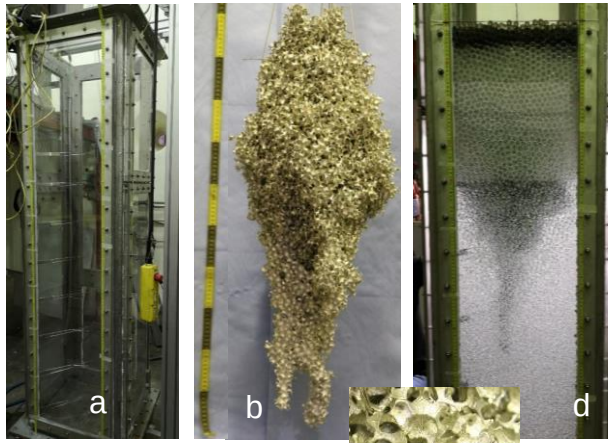

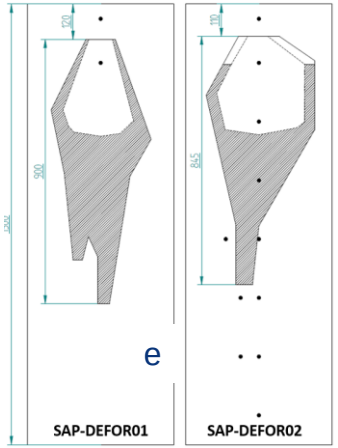

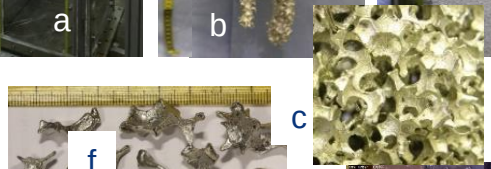





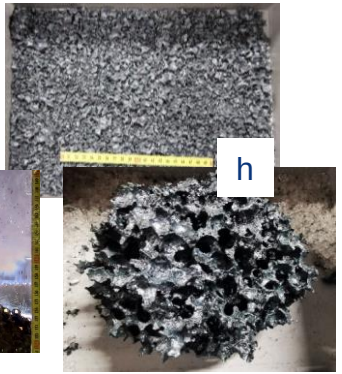

DEFOR01/02 (metal): Exteremely filigree metal structures, low amount of loose debris

DEFOR03: small bulk part, very brittle, large amount of loose debris

Smooth melt interaction, high porosity, suspended structures

Performed Experiments (3)

“Dry” Pools, SAP-FRA tests 01-03 (Karlstein, Germany), Thermite

- FRA01, sheet metal insert before the test (a)
- FRA01, thermite generator & test section (b)
- FRA01, pool surface during melt impact (c)
- FRA03, two crucibles, jet inflow (d)
- FRA01, fragments of solid metal/oxide (e)
- FRA01, ingot and remaining SAP particles after opening of the test section (f)
- FRA03, ingot cleaned of SAP particles (g)











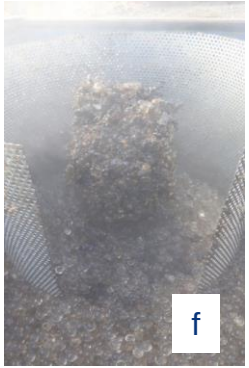



FRA01/02: pool depth <1 m, some melt penetrated to the bottom and spread at the floor

FRA01/02/03: as in DEFOR: highly porous solid structures, partially filled with later-released oxidic melt, low amount of loose debris, SAPs mostly intact (even inside solid porous debris!)

 © Framatome - All rights reserved

C1 - Framatome Restricted / Framatome know-how / Export Control - AL : N ECCN : N

Performed Experiments (4)

Conclusion from “Dry” SAP pools

- Tests showed that metal melts even with conservatively high superheat do not destroy the SAPs at large scale, which is attributed to the particles thermal stability.
- It is therefore concluded that “Dry” SAP pools underneath the RPV can prevent steam explosion for a wide range of melt release conditions.
- “Dry” pools further result in highly porous, coherent structures inside the SAP-pool, which are well coolable in the short and long term.
- Further investigations:
  - Thermal decomposition of SAP’s
  - Jet release into “Wet pools”
  - Underwater spreading in “Wet pools”

 © Framatome - All rights reserved

C1 - Framatome Restricted / Framatome know-how / Export Control - AL : N ECCN : N

Performed Experiments (5)

“Wet” Pools, SAP-FRA tests 04-06 (Karlstein, Germany), similar conditions as used in **“Dry”** tests

- FRA05, jet inflow (impact of jet velocity) (a)
- FRA06, jet inflow (b)
- FRA04, coarse metallic/oxidic fragments (c)
- FRA06, retrieved debris (d)
- FRA06, debris classified by dimension, largest fraction between 10 mm and 25 mm (e)
- FRA06, axial melt progression, jet front progression and decrease in progression speed (f)
- FRA06, thermocouple arrangement (g)











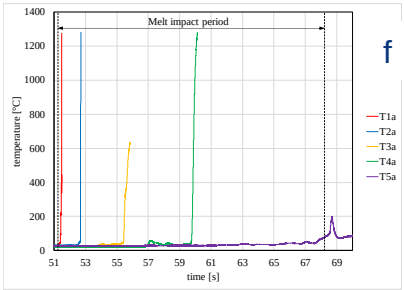

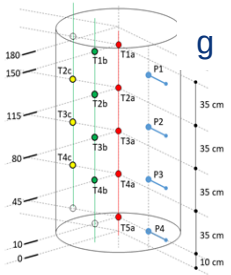

Absence of energetic interactions in all tests,

High degree of fragmentation, but no large structures

At the applied mass flow rate the jet entry velocity has limited effect on melt front progression

 © Framatome - All rights reserved

C1 - Framatome Restricted / Framatome know-how / Export Control - AL : N ECCN : N

Performed Experiments (6)

Preliminary Conclusions on Melt Jets entering “Wet” SAP pools

- **In the applied range of metal/oxide melt release conditions (rate: <4 kg/s, superheat: up to 600 K) the tests did not result in energetic reactions and showed good fragmentation. The created debris is of large size (mostly in the range of 1..10 cm) the which promotes coolability.**
- **The conditions investigated in the “Wet” pool tests are considered representative for a wide range of prototypic melt release conditions (incl. oxidic melt jet through failed RPV bottom penetrations).**
- **Further investigations:**
  - **Melt jets of higher release rate (thermite)**

 © Framatome - All rights reserved

C1 - Framatome Restricted / Framatome know-how / Export Control - AL : N ECCN : N

Performed Experiments (7)

Test in “Wet” SAP pool with high thermite mass (2 t) and high jet diameter (10 cm), Analysis still ongoing.

- **Jet did not fragment well in the provided 2.5 m SAP pool.**
- **Melt penetrated the bottom end entered the outer water space (without SAPs)**
- **During spreading at the support structure / concrete energetic interactions occured.**

Shows limits for the fragmentation efficiency of “Wet” pools

No steam explosion during jet-water interaction

Recalls the risk of stratified explosions in case no counter-measures are taken

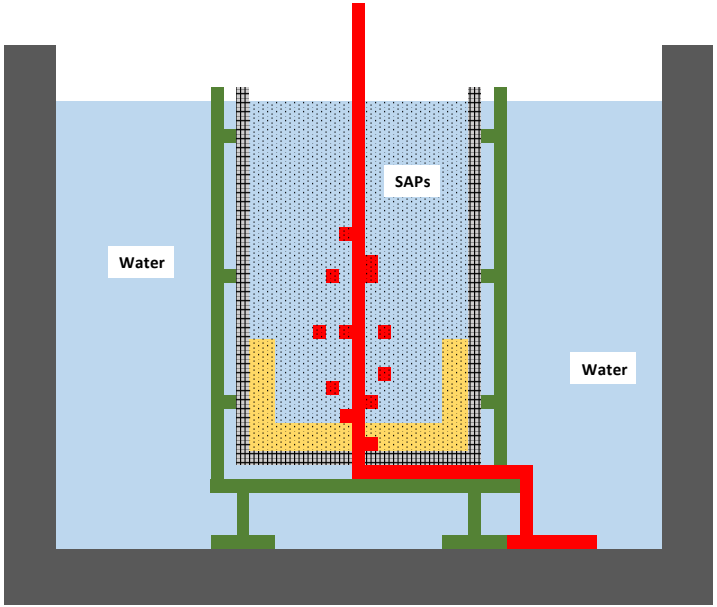

Estimated melt progression

Performed Experiments (8)

In PULiMS tests (KTH Stockholm) stratified steam explosions were repeatedly observed during underwater melt spreading.

PULiMS-E6 test was replicated, now with an overlying SAP pool

- Principal scheme of the test facility (a)
- Melt jet entering SAP pool (b)
- Melt jet entering SAP pool + melt spreading (c)
- Melt spreading detail (d)
- Example of solid debris structure (e)
- Solid spread melt: top view (f)

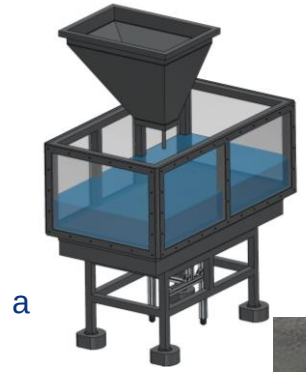







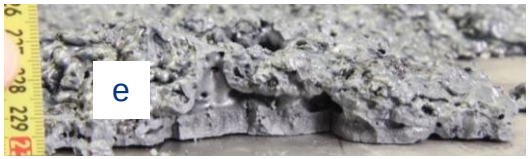



Rather symmetric distribution (steel surface)

Only small fraction of fragmented debris at the top, mainly coherent cake with layered porous structure

No energetic interactions (local and global)

 © Framatome - All rights reserved

C1 - Framatome Restricted / Framatome know-how / Export Control - AL : N ECCN : N

Summary and Outlook

“Dry” SAP pool reliably suppress steam explosions and result in coolable debris configurations. Also for the bounding case of “Wet” SAP pools the performed experiments indicate strong positive impact on steam explosions suppression and melt jet fragmentation.

Further experiments on the efficiency of “Wet” SAP pools and on underwater spreading with thermite melt (in analogy to earlier explosive tests) are planned.

> *“Corium spreading under water and its possible consequences”, ERMSAR 2017, Warsaw, Poland, May 16-18, 2017*

In parallel, an optimization / customization of the SAP material for nuclear application is foreseen (thermo-mechanical / radiological properties, prevention of recriticallity, etc.) together with the development of back-fitting systems plus adapted SAM procedures.

Partners interested in participating to this development and bringing the technology to application in NPPs are welcome

- Patent (DE 102019126049 B3), PCT (PCT/EP2020/076521)
- Contact: torsten.keim@framatome.com

Overview of Experimental Conditions

	DEFOR01/02	DEFOR03	FRA01/02/03	FRA04	FRA05	FRA06	MS01
Melt type	tin	Bi_2O_3-WO_3		aluminum/iron-oxide thermite			Bi_2O_3-WO_3
Melt mass, kg	30	27	17 - 50	24	24	48	31
Melt temp. (funnel), °C	455 - 625	1073		~2100			1082
Melt superheat (funnel), K	223 - 393	173		~600/~30 (iron/alumina)			212
Duration melt release, s	~7	6.5	12 - 19	14	13	17/12	9.0
Jet free fall height, m	0.23	0.23	0.30	0.30	2.10	0.30	0.21
Impact velocity*), m/s	3.3	3.1	~3	3.0	6.5	3.2	3.1
SAP pool height, m	1.50	1.50	0.77 - 1.53	1.50	1.50	1.70	0.19
SAP pool temperature, °C	22	22	11 - 14	~24	~28	~27	70
SAP pool type	„dry“	„dry“	„dry“	„wet“	„wet“	„wet“	„wet“

Legal Notice

Editor and Copyright 2022: Framatome GmbH – Paul-Gossen-Straße 100 – 91052 Erlangen, Germany. It is forbidden to reproduce the present publication entirely or partially without prior consent in whatever form. Legal action may be taken against any infringer and/or any person breaching the aforementioned conditions.

Subject to change and error without notice. Illustrations may differ from the original. The contained statements and information are for advertising purposes only and do not constitute an offer of contract. They shall neither be construed as a guarantee of quality or durability, nor as warranties of merchantability or fitness for a particular purpose. These statements, even if they are future-oriented, are based on information that was available to us at the date of publication. Type, quantity and characteristics of goods and services are subject to formal individual formal contracts.

framatome

Thank you for your attention!



To discover more about how we can help, visit us at
www.framatome.com/solutions-portfolio

ASSESSMENT OF EX-VESSEL CORIUM COOLABILITY IN THE CONTAINMENT OF THE VVER-1000 REACTOR AS A MEASURE OF SEVERE ACCIDENT MITIGATION

Miroslav Kotouč, Tomáš Janda and Petr Vokáč
ÚJV Řež, a. s.
Hlavní 130, Husinec-Řež, 250 68, Czech Republic
miroslav.kotouc@ujv.cz; tomas.janda@ujv.cz; petr.vokac@ujv.cz

ABSTRACT

After the Fukushima accident and the consequently conducted European stress-tests, which aimed at identification of weaknesses of European nuclear power plants (NPP) with regard to severe accidents (SA), it was decided to strengthen the robustness of Czech VVER energetic reactors. This paper aims to describe a feasibility study, recently carried out, of an alternative strategy to mitigate a hypothetical SA at the Temelin NPP (equipped with 2 VVER-1000/320 reactors). Due to technical and organizational constraints, the strategy of in-vessel melt retention (IVMR) could not be adopted for the Temelin units. Therefore, the investigation of an alternative ex-vessel corium cooling (ExVC) strategy for maintaining the integrity of the containment (CTMT), which constitutes the last barrier to fission products (FP) release into environment, was initiated. This strategy would consist of allowing spreading of the corium, evacuated from the breached reactor pressure vessel (RPV), onto a large area and its consequent water top-cooling. The alternative ExVC strategy was assessed using appropriate computational tools, consisting of the integral SA analysis code MELCOR 2.2 and the detailed mechanistic codes MELTSPREAD (for corium spread-ability assessment) and CORQUENCH (for corium cool-ability assessment). The MELCOR code was used to simulate 2 qualitatively different SA scenarios: an unmitigated large break loss-of-coolant accident (guillotine break LOCA), representing rather a fast-progression scenario with steam starvation conditions, and a station black-out (SBO), representing rather a slow-progression scenario with the availability of steam for core components oxidation. The MELTSPREAD code was then used to assess corium capabilities to spread over the provided spreading area, and finally the CORQUENCH code was employed to assess the proneness of corium to be cooled down by top-flooding. Besides the overview of the employed methods and some partial conclusions (the ExVC strategy assessment is still ongoing), a link to the international project OECD/NEA ROSAU and the Czech national project CORIUM is provided to demonstrate the experimental back-up to the conclusions coming out of the numerical simulations.

KEYWORDS
VVER-1000, ex-vessel corium cooling, MELCOR, MELTSPREAD, CORQUENCH

1. INTRODUCTION

Two units of the VVER-1000/320-type of reactor are operated in Czech Republic at the Temelin NPP. As part of the Czech national action plan, which resulted from the outcomes of the European stress tests having been carried out after the Fukushima accident (2011), analyzes of the possibility of enhancing the plant's safety by additional safety measures have been carried out. The main purpose of adding additional safety

measures is to cope with SAs, the main goal being to maintain the integrity of the CTMT as it acts as a last barrier for the FPs before their release into the environment. Given the current status of the Temelin NPP units, the measures to be implemented are those aiming at preventing late containment failure. Phenomena such as CTMT bypass, direct CTMT heating or hydrogen blasts are eliminated either by the design or by additional safety measures, already implemented – such as H_2 mitigation system, based on passive autocatalytic recombiners or a primary circuit (PC) depressurization system, based on current pressure-operated relief valves (PORV).

One of the initially considered options assuring the CTMT basemat integrity in a long-term, was implementation of the IVMR strategy. The IVMR strategy is one of SA management (SAM) measures, first investigated for relatively low-powered reactors [1]. First design application of this strategy was done for the AP-600 reactor [2]. Besides implementing the strategy for new reactor designs, first Gen-II NPPs were back-fitted with measures allowing for the IVMR strategy (e.g. Loviisa, Dukovany, Paks or Jaslovské Bohunice/Mochovce, which are the VVER-440-type of reactors located, respectively, in Finland, Czechia, Hungary and Slovakia). After the Fukushima Dai-ichi nuclear accident, investigations of the possibility of backfitting also high-output-power NPPs with the IVMR concept were accelerated and an international European Commission (EC) project, funded within the Horizon 2020 framework, was launched. It was entitled "In-Vessel Melt Retention Severe Accident Management Strategy for Existing and Future NPPs", abbreviated as the H2020 "IVMR" project [3]. Within this project, an experimental device named THS-15 was set up at UJV Rez premises [4]. The device is a full-length representation of the VVER-1000 reactor outer surface and part of the surrounding cavity, constituting thus a channel for testing the vessel outer surface cooling efficiency. One of the outcomes from the numerous experiments carried out at the THS-15 facility was the confirmation that critical heat flux is high enough to allow successful vessel cooling [5]. However, the consequent technical and organizational feasibility study ruled out the possibility of IVMR strategy implementation for both operated VVER-1000 units at the Temelin NPP. There are several reasons for that. First, the reactor within the concrete cavity (**Figure 2**) is not equipped with an adjacent biological shielding – the concrete walls of the cavity, lined with several layers of thin steel sheets (see later for detailed description), act themselves as a radiation shielding. Therefore, the reactor cavity structures are highly activated and it is extremely difficult to perform design changes in the vicinity of the reactor. Second, the RPV inspection machine, which is located behind the hermetic steel door (see **Figure 2**), is employed during every outage to inspect the RPV outer surface. If a deflector, channeling and smoothing the flow around the vessel, or any other device, needed for the IVMR strategy successful implementation, are required to be installed within the reactor cavity, the inspection machine's pathway could be blocked. And, finally, the recirculation sump is located at the very bottom of the VVER-1000 CTMT, i.e. under the floor of the reactor cavity which is to be flooded. Thus, an active system would be necessary to continuously provide the reactor cavity with water inflow. Hence, because of the fore-mentioned reasons, the IVMR strategy was suspended. Instead, the implementation of other SA mitigation measures, such as filtered CTMT venting system (FCVS) or hardened in-vessel injection system (being part of DAM – diverse and alternative means) is currently underway. At the same time, the feasibility study of corium localization within the CTMT after RPV failure, hereafter denoted as the "ExVC strategy", was launched.

The suggested ExVC strategy relies on provisions allowing spreading of the corium[1], breached from the failed RPV lower plenum, onto a large area where it would be cooled down by water top-flooding. The pour of the corium shall be first onto a dry reactor cavity floor (to the left from the concrete door in **Figure 2**), avoiding thus a steam explosion, and consequently it would spread onto a previously flooded floor of an adjacent room entitled GA302 (to the right from the steel door in **Figure 2**; the floor elevation in this room is 0.6 m lower than the floor in the reactor cavity room). It is important to ensure that the reactor cavity is dry at the moment of RPV failure, which precludes a "classical" steam explosion (i.e. the steam explosion which is triggered by superheated melt being poured into a deep mass of subcooled water; such

[1] *Corium* stands for a mixture of solid debris and molten core material, both in-vessel or ex-vessel.

configuration leads very often – and sometimes unintentionally, as the DEFOR (KTH) experiments showed – to highly energetic steam explosion). However, it was shown ([17]) that a "stratified" steam explosion (SSE) may be triggered when a hot melt is steadily covered with water. Such a situation could possibly set in when the corium from the reactor cavity escapes into the stepped-down floor in the neighboring room GA302, already flooded. However, the advantage of immediate corium cooling, allowing its prompt solidification, is of highest importance. An insight into the issue of melt being spread under-water is to be given within the OECD/NEA ROSAU project ([14]), which investigates corium spreading and cooling in a flooded cavity. UJV Rez being part of the ROSAU project (with the support of the Czech utility CEZ), the outcomes of the project will shed light on the corium under-water spread-ability in a complex manner.

The aim of immediate corium spreading from the reactor cavity is to obtain coolable configuration of thin layer of corium. Even if the onset of MCCI is not prevented, subsequent processes of water ingression (WI) and melt eruptions (ME) are deemed to enhance cooling sufficiently. Hence, the concrete ablation would be stopped and containment integrity would be maintained. The two crucial phenomena – WI and ME – were extensively studied in the past within experimental projects, e.g. MACE or MCCI ([7]). Enhancement of cool-ability of the top-flooded molten core, considering the effects of both phenomena, was consequently implemented both into specialized codes, such as CORQUENCH (see later) and into integral SA analysis codes, e.g. ASTEC and MELCOR ([8,9]). It is known that the WI and ME phenomena (see **Figure 1**) drastically enhance coolability of a melt with crust atop on it; the heat transfer rate from flooded corium might reach up to several hundreds of kW/m^2, see **Figure 3** (if the corium is not mixed with products of concrete ablation yet). Such heat transfer enhancement by the effects of WI and ME is substantial and is of an order higher than simple heat conduction from the crust.

The investigated ExVC strategy was assessed using a set of computational tools, consisting – in the order of employment – of: 1. the integral SA analysis code MELCOR 2.2 ([10,11]), 2. the detailed mechanistic code MELTSPREAD for corium spreading ([12]) and 3. the detailed mechanistic code CORQUENCH for corium cooling with the presence of WI and ME phenomena ([13]).

In order to support the computational analyses with experimental data, UJV Rez joined the international project ROSAU (Reduction of Severe Accident Uncertainties, 2019-2024 [14]), organized by the OECD/NEA. The experiments, conducted at Argonne National Laboratory (ANL), aim at filling knowledge gaps for melt spreading (namely in the under-water configuration, varying the melt's metal content, initial temperature and pour rate) and corium cooling by water top-flooding (varying corium chemical composition and type of basemat – refractory vs. concrete).

In addition to the ROSAU project, a Czech national project CORIUM was launched at CV Rez (subsidiary of UJV Rez) in order to investigate: 1. corium properties (density and viscosity) at high temperatures and 2. the impact of corium on internal RPV structures or on a thermal shielding, located at the reactor cavity floor. The former is crucial for numerical investigation of corium spreading, the latter sheds light on possible damage caused to structures by the impacting corium. The project was launched in 2020, therefore only preliminary data are available up to the date. The unique "cold crucible" device, which is used to generate the prototypic melt, is described e.g. here [15].

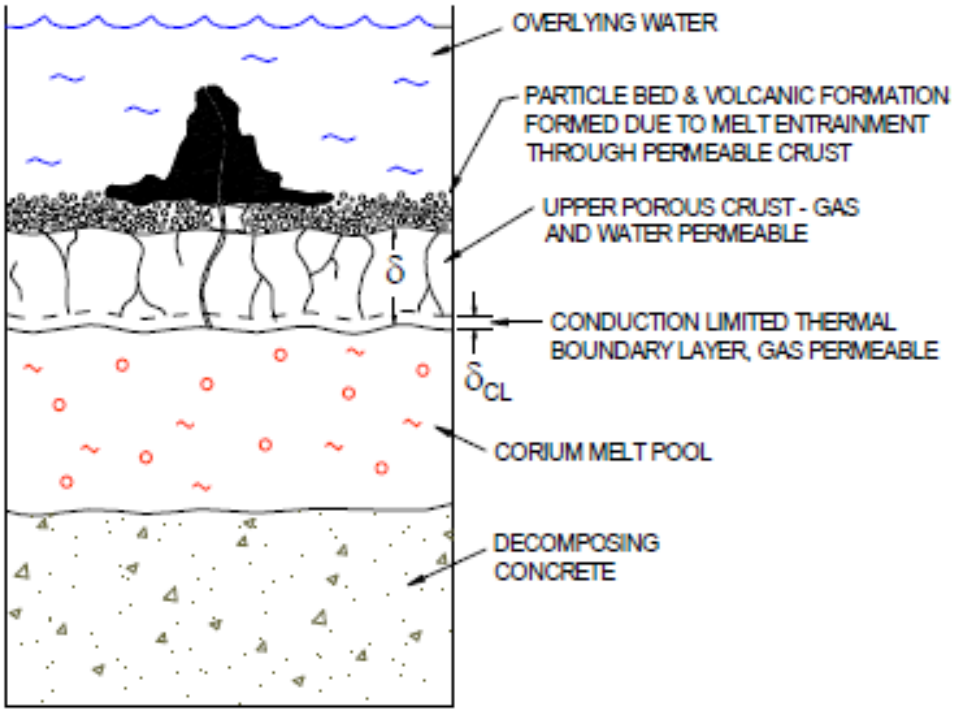

Figure 1 Principle of WI and ME phenomena and the mechanism of enhanced corium cooling. Picture taken from [13].

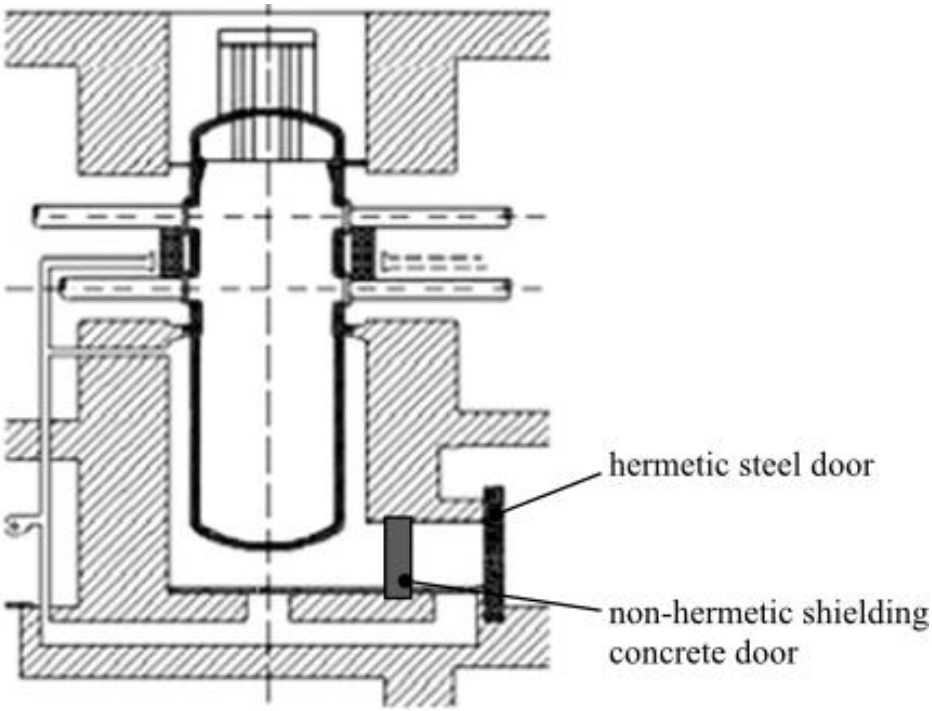

Figure 2 Schematic view of the VVER-1000 reactor cavity. Figure taken from [6].

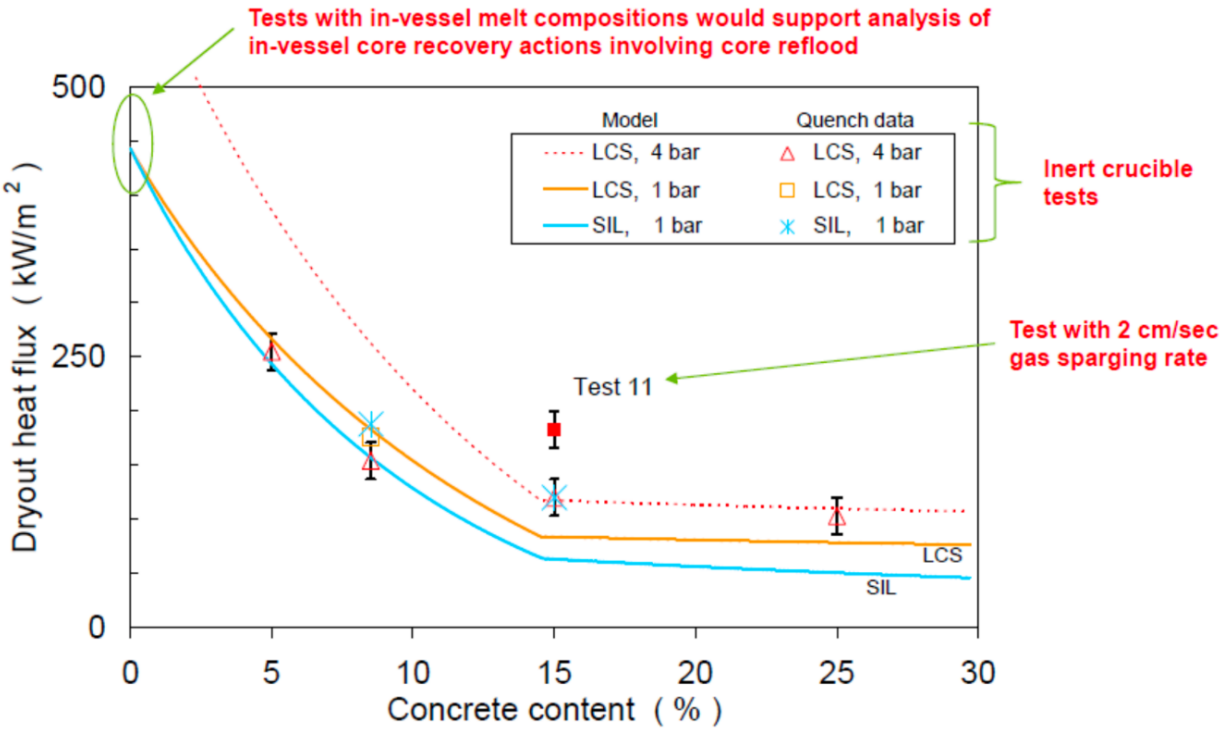

Figure 3 Heat flux density from flooded corium if water ingression and melt eruptions phenomena take place. Graph taken from [14].

2. MELCOR CALCULATION: INITIAL AND BOUNDARY CONDITIONS FOR THE CONSEQUENT CORIUM EX-VESSEL BEHAVIOR SIMULATION

In order to obtain initial conditions of the corium ejected from the breached RPV into the reactor cavity, 2 qualitatively different SA scenarios were simulated using the MELCOR code: a fast-progression large break LOCA scenario with steam starvation conditions and a slow-progression SBO scenario. The latter used a SAM measure consisting in depressurizing the PC and, in order to enhance the degree of core components oxidation, a SAM measure consisting in injecting additional water into the degraded core by the use of low-pressure injection system. The LOCA scenario, due to the unavailability of steam, is typical with high decay heat and a large fraction of unoxidized Zr in the corium. On the other hand, the SBO scenario – due to its later RPV failure – is typical with lower decay heat and, thanks to the injection of additional water, a lower fraction of unoxidized Zr in the corium.

Detailed description of the input model for the MELCOR 2.2.18019 calculation is beyond the scope of present paper, however, some basic features are given in the following paragraph and are deducible from the nodalization scheme shown in **Figure 4**. The core is represented with 6 radial rings and 35 axial levels (including the lower plenum (LP) domain), creating thus a grid of cells for core degradation computation (the red-line grid in the upper part of the scheme). Core components are represented with colored blocks, each color corresponding to a different material. Thermo-hydraulic (T-H) nodes are shown as blocks of different colors and are connected with flow paths. Within the RPV region, every 2 core cells are coupled to 1 T-H node. The 4th PC circulation loop is depicted, with the pressurizer (connected with surge line) and a quench tank.

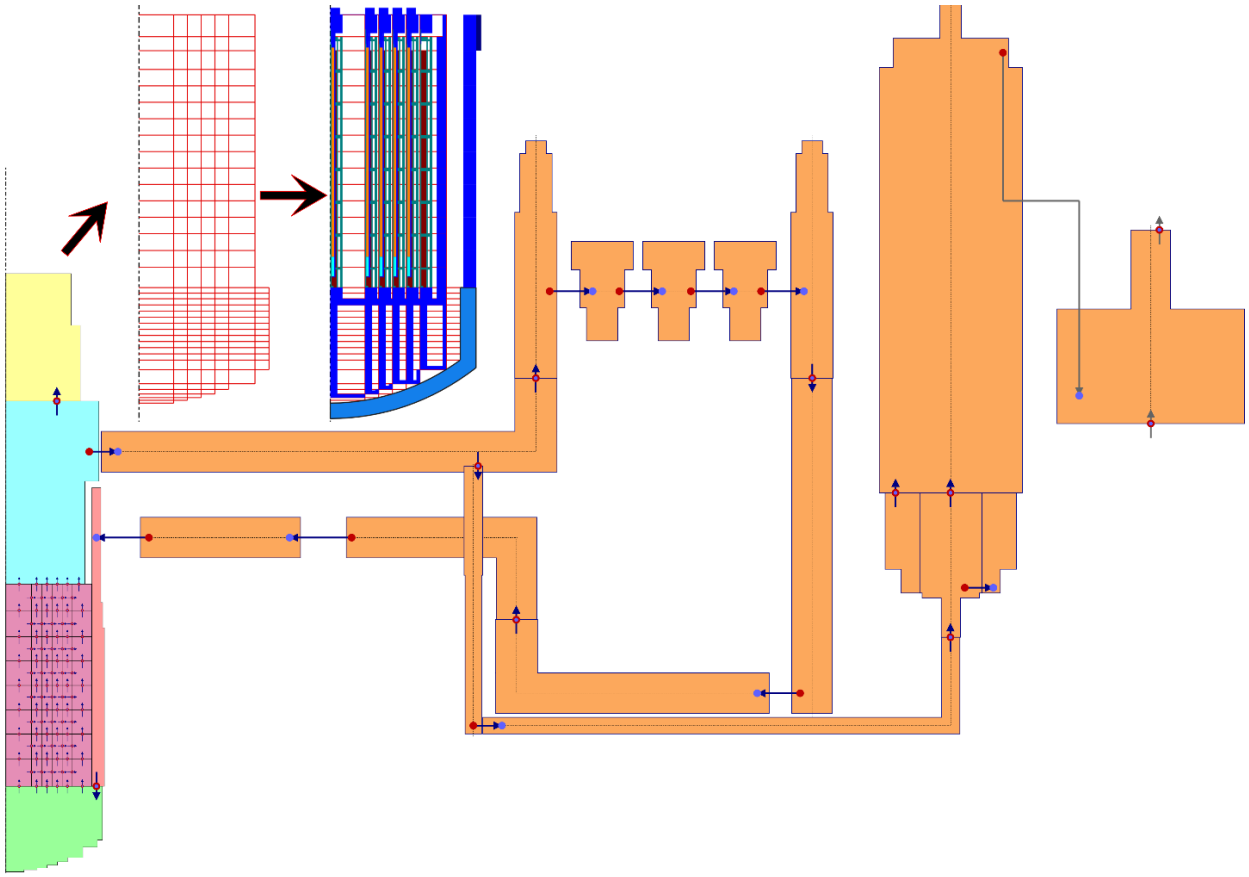

Figure 4 Nodalization scheme of the VVER-1000 reactor and PC.

To illustrate the differences in corium state at the moment of RPV breach for both simulated scenarios, 4 comparative graphs are presented (**Figure 5** to **Figure 8**). In all 4 graphs, LOCA scenario results are plotted with thick solid lines, whereas SBO scenario results are plotted with thin dashed lines (and the same color). Due to proprietary constraints, the y-axis values are hidden; however, the figures are meant to be mainly comparative, i.e. indicating the qualitative differences between the two considered scenarios.

From the decay heat history (**Figure 5**), time of RPV lower head (LH) failure may be deduced: 1.98 h (LOCA) vs. 8.22 h (SBO). The total decay heat is the same for both scenarios, the gap between the total decay heat and core decay heat indicates the amount of FPs released from the fuel. At the time of RPV breach, decay heat for the cavity is by 2 MW higher for the LOCA scenario. **Figure 6** indicates higher oxidation degree for the SBO scenario. The oxidation kinetics is the parabolic one, as implemented in the MELCOR code ([11]):

$$d(W^2)/dt=K(T). \quad [1]$$

The temperature-dependent constant K(T) is of the classical, Arrhenius form:

$$K(T)=A*\exp(-B/T), \quad [2]$$

with the constants A and B being adjustable by the user. Thus, proper values were set in order to accommodate the breakaway oxidation phenomenon and the specifics related to the Nb-1 % E110 cladding alloy. The time shift between the LOCA and the SBO scenarios is due to the fact that within the LOCA, coolant is lost immediately and hence, steam starvation conditions set in rather quickly. On the other hand,

the coolant boils off rather slowly within the SBO scenario and so is the overall SA progression. **Figure 7** shows that more molten material (curves in green – oxidic molten pool and in blue – metallic molten pool, respectively) is evacuated for the LOCA scenario; in the case of SBO scenario, the RPV is subject to a slightly elevated pressure, which precipitates creep rupture of the vessel, and, consequently, less time is available for the solid debris (red curve) to melt within the LP. Finally, **Figure 8** shows lower temperature of the convecting metallic molten pool within the LP for the SBO scenario, temperature of the convecting oxidic molten pool being comparable for both scenarios.

The corium composition at the moment of RPV failure for the LB LOCA and SBO scenarios, respectively, is given in **Table 1**.

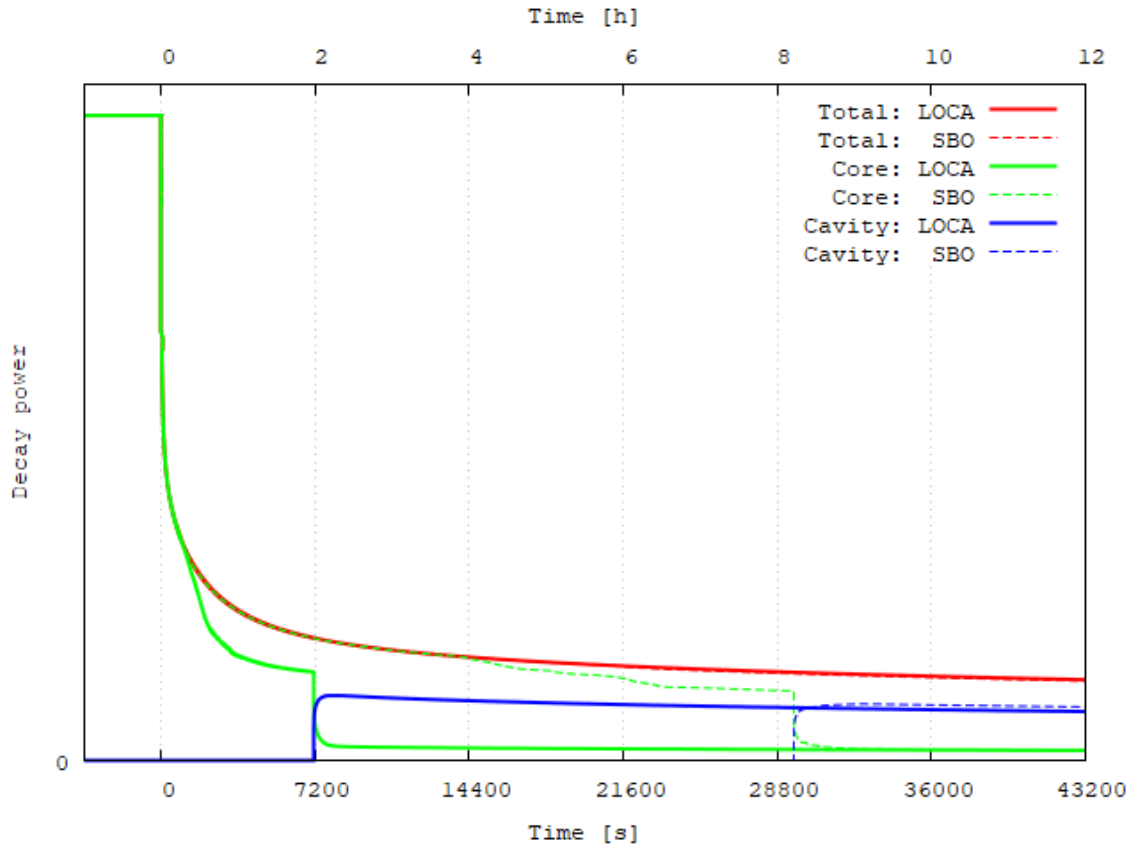

Figure 5 Decay power in different locations.

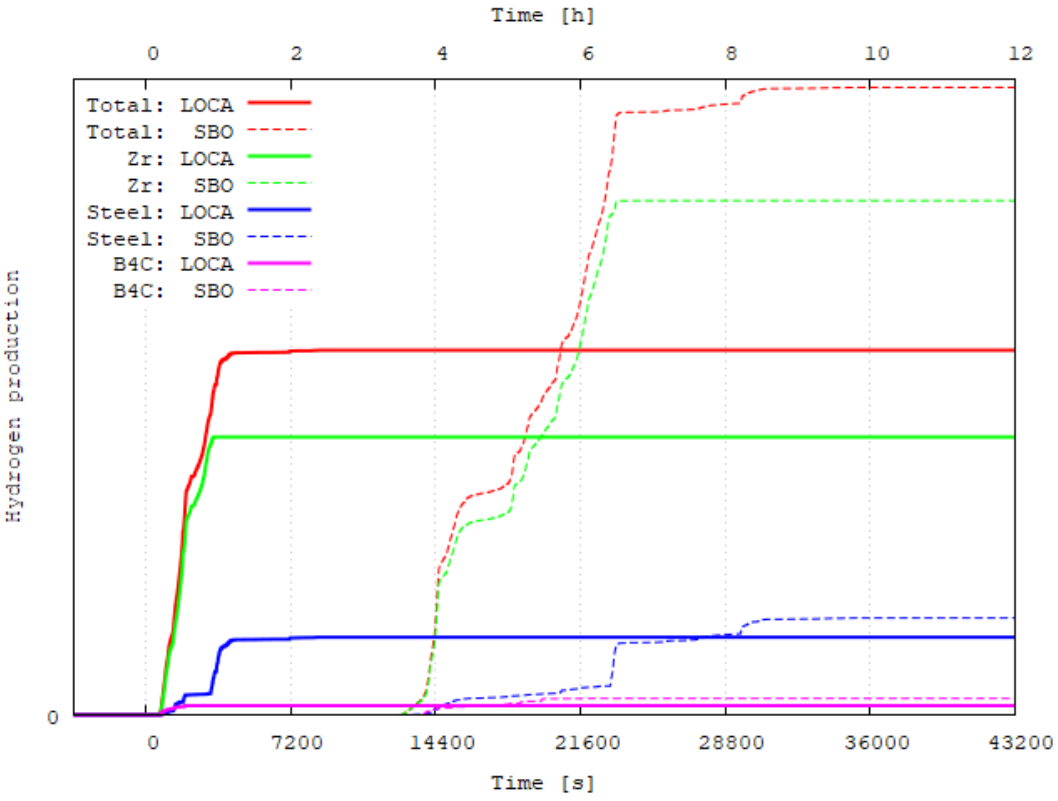

Figure 6 Production of hydrogen from various oxidation processes.

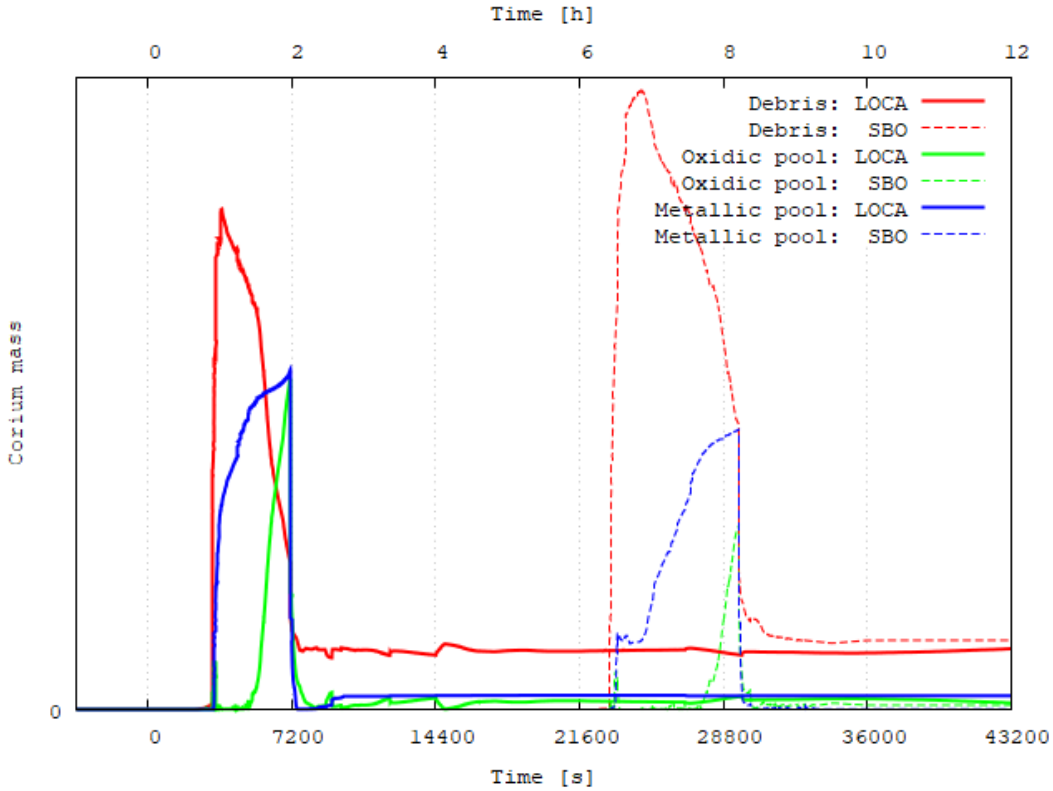

Figure 7 Mass of solid debris (unmolten material, in red) and oxidic/metallic molten pools (in green and blue, respectively) in the LP.

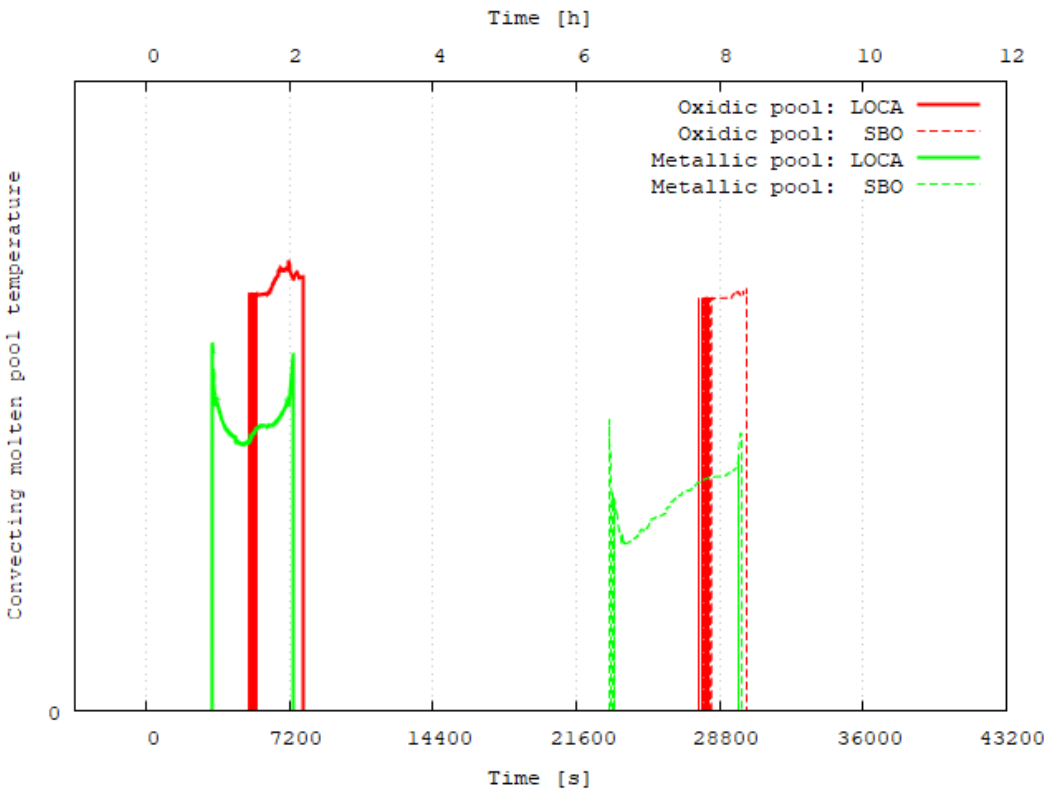

Figure 8 Temperature of oxidic/metallic pool in the LP.

Corium component	G-LOCA %	SBO %
FeO	0.40	0.77
Fe2O3	0.40	0.77
Fe3O4	0.40	0.77
Fe	23.31	21.55
Zr	14.34	12.22
ZrO2	5.86	8.66
B4C	0.15	0.14
UO2	55.13	55.11
Total	100.00	100.00

Table 1 Corium composition for both evaluated SA scenarios.

3. MELTSPREAD CALCULATION: SPREAD-ABILITY

A corium that is poured from the failed RPV must be spread first in a cylindrical-geometry of reactor cavity, then it must flow through a narrow corridor connecting the reactor cavity with a neighboring room (GA302, see **Figure 9** for the situation). At the point where the corridor enters into the room GA302, there is a down step of 0.6 m. The corridor is closed by two different doors: the first door is closer to the reactor cavity and is made of concrete. It has two wings that open against the corium flow. The purpose of the door is radiation shielding. The second door is situated at the point where the corridor enters the GA302 room and it is made

of steel. It is hermetically sealed during normal plant operation to ensure correct functioning of reactor cavity ventilation and cooling. Within the feasibility study performed, it turned out that a provision, allowing for quasi-immediate escape of the corium through the concrete door, shall be implemented. The concrete technical solution was not investigated as it is beyond the scope of the research project. Similarly, the hermetic steel door shall be automatically opened after the entrance into SA (before RPV failure). Part of the GA302 room would be dedicated for melt spreading and would be flooded by water prior to RPV failure. The spreading area is limited by corium spreading barriers that will prevent the corium from reaching a hermetic boundary of the CTMT. The spreading area is 25 m^2 in the reactor cavity and 64 m^2 in the room GA302, which is enough to successfully localize and cool down the corium (see calculation results later).

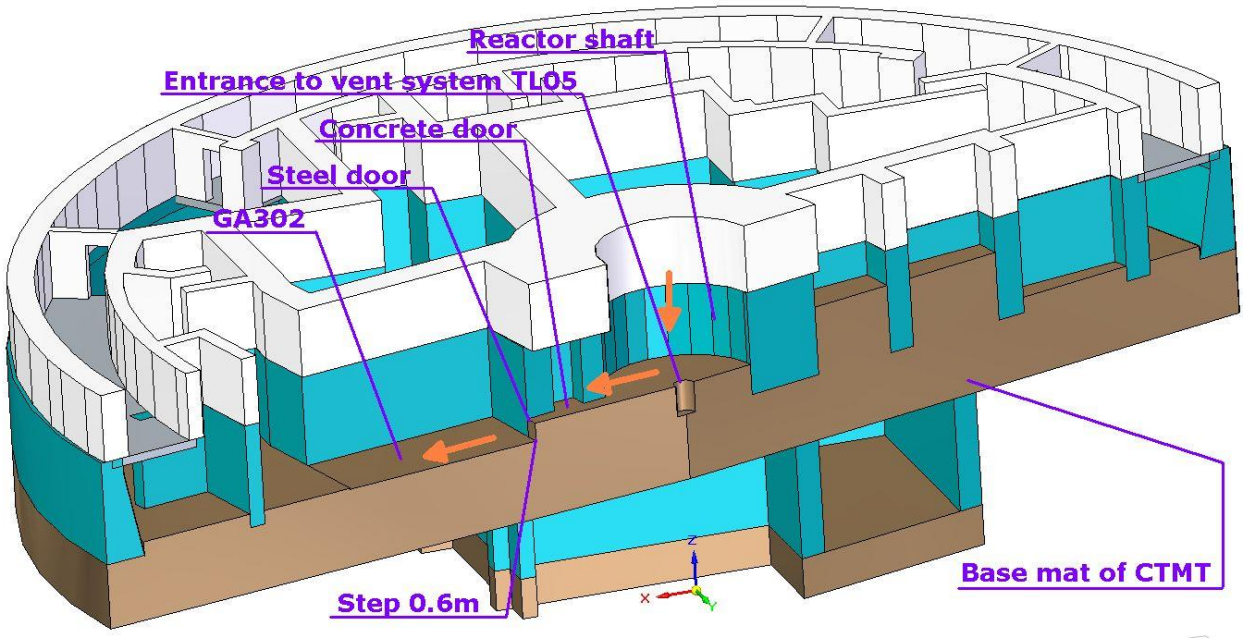

Figure 9 Corium spreading path in the geometry of the Temelin CTMT.

The MELTSPREAD 3.0 code, developed in ANL [12], was used for mechanistic assessment of corium spreading. The spreading area of the reactor cavity, the corridor and the GA302 room was divided into roughly 400 nodes (dimensions of arrays in the MELTSPREAD source code had to be increased to allow that quantity of nodes), each of them being approximately 25mm wide.

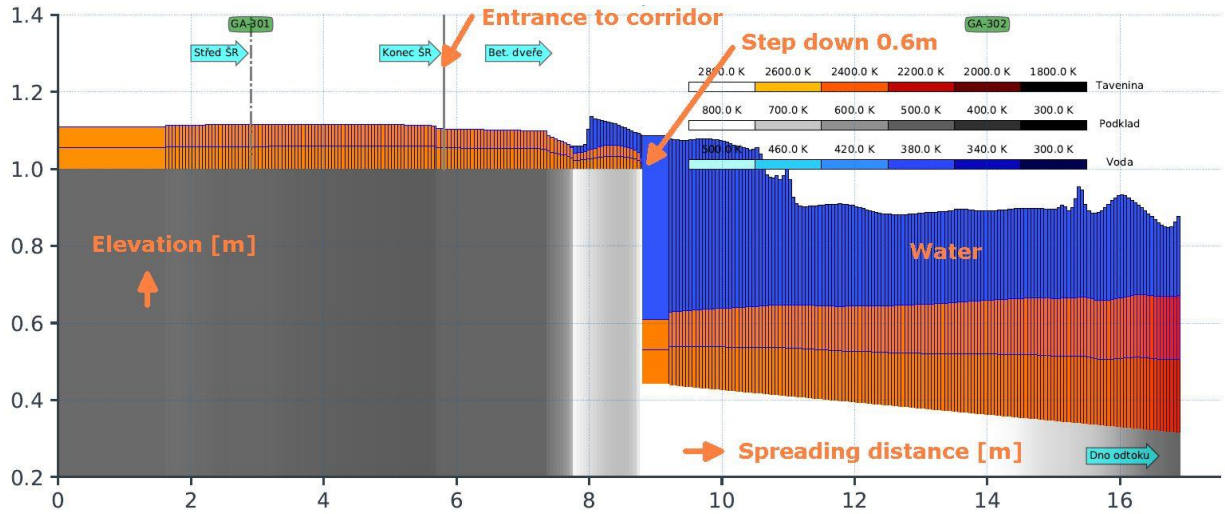

Figure 10 Example of MELTSPREAD calculation visualization using Python programmed visualization tool.

MELTSPREAD 3.0 envisages Newtonian melt flow. The "Ramacciotti" effective viscosity enhancement is assumed for the flow of slurries. Due to non-Newtonian effects, melt undergoing freezing could exhibit a greater resistance than calculated in the investigated analyses – the current results could thus be rather optimistic. As for the solidification model, a simple model, using a constant called ALPMAX, is used: if this constant is set to 1.0, then the maximum solid fraction in the melt at which the material is declared to be a solid (in code MELTSPREAD) is equal to 1.0. Once this limit is reached, the material is immobilized and incorporated into the substrate.

There are a few uncertain parameters, the variation of which has significant influence on results of corium spreading. Thus, sensitivity studies were conducted in order to assess the importance of these parameters.

The first parameter is corium temperature at time of corium pouring from RPV, it has direct influence on corium viscosity, which is a crucial parameter of corium flow and spreading. In RPV LP the corium has different temperature in different locations. This means that near the RPV wall, there are probably solid debris or crust that is cooler than corium in the center of the pool in the LP. With continuous change of temperature dependent on location, it is difficult to determine some average temperature of corium escaping from RPV. Fortunately, calculation of average temperature can be avoided. The MELTSPREAD code uses correlations for corium viscosity estimation based on volumetric fraction of solid phase in liquid corium (in our study the Ramacciotti correlation was chosen). Hence, the data from MELCOR calculation were used for estimation of solid/liquid (i.e. debris/molten corium) ratio at the time of RPV failure. The obtained volumetric solid fraction was then compared to a solid fraction obtained by the MELTSPREAD code at a certain temperature. Thus, the temperature in MELTSPREAD was varied so that the solid fraction matched the MELCOR-calculated solid fraction, and that temperature was used as initial corium temperature prior to spreading. With such a trick the spread-ability was deemed to be correct – as it is dependent on the solid fraction within the melt, the initial temperature varying slightly from that predicted by the MELCOR code. Thanks to high thickness of the VVER-1000 RPV wall (200 and 244 mm in the cylindrical and elliptical part, respectively), the wall fails relatively late and thus the corium in the LH has enough time to melt. Repeated calculations by MELCOR and ASTEC codes indicated that the volumetric solid fraction in the corium was about 12-14 % at the time of RPV failure in various scenarios.

The solution described in the paragraph above resolves the task of finding an average temperature for the molten material being evacuated from the breached RPV; in the LP, the temperature is not homogeneous in its volume. Corium close to the RPV wall is colder than in the center of the pool. It may be assumed that

the corium temperature varies between solidus and liquidus temperatures depending on its location within the lower plenum. Colder corium contains more solid parts floating in the liquid than hotter corium. The volumetric fraction of solid phase in the molten corium pool influences its viscosity, which is a key property for spreading estimation. The MELCOR code can easily deliver data of solid/liquid material in the LP right before RPV failure. This would define the total volume of solid fraction in the RPV before corium pouring and spreading, which is a key property for viscosity calculation using the MELTSPREAD-built-in correlations, e.g. the Ramacciotti correlation.

The second uncertain parameter is the RPV rupture cross section. Mass flow of poured corium onto the spreading area has significant impact on spreading ability. MELCOR code predicts corium evacuation from the RPV through a rupture the cross-section of which is only roughly calculated (either a user-defined cross-section is used or the whole failed LH node's area is used; the hole is moreover ablated by the flowing corium). Hence, a sensitivity study was performed: the corium pour rate was decreased down to five times to cover less favorable situation for spreading. For low corium mass flow rates MELTSPREAD calculations often did not end up with useful results, as a front crust formed – and never broke again (a model of front crust breach is still missing in the code). Hence, the calculations ended up with deep pool of liquid corium un-physically held up by thin front crust. Future release of MELTSPREAD code should also contain the model of front crust break-up, which would allow a continued spreading after the crust is predicted to collapse.

The third uncertain parameter is the dependance of solid fraction in the melt on temperature. MELTSPREAD allows user to set this relation as a set of interpolation points. For prototypical corium poured from failed RPV, this knowledge can be obtained from equilibrium quaternary phase diagram U-Zr-Fe-O. This set of points will vary with each new corium material composition. Composition of corium in time of RPV failure changes with the accident scenario. Knowledge of the quaternary diagram U-Zr-Fe-O is thus crucial for further work. Without knowing the exact dependance of solid fraction between the melt solidus and liquidus temperature, a sensitivity study was performed again: an "optimistic" and "pessimistic" dependencies were defined, the former characteristic with rather low solid fraction at high temperatures and the latter characteristic with rather prompt solidification when cooling down from the initial temperature.

Even though MELTSPREAD 3.0 has not a model of hydraulic resistance of walls to flowing corium, there were done some calculations to estimate minimal flow area of apertures that must be made into the concrete door to allow successful corium evacuation from the reactor cavity into the GA302 room. Future release of MELTSPREAD should already contain the flow resistance model.

There is also a reactor cavity cooling ventilation system TL05 in the middle of reactor cavity that can be filled with the poured corium as there is an entrance into this system – albeit covered by a steel thermal shielding (see later for more detailed description). A separate model for MELTSPREAD, representing part of the ventilation duct, was prepared (considering the constraints of not being capable of modeling wall friction) and calculations simulating corium inflow and spreading in the ventilation were launched. According to these calculations, approximately 4 m^3 of corium can possibly enter into the ventilation of TL05 and ablate the concrete slab.

Corium spreading on dry vs. wet surface in the room GA302 was extensively studied (see **Figure 10** for a snapshot from such a calculation with water-flooded GA302 prior to spreading). Calculations showed that there is no significant difference between spreading of corium on a dry floor and in the pool of saturated water.

The thermal shielding (TS) structure, located on the floor of the reactor cavity, consists of several tens of very thin stainless-steel sheets, stacked and equally distanced. The gaps, separating the sheets, are filled with the air. This system of stacked stainless-steel sheets is enclosed within a box made of carbon-steel. An

investigation was carried out to assess how the TS would behave when the melt, ejected from the RPV, impacts it. Two situations were envisaged: first, the TS would not collapse under the weight of the impacting corium, and second, the TS would be destroyed by the impacting corium. For the first case envisaged, the floor with the TS would remain flat – as it is (without any deformation). For the second case envisaged, the floor would form a sag. MELTSPREAD simulation for the second case, i.e. the sag geometry, showed that such an obstacle is not preventing the corium from flowing from the reactor cavity, through the sag under the concrete door, further on into the neighboring room GA302.

Moreover, sensitivity calculations that included uncertainty in corium pouring mass flow rate were carried out. The MELCOR-predicted corium mass flow rate (approximately 70 % of the melt would be evacuated from the breached RPV within 5 min) was increased/decreased to investigate the corium spreadability. The following findings was made: lower pouring mass flow rate resulted in front crust formation in the front of the spreading corium, as MELTSPREAD 3.0 is not able to break that crust once it solidifies. That results in non-physical state in which relatively deep pool of liquid corium is held by relatively thin front crust. The crust is not broken by hydrostatic pressure nor it is molten by liquid corium. This flaw of the MELTSPREAD code prevented several calculations to be finished with physically convenient results. Another sensitivity study, concerning the quality of the melt pour, was made: initially, it was assumed that after the RPV ruptures, corium starts to flow out as well mixed mixture of metallic and oxidic corium. Further, sensitivity analyses were made with separate metallic/oxidic pouring (one following the other). It turned out that the impact of different order of oxidic/metallic melt evacuation from the RPV has a large impact on the corium spreadability.

4. CORQUENCH CALCULATION: COOL-ABILITY

After successful evacuation of corium from the reactor cavity into the room GA302, calculations with the CORQUENCH 4.0, developed in ANL [13], were carried out to assess the rate of concrete floor ablation and corium cool-ability. As the initial and boundary conditions the results from MELTSPREAD calculations were used. MELTSPREAD itself can prepare input for CORQUENCH calculations as there is a possibility of transforming relatively large groups of MELTSPREAD nodes into a simpler geometry in CORQUENCH, representing the cavities. Those cavities have corium mass and composition specified alongside with other physical parameters taken over from MELTSPREAD calculations. The area of reactor cavity, corridor, room GA302 and ducts of the ventilation system TL05 was subdivided into several cavities that were investigated separately.

The reactor cavity as modeled with a node (cavity) of cylindrical geometry and with three layers of different materials, representing the TS, the serpentine concrete and the siliceous concrete. After evacuation of major mass of corium from the reactor cavity, the residue of corium in the reactor cavity consists only of a thin layer (10 to 15 centimeters) which solidifies quickly (in the order of minutes) even without being flooded by water. The same situation is in the corridor, where rectangular geometry with two opposing inert walls was modeled.

Majority of corium mass is located in the room GA302, where it forms a 40 cm thick layer and it is flooded by water (using a dedicated system for severe accident with independent mobile power and water sources). A rectangular geometry node was used to represent the room GA302. The ablation of concrete floor is stopped roughly after half an hour of cooling, quickly followed by complete solidification of corium. Coolant supply interruption (up to 50 hours) scenarios were also investigated. Preliminary results show that even such disruptions in water supply did not have a major effect on the corium cool-ability and in any case the integrity of the CTMT basemat was not jeopardized; in the worst case, approximately one-meter-thick layer of the CTMT basemat was ablated.

Further focus was dedicated to the ventilation system TL05, filled with the corium (assuming that the TS would be breached). Three parts of the ventilation duct were modeled to faithfully represent the whole ventilation system. Tubes with circular profile were replaced by rectangular profile. Water cannot access the ventilation if it is full of hot corium, therefore all calculations were done with dry floor conditions. The results showed that ablation is stopped, and corium partially solidifies after several hours due to corium mixing with concrete ablation products and decay heat decrease.

The last part of computational effort was invested into an integral analysis using the MELCOR code again – an assessment of CTMT pressurization was performed, oriented on the risk of hydrogen deflagrations and fission products release. The results from MELTSPREAD and CORQUENCH were used as boundary conditions for MELCOR. The CORCON code, implemented in the MELCOR as the module (the CAV module) responsible for molten core concrete interactions (MCCI), allows the user to tweak sensitivity coefficients and multiplication constants so that the MCCI process behaves in a desired manner. Thus, the CORQUENCH-calculated produced hydrogen, steam, were matched while "tuning" the CAV module parameters, independently in each cavity. Moreover, MELCOR allows the user to define corium spreading in each cavity, using a table of time-radius. Rupture elevations between particular cavities can be set by the user to permit an overflow of specified amount of corium to the next cavity.

5. EXPERIMENTAL BACKUP

The international OECD/NEA project ROSAU aims at reducing the uncertainties of dryout heat flux (DHF) for the in-vessel type of corium – i.e. corium without products of concrete ablation. Indeed, the correlation based on historical Small-Scale Water Ingression and Crust Strength experiments (see **Figure 1**, [14] and [16]) is not supported with experimental data for the 0 % concrete content in the melt, which is the case of ex-vessel melt being flooded immediately after breaching the RPV. Therefore, an apparatus for wet MCCI was made (see **Figure 11**) and is being used to investigate the top-flooded corium cooling capabilities.

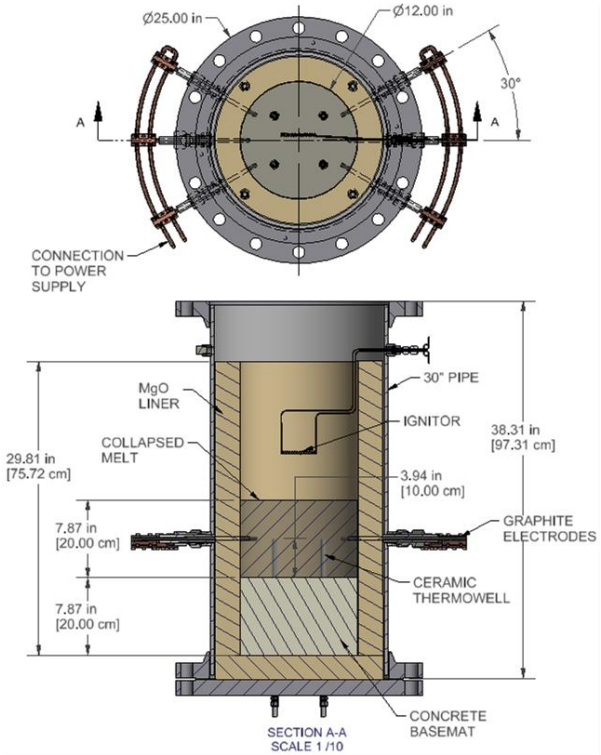

Figure 11 The test apparatus for corium cooling by water top-flooding investigations within the ROSAU program [14].

The Czech national experimental program CORIUM provided (as of the end of 2021) some valuable results concerning the study of corium impact on the TS. The experiment was carried out with 5 kg of prototypic corium (59.4 wt% of UO_2, 31.3 wt% of ZrO_2 and 9.3 wt% of Fe_2O_3) produced in the cold crucible, which was poured on the specimen representing part of the TS. A post-test examination (**Figure 12**) showed that the corium did not breach completely the TS structure.

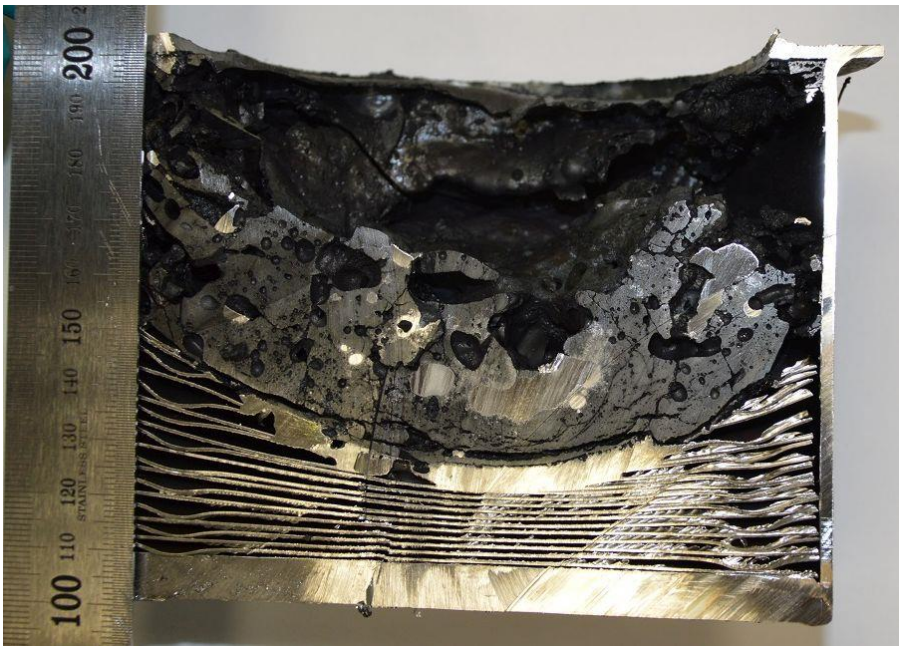

Figure 12 A preliminary snapshot of the TS being attacked by corium.

6. CONCLUSIONS

A sequence of numerical analyses was performed in order to assess, in the first approach by deterministic analyses, the feasibility of the ExVC strategy for the VVER-1000 reactor. First, the MELCOR code was used to obtain BCs for the corium before its spreading, considering 2 qualitatively different SA scenarios (LB LOCA and SBO, respectively characterized by higher decay heat and low oxidation degree and lower decay heat and higher oxidation degree at the instant of RPV breach). Further, the MELTSPREAD code was used to assess corium spread-ability in the geometry of reactor cavity, tunnel and the neighboring room GA302, moreover considering the ventilation duct in the center of reactor cavity. Both cases – dry and wet spreading – were considered. Finally, the CORQUENCH code was used to assess the possibilities of corium cooling by water top-flooding, considering also the cases of dry MCCI. As an outcome, it can be concluded that if provisions were made for the corium to enable its escape from the reactor cavity immediately after being poured from the RPV, and if immediately flooded, the CTMT basemat ablation may be slowed down or even stopped. The numerical study was supported by outcomes from the still ongoing Czech experimental project CORIUM (indicating the risk of the TS being destroyed by the poured corium and providing some corium properties at high temperatures, namely viscosity and density), and will be supported by the outcomes from the international ROSAU project, when the pertinent tests (especially the spreading tests and quenching tests with concrete basemat) are executed. A final remark concerns the uncertainties of the calculations: as still many uncertainties exist, a ROAAM (Risk Oriented Accident Analysis Methodology) is ongoing, in parallel, to the described deterministic assessment.

REFERENCES

1. T. G. Theofanous et al., "In-Vessel Coolability and Retention of a Core Melt," *DOE/ID-10460 Vols. I and II* (1996).
2. J. L. Rempe et al., "Potential for AP600 in-vessel retention through ex-vessel flooding," *Technical Evaluation Report, INEEL/EXT-97-00779* (1997).
3. "In-Vessel Melt Retention Severe Accident Management Strategy for Existing and Future NPPs," https://cordis.europa.eu/project/id/662157 (2015-2019).
4. J. Zdarek et al., "Final report on full scale tests," *WP 4 – HORIZON 2020 IVMR D 4.4* (2019).
5. D. Batek and J. Zdarek, "THS-15 Experiment: ERVC in VVER-1000 design," *Proceedings of the International Seminar on In-vessel retention: outcomes of IVMR project*, Juan-les-Pins, France, January 21-22, 2020.
6. B. R. Sehgal et al., *Nuclear Safety in Light Water Reactors – Severe Accident Phenomenology*, ELSEVIER, Amsterdam, The Netherlands (2012).
7. F. Robledo et al., "State-of-the-Art Report on Molten Corium Concrete Interaction and Ex-Vessel Molten Core Coolability", OECD, NEA/CSNI/R(2016)15, 2017.
8. P. Chatelard, "Brief overview of the ASTEC V2.1 major version," *Proceedings of the 6th ASTEC Users' Club*, Bologna, Italy, February 23-26, 2015.
9. B. Beeny, "MELCOR 2019 Workshop CAV Package Water Ingression and Melt Eruption Models," *Proceedings of the CSARP/MCAP Meeting*, Albuquerque, USA, June 3-7, 2019.
10. L. L. Humphries et al., "MELCOR Computer Code Manuals, Vol. 1: Primer and Users' Guide, Version 2.2.18019", Sandia National Laboratories, January 2021.
11. L. L. Humphries et al., "MELCOR Computer Code Manuals, Vol. 2: Reference Manual, Version 2.2.18019", Sandia National Laboratories, January 2021.
12. M. T. Farmer, "The MELTSPREAD Code for Modeling of Ex-Vessel Core Debris Spreading Behavior, Code Manual – Version 3.0", Argonne National Laboratory, September 2018.
13. M. T. Farmer, "The CORQUENCH Code for Modeling of Ex-Vessel Corium Coolability under Top Flooding Conditions Code Manual – Version4.1-beta", Argonne National Laboratory, August 2018.
14. J. Licht, "STATUS OF THE OECD REDUCTION OF SEVERE ACCIDENT UNCERTAINTIES (ROSAU) TEST PROGRAM", *Proceedings of the CSARP/MCAP Meeting*, Virtual (MS Teams), June 7-11, 2021.
15. I. Poznyak and J. Hrbek, "Cold Crucible Laboratory," *Proceedings of the Nuclear Technologies for the 21st Century*, Rez, Czech Republic, September 13, pp. 98-104 (2017).
16. S. Basu et al., "Significance of the OECD-MCCI Program in Relation to Severe Accident Uncertainties Evaluation", *Proceedings of the Workshop on Evaluation of Uncertainties in Relation to Severe Accidents and Level 2 Probabilistic Safety Analysis*, Aix-en-Provence, France, November 7-9, 2005.
17. A. Konovalenko et al., "Experimental Results on Pouring and Underwater Liquid Melt Spreading and Energetic Melt-coolant Interaction", *Proceedings of the 9th International Topical Meeting on Nuclear Thermal-Hydraulics, Operation and Safety (NUTHOS-9)*, Kaohsiung, Taiwan, September 9-13, 2012.

ASSESSMENT OF EX-VESSEL CORIUM COOLABILITY IN THE CONTAINMENT OF THE VVER-1000 REACTOR AS A MEASURE OF SEVERE ACCIDENT MITIGATION

Miroslav Kotouč
Tomáš Janda
Petr Vokáč
& the team of CV Rez's „Cold Crucible“

May 17th, 2022

The 10th European Review Meeting on Severe Accident Research (ERMSAR2022)
Akademiehotel, Karlsruhe, Germany, May 16-19, 2022

Skupina ÚJV
LIDÉ I INOVACE I TECHNOLOGIE

OUTLINE

1. Situation at the Czech Temelin NPP (2x VVER-1000)
   - On-vessel melt retention (IVMR) vs. ExVC (Ex-Vessel Corium Cooling)
2. Basic principles of corium spread-ability and cool-ability
   - Water ingression (WI), melt eruptions (ME), dryout heat flux (DHF)
3. Numerical codes employed & main results
   - MELCOR (in-vessel degradation)
   - MELTSPREAD (corium spreading)
   - CORQUENCH (corium cooling)
4. Experimental backup
   - OECD/NEA *ROSAU*
   - Czech national project *CORIUM*
5. Conclusions

CONTEXT: UNMITIGATED SA AT THE TEMELIN NPP

- Severe accident (SA):
  - core degradation
  - solid debris and molten pool (corium) formation
  - relocation/slumping into the lower plenum (LP)
  - large stratified molten pool formation
  - RPV failure
  - corium spreading onto the containment (CTMT) basemat

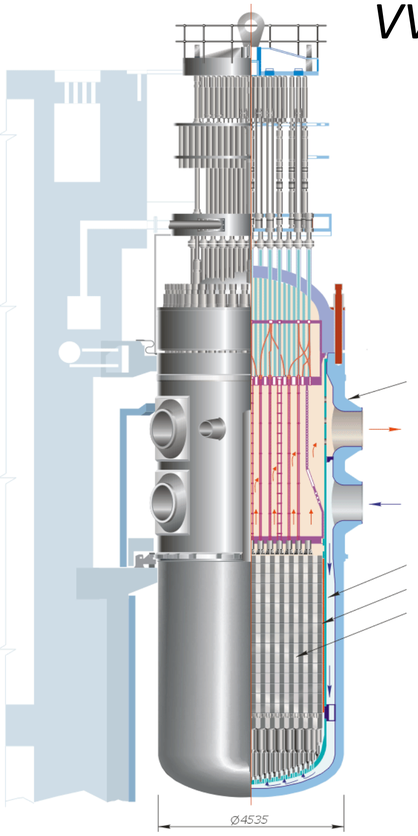

VVER-1000/320:

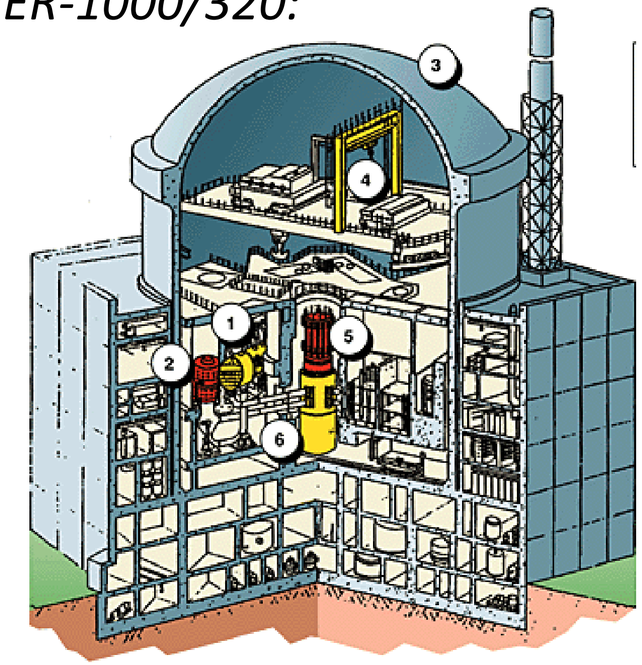

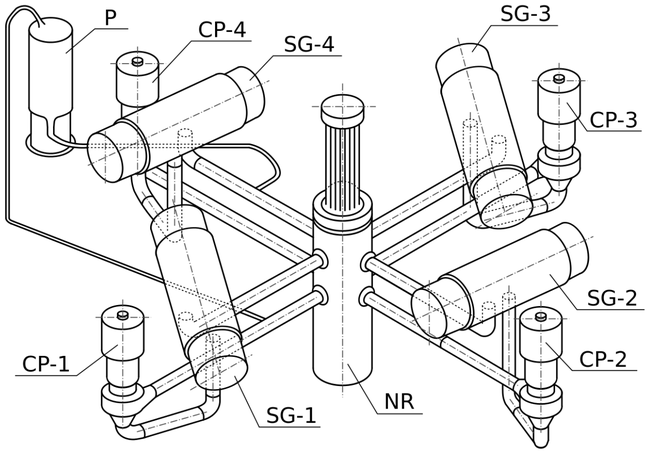

CONTEXT: DANGER OF CTMT MELT-THROUGH

- If the ejected molten corium is not cooled-down on the CTMT floor,

- after several days the CTMT basemat fails => release of radioactive (RA) substances into the non-hermetic rooms => „large RA release“

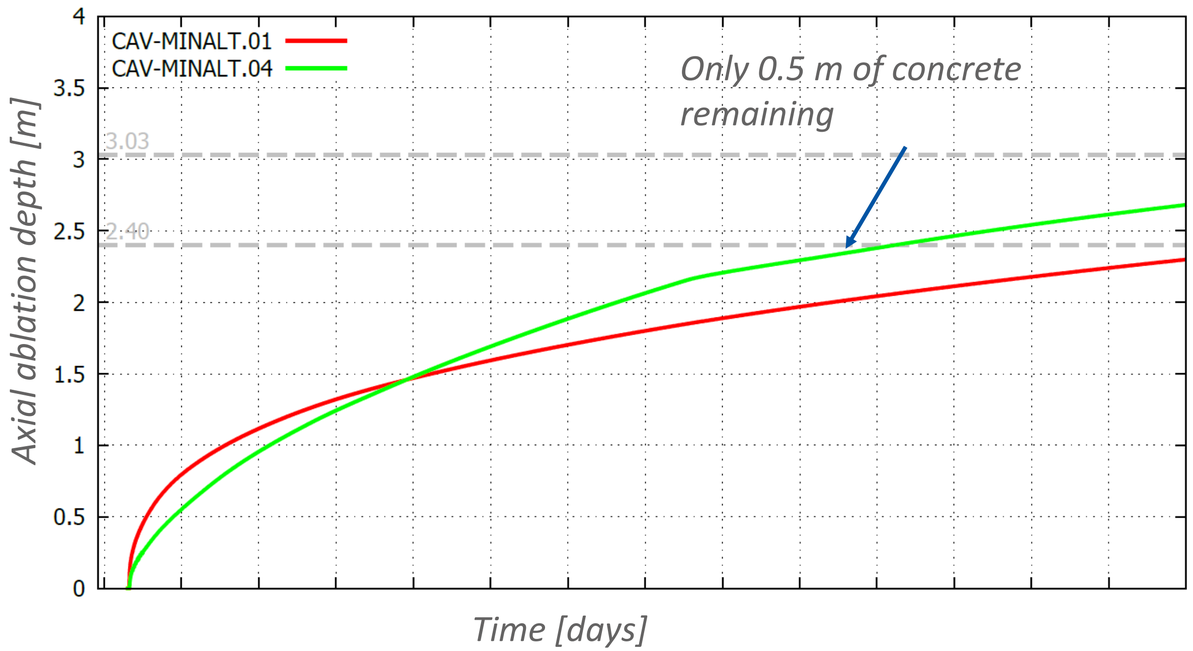

IAEA Safety Standards

for protecting people and the environment

Safety of Nuclear Power Plants: Design

Specific Safety Requirements
No. SSR-2/1 (Rev. 1)

IAEA
International Atomic Energy Agency

5.31. The design shall be such that the possibility of conditions arising that could lead to an early radioactive release or a large radioactive release is ‘practically eliminated’.[16]

SA COPING AT TEMELIN NPP

- IVMR (In-Vessel Melt Retention)
  - Not feasible due to technical constraints
- Instead, the implementation of additional SA mitigation measures was initiated, among others:
  1. **In-Vessel Retention by In-Vessel Injection (IVR-IN)**
     - Part of diverse and alternative means (DAM)
     - Based on additional pump & external water reservoir
       - Injection into the reactor coolant system (RCS) up to 2.5 MPa
       - Suction from an external water tank
  2. **Filtered CTMT venting system (FCVS)**
     - Dry filter method (DFM) to be implemented
- However, to eliminate most of the residual risks



- ExVC – strategy investigation initiated

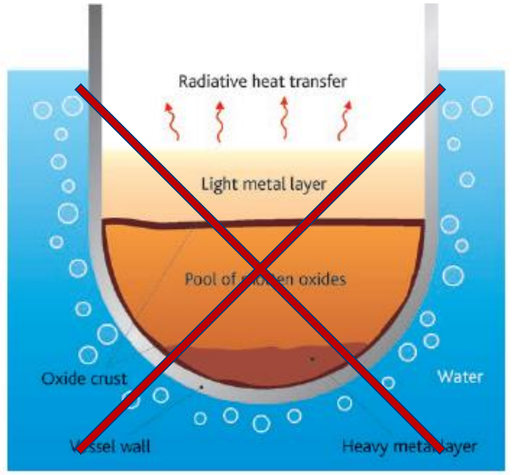

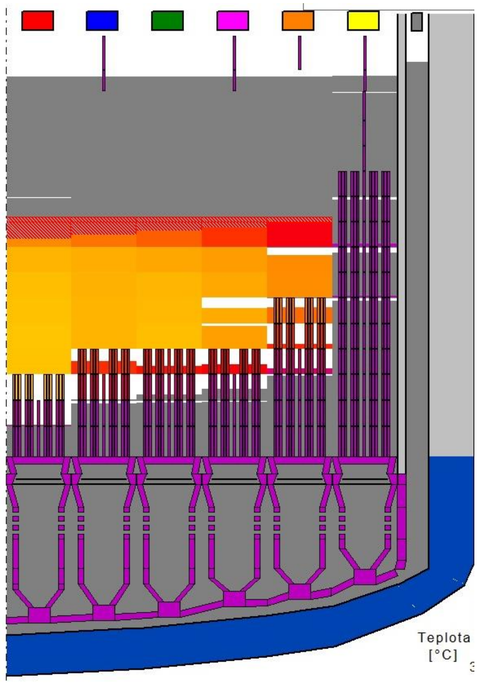

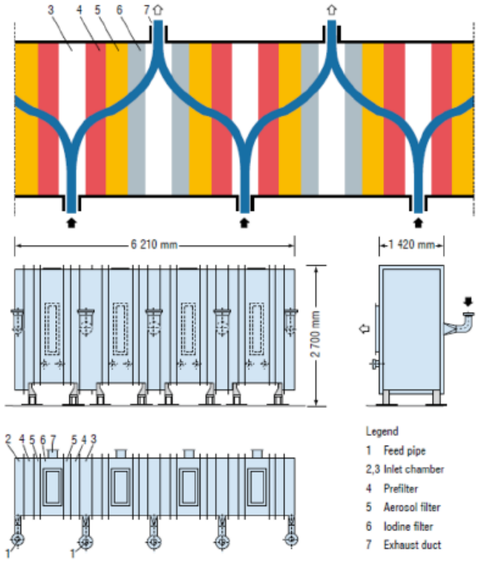

Westinghouse

FP	DF
Aerosols	10 000
Iode I2	> 10 000
Iode organ	> 100*

EXVC STRATEGY: SITUATION AT TEMELIN NPP

- After the RPV is breached, the melt has to overcome:
  1. Non-hermetic shielding concrete door
     - Must be „breachable“ for the melt
  2. Hermetic steel door
     - Must be already open prior to melt attack

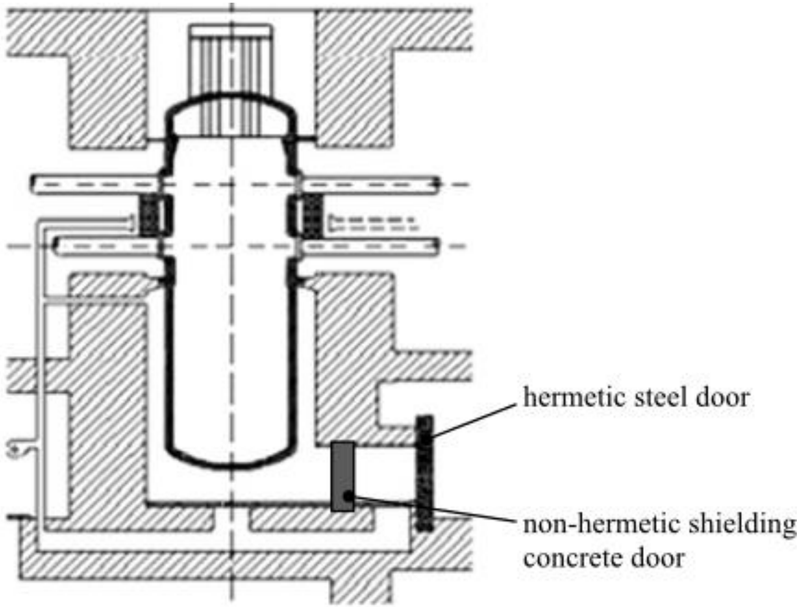

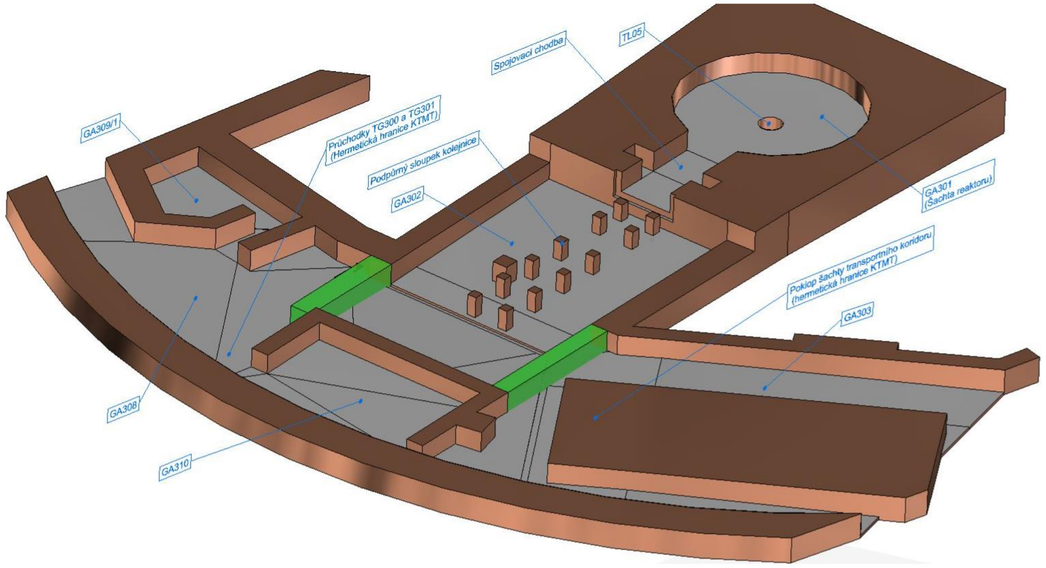

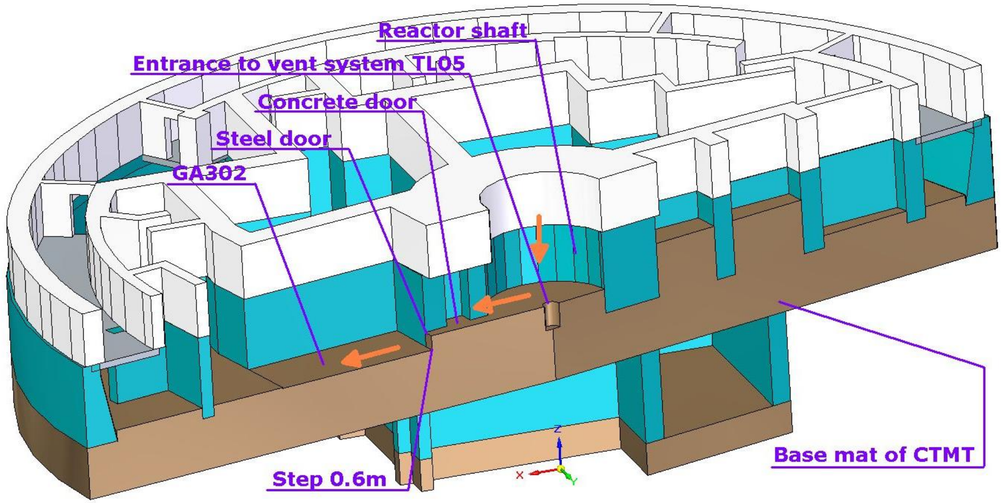

EXVC STRATEGY: COOLING MECHANISMS

- Mechanisms of corium cooling:
  - Concrete (ablation + conduction)
  - Top-radiation onto cooler surfaces
  - Nucleate boiling (if top-flooded)
  - ***Water ingression (WI)***
  - ***Melt eruptions (ME)***

- Assessment of succesful ExVC strategy application:
  - Numerical analyses
  - Experimental backup

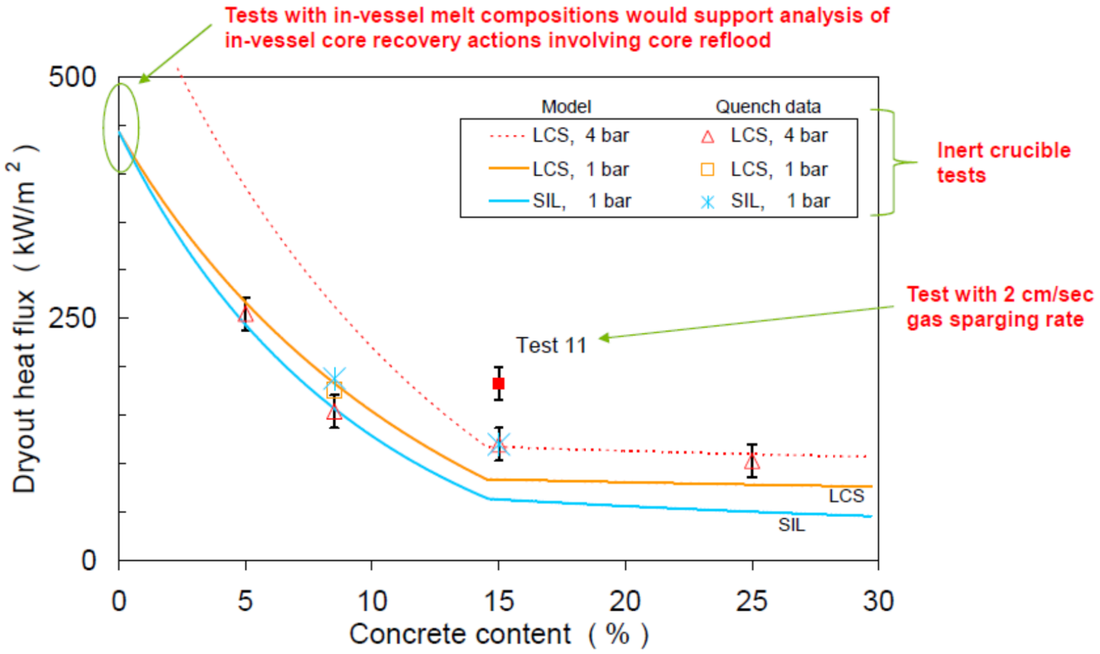

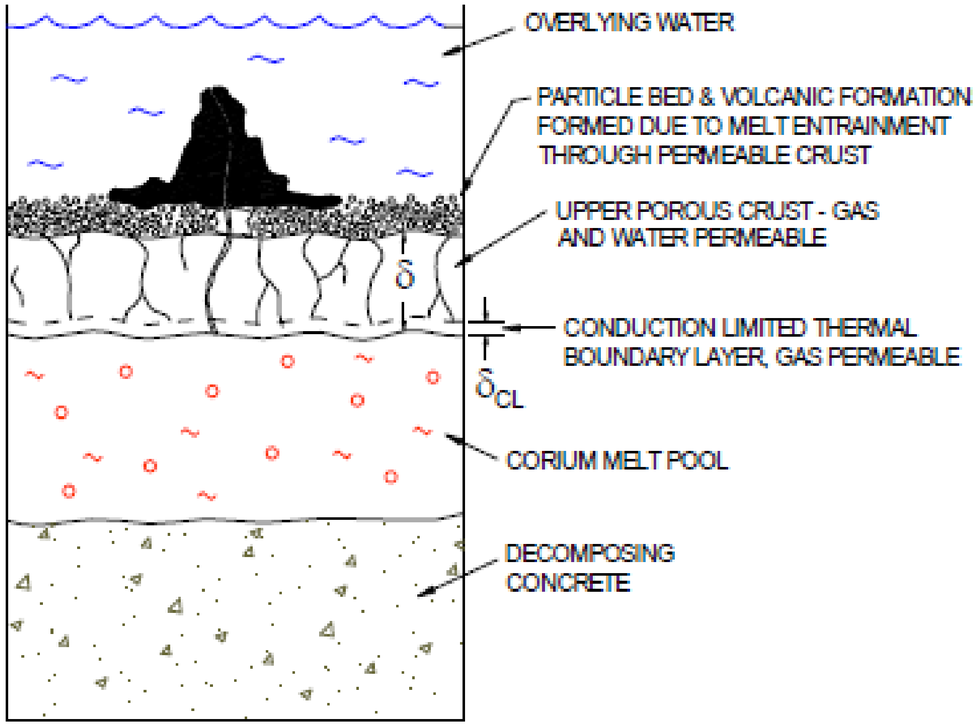

EXVC: NUMERICAL TOOLS USED

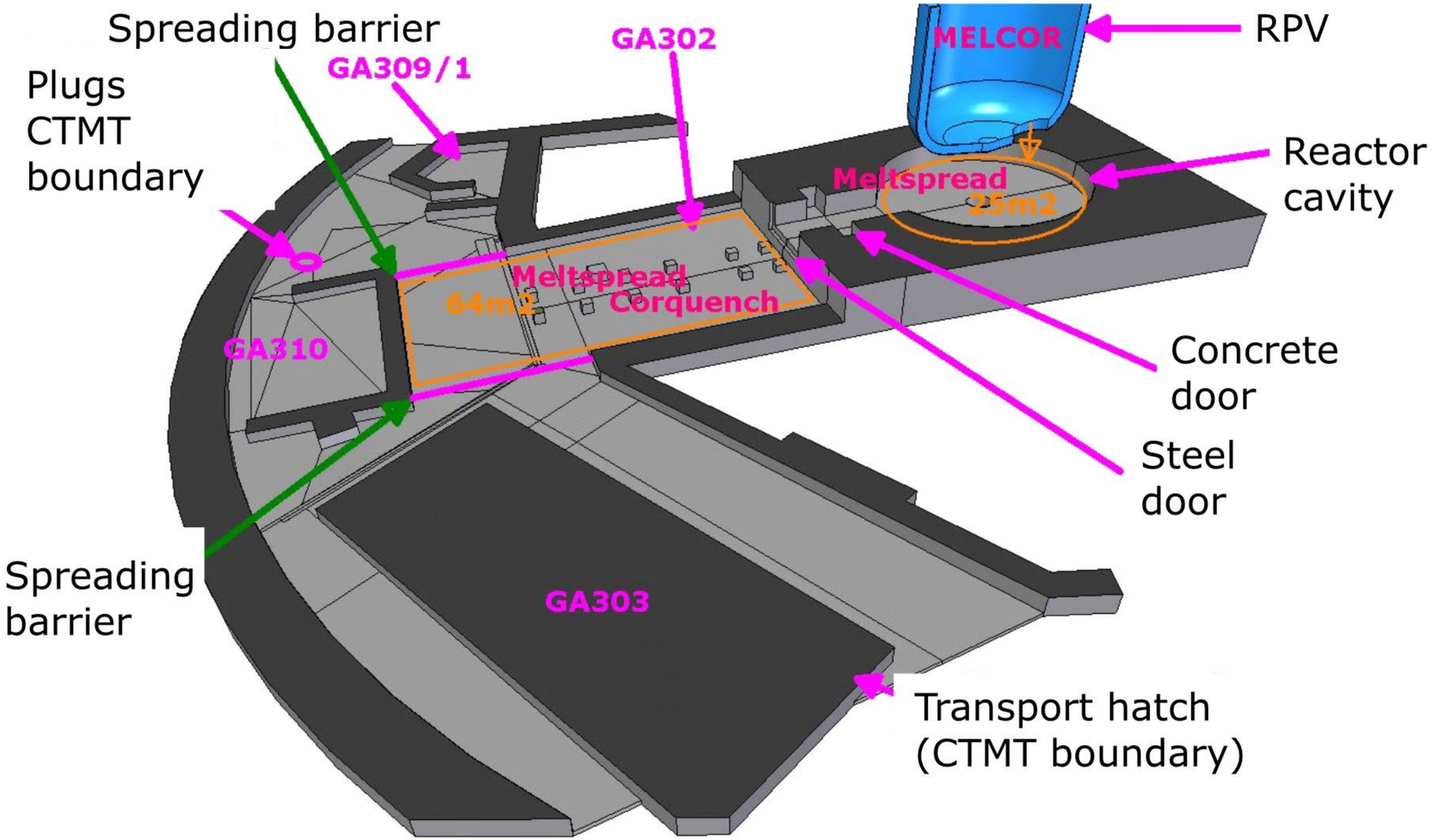

CALCULATION OF IN-VESSEL SA PROGESSION

- **MELCOR**: SNL (USA)
- Integral, lumped parameter (LP) code for SA progression
- Assessment of RPV-ejected corium: *mass, composition, temperature, solid fraction*
- Variation of: SA scenario (LB LOCA vs. SBO => decay heat, oxidation degree, …)

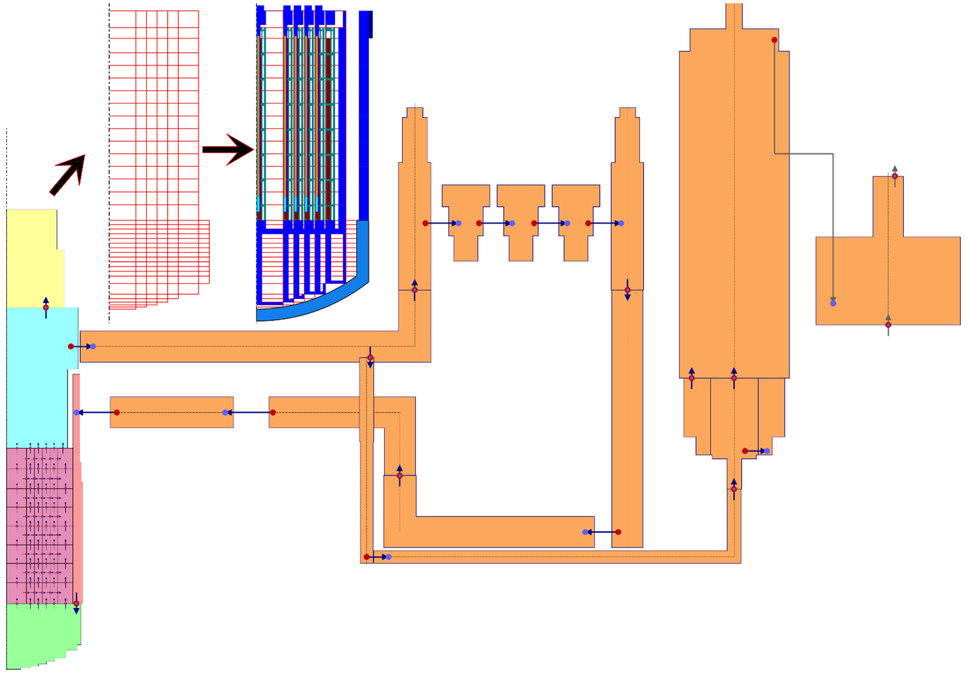

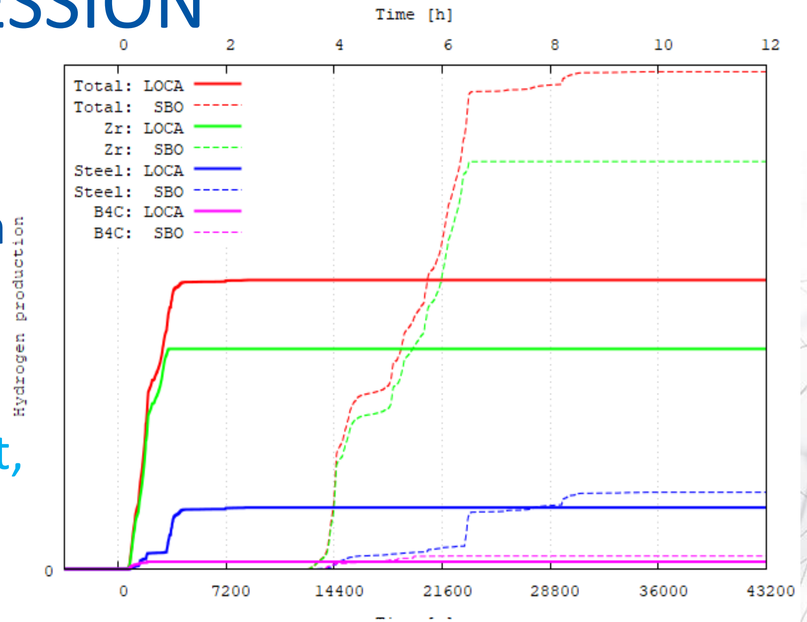

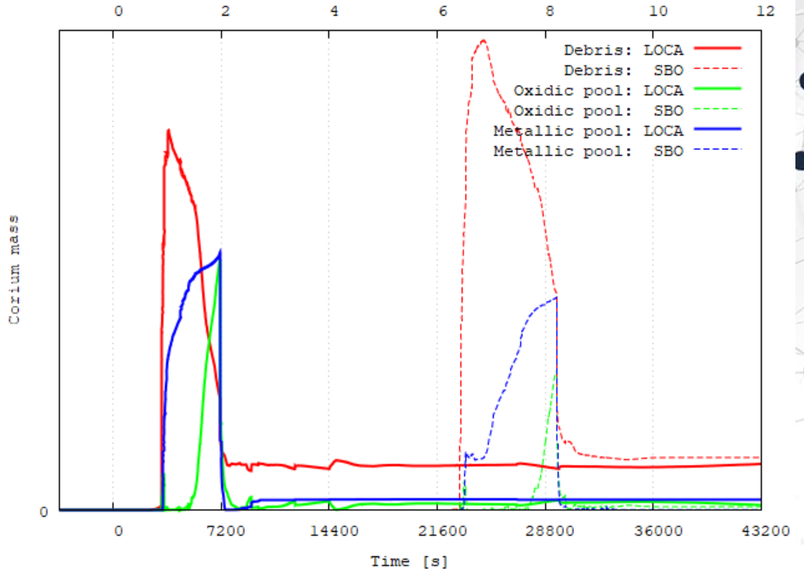

CALCULATION OF CORIUM SPREADING

- **MELTSPREAD**: ANL (USA)
- 1D corium movement in a geometrically complex channels: widening/narrowing, obstacles, steps, etc.) for corium thickness & front velocity calculation
- Takes into account: corium cooling & solidifying, heating of concrete, gas production, metals oxidation, convective heat losses from the top
- Viscosity evaluation based on user-defined solid fraction in the melt: f(T)
- Variation of: melt pour rate, melt composition (ox./met.), spreading in dry/wet conditions

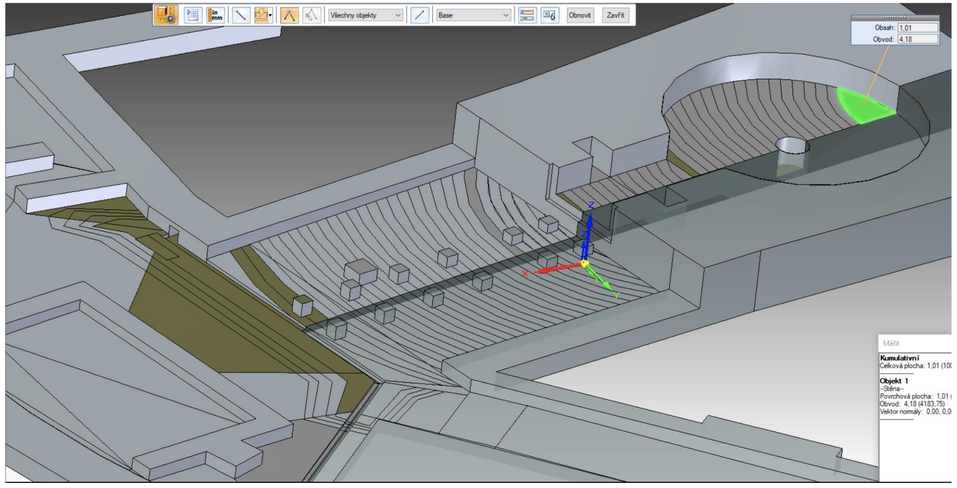

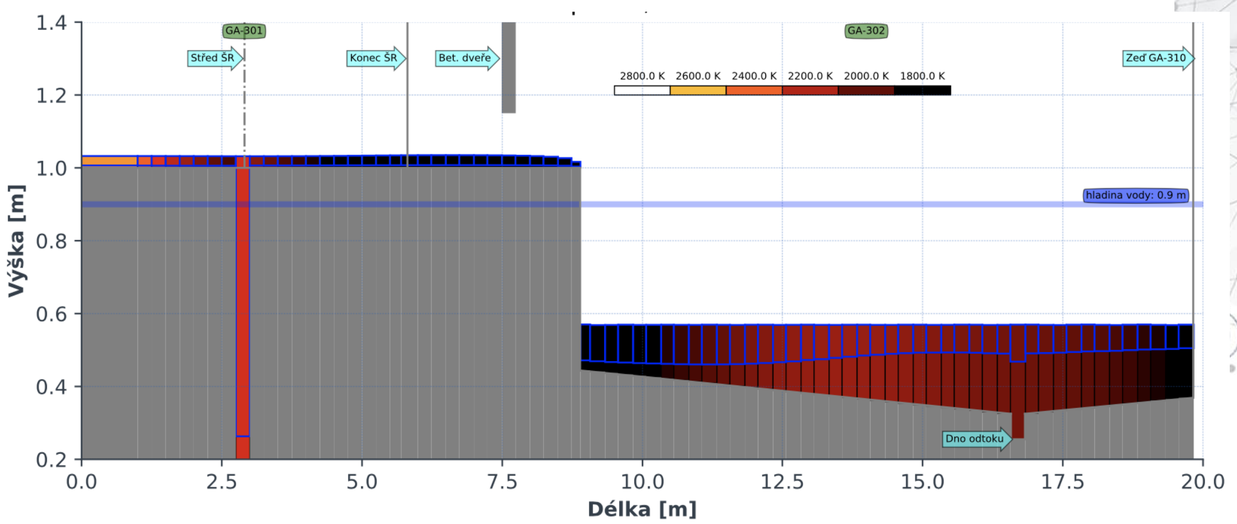

CALCULATION OF CORIUM COOLING

- **CORQUENCH**: ANL (USA)
- 1D (or pseudo-2D) erosion of concrete by the melt
- Considers concrete ablation & conduction, crust/slag formation, oxidation, heat losses from the upper surface: *radiation* (dry cavity), *convection* (flooded cavity) including WI & ME
- Only 1 phase in the melt, i.e. no stratification (oxidic vs. metallic melt)
- Variation of: area of spreading, water presence (incl. inflow interruptions)

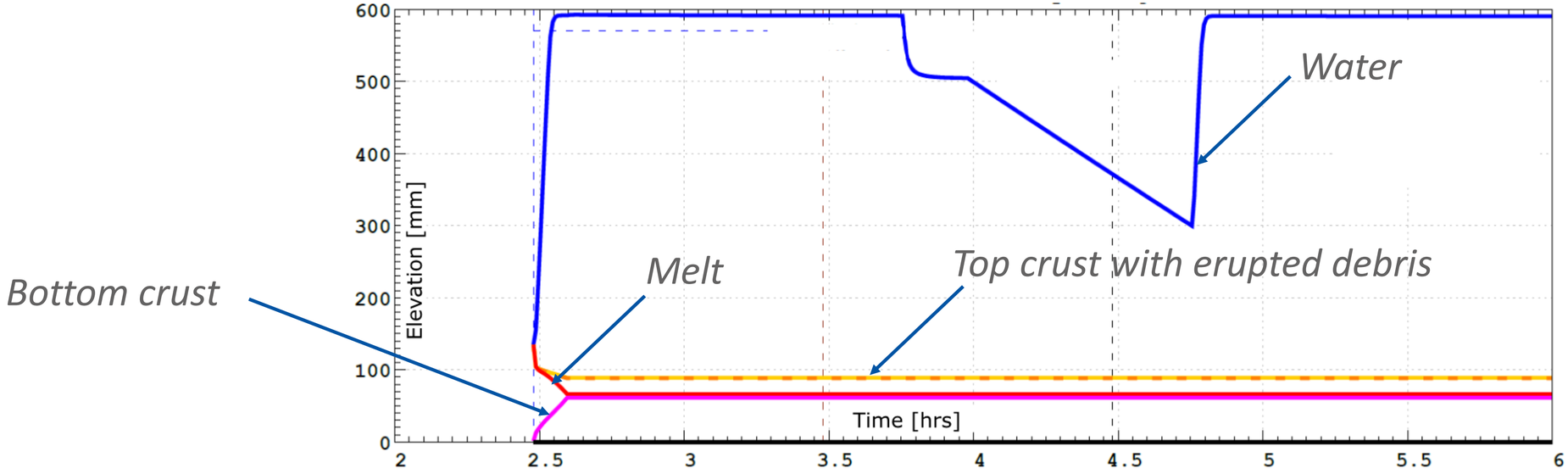

EXPERIMENTAL BACKUP: OECD/NEA ROSAU

- **R**eduction **O**f **S**evere **A**ccident **U**ncertainties (ANL, USA); 2019-2024
- Prototypical corium composition: UO_2 + Zr + ZrO_2 + Cr (+ concrete + Fe)
- Thermite heating => no decay power representation
  - Though possibility of direct electrical heating for cool-ability tests
- Unique occasion for validation of:
  - **MELTSPREAD** – melt spreading tests (**MST** – *see the next slide*)
  - **CORQUENCH** – debris cooling and MCCI (**DCAM** – *see the 2nd next slide*)

Corium cooling by water top-flooding:





Dry drop test:





Wet drop test:



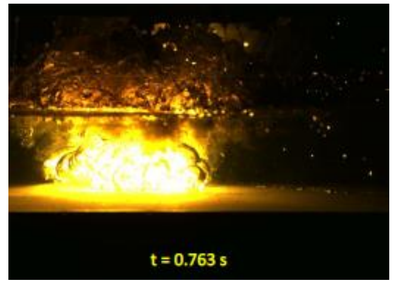

ROSAU: MELT SPREAD-ABILITY (MST)

- 300 kg of melt
- Varying parameters:
  1. Amount of water in the channel
  2. Metal content in the melt
  3. Melt temperature
  4. Melt pour rate
  5. „Dam-break“ case

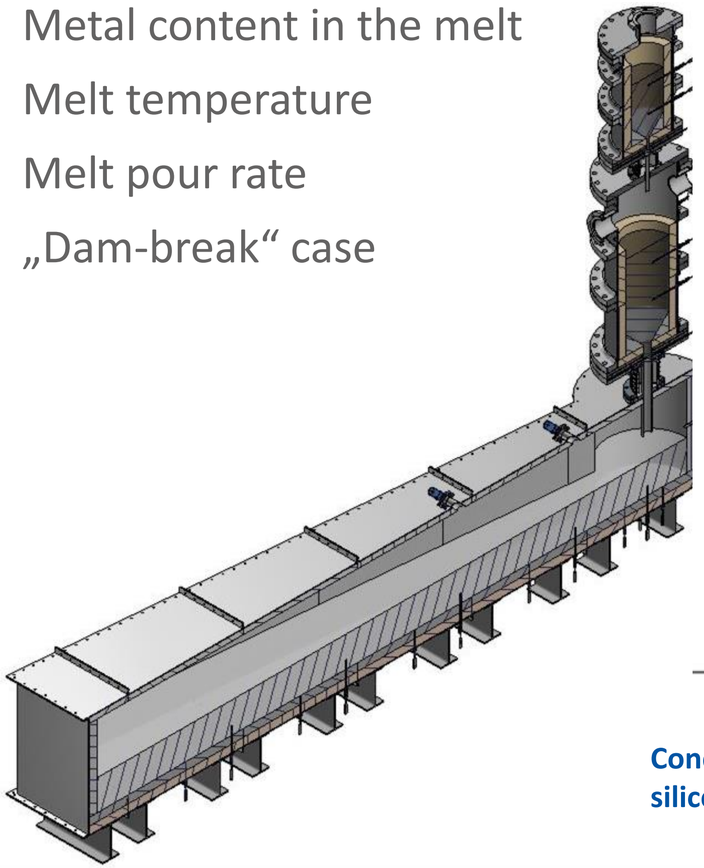

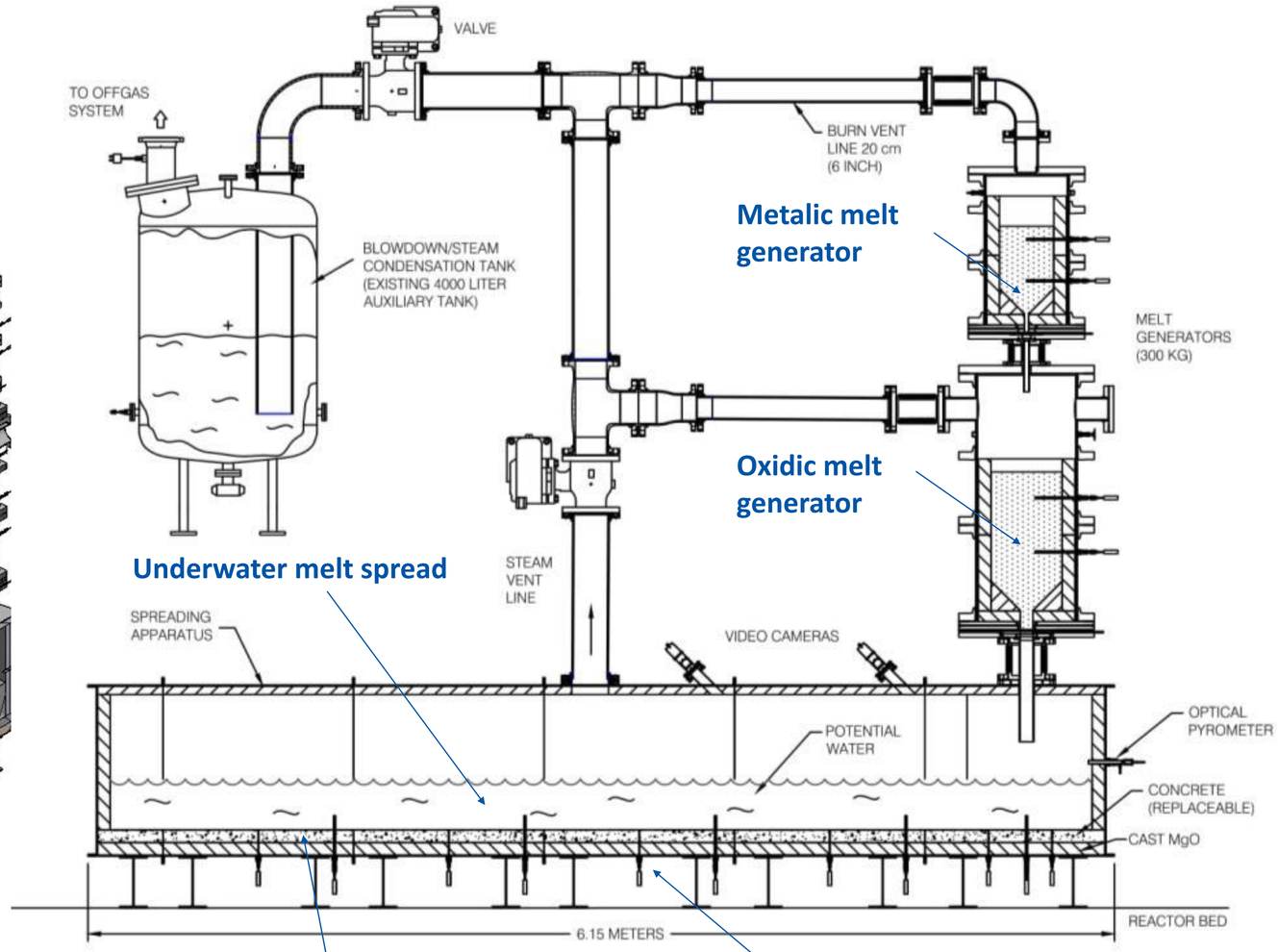

ROSAU: MELT COOL-ABILITY (DCAM)

- 100 kg of melt
- Varying parameters:
  1. Refractory or concrete basemat
  2. Metal content in the melt
  3. Siliceous/LCS concrete

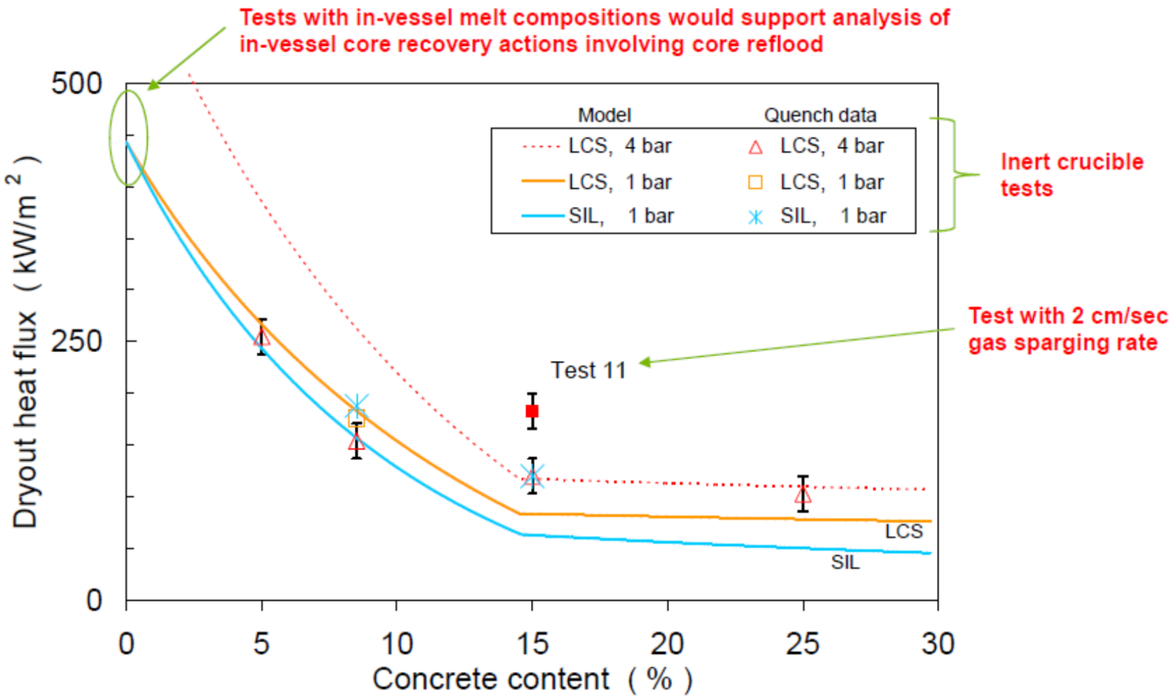

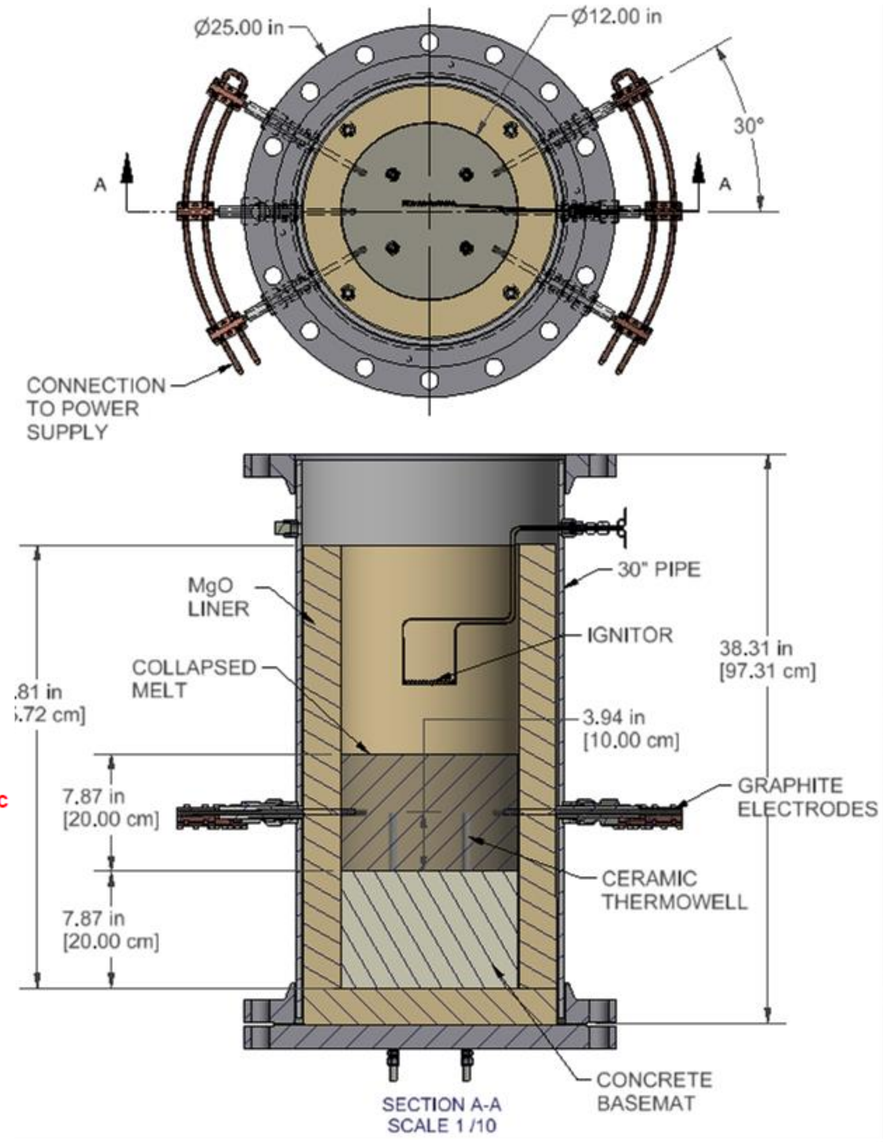

EXPERIMENTAL BACKUP: CZECH NAT. PR. CORIUM

- Cold crucible apparatus at CV Řež

1. **Corium parameters assessment at high temperatures**
   - Viscosity
   - Density
2. **Interaction of corium with solid structures: in-/ex-vessel**
   - Core barrel LH
   - Cavity thermal shielding

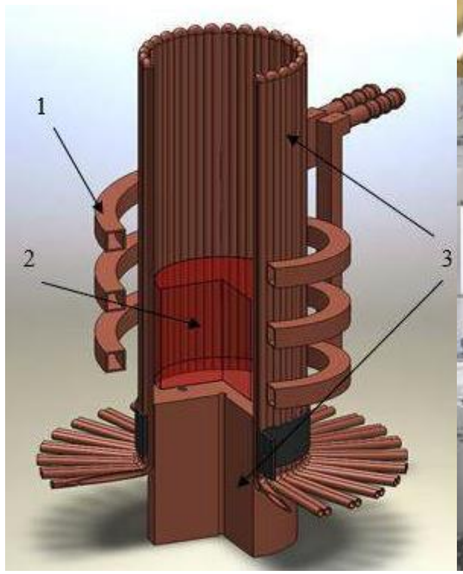



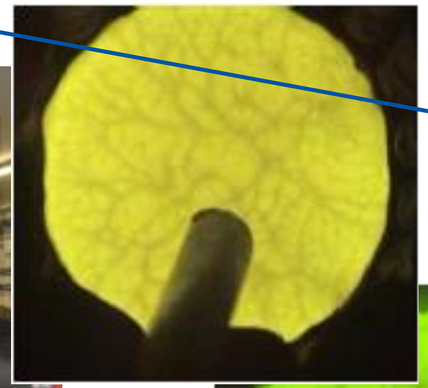

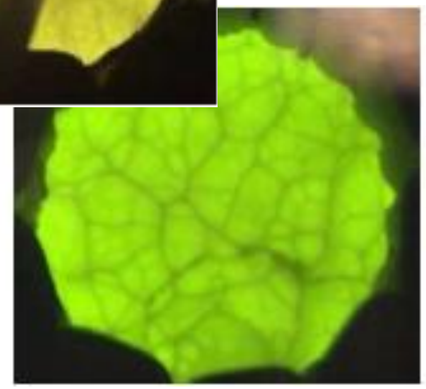

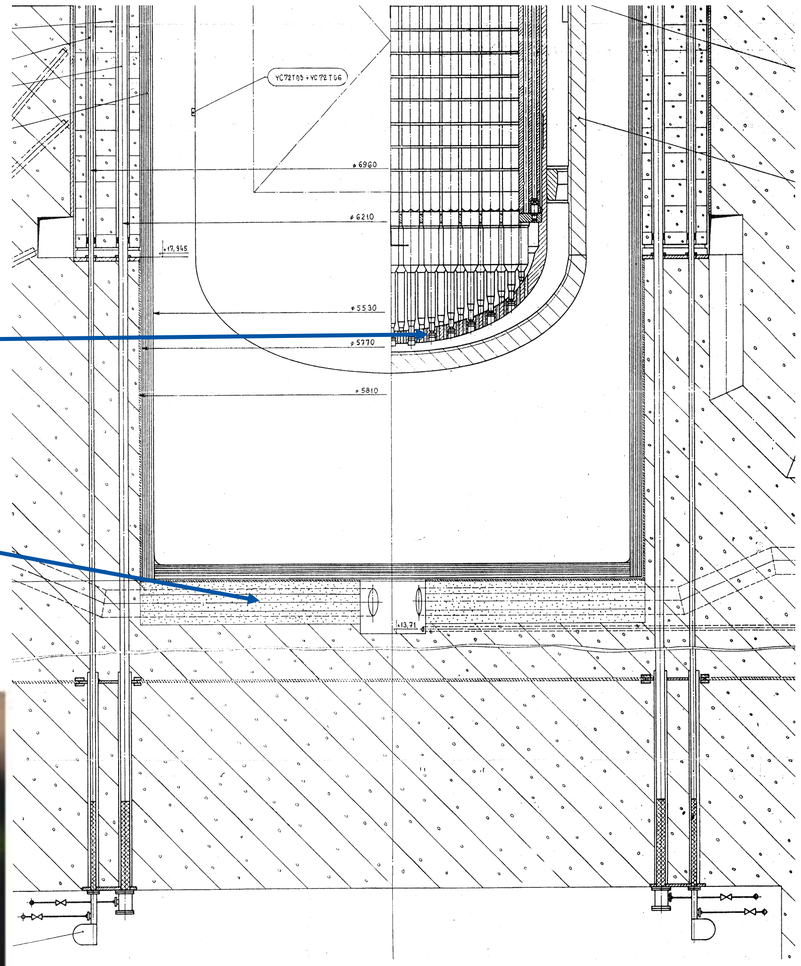

CORIUM ⇔ CORE BARREL

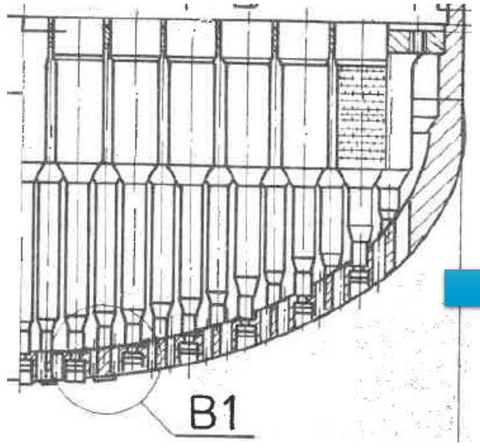

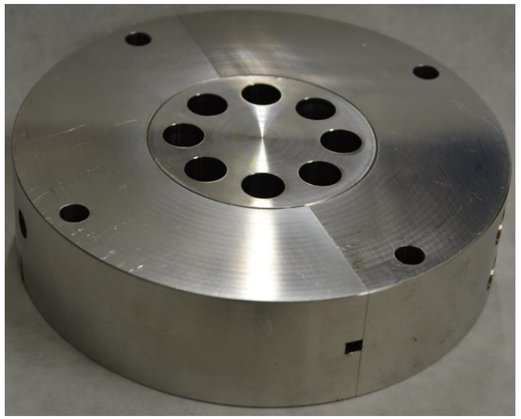



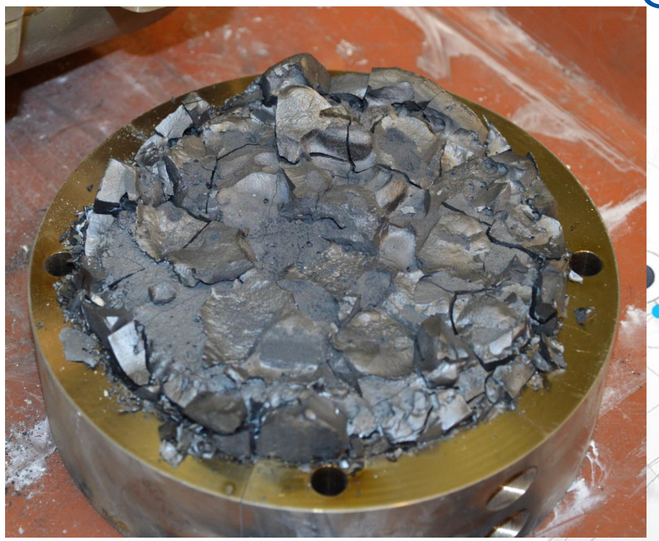





CORIUM ⇔ THERMAL SHIELD

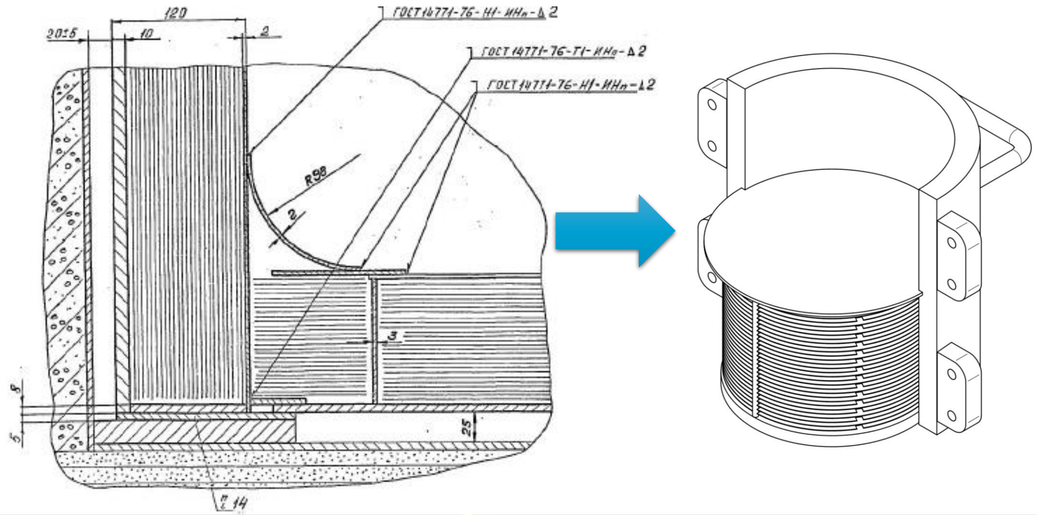

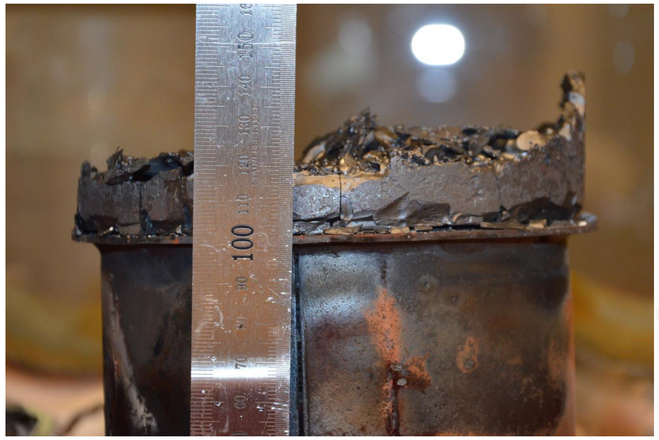





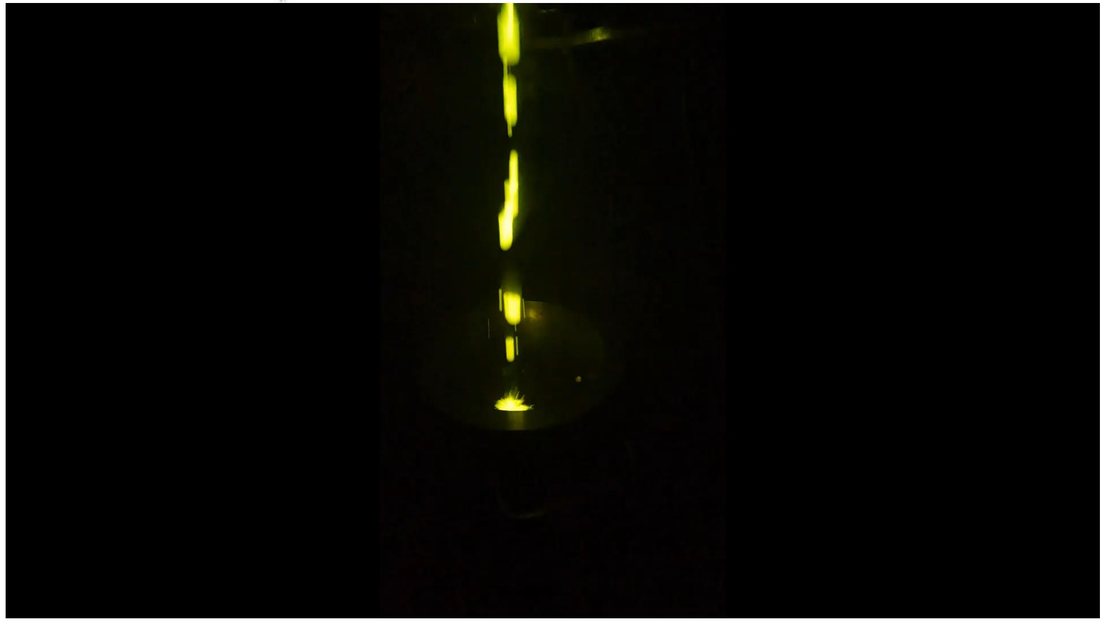



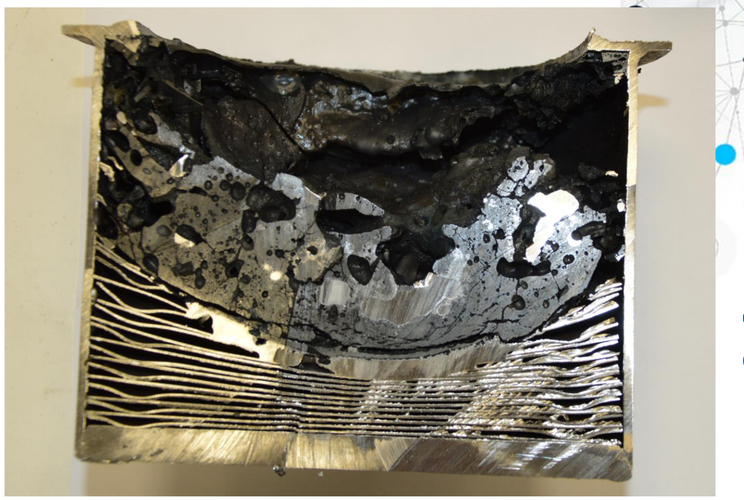

CONCLUSIONS

- As the IVMR strategy is not feasible (due to technical constraints) for the Temelin NPP (VVER-1000 reactor), and as the complementary SA measures currently being implemented, namely
  - IVR-IN and
  - FCVS,
- are not solely and undeniably assuring the maintenance of CTMT integrity,



- the investigation of the possibility of ExVC was launched, using both

1. analytical results
   - MELCOR => corium properties at the moment of RPV breach for 2 qualitatively different scenarios
   - MELTSPREAD => corium spread-ability on dry basemat/under water, varying the initial conditions
   - CORQUENCH => corium cool-ability on dry basemat/under water, varying the boundary conditions
2. experimental outcomes
   - OECD/NEA ROSAU => large-scale experiments (DCAM & MST)
   - Czech national CORIUM => corium properties & interactions with core barrel/thermal shield

Thank you for your attention!

ÚJV Řež, a. s.
Hlavní 130, Řež
250 68 Husinec, Czech Republic

e-mail: miroslav.kotouc@ujv.cz
www.ujv.cz

Skupina ÚJV
LIDÉ | INOVACE | TECHNOLOGIE

EXPERIMENT AND NUMERICAL SIMULATIONS ON SFR CORE-CATCHER SAFETY ANALYSIS AFTER RELOCATION OF CORIUM

B. Bigot[1], X. Gaus-Liu[2], R. Clavier[1], C. Journeau[3], F. Payot[5], T. Cron[2], P.E. Angeli[4], M. Peybernes[1] and B. Fluhrer[2] *

[1] : CEA, DES,IRESNE,SMTA,LMAG,
Cadarache – 13108 Saint Paul-lez-Durance - FRANCE
barbara.bigot@cea.fr; remi.clavier@cea.fr; mathieu.peybernes@cea.fr

[2] : Karlsruhe Institute of Technology (KIT)
Hermann-von-Helmholz-Platz 1, Eggenstein-Leopoldshafen, 76344 Germany
xiaoyang.gaus-liu@kit.edu; Thomas.cron@kit.edu; Beatrix.fluhrer@kit.edu

[3] : CEA, DES,IRESNE,SMTA,LEAG,
Cadarache – 13108 Saint Paul-lez-Durance - FRANCE
christophe.journeau@cea.fr

[4] : CEA, DES,ISAS,DM2S,STMF,LMSF,
Saclay – 91191 Gif-sur-Yvette cedex - FRANCE
pierre-emmanuel.angeli@cea.fr

[5] : CEA, DES,IRESNE,DER,DIR,
Cadarache – 13108 Saint Paul-lez-Durance - FRANCE
frederic.payot@cea.fr

ABSTRACT

In-vessel core catcher is a safety design feature of European type Sodium-Cooled Fast Reactor (ESFR) to guarantee the reactor integrity during a postulated core-melt accident. The core catcher has the function to collect the relocated melt derived from the upper core area and to prevent local thermal attack of melt on the reactor vessel. The thermodynamics of the melt with decay heat and its heat transfer at the core catcher boundaries will be studied experimentally at KIT and numerically at CEA.
A new large-scale 3D vessel, ESFR-LIVE, is built at KIT imitating the geometry of the core-catcher in a diameter scale of 1:6. The lower part of the vessel is a truncated cone and the upper part is a cylinder. All the vessel boundaries are enclosed in a water-cooled vessel and the melt surface was cooled by a cooling lid. The decay power is simulated by four planes of resistance heater with a total power up to 86 kW. The melt pool geometry can be variated by shifting the upper lid and/or crust-building at the bottom. Measurable parameters are bulk temperature and boundary temperature of the melt, 3D vessel wall temperatures and heat flux. The simulant of oxide melt is eutectic NaNO3-KNO3 mixture allowing operation temperature up to 400 °C. Results of similarity comparisons indicate that Ra of the experiment is comparable to the reactor case, thus the experiment can capture both general heat transfer characteristics and local heat transfer details.

* Footnote, if necessary, in Times New Roman font and font size 10

Two test series, LIVE-CC1 and LIVE-CC2, have been carried out in August and September 2021 respectively. The result analysis are under progress. In this article, a first computational Fluid Dynamics (CFD) post-test calculation with TrioCFD code is performed on the cylindrical configuration of the melt pool′, simulating the 3rd pool heating configuration of LIVE-CC1 test. A direct numerical simulation is run by using High Performance Computing on 64 million of mesh nodes on a quarter of geometry of the melt pool. A mesh resolution analysis is performed, followed by a study interpreting the melt velocity, temperature and heat fluxes. Experimental tests were carried out end of 2021 and the results analysis are under progress.

KEYWORDS
In-vessel melt retention, ESFR-LIVE, core catcher, experiment, numerical simulation

1. INTRODUCTION

The study bears one of the aim of EU H2020 ESFR-SMART project [1] to improve the understanding and provide quantitative estimation on the heat transfer of corium after relocation in a SFR-core catcher to ensure the safety criterial in the long term. Although many previous studies have been reported on the heat transfer behaviour on a cavity filled with corium and cooled at all boundaries, such as the study of the PWR/VVER in-vessel melt retention at the reactor lower head [2-5], the results of these studies cannot be transferred directly to the core-catcher heat transfer due to the difference in the geometry, which effects the turbulent flow extensively. Comparing to the reactor lower head in spherical or torispherical geometry, the corium pool in core catcher is very shallow, which has limited sidewall area for the heat transfer. For the overall heat transfer, understanding both the heat transfer coefficients at the upper surface and at the lateral wall are important, since the balance of the two heat rates influences the lateral heat flux. For the case of localized heat flux, critical hotspot on the vessel wall should be identified for the design of robust core-catcher wall structure. To provide reliable data to limit above uncertainties, a new facility with core-catcher cavity character is constructed at KIT and has been commissioned in the summer 2021. The results analysis are under progress. The new facility will provide local heat flux and the general heat transfer ratio of upper surface to sidewall, the bulk pool temperatures, pool boundary temperatures, wall inner surface and outer surface temperatures. The great advantage of the experiment is that the corium pool geometry and the pool height are variable, and the power input density is much higher than the earlier facility LIVE-3D [6]. This study provides the technique details of the facility, similarity analysis and three pre-test calculations. A numerical analysis is also presented as a first post-test calculation on a cylindrical geometry of the melting pool. A Computation Fluid Dynamic (CFD) using the TRIO-CFD code was performed by running a Direct Numerical Simulation (DNS) with 64 million of meshes nodes for a quarter of cylindrical geometry. A mesh resolution analysis was carried out due to an internal Rayleigh number value of $1.8 \cdot 10^{11}$. For this, the characteristic turbulent scales were investigated. Temperature and velocity fields are also presented as well as an evaluation of the heat fluxes distribution received by boundary surfaces.

2. TEST FACILITY

2.1. Test vessel and cooling system

The new-built ESFR- LIVE test vessel is integrated in the LIVE experimental platform [5] and is located at the same position as the former LIVE3D test, see Fig. 1. Besides the test vessel, the platform includes logistic of melt preparation, pouring and recycling, cooling water supply, power supply and control, and data acquisition system. An external heating furnace is used for the melt preparation, pouring, extraction and storage. The experiment begins generally with the melt pour from the heating furnace via a pouring spout into the test vessel and is terminated by melt extraction from the test vessel back to the heating furnace.

The ESFR-LIVE test vessel simulates the typical tray geometry of an in-vessel SFR core catcher, whose cavity has a geometry of truncated cone in the lower part, and cylinder in the upper part. The inner diameter of the upper cylinder is 1 m, and thus is in 1:6 length scale. The total height of the test vessel inner cavity is 0.38 m, and provides the flexibility of the pool height and the position of the cooling lid. The truncated cone is 0.08 m in height, thus corresponding to 1:1 scale of the prototype geometry. The inclined sidewall is 20° to the horizontal orientation. The test vessel is made stainless steel and in 0.015 m thickness. The external cooling of liquid Na is simulated by water in ground temperature. A cooling vessel encloses the test vessel and creates a cooling channel of 0.06 m in width. Cooling water flows in at the bottom and flows out at four outlets at the vessel upper edge. The flow rate is controlled to enable a certain difference between the water inlet and outlet temperature.

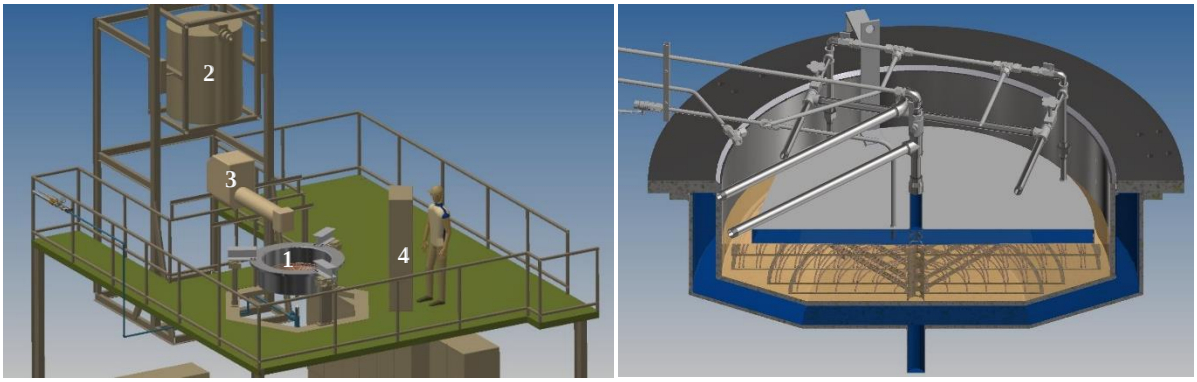

Figure 1: Left: LIVE experimental platform with ESFR-LIVE facility. 1- ESFR test vessel, 2 - heating furnace for melt preparation, 3 - pouring spout, 4 - instrumentation board. Right: ESFR-LIVE test vessel with all boundary cooling system.

The top surface of the vessel can be either cooled with a water-cooled lid or be insulated by covering an insulation lid, see Fig. 1. The upper cooling lid is a water-cooled container, which has four inlets at the periphery and one outlet at the central of the lid. The cooling lid position is flexible and can be placed from the bottom part of the cylindrical part upwards. The direct contact between the melt surface and the cooling lid is controlled regularly.

2.2. Heating system

Four planes of resistance heating element are designed to simulate the decay heat of the corium, which are named HE1 to HE4 from the bottom upwards, as shown in Fig. 2. Two planes are located in the truncated cone (HE1 and HE2) and the other two are located in the cylindrical part (HE3 and HE4). The upper two

heating planes can be removed individually to enable different pool heights at the top boundary. The total heating power can reach 86.5 kW. The cross diameter of the heating cable is 4 mm, and the cables are formed spirally with even distance. Some heating planes are in duplex winding to enable high power inputs. All the heating planes can be controlled individually and thus variations of the height of the truncated part is

The top surface of the vessel can be either cooled with a water-cooled lid or be insulated by covering an insulation lid, see Fig. 1. The upper cooling lid is a water-cooled container, which has four inlets at the periphery and one outlet at the central of the lid. The cooling lid position is flexible and can be placed from the bottom part of the cylindrical part upwards. The direct contact between the melt surface and the cooling lid is controlled regularly.

Four planes of resistance heating element are designed to simulate the decay heat of the corium, which are named HE1 to HE4 from the bottom upwards, as shown in Fig. 2. Two planes are located in the truncated cone (HE1 and HE2) and the other two are located in the cylindrical part (HE3 and HE4). The upper two heating planes can be removed individually to enable different pool heights at the top boundary. The total heating power can reach 86.5 kW. The cross diameter of the heating cable is 4 mm, and the cables are formed spirally with even distance. Some heating planes are in duplex winding to enable high power inputs. All the heating planes can be controlled individually and thus variations of the height of the truncated part is possible by shutdown the one or two of the lower heaters. Correspondingly, bottom crust grows upwards till the level of the lowest heater in operation.

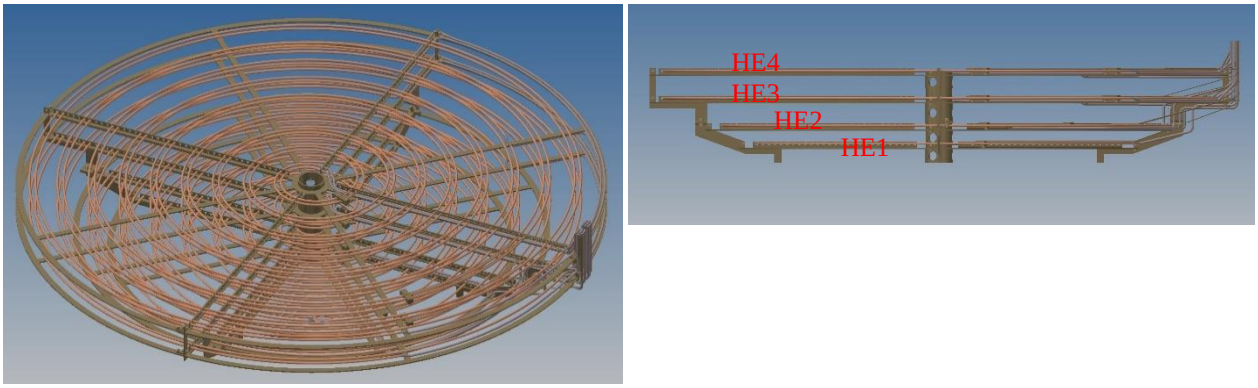

Figure 2: Heating system of ESFR-LIVE.

2.3. Instrumentations and simulant material

The instrumentation of the ESFR-LIVE includes:

- 44 pairs of thermocouples (TCs) measuring vessel wall inner temperature (IT) and outer surface temperature (OT) on 4 azimuth axils. At each axil 11 pairs TC are arranged in the order of 3 pairs at the bottom plate, 3 pairs at the truncated cone vessel wall and 5 pairs at the cylindrical vessel wall. Local heat fluxes can be obtained based on the temperature difference between a IT/OT pair at one position.
- 49 TCs measuring melt temperature (MT) are arranged in the angle of 45°, as shown in Fig. 3. The symmetrical arrangement of the MTs under the heating planes are used for the examination of the

symmetricity of 3-D thermo-hydraulics of the melt pool, and the additional MT planes and the wall-near TCs at azimuth 45° can provide more details of the crust positions.

- Instrumentation at the top cooling lid: three thermocouple trees (DCT) and four surface temperature TCs (DIT) are arranged at the bottom plate of the cooling lid to measure the interface temperature at the crust / lid and the top boundary temperature.
- Cooling water flow rate, inlet temperature and outlet temperature for the estimation of the integral waterside heat removal rate at the vessel wall and at the melt surface.
- Weight change of the vessel.
- Temperature upper limit control with automatic shutdown for all heaters.

The data signals are recorded with the Labview program of National Instruments. The simulant material of the corium melt is the eutectic NaNO3- KNO3 mixture with the melting temperature of 220 °C. The low melting temperature enables a large super heat range between 220 °C and 400 °C. In addition, its simple non-mushy-zone solidification character simplifies physical modelling.

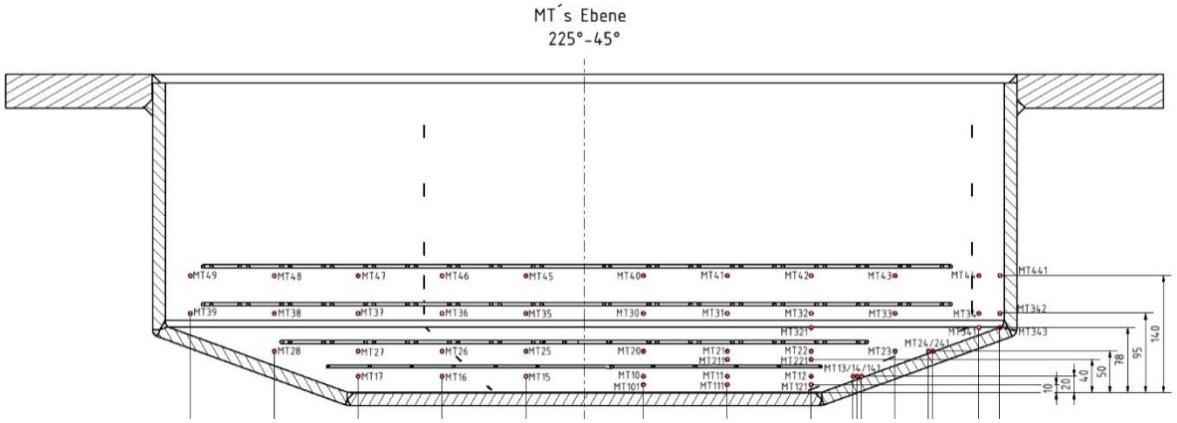

Figure 3: TC positions for melt temperature measurement.

3. TEST DEFINATION AND SIMILARITY ANALYSIS

Two test series are have been carried out in ESFR-LIVE: one series with a pool volume to the highest heater, the other series with the melt only filling the truncated cone part. In the first test series, LIVE-CC1, which is the object of this article, the lower part of melt pool geometry will be variated by shutdown the two lower heaters HE1 and HE2 one by one, as shown in Table 1. The liquid melt below the operating heaters will be solidified due to the bottom cooling and very low downward heat transfer rate. Several power levels will be performed for each of the pool geometry to obtain the heat transfer characteristic under a large range of Ra and heat flux.

Table 1 Test conditions in the test series LIVE-CC1.

Melt pool configuration	CC1-1	CC1-2	CC1-3
Heaters in operation	HE1 - HE4	HE2 - HE4	HE3 - HE4
Height in truncated cone part, m	0.08	0.05	0
Height in cylinder part, m	0.1	0.1	0.1

Total pool height, m	0.18	0.15	0.1
Number of power levels	4	3	2

The similarity of the geometry, thermophysical properties and thermodynamic of the ESFR-LIVE experiments are compared with the reactor case to verify the applicability of the experimental result. In Table 2 comparisons are given on the comparison in geometry, material properties and thermodynamic similarities. The thermodynamic parameters of ESFR-LIVE are estimated for the power of 67 kW in the case of CC1-1 (see Table 1). Three heat transfer calculation methods are carried out: a) applying external Ra number by suiting the boundary temperature, performed by KIT, b) applying internal Ra number by applying the power input density, performed by CEA and c) numerical calculation applying Tri-CFD and using a LES model, performed by CEA, which will be introduced in the following section. For the numerical results, only the lateral heat flux at the cylindrical wall. is shown here.
The corium in the reactor case is assumed as UO2 with the properties given by Kim [7] and Harding [8]. The properties of the eutectic nitrate melt are referred in [9] . The equations of external Ra number and internal Ra number are given in Eq. (1) and Eq. (2) respectively. The ESFR-LIVE melt pool has the same height as reactor corium pool. The radius/height aspect ratio of the experiment is 10 in ESFR-LIVE, which is large enough to neglect the lateral boundary effect on the upwards heat transfer. The thermodynamic similarity, characterised by both internal Ra and external Ra are in the same order as the reactor case. Three sets of heat flux are presented, which show the similar trend of heat flux ratio in top surface to lateral surface but in different values to some extent.
The heat transfer calculation undergoes certain uncertainty due to the selection of the Nu~Ra correlations. For the method a), which applies external Ra, the Globe & Dropkin correlation [10] in Eq. (3) is used for the upper surface heat transfer, and the Churchill & Chu correlation [11] in Eq. (4) is used is for the sidewall heat transfer. For the method b), whereas the internal Ra is applied, Steinberner and Reinecke Correlations [12] for a rectangular cavity with an aspect ratio A=1 are applied, as given in Eq. (5) and Eq. (6) for the upper and lower surfaces heat transfer and in Eq. (7) for sidewall heat transfer [13].

Table 2: Similarity studies and heat flux predictions.

	Reactor / Oxid melt	**ESFR-LIVE**	**Scale experiment/reactor**
Cavity geometry			
D, Diameter, m	6	1	1:6
Dh, Height /Characteristic length, m	0.18	0.18	1:18
A, Aspect ratio: diameter / height, -	60	10	1:6
Material properties			
ρ, Density, kg/ m³	8703 [7]	1747	0.2
μ, Dynamic viscosity, Pa·S	$4.035 \cdot 10^{-3}$ [7]	$3.102 \cdot 10^{-3}$	0.77
λ, Thermal conductivity, W/m/K	3.52 [7]	0.459	0.13
β, Thermal expansion rate, 1/K	$1.05 \cdot 10^{-4}$	$3.81 \cdot 10^{-4}$	3.65:1
Cp, Thermal capacity, J/kg/K	485 [8]	1492	3.08:1
Pr	0.556	10.092	18.2:1
Thermodynamics and Heat transfer			
Superheat, K	327	70	
Power input, kW	30711	67	0.002
Internal Ra	$3.37 \cdot 10^{11}$	$9.18 \cdot 10^{11}$	2.72

External Ra	$2.59 \cdot 10^9$	$2.50 \cdot 10^9$	0.97
q lat_ext. Ra, kW/m²	1330	36.9	0.028
q up ext. Ra, kW/ m²	729	24.8	0.034
q lat, int. Ra, kW/m²	842.3	28.4	
q up, int. Ra, kW/m²	$1 \cdot 10^3$	37.7	
q lo, int. Ra, kW/m²	110.5	3.4	

$$Ra_{ex} = Gr \cdot Pr = \frac{g\beta \Delta T L^3}{\alpha \nu}, \quad (1)$$

$$Ra_i = Gr \cdot Pr \cdot Da = \frac{g\beta \dot{q} L^5}{\alpha \lambda \nu}, \quad (2)$$

$$Nu_{up} = 0.069 Ra_{ex}^{1/3} Pr^{0.074}, \qquad Ra : 3 \cdot 10^5 - 7 \cdot 10^9;\ Pr: 0.02\text{-}8750, \quad (3)$$

$$Nu_{sd} = \left\{ 0.825 + \frac{0.387 Ra_{ex}^{\frac{1}{6}}}{\left[1+\left(\frac{0.492}{\mathrm{Pr}}\right)^{9/16}\right]^{\frac{8}{27}}} \right\}^2, \qquad Ra < 10^{12},\ all\ Pr \quad (4)$$

$$Nu_{up} = 0.345 Ra_i^{0.233}, \qquad Ra: 5 \cdot 10^{12} \sim 3 \cdot 10^{13},\ Pr \sim 7 \quad (5)$$

$$Nu_{lo} = 1.389 Ra_i^{0.095}, \qquad Ra: 5 \cdot 10^{12} \sim 3 \cdot 10^{13},\ Pr \sim 7 \quad (6)$$

$$Nu_{sd} = 0.85 Ra_i^{0.19}, \qquad Ra: 5 \cdot 10^{12} \sim 3 \cdot 10^{13},\ Pr \sim 7 \quad (7)$$

The applicability of the three methods on the heat transfer calculation of the corium in a SFR core catcher will therefore be assess with respect to the experiment result. All the methods show that the lateral heat flux is considerably higher than the top surface heat flux. However, due to the large area at the upper surface the upwards heat transfer will considerably contribute the overall heat removal, and reduce the bulk temperature, which in return reduces effectively the thermal load on the lateral wall.

4. NUMERICAL SIMULATION

For numerical study, cylindrical configuration of the melt pool of the ESFR-LIVE experiment facility is chosen corresponding to the CC1-3 pool configuration (height of 0.1m and radius of 0.5m) where only the HE3 and HE4 heaters are on (Fig.2 and 3, Table 1). For this configuration, the pool belo0w the cylindrical part (conic part) is frozen with the HE1 and HE2 heaters turned off and the internal power is equal to 44kW for a test phase of the experiment. Physical numerical conditions are close to the operating condition of the experiment.

4.1. Model description

Numerical simulation with the TrioCFD code [14] was used for the post-test calculation, by which the incompressible Navier-Stokes equation (in Eq. (8) and Eq. (9)), under Boussinesq approximation (in Eq. (10)), and the heat equation (in Eq. (11)) were solved.

$$\nabla \vec{v} = 0, \tag{8}$$

$$\rho_0 \left(\frac{\partial \vec{v}}{\partial t} + \vec{v}.\nabla \vec{v} \right) = -\nabla P + \mu \Delta \vec{v} + \rho \vec{g}, \tag{9}$$

$$\rho = \rho_0 (1 + \beta (T - T_0)), \tag{10}$$

$$\rho_0 C_p \left(\frac{\partial T}{\partial t} + \vec{v}.\nabla T \right) = \lambda \Delta T, \tag{11}$$

With the velocity $\vec{v}$, the temperature T, the pressure P and the gravity $\vec{g}$. The physical properties are defined in Table 2, and the reference density ρ_0 taken at the initial temperature T_0.
A direct numerical simulations (DNS) is performed on 64 million of mesh nodes (meshes sizes between 0.2 and 0.9 mm) on a quarter of geometry of the melt pool due to the high number. Calculation domain is composed of lower, upper and lateral physical surfaces, and symmetry faces I and II corresponding to the truncated cylinder as illustrated in Fig. 4.

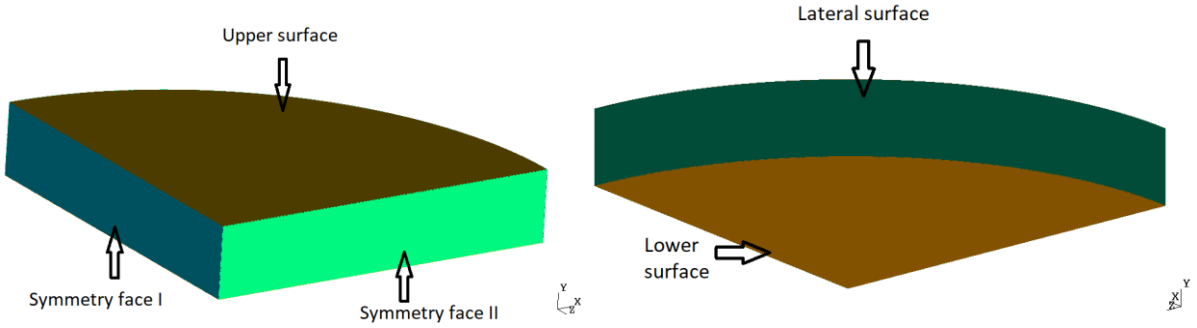

Figure 4: DNS calculation domain based on the quarter of the cylindrical upper part of the experimental device corresponding to a specific experimental phase of LIVE-CC1. "lower surface", "upper surface" and "lateral surface" are physical surfaces of melt pool. Symmetry faces I and II are virtual surfaces of the truncated cylinder section.

The fluid physical properties are presented in Table 2 with an initial temperature of 548K. In first approximation, these physical properties values kept constant during the calculations (low temperature amplitudes). The boundary temperature of the lower, upper and lateral surfaces is set to 495K (liquidus temperature of the eutectic mixture). No slip condition of the velocity field is imposed on these surfaces (e.g. fluid velocity is zero at these boundaries) and the fluid initially rest. For symmetry faces I and II, a

slipping symmetry boundary condition is imposed for the velocity and the thermal flux (adiabatic condition). A power of 11kW is set with a uniform spatial distribution (corresponding to the power of 44kW on the complete cylindrical configuration), and the internal Rayleigh number is equal to $1.3\cdot 10^{11}$. This internal power corresponds to a test phase of the experiment where the HE1 and HE2 heaters are turned off after having reached the maximum power phase of 67kW (four heaters on) on the total (cylindrical and conical) geometry.

In order to ensure that the meshing is sufficiently fine, a characteristic turbulence scales study is performed during the statistically stationary regime. Therefore, Kolmogorov, l_ν, and Batchelor, l_α, scales are investigated and express as:

$$l_\nu = \left(\frac{\nu^3}{\epsilon}\right)^{1/4}, \forall\, Pr, \tag{11}$$

$$l_\alpha = \left(\frac{\alpha^2\nu}{\epsilon}\right)^{1/4}, Pr > 1, \tag{12}$$

With, the kinematic viscosity $\nu = \mu/\rho$, the thermal diffusivity $\alpha = \lambda/\rho c_p$ and the turbulence dissipation rate $\epsilon = \nu\, \overline{\frac{\partial v_i'}{\partial x_k}\frac{\partial v_i'}{\partial x_k}}$ which is the mean square of the turbulent velocity gradient, $\frac{\partial v_i'}{\partial x_k}$, expressing the turbulence kinetic energy converted into thermal internal energy at the small scales. These scales characterize the spatial scales below the flow which becomes viscous or diffusive and thus efficiently dissipate kinetic or thermal energy. Ratios of the local Kolmogorov and Batchelor scales with the local meshes sizes are computed and illustrated in Fig 5 and Fig. 6 with a meshes numbers distribution and a cross section visualization of the computation domain. The ratios show that the meshes sizes are mainly lower than Kolmogorov scale (only 10 % of the meshes over the totally $64\cdot 10^6$ mesh nodes is not resolved with a ratio between 0.8 and 1) and are, however, larger than Batchelor scale with a ratio between 0.2 and 0.8. The region supporting the unresolved Kolmogorov and Batchelor scales are mainly the convective part of the domain. According to these observations, the DNS computation is relatively well resolved with regard to the Kolmogorov scale and is slightly under resolved with regard to the Batchelor scale, but nevertheless allows having suitable first post-test calculation results.

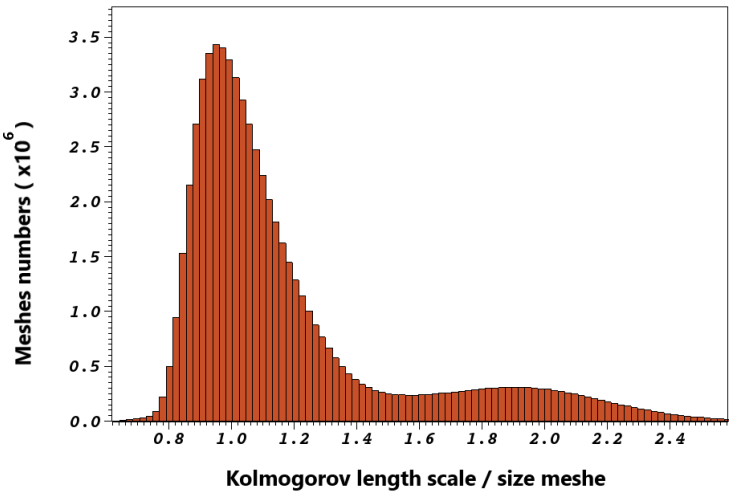

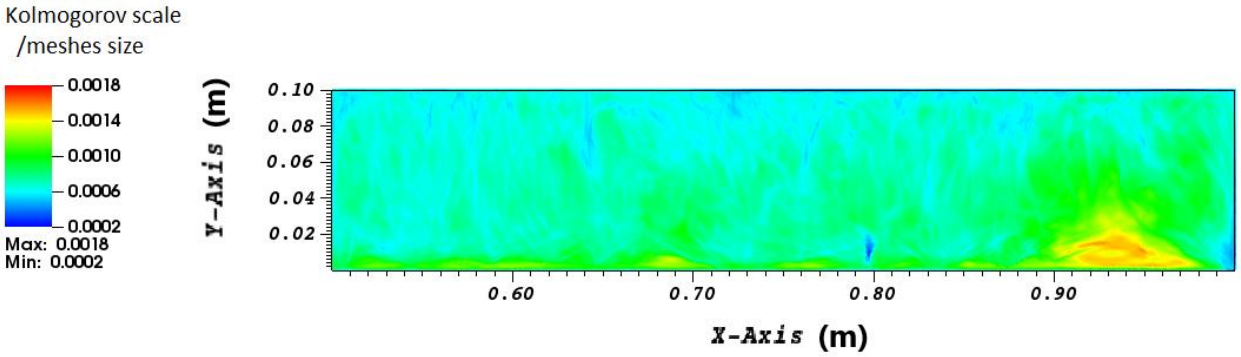

Figure 5: Ratio between local Kolmogorov scale and local meshes size: meshes number distribution (upper) and cross section of the computational domain (lower).

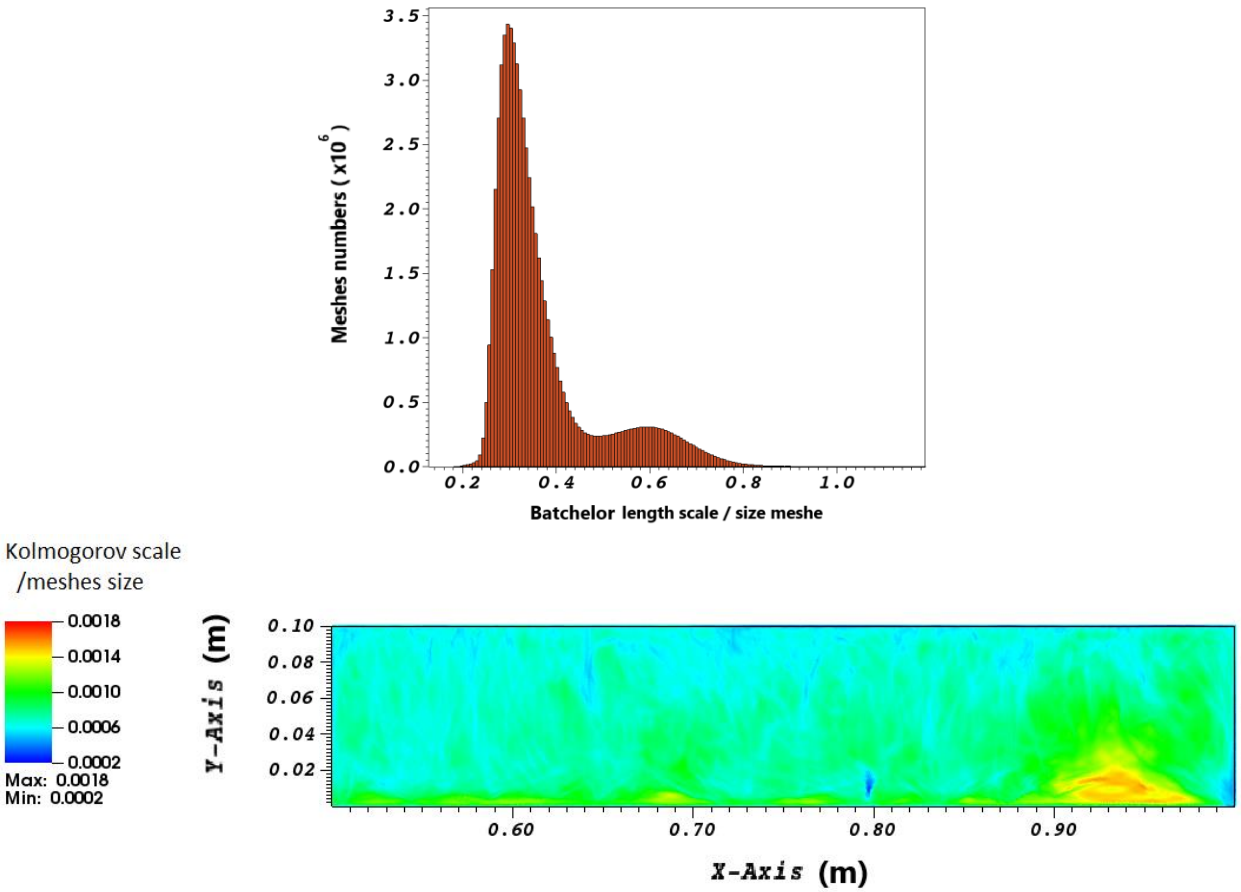

Figure 6: Ratio between local Batchelor scale and local meshes size: meshes number distribution (upper) and cross section of the computational domain (lower).

4.2. First post-test results of the numerical simulation

Fig. 7 shows the velocity and temperature fields in a statistically stationary regime and statistically averaged in this regime for a power of 11 kW (corresponding to 44kW for complete domain). Flow presents convective vortices characteristics to a natural Rayleigh-Bénard convection sustained by internal volumetric power density and with an external wall coolant. The temperature field presents a stratification with two distinct zones with a thin lower conductive region (corresponding to the low velocity region) with a temperature gradient and a stratification (as illustrated in Fig 9) and a larger upper region with uniform temperature (corresponding to the convective region). The minimal and maximal temperature are 495K (liquidus temperature) and 572K with a volume average temperature of 542K.

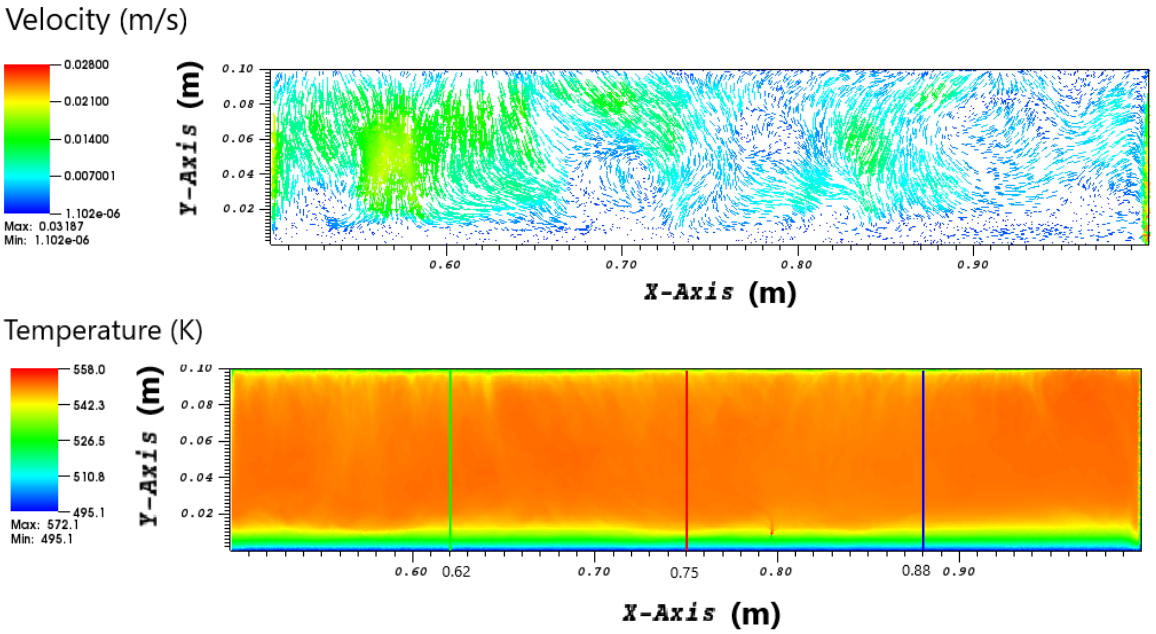

Figure 7: Cross-section of the velocity (top) and temperature (bottom) fields in the device during the statistically stationary regime and statistically averaged in this regime.

Fig. 8 presents three temperatures profiles similar plotted along the height (y-axis) of the calculation domain at the x-axis positions corresponding nearly to the quarter (x=0.62m), middle (x=0.75m) and three quarter (x=0.88m) of the domain length (the profile lines are drawn in the temperature fields of Fig. 7) . These profiles allow measuring the thickness of the conductive thin region which is around 2cm. The convective region (with uniform temperature) fills the rest of calculation domain with an observable upper thermal boundary layer.

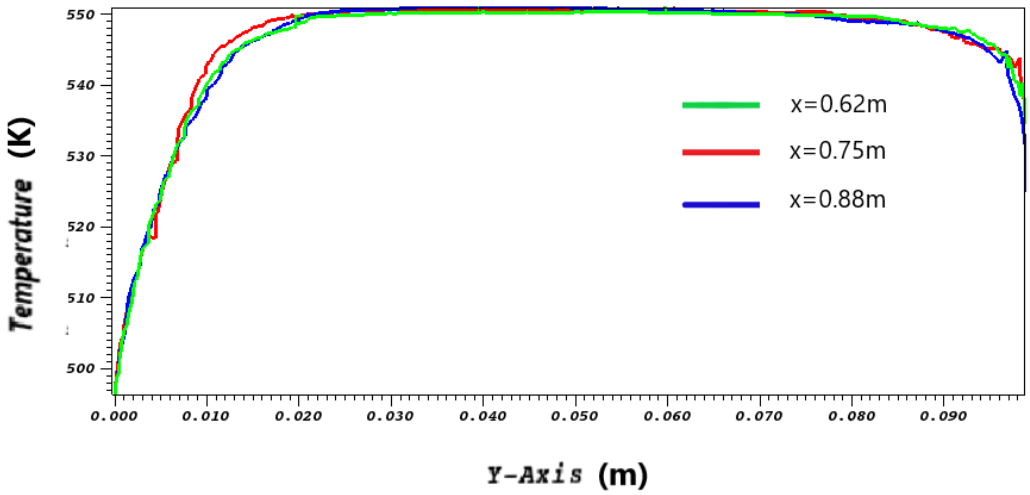

Figure 8: Temperature profiles along the height (y-axis) of calculation domain during the statistically stationary regime for 3 x-axis positions (0.62m, 0.75m and 0.88m) chosen along the domain length. Profile lines are depicted in temperature fields of Fig. 7.

Fig. 9 shows the instantaneous temperature field in a statistically stationary regime. The upper boundary is characterized by thermal plume instabilities as expected, and the interface between the convective and conductive region presents Kelvin-Helmholtz instabilities.

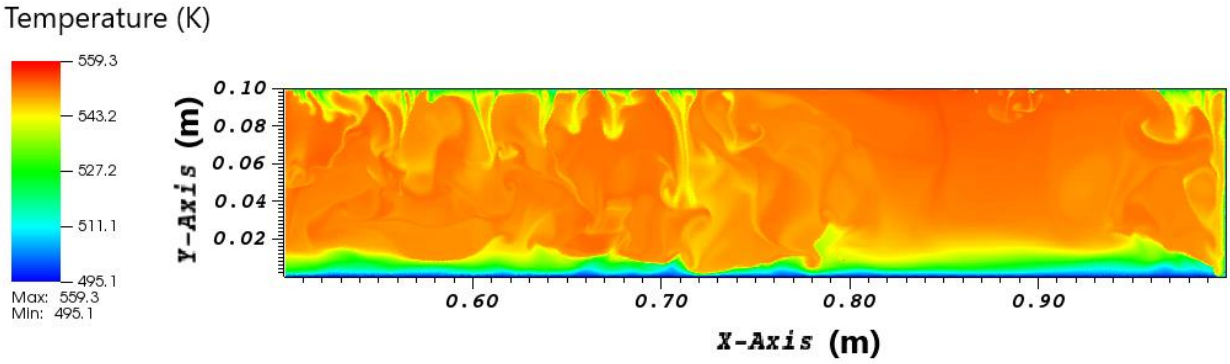

Figure 9 : Cross-section of the instantaneous temperature (bottom) fields in the device during the statistically stationary regime.

In order to estimate the thermal stress distribution on the device surfaces, the average heat rates and heat fluxes transferred to these interfaces were calculated during the statistically stationary regime and are presented in Table 4. The average heat rates distribution indicates that the upper surface supports three-quarter of the total heat rate (11kW) transferred to the surfaces with a value equals to 74 %. The lateral surface takes a significant flux close to 20%. Finally, the lower surface only receives 6%. As expected, the slipping boundary faces I and II (see Fig 4) do not receive any heat rate.

Table 3: Average heat rate (%), and heat flux (kW/m2) from the CFD calculation and the predictions (given by the Steinberner and Reinecke Correlations [12, 13] in Eq. (5), Eq. (6) and Eq. (7)) received by the upper, lower and lateral surfaces. For the CFD calculation, heat rates and heat fluxes are averaged during the stationary statistically regime for an internal power of 11kW (corresponding to 44kW on the complete cylindrical domain).

	« Lower » surface	« Upper » surface	« Lateral » surface
Heat rate from CFD (%)	6	74	20
Heat flux from CFD (kW/m^2)	3.4	41.4	27.03
Heat rate prediction (%)	8	69	23
Heat flux prediction (kW/m^2)	3.99	33.85	27.75

The upper, lower and sidewall heat fluxes are compared to the predictions given by the Steinberner and Reinecke Correlations [12, 13] (see Eq. (5), Eq. (6) and Eq. (7)). Here, the predictions are applied to a cylindrical geometry with an aspect ratio of 10 and an internal Rayleigh number of $1.3\cdot 10^{11}$. The mean temperature calculated during the stationary statistically regime is 550K leading to a superheat equal to 55K with a liquidus temperature of 495K. The results between the fluxes of the calculation and those of predictions are relatively in good agreement: Upper fluxes are larger than sidewall fluxes and lower fluxes are the weakest; sidewall and lower fluxes (between CFD calculation and correlation) values are very close; and an underestimation of around 20% for the upper flux is given by the prediction and explained by the different aspect ratios: experiment performed in rectangular cavity with an aspect ratio of 1 for the correlations, and simulation of a quarter cylinder with an aspect ratio of 10 for the CFD calculation. The comparison of the heat rates between CFD calculation and correlations shows close values with an overestimation (around 15%) of the lateral and lower heat rates and underestimation (7%) of the upper heat rate for the correlations predictions. These discrepancies are also explained by the different aspect ratios.

5. CONCLUSION

A new facility in form of a SFR- core catcher is built to provide reliable data for the understanding of heat transfer and ablation behaviour of a corium pool after its relocation in a SFR in-vessel core-catcher. The thermodynamic and material features of the experiment are very similar as those of an oxide corium pool. The flexible design and high power input enable a wide range of prediction. The paper presents the results of three pre-test calculations, which have shown similar trends but different values on the heat fluxes at the upper surface and lateral surface. Experimental results are expected to verify empirical correlations and validate the numerical study. Two series of experiments have been carried. The simulation results are currently being validated with the experimental results.
A first Computational Fluid Dynamics (CFD) post-test calculation with TrioCFD code was performed on the cylindrical configuration of the melt pool. A mesh resolution analysis were presented, followed by a study interpreting the melt velocity, temperature and heat fluxes distribution over the surfaces. Heat rates and fluxes predictions based on Steinberner and Reinecke correlations were calculated and compared to the heat rates and fluxes of the CFD calculation. The comparison is encouraging and shows a relative good agreement considering different aspect ratios between predictions and CFD calculation. DNS is a first step that allows calibrating a Large Eddy Simulation (LES) calculation on the complete cylindrical domain. This LES calculation is undergoing and will allow comparing, among other things, the heat flux distribution obtained with the DNS calculation and with the experiment test analyses.

ACKNOWLEDGMENTS

The experimental study is financially supported by the EU-H2020 Project ESFR-SMART with the Project Number 754501 and Germany federal government Helmholtz Society. The numerical work was granted access to the HPC resources of the CEA's Very Large Computing Centre (TGCC) under the allocation 2021 A0012A07691 made by GENCI.

REFERENCES

1. EU H2020 ESFR-SMART Project. Available from: http://esfr-smart.eu/.
2. T.G Theofanou,. and S. Angelini, "Natural convection for in-vessel retention at prototypic Rayleigh numbers", *Nuclear Engineering and Design*, **200**, pp. 1-9 (2000).
3. Bonnet, J.M. and J.M. Seiler, "Thermal Hydraulic Phenonena in Corium Pools: the BALI Experiment", in ICONE-7. Tokyo, Japan. p. ICONE-7057, (1999).
4. M. Helle, O. Kymäläinen, and H. Tuomisto, "Experimental COPO II data on natural convection in homogeneous and stratified pools*", in 9th International Topical Meeting on Nuclear Reactor Thermal Hydraulics* (NURETH-9), San Francisco, USA (1999).
5. X. Gaus-Liu, et al., "Core melt solidification characteristics in RPV lower head. Experimental results from live-tests", *in Proceedings of the 17th International.Conference.on Nuclear Engineering* (ICONE-17), Bruxelles, ICONE17-75450, (2009).
6. X. Gaus-Liu, et al., "LIVE L4 and LIVE L5L experiments on melt pool and crust behaviour in the RPV lower head", *in 14th International.Topical Meeting on Nuclear Reactor Thermalhydraulics* (NURETH-14), Proc.on CD-ROM NURETH14-26 Toronto, Canada, September 25-30, (2011).
7. W.K. Kim, J.H. Shim, and M. Kaviany, "Thermophysical properties of liquid UO 2, ZrO 2 and corium by molecular dynamics and predictive models", *Journal of Nuclear Materials, **491**,* pp. 126-137 (2017).
8. J.H. Harding, D.G. Martin, P.E. Potter, *Thermophysical and thermochimical properties of fast reactor materials*, European Comission (1989).
9. G.J. Janz, et al., "Physical properties data complications relevant to Energy storage II. Molten salts: Data on single and multi-component salt systems", in NSRDS-NBS 61, *Part II. National Bureau of Standards*, U.S. Department of Commerce: New Work, (1979).
10. S. Globe, and D. Dropkin, "Natural-Convection Heat Transfer in Liquids Confined by Two Horizontal Plates and Heated From Below", *Journal of Heat Transfer*, **81**, pp. 24-28, (1959).
11. S.W.Churchill, and H.H.S. Chu, "Correlating Equations for Laminar and Turbulent Free Convection from a Vertical Plate", *International Journal of Heat and Mass Transfer*, **18**, pp. 1323-1329, (1975).
12. U. Steinberner, and H.-H. Reinecke, "Turbulent buoyancy convection heat transfer with internal heat sources, ", *in 6th International Hear Transfer Conference,* Toronto, Canada (1978)
13. R.R. Nourgaliev, T.N. Dinh, and B.R. Sehgal, "Effect of fluid Prandtl number on heat transfer characteristics in internally heated liquid pools with Rayleigh numbers up to 10^{12}", *Nuclear Engineering and Design*, **169**(1), pp. 165-184, (1997).
14. Code TrioCFD, CEA. Available from: http://www-trio-u.cea.fr.

Experiment and Numerical Simulation on Long-Term Ablation of SFR Core-Catcher

FROM RESEARCH TO INDUSTRY

B. Bigot, R. Clavier, C. Journeau, F. Payot (CEA,DES,IRESNE)
X. Gaus Liu, T. Cron, B. Fluhrer (KIT)
P.E. Angeli (CEA,DES, ISAS) , M. Peybernes (EPFL)

IRESNE I DTN I SMTA I LMAG

Research Institute for Nuclear Systems for Low Carbon Energy Production

ERMSAR 2022

Core-Catcher design for ESFR reactor

IRESNE | DTN | SMTA | LMAG

Research Institute for Nuclear Systems for Low Carbon Energy Production

French Alternative Energies and Atomic Energy Commission - www.cea.fr

ESFR Core Catcher design ► Context

- Core-catcher (CC) design for european SFR surrounded by Na cooling system
- Safety device : recovering corium (discharging tubes) during a core-melting accident to guarantee the integrity of the SFR
- Geometry : truncated cone under a cylinder with a diameter of 10m

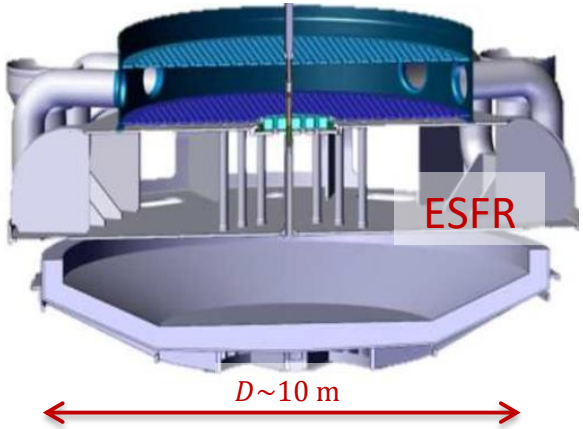

- Corium (oxide) pool :
  - $Ra_i \sim 3 \times 10^{11}$ (moderately turbulent), $\mathrm{Pr} \sim 0.56$ (diffusive effects > viscous effects), $\epsilon \sim 10$
  - surrounded by crust (at the walls) and heated by residual power density due to fission products
- Needs to better understand the thermal load of the corium to evaluate the CC sturdiness
- A new experimental facility, LIVE-ESFR, carried out at KIT and numerical simulations performed in CEA within the ESFR-SMART European project
  -> thermalhydraulic study to characterize heat transfer (to the walls) and optimize the CC design

Document owned by the CEA - Reproduction and distribution outside the CEA subject to the issuer's authorization

Experimental approach: the LIVE-ESFR program

IRESNE* I *DTN* I *SMTA* I *LMAG

Research Institute for Nuclear Systems for Low Carbon Energy Production

French Alternative Energies and Atomic Energy Commission - www.cea.fr

LIVE-ESFR program ► Objectives & overview

- Geometry of the ESFR CC
  - 3D experimental device
  - 1:10 scale in diameter : 1 m external diameter vs ~10 m for the reactor case
  - 1:1 scale in height : 20 cm, representative of the oxide melt
  - Conic part inclination: $\theta = 20°$

- Simulant material :
  - Eutectic mixture KNO_3-$NaNO_3$

- Water cooling system surrounding the pool

- Simulant material pool:
  - $Ra_i \sim 10^{8-12}$, $Pr \sim 10$ et $\epsilon \geq 5$
    vs $Ra_i \sim 3 \times 10^{11}$, $\mathrm{Pr} \sim 0.56$, $\epsilon \sim 10$ for the reactor case
    → Ra_i & ϵ : representative of the oxide pool
    → Pr : dissipative / viscous effects inverted

- Expected results
  - Melt temperature
  - Crust position
  - Heat flux at wall
  - Heat rate through sidewall, from external waterside and from top water side

→ Nu ~ Ra_i heat flux correlations

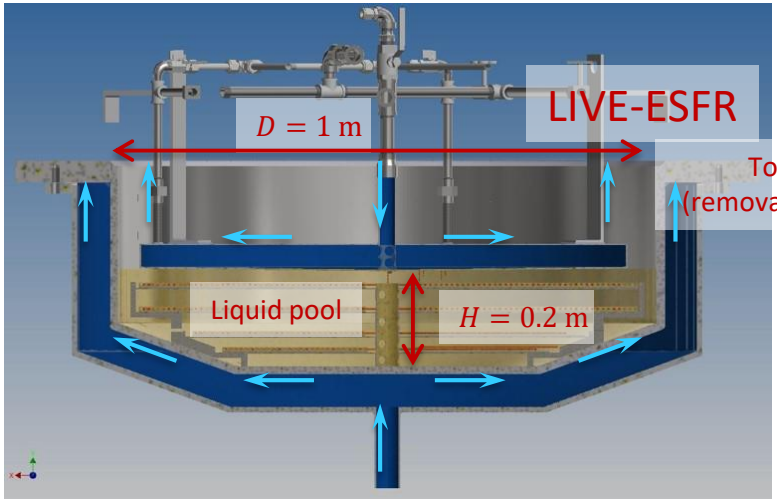

Document owned by the CEA - Reproduction and distribution outside the CEA subject to the issuer's authorization

Heating system

- Electric heaters distributed into the pool to simulate the decay heat

Heating plane	HE1	HE2	HE3	HE4
H [mm]	30	60	105	160
P_{max} [kW]	10.27	39.47	40.81	22.34

- HE3 and HE4 can be removed, each heater may be operated or disabled separately

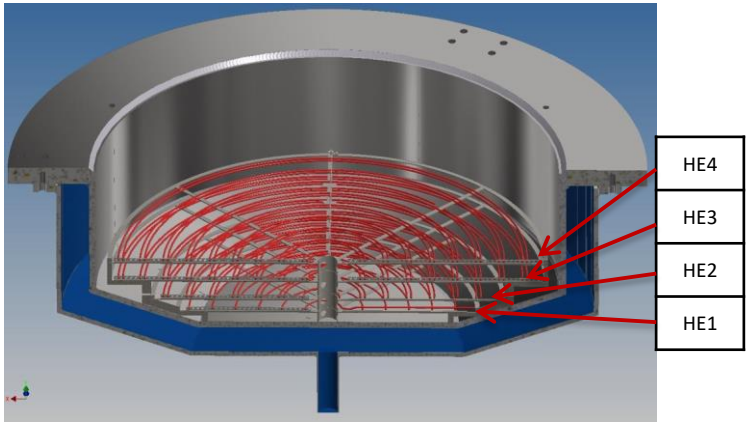

Document owned by the CEA - Reproduction and distribution outside the CEA subject to the issuer's authorization

Boundary conditions

- Water cooling at the bottom and in the (removable) top lid
  - Crust on all boundaries if the top cooling lid is used
  - Free upper surface if the top cooling lid is not used

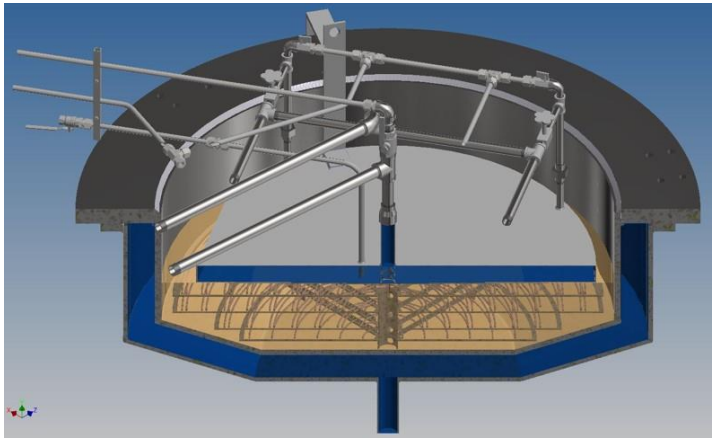

Melt with top lid → upper crust

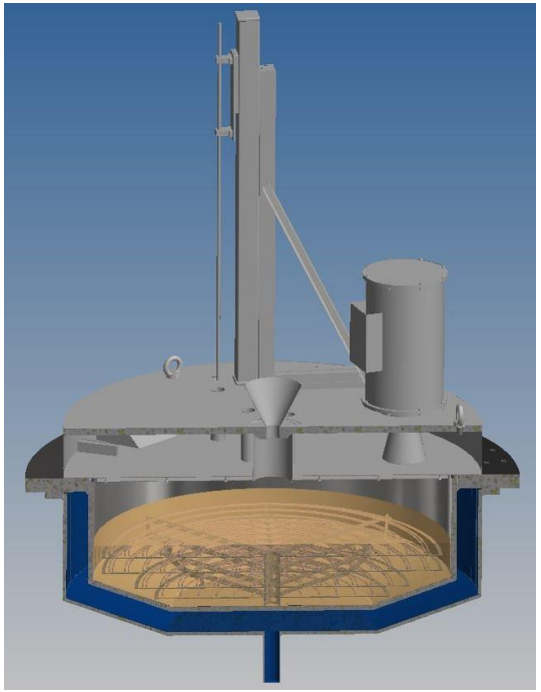

Melt without top lid
→ free upper surface

Document owned by the CEA - Reproduction and distribution outside the CEA subject to the issuer's authorization

CC1 test : Experimental configurations

Main phases	Sub-phases	Heaters in operation	P (kW) / $\dot{q}$ (kW/m³)
Phase 0 (melt pour)		*HE1. HE2. HE3. HE4 after melt pour*	*67kW after melt pour*
Phase 1	1a	HE1, HE2, HE3, HE4	67 /569
	1b	HE1, HE2, HE3, HE4	50 /425
	1c	HE1, HE2, HE3, HE4	20 /170
	1d	HE1, HE2, HE3, HE4	67 /569
	1e	HE1, HE2, HE3, HE4	35 /297
Phase 2	2a	HE2, HE3, HE4	32 /296
	2b	HE2, HE3, HE4	65 / 620
	2c	HE2, HE3, HE4	46 /426
Phase 3	3a	HE3, HE4	36 / 458
	3b	HE3, HE4	44 /560
	3c	HE3, HE4	28 /357
	3d	HE3, HE4	22 /280
Phase 4 (End)		*HE1, HE2, HE3, HE4*	*variable*

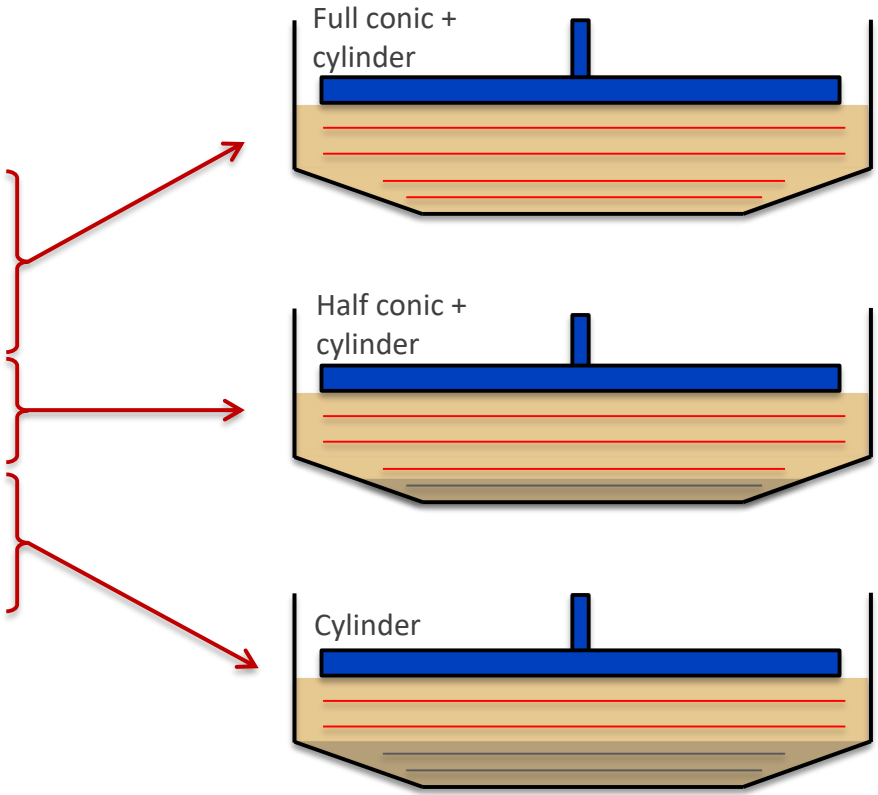

Document owned by the CEA - Reproduction and distribution outside the CEA subject to the issuer's authorization



CFD approach: numerical simulations with TRIOCFD of homogeneous pool in turbulent natural convection

IRESNE I DTN I SMTA I LMAG

Research Institute for Nuclear Systems for Low Carbon Energy Production

First numerical post-test

- CC1 tests phase 3b

Main phases	Sub-phases	Heaters in operation	P (kW) / $\dot{q}$ (kW/m³)
Phase 1	1a	HE1, HE2, HE3, HE4	67 /569
	1b	HE1, HE2, HE3, HE4	50 /425
	1c	HE1, HE2, HE3, HE4	20 /170
	1d	HE1, HE2, HE3, HE4	67 /569
	1e	HE1, HE2, HE3, HE4	35 /297
Phase 2	2a	HE2, HE3, HE4	32 /296
	2b	HE2, HE3, HE4	65 / 620
	2c	HE2, HE3, HE4	46 /426
Phase 3	3a	HE3, HE4	36 / 458
	3b	HE3, HE4	44 /560
	3c	HE3, HE4	28 /357
	3d	HE3, HE4	22 /280

Numerical set up

- Direct Numerical Simulation
- Incompressible Navier-Stokes (Boussinesq approx.) and heat equations
- Simulant material physical properties
- Calculation domain : quarter cylinder
- $\dot{q} = 560\ kW/m^3 \longleftrightarrow$ P= $11kW$
  - → Uniform power density
- $Ra_i = 1.3 \times 10^{11}$, $Pr = 10$, $\epsilon = 10$,

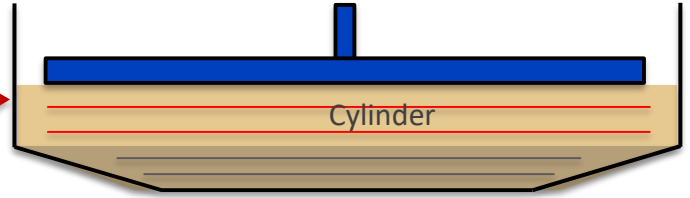

Document owned by the CEA - Reproduction and distribution outside the CEA subject to the issuer's authorization

CFD simulation ► calculation domain

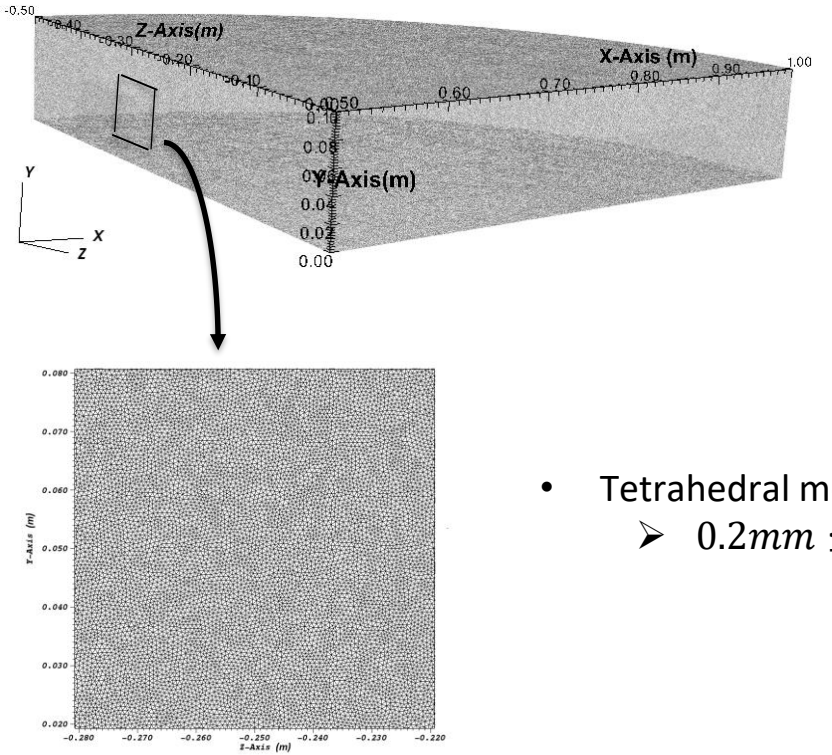

- Calculation domain : quarter cylinder
  - ➢ Partial geometry due to calculation time cost
- Phase 3b test dimensions :
  - 10cm thick,
  - 1m in diameter

- Tetrahedral meshing over 64 million of meshes
  - ➢ $0.2mm \leq \Delta x \leq 0.9mm$

Document owned by the CEA - Reproduction and distribution outside the CEA subject to the issuer's authorization

CFD simulation ► Boundary and initial conditions

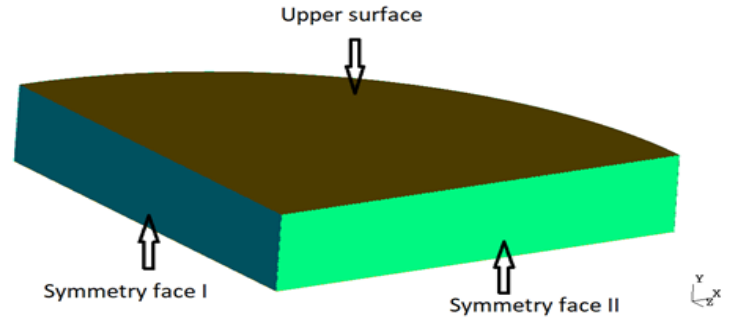

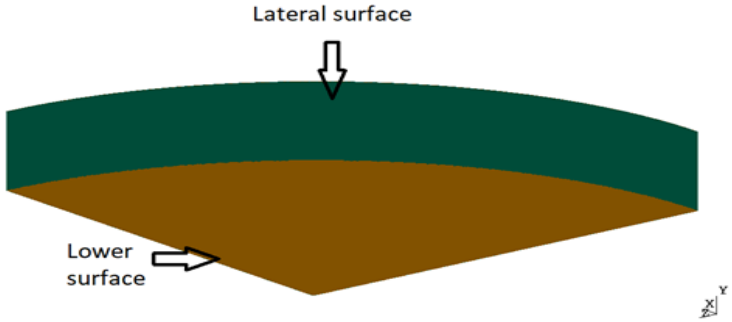

- Physical boundary surfaces :
  - liquidus temperature (495K)
    - ➢ no crust modelling (next step)
  - no slip condition
- Virtual “symmetry” faces
  - Adiabtic and no slip conditions
- Fluid initially in rest with uniform temperature
  - 548 K : a few degrees below the average measured temperature for phase 3b

Document owned by the CEA - Reproduction and distribution outside the CEA subject to the issuer's authorization

Small scales of turbulent flow :

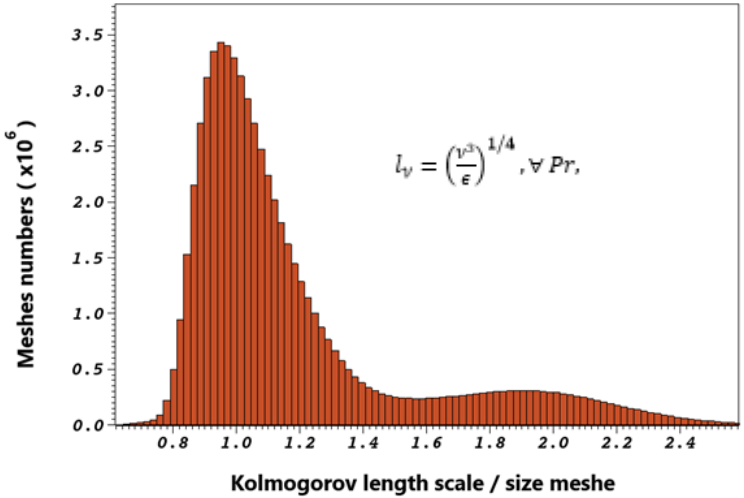

- Kolmogorov viscous scales :
  - 90% meshes resolved :

$$0.6 \leq \frac{\ell_K}{\Delta x} \leq 2.6$$

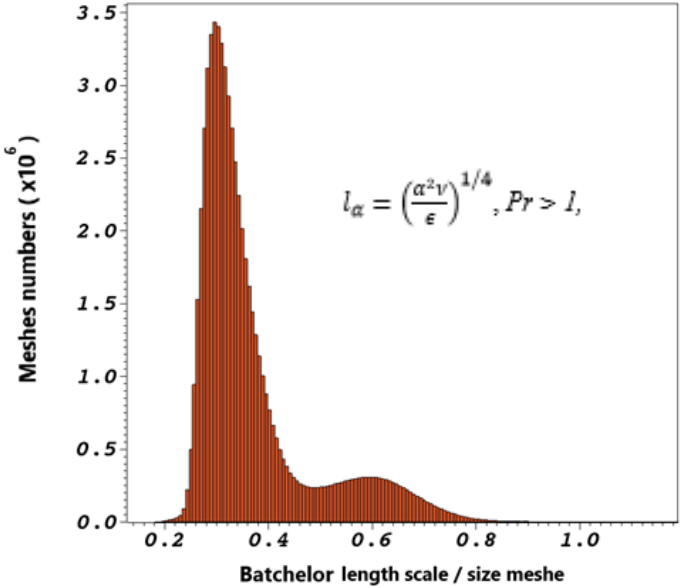

- Batchelor thermal scales:
  - Meshes slightly under resolved :

$$0.2 \leq \frac{\ell_B}{\Delta x} \leq 0.8$$

→ <u>Suitable calculation !?</u>

Document owned by the CEA - Reproduction and distribution outside the CEA subject to the issuer's authorization

CFD simulation ► results : Temperature & velocity fields snapshots at steady state

- Horizontal slice at :

Temperature

y = 0.5cm

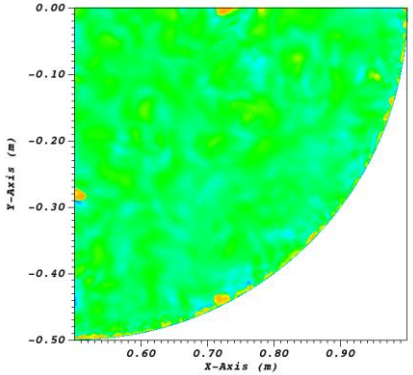

y = 5cm

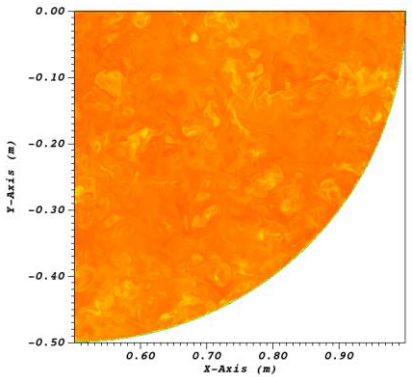

y = 9.5cm

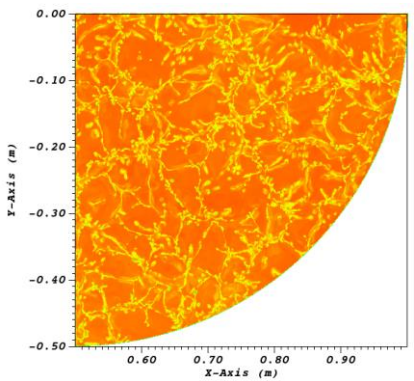

Velocity

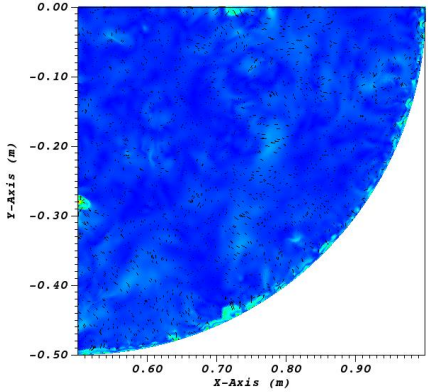

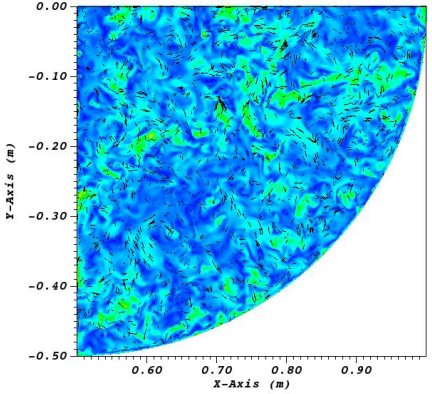

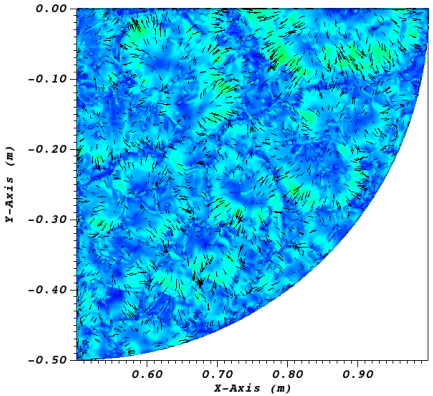

- 3D temperature field :

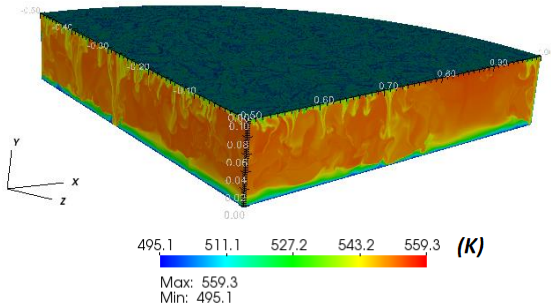

- Slice of velocity field at azimut 60°:

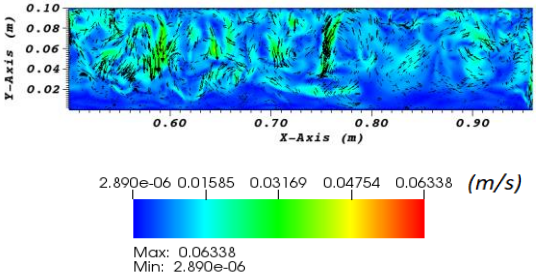

Document owned by the CEA - Reproduction and distribution outside the CEA subject to the issuer's authorization

Average velocity and temperature fields at steady state (at azimut 45°)

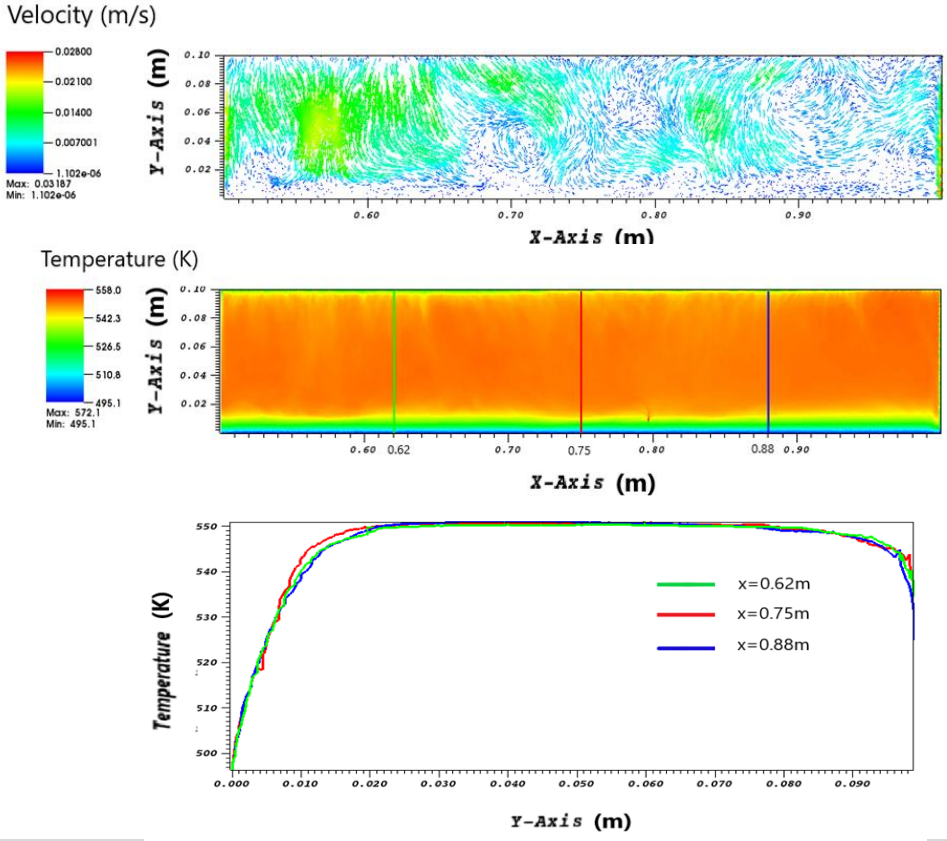

- Large upper convective region (80% of height)
  - vortex structures of natural convection
  - uniform temperature field
- Thin lower conductive region
  - weak velocity field
  - Temperature gradient (stratification)
- Lateral boundary layer with large downward velocity due to fluid cooling
- Upper thermal boundary layer

Document owned by the CEA - Reproduction and distribution outside the CEA subject to the issuer's authorization

Thermal distribution on the device surfaces compared to literature prediction

	« Lower » surface	« Upper » surface	« Lateral » surface
Heat rate from CFD (%)	6	74	20
Heat flux from CFD (kW/m^2)	3.4	41.4	27.03
Heat rate prediction (%)	8	69	23
Heat flux prediction (kW/m^2)	3.99	33.85	27.75

- CFD : upper and lateral surfaces support 75% and 20% of total heat rate
- Heat predictions based on Steinberner & Reinecke correlations (1978) for rectangular cavity with $\epsilon = 1$
- Good agreement and encouraging comparison between CFD results and predictions considering different ϵ (~10 for CFD calculation):
  - Close values for lateral surface
  - Main difference for upper surface explained by different values of ϵ
- Next step : results of LES calculation (already done) to compare to “1/4” DNS results and experiment results

Document owned by the CEA - Reproduction and distribution outside the CEA subject to the issuer's authorization

Prospects

Summary & Prospects

LIVE-ESFR experiments

✓ CC1 and CC2 tests (ESFR-SMART project) were carried out in August & November 2021

- CC1 and CC2 tests analysis at KIT (under progress)
  - Heat flux profiles : side, bottom and top, for all power plateaus and all configurations
  - Nu ~ Ra_i correlations

CFD calculation

✓ Performing a 3D DNS over partial geometry for the CC1 phase 3b:
  - ✓ Characteristic flows (velocity and temperature) of the natural convection within wall-cooled pool were observed as expected with some specificity of cylindrical configuration
  - ✓ Heat flux calculation and comparison to the predictions with a good agreement

- Complete the analysis of CC1 phase 3b test with LES calculation and compute heat predictions
- Post-test calculation of CC2 with a truncated cone configuration
- Calculation with physical properties of an homogeneous oxide pool (Pr <0.5)
- Modeling of melting/solidification front to take into account a crust at walls (mid term)

Document owned by the CEA - Reproduction and distribution outside the CEA subject to the issuer's authorization



FROM RESEARCH TO INDUSTRY

IRESNE** I **DTN** I **SMTA** I **LMAG

Research Institute for Nuclear Systems for Low Carbon Energy Production

French Alternative Energies and Atomic Energy Commission - www.cea.fr

The 10th European Review Meeting on Severe Accidents Research

Severe Accident Research Eleven Years after the Fukushima Accident

May 16-19, 2022, Karlsruhe, Germany

Technical Session 4-1: Severe Accident Scenarios in Innovative Systems

Chairs: H. U. Rehman (IAEA), F. Rocchi (ENEA)

ID338	**Analysis of BDBA sequences in a generic IRIS reactor using ASTEC code** P. Maccari (ENEA)	**Paper** **Presentation**
ID276	**Severe Accident Analysis Research at CNL for Small Modular and Advanced Reactor Designs** A. Morreale (CNL)	**Paper** **Presentation**
ID304	**MELCOR Integrated Severe Accident Code Scoping Uncertainty Study of Heat Pipe Reactor Accident Progression** D. Luxat (SNL)	**Presentation**
ID305	**MELCOR Integrated Severe Accident Code Demonstration Uncertainty Study of High-Temperature Gas-cooled Reactor Accident Progression** D. Luxat (SNL)	**Presentation**

Analysis of BDBA sequences in a generic IRIS reactor using ASTEC code

Pietro Maccari
ENEA, Italy
pietro.maccari@enea.it

Giuseppe Agnello
ENEA, Italy
Università degli Studi di Palermo, Italy
giuseppe.agnello04@unipa.it

Fulvio Mascari
ENEA, Italy
fulvio.mascari@enea.it

Stefano Ederli
ENEA, Italy
stefano.ederli@enea.it

ABSTRACT

Integral Severe Accident (SA) codes are aimed at providing an exhaustive coverage of all the main phenomena taking place in a core melt accident. Today, these deterministic codes have reached a high level of maturity for the simulation of operating reactors and the nuclear technical community is starting to extend their applicability to advanced reactor designs, as Small Modular Reactor (SMR). In the framework of the NUGENIA TA-2 ASCOM (ASTEC COMmunity) collaborative project, a generic input-deck based on the IRIS design has been developed for the ASTEC code. The generic SMR ASTEC model has been already proved able to simulate the main thermal-hydraulic phenomena driving the passive mitigation of a SBLOCA in Design Basis Accident (DBA) conditions. The same initiator event, regarding the guillotine break of a Direct Vessel Injection (DVI) line, will be assumed for the simulation of beyond-design scenarios by considering the unavailability of selected passive safety systems. The results of the ASTEC simulations of four Beyond Design Basis Accidents (BDBAs) (study carried out with ASTEC V2.2, IRSN all rights reserved, [2021]) will be analyzed and discussed against the reference DBA sequence in the present paper. This study is aimed at proving the first insights about the capability of the ASTEC model of a generic IRIS reactor to be used in BDBA and in SA analyses, if significant core degradation takes place. In addition, it characterizes the role played by each safety system in SMR passive mitigation strategy and give the possibility to characterize the phenomenologies specific of SMR designs.

KEYWORDS
SMR, BDBA sequence, passive safety systems, SA, SA code

1. INTRODUCTION

The international nuclear technical community, taking into account the experience of operating Light Water (LW) fission Nuclear Power Plants (NPPs), in the last decades started to develop advanced reactors, designed to improve the safety features, the economic efficiency and to reduce the capital costs [1]. Many new advanced reactors design adopt passive mitigation strategies based on natural circulation for the removal of the core power during accidental transient conditions, or even in nominal operation [2,3]. In this framework, advanced Small Modular Reactors (SMRs), using passive safety systems, are particularly interesting because of the potential economic and safety advantages [4]. SMRs are usually classified as reactors having a maximum power output of 300 MWe [4] that, in relation to the safety, it determines a lower decay power to be removed in postulated accidental scenarios. LW SMRs, using passive mitigation strategies, are in general characterized by common features with the current operating large-LWR and by other specific features typical of their evolutionary designs, providing inherent safety advantages that reinforce the first three levels of the Defence-in-Depth (DiD) principle. In this view, integral Severe Accident (SA) codes, such as ASTEC [5,6], MELCOR [7], etc., developed for the simulation of operating reactors, have reached a high level of maturity and, today, the international nuclear technical community is starting to analyze their applicability to advanced designs. In particular, in order to apply a SA code for the design of accident management's strategy in SMR or for a safety review process, the code simulation capabilities should be tested for integral configurations, compact containments and the passive mitigation strategy of a SMRs. In the framework of the NUGENIA TA-2 ASCOM (ASTEC COMmunity) collaborative project [8,9], coordinated by IRSN, a generic input-deck based on the IRIS (International Reactor Innovative and Secure) design [10,11] has been developed with the SA code ASTEC V2. The generic IRIS nodalization was proved able to simulate the main thermal-hydraulic phenomena driving the passive mitigation of a Small Break Loss of Coolant Accident (SBLOCA) in DBA conditions [12]. The application of a SA code to simulate a SMR design in BDBA and core degradation conditions could lead to valuable conclusions regarding the capability of the code to simulate the main thermal-hydraulic and core degradation phenomena in integral configuration and in smaller containment (characterized by a reduced containment-volume/core-power ratio compared to large-LWR). Besides this purpose, the simulation of BDBAs add valuable information regarding the role played by each passive system in the mitigation strategy with respect to the DBA sequence. In the present work, the generic ASTEC nodalization of the IRIS reactor has been used for the development of four BDBA scenarios. The four scenarios have been postulated in view of providing the first insights about the capability of the ASTEC model of a generic IRIS reactor to be used in BDBA and in SA analyses, to characterizes the role played by each safety system in SMR passive mitigation strategy and give the possibility to characterize the phenomenologies specific of SMR designs. The ASTEC simulations results have been analyzed and discussed against the reference DBA simulation.

2. DESCRIPTION OF IRIS-LIKE REACTOR DESIGN

IRIS is an integral, modular, medium power (300 MWe) Pressurized Water Reactor (PWR), developed by an international consortium led by Westinghouse and involving several Universities, companies and organizations [13,14]. The SMR design consists of a Reactor Pressure Vessel (RPV) which includes all the reactor Primary Coolant System (PCS) components: the reactor core, the Pressurizer (PRZ), Control Rod Drive Mechanism (CRDM), Steam Generators (SG), primary coolant pumps. The integral arrangement of the PCS layout avoids high pressure components outside the RPV and large primary vessel penetration, eliminating the possibility of Large Break LOCAs (LBLOCAs) and reducing the number of possible SBLOCAs (safety by design concept) [15-17]. As shown in Figure 1, the reactor core locates in the bottom part of the RPV and the PRZ is integrated in the upper head. The primary coolant coming from the core outlet, flows upward through the inner riser channel and reaches the top part of the circuit. The RPV of IRIS is placed in a spherical containment, as shown in Figure 2, in which most of the passive safety systems are located. The spherical containment is itself part of the passive safety approach, and in case of LOCA is directly involved in the mitigation strategy [15]. The reactor passive safety systems includes: an Emergency

Heat Removal System (EHRS) consisting of 4 independent trains working in natural circulation, each of which is connected to a pair of the 8 SGs; 3 trains of an Automatic Depressurization System (ADS), on the head of the RPV, dumping steam in the pool of the same Quench Tank (QT) which is located in the Drywell (DW); 2 Emergency Boration Tanks (EBTs), to inject water for gravity; two bigger tanks as Long term Gravity Make-up System (LGMS); 2 Pressure Suppression System (PSS) tanks connected to the DW through a vent pipe. The PSS are the largest tanks and besides limiting the containment pressurization, this system is also employed to fill the Reactor Cavity (RC) of water in the mitigation strategy. Each of the 2 EBT, LGMS, and PSS tanks belongs to one of the 2 independent lines, as the one reported in Figure 2. The PSS tank and the LGMS tank, belonging to the same line, are connected through an open vent pipe which keeps in communication the top parts of the two tanks, maintaining the two tanks at the same pressure (see Figure 2). The EBTs and LGMS tanks on the same line can inject cooling water in the vessel through a Direct Vessel Injection lines (DVIs) once the respective valves are opened. The energy removed by natural circulation in the EHRS is transferred to two Refueling Water Storage Tanks (RWSTs), acting as heat sink and located outside the containment.

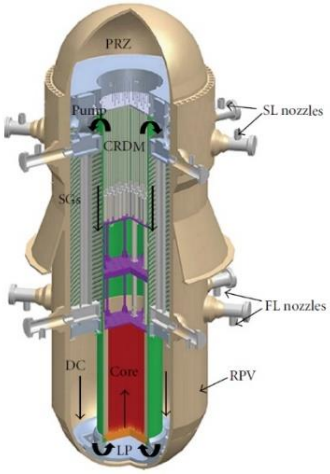

Figure 1. IRIS integral reactor vessel layout [10]

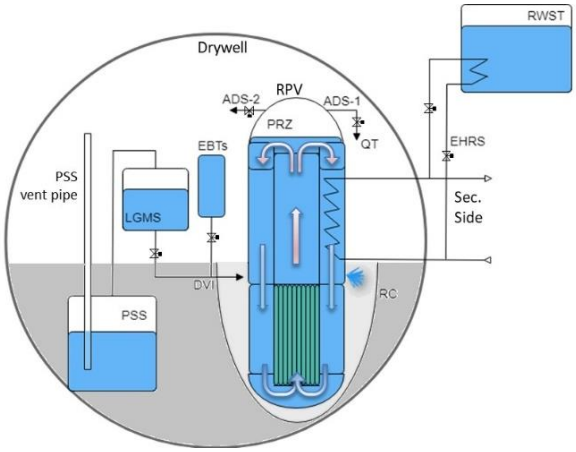

Figure 2. Scheme safety systems for a generic IRIS reactor (for the sake of simplicity, only one line is reported for redundant systems) [12].

2.1. IRIS passive mitigation strategy for a DVI line double ended break

The DBA sequence selected for the presented study is a double-ended break of one of the two DVI lines (2-inches of diameter); considering the availability of all the emergency passive safety systems. The SBLOCA considered is the lower elevation possible LOCA and the most challenging accidental scenario. The passive mitigation strategy consists in the opening of specific safety valves which activate specific safety systems, consequently to the triggering of set-point signals. The DVI line-A is considered as the broken line and the DVI line-B as the intact one.

The main phenomenology of the DBA sequence is described in the following [13,16,17]:

a) The accident initiator event is the guillotine break of the DVI line-A; it is followed by the RPV blowdown and depressurization. The containment pressure starts to increase and causes the transfer of a hot steam-gas mixture from DW to PSS tanks through the PSS vent lines. It determines the steam condensation underwater, limiting the DW pressurization. The PSS and LGMS tanks pressure increases

driven by the containment pressure trend. The RC is slowly filled by the primary water flowing from the break and by the steam condensation on the DW metal surfaces.

b) When the containment pressure value reaches the set-point, the S-signal (Safety) triggers the reactor SCRAM, the secondary-side lines isolation and the opening of two of the four EHRS loops. Due to the SCS isolation, the SCS pressure rapidly increases to the saturation point. Natural circulation starts in the EHRS loops 1 and 2, with the transfer of power to the RWST water, contributing to the RPV cooling and depressurization.

c) The primary pumps coast down is activated by the low PRZ level signal. The decrease of pump delivery pressure determines the automatically opening of the RI-DC check valves, increasing the core cooling by only natural circulation.

d) When the low PRZ pressure set-point is reached, the LM-signal (LOCA Mitigation) occurs actuating the ADS stage-1, the EBTs and the two EHRS remaining loops. Due to the EBT valves opening, cold borated water starts to be injected through the two DVI lines by gravity, while the broken loop (line-A) drops the EBT water inside the RC. The ADS stage-1 discharges steam from the PRZ head to a QT, increasing the PRZ depressurization rate and the equalization between RPV and containment pressures. The energy removal from the PCS is increased by the actuation of all the EHRS loops.

e) The low RPV-Containment Differential Pressure (DP) signal, activated by the RPV and DW pressures equalization, determining the opening of the valves connecting the LGMS line-B to the RPV (through the intact DVI line) and the LGMS line-A to the RC (through the broken DVI line). Steam condensation on the containment walls and heat removal from primary side due to the EHRS intervention causes the containment and the RPV pressure decreases. When DW pressure decreases below PSS pressure, the PSS water is pushed inside the PSS vent pipes to the top end and fills the RC above the break level.

f) When the LGMS mass reaches the low water mass signal, the ADS stage-2 valves are opened permitting steam circulation between RPV and DW. During the long-term cooling phase, the core is kept filled and cooled by the water available from RC, the power removed by the EHRS system and the heat losses to the environment through the DW metal surfaces.

3. DESCRIPTION OF ASTEC CODE AND ASTEC NODALIZATION OF THE GENERIC IRIS-LIKE REACTOR

The ASTEC code [18,19,20] (Accident Source Term Evaluation Code), developed by the French “Institut de Radioprotection et de Sûreté Nucléaire” (IRSN), aims at simulating an entire Severe Accident (SA) sequence in nuclear water-cooled reactors from the initiating event through the release of radioactive elements out of the containment [21]. ASTEC features a modular structure and each module is aimed at simulating a specific set of physical phenomena or related to a specific reactor zone. The main applications of the ASTEC code are source term evaluation studies, Probabilistic Safety Assessment level-2 (PSA2) studies, accident management studies, etc. [22]. In the present work, the modules CESAR, CPA, ICARE, SOPHAEROS and ISODOP of ASTEC have been implemented in the generic IRIS reactor model. The CESAR module is dedicated to the simulation of coolant systems thermal-hydraulics, it is a two-phase system code based on a two-fluid 5 or 6-equations thermal-hydraulic model. CPA is the ASTEC module with the purpose of simulating all the relevant thermal-hydraulic processes and plant states taking place in the containment of a LWR. ICARE is the module dedicated to core internals heat-exchange and in-vessel degradation phenomena. ICARE implements mechanical models, processes chemical reactions, incorporates fission product release (by coupling with ELSA) and describes core thermal behavior, degradation and relocation in the Lowe Plenum (LP), until the rupture of the Lower Head (LH) wall. The ISODOP module simulates the decay of Fission Products (FPs) and actinide isotopes and it allows to estimate the decay heat and the isotopes inventory in the different zones of the reactor. SOPHAEROS is in charge of simulating the transport of vapors and aerosols FPs in the RPV and in the containment, accounting

for the chemical reactions and speciation. The ASTEC version used is the V2.2 beta, with a 5-equation model for CESAR.

3.1. ASTEC nodalization of the generic IRIS-like reactor

In order to develop the ASTEC nodalization of the generic IRIS-like SMR, no proprietary data have been used; therefore, the main geometric information have been determined by scaling the data available from the SPES-3 facility [14,15,17] or by engineering evaluation. The public general data available for the IRIS reactor can be found in [10,11]. The approach followed in the generic IRIS modelling with ASTEC V2 aims at accurately simulating the thermal-hydraulics of RPV and passive safety systems. For this reason, CESAR (Figure 3) has been used for the nodalization of the primary systems (top half of RPV); secondary system (feed and steam lines; SGs) and most of the passive safety systems. The lower half of RPV, including the core, has been modelled with ICARE (Figure 4).

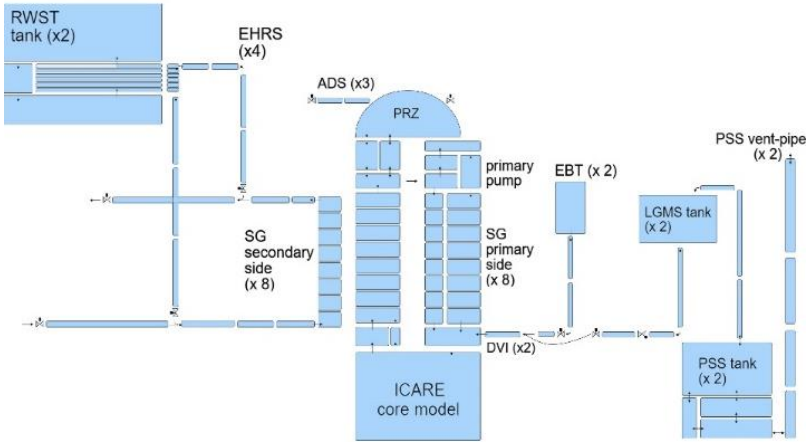

Figure 3. Scheme of CESAR IRIS reactor nodalization of the PCS, secondary coolant system and passive safety systems [15].

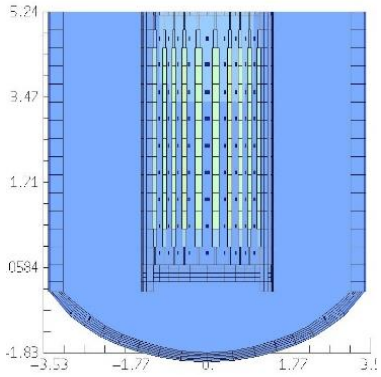

Figure 4. Scheme of ICARE IRIS reactor nodalization of the RPV and core [15].

CPA completes the thermal-hydraulic nodalization modeling the spherical containment (DW and RC). A more detailed description of the thermal-hydraulic nodalization adopted can be found in [12]. The reactor meshing considered by SOPHAEROS includes the RPV volumes and all the zones of the containment. The FPs initial inventory provided to ISODOP for the calculation of decay heat and of isotopes transmutation has been estimated with an ORIGEN-ARP code [23] calculation, by assuming a four-year fuel cycle lifetime, for an average burnup of 40000 MWd/tU. The corresponding FPs inventory (and decay heat) is distributed in the core considering the axial - radial profiles using dedicated factors in the FPEVOL structure of the code.

4. ASTEC SIMULATION OF DBA AND BDBA SEQUENCES

4.1 Simulation of DBA sequence

A simulation of the reference DBA sequence for the IRIS reactor (described in Section 2.1) has been performed after 2000 s of steady-state simulation, needed to reach the reactor nominal conditions. The DBA transient is initiated (t = 0 s) at the opening of the DVI break. The calculation has been carried out for 70000

s and the results have been described and discussed in previous works [12,24]. The main timings of the DBA simulation have been summarized in Table 1.

4.2 Simulation of BDBA sequences

4.2.1 Assumptions for the BDBA simulations

Considering as reference the DBA simulation sequence, four BDBA scenarios have been assumed by starting from the same steady-state simulation and initiator event. In all the scenarios it is assumed the failure of different selected passive safety systems, which would be activated by the opening of valves at specific set-points (see Section 2.1). Indeed, despite passive systems work thanks to natural-driven forces, their activation is based on electric signals and the opening of valves that, as an extreme hypothesis, have been considered to fail. The 4 assumed BDBA scenarios are: failure of EBTs, failure of EBTs and LGMS, failure of EHRS and ADS st-1, failure of EBTs, LGMS, EHRS and ADS. The activations of the considered safety systems follow the same control logics of the reference DBA (see Section 2.1). The passive safety systems that guarantee the operability in all the scenarios are: PSS system, opening of the RI-DC valves. Furthermore, the thermal-hydraulic coupling between RPV, containment and PSS can be considered as a passive mitigation strategy that is always available. The reactor containment failure is assumed in case of internal pressure greater than 13.5 bar (design pressure of an IRIS-like containment). In this condition, a large breach is assumed to open and to directly connect the top part of the DW to the environment, determining the containment depressurization to the atmospheric pressure. The 4 calculations have been initiated by starting from the same steady-state; the opening of the 2-inch break of DVI line-A is considered to take place at the Start Of the Transient (SOT) (t = 0 s). The main timings of the simulation results are summarized in Table 1 and the plots of the main Figure of Merit (FOMs) have been reported from Figure 5 to Figure 10 against the reference DBA results.

Table 1. Timings of main events in the 4 BDBA sequences and the reference DBA.

Event [s]	Reference DBA	EBT failure	EBT, LGMS 1failure	EHRS, ADS st-1 failure	All failure
Break	0	0	0	0	0
High Containment P. set-point	29	29	29	29	29
Low PRZ P. set-point	134	134	134	302	302
EBT-B empting	1650	-	-	2400	-
EBT-A empting	320	-	-	580	-
Low ΔP RPV-Cont. set-point	1330	1375	1375	16905	26960
RC level at DVI level	4100	5200	5200	14900	74000
Low LGMS mass set-point	17800	18000	-	132150	-
LGMS-B empting	25500	25600	-	155000	-
LGMS-A empting	20600	21500	-	135000	-
RWST water boiling	48000	48000	55000	-	-
Cladding failure	-	-	-	7800	9170
Corium relocation in LP	-	-	-	91560	111600
Containment failure	-	-	-	133950	113050

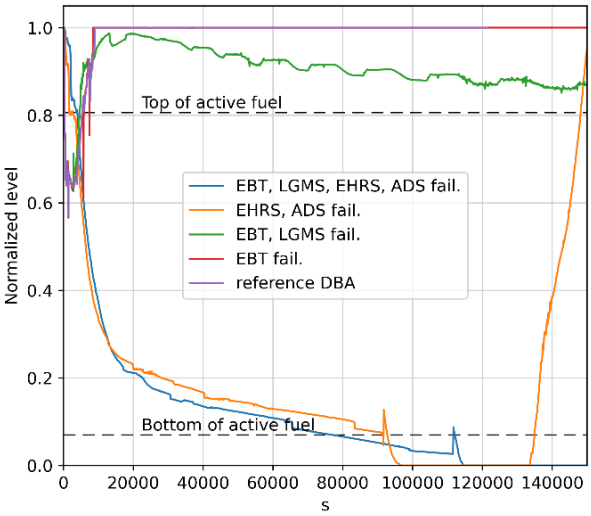

Figure 5. Normalized value of averaged collapsed level in the core (upper and lower core plates elevations taken as reference).

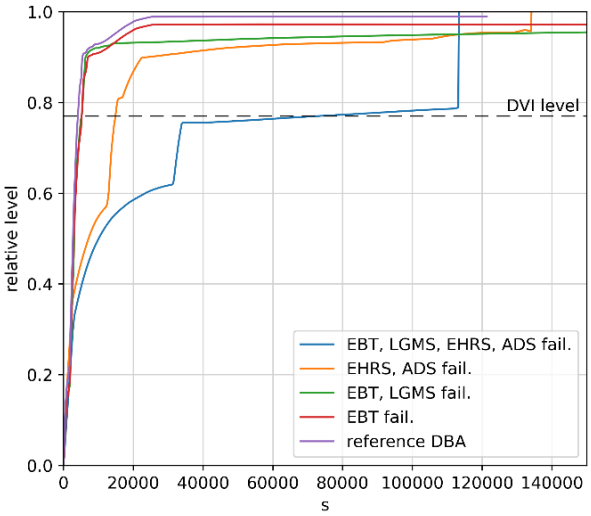

Figure 6. Normalized value of water level in the RC, with respect to the RC total elevation.

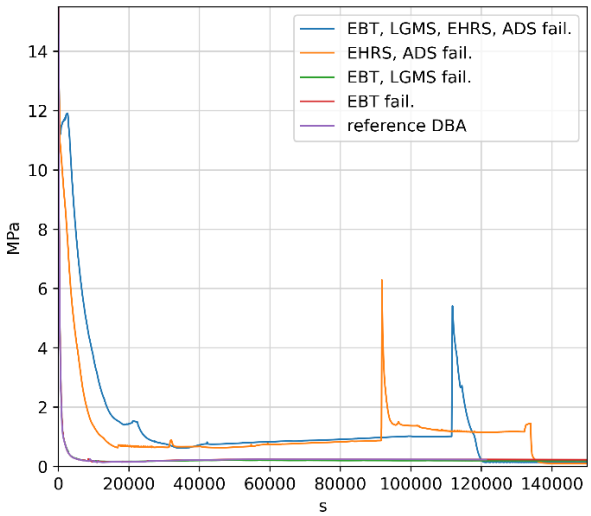

Figure 7. PCS pressure (PRZ).

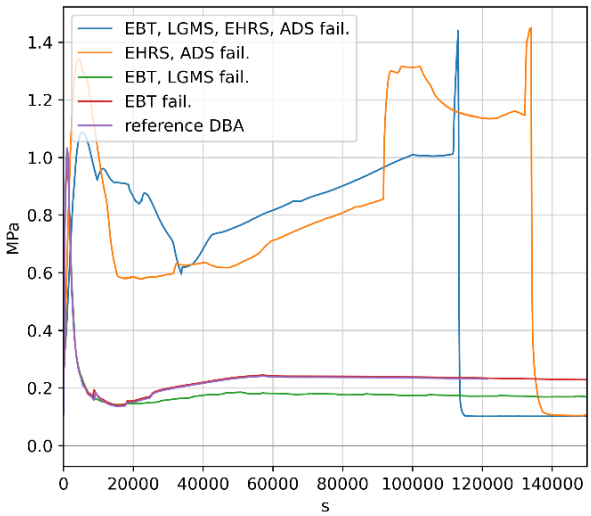

Figure 8. Containment pressure.

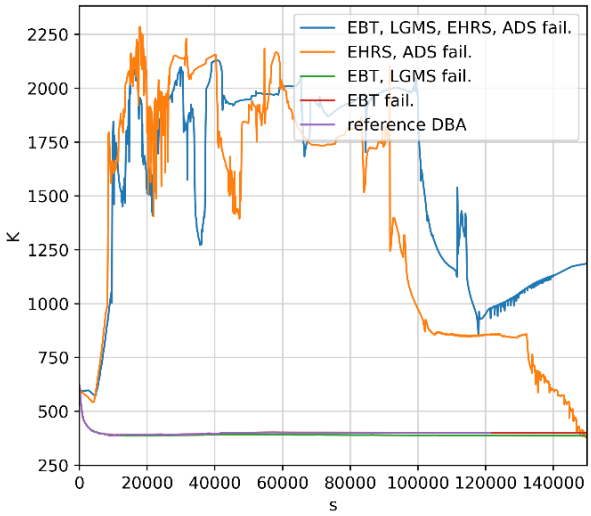

Figure 9. Core outlet temperature.

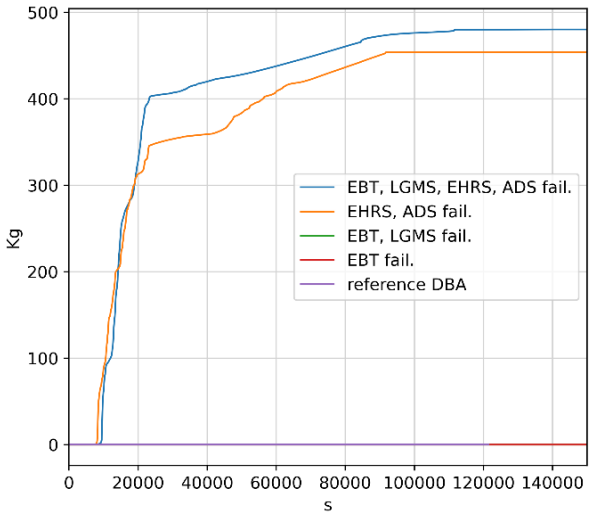

Figure 10. Total hydrogen mass production.

4.2.2 Results of EBTs failure scenario

From a qualitative and phenomenological point of view, the EBTs injection failure scenario is similar with respect to the reference DBA sequence. The lack of EBT cold water injection determines a slight reactor cooling and depressurization delay as shown in Table 1. A slightly lower RC water level at the end of the transient is observed due to the lack of EBTs injection.

4.2.3 Results of EBTs and LGMS failure scenario

The present transient shows a qualitative trend of the core water level decrease during the RPV depressurization and core refill (Figure 7) preventing any core heat-up (Figure 9). The RPV depressurization effect of the ADS st-1 openings and the EHRS power removal mitigates the coolant blowdown from the break. The EHRS in natural circulation permits the core cooling preventing any core damages. As shown in Figure 5, due to the lack of LGMS injection, the final core level is lower than the previous scenarios (DBA and EBTs failure). At the end of the simulated transient, the water level is above the top of active fuel, slowly keeping to decrease due to the coolant evaporation. With respect to the previous scenario, a phenomenological difference is related to the coupling between RPV and containment: considering that the water level in the RC reaches and overcomes the DVI level with very similar timing (Figure 6, Table 1), it has to be observe that the present transient does not feature a backward water flow through the break keeping the RPV water level at the same level as the RC (Figure 5 and Figure 6). It should be attributed to the lack of opening of ADS st-2, activated by “LGMS low water mass signal” never reached in this scenario (Table 1). Indeed, in the present scenario only ADS-st1, connecting the PRZ to the pool of the QT, valves have been opened. Considering the smaller size of ADS st-1 compared to the ADS st-2, a small over pressurization of RPV with respect to containment (of about 0.3 bar = 3 m of water head) is observed. For this reason, no backward water flowing through the break is simulated by the code in the present calculation.

4.2.4 Results of EHRS and ADS st-1 failure scenario

The lack of ADS-st1 opening and of EHRS heat removal determines the delay of the containment-RPV low differential pressure set-point ($\Delta P < 0.5$ bar) activation, as shown in Table 1. As a consequence, the water level does not decrease enough to avoid the core uncover in the first part of transient (0 - 10000 s). The

impossibility to cool the uncovered core (despite the intact EBT injection) leads to the start of degradation at around 7800 s after the SOT. The RPV–containment low DP-signal arrives at about 16905 s after the SOT (Table 1), opening at this point the LGMS valves. During the core degradation, steam and incondensable gases produced and the lack of the EHRS cooling maintain the containment and the RPV pressure between 6 and 9 bar, as can be observed in Figure 7 and Figure 8. The higher RPV pressure (with respect to the safety systems line) prevents any injection of LGMS water into RPV (through the intact DVI line); while a slow LGMS injection into the containment (through the broken DVI line) takes place. In addition, the RC water level, which has reached the break elevation at 14900 s after the SOT, is not allowed to refill the core due to the RPV pressurization. Core degradation advances until the bottom support plate failure and corium relocation in the LP (slumping) takes place at 128100 s after the SOT. The vaporization of LP water causes a very high-pressure peak in the RPV (about 63 bar), which is followed by a steep containment pressurization, up to around 13 bar, very close to the containment design pressure of 13.5 bar. After the slumping, the systems feature a stable phase with RPV pressure at around 13 bar, during which the corium is retained in the LP externally cooled by the RC water. At 111600 s after the SOT, the low water mass in the LGMS tank-A triggers the "Low LGMS mass set-point", opening the ADS st-2 valves. As a consequence, the RC water is allowed to flow back through the break, interacting with the hot corium pool and, hence, producing overheated steam which quickly increases again the RPV and the containment pressures. As a consequence, the containment fails at 113050 s and this leads to a fast depressurization of all the reactor systems to the atmospheric pressure and, as expected, by a large release of hydrogen, steam and FPs to the environment zone. The ASTEC visualization of the core degradation is reported in Figure 11, considering four timings of the core degradation sequence. The RC water keeps entering in the RPV through the break, completely filling the core. The final state of the reactor, at 150000 s after the SOT, features the corium retained in the LH and submerge by water, as reported in the last time of Figure 11. The possibility of an In-Vessel Melt Retention (IVMR) strategy within this final configuration (internal and external core cooling) should be investigated in further analyses. From a preliminary study, there seems to be promising possibilities to retain the corium in the LP by both internal and external cooling.

4.2.5 Results of EBTs, LGMS, EHRS and ADS st-1 failure scenario

As can be inferred at first sight of Figure 5 and Figure 10, the present scenario presents a similar phenomenological behavior to the one above described (failure of EHRS and ADS stage-1). The first phases of transient, before the onset of core oxidation, features some discrepancies with respect to the previous scenario: due to the lack of the EBTs cold water injection in RPV, the core temperature and primary pressure remain slightly higher; while, on the contrary, the containment pressure increase is much stronger in the previous scenario, where the pressurized water of the EBT (at the primary pressure) connected to the broken DVI is flashed in the containment. The onset of core oxidation and degradation arrives within a similar timing in the two SA scenarios, as can be inferred by looking at Table 1 and at the hydrogen generation in Figure 10. The core degradation evolution of the present scenario features a very similar qualitative behavior to the previous one, as can be observed by looking at the hydrogen production (oxidation processes) and at the temperature evolution, in Figure 9 and Figure 10 respectively. The slumping arrives 20000 s later in this last scenario with respect to the previous one and a similar primary pressure peak is predicted by the code in the RPV, as shown in Figure 7. The containment pressure increase follows the fast RPV pressurization. However, in this case, due to the initial higher pressure before the corium slumping, the containment reaches the failure pressure of 13.5 bar at this point, determining an earlier opening to the environment and depressurization. After the containment failure, the lack ADS-st2 valves opening makes the RPV pressure to remain higher than the containment pressure along all the sequence (with a minimum over-pressurization value of 0.4 bar). As a consequence, a reverse flow through the break refilling the core is never predicted in this scenario. At the end of the sequence (150000 s), the corium is retained in the LP and the LH structures is cooled only by the external water in the RC (Figure 12). It is evident that the possibility of IVMR retention within this configuration has a lower possibility to succeed.

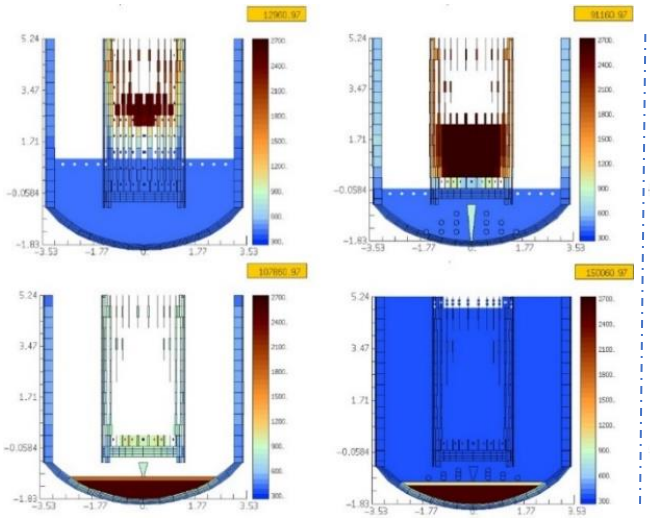

Figure 11. ASTEC - ICARE mask of core degradation evolution for the ADS st-1 and EHRS failure scenario.

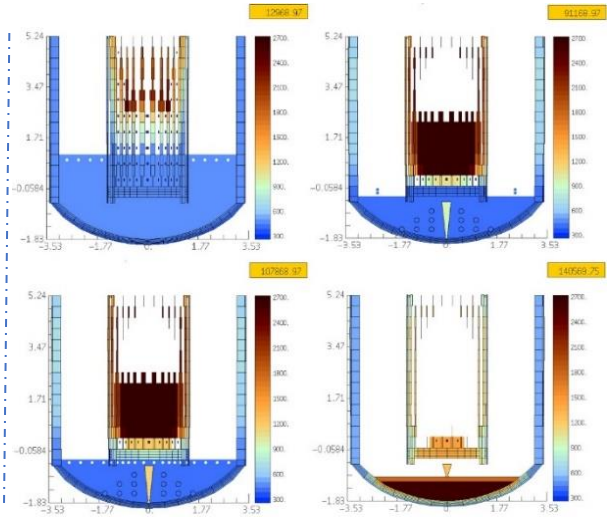

Figure 12. ASTEC - ICARE mask of core degradation evolution for the EBTs, LGMS, EHRS and ADS st-1 failure scenario.

5. CONCLUSIONS

In the present analysis, four BDBA simulations in a generic IRIS reactor have been carried out using the SA code ASTEC V2.2 beta and assuming the double-ended break of one of the two DVI lines. The actuation failure of different selected passive systems has been postulated: failure of EBTs; failure of EBTs and LGMS; failure of EHRS and ADS st-1; failure of EBTs, LGMS, EHRS and ADS. From the analysis of the results, the accident mitigation achieved in the first scenario (EBTs failure) and the partial mitigation of the second scenario (failure of EBTs and LGMS) show a safety margin guaranteed by the passive mitigation strategy even in the case of multiple failures of the passive injection systems. Accordingly, the results underline the crucial role played by EHRS and ADS systems in the passive mitigation strategy: the actuation of ADS st-1 ad EHRS guarantees the depressurization of the PCS and the pressurization of containment (in safety conditions), anticipating the pressure equalization between the two systems and mitigating the blowdown of coolant from RPV and, consequently, avoiding core damages. The following decrease of containment pressure below the PSS pressure guarantees the RC flooding (from PSS vent-pipes) and the LGMS injection. The effect of ADS st-2 is also underlined: in the presented analyses, the core refill is predicted to take place only in case of ADS st-2 opening (EBTs failure scenario; EHRS, ADS st-1 failure scenario). If ADS st-2 valves are closed, indeed, the RPV remains pressurized and water cannot flow back through the break from the RC.

Two IVMR configurations have been observed in the described SA scenarios (Figure 12 and 13). The first one, obtained in this study with EBTs, LGMS, EHRS and ADS st-1 failure, is a traditional IVMR configuration in which most of decay-heat is removed by the external RC water thorough the LH structure, and a corium stratification with focusing effect is present. The second IVMR configuration in this study is obtained when the EHRS and ADS st-1 fail, and it features a corium cooling from both the external water in RC and the internal water on the top of the corium pool, removing heat directly from the top metallic layer. The large heat removed by water from the top of the corium pool could mitigate the focusing effect and may prevent from high heat-flux to a limited LH surface. Further investigations are necessary to characterize the ASTEC code IVMR modelling capability in integral SMR configuration, in the view of characterizing its feasibility in a safety review process.

The present study is important to highlight the possibility of SA sequences, due to the not operation (or partial operation) of passive systems, characterized by specific phenomenology (e.g. IVMR with top water cooling, systems coupling during core degradation, etc.) not observed before for larger power reactor. These phenomenologies, due to the peculiarity of these reactors (the integral geometry, the intimate thermal-hydraulic coupling between the primary coolant system and the containment, the effect of the operation of the passive systems in a BDBA sequence, etc) coupled with the evolution of core degradation, needs to be thoroughly investigated. In addition, the failure of the containment in one of the reported scenarios underlines the importance to further study SA transient in smaller containment (characterized by a reduced containment-volume/core-power ratio compared to large-LWR) including hydrogen risk.
About the ASTEC performances, the activity gives the first insights about the capability of the code to capture different accidental sequences due to the partial or total not operation of the passive system in a SMR. Further research activity is necessary to identify code model development needs in term of further validation and the needs of further experimental program specifically developed for SMR configurations.

NOMENCLATURE

ADS: Automatic Depressurization System; **ASTEC**: Accident Source Term Evaluation Code; **BDBA**: Beyond Design Basis Accident; **CRDM:** Control Rod Drive Mechanism; **DBA**: Design Basis Accident; **DC**: Downcomer; **DiD**: Defence-in-Depth; **DP**: Differential Pressure; **DVI**: Direct Vessel Injection; **DW**: Drywell; **EBT**: Emergency Boration Tank; **EHRS**: Emergency Heat Removal System; **IRIS**: International Reactor Innovative and Secure; **IRSN**: Institut de Radioprotection et de Sûreté Nucléaire; **IVMR**: In-Vessel Melt Retention; **LBLOCA**: Large Break Loss Of Coolant Accident; **LGMS**: Long-term Gravity Make-up System; **LH**: Lower Head; **LP**: Lower Plenum; **LW**: Light Water; **NPP**: Nuclear Power Plant; **PCS**: Primary Coolant System; **PRZ**: Pressurizer; **PSS**: Pressure Suppression System; **PWR**: Pressurized Water Reactor; **QT**: Quench Tank; **RC**: Reactor Cavity; **RPV:** Reactor Pressure Vessel; **RWST**: Refueling Water Storage Tank; **SA**: Severe Accident; **SBLOCA**: Small Break Loss of Coolant Accident; **SCS**: Secondary Cooling System; **SG**: Steam Generator; **SMR**: Small Modular Reactor; **SOT**: Start Of the Transient.

REFERENCES

1. F. Mascari, B. G. Woods, K. Welter, F. D'Auria, A. Bersano, P. Maccari, Small Modular Reactors and insights on passive mitigation strategy modeling, OECD/NEA/CSNI Specialists Meeting on Transient Thermal-hydraulics in Water Cooled Nuclear Reactors (SM-TH) – Dec. 14-17, 2020 - CIEMAT, Madrid (Spain).
2. IAEA-TECDOC-1391, 2004, Status of Advanced Light Water Reactor Designs, 2004.
3. F. Mascari, PhD Thesis on "Natural Circulation and Phenomenology of Boron Dilution in the Pressurized Water Reactors (Circolazione Naturale e Fenomenologie di Boron Dilution in Reattori ad Acqua in Pressione), Università degli Studi di Palermo, 2010.
4. IAEA, Advances in small modular reactor technology developments, A supplement to: IAEA Advanced Reactors Information System (ARIS) Vienna, 2014. https://aris.iaea.org/Publications/IAEA_SMR_Booklet_2014.pdf
5. P. Chatelard, S. Belon, L. Bosland, L. Carénini, O. Coindreau, F. Cousin, C. Marchetto, H. Nowack, L. Piar, L. Chailan, "Main modelling features of the ASTEC V2.1 major version", *Annals of Nuclear Energy*, **93**, 83–93, 2016. https://doi.org/10.1016/j.anucene.2015.12.026
6. P. Chatelard, N. Reinke, S. Arndt, S. Belon, L. Cantrel, L. Carénini, K. Chevalier-Jabet, F. Cousin, J. Eckel, F. Jacq, C. Marchetto, C. Mun, L. Piar, "ASTEC V2 severe accident integral code main features, current V2.0 modelling status, perspectives", *Nuclear Engineering and Design*, **272**, p.119-135, 2014.

7. MELCOR Computer Code Manuals, Vol.1: Primer and Users' Guide, SAND 2015-6691 R; Vol. 2: Reference Manual, SAND 2015-6692 R; Vol. 3: MELCOR Assessment Problems, SAND 2015-6693 R; Sandia National Laboratories, USA.
8. P. Chatelard, ASCOM project overview and description of work, SARNET-ASCOM-COORDI-P1, 2018.
9. NUGENIA TA-2: ASCOM project (2018-2022). https://snetp.eu/portfolio-items/ascom/
10. IRIS International Reactor Innovative and Secure, IRIS Plant Overview, 2002. https://www.nrc.gov/docs/ML0336/ML033600086.pdf.
11. IRIS Plant Description Document, WCAP-16062-NP Revision 0, Westinghouse Non-Proprietary, March 21, 2003. https://www.nrc.gov/docs/ML0336/ML033600112.pdf
12. P. Maccari, F. Mascari, S. Ederli, P. Meloni, and S. Manservisi, "ASTEC code DBA analysis of a passive mitigation strategy on a generic IRIS SMR", *Annals of Nuclear Energy*, **156**, p. 108 194, 2021. https://doi.org/10.1016/j.anucene.2021.108194
13. M. Carelli, L. Conway, M Dzodzo, A. Maioli, L. Oriani, G. Storrick, B. Petrovic, A. Achilli, G. Cattadori, C. Cogiu, R. Ferri, "The SPES3 experimental facility design for the IRIS reactor simulation", *Science and Technology of Nuclear Installations*, Article ID 579430, 12 pages, 2009. https://doi.org/10.1155/2009/579430
14. R. Ferri, C. Congiu, Conceptual design of SPES3-IRIS facility, SIET 01 334 RT 07 Rev.1. Piacenza (I), September 5th, 2008.
15. R. Ferri, F. Mascari, P. Meloni, G. Vella, TRACE and RELAP5 Codes for Beyond Design Accident Condition Simulation in the SPES3 Facility, 2012, 20th International Conference on Nuclear Engineering and the ASME 2012 Power Conference. American Society of Mechanical Engineers Digital Collection, 2012.
16. A. Achilli, C. Congiu, R. Ferri, F. Bianchi, P. Meloni, D. Grgić, M. Dzodzo, SPES3 facility RELAP5 sensitivity analyses on the containment system for design review, Science and Technology of Nuclear Installations, 2012, Article ID 173637, 19 pages, 2012.
17. R. Ferri, SPES3-IRIS facility RELAP5 sensitivity analyses on the containment system for design review, no. SIET 01 526 RT 09 Rev.0, 2010.
18. L. Chailan, A. Bentaïb, P. Chatelard, Overview of ASTEC code and models for Evaluation of Severe Accidents in Water Cooled Reactors, IAEA Technical Meeting on Status and Evaluation of Severe Accident Simulation Codes for Water Cooled Reactors, Vienna (Austria), October 9-12, 2017.
19. L. Laborde et al., Overview of the ASTEC V2.2 integral code, Report IRSN-2021-00298, (2021)
20. P. Chatelard, L. Laborde, Synthesis of the ASTEC V2.2 code validation vs. experimental data, 10th European Review Meeting on Severe Accident Research (ERMSAR-2022), Karlsruhe, Germany, May 16-19, 2022.
21. F. Mascari, J. C. De La Rosa, M. Sangiorgi, G. Bandini, Analyses of an Unmitigated Station Blackout Transient in a Generic PWR-900 with ASTEC, MAAP and MELCOR Codes, NUREG/IA-0515, published by U.S. Nuclear Regulatory Commission, 2019.
22. C. Caroli, L. Bellenfant, H. Bonneville, S. Phoudiah, J. Chambarel, R. Cozeret, E. Veilly, E. Raimond, Examples of recent and on-going reactor accident analysis with the ASTEC integral code at IRSN, 7th European Review Meeting on Severe Accident Research (ERMSAR 2015), Marseille (France), March 24-26, 2015.
23. B. T. Rearden, M. A. Jessee, Scale code system, Oak Ridge National Lab.(ORNL), Oak Ridge, TN (United States), ORNL/TM-2005/39 Version 6.2.3, March 2018.
24. P. Maccari, J. A. Zambaux, A. Bersano, BEPU analysis of a 2-inches DVI line break in a generic IRIS SMR by ASTEC-RAVEN coupling, EUROSAFE Forum 2021, Paris, France, November 22-23, 2021.

Italian National Agency for New Technologies,
Energy and Sustainable Economic Development

ALMA MATER STUDIORUM
UNIVERSITÀ DI BOLOGNA

Analysis of BDBA sequences in a generic IRIS reactor using ASTEC code

10th European Review Meeting on Severe Accidents Research - ERMSAR 2022
May 16-19 2022

Pietro Maccari*; Giuseppe Agnello**; Fulvio Mascari*; Stefano Ederli*

**ENEA Italian National Agency for New Technologies, Energy and Sustainable Economic Development – Via Anguillarese, 301 - 00123 Roma, Italy*
***Università degli Studi di Palermo, Dipartimento di Ingegneria – Viale delle Scienze, Edificio 6, 90128, Palermo, Italy*

OUTLINE

- Introduction
- The IRIS reactor
- ASTEC V2.2 modelling of IRIS
- ASTEC simulation of DBA sequence
- ASTEC simulation od BDBA sequences
- Conclusions and remarks

OUTLINE

- Introduction
- The IRIS reactor
- ASTEC V2.2 modelling of IRIS
- ASTEC simulation of DBA sequence
- ASTEC simulation od BDBA sequences
- Conclusions and remarks

Advanced Small Modular Reactors (SMRs)

Small Modular Reactors:

Advanced Reactors with an electric power up to 300 MWe, built and assembled in factories and transported as modules to the site for the installation of many identical unites**.**

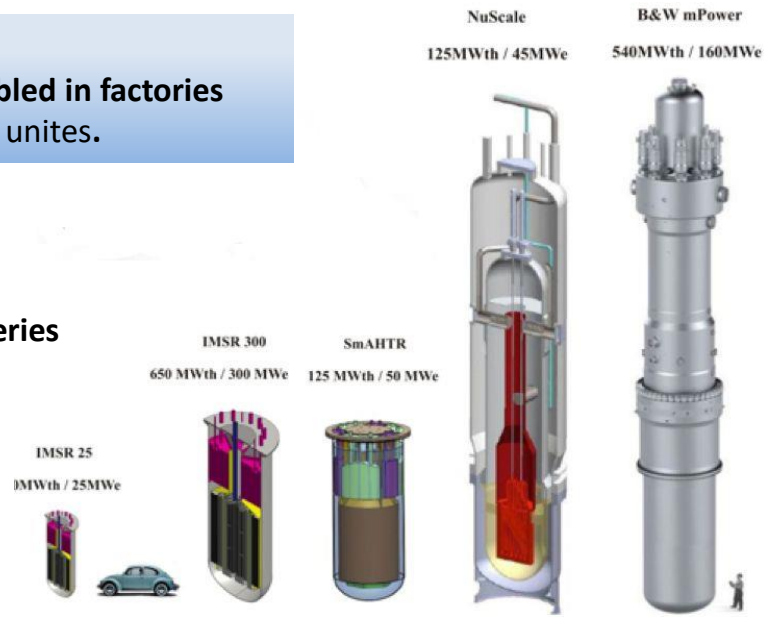

Potential Advantages:

❖ **Economic advantages** (smaller size, modularity):

- **Lower capital costs** for each unit;
- **Simpler and standardized** design -> possibility of **manufacturing in series** lowering construction times.

❖ Suitability for **innovative energy applications**:

- Cogeneration & non-electric applications (e.g. water desalination, industrial applications, Hydrogen production);

❖ **Flexibility**: suitable for energy needs in **remote areas** and for **micro-grids**.

❖ Potential for **enhanced safety** thanks to "**inherent" safety features;**

Based on well known technology: Based on the technology of current LWR (core part geometry and materials, Regulatory & operating experience)



New Thermal-hydraulic features and phenomena

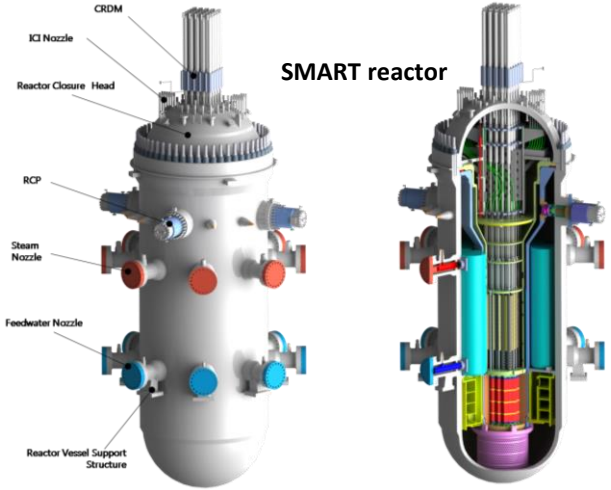

SMART reactor

Due to the **innovative design of SMR** (integral configuration, passive safety systems)
→ SMR may be **characterized by new thermal-hydraulic features and phenomena** specific of their design:

a) Containment interactions with the RCS (strong coupling and feedback effects);
b) Low pressure phenomena (e.g. natural circulation, influence of non-condensable gases, liquid stratification, gravity-driven reflooding, etc.);
c) Phenomena related specifically to new systems or reactor configurations.

- **Specific experimental investigations** in **separated test facilities and integral test facilities** has been necessary to **extend the "assessment database" of SMR**.
- International **code application activities** have been carried out (or are in progress) **to validate thermal-hydraulic codes against SMR thermal-hydraulic features.**

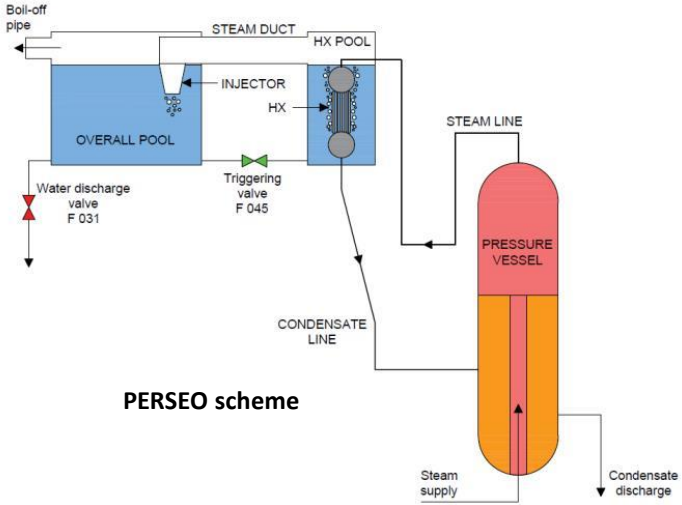

PERSEO scheme

SA codes modelling of SMR

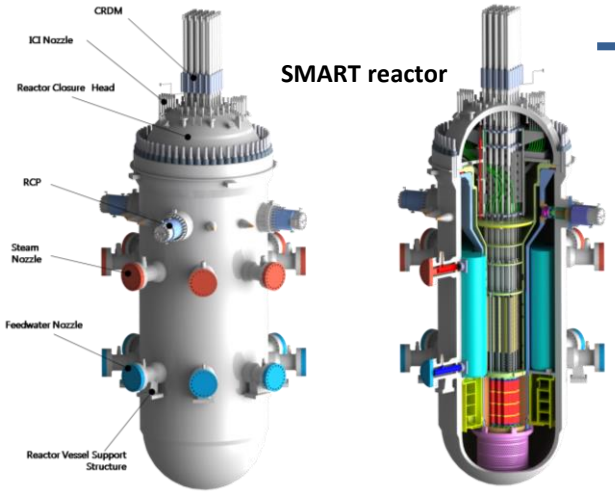

SMART reactor

→ Also **Severe Accident codes need to be validated for SMR applications**

❖ The **thermal-hydraulic module / package** should be **validated** against relevant **experimental campaigns** specific for SMR thermal-hydraulics;

❖ Regarding core **degradations and FPs transport modules / packages**:

- ➢ **New phenomena, features, accidental configurations specific of SMR in SA conditions should be identified;**
- ➢ New experimental activities and research programs should be planned.

(The new research projects SASPAM is going to start)

→ As a first step of **ASTEC code assessment** for advanced SMR, in the framework of the **NUGENIA TA-2 ASCOM** project, a **generic input-deck of the IRIS SMR** has been developed with the **ASTEC code**.

- ➢ Test the code capability in the prediction of the main thermal-hydraulic and SA phenomena and underlines code needs;
- ➢ Test the modelling capability of the code for advanced SMR design and provides modelling guidelines.

OUTLINE

- Introduction
- **The IRIS reactor**
- ASTEC V2.2 modelling of IRIS
- ASTEC simulation of DBA sequence
- ASTEC simulation od BDBA sequences
- Conclusions and remarks

The IRIS reactor

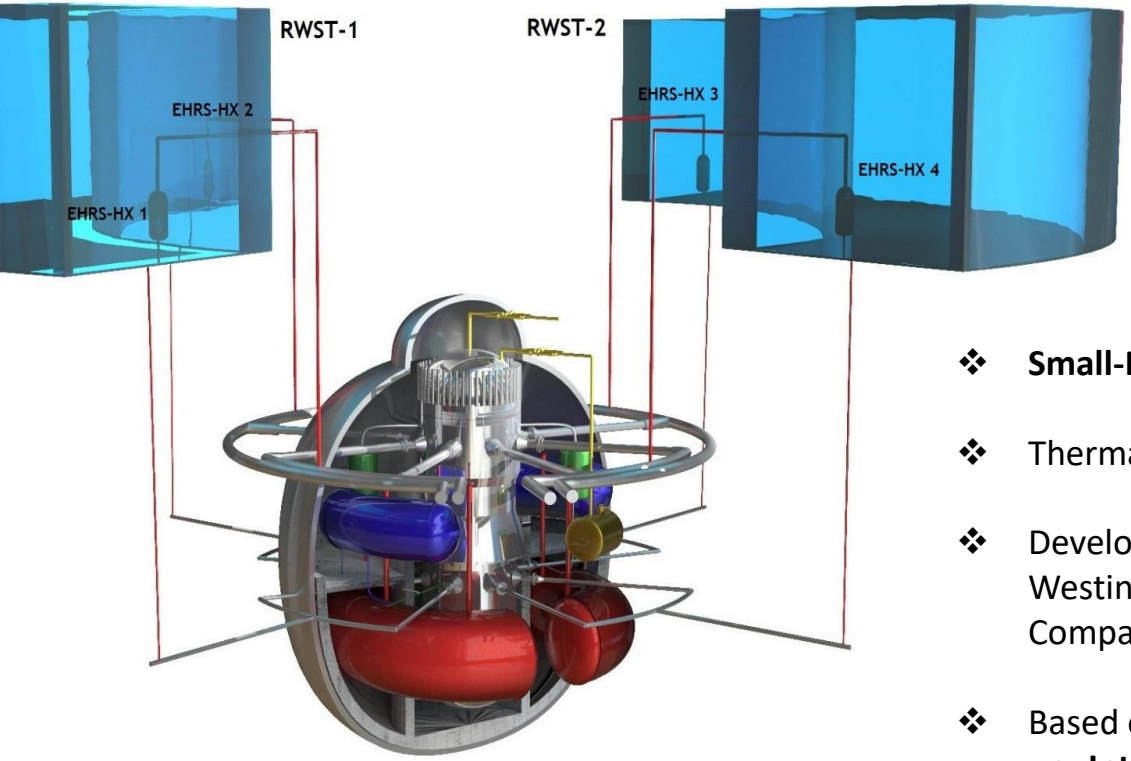

IRIS: International Reactor Innovative and Secure

- **Small-Power** modular integral **Light Water Reactor**;
- Thermal power of **1000 MWt (~ 300 MWe)**;
- Developed by an international consortium led by Westinghouse and including several international Companies and Universities;
- Based on a **safety-by-design** philosophy:
  - **Integral configuration**;
  - Adoption of only **Passive Safety Systems.**

The IRIS reactor

IRIS reactor layout:

The **RPV** includes all the main reactor **coolant Primary System** components:

- Core;
- Pressurizer;
- 8 Downcomer primary-side Steam Generator;
- 8 Immersed Pumps;
- Control Rods Drive Mechanism;

Secondary sides:

- **8 SG Helical Coil** bundles, immersed in the 8 downcomer primary lines;
- 8 Steam Lines and 8 Feed Lines.

Spherical cointainment:

- Contains most of the Passive Safety Systems;
- Designed to be thermo-hydraucally coupled with the RPV during accident conditions.

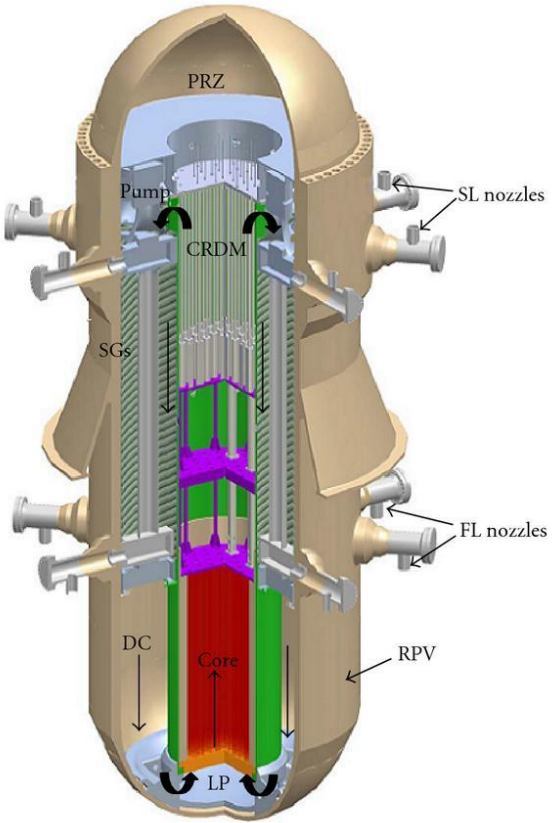

IRIS reactor features: Passive Safety Systems

IRIS plant scheme:

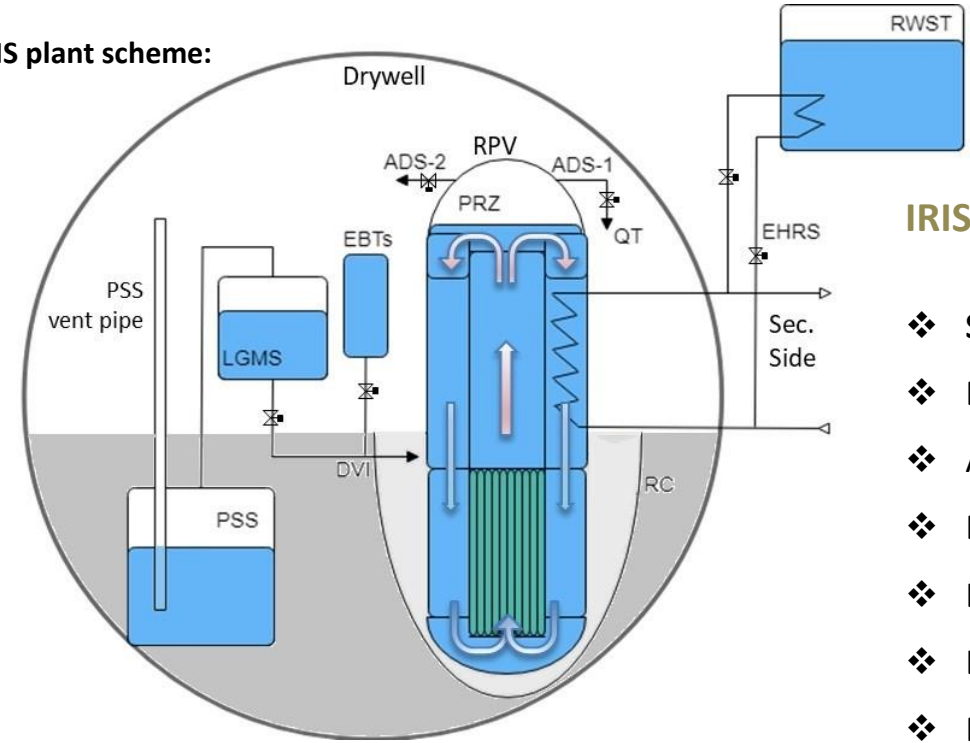

IRIS Passive Safety Systems:

- **Spherical containment (RC, DW)**
- Emergency Heat Removal System **(EHRS)** → **x 4 loops**
- Automatic Depressurization systems (**ADS st-1 / 2**)
- Direct Vessel Injection lines (**DVI**)
- Emergency Boration Tanks (**EBTs**)
- Long term Gravity Makeup System (**LGMS**)
- Pressure Suppression System (**PSS**)

x 2 lines

OUTLINE

- Introduction
- The IRIS reactor
- **ASTEC V2.2 modelling of IRIS**
- ASTEC simulation of DBA sequence
- ASTEC simulation od BDBA sequences
- Conclusions and remarks

ASTEC V2.2 modelling of a generic IRIS design

IRIS plant scheme:

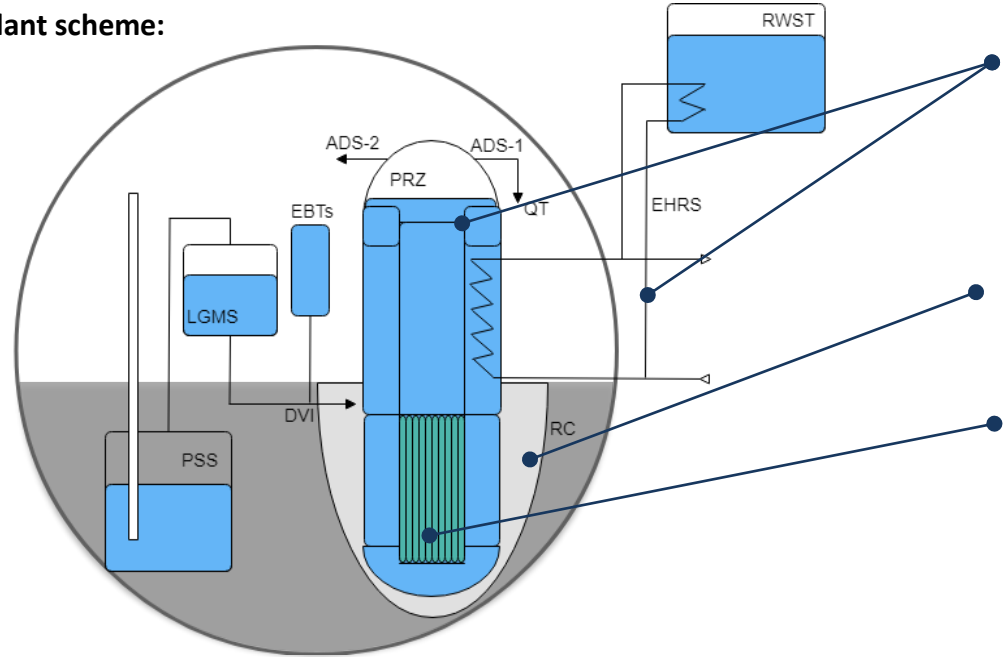

CESAR: Thermal-hydraulics calculation in
- Primary system;
- Secondary system;
- EHRS, EBT, LGMS, PSS, ADS, DVI

CPA: Thermal-hydraulics calculation in Containment and QT

ICARE: Core components modelling and In-Vessel degradation phenomena

SOPHAEROS: FPs transport in Primary system and containment

ELSA; **ISODOP**

Reactor geometric data have bee taken from open available sources avoiding proprietary data

ASTEC modelling of a generic IRIS design: CESAR module

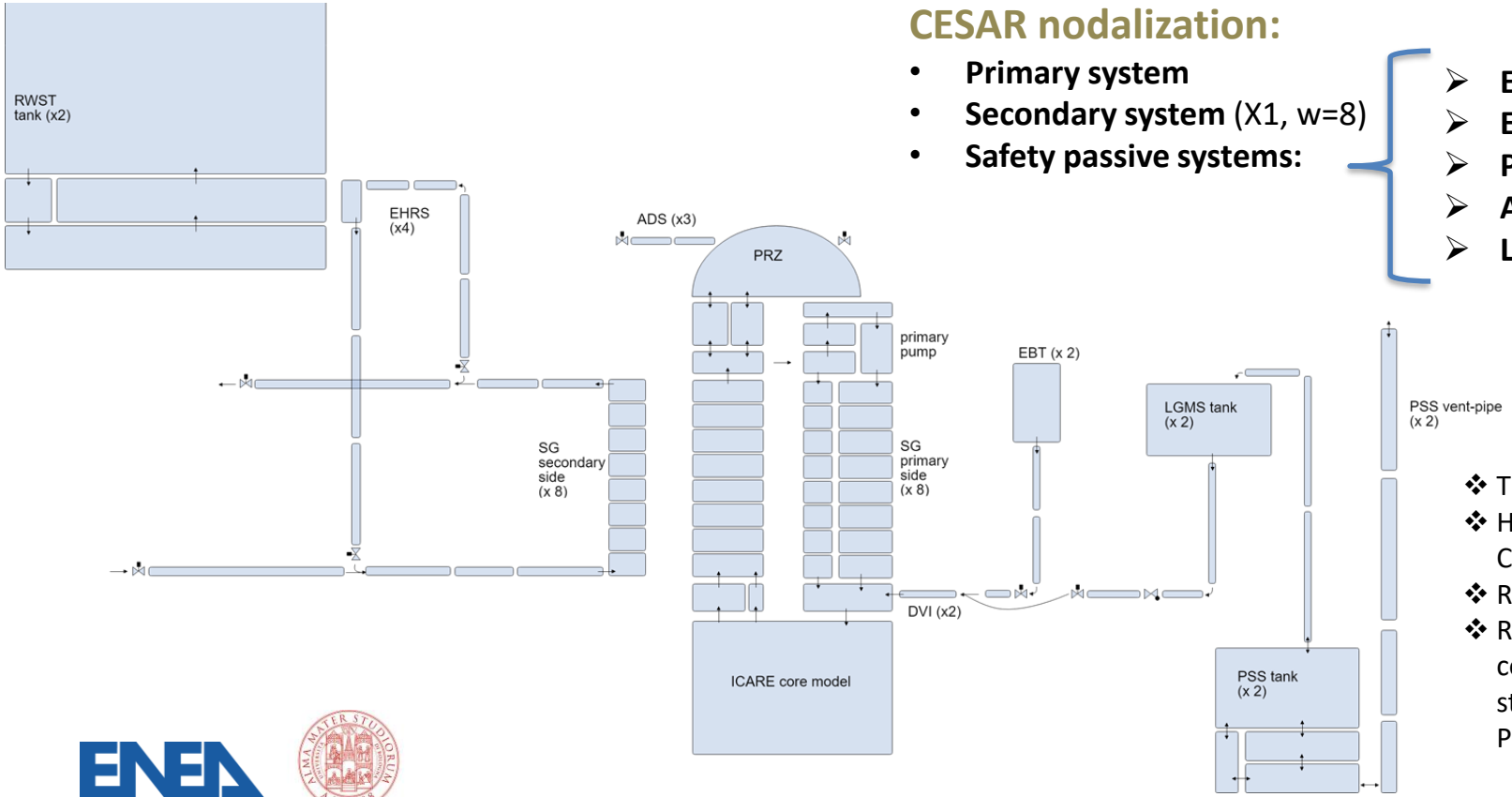

CESAR nodalization:

- **Primary system**
- **Secondary system** (X1, w=8)
- **Safety passive systems:**
  - **EHRS** (x1, w=4)
  - **EBTs** (x2)
  - **PSS** (x2)
  - **ADS** (x2)
  - **LGMS** (x2)

- Thermal structures;
- Heat losses to the Containment;
- Reactor logics;
- Reactor auxiliary components for steady state (pumps, PRZ heaters and spry)

ASTEC modelling of a generic IRIS design: ICARE module

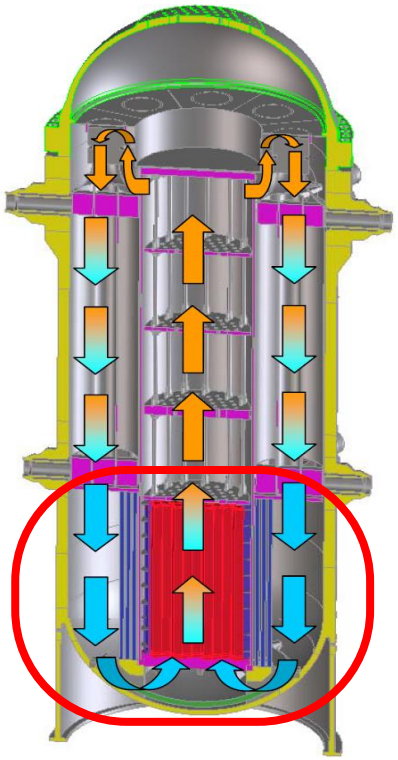

2-D Cylindrical symmetric ICARE model

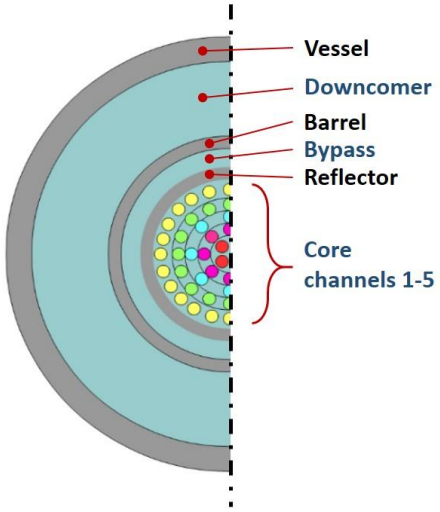

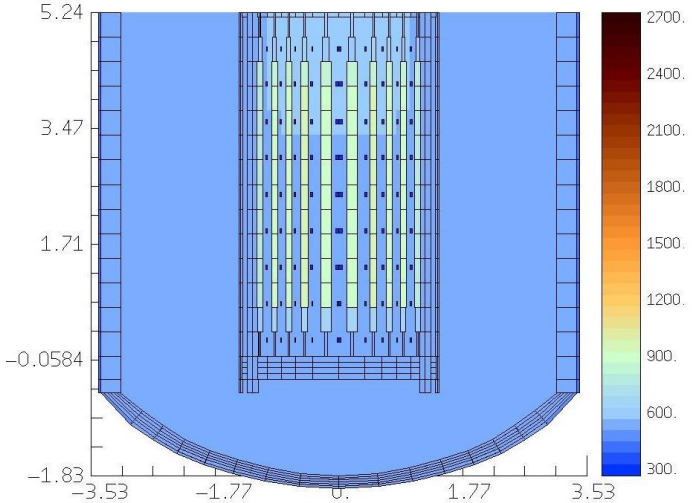

Radial discretization

- **7 Fluid channels**: 5 fuel rods channels, Bypass, Downcomer
- **Macro Components**: Fuel rods, Control rods, Nozzles, Reflector, Barrel, Vessel, Spacer Grids, Support Plates.

Axial discretization

- 16 **axial core regions** + lower-plenum volume
- **Lower head**: 6 radial meshes, 9 axial meshes

ASTEC modelling of a generic IRIS design: CPA module

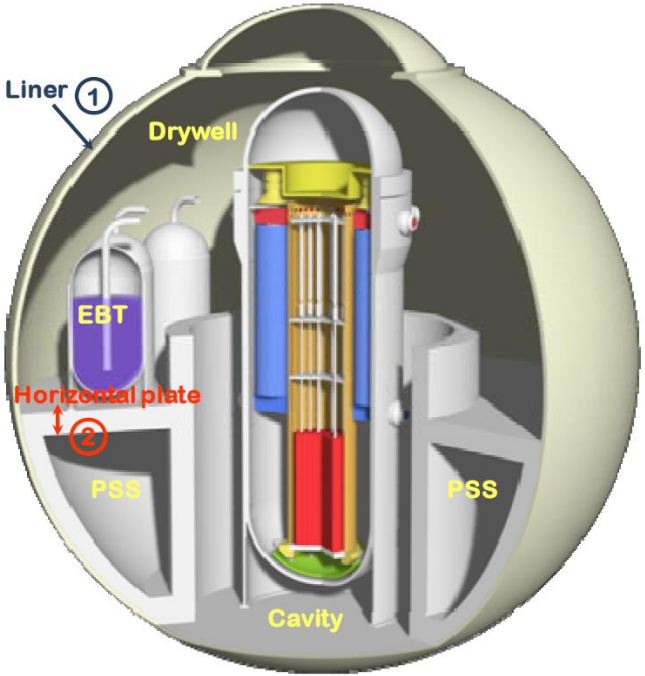

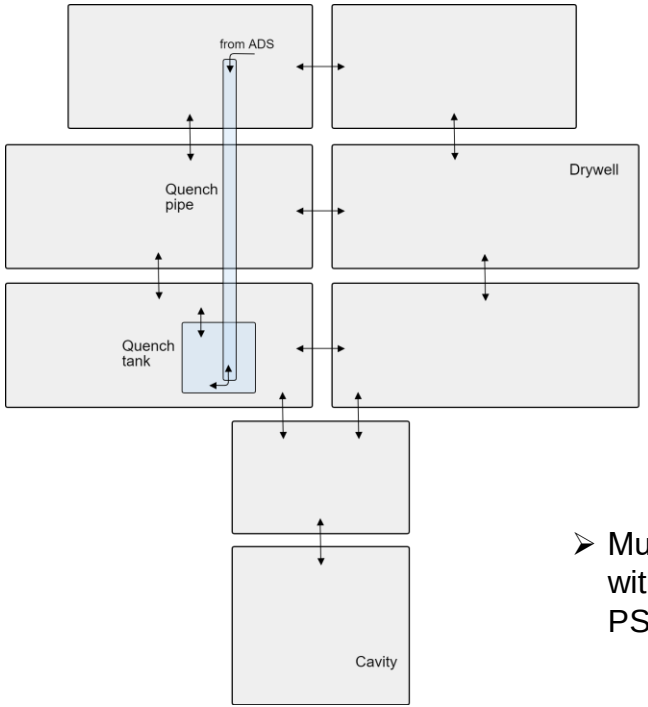

CPA nodalization:

- **Drywell**
- **Reactor Cavity (RC)**
- **Quench Tanks (QT)**
  & Quench pipe

- Thermal Structures;
- Heat losses to Env.;

- Multiple ‘’BREAK‘’ connections with CESAR (DVI break, ADS, PSS vent X 2)

ASTEC modelling of a generic IRIS design: other modules

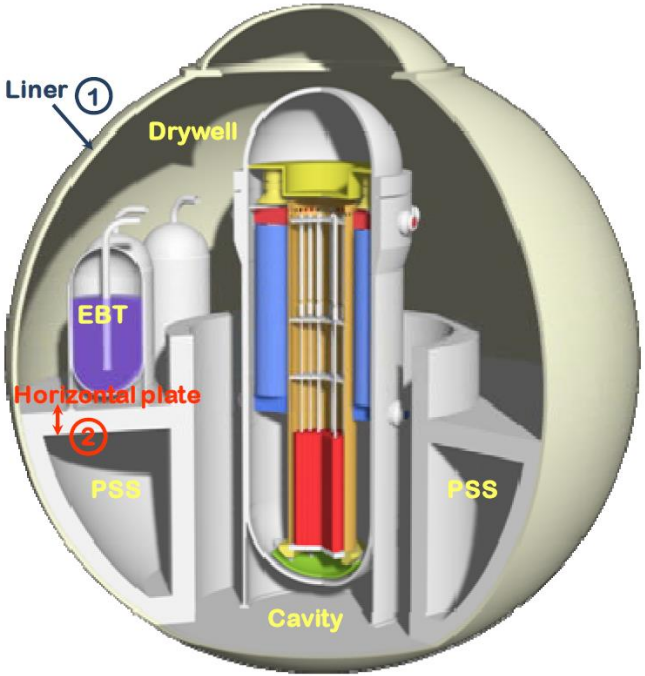

SOPHAEROS

Has bee **activated for the calculation of FPs transport** in RPV volumes and in the Containment;

ISODOP

Has been **provided with the initial FPs inventory** (ORIGEN-ARP code calculation considering a BU of 40000 MWd/tU);

ELSA

Has bee activated for the calculation of **FPs release from core** .

Code calculation: Steady - State simulation

Parameters	Ref. Reactor	ASTEC	Discr(%)
PRZ P (bar)	155.13	154.97	0.1%
Primary flow (Kg/s)	4800.0	4857.0	1.19%
Inlet Core T (K)	565.15	570.5	1.1%
Outlet Core T (K)	601.55	601.56	0.002%
RCS Vol. (m^3)	455,0	460.4	1.18%
Core power (MW)	1000.0	1000.0	0%
SG outlet pressure (bar)	58.3	58.0	0.51%
SG inlet temperature (K)	479.0	493.0	0.80%
SG outlet temperature (K)	594.0	595.0	0.17%
SG mass flow rate (kg/s)	62.9	62.9	0.00%

Pressure in primary volumes

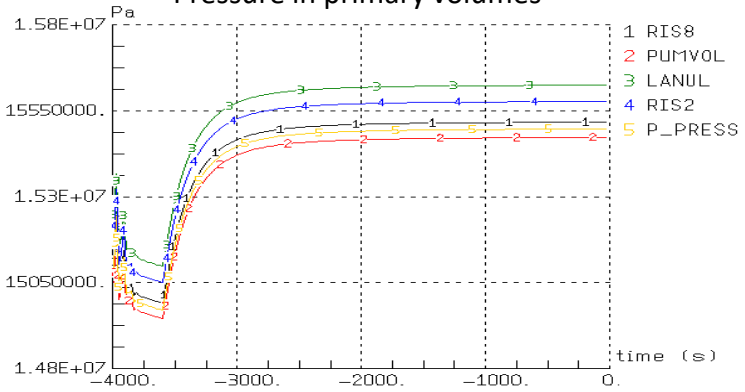

Heat flux in PRZ heaters

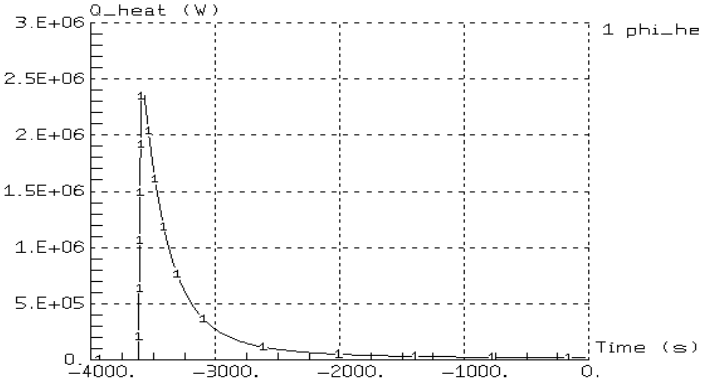

OUTLINE

- Introduction
- The IRIS reactor
- ASTEC V2.2 modelling of IRIS
- **ASTEC simulation of DBA sequence**
- ASTEC simulation od BDBA sequences
- Conclusions and remarks

Code calculation of DBA sequence: 2 in DVI break

A DBA scenarios have been simulated with the **ASTEC** input-deck of the generic **IRIS**, by **assuming a 2-in break of a DVI-line**. **All the passive safety systems** are considered **available.**

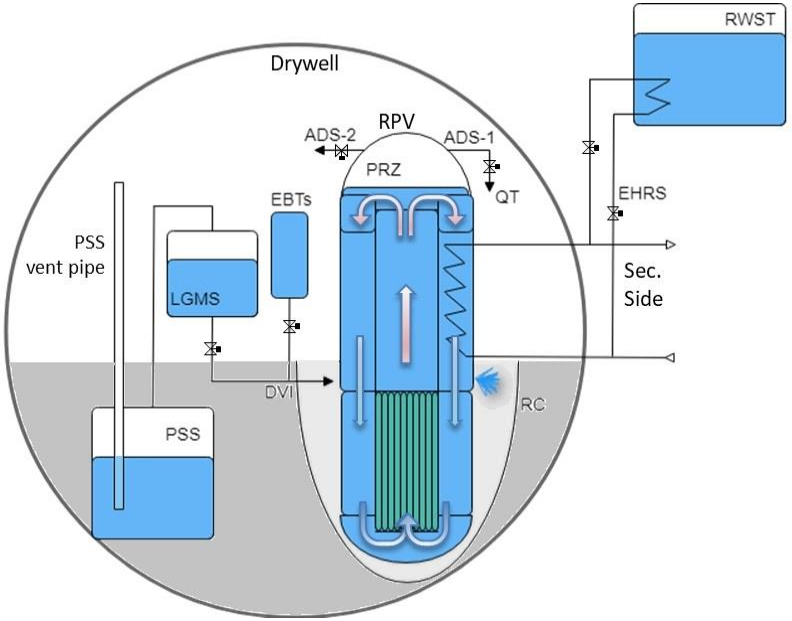

Objectives:

- Qualitative investigation of the thermal-hydraulic phenomena prediction by the code for the different passive safety systems.
- Find possible code models needs;
- Propose a nodalization approach suitable for SRMs for ASTEC users

Results and conclusions of code calculation: 2 in DVI break

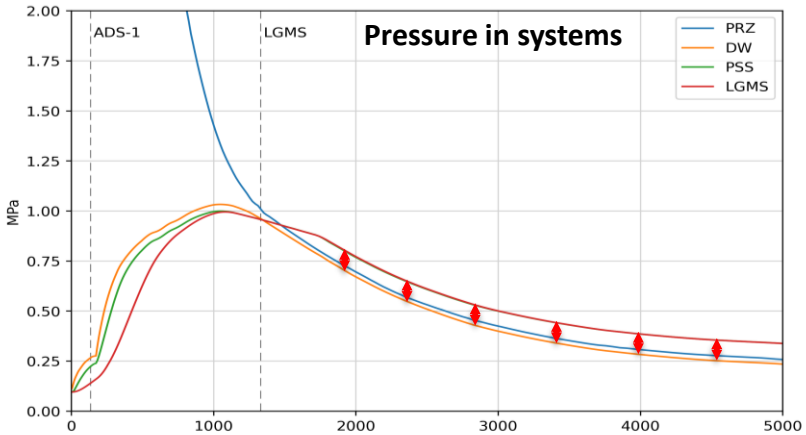

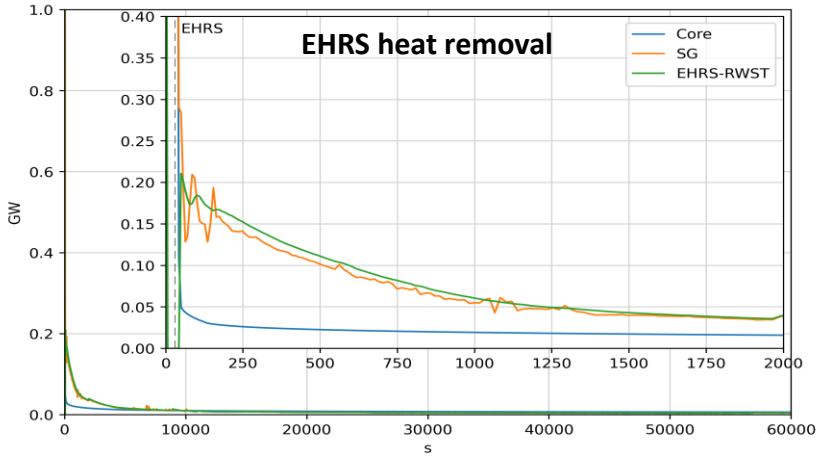

The ASTEC code with the adopted **nodalization approach** has been able to **reproduce the main expected thermal-hydraulic phenomena** driving in **the passive mitigation strategy**:

- The **thermal-hydraulic coupling** between **containment**, **RPV** and **passive safety systems**, which allows the success of the passive mitigation strategy, has **been simulated**.
- Phenomena of direct **interaction** of **hot gas and steam injected inside PSS water**, limiting DW pressurization.
- **Natural circulation** is predicted **in the EHRS loops, RWST** and **RPV**, allowing the removal of decay heat from the RPV.

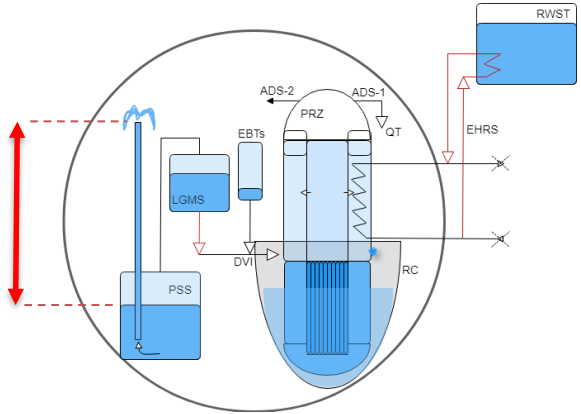

OUTLINE

- Introduction
- The IRIS reactor
- ASTEC V2.2 modelling of IRIS
- ASTEC simulation of DBA sequence
- **ASTEC simulation od BDBA sequences**
- Conclusions and remarks

Code calculation: BDBA sequences

4 BDBA scenarios have been simulated by **assuming the actuation failure** of selected **safety systems** within the **reference DBA scenario** (2-in break of DVI-line), and by starting from the same steady-state calculation.
(Only selected significant cases have been chosen with the aim to provide a better characterization of the role played in the mitigation strategy by the passive safety systems).

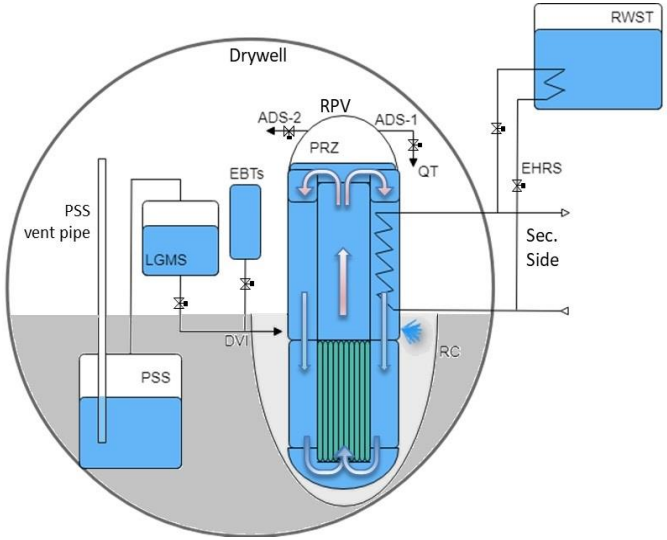

The **4 scenarios** are characterized by:

- **Failure of EBTs;**
- **Failure of EBTs and LGMS;**
- **Failure of EHRS and ADS st-1;**
- **Failure of EBTs, LGMS, EHRS and ADS.**

➢ The **BDBA** simulations results have been analyzed by comparing selected FOMs with respect to the **reference DBA sequence**.

Code calculation: BDBA sequences

- **Failure of EBTs injection**: **Success** of the passive mitigation strategy;
- **Failure of EBTs and LGMS injection: Success** of the passive mitigation strategy;
- **Failure of EHRS and ADS st-1: Failure** of the passive mitigation strategy and consequent SA;
- **Failure of EBTs, LGMS, EHRS and ADS: Failure** of the passive mitigation strategy and consequent SA;

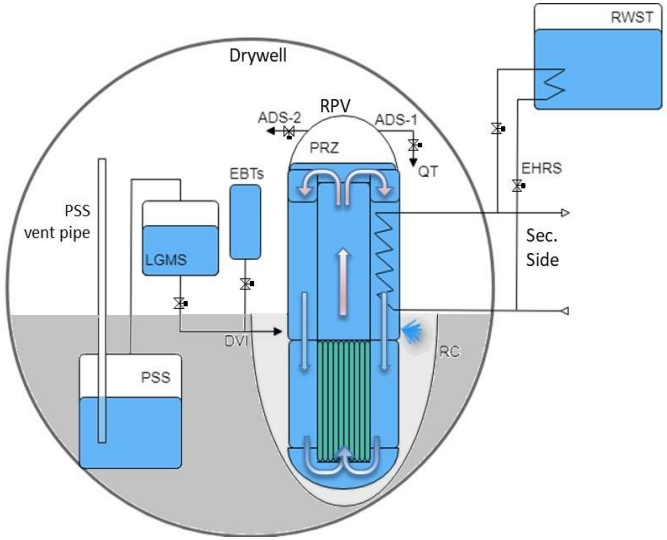

Event [s]	Reference DBA	EBT failure	EBT, LGMS 1failure	EHRS, ADS st-1 failure	All failure
Break	0	0	0	0	0
High Containment P. set-point	29	29	29	29	29
Low PRZ P. set-point	134	134	134	302	302
EBT-B empting	1650	-	-	2400	-
EBT-A empting	320	-	-	580	-
Low ΔP RPV-Cont. set-point	1330	1375	1375	16905	26960
RC level at DVI level	4100	5200	5200	14900	74000
Low LGMS mass set-point (ADS st-2)	17800	18000	-	132150	-
LGMS-B empting	25500	25600	-	155000	-
LGMS-A empting	20600	21500	-	135000	-
RWST water boiling	48000	48000	55000	-	-
Cladding failure	-	-	-	7800	9170
Corium relocation in LP	-	-	-	91560	111600
Containment failure	-	-	-	133950	113050

Comparison of BDBA calculations: **Core collapsed level**

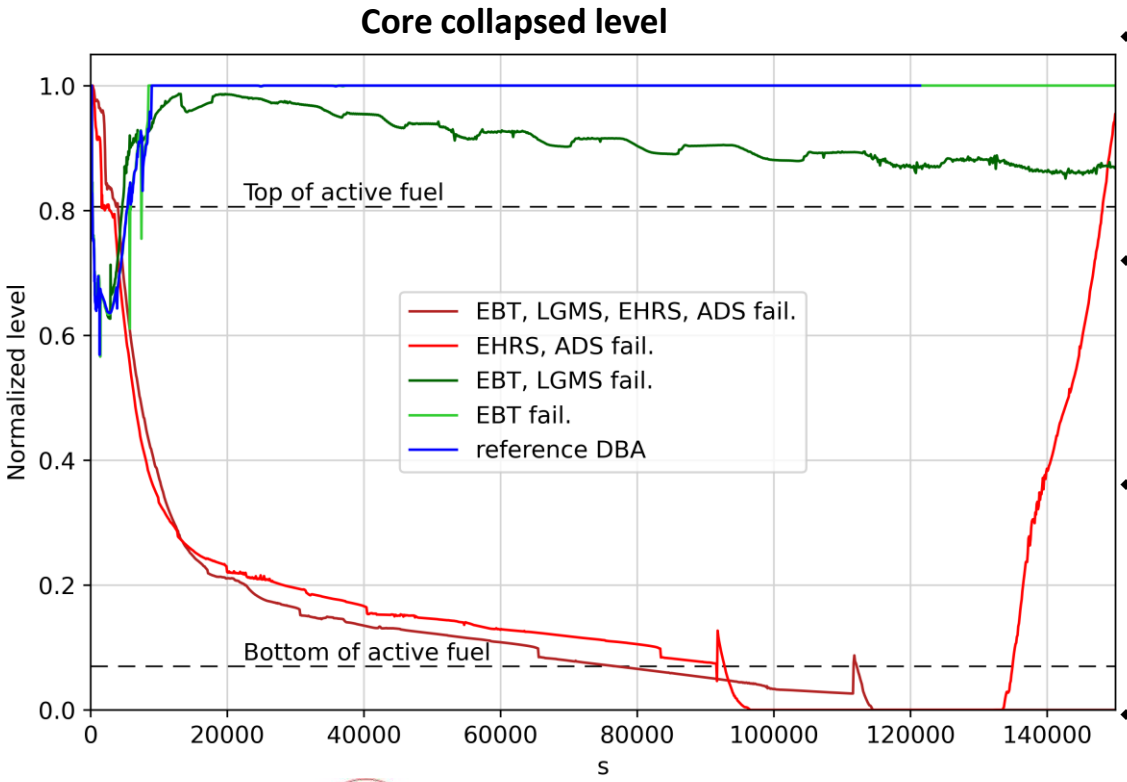

- **The final core lever is restored above the TAF** only in the 2 **Successful scenarios:**
  - **EBTs failure;**
  - **EBTs, LGMS failure.**
- The **early core level decrease** in the **Successful scenarios** is due to the **opening of the ADS st-1**, enhancing the core water boiling.
- In the scenario of **EBTs and LGMS failure**, at calculation end (150000 s) the level is still decreasing: **ADS st-2 opening failure** prevent the water flow back through the breack
- In the two **Failure scenarios** the core level decreases leading to a **severe accident**.

Comparison of BDBA calculations: **RC water level**

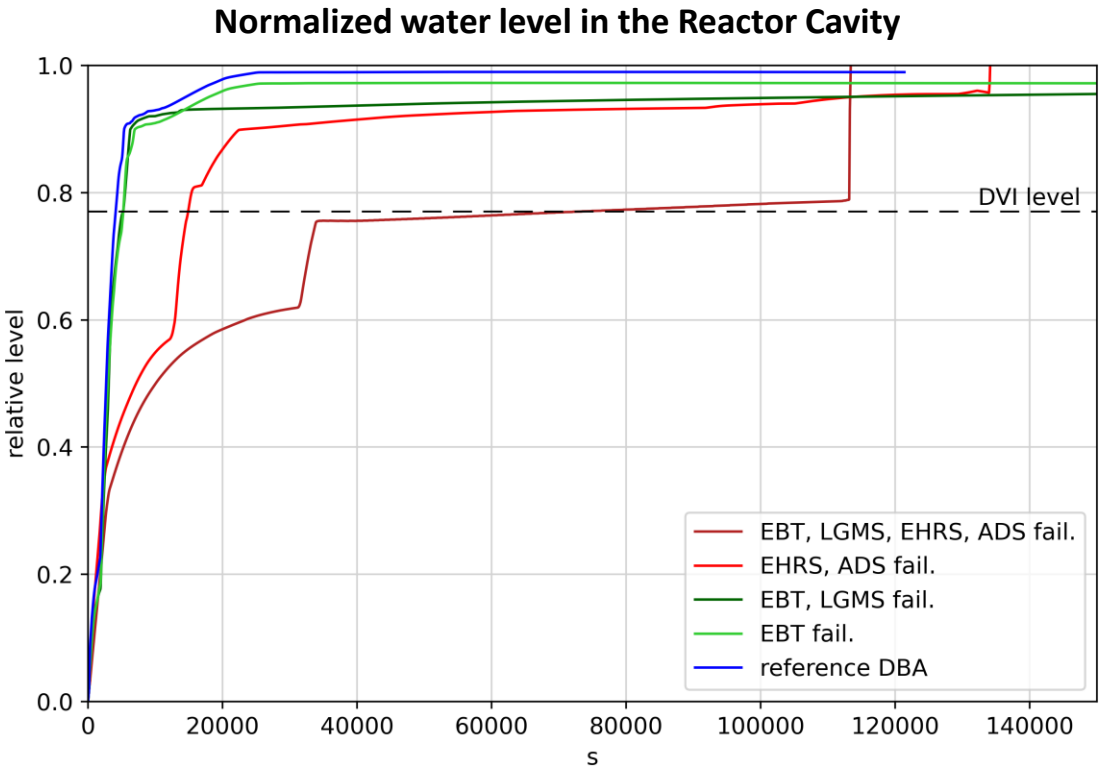

- In the 2 **Successful scenarios**, the correct operation of the passive mitigation strategy (inversion of containment and PSS pressures) allow the **RC to be filled above the break level** at early timings.

- In the **Failure scenarios** the **RC filling** is only due to the water flowing out of the break and of the EBTs and LGMS tanks.

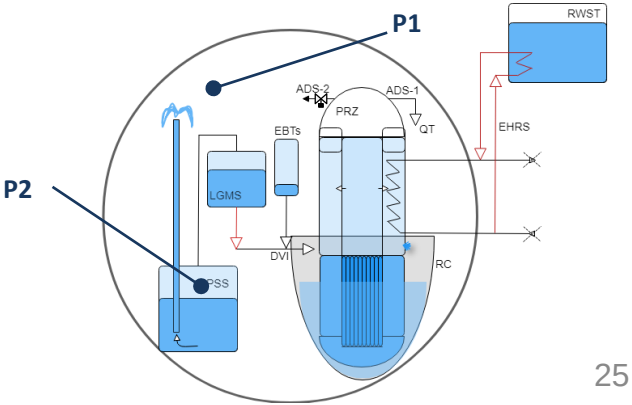

Comparison of BDBA calculations: **Primary pressure**

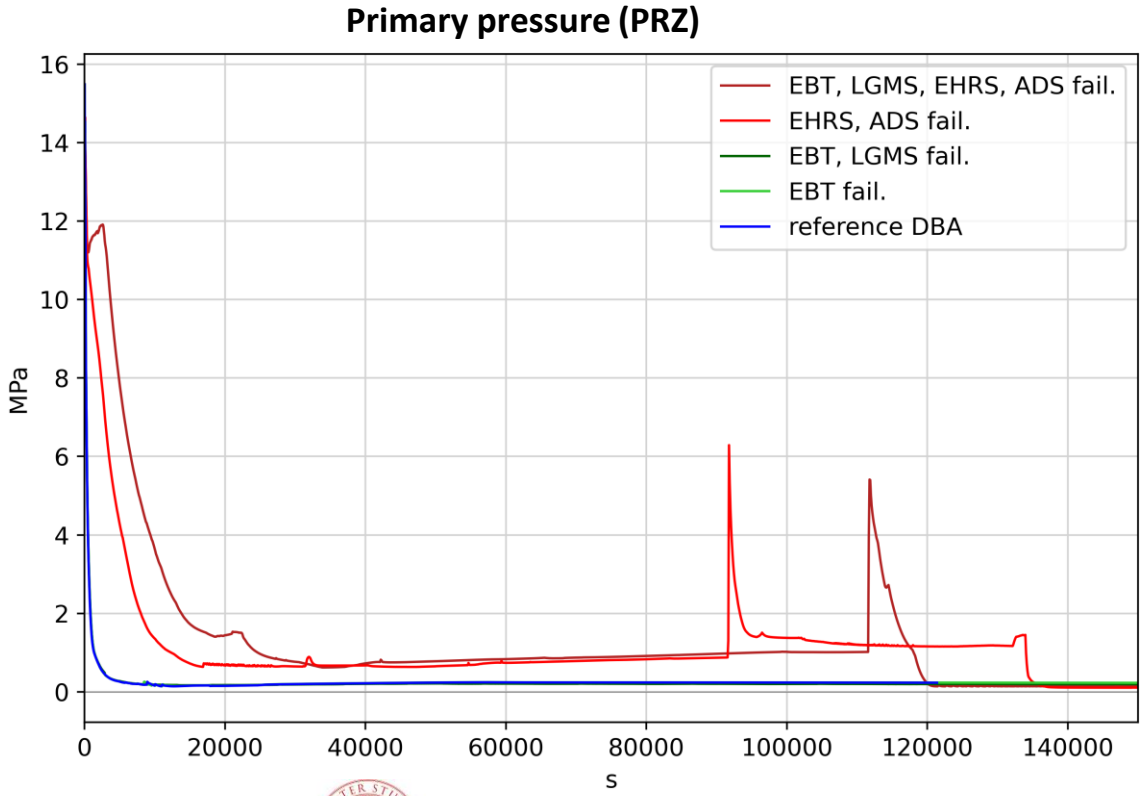

- **Faster RPV depressurization** in the 2 **Successful scenarios** is due to:
  - **opening of ADS st-1**;
  - Natural circulation **removal power of EHRS**.

A fast **depressurization of RPV and equalization with the containment pressure** is important to guarantee the **mitigation of the leak through the** break, avoiding the core uncovery.

- The high **pressure peaks** in the **Failure scenarios** are caused by the **corium slumping in the LP** in the two SA.

Comparison of BDBA calculations: **Containment pressure**

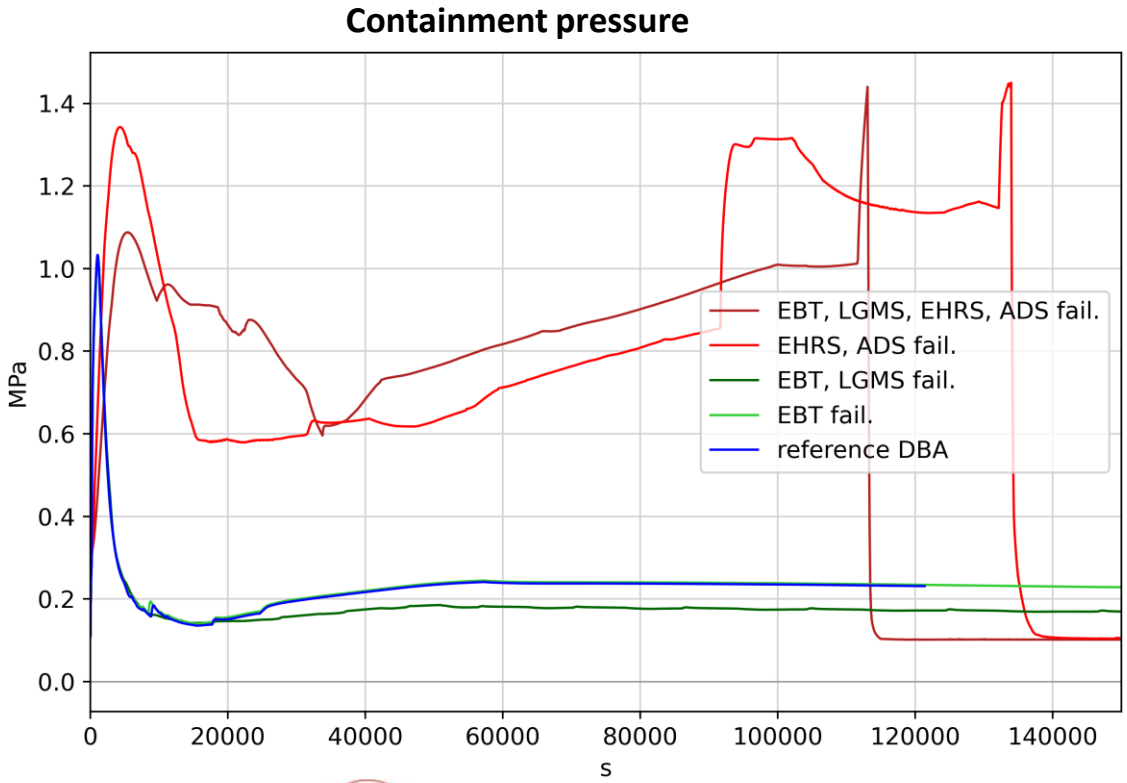

- **Containment pressurization** is faster in scenarios in which the **ADS st-1** is in operation (**Successful scenarios**). It leads to a **earlier equalization with RPV** pressure and **mitigation of the break leak.**

- In the 2 **Failure scenarios** the containment design pressure (13.5 bar) is reached:
  - After the corium slumping in the LP in the EBT, LGMS, EHRS, ADS failure scenario;
  - During the IVMR in the EHRS, ADS failure scenario.

Comparison of BDBA calculations: **Core T and H_2 production**

Core outlet temperature

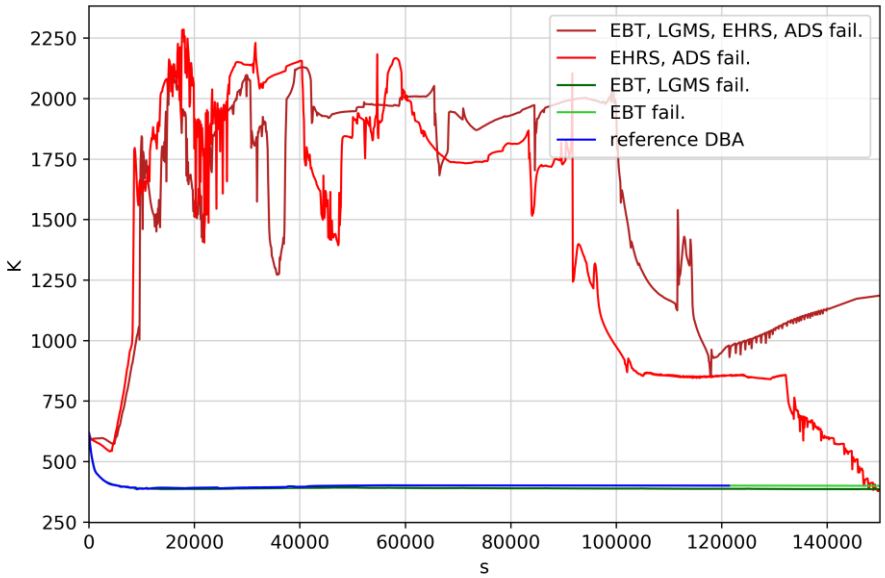

❖ The two failure scenarios features a similar degradation evolution.

H_2 production

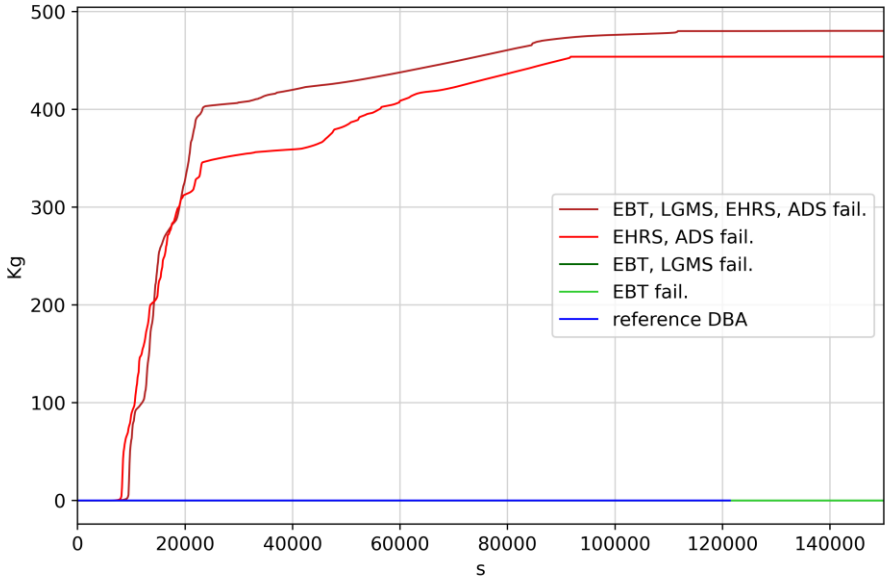

❖ The lower-plate failure takes place earlier in the worst scenario as expected (failure of EBTs, LGMS, EHRS, ADS).

Comparison of BDBA calculations: **Core degradation**

EHRS, ADS failure scenario

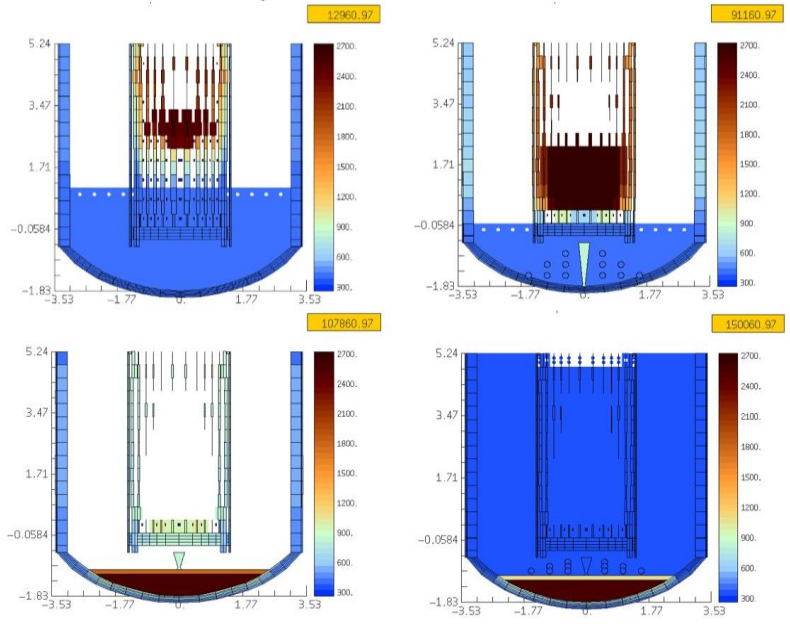

EBTs, LGMS, EHRS, ADS failure scenario

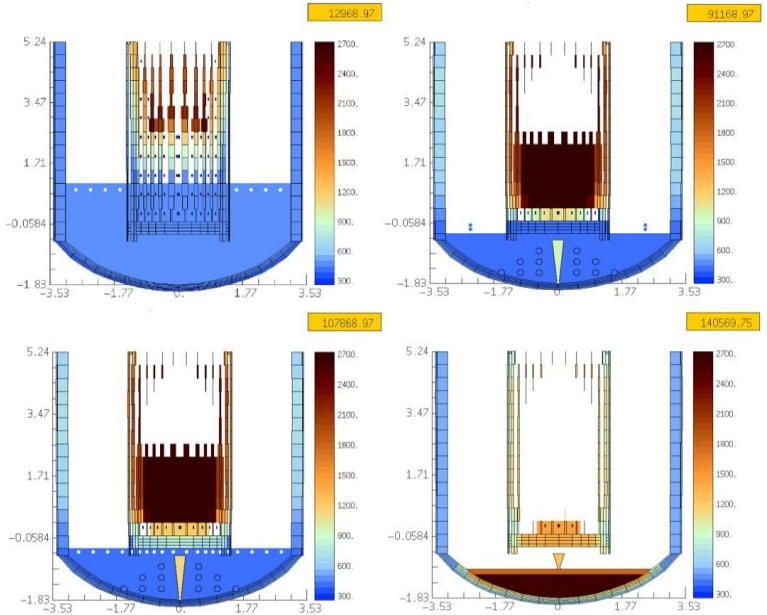

- The two **failure scenarios** features **a similar core degradation**, except for the **core refill from RC water** in the **EHRS, ADS failure scenario**, following the **ADS st-2 opening** (complete RPV depressurization).
  - High steam production and reactor pressurization.
  - Final **"new" IVMR configuration: corium submerged in water** (code applicability for this configuration should be further investigated).

OUTLINE

- Introduction
- The IRIS reactor
- ASTEC V2.2 modelling of IRIS
- ASTEC simulation of DBA sequence
- ASTEC simulation od BDBA sequences
- Conclusions and remarks

Conclusions and remarks

- The **4 BDBA simulation** shows the **applicability of the SMR ASTEC input-deck to several scenarios**, by assuming different combinations of systems failures.

- The **comparison of BDBA simulations** add valuable information regarding the **characterization** of each **passive safety systems in BDBA and SA** conditions:
  - **EHRS** and **ADS st-1 systems play a main role in the mitigation:** their operation seems to be a necessary criteria to guarantee the safety of the system during the postulated accident (2-in break of a DVI).
  - The effect of **ADS st-2** is also underlined: it allows the core refill from RC even in SA conditions.

- The study highlight the possibility that **SMRs in SA conditions** may be **characterized by specific phenomenology** (e.g. **IVMR with top water cooling**, systems coupling during core degradation, etc.) **not observed before for traditional size reactors**. Such phenomena **needs to be thoroughly investigated in future studies**.

- The activity gives first insights about the capability of ASTEC to capture different accidental sequences due to the partial or total not operation of the passive systems in a SMR. **Further research activity** specifically developed for SMR configurations **is necessary to identify ASTEC models development needs in term of further validation**.

Thank you for your attention

Pietro Maccari

pietro.maccari@enea.it

SEVERE ACCIDENT ANALYSIS RESEARCH AT CNL FOR SMALL MODULAR AND ADVANCED REACTOR DESIGNS

Andrew C. Morreale*, David W. Hummel, Luke S. Lebel, Yu-Shan (Sammy) Chin, Raymond S. Dickson, Kurt Stoll, and Christopher Maxwell
Canadian Nuclear Laboratories, Ltd. (CNL)
286 Plant Road, Chalk River, Ontario, K0J 1J0, Canada
andrew.morreale@cnl.ca; david.hummel@cnl.ca; luke.lebel@cnl.ca; sammy.chin@cnl.ca; raymond.dickson@cnl.ca; kurt.stoll@cnl.ca; christopher.maxwell@cnl.ca
*corresponding author

ABSTRACT

Across the world, small modular reactor (SMR) and advanced reactor designs are being explored to address demand for carbon-free energy generation. Canadian Nuclear Laboratories (CNL), in its capacity as Canada's national nuclear laboratory, conducts research to support the development and deployment of SMRs for both remote (off-grid) locations and grid-level applications. This includes a robust technical program to support research, development, and licensing activities. One of the major focus areas is severe accident scenarios and the associated radionuclide source terms. The CNL safety analysis and severe accident research program for SMRs includes the identification of relevant phenomena and research gaps, experimental investigation, evaluation of postulated accident scenarios, assessment of potential source terms, and the impacts of small modular designs on emergency planning zones. CNL is leveraging its extensive experience in CANDU to develop capabilities in safety analysis and severe accidents related to SMR designs including small light water reactors (integral pressurized water reactors, iPWR, and small boiling water reactors, BWR), high temperature gas reactors (HTGR), and molten salt reactors. Experimental programs related to specific phenomena such as fission product behaviour inside innovative iPWR containments, air ingress into HTGR cores, fission product releases from molten salts under accident conditions, and UO_2 corium behaviour and molten corium-concrete interaction are currently being pursued. Analysis efforts include integrated severe accident analysis of SMR designs and the evaluation of accident source terms and dose consequences. The technological focus of this research is guided by the SMR deployment landscape in Canada, based on proposed new build efforts and vendor designs under review by the Canadian Nuclear Safety Commission. CNL supports the needs of both Canadian government stakeholders and reactor vendors in the deployment of small modular reactor technologies in Canada.

KEYWORDS
Small Modular Reactors, source term, molten salt, high temperature gas cooled reactors (HTGR), integral PWR, small BWR

1. INTRODUCTION

Nuclear energy is receiving renewed interest across the world as an avenue for carbon free energy generation, which includes the development of advanced nuclear designs in the form of small modular reactors (SMRs). Multiple technologies and various sizes of SMRs are being explored, which are designed to meet different needs and to open new markets for nuclear energy. The principal deployment opportunities for SMRs in Canada are micro-sized reactors (5-15 MWe) designed for remote locations and industry sites, and grid-scale SMRs (50-300 MWe) for electricity generation. Canada has expressed great interest in the

deployment of SMR technologies, demonstrated by the government support for the research, development and licensing activities to bring these technologies to market. Canadian Nuclear Laboratories (CNL) is Canada's premier nuclear science and technology organization and is a major component of this effort through a robust technical program to support research, development, and licensing activities. A major area of this program is reactor safety analysis for licensing including the analysis of accident scenarios and potential radionuclide source terms.

The SMR reactor safety and severe accident research program at CNL is composed of experimental and modelling efforts to investigate areas of interest and facilitate their deployment. This includes identification of important phenomena and gaps in understanding, experimental investigation, evaluation of postulated accident scenarios, assessment of potential source terms, and the impacts of SMR designs on emergency planning zones. The investigation of SMR technologies at CNL benefits from extensive safety analysis and severe accident experience in support of the CANDU industry over several decades. The SMR research program at CNL is exploring multiple SMR designs, including water cooled designs (integral pressurized water reactor, iPWR; small boiling water reactors, BWR), high temperature gas cooled reactors (HTGR, including cylindrical compact and pebble bed designs), and molten salt designs. In addition, CNL is exploring heat pipe reactors to assess any specific concerns in the operation of these designs. Experimental and modelling efforts are being applied in these areas to understand specific phenomena relevant to these technologies, accident scenarios, and potential radionuclide release consequences. Other SMR designs (e.g. sodium fast reactors, etc.) may be added to CNL research programs based on the deployment landscape in Canada and potential interest of utilities, vendors, and government.

Initial CNL research into SMR designs in the area of severe accidents began with investigations of relevant phenomena and special conditions unique to these designs (e.g. small externally cooled containments in iPWR, air ingress in HTGR). These initial investigations also included phenomena identification and ranking table (PIRT) exercises conducted by CNL with input from international experts. These PIRT exercises sought to identify the relevant phenomena and present knowledge level for postulated severe accident conditions in certain SMR types. PIRTs were conducted for HTGR [1] and molten salt reactor (MSR) concepts [2]. In addition to this work, preliminary assessments of radiological consequences of limiting accidents for various SMR technologies were conducted. This included postulated accident scenarios, generic radionuclide inventories and estimated source terms based on release timing and time function release rates [3]. Information from these PIRTs and early generic analysis efforts have informed the refined experimental and modelling program in the area of severe accidents discussed herein. The research program is continually evolving and the focus is narrowing to the more specific technologies and designs that are moving closer to deployment.

The experimental programs, discussed in Section 2, include a variety of campaigns across the different reactor technologies including aerosol behaviour inside iPWR containments, air ingress into HTGR cores, and molten salt characterization and fission product release. There are also parallel investigations into UO_2 corium behaviour and molten corium-concrete interaction conducted in the CANDU space that may have bearing on certain SMR designs (i.e. water cooled with UO_2 fuel). The modelling and analysis work, presented in Section 3, includes integrated severe accident analysis of SMR designs and the evaluation of accident source terms and dose consequences. There are also additional modelling efforts focused on molecular dynamics of fission products in molten salts. The modelling and analysis efforts are also being used to support CNL participation in international projects discussing the potential implications for emergency planning zones (EPZ) of SMR designs to ensure reasonable emergency preparedness and response requirements are set out for the licensing and operation of these plants. CNL maintains connections to the international community through participation in such project and working groups run by the International Atomic Energy Agency (IAEA) and the Organization for Economic Cooperation and Development Nuclear Energy Agency (OECD-NEA).

CNLs strategy for SMR severe accident research, discussed in Section 4, is continually informed by the small modular reactor landscape in Canada including the proposed reactor technologies under vender design (and eventual licensing) review with the Canadian Nuclear Safety Commission (CNSC) and actively proposing deployment at sites in Canada. The technical program at CNL to support the research, development, and licensing activities is designed to support the needs of both Canadian government stakeholders and reactor vendors in the deployment of SMR technologies in Canada.

2. EXPERIMENTAL CAMPAIGNS RELATED TO SMR

Based on the gaps identified in the PIRT studies for the relevant SMR and advanced reactor technologies, CNL embarked on experimental programs to address important issues. The major identified gaps are design specific and focus on phenomena with limited information that can have relevant impacts on severe accident progression and radionuclide source term. For water cooled SMRs, the designs often feature innovative passive safety systems that can operate based on natural circulation, in order to forego the use of active systems like pumps that require external power. Such passive systems generally rely on a large external water pool as the heat sink that enables them to function, and some designs even have their small, high pressure steel containment vessels directly (either fully or partially) immersed in the pool. These immersed containment approaches are different from the larger dry containments of the large light water reactors (LWRs) and can have effects on the thermalhydraulic and fission product behaviour in the containment during an accident scenario. The current experimental focus is on iPWR designs, but the efforts in this area will be leveraged to investigate the small-BWR designs that make up the other major water cooled SMRs. High Temperature Gas Reactors and molten salt designs are quite different from each other and from the water-cooled reactor fleets currently operating in Canada and across the world. These designs also employ passive safety systems and rely on the specific nature of their designs and coolants to avoid or mitigate potential accidents. The primary concerns for HTGR is the effects of changing coolant flow conditions during an accident transient leading to the potential for air ingress and the possibility of oxidation of high temperature graphite. In terms of molten salt designs, there is high reliance on molten salt coolant to provide containment/retention of fission products during an accident scenario and thus the level of retention and potential for fission product release has become an area of significant interest.

2.1. iPWR Related Experiments

The iPWR experiments are focused on passive cooling innovations and specifically immersed containment systems. These include, for example, passive emergency core cooling systems that use steam that has re-condensed in containment as the water source, and pass it back into the core through a series of check valves [4]. The heat is generally transferred to large external water pools that are part of the design. CNL is investigating certain aspects of these immersed containment systems including:

- Thermal-hydraulic conditions (including the impact of non-condensable gases, e.g., hydrogen)
- Radionuclide transport (including the role of diffusiophoresis as a deposition mechanism)
- Radionuclide leakage from containment and retention in the outer water pool

The first phase of CNL experiments focuses on exploring the thermalhydraulic and radionuclide transport conditions that might be encountered in iPWR containment during an accident, and on quantifying the degree of diffusiophoresis-enabled aerosol deposition. Following a break or coolant discharge inside the containment vessel, the substantial heat sink of the outer pool results in significant condensation on the containment vessel wall, which also drives diffusiophoretic wall deposition of radionuclide-containing aerosols. Experiments, conducted in a 3.66 m tall rectangular vessel with a simplified iPWR containment-like geometry (the Strong Condensation Containment Apparatus, SCCA, shown in **Figure 1**), measured condensation and heat transfer rates, thermal stratification, and aerosol deposition rates for a variety of steam injection flow rates. Aerosol deposition was evaluated by tracking the transfer of surrogate (NaCl) aerosols in the condensate and Phase Doppler Anemometry observation of the near-wall particle size and velocity.

Initial experiments were conducted in March 2021 with steam and aerosol injection, and with the system open to atmosphere analogous to a loss-of-containment isolation beyond design basis accident. Some of these experimental results (gas temperatures and aerosol collection rates for several trials with different steam flows) are presented in **Figure 1** as well. The development of a hot steam layer overlying a cooler air layer in the volume was observed in all the tests, where the thickness of the steam layer grew or shrank with the steam injection rate. The steam condensation rate increased proportionally with the thickness of the steam layer. The total aerosol deposition rates plateaued at a fixed value (matching a fixed proportion to the injection rate), with the airborne concentrations deceasing as they were diluted throughout the thicker steam layer. An important observation is that aerosols were largely trapped in the upper steam layer, and became much more concentrated in the air at low steam flows. This stratification-induced trapping effect could have implications for source term analyses. The next phase of the experiments will focus on the impact of light non-condensable gases, using helium as an analog for hydrogen.



a) experimental apparatus

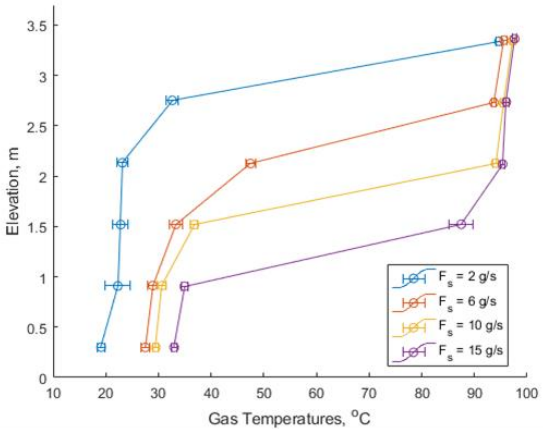

b) temperature stratification in the experimental volume

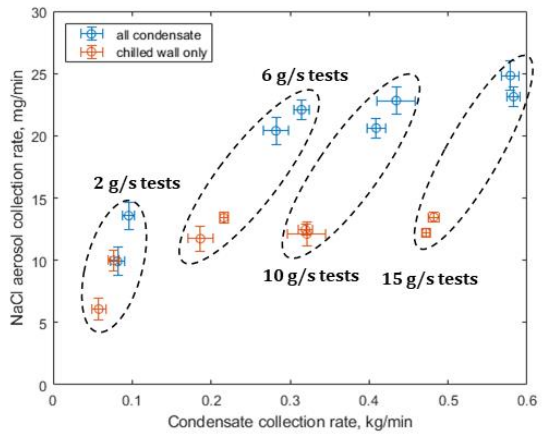

c) NaCl aerosol collection rate versus water condensate collection rate

Figure 1. Overview of Experimental Results from the Strong Condensation Containment Apparatus (SCCA)

2.2. HTGR-Related Experiments

A phenomenon that was highlighted by the HTGR severe accident PIRT exercise was the transition from a stagnant flow condition to bulk natural circulation of air within the core following a postulated break of the co-axial inlet/outlet duct. The timing of this transition appears uncertain, and the impact of bulk natural circulation of air on graphite oxidation would be significant [1]. CNL has begun designing an experimental apparatus to measure the onset of natural circulation of air in a HTGR vessel.

The High Temperature Air Ingress Facility (HTAIF) is intended to be located within CNL's existing Large Scale Containment Facility (LSCF). The apparatus will be close to full vertical scale for a HTGR-type SMR vessel (approximately 5 m) and will possess a stainless steel structure capable of maintaining temperatures in excess of 700°C (electrically heated) for several days. Initially filled with stagnant helium, the onset of natural circulation of air will be determined by temperature and indirect gas concentration measurements inside the vessel. Engineering design of the HTAIF is currently in progress.

Through a cooperative action plan signed by Atomic Energy of Canada Limited (AECL), Natural Resources Canada (NRCan), and the United States Department of Energy (U.S.DOE), CNL has also had collaborative discussions with Oregon State University (OSU). OSU is home to the High-Temperature Test Facility (HTTF), a one-quarter scale representation of the General Atomics Modular HTGR concept designed to operate at reduced pressure (0.8 MPa) but full accident temperature (1600°C) for integral thermalhydraulics testing [5]. The HTTF was constructed as part of the U.S.DOE's Next Generation Nuclear Plant Program [6]. Aside from getting access to experimental data that supports CNL's own model development and benchmarking work, CNL staff have also visited OSU to gain insights from the design and construction experience of the HTTF. Lessons learned from this experience are being applied to the design of CNL's HTAIF.

Verification of core concepts and components intended for the HTAIF has, meanwhile, been occurring within the LSCF. A method to measure helium/air concentration based solely on differential pressure has been successfully tested. Traditional gas concentration sensors are unsuitable with ≥700°C gases, and the withdrawal and cooling of gas samples prior to measurement would be disruptive to the development of the natural circulation inside the vessel. The differential pressure technique was demonstrated to be capable of tracking the ingress of air in the proposed geometry. Testing of a novel cartridge heater concept that could electrically heat the HTAIF to ≥700°C will be occurring within the LSCF in early 2022.

2.3. MSR-Related Experiments

CNL has been developing broad experimental capabilities to support research and development of MSRs. This includes development of experimental protocols for characterization and verification of key transport and thermodynamic properties of fuel and coolant salts, the study of corrosion of materials in contact with the salts, and the development of facilities for synthesis of actinide fluorides and chlorides. One topic of specific interest to MSR safety is the behavior of fuel salts in postulated accident conditions, particularly the ability of the salt to retain fission products.

CNL performed preliminary tests of fission product releases from molten salt fuels in early 2018. These tests made use of previously irradiated UO_2 fuel that was trace re-irradiated within CNL's National Research Universal (NRU) reactor to create a concentration of shorter-lived fission products including ^{131}I (half-life of approximately 8 days). A technique was devised to convert the UO_2 fuel into a halide salt within a hot cell while retaining the majority of fission products within the sample. The newly created salt fuel was then exposed to inert and oxidizing conditions inside an experimental furnace that could heat the salt past its melting point to temperatures in excess of 1000°C. The release of fission products from the salt was measured via gamma spectrometry through a combination of direct view of the salt, measurement of the gas

stream, and post-test scanning of deposition on the furnace tubes. Publication of the test results in the open literature has been delayed because questions have been raised regarding the efficacy of the conversion from UO_2 to halide salt within the cell.

As a follow up to the preliminary tests, CNL is designing new experiments that will measure fission product releases from molten salt fuels under much more tightly-controlled conditions of purity and oxygen content. These experiments will make use of specially designed salts with pre-established concentrations of actinides and fission product simulants ("simsalts") informed by reactor physics calculations. The first experiment will be performed entirely with stable isotopes as fission product simulants. The possibility of irradiating these "simsalt" fuels in a research reactor, and then transferring the irradiated salts to CNL's hot cell facilities for a similar measurement of fission product release, is currently being investigated.

3. SEVERE ACCIDENT ANALYSIS FOR SMR

CNL has been developing modelling capabilities to support analysis of normal operation and design basis accidents in advanced reactors and SMRs. Analyses of beyond design basis accidents, including severe accidents, typically involved different phenomena and often make use of different modelling tools than the design basis analyses. For the advanced reactor and SMR technologies of interest, the requirements for analysis of beyond design basis events are often unclear, and in some cases, there is no consensus that a credible severe accident condition even exists. CNL has been performing preliminary analyses of postulated accidents to develop modelling capabilities that may be required in the future, and performing scoping-level assessments that may inform and bound emergency preparedness and response considerations. The extent of the severe accident analysis of a particular SMR system is planned to take a graded approach in line with the size, potential radionuclide source term, and the phenomena encountered. CNL has the capabilities to tailor analysis to the level necessary to meet the needs for regulatory and licensing efforts.

3.1. Light Water Cooled SMR Related Analysis

Given the technological readiness level, availability of design information, and the similarities to currently deployed technologies, light water cooled SMR analysis is the area furthest ahead at CNL, specifically focused on iPWR designs. CNL has leveraged its experience in large LWR analysis with the MELCOR [7] integrated severe accident analysis code, gained mainly through Fukushima Daiichi related analysis efforts under OECD-NEA projects [8] [9], but also through efforts on severe accident analysis of large PWRs currently underway. These efforts help CNL to better understand the accident progression in large LWRs and the potential source terms of an accident near the US-Canada border. This modelling and analysis experience with large LWRs has also been beneficial in developing severe accident models and performing analysis on their SMR counterparts (e.g. iPWR and small-BWR).

For iPWR, a model has been developed in MELCOR for a generic submerged containment NuScale-like [4] design and includes the reactor pressure vessel, containment vessel and operating pool for a single unit (**Figure 2**). The decay heat removal system (DHRS), and passive core cooling through the system of reactor vent valves (RVVs; flow path 199 in **Figure 2**) and reactor recirculation valves (RRVs; flow path 299 in **Figure 2**) is also modeled. The use of the containment vessel, RVVs, RRVs, and the operating pool as the ultimate heat sink allows for full passive cooling of the reactor core in a station blackout scenario. As mentioned earlier in relation to the experiments, such passive cooling systems can result in phenomena such as steam stratification and air ingress in the event of failure of the containment vent line. The detail of this model allows for investigation into these phenomena, which can impair passive cooling (if there are steam losses) and may also affect fission product deposition on the containment walls and release to the environment [10]. The generic iPWR model at CNL is currently being used to analyze various severe accident scenarios to determine the accident progression and evaluate the potential source terms to the environment.

In addition to the full accident simulations for iPWR, benchmarking activities for the SCCA experiments, discussed in Section 2.1 are planned to compare the experimental results to code analysis with the GOTHIC (containment), STAR-CCM+ (computational fluid dynamics), and the MELCOR (severe accident) codes.

The other major type of light water cooled SMR designs is the small-BWR design. CNL is beginning its evaluation of this design in 2022 and will be leveraging its experience with MELCOR analysis of large BWRs (Fukushima Daiichi) along with the efforts in natural circulation and passive cooling phenomena common to iPWRs and small-BWR. The interest in small-BWR is driven by the proposed construction of a GE-Hitachi BWRX-300 by Ontario Power Generation at their Darlington site [11], which will dictate the modelling and analysis work on small-BWR. Development of a grid-sized (~300 MWe) small-BWR MELCOR model will be conducted in 2022, with preliminary analysis of severe accident scenarios to estimate source terms to follow in 2023.

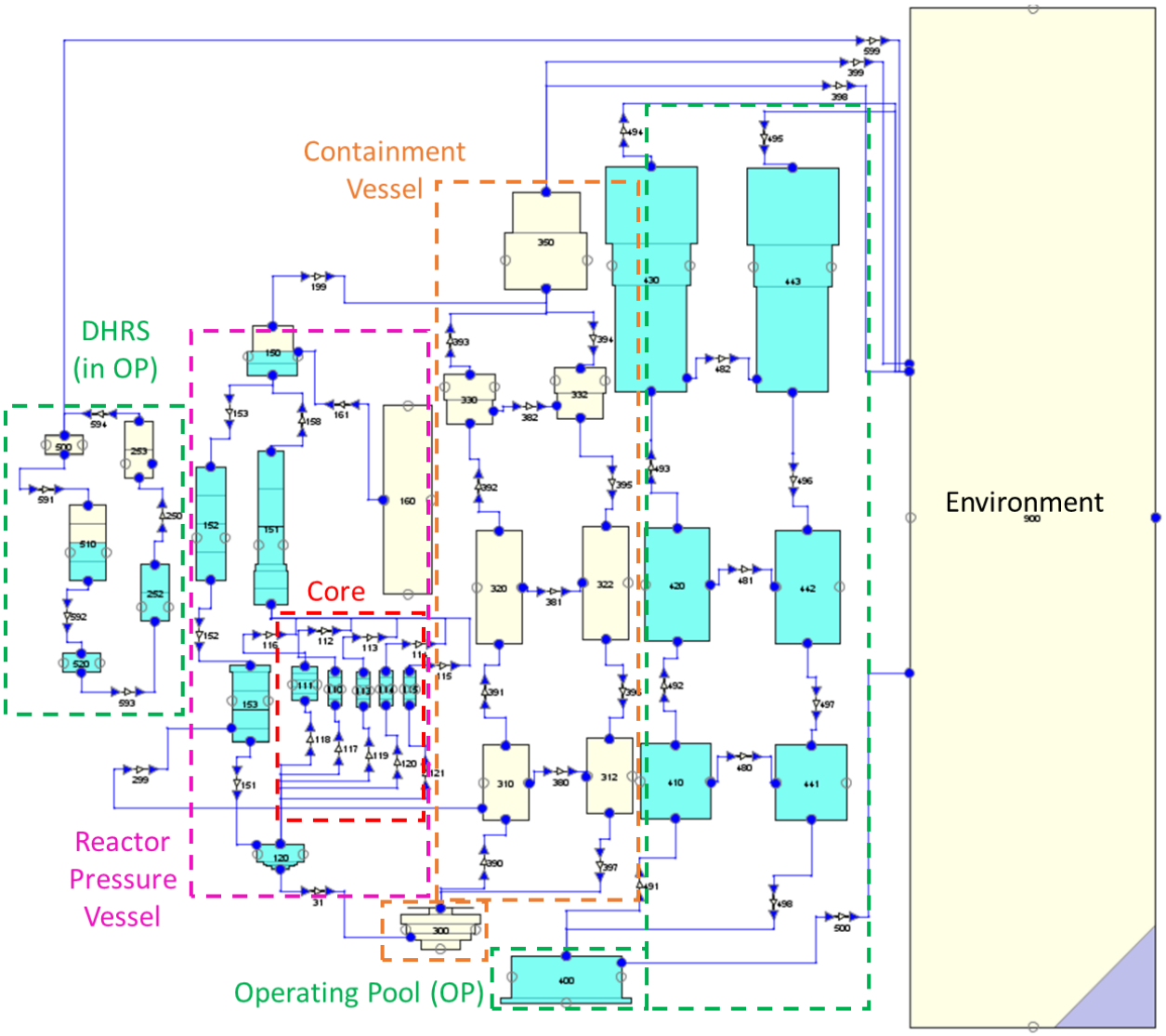

Figure 2. MELCOR Model of Generic iPWR with Submerged Containment [10]

CNL is also extending its SMR severe accident analysis efforts with the application of uncertainty and sensitivity analysis tools. Considering the maturity of the generic iPWR MELCOR model and analysis, it will be used first in the application of the sensitivity/uncertainty tools, such as DAKOTA or SUSA. This work leverages CNL efforts within the IAEA Cooperative Research Project (CRP) on Advancing the State-of-Practice in Uncertainty and Sensitivity Methodologies for Severe Accident Analysis in Water-Cooled Reactors, where CNL is conducting sensitivity and uncertainty analysis on CANDU severe accidents with the MAAP-CANDU and SUSA codes [12]. Following the uncertainty/sensitivity efforts conducted with iPWR, the application will be extended to small-BWR analysis and eventually to other non-LWR SMRs. The United States Nuclear Regulatory Commission (US NRC) is working with its national laboratory partners to demonstrating the capability of MELCOR to analyze such designs.

3.2. High Temperature Gas Reactor SMR Related Analysis

As mentioned above, US NRC, along with Oak Ridge National Laboratories and Sandia National Laboratories (SNL), are performing generic severe accident calculations of non-LWR SMR designs in an effort to develop better understanding of the accident progression and source terms as well as to ensure that the SCALE and MELCOR code capabilities are sufficient to accurately represent these complex designs. The severe accident modelling and analysis effort [13] uses non-proprietary generic reactor designs covering the major types of non-LWR SMRs including a heat pipe reactor, a pebble bed HTGR, a pebble bed fluoride salt-cooled high temperature reactor (FHR), a molten salt reactor, and a sodium cooled fast reactor. The analysis of the first three designs were conducted in 2021 and the analysis of the remaining two is planned for 2022. The non-proprietary input decks and analysis information will be made available from SNL by request, following the release of the latest MELCOR version in 2021 December. Information generated from these studies will be an important resource for CNL severe accident analysis efforts in the non-LWR space.

In the HTGR severe accident analysis space, CNL is focused on a grid-sized pebble bed gas cooled reactor design using TRISO type fuel. This is similar to the X-Energy Xe-100 design [14] that was a proposed option for the OPG SMR new build at Darlington (ultimately a small-BWR from GE-Hitachi was selected for this new build). The Xe-100 represents a well-developed design that is likely to attract interest in Canada, specifically for its ability to generate high temperature process gas as well as electricity. This makes the design of interest to hydrogen generation, and oil sands extraction industries. CNL is in the process of producing a MELCOR model of a generic pebble bed gas cooled design similar to the Xe-100. As mentioned, the US NRC studies on a generic pebble bed cooled HTGR will be a valuable resource to guide this model development and the subsequent analysis efforts planned at CNL in 2022.

The other important gas-cooled reactor design being developed in Canada is the proposed construction of a micro modular reactor design at the Chalk River Laboratories. Global First Power is undergoing the formal CNSC licensing process in order to build and operate a 5 MWe (15 MWth) Micro-Modular Reactor (MMR) from the Ultra Safe Nuclear Corporation. As this high temperature gas cooled design is destined for deployment at a CNL site, CNL will be working with both the reactor vendor and the regulator to provide support. While the extent of the support regarding severe accident analysis is yet to be determined, CNL has the capability to support a range of analysis from bounding calculations, design basis analysis, to full integrated severe accident code analysis.

3.3. Molten Salt Related Analysis

Molten salt cooled SMR designs are also of interest in Canada but are somewhat behind other SMR types (water-cooled, high temperature gas cooled) in their technological readiness level and projected deployment. Thus the research in this area is still focused on the major gaps identified in molten salt SMR PIRT [2], where fission product retention in molten salts is most relevant for severe accidents. Molten salt fission

product behaviour research efforts include the experimental work discussed in Section 2.3, and molecular dynamics modelling of molten salts discussed later in this section.

In terms of integrated severe accident analysis, CNL will be evaluating relevant molten salt cooled designs nearing deployment in Canada. A thorough review of the US NRC analysis efforts for a pebble bed FHR, and a reactor with molten salt fuel, will be included in this assessment. Future integrated severe accident analysis of molten salt-cooled designs will likely follow a similar path to the water-cooled and high-temperature gas designs, with the selection of a representative generic design, the development of a model (likely using MELCOR), and an assessment of relevant severe accident scenarios.

3.3.1. Molecular dynamics simulations of molten salts

Computer-based simulations of salt behaviour can be a valuable contribution to the interpretation and understanding of experimental results. As such, the capability to predict salt properties has been developed at CNL. Molecular dynamics (MD) simulations, based on polarizable interatomic potentials, have been conducted to predict thermophysical properties of molten salts and their mixtures. The density, heat capacity, thermal conductivity and viscosity of nitrate salts were estimated with good accuracy when compared to available experimental data [15]. Additionally, microscopic details of the salt structure were predicted.

Subsequently, MD simulations have focused on the behaviour of dissolved species in molten salts, and their effects on the solvent salt properties. In the model system of FLiNaK salt, the behaviour of the fission gases Xe and CsI was examined, and details of their solvation environment and their diffusivity were revealed. Also, alchemical free energy calculations were conducted to determine the free energy of solvation for these species, which matched trends observed experimentally [16]. Future computational work at CNL will involve expanding the interatomic potential to include other salts and dissolved species, as well as an examination of density functional theory-based MD simulations.

3.4. Emergency Planning Zones for SMRs

Many SMR and advanced reactor vendors have a goal to reduce the size of the emergency planning zone around the plant. International standards require that EPZs be established around any nuclear facility where there is the possibility that an event could cause radiation doses to persons off-site, thus warranting urgent protective actions. Consideration is typically given to very low probability events to ensure an appropriate envelope or planning basis for emergency preparedness and response.

CNL has been participating in an IAEA CRP on the development of approaches, methodologies and criteria for determining the technical basis for EPZ for SMRs [17]. A focus of this CRP has been formulating the event criteria and technical aspects to be considered when establishing the size of an EPZ around SMRs. The CRP is nearing completion and a technical document (IAEA-TECDOC) publication will be generated to summarize the project outcomes.

Recognizing that EPZs are determined based on low probability events with the potential for significant consequences, CNL has also performed an initial scoping-level assessment of potential postulated “limiting” reactor accidents (with respect to source terms) for different SMR technologies [3]. Source terms for these accidents were generated from data that was available in the open literature. These source terms were then input to an atmospheric dispersion and dose assessment model, and the resulting doses were compared against a similar assessment of a severe accident in a contemporary large water-cooled reactor. The study concluded that the smaller radionuclide inventory available for release from the SMRs inherently reduced the dose consequence for hypothetical limiting accidents. For SMR technologies that may retain most fission products under any credible accident condition, typical evacuation criteria are not exceeded greater than

1 km from the plant. The reduced dose consequences from these limiting accidents suggests that smaller EPZs may be suitable for these SMRs without increased risk of radiation dose to the public [3].

CNL is presently investigating the development of a framework that may be used to establish EPZ size around SMRs and advanced reactors. Preliminary investigations have suggested that, at least in Canada, there is no consensus among the various stakeholders on what would serve as an appropriate emergency planning basis for these reactor technologies. The selection and justification of appropriate planning basis, including the particular events and accident conditions for which source terms are generated, is considered a priority within this work.

4. STRATEGY FOR SMR SEVERE ACCIDENT RESEARCH

In the Canadian context there are multiple SMR technologies of interest and successful deployment of SMR technology requires support of research, development, and licensing activities. There is also uncertainty about which technologies will be first to market and even more as to which technologies will ultimately be successful. CNL, as Canada's premier nuclear science and technology organization, supports the needs of both Canadian government stakeholders and reactor vendors in the deployment of small modular reactor technologies in Canada.

The approach to SMRs at CNL has evolved from an agnostic development of understanding and tools to a more targeted application of CNL capabilities and skills in the assessment of specific phenomena of concern and to specific designs nearing deployment in Canada. In terms of severe accidents, initial PIRT assessments of reactor technologies to determine important phenomena and knowledge gaps were used to determine specific experimental and analysis research programs. Some of these programs have yielded results and further efforts have been identified. Ultimately the information generated by the phenomena specific research will be used to improve analysis tools to more accurately determine accident progression and consequences. CNL seeks to develop in-house tools and capabilities, and to contribute to relevant third-party tools and to the broader international body of knowledge on SMR severe accidents. CNL maintains good partnerships/collaborations with other research institutions and international communities. In terms of integrated severe accident analysis codes, CNL maintains an effective working relationship with the MELCOR code developer, SNL, and there are good connections between CNSC and the US NRC in the regulatory space.

In terms of the international community CNL is involved in several SMR related projects and working groups conducted under the IAEA, OECD-NEA and the Generation IV International Forum (GIF). As mentioned above, CNL is participating in the IAEA CRP on EPZs for SMRs, has membership on the GIF Risk and Safety Working Group (RSWG), and the OECD-NEA Expert Group on Small Modular Reactors (EG-SMR). CNL also participates in the US-NRCs Cooperative Severe Accident Research Project (CSARP) and MELCOR Code Assessment Project (MCAP), maintaining a good connection with the MELCOR user group and code developers.

5. CONCLUSIONS

SMRs and advanced reactors are an innovative carbon-free energy generation technology and there is significant push both internationally and in Canada for the development and deployment of these technologies. Government support for SMR deployment in Canada includes a supportive environment for research and development. As Canada's premier nuclear science and technology organization, CNL is a significant part of this, establishing and conducting technical research programs supporting SMR development and licensing. Reactor safety is the major component in licensing and CNL is conducting experimental and analysis work to better understand specific phenomena, concerns and research gaps related to the safety of SMR designs. Experimental programs including investigations into water- cooled SMR

passive cooling systems, air ingress into HTGR cores, and molten salt fission product retention provide valuable data on critical phenomena to better understand accident progression and potential consequences. Analysis efforts both support and augment the experiments, including molecular modelling of molten salts, benchmarking of experiments, and integrated severe accident analysis of different SMR designs (water-cooled, HTGR, molten salt). CNL participates in the international community to support SMR development through projects and working groups run by IAEA, OECD-NEA, and GIF. CNL's technical program is flexible and the focus is guided by the SMR deployment landscape in Canada and on best meeting the needs of both industry and regulatory stakeholders.

ACKNOWLEDGMENTS

Much of the work discussed herein and CNL participation in various international working groups, projects and initiatives is funded through the AECL Federal Nuclear Science and Technology Program.

REFERENCES

1. D. W. Hummel, Y-S. Chin, A. Prudil, A. Williams, E. Masala, G. Waddington, M. Edwards, P. Yakabuskie, T. Jafri, T. Tran, Xianmin Huang, and Z. Liang, "Results of a Phenomena Identification and Ranking Table (PIRT) Exercise for a Severe Accident in a Small Modular High-Temperature Gas-Cooled Reactor", *CNL Nuclear Review*, **Vol. 8, No. 2** (2019). doi: 10.12943/CNR.2019.00006
2. D.W. Hummel, Y-S. Chin, A. Prudil, A. Williams, D. Cluff, D. Mancey, E. Merle, F. Adams, L. Lebel, M. Salay, R. Dickson, S. Beils, T. Jafri, T. Tran, X. Huang, "Results of a Phenomena Identification and Ranking Table (PIRT) Exercise for a Severe Accident in Molten Salt Small Modular Reactors," Submitted to the *4th International Conference on Generation IV and Small Reactors (G4SR-4)*, Toronto, Canada, October 3-6 2022.
3. D.W. Hummel, S. Chouhan, L. Lebel, A.C. Morreale, "Radiation dose consequences of postulated limiting accidents in small modular reactors to inform emergency planning zone size requirements", *Annals of Nuclear Energy,* **Vol. 137**, 107062 (2020). https://doi.org/10.1016/j.anucene.2019.107062
4. J. N. Reyes, "NuScale plant safety in response to extreme events," *Nuclear Technology*, **178**(2), pp. 153-163 (2012).
5. M.A. André, R.A. Burns, P.M. Danehy, S.R. Cadell, B.G. Woods, and P.M. Bardet, "Velocimetry During Depressurized Conduction Cooldown Events in the HTTF", *Nuclear Engineering and Design*, **Vol. 341**, pp. 406–414 (2019). doi: 10.1016/j.nucengdes.2018.11.026
6. J.N. Reyes, J.T. Groome, B.G. Woods, B. Jackson, and T.D. Marshall, "Scaling Analysis for the High Temperature Gas Reactor Test Section (GRTS)", *Nuclear Engineering and Design*, **Vol. 240**, pp. 397–404 (2010). doi: 10.1016/j.nucengdes.2009.03.020
7. Sandia National Laboratory (SNL), "MELCOR Computer Code Manuals, Version 2.2-14959, Vol. 2 Reference Manual", SAND2019-12537, (2019)
8. A.C. Morreale, "Simulation of the Fukushima Daiichi Unit 2 Severe Accident With MELCOR 2.1", *Proceedings of the 18th International Topical Meeting on Nuclear Reactor Thermal Hydraulics (NURETH-18)*, Portland, OR, USA, August 18-22, 2019.
9. A.C. Morreale, "Refined Melcor Analysis of the Fukushima Daiichi Unit 2 Accident", *Proceedings of the 19th International Topical Meeting on Nuclear Reactor Thermal Hydraulics (NURETH-19)*, Brussels, Belgium, March 6-11, 2022.
10. L.S. Lebel, A. Morreale, K. Batten, T. Clouthier, "iPWR Containment Aerosol Deposition Experiments", *Proceedings of the 19th International Topical Meeting on Nuclear Reactor Thermal Hydraulics (NURETH-19)*, Brussels, Belgium, March 6-11, 2022.
11. Ontario Power Generation, "OPG Advances Clean Energy Generation Project", 2021 December 2. https://www.opg.com/media_releases/opg-advances-clean-energy-generation-project/

12. S.M. Petoukhov, A.C. Morreale, and M. Kloos "An Assessment of Uncertainties and Sensitivities in Severe Accident Progression Simulation for a Generic CANDU 6 Plant", *Proceedings of the 40th Annual Conference of the Canadian Nuclear Society,* Virtual Conference, June 6-9, 2021.
13. US NRC, "NRC Non-Light Water Reactor (NonLWR) Vision and Strategy, Volume 3 – Computer Code Development Plans for Severe Accident Progression, Source Term, and Consequence Analysis", ML20030A178 Rev. 1, January 31, 2020. https://www.nrc.gov/docs/ML2003/ML20030A178.pdf
14. X-Energy "Xe-100", https://x-energy.com/reactors/xe-100
15. C. I. Maxwell, M. Saoudi, and J. Pencer. "Development of a Polarizable Interatomic Potential for Molten Lithium, Sodium, and Potassium Nitrate," *Journal of Physical Chemistry B*, **124.23**, pp 4751-4761 (2020).
16. C. I. Maxwell, "Molecular Dynamics Study of Fission Gas Behaviour and Solubility in Molten FLiNaK Salt", *Journal of Nuclear Materials* (In Press-2021).
17. International Atomic Energy Agency, "Development of Approaches, Methodologies and Criteria for Determining the Technical Basis for Emergency Planning Zone for Small Modular Reactor Deployment", IAEA CRP I31029. https://www.iaea.org/projects/crp/i31029

Canadian Nuclear Laboratories | Laboratoires Nucléaires Canadiens

Severe Accident Analysis Research at CNL for Small Modular and Advanced Reactor Designs

Andrew C. Morreale*, David W. Hummel, Luke S. Lebel, Yu-Shan (Sammy) Chin, Raymond S. Dickson, Kurt Stoll, and Christopher Maxwell

Canadian Nuclear Laboratories (CNL)

The 10th European Review Meeting on Severe Accident Research (ERMSAR-2022), Akademiehotel, Karlsruhe, Germany, May 16-19, 2022



GE Hitachi BWRX-300 Single plant concept art:
- Successful bid for new SMR construction in Ontario, Canada

Outline

- Introduction
  - CNL's role in Small Modular Reactor (SMR) deployment and research areas
- Experimental Campaigns Related to SMRs
  - iPWR (integral Pressurized Water Reactor) Experiments
  - HTGR (High Temperature Gas Reactor) Experiments
  - Molten Salt Related Experiments
- Severe Accident Analysis for SMRs
  - Light Water Cooled SMR Analysis (iPWR and small Boiling Water Reactors, BWRs)
  - HTGR Analysis
  - Molten Salt Related Analysis
  - SMR Emergency Planning Zones
- Strategy for SMR Severe Accident Research
- Conclusions

Introduction

- SMRs are a source of carbon free energy with opportunity for deployment in Canada
  - Micro sized (5-15 MWe or 15-45 MWth) and grid-scale (50-300 MWe or 150-1000 MWth)
  - CNL's robust technical program supports SMR research, development, and deployment.
- CNL SMR reactor safety program combines experimental and modelling efforts:
  - Benefits from extensive experience supporting CANDU safety analysis over several decades.
  - Objective is to investigate areas of interest and facilitate SMR deployment.
    - Identification of important phenomena/knowledge gaps and investigation via experiments and modelling
    - Evaluation of postulated accident scenarios and potential source terms, and assessment of the impacts of SMR designs on emergency planning zones.
  - Designs currently under exploration include iPWR, small BWR, HTGR, and molten salts.
    - Includes both grid scale and micro-sized designs
    - Efforts based on SMR deployment landscape in Canada and interests of utilities, vendors, and government.
- CNL also maintains connections with the international community, participates in joint projects, and is exploring commercial projects with reactor vendors.

Introduction - 2

- Initial SMR research plans were technology agnostic and began with investigations of relevant phenomena/special conditions including phenomena identification and ranking tables (PIRTs)
    - Identify relevant phenomena and present knowledge level for postulated severe accident conditions in certain SMR types (PIRTs conducted for HTGR and molten salt reactors)
- Preliminary assessments of radiological consequences of limiting accidents for various SMRs
    - Postulated accident scenarios, generic radionuclide inventories and estimated source terms based on release timing and time function release rate.
- PIRTs and early generic analysis efforts used to inform/refine severe accident research program
    - Research program is continually evolving and the focus is narrowing to more specific technologies and designs that are moving closer to deployment.
- CNL SMR Severe Accident Research includes:
    - **Experimental programs:** iPWR containment thermal-hydraulics and aerosol behaviour, HTGR air ingress, molten salt behaviour, and parallel investigations into UO_2 corium behaviour (CANDU space).
    - **Modelling and analysis:** integrated severe accident analysis of SMRs (evaluation source terms/dose consequence) and molecular dynamics of fission products in molten salts.

Experimental Campaigns

- Based on gaps identified in the PIRT studies (HTGR, MSR) and other important phenomena
  - Focused on phenomena with limited information that can impact severe accident progression and source term.
- **Water cooled SMRs:** exploration of passive safety systems using natural circulation, containment vessel and operating pool configurations, and effects of smaller containments.
  - Behaviour of thermalhydraulics and fission products is different from large reactors.
  - Initial focus on iPWR, but efforts being leveraged to expand to investigate small-BWRs
- **High temperature gas reactors:** studying effects of changing coolant flow conditions during an accident leading to potential for air ingress and possible oxidation of high temperature graphite.
- **Molten salt designs:** investigation of fission product (FP) behaviour/retention in the salt under accident conditions to understand the impact on fission product source term.
  - Preliminary FP release tests from fuel salt in hotcell (2018)
  - Designing new FP release experiments using "simsalts" (contain actinides and FP simulants)
  - **"simsalt" tests:** 1) stable isotopes; 2) possible irradiation of "simsalt" in a research reactor

IPWR Experiments

- Investigating iPWR immersed containment configurations
  - Thermal-hydraulic conditions:
    - Including the impact of non-condensable gases, e.g., hydrogen)
  - Radionuclide (RN) transport:
    - RN retention and leakage from containment.
    - Including the role of diffusiophoresis as a deposition mechanism
- Phase 1 experiments in the SCCA (March 2021)
  - Aerosol deposition (diffusiophoresis-enabled) on containment walls during accident conditions
  - Analogous to loss-of-containment isolation accident
    - Steam and aerosol injection; vessel open to atmosphere
  - All tests saw hot steam overlaying cooler air
    - Steam layer thickness varied with injection rate and condensation increased proportional to steam thickness
    - Aerosol deposition rates plateau (in line with injection rate) and airborne concentrations decrease (diluted by thicker steam layer)
- Phase 2 experiments will explore helium injection

Strong Condensation Containment Apparatus (SCCA)

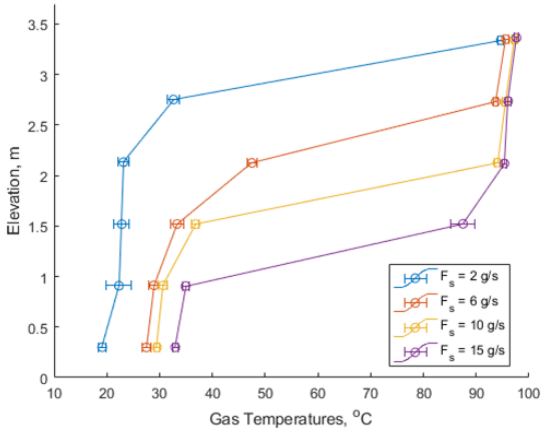

Temperature stratification in the experimental volume

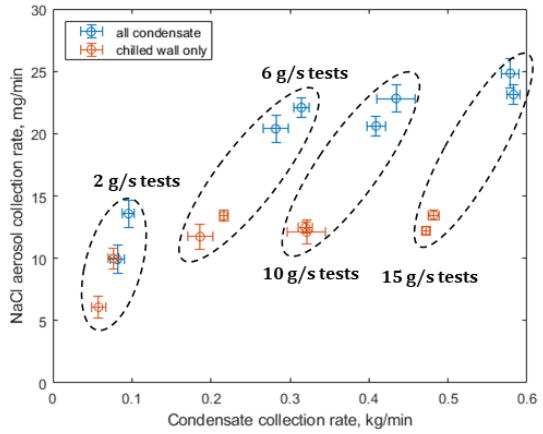

NaCl aerosol collection rate versus water condensate collection rate



HTGR Experiments

- Exploration of transition from stagnant flow to bulk natural circulation of air within the core following a postulated break of the co-axial inlet/outlet duct: **Air ingress and potential for graphite oxidation**
  - Apparatus under design to measure the onset of natural circulation of air in a HTGR vessel
  - High Temperature Air Ingress Facility (HTAIF): Engineering design currently in Progress
    - Full vertical scale for HTGR-type SMR vessel (~5 m); SS structure; temp. > 700°C (electrically heated) for several days
    - Initially filled with stagnant He; determine onset of natural circulation of air via temperature and indirect gas concentration measurements inside the vessel.
  - Also exploring a smaller scale apparatus to investigate air ingress into HTGR vessel.
  - Verifying core concepts/components intended for the HTAIF and/or other smaller apparatus
    - Method for differential pressure measurement for helium/air concentration
    - Testing (in early 2022) of a novel cartridge heater concept to heat HTAIF to ≥700°C
- AECL/Natural Resources Canada/US Department of Energy collaboration = access to DOE experiments
  - Oregon State High-Temperature Test Facility (HTTF) – ¼ scale General Atomics HTGR concept
    - Operates at reduced pressure (0.8 MPa) but full accident temperature (1600°C) for integral thermalhydraulics testing
  - CNL accessing HTTF experimental data to support model development and benchmarking work.
  - CNL visited OSU to gain insights from HTTF design/construction; apply lessons learned to HTAIF.

Molten Salt Experiments

- Developing broad experimental capabilities to support research and development of MSRs
  - Characterization and verification of the thermodynamic properties of salts
  - Corrosion of materials in contact with the salts
  - Development of facilities for the synthesis of actinide fluorides and chlorides.
- Fuel salt FP behaviour accident conditions: **FP retention**
  - Trace re-irradiated UO_2 fuel converted into a halide salt (retaining majority of fission products)
  - Salt fuel was then exposed to inert and oxidizing conditions inside furnace (>1000°C)
  - FP release measured via gamma spectrometry
    - (direct view + gas stream + furnace tube scan post test)
  - Publication delayed due to questions raised on efficacy of conversion from UO_2 to halide salt

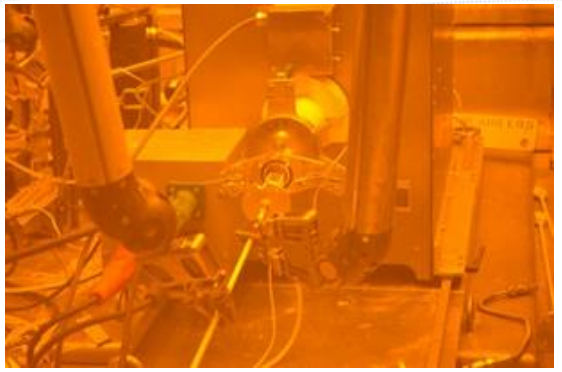



Top: Fission product release furnace in hot cell + instrument readings
Bottom: Diagram of molten salt fission product release experiment

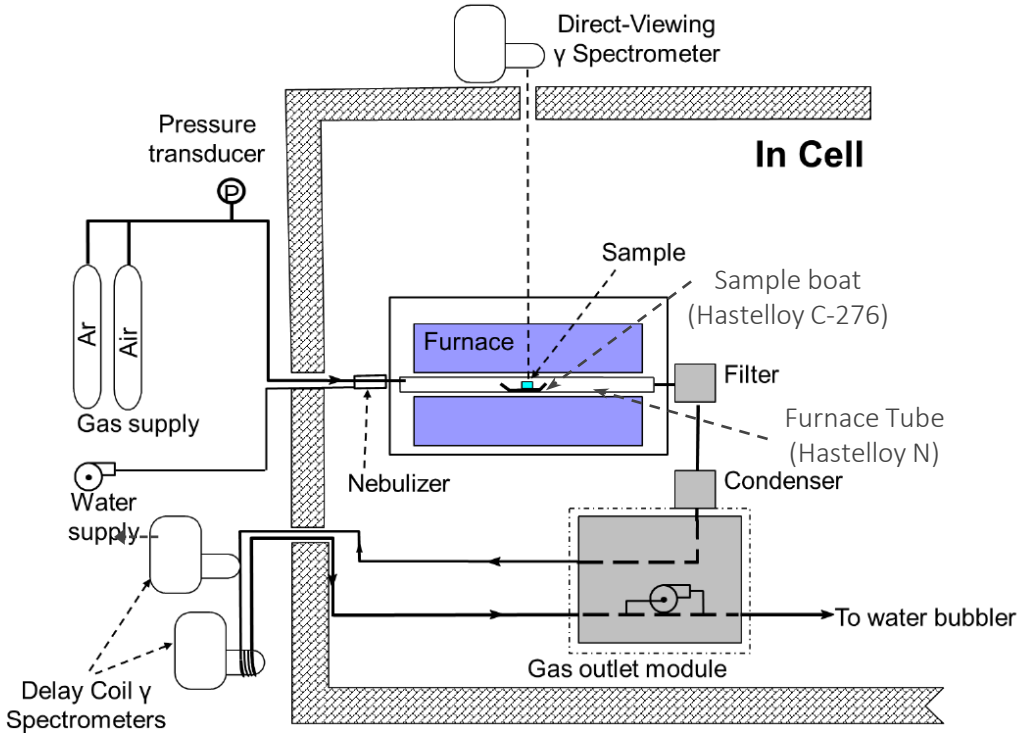

Modelling and Analysis

- For advanced reactor and SMR technologies, requirements for analysis of beyond design basis events are often unclear, and in some cases no consensus exists for a credible severe accident
  - CNL developing future modelling capabilities and understanding for emergency response
    - Preliminary analyses of postulated accidents, and scoping-level assessments that may inform and bound emergency preparedness and response considerations.
  - Capable of tailoring analysis to the level necessary to meet regulatory/licensing needs
    - Graded approach to the extent of the severe accident analysis of a particular SMR system in line with the size, potential radionuclide source term, and the phenomena encountered.
- **Water cooled SMRs:** integral accident analysis of iPWR and small-BWR (upcoming) systems.
  - MELCOR analysis of iPWR station blackout + containment behaviour (SCCA benchmark)
- **High Temperature Gas Reactors:** assessment of severe accident code applicability to HTGR severe accident analysis (MELCOR found suitable) and development of generic pebble bed HTGR model.
- **Molten salt designs:** investigation of molten salt coolant designs and early integral analysis efforts
- **Future plans:** exploration of heat pipe reactor designs, and investigation of sodium cooled designs

Water-cooled Reactor Analysis

- Generic iPWR, MELCOR modeling/analysis
  - SBO + passive cooling/containment failure to look at accident progression/source term.
    - e.g., loss of DHRS, containment failure and air ingress, and failure of operating pool heat sink
- Code benchmarking of the SCCA experiments
  - GOTHIC (containment), STAR-CCM+ (CFD), and MELCOR (severe accident) codes.
- Leveraging iPWR (passive cooling) and large-BWR experience (Fukushima Daiichi) for small-BWR effort
  - GE-Hitachi BWRX-300 (OPG Darlington)
    - Develop generic small-BWR MELCOR model (2022)
    - Severe accident source term analysis (2023)
- Application of uncertainty and sensitivity (U&S):
  - DAKOTA (or SUSA) application to MELCOR
    - First application is to severe accident analysis of iPWR and then to small-BWR and non-water-cooled SMRs
    - Leverages CNL participation in IAEA CRP (U&S methodologies for severe accident analysis in water-cooled reactors)

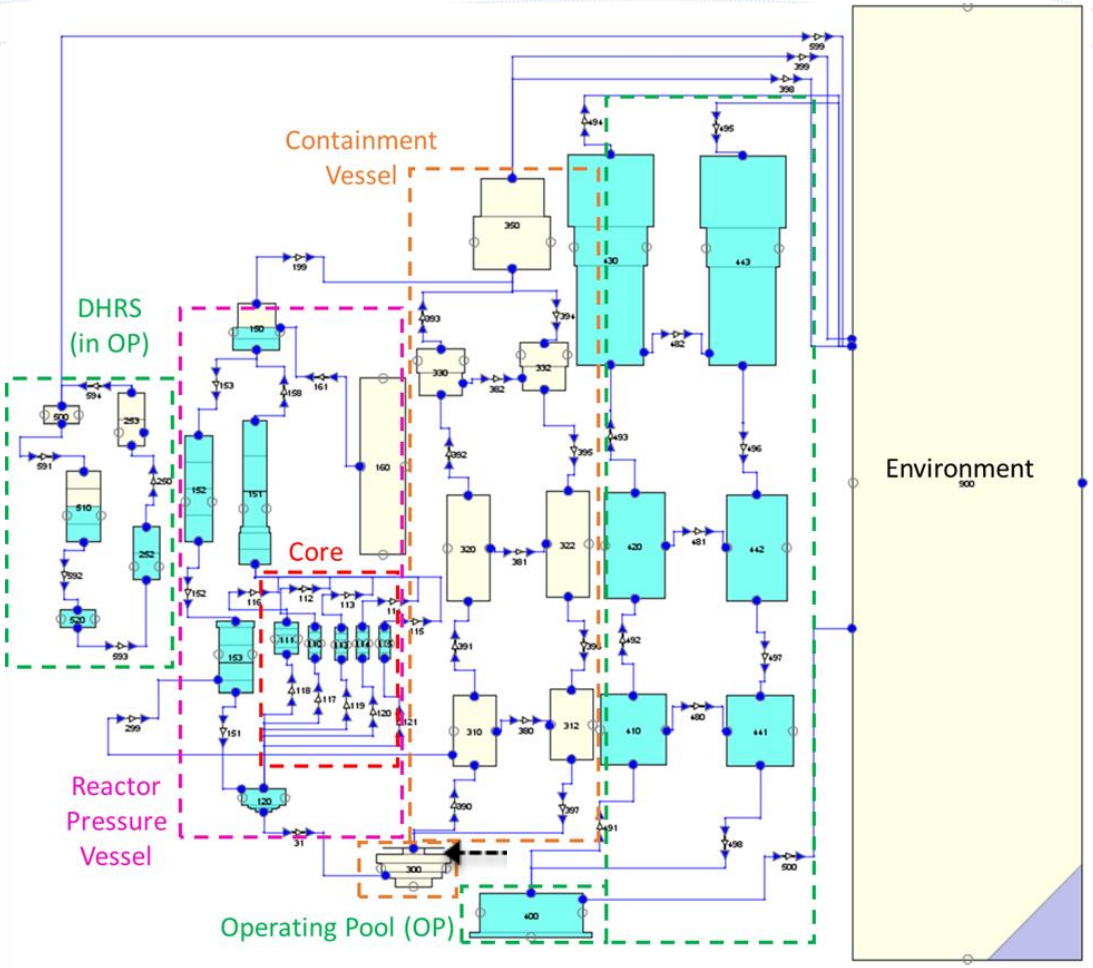

CNL MELCOR Model of Generic iPWR

HTGR Modelling and Analysis

- CNL assessing severe accident analysis tools and beginning integral analysis efforts
- Focus on grid scale pebble bed HTGR and assessing analysis needs for micro-HTGRs
  - X-Energy (Xe-100 design) proposed for OPG SMR new build at Darlington
    - While not selected, it is a well-developed design likely to attract interest in Canada due to capability for combined electricity and process heat (valuable to industry: H_2 and oil sands)
  - USNC MMR planned build at Chalk River (determining analysis needs)
- Assessment of suitable integral analysis tools found MELCOR to be a good option
  - Based on literature review and the US NRC non-LWR Analysis Project, which included analysis of a non-proprietary generic pebble bed HTGR
- CNL developed an initial SMR-sized pebble bed HTGR model, analysis begins soon
  - Generic pebble bed HTGR model based on Xe-100 and PBMR-400
    - Model was developed from open literature (focused on Xe-100 with supplementary and missing information based off of PBMR-400) and is non-proprietary.
    - Model and analysis to be compared with US NRC non-LWR efforts with HTGR
  - Analysis to focus on relevant accident scenarios and investigate air ingress.

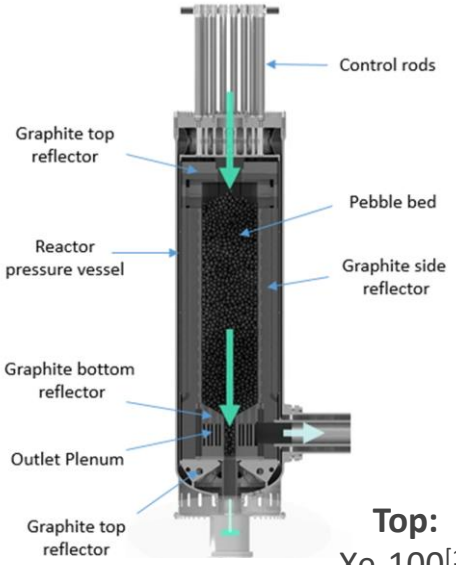

Top: Xe-100[1]

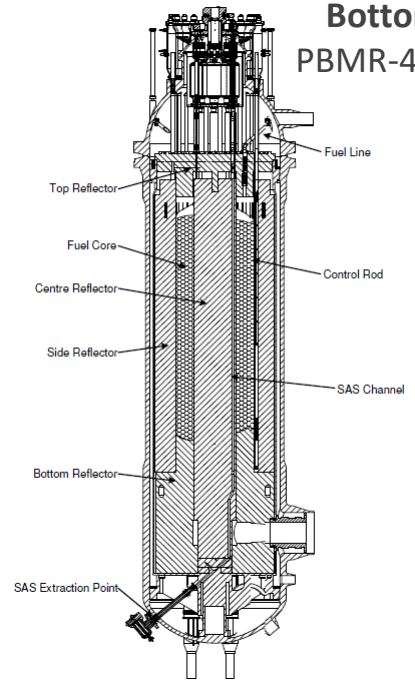

Bottom: PBMR-400[2]

[1] X-energy, "Reactor: Xe-100", https://x-energy.com/reactors/xe-100; [2] P. J. Venter, M. N. Mitchell and F. Fortier, "PBMR REACTOR DESIGN AND DEVELOPMENT", in 18th International Conference on Structural Mechanics in Reactor Technology (SMiRT 18), Beijing, 2005.

Molten Salt Modelling and Analysis

- CNL research focused on major gaps identified in PIRT (e.g. fission product behavior and retention in salts) and early investigation into MSR designs (e.g. Terrestrial IMSR)
- **Integral analysis:** Code assessment + evaluation of designs proposed to deploy in Canada
  - Review US-NRC non-LWR analysis of pebble bed FHR (salt cooled), and molten salt fuel reactor
  - CNL molten salt reactor analysis will follow similar path to other technologies (e.g. LWR, HTGR)
    - 1) Select representative generic design, 2) develop model, and 3) assess relevant severe accident scenarios.
- Molecular dynamics (MD) simulations of molten salts (salt properties and FP behaviour)
  - MD simulations (based on polarizable interatomic potentials) conducted:
    - Predicted thermophysical properties of molten salts and their mixtures
    - Estimation of density, heat capacity, thermal conductivity and viscosity of nitrate salts had good accuracy compared to available experimental data.
  - Behaviour of dissolved species (FPs) in molten salts, and effects on solvent salt properties
    - Fission gasses (Xe and CsI) in FLiNaK salt examined based on solvation and diffusivity and alchemical free energy calculations showed free energy of solvation matched experimental trends observed experimentally
  - Future efforts will include investigation of other salts/dissolved species as well as examining density functional theory-based MD simulations.

SMR Emergency Planning Zones (EPZs)

- International standards require EPZs for nuclear facilities where possible events could cause off site consequences (i.e. radiation doses) warranting urgent protective actions.
  - EPZs based on very low probability events with potential for significant consequences
  - Need to ensure appropriate envelope/planning basis for emergency preparedness/response.
  - A common goal of SMR/AR vendors is to reduce the size of EPZs compared to current plants

- CNL previously performed an initial scoping-level assessment of potential postulated "limiting" reactor accidents with respect to radionuclide (RN) source terms for different SMR technologies
  - Atmospheric dispersion/dose consequence analysis (source terms from open literature data).
    - Compared SMR results (HTGR, Molten Salt Reactor, Lead Cooled Fast Reactor, and iPWR) to a similar severe accident assessment for a contemporary large water-cooled reactor.
  - Smaller RN inventories in SMRs reduce dose consequence for hypothetical limiting accidents.
  - Reduced dose consequences from these limiting accidents suggests that smaller EPZs may be suitable for these SMRs without increased risk of radiation dose to the public.

SMR Emergency Planning Zones (EPZs) - 2

- CNL is participating in IAEA Cooperative Research Project on the technical basis of EPZ for SMR, which is focused on:
  - Development of EPZ approaches, and methodologies
  - Formulating event criteria and technical aspects to consider when establishing the size of an EPZ around SMRs.

- CNL is investigating development of a framework to establish EPZ size for SMRs/advanced reactors.
  - An appropriate emergency planning basis needs to be determined for these reactor technologies.
  - Preliminary investigations suggest a lack of consensus among various stakeholders in Canada
  - Major priorities of this effort will include:
    I. Selection and justification of an appropriate planning basis
    II. Determination of particular events and accident conditions for which source terms should be generated.

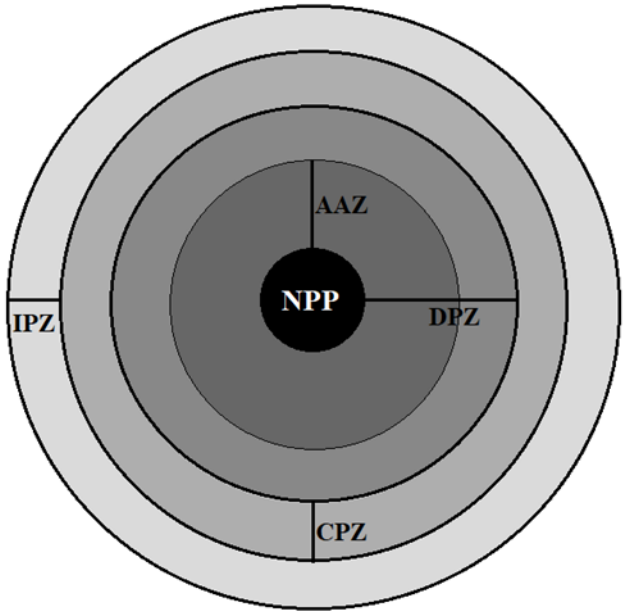

EPZs Defined in the Ontario Provincial Nuclear Emergency Response Plan (PNERP)
AAZ – Automatic Action Zone
DPZ – Detailed Planning Zone
CPZ – Contingency Planning Zone
IPZ – Ingestion Planning Zone

CNL SMR Research Strategy

- Canadian SMR landscape includes multiple technologies and successful deployment will require support of research, development, and licensing activities.
    - Uncertainty on first to market technologies, and even more as to those ultimately successful.
    - CNL supports both government stakeholders and reactor vendors in SMR deployment.
- CNL's approach to SMRs evolves as the market matures and the landscape changes
    - Initial technology agnostic development of understanding/tools moving towards targeted applications of capabilities to assess specific phenomena for designs nearing deployment.
- Severe accident research has progressed:
    - Initial PIRTs (identifying phenomena and gaps) → specific experimental and analysis research programs → some results generated helping to identify further efforts
    - Ultimately data from phenomena specific research will be used to improve analysis tools to more accurately determine accident progression/consequences.
- CNL is developing in-house tools and capabilities, and contributing to relevant third-party tools and the broader international body of knowledge on SMR severe accidents.

CNL SMR Research Strategy - 2

- Significant CNL involvement in the international community for SMR related research
  - Participating in the IAEA CRP on Emergency Planning Zones for SMRs,
  - Membership in Gen. IV International Forum (GIF) Risk and Safety Working Group (RSWG),
  - Charing and participating in OECD-NEA Expert Group on Small Modular Reactors (EG-SMR).
  - CNL organizes Gen IV and Small Reactors Conference: **G4SR-4 October 2022 in Toronto!**

- International severe accident community and SMR development collaborations:
  - Collaboration with other research institutions and participation in international meetings.
    - Participation in the ERMSAR Conference and exploring relevant EU projects on SMRs
  - CNL and CNSC participate in US-NRCs Cooperative Severe Accident Research Project (CSARP) and MELCOR Code Assessment Project (MCAP)
    - Good connections between CNSC and US NRC in the regulatory space and CNL maintains a good working relationship with the MELCOR code developers at SNL and connections to the international MELCOR user group.

Conclusion

- Significant push both Internationally and in Canada to develop and deploy SMR/Advanced Reactors
- Canadian government provides supportive environment for R&D to aid in SMR deployment.
  - CNL (Canada's premier nuclear science and technology organization), is establishing and conducting technical research programs supporting SMR development/licensing.
  - CNL's technical program is flexible, focus is guided by the SMR deployment landscape in Canada, and designed to best meet needs of both industry and regulatory stakeholders.
- Reactor safety is the major component in licensing and CNL is working to better understand specific phenomena, concerns and research gaps related to the safety of SMR designs.
  - **Experimental programs:** water-cooled SMR passive cooling, HTGR air ingress, and molten salt fission product retention.
    - Provide valuable data on critical phenomena to better understand accident progression/consequences.
  - **Analysis efforts:** experimental benchmarking, molecular modelling of molten salts, and integrated severe accident analysis SMR designs (water-cooled, HTGR, molten salt).
- CNL participation in the international community to support SMR development
  - Participating in projects and working groups run by IAEA, OECD-NEA, and GIF.

Thank you for your attention
Questions?

Acknowledgements:

- Much of the work discussed herein and CNL participation in various international working groups, projects and initiatives is funded through through the Atomic Energy of Canada Limited (AECL) Federal Nuclear Science and Technology Program

Andrew Morreale, Research Scientist

Thermalhydraulics and Safety Analysis Branch

Advanced Reactors Directorate

andrew.morreale@cnl.ca

Sandia National Laboratories

Securing the future of Nuclear Energy

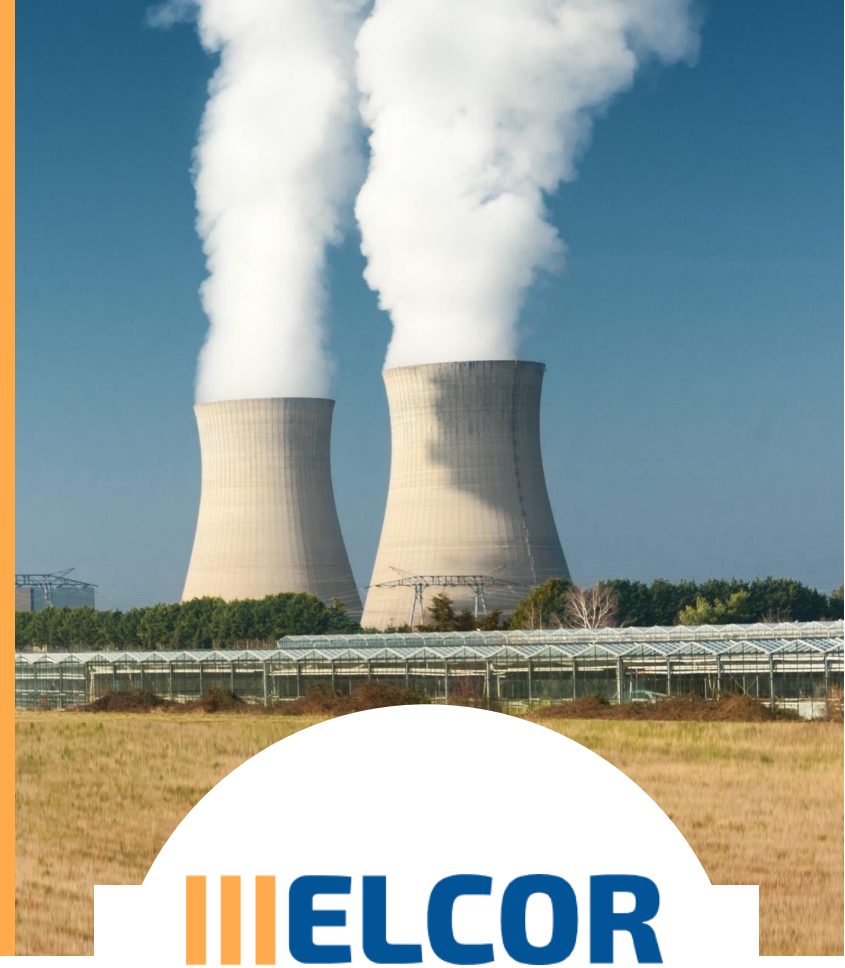

MELCOR

MELCOR Integrated Severe Accident Code Demonstration and Sensitivity Study of Heat Pipe Reactor Accident Progression

K.C. Wagner, C. Faucett, R. Schmidt, and D.L. Luxat
Nuclear Energy Safety Modeling and Analysis (8852)

U.S. DEPARTMENT OF ENERGY NNSA

Sandia National Laboratories is a multimission laboratory managed and operated by National Technology and Engineering Solutions of Sandia, LLC., a wholly owned subsidiary of Honeywell International, Inc., for the U.S. Department of Energy's National Nuclear Security Administration under contract DE-NA0003525.

NRC Capability Readiness for non-LWRs

ELCOR

Public Workshop: SCALE/ MELCOR Non LWR Source Term Demonstration Project

Heat pipe reactor – June 29, 2021
Gas cooled reactor – July 20, 2021
Pebble bed molten-salt-cooled reactor – Sept 14, 2021

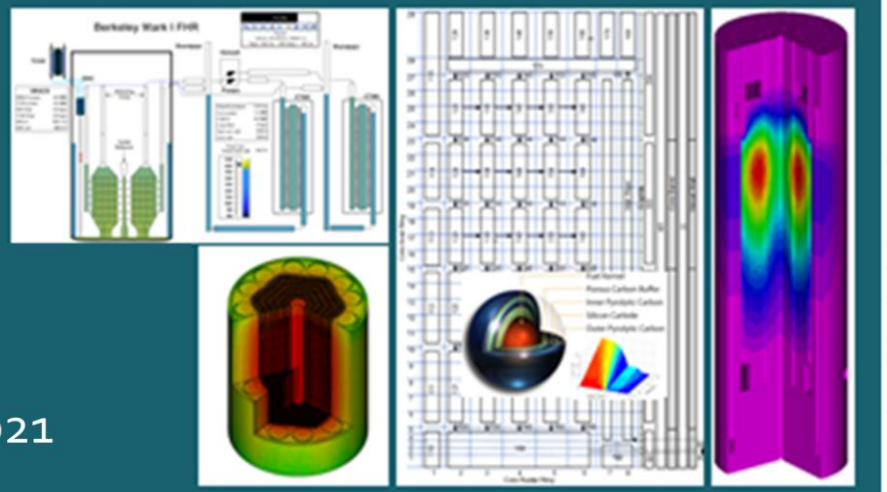

For More Information

Coming in 2022

Molten-salt fueled reactor
Sodium-cooled fast reactor

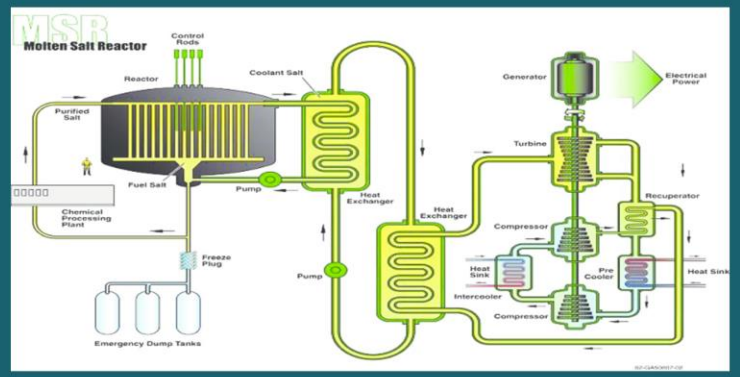

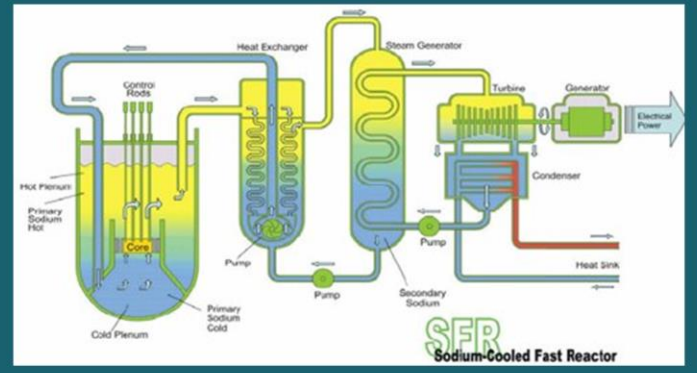

MELCOR Heat Pipe Reactor Modeling

When present, HPs replace conventional convective heat transfer between the fuel and coolant channel with the energy transfer from the fuel to the evaporative region of the HP.

HP models are special components within the COR package.

Heat rejection from the HP model at the condensation interface is transferred to the CVH package.

Basic geometry of a heat pipe is assumed to be a circular cylinder characterized by a relatively small set of geometric values, e.g.:

- R_O outside radius of heat pipe wall (m),
- R_I inside radius of heat pipe wall (m),
- D_{wick} thickness (or depth) of the wick (m), and
- ϕ_{wick} porosity of the wick (-).

Axial lengths of the condenser, adiabatic, and evaporator sections are implicitly defined by the COR package cells that these regions are associated with.

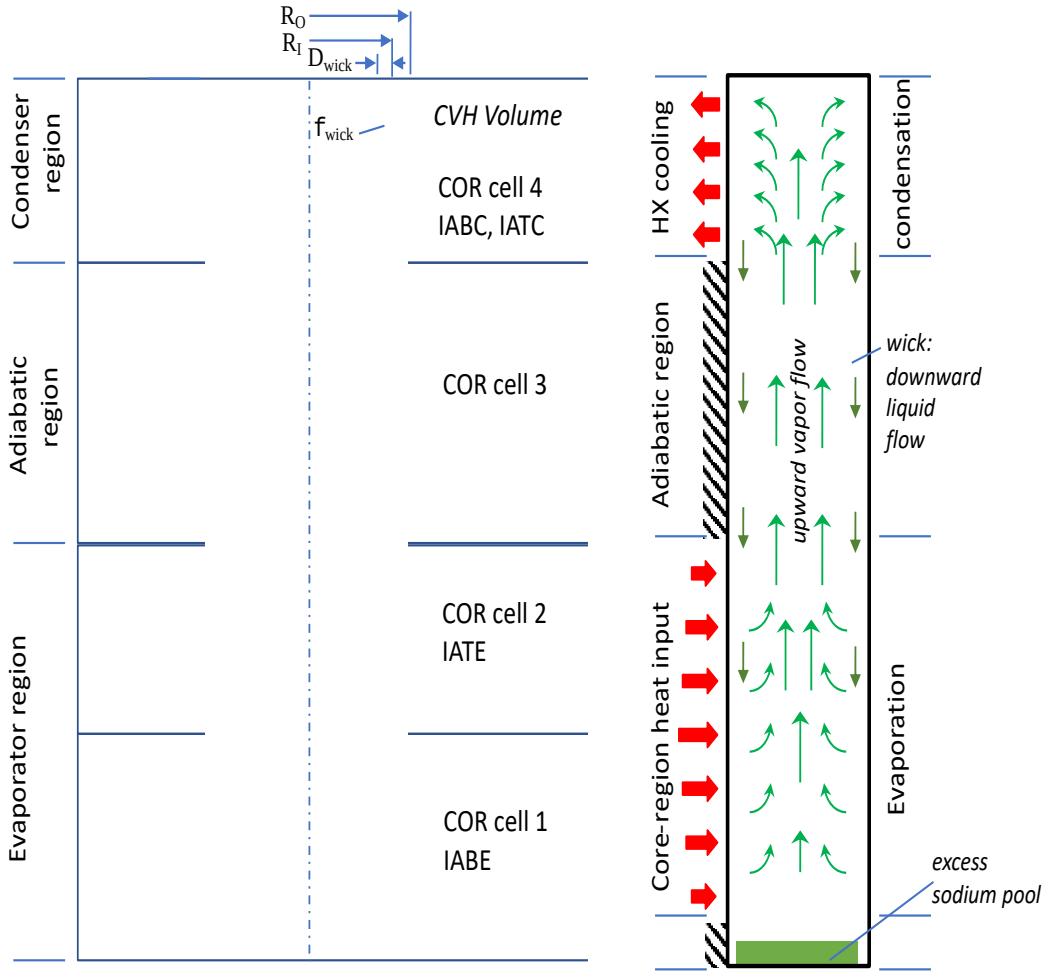

A Generic Heat Pipe

MELCOR Model of INL Design A – Reactor

Reactor modeling

- 2-D reactor nodalization
  - 14 axial levels
  - 15 radial rings
- 14 concentric rings of heat pipes (width of ~1 fuel assembly)
- Center ring models the emergency control rod guides
- Top and bottom reflectors are in axial levels 1 and 13
- Heat pipes transfer heat to the secondary Brayton air cycle in axial level 14
- Core region is surrounded by stainless steel shroud, alumina reflector, core barrel, and B_4C neutron shield

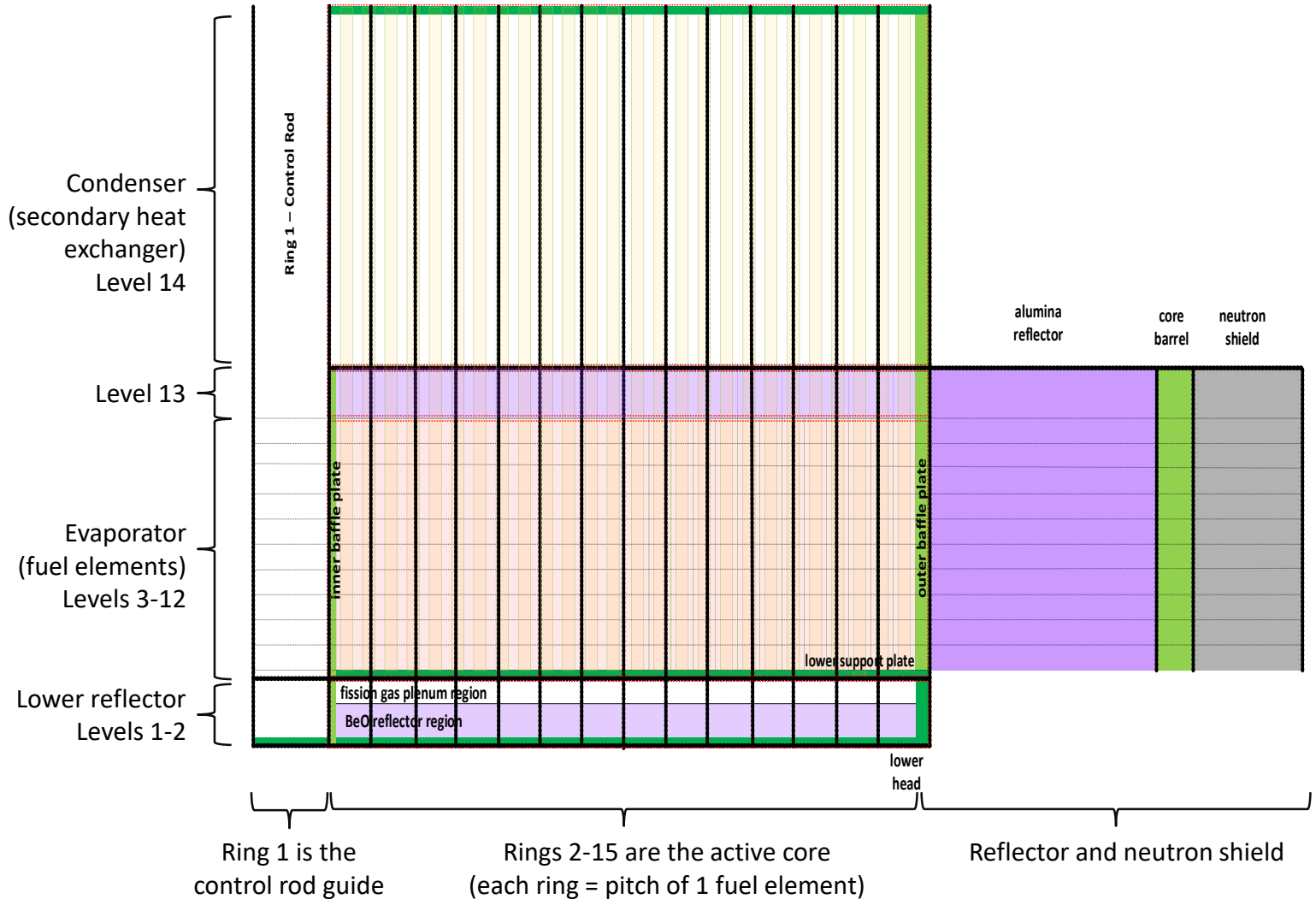

Reactor Vessel – Release Pathways

Release from fuel to reactor vessel

- Stainless-steel cladding failure at 1650 K

Release from reactor vessel to reactor building

- Assumed reactor vessel leakage

Heat-pipe release path

- Requires heat-pipe wall failure in two places
  - Creep rupture followed by melting
- Creep rupture failure in the heat-pipe condenser region (secondary system region) could lead to reactor building bypass

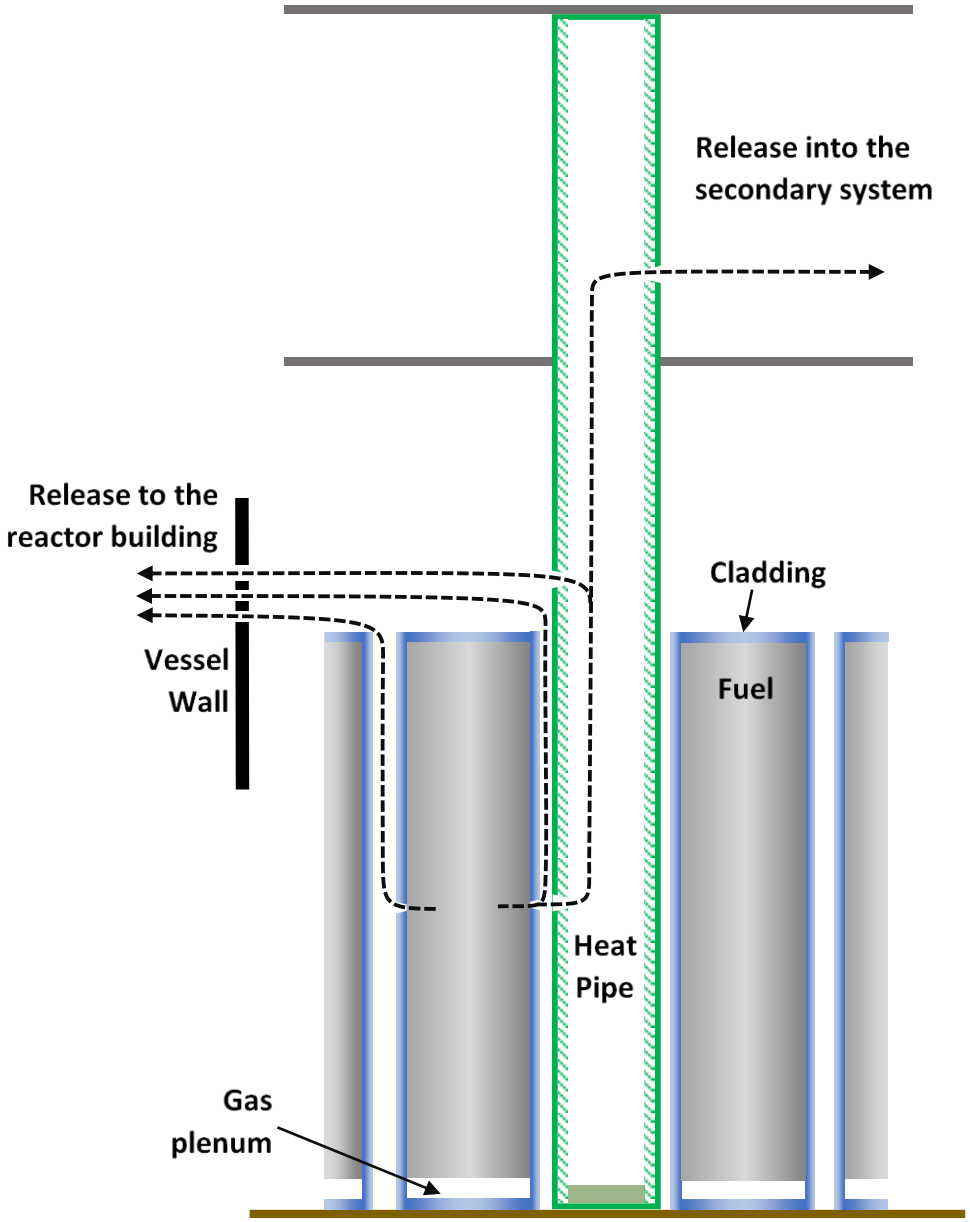

Enclosure Building Nodalization

LANL and INL HPR descriptions did not address the enclosure building

Modeling includes internal building circulation flow paths

- Natural circulation into and out of the reactor cavity
- Natural circulation within the building

Building leakage addressed parametrically

- Base leakage similar to the reactor building surrounding the BWR Mark I containment

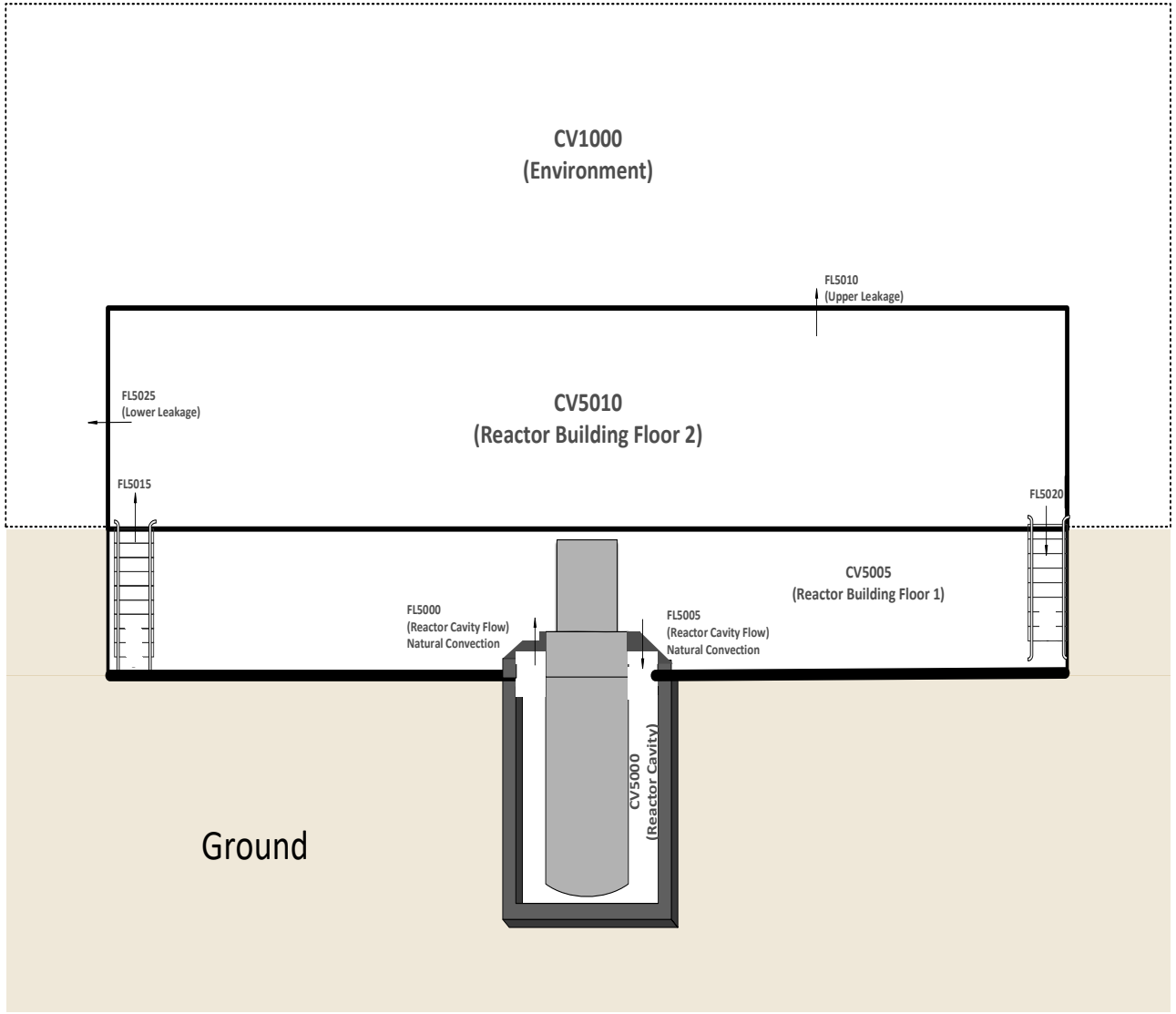

Description of the TOP Scenario

Transient Overpower (TOP) scenario selected for demonstration calculations
- Control drums malfunction and spuriously rotate “outward”

Modeled as linear reactivity insertion rate in $/second
- Safety control rods assumed to insert when peak fuel temperature exceeds 2200 K
- Strong feedback coefficient creates linear power increase

Performed sensitivity analysis to show how MELCOR could be used to gain insight into key source term drivers
- Sensitivities focused on source term and HPR parameters
- Previous LWR parameters do not necessarily translate to HPR uncertainties

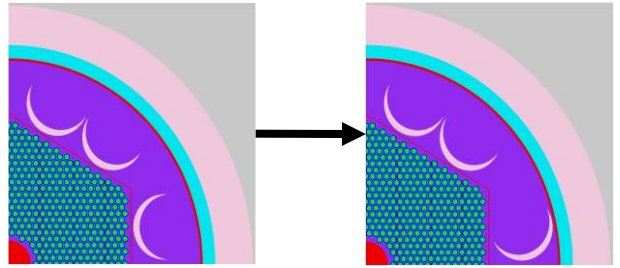

t = -5000 s | **t = 0 s** | **T_{max} = 2200 K** | **t = 24 h**

Steady-State	Reactivity Insertion	Post-SCRAM
• Initialization • Fuel temperature stabilizes	• Power increase • Temperature rise • Heat pipe failure • Core damage • Fission product release	• Radial cooling by natural processes • Fission product release and transport

Transient Overpower (TOP) Base Scenario (1/7)

The control drums start rotating at t=0 sec, which leads to an increase in the core power over 0.9 hr

- Negative fuel temperature reactivity feedback limits the rate of power increase

The core steadily heats until the maximum heat flux location reaches the boiling limit

- The heat transfer rate is limited above the boiling limit, which leads to a rapid heatup rate
- The SS cladding is assumed to fail at 1650 K (just below its melting point), which starts the fission product releases into the reactor
- The reactor is assumed to trip at 2200 K

Radial heat dissipation and heat loss to the reactor cavity passively cools the core

- No active heat removal (secondary system trips and isolates)

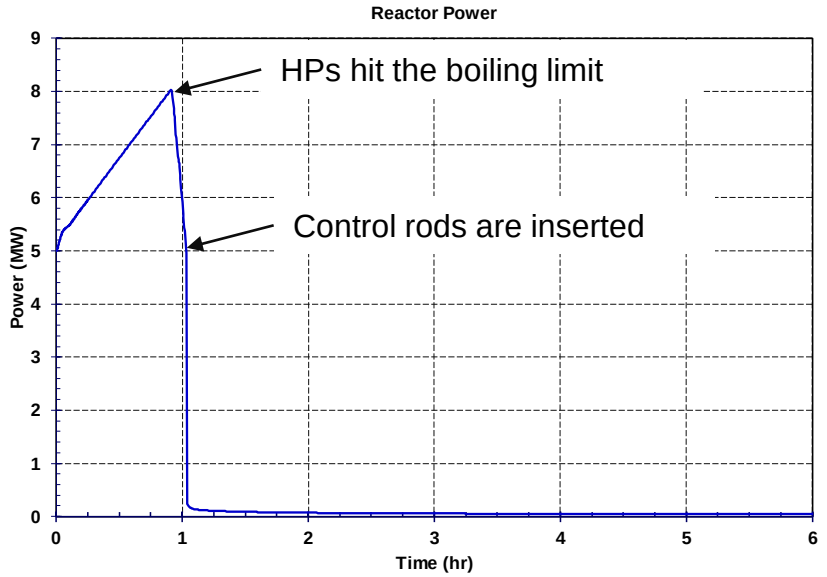

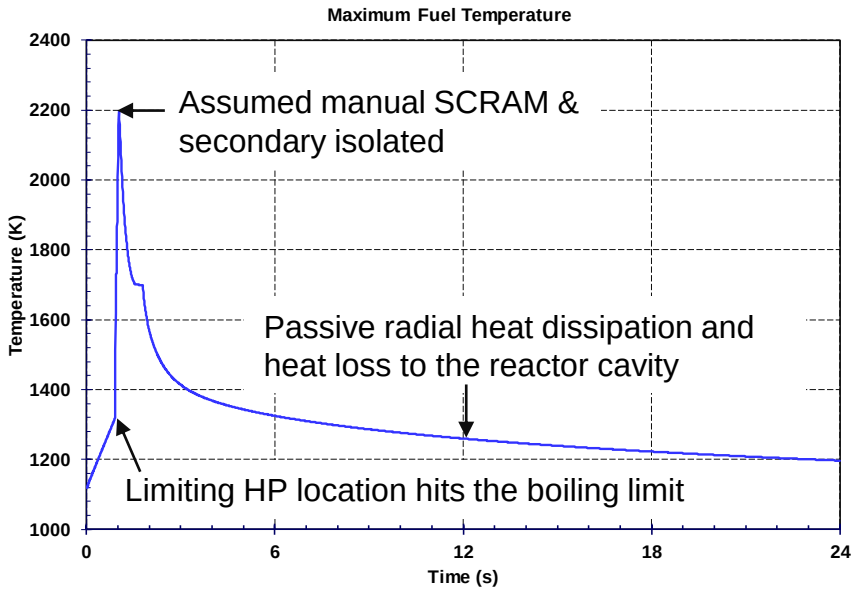

Transient Overpower (TOP) Base Scenario (2/7)

The HP performance limits at the highest heat flux location show a steady heatup to the boiling limit

- Once the boiling limit is reached, there is a rapid heatup over the next minute
  - The fuel rapidly heats to melting conditions
  - SS cladding fails at 1650 K
  - SS HP wall also fails at 1650 K
- The start of the fission product release occurs through the failed cladding locations

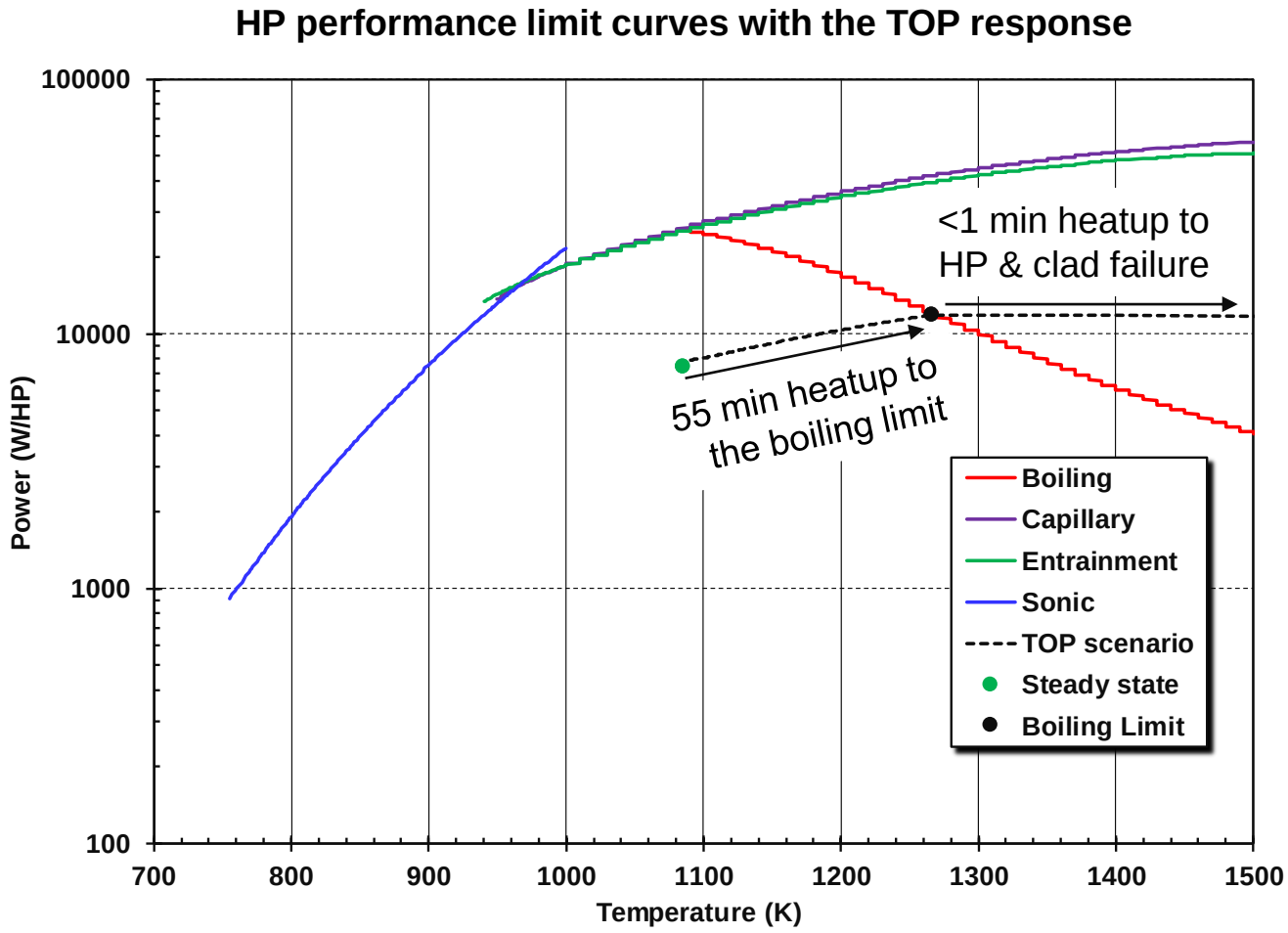

Transient Overpower (TOP) Base Scenario (3/7)

Cladding failure at 1650 K resulting in fission product release

- HPs that exceeded the boiling limit rapidly heat to cladding failure (1650 K)
- ~20% of the 1134 HPs and fuel elements failed
- HP depressurization on failure drive release from the vessel

Iodine releases also depend on time at temperature

- Fuel release – 1.4% of core inventory
- Environmental release – 0.0008% of core inventory

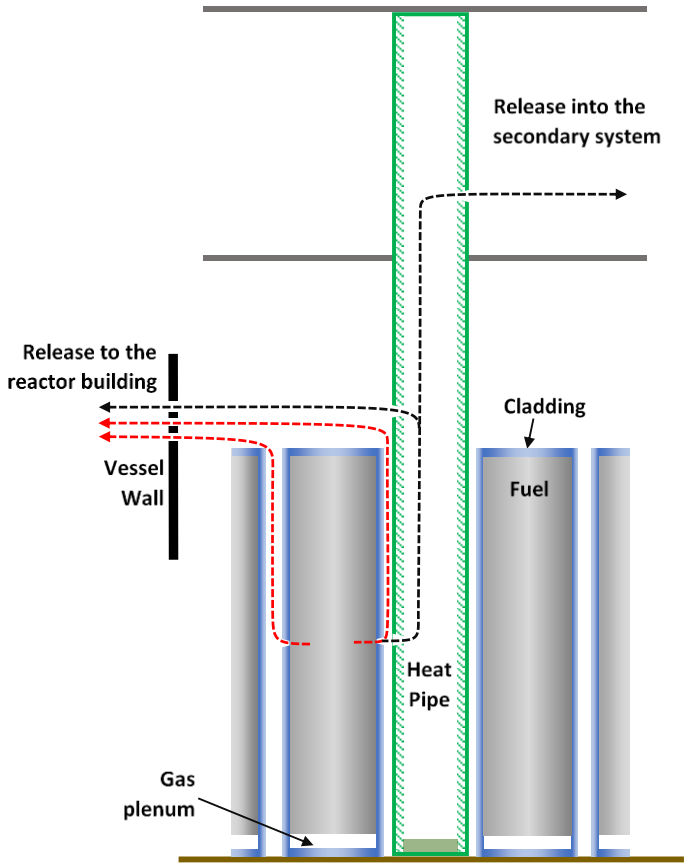

- Vessel leakage is 1.6 in^2
- Building leakage is 1.8 in^2

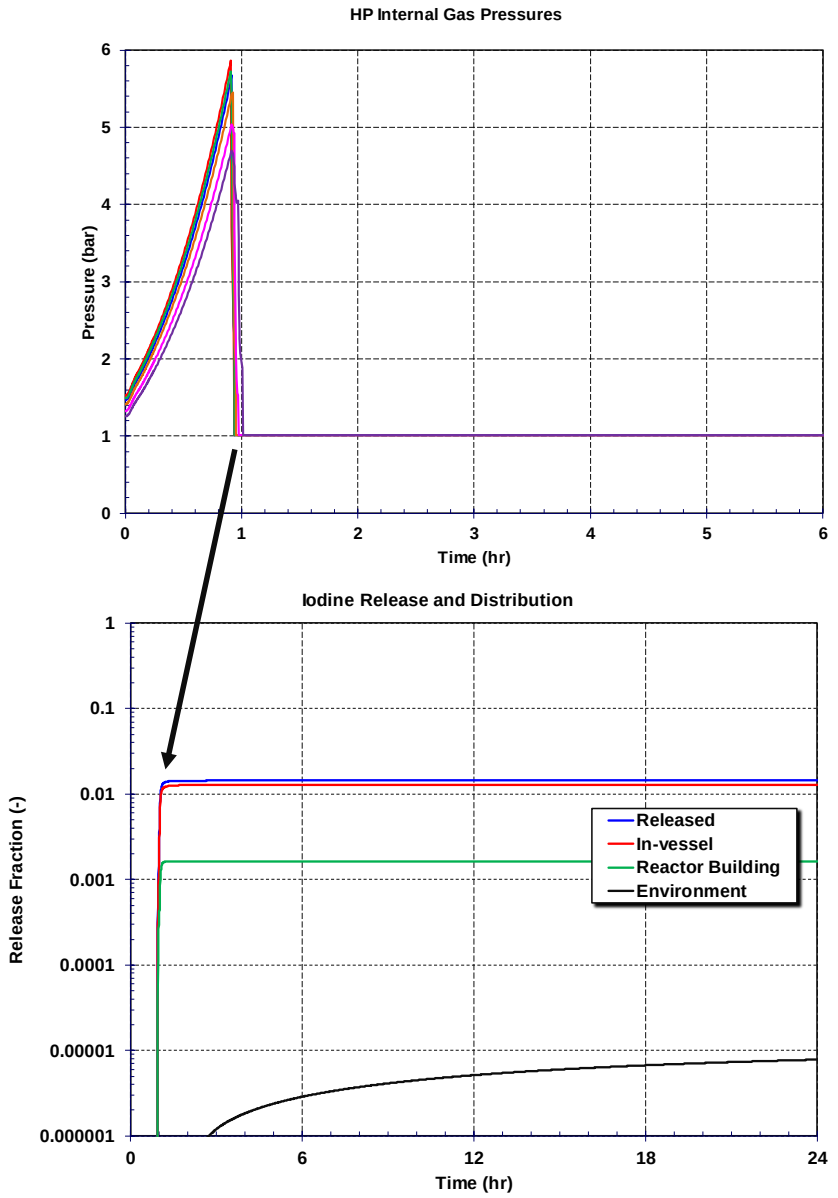

Transient Overpower (TOP) Base Scenario (4/7)

The HPs could be challenged by creep failure at high temperature and pressure

- The HP gas heats and pressurizes during the TOP scenario
- The HP depressurizes after the wall fails shortly after reaching the boiling limit
  - Creep accumulation effectively stops upon HP wall failure without ΔP stress
- For HPs that do not reach the boiling limit, the HP pressure initially drops due to secondary system removing heat

HP creep failure is monitored using Larson-Miller correlations

- TOP base scenario shows maximum creep is ~0.07 (failure = 1)
- Creep failures in the condenser can create a bypass leak path to the environment

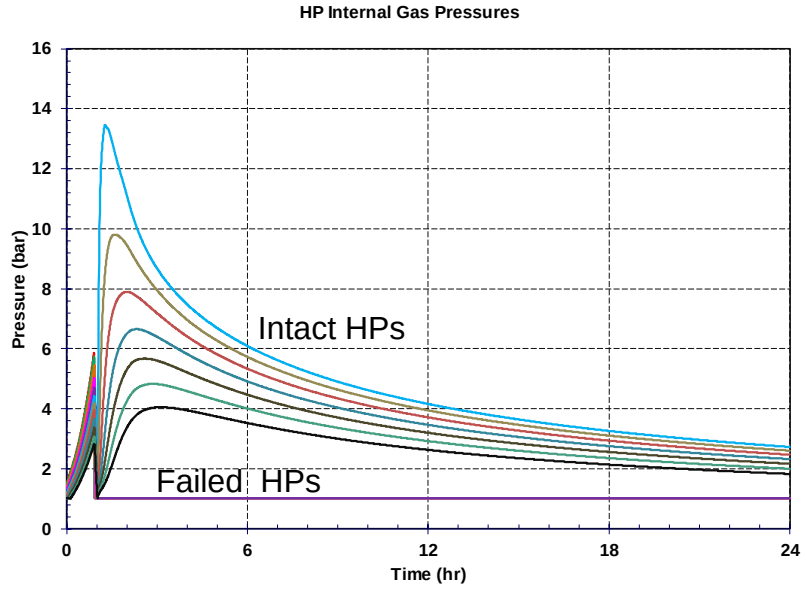

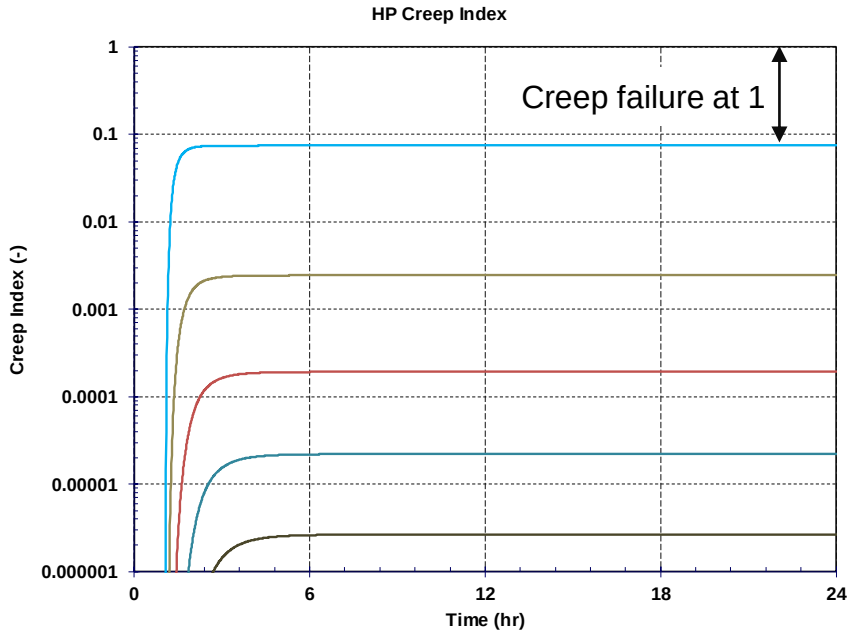

Transient Overpower (TOP) Base Scenario (5/7)

Fission products are retained in the fuel or deposit on their way to the environment

- The cladding remained intact for ~80% of the fuel elements
- 98.4% of the iodine fission product inventory is retained in the fuel due to limited time at high temperature

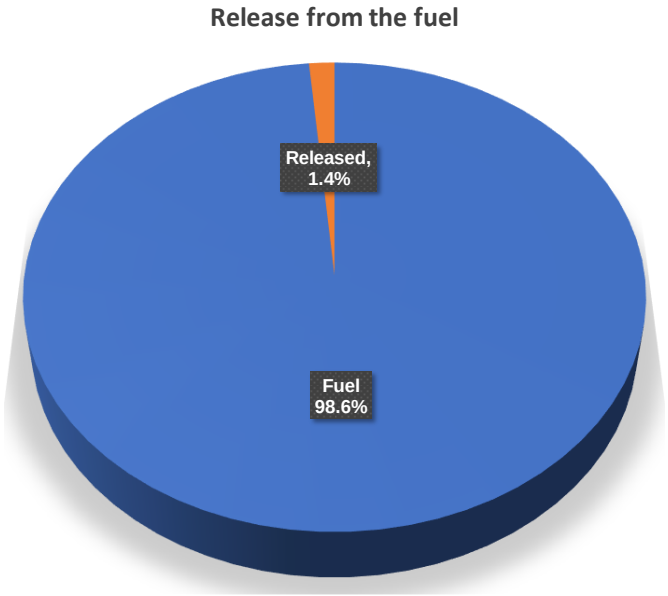

- The vessel retains 89% of the released iodine radionuclides
  - HP depressurization after failure is primary release mechanism
- The reactor building retains 11% of the radionuclides in the base case
  - BWR reactor building leak tightness used for the base case
  - No strong driving pressure to cause leakage

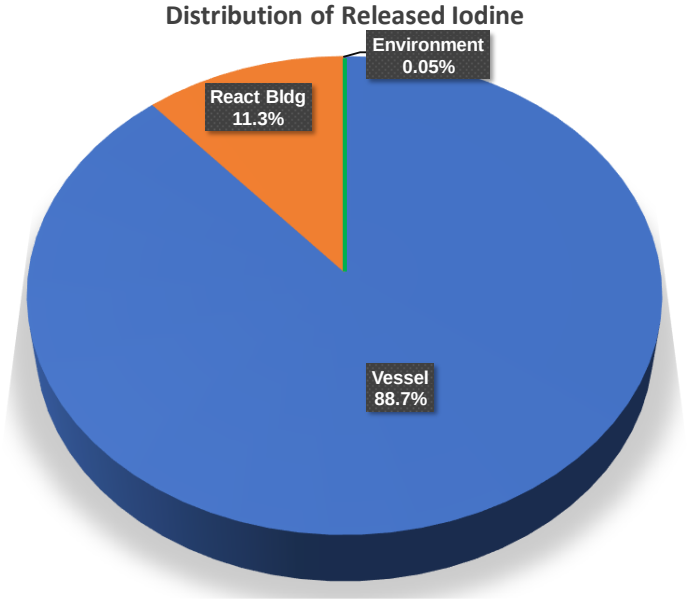

Transient Overpower (TOP) Base Scenario (6/7)

A series of calculations were performed to investigate the sensitivity of the source term magnitude to reactor building leakage effects

- The design specifications of the reactor building were assumed
  - The base result (1X) assumed a BWR reactor building value
  - 10X and 100X reflects higher design leakage and/or building damage
- Building leakage is driven by a very small temperature gradient to the environment (~5-7 ℃)
  - Leakage is approximately linear with leakage area (1X is ~1.8 in2)

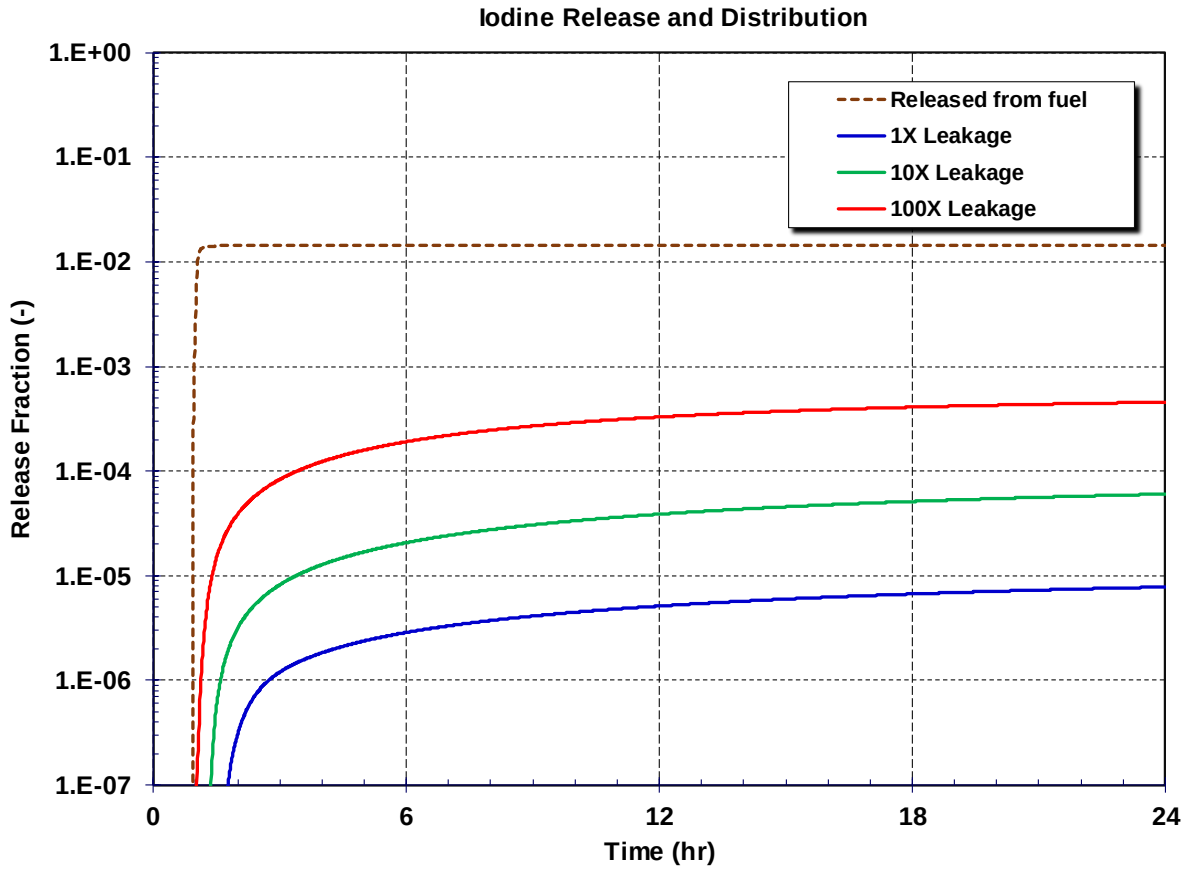

Transient Overpower (TOP) Base Scenario (7/7)

A series of calculations were performed to investigate the impact of an external wind

- External wind effects are included in DOE facility safety analysis where there also are not strong driving forces
  - Wind increases building infiltration and exfiltration
  - Upwind and downwind leakage pathways
- Wind effects are modeled as a Bernoulli term
  - $dP = \frac{1}{2}\rho C_p v^2$
  - ASHRAE building wind-pressure coefficients

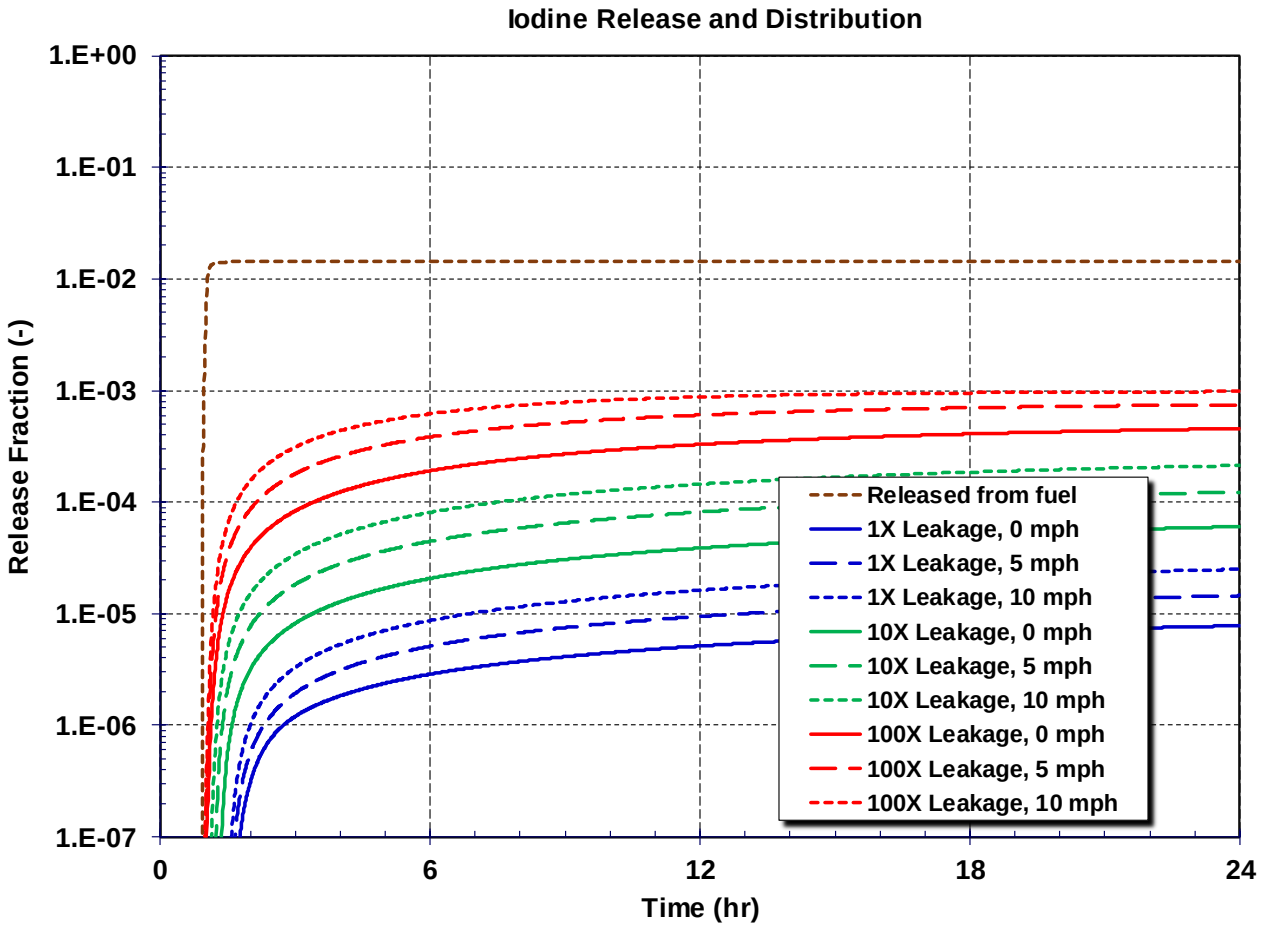

External wind modeling ref:

"MELCOR Computer Code Application Guidance for Leak Path Factor in Documented Safety Analysis," U.S. DOE, May 2004.

Building wind pressure coefficients.

ASHRAE, 1977, Handbook of Fundamentals, American Society of Heating, Refrigerating and Air-Conditioning Engineers, Inc, 1997.

Parametric Uncertainties – Capability Demonstration

Component	Parameter	Ranges
Heat Pipes	Heat Pipe Failure Location	Condenser (50%) / Evaporator (50%)
	Initial non-functional HPs	0% - 5%
Core	Gaseous Iodine Fraction (-)	0.0 - 0.05
	Reactivity Insertion Rate ($/s)	$0.5x10^{-4}$ - $1.0x10^{-3}$
	Total reactivity feedback	-0.0015 to -0.0025
Vessel	Fuel Element Radial View Factor Multiplier (-)	0.5 - 2.0
	Vessel Emissivity (-)	0.125 - 0.375
	Total Leak Area (m^2)	$2x10^{-5}$ - $2x10^{-3}$
	Vessel and Vessel Upper Head HTC (W/m-K)	1 – 10
Confinement	Cavity entrance open fraction	100% (90%) - 1% (10%)
	Cavity Emissivity (-)	0.125 – 0.375
	Wind Loading (m/s)	0 – 10
	Total Leak Area Multiplier (-)	1 - 100
Scenario	Peak fuel temperature for safety rod insertion (K)	1300 – 2200

Heat Pipe Response

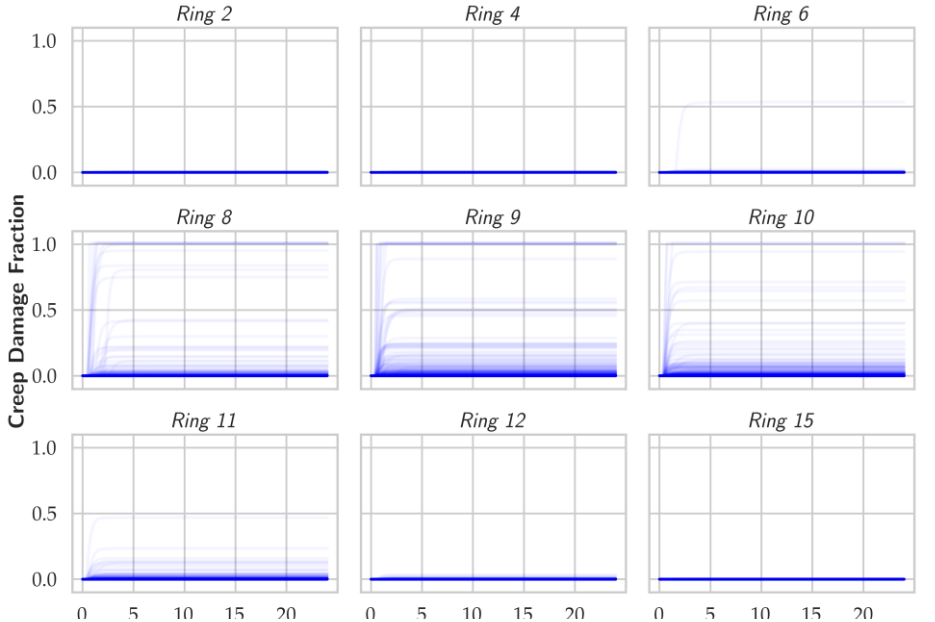

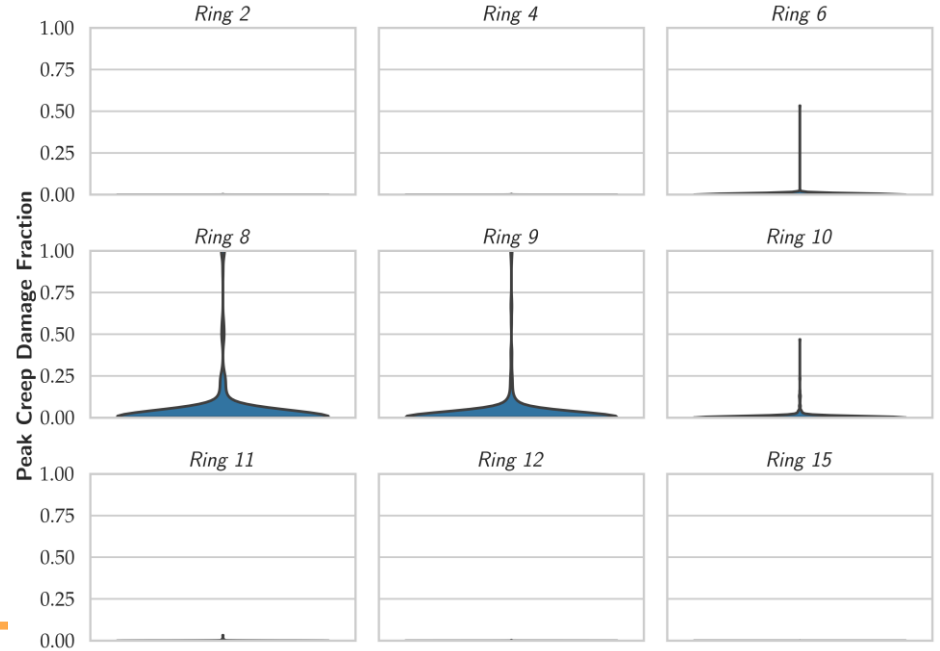

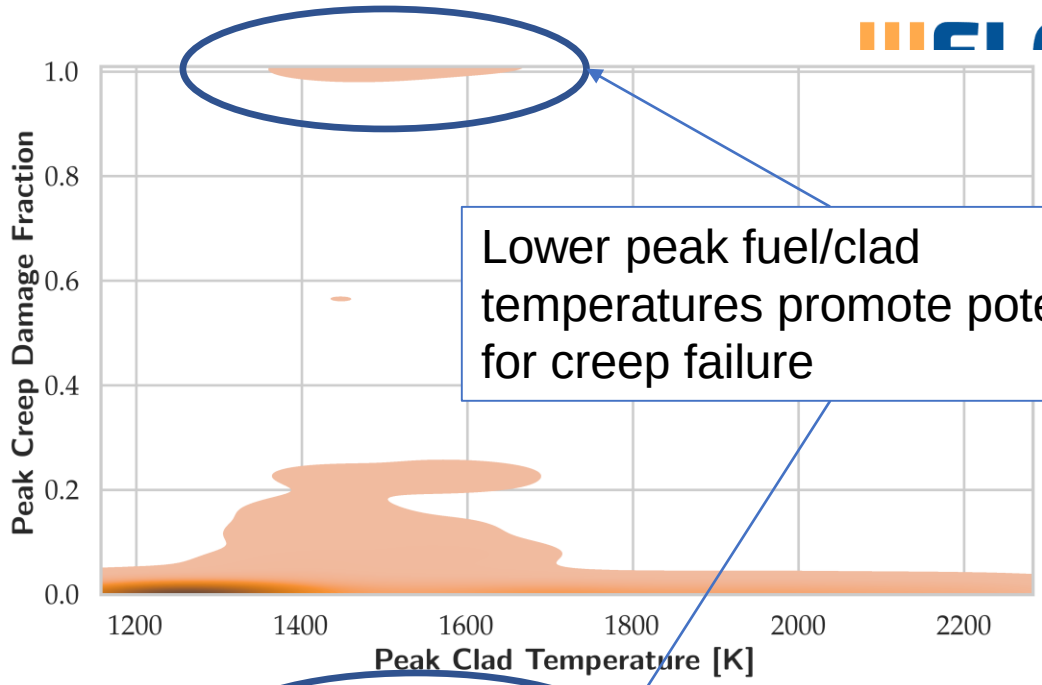

Lower peak fuel/clad temperatures promote potential for creep failure

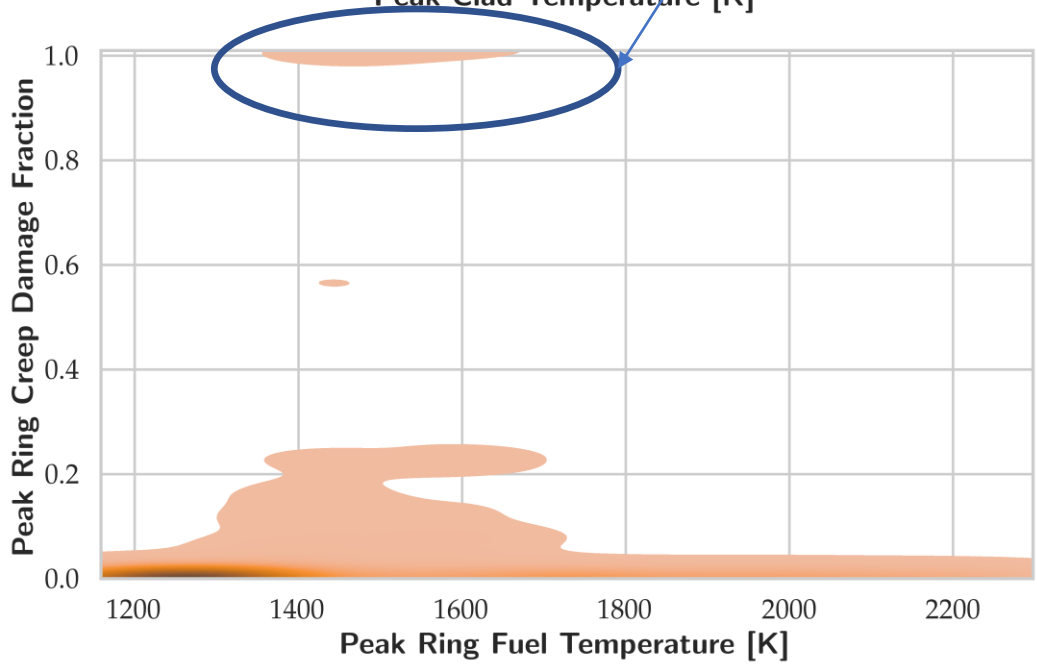

Fission Product Release from Fuel Characterization

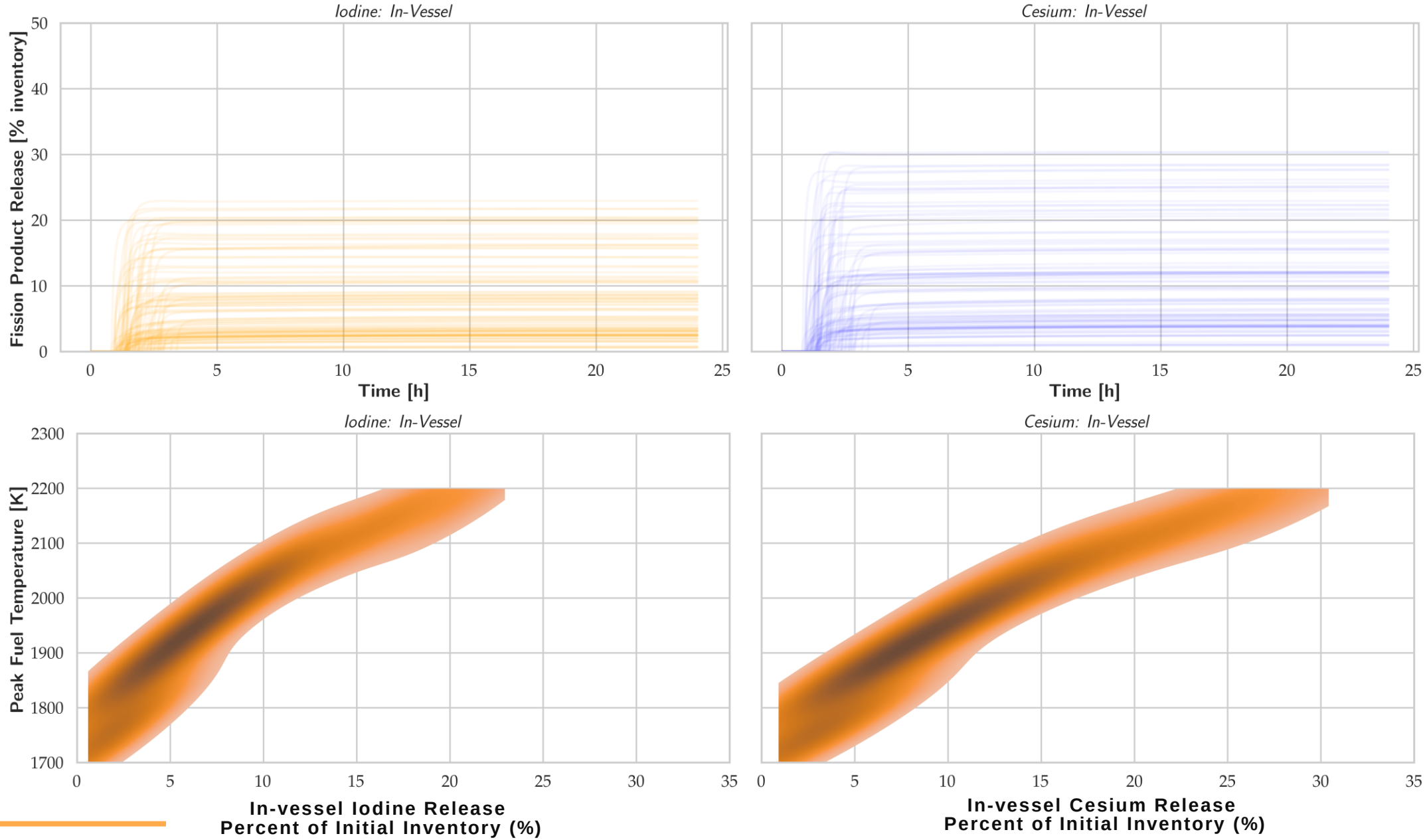

Fission Product Transport Characterization

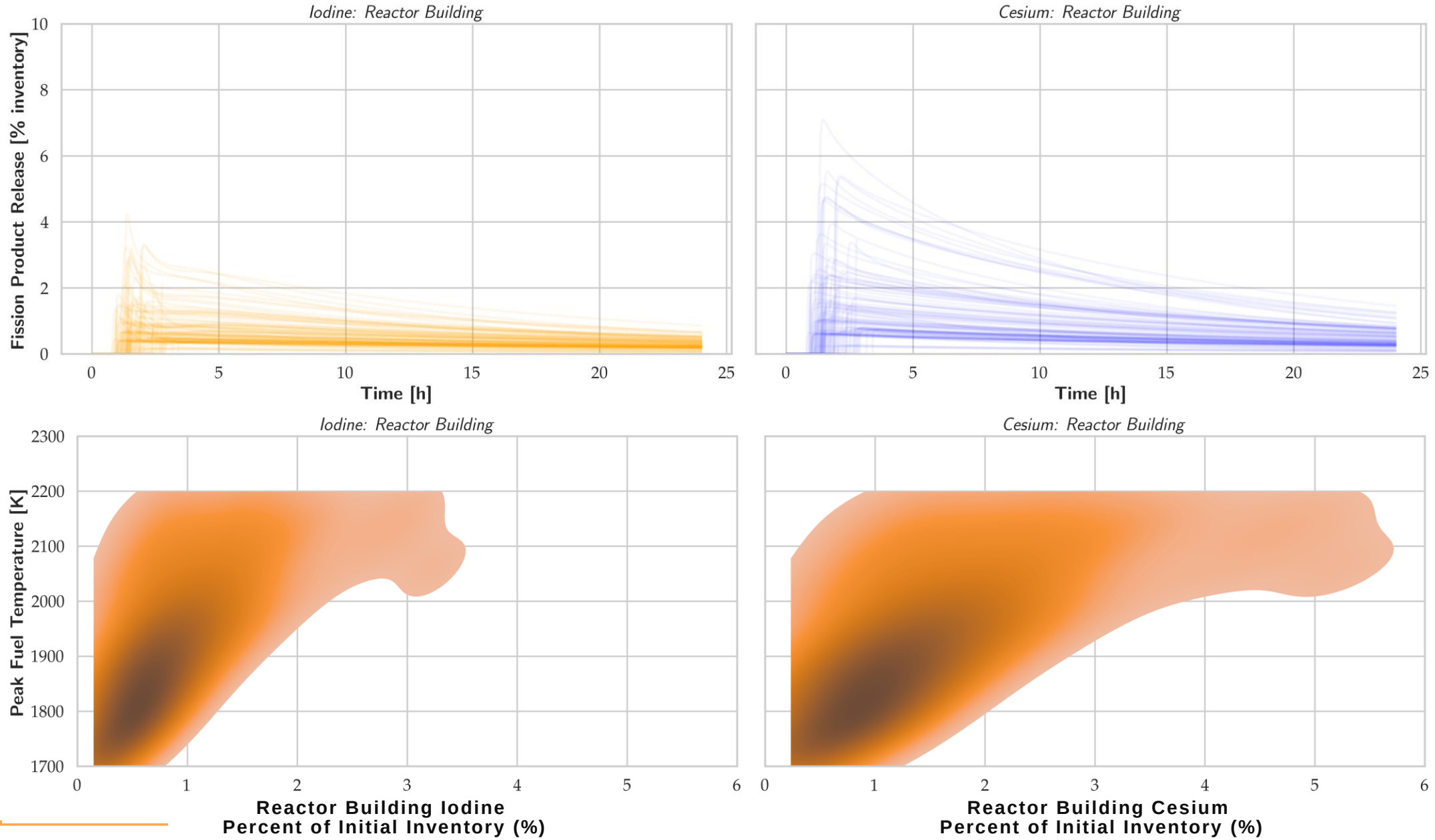

Fission Product Release to Environment

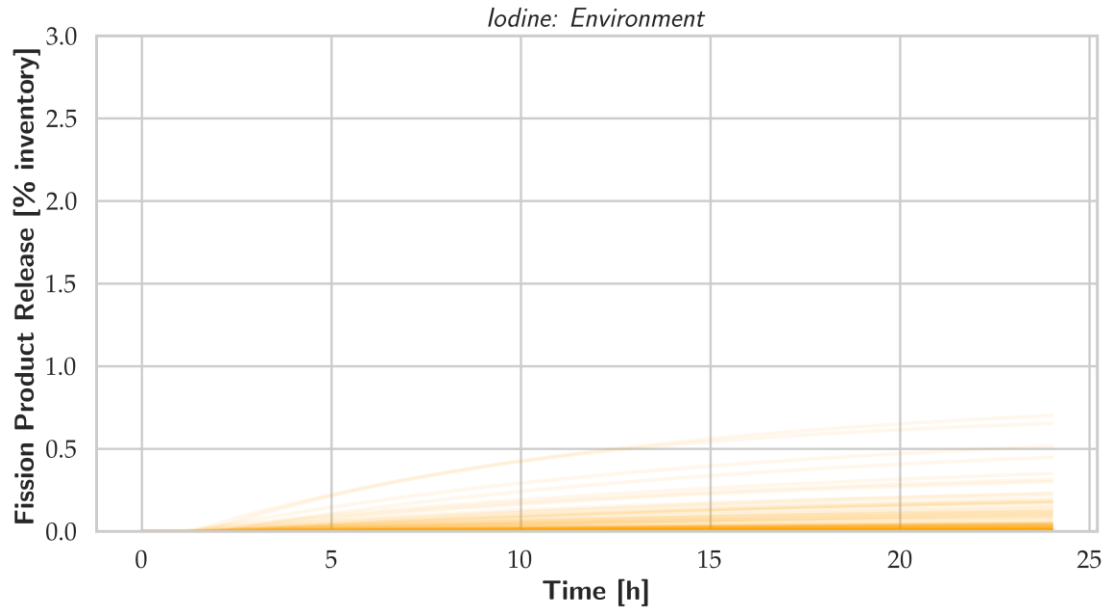

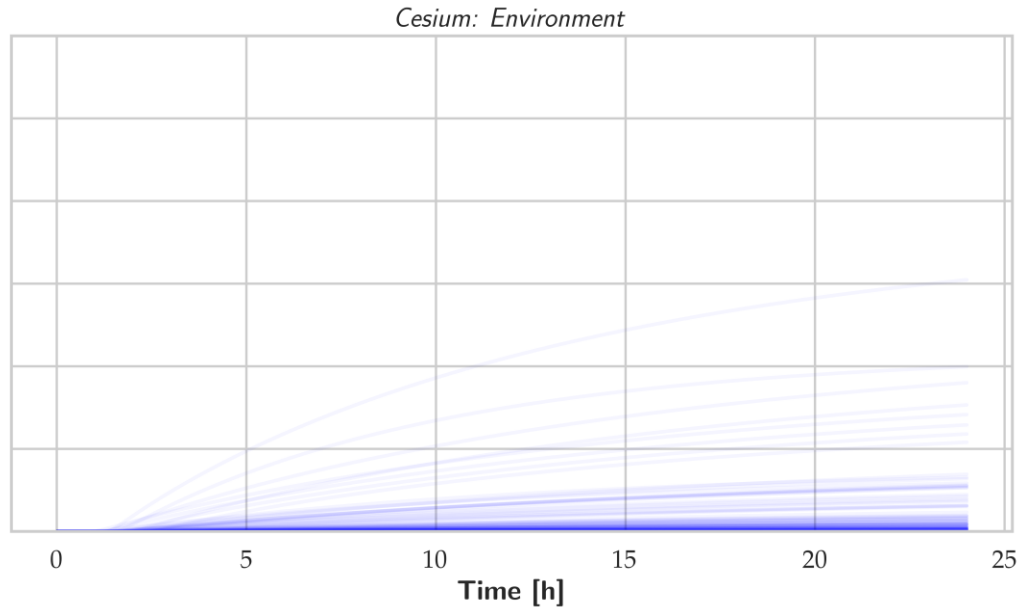

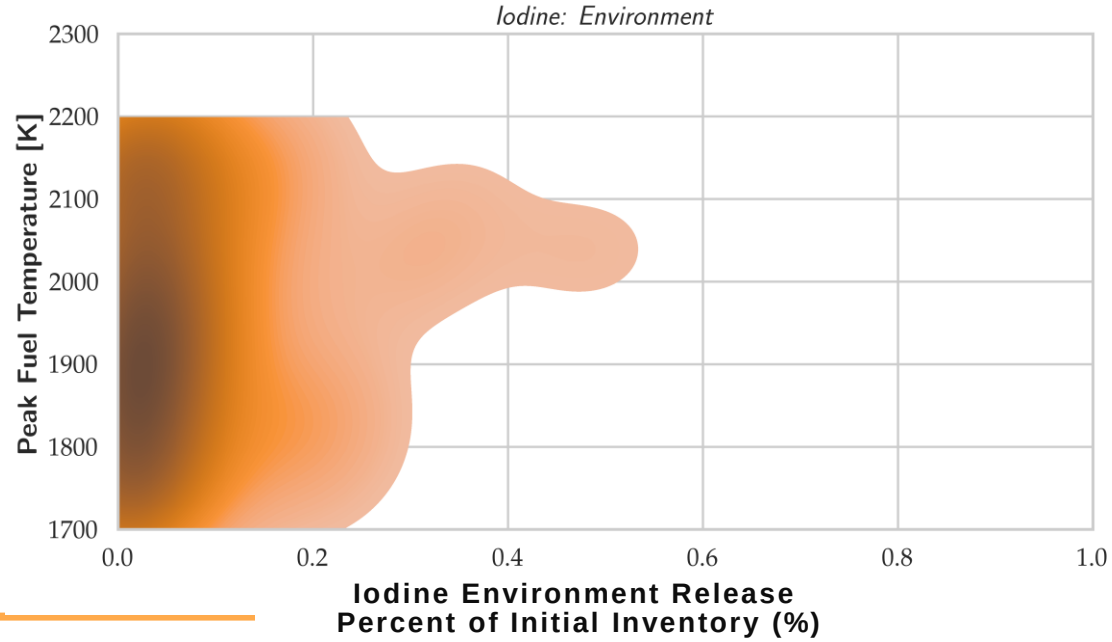

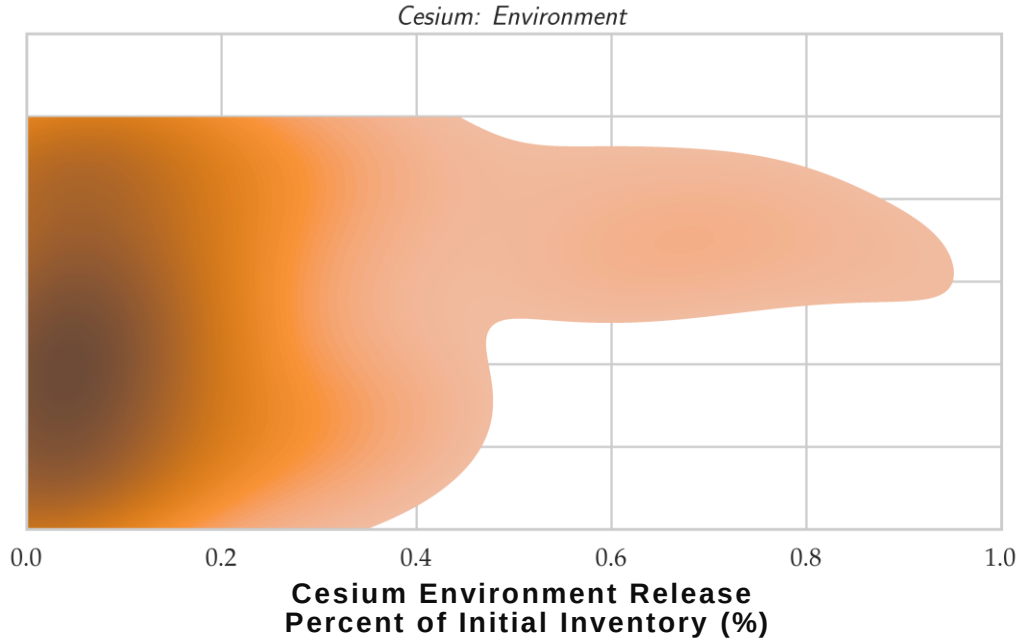

Sandia National Laboratories

Securing the future of Nuclear Energy

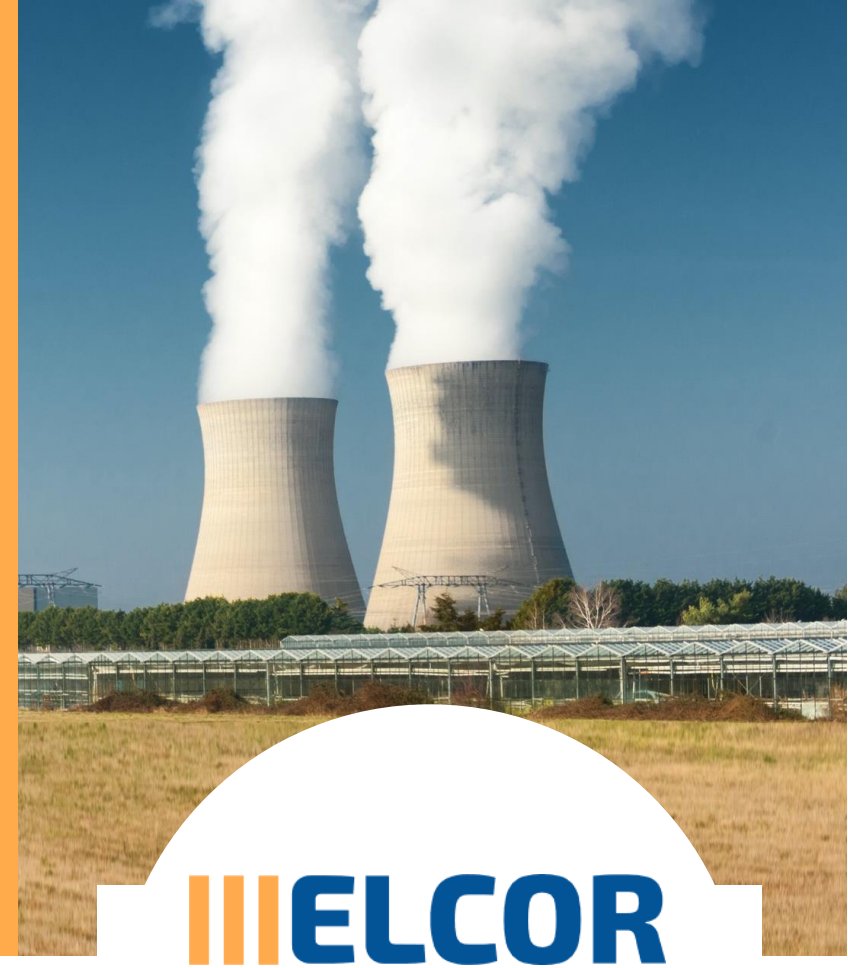

ELCOR

Thanks for your attention!

Sandia National Laboratories is a multimission laboratory managed and operated by National Technology and Engineering Solutions of Sandia, LLC., a wholly owned subsidiary of Honeywell International, Inc., for the U.S. Department of Energy's National Nuclear Security Administration under contract DE-NA0003525.

Sandia National Laboratories

Securing the future of Nuclear Energy

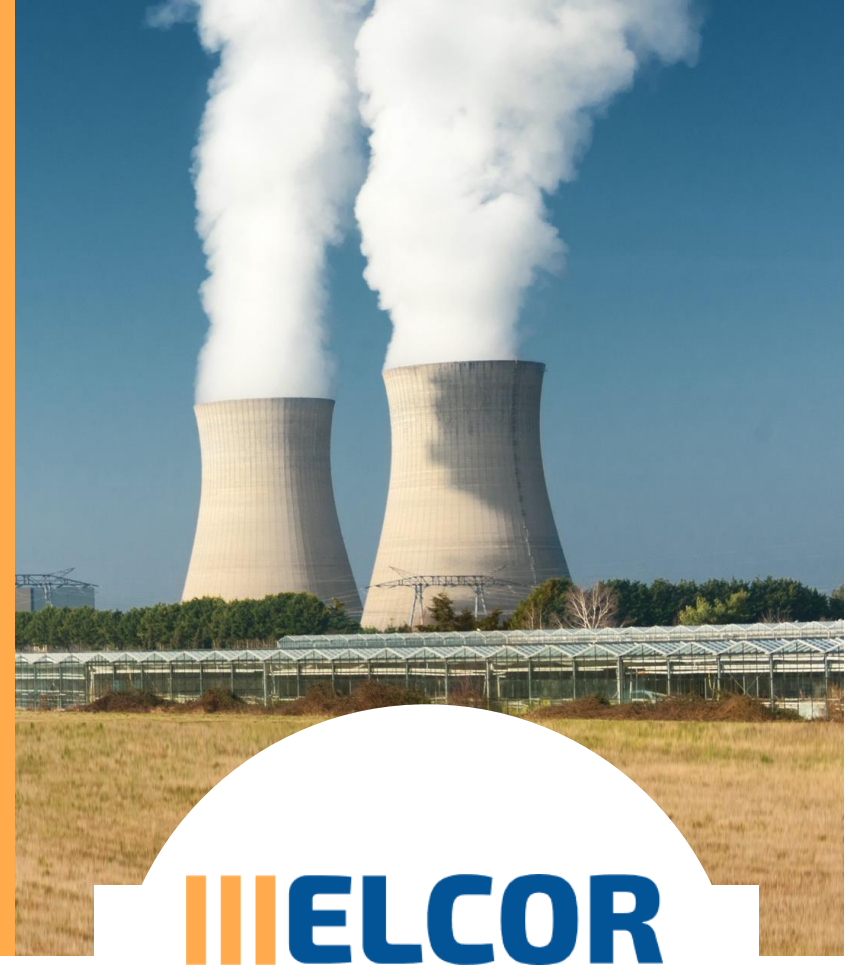

MELCOR

MELCOR Integrated Severe Accident Code Demonstration and Sensitivity Study of HTGR Accident Progression

K.C. Wagner, B. Beeny, and D.L. Luxat
Nuclear Energy Safety Modeling and Analysis (8852)

Sandia National Laboratories is a multimission laboratory managed and operated by National Technology and Engineering Solutions of Sandia, LLC., a wholly owned subsidiary of Honeywell International, Inc., for the U.S. Department of Energy's National Nuclear Security Administration under contract DE-NA0003525.

MELCOR HTGR modeling

Fission product release

- Release from TRISO kernel
- Radionuclide distributions within the layers in the TRISO particle and compact
- Release to coolant

Other core models

- Graphite oxidation
- Intercell and intracell conduction
- Convection & flow
- Point kinetics
- Dust generation and resuspension

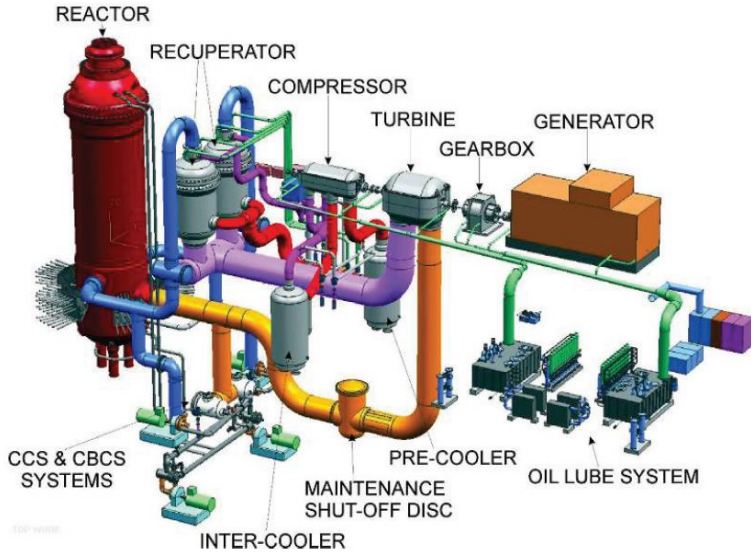

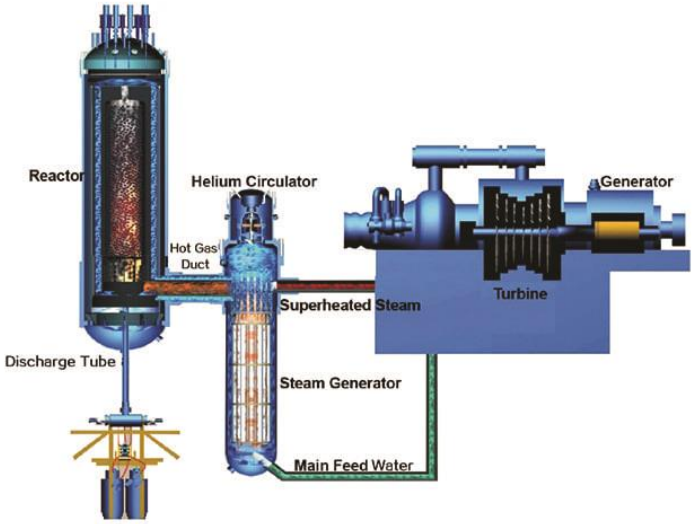

HTGR Radionuclide Diffusion Release Model

Intact TRISO Particles

- One-dimensional finite volume diffusion equation solver for multiple zones (materials)
- Temperature-dependent diffusion coefficients (Arrhenius form)

$$\frac{\partial C}{\partial t} = \frac{1}{r^n}\frac{\partial}{\partial r}\left(r^n \boldsymbol{D}\frac{\partial C}{\partial r}\right) - \lambda C + \beta \qquad D(T) = D_0 e^{-\frac{Q}{RT}}$$

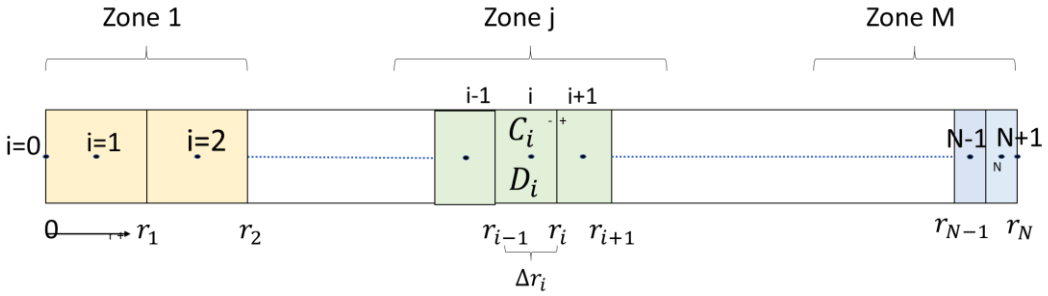

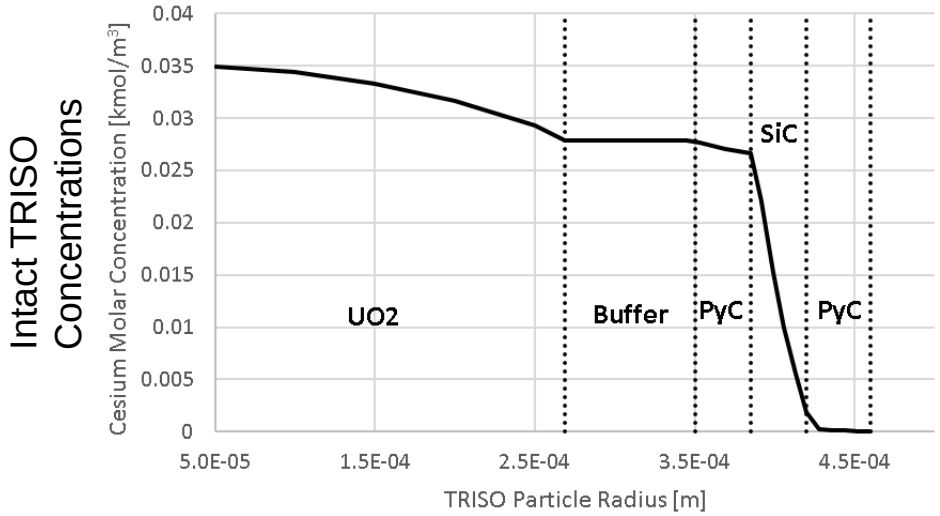

Diffusivity Data Availability

Radionuclide	UO_2	UCO	PyC	Porous Carbon	SiC	Matrix Graphite	TRISO Overall
Ag	Some	Not investigated	Some	Not found	Extensive	Some	Extensive
Cs	Some		Some		Extensive	Some	Some
I	Some		Some		Some	Not found	Not found
Kr	Some		Some		Not found	Some	Some
Sr	Some		Some		Extensive	Some	Some
Xe	Some		Some		Some	Some	Not found

Data used in the demo calculation

[IAEA TECDOC-0978]

	FP Species							
	Kr		Cs		Sr		Ag	
Layer	D (m^2/s)	Q (J/mole)	D (m^2/s)	Q (J/mole)	D (m^2/s)	Q (J/mole)	D (m2/s)	Q (J/mole)
Kernel (normal)	1.3E-12	126000.0	5.6-8	209000.0	2.2E-3	488000.0	6.75E-9	165000.0
Buffer	1.0E-8	0.0	1.0E-8	0.0	1.0E-8	0.0	1.0E-8	0.0
PyC	2.9E-8	291000.0	6.3E-8	222000.0	2.3E-6	197000.0	5.3E-9	154000.0
SiC	3.7E+1	657000.0	7.2E-14	125000.0	1.25E-9	205000.0	3.6E-9	215000.0
Matrix Carbon	6.0E-6	0.0	3.6E-4	189000.0	1.0E-2	303000.0	1.6E00	258000.0
Str. Carbon	6.0E-6	0.0	1.7E-6	149000.0	1.7E-2	268000.0	1.6E00	258000.0

Iodine assumed to behave like Kr
CORSOR-Booth LWR scaling used to estimate other radionuclides

Reactor Vessel and Core

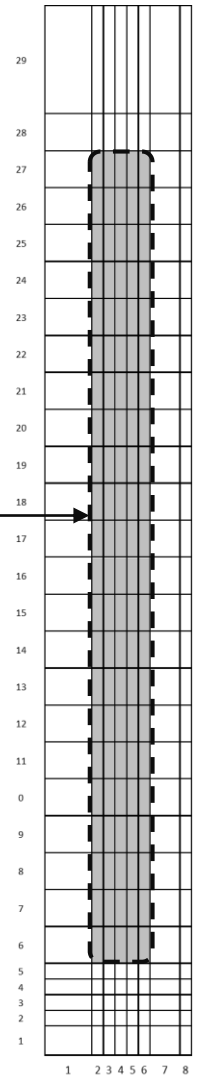

Vessel core package nodalization
(8 rings x 29 axial levels)
Correct aspect ratio

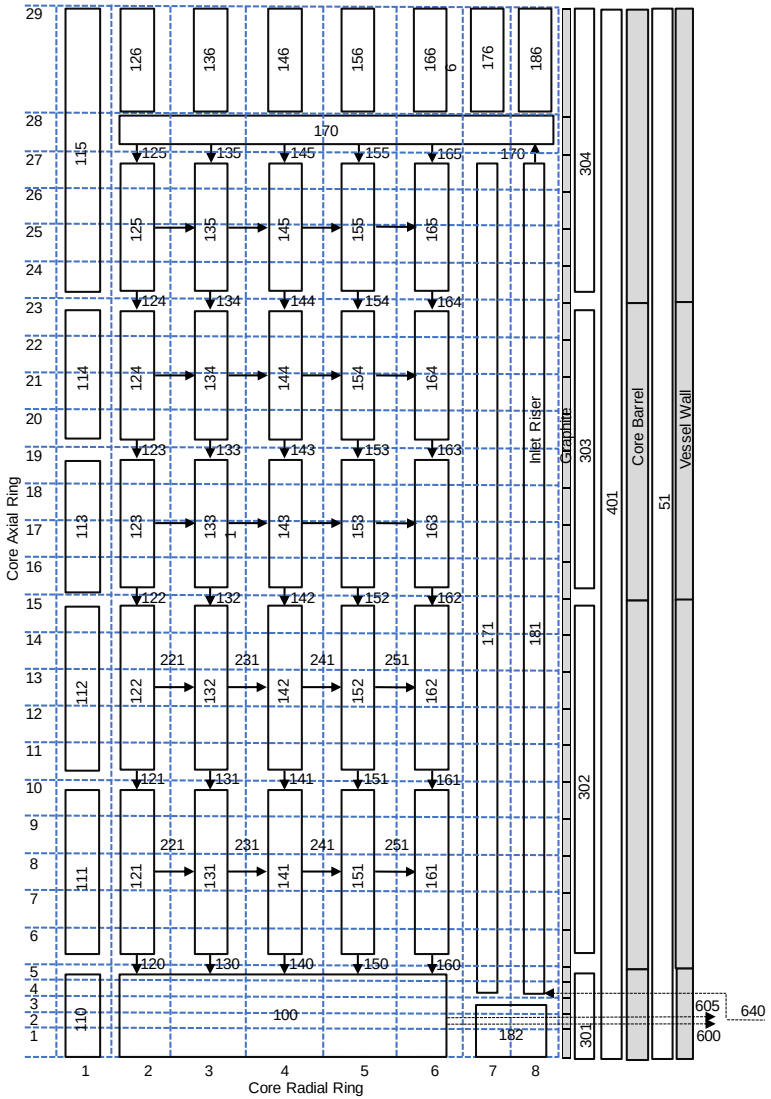

Vessel control volume, flow path, and heat structure
nodalization with core package boundaries in blue

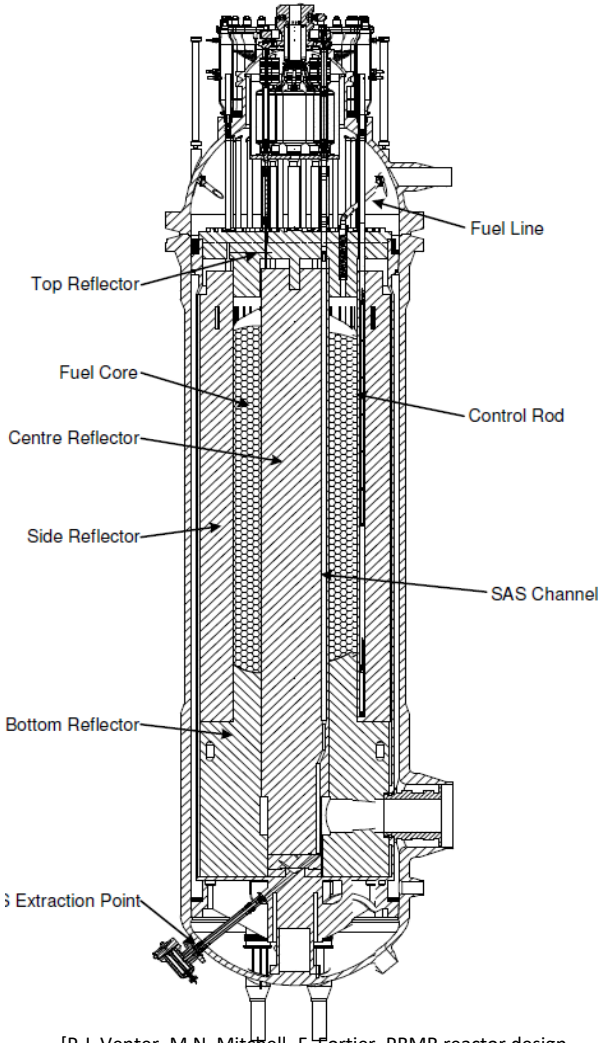

[P.J. Venter, M.N. Mitchell, F. Fortier, PBMR reactor design and development, in: Proceedings from the 18th International Conference on Structural Mechanics in Reactor Technology (SMiRT 18), Beijing, China, Aug. 2005]

Reactor Building

Nodalization guided by NGNP layout

- Passive air-flow Reactor Cavity Cooling System (RCCS)

Leakage assumed to be the same as BWR Mark I reactor building surrounding the containment

- 100% vol/day at 0.25 psig

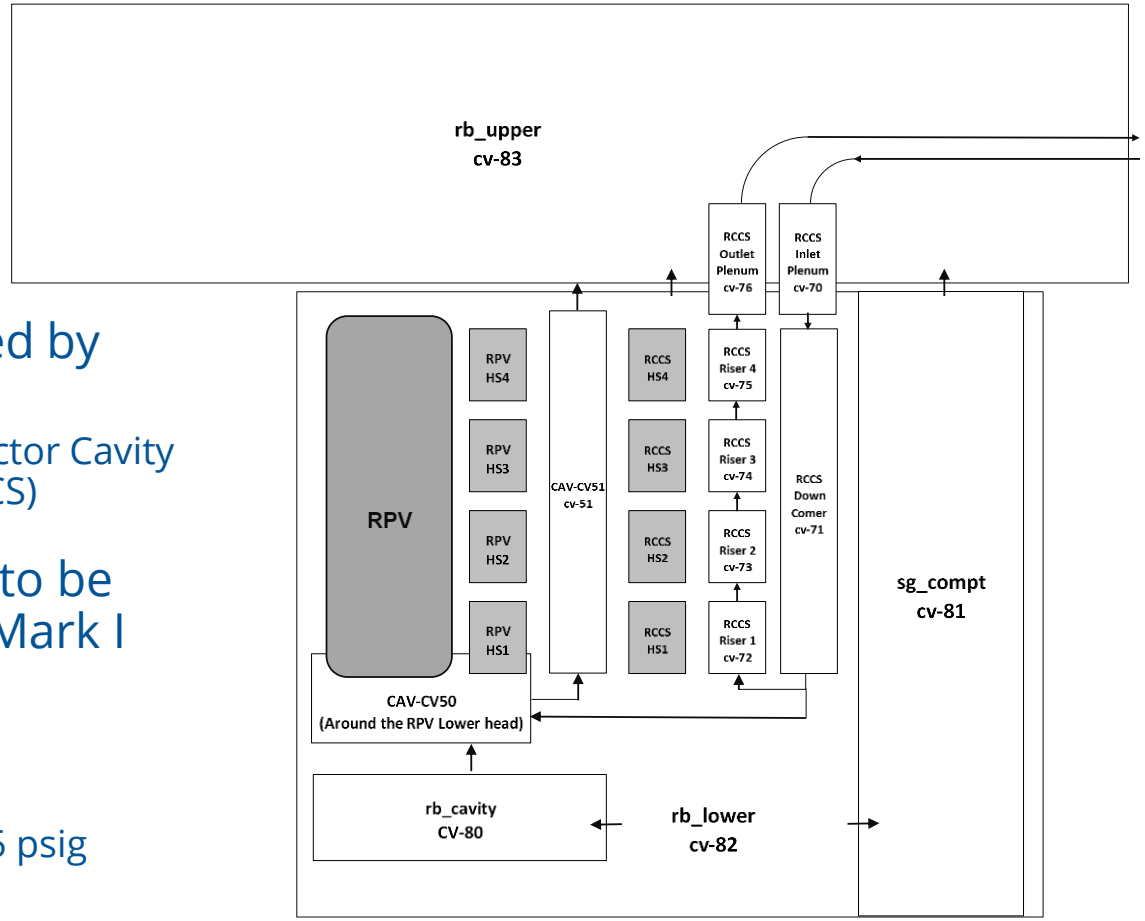

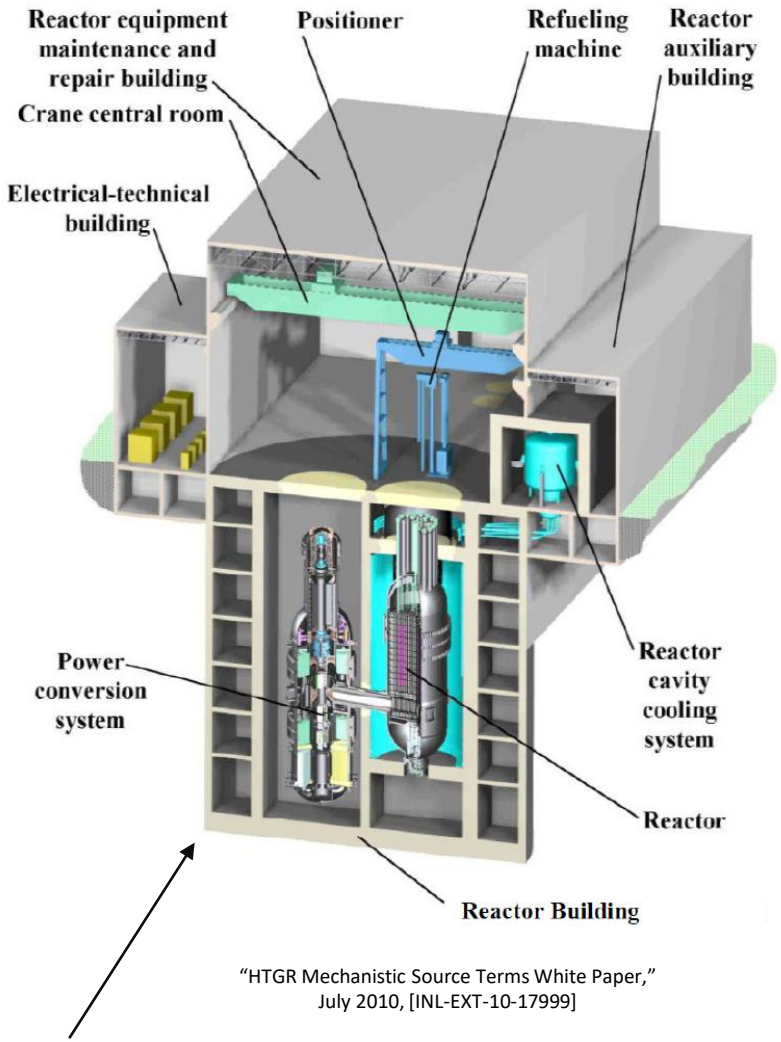

"HTGR Mechanistic Source Terms White Paper," July 2010, [INL-EXT-10-17999]

Picture above shows a water-cooled RCCS but demo model uses air-cooled RCCS.

Recirculation Loop and Secondary Heat Removal

Recirculation system and secondary heat removal

- Recirculation loop and secondary heat removal provide boundary conditions to the vessel
  - Flow rate
  - Heat removal & inlet temperature

Pipe break nodalization allows counter-current natural circulation flow

- MELCOR counter-current flow model used to represent adjacent stream drag forces
- Geometry similar to PWR hot leg natural circulation [NUREG-1922]
- Allows for air ingression

Scenario: depressurized loss of forced circulation (DLOFC)

- Assumes double-ended break of the hot leg

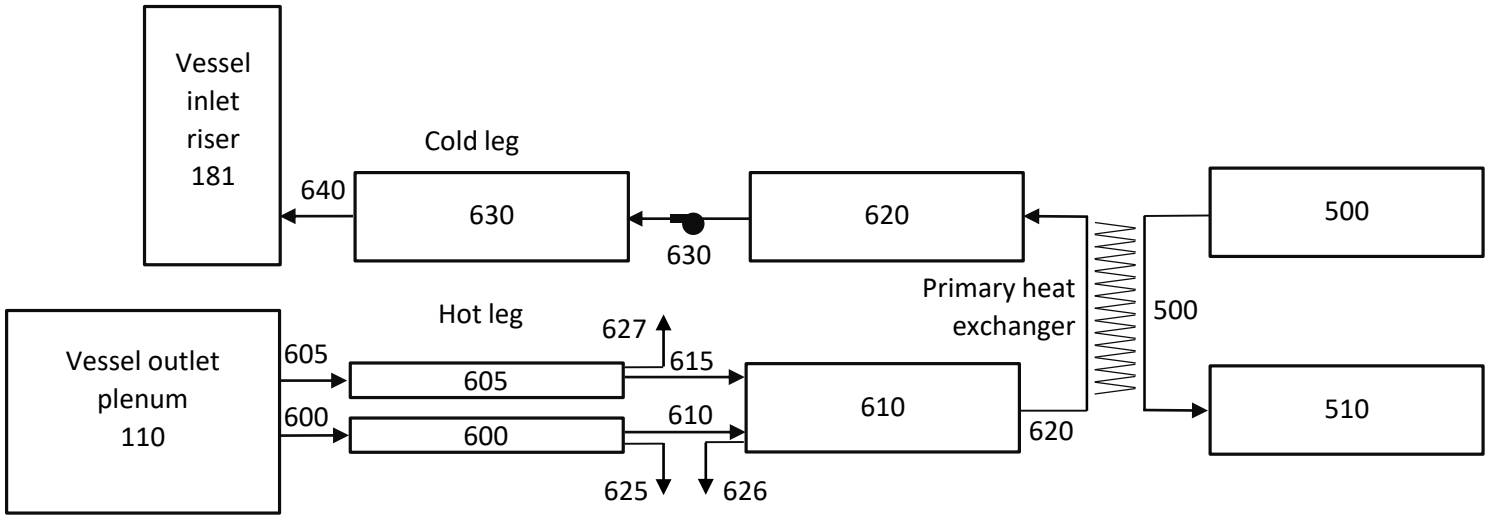

DLOFC Scenario

DLOFC is initiated after 900 days of operation

- Long-term fission product concentrations developed in TRISO and pebble
- 24 kg/yr graphite dust generation based on German AVR experience
- TRISO initialized with 10^{-5} failure fraction during the steady state

Provisions for air ingression

Reactor cavity cooling system (RCCS) is operational

Sensitivity calculations to explore variations in the model response to uncertainty in input parameters

DLOFC Reference Case Results (1/7)

Following pipe break

- Control rods insert to terminate fission
- The vessel depressurizes in seconds as the high-pressure helium escapes out both sides of the broken pipe
- Peak velocity in the pebble bed is 45 m/s (normal flow rate is 11-18 m/s)

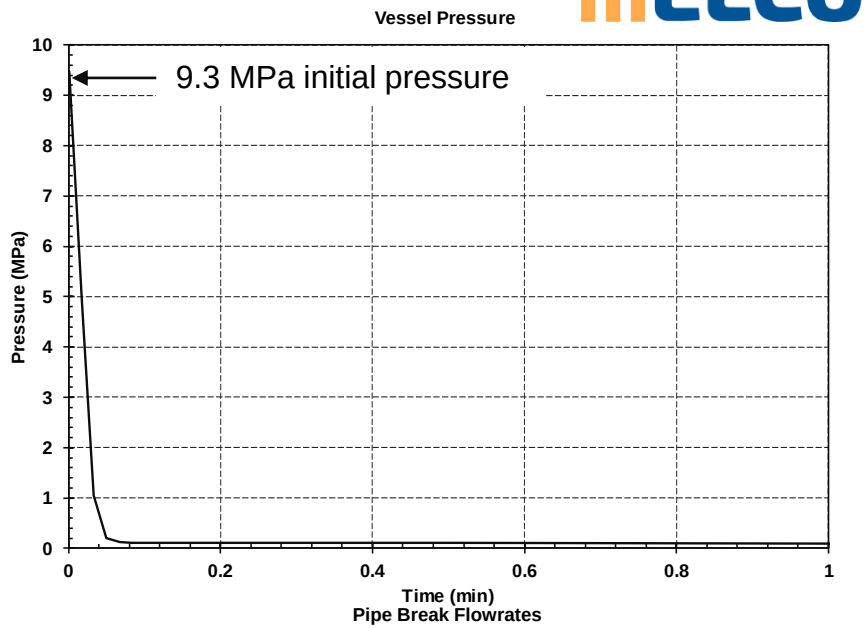

Counter-current flow established on the vessel side of the pipe break

- Hot gases from the exit plenum escape on the top side of the broken hot leg pipe and cooler gases enter along the bottom of the pipe

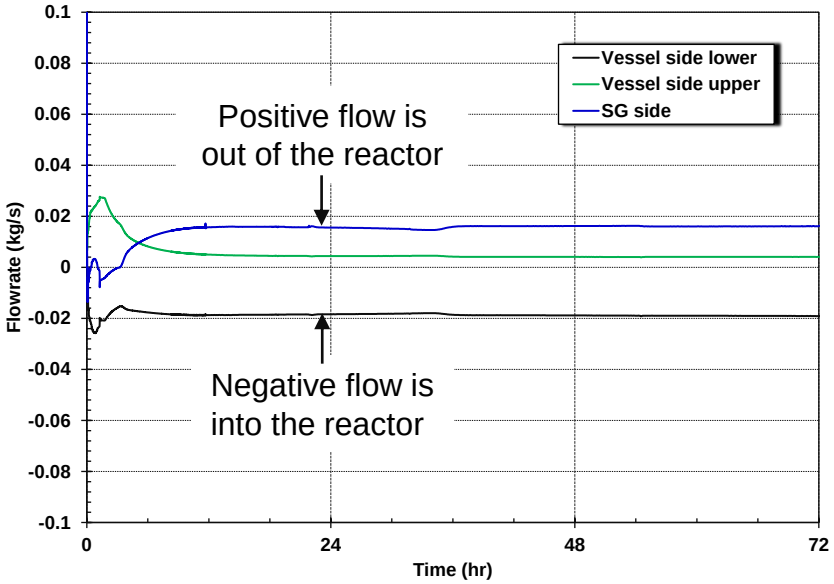

DLOFC Reference Case Results (2/7)

In-vessel natural circulation flow after blowdown

- Upward flow in the inner region of the core where the fuel temperatures and decay power heating are higher
- Downward flow in the outer region of the core where the fuel temperatures and decay power heating are lower
- Flow increases when the fuel starts to cool

The fuel temperatures in the inner region of the pebble bed shift from cooler at inlet and hot at the outlet due to the flow reversal

- The axial fuel temperatures are affected by the local decay heat power (highest in the center) and the flow direction
  - During normal operation, the fuel at the exit (bottom) is the hottest
  - The exit becomes the coolest location (low power and cooler gases entering from the exit plenum)

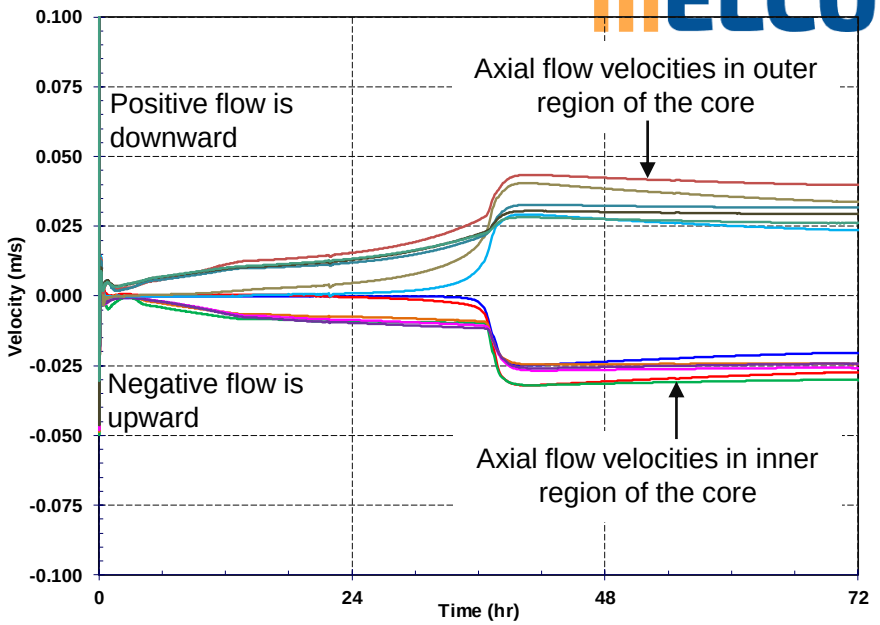

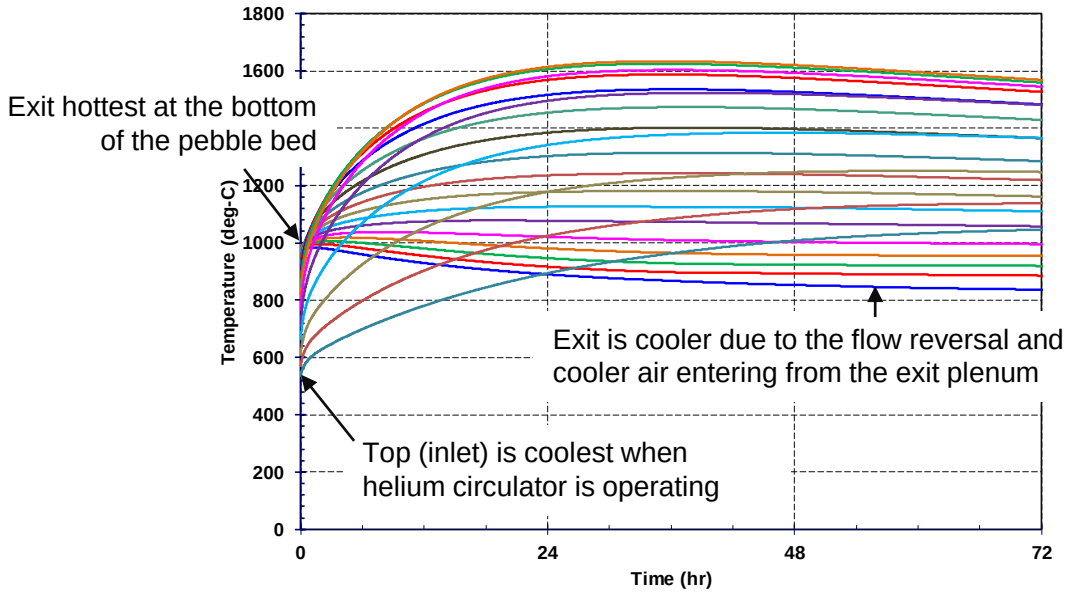

DLOFC Reference Case Results (3/7)

The core heatup is dominated by the decay heat

- The air oxidation power is relatively small at <25 kW
- Although the vessel is thermally-stratified with a low exit path, a small natural circulation flow persists to bring air into the vessel
  - Pebble bed inlet and circulation velocities are <0.04 m/s

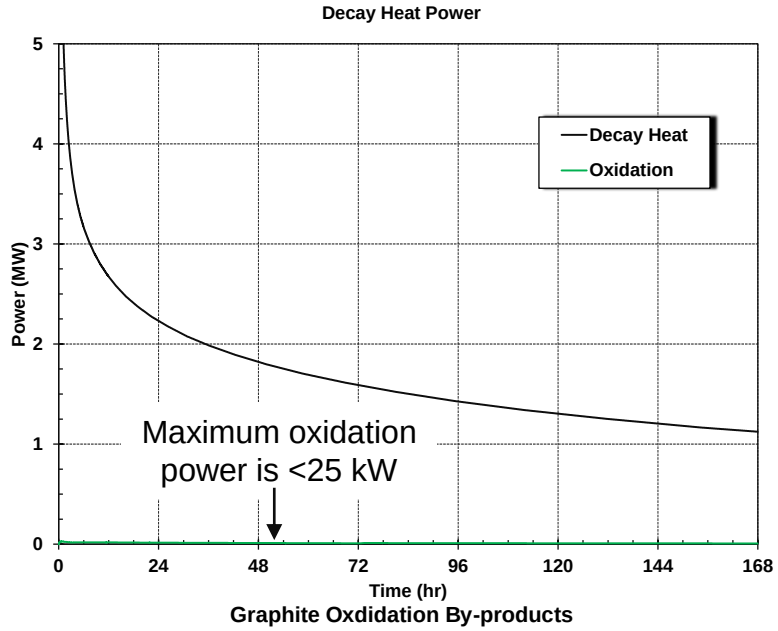

The graphite oxidation produces significant quantities of CO and CO_2

- Approximately 50% of the oxidation occurs in the graphite reflector structures around the inlet plenum and 50% in the lower portion of the pebble bed.
- ~1% of the pebble matrix oxidized after 168 hr
  - 17% peak pebble oxidation at the bottom center

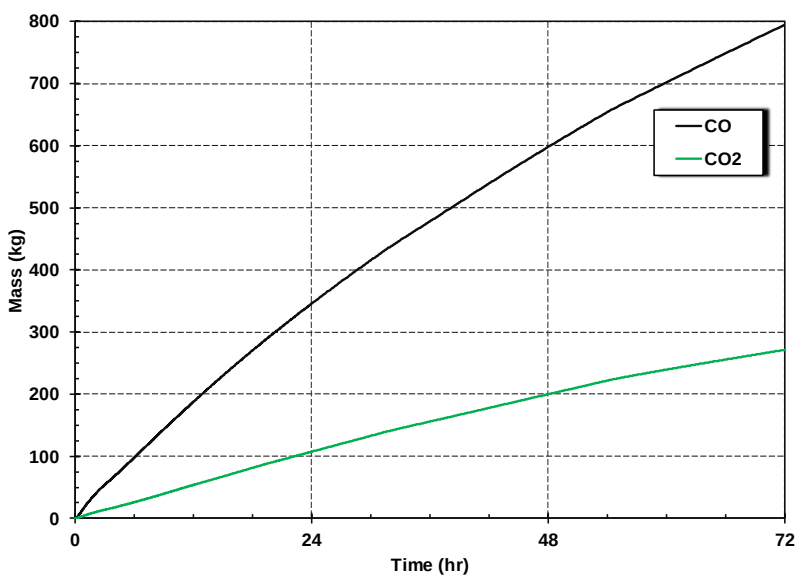

DLOFC Reference Case Results (4/7)

Potential for combustion in the reactor building

- MELCOR lower limit for CO combustion with an ignition source is 12.9% (~2X higher than for hydrogen)
- Highly dependent on local concentrations and building design and interconnectivity
- Demo reactor building assumes high inter-connectivity
  - Allows air and CO circulation
- No CO burns were predicted through 168 hr

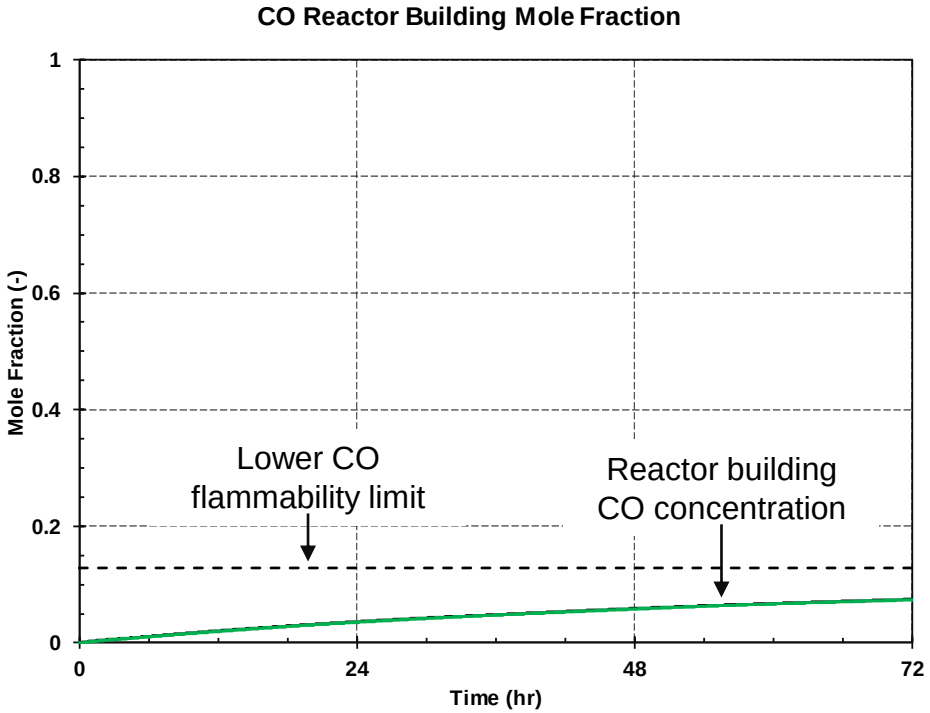

DLOFC Reference Case Results (5/7)

MELCOR predicts release and transport from fuel to the environment

- Fuel heat-up
- TRISO layers – Initial failure fraction + failures during heat-up
- Pebble matrix and pebble outer shell – Higher diffusivity at elevated temperatures, recoil, and air oxidation
- Primary system – Failed with the initiating event
- Reactor building – Design leakage

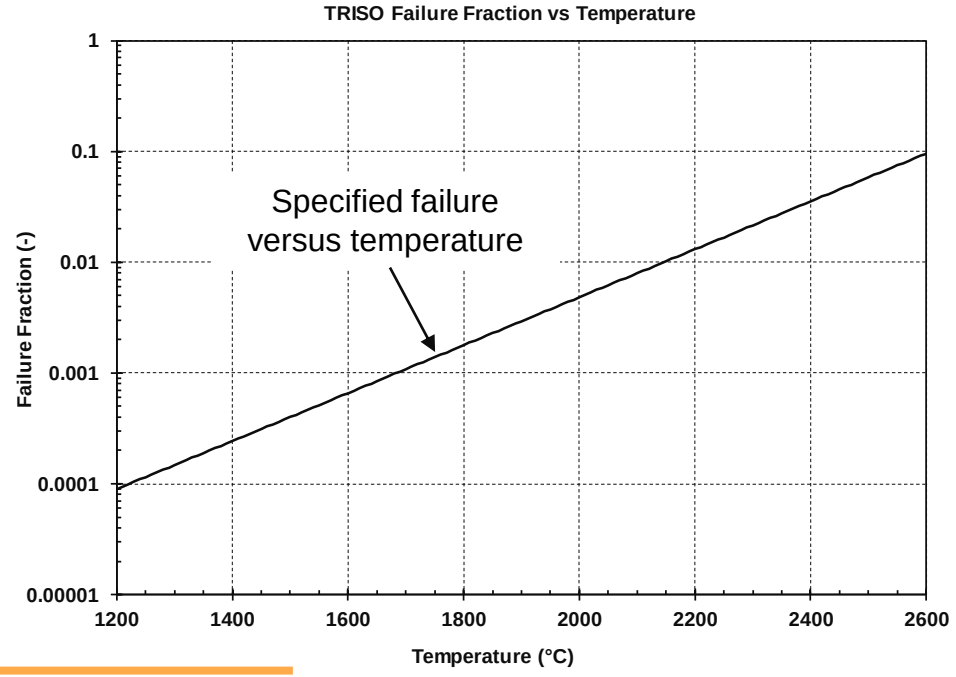

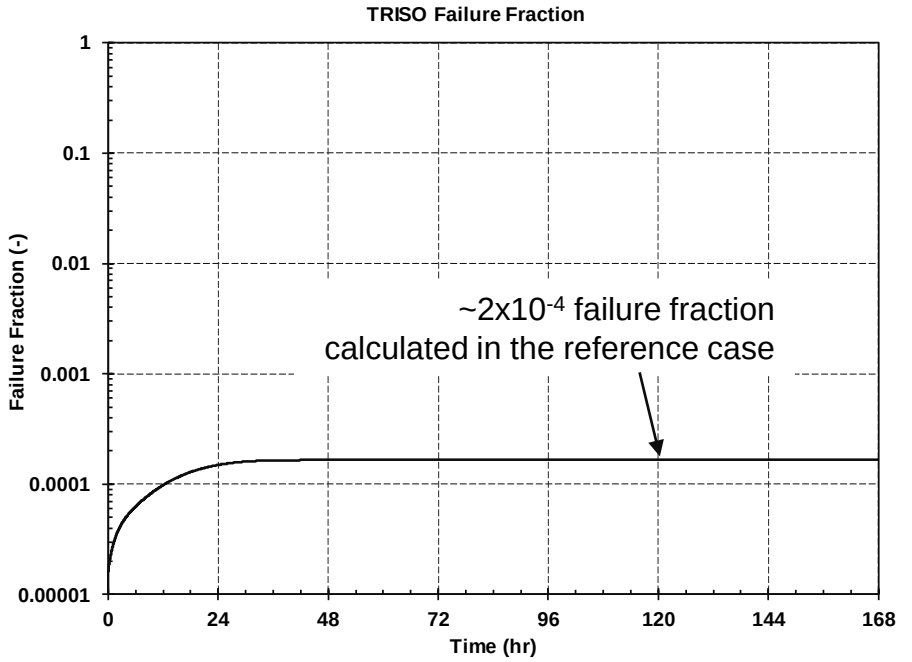

DLOFC Reference Case Results (6/7)

The impact of the low TRISO failure fraction leads to small releases

- Iodine diffusivity assumed to be same as krypton
- Assumes most iodine reacts with cesium
- Larger cesium release due its the higher diffusivity
- Ag release to the environment is 1.2×10^{-3} (highest diffusivity)

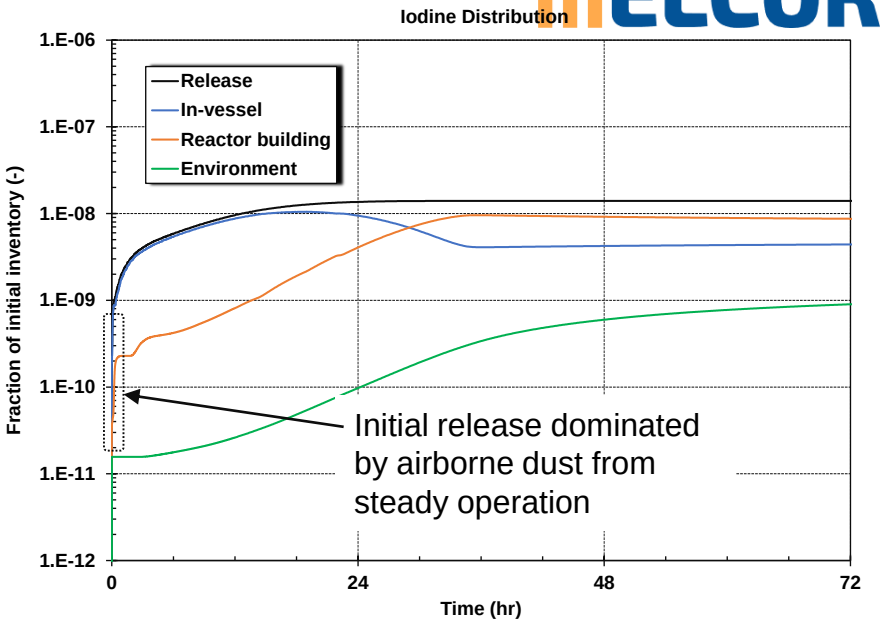

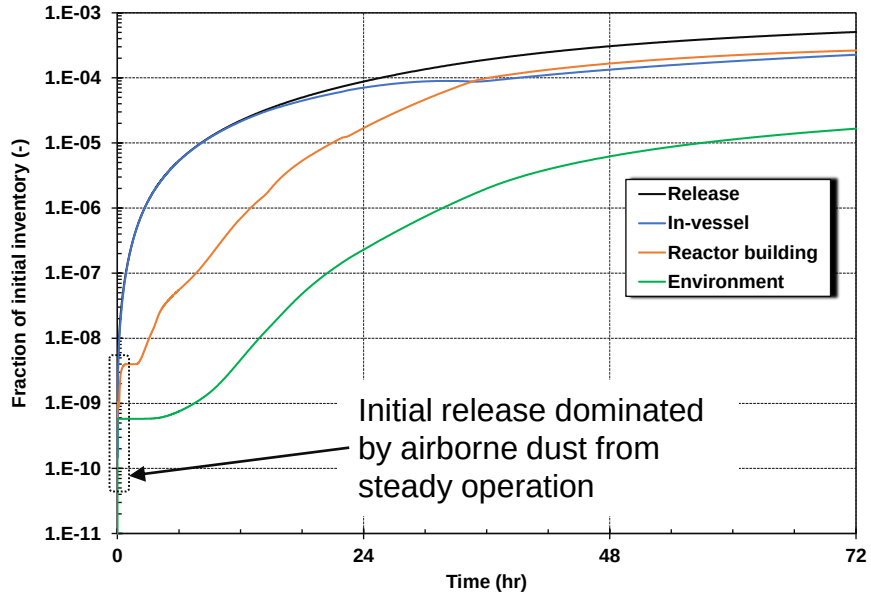

DLOFC Reference Case Results (7/7)

Of the small release from the fuel…

34% and 62% of iodine and cesium, respectively, retained in the vessel

- Thermally-stratified orientation limits vessel releases
- Low flowrate combined with aerosol deposition
- Inclusion of graphite oxidation reaction products (CO and CO_2) promotes more flow and therefore more releases from the vessel

58% and 34% of iodine and cesium, respectively, retained in the reactor building

- No strong driving force for reactor building leakage
  - Reference model uses a hole size equivalent to 100% leakage per day at a design pressure of 0.25 psig (3.2 in^2)

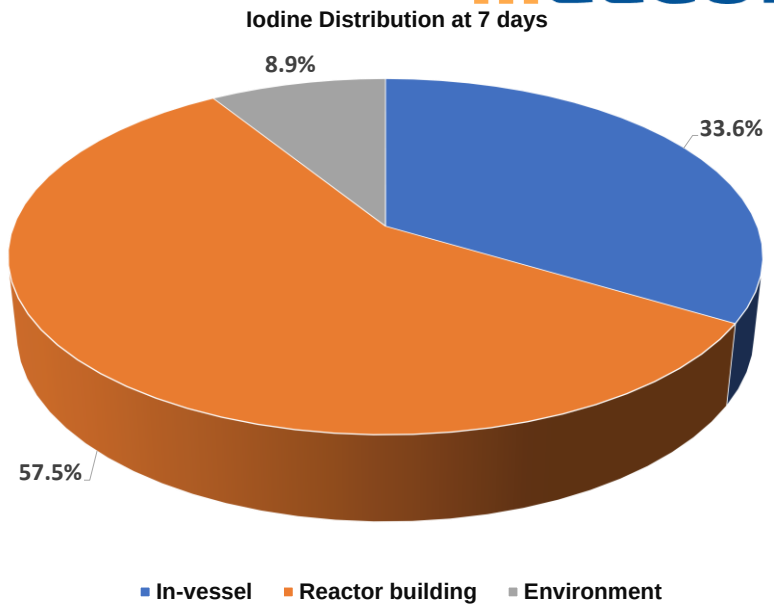

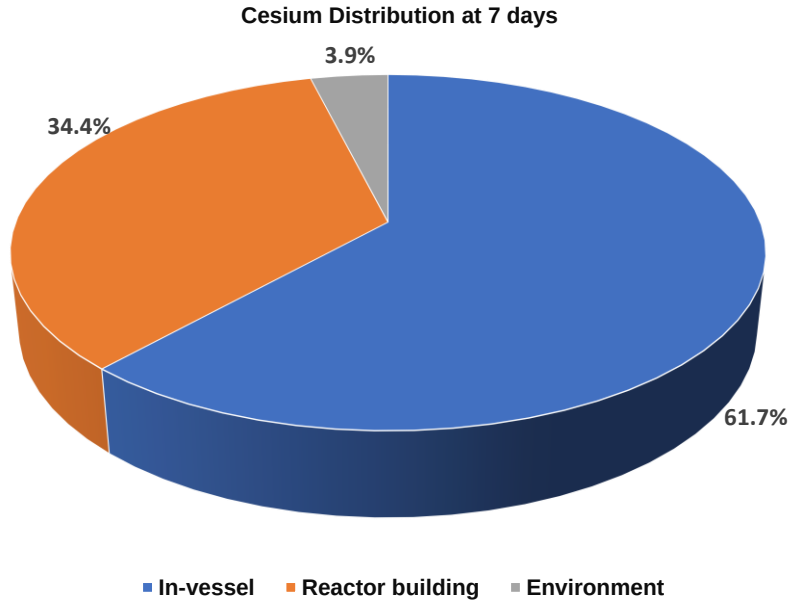

MELCOR can be used to explore the variability of the results to uncertainties

Model	Parameter	Distribution	Range
TRISO Model Parameters	Initial TRISO Failure Fraction (fraction of inventory)	Log uniform	10^{-5} – 10^{-3}
	TRISO Failure Rate Multiplier (-)	Log uniform	0.1 – 10.0
	Intact TRISO Diffusivity Multiplier (-)	Log uniform	0.001 – 1000.0
	Failed TRISO Diffusivity Multiplier (-)	Log uniform	0.001 – 1000.0
	Matrix Diffusivity Multiplier (-)	Log uniform	0.001 – 1000.0
	TRISO Pebble Emissivity (-)	Uniform	0.5 – 0.999
	TRISO Pebble Bed Porosity (-)	Uniform	0.3 – 0.5
	TRISO recoil fraction (-)	Uniform	0 – 0.03
Radionuclide Model Parameters	Shape Factor (-)	Uniform	1.0 – 5.0
	Gaseous Iodine Multiplier (Base = 5% I_2)	Uniform	0.02 – 1.0
Design Parameters	Graphite Conductivity Multiplier (-)	Uniform	0.5 – 1.5
	Decay Heat Multiplier (-)	Uniform	0.9 – 1.1
	RCCS Blockage Multiplier (-)	Log uniform	0.001 – 1.0
	RCCS Emissivity (-)	Uniform	0.1 – 1.0
	Reactor Building Leakage Multiplier (-)	Log uniform	0.1 – 100.0
	Wind speed (m/s)	Uniform	0 - 10

UO2 Thermal Response

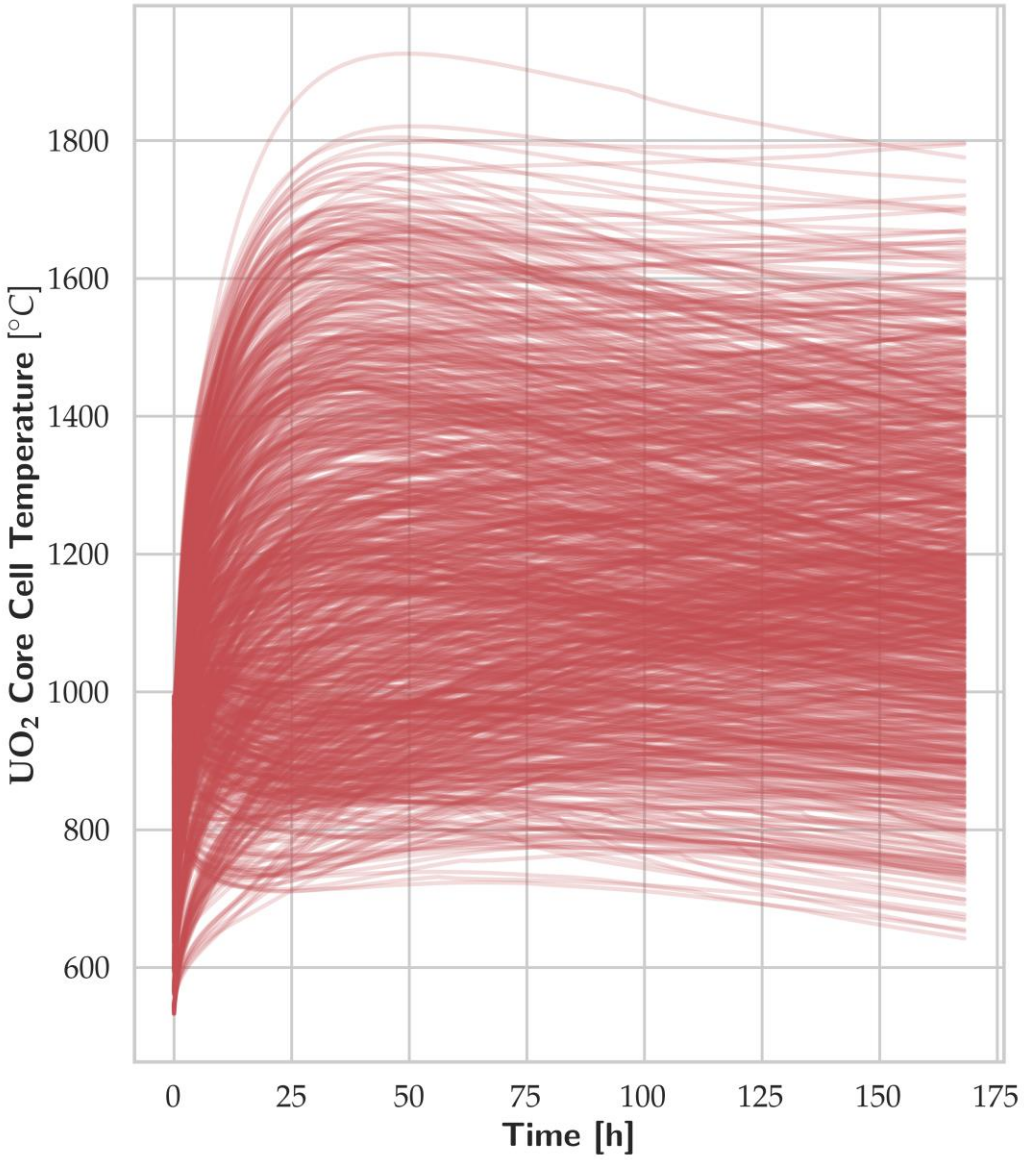

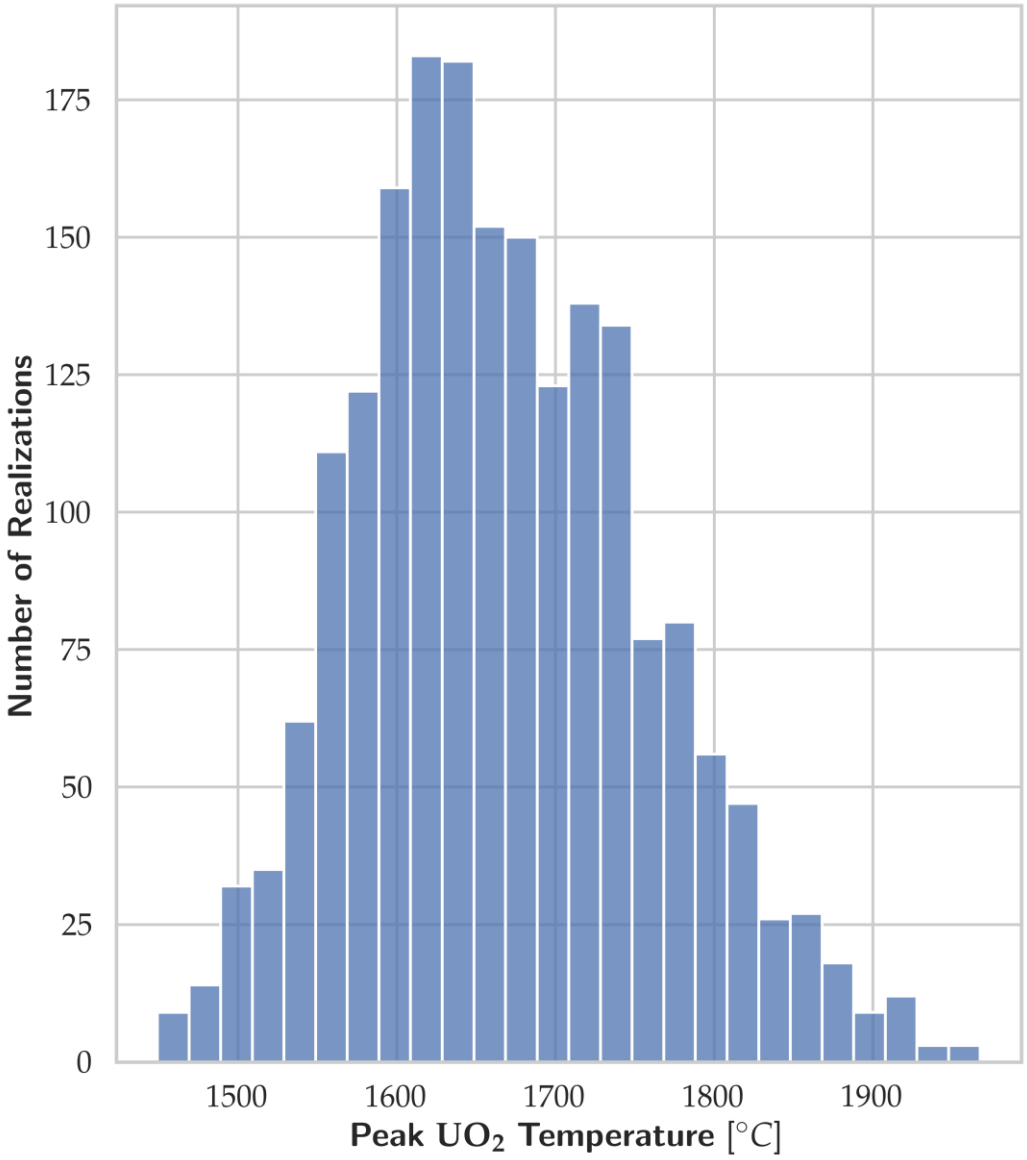

UO2 Thermal Transient Evolution

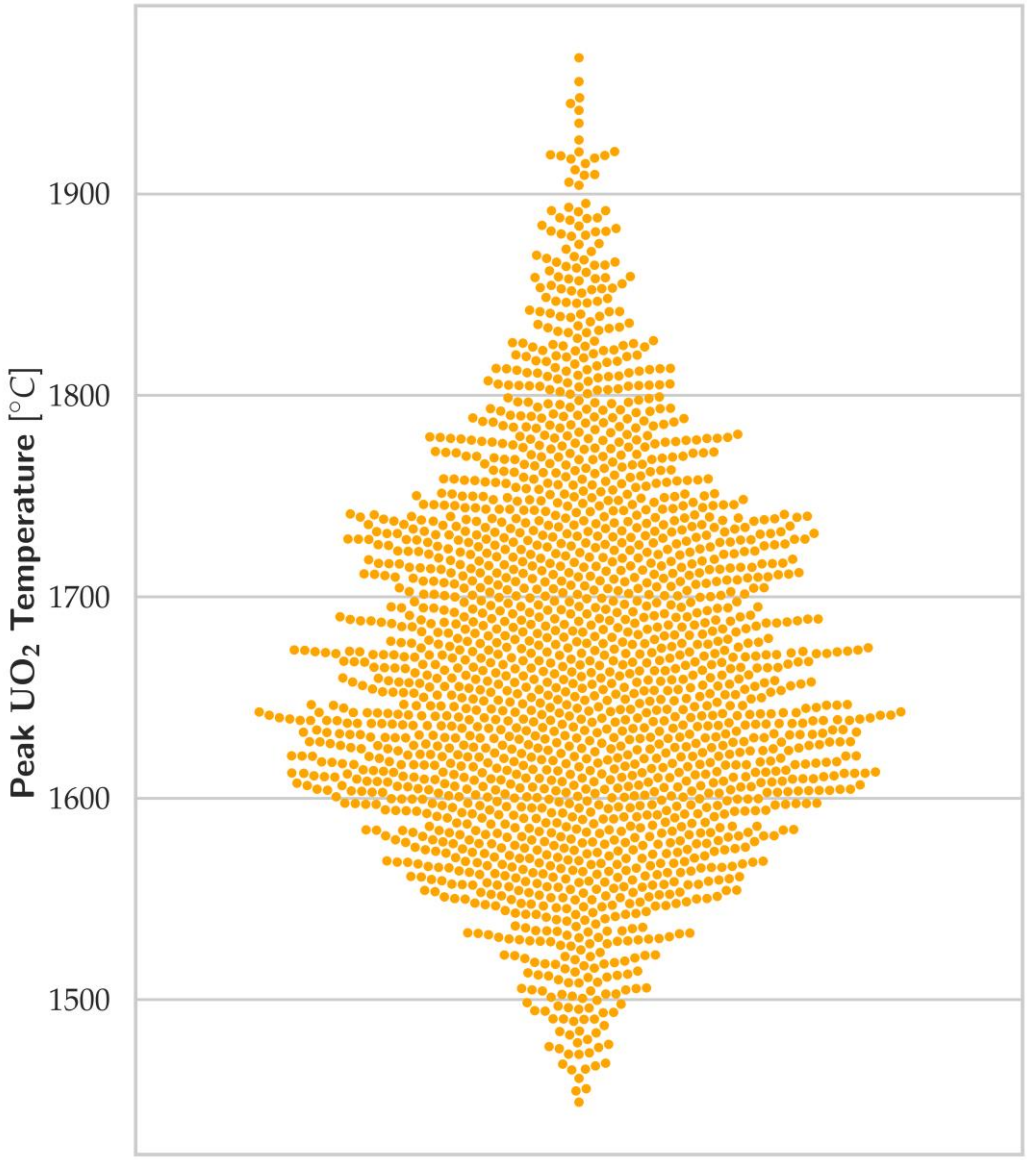

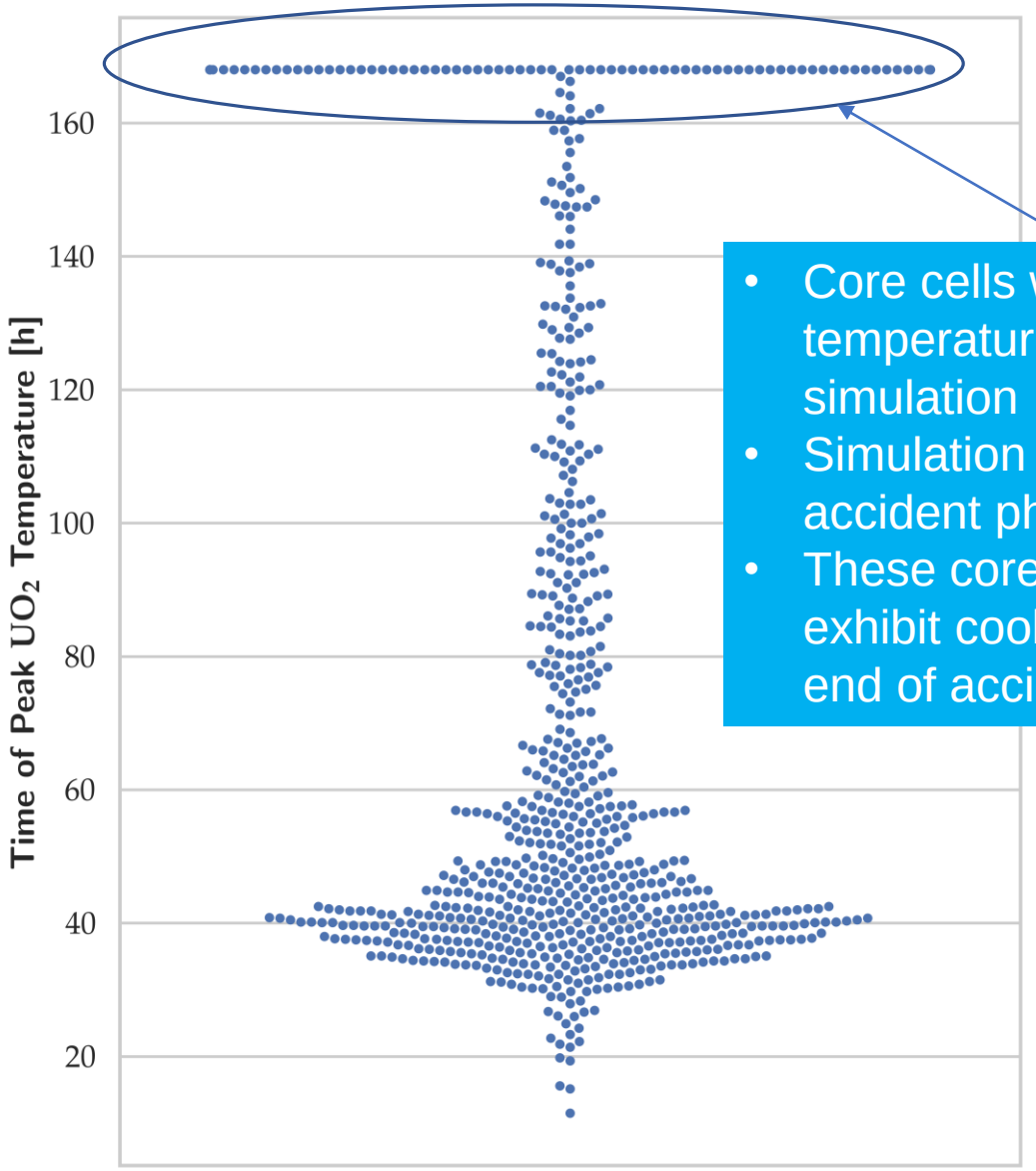

- Core cells with peak fuel temperatures at end of simulation
- Simulation time denoted as accident phase
- These core cells do not exhibit cooldown prior to end of accident phase

TRISO Particle Failure

Long-term TRISO particle failure possible for core cells exhibiting prolonged over-temperatures

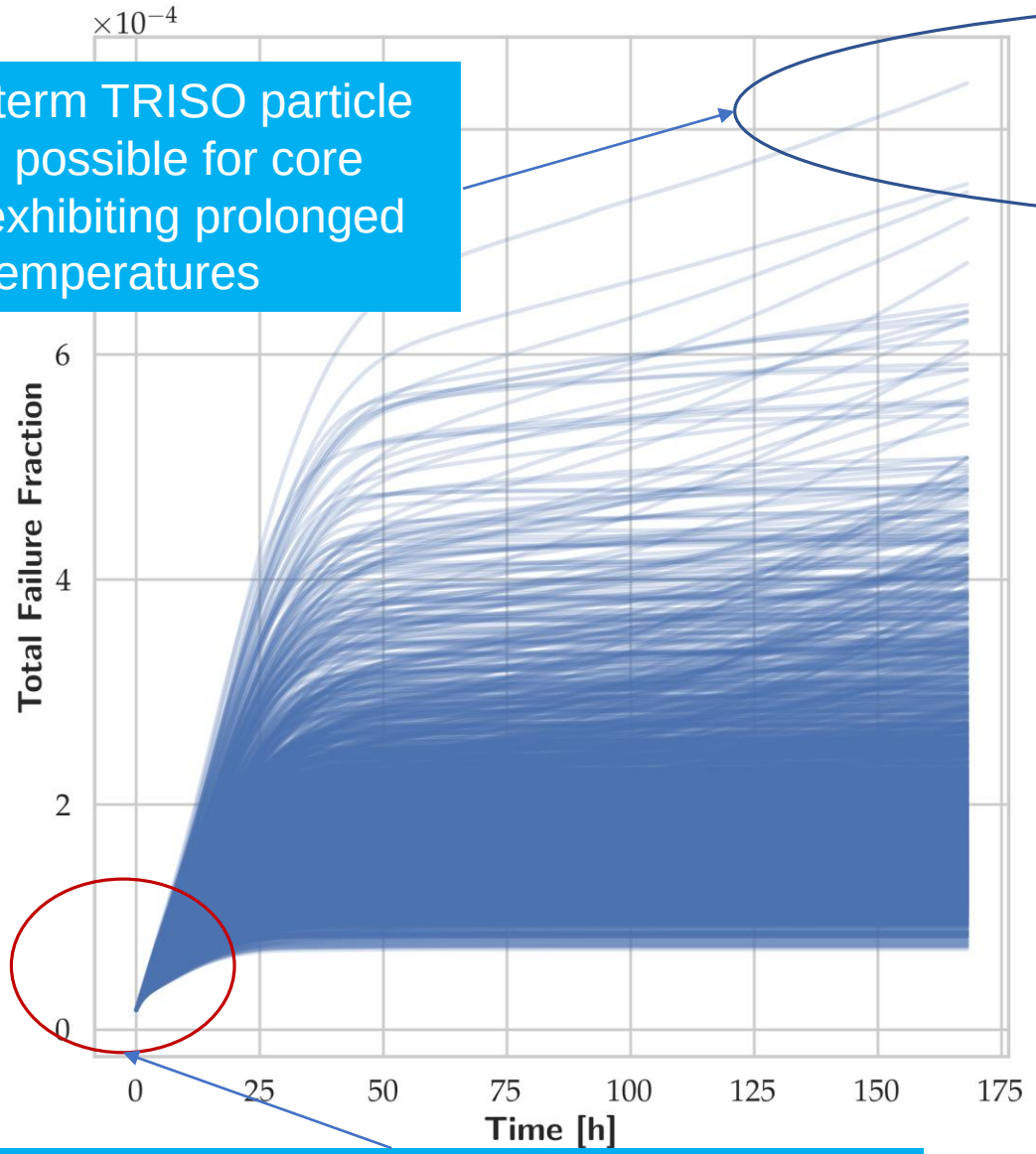

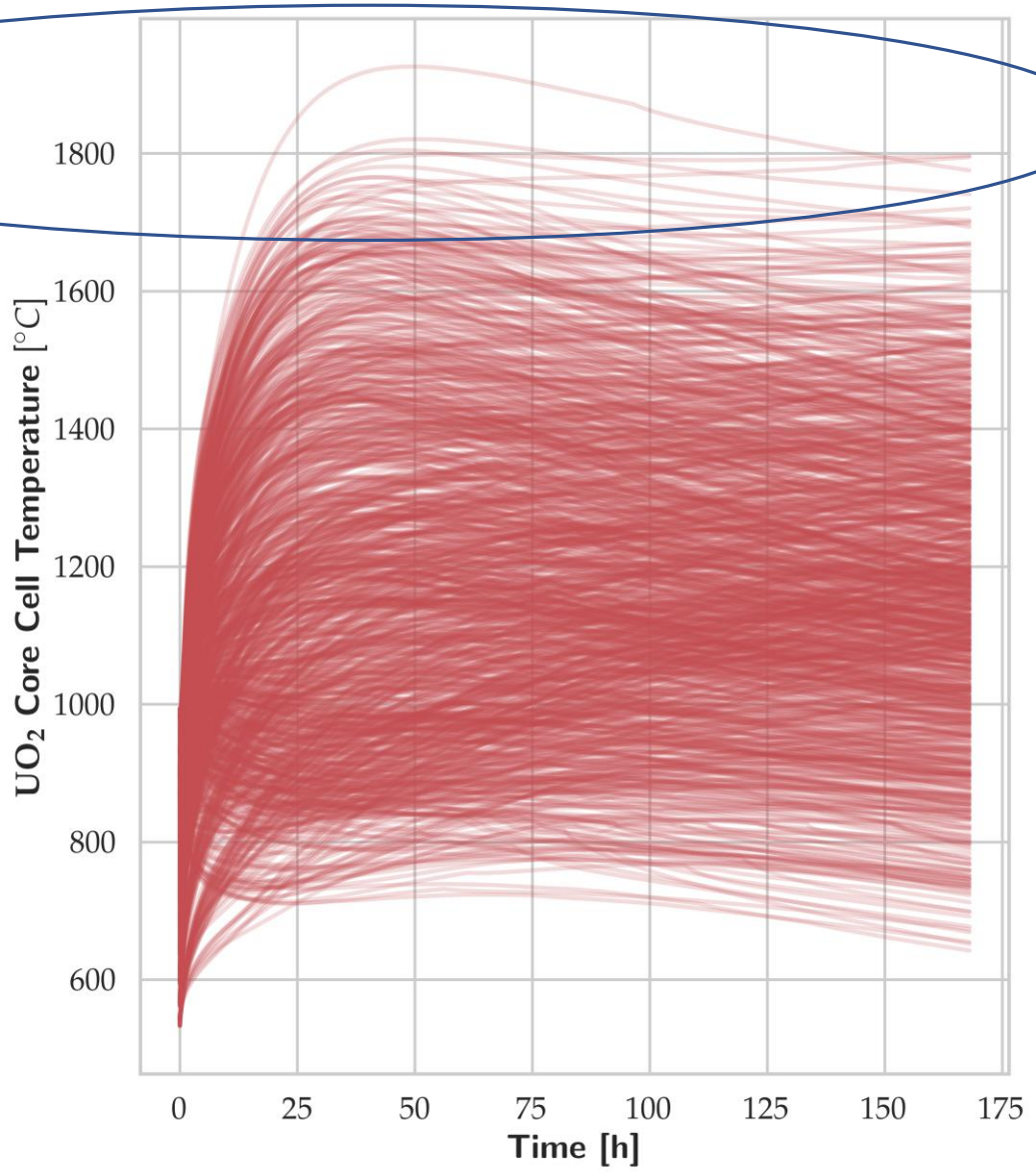

Initial distribution of failed TRISO particles

Evolution of TRISO Particle Failures

Long-term failures of TRISO particles at lower rate but driven by prolonged period of elevated fuel temperature

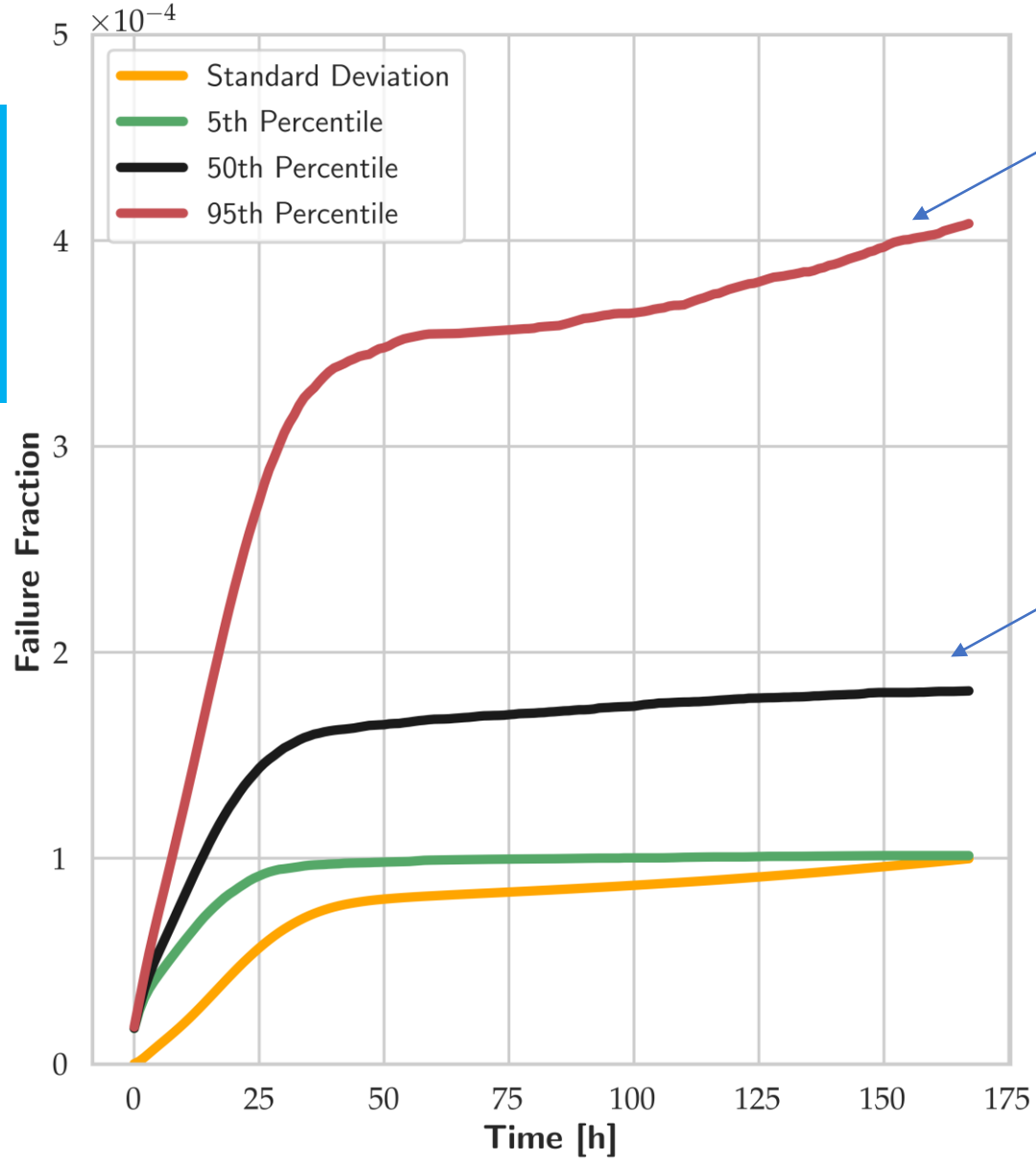

Tails of realizations contributing to longer term growth of TRISO particle failures

50th percentile reasonably stable in the long-term

Rapid growth in failure fraction driven by the early temperature excursion

Lower rates of failure entirely driven by early temperature excursion
Variability in peak fuel temperature and cooldown transient dominates higher failure rate realizations

Role of Decay Heat Rejection – Latest Time to Peak Fuel Temperature

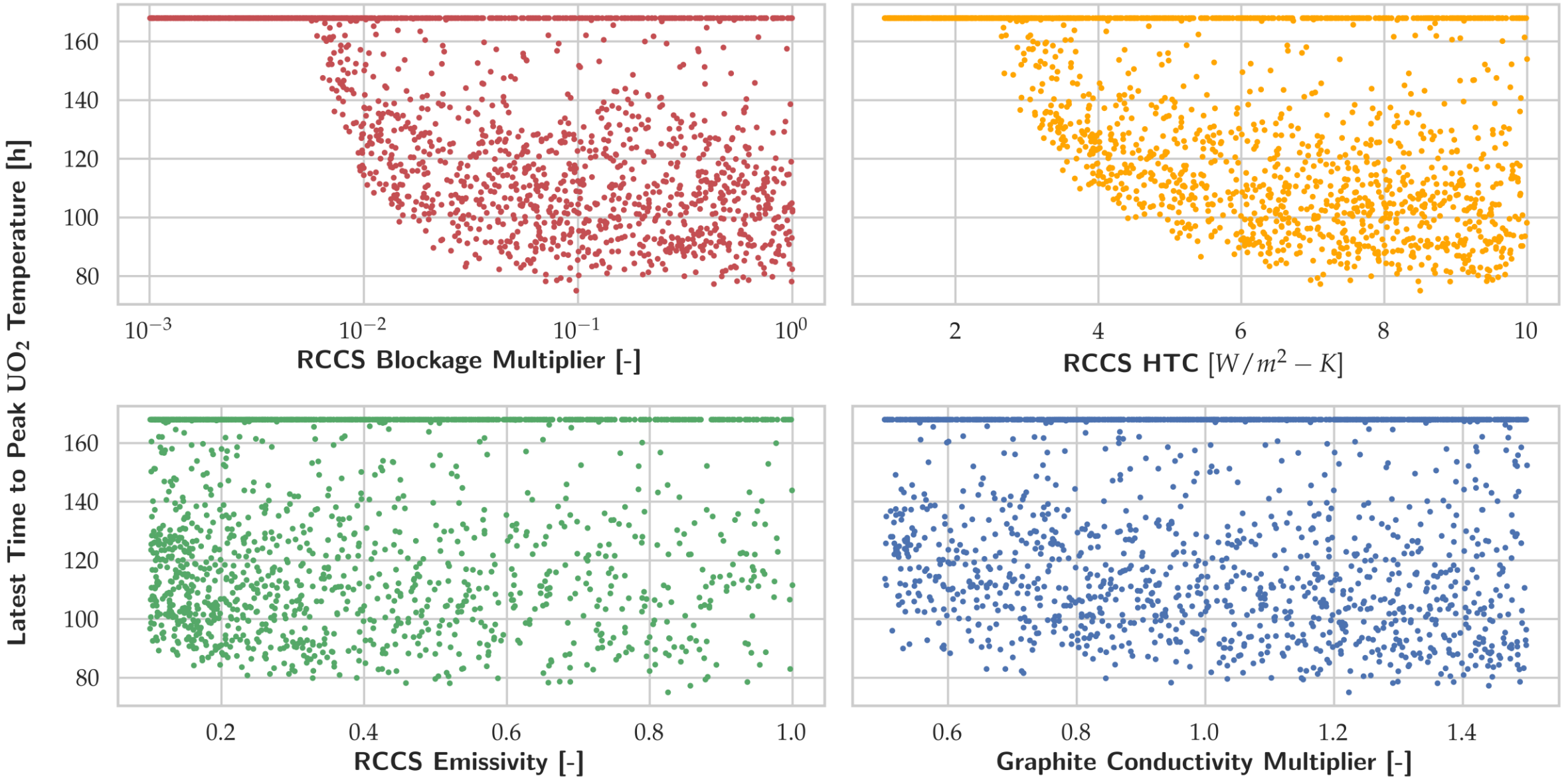

Role of Decay Heat Rejection – Peak Fuel Temperature

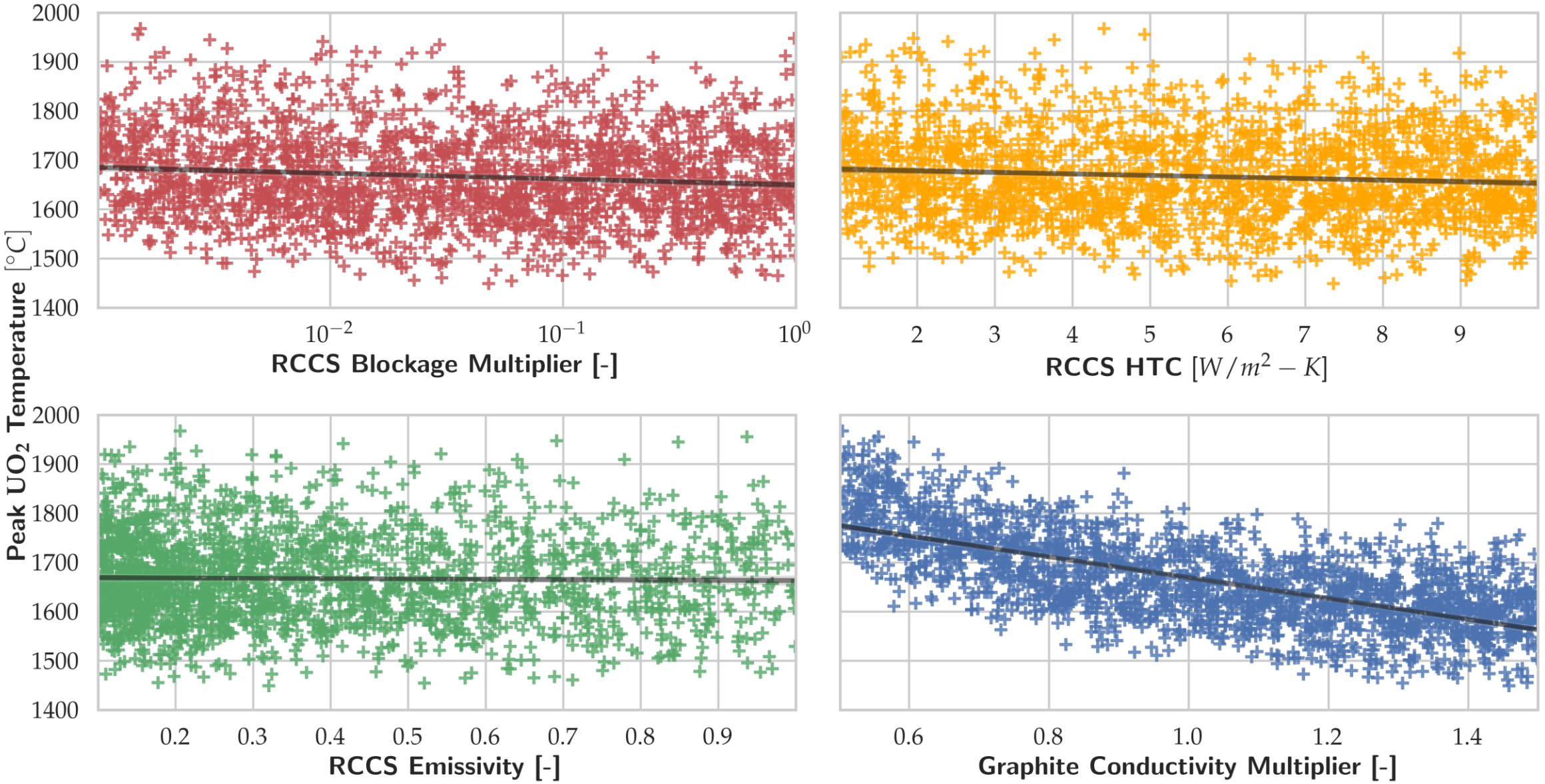

Sandia National Laboratories

Securing the future of Nuclear Energy

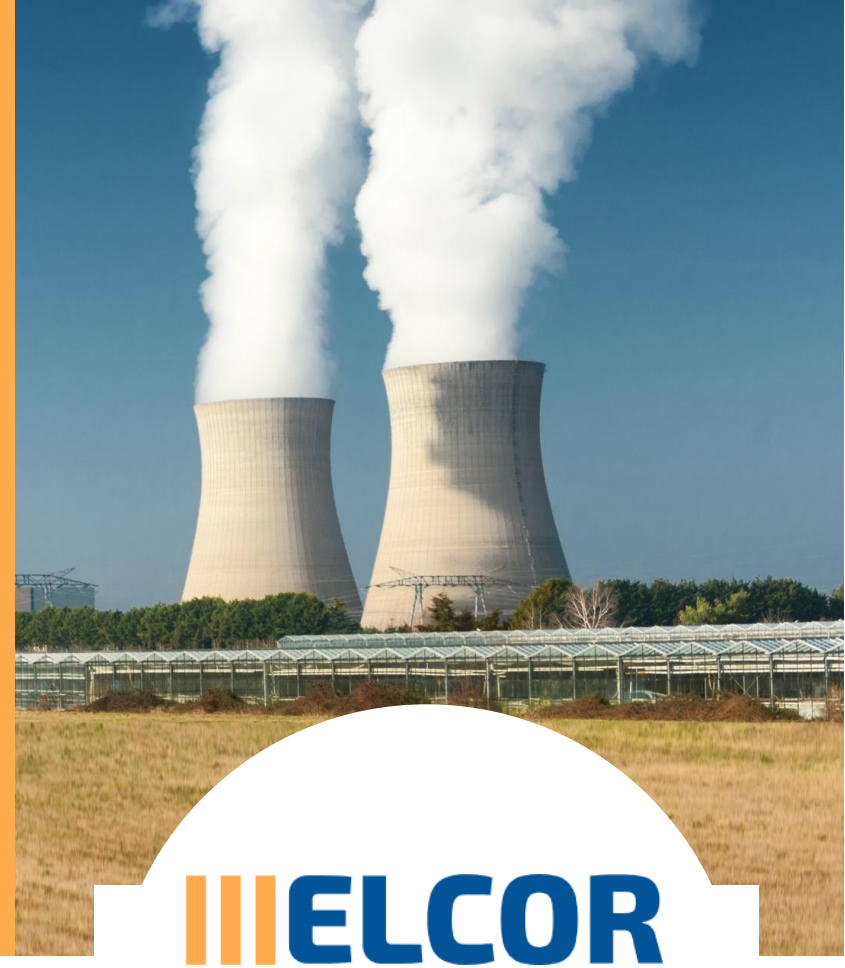

ELCOR

Thanks for your attention!

Sandia National Laboratories is a multimission laboratory managed and operated by National Technology and Engineering Solutions of Sandia, LLC., a wholly owned subsidiary of Honeywell International, Inc., for the U.S. Department of Energy's National Nuclear Security Administration under contract DE-NA0003525.

The 10th European Review Meeting on Severe Accidents Research

Severe Accident Research Eleven Years after the Fukushima Accident

May 16-19, 2022, Karlsruhe, Germany

Technical Session 5-1: Source Term

Chairs: N. Girault (IRSN), S. Gupta (Becker Techn.)

ID328	**Research needs on Source Term: a CSNI/WGAMA perspective** L. E. Herranz (CIEMAT)	**Paper** **Presentation**
ID292	**Fission Product Behaviour in Severe Accident Condition: Focus on Information gained from VERCORS/VERDON Analytical Programs** Y. Pontillon (CEA)	**Paper** **Presentation**
ID268	**Experimental study of CsI revaporization behavior in RCS condition after a SA** E. Le Fessant (IRSN)	**Paper** **Presentation**
ID269	**Experimental study on the feasibility for noble gases (Xe, Kr) trapping using Metal-Organic Framework** J. Nguyen-Sadassivame (IRSN)	**Paper** **Presentation**

RESEARCH NEEDS ON SOURCE TERM: A CSNI/WGAMA PERSPECTIVE

Luis E. Herranz
CIEMAT
Avenida Complutense 40, 28040 Madrid, Spain
luisen.herranz@ciemat.es

Didier Jacquemain
OECD/NEA
NEA offices, Boulogne-Billancourt, France
Didier.jacquemain@oecd-nea.org

ABSTRACT

The investigations conducted worldwide in the last 15 years on different aspects of Source Term in a nuclear accident, and particularly in the frame of the Nuclear Energy Agency (NEA) of the OECD, has resulted in a significant enlargement of the available database and an enhancement of the modelling capabilities. The Working Group on Accident Management and Analysis (WGAMA) of the Committee on Safety of Nuclear Installation (CSNI) of NEA faced with the challenge of identifying gaps and remaining uncertainties that might have a sizeable impact on nuclear safety, and to discuss the best way to address them. Four open issues, not or hardly addressed in previous investigations, were highlighted: fission products remobilisation resulting in delayed releases; source, behavior and mitigation of fine radioactive particles hard to remove from the gas atmosphere; completion of the database on organic iodides; fission product leaching up to decommissioning. In addition, two major points were made: the need to further and better exploit the data available to bring them to their maximum usefulness for plant applications and the data scalability to anticipated conditions. The significance of leak paths for the eventual Source Term to the environment was mentioned to be a "need" in the research agenda.

KEYWORDS
Source Term, CSNI/WGAMA, research issues

1. INTRODUCTION

In the last 15 years a good number of international projects have been carried out on Source Term, both under the auspices of CSNI and beyond. As for CSNI, in the last years, BIP (NEA, 2020a), STEM (NEA, 2018) and THAI (NEA, 2016a; NEA 2021b) projects have provided important data on key aspects of Source Term, like iodine and ruthenium behaviour in the containment on the short and long term, including revolatilization from surfaces and pools or even the effect of mitigation systems (PARs, …). In addition, there have been a number of projects, like the NEA BSAF (Pellegrini, 2019) projects and the most recent TCOFF, PreADES (Nakayoshi, 2020) and ARC-F (Nakatsuka, 2018) projects, which have been set up in the wake of the Fukushima Daiichi accident and are closely related to Source Term. No less important, activities like those addressed within the WGAMA group on Long Term Management of accidents in Nuclear Power Plants (LTMNPP) (NEA, 2021a) and the FASTRUN exercise (NEA, 2015a) have provided and are providing elements for discussion in the area of Source Term. It is worth emphasizing that in Spring

2015 an international workshop on iodine was organized by WGAMA and a set of recommendations, partially addressed in the recently ended or about ending projects, were given (NEA, 2016b).

Beyond the CSNI, the SARNET framework provided a good progress on Source Term (Herranz, 2015) and framed a good number of small and mid-scale experimental projects on release and transport of fission products; no less important, interpretation work of the key PHEBUS-FP experiments was also conducted under the SARNET sponsorship, among which the so called PHEBUS FPT3 benchmark (Di Giuli, 2016) is worth mentioning, as it has been the last integral code benchmark broadly participated with the main focus on fission product and aerosols release and transport. Other projects also provided meaningful achievements in different aspects of Source Term, including mitigation, like VERCORS (Ducros, 2013), ISTP (EPICUR, VERDON and CHIP testing) (NEA, 2016b; Pontillon, 2017), ARTIST (Lind, 2019), PASSAM (Albiol, 2018), etc.

After such significant work conducted and the database having been so enlarged, the CSNI/WGAMA working group organized a workshop with a two-fold purpose: to identify the knowledge gaps and remaining uncertainties in the Source Term area, that might have a sizeable impact on nuclear safety; and to discuss the best way to address them with the existing and/or future methods, analytical tools and facilities, if needed. The scope was limited to water cooled reactors and conventional types of fuels.

In next sections the main outcomes and, most importantly, recommendations made during the workshop are summarized. Nonetheless, paper writing is notably changed with respect to the reference report produced (NEA, 2020b) and some differences might be noted on the way to convey the messages, but not on the essence that came out from the workshop

2. KEY BACKGROUND

Some of the major milestones in the last 20 years closely related to Source Term research evolution are displayed in Figure 1. State of the Art Reports (SOAR) by NEA have become references in different fields. Such is the case of the SOARs on nuclear aerosols (NEA, 2009) and iodine chemistry (NEA, 2007). Just taking these reports as the start line for discussion, a number of issues are highlighted for both nuclear aerosols and iodine chemistry. Some are still standing: the shape of aerosols, which might be investigated through uncertainty and sensitivity analyses; aerosol resuspension, which might pose a threat in by-pass sequences; particle break-up, on which no data is available for prototypical nuclear aerosols; deposit revaporization, which impact in risk-dominant sequence might be significant; re-entrainment, which in case of contaminated pools reaching saturation conditions might turn into an unexpected late source of radioactivity. Regarding iodine chemistry, some issues haven not yet been worked out: the impact of chemical kinetics in radionuclide transport in the primary circuit; the large uncertainties in key conditions for iodine chemistry, like the sump pH; the adsorption/desorption of iodine onto/from containment surfaces; the production of organic iodides from any substrate and/or homogeneous reaction; and, the iodine chemical reactivity at the secondary side of a steam generator undergoing an steam generator tube rupture (SGTR) severe accident sequence. Some of these matters, though, have been addressed in projects that came after SOARs, as discussed next.

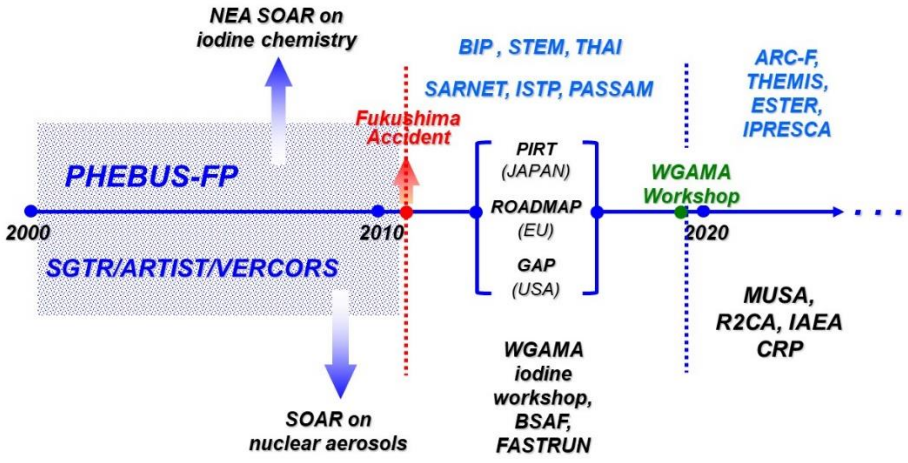

Figure 1. Major chronological milestones of the recent international Source Term research.

The PHEBUS-FP project has likely been the most significant contribution to Source Term as it was a unique chance to examine chemical and physical forms taken by radionuclides along an accident (Haste, 2013). Nonetheless, there have been other major contributions after it, like ARTIST (Lind, 2019), which tested containment by-pass sequences (i.e., SGTR severe accident sequences), OECD/NEA BIP (Glowa, 2016), OECD/NEA STEM (Mun, 2015), mainly dealing with iodine chemistry, OECD/NEA THAI (Gupta, 2016), and VERDON (Pontillon, 2017). Additionally, the SARNET network made relevant contributions in this period, as reported in (Herranz, 2015). All the research referenced here has resulted in a better understanding of fission products release from fuel and transport. Some of their insights deserve being stood out:

- Releases from fuel were mostly adequately predicted for iodine and caesium. Release for tellurium (Te) and molybdenum (Mo) and other less volatile FP are more complex to model as they are sensitive to oxidative or reducing conditions.
- Aerosol behavior and transport was estimated reasonably, despite particles form and composition remain uncertain.
- In scenarios with Mo release, Cs_2MoO_4 has been credited as the main chemical species transporting caesium to containment and beyond.
- Long-run iodine concentration in the gas phase might not come from in-containment sumps, as previously assumed, and some other sources of gaseous iodine, including organic iodides, might be considered.
- Small iodine-containing particles might be formed from airborne iodine through oxidation in containment gas phase.

In spite of the major progress reported, further work is considered necessary in the following issues: deeper analyses of the VERDON release tests; of iodine-paint interactions under realistic conditions (i.e., paint aging, competition with other reactive species, doses, etc.); particles form in the primary circuit; iodine interactions with water contaminants (complications associated to contaminated waters have not been thoroughly addressed so far).

In the years after the Fukushima-Daiichi accidents, a number of Phenomena Identification Ranking Tables were conducted worldwide on severe accidents and their insights are worth being considered. In Europe, such an initiative traced back in the early years of the 21st century with the EC EURSAFE project (Magallon, 2005) and a periodic update has been reported in the ERMSAR conferences. The latest one (Manara, 2019) brought up two major issues as still deserving further attention (other issues being investigated at the time

in international frames like NEA projects were disregarded): fission product release and transport under oxidation conditions (in particular, air ingress for high burnup and MOX fuel with special attention to semi-volatile Mo and low volatile Ruthenium (Ru)) and high temperature chemistry in the reactor coolant system (RCS), as a need for modelling phenomena like revaporization. The so-called American PIRT (Bunt, 2015) was a high-level exercise specifically addressing Station BlackOut (SBO) accidents which did not include any issue on Source Term, although, for example, it made insightful statements regarding emergency core cooling system equipment performance for ex-vessel debris coolability and limiting core-concrete interaction, and it underlined that uncertainties related to core degradation might overshadow other uncertainty sources. A specific Source Term PIRT based on findings during the Fukushima-Daiichi accident was developed by Japan (Suehiro, 2015). Mostly based on engineering judgement, in-vessel release related phenomena to source term and condensation, revaporization and adsorption phenomena were highly ranked as key mechanisms for radionuclide behavior in the reactor pressure vessel, the primary circuit and the steam line.

The Fukushima-Daiichi accidents should be seen as a source of data that might help to reduce model uncertainties, but no less important, the accidents drew attention to Source Term phenomena that might happen in a longer time horizon than the initial stages of an accident; in other words, long-term effects should not be neglected without proper consideration.

3. RECENT PROGRESS and CURRENT STATUS

This section focuses on the latest achievements made, both experimental and analytical, and the major findings that have come out so far from the Fukushima-related research concerning Source Term. Main Source Term related phenomena are summarized in Figure 2. Experimentally, major source term findings might be better summarized if the fission product research is split into release from the fuel, chemistry and transport in RCS and RCB (reactor containment building) and mitigation.

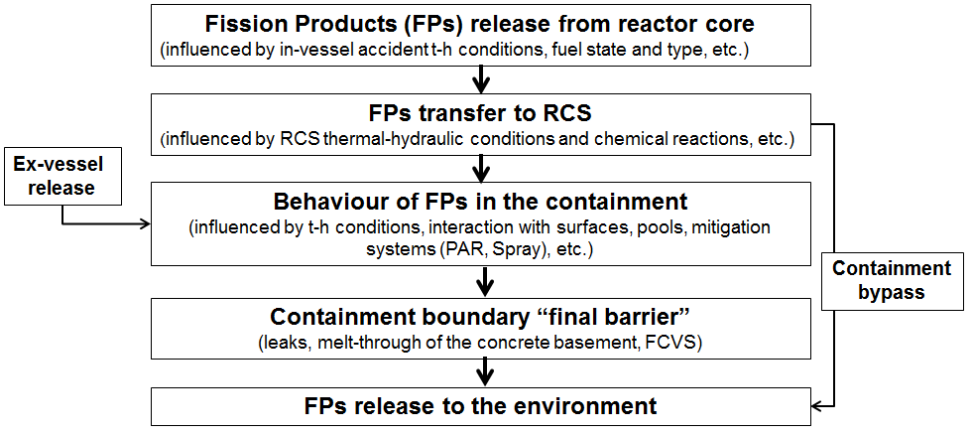

Figure 2. Main phenomena related to Source Term.

As for release, the "in-vessel" database already existing (HI/VI (US), CRL (Canada), VEGA (Japan), HEVA/VERCORS (France), PHEBUS-FP (France), …) has been enlarged with ISTP/VERDON –CEA, France) tests, as mentioned above, and a classification has been proposed: volatile FPs (Noble Gases, Cs, I, Te and others), semi-volatile FPs (Mo, Ba, Rh, etc.), low volatile FPs (Sr, Ru, La and others), non-volatile FPs (Zr, Nd, Pr) and actinides (also non-volatiles). Major observations were highlighted:

- Higher release kinetics for volatile FPs for high burn-up and MOX fuel in comparison to low burn-up UO_2 fuel, starting at a rather low temperature.
- Substantial release in oxidizing conditions for Mo (steam environment) and Ru (air ingress) and in reducing conditions for Ba.

As for the ex-vessel, there seems to be still some matters worth investigating:

- Aerosol releases from boiling sumps might have potential relevance and the knowledge is incomplete to address some accident scenarios.
- Delayed releases due to remobilization of a fraction of fission product deposits, by mechanisms like revaporization, resuspension and/or revolatilization might have relevance in the magnitude and/or timing of Source Term, and very limited knowledge does exist on these phenomena. Long-term leaching must be considered among those uncertain phenomena.

As for transport through RCS, there are still some uncertainties, particularly, those affecting iodine and ruthenium speciation:

- Effect of various gaseous and aerosol species/impurities on the volatilization of both elements.
- Formation of organic iodine from sources other than transfer from pools and reactions with paints.
- Production and behaviour of small iodine oxide particles in the containment atmosphere.
- Nature and amount of potential water pool contaminants/impurities should be given proper consideration, as they might strongly affect both FP release and transport.

Finally for release mitigation, the performance of safety systems under realistic conditions would notably strengthen their reliability under BDBA.

Review of the modelling of FP releases, in-RCS and in-containment transport and chemistry and mitigation in integral codes like ASTEC, AC2, MELCOR and MAAP under prevailing conditions during accidents, indicate some still open issues (mostly in accordance with what is noted experimentally):

- Late in-vessel releases, ex-vessel molten pool releases, fuel leaching and release from Accident Tolerant Fuels (ATFs) need further analytical development and validation.
- On RCS transport and chemistry, remobilization mechanisms need further development from their current status, as well as any via of gas iodine generation.
- In containment, the matters needing further investigation are iodine oxides reactivity, production of gaseous organic iodides through homogeneous reactions, and containment natural leakages.

Aside specific issues, the use of Uncertainty and Sensitivity Analysis (UaSA) at plant scale studies would be necessary to assess the dominating uncertainties and sensitivities of all the issues listed above.

Additionally, to thoroughly review experimental campaigns and modelling status, an objective assessment of the learnings from the Fukushima-Daiichi accident unfolding in Units 1 – 3 should be considered. Some interesting observations have been made either onsite or through NEA Fukushima-Daiichi related projects:

- Influence of FP deposits on upper vessel structures on FP delayed release through the potential chemisorption of some species (e.g. CsOH) and later revaporization.
- Strong effect of FP chemical speciation on transport and behaviour depending on prevailing boundary conditions, like high steam content and temperature in BWR dry-well and pH in BWR suppression pool.

- Conditions in suppression pools in terms of temperature and injection flow rates might have gone higher than in previous studies and the possibility of having iodine species revolatilization has not been ruled out with the current knowledge of the accident scenarios, in which variables as important as suppression pool pH is unknown.
- Strong effect of leak paths definition between RCV and containment and between containment and reactor building (Figure 3); both definition of flow-paths and phenomena governing the transport and deposition of particles entail huge uncertainties. Effects of accident management measures, such as water injection and resulting pressurization effects should be examined more thoroughly.
- Leakages of FPs through aqueous pathways; very little has been done in the past on it and it turned out to be one of the main release path to the environment.

According to the Fukushima-Daiichi accident unfolding, it would be recommendable to pay attention to some of the issues listed above not just from a reactor perspective, but also from a spent fuel pool one.

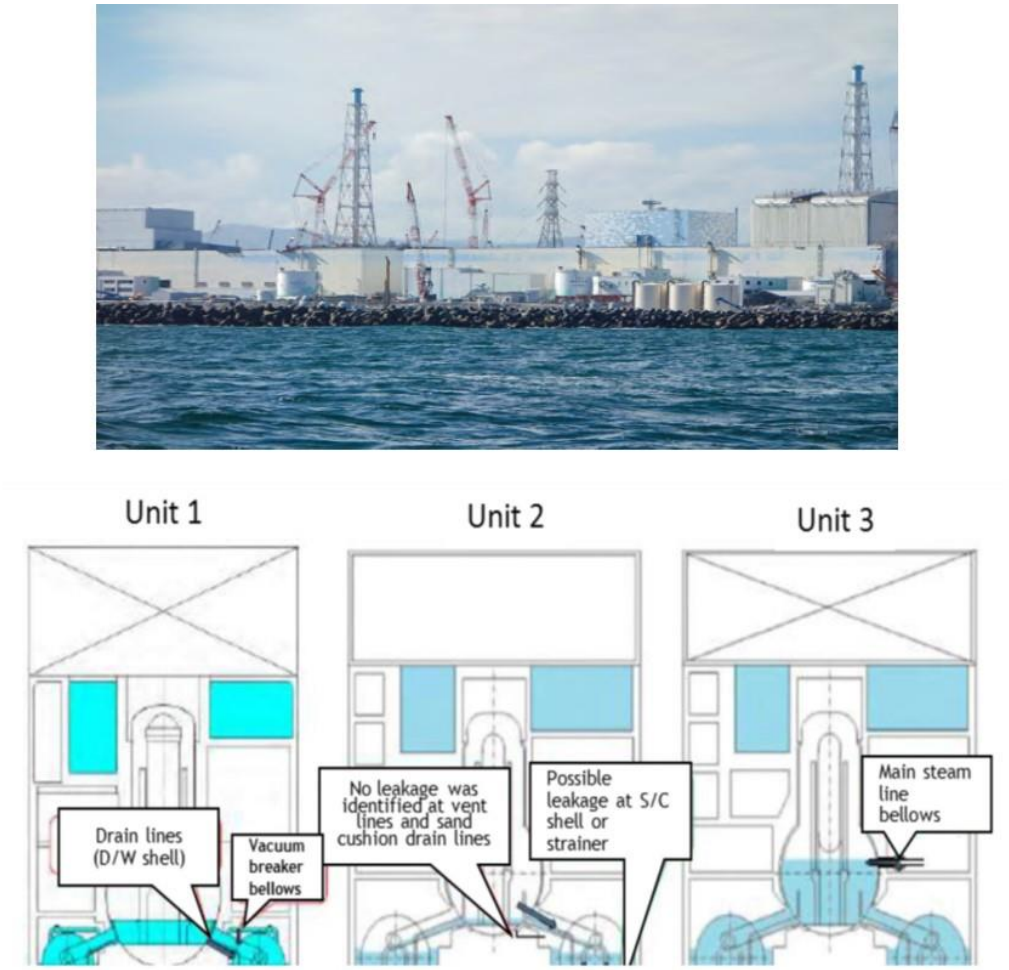

Figure 3. Illustration of possible leak paths in the damaged units at Fukushima Daiichi, reproduced from NEA, 2021a.

4. SUMMARY

This section gives an integral vision of issues previously discussed, from the background to the current status, regardless whether the motivation stems from lack of data or/and immature (if any) model. Important

is that the assessment made here is not quantitatively supported; i.e., in no case there is analytical support that allows estimating how significant any of the issues listed next might eventually affect Source Term to the environment. In other words, the outcome of the assessment made in this paper should be strengthened by outcomes from projects like H2020 MUSA and IAEA CRP on severe accident uncertainties; particularly MUSA, focused on Source Term Figures of Merit (FOMs), will bring sound insights into the sources and magnitude of uncertainties dominating Source Term estimates and, as a consequence, they should be instrumental in defining well-targeted Source Term research in the mid-and long-term.

The list and bases of the major issues identified may be expressed as follows:

- FP release. Even though a large progress has been achieved, there are some areas worth visiting. This is the case of SGTR and LOCA DBA and DEC-A sequences, which are investigated in the H2020 R2CA project. What seems drawing more attention after the Fukushima-Daiichi accident are the so called long-term releases that strongly depend on the core degradation phenomena and then fuel debris ageing and leaching. These issues would need at least a review of existing models to assess the present predictive capability. They are of interest for management of an accident on the long term, including waste streams and decommissioning. A different matter is the need of investigating releases from the ATFs, which should be articulated consistently with other ongoing initiatives on ATF research.
- Delayed FP releases by remobilization phenomena. Observed in Fukushima-Daiichi and proved in Source Term experiments, this potential contribution to radiological releases is worth investigating in their multiple ways (revaporisation, revolatilization, reentrainment and resuspension) with delayed formation of radioactive fine particles and gas. Some aspects are currently being investigated in the NEA ESTER and THEMIS projects. It would be worth reviewing existing knowledge and data in the area to focus additional investigations, if needed.
- High temperature chemistry in RCS. This issue has been experimentally investigated recently and new models addressing control rod effect (Sg/In/Cd allow and B) on fission product transport are being presently developed. High temperature chemistry in RCS needs to be investigated related to enhancing knowledge on remobilization phenomena which are very much dependant on chemical interactions at surfaces. Some aspects are currently addressed in the NEA ESTER project.
- Pool scrubbing. As highlighted in the EC PASSAM project, this issue lacks a systematic approach and a full scope investigation addressing conditions hardly explored so far, with particular emphasis on saturated pools and high injection velocities. In this research, a deep study of hydrodynamics is recognized to be of vital importance. The NUGENIA IPRESCA project, the NEA THEMIS project (Figure 4) and the WGAMA BCAPFIS activity are currently being conducted to address this.
- Fine particle behavior in containment. Several mechanisms can produce particles in the sub-micronic range. Their potential for remain airborne, interact with iodine, affect safety systems (and viceversa) and the lower efficiency of filtration systems to retain them, recommend to conduct experimental investigations after reviewing the current knowledge and data available. Some investigations have started in NEA THEMIS project.
- Organic iodides (OrgI) in containment. Despite the efforts made in last experimental programs to identify the major sources of OrgI, there are evidences that something is still missing in the current modeling to match observations made in the long-run of PHEBUS-FP tests. Related investigations have recently been undertaken in the NEA ESTER project in the EPICUR facility (Figure 5). It would be worth reviewing existing knowledge and data in the area, following ESTER completion, to focus additional investigations, if needed.

Beyond the specific issues listed, forthcoming ST research should be recommended bringing on board a few related aspects:

- Full and thorough exploitation of existing data should be pursued. Critical reviews of the existing databases and integral application (if suitable) for model development and validation should be part of the research agenda.
- Realistic conditions as the presence of impurities in the system, the multicomponent nature of aerosols, the high temperature and doses anticipated, the boiling conditions in sumps, and more importantly the results scaling to NPPs need to be addressed. In other words, any new forthcoming initiative should be conceived to further and better exploit the data available to enhance NPP safety.
- Significance of leaking pathways when analyzing accident sequences (direct information coming from OECD/NEA BSAF and ARC-F projects). System failures and leaks play an outstanding role in any Source Term prediction to the environment. Any reduction of uncertainties affecting leak path definition in a severe accident analysis would have a strong effect on the results. Specialist groups under CSNI, like WGIAGE and WGAMA, might be the right framework to address this point.

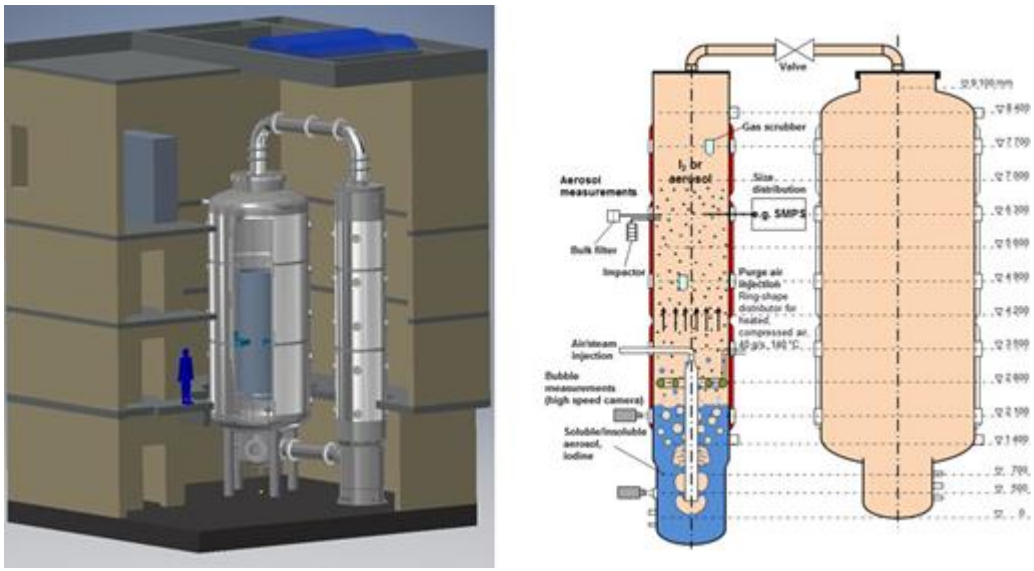

Figure 4. Illustration of experimental configuration for pool scrubbing investigations in the THAI+ facility at Becker Technologies, reproduced from NEA, 2021b.



Figure 5. Picture of the IRSN EPICUR irradiator and loop used for containment iodine chemistry investigations reproduced from NEA, 2016b.

Just as an additional leading support to forthcoming Source Term research, regulatory concerns on Source Term should be also considered. In the particular case of USNRC (Lee, 2018), these are the ones that may be highlighted:

- The ability of analytical tools to assess the efficacy of mitigation systems in the Defence-in-Depth approach and the siting and emergency planning, the safety issue resolution, the risk-informed decision making, and the testing of SAMGs (Severe Accident Management Guidelines) effect.
- Modern modelling techniques used in aerosol transport in the RCS, the enhancement of numerics, the potential effect of "fractal" collision kernels or the actual nature of aerosols (can PHEBUS-FP observations being adopted as fully prototypical?).
- Radionuclide releases and behaviour in New Generation of Nuclear Power (NGNP). In addition, the Uncertainty Quantification (UQ) approach to be used in severe accident analysis, particularly in the frame of new Source Term to be defined in high burnup and MOX fuels, was highlighted as a key element in the forthcoming research on Source Term.

At the time this paper is written, there are already a number of projects ongoing that are addressing some of the specific issues highlighted here. Particularly fitted to the purpose are: OECD/NEA THEMIS, addressing safety systems performance, like pressure suppression pools (Gupta, 2021), OECD/NEA ESTER, focused on delayed releases (NEA, 2020c) or OECD/NEA ARC-F (Nakatsuka, 2018), which among other topics payed attention to fission products leak paths in the Fukushima-Daiichi accidents. In addition, complementary projects related to Severe Accident and, particularly, Source Term uncertainties are being conducted in frameworks other than NEA, as cited above (H2020 MUSA and IAEA CRP on uncertainties). It is firmly believed that the outcomes from these projects should be used together with the outcomes of the workshop here reported to outline what might be the strategic R&D on Source Term in the coming decade.

Finally, another emerging question that was not extensively discussed during the workshop but will need some attention is: are there any specific Source Term aspect that would need to be further investigated related to the foreseen deployment of advanced fuels, including ATFs, and advanced reactor designs, including SMRs. Such an assessment should be undertaken to support in particular licensing and deployment of proven or high TRL concepts.

ACKNOWLEDGEMENTS

The authors thank the members of the Working Group on the Analysis and Management of Accidents (WGAMA) for their contribution and active participation in the workshop and the WGAMA Bureau members for their support and wise advising during the preparation of the workshop. Special thanks are also due to R. Lee (United States of America), L.E. Herranz (Spain), M. Berdai (France), S. Gupta (Germany), C. Mun (France), Y. Maruyama (Japan), and D. Jacquemain (France) for preparing the material and presentations that structured the workshop.

REFERENCES

Albiol T. et al., 2018, Main results of the European PASSAM project on severe accident source term mitigation, Annals of Nuclear Energy, Vol. 116, pp. 42-56., 10.1016/j.anucene.2018.02.024.
Bunt R., Corradini M., Ellison P., Farmer M.T., Francis M., Gabor J., Gauntt R., Henry C., Linthicum R., Luangdilok W., Lutz R., Paik C., Plys M., Rabiti C., Rempe J., Robb K., Wachowiak R., 2016, Reactor safety gap evaluation of accident tolerant components and severe accident analysis. 16th International Topical Meeting on Nuclear Reactor Thermal Hydraulics (NURETH-16), August 30–September 4, 2015, Chicago (IL), United States.

Di Giuli M. et al., 2016, SARNET benchmark on Phébus FPT3 integral experiment on core degradation and fission product behaviour, Annals of Nuclear Energy, Vol. 93, pp. 65-82.
Ducros G. et al., 2013, Synthesis of the VERCORS experimental programme: Separate-effect experiments on Fission Product release, in support of the PHEBUS-FP programme, Annals of Nuclear Energy, Vol. 61, pp. 75-87.
Glowa G.A., Moore C.J., Boulianne D., 2016, Main outcomes of the OECD Behaviour of Iodine Project, pp. 153-164, in NEA, 2016, International Iodine Workshop Summary Report, NEA/CSNI/R(2016)5.
Gupta, S., Freitag, M., Poss, G., 2021, THAI experimental research on hydrogen risk and source term related safety systems. Front. Energy Vol. 15, pp. 887–915. https://doi.org/10.1007/s11708-021-0789-1.
Haste T., Payot F., Bottomley P.D., 2013, Transport and deposition in the Phébus FP circuit. Annals of Nuclear Energy, Vol. 61, pp. 102-121. https://doi.org/10.1016/j.anucene.2012.10.032.
Herranz L.E., Haste T., Kärkelä T., 2015, Recent advances in the source term area within the SARNET European severe accident research network, Nuclear Engineering and Design, Vol. 288, pp. 56-74. https://doi.org/10.1016/j.nucengdes.2015.03.014.
Lee R., 2018, Some points for discussion @ Workshop on Source Term Presentation delivered at the Source Term Workshop organized by CSNI/WGAMA, Paris (France).Lee R., 2018. Some points for discussion @ Workshop on Source Term. Presentation delivered at the Source Term Workshop organized by CSNI/WGAMA, Paris (France).
Lind T., Guentay S., Herranz L.E., Suckow D., 2019, A summary of the ARTIST: Aerosol retention during SGTR severe accident. Annals of Nuclear Energy, Vol. 131, pp. 385-400, https://doi.org/10.1016/j.anucene.2019.04.006.
Magallon D., Mailliat A., Seiler J.M., Atkhen K., Sjövall H., Dickinson S., Jakab J., Meyer L., Buerger M., Trambauer K., Fickert L., Sehgal B.R., Hozer Z., Bagues J., Martin-Fuentes F., Zeyen R., Annunziato A., El-Shanawany M., Guentay S., Tinkler C., Turland B, Herranz L.E., 2005, European expert network for the reduction of uncertainties in severe accident safety issues (EURSAFE), Nuclear Engineering and Design, Vol. 235, 2–4, pp. 309-346, https://doi.org/10.1016/j.nucengdes.2004.08.042.
Manara D., Jacquemain D., Van Dorsselaere J.P., Bottomley P.D., Adorni M., Journeau C., Pontillon Y., Lind T., Herranz L.E., Rocchi F., Schaffrath A., de la Rosa J.C., Bechta S., Duspiva J., Kljenak I., Dejardin P., 2019, Severe accident research priority ranking: a new assessment eight years after the Fukushima Daiichi accident. The 9th European Review Meeting on Severe Accident Research (ERMSAR2019), Prague, Czech Republic, March 18-20, 2019. https://ftp.ermsar2019.com/ERMSAR%202019%20-%20Final%20Papers/98.%20Manara%20D.pdf.
Mun C., Bosland L., Cantrel L., Colombani J., Leroy O., Ohnet M.N., Albiol T., 2015, OECD/NEA STEM project and its follow-up STEM2, International Iodine Workshop Summary Report, NEA/CSNI/R(2016)5, pp. 172-179.
Nakatsuka T., Maeda T., Sugiyama T., Maruyama Y., 2018, Outline of the OECD/NEA ARC-F Project, Proceedings of 18th International Topical Meeting on Nuclear Reactor Thermal Hydraulics (NURETH-18), August 18-23 2019, Portland (OR), United States.
Nakayoshi A. et al., 2020, Review of Fukushima Daiichi Nuclear Power Station debris endstate location in OECD/NEA preparatory study on analysis of fuel debris (PreADES) project, Nuclear Engineering and Design, Vol. 369, 110857 https://doi.org/10.1016/j.nucengdes.2020.110857
NEA, 2021a, Long Term Management and Actions for a Severe Accident in a Nuclear Power Plant, Status report, NEA N°7506.
NEA, 2021b, OECD/NEA THAI-3 Project Final Report, NEA/CSNI/R(2021)8.
NEA, 2020a, OECD/NEA BIP-3 Final Report, NEA/CSNI/R(2020)14.
NEA, 2020b, CSNI/WGAMA Source term workshop 2019, NEA/CSNI/R(2020)4.
NEA, 2020c, NEA ESTER project, https://www.oecd-nea.org/jcms/pl_58926/experiments-on-source-term-for-delayed-releases-ester-project
NEA, 2018, OECD/NEA STEM Final Summary Report, NEA/CSNI/R(2018)6.

NEA, 2016a, Aerosol and Iodine Issues, and Hydrogen Mitigation under Accidental Conditions in Water Cooled Reactors - Thermal-hydraulics, Hydrogen, Aerosols and Iodine (THAI-2) Project - Final Report, NEA/CSNI/R(2016)8.
NEA, 2016b, International Iodine Workshop Summary Report, NEA/CSNI/R(2016)5.
NEA, 2015a, Benchmarking of Fast-running Software Tools Used to Model Releases During Nuclear Accidents, NEA/CSNI/R(2015)19.
NEA, 2015b, Benchmark Study of the Accident at the Fukushima Daiichi Nuclear Power Plant (BSAF Project) - Phase I Summary Report, NEA/CSNI/R(2015)18.
NEA, 2009, State of the art report on nuclear aerosols, NEA/CSNI/R(2009)5.
NEA, 2007, State of the art report on iodine chemistry, NEA/CSNI/R(2007)1.
Pellegrini M. et al., 2019, Main Findings, Remaining Uncertainties and Lessons Learned from the OECD/NEA BSAF Project, in *Proceedings of the 18th International Topical Meeting on Nuclear Reactor Thermal Hydraulics, NURETH-18*, pp. 1147-1162, American Nuclear Society (ANS).
Pontillon Y., Geiger E., Le Gall C., Bernard S., Gallais-During A., Malgouyres P.P., Hanus E., Ducros G., 2017, Fission products and nuclear fuel behaviour under severe accident conditions part 1: Main lessons learnt from the first VERDON test. Journal of Nuclear Materials, Vol. 495, pp. 363-384, https://doi.org/10.1016/j.jnucmat.2017.08.021.
Suehiro S., Sugimoto J., Hidaka A., Okada H., Mizokami S., Okamoto K., 2015, Development of the source term PIRT based on findings during Fukushima Daiichi NPPs accident, Nuclear Engineering and Design, Vol. 286, pp. 163-174. https://doi.org/10.1016/j.nucengdes.2015.02.005.

Research Needs on Source Term: A CSNI/WGAMA Perspective

Luis E. Herranz

Unit of Nuclear Safety Research
CIEMAT (Spain)

Didier Jacquemain

Nuclear Safety Division
OECD/NEA (pARIS)

This work was done in the frame of the OECD/WGAMA

NEA NUCLEAR ENERGY AGENCY

CONTENTS

- BACKGROUND
- THE WORKSHOP
- LATEST RESULTS
- FINAL REMARKS

BACKGROUND

FP Mapping in Severe Accidents

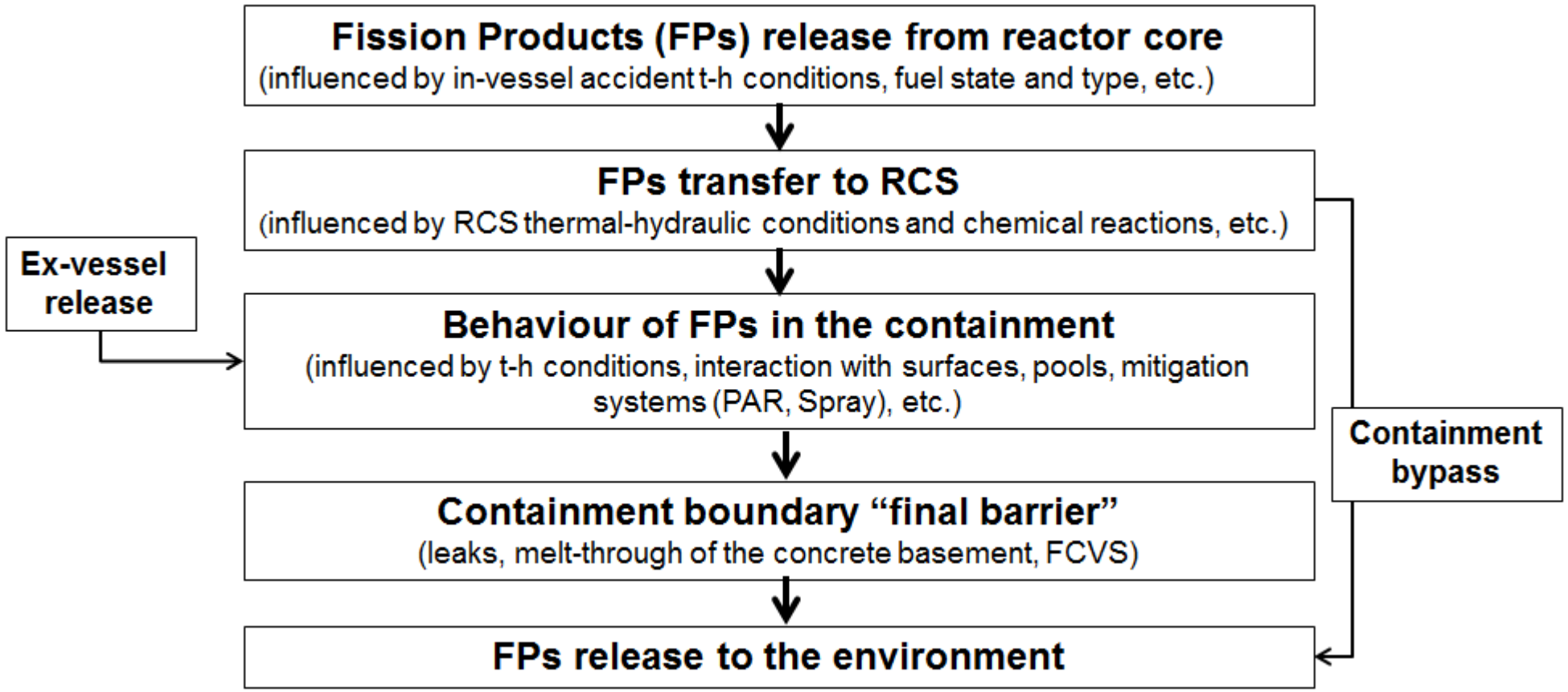

Recent Progress on Source Term

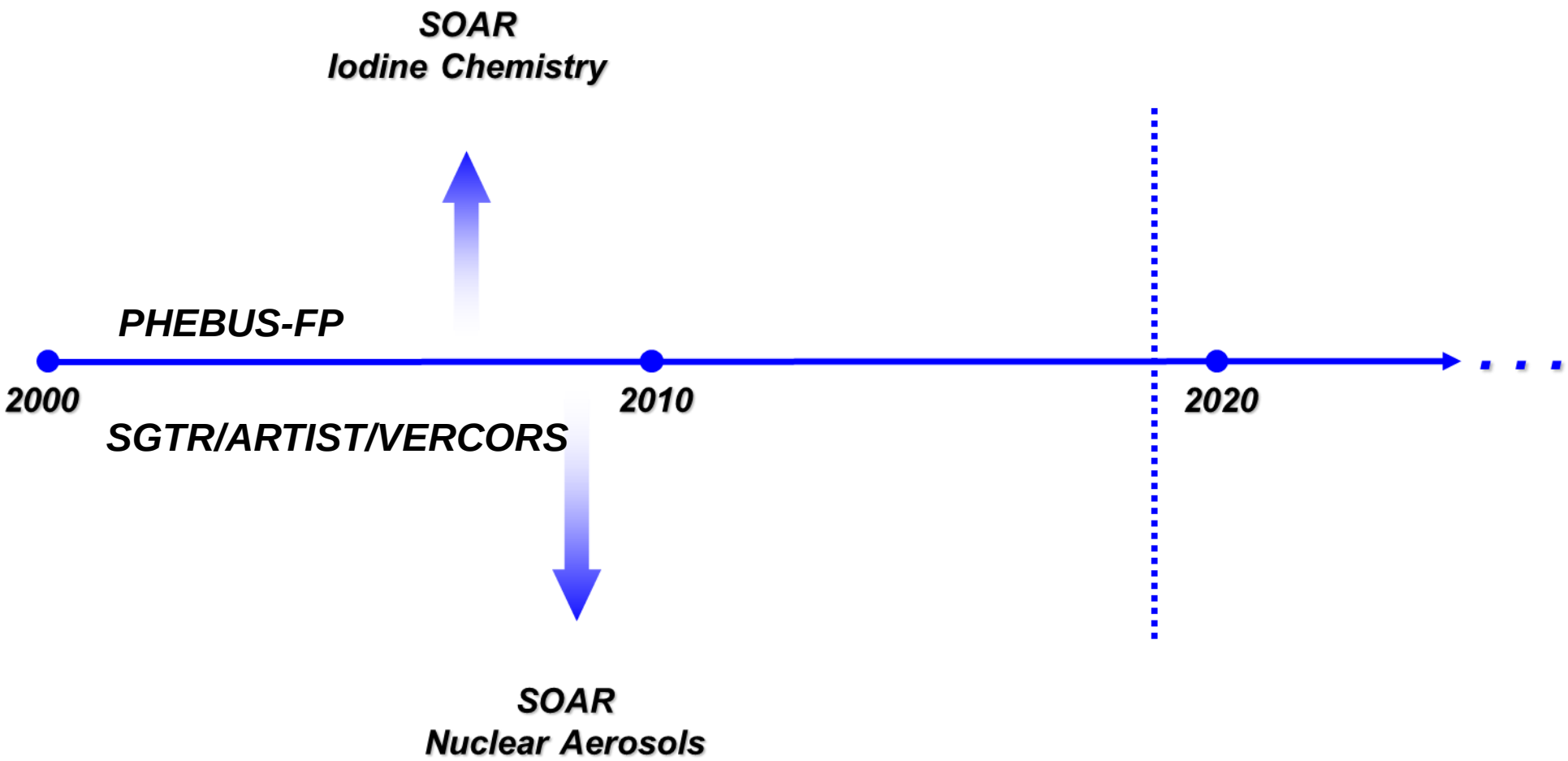

Recent Progress on Source Term

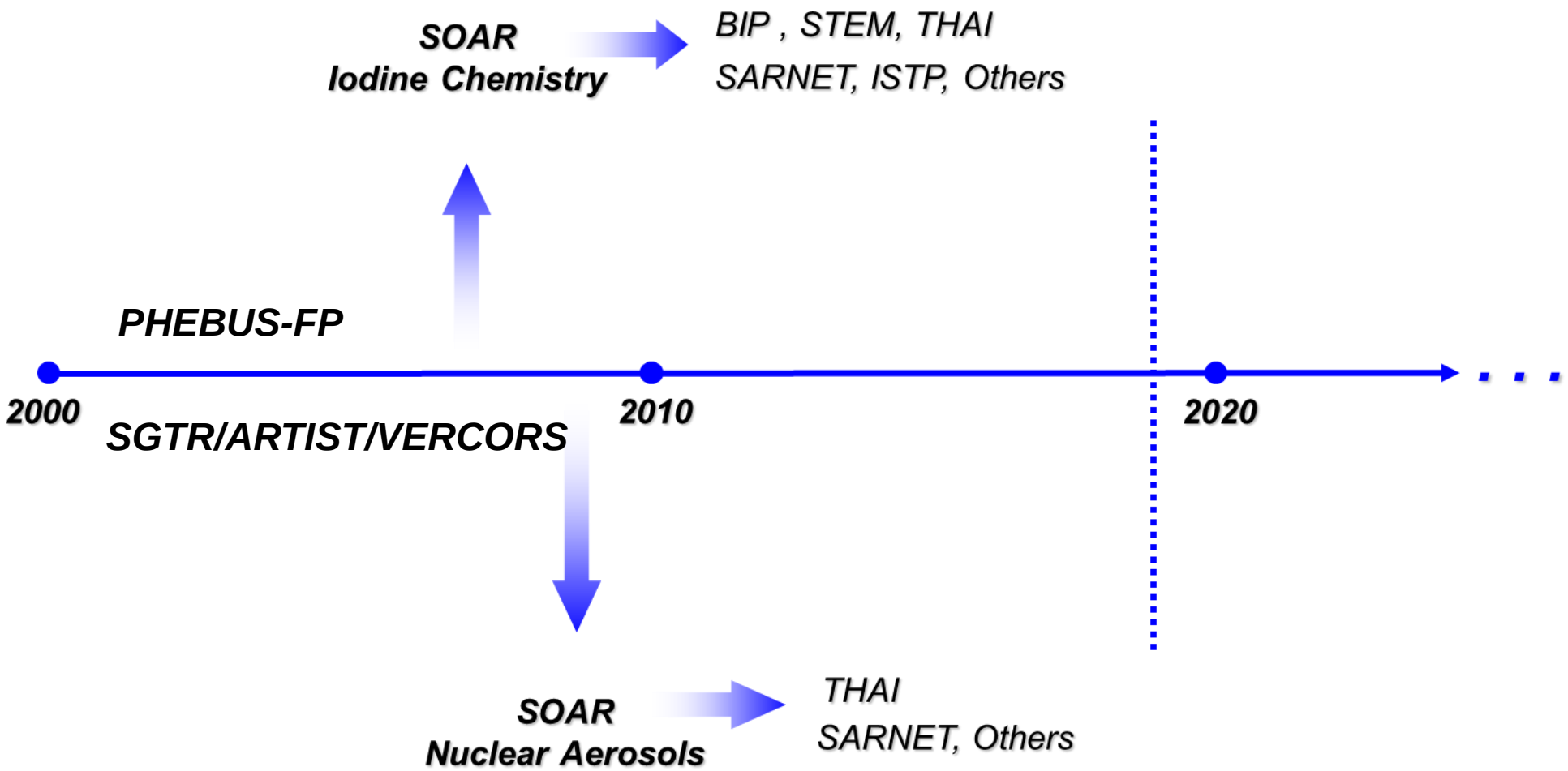

Recent Progress on Source Term

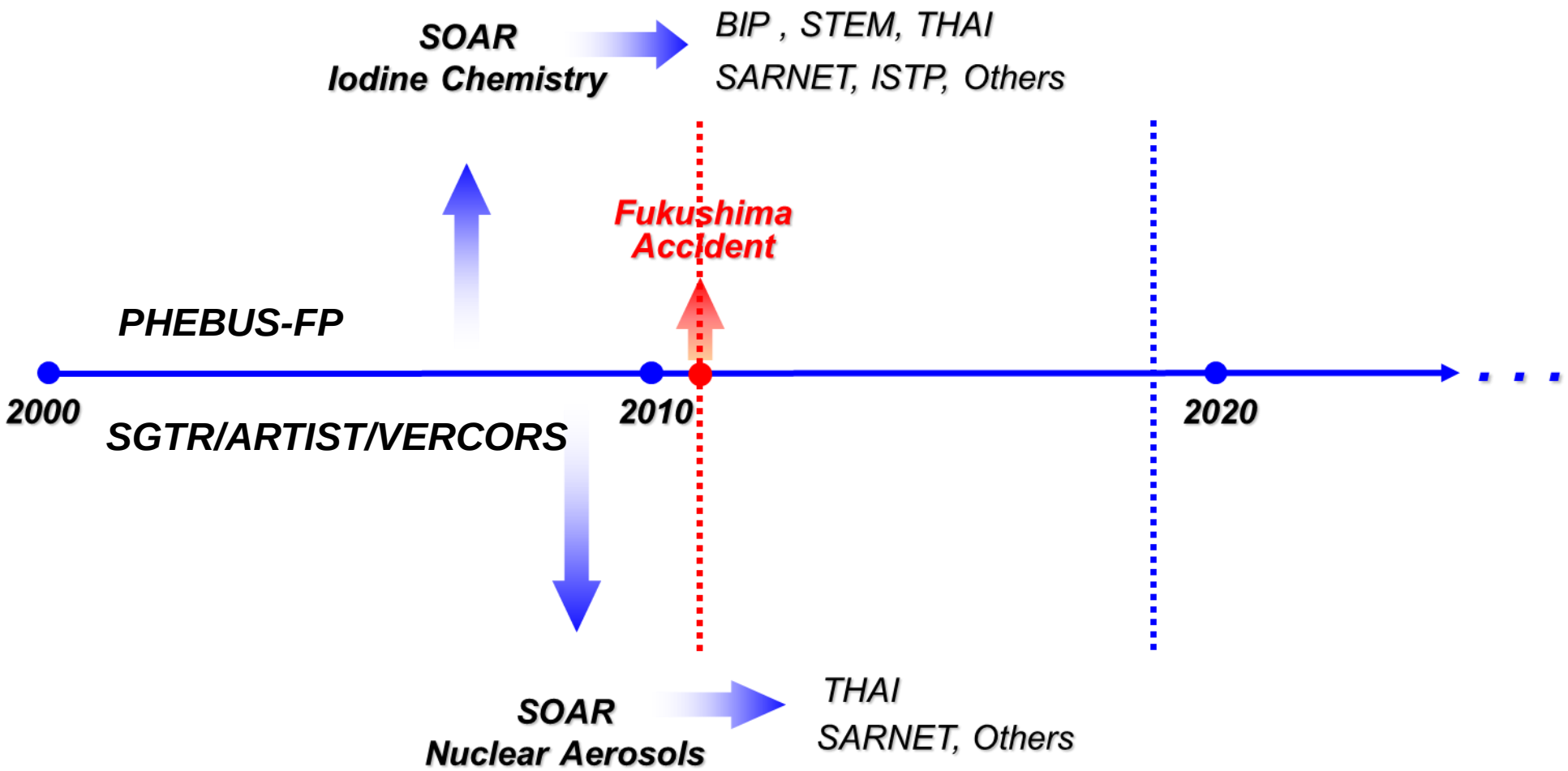

Recent Progress on Source Term

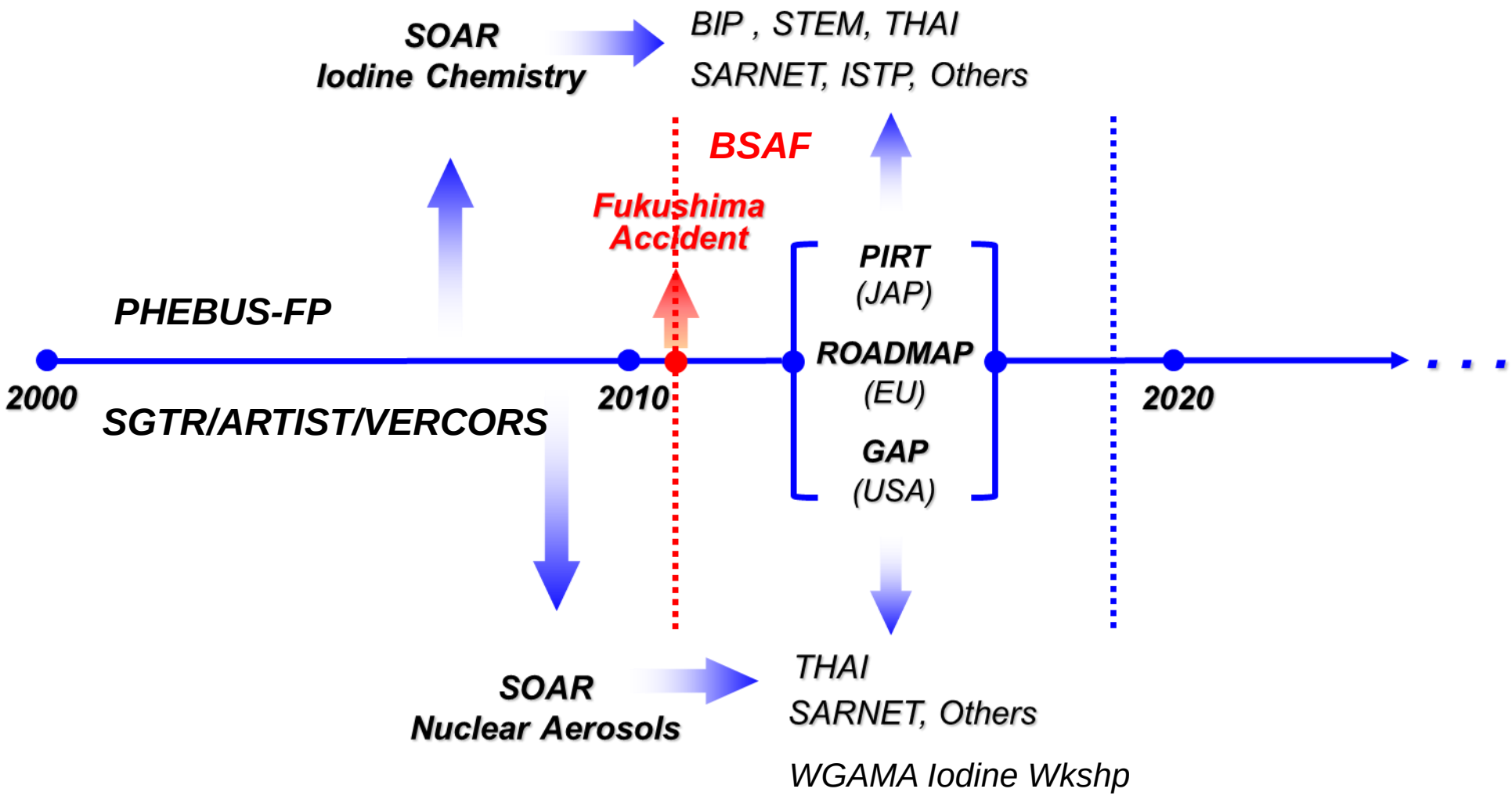

Recent Progress on Source Term

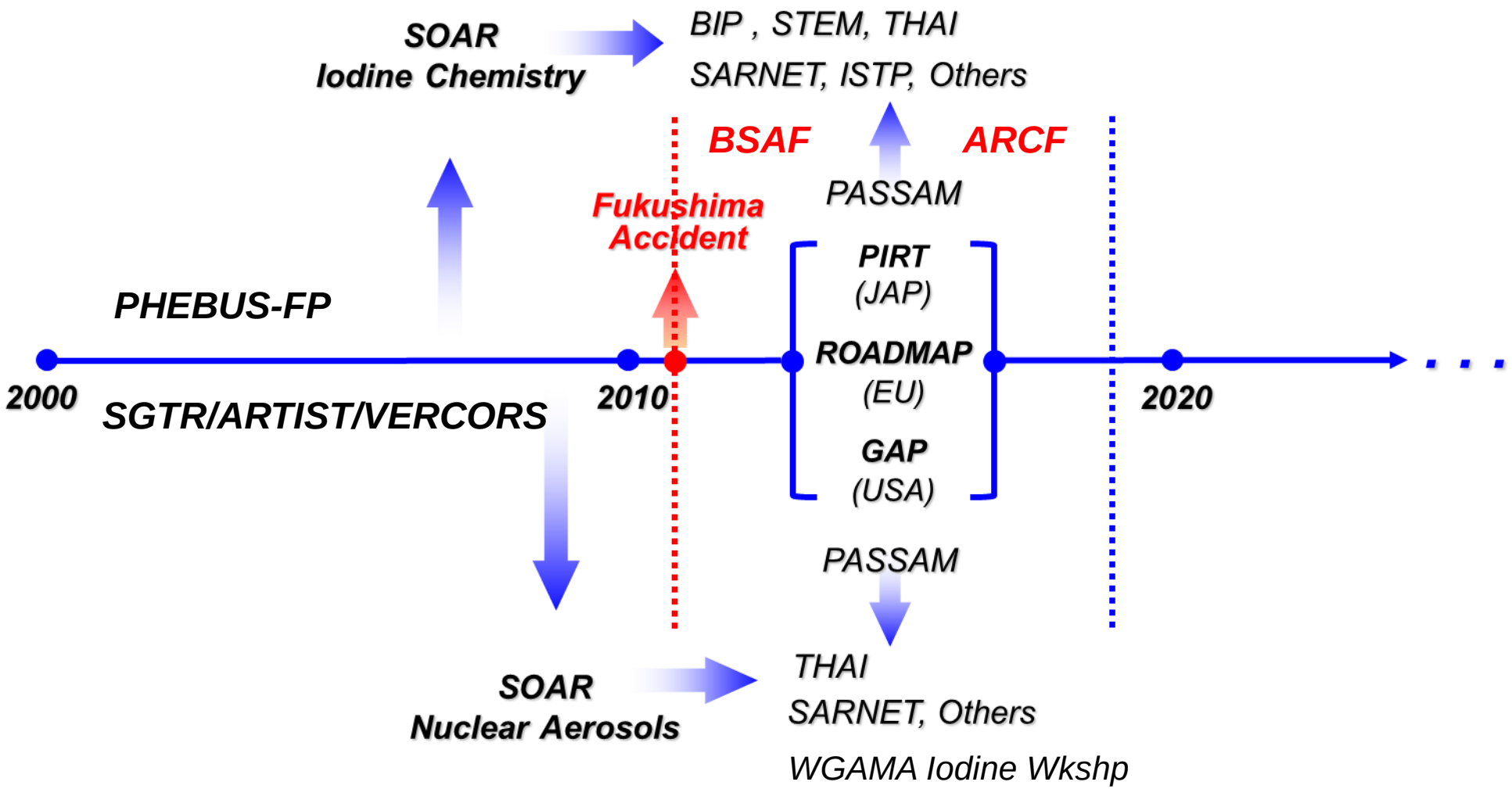

Recent Progress on Source Term

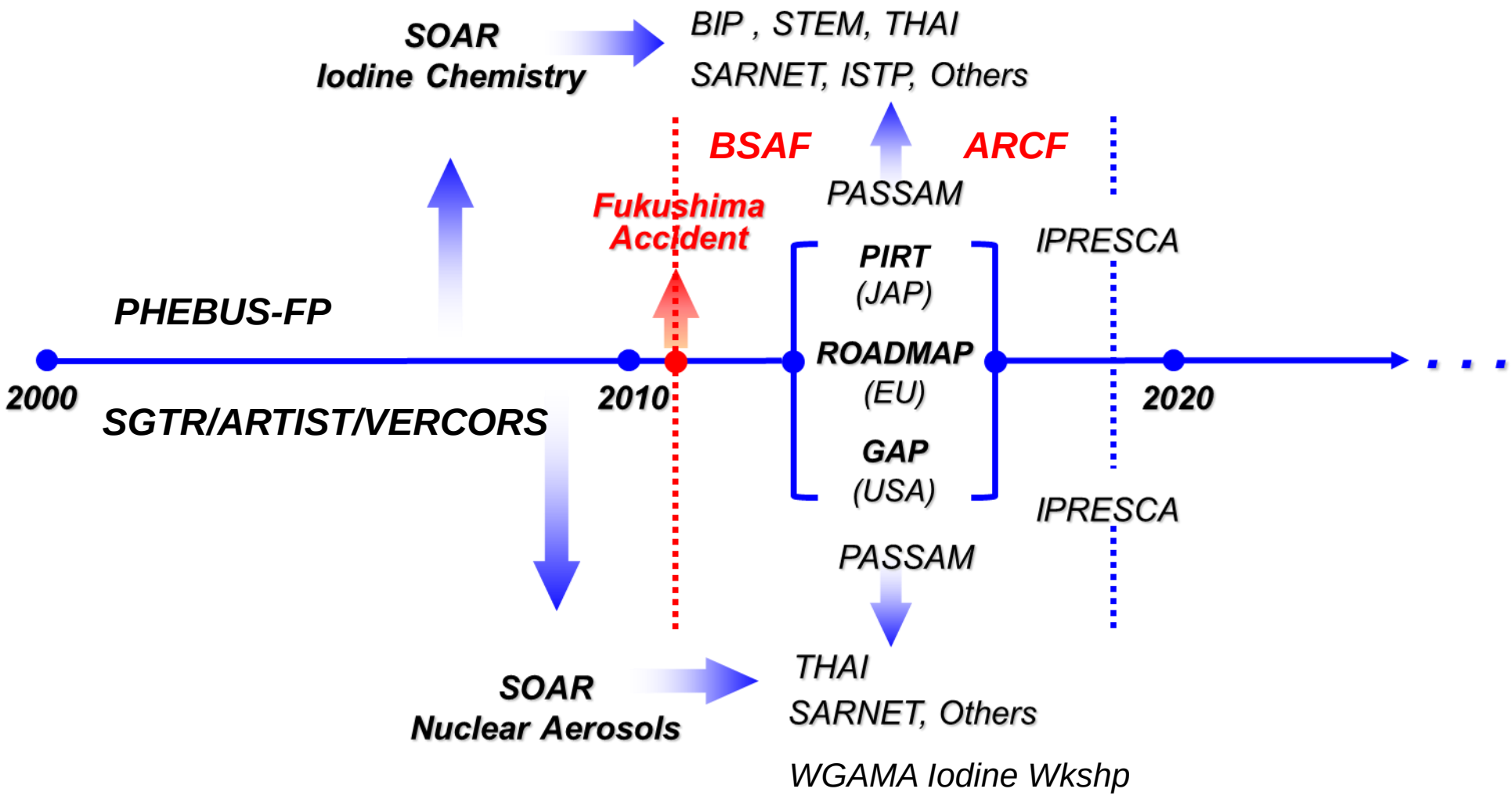

Recent Progress on Source Term

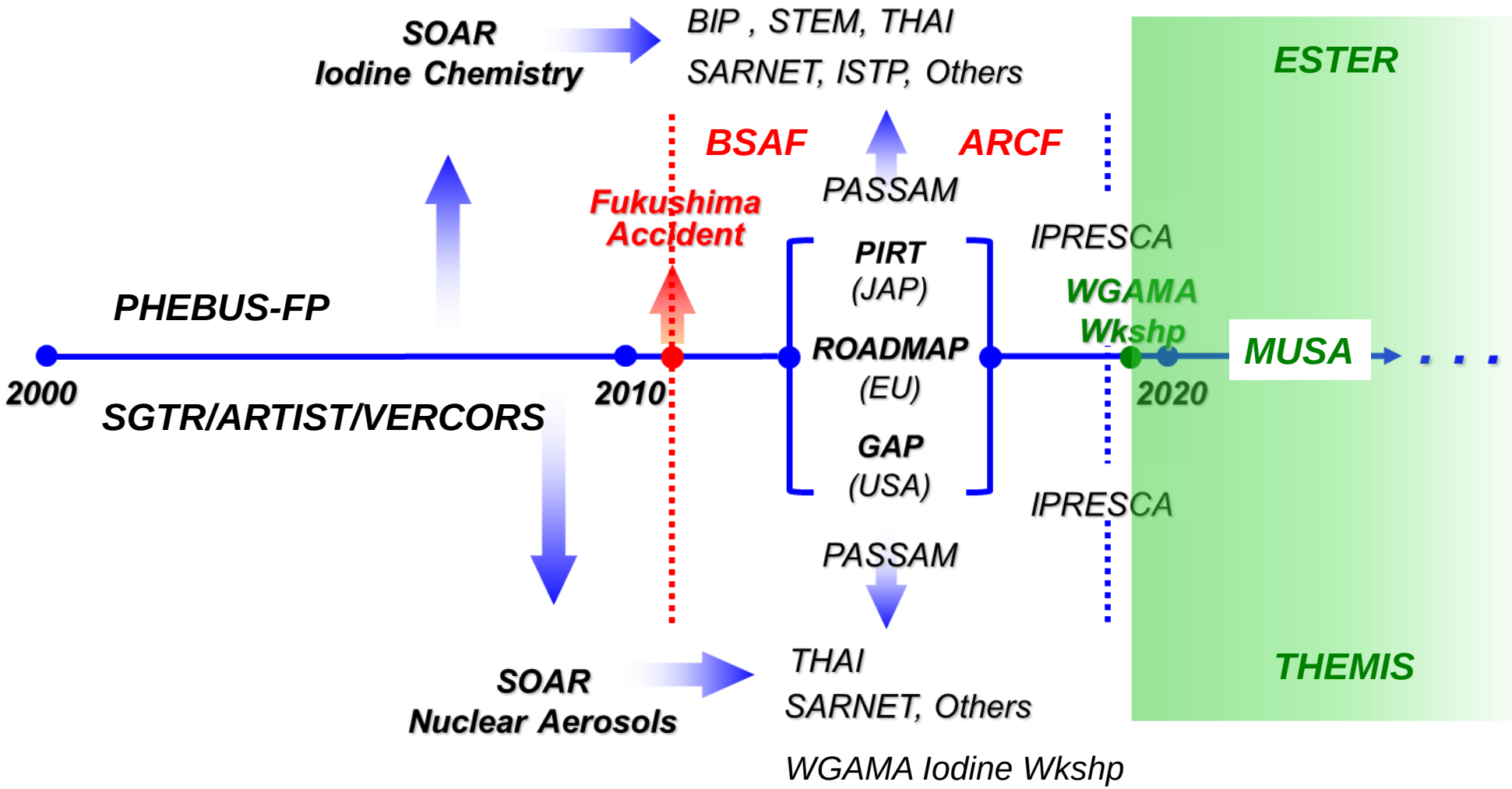

Synthesis

- *Extensive research on Source Term in the last 15 years.*
- *PHEBUS-FP; ISTP; SARNET; ARTIST; VERCORS; EU-PASSAM; VERDON; …*
- *Recent OECD/NEA projects just finished (BIP; STEM; THAI).*
- *Post-Fukshima projects closely related (OECD-BSAF; TCOFF; PreADES).*
- *WGAMA-related activities..*

- *Analytical developments of phenomenological models and "fast" approaches.*

THE WORKSHOP

Objectives

To carry out a comprehensive and deep reflection (Workshop) *aimed to*

- ***Identify the main "safety-significant" knowledge gaps and uncertainties*** *still remaining*
- ***Discuss the best way to address them*** *with existing and/or innovative methods, if needed.*

Source Term

(Water Cooled Reactors & established types of fuels)

(January, 2019)

Main Ingredients

- ***Knowledge basis***
  - ***PHEBUS-FP***
  - ***SOARs*** *(nuclear aerosols; iodine chemistry)*
  - ***PIRTs*** *(Europe; USA; Japan)*
- ***Recent progress***
  - ***Experimental data and analytical development***
  - ***Insights from Fukushima*** *(data & projects outcomes)*

SOAR on Iodine Chemistry

(NEA/CSNI/R(2007)1)

- *Gas phase chemistry and formation of I_{gas} in the RCS.*
- *Production of RI_{gas} from painted surfaces.*
- *Effect of impurities on oxidation/reduction in the liquid phase.*
- *Iodine in the secondary side of SG.*
- *I_{gas} – air radiolysis products.*
- *RI formation in liquid phase (homogeneous & heterogeneous).*
- *pH evolution in the sump.*
- *Dose rate & type.*
- *Amount of Ag and its oxidation state in sump water.*
- *Mass transfer parameters.*
- *Adsorption/desorption rates on/from different surfaces.*

SOAR on Nuclear Aerosols

(NEA/CSNI/R(2009)5)

- *Charge effects.*
- *Mixed aerosols in condensing atmospheres (hygroscipity; density).*
- *Mechanical resuspension (sudden RCB breach; H2 burn).*
- *Reentrainment from pools (realistic conditions).*
- *Pool scrubbing (high gas velocities; submerged structures; surfactants; etc.).*
- *Removal by sprays.*
- *Influence of recombiners (I_{gas} formation; realistic conditions).*
- *H_2 burn effects on airborne particles (MI → I_{gas}).*
- *Release from MCCI*
- *Penetration through leak paths.*
- *Interaction of nuclear and fire aerosols.*

Severe Accident Research Priorities

(NED, 2014)

- *FP release during reflooding in the late phase (corium leaching).*
- *FP release under oxidizing conditions (Ru) for ↑Bup and MOX.*
- *High temperature chemistry.*
- *FP revaporization from RCS deposits.*
- *Source terms from SFPs*
- *Pool scrubbing under boiling conditions.*
- *Long term stability of deposits.*
- *Iodine interactions with aerosols.*
- *I_xO_y aerosols formation/destruction.*
- *Gas iodine production (impurity effects).*

The Latest Results from SARNET2

(ATW, 2016)

- *FP revaporisation from deposits on circuit surfaces.*
- *High temperature chemistry.*

- *I_xO_y aerosols stability.*
- *Gas iodine production (homogeneous & heterogeneous).*
- *In-containment Ru behaviour (revaporization & in-gas persistence).*
- *Data scaling (conditions & size).*

Source Term PIRT on Fukushima

(NED, 2015)

- *Radionuclide release from molten fuel.*
- *Iodine & Caesium speciation in the presence of B_4C.*
- *FP/aerosol leakages through penetrations, gaskets, instruments, etc.*
- *Late migration of radioactive material (AM).*
- *Effects of sea water .*
- *Iodine release from R/B contaminated water.*

Reactor Safety Gap Evaluation

(NS&E, 2016)

- *Effect of raw water on FP/aerosols transport.*
- *Thdycs of FP species in ↑T with ↑PH2Ov and ↑PH2.*
- *Effect of radiation ionizing gas within RCS.*

- *Vapor interactions with aerosols and surfaces.*
- *Effects of H_2/H_2O and H_2/CO gas mixtures on pool scrubbing at ↑P and saturation.*

Open Issues

- *FP releases (LOCA; SGTR).*
- *High temperature chemistry.*
- *Pool scrubbing.*
- *Fine particles behavior in containment.*
- *OrgI in containment.*
- *Remobilization phenomena (delayed releases).*

Open Issues

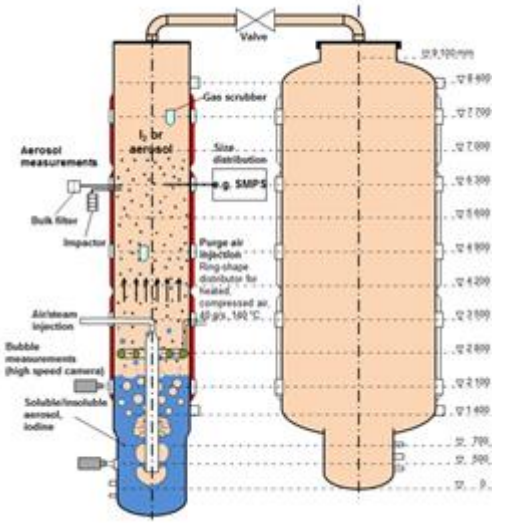

- *FP releases (LOCA; SGTR)* → *EU-R2CA*
- *High temperature chemistry* →
- *Pool scrubbing.* → *TA2/IPRESCA; OECD/THEMIS*
- *Fine particles behavior in containment.* → *OECD/THEMIS*
- *OrgI in containment.* → *OECD/ESTER*
- *Remobilization (delayed releases).* → *OECD/THEMIS, /ESTER*



ATFs!

Major Observations

- *The need for realistic conditions (or "bridging" extrapolation)* → *"Scalable" data!*
- *Outcomes from MUSA (& R2CA)!* → *Efficient "funding"!*
- *Fission products paths & boundary conditions*



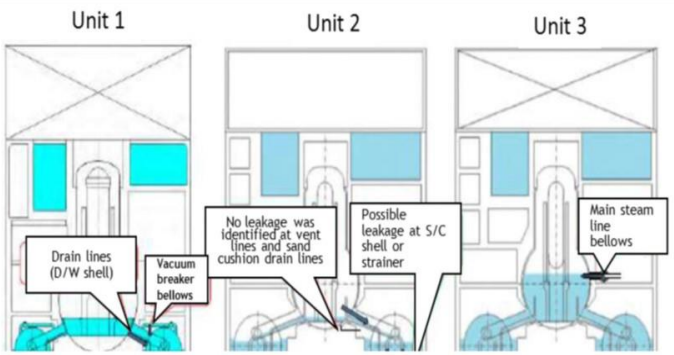

SUMMARY

- ***Substantial progress in Source Term knowledge.***
- ***Mitigation: a fundamental axis of any Source Term matrix.***
- ***Fukushima highlighted remobilization, SFPs, leak paths, BCs!*** *(more-to-come)*
- ***Trade-off necessary between "assimilation" and "infrastructures".***
- ***Scalability of data from initial project stages.***
- ***"Risk-informed" research!***

Thank you for your attention!

FISSION PRODUCT BEHAVIOUR IN SEVERE ACCIDENT CONDITION: FOCUS ON INFORMATION GAINED FROM VERCORS/VERDON ANALYTICAL PROGRAMS

Y. Pontillon, F. Audubert, P. Bros, I. Moysan, J. Sercombe, B. Teisseire
CEA, IRESNE/DEC
Cadarache F-13108 Saint-Paul-Lez-Durance, France
yves.pontillon@cea.fr

ABSTRACT

In the case of a hypothetical Severe Accident (SA) in a light water reactor - loss of coolant, failure of safety systems, core degradation with fuel meltdown, … - Fission Products (FPs) and other radioactive materials would be swept out into the containment and, in the event of containment failure, due to the accident, radioactivity would be released into the environment. The knowledge of the ratio of radioactivity released from the core to the environment, i.e. the determination of the "source term", is of prime and crucial importance for the overall assessment of nuclear power plant safety.

Partly due to the impact of the TMI (Three Mile Island, 1977) and Chernobyl (1986) and Fukushima accidents, and to better assess the consequences of such situations, a number of R&D programs have been conducted in this area of research throughout the world. In France, the IRSN (Nuclear Radioprotection and Safety Institute) and EdF (Electricité de France) in collaboration with the CEA (Commissariat à l'Energie Atomique et aux Energies Alternatives) have initiated several experimental programs devoted to the source term of fission products and actinides released from PWR fuel samples in SA conditions.

Within this framework, technical facilities, set up in shielded hot cells, have been developed around the so-called "VERCORS/VERDON" programs. Theirs aims were to quantify the release kinetics of FPs from irradiated nuclear ceramics, quantify the nature of the vapors and aerosols emitted (particle size analysis and chemical composition), and understand how the fuel degrades. The corresponding analytical experiments, conducted in a shielded hot cell, can be considered as complementary to in-pile integral experimental programs such as "PHEBUS FP" and similar to analytical ones conducted in other countries (i.e. the HI/VI program in the USA, the CRL program in Canada and the VEGA program in Japan).

This paper gives an overview of the mains results gained thanks to VERDON and VERCORS programs, with a special emphasis on fuel relocation temperature, high burn-up and MOX fuel effects on Fission Product release. The well known FP classification into four main volatility classes will be detailed and its utility, in order to assess the fuel performance code ALCYONE developed at the CEA fuel study department, presented and discussed.

KEYWORDS
Severe Accident, Source Term Quantification, VERDON, VERCORS

1. INTRODUCTION

One of the most important areas of research concerning a hypothetical severe accident in a Light Water Reactor (LWR), at both a French and an international level, is determining the source term, i.e. quantifying

the nature, release rate and total released fraction of fission products (FP) and other radioactive materials. This is in great part due to the consequences of the Three Mile Island (1979), Chernobyl (1986) and more recently Fukushima accidents (2011). In the course of this type of scenario, the chain of events can effectively result in primary coolant boiling and draining, meaning that it is no longer cooling the core. One direct result is the core melting and the release of FP and structural and/or activated control rod elements (*e.g.* activation products, AP) into the containment building. If there is a failure in the various protective barriers, the FP/AP can leak out of the containment building and be released into the environment.
A large number of research programs have thus been undertaken on this subject in various countries. In line with this approach, IRSN (France) has been the driving force and has conducted programs specifically focusing on determining the source term, with particular efforts devoted to **understanding the mechanisms** that lead to the release of FP, since only a very complete knowledge of the phenomena governing the behaviour of FP/AP under such constraints will make it possible to define the actions that need to be planned (and/or performed) to minimise emissions and optimise the protection of both the people and the environment. In this general context, the HEVA [1]/VERCORS [2] programs were thus initiated by the CEA. VERCORS has considerably broadened the field of application by exploring higher temperatures and by testing a wider range of fuels (UO_2, MOX, debris bed configurations, high burn-ups) in a more complex experimental installation with improved instrumentation. It was composed of 17 tests which were conducted over 14 years, in accordance with 3 experimental phases. A first series of six tests (VERCORS 1 to VERCORS 6) was conducted between 1989 and 1994 on UO_2 fuels in a higher temperature range than the preceding HEVA phase, close to the fuel relocation [3]. This series made it possible to integrate certain FP with low volatility into the HEVA results database. Two series of tests –VERCORS HT and RT– were then conducted alternately throughout 1996-2002 allowing the data base extension to the less volatile FP. Their aim was to quantify the released fractions and release rates of FP from irradiated nuclear ceramics (UO_2 or MOX, typically three PWR pellets in their original cladding), quantify the nature of the gases and aerosols emitted (particle size analysis and chemical composition), and understand how the fuel degrades. According to HEVA/VERCORS series, fuel burn ups ranging from 19 GWd/t to 72 GWd/t were investigated. These experimental sequences were carried out in a very high activity cell and were commonly considered to be complementary to the PHEBUS FP [4] integral tests and comparable with certain tests carried out abroad: HI/VI [5] in the United States, VEGA [6] in Japan or the program conducted at the CRL in Canada [7]. The experimental results of this program are used to (a) define the envelope values for released fraction within the scope of assessing reference source terms for all French PWRs, and (b) validate the semi-empirical or mechanistic models regarding FP release and transport while qualifying the simulation codes by integrating these models [8], [9], [10], [11].
However, major uncertainties still remain in some fields, concerning the assessment of risks for populations and the environment [12]. As a consequence, it has been decided to build a co-operative research program between teams involved in severe accident (SA) phenomenology all over the world (US-NRC, IRSN, CEA, EDF, GDF Suez, PSI, European Commission, EACL, KAERI), based on separate-effect experiments and called “International Source Term Program (ISTP)”. The results of these separate-effect experiments would allow improving models used for Source Term evaluation studies. Four main R&D research axes have been included in this program: (1) iodine behaviour in the reactor coolant system and the containment, (2) study of the boron carbide effect on fuel degradation and FP release, (3) study of the air effect on fuel and FP behaviour and (4) study of the fission product release from the fuel.
As far as the source term quantification is concerned, four VERDON tests were considered. They were devoted to FP release from high burn-up UO_2 fuel, MOX fuels and air ingress scenario. They were performed in the VERDON laboratory at the CEA Cadarache Centre.

This paper recalls, in section 2, the main characteristics of the experimental facilities together with the corresponding experimental grids with special emphasis on the last part of the program dedicated to the VERDON tests. Section 3 proposes an overview of the main results gained thanks to these programs, with

a special emphasis on fuel relocation temperature, high burn-up atmosphere and MOX fuel effects on Fission Product release and how these databases can be used in order to asses the fuel performance code ALCYONE developed at the CEA fuel study department, and recently extended to SA conditions.

2. SEVERE ACCIDENT LABORATORY AND EXPERIMENTAL GRIDS

2.1. The VERDON Laboratory and sample

In the course of the 25 years of the program, the test loop underwent several adaptations and upgrades to meet the experimental requirements. This involved following the evolution of the program objectives, e.g., increasing the final test temperature, and making constant technological improvements to the materials and instruments so as to produce increasingly more reliable results (gamma spectrometer acquisition chain with a very high counting rate, for example). The laboratory itself has undergone significant changes and was ultimately transferred from CEA-Grenoble to CEA-Cadarache for the launch of the VERDON program. We will describe this latest version of the laboratory below because it corresponds to the most recent one and which is still operational.

The four ISTP VERDON tests were conducted in a dedicated laboratory at the LECA-STAR facility [13]. It is constituted of two high activity cells (called C4 and C5) and a glove-box, as illustrated in Figure 1. The C4 cell is dedicated to the sample reception, pre/post-tests gamma scanning and loop element storage. The C5 cell contains the experimental circuit itself (i.e. VERDON loop, including two configurations). It is dedicated to the accidental sequence realisation and to on-line measurements. The glove-box main functions are to analyse and store the fission and carrier gases.

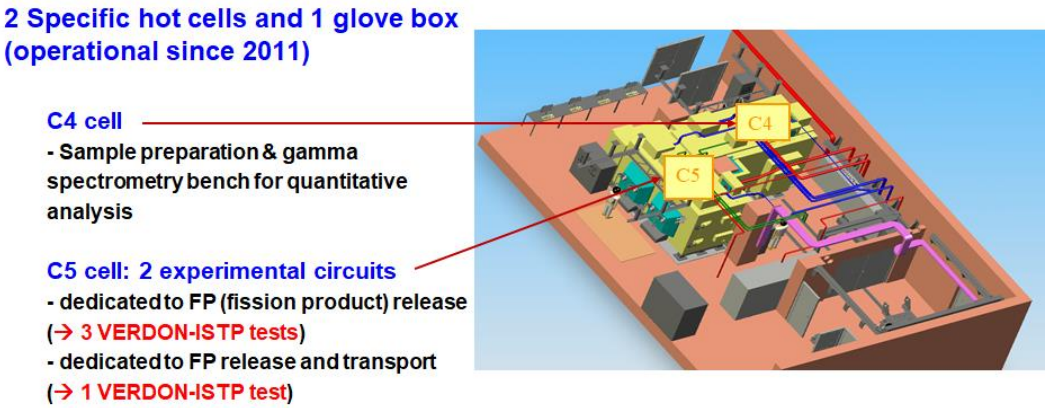

Figure 1: Schematic view of the VERDON laboratory.

The VERDON loops configurations are illustrated in Figure 2. In its release configuration (CER, Figure 2a) the experimental loop is constituted of (along the path of gas flow): (a) the fluid injection system, (b) the furnace, (c) an aerosol filter located directly on the top of the furnace (its filtering part is constituted of stainless steel poral® which function is to stop all the fission products under aerosol forms. The aerosol filter is heated at 150°C±10%), (d) a May-Pack filter, filled with zeolite (impregnated with silver) in order to trap potential molecular iodine and heated at 150°C±10% to avoid condensation, (e) a condenser the function of which is to condense steam from the experimental gas and to recover the water for analysis, (f) a final safety filter, which filtering part is constituted of stainless steel poral®, in order to stop any residual trace of fission products (other than gaseous Xe, Kr). Upstream from the condenser, the circuit is constituted of stainless

steel tubes heated at 150°C±10%. Downstream, the condenser is linked to the final safety filter. Outside of the cell, a "linking line" is used to make the junction between the C5 cell and the gloves box.

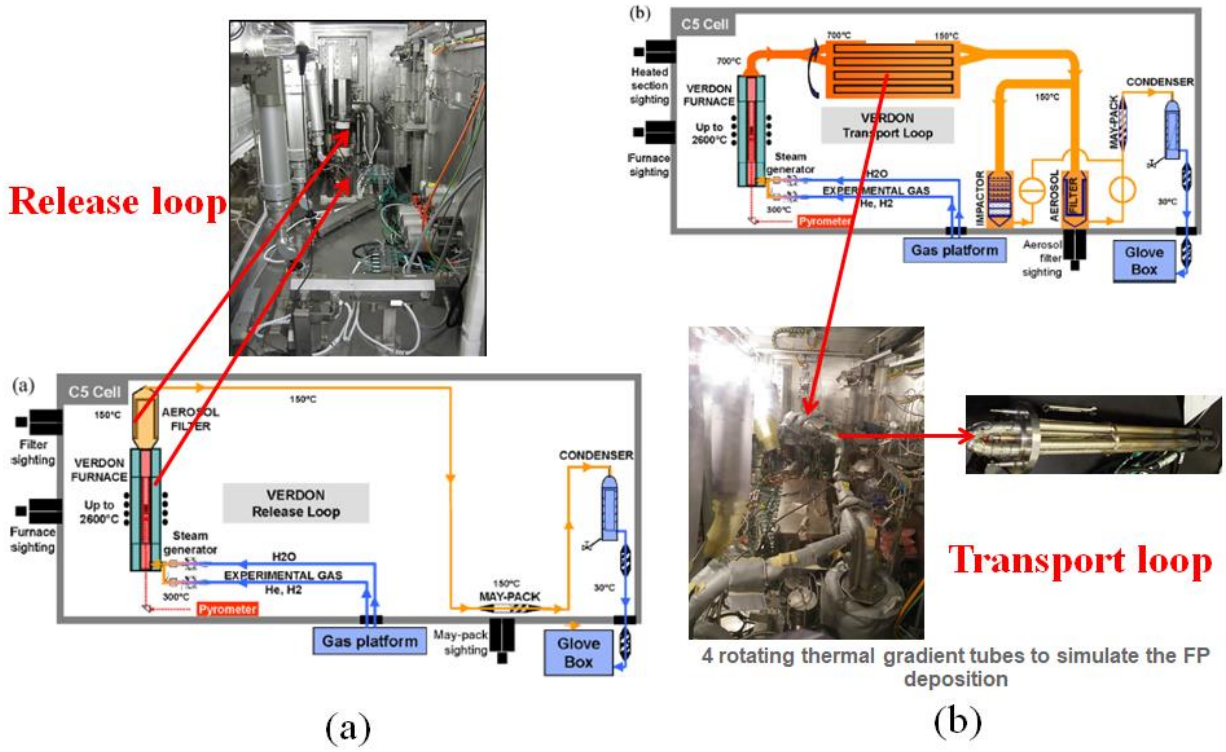

Figure 2: The so-called: (a) release experimental loop (CER) and (b) transport experimental loop (CET)

The VERDON loop in its transport configuration (CET, Figure 2b), in addition to FP release objective, is also dedicated to the study of FP transport (deposits and their potential re-volatilization). It is constituted above the furnace of: (a) a section heated at 700°C; (b) a multiple thermal gradient tubes (TGTM) in which the temperature along the outlet of four Inconel tubes (700 mm length, ~20 mm diameter) is linearly decreasing from 730°C to 140°C. Downstream from the TGTM, the fluid goes through a 150°C heated Inconel section and goes successively to: (a) an aerosol filter or (b) a cascade impactor composed of a succession of 6 impaction stages designed to collect the aerosols on drilled discs with decreasing diameter openings from 1.2 mm to 0.2 mm, two successive batteries of beds designed to collect submicronic aerosols and finally a Poral® filter (grade-3). The impactor operates for few minutes at the end of the test in order to quantify the particle size distribution of the aerosols. It is heated to allow 150°C in the impactor. The May-Pack filter and the condenser are similar to those of the release loop and located downstream of the aerosol filter and cascade impactor. Downstream, the condenser is linked to a P4VP filter made of "polyvinylpyridine" in order to trap the gaseous ruthenium tetra-oxide potentially produced during the experiment.

In both configurations, the VERDON furnace is based, as the previous VERCORS one, on induction technology. Schematically, it is constituted of a coil surrounding a tungsten susceptor tube, which is the heating component of the furnace. A high frequency power supply generates a current in the coil. By electro-magnetic coupling, a current is generated into the susceptor tube and the corresponding electric energy is converted to thermal energy by Joule effect, leading to the heating of the susceptor tube. Then, the fuel sample, located at the centre of the susceptor tube, is heated, mostly by thermal radiation.

FP release kinetics is measured by means of three complementary on line gamma spectrometry stations and one micro gas chromatography apparatus:

- One gamma station is aimed directly at the fuel sample and used during all the test. This gamma station makes it possible to qualitatively measure the FP remaining in the fuel as a function of temperature, which explains why a relatively imprecise quantification of the release kinetics was obtained. The two advantages of this station come (i) from its ability to measure directly at the source (all the FP were measured, unlike at the other stations where deposits upstream could occur) and (ii) for its ability to indicate the precise moment when the fuel relocates by detecting the disappearance (or significant decrease) in the signal of non-volatile FP. This last point was well illustrated in the case of the VERCORS series [2, 14]. This gamma station is also used in order to perform pre and post qualitative gamma scanning of the sample inside the furnace respectively before and after the accidental sequence.
- One other gamma station is aimed at the large-capacity aerosol filter. It provides a very precise measurement of the FP deposited at this point, where most of the volatile FP were found. It is highly complementary with the previous station (fuel sight).
- The last gamma station is aimed at the May-Pack (CER configuration only) and allows measuring potential gaseous iodine during the test.

The gas analysis can be also performed on-line by a micro gas chromatograph (μGC) localized inside the glove box. The μ-GC extends the analysis of active gases to all the gases.

With the exception of 2 tests[1], the fuel samples were composed of a PWR section containing 3(2) pellets in their original cladding. The samples were obtained from father rods irradiated for several years in some EDF nuclear power plants. At each end, half a fresh pellet of depleted UO_2, blocked against the fissile column and maintained by crimping, was used to seal the rod without any specific action to ensure the tightness (Figure 3a). Each assembly was systematically controlled by X-ray (Figure 3b).

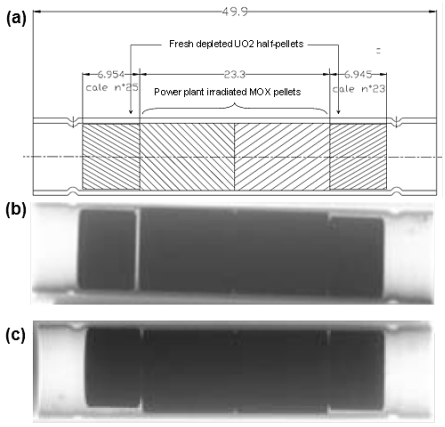

Figure 3 : Typical VERDON samples, Schematic dimensions in mm (a) and radiography of the VERDON-3 (b) and VERDON-4 (c) samples

In most of the tests, the sample was re-irradiated for several days in a pool-type material testing reactor (MTR) of the CEA (SILOE or OSIRIS) so as to rebuild the inventory of FP with short half-lives[2] at a gamma

[1] RT3 and RT4 were carried out with an initial fuel configuration in the form of debris beds to simulate the advanced phase of a severe accident (see hereafter).

[2] These FP with short half-lives (important in terms of their radiological consequences) include a number of volatile

spectrometry detection level similar to that of FP with long half-lives (obtained after base irradiation in a PWR). This short period of re-irradiation at low power in the reactor (typically between 10 and 20 W/cm for 6 to 10 days) did not result in any additional FP release.

2.2. The VERCORS/VERDON experimental grids

The main parameters explored throughout the VERCORS program were: temperature and duration of the final plateau, the oxidizing-reducing conditions of the vector fluid, the burn-up of the sample, and finally the nature and initial state of the fuel (UO_2 or MOX, initial configuration "rod" or "debris beds"). For most of the tests[3], an intermediate temperature plateau (1300°C or 1500°C depending on the test) was produced in a steam and hydrogen atmosphere so as to fully oxidize the cladding before the temperature ramp up to the final plateau. For the HT2 and HT3 tests, plus all the RT tests, this intermediate plateau was followed by a succession of 10-minute plateaus every 100°C from 2000°C or 2100°C until the sample collapsed.

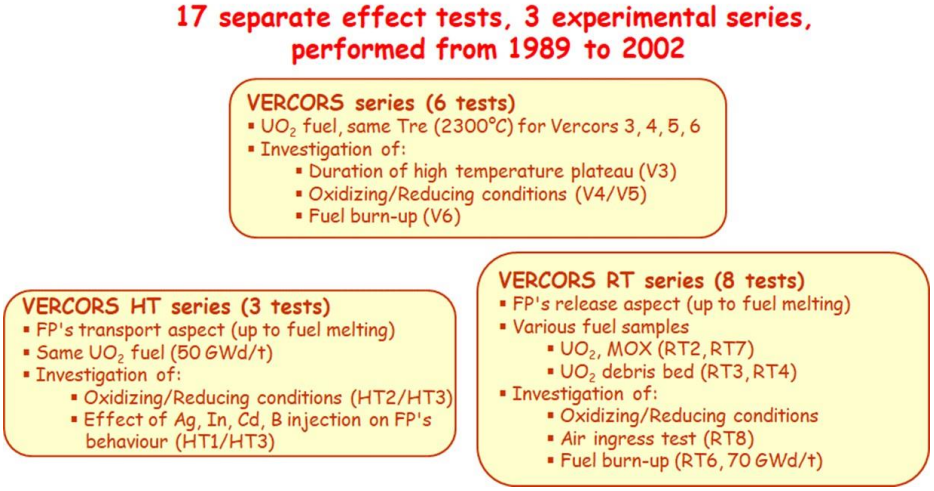

Figure 4 : VERCORS experimental grids (VERCORS 1 to 6, RT and HT series)

The main parameters explored throughout the 4 VERDON tests (Table 1) were the maximal temperature, the oxidizing-reducing conditions of the carrier fluid, the high burn-up and the nature of the fuel sample (UO_2 or MOX). For the four tests, an intermediate temperature plateau was performed at 1500°C (in a steam and hydrogen atmosphere for VERDON-1 and -3, pure steam for VERDON-2 and -4) in order to fully oxidize the cladding before the temperature ramps up to the final phase of the test. The duration of this intermediate plateau was about 10-15 minutes, except for VERDON-1 for which it was 50 minutes long.

During the first VERDON-1 test, the good performances of the VERDON loop in terms of tightness, thermal-hydraulics, furnace ceramics behavior, etc.… and of the gamma scanning and sighting have been clearly demonstrated. As a consequence it was asserted that the VERDON facility was technology-approved. The comparison with VERCORS RT6 (same fuel, same thermal history, same atmosphere, etc…) has been possible and conclusive: similar FP released fractions at 1500°C. The VERDON loop was then

FP isotopes (iodine and tellurium), fission gases (xenon) and low volatile FP (zirconium, niobium, molybdenum, ruthenium, barium, lanthanum, cerium, etc.)

[3] With the exception of VERCORS 1, 3 and 6, where cladding oxidation occurred during the temperature ramp up to the final plateau

qualified in "release configuration", in continuity with the VERCORS experiments. The VERDON-2 test concerns high burn-up MOX fuel behavior - and corresponding FP release and transport - under air ingress conditions. One of the main goals of this test concerns the transport/re-volatilization study of ruthenium and previously deposited volatile fission products in the RCS of a nuclear power plant, thanks to the TGTM of the Transport configuration. VERDON-3 and -4 are two complementary experiments. Their main objective is the quantification of FP release from a high burn up MOX fuel under steam oxidizing conditions for VERDON-3 and hydrogen reducing conditions for VERDON-4. Both tests were conducted at high temperature but without reaching global fuel relocation and with a follow-up of semi-volatile fission products in order to expect interesting post-test micro-analysis. They were performed with the Release Circuit.

Table 1: Main characteristics of the 4 VERDON-ISTP tests

Test	**VERDON-1**	**VERDON-2**	**VERDON-3**	**VERDON-4**
Date of test	09-2011	06-2012	04-2013	10-2014
Fuel	UO_2	MOX	MOX	MOX
PWR irradiation	Gravelines	Chinon	Chinon	Chinon
Local burn-up (GWd/t)	72	60	60	60
Re-irradiation	Osiris	Osiris	Osiris	Osiris
Test conditions (after oxidation plateau)				
Atmosphere	Mixed H_2O steam+H_2 (He at the end)	Mixed H_2O steam +air	H_2O steam	H_2
H_2O steam flow rate (mg/s)	0.3	2.6	2.5	0
H_2 flow rate (mg/s)	0.33	0	0	0.4
Air flow rate (mg/s)	0	4.2	0	0
End of the test				
Max fuel temperature (°C)	2610	2100	2300	2530

3. VERCORS-VERDON MAIN RESULTS

3.1. Fuel collapse temperature

One of the main important point that can be highlighted thanks to the VERCORS/VERDON results is related to the fuel collapse temperature. Indeed, as shown in Figure 5, systematic fuel collapse has been detected for a temperature range of 2000-2350°C during the VERCORS tests, whatever the burn-up from 47 GWd/t to 70 GWd/t; thus without no great effect of burn-up. Only VERDON-1 reached a higher temperature (2600°C). But, whatever the atmospheric conditions of the test, the temperature at which the fuel loses its integrity is systematically inferior to the melting point of UO_2. One can also note that fuel collapse temperature decreases in oxidizing conditions. This point is well highlighted by the comparison of the HT1 and HT2 tests and the RT6 and VERDON-1 tests, which were performed on the same fuel section for HT1 and HT2 on one side, and for RT6 and VERDON-1 [15], on the other side. In reducing conditions HT1 and VERDON-1 fuel collapsed respectively around 2250°C and 2600°C against 2030°C and 2130°C in oxidizing conditions, respectively for HT2 and for RT6.

Many thermodynamic studies coupled to detailed microstructural examination of VERCORS/VERDON samples have confirmed the general process involved in fuel degradation during the tests [16, 17, 18, 19, 20] assuming a progressive dissolution of UO_2 coming from the fuel matrix by the liquid $U_yZr_{1-y}O_{2\pm x}$ phase originally formed at the periphery when temperature is increased:

- First, Zr-U interdiffusion occurs until a certain $U_yZr_{1-y}O_{2\pm x}$ composition is reached.

- Melting of this $U_yZr_{1-y}O_{2\pm x}$ phase occurs as soon as the composition meeting the minimum melting temperature is reached.
- The molten phase then penetrates through the cracks of the pellet leading to the progressive dissolution of the fuel by $U_yZr_{1-y}O_{2\pm x}$.
- The melt is then reduced as the temperature increases.

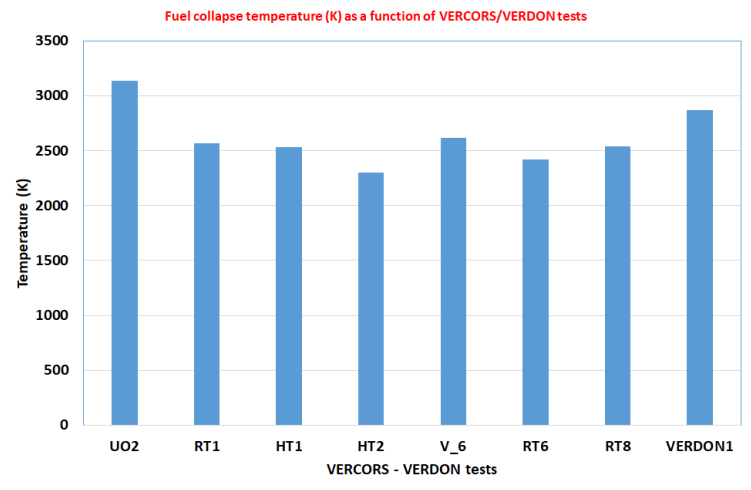

Figure 5: Fuel collapse temperatures recorded during some VERCORS/VERDON tests.

3.2. Fission product volatility classification

According to their releases recorded during the VERCORS program [2, 3, 15, 20], FPs could be classified into four categories: (1) the usual **volatile FPs** including fission gases, iodine, caesium, antimony, tellurium, cadmium, rubidium and silver**, (2) Semi-volatile FPs**, composed of molybdenum, rhodium, barium, palladium and technetium, (3) **Low volatile FPs**, composed of ruthenium, niobium, strontium, yttrium, lanthanum, cerium and europium and (4) **Non-volatile FPs**, composed of zirconium, neodymium and praseodymium. The main characteristics of each family are described below except for the last one since corresponding FP released fractions are too low to be measured by gamma spectrometry under even the most severe of the test grids presented here.

3.2.1. Volatile FPs behavior under SA conditions

Volatile FP have a high or even almost complete release for temperatures representative of a SA. The nature of the test (fuel type, initial geometry, atmosphere at the end of the test, etc.) essentially affects the release kinetics of these species and has little effect on the released fraction if temperature representative of SA is reached during the test.
Due to their radiological consequences in case of SA, we will focus in this paper only on Caesium and Iodine (details regarding the others FPS can be found in [2, 3, 15, 20]). Although the global release of these two FP did not depend (or only very little) on the test conditions at temperatures higher than 2300°C, it was quite different for their **release kinetics**. Inter-comparison of all the tests in the VERCORS/VERDON grid makes it possible to highlight that:

- for temperatures superior to 1200°C, the release kinetics of Cs and I are almost identical,

- the influence of key parameters - such as the burn-up, atmosphere, fuels (MOX or UO_2), and its initial geometry (intact or debris bed) - on the release kinetics. It was also possible to identify the influence of one of these parameters on another. From a general point of view, the release rate increases with the burn-up, in oxidizing condition and with MOX compared to UO_2 fuels.

To illustrate **the impact of the burn-up** on the release kinetics of iodine and caesium, Figure 6a compares tests VERDON-1 (UO_2 6 cycles) and **VERCORS RT1 (UO_2 4 cycles which can be considered as reference test with a moderate burn-up of 47.3 GWd/t)**. An unequivocal effect on the rate of iodine and caesium release kinetics is visible. At the end of the cladding oxidation plateau, caesium release was around four times higher for VERDON-1 than for RT1.
The influence of **the nature of the fuels** (MOX versus UO_2), which has already been highlighted [2, 15] by comparison between VERCORS RT2 (MOX, 45,6 GWd/t) and **VERCORS RT1**, was clearly confirmed by the comparison between tests VERDON -2, -3 -4 (MOX fuels at 60 GWd/t) and **VERCORS RT1**. Whatever the atmosphere of the tests and up to the end of the cladding oxidation plateau, the volatile (Cs/I) FP release kinetics is faster for MOX compared to UO_2 fuels (Figure 6b).

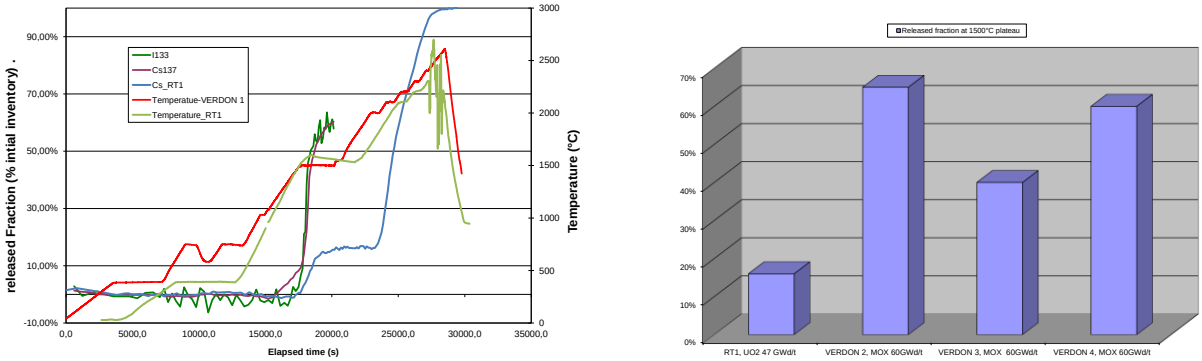

Figure 6: (a) I and Cs release kinetics for VERDON-1 and VERCORS RT1 (b) Release at 1500°C (after 10 minutes plateau) during VERDON -2, -3, -4 and VERCORS RT1.

Besides, the "LOCA" plateau (15 min at 1200°C), performed for VERDON 3 and 4, makes it possible to highlight a discrepancy between the iodine (^{131}I, ^{133}I) and caesium (^{134}Cs, ^{137}Cs) behaviour (Figure 7a, VERDON 3 example). At this stage, a 10% release has been recorded for the caesium whereas the iodine seems not to be released. This can be interpreted as a difference in the behaviour between long (caesium) and short (iodine) half-life species:

- Long half-life nuclides are quasi uncreated during the irradiation in the OSIRIS MTR. Thus, their repartition inside the fuel pellets is mainly determined by the fuel thermal history during base irradiation in EDF nuclear power plant. In the case of caesium, diffusion occurs to the grain boundaries and its distribution inside the fuel pellet includes inter- and intra-granular parts. In addition, a strong axial and radial migration leading to an accumulation at the pellets boundaries has been observed on this particular rod. This behaviour can explain the early release recorded during the "LOCA" plateau.
- Short half-life nuclides, unlike the previous ones, completely disappear from the fuel pellets a few days after the end of the power plant irradiation. Thus, their repartition inside the VERDON fuel sample is only due to the MTR irradiation and they are mainly located in intra-granular position in the fuel pellets. This repartition inside the fuel microstructure can explain the delay in the release of the short half-life iodine species compared to the long half-life caesium ones.

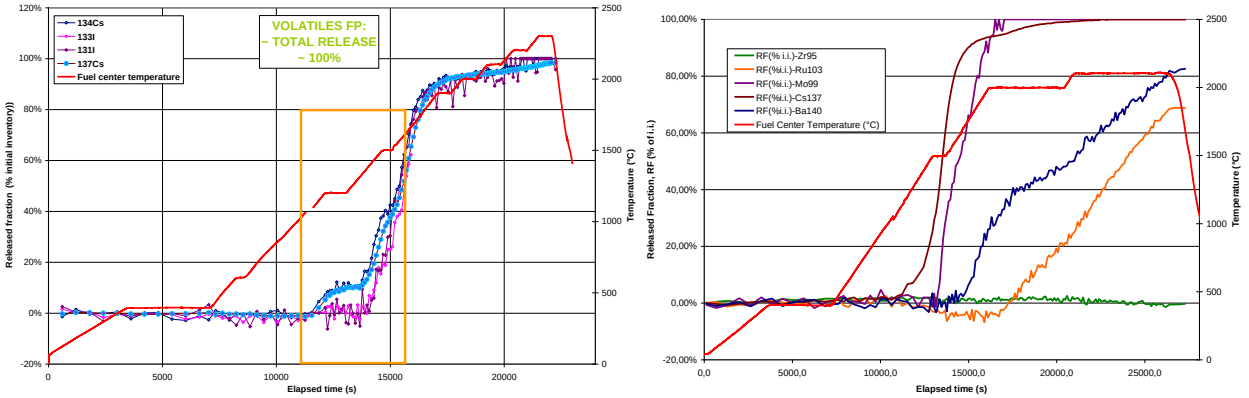

(a) (b)

Figure 7: (a) I and Cs release rate at low temperature simulating LOCA conditions (VERDON-3), (b) FP release measured during VERDON 2 (air ingress scenario).

3.2.2. Semi volatile FP behavior under SA conditions

Semi-volatile FP have released fractions that can attain 50% to 100%, but their redeposit are close to the emission point. In addition, the high sensitivity of the kinetics and released fractions to the oxidizing conditions of the tests – already demonstrated during the VERCORS program – were confirmed with VERDON. For instance, Mo release increased under oxidizing conditions through the formation of volatile species. On the contrary, the release of rhodium and barium increased under reducing conditions. This latter point seems to be less pronounced during VERDON tests on MOX fuels. Table 2 shows Ba and Mo releases for UO_2 fuels **at T=2270K** during the VERCORS 4, 5 and RT6 tests in order to emphasize the effect of the atmosphere on the release of these two FPs. These behaviour could be interpreted thanks to FP speciation occurring before and during the thermal sequences (see [8, 9, 21, 22, 23]).

Table 2: Mo and Ba release quantified after VERCORS 4, 5 and RT6 tests

	Vercors 4 (Red.)	Vercors 5 (Ox.)	Vercors RT6 (Ox.)
T(°K)	2270	2270	2270
R(Ba)	0%	0%	40%
R(Mo)	10%	70-80%	100%

3.2.3. Low volatile FP behavior under SA conditions

Low volatile FP have low, yet significant, released fractions of around 3% to 10% on average, but these values can attain 20-40% (even higher) in the case of some FP under particular conditions, e.g. oxygen potential or high burn-up. This is the case for Ru in the case of VERDON 2 (Figure 7b), in which 60% of release has been measured after 1 hour at 2000°C and 1.5h at 2100°C. In addition, the FP in this category are essentially re-deposited in the high temperature section of the test loop, i.e. near the fuel (emission point). Furthermore, it also appears that reducing conditions encourage the release of strontium, cerium, europium and lanthanum, whereas oxidising conditions enhance the ruthenium release.

3.2.4. Mechanistic code validation at the CEA fuel study department

Historically, most severe accident codes rely on simplified thermodynamic calculations, as detailed in a recent review of thermodynamically informed nuclear fuel codes [24]. Advanced thermodynamic calculations rely on the contrary on the Gibbs Energy Minimization technique. One difficulty in the modeling of severe accident sequences with this approach is related to the necessary inclusion of fission gas release kinetics and accurate FP speciation to properly assess the FP release. Recently, the coupling between thermochemical equilibrium calculations and fission gas release already implemented in the fuel performance code ALCYONE [25] has been extended to SA conditions. Detailed explanation and methodology used can be found in [21]. The main goal here is to highlight how the VERCORS/VERDON database can be used in order to identify/propose new species in the global speciation FP process, which occurs during the accidental thermal sequence.

In their analysis of the VERCORS/VERDON tests, Riglet-Martial et al. [22] pointed out that the molybdenum over cesium release fractions %Mo(t)/%Cs(t) during the oxidation temperature plateau was close to 2/3, which is more representative of the formation of cesium dimolybdate $Cs_2Mo_2O_7(g)$ rather than cesium molybdate $Cs_2MoO_4(g)$. To evaluate the potential formation of $Cs_2Mo_2O_7(g)$ during the VERCORS tests, the thermodynamic functions for the solid, liquid and gaseous compounds of $Cs_2Mo_2O_7$ were assessed from recently published studies and added to the current thermodynamic database. The assessment calculations (performed in our group) is out of the scope of the present paper. Recalculation of the molybdenum release during the VERCORS 4 test including $Cs_2Mo_2O_7(s,l,g)$ is presented Figure 8. These results clearly demonstrate that this species could have a predominant role in the mechanisms involved in semi volatile FP release.

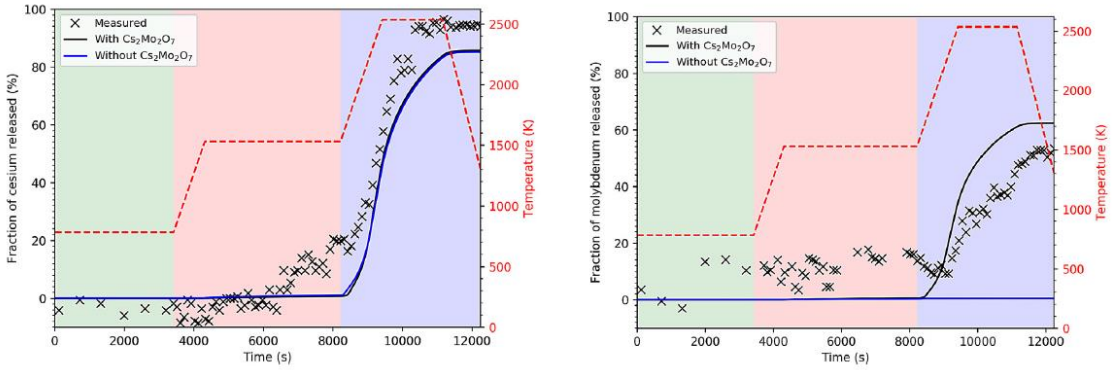

Figure 8 : Calculated fractions of Cs (left) and Mo (right) released during the VERCORS 4 test with and without $Cs_2Mo_2O_7$ in the database compared to measured values, the colors "green, pink and blue" of the figure background correspond to the 3 main parts of the test, namely respectively the thermalization of the experimental loop, the so-called oxidation plateau of the cladding and the final phase of the test at high temperature

4. CONCLUSIONS

We present in this paper the main characteristics of the experimental VERCORS/VERDON facilities (with the corresponding experimental grids) together with an overview of the mains results gained thanks to these programs, with a special emphasis on fuel relocation temperature, high burn-up and MOX fuel effects on Fission Product release and finally how these databases can be used in order to assess the fuel performance code ALCYONE developed at the CEA fuel study department and recently extended to SA conditions.

The expertise acquired throughout the VERCORS/VERDON program associated with the major results obtained (notably the FP classification into categories of volatility) have made it possible to assess, almost in real time, the state of degradation of the Fukushima cores, and the origin of release (core versus pool)

[26]. The CEA analyzes that followed the accident also made it possible to quantify the fractions released for all the FPs of interest (OECD project framework, BSAF 1 and 2).

REFERENCES

[1] Leveque et al., 1994. "*The HEVA experimental programme*". Nucl. Technol. 108, 33-44
[2] Pontillon, et al.. "*Behaviour of fission products under severe PWR accident conditions: the VERCORS experimental programme - Part 1: General description of the programme - Part 2: Release and transport of fission gases and volatile fission products - Part 3: Release of low-volatile fission products and actinides*", Nucl. Eng. Des. 240 (2010) 1843-1881.
[3] Ducros G. et al., 2001. "*Fission Product release under severe accidental conditions; general presentation of the program and synthesis of VERCORS 1 to 6 results*". Nucl. Eng. Des. 208, 191-203
[4] Schwarz et al., 2013. "*PHEBUS-FP final seminar, special issue*", Annals of Nuclear Energy 61 (2013) 1-230.
[5] Lorenz R.A., Osborne M.F., 1995. "*A summary of ORNL fission product release tests with recommended release rates and diffusion coefficients*". Report ORNL/TM-12801 - Nureg/CR-6261
[6] Hidaka A., 2011. "*Outcome of VEGA Program on Radionuclide Release from Irradiated Fuel under Severe Accident Conditions*", Journal of Nuclear Science and Technology, vol. 48, (2011), 85-102
[7] Lui Z. et al., 1994. "*A summary of CRL fission product release measurements from UO2 samples during post-irradiation annealing (1983-1992)*". Report COG-92-377
[8] Veshchunov, et al., 2003. "*Development of the mechanistic code MFPR for modelling fission product release from irradiated UO2 fuel (part 1). Development and validation of new models*". In: Proceedings of ENS Topfuel 2003, Würzburg, Germany
[9] Dubourg, R., Nicaise, G., 2003. "*Development of the mechanistic code MFPR for modelling fission product release from irradiated UO2 fuel (part 2). Application to integral tests VERCORS 4–5 and PHEBUS FPT0*". In: Proceedings of ENS Topfuel 2003, Würzburg, Germany
[10] Brillant G., Marchetto C., Plumecocq W., 2010. "*Ruthenium release from fuel in accident conditions*", Radiochim. Acta, 98(5), p.267-275, 2010
[11] Beuzet E. et al., 2012. "*Ruthenium release modelling in air and steam atmospheres under severe accident conditions using the MAAP4 code*", Nucl. Eng. Des. 246 (2012) 157-162
[12] Clement, B., "*The Phebus Fission Product and Source Term International Programs*", Int. Conf. Nuclear Energy for New Europe 2005 Bled, Slovenia, September 5-8, 2005
[13] Ferroud-Plattet M.P. et al., 2009, "*CEA VERDON Laboratory at Cadarache: new hot cell facilities devoted to studying irradiated fuel behaviour and fission product releases under simulated accident conditions*", Proc. HotLab Int. Conf., Prague, Czech Republic, 2009.
[14] Pontillon, Y. et al., 2005. "*Study of the active role played by UO_2–ZrO_2–PF interactions on irradiated fuel collapse temperature from VERCORS tests*". J. Nucl. Mater. 344, 265-273.
[15] Pontillon, Y., et al., Fission products and nuclear fuel behaviour under severe accident conditions. Part 1: main lessons learnt from the first VERDON test. *Journal of Nuclear Materials*, 495:363–384, 2017.
[16] Geiger E. *et al.*, « Fission products and nuclear fuel behaviour under severe accident conditions part 2: Fuel behaviour in the VERDON-1 sample », *J. Nucl. Mater.*, vol. 495, nº Supplement C, p. 49-57, 2017.
[17] Manara D. et al., Melting of stoichiometric and hyperstoichiometric uranium dioxide. *Journal of Nuclear Materials*, 342(1-3):148–163, 2005.
[18]Barrachin M. et al., New modelling of the U–O– Zr phase diagram in the hyper-stoichiometric region and consequences for the fuel rod liquefaction in oxidising conditions. *Journal of Nuclear Materials*, 375(3):397–409, 2008.
[19] Geiger E. et al. Modelling nuclear fuel behavior with TAF-ID: Calculations on the VERDON-1 experiment, representative of a nuclear severe accident. *Journal of Nuclear Materials*, 522:294–310, 2019.
[20] Le Gall, C. et al., ; MOX fuel microstructural evolution during the VERDON-3 and 4 tests, Journal of Nuclear Materials, 531, , 152015, 2020
[21] Sercombe J. et al., this proceedings
[22] Riglet-Martial Ch. et al., Speciation and release kinetics of the fission products Mo, Cs, Ba and I from nuclear fuels in severe accident conditions. In
Topfuel conference, Prague, Czech Republic, 2018.
[23] Germain A. et al., « Modeling high burnup fuel thermochemistry, fission product release and fuel melting during the VERDON 1 and RT6 tests", *J. of Nucl. Mat.*, **In Press**, (2021).
[24]Piro, M.H.A. Thermodynamically Informed Nuclear Fuel Codes—A Review and Perspectives. *Thermo*, 1(2):262–285, 2021.
[25] Baurens B. et al., "3D thermochemical–mechanical simulation of power ramps with ALCYONE fuel code", *J. of Nucl. Mat.*, **452**(1), pp. 578-594, (2014).

[26] Ducros G., et al., "Main lessons learnt from Fission Product release analysis, for the understanding of Fukushima NPP status, ANS Winter meeting, November 11-15, 2012

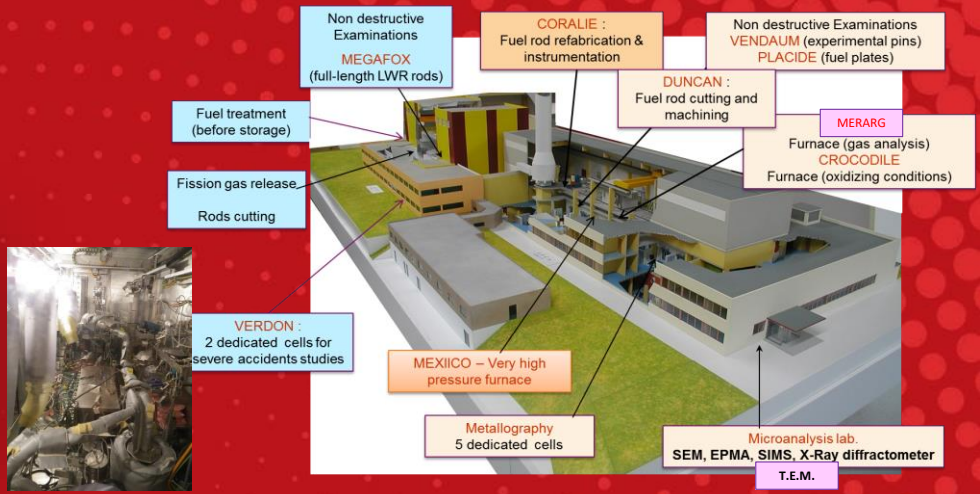

DE LA RECHERCHE À L'INDUSTRIE

FISSION PRODUCT BEHAVIOUR IN SEVERE ACCIDENT CONDITION: FOCUS ON INFORMATION GAINED FROM VERCORS/VERDON ANALYTICAL PROGRAMS

Y. Pontillon, F. Audubert, P. Bros, I. Moysan, J. Sercombe, B. Teisseire

CEA, IRESNE/DEC

General Context

- Severe nuclear reactor accident vs nonnuclear industrial facility?
  - Potential high radiological consequences, due to the amount of radioactive products released in the environment

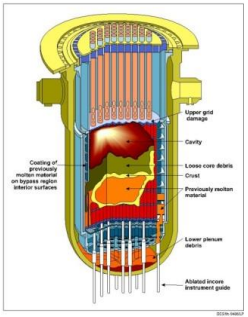

- Feedback from the 3 major Severe Accidents leading to an extensive core melting
  - TMI-2 (1979): **very low** release
  - Chernobyl (1986): **very high** release
  - Fukushima (2011): **still uncertainties** on the release amounts



➢ Importance to get a reliable assessment of the potential Source Term
  - **Program like VERDON/VERCORS** to improve the Source Term assessment



Context of the VERCORS/VERDON program (Source Term assessment)

- The objectives are as follows :
  - ***Build a realistic data base*** ***(****FP behaviour)*
  - *Improve and validate* ***models*** *used in* ***codes*** *describing the FP release to the environment during a severe accident sequence,*
  - *Input data for* ***Probabilistic Safety Assessment*** *(PSA) level 2*

FP source term determination in severe-accident conditions :

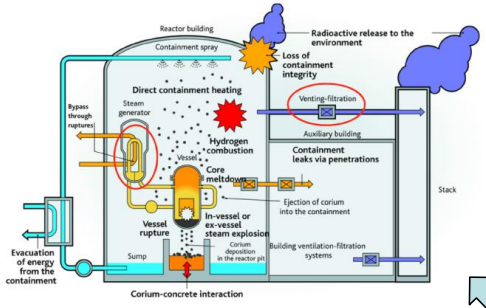

How ?

Analytical experiments on small samples

Up to loss of fuel integrity

Results complementary to those obtained

by the international PHEBUS FP program (integral experiments)

- The VERDON Laboratory
- SA Conditions in hot cell ?
- Status and main results of the programs (including VERCORS)
- Input data for SA codes ?
- Fukushima accident analysis ?

VERDON: a Severe Accident laboratory

Follow-up of the previous VERCORS laboratory (CEA Grenoble) with improved instrumentation

- **2 Specific hot cells and 1 glove box (operational since 2011)**

C4 cell

- Sample preparation & gamma spectrometry bench for quantitative analysis

C5 cell: 2 experimental circuits

- dedicated to FP (fission product) release (→ 3 VERDON-ISTP tests)
- dedicated to FP release and transport (→ 1 VERDON-ISTP test)

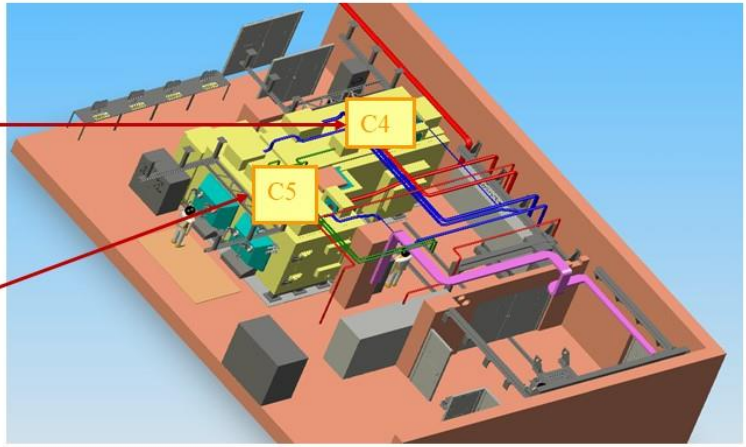

Ferroud-Plattet M.P. et al.,, Proc. HotLab Int. Conf., Prague, Czech Republic, 2009.

How to simulate SA conditions in hot cell (1/2)?

A. Gallais-During, Nuclear Engineering and Design 277: 117-123, 2014

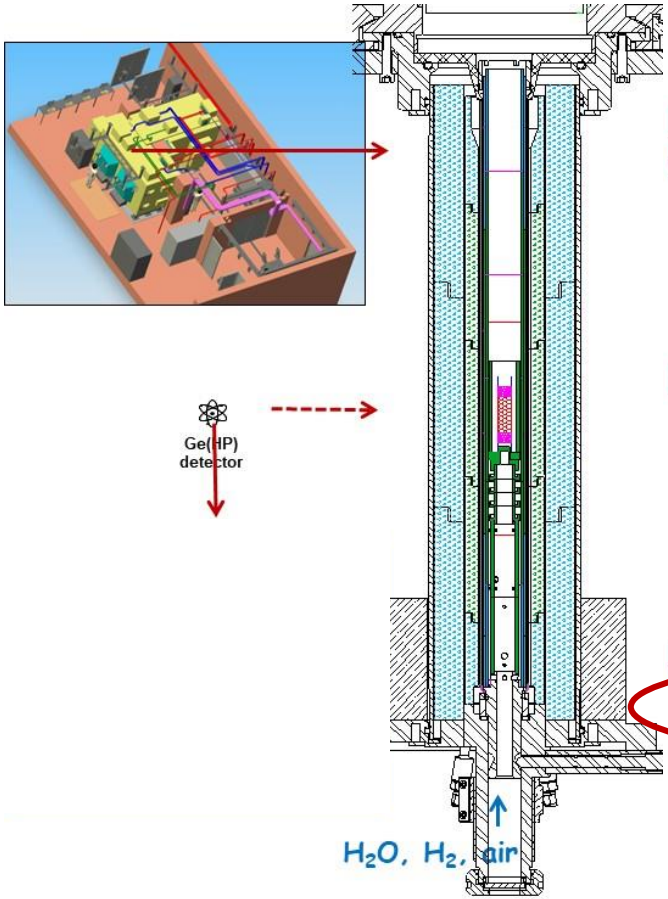

High Temperature Inductive furnace based on refractory ceramic materials (CEA design)

- *Temperature up to fuel melting*
- *Swept by steam/hydrogen/air …*

Fuel sample

- *Extracted from PWR rod*
  - 2-3 pellets in their original cladding
- *Re-irradiation at low power in OSIRIS*
  - Rebuild short half-life FP inventory

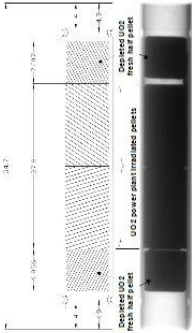

Fission Product measurements

- *On-line gamma spectrometry at high counting rate*
  - Kinetics release
- *Post-test gamma scanning and chemical analysis*
  - FP balance

How to simulate SA conditions in hot cell (1/2)?

A. Gallais-During, Nuclear Engineering and Design 277: 117-123, 2014
Y .Pontillon et al., J. Nucl. Mater., 2017

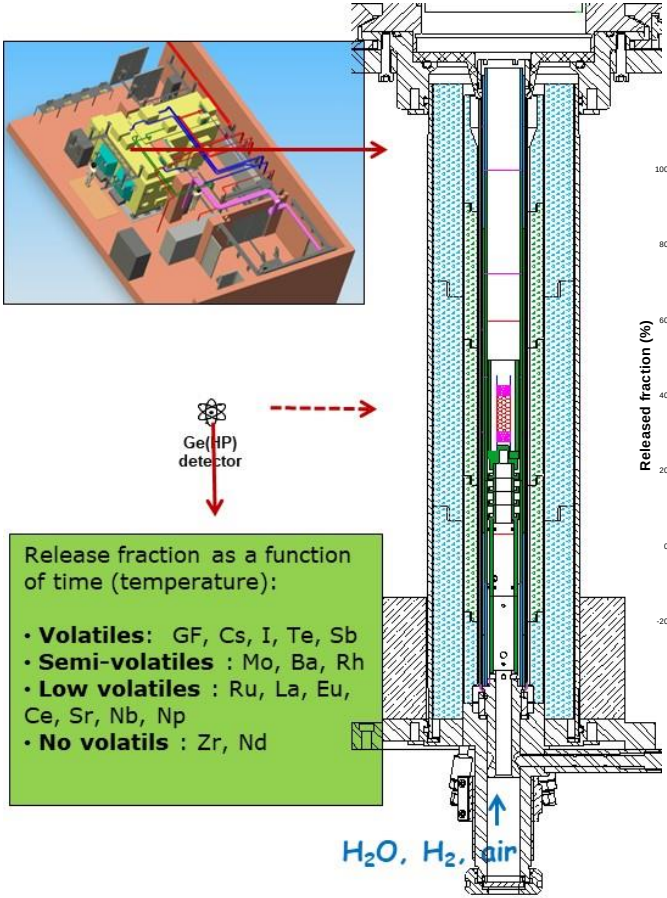

Release fraction as a function of time (temperature):

- **Volatiles**: GF, Cs, I, Te, Sb
- **Semi-volatiles** : Mo, Ba, Rh
- **Low volatiles** : Ru, La, Eu, Ce, Sr, Nb, Np
- **No volatils** : Zr, Nd

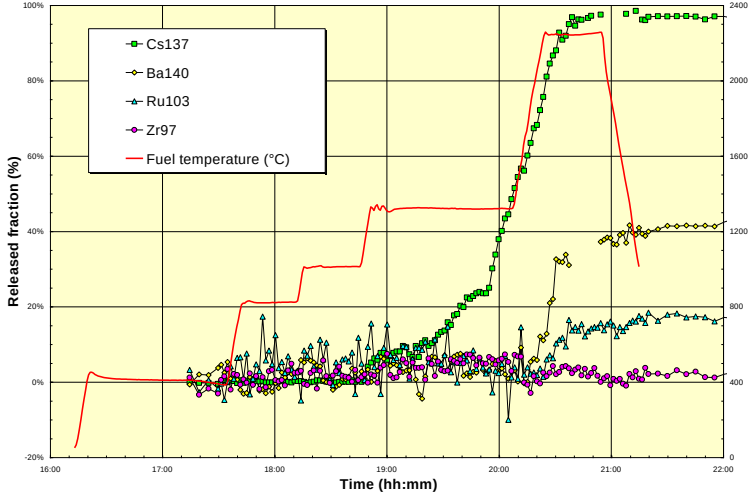

How to simulate SA conditions in hot cell (1/2)?

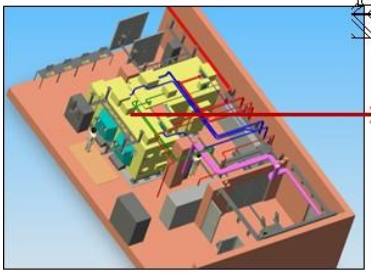

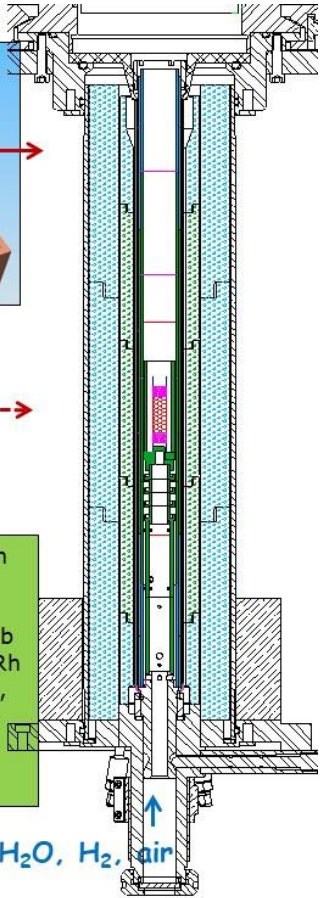

Release fraction as a function of time (temperature):

- **Volatiles**: GF, Cs, I, Te, Sb
- **Semi-volatiles** : Mo, Ba, Rh
- **Low volatiles** : Ru, La, Eu, Ce, Sr, Nb, Np
- **No volatils** : Zr, Nd

A. Gallais-During, Nuclear Engineering and Design 277: 117-123, 2014
Y .Pontillon et al., J. Nucl. Mater., 2017

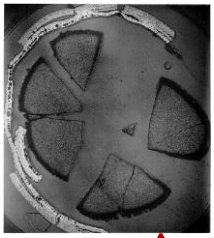

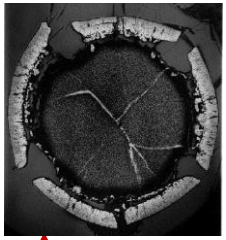

Fuel relocation detection

Fuel collapse

Intact fuel

Relocated fuel

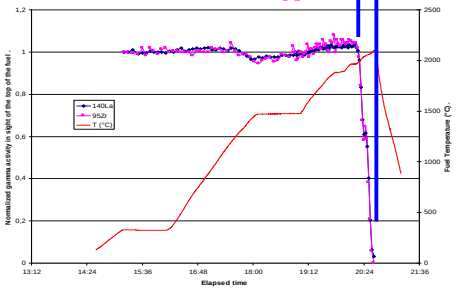

Status of the VERCORS/ VERDON programs

17 separate effect tests, 3 experimental series, performed from 1989 to 2002

VERCORS

VERCORS series (6 tests)
- UO_2 fuel, same Tre (2300°C) for Vercors 3, 4, 5, 6
- Investigation of:
  - Duration of high temperature plateau (V3)
  - Oxidizing/Reducing conditions (V4/V5)
  - Fuel burn-up (V6)

VERCORS HT series (3 tests)
- FP's transport aspect (up to fuel melting)
- Same UO_2 fuel (50 GWd/t)
- Investigation of:
  - Oxidizing/Reducing conditions (HT2/HT3)
  - Effect of Ag, In, Cd, B injection on FP's behaviour (HT1/HT3)

VERCORS RT series (8 tests)
- FP's release aspect (up to fuel melting)
- Various fuel samples
  - UO_2, MOX (RT2, RT7)
  - UO_2 debris bed (RT3, RT4)
- Investigation of:
  - Oxidizing/Reducing conditions
  - Air ingress test (RT8)
  - Fuel burn-up (RT6, 70 GWd/t)

VERDON

Test	Performed	Fuel	Circuit	Atm	Temperature (°C)	Main Objectives
VERDON-1	2011-09	UO2, 72 GWd/t **Re-irradiated** (OSIRIS)	Release	Reducing, H2/H20 molar ratio = 10	2600	High burn up effect on FP release kinetics / High temperature behaviour
VERDON-2	2012-06	MOX, 60 GWd/t **Re-irradiated** (OSIRIS)	Transport	Mixed steam-air conditions: 50-50%	2100	Air ingress / Ru release / Iodine revolatilisation
VERDON-3	2013-04		Release	Oxidising	Up to the limit of fuel melting	Complementary tests / FP behaviour under steam-hydrogen atm
VERDON-4	**2014-10**		Release	Reducing		

Typical thermal transient apply during VERCORS/ VERDON tests

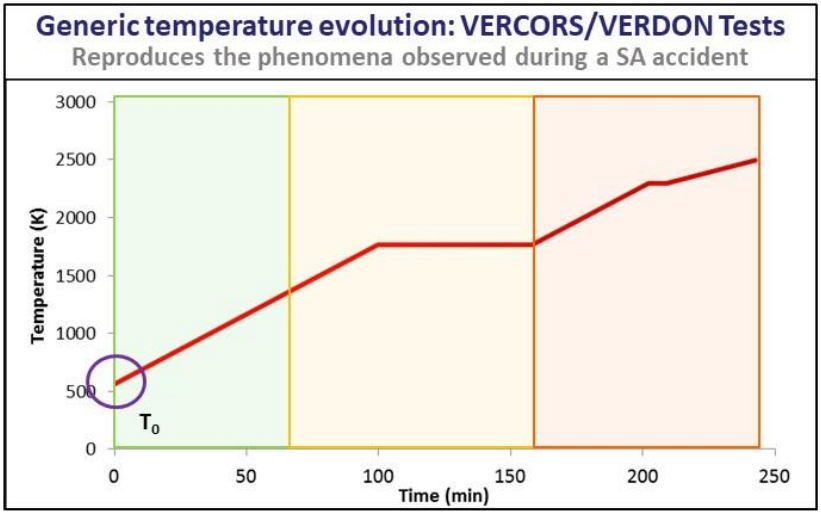

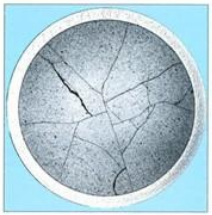

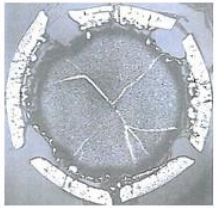

Five stages are considered

Initial State	Heat-up of fuel rods	Cladding oxidation	Further heating of fuel rods	Fuel collapse, if requested
Nuclear fuel as irradiated	Temperature ramp Neutral atmosphere	Oxidation plateau	High Temperature Red/Ox atmosphere	

Main lessons learnt from VERCORS/ VERDON programs:
Fuel collapse Temperature ?

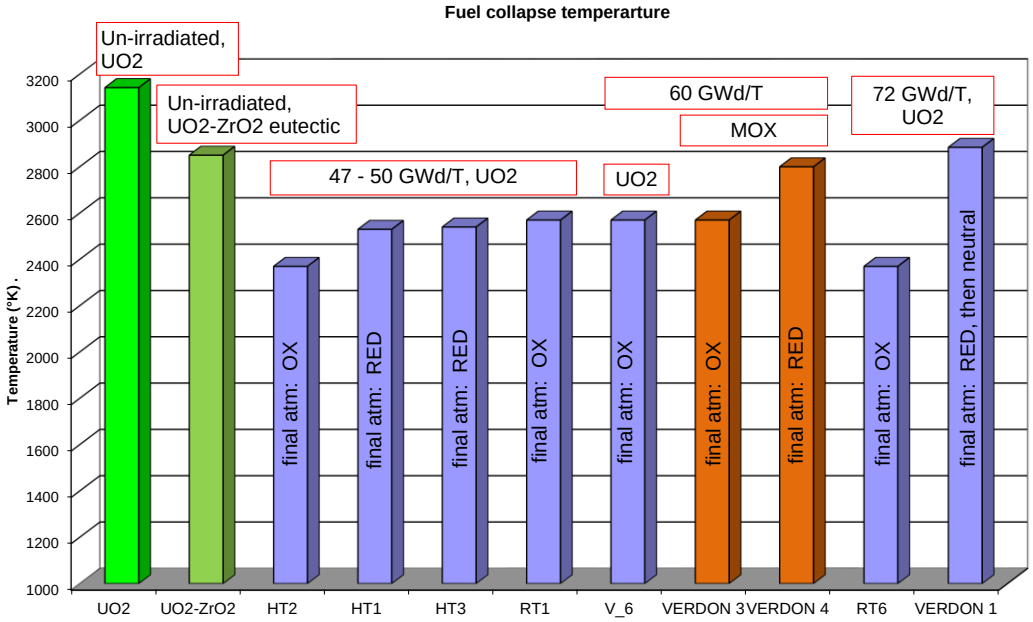

- Systematically inferior to the melting point of UO_2
- Atmosphere effect T-Red. > T-Ox.
- Progressive dissolution of UO_2 coming from the fuel matrix by the liquid $U_yZr_{1-y}O_{2\pm x}$ phase originally formed at the periphery when temperature is increased

Main lessons learnt from VERCORS/ VERDON programs: FP volatility ?

- Volatile FP: (Kr, Xe), Cs, I, but also Te, Sb, Rb, Ag, Cd
  - ***Nearly complete release when reaching fuel melting***
  - *Retention in the primary circuit*
    - Lower for iodine, compared to Cs and Te
    - High for Sb and Ag → behaviour similar to semi-volatile FP in terms of transport in the RCS
- Semi-volatile FP: Mo, Ba, Rh, Pd, Tc
  - ***Release can be as high as for volatile FP**, but:*
  - *High sensitivity to oxygen potential*
    - Higher volatility of Mo in oxidising conditions, of Ba in reducing conditions
  - *High retention in the primary circuit*
- Low volatile FP: Sr, Y, Nb, Ru, La, Ce, Eu
  - ***Released fraction generally from some % to 10%,** but*
    - Potentially higher release (~30-40%) at high burn-up and/or for highly oxidising conditions for some of them (Ru under air ingress conditions)
  - *Very high retention in the primary circuit, as well as in the upper structure of the reactor vessel*
  - ➢ ***Detection of theses FP in the environment can be considered as a signature of core melting***
- Non volatile FP: Zr, Nd, Pr
  - ***No significant release** measured up to now (<1%)*
- Actinides: U, Np similar to low volatile, Pu to non volatile

Pontillon, Y., et al., *Journal of Nuclear Materials*, 495:363–384, 2017

Main lessons learnt from VERCORS/ VERDON programs: Volatile FPs ?

VERDON 3/4, Fuel nature impact ? MOX versus UO_2

- **Very fast release kinetics (Cs):**

Fuel	T°/ Time	RF(Cs, %)
UO_2 4 cycles (VERCORS RT1)	1500°C / 10 min	20%
UO_2 6 cycles (VERDON-1)	1500°C / 10 min	40%
MOX 4 Cycles (VERDON 2/3/4)	1500°C / 10 min	40-50%

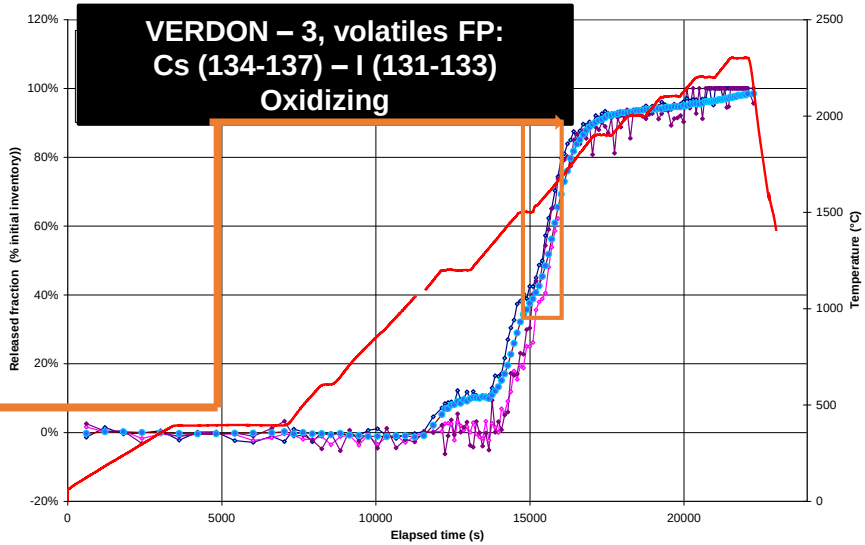

Y. Pontillon, et al.. In International OECD/NEA-NUGENIA/SARNET Workshop on the "Progress in Iodine Behaviour for NPP Accident Analysis and Management", Marseille, 2015

Main lessons learnt from VERCORS/ VERDON programs: Semi-Volatile FPs ?

	Vercors 4 (Red.)	Vercors 5 (Ox.)	Vercors RT6 (Ox.)
T(°K)	2270	2270	2270
R(Ba)	0%	0%	40%
R(Mo)	10%	70-80%	100%

VERCORS/VERDON, Atmosphere impact ?

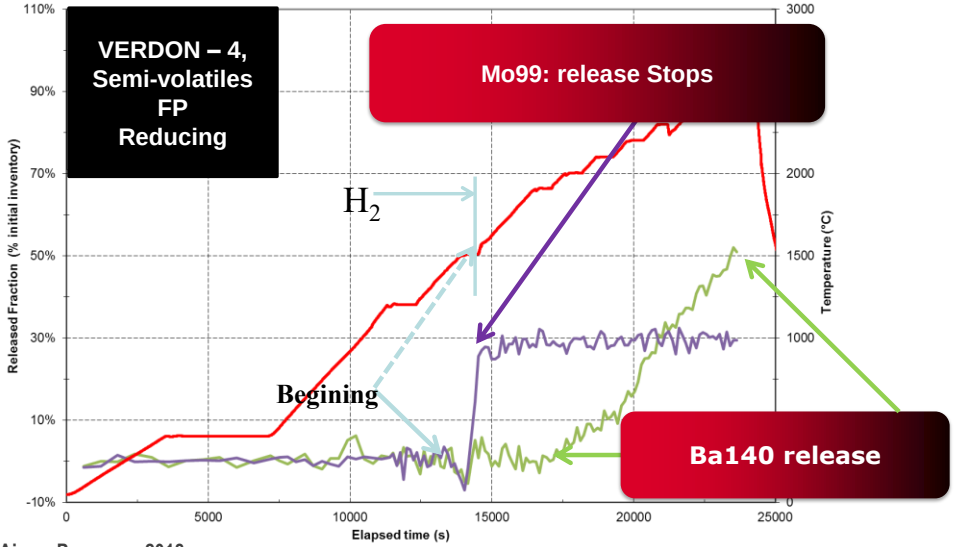

Y. Pontillon, et al.. In International VERDON Seminar, Aix en Provence, 2018

Main lessons learnt from VERCORS/ VERDON programs:
Input data for SA code ?

VERCORS 4

Calculated fractions of Cs

Calculated fractions of Mo

CEA ALCYONE fuel performance code

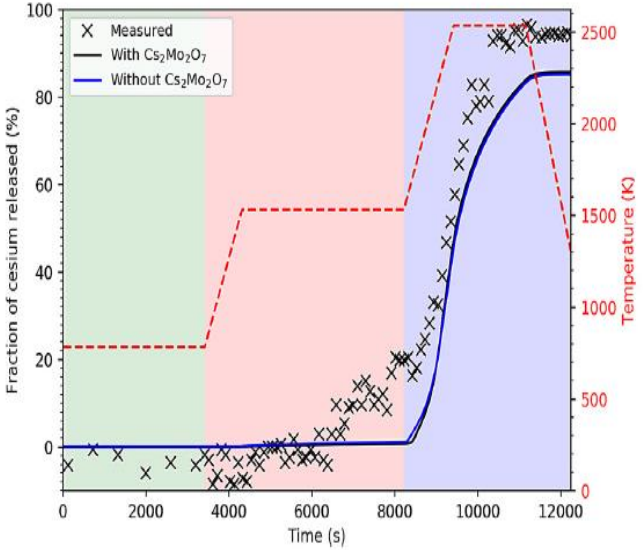

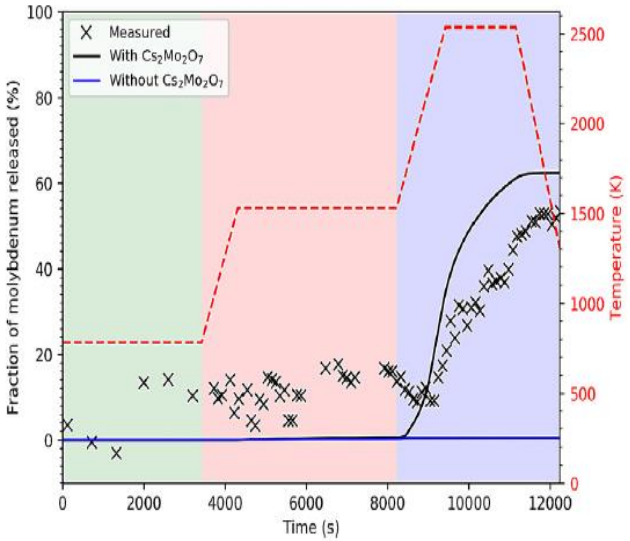

with and without $Cs_2Mo_2O_7$ in the database

Sercombe J. et al., this proceedings ; Riglet-Martial Ch. et al., *Topfuel conference*, Prague, Czech Republic, 2018.

Main lessons learnt from VERCORS/ VERDON programs: Fukushima accident analysis ?

1. Main origin of the FP release
2. Assessment of cores degradation

- $^{131}I/^{137}Cs$ ratios for samplings taken at the exit discharge canal of units 1 to 4 (decay corrected to March 11, 2011)

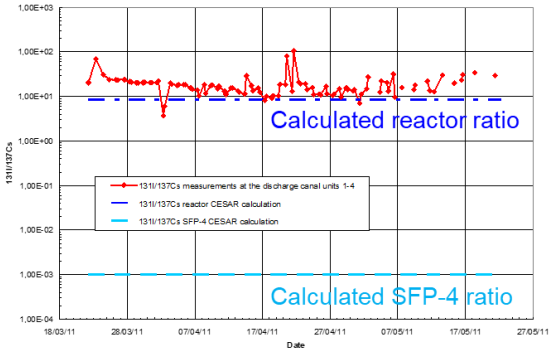

- $^{136}Cs/^{137}Cs$ ratios for atmospheric samplings coming from the CTBTO network (decay corrected to March 11, 2011)

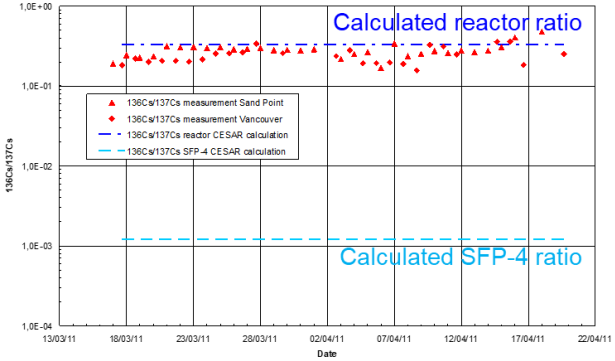

➢ The main origin of the FP release comes from the reactors and not from the SFP

[1]: Ducros G. et al., "Main lessons learnt from Fission Product release analysis, for the understanding of Fukushima Dai-ichi NPP status", ANS winter meeting, November 11-15, 2012

Main lessons learnt from VERCORS/ VERDON programs: Fukushima accident analysis ?

1. Main origin of the FP release
2. Assessment of cores degradation

[1]: Ducros G. et al., "Main lessons learnt from Fission Product release analysis, for the understanding of Fukushima Dai-ichi NPP status", ANS winter meeting, November 11-15, 2012

- Atmospheric sample collected at Takasaki on March 22, 2011, and analysed by the CEA (CTBTO network)

Radionuclide	Type	Core inventory calculation (TBq/tM)	Measured activity concentration (Bq/m3)	Fr
Rb86	Volatile	2,42E+01	2,83E-04	9,13E-01
Nb95	**Low volatile**	**4,11E+04**	**2,88E-04**	**5,49E-04**
Mo99	**Semi-volatile**	**3,55E+03**	**4,11E-03**	**9,06E-02**
Ru103	**Low volatile**	**2,95E+04**	**4,95E-05**	**1,32E-04**
Ag110m	Volatile	4,65E+01	6,55E-05	1,10E-01
Sb125	Volatile	1,98E+02	3,21E-04	1,27E-01
Te127m	Volatile	3,01E+02	6,03E-03	1,57E+00
Te129	Volatile	1,92E+03	3,47E-02	1,41E+00
Te129m	Volatile	1,92E+03	5,49E-02	2,23E+00
Te132	Volatile	3,21E+03	1,00E-01	2,44E+00
I131	Volatile	9,87E+03	2,18E+00	1,73E+01
Cs134	Volatile	2,75E+03	3,63E-02	1,03E+00
Cs136	Volatile	5,40E+02	5,54E-03	8,04E-01
Cs137	Volatile	2,77E+03	3,54E-02	1,00E+00
Ba140	**Semi-volatile**	**2,47E+04**	**2,87E-04**	**9,10E-04**

- Consistent Fr values for volatile and semi-volatile FP
- Validation of the presence of low volatile FP (^{95}Nb, ^{103}Ru), with Fr values consistent with a core melting signature

- $Fr = (Rn/Rn_0)/(^{137}Cs/^{137}Cs_0)$ with Rn_0 : Initial core inventory of each RN

Conclusion

- Larger database regarding FPs release in SA conditions
- Main results :
  - Fuel collapse temperature
  - Categories of FP volatility, impact of fuel nature and atmosphere on release rate and total release
- Can be used in order to assess:
  - Fuel performance code (models)
  - Fukushima accident (few days after the beginning)

Thank you

EXPERIMENTAL STUDY OF CsI REVAPORIZATION BEHAVIOR IN RCS CONDITION AFTER A SA

E. LE FESSANT[1*], A. C. GREGOIRE[1], C. TORNABENE[1], G. BOURBON[1], L. CANTREL[1]
Institut de Radioprotection et de Sûreté Nucléaire, PSN-RES
Cadarache, F-13115 Saint Paul Lez Durance, France
*Corresponding author: elouan.lefessant@irsn.fr

J. F. PAUL[2], A. S. MAMEDE[2]
Univ. Lille, CNRS, Centrale Lille, ENSCL, Univ. Artois, UMR 8181 – UCCS – Unité de Catalyse et Chimie du Solide
F-59000 Lille, France

ABSTRACT

During a Severe Accident (SA) occurring in a nuclear power plant, many Fission Products (FP) are released from the degraded fuel and are transported in the Reactor Coolant System (RCS). Depending on their volatility, FP can be partially deposited in the RCS and for a part can reach the containment from where they may be released into the environment in case of early containment failure or venting procedure. This was the case for the Fukushima Daiichi (FD) accident with important FP releases occurred with delayed releases up to several weeks after the start of the accident. These releases affected the counter-measure protocol and post-accidental management phases. One FP of importance is iodine. If early phase releases were well predicted by SA simulation codes, delayed releases were not correctly predicted by default [1]–[3]. Such delayed releases can be attributed to the revaporization of deposits inside the RCS which were not yet modeled in the SA simulation tools. Past experiments evidenced the possible revaporization of CsI[4]. In one of these experiments [4], CsI powder (1-10 g) was revaporized under two different temperatures (400 and 650°C) with different atmosphere compositions (H_2/steam, steam and air atmosphere). Revaporized iodine species were too low to be discussed at 400°C. However, at 650°C the presence of revaporized gaseous iodine species increased with more oxidative atmospheres. In recent work [5], CsI aerosol synthetic deposits were heated using thermal ramps up to 750°C under a wide range of air/steam atmospheres. The main results obtained highlight the importance of the atmosphere composition on CsI revaporization. In fact, under an oxidative atmosphere, the proportion of molecular iodine formed (I_2) increases.
However, up to this day, no exhaustive analytical study of iodine revaporization with isotherms and influence of oxygen concentration has been performed.
This study is scheduled within the OECD/NEA/ESTER project (2020-2024). The present work aims at determining CsI revaporization mechanisms and quantifying iodine revaporized species in isotherm conditions (temperature between 200°C and 530°C) and oxygen partial pressure (between 1.10^{-4} and 4.10^{-2} atm). Thanks to a new experimental setup coupled with ICP-MS analysis and surface ToF-SIMS and XPS characterizations, Cs and I speciation are determined and quantified. On the one hand, with a steam/air atmosphere (oxygen partial pressure at 4.10^{-2} atm) significant iodine revaporization is observed resulting in the transport of both gaseous and aerosols I species. On the other hand, when oxygen partial pressure increases, gaseous iodine species revaporization increases with different natures of iodine species.

KEYWORDS
CsI, revaporization, isotherms, oxygen partial pressure

1. INTRODUCTION

The assessment of the source term in case of a SA of a PWR is the main issue for the evaluation of the radiological consequences of such accidents. Fission products vapor or aerosol released from the reactor core region can be deposited on the surface of the Reactor Coolant System (RCS) piping or transported into the containment building. In Fukushima Daiichi accident, FP were released into the environment like I or Cs, following the containment failure of FD units 2, 1, and 3 respectively. These releases lasted up to several weeks after the accident started. Such delayed releases impacted the crisis management and the post-accidental management phases.

Within the framework of the international project OECD BSAF-2 dedicated to the FD accident analyses, two specific points concerning the delay in the releases were highlighted [6]:

- Delayed releases were significant (up to 1/10th of the direct releases) but are poorly simulated by SA softwares (ASTEC, MAAP, MELCOR, SAMPSON, THALES) in their reference version. A comparison between simulations (ASTEC Code/ IRSN) and measurements is described in Figure 1 [1]–[3]. For the first 6 days, simulation and measurements were consistent but after 6 days, some discrepancies are observed with a difference up to a 100-factor;

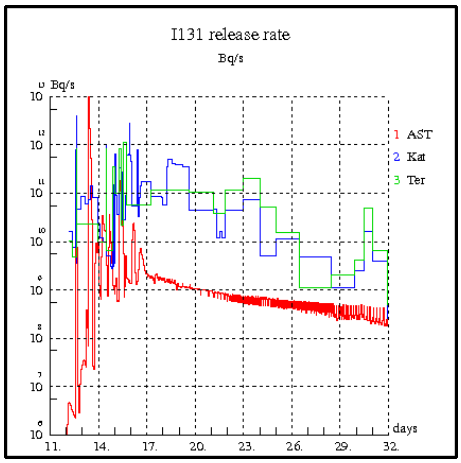

Figure 1: ASTEC simulation (red [1]) and on-field measurement (blue [2] and green [3]) of ^{131}I released during the Fukushima Daiichi accident.

- These discrepancies may be attributed to chemical revaporization of FP deposits inside the reactor rather than gas re-entrainment from the sump [1].

Previous experiments evidenced the possible revaporization of CsI. This phenomenon was partially studied for the last 20 years to improve the assessment of late-phase releases. CsI revaporization in steam atmosphere is reported to start below 500°C and to finish around 750°C. CsI is the main specie identified in steam and steam/hydrogen conditions. In presence of air, the release of gaseous iodine compounds was mentioned [7]; CsI powder was revaporized at two different temperatures (400°C and 650°C) under different atmosphere compositions (H_2/steam, steam and air/steam atmospheres). Revaporized iodine species were too low to be discussed at 400°C. However, at 650°C with more oxidative atmospheres, the presence of revaporized gaseous I species increased [4]. More recent work of D. Obada [5] (ANR MiRE project) focused on revaporization studies of CsI aerosol deposits in temperature ramp (250-750°C). This work highlighted the importance of the atmosphere composition on revaporization of the CsI aerosol deposits. Under pure air, iodine (I) was released mainly as molecular iodine (I_2) up to 90% of the initial I deposit whereas, under pure steam, CsI aerosols were formed. For a mixed air/steam atmosphere, iodine revaporization occurs partially

through I_2 formation (20-30%) and CsI aerosol (70-80%), regardless of the air/steam ratio and temperature. In addition, D. Obada demonstrated that the deposition method (aerosol deposition or vaporization/condensation method) did not impact the revaporization.
However, no exhaustive analytical study of iodine revaporization with isotherms and the influence of oxygen concentration has been performed.
This study is ongoing within the OECD/NEA/ESTER project. The present work aims at determining CsI revaporization mechanisms and quantifying cesium and iodine revaporized species in isotherm conditions (temperature between 200°C and 530°C) and variable oxygen partial pressures (between 1.10^{-4} and 4.10^{-2} atm). Thanks to a new experimental setup coupled with ICP-MS analyses, surface ToF-SIMS and XPS characterizations, Cs and I speciation are determined and quantified. With this information, a revaporization reaction is proposed according to the experimental results.

2. EXPERIMENTAL

2.1. Experimental protocol

To be as representative as possible of a SA in the RCS, the experimental protocol was divided into 4 steps:
1) Substrate preparation: during a SA, RCS Stainless Steel (SS) is oxidized by the temperature rise combined with steam. Hence, coupons (1.2 cm^2) of SS representative of RCS (304L) are oxidized to simulate the RCS oxidation. These pieces of oxidized SS will be used as substrate for aerosol deposits;
2) FP deposition process: a previous study [5] showed that deposits obtained by aerosol impaction at room temperature behave as deposits obtained at higher temperatures. Thus aerosol deposition was carried out at room temperature. Aerosols are generated by nebulization-drying and next deposited by impaction on the SS oxidized sample;
3) CsI revaporization: deposits are vaporized in the ATMIRE experimental revaporization setup to simulate FP revaporization.
4) Post-test analyses.
The first two-steps were detailed in a previous study [5] and will not be detailed here.

2.1.1. CsI revaporization protocol

ATMIRE (Figure 2) is an experimental setup dedicated to the identification and quantification of revaporized I compounds. It is composed of an alumina tube (Anderman Ceramics; 100 cm; internal diameter = 30 mm) placed in an oven (Vecstar, 50 cm, Tmax = 1600°C). Sections of the tube are kept after the oven at high temperature thanks to two heating shells downstream (Watlow, 15 cm, Tmax = 1000°C) and heating strips (Watlow, 25 cm, Tmax = 200°C) upstream. The tube is equipped with tight flanges upstream and downstream to control the inner atmosphere. Revaporization has been studied under different atmospheres, generated by a Steam Generator (SG) delivering the gas mixture in known proportions. The steam generation has been obtained by water nebulization in a gas flow heated in the vaporizer at 450°C. Water and gas flows are monitored using a thermal mass flowmeter (Bronkhorst, 0.02 to 1 $Nl.min^{-1}$ for gas) and a coriflow mass flowmeter (Bronkhorst, 2-100 $g.h^{-1}$ for water). During experimentation, the SG can be used with either Ar or air (20% O_2/80% N_2) as carrier gas.
The tube is fitted with a preoxidized Stainless Steel (SS) liner in the revaporization zone to improve the setup representativity towards the RCS. Samples are placed on removable support (instrumented with a K-type thermocouple) allowing to insert samples when the thermal condition is reached in the whole line. This support carries two samples in each test, one for surface analyses and another one (leached by sodium hydroxide solution) for quantitative elemental analyses.
Downstream of the tube, 2 main types of lines are connected:

- An “oxygen line” dedicated to the measurement of oxygen partial pressure in the atmosphere before and after revaporization;
- A “trap line” to recover every species transported in the tube. This line is made of two biphasic traps followed by a PTFE filter and a last sodium hydroxide trap. The biphasic trap is composed of toluene (organic phase) and nitric acid (aqueous phase; 0.015 M). The main purpose of this trap is to separate I_2 (in the organic phase) from CsI aerosols (in the aqueous phase). This line can be simple or doubled (Figure 2) depending on experimental conditions. During each test, only one line is used at the same time. Thus, the second one can be changed to a new one to allow sequential analyses (minimal operation duration for each line is 1 h).

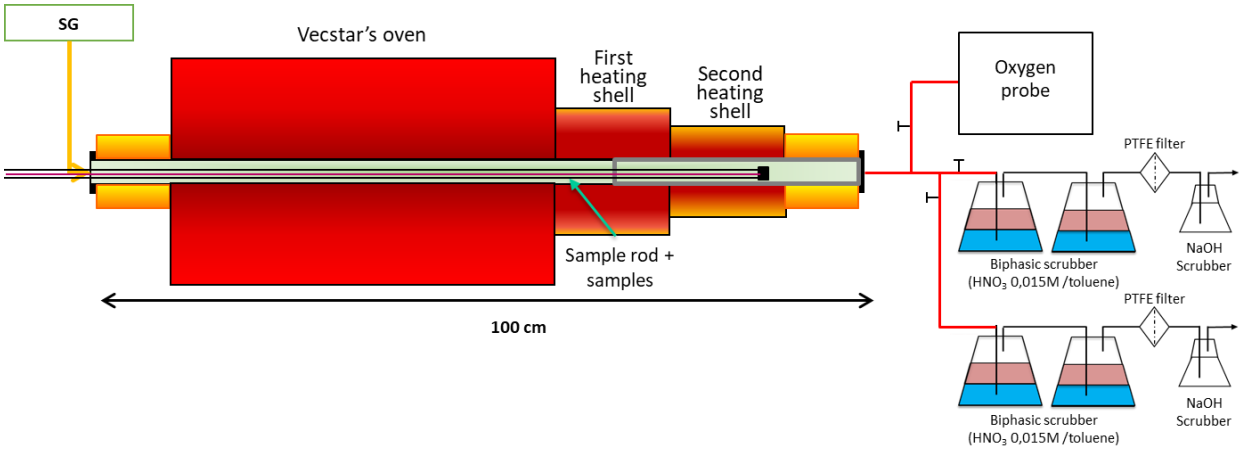

Figure 2: ATMIRE setup.

A typical experimental sequence comprises six steps:
1) First the thermohydraulic conditioning of the setup is performed. In this step, the oven and shells are heated until their set point under argon flow. The minimal setpoint of the entire ATMIRE setup is 150°C to avoid steam condensation. Simultaneously, steam flow flowrate is checked by generating/condensing steam and weighing the condensate. Samples are placed on the sample rod in a cold zone (close to downstream flange, 150°C).
2) The first oxygen measurement is carried out. Once the thermohydraulic conditions are set up, the oxygen line is opened to measure the oxygen concentration in the atmosphere.
3) The revaporization test begins by moving the samples in the revaporization zone thanks to the sample rod. Outlet supplies are switched from the oxygen probe to gas trap lines.
4) Revaporization phase ends with replacing the sample in the cold zone. Meanwhile, the outlet gases are directed into the oxygen line for the second oxygen measurement.
5) At the end of the test, steam injection is stopped and only argon passes through the experimental setup, the oven cools down thanks to natural convection.
6) ATMIRE set up is finally dismantled, one SS sample is recovered for surface characterization (residue). The other one and the whole line are washed with a sodium hydroxide solution (0.1 M). Elemental analysis (ICP MS) allows the determination of overall I and Cs distribution after revaporization. Biphasic trap solutions are separated and the aqueous solution is analyzed by ICP-MS analysis. The organic solution is analyzed by UV-Vis to determine I_2 concentration. Then, organic solutions are mixed with sodium hydroxide (0.1 M) for 15 min for I extraction from the organic phase. This step is reproduced twice and extractions solutions are finally analyzed by ICP-MS.

2.1.2. Post-test analysis

Both surface and elementary analyses are performed to characterize the substrate surface, the FP deposit before and after revaporization and the revaporized species. All analytical instruments used in this work are detailed in Table I.

Table I: Analytical techniques used with the associated objectives

Objectives	Analytical technics	Expected information
Initial deposit quantification and post-test elemental distribution	Inductively Coupled Plasma Mass Spectrometry (ICP-MS)	Elemental concentration for all lixiviation solutions
Revaporized species identification	UV-Visible spectrometry	Determination and quantification of I_2 in toluene phase and IO_3^- in sodium hydroxide aqueous phase
	Ion-Selective Electrode (ISE) for iodide	Iodide (I^-) quantification
Identification of residue species	X-ray photoelectron Spectrometry (XPS)	Determination of oxidation degree and relative quantification of the deposit after revaporization
	Time-of-Flight Secondary Ion Mass Spectrometry (ToF-SIMS)	Determination of some part of molecules to determine the initial species
Oxygen quantification	Oxygen probe	Quantify oxygen in the revaporization atmosphere by measuring oxygen partial pressure

ICP-MS analyses were performed on a VARIAN 810 MS device. The elements analyzed were ^{133}Cs, ^{127}I in a NaOH 0.1 M matrix. Internal standards used were ^{128}Te and ^{130}Te to correct the signal deviation during analyses. ICP-MS measurements uncertainties were estimated [8] based on the EURACHEM/CITAC method [9]. Uncertainties were found to be +/- 8% at a 95% confidence level.

UV-Vis analyses were performed with an Agilent Cary 8454 spectrometer. This spectrophotometer is equipped with deuterium and tungsten sources of light. I_2 in toluene complex is detected on the UV-Vis at 309 and 498 nm with different quartz cell lengths (0.5, 1 and 10 mm) to obtain an absorbance between 0.1 to 1 (u.a.). Measurements uncertainties of UV-Vis in such conditions were estimated [8] based on the EURACHEM/CITAC method [9]. Uncertainties were found to be +/-7% at a 95% confidence level. IO_3^- in sodium hydroxide are measured thanks to the Dushman reaction [10] at 288 and 350 nm [11]. Uncertainties were found to be +/-10% at a 95% confidence level with the same method as I_2.

Quantification of I^- by ISE was performed by a specific electrode previously calibrated (Thermoscientific) with a measure based on the NERNST equation. Uncertainties were found to be +/-10% at 95% [12].

XPS measurements were carried out at the UCCS laboratory at the University of Lille on a Kratos AXIS UltraDLD spectrometer equipped with a monochromatic Al Kα source (1486.6 eV). The analyzer was operated in constant pass energy of 40 eV using an analysis area of approximately 700 µm x 300 µm. Calibration was realized by using the C 1s component of carbon at BE (binding energy) = 284.8 eV. Quantification and decomposition were carried out using CasaXPS software. Binding energy value uncertainties is +/-0.1 eV and uncertainty on quantitative elemental analysis is +/- 10%.

ToF-SIMS analyses were carried out at the UCCS laboratory at the University of Lille using a TOF-SIMS V instrument (IONTOF GmbH). Pulsed Bi^+ primary ions have been used for analyses (25 keV, ≈1 pA).

Oxygen measurements were studied with a Jok'air analyzer designed by SETNAG. This analyzer was equipped with a MicroPoas sensor and an oven to maintain the sensor at 650°C. Measurements uncertainties were estimated by SETNAG at 2% of each measure at a 95% confidence level.

2.2 Test grid

Different isotherms and oxygen partial pressures were investigated to highlight potential impacts. Parameters range and number of tests are detailed in Table II. For each parameter, the focus is mainly placed on the global revaporization kinetics, the revaporized iodine speciation kinetics and the residue speciation.

Table II: CsI revaporization test grid

Studied parameters	Parameters	Number of tests
Temperature plateau	From 215°C to 523°C	5
Oxygen concentration	From 9.10^{-5} to 4.10^{-2} atm	5

Results are presented in terms of element distribution. The ATMIRE facility is divided into 3 zones allowing the determination of:

- Residual mass: mass recovered on the sample. This represents the mass of Cs and I not revaporized during the test;
- Redeposited mass: mass recovered in the SS liner (and flanges). This represents the Cs and I mass revaporized and redeposited in a heated zone (> 200°C). The temperature decreases sharply with a gradient at -5 °C per cm (for low-temperature test) up to -38°C per cm for high-temperature test. Thus, deposits found in the tube are at lower temperature than sample. The revaporisation kinetics decreases sharply when the temperature decreases so the revaporisation of deposit in the tube is not considered to be significant;
- Transported mass: mass recovered downstream the flange (in the cold zone, < 150°C).

For a given element, the revaporized mass is calculated by the sum of redeposited mass and transported mass. Revaporization kinetics are obtained by dividing revaporized mass by the test duration assuming a steady-state for all tests.

Concerning speciation of revaporized iodine, sample lines with biphasic scrubbers allow to identify the following species:

- Iodine found in toluene phases from the biphasic trap is considered as I_2 trapped in this phase;
- Iodine found in the aqueous phase is assumed to be transported:
  - As a CsI aerosol if I/Cs molar ratio is below 1.25;
  - As a mixture of gaseous iodine and CsI aerosol if I/Cs molar ratio is over 1.25. The excess of I is considered as I gas species.

The sum of I_2 and I gas species are the gaseous I species.

3. RESULTS

3.1. Influence of temperature

Based on the methods presented in the previous section, five tests were performed featuring temperature plateau from 200°C up to 530°C. For this part, revaporization tests were performed from CsI deposit (I/Cs = 1) with an atmosphere featuring a mixture of steam/air (80%/20%) and a 0.5 Nl.min^{-1} total flow at atmospheric pressure. Test duration was varied from 3 h up to 6 h.

3.1.1. Revaporization kinetics

Cs and I revaporization kinetics depending on temperature plateaus are presented in Figure 3. When temperature increases, Cs and I revaporization kinetics increase. Cs and I revaporization kinetics remain low for moderate temperature. However, above a threshold, revaporization kinetics rise for both Cs and I with a greater increase for I. At the highest tested temperature, Cs revaporization rate seems to reach a maximum value, which is not the case for I. Thus, difference between I and Cs revaporization kinetics is increasing with temperature.

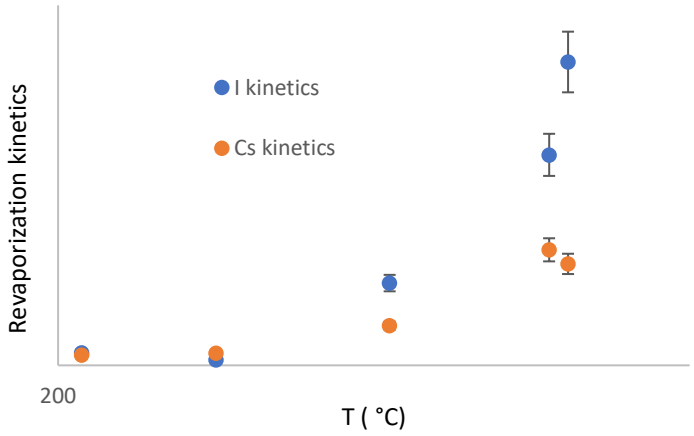

Figure 3: Iodine revaporization kinetics depending on temperature plateau.

3.1.2. Speciation of revaporized iodine

A particular focus is placed on I revaporization speciation. Figure 4 shows the release kinetics of CsI and gaseous I depending on temperature. Tests at the lowest temperatures are difficult to interpret due to the low mass revaporized. When the revaporization temperature increases, the gaseous I and I_{CsI} kinetics increase. However, gaseous I kinetics increases more than I_{CsI} kinetics.

The speciation of I_{gas} was studied using leaching solutions (sodium hydroxide, 0.1 M) downstream the alumina tube. An analysis by iodine specific-electrodes and UV-Vis spectrometry was performed to determine iodine speciation (in sodium hydroxide solution).

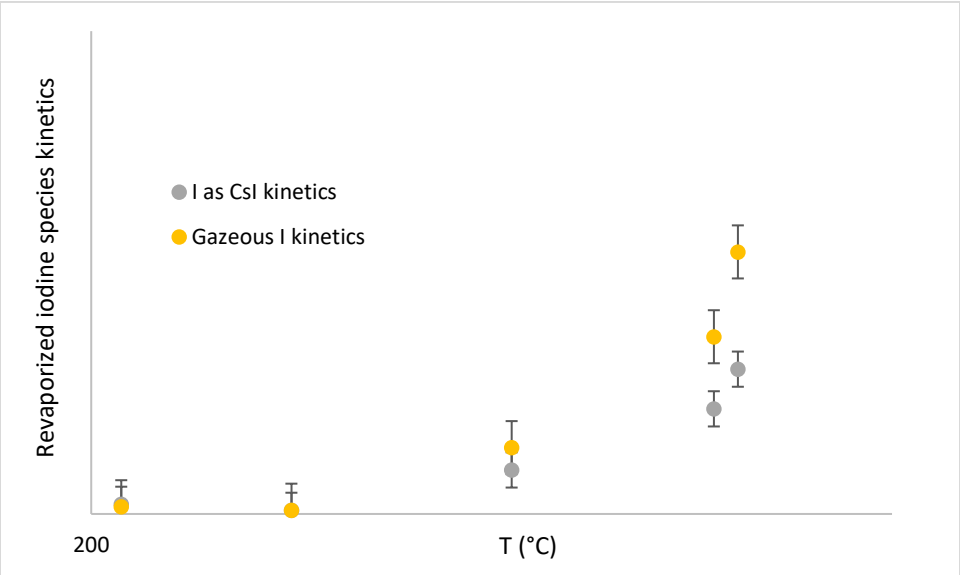

Figure 4: Revaporized iodine species kinetics depending on isotherms.

3.1.3. Residue speciation

XPS analyses were performed on SS samples after thermal treatment for residues characterization. Atomic surface composition is detailed in Table III. Cs and O dominate the surface composition whereas substrate elements in the oxide layer are minor (Fe, Mn, Cr and Ni). Thus, the extreme surface is composed of residual Cs compounds.

Table III: Surface composition obtain by XPS analysis on sample after revaporization at 523°C

Elements	O as hydroxide (OH)	O as metal oxide (O^{2-})	Cs	Fe	Mn	Cr	Ni
Atomic percentage (%)	27.5	40.2	26.7	0.8	3.2	0.7	1.0

The study of Cs chemical shift is not relevant for Cs speciation as Cs^+ displays very close binding energy whatever its chemical environment (724 eV for Cs 3d 5/2 [13]). The focus is then placed on other elements. First, chromium is analyzed (Cs-Cr mixed oxide observed in the literature [5], [14], [15]). Cr 2p chemical shift at 575.5 eV [13] shows the presence of Cr (+III) only; Cr (+VI) is not detected (chemical shift at 580 eV for Cr +VI 2p [13]). Thus, Cs-Cr mixed oxide forms can be excluded.

XPS spectra of O 1s features a broadened peak around 530 eV (Figure 5) which could be decomposed in O as hydroxide contribution (531.4 eV [13], 27.5% of surface atomic percentage) and O as oxide contribution (529.4 eV [13], 40.2% of surface atomic percentage).

Given the close atomic percentage of Cs and O as hydroxide on the surface, the presence of CsOH can be assumed. Complementary surface analyses by ToF-SIMS (Bi^+ beam) revealed the presence of a significant amount of CsO^+ fragments confirming the hypothesis of CsOH residue on the sample.

All iodine detected in the residue are considered as CsI species. All Cs in excess are considered as CsOH.

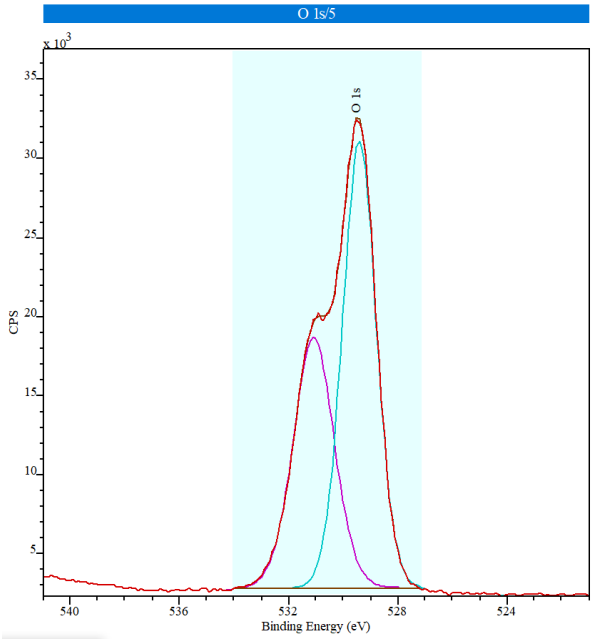

Figure 5: XPS spectrum of SS coupon after revaporization at 523°C. O 1s binding energy range. O 1s can be decomposed into two contributions: O as OH (531.1 eV) and O as in metal oxide (529.4 eV).

3.2. Oxygen content influence

Oxygen has a strong influence on CsI revaporization and gaseous I release [16]. Oxygen concentration influence is studied in the revaporization atmosphere with an oxygen partial pressure (P_{O2}) measured between 10^{-5} and 10^{-1} atm. P_{O2} study was performed from CsI deposit (I/Cs = 1) with an isotherm between 510°C and 520°C and a 0.5 Nl.min^{-1} total flow (mixture of Ar/air). Test duration was 3 h.

3.2.1. Kinetics of release from the deposit

Cs and I revaporization kinetics depending on oxygen partial pressure are presented in Figure 6. With increasing oxygen partial pressure, iodine revaporization kinetics increases. For Cs revaporization kinetics, O_2 accelerates Cs revaporization but in a lesser extent and reaches a plateau at high partial pressure. In addition, like in the temperature plateau study, there is a significant difference between I and Cs revaporization kinetics for high oxygen concentrations.

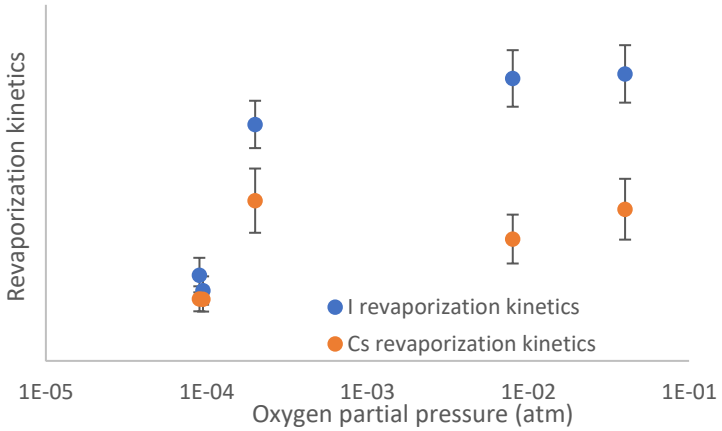

Figure 6: Iodine revaporization kinetics depending on oxygen partial pressure.

3.2.2. Chemical speciation

The iodine forms (aerosol/ gas) released are a mix between CsI and gaseous iodine whose proportions depend on oxygen partial pressure.
With increasing oxygen partial pressure, I/Cs ratio on the residue decreases, indicating an enrichment in Cs of the residue. At low oxygen partial pressure, the residue is assumed to be CsI. At higher oxygen partial pressure, the residue is a mixture of CsI and CsOH, according to XPS and ToF-SIMS analyses performed previously.

4. DISCUSSION/CONCLUSION

Analytical experimental work within the ESTER program focuses on the revaporization of synthetic FP deposits (on the most expected species which could be sources of volatile iodine in case of late-phase releases). The purpose is to understand revaporization phenomena to depict/characterize a mechanism that took place in FD and led to late releases.
Revaporization of CsI deposits under different isotherms and different oxygen partial pressure was studied.

This study highlights the importance of temperature and oxygen partial pressure for CsI revaporization. This revaporization rises more than 25 times within the temperature range. This rise is combined with a quicker increase of revaporization under gaseous form than under CsI form. Thus, two mechanisms could take place simultaneously: a vaporization mechanism (ruled by the CsI vapor pressure) and a splitting mechanism. This second mechanism takes place at the CsI aerosol surface with a solid-gas reaction. This solid-gas reaction is strongly affected by the oxygen concentration in the revaporization atmosphere.
One possibility of gaseous iodine formation was set in using DFT calculations between CsI and O_2 [5], a first revaporization reaction is proposed (Equation 1):

$$\mathbf{CsI + O_2 \rightarrow CsO^{\bullet} + IO^{\bullet}} \qquad (1)$$

The O_2 molecules can react on the CsI particles to form in the first step the radical species $IO^{\bullet}$, but this reaction is only possible on the surface defects [5]. $CsO^{\bullet}$ is presumed to become CsOH in the presence of steam. However, the pathway between $IO^{\bullet}$ (oxidation degree at +I) and gaseous iodine species (with an iodine oxidation degree at –I) is still under investigation.

ACKNOWLEDGMENTS

The authors thank Dr. N. Nuns and Dr. P. Simon for the XPS and ToF SIMS analyzes. This work was supported by the partners (NRC, GRS, SSM, NRA, EDF, VTT and KINS) of the OECD/ESTER program.

REFERENCES

[1] F. Cousin, H. Bonneville, C. Bouillet, D. Didier, and D. Jacquemain, "Analysis of fission products behavior and environmental releases during the Fukushima-Daiichi accident by direct and inverse approach at IRSN," IRSN, 2020.

[2] G. Katata *et al.*, "Detailed source term estimation of the atmospheric release for the Fukushima Daiichi Nuclear Power Station accident by coupling simulations of atmospheric dispersion model with improved deposition scheme and oceanic dispersion model," *Atmospheric Chemistry & Physics Discussions*, vol. 14, no. 10, pp. 14725–14832, 2014, doi: 10.5194/acpd-14-14725-2014.

[3] H. Terada, G. Katata, M. Chino, and H. Nagai, "Atmospheric discharge and dispersion of radionuclides during the Fukushima Dai-ichi Nuclear Power Plant accident. Part II: verification of the source term and analysis of regional-scale atmospheric dispersion," *Journal of Environmental Radioactivity*, vol. 112, pp. 141–154, Oct. 2012, doi: 10.1016/j.jenvrad.2012.05.023.

[4] J. Kalilainen, T. Kärkelä, R. Zilliacus, U. Tapper, A. Auvinen, and J. Jokiniemi, "Chemical reactions of fission product deposits and iodine transport in primary circuit conditions," *NUCL ENG DES*, vol. 267, pp. 140–147, 2014, doi: 10.1016/j.nucengdes.2013.11.078.

[5] D. Obada *et al.*, "Chemical stability of caesium iodide deposits in air/steam atmosphere," *Journal of Hazardous Materials*, p. 124519, Nov. 2020, doi: 10.1016/j.jhazmat.2020.124519.

[6] T. Lind *et al.*, "Overview and outcomes of the OECD/NEA benchmark study of the accident at the Fukushima Daiichi NPS (BSAF), Phase 2 – Results of severe accident analyses for unit 3," *Nuclear Engineering and Design*, vol. 376, p. 111138, May 2021, doi: 10.1016/j.nucengdes.2021.111138.

[7] A. Auvinen, K. E. J. Lehtinen, J. Enriquez, J. K. Jokiniemi, and R. Zilliacus, "VAPORISATION RATES OF CsOH AND CsI IN CONDITIONS SIMULATING A SEVERE NUCLEAR ACCIDENT," *Journal of Aerosol Science*, vol. 31, no. 9, pp. 1029–1043, Sep. 2000, doi: 10.1016/S0021-8502(00)00027-6.

[8] M. Gouello, "Chimie de l'iode et composition des aérosols dans le circuit primaire d'un réacteur nucléaire en situation d'accident grave," PHD Thesis, Institut National Polytechnique de Grenoble - INPG, 2012. Accessed: Jun. 04, 2020. [Online]. Available: https://tel.archives-ouvertes.fr/tel-00832204

[9] "Quantifying Uncertainty." https://www.eurachem.org/index.php/publications/guides/quam (accessed May 04, 2021).

[10] G. Schmitz, "Kinetics of the Dushman reaction at low I− concentrations," *Phys. Chem. Chem. Phys.*, vol. 2, no. 18, pp. 4041–4044, Jan. 2000, doi: 10.1039/B003606O.

[11] R. O. Rahn, "Determination of iodide formed from inorganic iodine in aqueous solution," *Analytica Chimica Acta*, vol. 248, no. 2, pp. 595–602, Aug. 1991, doi: 10.1016/S0003-2670(00)84681-4.

[12] L. Martinet, "Rapport de qualification du dosage des iodures," IRSN, SERC1-2011-045-DI.

[13] A. Naumkin, A. Kraut-Vass, S. Gaarenstroom, and C. Powell, "X-ray Photoelectron Spectroscopy Database XPS,Version 4.1, NIST Standard Reference Database 20." National Institute of Standards and Technology, 1989. doi: 10.18434/T4T88K.

[14] H. Shibazaki *et al.*, "Revaporization of a CsI Aerosol in a Horizontal Straight Pipe in a Severe Accident Condition," *Nuclear Technology*, vol. 134, no. 1, pp. 62–70, Apr. 2001, doi: 10.13182/NT01-A3186.

[15] K. Sasaki, K. I. Fukumoto, T. Oshima, T. Tanigaki, and U. Masayoshi, "Microstructure analysis for chemical interaction between cesium and SUS 316 steel in fast breeder reactor application," *Proceedings of the 2012 International Congress on Advances in Nuclear Power Plants - ICAPP '12*, 2012, Accessed: Jul. 21, 2021. [Online]. Available: http://inis.iaea.org/Search/search.aspx?orig_q=RN:44065706

[16] D. Obada, A.-S. Mamede, N. Nuns, A.-C. Grégoire, and L. Gasnot, "Combined ToF-SIMS and XPS characterization of 304L surface after interaction with caesium iodide under PWR severe accident conditions," *Applied Surface Science*, vol. 459, pp. 23–31, Nov. 2018, doi: 10.1016/j.apsusc.2018.07.212.

[18] B. R. Bowsher, "Fission-product chemistry and aerosol behaviour in the primary circuit of a pressurized water reactor under severe accident conditions," *Progress in Nuclear Energy*, vol. 20, no. 3, pp. 199–233, 1987, doi: 10.1016/0149-1970(87)90006-0.

RÉPUBLIQUE FRANÇAISE
Liberté
Égalité
Fraternité

UCCS
UNITÉ DE CATALYSE ET CHIMIE DU SOLIDE

IRSN
INSTITUT DE RADIOPROTECTION ET DE SÛRETÉ NUCLÉAIRE

REVAPORIZATION STUDY OF FISSION PRODUCT DEPOSITS UNDER SEVERE ACCIDENT CONDITIONS (ESTER PROJECT)

Elouan Le Fessant
PSN-RES/SEREX/L2EC

Director: Dr. Jean-François PAUL, Professeur
Univ. Lille, CNRS, Centrale Lille Institut, Univ. Artois, UMR 8181 – UCCS – Unité de Catalyse et Chimie du Solide, F-59000 Lille, France

Co-Director: Dr. Anne-Sophie MAMEDE, Maître de Conférences
Univ. Lille, CNRS, Centrale Lille Institut, Univ. Artois, UMR 8181 – UCCS – Unité de Catalyse et Chimie du Solide, F-59000 Lille, France

IRSN supervisor: Dr. Anne-Cécile GREGOIRE
PSN-RES/SEREX/L2EC

IRSN/FRM-296 ind. 06

MEMBRE DE ETSON

Université de Lille

cnrs

UNIVERSITÉ D'ARTOIS

centralelille

institut Chevreul

Late FP release in a SA: special case of Iodine in Fukushima Daiichi

Severe accident → Release of FP into containment building (CB) → **CB leakages** → Release of FP into the environnement → **Identify and quantify FP source term in case of delayed releases**

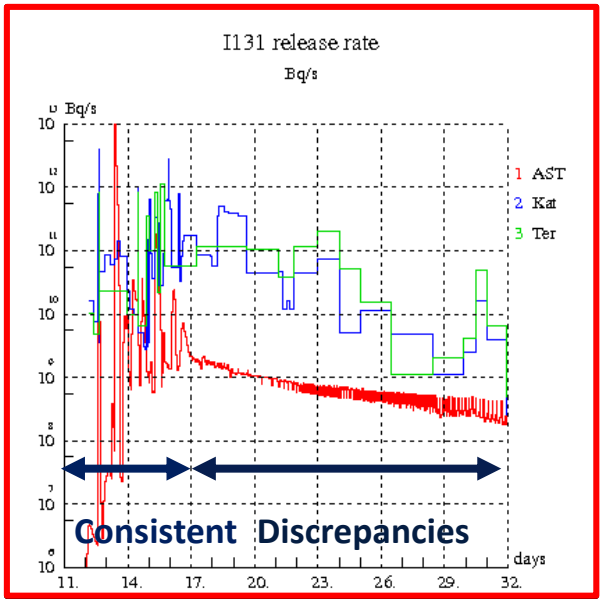

Radioelement measurement (^{131}I,…) were performed nearby the powerplant
(Blue and green curves)

ASTEC code predictions (red curve)

Discrepancies due to late releases and partially attributed to the fission products revaporization.

Focus is made on the gaseous iodine released

Which phenomena are involved in revaporization ?

Bonneville H. *et al.*, 2019 ; Katata G. *et al.*, 2015 ; Terada H. *et al.*, 2012

Revaporization during a severe accident

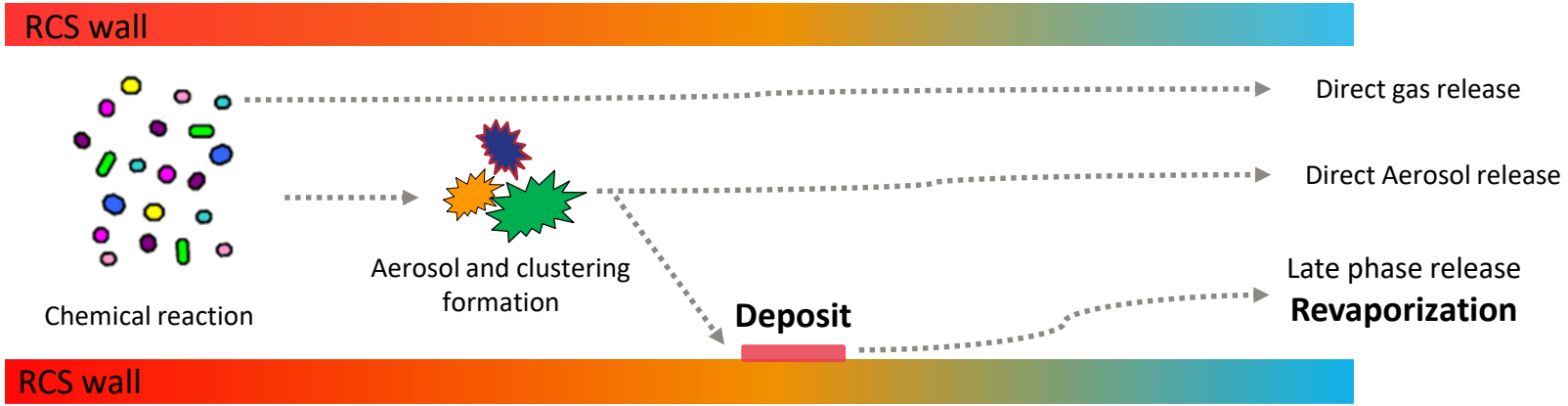

- Nature and surface state of the substrate
- Fission Products deposits
- Thermal-hydraulic conditions

Identify and quantify the revaporized species to define reaction pathway

Focus on cesium iodine (CsI) revaporization

CsI revaporization: recent literature data

CsI is the most probable iodine salt formed during a severe accident (Cs/I ~ 10 for a PWR)

VTT experimentation

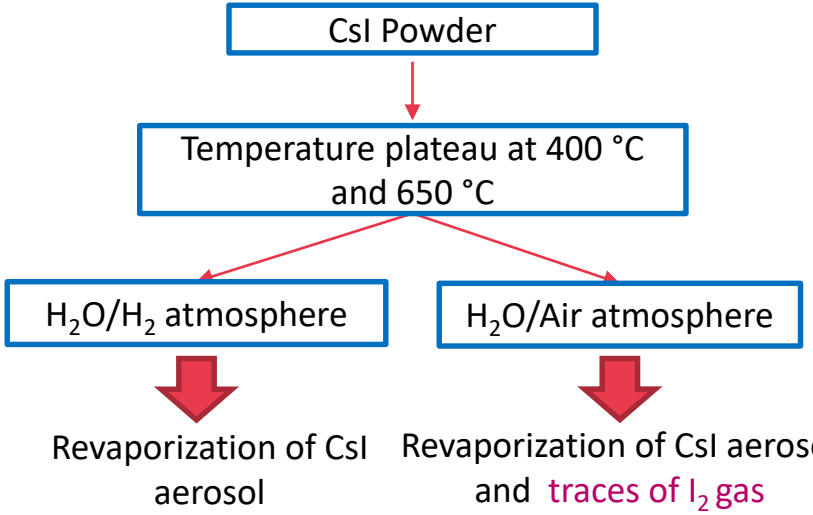

IRSN (MiRE project) experimentation

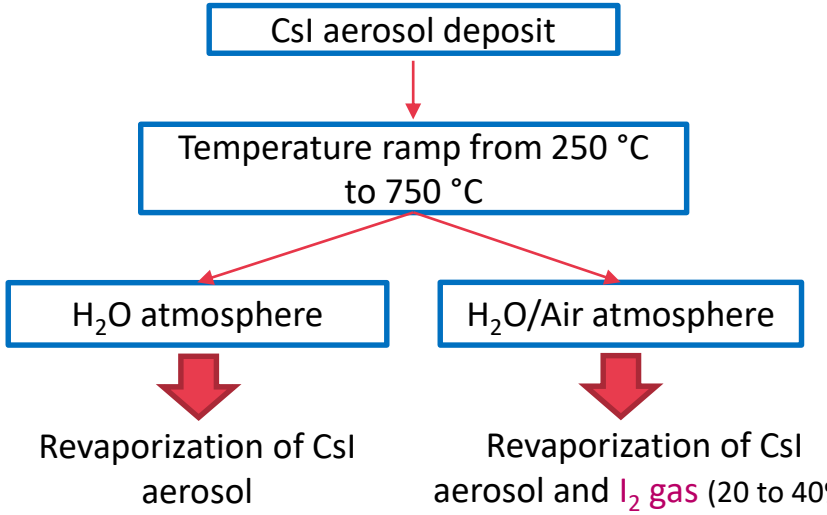

What are the key parameters of gaseous iodine formation?
Which are the main reaction pathway?

Gouëllo M. *et al.*, 2018 ; Obada D. *et al.*, 2020.

Methodology: ATMIRE experimental setup

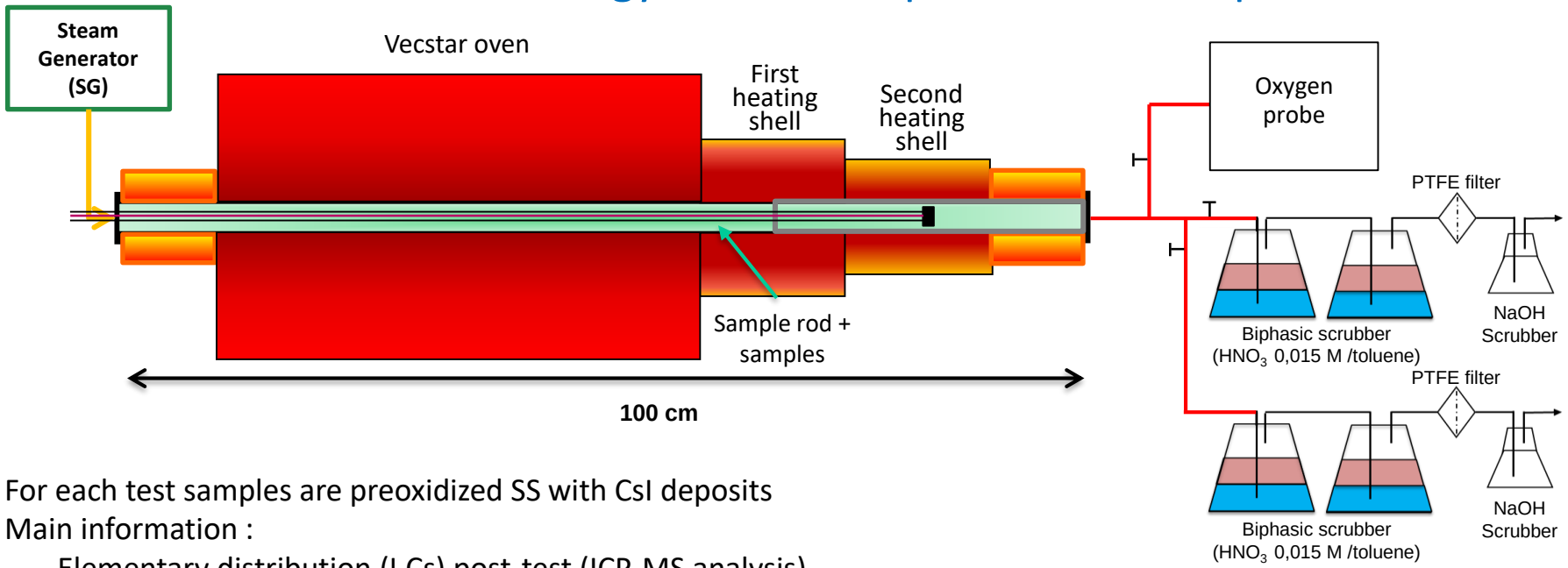

For each test samples are preoxidized SS with CsI deposits

Main information :

- Elementary distribution (I,Cs) post-test (ICP-MS analysis)
- Quantification of I_2 species (UV-Vis analysis of toluene)
- Nature of the residue (XPS and ToF-SIMS analysis)

ATMIRE: Atmosphere and Temperature monitored for Iodine Revaporization Experiments

Methodology: ATMIRE experimental setup

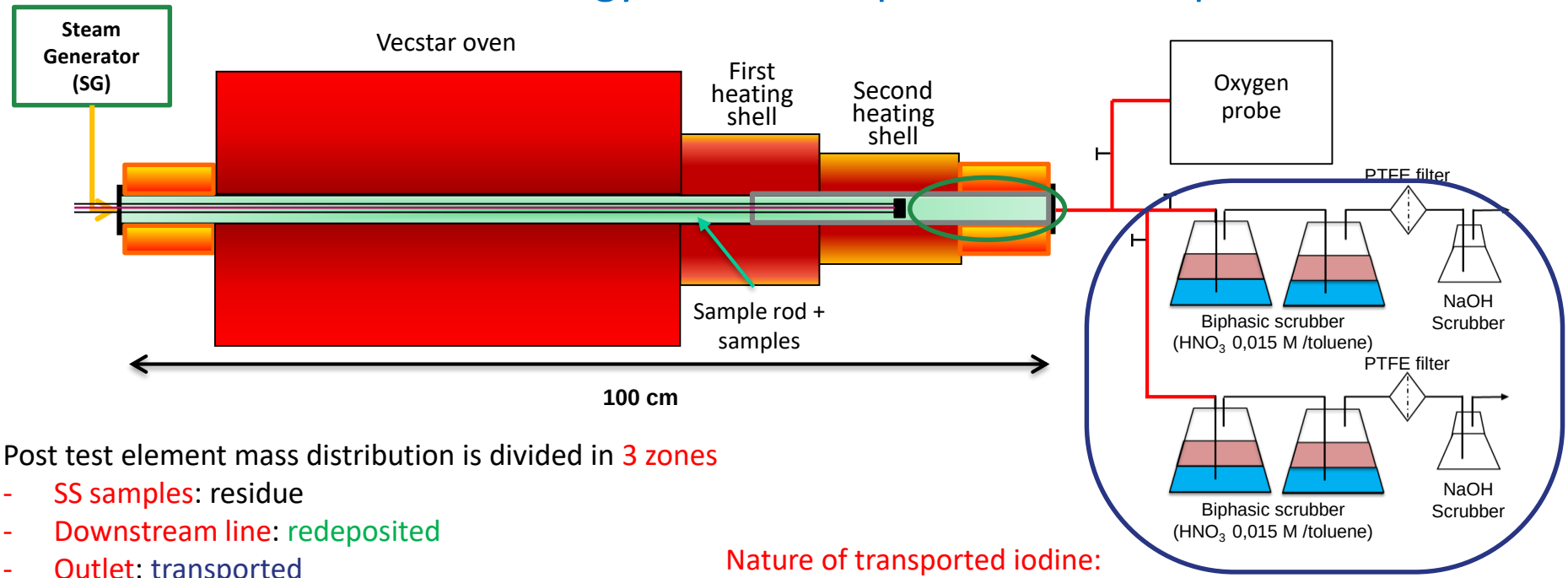

Post test element mass distribution is divided in 3 zones

- SS samples: residue
- Downstream line: redeposited
- Outlet: transported
- Σ redeposited + transported = revaporization

Nature of transported iodine:

- I in toluene phase → I_2
- If I/Cs > 1.25 → I in excess is considered as I_{gas}
- Other I is considered as CsI aerosol
- Σ I_2 + I_{gas} = gaseous iodine

ATMIRE: Atmosphere and Temperature monitored for Iodine Revaporization Experiments

Temperature influence

Experimental conditions:
Isotherm treatment between 200 and 550 °C
Test duration: from 3 to 6 h depending of the test
Atmosphere composition: 80% H_2O / 20% Air
Oxygen partial pressure: 0.04 atm

Iodine revaporization kinetics increases with T

Difference between Cs and I revaporization increases with T

Gaseous iodine proportion increases with T

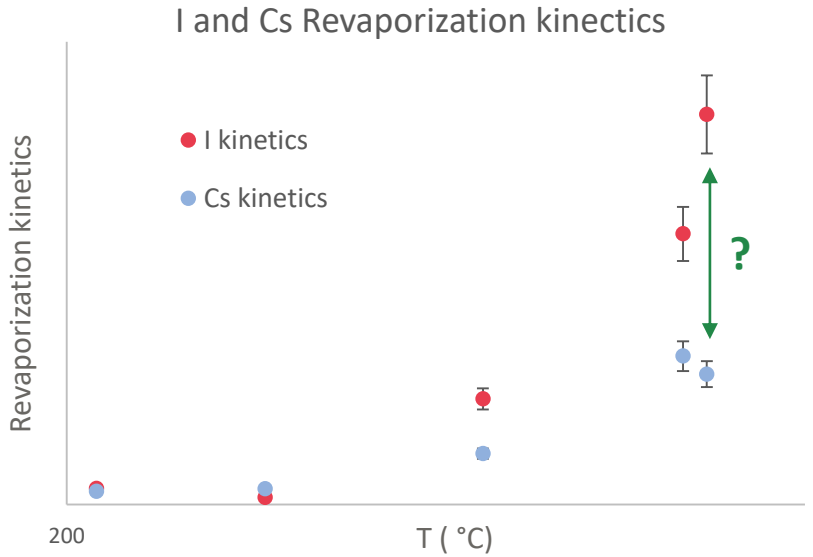

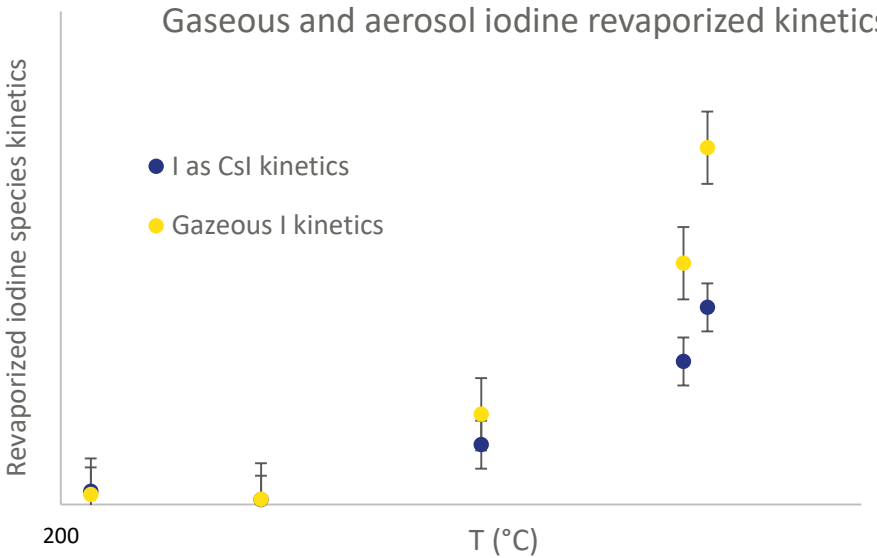

Surface analysis: Cs speciation in sample

XPS semi-quantification table

Elements	O as hydroxide (OH)	O as metal oxide (O^{2-})	Cs	Fe	Mn	Cr	Ni
Atomic percentage (%)	27.5	40.2	26.7	0.8	3.2	0.7	1.0

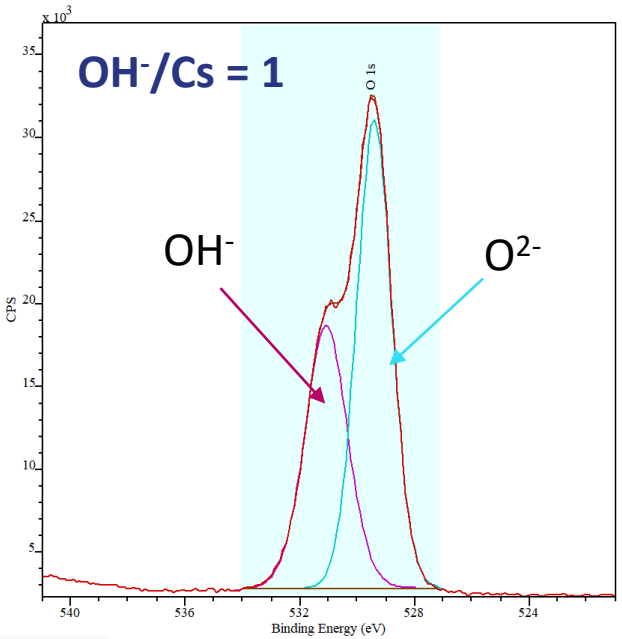

XPS spectrum
(O 1s binding energy)

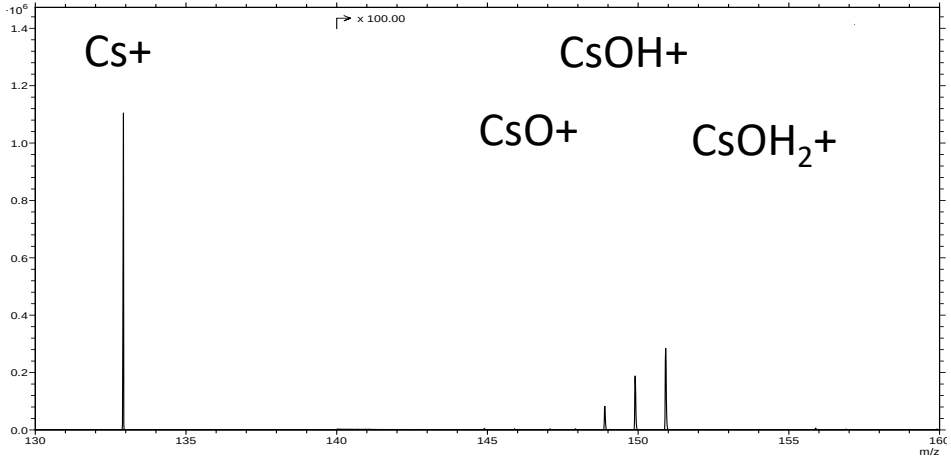

ToF-SIMS spectrum
(between 130 and 160 m/z ; Bi+ beam)

After revaporization, Cs residue seems to be CsOH species

Oxygen partial pressure influence

Experimental conditions:
Isotherm treatment between 500 and 520 °C
Test duration: 3 h
Atmosphere composition: 80% H_2O / 20% Air or Ar
Oxygen partial pressure: from 10^{-4} to 0.04 atm

Iodine revaporization kinetics and gaseous iodine proportion increase with oxygen partial pressure

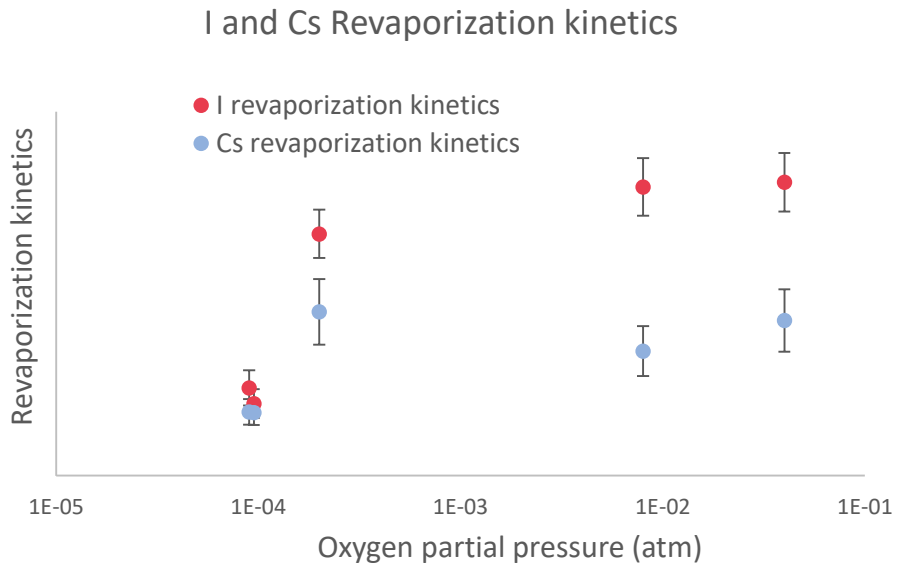

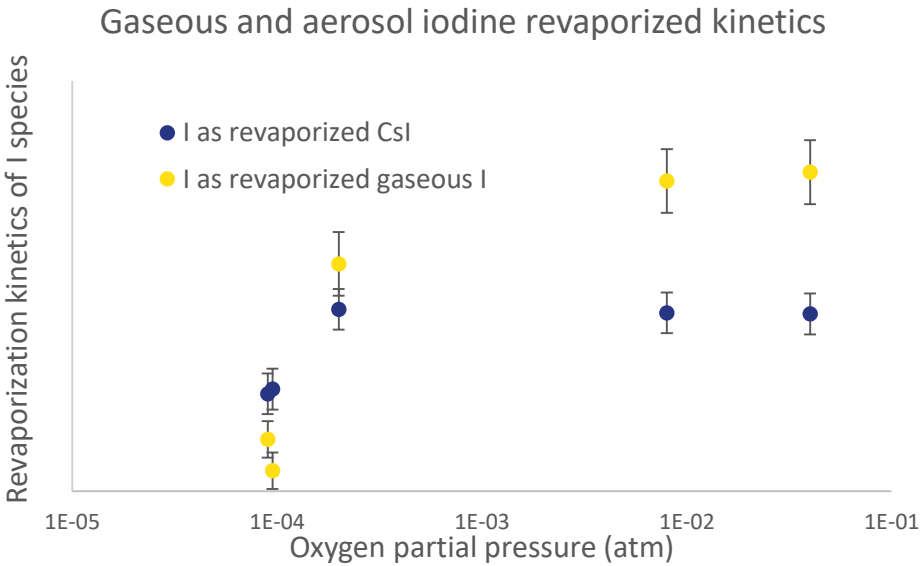

Experimental conclusions on CsI revaporisation

I revaporization kinetics ↗ when P_{O2} and T°↗

Gaseous I fraction ↗ when P_{O2} and T° ↗

Cs is under CsOH form on samples after thermal treatment

Global reaction possible according to experimental results

$$\mathbf{2\ CsI + \frac{1}{2} O_2 + H_2O \rightarrow 2\ CsOH + Gazeous\ I\ ?}$$

Which species of gaseous iodine is thermodynamically favored?

Thermochemistry analysis

Gibbs energy for possible reactions between CsI, O_2 and H_2O at 700K:

$$CsI_{(s)} + \frac{1}{4}O_{2_{(g)}} + \frac{1}{2}H_2O_{(g)} \leftrightarrow CsOH_{(s)} + \frac{1}{2}I_{2_{(g)}} \qquad \Delta_rG°_1 = +104 \text{ kJ.mol}^{-1}$$

$$CsI_{(s)} + H_2O_{(g)} + \frac{1}{2}O_{2_{(g)}} \leftrightarrow CsOH_{(s)} + HOI_{(g)} \qquad \Delta_rG°_2 = +127 \text{ kJ.mol}^{-1}$$

However, effect of dilution ($P_{H20} + P_{O2} >> P_{I\ gas}$) and reaction stochiometry:

$$P_{I_2} = (K_1 * (P_{H2O})^{0.5} * (P_{O2})^{0.25})^2 = 4.6\ 10^{-17} \text{ atm}$$

$$P_{HOI} = (K_2 * (P_{H2O}) * (P_{O2})^{0.5}) = 5.3\ 10^{-11} \text{ atm}$$

$P_{H20} + P_{O2} >> P_{I\ gas}$ lead to the formation of HOI instead of I_2

Conclusion on CsI revaporisation

The revaporization reaction leading to vaporization of gaseous iodine seems to be

$$\boldsymbol{CsI + \frac{1}{2}O_2 + H_2O \rightarrow CsOH + HOI}$$

in the condition of an atmosphere H_2O/air

Thus, the formation of gaseous iodine is linked to:

- the temperature
- the water partial pressure
- the oxygen partial pressure

Thank you for your attention

Acknowledgment to all the partner involved in the OECD/ESTER project
and the analytical platform team at the Chavreul institute

Development of an experimental test bench for dynamic adsorption of noble gases (Xe, Kr) by porous Metal-Organic Framework materials

Julie Nguyen-Sadassivame, Philippe Nérisson and Laurent Cantrel
Institut de Radioprotection et de Sûreté Nucléaire
BP 3, 13115 Saint-Paul-Lez-Durance Cedex
julie.nguyensadassivame@irsn.fr; philippe.nerisson@irsn.fr; laurent.cantrel@irsn.fr

Christophe Volkringer, Thierry Loiseau, Jérémy Dhainaut and Sébastien Royer
Univ. Lille, CNRS, Centrale Lille, Univ. Artois, UMR 8181 - UCCS - Unité de Catalyse et Chimie du Solide, F-59000 Lille, France
christophe.volkringer@centralelille.fr; thierry.loiseau@univ-lille.fr; jeremy.dhainaut@univ-lille.fr; sebastien.royer@univ-lille.fr

ABSTRACT

Xenon and krypton are noble gases produced from fission reactions in nuclear fuel. During accidental situations, their potential releases can lead to significant radioactive doses in the short and medium terms, particularly for on-site operators. These radioactive isotopes have various half-lives, from few days (5.3 days for ^{133}Xe, short term nuclear accident tracer) to several years (10.8 years for ^{85}Kr). Due to their low reactivity and very high volatility, these gases are difficult to trap (nuclear mitigation) and separate (industrial applications).
Until recently, the capture of these noble gases had never been thoroughly investigated because only complex and expensive methods or processes were accessible, making them difficult to implement in industry. However, since a decade, relatively new porous materials named Metal-Organic Frameworks (MOFs) have demonstrated efficient trapping capacities towards volatile compounds, notably the capture of gaseous fission products such as volatile iodine or ruthenium tetroxide, as well as trapping of CO_2. Indeed, these 3D hybrid metal-ligand materials, showing structural flexibility and variable pore diameters, can be functionalized in order to improve gases sorption.
The objective of this work is to study the feasibility of noble gases trapping by innovative porous materials such as MOFs in a nuclear context. This will contribute to better characterize the efficiency of filtration or purification devices (mitigation processes), to reduce radioactive releases under normal and accidental operations.
A first study has been carried out on a reference copper-based MOF called HKUST-1. Its efficiency for Xe and Kr sorptions, along with Xe/Kr selectivity, have been examined under static conditions as well as under dynamic conditions on the SAFARI homemade experimental bench at IRSN. This is an essential step before testing other promising materials less described in the literature. Thanks to SAFARI test bench, we can also analyze the effect of thermohydraulic conditions representative of accidental situations (flow velocity, temperature, humidity...) over the capture of noble gases. First results with HKUST-1 are presented.

KEYWORDS
Noble gases, Metal-Organic Frameworks, trapping, severe nuclear accident, experimental study

1. INTRODUCTION

Xenon and krypton are noble gases naturally present in the atmosphere at concentrations around 0.087 ppmV and 1.14 ppmV, respectively. They are produced industrially as by-products of the cryogenic distillation of air, (nitrogen-oxygen separation, widespread technique though very energy consuming). In industry, xenon and krypton have different uses such as lighting or insulation. These gases also find medical uses, for imaging and anesthesia. In addition, xenon is used as a probe for NMR (Nuclear Magnetic Resonance) or as a fuel for space propulsion (ion engine). The capture and separation of xenon and krypton is therefore an economic issue but also a nuclear safety issue. Indeed, radioactive isotopes such as ^{133}Xe and ^{85}Kr are produced by nuclear fission of uranium and have half-lives of 5.3 days and 10.8 years respectively. These gases are not toxic as such, but they contribute to an accumulation of significant radioactive doses in the environment following nuclear tests, spent nuclear fuel reprocessing, production of medical isotopes or during a hypothetic nuclear severe accident on a NPP (Nuclear Power Plant).
Noble gases chemical inertia and high volatility make them difficult to trap and separate. Their capture using porous materials such as activated carbons or zeolites is reported in literature [1-4]. Moreover, for the past ten years, a new class of hybrid materials called Metal-Organic Frameworks (MOFs) has demonstrated remarkable performance in gas capture, selectivity and storage [5]. It concerns notably CO_2 [6] and fission products such as volatile iodine [7-8] or ruthenium tetroxide [9]. MOFs are crystalline materials made up of organic ligands and metal clusters (hence hybrid). They offer advantages such as high porosity (up to 7000 m^2/g) [10], an infinity of possible structures and an unlimited functionalization by the choice of organic ligands or by doping with metallic particles. A judicious choice of the metal cluster (Al, Zr) can also make them resistant to radiations [11]. Different studies have been conducted for the capture of noble gases by MOFs under static and dynamic conditions (gas flow through MOF, less frequently studied) [12-13]. However, very few studies have been carried out under conditions representative of a nuclear accident: flow velocity through material, temperature, humidity, gas mixture, etc… Such data would be critical in the long term, notably to contribute to improve Filtered Containment Venting Systems (FCVS) [14] implemented on NPPs for mitigation of airborne releases, or equivalent devices in reprocessing plants.
To contribute to this latter point, after a state of the art in static and dynamic conditions, this paper presents the development of an experimental test bench allowing the dynamic study of noble gases adsorption (Xe, Kr) by MOFs and selectivity, under nuclear accident conditions listed above. This device named SAFARI, initially used for volatile iodine and RuO_4(g) capture [15-16], is adapted for the study of noble gases capture, notably with the development of an online analysis method for noble gases by gas chromatography coupled with a mass spectrometer. In this work, the reference copper-based material HKUST-1 was synthesized. This MOF compound has two different pore sizes (5 Å and 15 Å) offering opened and polarizing metal sites, favorable for Xe and Kr adsorptions [17]. Its trapping capacities for noble gases in dynamic conditions will be compared to those obtained in static conditions in a previous step of this work. This experimental campaign with reference material will permit to validate SAFARI for noble gas studies, in order later on to test other promising MOF materials less described in the literature.

2. STATE OF THE ART ON NOBLE GAS TRAPPING

2.1. Static studies

Numerous studies discuss the adsorption of noble gases in porous materials such as MOFs [13] [18]. These studies are carried out under so-called static conditions, using a gas adsorption analyzer. This consists in inserting pure gas (Xe or Kr) into the material at fixed temperature; then gas-phase pressure variation is measured as a function of the adsorbed gas volume. Literature has highlighted the main parameters for optimizing the adsorption of noble gases in porous materials:

- Temperature: as it increases, the adsorption capacities are reduced due to the fact that gases become more volatile [19], thus limiting solid-gas interactions;

- Pressure: the adsorption capacities strongly increase with pressure. It is notably highlighted by Mueller *et al.* [20] for noble gases adsorption in MOF-5 at high pressure;
- Specific surface area: the general trend in the literature shows that the maximum adsorption capacities of noble gases are obtained for materials with high specific surface area (SSA), generally greater than 1000 m²/g. For example, xenon adsorption record is 7.1 mmol/g in PCN-14 (SSA = 2138 m²/g) and 1.4 mmol/g for krypton in NOTT-100 (1619 m²/g) at ambient temperature and pressure [21];
- Pore size: this important parameter can influence the selective adsorption of Xe/Kr. Selectivity S under static conditions is defined such as:

$$S_{Xe/Kr} = \frac{k_{H(Xe)}}{k_{H(Kr)}} \quad (1)$$

$$q = k_H P \; and \; k_H = B q_m \quad (2)$$

With q the adsorbed amount (cm^3/g), P the pressure (bar), k_H the Henry constant ($cm^3/g/bar$), B the Langmuir constant (bar^{-1}) and q_m the monolayer or saturated amount adsorbed (cm^3/g).
Indeed, when this size is close to the kinetic diameter of Xe atom (4.10 Å), interactions are favored between the gas and the framework or the unsaturated material sites. Therefore, this makes it possible to create an induced dipole between the electronic cloud of the gas and the MOF. The kinetic diameters of the other gases (N_2, O_2, CO_2, etc.) being smaller, they interact less with the material. On the other hand, MOFs belonging to this category do not have high adsorption capacities due to their low specific surface (generally less than 500 m²/g) [12]. Material SBMOF-1 is a good example since it holds the record of 16 for Xe/Kr selectivity, at 298 K and 1 bar [22]. Indeed, this solid has no unsaturated sites or high porosity (145 m²/g) but it presents pore sizes (4.5 Å) very close to the kinetic diameter of Xe atom;
- Functionalization of the ligand by specific groups: Lee *et al.* [23] presented the adsorption of Xe and Kr in functionalized UiO-66-X (with X = $-NH_2$, $-(OMe)_2$, $-NH_2(OMe)_2$ and $-F_4$) at 283 K and 1 bar. Xe adsorption capacity obtained in UiO-66-NH_2 (SSA = 1274 m²/g) is 2.3 mmol/g, greater than the original UiO-66 (1.3 mmol/g) while its specific surface is higher (1706 m²/g). This functionalization of the ligand also has an impact on Xe/Kr selectivity [23] since it modifies functional groups electron density: $-NH_2(OMe)_2$ (14.4) > $-NH_2$ (11.4) > $-(OMe)_2$ (9.5) > $-F_4$ (7.4). The adsorption mechanisms involved are the Van der Waals forces because noble gases are uncharged and non-polar while they remain polarizable (Xe more than Kr). This is also shown by Meek *et al.* [24] on the adsorption of Xe and Kr at ambient temperature and pressure on halogenated IRMOF-2 [Zn_4O(2-X-1,4—BDC)$_3$] with X = F, Cl, Br or I. Thus, Xe/Kr selectivity increases with halogen size and so its polarizability: -I (4.17) > -Br (3.9) > Cl (3.7) > F (3.4). Perry *et al.* [21] studied noble gases adsorption in MOF-74-M (M = Co, Mg, Ni or Zn), containing open metal sites. They showed that adsorption and interaction energies increase with the polarizability of the gas. MOF-74-Co achieved the best selectivity (10.4), but no clear trend was defined between interaction energies and the nature of the open metal sites. On the other hand, this type of material obtained overall better performance due to the charge density of the unsaturated sites and its cylindrical and uniform structure (pore size of 11 Å).

2.2. Dynamic studies

As mentioned before, these works are much less conducted than static studies [12]. Dynamic breakthrough experiments allow concluding on the real potential of adsorbents. Breakthrough experiments involve a gas-mixture flow at different concentrations through a material, under fixed conditions of temperature and pressure (around 298 K and 1 bar for all reported studies). For a porous material, dynamic studies generally lead to adsorption capacities lower than under static conditions. Parameters influencing static adsorption,

mentioned in section 2.1, also have an impact on the breakthrough time (*i.e.* time when the target gas is detected downstream the material, at the outlet of the device).
Liu *et al.* [25] carried out dynamic breakthrough experiments on HKUST-1 and MOF-74-Ni materials. These materials were selected for their open metal sites, favorable to noble gases adsorption, and also for their different structures and pore sizes. A gas-mixture flow containing 1000 ppmV Xe or 1000 ppmV Kr in air was flowed through the material. The breakthrough times were around 8 min with xenon through the 2 solids, while krypton was detected downstream the MOF almost immediately after injection. Besides, Xe adsorption capacity was slightly higher in MOF-74-Ni (9.3 mmol/kg) than in HKUST-1 (8.5 mmol/kg), due to the stronger interaction between open metal sites of MOF-74-Ni and Xe. Conversely, Kr adsorption was slightly higher in HKUST-1 (2.0 mmol/kg) than in MOF-74-Ni (1.8 mmol/kg), owing to its bimodal pore sizes. In addition, this study showed that the gas-mixture concentration influences Xe/Kr selectivity, regardless of the material. Indeed, with a 80/20 (V/V) Xe/Kr gas-mixture, the relating Xe/Kr selectivity was lower than with a 20/80 (V/V) Xe/Kr gas mixture Xe/Kr. Selectivity S under dynamic condition is defined such as:

$$S_{Xe/Kr} = \frac{x_{Xe}/y_{Xe}}{x_{Kr}/y_{Kr}} \quad (3)$$

With x_i the adsorbed mole fractions and y_i the mole fractions in the upstream bulk gas for each species i.
Material SBMOF-1 [22], mentioned previously, achieved a record breakthrough time of 55 min for Xe and 8 min for Kr, with a 400 ppmV/40 ppmV Xe/Kr gas-mixture in air. Moreover, this solid presented an exceptional Xe adsorption capacity of 13.2 mmol/kg. In addition, its low porosity and the absence of unsaturated sites give it great stability even in the presence of water. Finally, the breakthrough time can be increased by the doping of MOF structures with metallic particles, as conducted by Wang *et al.* [26] on MOF-303 which was silver-doped. Despite a reduced specific surface of MOF-303@Ag (716 m^2/g) compared to the initial MOF-303 (1343 m^2/g), the breakthrough time of Xe (20/80 (V/V) Xe/Kr gas mixture, room temperature and pressure) was increased by 25 min/cm^3, thanks to the silver doping. Indeed, its pore size becomes close to the kinetic diameter of Xe atom, which favors Xe retention as mentioned in section 2.1.
All these dynamic breakthrough experiments were conducted at ambient temperature and pressure, which is not representative of a nuclear accident. In contrast, herein, the objective is to be able to evaluate the effect of severe thermohydraulic conditions over the capture of Xe and Kr by MOF materials.

3. MATERIAL AND METHODS

As mentioned above, copper-based MOF HKUST-1 has been chosen for this first step of noble gases trapping study, given it is a reference material, which synthesis in large-scale quantities is mastered and well referenced. Besides, previous studies exist in the literature for standard conditions (Liu *et al*., cf. section 2.2), to compare the results.

3.1. Synthesis of HKUST-1 material

The HKUST-1 large-scale synthesis conducted in the present study was derived from the protocol proposed by Giovine *et al.* [27]. 238,56 g (1,03 mol) of $Cu(NO_3)_2.2.5H_2O$ and 143,14 g (0.68 mol) of trimesic acid were dissolved in 5 L of 50/50 (V/V) water/ethanol liquid mixture, inside a 8 L autoclave (Figure 1). The solution was heated at 110 °C during 23 h under stirring. The obtained suspension was thereafter centrifuged 3 times with ethanol à 60 °C, to recover blue crystals. These latter were dried at 70 °C during 12 h, prior to be activated at 110 °C during 12 h under vacuum then kept in glove box. The activated material was dark blue/purple, attesting that the material was effectively dried.



Figure 1. Picture of the 8 L autoclave used for the synthesis of HKUST-1 in which the solution is stirred and thermostated.

3.2. Characterization of HKUST-1 material

Powder X-ray diffraction diagram has been registered at ambient temperature using a diffractometer Bruker D8 Advance A25. N_2 adsorption-desorption isotherm at 77 K until 1 bar has been measured with a Micromeritics ASAP 2020 porosimeter. BET specific surface is calculated on the range $0.015 \leq P/P_0 \leq 0.30$. Before each measurement, the material is heated under a primary vacuum (5 Pa) at 110 °C during 12 h. Figure 2 presents both PXRD diagram and N_2 adsorption-desorption isotherm obtained for as-synthetized HKUST-1.

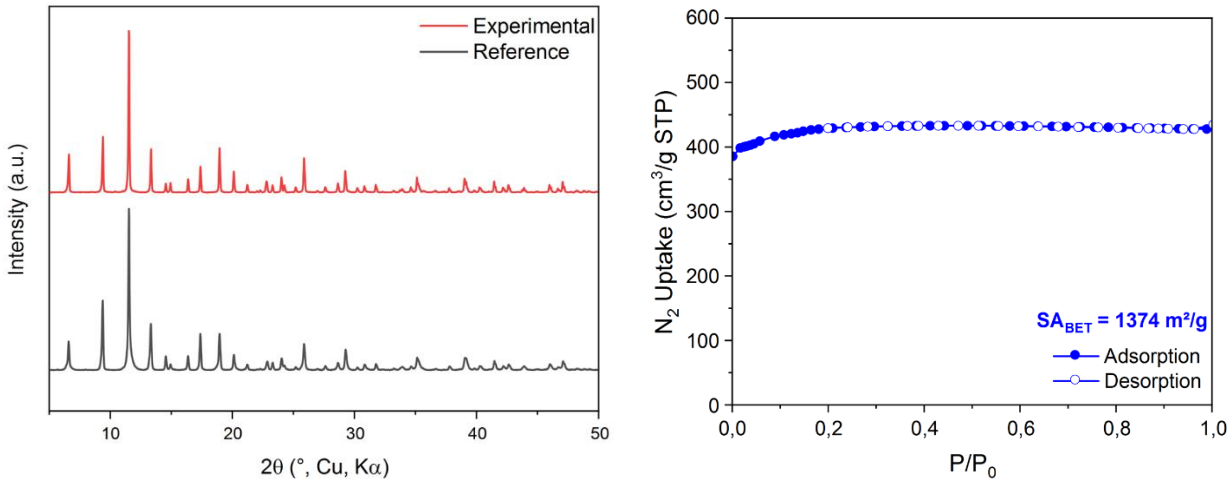

Figure 2. Left: PXRD patterns of activated HKUST-1 (top) and reference (bottom); Right: N_2 adsorption-desorption isotherm, related to a BET specific surface area value of 1374 $m^2.g^{-1}$.

3.3. Noble gases (Kr, Xe) analysis

Noble gases analysis is performed continuously online by gas chromatography coupled to a mass spectrometer (GC-MS). Gas chromatography module (Agilent 7820A, injection split/spliless) is made up of a pre-column (Agilent J&B PoraBond Q with two particle traps) of sizes 3 µm×0.25 mm×25 m. This permits heavy gases to be evacuated through a 6-way valve and allows light gases to reach the second column with molecular sieve (Agilent J&W CP-Molsieve 5 Å) of sizes 30 µm×25 µm×25 m. Isotherm analysis is done at 130 °C, with a carrier gas flowrate (helium) of 1 mL/min in the first column and 5 mL/min in the second column. The sampling loop volume, driven by a 6-way valve, is 1 mL and the split ratio is 150:1. The sampling loop is continuously swept by the SAFARI bench outlet gas flow. The 6-way valve is then programmed to inject the volume of the loop into the separation columns using the carrier gas. The uncertainty of the measurement is 10 %.
The mass spectrometry module (Agilent 5977B GC/MSD) allows ionization of the sample by electron impact (EI) at 230 °C and mass analysis by a quadrupole at 150 °C.
Commercial gas cylinders titrated at 1000 ppmV and 100 ppmV in Xe and Kr separately are diluted on a dedicated dilution bench, to obtain standard samples for apparatus calibration. High purity helium (99.99%) is used as carrier gas.

3.4. Experimental test bench SAFARI

Dynamic breakthrough experiments are carried out on the SAFARI test bench (Figure 3), at IRSN (Institute for Radioprotection and Nuclear Safety, Cadarache, France). This experimental device allows the injection of xenon and/or krypton diluted in air through a bed of adsorbent material. The flow downstream the adsorbent bed is analyzed online by GC-MS (see section 3.3). Before each gas adsorption experiment, the material is activated at 110 °C for 1 hour. Then, the cylindrical glass column (diameter 2 cm) containing a 1 cm height bed of dried adsorbent (1.8 g of HKUST-1) on a sintered filter, is placed in SAFARI test bench, as shown on Figure 3. Heating cords and heat insulators are placed around the column, as well as a thermocouple to regulate the temperature. Before and after each xenon and/or krypton breakthrough experiment, the line is swept with dry air at 1 cm/s. This procedure is applied for each test. Steam can also be added to the gas stream at a desired flowrate, to reach the target relative humidity. In dynamic experiments, xenon (or krypton) diluted in air at 500 ppmV or 400/40 ppmV Xe/Kr gas mixture, are injected at a rate corresponding to 1 cm/s in the glass column through the material. Gases are injected from the top of the column and a glass bubbler is placed at the outlet to condense the water vapors (for tests involving steam) before injection into the GC-MS. Improving the online GC-MS analysis for Xe and Kr is part of this work: the GC-MS outflow gas sampler is programmed to inject a known volume into the separation columns, at periodic intervals. This permits to obtain a more regular sampling (every 3 min) and a curve with more points.

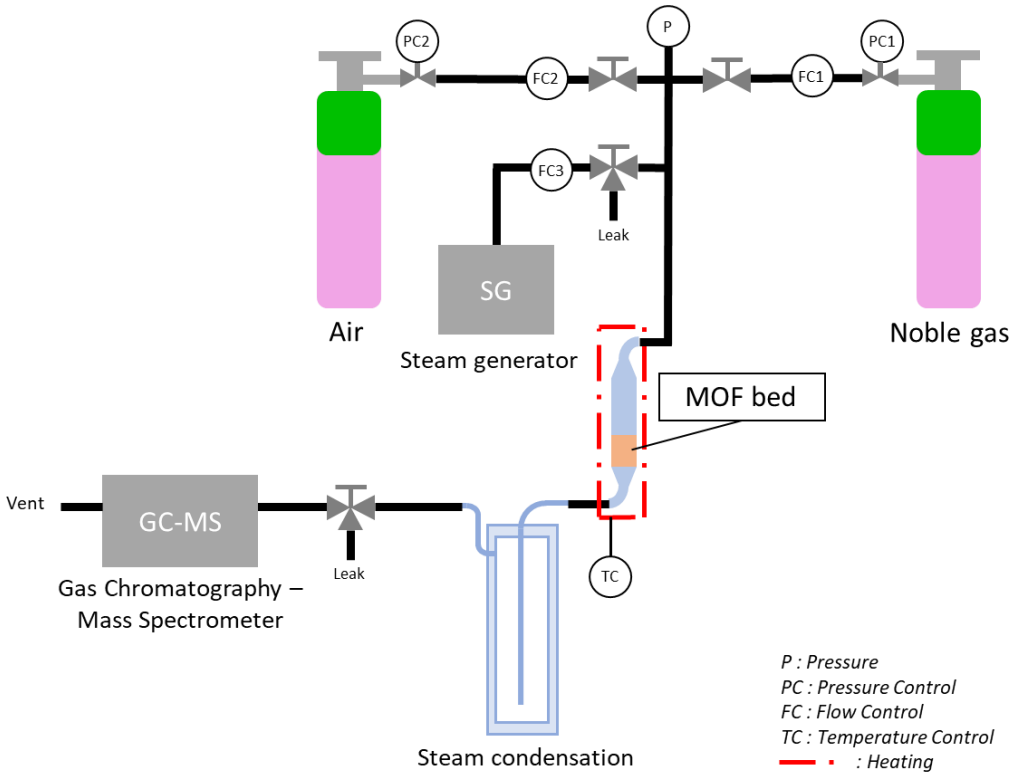

Figure 3. Experimental test bench SAFARI for dynamic adsorption of noble gases into a MOF sample.

4. RESULTS AND DISCUSSION

The first dynamic experiments series performed on SAFARI bench for noble gases adsorption in HKUST-1 have permitted to investigate:

- Selectivity of Xe/Kr adsorption in HKUST-1 at ambient temperature;
- Influence of temperature on noble gases adsorption;
- Influence of humidity on noble gases adsorption;
- Comparison with results obtained in static conditions.

These points are detailed below.

4.1. Selectivity of Xe/Kr adsorption in HKUST-1 at ambient temperature

Figure 4 below presents the monitoring of Xe and Kr concentrations, measured with GC-MS downstream the MOF HKUST-1 bed as a function of the experiment time. The test is performed at ambient temperature with a dry airflow such as [Xe] = 400 ppmv and [Kr] = 40 ppmv upstream the MOF. The dash curves correspond to the experiment without material (blank test) and the line curves are the breakthrough test with MOF HKUST-1.

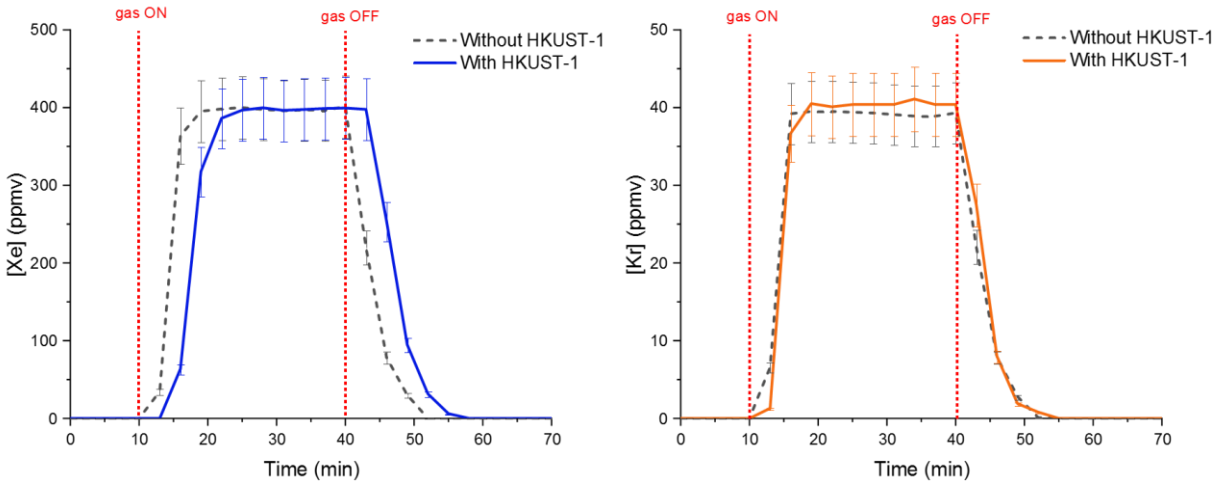

Figure 4. Xe (left) and Kr (right) breakthrough curves in HKUST-1 material on SAFARI test bench. $[Xe]_{upstream}$ = 400 ppmV, $[Kr]_{upstream}$ = 40 ppmV, 22 °C, 1 bar. Velocity: 1 cm/s.

According to breakthrough curves on Figure 4:

- Breakthrough time (*i.e.* time when the signal attesting noble gas presence is detected downstream the HKUST-1, compared to this time in blank test, taking into account injection and timeout due to GC-MS measurement) is around 5 min for Xe and 0 min for Kr;
- Trapping capacities are estimated at 5.68 $mmol_{Xe}/kg_{MOF}$ and 0.064 $mmol_{Kr}/kg_{MOF}$ (integration method, equation 4).

$$q = \frac{Q_v \int_0^{t_s} (C_{blank} - C) dt}{V_m W} \quad (4)$$

With q the adsorbed amount of the gas (mol/g), Q_v the injected gas flow rate (cm^3/min) in the Standard Temperature and Pression (STP), t_s the time of bed saturation (min), C_{blank} and C the Xe or Kr concentrations in the flow respectively for blank test and test with MOF (ppmV), V_m the molar volume (m^3/mol) in the STP and W the mass of the activated adsorbent material (g).

These results confirm the selectivity of Xe over Kr in HKUST-1, noted $S_{Xe/Kr}$, (cf. equation 3 in section 2.2). Indeed, with trapping capacities determined above, $S_{Xe/Kr}$ = 8.9 in HKUST-1. This selectivity can be associated to gas atomic diameters compared to pore sizes. This value is higher than data provided by Liu *et al.* [25], where $S_{Xe/Kr}$ = 4.3 is obtained experimentally using HKUST-1. This gap can be explained by differences in experimental conditions, especially upstream concentrations ([Xe] = [Kr] = 1000 ppmV for Liu et *al.*), gas velocity through the MOF and MOF properties such as shaping. Liu *et al.* also mention a selectivity of 2.6 obtained with Xe/Kr mixture of pure gases (volume ratio 20:80), and the corresponding value predicted with GCMC simulation by Ryan *et al.* [28], where $S_{Xe/Kr}$ was determined to be of 8.1 in HKUST-1 (higher than experimental results of Liu *et al.*). These values confirm the strong dependence of selectivity on the operating parameters, even if the order of magnitude remains the same.

4.2. Influence of temperature

Figure 5 presents the breakthrough curves obtained for Xe and Kr in HKUST-1 at 50 °C in dry air.

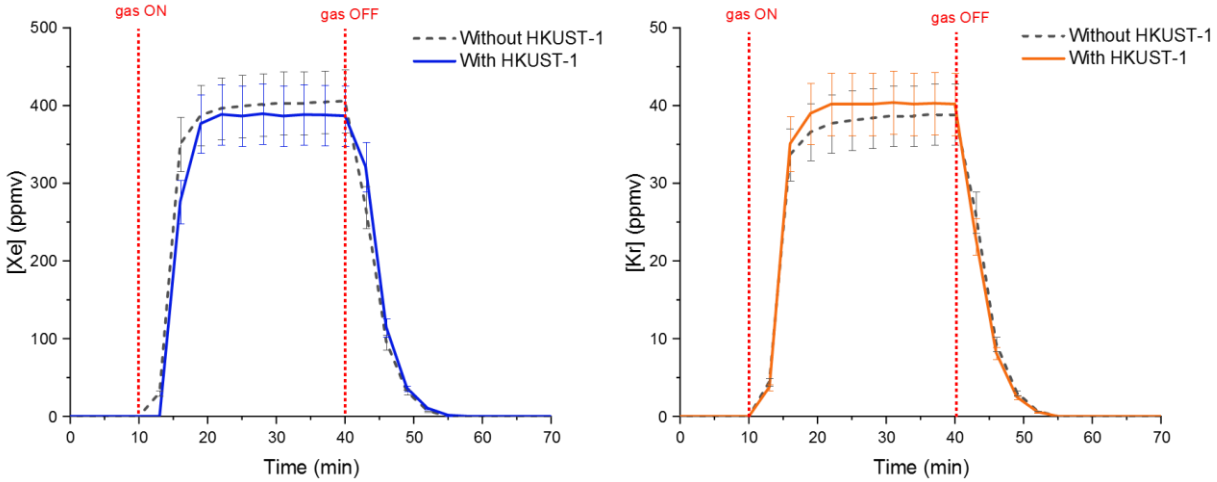

Figure 5. Xe and Kr breakthrough curve in HKUST-1 material on SAFARI test bench. Influence of temperature. $[Xe]_{upstream}$ = 400 ppmV, $[Kr]_{upstream}$ = 40 ppmV, 50 °C, 1 bar. Velocity: 1 cm/s.

The breakthrough curves on Figure 5, compared to curves presented on Figure 4, show that breakthrough time of Xe in HKUST-1 decreases from 5 min to 3 min when temperature increases (0 min for Kr in both cases). It highlights that adsorption capacities of Xe decreases with temperature as expected. This can be explained by the increase in volatility of gases with temperature.

4.3. Influence of humidity

Figure 6 presents the breakthrough curves obtained for Xe and Kr in HKUST-1 at 50 °C, for a relative humidity RH = 30%. It corresponds to a steam flowrate of 0.28 $g.h^{-1}$.

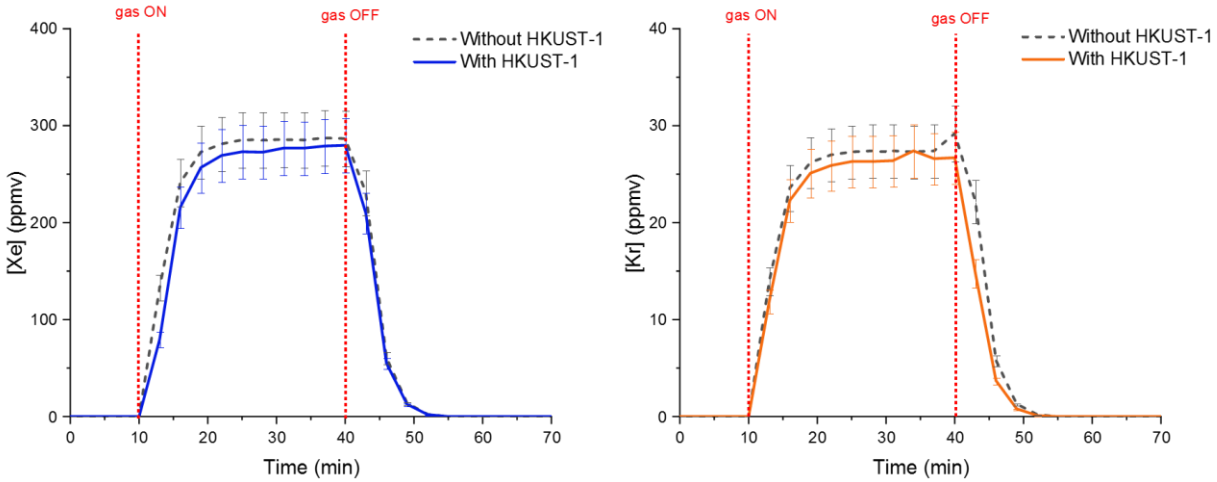

Figure 6: Xe and Kr breakthrough curve in HKUST-1 material on SAFARI test bench. Influence of humidity. $[Xe]_{upstream}$ = 300 ppmV, $[Kr]_{upstream}$ = 30 ppmV, 30% RH, 50 °C, 1 bar. Velocity: 1 cm/s.

The breakthrough curves on Figure 6, compared to curves presented on Figure 5, show breakthrough time of Xe in HKUST-1 decreases to zero min when RH increases (0 min for Kr in both cases).It highlights that

adsorption capacities of Xe decrease when RH increases. This can be explained by the competition between Xe and water molecules to fill the pores.

4.4. Comparison to static tests

As mentioned in the introduction, HKUST-1 trapping capacities for noble gas have been tested in static conditions in a first step of this work. More precisely, adsorption isotherms of Xe and Kr in HKUST-1 have been established (Figure 7), thanks to the same apparatus as that used for BET specific surfaces measurements (see section 3.2), with pure Xe or Kr gas instead of N_2. These curves allow to determine Xe and Kr adsorption capacities CS and selectivity $S_{Xe/Kr}$ in HKUST-1 in static conditions. Some of them are, reported in Table 1, to compare with dynamic conditions.

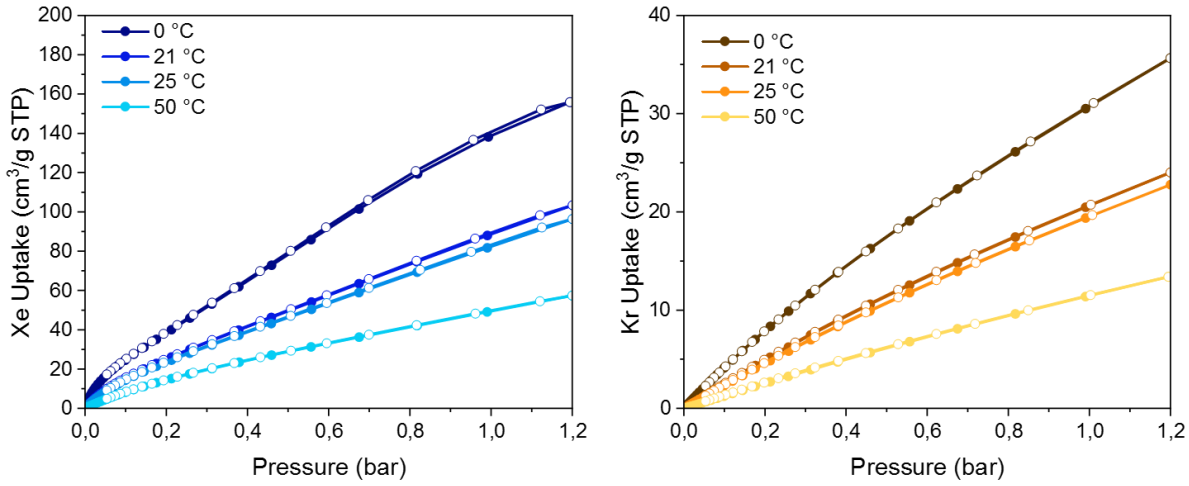

Figure 7 : Adsorption isotherm of Xe (left) and Kr (right) under static conditions in the temperature range of 0 to 50 °C.

Table 1: Comparison of Xe and Kr adsorption capacities (CS) and selectivity in HKUST-1 in dry gas, in static and dynamic conditions (1 bar). Influence of temperature.

Température (°C)	***CS_{Xe} (mmol/g)*** *static*	***CS_{Xe} (mmol/kg)*** *dynamic*	***CS_{Kr} (mmol/g)*** *static*	***CS_{Kr} (mmol/kg)*** *dynamic*	***$S_{Xe/Kr}$*** *Static Equation 1*	***$S_{Xe/Kr}$*** *Dynamic Equation 3*
22	3.64	5.68	0.84	0.064	9.7	8.9
50	1.83	1.94	0.43	0.00	9.1	-

Results listed in Table 1 show the same trend linked to temperature increase between static and dynamic tests, namely that adsorption capacities decrease while temperature increases. It also highlights the most important quantities of noble gases adsorbed in static conditions. It is logically explained using pure gases under pressure for static experiments, compared to diluted flows used in dynamic studies.

5. CONCLUSIONS

This work aims to determine the feasibility of trapping noble gases using a new class of so-called "hybrid" materials named Metal-Organic Frameworks (MOFs). Literature review made it possible to highlight the

main parameters influencing the adsorption capacities of noble gases into MOFs, as well as their Xe/Kr trapping selectivity. Up to now, very few studies reported adsorption studies under dynamic conditions, representative of a hypothetical accidental scenario impacting nuclear plants (noble gases concentrations, temperature, humidity, etc.).

So, objectives of this work were to identify and characterize a reference MOF, and to evaluate its noble gas adsorption capacities under dynamic conditions. For this latter point, described in this paper, a method has been developed and improved on SAFARI test bench. Thereby, the reference MOF called HKUST-1 has been synthetized and characterized. The Xe and Kr adsorption study performed with HKUST-1 provides very encouraging results, allowing the test bench validation. Indeed, Xe retention inside the MOF and selectivity of Xe over Kr are confirmed, in accordance with literature results. Besides, influences of temperature and humidity have been investigated to reach more representative conditions of the nuclear severe accidents context. Thus, the increase in temperature or RH lead to a decrease in the adsorption of noble gases. In line, additional experimental tests are in progress, dealing with more severe conditions (up to 150 °C, higher RH, higher velocity through the MOF).

The next step of this work is to perform static tests with new MOFs, to select potential promising compounds for noble gas trapping. It concerns notably MOFs such as MIL-100 or MOF-303, given their suitable synthesis processes, pore sizes and Ag-doping possibilities. The most efficient MOFs in these conditions will be tested later in dynamic and representative conditions (T, RH,…) on SAFARI test bench. Results obtained with HKUST-1 will be presented at ERMSAR 2022.

ACKNOWLEDGMENTS

This work was performed in the French Institut de Radioprotection et de Sûreté Nucléaire (IRSN) and Unité de Catalyse et Chimie du Solide (UCCS, Lille), with the financial support of NUVIA Company.

REFERENCES

1. R. E. Bazan, M. Bastos-Neto, A. Moeller, F. Dreisbach, R. Staudt, Adsorption equilibria of O2, Ar, Kr and Xe on activated carbon and zeolites: single component and mixture data. *Adsorption*. **17**, 371–383 (2011).
2. K. Munakata, S. Kanjo, S. Yamatsuki, A. Koga, D. Ianovski, Adsorption of noble gases on silver-mordenite. *Journal of Nuclear Science and Technology*. **40**, 695–697 (2003).
3. D. Ianovski *et al.*, Adsorption of Noble Gases on H-Mordenite. *Journal of Nuclear Science and Technology*. **39**, 1213–1218 (2002).
4. D. W. Underhill, The adsorption of argon, krypton and xenon on activated charcoal. *Health Phys.* **71**, 160–166 (1996).
5. S. Ma, H.-C. Zhou, Gas storage in porous metal–organic frameworks for clean energy applications. *Chemical Communications*. **46**, 44–53 (2010).
6. J. Liu, J. Tian, P. K. Thallapally, B. P. McGrail, Selective CO2 Capture from Flue Gas Using Metal–Organic Frameworks—A Fixed Bed Study. *J. Phys. Chem. C*. **116**, 9575–9581 (2012).
7. M. Leloire *et al.*, Stability and radioactive gaseous iodine-131 retention capacity of binderless UiO-66-NH2 granules under severe nuclear accidental conditions. *Journal of Hazardous Materials*. **416**, 125890 (2021).
8. M. Chebbi, B. Azambre, C. Monsanglant-Louvet, B. Marcillaud, A. Roynette, L. Cantrel, Effects of water vapour and temperature on the retention of radiotoxic CH3I by silver faujasite zeolites. *Journal of Hazardous Materials*. **409**, 124947 (2021).
9. S. Chibani, M. Badawi, T. Loiseau, C. Volkringer, L. Cantrel, J.-F. Paul, A DFT study of RuO_4 interactions with porous materials: metal–organic frameworks (MOFs) and zeolites. *Phys. Chem. Chem. Phys.* **20**, 16770–16776 (2018).

10. I. M. Hönicke, I. Senkovska, V. Bon, I. A. Baburin, N. Bönisch, S. Raschke, J. D. Evans, S. Kaskel, Balancing mechanical stability and ultrahigh porosity in crystalline framework materials. *Angewandte Chemie International Edition*. **57**, 13780–13783 (2018).
11. C. Volkringer *et al.*, Stability of metal–organic frameworks under gamma irradiation. *Chem. Commun.* **52**, 12502–12505 (2016).
12. D. Banerjee, C. M. Simon, S. K. Elsaidi, M. Haranczyk, P. K. Thallapally, Xenon Gas Separation and Storage Using Metal-Organic Frameworks. *Chem.* **4**, 466–494 (2018).
13. K. Jin, B. Lee, J. Park, Metal-organic frameworks as a versatile platform for radionuclide management. *Coordination Chemistry Reviews*. **427**, 213473 (2020).
14. D. Jacquemain *et al.*, "OECD/NEA/CSNI status report on filtered containment venting" (Organisation for Economic Co-Operation and Development, 2014).
15. P. Nerisson, H. Hu, J. F. Paul, L. Cantrel, C. Vesin, Filtration tests of gaseous ruthenium tetroxide by sand bed and metallic filters. *J Radioanal Nucl Chem*. **321**, 591–598 (2019).
16. M. Leloire, thesis, Université de Lille (2021).
17. B. J. Sikora, C. E. Wilmer, M. L. Greenfield, R. Q. Snurr, Thermodynamic analysis of Xe/Kr selectivity in over 137000 hypothetical metal–organic frameworks. *Chemical Science*. **3**, 2217–2223 (2012).
18. A. Abramova, N. Couzon, M. Leloire, P. Nerisson, L. Cantrel, S. Royer, T. Loiseau, C. Volkringer, J. Dhainaut, Extrusion-Spheronization of UiO-66 and UiO-66_NH2 into Robust-Shaped Solids and Their Use for Gaseous Molecular Iodine, Xenon, and Krypton Adsorption. *ACS Applied Materials & Interfaces* (2022).
19. A. Soleimani Dorcheh, D. Denysenko, D. Volkmer, W. Donner, M. Hirscher, Noble gases and microporous frameworks; from interaction to application. *Microporous and Mesoporous Materials*. **162**, 64–68 (2012).
20. U. Mueller, M. Schubert, F. Teich, H. Puetter, K. Schierle-Arndt, J. Pastre, Metal–organic frameworks—prospective industrial applications. *Journal of Materials Chemistry*. **16**, 626–636 (2006).
21. J. J. Perry IV, S. L. Teich-McGoldrick, S. T. Meek, J. A. Greathouse, M. Haranczyk, M. D. Allendorf, Noble gas adsorption in metal–organic frameworks containing open metal sites. *The Journal of Physical Chemistry C*. **118**, 11685–11698 (2014).
22. D. Banerjee *et al.*, Metal–organic framework with optimally selective xenon adsorption and separation. *Nature Communications*. **7**, ncomms11831 (2016).
23. S.-J. Lee, S. Kim, E.-J. Kim, M. Kim, Y.-S. Bae, Adsorptive separation of xenon/krypton mixtures using ligand controls in a zirconium-based metal-organic framework. *Chemical Engineering Journal*. **335**, 345–351 (2018).
24. S. T. Meek, S. L. Teich-McGoldrick, J. J. Perry, J. A. Greathouse, M. D. Allendorf, Effects of polarizability on the adsorption of noble gases at low pressures in monohalogenated isoreticular Metal–Organic Frameworks. *The Journal of Physical Chemistry C*. **116**, 19765–19772 (2012).
25. J. Liu, P. K. Thallapally, D. Strachan, Metal–Organic Frameworks for Removal of Xe and Kr from Nuclear Fuel Reprocessing Plants. *Langmuir*. **28**, 11584–11589 (2012).
26. H. Wang, Z. Shi, J. Yang, T. Sun, B. Rungtaweevoranit, H. Lyu, Y. Zhang, O. M. Yaghi, Docking of CuI and AgI in Metal–Organic Frameworks for Adsorption and Separation of Xenon. *Angewandte Chemie*. **133**, 3459–3463 (2021).
27. R. Giovine, F. Pourpoint, S. Duval, O. Lafon, J.-P. Amoureux, T. Loiseau, C. Volkringer, The Surprising Stability of Cu3(btc)2 Metal–Organic Framework under Steam Flow at High Temperature. *Crystal Growth & Design*. **18**, 6681–6693 (2018).
28. P. Ryan, O. K. Farha, L. J. Broadbelt, R. Q. Snurr, Computational screening of metal-organic frameworks for xenon/krypton separation. *AIChE Journal*. **57**, 1759–1766 (2011).

DEVELOPMENT OF AN EXPERIMENTAL TEST BENCH FOR DYNAMIC ADSORPTION OF NOBLE GASES (Xe, Kr) BY MOF TYPE POROUS MATERIALS

ERMSAR 2022 – 18/05/2022

Ph.D student: **Julie NGUYEN-SADASSIVAME**, 2nd year
Thesis director: **Pr. Christophe VOLKRINGER**, Centrale Lille, UCCS
Thesis co-director: **Dr. Thierry LOISEAU**, CNRS, UCCS
Tutor: **Dr. Philippe NERISSON**, IRSN
Nuvia correspondent: **Mr. Philippe CHANTEREAU**

IRSN/FRM-296 ind. 06

SEVERE ACCIDENT AT A NUCLEAR FACILITY: EXAMPLE OF THE PWR

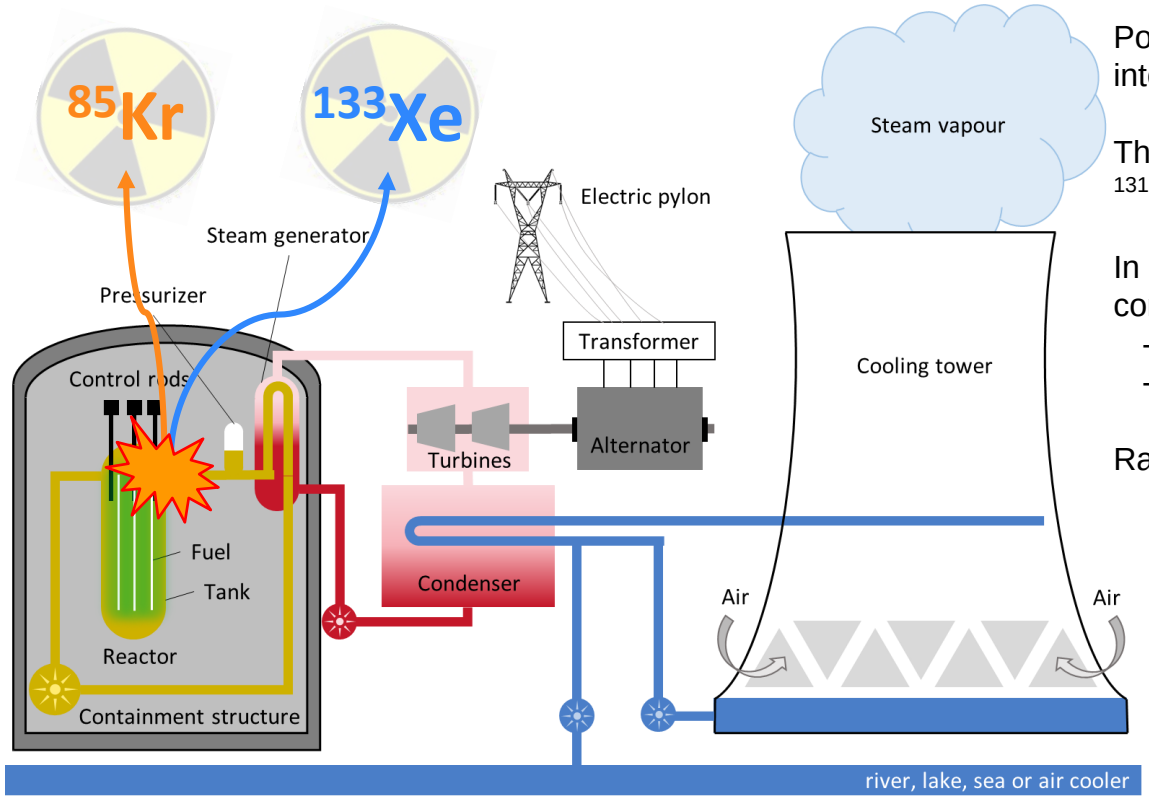

Potential **release** of FPs into the containment and even into the environment.

The first FPs to be released are the **most volatile** (^{129}I, ^{131}I, ^{103}Ru, ^{106}Ru, ^{3}H, ^{14}C…) including noble gases.

In an emergency shutdown, a 900 MWe reactor can contain:

- **22 kg of Kr** (2.32% of total activity)
- **307 kg of Xe** (4.33% of total activity)

Radioactive half-life:

^{85}Kr = 10.8 years

^{133}Xe = 5.3 days

D. Jacquemain, IRSN. edp sciences, **2013**

SEVERE ACCIDENT (SA) ON A NUCLEAR FACILITY: EXAMPLE OF THE PWR

In case of SA, **two antagonistic objectives**:

- Decrease the pressure of the containment to maintain its integrity
- Prevent the propagation of FPs into the environment

→ Implementation of FCVS (Filtered Containment Venting System) on french PWR:

- ✓ Designed for aerosols (particles from 100 µm to 10 nm in suspension in a gas)
- ○ Not suitable for volatile (gaseous) molecular compounds

Capture and storage of noble gases by microporous materials under SA conditions

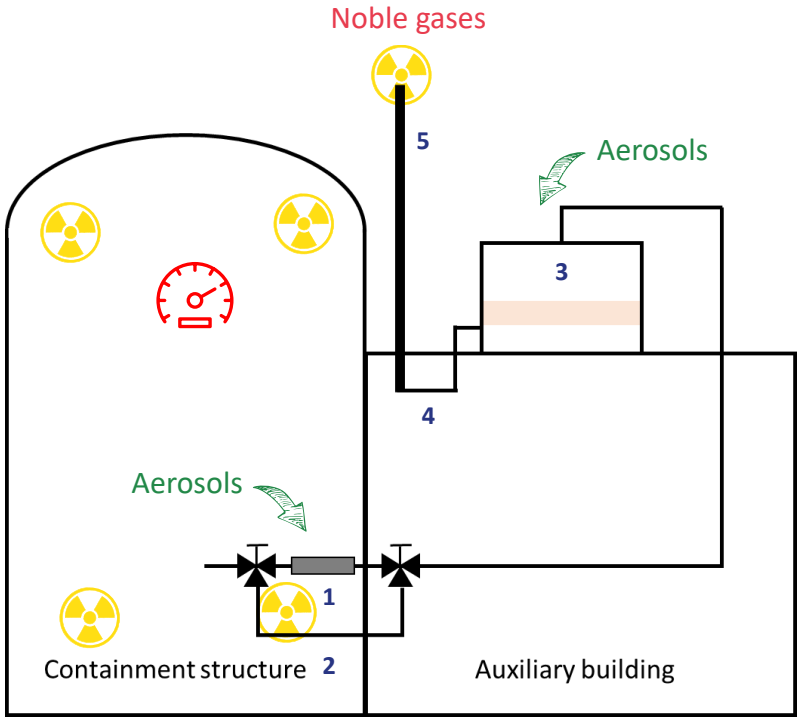

1 Metal pre-filter
2 By-pass
3 Sand filter
4 Radioactivity measurement
5 Chimney

D. Jacquemain *et al.*, Organisation for Economic Co-Operation and Development, report n°45089842, vol. 45, **2014**

NOBLE GASES TRAPPING BY MOF TYPE MICROPOROUS MATERIALS IN SEVERE ACCIDENT CONDITIONS

Synthesis and characterization of MOFs
Static study:

- Adsorption of NG at ≠ temperatures (0 – 50 °C)
- Influence of silver doping on NG adsorption
- Identification of promising MOFs



Dynamic study (filtration):

- Development of SAFARI test bench with on-line analysis by GC-MS
- Adsorption of NG under SA conditions at the FCVS:
  - NG concentrations
  - Temperature (150 °C)
  - Humidity (20-30 %w)
  - Gas velocity (10 cm/s)



A MOF ? WHAT IS THIS ? WHY ?

METAL-ORGANIC FRAMEWORK (MOF)

- Microporous (3 - 70 Å) → ↗ **Selectivity**
- Specific surface area < 7000 m²/g → ↗ **Storage**
- Many possible structures
- Unlimited functionalization
  → ↗ **Adsorption**
- SA conditions resistant (Al, Zr)

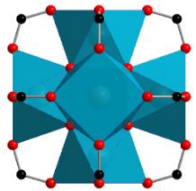

Zirconium cluster
$[Zr_6O_4(OH)_4]$



Terephthalic acid
$[C_8H_6O_4]$

120 °C/24h

DMF/FA

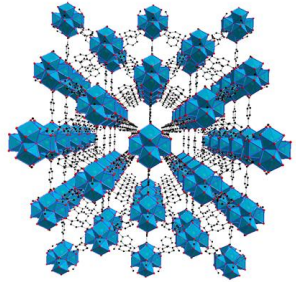

UiO-66

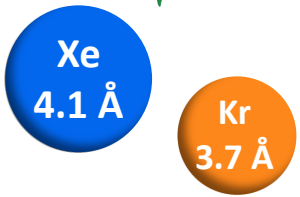

- Electron cloud polarization
- Selectivity Xe/Kr

C. Volkringer et al., Chem. Commun., vol. 52, p. 12502-12505, **2016**

A MOF ? WHAT IS THIS ? WHY ?

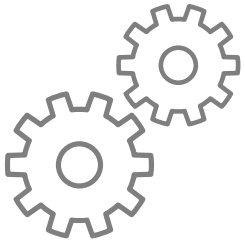

- Many studies for radionuclide capture (I, Ru…)
- Many studies in static, less in dynamic conditions for the adsorption of NG
- → Not in SA conditions

Is it possible for MOFs to trap noble gases under SA conditions?

- ✓ Development of an experimental test bench and on-line analysis by GC-MS
- ✓ Test bench functional validation using reference material
- ✓ Test of promising MOFs

K. Jin et al., Coordination Chemistry Reviews, vol. 427, p. 213473, ***2020***

M. Leloire et al., Journal of Harzardous Materials, vol. 416, p. 125890, ***2021***

HKUST-1 : PRESENTATION

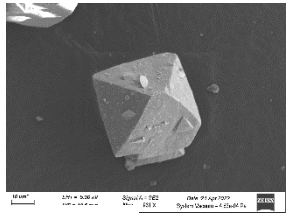



$$Cu(NO_3)_2.2{,}5H_2O + \text{Trimesic acid} \xrightarrow[EtOH/H_2O]{110\ °C/24h}$$

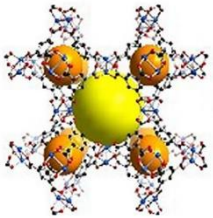



- Commercialized (Basolite® C 300 by BASF)
- Used in many studies for FPs trapping (I, U…)

Sava et al., Chemistry of Materials, vol. 25, p. 2591-2596, ***2013***
Feng et al., Colloids and Surfaces A: Physicochemical and Engineering Aspects, vol. 431, p. 87-92, ***2013***

- High specific surface area (1000 - 1800 m²/g)
- 2 pore sizes (5 et 15 Å)
- Material for test bench validation:
  - Good results in static condition
  - Dynamic comparison

J. Liu et al., Langmuir, vol. 28, p. 11584–11589, ***2012***

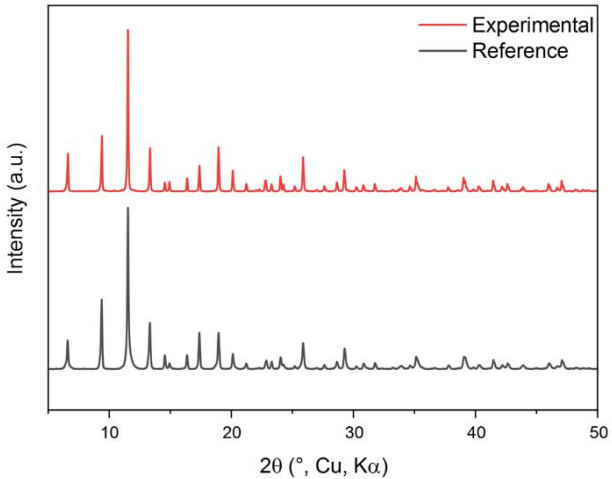

➢ m_{exp} = 220 g



Steel autoclave 8 L

HKUST-1: STATIC STUDY

Gas adsorption analyzer:

- Specific surface BET by N_2 adsorption at 77 K (m^2/g)
- Adsorption capacity of pure NG until 1.2 bar (cm^3_{gas}/g_{MOF}) : 0 °C < T < 50 °C
- Enthalpies of adsorption (kJ/mol)

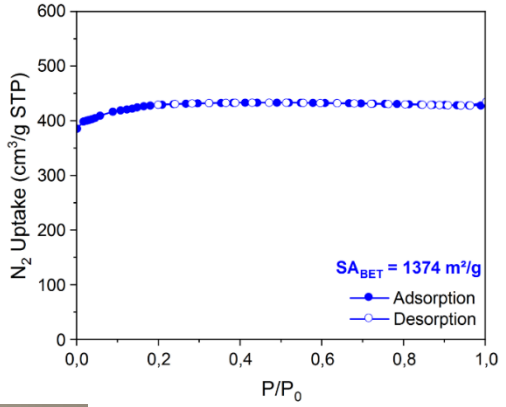

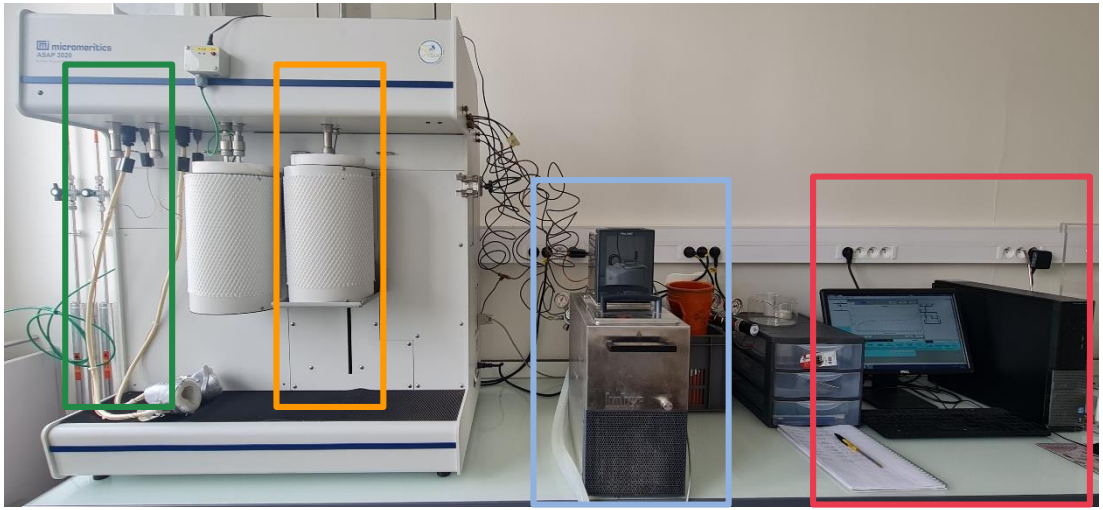

Degassing 12h/110 °C

Adsorption (N_2, Xe or Kr)

Temperature control

Computer

RESULTS OF STATIC MEASUREMENTS AT DIFFERENT TEMPERATURES

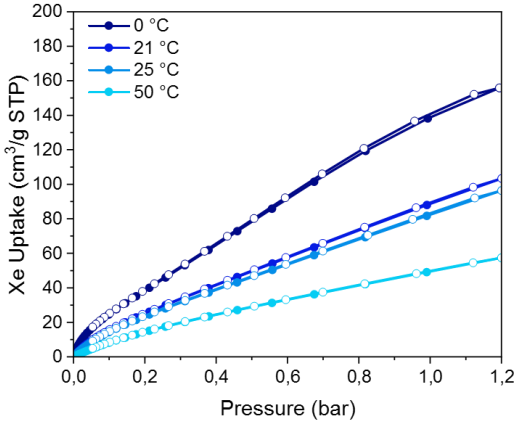

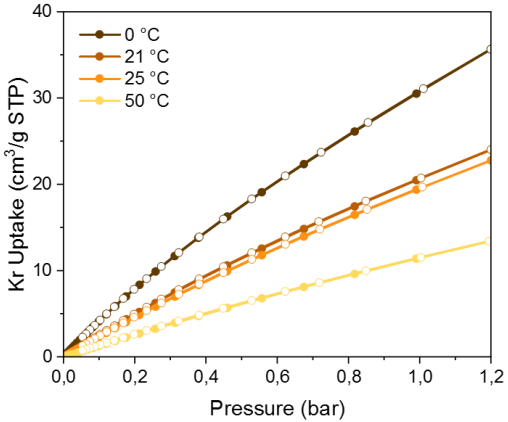

Adsorption capacities ↘ when T ↗

	Specific surface (m^2/g) N_2 77K	Temperature (K)	Adsorption (cm^3/g STP)	
			Xe (1 bar)	Kr (1 bar)
HKUST-1 **Large scale : this study**	1374	294	89	21
HKUST-1[1] **Low scale synthesis**	1844	292	112	25
Zeolite (ZSM-5)[2] **Silver free**	432	298	40	18
Activated carbon[3]	793	298	74	25

	Qst_{min} (kJ/mol)		Qst_{max} (kJ/mol)	
	Xe	Kr	Xe	Kr
HKUST-1 **This study**	18	17	28	18
HKUST-1[4]	20	16	27	19

[4] *A. Soleimani Dorcheh et al., Microporous and Mesoporous Materials, vol. 162, p. 64-68,* ***2012****.*

[1] *J. J. Perry IV et al., The Journal of Physical Chemistry C, vol. 118, p.11685-11698,* ***2014***
[2] *Y. Yu et al., Journal of Environmental Chemical Engineering, vol. 10,* ***2022***
[3] *Q. Wang et al., Sci. China Chem., vol. 59, p. 643-650,* ***2016***

HKUST-1: DYNAMIC STUDY

Experimental test bench SAFARI GR:

- Flow of a gas mixture at different concentrations and temperatures

Gas flow → MOF → Detection

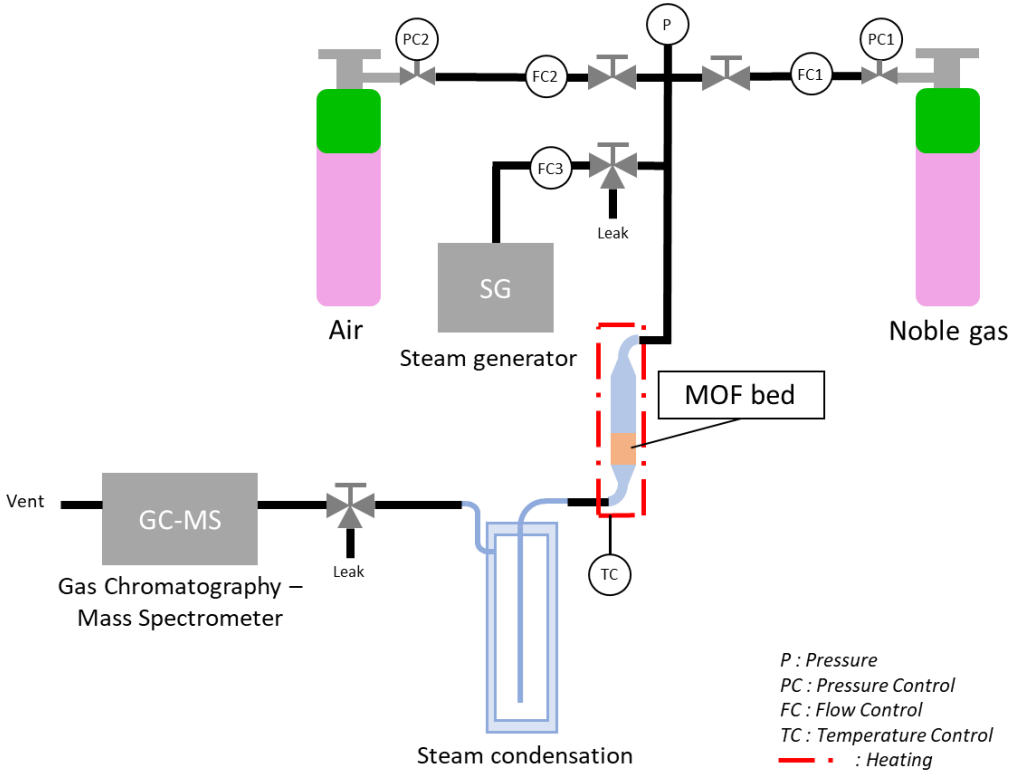

HKUST-1: DYNAMIC STUDY



GC-MS on-line analysis



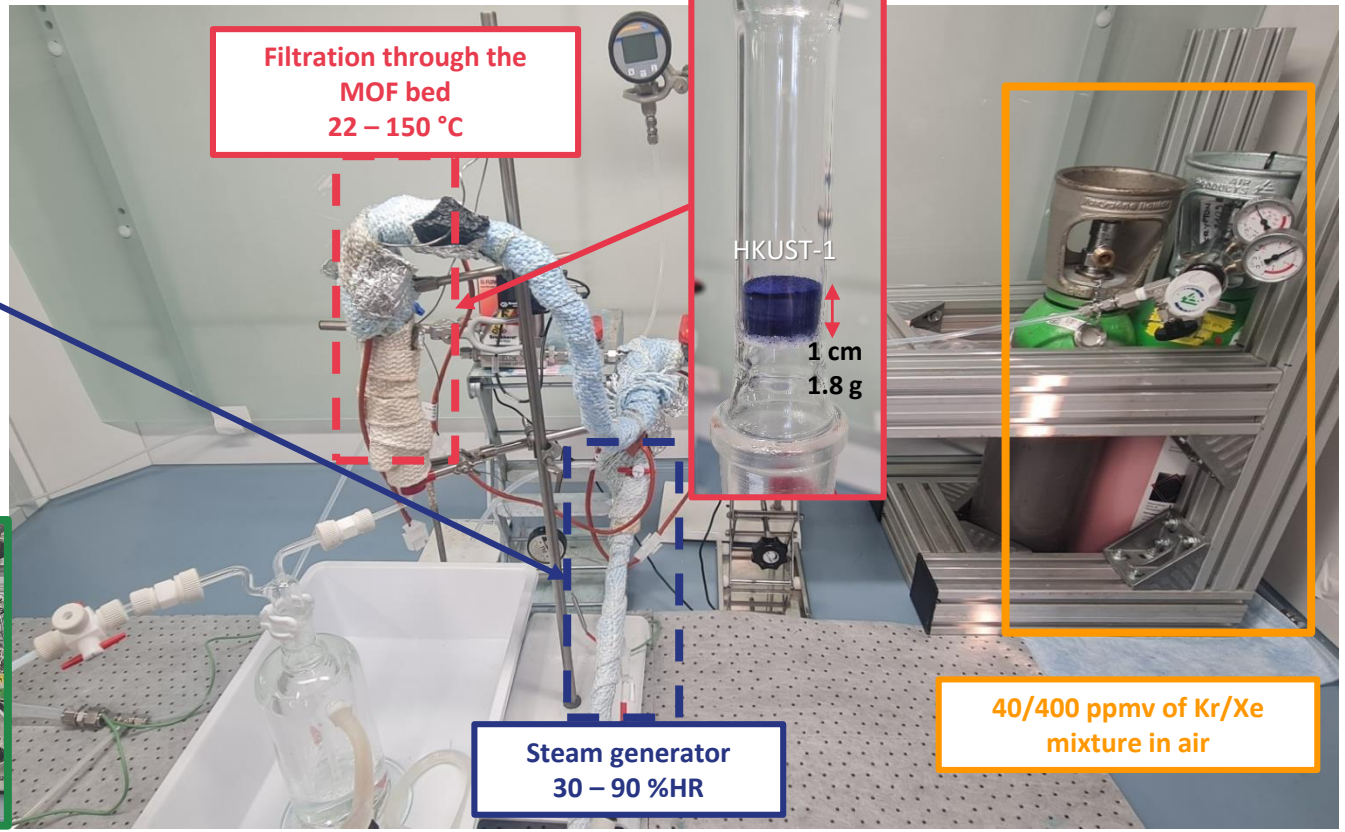

RESULTS OF DYNAMIC MEASUREMENT: BREAKTHROUGH CURVES AT 22 °C, 1 BAR, 1 CM/S

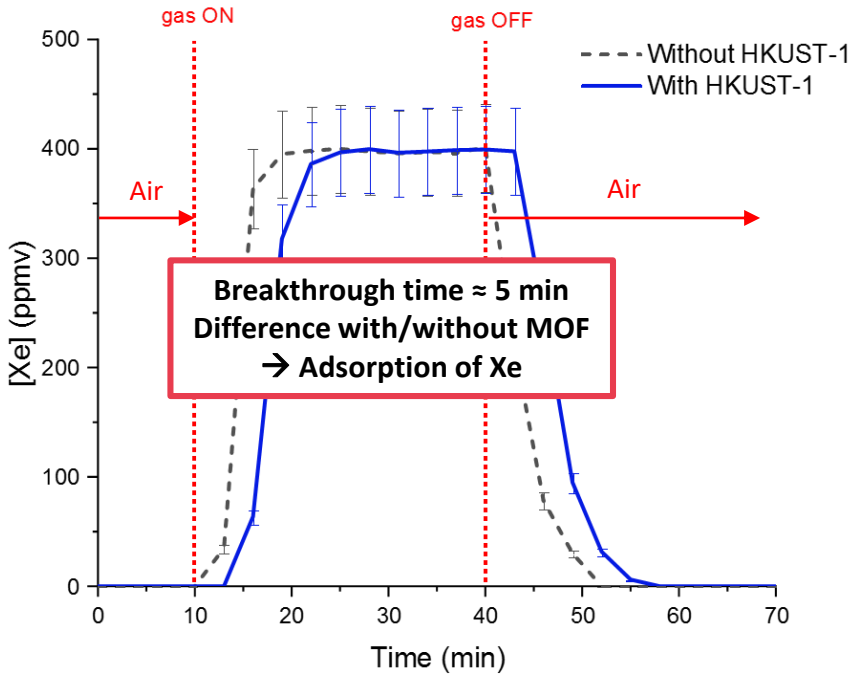

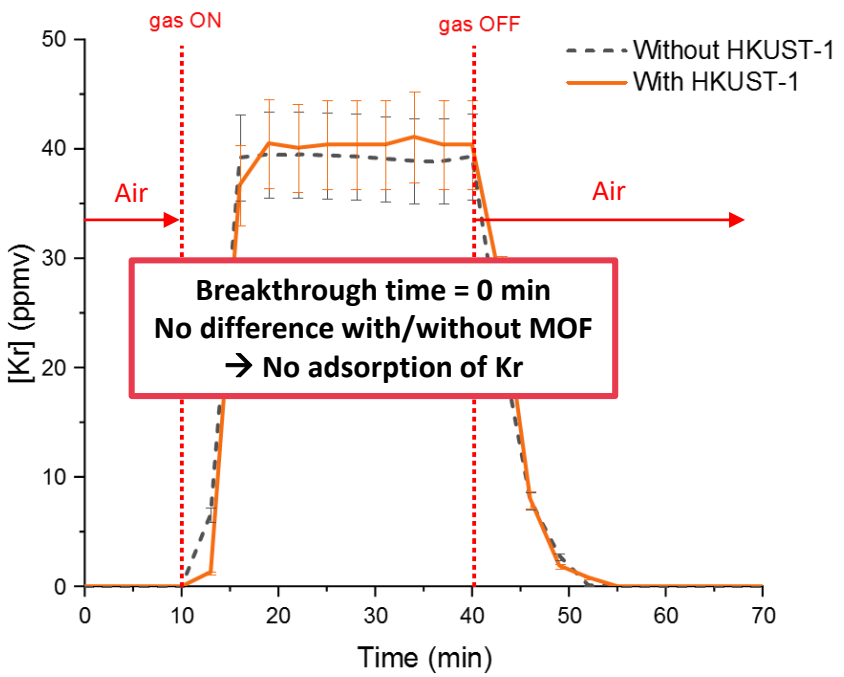

Breakthrough time: time when the target gas (Xe or Kr) is detected downstream the MOF

RESULTS OF DYNAMIC MEASUREMENT: BREAKTHROUGH CURVES AT 50 °C, 1 BAR, 1 CM/S

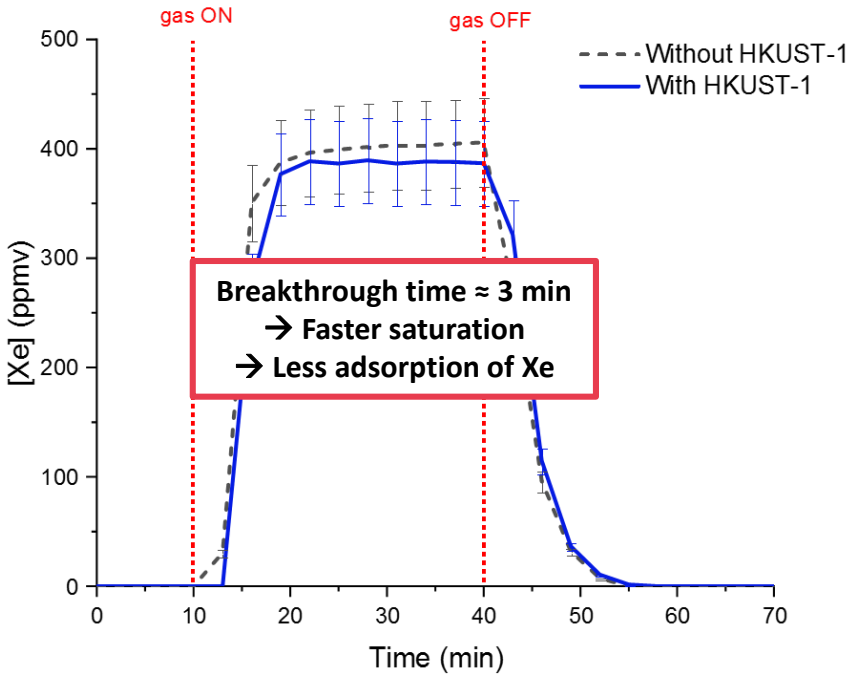

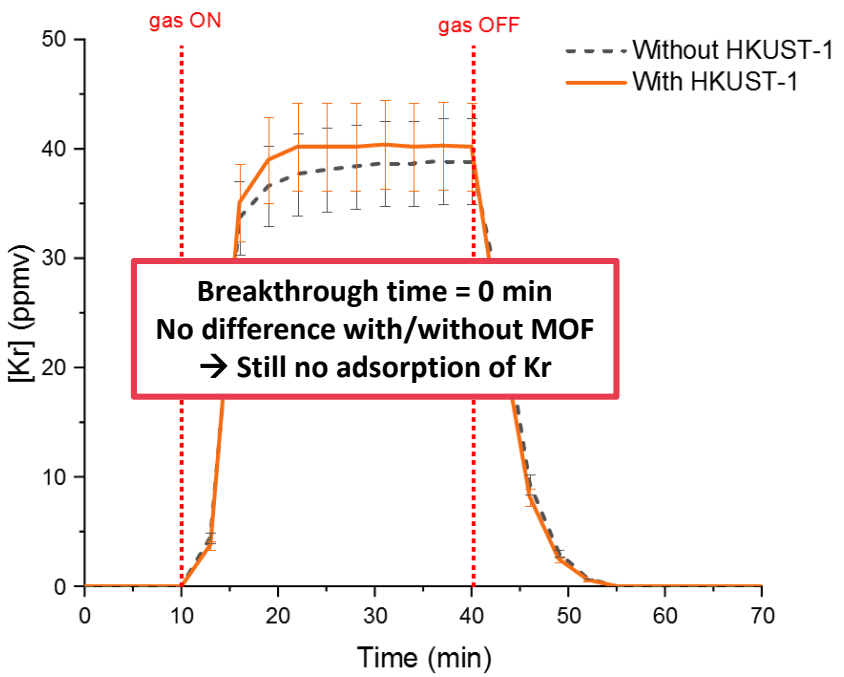

RESULTS OF DYNAMIC MEASUREMENT: BREAKTHROUGH CURVES AT 50 °C, 30% HR 1 BAR, 1 CM/S

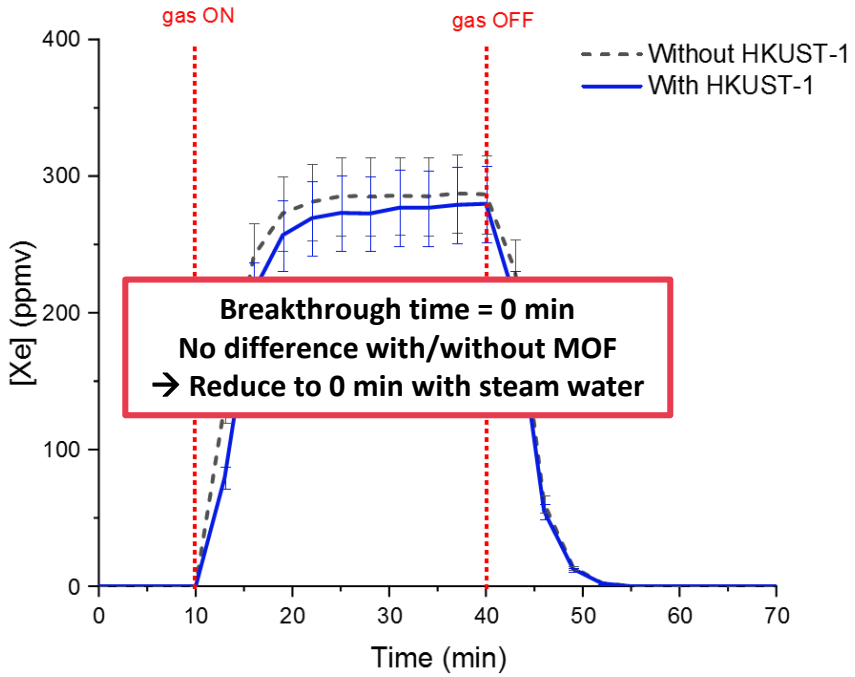

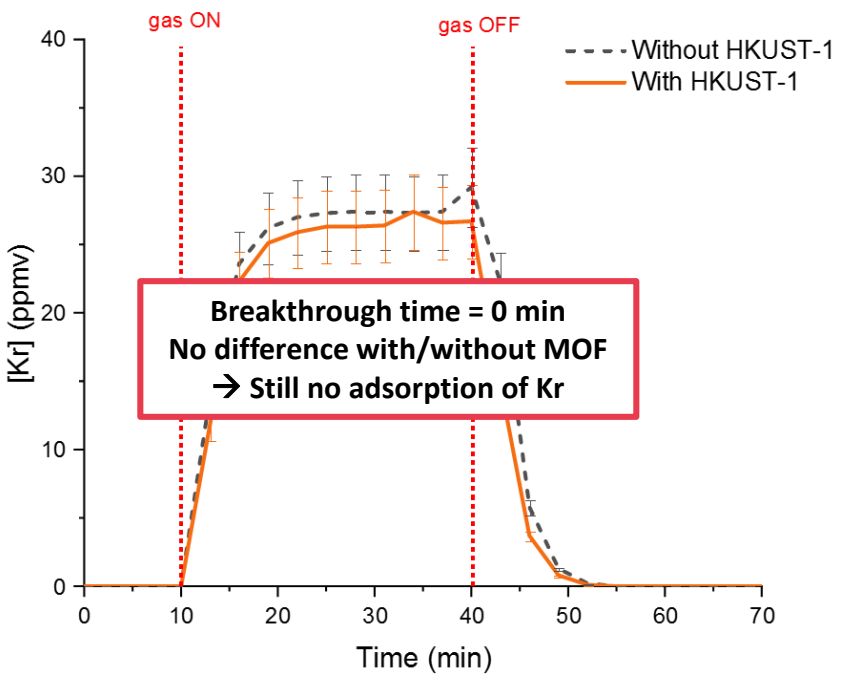

COMPARISON OF XE AND KR ADSORPTION CAPACITIES AND SELECTIVITY AT 1 BAR AND DIFFERENT TEMPERATURES

	Static Single component			Dynamic Kr/Xe at 40/400 ppmv/Air		
Temperature (°C)	CS_{Xe} (mmol/g)	CS_{Kr} (mmol/g)	$S_{Xe/Kr}$	CS_{Xe} (mmol/kg)	CS_{Kr} (mmol/kg)	$S_{Xe/Kr}$
22	3.64	0.84	9.7	5.68	0.064	8.9
50	1.83	0.43	9.1	1.94	0.00	-
50 + 30% HR	-	-	-	0.00	0.00	-

- Adsorption capacities ↘ when temperature ↗ = same trend as the static study
- Consistent selectivity static/dynamic/literature

CS : Capacity Sorption

- HKUST-1 study: reference material for the SAFARI bench development
  - Static:
    - » High T = less trapping as expected
    - » Enthalpies of adsorption consistent with literature
  - Dynamic:
    - » Results at ≠ T consistent with the static study
    - » Adsorption of Xe by this MOF at ambient T
    - » Presence of steam water reduces the breakthrough time
    - » SAFARI test bench now operational for the filtration of NG
- Select potentially promising compounds:
  - Test under static conditions
  - Suitable synthesis protocol and pore sizes
  - Ag-doping possibilities
- Most efficient will be tested on SAFARI bench in dynamic and representative SA conditions

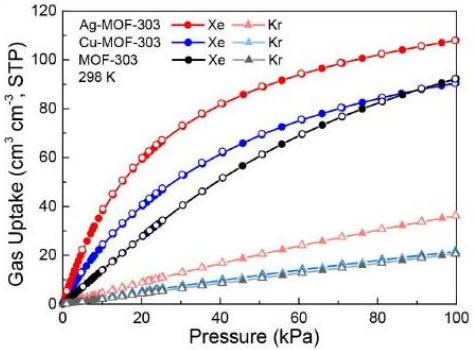

Wang et al., Angewandte chemie, vol. 133, p. 3459-3463, ***2021***

ACKOWLEDGMENTS

Pr. C. VOLKRINGER
Dr. T. LOISEAU
Dr. S. DUVAL
Dr. N. HENRY
Dr. J. DHAINAUT
Pr. S. ROYER

D. ANDRIOTOU
P. HARDY
O. PLASTIRAS
A. FLAMENT
P. HENRIQUE
…

Dr. N. COUZON
Dr. A. ABDALLAH
M. BAKOUCHE

P. CHANTEREAU
R. SARRAF

Dr. P. NERISSON
Dr. L. CANTREL
Dr. C. LE GALL
Dr. A-C. GREGOIRE
Dr. S. MORIN
C. TORNABENE
L. MARTINET
G. BOURBON

C. ALVAREZ-LE MAOUT
E. LE FESSANT
M. DAURY
A. MINNE
…

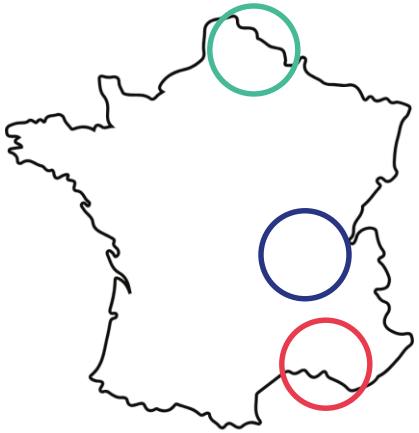





Thank for your attention !



ENTHALPIES OF ADSORPTION

$$-\Delta H = R\frac{\partial \ln(P)}{\partial(1/T)}$$

- Solid-gas interaction force expressed by the enthalpy of adsorption
- Determinated by a manual method with adsorption isotherm at different T
- 17 < -ΔH < 40 kJ/mol

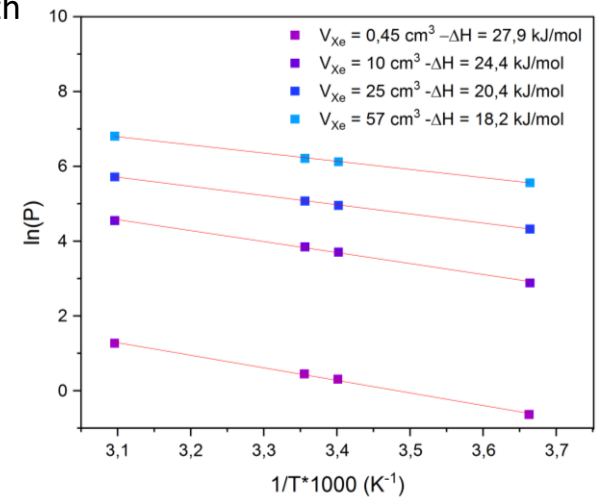

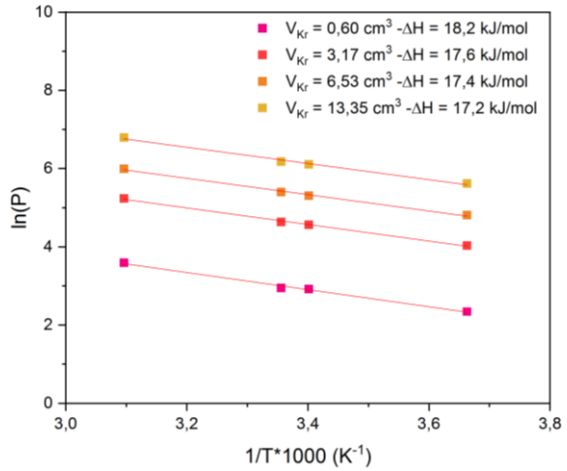

PRINCIPLE OF ON-LINE GC-MS ANALYSIS

- Outgoing flow from SAFARI bench loads the injection loop (V1 OFF, load position)
- Unload the injection loop during 30 sec to inject the sample into the column of GC (V1 ON, inject position)
- V1 switches back to OFF (load position)

→ Injection every 3 min during a 70 min run

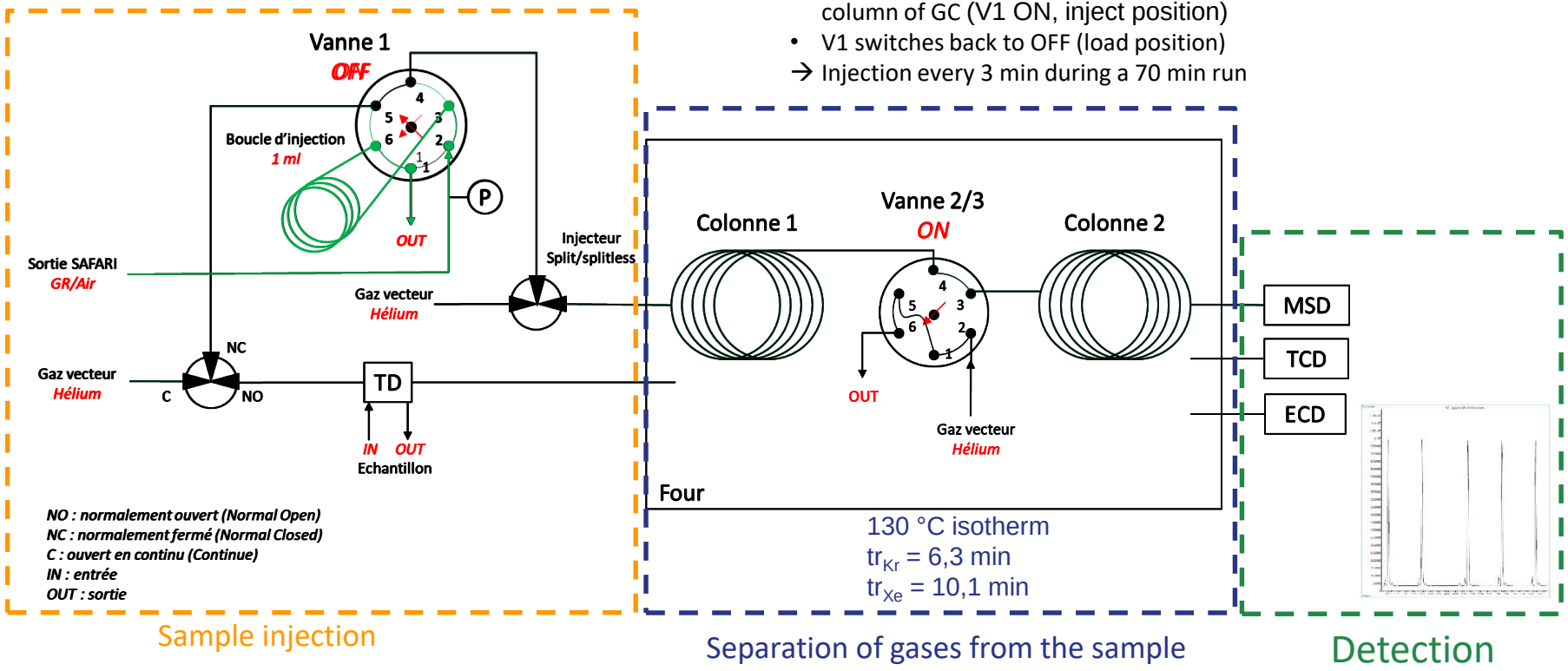

Sample injection

Separation of gases from the sample

Detection

CALCULATION OF SELECTIVITY IN STATIC OR DYNAMIC CONDITION

Static

$$S_{Xe/Kr} = \frac{k_{H(Xe)}}{k_{H(Kr)}}$$

k_H: Henry constant is determined by the linear Langmuir equation at very low pressure ($R^2 > 0.999$) on the adsorption isotherm

Dynamic

$$S_{Xe/Kr} = \frac{x_{Xe}/y_{Xe}}{x_{Kr}/y_{Kr}}$$

x: molar fraction adsorbed
y: molar fraction in the gas phase

[CALCULATION OF ADSORPTION CAPACITIES FROM BREAKTHROUGH CURVES

$$q = \frac{Q_v \int_0^{t_s} (C_{blank} - C)dt}{V_m W}$$

t_s : time at saturation

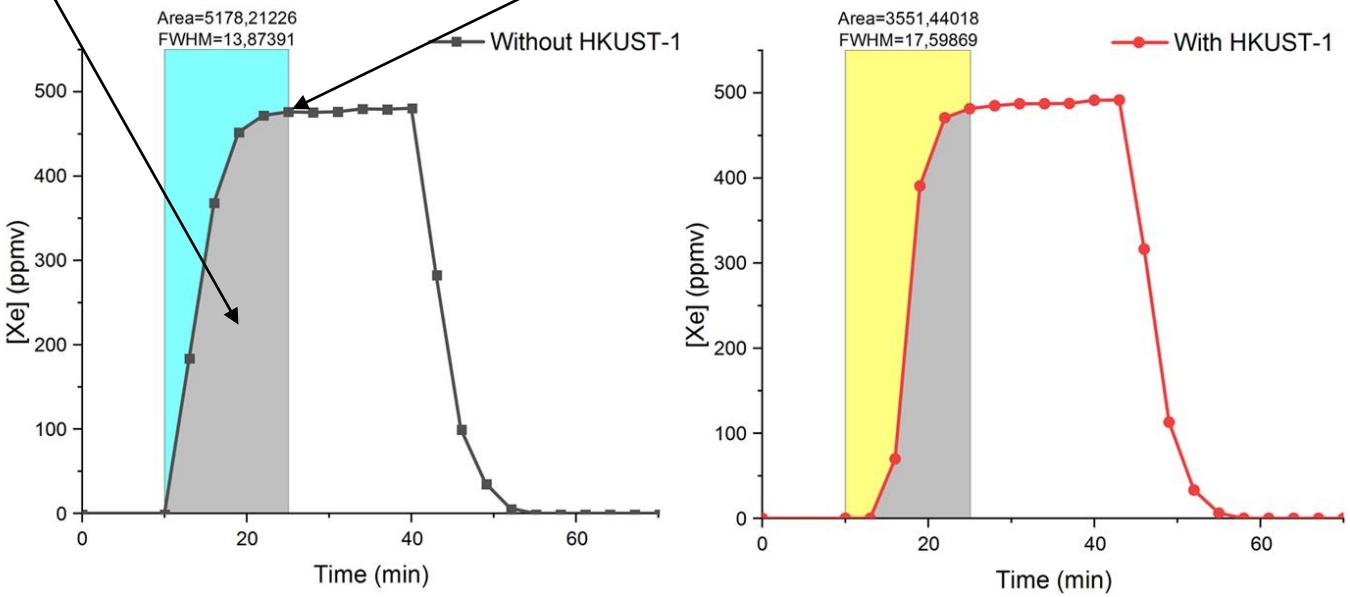

Calculation of NG concentration at an emergency shutdown

- T_{max} = 150 °C
- P_{max} = 5 bar
- $V_{C\ 900\ MWe}$ = 60 000 m^3

m_{Xe} = 307 kg → 270,7 ppmv
m_{Kr} = 22,1 kg → 30,5 ppmv

T (°C)	P (bar)	[Xe] (ppmv)	[Kr] (ppmv)
25	1	954	107
150	5	271	31

Industrial applications

- Sensors
- Drug delivery
- Gas storage
- Separation/purification
- Heterogenous catalysis
- …

➢ More academic applications than industrial



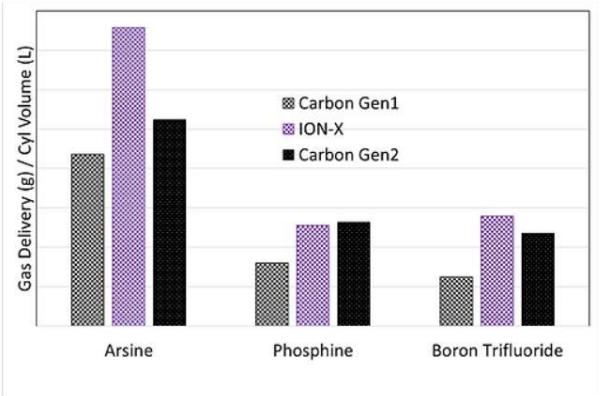

Figure 4. Dopant gas delivery comparison (down to 20 torr) between carbon-based incumbent products and ION-X

Numat Technologies

The 10th European Review Meeting on Severe Accidents Research

Severe Accident Research Eleven Years after the Fukushima Accident

May 16-19, 2022, Karlsruhe, Germany

Technical Session 7-1: Hydrogen and Containment Related issues

Chairs: M. Hupp (Framatome GmbH), I. Kljenak (IJS)

ID340	**Results of metallographic analysis of the QUENCH-20 bundle with B4C absorber** J. Stuckert (KIT)	**Paper** **Presentation**
ID315	**Status of Modeling of FeCrAl Claddings in Severe Accident Codes and Application on the QUENCH-19 Experiment** T. Hollands (GRS)	**Paper** **Presentation**
ID284	**Current understanding of high-temperature oxidation phenomena during air ingress scenarios** S. Park (Lee & Co)	**Paper** **Presentation**
ID356	**THAI Experiments on Iodine Behavior in a Room Chain Representing Flow Conditions in Large Containments** M. Freitag (Becker Technologies)	**Paper** **Presentation**

10TH CONFERENCE ON SEVERE ACCIDENTS RESEARCH
May 16-19, 2022 – Karlsruhe, Germany
ERMSAR 2022

RESULTS OF METALLOGRAPHIC ANALYSIS OF THE QUENCH-20 BUNDLE WITH B4C ABSORBER

J. Stuckert, U. Peters, U. Stegmaier, M. Steinbrück
Karlsruhe Institute of Technology
Hermann-von-Helmholtz-Platz 1, 76344 Eggenstein-Leopoldshafen
juri.stuckert@kit.edu

ABSTRACT

Experiment QUENCH-20 with BWR geometry simulation bundle was conducted at KIT on 9th October 2019 in the framework of the international SAFEST project. The test bundle mock-up represented one quarter of a BWR fuel assembly with 24 electrically heated fuel rod simulators and two B_4C control blades. The rod simulators were filled with Kr to inner pressure of 5.5 bar at peak cladding temperature of 900 K. The pre-oxidation stage in the flowing gas mixture of steam and argon (each 3 g/s) and system pressure of 2 bar lasted 4 hours at the peak cladding temperature of 1250 K. During the following transient stage, the bundle was heated to a maximal temperature of 2000 K. The cladding radial extensions and failures due to inner overpressure (about 4 bar) were observed at temperature about 1700 K and lasted about 200 s. During the period of rod failures also the first absorber melt relocation accompanied by shroud failure were registered. The interaction of B_4C with steel blade and ZIRLO channel box was observed at elevations 650…950 mm with formation of eutectic melt. The typical components of this melt are (Fe, Cr) borides and ZrB_2 precipitated in steel or in Zr-steel eutectic melt. Massive absorber melt relocation was observed 50 s before the end of transition stage. Small fragments of the absorber melt moved down to the elevation of 50 mm. The test was terminated with the quench water injected with a flow rate of 50 g/s from the bundle bottom. Fast temperature escalation from 2000 to 2300 K during 20 s was observed. As result, the metal part (prior β-Zr) of claddings between 550 and 950 mm was melted, partially released into space between rods and partially relocated in the gap between pellet and outer oxide layer to 450 mm. The bundle elevations 850 and 750 mm are mostly oxidized with average cladding ECR 33%.

KEYWORDS
BWR test bundle, cladding oxidation, eutectic melt relocation, reflood, temperature escalation

1. INTRODUCTION

The main objective of the QUENCH program at KIT is the investigation of the hydrogen source term and materials interactions during LOCA and the early phase of severe accidents including reflood [1-3]. Bundle experiments as well as separate-effects tests are conducted to provide data for the development of models and the validation of severe fuel damage code systems. The QUENCH bundle facility is an out-of-pile bundle facility with electrically heated fuel rod simulators and extensive instrumentation. So far, 20 experiments with various severe accident scenarios as well as a series of 7 DBA LOCA experiments were conducted. Two of the bundle tests on severe accident were performed with PWR geometry containing central B_4C neutron absorber rod: QUENCH-07 [4] and QUENCH-09 [5]. Numerous accompanying single control rod tests were performed at KIT and showed a complicated eutectic interaction between B_4C, stainless steel and zirconium with formation of different borides [6, 7]. The last severe accident test QUENCH-20 was the first test performed in the QUENCH facility with BWR geometry simulation bundle [8].

2. TEST FACILITY

The general scheme of the test section is given in Fig. 1. The test rods were arranged within the bundle as shown in the schematic cross section of Fig. 2. The rod cladding of the fuel rod has 9.84 mm outside diameter and 8.63 mm inner diameter. The materials used in this test consisted of Zircaloy-2 cladding tubes with inner liner (LK3/L). The composition of the LK3 and L materials can be found in Table 3.

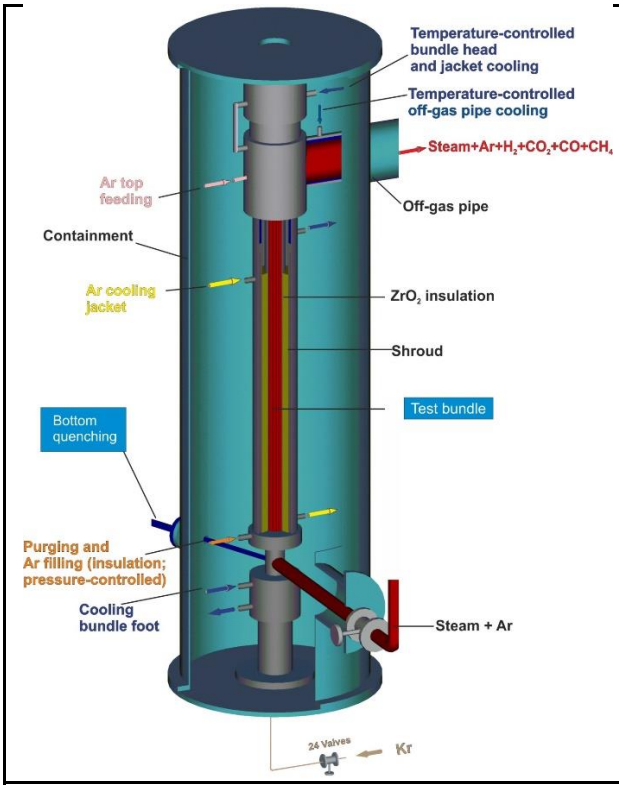

Figure 1. Containment and test section

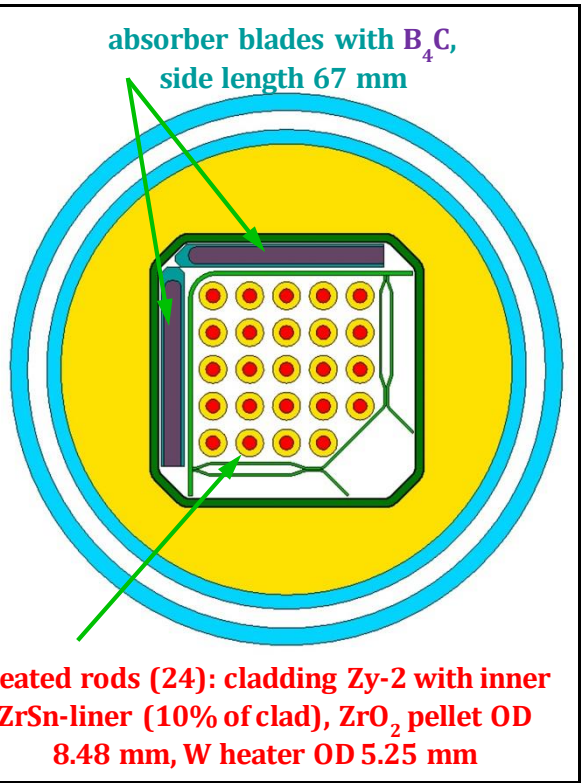

Figure 2. Cross section of test section with ¼ SVEA-96 OPTIMA2 assembly

The test bundle is approximately 2.5 m long and is made up of 24 heated fuel rod simulators. Heating is electric by 5.25 mm diameter tungsten heaters installed in the rod centers, and the bundle section heated by tungsten heaters between bundle elevations 0 and 1024 mm. Molybdenum heaters and copper electrodes are connected to the tungsten heaters at one end and to the cable leading to the DC electrical power supply at the other end. The tungsten heaters are surrounded by annular ZrO_2 pellets simulating UO_2 fuel. The Mo heaters and Cu electrodes are coated with ZrO_2 layer (about 200 µm thickness) to avoid an electrical contact to the cladding inner surface. All the test rods were filled with Kr at a overpressure of approximately 0.35 MPa after bundle heating to cladding peak temperature of 900 K. The system pressure maintained at about 0.2 MPa. The fuel rod simulators are held in position by five grid spacers at bundle elevations -200, 50, 550, 1050 and 1410 mm. All five grid spacers were the standard Westinghouse Inconel X750 spacers. Two steel blades with horizontal B_4C absorber pins were filled with helium (0.12 MPa) and inserted between channel box and shroud. The composition of the steel blade is the following (low carbon alloy AISI 316L SS): Fe, Cr (17%), Ni (11%), Mo (2.5%), [Si, P, S (<1%)]. One corner rods was installed in the water channel and was designed to be withdrawn from the bundle to check the amount of oxidation and hydrogen absorption at specific time. This corner rod was withdrawn at the end of pre-oxidation stage.

The test bundle is surrounded by an octagonal shroud of Zr 702, then by ZrO_2 fiber insulation extending from the bottom (-300 mm) to the upper end of the heated zone (+1024 mm) and a double-walled cooling

jacket of Inconel 600 (inner)/stainless steel (outer) over the entire length. The annulus between shroud and cooling jacket with the fiber insulation is purged (after several cycles of evacuation) and then filled with stagnant argon. This annulus is connected to a flow- and pressure-controlled argon feeding system in order to keep the pressure constant at the target of 0.3 MPa (beyond this pressure gas is released by feeding system). It must prevent an access of steam from the test bundle to the annulus after possible shroud failure, after which argon is supplied continuously. The 6.7 mm annulus of the cooling jacket is cooled by argon from the upper end of the heated zone to the bottom of the bundle and by water in the upper electrode zone. Both the absence of ZrO_2 insulation above the heated region and the water cooling are to avoid too high temperatures of the bundle in that region.

For temperature measurements the test bundle, shroud, and cooling jackets are equipped with thermocouples. The thermocouples attached to the outer surface of the rod cladding at elevations between -250 and 1350 mm are designated "TFS" for all heated rods. The shroud thermocouples (designation "TSH") are mounted at the outer surface between -250 and 1250 mm. The thermocouples installed at the blade side at the bundle elevations 250, 350 and 450 mm are designated as TBL. The thermocouples mounted at the channel box at elevations 350 and 450 mm are designated as TCH.

The release of gas spezies is analyzed by a quadrupole mass spectrometer Balzers "GAM300" located at the off-gas pipe of the test facility. The ion currents representing the concentrations of the respective gases are determined. From these data the mass production rate of hydrogen as well as of the other gases is calculated with the ratio of the partial pressure of the particular gas and that one of argon (carrier gas) and multiplied by the argon flow rate through the test bundle.

3. EVENTS DURING TEST PERFORMANCE

In the QUENCH-20 experiment the test sequence can be distinguished in the following stages:

Pre-oxidation	0000 – 14416 s,
Heat-up	14416 – 15882 s,
Quench	15882 – 16375 s with water flow rate 50 g/s.

The scheme of test performance is depicted in Fig. 3.

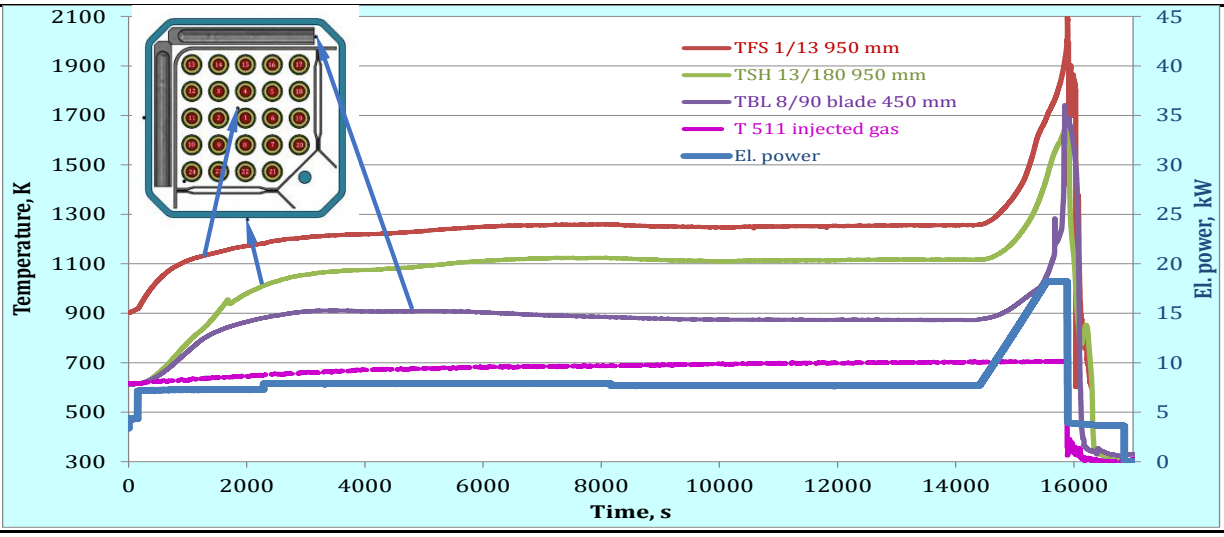

Figure 3. Test scenario

The hottest elevation of the QUENCH-20 was the level 950 mm similar to most former QUENCH bundle tests. To determine the axial temperature profile at a certain time, the average value of all thermocouple

readings of certain bundle elevation were calculated separately for claddings and shroud. Fig. 4 presents these axial temperature distributions on the end of the pre-oxidation stage and on the end of transient. For both time points, the hottest region was near to the elevation 950 mm. However, there is a significant temperature increase between 450 and 1050 mm during the transient stage.

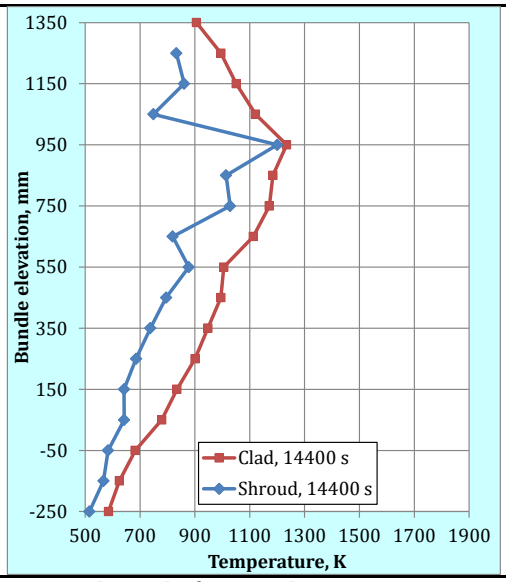

on the end of pre-oxidation (14400 s)

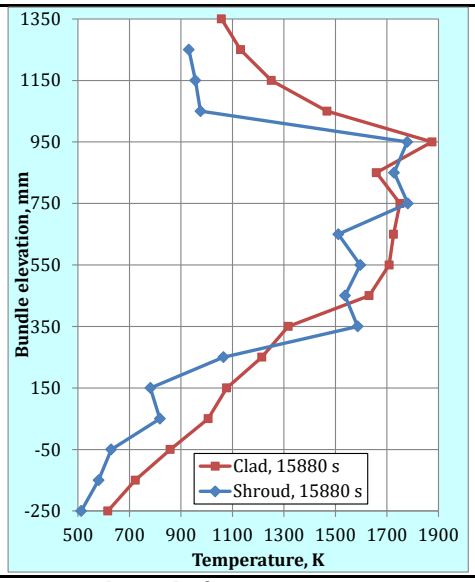

on the end of transient (15880 s)

Figure 4. Axial temperature profiles of outer cladding surfaces and outer shroud surface

According to rod pressure drops, the cladding failures occurred during the transient stage, probably at temperature about 1700 K measured to the failure time point at the elevation 950 mm. Simultaneous release of Kr was registered by mass spectrometer, which shown seven Kr peaks corresponding to seven rod groups failed during about 200 s. In the first group, the rods 8, 1, and 4 of internal group were failed. The last group consists of rods 17 and 12 located at bundle periphery. The failure sequence from internal to outer rods; this is due to the radial temperature profile, decreasing from the center rod to the shroud. The absorber blade failures were registered by He release. The corresponding absorber melt relocations to the elevations of 250…450 mm were indicated during the transient stage by the TBL thermocouple installed at these elevations (Fig. 5).

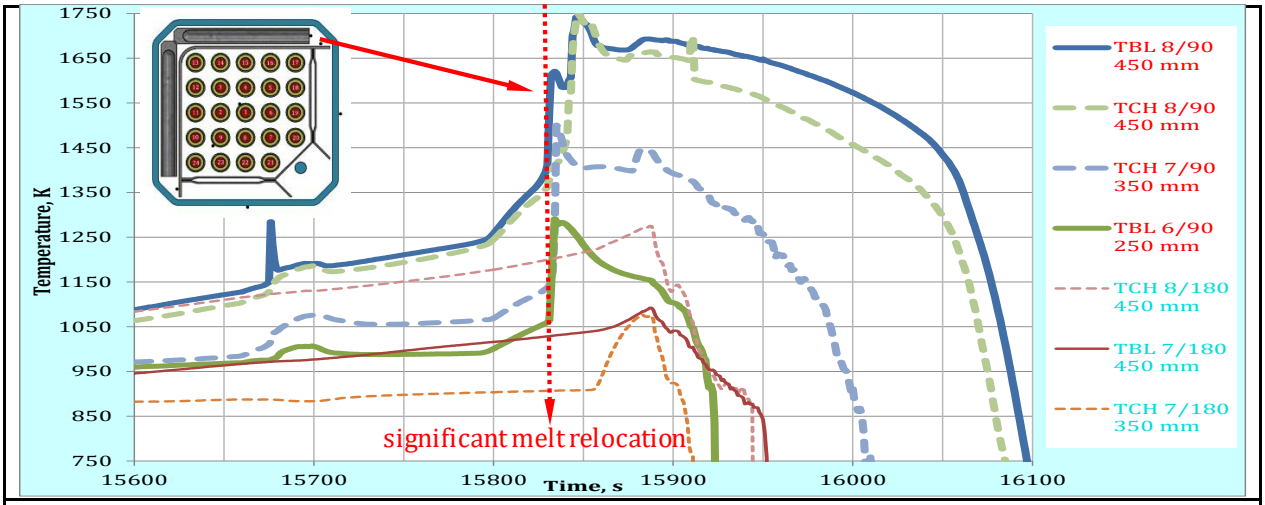

Figure 5. Absorber melt relocation from hottest bundle elevations to elevations 250…450 mm

The quench water injection was initiated at 15891 s. The maximum cladding temperature achieved during the test was recorded with the TFS 1/13 thermocouple at the time of quenching and amounted to 2098 K. During the quench stage, mass spectrometer registered release of following products of B_4C oxidation by steam: significant amounts of CO (12.6 g), and CO_2 (9.7 g) as well as relative small mass of CH_4 (0.4 g). This corresponds to following chemical reactions:

$$B_4C(s)+7H_2O(g)=2B_2O_3(l)+CO(g)+7H_2+[732\ kJ/mol\ \&\ 1600\ K] \quad (1)$$
$$B_4C(s)+8H_2O(g)=2B_2O_3(l)+CO_2(g)+8H_2+[761\ kJ/mol\ \&\ 1600\ K] \quad (2)$$
$$B_4C(s)+6H_2O(g)=2B_2O_3(l)+CH_4(g)+4H_2+[959\ kJ/mol\ \&\ 1600\ K] \quad (3)$$

Steam reacts with liquid boron oxide to form volatile boric acids:

$$B_2O_3(l)+H_2O(g)=2HBO_2-[329\ kJ/mol\ \&\ 1600\ K] \quad (4)$$
$$B_2O_3(l)+3H_2O(g)=2H_3BO_3+[42\ \ kJ/mol\ \&\ 1600\ K] \quad (5)$$

Boron oxide self directly evaporates temperatures above 1500 °C

The calculations, based on the relations (1)…(3) and measured data, showed that the corresponding mass of reacted B_4C was 38.4 g (4.3% from the total mass of B_4C pins), and additionally to released CO (12.6 g), CO_2 (9.7 g)and CH_4 (0.4 g) gases were formed 96.8 g B_2O_3 and released 10 g hydrogen. The total energy release due to boron carbide oxidation is about 500 kJ. The integral hydrogen release registered by mass spectrometer during the whole test was 57.4 g, from that 32 g during the quench stage.

4. METALLOGRAPHIC EXAMENATION

The test bundle was encapsulated in epoxy resin. After epoxy hardening during about three weeks, the bundle was cut into slices. Fig. 6 shows top views of grinded and polished cross sections between elevations 50 and 950 mm. The cladding melt was partially released into the space between rods at the bundle elevations 555…950 mm, whereas the eutectic absorber melt at elevations 450…950 mm.

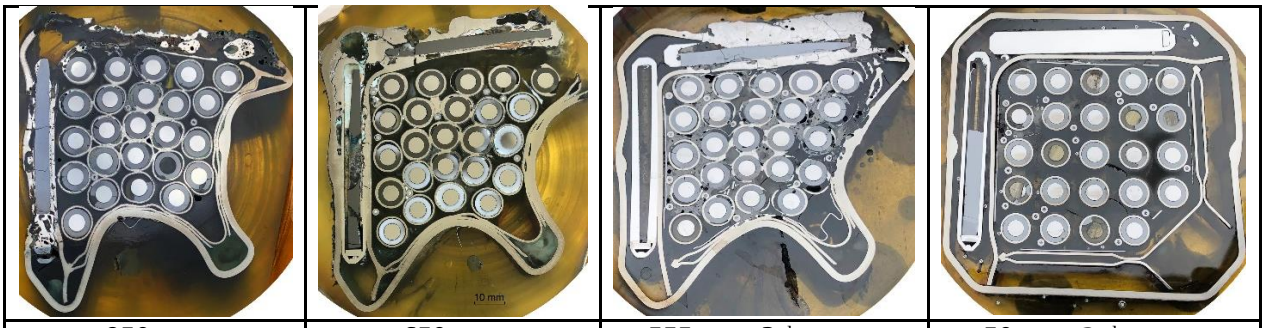

950 mm	650 mm	555 mm, 3rd spacer	50 mm, 2nd spacer

Figure 6. Overview of polished cross sections; formation of eutectic absorber melt.

The shroud was ductile deformed at angle positions 90° and 180° at bundle elevations above 350 mm due to higher gas pressure outside the shroud. This caused squeezing of bundle and two grid spacers (at 550 and 1050 mm) in directions to 0° and 270° and led to the narrowing of the cooling channels between the rods.

At elevations 1050 and 555 mm, only small fragments of Inconel spacer grids remained on the periphery of the bundle. At four contact points of spacer cell to cladding, the spacer grids at these elevations could melted locally due to the eutectic interaction of Ni of the grids with Zr of the claddings at about 1480 K. However, the main part of spacers was melted at the end of the transient (melting point of Inconel X-750 is 1610 K).

At the elevations of 450...950 mm, a detailed measurement of all characteristic layers of each cladding was carried out. Fig. 7 presents a comparison of the thicknesses of the outer oxide layers of all claddings at three bundle elevations.

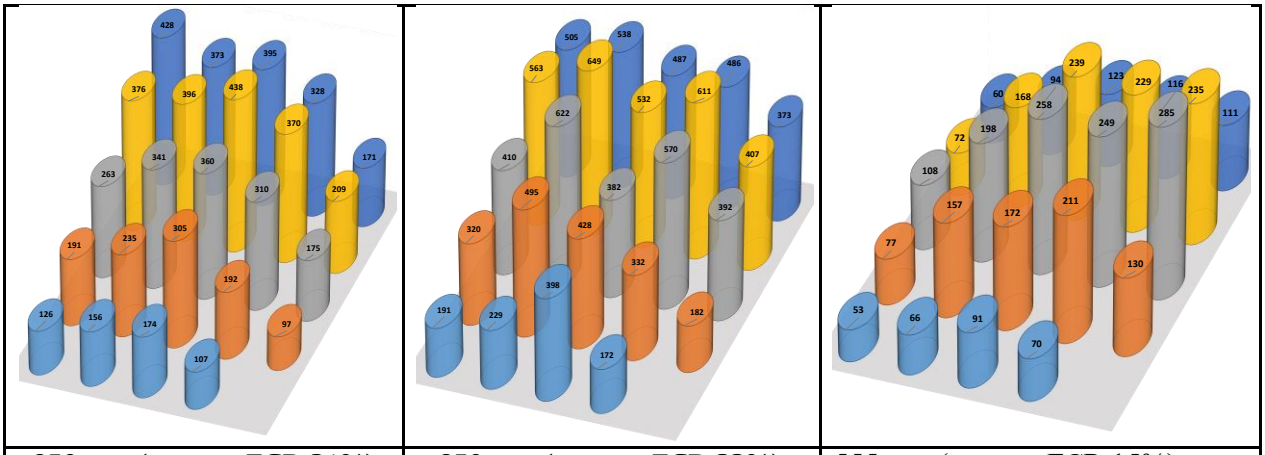

950 mm (average ECR 31%)	850 mm (average ECR 33%)	555 mm (average ECR 15%)

Figure 7. Comparison of oxide thickness for different rods at different elevations

4.1. Elevation 950 mm

The peak cladding temperature about 2100 K was measured at the central rod during the quench stage. The absorber blade at the angle position 0° is strongly destroyed due to eutectic interactions. The B_4C pin is practically absent at this position, whereas the B_4C pin at the angle position 270° was only not significantly attacked by melt formed due to interaction of stainless steel blade with Zr-based cannel box and shroud. Small molten pools were formed around the central rod by cladding melt released through the failed oxide layers of claddings. This cladding melt is mixed with spacer melt relocated from 1050 mm and steel melt from absorber blades. The gap between pellets and cladding was increased (lift-off) during the pre-oxidation stage due to rod inner overpressure of Kr. The cladding melt was partially released outside the claddings of inner rods 1…9 and mixed with spacer melt and absorber steel melt. The spacer melt from 1050 mm and from the steel absorber plate has penetrated between α-Zr(O) layers of rods (Fig. 8). The inner cladding surface of several rods was also partially oxidized due to steam penetration in the gap or due to interaction with pellet.

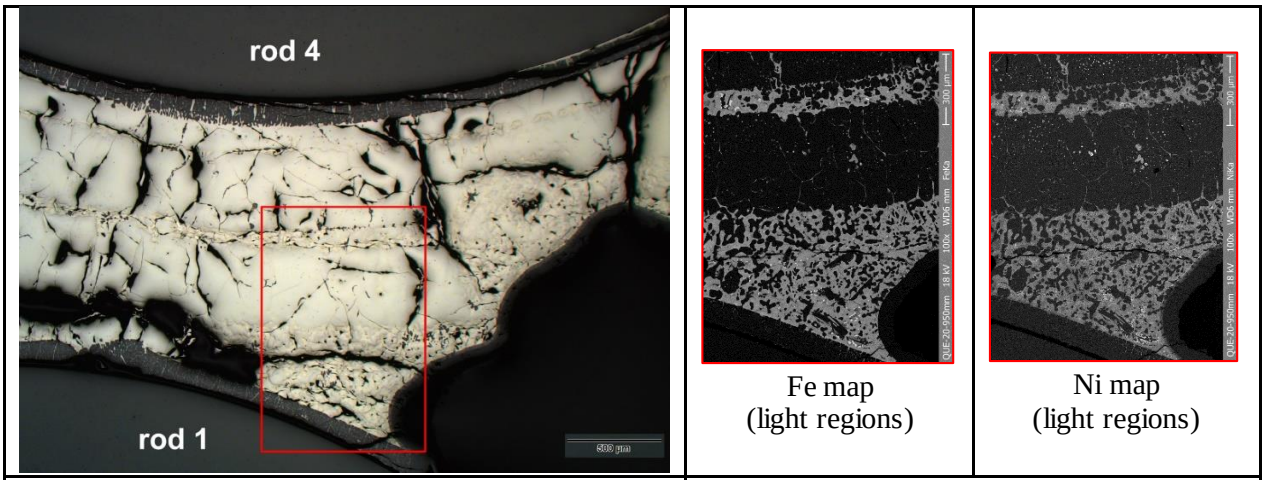

melt penetrated between α-Zr(O) layers of rods 1 and 4

Fe map
(light regions)

Ni map
(light regions)

EDX mapping of melt between rods 1 and 4

Figure 8. Spacer melt (Ni containing) at 950 mm relocated from 1010 mm

The claddings of peripheral hot rods along the absorber blades were strong oxidized and partially melted. The claddings of rods 13, 14 and 15 were failed at the contact with water channel and absorber blade. The corresponding Zr/SS eutectic melt, containing ZrB_2 and (Fe, Cr) chunks, penetrated under cladding and distributed along the entire perimeter of the cladding under the outer oxide layer (Fig. 9). Part of the oxide layer was dissolved and formed ceramic precipitates in the melt. The phenomenology of this process was investigated and described in [9]. The claddings of the relatively cold peripheral rods (e.g. rod #20) were only moderately oxidized without melting. The water wings and the shroud were also only moderately oxidized in this relatively cold region.

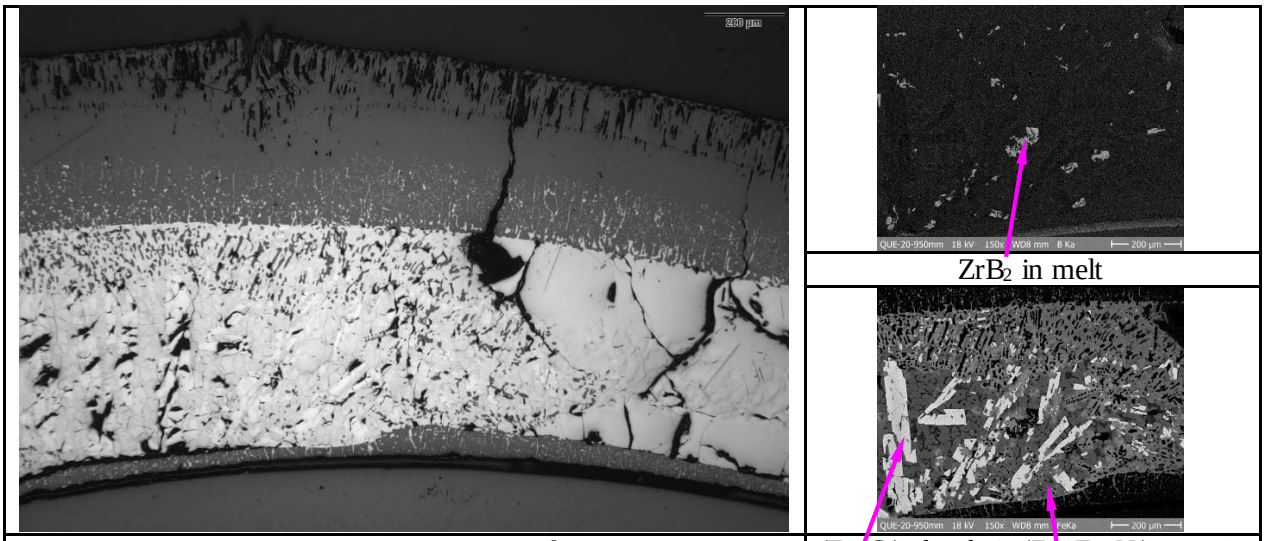

Figure 9. Optical view and SEM/EDX mapping for rod #13 at bundle elevation 950 mm

4.2. Elevation 750 mm

Similar to 950 and 850 mm, the B_4C pin inside the absorber blade reacted with stainless steel of the absorber blade and partially dissolved (Fig. 10). The detailed SEM/EDX analysis of the eutectic melt around the B_4C pin revealed formation of equiaxed (Fe, Cr) borides near to pin and the needle-shape ZrB_2 near to Zr-based channel box, in full accordance with the structures observed in [7].

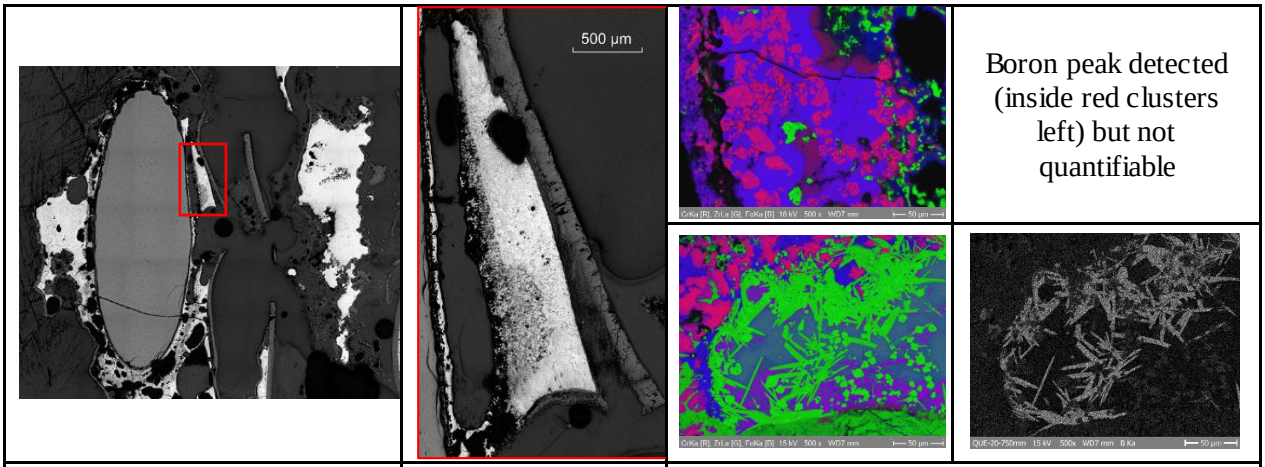

Figure 10. Interaction of B_4C with steel blade and ZIRLO channel box at 750 mm

The cladding melt released inside the group of inner rods #1…#9 formed several molten pools with steam channels with oxidized edges. The pellet-cladding gaps of inner rods #1…#4 were filled with molten cladding metal or the voids were formed here due to downwards melt relocation. For the more cold inner rods #5…#9, the gaps were mostly free from the melt. For the hot peripheral rods #10…#17, the eutectic melt (formed due to interaction of stainless steel blades with ZIRLO bundle parts) filled the entire gap and contacted the pellet (Figs. 11, 12). The presence of zirconium borides in the melt of these claddings confirms the penetration of melted elements of the absorber blade under the outer oxide layer of claddings (Fig. 13). For the relatively cold peripheral rods #18…#22, the gap (formed during the lift-off of the cladding due to Kr overpressure) was free from the melt. The claddings of the last two peripheral rods #23 and #24, which are in turn in the hot bundle area, were partially melted (especially for rod #24), and the melt contacted pellet and the outer oxide layer.

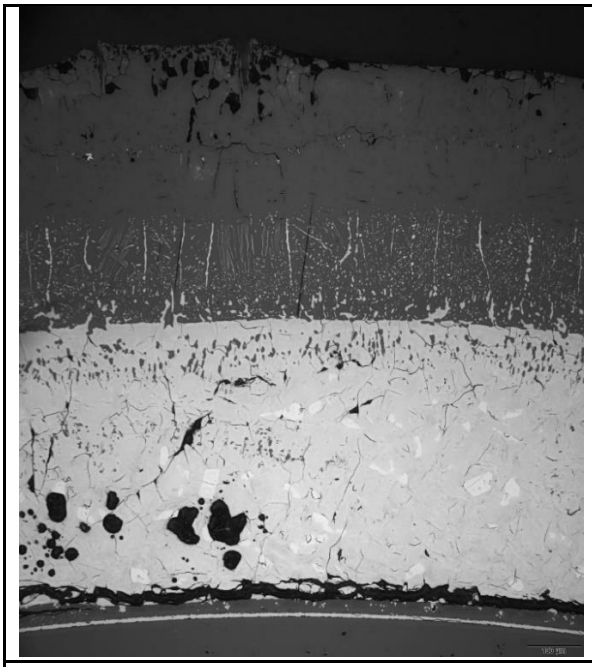

Figure 11. Microstructure of cladding #12 at bundle elevation 750 mm, 0: few (Fe,Cr) chunks in the eutectic Zr/steel melt



Figure 12. Microstructure of cladding #17 at bundle elevation 750 mm, 45°: numerous (Fe,Cr) chunks in the eutectic Zr/steel melt

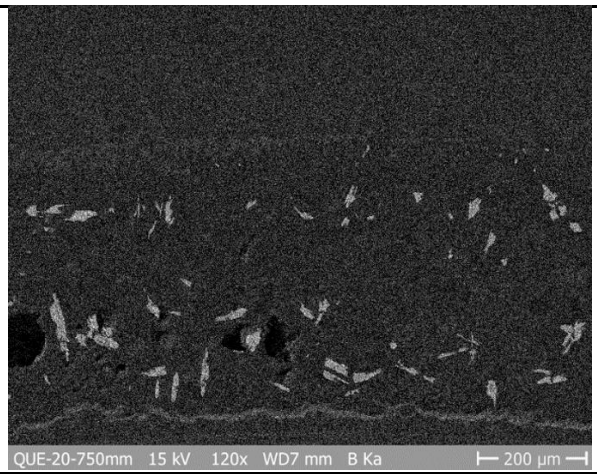

B map

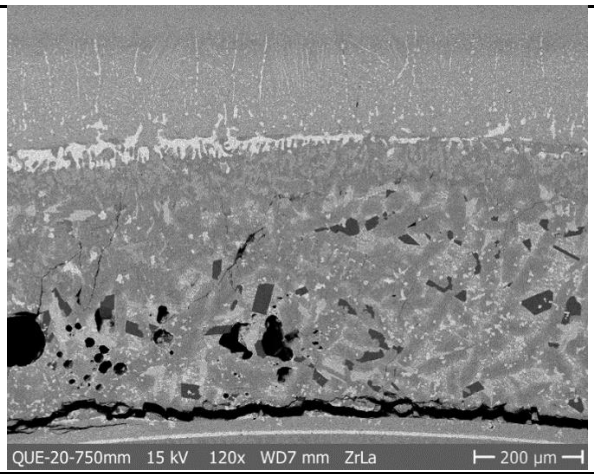

Zr map

Figure 13. SEM/EDX mapping of zirconium borides in the eutectic melt of rod #12 at 750 mm

4.3. Elevation 550 mm

Temperature peaks on the shroud (azimuthal side 0°) during the transient indicate the relocation of the Zr-SS eutectic melt here from the upper bundle elevations. The interaction of the melt with the B_4C pins was minimal. Cladding oxidation was moderate and more pronounced in the center of the bundle. Only small fragments of Inconel spacer grids (about 70% Ni) remained on the periphery of the bundle. In the center of the bundle, the spacer grids at these elevations were melted firstly due to the eutectic interaction of the nickel of the grids with the zirconium of the claddings: the deepest eutectic temperature is 1233 K. At a later stage of the transient, the melting point of the Inconel spacer (1610 K) was exceeded. The melt partially relocated down, and partially penetrated under the damaged claddings (Fig. 14). This melt characterized by the formation of Zr precipitates distributed over the eutectic melt.

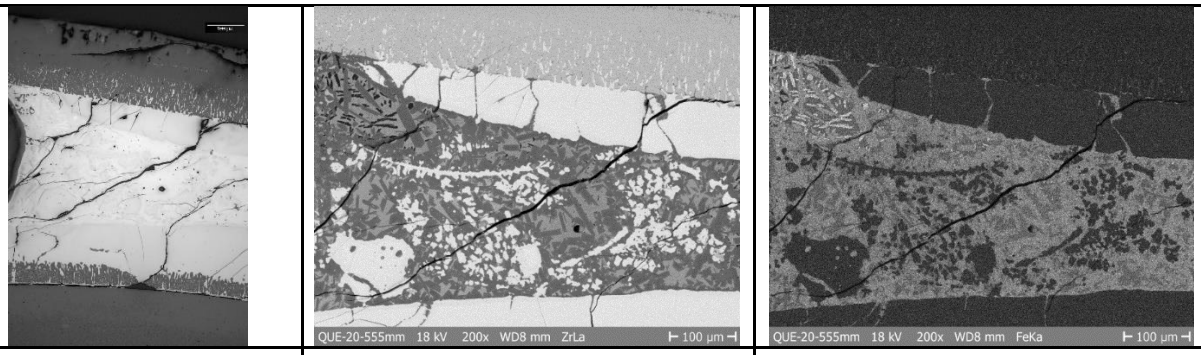

cladding and pellet layers	α-Zr(O) precipitates in melt	eutectic melt (Fe, Ni, Zr containing)

Figure 14. Optical view and SEM/EDX mapping for rod #3 at bundle elevation 550 mm

The claddings of the outer rods were less damaged than those of the inner ones, but the eutectic melt formed here was penetrated into the gap and distributed between inner and outer α-Zr(O) layers too. It is interesting to note that if the zirconium-nickel eutectic prevails in the melt for the hotter and more damaged inner rods, then the zirconium-iron-chromium eutectic dominates in the less damaged outer rods. This is clear too seen from the comparison of the SEM/EDX analysis of rods 9 and 10 (Fig. 15). Sometimes for the outer rods, the formation of (Fe, Cr) chunks in the (Zr, Ni) eutectic melt is observed.

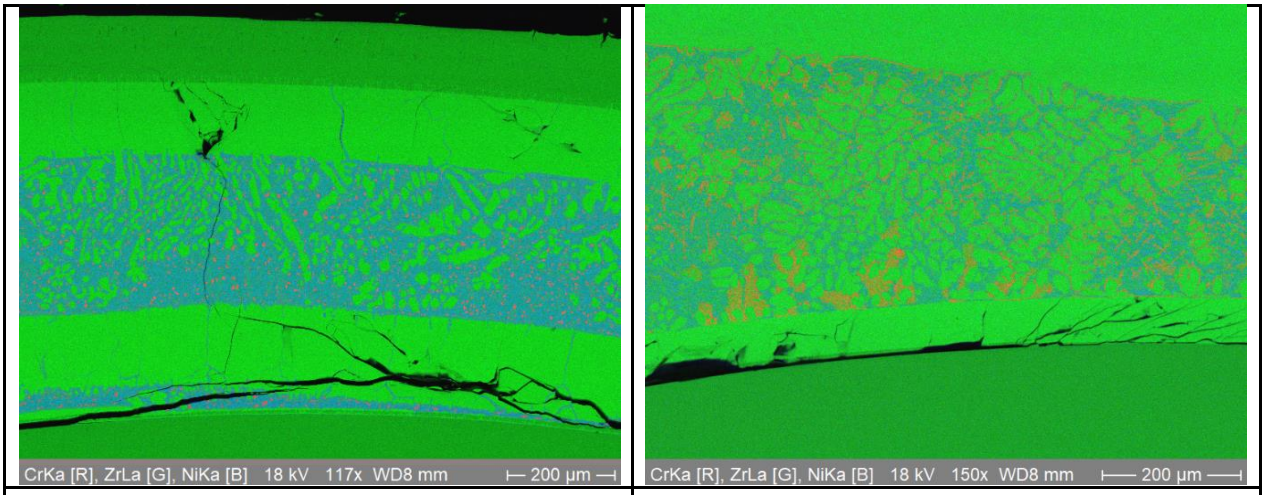

rod #9: more Ni in melt (intensive blue)	rod #10: less Ni in melt (light blue)

Figure 15. SEM/EDX mappings for rods #9 and #10 at bundle elevation 550 mm

5. CONCLUSIONS

Experiment QUENCH-20 with BWR geometry simulation bundle was successfully conducted at KIT on 9th October 2019 in the framework of the international SAFEST project. The test bundle mock-up represented one quarter of a BWR fuel assembly with 24 electrically heated fuel rod simulators and two B_4C control blades. The rod simulators were filled with Kr to inner pressure of 5.5 bar at peak cladding temperature of 900 K. The pre-oxidation stage in the flowing gas mixture of steam and argon (each 3 g/s) and system pressure of 2 bar lasted 4 hours at the peak cladding temperature of 1250 K. The Zry-4 corner rod, withdrawn at the end of this stage, showed the maximal oxidation at elevations between 930 and 1020 mm with signs of breakaway. During the transient stage, the bundle was heated to a maximal temperature of 2000 K. The coolability of bundle was decreased by its squeezing due to the shroud ductile deformation caused by overpressure outside the shroud. The cladding radial extensions and failures due to inner overpressure (about 4 bar) were observed at temperature about 1700 K and lasted about 200 s.

During the period of rod failures also the first absorber melt relocation accompanied by shroud failure were registered. The interaction of B_4C with steel blade and ZIRLO channel box was observed at elevations 650…950 mm with formation of eutectic melt. The typical components of this melt are (Fe, Cr) borides and ZrB_2 precipitated in steel melt or in Zr-steel eutectic melt. Massive absorber melt relocation was observed 50 s before the end of transition stage. Small fragments of the absorber melt moved down to the elevation of 50 mm. The melting point of Inconel spacer grids at 500 and 1050 mm was reached also at the end of the transition stage. The Inconel melt from the elevation 1050 mm relocated downwards through hot bundle regions to the Inconel grid spacer at 550 mm and later (during the escalation caused by quench) to 450 mm. This melt penetrated also under damaged cladding oxide layer and formed molten eutectic mixtures between elevations 450 and 550 mm.

The test was terminated with the quench water injected with a flow rate of 50 g/s from the bundle bottom. Fast temperature escalation from 2000 to 2300 K during 20 s was observed. As result, the metal part (prior β-Zr) of claddings between 550 and 950 mm was melted, partially released into space between rods and partially relocated inside the gap between pellet and outer oxide layer to 450 mm. It should be noted the positive role of the oxide layer, which does not allow the melt to completely escape into the inter-rod space - and thereby limiting the possibility of interaction of a large amount of melt with steam, which could significantly increase the exothermic oxidation processes and the escalation of temperatures.

The distribution of the oxidation rate within each bundle cross section is very inhomogeneous: whereas the average outer ZrO_2 layer thickness for the central rod (#1) at the elevation of 750 mm is 465 µm, the same parameter for the peripheral rod #24 is only 108 µm. The average oxidation rate of the inner cladding surface (due to interaction 1) with steam, 2) with pellets) is about 20% in comparison to the outer cladding oxidation. The bundle elevations 850 and 750 mm are *mostly* oxidized with average cladding ECR 33% due to: 1) downwards shift of the temperature maximum from 950 mm (ECR 31%) during transient and quench, 2) due to cladding melt relocation inside and outside the rods from 800…1000 mm to lower bundle elevations. The oxidation of the melt relocated inside rods was observed at elevations 550…950 mm.

The mass spectrometer measured release of CO (12.6 g), CO_2 (9.7 g) and CH_4 (0.4 g) during the reflood as products of absorber oxidation; corresponding B_4C reacted mass was 41 g or 4.6% of total B_4C. It is significantly lower than in the PWR bundle tests QUENCH-07 and QUENCH-09 containing central absorber rod with B_4C pellets inserted into a thin stainless steel cladding and Zry-4 guide tubes (20% and 50% reacted B_4C correspondingly [5]). Hydrogen production during the reflood amounted to 32 g during the reflood (57.4 g during the whole test) including 10 g from B_4C oxidation.

ACKNOWLEDGMENTS

The QUENCH-20 experiment was performed in the framework of the SAFEST project in cooperation with Swedish Radiation Safety Authority (SSM), Westinghouse Sweden, GRS and KTH and supported by the KIT program NUSAFE. Personal thanks to Mr. Isaksson (SSM), Mr. Bechta (KTH), Mr. Hollands (GRS), Ms. Korske (Westinghouse) for their help and fruitful cooperation. The bundle materials and absorbers were provided by Westinghouse Sweden. The authors thank particularly J. Moch (KIT) for bundle preparation

REFERENCES

1. J. Stuckert, M. Steinbrueck, M. Grosse, "Experimental program QUENCH at KIT on core degradation during reflooding under LOCA conditions and in the early phase of a severe accident," *Proceedings of Meeting on Modelling of Water Cooled Fuel Including Design Basis and Severe Accidents*, Chengdu/China, 28 October–1 November 2013, IAEA-TECDOC-CD-1775, pp. 281-297, https://www-pub.iaea.org/MTCD/Publications/PDF/TE-1775_CD_web.pdf (2013).

2. T. Haste, M. Steinbrück, M. Barrachin, O. de Luze, M. Grosse, J. Stuckert, "A comparison of core degradation phenomena in the CORA, QUENCH, Phébus SFD and Phébus FP experiments," *Nuclear Engineering and Design*, **283**, pp. 8–20 (2015), https://doi.org/10.1016/j.nucengdes.2014.06.035.

3. M. Steinbrück, M. Große, L. Sepold, J. Stuckert. "Synopsis and outcome of the QUENCH experimental program", *Nuclear Engineering and Design*, **240** (7), pp. 1714-1727, (2010), https://doi.org/10.1016/j.nucengdes.2010.03.021.

4. M. Steinbrück, C. Homann, A. Miassoedov, G. Schanz, L. Sepold, U. Stegmaier, H. Steiner, J. Stuckert. „Results of the B_4C control rod test QUENCH-07", *FZKA-6746* (2004), https://doi.org/10.5445/IR/270058023.

5. M. Steinbrück, A. Miassoedov, G. Schanz, L. Sepold, U. Stegmaier, H. Steiner, J. Stuckert. „Results of the QUENCH-09 experiment with a B_4C control rod", *FZKA-6829* (2004), https://doi.org/10.5445/IR/270059406.

6. P. Hofmann, M. Markiewicz, J. Spino. "Reaction Behaviour of B_4C Absorber Material with Stainless Steel and Zircaloy in Severe LWR Accidents", *KfK 4598*, CNEA NT -10/89, (1989), https://doi.org/10.5445/IR/270027893.

7. M. Steinbrück. "Degradation and oxidation of B_4C control rod segments at high temperatures", *Journal of Nuclear Materials*, **400** (2), pp. 138-150, (2010), https://doi.org/10.1016/j.jnucmat.2010.02.022.

8. J. Stuckert, M. Große, J. Laier, J. Moch, U. Peters, U. Stegmaier, M. Steinbrück. „Results of the QUENCH-20 experiment with BWR test bundle", *NUSAFE 3576 (2022)*.

9. P. Hofmann, J. Stuckert, A. Miassoedov, M.S. Veshchunov, A.V. Berdyshev, A.V. Boldyrev. "ZrO_2 dissolution by molten zircaloy and cladding oxide shell failure. New experimental results and modelling", FZKA-6383, https://doi.org/10.5445/IR/270046616.

Karlsruhe Institute of Technology

Institute for Applied Materials

Results of metallographic analysis of the QUENCH-20 bundle with B_4C absorber

J. Stuckert, U. Peters, U. Stegmaier, M. Steinbrück

Institute for Applied Materials; Program NUSAFE

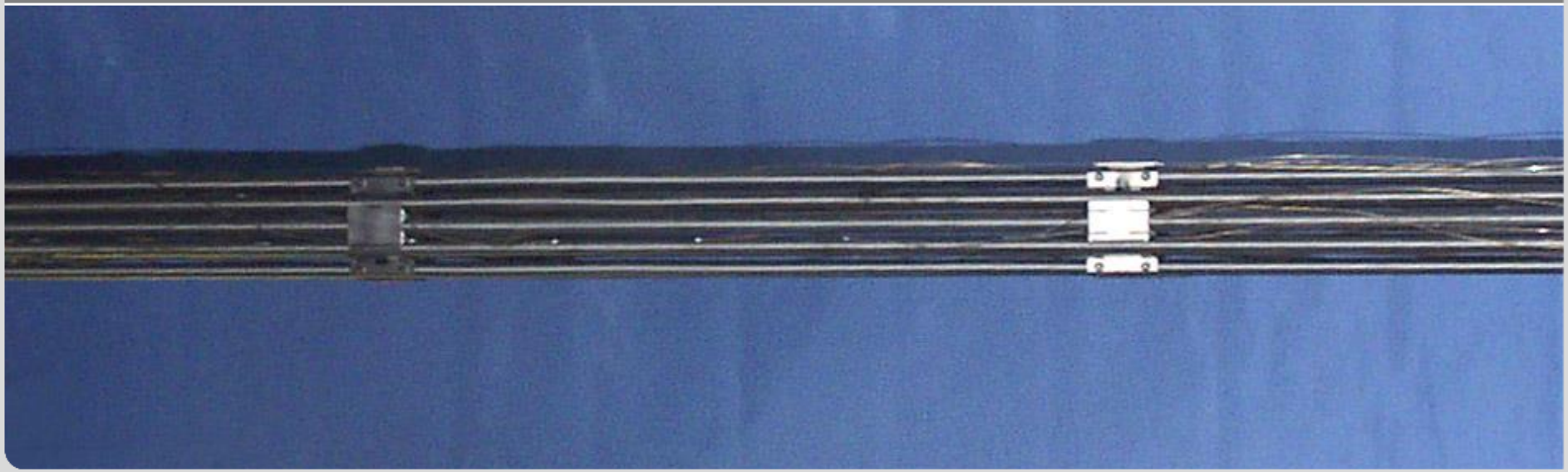

QUENCH-20 (SAFEST): Choice of BWR elements, which should be simulated during QUENCH-SAFEST

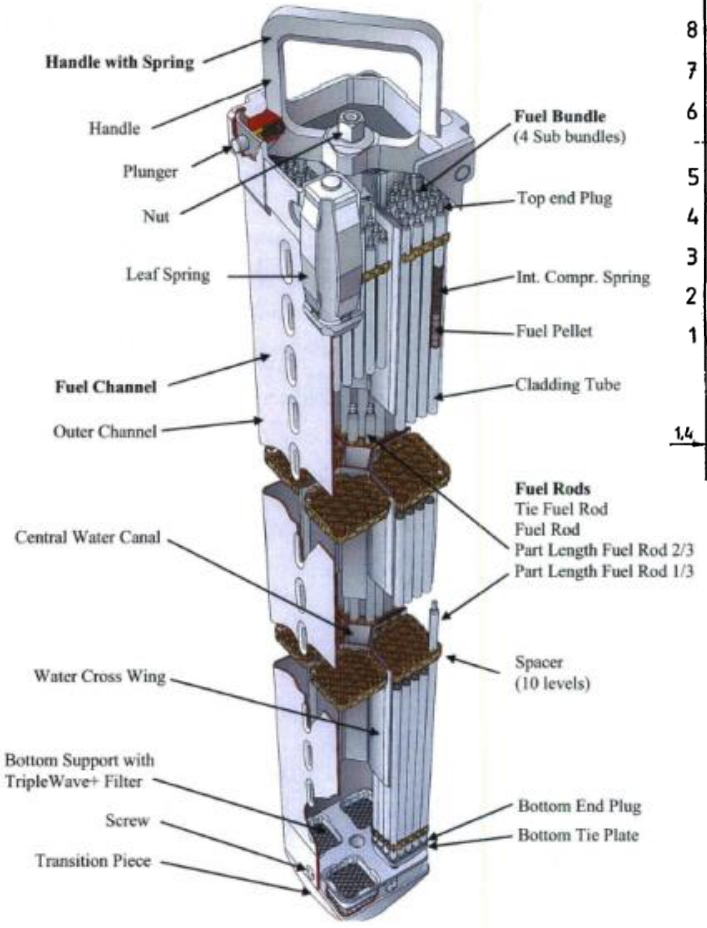

assembly SVEA-96 Optima

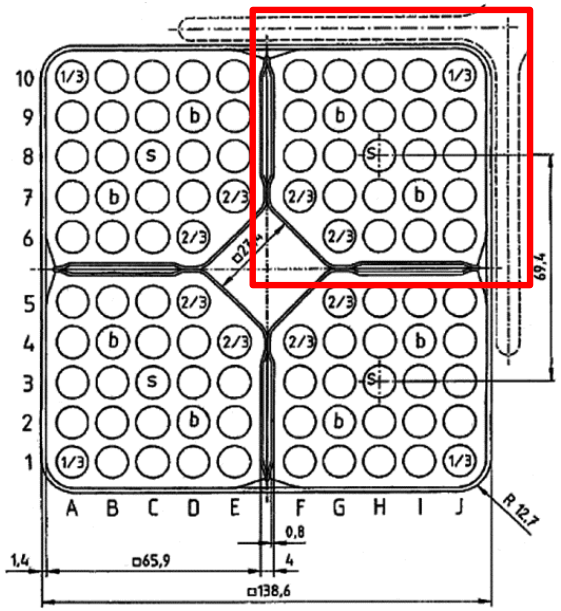

assembly cross section

***SSM/Sweden proposal for SAFEST*: study of high temperature degradation of BWR assembly mock-up in QUENCH facility: 1) melt formation due to eutectic material interaction inside absorber cross, 2) melting of claddings.**

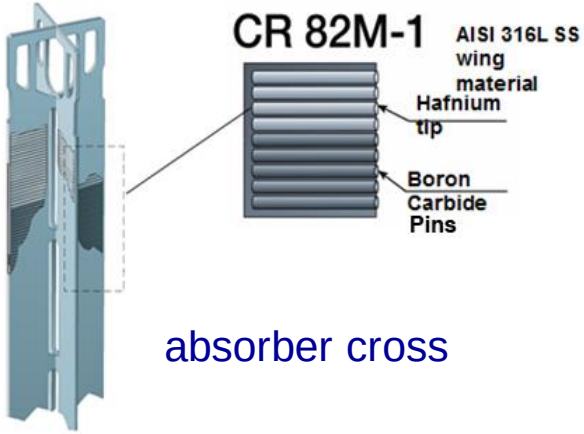

absorber cross





horizontal holes for B_4C pins

QUENCH-20: suggested test bundle composition (¼ SVEA-96 OPTIMA2 assembly)

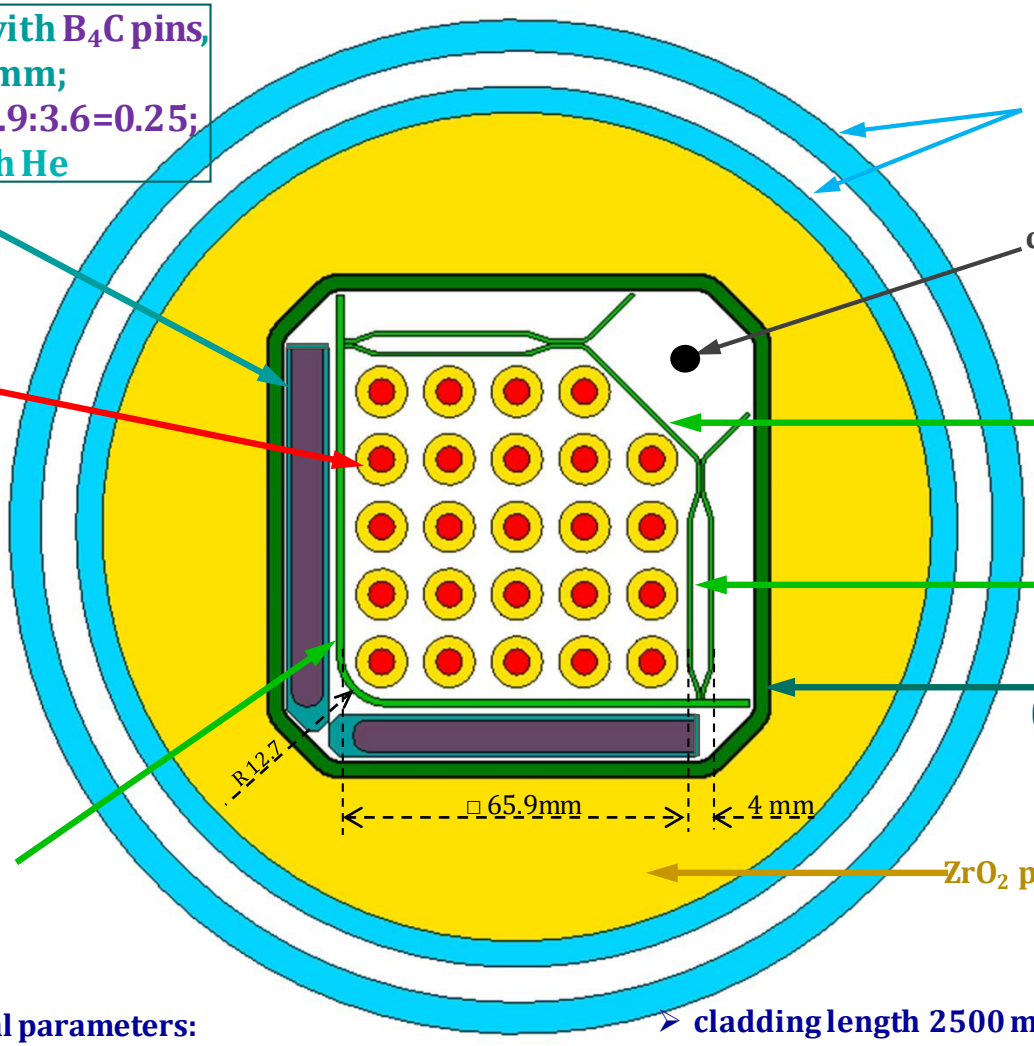

absorber steel blades with B_4C pins, side length 67 mm; mass ratio B_4C:steel=0.9:3.6=0.25; holes filled with He

pressurized (5.5 bar Kr) heated rods (24):

cladding Zy-2 with inner ZrSn-liner (10% of clad),

ZrO_2 pellet OD 8.48±0.05 ID 5.45±0.1 mm, length 11 mm,

W heater OD 5.25±0.025 mm

advanced low tin ZIRLO fuel channel box, wall thickness 1.4 mm

Inconel cooling jacket, inner tube ID=158.3 mm

corner rod (Zry-4, OD 6 mm)

water channel box (ZIRLO), side length 27.4 mm

water cross wing (ZIRLO), wall thickness 0.8 mm

Zr shroud 90 mm x 114 mm (inner clearance dimensions), wall thickness 3 mm

ZrO_2 porous thermal insulation

Geometrical parameters:

- bundle pitch 12.898 mm;
- outer diameter of claddings 9.84 mm;
- thickness of claddings 0.605 mm;
- absorber blades: thickness 8.05 mm

- cladding length 2500 mm
- absorber and cannel box lengths 1600 mm
- water gap between channel box and absorber blade 2.5 mm (nominal inter-assembly gap in BWR-PROTEUS core is 13.8 mm -> water gap 2.875 mm)

QUENCH-20: test progress

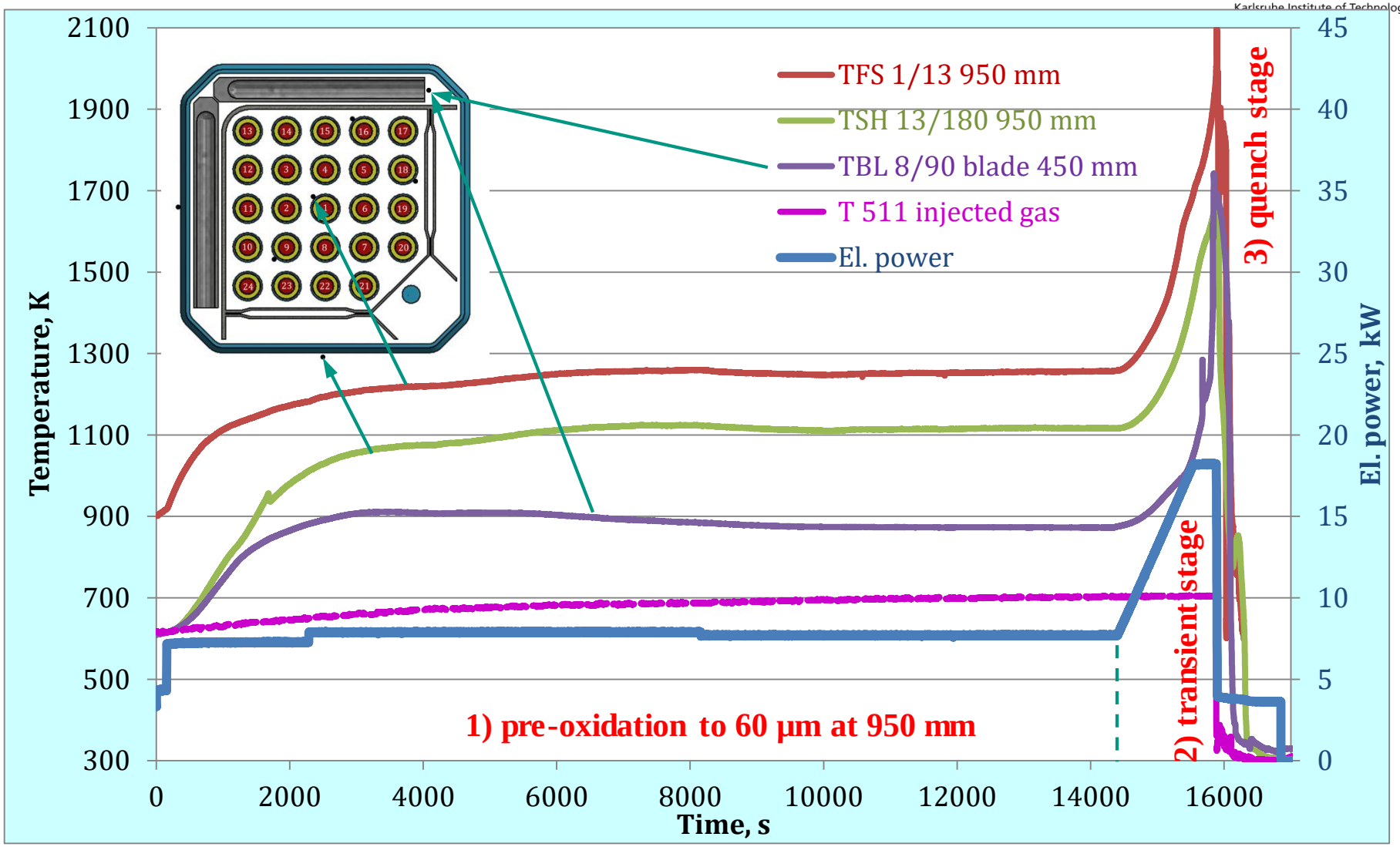

gas injection: Ar 3g/s during the whole test; superheated steam 3 g/s until the quench initiation

QUENCH-20: axial temperature profiles of outer cladding surfaces and outer shroud surface (TC readings averaged through the cross-section for each elevation)

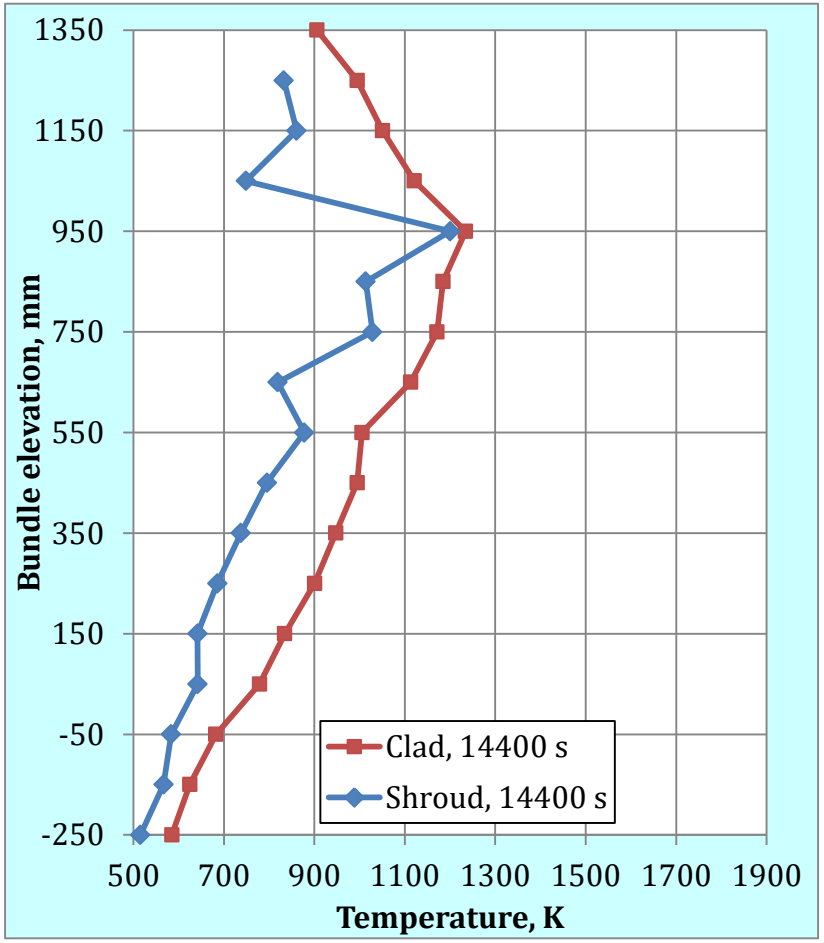

on the end of pre-oxidation (14400 s)

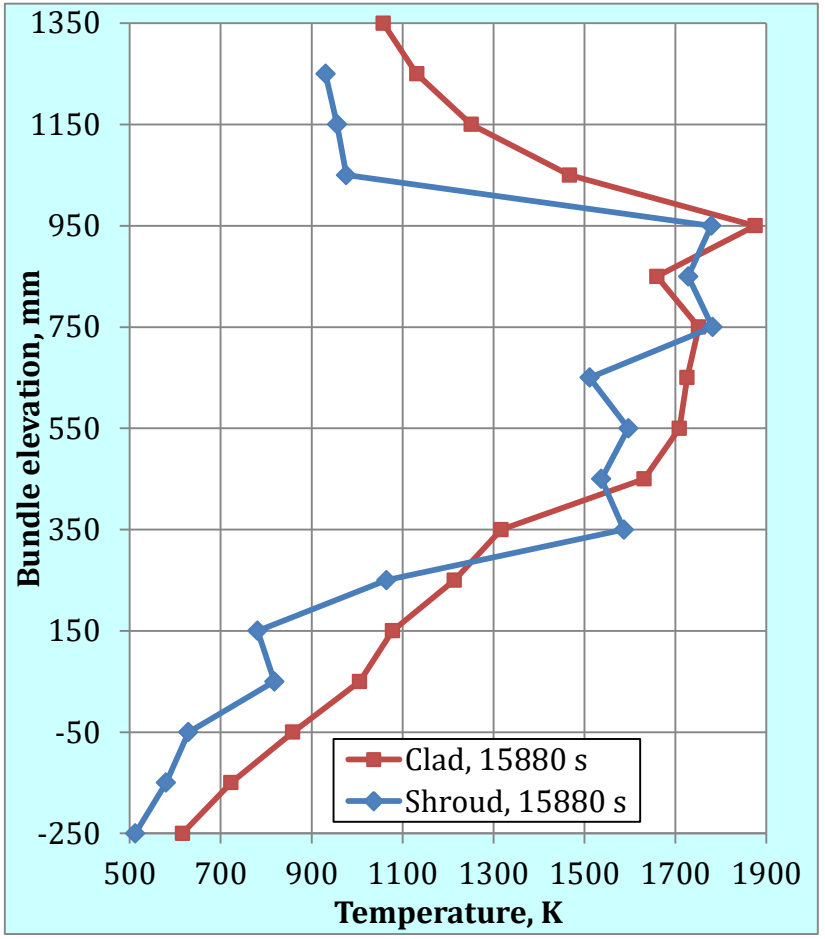

on the end of transient (15880 s)

QUENCH-20 bundle surrounded by shroud: post-test view

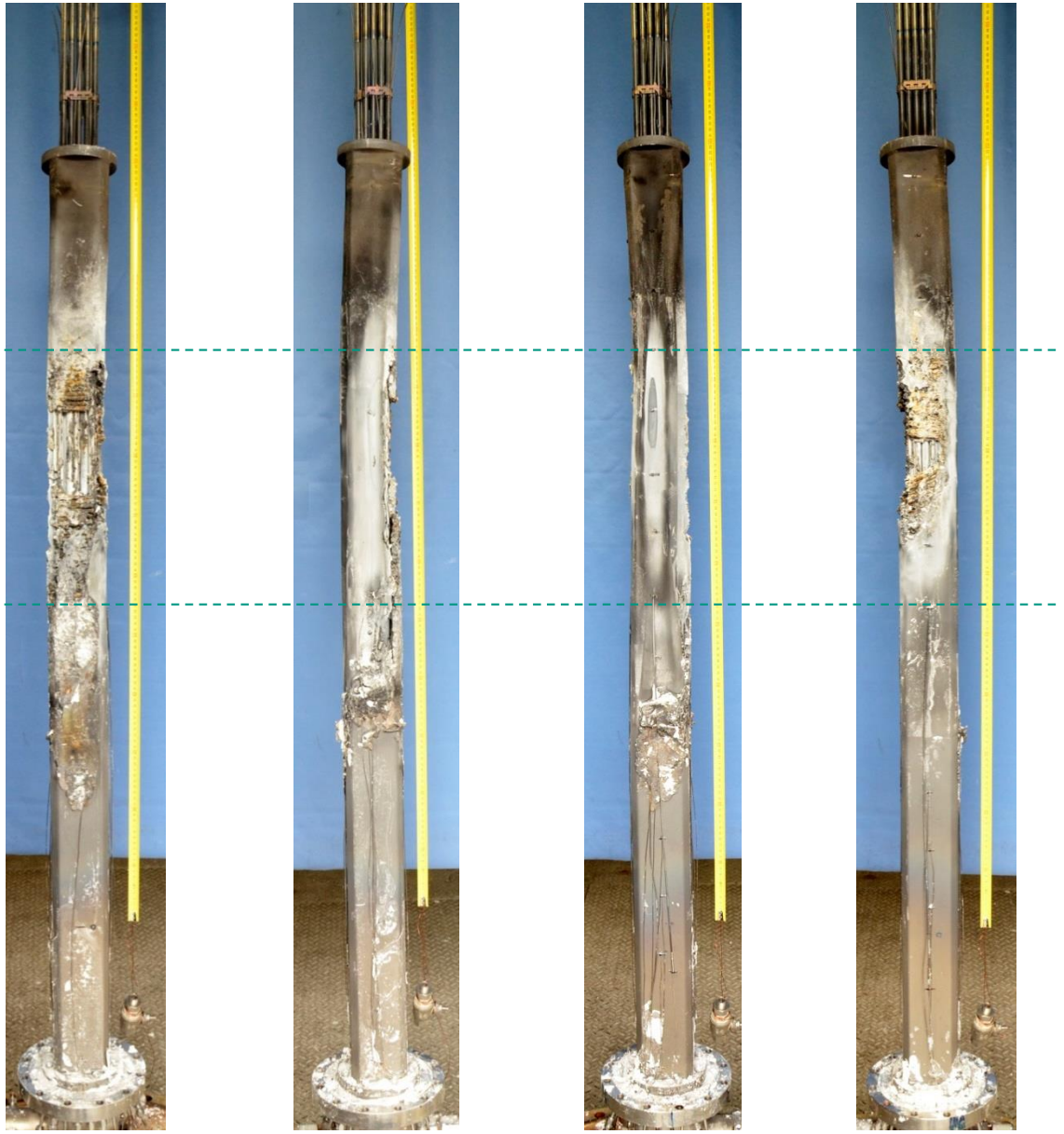

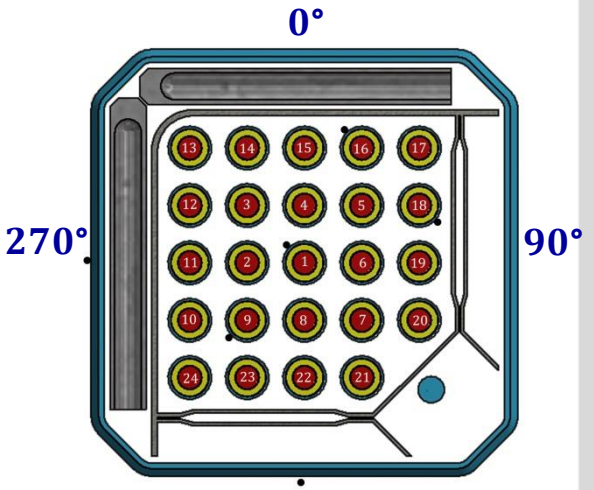

bundle cross-section, top view

QUENCH-20 bundle surrounded by shroud: post-test view

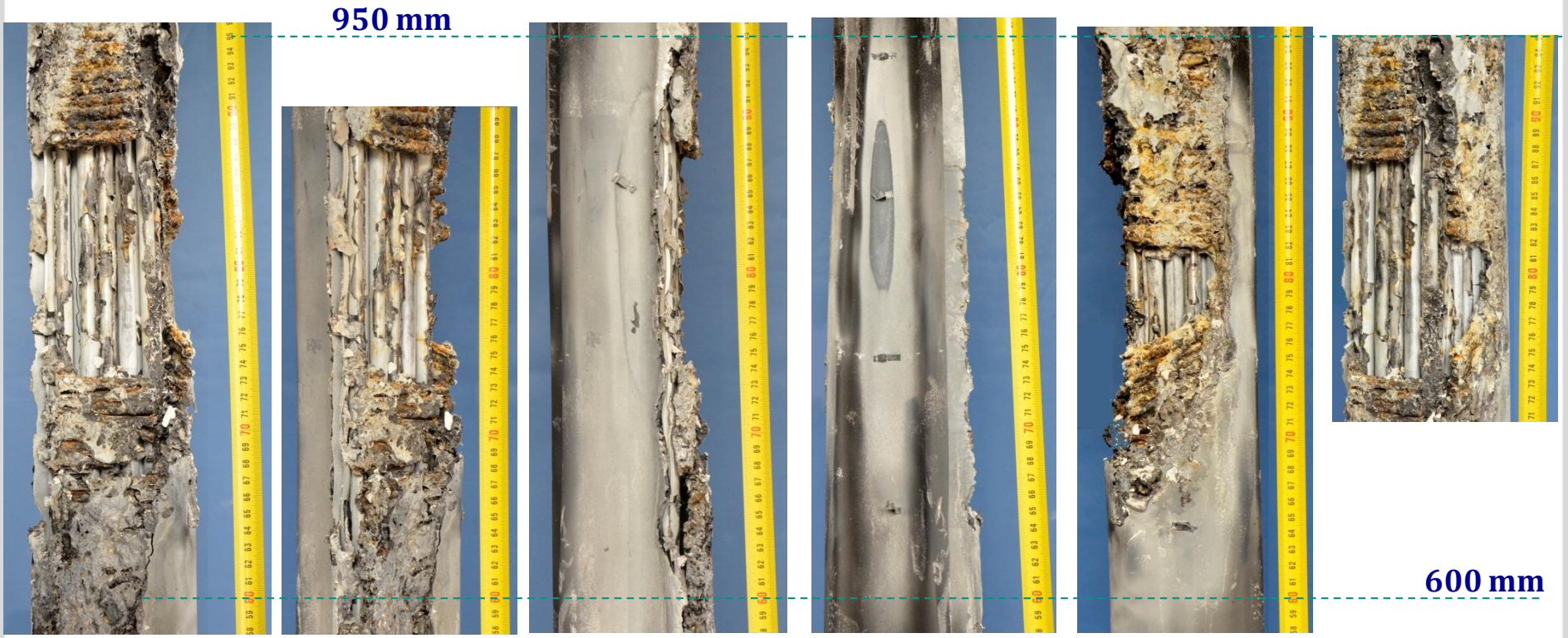

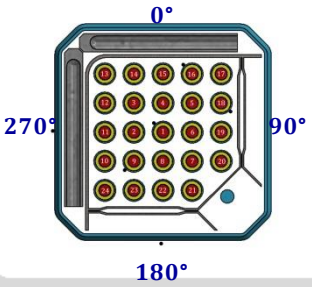

Strong degradation of absorber blades, channel box and shroud between elevations 650 and 950 mm at angle positions 0° and 270°

Piece of absorber blade broken away between 750 and 800 mm, 0°: eutectic interaction of B_4C pins with SS blade

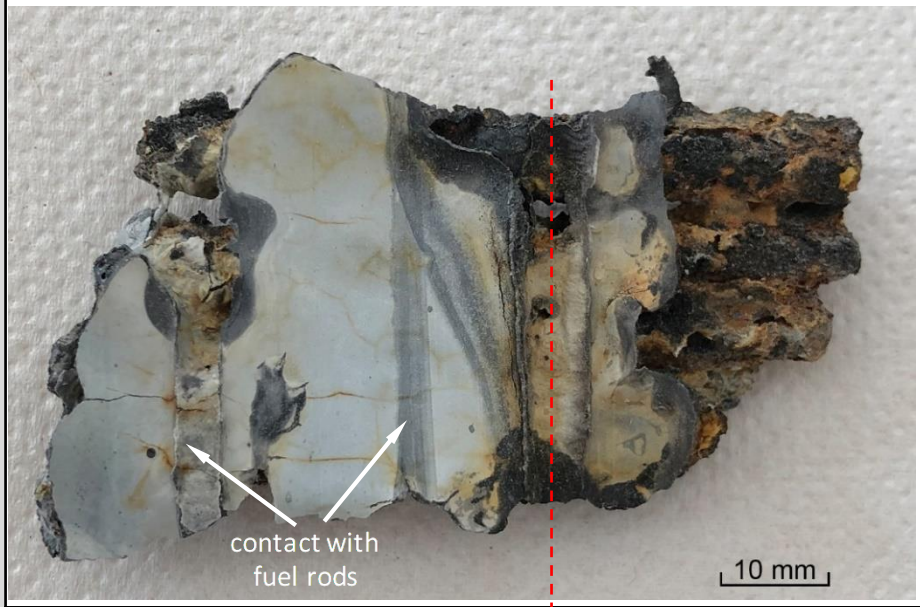

back side view: absorber blade covered by **oxidized channel box**



front side view: oxidized eutectic SS blade – B_4C absorber pins

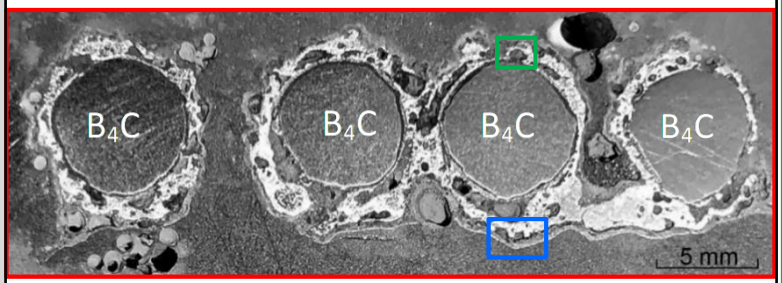

cross section of four B_4C pins interacted with steel blade

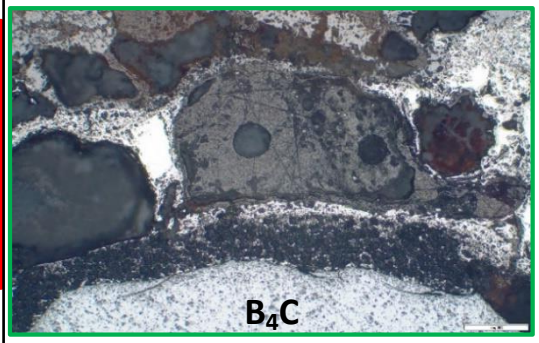

interaction B_4C - stainless steel

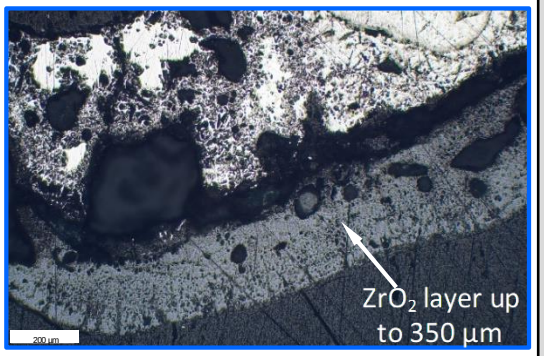

interaction B_4C - stainless steel - ZIRLO

Karlsruhe Institute of Technology
IAM Institute for Applied Materials

Overview of polished cross sections:
formation of eutectic absorber melt at elevations 450…950 mm;

deformation of Zr shroud and ZIRLO channel box at ≈900 °C due to outer overpressure of 1 bar

			
1150 mm	1050 mm, bottom of 4th spacer	950 mm	850 mm
		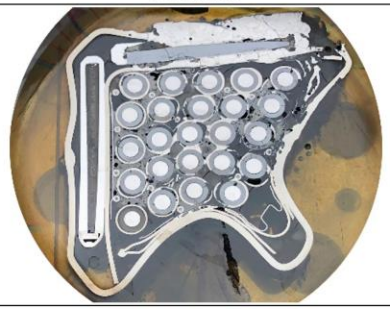	
750 mm	650 mm	555 mm, middle of 3rd spacer	450 mm
			
350 mm	250 mm	50 mm, bottom of 2nd spacer	

QUENCH-20: absorber melt relocation from hottest bundle elevations to elevations 250-450 mm (indication by TCs)

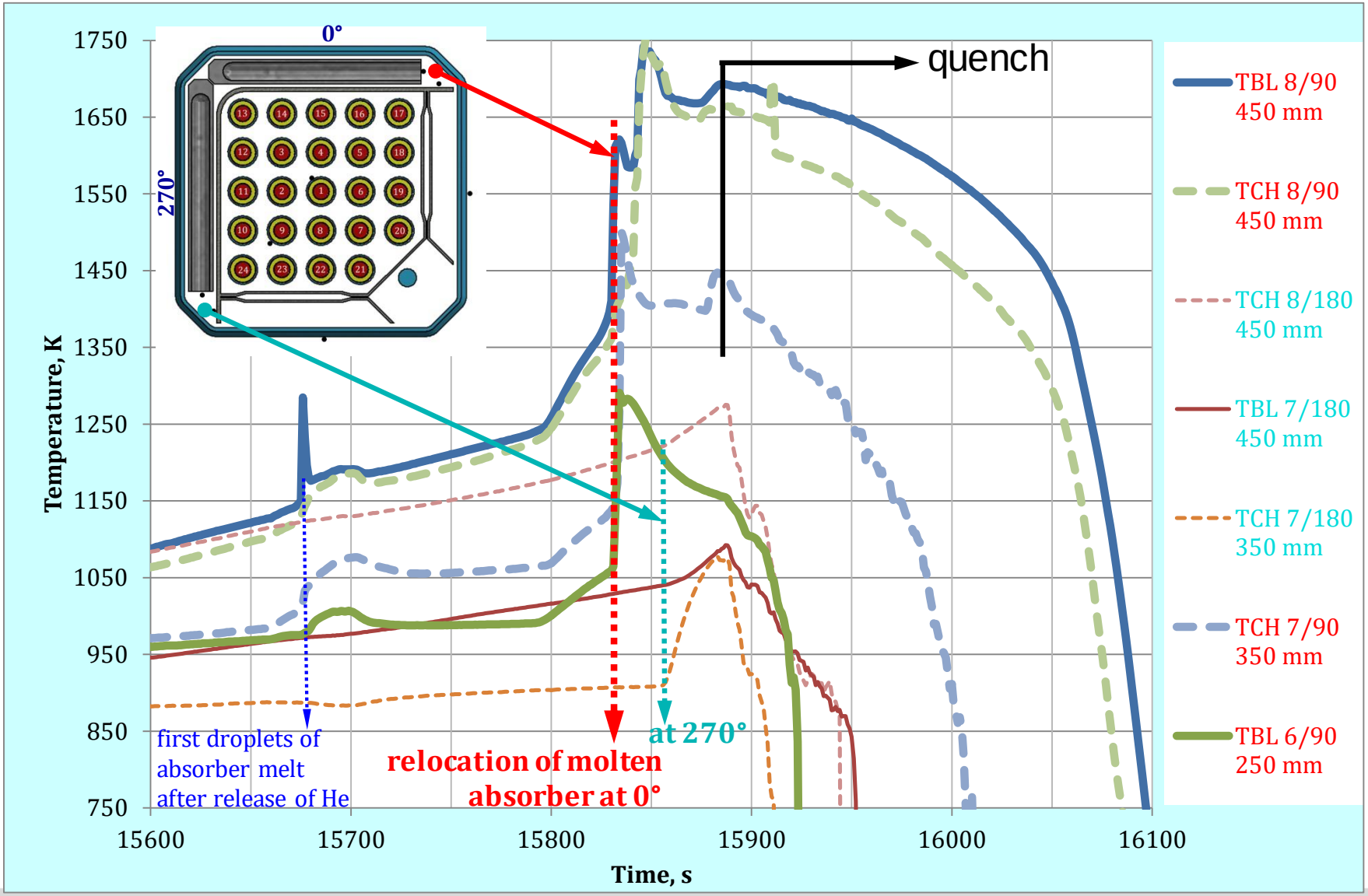

750 mm: interaction of stainless steel blade with B_4C and ZIRLO channel box

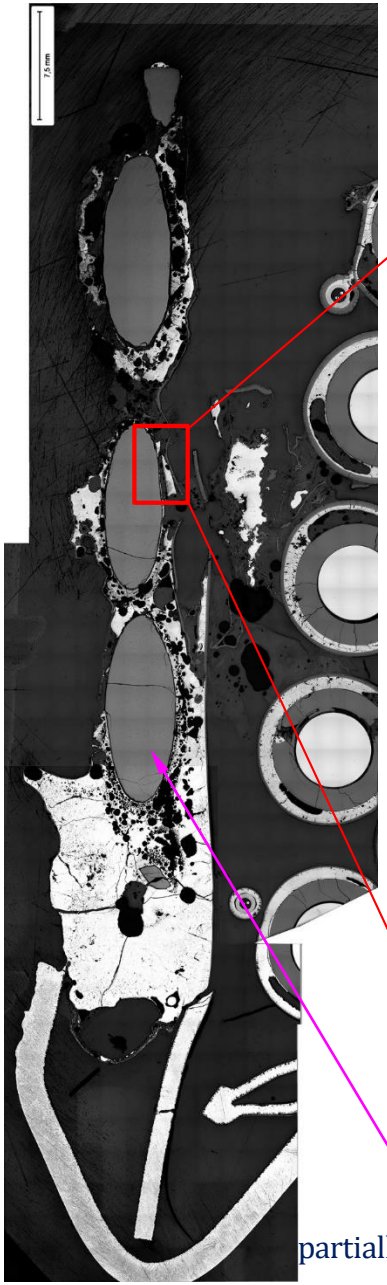

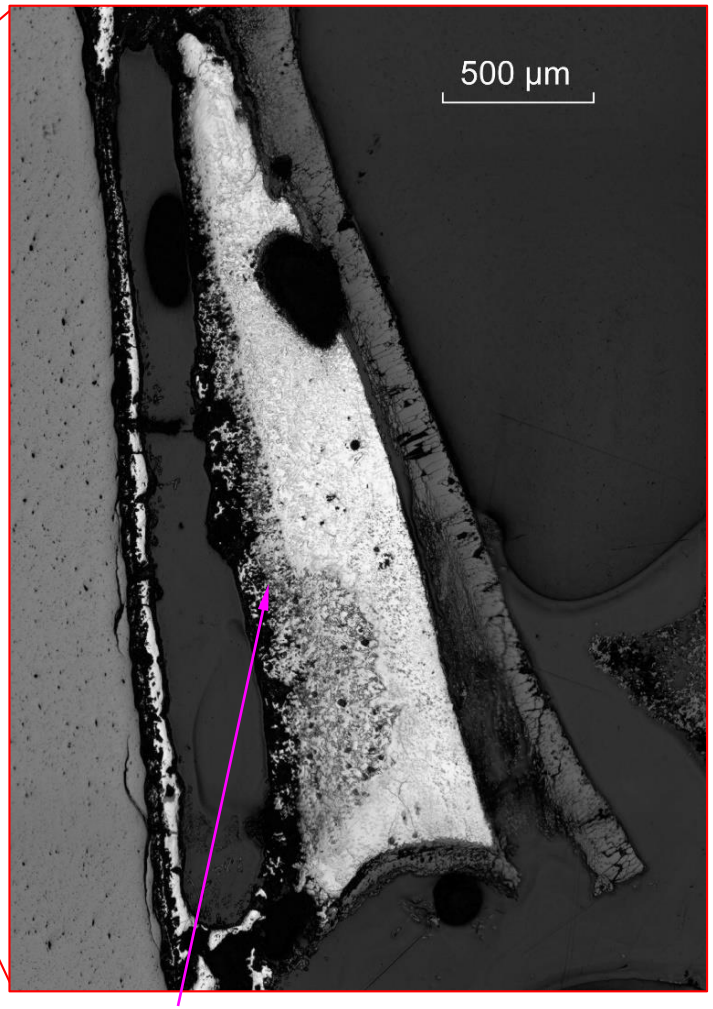

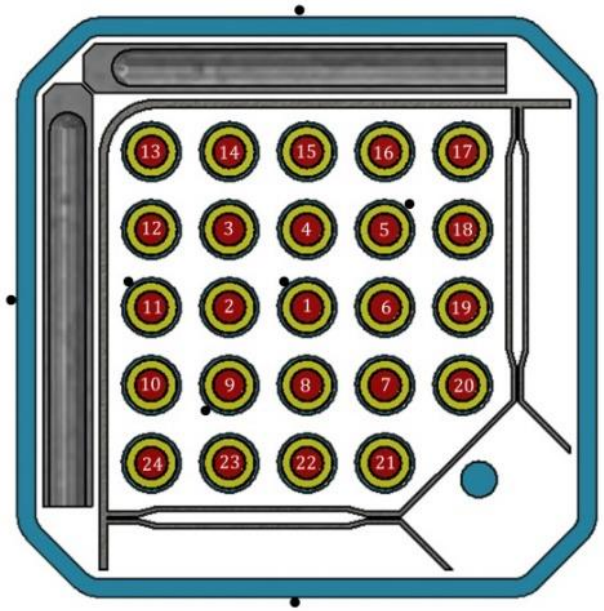

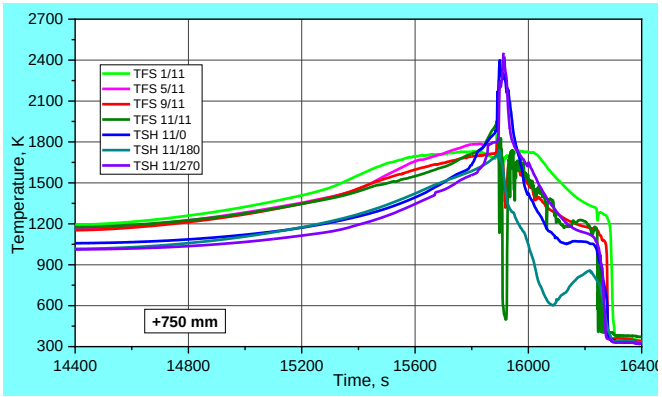

eutectic interaction B_4C pin ↔ SS blade at T>1500 K;

partially dissolved B_4C pin

750 mm: SEM/EDX investigation of interaction of B_4C with steel blade and ZIRLO channel box

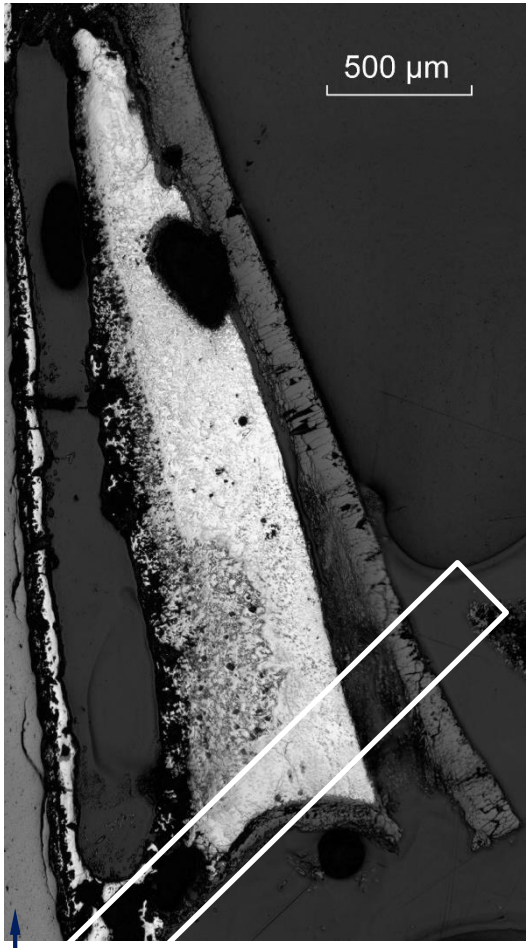

B_4C pin

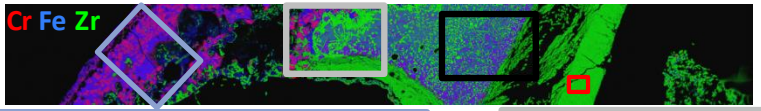

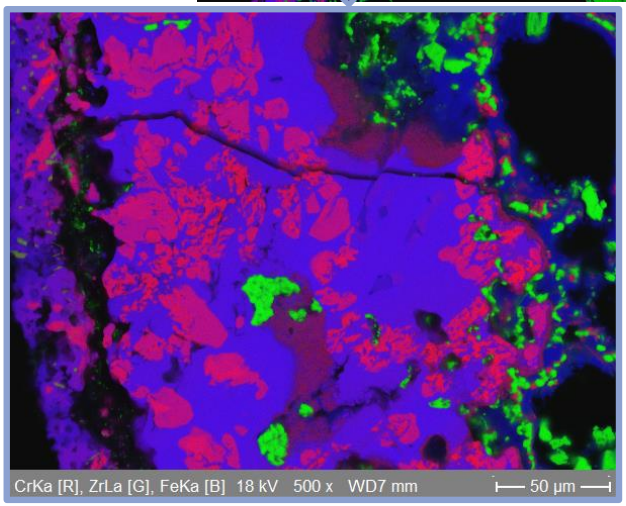

stainless steel blade: (Fe, Cr) boride (red) in steel melt (blue)

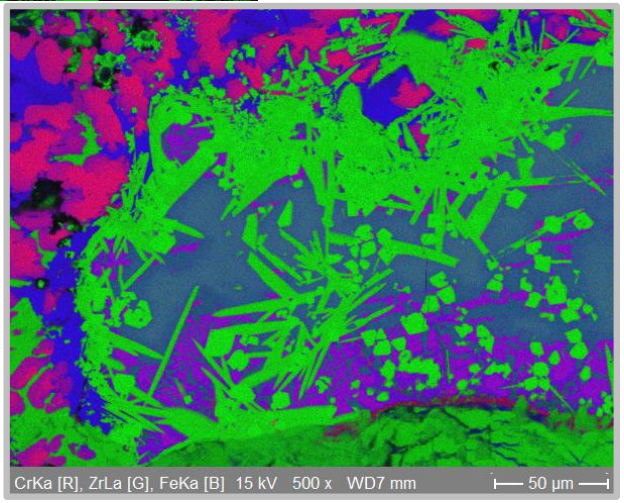

ZrB_2 needle precipitates in Zr-steel eutectic melt

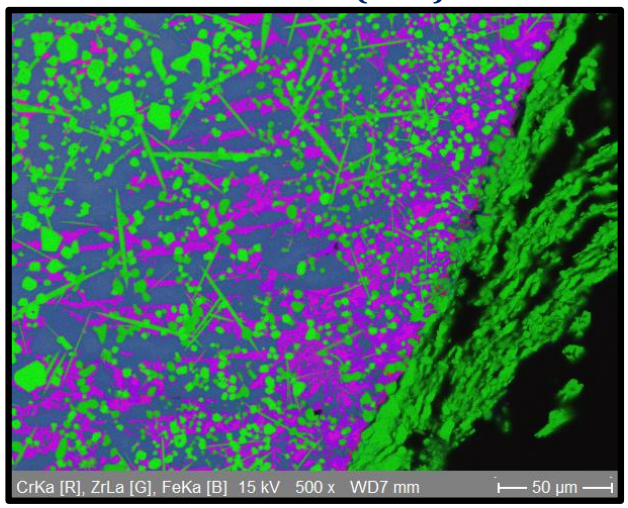

ZrB_2 needle precipitates in Zr-steel eutectic melt

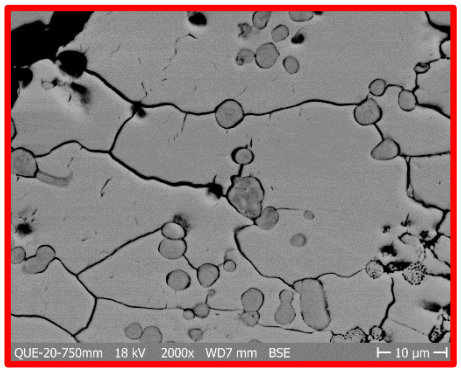

ZrO_2 layer of ZIRLO channel box

750 mm: SEM/EDX investigation of interaction of B_4C with steel blade and ZIRLO channel box

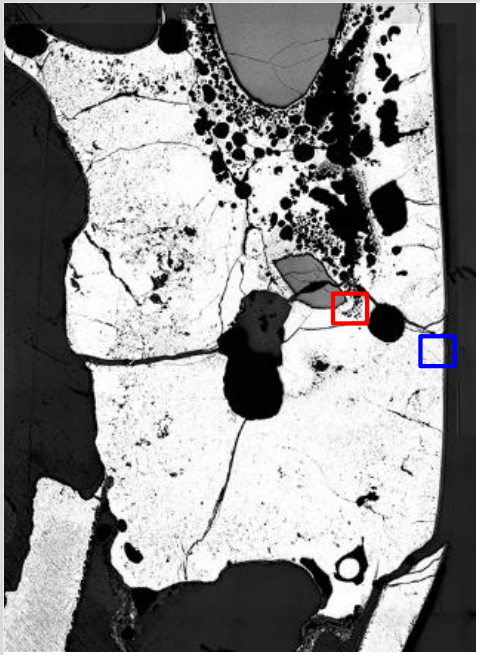

contact steel blade with ZIRLO channel box

B_4C

(Fe, Cr) precipitates
(partially borides)
in Fe melt

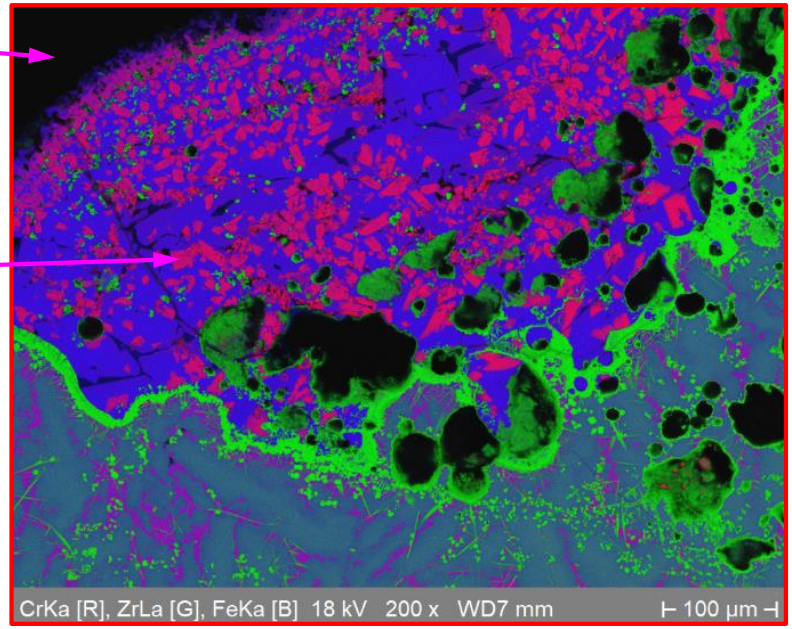

contact B_4C with steel blade

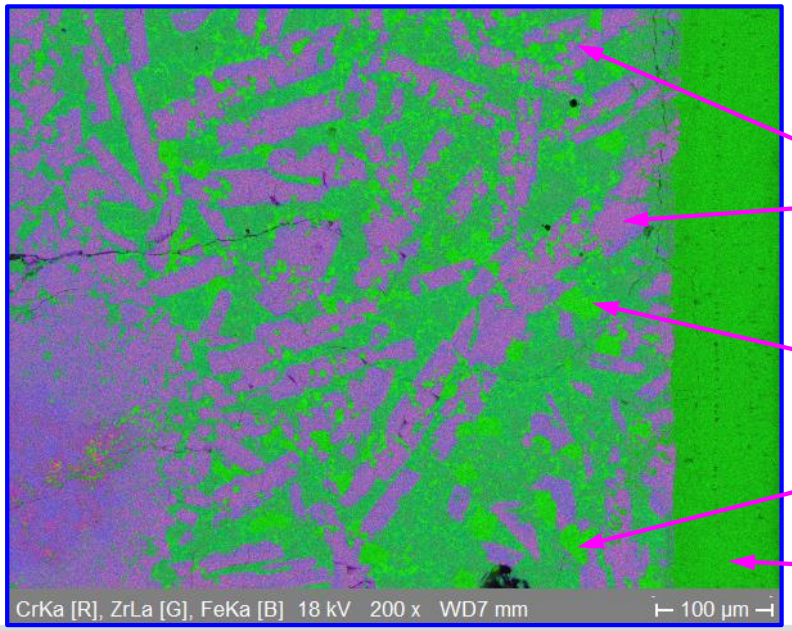

(Fe, Cr) precipitates
in (Ni, Fe, Zr) melt

ZrB_2 precipitates in
(Ni, Fe, Zr) melt

ZrO_2

QUENCH-20: reaction of B_4C with steam

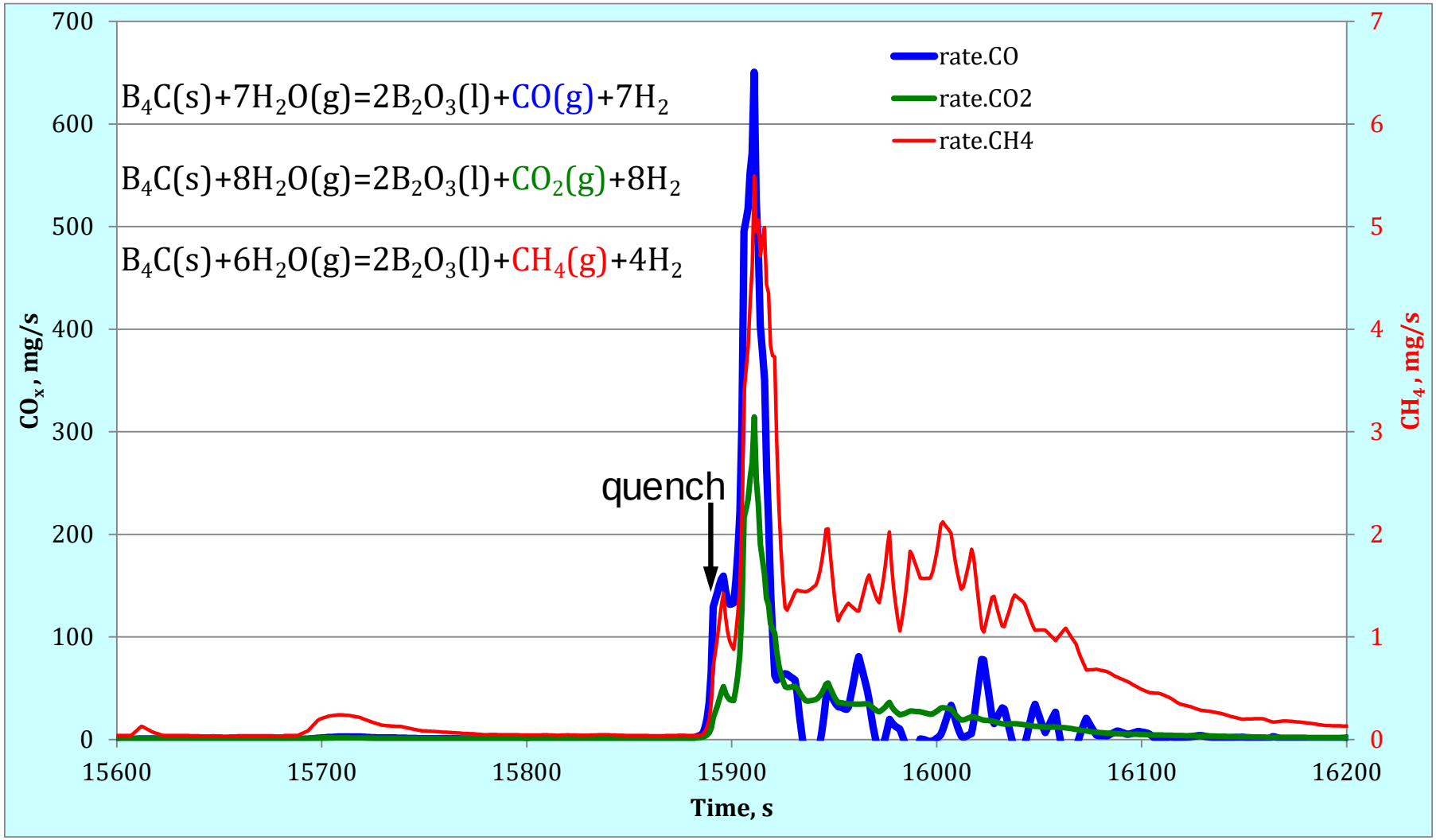

only small release of CH_4 before quench; CO and CO_2 formation firstly in the quench stage

QUENCH-20: reaction of B_4C with steam, integral gas release

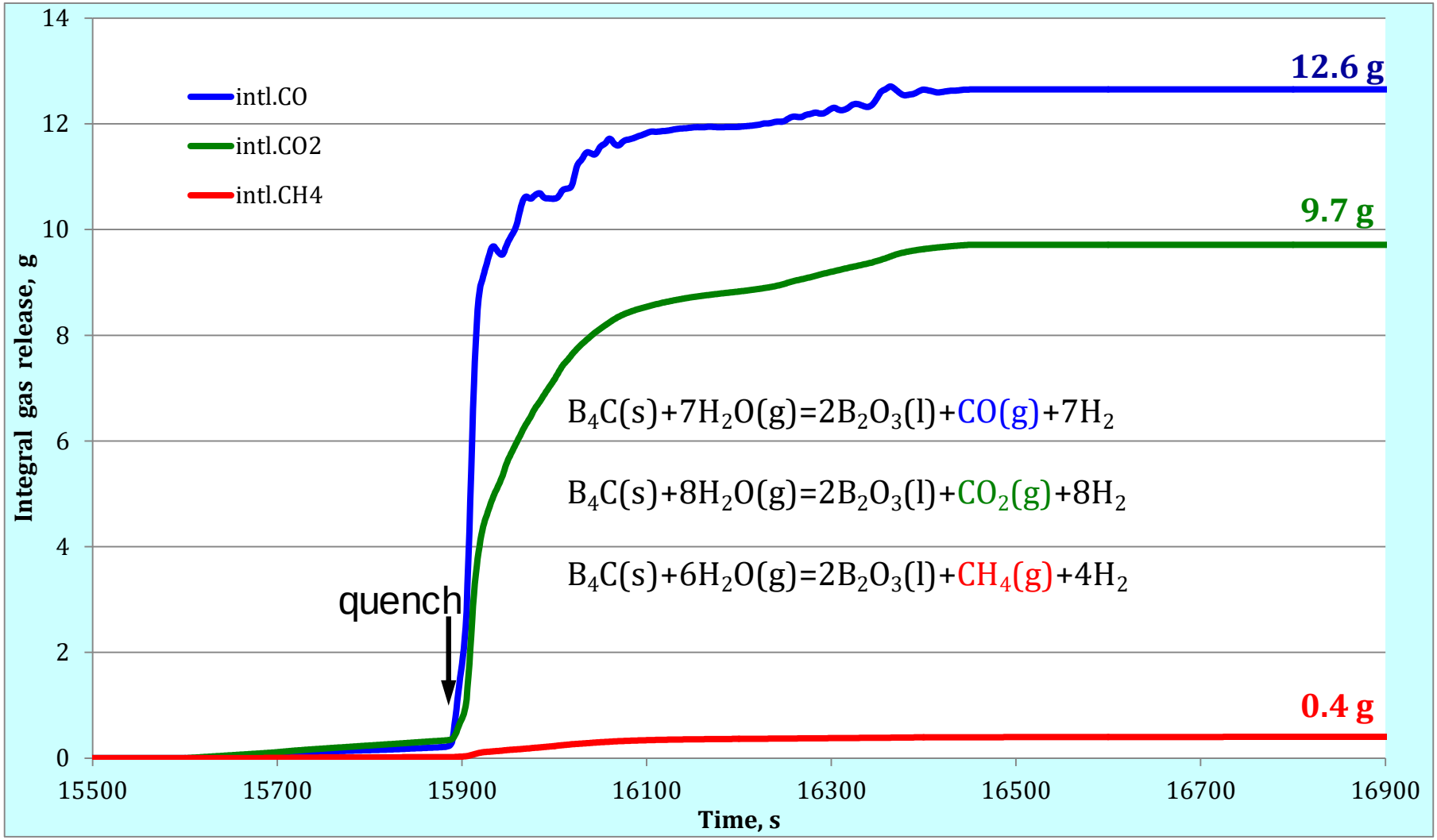

According to CO_x and CH_4 release: corresponding mass of B_2O_3 is 96.8 g; H_2 is 10.0 g; reacted B_4C 41 g, i.e. 4.6% of total B_4C mass (900 g)

QUENCH-20: hydrogen release

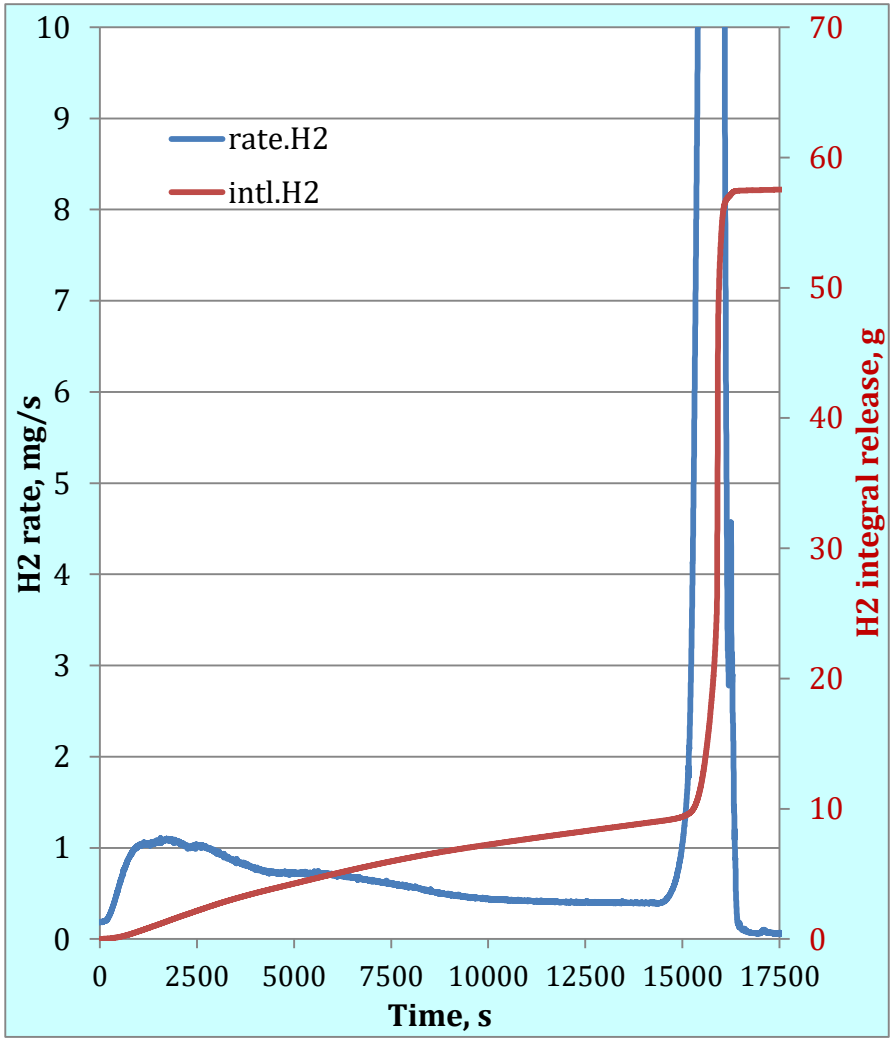

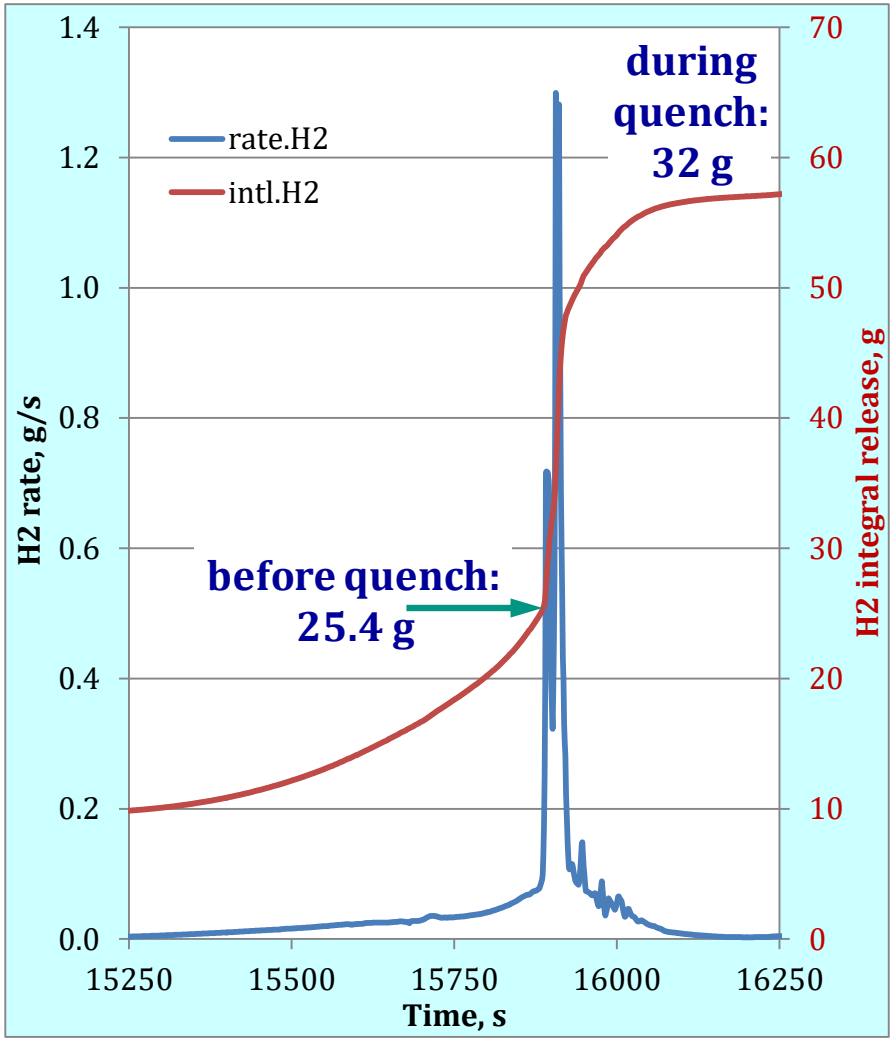

H_2 release during the whole test: 57.4 g;
before quench – interaction of steam with Zry,
during quench – steam interaction with Zry and absorber

H_2 release during quench:
22 g (from Zry and molten steel) +
+ 10 g (from B_4C)

Average thicknesses of outer ZrO_2 for each cladding at the bundle elevations 450…950 mm; *not symmetrical distribution of oxidation degree across the bundle due to influence of absorber blades*

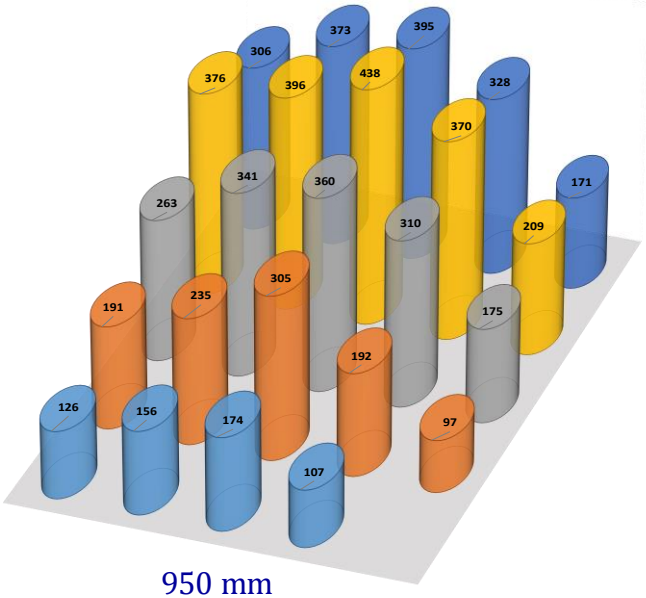

950 mm
(*ECR 17…47%; avg. 31%)*

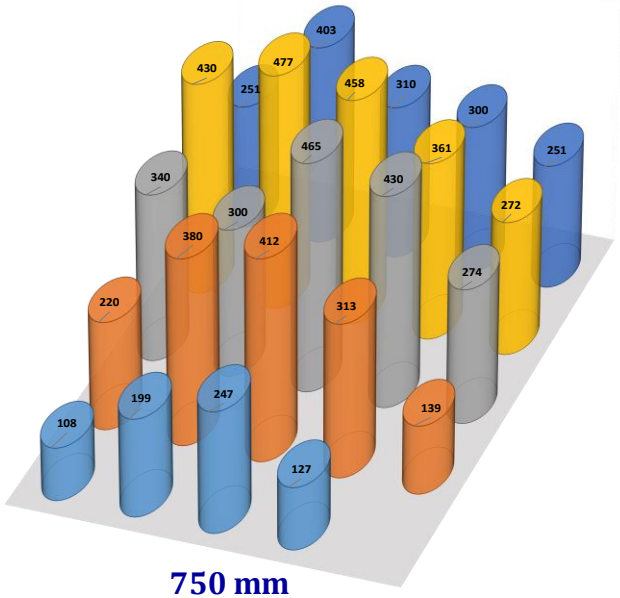

750 mm
(ECR 18…49%; avg. 33%)

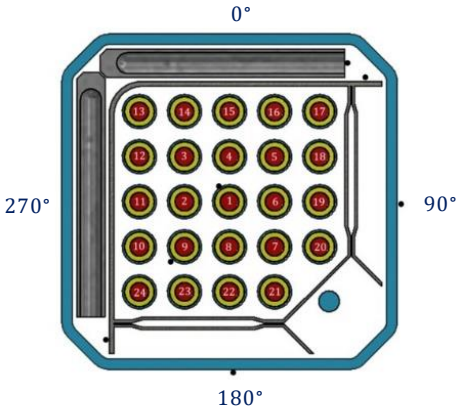

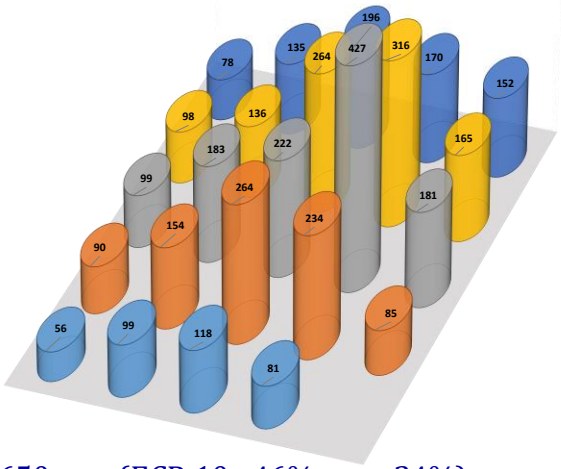

650 mm (ECR 10…46%; avg. 24%)

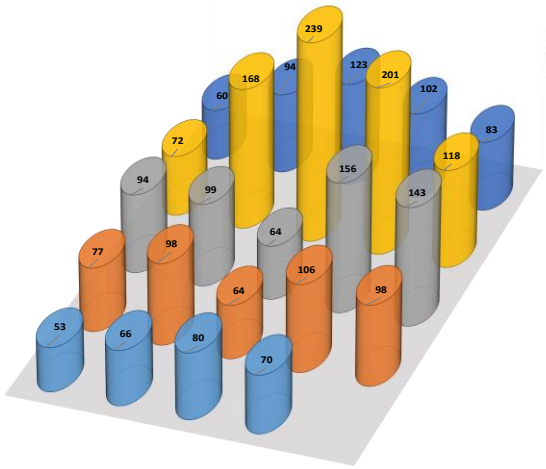

555 mm (grid spacer) (*ECR 6…22%; avg. 15%*)

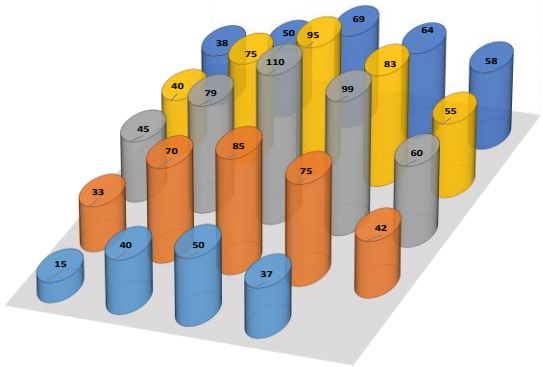

450 mm (*ECR 7…19%; avg. 14%*)

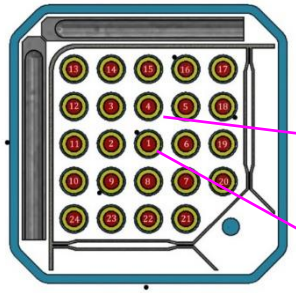

Cladding behavior of relatively hot inner rods at 950 mm

Karlsruhe Institute of Technology

central rod (#1)

inner rod (#4)

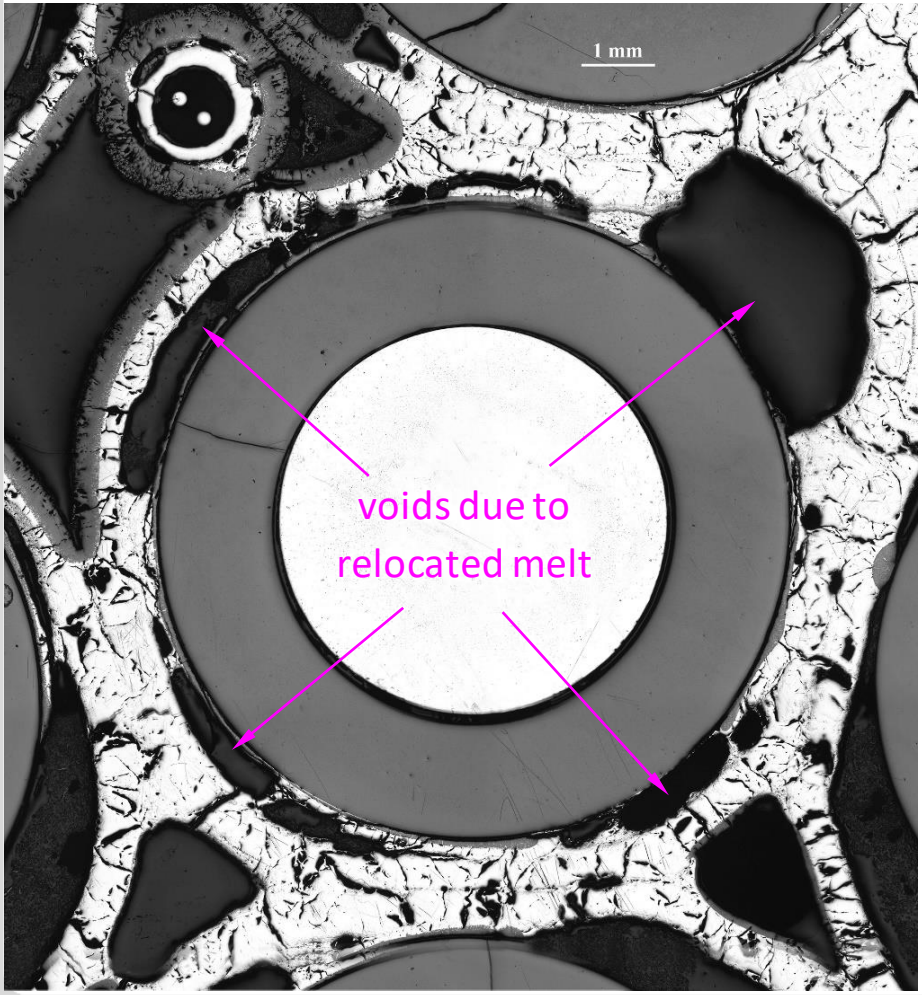

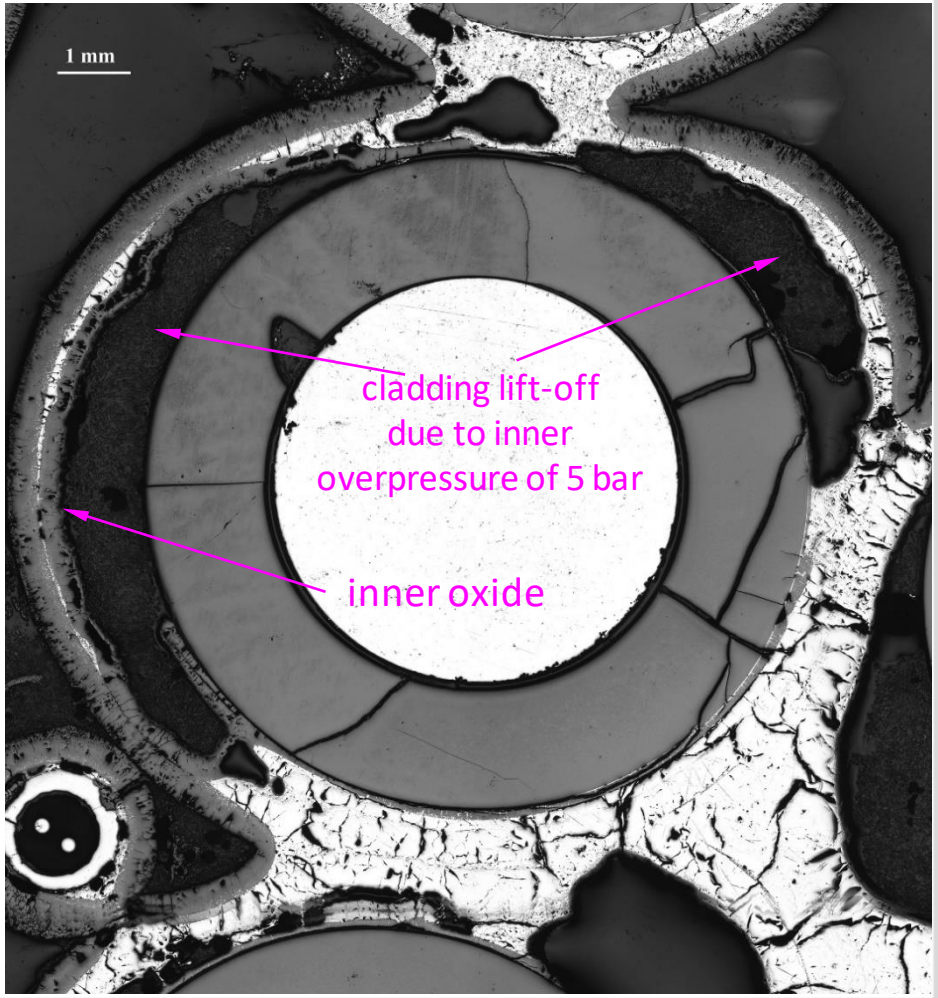

Layer composition for peripheral road #12 at 950 mm: *not melted and melted β-Zr depend on the angle position*

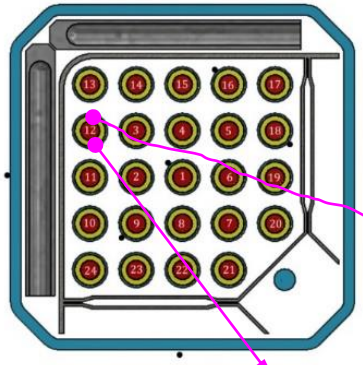

"cold" at 180°

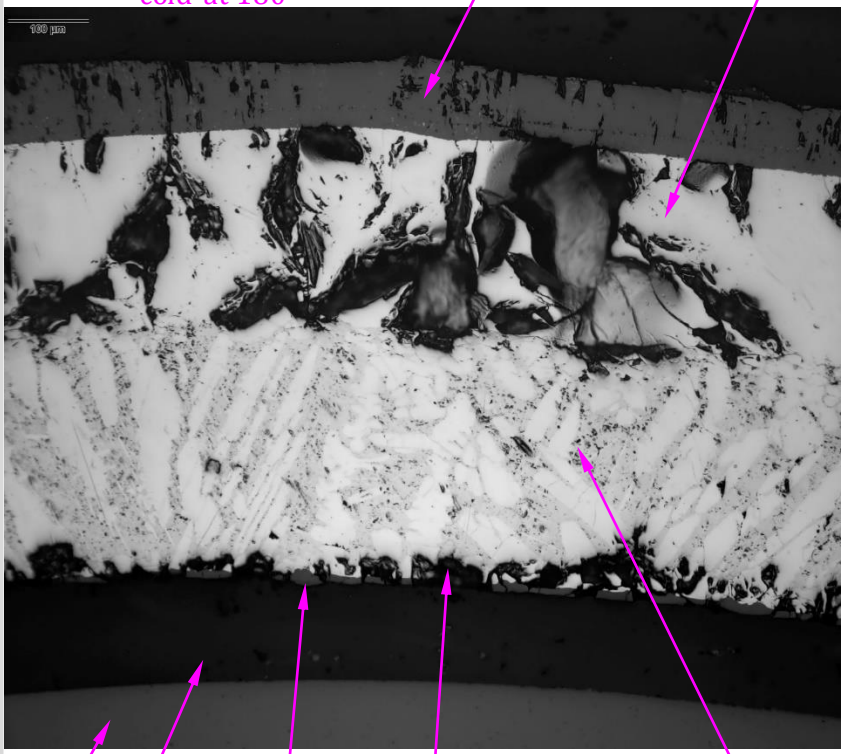

"hot" at 0°

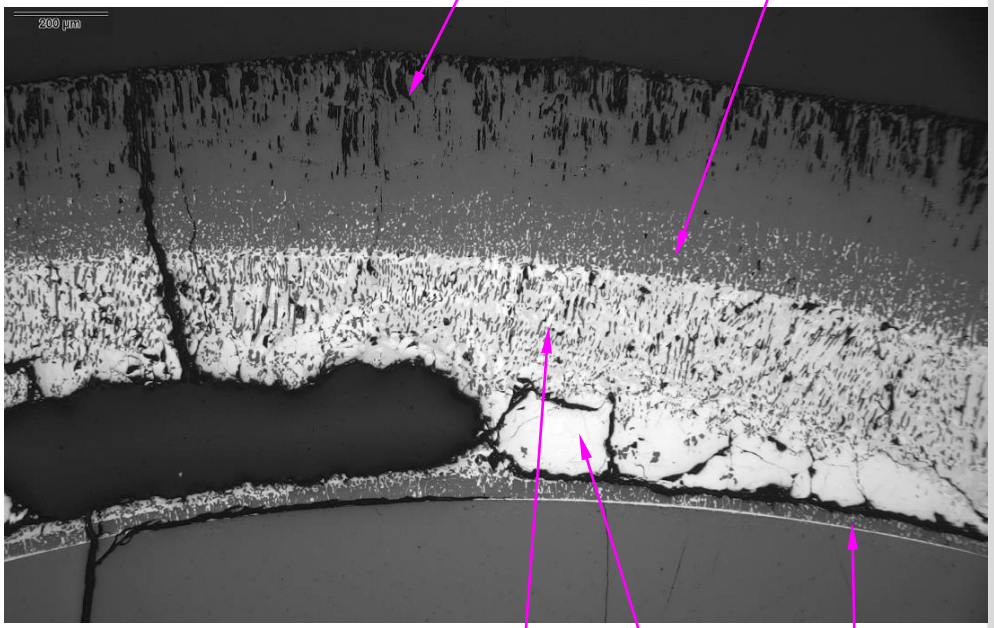

750 mm: micro structure of claddings



internal rod #2 at 315°: melted and frozen β-Zr between outer α-Zr(O) and inner ZrO_{2-x}



peripheral rod #12 at 0°: partially oxidized metal melt between outer and inner ZrO_2

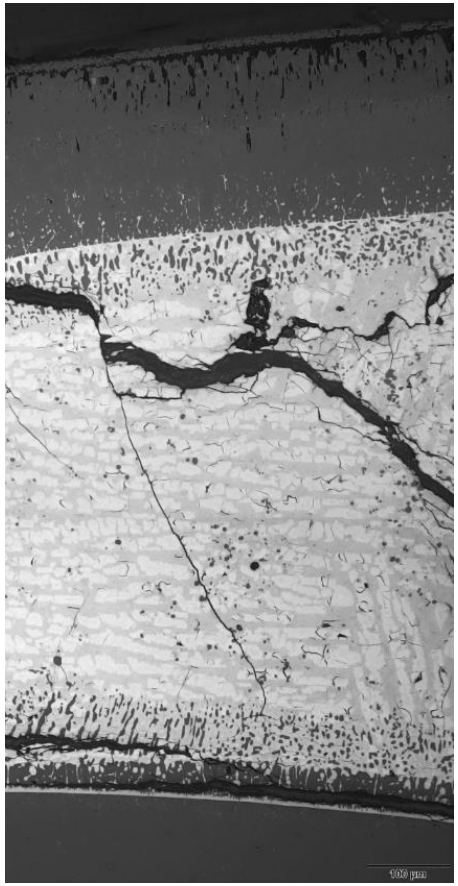

peripheral rod #17 at 45°: partially oxidized metal melt between outer and inner ZrO_2

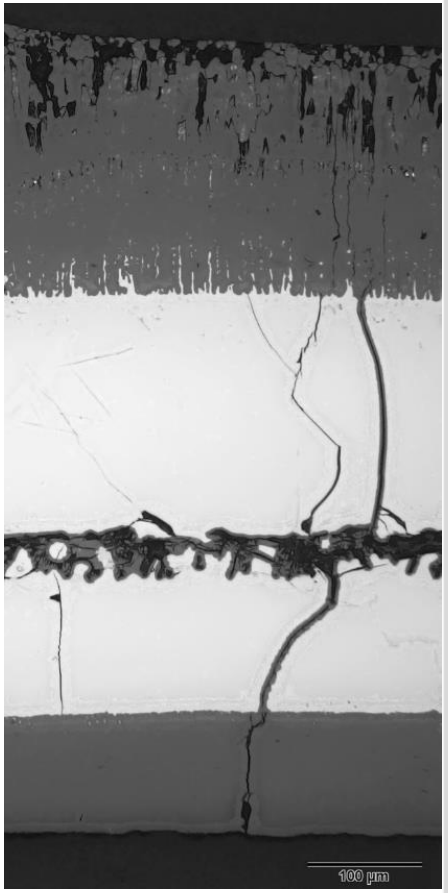

peripheral rod #21 at 315°: not melted metal, oxidation of cracks

Elevations without and with grid spacer

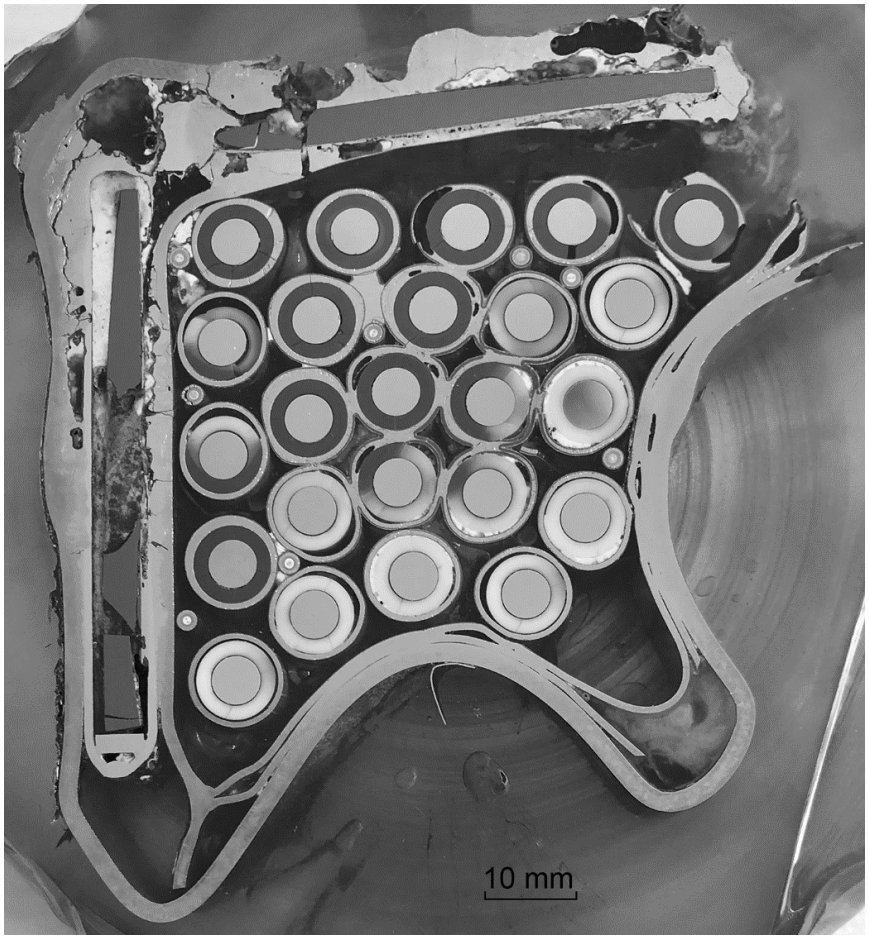

650 mm:
1) local blockages between several rods,
2) dark pellets contacted with inner melt: oxygen transport to melt
(white pellets had no contact with melt)

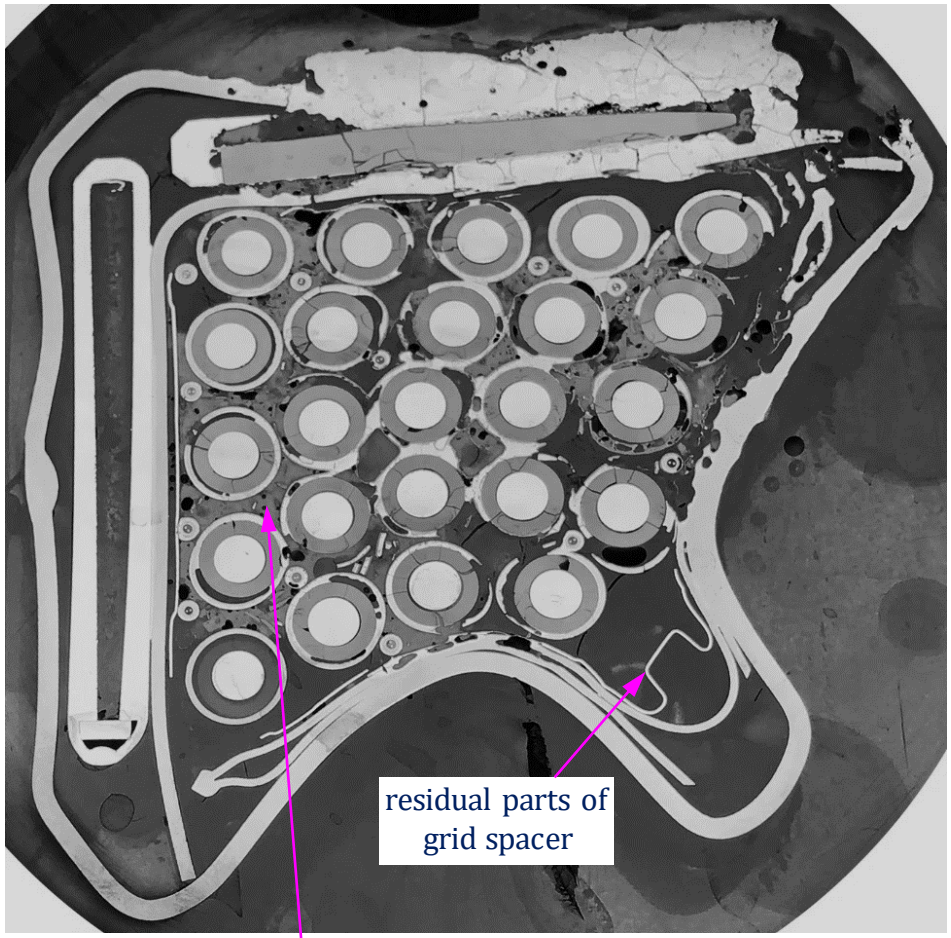

550 mm:
strong bundle blockage by melt collected inside
partially *molten* grid spacer

450 mm: eutectic (*Inconel* spacer/ZIRLO clad) melt relocated inside the rod from 550 elevation

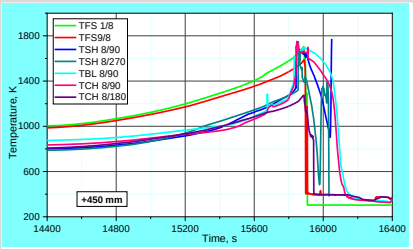

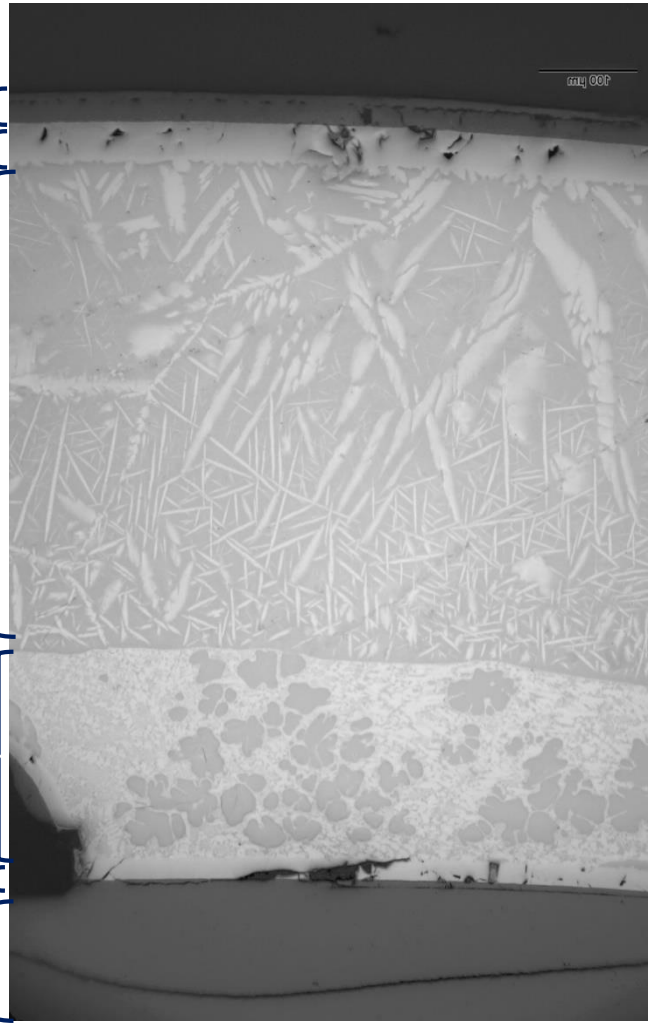

optical observation of cladding at 450 mm

SEM/EDX mapping at 450 mm (main element is white)

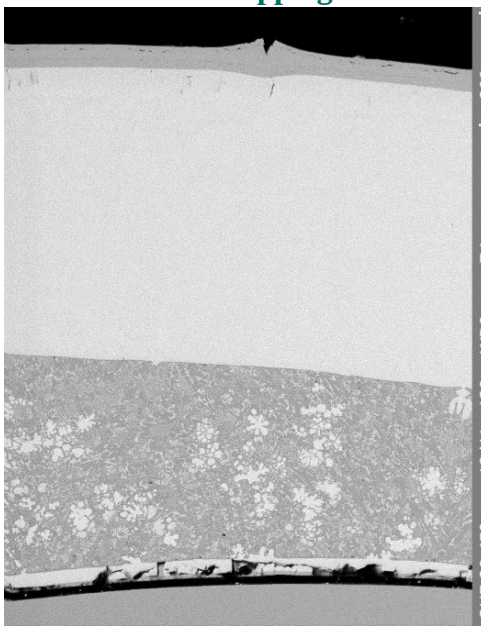

Zr map

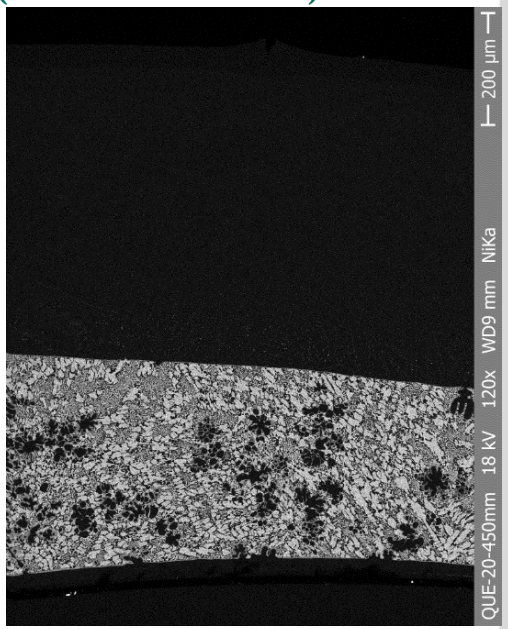

Ni map: Ni as main component of molten INCONEL spacer was relocated down in the gap between cladding and pellet

SEM/EDX mapping at 550 mm (Ni is blue)

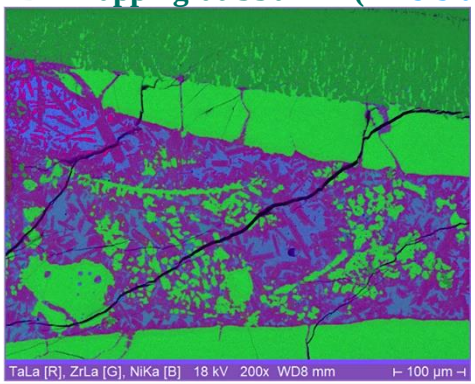

Summary and conclusions

- The QUENCH-20 test bundle mock-up represented one quarter of a BWR fuel assembly with 24 electrically heated fuel rod simulators and B_4C control blade. The pre-oxidation stage to ZrO_2 thickness >55 µm lasted 4 hours at the peak cladding temperature of 1250 K.
- During the transient stage, the bundle was heated to a maximal temperature of **2000 K**. The eutectic interaction of B_4C with steel blade and ZIRLO channel box was observed at elevations 650…950 mm with formation of eutectic melt. The typical components of this melt are (Fe, Cr) borides and ZrB_2 precipitated in steel or in Zr-steel eutectic melt.
- *Massive absorber melt relocation was observed 50 s before the end of transient stage and was localized between shroud and channel box*.
- The test was terminated with the quench water injected with a flow rate of 50 g/s from the bundle bottom. Fast *temperature escalation* from 2000 to **2300 K** during 20 s was observed. The mass spectrometer measured *release of CO (12.6 g), CO_2 (9.7 g) and CH_4 (0.4 g) during the reflood as products of absorber oxidation; corresponding* ***B_4C mass reacted*** *with steam was 41 g or* ***4.6% of total B_4C***.
- Cladding melt was formed at elevations 650…1000 mm and relocated to lower bundle elevations *inside* and outside rods to elevations 450…550 mm, where was mixed with molten Inconel grid spacer. Residual parts of claddings were oxidized with the highest oxidation degree ECR 33% at the elevation 750 mm.
- Hydrogen production during the reflood amounted to **32 g** (57.4 g during the whole test) including ***10 g from B_4C oxidation***.

Acknowledgment

The QUENCH-20 experiment was performed in the framework of the SAFEST project in cooperation with Swedish Radiation Safety Authority (SSM), Westinghouse Sweden, GRS and KTH and supported by the KIT program NUSAFE. Personal thanks to Mr. Isaksson (SSM), Mr. Bechta (KTH), Mr. Hollands (GRS), Ms. Korske (Westinghouse) for their help and fruitful cooperation. The bundle materials and absorbers were provided by Westinghouse Sweden.

The authors would like to thank all colleagues involved in the post-test investigations.

Thank you for your attention

http://www.iam.kit.edu/awp/163.php

http://quench.forschung.kit.edu/

STATUS OF MODELING OF FeCrAl CLADDINGS IN SEVERE ACCIDENT CODES AND APPLICATION ON THE QUENCH-19 EXPERIMENT

Thorsten Hollands, Liviusz Lovasz
Gesellschaft fuer Anlagen- und Reaktorsicherheit (GRS) gGmbH
Boltzmannstrasse 14, 85748 Graching, Germany
thorsten.hollands@grs.de, liviusz.lovasz@grs.de

Fabrizio Gabrielli
Karlsruhe Institute of Technology (KIT)
Hermann-von-Helmholtzplatz 1, 76344 Eggenstein-Leopoldshafen, Germany
fabrizio.gabrielli@kit.edu

Laure Carénini
Institut de Radioprotection et de Sûreté Nucléaire (IRSN)
13115 St Paul lez Durance, France
laure.carenini@irsn.fr

David L. Luxat, Jesse Phillips
Sandia National Laboratories (SNL)
Albuquerque, New Mexico, USA
dlluxat@sandia.gov, jphill@sandia.gov

ABSTRACT

Zirconium based claddings have been widely used for decades due to their good mechanical properties, corrosion resistance and low neutron absorption at operational conditions. At elevated temperatures, these claddings have some negative characteristics such as the occurrence of exothermic oxidation reactions in steam or air environments. This has motivated research and development of Accident Tolerant Fuel (ATF) and Cladding (ATC) materials, which has begun prior to the Fukushima Daiichi nuclear power plant core melt events though these events have highlighted the importance of developing such new materials. The new materials should be more resistant to oxidation, exhibiting significantly slower oxidation kinetics compared to the Zr-based alloys used in typical light water reactors. This should reduce the hydrogen generation rate along with the rate and magnitude of energy generation in the core due to oxidation after uncovering of the core. This can result in an increased time to introduce accident mitigation measures. One of the accident tolerant cladding materials under intensive investigation and testing is FeCrAl – at 1200°C, the oxidation rate is several orders of magnitudes smaller than a typical zirconium-based cladding. In conjunction with experiments, code modelling capabilities for DBA and DEC analyses must be improved for the analysis of systems including such materials. In addition to material properties, suitable oxidation kinetics models must be implemented to properly predict the ATF/ATC behavior under DBA and DEC conditions. The capability to model FeCrAl varies across three severe accident codes AC2/ATHLET-CD, ASTEC, and MELCOR and will be described in detail in the paper. To validate the performance of such integral codes to model FeCrAl cladding behavior, the QUENCH-19 experiment performed at KIT in 2018 is employed in this study. The results of the simulations show good agreement with the measured temperature. Hydrogen generation exhibits a sensitive dependence to the chosen material and associated oxidation correlation, which is quite sensitive to the FeCrAl composition. This can result in a significantly different amount exothermic energy generation.

KEYWORDS
Accident Tolerant Fuel, QUENCH-19, Core Degradation, Severe Accident Codes

1. INTRODUCTION

The investigation of ATF (Accident Tolerant Fuels) materials had already started before the accident at the Fukushima Daiichi plant in 2011, but after this event the development of new materials with significantly improved behavior under accident conditions was considered an important issue for the safety of light water reactors. A main feature of the new ATF cladding materials is a significantly reduced kinetics of steam oxidation, which is accompanied by slower heating and therefore a longer time period before temperatures reach the melting point compared to zirconium-based cladding currently used in LWRs. One of the materials studied is FeCrAl: at 1200°C, the oxidation rate of FeCrAl is about a factor of 1000 lower than for zirconium. A slower reaction of FeCrAl with steam therefore reduces the rate of hydrogen generation, slowing down the pressure build-up in the pressure vessel and delaying the onset of hydrogen release into the containment [1], [2].

2. CURRENT STATUS OF ATF MODELING IN SEVERE ACCIDENT CODES

To consider the above-mentioned topic about ATF and especially FeCrAl oxidation commonly used severe accident codes are extended in the way that the currently implemented Zr oxidation models are adopted for this kind of oxidation. This chapter deals with short descriptions about ATF oxidation in AC²/ATHLET-CD, ASTEC and MELCOR (cp. [3]).

2.1. AC²/ATHLET-CD

ATHLET-CD has been used many times for pre- and post-test calculations to support the QUENCH experimental program. The simulation of oxidation processes is very complex; oxidation models were developed and validated over the years with a strong cooperation with KIT to be able to predict the fuel cladding behavior during a nuclear accident. Most of these models were, however, developed for the oxidation of zirconium based claddings. New materials require adjustments and improvements also in the existing models.
The currently available modelling of ATF oxidation in ATHLET-CD is described in the following [4].
The deduced models were developed for Kanthal APM material with a composition of 69 % Fe, 21.6 % Cr, 4.9 % Al (+ 4.5 % others). It is assumed that due to the oxidation only Al_2O_3 is produced, which then forms a protective layer of α-Al_2O_3, i.e. corundum [7].
The oxidation of the specific ATF material can be summarized by the following (cp. [4])

$$Fe_xCr_yAl_z + \frac{z}{2} \cdot 3\,H_2O \longrightarrow Fe_xCr_y + z \cdot Al_2O_3 + \frac{z}{2} \cdot 3\,H_2 + z \cdot \Delta h \qquad (1)$$

where
Δh energy release during oxidation = $9.3 \cdot 10^5$ J/mol = $9.32 \cdot 10^6$ J/kg FeCrAl
x, y, z composition of FeCrAl molar masses of x = 1.307, y = 0.404 and z = 0.215

A parabolic law was used to determine the oxidation rate that was derived from the analytical solution of the diffusion equation, similarly to the method for the oxidation of zirconium:

$$dW^2 = K \cdot dt \longrightarrow \frac{dW}{dt} = \frac{K}{2W} \qquad (2)$$

where:

W	m_{ox}/ (surface area) in [kg/m^2]
m_{ox}	mass of the resulting oxide (Al_2O_3) [kg]
K	reaction rate in [kg^2/m^{4}s]
dt	time step [s]

The reaction rate is determined by the following Arrhenius equation:

$$K = A \cdot exp(-B/RT) \cdot g(ps) \tag{3}$$

where:

R	universal gas constant (J/mol/K)
T	cladding temperature [K]
$g(p_s)$	reduction factor to consider steam starvation ($0 \leq g(p_s) \leq 1$)
A, B	rate constants as given by KIT for KANTHAL APMT /HOL 19/: A = 3.1 kg^2/m^4/s, B = 2.78519 · 10^5 J/mol.

Figure 1 shows the currently implemented FeCrAl correlations implemented in ATHLET-CD in comparison to Zr oxidation correlations, which shows that FeCrAl oxidation is much slower compared to Zr.

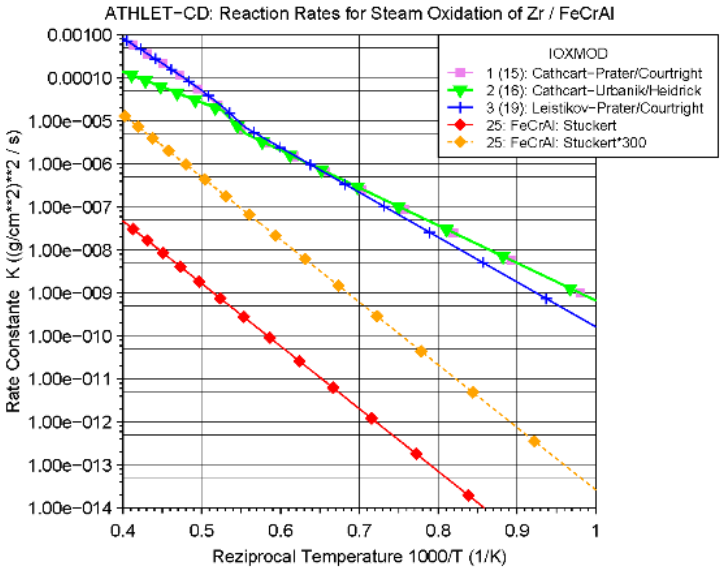

Figure 1. Zr and FeCrAl oxidation correlations implemented in ATHLET-CD [4].

ATHLET-CD uses the material properties (density, heat capacity, melting temperature, etc) of the cladding, which is user input. If FeCrAl (or any other) material is used, these values have to be changed from the standard Zr values.
The user has the option to implement their own ATF correlation. In this case the user has to explicitly add the following values in the input deck: A, B, Δh and the temperature validity range of the correlation.

2.2. ASTEC

Cladding oxidation model in ASTEC code has been developed and validated for zirconium based claddings [5] [6]. No specifics models are currently available to simulate ATF oxidation. However, thanks to the versatility of the code, it is possible for the user to adapt the general oxidation model formulated as parabolic rate approach to other kinetics representative of ATF (cp. [3]).

$$m_o(t+dt) = S.\left(\left(\frac{m_o(t)}{S}\right)^{\frac{1}{model}} + AGAIN.e^{-\frac{BGAIN}{R.T}}dt\right)^{model} \quad (4)$$

$$e_{ZrO2}(t+dt) = \left(\left(e_{ZrO2}(t)\right)^{\frac{1}{model}} + ATHIC.e^{-\frac{BTHIC}{R.T}}dt\right)^{model} \quad (5)$$

Parameters AGAIN, BGAIN as well as ATHIC, BTHIC can be modified for the evaluation of respectively the mass gain and the oxide layer thickness. For the simulation of FeCrAl, it was decided [3] to use available data for oxidation of Cr. Those data and associated fitting function from CEA are presents in Figure 2 (black curve).

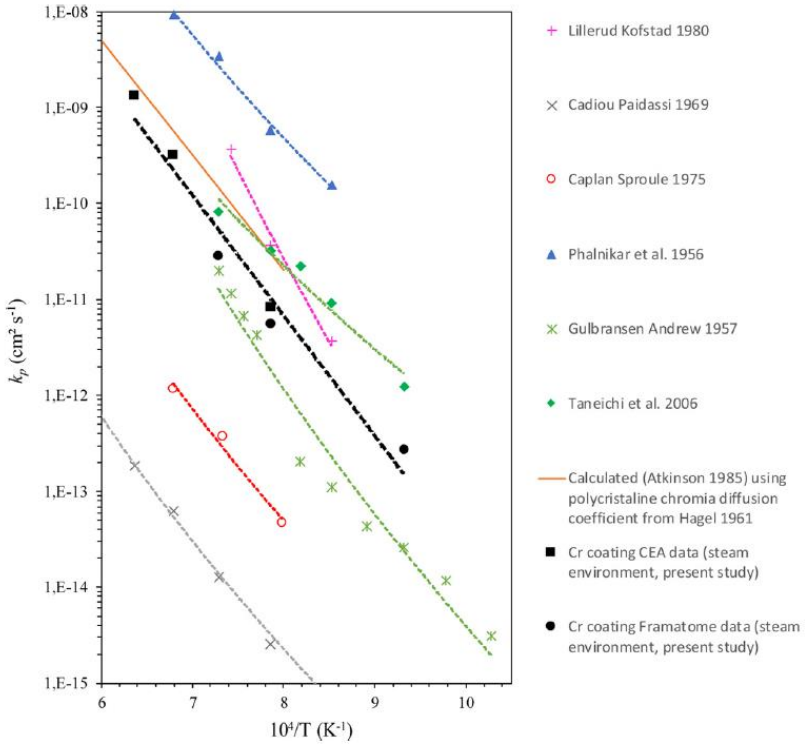

Figure 2. FeCrAl oxidation correlations [3].

In addition to the oxidation kinetics, the material properties of FeCrAl has to be implemented in the input deck by the user.

2.3. MELCOR

In general, the MELCOR oxidation model is a parabolic rate expression for the metallic reaction. While alumina formation maybe assumed for the QUENCH-19 experiment given the accident duration and temperatures, the MELCOR oxidation model does not distinguish between constituents of materials. A single oxide mass conversion of a material into its oxide form is performed. Therefore, preferential oxidation of aluminum is not modeled and instead the oxidation of FeCrAl forming a singular FeCrAl-oxide is modeled (cp. [3]):

$$Fe+4/3\cdot H_2O \rightarrow 1/3\cdot Fe_3O_4+4/3\cdot H_2 \quad (6)$$

$$Cr+3/2\cdot H_2O \rightarrow 1/2\cdot Cr_2O_3+3/2\cdot H_2 \quad (7)$$

$$Al+3/2\cdot H_2O \rightarrow 1/2\cdot Al_2O_3+3/2\cdot H_2 \quad (8)$$

Experimental data from the supplied references were employed to compute the constants A and B for the rate constant, K, seen in the expression below. The weight gain due to solid-state diffusion of oxygen through an oxide is expressed by the following parabolic rate equations (cp. [3])

$$\frac{dW(t)^2}{dt} = K(t) \quad (9)$$

$$K = A \cdot exp(-B/T) \quad (10)$$

The experimental data employed provides the weight gain for coupon samples; therefore, the metallic reaction rate is a conversion of the oxygen uptake. Assumed oxide forms (Fe_3O_4, Al_2O_3, and Cr_2O_3) are needed both to convert the oxygen uptake into reacted mass as well as to approximate the oxide physical properties.

3. QUENCH FACILITY AND TEST CONDUCT

3.1. Facility Description

Figure 3 shows a schematic representation of the QUENCH test facility [8]. In addition to the gas inflow line (steam and argon as carrier gas), there is a line for the inflow of the quench water at the bottom of the test area. The outflow of steam, argon and hydrogen is realized via a temperature-controlled outlet line at the bundle head to avoid condensation of steam at the bundle outlet. The electrically heated rod bundle with a heated length of 1024 mm consists of 24 heated fuel rod simulators with FeCrAl(Y) cladding and 8 corner rods made of FeCrAl (Kantal APM), as shown in cross-section in Figure 4. The heated rods contain a 5 mm diameter tungsten heating rod in the center surrounded by annular ZrO_2 pellets to simulate the UO_2 fuel. As can be seen from the comparison of a fuel rod simulator of the QUENCH-15 test used as a reference test with that of QUENCH-19, the cladding of QUENCH-19 is much thinner (381 µm) than that of the reference test (572 µm), whereas the ZrO_2 pellet is slightly thicker. The rod bundle is held in position by 4 FeCrAl(Y) spacers as well as a lowest spacer grid made of Inconel. The beginning of the heated zone corresponds to the bundle height 0 mm.

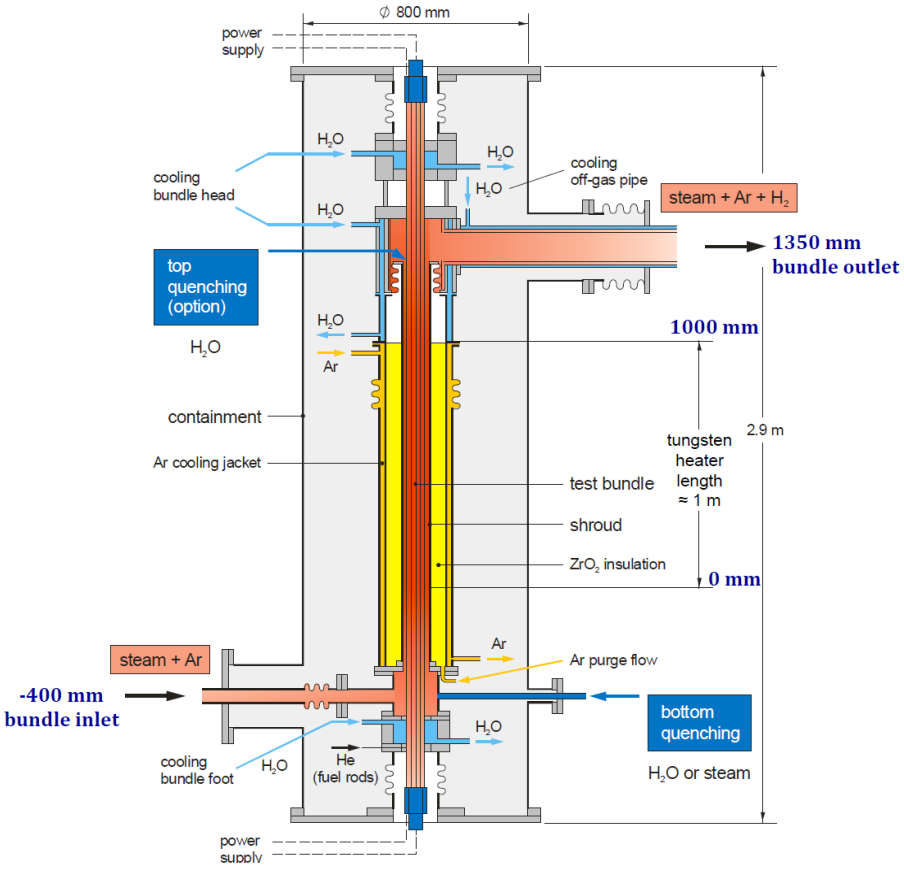

Figure 3. QUENCH facility [8].

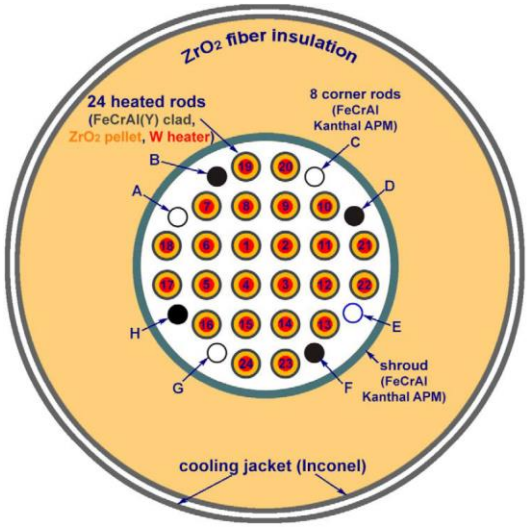

Figure 4. QUENCH-19 test bundle [8].

The 8 corner rods are divided into 4 each consisting of an FeCrAl cladding tube with temperature sensors (A, C, E, G) or solid FeCrAl rods of 6 mm diameter (B, D, F, H). The latter are pulled out of the bundle during different phases of the test to check the extent of oxidation during the test.

The test bundle is surrounded by a 3 mm thick shroud made of FeCrAl (Kantal APM), to which a 34 mm thick ZrO_2 insulation and a double-walled cooling tube made of Inconel (inside) and stainless steel (outside) connect (cooling jacket), with the intervening annular space filled with argon. Above the heated length, the cooling jacket is cooled with water to avoid excessive temperatures at the bundle head.
The fuel rod simulators, shroud and cooling jacket are equipped with thermocouples at different heights and in different directions. The released hydrogen and the outflowing mass flows are recorded with a mass spectrometer.

3.2. QUENCH-19 Test Conduct

Figure 5 shows the course of the QUENCH-19 experiment in comparison to the reference test QUENCH-15 [8]. The gradual increase in the electrical power output up to a maximum value of 18.12 kW is identical in both experiments. While in test QUENCH-15 a temperature excursion had already occurred when this power was reached, and the power was therefore switched off, test 19 showed a temperature that was approx. 500°C lower. For this reason, a power plateau was maintained at a constant value of 18.32 kW until, after the maximum temperature rose to 1455 °C, the power was first reduced to 4.34 kW and finally switched off completely.
With regard to the feed-in mass flows of steam and argon, the comparison shows that the argon inflow rate of 3.5 g/s was identical for both tests, but the inflow rate for steam was slightly higher for QUENCH-19 than for QUENCH-15 (3.8 g/s and 3.2 - 3.4 g/s, respectively). The temperature of the inflowing steam and argon mixture is also about 80°C lower for QUENCH-19 at 640°C at the beginning of the test compared to the comparison test. Thus, the comparison of these similar but not identical boundary conditions already provides a first indication of a possible reason for the difference of 200°C occurring at the plateau of the maximum temperature already during the pre-oxidation phase, in which the different oxidation behavior should not yet have a major influence.
After a maximum cladding tube temperature of 1455°C was reached in the current experiment, the water inflow was started at ~9100 s simultaneously with the reduction of the electrical power. While no temperature excursion was measured at the height of the maximum bundle temperature (850 mm), at the height of 1050 mm a brief increase can be recognized in the measured course even before the start of the feed, which, however, did not reach the melting temperature of 1500°C. The temperature excursion is also visible at the height of the maximum bundle temperature (850 mm). With the water injection of 46 g/s, the bundle is cooled down quickly.
The integral hydrogen production during the test was 9.2 g compared to 47.6 g for the QUENCH-15 test with a much shorter period of high electric power. While only a small fraction of 0.3 g was released during the pre-oxidation phase, there was a large increase after the maximum temperature had exceeded 1400°C.

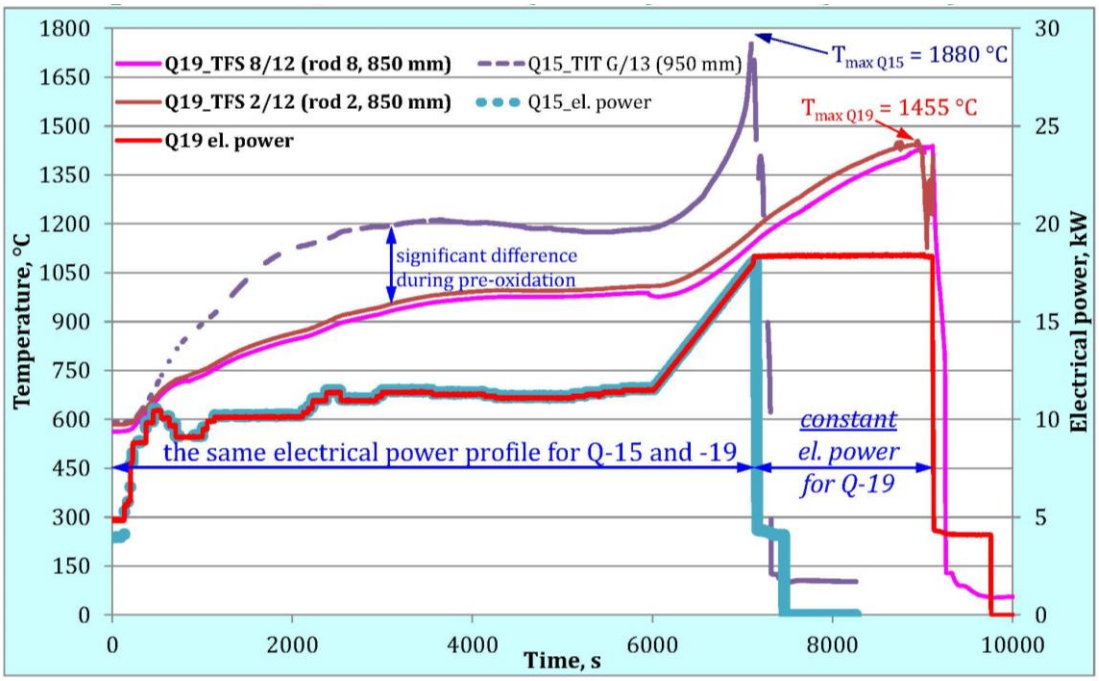

Figure 5. QUENCH-19 test conduct [8].

4. SIMULATION OF QUENCH-19

The simulation of QUENCH-19 was performed with the following codes applied by GRS, KIT and SNL:

- ATHLET-CD as part of the code package AC² by GRS
- ASTEC by KIT
- MELCOR by SNL

For the thermal hydraulics and core degradation processes the established and validated models of these codes were applied, while for FeCrAl oxidation the above mentioned models were used. For the simulation with ATHLET-CD an alternative correlation for the ORNL alloy B136Y3, which was used for the claddings in QUENCH-19 [9], was used.

Generally, the results of the simulations show that the codes are able to predict the thermal behavior of a bundle equipped with FeCrAl cladding, grid spacer and shroud as shown in Figure 6 and Figure 7. In both figures the simulated results represent rods which are located in the intermediate ring (cp. Figure 4), but the radial profile is in general not very developed in all three simulations as it was observed in the experiment due to the wetted shroud insulation. In the lower bundle MELCOR overestimates the measured temperature significantly while ASTEC and ATHLET-CD are closer to the measured temperatures (Figure 6, left). At a middle bundle elevation the deviations between the numerical results are not that pronounced and all are in the range of the measured data of the innermost or intermediate rods (Figure 6, right). For both regions (lower and middle) the qualitative behavior is captured by the codes and show no temperature escalation.

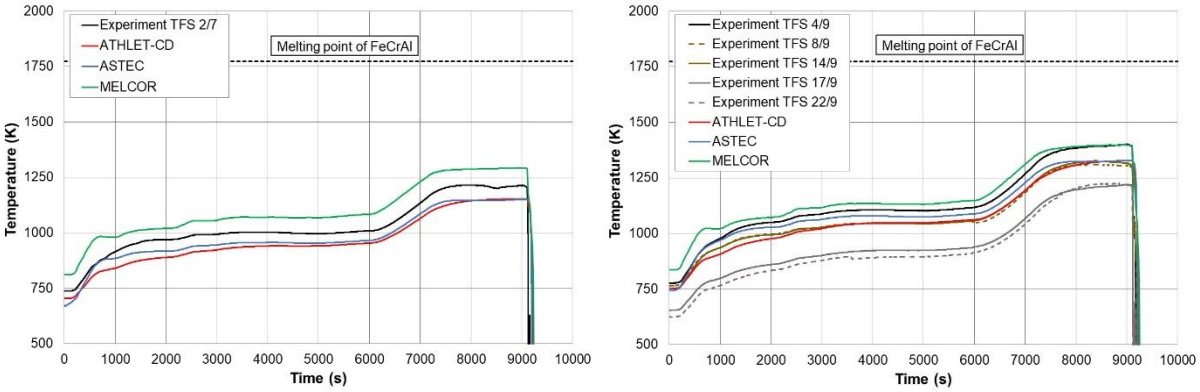

Figure 6. Measured and calculated cladding temperatures at 350 mm (left) and 550 mm (right).

In the upper bundle region the temperatures observed in the experiment reach the melting point of FeCrAl and first local melting was observed even at lower temperatures due to eutectic formation. At 850 mm no simulation reaches the melting temperature although MELCOR overestimates the measured temperatures while ASTEC and ATHLET-CD are in close agreement to the experiment (Figure 7, left). The high temperature in the MELCOR simulation cannot significantly caused by the oxidation of FeCrAl because on the one hand the oxidation in the MELCOR simulation is much smaller than observed in the experiment and on the other hand the exothermal character is not as exothermal as for Zr oxidation due to the slower kinetics. The reason for the overestimation needs to be further investigated. At the highest heated elevation (950 mm) the results of all three simulations are closer to each other, but all overestimate the measured values (Figure 7, right). For ASTEC and MELCOR temperatures in the melting region are predicted, but melt oxidation seems not to play a role in the simulation in contrast to what is assumed for the experiment. ATHLET-CD does neither reach the theoretical melt temperature of FeCrAl nor the one of first melting in the test.

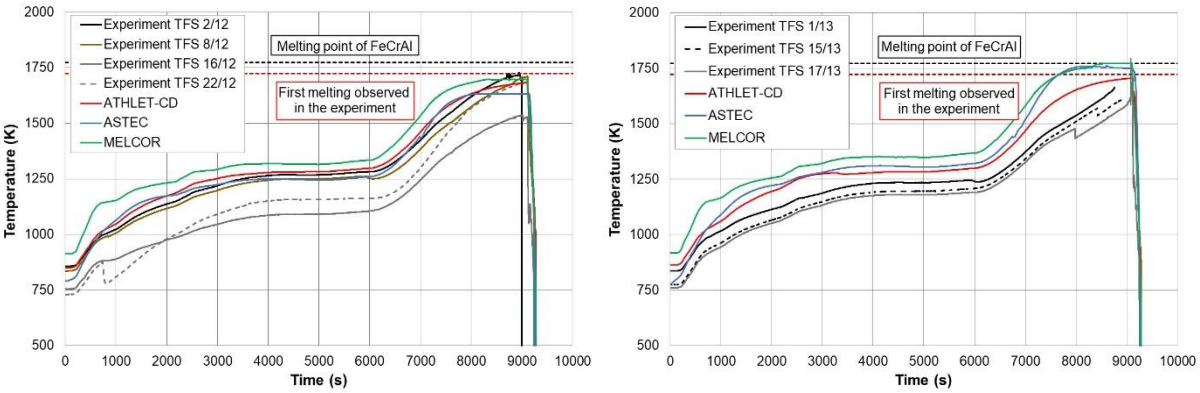

Figure 7. Measured and calculated cladding temperatures at 850 mm (left) and 950 mm (right).

To the fact that the FeCrAl oxidation is orders of magnitude smaller than for Zr oxidation the resulting additional heat impact is smaller although the FeCrAl oxidation is significantly exothermic. Thus, the interaction between the thermal behavior as discussed above and the

hydrogen generation is not very pronounced. This leads to the results, that even with moderate temperatures like in the ASTEC simulation the hydrogen generation is higher than in the experiment as well as compared to the other simulations. Figure 8 shows that ASTEC overestimates the hydrogen generation already during pre-oxidation and the transient phase, while ATHLET-CD underestimates the hydrogen production in the first phases but increases significantly during the end of the transient phase and during quenching. This could be explained by the higher oxidation kinetics even at lower temperatures in the ASTEC correlation compared to the applied correlation used in ATHLET-CD. Both simulations roughly predict the final integral value of the experiment, but with another kinetic due to the chosen correlation. In contrast to that MELCOR significantly underestimates the hydrogen production and predicts only approximately 5 % of the integrated measured mass, although the temperatures are along the whole bundle overestimated.

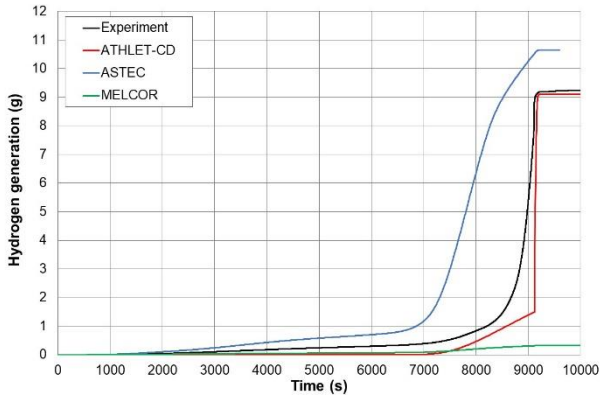

Figure 8. Measured and calculated hydrogen generation.

5. CONCLUSIONS

Accident Tolerant Fuel (ATF) with accident tolerant claddings are of high interest for future fuel assembly developments due to their low oxidation potential which could increase the margins for accident management measures to mitigate severe accident progressions with significant core degradation and melting up to RPV failure. Several ATF concepts are under investigation, one of these is FeCrAl cladding. To be able to predict the behavior of ATF correctly and to be able to evaluate emergency measures, severe accident codes need to be improved. Therefore, the codes AC²/ATHLET-CD, ASTEC and MELCOR were extended to consider FeCrAl claddings with respect to the material properties and oxidation behavior. The extended model basis is evaluated by comparison with the experiment QUENCH-19 which dealt with FeCrAl claddings and components.

The results of the simulation show that the qualitative thermal behavior of the experiment can be predicted by all codes, but the quantitative agreement to experiment differs for the three simulations. While MELCOR overpredicts the temperatures along the whole bundle, AC²/ATHLET-CD and ASTE$C are closer to the experiment, except the highest heated elevation. Due to the smaller interaction between thermal behavior and oxidation compared to Zr the calculated hydrogen generation show a different picture. AC²/ATHLET-CD and ASTEC approximately predict the measured final value with different kinetics, MELCOR significantly underestimates the hydrogen generation leading to only 5 % of the experimental value. These results lead to the conclusion that the FeCrAl models need to be further investigated, improved and validated also against a wider experimental data base to be able to do robust predictions for emergency measures.

ACKNOWLEDGMENTS

The work of GRS is sponsored by the German Federal Ministry for the Environment, Nature Conservation, Nuclear Safety and Consumer Protection (BMUV).

REFERENCES

1. NEA, “State-of-the-Art Report on Light Water Reactor Accident-Tolerant Fuels”, NEA No. 7317, Nuclear Energy Agency, Organisation for Economic Co-Operation and Development, 2018.
2. IAEA, “Analysis of options and Experimental Examination of Fuels for Water Cooled Reactors with Increased Accident Tolerance (ACTOF)”, Final Report of a Coordinated Research Project, IAEA-TECDOC-1921, International Atomic Energy Agency, Vienna, 2020.
3. F. Gabrielli et al., “ATF modelling in Severe Accident Codes”, Proceedings of the 26th International QUENCH Workshop, 6-9 December 2021, Virtual event organized by Karlsruhe Institute of Technology Karlsruhe, Germany, Editor: Martin Steinbrück, DOI: 10.5445/IR/1000141824.
4. L. Lovasz et al., “ATHLET-CD 3.3 User's Manual, Models and Methods”, GRS-P-4/Vol. 2 Rev. 0, Gesellschaft für Anlagen- und Reaktorsicherheit (GRS) gGmbH, November 2021.
5. O. Coindreau et al., “ASTEC V2.1 Physical modelling of the ICARE module”, IRSN PSN-RES/SAG/2016-00422, March 2017.
6. P. Chatelard and L. Laborde, “Synthesis of the ASTEC V2.2 code validation against experimental data”, Proceedings of ERMSAR 2022 conference, 16-19 May 2022, Karlsruhe, Germany.
7. ORNL, “Handbook on the Material Properties of FeCrAl Alloys for Nuclear Applications”, ORNL/SPR-2018/905, Oak Ridge National Laboratory, U.S. Department of Energy (DOE), 18. ed., 68 p., 2018.
8. J. Stuckert et al., “First results of the bundle test QUENCH-19 with FeCrAl claddings”, Proceedings of the 24th International QUENCH Workshop, 13-15 November 2018, Karlsruhe Institute of Technology Karlsruhe, Germany, Editor: Martin Steinbrück, DOI: 10.5445/IR/1000088229.
9. C. Kim et al.: Oxidation Kinetics of Nuclear Grade FeCrAl Alloys on Steam in the Temperature Range 600-1500°C, Proceedings of TopFuel 2021, 24-28 September 2021, Santander, Spain.

STATUS OF MODELING OF FeCrAl CLADDINGS IN SEVERE ACCIDENT CODES AND APPLICATION ON THE QUENCH-19 EXPERIMENT

Thorsten Hollands[1], Liviusz Lovasz[1], Fabrizio Gabrielli[2], Laure Carénini[3], David L. Luxat[4], Jesse Phillips[4]

[1]: GRS gGmbH, Boltzmannstr. 14, 85748 Garching, Germany

[2]: KIT, Hermann-von-Helmholtz-Platz 1, 76344 Eggenstein-Leopoldshafen, Germany

[3]: Institut de Radioprotection et de Sûreté Nucléaire (IRSN),13115 St Paul lez Durance, France

[4]: Sandia National Laboratories (SNL), Albuquerque, New Mexico, USA

The 10th European Review Meeting on Severe Accident Research (ERMSAR2022)

Akademiehotel, Karlsruhe, Germany

May 16-19, 2022

Content

- Motivation
- ATF Modelling in Severe Accident Codes
- QUENCH-19
  - Bundle Configuration
  - Test Conduct
- Simulation Results
- Conclusions and Outlook

Motivation

- The investigation of ATF (Accident Tolerant Fuels) materials had already started before the accident at the Fukushima Daiichi plant in 2011
- A main objective for new ATF cladding materials is a significantly reduced kinetics of steam oxidation, which is accompanied by slower heating and therefore a longer time period before temperatures reach the melting point compared to zirconium-based cladding currently used in LWRs
- One of the materials studied is FeCrAl: at 1200°C, based on the composition the oxidation rate of FeCrAl could about a factor of 1000 lower than for zirconium. A slower reaction of FeCrAl with steam therefore reduces the rate of hydrogen generation, slowing down the pressure build-up in the pressure vessel and delaying the onset of hydrogen release into the containment

➢ The experiment QUENCH-19 was performed at KIT to investigate FeCrAl as cladding material

➢ Additionally, the modelling capabilities of severe accident codes were extended to be able to consider ATF. These new models need validation

ATF Modelling
– AC²/ATHLET-CD –

- Assumption: Al oxidized only

$$Fe_xCr_yAl_z + z/2 \cdot 3\ H_2O \rightarrow Fe_xCr_yAl_{2z}O_{3z} + z/2 \cdot 3\ H_2 + z \cdot \Delta h\ (\Delta h = 9.3 \cdot 10^5\ J/mol)$$

- Oxidation Rate → Parabolic law derived from the analytical solution of the diffusion equation (as for Zr):

$$dW^2 = K(T) \cdot dt$$

W: m_{Ox}/A [kg/m²], K: reaction rate [kg²/m⁴ s], t: time [s])

- Reaction rate from the Arrhenius formulation:

$$K = A \cdot e^{-B/(RT)}$$

R = 8.134 J/mol K, T: cladding Temperature [K],

A, B: rate constants

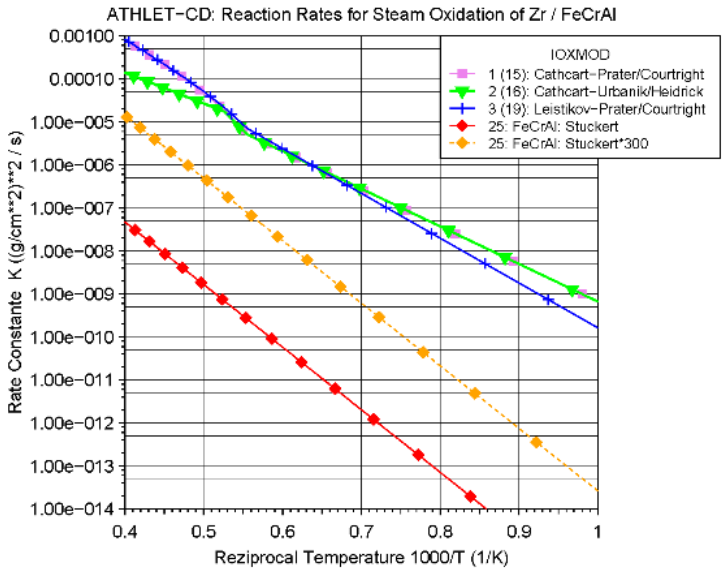

ATF Modelling
– ASTEC –

- Modifying the laws for oxygen mass gain and oxide thickness growth in the database relevant to the cladding steam oxidation
- Assumptions: 1) No temperature dependency considered 2) Δh of Zr employed

$$m_o(t+dt) = S.\left(\left(\frac{m_o(t)}{S}\right)^{\frac{1}{model}} + AGAIN.e^{\frac{-BGAIN}{R.T}}dt\right)^{model}$$

$$e_{ZrO2}(t+dt) = \left(\left(e_{ZrO2}(t)\right)^{\frac{1}{model}} + ATHIC.e^{\frac{-BTHIC}{R.T}}dt\right)^{model}$$

- Brachet correlation is considered
- Fitting functions for weight gain and thickness grown of the oxide layer provided by J. Stuckert (KIT)

$$\Delta m = 19.62 \cdot e^{-\frac{123783}{R \cdot T}} \cdot \sqrt{t}$$

$$\delta = 0.00377 \cdot e^{-\frac{123783}{R \cdot T}} \cdot \sqrt{t}$$

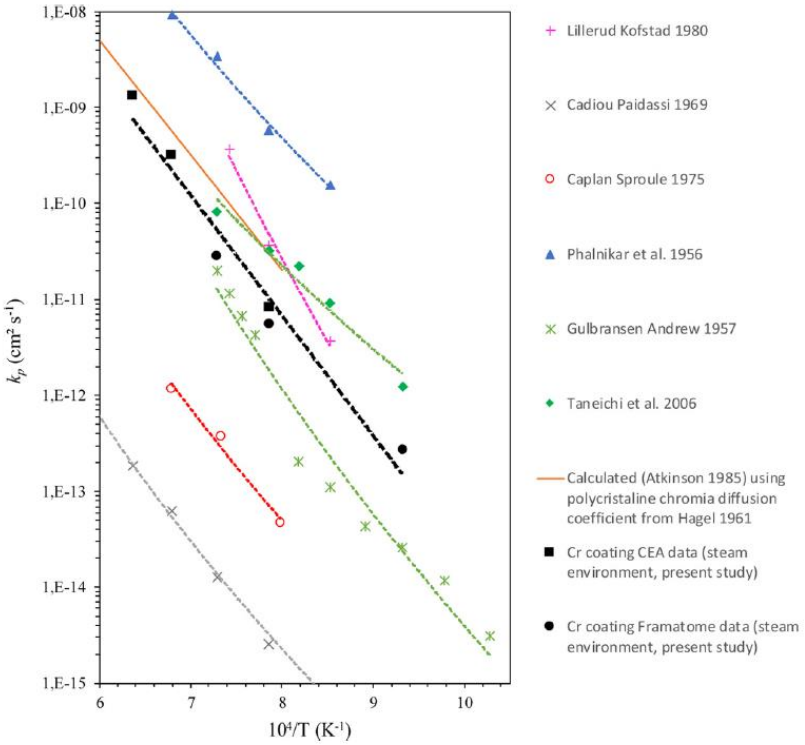

F. Gabrielli et a.: ATF modelling in Severe Accident Codes, Proceedings of the 26th International QUENCH-Workshop, 2021

ATF Modelling
– MELCOR –

- Based on prior work by INL/ORNL
- Reaction rates apply data from Pint, et.al., prior to breakaway
- Oxygen uptake data is converted to metal reacted and standard units
- Must assume prevailing oxides to convert from oxygen to metal reacted
  - $Fe+4/3\cdot H_2O \rightarrow 1/3\cdot Fe_3O_4+4/3\cdot H_2$
  - $Cr+3/2\cdot H_2O \rightarrow 1/2\cdot Cr_2O_3+3/2\cdot H_2$
  - $Al+3/2\cdot H_2O \rightarrow 1/2\cdot Al_2O_3+3/2\cdot H_2$
  - $K = 4360 \cdot e^{-(41376/T)}$
- Parabolic law:

$$dW(t)^2/dt = K(t)$$

$$K = 4360 \cdot e^{-(41376/T)}$$

- New MELCOR modeling allows specifying all the reaction parameters

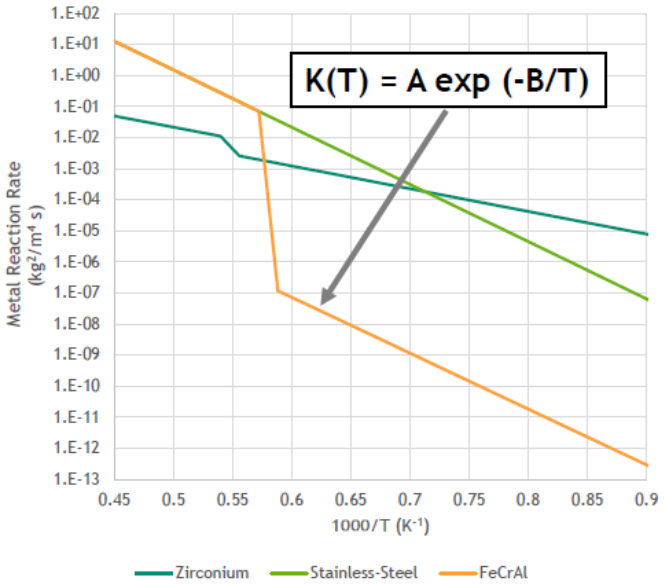

F. Gabrielli et a.: ATF modelling in Severe Accident Codes, Proceedings of the 26th International QUENCH-Workshop, 2021

ATF Modelling
– Summary of FeCrAl Correlations –

- Recommended correlations

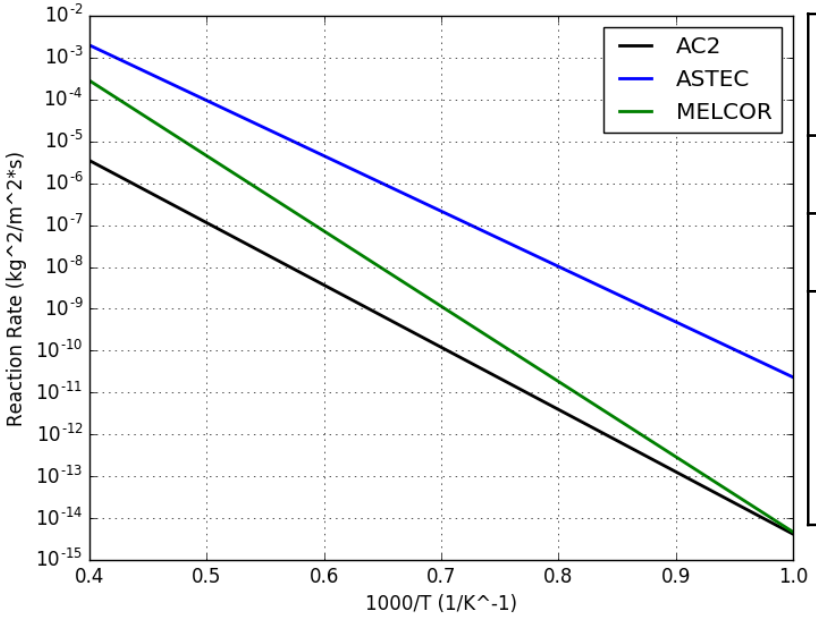

Code	Oxidation of	Enthalpy (J/kg)
AC²/ATHLET-CD	Al	$9.36 \cdot 10^6$
ASTEC	Zr	$-1.21 \cdot 10^7$
MELCOR	Fe (74 wt.%)	$-2.495 \cdot 10^5$
	Cr (21 wt.%)	$2.442 \cdot 10^6$
	Al (5 wt.%)	$1.51 \cdot 10^7$

F. Gabrielli et a.: ATF modelling in Severe Accident Codes, Proceedings of the 26th International QUENCH-Workshop, 2021

- For the current investigations the following correlation is used in AC²/ATHLET-CD:

$$K = \begin{cases} 9.62 \times 10^{-12} [\mathrm{g}^2/\mathrm{cm}^4\mathrm{s}], & T \leq 1473\ \mathrm{K} \\ A_B \exp\left(\frac{-E_B}{RT}\right), & 1473\ < T < 1648\ \mathrm{K} \\ A_{Fe} \exp\left(\frac{-E_{Fe}}{RT}\right), & T \geq 1648\ \mathrm{K}\ (melting\ point\ of\ FeO) \end{cases}$$

C. KIM et al.: OXIDATION KINETICS OF NUCLEAR GRADE FeCrAl ALLOYS IN STEAM IN THE TEMPERATURE RANGE 600-1500°C, TopFuel 2021

QUENCH-19
– Bundle Configuration –

- Performed at KIT 2018
- FeCrAl claddings to investigate the cladding material behavior under SA conditions
- Scenario: similar to QUENCH-15 with Zirlo cladding
  - same bundle geometry
  - same electrical power input
- Bundle configuration made of different FeCrAl compositions:
  - 24 heated rods with tungsten heater and ZrO_2 pellet
  - 8 corner rods
  - 5 spacer grid
  - Shroud

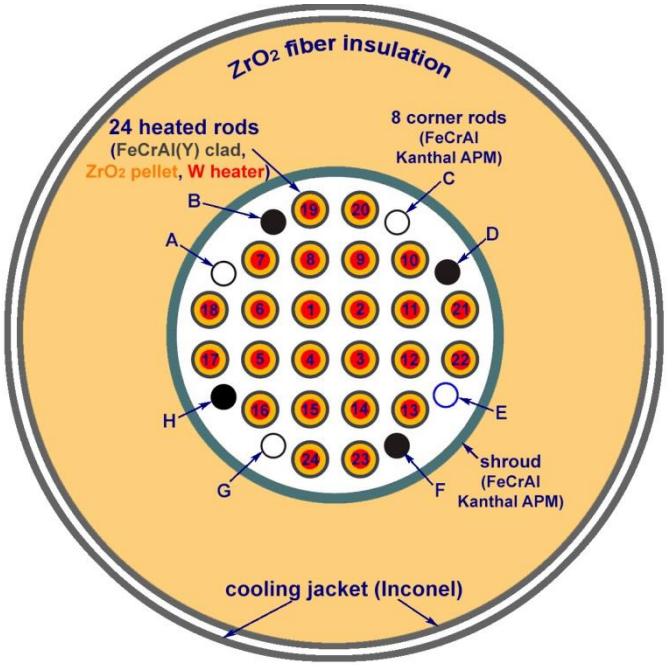

Source: KIT

QUENCH-20
– Test Conduct –

- Pre-Oxidation Phase 0 – 6020 s
- Transient Phase 6020 – 9106 s
- Quench Phase 9106 – 10000 s

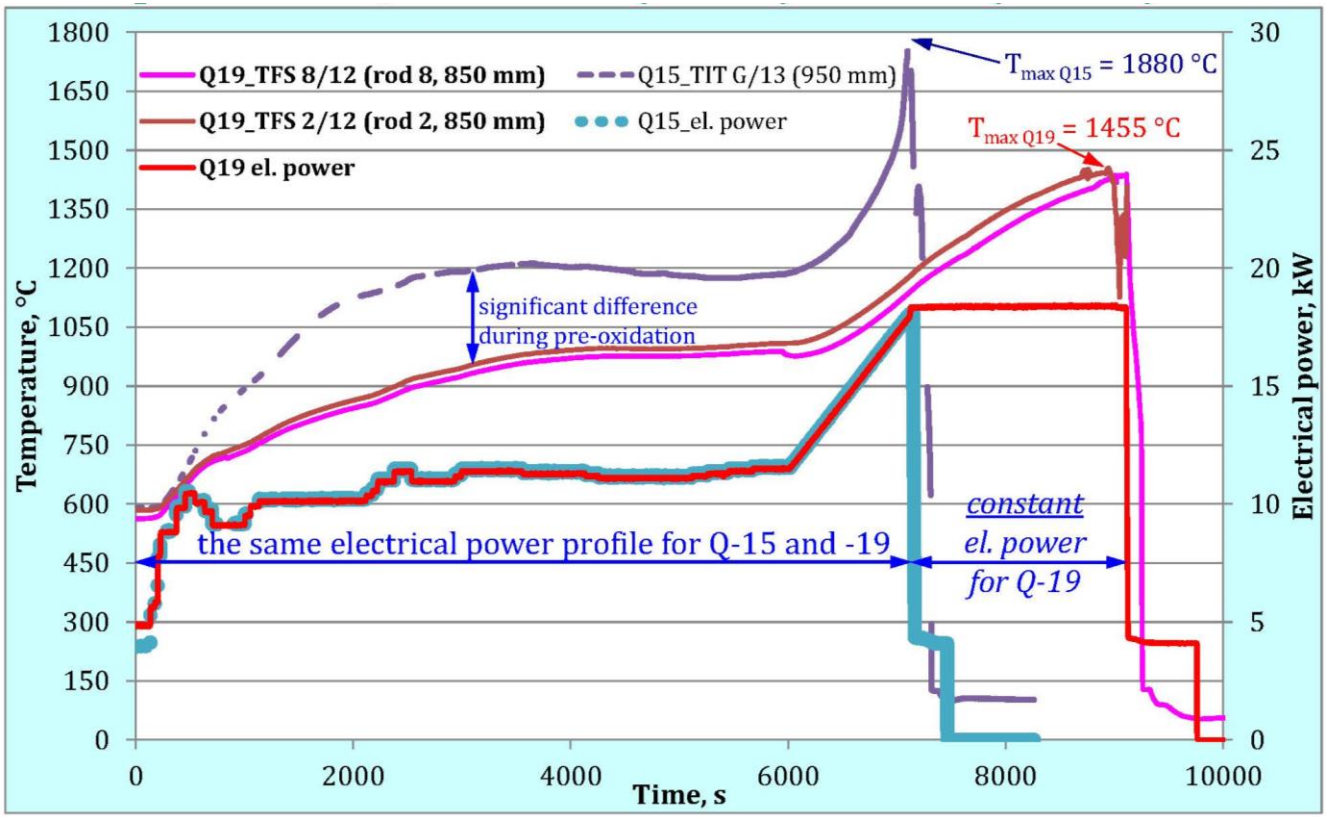

Source: KIT

Simulation Results
– Cladding Temperatures at 350 mm –

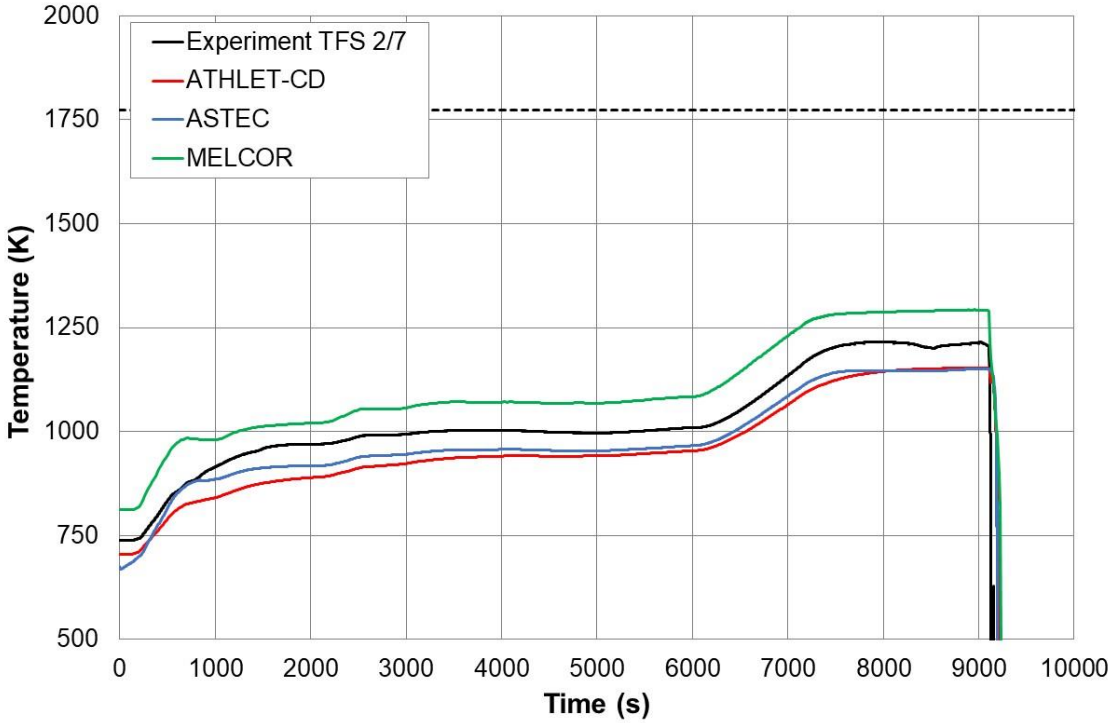

- The simulations predict the measured temperature in the lower bundle elevation qualitatively correct without temperature escalation as in the test
- MELCOR overestimated the experimental value while ATHLET-CD and ASTEC underpredicts it

Simulation Results
– Cladding Temperatures at 550 mm –

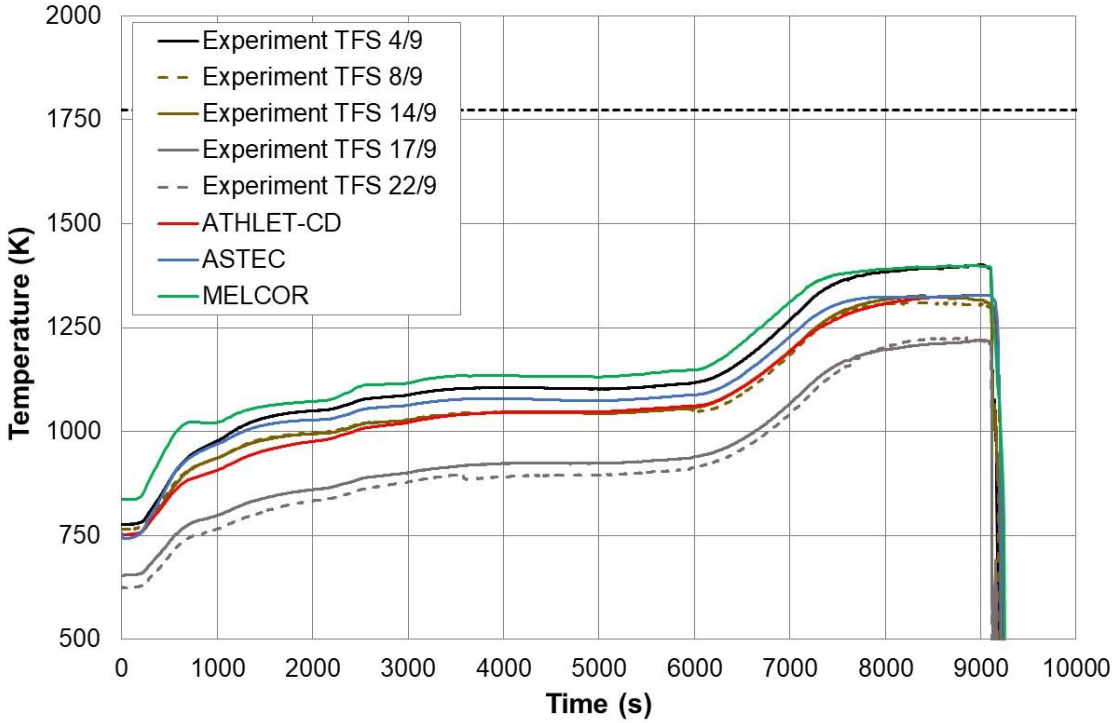

- The simulations predict the measured temperature in the middle bundle elevation qualitatively correct without temperature escalation as in the test
- The simulated cladding temperatures capture the temperatures of the inner rods
- The strong radial profile in the experiment is not predicted by any code

Simulation Results
– Cladding Temperatures at 850 mm –

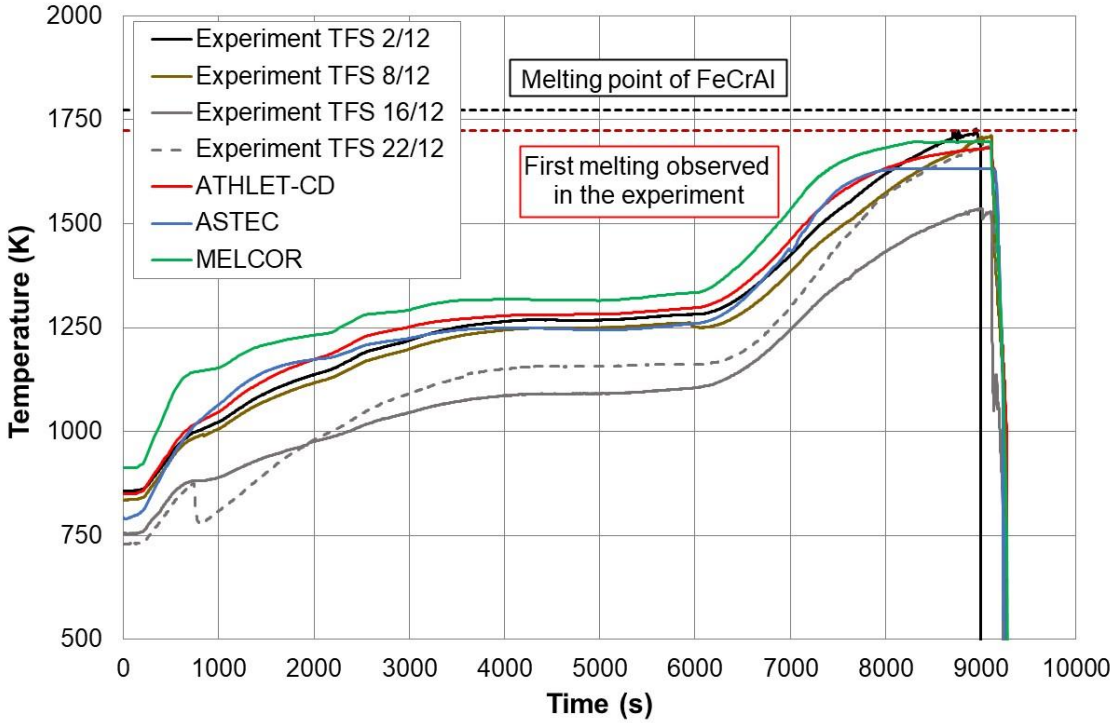

- The qualitative experimental temperature evolution is precited by the codes without temperature escalation at the end of the transient and quenching phase
- ATHLET-CD and ASTEC are in general close to the measured temperature while MELCOR overestimates especially in the pre-oxidation phase

Simulation Results
– Cladding Temperatures at 950 mm –

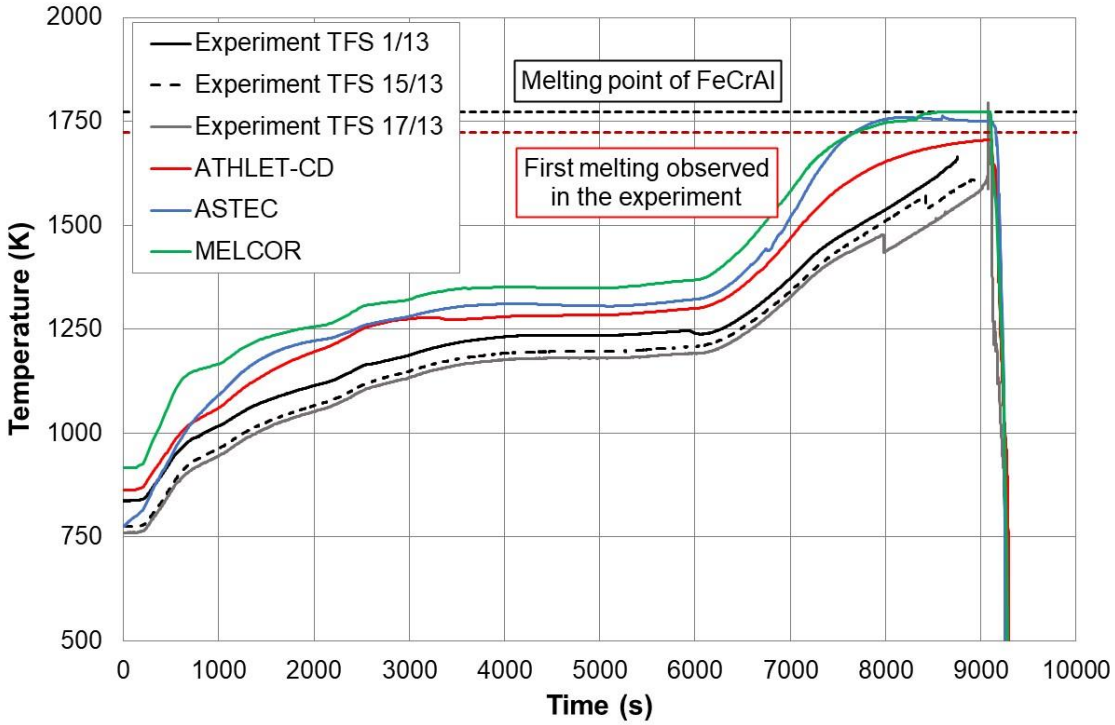

- All codes overpredict the measured temperatures
- No escalation is predicted by any code although ASTEC and MELCOR reaches temperatures close the melting temperature of FeCrAl

Simulation Results
– Hydrogen Generation –

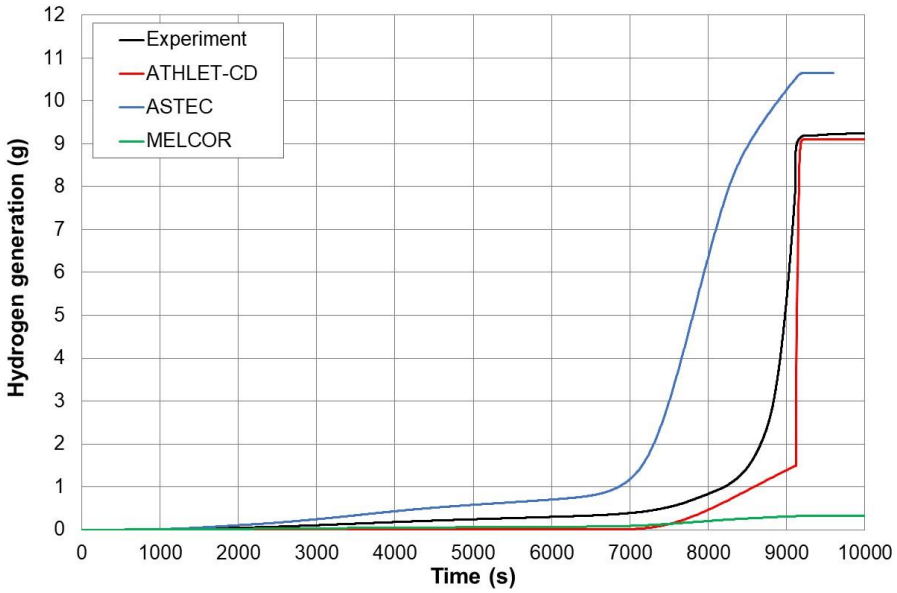

- The experimental integrated mass of hydrogen is predicted by ASTEC and ATHLET-CD, but the qualitative evolution in both codes differ strongly
  - ASTEC overestimates already in the pre-oxidation phase
  - ATHLET-CD show a significant increase at the end of transient and quenching
- MELCOR strongly underestimates the hydrogen generation although the temperatures are overestimated nearly the whole test

Conclusions and Outlook (II)

- The capabilities of the codes AC²/ATHLET-CD, ASTEC, and MELCOR were extended to simulate ATFs
- Dedicated models to calculate FeCrAl material and its oxidation has been implemented in the codes
- The experiment QUENCH-19 performed at KIT was considered to validate the recently implemented models
- With respect to the temperatures the results of the simulations show that
  - The qualitative evolution is generally captured for all elevations
  - The MELCOR overestimates the temperature, while AC²/ATHLET-CD and ASTEC are closer to the experiment in the lower and middle bundle elevations and overestimates the temperatures especially in the upper bundle elevation
  - The observed radial gradient due to the wetted insulation is not captured by any code

Conclusions and Outlook (II)

- The hydrogen generation varies strongly between the codes
  - AC²/ATHLET-CD and ASTEC predict the integral value of the experiment, but with a completely different evolution
  - MELCOR underpredicts the measured mass significantly although the temperatures are consequently overestimated
- The results show that the hydrogen generation strongly depends on the chosen correlation, which differ significantly depending on the FeCrAl composition

➢ ATF will play a major role for future developments and safety assessments

➢ The models need to be further improved also with respect to other ATF concepts to allow robust predictions

➢ Therefore, also the experimental basis needs to be expanded

Acknowledgements

- The work of GRS is sponsored by the German Federal Ministry for the Environment, Nature Conservation, Nuclear Safety and Consumer Protection (BMUV).

Supported by:

Federal Ministry
for the Environment, Nature Conservation,
Nuclear Safety and Consumer Protection

based on a decision of
the German Bundestag

Thank you for your Attention!

Current understanding of high-temperature oxidation phenomena during air ingress scenarios

Sanggil Park*
Lee & Ko
Corresponding Address
sanggil.park@leeko.com

Terttaliisa Lind
Paul Scherrer Institute
terttaliisa.lind@psi.ch

Jonathan Birchley
formerly Paul Scherrer Institute
birchley@hotmail.com

Martin Steinbrueck
Karlsruhe Institute of Technology
martin.steinbrueck@kit.edu

ABSTRACT

Zirconium alloys are used as cladding materials in light water reactors acting as a safety barrier against a release of radioactive materials during operation and in case of reactor core uncovery in severe accident scenarios. It has long been recognized that overheated cladding undergoes exothermic oxidation in steam, leading to the generation of hydrogen. Under such circumstances, the oxidation rate would typically be limited by the rate of oxygen diffusion through the oxide layer which builds up on the cladding surface, provided the layer remains undamaged. However, exposure to air can lead to accelerated oxidation since the effect of nitrogen degrades the oxide layer which hence becomes a less effective barrier, resulting in faster oxidation kinetics.
The knowledge collected in past studies has helped to identify two major behaviors of nitrogen during air oxidation. One is the nitriding, which causes the formation of a micro-porous layer, and the other is the re-oxidation of the nitride cladding, which results in a macro-cracked oxide layer due to the volume changes of the involved phases leading to faster oxidation kinetics. During a reactor accident, both reactions occur simultaneously and therefore it is hard to understand their mechanisms based on existing experimental data. For this reason, a series of experiments are conducted to understand better the phenomena of nitriding and re-oxidation during the air oxidation. This paper presents firstly the review of air oxidation phenomena from the past studies, and it provides the updated understanding of air oxidation phenomena from the present studies.

KEYWORDS
Zirconium alloy, air ingress scenario, air oxidation, nitriding, re-oxidation

* This work was conducted in the frame of PhD thesis and performed at both Paul Scherrer Institute and Karlsruhe Institute of Technology.

1. REVIEW OF PHENOMENA OF AIR OXIDATION OF ZIRCONIUM ALLOY CLADDING FROM PAST STUDIES

During air oxidation of zirconium, both oxidation and nitriding occur. The overall process of air oxidation of zirconium is summarized in [1] as follows.

(1) $O_2 + Zr \rightarrow ZrO_2$ and/or $xO_2 + 2Zr \rightarrow 2Zr(O_x)$: zirconium reacts with oxygen and forms zirconium oxide and/or α-Zr(O) by absorbing oxygen. The dissolved oxygen can stabilize the α-Zr(O) at high temperature until the melting temperature.

(2) $O_2 + 2ZrO + 2V_o^{(2+)} + 4e^- \rightarrow 2ZrO_2$: in the oxide layer, oxygen anions diffuse to the metal and the oxygen vacancies move to the oxide surface to react with additional oxygen in air. After oxygen is sufficiently decreased, nitrogen can react.

(3) $½\ N_2 + 2ZrO + 2V_o^{(2+)} + 4e^- \rightarrow ZrN + ZrO_2$: nitrogen reacts with zirconium through the previously developed oxygen vacancies in the oxide and forms ZrN (i.e. $1/2N_2 + Zr \rightarrow ZrN$).

(4) $ZrN + O_2 \rightarrow ZrO_2 + ½\ N_2$: ZrN is oxidized by newly-incoming oxygen and forms zirconium oxide and nitrogen gas is released.

Chemical heat is released during air oxidation. The reaction enthalpies of each step at room temperature (25°C) are given in the following.

- Zirconium oxidation by oxygen: $O_2 + Zr \rightarrow ZrO_2$ $\triangle H_{rxn}$ = -1094.8 kJ/mol Zr
- ZrN formation: $½\ N_2 + Zr \rightarrow ZrN$ $\triangle H_{rxn}$ = -365.4 kJ/mol Zr
- ZrN re-oxidation: $ZrN + O_2 \rightarrow ZrO_2 + ½\ N_2$ $\triangle H_{rxn}$ = -729.4 kJ/mol Zr

Nitrogen reacts with zirconium only when oxygen concentration in the gas phase is low. The P_{O2}/P_{N2} diagram which indicates the stability regions of Zr, ZrO_2 and ZrN is calculated in [2] as seen in Fig 1. The stability diagram shows that ZrN is stable only at very low oxygen partial pressure. Therefore, ZrN is formed under a locally or globally very low oxygen partial pressure after a sufficient consumption of oxygen [2].

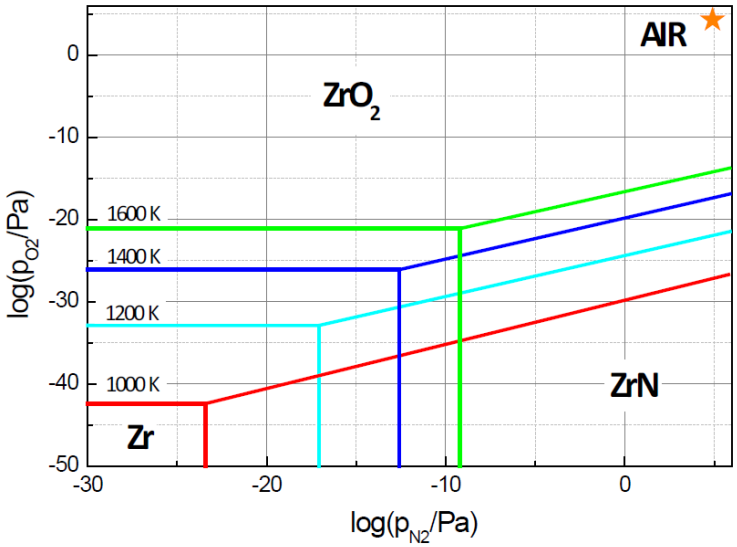

Figure 1. P_{O2}/P_{N2} stability diagram (excerpted from [2])

From the results of separate-effect tests performed by Steinbrueck et al. [2], nitrogen minimally reacts with pure zirconium and β-Zr(O). However, nitrogen readily reacts with α-Zr(O) and sub-stoichiometric oxide when oxygen is almost fully consumed. The sub-stoichiometric oxide ZrO_{2-x} is in equilibrium with oxygen-stabilized α-Zr(O) according to the Zr-O phase diagram. Under this locally almost oxygen starvation condition at the metal-oxide interface, the nitrogen reacts with α-Zr(O) and sub-stoichiometric oxide.

In addition, pores are formed during ZrN formation due to a volume mismatch between ZrN and ZrO_2 [3]. According to Duriez et al. [4], as the further oxidation occurs towards the metals the newly formed inner-oxide at the interface between the oxide layer and the metal pushes the formed ZrN outwards. Conseuqently, the ZrN is embedded in the oxide. This process continues as oxygen from the newly-incoming air partially oxidizes the previously formed ZrN and forms the ZrO_2 again while the nitrogen is released to the atmosphere or combine again with unoxidized Zr atoms near the interface where the oxygen partial pressure is sufficiently low. The different molar volumes of ZrN (14.8 cm^3) and ZrO_2 (21.7 cm^3), lead to 46.6% ($\Delta V_{ZrN \rightarrow ZrO_2}/V_{ZrO_2}$ = 6.91/14.8) of volume increase during oxidation of ZrN. Due to this significant volume expansion, the oxide scale experiences local stresses which lead to very porous oxide and cracks in the oxide allowing air to penetrate deeper as a gas.

This nitride-assisted degradation is self-sustaining. Some amount of the generated nitrogen during the oxidation of ZrN would be trapped in the oxide and it is available for further ZrN formation. Also, released nitrogen is available for further reaction with the oxygen stabilized α-Zr(O) phase under local oxygen starvation [5].

Fig 2 illustrates the oxide layer of Zircaloy-4 in air oxidation and it gives the information of mechanisms of ZrN formation and its oxidation.

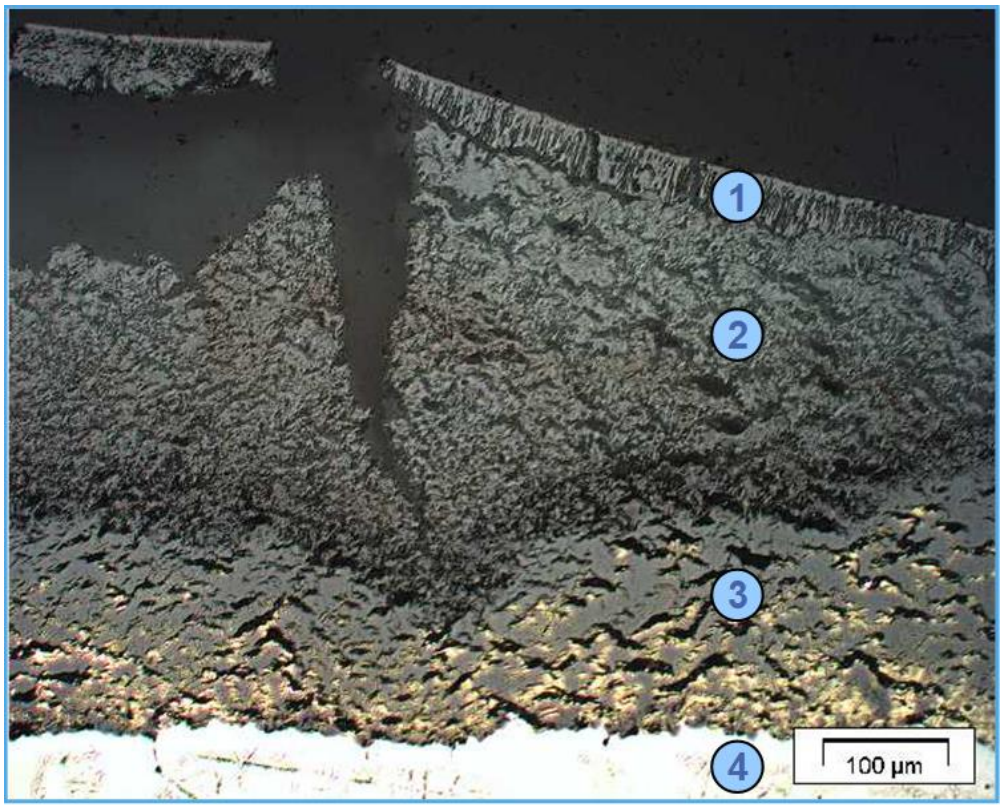

Figure 2. Mechanism of air oxidation (adopted from [6])

Region 1: initially formed dense oxide ZrO_2 – the most outer region: the dense and columnar oxide that was formed during pre-transition period (i.e. before the breakaway). Through the imperfections in oxide scale, air accesses to the interface between the oxide and the metal and oxidizes the metal. The oxygen is almost starved locally and nitrogen reacts with the oxygen stabilized α-Zr(O) or sub-stoichiometric oxide.

Region 2: porous oxide after oxidation of ZrN – ZrN converts to ZrO_2 region: ZrN is oxidized by newly incoming air and converted to oxide. Due to the significant volume increase in the oxide, cracks are formed by compressive stresses.

Region 3: ZrO_2/ZrN mixture – ZrO_2/ZrN mixtures are stable according to the stability diagram as shown in Fig 2.

Region 4: α-Zr(O) – At the oxide-metal interface, the oxygen is almost starved locally and nitrogen reacts actively with the oxygen stabilized α-Zr(O).

As explained above in this chapter, the understanding on the oxidation and nitriding from the past studies is still rather empirical and phenomenological. It is based on the Zr-O binary system and partly on the Zr-N binary system as well on the $p(O_2)/p(N_2)$ stability diagram. For this reason, only binary compounds, ZrO_2 and ZrN, are involved in the oxidation and nitriding process.

2. CURRENT UNDERSTANDING OF AIR OXIDATION PHENOMENA FROM THE PRESENT STUDY

In the present study, a series of separate-effect tests was conducted under different boundary conditions by separating each reaction phase, pre-oxidation, nitriding, and re-oxidation, respectively. In addition, tests

under identical conditions were repeated to assure the reproducibility of the behavior. The series of tests were conducted in two temperature regimes. One is the breakaway temperature regime (< 1050°C) and the other is the non-breakaway temperature regime (> 1050°C). Based on findings from analyses of test data from both temperature regimes, current understanding and its limitation on the behavior of pre-oxidation, nitriding and re-oxidation is presented in this chapter.

2.1. Current understanding on the behavior of pre-oxidation

In the pre-oxidation phase, the breakaway occurs after a certain oxidation time in the low-T regime (< 1050°C), but it does not occur in the high-T regime (> 1050°C). During pre-oxidation phase an important phenomenon for the further reaction with nitrogen is the development of alpha-Zr(O) during pre-oxidation since the alpha-Zr(O) reacts actively with nitrogen. The end products of pre-oxidation are alpha-Zr(O) and oxide. Steinbrück [2] reported that pure Zircaloy-4 was only slowly nitrided, and only oxidized metal was nitrided. As shown in Fig 3, alpha-Zr(O) was significantly nitrided whereas pure Zr metal (β-Zr) showed almost no reaction with nitrogen. In addition, the sub-stoichiometric oxide was nitrided significantly slower than the alpha-Zr(O) as seen in Fig 3.

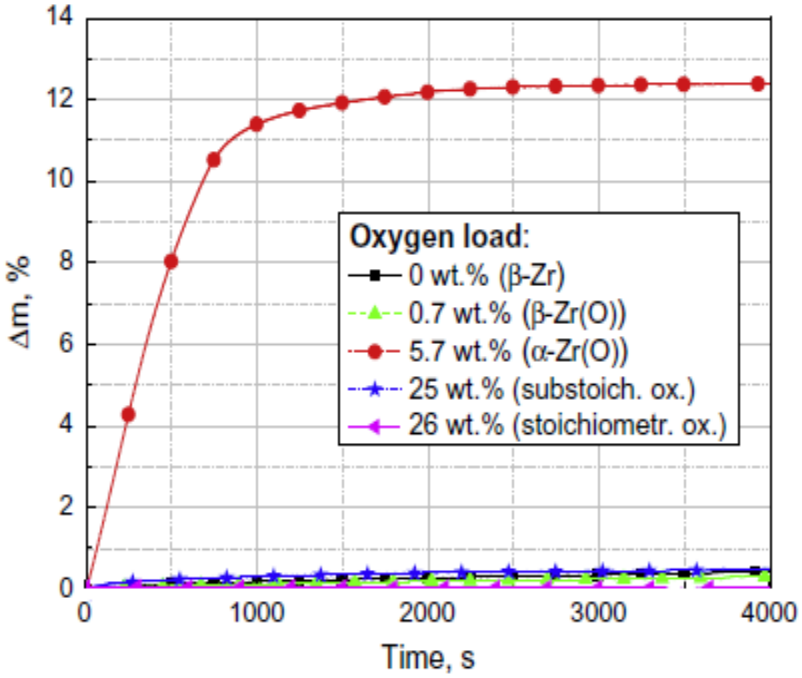

Figure 3. Nitriding mass gain of Zry-4 during nitriding at 1200°C (excerpted from [2])

In some of the tests conducted in this study, there might be a chance of starvation due to a low flow rate of oxygen gas during pre-oxidation, and it would affect the formation of alpha-Zr(O). However, this effect was not studied in detail. Future studies will be needed to vary the oxygen gas flow rate from high to very low to see the growth rate of alpha-Zr(O). As long as oxide is formed, oxygen starvation would only affect oxide scale growth. Only if the oxygen flow is so low that no oxide scale is formed, alpha phase formation would be dependent on gas flow.

The alpha-Zr(O) formation slows down because itself becomes thicker with time, similar to the oxide scale development. However, it is noted that during the breakaway alpha-Zr(O) is much thinner than expected from the oxide thickness. Because the oxide formation is much faster (linear reaction rate) than the alpha-Zr(O) formation (parabolic reaction rate, possibly even slower due to oxygen barriers at radial cracks).

As previously mentioned, it is critical to know the state of alpha-Zr(O) at the end of pre-oxidation for its amount, location and oxygen content. However, this study only focuses on the end state of nitriding and re-oxidation. In other words, no examinations were made after the pre-oxidation.

2.2. Current understanding on the behavior of nitriding

The nitriding behavior was strongly dependent on temperature, below and above 1050°C. In the low-T regime (< 1050°C), nitriding behavior was classified into two groups: "NT initially developed" and "NT slow". However, in the high-T regime (> 1050°C), nitriding behavior was classified into four groups: "NT initially developed", "NT fast", "NT transition" and "NT slow".

The main difference is internal nitriding at the metal-oxide interface for 900-1000°C and initially external nitriding for 1100-1200°C. Fig 4 shows the internal nitride at 1000°C after the pre-oxidation of 20 min and 60 min, respectively and both external and internal nitride at 1100°C after the pre-oxidation of 10 min

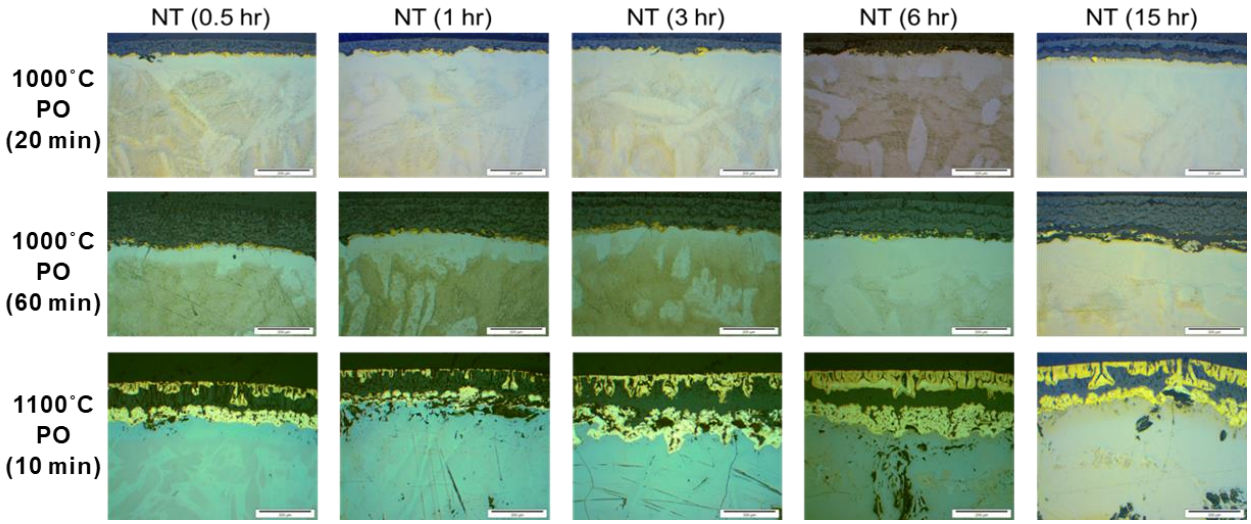

Figure 4. Nitrided Zircaloy-4 samples after the pre-oxidation

In case of tests below 1050°C (900-1000°C), the main source of nitriding in the phase of "NT initially developed" seems to be the already developed alpha-Zr(O) during pre-oxidation. For this reason, the "NT initially developed" was dependent on the pre-oxidation history of the tests. With longer pre-oxidation time (i.e. higher amount of already developed alpha-Zr(O)), a higher mass gain of "NT initially developed" was achieved. First, the nitrogen is taken up by the already developed alpha-Zr(O) phase and forms the nitride after the solubility limit of nitrogen in the alpha-Zr(O,N) is reached/exceeded. However, for the "NT slow", its main source might be the further developed alpha-Zr(O) during the nitriding time, because the mass gain of "NT slow" was proportional to the nitriding time, but not to the pre-oxidation time. During the nitriding period, the oxygen diffused from the oxide to the metal, and it further developed the alpha-Zr(O).

The simple schematics of the mechanistic behavior are drawn in Fig 5 based on the findings and analyses of tests data below 1050°C (900-1000°C).

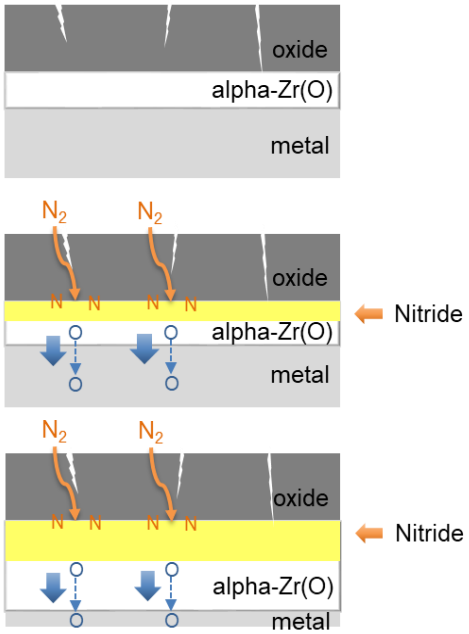

Figure 5. Schematics of nitriding behavior (tests below 1050°C)

As shown in Fig 5, nitrogen firstly accesses through imperfections in the oxide to the alpha-Zr(O), which has been previously developed during the pre-oxidation (i.e. "already developed alpha-Zr(O)"), and forms the nitride at the oxide-metal interface. This happens during the "NT initially developed". At the same time, oxygen diffuses to the inner metal part by developing further alpha-Zr(O) (i.e. "further developed alpha-Zr(O)"), and the nitrogen reacts with this further developed alpha-Zr(O) after the nitriding of the already developed alpha-Zr(O). This happens during the "NT slow".

For the ZrN phase to be stable, a very low oxygen partial pressure (below ca. 10^{-30} Pa at 1000°C) is required according to the P_{O2}/P_{N2} stability diagram as shown in Fig 1. For this reason, the ZrN phase can be stabilized in the oxygen deficient region. As shown in Fig 6, the nitride was mostly formed at the metal-oxide interface. Through the imperfections in oxide such as cracks by the breakaway oxidation, the nitrogen accesses to the oxide-metal interface. At the interface, the oxygen concentration is locally lower than the overall oxide scale since oxygen is continuously diffusing into the metal and forms the alpha-Zr(O). Thermodynamically, the oxygen partial pressure is determined by the Zr/ZrO_2 equilibrium, which is lower than the ZrO_2/ZrN equilibrium according to Fig 1.

However, it is highly noted that the nitriding occurred not only at the oxide-metal interface but also on the external surface of the oxide layer. At 1100-1200°C, the external nitride was developed first on top of the oxide layer and the inner nitride developed later.
In case of tests above 1050°C (1100-1200°C), the reaction rate of "NT initially developed" was around 200 times higher than that of tests at 1000°C. After the "NT initially developed", the "NT fast" was continued. During the "NT fast", the nitriding rate kept increasing and reached the local maximum. After reaching the local maximum, the "NT transition" followed and the nitriding rate kept decreasing until reaching the "NT slow". For the duration of "NT slow", the nitriding rate was very low and kept an almost constant value.

As shown Fig 4, it was found that the nitride was also formed at the top of the oxide surface. This external nitride was formed during the "NT initially developed" and "NT fast". It seems that the oxygen diffusion from the oxide to the metal creates points of attack for the nitrogen, which could be vacancies in sub-stoichiometric oxide or even alpha-Zr(O) phase. The incoming nitrogen reacts with this alpha-Zr(O) and sub-stoichiometric oxide to form the external nitride. As the nitriding duration increased, this external nitride

layer became thicker and nitrogen accessed through the imperfections to the already developed alpha-Zr(O) near the oxide-metal interface. The main source of nitriding during "NT transition" seems to be the already developed alpha-Zr(O). After nitriding the already developed alpha-Zr(O), the nitrogen would react with the further developed alpha-Zr(O) which was formed at the inner metal layer. The main source of nitriding during "NT slow" seems to be the further developed alpha-Zr(O). For this reason, the mass gain of "NT slow" was proportional to the nitriding time during the tests. The simple schematics of the mechanistic behavior are drawn in Fig 6 based on the findings and analyses of tests data above 1050°C (1100-1200°C).

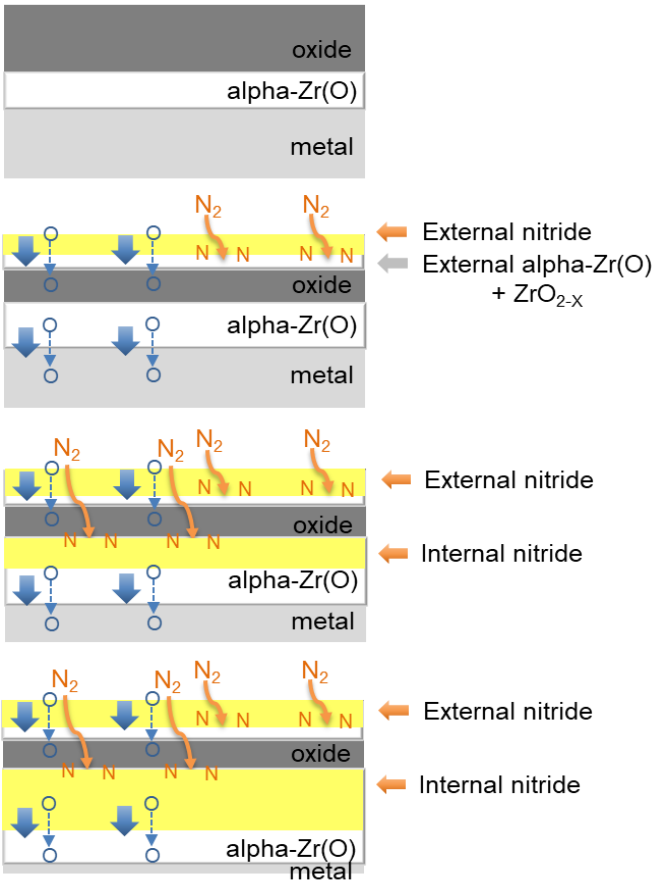

Figure 6. Schematics of nitriding behavior (tests above 1050°C)

As shown in Fig 6, the oxide scale is dense, and the oxygen diffuses from the surface of oxide to the inner part. The external alpha-Zr(O) and the sub-stoichiometric oxide are developed, they are nitrided first by forming the external nitride layer. This happens during the "NT initially developed" and "NT fast". The nitrogen invades to the oxide-metal interface and reacts with the already developed alpha-Zr(O) by forming the internal nitride layer during the "NT transition". At the same time, oxygen diffuses continuously and develops the further alpha-Zr(O). The nitrogen reacts with this further developed alpha-Zr(O) by forming additional internal nitride during the "NT slow".

As seen in Fig 5 and 6, the nitride development is quite different by temperature. At 900-1000°C, the nitride was observed at the oxide-metal interface. At 1100-1200°C, the external nitride was developed first on top of the oxide layer and the internal nitride developed later.

2.3. Current understanding on the behavior of re-oxidation

During the re-oxidation phase, there are two different reactions. One is the "re-oxidation of nitride" and the other is the "further oxidation of remaining metal". However, both reactions happen simultaneously at each different location, not sequentially. As described before, the nitride formation was different at both low (900-1000°C) and high (1100-1200°C) temperatures.

At temperature below 1050°C, the nitride was formed mostly at the oxide-metal interface (see the schematic in Fig 5). The incoming oxygen may firstly react with the nitride at the oxide-metal interface causing massive oxide layer degradation. As already described in chapter 1, around 46.6% ($\Delta V_{ZrN \rightarrow ZrO_2}/V_{ZrO_2}$ = 6.91/14.8) of volume expansion is accompanied with the re-oxidation of ZrN. This significant oxide degradation would promote the further oxidation of the remaining metal below the nitride layer.

At temperature above 1050°C, the nitride was firstly formed on the top of the oxide surface and only later at the oxide-metal interface and inner metal part (see the schematic in Fig 6). Firstly, the incoming oxygen re-oxidized the external nitride. From the analysis of metallography of post-test samples at 1100-1200°C as shown in Fig 7, it was found that the external nitride was firstly re-oxidized and forming porosity on the top of the dense oxide layer. However, the internal nitride layer remained almost intact just below the dense oxide layer. It seems that this intact internal nitride layer was protected by the dense oxide layer.

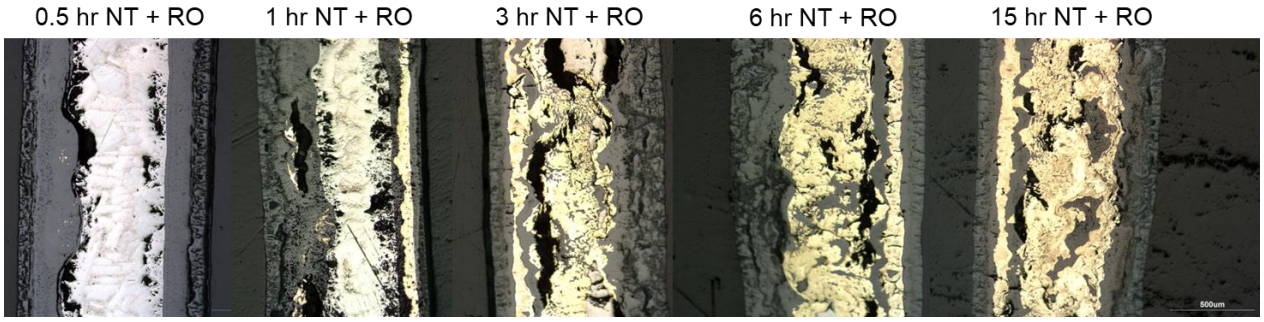

Figure 7. Re-oxidized Zircaloy-4 samples after the pre-oxidation and nitriding (tests at 1050°C)

In the beginning of re-oxidation period, the incoming oxygen re-oxidizes the nitride (i.e. the internal nitride for low temperature tests (900-1000°C) and the external nitride for high temperature tests (1100-1200°C)) and oxidizes the metal near the edge at the top of sample. These two reactions would lead to the accelerated kinetics in the beginning of re-oxidation period. After re-oxidizing the nitride, it follows further oxidation of remaining metal oxidation and its kinetic rate is slightly lower than that of the accelerated kinetics.

3. CONCLUSIONS

In this paper, the current understanding on the air oxidation of zirconium alloy cladding is presented. The air oxidation may occur in the air ingress scenarios at both reactor and spent fuel pool in the nuclear power plant. During such scenarios, nitrogen plays a major role after the pre-oxidation by a nitriding of oxidized metal and a re-oxidation of nitride. The past studies identified the overall behavior of nitriding and re-oxidation, but its detailed mechanism was not investigated sufficiently. For this reason, a series of tests has been performed to better understand individual phenomena of pre-oxidation, nitriding and re-oxidation during the air oxidation. Each reaction mechanism was divided into two temperature regimes, low-T (< 1050°C) and high-T (< 1050°C) as shown in Fig 8.

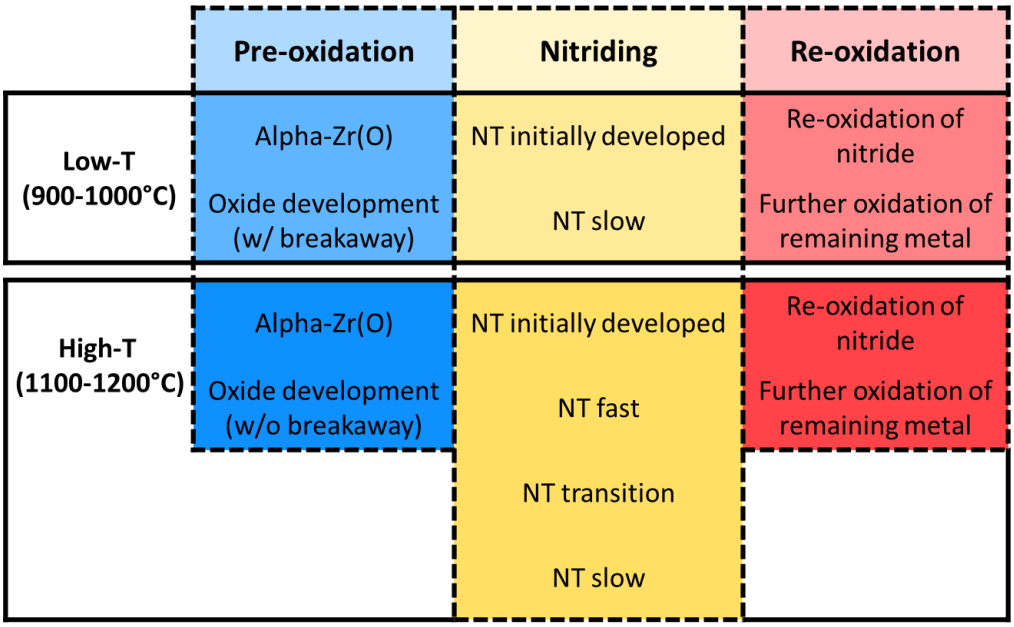

Figure 8. Summary of air oxidation behavior

Based on numerous tests data and their analyses, the current understanding on the behavior of air oxidation was significantly updated compared to the past understanding.

NOMENCLATURE (IF NEEDED)

PO: Pre-oxidation
NT: Nitriding
RO: Re-oxidation

ACKNOWLEDGMENTS

The project was financially supported by the Swiss Federal Nuclear Safety Inspectorate ENSI.

REFERENCES

1. M. Grosse, Nuclear Corrosion Science and Engineering, A volume in Woodhead Publishing Series in Energy (2012) 265-300.
2. M. Steinbrück, Journal of Nuclear Materials 447 (2014) 46-55.
3. C. Duriez, M. Steinbrück, D. Ohai, T. Meleg, J. Birchley, T. Haste, Nuclear Engineering and Design 239 (2009) 244-253.
4. C. Duriez, T. Dupont, B. Schmet, F. Enoch, Journal of Nuclear Materials 380 (2008) 30-45.
5. M. Steinbrück, M. Böttcher, Journal of Nuclear Materials 414 (2011) 276-285.
6. M. Steinbrück, M. Grosse, “Deviations from parabolic kinetics during oxidation of zirconium alloys”, (2015) ASTM Special Technical Publication, STP 1543, pp. 979-1001.

PAUL SCHERRER INSTITUT

PSI



Dr. Sanggil Park

Current understanding of high-temperature oxidation phenomena during air ingress scenarios

ERMSAR2022, 18 May 2022

PAUL SCHERRER INSTITUT

Content

1. **Background**
2. **Experimental Set-up**
3. **Results and Discussion**
4. **Open Issues**
5. **Summary and Conclusion**

Overview of air oxidation of Zicaloy-4

- Steam oxidation: $2H_2O+Zr \rightarrow ZrO_2+2H_2$ $\Delta H_{rxn}=-616$ kJ/mol Zr
- Oxygen oxidation: $O_2+Zr \rightarrow ZrO_2$ $\Delta H_{rxn}=-1094.8$ kJ/mol Zr

ca. 1.8 times heat release

- Nitriding: $1/2N_2+Zr \rightarrow ZrN$ $\Delta H_{rxn}=-365.4$ kJ/mol Zr
- Re-oxidation: $ZrN+O_2 \rightarrow ZrO_2+1/2N_2$ $\Delta H_{rxn}=-729.4$ kJ/mol Zr

Cladding degradation by nitriding and re-oxidation

ΔH_{rxn} at room temperature

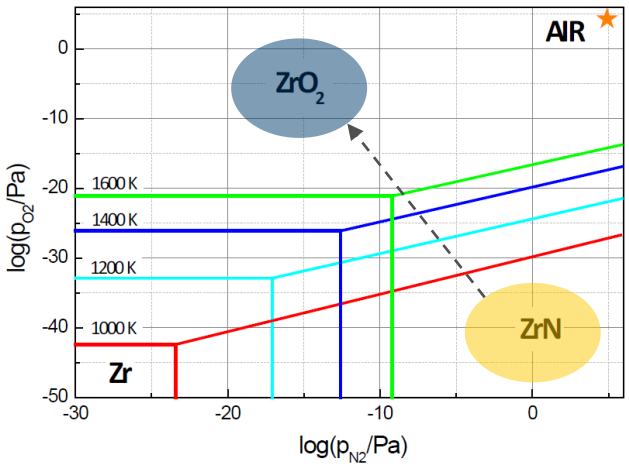

- **Nitriding** of pre-oxidized Zry-4 cladding leads to micro porous and less coherent oxide scale.

$$\bar{V}_{ZrN}/\bar{V}_{ZrO_2} = 0.68$$

- **Re-oxidation** of nitrided pre-oxidized Zry-4 cladding leads to macro cracked oxide scale.

$$\bar{V}_{ZrO2}/\bar{V}_{ZrN} = 1.47$$

Background

Knowledge gap of the past studies

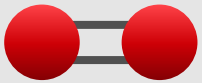

O_2

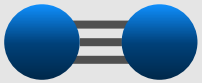

N_2



Zry-4 cladding oxidation for 1 hour at 1000˚C in air*

- Simultaneous reaction of NT & RO
- Hard to differentiate one from another



Detailed individual behavior of NT & RO

Interrelationship b/w PO, NT and RO



*M. Steinbrück et al., Prototypical Experiments on Air Oxidation of Zircaloy-4 at High Temperatures, KIT, FZKA 7257, January 2007

Experimental set-up

Test matrices and facilities

Temperature	Pre-oxidation (O_2/Ar)	Nitriding (N_2/Ar)	Re-oxidation (O_2/Ar)
900-1200°C	X	X	
	X	X	X

- **Test temperature**: "**Low-T**" breakaway regime (900 and 1000°C) and "**High-T**" non-breakaway regime (1100 and 1200°C)
- **Different experimental boundary condition**: to verify whether or not the behavior of pre-oxidation, nitriding and re-oxidation are independent of the experimental boundary conditions
- **Reproducibility**: each test of identical condition was repeated.

Setaram TAG system (1st series)

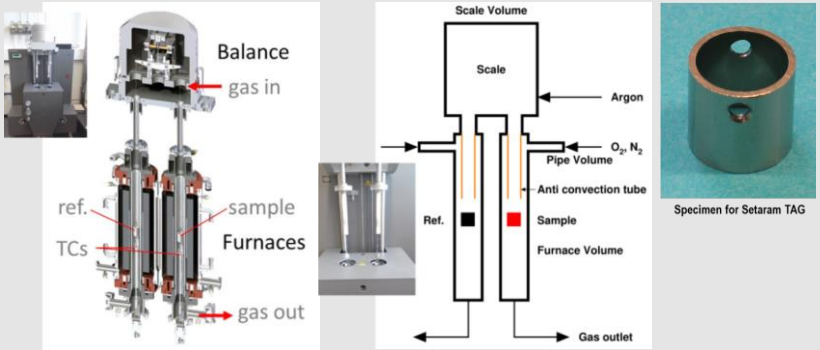

Netzsch STA-409 system (2nd series)

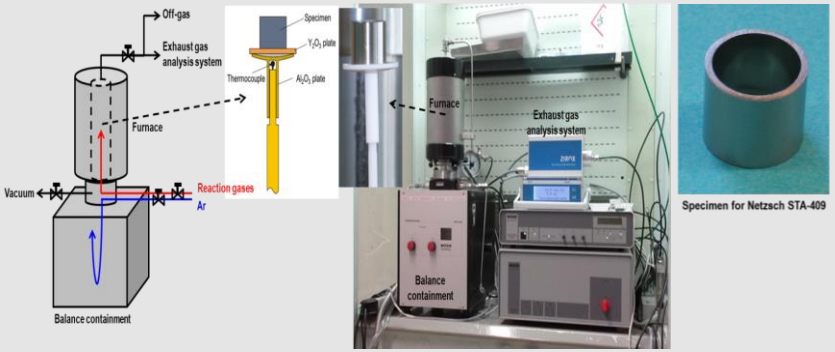

Experimental set-up

Post-test examination methods

Methods	Target Samples	Investigation
Optical microscopy	All samples	Horizontal cross sectional surface Vertical cross sectional surface
Raman spectroscopy	 Specific oxidized /nitrided sample (Zr-O-N ternary phase investigation)	Local phase identification
SEM		Locally magnified surface morphology
EDS		Local composition analysis
WDS		Local composition analysis
XPS		Local phase identification
XRD		Identification of crystalline phases

Results and Discussion

Overview of behavior

	Pre-oxidation	Nitriding	Re-oxidation
Low-T (900-1000°C)	Alpha-Zr(O) Oxide development (w/ breakaway)	NT initially developed NT slow	Re-oxidation of nitride Further oxidation of remaining metal
High-T (1100-1200°C)	Alpha-Zr(O) Oxide development (w/o breakaway)	NT initially developed NT fast NT transition NT slow	Re-oxidation of nitride Further oxidation of remaining metal

Results and Discussion

Pre-oxidation

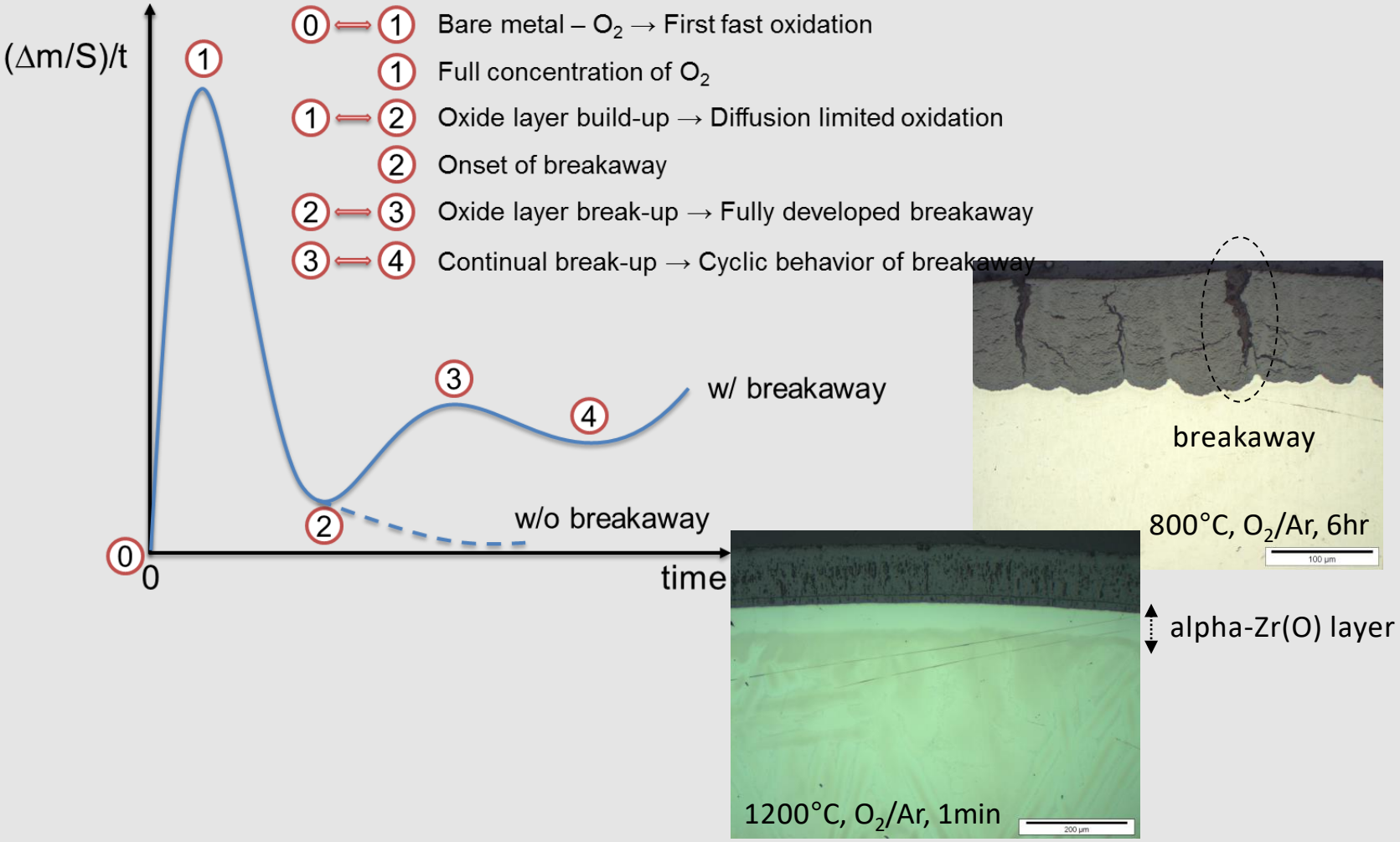

*Note: micrographs are taken from other tests just for the explanation. Current tests were not finished only after the pre-oxidation.

Results and Discussion

Transition from Pre-oxidation to Nitriding

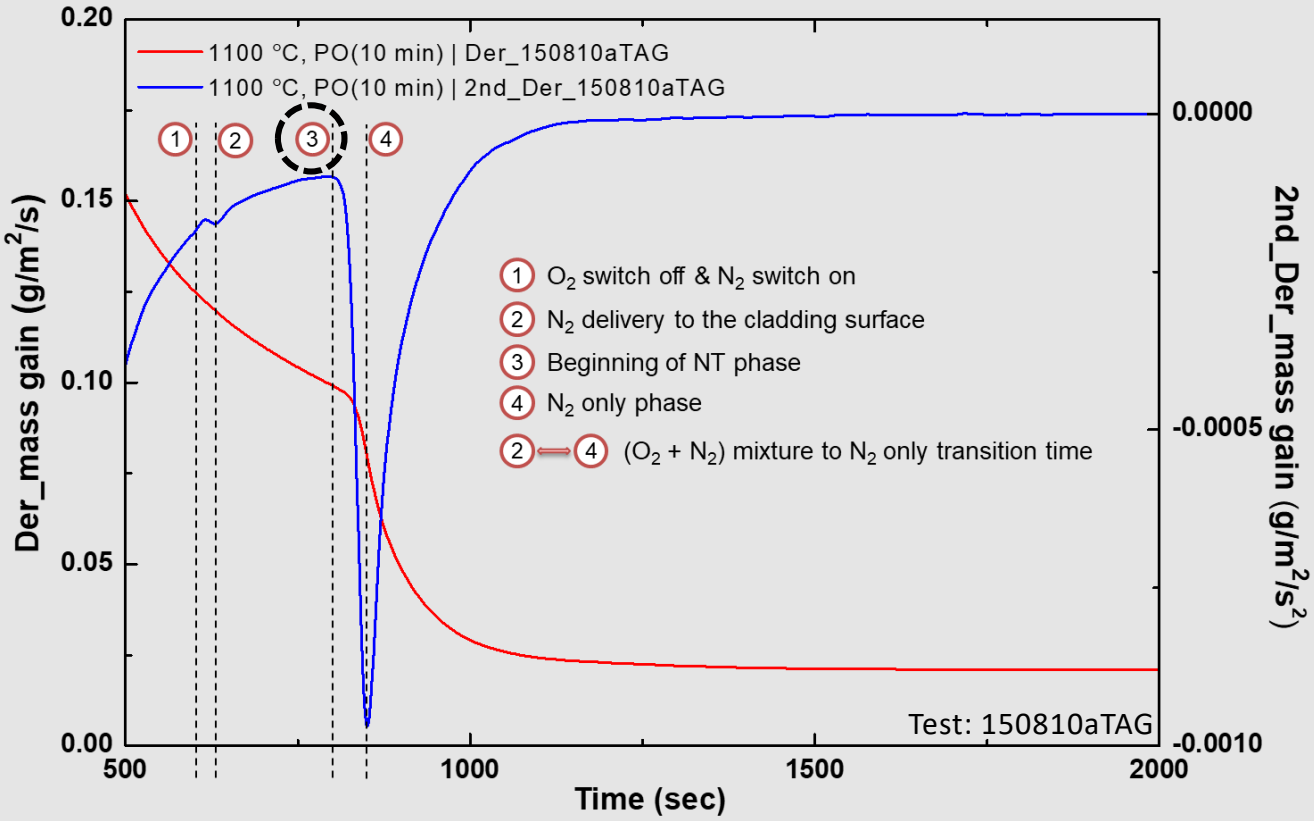

- **Depletion of remaining O_2**: by the twin effects of O_2 uptake and O_2 purging
- **Open issue**: resolution of the amount of NT phase mass gain by uptake of residual oxygen

Results and Discussion

Low-T (900-1000°C) Nitriding

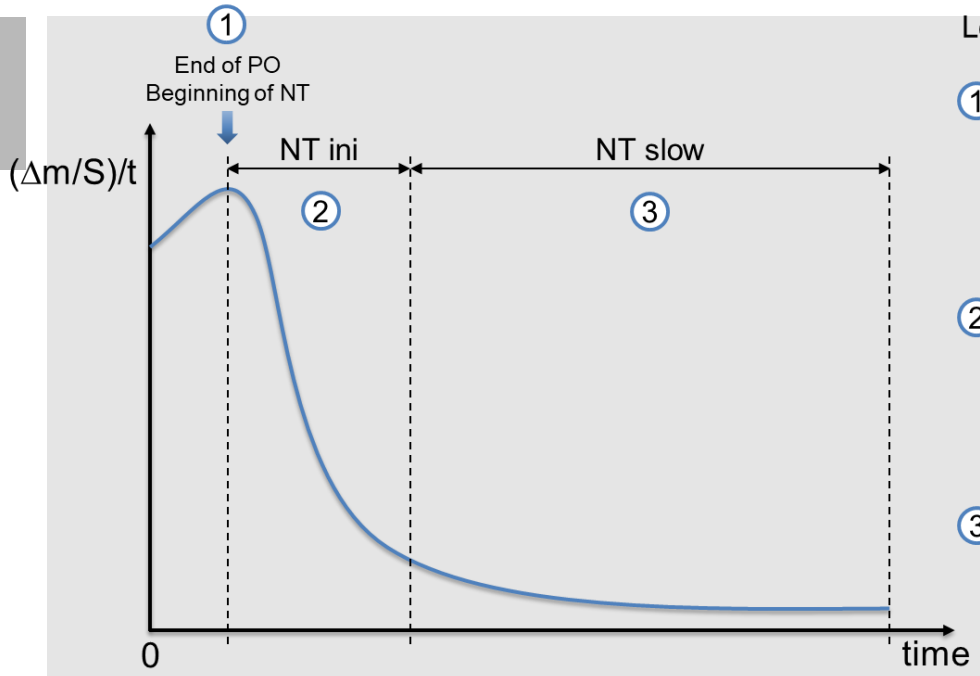

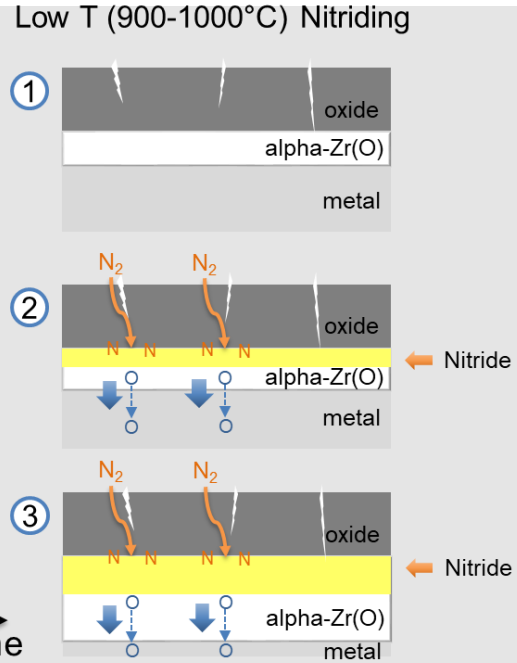

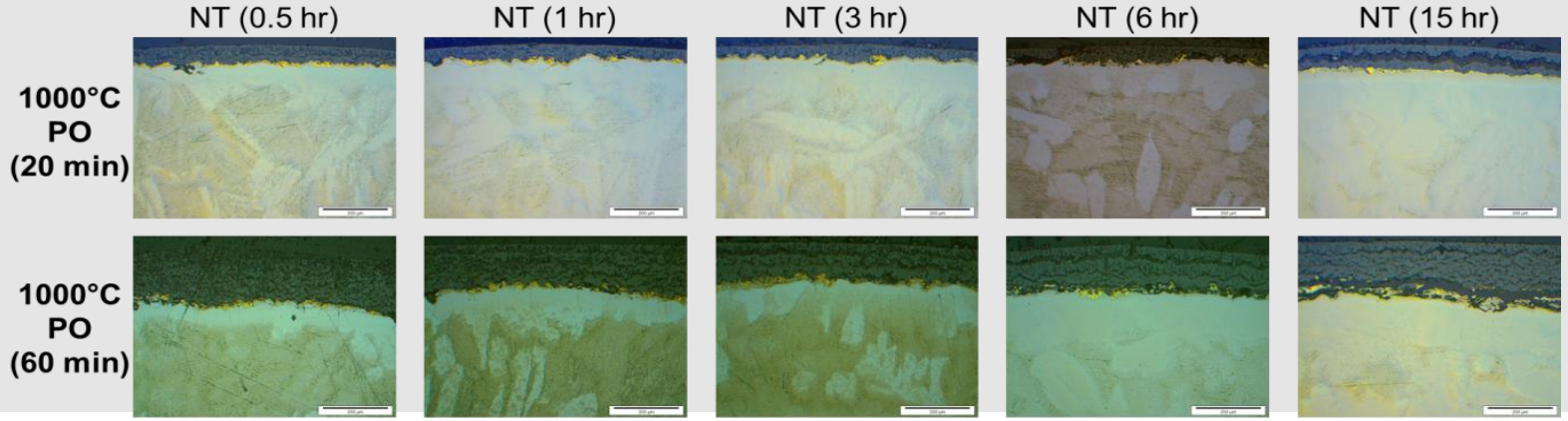

Results and Discussion

Low-T (900-1000°C) Nitriding

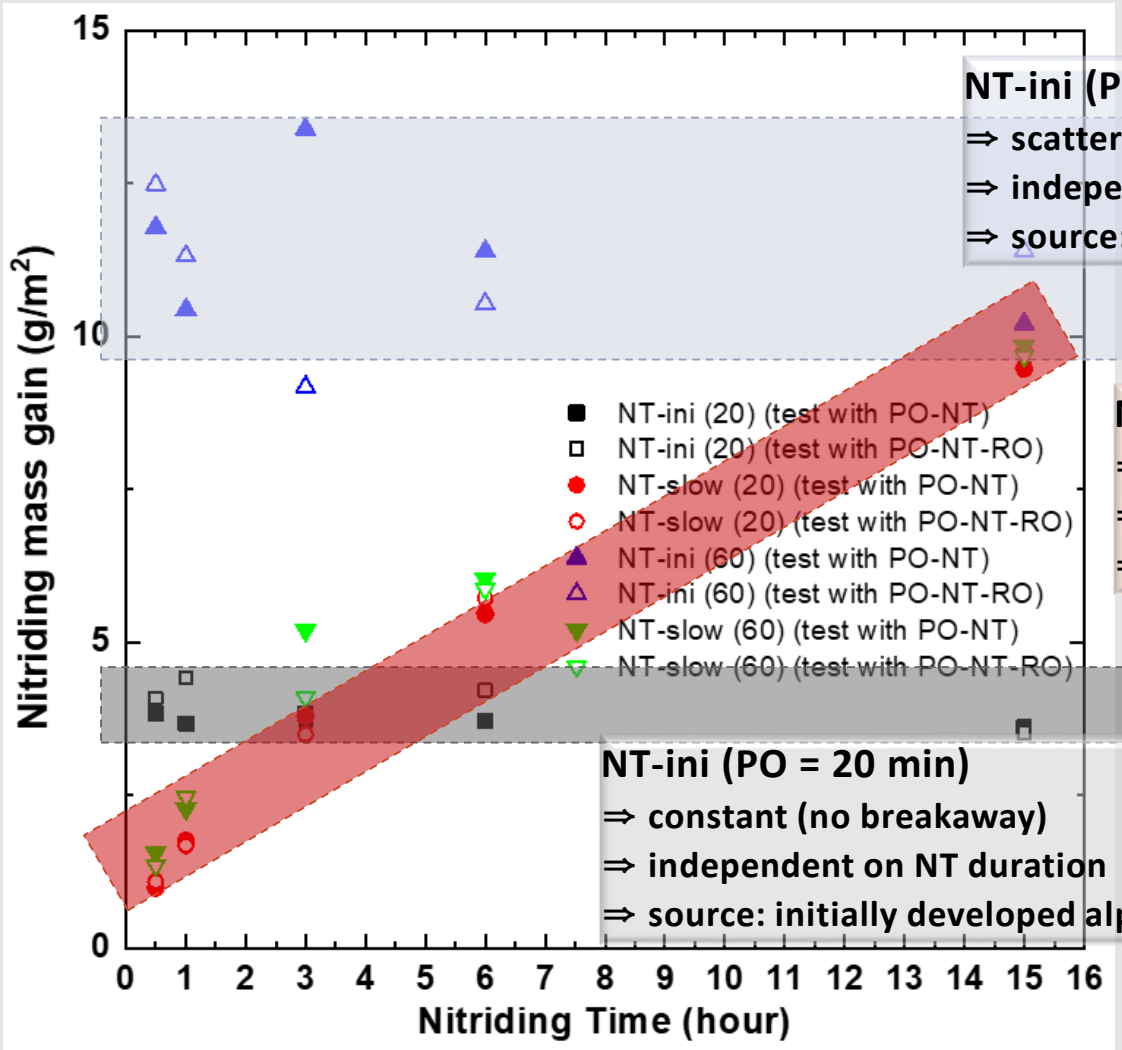

NT-ini (PO = 60 min)
⇒ scattering due to the breakaway
⇒ independent on NT duration
⇒ source: initially developed alpha-Zr(O)

NT-slow (PO = 20 & 60 min)
⇒ dependent on NT duration
⇒ independent on PO duration
⇒ further developed alpha-Zr(O)

NT-ini (PO = 20 min)
⇒ constant (no breakaway)
⇒ independent on NT duration
⇒ source: initially developed alpha-Zr(O)

High-T (1100-1200°C) Nitriding

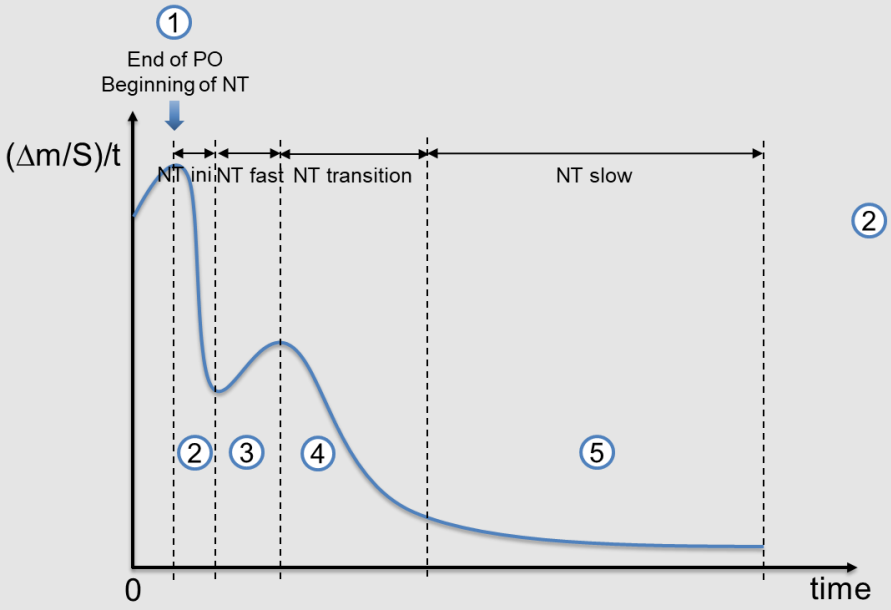

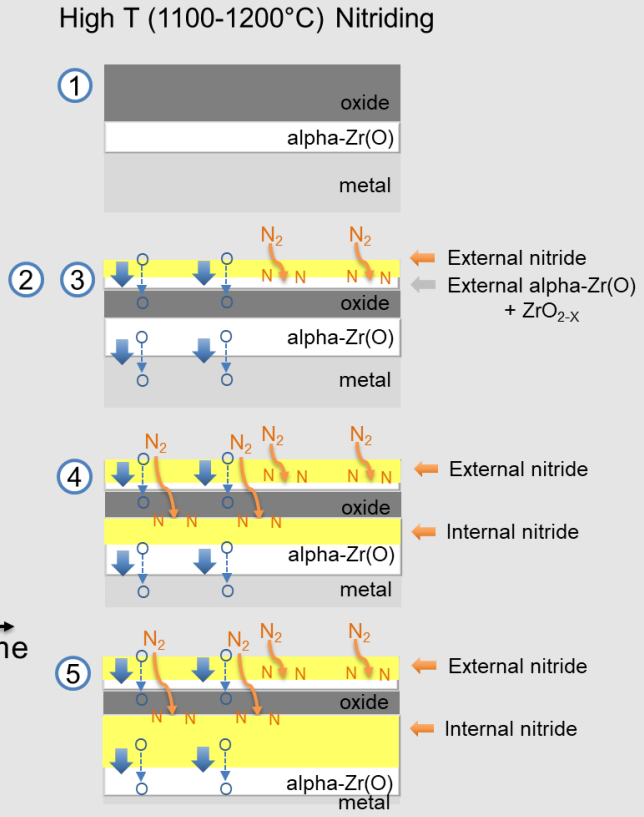

1100°C PO (10 min)

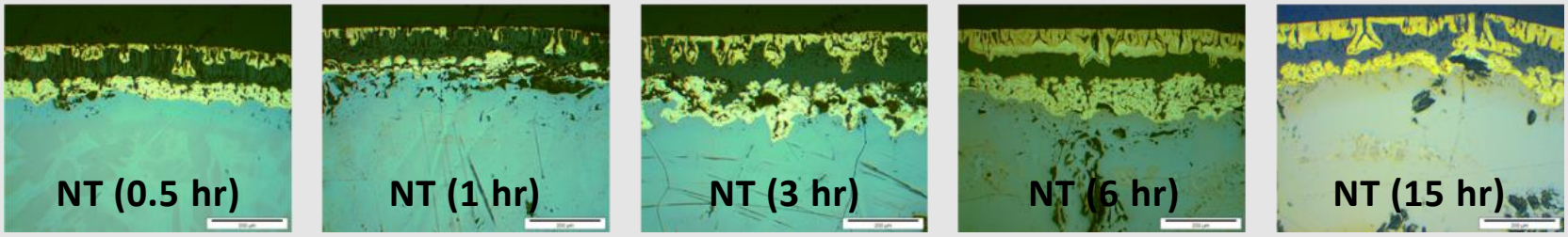

Results and Discussion

High-T (1100-1200℃) Nitriding (NT ini + fast → External ZrN)

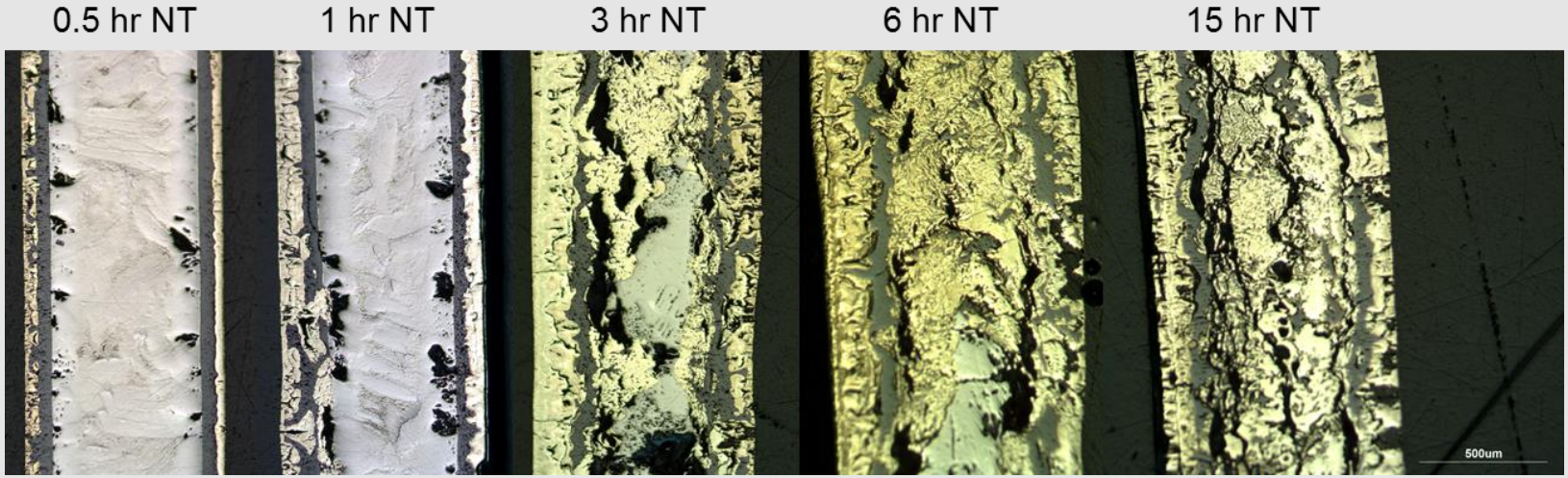

- The **external nitride was firstly formed uniformly on the top of oxide layer**. This external nitride layer became thicker as nitriding duration increased.
- Due to the **protectiveness of oxide scale (no breakaway temperature regime)**, nitrogen reacted the external alpha-Zr(O) and/or sub-stoichiometric oxide.
- As nitriding duration increased, the external layer became thicker and **nitrogen invaded into the inner metal layer and converted to the internal nitride layer**.

Results and Discussion

High-T (1100-1200°C) Nitriding (NT transition)

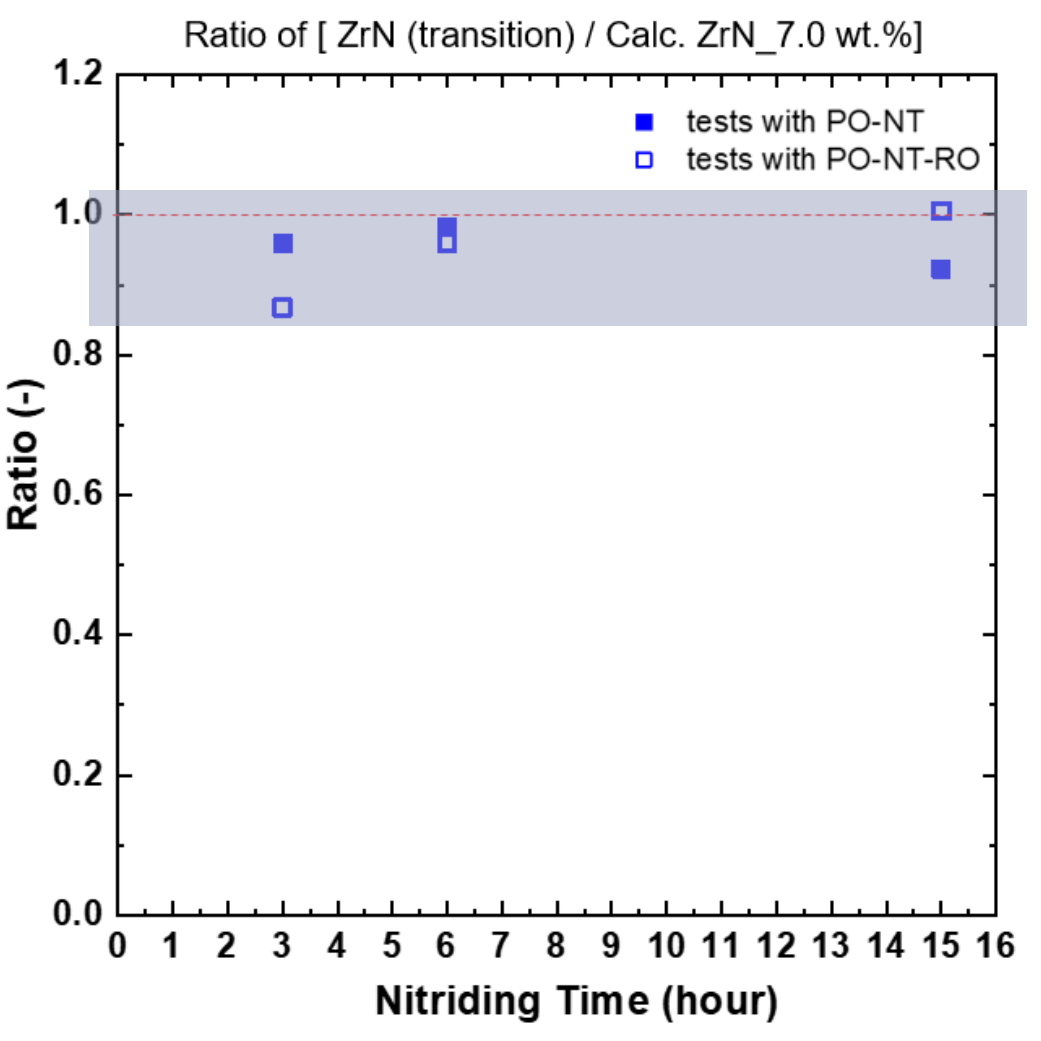

Source of nitriding in the process of "NT transition"

⇒ initially developed alpha-Zr(O) during pre-oxidation

"ZrN (transition)"

= mass gain from "NT transition"

"Calc. ZrN_7.0 wt.%"

= mass gain if the 7.0 wt.% of initially developed alpha-Zr(O) is converted to the ZrN.

Results and Discussion

High-T (1100-1200°C) Nitriding (NT slow)

Mass gains of "NT slow" ⇒ Proportional to nitriding time

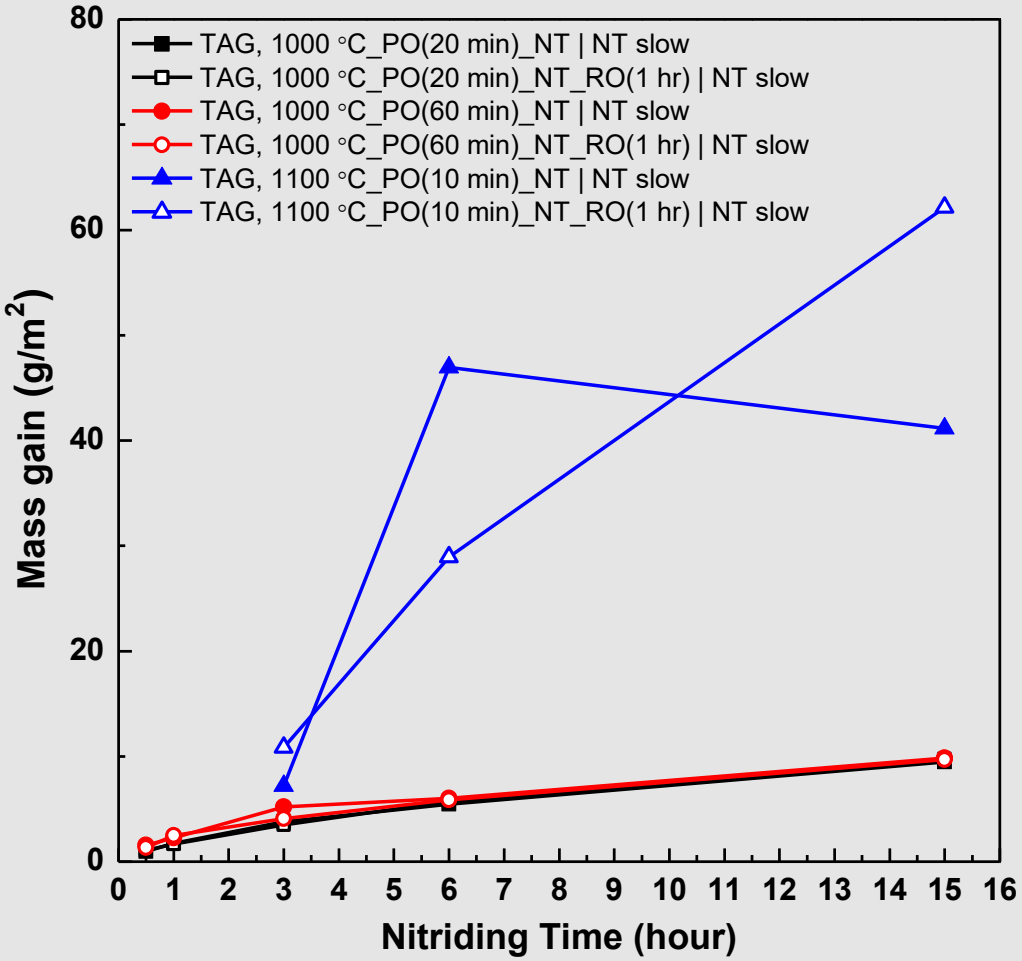

Source of nitriding in the process of "NT slow"

⇒ further developed alpha-Zr(O) by the oxygen diffusion from the oxide to metal during the nitriding time.

Results and Discussion

Low-T (900-1000°C) Re-oxidation

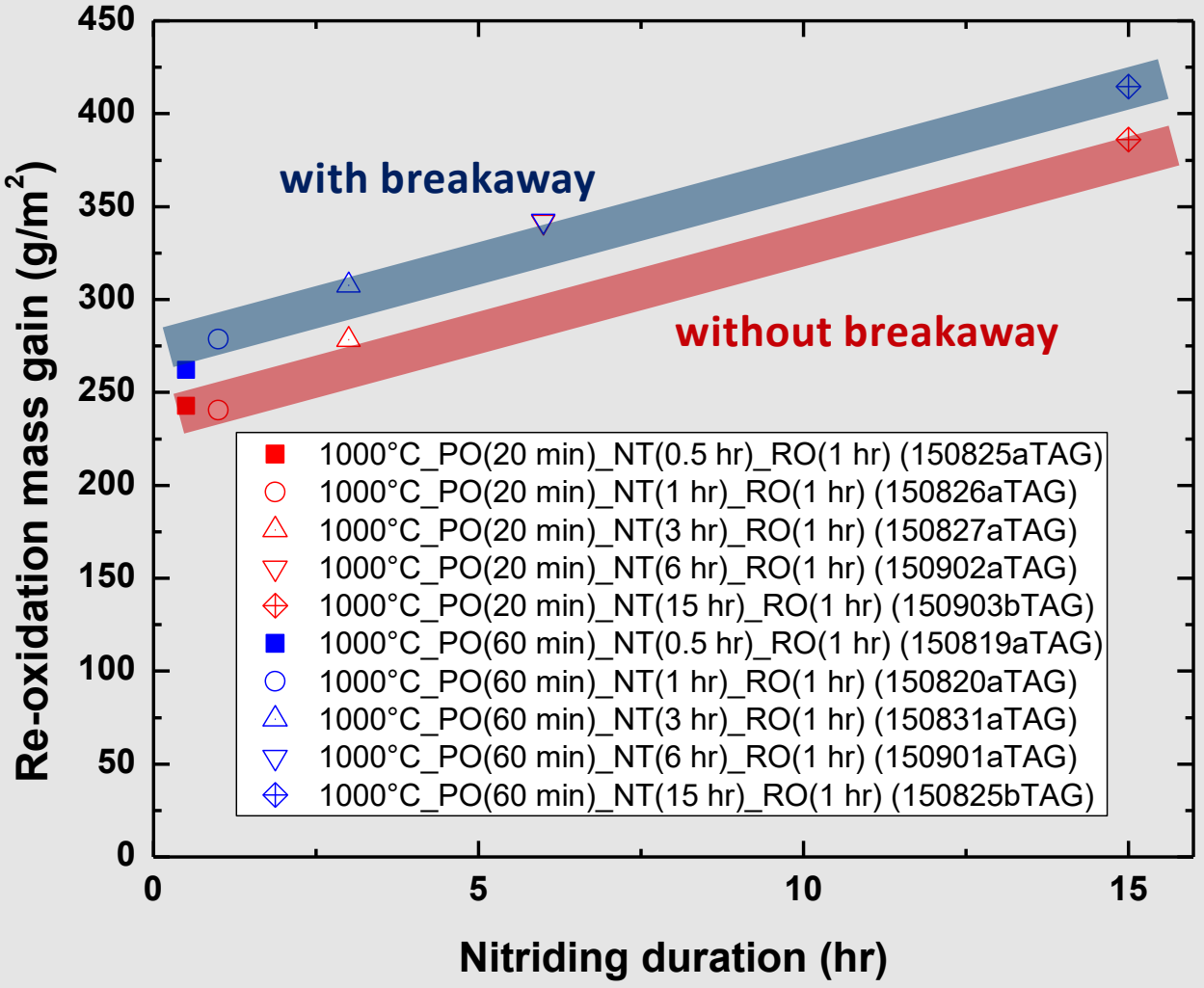

Results and Discussion

High-T (1100-1200°C) Re-oxidation

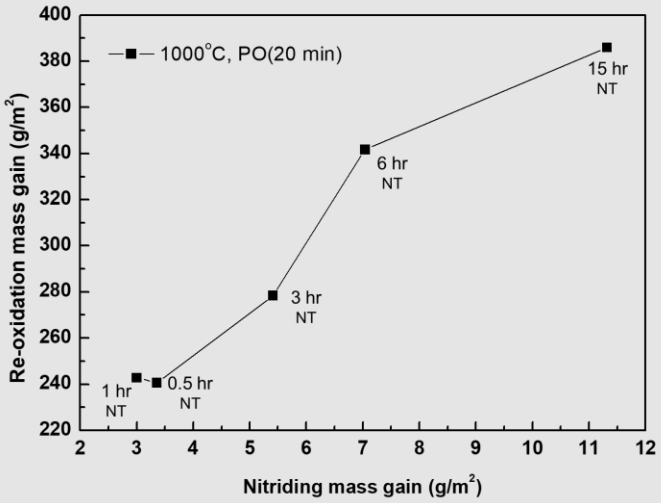

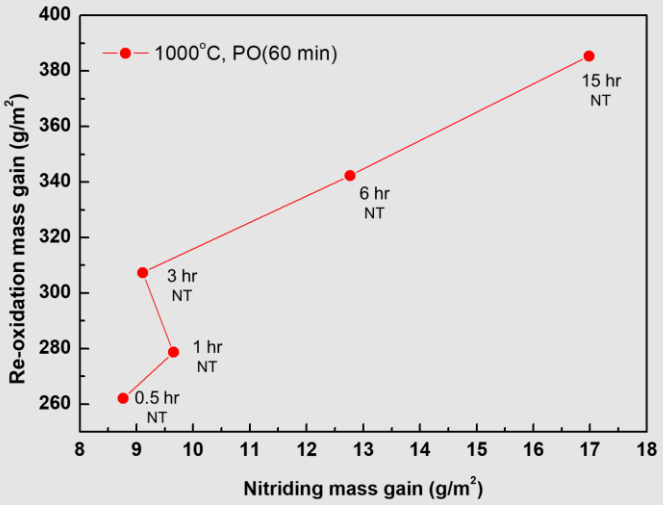

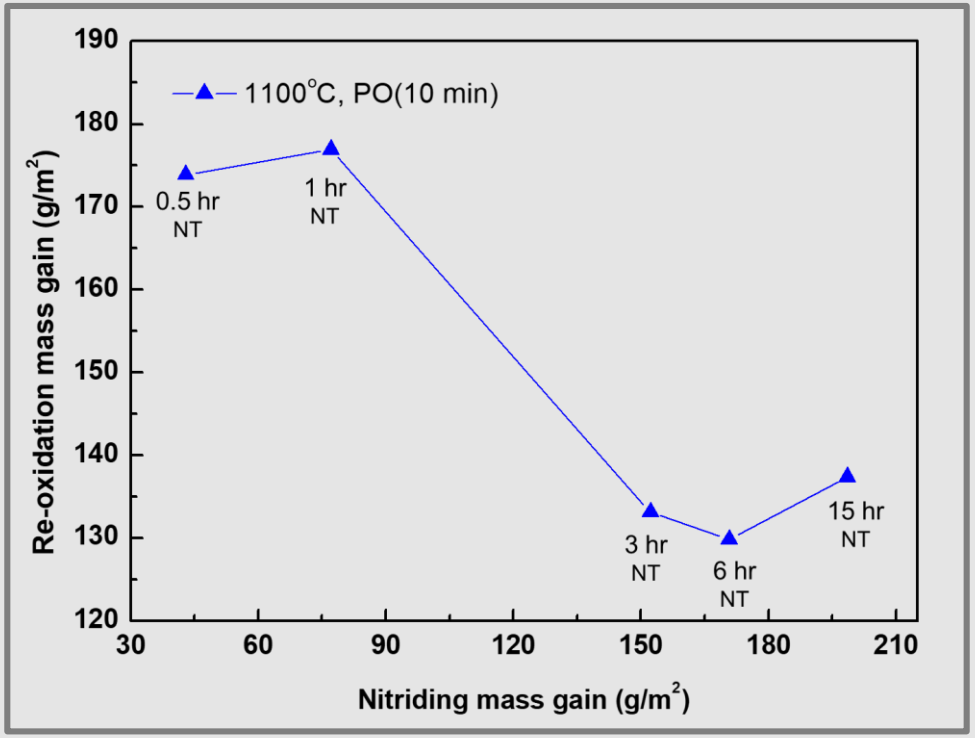

The mass gain of re-oxidation shows a **decreasing trend in tests at 1100°C** as a function of both nitriding duration and mass gain.

Results and Discussion

High-T (1100-1200°C) Re-oxidation

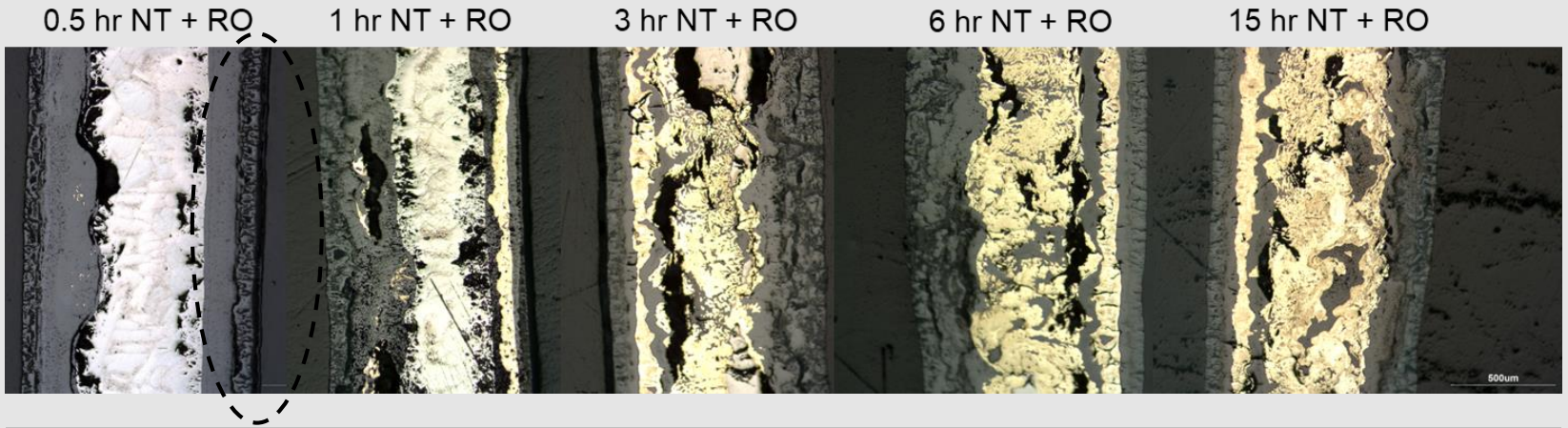

- <u>Re-oxidation of the external nitride</u> by newly incoming O_2.
- <u>Very porous re-oxidized layer</u> on a top of the relatively dense oxide layer.
- Dense oxide layer may delay the diffusion of oxygen to the internal nitride.



Nitriding from the external site to the internal site

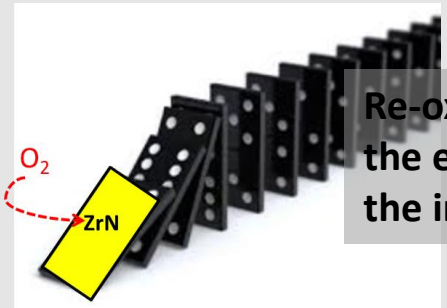

Re-oxidation from the external site to the internal site

Results and Discussion

Nitriding and Re-oxidation Correlations

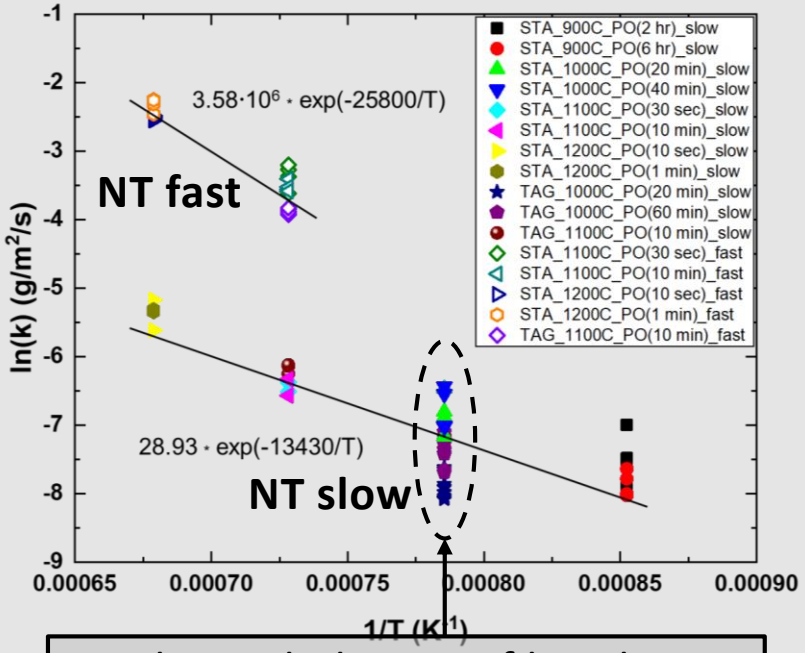

Stochastic behavior of breakaway may cause this scattering of data

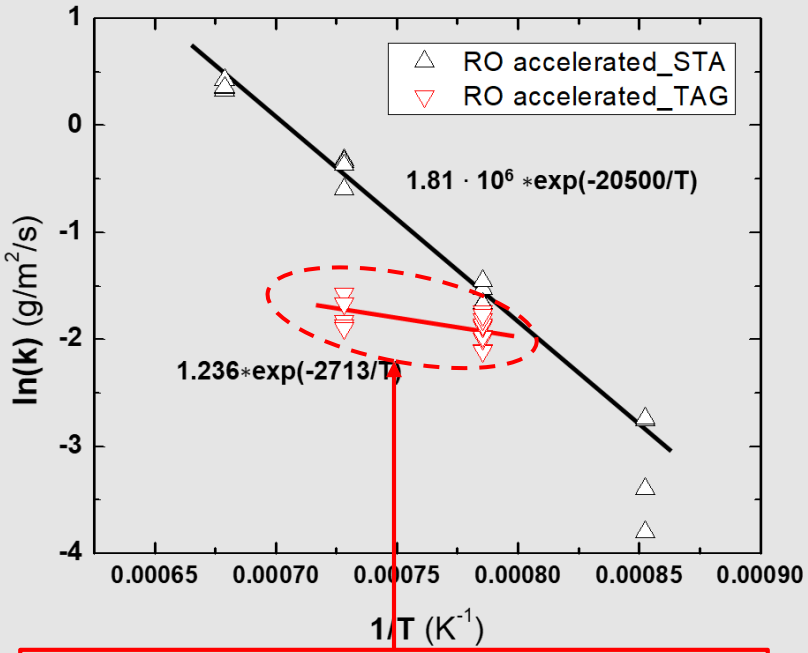

Lower flow rate and poorer mixture in the TAG tests than STA tests

RO mass gains (RO = 60 min)

⇒ **240 g/m² to 380 g/m²**

(TAG tests data)

- Urbanic-Heidrick (at 1000°C and RO = 60 min): **153.63 g/m²**
- Cathcart-Pawel (at 1000°C and RO = 60 min): **134.12 g/m²**
- Leistikow-Schanz (at 1000°C and RO = 60 min): **115.88 g/m²**

Results and Discussion

Raman Investigation: Target sample: 1200°C_PO(1 min)_NT(30 min)

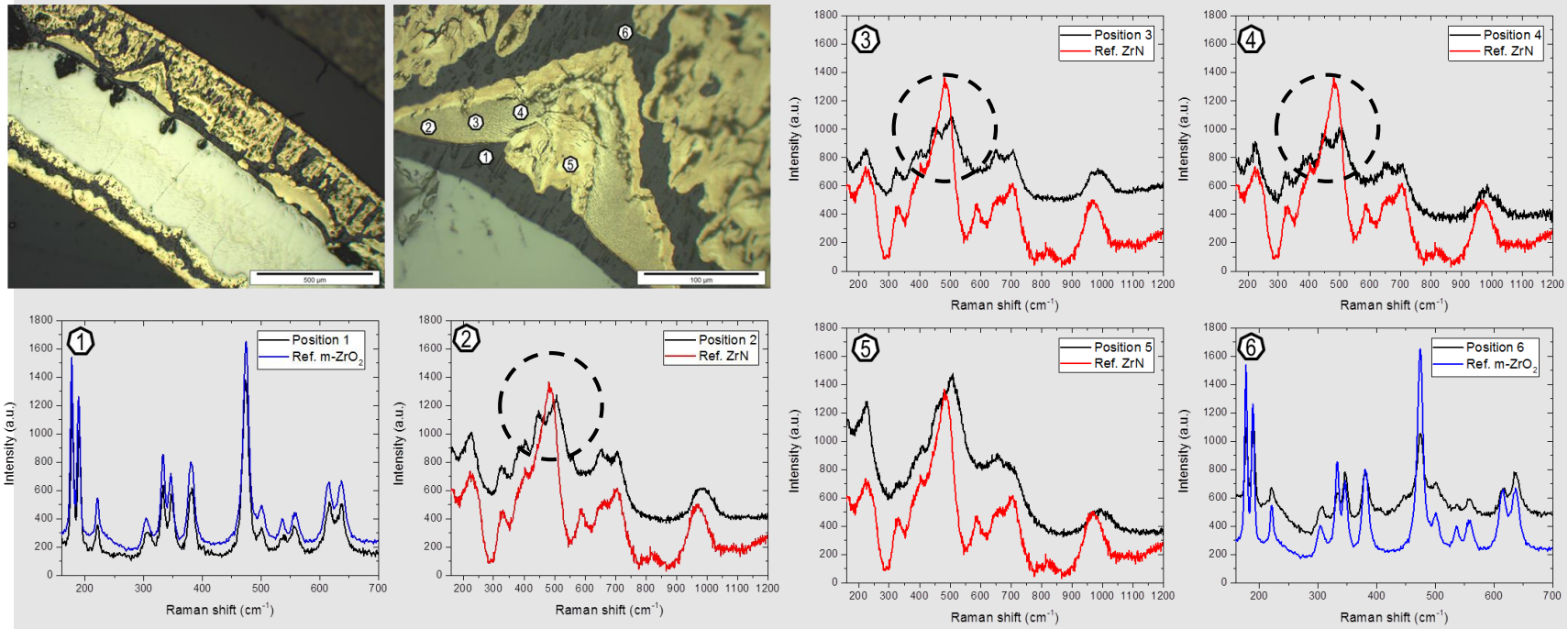

- Bright golden-yellow phase: ZrN
- **Dark golden-yellow phase: unknown twin peaks at 452 cm^{-1} and 502 cm^{-1}**
- Among 18 Raman active modes of m-ZrO_2, peak of 502 cm^{-1} is assigned to O-O bonding. **One of the unknown twin peaks at 502 cm^{-1} might be assigned to an O-O bonding of m-ZrO_2.**

Results and Discussion

Raman Investigation: Target sample: 1200°C_PO(1 min)_NT(30 min)

Characteristic peak of (MTe_3O_8 (M = Zr, Sn, Ti))

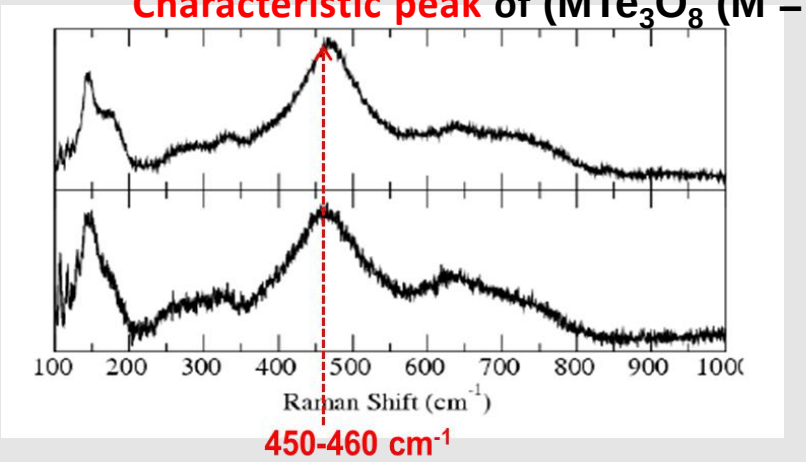

$2ZrO_2 + N_2 \rightarrow Zr_2ON_2 + 3O$

and/or;

$½\ ZrO_2 + ½\ Zr_3N_4 \rightarrow Zr_2ON_2.$

- **The peak of 452 cm^{-1} might be a peak of Zr-O-N phase.**
- **Zr_2ON_2 phase: optically yellow**

➢ Based on literature finding regarding the characteristic Raman peak of Zr_2ON_2 and the same crystal structure (MTe_3O_8 (M = Zr, Sn, Ti)), **Raman spectra of Zr_2ON_2 may have a characteristic peak around 450-460 cm^{-1}**.

Open issues

Remaining issues

- Quantification of the initially developed alpha-Zr(O) during PO
- Quantification of the further developed alpha-Zr(O) during NT
- Resolution of the amount of NT phase mass gain that was uptake of residual oxygen
- Experimental conditions as compared to a reactor and/or SFP case
- Sample's edge effect on the reaction behavior

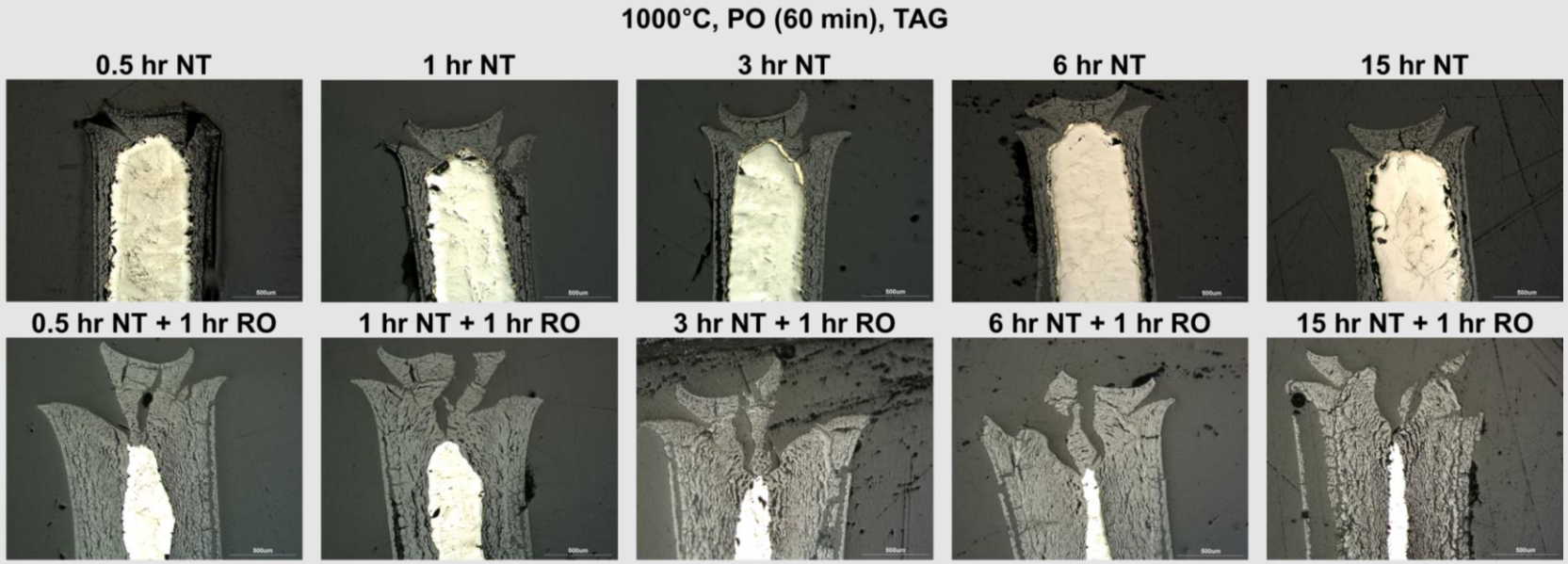

Summary and Conclusion

- **(Tests)** performed by **separating each reaction phase**, pre-oxidation (PO), nitriding (NT), and re-oxidation (RO) **to study the individual and interrelated behavior of each reaction**.
- **(Pre-oxidation)** performed in O_2/Ar
  - Low-T (< 1050°C): alpha-Zr(O) + oxide scale breakaway or not
  - High-T (> 1050°C): alpha-Zr(O) + non-breakaway oxide
- **(Nitriding)** performed in N_2/Ar
  - Low-T (< 1050°C): "**NT initially developed**" and "**NT slow**"

    ⇒ **Internal nitride** (from oxide-metal interface to the inner metal part)
  - High-T (> 1050°C): "**NT initially developed**", "**NT fast**", "**NT transition**", and "**NT slow**"

    ⇒ **External nitride** (NT ini + NT fast) + **Internal nitride** (NT tran + NT slow)

Summary and Conclusion

- **(Re-oxidation)** performed in O_2/Ar
  - Two main different reactions: "**re-oxidation of nitride**" and "**further oxidation of remaining metal**"
  - Both reactions occurred simultaneously at each different location, not sequentially.
- **(Post-test investigation)** performed to identify the possibility of existence of ternary Zr-O-N phases in the nitrided sample.
  - From the **Raman investigation, the existence of ternary Zr-O-N phase (Zr_2ON_2) was highly suspected**.
- **(A note of caution for a future modeling)**
  - **Thermobalance tests are different from the reactor and SFP conditions**.
  - **Code model using results of this study should be validated by integral test**.


Thank you for your attention!

Back-up slide

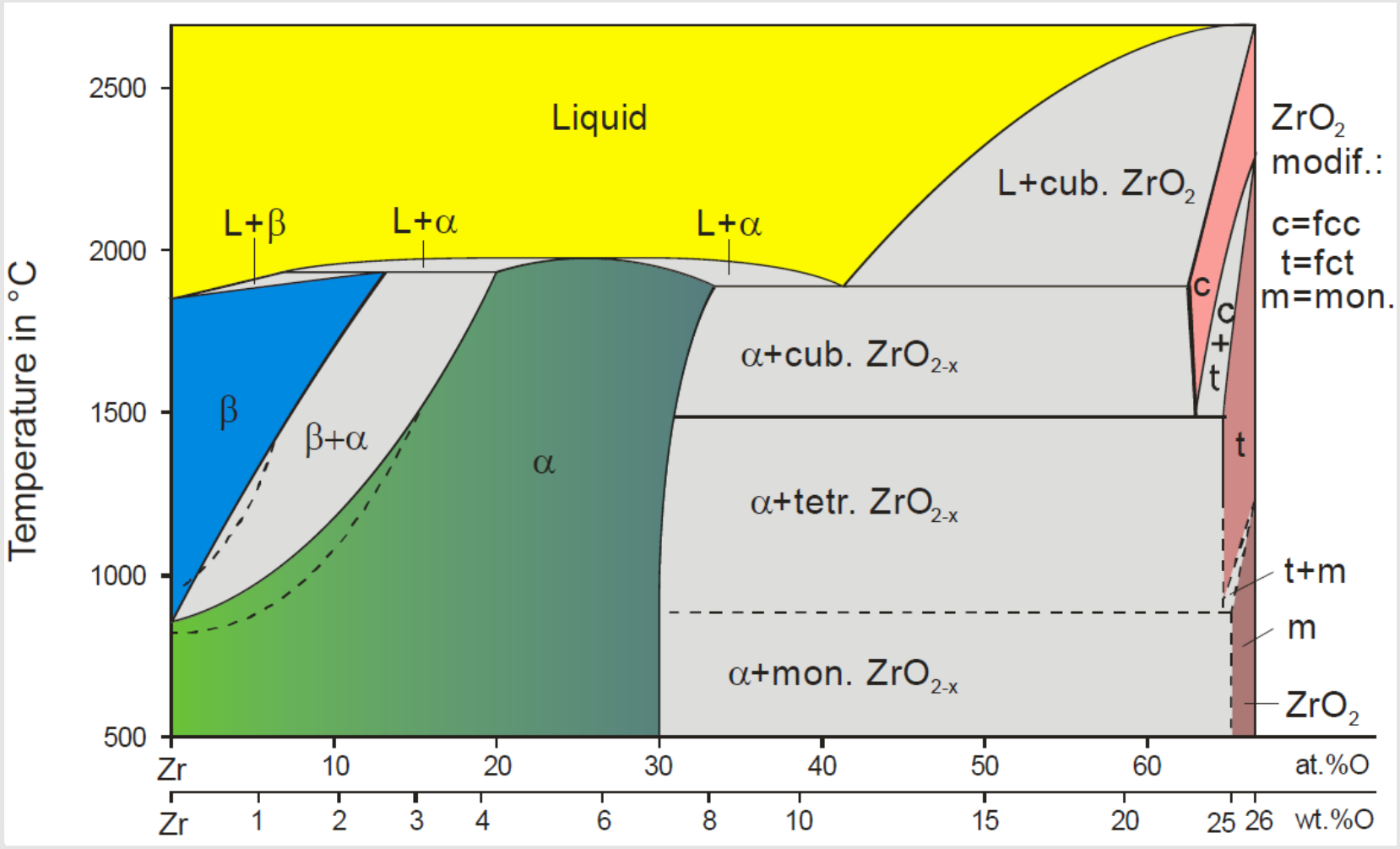

Back-up slide

Air ingress scenarios

- into the **reactor core** at the late phase of SAs after RPV failure
- into the **reactor core** during mid-loop operation to do refueling
- into the **spent fuel pool** during LOCA
- into the **dry storage cask** by the mis-handling

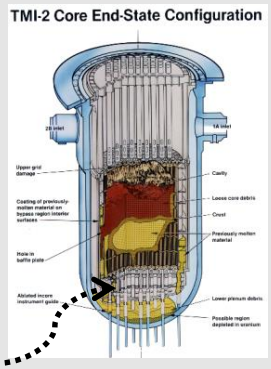

Air

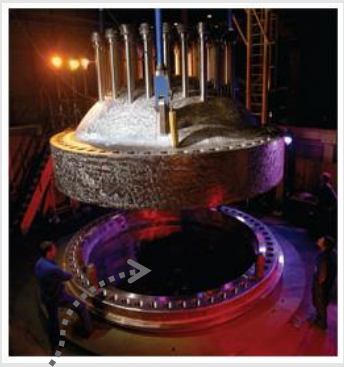

Air







Air

THAI EXPERIMENTS ON IODINE BEHAVIOR IN A ROOM CHAIN REPRESENTING FLOW CONDITIONS IN LARGE CONTAINMENTS

M. Freitag, E. Schmidt, B. von Laufenberg
Becker Technologies GmbH
Rahmannstr. 11, 65760 Eschborn, Germany
freitag@becker-technologies.com

G. Langrock and F. Funke
Framatome GmbH
Paul-Gossen-Str. 100, 91052 Erlangen, Germany
gert.langrock@framatome.com

ABSTRACT

Iodine which can be released into the containment during a severe accident, is considered one of the most important nuclides with potential for public dose. Significantly different iodine concentrations can be expected in the individual compartments and rooms of large containments, due to geometrical constraints and the strong dependence of many iodine reactions on local thermohydraulic conditions. Such inhomogeneity may be relevant for organic iodide formation which depends on the concentration of deposited I_2 and the dose rate.

The objective of the two tests Iod-33 and Iod-35 was to measure the distribution of iodine along a convective flown-through room chain. This arrangement shall simulate the pathway of iodine from the locations of release (primary loop rupture) or formation (sump) along the plant rooms up to the dome of the containment and back. With respect to iodine, the aims were to measure the distribution and mixing of gaseous iodine in different rooms, the decrease of gaseous iodine by its deposition on painted surfaces, and the distribution of deposited iodine on the different painted surfaces.

The two tests were performed in the two vessel THAI$^+$ facility with additionally installed painted surfaces (painted with Gehopon epoxy paint) under superheated and condensing conditions. The main part of the painted surface area was provided in the form of painted steel sheets and arranged to form two intermediate floors within the THAI test vessel including small flow openings. Gaseous iodine was injected over several hours into the room chain in which a slow convection was established by means of differential heating.

The gaseous I_2 concentration inside the THAI$^+$ facility increased continuously until the I_2 injection was terminated. Simultaneously, the iodine deposition onto the painted surface increased. The gaseous I_2 concentration decreased rapidly after stopping the I_2 injection, in favor of a continuation of the I_2 deposition on painted surfaces. The multi-compartment effect along the room chain has been demonstrated by the test results and the data allows for further development and validation of the I_2/paint reaction model of severe accident codes.

KEYWORDS
Severe Accident, Containment, Fission Products, Iodine, THAI, Multi-compartment

1. INTRODUCTION

Iodine which can be released into the containment of nuclear facilities can be distributed non-homogenous due to its volatility and due to its appearance in different chemical compounds which have different chemical reactivities. In medium- and long-term accident transients a steady-state large flow loop might establish in containments like German KONVOI in which iodine will be transported. The objective of tests Iod-33 and Iod-35 was to measure the distribution of iodine along a convective flown-through room chain in the THAI$^+$ facility, Fig. 1. This arrangement shall simulate the pathway of iodine from the locations of release (e.g. primary loop rupture) or formation (e.g. radiolysis in the containment sump) along the plant rooms up to the dome of the containment and back through the auxiliary rooms (next to the containment shell). With respect to iodine, the aims were to measure

(1) the distribution and mixing of gaseous iodine in different rooms,
(2) the decrease of gaseous iodine by its deposition on painted surfaces,
(3) the distribution of deposited iodine on the different painted surfaces.

Under accident conditions the process of iodine deposition on paint plays a crucial role for the radiolytic organic iodide formation which depends on the iodine concentration on paint and the dose rate. The I_2/paint interaction in a severe accident (SA) containment atmosphere has a significant influence on the fraction of gaseous iodine, as was shown in a COCOSYS/AIM sensitivity analysis [1, 2].

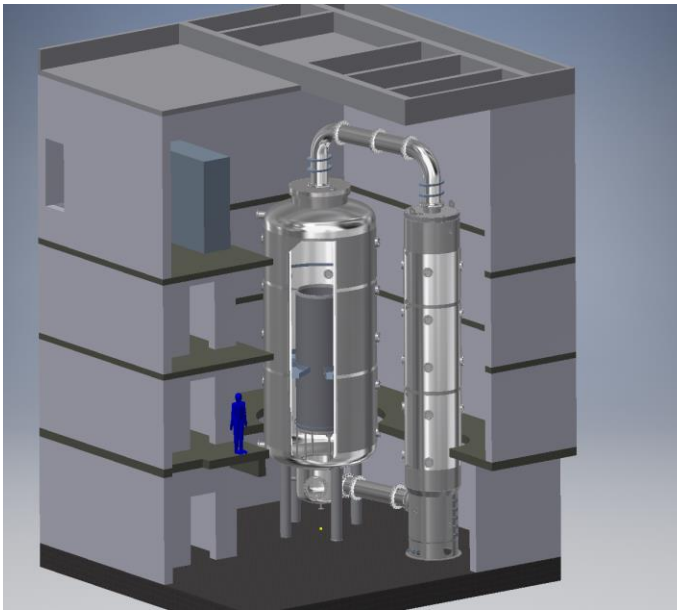

Figure 1. THAI$^+$ facility and building; condensate trays and the TTV inner cylinder were not installed, instead two intermediate floors were inserted

In addition to an inhomogeneous distribution of gaseous I_2 in a multi-compartment or room-chain geometry also an inhomogeneous iodine loading of the paint surfaces is expected. It is mainly influenced by the ratio of convection velocity and adsorption velocity. According to the I_2/paint model [3] which was based mainly on OCED/NEA BIP data [4, 5], also the fraction of physisorbed iodine and, hence, easily releasable I_2 shall have a strong influence on the iodine distribution. Measuring the expected inhomogeneous iodine deposition on paint can be easier accomplished in a two-vessel system like the THAI$^+$ configuration with well-defined convection loops than in the previous one-vessel multi-

compartment geometry. Previously performed multi-compartment tests were not designed for such measurements.

2. TEST CONFIGURATION, INSTRUMENTATION AND TEST TRANSIENT

The thermal hydraulics of the tests Iod-33 and Iod-35 was intended to generate well controlled steady-state conditions with respect to pressure, temperature and relative humidity. Differential heating of the two vessels with higher temperatures at the THAI test vessel (TTV, 60 m^3 and 9.2 m tall, 3.2 m in diameter) was used to generate a large convection loop with upward gas velocities inside the TTV and downward gas transport inside the parallel attachable drum (PAD, 18 m^3 and 9.7 m tall, 1.6 m in diameter). The cylindrical part of both vessels is double-walled, the inner and outer wall being 22 mm and 6 mm thick, respectively. The 16.5 mm gap between the walls is filled with thermal oil of the wall heating/cooling system. Driving force for the natural convection was a wall temperature difference of few K. A sketch of the configuration is shown in Fig. 2. All standard internals (inner cylinder and lateral condensate trays) were removed from the TTV. Two intermediate floors coated with decontamination paint (Gehopon epoxy paint) were installed in the TTV, at heights H = 4.08 m and 6.64 m, dividing the vessel into the three compartments TTV-U(p), TTV-M(iddle), and TTV-L(ow), Fig. 3. One flow opening in each floor of about 0.19 m^2 was inserted, see Fig. 3.

The painted surface area of test Iod-33 amounted to 29.8 m^2 consisting of the two intermediate floors (28.8 m^2) and three small painted surfaces installed in the three compartments of the TTV. The small coupons allowed to monitor the local iodine deposition with three scintillation detectors sensitive to ^{123}I radiation. In addition to the intermediate floors two coolers, each with 3.72 m^2 surface and coated with decontamination paint, were installed inside the PAD in test Iod-35. The thickness of the paint on each side of the coupons was 150 - 200 µm after natural drying, as specified. All painted surfaces were artificially pre-aged, by thermal treatment for 21.1 h at 160 °C in air atmosphere, which is a THAI standard procedure.

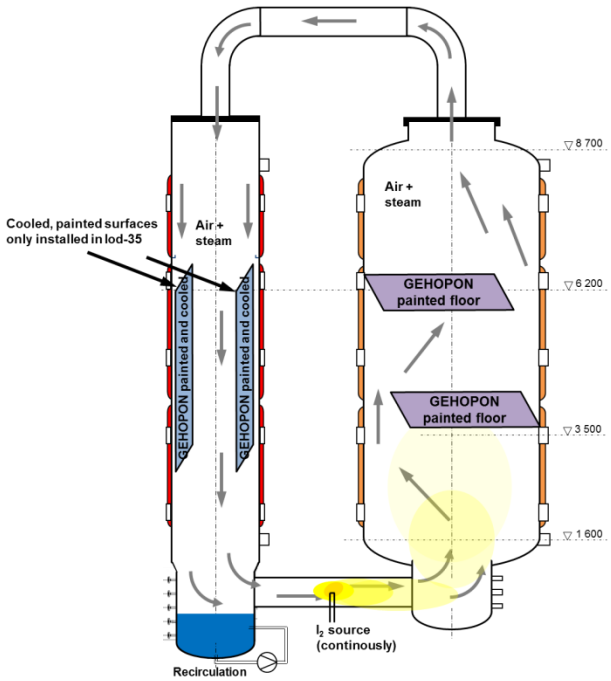

Figure 2. THAI$^+$ configuration with intermediate floors in TTV, painted coolers (Iod-35) and recirculated sump in PAD, and iodine injection into lower connecting pipe

The long-term injection of gaseous iodine through a small pipe (d_i = 4 mm) into the lower inter-connecting pipe was located at H = 0.65 m (vertical center of the connecting pipe) and 2.255 m away from the centerline of the TTV. The injection pipe was horizontally mounted and extended 100 mm from the DN500 pipe wall into the pipe. The resulting jet in cross-flow was characterized by a velocity ratio of about r = 8 and a diameter ratio of D_i/d_i = 122. The penetration depth of the jet in cross-flow was $(3…4) \cdot r \cdot d_i \sim 96…128$ mm, such that optimal mixing was achieved at the centerline of the connecting pipe. Direct wall impingement of the released iodine was excluded due to the velocity ratio and the very high diameter ratio. The injection technique was based on the recently developed long-term I_2 source and is described in detail in [6].

The PAD sump was filled with about 1 m^3 of decalcified water and chemically conditioned at pH 2 (Iod-35) and pH 1.5 (Iod-33) which was continuously recirculated with a pump.

2.1. Instrumentation

Beside thermal hydraulic instrumentation which recorded the wall, gas and sump water temperature distribution, the vessel pressure and relative humidity and the flow along the room-chain, dedicated iodine instrumentation was used to trace the gaseous iodine concentration along the room chain, its deposition onto the paint, the concentration inside the sump water or the condensate and to resolve the iodine speciation.

Calibrated 1.5 mm NiCr-Ni thermocouples for temperature measurement (accuracy ± 0.3 K for calibration range of 0 - 130 °C) were positioned at various measurement locations inside the $THAI^+$ configuration and onto the surfaces of the vessels. Piezoresistive pressure transmitters were installed to measure the absolute vessels' pressure during the tests. The relative humidity was measured by three Testo humidity sensors (type 6610 with control unit 6681) distributed along the room-chain.

A unique measurement device (Minimal encroaching turnable stream-wise anemometers: METUSA) was installed into the upper connection pipe which allowed determining the volumetric flow being exchanged between the two vessels. By turning the pipe section by 360°, six installed vane wheels run along a circular path recording the gas flow distribution.

The gaseous iodine distribution was measured by 8 gas scrubbers, six of them installed inside the TTV and two inside the PAD. The six gas scrubbers of the TTV were distributed such that a pair of gas scrubbers was installed in each sub-compartment in test Iod-33, Fig. 3 (left). This was modified in Iod-35 where each of the three sub-compartments TTV-U, TTV-M, TTV-L was monitored by one gas scrubber, one gas scrubber was installed in each of the two flow openings between theses compartments, and one gas scrubber was installed inside the sump compartment, Fig. 3 (right). The absorber liquid of the gas scrubbers was an aqueous solution of 0.2 wt% sodium hydroxide and 0.5 wt% sodium thiosulfate, pH = 13. This absorber efficiently traps gaseous I_2 to measure the I_2 concentration in the gas phase. An additional iodine measurement was performed in TTV-M by wide spectral light absorption spectroscopy, which provides a continuous, in-line, and non-intrusive measurement of gas-borne iodine at a rate of 1 Hz.

Two Maypack filter stations were operated to discriminate the chemical iodine forms. The iodine forms, as usually relevant in THAI, were discriminated through a sequence of 5 filter cartridges with different absorbers. The trapping of the iodine species in flow direction downstream the vessel was:

- Iodine in aerosol form: 1 x Emfab TX40H120-WW
- I_2: 2 x DSM-11 (silicic acid, potassium iodide impregnated)
- Organic iodide: 2 x charcoal (activated, potassium iodide impregnated)

To avoid condensation during sampling, Maypack filters were overheated with respect to the vessel atmosphere.

The iodine concentration of the PAD sump and the concentration inside the condensate created at the coolers, only in test Iod-35, were determined by means of frequent sampling.

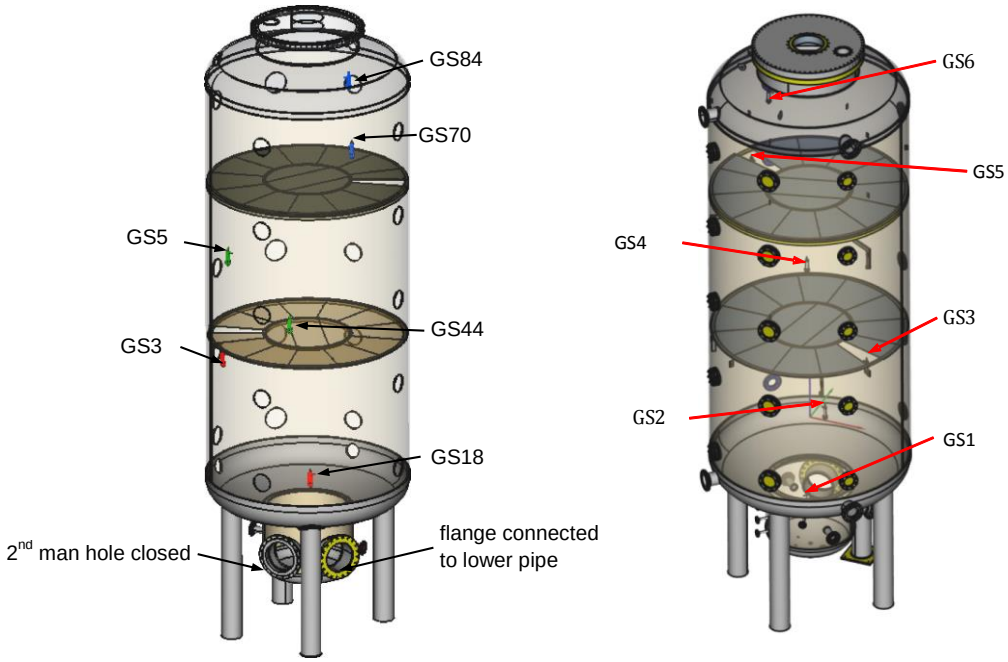

Figure 3. Gas scrubber arrangement inside TTV test Iod-33 (left) and test Iod-35 (right)

2.1. Test transient

The test procedure for both tests Iod-33 and Iod-35 consisted of a preconditioning phase followed by two main test phases:

0. Preconditioning phase to establish initial conditions in the THAI facility, including heating and generation of dedicated steam concentration, by sump water heating and steam injection into the TTV. Generation of slow steady-state convective flow through the room chain. In Iod-35, steady state condensation rates were established at the cooled painted surfaces inside the PAD.
1. Continuous I_2 injection and deposition of I_2 onto the painted surfaces (and steel surfaces)
2. I_2 injection terminated and ongoing deposition of I_2 onto the painted surfaces (and steel surfaces)

The initial test conditions are listed in Table I. The desired thermal hydraulic conditions have been achieved by controlled heating of the TTV and PAD walls and a controlled heating of the sump water stored in the PAD vessel. The convection velocity was measured by the METUSA system inside the upper connection line, resulting into 95 L/s in Iod-33 and 105 L/s in Iod-35, Fig. 4. Steam was injected into the TTV at small flow rate and condensed at the cooled painted surface installed inside the PAD in test Iod-35. The flow rate of injected steam was regulated to maintain constant pressure in the vessels. The time t = 0 h is defined as time of starting the I_2 injection. The injection of iodine lasted for 5 h in Iod-33 and 5.47 h in Iod-35.

Table I. Comparison of the actual test conditions as measured in Iod-33 and Iod-35

Test	P (bar)	T (°C)	T_{TTV} (°C)	T_{PAD} (°C)	c_{Steam}(vol%)	PAD sump	Injected I_2
Iod-33	1.40 (abs)	80 - 82 (PAD) 83 - 89 (TTV)	89.5 - 91.5 (wall)	79.5 - 80.5 (wall)	18.4	1037 L at 66 °C pH 1.5 (H_3PO_4,)	0.862 ± 0.015 g
Iod-35	1.51 (abs)	76 - 84 (PAD) 80 - 88 (TTV)	88.5 - 91 (wall)	74 - 83.5 (wall)	25.4	1007 L at 70 °C pH 2 (H_3PO_4)	0.844 ± 0.016 g

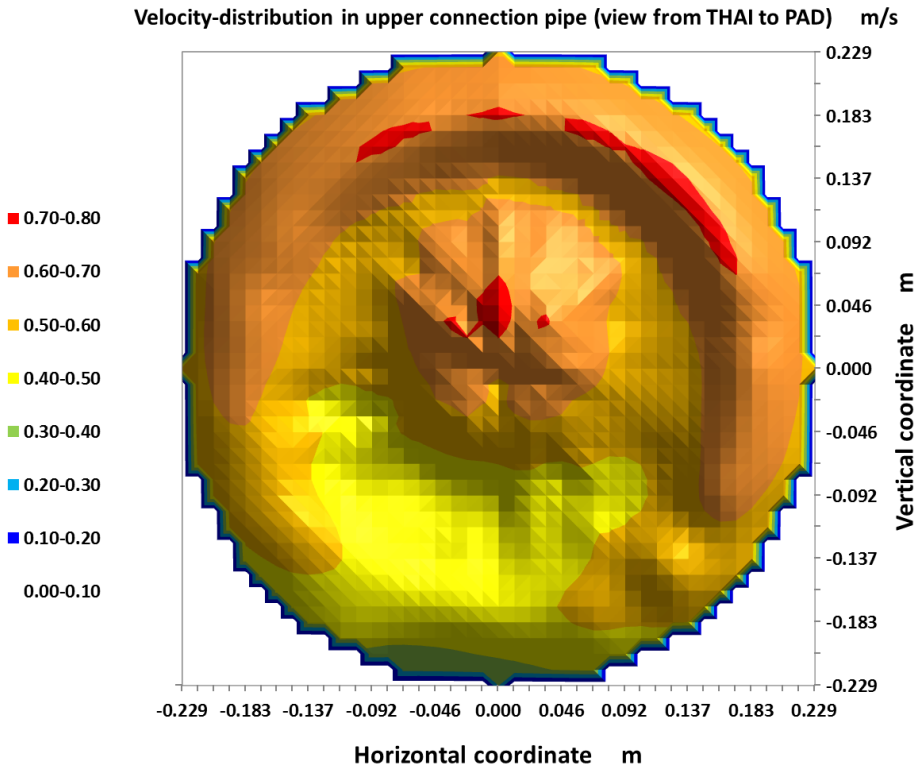

Figure 4. METUSA measurement of test Iod-35, average velocity distribution

3. TEST RESULTS

Fig. 5 shows the gas temperatures inside the three sub-compartments of the TTV, at the upper end of the PAD and the lower section of the PAD as well as the water temperature inside the PAD sump compartment. The temperature distribution clearly indicates the long term steady state conditions during the iodine injection and during the subsequent iodine deposition phase. Gas atmosphere driven by the natural convection entered the TTV sump compartment through the lower connecting pipe at around 80 °C. The gas was heated continuously during its ascent by heat transferred from the TTV vessel walls until it entered the PAD through its top flange at about 87-88 °C. The gas cooled down while descending the PAD due to the lower wall temperatures to about 81 °C in Iod-33. The steam condensation at the cooler surface in Iod-35 reduces the gas temperature in this test down to about 77 °C before the gas enters the lower connecting pipe. The steam injection and cooler operations was terminated at t = 9.37 h in Iod-35 which generated a slow transient until the gas temperature stabilize again. The sump water temperature in test Iod-33 was slightly cooler than in Iod-35, corresponding to slightly smaller steam concentration of about 19 vol.-% in Iod-33 compared to 26 vol.-% Iod-35.

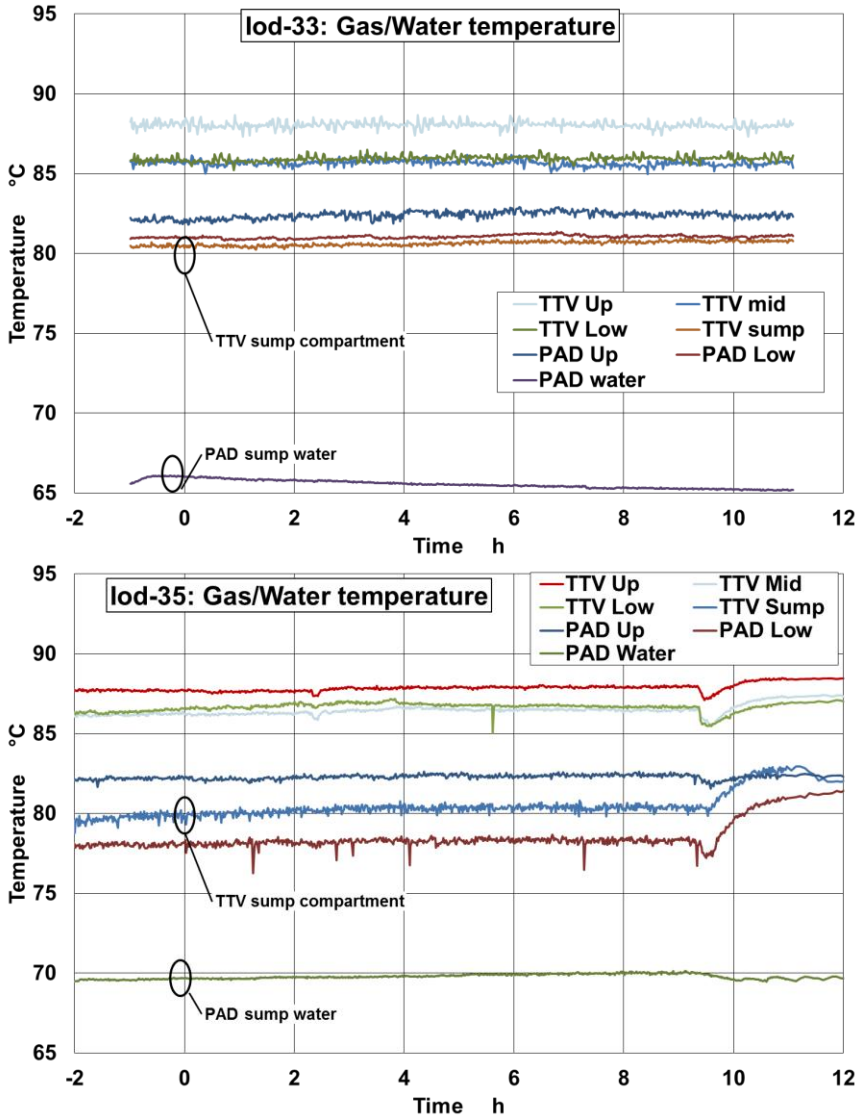

Figure 5. Iod-33 (top) and Iod-35 (bottom) gas temperature in compartments along the room chain and water temperature inside PAD sump

The initial conditions, the total mass of injected I_2 and the durations of the iodine injection in both tests were considerably similar (Iod-33: t = 20 min to 300 min and Iod-35: t = 20 min to 328 min). The behavior of the gaseous I_2 concentration was similar in both tests, cf. Fig 6, but the rearrangement of gas scrubber positions in test Iod-35 revealed the multi-compartment effect more pronounced in the corresponding test. The additional painted surfaces and the steam condensation at these surfaces provided no significant differences between the iodine concentrations in TTV-U (measured with GS6) and the PAD atmosphere (measured with GS75P and GS40P) in test Iod-35. The level of gaseous iodine concentrations was approximately the same as in test Iod-33.

After iodine injection was finished the iodine in the gas phase depleted quickly in both tests. While the iodine decreases, the multi compartment effect was conserved. This indicates a release of physisorbed iodine from the steel walls at the lower compartment of the TTV and a transfer to the painted surface which finally chemisorbed. The LASI and the gas scrubber measurements converged towards a stable low iodine concentration in test Iod-33, which was in the order of the detection limit, but the iodine concentration in test Iod-35 reduced continuously until the measurements were terminated.

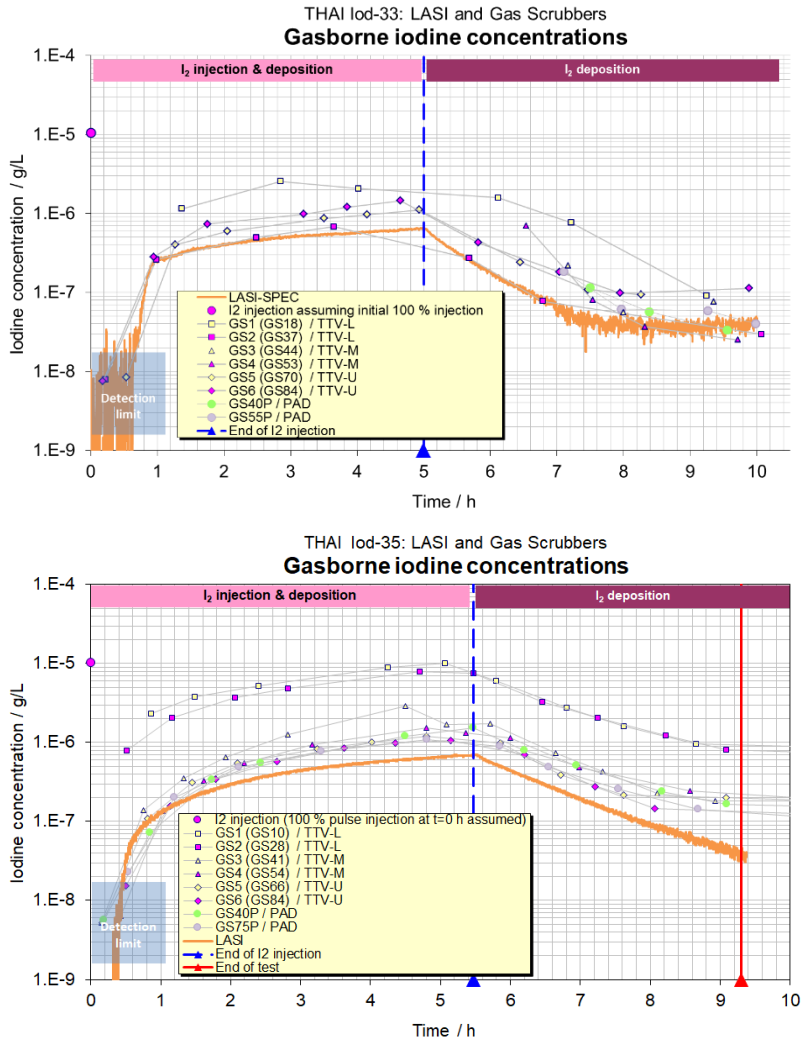

Figure 6. Iod-33 (top) and Iod-35 (bottom) LASI-SPEC and gas scrubber results

The I_2 concentrations recorded with the LASI are provided with a temporal resolution of 0.5 min in order to reduce the signal to noise ratio which is noticeably higher when using the recording frequency of the system (1 Hz). The detection limit of the system is comparable to the gas scrubbers, i.e. approximately 2E-8 g/L. LASI was capable to temporally resolve the increase and decrease of gaseous I_2 concentrations. The I_2-concentration increased initially fast and then slower until the end of the iodine injection which could not be resolved by the gas scrubbers. After the iodine release was stopped, the iodine concentration reduced on a perfect exponential slope. The absolute I_2 concentration deduced from the LASI were noticeably smaller than the gas scrubber concentrations in Iod-35 but in well agreement in Iod-33. Using the neighboring gas scrubber to calibrate the device would improve the absolute data of LASI.

The ratio between inorganic and organic iodine detected by the Maypack filters was also similar in both tests, considering that the sampling position was changed from TTV (Iod-33) to PAD (Iod-35) , Fig 7. The amount and fraction of organic iodide increased continuously throughout the test. Final RI concentrations in the late phase of Iod-35 were around 5-8E-9 g/L, the fraction 0-5 % at MP06 and 0-13 % at MP77P.

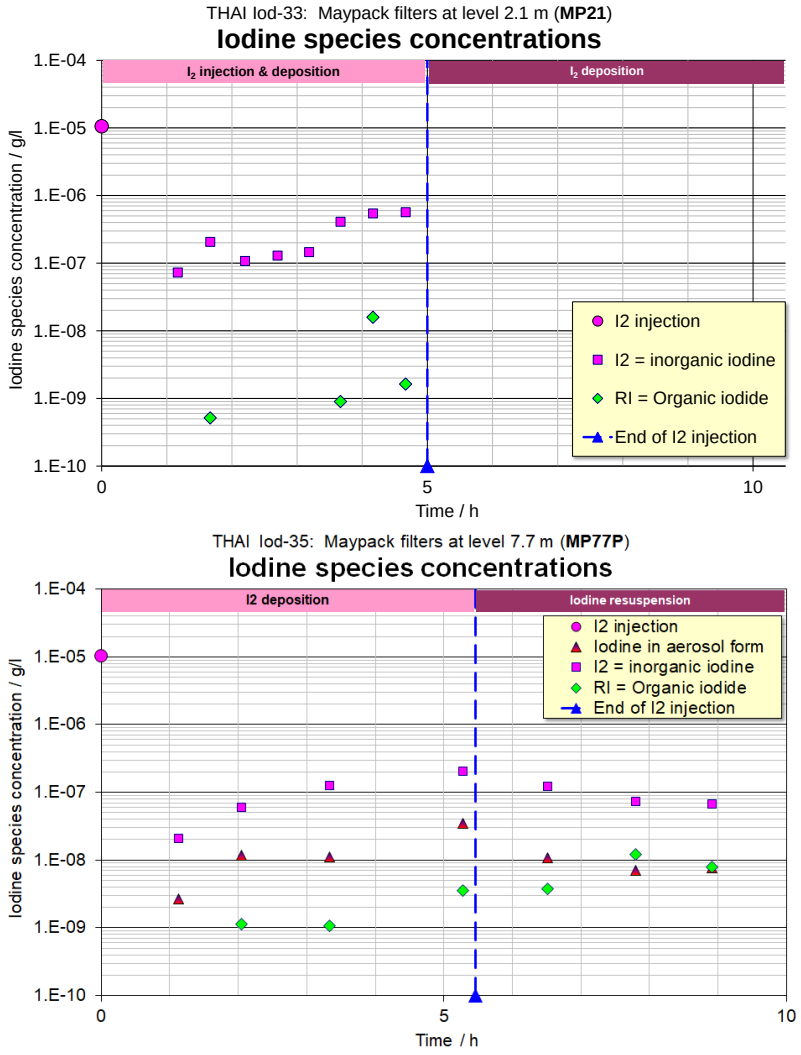

Figure 7. Iod-33 (top) and Iod-35 (bottom) Iodine speciation by Maypack measurements

The depletion rate and the absolute depletion of iodine of the painted surfaces showed a quite similar behavior in both tests. The absolute mass of iodine which was detected in the PAD sump water was very small in test Iod-33 with about 6.5 mg at t = 5 h, when the injection was stopped. The iodine concentration in the sump water of test Iod-35 was 13 times higher, even though the water inventory in both tests was quite similar (1005 to 1035 L in Iod-35 and 1037 L in Iod-33) as well as the water temperature, the state of mixing and the pH. The difference might originate at least partially from iodine which condensed together with steam in the lower connecting pipe and both being transferred into the PAD sump. However, simulations of validated SA codes, like COCOSYS AIM are required to investigate the likeliness of this further.

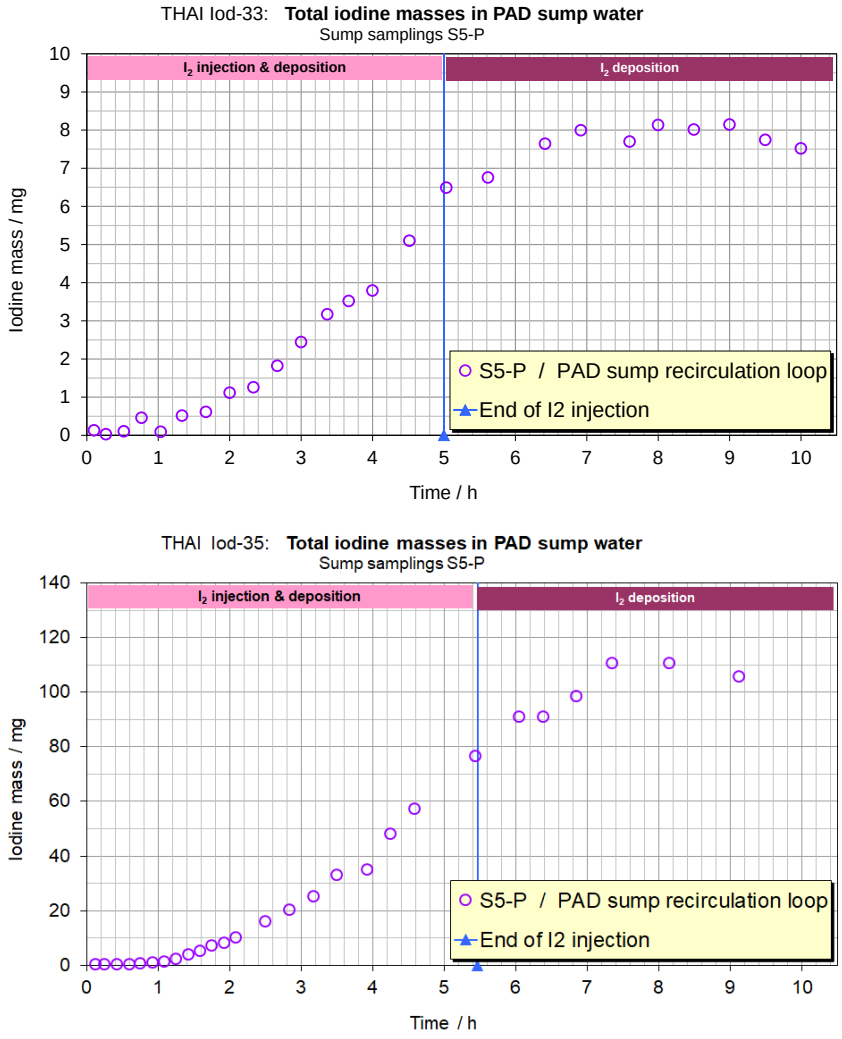

Figure 8. Iod-33 (top) and Iod-35 (bottom) Measurement of iodine in the PAD sump

4. CONCLUSIONS

The distribution of gaseous I2 along a convective flow loop through a room chain was investigated in the THAI+ facility under superheated (Iod-33) and condensing (Iod-35) conditions. In a reactor containment, the geometry mimics the path from the release (break in the primary circuit) or source (containment sump) through the plant rooms to the dome and back. Gaseous iodine (I_2) was injected into the flow loop which

circulates between the two vessels over several hours. The continuous long-term I_2 feed led to a continuous increase in the iodine concentration in the gas phase, with concentrations decreasing along its flow path, and a deposition of iodine on both, dry and wet painted surfaces in the TTV. The gaseous I_2 concentration decreases as soon as the I_2 injection was terminated and, at the same time, the multi-room effect also decreased. Due to the consistent set of temporal resolved iodine measurement results in the gas phase, sump and on the paint surfaces, the two experiments provides valuable data for the development and validation of the I2 paint models in SA codes.

ACKNOWLEDGMENTS

The THAI test programs which included Iod-33 and Iod-35 were funded by the German Federal Ministry for the Environment, Nature Conservation, Nuclear Safety and Consumer Protection under grant numbers 1501547 and 1501594, on the basis of a decision by the German Bundestag.

The authors further acknowledge the contribution of Sara Beck, GRS gGmbH by performing design calculations for the iodine multi compartment tests.

REFERENCES

List references here, according to their first use in the paper. Include the following information (as applicable). Do not include these sentences in the full paper.

1. Weber, G.; Krzykacz-Hausmann, B.; Funke, F.: Unsicherheits- und Sensivi-tätsuntersuchung der COCOSYS-AIM-Ergebnisse zum Iodverhalten im PHE-BUS-Versuch FPT1. GRS-A-3676, Juli 2012
2. Weber, G.; Krzykacz-Hausmann, B.; Funke, F.; Klein-Hessling, W.: Uncertainty and Sensitivity Analysis on the Iodine Model in the Containment Code COCOSYS. NUTHOS-10 Conference, Okinawa, Japan, 14-18 Dec. 2014
3. S. Beck, G. Weber, Das neue Iod/Farbe-Modell in AIM-3 für trockene Bedin-gungen und die Validierung an THAI-Versuchen, GRS, Technische Notiz, GRS - V – RS 1532 - 1/2015, September 2015
4. G. Glowa, C. Moore, D. Boulianne: Behaviour of Iodine Project: Final report on iodine adsorption studies, BIP project; AECL Report 153-126530-440-013 Rev.0, December 2011
5. G. Glowa, C. Moore, D. Boulianne, J. Mitchell: Behaviour of Iodine Project 2: Final Report, BIP2 project; AECL Report 153-126530-440-019 Rev.0, Novem-ber 2014
6. Langrock, G.: Development and qualification of a system to constantly inject gaseous I2 radio-tracered with ^{123}I over several hours into test facilities ("Long-term I2 source"). Final Report, Framatome GmbH, D02-ARV-01-151-441A, 2019

THAI EXPERIMENTS ON IODINE BEHAVIOR IN A ROOM CHAIN REPRESENTING FLOW CONDITIONS IN LARGE CONTAINMENTS

On behalf of:

Federal Ministry
for the Environment, Nature Conservation,
Nuclear Safety and Consumer Protection

of the Federal Republic of Germany

M. Freitag, E. Schmidt, B. von Laufenberg,
G. Langrock and F. Funke

Becker Technologies GmbH, Rahmannstr. 11, 65760 Eschborn, Germany
freitag@becker-technologies.com
Framatome GmbH, Paul-Gossen-Str. 100, 91052 Erlangen, Germany
gert.langrock@framatome.com

ERMSAR 2022
MAY 16-19, 2022 — KARLSRUHE, GERMANY

NUGENIA TA2 Severe Accidents
Nuclear Generation II&III Alliance

SNETP
Sustainable Nuclear Energy
Technology Platform

Content

- Background/Objective
- THAI test facility
- Set-up of tests Iod-33 and Iod-35
- Experimental results and interpretation
- Evaluation and Summary

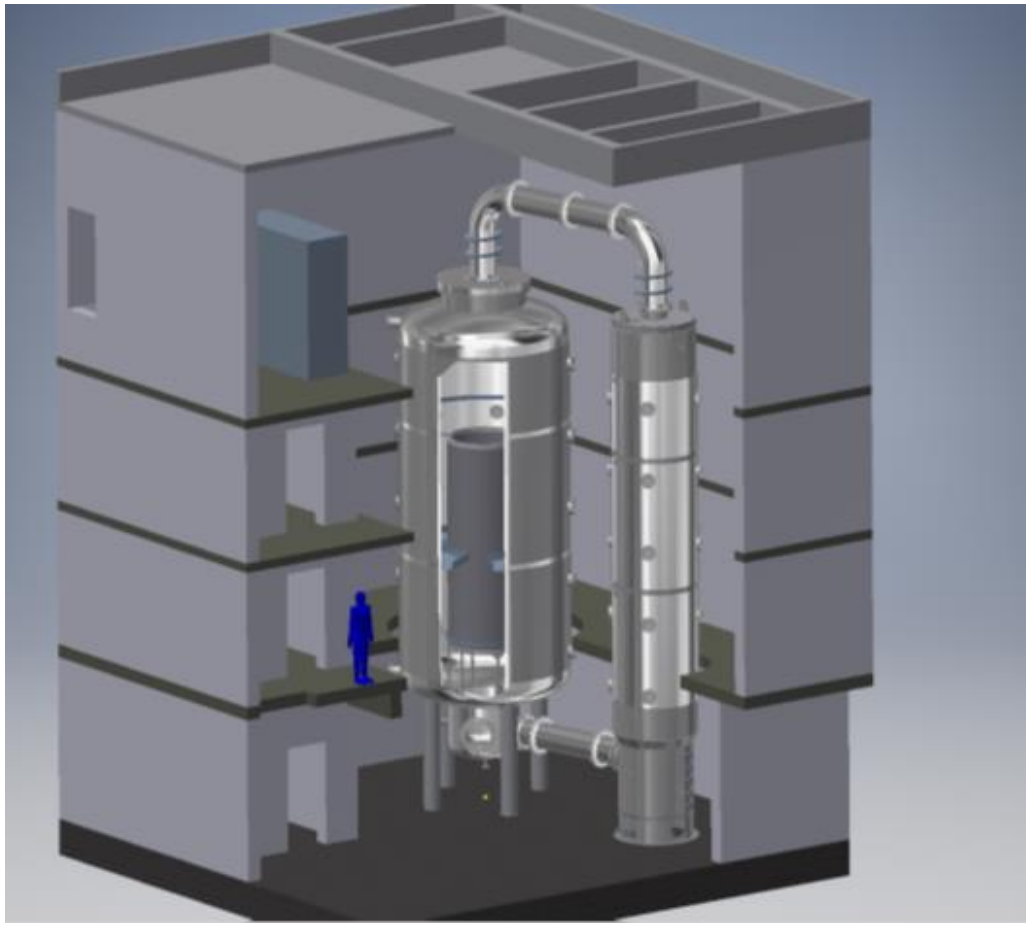

Overall objectives of THAI

- To provide **experimental data bases** for development and validation of containment specific **Lumped Parameter** and **CFD Codes** used in the area of reactor safety analyses
- To investigate specific issues for **LWR (PWR, BWR) under severe accident conditions**:
  - **Thermal hydraulics** and hydrodynamics of water pools,
  - **Hydrogen** distribution, combustion and mitigation systems (e.g. PAR), and
  - **Fission product** (Aerosol and Iodine) behavior, source term and mitigation systems (FCVS)

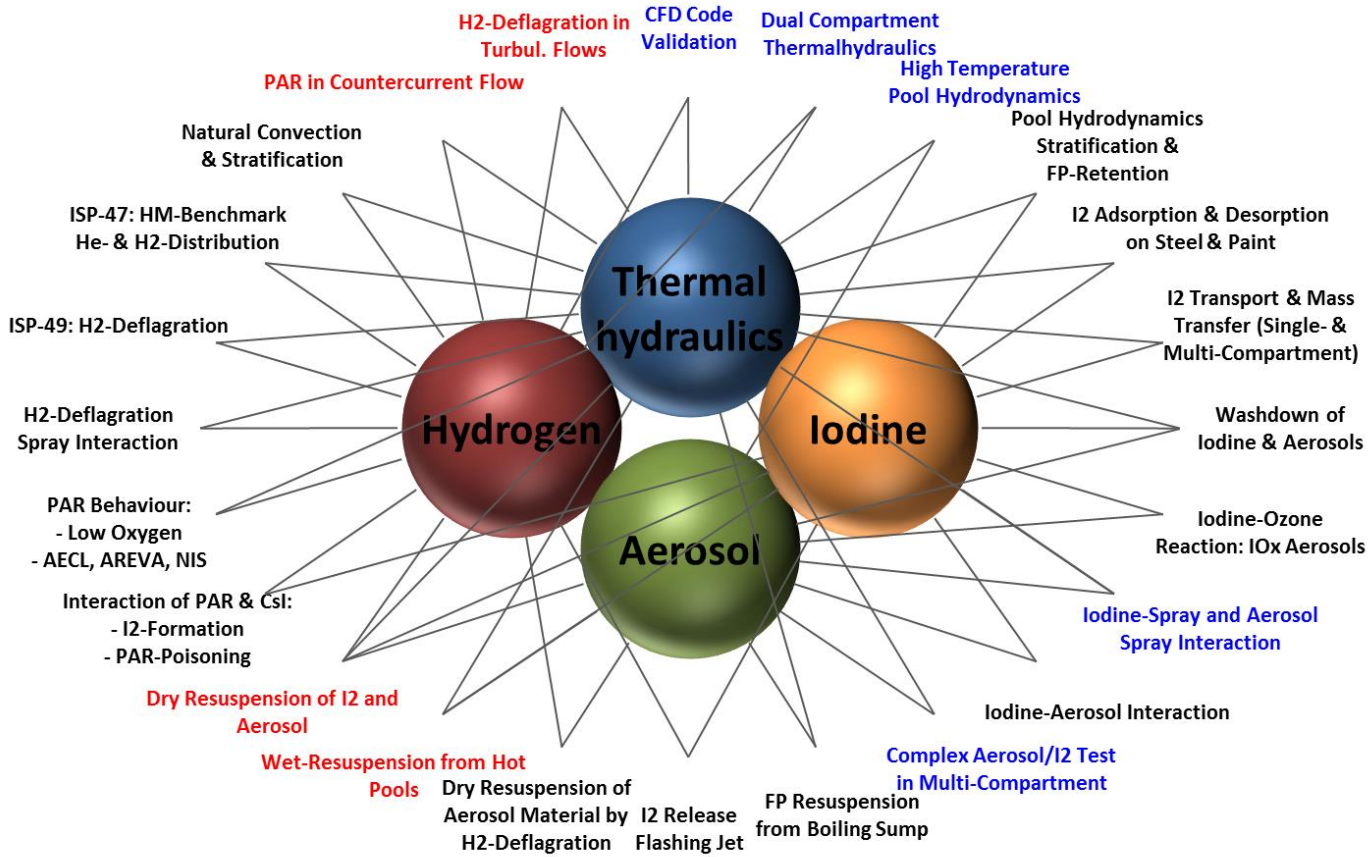

Background / Objective

Iodine:

- can be released into containments during a severe accident
- is considered one of the most important nuclides with potential for public dose
- significantly different iodine concentrations can be expected in compartments and rooms
- inhomogeneity may be relevant for organic iodine formation and the dose rate
- I as g ne and in aerosol form

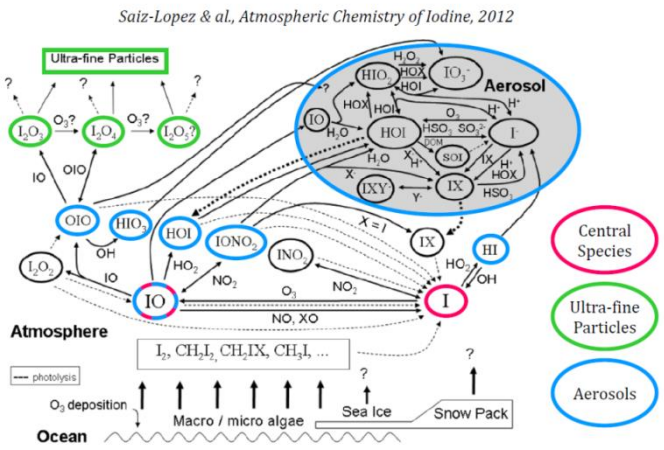

Simulation Results – local I_2 concentrations in the containment

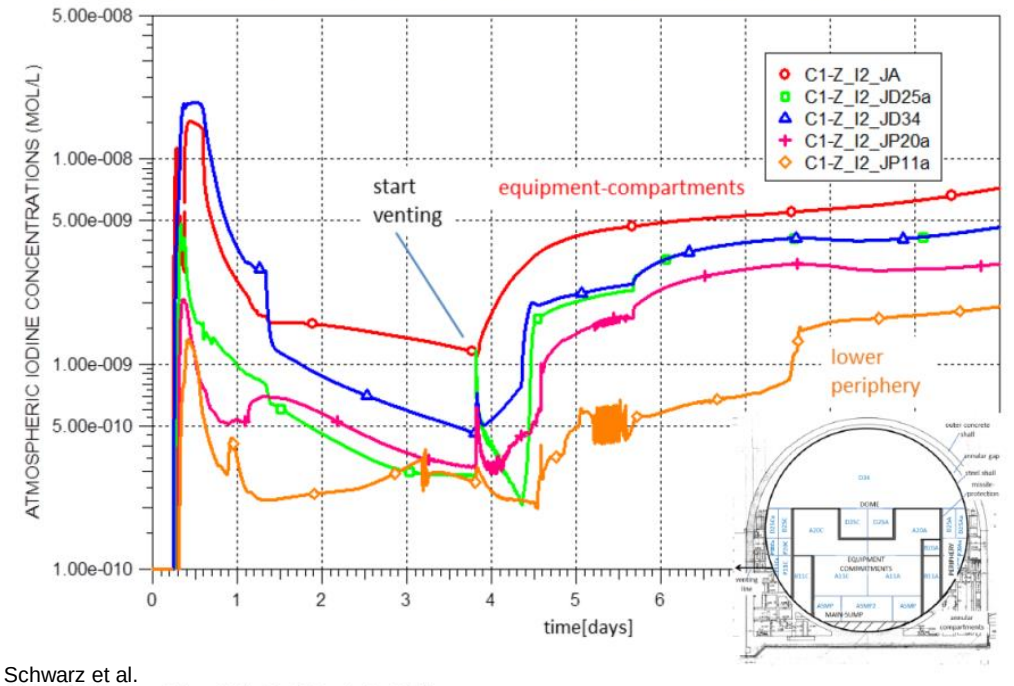

Schwarz et al.
5th COCOSYS user workshop, Berlin 28 – 30 September 2015

20

Background / Objective

THAI room chain tests shall simulate I_2 transport along typical flow loops in large containments:

- starting a pathway of iodine from the locations of release (e.g. pr imary loop rupture)
- or formation (e.g. radiolysis in the containment sump)
- along the plant rooms up to the dome of the containment
- and back through the auxiliary rooms (next to the containment s hell)

Measurement data for code validation purpose:

1. the distribution and mixing of gaseous iodine in different rooms,
2. the decrease of gaseous iodine by its deposition on painted sur faces,
3. the distribution of deposited iodine on the different painted surfaces.

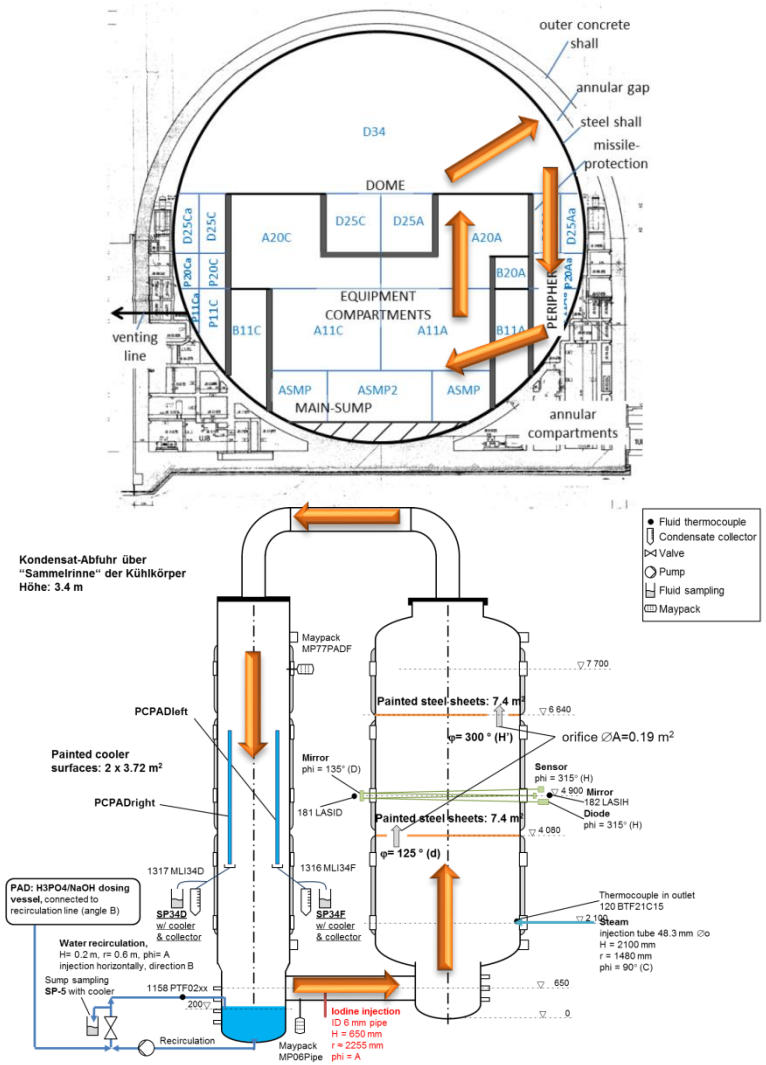

THAI+ -Test-Facility



Specifications

- 80 m^3 total gas volume
- 11.3 m height, vessel diameters:
  - 3.2 m (THAI)
  - 1.6 m (PAD)
- Design P/T: 14 bar at 180 ˚C
- Pressure resistent for H_2-deflagrations
- Stainless Steel, 22 mm



Unique Features

- Handling of hydrogen and carbon monoxide
- Licensed for use of radiotracer I^{123}
- Modularity, i.e. single or dual system and internals
- Ability to investigate passive safety systems at technical scale under SA-conditions

Test set-up and instrumentation

Specific test set-up Iod-33 and Iod-35:

- 3 compartments in TTV
- 2 intermediate floors in TTV painted with Gehopon epoxy paint (~ 30 m^2)
- 2 coolers paint coated with Gehopon in PAD (~7.5 m^2, **only Iod-35**)
- Gehopon was thermally pre-aged equivalent to 15 years
- Sump in lower section of PAD with 1 m^3 of decalcified water and chemically conditioned at pH 2 (Iod-35) and pH 1.5 (Iod-33)

Instrumentation

- Pressure, temperature (gas and wall thermocouples), relative humidity
- Steam feed rate and steam condensation rates
- Volumetric flow in upper connecting pipe
- I_2 injection rate
- I_{total}: by gas scrubbers with thiosulfate solution
- I_2 gas concentration by LASI (qualified light absorption at THAI)
- Iodine discrimination by Maypack filters

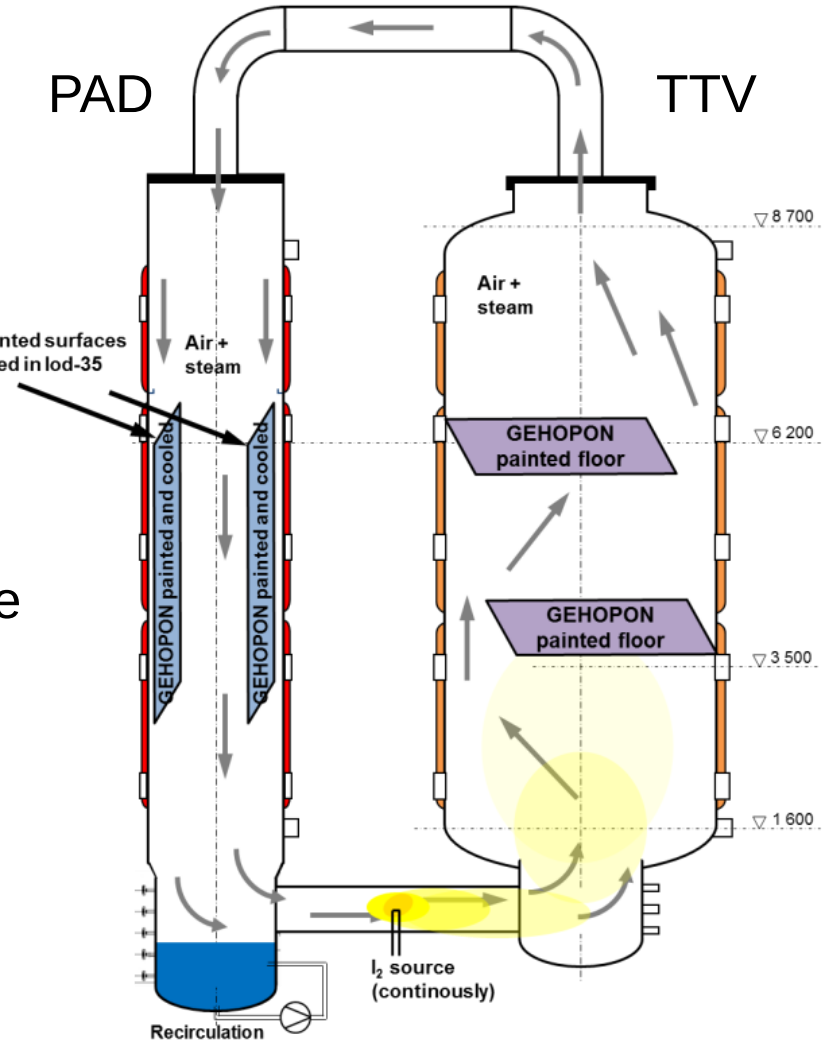

Test transient

Test conditions:

Test	P (bar)	T (°C)	T_{TTV} (°C)	T_{PAD} (°C)	c_{Steam}(vol%)	PAD sump	Injected I_2
Iod-33	1.40 (abs)	80 - 82 (PAD) 83 - 89 (TTV)	89.5 - 91.5 (wall)	79.5 - 80.5 (wall)	18.4	1037 L at 66 °C pH 1.5 (H_3PO_4,)	0.862 ± 0.015 g
Iod-35	1.51 (abs)	76 - 84 (PAD) 80 - 88 (TTV)	88.5 - 91 (wall)	74 - 83.5 (wall)	25.4	1007 L at 70 °C pH 2 (H_3PO_4)	0.844 ± 0.016 g

Experimental procedure:

Preconditioning:

- Facility heating to 90 °C, sump water heating and steam injection into the TTV.
- Generation of slow steady-state convective flow through the room chain.
- In Iod-35, steady state condensation rates were established at the cooled painted surfaces inside the PAD

1. **Phase (0 … 5.5 h)**
   - Continuous I_2 injection (~ 0.16 g/h) and deposition of I_2 onto the painted surfaces (and steel surfaces)
2. **Phase: (5.5 … 10 h)**
   - I_2 injection terminated and ongoing deposition of I_2 onto the painted surfaces (and steel surfaces)

Iod-33 and Iod-35: Thermohydraulics

Results of Iod-33:

- Gas temperature ranges from 80 to 88 °C
- Water temperature at 65 °C (control of relative humidity)
- Long term steady-state conditions
- Slightly higher temperature in “heated” large TTV where gas ascends compared to “cooled” small PAD where gas descends
- 19 vol.-% steam in Iod-33

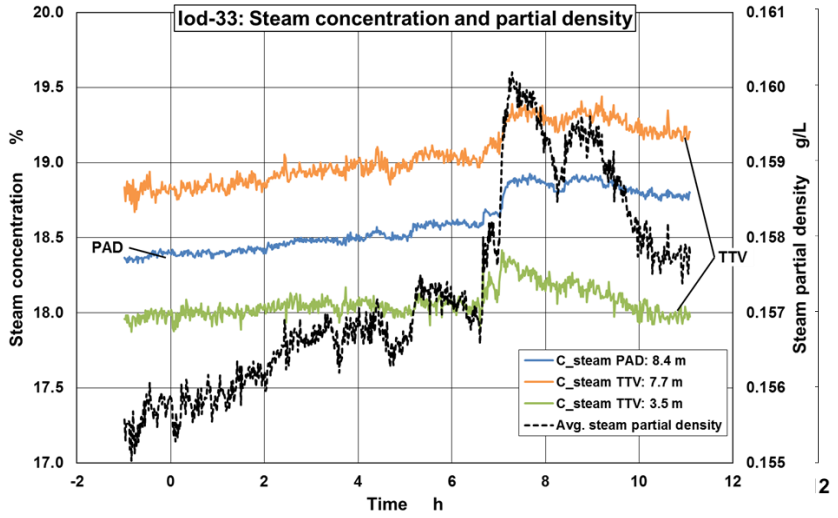

Results of Iod-35:

- Same principal characteristics, but
- Slightly higher temperature in TTV (steam injection)
- Slightly lower temperature in PAD (condensation at coolers)
- Elevated sump water temperature (thermal equilibrium with r.H.)
- 26 vol.-% steam in Iod-35

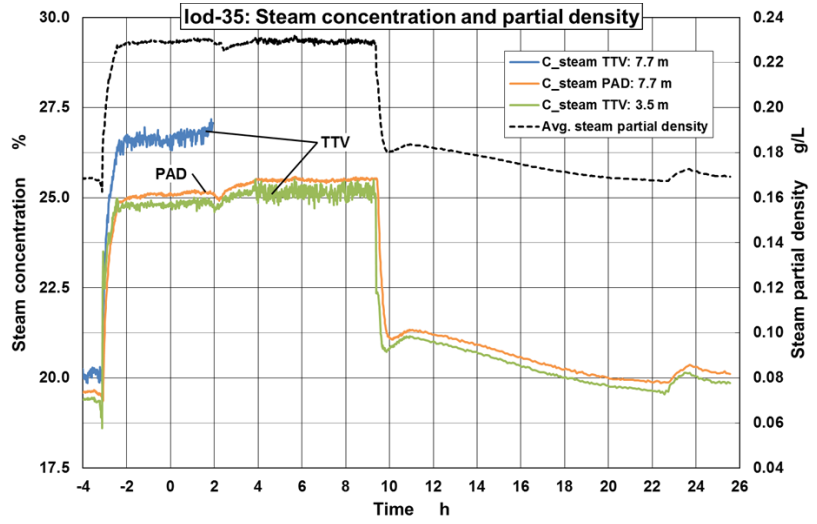

Iod-33 and Iod-35: Thermohydraulics

Results of Iod-33 and Iod-35

- Gas velocities measurement in the upper connecting pipe
  - Iod-33: 95 l/s → 14 min flow through of system
  - Iod-35: 105 l/s → 12.6 min flow through of system

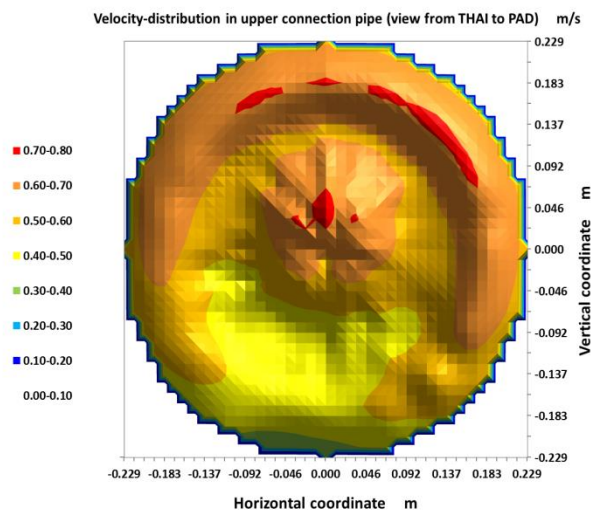

Steam injection and condensation in Iod-35:

- Injected steam (4 g/s) supports the flow loop
- Condensation at
  - PAD sump
  - Cooler A operated at 2.5 and
  - Cooler B at 5 kW, respectively

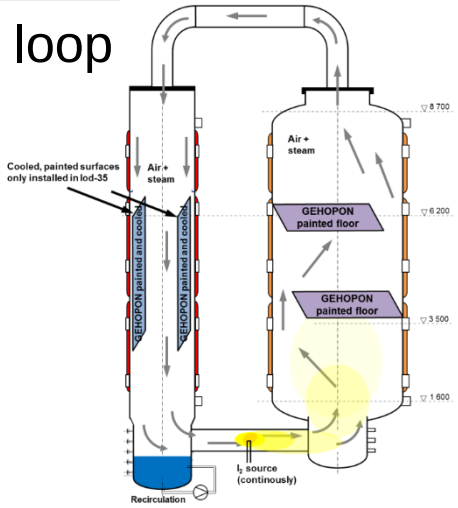

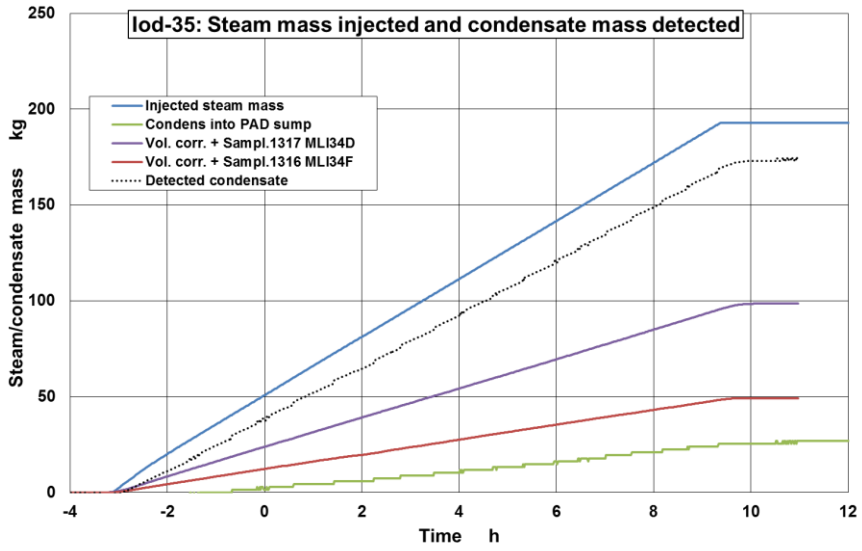

Iod-33: Gaseous I_2 distribution

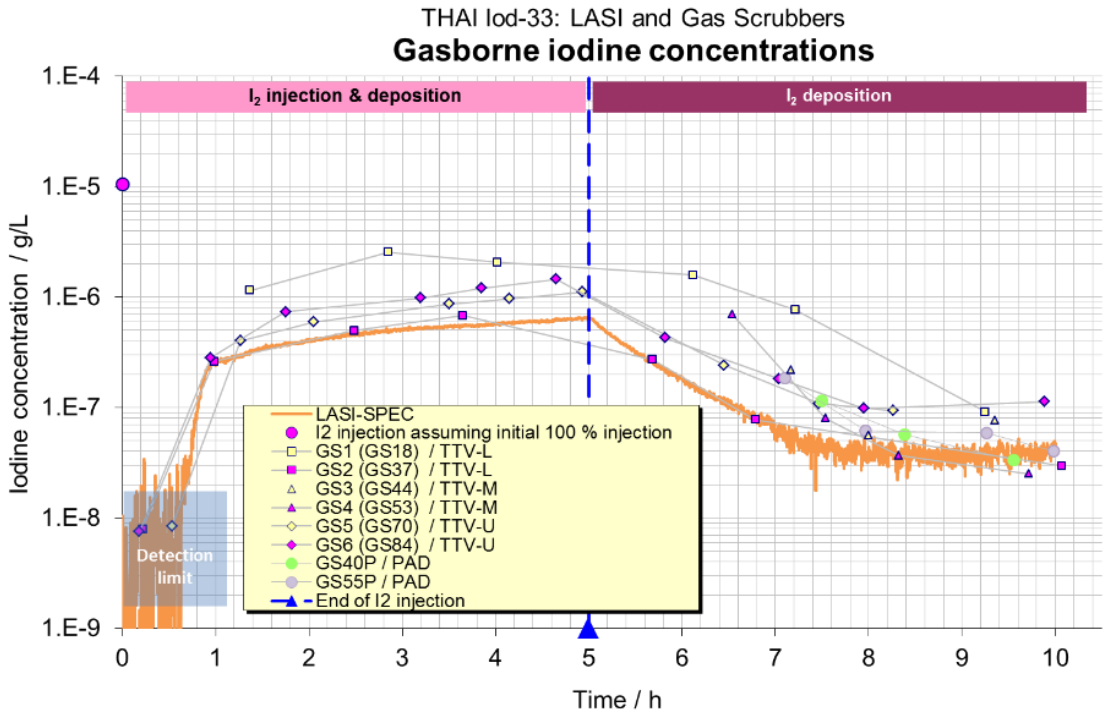

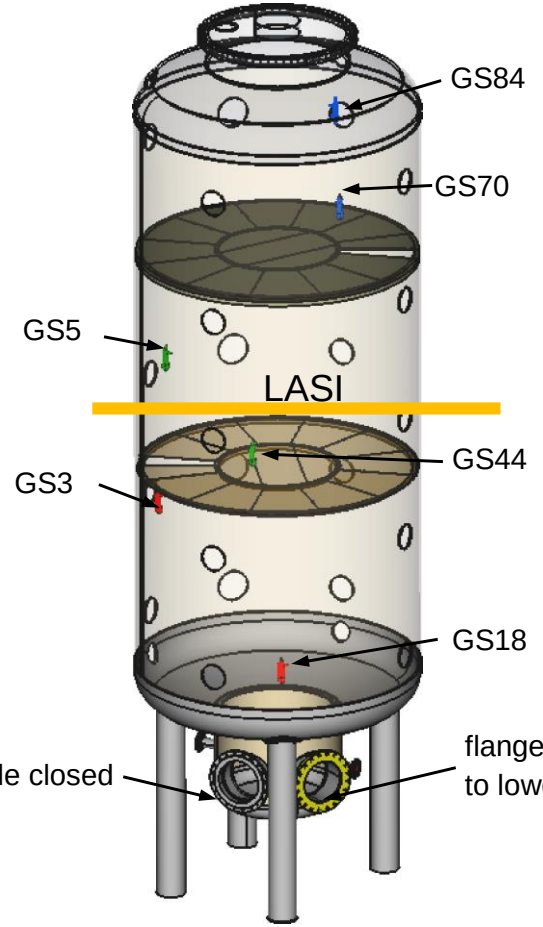

- I_2 concentration increases rapidly after starting the constant I_2 release
- Steady, but slower increase until injection is stopped
- Exponential decrease after I_2 injection was stopped
- Remaining plateau concentration indicates balance of gaseous and deposited I_2

Iod-35: Gaseous I_2 distribution

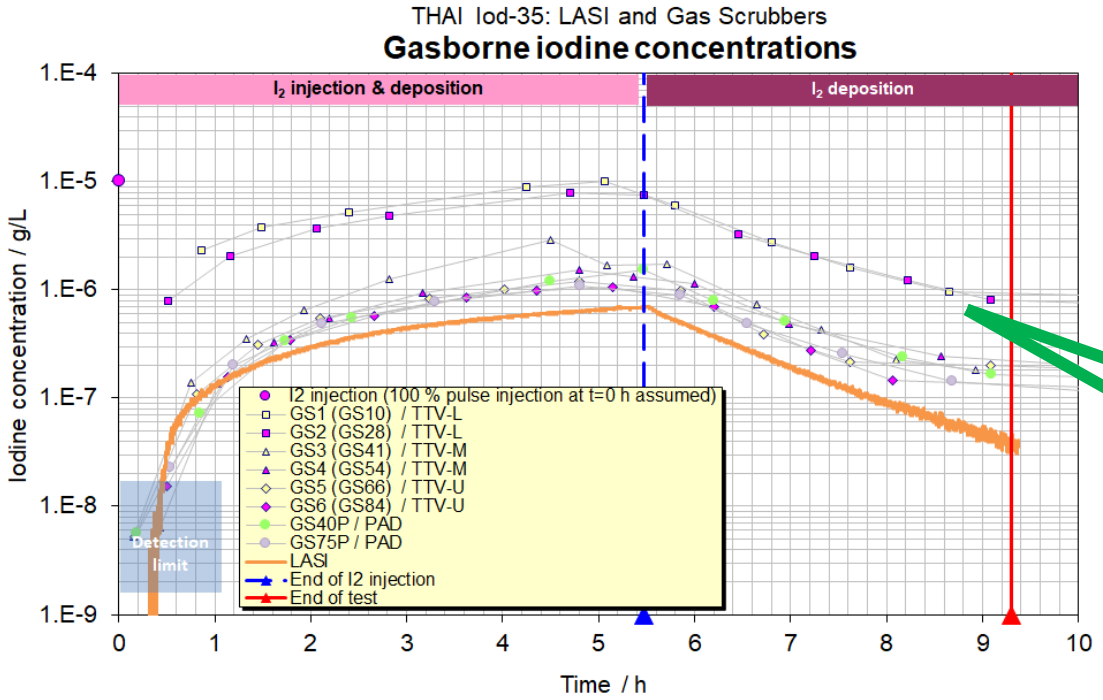

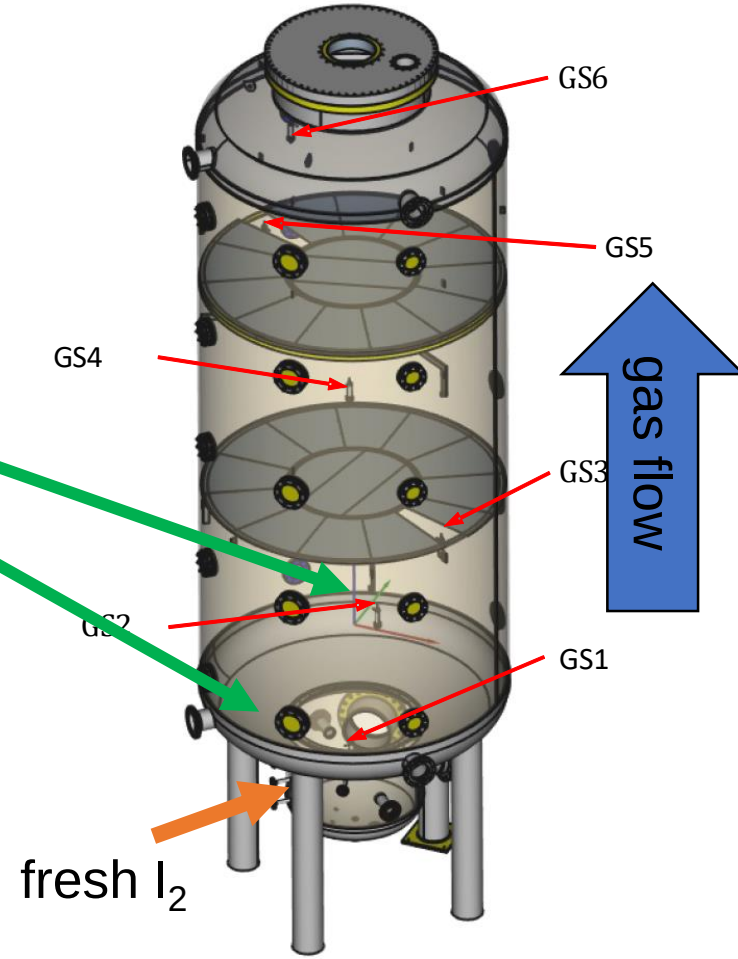

- Same characteristic **and** well developed multicompartment effect
- Multicompartment effect remained after stopping I_2 release indicating release of physisorbed I_2 from steel walls
- Transport of physisorbed I_2 to painted surfaces and final chemisorption
- LASI provides high resolution online signal of I_2 gas concentration (unscaled)

Iod-33 and Iod-35: Iodine species

Both tests showed:

- molecular I_2 is dominating species
- aerosol and organic iodine on similar levels
- organic iodine levels increased continuously throughout the test,
  late phase of Iod-35 were around 5-8E-9 g/L, i.e. fraction 0-10 %
- Iodine loading on paint and steel increased linear during injection and gradually in phase 2

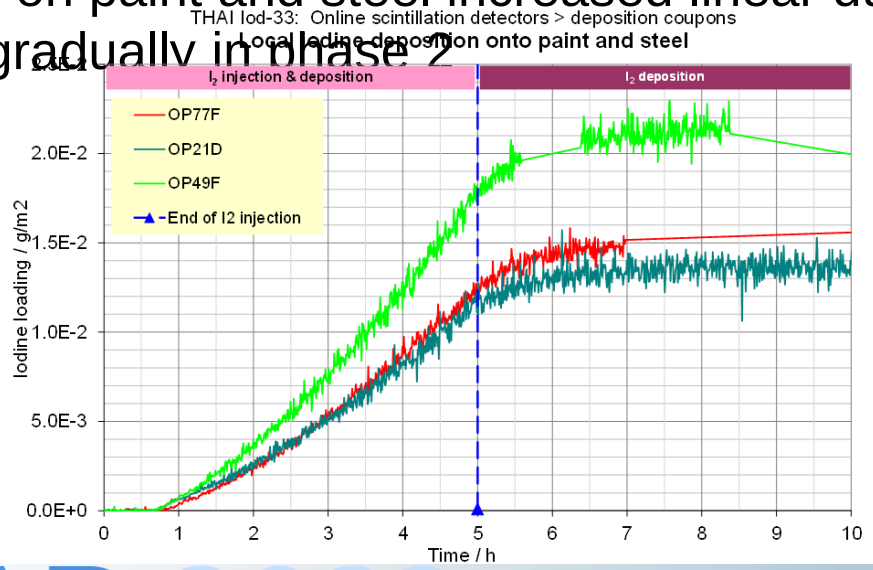

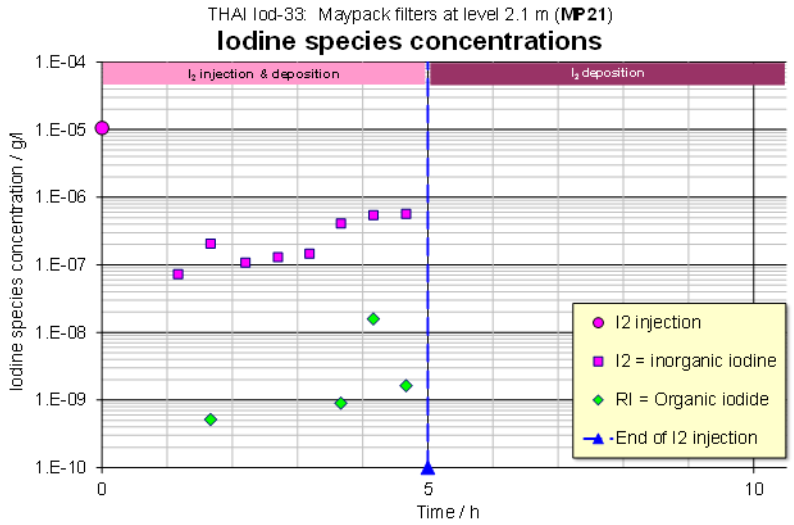

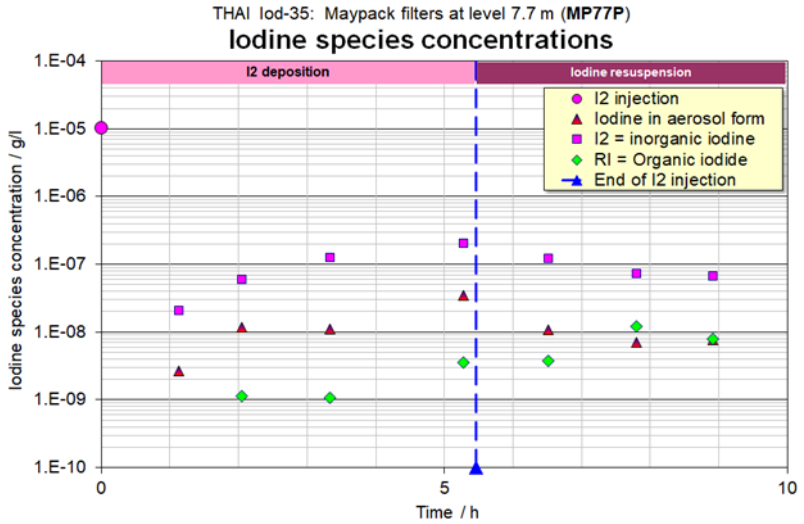

Iodine in condensate (Iod-35)

Results of Iod-33 and Iod-35

- I_2 transfer into sump in iod-33 by mass transfer only
- I_2 transfer into sump in iod-35 by mass transfer and steam condensation -> $I_{2,\,liq.}$ is 13 times higher
- Consequence of finding must be investigated and interpreted by validated SA-Codes (e.g. COCOSYS AIM)

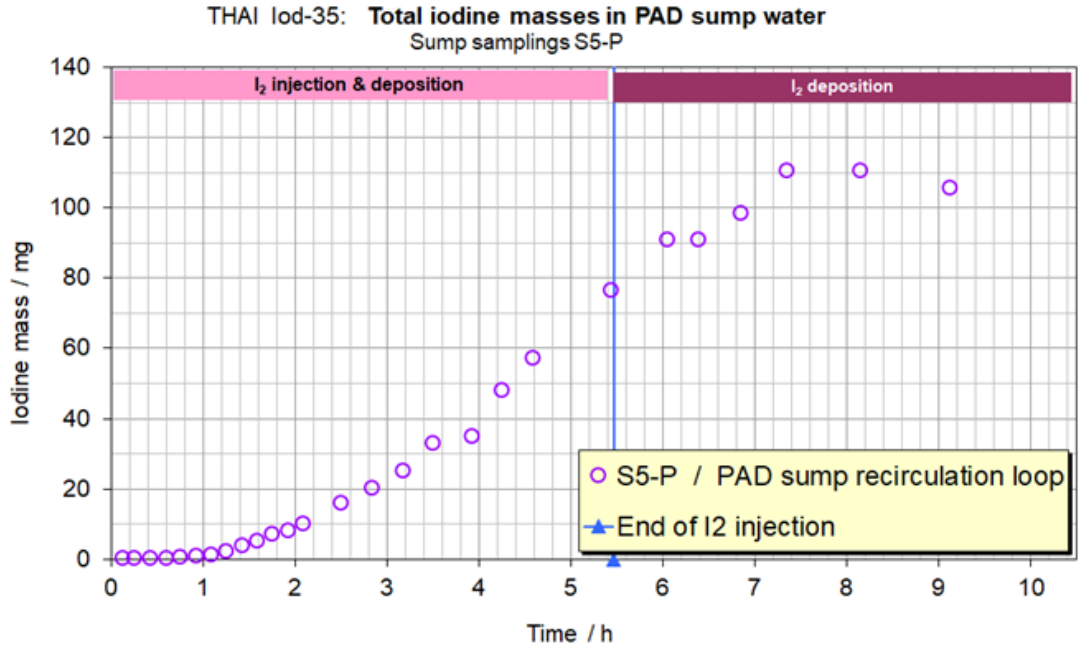

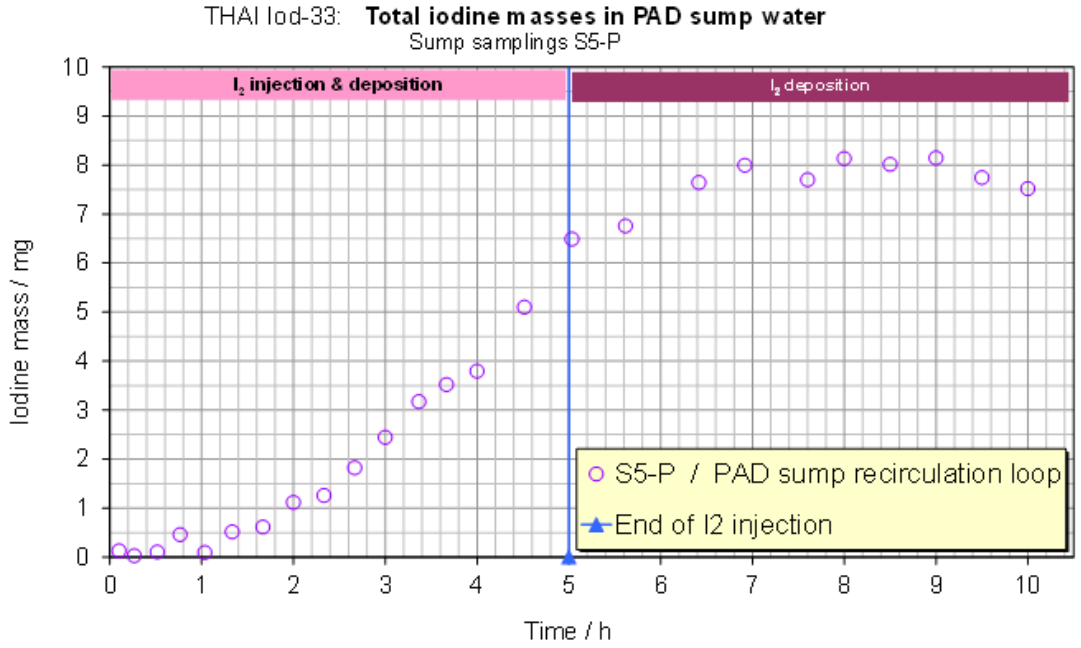

Conclusions and outlook

- Distribution of gaseous I_2 along a convective flow loop through a room chain was investigated in the THAI+ facility
  - under superheated (Iod-33) and
  - condensing (Iod-35) conditions
- Geometry mimics the path from the release (break in the primary circuit) or source (containment sump) through the plant rooms to the dome and back.
- Gaseous iodine (I_2) was injected into the flow loop which circulates between the two vessels
- The continuous long-term I_2 feed led to a continuous increase in the iodine concentration in the gas phase, with concentrations decreasing along its flow path, and a deposition of iodine on both, dry and wet painted surfaces in the TTV.
- Consistent set of temporal resolved iodine measurement: gas phase, sump, painted surfaces, tests provide excellent data for the development and validation of the I_2 paint models in SA codes
- Next in THAI program will be the investigation on the effect of deflagrations impacting the performance of decontamination paint

Acknowledgements

This work was funded by the German Federal Ministry for the Environment, Nature Conservation, Nuclear Safety and Consumer Protection under grant numbers 1501547 and 1501594 on the basis of a decision by the German Bundestag. The authors gratefully acknowledge the sponsorship by the German Federal Ministry for the Environment, Nature Conservation, Nuclear Safety and Consumer Protection .

On behalf of:

Federal Ministry
for the Environment, Nature Conservation,
Nuclear Safety and Consumer Protection

of the Federal Republic of Germany

The 10th European Review Meeting on Severe Accidents Research

Severe Accident Research Eleven Years after the Fukushima Accident

May 16-19, 2022, Karlsruhe, Germany

Poster Session		
ID267	**Organic Iodides trapping using silver-exchanged zeolites in conditions representative of a French pressurized water reactor severe accident** C. Le Gall (CEA)	**Paper** **Poster**
ID283	**THE EVOLUTION OF SEVERE ACCIDENT RESEARCH AT CHALMERS UNIVERSITY OF TECHNOLOGY – STATE-OF-THE-ART** A.-E. Pasi (Chalmers University)	**Paper** **Poster**
ID288	**Extending Capabilities of the ASTEC Severe Accident Code to Simulate Accident Sequences of Generic BWR4 Mark1** O. Murat (KIT)	**Paper** **Poster**
ID345	**IVMR system. Analytical justification results for VVER-440/V-213** O. Mazurok (ES Group)	**Paper** **Poster**
ID357	**The NewPLINIUS project: France future prototypic corium experimental platform for severe accident R&D** C. Journeau (CEA)	**Paper** **Poster**
ID358	**Evaluation of Long-Term Containment Cooling System (LTCCS) concepts for reactor facility VVER-1000/V-320** V. Ivanov (ES Group)	**Poster**
ID360	**TOP FLOODING TESTS OF PROTOTYPIC CORIUM ON MERELAVA FACILITY** V. Bouyer (CEA)	**Paper** **Poster**
ID362	**FAN COOLER IMPACT UNDER A TLOFW ACCIDENT IN A NEW SMR IN DESIGN PHASE** M. R. Gual (University of São Paulo)	**Paper** **Poster**
ID386	**Development of CFD Code for Prediction and Improvement of Core-Catcher Performance** Sangmin Kim (KAERI)	**Paper** **Poster**

The 10th European Review Meeting on Severe Accident Research (ERMSAR2022) **Log Number: 267**
Akademiehotel, Karlsruhe, Germany, May 16-19, 2022

Organic Iodides trapping using silver-exchanged zeolites in conditions representative of a French pressurized water reactor severe accident

C. Le Gall[1 *], P. Nérisson[1], L. Hurtado[1], C. Tornabene[1], O. Leroy[1], C. Cunin[1], C. Duffieux[1], H. Houjeij[2], M. Chebbi[2], C. Monsanglant-Louvet[2], A. Piton[3], B. Azambre[3], Brice-Loïc Renard[4], Michel Molière[5] and L. Cantrel[1]

[1]: Institut de Radioprotection et de Sûreté Nucléaire, PSN-RES, SEREX,
13115 Saint-Paul-lez-Durance CEDEX
[2]: Institut de Radioprotection et de Sûreté Nucléaire, PSN-RES, SCA,
91192 Gif-sur-Yvette CEDEX
[3]: Laboratoire de Chimie et Physique-Approche Multi-échelle des Milieux Complexes,
Institut Jean Barriol CNRS, Université de Lorraine, 57500 Saint-Avold
[4]: SOMEZ, Parc Marcel Dassault, 470 rue Alberto Santos Dumont, 34430 Saint-Jean-Michel-de-Védas
[5]: Consultant for SOMEZ and research associate at UTBM-ICB, 90010 Belfort CEDEX

* Corresponding author: claire.legall@irsn.fr

Abstract

In case of a nuclear severe accident leading to a pressurization of the containment building, the in-depth defense system allows controlled venting of the containment to lower the pressure and maintain the integrity of the structure. In France, this procedure is called U5 and requires a dedicated line including a metallic pre-filter and a sand bed filter ("dry" FCVS: Filtered Containment Venting System), which both limit emissions of radioactive species in the environment.

As far as aerosols are concerned, a large number of studies demonstrated the efficiency of this system, consistently with its design, but also highlighted its weaknesses, notably towards gaseous forms of iodine [1], [2]. Yet, iodine is a highly reactive and volatile fission product which may have huge radiological impacts if released to the outside. In case of a severe accident, iodine is mainly released under two volatile types of compounds: molecular Iodine (I_2) and organic iodides (CH_3I being the most volatile).

Within this context, the MiRE ANR project aims notably at developing and characterizing new trapping methods in order to limit the dissemination of volatile iodine species in the environment in case of containment venting. Among possible adsorbents, zeolites have been identified as a promising solution [3], [4] thanks to their thermal stability, radiation resistance, large specific surface areas and tunable properties [5]–[7]. More precisely, silver-exchanged zeolites are able to capture irreversibly iodine species through the formation of thermally stable (up to 500 °C) and insoluble AgI precipitates [5], [8].

To assess their performances under conditions more representative of French FCVS (normal and accidental), three silver-exchanged zeolites were thus tested at IRSN in a large variety of thermohydraulic conditions (temperature, humidity, apparent velocity, irradiation, pollutants…). Their trapping performances towards I_2 and CH_3I were thus determined on different experimental benches and facilities: SAFARI and EPICUR at IRSN Cadarache, BRIOCH and PERSEE at IRSN Saclay. Aging tests and characterizations of the zeolites were carried out at LCPA2MC. All these tests proved the irreversibility and stability of iodine trapping under irradiation and the very interesting performances of zeolites at low humidity. However, very high water fractions in the carrier gas as well as potential ageing due to SO_x or NO_x affect the efficiency of iodine capture on these materials.

Keywords: Silver-exchanged zeolites, organic iodine, severe accident, U5 procedure.

References: [1] T. Albiol *et al.*, *Ann. Nucl. Energy*, 2018. [2] O. Leroy *et al*, *J. Radioanal. Nucl. Chem.*, 2019. [3] O. Leroy *et al.*, IRSN/2019-00884, MiRE 135-2019, 2019. [4] M. Chebbi *et al.*, *J. Hazard. Mater.*, 2021. [5] M. Chebbi,PhD. Thesis, Université de Lorraine, 2016. [6] E. R. Vance *et al.*, *J. Mater. Sci.*, 1982. [7] A. G. Evans, Du Pont de Nemours (E.I.) and Co., DP-MS--78-5, 1978. [8] Y. Nan *et al.*, *AIChE J.*, 2017.

CH_3I trapping using silver-exchanged zeolites in conditions representative of a NSA occurring on French PWR

C. Le Gall[1], P. Nérisson[1], L. Hurtado[1], C. Tornabene[1], O. Leroy[1], C. Cunin[1], C. Duffieux[1], L. Cantrel[1], H. Houjeij[2], M. Chebbi[2], C. Monsanglant-Louvet[2], A. Piton[3], B. Azambre[3], B.-L. Renard[4], M. Molière[5]

[1] *IRSN, PSN-RES, SEREX, 13115 Saint-Paul-Lez-Durance, France*
[2] *IRSN, PSN-RES, SCA, 91192 Gif-sur-Yvette, France*
[3] *LCP-A2MC, Institut Jean Barriol CNRS, Université de Lorraine, 57500 Saint-Avold, France*
[4] *SOMEZ, Parc Marcel dassault, 470 rue Alberto Santos Dumont, 34430 Saint-Jean-Michel-de-Védas, France*
[5] *Consultant for SOMEZ and research associate at UTBM-ICB, 90010 Belfort CEDEX, France*

Further tests to better assess the AgClino behavior

(preparation protocol, pre-heating, pre-saturation with H_2O, aerosols deposit)

4

BRIOCH

100°C, 0%$_{R.H.}$, 10 cm.s^{-1}, [CH_3I] = 10 ppm$_v$

Batches of AgClino obtained with synthesis protocole of March 2021 are less efficient twards CH_3I capture

Characterizations before and after test
DRS-UV-Visible [4], SEM-EDX, FTIR-ATR

More Ag^0 in 2021 batches
Strong reducing effect of CO on Ag [5]
Stable AgI formed after CH_3I exposition

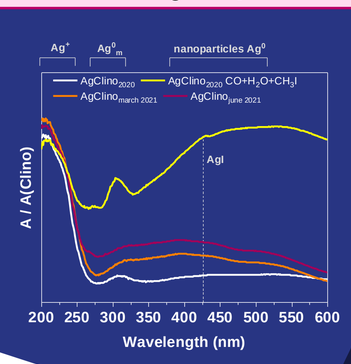

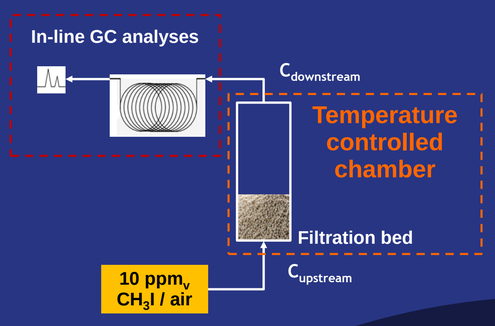

SAFARI

140°C, 0-50%$_{R.H.}$, 0-3.2 bar, 10 cm.s^{-1}, [CH_3I] = 40 ppm$_v$, CO, 3 h

$DF_{CH_3I} > 10^3$ up to 42%$_{mass}$ H_2O (40%$_{R.H.}$)
Drop of performance for higher H_2O content
$DF_{CH_3I} > 10^3$ in closer conditions to NSA (CO, H_2O)

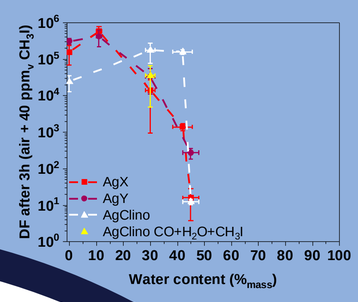

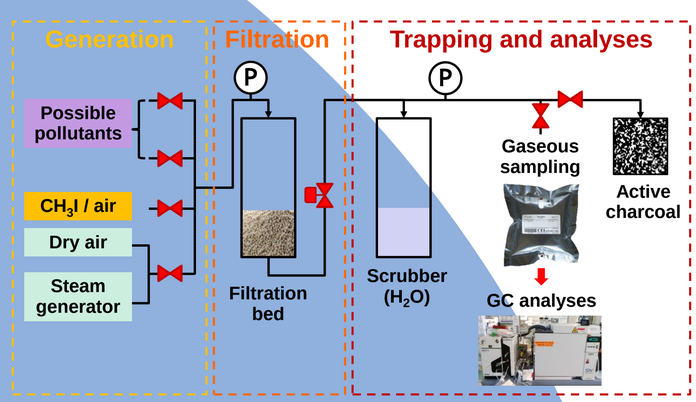

1

0,1 ppm$_v$ < [CH_3I], [I_2] < 1 ppm$_v$ [1]
[H_2O] ≤ 70%$_{wt}$ (HR ≤ 73% at 5 bar) [2]
[CO] ≤ 15%$_{wt}$ [2]

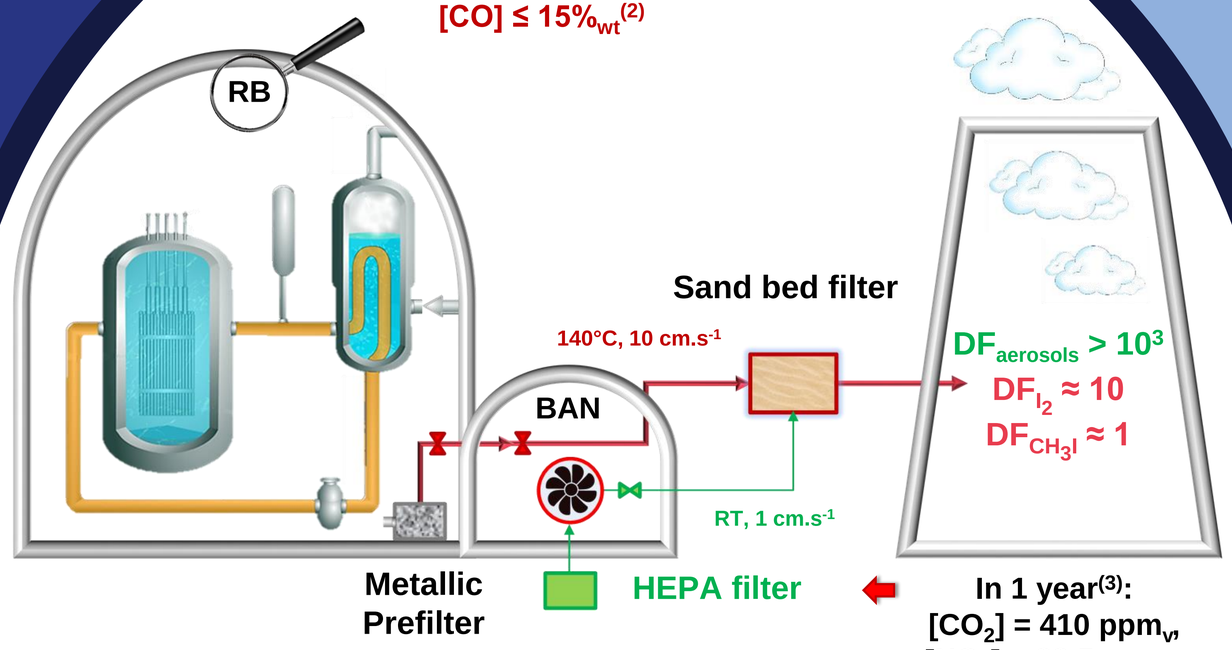

In 1 year [3]:
[CO_2] = 410 ppm$_v$,
[NO_2] = 23,5 ppm$_v$,
[SO_2] = 0,002 ppm$_v$

EPICUR

120°C, 80%$_{R.H.}$, 3.5 bar,
2 cm.s^{-1}, 27 kGy

Stable I retention by AgClino under irradiation after 30 h of irradiation

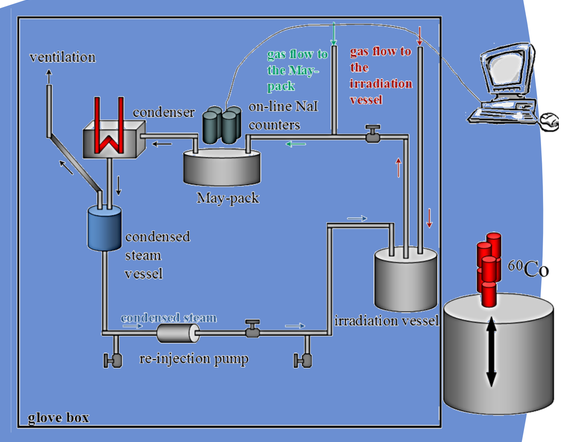

PERSEE

80°C, 10%$_{R.H.}$, 10 cm.s^{-1}, [CH_3I] = 0.15 ppm$_v$
30 min of injection, 1 h of elution

Total retention of CH_3I on AgX, AgY and AgClino zeolites

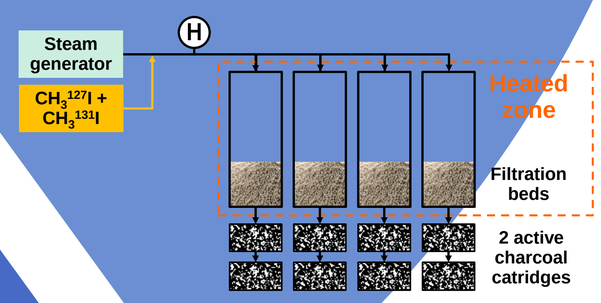

Ageing bench

R.T., 0%$_{R.H.}$, CO_x, SO_2, NO_2,1 cm.s^{-1}

Ag coalescence on AgClino exposed to NO_2 and SO_2 : $AgNO_3$? ($N/Ag_{EDX} \approx 1$)

AgY sensitive to NO_2 (↘ of $Q_{5\%\ CH_3I}$ by 76% after 28 y) but not to SO_2 (until 55 y)

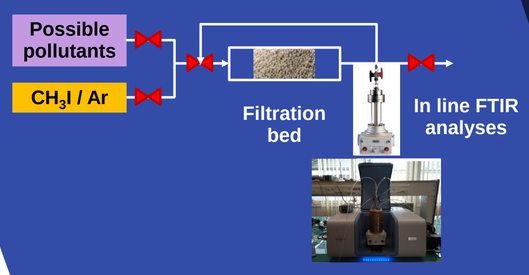

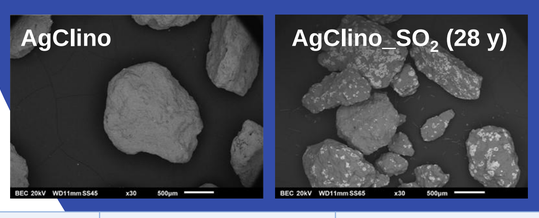

	Q_{sat} SO_2 ($mg_{CH_3I}.g^{-1}$)	Q_{sat} NO_2 ($mg_{CH_3I}.g^{-1}$)
AgY	218 (5700 y)	-
AgClino	11 (350 y)	20 (228 y)

2

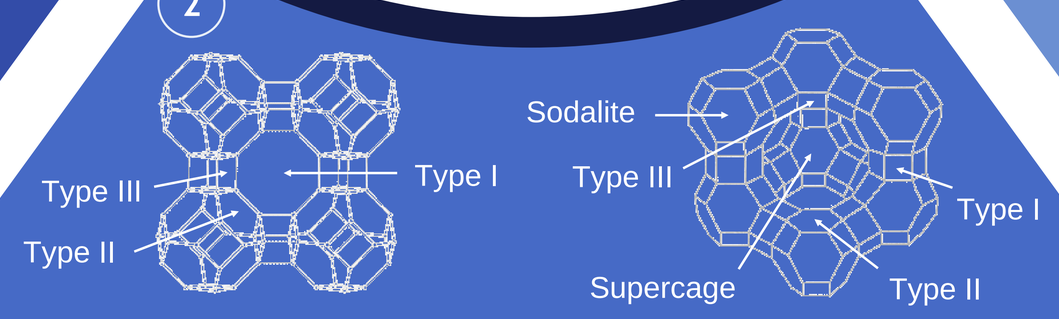

AgClino (natural Clinoptilolite)

S_{BET} = 20 m².g^{-1}
Si/Al = 5
%Ag = 10 %$_{mass}$

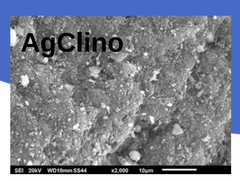

AgX and AgY (faujasites)

S_{BET} = 251 and 690 m².g^{-1}
Si/Al = 1.2 and 2.5
% Ag = 35 and 22 %$_{mass}$

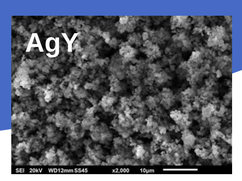

3'

After ageing under normal operating conditions

3

Under severe accident conditions

Need for improving volatile I trapping on French FCVS

PIA RSNR MiRE project (2014-2022)

Silver-exchanged zeolites

Performances towards CH_3I retention ?

[1] Herranz *et al.*, *Annals of Nuclear Energy* **(2014)**
[2] Réunion de clôture MiRE I **(2019)**
[3] Le Gall *et al.*, Internal report IRSN/2020-00248 **(2020)**
[4] Chebbi *et al.*, *J. Phys. Chem. C* **(2016)**
[5] Akolekar *et al.*, *Journal of Molecular Catalysis A: Chemical* **(2000)**

THE EVOLUTION OF SEVERE ACCIDENT RESEARCH AT CHALMERS UNIVERSITY OF TECHNOLOGY – STATE-OF-THE-ART

Pasi, Anna-Elina
Chalmers University of Technology
Department of Chemical and Biological Engineering
SE-412 96 Gothenburg, Sweden

pasia@chalmers.se

ABSTRACT

What does it take to create a valid tool for analyzing severe nuclear accidents? To be able to construct an accurate model of a nuclear accident from start to finish, from releases to management, the details and data needed is substantial. Where is this data obtained? From basic research that provides the results, reactions, and reconstruction details which, when rightly applied, will help to set the carefully constructed model to the high accuracy that is needed to validly analyze, assess, and most importantly minimize the consequences of a severe nuclear accident. This type of fundamental work has been performed at Chalmers University of Technology for decades for various fission products, and it is not an overstatement to say that Chalmers is still in the forefront of severe accident chemistry research. The results obtained for iodine, ruthenium and most recently for tellurium source term have been highly appreciated and the work continues closely alongside other nuclear accident experts. The future of severe accident research at Chalmers aims to couple experimental work closer together with modeling which strengthens the overall severe accident research concept. This paper attempts to present the evolution of severe accident research conducted at Chalmers University of Technology through a review of the state-of-the-art. The aim is to put fundamental chemistry research into severe accident context and present the valuable assets it holds as well as pave the way for possible future collaborations.

KEYWORDS
Source term, iodine, ruthenium, tellurium, chemistry

1. INTRODUCTION

For as long as nuclear power has been in commercial operation, safety has been of highest priority. Despite the growing interest towards the energy atoms hold from the 1950s and 60s all the way to today, nuclear power has had a stigma of unreliability and uncertainty around it. In the early era of commercial use of nuclear energy, the concerns revolved around military use of nuclear materials that had been demonstrated just years prior. There concerns were replaced by nuclear reactor accidents which awoke concerns in terms of the safety of nuclear power. The accidents that have occurred, one might say in regular intervals, have not only resulted in social bias and stigma but also in development and need for severe accident research. From the early days of WASH reports[1] to current advanced modeling codes and complex experimental programs, severe accident research has provided crucial data that has and will be used to assure safe use of nuclear power.

If we investigate the history of experimental severe accident research worldwide, the focus lies in advanced experimental programs such as PHEBUS[2], [3], VERCORS[4], THAI[5] and BIP[6]. These programs have focused on the progression of a core melt accident, release behavior of fission products in variety of conditions and the complexity of fission product behavior, mostly iodine. The access to large and complex experimental facilities as used in PHEBUS and VERCORS have been crucial in investigating severe accident phenomenology in moderately realistic conditions. To complement these large experimental programs, the THAI and BIP have focused on individual phenomena like hydrogen risk and iodine behavior. In addition, the Nuclear Energy Agency (NEA) of the OECD has produced a wide range of valuable results for both individual elements and their behavior [7] as well as phenomena taking place during an accident [8]. The international working group is still active in SA research and keep adding to the already extensive collection of results. These programs and collaborations have laid the foundation and continue to be the benchmark of severe accident and especially source term research.

The content of these SA projects and others have obviously been affected by the events occurred before, during and after the programs. The VERCORS program was initiated in 1989, just a couple years after the Chernobyl accident, and the program ran until 2002. In parallel with the VERCORS project, PHEBUS started in 1988 and the end report for the last test was published in 2010, just a few months before the Fukushima accident. Although the program was finished before the Fukushima accident, the PHEBUS results have been crucial in developing severe accident modelling codes and understanding the severe accident phenomenology.

Where does Chalmers University of Technology fit in? Looking at the timeline in Figure 1, severe nuclear reactor accident research started in the mid 1980s when Chalmers was part of extensive study on severe accident methodology in Swedish nuclear power stations. The research at Chalmers was related to the effect of cable pyrolysis on sump pH and the source term of actinides and fission products. The data can be found in Reactor Accident Mitigation Analysis (RAMA) report published in 1985[9]. Since then, Chalmers has contributed to severe nuclear accident research, experimental and modeling, taken part in international projects and filled some uncertainties left from the large-scale programs. The research, both modeling and experimental, has focused mostly on the source term of various fission products and the aim has been produce data that could be used for code validation in the future. This state-of-the art will provide the collected data produced by the researchers at Chalmers over the past few decades, explain the aim of each research topic and present the current status and future of the severe nuclear reactor accident group at Chalmers University of Technology.

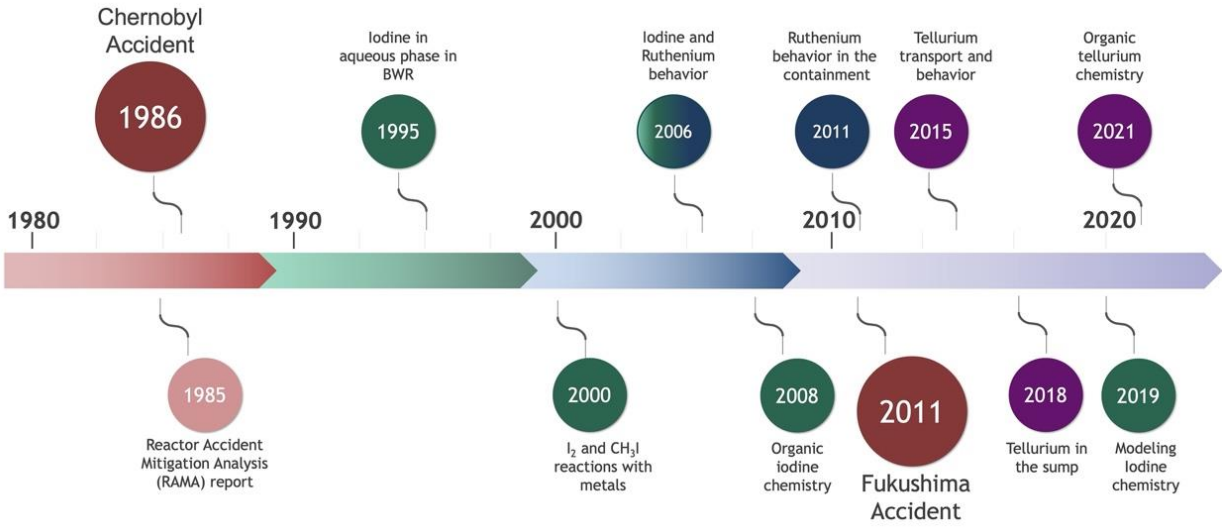

Figure 1. Timeline of the SA research performed at Chalmers University of Technology.

2. SEVERE ACCIDENT RESEARCH AT CHALMERS

Severe accident research at Chalmers has been active since around the mid 1990s. Around this time, the first PhD student was employed, and the SA group was formed. Since then, the research has been consistent and ever evolving. The researchers at Chalmers have focused on mainly three fission products: iodine, ruthenium and tellurium. Moreover, the phenomena studied include both gas and liquid phase, different surfaces, temperatures and accident management systems. The following sections introduce the different eras of severe accident research conducted at Chalmers over the years and the main results from each project.

2.1. Iodine

If all severe accident research is compiled together, majority of it is related to iodine. The reason iodine is in the center focus is its high volatility, risk of thyroid cancer and complex chemistry. Therefore, the severe accident research conducted at Chalmers started with iodine. The coming sections present the main results of the iodine related research between the year 2000 and 2015.

2.1.1. Iodine-metal surface interactions

The iodine research started by building a small-scale model of a BWR containment in a form of an apparatus for online gas and liquid measurement (Figure 2.)[10]. The two-loop system equipped with two NaI detectors enabled the simultaneous measurement of partitioning of radioactive iodine between gas and liquid phase. The whole setup was made from glass to inhibit iodine sticking to any surfaces and the temperature was controlled by placing the entire system in a temperature box.

Once the setup had been tested and validated for iodine partitioning, it was used to study interactions between I_2 or CH_3I and reactive metals[9]. The metals studied were copper, zinc and aluminum and the uptake of iodine species was investigated in temperatures 25, 50 and 70°C. The respective metal was held in the gas or aqueous phase of the apparatus with a specially designed glass hook and the concentration of iodine was measured continuously in both gas and liquid phase with the NaI detectors. The results suggest that I_2 has high affinity towards all the three metals in the gas phase and that the reaction rates are temperature dependent. The concentration drops initially in the gas phase rapidly, but the deposition slows down after some minutes. This is demonstrated in the aluminum I_2 results in Figure 3. For methyl iodide, the uptake was significantly lower on the metals. In aqueous phase, only copper showed any significant iodine uptake. This was explained by the high solubility of zinc and aluminum iodides in the aqueous phase.

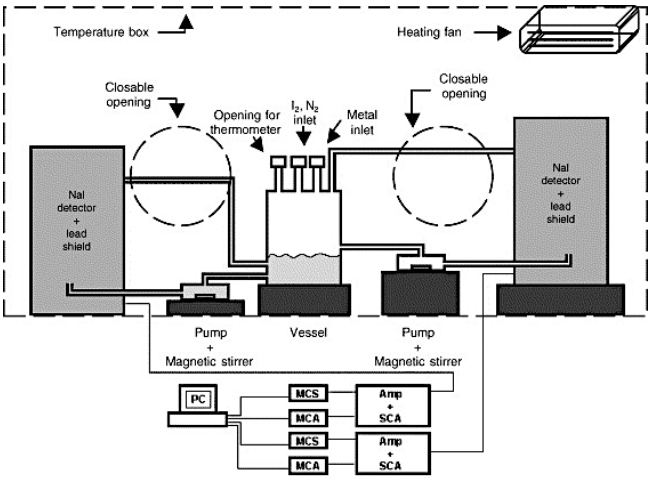

Figure 2. Apparatus for online measurement of iodine in gas and aqueous phase[10]**.**

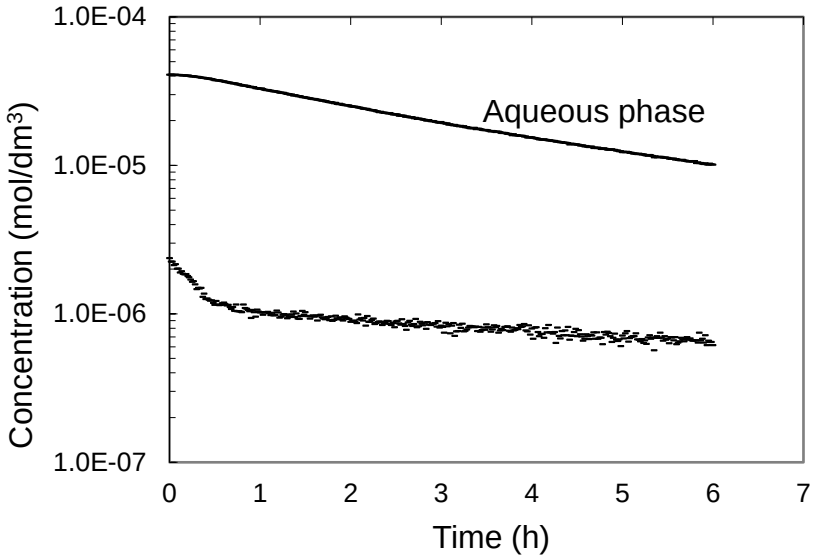

Figure 3. Results from experiment with aluminum and I_2 at 50 °C illustrating the I_2 deposition trend under humid conditions[11]**.**

2.1.2. Iodine modelling

One of the main goals of the experimental work performed at Chalmers is to produce results which can be implemented in severe accident codes. The chemistry data of many of the codes is very limited and require a lot of improvements. We at Chalmers have recently started incorporating modelling to some of the earlier data produced at the severe accident group. The first attempt was to simulate the iodine-metal interactions performed experimentally in the early 2000s[11]. The work was performed with MELCOR to evaluate the deposition models already existing in the code. For this, a containment model (Fig. 4) was constructed to simulate the setup used in the experiments presented in Figure 2[10]. During this work, the need for code development was clearly highlighted due to inconsistent results produced by the code compared to the experimental data. Through extensive work, we were able to produce comparable data which will be published later this coming year. The main result, however, was concluded to be the lack of chemistry data in the code and the need for improvement even for the most significant radionuclides.

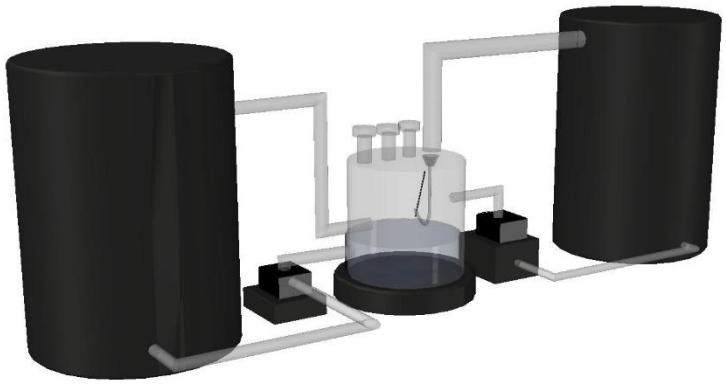

Figure 4. The simulated setup used for modelling iodine-metal interactions.

2.1.3. Chemistry of organic iodides

In 2010 the focus was shifted towards organic chemistry of iodine in accident scenarios. Severe accident-related organic iodide research has been carried out for decades and the concern about volatile iodine species was recognized already before any major accidents[12]–[15]. First extensive report, WASH-1233 by Postma and Zavadoski (1972)[16] presented data on measurement and formation of organic iodides. Another review on organic material and iodine interactions was published by Wren et al., (1999)[17] which presented, then current, results mainly on formation of organic iodides in the sump from dissolved organic solvents. Despite the wide range of experiments performed worldwide, organic iodine chemistry still is in the focus of severe accident research. The work performed at Chalmers including organic iodine chemistry started around 2010 although methyl iodide had already been part of some experiments earlier. The work from 2010 onwards really focused on the formation and management of not only methyl iodide but also other organic iodide species. In addition, the work included characterization of paint used in nuclear facilities, mainly Swedish power plants[18]. Moreover, this work was also recognized in an extensive review on iodine-paint interactions as part of the Severe Accident Research Network (SARNET)[19].

The main results for organic iodides relate to the formation of various organic iodides from paint solvents in liquid phase. Experiments were performed using paint solvents identified in previous studies: texanol ester alcohol and Stoddard solvent (white spirit). Samples were prepared by dissolving 1 g of iodine in 15 ml of paint solvent and exposed to gamma irradiation in a ^{60}Co Gammacell 220 between 1.7 and 3700 kGy at a dose rate 14 kGy/h. Samples were analyzed for iodine concentration (UV/VIS) and speciation (GC-MS)[20].

The main species formed from dissolved iodine and texanol ester was found to be isopropyl iodide. The formation of isopropyl iodide as a function of irradiation dose is presented in Figure 5. The white spirit solution also produced organic iodides that were identified as various alkyl iodides (methyl, ethyl, propyl butyl iodide). However, the amounts were too low for a reliable quantification. The concentration of iodine and the consumption with different paint solvents could be measured and it was observed that majority of iodine was consumed and likely converted into organic iodides. These results showed that methyl iodide is not the only organic iodine species potentially formed during a severe accident and raised the concerns in the uncertainties of the behavior and management of volatile iodine.

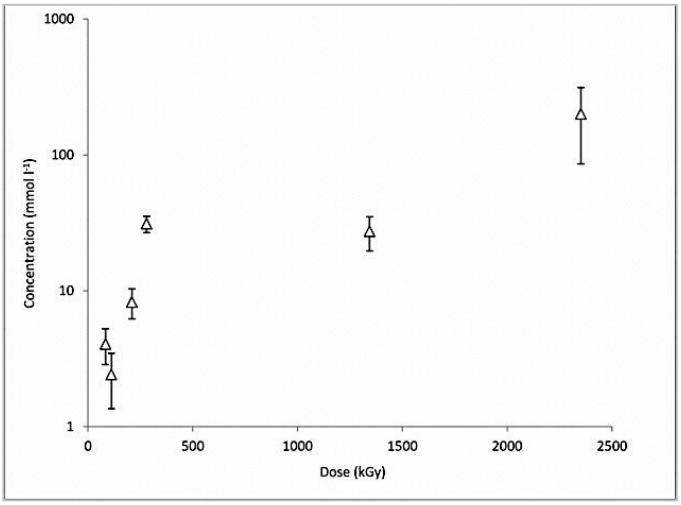

Figure 5. Formation of isopropyl iodide during the irradiation (14 kGy/h) of a texanol-elemental iodine solution under gamma irradiation[20]**.**

2.2. Ruthenium

To step away from the mainstream severe accident research topics and to also give the modelling community time to implement the new results, one of the more understudied radionuclides, ruthenium, was chosen. Although ruthenium is not as volatile as iodine, cesium or tellurium, significant activities have been released during the two major accidents. The ^{103}Ru and ^{106}Ru releases during the Chernobyl accident are both comparable to those of iodine and cesium[21]. The research involving ruthenium is mainly focusing on the different oxides of ruthenium, since metallic ruthenium is only moderately volatile but in case of an air ingress, different ruthenium oxides can form, which are more volatile than the elemental species. Before Chalmers research, various experiments studying volatilization of ruthenium oxides in oxidizing atmospheres had been performed. One of the major ones was PHEBUS-RUSET program in 2002. Research at Chalmers focused on the ruthenium transport and behavior in the containment, mainly deposition and possible re-volatilization of ruthenium oxides. In addition, VTT in Finland was also active in ruthenium SA research, which resulted in collaboration between Chalmers and VTT on a study of ruthenium transport in the reactor coolant system[22]. The following sections present the main results from ruthenium research conducted at Chalmers.

2.2.1. RuO_4 interactions with surfaces

One of the containment related ruthenium studies was the interactions of ruthenium tetroxide, RuO_4 with paint and metal surfaces[23]. The experiment was meant to provide insight into the nature of RuO_4 deposition and to identify the deposited ruthenium species. This study provided information on the ruthenium behavior in the containment and was then used later for possible re-volatilization experiments.

The experimental setup was constructed from four sections: production of RuO_4 from $RuCl_3$ with $K_2S_2O_8$ and ^{103}Ru tracer, deposition of RuO_4 and trapping of excess RuO_4. The produced RuO_4 was flushed with nitrogen gas to the reaction vessel where the respective surface, paint, zinc, copper or aluminum, was placed. The excess RuO_4 was trapped by a hydroxide solution filled flask. Surface samples were analyzed with various surface analysis techniques (SEM/EDS, ESCA, EXAFS) to determine the speciation of the deposited ruthenium compounds.

The results for RuO_4 deposition on different surfaces are collected in Table I. In terms of the nature of the deposits, it was found that ruthenium was deposited as RuO_2, and the outer layer was hydrated forming ruthenium oxy-hydroxide species. This led to differences in speciation of the hydrolyzed outer layer species compared to the more crystallized RuO_2 in the bulk. The amount of deposition on the metal surfaces seemed to vary. The highest deposition was on aluminum and the lowers on zinc and copper in dry atmosphere. Proposed explanation was the differences between the oxide layers formed on the surface of the metals and due to high oxygen density of the aluminum surface, it is more attractive to RuO_4.

Table I. Deposition of ruthenium in µg/cm2 on metallic surfaces in dry and humid atmosphere.

Dry atmosphere			Humid atmosphere		
Zinc	**Copper**	**Aluminum**	**Zinc**	**Copper**	**Aluminum**
2.7 ± 0.5	9.4 ± 0.2	103.3 ± 0.6	15.3 ± 0.3	18.0 ± 0.3	31.6 ± 0.6
0.76 ± 0.02	0.4 ± 0.1	86.8 ± 0.7	13.2 ± 0.2	12.1 ± 0.2	24.8 ± 0.5
2.2 ± 0.4	2.5 ± 0.5	98.4 ± 0.6	18.5 ± 0.3	19.2 ± 0.4	38.9 ± 0.7

2.2.2. Re-vaporization of ruthenium deposits

Another ruthenium related work was the study on possible re-vaporization of ruthenium deposits in the containment. This was a continuation to the previous deposition experiments. The aim was to investigate whether gamma irradiation can oxidize RuO_2 to the volatile RuO_4 form via air radiolysis products. Same metal and paint surfaces were used and the deposition prior to irradiation was performed in the same way as described in Section 2.2.1. The samples were irradiated with ^{60}Co gammacell 220 giving a dose rate of around 11 kGy/h up to 264 kGy and this was done in both dry and humid atmospheres. Quantification of the vaporized ruthenium was measured using ^{103}Ru radiotracer.

Results for re-vaporization of ruthenium from painted surfaces are presented in Figure 6. In dry atmosphere, no vaporization was observed indicating that the amount of air radiolysis products is not sufficient in oxidizing ruthenium. On contrary, in humid atmosphere, vaporization was observed which suggests that oxidizing water radiolysis products are sufficient to potentially oxidize RuO_2 to volatile RuO_4. In terms of metal surface samples, strong corrosion was observed that also led to loosely held ruthenium deposits and some of the deposition fell off. The highest loss of ruthenium was from zinc surface, but it could not be determined accurately how much was lost due to re-vaporization and the fraction physically falling off.

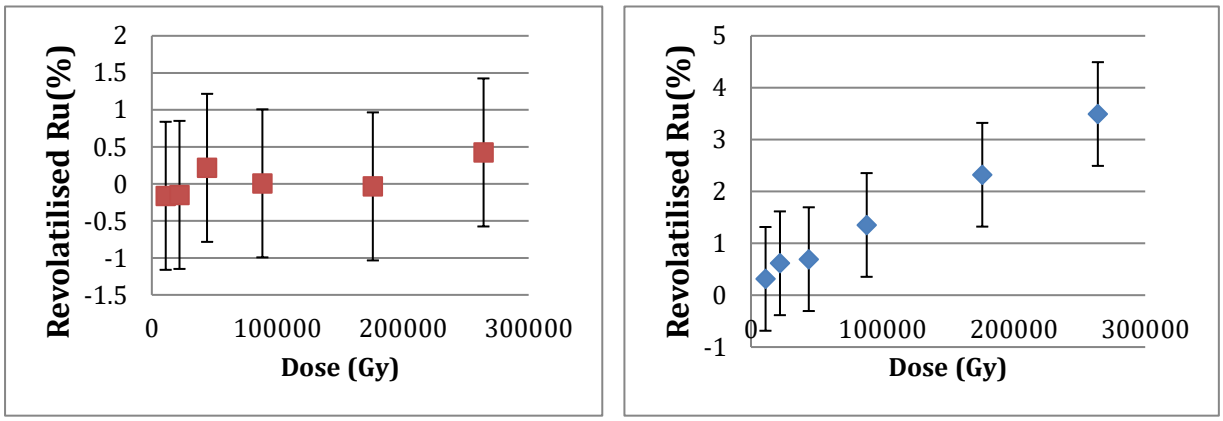

Figure 6. Re-vaporization of RuO_4 in dry (left) and humid (right) atmospheres [24].

2.3. Tellurium

To continue studying the potentially important nuclides traditionally receiving less attention in severe accident research, tellurium was selected. Moreover, tellurium has been the center of SA research at Chalmers in the past years. Tellurium is categorized as a volatile fission product like cesium and iodine. In fact, the tellurium releases from the major accidents are comparable to those of iodine and cesium. However, comparing the tellurium SA chemistry to that of iodine or cesium, the data is scarce. Previous studies have focused on tellurium behavior in the fuel and its release from the core[25], interactions with the cladding[26] and speciation in various atmospheres[27]. However, when searching for data on tellurium behavior in the containment the information is lacking. Therefore, Chalmers researchers have taken means to fill in the gaps and provide this information through bench-scale experiments in containment relevant conditions. Experiments include studies on tellurium transport in the reactor coolant system (RCS), efficiency of the containment spray system on tellurium species, behavior of tellurium in the sump and formation of organic tellurides from aqueous solution. All these topics will be introduced briefly in the following sections.

2.3.1. Transport of tellurium in the reactor coolant system (RCS)

Before entering the containment building, the released fission products will be transported through the RCS. This phenomenon was studied for tellurium as a collaboration project with VTT Research Center of Finland and University of Oslo[26]. In addition, Nuclear Research Center UJV Řež in Czech Republic had a part in the analysis process of the samples. The experimental facility is presented in Figure 7 which consisted of two tubular furnaces, one where metallic tellurium precursor was heated to the set point of 810 K before flushed to the second furnace that acted as the reaction zone set to 1500 K. Experiments were conducted in various atmospheres and conditions which are all complied and presented in Table II.

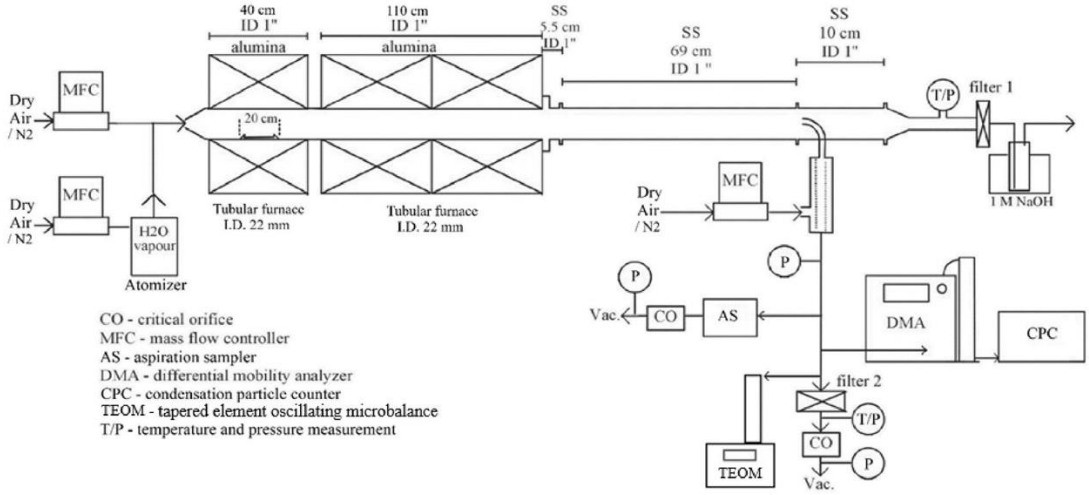

Figure 7. Schematic of the experimental facility used in tellurium transport experiments[28]**.**

Table II. Experimental matrix in tellurium transport experiments.

Condition	Experiment	Gas	Temperature [K]	Humidity [ppmV]	Caesium iodide [M]
Oxidizing	1	Air	1500	Dry	Dry
	2	Air	1500	$2.1 \cdot 10^4$	
	3	Air	1500	$2.1 \cdot 10^4$	0.15
Inert	4	Nitrogen	1500	Dry	
	5	Nitrogen	1500	$2.1 \cdot 10^4$	
	6	Nitrogen	1500	$2.1 \cdot 10^4$	0.15

The main results of the tellurium transport experiments are collected in Figure 8. There, the fractions of tellurium found on the filters and liquid traps are presented. The highest transport of tellurium was in oxidizing conditions and especially in humid oxidizing atmosphere. This is supported by previous work related on tellurium volatility which suggests that humidity influences the volatilization. In inert atmosphere, the tellurium transport was significantly lower. Almost all the transported tellurium was in aerosol form and found on the filters and only a very small fraction if any was measured in the liquid traps. The tellurium found in the traps was concluded rather be aerosols leaking from the side of the filter than gaseous tellurium species.

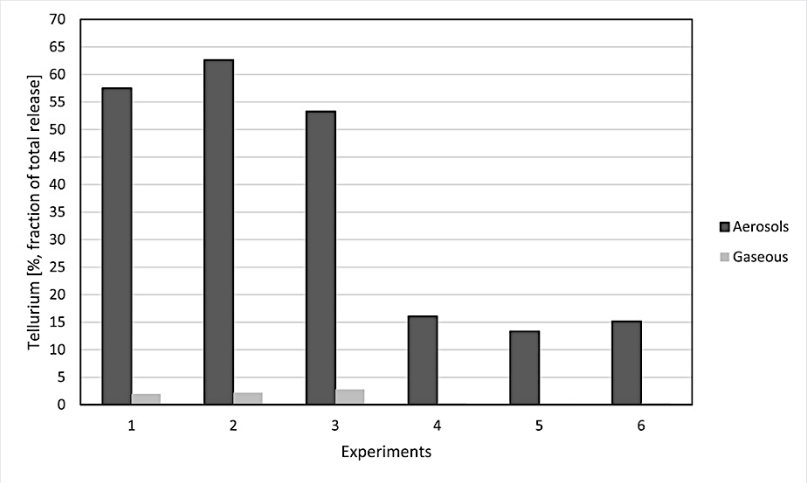

Figure 8. The transported aerosol and gaseous tellurium fractions[28]**.**

2.3.2. Tellurium removal by the containment spray system (CSS)

Although majority of the work performed at Chalmers over the years has been bench scale experiments focusing on detailed phenomena, more applied work related to tellurium source term and especially management has been published. This was the study on the effectiveness of the containment spray system (CSS)[29]. The was a second part of the collaboration between Chalmers, VTT Technical Research Center of Finland and University of Oslo.

The aim of the work was to study the efficiency of the CSS with changing parameters such as the composition of the spray solution, atmosphere, tellurium precursor and effect of cesium iodide. The experimental facility contained two sections: a furnace where the respective tellurium precursor was vaporized and the containment model unit with a spray nozzle on top. The varying parameters, tellurium precursor, temperature, atmosphere, humidity, are compiled and presented in Table III. In addition to these parameters, three different spray solutions were used: **I** 18 MΩ deionized water, **II.** Alkaline borate solution (0.23 M H_3BO_3, 0.15 M NaOH) **III.** Alkaline borate solution with sodium thiosulphate (0.23 M H_3BO_3, 0.15 M NaOH and 0.064 M $Na_2S_2O_3$). The pH of both chemical spray solutions was around 9.3, whereas pH was close to neutral for MilliQ water.

Table III. Experimental matrix used in the spray experiments.

Experiment [#]	Precursor	Temperature [K]	Atmosphere	Humidity[a]	CsI[b]
1	TeO_2	1150	Air	No	No
2	TeO_2	1150	Air	Yes	No
3	TeO_2	1150	Air	Yes	Yes
4	Te	810	Air	No	No
5	Te	810	Air	Yes	No
6	Te	810	Air	Yes	Yes
7	Te	810	Nitrogen	No	No
8	Te	810	Nitrogen	Yes	No
9	Te	810	Nitrogen	Yes	Yes

[a] Humidity content of the gas flow that entered the spray chamber was 21000 ppmV
[b] CsI content of the atomizer supply bottle was 0.15

The spray efficiency results are presented in Figure 9. As observed, overall, the removal efficiencies were relatively high, up to 99 % with three exceptions. Firstly, Experiment 5 with tellurium in humid air is not in line with the other experiments. In addition to the removal efficiency of Exp. 5, the overall mass of tellurium transported was significantly lower than in all the other experiments and therefore, experimental error was suspected, and the removal efficiency results should be taken with hesitation. The removal efficiency was lowest in nitrogen atmosphere. However, CsI in the flow increased the removal efficiency which was concluded to be due CsI particles colliding and coagulating with tellurium aerosols. In all experiments, there was a slight increase in the removal from water to chemical spray, however, we suspect that this was not due to chemical reactions but more related to physical removal processes.

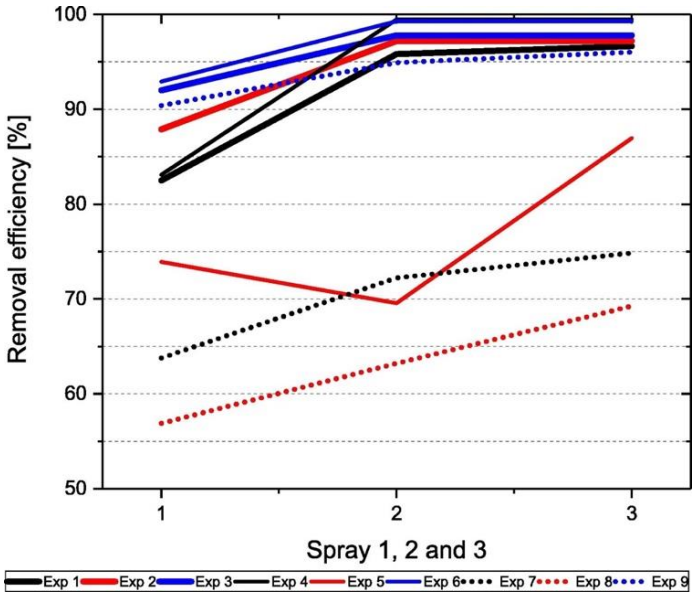

Figure 9. Removal efficiencies for the tellurium aerosols in Experiments 1 to 9. Spray 1: MilliQ water, Spray 2: Alkaline borate buffer, Spray 3: Alkaline borate buffer with sodium thiosulphate[29]**.**

2.3.3. Tellurium behavior in the sump

After being flushed by the containment spray system, tellurium species end up on the bottom of the containment also called the sump. The sump is a complex mix of compounds origination from the spray system, pH control and primary circuit. In addition, the sump can consist of various dissolved species and released radionuclides. All this makes the sump a very complicated matrix and the reactions to consider are endless. The complexity of the sump coupled with the varying chemistry of tellurium makes it nearly impossible to predict the behavior of tellurium in the sump during an accident. Therefore, this was one of the studies conducted at Chalmers. The aim was to investigate the behavior of tellurium dioxide in sump conditions under gamma irradiation.

The experiments were done by comparing two different solutions: alkaline borate solution with and without sodium thiosulphate. Samples consisting of one of the solutions and TeO_2 were either irradiated or kept in a heating cabinet in the same temperature as the gammacell 220. Samples were irradiated up to 1.2 MGy and analyzed for tellurium concentration and speciation. Here, the main results are presented graphically in Figure 10.

Two phenomena were observed: in alkaline borate solution under gamma irradiation, oxidation of TeO_2 occurred to Te(VI) species. This was confirmed by speciation analysis and supported by increase in concentration of Te with increasing dose due to the higher solubility of Te(VI) compared to Te(IV)O_2. In comparison, when sodium thiosulphate was present, TeO_2 reduced to elemental tellurium, also confirmed by speciation analysis. Elemental Te is very insoluble in aqueous solution and therefore, the concentration of tellurium decreased in these samples. All the reactions were generated by water radiolysis products. Due to the complex chemistry of tellurium, it can reduce with both oxidizing and reducing species and therefore appear as different species depending on the prevailing conditions. In the absence of thiosulphate, TeO_2 can react with oxidizing radicals whereas in the presence of it, the oxidizing radicals are scavenged, and tellurium reacts with reducing species to form elemental tellurium. These results provide information on the speciation of tellurium in the sump and lays a foundation for further studies on tellurium behavior in accident conditions by showing how tellurium can adapt different speciation depending on the surroundings and therefore be either in insoluble form or in the solution and consequently react further with other available species.

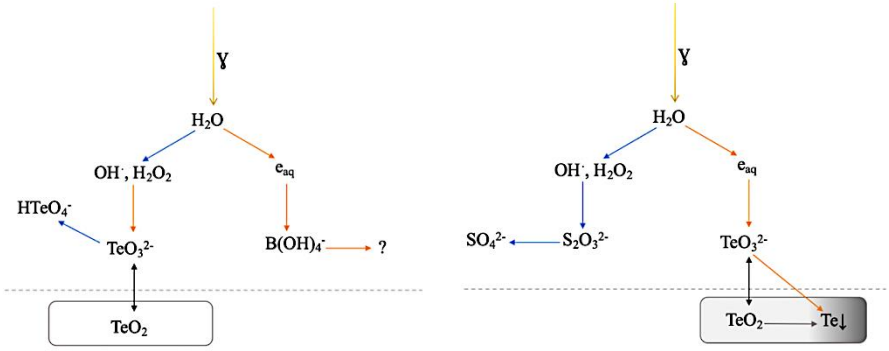

Figure 10. Graphical presentation of tellurium behavior in the sump[30]**.**

2.3.4. Organic tellurium chemistry

The most recent work has focused on the organic tellurium chemistry. The basis of investigating organic telluride formation and behavior lies on the concern of their volatility and the fact that other fission products like iodine is known to form volatile organic species. As far as we know, there has not been any extensive study related to organic tellurium chemistry in severe accident conditions and the mentions of organic tellurium species in severe accident literature has been using analogs from other disciplines.

Organic telluride experiments performed at Chalmers investigated the potential formation of volatile species in aqueous phase in the presence of various paint solvent, and under gamma irradiation. The aim was to investigate whether tellurium dissolved in the sump will react with organic radicals to form volatile compounds. This is, as far as the author is aware, the first ever study of organic telluride formation from the containment sump. This study is the first stage of investigating organic tellurium chemistry, the quantification and consequently determination of the relevance will be part of the future work.

The experiments were conducted by preparing samples containing tellurium dioxide and respective paint solvent in alkaline borate solution. The paint solvents chosen for this work were texanol ester alcohol, methyl isobutyl ketone (MIBK) and toluene, all of which are compounds found in common

paint used in nuclear facilities. In addition, these solvents have been used in several severe accident-related experiments in the past studying radiolytic formation of organic iodides[20], [31].
What should be highlighted is the evidence of organic telluride formation from paint solvents. The results did show evidence of the formation and the main species were identified as various organic tellurides. Two of the used paint solvents, texanol and MIBK produced organic tellurides which were identified as diisopropyl telluride and methyl isobutyl telluride, respectively. The analysis and identification were done by gas chromatography mass spectrometry (GC-MS) and the mass spectrum of diisopropyl telluride formed from texanol and TeO_2 under gamma radiation is presented in Figure 11. The evidence of the formation of organic tellurides initially justifies the importance of further studying the volatile tellurium species. The need for quantification and effectiveness of safety measures needs to be investigated to be able to determine the harmfulness and relevance of organic tellurides in accident conditions.

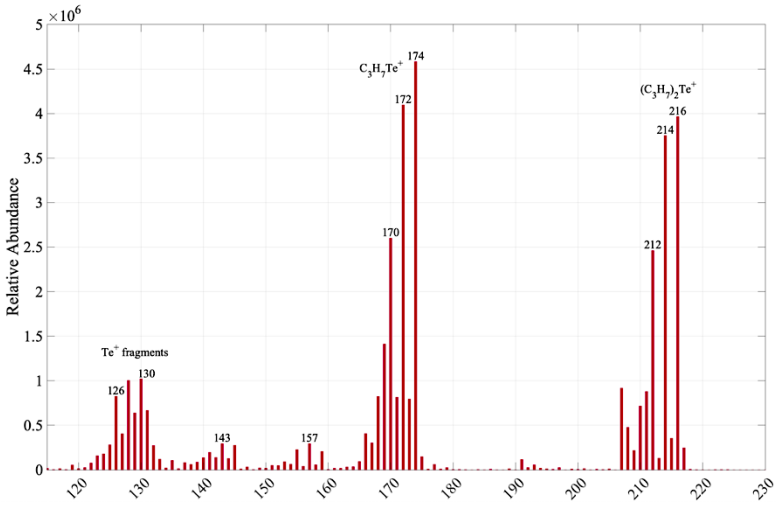

Figure 11. Mass spectrum of diisopropyl telluride formed from irradiated solution of texanol ester and tellurium dioxide

3. SUMMARY AND PROSPECT

The work done at the severe accident group at Chalmers has provided valuable information on the source term of iodine, ruthenium and tellurium. From fundamental bench-scale experiments to international collaborations, Chalmers has been and still is active on the field. Results presented here aim to give an overview of the work performed at Chalmers during the past decades. More detailed description and results can be found in scientific publications of the respective topics. The goal for the future is to continue the quality research but also step closer towards applying the experimental results to severe accident codes and collaborate with international experts on this discipline. This will strengthen the overall source term assessments and improve the quality of data produced at Chalmers University of Technology.

ACKNOWLEDGEMENT

We would like to thank Accident Phenomena Risk Importance (APRI), Swedish Radiation Protection Authority (SSM) and Nordic Nuclear Safety Research (NKS) for supporting the work throughout the years.

REFERENCES

1. U.S. Nuclear Regulatory Commission, "Reactor safety study: An assessment of accident risks in U.S. commercial nuclear power plants (WASH-1400 Appendices III and IV)," (1975).
2. P. March and B. Simondi-Teisseire, "Overview of the facility and experiments performed in Phébus FP," *Ann. Nucl. Energy*, vol. **61**, pp. 11–22, (2013).
3. M. Laurie, P. March, B. Simondi-Teisseire, and F. Payot, "Containment behaviour in Phébus FP," *Ann. Nucl. Energy*, vol. **60**, pp. 15–27, (2013).
4. Y. Pontillon, G. Ducros, and P. P. Malgouyres, "Behaviour of fission products under severe PWR accident conditions VERCORS experimental programme - Part 1: General description of the programme," *Nucl. Eng. Des.*, vol. **240**(7), pp. 1843–1852, (2010).
5. OECD/NEA, "Aerosol and Iodine Issues, and Hydrogen Mitigation under Accidental Conditions in Watercooled Reactors: Thermal-hydraulics, Hydrogen, Aerosols and Iodine (THAI-2) Project - Final Report," no. NEA/CSNI/R(2016)8, (2017).
6. G. A. Glowa, C. J. Moore, and J. M. Ball, "The main outcomes of the OECD Behaviour of Iodine (BIP) Project," *Ann. Nucl. Energy*, vol. **61**, pp. 179–189, (2013).
7. Clément, Bernard, Laurent Cantrel, Gérard Ducros, Friedhelm Funke, L. Herranz, Adolf Rydl, Gunter Weber, and Clara Wren. State of the art report on iodine chemistry. No. NEA-CSNI-R--2007-01. OECD, (2007).
8. Allelein, Hans-Josef, Ari Auvinen, Joanne Ball, Salih Güntay, L. Enrique Herranz, Akihide Hidaka, Alain V. Jones, Martin Kissane, Dana Powers, and Gunter Weber. "State of the art report on nuclear aerosols." OECD/NEA,(2009).
9. K. Johansson, "RAMA Final report January 1985". No. RAMA--85-2. Swedish Nuclear Power Inspectorate, (1985).
10. H. Glänneskog, Y. Albinsson, J. O. Liljenzin, and G. Skarnemark, "Apparatus for on-line measurements of iodine species concentration in aqueous and gaseous phases," *Nucl. Instruments Methods Phys. Res. Sect. A Accel. Spectrometers, Detect. Assoc. Equip.*, vol. **498**(1–3), pp. 517–521, (2003).
11. H. Glänneskog, "Interactions of I2 and CH3I with reactive metals under BWR severe-accident conditions," *Nucl. Eng. Des.*, vol. **227**(3), pp. 323–329, (2004).
12. R. K. Hilliard, A. K. Postma, J. D. McCormack, and L. F. Coleman, "Removal of Iodine and Particles by Sprays in the Containment Systems Experiment," *Nucl. Technol.*, vol. **10**(4), pp. 499–519, (1971).
13. A. Habersbergerová and B. Bartoníček, "Radiolysis of iodine compounds in model systems of PWR," *Radiat. Phys. Chem.*, vol. **21**(3), pp. 289–293, (1983).
14. D. O. Campbell, A. P. Malinauskas, and W. R. Stratton, "The Chemical Behavior of Fission Product Iodine in Light Water Reactor Accidents," *Nucl. Technol.*, vol. **53**(2), pp. 111–119, (1981).
15. R. J. Lemire, J. Paquette, D. F. Torgerson, D. J. Wren, and J. W. Fletcher, "Assessment of Iodine Behaviour in Reactor Containment Buildings from a Chemical Perspective," Atomic Energy of Canada Ltd., (1981).
16. A. K. Postma and R. W. Zavadoski, "Review of Organic Iodide Formation under Accident Conditions in Water-Cooled Reactors," vol. **1233**, p. 72, (1972).
17. J. C. Wren, J. M. Ball, G. A. Glowa, and J. Clara Wren, "The Interaction of Iodine with Organic Material in Containment," *Nucl. Technol.*, vol. **125**(3), pp. 337–362, (1999).
18. S. Tietze, M. R. S. J. Foreman, C. H. Ekberg, and B. E. Van Dongen, "Identification of the chemical inventory of different paint types applied in nuclear facilities," *J. Radioanal. Nucl. Chem.*, vol. **295**(3), pp. 1981–1999, (2013).
19. L. Bosland *et al.*, "Iodine–paint interactions during nuclear reactor severe accidents," *Ann. Nucl. Energy*, vol. **74**, no. C, pp. 184–199, (2014).
20. S. Tietze, M. RStJ Foreman, and C. H. Ekberg, "Formation of organic iodides from containment paint ingredients caused by gamma irradiation," *J. Nucl. Sci. Technol.*, vol. **50**(7), pp. 689–694, (2013).

21. UNSCEAR, "SOURCES AND EFFECTS OF IONIZING RADIATION (annex D)," United Nations, New York, (2008).
22. I. Kajan, T. Kärkelä, A. Auvinen, and C. Ekberg, "Effect of nitrogen compounds on transport of ruthenium through the RCS," *J. Radioanal. Nucl. Chem.*, vol. **311**(3), pp. 2097–2109, (20179.
23. I. Kajan, H. Lasseson, I. Persson, and C. Ekberg, "Interaction of ruthenium tetroxide with surfaces of nuclear reactor containment building," *J. Nucl. Sci. Technol.*, vol. **53**(9), pp. 1397–1408, (2016).
24. I. Kajan, H. Glänneskog, J. Thorn, and C. Ekberg, "Impact of gamma radiation on the ruthenium deposited materials in a nuclear power plant," *J. Radioanal. Nucl. Chem.*, vol. **309**(2), pp. 743–749, (2016).
25. R. De Boer and E. H. P. Cordfunke, "The chemical form of fission product tellurium during reactor accident conditions," *J. Nucl. Mater.*, vol. **240**(2), pp. 124–130, (1997).
26. R. De Boer and E. H. P. Cordfunke, "Reaction of tellurium with Zircaloy-4," *J. Nucl. Mater.*, vol. **223**(2), pp. 103–108, (1995).
27. A. P. Malinauskas, J. W. Gooch Jr, J. D. Redman, and J. W. Gooch, "The Interaction of Tellurium Dioxide and Water Vapor," *Nucl. Appl. Technol.*, vol. **8**(1), pp. 52–57, (1970).
28. F. Espegren *et al.*, "Tellurium transport in the RCS under conditions relevant for severe nuclear accidents," *Prog. Nucl. Energy*, vol. **139**, p. 103815, (2021).
29. T. Kärkelä, A. E. Pasi, F. Espegren, T. Sevón, U. Tapper, and C. Ekberg, "Tellurium retention by containment spray system," *Ann. Nucl. Energy*, vol. 164, p. 108622, Dec. 2021.
30. A.-E. Pasi, H. Glänneskog, M. R. S.-J. Foreman, and C. Ekberg, "Tellurium Behavior in the Containment Sump: Dissolution, Redox, and Radiolysis Effects," *Nucl. Technol.*, **207**(2), pp 217-227, (2020).
31. K. MORIYAMA *et al.*, "Experiments on the Release of Gaseous Iodine from Gamma-Irradiated Aqueous CsI Solution and Influence of Oxygen and Methyl Isobutyl Ketone (MIBK)," *J. Nucl. Sci. Technol.*, vol. **47**(3), pp. 229–237, (2010).

THE EVOLUTION OF SEVERE ACCIDENT RESEARCH AT CHALMERS UNIVERSITY OF TECHNOLOGY – STATE-OF-THE-ART

Anna-Elina Pasi
Chalmers University of Technology
Department of Chemistry and Chemical Engineering
Nuclear Chemistry
pasia@chalmers.se

Introduction

Severe nuclear reactor accident research at Chalmers has been active since around the mid 1990s, and focused mostly on the source term of various fission products. Since then, the research has been consistent and ever evolving. The researchers at Chalmers have focused mainly on three fission products: iodine, ruthenium and tellurium. Moreover, the phenomena studied have included both gas and liquid phases, different surfaces, temperatures and accident management systems. One of the main advantages at Chalmers has been the use of Gammacell220 ^{60}Co source which has enabled the investigation of the effect of ɣ-radiation on the chemistry of fission products. Results on especially re-volatilization of fission products via reactions with radiolysis products into more volatile species have been highly appreciated. In addition, we have started incorporating SA modelling of the chemical reactions into our work and the aim is to strengthen that through future collaborations.

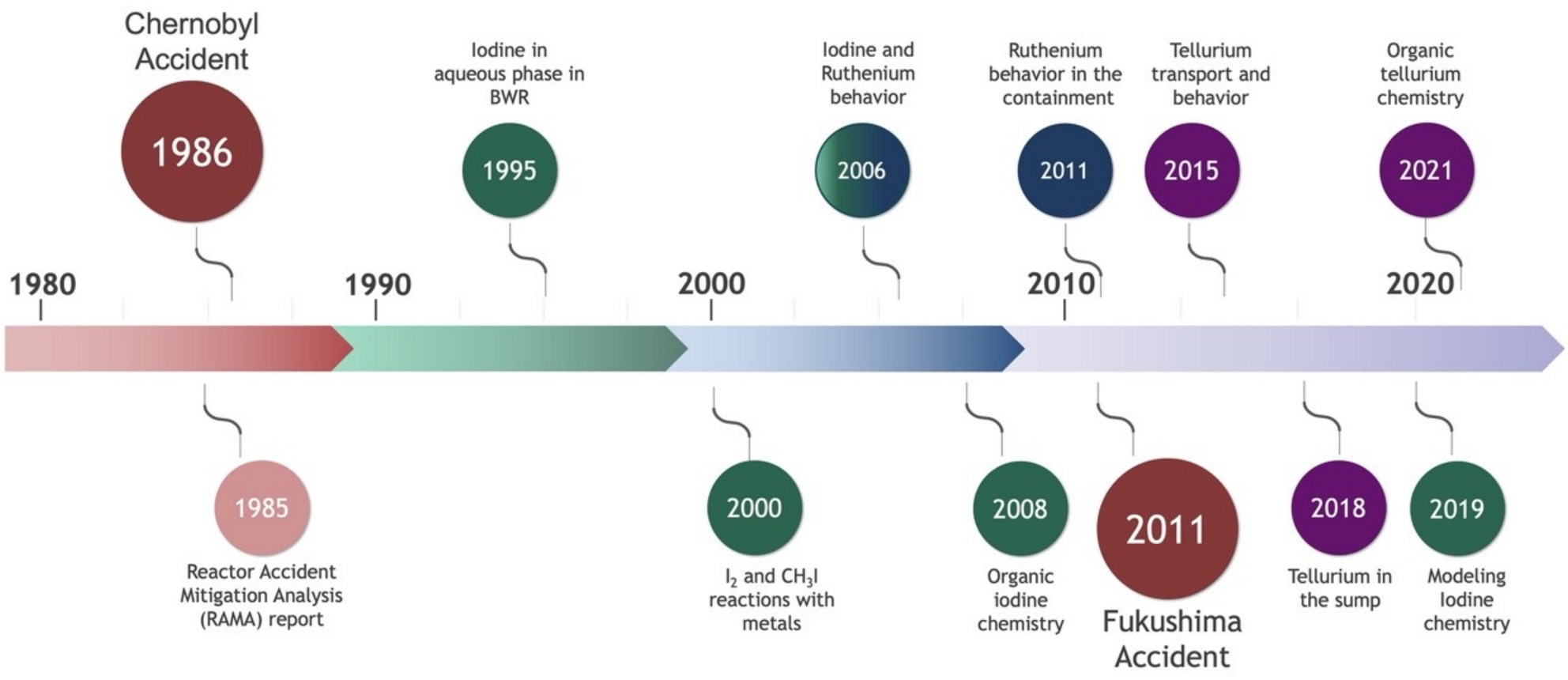

Iodine

- **Metal surface interactions**
  - I_2 adsorps on Al, Zn and Cu in gas phase, CH_3I less
  - Aqueous phase only on Cu
- **Formation and chemistry of organic iodides**
  - Various organic iodides formed from paint solvents (methyl, ethyl, propyl, butyl iodide)
- **Iodine modelling**
  - Metal-surface interactions were simulated
  - Successful in replicating the results but limited by chemical reactions available in the codes

Ruthenium

- **Interactions with surfaces**
  - Ru deposits on metal surfaces (Al, Zn, Cu) as RuO_2 or in hydrated form
- **Re-vaporization of Ru deposits under ɣ-irradiation**
  - No desorption in dry atmosphere→ Air radiolysis products not sufficient to oxidize RuO_2 to RuO_4
  - Re-vaporization occurs in humid atmosphere due to water radiolysis products

Tellurium

- **Transport through the RCS**
  - Atmosphere and humidity govern the volatility
- **Chemistry and behavior in the containment**
  - Radiolysis changes the speciation in the sump → Te solubility increases
  - Reacts with both Red and Ox radiolysis products
- **Organic tellurides from paint solvents**
  - Tellurium forms volatile organic species under ɣ-irradiation from texanol and MIBK
  - Concern about volatility, stability and management

10th European Review Meeting on Severe Accident Research
16-19th of May 2022
AkademieHotel Karlsruhe, Germany

ACKNOWLEDGEMENT:

Strål säkerhets myndigheten
Swedish Radiation Safety Authority

nks
Nordic nuclear safety research

APRI
Accident **P**henomena
Risk **I**mportance

VTT

Extending Capabilities of the ASTEC Severe Accident Code to Simulate Accident Sequences of Generic BWR4 Mark1

Onur Murat, Victor-Hugo Sanchez Espinoza
Karlsruhe Institute of Technology, Institute of Neutron Physics and Reactor Technology,
Hermann-von-Helmholtz-Platz 1, D-76344 Eggenstein-Leopoldshafen

onur.murat@partner.kit.edu
victor.sanchez@kit.edu

Abstract

Fukushima Daiichi severe accidents were the last major nuclear events which emphasizes the safety status of the nuclear power plants. Impact of the accidents made a necessity to reevaluate safety status of the current operating power plants to enhance the understanding of the accidents and making development and improvements of severe accident management guidelines. In order to assess the safety integrity of the power plants, severe accident codes such as ASTEC were employed to simulate the severe accident transients from initiating event to core degradation and release of radioactive materials.

Peach Bottom Unit-2 is BWR4 Mark-1 type nuclear power plant model was created by using ASTEC V2.2.b version. Selection of the plant based on the previous U.S.NRC severe accident risk assessment studies which includes Peach Bottom Unit-2 BWR type participant. Transient scenario short-term SBO was selected and assumption of all the heat removal systems and emergency core cooling systems (ECCS) were not available employed. Calculation time interval was until the pressure vessel failure.

The results showed that hydrogen generation consists of oxidation of fuel claddings, canisters and control structures which are in cylindrical geometry. Since the hydrogen production comes from boron carbide is in considerable amount and eutectic interactions also plays important role during early phase of severe accidents, definition of control structure in correct geometry with oxidation, chemical interaction and material relocation models needs to be performed. In order to fulfill that, development of integral BWR type plant models will be main goal of the work.

After the model implementations, investigation of severe accident management strategies with validated code version will be performed by aiming to avoid failure of pressure vessel or containment.

Keywords: BWR4, Peach Bottom, SBO, ASTEC

Karlsruhe Institute of Technology

Institute for Neutron Physics and Reactor Technology (INR)

Peach Bottom Unit-2 ASTEC V2.2.0.1 Model and Stationary Plant Results

Onur Murat*,[a]

[a]Karlsruhe Institute of Technology, Institute for Neutron Physics and Reactor Technology, Hermann-von-Helmholtz-Platz 1, D-76344 Eggenstein-Leopoldshafen, Germany

Motivation

- The severe accidents at Fukushima Daichii emphasized the importance of the SAMGs and preventive actions based on the severe accident tools prediction capabilities of the accident progression.
- In order to further extend the modeling capabilities of the European reference Accident Source Term Evaluation Code (ASTEC)[1] to simulate severe accident scenarios in BWR type reactors, a KIT/IRSN collaboration was established.

ASTEC Model of a generic Peach Bottom Unit-2 NPP

- The latest release of the ASTEC code (V2.2.0.1) employed.
- Peach Bottom Unit-2 type-1 initial fuels selected for core loading.
- Sub-channel structure BOX4SIDE (BWR-specific) placed to model the fuel channel boxes.

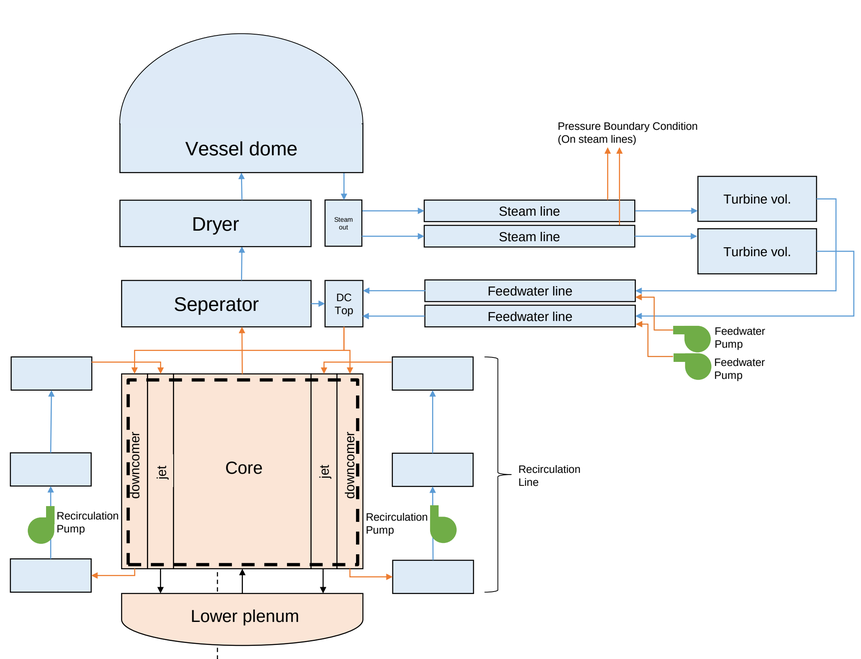

Peach Bottom Unit-2 ASTEC Model Water Cycle (ICARE+CESAR Domain)

Current Capabilities of ASTEC V2.2.0.1 related with BWR specific structures

	Geometry	Chemical Interaction	Mechanical Integrity	Molten Material Movement
Fuel Channel Box	BOX4SIDE rectangular structure is available	Oxidation, Eutectic Interactions	Loss of integrity available	Mass transfer to MAGMA and corium movement
Absorber Blade*	Only cylindrical definition is available	Oxidation, Eutectic Interactions	Loss of integrity available	Mass transfer to MAGMA and corium movement
Water Rods	Water rods can be defined inside BOX4SIDE (1 Structure allowed)	Oxidation, Eutectic Interactions	Loss of integrity available	Mass transfer to MAGMA and corium movement
Guide tubes (Lower plenum structures)	Cylindrical and Plate type structures	N/A	Only melting of the structure is available	N/A

**Absorber Blade chemical interactions, mechanical integrities and material movement definitions valid for cylindrical definition.*

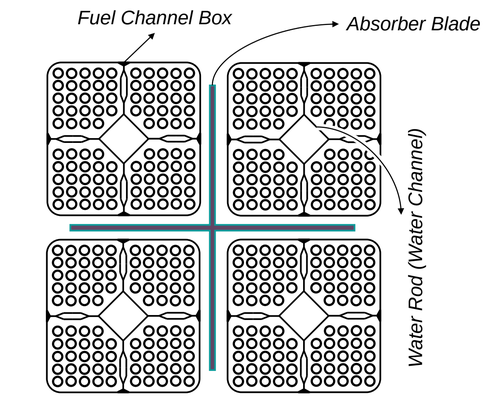

Example of BWR type fuel: SVEA-96 Optima-2

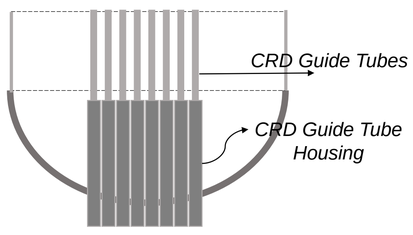

BWR Lower plenum with inner structures representation

Reference Design Parameters[2]		**ASTEC**
Core Power (MW)	3293	**3293**
Feedwater mass flow rate (kg/s)	1679.68	**1691.03**
Total mass flow rate (kg/s)	12914.78	**12903.35**
Core mass flow rate (kg/s)	11336.75	**11285.27**
Bypass mass flow rate (kg/s)	1578.03	**1618.08**
Steam mass flow rate (kg/s)	1685.98	**1691.03**
Steam temperature at dome (K)	559.29	**559.28**
Core outlet temperature (K)	560.48	**559.48**
Core inlet temperature (K)	548.53	**547.96**
Feedwater temperature (K)	464.32	**464.32**
Dom pressure (MPa)	7.033	**7.033**
Pressure drop over sep. and dryer (MPa)	0.103	**0.0156**
Core outlet pressure (MPa)	7.1564	**7.051**
Bundle pressure drop (MPa)	0.081	**0.084**
Core inlet pressure (MPa)	7.3084	**7.135**
Core exit void fraction	0.65	**0.679**
Core avg. void fraction	0.304	**0.472**
RPV water level (m)	14.326	**14.9**

Outlook

- Simulation of a ST-SBO accident scenario including in-vessel and ex-vessel progression (Early figures presented on the right side).
- Source term evaluation and analysis of the fission product transport through vessel and containment domain including enviromental release.
- Analysis of the performance of the new BWR-specific ASTEC capabilities and related model implementation.

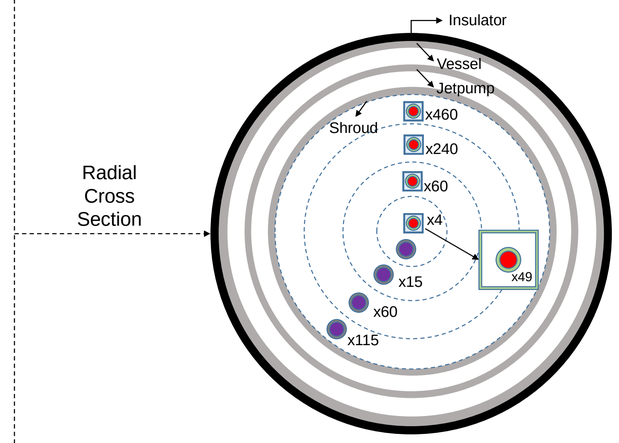

Peach Bottom Unit-2 ASTEC Model ICARE Module Core Radial Meshing

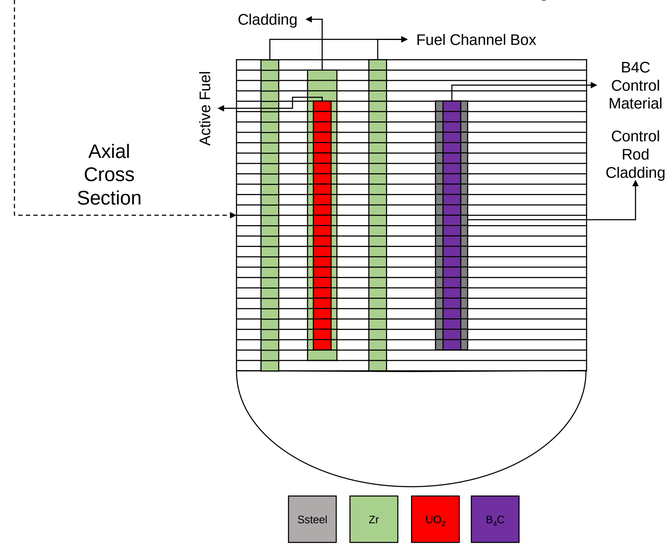

Peach Bottom Unit-2 ASTEC Model ICARE Module Core Axial Meshing

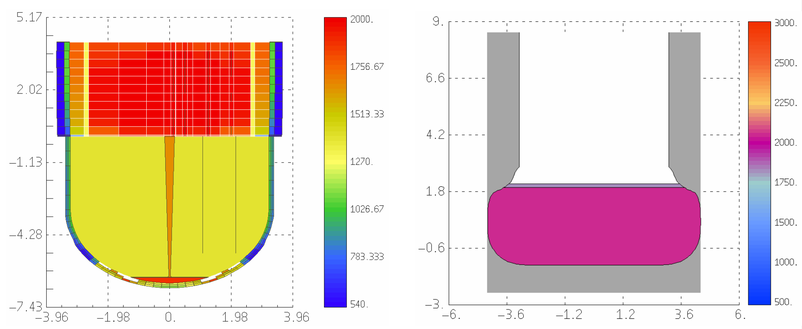

Peach Bottom Unit-2 ASTEC Model Core Degradation up to Vessel Failure and Cavity Ablation Figures resulted by SBO scenario

*Correspoding Author is funded by Republic of Turkey Ministry of National Education during his Ph.D. studies. E-Mail address: onur.murat@partner.kit.edu

[1] Chatelard, P., Belon, S., Bosland, L., Carenini, L., Coindreau, O., Cousin, F., Marchetto, C., Nowack, H., Piar, L., Chailan, L., 2016. Main modelling features of the ASTEC V2.1 major version. Ann. Nucl. Energy 93, 83-93. https://doi.org/10.1016/janucene.2015.12.026.

[2] Larsen, N., 1978. Core Design and Operating Data for Cycles 1 and 2 of Peach Bottom 2, NP-563, California: General Electric Company.

IVMR system. Analytical justification results for VVER-440/V-213

Mazurok Ph.D., Oleksandr
Energy Safety Group (ES Group), Kyiv, Ukraine

Abstract

To date, a set of "Post-Fukushima" modernizations has been implemented for Ukrainian NPPs with a VVER-440/V-213 reactor, which allow maintaining the integrity of the confinement for severe accidents (SA) with Station Blackout (SBO) for 72 hours. For example, implemented such modernizations as: In-Vessel Melt Retention (IVMR) system, hydrogen removal systems, etc.
The implementation of IVMR system for Rivne NPP Unit 1,2 with VVER-440/V-213 was carried out by the company VUEZ a.s., together with the company ES Group. ES Group has developed technical documentation and analytical justifications for IVMR system.
This poster provides information about analytical justification of an IVMR system for WWER-440/V-213 Rivne NPP Unit 1,2.
Modeling of a SA was performed with model for the codes MELCOR and RELAP5. The MELCOR model considers reactor coolant system, core, confinement, and all heat sources in the confinement (including PARs).
The results of the thermo-hydraulic simulation of the operation IVMR system in SA conditions showed that for SA with SBO, as well as with leaks of the primary of different diameters, the IVMR system performs its functions of maintaining the integrity of the RPV and heat dissipation of the residual energy generated inside the reactor. For all SA scenarios considered, the pressure in the confinement does not exceed the design limit of 2.5 kgf/cm² (abs). Due to the presence of passive hydrogen recombiners in confinement, the conditions for detonation of hydrogen are not formed during the operation of IVMR in confinement.
It should be added that after melt retention, there is a need for long-term cooling of the confinement. Based on the results of preliminary MELCOR calculations some conclusions have also been drawn in this regard.

Keywords: IVMR, confinement, VVER-440/V-213, safety system, SA

10TH EUROPEAN REVIEW MEETING ON SEVERE ACCIDENTS RESEARCH
ERMSAR 2022
MAY 16-19, 2022 — KARLSRUHE, GERMANY

IVMR system. Analytical justification results for VVER-440/V-213

Oleksandr Mazurok, Vadym Ivanov, Vyacheslav Bliednykh, Oleksandr Mykhailenko, Artem Tiurin
ES Group Europe s.r.o., Plzeň, Česká Republika
ES Group LLC, Kyiv, Ukraine

ENERGY SAFETY GROUP

Introduction

The implementation of in-vessel melt retention system (IVMR) for Rivne NPP Unit 1,2 with VVER-440/V-213 is carried out by the company VUEZ a.s., together with the company ES Group, which develops technical documentation and the necessary calculation-analytical justifications.
This poster presents the results of analytical justification for IVMR system for VVER-440/V-213 and estimate efficiency of Long-Term Containment Cooling System (LTCCS) concept .

In the framework of the calculation justification of the IVMR system for SA with station blackout (SBO) of the VVER-440 power unit, the simulation of processes in the reactor, in the reactor shaft, in the IVMR circulation loop, including the SG boxes, was performed.

For simulation, models developed based on the codes MELCOR, RELAP5, ANSYS were used. Thermohydraulic analysis was performed for SA scenarios with:

- SBO without primary's leaks;
- SBO with primary's leaks, including maximal primary's leak Dn500.

Strength analyzes for reactor pressure vessel (RPV) were performed under the conditions of the considered SA scenarios.

An assessment of the radiation consequences for SA in which the IVMR system operates were performed.

As part of the analysis of the consequences of various failures, an analysis has been made of the situation in which, during operation of the IVMR system, the reactor vessel is fail (hole in the reactor vessel). The calculation results showed that, provided there is no steam explosion:

- the corium resulting from the RPV is distributed among the service areas located below the RPV;
- corium is effectively cooled by coolant;
- the corium hardens, lingering on the service areas of the RPV, does not form a compact molten pool at the lower elevation of the reactor shaft room.

The results of simulation showed that the IVMR system, even in the case of a hypothetical RPV penetration, does not violate the integrity of the concrete reactor shaft.

The calculation results showed that the IVMR system performed its functions for all SA scenarios considered in the analysis.

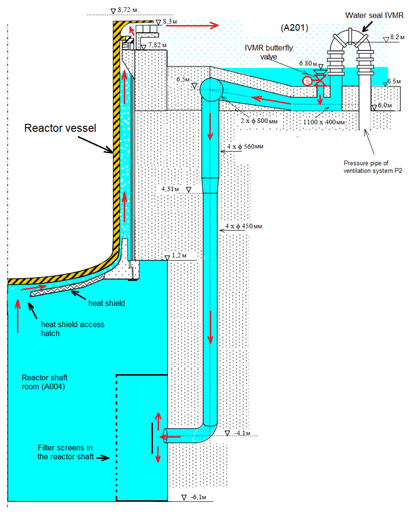

Schematic illustration of the IVMR circuit

The structural elements of the IVMR system implemented at the power unit as part of the project:

- The filling of reactor shaft room VVER-440 was carried out along the air ducts of the recirculation cooling system of the reactor shaft (P2). As part of the implementation of the IVMR system project, two electric actuator butterfly valves DN500 were installed in the SG boxes on the air ducts (P2).
- to prevent the flow of coolant (when filling the reactor shaft through the P2 air ducts) from the SG boxes to the reactor facility ventilation center, a hydraulic shutter is installed between the butterfly valve and the pressure of the P2 system;
- the butterfly valves installed at the +6.500 mark of the SG box are protected from debris and mechanical influences by the lattice structure;
- mesh filters are installed in the reactor shaft to hold fragments of thermal insulation and other small fragments of debris that appear during accidents with a coolant leak;
- in the heat shield of the RPV elliptical bottom, the project provides a hatch with a lever-float drive of passive action.

Methodological approach to the calculated justification

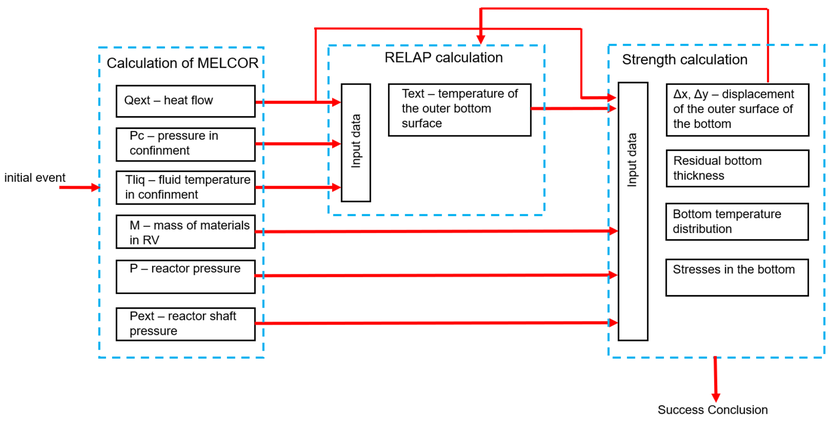

The general scheme of calculation analysis involves the consistent use of several calculation codes:

- General parameters of the primary circuit , the bottom of the RPV and confinement are determined in the calculation by the MELCOR code;
- Based on the results of the MELCOR analysis, the input data for the refinement calculation of the circulation loop model on the RELAP5 code are determined;
- Based on the RELAP5 and MELCOR calculations, the input data for the RPV Strength Analysis (ANSYS) is determined;
- Based on the strength analysis data, it is concluded that the RPV cooling process is successful;
- Initial data for assessing the radiation consequences of the implementation of IVMR are determined in the calculation of MELCOR.
- RELAP5 code model is a dedicated IVMR circulation loop. Separate use of the RELAP5 code is associated with wider capabilities for modeling flow hydraulics in the narrow RPV cooling gap;
- Strength analysis, in turn, gives RPV bottom movements that must be considered in the RELAP5 model;
- MELCOR and RELAP5 calculations are carried out sequentially, the calculation time is 3 days. The time between these calculations is agreed;
- When transmitting data on the heat flux, it is processed to bring it to the real elliptical geometry of the bottom and allowance for the safety factor. All data processing procedures are described in the report.

MELCOR model nodalization

The model structurally consists of the following main parts:

- primary circuit model;
- secondary circuit model;
- reactor core model;
- model the reactor bottom;
- model of tight barriers;
- model of the reactor core and the bottom area of the reactor;
- model of discharge of borated water from bubbler plates;
- model of the circulation loop IVMR;
- model of the concrete shaft of the reactor;
- model of PAR.

Validation of the MELCOR Model:

- application of code developer recommendations;
- stationary setting;
- confinement leak detection according to experimental data.

Nodalization of the IVMR circulation loop model for the MELCOR code

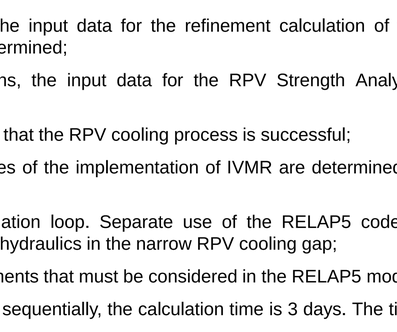

Core and bottom nodalization for the MELCOR code

Modeling assumptions with the MELCOR code

As part of the calculation justification of IVMR, severe accidents were simulated with a long SBO (up to 72 hours). The criterion for the initiation of the IVMR system is achieved when the criterion for the transition from design basis accident management instructions to SAMG procedures is reached - the temperature at the outlet of the core> 450 ° C.

The main goals of MELCOR simulation were:

- modeling processes in confinement during a severe accident;
- calculation of parameter changes along the IVMR path;
- confirmation of the adequacy of the water supply in confinement for 72 hours of a severe accident;
- obtaining initial data for thermal-hydraulic calculation of the IVMR path parameters using the RELAP5 code;
- obtaining initial data for strength analysis of RPV and assessment of radiation consequences.

Scenarios list (MELCOR):

- Scenario 1. Double-sided break 500 mm (cold leg) with SBO and a start of IVMR system on 1200s (MELCOR).
- Scenario 2. Primary leak 200 mm (cold leg) with SBO and a start of IVMR system on 1300s (MELCOR).
- Scenario 3. Primary leak 50 mm (cold leg) with SBO a start of IVMR system on 6500s (MELCOR).
- Scenario 4. SBO and a start of IVMR system on 45000s (MELCOR).
- Scenario 5. SBO with depressurization primary circuit by opening of pressurizer's safety valves, with the opening of primary emergency gas removal system valves, and a start of IVMR system on 45000s (MELCOR).
- Scenario 6. SBO, with depressurization primary circuit by opening of pressurizer's safety valves, with the opening of primary emergency gas removal system valves, and a start of IVMR system on 45000s and the subsequent closure of Pressurizer's safety valves for 49000s (MELCOR).
- Scenario 7. SBO, with the opening of primary emergency gas removal system valves and a start of IVMR system on 45000s (MELCOR).

RELAP5 model nodalization

The IVMR loop model consists of the following main parts:

- model of the pipeline for supplying water from the SG boxes;
- reactor shaft room model;
- model of cooling gap between thermal shield and bottom of RPV;
- model of the gap between the cylindrical part of the RPV and the thermal insulation of the reactor shaft.

The model is prepared for radial expansion options for the RPV bottom half-axis by 10, 12 and 15 mm

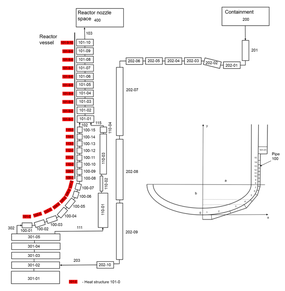

IVMR circulation line nodalization for RELAP5 model

Validation of the RELAP Model

Validation of the model in the CERES experiments (1:40 in azimuth, 1: 1 in elevations, one-dimensional cooling loop with the geometry of the VVER-440/ V-213 heat shield).
Considered:

- cold gaps size;
- narrower gaps size.

A good agreement between the temperature of the liquid, the wall and the period of oscillation of the parameters

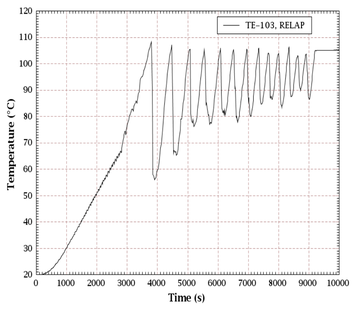

RELAP5 fluid temperature

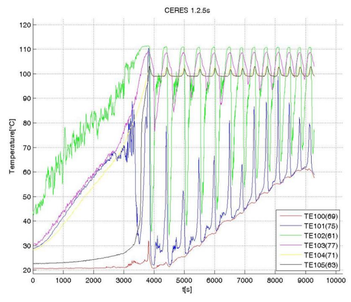

Liquid temperature according to the results of the experiment at the CERES installation

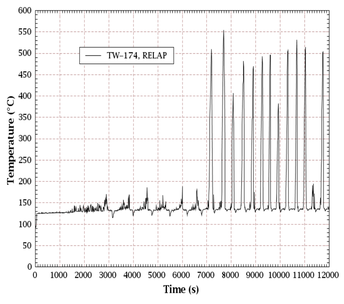

Wall temperature for RELAP5 narrow gap version

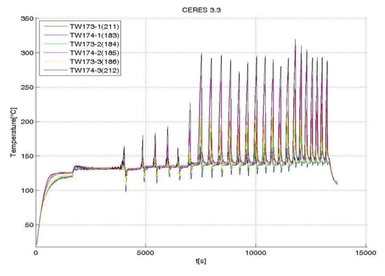

Wall temperature for the option with a narrow gap according to the results of the experiment at the CERES installation

Assumptions in RELAP Modeling
The RELAP calculations are consistent with the MELCOR calculations in time, when water begins to flow into the reactor shaft.
The main goals of RELAP computational modeling are:

- obtaining initial data on the temperature of the outer wall RPV for strength analysis of RPV;
- calculation of parameter changes along the IVMR path.

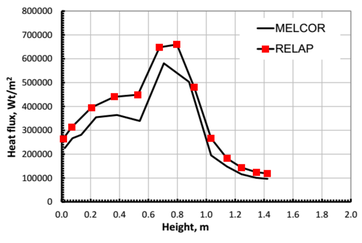

The dependence of the heat flux on the outer surface of the bottom RPV for a large leak with SBO (Scenario 1)

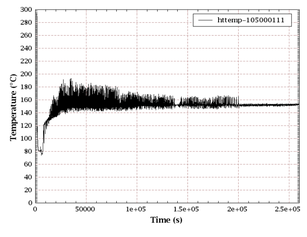

The temperature of the outer surface of the bottom RPV for hydraulic element 100-05 for a large leak with SBO (Scenario 1)

RPV Strength Analysis
The results of the strength calculations (ANSYS) indicate the fulfillment of the integrity conditions for all criteria: brittle strength, penetration of the wall, providing a gap between the RPV and the heat shield for reliable cooling, viscous plastic collapse.

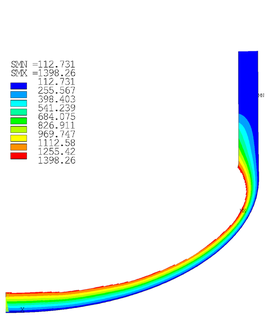

Distribution of the bottom temperature RPV for a large leak with blackout (Scenario 1), 42000 s

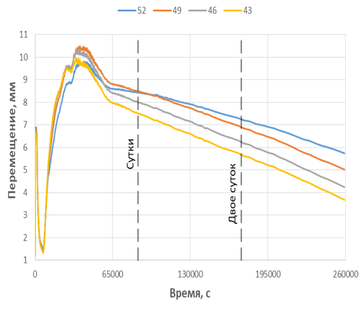

Moving the nodes of the elliptical bottom in the radial direction (Scenario 1)

Thermo-hydraulic simulation results

The results of the thermo-hydraulic simulation with IVMR system operation in SA conditions showed that for SA with SBO, as well as with superimposing leaks of the first circuit of different diameters, the system performs its functions of maintaining the integrity of the RPV and heat dissipation of the residual energy generated by inside the reactor. The coolant supply to ensure the operation of the natural circulation loop IVMR is enough for 72 hours. For all SA scenarios considered, the pressure in the confinement does not exceed the design limit of 2.5 kgf/cm² (abs). Due to the presence of passive hydrogen recombiners in confinement, the conditions for detonation of hydrogen are not formed during the operation of IVMR in confinement.

If a severe accident continues for a longer period (more then 72 hours), the Long-Term Containment Cooling System (LTCCS) required.

Causes: Example of MELCOR results for SA analysis of IVMR system for Rivne NPP Unit 2 - Scenario: "LOCA 50 mm (cold leg) with SBO".

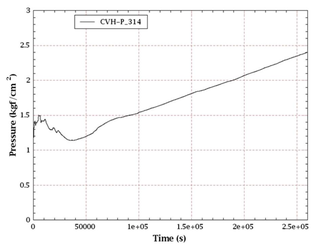

Pressure in confinement

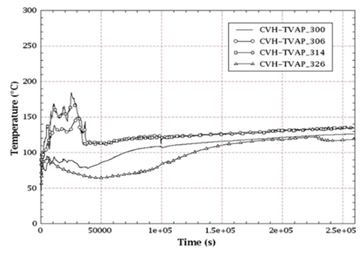

Temperature in confinement

The simulation of the IVMR system operation in the MELCOR code has shown that without long-term heat removal from containment the pressure are continuously increasing and after 72 hours can reach the design upper limit values (P=2.5 kgf/cm² (245 kPa) abs.).

Decay heat in the core of VVER-440/V-213

Calculations have shown that within 3 days without the operation of the LTCCS, the parameters in the confinements remain within acceptable limits.
After 2-3 days of severe accident the LTCCS heat exchanger capacity should be not less than the core power generated after 2÷3 days ~ 6 MW.

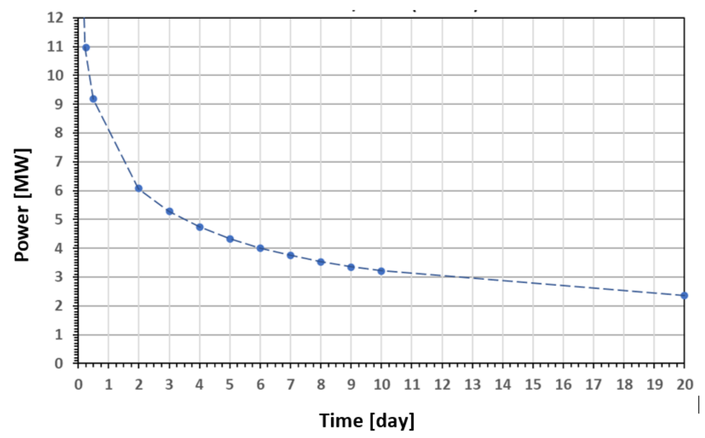

Main criteria of LTCCS:

Criteria for choosing the LTCCS concept:

- all elements of the system must work without electricity power supply;
- simplicity of design;
- reliability;
- use of the existing infrastructure at the NPP (water tanks, water channel, mobile pumping units, etc).

Estimated calculations for the LTCCS concept.

As a result of a qualitative analysis of various concepts, the LTCCS concept with active elements was selected for computational analysis.
LTCCS concept with active elements:

- turbine driven pumps;
- heat exchanger;
- spray nozzles;
- mobile pump.

The basis for this LTCCS concept is the simplicity and reliability of application in SA conditions. To remove heat from the containment to the final heat sink this concept requires only water source from a mobile pumping unit. The flow of water from an external mobile pumping unit drives the turbine of the sprinkler turbo-driven pump. At the same time, these water removes heat through the LTCCS heat exchanger and transports the heat to the final heat sink outside the power unit. This LTCCS has no electrical parts, switches or controls. Not affected by fire and flooding. LTCCS elements placed in confinement must be qualified for severe accident conditions.

Proposed LTCCS configuration for VVER-440/V-213

The system includes turbine driven pumps providing flow rate of 210 m³/h.
The cooling water from mobile outside source drives turbine driven pumps, cools spray water in the LTCCS heat exchanger and flows out of confainment.
Spray water is taken from the floor and pumped to the spray nozzles by turbine pumps.
The concept uses open circuit heat removal to the heat sink.

Example of LTCCS analysis results
The calculation is performed for the RNPP Unit 2 (VVER-440/B-213), model for MELCOR code, initial conditions for reactor - nominal power.
Scenario 1: «Severe accident with SBO, activation IVMR system start at 45000s after reactor shutdown, LTCCS start at 200,000 sec (55 hours)»:

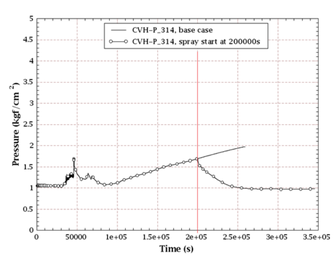

Pressure in the SG boxes (abs.)

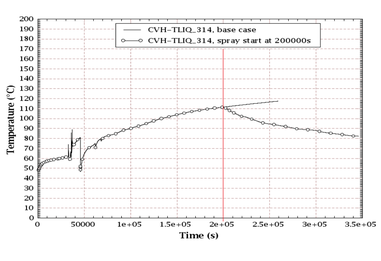

Coolant temperature in the of SG boxes

Based on the results of preliminary MELCOR calculations of the LTCCS operation, it was concluded that for VVER-440/V-213 power units operated in Ukraine, the use of LTCCS with a turbine-driven pumps allows maintaining a minimal pressure and temperature in the confinement. This ensures the integrity of the confinement VVER-440 in the long term and minimizing the release of radioactive into environment.

Recommendations for further improvement of the safety level of the power unit under SA conditions:

The introduction of an LTCCS for removing heat from confinement
The radiation effects of SA on the environment and the public can be reduced by maintaining a minimum pressure in confinement and sedimentation of radioactive aerosols. For this purpose, the most effective use of the sprinkler system. However, in the conditions with SBO and unpredictable damage to its infrastructure that caused SA, the use of a standard sprinkler system is likely to be problematic. In this regard, we recommend the introduction of an alternative confinement heat removal system at the power unit, which could remove the residual heat from confinement to the final absorber and maintain the confinement pressure at a level close to atmospheric pressure, without standard power supply and heat removal systems. The implementation of this modernization will reduce the leakage of radioactive gases and aerosols into the environment during SA by several times.

The NewPLINIUS project: France future prototypic corium experimental platform for severe accident R&D

C. Journeau

CEA, DES, IRESNE

DTN, SMTA, Severe Accident Experimental Laboratory, Cadarache,

F 13108 Saint-Paul-lez-Durance, France

christophe.journeau@cea.fr

Abstract

In order to improve the understanding and modelling of corium behavior, experiments are needed both for LWRs and Gen IV fast reactors. This has been stressed for instance in Europe by SNETP in its Identification of Research Areas in Response to the Fukushima Accident and by the SAFEST roadmaps.
Thanks to France Recovery plan, CEA is preparing a new experimental platform, newPLINIUS, to replace the aging current PLINIUS platform and extend experimental capabilities to more representative masses. This new versatile facility, shall be devoted to both water and sodium-cooled reactor severe accident experimental simulation.
It will mainly be composed of:

- A furnace able to melt 100 kg of corium including nuclear fuel (depleted UO2);
- An experimental hall devoted to Fuel Coolant Interaction tests with high energy X-ray imaging;
- A sodium circuit to conduct experiments with corium and sodium;
- A second experimental hall in which experiments can be carried out with up to 500 kg of uranium thermite;
- A steam quenching system,
- A corium load workshop, storage and service rooms.
- Two small scale facilities to study thermo-physical properties of corium and material interactions.

In the first years of the new platform a test section dedicated to corium jet fragmentation in sodium and one for ex-vessel water cooling of corium will be commissioned and used. Other advanced test section will be used on this versatile platform during the following decades.

ERMSAR 2022
MAY 16-19, 2022 — KARLSRUHE, GERMANY

THE NEW PLINIUS PROJECT: FRANCE FUTURE PROTOTYPIC CORIUM EXPERIMENTAL PLATFORM FOR SEVERE ACCIDENT R&D

Christophe JOURNEAU, Viviane BOUYER, Jules DELACROIX, Arthur DENOIX, Cyril MATTASSOGLIO, Pascal PILUSO, Pascal SAUVECANE, Christophe SUTEAU, Frédéric PAYOT, Fanny DERASSE
CEA, DES, IRESNE (Research Institute for Nuclear Systems for Low Carbon Energy Production)
Cadarache, F-13108 Saint-Paul-lez-Durance, France

CONTEXT

In order to improve the understanding and modelling of corium behavior, experiments are needed both for LWRs and Gen IV fast reactors.

This has been stressed for instance in Europe by SNETP in its Identification of Research Areas in Response to the Fukushima Accident and by the SAFEST roadmaps.

Thanks to France Recovery plan, CEA is preparing a new experimental platform, NEW PLINIUS (*provisional name),* to replace the aging current PLINIUS platform and extend experimental capabilities to more representative masses with the use of innovative instrumentation.

Ambition : to cover and to experimentally simulate for the next decades the full range of phenomena involved during Severe Accident for Gen, 2, 3, 3+ and 4 nuclear reactors

LAYOUT

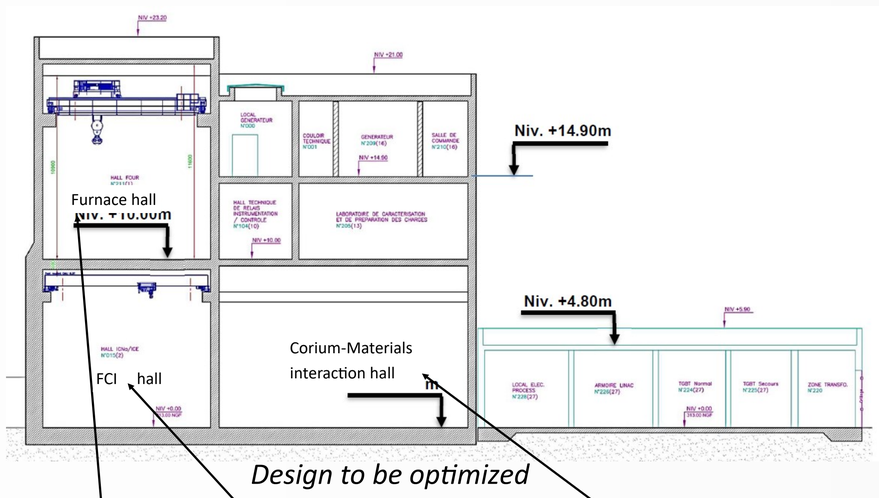

- A **furnace** able to melt **100 kg of UO_2**-containing prototypic corium currently undergoing system qualification tests
- An experimental hall dedicated to **Fuel Coolant Interaction** with **X-ray imaging**
- A sodium circuit to conduct **large-scale corium + sodium experiments**
- A 2nd hall to carry out experiments with up to **500 kg uranium thermite**
- A steam quenching system for **LWR cooling experiments**
- A corium load workshop, storage and service rooms
- Small scale facilities to study thermophysical properties and liquid layers.



Cold crucible induction Furnace

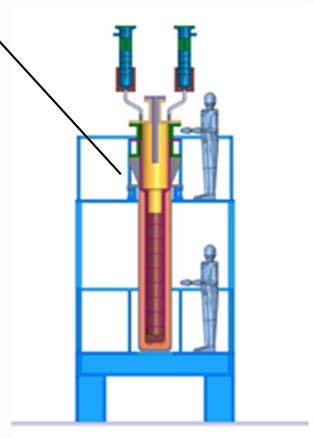
Fragmentation in Na (FR) test section

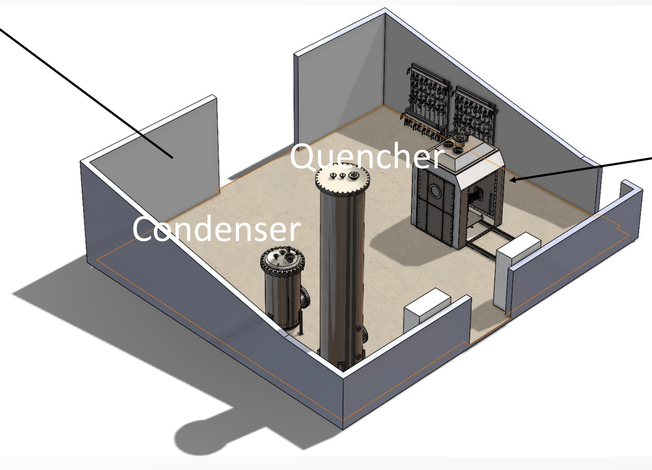

PARIOU Test section for corium top flooding

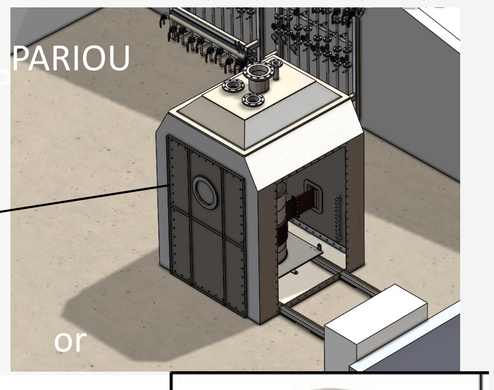

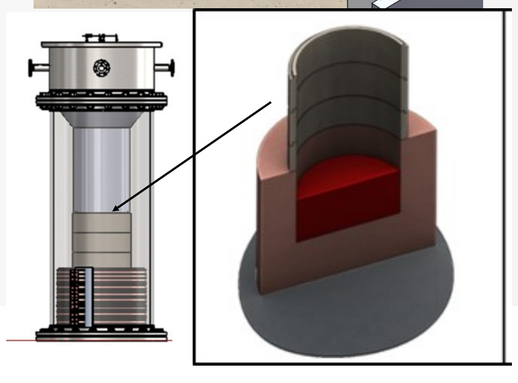



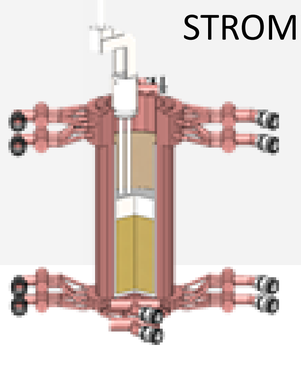

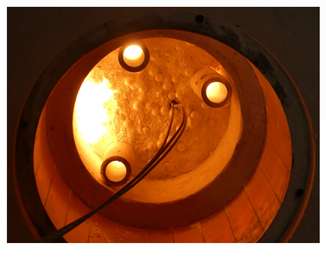

Designs to be optimized

SCHEDULE

Site pre-selected. Geotechnical and ecological surveys under finalization.
Choice of contractor: mid 2022
Design and construction contract: end 2022
Commissionning expected end 2026
1st Test section: PARIOU (**MCCI and top flooding**)
2nd test section 2027 : FR (corium fragmentation in Na)
Further test sections to be housed in NEW PLINIUS according to the experimental program needs.







NEW PLINIUS designed to operate for 3-4 decades at CEA Cadarache site.
NEW PLINIUS is open to international collaborations and is **planned to be partly operated as an international user facilty.**

10TH EUROPEAN REVIEW MEETING ON SEVERE ACCIDENTS RESEARCH

ERMSAR 2022

MAY 16-19, 2022 — KARLSRUHE, GERMANY

Evaluation of Long-Term Containment Cooling System (LTCCS) concepts for reactor facility VVER-1000/V-320

Vadym Ivanov, Oleksandr Mazurok, Vyacheslav Bliednykh, Oleksandr Mykhailenko, Artem Tiurin
ES Group Europe s.r.o., Plzeň, Česká Republika
ES Group LLC, Kyiv, Ukraine

ENERGY SAFETY GROUP

Introduction

To date, a set of “Post-Fukushima” modernizations has been implemented for Ukrainian NPPs with a VVER-1000\V-320 reactor , which allow maintaining the integrity of the containment for severe accidents (SA) with station blackout (SBO) for 72 hours.

For example, implemented such modernizations as: Filtered Containment Venting System (FCVS), hydrogen removal systems (PAR), water injection to the spent nuclear fuel storage pools from mobile water sources, etc.).

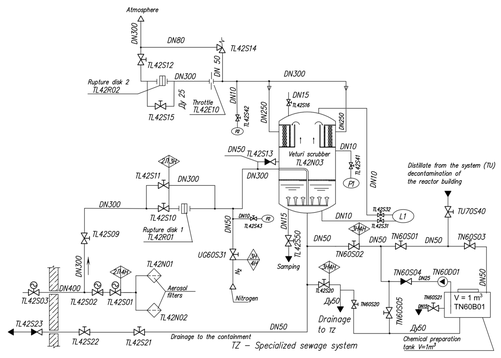

The main technical characteristics of the FCVS:

Setpoints of the containment pressure (beginning/stop venting) - 5.0 kgf/cm²/3.0 kgf/cm².

The mass flow rate of vapor-gas mixture for $P_{containmant}$ = 5.0 kgf/cm² (abs.) - 7.41 kg/s

System operability without replenishing the filter solution - 72 hour

Long-Term Containment Cooling System (LTCCS) concepts

Currently, no solution has been found for the implementation of In-Vessel Melt Retention (IVMR) technology for old VVER-1000 reactors. In the case of SA for a VVER-1000 with a long-term SBO it is not possible to prevent the ex-vessel phase of the SA.

Long-term heat removal from the molten corium and containment by Long-Term Containment Cooling System (LTCCS) allow maintaining the integrity of the containment floor.

As a result of the analysis the available information on the proposed concepts of passive LTCCS for VVER-1000, we concluded that, considering the design features of old VVER-1000 implementation of passive LTCCS for old VVER-1000 impossible (because: lack of the necessary range of reserve penetrations in the containment wall or base plate of containment, lack of sufficient free space in the containment for installation of LTCCS heat exchangers, problems with the installation of equipment on the power unit building for heat exchanger with environment, etc.).

As a result of a qualitative analysis of various concepts, the LTCCS concept with active elements (turbine driven pumps) was selected for further computational analysis. The main requirements for choosing LTCCS concept - simplicity and reliability of application in SA conditions.

LTCCS concept contains such elements:

- turbine driven pump
- heat exchanger
- spray collectors with nozzles
- mobile diesel pumping unit (MDPU).

To transfer heat from the containment to the final heat sink requires only supplying of a water flow from a MDPU which drives turbine of the sprinkler pump. At the same time, this water removes heat from containment through the LTCCS heat exchanger and transports the heat to the final heat sink outside the power unit. This LTCCS hasn't electrical parts, switches or controls. This concept is practically unaffected by such extreme influences as fires and flooding in the building of power unit .

LTCCS elements placed in containment must be qualified for severe accident conditions

There are two options for placing LTCCS:

- turbine driven pump inside of the containment (at elevation level 13.7 m);
- turbine driven pump outside of the containment (at elevation level of 0.0 m or -4.2 m).

Both LTCCS placement options have advantages and disadvantages:

- if turbine driven pump is installed inside the containment, pipelines and equipment with highly radioactive water will be inside the containment. In this case, LTCCS has no connections with other safety systems. But there is a risk of pump cavitation when the pumped water has a temperature close to the saturation temperature.
- if a pump with a turbine drive is installed outside the containment due to the additional hydrostatic pressure in the pump no risk of pump cavitation, but in this case the pipelines and equipment with highly radioactive water will be outside the containment and for connection to the sump, it is necessary to connect to the safety systems pipelines

Preliminary calculations say that it is possible to operate a turbine driven pump in the SA conditions without cavitation when pump installed inside of the containment , but these issues require more detailed research during the system design process.

LTCCS sketch diagram with pump and heat exchanger placement inside the containment at elevation level 13.7 m:

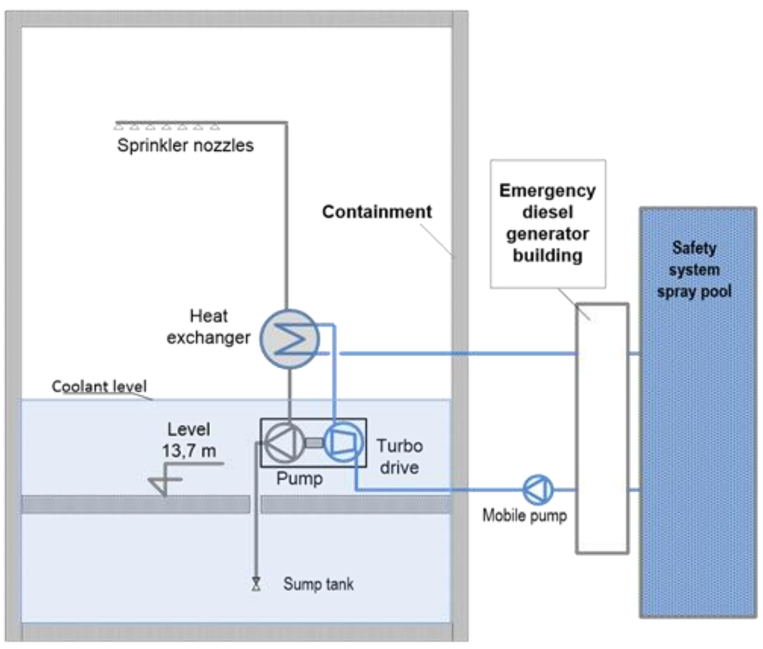

Placement of a two-channel LTCCS outside of the containment

Various options for implementing LTCCS were considered, including concept two-channel LTCCS outside of the containment with the function of cooling the reactor core. This concept uses a turbine driven pump with a head of about 110 m. This pressure is sufficient for pumping the coolant into the primary circuit after of its forced decompression.

As a result of modernization, we get LTCCS:

- with the additional function of ensuring the integrity of the reactor vessel;
- LTCCS is not afraid of fires and flooding in NPP buildings.

Sketch two-channel LTCCS diagram with placement active components outside of the containment (colored lines), and possible points of connection with pipelines of safety systems:

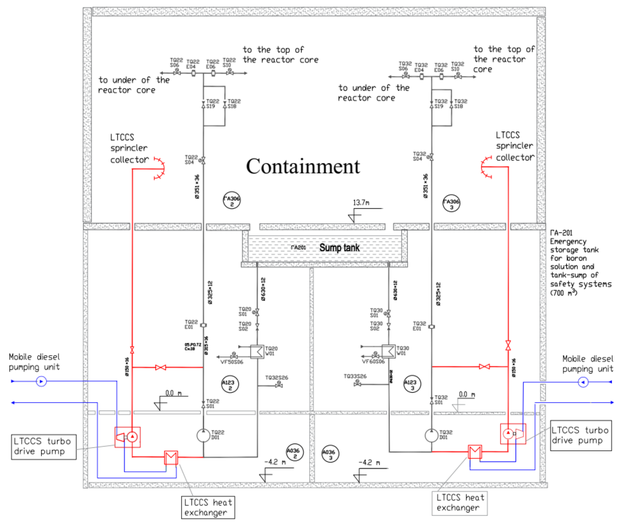

MELCOR code calculations results of LTCCS operation

The calculations were performed for a system with LTCCS pumps located in a containment, with minimal pump head characteristics.

Calculation model.

- modeling of a SA is performed with VVER-1000 model for the MELCOR code, that is previously used for the analytical justification of FCVS for power unit №1 of Zaporizhia NPP, Ukraine (ZNPP-1).
- the model of LTCCS has been added as spray sources with calculated spray water temperature after heat exchanger.

Initiating event and initial conditions

- for a preliminary analysis, a series of calculations is performed for severe accident with SBO initiating event (without leaks in the primary circuit).
- the personnel actions on the primary depressurization (opening PORVs), operation of the FCVS and LTCCS are assumed.
- initial conditions for NPP units - nominal power

Calculation model

Modeling of a SA is performed with VVER-1000 model for the MELCOR code, that is previously used for the analytical justification of FCVS for power unit ZNPP-1.

The model of LTCCS has been added as spray sources with calculated spray water temperature after heat exchanger.

Initiating events:

For a preliminary analysis, a series of calculations is performed for SA with SBO initiating event (without leaks in the primary circuit).

Initial conditions for NPP units - nominal power.

Calculation model.

Modeling of a SA is performed with VVER-1000 model for the MELCOR code, that is previously used for the analytical justification of FCVS for power unit ZNPP-1.

The model of LTCCS has been added as spray sources with calculated spray water temperature after heat exchanger.

Initiating events.

For a preliminary analysis, a series of calculations is performed for severe accident with SBO initiating event (without leaks in the primary circuit).

Initial conditions for NPP units - nominal power.

LTCCS characteristics

After the iterative calculations, the following technical LTCCS characteristics are selected:

- spray pump head pressure - 25 m;
- spray pump flow - 420 m³/h;
- MDPU water flow - 400÷450 m³/h;
- LTCCS heat exchanger ~20 mW.

Series of calculations.

Calculations Series #1, 2 - evaluation of the efficiency of heat removal from the containment using LTCCS+FCVS, for specified start time for LTCCS, assessment of the impact of the installation height of the spray LTCCS collector.

Calculations Series # 3 - evaluation of LTCCS efficiency in case of failure to close FCVS (venting through the FCVS until the end of the calculation);

Calculations Series # 4 - evaluation of the possibility of long-term heat removal using only venting through FCVS and refill of the containment with water from a mobile external source.

Preliminary calculation results.

Series #1 of calculations

The LTCCS spray collector is modeled in the containment at elevation ~19 m (~5 m above the floor containment). In this series of calculations, LTCCS runs at different times.

Setpoints for start venting by FCVS P = 5 kgf/cm² and stop venting P=3kgf/cm² containment abs. pressure.

The graphs show, a comparison of the calculation results:

- if only the FCVS is in operation (line without markers)
- if FCVS and LTCCS is in operation (lines with markers, “..spray start….” and specified start time for LTCCS.

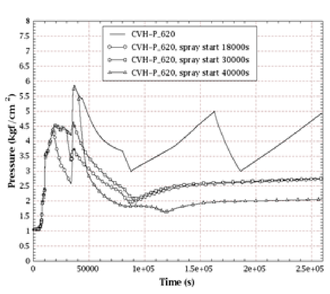

Containment pressure

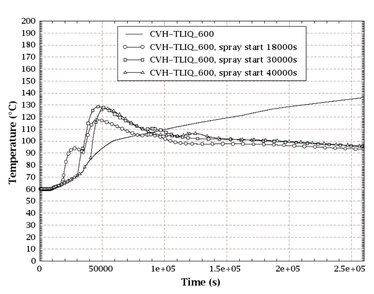

Coolant temperature in the sump

The calculation results show that if LTCCS is started before reaching the FCVS opening setpoint, start of venting by FCVS may not occur.

Series #2 of calculations

In this series of calculations, the scenarios are the same as in series #1, the difference is in the height of the sprinkler collector. LTCCS spray collector is divided in two equal parts (one part to elev. 19 m, as in previous series #1, and second part to elev. 24 m).

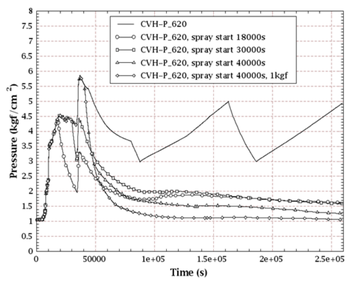

Containment pressure

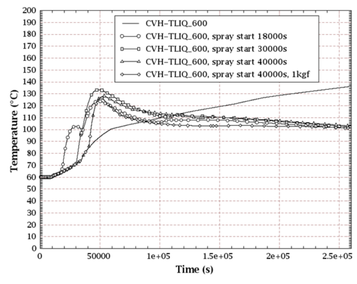

Coolant temperature in the sump

Series of calculations # 3

Series #3. Start FCVS venting after reaching the pressure setpoint in the containment of 5 kgf/cm² and venting open until the end of the calculation, LTCCS start at 40 000 s.

The operation of the LTCCS allows to reduce the pressure in the containment to atmospheric and to reduce radioactive emissions even in case of failure to close the FCVS.

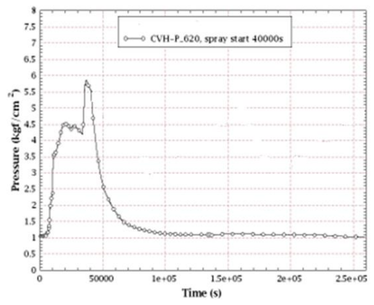

Containment pressure

Series of calculations # 4

The purpose of the calculation in this series is to check the possibility of long-term heat removal without LTCCS, using FCVS and water injection into the containment.

In this series of calculations start FCVS venting after reaching the pressure setpoint in the containment and venting remains open until the end of the calculation. In this scenario no LTCCS operation, water is injected into the containment (water temperature 30°C, flow rate 10 kg/s).

The containment pressure is stabilized nearly 3.0 kgf/cm² and decreasing to ~ 2.5 kgf/cm². In these case radioactive gases are released into the environment a long time. This heat removal method from the containment can be applied only as temporarily.

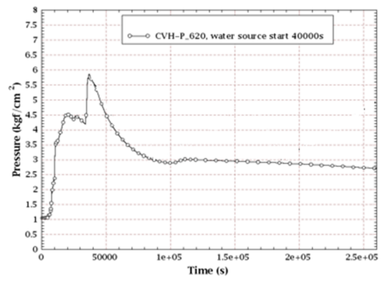

Containment pressure.

Assessment of the Impact of LTCCS operation on hydrogen safety.

The calculation results have confirmed the provision of hydrogen safety during the operation of the LTCCS. Below is a graph characterizing the change in the composition of the vapor-gas mixture during the development of a severe accident for the start of LTCCS on 30000 seconds after the reactor shutdown (Series of calculations # 1).

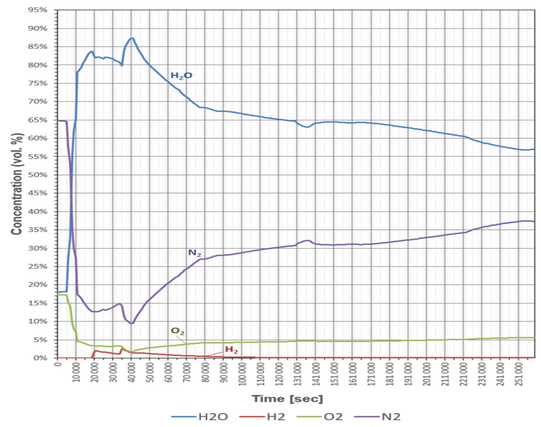

Assessment of the danger of vacuumizing the containment when the standard sprinkler system is turned on.

The results of the performed calculations showed that the inclusion of LTCCS allows to reduce the operating time of the venting through the FCVS, and in the case of early activation of the LTCCS, it makes it possible to exclude the achievement of the venting opening setpoint. As a result, the release of non-condensable gases into the environment will be either significantly reduced or completely eliminated. Accordingly, after the application of LTCCS, if the power supply of the power unit's safety systems is restored and the standard sprinkler system is turned on, the danger of vacuuming the containment is practically excluded.

CONCLUSIONS

- The preliminary analysis of LTCCS concept has shown successful long-term heat removal from VVER-1000 containment in case of SA with ex-vessel phase.
- Preliminary estimations of system specifications have shown that LTCCS heat exchanger capacity 20 MW and spray total flow 420 m³/h are sufficient for this purpose.
- In case of early LTCCS start the FCVS setpoint might be not reached.
- The design of LTCCS with upper located spray collector is more efficient for heat removal.
- Preliminary analysis have shown that hydrogen detonation conditions are not reached during LTCCS operation and if case turned on standard sprinkler system.
- Application of LTCCS decreases loss of non-condensable gases from containment to the environment during venting through the FCVS. As a result, the risk of "vacuuming" of the containment after the start of the standard sprinkler system is significantly reduced.
- The location of the two-channel LTCCS outside the containment can add an additional function to the LTCCS - ensuring the integrity of the reactor vessel as a result of cooling the reactor core during the SA after the decompression of the first circuit.

TOP FLOODING TESTS OF PROTOTYPIC CORIUM ON MERELAVA FACILITY

Bouyer PhD, Viviane

Commissariat à l'énergie atomique et aux énergies alternatives

Centre de Cadarache – Bât.219- 13108 St Paul Lez Durance cedex

viviane.bouyer@cea.fr

Abstract

Top flooding tests of prototypic corium are conducted on MERELAVA, the advanced facility of the PLINIUS severe accident platform of the CEA. This facility extends the existing experimental database on water ingression cooling to mixture of oxide and steel prototypical corium melt compositions, including uranium oxide. Indeed, different cooling behaviours could be observed due to the presence of a metallic phase.

MERELAVA have been developed in the frame of the MIT3BAR project on Mitigation of the risk of melting through the basemat which is carried out within the framework of the RSNR initiative funded by the French Government with EDF and Framatome partnership.

The initial step of the project consisted in transient tests with no sustained heating of corium. Corium melting is obtained using thermite reaction. Three experiments have been performed: first experiment ME-U1 was devoted to the flooding of an oxidic melt; second and third experiments, ME-U2 and ME-U3 respectively, consisted in the flooding of oxidic and metallic melts.

This poster presents the functioning of MERELAVA facility and gives the principal characteristics of the 3 tests (i.e. test section configuration and flooding parameters). Preliminary measurements results concerning gas and vapour flow rate are synthesized, as well as details about dismantling and observations of post-test corium blocks.

The objective of the second step of the project is to perform steady state experiments with 1D concrete ablation and thus study gas sparging effect on water ingression. A new lower part of the MERELAVA test section has been manufactured enabling the use of induction heating to simulate residual power in the corium. Some information about the design of the next top flooding test with induction heating is given.

Acknowledgements: This work has been performed with the financial help of the French government through the 'Programme d'Investissement d'Avenir" under convention number ANR-11-RSNR-0014.

ERMSAR 2022
MAY 16-19, 2022 — KARLSRUHE, GERMANY

IRESNE.

TOP FLOODING TESTS OF PROTOTYPIC CORIUM ON MERELAVA* FACILITY

V. Bouyer, C. Journeau, A. Denoix, P. Sauvecane

CEA, DES, IRESNE, DTN, SMTA, LEAG, Cadarache F-13108 Saint-Paul-Lez-Durance, France

OBJECT

Top flooding tests of prototypic corium are conducted on **MERELAVA facility of the PLINIUS severe accident platform of the CEA** in the MIT3BAR project. This facility extends the existing experimental database on water ingression cooling to **mixture of oxide and steel prototypical corium** melt compositions, including uranium oxide.

MIT3BAR project objective stands on the realization of **5 top flooding tests** with **3 transient** tests i.e. without sustained heating of corium and **2 MCCI tests** in a 1D configuration **with induction heating** of corium.

This poster presents the main results of the three transients tests and the design of the first test with sustained heating.

*MERELAVA has been developed in the frame of the MIT3BAR project on Mitigation of the risk of melting through the basemat which is carried out within the framework of French government "Investments for Future" programme, with EDF and Framatome partnership. **This facility is to be opened to international users.***

MERELAVA FACILITY

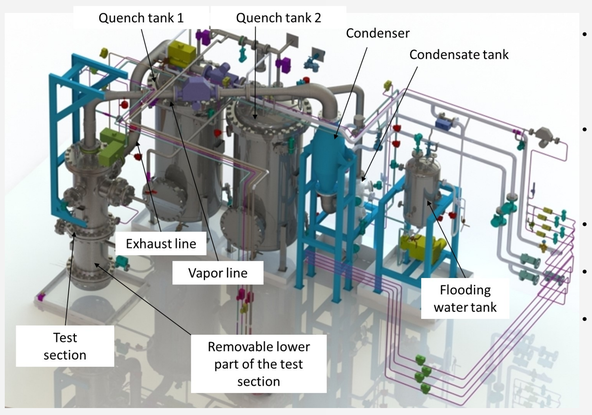

3D VIEW ON MERELAVA 3D

- Up to **80 kg of corium molten by thermitic reaction** in a zirconia crucible
- Water tank for injection : **100 liters**. Water is heated at 95°C
- **Water injection flow between 3 and 15 liters/s**. Injection with fixed steps of maximum 9 liters is required by safety rules
- Quench tank 1 (normal functioning) : cool gases from thermitic reaction and proceed to evacuation of gases formed during reaction and flooding of metallic corium.
- Quench tank 2 operates in case of overpressure greater than 3 bar in the test section
- Temperature measurements of the vessel, the crucible and the corium pool
- Determination of mass flow rate from the upper surface of the pool :
  - **Vapor flow at the exit of the test section** (flowmeter)
  - **Quantity of condensed water** (level in the condensate tank using a radar meter and a differential pressure transmitter)

TEST SECTION

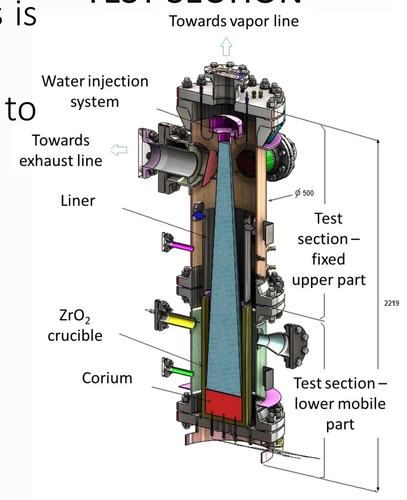

CONFIGURATION OF TOP FLOODING TESTS

- Tests with no ablation
- ZrO2 crucible (270 internal diameter / 30 mm thick)
- Initial pressure is 1 bar
- ME-U1 was the functioning test, using the same corium composition as the one used in SSWICS7 ANL test;
- ME-U2 was the first test with a 15wt% of steel in the corium
- ME-U3 was the second test with a 15wt% of steel and a larger amount of concrete

Test number	ME-U1	ME-U2	ME-U3
Corium composition (%wt) Type of concrete is siliceous	UO2/ZrO2/Concrete/ Cr : 64/26/4/6*	UO2/ZrO2/Concrete/ Steel : 54/23/8/15	UO2/ZrO2/Concrete/ Steel : 50/21/14/15
Protection of the crucible	ZrO2 felt on the inner wall	30 mm thick concrete on the outer wall	30 mm thick concrete on the outer wall
Initial thermite mass	75	64	58
Heating temperature of test section walls and vaport line	~110 à 120°C	~110 à 120°C	Upper test section and vapor line at 120°C Lower test section at 90°C
Water injection flow (l/s)	8.4±1	8±1	8,8±0.9
Quantity of water injected	13 injections of about 7±0,2 l	9 injections of about 8,5±0,5 l	9 injections of about 8,5±0,9 l

TEST SECTION WITH INDUCTION HEATING

Induction generator of 400 kW – [70-300 kHz] to simulate the residual

1D MCCI test with flooding is under preparation and should be realized at the end of 2022

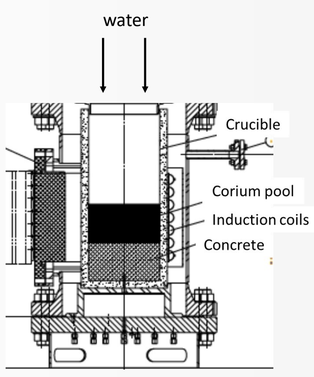

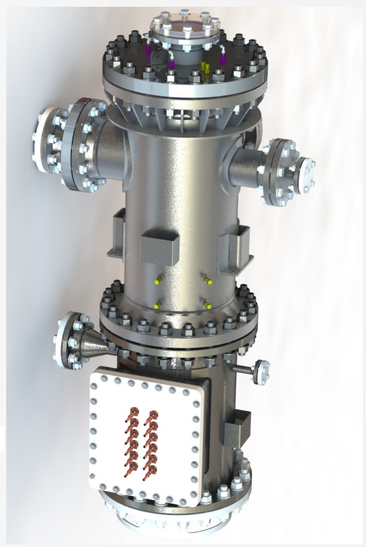

RESULTS

Test number	ME-U1	ME-U2	ME-U3
Solidified corium pool mass (kg)	45	39.6	40
Solidified corium pool height (cm)	~12	~11.5	~13
Maximum pressure (bar)	0.3	0.7	0.7

ME-U1



ME-U2



ME-U3



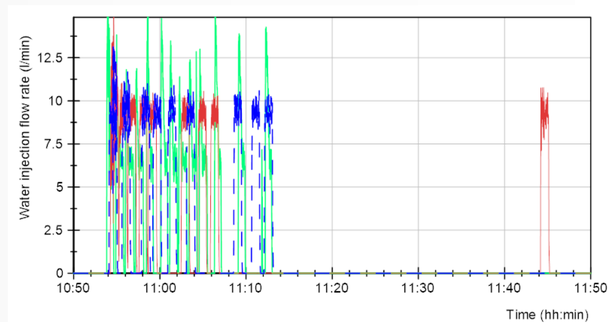

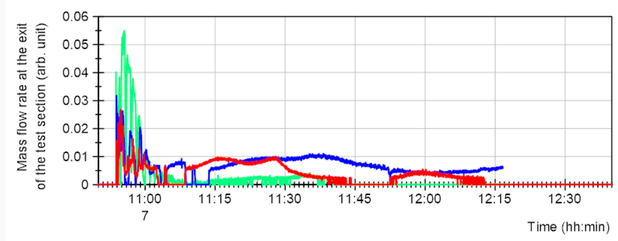

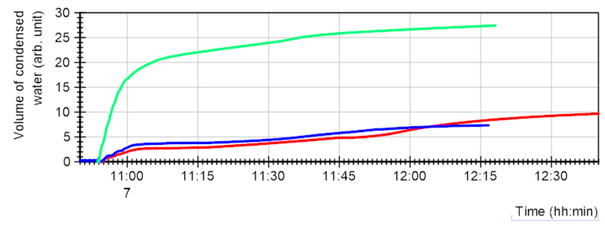

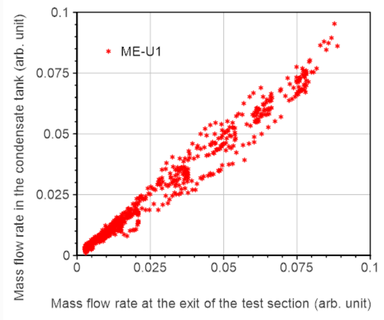

- First test ME-U1 with only 6%Cr validated the functioning of MERELAVA facility and put in evidence a quite satisfactory fit between the two independent measurements of mass flow rate
- On the contrary, ME-U2 and ME-U3 tests with steel and concrete showed a high discrepancy between both measurements, due to the presence of uncondensable gases (H_2). Gas flow measurements are thus used to analyse those tests.

STUDY OF TLOFW SEVERE ACCIDENT OF A SMR WITH FANCOOLER AS MITIGATION MEASURE USING MELCOR

Maritza R. Gual[1], Nathália N. Araújo[1], Marcos C. Maturana[1], Ulisses A. Maciel Neto[1] and Marcelo R. Martins[1]

[1]: Analysis, Evaluation and Risk Management Laboratory (LabRisco), Polytechnic School of the University of São Paulo. Av. Prof. Mello Moraes, 2231, 05508-030, São Paulo – SP, BRAZIL

maritza.gual@labrisco.usp.br, nathalia.araujo@labrisco.usp.br, marcos@labrisco.usp.br, ulisses.neto@labrisco.usp.br, and mrmartin@usp.br

Abstract

The simulation of severe accidents is essential for the development of Probabilistic Safety Analysis and the Safety Analysis Report, which are documents required for the licensing and operation of a nuclear power plant. In the Level 1 Probabilistic Safety Analysis (PSA) (for transients) performed, it was analyzed different severe accident progressions that appears with the dominant contribution to the Core Damage Frequency (CDF).

Various severe accidents analysis (SAA) has already been carried out in the author's laboratory: Loss of Feed Water Accident (LOFW) of steam generator, LOFW of steam generator combined with an Anticipated Transient Without Scram (ATWS), Total Loss of Feed Water Accident (TLOFW), Total Loss of Feed Water Accident (TLOFW) with mitigation measure, and Loss of Coolant Circulation Accident in Spent Fuel Pool (SFP). This work presents a strategy of severe accident mitigation prepared for a very small modular reactor (vSMR) of Pressurized Water Reactor (PWR) type, and two scenarios are compared: the Total Loss of Feed Water (TLOFW) severe accident with and without mitigation measure inside containment. The reference PWR is designed with an electrical capacity of 48 MWt (11 Mwe).

The deterministic computer code MELCOR v. 2.2 was used to analyze two severe accident scenarios: TLOFW with and without CFC operating. The MELCOR code is an integrated platform capable of simulating the main phenomena of a severe accident and has been used to simulate accidents in different designs of nuclear plants and spent fuel pools. It is intended to perform the sensitivity analysis in future works such as the use of Containment Fan Cooler (FC) distributed in different compartment of containment during of a hypothetical TLOFW accident, the use of the passive containment systems only, a case of different size and localizations of mitigation systems, etc. In addition, the sensitivity analysis of the parameters used in the model (a fans coolers activation time, time step, nodalization of containment, etc.) will also be effectuated to suggest improvements in the system design.

Keywords: Severe Accident Analysis, TLOFW, MELCOR, vSMR.

ERMSAR 2022
MAY 16-19, 2022 — KARLSRUHE, GERMANY

FAN COOLER IMPACT UNDER A TLOFW ACCIDENT IN A NEW SMR IN DESIGN PHASE

M.R. Gual[1], N.N. Araújo[2], U.A. Maciel Neto[3], M.C. Maturana[4], M.R. Martins[5]
Analysis, Evaluation and Risk Management Laboratory (LabRisco), University of Sao Paulo
[1]maritza.gual@labrisco.usp.br, [2]nathalia.nunes@labrisco.usp.br, [3]ulisses.neto@labrisco.usp.br, [4]marcos@labrisco.usp.br, [5]mrmartin@usp.br

INTRODUCTION

The reactor considered in this paper refers to a new design of nuclear reactors that enters in the group of Very Small Modular Reactors (vSMR) [1]– a subcategory proposed for SMRs under about 15 MWe, proposed for power supply in remote communities [4]. The objective of this work is to evaluate the mitigation effect of Containment Fan Coolers (CFCs) in a generic PWR nuclear power plant (NPP) under a hypothetical total loss of feedwater (TLOFW) accident using the MELCOR code.

NPP MODELING USING MELCOR

The PWR containment is basically a horizontal cylindrical hull, as shown in Figure 1. The containment vessel is submersed in the shielding pool.

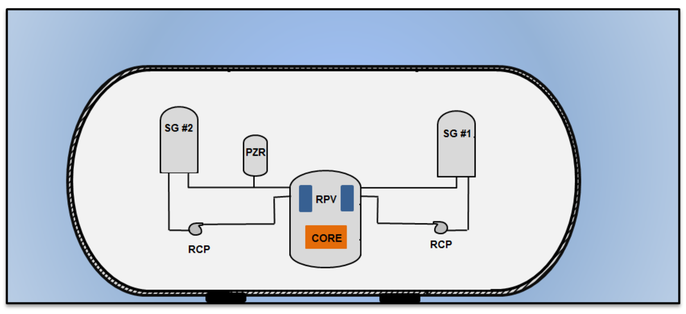

Figure 1: The reference reactor cooling system model.

The main modeled heat structures were the core vessel and their structures, PRZ, baffle, SGs tubes and containment are shown in Figure 2 [3].

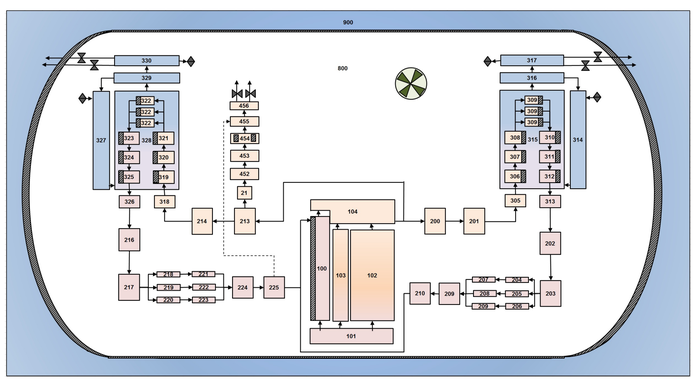

Figure 2: Reactor cooling system nodalization.

In Table 1, the main parameters of SMR are presented [2].

Table 1: Main parameters of SMR

Parameter	Nominal value
Thermal Power, MWt	48.00
Electrical Power, MWe	11.00
Reactor pressure, MPa	13.10
Core inlet temperature, K	537.95
Core outlet temperature, K	558.08
SG pressure, MPa	3.77
SG temperature, K	519.15
SG liquid level, m	2.53
SG steam flow rate, kg/s	40.00
Feed water flow rate, kg/s	9.45

In the Internal Events PSA Level 1 (for transients) for the reference plant, the Excessive-LOCA initiating event appears in the cut set with the high frequency – the dominant contribution to the Core Damage Frequency (CDF) of the plant [5]. The hypothetical TLOFW accident was chosen for this study because its CDF is very high when compared to other accidents, as described in Table 2.

Table 2: Cut set with the highest frequency in the PSA Level 1

Event Description	Event Probability	Cut Set Frequency (/yr)
LOFW	1.77E-01	
Plant is at power operation based on annual availability	1.00E+00	
Flag to enable transient events	1.00E+00	
Failure of operator manual trip from control room	5.10E-02	1.63E-07
Reactor protection system (RPS) fail to send reactor trip	1.80E-05	
Transient w/o SCRAM (ATWS) and Moderator Temperature Coefficient (MTC) is not acceptable	1.00E+00	

INITIAL CONDITION AND ACCIDENT PROGRESSION

The initial conditions of the several accidents considered in this work are given in the Table 3.

Table 3: Initial conditions of the analysis

Initial conditions
1. The reactor is operating at the initial nominal power 100%.
2. The SCRAM system is available and operational.
3. Feed Water Pumps (FWPs) in secondary loop fail to start.
4. An Auxiliary Feed Water (AFW) and Emergency Feed Water (EFW) system fails to start.
5. SG safety and relief valves are available and operational
6. Safety relief valve and spray valve of PRZ is available and operational.
7. Passive residual heat removal through SG fails to start.
8. Passive residual heat removal heat exchanger (PRHR HX) submerged in water pool is not available.

The Table 4 presents th chronology of main events for the two scenarios considered.

Table 4: Chronology of main events (in seconds) after both postulated accidents

Event	TLOFW without CFCs	TLOFW with CFCs
Steady state	0.0	0.0
Transients occurred	200.0	200.0
Reactor tripped (SCRAM occurs successful)	207.0	207.0
Dry out of SGs	479.0	479.0
Beginning the oxidation and H_2 generation	660	660
CFCs activation	not	700.0
Fuel cladding melting	960.0	not
RPV fails and core start to relocate	1600.0	not
CFCs deactivated	not	4000
Deflagration starts	4791.3	not
Containment fails	not	not

RESULTS AND DISCUSSION

The chart below shows and compares the containment pressure in TLOFW with fan cooler activated and without fan cooler activated.

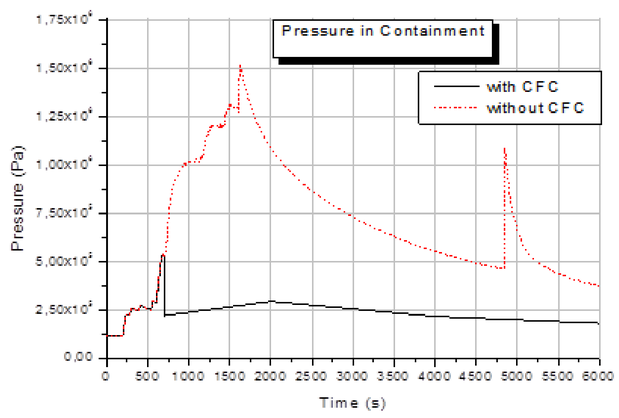

The fan cooler reduces the containment temperature. The CFCs provides the heat removal capacity to maintain containment temperature below 346 K during the accident.

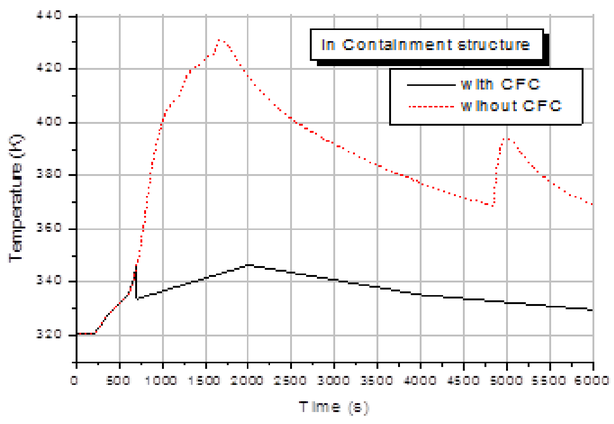

The fan coolers can result in steam decreasing and deinertization of the containment atmosphere.

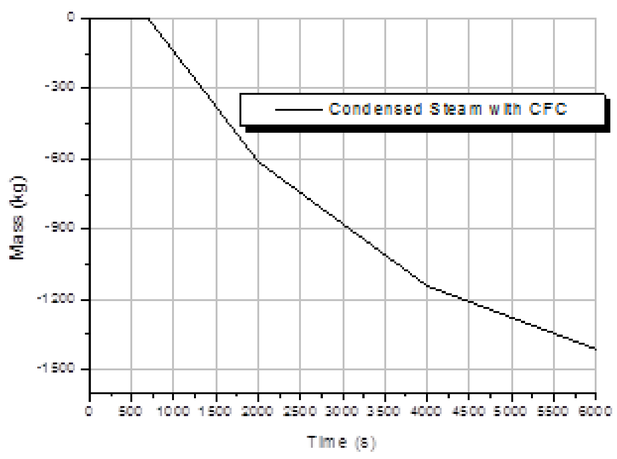

From a comparative study for cases it was concluded that the CFCs is effective for maintain the temperature and pressure of containment below during the severe accident.

Table 5: Major temperature and pressure reached in containment during TLOFW with and without CFCs

Variable	Without CFCs	Maximum valor reached with CFCs
Temperature (K)	431.00	346.00
Pressure (Pa)	1.5E+06	2.95E+05

CONCLUSIONS

The main conclusion of this work is that fan coolers can be effective in controlling the gradual over pressurization in the containment. The fan cooler contributes to the reduction in temperature of the containment atmosphere and the heat removal.

References

[1] International Atomic Energy Agency. Status of Small and Medium sized Reactors Designs: A Supplement to the IAEA Advanced Reactors Information System (ARIS). Technical report, 2012.

[2] N. N. Araujo, M. C. Maturana, and M. R. Gual. MELCOR steady state calculation of the generic PWR of 40 MWth. *Brazilian Journal of Radiation Sciences*, 08(03A):01–19, 2020.

[3] N. N. Araujo, M. C. Maturana, and M. R. Gual. Unmitigated Severe Accident Analysis for a PWR using MELCOR. *Progress in Nuclear Energy*, 128, 2020.

[4] World Nuclear Association. Small Nuclear Power Reactors. Available at https://www.world-nuclear.org/information-library/nuclear-fuel-cycle/nuclear-power-reactors/small-nuclear-power-reactors.aspx (2022/05/05).

[5] Maturana M. C.and Bruno L. L. and Martins M. R. Application of Fire PSA in Defining System Reliability Criteria: Detection and Suppression Systems in I&C Electrical Panel Room. In *Proceedings of Probabilistic Safety Assessment and Management – PSAM 14*, Los Angeles, CA, September 2018.

Development of CFD Code for Prediction and Improvement of Core-Catcher Performance

Sangmin Kim[1], Keunsang Choi[1] and Jeahoon Jung[1]
[1]: Korea Atomic Energy Research Institute, 111, Daeduk-daero 989, Daejeon, Korea

ksm0226@kaeri.re.kr

Abstract

The PECS (Passive Ex-vessel corium retaining and Cooling System) is installed inside EU-APR1400 to prevent leaking corium from contacting concrete under ex-vessel accident. The PECS consists of a core-catcher and coolant filled in the cavity. When high-temperature corium contacts with the upper part of the core-catcher, the cooling water naturally circulates due to the heat and continuously cooling the core-catcher. The CE-PECS (Cooling Experiment-PECS) test was conducted by KAERI (Korean Atomic Energy Research Institute) to evaluate the performance of cooling water circulation in PECS. In this experimental study, the heat from melting corium was realized by installing heating blocks on the upper part of the core-catcher. And like PECS, the lower part of the core-catcher is filled with coolant. In the experiment, as electric power was applied to the heating blocks and the temperature of the core-catcher increased, the cooling water circulated naturally and finally the temperature of the core-catcher was stabilized.

In this study, the code was developed based on OpenFOAM-v2006 for CFD simulation of PECS. Since the actual PECS is a very-large scale structure, the computation load is very heavy when performing CFD. To solve this problem, we focus on minimizing the number of cells in the mesh. Only about 50,000 cells were used in the calculation area of 10 m $\times$ 3 m.

The code includes the calculation of CHT (conjugate heat transfer), boiling-condensation phase change at walls and gas-liquid two-phase flow. As a result of performing CFD analysis by benchmarking CE-PECS test, it showed high accuracy in circulating flow rate and temperature change of the cooling water. However, when a very high heat flux was set in simulation, the calculation of the code was unstable due to the limitation of computational cell size. This code can be used to predict and improve cooling performance of the PECS.

Keywords: CFD, PECS, core-catcher, ex-vessel, coolability

Development of CFD Code for Prediction and Improvement of Core-Catcher Performance

Sangmin Kim [a*], Keunsang Choi[a], Jeahoon Jung[a]
[a]Korea Atomic Energy Research Institute, 111, Daeduk-daero 989, Daejeon, Korea
*Corresponding author: ksm0226@kaeri.re.kr

KAERI Korea Atomic Energy Research Institute

Introduction

The PECS (Passive Ex-vessel corium retaining and Cooling System) is installed inside EU-APR1400 to prevent leaking corium from contacting concrete under ex-vessel accident. The CE-PECS (Cooling Experiment-PECS) test was conducted by KAERI (Korean Atomic Energy Research Institute) to evaluate the performance of cooling water circulation in PECS.

In this study, the code was developed based on OpenFOAM-v2006 for CFD simulation of PECS. The code includes the calculation of CHT (conjugate heat transfer), boiling-condensation phase change at walls and gas-liquid two-phase flow. The accuracy of the code was determined based on the flow rate and temperature change of the cooling water in the cooling channel according to the heat flux over time.

PECS

- PECS and core-catcher in EU-APR1400

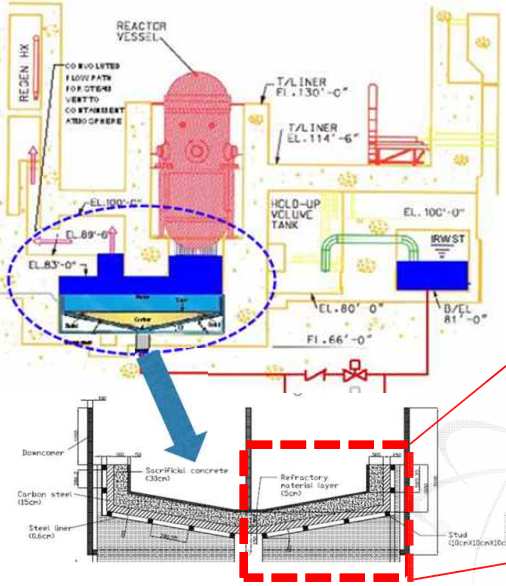

CE-PECS

- Schematic of the CE-PECS test facility (KAERI)

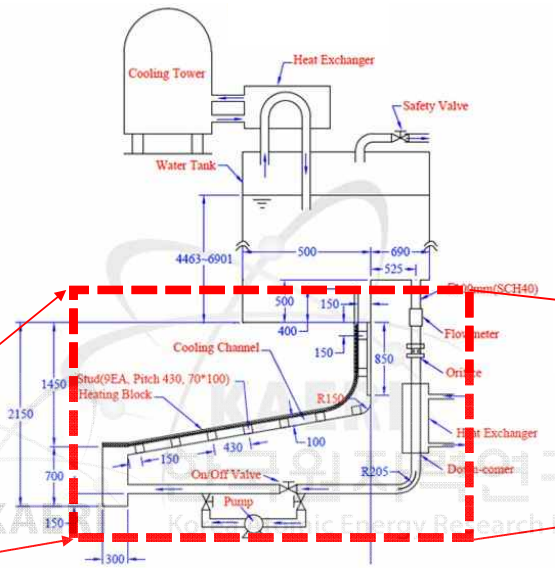

CFD

- Mesh system of CE-PECS test facility

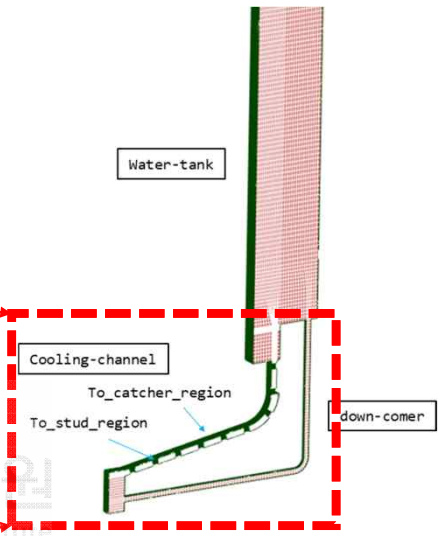

Method and Result

CFD solver for simulating was developed based on **chtMultiRegionTwoPhaseEulerFoam** in OpenFOAM.

- Heat flux at the wall

Total wall heat flux	$q''_w = q''_c + q''_e + q''_q$
Evaporation heat flux	$q''_e = \frac{\pi}{6} d_w^3 \rho_v f N'' (i_{g,sat} - i_l)$
Nucleation site density (LemmertChawla)	$N'' = [210\,(T_w - T_{sat})]^{1.805}$
Bubble departure frequency (Cole)	$f = \sqrt{\frac{4g(\rho_l - \rho_v)}{3D_d\rho_l}}$
Bubble departure diameter (Tolubinski-Kostanchuk)	$d_{ref} exp\left(\frac{-T_{sat} - T_l}{45}\right)$
Quenching heat flux	$q''_q = A_q \frac{2\lambda_l (T_w - T_l)}{\sqrt{\frac{\pi}{f}\frac{\lambda_l}{\rho_l c_{pl}}}}$
Convective heat flux	$q''_c = (1 - A_q) h_c (T_w - T_l)$

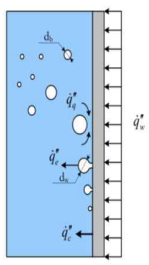

- CE-PECS T8-4 experiment conditions and Location of HBs

Coolant level	7.56 m
Initial coolant temperature	89 ℃
Total heating time	2830 s
Total power	123.3 kW (75%)
Average heat flux in HB #1	60.9 kW/m²
Average heat flux in HB #2	46.4 kW/m²
Average heat flux in HB #3	89.1 kW/m²
Average heat flux in HB #4	98.3 kW/m²
Average heat flux in HB #5	150.3 kW/m²
Average heat flux in HB #6	220.9 kW/m²
Average heat flux in HB #7	261.0 kW/m²

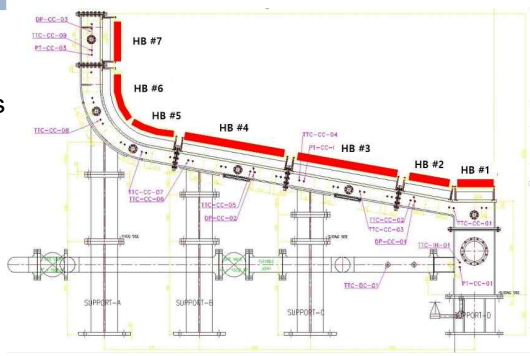

- Coolant mass flow rate at the inlet of the cooling channel

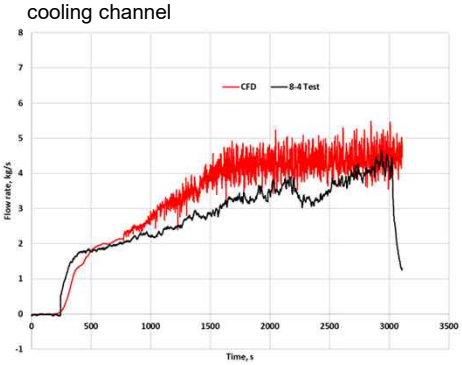

- Coolant temperature change at the inlet of the cooling channel

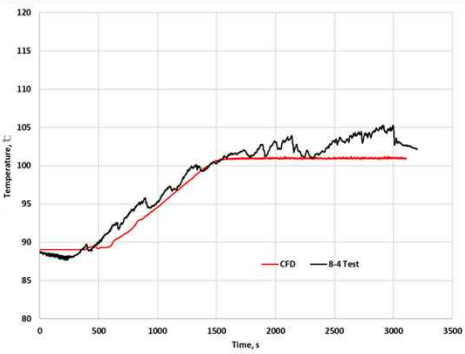

Conclusion

In an ex-vessel situation, it is most important to cool the molten corium well. Therefore, it is necessary to verify whether the coolant circulates properly in PECS through experiments and CFD analysis.

As a result of benchmarking and simulating the CE-PECS T8-4 experiment, the flow rate and temperature rise trends were well predicted.

We expect to find ways to improve and to verify the cooling performance of the core catcher by using this CFD code.

The 10th European Review Meeting on Severe Accidents Research

Severe Accident Research Eleven Years after the Fukushima Accident

May 16-19, 2022, Karlsruhe, Germany

Technical Session 5-2: Source Term

Chairs: T. Lind (PSI), S. Gupta (Becker Techn.)

ID294	**Pool scrubbing in Unit 1 of Fukushima Daiichi** L. E. Herranz (CIEMAT)	**Paper** **Presentation**
ID298	**Bubbles dynamics under pool scrubbing conditions for iodine compounds trapping applications** M. Farhat (IRSN)	**Paper** **Presentation**
ID329	**New pool scrubbing correlations based on reliable data** L. E. Herranz (CIEMAT)	**Paper** **Presentation**
ID332	**The R2CA project for a better evaluation of radiological consequences under Design Basis Accidents and Design Extension Conditions in LWRs: Motivation and first results** N. Girault (IRSN)	**Paper** **Presentation**

POOL SCRUBBING IN UNIT 1 OF FUKUSHIMA DAIICHI

Luis E. Herranz
CIEMAT
Avenida Complutense 40, 28040 Madrid, Spain
luisen.herranz@ciemat.es

ABSTRACT

Under the frame of OECD/BSAF and ARC-F projects, CIEMAT estimated that around 40% of the Cesium initial inventory in the reactor core and nearly 60% of the Iodine one of the Unit 1 of Fukushima Daiichi, got absorbed in the suppression pool. CIEMAT has critically reviewed the bases of the MELCOR pool scrubbing module, including the major assumptions and approximations underneath, under the prevailing conditions in Unit 1 of Fukushima Daiichi during fission product scrubbing. The results have shown that most fission product mass is retained in the water nearby the injection point as a consequence of diffusiophoresis and inertial mechanisms. However, some of the approximations underneath the corresponding models have been found to be questionable and some new formulations have been considered and implemented within the stand-alone SPARC-90 code, which is the basis of the MELCOR models for pool scrubbing. In particular, a model capable of describing the scrubbing effect of jet injection has been implemented. This work presents better-fitted models for the scenario and, after implementing them into the SPARC-90 code, the resulting moderate quantitative impact on the accident scenario of Unit1 in Fukushima Daiichi, has been discussed to be well within the uncertainty range associated to the original code estimates. However, updating of MELCOR concerned models for fission products trapping in pools is highly recommended for physical consistency.

KEYWORDS
Pool scrubbing, jet regime, Fukushima Daiichi

1. INTRODUCTION

Under the frame of OECD/BSAF and ARC-F projects, CIEMAT estimated that around 40% of the Cesium initial inventory in the reactor core and nearly 60% of the Iodine one of the Unit 1 of Fukushima Daiichi, got absorbed in the suppression pool (Herranz & López, 2020). Recent studies of the bases of severe accident (SA) models of fission product trapping in suppression pools have found weaknesses worth further investigation (Herranz et al., 2014). As a consequence, CIEMAT has critically reviewed the bases of the MELCOR pool scrubbing module, including the major assumptions and approximations underneath, under the prevailing conditions in the Unit 1 of Fukushima Daiichi during fission product scrubbing.

Based on the results referred above, a quantification of uncertainties affecting the prediction of the suppression pool decontamination was conducted with SPARC-90 (Herranz et al. 2019) and with MELCOR 2.2 (Herranz & Bocanegra, 2020). It was found that the high decontamination factors (DF) estimated would be affected by uncertainties around 2 orders of magnitude. The subsequent sensitivity analysis showed that the DFs did notably correlate with carrier gas composition and particles inertia.

This paper collects every piece developed by CIEMAT in the investigation of pool scrubbing in Unit 1 of Fukushima and show a final comparison of the different predictions resulting from adapting the in-code existing formulations of the governing phenomena to the prevailing conditions in Unit 1 of Fukushima Daiichi.

2. KEY BACKGROUND

Modelling the SBO accident in Unit 1 of Fukushima with MELCOR 2.2 (Herranz & López, 2020), allowed determining the major boundary conditions of FP scrubbing in the suppression pool. By using them to build up SPARC-90 input decks, the scrubbing was described through the calculation of 15 time-point decontamination factors (i.e., ratio between the mass coming into the pool and the mass leaving the pool surface). The results of the study were reported by Herranz et al. (2020) and are synthesized in Fig. 1. In short, the retention efficiency was estimated to be at all times over 99% (DF>100) and most times over 99.9% (DF>1000). Nevertheless, it is worth recalling that DFs over 100 become very sensitive to uncertainties in the retention efficiency and caution should be taken if they are to be credited (Fontanet et al., 2009). Therefore, even if large DF changes are observed in consecutive times, they do not mean such abrupt changes in terms of scrubbed mass.

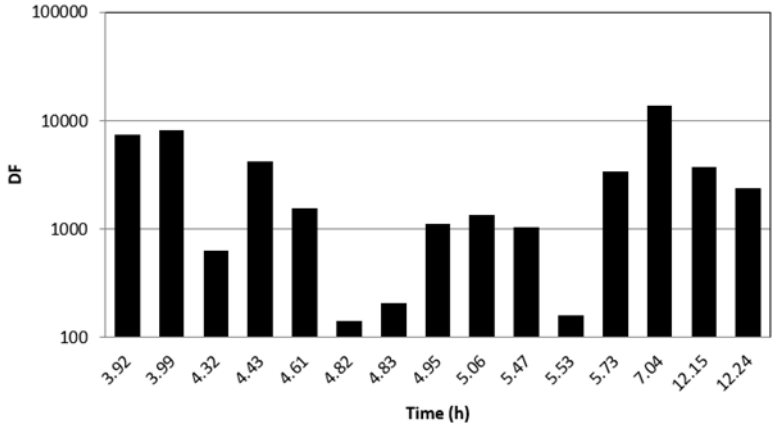

Fig. 1. DFs predicted during the FP injection in the suppression pool

The DF uncertainty was quantified by Herranz et al. (2019) by using the DAKOTA/SPARC-90 suite and characterizing the input variable uncertainties through an engineering judgement "informed" by MELCOR calculations. As shown in Fig. 2 for two specific times (5.06 h and 5.53 h), regardless the DF value (>10^3 and >10^2, respectively), the uncertainty range estimated extends over two orders of magnitude. The complementary sensitivity analysis conducted (Fig. 3) indicated that DFs in the scenario simulated were particularly sensitive to gas composition and particle characteristics, which highlighted the potential significance of phase changes and particle inertia as major drivers of radioactive absorption in the water pool.

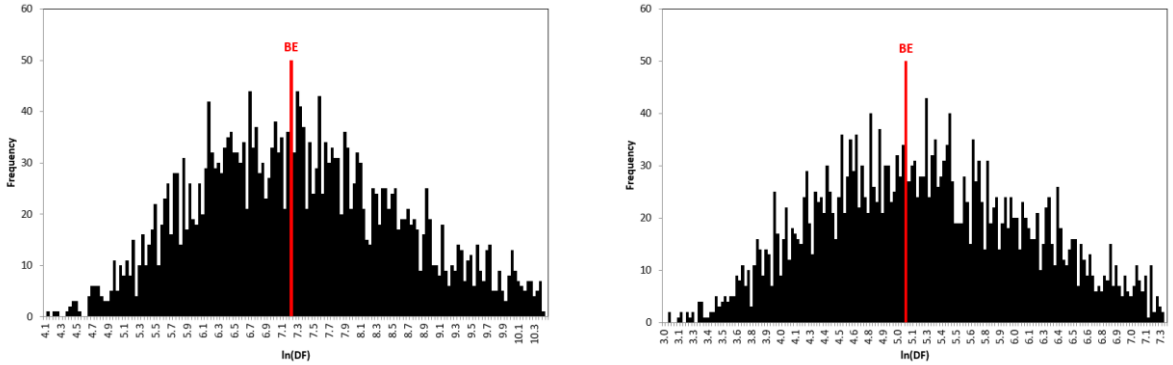

a. 5.06 h b. 5.53 h

Fig. 2. DF distributions

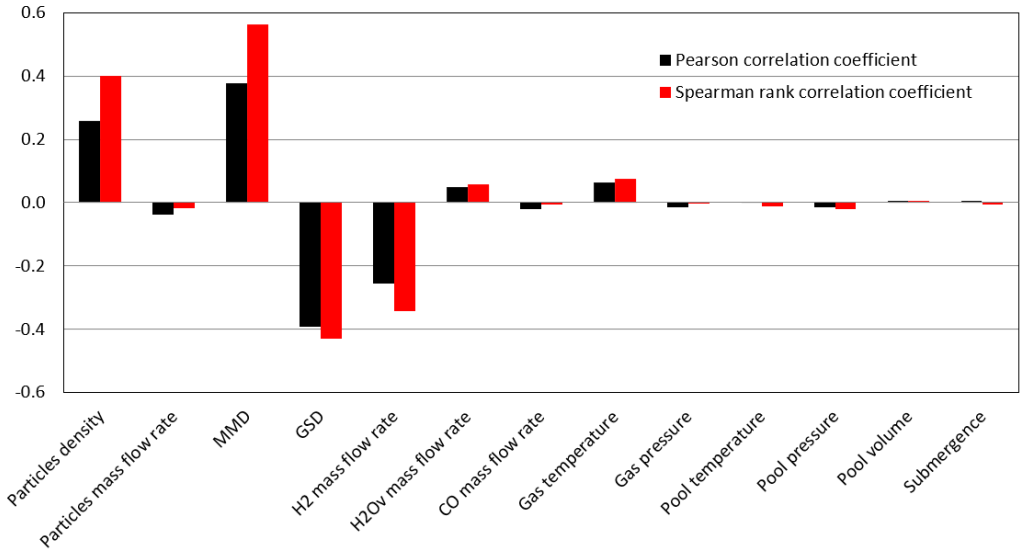

Fig. 3. Pearson and Spearman coefficients for DF (5.06 h)

The sensitivity results were consistent with the best estimate results of SPARC-90, which analysis indicated that most of the fission product mass was scrubbed in the nearby of the injection zone and that the dominant removal mechanism by far was steam condensation with inertial impaction contributing significantly (Fig. 4 a and b). As for the difference noted in mass flow rate of H_2 and CO, the reason underneath is nothing to do with the non-condensible nature of both gases, but with the fact that most fission products injection in the suppression pool occurred during the in-vessel phase of the accident, under which H_2 was the dominant non-condensible gas in the mixture. It is also worth mentioning that pool remains substantially sub-cooled during the fission product scrubbing (time length addressed in this paper) and got near saturation long after the main fission product release phase (about 2.5 days after the in-vessel injection period addressed in this work).

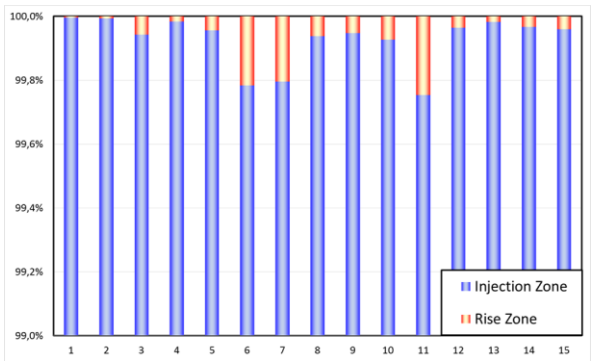

a. Scrubbing share (mass %)

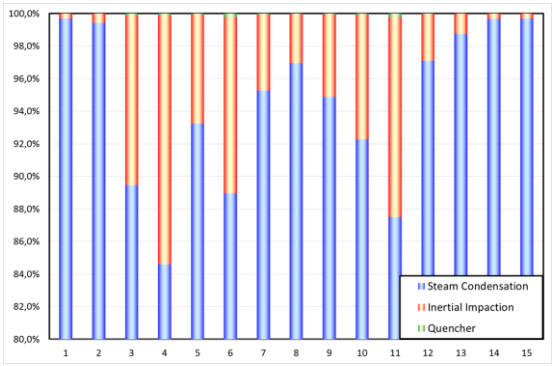

b. Removal mechanisms contribution (mass %)

Fig. 4. Driving decontamination mechanisms in the suppression pool

3. RECENT PROGRESS and CURRENT STATUS

3.1. Steam condensation

Steam condensation is subject to several approximations. First, it is assumed that it is the first process occurring to the carrier gas when approaching the pool whenever the saturation ratio (i.e., ratio between steam partial pressure and saturation pressure) is greater than 1.0. Second, it is assumed that the carrier gas equilibrates instantaneously with pool. In other words, right at the pool inlet and before undergoing any other process, steam partial pressure meets the condition,

$$p_{steam} = p_{sat}\ (T_{pool}) \qquad \text{Eq. 1}$$

and the steam exceeding such pressure is automatically condensed; consequently, particles airborne in the corresponding volume fraction are moved out the gas bulk. Both hypotheses are supported by Moody and Nagy (1983), who reported that such equilibrium condition takes a characteristic time of 0.03 s.

By adopting such approximations and doing some algebra one may get to the expression of the so called "early condensation" DF:

$$DF_{ec} = \frac{x_{nc}^{eq}}{x_{nc}^{in}} \qquad \text{Eq. 2}$$

However, SPARC-90 formulation includes a multiplicative factor of 3.0. Even though an internal comment within SPARC-90 source code says that such a factor was recommended by F.J. Moody, its technical support has not been found anywhere in the open literature. As introducing this enhancing factor is not conservative, Eq. 2 is considered a better approximation to the so called early condensation DF. A new calculation of mechanisms contribution removing the unsupported factor 3.0 from DF_{ec} is shown in Fig. 5. As expected, inertial impaction notably grows at all calculated times, being responsible for more than 30% FP removal at several time points. This along with the questionable instantaneous nature of steam condensation in the presence of non-condensable, highlights the relevance of inertial impaction in the decontamination process.

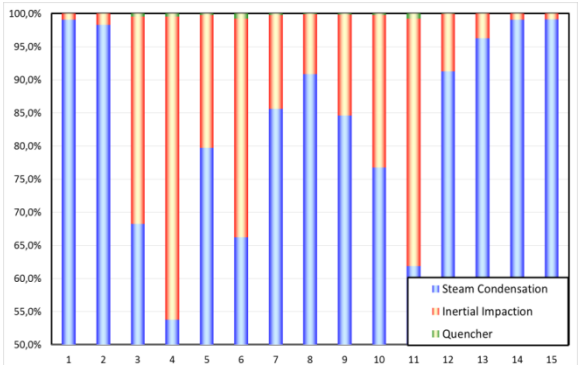

Fig. 5. Re-assessment of the relative effect of steam condensation in Unit 1 (mass %).

3.2. Inertial impaction

The equation implemented in SPARC-90 was derived from data taken by Ranz & Wong (1952) for a flat plate impactor where monodisperse particles were thrown through a rectangular injector. However, the topology of Ranz and Wong data that better fits the pool scrubbing scenario were the ones corresponding to a round injector, so that the original equation has been replaced by

$$\varepsilon_{imp} = 1 - \frac{1}{1+\exp(\frac{\sqrt{Stk}-0{,}38}{0{,}047})} \qquad \text{Eq. 3}$$

Fig. 6 shows results from this sigmoid equation along with those from SPARC-90 one as a function of the root squared of Stokes non-dimensional number ($Stk\ \ (i) = \frac{\rho_i\ d_i^2\ V_e}{18\ \mu\ l}$); the Ranz and Wong data are also included

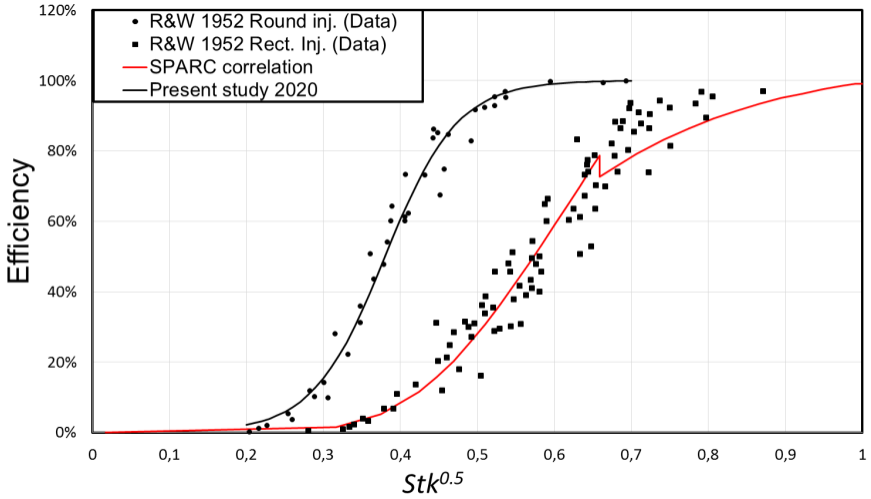

Fig. 6. Data and correlations for inertial impaction.

In other words, inertial impaction would play a more significant role at the entrance.
Another point remaining to better assess the relative contribution of inertial impaction with respect to steam condensation refers to the SPARC-90 hypothesis on the instantaneous thermal equilibrium assumed. This entails that inertial impaction is calculated right after steam condensation. A literature survey on steam condensation in the presence of non-condensible within bubbles, show characteristic times in the range of 10-2 s (Qu et al., 2015, 2017). Based on the classical formulation of mass removal by any mechanism and adapting it to the globule topology, one may derive the following expression for the characteristic time for impaction might be estimated through,

$$t_{imp} = \frac{\pi D_{gl}^3}{\dot{V}_{in} ln\ DF_{imp}} \qquad \text{Eq. 4}$$

By using the information during the fission product injection in Fukushima Daiichi, t_{imp} is expected to be between $5 \cdot 10^{-3}$ s and $4 \cdot 10^{-2}$ s. That is, the same order of magnitude as the steam condensation characteristic time.
Given that there is not a sound foundation to assume a fix sequence in the occurrence of the two phenomena, a parametric analysis to check the effect of switching order of the two removal mechanisms in the injection DF, one may realize (Fig. 9) that no effect should be anticipated on scrubbing efficiency or on size distribution of particles remaining gas-borne in the globule. A plausible hypothesis underneath considering steam condensation first is assuming it occurs at the submerged region of the injector.

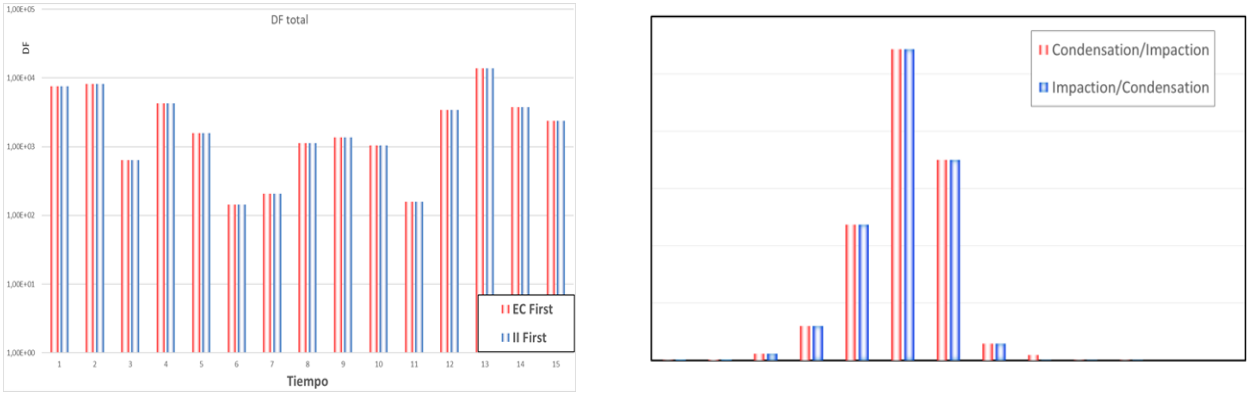

a. Entry region DF b. Airborne particle size distribution

Fig. 7. Impact of the calculation sequence of decontamination mechanisms

As a result, after introducing the modifications presented in this section in SPARC-90, the effect of the two mechanisms governing scrubbing in the 15 times describing the fission product injection changes substantially (dotted line in Fig. 8), it is observed that at some times inertial mechanisms had a non-negligible effect. One may note that the relative contribution to the mass depletion (%) in the entry region is practically the same as in Fig. 6. In other words, the most significant effect of the corrections introduced is dropping the factor 3 from the calculation of the diffusiophoretic deposition at the pool entry.

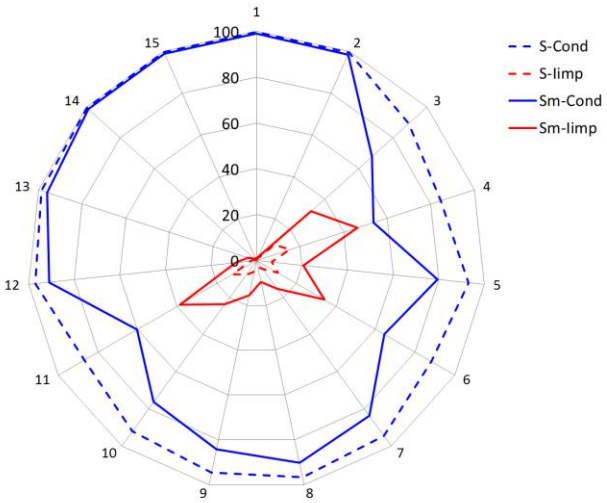

Fig. 8. Relative contribution of steam condensation and inertial impaction

4. JET REGIME

Inertial impaction formulation in SPARC-90 assumes that the gas entering the pool forms a globule that grows until buoyancy force exceeds the adhesion force and it moves upwards through the pool towards the surface. During that period of time a fraction of the particles carried by the gas are unable to follow the gas streamlines and hit the globule front surface thrown by their own inertia. However, under the conditions prevailing in Unit 1 during FP injection into the suppression pool (Fig. 9), gas moves so rapidly that it forms a submerged jet ($We \geq 10^5$).

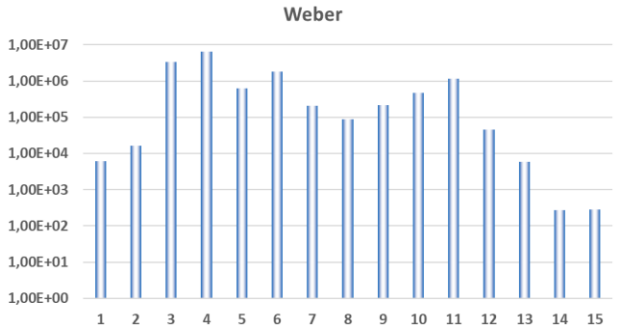

Fig. 9. Weber nondimensional number at 15 time points during fission product injection in the suppression pool of Unit 1.

This new regime means a drastically different interaction between gas and water and, as a consequence, mechanisms responsible for particle removal are unlikely to be described by the SPARC-90 approximation to inertial impaction. These two scenarios (injection regimes) are depicted in Fig. 10 and a deeper discussion might be found in Herranz et al. (2018).

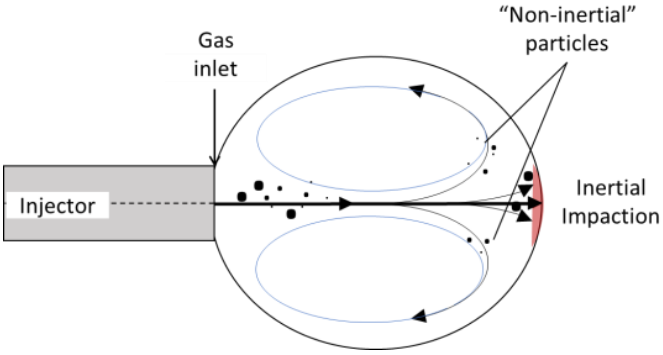

a. Globule regime

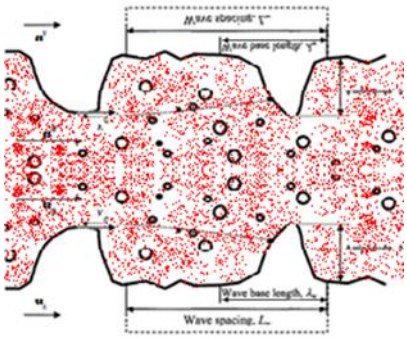

b. Jet regime

(red: particles; blank: water droplets)

Fig. 10. Sketch of injection regimes at the entry of suppression pools

Recently, there have been a number of attempts to model the particle depletion in the jet injection regime, from empirical (Herranz et al., 2018) to pseudo-mechanistic approaches (Berna et al. 2016; Yan et al. 2020). The results of implementing both new approximations for the jet injection regime in the SPARC-90 source code are shown in Fig. 11. Fig. 11(a) displays the retention efficiency at the entry of the pool and Fig. 11(b) does in the entire pool. The main observation is the noticeable difference in the entry region: whenever particles are dragged into the pool in jet regime the empirical correlation sets a limit on the maximum efficiency (98%) linked to the shortcomings of the database used to derive it, while the model calculates efficiencies always lower than the one from the empirical calculation. Even more

interesting, both are estimated to be lower than the one estimated in the globule regime. Given the large uncertainties associated with both jet regime formulations and the high efficiency estimated in all the cases ($\geqslant$ 92.5%), it is not worth discussing these discrepancies in further detail. Interesting enough though, in the overall retention efficiency in the pool differences persist but again they are less than 1%. What might be of some concern is that there are specific conditions in which the globule approximation adopted by SPARC-90 provides the highest value of the retention efficiency. By translating these differences in terms of the total DF (Fig. 12), and bearing in mind that the SPARC-90 uncertainties for each time point were estimated (Herranz et al., 2020) to be about 2 orders of magnitude, the discrepancies stemming from better modelling retention under jet regime are well within that range.

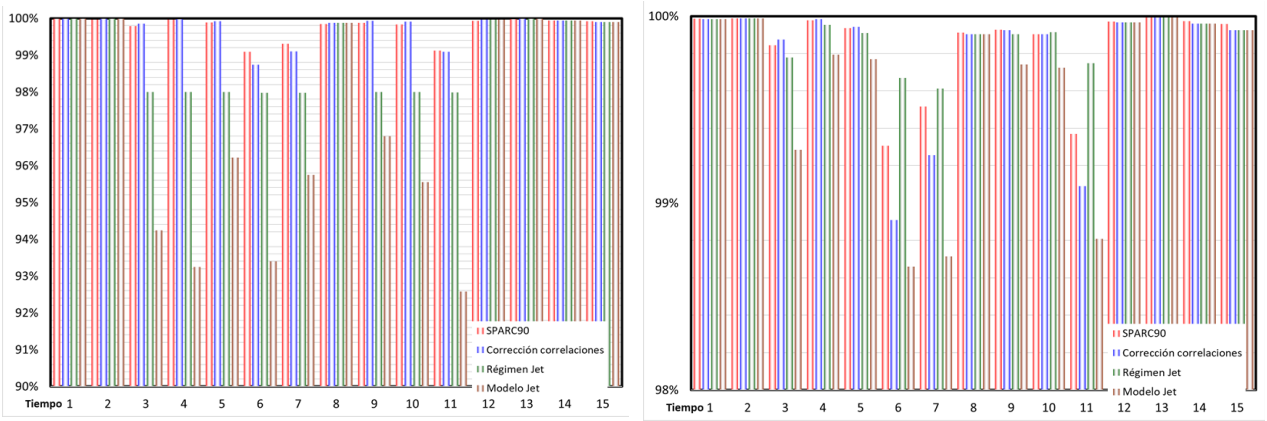

a. Retention efficiency at the entry region b. Total retention efficiency in the pool

Fig. 11. The effect of jet injection on pool scrubbing in Unit 1 of Fukuhsima Daiichi

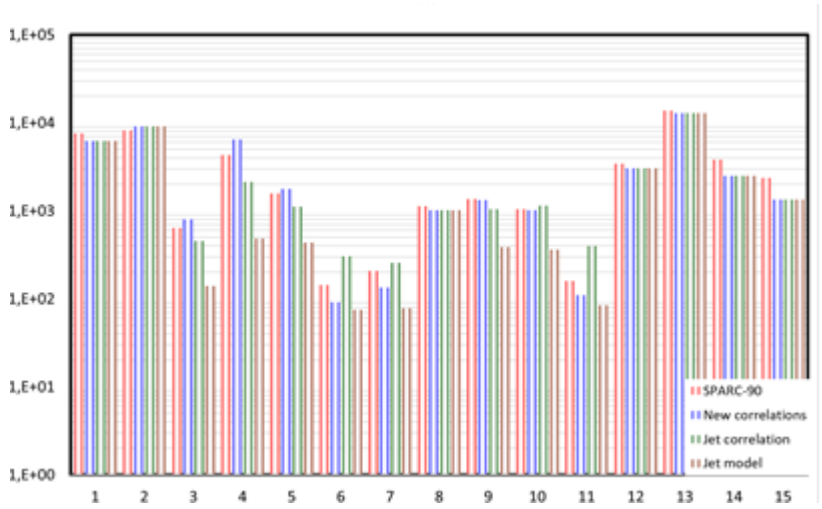

Fig. 12. DF estimates at 15 time points during fission products injection in the suppression pool of Unit 1of Fukushima Daiichi.

Finally, Table 1 shows the overall DF in the suppression pool of the Unit 1 of Fukuhsima Daiichi according to all the approximations made in this study. As said above, discrepancies between the original SPARC-90 estimates and any of the two jet formulations are around a factor of 2.0, much closer than the

uncertainty band associated with original predictions (two orders of magnitude). Therefore, even if physical consistency requires having jet retention properly modeled, the calculations done so far seem to indicate that quantitative differences will not change the overall picture of pool scrubbing in Fukushima Daiichi.

Table 1. Integrated DF from the approximations in the present study.

	SPARC-90	**SPARC-90mod**	**Jet correlation**	**Jet model**
m_{in} (kg)	45.29			
m_{out} (kg)	0.085	0.117	0.059	0.192
DF	5.35E+02	3.86E+02	7.69E+02	2.37E+02

5. FINAL REMARKS

This work deepens in the retention of fission products in the suppression pool of Fukushima Daiichi, according to the model postulated with the MELCOR 2.1 code. Some important highlights can be drawn from this study:

- The suppression pool was an efficient trap of fission products carried by steam and hydrogen entering through the quencher. An overall DF higher than 100 might be considered a "ground value"; in other words, more than 99% of fission products reaching the pool were trapped.
- Most of fission products carried into the suppression pool would have been absorbed in the region around the injection point.
- The governing mechanisms responsible for fission products absorption within the pool would have been diffusiophoresis (driven by steam condensation onto gas-water interface) and inertial mechanisms capable of dragging particles out of the gas streamlines towards the interface.

These highlights can be considered generic and independent of the code shortcomings and/or the in-code modelling of the prevailing phenomena. Nonetheless, the present study has led to:

- A more sound formulation of steam condensation, which although still based on instantaneous thermal equilibration of carrier gas and water, removes an unjustifiable 3.0 factor.
- A refinement of the inertial impaction correlation derived by using what considered the proper database.
- A demonstration of that the sequential order in which the effects of removal mechanisms are calculated (first diffusiophoresis and, then, inertial impaction) does have no influence on the decontamination at the entry region. The same retention efficiency and equally sized airborne particles, result from the calculation no matter the calculation order.

By enlarging the modelling capabilities to encompass jet regime, this work has shown that:

- Jet scrubbing retention in the Unit 1 of Fukushima Daiichi would have resulted in no drastic discrepancies with respect to what initially predicted, despite the extreme differences of inertial removal mechanisms with respect to the globule scrubbing. The reason for this is likely the dominant nature of particle removal due to steam condensation.
- Reducing the uncertainties associated to pool scrubbing estimates in the Unit 1 of Fukushima Daiichi would require an accurate determination of boundary conditions like steam content in the carrier gas and water temperature than enhanced modelling of removal mechanisms.

ACKNOWLEDGEMENTS

The authors thank the partners in the Program Review Group of the OECD/ARC-F project for their interest and motivating and inspiring questions and comments along the project.

REFERENCES

Berna C., Escrivá A., Muñoz-Cobo J.L., Herranz L.E., "Enhancement of the SPARC90 code to pool scrubbing events under jet injection regime", Nuclear Engineering and Design 300, 563-577, 2016.

Bocanegra R., Herranz L.E., 2020. The importance of characterizing input uncertainties in severe accident analyses. The effect on pool scrubbing modeling in a Fukushima Unit 1 sequence. Annual Meeting of the Spanish Nuclear Society, Virtual meeting, 2020.

Fontanet J., Herranz L.E., Ramlakan A., Naicker L., 2009. Modelling of HTR confinement behaviour during accidents involving breach of the helium pressure boundary. Science and Technology of Nuclear Installations, Vol. 2009, Special Issue on Innovative Gas-Cooled Reactors, 687634, 11 pp., https://doi.org/10.1155/2009/687634.

Herranz L.E., Tardáguila R.D., Berschart T., Lind T., Morandi S.; 2014. Remaining issues in pool scrubbing: major drivers for experimentation within the EU-PASSAM project. Proceedings of ICAPP 2014, Charlotte (USA), April 6-9, 2014.

Herranz L.E., Aguado C., Sánchez F.; 2019. Uncertainty quantification of in-pool fission product retention during BWR station BlackOut sequences. Annals of Nuclear Energy, 141, 107290, https://doi.org/10.1016/j.anucene.2019.107290

Herranz L.E., López C; 2020. Challenges and sensitivities in the modelling of Fukushima Daiichi Unit-1 unfolding with MELCOR 2.2. Annals of Nuclear Energy 141, 107348. https://doi.org/10.1016/j.anucene.2020.107348.

Fontanet J., Herranz L.E., Ramlakan A., Naicker L., 2009. Modelling of HTR confinement behaviour during accidents involving breach of the helium pressure boundary. Science and Technology of Nuclear Installations.

Moody, F. J., Nagy, S.G.; 1983. Estimated Effects of Interfacial Vaporization on Fission Product Scrubbing. Proceedings of ANS-ENS International Meeting on Light Water Reactor Severe Accident Evaluation, LaGrange Park, lllinois.

Qu, X., Revankar, S. T., & Tian, M. (2017). Numerical simulation of bubble formation and condensation of steam air mixture injected in subcooled pool. Nuclear Engineering and Design, 320, 123-132. https://doi.org/10.1016/j.nucengdes.2017.04.009

Qu, X., Tian, M., Zhang, G., & Leng, X. (2015). Experimental and numerical investigations on the air–steam mixture bubble condensation characteristics in stagnant cool water. Nuclear Engineering and Design, 285, 188-196. https://doi.org/10.1016/j.nucengdes.2014.12.031

Ranz, W.E. y Wong, J.B. (1952). Impaction of Dust and Smoke Particles on Surface and Body Collectors. Ind. Eng. Chem., 44(6): 1371-1381. doi: 10.1021/ie50510a050

Pool Scrubbing

in

Unit 1 of Fukushima Daiichi

Luis E. Herranz

Unit of Nuclear Safety Research
CIEMAT (Spain)

This work has been done in the frame of the OECD/ARC-F Project

SNETP Sustainable Nuclear Energy Technology Platform

NUGENIA TA2 Severe Accidents Nuclear Generation II&III Alliance

How much
uncertainties in pool scrubbing modeling
could affect predictions of
FPs trapping in the 1F1 accident?

CONTENTS

- BACKGROUND
- MODELING GOVERNING PHENOMENA
- LATEST RESULTS
- FINAL REMARKS

BACKGROUND

Suppression Pool Modeling

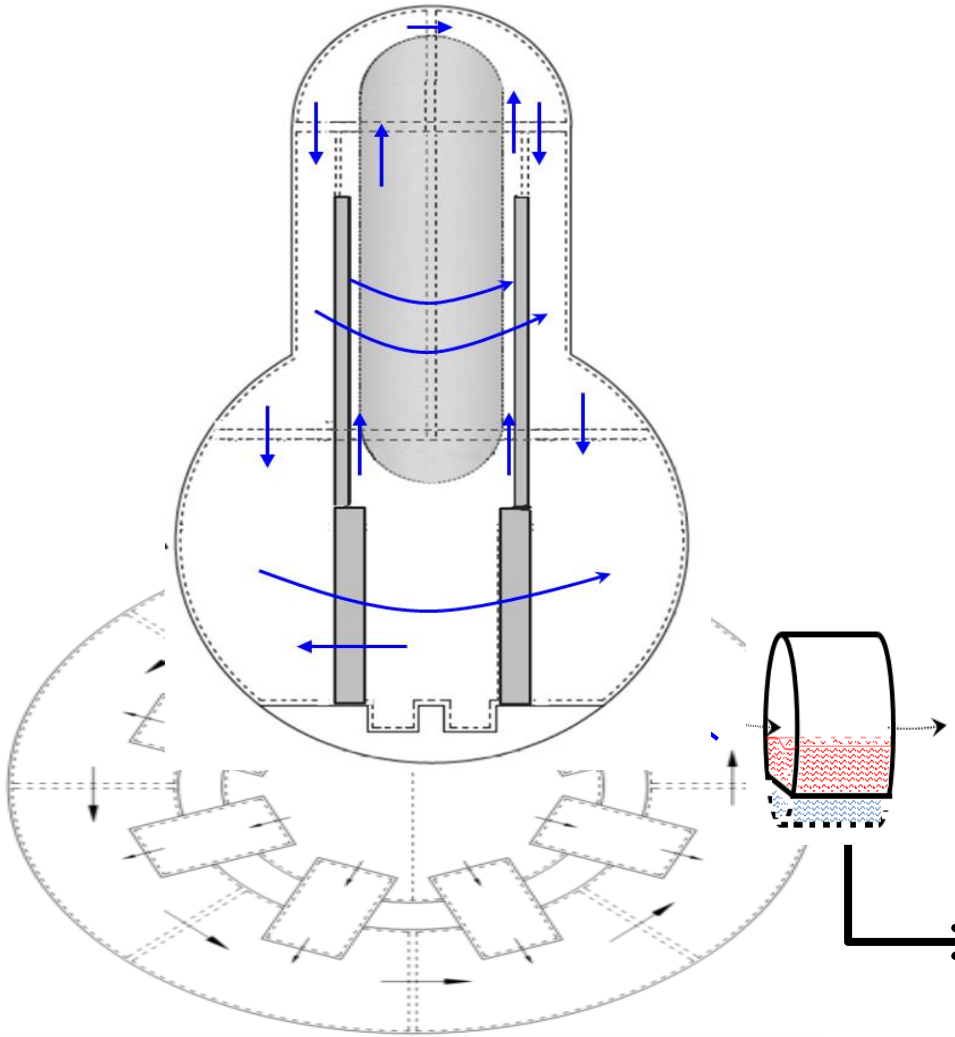

RPV Concentration

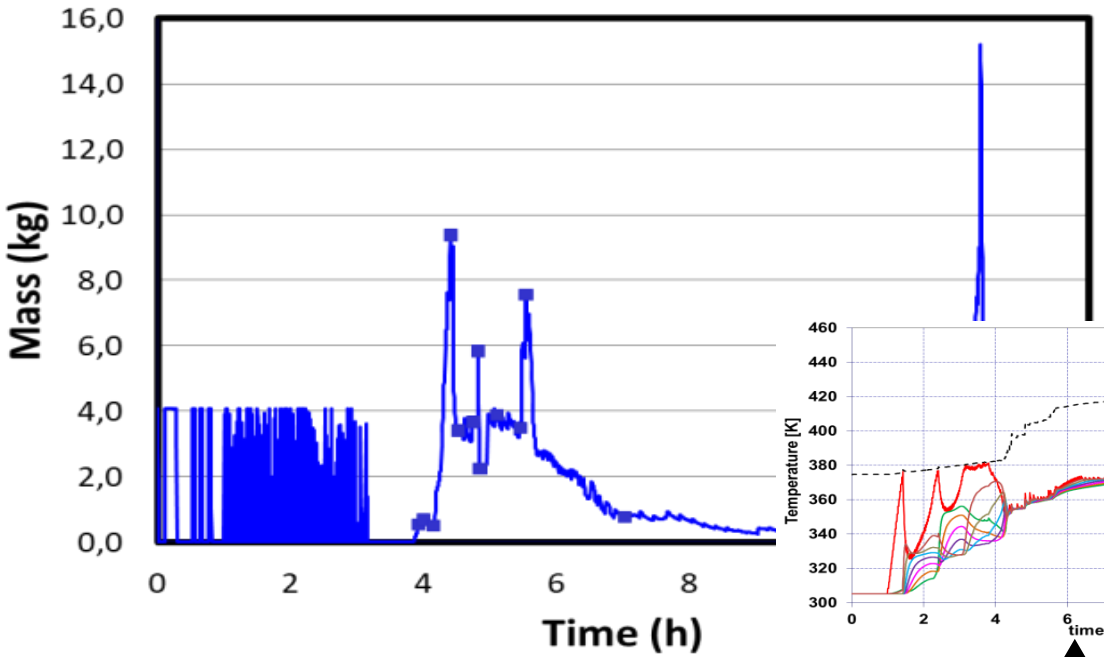

"Perfect stratification" approach.

MELCOR Estimates

"SRV Efficiency"

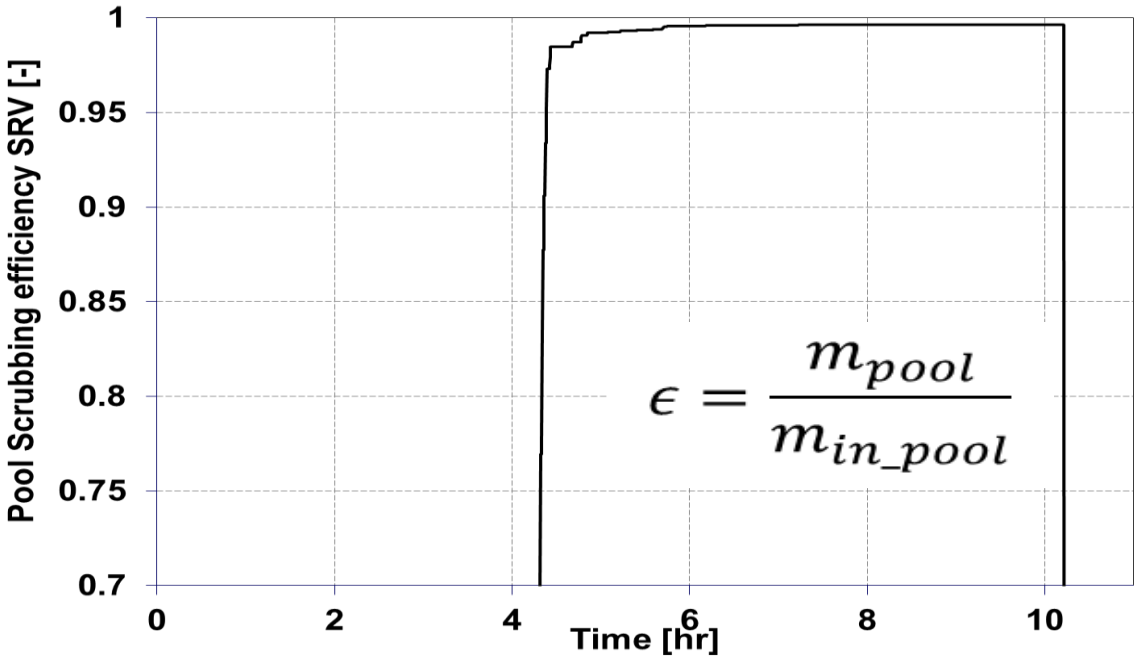

"WW Efficiency"

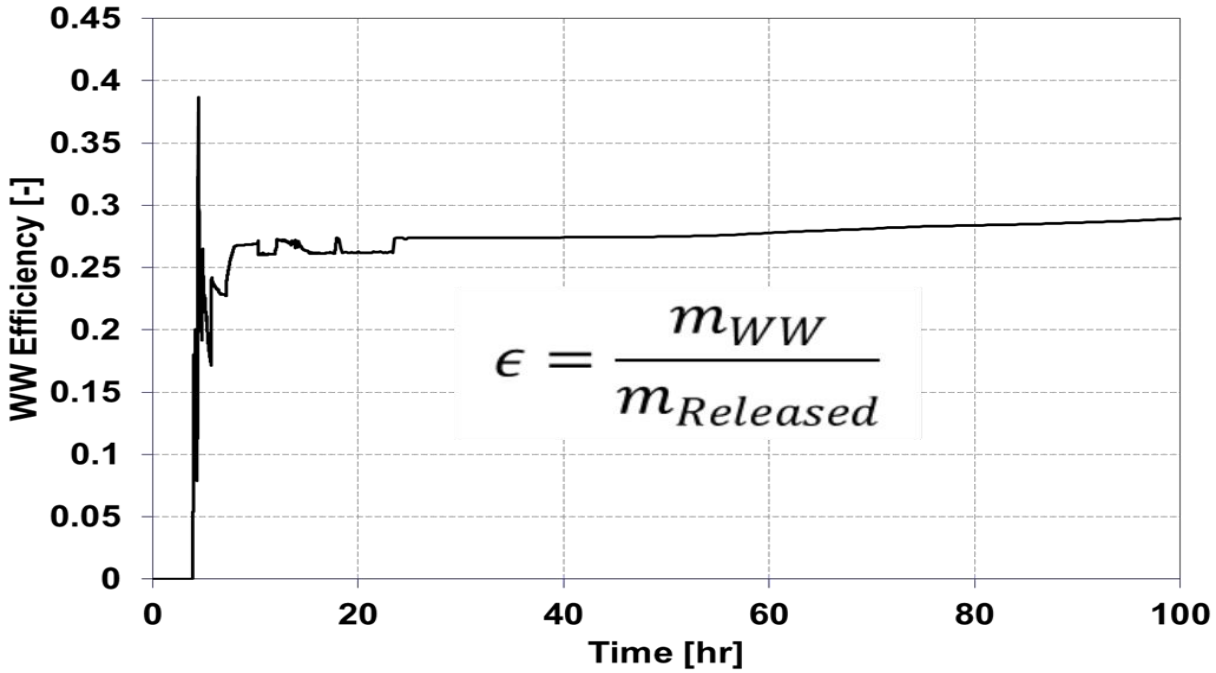

A substantial fraction of FPs might not have reached WW pool (RPV;DW)!

SPARC90 DF Estimates

	time (h)	DF	η (%)
Time 1	3.92	7.8E+03	99.99%
Time 2	3.99	8.1E+03	99.99%
Time 3	4.32	6.4E+02	99.84%
Time 4	4.43	4.3E+03	99.98%
Time 5	4.61	1.6E+03	99.94%
Time 6	4.82	1.4E+02	99.31%
Time 7	4.83	2.1E+02	99.52%
Time 8	4.95	1.1E+03	99.91%
Time 9	5.06	1.4E+03	99.93%
Time 10	5.47	1.4E+03	99.90%
Time 11	5.53	1.6E+02	99.37%
Time 12	5.73	3.4E+03	99.97%
Time 13	7.04	1.4E+04	99.99%
Time 14	12.15	3.8E+03	99.97%
Time 15	12.24	2.4E+03	99.96%

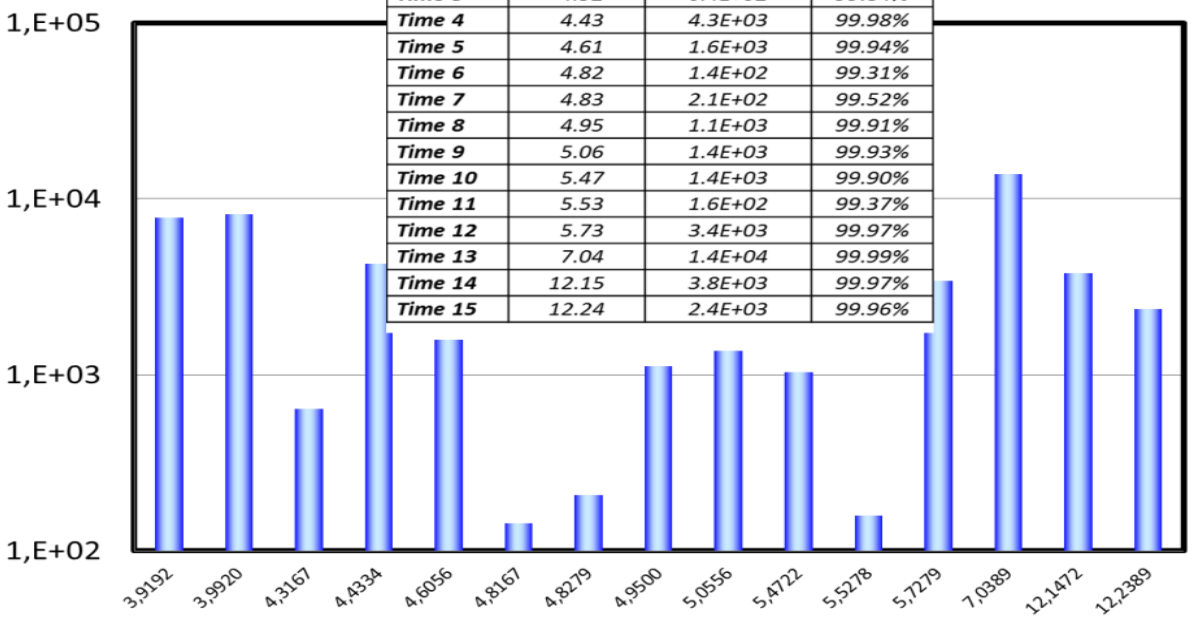

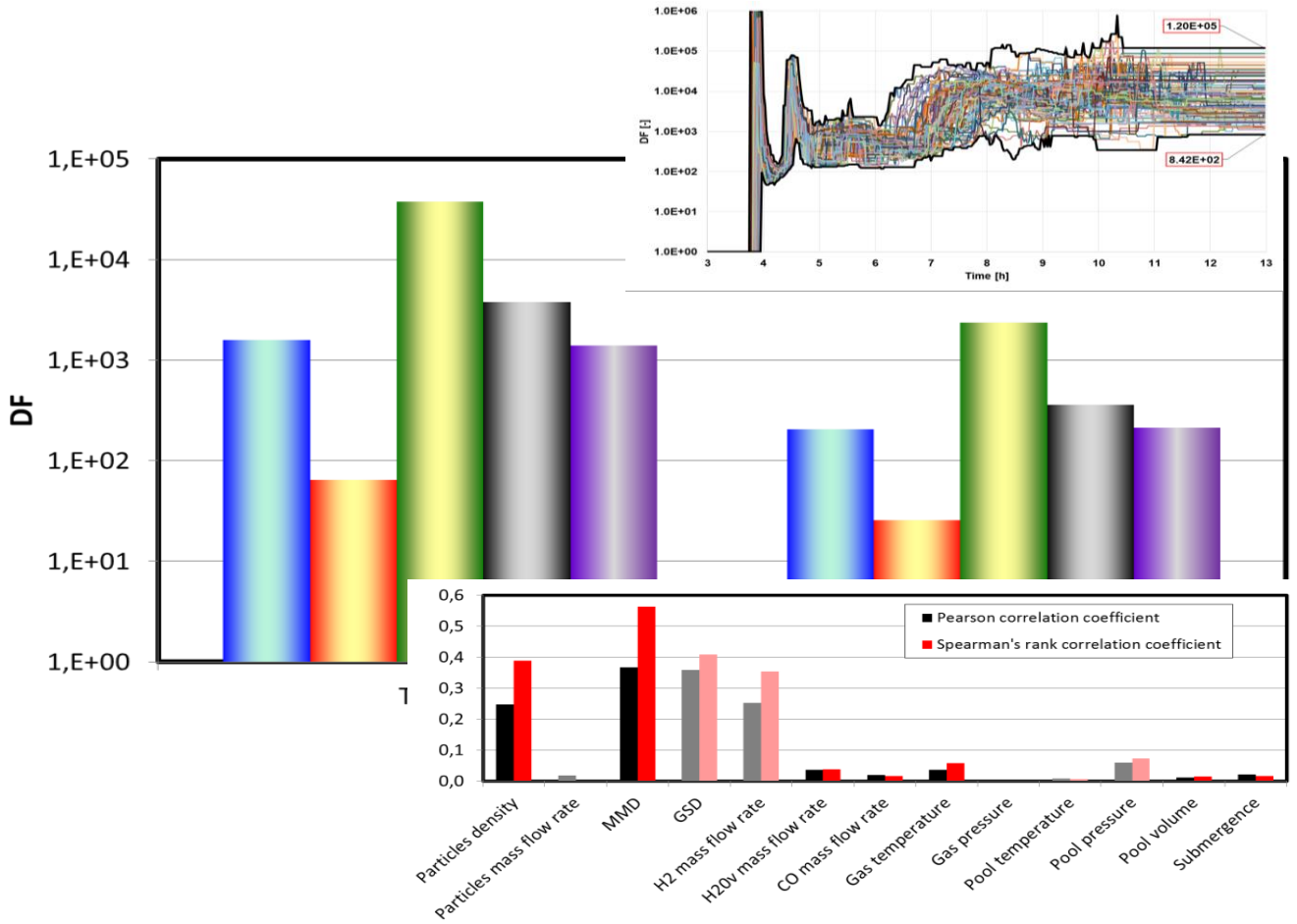

MODELING GOVERNING PHENOMENA

Identification

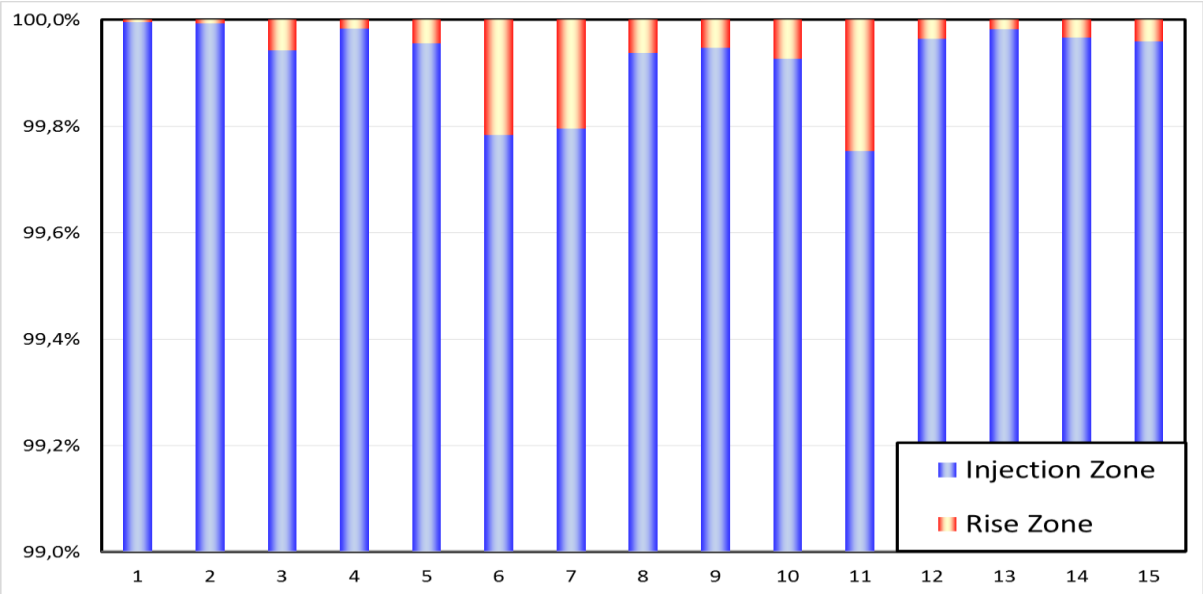

Scrubbing Share

(mass %)

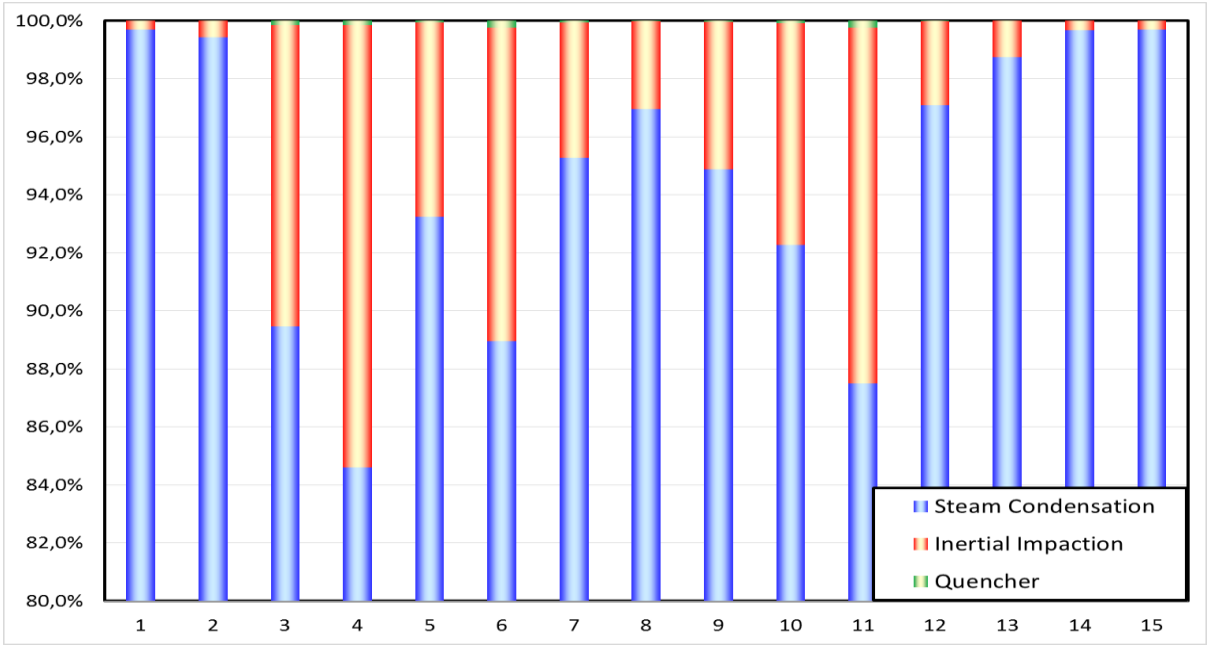

SPARC Formulation Enhancements

- **Steam condensation** $S \geq 1.0 \rightarrow p_{steam} = p_{sat}(T_{pool})$ $DF_{EC} = \frac{{X_{nc}}^{eq}}{{X_{nc}}^{in}}$

  Hypo: *"Instantaneous thermodynamic equilibrium"*

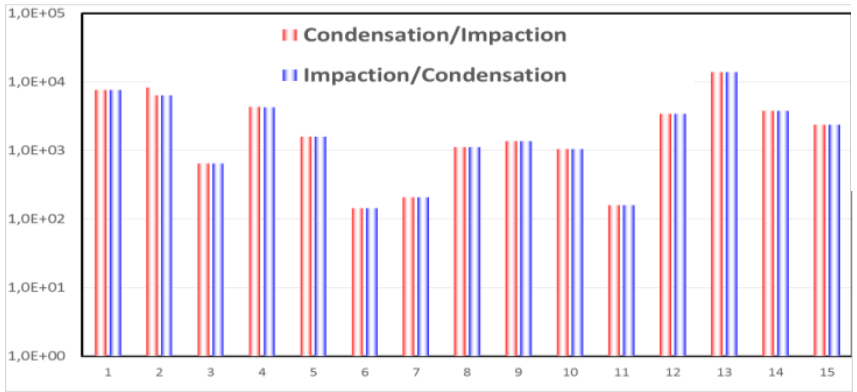

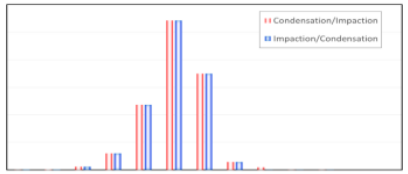

- **Inertial impaction**

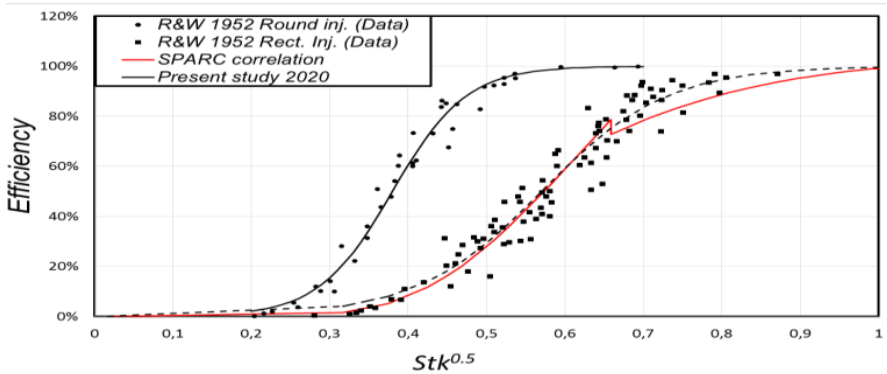

Ranz & Wong, 1952

$$\varepsilon = 1 - \frac{1}{1 + \exp\left(\frac{\sqrt{Stk} - 0{,}38}{0{,}047}\right)}$$

Enhancement Effect

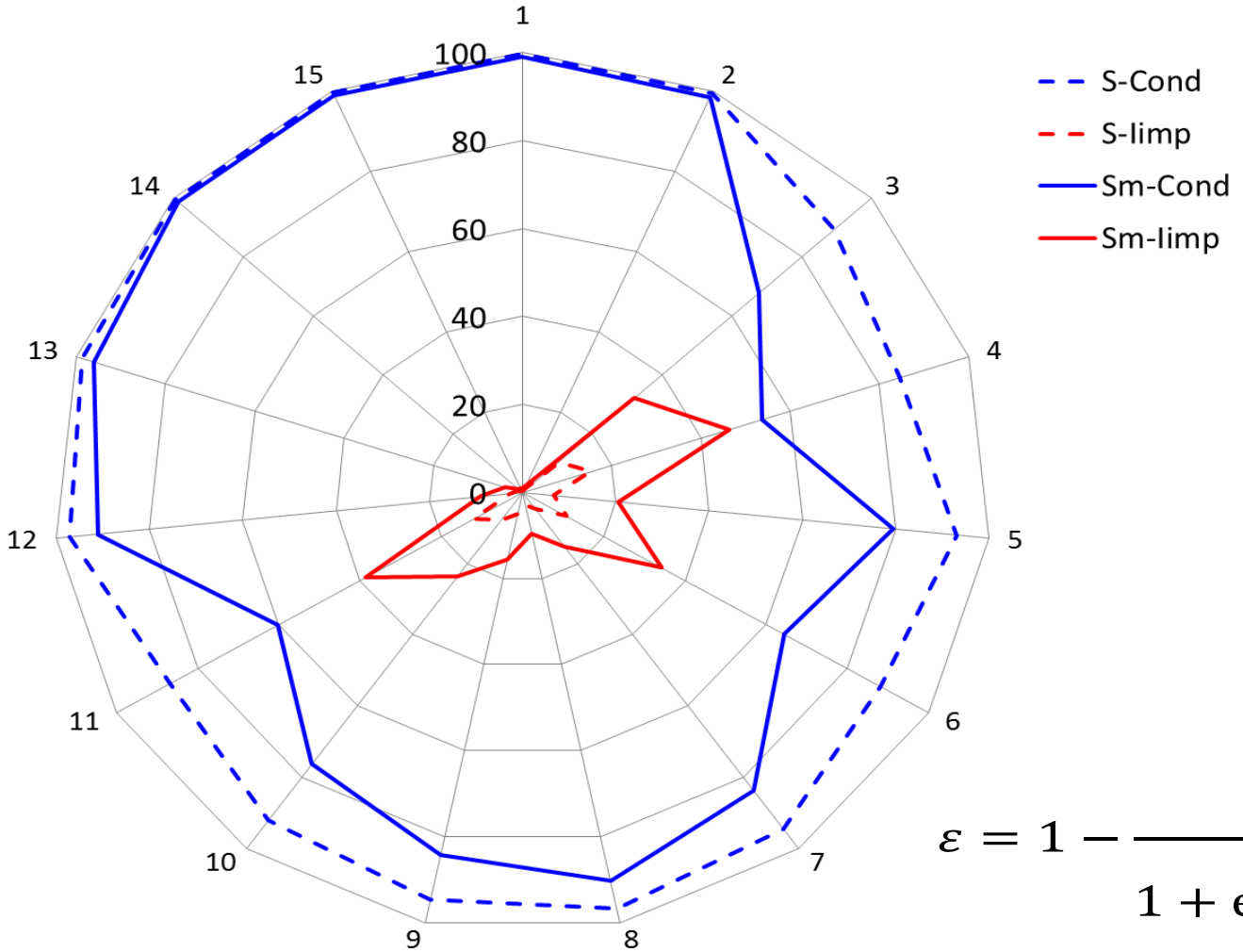

$$DF_{EC} = \frac{{X_{nc}}^{eq}}{{X_{nc}}^{in}}$$

$$\varepsilon = 1 - \frac{1}{1 + \exp\left(\frac{\sqrt{Stk} - 0{,}38}{0{,}047}\right)}$$

SPARC Extension

Jet Regime

(We≥10^5)

About 70% of the mass entered the pool under jet injection regime (We≥10^5)

SPARC-90

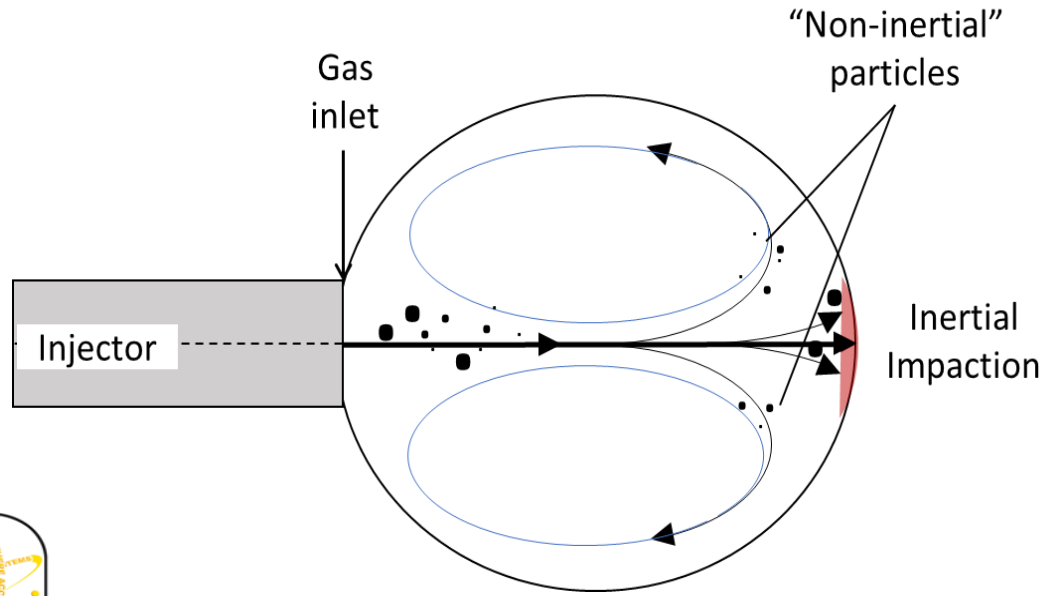

1F-Unit 1

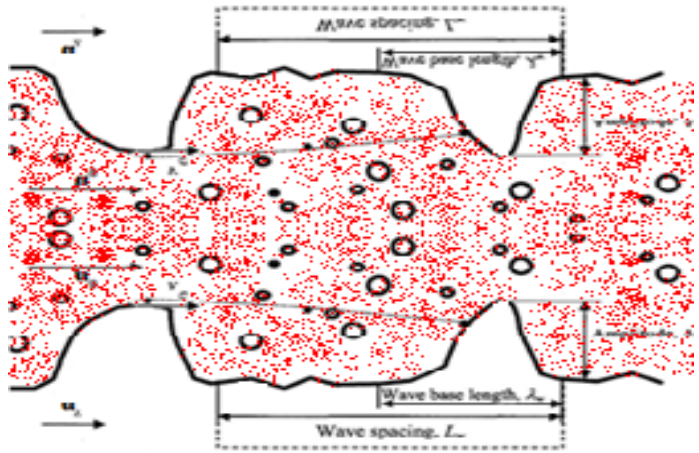

Pool Scrubbing

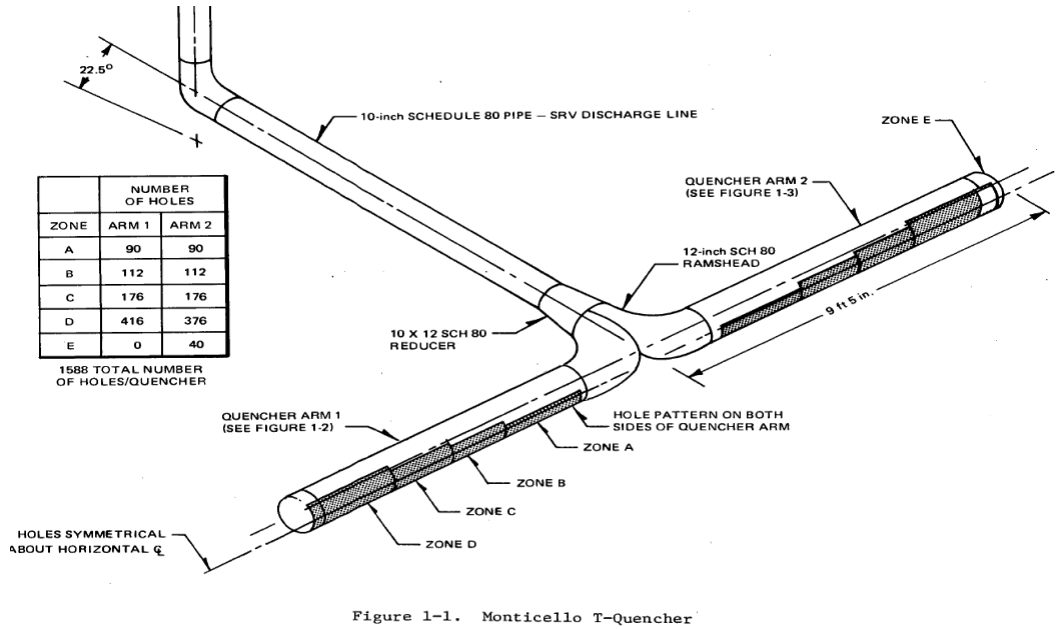

ZONE	NUMBER OF HOLES ARM 1	ARM 2
A	90	90
B	112	112
C	176	176
D	416	376
E	0	40

1588 TOTAL NUMBER OF HOLES/QUENCHER

Figure 1-1. Monticello T-Quencher

We Number

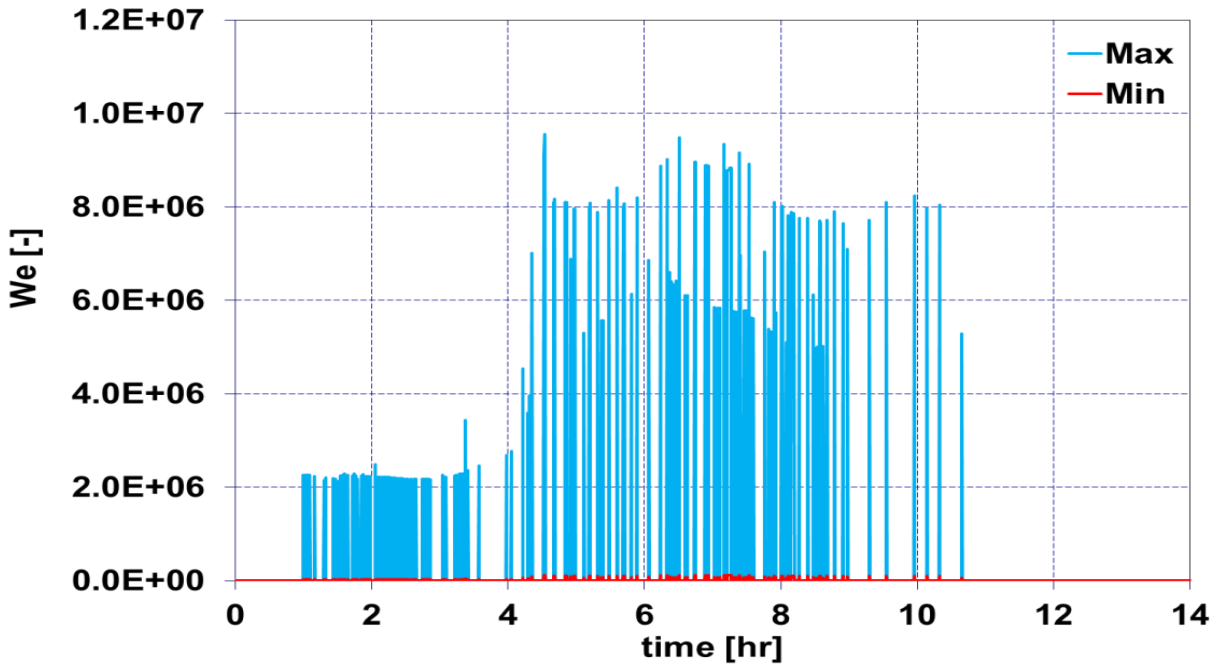

$$We = \frac{\rho_p \cdot v_g^{\,2} \cdot d_g}{\tau}$$

Jet Modeling

- ***Semi-empirical correlation*** *(Herranz et al., 2018)*

$$\varepsilon[\%] = \frac{0{,}98}{1 + 1{,}0847\,\exp(-1{,}0528\,10^{8}\,Stk^{3{,}7885} - 0{,}7257\,S)} * 100$$

- ***"Analytical" correlation*** *(Berna et al., 2012 "like": Yan et al. 2020)*

$$\boldsymbol{\eta_t = 1 - (1 - \eta_b)(1 - \eta_d)}$$

Gas-liquid interface

Droplets

$$\eta = 1 - \left(1 - \eta_{\text{impact}}\right) \cdot \left(1 - \eta_{\text{intercep}}\right) \cdot \left(1 - \eta_{\text{diff}}\right)$$

Latest Results (1)

Inlet region

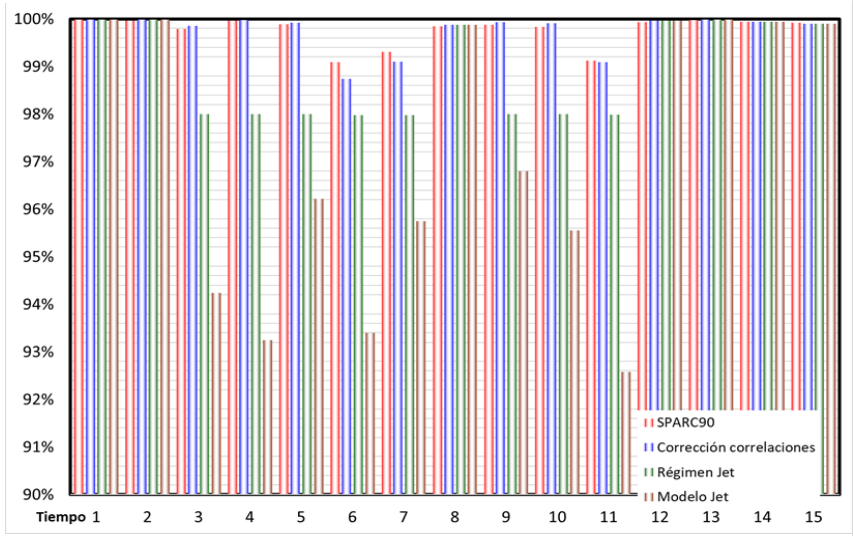

Entire pool

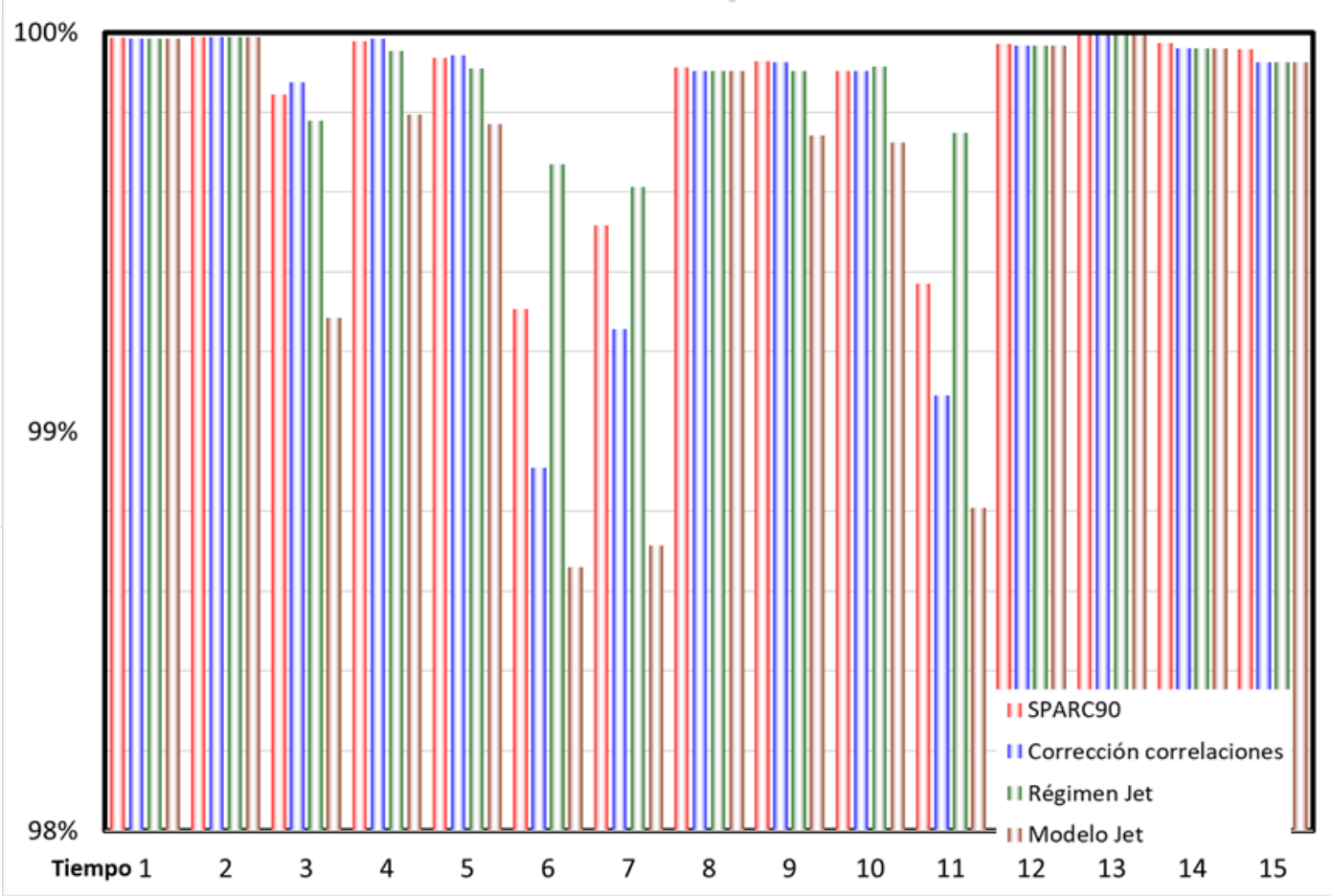

Scrubbing Share

(mass %)

Latest Results (2)

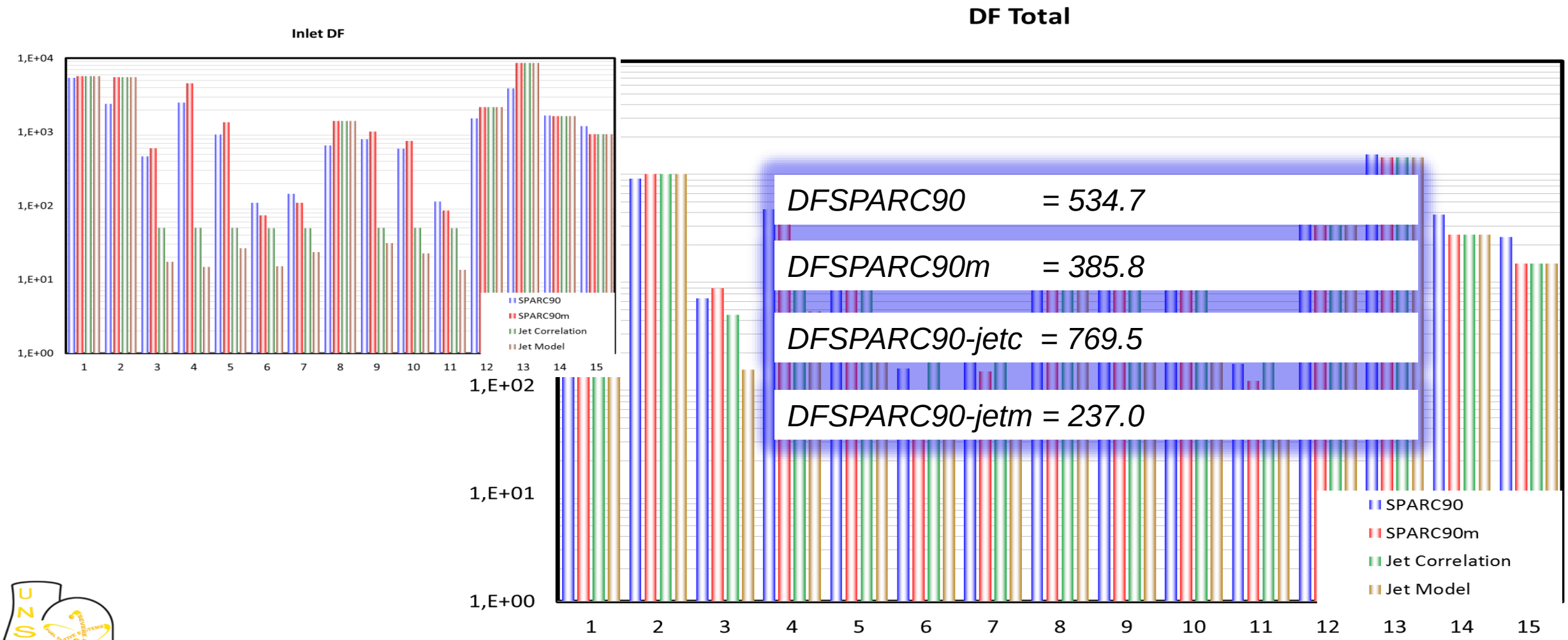

FINAL REMARKS

- ***Uncertainties affecting pool scrubbing DF in 1F1 are dominated by the prevailing boundary conditions:***
  - *Postulated scenario.*
  - *Assumptions made as for carrier gas and pool thermal state.*

- ***The quantitative impact of model uncertainties have a moderate quantitative impact.***
  - *Huge uncertainties in high DF domain (not much effect, though).*
  - *Still huge uncertainties in jet scrubbing modeling.*

- ***Most mass likely retained in the inlet nearby***
  - *Phase change was responsible for most mass retention*
  - *In-bulk mechanisms hardly play any role.*

Thank you for your attention!

Bubbles dynamics under pool scrubbing conditions for iodine compounds trapping applications

M. FARHAT[1,2], P. NERISSON[1], M. CHINAUD[2], Olivier VAQUELIN[2], L. CANTREL[1]

[1]: Institut de Radioprotection et de Sûreté Nucléaire (IRSN), 13115 St Paul Lez Durance
[2]ds: Aix-Marseille Université, IUSTI UMR 7343, 5 rue Enrico Fermi, 13453 Marseille

Mohamad.Farhat@irsn.fr

ABSTRACT

Accident management systems are highly regarded in the designing of nuclear power plants, in order to mitigate as much as possible the radiological consequences of accidents. Wet FCVS is one of these systems that aims to trap fission products in liquid bath by pool scrubbing as well as suppression pool in BWR.
Relying on set of bubble dynamics and retention mechanisms, it is essential to characterize the relevant hydrodynamics in pool scrubbing conditions, for the development and assessment of models. Injecting air induces bubble-bubble interactions which provoke, depending on the flow rate, random formation of bubbles affecting their size, shape, and frequency of bubbling.
Experimental work is carried out to reveal the impact of these interactions on the formation of bubbles at a submerged orifice. Based on the different bubble's morphologies that have been observed, we first investigated the bubble-bubble interactions and then classified different bubbling regimes depending on the position of bubbles' coalescence. The biggest bubble formed above the orifice, after the coalescence of bubbles, is referred by a globule. On the basis of the morphological description of bubbles throughout our experiments, two approaches in characterizing the bubbles sizes were developed. The first conventional approach is based on the assumption of single bubbling formation and spherical shape of bubbles. Upon this approach, the comparison of characteristic bubble size V_b, which is computed after determining the bubble departure frequency f_b, shows a good agreement with literature models. However, this approach is not consistent with flow morphology experimentally observed. Therefore, and through a proposed phenomenological approach, we aimed to characterize experimentally the globule formation frequency f_G and its volume V_G, by tracking the globules formation through image processing and reconstructing bubble shape with axisymmetric assumption. Experimental work characterizing bubble dynamics in the injection zone for different flow conditions (orifice diameter, injection flowrate, and submergence) is presented. In parallel, decontamination factors (DF) for iodine compounds are experimentally determined, in order to be able in the long term to correlate iodine trapping with hydrodynamics considerations.

Keywords: Pool scrubbing, bubble dynamics, aperiodic formation, bubble volume

1. INTRODUCTION

In a severe nuclear accident where a significant damage of reactor fuel results in partial or complete core meltdown, fission products can be transported by various natural processes (chemical reactions, aerosol behaviour, condensation, etc.) into the containment or environment. The PWR (Pressurized Water Reactor) nuclear facilities are therefore featured and equipped with accident management systems designed to prevent potential abnormal situations and limit their hazardous consequence in case of any accident. One of these

systems is the Filtered Containment Venting System, FCVS [1], which aims to prevent containment failure (removing heat and attenuating pressure) by venting its atmosphere comprising fission products into liquid pools [2]. Pool scrubbing can also occur in SGTR (Steam Generator Tube Rupture) accidental situation on PWR and in pressure suppression pools on BWR (Boiling Water Reactor). This bubbling of the gaseous radioactive material leads to the formation of bubbles. During their rise along the pool, fission products can reach the bubble surface due to mass transfer mechanisms, then, are trapped in the liquid pool. This phenomenon, known as pool scrubbing, has the potential to reduce the release of radioactive species to environment. Pool scrubbing relies on set of bubble dynamics and mass transfer mechanisms into the liquid phase, which are dependent of different flow conditions. For that, extensive experimental programs have been conducted to characterize the bubble hydrodynamics and retention of mixtures carried by injected gas into liquid pools [3]. Yet, developed pool scrubbing codes (BUSCA, SUPRA, SPARC) have not shown accurate simulations for the existing experimental databases in determining decontamination factor (DF). The latter refers to retention efficiency as it is the ratio of fission product mass flowrate entering the pool to the fission product mass flow rate leaving it.

$$DF = \frac{\dot{m}_{in}}{\dot{m}_{out}}$$

Large effort is ongoing in the frame of the IPRSECA project to cover this issue.
In order to improve the pool scrubbing and retention modelling, a better characterization of bubble hydrodynamics should be performed, apart from classical assumptions, and considering different encountering phenomena. Since massive research have been conducted to characterize the behavior and dynamics of bubble formation [4-6], however few of them aimed to characterize the chaotic behavior bubbling [7-8]. That is because in high flowrate injection systems, bubble-bubble interactions is considered to be key of nonlinear behavior of bubbles**,** as inertial effects over dominate the interfacial – viscous forces**.** In Farhat et al. [9], it is reported that classical approaches to characterize the bubble dynamics are not consistent with the flow morphology. There is a large uncertainty for classical models in predicting the bubbles sizes, therefore, the corresponding mass transfer. Kyriakides [8] et al. stated that beyond a certain flowrate, an irregular large bubble is formed after the coalescence of several bubbles just above the orifice, which is characterized phenomenologically in Farhat et al.

In the pool scrubbing facility there are three hydrodynamic zones in the pool. Each zone has its specific contribution depending on different removal mechanisms. There is an injection zone where there is the globule bubble formation, then the transition zone where globule breaks up during its rising and finally there the bubble rise zone which is identified as a horizontally expanding bubble swarm that consists of tiny equal sized bubbles. Given that significant retention in expected by some authors in the injection zone [10], experimental work is carried out in the present study to characterize the bubble dynamics in this zone.

Thus, in the present study, experimental work is carried out to characterize the bubble dynamics in the injection zone for different flow conditions (orifice diameter, injection flowrate, and submergence). An optical technique was implemented in order to characterize the globule formed from different orifices sizes at different flow rates and pool submergence. Besides, first experiments of DF measurements have been performed simultaneously, for CsI aerosols. Finally, the dependence of the decontamination factor on the injection flow rate and Weber number, $\mathrm{We} = \frac{\rho_g {U_{inj}}^2 d_o}{\sigma} = \frac{16\,\rho_g {Q_{inj}}^2}{\sigma\pi^2 {d_o}^3}$, will be discussed.

2. EXPERIMENTAL WORK

Different techniques have been used in the literature for investigation of bubbling through submerged orifice [11-14]. At high flowrates, bubbles behavior limit the capability of techniques that provide local measurements, due to the bubble-bubble interactions. In our experiments, bubble hydrodynamics

measurements are carried out mainly with a high-speed camera technique, and based on images processing, allowing tracking of bubbles evolution. In parallel, DF measurements are performed by determining CsI quantities upstream and downstream the liquid bath, using chemical analysis techniques.

2.1. Experimental setup

The experimental tests were carried out on TYFON (Trapping and hYdrodynamics of FissiON products behaviour in pool scrubbing) facility, shown on figures 1 and 2. The facility is designed to perform experiments coupling hydrodynamic, thermal hydraulic, and decontamination factor measurements for various FP compounds (iodine compounds such as volatile I_2 or CH_3I, aerosols). Eventually, this allows to investigate the dependence of the bubble hydrodynamics and decontamination factor on the different experimental aspects.
Air is injected from single nozzle (2 mm, 5 mm, 10 mm, 20 mm, and 50 mm) submerged in a stagnant liquid column. The bubble column is of 500 mm internal diameter and afford pool submergence of 1.3 m, which corresponds to a volume of 250 L. The interior walls of the column are made up of stainless steel ‘‘mirror polished’’ to effectively prevent the adsorption of iodine composites on its surfaces. Moreover, it is equipped with six transparent windows permitting visualization of flow using the high-speed camera ‘’Phantom Speed sense” VEO-E’’, which could take 3000 images per second at 1280 × 800 pixels.



Figure 1- TYFON facility

The column is thermally insulated, and the liquid bath can be heated up to 90°C according to heating cords around the column external surface. Five thermocouples are distributed between the injection and the height of the free surface of the pool, to maintain the temperature's measurement of the pool.

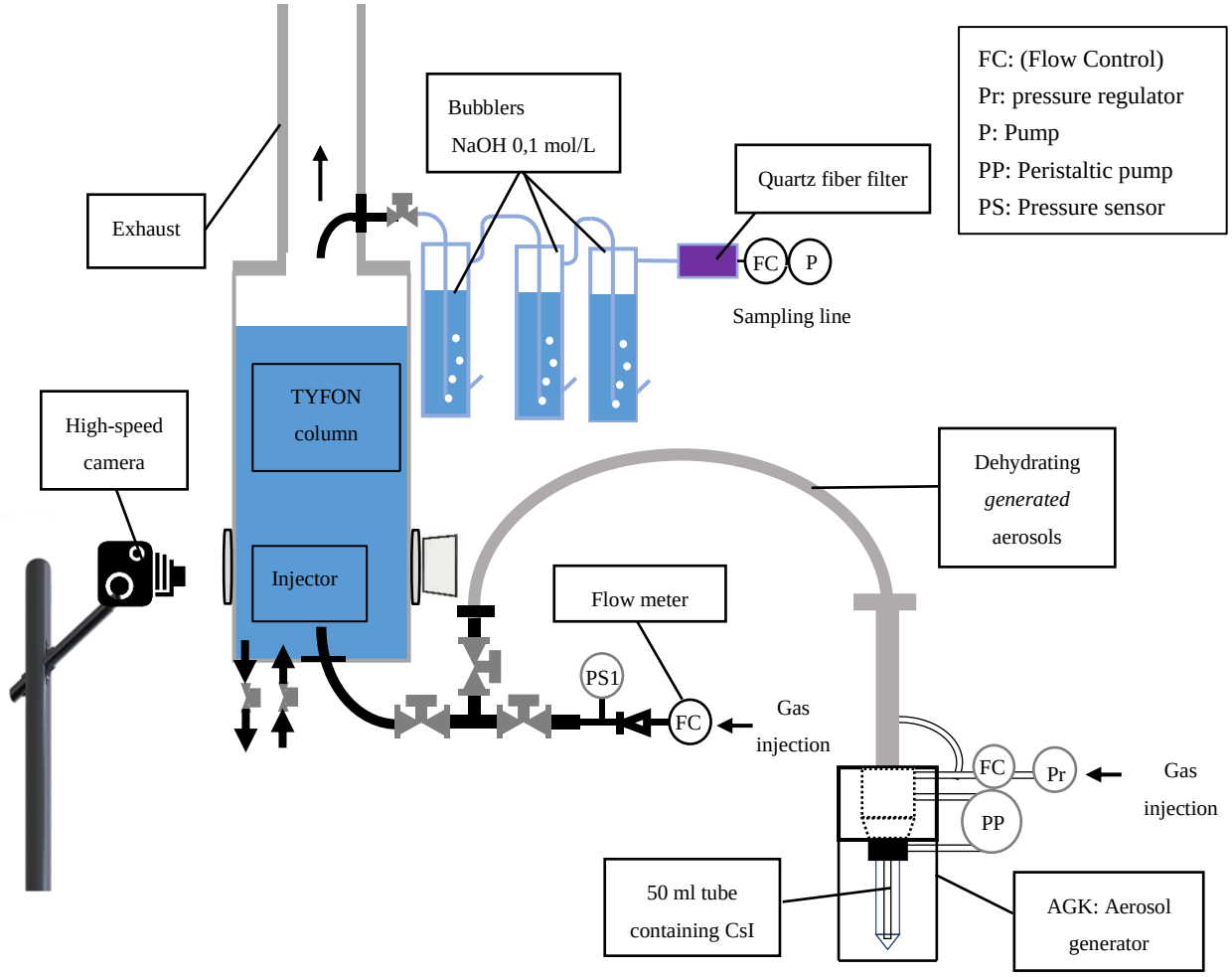

Figure 2- Schema of the experimental setup in CsI injection configuration

2.2. Data treatment

The measurement system of bubble hydrodynamics is composed of a high-speed camera, a LED light source with a diffuser, and associated to the Dantec-Dynamics software. A high-speed camera is used to obtain the flow visualizations and describe the bubble shapes and sizes by image processing. Acquisition of images is performed with 2500 images per second, lasting for 30 seconds.

A background light is used on the opposite window to the camera, in order to compensate the illumination while setting low aperture values of the camera. The latter serves in decreasing the obscurity of images due to the rapid motion of bubbles.

The contrast of the raw images are adjusted and blurred to reduce background noise. This is followed by removing noise from images through filtering the grey-scale images using a pixel-wise adapting low-pass

wiener filter. Thereafter, the contours of structures are detected using the edge-detection algorithm as shown in figure 3.

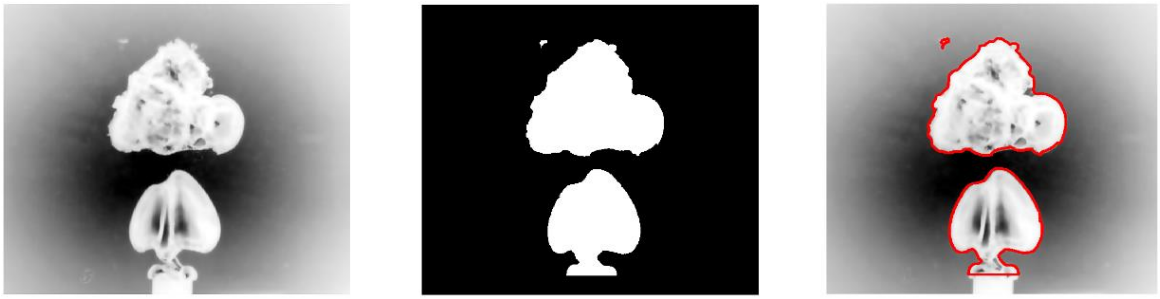

Figure 3- Image processing; (a): Sobel filter, (b): Binarization, (c): Detection of contours

2.3. Globule characterization

The formation and rising process along the pool exhibit different behavior and regimes. Thanks to the different phenomenology encountered in each zone, it is possible to distinguish the onset of each zone. There is an injection zone where there is the globule formation, which is the biggest bubble formed above the orifice, after the coalescence of bubbles. Then the bubbles break up during the rising flow (break up zone) and finally there is a zone with the bubble swarm (bubble rise zone, where bubbles reach their terminal velocities).

2.3.1 Globule frequency

For the frequency of globule, an event is recorded when a complete formation of a globule is achieved. The latter takes in consideration the coalescences of two or more or bubbles and the re-attachment of the formed structure to the orifice. The quantification of the globules formation is done through analyzing a chronograph of bubbles evolution. Therefore, we are capable of differentiating between the events of bubbles departure and globule formation [9].

2.3.2. Globule Volumes

At the instant where a detected structure is detached finally from the orifice, the globule volume is computed numerically by considering a unitary volume corresponding to a pixel in a binarized image. Then a cylindrical revolution of the pixels is assumed around an equidistant line with ax-symmetric assumption.

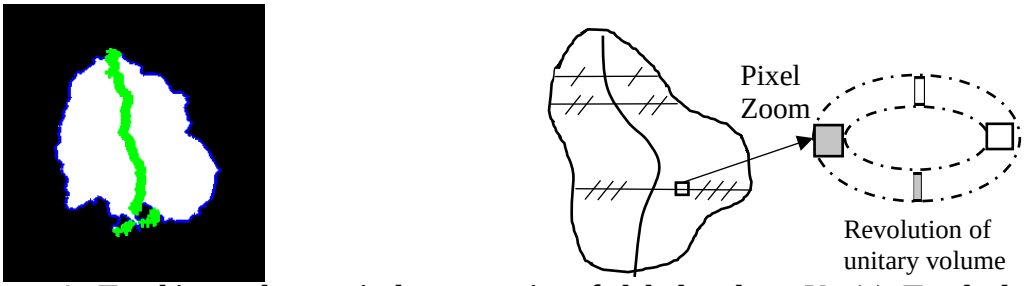

Figure 4-: Tracking and numerical computation of globule volume $V_{G;}$ (a): Tracked globule, (b): Schema of unitary volume of a pixel

Thus, the volume of revolution (1-pixel torus) is computed for each pixel (rotation, see figure 4). Therefore, the volume of each cylindrical slice of the structure is the sum of all 1-pixel torus volumes of the corresponding slice. Finally, the volume of the structure is the sum of all cylinder volumes calculated along the equidistant line. This phenomenological approach is validated by comparing Q_{exp} (V_G, f_G) to the real injected flowrate Q_{real}, which are consistent [9] (see results below).

2.4. DF measurements

Cesium iodide aerosols were injected into the TYFON facility, using Palas AGK 2000 generator. The median mass aerodynamic diameter (MMAD) for CsI aerosols is 1 µm (dispersion $\sigma_g = 1.8$). The mean aerosol flow rate is between 0.2 and 0.4 mg.min^{-1}.A sampling system (shown in figure 2) is used downstream the bath to measure outlet CsI concentration.

The amount of CsI aerosols injected is the sum of the amount of CsI trapped in the pool with the amount of CsI transferred through the pool, which is measured in the sampling system. Taking in consideration the aerosol deposition on the surfaces, notably in the sampling system (isokinetic cane, pipes) in addition to the deposition on the quartz filter, sample washing is done to collect all the deposited quantity of CsI aerosols. All the liquid samples are then analyzed by inductively coupled plasma - mass spectrometry ICP-MS.

3. RESULTS AND DISCUSSION

In pool scrubbing scenarios, tests parameters may favor or hinder the retention of fission products. It is therefore important to investigate the influence of these parameters on the bubble dynamics in order to correlate with decontamination factor measurements. In the following paragraphs, the possible impacts of contamination, injection flow rate, orifice size, and pool submergence, are characterized on the globule formation in the injection zone. At this stage, all the presented results have been obtained at ambient temperature for gas and liquid bath.

3.1. Effect of contamination

In our test conditions, it was experimentally checked that there is no significant change in the globule volume when feeding the carrier gas by these CsI particles, as shown in the figure 5.

This may be due to the low concentration of aerosols depositing on the globules, this is consolidated by the ratio in size of the aerosol's particles to globule volume [15]: for We = 0,077, this ratio is around 4.4×10^{-3}.

3.2. Variation of test conditions

Five orifices were used to compare their influence on the globule size. For the 50 mm orifice, no globule formation was observed. Instead, a swarm of smaller bubbles was formed within the tips of the orifices. This can be due to the weak effect of surface tension (orifice – air – water) in front of the inertial and gravitational forces. For the other orifices (2 mm, 5 mm, 10 mm, 20mm), globule formation was characterized for different injection flowrates and pool submergence.

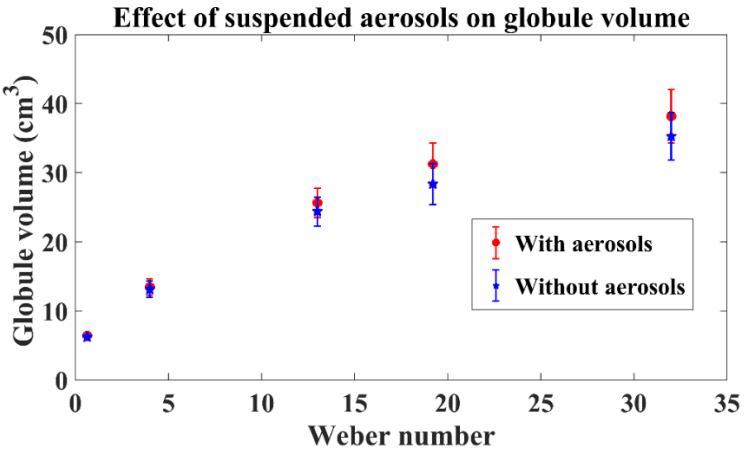

Figure 5- Effect of aerosol suspension on globule volume at ambient temperature

3.2.1- Effect of orifice size

In the figure 6, the globule volume is presented as function of Weber number that varies due to both the orifice size and injection flow rate. A significant increase in globule volume is shown with higher orifice size for same Weber number.

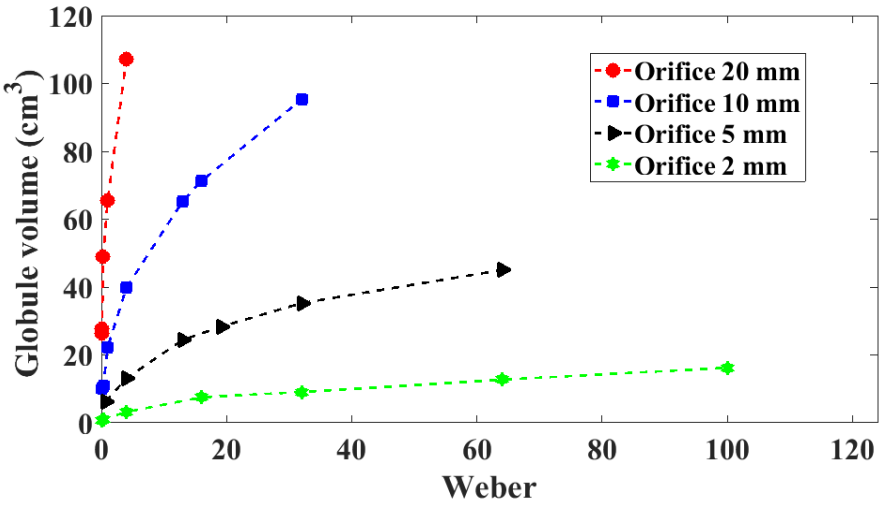

Figure 6- Variation of globule volume for different orifices

Owing to the strong dependence of Weber number on the orifice size, and in order to differentiate between the contribution of orifice size and injection flow rate, the impact of gas flow rate for different orifices is presented in figure 7.

Despite the size of orifice, comparable values of globule volumes for same flow rate are maintained. For orifice of 20 mm, there is slight increase which is due to the higher formation time needed in order to form bubbles between the tips of the orifice, as shown in figure 7. Figure 8 illustrates and consolidates this statement, where the globule frequency of 20 mm orifice is smaller than other globule frequencies of different orifices sizes.

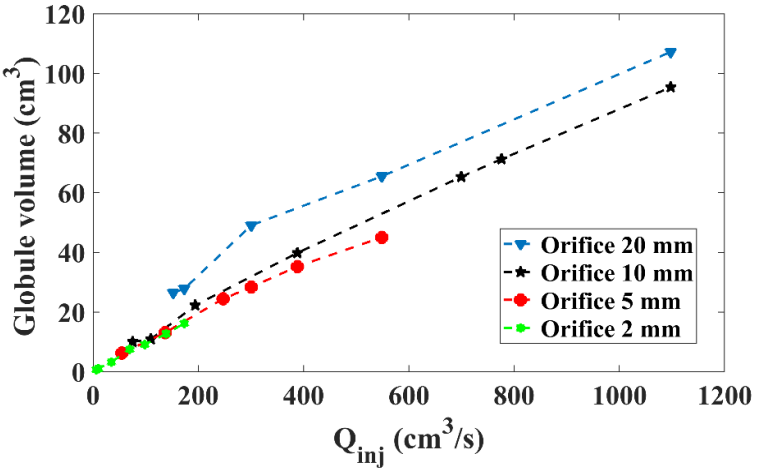

Figure 7- Variation of gluble volume as function of injection flowrate

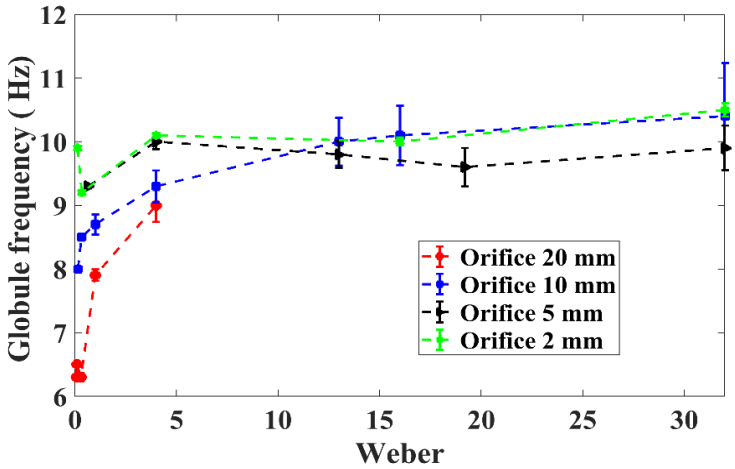

Figure 8- Globule frequency for different orifices at ambient temperature

Moreover, we assume that $Q_{calc} = V_G \times f_G$, where V_G and f_G are respectively the volume and frequency of the globules. This assumption stems from the fact the formation of globule is common and relevant along the different flow morphologies. Therefore, as explained in [9] to validate the method (cf. section 2.3.2), the injection flowrate Q_{real} must be correlated to the volume of globule V_G formed at frequency f_G. Figure 9 shows that the experimental data fits reasonably the actual injection flowrate for the different orifices.

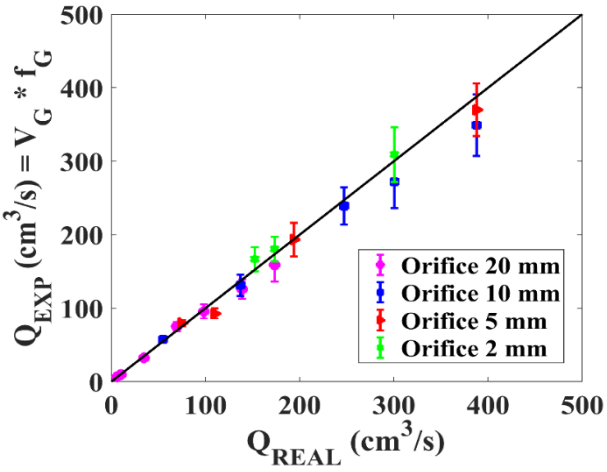

Figure 9- Validation of experimental flowrate with actual flowrate

3.2.2 Effect of pool submergence

According to Kumar and Kuloor [16], above a certain altitude of the pool surface, volume of bubbles forming at a submerged orifice for a constant air flow rate are not affected. Nevertheless, it may affect the bubble volume appreciably in the intermediate region.

The pool submergence was set to 5 different altitudes according to Y_{max} which refers to the altitude of the injection zone (i.e.: the onset of breakup zone where the globule starts fragmentation).

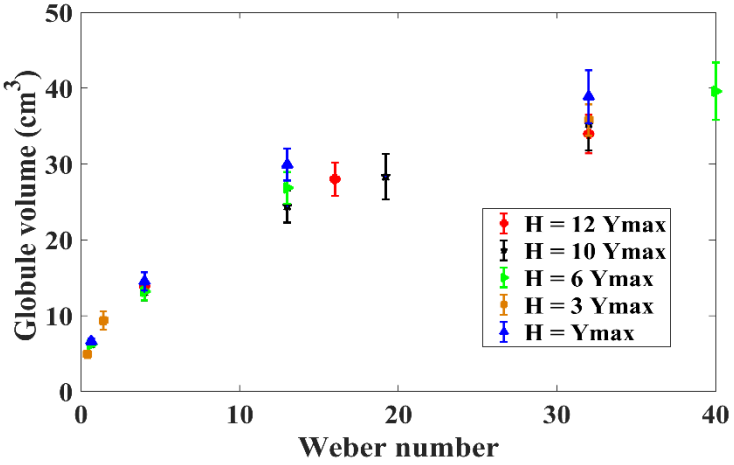

Figure 10- Globule volume for different pool submergences at ambient temperature

For a given We, no significant variation was found on the volume of globule except at the lowest submergence where H = Y_{max}, as shown in figure 10. At this altitude, the globule undergoes a bit larger expansion due to less hydrostatic pressure on the interface of the bubble. However, and despite the variation hydrostatic pressure, the inertial effects over dominate the latter mechanism

3.3. Effect of Weber Number on Decontamination Factor

First tests were carried out to investigate mainly the dependence of DF on gas flowrate, consequently Weber number. The parameters of the test are shown in table 1.

Table 1- Tests conditions of DF measurements

Test	We	Air temperature (°C)	Water temperature (°C)	Orifice size (mm)	Pool Submergence (m)
1	0.08	25	25	20	1
2	4.9	25	25	5	1
3	32	25	25	5	1
4	205	25	25	5	1
5	350	25	25	5	1

Zhao et al. [17] considered a critical Weber number $We_{critical}$ for transition from bubbling to jetting regime. This critical Weber number was given by: $We_{critical} = 10.5 \left(\rho_l/\rho_g\right)^{0.5}$ such that $We_{critical} = 316$. According to this criterion, it is considered that different bubbling regimes were examined.
The impact of gas injection flowrate on the retention of aerosols varies between bubbling and jetting regimes. In fact, this parameter prompts counter effect removal mechanisms (gravitational settling, gas residence time, jet impaction, centrifugal impaction).
At very low Weber number, the decontamination factor was found to be relatively high due to high residence time. Moreover, low bubble rising velocities prompts gravitational settling of aerosols. As Weber number increases, DF starts to decrease significantly due to the attenuation of the latter mechanisms. In the regime where it can be described as transition regime ($100 < We < 300$), DF tends to have a similar value. However, as Weber number increases beyond the transition regime, DF tends to increase when the flow is described as jetting regime ($We = 350$). In our test conditions, DF is lower than ~50.
In the latter regime, two main removal mechanisms are present: inertial impaction (deposition velocity of impaction proportional to injection velocity) and surface exchange. When gas flow rate increases in jetting regimes, smaller bubbles in the bubble rise zone are obtained due to a stronger inertial breakup [18], thus provoking higher interfacial area and generally lower terminal velocities[1] [19], inducing higher residence time of bubbles in the bath.

4. CONCLUSIONS

Flow structure in pool scrubbing conditions, where for example air is injected at high momentum, exhibits different patterns than in conventional experiments. That recalls for approaches that could better describe the bubble hydrodynamics due to the different encountered phenomena. Within this concept and its relevance in nuclear safety, experimental work is carried out, in a first step at ambient temperature, to characterize the bubble hydrodynamics in the injection zone. Air is injected from submerged orifices of different sizes, at different flowrates, and through pools of water of different altitudes.
The presence of CsI aerosols has no influence on the globule dynamics, where the respectively large globule volumes can afford the deposition without interfering their surface tension.
Comparable globule volumes and frequencies were reported for the small orifices (2, 5, and 10 mm), where globule volume increases with the injection flowrate. For the large orifice (20 mm), the increase formation time results in a larger globule volume and smaller globule frequency. The phenomenological approach

[1] On the graph plotting terminal velocity vs bubble size, even if the overall curve shape is increasing, a local maximum can be observed for bubble diameter around 1 mm [19].

implemented to determine the globule volume is validated by comparing Q_{calc} (V_G, f_G) to the real injected flowrate Q_{inj}.
Regarding the pool submergence, negligible influence on globule volume was reported where experiments were carried at constant flow and pressure conditions. The dominant mechanisms in the injection zone near the orifice attenuates the effect of hydrostatic pressure induced by the pool submergence.
In fact, while an increase in gas flowrate favors the inertial and centrifugal impaction, it hinders the residence time and gravitational settling. Apparently, in bubbling regimes, the latter mechanisms dominate over the mechanisms induced by the increase of gas flowrate (i.e., inertial and centrifugal impaction, large surface exchange), whereas these phenomena dominate over the residence time once jetting regime reached. In other words, for a given test conditions, the DF variation as a function of We should tend to have a minimum. Beyond this minimum, residence time and gravitational settling effects dominate and above it, effects linked to jetting regime listed above dominate.
Later on, tests will be performed to evaluate the influence of liquid pH and temperatures of bath and/or gas on DF. Besides, DF will be measured for volatile iodine species (I_2, CH_3I).

ACKNOWLEDGMENTS

This work was performed in the French Institut de Radioprotection et de Sûreté Nucléaire (IRSN), with the financial support of French Région Sud- Provence-Alpes-Côte d'Azur and Electricité de France (EDF).

Nomenclature

d_0	Orifice diameter	[m]
Q_{inj}	Injected air volume flow rate	[$m^3.s^{-1}$]
Q_{calc}	Calculated volume flow rate	[$m^3.s^{-1}$]
V_G	Globule volume	[m^3]
U_{inj}	Gas injection velocity	[$m.s^{-1}$]
We	Orifice Weber number:	[-]
$We_{critical}$	Critical Weber number	[-]
Ymax	Height of injection zone	[m]
Greek symbols		
ρ_g	Gas density	[$kg.m^{-3}$]
ρ_l	Liquid density	[$kg.m^{-3}$]
σ	Surface tension	[$N.m^{-1}$]

REFERENCES

1. D. Jacquemain, S. Guentay, S. Basu, M. Sonnenkalb, L. Lebel, J. Ball, H. Allelein, M. Liebana, B. Eckardt, N. Losch, et al., "Oecd/nea/csni status report on filtered containment venting," tech. rep., Organisation for Economic Co-Operation and Development, 2014.
2. Sehgal, Bal Raj, ed. *Nuclear safety in light water reactors: severe accident phenomenology*, Academic Press, 2011.
3. Swiderska-Kowalczyk, M., Escudero-Berzal, M., Marcos-Crespo, M., Martin-Espigares, M., & Lopez-Jimenez, J. *State-of-the-art review on fission product aerosol pool scrubbing under severe accident conditions*, 1996.
4. J. Davidson and B. Schuler, "Bubble formation at an orifice in a viscous liquid," *Transactions of the Institution of Chemical Engineers*, **vol. 38**, pp. 144–154, 1960.
5. E. Gaddis and A. Vogelpohl, "Bubble formation in quiescent liquids under constant flow conditions," *Chemical Engineering Science*, **vol. 41**, no. 1, pp. 97–105, 1986.

6. M. Jamialahmadi, M. Zehtaban, H. Müller-Steinhagen, A. Sarrafi, and J. Smith, "Study of bubble formation under constant flow conditions," *Chemical Engineering Research and Design*, **vol. 79**, no. 5, pp. 523–532, 2001.
7. R. Mosdorf and T. Wyszkowski, "Experimental investigations of deterministic chaos appearance in bubbling flow," *International journal of heat and mass transfer*, **vol. 54**, no. 23-24, pp. 5060–5069, 2011.
8. N. Kyriakides, E. Kastrinakis, S. Nychas, and A. Goulas, "Bubbling from nozzles submerged in water: transitions between bubbling regimes," *The Canadian journal of chemical engineering*, **vol. 75**, no. 4, pp. 684–691, 1997.
9. Farhat, M., Chinaud, M., Nerisson, P. and Vauquelin, O., 2021. Characterization of bubbles dynamics in aperiodic formation. *International Journal of Heat and Mass Transfer*, **vol. 180**, p.121646.
10. Lee, Yoonhee, Yong Jin Cho, and Inchul Ryu. "Preliminary analyses on decontamination factors during pool scrubbing with bubble size distributions obtained from EPRI experiments." *Nuclear Engineering and Technology* 53.2 (2021): 509-521.
11. Q. Cai, X. Shen, C. Shen, and G. Dai, "A simple method for identifying bubbling/jetting regimes transition from large, submerged orifices using electrical capacitance tomography (ect)," *The Canadian Journal of Chemical Engineering*, **vol. 88**, no. 3, pp. 340–349, 2010.
12. J. Cieslinski and R. Mosdorf, "Gas bubble dynamics—experiment and fractal analysis," *International Journal of Heat and Mass Transfer*, **vol. 48**, no. 9, pp. 1808–1818, 2005.
13. V. Badam, V. Buwa, and F. Durst, "Experimental investigations of regimes of bubble formation on submerged orifices under constant flow condition," *The Canadian Journal of Chemical Engineering*, **vol. 85**, no. 3, pp. 257–267, 2007.
14. Y. Abe, K. Fujiwara, S. Saito, T. Yuasa, and A. Kaneko, "Bubble dynamics with aerosol during pool scrubbing," *Nuclear Engineering and Design*, **vol. 337**, pp. 96–107, 2018.
15. Hinds, William C. *Aerosol technology: properties, behavior, and measurement of airborne particles*. John Wiley & Sons, 1999.
16. R. Kumar and N. Kuloor, "The formation of bubbles and drops," *Advances in chemical engineering*, **vol. 8**, pp. 255–368, 1970.
17. Y.-F. Zhao and G. A. Irons, "The breakup of bubbles into jets during submerged gas injection," *Metallurgical Transactions B*, **vol. 21**, no. 6, pp. 997–1003, 1990.
18. A.T. Wassel, A.F.Mills, D.C. Bugby and R.N. Oehlberg. "Analysis of radionuclide retention in water pools", *Nuclear engineering and design*, ***90*(1)**, pp.87-104, 1985.
19. R. Clift, J.R. Grace and M.E. Weber. *Bubbles, drops and particles.* Chapter 7, Academic Press, New York – San Francisco - London, 1978

RÉPUBLIQUE FRANÇAISE
Liberté
Égalité
Fraternité

IRSN
INSTITUT DE RADIOPROTECTION ET DE SÛRETÉ NUCLÉAIRE

BUBBLES DYNAMICS UNDER POOL SCRUBBING CONDITIONS FOR IODINE COMPOUNDS TRAPPING APPLICATIONS

M. FARHAT, P. NERISSON, M. CHINAUD, O. VAQUELIN, L. CANTREL

IRSN/ERM-296 ind. 06

MEMBRE DE ETSON

ERMSAR 2022 – Karlsruhe, Germany

Région PACA
Aix*Marseille université
IUSTI LABORATOIRE AIX MARSEILLE UNIVERSITÉ CNRS

OUTLINE

- Context
- Materials & methods
- Hydrodynamics
- DF measurements

$$DF = \dot{m}_{in} / \dot{m}_{out}$$

- Conc. & Perspect.

Pool scrubbing

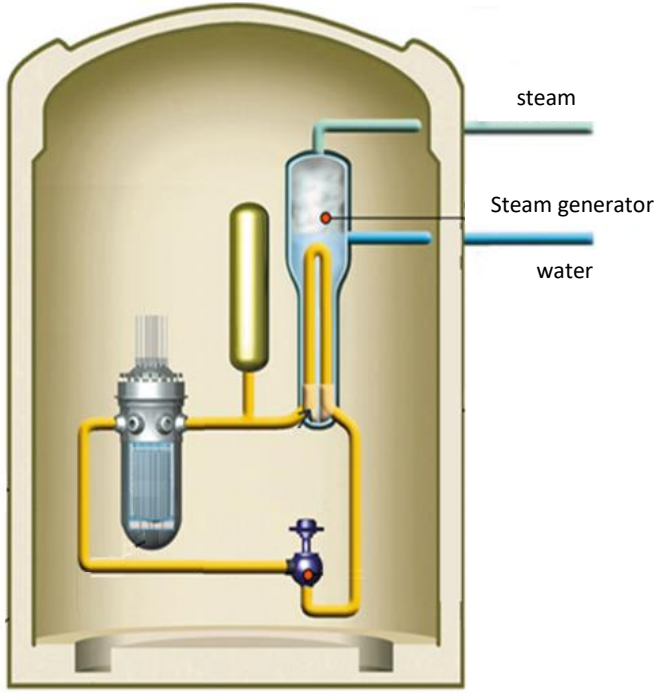

Containment building of PWR

Pool scrubbing

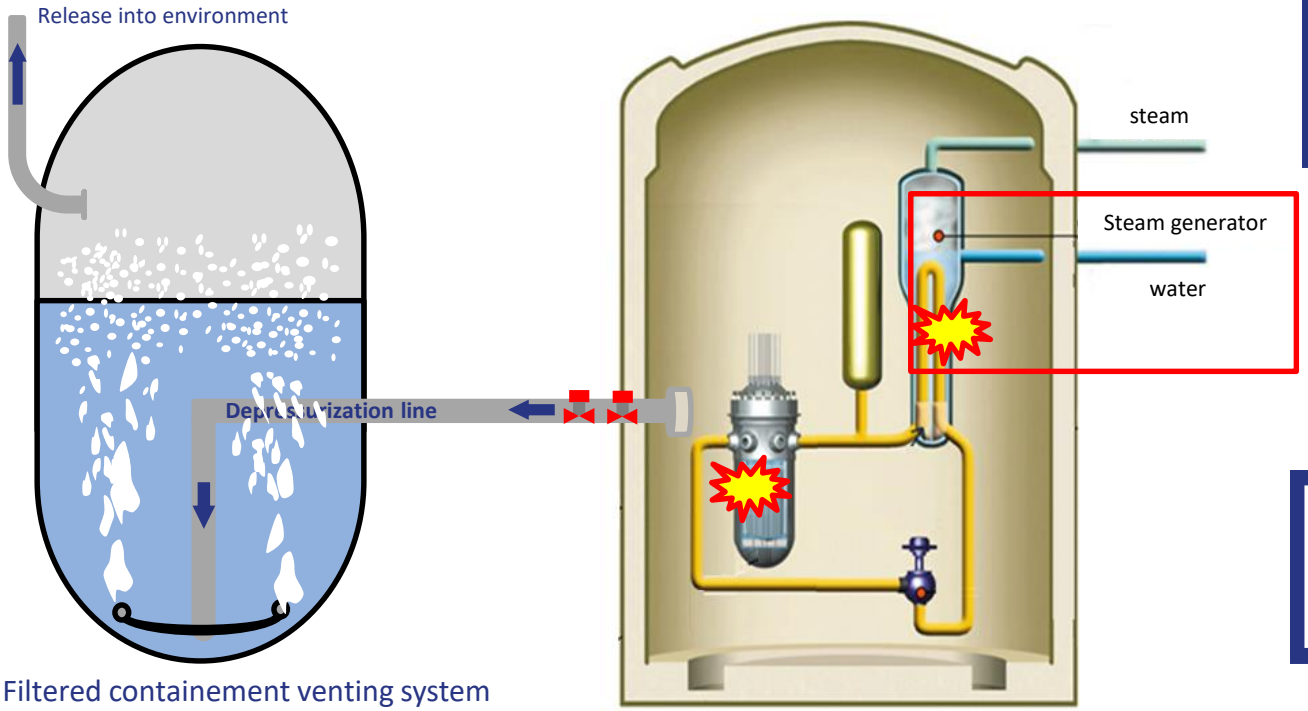

Filtered containement venting system (FCVS)

Containment building of PWR

MITIGATION OF THE RELEASED FISSION PRODUCTS:

WET FCVS

STEAM GENERATOR TUBE RUPTURE (ACCIDENTAL SITUATION SGTR)

Pool scrubbing



Filtered containement venting systems

Ref: https://www.idom.com/en/project/design-of-the-filtered-containment-venting-system-in-asco-and-vandellos-ii-nuclear-power-plants/

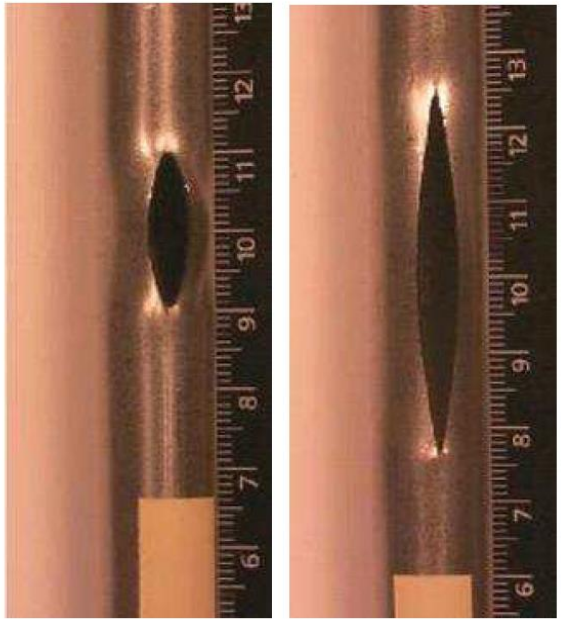

Ruptures of tubes SG

Ref: Cartonnet, A. (2013). *Contribution à l'étude du rejet à l'environnement de l'iode radioactif lors d'une séquence accidentelle de type RTGV* (Doctoral dissertation, Thesis.

State of art, uncertainties, and objectives

- Experimental databases haven't yet characterized the overall phenomena encountered in the pool scrubbing.
- Conventional theoretical models and assumptions for the descriptions of pool scrubbing are implemented in codes.
- The code‘s validity extends only over the range of conditions encompassed by the data they were based on.

Establishing advanced experimental database ➔ ASTEC code

Hydrodynamic characterization in the injection zone and global decontmination factor measurements

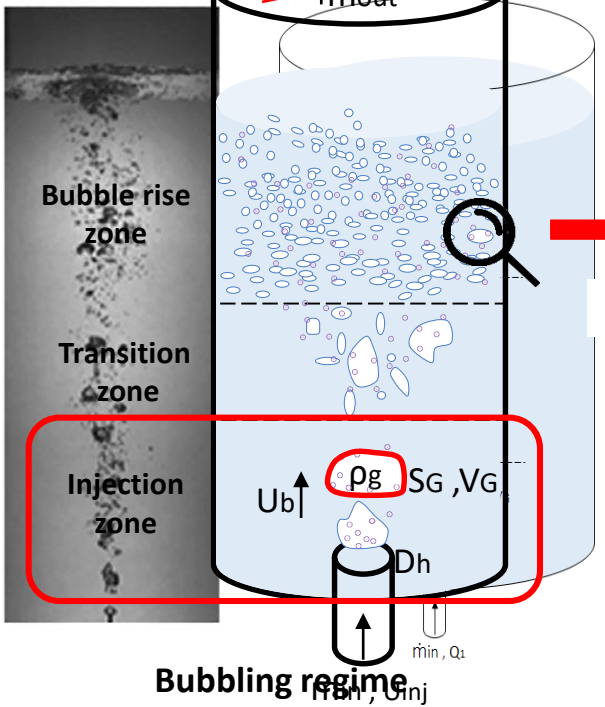

Bubbling regime

$We = \frac{D_h U_{inj}^2 \rho_g}{\sigma}$

Equivalent to

Brownian diffusion $\frac{16\, Q_{inj}^2 \rho_g}{\pi^2 D_h^3 \sigma}$

- D_h: Orifice diameter
- ρ_g: gas density
- σ : *surface tension*

Inertial impaction

Condensation

Gravitational sedimentation

Transfer by chemical reactions
(decomposition, hydrolysis,oxidation)

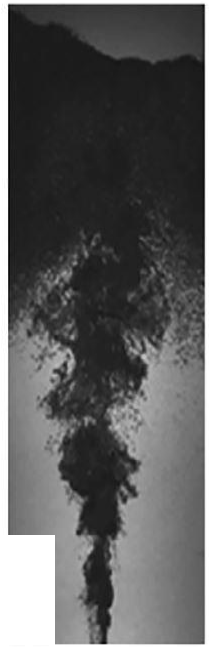

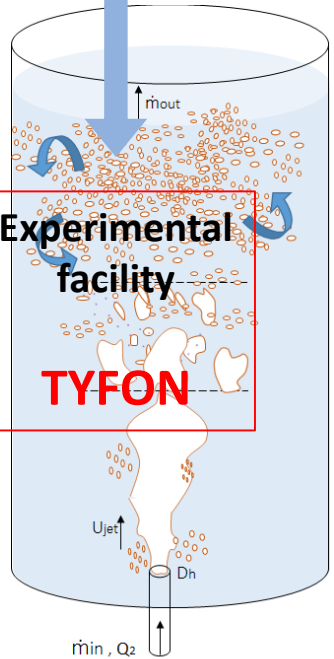

Jet regime

MATERIALS & METHODS



Experimental setup: TYFON





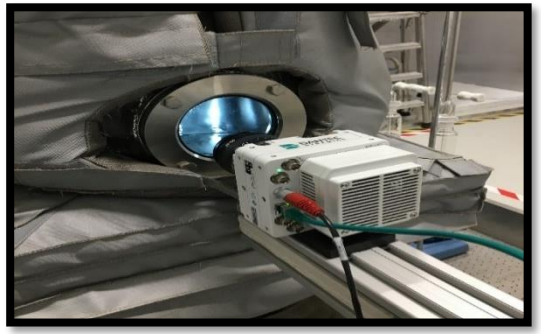

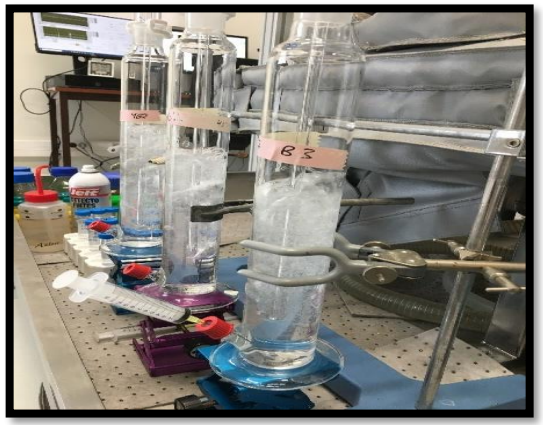

Data treatment & analysis

Physical aspects



Image processing



Tracking and characterization of globules formation

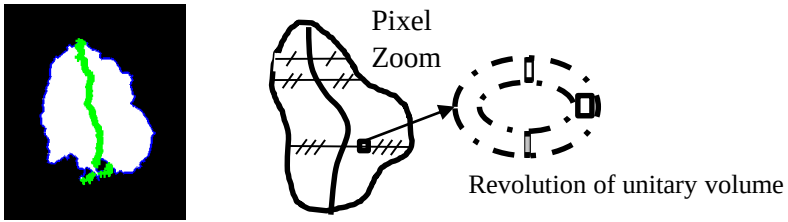

Globule volume computation

Chemical aspects



Aerosol generator AGK 2000 Palas



ICPMS

Analysing liquid samples

quantification of trapping

HYDRODYNAMICS

Hydrodynamics

- Hydrodynamic measurements of globules fomation in the injection zone

- Examination of influences : **- Carrier gas contamination** **- Injection flowrate**
  - Orifice size **- Water level (submergence)**

D_h= 2 mm

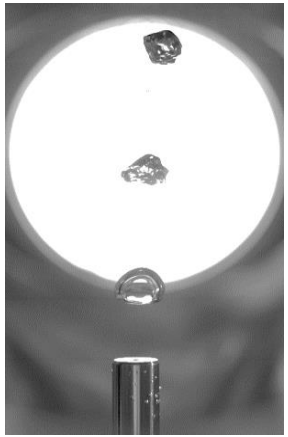

D_h= 5 mm

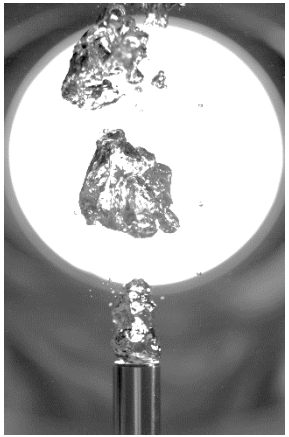

D_h= 10 mm

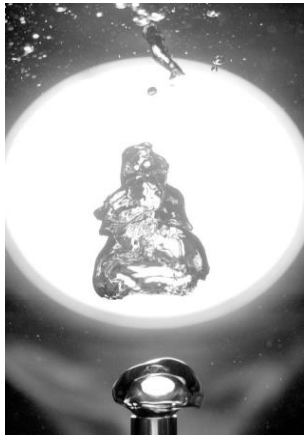

D_h= 20 mm

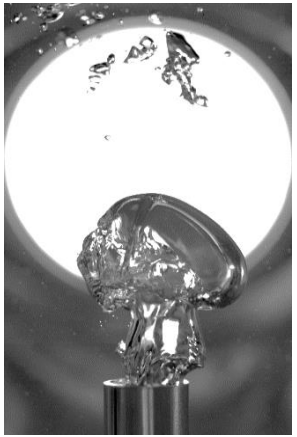

Globule volume

- *Mohamad Farhat, Maxime Chinaud, Philippe Nerisson, and Olivier Vauquelin. "Characterization of bubbles dynamics in aperiodic formation." International Journal of Heat and Mass Transfer 180 (2021): 121646.*

Classical approach

$$d_b \approx \sqrt[3]{\frac{6 * V_b}{\pi}}$$

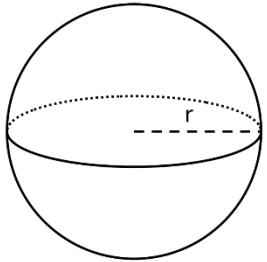

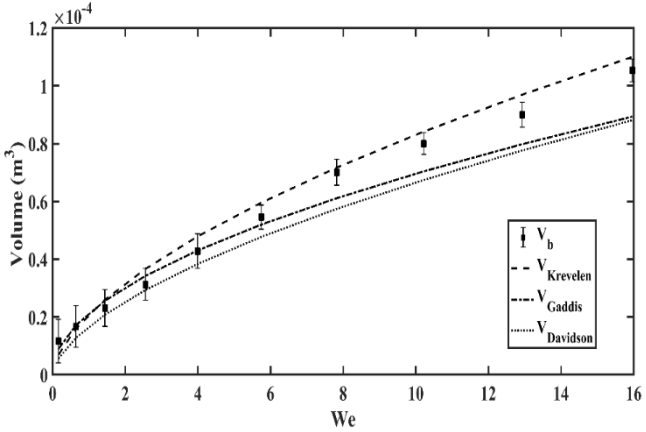

Phenomenological appraoch



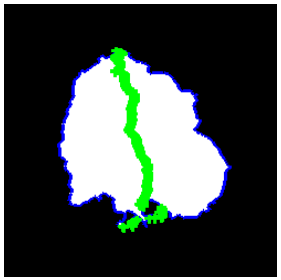

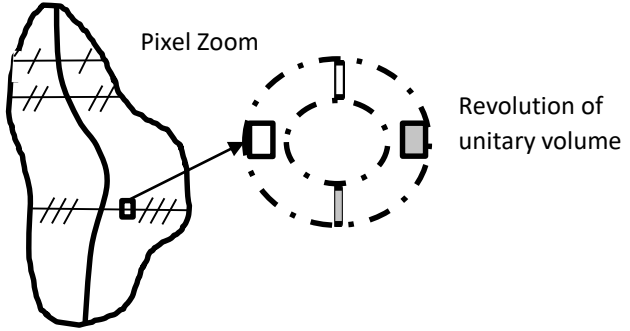





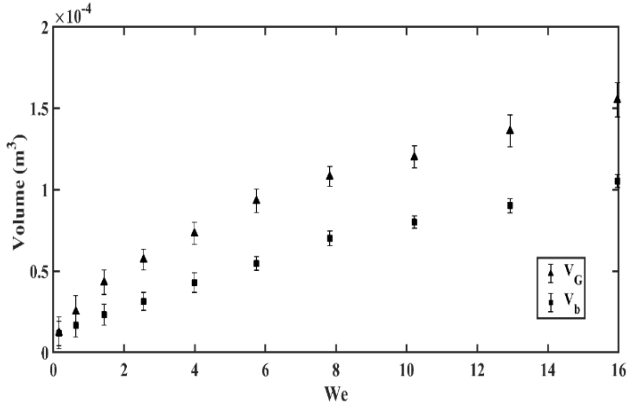

Hydrodynamics

- **Carrier gas contamination**

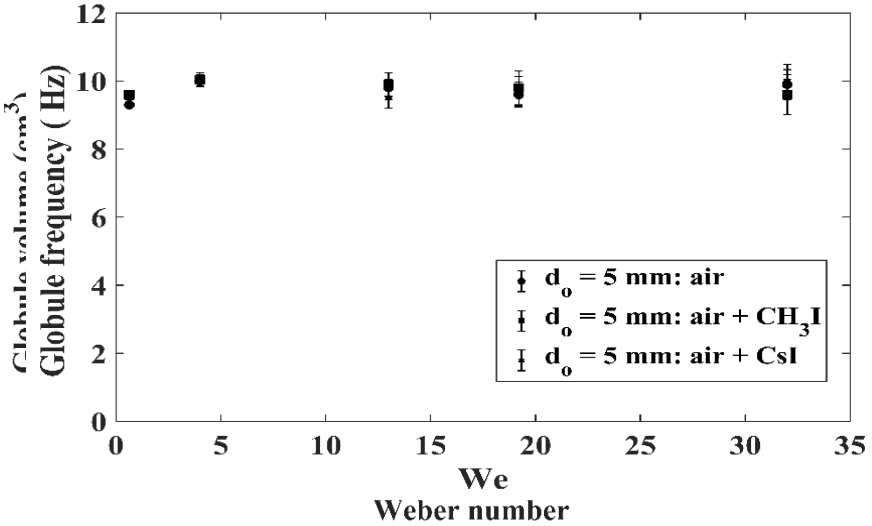

- **Submergence**

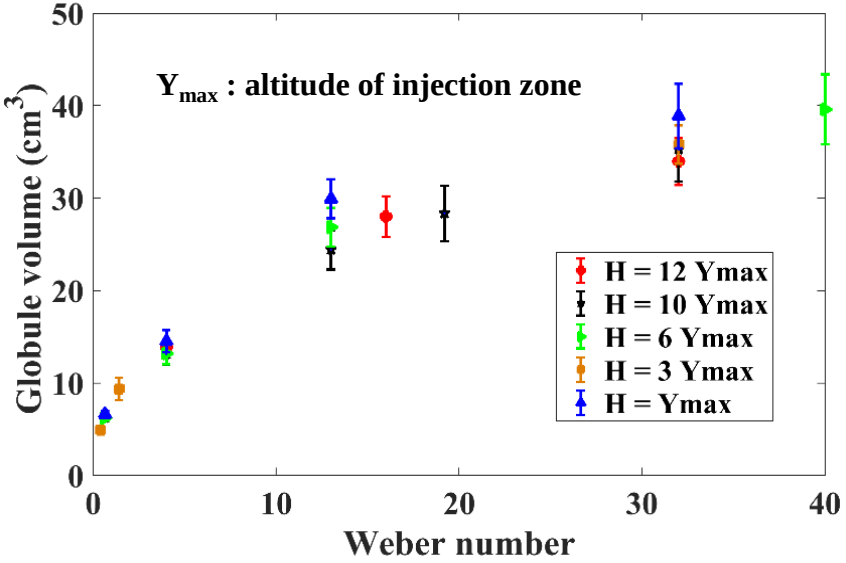

- No influence on the formation process of globules
- Negligible influence on globule volume with the variation of submergence.

Hydrodynamics

- **Orifice size & injection flow rate**

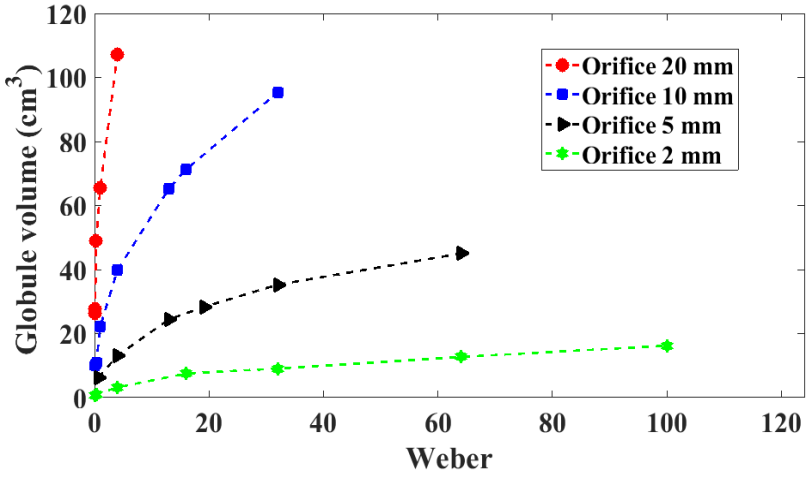

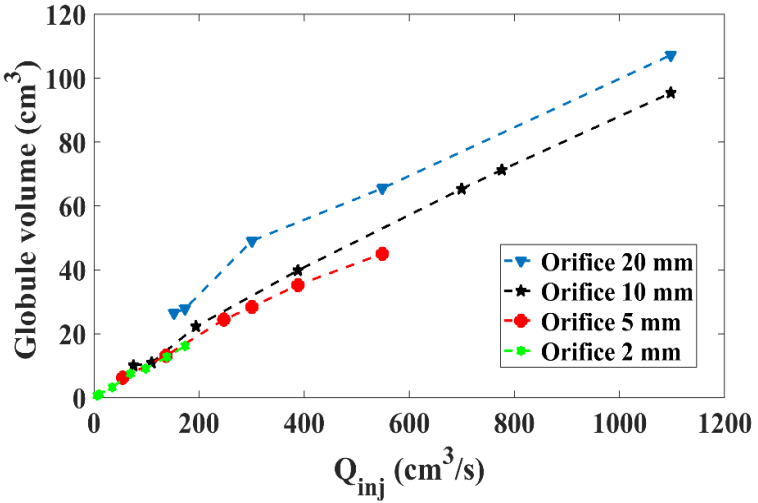

$$We = \frac{16\, Q_{inj}^{2} \rho_g}{\pi^2 D_h^{3} \sigma}$$

- Implication of orifice size into Weber number ➔ divergence of globule volumes as function of Weber
- Comparable globule volumes with different orifices at same conditions ➔ frequency ?

Hydrodynamics

- *Mohamad Farhat, Maxime Chinaud, Philippe Nerisson, and Olivier Vauquelin. "Characterization of bubbles dynamics in aperiodic formation." International Journal of Heat and Mass Transfer 180 (2021): 121646.*

Globules frequency and validation of globule characterization

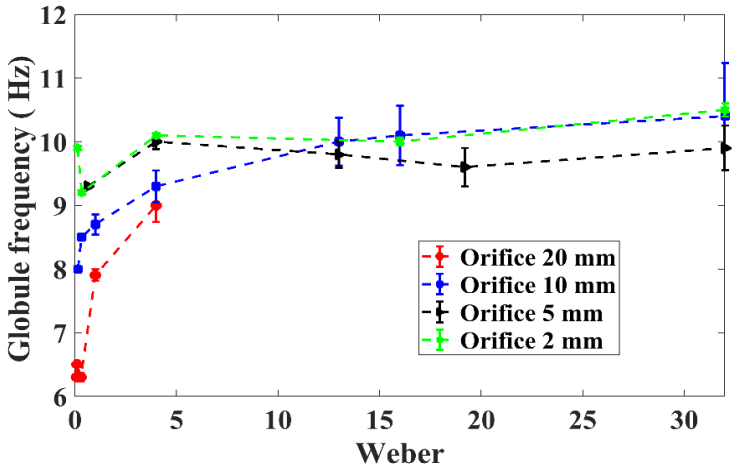

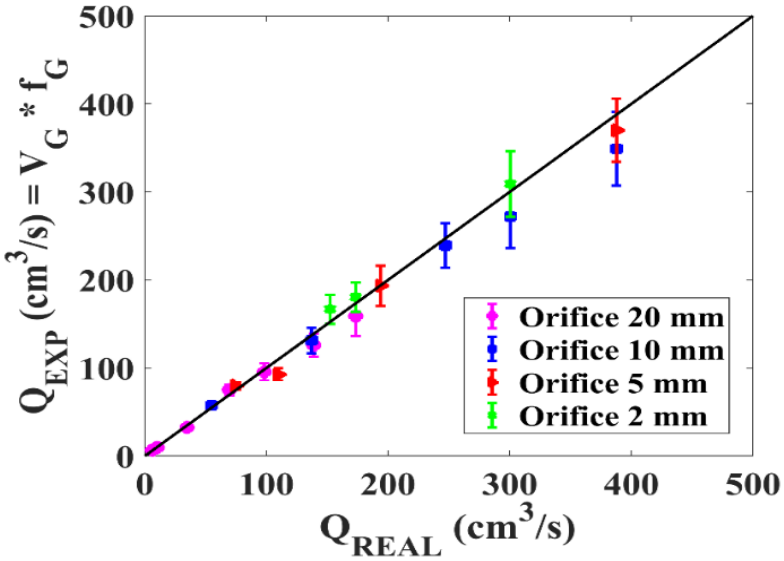

- Stable frequency, maximum frequency up to a certain flowrate (**Dh= 20 mm**).
- Valdiation of globule approach by comparing experimental to real flowrate

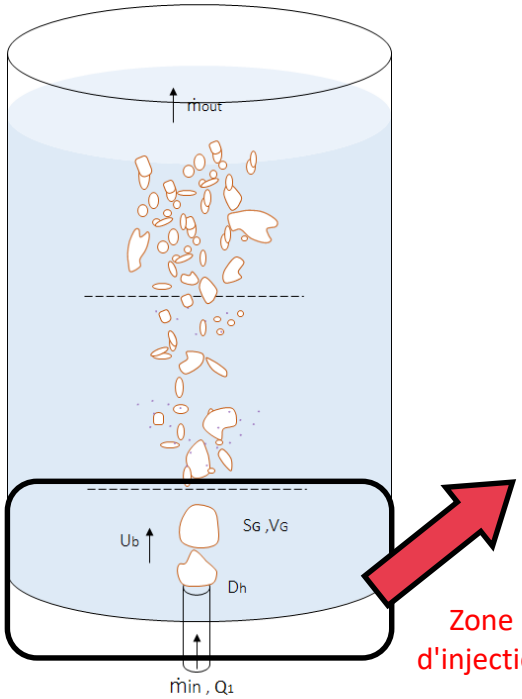

Zone d'injection

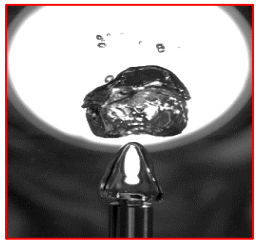



Morphology Bubbling - Jet

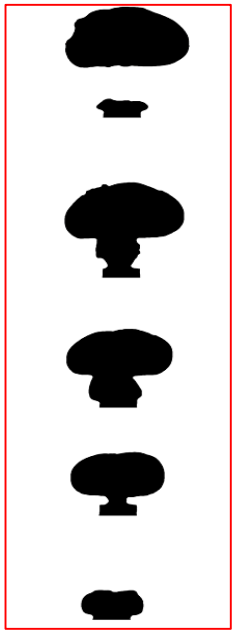

Formation frequency

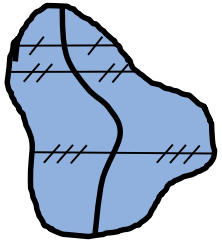

Volume

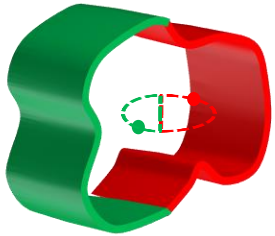

Surface area

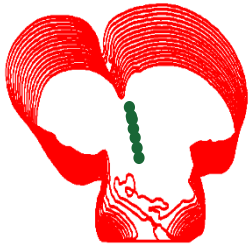

Formation velocity

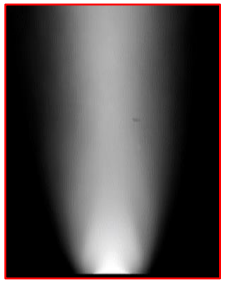

Void fraction

*Références

- *Mohamad Farhat, Maxime Chinaud, Philippe Nerisson, and Olivier Vauquelin. "Characterization of bubbles dynamics in aperiodic formation." International Journal of Heat and Mass Transfer 180 (2021): 121646.*
- *Farhat M. Etude expérimentale de l'hydrodynamique du barbotage pour différents régimes :application au piégeage des iodes. Rapport d'avancement de première année de thèse. Rapport IRSN/2020-00691, 2020.*

DF MEASURMENTS

DF measurements of CsI

- Hydrodynamics: No impact of aerosols contmaination.
- $DF = \dot{m}_{in} / \dot{m}_{out}$
- The tests covered bubbling and jet regimes (0.07 < We < 1000).
- Effects:

  - Injection flowrate (We)

  - Submergence

  -Gas temperature

  -Pool temperature

  -pH

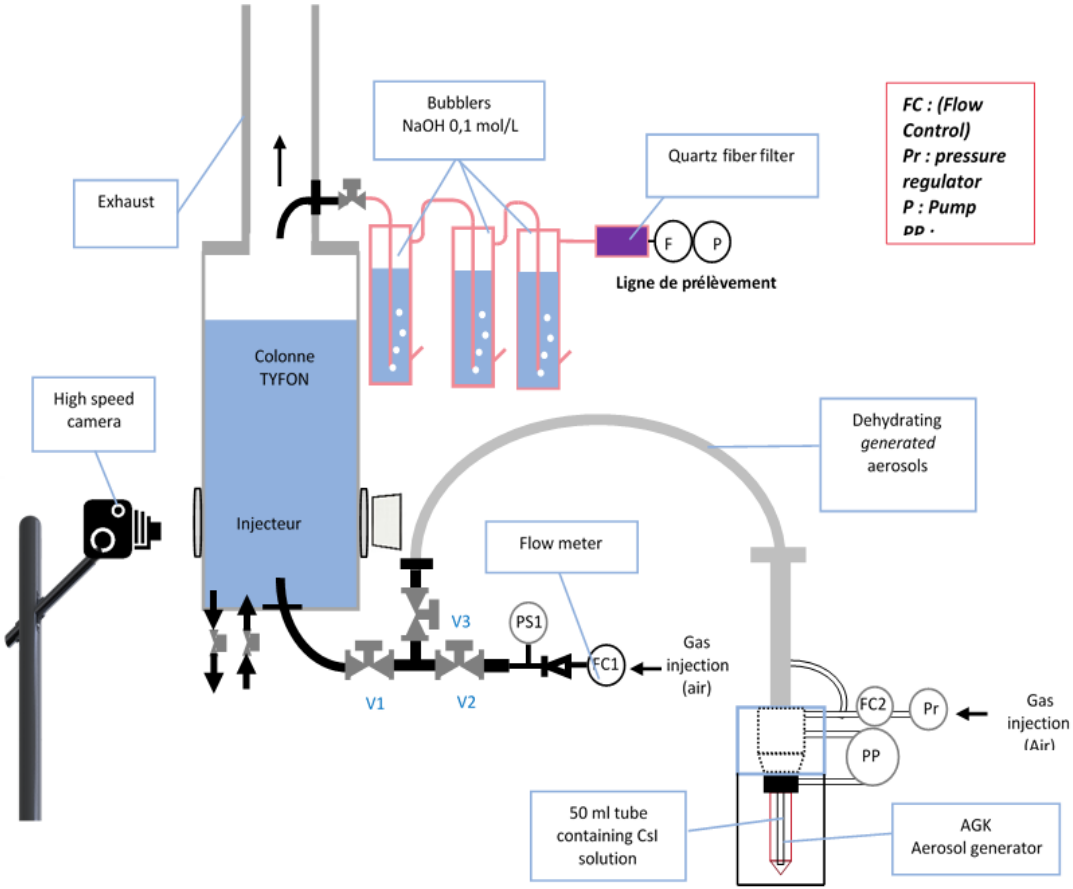

Some results

- DF vs submergence.

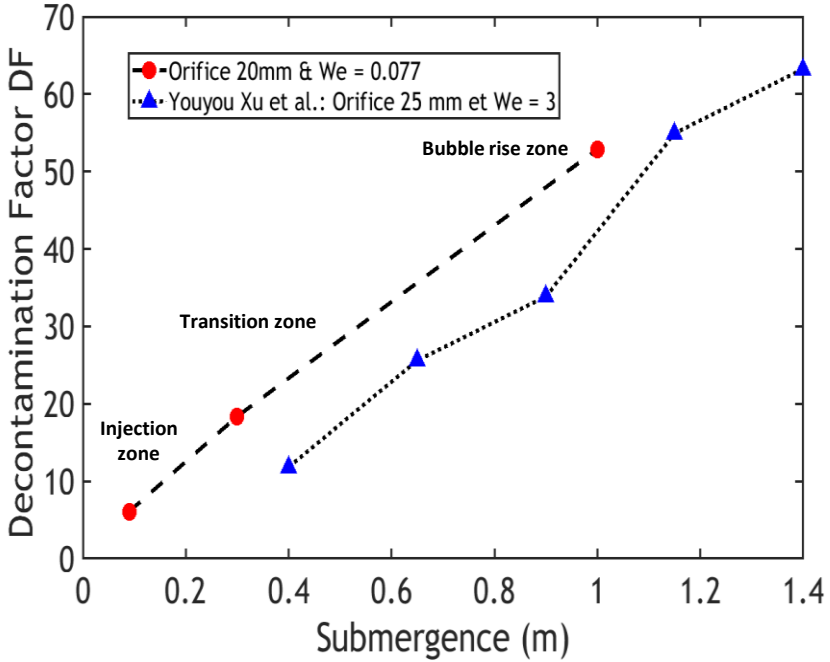

- A minimum of DF in intermediate regimes.

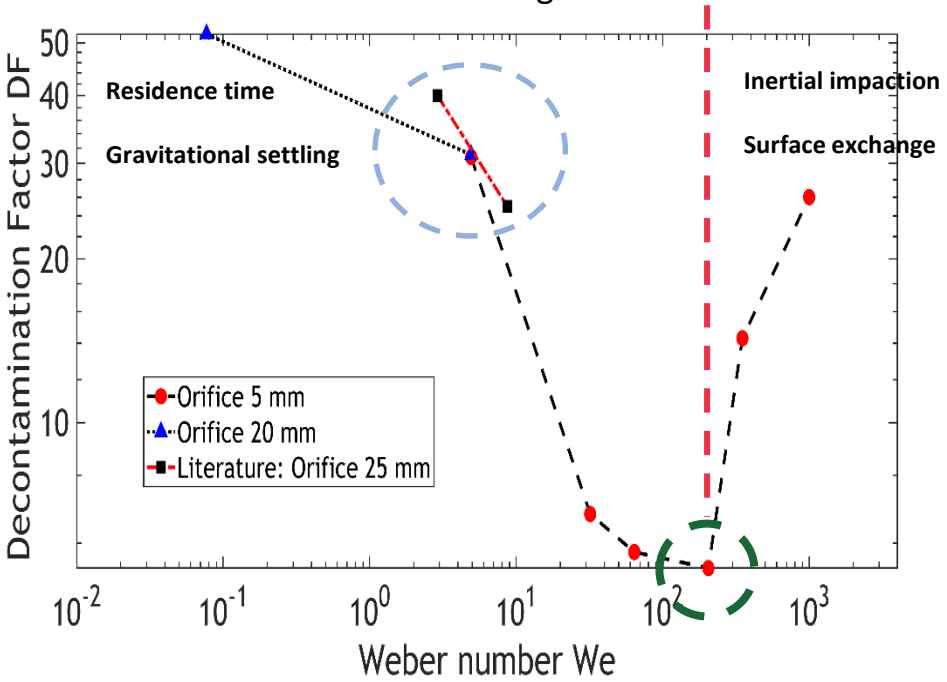

- Capability of Weber, comprising the variation of orifice's size and injection flowrate, in characterization of DF.

Ref: Xu, Youyou, et al. "Experimental study on aerosol behavior in water pool scrubbing under severe accident conditions." *International Journal of Advanced Nuclear Reactor Design and Technology* 2 (2020): 111-116.

DF measurements of CH_3I

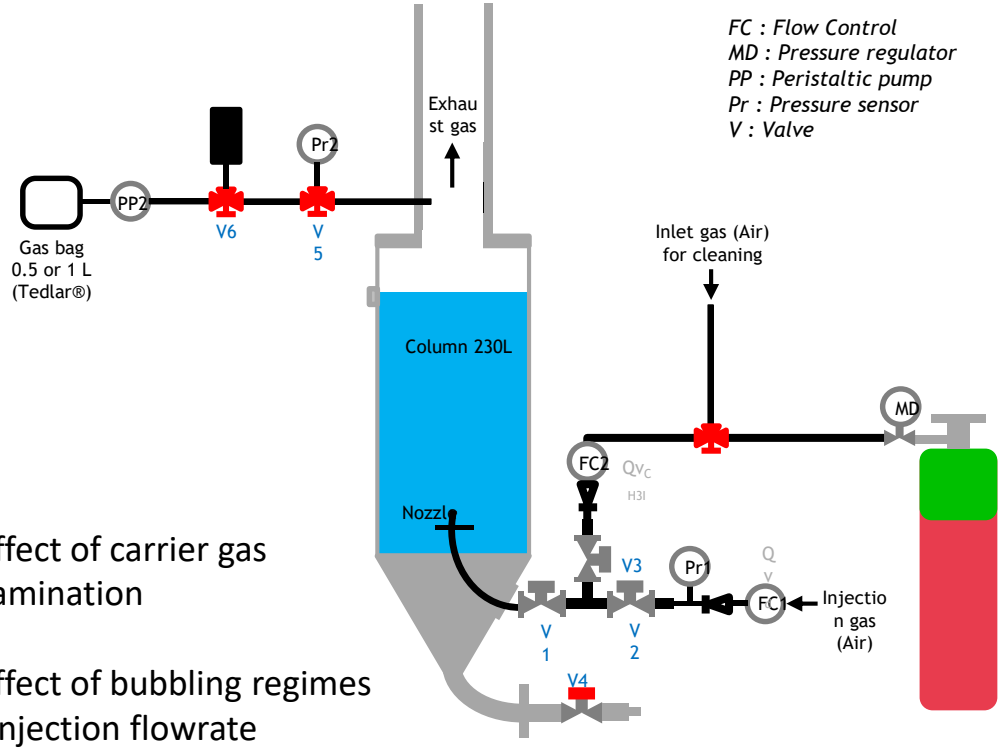

- No effect of carrier gas contamination
- No effect of bubbling regimes and injection flowrate (0.07 < We < 3000).

Pool scrubbing of IodoMethane					
TYFON	Conditions				DF
Test	Matrix	Temp. gas	Temp. pool	Weber	
PIM 1	Alcaline (pH = 12)	25 °C	25 °C	0,077	1,3
PIM 2	Alcaline (pH = 12)	70 °C	70 °C	0,077	2,4
PIM 3	Alcaline (pH = 12)	25 °C	25 °C	64	1,0
PIM 4	Alcaline (pH = 12)	70 °C	25 °C	350	1,2
PIM 5	Alcaline (pH = 12)	70 °C	70 °C	350	1,6
PIM 6	Alcaline (pH = 12)	70 °C	25 °C	1000	1,1
PIM 7	Alcaline (pH = 12)	25 °C	25 °C	1000	1,0
PIM 8	Alcaline (pH = 12)	25 °C	25 °C	3000	1,1
PIM 9	Alcaline (pH = 13)	70 °C	70 °C	0,077	5,6

CONCLUSION & PERSPECTIVES

Conclusion

1 – Hydrodynamics

- Capability and validity of phenomenological approach in characterizing globule volumes in the injection zone
- Negligible influence on the globule dynamics due presence of CH_3I or CsI aerosols in the composition of the carrier gas
- Negligible influence of pool submergence (level of water in the pool)
- Globule volumes is mainly affected by the gas flow rate as the frequency of formation is independent at high flowrates

2 – DF measurments

- Pool scrubbing trapping CsI aerosols is affected significantly by hydrodynamic aspects & week retention of CH_3I
- Competition of aerosol removal mechananisms and existence of a minimum trapping
- Capability of Weber number in characterizing the DF

Perspectives

DF measurements on CsI at high Weber number: We > 10^4

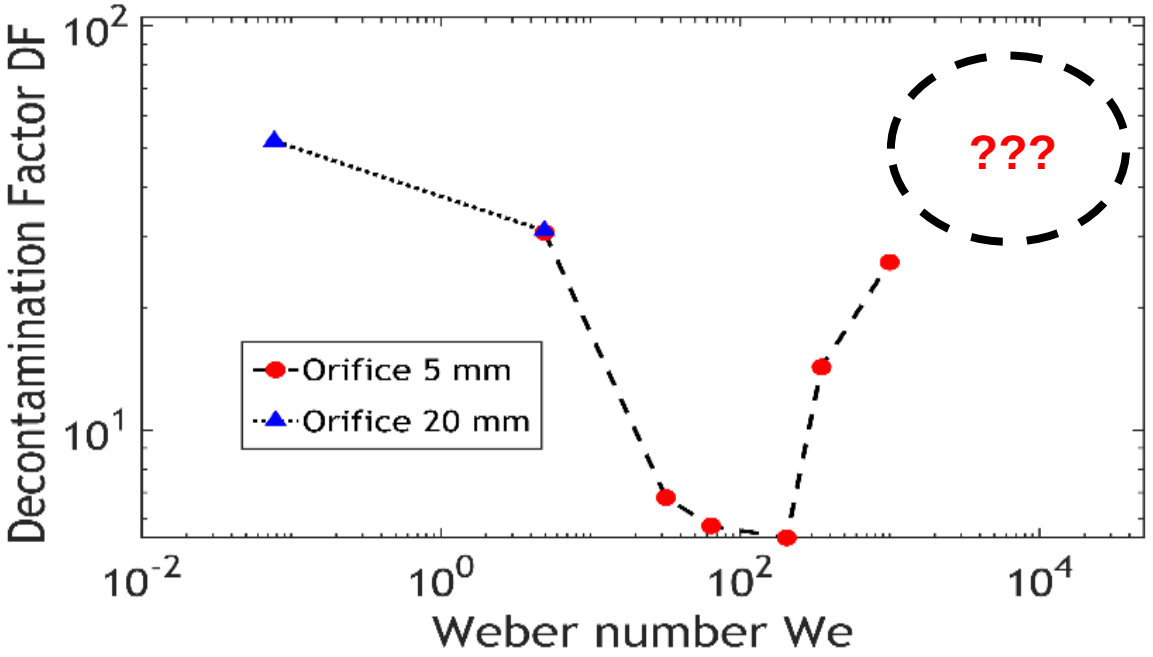

Perspectives

Trapping of elemental I_2

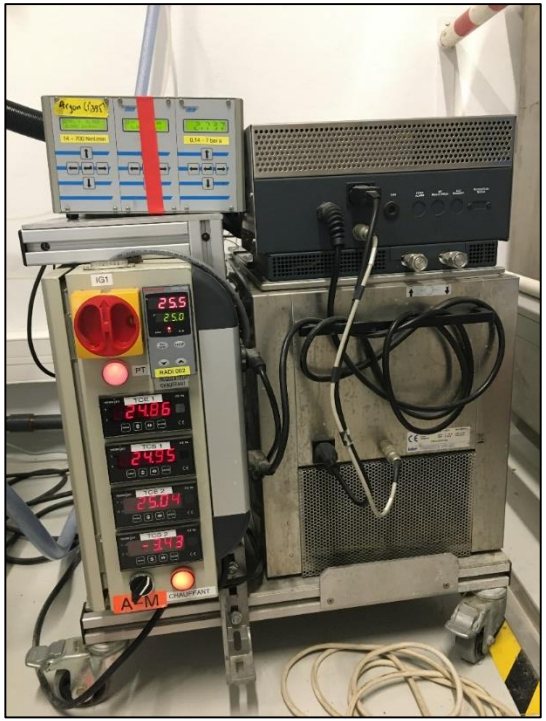

I_2 generator





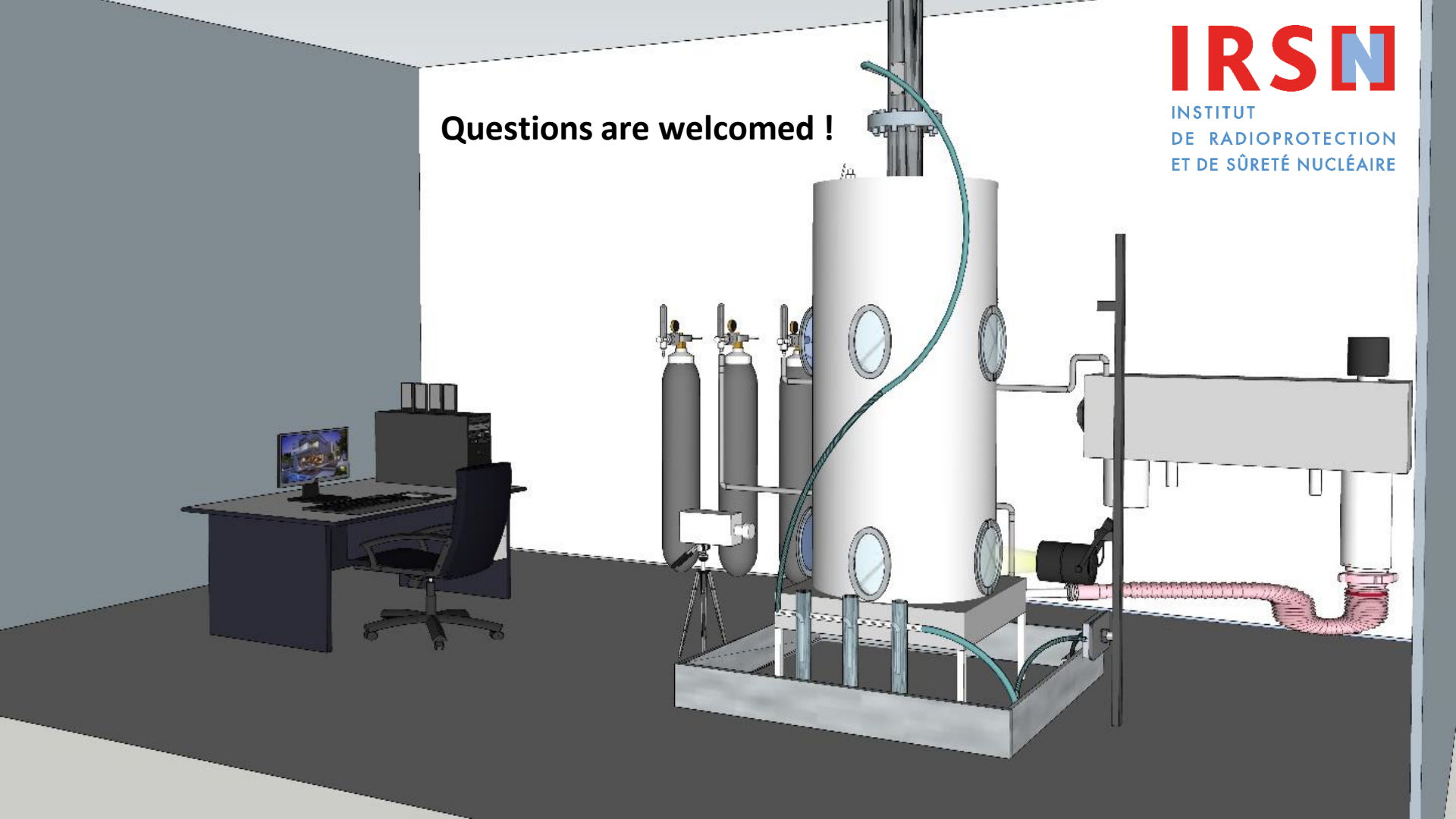
Questions are welcomed !
IRSN
INSTITUT
DE RADIOPROTECTION
ET DE SÛRETÉ NUCLÉAIRE

Récapitulatif des essais Pool scrubbing of IodoMethane													
TYFON	Conditions							débit total Nl/min	débit air Nl/min	débit CH3I Nl/min	[CH3I] inlet ppm	[CH3I] outlet ppm	DF
Essai	Mâtrice	[CH3I]	Air Temp	Water Temp	Water level cm	Orifice size mm	Weber						
PIM 1	Alcaline (pH = 12)	5 ppm	25 °C	25 °C	100	20	0.077	9.21	9.16	0.05	4.71	3.67	1.28
PIM 2	Alcaline (pH = 12)	5 ppm	70 °C	70 °C	100	20	0.077	8.07	8.03	0.04	4.68	1.98	2.36
PIM 3	Alcaline (pH = 12)	5 ppm	25 °C	25 °C	100	5	64	33.18	33.01	0.16	5.05	5.09	0.99
PIM 4	Alcaline (pH = 12)	5 ppm	70 °C	25 °C	100	5	350	70.12	69.77	0.35	4.75	3.81	1.25
PIM 5	Alcaline (pH = 12)	5 ppm	70 °C	70 °C	100	5	350	68.02	67.68	0.34	4.73	4.52	1.05
PIM 6	Alcaline (pH = 12)	5 ppm	70 °C	25 °C	100	5	1000	121.96	121.35	0.61	4.91	4.5	1.09
PIM 7	Alcaline (pH = 12)	5 ppm	25 °C	25 °C	100	5	1000	131.15	130.5	0.65	4.84	4.71	1.03
PIM 8	Alcaline (pH = 12)	5 ppm	25 °C	25 °C	100	5	3000	227.15	226.03	1.12	4.88	4.63	1.05
PIM 9	Alcaline (pH = 13)	5 ppm	70 °C	70 °C	100	20	0.077	8.07	8.03	0.04	6.72	1.2	5.60
Reproduce PIM 1	Alcaline (pH = 12)	5 ppm	25 °C	25 °C	100	20	0.077	9.207	9.161	0.046	4.68	3.51	1.33
Reproduce PIM 2	Alcaline (pH = 12)	5 ppm	70 °C	70 °C	100	20	0.077	8.07	8.03	0.04	6.72	2.73	2.46

$$CH_3I + OH^- \rightarrow I^- + CH_3OH$$

- La vitesse de décomposition de CH3I augmente avec la température du bain.
- Vitesse d'hydrolyse augmente avec pH.
- Importance de caractériser la chimie adéquate de l'eau (additifs, pH, réactions, collage..) pour la rétention de CH_3I.

Etude de l'hydrodynamique des bulles et le piégeage de l'iode dans le banc d'essai TYFON

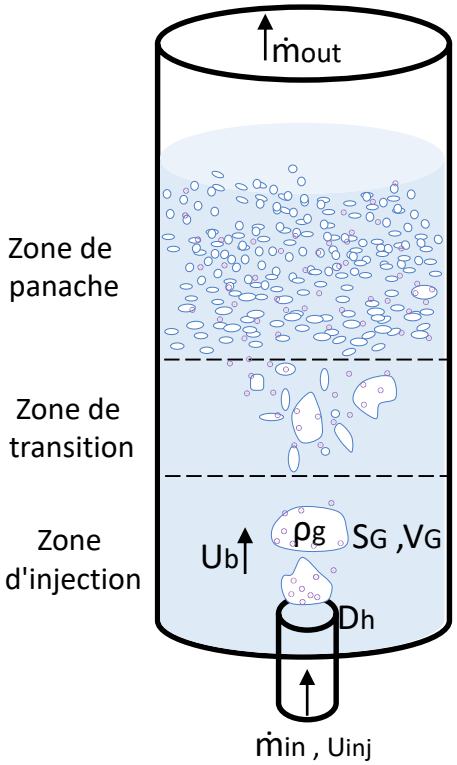



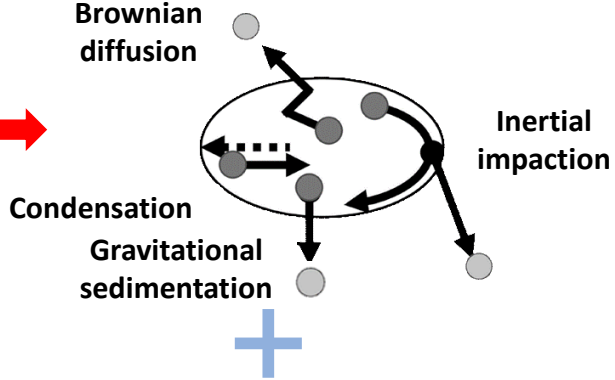

Montage expérimental

TYFON

Transfert par réactions chimiques

(décomposition, hydrolyse, l'oxydation radiolytique)

Objectifs de la thèse

Aspects physiques

Caractériser l'hydrodynamique des bulles :

1. Morphologie
2. Taille (volume, surface)
3. Vitesse
4. Taux de vide

Aspects chimiques

- Quantifier la rétention des composés iodés
- Déterminer les conditions optimales

$$DF = \dot{m}_{in} / \dot{m}_{out}$$

Valider/améliorer la modélisation existante du barbotage (code ASTEC)

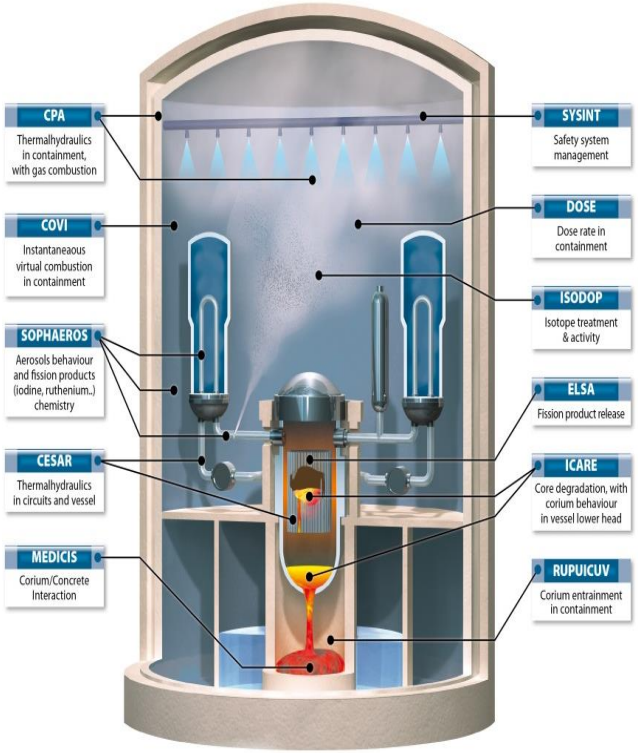

Structure du logiciel ASTEC et principaux modules

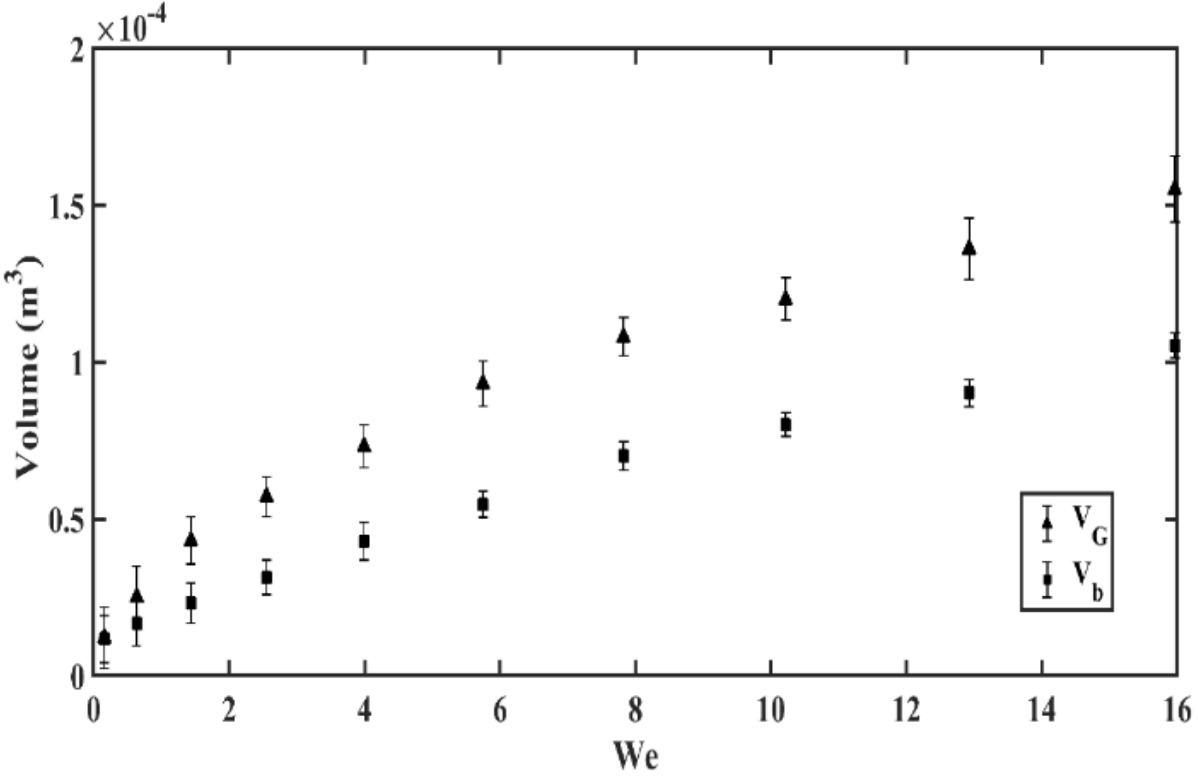
×10^-4
2
1.5
1
0.5
0
Volume (m^3)
0
2
4
6
8
10
12
14
16
We
V_G
V_b

New pool scrubbing correlations based on reliable data

Luis E. Herranz, Francisco Sánchez
CIEMAT
Avenida Complutense 40, 28040 Madrid, Spain

luisen.herranz@ciemat.es; fra.sperez@gmail.com

Abstract

The removal of aerosol particles and vapors in gas bubbles moving through a water pool is known to be an efficient means to reduce source term to the environment during severe accidents, as it happened in the Fukushima Daiichi accident. Based on the experimental data reported until 2016, this paper analyses and discusses the trends of DF (Decontamination Factor) with injection depth, particle size, gas flowrate and steam fraction. The analysis done indicates that the depth effect on DF depends on particle size and the injector diameter. As for particle size, the bigger the particle, the higher the DF; however, a sound correlation cannot be set as such dependence is strongly dependent on other variables too. The effect of submerged structures on DF has been shown to be minor. When coming to flowrate or steam content, even though the effect is observed, correlations are just too inaccurate to be given any quantitative credit.

Keywords: Source Term, pool scrubbing, DF correlations

1. INTRODUCTION

In the Fukushima Daiichi accidents, suppression pools played a major role in mitigating Source Term to the environment, according to the results coming from OECD projects, like BSAF (Pellegrini et al., 2019) and/or ARC-F. Nonetheless, the removal of contaminant particles and/or vapors carried by a gas when passing through an aqueous pool (pool scrubbing), is not restricted to BWR reactors (i.e., secondary side of a steam generator during SGTR; reactor building during V sequences; overlying water during molten materials interaction (MCCI) with basemat concrete; operation of filtered containment venting systems.

Since the 80's last century databases were built and some reviews were published in the 90's (Ramsdale et al., 1992; Escudero et al., 1995; Fischer and Häfner, 1993)). More recently, Herranz et al. (2014) critically summarized the database providing a general overview and highlighting the need to conduct a deep assessment of the individual programs, in which fundamental issues were critically reviewed. Since then an extensive compilation of the literature available from all the open sources since the very old times till 2016 was conducted and data retrieved to be stored electronically. A summary of the work has been recently presented by Herranz & Gupta (2022); individual references to the experimental programs considered in this work can be found in the given reference.

Herranz & Gupta (2022) presented a synthetic table (Table 1) in which more than 500 experiments were scrutinized and categorized according the type of support they can provide, from fit-for-validation (QfV) to unfit-for-validation (NoU), with an intermediate category named useful for understanding (UfU). Less than 12% met the conditions required concerning availability and completeness of information and DF (Decontamination Factor) accuracy for them to be considered valuable for validation.

One of the major drawbacks noted in most programs included in the database (Herranz et al., 2014) was the lack of a systematic analysis of the parameters influencing pool scrubbing. This paper is an attempt to conduct such an analysis and, whenever possible, to derive an empirical expression consistent with the data

included in the database. This work has been conducted under the frame of the IPRESCA project, led by Becker Technologies, in the frame of SNETP/NUGENIA/TA2.

Table 1. Classification of pool scrubbing experimental programs

PROGRAM	# TESTS	QfV	UfU	NoU
UKAEA (1965-1966)	>47			X
GE (1982)	18		X	
EPRI (1982-1986)	>151		X	
EPSI (1983-1991)	>7			X
POSEIDON-I (1987)	>100		X	
JAERI (1987)	~70		X	
ACE (1988-1992)	9	X		
LACE-España (1990-1992)	11	X		
SPARTA (1992)	1			X
RCA (1995)	4	X		
POSEIDON-II (1998)	17	X		
AASC-PS (1999-2000)	4	X		
SG-Experiments (2000-2012)	9	X		
PASSAM-RSE (2013-2017)	6	X		
PASSAM-CIEMAT (2013-2017)	7	X		
PASSAM-AREVA (2013-2015)	>21		X	
TOTAL # TESTS	>482	67	>360	>55

2. TRENDS OF DECONTAMINATION FACTOR

Based on the pool scrubbing database built up, the DF (ratio of the incoming mass into the pool and the outgoing mass from the pool) tendencies with the four experimental variables more profusely explored in experimental pool scrubbing programs (i.e., submergence, AMMD[1], flowrate and steam fraction) have been plotted in Fig. 1 (a through d). Two observations should be made: first, the data considered have been those from QfV and UfU programs; second, the data displayed from each experimental program are those which boundary conditions, other than the variable being explored, have similar or the same values, so that the effects of other variables are minimized as much as possible. It is worth noted that the error bars in the plots mean either the experimental error reported by the authors or the range of values explored in the program.

As observed, it is not possible to set clear global trends when considering data points coming from all the experimental programs. Differences in aspects such as experimental set-ups or the boundary conditions other than the variable explored, as well as the large uncertainty associated to data sometimes, prevent from setting firm tendencies of DF. Therefore, no conclusion on DF trends might be reached by using the database as a whole. Then, the next step is to explore those trends through assessing the individual programs that addressed each of those effects. Mathematical equations have been derived only for those cases with more than three values of the independent variable (i.e., submergence, AMMD, flowrate or steam fraction).

In the sections below, data uncertainties have been included whenever the references supporting the data included them. As for the validity ranges of each of the correlations given in the sections below, they would be those corresponding to the experimental series/programs from which the equations have been derived. Whenever feasible, a determination coefficient (R^2) has been calculated; no threshold has been set to assess the correlations reliability, since R^2 is mostly used to discuss the specific trend found and its consistency with data.

[1] Aerodynamic Mass Median Diameter

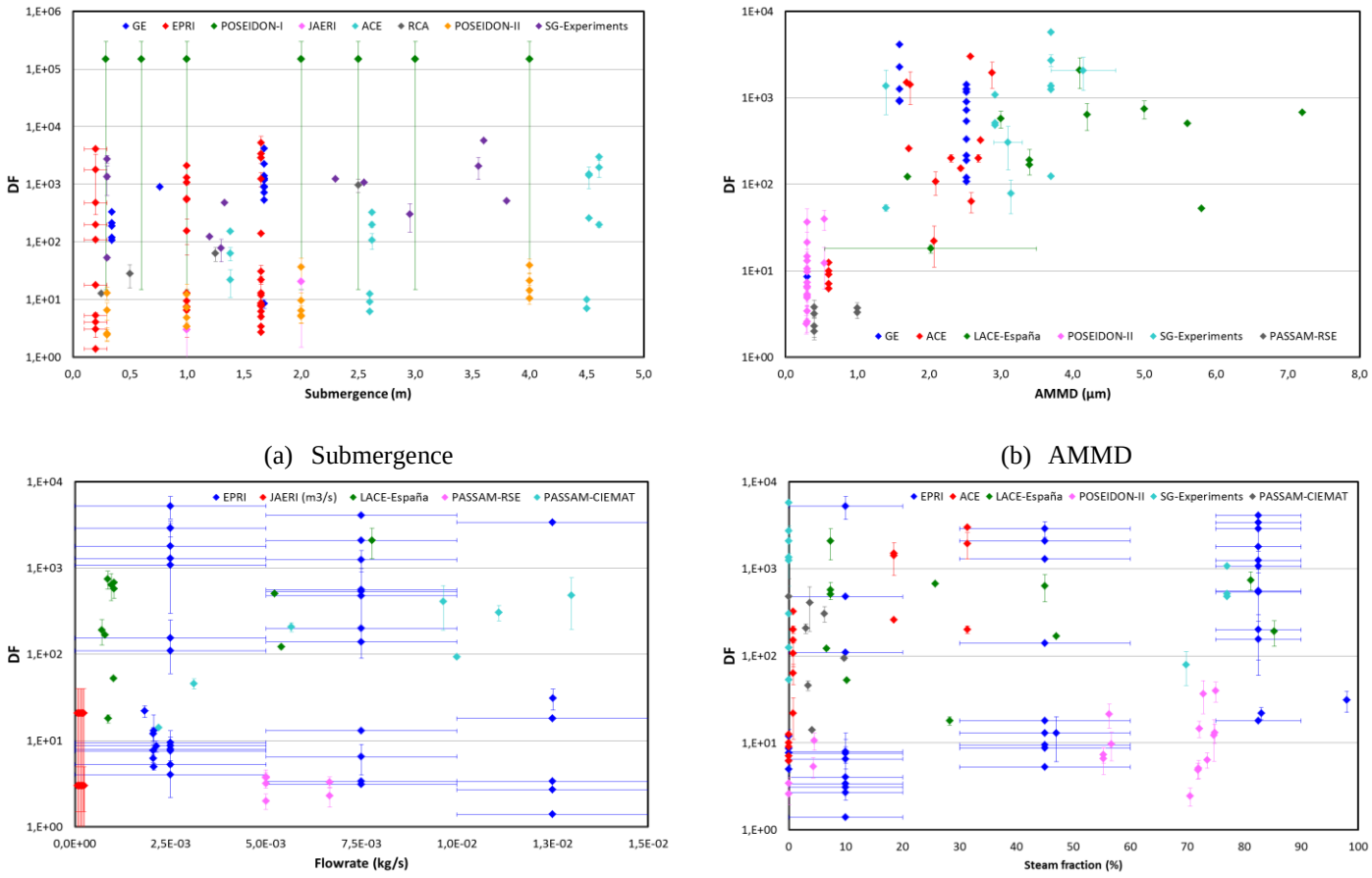

(a) Submergence

(b) AMMD

(c) Flow rate

(d) Steam fraction

Figure 1. DF measurements vs. key pool scrubbing variables

2.1. Submergence

In order to assess the submergence (Sub) effect on DF some a priori considerations need to be made. Given the direct relation between submergence and in-pool residence time (i.e., the time that takes the contaminant to move from the injection point to the pool surface), the influence of submergence on DF will be different if there are submerged structures in the water that might heavily affect the gas hydrodynamics (Betschart et al., 2020) or if radioactive contaminants within the bubble are in different physical phase (i.e., condensed vs vapour) since they would be subject to different scrubbing mechanisms. Therefore, experiments having immersed surfaces or injecting vapour chemical forms of some nuclides will be given specific attention.

Out of the nine experimental programs addressing submergence as a variable, only six of them tackle with particle scrubbing within pools free of any immersed surface (GE, EPRI, JAERI, ACE, RCA and POSEIDON-II). EU-SGTR and ARTIST-I dealt with particle scrubbing with submerged structures and POSEIDON-I investigated iodine vapour scrubbing. The submergence ranges were different in each program (as shown in the x axes of the graphs below).

Usefulness of some of these datasets, though, is heavily conditioned for different reasons. In the case of GE (Fig 2(a)), even though there is a visible trend, the deeper the submergence the higher the DF, no mathematical description has been derived, though, since there is just a single point in between the lower and the upper bound of the submergence interval. In the EPRI experimental program (Fig 2(b)), where different colours have been used for experimental campaigns with similar features other than submergence (grey data points are the only ones with particle diameters over 2.5 μm; the rest of data, particle diameters were smaller than 0.5 μm), to set a trend is not possible because of the large uncertainty associated to data. Finally, the JAERI program, in which all the tests had similar boundary conditions, include just few largely uncertain experimental points (Fig. 2(c)). The ACE experimental program (Fig. 2(d)) also shows a clear growing trend with submergence, except in the case of DOP particles, probably due to the small particle size of DOP (0.6 μm).

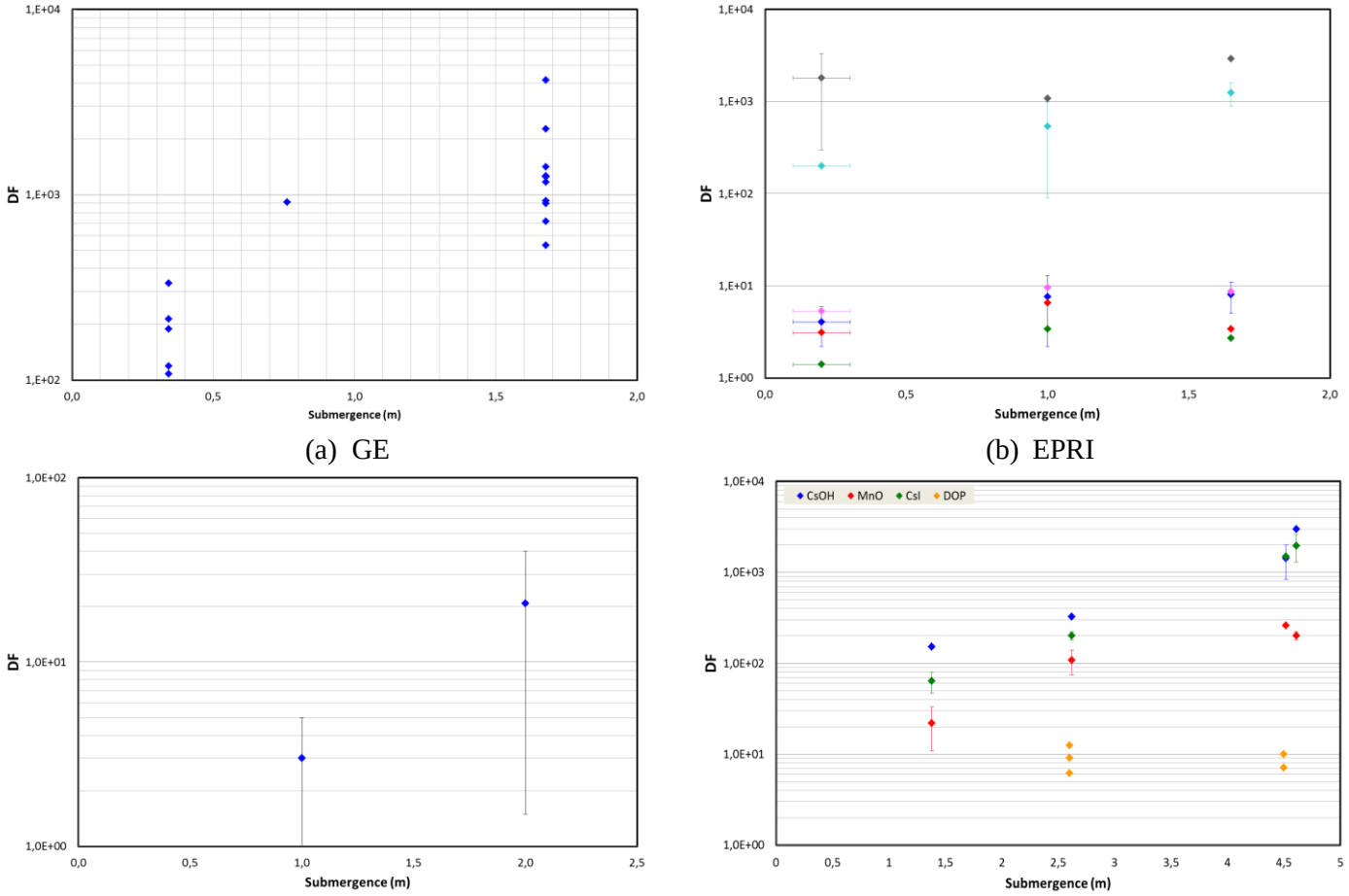

(a) GE (b) EPRI

(c) JAERI (d) ACE

Fig. 2. Decontamination factor vs submergence (GE; EPRI; JAERI; ACE)

Contrary to the previous programs, there are two experimental programs that have allowed deriving mathematical expressions to express the DF trend with submergence (Fig. 3): RCA and POSEIDON-II. In the RCA program (Fig. 3(a)) the submergence was the only variable changed, the rest of boundary conditions were just kept at equal or very similar values; a growing exponential correlation, with an R^2 higher than 0.98, was derived at the time (Herranz et al., 1997). The POSEIDON-II tests (Fig. 3(b)), when

the effect of steam fraction was singled out, a similar trend was found with an R^2 of at least 0.93, the highest one (0.996) being the one with no steam.

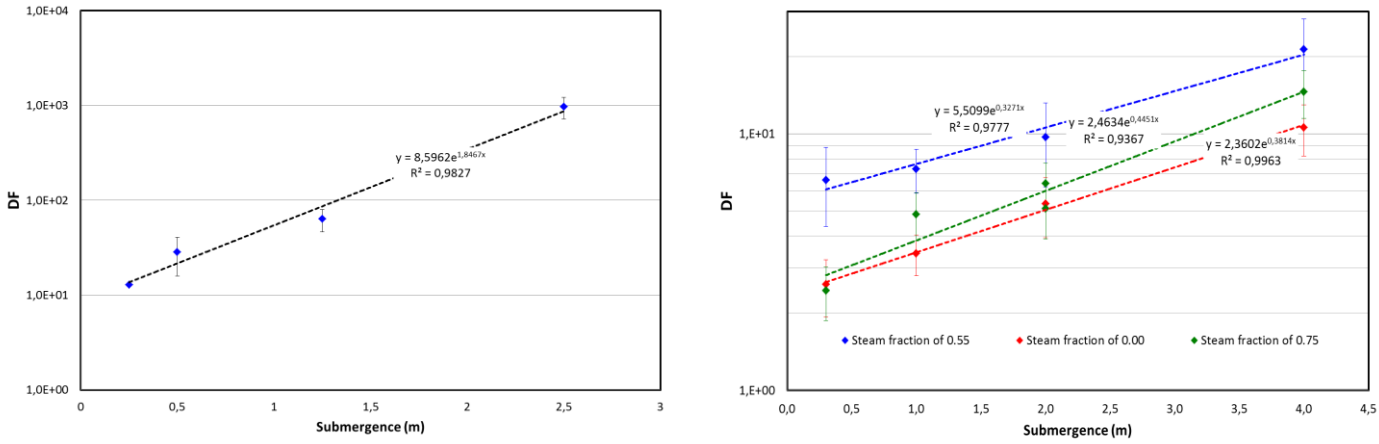

(a) RCA (b) POSEIDON II

Fig. 3. Decontamination factor vs submergence (RCA; POSEIDON)

A joint analysis of both experimental programs allows setting the following general trend to describe the DF dependence on submergence:

$$DF = a \cdot \exp(b \cdot Sub) \quad (1)$$

This exponential equation, already proposed and discussed by Herranz et al. (1997), is consistent with the relation between in-pool residence time of bubbles and submergence. However, when looking for the best a and b coefficients for each of the experimental sets (Table 2), one may observe that other experimental conditions also affect the DF-S relation. The sensitivity of submicron particles removal (0.3- 0.5 µm particles were used in POSEIDON II) to water depth is softer than for micron particles (1.1 – 1.3 µm in RCA), as shown by the b values in Table 2. This is consistent with the fact that under most conditions the dominant removal mechanism is centrifugal deposition, which is proportional to the particle diameter squared (Fuchs, 1964). In addition, there might be an effect of the injector diameter: the smaller the injector, the larger the "effective submergence" (i.e., water depth from the location at which a bubble swarm is formed and its average bubble size is steady up to the pool surface). The primary globule diameter was shown by Paul et al. (1984) to be a function of the injector diameter and this, in turn, influences the transition length to a steady bubble swarm (transition region). Therefore, the smaller the injector diameter, the smaller the globule and, consequently, the deeper the "effective submergence".

Table 2. Parameters in the $DF = f(Sub)$ correlation

	a	b	d_{inj} (mm)
RCA	8.5962	1.8467	10.0
POSEIDON-II #1	5.5099	0.3271	20.0
POSEIDON-II #2	2.3602	0.3814	20.0
POSEIDON-II #3	2.4634	0.4451	20.0

For steam generator experiments, EU-SGTR and ARTIST-I programs, submerged structures were embedded in the experimental set-up. By plotting both programs' data points together, a growing trend of DF with submergence is observed. However, the number of data points and the differences in the testing conditions prevent from deriving an acceptable exponential correlation, as shown in Fig. 4, and the best fit yields R^2 hardly over 0.5.

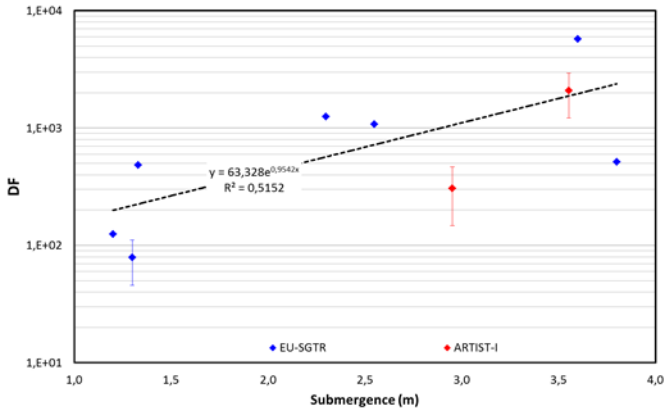

Fig. 4. Decontamination factor vs submergence in setups with submerged structures

Finally, for the POSEIDON-I experiments (vapour I_2 injection) the exponential growing trend with submergence shows correlations with determination coefficients (R^2) greater than 95% (Fig. 5). Note that only those test groups that have at least four submergence values have been considered. Four data sets, with different size of injector, are drawn. It is observed that injector size has an effect on the DF slope with submergence: the bigger the injector the less sensitivity of DF to submergence. As discussed above, this is related to the close link between bubbles residence time in pool and the "effective submergence".

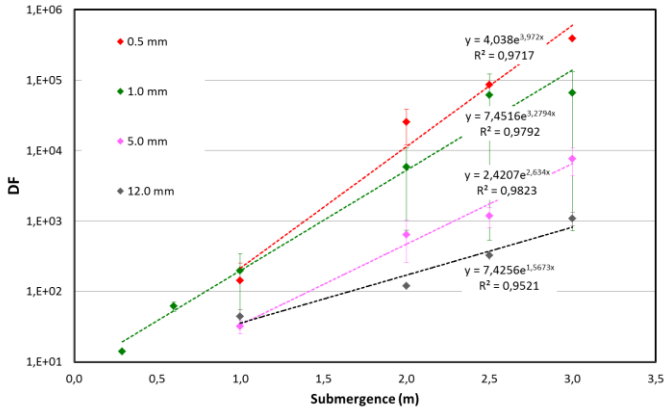

Fig. 5. Decontamination factor vs submergence for vapours (POSEIDON I)

Interestingly, the pre-factor and exponential coefficients of the data points with injector diameter 12 mm are notably similar to those of RCA (10 mm), Table 3. Given the different nature of particles and vapours absorption in the pool, this might support the discussion held on the "effective submergence" above.

Table 3. Parameters in the $DF = f(S)$ correlation

	a	*b*	d_{inj} (mm)
POSEIDON-I #4	7.4256	1.5673	12.0
RCA	8.5962	1.8467	10.0

2.2. AMMD

The AMMD effect on DF was studied by six of the experimental programs in Table 1 (GE; ACE; LACE-España; POSEIDON-II; PASSAM-RSE; ARTIST). Unlike submergence, in the case of particle size the number of data points with different AMMDs under similar boundary conditions is in most experimental programs less than four. This means that a correlation between DF and AMMD cannot be reliably derived, except in the case of immersed surfaces, as will be discussed at the end of this section. In the plots shown, GSD[2] will be included in brackets within the program heading.

There are 3 experimental programs that explored this sensitivity but could not give sound insights: GE, ACE and LACE-España. In the GE experimental program (Fig. 6(a)), data scatter prevents from observing an explicit trend of DF with AMMD. Such a lack of sensitivity might stem from two main factors: on one side, the small injector size ($d_{inj} < 10^{-4}$ m) would have resulted in a bubble swarm formation pretty close to the injection point, so that the effective submergence was heavily enhanced and other effects were shadowed; on the other, the bubble rise velocity (~0.3 m/s) was low enough as for removal mechanisms to become very efficient. Anyway, at the high DF values measured, experimental errors are expected to result in large DF intervals. The ACE program (Fig. 6(b)) was *a priori* a good candidate to settle the sensitivity of DF with particle size, as several AMMDs were explored in its test matrix; however, the proximity of different sizes of particles and the use of different nature particles (i.e., soluble - CsOH and CsI -, and unsoluble, MnO) in tests with similar boundary conditions (AA1 and AA3), makes it hard to set any certain trend. LACE-España (Fig. 6(c)) experiments had also potential to find out the DF sensitivity with particle size. Nonetheless, multiple reasons hindered it: first, just two particle diameter values were tested for each steam fraction; second, in all the cases GSDs were larger than 2.5 and in each pair of data points at the same steam fraction, the GSDs were notably different (one of them being over 3.5 typically); and, finally, one of the experiments, despite having a GSD around 1.6, showed a bi-modal distribution, which makes it hardly comparable to any other.

Qualitative tendencies might be observed in POSEIDON-II and PASSAM-RSE (Fig. 7); however, in both cases data were not enough to derive a correlation out of them. In both cases, though, a growing trend might be perceived, but just two rather scattered size points were reported.

Within the SG-Experiments (Fig. 8), an increasing trend is observed in ARTIST-I and ARTIST-II data when the inlet gas pressure is atmospheric. For the ARTIST-II tests, with high injection pressure, the error band overlap prevents from firmly setting any trend, although a growing tendency might be observed. Given that the experimental set-up of ARTIST-I and –II was similar, a correlation with an R^2 of 0.97 has been derived for the low injection pressure data (AMMD in μm):

$$DF_{ss} = 7.1 \cdot \exp(1.355 \cdot AMMD) \quad (2)$$

[2] Geometric Standard Deviation

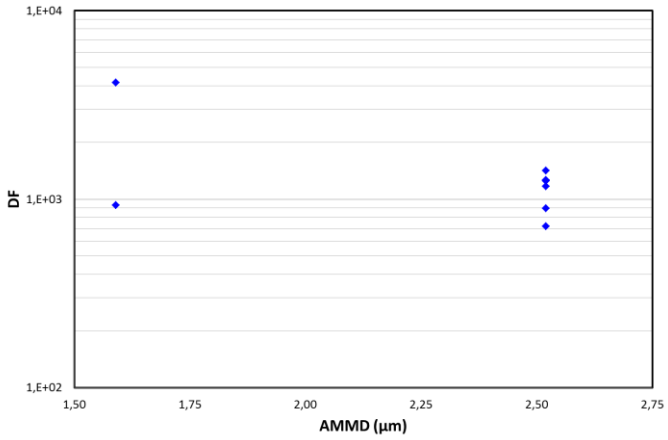

(a) GE (GSD, 2.06-2.43)

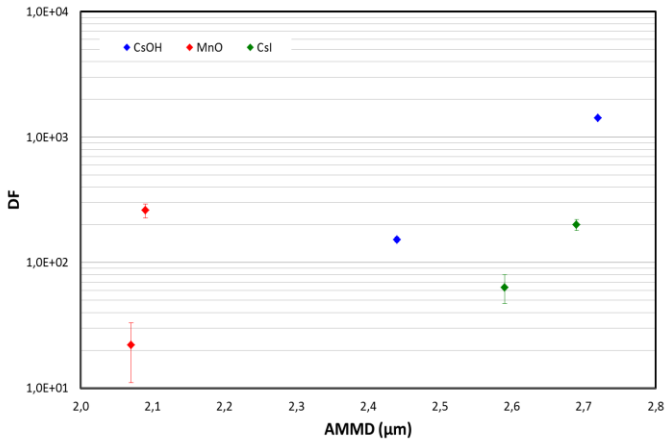

(b) ACE (GSD, 1.53-2.36)

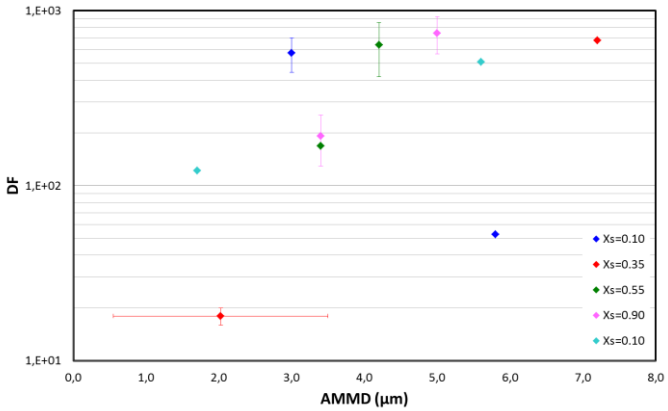

(c) LACE-España (GSD, 1.4 – 5.4)

Fig. 6. Decontamination factor vs AMMD (GE; ACE; LACE-España)

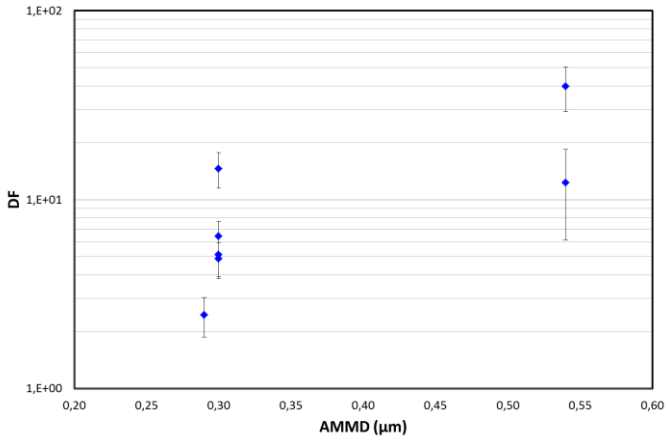

(a) POSEIDON-II (GSD, 1.36 – 1.73)

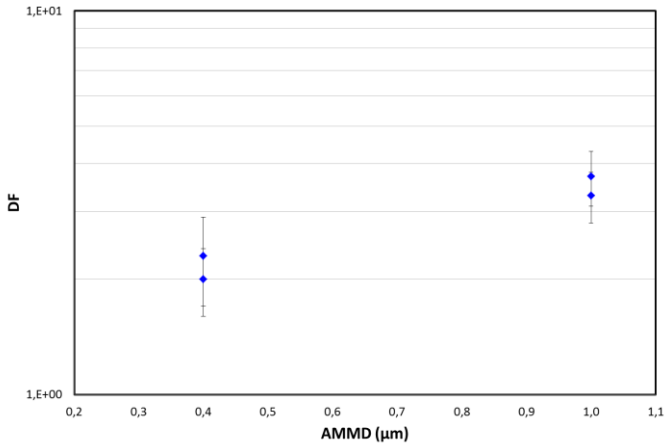

(b) PASSAM-RSE (GSD, 1.19 – 1.3)

Fig. 7. Decontamination factor vs AMMD (POSEIDON-II; PASSAM-RSE)

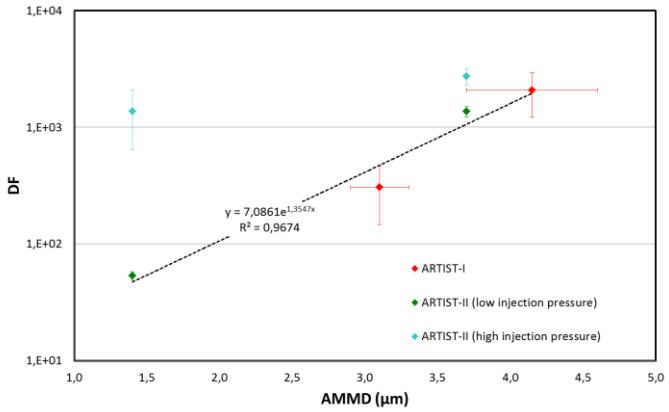

Fig. 8. Decontamination factor vs AMMD in the steam generator experiments (GSD, 1.2 – 3.0)

In summary, observations indicate the bigger the particle, the higher the DF. In the case of immersed surfaces, this qualitative statement may be translated into a numerical correlation for low injection pressure data. However, for the rest of data a sound correlation describing the impact of particle size on DF cannot be soundly derived. In fact, according to the large DF differences shown in some experimental programs (ACE and POSEIDON-II) for rather similar aerosol sizes, it seems that DF sensitivity to particle diameter is strongly dependent on other boundary conditions.

To support the above statement, a very simple exercise has been conducted. By neglecting the GE and LACE data points for the reasons given above and assuming that the DF higher than 300 in the ACE program should be attributed to changes in other variables than particle size, an exponential correlation might be derived (Fig. 9),

$$DF_{ns} = 3.0 \cdot \exp(1.365 \cdot AMMD) \tag{3}$$

but the resulting R^2 does not even reach 0.7 (0.668), which indicates a rather poor correlation.

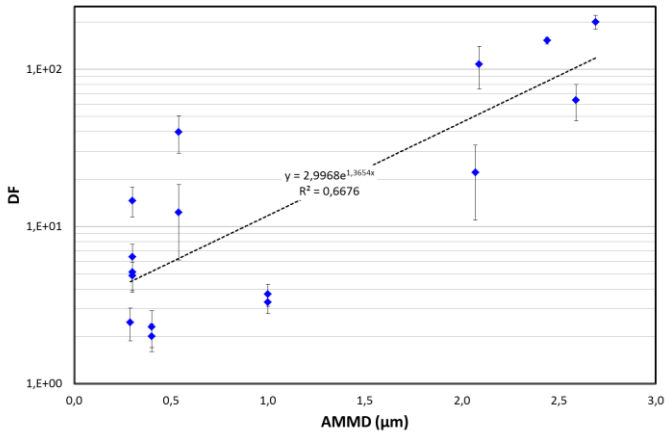

Fig. 9. DF vs AMMD for data with DFs less than 300

The above expression, despite not being recommended for assessing the particle size effect on DF, highlights an interesting feature of such sensitivity: in scenarios with submerged structures DF should be expected to be higher, but its dependence on particle size is roughly the same than in structures-free pool scenarios. In mathematical terms:

$$DF_{ss} = DF_{ns} \cdot 2.4 \cdot \exp(-0.01 \cdot AMMD) \quad (4)$$

2.3. Flowrate

DF sensitivity with carrier gas flowrate was given less attention than submergence but, even so, five experimental programs addressed the issue (EPRI; JAERI; PASSAM-RSE; LACE-España; PASSAM-CIEMAT).

Given the uncertainty in the DF measurements and the definition of flowrate values in intervals, the EPRI experimental program (Fig. 10(a) and (b)) does not provide valuable insights into the effect of flowrate on DF. Nonetheless, the plots indicate that flowrate is not the variable that determines the DF level; in other words, in the flowrate interval explored, flowrate was not a dominant variable for DF when compared to others like steam fraction, submergence or particle size, which were really the ones determining the DF. Observations from JAERI data are similar: data were given in so broad DF bands that it is hard to identify a trend of DF with flowrate; namely, gas flowrate was not the dominant variable on DF, submergence was. Few PASAM-RSE experiments addressed the effect of flowrate on DF while using two different particle sizes. Even though the data might indicate that the flowrate effect (growing or decreasing) is dependent on particle size, the scarcity of data points and the DF error bands recommends not drawing any conclusion. In addition, the moderate submergence (1.0 m) and the upward direction of injection might have substantially affected the DF measurements and its sensitivity.

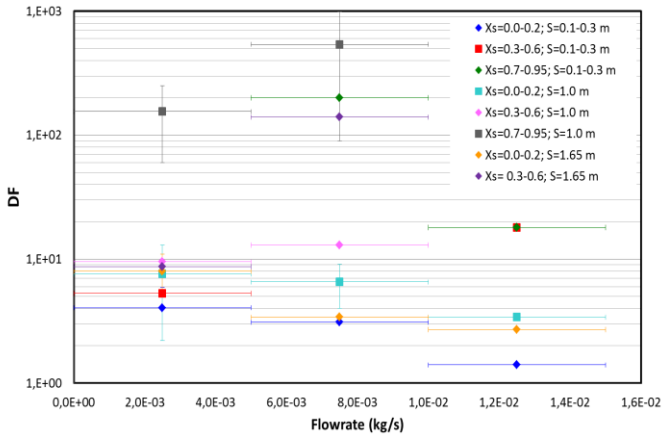

(a) EPRI (small particles, 0.4 μm AMMD)

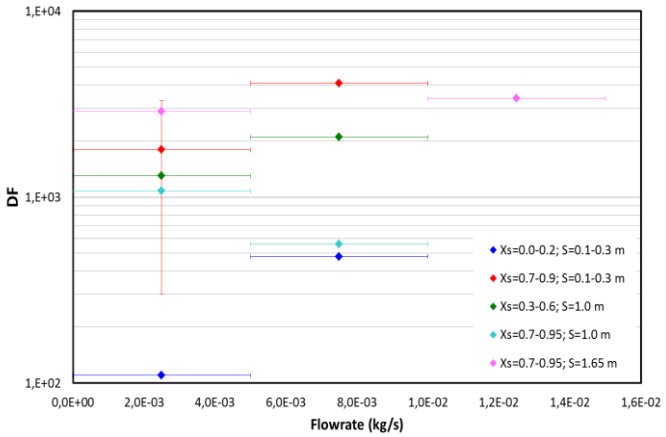

(b) EPRI (large particles, 2.7 μm AMMD)

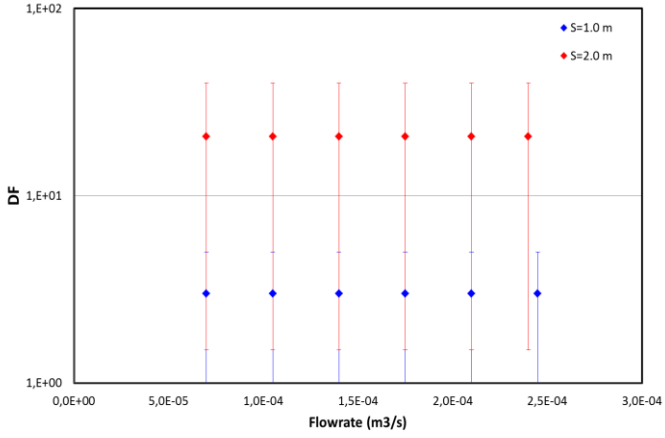

(c) JAERI

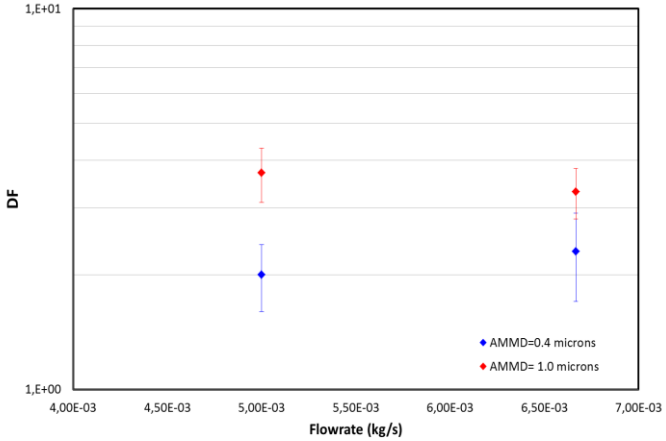

(d) PASSAM-RSE

Fig. 10. DF vs Flowrate (EPRI; JAERI; PASSAM-RSE)

Contrary to the previous programs, LACE-España and PASSAM-CIEMAT allowed identifying a growing trend of DF with flowrate (Fig. 11). The difference is that, while just two data points can be properly compared in the case of LACE-España, which prevents from deriving any correlation, in PASSAM-CIEMAT campaign a sharp increasing followed by an asymptotic tendency was reported by Herranz et al. (2018). In fact, by including jet scrubbing data from other programs, they proposed an approximate equation describing the scrubbing efficiency as a function of the Stokes number (Stk) and the saturation ratio (S) (R^2=0.8):

$$\varepsilon[\%] = \frac{0.98}{1+1.0847\cdot\exp(-1.0528\cdot 10^{8}\cdot Stk^{3.7885}-0.7257\cdot S)}\cdot 100 \quad (5)$$

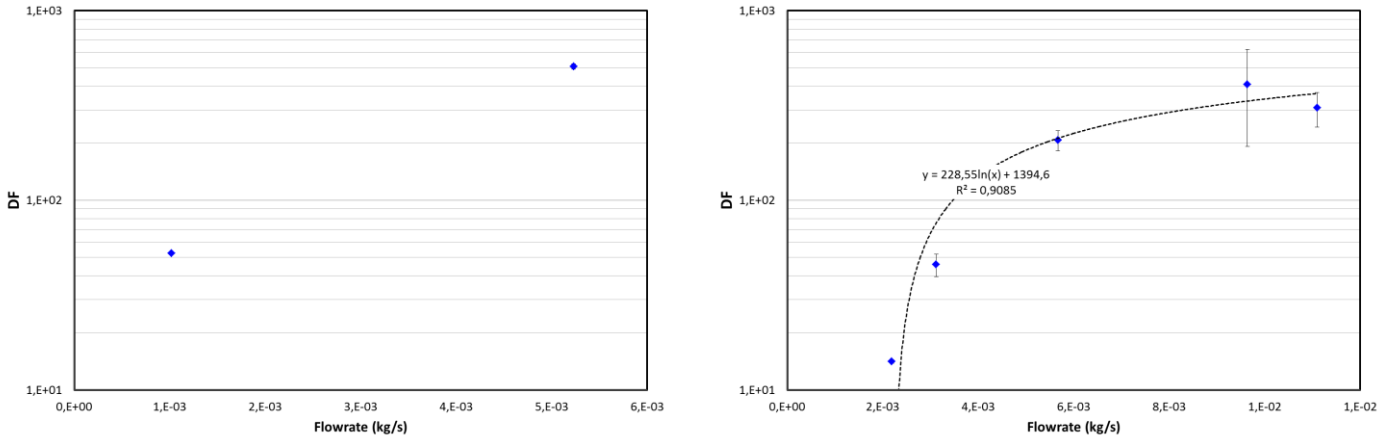

(a) LACE-España (b) PASSAM-CIEMAT

Fig. 11. Decontamination factor vs flowrate (LACE-España; PASSAM-CIEMAT)

2.4. Steam fraction

The effect of steam fraction (X_s) on DF has been explored in six experimental programs (EPRI; ACE; LACE-España; POSEIDON-II; PASSAM-CIEMAT; EU-SGTR). As steam fraction speaks out about the potential condensation of steam in the carrier gas, the analysis below has been conducted in terms of saturation ratio (S), which better embraces such a potential as it considers the pool thermal state ($S = \frac{p_v}{p_{sat}(T_{pool})}$).

The EPRI program explored three ranges of steam fraction in the carrier gas (low, medium and high). DF measurements ranged (Fig. 12) over at least 3 orders of magnitude. By grouping data according to particle size and pool thermal conditions, some observations can be made. Data of small particles (0.40 μm) in hot pools indicate just a slight growth of DF with Xs, which is consistent with the fact that likely no or hardly condensing conditions were attained at high pool temperature and, if the experimental error is accounted for, not even that slight tendency can be rigorously credited. Contrarily, when the pool is at ambient temperature, 5 out of 7 groups identified representing similar test conditions showed a remarkable effect of Xs on DF, whereas the 2 other cases does not have one data point at high Xs. This trend at cold pool conditions cannot be stated so firmly when big particles (2.70 μm) are used (only 2 out of 5 groups experience a DF growth with Xs; and the others show no change or, even, a reducing trend), though.

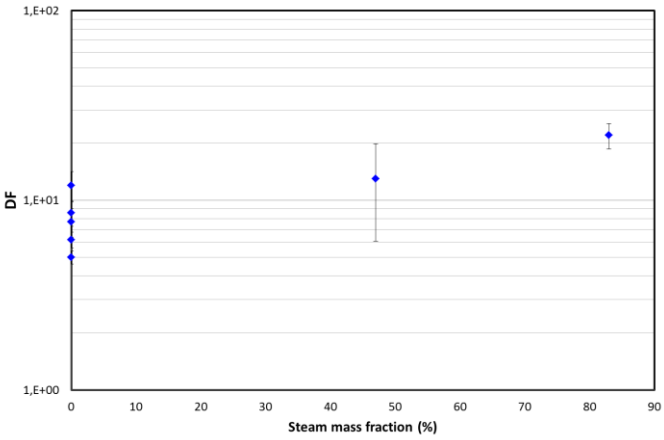

(a) 0.4 μm; 373 K

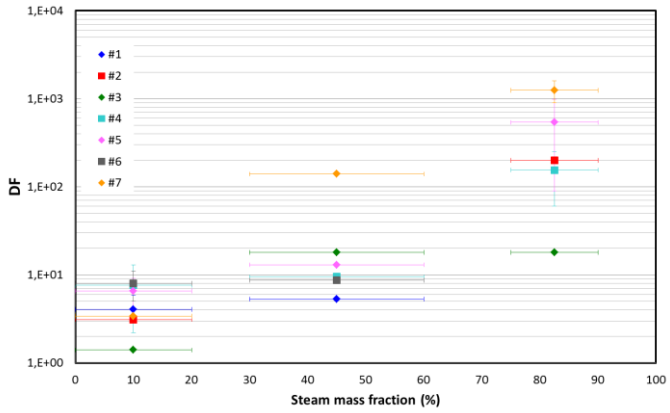

(b) 0.4 μm; 293,15 K

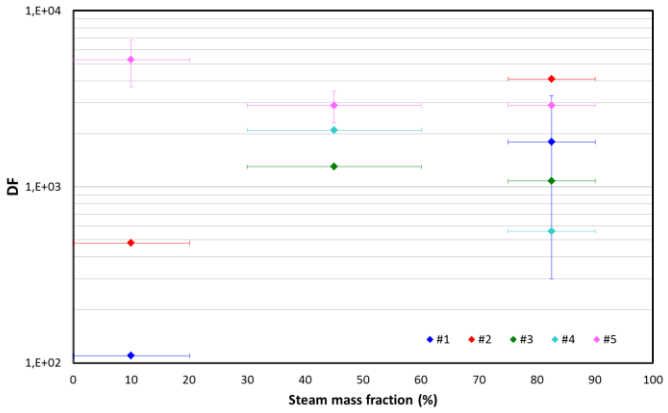

(c) 2.7 μm; 293.15 K

Fig. 12. Decontamination factor vs steam mass fraction (EPRI)

The ACE program (Fig. 13) was characterized by S values over 1.0 (i.e., condensing conditions for all aerosol compounds used). Only MnO DF grows about a factor of 2.0 when S increases nearly an order of magnitude. The soluble aerosols (CsI and CsOH), apparently, show a decreasing trend, although if the DF error is considered, no tendency should be noted.

LACE-España and POSEIDON-II programs (Fig. 14) included tests with saturation ratios below and over 1.0. Even though for different reasons, no trend may be drawing from any of them. In the former, the big particles size (3-6 μm AMMD) and the large distributions scatter (GSD > 2.5) were likely behind this lack of trend. The latter, even if submergence grouped according submergence, not a firm trend is observed.

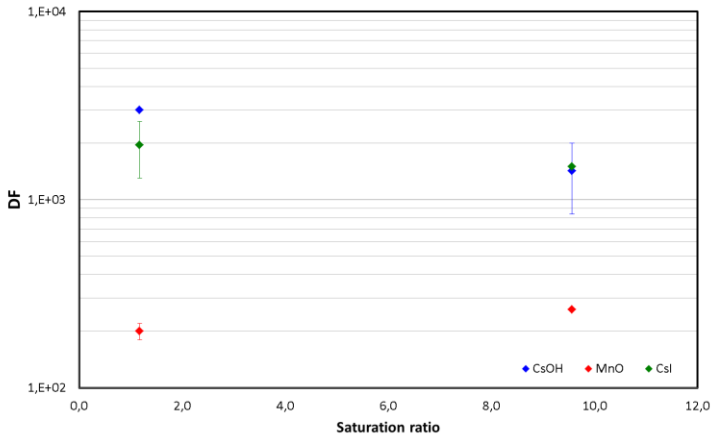

Fig. 13. Decontamination factor vs saturation ratio (ACE)

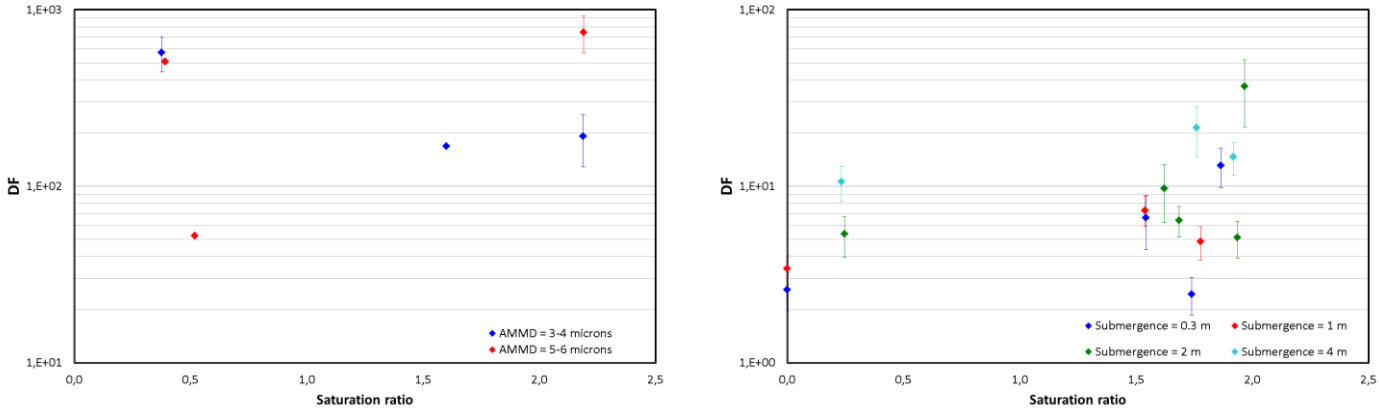

(a) LACE-España (b) POSEIDON-II

Fig. 14. Decontamination factor vs saturation ratio

PASSAM-CIEMAT (Fig. 15(a)) data draw a decreasing trend of DF with S (ranging from 0 to more than 4.0) at high flowrates (just two data points at low flowrates). Nonetheless, when the experimental error is considered, 3 out of the 4 tests data should be considered the same value; namely, no trend can be soundly supported. As in the case of PASSAM-CIEMAT, the EU-SGTR experiments were conducted at S ranging from 0 to more than 3.0 (Fig. 15(b)). The points at low and medium submergence look not to be sensitive to S, so that just 2 data points at submergences close to 4.0 show a DF decreasing trend of about an order of magnitude in the upper ranges of DF values (from about 6000 to 500); again, no trend should be withdrawn from the SG-Experiments database either.

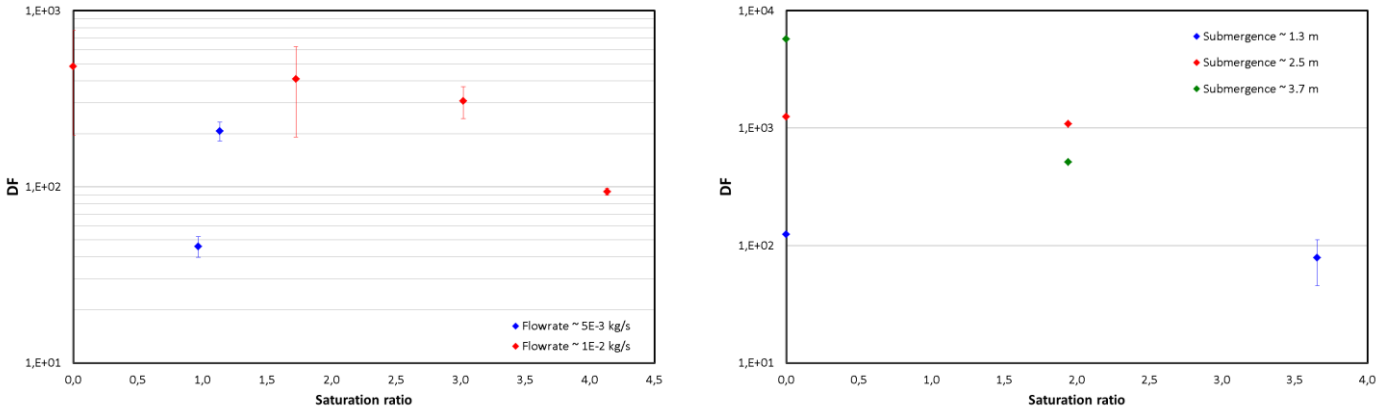

a. PASSAM-CIEMAT b. EU-SGTR

Fig. 15. Decontamination factor vs saturation ratio

3. MAIN INSIGHTS

Based on a comprehensive data base collected from the open literature on pool scrubbing experimental research since the 60's of last century to 2016, an analysis of the major trends observed has been conducted. In addition to the observations and discussions held in the previous sections, some key insights may be drawn from this work:

- Pool scrubbing experimental research was conducted mostly lacking a systematic parametric analysis of the variables influencing the process (i.e., more than a single parameter was usually changed in each experiment). Given the complexity of the interlink between phenomena of different nature (i.e., aerosol physics, heat transfer, gas-water hydrodynamics), it made hard a quantitative interpretation of the effects of individual parameters.
- Pool scrubbing scenarios experimentally investigated addressed a broad range of conditions (likely due to variability of conditions in different reactor designs and sequences). Given the influence of boundary conditions set on the effects of key variables on DF, drawing any conclusion on a specific effect based on data from all the programs that explored it, is just not possible.
- Experimental uncertainties play a key role when deriving tendencies based on data, particularly when DF values go over 100. In many cases, apparent trends based on data points vanish when uncertainties are considered and cannot be rigorously supported.
- DF correlates exponentially with pool submergence showing high determination coefficients for both particles and gases, which is consistent with the close relation between submergence and residence time. The correlation is notably affected by particle size and injector diameter; the latter being a direct factor in what has been called "effective submergence". Presence of submerged structures does not break up the correlation trend, although further data would be needed to reach a reliable equation to apply.
- DF correlation with particle size, even though analytically supported, cannot be strictly sustained through data, except in the case of immersed surfaces at low inlet pressure (i.e., near atmospheric pressure). In other words, there might be other influencing boundary conditions in the scrubbing processes that seem to blur the size effect. According to data discussion, the presence of surfaces within the pool would hardly affect the size effect on DF.
- Uncertainties and/or scarcity of data prevent from deriving a soundly supported correlation of DF with flowrate. A growing sigmoidal trend was proposed, though, based on data acquired in the jet injection domain, but still the determination coefficient was considered too low as to be reliable.

- Steam fraction effect on DF is better investigated in terms of saturation ration at the pool conditions. Even so, the data available are far from allowing set even qualitative observations, this meaning that the effect explored must be affected and even hidden by others that hinder settling any equation.

The work here reported might be a valuable asset both for validation and verification of pool scrubbing models and codes and for optimization of future experimentation where further data might bring new insights and/or sound support to those shown in previous sections. Once all these data have been retrieved from old archives and peerly reviewed, it would be natural to continue enlarging the database with the material produced from 2017 on under a proper framework, like the IPRESCA project.

References

Betschart T., Lind T., Prasser H-M, 2020. Investigation of two-phase flow hydrodynamics under SGTR severe accident conditions. NED 366. https://doi.org/10.1016/j.nucengdes.2020.110768.

Escudero Berzal M., Marcos Crespo M.J., Swiderska-Kowalczyk M., Martin Espigares M., Lopez Jimenez J., 1995. State of the art review on fission products aerosol pool scrubbing under severe accident conditions, Final report, Report EUR 16241 EN, ISSN 1018-5593.

Fischer K., Häfner W. 1993. Review of Pool Scrubbing Experiments and Theoretical Models. 10th European Pool Scrubbing Meeting, 1993.

Herranz L.E., Tardáguila R., Berschart T., Lind T., Morandi S., 2014. Remaining Issues in Pool Scrubbing: Major Drivers for Experimentation within the EU-PASSAM Project, Proceedings of ICAPP '14, Charlotte, USA, April 6-9, 2014, Paper 14156.

Herranz L.E., Gupta S., 2022. Validation matrix for pool scrubbing models. Proceedings of the Nuclear Reactor THermalhydrulics conference, NURETH-19, Online, March 7-10 2022.

Pellegrini M., Herranz L., Sonnenkalb M., Lind T., Maruyama Y., Gauntt R., Bixler N., Morreale A., Dolganov K., Sevon T., Jacquemain D., Journeau C., Song J.H., Nishi Y., Mizokami S., 2020. Main Findings, Remaining Uncertainties and Lessons Learned from the OECD/NEA BSAF Project. Nuclear Technology, DOI: 10.1080/00295450.2020.1724731.

Ramsdale S.A., Bamford G.J., Fishwick S., Starkie H.C., 1992. Status of Research and Modelling of Water-Pool Scrubbing, Final Report, Commission of the European Communities, Directorate-General XIII, EUR 14566 EN, November 1992.

New Pool Scrubbing Correlations based on Reliable Data

Luis E. Herranz, F. Sánchez

Unit of Nuclear Safety Research
CIEMAT (Spain)

This work has been done in the frame of the IPRESCA Project

SNETP Sustainable Nuclear Energy Technology Platform

NUGENIA TA2 Severe Accidents Nuclear Generation II&III Alliance

CONTENTS

- INTRODUCTION
- OBJECTIVE & SCOPE
- DF TRENDS
- MAJOR INSIGHTS

INTRODUCTION

Motivation

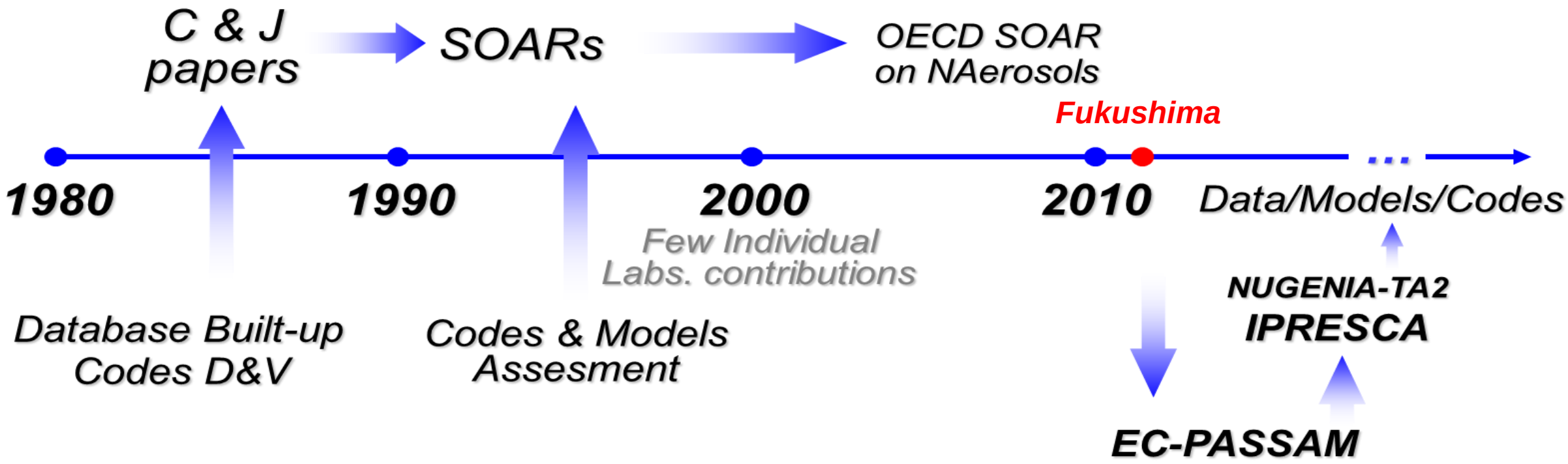
C & J papers
SOARs
OECD SOAR on NAerosols
Fukushima
1980
1990
2000
2010
...
Data/Models/Codes
Few Individual Labs. contributions
Database Built-up Codes D&V
Codes & Models Assesment
NUGENIA-TA2
IPRESCA
EC-PASSAM

The Path Forward

The "understanding domain"

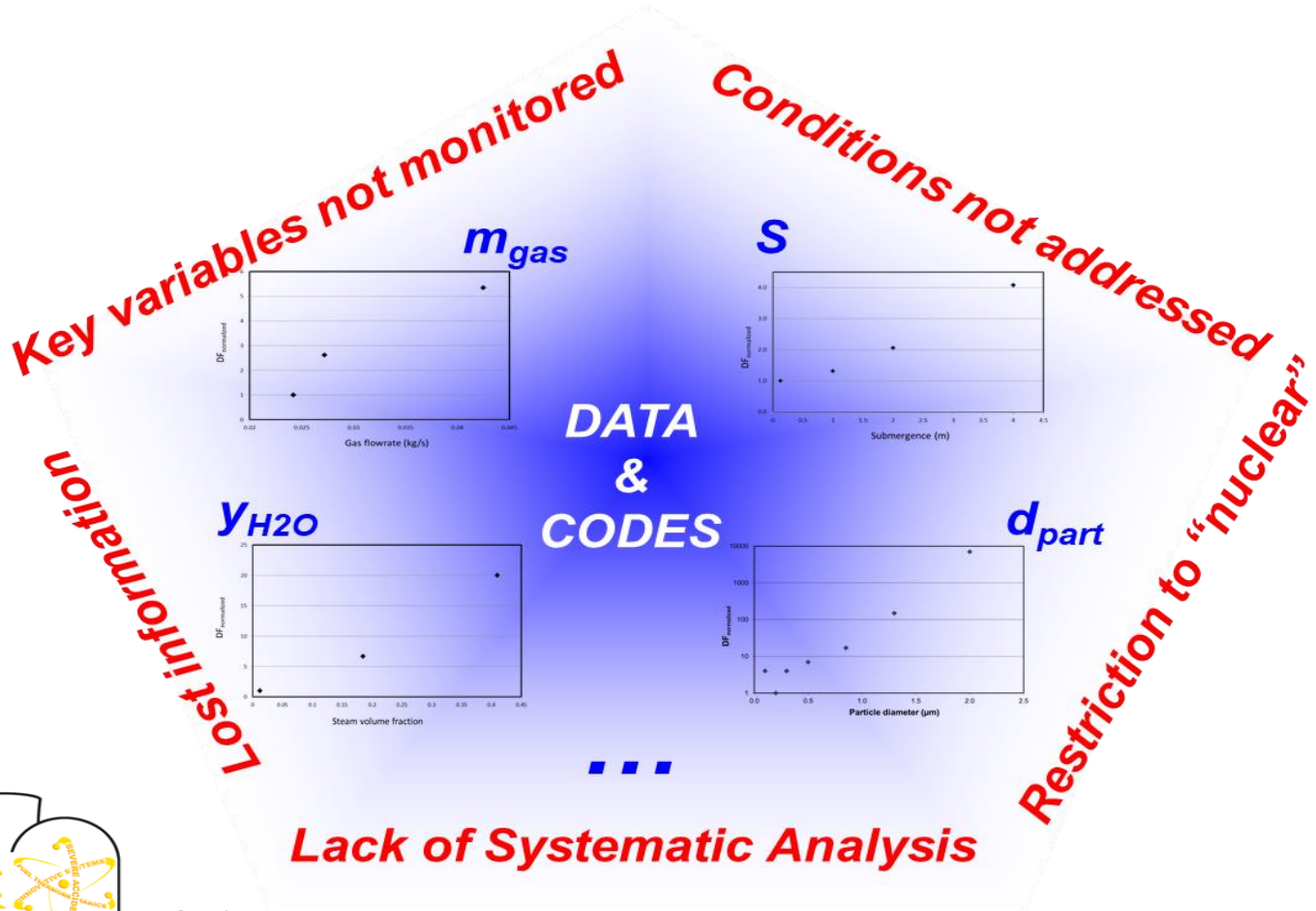

i. Data "hunting"

ii. Data "rationalization"

iii. Critical review

iv. Data analysis

Test Classification

- **Target variable:** Decontamination Factor (DF)

$$DF = \frac{1}{1-\varepsilon}$$

- **Test category:**
  - Qualified for validation (QfV);
  - Useful for understanding (UfU);
  - Non-useful (NoU);

NoU → QfV

- Access to main articles/reports
- Test characterization
- Explanation on DF derivation
- Data errors reported
- Insights (at least) on hydrodynamics

Nuclear Technology (NURETH-19)
"Validation matrix for pool scrubbing models"

Disclaimer

Criticism raised on what remains from the projects at present

Pool Scrubbing Project Classification

PROGRAM	# TESTS	QfV	UfU	NoU
UKAEA (1965-1966)	>47			X
GE (1982)	18		X	
EPRI (1982-1986)	>151		X	
EPSI (1983-1991)	>7			X
POSEIDON-I (1987)	>100		X	
JAERI (1987)	~70		X	
ACE (1988-1992)	9	X		
LACE-España (1990-1992)	11	X		
SPARTA (1992)	1			X
RCA (1995)	4	X		
POSEIDON-II (1998)	17	X		
AASC-PS (1999-2000)	4	X		
SG-Experiments (2000-2012)	9	X		
PASSAM-RSE (2013-2017)	6	X		
PASSAM-CIEMAT (2013-2017)	7	X		
PASSAM-AREVA (2013-2015)	>21		X	
TOTAL # TESTS	**>482**	**67**	**>360**	**>55**

Major Insights

- …
- *Particle size range vastly explored.*
- *Presence of steam in the carrier gas composition sufficiently addressed.*
- *Slow gas flow rates notably populate the test matrix.*
- *Submergence broadly addressed.*
- …

Major Insights

- …
- *Particle size range vastly explored.*
- *Presence of steam in the carrier gas composition sufficiently addressed.*
- *Slow gas flow rates notably populate the test matrix.*
- *Submergence broadly addressed.*
- …
- *Lack of a **systematic analysis** of the most influencing parameters !*

OBJECTIVES & SCOPE

Objectives

- ***To conduct a systematic analysis of the data in the DB (QfV; UfU).***
- ***To derive analytical expressions, whenever feasible.***

$$DF = f_1\,(Sub)$$
$$DF = f_2\,(d_{part})$$
$$DF = f_3\,(y_s)$$
$$DF = f_4\,(\Phi)$$

Trends Investigated

Experimental program	Thermalhydraulics		Carrier gas		Particle/Gas characteristics			Injector		
	Tpool	Tgas	Y_{H2O}	Flow rate	Compound	d_{part}	[parts]	Configuration	Diameter	Submergence
GE	x	x				X	x			X
EPRI			X	X						X
POSEIDON-I									x	X
JAERI				X			x			X
ACE	x		X		x	X				X
LACE-España			X			X		x		
RCA										X
POSEIDON-II	x		X			X				X
AASC-PS										
SG-Experiments			X	X		X				X
PASSAM-RSE				X		X				
PASSAM-CIEMAT			X	X						
PASSAM-AREVA	x									

DF TRENDS

Global Trends

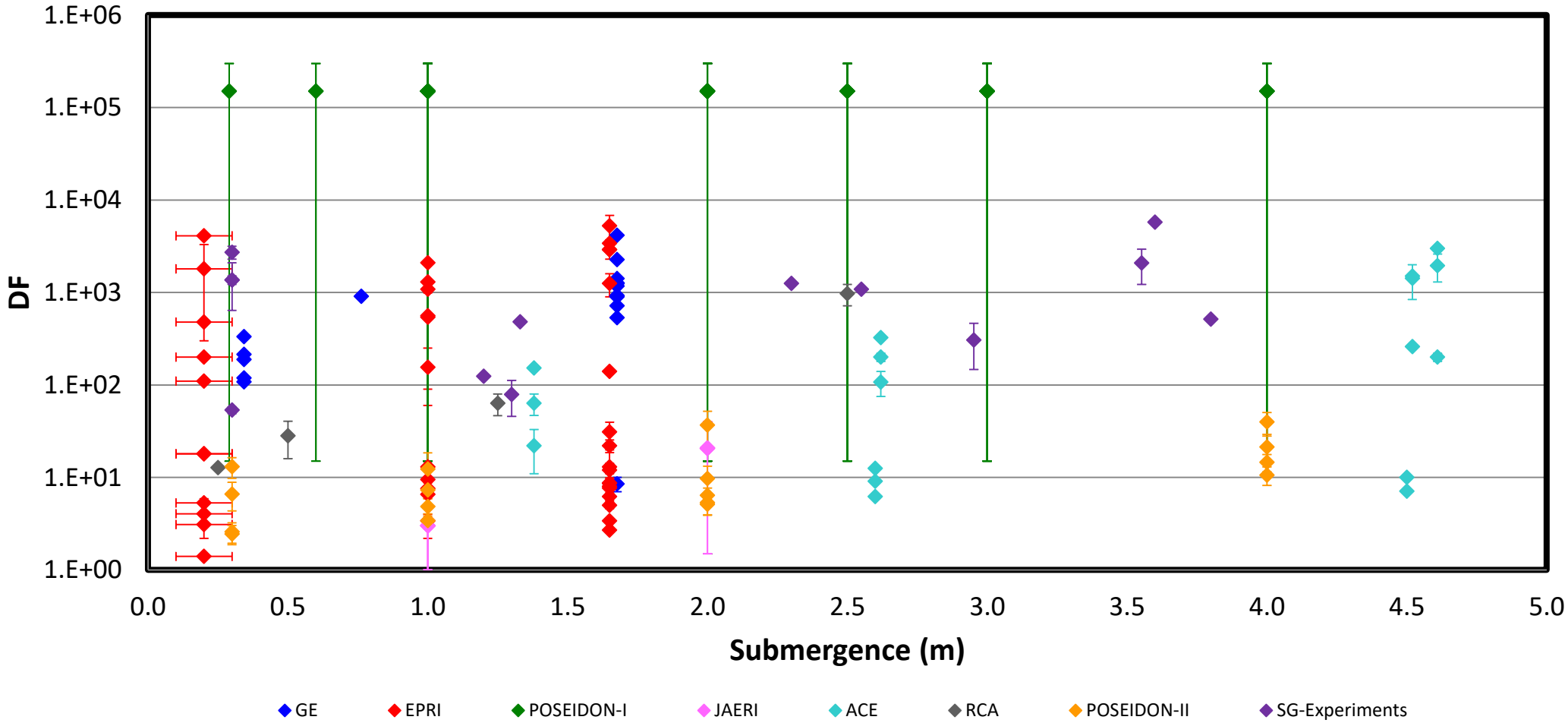

Global Trends

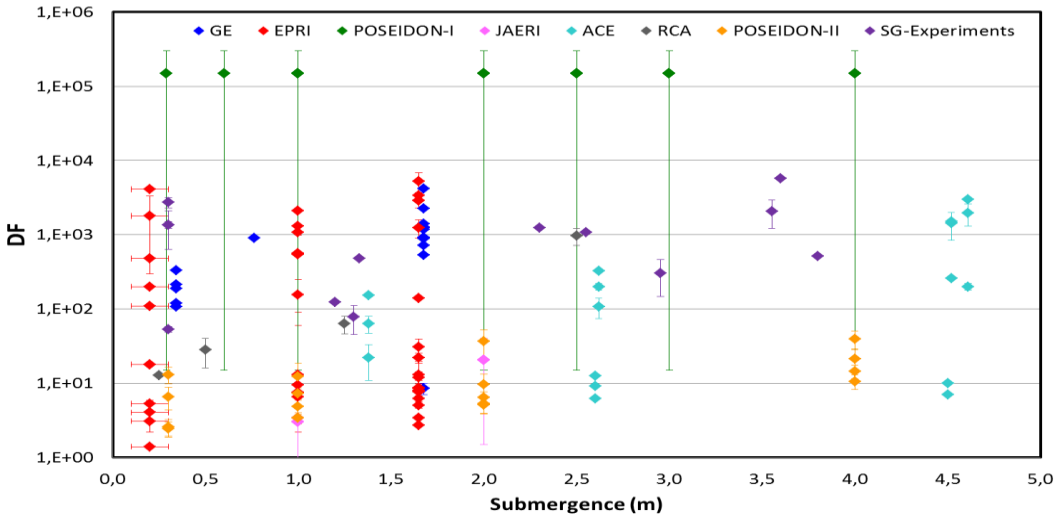

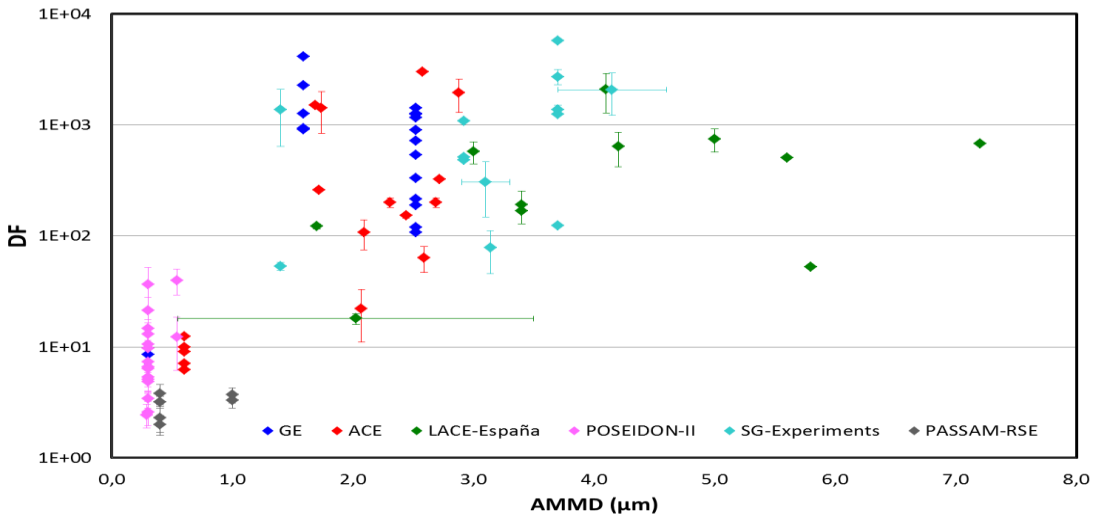

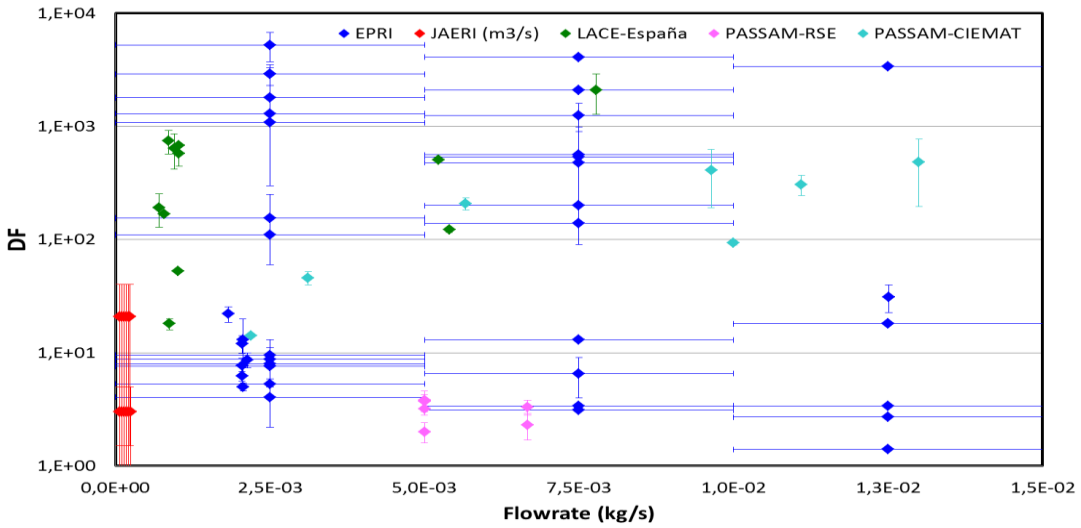

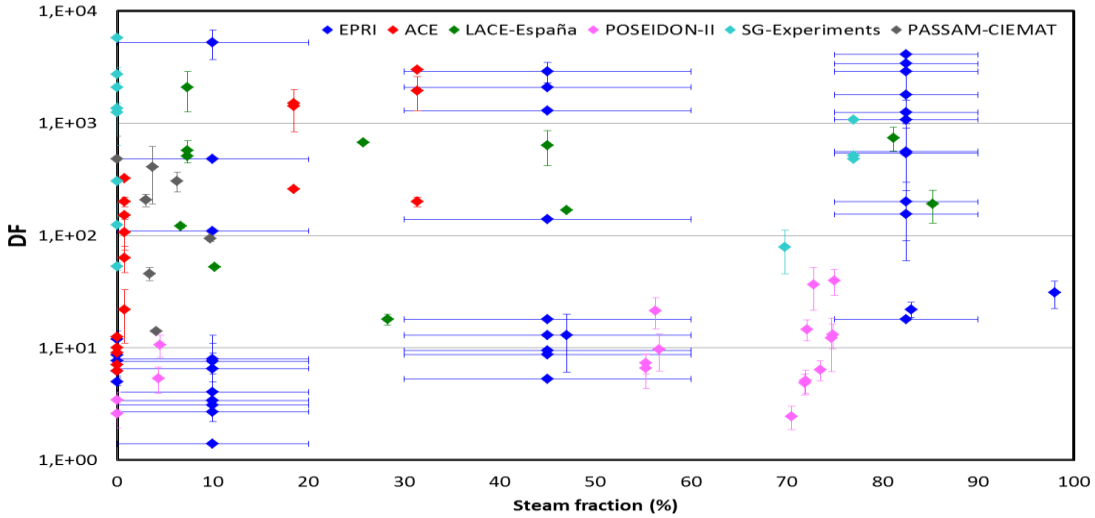

Global Trends

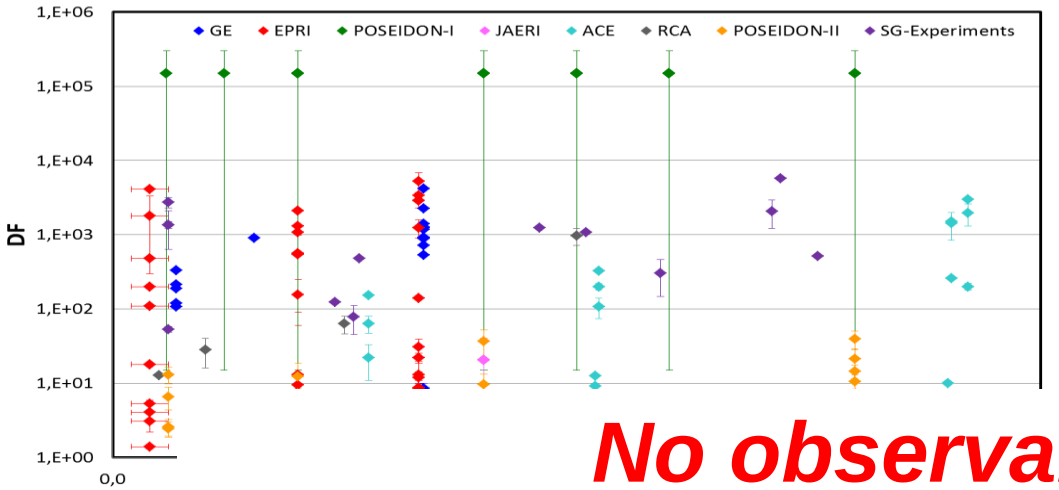

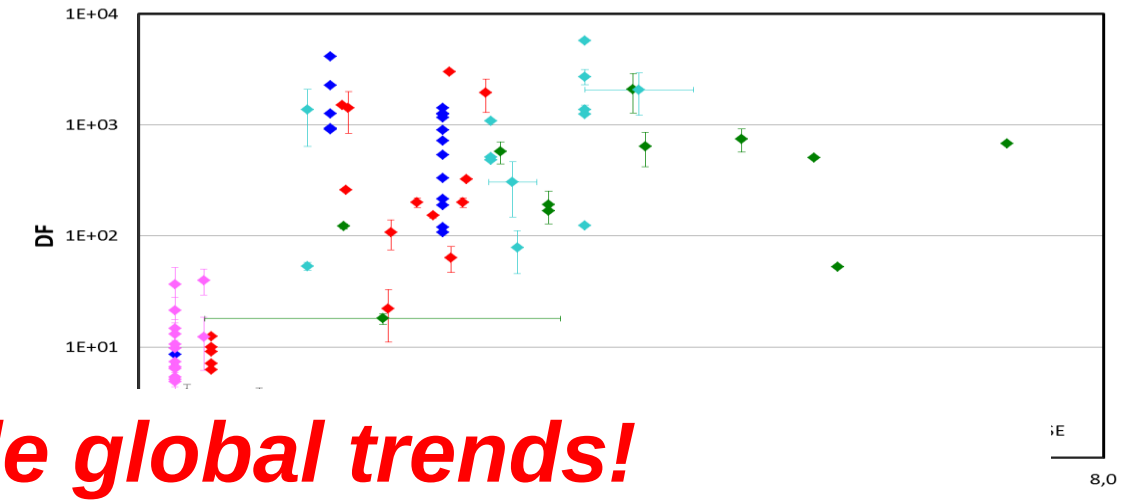

No observable global trends!

(experimental set-ups, other BCs, data uncertainty)

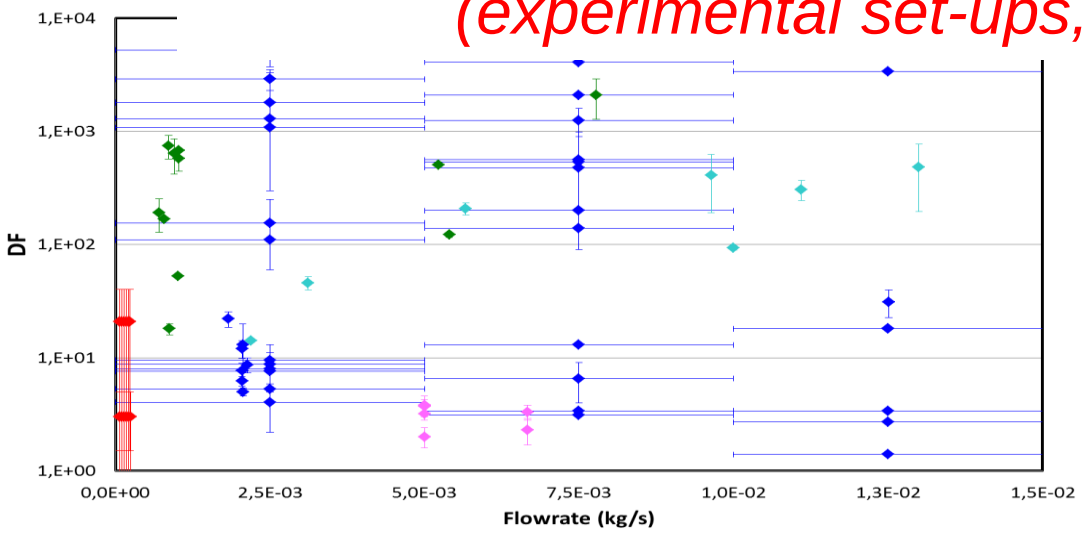

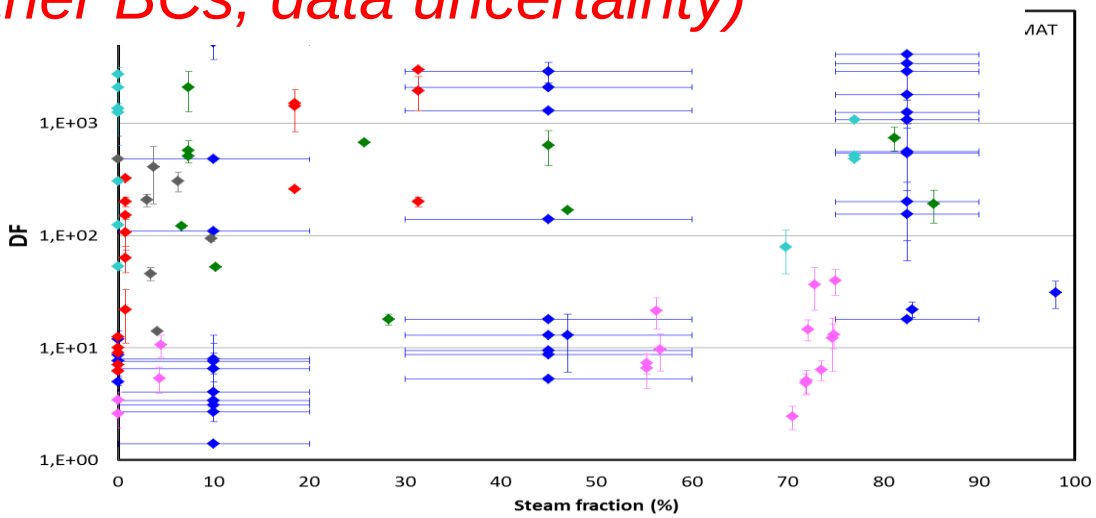

Submergence (1)

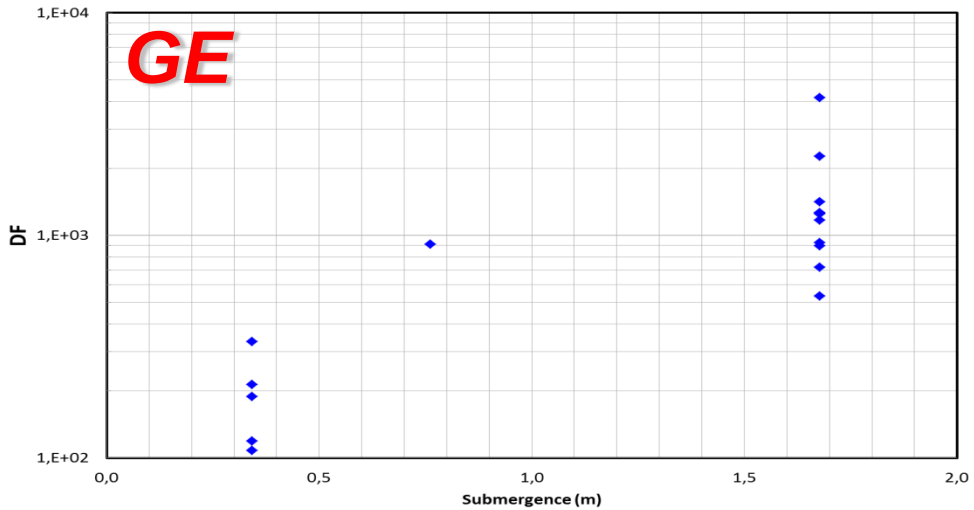

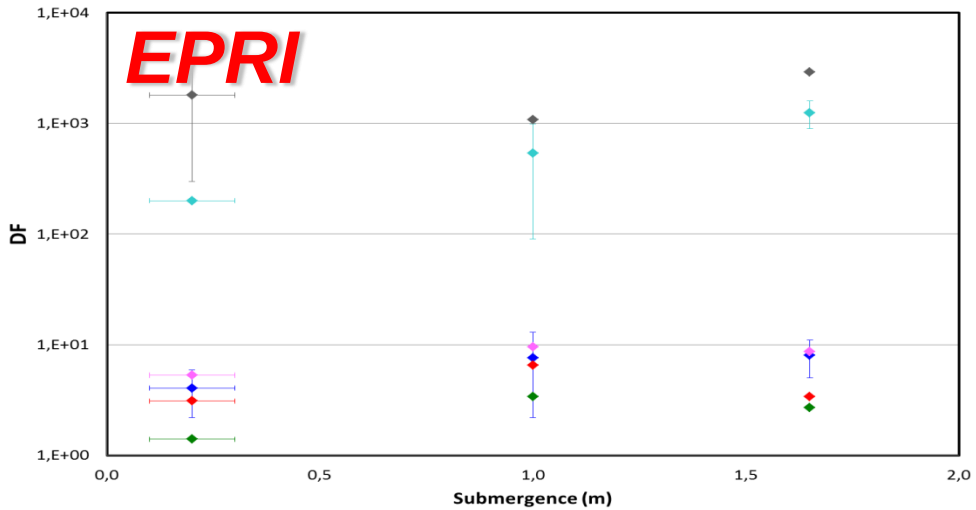

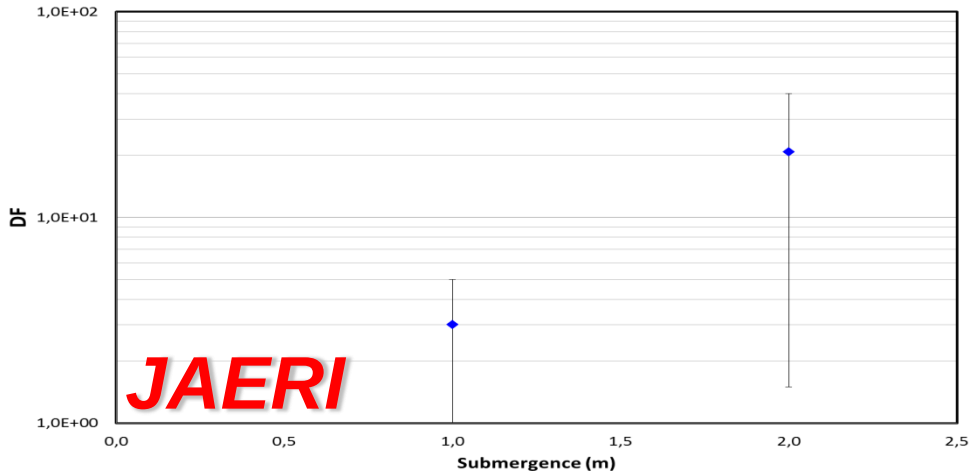

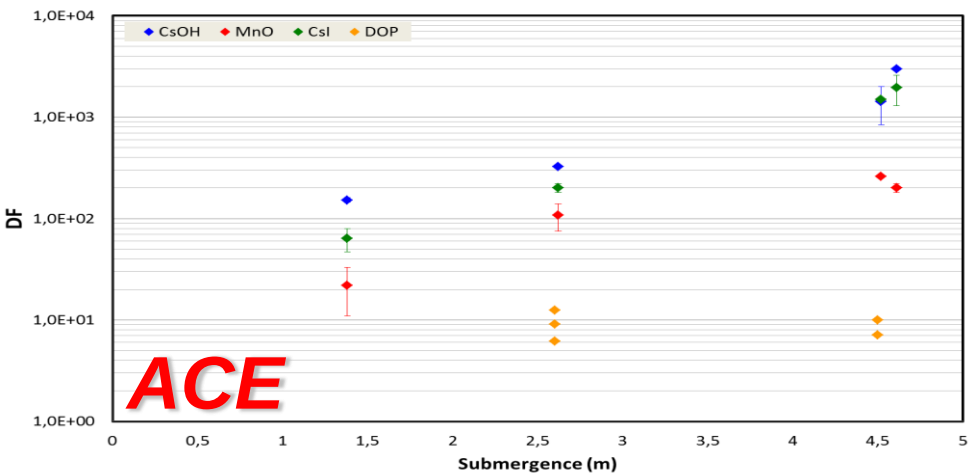

Submergence (2)

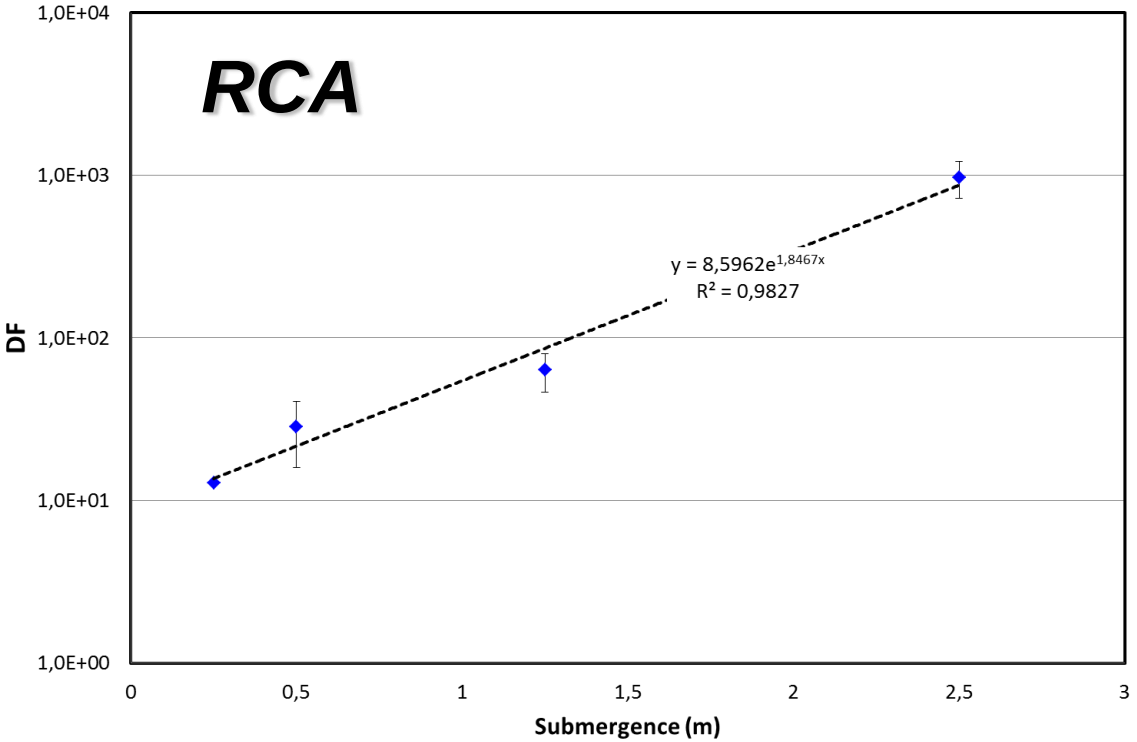

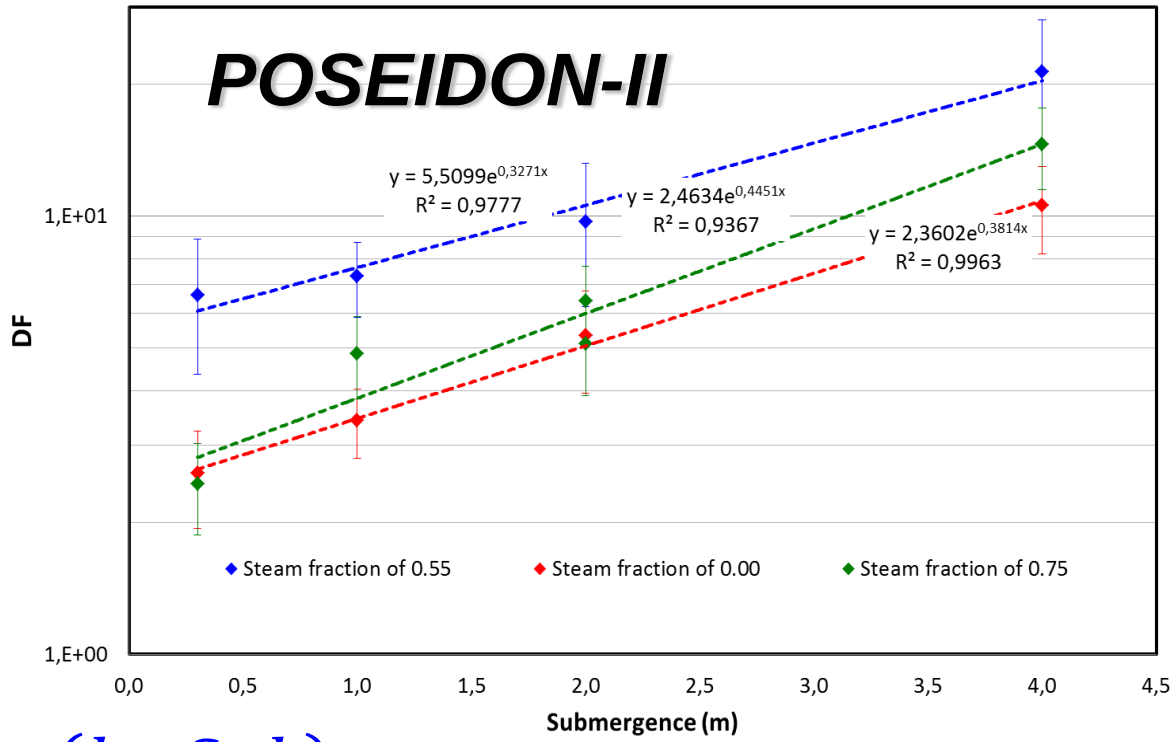

$$DF = a \cdot \exp(b \cdot Sub)$$

- *Particle size (1.2 μm vs. 0.3 μm)*
- *"Effective submergence" (POSEIDON-I)*

Submergence (3)

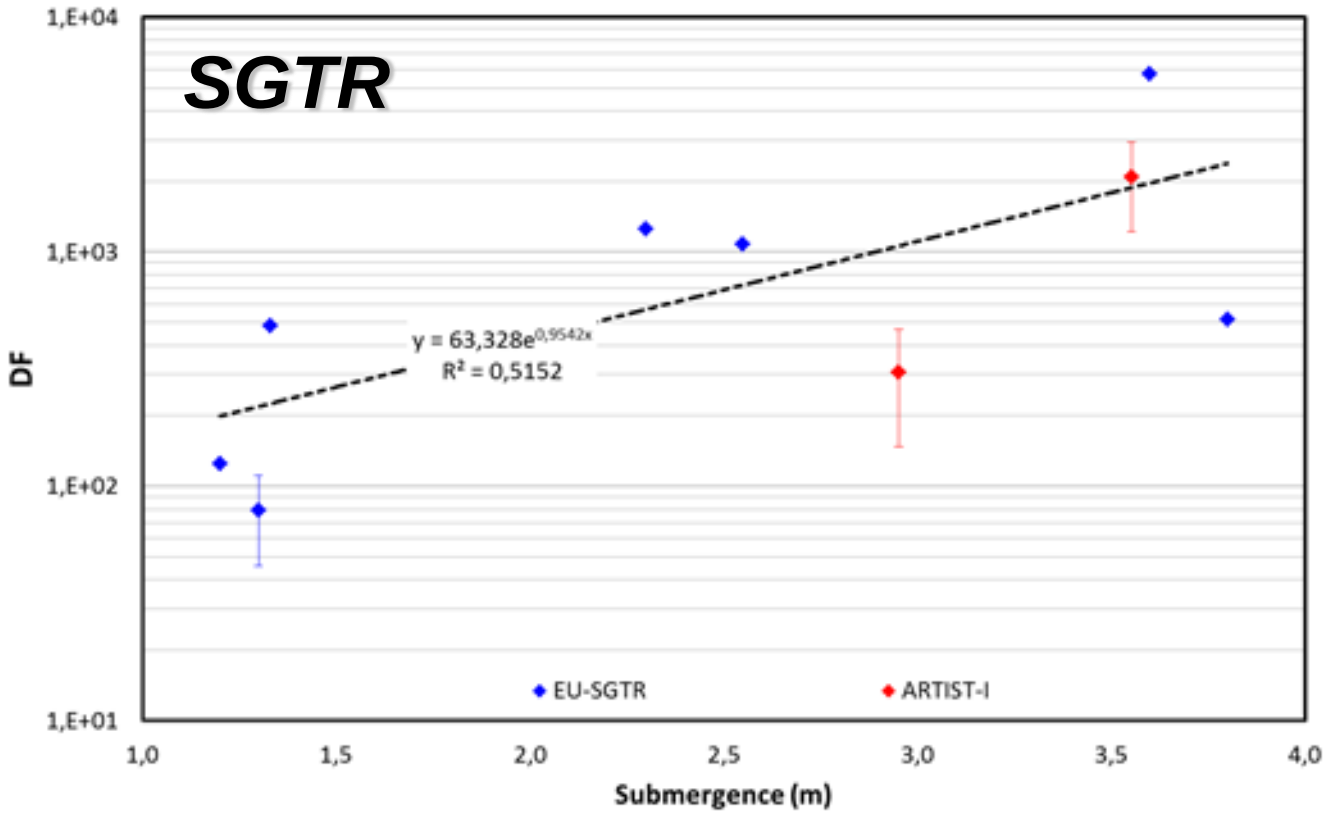

$$DF = a \cdot \exp(b \cdot Sub)$$

AMMD

GE *Data scatter*

LACE-E *Big GSDs*

ACE *Too similar AMMDs; different particles nature*

POSEIDON-II & RSE *Just 2 ≠ diameters*

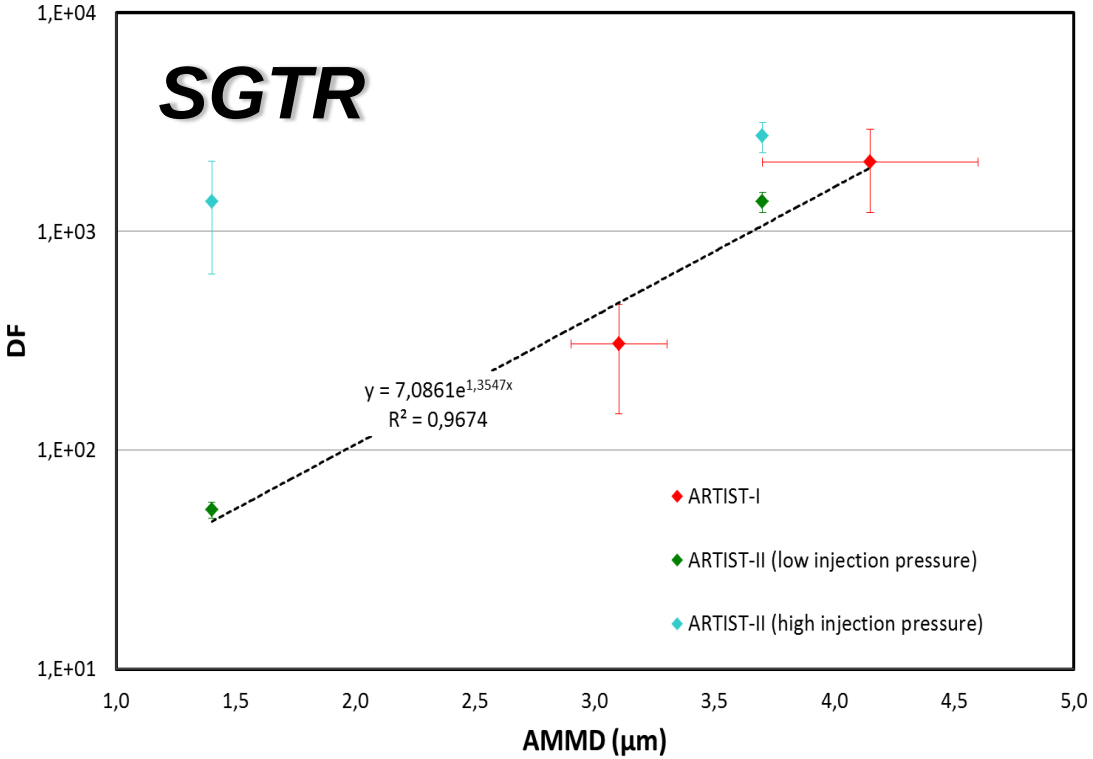

$$DF_{SS} = a \cdot \exp(b \cdot AMMD)$$

- *Neglect GE & LACE-E*
- *ACE DF data < 300*

$$DF_{SS} = DF_{NS} \cdot 2.4 \cdot \exp(-0.01 \cdot AMMD)$$

MAJOR INSIGHTS

Generic Insights

- ***Nearly impossible to set the individual quantitative effect of key variables on DF:***
  - *Pool scrubbing DB (60's – 2016) lacks a systematic parametric approach.*
  - *Diversity in the range of conditions of different programs.*
- ***Data uncertainties prevent sound support of apparent trends (DF>100).***
- ***Hard to validate models and codes on the explored database!***
  New data might overcome this drawback (IPRESCA and/or THEMIS projects).

Specific Insights

- ***DF exponentially correlates with submergence***

$$DF = a \cdot \exp(b \cdot Sub) \quad R^2 > 0.95$$ *Particles & vapors (I_2)*

(d_{part} ; "Effective submergence" D_{inj})

Submerged structures do not break the trend (further data needed, though).

- ***DF correlation with particle size cannot be sustained through data,*** *except*

$$DF_{SS} = a \cdot \exp(b \cdot AMMD)$$ *(low pressure)*

Submerged structures enhance but hardly change the DF dependence on size.

Specific Insights

- ***DF correlation with flowrate is not data-supported*** *(uncertainties & scarcity)*
  A growing sigmoidal trend proposed for jet injection domain (too low R^2)

- ***DF correlation with Y_s better investigated in terms of Saturation ratio.***
  Existing data do not support even qualitative observations.

Thank you for your attention!

THE R2CA PROJECT FOR EVALUATION OF RADIOLOGICAL CONSEQUENCES AT DESIGN BASIS ACCIDENTS AND DESIGN EXTENSION CONDITIONS FOR LWRs: MOTIVATION AND FIRST RESULTS

N. Girault[1*], F. Mascari[2], N. Muellner[3], A. Berezhnyi[4], M. Cherubini[5], A. Malkhasyan[6], T. Kaliatka[7], P. Bradt[8], M. Salmaoui[8], P. Van-Uffelen[9], A. Arkoma[10], Z. Hozer[11], M. Jobst[12], L. Luzzi[13], A. Kecek[14], D. Gumenyuk[15], E. Pouillier[16], L. E. Herranz[17]

[1]: Institut de Radioprotection et de Sûreté Nucléaire (IRSN), 13115 Saint-Paul-lez-Durance, France
[2]: Agenzia Nazionale per le Nuove Tecnologie, L'Energia e lo Sviluppo Economico Sostenibile (ENEA), 40129 Bologna, Italy
[3]: University of Natural Ressources and Life Sciences (BOKU), 1190 Wien, Austria
[4]: Analytical Research Bureau for NPP Safety (ARB), Kiev, Ukraine
[5]: Nuclear and Industrial Engineering (NINE), 55100 Lucca, Italy
[6]: Bel V, 1070 Brussels, Belgium
[7]: Lithuanian Energy Institute (LEI), Breslaujos g. 3, Kaunas, Lithuania
[8]: Tractebel Engineering (TE), 1000 Brussels, Belgium
[9]: European Commission, Joint Research Center (JRC) Karlsruhe, Germany
[10]: VTT Technical Research Centre of Finland, 02044 Espoo, Finland
[11]: Centre for Energy Research (EK), 1121 Budapest, Hungary
[12]: Helmholtz-Zentrum Dresden-Rossendorf, D-01328 Dresden, Germany
[13]: Politecnico di Milano (POLIMI), 20156 Milan, Italy
[14]: Ustav Jaderneho Vyzkumu (UJV), Rez, Czeh Republic
[15]: State Scientific and Technical Centre for Nuclear and Radiation Safety (SSTC-NRS), 03142 Kiev, Ukraine
[16]: Electricité de France (EDF), 77250 Moret-sur-Loing, France
[17]: Centro de Investigationes Energética, Medioambientales y Tecnologicas (CIEMAT), 28040 Madrid, Spain

ABSTRACT

The numerous research programs initiated after the Fukushima Daiichi Nuclear Power Plant (FDNPP) accident led to considerably increase the predictability of Severe Accidents (SA) and consequences, to assess SA Management (SAM) strategies and reinforce the diagnosis and prognosis tools for Emergency Preparedness and Response (EP&R). These consolidated evaluations by lowering down the risks associated to all main categories of SA conditions, confirmed the conservatisms in Design Basis Accident (DBA) radiological consequence evaluations, which prevents an accurate quantification of the gains brought by additional safety measures or devices. At the same time the safety analyses approach reviews initiated in Europe after FDNPP accident highlighted the importance to also consider Design Extension Conditions (DEC) for which specific provisions have to be designed to strengthen the Nuclear Power Plant (NPP) safety level.
The 4-year Reduction of Radiological Accident Consequences (R2CA) collaborative project started in 2019 in the frame of the Horizon-2020 Program of the European Commission, brings together 17 partners from 11 countries around the best-estimate evaluations of radiological consequences (RC) from Light Water-cooled

* Corresponding author: nathalie.girault@irsn.fr

Reactors (LWR) and, in corollary, around proposals for improvements of NPP accident management strategies and safety devices, including dedicated instrumentation, Accident Tolerant Fuels (ATF) and early diagnosis tools. The project addresses a broad scope of LWR designs from Gen II, III and III+ through the analyses of bounding scenarios of Loss Of Coolant Accidents (LOCA) and Steam Generator Tube Rupture (SGTR) transients and explores DBA and DEC-A conditions.
This paper summarizes the main motivations of the R2CA project and its expected results as well as the main progresses made in the Work Package (WP) dedicated to the improvement of evaluation methodologies and calculation tools. The work started by comparative reviews of release evaluation methodologies, available simulation tools within the project consortium and supporting experimental databases. The first set of reactor calculations using existing evaluation methodologies, calculation schemes and available calculation tools were also provided and analysed. Gained results and their analyses, synthesized in this paper, show possible improvements for the evaluation methodologies and models in currently applied calculation schemes and tools. These improvements are planned to be performed and evaluated further in the project.

KEYWORDS
LOCA, SGTR, DBA, DEC-A, Radiological Consequences

1. INTRODUCTION

The behaviour of NPPs during postulated accidents, including SAs, have been widely studied since several decades. Numerous simulation tools have been developed to consider the complexity of all the thermal-hydraulics, thermo-mechanical and chemical phenomena potentially occurring during the successive phases of SAs, up to the releases and transport of fission products (FPs) into the environment. These simulation tools have been currently used for safety analyses, to check the compliance of the safety features of a NPP with the safety requirements and increase the predictability of SA progression. They also have greatly helped the development, assessment and optimization of SAM strategies to prevent SA or to mitigate their consequences. The R&D efforts on the evaluation of SA progression and consequences have been especially strengthened after the FDNPP accident, as well as the reinforcement of SA simulation tools for EP&R diagnosis and prognosis activities. It led to consolidated evaluations of SA progression and their consequences on one hand and to improvements of SAM and mitigation strategies and devices on the other hand that have been further integrated in level 2 PSA. The post-processing of these PSA results, in turn, highlighted the effective reduction of the risks associated to all main categories of SA conditions. They also confirmed that the evaluations of radiological consequences of accidents within the DBA domain usually are done with very conservative deterministic assumptions mostly based on decoupled approaches which prevents for an explicit quantification of the gains, notably in terms of RC, of additional safety measures or devices. Finally, an additional outcome of the reviews of safety analysis approaches made in particular in Europe after FDNPP accident was the importance to strengthen globally the assessment of the safety level of NPPs by considering additional accidental situations (DEC) more severe than those integrated during the design of the plants (i.e. additional events or combination of events) for which specific provisions have to be designed.
The R2CA (Reduction of Radiological Consequences of design basis and design extension Accidents) launched in 2019 is a 4-year HORIZON-2020 EURATOM project coordinated by IRSN and gathering 17 partners (utilities, TSOs, universities and research organizations, consulting and engineering companies) from 11 European countries balanced between Western and Eastern Europe around a consolidated assessment of RC of selected DBA and DEC-A (without significant core degradation and melting) reactor accidental situations, focusing on LOCA and SGTR transients. The project also intends to propose the improvement of NPP accident management strategies and devices to reduce the radiological consequences of these accidents for GEN II, III and III+ reactors under operation or foreseen in the next future in Europe through the performance of innovative R&D work (i.e. on expert systems for accident diagnosis/prognosis, ATFs). The analysed reactor cases will be mostly PWRs, VVERs while BWR-4 and EPR will also be investigated.

The project objectives and means are described respectively in section 2 and 3 while the first reactor calculation results are detailed in section 4. Final remarks and future work is given in section 5.

2. OBJECTIVES AND STRUCTURE OF THE R2CA PROJECT

Though DBA have been largely studied in the past, their RC were generally evaluated with specific assumptions, such as for LOCA, on the barrier loss of integrity on one side and on their consequences (i.e. FP releases into the environment) on the other side. These evaluations were generally very conservative. Only few best-estimate evaluations of RC have been performed whereas these evaluations are essential to optimize the SAM actions and to explore the potentiality of new safety measures and devices to reduce the consequences. The project intends to improve these evaluations through existing simulation tool upgrading/model developments and new modelling approaches related to both accident progression and source term estimation up to the environment.
More specifically, during the 4-year project, it is intended to:

- Make a comparative assessment of existing results, assumptions, models and simulation tools, calculation schemes and evaluation methodologies that are applicable to evaluate the safety margins of various types of existing or foreseen reactors in Europe within DBA and DEC-A conditions, through the RC evaluation of bounding scenarios;
- Provide improved models, upgraded simulation tools, enhanced calculation schemes and consistent approaches allowing assessing the degree of conservatism/empiricism/arbitrariness used in some existing RC evaluation methodologies and deriving more realistic or best estimate evaluations;
- Elaborate guidelines for harmonization of the methodologies for RC evaluation under DBA and DEC-A conditions applicable to operating and foreseen NPPs;
- Derive from these upgraded methodologies some rationales for the optimization of EP&R actions and highlight their application in dedicated tools;
- Provide analytical rationales to support the development of innovative measures, devices and tools for the anticipated diagnosis of accidents, their management and the mitigation of their consequences for both existing and foreseen reactor concepts.

Main R&D efforts will be paid on model/calculation scheme improvements where different kind of simulation tools, whether they are integral (i.e. tackling globally all the processes from the initiating events up to the environmental releases) or detailed (i.e. addressing part of the phenomenology only), will be considered. Detailed simulation tools will be used to support the reassessment of the past experimental database on fuel rod clad failure, FP release and transport up to the environment as well as to inform low fidelity model of more integral simulation tools (including the determination of the associated uncertainties) or to perform numerical experiments to investigate still open issues.
Often more than one code will be needed to consider the phenomena occurring in normal operation and during transients, the different modelling scales (from grain-scale modelling tools to integral codes), resulting in calculation chains in which data is passed from one code to another. Statistical methodologies or extension approaches will be used for the whole core thermomechanical modelling in LOCA transient analyses.

Full range simulation of reactor cases will be made up to the evaluations of the RC. However, the R&D and methodological efforts within the project will be focused on the determination of the consequences up to the environmental source term while the RC will be addressed in a more generic way through a simplified RC evaluation tool that was built at the beginning of the project.
The achievement of all these objectives will be assured by a detailed work program established for each of the four technical WPs of the project which are dedicated to:

- The evaluation of existing methodologies, simulation tools and database for RC quantification (WP2, METHODOLOGY) and to the performance of reactor case simulations
- The improvement of simulation tools dedicated to the evaluation of RC of LOCA accidents under DBA and DEC-A conditions (WP3, LOSS OF COOLANT ACCIDENT)

- The improvement of simulation tools dedicated to the evaluation of RC of SGTR accidents under DBA and DEC-A conditions (WP4, STEAM GENERATOR RUPTURE)
- The identification and evaluation of gains of potential new accident management actions and devices (including new instrumentation and ATF) as well as to the exploration of prognosis evaluation tool capabilities for accidental configuration anticipation through artificial intelligence functionalities or expert systems.

3. AVAILABLE MEANS

The improvements and harmonization of the methodologies for evaluation of RC of LOCA and SGTR bounding scenarios under DBA and DEC-A conditions heavily rely on dedicated simulation tools and on their validation. Therefore, the first activities performed within the project consisted of reviews of existing models and simulation tools that will be used within the project and of review of experimental database relevant for their validation and re-assessment.

3.1. Simulation tools

The simulation tool review covered the capabilities of the available codes including both system codes and codes focusing on a part of the phenomenology and mainly consist in a comparison of the models included in the different codes with an emphasis on the FP behaviour. A review of the combined use of these codes in implementation of the evaluation methodologies was also carried out. More than 20 simulation tools were reviewed, including both established tools that originate from the development work done for decades, as well as newer tools that have been developed just recently. This review covers fuel performance (transient and normal operation), sub-channel and system thermal-hydraulics, radionuclides behaviour and integral system simulation tools. Simulation tools modelling only the steady-state operation have also been included in the review (i.e. FRAPCON, FUROM, TRANSURANUS…) as they produce initial conditions for the transient codes and are an integral part of the calculation chain. Also codes with a large variety of levels to simulate the overall behaviour of a transient, (e.g. for LOCA thermal-hydraulics, there are system codes including thermal-hydraulics and reactor dynamics/physics, thermal-hydraulics codes, reactor dynamics codes, and stand-alone or coupled CFD simulations) were considered.
The review helped to understand the status of modelling capabilities of LOCA and SGTR but also to pinpoint the required development needs of each code. During the R2CA project, both simulation tools and the methods how those tools are applied are likely to be upgraded. Improvements are planned for modelling the phenomena addressed in the project, simulation tool coupling, whole reactor core modelling and nodalization. Beyond the R2CA project some of the simulation tools have already been assessed against each other in dedicated benchmark exercises [1]. Thus, within the project the re-assessment of simulation tools will be essentially performed against experimental data.

3.2. Experimental database

As simulation tools used for safety analyses have to go through a verification and validation process against numerous and various data, a review of relevant available data for code development and model re-assessment against DBA and DEC-A conditions has been done [2]. Measurements from separate effect and integral experiments but also existing information from the monitoring of normal operation states and transients in NPPs were thus selected. The review includes the experiments targeting the fuel rods and/or cladding rupture, as well as the FP releases from fuel rods and their transport up to the environment. The selected tests cover:

- Fuel failure during LOCA: PBF, FR-2, ACCR, ANL, FLASH, Halden LOCA, Studsvik LOCA with various clad types investigating burst and brittle Zr alloy failures, fuel pellet fragmentation and dispersal.
- Fuel failure during SGTR (expected for defective rods potentially suffering from secondary defects): related experiments on hydrogen uptake by Zr alloys and their subsequent embrittlement.

- Activity release from fuel (LOCA conditions): several separate effect test were selected: VERDON, VERCORS, GASPARD (separate effect tests) and ACRR, FLASH, Halden-LOCA & FGR, LOFT LP-FP (integral tests).
- Activity release from fuel (SGTR conditions): iodine spiking measurements in PWRs/VVERs and DEFECT/ DEFEX separate effect test series (on leaching fuel pellet samples providing information on secondary defects and water logged fuel rod phenomena).
- Activity transport (in LOCA conditions): VERCORS, VERDON, BIP, THAI and STEM projects investigating FP transport/chemistry within primary circuit and containment conditions (especially iodine chemistry). Data from the OECD-IAEA Paks fuel project and NPP events with pressurizer safety valve stuck open will also be considered.
- Activity transport (in SGTR conditions): BIP, MARVIKEN FSCB, STEM test series (simulating the FP transport in SG) and the ARTIST project (focusing on aerosol trapping in SG). Some NPP measured events (i.e. VVER steam generator collector cover lift-up) will also be considered.

4. REACTOR CASE SIMULATIONS

The first run of reactor cases simulations selected by a dedicated group have been performed using existing simulation tools of various details at different scales in various calculation schemes. In total 13 organizations participated in this task. These organizations have provided LOCA and/or SGTR simulations for VVER, PWR, EPR and BWR type reactors at DBA and/or DEC-A conditions. Some partners used generic reactor models and other partners used real plant configurations.

4.1. Main outcomes of LOCA calculations

For the modelling of LOCA accidents and for the evaluation of their radiological consequences, many phenomena and processes taking place in the reactor core, main reactor cooling circuit and containment need to be considered. These are mostly dealing with thermal-hydraulic, thermo-mechanical, FP behaviour and chemistry. Various methodologies based on different modelling computer codes or process assessment methods were used by the R2CA partners for the simulation of the phenomena and processes occurring during LOCA accidents. R2CA partner's simulations were based on their own experience, commonly used methods in their countries, and existing modelling codes to get the main results of thermal-hydraulic (core, primary circuit and containment) and fuel rod thermo-mechanical analysis as well as far as possible evaluation results of FP release and transport.

In general, summarizing modelling approaches used by different partners, it is possible to distinguish 3 types:

1. The thermal-hydraulic and thermo-mechanical analysis were provided by simulation tools. FP transport and behaviour in the primary circuit and containment (whose releases from fuel were evaluated from the thermo-mechanical analysis) were also simulated by computer codes. For this analysis partners used complex coupled and detailed computer codes.
2. Detailed thermal-hydraulic and thermo-mechanical analyses were provided. However, conservative/empirical assumptions for the FP releases and behaviour were made.
3. The thermal-hydraulic analysis was provided but the thermo-mechanical analysis was not provided i.e. the fuel rod clad failure was not calculated. Instead of this, some assumptions were made. Taking them into account, the FP behaviour was then simulated using computer codes.

In total 9 partners analysed VVER (440 and 1000), PWR (900 and Konvoi), EPR-1600 and BWR-4 type reactors. Gained calculation results vary in wide range (Table 1 and Table 2). The calculated PCTs for the DBA case is varying from ~750 °C to ~1100 °C while for DEC-A case calculations the temperature varies from ~720 °C to ~2250 °C. Beyond the differences in the used simulation tools and their coupling schemes, the wide range of the received calculation results in terms of PCTs, number of fuel rod ruptures and activity released to the environment is due to many other factors, such as:

- Reactor types and their designs.
- Modelling approaches, such as core nodalization method.
- Individual assumptions for the initial parameters and conditions. Some partners used the realistic initial conditions, however some used conservative (e.g. initial reactor power up to 104% was assumed).
- Boundary conditions used for the calculations, for example HPIS and LPIS flowrate characteristics, applying single and dependent ECCS failures, etc.

Mentioned differences caused differences in PCTs calculated by partners and these differences were also reflected in other analysed parameters (thermo-mechanical analysis, number of failed rods, etc.).

Partners who provided thermo-mechanical analysis generally found, that there is no damage of fuel cladding in the case of analysed LOCA under DBA conditions and even in some cases under DEC-A conditions. For that reason, in some cases, several sensitivity calculations were performed and the calculations were penalized by using pessimistic conditions and hypotheses (for instance increasing the linear heat rate, the initial reactor power, etc.) to meet the conditions of clad failures. Whatever the level of refinement for the fuel thermo-mechanical calculations were, very often, decoupled approaches were used for the FP releases (for the DBA and DEC-A case analysis) to containment and then to environment. In some calculations an average initial gap inventory was assumed for all the fuel rods and the gap content of the failed fuel rods during the LOCA transient was assumed to be released to the primary circuit. In others calculations, more conservative assumptions were used where the failure of all the core fuel rods was considered and their corresponding gap content instantaneously released and transported to the containment or directly transferred to environment (in the case where the containment is not modelled) during the transient.

Regarding the radioactivity released into environment, calculation results show that they are differing by 2 orders of magnitude for the VVER and PWR type reactors (for DBA and DEC-A cases). Activities were released into the environment from containment design leakages. For these evaluations, partners also considered different approaches. Most of the partners used simulation tools to calculate the release function in time considering the pressure difference between containment and environment while others used conservative assumptions, for example considering the maximal containment design pressure for the calculation of FP release to environment.

Though the above listed differences in modelling approaches and assumptions could affect the range of the calculated integral activity released into the environment, several other factors play an important role. Indeed, the total activities released into the environment consists of the activities released into the environment carried by aerosols, together with liquid and gas releases depending on the assumptions made by partners (filtered or non-filtered releases, operation of venting system, etc.). Thus, they strongly depend on the calculated or assumed containment inventory, on the FP distribution between the liquid and gaseous phases and for the iodine on whether chemistry is considered or not.

Activities released into the environment from liquid were always found small while activities released through aerosols were dependant on pressure, temperature, steam content in the containment, mass and energy of water, steam release from the primary circuit into the containment, accident management strategies and other factors. As these aerosols are likely to condense onto containment surfaces and/or settle down to the containment sump, the calculated containment activity in the gas phase decreases and thus the activity likely to be released into the environment also decreases with time. The main and more important contribution on the total activity release is the gaseous release through design leakage, which depends on the containment pressure. This activity release does not stop throughout the entire transient under consideration but continuously decrease as the pressure in the containment is decreasing. Thus, it is important to consider a rather long time of calculation even if during the long term phase the activity increase in the environment is relatively low comparing to initial phase.

Reactor type	**Partner** **Used simulation tools** **Main assumptions**	**Scenario (Initial event + failures)**	**Power[i] (% P_N)**	**PCT (°C)**	**Burst FA[ii] (%)**	**Activity in environment (Bq) at time (s)**
VVER 440	Partner – ARB T-H: ATHLET T-M: not performed FP: COCOSYS	DEGB in CL; LOOP Failure of DG-1	104	~1050	100[a]	~6.0 10^{15} at 80000
	Partner – EK T-H: ATHLET T-M: FUROM and FRAPTRAN mod. EK FP: CONTAIN+EK methodology	DEGB in CL; $^2/_3$ LPIS available	100	~900	100[a]	~9.5 10^{13} at 128
VVER 1000	Partner – ARB For T-H, T-M and FP same as VVER 440	DEGB in CL; LOOP Failure of DG-1	104	~1100	100[a]	~5.5 10^{11} at 1400
	Partner – SSTC-NRS T-H: RELAP5 T-M: not performed FP: MELCOR	DEGB in CL; LOOP	104	~880	100[a]	~1.6 10^{13} at 60000
	Partner - UJV-NRI T-H: ATHLET T-M: TRANSURANUS FP: COCOSYS	DEGB in CL; $^3/_4$ HA available; $^1/_3$ HPIS & LPIS available	104	~860	100[a]	~1.6 10^{11} at 60000
PWR 900	Partner – IRSN T-H, T-M, FP: ASTEC	DEGB in CL; LOOP Failure of ½ DG	104	~750	~33[c]	~3.5 10^{13} at 180000
PWR 900 Generic	Partner – ENEA T-H, T-M, FP: ASTEC	DEGB in CL; LOOP Failure of ½ DG	100	~860	12.7[c]	6.1 10^{12} at 180000
PWR Konvoi	Partner – HZDR T-H, T-M, FP: ATHLET-CD	DEGB in CL; LOOP	106	~1050	10[c]	~5.84 10^{14} at 86400
EPR 1600	Partner – VTT T-H: GENFLO, APROS T-M: FRAPTRAN-GENFLO FP: not performed	DEGB in CL; LOOP Delay of DG start	102	~900	1.4[c]	–

i: Operational power at beginning of the transient in % of nominal power P_N
ii: % of burst Fuel Assemblies: [a]: assumed & [c]: calculated

Table 1. LOCA analysed scenarios and main calculation results (DBA conditions).

Reactor type	**Partner.** **Used simulation tools** **Main assumptions**	**Scenario (Initial event + failures)**	**Power[i] (% P_N)**	**PCT (°C)**	**Burst FA[ii] (%)**	**Activity in environment (Bq) at time (s)**
VVER 440	Partner – ARB T-H, T-M, FP: as DBA	DBA + failure of CSS	100	~720	100[a]	~2.8 10^{14} at 60000
VVER 1000	Partner – ARB T-H, T-M, FP: as DBA	DBA + failure of CSS	100	~890	100[a]	~3.5 10^{11} at 1800

	Partner - SSTC-NRS T-H, T-M, FP: as DBA	DBA + failure of CSS	100	~900	100[a]	~4.6 10^{13} at 60000
	Partner – VTT. T-H: GENFLO, APROS T-M: FRAPCON, FRAPTRAN-GENFLO FP: not performed.	DEGB in CL; LOOP Failure of CSS	104	~890	no damage[c]	–
PWR 900	Partner – IRSN T-H, T-M, FP: as DBA	DEGB in HL; Failures of ECCS, Delay of SIS start by operators (33 min).	100	~1000	70[c]	~1.2 10^{14} at 180000
PWR 900 generic	Partner – ENEA T-H, T-M, FP: as DBA	DEGB in HL; Failures of ECCS, Delay of SIS start by operators (36.5 min).	100	~2250 at 5th ring; ~1250 in others	70[c]	~8.7 10^{13} at 180000
PWR Konvoi	Partner – HZDR T-H, T-M, FP: as DBA	DBA Failure in ECCS	106	~1160	10[c]	~5.84 10^{14} at 86400
BWR-4 generic	Partner – LEI T-H, T-M, FP: ASTEC	DEGB in main recirculation pipe; Failure of ECCS, except LPCI	100	~830	55[c]	~5.3 10^{14} t 200000

i: Operational power at beginning of the transient in % of nominal power P_N
ii: % of burst Fuel Assemblies: [a]: assumed & [c]: calculated

Table 2. LOCA analysed scenarios and main calculation results (DEC-A conditions).

4.2. Main outcomes of SGTR calculations

For the modelling of SGTR accident, it is needed to consider many phenomena and processes taking place in the reactor core (spiking), main reactor cooling circuit, affected SG, intact SGs, available ECCS. These are mostly thermal-hydraulic questions which should be solved. For the low temperatures calculated in the SGTR transient, fuel failure could not be expected. To evaluate possible activities in the reactor cooling circuit, then in the affected SG and environment, it is needed to estimate FP release during accident from leaking fuel rods and their transfer from the primary circuit, then to the affected SG, and from there to the environment.
There are different methodologies used with different modelling tools or process assessment methods for the evaluation of the phenomena and processes during SGTR accident. R2CA project partners, based on their experience, have chosen methods and modelling tools in order simulate appropriate SGTR scenarios and to get results of thermal-hydraulic analysis as well as evaluate the FP release and transport.
In total 9 partners analysed VVER (440 and 1000), PWR (900, 1000 and 1300) type reactors. SGTR transients under DBA and DEC-A conditions were simulated. However, the initiator was not the same for all partners (double-ended break of one or several SG tube(s) (with different break diameters) and SG cover lift-up in VVERs, double-ended break of one or several SG tube(s) on top or bottom U-tube bundle in PWRs). Due to some technology differences and provided individual assumptions for the initial and boundary conditions (additional single/multiple failure(s), best estimate/penalized parameters), individual results were slightly different from each other (Table 3 and Table 4):

- For PWR reactor type, the calculated integral activity released to the environment is in the range from ~1.166E+9 Bq to 2.69E+14 Bq. The lowest value was reached by CIEMAT PWR-1000 DEC-A analysis in which the secondary to the environment discharge is limited by considering an isolable SLBOUT.

- For VVER-440 reactor type, the calculated integral activity released to the environment is in the range from ~2.0e+13 Bq to 4.6E+14 Bq.
- For VVER-1000 reactor type, the calculated integral activity released to the environment is in the range from ~4E+13 Bq to 2.23E+15 Bq.

The calculation results show that the results may differ up to 2 orders of magnitude. These differences could be caused by many reasons:

- The differences in the SGTR break sizes, the SIS duration, automatic procedures and operator actions, differences in the secondary to environment discharge capacities (considering or not) isolable/non isolable SLB, SG relief and SV discharge capacities, setpoints, failures, etc).
- Pressure in the primary side which is impacted by considering (or not) some assumptions (reactor scram signals, decay heat, reactor coolant pumps trip, cooling of the primary by the intact SG Relief valves, HPIS and LPIS failure/flowrate characteristics, etc.).
- Pressure in the affected SG which is also impacted by considering (or not) some assumptions (additional isolable/non isolable SLB, failure of the affected SG RV and/or SV to close, failure of intact SG RV to open, closure of the MSIV, isolation of the main/auxiliary feedwater, etc.).
- Realistic/Conservative initial conditions, for example initial reactor power of 104% was assumed by some partners.
- Difference in initial fuel inventory.
- Difference in the postulated number of defective fuel rods.
- Some partners calculated activity of only most important isotopes, others give total activity values.
- Different timing of the FP release into the containment determined by participants.
- Modelling (or not) of the spiking, pre-spiking, atomisation, flashing and partitioning phenomena.
- Considering (or not) the deposition and dilution of isotopes in the affected SG.

Reactor type	**Partner.** **Used simulation tools** **Main assumptions**	**Scenario** **(Initial event + failures)**	**Power[i]** **(% P_N)**	**Activity in environment (Bq)** **at time (s)**
VVER 440	Partner – ARB T-H: ATHLET 3.2 FP: COCOSYS	SG collector lift up or DEGB (1,2 or 3 tubes of several Φ) SG SV stuck open +LOOP	103.5%	2E+13 to 4.6E+13 at 250 to 18000
	Partner – EK TH: RELAP5 Mod 3.3 FP: RING	SG hot collector lift up or DEGB (3 tubes)	103.7%	Not evaluated
VVER 1000	Partner – ARB TH: ATHLET 3.2 FP: COCOSYS	SG collector lift up or DEGB (1,2 or 3 tubes of several Φ) SG RV stuck open+LOOP	104%	4E+13 to 2.4E+14 at 5000 to 9000
	Partner – SSTC-NRS TH: RELAP5 Mod 3.2 FP: Not performed, Assumed 100% release of FP from primary circuit to environment	SG collector lift up LOOP+failure of $^1/_3$ HPIS and LPIS	104%	7.79E+13 at 10000
	Partner – UJV-NRI TH: ATHLET 3.1 FP: Conservative and simplified methodology	DEGB (1 tube) SG RV stuck open +LOOP	104%	2.23E+15 at 22000

	Partner – BOKU TH: RELAP5-3D 4.0.3 FP: Not performed.	SG hot collector lift up SG RV stuck open +LPIS not considered	100%	Not evaluated
PWR 900	Partner – IRSN TH, FP: ASTEC 2.2	DEGB (1 tube) top or bottom of U-tube bundle One intact SG RV blocked closed	102%	4.7E+13 to 2.69E+14 at 4000
PWR 1000	Partner – TRACTEBEL TH, FP: RELAP5 Mod 2.5	DEGB (1 tube) SG RV stuck open	100%	2.18E+10 at 3250
	Partner – Bel V TH: CATHARE2/V2.5_3/mod8.1 FP: VBA script	DEGB (1 tube) SG RV stuck open	100%	1.90E+11 at 5000
	Partner – CIEMAT TH, FP: MELCOR2.2	DEGB (1 tube) SG RV stuck open (closed after 30 minutes)	100%	2.39E+9 at 1800
PWR 1300	Partner – BOKU TH: RELAP5-3D 4.0.3 FP: Not performed	DEGB (1 tube) Failure of 2/4 HPIS/LPIS pumps and 2/4 EFW	100%	Not evaluated

i: Operational power at beginning of the transient in % of nominal power P_N

Table 3. SGTR analysed scenarios and main calculation results (DBA conditions).

Reactor type	**Partner. Used simulation tools Main assumptions**	**Scenario (Initial event + failures)**	**Power[i] (% P_N)**	**Activity in environment (Bq) at time (s)**
VVER 440	Partner – ARB TH: ATHLET 3.2 FP: COCOSYS	SG collector lift or DEGB (1,2 or 3 tubes) SG SV+ RV stuck open +LOOP	103.5%	2E+13 to 4.6E+13 at 250 to 16000
VVER 1000	Partner – ARB TH: ATHLET 3.2 FP: COCOSYS	SG collector lift up or DEGB (1,2 or 3 tubes) SG RV + SV stuck open +LOOP	104%	4E+13 to 2.4E+14 at 5000 to 8000
	Partner – SSTC-NRS TH: RELAP5 Mod 3.2 FP: Not performed, Assumed 100% release of FP from primary circuit to environment	SG collector lift up SG RV stuck open+LOOP+failure of 1/3HPIS/LPIS	104%	7.79E+13 at 9000
	Partner – BOKU TH: RELAP5-3D 4.0.3 FP: Not performed.	DEGB (1 tube) and simultaneous SLB +Failure of HPIS and accumulators SG hot collector lift up+SG RV stuck open+Failure of LPIS	100%	Not evaluated
PWR 1000	Partner – TRACTEBEL TH, FP: MELCOR2.2	DEGB (3 tubes) and simultaneous SLB out of containment (non isolable)+LOOP	100%	1.408E+11 molecular iodine 1.063E+11 Noble gases at 4570

	Partner – Bel V TH: CATHARE2/V2.5_3/mod8.1 FP: VBA script	DEGB (3 tubes) and simultaneous SLB out of containment (non isolable)+LOOP	100%	4E+11 at 5000
	Partner – CIEMAT TH, FP: MELCOR2.2	DEGB (3 tubes) and simultaneous isolable SLB+LOOP	100%	1.166E+9 at 3000
PWR 1300	Partner – BOKU TH: RELAP5-3D 4.0.3 FP: Not performed.	DEGB (1 tube) +SG RV stuck open +Failure of LPIS	100%	Not evaluated

i: Operational power at beginning of the transient in % of nominal power P_N

Table 4. SGTR analysed scenarios and main calculation results (DEC-A conditions).

5. FINAL REMARKS AND FUTURE WORK

The R2CA project intends to provide best-estimate calculations of the RC of both LOCA and SGTR bounding scenarios under DBA and DEC-A conditions from operating and foreseen NPPs in Europe. An update of the existing methodologies used in the different countries involved for environmental release evaluations is then foreseen where guidelines for harmonizing them will be also proposed at the end of the project.
The work started with a thorough review of available simulation tools capabilities and a selection of relevant experimental data to support the improved tools and their models verification and validation. The first runs of reactor calculations covering a large amount of LWR designs and a wide range of LOCA and SGTR accidents were also completed. The differences in studied reactor designs, used methodologies and assumptions led to 2 order of magnitude difference for the radioactive releases of some major FP. These differences will then also lead to differences in the calculated RC for the population and will affect in turn the decision making processes in post-accidental scenarios.
The first set of calculation results allowed to highlight where improvements in the simulation tools and modelling approaches could be made to better estimate the environmental releases during evaluated transients and then adjust the decision making processes. Improvements will be made during the project and some are already in progress. They can be roughly divided into four main categories:

1. Improvements of plant models (i.e. by updating approach of core modelling, upgrading nodalization).
2. Improvements of calculation chains and methodologies (i.e. by coupling of more mechanistic simulation tools, using statistical approaches for evaluating the number of fuel clad burst).
3. Improvement of computational models at different levels of details (i.e. by developing new cladding burst models better corresponding to the experimental data, by refining clad burst criteria, including user-driven correlations (like iodine spiking modelling)).
4. Developments/improvements of mechanistic modelling for a detailed modelling of important processes (i.e. fuel rod clad deformation and rupture, clad secondary hydriding, high burn-up structure growth and associated FP releases, FP releases from fuel rod gaps, atomisation, flashing processes in failed SG). These detailed improvements could help to improve the prediction of low-informed models.

ACKNOWLEDGMENTS

This paper has been possible thanks to the work of all the partners of the project who are thanked here for their contribution.
This project has received funding from the Euratom research and training programme 2014-2018 under grant agreement No 847656.

REFERENCES

1. IAEA, 2019. Fuel modelling in accident conditions (FUMAC). Final report of a coordinated research project. IAEA-TECDOC-1889. www-pub.iaea.org/MTCD/Publications/PDF/TE-1889web.pdf (accessed: 25 Feb. 2020)
2. Hozer, Z. et al., "Review of experimental databases for SGTR and LOCA analyses", TOPFUEL Conference, October 2021, Santander (Spain).

Abbreviations

Abbre-viation	Description
ATF	Accident Tolerant Fuels
BWR	Boiling Water Reactor
CFD	Computational Fluid Dynamics
CL	Cold Leg
CSS	Containment Spray System
DBA	Design Basis Accident
DEC	Design Extension Conditions
DEGB	Double-ended guillotine break
DG	Diesel Generator
ECCS	Emergency Core Cooling System
EFW	Emergency Feed Water
EPR	European Pressurized Reactor
EP&R	Emergency Preparedness and Response
FDNPP	Fukushima Daiichi Nuclear Power Plant
FG	Fission Gas
FGR	Fission Gas Release
FP	Fission product
HA	Hydro Accumulator
HL	Hot Leg
HPIS	High-Pressure Injection System
IAEA	International Atomic Energy Agency
IRSN	Institut de Radioprotection et de Sûreté Nucléaire
IS	Injection System
LOCA	Loss of Coolant accident
LOOP	Loss Of Off-site Power
LPCI	Low Pressure Coolant Injection

Abbre-viation	Description
LPIS	Low-Pressure Injection System
LWR	Light-water Reactor
NPP	Nuclear Power Plant
OECD	Organisation for Economic Cooperation and Development
PCT	Peak cladding temperature
PSA	Probabilistic Safety Assessment
PWR	Pressurized Water Reactor
RC	Radiological consequences
R2CA	Reduction of Radiological Accident Consequences
R&D	Research & Development
RN	Radio Nuclide
RV	Relief Valve
SA	Severe Accidents
SAM	Severe Accident Management
SG	Steam generator
SGTR	Steam Generator Tube Rupture
SIS	Safety Injection System
SLB	Steam Line Break
SLBOUT	Steam Line Break outside containment
SV	Safety Valve
TSO	Technical Support or Safety Organization
VBA	Visual Basic for Applications
VVER	Vodo-Vodjanoi Energetitsjeski Reactor (Water-Water Energie Reactor)
WP	Work Package

ERMSAR 2022

THE **R2CA** PROJECT FOR EVALUATION OF RADIOLOGICAL CONSEQUENCES AT DESIGN BASIS ACCIDENTS AND DESIGN EXTENSION CONDITIONS FOR LWRS: MOTIVATION & FIRST RESULTS

Nathalie Girault (IRSN), Tadas Kaliatka (LEI), Mohamed Salmaoui (TE)

F. Mascari (ENEA), N. Muellner (BOKU), A. Berzhnyi (ARB), M. Cherubini (NINE), A. Malkhasyan (BelV), P. Van-Uffelen (JRC), A. Arkoma (VTT), Z. Hózer (EK), M. Jobst (HZDR), L. Luzzi (POLIMI), A. Kecek (NRI), D. Gumenyuk (SSTC), E. Poullier (EDF), L. Herranz (CIEMAT)

Content

- **O**verview of the R2CA project
- **M**ethodologies
- **R**eactor calculations (LOCA, SGTR)
  - Modelling approaches
  - Main outcomes & few figures
- **O**n-going R&D work
- **F**inal remarks

Overview of the H2020-R2CA project (2019-2023)

Reduction of **R**adiological **C**onsequences of design basis & design extension **A**ccidents: https://r2ca-h2020.eu

- 17 partners in Europe: academic & research organisations, operators, TSOs
- Main objectives
  - Evaluate more realistic safety margins through RC evaluation of bounding scenarios (reduction of some conservatisms & decoupling factors) + uncertainties
  - Increase NPP safety by developing AMPs and a smart tool for early diagnosis of accidents (incl. guidelines for new safety devices & some ATF evaluations)

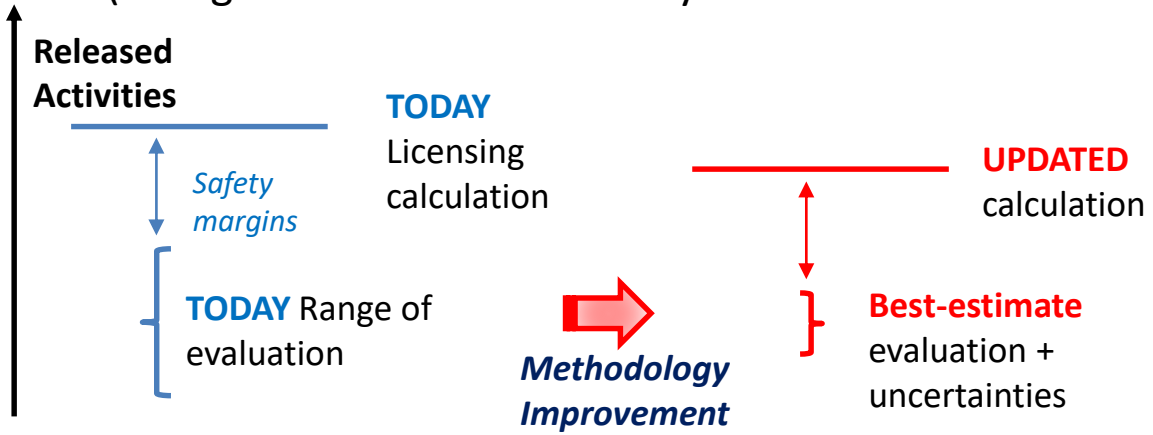

- Scope
  - ✓ DBA& DEC-A conditions
  - ✓ LOCA & SGTR scenarios
  - ✓ PWRs, EPR, VVERs & BWR

Overview of the H2020-R2CA project (2019-2023)

- **K**ey challenging areas
  - Formulation of best-practices for RC calculations of LOCA and SGTR scenarios & harmonisation of methodologies for a large variety of existing (foreseen) NPPs
    - ✓ Best-estimate approaches reducing some conservatisms & decoupling factors
    - ✓ Derivation in principles for EP&R optimisation (i.e. population protection measures)
  - Developments of technological innovations for RC reduction (innovative devices, AMPs, diagnosis tools)
    - ✓ Improvement of AMPs: optimized procedures (algorithms), use of neural network
    - ✓ Elaboration of an expert system prototype based on AI for identification of rod defects for RCS activity variations

Overview of the H2020-R2CA project (2019-2023)

- **M**ain expected Achievements
  - Improvemts of calculation chains for RC evaluation and of a large variety of simulation tools at different scales (mechanistic/detailed, meso, integral)
    - ✓ Updated models in integral codes & in more detailed/specific codes (for FP releases/transport/behaviour, fuel performance & clad behaviour/failure)
    - ✓ Additional simulation tool coupling (i.e. for providing details to low-informed tools)
    - ✓ Updated (statistical) or new (multi-scale mixed) approaches for core meshing (LOCA)
  - Better evaluations of LOCA & SGTR RC for different reactor concepts
    - ✓ Through application of a simple methodology (bi-gaussian plume model for dispersion) + conversion to health effect on human body (dose by inhalation, external exposure and equivalent thyroid dose)
  - Evaluation of innovative devices (i.e. near-term ATF concepts) & new AMPs with the updated calculation chains

Overview of the H2020-R2CA project (2019-2023)

Detailed codes

T/H transient

Fuel rod failure

Radionuclide releases from fuel

RCP physics & chemistry of radionuclides

Containment controlled & uncontrolled leaks

Integral codes

Selection of bounding LOCA scenarios for each reactor type

Perform simulations according to **existing approach** (i.e. regulatory practices in each country)

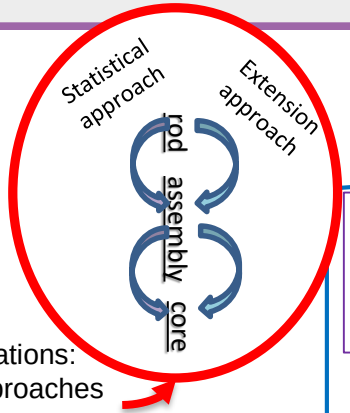

1- Improve whole core simulations: statistical vs extension approaches

2- Improve fuel rod failure models: clad burst criteria…

3- Improve FP-release models: from fuel oxidation, High Burn-up Structure…

Etc…

Model improvements and calculation chain upgrading

Perform simulations according to the **Best-Estimate approach (new method)**
Use the same scenarios

Show advantages of new methods compared to existing approach

Reduction of some conservatisms (decoupling factors)

Uncertainty evaluation

Methodologies

- **R**eview of existing evaluation methodologies for LOCA/SGTR scenarios
  - PWRs (900, 1000, 1300), VVERs (440, 1000), BWR-4
  - From isotopic inventories to environmental FP releases
- **V**arious methodologies originate from very different contexts
  - Reactor licensing (regulatory guidelines), probabilistic risk assessment studies, R&D work
  - Old/new studies, very simple/conservative to much more complex
  - Only few hypotheses/assumptions similar

    ✓ *Long time irrad. history, 100% gap release of failed rods in LOCAs, no retention in RCS*

    → *Significant differences in evaluated FP releases*
- **I**dentification of major sources of uncertainties/gaps in ST evaluation
  - Refine requirements for modelling improvements (models & code interlinkages)

    ✓*Model comparison charts (more than 20 codes: from reactor dynamics &T/H to FP behavior*)
  - Support for methodology improvement/harmonization (to be performed at project end)

Reactor calculations: modelling approaches

- **For LOCA** 3 types of modelling approaches
  - Complex modelling with (coupled) computer codes : simulations of T/H, thermo-mechanics analysis (incl. FP releases from fuel), FP transport and behavior in containment
  - Detailed T/H & thermo-mechanics but for FP release/behavior conservative assumptions
  - Detailed T/H but for thermo-mechanics conservative assumptions (i.e. entire & instantaneous release of gap content at transient start or 100% rod failure…)

- **For SGTR** various levels of modeling
  - Common features: no simulation of clad defect formation & FP retention in SG upper structures, detailed T/H in I^{ary} and to a less extent in II^{ary} circuits
  - For FP release from defective fuel rods either simple models (RING) or assumptions for I^{ary} circuit activity S.-S. & transient evolution (iodine spike) often based on NPP feedbacks
  - For FP (esp. iodine) either detailed behavior modelling (incl. gas/liquid partition, flashing, atomization) or simplified modelling (only partitioning considered)

Reactor calculations: main outcomes

- **R**eleased activity for VVERs & PWRs significantly differ (>2 orders magnitude)
  - LOCA: noble gas releases (esp. Xe) via design leakages mostly dominate environt activity
    Iodine depending on scenarios (CSS actuation..) can also play a significant role
  - SGTR: released activity/isotopic composition depend on scenarios (SG overflow, dry-out..)
    and calc. details (from only iodine (I_2) to a more complete list of FP)
- **M**ost impactful parameters/assumptions for activity releases in LOCAs
  - Failed fuel rod fraction (1,4 → 100% in DBA 10 → 100% in DEC-A)
    - ✓ *When T/M analyses performed generally low PCTs are predicted (750°C- 1100°C)*
    - ✓ *Burst rods/FAs function of core meshing, FA grouping & initial parameters (P_{core}, P_{ax}/P_{rad}, $P_{int\ rod}$…)*
  - Containment liquid/gas partitioning at break, CSS operation/efficiency for iodine
  - Containment leak rates (single/double containment, design leakages…)
- **M**ost impactful parameters/hypotheses for activity releases in SGTRs
  - I^{ary} coolant activity : iodine steady-state & transient activity (spike ranges: 1-35)
  - Liquid/gas iodine partition in failed SGs & considered phenomena (flashing, atomization)
  - Liquid releases (SG overflow)

LOCA reactor calculations: few figures

- **DBA** Large Break transients in cold leg (+LOOP)

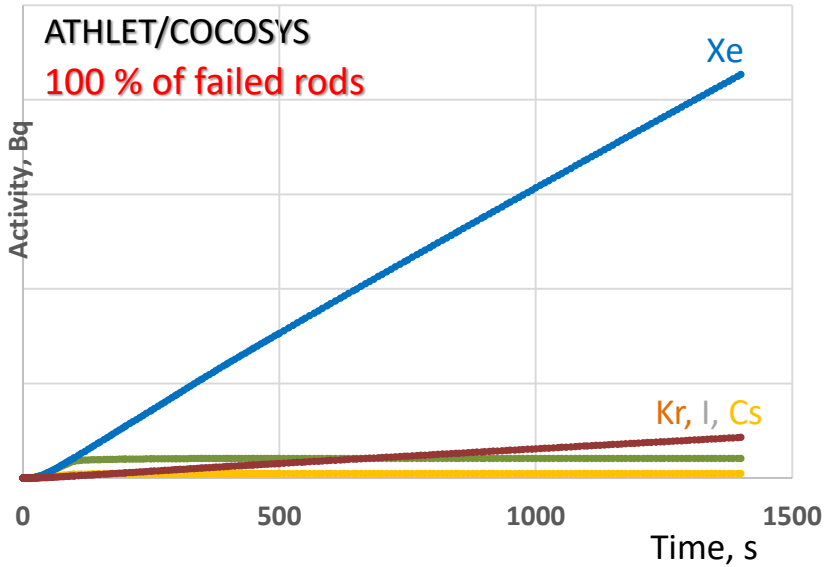

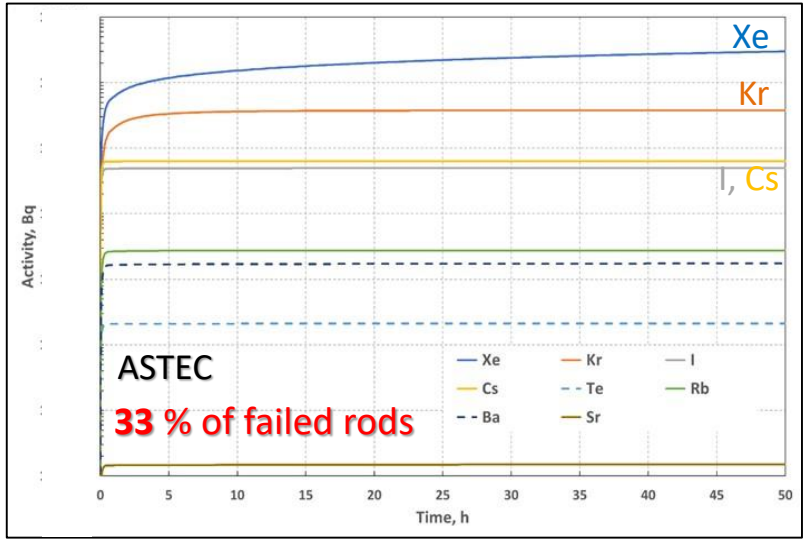

Release kinetics only depends on Cont pressure
(linear release of Xe, Kr activity at short term)
Released activity quite similar for DBA/DECA

Releases fonction of failed rod number (higher in DEC-A)
Iodine activity contribution fonction of scenarios ~1 to 20%

SGTR reactor calculations: few figures

- **DBA** 1 or several tube ruptures (immersed or uncovered) & RV stuck open

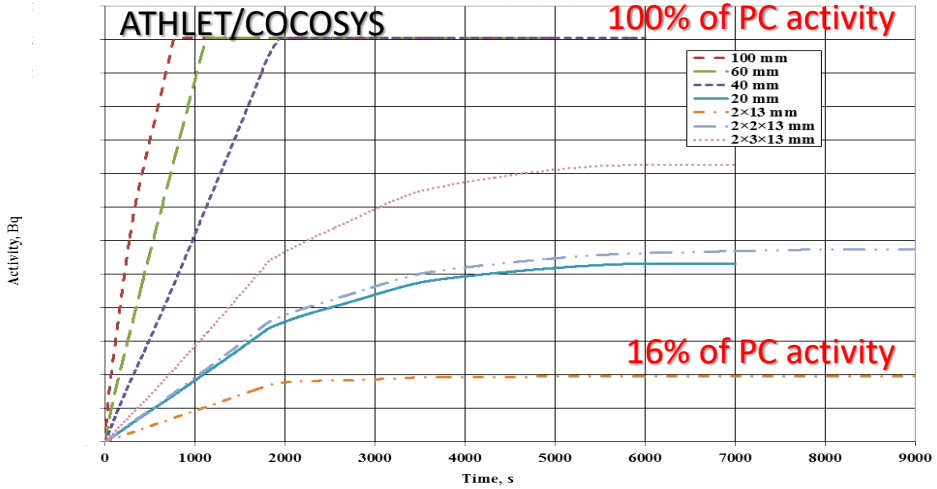

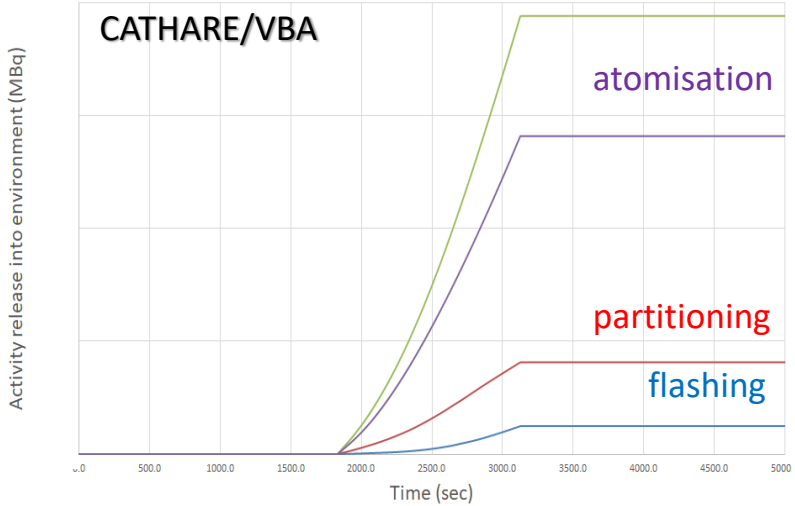

– Released activity kinetics function of scenarios (steam or liquid) & activity releases mainly driven by noble gases and iodine (~60%)
  ✓ *Isotopic compo. function of assumptions on pre &-spiking primary coolant activities & partition coefficient*
– In non-flooded SG scenarios importance of jet atomisation in iodine environ[t] release (low partitioning factor)

On-going R&D work (LOCA)

- Failed rod number: re-analysis of burst failure database, best-estimate (+ upper, lower, mean) exponential true stress models developed, new core modeling approaches under developt (mixed meshing (3D meshed+ equivalent rods, FA grouping)

- Fuel rod transient behavior: re-analysis of HRP (burst, gas flow/axial gas transport, high BU) tests, revised models for High Burn-up structure formation/growth, fuel performance & FP release code coupling

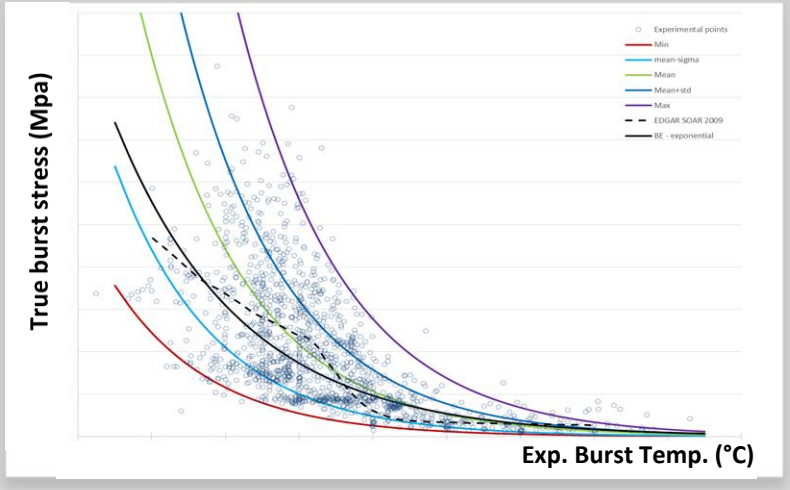

from Taurines, T. (IRSN)

On-going R&D work (SGTR)

- FP releases (from defective rod): updated correlations for iodine spike and partitioning, detailed models under developt for gap releases in normal/transient conditions

- Clad secondary hydriding (in defective rods): new tests performed (Zr4/E110), model developments for gas transport, clad hydriding (H_2 uptake, radial re-distribution, hydride precipitation/dissolution)

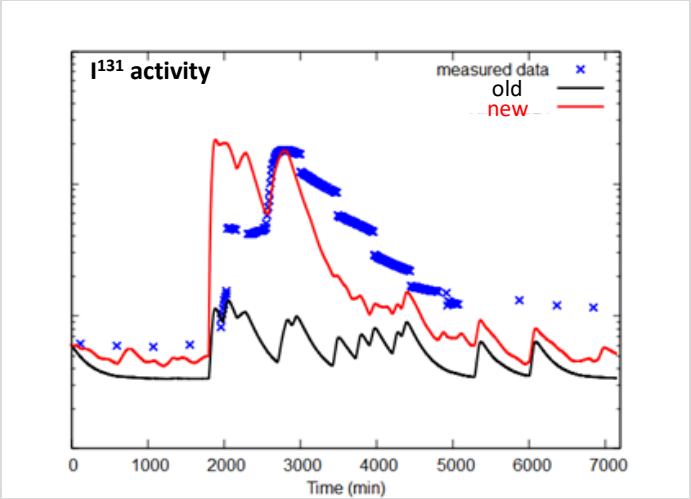

from Hózer, Z. and al. (EK)

Final remarks

- **R2CA** supports a better source term evaluation to help decision making process in post-accid. phase through reduction of some conservatisms
- **M**ethodology review & 1st reactor calc. highlight significant differences in VVER/PWR/BWR release evaluation approach for DBA & DEC-A
  - ✓ Orders of magnitude in calc. released activities for LOCA and SGTR bounding scenarios
- **S**imulation tool review & 1st set of calc. path the way to improvements
- **D**ifferent kinds of improvements are in progress
  - ✓ Updated approach of core modelling & nodalisation
  - ✓ Enhanced tool coupling, use of mechanistic models to improve low-informed tool prediction
  - ✓ Upgraded simulation tools/models at different levels of details for most impacting processes regarding environmental radioactive releases

- 11 presentations in Conference (2021/22): NENE, SNE, TOPFUEL, NURETH19…
- 2 journal papers (Nucl. Eng and Tech.)
- 1 ANE special issue expected for Automn 2022
- All public deliverables archived in Zenodo (R2CA project community) and shared through social networks & R2CA public website (https://r2ca-H2020.eu)

✓ EUG to be organized at project end/ Contact : nathalie.girault@irsn.fr & fulvio.mascara@enea.it

Thank you!

This paper has been possible thanks to the work of all the project partners.
This project has received funding from the Euratom research and training programme 2014-2018 under grant agreement No 847656.

The 10th European Review Meeting on Severe Accidents Research

Severe Accident Research Eleven Years after the Fukushima Accident

May 16-19, 2022, Karlsruhe, Germany

Technical Session 6-1: Severe Accident Modeling and Code Development

Chairs: E.-M. Pauli (Framatome), F. Gabrielli (KIT)

ID302	**Synthesis of the ASTEC V2.2 code validation vs. experimental data** P. Chatelard (IRSN)	**Paper** **Presentation**
ID266	**Development of Severe Accident Code CORVES for Analysing In-Vessel Degradation Phase of Severe Accident in VVER-1000 Reactor** S. Sil (NPCIL)	**Paper** **Presentation**
ID303	**Modeling of Fission Product Release during Severe Accidents: Overview of Recent Developments in the Fuel Performance Code Alcyone** J. Sercombe (CEA)	**Paper** **Presentation**
ID313	**A Simplified Core Catcher Model for the Containment Code AC2/COCOSYS** C. Spengler (GRS)	**Paper** **Presentation**

SYNTHESIS OF THE ASTEC V2.2 CODE VALIDATION AGAINST EXPERIMENTAL DATA

Patrick Chatelard and Laurent Laborde
Institut de Radioprotection et de Sûreté Nucléaire
IRSN/PSN-RES/SAM, Saint Paul lez Durance cedex 13115, France
patrick.chatelard@irsn.fr; laurent.laborde@irsn.fr

ABSTRACT

Significant efforts are being continuously put for many years into the assessment of the severe accident integral code ASTEC developed by IRSN, through comparison either with results of the most important international experiments or with results of other severe accident simulation codes. These efforts are done in priority by IRSN code developers, and then also by partners, in particular in the frame of the on-going SNETP-NUGENIA ASCOM project. This paper relates to the ASTEC V2.2 version that was released in 2021 to the ASTEC community. It aims at providing a synthesis of its assessment vs. experimental data. For that purpose, the ASTEC validation strategy and ASTEC V2.2 validation matrix are firstly introduced. Then some V2.2 results are discussed for a few representative applications that cover diverse aspects of in-vessel and ex-vessel severe accident phenomenology. Finally, main lessons drawn from this large validation task are summarized, along with an evaluation of the current physical modelling relevance and how it relates to the state-of-the-art. Based on those outcomes, the ASTEC V2.2 validity domain is specified and some prospects for further improvements are put forward.

KEYWORDS
ASTEC, severe accident simulation code, validation

1. INTRODUCTION

The Severe Accident (SA) integral code ASTEC [1], developed by the French Institut de Radioprotection et de Sûreté Nucléaire (IRSN), aims at simulating an entire SA sequence in a nuclear water-cooled reactor from the initiating event up to the release of radioactive elements out of the containment. The 3rd major version of the ASTEC V2 series, V2.2 [2], was released in 2021 to the ASTEC community. With respect to former V2.1 [3], main progress was on physical models and new code capabilities, but also on physico-numerical issues (improved robustness and reduced sensitivity to cliff-edge effects). As to the physical models' validation, significant efforts are being continuously put for many years into the assessment of the code through comparison either with data of the most important international experiments or with results of other SA simulation codes. These efforts are done in first priority by IRSN code developers, and then also by partners, notably in the frame of the on-going SNETP-NUGENIA ASCOM collaborative project [4]. In continuity to former validation tasks [5] [6], the ASTEC V2.2 assessment has been carried out against a wide experimental data covering main SA physical phenomena while following up in parallel the full scale code-to-code benchmarks activity on various transients for different types of LWRs.

The present paper is exclusively focused on the validation vs. experiments, meaning that the ASTEC assessment by means of code-to-code benchmarks on reactor SA sequences is not tackled in the following. This paper recalls firstly the general approach for ASTEC V2 validation before displaying the composition of the ASTEC V2.2 validation matrix. Some validation results are then discussed for a few representative applications that cover both in-vessel and ex-vessel processes. Finally, the main lessons drawn from this

quite large validation task are summarized, along with an evaluation of the current physical modelling relevance and how it relates to the current state-of-the-art. Based on those outcomes, the ASTEC V2.2 validity domain is specified and some prospects for further improvements are put forward.

2. VALIDATION STRATEGY FOR THE ASTEC V2 SERIES

ASTEC V2.2 benefits of course from the intensive validation of former V2.1, V2.1.1 and V2.2b versions that was carried out between 2015 and 2021 not only by IRSN but also by foreign partners in the frame of the successive CESAM FP7 [7] and NUGENIA ASCOM projects (e.g. [8] [9] [10] [11] [12]). That being said, the ASTEC V2.2 validation is supported by its own large set of French and international experiments that cover most aspects of SA phenomenology. While most of the experiments that were analyzed few years ago with V2.1 have been again recalculated with V2.2, the ASTEC V2 validation matrix was being enlarged from time to time in order to continuously account for the newly available experiments in the field of SA. The V2.2 validation matrix includes three different types of experiments: 1) Separate-Effect Tests (SETs) focused on a single phenomenon; 2) Coupled-Effect Tests (CETs) addressing a few phenomena; 3) integral applications that allow checking the completeness of the modeling with respect to significant phenomena and their coupling. For the latter, one may notably mention the TMI-2 and Fukushima-Daiichi accidents, and four integral experiments of the Phébus FP program that coupled all the modules involved for the primary circuit and the core, and for the containment. Overall, the ASTEC V2.2 validation matrix comprises more than 300 experimental tests conducted at various scales in more than 50 different in-pile and out-of-pile facilities worldwide. The contents of the ASTEC V2.2 validation matrix is displayed below in Tables I and II, for in-vessel and ex-vessel processes, respectively.

Table I. Main experiments used for the validation of the ASTEC V2.2 in-vessel physical models

Domain	Physical phenomena	Facility/ Program	Experiments
Thermal-hydraulics in primary and secondary circuits	Two-phase flow, heat transfers, wall friction, interface friction, phase separation, condensation…	Moby Dick, Patricia GV, Rebeca, Cosi, Coturne…	Numerous SETs
	Complete T/H behavior in the RCS	BETHSY	#9.1b (*ISP-27*), #5.2e, #6.4, #6.9
Core degradation	Boron carbide oxidation	VERDI	16 tests
	Zircaloy oxidation under air flow	MOZART	7 tests
	Corium oxidation	SKODA-UJP	18 tests
	Reflooding of intact core	PERICLES	48 tests
	Reflooding in debris bed	PRELUDE	12 tests
	Reflooding in debris bed (larger scale)	PEARL	33 tests
	Core degradation (early & late phase)	PHEBUS FP	FPT1, FPT2, FPT3
	In-core debris bed & molten pool behavior	PHEBUS FP	FPT4
	Core reflooding	QUENCH	#3, #11, #10, #16
	Delayed core reflooding	QUENCH	#17
Corium behaviour in the lower head	Corium-water interaction	FARO	#14 (*ISP-39*), #24
	Late phase degradation	LIVE	L1, L6
	Corium-structure interactions	MASCA	21 tests
	Vessel lower head thermal-mechanical loading	OLHF	#1
RCS and vessel processes	RCS thermal-hydraulics & vessel degradation	TMI-2 real accident	Phases 1 to 4

Fission products and aerosols behaviour in the RCS	FP release from fuel	VERCORS	#4, #5
	FP release from fuel	VERDON	#1, #5
	Diffusiophoresis aerosol deposition	TUBA	TD07
	Interaction between FP vapor & aerosols	FALCON	#18 (*ISP-34)*
	Deposition & resuspension of aerosols	STORM	#11 (*ISP-40*)
	Iodine transport & chemical behavior (speciation) in the RCS	CHIP/CHIP+	12 tests
	Ruthenium transport & chemical behavior (speciation) in the RCS	START	6 tests

Table II. Main experiments used for the validation of the ASTEC V2.2 ex-vessel physical models

Domain	Physical phenomena	Facility/ Program	Experiments
Th.-hydraulics in ERVC circuit	Th.hydraulics in vessel external cooling circuit (*case of IVR strategy implementation*)	ULPU V	#10
Thermal-hydraulics in containment	Containment T/H and H_2 distribution	TOSQAN	ISP-47
	Cont. T/H and H_2 distribution	MISTRA	ISP-47
	Filmwise condensation on containment walls	TOSQAN	#1, #9b
	Contain. T/H with spray activation	TOSQAN	#115
	Contain. T/H, H_2 stratification with spray	PANDA	PE1
	Contain. T/H and H_2 stratification	THAI HM	#2
	Contain. T/H and H_2 deflagration	THAI HD	#22 (*ISP-49*)
	Contain. T/H and H_2 PAR behavior	THAI HR	#1, #11, #12, #22
	Flame propagation (H_2-air mixture)	ENACCEF	#153
	Flame propagation (H_2-air-steam mixture)	ENACCEF	ISP-49, XH2
Th.-hydraulics and aerosols in containment	Cont. T/H and aerosols behavior	VANAM	M3 (*ISP-37*)
	Cont. T/H and aerosols behavior with spray	CSE	A10
	Filtration by pool scrubbing	PSI	6 tests
Iodine and Ruthenium chemistry in containment	I_2 formation in sump and adsorption surfaces	CAIMAN	#97-02 (*ISP-41*)
	Iodine volatility in the containment	PHEBUS RTF	#1, #3, #6
	I^- radiolytic oxidation, mass transfer on paints	SREAS	#01
	Iodine release from Epoxy paint under irradiation	EPICUR LD	#1, #2, #3, #5, #6
	CH_3I desorption from Epoxy paints	BIP2	RAD-EPICUR-A1
	Interaction of I_2 with stainless steel	BIP	G1
	Iodine mass transfer & adsorption on steel wall	THAI	#9
	Silver/iodine interactions in sumps	SIEMENS-IPSN	6 tests
	RuO_2 decomposition on paint under irradiation	IRSN	4 tests
	AgI decomposition	EPICUR MC	Aer1
	IOx formation	PARIS	2 tests
	IOx decomposition	STEM2	6 tests
	All iodine & ruthenium chemistry-related phenomena	Phébus FP	FPT1 (*ISP-46*), FPT2, FPT3
DCH	Dispersion of hot corium from the reactor pit	DISCO	FH03
Corium Concrete Interaction	LCS concrete (8 wt. %)	CCI	#2, #8
	Siliceous concrete (15 and 6 wt. %)	CCI	#3, #7
	Siliceous concrete (14 wt. %)	VULCANO	VBU5, VBU6

3. OVERVIEW OF THE ASTEC V2.2 VALIDATION

This section aims to provide a comprehensive picture of the ASTEC V2.2 validation achievements. For that purpose, results of some simulations are depicted for a few experiments. Those peculiar code-to-data comparisons are selected to be representative of the ASTEC V2.2 whole validation process. However, since those few examples concern only a sub-set of the entire set of ASTEC V2 modules, this chapter is itself sub-divided into separate sub-sections (each one being focused on a SA key physical phenomenon) in order to provide a somewhat exhaustive view of the ASTEC V2 whole validation process, independently from the provision or not within the paper of an illustration of related results.

3.1. Thermal-Hydraulics in the Reactor Cooling System (RCS)

In ASTEC, CESAR is the module dealing with the two-phase thermal-hydraulics in the primary (including the vessel) and secondary circuits. The validation matrix that was considered to evaluate the physical relevance of the ASTEC V2.2 CESAR models to cope with RCS phenomena (see Table I) covers both DBA basic phenomena (including tests addressing shut-down states) and, to some extent, SA conditions. A brief summary of the main lessons drawn from the code-to-data assessment in the field of RCS thermal-hydraulics is provided later in Section 4. Details about these various ASTEC V2.2 CESAR simulations may be found in [13] [14] [15] [16].

3.2. Core Degradation

In ASTEC, all in-vessel degradation processes (i.e. in the core and in the vessel lower head) are simulated by the ICARE module. The validation matrix that was considered to evaluate the suitability and capability of the ASTEC V2.2 ICARE core degradation models (see Table I) includes both ICARE stand-alone applications and CESAR/ICARE coupled applications.

To illustrate such validation tasks, attention is directed hereafter at one of the works that was performed to assess the CESAR/ICARE coupled modules vs. the PEARL debris bed reflooding tests. Being part of the PROGRES experimental program [17], the IRSN PEARL facility aims at improving the understanding of the factors governing the coolability of large heated debris beds. The PEARL test section (Fig.1a) is composed of a long quartz tube (diameter 540 mm) filled with a 500 mm high debris bed made of stainless steel balls. It is surrounded by a bypass zone made of twice larger quartz balls representing a quasi-intact region at the periphery of a degraded core. The bed is heated by induction with a specific power of 150 W/kg, representative of the decay heat one hour after SCRAM in a generic PWR. In the tests presented hereafter, water is injected at the bottom of the test section (bottom flooding).

The device is modelled in ASTEC by 3 axial channels for the debris bed plus one channel for the bypass, surrounded by an adiabatic wall, and a 50 mm axial nodalization is applied. The bed initial temperature is set to the experimental value measured at the reflooding onset (t=0s). A constant pressure boundary condition is applied at the top while water is injected from the bottom following experimental conditions. Figures 1b and 1c indicate examples of comparison between ASTEC calculation and experiments [18]. The presented tests D5-2 and D1-7 are both performed with the same debris bed geometry, water velocity and initial temperature, and only differ by the imposed pressure (respectively 5 bars and 1 bar). The evolution of the steam mass flow rate at the test section outlet is well reproduced in both tests, as well as the quench front progression in the bed centre (R=0 mm) and periphery (R=220 mm). In particular, the impact of pressure on the reflooding is well captured: while a flat quench front profile is observed in the D5-2 test with a short reflooding time, the quench front progression in D1-7 is faster in the periphery compared to the centre, and the reflooding time is much longer.

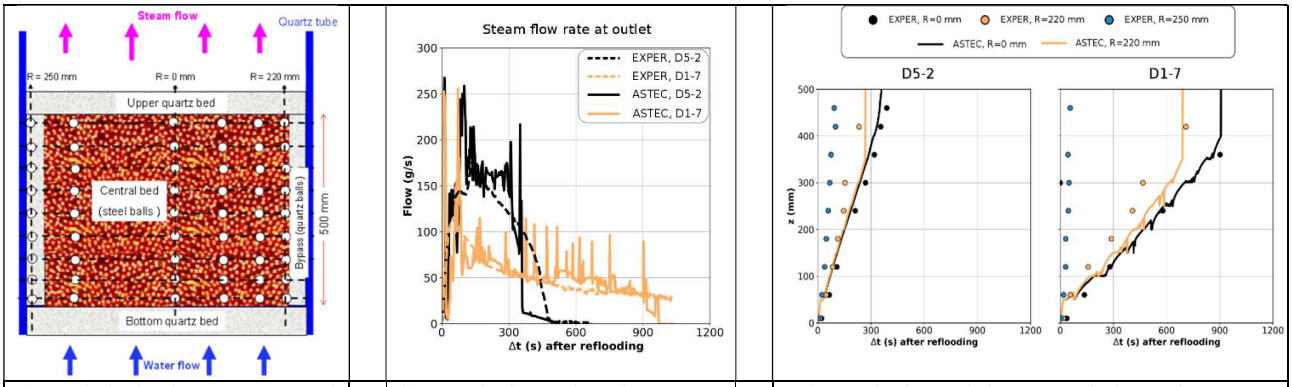

a) Debris bed structure and instrumentation

b) Evolution of outlet steam flow rate in D5-2 and D1-7

c) Evolution of the quench front for tests D5-2 (5 bar) and D1-7 (1 bar)

Figure 1. PEARL

Besides this example, a summary of the main lessons which have been drawn from the whole code-to-data assessment in the field of core degradation is provided later in Section 4. To get more details about these numerous ASTEC V2.2 CESAR/ICARE simulations, one may refer to [15] [16] [18] [19].

3.3. Corium Behavior in the Vessel Lower Head and ERVC issues

As already mentioned, the ICARE module also deals with the corium behavior after its slumping into the lower head. Besides, in case of situations with an In-Vessel Retention (IVR) strategy implementation, the CESAR module is also of interest to model the external reactor vessel cooling (ERVC) circuit. The main lessons that were drawn from the code-to-data assessment relating to the corium behavior in lower head are summarized in Section 4. More details about these ASTEC V2.2 analyses are given in [15] [16] [20].

3.4. Fission Products Release from the Core

In ASTEC, the fission products (FP) release from the core components is simulated by the ELSA module that is tightly coupled with the ICARE module. The validation matrix that was considered to evaluate the physical relevance of the ASTEC V2.2 FP release models remains today limited to a few VERCORS and VERDON tests [16]. Indeed, apart from these two experiments, the validation status of the ASTEC V2.2 ELSA models today still relies upon the one issued from the validation of the V2.1 former series, keeping in mind that only very few modelling evolutions were implemented in the ELSA module from V2.1 to V2.2. The main lessons that had been drawn from that V2.1 assessment are summarized in [15].

3.5. Fission Products and Aerosols Transport and Chemistry in RCS

In ASTEC V2.2, all FP/aerosols phenomena (i.e. transport and chemistry of FPs/aerosols in both RCS and containment) are simulated by the SOPHAEROS module. The validation matrix that was considered to evaluate the physical relevance of the SOPHAEROS models in the RCS domain is shown in Table I.

To illustrate such validation tasks, attention is directed hereafter at some of the works performed to assess the SOPHAEROS modeling for iodine gaseous phase chemistry kinetics in the RCS vs. the CHIP and CHIP+ data. The CHIP experimental program, operated at IRSN as part of the International Source Term Program [21], aimed to obtain data on iodine speciation under different circuit boundary conditions in presence of other FPs (Cs, Mo) and control rod materials (Ag, In, Cd, B). The CHIP experiments consist in analyzing the behavior of selected elements transported in a controlled thermal gradient tube flow. The

test line is composed of a high temperature alumina tube at the entrance followed by a stainless steel tube where the fluid is cooled down and where chemical reactions take place, producing aerosols and gases.

Validation results are displayed in Table III for two tests (tests "Cd-Mo-Cs-I" and "Ag-Cd-B-Mo-Cs-I") that were part of the CHIP+ program. For each injected element, the comparison between the ASTEC prediction and the experimental data is focused on the deposited masses in the alumina and steel tubes, respectively, and thus the transported mass flowing out from the test line. In both tests, the SOPHAEROS kinetic modelling implemented in ASTEC V2.2 gives a satisfactory estimation of the iodine total transport (gas+aerosols) along the CHIP+ test line. Cesium and molybdenum transport is also reasonably predicted, though a bit overestimated, notably for the second test loaded with several control rod materials. On the contrary, the transport of Cadmium (Cd) and Silver (Ag) is largely overestimated by ASTEC in the second test because of a large underestimation of the Cd and Ag deposited masses in the high temperature zone.

Table III. Deposition & Transport of Elements along the CHIP Line (in % of element mass injected)

Experiment and selected elements	Deposited in high temperature zone *(% ii.)*		Deposited in transport zone (stainless steel tube) *(% ii.)*		Released at the outlet of the test line *(% ii.)*	
"CdMoCsI"	**Experiment**	**ASTEC**	**Experiment**	**ASTEC**	**Experiment**	**ASTEC**
Iodine	0.00%	0.00%	13.20%	19.28%	86.80%	80.72%
Cesium	10.00%	1.66%	16.50%	16.06%	73.50%	82.28%
Molybdenum	30.60%	11.18%	10.30%	28.44%	59.10%	60.38%
"AgCdBMoCsI"	**Experiment**	**ASTEC**	**Experiment**	**ASTEC**	**Experiment**	**ASTEC**
Iodine	0.00%	2.70%	7.20%	11.76%	92.80%	85.53%
Cesium	14.30%	1.47%	10.10%	10.99%	75.60%	87.54%
Molybdenum	25.50%	3.25%	9.10%	10.68%	65.40%	86.06%
Cadmium	33.10%	0.00%	24.20%	18.50%	42.70%	81.50%
Silver	48.50%	17.16%	7.80%	9.01%	43.70%	73.83%
Boron	1.00%	0.03%	1.80%	1.51%	97.20%	98.46%

Overall, the good results obtained for the iodine transport in most CHIP/CHIP+ experiments confirm the physical relevance of the current iodine gaseous phase chemistry kinetics modelling in the RCS. For other elements, results alternate among reasonable (e.g. fuel elements) and inadequate (control rod elements). Improvements are expected from IRSN on-going modelling works to ensure SOPHAEROS accounting for non-congruent condensation phenomena. A summary of the main lessons that have been drawn from the code-to-data assessment relating to the FP/aerosols behavior in the RCS is provided later in Section 4. More information about those ASTEC V2.2 SOPHAEROS analyses are displayed in [15] and [16].

3.6. Thermal-Hydraulics in Containment

In ASTEC, CPA is the module dealing with containment thermal-hydraulics, including all phenomena related to hydrogen risk (H_2 distribution, combustion and recombination). The validation matrix that was considered to evaluate the suitability of the CPA models to address those issues is supplied in Table II.

To briefly illustrate the numerous validation tasks relating to containment thermal-hydraulics, attention is directed hereafter at the work that was performed to assess the CPA module vs. the TOSQAN ISP-47 test. This experiment, operated by IRSN, aimed to study steam condensation on walls, notably in presence of non-condensable gas. For that purpose, the ISP-47 test included three steady states with air-steam mixture and one steady state with air-steam-helium mixture [22].

The global thermal-hydraulics behavior of the TOSQAN ISP-47 test is mainly governed by steam injection and wall condensation (pressurization due to steam and helium injection and depressurization due to condensation on cold wall). Each steady state, characterized by a pressure level (Fig.2a), is reached when the condensation mass flow rate (Fig.2b) is equal to the steam injection mass flow rate. As shown on those figures, the ISP-47 thermal-hydraulics behavior is very well captured by the ASTEC V2.2 CPA simulations for the four steady-states. The fluid temperature evolution is also reasonably predicted during both the pressurization and depressurization phases.

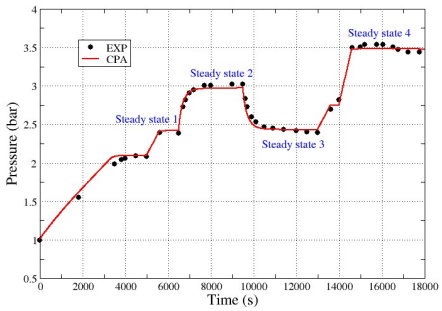

a) Pressure evolution

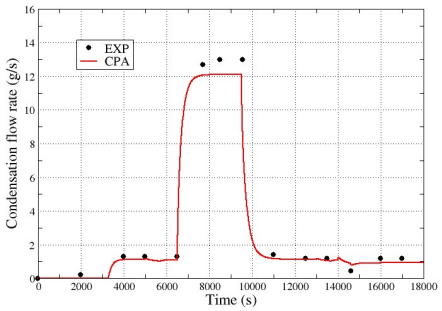

b) Condensation flow rate

Figure 2. TOSQAN ISP-47

A summary of the main lessons that have been drawn from the code-to-data assessment in the field of the containment thermal-hydraulics is provided later in Section 4. To get more details about these numerous and rather different ASTEC V2.2 CPA simulations, one may refer to [15] and [16].

3.7. Thermal-Hydraulics and Aerosols Behavior in Containment

As already mentioned, the SOPHAEROS module also deals with the behavior of FPs and aerosols in the containment, in addition to the RCS domain. The validation matrix that was used to evaluate the physical relevance of the SOPHAEROS models to cope with those containment phenomena is supplied in Table II. The CPA/SOPHAEROS coupling was activated to simulate the integral tests while pool-scrubbing SETs have been analyzed using SOPHAEROS in its stand-alone running mode. A summary of the main lessons that have been drawn from the code-to-data assessment related to behavior of FPs and aerosols in the containment, along with their coupling to the thermal-hydraulics, is provided later in Section 4. More details about these ASTEC V2.2 CPA/SOPHAEROS analyses may be found in [15] and [16].

3.8. Iodine and Ruthenium Chemistry in Containment

In ASTEC V2.2, the SOPHAEROS module also addresses in a detailed manner the chemical behavior of iodine and ruthenium compounds (vapors and aerosols) in containment. The validation matrix that was assumed to assess the suitability of the SOPHAEROS iodine models is given in Table II.

To illustrate very shortly such validation extended tasks, attention is directed hereafter at the work that was performed to assess the SOPHAEROS containment iodine chemistry models vs. the PHEBUS RTF1 test. The RTF1 test, that had been operated at AECL at the end of the 90s as a part of the ISP-41 [23], dealt notably with the radiolysis of iodide ions I^-, leading to the formation of I_2 in the sump and its transfer

to the gaseous phase where it was adsorbed on a dry paint surface. So, the main issue of this validation task was to check how fast iodide ions I^- were converted into gaseous I_2 and how much gaseous organic and inorganic iodine remained in gaseous phase all over the irradiation. As shown on Fig.3, the ASTEC V2.2 prediction of the iodine distribution in aqueous phase, gaseous phase and on painted surfaces was quite good using recommended values for steel and paint adsorption rate constants.

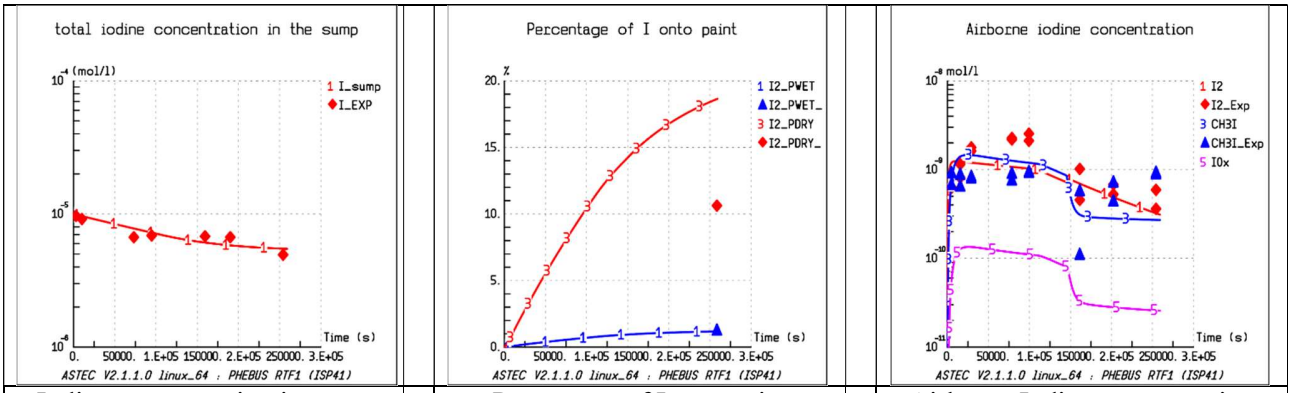

Iodine concentration in sump	Percentage of I onto paint	Airborne Iodine concentration

Figure 3. PHEBUS RTF

Main lessons that have been drawn from the code-to-data assessment relating to the iodine and ruthenium chemistry in the containment are summarized later in Section 4. To get more details about these diverse ASTEC V2.2 SOPHAEROS simulations, one may refer to [15] and [16].

3.9. Direct Containment Heating

In ASTEC the Direct Containment Heating (DCH) is modelled in a rather simple manner, with main goal to limit the number of user parameters that are unknown particularly in reactor cases. The ASTEC V2.2 DCH models were validated on five tests from the KIT DISCO experimental program, focusing on the DISCO-HOT FH series addressing French 1300 MWe PWRs. A brief summary of the main issues learnt from this assessment is provided in Section 4. More details may be found in [15] and [16].

3.10. Molten Core Concrete Interaction

In ASTEC, MEDICIS is the module dealing with Molten Core Concrete Interaction (MCCI). The validation matrix that was considered to evaluate the physical consistency of the ASTEC V2.2 MEDICIS models is shown in Table II. A summary of the main outcomes that have been drawn from the code-to-data assessment in the field of MCCI (either dry CCI or CCI with top flooding) is provided in the next section. To get more details about these ASTEC V2.2 MEDICIS analyses, one may refer to [15] and [16].

4. MAIN OUTCOMES FROM ASTEC V2.2 VALIDATION vs. EXPERIMENTS

For primary and secondary circuit thermal-hydraulics, the ASTEC V2.2 models have been successfully reassessed vs. numerous SETs (Moby-Dick, Coturne, Rebeca, Cosi, Patricia, Takeuchi…) covering basic key phenomena such as critical flow-rate, flashing, interfacial friction, wall heat transfer, interfacial heat transfer and reflooding of a full-scale western-PWR fuel rod assembly (PERICLES). Good results have been also obtained on several BETHSY integral tests with RCS loops as well as on the TMI-2 scenario.

For core degradation early phase phenomena such as core heat-up, oxidation and hydrogen production, results of the ASTEC V2.2 simulations of several Phébus FP and QUENCH integral experiments are quite good. Furthermore, the core final state is also rather well estimated for all Phébus FP and QUENCH transients. Those results show the overall consistency of the updated early-to-late transition phase modeling now available in V2.2 to trigger the fuel rod embrittlement and subsequent relocation of materials combining the flowdown of solid/liquid melts with the possible formation and collapse of fragmented debris. ASTEC V2 results are also satisfactory on TMI-2 up to the final quenching. Conversely, the large hydrogen peak observed during the quenching phase is still underestimated by ICARE. As concerns air ingress transients, while promising results could be obtained against two QUENCH air tests using a preliminary nitriding model, modelling efforts in that field shall continue.

Focusing on late degradation phase models, nice results have been achieved on Phébus FPT4 (test starting in a debris bed geometry), using the combined magma-debris models in the core region. Good results have been also obtained against PRELUDE and PEARL data addressing the reflooding of severely damaged cores, thus confirming the global physical consistency of the ASTEC new model dealing with two-phase flows in porous media. The ICARE modelling for the corium behavior in the lower head is relevant too, as exhibited by the satisfactory simulations of several LIVE and MASCA tests that were focused on heat transfers in corium molten pools and interaction between corium and structural materials, respectively. Finally, the ASTEC V2.2 lower head failure model was also successfully validated vs. the OLHF-1 experimental data, providing a consistent evaluation of the rupture time and localization.

For FP release from core components, good V2.2 results (and even excellent for volatile species) have been obtained on a few VERCORS and VERDON tests, while the planned update of the ELSA models validation vs. other SETs as well as vs. Phébus FP integral tests had to be postponed to mid-2022.

Regarding FP/aerosol behavior in the primary circuit, the ASTEC V2.2 results are reasonable on FP transport and deposition, as experienced on TUBA, FALCON and STORM tests. As concerns physical processes that directly drive the amount of iodine to be released under a gaseous form into the containment, suitable results have been also obtained in the field of element chemical speciation in the RCS. In particular, the {Cs-Mo-I-O-H} new models implemented in SOPHAEROS enabled a good prediction of the CHIP PL experimental trends. Those promising results have been then confirmed vs. several tests of the CHIP+ program with control rod materials, apart from the Ag behavior. So, the numerous simulations that have been performed vs. the CHIP and Phébus FP experimental data have clearly highlighted the significant progress that has been brought by the implementation in ASTEC V2.2 of an RCS gaseous phase chemistry kinetics dedicated modelling. Nonetheless, R&D works are still being continued at IRSN on the chemical behavior of multi-element compounds (e.g. on {I-O-H-Cs-Mo-Ag-Cd-B} system), while progressively ensuring SOPHAEROS accounting for non-congruent condensation phenomena.

For containment thermal-hydraulics, the relevant simulations of the TOSQAN, THAI-HM and PANDA experiments confirmed the overall consistency of the CPA models to deal with mass and heat transfers (e.g. condensation/evaporation, thermal stratification) or hydrogen distribution in the containment under SA conditions. As to the modelling of the mitigation systems operating in the containment, the simulations of selected TOSQAN and PANDA tests proved the global ability of CPA models to deal correctly with spray condensation phenomena. The simulations of several THAI-HR tests showed that CPA can rather well predict the behavior of concurrent types of operating PARs under various transient conditions. Regarding hydrogen combustion, reasonable results could also be obtained vs. THAI-HD and ENACCEF tests using the flame front propagation model. However, open questions still exist applying this model to real plants, as the CPA-FRONT model parameters were determined in relatively small test facilities. So, their application in rougher nodalization with larger control volumes requires to be further assessed.

Regarding the behavior of FPs and aerosols in containment, satisfactory results have been obtained on integral experiments (VANAM, CSE, Phébus FP) using the ASTEC V2.2 SOPHAEROS module. Those rather fair results confirm the physical relevance of the SOPHAEROS containment new modelling that is now replacing the former V2.0 CPA-AFP sub-module. However, these good results concern mostly the evolution of the species in the gaseous atmosphere or on the walls (suspended and depleted) while the predictions of pool scrubbing experiments still exhibited some modelling deficiencies. In that respect, a new pool scrubbing model is being currently under development at IRSN, aimed at removing the observed weakness in that field.

Over the past decade, the ASTEC V2 models dealing with iodine chemistry in containment have been continuously improved in close link with the production of new experimental data successively acquired in the frame of the OECD STEM, STEM2, BIP, BIP2 and BIP3 international projects and the ANR MIRE French domestic project. Most of these SOPHAEROS improvements related to the iodine volatility in gaseous atmosphere aimed to better evaluate the formation/decomposition of inorganic and organic iodine species under irradiation. The treatment of iodine aerosols and oxides was also largely improved. All those modelling evolutions have been then successfully validated vs. numerous SETs. Moreover, in comparison to V2.0, a better agreement with experimental data could notably be achieved for all Phébus FP tests on the evolution of both molecular iodine and organic iodine concentrations in the containment. In summary, those updated validation tasks confirmed that the ASTEC V2.2 modelling of the iodine behavior in the containment is at the state-of-the-art of the R&D knowledge. Finally, though based on a less extended validation matrix in comparison to iodine, the V2.2 modelling of the ruthenium chemistry looked also close to the state-of-the-art, as proved by the quite relevant simulations of IRSN dedicated experiments. That's being said, there are still open issues to be better addressed, such as mid to long term releases.

Regarding DCH, the ASTEC V2.2 new model was successfully assessed vs. DISCO FH experiments. Indeed, despite its simplifications, this new modelling of the DCH process gave satisfactory results while allowing reducing the number of user parameters which are unknown particularly in reactor cases.

For MCCI in dry conditions, the fair agreement noted between ASTEC V2.2 simulations and experimental data on several CCI and VULCANO experiments for the 2-D ablation kinetics and the final cavity shape, as well as for the ablated concrete mass, showed basically the relevance of the set of assumptions and models used for both considered concrete types (LCS and siliceous). The main still unresolved issue for the 2-D ablation in dry conditions remains likely the long-term behavior of the solid accumulation or crust possibly built-up at the cavity bottom very early during MCCI in case of siliceous concrete. For MCCI under water, the CCI-7 and CCI-8 experiments were selected to make a first assessment of the ASTEC MEDICIS new models specifically addressing top quenching phenomena arising during MCCI, such as melt ejection and boiling heat transfer at the corium-water interface, including water ingression. The overall behavior predicted by MEDICIS sounded reasonable, although the analyses need to be thoroughly studied. Nonetheless, one must keep in mind that these top quenching models are a priori poorly adapted to the possible anchored crust process and cannot reflect the intermittency of melt ejection. More R&D is therefore still needed on MCCI top quenching regarding these two processes. In that respect, IRSN currently actively participates with ASTEC in the on-going OECD ROSAU experimental program.

Finally, to complement those huge validation tasks carried out vs. experimental data at different scales, a so-called "validation at plant scale" work is also being realized. In that respect, in addition to the recurrent simulation of the TMI-2 real accident transient, the analyses of the Fukushima-Daiichi accidents are being also periodically updated to further assess the ICARE few specific models that aim to better cope with BWR core geometries [3]. Besides, those analyses emphasized the need for extending the modelling from the short to the long term to better address the delayed releases and resuspension related phenomena [24] [25]. Hence, the ASTEC modelling in those fields will be further improved, accounting for the data that was already obtained from some OECD recent R&D programs (STEM2, BIP3) or could come from the

on-going OECD ESTER project. Moreover, many other ASTEC V2.2 plant analyses are being performed by foreign partners involved in the NUGENIA ASCOM project [4]. These independent plant applications, which often consist of code-to-code benchmark studies, aim at bringing complementary lessons about the ASTEC V2 overall modelling capabilities to calculate complete SA sequences on diverse types of NPPs.

5. CONCLUSIONS

The main conclusion that can be drawn from these very extended validation activities of the V2.2 major version is that most ASTEC models are today at the state of the art, in particular FP models that are directly driving the evaluation of the final source term to the environment in case of a severe accident.

ASTEC V2.2 can be considered as a suitable tool to calculate various SA sequences initiated at either reactor power state or shut-down state on different types of NPPs. In particular as demonstrated by both IRSN and many ASCOM foreign partners, ASTEC V2.2 can be used to perform Gen.II PWR and VVER once-through best-estimate calculations, while providing the actual capability for simulations of technical means for mitigation of SA consequences as well as for simulation of typical SAM actions. For BWRs, the V2.2 containment models and source term models are also considered as physically relevant while the core new degradation models, although proved to be rather consistent, likely need to be further assessed. ASTEC V2.2 can also be used to perform best-estimate safety analyses on EPR, as done at IRSN. Moreover, as demonstrated by several partners, ASTEC V2.2 appears to be also a useful tool to investigate the progression of severe accidents in NPPs relying on the in-vessel melt retention strategy.

Modelling efforts will continue to keep ASTEC models at the state of the art and thus further improve the simulations of SA relating to various types of Gen.II and Gen.III plants. Besides, both the development of a few new specific models and the improvement of some existing ones are required to enlarge the scope of best-estimate analyses to other innovative NPPs and nuclear installations, and in particular to consolidate the promising first ASTEC V2.2 applications to SMRs [26] while better addressing accidents occurring in spent fuel pools [27]. Anyhow, ASTEC shall remain a repository of knowledge gained from international R&D for SA phenomenology. For that purpose, physical models will be continuously updated according to the interpretation of current and future experimental programs executed in an international frame. Meanwhile, the ASTEC assessment activities will of course continue both at IRSN and outside IRSN through foreign partners' contributions to be mostly realized in the frame of the ASCOM on-going project.

ACKNOWLEDGMENTS

The authors would like to associate to this article the whole IRSN ASTEC development team who very actively contributed to the ASTEC V2.2 validation tasks, as well as the foreign organizations who also brought afterward a valuable contribution to the ASTEC V2 assessment tasks in the frame of both the international ASTEC Users' Club network and the SNETP-NUGENIA ASCOM collaborative project.

REFERENCES

1. L. Chailan et al., "Overview of ASTEC code and models for Evaluation of Severe Accidents in Water Cooled Reactors", *Proceedings of the IAEA Technical Meeting on Status and Evaluation of Severe Accident Simulation Codes for Water Cooled Reactors*, Vienna (Austria), October 9-12, (2017)
2. L. Laborde et al., "Overview of the ASTEC V2.2 integral code", Report IRSN-2021-00298, (2021)
3. P. Chatelard et al., "Main modelling features of ASTEC V2.1 major version", *Annals of Nuclear Energy*, **93**, pp.83-93, (2016)
4. SNETP NUGENIA TA2 ASCOM, https://snetp.eu/project-portfolio/, (2018)
5. P. Chatelard et al., "Overview of ASTEC V2.0r1 validation", *Nuclear Engineering and Design*, **272**, pp.136-151, (2014)

6. M. Buck et al., "Synthesis of validation of ASTEC V2.1rev0 and rev1 versions", CESAM FP7 Deliverable referred to as "*CESAM-D20.25*", (2017)
7. H. Nowack et al., "CESAM - Code for European Severe Accident Management, EURATOM project on ASTEC improvement", *Annals of Nuclear Energy*, **116**, pp.128-136, (2018)
8. A.K. Mercan et al., "Validation of ASTEC 2.1 using QUENCH-12 for VVER reactors", *Proceedings of the 9th European Review Meeting on Severe Accident Research (ERMSAR-2019)*, Prague, Czech Republic, March 18-20, 2019
9. O. Murat et al., "Preliminary validation of ASTEC V2.2 with the QUENCH-20 BWR bundle experiment", *Nuclear Engineering and Design*, **370**, (2020)
10. F. Gabrielli et al., "U&S analyses applied to ASTEC results for QUENCH-08 test", *Annals of Nuclear Energy*, in press, (2021)
11. M. Gouëllo et al., "Interaction between Cesium iodide particles and gaseous boric acid in a flowing system through a thermal gradient tube (1030K to 450K) and analysis with ASTEC/SOPHAEROS", *Progress in Nuclear Energy*, **138**, (2021)
12. M. Kotouc, "Simulation of external reactor vessel cooling with the ASTEC code – Validation on experiments performed at the THS-15 (VVER-1000) facility", *Proceedings of the 19th International Topical Meeting on Nuclear Reactor Thermal Hydraulics (NURETH-19)*, Brussels, Belgium, March 6-11, 2022
13. I. Gomez Garcia-Torano and L. Laborde, "Validation of selected CESAR friction models of the ASTECV21 code based on Moby Dick experiments", *Journal of Nuclear Engineering and Radiation Science*, **5**, (2019)
14. I. Gomez-Garcia-Torano et al., "Overview of the CESAR thermalhydraulic module of ASTEC V2.1 and selected validation studies", *Proceedings of International Youth Nuclear Congress (IYNC2018)*, Bariloche, Argentina, March 11-17, 2018
15. P. Chatelard, "ASTEC V2.1 final validation report", Report IRSN-2019-00717, (2019)
16. L. Laborde et al., "ASTEC V2.2 physical validation", Report IRSN-2021-00272, (2021)
17. PROGRES program, *https://www.irsn.fr/EN/Research/Research-organisation/Research-programmes*
18. I. Gomez-Garcia-Torano et al., "Reflooding of degraded cores in ASTEC V2.1: modelling and validation on PEARL experiments", submitted to *Nuclear Engineering and Design.*
19. I. Gomez-Garcia-Torano and L. Laborde, "Modelling reflooding of intact core geometries in ASTEC V2.1: Improvements and validation on PERICLES experiments", *Nuclear Engineering and Design*, **378**, 111157, (2021)
20. L. Laborde et al., "External Reactor Vessel Cooling modelling in ASTEC V2.1 code", *Proceedings of the 12th International Topical Meeting on Nuclear Thermal-Hydraulics, Operation and Safety (NUTHOS-12)*, Qingdao, China, October 14-18, 2018
21. ISTP program, *https://www.irsn.fr/EN/Research/Research-organisation/Research-programmes*
22. J. Malet et al., "OECD International Standard Problem ISP-47 on containment thermal-hydraulics: Conclusions of the TOSQAN part", *Nuclear Engineering and Design*, **240**, pp. 3209-3220, (2010)
23. J. Ball et al., "International Standard Problem n°41, Containment Iodine Computer Code Exercise Based on a Radioiodine Test Facility (RTF) experiment", OECD/NEA/CSNI/R(2000)6, Vol 2, (2000)
24. C. Bouillet et al., "OECD/NEA BSAF project (Benchmark on Study of the Accident at the Fukushima Daiichi NPPs), IRSN contribution to BSAF Phase II", IRSN/PSN-RES/SAG/2018-00065, (2018)
25. P. Chatelard et al., "Contribution of ASTEC numerical simulations to the understanding of the Fukushima accidents", *Proceedings of the IAEA Workshop on advances in understanding the progression of severe accidents in Boiling Water Reactors*, Vienna, Austria, July 17-21, 2017
26. P. Maccari et al., "Analysis of BDBA sequences in a generic IRIS reactor using ASTEC code", *Proceedings of the 10th European Review Meeting on Severe Accident Research (ERMSAR-2022)*, Karlsruhe, Germany, May 16-19, 2022
27. O. Coindreau et al., "Uncertainty quantification for a severe accident sequence in an SFP in the frame of the H-2020 MUSA Project: first outcomes", *Proceedings of the 10th European Review Meeting on Severe Accident Research (ERMSAR-2022)*, Karlsruhe, Germany, 16-19 May 2022

RÉPUBLIQUE FRANÇAISE
Liberté
Égalité
Fraternité

10TH CONFERENCE ON
SEVERE ACCIDENTS RESEARCH
May 16-19, 2022 – Karlsruhe, Germany
ERMSAR 2022

IRSN
INSTITUT DE RADIOPROTECTION
ET DE SÛRETÉ NUCLÉAIRE

VALIDATION OF THE IRSN ASTEC V2.2 SEVERE ACCIDENT INTEGRAL CODE

Patrick CHATELARD *(on behalf of the ASTEC team)*
IRSN/PSN-RES/SAM

The 10th European Review Meeting on Severe Accidents Research
Karlsruhe, Germany - May 16-19, 2022

IRSN/ERM-296 ind. 06

MEMBRE DE
ETSON

Contents

1. **Introduction**
   - ASTEC V2.2 version
   - ASCOM collaborative project
2. **ASTEC V2.2 validation strategy and validation matrix**
3. **Few illustrations of the ASTEC V2.2 validation vs. experimental data**
4. **Synthesis of the ASTEC V2.2 validation vs. experimental data**
5. **General conclusion on the ASTEC V2.2 main capabilities for LWR analyses**

ASTEC V2.2 (current version on production) & ASCOM project

ASTEC : integral code developed at **IRSN** for simulation of severe accidents (SA) in present/future Water-Cooled Reactors (PWR, incl. VVER, BWR, SMR and CANDU), from the accident initiating event until radioactive release out of the containment

ASTEC main issue: to remain a **state-of-the-art tool for source term calculations**

- Most modelling is mechanistic, only sometimes simplified
- **Repository of knowledge of severe accident phenomenology**

ASCOM project: on-going R&D collaborative project, coordinated by IRSN since 2018, that takes place under the **NUGENIA TA2** aegis

- ASTEC V2.2 supplementary assessment by partners (with both **validation vs. experiments** and **benchmarks with other codes on plant applications** for various NPP types)
  ➔ Sharing experience and best practice is essential for running reliable NPP calculations
- Development of new ASTEC generic open plant input decks (e.g. for LWR-SMRs)

ASTEC V2.2 general architecture



- **ASTEC makes use of independent program units (so-called modules), each one being in charge of a set of phenomena in a given domain (circuit, vessel, containment…)**
  - **The modules exchange data through a main database resident in memory**
  - **The high level of modularity allows easy validation of physical models vs. experiments**

General approach for ASTEC validation

Four-tier validation approach (benefits from ASTEC code modularity):

1. **Separate-Effect-Tests** (SETs) focusing on only 1 physical phenomenon
2. **Coupled-Effect-Tests** (CETs) focusing on a set of physical phenomena
3. **Integral tests** (IT) to check the coupling of physical models and that no essential phenomenon was forgotten or neglected
   → *Example of **Phébus FP** integral experiments at IRSN*
4. **R**epresentative **simulations at plant scale** for few reference sequences

Very large validation matrix, covering all SA phenomena through **more than 300 experiments** (conducted at various scales in ~70 different facilities worldwide):

- Major (past, on-going) French and international experimental programs, along with most ISPs

Systematic regression testing through a weekly application of a significant sub-set (~250 tests) of the whole validation matrix (automatic comparison of reference validation results with current ones thanks to an adequate instrumentation of the ASTEC validation input decks)

Validation of late phase core reflooding models

Focus on **ASTEC V2.2** (***ICARE/CESAR modules***) validation on **PEARL** large heated debris bed experiments (IRSN facility)

- The D5-2 and D1-7 selected tests only differ by the imposed pressure (respectively 5 bars and 1 bar)
- Right evaluation of the steam mass flow rate evolution at the test section outlet in both tests
- Good results also for the quench front progression in the bed centre (R=0 mm) and periphery (R=220 mm)

➔ **The th.hydraulics conditions are well predicted.** In particular, **the impact of pressure on the reflooding is well captured**: while a flat quench front profile is observed in the D5-2 test with a short reflooding time, the quench front progression in D1-7 is faster in the periphery compared to the centre, and the reflooding time is much longer

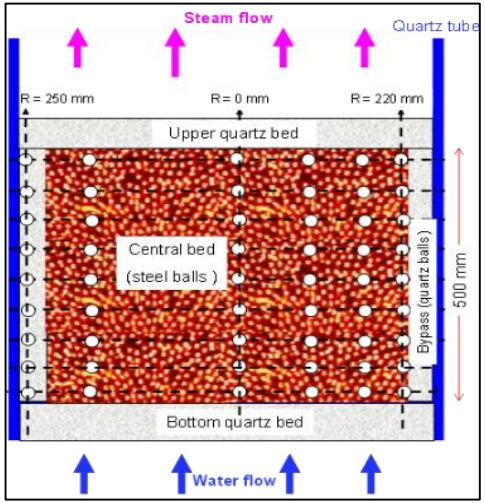

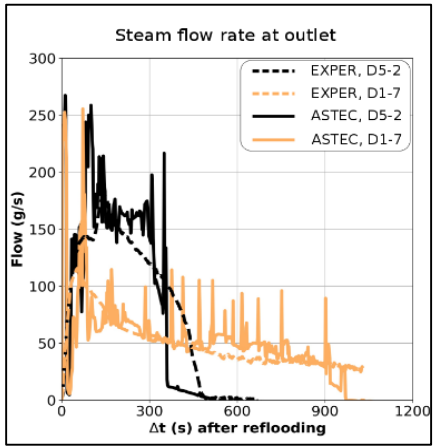

Evolution of outlet steam flow rate in D5-2 (5 bar) and D1-7 (1 bar)

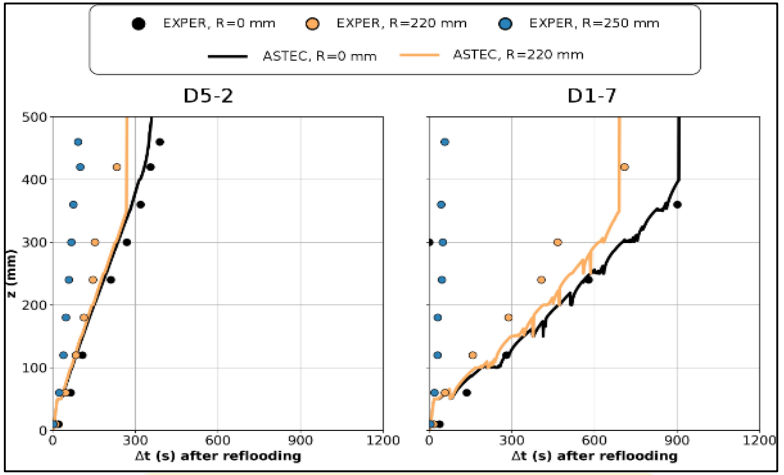

Evolution of the quench front for tests D5-2 (5 bar) and D1-7 (1 bar)

Validation of FP/aerosol transport & chemistry models in the RCS

Focus on the **ASTEC V2.2** (***SOPHAEROS module***) validation on two **CHIP+** experiments (TGT device operated at IRSN)

- Satisfactory estimation of the **iodine** total transport (gas+aerosols) along the CHIP+ test line
- The transport of **cesium** and **molybdenum** is also reasonably predicted, although a bit overestimated
- On the contrary, the transport of **Cadmium** and **Silver** is largely overestimated by ASTEC, notably in the second test

➔ **Overall good enough results confirming the physical relevance of the current iodine gaseous phase chemistry kinetics modelling in the RCS.** For other elements, improvements are really expected from some IRSN on-going modelling works that aim to ensure SOPHAEROS accounting for non-congruent condensation phenomena

Experiment and selected elements	Deposited in high temperature zone (alumina tube) (% ii.)		Deposited in transport zone (stainless steel tube) (% ii.)		Released at the outlet of the test line (downstream steel tube) (% ii.)	
Test "CdMoCsI"	**Experiment**	**ASTEC**	**Experiment**	**ASTEC**	**Experiment**	**ASTEC**
Iodine	0.00%	0.00%	13.20%	19.28%	86.80%	80.72%
Cesium	10.00%	1.66%	16.50%	16.06%	73.50%	82.28%
Molybdenum	30.60%	11.18%	10.30%	28.44%	59.10%	60.38%
Cadmium	3.00%	0.00%	41.30%	24.74%	55.70%	75.216%
Test "AgCdBMoCsI"	**Experiment**	**ASTEC**	**Experiment**	**ASTEC**	**Experiment**	**ASTEC**
Iodine	0.00%	2.70%	7.20%	11.76%	92.80%	85.53%
Cesium	14.30%	1.47%	10.10%	10.99%	75.60%	87.54%
Molybdenum	25.50%	3.25%	9.10%	10.68%	65.40%	86.06%
Cadmium	33.10%	0.00%	24.20%	18.50%	42.70%	81.50%
Silver	48.50%	17.16%	7.80%	9.01%	43.70%	73.83%
Boron	1.00%	0.03%	1.80%	1.51%	97.20%	98.46%

Validation of containment thermal-hydraulics models

Focus on the **ASTEC V2.2** (***CPA module***) assessment on IRSN **TOSQAN** experiments (**7 m³ test facility**)

- TOSQAN **ISP47** (condensation test): Condensation flow and pressure well reproduced
- TOSQAN **T115** (spray test): Pressure and average atmosphere temperature well reproduced

➔ **Overall consistency of the ASTEC models to deal with mass and heat transfers in the containment**

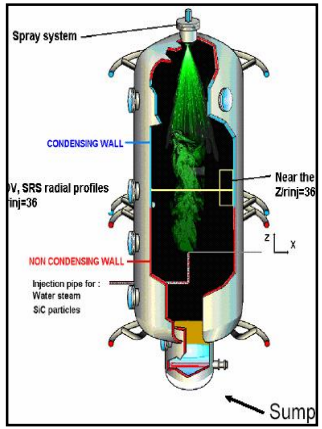

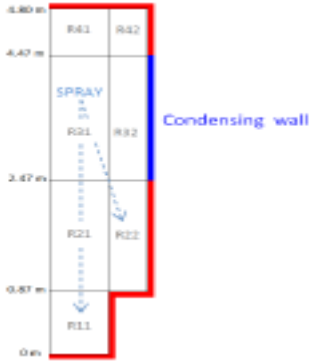

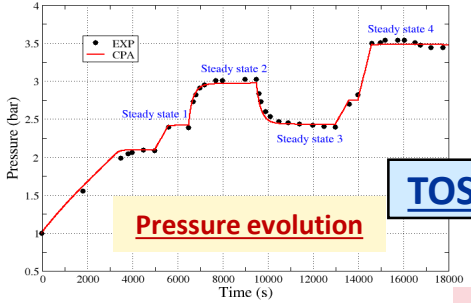

Pressure evolution

TOSQAN ISP47

Condensation mass flow rate

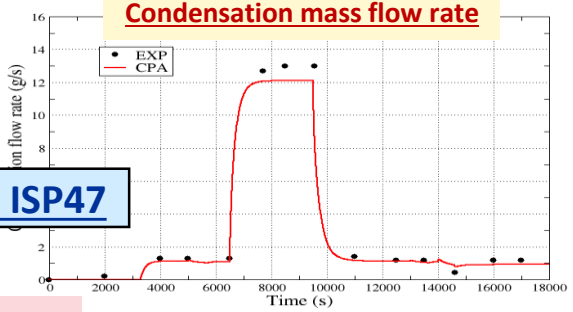

ASTEC results **in red curves**

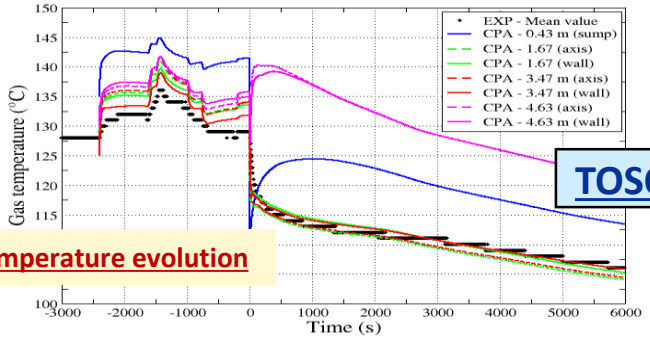

Gas temperature evolution

TOSQAN T115

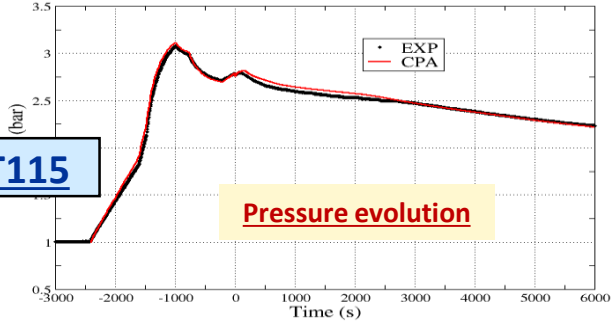

Pressure evolution

Validation of models for iodine behaviour in containment

Focus on the **ASTEC V2.2** ***(SOPHAEROS module)*** validation on **PHEBUS RTF1** experiment (AECL/CNL facility)

- Volume 300 l with painted and steel surface
- **Test conditions**: Injection of iodide ions I^- in presence of epoxy paints and on-line measurement of iodine speciation in gas and liquid

➔ **Overall good agreement of iodine concentrations in sump** (*left figure*) **and in atmosphere** (*as depicted on right figure for both gaseous iodine* I_2 *and organic iodides* CH_3I *)*

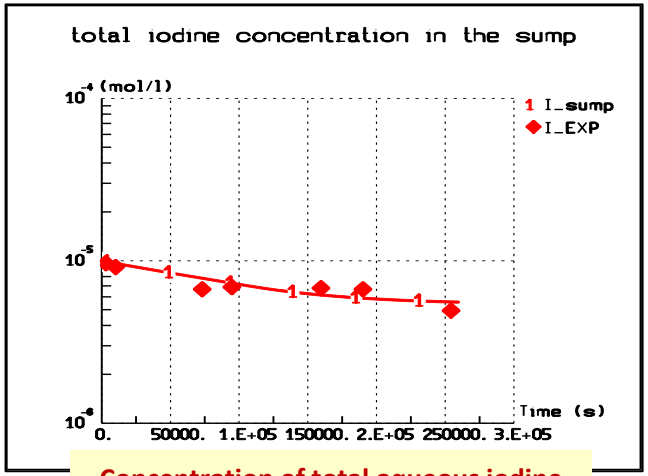

Concentration of total aqueous iodine

ASTEC results **in solid lines**

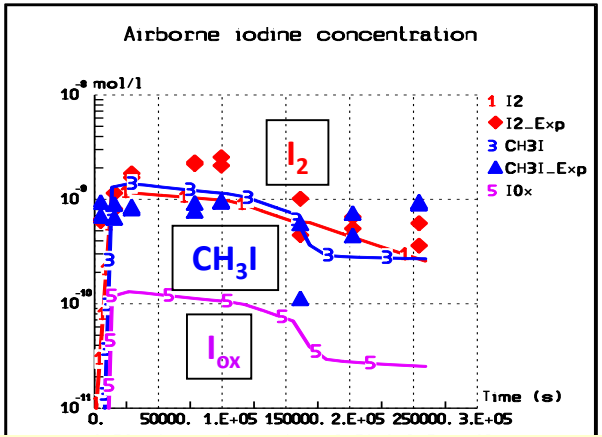

Concentration of iodine species in gaseous phase

Validation of MCCI models (1/2)

Focus on the **ASTEC V2.2** ***(MEDICIS module)*** validation on **CCI** experiments (ANL)

- Illustration of ASTEC results on MCCI **dry tests** for 2 different types of concrete

➔ **Good enough agreement on ablation kinetics and final cavity shape for both tests**

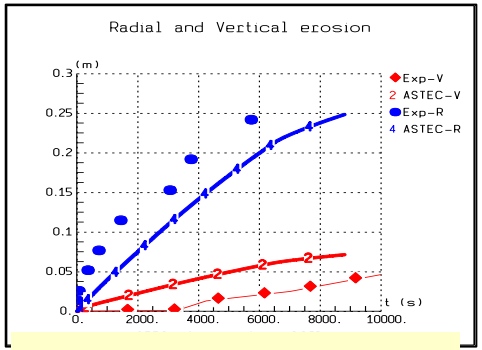

Lateral and axial ablation kinetics

CCI-3 test with Siliceous concrete

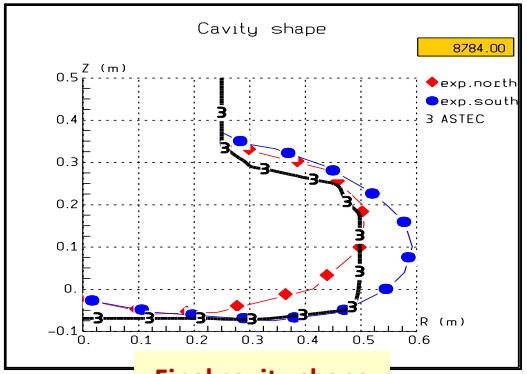

Final cavity shape

ASTEC results **in solid lines**

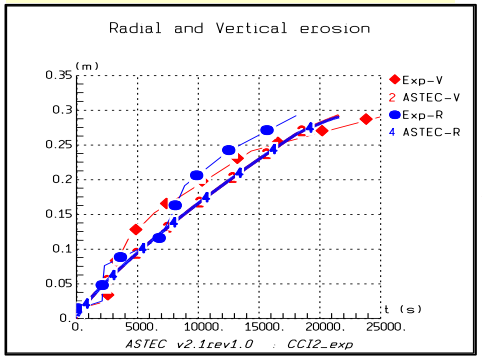

CCI-2 test with LCS concrete (limestone / common sand)

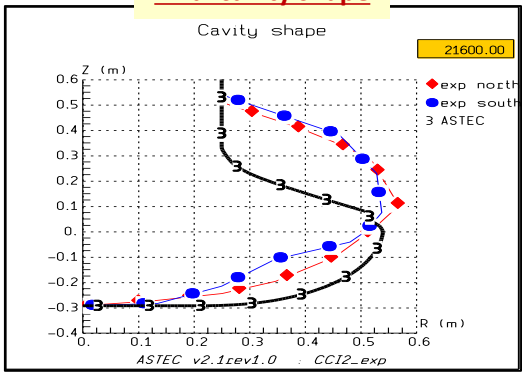

Validation of MCCI top flooding models

ASTEC V2.2 ***(MEDICIS module)*** validation on **CCI-8** experiment (LCS concrete) with early top cooling

- The axial ablation kinetic is quite well reproduced. In contrast, ASTEC/MEDICIS does not predict correctly the delayed start of the sidewall erosion.
- As to the rest of the transient, without any crust anchoring prediction, MEDICIS predicts a significant ejected corium mass, leading to the formation of a substantial particle bed, that seems not correct.

➔ **Promising results have been obtained**, but open modelling issues still remain, in particular concerning the crust behaviour

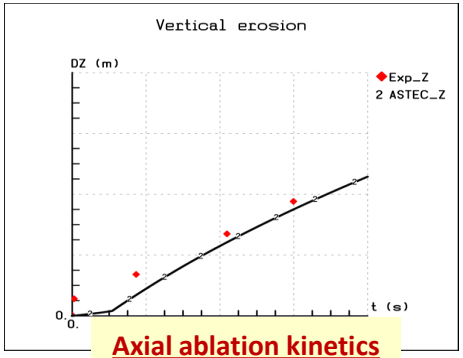

Axial ablation kinetics

ASTEC results **in solid lines**

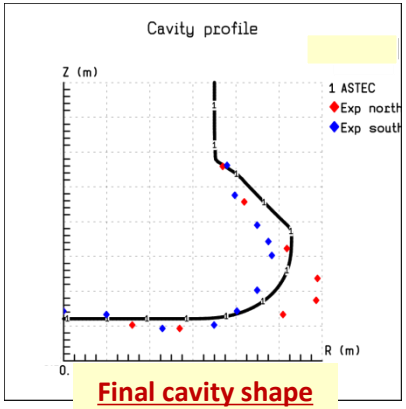

Final cavity shape

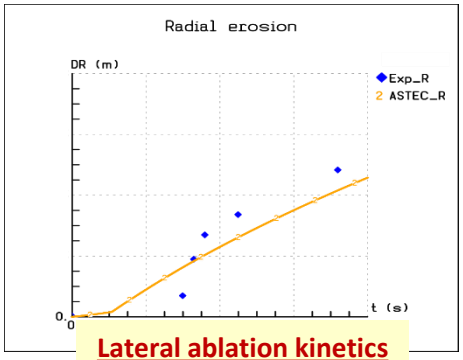

Lateral ablation kinetics

Summary of the ASTEC V2.2 validation vs. experimental data (1/3)

Thermalhydraulics in circuits

- **Successful reassessment vs. numerous SETs** belonging to the CATHARE code validation matrix
- **Good results on integral tests** addressing DBAs at power state conditions (as well as on TMI-2)
- Reasonable results on integral tests (BETHSY) related to shut-down state initial conditions

Core degradation

- **Quite fair results for both in-core early-phase** (heat-up, H_2 production, …) **and late phase models** (2D relocation, debris bed and/or molten pool formation,…) **as well as on the corium behaviour in the vessel lower head**
  - *But the model of particulate debris formation still needs to be consolidated at different scales*
  - *Besides, **ATF** technology constitutes of course another challenging modelling issue for ASTEC*
- Very **promising results using the porous media modelling in case of reflooding of a degraded core**
  - Relevant prediction of the main thermal-hydraulics parameters on PRELUDE/PEARL
  - *But the large hydrogen peak observed during TMI-2 quenching phase is still underestimated*

FP release

- Good results for volatile and semi-volatile FPs (even excellent for volatile species) and reasonable results (slight underestimation) for low-volatile FPs

Summary of the ASTEC V2.2 validation vs. experimental data (2/3)

FP/aerosol transport & chemistry in the RCS

- Good enough results on FP transport and chemistry, with a **significant improvement on the modelling of speciation processes**
- In particular, the importance of the gas chemistry kinetics with respect to the final Source Term (e.g. iodine partition at the break) has been confirmed by **Phébus FP** and **CHIP+** post-test analyses and ASTEC related validation
  - ➢ *Modelling improvements are underway on basis of **CHIP+** and **START** experimental data*
    - ➔ *account in SOPHAEROS for non-congruent condensation phenomena*
  - ➢ *Other modelling improvements are planned as a feed-back from on-going OECD **ESTER** program*
    - ➔ *notably on the remobilization of FP deposits that might contribute to delayed releases*

Containment response

- **Satisfactory results on both thermal-hydraulics** (mass/heat transfers, but also hydrogen combustion & recombination) **and aerosols behaviour**
- **But** confirmation of the **not relevant treatment of pool-scrubbing phenomena**
  - ➢ *Fully new model currently under development and validation at IRSN*

Summary of the ASTEC V2.2 validation vs. experimental data (2/2)

Iodine chemistry in the containment

- **Global trends are well reproduced**
  - *such as on formation/decomposition of organic and inorganic iodine species under irradiation, behaviour of iodine aerosols and oxides…*
- **Iodine behaviour modelling at the current state of the art**
  - *But modelling improvements will continue as a feed-back from on-going OECD **ESTER** program*

DCH

- Suitable new correlation (*based on DISCO test analyses*) to predict the corium dispersion in containment, allowing reducing the number of user parameters which are unknown particularly in reactor cases

MCCI

- **Basic relevance of the set of models and assumptions**, as illustrated by the quite good results obtained against MCCI tests **in dry conditions** for both siliceous and LCS concrete
- **Promising results obtained** vs. CCI latest experiments using the new coolability models **in conditions of corium top quenching during MCCI**
  - *But modelling improvements will continue as a feed-back from on-going OECD **ROSAU** program*

General conclusion on the ASTEC V2.2 capabilities for LWRs

Main outcome of the physical validation tasks

- **Most physical models are at to the current state of the art** (**notably FP models**)

Main outcomes for full scale analyses (from both IRSN PSA-2 studies and partners' works performed or shared in the frame of the ASCOM project)

- Significant progress was achieved on the code robustness and stability, along with a valuable **reduction of the numerical dispersion of the code results**
- Adequate tool to simulate **most SA scenarios in various types of Gen.II NPPs** (**PWR**, **VVER, BWR**) **and Gen.III NPPs** (both **EPR** with external core catcher and NPPs relying on the **IVMR** strategy with ERVC) **for both normal power** and **shutdown states**,
  - along with the capability to simulate most **safety systems** and **SAM measures**
- Useful tool to study SA scenarios in **SFPs** (*one can notably refer to the on-going works in **MUSA***)
- Promising results yet obtained on **SMR** accident analyses (*e.g. ENEA/UNIBO works in **ASCOM***)
  - Passive Systems modelling to be further assessed in **PASTELS** and **SASPAM-SA** Euratom projects

In Memory of Martin Kissane

Acknowledgements

The lecturer wishes to thank
the whole ASTEC team from IRSN,
as well as
the ASCOM project partners who contributed
to the validation of ASTEC V2.2

Appendix 1

ASCOM project overview

ASCOM project (1/2)

ASCOM Project conduct

- **4-year long in-kind R&D project** (*Oct. 2018 - Sept. 2022*) **coordinated by IRSN** in the frame of the **NUGENIA TA2 (SARNET)**

ASCOM Project objectives

- ASCOM main objective is to help amplify and accelerate the on-going process of making ASTEC a fully reliable tool for **SA analyses and accident management** in a **wide range of nuclear safety applications** by **strengthening the various R&D activities of the ASTEC COMmunity in a consistent way**

ASCOM Project partnership

- Today, ASCOM gathers about **20 partners** (TSO, research, universities, industry) :
  - **IRSN**, **EDF R&D** (France), **KIT**, **RUB PSS** (Germany), **Tractebel-ENGIE** (Belgium), **JRC** (EC,) **CIEMAT** (Spain), **ENEA**, **Univ.Bologna** (Italy), **NUBIKI** (Hungary), **IVS** (Slovakia), **UJV** (Czech Rep.), **INRNE** (Bulgaria), **RATEN ICN** (Romania), **IJS** (Slovenia), **FER** (Croatia), **LEI** (Lithuania), **VTT** (Finland)
  - **Energorisk** (Ukraine)
  - **NSC** (China), **NUS** (Singapore)

ASCOM project (2/2)

ASCOM project structure

- 5 Work-Packages, whose major ones cover:
  - **Continuous validation** of ASTEC V2 series
  - **ASTEC applications at plant scale**, **along with cross-walk activities** with other reference SA analysis codes (**MELCOR, MAAP, …**) for Gen.II LWRs
  - **Development of few new "generic" reference open input decks** to extend the ASTEC V2 applicability to some other kinds of nuclear installations, in priority **SMR**s and **SFP**s

Yearly workshops

- KoM and 1st workshop held in Autumn 2018 and 2019, respectively
- 2nd workshop delayed due to Covid-19 ➔ virtual event held in May 2021
- Final workshop to be hosted by IRSN in September 2022

A crucial community for best-estimate calculations

- SA codes necessitate experienced users

  ➔ **Sharing experience and best practice is essential for running reliable calculations**

Appendix 2

Main experimental programmes considered in the ASTEC V2.2 validation matrix

Overview of the ASTEC V2 validation matrix main contents (1/4)

- **Most OECD/NEA/CSNI ISPs are considered**
  - **27** (**BETHSY**): Thermal-hydraulics in western-type PWR RCS
  - **33** (**PACTEL**): Thermal-hydraulics in VVER RCS
  - **45** (**QUENCH**): Core reflooding
  - **34** (**FALCON**): Gas transport and chemistry in the RCS
  - **37** (**VANAM**): Containment spray and H_2 distribution in containment
  - **39** (**FARO**): Corium slump and fragmentation
  - **40** (**STORM**): Aerosol resuspension in the RCS
  - **41** (**ACE-RTF**, **CAIMAN**): Iodine behaviour in containment
  - **44** (**KAEVER**): Aerosol depletion and thermal-hydraulics in containment
  - **46** (**Phébus-FPT1**): Integral test
  - **47** (**TOSQAN-MISTRA-ThAI**): Thermal-hydraulics in containment with spray operation
  - **49** (**ThAI-ENACEFF**): Hydrogen combustion in containment

Overview of the ASTEC V2 validation matrix main contents (2/4)

- **Other OECD projects' experiments**
  - **LHF/OLHF**, **RASPLAV/MASCA**, **ThAI**, **PANDA SETH-II**, **STEM/STEM2**, **BIP/BIP2**, **ESTER**, **OECD-CCI**, **ROSAU**…
- **Most of the other recent or on-going key-experiments worldwide**
  - All **Phébus-FP** in-pile integral tests
  - **SKODA-UJP** on corium oxidation
  - **PBF SFD** and **LOFT LP** on core degradation
  - **QUENCH** on core reflooding
  - **PERICLES** on a PWR fuel rod assembly reflooding
  - **PRELUDE**, **PEARL**, **DEBRIS** on severely degraded core reflooding
  - **LIVE** on corium pool behaviour in vessel lower head
  - **CORDEB** & **CORDEB2** on corium/debris behaviour in vessel lower head
  - **CERES**, **RESCUE-2**, **ULPU-V**, **THS-15** on ERVC loop

Overview of the ASTEC V2 validation matrix main contents (3/4)

- **Most of the other recent or on-going key-experiments worldwide** (cont'd)
  - **VERCORS** and **VERDON** on fission products release from fuel
  - ISTP/**CHIP**, **CHIP+** and **EXSI** on iodine behaviour in RCS
  - **START** on ruthenium behaviour in RCS
  - **EPICUR** on iodine behaviour in containment
  - **STEM** & **STEM2** on Source Term mitigation
  - **ThAI** on containment th.hydraulics, including notably hydrogen behaviour (H_2 distribution, H_2 combustion, H_2 recombination…)
  - **VTT** experiments on pool scrubbing
  - **DISCO** on DCH
  - **VULCANO** and **CCI** on MCCI
- **along with several VVER-specific experiments**
  - **PACTEL**, **QUENCH-VVER**, **CODEX-VVER**, **CERES**, **RESCUE-2**, **THS-15**…

Overview of the ASTEC validation matrix main contents (4/4)

Illustration of a detailed validation matrix (*here for* CESAR ***module***)

Validation of the physical laws: Separate Effect Tests

Main phenomena	Experiment	Mechanical Transfer	Interfacial Heat Flux	Wall Heat Flux
Critical flow rate	SMD long nozzle	Yes	Yes	
	SMD short nozzle	Yes	Yes	
	REBECA	Yes	Yes	
Reflooding 1D	PERICLES Reflooding	Yes	Yes	Yes
Swollen water level volume	PERICLES boil up			Yes
Wall friction	MD	Yes		
Wall heat flux	COTURNE	Yes	Yes	Yes
Condensation	COSI (Accu)		Yes	

Component validation

Component	Experiment
Steam Generator	PATRICIA GV1 GV2
	Comparison with CATHARE
Pressurizer	Comparison with plant results

Integral tests

Experiment	Scenario
BETHSY	LOCA (2 inches cold leg break): 9.1b
	LOCA (6 inches hot leg break) : 6.4
	Total loss of Feed-Water : 5.2e
	Cold shut-down conditions : 6.9f

DEVELOPMENT OF SEVERE ACCIDENT CODE CORVES FOR ANALYSING IN-VESSEL DEGRADATION PHASE OF SEVERE ACCIDENT IN VVER-1000 REACTOR

Sil Sitesh*, P. Krishna Kumar, Pandey Y.K.
Nuclear Power Corporation of India Ltd.
Mumbai 400 094, India
ssil@npcil.co.in; pkrishnakumar@npcil.co.in; ypandey@npcil.co.in

ABSTRACT

Analysis of accident progression during postulated severe accident scenarios is an integral part of safety studies for nuclear reactor and facilities. Severe accident progression in VVER-1000 reactors can be categorized into two stages: in-vessel phase and ex-vessel phase. As part of analysis tool development for severe accident analysis, a computer code 'CORVES' for modelling degradation of reactor core and other internal components during in-vessel phase of PWR has been developed. A range of complex physico-chemical phenomena occurring during in-vessel phase viz. core uncovery and heat-up, oxidation reaction, fuel melting, degradation of structural materials, slumping of corium in the lower plenum, heat transfer of molten corium pool in the lower plenum and subsequent Reactor Pressure Vessel (RPV) failure has been modelled in 'CORVES' code. The code estimates duration of complete core uncovery, hydrogen generation, fuel melt, and lower grid plate failure, relocation of corium in the lower plenum and heat-up & failure of RPV.
In the present study Large Break Loss of Coolant Accident (LB-LOCA) along with extended Station Black Out (ESBO) has been considered as the representative core melt scenario for VVER-1000 reactor. In the scenario, the effect of water injection from passive hydro-accumulators has also been evaluated and critical parameters viz. time core uncovery & Fuel heatup, hydrogen generation, RPV failure time has been predicted by 'CORVES' code.
Results of this study provide analytical insight into the severe accident progression which is instrumental for development of Severe Accident Management Guidelines (SAMG).

KEYWORDS
Severe Accident; In-Vessel Phase; Core Melt; SAMG; VVER

1. INTRODUCTION

Severe accident is a Design Extension Condition (DEC) which involves extensive degradation of fuel rods and partial/complete core melting occurring due to multiple failures of safety systems [1]. Core degradation/melting happens due to lack fuel cooling and subsequently molten corium flows through the lower plenum. After Reactor Pressure Vessel (RPV) failure corium flows out of RPV and into core catcher. Such severe accident progression sequence is generally categorized into two phases; In-vessel phase and Ex-vessel phase. A series of experimental and theoretical studies have been performed worldwide in order to develop computational models for different physico-chemical phenomena associated with severe accident. Incorporating such models into an integrated computational tool for simulating accident progression sequence in a commercial reactor is of utmost importance to provide analytical support for development of Severe Accident Management Guidelines (SAMG).

As part of analysis tool development for severe accident analysis, a computer code 'CORVES' for modelling degradation of reactor core and other internal components during in-vessel phase of PWR has been developed. In the present study Large Break Loss of Coolant Accident (LB-LOCA) along with extended Station Black Out (ESBO) has been considered as the representative core melt scenario for VVER-1000 reactor.

2. BRIEF DESCRIPTION OF VVER 1000 REACTOR

The Reactor considered for this analysis is VVER-1000 reactor. This type of reactor is a pressurized light water with 1000 MW electrical power. There are four loops of reactor coolant system which consist of RPV and its internals, RCP (Reactor Coolant Pump), horizontal SG (Steam Generator) and MCP (Main Coolant Pipelines).To increase the reliability of safety systems, enhanced Passive ECCS system comprising two stages of hydro-accumulators (HA) have been provided. HA-1 system consists of 4 tanks each having 50 m^3 water inventory at 5.89 MPa pressure by nitrogen pressurization. HA-2 system consists of 8 tanks each having 120 m^3 of water inventory. During LOCA scenario when RCS pressure drops below 5.89 MPa HA-1 system starts adding water to RPV and HA-2 actuates when RCS pressure drops below 1.5 MPa [2].
Reactor core inside RPV consists of 163 hexagonal fuel assemblies. Apart from reactor core, other reactor internal components such as core barrel, core baffle and protective tube unit on top of core are made of steel. The schematic of RPV is shown in Figure-1.

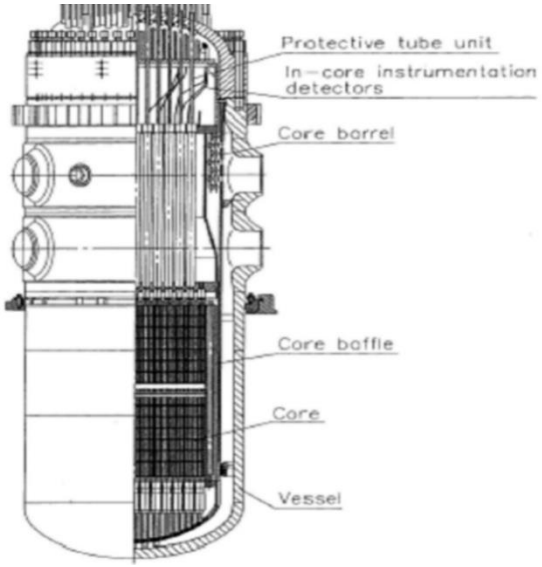

Figure 1. Schematic of RPV and its internals [3]

3. COMPUTER CODE CORVES AND VVER-PLANT MODEL

3.1. Modelling Assumptions:

The following assumptions are taken for simplification of the analysis:

- The clad and fuel is assumed to be lumped into a single structure.
- Surface area for oxidation has been assumed to be constant during core degradation phase.
- 1-D Radiation in the radial direction has been considered for heat transfer modelling in the core.
- The molten fuel node after complete melting is assumed to be instantaneously relocated on the top of the grid plate.

- If core water inventory is not emptied, the relocating molten fuel is assumed to be fully quenched before settling on top of the grid plate. The relocated debris/corium mixture is assumed to be uniformly distributed on top the grid plate.
- The stratification of the molten corium in the lower plenum of RPV has been assumed instantaneously after the complete re-melting of the debris in the lower plenum.
- Temperature based failure criterion (1500 K) has been assumed for the failure of RPV and grid plate.
- Major decay heat is assumed to be in the oxidic phase and the remaining decay heat is to be released in the metallic phase in the stratified molten pool.
- The outer boundary of RPV has been assumed as insulated.

3.2. Geometric Modelling:

For modelling of in-vessel degradation phase, following components have been modelled [Figure -2]:

- Reactor core:

The reactor core has been discretized into two radial zones with 100 and 63 Fuel assemblies (FA) located at inner radial zone and outer radial zone respectively. In each radial zone fuel rod is discretized into 20 axial nodes.

- Baffle:

In the periphery of the core the baffle has been modelled as one dimensional vertical structure. The baffle structure is also discretized into 20 axial nodes.

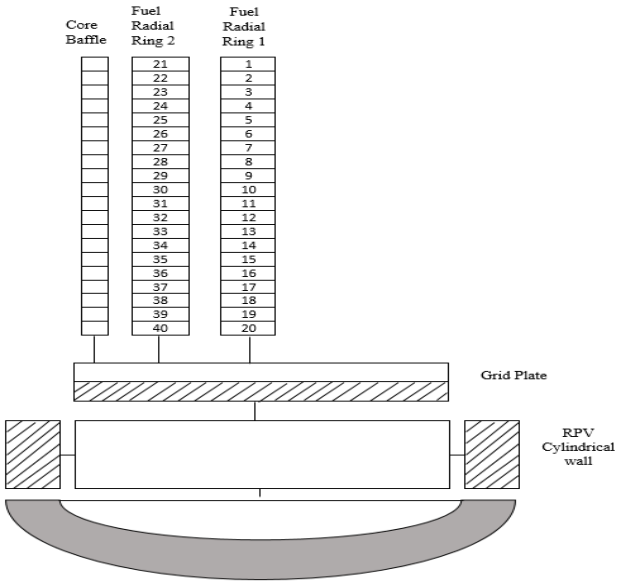

Figure 2. Reactor Core and RPV internals Model

- Grid plate:

At the bottom of the core, all the mass of grid plate, bottom portion of core barrel and its associated components has been lumped into an equivalent horizontal plate-type structure.

- Lower Plenum

Corium/debris in the lower plenum has been considered as a single volume before stratification. After stratification two different volumes (metallic and oxidic layer) has been considered.

- Cylindrical section of the RPV wall

Cylindrical section of RPV wall has been as a single volume.

3.3. Physical modelling:

The modelling of in-vessel phase has been divided in to following sub-modules in accordance with the anticipated accident progression:

- Uncovery of fuel
- Heat-up of fuel
- Oxidation of clad and hydrogen generation
- Heat transfer between debris and grid plate and grid plate failure
- Heat transfer in lower plenum molten pool and RPV failure

Core uncovery rate due to decay heat as well due to evaporation during falling of debris in core water pool has been modelled. Temperature change of any fuel node after uncovering is calculated taking into account decay heat of that node, reaction heat due to Zr oxidation and heat removal through radiation mode. Clad oxidation with steam is modelled with Parabolic correlation with rate constant described by Arrhenius' equation. Molten corium relocated on top of the grid plate is lumped into a single volume. Before melting of debris is started, conductive heat transfer between debris and grid plate has been considered. Once melting begins, convective heat transfer mode is activated. After the failure of grid plate the molten corium/debris relocates to lower plenum of RPV and the remaining water inventory in the lower plenum boils-off leading to partial solidification of the corium. Further re-melting of solidified debris has been modelled. Once the melting fraction of the corium becomes one, the molten corium pool is considered to be stratified into two layers; metallic layer on top and oxidic phase at the bottom layer. Subsequently, the temperature increase of the cylindrical section of RPV wall due to heat transfer from the adjacent metallic layer (focusing effect) is estimated until the temperature based RPV failure criteria is reached.

4. RESULTS AND DISCUSSIONS

Initial thermal-hydraulic calculations until core heat –up post HA-2 emptying have been analysed by RELAP5/SCDAP code. To maintain continuity with the RELAP5/SCDAP calculations, end-state parameters (void fraction, density of core coolant and fuel temperatures) obtained from RELAP5/ SCDAP calculation have been used as initial conditions for core degradation analysis by CORVES code. Chronology of events like beginning of oxidation, molten pool formation in the core, first material slump in the lower plenum and lower head of RPV failure is tabulated in Table I.

Table 1. Sequence of events

Time (sec /hours)	Event	Remarks
0/0	Initiation of event LOCA and SBO	
86400.0/24.0	Termination of borated water supply from HA-2	Exhaust of borated water inventory in HA-2
95000.0/26.4	Starting of fuel heat up	Impairment of heat removal
95975.0/26.7	Initiation of hydrogen generation in the core due to oxidation reactions	T> 1000 K
96354.0/26.8	Rupture of fuel rod claddings	T> 1473 K
96439.0/26.8	Initiation of fuel damage in the core	T> 2850 K
98907.0/27.5	Corium relocation to lower plenum	$T_{GRID\ PLATE}$> 1500 K
100857.0/28.0	Damage of reactor vessel and output of melt	T_{VESSEL}> 1500 K

Initiating event i.e. double ended guillotine rupture of cold leg along with SBO occurs at 0.0 second. After emptying of the hydro accumulators HA-2 in 24 hours (86400 sec), CORVES code calculation is started from 95000 sec. From 95000.0 sec the fuel rod temperature begins to rise as the reactor uncovery due to water boiling in the core takes place. as shown in Figure 3. When fuel element temperature crosses 1300 K due to higher oxidation rate, fuel temperature increases very sharply.

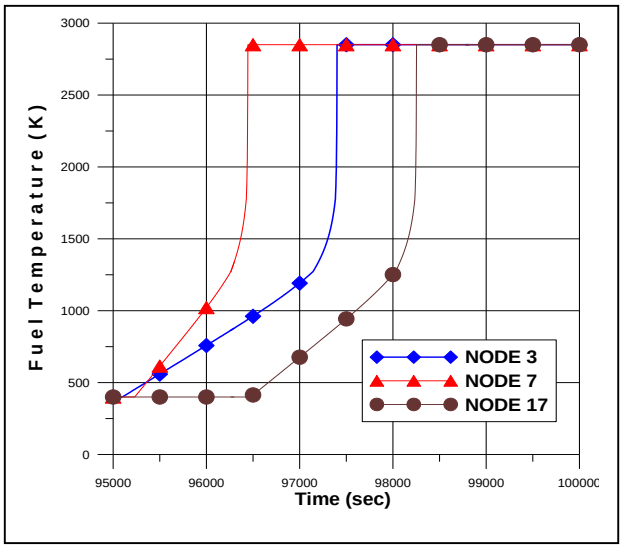

Figure 3. Temperature Field after Core Uncovery

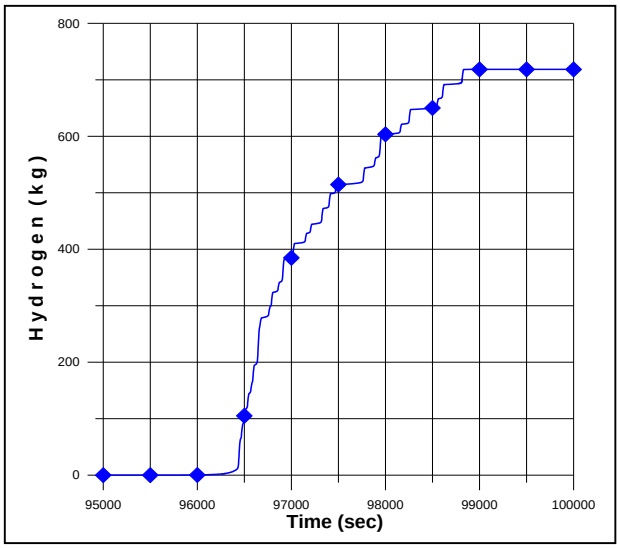

Figure 4. Cummulative Hydrogen Generation

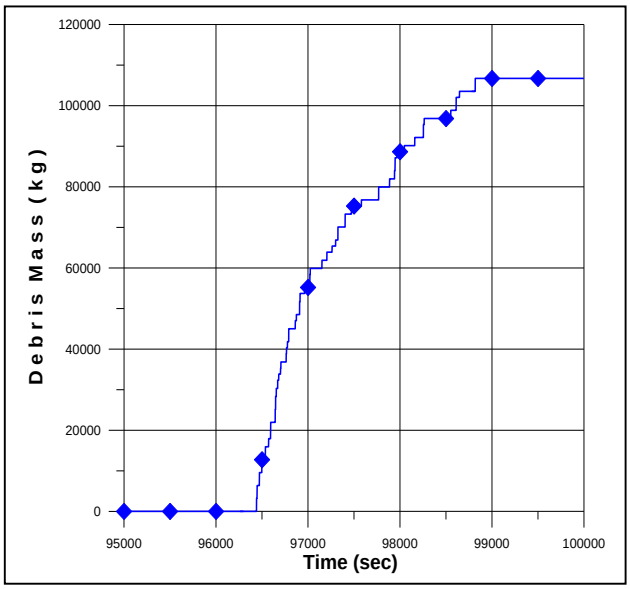

Figure 5. Debris Generation at lower plenum

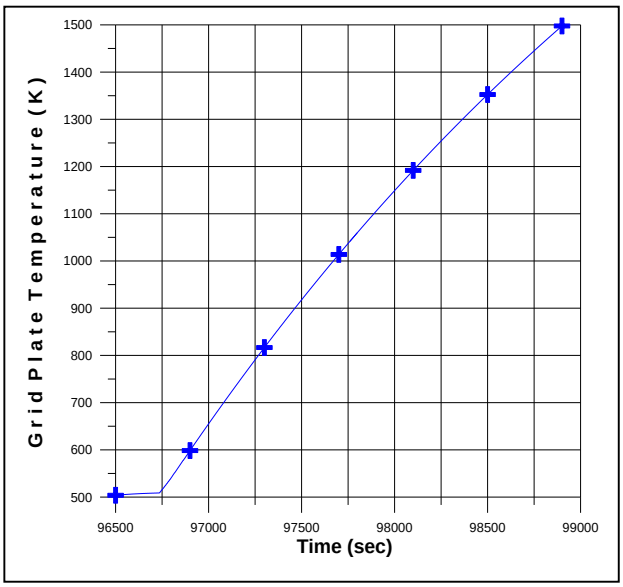

Figure 6. Grid Plate Temperature

Initiation of hydrogen release in the core corresponds to reaching the temperature 1000K and occurs in 95975.0 sec after onset of the accident as shown in Figure-4. As the clad surface gets oxidized, due to presence of oxidic layer diffusion of oxygen through clad surface becomes difficult and the hydrogen generation rate decreases.

About in 26.8 hours the fuel temperature reaches the value of 2850 K and melting of the core begins the generated corium moves downward and falls on to the bottom grid plate. Variation of debris mass during in-vessel phase with time is shown in Figure 5 and Figure 6 shows temperature variation of bottom grid plate. Once the bottom plate fails, the corium relocates to the lower plenum of Reactor pressure vessel. After corium components melt and mix, the corium pool becomes stratified. Heavy oxide fractions containing uranium and zirconium oxides settle down. Relatively lighter metal fractures with zirconium and steel float thus forming a top metal layer. It is assumed in the modelling that RPV failure takes place in its cylindrical part corresponding to the metal layer area due to focusing effect. The failure of RPV is predicted to occur 28.0 hours after the initiation of the accident and subsequently molten corium relocates into core catcher.

A scenario of early core melt (with taking credit of only HA-1) has been analysed and results were compared with ASTEC analysis of VVER-1000/320 reactor [4]. Overall the global progression of events are in good agreement.

5. CONCLUSION

An end-to-end analysis of in-vessel degradation sequence in VVER-1000 taking into account a range of physico-chemical phenomena has been performed for a representative severe accident sequence. Critical safety parameters viz. time for core uncovery & Fuel heatup, hydrogen generation, RPV failure time has been predicted by 'CORVES' code. Due to presence of second stage hydro-accumulator initiation of core degradation starts after 24 hours from the initiating event and RPV failure takes place after 4 hours from the emptying of second-stage hydro-accumulator. Results of this study provide analytical insight into the severe accident progression which is instrumental for development of Severe Accident Management Guidelines (SAMG).

REFERENCES

1. Safety Reports Series No. 56,2008, Approaches and Tools for Severe Accident Analysis for Nuclear Power Plants, International Atomic Energy Agency
2. Agrawal S.K. et al, "The VVERs at KudanKulam", *Nuclear Engineering and Design*, **236**, pp. 812-835 (2006)
3. Jafarikia S. et. al, "Contribution of Production and loss terms of fission products on in-containment activity under severe accident condition for VVER- 1000", *Nuclear Engineering and Technology,* **51**(1), pp 125-137 (2019)
4. Chatterjee B. et. al, "Analyses for VVER- 1000/320 reactor for spectrum of break sizes along with SBO", *Annals of Nuclear Energy*, **37**, pp 359-370(2010)

.

Development of Severe Accident Code ‘CORVES’ for Analysing In-Vessel Degradation Phase of Severe Accident in VVER-1000 Reactor

S. Sil*, P. Krishna Kumar, Y.K.Pandey

E-mail : ssil@npcil.co.in



10th European Review Meeting on Severe Accident Research (ERMSAR2022), May 16-19, 2022

Outline

- Salient Features of VVER-1000
- Passive Safety Systems of VVER-1000
- CORVES development
- Modelling Assumptions
- Geometrical Modelling
- Physical Modelling
- Results & Discussions
- Conclusion
- References

Salient Features of VVER-1000

- Rated Nuclear power: 3000 MW
- Four loop heat transport system
- Pressurizer system connected to hot leg of one loop
- No. of FAs in the core:163
- Shell and Tube Type Horizontal SGs

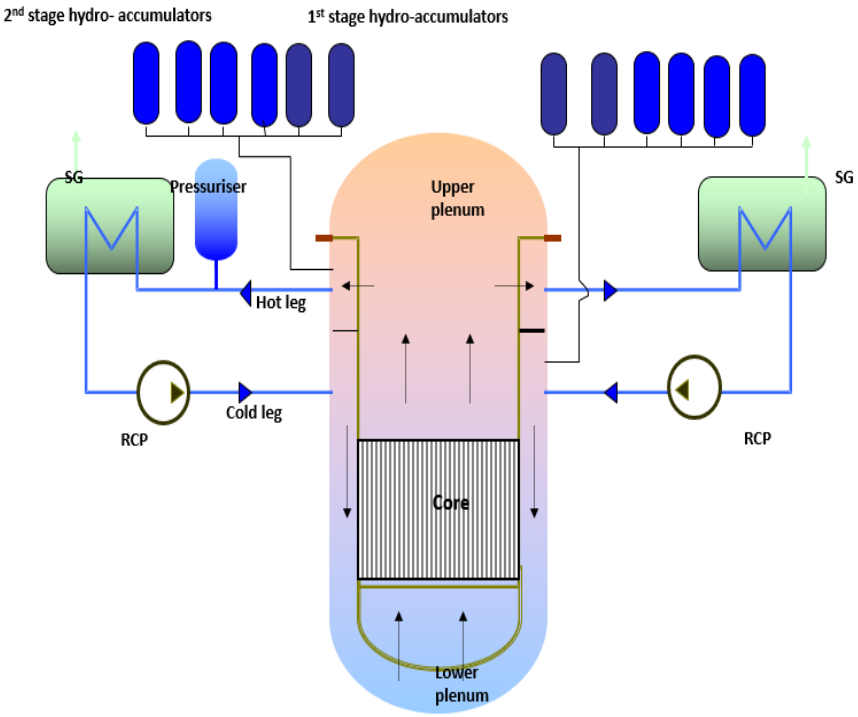

Salient Features of VVER-1000

- Reactor vessel is designed to contain the vessel internals and fuel assemblies of the core.
- RPV houses core barrel which is a cylindrical vessel with perforated elliptical bottom.
- Fuel assemblies are fixed in the specified locations at the bottom of the core barrel.
- Core Baffle placed on the periphery of the core acts as shield for neutron flux and protects RPV

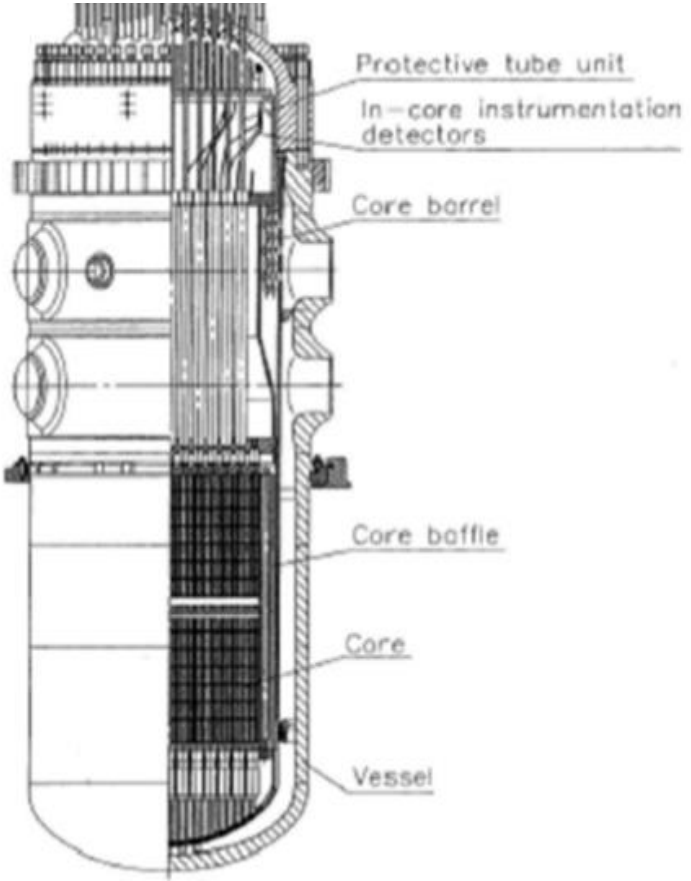

Passive Safety Systems of VVER-1000

Apart from active safety systems following important passive safety systems exist:

- High pressure passive ECCS system (HA-1)
- Low pressure passive ECCS system (HA-2)
- Passive Heat Removal System
- Core Catcher
- Passive Catalytic Hydrogen Re-combiners

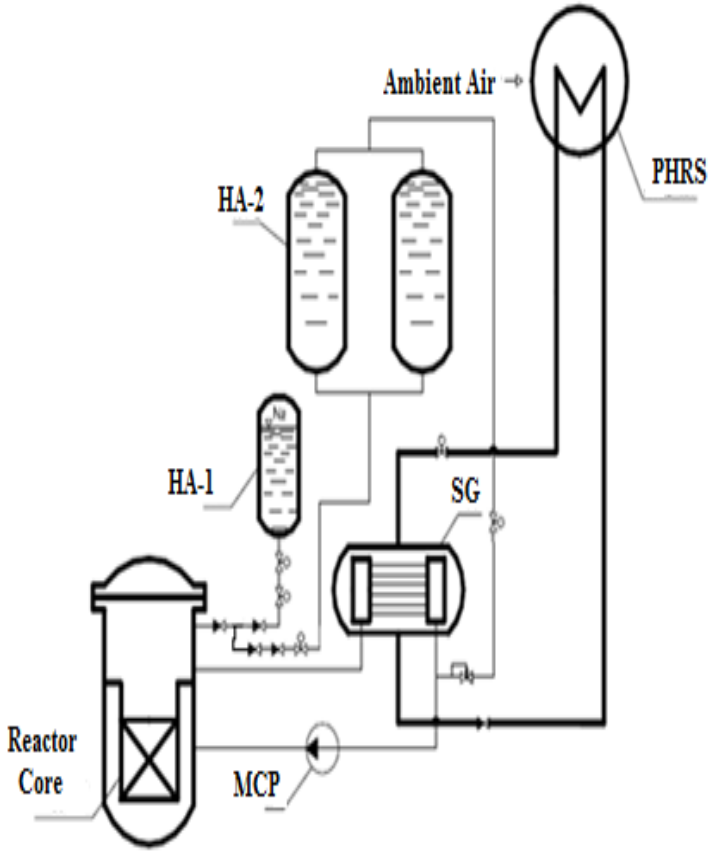

Passive Safety Systems of VVER-1000

1st Stage Hydro-accumulator

- Passive injection of water directly into the core when primary pressure drops below set point
- Four hydro accumulators kept pressurized to with Nitrogen
- Injections from passive accumulator are from both top & bottom of the core and inject directly to RPV (Combined Top and Bottom Flooding)

2nd Stage Hydro-accumulator

- Supplies Borated water into the core and Maintains the inventory in the core for 24 hrs with HP accumulators along with PHRS
- Combined Top and Bottom Flooding
- Designed Flow Profiling done in such a way to match decay heat removal

Passive Safety Systems of VVER-1000

System ensures long-term removal of reactor core decay heat in absence of all power supplies

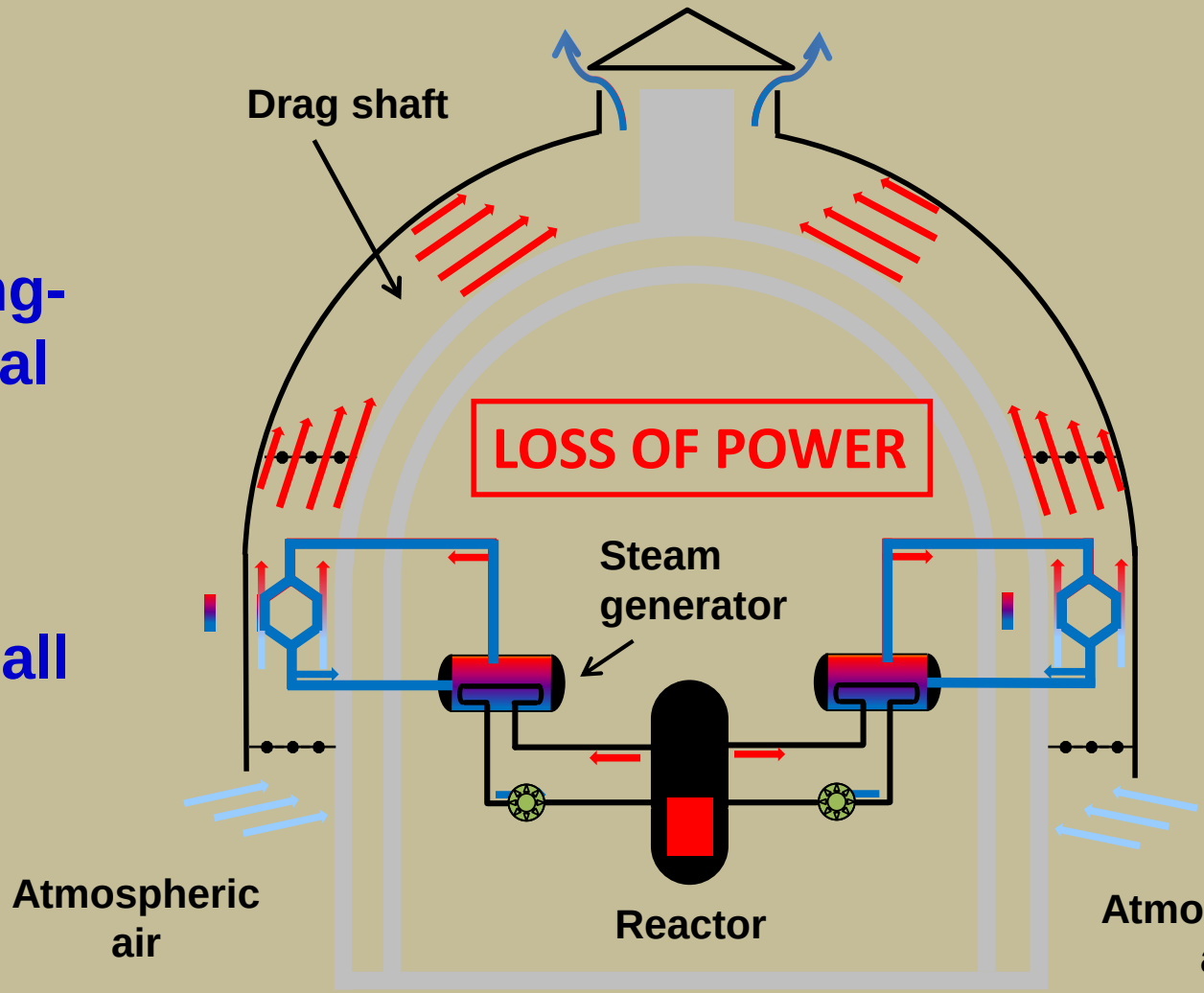

Passive Safety Systems of VVER-1000

Passive Heat Removal System (PHRS

- Removes core residual heat due to non-availability of normal heat removal system during Station Blackout (SBO)
- Four independent cooling circuits
- Steam from SG is continuously passing through PHRS HX
- Together with 2nd stage hydro accumulators remove decay heat under LOCA+ SBO

Severe Accident Scenario in VVER-1000

- Severe accident partial/complete core melting occurring due to multiple failures of safety systems

- In-vessel phase : Initiating event to core degradation until RPV failure

- Ex-Vessel phase: Corium relocation into core catcher and interaction with sacrificial material

‘CORVES’ Code Development

- In-house Computer Code development for Severe Accident analysis for end-to-end analysis
- ‘**CORVES’ code** for modelling degradation of reactor core and other internal components during **in-vessel phase** of PWR
- Prediction of critical safety parameters: Hydrogen generation, RPV failure time
- Capable of analysing in-vessel phase of core melt scenario occurring from any type of initiating events

Modelling Assumptions

➢ **Core Region:**

- The clad and fuel lumped into a single structure.
- The molten fuel node after complete melting is assumed to be instantaneously relocated on the top of the grid plate.

➢ **Lower Plenum Region:**

- The stratification of the molten corium in the lower plenum of RPV has been assumed instantaneously after the complete re-melting of the debris in the lower plenum.
- Major decay heat is assumed to be in the oxidic phase and the remaining decay heat is to be released in the metallic phase of molten pool.
- Temperature based failure criterion (1500 K) has been assumed for the failure of RPV and grid plate.

Geometrical Modelling

- **Reactor core:**
  - Radial discretization : Two Radial Zones
  - Axial discretization : 20 Axial Nodes
- **Baffle:**
  - One-dimensional Vertical structure
- **Grid plate:**
  - Core Bottom plate, lower elliptical section of core barrel and associated structure
  - Horizontal Plate-type structure
- **Lower Plenum**
  - Single volume before stratification
  - Two stratified layer: Top Metallic layer and bottom oxide layer
- **Cylindrical section of the RPV wall**

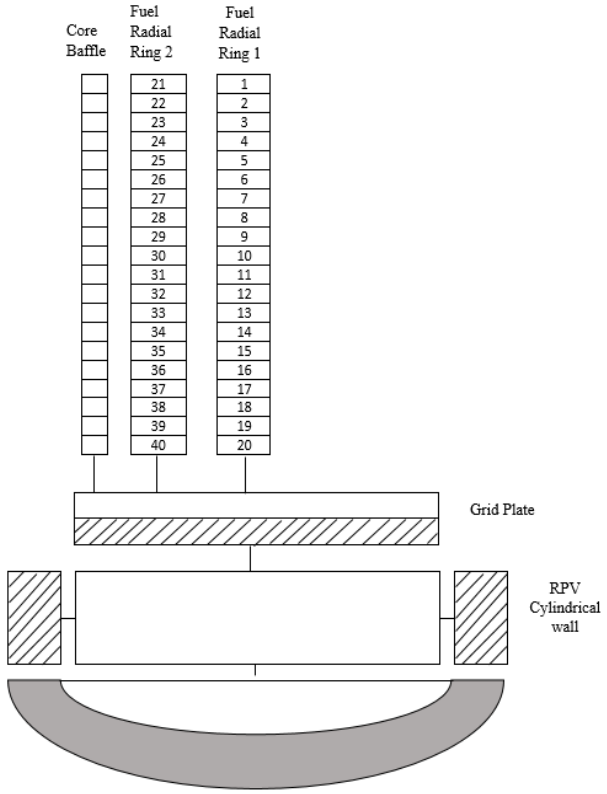

Reactor Core and RPV internals Model

Physical Modelling

- **Uncovery of fuel**
  - Decay heat as well due to evaporation during falling of debris in core water pool
- **Heat-up of fuel**
  - Decay Heat + Reaction Heat
- **Oxidation of clad and hydrogen generation**
  - Parabolic correlation
  - Different rate constant for different temperature regime
- **Heat transfer between debris and grid plate and grid plate failure**
  - Conductive heat transfer before debris melting starts
  - Convective heat transfer after debris melting
- **Heat transfer in lower plenum molten pool and RPV failure**
  - Debris remelting
  - Natural convection in molten pool
  - Focussing effect

Analysed Scenario

- Representative core melt scenario of VVER-1000
- Large Break Loss of Coolant Accident (LB-LOCA) along with extended Station Black Out (ESBO)
- Core heat-up starts after 24 hours due to HA-2 emptying
- Subsequently core degradation and later RPV failure takes place

Initial and Boundary conditions

- Calculation by ‘CORVES’ code starts after Initial thermal-hydraulic calculations by RELAP5/SCDAP code
- RELAP5/SCDAP analysis spans from initiating event until core heat–up post HA-2 emptying
- Initial conditions for ‘CORVES’ analysis extracted from RELAP analysis end-state (void fraction, density of core coolant and fuel temperatures)
- Adiabatic boundary condition applied at RPV outer wall

Results and Discussions

Time (hours)	Event	Remarks
0	Initiation of event LOCA and SBO	
24.0	Termination of borated water supply from HA-2	Exhaust of borated water inventory in HA-2
26.4	Starting of fuel heat up	Impairment of heat removal
26.7	Initiation of hydrogen generation in the core due to oxidation reactions	T> 1000 K
26.8	Initiation of fuel damage in the core	T> 2850 K
27.5	Corium relocation to lower plenum	$T_{GRID\ PLATE}$> 1500 K
28.0	**Damage of reactor vessel and melt discharge**	**T_{VESSEL}> 1500 K**

Results and Discussions

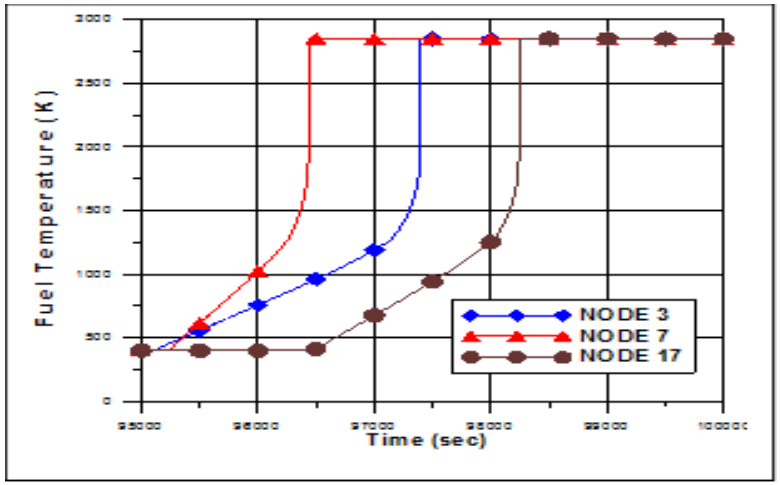

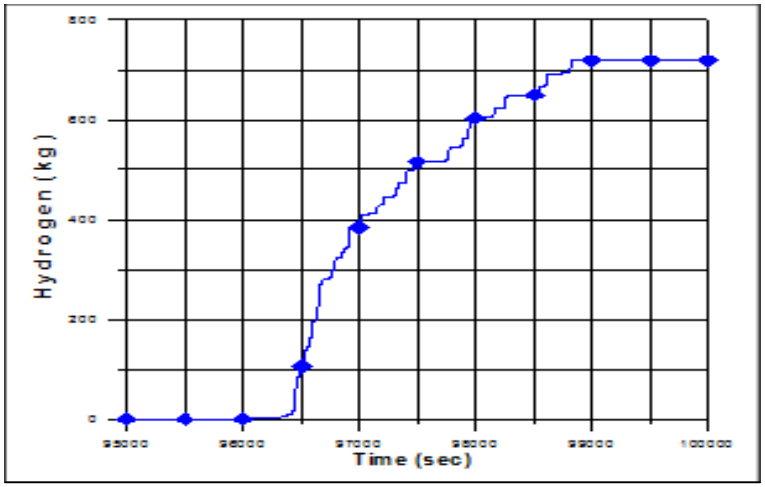

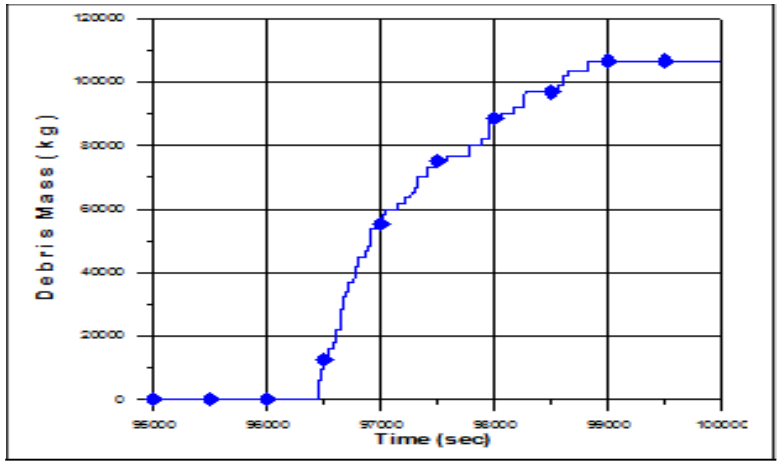

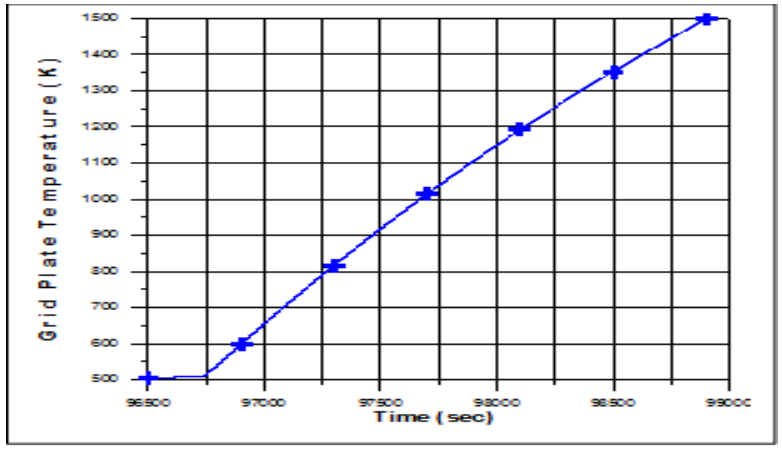

Conclusion

- End-to-end analysis of in-vessel degradation sequence in VVER-1000 taking into account a range of physico-chemical phenomena
- Estimation of Critical safety parameters: time for core uncovery & Fuel heatup, hydrogen generation, RPV failure time
- RPV failure takes place after 4 hours from the emptying of second-stage hydro-accumulator
- Analytical insight into the severe accident progression

References

1. Safety Reports Series No. 56,2008, Approaches and Tools for Severe Accident Analysis for Nuclear Power Plants, International Atomic Energy Agency

2. Agrawal S.K. et al, “The VVERs at KudanKulam”, Nuclear Engineering and Design, 236, pp. 812-835 (2006)

3. Jafarikia S. et. al, “Contribution of Production and loss terms of fission products on in-containment activity under severe accident condition for VVER- 1000”, Nuclear Engineering and Technology, 51(1), pp 125-137 (2019)

4. Chatterjee B. et. al, “Analyses for VVER- 1000/320 reactor for spectrum of break sizes along with SBO”, Annals of Nuclear Energy, 37, pp 359-370(2010)

NPCIL: Working towards green Future

Thank You



MODELING OF FISSION PRODUCT RELEASE DURING SEVERE ACCIDENTS: OVERVIEW OF RECENT DEVELOPMENTS IN THE FUEL PERFORMANCE CODE ALCYONE

J. Sercombe*, A. Germain, C. Riglet-Martial, C. Introïni, L. Noirot, Y. Pontillon
CEA, IRESNE/DEC
13108 Saint-Paul-lez-Durance, France
jerome.sercombe@cea.fr

ABSTRACT

ALCYONE fuel performance code co-developed by CEA-EDF-FRAMATOME within the PLEIADES computational environment, originally devoted to nominal irradiation conditions only, has been extended in the past years to accidental conditions (LOCA, RIA…). Following a previous work done on Pellet Cladding Interaction (PCI) where irradiated fuel thermochemistry and fission gas release have been coupled in ALCYONE, the coupling scheme has been adapted to Severe Accident (SA) conditions. The Thermodynamic Data Base (TDB) used for nominal irradiation conditions (called TBASE, adapted from the SGPS-SGTE database with a simplified solid solution model for the U-O-Pu-FP system) has been extended to include the compounds likely to form during the oxidizing conditions at hold during a SA. To test the coupling, a specific fission gas release model, where all the gases formed during a typical sequence are assumed to be released at the same rate, has been coupled to the thermochemical equilibrium calculations. The coupling has been checked by comparing the simulation results to on-line measures of FP release (Xe, I, Te, Cs, Mo and Ba) during the VERCORS 4/5, RT6 and VERDON 1 tests. The sensitivity to external conditions ($He/H_2O/H_2$ content in the furnace) and fuel-clad interactions has been assessed, confirming the predominance of thermochemistry on the release of semi-volatile FPs (Mo and Ba). The versatility of the coupling has been checked by using a more complex TDB in the simulations, i.e., the Thermodynamics of Advanced Fuels - International Database (TAF-ID). Release of low- and non-volatile FPs, fuel-clad melting have been successfully investigated.

KEYWORDS
Severe Accident, Source Term Quantification, modeling, VERCORS/VERDON, fuel performance code

1. INTRODUCTION

During a Severe Accident (SA), Fission Product (FP) release can occur with potential environmental consequences. It is therefore of primary importance to well understand the phenomena behind FP release. Experimental programs have been launched worldwide to study and quantify FP release during SAs. Among them, separate-effect tests were performed at the CEA in 2 different programs: VERCORS [1] and VERDON [2]. These tests were launched to study the impact of several parameters on FP release: burnup of the fuel, geometry of the fuel fragments, oxidizing/reducing atmosphere... The comparison of annealing tests with similar temperatures and atmospheric conditions but performed on medium (~38 GWd/tU) and high burnup fuel samples (~72 GWd/tU) showed the acceleration with burnup of the FP release kinetics.

* Corresponding author

SA codes generally consider the fuel pellet as a single entity characterized by an average burnup and FP content [3]. While this hypothesis is convenient to reduce the computational time, it is far from the fuel state after irradiation in a commercial Pressurized Water Reactor (PWR). Due to the build-up of Pu at the fuel pellet rim, the fission rate increases at the pellet periphery leading to much higher quantities of FPs and burnup in this region as irradiation proceeds. The development of the High Burnup Structure (HBS) at the pellet rim with a specific microstructure and an increased potential for fission gas release is one of the consequences of this non-uniform irradiation [4]. The strong radial temperature gradient at hold during nominal irradiation is another reason for the pronounced inhomogeneity of the fuel samples. These aspects are taken into account in more or less details in fuel performance codes but they are generally not considered in SA simulations. In recent years, some tentative coupling between the fuel performance code TRANSURANUS and the thermochemical - gas diffusion code MFPR [5] have been presented in this aim [6].

In this paper, the coupling between thermochemical equilibrium calculations and fission gas release already implemented in the fuel performance code ALCYONE [7] is extended to SAs. After a brief presentation of ALCYONE, the Thermodynamic DataBases (TDB) available and the burnup dependent Fission Gas Release (FGR) model developed for SAs are described. Simulations of four tests (VERCORS 4 and 5, RT6 and VERDON 1) performed on two fuel rods pre-irradiated in commercial reactors are then proposed. Comparison of volatile, semi-, low- and non-volatile FP releases with measurements are used to assess the quality of the TDBs in the simulations. The fuel rod melting temperatures during the RT6 and VERDON 1 tests are also estimated and compared to the measured fuel "collapse" temperatures.

2. ALCYONE FUEL PERFORMANCE CODE

ALCYONE is a fuel performance code co-developed by the CEA, EDF and FRAMATOME within the PLEIADES computational environment. Multi-dimensional modeling (1.5D, 2D, 3D) of a fuel rod in normal and accidental conditions (Reactivity Initiated Accident, Loss of Coolant Accident) is available in the code [8]. In this work, only the 1.5D calculation scheme is considered. As illustrated in Figure 1, the fuel rod is discretized axially in slices and radially in annular rings.

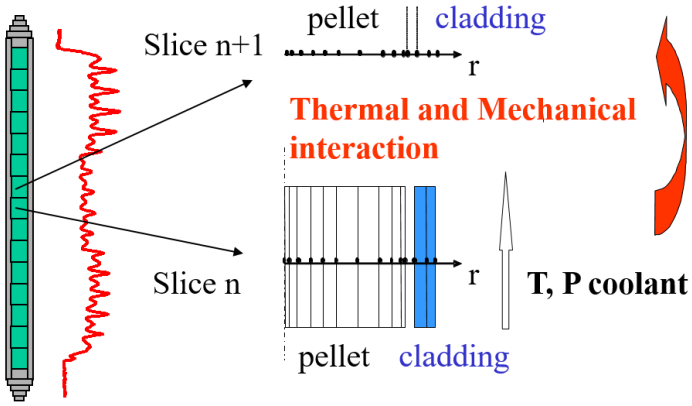

Figure 1. Typical fuel rod discretization in the 1.5D scheme of ALCYONE.

A typical ALCYONE simulation of the fuel rod behavior during nominal irradiation relies on the 4 main following solvers:

- a thermo-mechanical solver to assess the stresses and the temperatures within the fuel pellet and the cladding rings,

- a neutronic-based solver to estimate the U and Pu fission-related power deposition within the fuel pellet rings as well as the local FP content,
- a fission gas solver to assess the Fission Gas Release (FGR) as well as the fuel swelling caused by FPs (including only the noble gases, i.e., Xe and Kr) within the fuel pellet rings,
- a thermochemical solver to estimate the compounds (composition and nature) formed by reaction between the FPs, actinides and oxygen within the fuel pellet rings.

The thermo-mechanical solver is based on the Finite Element (FE) code CAST3M and provides the solution of the thermal heat balance equation and of the mechanical equilibrium equation for the fuel-clad system at hand with potential contact between the pellet and the cladding. Thermo-mechanical iterations are performed until convergence is reached on a number of criteria related to temperature, stress, fuel-pellet gap and fuel swelling. More details can be found in reference [9].

The neutronic solver is called PRODHEL. The elements taken into account are: U, Pu, Am, Cm, Np, Xe, Kr, Cs, Rb, I, Br, Te, Se, Mo, Tc, Ru, Rh, Pd, Sr, Ba, Y, La, Nd, Pm, Eu, Gd, Ce, Pr, Nb and Zr. Overall, 199 isotopes of the FPs as well as 23 isotopes of the actinides are considered. The depletion and/or generation by radioactive decay and neutronic reactions of these isotopes is precisely assessed during the time spent by the fuel rod in the reactor. The database used for neutronic calculations is JEFF 3.1.1 [10].

A mechanistic fission gas solver is available in ALCYONE, named MARGARET [11]. It provides a detailed description of the state of noble gases (Xe, Kr) in each fuel rings, whether dissolved in the fuel grains, in bubbles/pores in the grains or at the grain boundaries, or released in the free volume of the rod. The formation of the High Burnup Structure (HBS) is also described. Coupled calculations of fuel swelling related to bubble nucleation and growth are provided.

The OPENCALPHAD thermochemical solver has been implemented in ALCYONE [12] to provide in each fuel ring an estimation of the state (gaseous, solid, liquid) and composition of the compounds likely to form by chemical interactions between actinides, FPs and oxygen. The TDBs used with this solver are the TBASE and the TAF-ID, as detailed in section 3. To reduce the chemical system, the FPs and actinides considered in the thermochemical calculations are grouped in 14 or 18 representative elements, depending on the TDB. In the case of the TBASE, the following representative elements are used: inert fission gases (Xe for Xe+Kr+He), volatile FPs (I for I+Br, Te for Te+Se+Ag+As, Cs for Cs+Rb), stable oxides (Ba for Ba+Sr, Zr for Zr+Nb), metallic FPs (Ru for Ru+Tc+Rh, Pd for Pd+Sn+Sb), Mo, FPs and actinides in solid solution in UO_2 (Ce for Ce+Pr, Eu for Eu+Sm, La for La+Y, Gd for Gd+Nd+Pm, Pu for Pu+Np+Am+Cm).

As illustrated by the scheme of Figure 2, a simulation with ALCYONE includes several interactions between the solvers that rely on each other for the initialization of input variables. Among the interactions of interest for this paper, it may be noticed that the initialization of thermochemical calculations (OPENCALPHAD) requires information from the neutronic solver PRODHEL (quantities of actinides and FPs) and from the thermomechanical solver CAST3M (temperature and mechanical pressure). OPENCALPHAD provides the composition of the chemical system at equilibrium in the fuel (gas phase, condensed phases, FPs dissolved in the uranium oxide matrix called solid solution in Figure 2). Evaluation of the FP release in each ring requires information (noble gas percolation flux) from the fission gas solver (MARGARET) and from thermochemistry (composition of the chemical system). Up to now, this scheme has been mostly used to study Pellet Cladding Interaction (PCI) failure of fuel rods during power ramps in experimental reactors [7][9] following irradiation in commercial reactors (base irradiation). In practice, ALCYONE simulations are therefore performed in two steps: first, the base irradiation of the fuel rod is assessed, second, the power ramp on part of the rod is simulated.

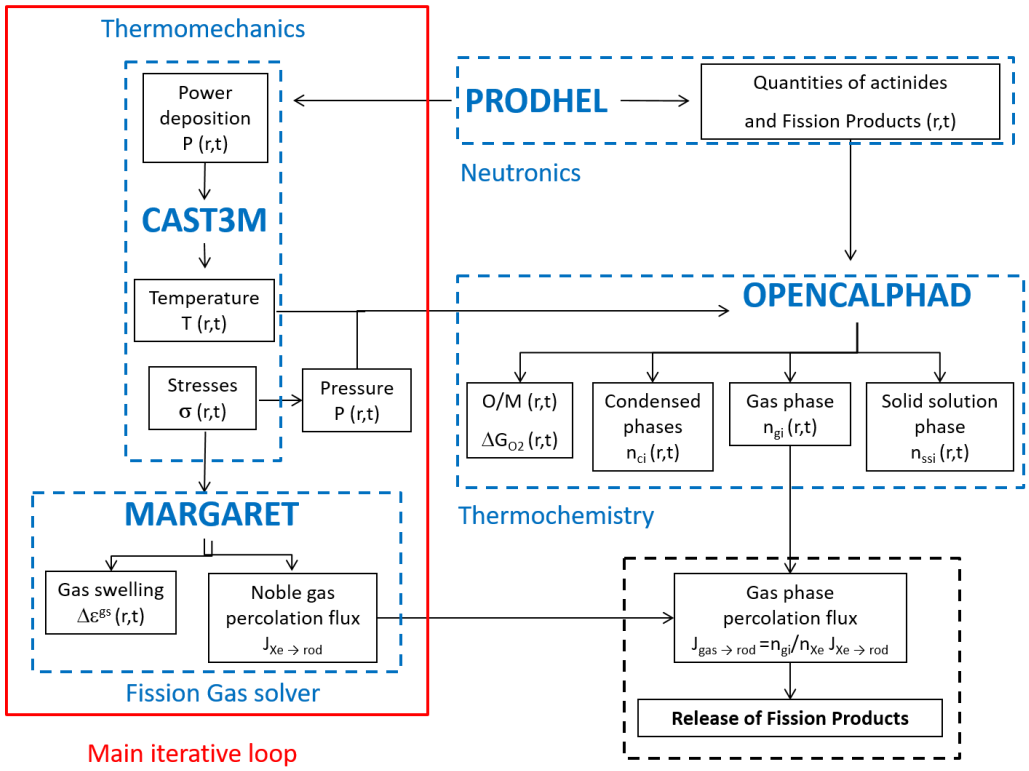

Figure 2. Schematic representation of the interactions in ALCYONE between the thermomechanical (CAST3M), neutronic (PRODHEL), Fission Gas (MARGARET), and thermochemical (OPENCALPHAD) solvers. (r,t) refer to the radial position of a ring and to a given time during the simulated irradiation sequence.

3. FUEL THERMOCHEMISTRY

The first TDB available in ALCYONE is called TBASE and was originally developed for nominal irradiation conditions. It has been extended for SA simulations since the formation of new compounds from the reaction with the carrier gas (He, H_2O, H_2, O_2...) is expected during SA simulations [13]. Validation of the thermochemical calculations on irradiated fuel with the updated TBASE and the OPENCALPHAD solver is based on cross-comparisons of results with similar calculations performed with the SGPS-SGTE TDB included in the FACTSAGE solver [14]. To improve the thermodynamic description of the Cs-Mo-Ba system in irradiated fuel, new compounds ($Cs_2Mo_2O_{7(s,l,g)}$ from experimental data recently published [15] and $ZrO_{2(ss)}$ from the Thermodynamics of Advanced Fuel – International Database [16] with (s) for solid, (l) for liquid, (g) for gas and (ss) for solid solution) have also been added, as detailed in reference [13]. The modeling of oxidation/reduction of the fuel that takes place during severe accidents relies on a solid solution model for the uranium, plutonium and dissolved FPs (mostly rare earth) already included in the TBASE. A thorough validation of the solid solution model on the U-O, U-Pu-O, U-Gd-O, U-La-O, U-Ce-O, U-Eu-O, U-Zr-O systems, on SIMFUELS (Simulated high-burnup nuclear fuel) and on irradiated fuels by comparing the calculated and measured fuel oxygen potential (i.e., RT ln p_{O2} with R the gas constant, T, the temperature and p_{O2} the oxygen partial pressure) is detailed in reference [17]. The assessment of the oxygen partial pressure in the fuel is essential to capture the chemical speciation of FPs during the VERCORS test sequences, as discussed in reference [18]. The TBASE is well suited for the simulation of volatile and semi-volatile FP release during SAs but does not describe fuel-clad melting at high temperatures.

To assess fuel-clad melting during SAs, thermochemical calculations in ALCYONE can be performed with the TAF-ID [16] where the liquid phases likely to appear at high temperatures are described. The thermodynamic modeling of oxide fuels in the TAF-ID rests largely on the description of the fluorite $(U,Pu)O_2$ phase from reference [19], where, apart from major and minor actinides, FPs may also occupy the cation sites, both at hypo- and hyperstoichiometric oxygen conditions. The liquid phases are described using the partially ionic two sublattice liquid model. The first sublattice is occupied by cations, and the second by anions, "hypothetical vacancies" and neutral species. This allows for both purely metallic and ionic liquids to be simulated by the same model. In the TAF-ID V8, 206 binary and 72 ternary sub-systems are assessed. The ternary sub-systems of interest for this work are: Ba-Mo-O, Ba-O-U, Ba-O-Zr, Ce-O-U, Cs-Mo-O, Cs-O-U, Cs-O-Zr, Gd-O-U, La-O-U, Mo-O-U, Mo-Pd-Rh, Mo-Pd-Ru, Mo-Rh-Ru, Nd-O-U, O-Pu-U, O-Pu-Zr, O-Sr-U, O-Sr-Zr, O-U-Zr, Pd-Rh-Ru, Pu-U-Zr. An extended description of the TAF-ID is given in reference [16]. The models behind the description of the U-O system in the TAF-ID include the solidus and liquidus temperatures measured by Manara [20]. The U-O phase diagram in the stoichiometric region of interest is plotted in Figure 3. The UO_2-ZrO_2 phase diagram from the TAF-ID reproduced in the same Figure shows the formation and melting of a UO_2-ZrO_2 eutectic at a temperature around 2500 °C, as expected from the known behavior of the system.

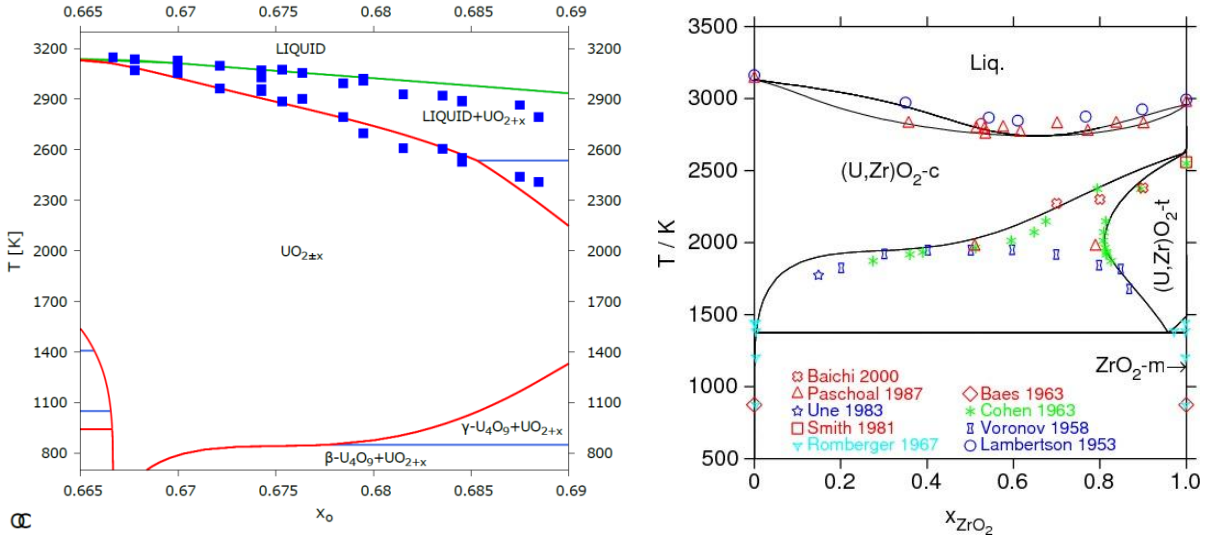

Figure 3. Left graph: U-O phase diagram as calculated with the TAF-ID and OC and experimental measurements of solidus and liquidus temperatures [20]. Right graph: UO_2-ZrO_2 phase diagram as calculated with the TAF-ID and experimental measures (reproduced from [21]).

4. FISSION PRODUCT RELEASE

As of today, the fission gas model available in ALCYONE (MARGARET) is not adapted to the conditions prevailing during SAs (uniform temperature in the fuel). In fact, it has been developed for normal irradiation conditions where the strong temperature gradient in the fuel pellet triggers the gas bubble transport from intragranular position to intergranular position. Negligible FGR is obtained in the case of a uniform temperature in the fuel. For this reason, a specific fission gas model has been implemented in ALCYONE for SAs. It describes the diffusion of all fission gases (noble gases and those formed from the chemical reactions between the other FPs) within an equivalent spherical fuel grain of radius a, according to the following equation:

$$\frac{\partial C}{\partial t} = \frac{1}{r^2}\frac{\partial}{\partial r}\left[Dr^2\frac{\partial C}{\partial r}\right] + \frac{\partial S_{FP}}{\partial t} \quad (1)$$

where C (mole/m^3) is the fission gas concentration, D (m^2/s) the effective diffusion coefficient and r the radial position in the equivalent sphere (m). The novelty in this model resides in the term $\partial S_{FP}/\partial t$ added to take into account the gases formed by reaction between the FPs, as calculated by OPENCALPHAD. During an annealing test, as bubbles form inside the grains and as there is no resolution by fission spikes, all the gases rapidly get trapped into the bubbles. So the gas transport within the grains is strongly believed to occur through intragranular bubble transport [22]. A unique gas transport mechanism (applied to the gases as a whole) is thus believed to be sufficient to describe the release of both noble and chemically reactive FP gases together. See reference [13] for an experimental justification of this hypothesis. The boundary condition is C(r=a, t) = 0 which is equivalent to an instantaneous release when gases reach the surface of the grain. The effective diffusion coefficient can be expressed as follows:

$$D(T) = D_0 \times e^{-\frac{Q}{RT}} \quad (2)$$

where D_0 (m^2/s) is a constant parameter, Q (J/mol) the activation energy, R (J/mol/K) the universal gas constant and T (K) the temperature. In previous works on the VERCORS/VERDON tests [13][23], the fit of the measured release rate curves of ^{133}Xe has led to the following parameters: Q = 188 kJ/mol, $D_0 = 1.09\ 10^{-11}$ m^2/s for a fuel sample of average burnup 38 GWd/tU, $D_0 = 2.17\ 10^{-10}$ m^2/s for a fuel sample of average burnup 72 GWd/tU. It must be emphasized that the impact of temperature, that present strong variations during the tests, was found to be reasonably well assessed with an activation energy of 188 kJ/mol, irrespective of the burnup. The impact of the burnup appears to be strong (factor 20 on D_0 when the burnup is approximately doubled) and cannot obviously be neglected in an ALCYONE simulation where a strong radial burnup gradient holds along the radius of the pellet. From a computational point of view, a simple and efficient way to account for the burnup dependency is to consider D_0 as a function of burnup. Using the D_0 identified previously from the ^{133}Xe release rate curves of the VERCORS/VERDON tests, and assuming that the Fission Gas Release versus burnup relation can be described by a quadratic function (with FGR=0 at 0 GWd/tU), the following function for D_0 has been identified:

$$D_0(\tau) = 3.61\ 10^{-9}(3.884\ 10^{-5}\tau^2 + 3.435\ 10^{-4}\tau\ )^2 \quad (3)$$

with τ the burnup (GWd/tU) and a the grain radius (m). The proposed function has been checked by comparing the calculated FGRs to measurements made during the GASPARD annealing test series on pre-irradiated fuels with average burnups between 48 and 103 GWd/tU [24].

During the simulation of the SA sequence, equation 1 is solved at each time step and in each pellet ring by the finite volume method, leading to an estimation of the gas flux J (in mole/m^2/s) at the grain boundary:

$$J = -D\left.\frac{\partial C}{\partial r}\right|_{r=a} \quad (4)$$

The release rate RR (in mole/s) at each time step of a FP indexed i is obtained from the following expression:

$$RR(FP_i) = \frac{\int_S JdS}{\int_V CdV}\int_V c_{FPi}dV \quad (5)$$

where $\int_V c_{FPi}dV$ (in mole) is the content of the i-th FP in the gas phase in the grain (from thermochemistry), $\int_V CdV$ is the total gas content in the grain (in mole), V the grain volume (in m^3) and S the surface of the grain (in m^2). As an alternative to solving equation 1, and since noble gases represent the bulk of the gas phase, the measured Xe release rate can be used to define the release rate $\int_S JdS$. More details on the fission gas release model are given in reference [24].

5. MODELING OF THE VERCORS/VERDON TESTS

The simulated VERCORS and VERDON tests are here briefly described. Four tests are considered to investigate the impact of fuel burnup on FP release. Two were performed on samples (3 pellet long) taken from the same fuel rod irradiated up to an average burnup of 38 GWd/tU [1] (VERCORS 4 and 5). The two others used similar samples (2 or 3 pellet long) taken from a fuel rod irradiated up to an average burnup of 72 GWd/tU (VERCORS RT6 [1] and VERDON 1 [2]).

The experimental sequence was very similar in the four tests. A first temperature plateau was performed at around 400 - 500 °C under an He flow. The temperature was then increased until reaching 1250 - 1300 °C (VERCORS 4 and 5) or 1500 °C (VERDON 1 and VERCORS RT6) under an oxidizing atmosphere (high H_2O flow rate). These conditions were maintained during 60 to 75 minutes depending on the test. This step aimed at fully oxidizing the cladding. After the oxidizing plateau, one or several temperature ramps were applied with one or more plateaus at intermediate levels. Two different conditions were used. During the VERCORS 4 and VERDON 1 tests, the carrier gas composition (H_2/He) ensured that reducing conditions hold in the furnace. During the VERCORS 5 and RT6 tests, the carrier gas consisted of water vapor (H_2O) with a small amount of hydrogen (H_2) in order to ensure oxidizing conditions in the furnace.

Before simulating the VERCORS/VERDON tests, a calculation is made with ALCYONE of the base irradiation of the two father rods to determine the radial burnup profiles as well as the radial FP profiles in the pellets of the tested samples. To this end, the father rods are discretized axially in 30 slices and radially in 45 elements (40 in the pellet and 5 in the cladding thickness). As shown in Figure 4, the fuel pellet mesh is refined at the periphery to better describe the formation of the HBS and the burnup/FP peaked profiles.

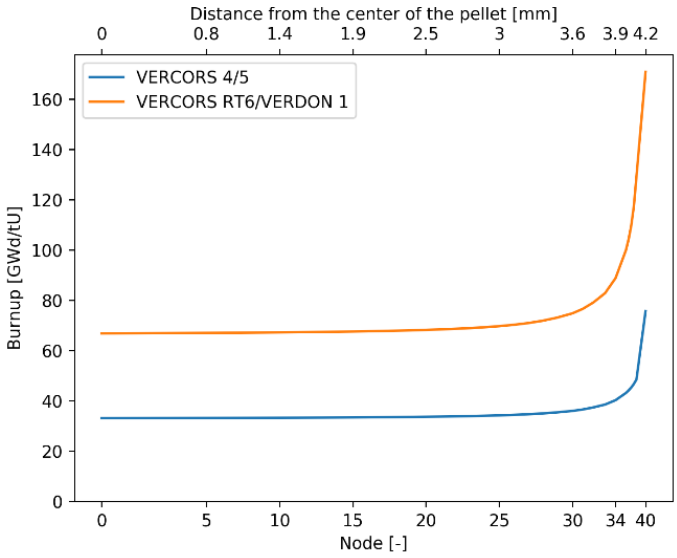

Figure 4. Calculated radial profiles of burnup in the fuel pellets used in the VERCORS 4/5 and RT6/VERDON 1 tests.

The radial burnup profiles are nearly flat from the center to the last mm of the pellet. At the pellet rim, the burnup approximately doubles: from ~35 GWd/tU till ~70 GWd/tU in the medium burnup fuel of the VERCORS 4/5 tests and from ~70 GWd/tU till ~170 GWd/tU in the high burnup fuel of the RT6/VERDON 1 tests. The radial profiles of a number of FPs and actinides of interest calculated at the end of the base irradiation in the two fuel samples are plotted in Figure 5. The same trend is obtained for all the FPs with a doubling of their content at the pellet rim compared to the pellet center. Among the actinides, Pu has a different behavior with a nearly threefold increase of its quantity at the pellet rim compared to the center.

These burnup and FP radial distributions are used to initialize the thermochemical equilibrium calculations and the fission gas model in each pellet ring during the simulations of SA tests that follow.

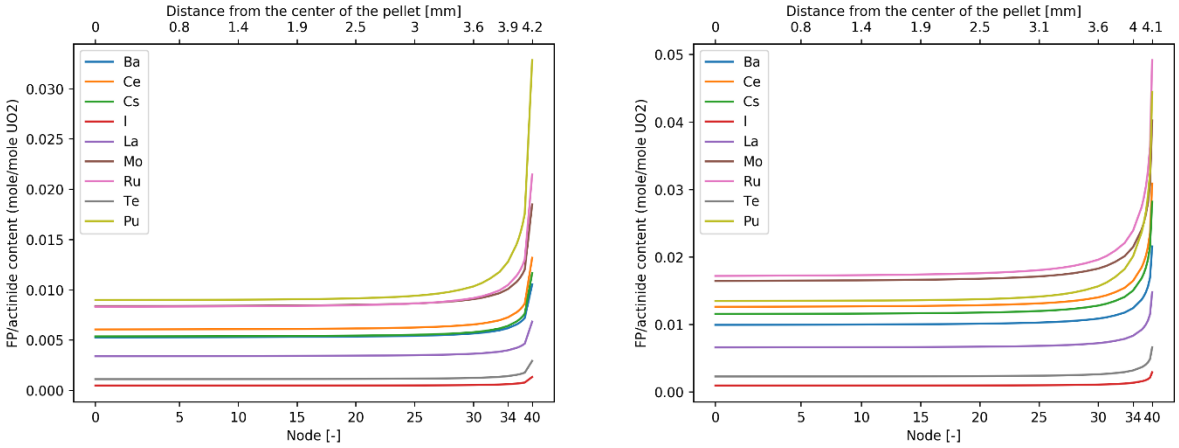

Figure 5. Calculated radial profiles of FPs and actinides in the fuel pellets used in the VERCORS 4/5 tests (left) and RT6/VERDON 1 tests (right).

A first set of simulations where the fuel thermochemistry is assessed with the TBASE, is proposed. Figure 6 presents the calculated release of volatile (iodine, tellurium and cesium) and semi-volatile FPs (molybdenum, barium) compared to measurements. The green background refers to an He atmosphere, the red background to an oxidizing atmosphere and the blue background to a reducing atmosphere. A very good agreement between calculations and measurements is obtained for the volatile FPs during the tests. This result is a consequence of the quasi-total volatilization of the FPs at low temperatures (< 1000 °C) and of the small impact of reducing/oxidizing conditions on their volatility. The release of iodine, cesium and tellurium is therefore mostly controlled by the fission gas release model.

The release of the semi-volatile FP molybdenum is generally hard to assess due to the strong impact of thermochemistry on the availability of this FP in the gas phase [13]. Refinement of the TBASE by considering cesium polymolybdates in the database ($Cs_2Mo_2O_7$) has improved the description of Mo release, as it can be seen during the 1500 °C oxidizing plateau of the RT6/VERDON 1 tests (black curves). The impact of oxidizing/reducing conditions after the oxidizing plateau is also well captured since the release of Mo is enhanced during the VERCORS 5 and RT6 tests compared to the VERCORS 4 and VERDON 1 tests. During the VERCORS 4 and the VERDON 1 tests, a stabilization of Mo release is observed after the oxidizing plateau in consequence of the reducing conditions at hand which lead to the precipitation of metallic Mo therefore suppressing Mo from the gas phase.

Ba release is also strongly dependent on thermochemistry and therefore complicated to assess. In a previous work [13], it was determined that the barium partial pressure in equilibrium with the fuel and the cladding depended on the quantity of ZrO_2 dissolved in the UO_2 solid solution as well as on the H_2O partial pressure. Optimization of the calculated Ba release in the VERCORS 4/5 tests was achieved by considering 2%/10% of the clad Zr in the system in reducing/oxidizing conditions, respectively. As it appears from Figure 7, there is a general agreement between the calculated and measured Ba release curves in all the tests (blue curves in the graphs on the right of Figure 6). The temperature at which release of Ba begins is well captured and is a consequence of the vaporization of barium molybdate and/or barium zirconate at around 1700°C.

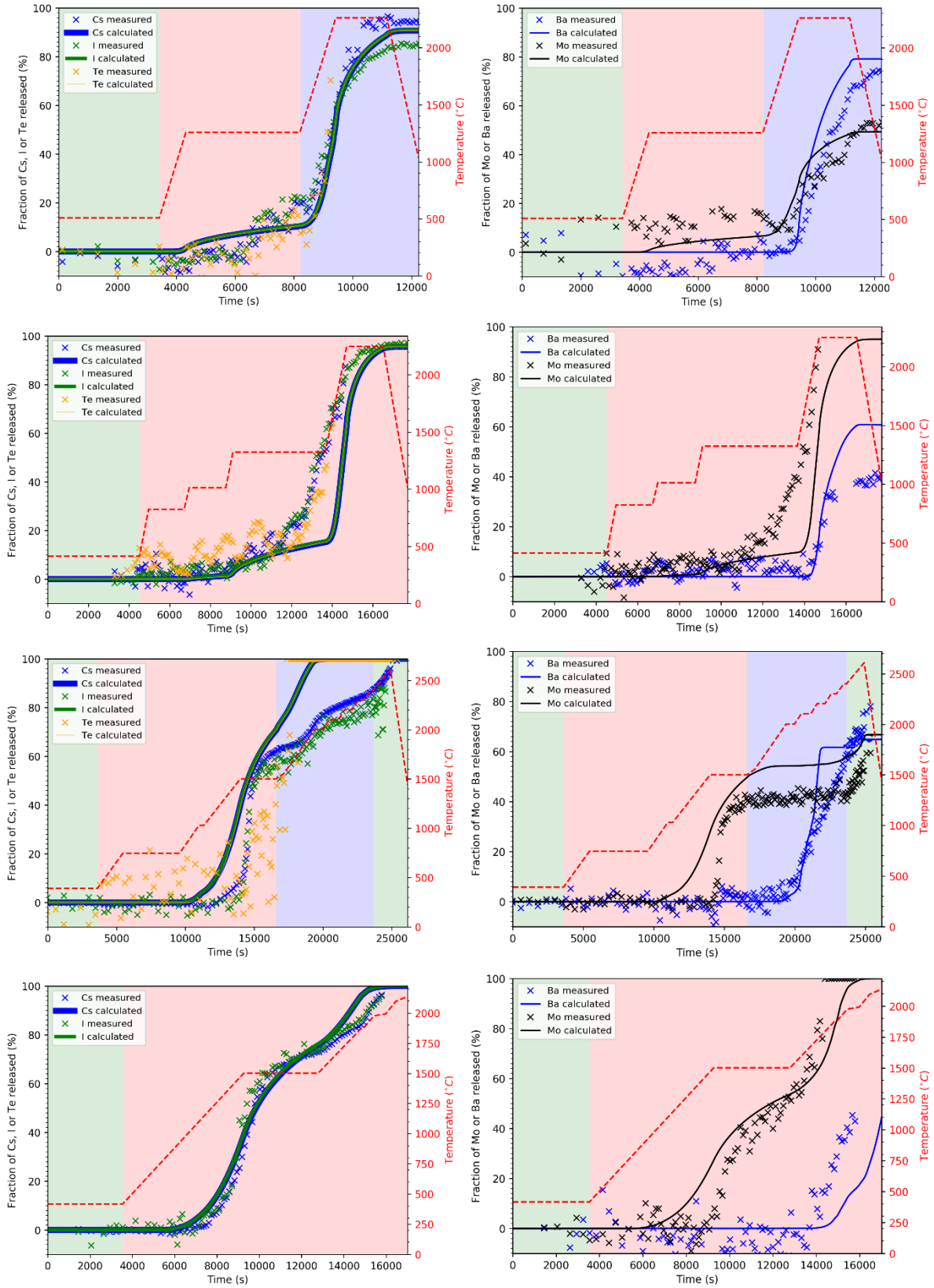

Figure 6. Measured and calculated fractions of I, Cs, Te (left) and Mo, Ba (right) released during the VERCORS 4 (1st row), VERCORS 5 (2nd row), VERDON 1 (3rd row) and RT6 (4th row) tests.

To assess the release of the low- / non-volatile FPs and the potential melting of the fuel rods during the VERDON 1 and RT6 tests (no melting recorded during the VERCORS 4/5 tests), ALCYONE simulations were performed with the TAF-ID instead of the TBASE. The same FGR model was used ("diffusion model" given by equation 1). As explained in section 4, the measured Xe release rate can be used as an alternative to define the release of the gas phase (model referred to as "Xe based model" in the next Figure). The calculated Released Fractions (RF) of a selection of FPs at the end of the simulations are compared in Figure 7 to measurements performed during the tests (on-line) or after the tests (residual FP content divided by initial FP content). Calculated data regarding uranium and plutonium are also indicated in the Figure.

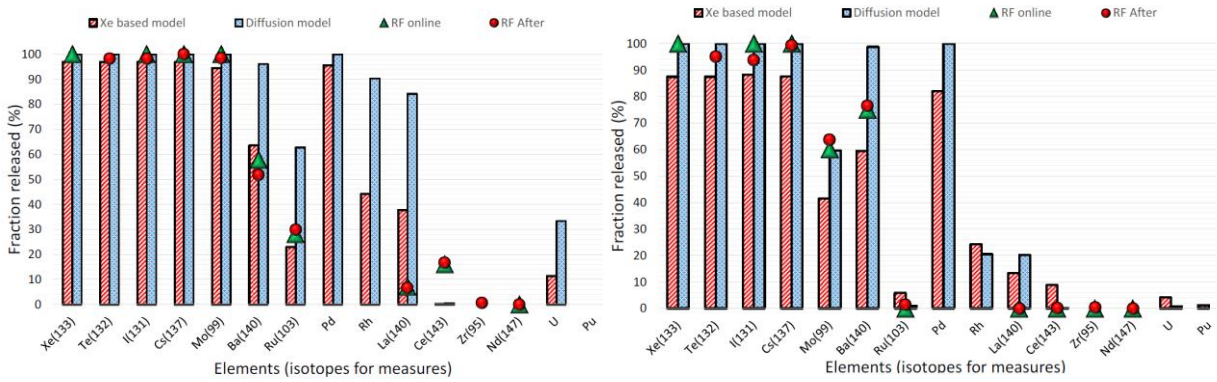

Figure 7. Calculated Released Fractions (RF) of the FPs during the RT6 (left) and VERDON 1 (right) tests compared to online and post-test measurements

As can be seen, there is a general agreement between calculated and measured RFs. The best match is obtained for the RT6 test with the measured Xe release rate (Xe based model). The diffusion model gives systematically conservative estimates of the FP final releases. Among the low volatile FPs, only La and to a lesser extent Ce releases seem respectively overestimated/underestimated by the coupled simulation. La speciation indicates the formation of gaseous LaO after the oxidizing plateau of the tests leading to non-negligible releases. A Ce oxide appears during the last part of the VERDON 1 test, which explains the calculated 9 % release in reducing conditions. Ru oxidation at high temperature is well captured by the simulations leading to a 23 % release during RT6 and 6 % during VERDON 1, in consistency with the measured 28.1 and 1.3 %. Note that another measurement for Ru (5 %) closer to the estimated 6 % is available from the quantity deposited in the VERDON testing device.

The non-volatile FPs include here Nd and Zr. Gaseous uranium trioxide is also formed at the end of the RT6 and VERDON 1 tests (at temperatures above 2200 °C). This leads to an 11.4 % / 4.1 % RF at the end of the RT6/ VERDON 1 tests (not measured after these tests). This increased RF in oxidizing conditions (RT6) and the magnitude of the RFs are in good agreement with the measurements by Inductively Coupled Plasma Mass Spectrometry (ICP-MS) during other VERCORS tests (between 1 and 10 % [25]). Plutonium RF (not measured) is on the contrary null, except during the very high temperature plateau of the VERDON 1 test (1.3 %). Chemical analyses of Pu after other VERCORS test series led to estimated RFs of less than 1 % [25], which agree well with the calculated 1.3 % during the VERDON 1 test.

In the VERDON 1 simulation, melting of a quasi-stoichiometric (U,Zr,FP)O_2 phase was obtained at a temperature between 2500 °C (beginning) and 2600 °C (full melting), in agreement with post-test observations [26] . No melting was predicted in the simulation of the RT6 test, in contradiction with the fuel collapse recorded at ~2200 °C. Independent calculations with the TAF-ID on the fuel composition (U-O and remaining FPs) obtained at 2200 °C during the RT6 simulation were performed to understand this discrepancy. Calculations were first performed without the cladding Zr (taken into account by default). They led to an Oxygen/Metal ratio in the fuel of 2.02, to a solidus temperature of 2267 °C and to a liquidus temperature of 2312 °C. Note that the impact of FPs on the melting temperature is taken into account in the

calculations but is small compared to that of the stoichiometry deviation of the fuel [16]. From these results, it is therefore inferred that the fuel center with no contact with the clad Zr melted first during the RT6 test, explaining the low collapse temperature of ~2200 °C.

6. CONCLUSIONS

This work presents the first simulations of SA sequences with the fuel performance code ALCYONE. The coupling between irradiated fuel thermochemistry and fission gas release available in ALCYONE has been adapted to SAs by the refinement of the thermodynamic database TBASE, the consideration of the carrier gas in the thermodynamic equilibria and by the development of a specific burnup dependent FGR model. Simulations of 4 tests performed during the VERCORS and VERDON programs on fuel samples pre-irradiated in commercial reactors up to average burnups of 38 and 72 GWd/tU have been analyzed to investigate the impact of the radial burnup, FP and actinide profiles on the FP release rates. The precise assessment of the state of the fuel prior to the SA sequence is one of the advantage provided by the fuel performance code ALCYONE. A reasonably good agreement between calculated and measured FP release rates during the four simulated tests was obtained with ALCYONE. The impact of oxidizing/reducing conditions on FP release rates was well reproduced in the case of the semi-volatile FPs Mo and Ba, showing the consistency of the thermodynamic modeling of the system. Detailed calculations with the TAF-ID and the same FGR model have furthermore shown the potential of this advanced TDB for capturing the release of low- or non-volatile FPs with the same coupling method. Differences in the fuel sample melting temperatures during the RT6 and VERDON 1 tests were also reasonably well explained by differences in oxidizing/reducing conditions during the tests and potential fuel-clad reaction.

The treatment of SAs in a fuel performance code originally dedicated to nominal irradiation simulations opens a wide range of potential sophistications of the models. First, the radial discretization of the fuel pellet and of the cladding provided in ALCYONE makes detailed calculations of the fuel rim - cladding interactions possible. Chemical reactions between the cladding and the FPs released from the fuel could thus be described. The cladding progressive oxidation controlled by the diffusion of oxygen in zirconia could easily be implemented. Finally, the proposed burnup dependent FGR model implemented in this work does not account for the precise evaluation of fission gas distribution within the fuel grains and grain boundaries that is provided by the MARGARET model in ALCYONE. A refinement of the mechanistic model MARGARET is necessary to catch the complexity of the release mechanisms during SAs. In this respect, a specific bubble transport mechanism associated to dislocations will be implemented in the future to ensure a proper modeling of the release of the FPs [5][22]. Specific VERDON tests could be proposed to support the modeling work.

ACKNOWLEDGMENTS

The authors would like to acknowledge the technical and financial support from FRAMATOME and EDF to this work.

REFERENCES

1. Y. Pontillon et al., “Behaviour of fission products under severe PWR accident conditions VERCORS experimental program. Part 1: General description of the program”, *Nucl. Eng. and Des.*, **240**(7), pp. 1843-1852 (2010).
2. Y. Pontillon et al., “Fission products and nuclear fuel behaviour under severe accident conditions. Part 1: main lessons learnt from the first VERDON test”, *J. of Nucl. Mat.*, **495**, pp. 363-384, (2017).
3. G. Brillant et al., “Fission product release from nuclear fuel. I. Physical modelling in the ASTEC code”, *Annals of Nuclear Energy*, **61**, pp. 88-95, (2013).

4. J. Noirot et al., "Heterogeneous UO_2 fuel irradiated up to a high burn-up: Investigation of the HBS and of fission product releases", *J. of Nucl. Mat.*, **442**(1-3), pp. 309-319, (2013).
5. M.S. Veshchunov et al., « Development of the mechanistic code MFPR for modelling fission-product release from irradiated UO_2 fuel", *Nucl. Eng. and Des.*, **236**(2), pp. 179-200, (2006).
6. T.R. Pavlov et al., « Towards a more detailed mesoscale fission product analysis in fuel performance codes: a coupling of the TRANSURANUS and MFPR-F codes", *Proceedings of the TopFuel conference*, Prague, Czech Republic, (2018).
7. B. Baurens et al., "3D thermochemical–mechanical simulation of power ramps with ALCYONE fuel code", *J. of Nucl. Mat.*, **452**(1), pp. 578-594, (2014).
8. V. Marelle et al., "Validation of PLEIADES/ALCYONE 2.0 fuel performance code", *Proceedings of Water Reactor Fuel Performance Meeting/TopFuel Conference*, Jeju Island, Korea, (2017).
9. J. Sercombe et al., *Comprehensive Nuclear Materials*, Chapter 2.14 - Modelling of pellet cladding interaction, Elsevier, Oxford, (2020).
10. JANIS 4.0 Java-based Nuclear Data Information System. https://www.oecd-nea.org/janis/.
11. L. Noirot. "MARGARET: A comprehensive code for the description of fission gas behavior", *Nucl. Eng. and Des.*, **241**(6), pp. 2099-2118, (2011).
12. C. Introïni et al., "Development of a robust, accurate and efficient coupling between PLEIADES/ALCYONE 2.1 fuel performance code and the OpenCalphad thermo-chemical solver", *Nucl. Eng. and Des.*, **369**, (2020).
13. A. Germain et al., "Coupled modeling of irradiated fuel thermochemistry and gas diffusion during severe accidents", *J. of Nucl. Mat.*, **560**, (2022).
14. C.W. Bale et al., « FactSage thermochemical software and databases — recent developments", *Calphad*, **33**(2), pp. 295-311, (2009).
15. A.L. Smith et al., "Structural and thermodynamic study of dicesium molybdate $Cs_2Mo_2O_7$: Implications for fast neutron reactors", *J. of Sol. State Chem.*, **253**, pp. 89-102, (2017).
16. C. Guéneau et al., "TAF-ID: An international thermodynamic database for nuclear fuels applications", *Calphad*, **72**, (2021).
17. P. Konarski, *Thermo-chemical-mechanical modeling of nuclear fuel behavior. Impact of oxygen transport in the fuel on Pellet Cladding Interaction*, PhD thesis, INSA Lyon, France, (2019).
18. Ch. Riglet-Martial et al., "Speciation and release kinetics of the fission products Mo, Cs, Ba and I from nuclear fuels in severe accident conditions", *Proceedings of the TopFuel conference*, Prague, Czech Republic, (2018).
19. C. Guéneau et al., "Thermodynamic modelling of advanced oxide and carbide nuclear fuels: description of the U–Pu–O–C systems", *J. of Nucl. Mat.*, **419**(1-3), pp. 145-167, (2011).
20. D. Manara et al., "Melting of stoichiometric and hyperstoichiometric uranium dioxide", *J. of Nucl. Mat.*, **342**(1-3), pp. 148-163, (2005).
21. A. Quaini et al., « Contribution to the thermodynamic description of the corium - the U-Zr-O system", *J. of Nucl. Mat.*, **501**, pp. 104-131, (2018).
22. L. Verma, *Spatialized study of the coupling between extended defects and mobile species in the nuclear fuel*, PhD thesis, Aix-Marseille University, France, (2019).
23. A. Germain et al., « Modeling high burnup fuel thermochemistry, fission product release and fuel melting during the VERDON 1 and RT6 tests", *J. of Nucl. Mat.*, **561**, (2022).
24. A. Germain et al., "Modeling of Fission Product release during Severe Accidents with the fuel performance code ALCYONE", *Nucl. Eng. and Des.*, **In Press**, (2022).
25. Y. Pontillon et al., « Behaviour of fission products under severe PWR accident conditions, the VERCORS experimental program - Part 3: Release of low-volatile fission products and actinides", *Nucl. Eng. and Des.*, **240**(7), pp. 1867-1881, (2010).
26. E. Geiger et al., "Modelling nuclear fuel behaviour with TAF-ID: Calculations on the VERDON-1 experiment, representative of a nuclear severe accident", *J. of Nucl. Mat.*, **522**, pp. 294-310, (2019).



DE LA RECHERCHE À L'INDUSTRIE

Modeling of Fission Product release during severe accidents: overview of recent developments in the fuel performance code ALCYONE

J. Sercombe, A. Germain, C. Riglet-Martial,

C. Introïni, L. Noirot, Y. Pontillon, Ph. Maugis

ERMSAR 2022 conference

May, the 18th, 2022

OUTLINE OF THE PRESENTATION

- ALCYONE fuel performance code
- Motivation for SA simulations
- Extension to severe accidents (source term)
  - ✓ Irradiated fuel thermochemistry
  - ✓ Fission Gas Release
- Simulations of the VERCORS / VERDON tests
- Conclusions

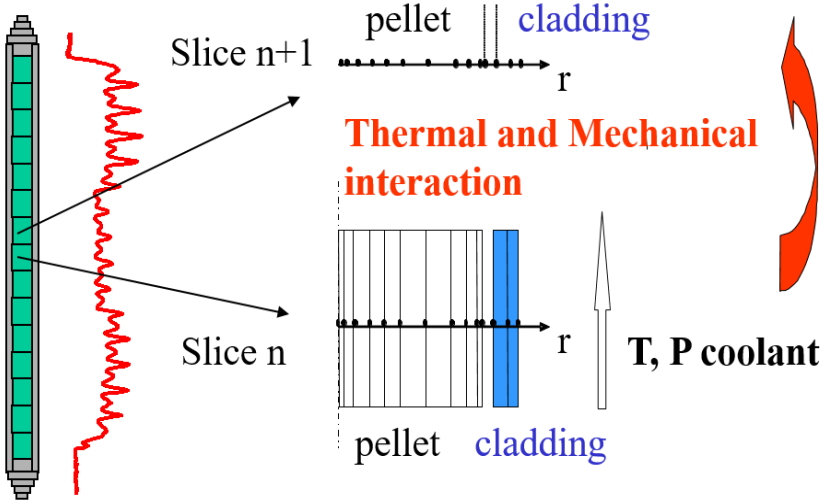

Typical fuel rod discretization in the 1.5D scheme of ALCYONE

ALCYONE 1.5D scheme is used to model the fuel rod behavior during:

- Nominal irradiation in PWR,
- Power ramps,
- RIA pulse tests,
- LOCA,
- pool and dry interim storage.

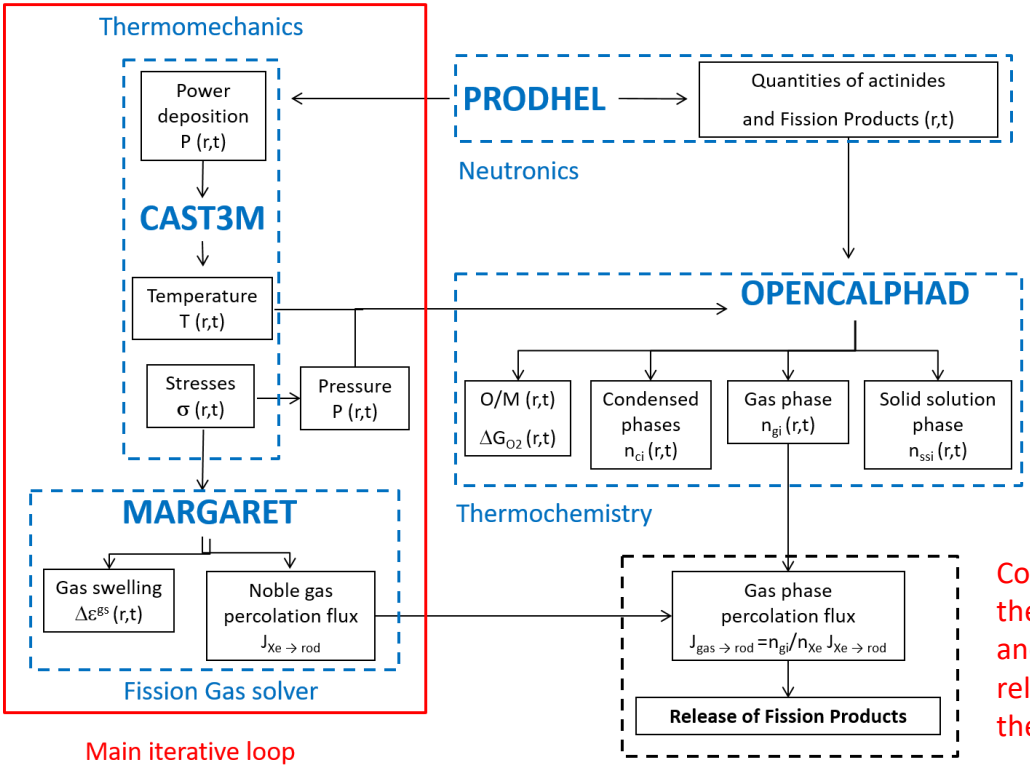

Controlled by thermochemistry and noble gas release (bulk of the gas phase)

Thermomechanics / Neutronics / Thermochemistry / Fission Gas solver → **Fission Product release**

- Irradiated fuel thermochemistry in ALCYONE:
  - ✓ inert fission gases (Xe for Xe+Kr+He),
  - ✓ volatile FPs (I for I+Br, Te for Te+Se+Ag+As, Cs for Cs+Rb),
  - ✓ stable oxides (Ba for Ba+Sr, Zr for Zr+Nb),
  - ✓ metallic FPs (Ru for Ru+Tc+Rh, Pd for Pd+Sn+Sb), Mo,
  - ✓ FPs and actinides in solid solution in UO_2 (Ce for Ce+Pr, Eu for Eu+Sm, La for La+Y, Gd for Gd+Nd+Pm, Pu for Pu+Np+Am+Cm).

- Chemical speciation obtained by Gibbs Energy Minimization:
  - ✓ Thermochemical solver OPENCALPHAD
  - ✓ Thermodynamic databases:
    - TBASE (gas species and secondary phases from SGPS, U-O solid solution model includes Pu-Ce-Eu-La-Gd-Zr) => solid-gas equilibria
    - TAF-ID (Thermodynamics of Advanced Fuels – International Database, OECD/NEA project) => melting assessment

OUTLINE OF THE PRESENTATION

- ALCYONE fuel performance code
- **Motivation for SA simulations**
- Extension to severe accidents (source term)
  - ✓ Irradiated fuel thermochemistry
  - ✓ Fission Gas Release
- Simulation of the VERCORS / VERDON tests
- Conclusions

- Validation of FP release in ALCYONE based on simulations of power ramps (for Iodine Stress Corrosion Cracking of Zr cladding)
- Comparison of simulation results to EPMA and SIMS measurements of volatile (Xe, Cs, I, Te) FPs at End Of Life (EOL)

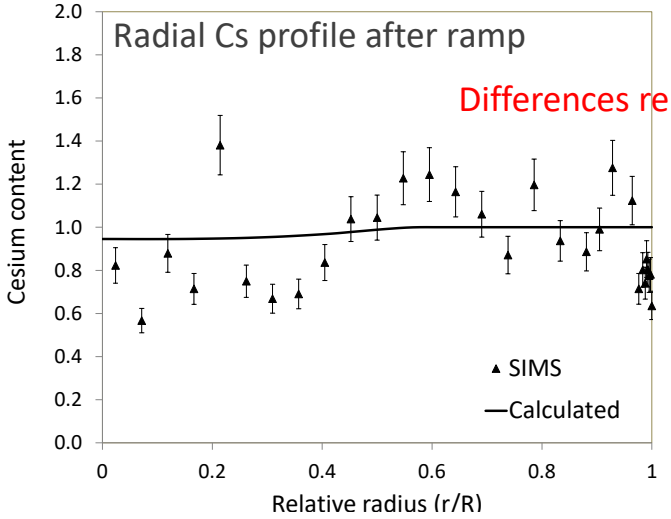

Differences related to thermochemistry

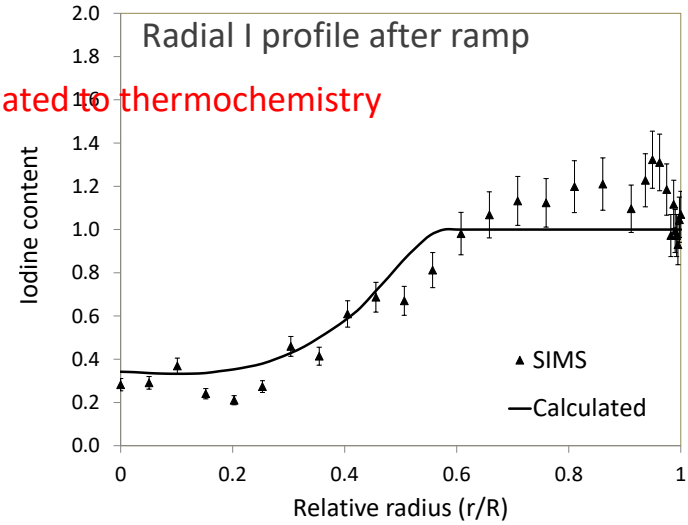

- **No data available on the FP release kinetics**

- The VERCORS and VERDON tests for SA conditions provide data on FP release kinetics (on line γ spectrometry)

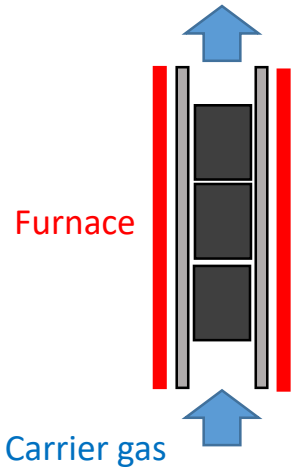

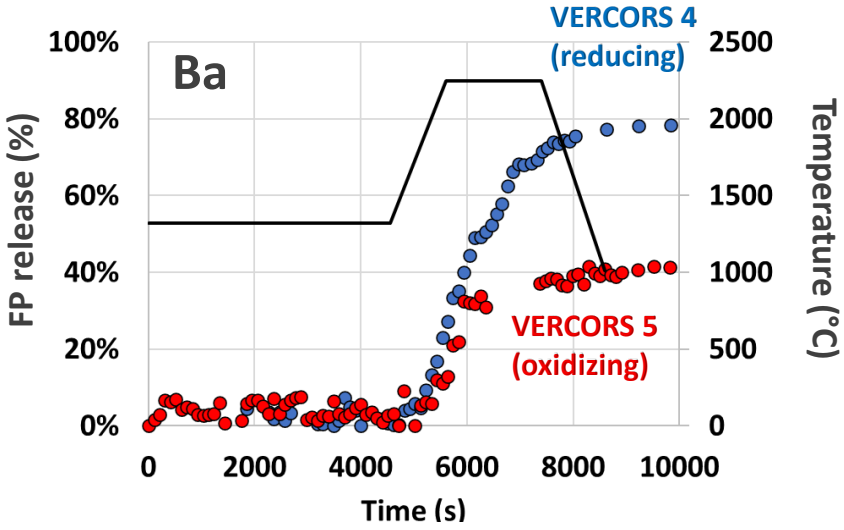

- FP release depends on the reducing / oxidizing external conditions (H_2O/H_2 ratio of the carrier gas)
- **Can ALCYONE scheme for power ramps reproduce these results?**

OUTLINE OF THE PRESENTATION

- ALCYONE fuel performance code
- **Motivation for SA simulations**
- **Extension to severe accidents (source term)**
  - ✓ **Irradiated fuel thermochemistry**
  - ✓ **Fission Gas Release**
- Simulation of the VERCORS / VERDON tests
- Conclusions

- Simulation of pre-accident state: OK
  - ✓ FP and Fission Gas distributions in the fuel radius
- Irradiated fuel thermochemistry:
  - ✓ TBASE: hydroxides and missing species forming in oxidizing conditions added (notably $Cs_2Mo_2O_{7(s,l,g)}$)
  - ✓ TAF-ID: already used for SA calculations
- Thermomechanics: OK but clad oxidation/failure is missing
- Fission gas transport and release:
  - ✓ available mechanistic models are limited to noble gases (Xe, Kr)
  - ✓ no transport mechanism activated in case of a uniform temperature in the fuel (SA conditions)
- **Development of a dedicated FG transport mechanism**

➢ Main assumptions:

✓ a single transport mechanism (diffusion in a fuel grain) is sufficient to model the release of all the FPs (volatile, semi- and low volatile)

$$\frac{\partial \boldsymbol{C}}{\partial t} = \frac{1}{r^2}\frac{\partial}{\partial r}\left(Dr^2 \frac{\partial \boldsymbol{C}}{\partial r}\right) + \boxed{\frac{\partial SFP}{\partial t}}$$

FPs in the gas phase (from TC calculations)
Necessary when noble gas release completed

C = noble gases + other FPs in gaseous compounds

r = fuel grain radius

✓ FPs are released at each time step in proportion to their concentration in the gas phase

Gas flux at the grain periphery

$$R(FP_i) = \frac{\int_S J dS}{\int_V C dV} \times \int_V \boxed{c_{FP_i}} dV$$

FP concentration in the gas phase

Gas concentration in the grain

➢ Strong coupling with thermochemistry

➢ Diffusion coefficient D(T) = $\mathbf{D_0}$ exp $\left(\frac{-Q}{RT}\right)$ estimated from the measured Xe release rates during the VERCORS / VERDON tests

VERCORS 5 (38 GWd/tU)

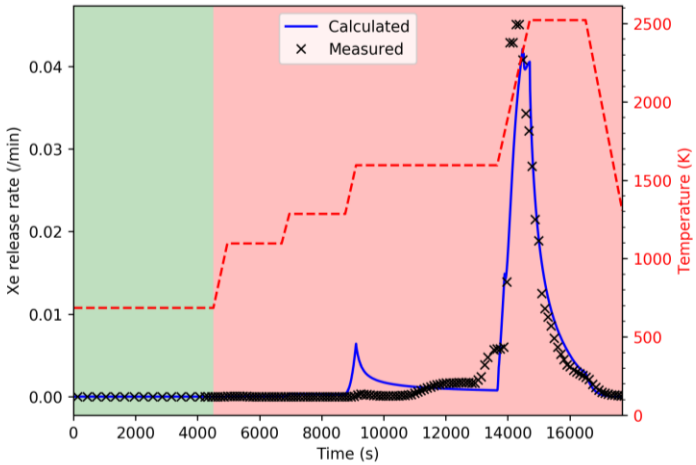

$D_0 = 1.09 \times 10^{-11}$ m²/s

Xe (/min)

VERCORS RT6 (72 GWd/tU)

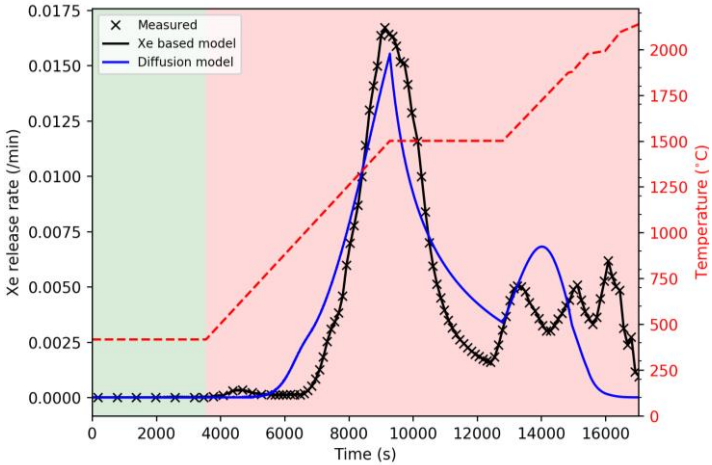

$D_0 = 2.17 \times 10^{-10}$ m²/s

➢ **We implemented a D_0(burnup) function (Q fixed)**

VERCORS 5 (38 GWd/tU)

Ba release (%)

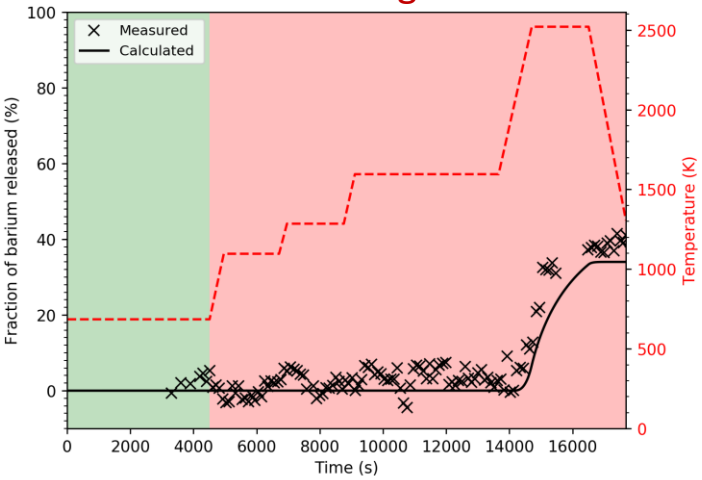

Ba

Ba speciation

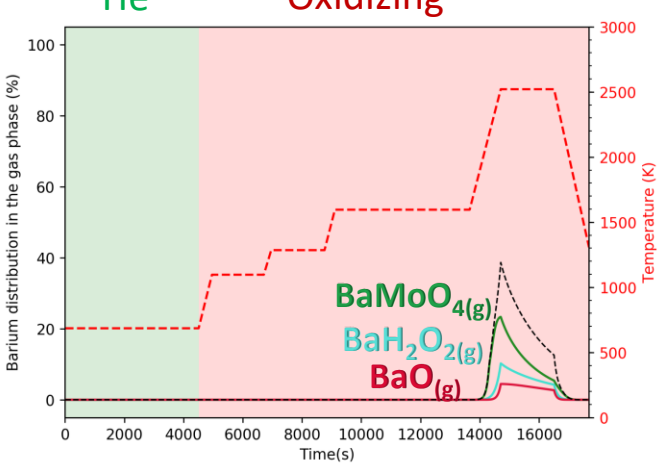

- **Ba release is mostly controlled by its availability in the gas phase (thermochemistry)**
- **Best agreement is obtained if 10% of the clad Zr is considered**

OUTLINE OF THE PRESENTATION

- ALCYONE fuel performance code
- Motivation for SA simulations
- Extension to severe accidents (source term)
  - ✓ Irradiated fuel thermochemistry
  - ✓ Fission Gas Release
- **Simulation of the VERCORS / VERDON tests**
- Conclusions

➢ Pre-accident state calculated by ALCYONE (radial profiles, 40 nodes)

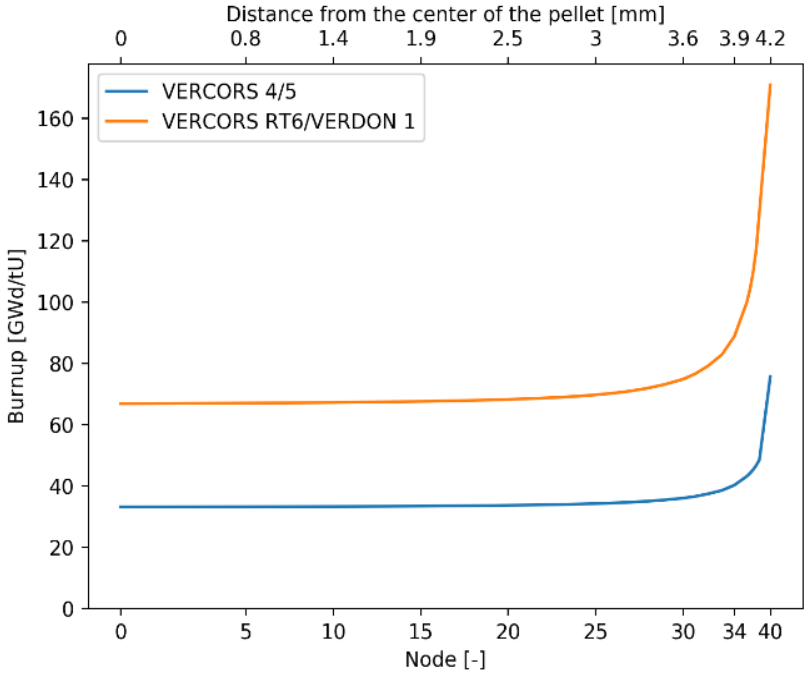

VERCORS RT6 / VERDON 1
~ 72 GWd/tU

VERCORS 4/5
~ 38 GWd/tU

➢ **Strong burnup increase at the pellet rim**

➢ Pre-accident state calculated by ALCYONE (radial profiles, 40 nodes)

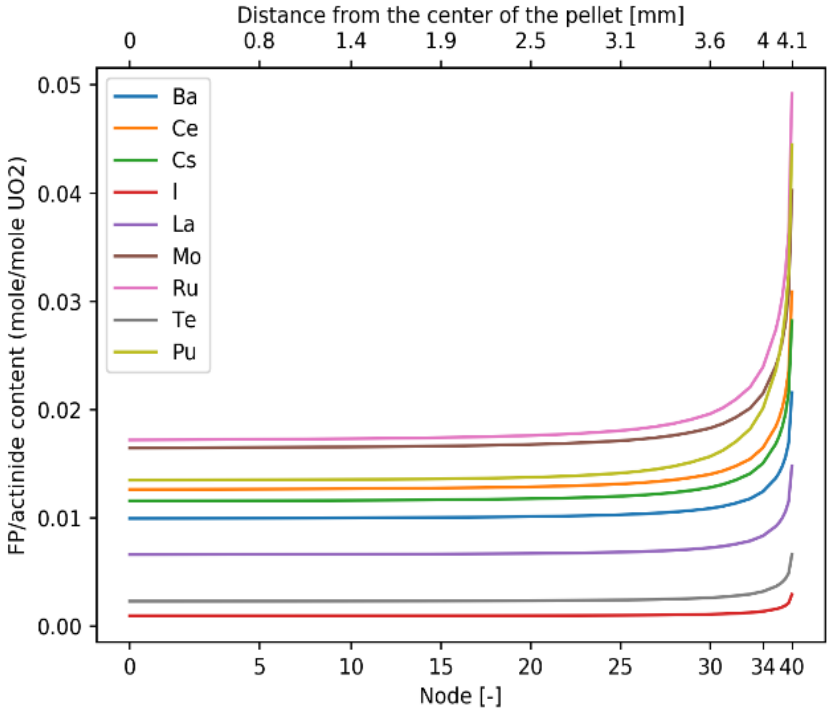

VERCORS RT6 /
VERDON 1
~ 72 GWd/tU

➢ **FPs / actinides increase at the pellet rim**

CALCULATED FP RELEASE RATES FROM THE WHOLE PELLET

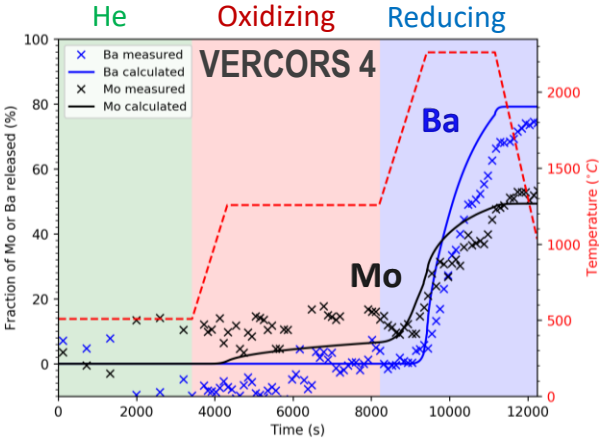

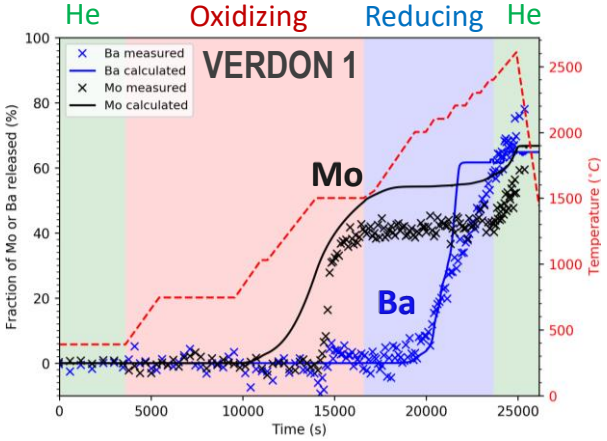

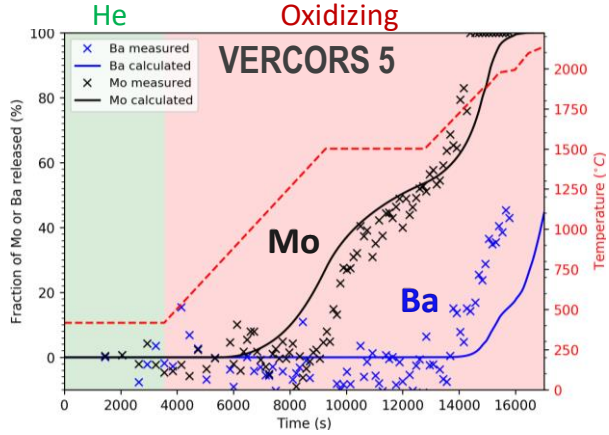

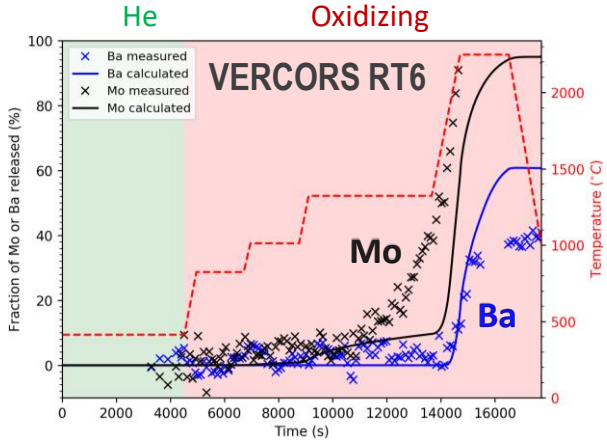

VERCORS 4
Mo release

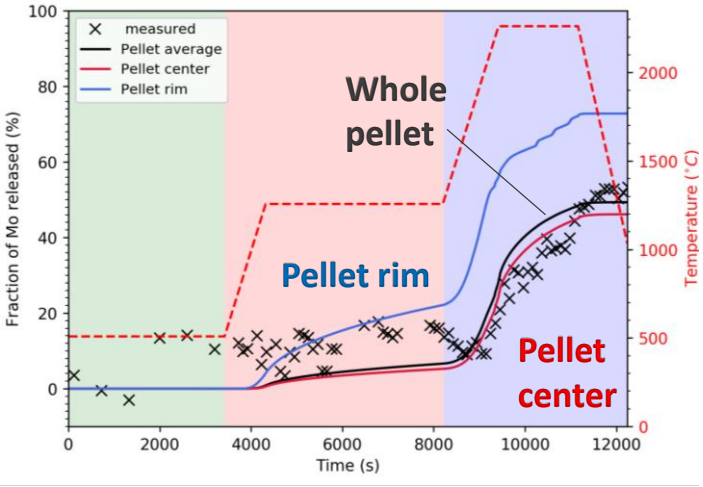

VERCORS 5
Mo release

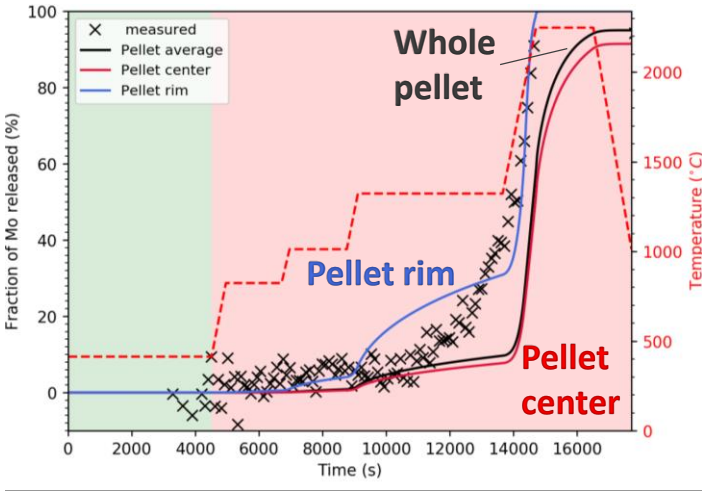

- A faster release is obtained at the pellet rim where the burnup and FP content are maximum / pellet center
- **The impact of the radial inhomogeneity of the pellet is not significant (Mo release rate of the whole pellet ≈ pellet center)**

VERCORS RT6
Mo speciation

Pellet center

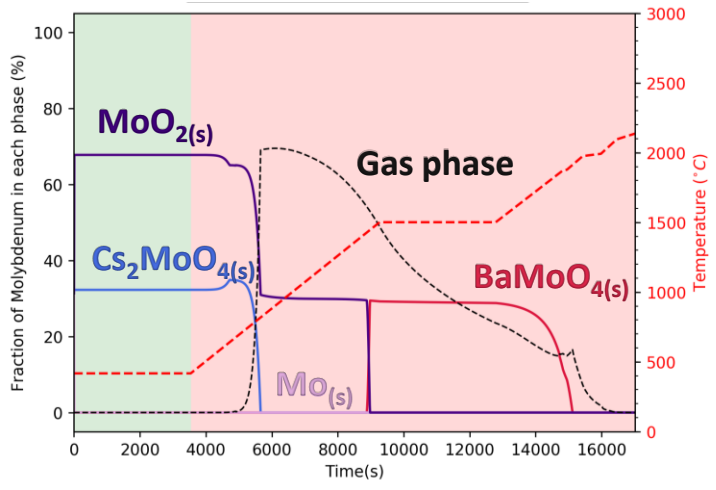

Pellet rim

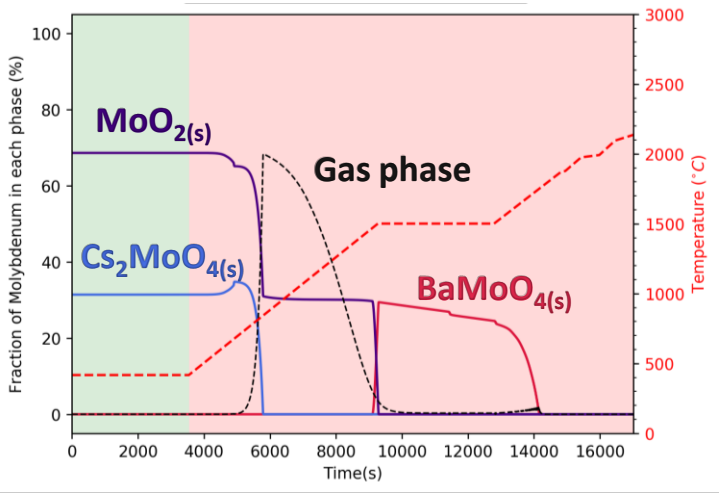

- The chemical speciation of Mo is independent of the radial position in the pellet
- **The faster release at the pellet rim is related to the faster gas diffusion with burnup increase**

CONCLUSIONS

- In this work, ALCYONE fuel performance code was extended to SA conditions to estimate FP release rates
- A unique gas transport mechanism is considered including volatile, semi-volatile and low volatile FPs
- The differentiation of FP release rates depends on the FP speciation given by the thermochemical calculations
- Simulations of four VERCORS/VERDON tests have shown good agreement between calculated / measured I, Cs, Te, Mo and Ba release rates
- The pronounced burnup and FP content increase at the pellet rim does not modify significantly the release of FPs from the whole pellet
- Work is in progress to use the mechanistic model MARGARET available in ALCYONE in SA simulations (intra- and inter-granular gas bubbles, HBS, …)

FOR MORE DETAILS

[1] J. Sercombe et al., “Modeling of Fission Product release during severe accidents: overview of recent developments in the fuel performance code ALCYONE”, this conference (2022).

[2] Y. Pontillon et al., “Fission Product behavior in severe accident condition: focus on information gained from VERCORS/VERDON analytical programs”, this conference (2022).

[3] A. Germain et al., “Coupled modeling of irradiated fuel thermochemistry and gas diffusion during severe accidents”, J. of Nucl. Mat., 560, (2022).

[4] A. Germain et al., « Modeling high burnup fuel thermochemistry, fission product release and fuel melting during the VERDON 1 and RT6 tests”, J. of Nucl. Mat., 561, (2022).

[5] A. Germain et al., “Modeling of Fission Product release during Severe Accidents with the fuel performance code ALCYONE”, Nucl. Eng. and Des., 392, (2022).

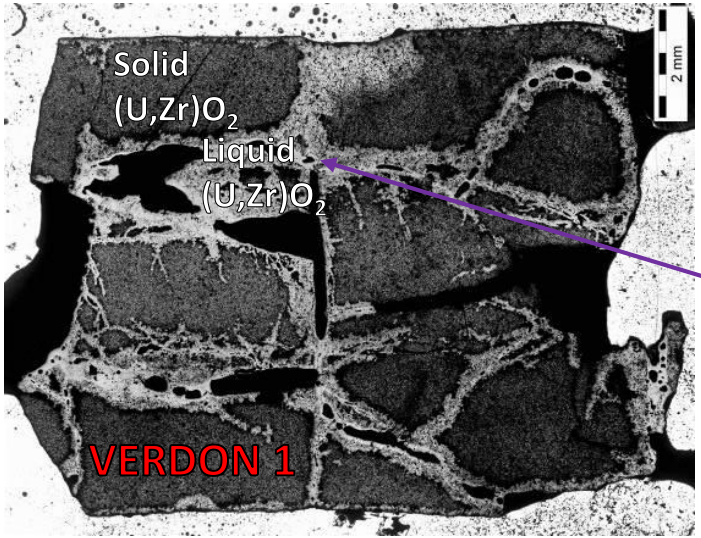

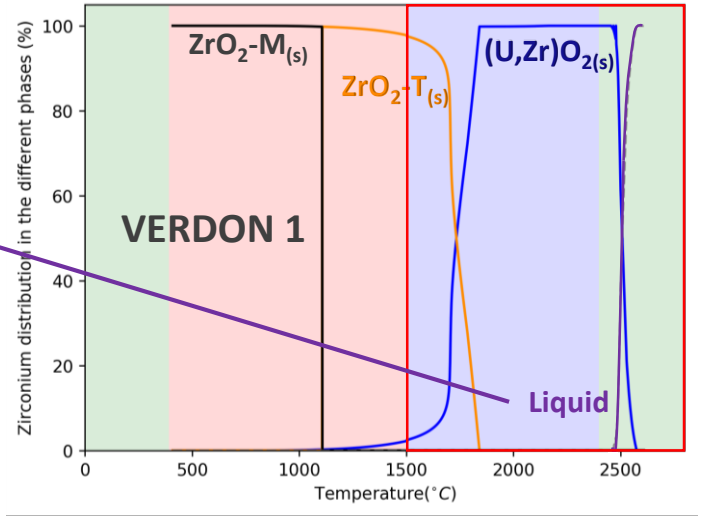

- **$(U,Zr)O_{2-x}$ melting in VERDON 1** is predicted by calculations **between 2500°C and 2600°C** → experimentally, signs of fuel-clad local melting were observed after the test



THANK YOU FOR YOUR ATTENTION

VERCORS 4 (38 GWd/tU)

Cs release (%)

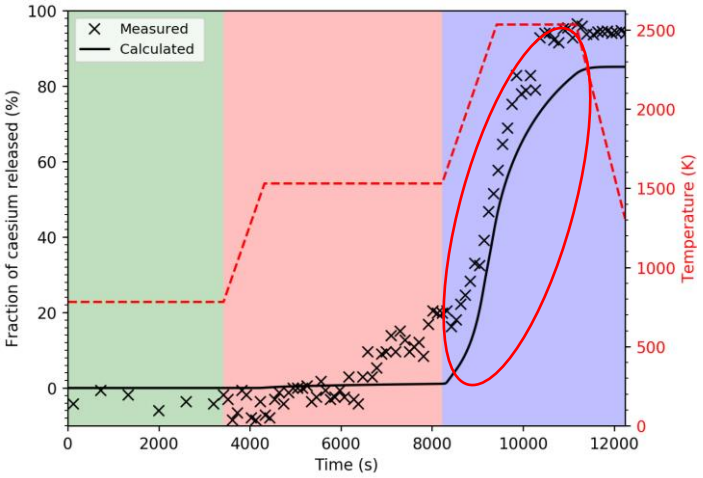

Cs

Cs speciation

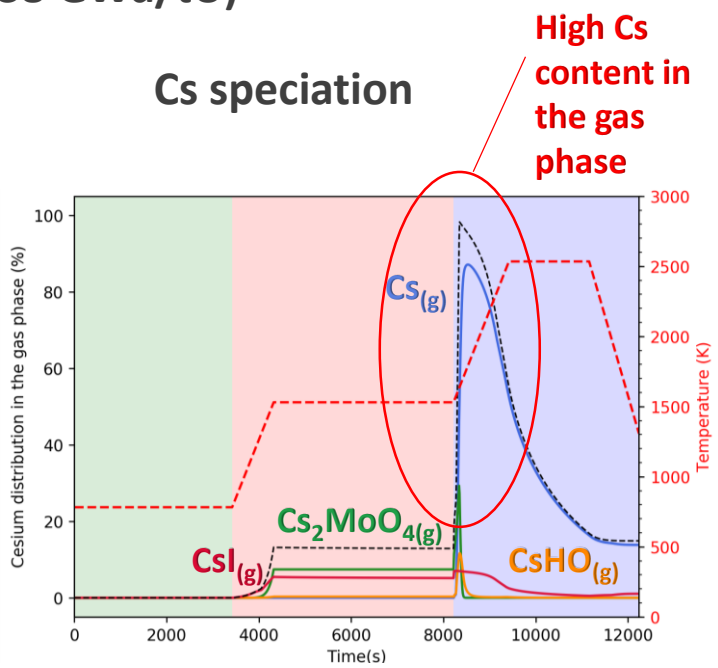

➢ **Cs release rate depends on both thermochemistry (availability in the gas phase) and fission gas diffusion kinetics**

A SIMPLIFIED CORE CATCHER MODEL FOR THE CONTAINMENT CODE AC²/COCOSYS

C. Spengler, I. Bakalov*
Gesellschaft für Anlagen- und Reaktorsicherheit (GRS) gGmbH
Schwertnergasse 1, 50667 Cologne, Germany
* Kurfürstendamm 200, 10719 Berlin
claus.spengler@grs.de, ivan.bakalov@grs.de

ABSTRACT

In Generation 3+ NPPs such as EPR or WWER-1200 the ex-vessel core catcher presents a key component of the severe accident mitigation concept. A simplified core catcher model in the containment code COCOSYS (part of AC² code package) is developed to consider core melt retention and cooling phenomena in core catchers for containment simulations. The model enables the characterization of the corium in the core catcher including processes in the corium conditioning phase (melting of sacrificial material in the core catcher, oxidation of metallic components, possible layer flip) and the long-term cooling phase (evolution of long-term corium pool bulk temperature and changes in physical state). The core catcher model is based on the existing molten corium / concrete interaction (MCCI) model in COCOSYS with additions for melt retention within water-cooled structures and can be adapted to reflect various core catcher design features of e. g. the EPR or the WWER.

The current state of the model, including basic assumptions, calculation methods, simplifications, and two application examples are outlined. The recalculation of the water-cooled basemat test OECD WCB-1 shows that the experimental data regarding e. g. the ablation of the sacrificial concrete on top of the water-cooled basemat, corium pool temperature and heat fluxes at water-cooled interfaces can be adequately reproduced by the COCOSYS simulation, when using empirical data for the heat transfer, including the MCCI phase. These empirical heat transfer data agree well with findings obtained from recent analytical work on MCCI tests. However, the model does not predict high local bottom plate temperatures as observed in the WCB-1 test due to a restriction of the model to quasi-steady state processes. The second calculation example demonstrates the current modelling features when applied to an axisymmetric geometry of a core catcher. With view to reactor-scale, the model is ready for a further verification, like e. g. comparison with other analytical core catcher approaches.

KEYWORDS
core catcher, melt stabilisation, containment, COCOSYS

1. INTRODUCTION

In case of severe accidents in light water reactors, the molten reactor core (corium) might be released from the reactor vessel to the containment. If there were no countermeasures, the interaction of the corium with containment structures could lead to a subsequent containment failure. A core catcher is a severe accident mitigation system for retention, stabilization, and long-term corium cooling during the ex-vessel phase. It is designed to provide long-term cooling of the ex-vessel corium by water circulation and thereby to avoid interaction of the corium with the concrete basemat, and, consequently, to reduce the generation of combustible gases and the risk of late containment failure.

For ex-vessel corium stabilization and cooling, various core catcher concepts exist which are tailored to specific plant designs and severe accident strategies. A crucible-type core catcher concept is provided in NPPs with WWER-1200 reactors [1] and collects the core melt directly beneath the RPV, thereby taking credit from simple corium slumping due to gravity. Moreover, the core melt stabilization system of the EPR includes a core catcher that provides a large horizontal corium spreading area, and the melt transfer due to spreading is part of the concept [2]. In both concepts the cooling of the core catcher structures and the top surface of the corium with water shall stabilize the corium in the core catcher in the long term.

Common to both concepts is further, that sacrificial material (SM) is placed inside the core catcher, which will be melted during the interaction with the corium before long-term cooling is established.

The SM shall:

- Absorb a significant part of the decay power of the corium into the melting of the SM.
- Ensure oxidation of zirconium and other metals by providing oxygen into the corium to reduce hydrogen release.
- Dilute the oxide corium with light molten materials with two positive effects for coolability:
    - Increase of the volume of the corium and thus its coolable surface.
    - Layer flip of the immiscible oxide and metal layers with a subsequent stable light oxide layer on top of the denser metal layer, which reduces the risk of potential energetic reactions between water and metal during top flooding condition.

With the computer code AC^2/COCOSYS conditions in light water reactor containments during normal operation, anticipated operational occurrences, design basis accidents and severe accidents can be simulated. Since the processes in core catchers during ex-vessel phenomena affect containment conditions, these processes need to be considered reasonably in containment simulations. The development of a generic core catcher model satisfies this requirement and ensures that retention and cooling phenomena in core catchers including processes related to SM are appropriately addressed.

2. MODEL DETAILS

2.1. Basic Assumptions

The core catcher model is based on the COCOSYS CCI (Core Concrete Interaction) module which describes the behaviour of corium relocated to the containment after RPV failure and its interactions with containment basemat structures [3]. The CCI module uses a melting approach for the decomposition of concrete [4]. Such melting approach is commonly used also in other computer codes like MEDICIS of the ASTEC code or CORCON of the MELCOR code for the simulation of MCCI [5]. In the core catcher model, the melting model is applied to the interaction of the corium with the SM and special features are added to consider the retention of the corium pool in the core catcher.

The main objective of the new core catcher model is to simulate the physical state of the corium pool during its interaction with the SM and thereafter the impact of the long-term-cooling of the corium on the containment thermal hydraulics. The core catcher model should be well-balanced regarding the level of detail in comparison with other COCOSYS models. Therefore, the following assumptions and simplifications are necessary:

- As long as there is SM between corium and the core catcher wall, thermal conduction into the wall is neglected. In the model, all the heat transferred from the corium to the SM is converted into the melting of the SM. This is a reasonable assumption for concrete-type SM. Concrete has a low thermal

conductivity. The same basic assumption is used by MCCI codes. The heat transfer between corium pool and core catcher sidewall starts at the time of first local contact between corium and core catcher cooling structure and grows with increasing contact area. The contact area grows with continuous melting of the SM until the maximum contact area is reached.

- A melting approach is used for the decomposition of the SM by the corium pool in the core catcher:

$$q = h_{\mathrm{eff}}\left(T_{\mathrm{pool}} - T_{\mathrm{dec}}\right) = v_{\mathrm{dec}}\varrho_{\mathrm{SM}}h_{\mathrm{dec,SM}}$$

  In the melting approach, the SM decomposition is related to the thermal heat flux q (W/m^2) from the melt pool with temperature T_{pool} to the interface of (unmolten) SM material at assumed decomposition temperature T_{dec}. This heat flux q is transferred into melting of a SM volume with density ϱ_{SM} and latent heat $h_{\mathrm{dec,SM}}$, with a linear decomposition velocity v_{dec} (m/s): $q = v_{\mathrm{dec}}\varrho_{\mathrm{SM}}h_{\mathrm{dec,SM}}$. The user provides empirical melting model parameters, including the heat transfer coefficient h_{eff} for the heat transfer between corium and SM. Such empirical heat transfer data can be derived from previous evaluation of specific experiments with the CCI model, if SM types have similar compositions like the concretes investigated so far, e. g. in MCCI experiments. Spengler et al. (2018) have performed an uncertainty and sensitivity analysis for the required CCI model parameters [4] for selected MCCI experiments.
- A dynamic configuration of the corium pool into layers can be considered using the configuration evolution criterion of the CCI model. The sequence of layers (i.e., oxide, metal) from bottom to the top is governed by the layer densities.
- In the model, the core catcher sidewall and bottom can be subdivided into several 1-dim heat structures, see Figure 1. When there is contact between the corium and a heat structure, the resulting heat flux is transferred to the whole (1-dim) heat structure. As first approximation, the user prescribes a constant heat transfer coefficient for the convection of corium at the core catcher wall. More detailed heat transfer models between corium and core catcher can be added, depending on the available experimental data.
- For the heat transfer at the water-cooled sides of the core catcher walls, correlations for convection flow and a pool boiling correlation (Rohsenow) are available.

2.2. Model Features

The erosion of the SM by the corium in the core catcher is simulated with the MCCI model in COCOSYS. In the example given in Fig 1, the core catcher is represented by the COCOSYS zones 1 and 2. The core catcher walls are represented by COCOSYS heat structures with one surface attached to zone 1 and the other surface attached to zone 2. The volume of the cooling channels is represented by the free volume of zone 1, which is filled with water to a large part. Zone 1 is basically a cylindrical volume in the lower part with an upward extension of an annular ring, both parts are axisymmetric. The water may pour on the top of the corium in zone 2, depending on a flow connection to zone 2.

Using this model, the axisymmetric surface area of the initial SM is defined by the user as a 2-dim series of points (r_i, z_i). Figure 2 shows an example of a SM layout.

The core catcher walls are represented by a set of axisymmetric wall segments (annuluses, central circular bottom segment) with strict horizontal or vertical orientation, defined by z_i = const. or r_i = const., respectively. Thus, bottom and sidewall structures are subdivided into several COCOSYS heat structures as shown in Figure 1. The volume of the SM as input to the calculation is then defined as the space confined by the axisymmetric r-z-profile of the SM surface (which can also be non-planar as depicted in Figure 2) and the horizontal and vertical core catcher walls.

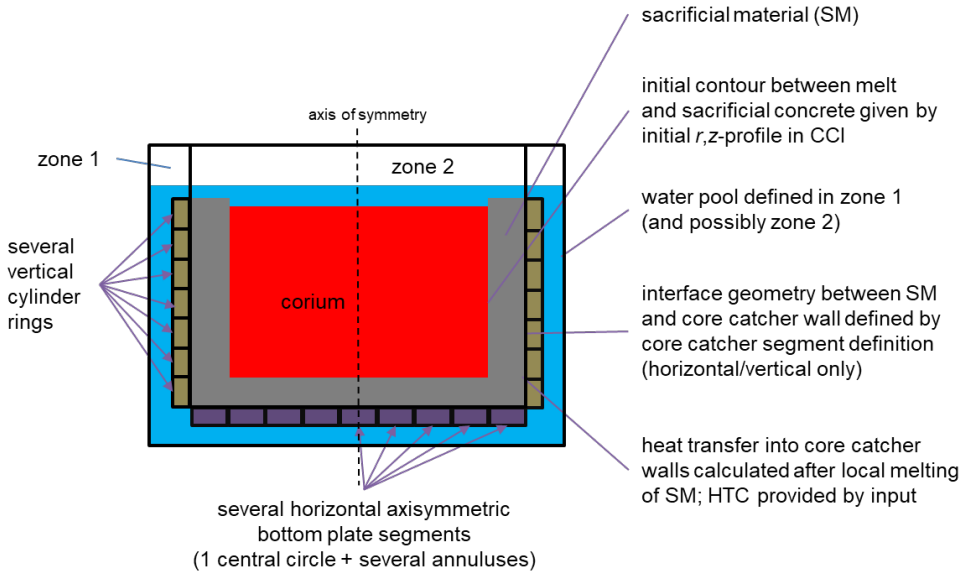

Figure 1. Basic approach of the core catcher model. Axisymmetric segmentation of core catcher side wall and bottom into several segments.

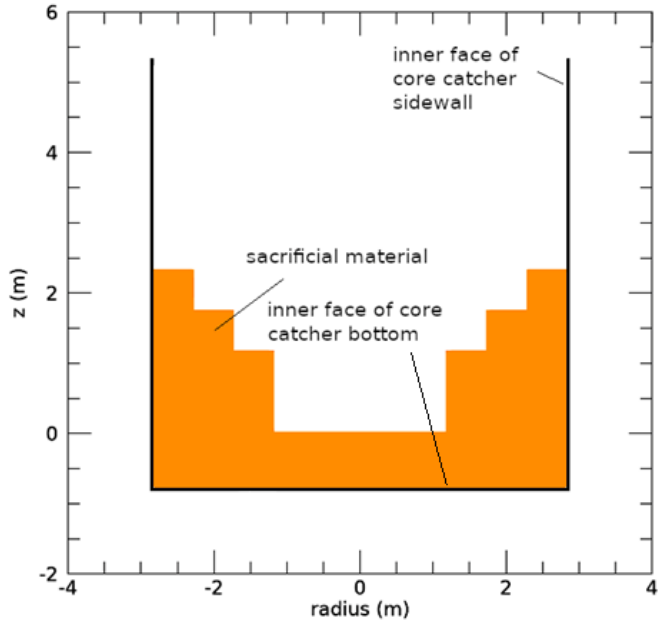

Figure 2. Geometrical arrangement of sacrificial material (SM) inside the core catcher.

Figure 2 gives an example for a core catcher layout with axisymmetric contour of sacrificial material and plane vessel walls at z = -0,8 m (bottom) and at r = 2,85 m (vertical side wall).

In this simulation methodology of a core catcher, four essential heat transfer interfaces are considered:

2.2.1. Heat transfer from the corium to the SM interface

In case the SM is a concrete-based type (like for the EPR concept) similar heat transfer mechanisms as investigated in MCCI experiments with oxide or metal melts using a range of concrete types (siliceous, limestone/common sand or serpentinite) can be expected. Heat transfer coefficients derived from such experiments are to be used only in combination with the corresponding assumption for concrete decomposition temperature T_{dec}. When using T_{dec} of about 1800 K, typical heat transfer coefficients in experiments with oxide melts were evaluated in the range of a few hundred W/(m^2 K) (e. g. ~ 300 W/(m^2 K) for the heat transfer at the bottom and ~ 1600 W/(m^2 K) for the heat transfer to the sidewall. The heat transfer coefficients are to be determined from the perspective of an effective (or apparent) approach, thus including all physical mechanisms involved (convection in liquid melt, conduction in solid agglomerates near the interface between melt and SM, effect of SM slugs and of gases potentially released at the interfaces) which are too complex to be considered by distinct mechanistic modelling. Any differences between heat transfer coefficients at horizontal and vertical interfaces are not subject of mechanistic modelling in the frame of this work. The particular values used are obtained from an uncertainty and sensitivity analysis performed for MCCI experiments in 2018 [4] as recommendation for best-estimate calculations for a scenario with oxide melt and siliceous concrete, in case that an anisotropic ablation is expected. With view to the specific concrete type used for the EPR core catcher, which differs to ordinary siliceous concrete by an increased content of iron oxides, indications from the HECLA experiments performed at VTT Finland and from VULCANO experiments at CEA Cadarache suggest a similar melting behaviour as compared to ordinary siliceous concretes [5]. For other cases, where the SM composition significantly differs from that of concrete, i.e., when it does not contain gases which will be released during melting, like e. g. for the WWER core catcher, a different heat transfer mechanism is expected. Experimental data for that system are not available. Since the uncertainty of heat transfer coefficient to be used at the concrete/SM interface is large (concluded from the uncertainty analysis [4] performed for MCCI experiments), the current state of the models allows the user to specify his own effective heat transfer coefficients in the input deck. No additional uncertainty analysis was performed on this point in the frame of this work.

2.2.2. Heat transfer at the upper surface of the corium

Heat is transferred from the corium pool to the water above, or to the atmosphere and upper structures of zone 2 if it is not flooded (Fig. 1). The same heat transfer models as available in the CCI model are used (boiling heat transfer to a water pool in the flooded condition; free or forced gas convection in combination with radiation for dry conditions). Models for corium coolability mechanisms under top flooded condition, such as bulk cooling, water ingression and melt eruption, as identified in the OECD MCCI experimental program [6] are not considered. The reason is that the effects of the first two mechanisms are limited, whereas the third mechanism involves unacceptable large uncertainties.

2.2.3. Heat transfer from the corium to the core catcher walls (inner face)

Heat is transferred from the corium pool to the core catcher wall and bottom when the SM is penetrated (Fig. 1). This phenomenology at this interface is different from the one between corium and SM or during MCCI since there are no gases (enclosed in concrete-type SM) which affect the heat transfer. After the SM has been melted and the corium is in direct contact with the core catcher cooling structures, there will be no longer any gas-induced enhancements of the heat transfer. In consequence, it is expected that the heat transfer will be smaller than in the case with SM. This is expected for the heat transfer to the bottom of the core catcher structures when the cooling induces a stable thermal stratification of the corium with not much convection in the thermal boundary layer. Heat transfer can be to a great extend governed by thermal conduction. Thermal conduction is usually subject of a 3D heat conduction analysis code which is out of the scope of COCOSYS for the simulation of the corium pool. Therefore, the user can specify a set of constant heat transfer coefficients in the input deck to approximate either the case of thermal conduction

(resulting in small heat transfer coefficients) or convective heat transfer (with larger heat transfer coefficients). The experimental data base is not very large for this condition. However, the OECD WCB-1 test [6] provides some valuable data for code validation.

2.2.4. Heat transfer from the core catcher wall (outer face) to the water

Heat is transferred from the structural segments to the water in zone 1. Depending on the flow conditions and the outer wall surface temperature, either free or forced convection, or flow boiling (in subcooled or saturated condition) may establish in the real system. A predictive modelling for this either requires a detailed 3D analysis for the two-phase flow using CFD codes or application of empirical correlations. CFD analyses are out of the scope of this work. The current model considers free convection heat transfer correlations as an approach to the more complicated real situation, knowing that empirical correlations are available only for idealized geometries (e. g. pipe flows). This is a reasonable simplification in the current state of model development, since the main objective for this work on the core catcher model in COCOSYS is to enable a reasonable evaluation of the containment behaviour in the long-term, including corium behaviour in the core catcher. The evaluation of critical heat flux conditions is out of scope of this model.

2.2.5. Effective interface area between corium and the SM

In some cases, the geometrical set-up of the SM according to Figure 1 (i.e., with a simple and plane layer of SM) may not be the best approach to reflect a real design. E. g. in the WWER core catcher concept, the SM provides some porosity and irregularities in the form of gaps and chinks, such that the corium can penetrate the SM more easily. Thus, the initial interface area between corium and SM is effectively larger than compared to the simplified compact set-up shown in Figure 1. To account for this in the model, the user has the option to provide an estimate of the initial factor $f_{\mathrm{geom},0} > 1$, by which the initial area should be virtually increased compared to the simple layer configuration. The initial heat transfer area between corium and SM is then scaled with $f_{\mathrm{geom}} > 1$, and the melting of SM volume is (based on increased virtual interface area) faster. During melting, $f_{\mathrm{geom}}(t)$ will decrease to 1 in the limit when the interface between corium and SM approaches the surface of the core catcher walls. This is tracked as a linear function of melted SM mass $m_{SM,\mathrm{melt}}(t)$ and initial available SM mass $m_{SM,0}$:

$$f_{\mathrm{geom}}(t) = 1 + \left(f_{\mathrm{geom},0} - 1\right) \frac{m_{SM,0} - m_{SM,\mathrm{melt\,(t)}}}{m_{SM,0}} \quad (1)$$

3. APPLICATION TO WCB-1 TEST

As discussed in section 2, there is only limited information on the heat transfer at the core catcher walls in open literature available. However, the experiment WCB-1 performed in the frame of the OECD MCCI-2 project allows to apply the core catcher model presented in section 2 to a realistic situation with view to the heat transfer. The specific objective of the WCB-1 test [6] [7] was to provide prototypic data on the evolution and stabilization of a core melt in a generic water-cooled core catcher design. In this test, a 100 % oxidized PWR corium including 8 wt.-% concrete was generated on the top of a basemat (Figure 3) and electrically heated. The basemat construction used in the WCB-1 test simulates a generic core catcher with a water-cooled steel plate at the bottom, and a 15 cm-thick concrete layer above. The bottom plate was cooled by water flowing through 5 channels with rectangular cross section. Sidewalls of the test section containing the corium were made of a refractory material with low thermal conductivity (MgO).

During the experiment, the water flowed through the bottom channels and the heated corium interacted with the concrete layer (Figure 3, left). Before the concrete was completely melted, the corium pool was flooded with water from the top, at t = 106 min. This defined the beginning of the “wet” operation phase (Figure 3, right).

As long as some remaining part of the concrete layer was left, the mechanism of concrete decomposition is considered as MCCI. MCCI heat transfer was recently simulated in COCOSYS using empirical assumptions for concrete decomposition temperature T_{dec} and effective heat transfer coefficients h_{MCCI}. Based on available experimental data from MCCI experiments with oxidic melt, the combination of $T_{\mathrm{dec}} \approx 1800\ K$ and $h_{\mathrm{MCCI,bot}} = 300\ \mathrm{W/(m^2K)}$ was identified as a reasonable universal approach (i.e. successfully tested for different experiments in different facilities) to describe the interaction of an oxide melt with the bottom concrete, considering that the presence of solidified corium near the bottom wall impacts the bottom heat transfer substantially. The magnitude of the given value for $h_{\mathrm{MCCI,bot}}$ could be interpreted as representative of thermal conduction through a 1 cm thick solid oxide layer (crust or mush attached to the bottom interface). The MCCI model in COCOSYS is not capable of considering 3-dim thermal conduction. Instead, a conduction-limited heat transfer is implemented with a small heat transfer coefficient by user-input.

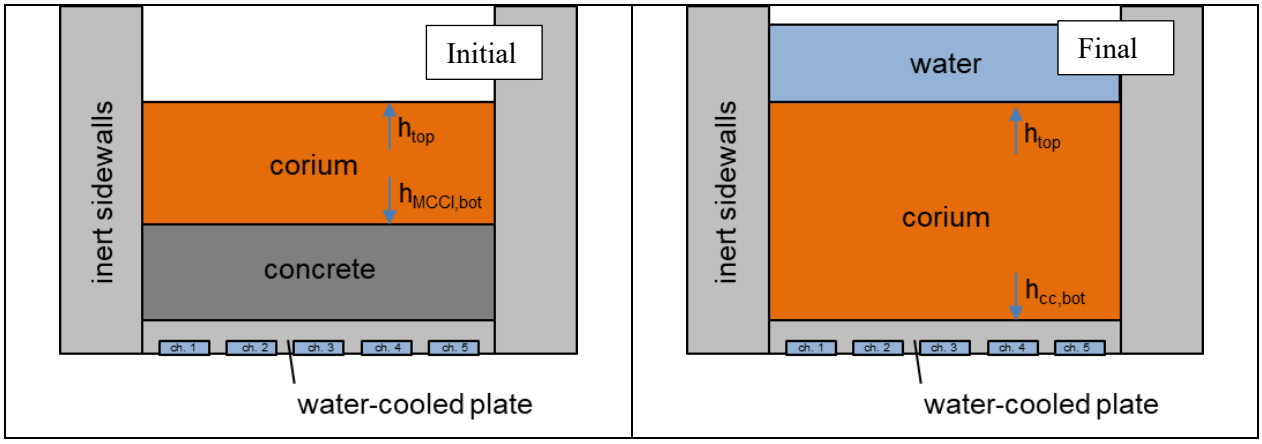

Figure 3. Initial set-up of WCB-1 test (left) during "dry" operation phase and final configuration (right) obtained during "wet" operation phase after concrete is molten.

When all the concrete (or the SM in a real core catcher concept) has been melted, Figure 3 (right), the heat transfer coefficient h_{cc} might be different to the MCCI situation because the processes at the interface are different (no melting/dissolution of SM). It is expected that an interface temperature will be established which is well below the melting temperature of the plate material (steel). Then, depending on the degree of solidification of the corium, either thermal conduction or free convection with internal heat sources would govern the heat transfer. However, code predictions for the degree of solidification and for the related viscosity of the corium in the boundary layer are highly uncertain. In a first approach, a constant value for the effective heat transfer coefficient under core catcher conditions, h_{cc}, is used, see below. More experimental investigations are required to provide predictive models for that. A first hint to realistic values is obtained from the code simulations for the WCB-1 test, presented hereafter.

In the experiment WCB-1, the heat flux to the water channels was measured. A rather low heat flux specific to surface area was obtained, in the order of $q < 30\ \mathrm{kW/m^2}$, see Figure 4.

Due to one of the basic assumptions listed in 2.1, heat transfer to the core catcher plate begins in the simulation when the erosion front arrives at the core catcher plate (in the calculation at time $t = 95$ min).

Because of the 1-dim boundary condition of the corium/concrete interaction (erosion) in the experiment WCB-1 (i.e., only in downward direction) the water-cooled surface areas (corium/SM interface, top surface)

remain constant during the interaction. Since both the internal power (heating power) and the assumed heat transfer coefficient $h_{\mathrm{MCCI,bot}}$ are constant, the calculation shows a constant corium pool temperature and a constant heat flux to the concrete during the "dry" interaction phase, resulting in a constant 1-dim erosion velocity (Figure 5). The calculated time duration until full concrete erosion (15 cm depth, 95 min) is calculated in good agreement with experimental indications for full concrete layer erosion (~ 100 min). However, measurements suggest that there was first a period with small erosion velocity (due to initial crust formation) followed by a period with large erosion velocity (failure of the crust), for which the COCOSYS simulation represents obviously an adequate "average" – this was also observed for other MCCI experiments with initial bottom crusts. The impact of initial crusts on experimental results is a known artefact and the transposition of the effect to reactor scale is not yet fully resolved. When focussing on long-term effects in reactor scale, the time frame with presence of initial crusts may play a minor role, and imposed heat transfer coefficients should be derived from quasi-steady state periods in MCCI experiments after failure of crust.

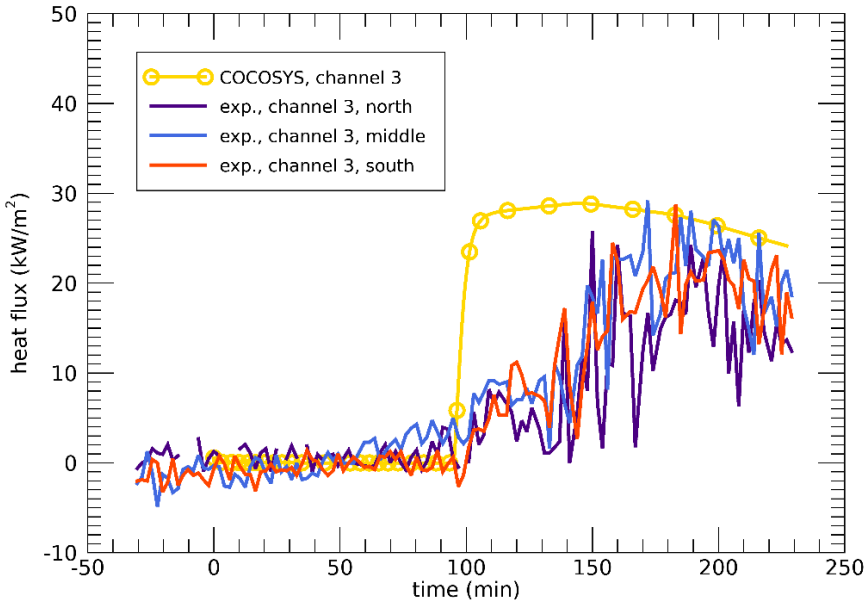

Figure 4. Comparison of COCOSYS results with WCB-1 data for the heat flux to the water-cooled channel 3.

The resulting heat transfer coefficient (htc) of the heat flow from the corium pool through the bottom plate to the water is basically a combination of three htc's:

i) convection/conduction in the corium: h_{cc}
ii) conduction in the thermal plate: $h_{\mathrm{cond}} = \lambda_{plate}/d_{plate}$
iii) convection in the water channel: h_{wat}

From parametric calculations with COCOSYS (not shown here) under variation of h_{cc} and h_{wat} (but with constant contact areas), it was concluded, that h_{cc} needs to be very small to obtain heat fluxes which are smaller than ~ 30 kW/m^2. The COCOSYS results in Figure 4 were obtained finally using h_{cc} = 15 W/(m^2 K) and $h_{\mathrm{wat}} \approx$ 700 W/(m^2 K). In this calculation h_{cc} is much smaller than h_{MCCI}, which implies that the cooling is efficient when the erosion front arrives near the cooled bottom plate, resulting in a thicker solidified layer than compared to the not-cooled MCCI situation. Thus, the effective h_{cc} (combining convection and conduction through solidified material) is very small, and the temperature drop between corium bulk and

top surface of the plate is sufficiently large so that the melting point of the steel (1400-1450 °C) is not reached (Figure 6).

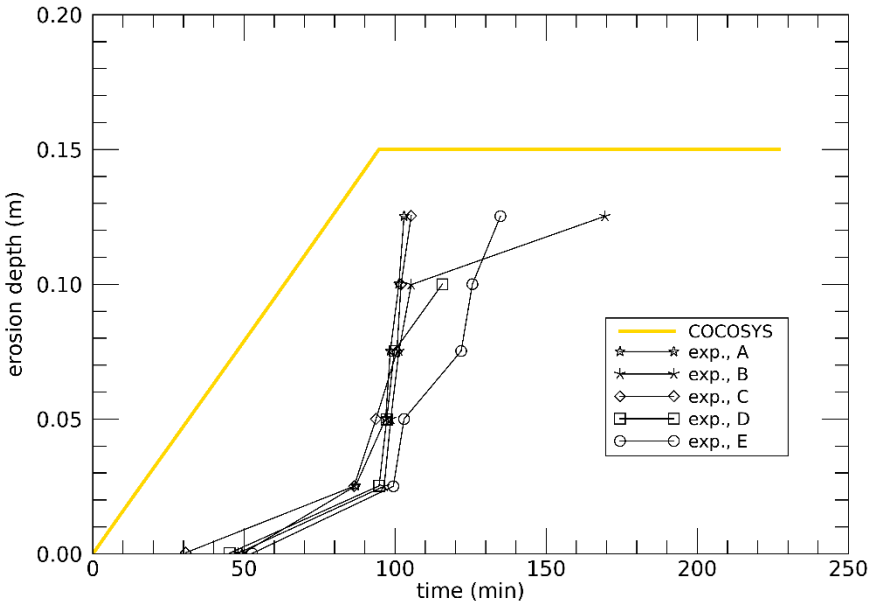

Figure 5. Comparison of COCOSYS results with WCB-1 data for erosion depth at different locations (A…E).

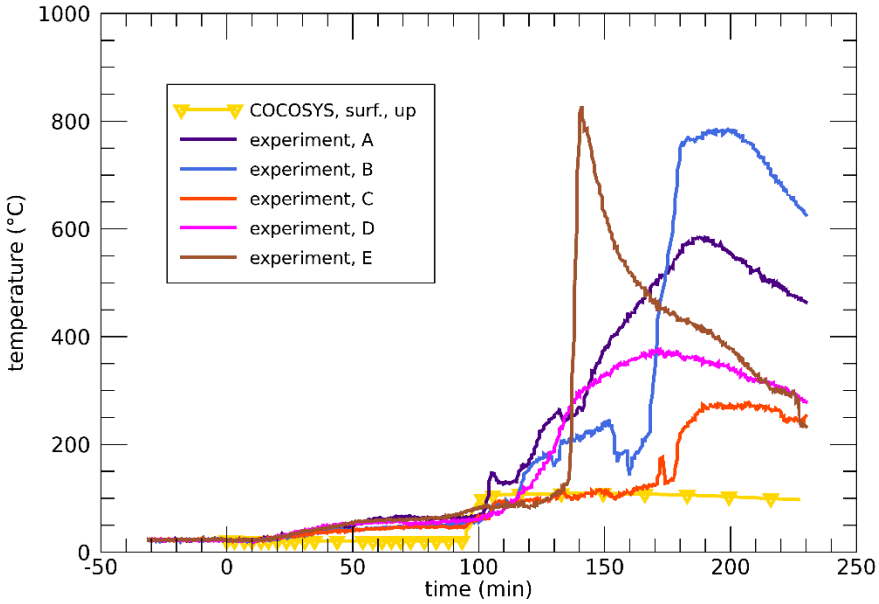

Figure 6. Comparison of COCOSYS results with WCB-1 data for plate top surface temperatures at different locations A…E.

Local temperature increases as observed in the WCB-test at several locations at the surface of the water-cooled plate (A-E) were not predicted. Maximum temperatures inside the steel plate above the channels are adequately captured in the COCOSYS simulation (Fig. 7). In consistency with the overestimation of heat

flux (Figure 4) the calculation slightly overestimates temperatures measured in the depth of 2 cm after calculated contact condition between melt and core catcher wall.

During the dry operation phase under MCCI conditions (t < 106 min in Figure 8), the maximum corium temperature is adequately simulated. This confirms the adequacy of the universal melting approach for the MCCI using empirical heat transfer coefficients.

The transition to the reduced heat transfer coefficient h_{cc} in the COCOSYS simulation, when corium gets in contact with the steel plate (at t = 95 min in the calculation), leads to a continuous increase of corium temperature, until the internal power is reduced at time 145 min (Figure 8). In contrast, the experiment shows a temperature drop (even before the flooding phase at t = 106 min) followed by an increase. The difference to the calculation is attributed to two effects in the experiment that have not been considered adequately in the simulation:

- The transient character of concrete decomposition in the experiment leads to a sudden mixing of a large cold concrete mass with the corium at around t = 100 min (Figure 5).
- The bulk cooling effect after top flooding leads to a strong peak in the heat flux extracted from the corium pool at its top interface in the time interval t = 106…120 min. This peak heat flux is not well captured in the COCOSYS calculation.

Both transient effects are later turned into quasi-steady-state behaviour, so that the slow cooling calculated with COCOSYS at reduced power after t = 145 min is again in good agreement with the experiment.

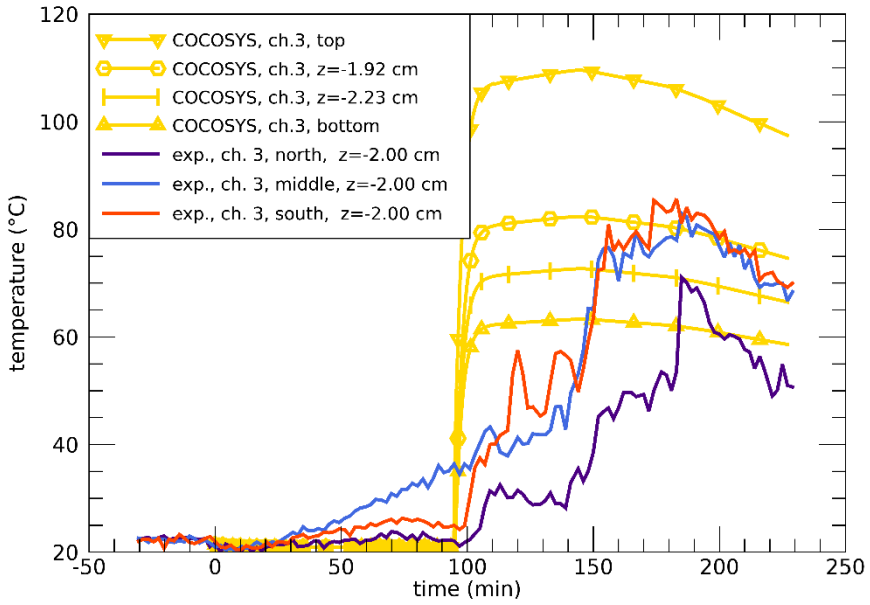

Figure 7. Comparison of COCOSYS results (lines with symbols) with WCB-1 data for temperatures inside steel plate, above channel 3.

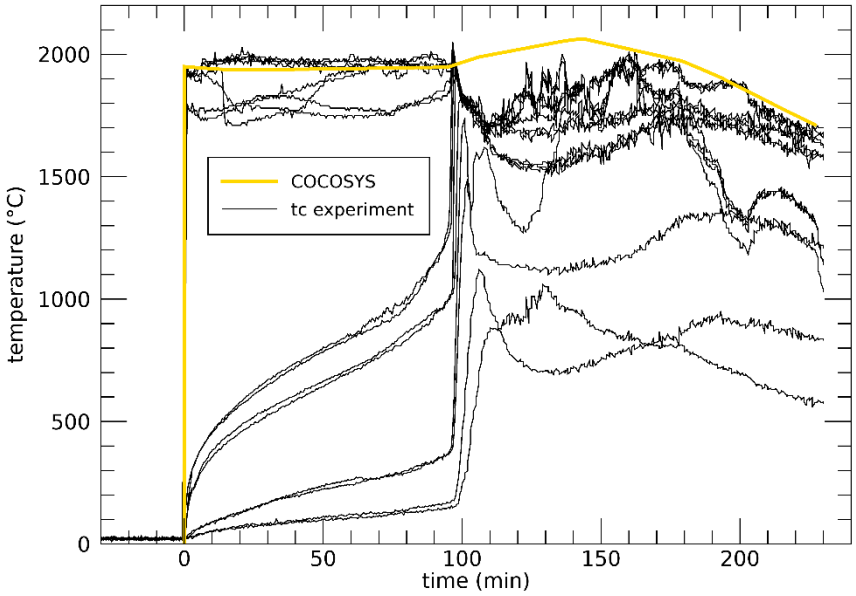

Figure 8. Comparison of COCOSYS results for corium temperature with WCB-1 thermocouple data in corium/SM.

4. APPLICATION TO A CRUCIBLE CORE CATCHER AND FIRST/PRELIMINARY RESULTS

The core catcher model was used for a simplified WWER-1200 simulation for which the geometry, material data and initial and boundary conditions are estimated.

The results of the model presented here are obtained for the exemplary axisymmetric core catcher geometry shown in Figure 2 as approximation to a WWER-1200 crucible core catcher type. Major initial and boundary conditions for this base case are estimated from available data in open literature [8]: The initial corium mass is assumed as 75000 kg oxide (88 wt.-% UO_2 and 12 wt.-% ZrO_2) and 75000 kg of metals (12000 kg zirconium + steel) at an initial temperature of about 2650 K. For simplification, the total corium mass is assumed to be present in the core catcher already at initial time t = 0 s.

The corium pool is considered as a homogeneously mixed melt layer throughout the calculation. The SM is assumed to be composed of Fe_2O_3 (61 wt.-%) and Al_2O_3 (39 wt.-%). The effect of elevated thermal conductivity compared to concrete-type SM is neglected with view to the melting approach used in the model. Decomposition temperature T_{dec} and enthalpy h_{dec} for the simulation of SM melting are assumed as 1800 K and 2.2 MJ/kg, respectively. A constant decay power of 20 MW is assumed. An initial increase of interface area with $f_{\mathrm{geom}} = 2$ is compared to the base case with $f_{\mathrm{geom}} = 1$ (Figure 9, left). In this calculation, it is assumed that the core catcher is not flooded from the top.

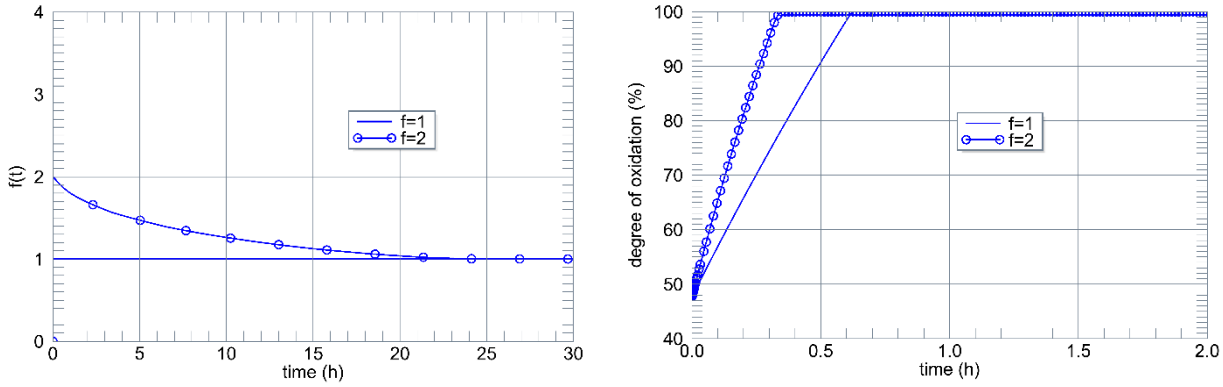

Figure 9. Evolution of $f_{\mathrm{geom}}(t)$ (left) and oxidation degree of zirconium inventory (right)

Depending on the choice of f_{geom}, a full oxidation of the zirconium inventory in this sample application is expected between 0.3 h and 0.6 h (Figure 9, right). Figure 10 shows the progression of the 2-dim interface profile between corium and SM. A quasi-steady state (input power ≈ output power) is obtained after approx. 8 h. The calculated corium temperature of the mixed layer is then steadily getting close to 1800 °C.

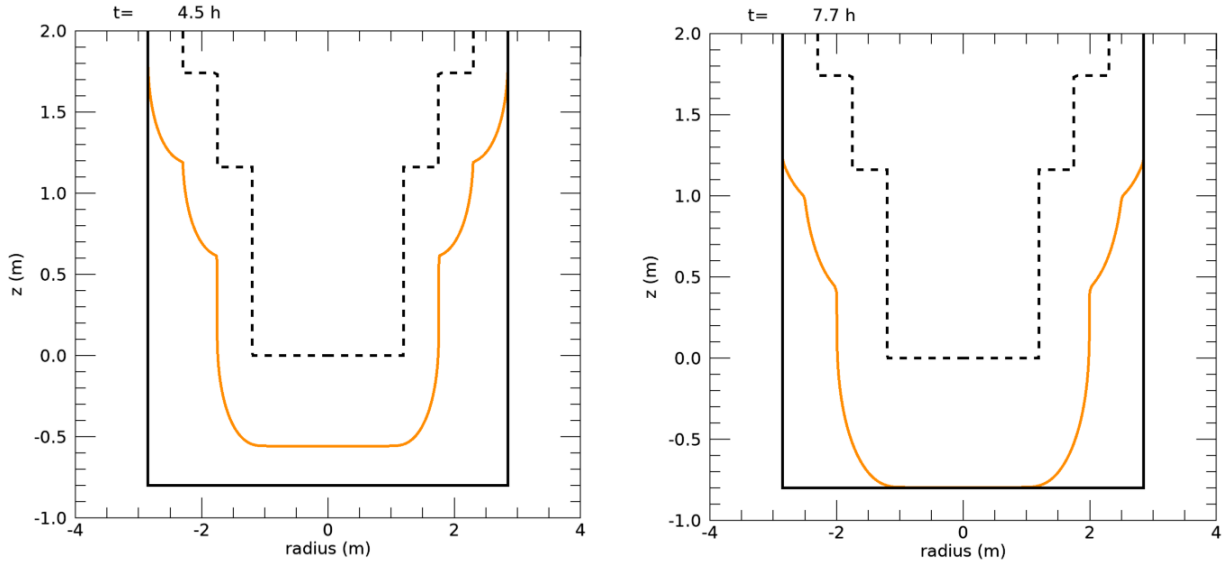

Figure 10. Time dependent contour (orange line) of the SM in relation to initial contour (dashed line) and vessel wall (solid line)

In a variation of the base case (not shown here) the corium configuration is considered as stratified, and the configuration evolution option is enabled. Here, a layer flip from the initial configuration with the heavy oxide layer at the bottom and the lighter oxide layer at the top to the inverse configuration (light oxide on top of the denser metal layer remaining) is obtained 0.6 h after start of the interaction between corium and SM. In this case, two quasi-steady layer temperatures are calculated: $T_{\mathrm{oxide}} \approx 1900$ °C, $T_{\mathrm{metal}} \approx 1550$ °C instead of a single layer temperature.

5. SUMMARY AND CONCLUSIONS

A core catcher model is developed for the containment code COCOSYS as part of the AC² code suite. Essentially, this model combines the existing CCI model in COCOSYS for simulation of the corium/sacrificial material interaction phase (MCCI phase) in the core catcher with a transition to a retention phase, in which the status of the corium is simulated with the help of empirical heat transfer coefficients between corium and water-cooled horizontal or vertical core catcher walls. During the MCCI phase, the model continuously calculates the melting of the sacrificial material, the corium oxidation and potentially a layer flip of stratified oxide and remaining metal layers in the core catcher. During the retention phase the model continuously calculates the heat transfer from the corium to the water-cooled interfaces as well as the physical state of the corium.

The model requires the input of an axisymmetric core catcher geometry, so that any non-axisymmetric design (like the EPR core catcher) shall first be scaled into an axisymmetric model. Designs, in which the initial interface area between corium and structural material is larger than that resulting from a single axisymmetric interface shape can be compensated via a time-dependent virtual increase of the interface area.

The model application to the WCB-1 test of the OECD MCCI-2 programme shows that the COCOSYS prediction of the concrete melting during the MCCI phase in a core catcher provides an adequate average of the behaviour observed in the experiment. In the second phase, after melting of the concrete layer, the thermal resistance between corium and the water-cooled bottom plate, as observed in the experiment, is very large compared to the thermal conduction in the bottom plate and the convection heat transfer in the channels. This large thermal resistance limits the overall heat transfer through the plate and is caused by a solidified corium layer or by a remaining concrete layer on the top of the water-cooled plate. For the base case calculation, the water-side heat transfer coefficient was in the order of 700 W/(m^2 K), which is by factor 2 smaller than approximations based on engineering correlations for forced turbulent boiling flows in pipes. The reduction by factor ~ 2 is reasonable to consider the potential effect of reduced wetting area, which might be expected during stratified or annular flow in horizontal channels, especially when only the upper half of the circumference is heated.

Discrepancies between code calculations and the experiment WCB-1 during the first phase (effect of initial crusts during dry operation phase) are attributed to transient effects, which cannot be considered in the current model, which is based on a lumped parameter approach, due to the complex phenomenology of initial crust behaviour known in MCCI experiments.

The high surface temperatures of the bottom plate measured in the WCB-1 experiment (Figure 6) could not be predicted by the calculation. It is assumed that they are caused by an artefact of the design of the instrumentation.

Furthermore, a sample application for a crucible-type core catcher of a WWER-1200 plant is presented in which the initial and boundary conditions in terms of masses, decay power, and geometry are estimated. For this type of core catcher, the validity of model assumptions for SM geometry and the neglect of heat transfer through non-ablated SM needs to be further investigated.

For a future verification and improvement of the model it would be beneficial to make a comparison with other calculations, e. g. performed with the SOCRAT/HEFEST[1] code (in which proprietary boundary conditions and a fine 2D mesh and 2D modelling were used) or with other experimental data, if available.

ACKNOWLEDGMENTS

The development and validation of COCOSYS is sponsored by R&D-projects RS1598 and RS1579 financed by the German Federal Ministry for the Environment, Nature Conservation, Nuclear Safety and Consumer Protection (BMUV).

REFERENCES

1. Y. Zvonarev, and Y. Semchenkov, "Strategy of Corium Localization for VVERs under Severe Accident Conditions," in *ERMSAR2019, The 9th European Review Meeting on Severe Accident Research (*2019).
2. M. Fischer, A. Henning, and R. Surmann, "The Core Melt Stabilization Systems of ARVEA NP's EPR and ATMEA1 Reactor," in *MCCI - Seminar,* OECD Nuclear Energy Agency (NEA), ed. (2010).
3. A. Wielenberg, L. Lovasz, P. Pandazis, A. Papukchiev, L. Tiborcz, P. J. Schöffel, C. Spengler, M. Sonnenkalb, and A. Schaffrath, "Recent improvements in the system code package AC^2 2019 for the safety analysis of nuclear reactors," Nucl. Eng. Design (2019).
4. C. Spengler, I. Bakalov, N. Reinke, and M. Sonnenkalb, "Uncertainty and Sensitivity Analyses in Support of Model Development and Validation of the Containment Module COCOSYS of the AC² Code – Application for Molten Corium/Concrete Interaction (MCCI)," in *NUTHOS-12, 12th International Topical Meeting on Nuclear Reactor Thermal-Hydraulics, Operation and Safety,* Chinese Nuclear Society (CNS), State Power Investment Corporation Limited (SPIC), eds. (2018).
5. OECD Nuclear Energy Agency (NEA), *State-of-the-Art Report on Molten Corium Concrete Interaction and Ex-Vessel Molten Core Coolability* (OECD/NEA, 2017).
6. M. T. Farmer, S. Lomperski, D. J. Kilsdonk, and R. W. Aeschlimann, *OECD MCCI-2 Project. Final Report* (2010).
7. M. T. Farmer, R. W. Aeschlimann, D. Kilsdonk, and S. Lomperski, "Category 2: Water-Cooled Basemat (WCB-1) Test Investigating Core Melt Stabilization Using a Water-Cooled Surface," in *MCCI - Seminar,* OECD Nuclear Energy Agency (NEA), ed. (2010).
8. Ю. А. Звонарев, *Оценка эффективности работы УЛР для ВВЭР-1200 (Проект АЭС-2006) с помощью кода ГЕФЕСТ-УЛР* (2011).

A Simplified Core Catcher Model for the Containment Code AC² / COCOSYS

C. Spengler, I. Bakalov

May, 16-19, Karlsruhe, Germany

ERMSAR 2022

ERMSAR 2022

MAY 16-19, 2022 — KARLSRUHE, GERMANY

Ex-Vessel core catcher designs in plants of gen. III+

Overall aim and requirements of a core catcher device in plants of Gen. III+ :

- To ensure retention and stabilisation (cooling) of molten corium inside the containment
- To limit the release of non-condensable gases (H_2, CO) and fission products
- To reduce the risk of ex-vessel steam explosions
- To ensure long-term sub-criticality of the corium
- To protect the reactor cavity against thermal and mechanical impact of corium

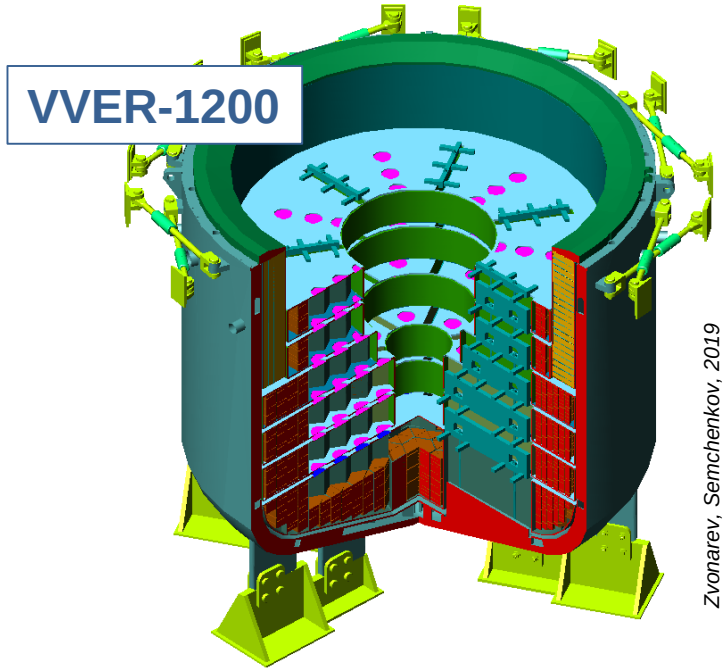

Zvonarev, Semchenkov, 2019

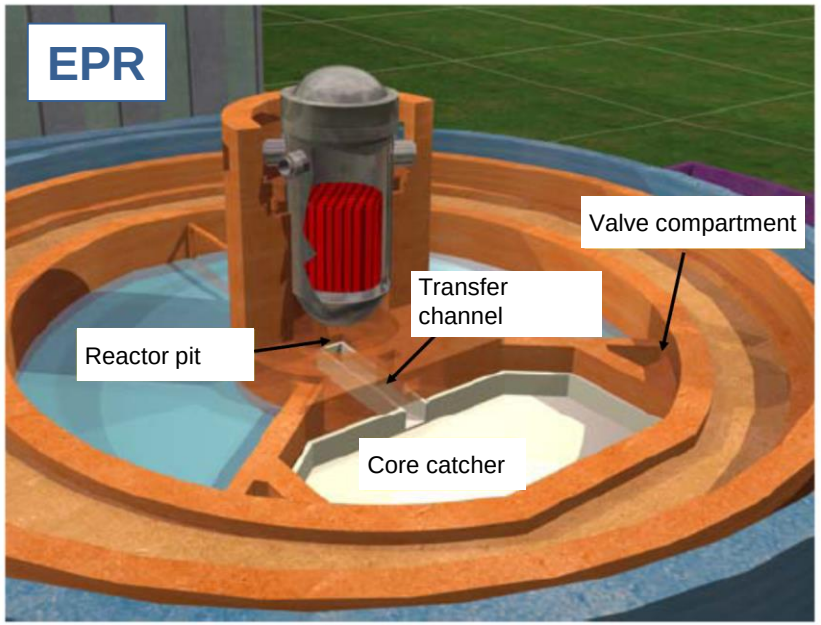

Fischer et al., 2010

AC² code package for simulation of incidents and accidents in LWR

AC² = ATHLET / ATHLET-CD + COCOSYS

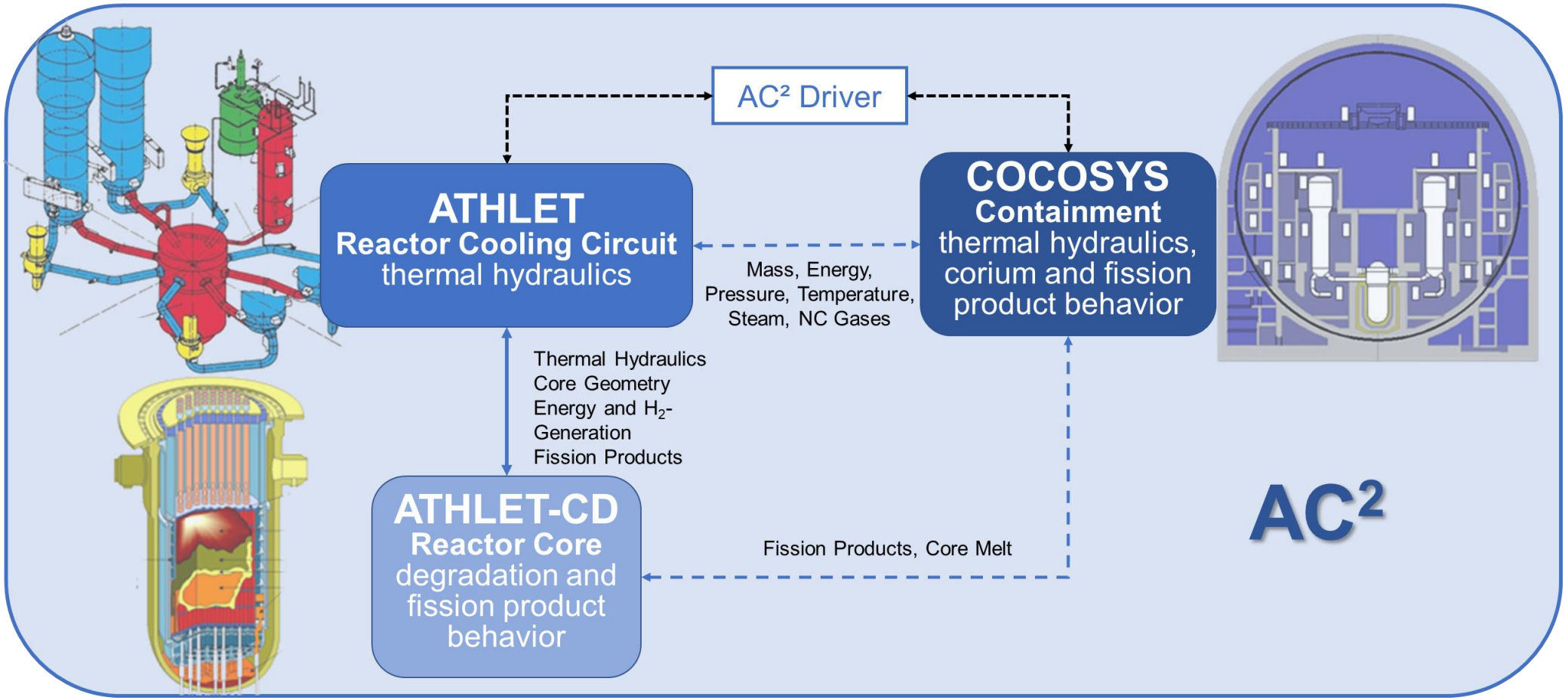

COCOSYS – COntainment COde SYStem for the analysis of containment phenomena in LWR

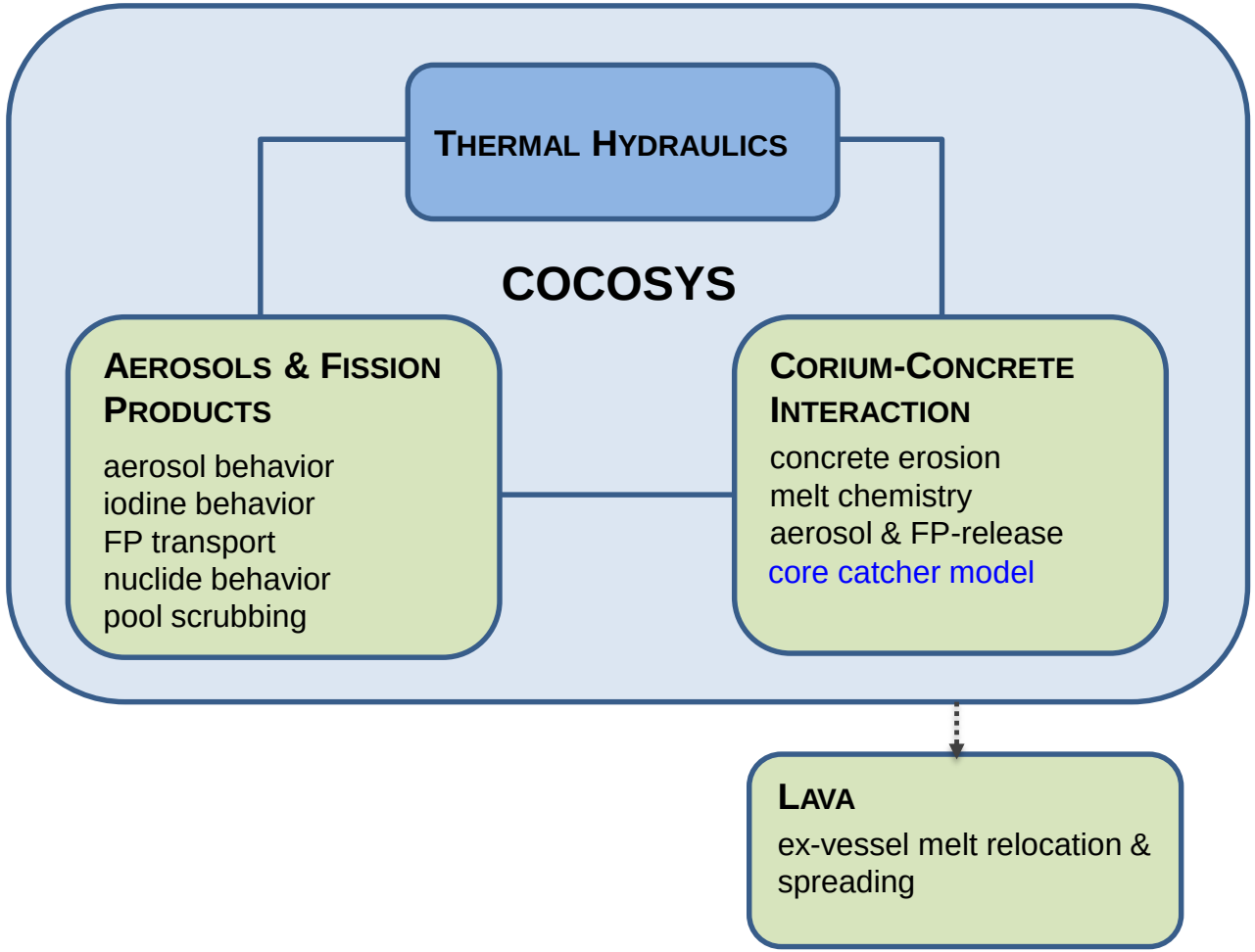

Objectives / requirements for the core catcher model in COCOSYS

- Model should be well balanced according to LP concept of the code
- Close the model gap in COCOSYS for the ex-vessel phase of the accident in plants with core catcher devices
  - Simulate stabilisation and cooling of molten core inside a core catcher in the containment in a severe accident analysis
  - Simulate the processes in a core catcher and their effects on the containment behaviour
    - Interaction of the core melt with sacrificial material
    - Oxidation of the metallic fraction in the melt and non-condensable gas generation
    - Stratification behaviour / layer flip of the corium in the core catcher
    - Temperatures inside the core catcher walls
    - External cooling of the core catcher walls (side and bottom)
    - Cooling of the core melt from the top
    - Steam release to the containment
    - Effects on free/forced water circulation in the containment
    - Effects on atmospheric convection inside containment

coupling with containment thermal-hydraulics and fission product behaviour

Outline of the core catcher model

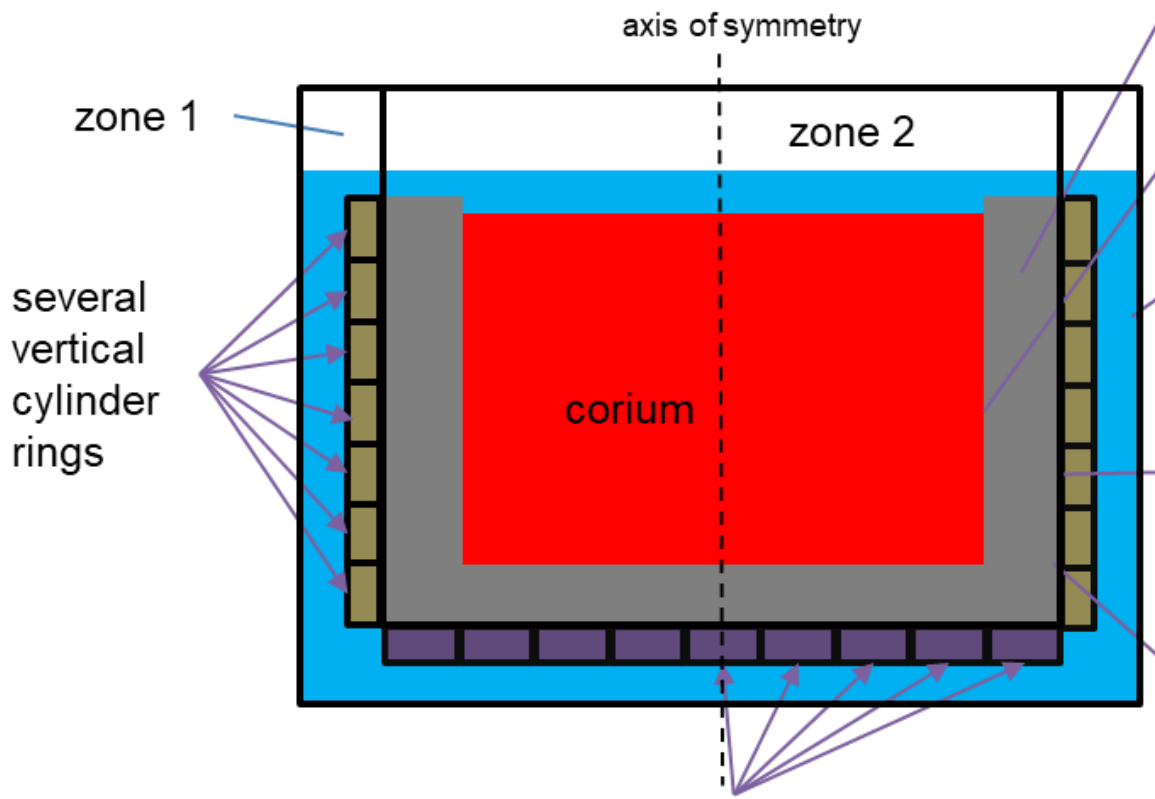

sacrificial material (SM)

initial contour between melt and sacrificial concrete given by initial *r*,*z*-profile in CCI

water pool defined in zone 1 (and possibly zone 2)

interface geometry between SM and core catcher wall defined by core catcher segment definition (horizontal/vertical only)

heat transfer into core catcher walls calculated after local melting of SM; HTC provided by input

Basic assumptions and simplifications

- Melting approach used for the decomposition of the SM by interaction with the melt (T_{dec}, H_{dec})
- Fast melting of the SM / neglecting the thermal conduction within SM during melting
- Homogeneous or two-layer configuration of the pool, triggered by relative densities of oxide and metal and superficial gas velocity
- Heat transfer to water by free convection / pool boiling correlation
- Core catcher cooling plates can be subdivided into vertical (sidewall) or horizontal (bottom) structures
- After melting of the SM: Heat flux calculated for sideward or downward contact between melt and core catcher wall injected in whole heat structure
- Elevated interface area between core melt and SM compared to simplified interface shape can be considered (e. g.: f_{geom} = 2).

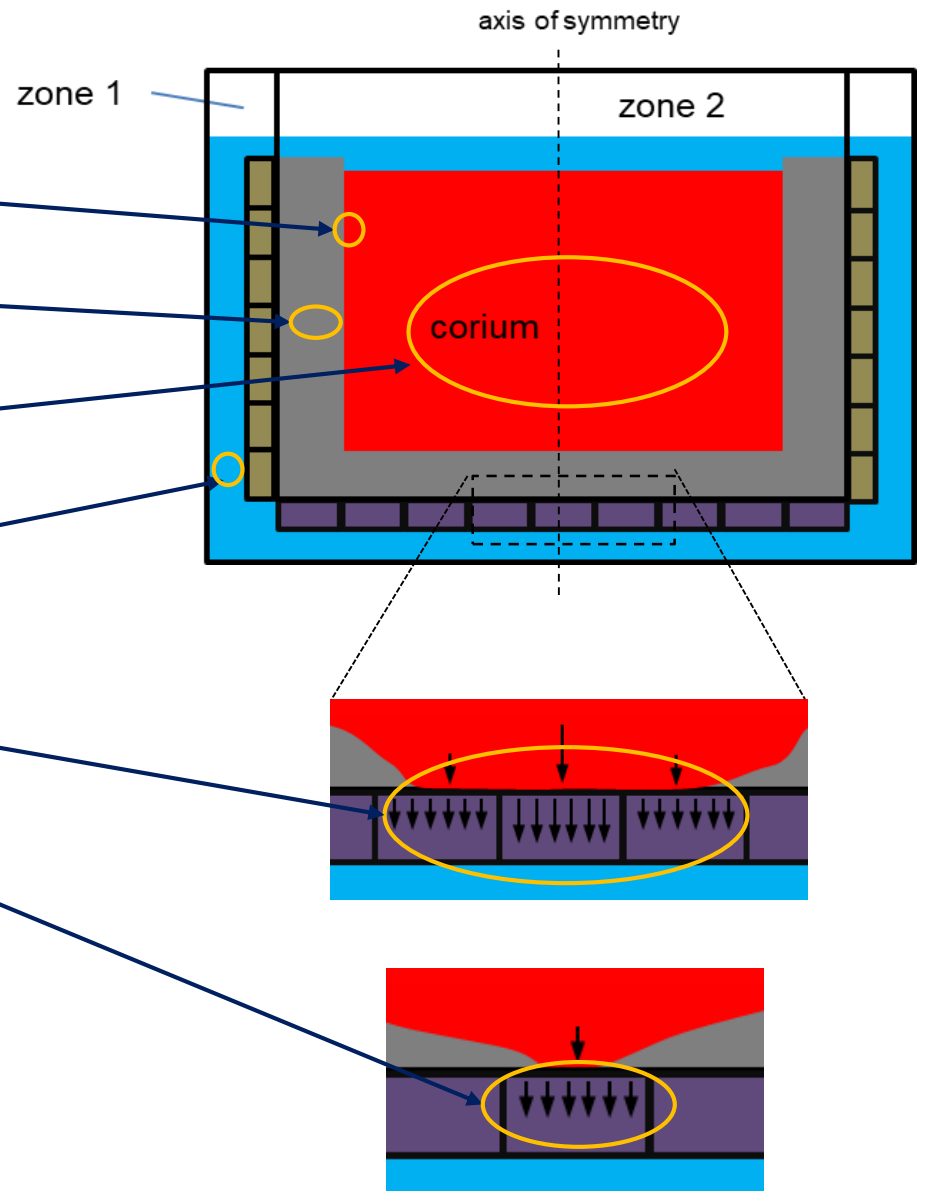

Assumptions on heat transfer to structures in the core catcher

- Heat transfer h_{MCCI} between corium bulk and SM assumed similar as for MCCI
  - Complex phenomenology involved
    - Reactions of corium with SM
    - Liquefaction of SM
    - Thermal convection
    - Solutal convection
    - Solidification of the melt
    - Gas release
  - Use of empirical effective heat transfer coefficients h_{MCCI} for heat transfer to SM using the MCCI model during decomposition of SM
- Heat transfer h_{cc} to core catcher wall is different:
    - Thermal convection
    - Solidification of the melt at the cold wall
  - Use of empirical effective heat transfer coefficients h_{cc} for heat transfer between the corium and vessel plate structures of the core catcher

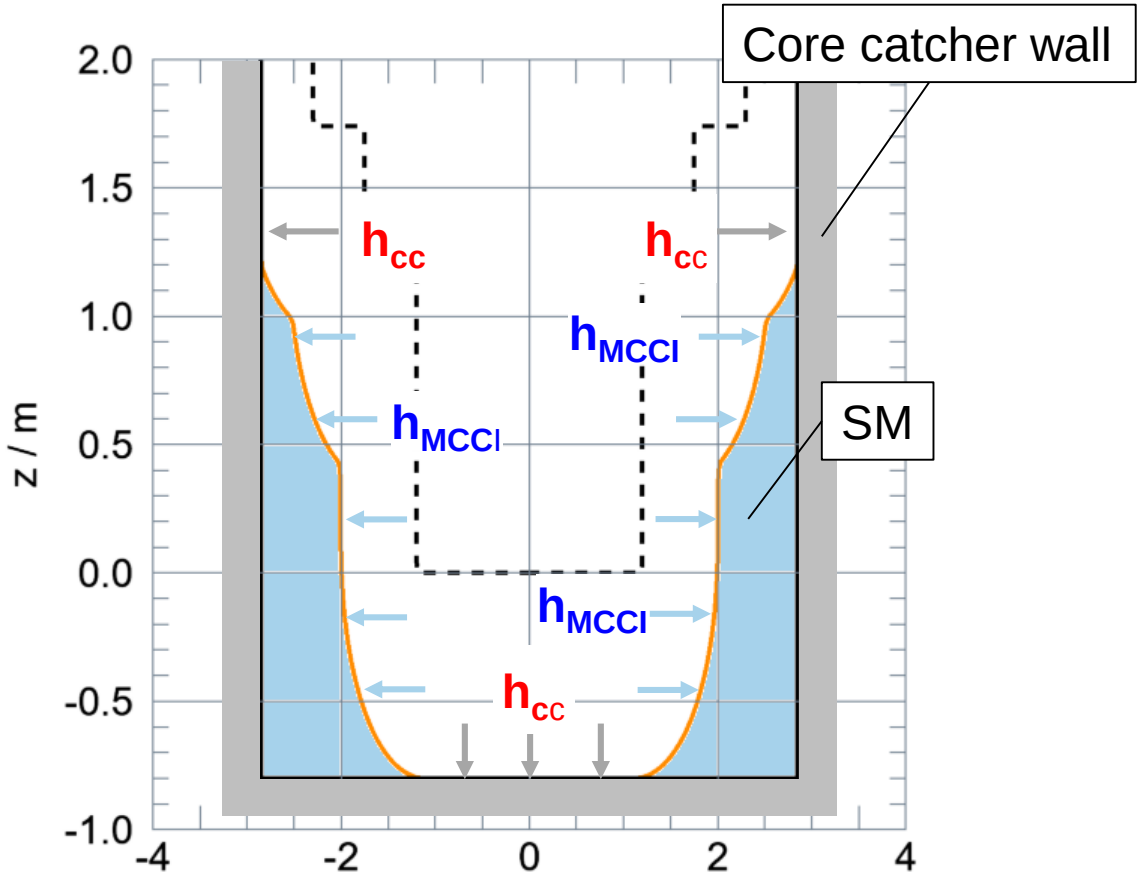

OECD-CCI2 Project: Water Cooled Basemat Test WCB-1

- Objective of WCB-1 test:
  - Provide prototypic data on the evolution and stabilization of a core melt in a generic water-cooled core catcher design for advanced plant applications
- Conditions of the experiment:
  - Square test section 50 cm × 50 cm
  - ~ 25 cm oxidic melt
  - UO_2 / ZrO_2 / concrete
  - T_0 = 1950 °C
  - Decay heat simulated by direct electric heating at constant power
  - Five cooling channels embedded in bottom stainless steel plate
  - 15 cm siliceous concrete as SM below corium pool
  - MgO sidewalls
  - Top surface of melt was flooded with water after 12.5 cm of axial concrete erosion

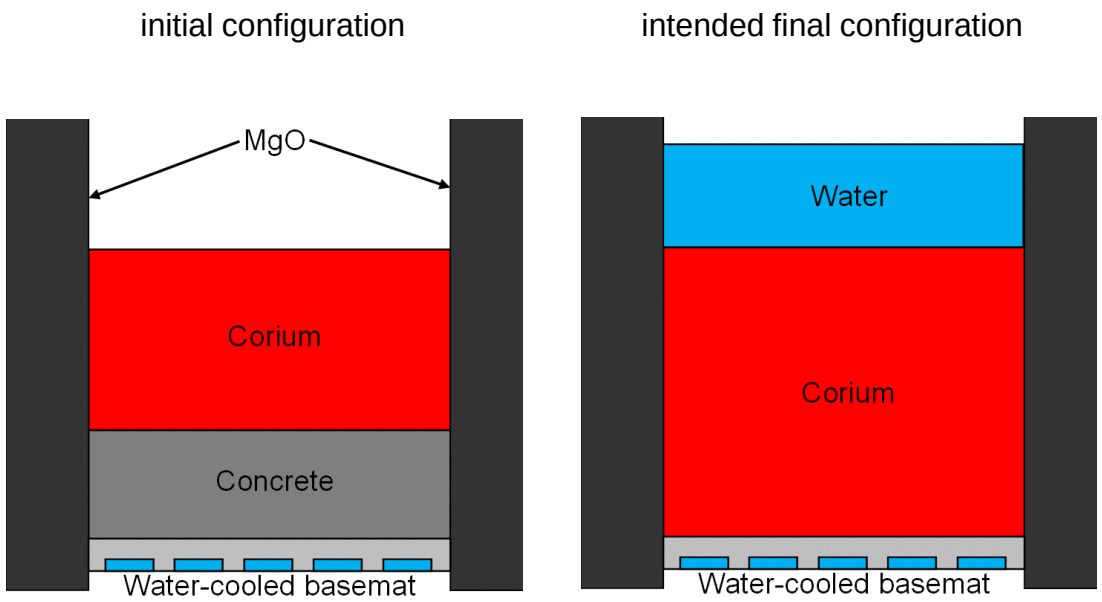

Results and Conclusions from WCB-1 Analysis with COCOSYS

- Confirmation, that empirical model parameters derived from earlier MCCI experiments are suitable as “average” approach during SM melting:
  - $T_{dec} \approx 1800$ K
  - $h_{MCCI} \approx 300$ W/(m^2 K) for bottom heat transfer coefficient during MCCI

Temperature

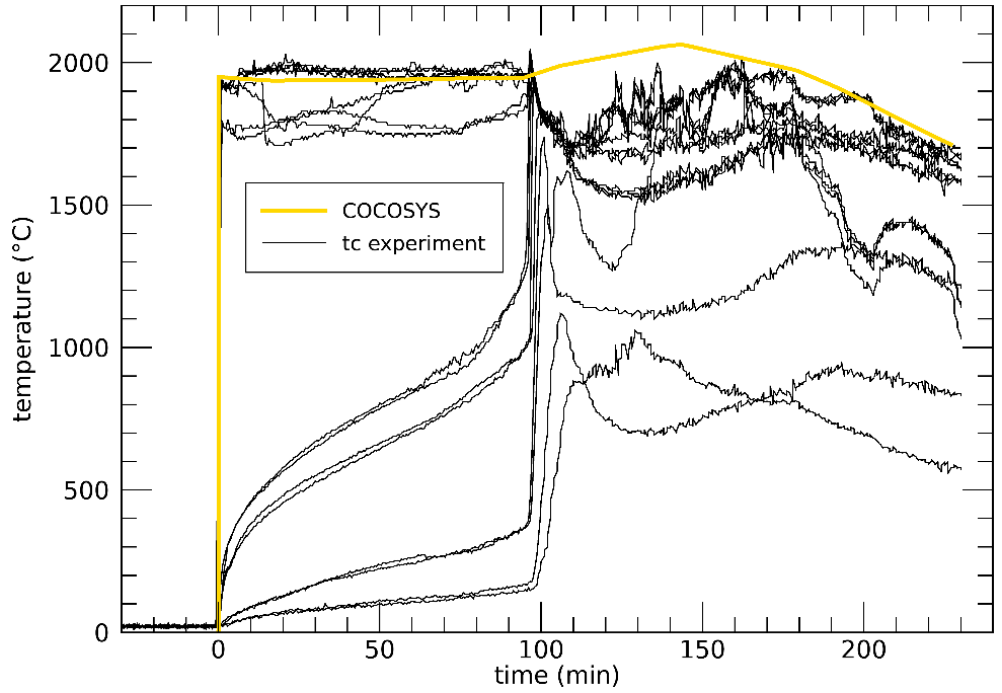

Concrete erosion depth

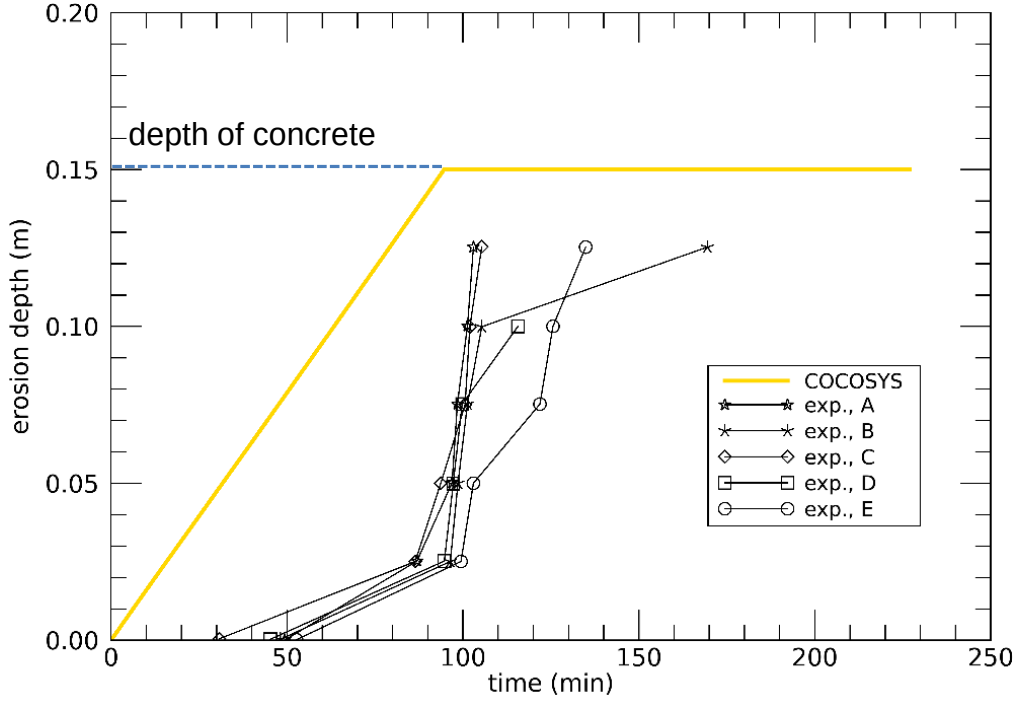

Results and conclusions from WCB-1 analysis with COCOSYS

- After SM melting, heat transfer to bottom plate seems to be very ineffective:
  - $h_{CC} \approx 15$ W/(m² K)
  - $\frac{\lambda}{d} \approx 550$ W/(m² K)
  - $h_{wat} \approx 700$ W/(m² K)
  - Thermal resistance is dominated by h_{CC}
  - h_{CC}: ~ thermal conduction through crust and remaining concrete
- Calculated interface temperature between melt and plate is well below solidification temperature of the corium
- Modelling of h_{CC} is difficult

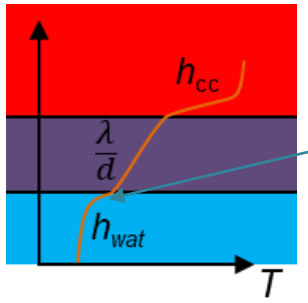

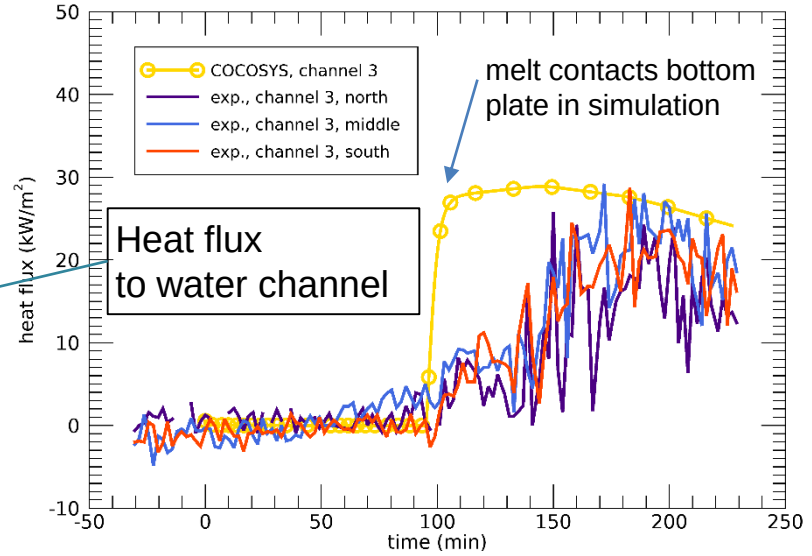

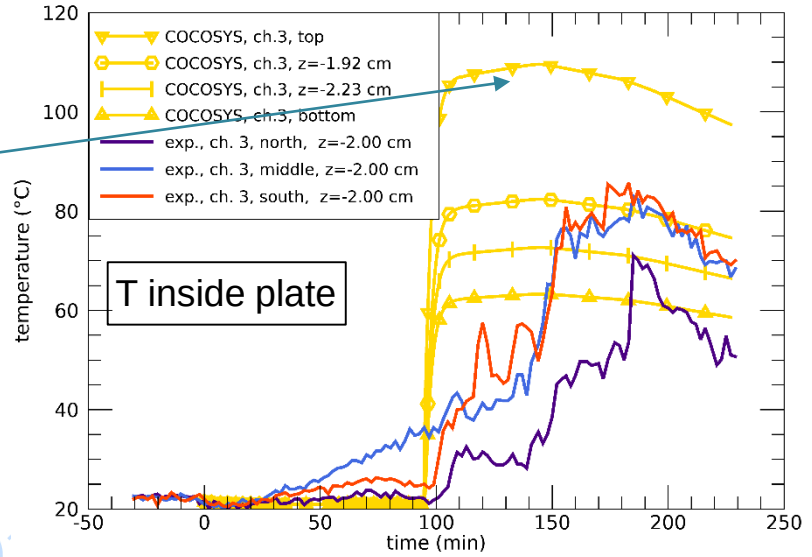

Sample application for a crucible type core catcher

Initial and boundary conditions estimated for a core catcher (based on few available data for VVER-1200 type) with some simplifications:

- 75 000 kg oxide (88 wt-% UO_2 / 12 wt-% ZrO_2)
- 75 000 kg of metals (steel + 12000 kg zirconium)
- P_{decay} = 20 MW = const.
- Single, homogeneously mixed layer (no layer flip considered)
- Corium pool in core catcher is complete at t = 0 s
- T_0 = 2650 K
- SM made of Fe_2O_3 (61 wt-%) and Al_2O_3 (39 wt-%)
- $T_{\mathrm{dec}} \approx$ 1800 K and h_{dec} ~ 2.2 MJ/kg for the simulation of SM melting
- Elevated thermal conductivity of specific SM is not considered
- External water cooling of the core catcher vessel walls
- In this example, the core catcher is not flooded from the top.

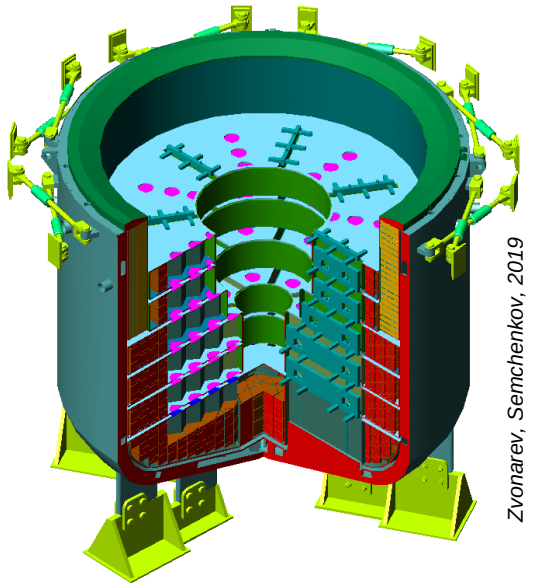

Zvonarev, Semchenkov, 2019

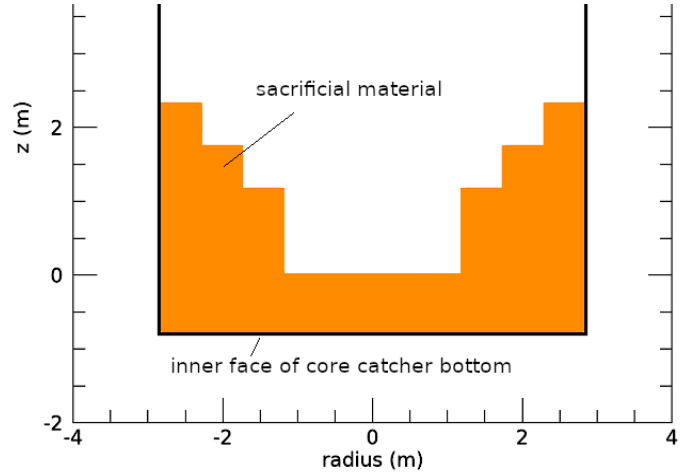

Sample application for a crucible type core catcher

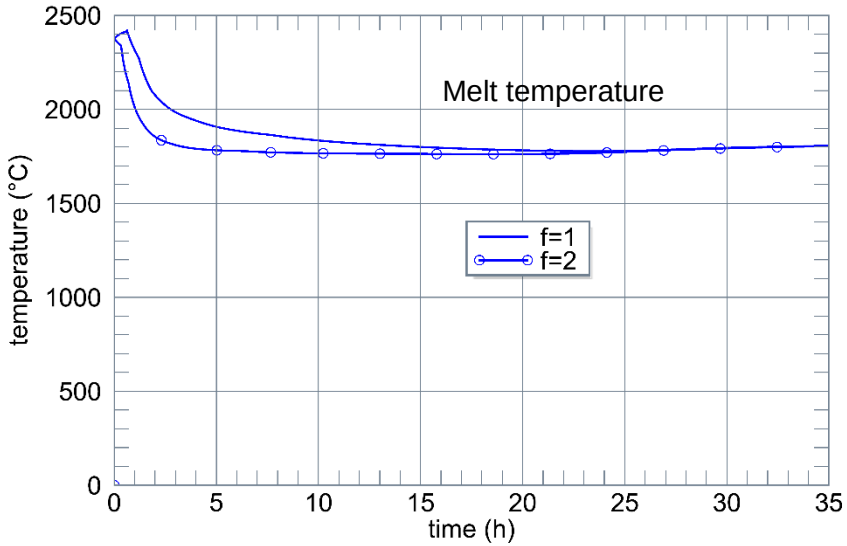

Contour of SM

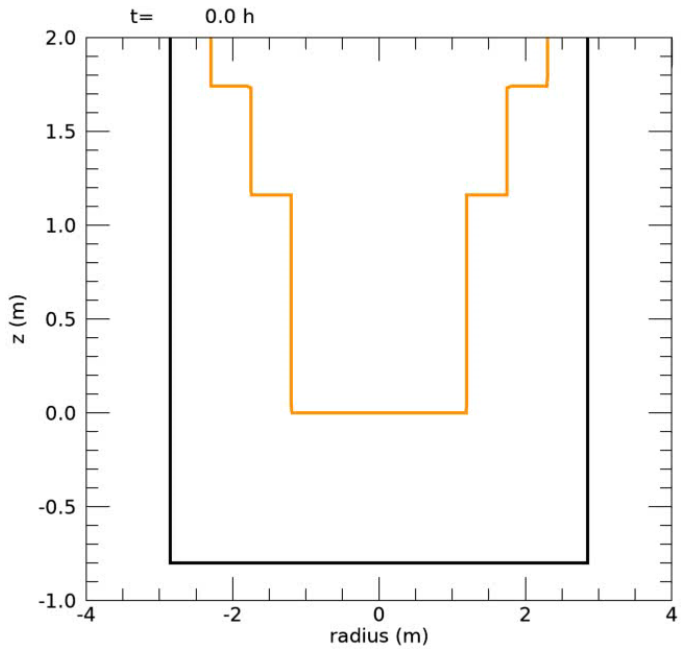

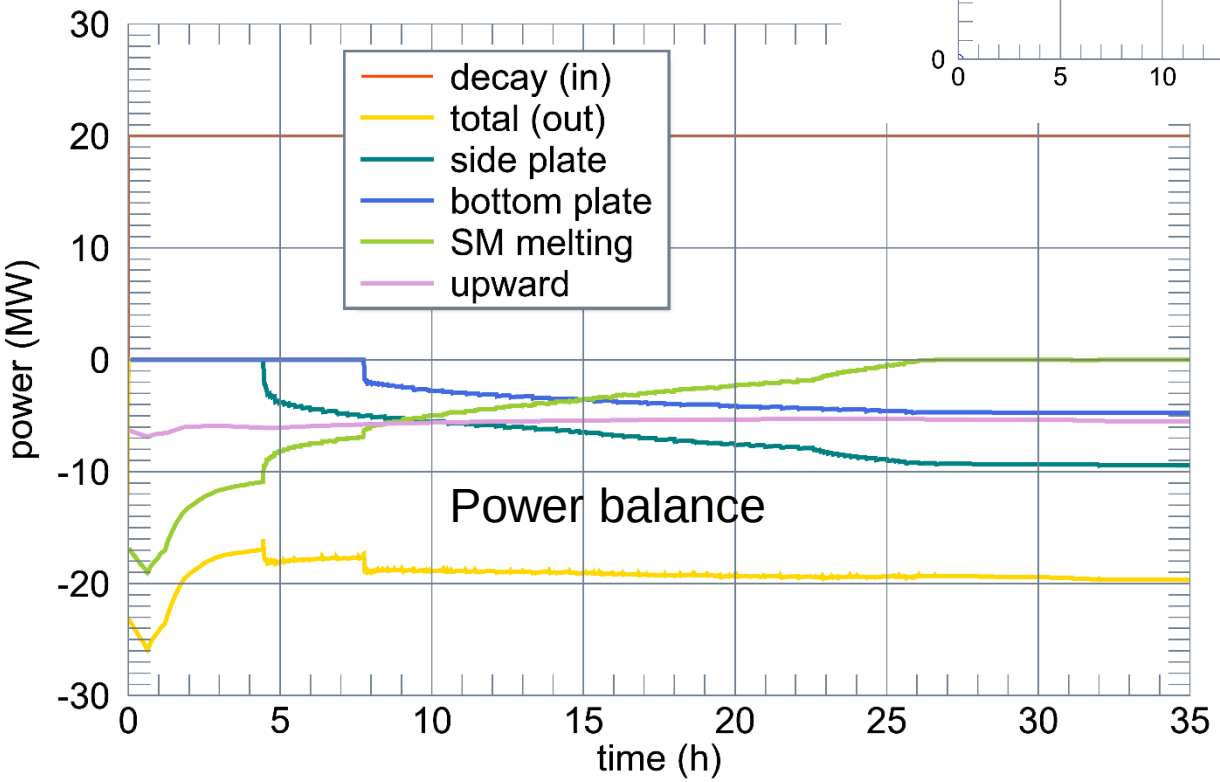

Summary and conclusions

A simplified core catcher model is developed for the containment code COCOSYS as part of the AC² code suite

- MCCI phase: approach for corium/sacrificial material interaction
  - Melting of SM
  - Oxidation of metals and generation of non-condensable gases
  - Potential layer flip
  - Flooding of melt from above
- Retention phase with (empirical) heat transfer coefficients to core catcher walls
  - Transfer of decay power into water passive flow around the core catcher walls and above the corium
  - Long-term temperatures of core melt and core catcher walls
- Use of empirical heat transfer coefficients for both phase to account for modelling uncertainties
- Application to OECD WCB-1 test
  - Adequate approximation of experiment
  - Limited heat transfer to the bottom interface in the conditions examined
- Sample application to a crucible-type core catcher
  - Results for roughly estimated VVER-1200 conditions are encouraging
  - Further improvement of the model requires the use of proprietary data and/or comparisons with available experiments or analyses performed with more mechanistic models (e.g. SOKRAT/HEFEST)

Acknowledgements

Supported by:



based on a decision of
the German Bundestag

The development and validation of COCOSYS is sponsored by R&D-projects RS1598 and RS1579 financed by the German Federal Ministry for the Environment, Nature Conservation, Nuclear Safety and Consumer Protection (BMUV).

The 10th European Review Meeting on Severe Accidents Research

Severe Accident Research Eleven Years after the Fukushima Accident

May 16-19, 2022, Karlsruhe, Germany

PLENARY SESSION: NEW ELEMENTS IN THE SA RESEARCH DOMAIN

Chairs: H. U. Rehman (IAEA), I. Kljenak (IJS)

Phenomena Identification Ranking Tables for Near Term Accident Tolerant Fuels (ATF) Applicable to Severe Accident Conditions
M. Khatib-Rahbar (Energy Research, Inc.)

SMR impact on SA research and community
P. Dejardin (TRACTEBEL)

Advanced decision support system: JRODOS Application for Ukraine
W. Raskob (KIT)

Innovation in Modeling
L. Chailan (IRSN)

10TH CONFERENCE ON SEVERE ACCIDENTS RESEARCH
May 16-19, 2022 – Karlsruhe, Germany
ERMSAR 2022

PHENOMENA IDENTIFICATION RANKING TABLES FOR NEAR-TERM ACCIDENT TOLERANT FUELS (ATF) APPLICABLE TO SEVERE ACCIDENT CONDITIONS

Mohsen Khatib-Rahbar
Energy Research, Inc.
6189 Executive Blvd
Rockville, Maryland 20852

ENERGYRESEARCHINC

European Review Meeting on Severe Accident Research, AkademieHotel Karlsruhe, May 2022

Round table: New elements in the SA research domain

IAEA
International Atomic Energy Agency

SNETP
Sustainable Nuclear Energy Technology Platform

NUGENIA TA2
Nuclear Generation II&III Alliance

NEA
Nuclear Energy Agency

Outline

- Objectives of the PIRT Panel
- Near-term ATFs
- Findings (including impact of high burn-up & enrichment) relative to FOMs*:
  - Accident progression (e.g., Oxidation, etc.)
  - Fission product release & transport (to containment for both PWRs & BWRs)

* Figures of Merit (FOM)

Objectives of PIRT Panel

- To evaluate the effects of ATF designs on severe accident behavior (including effect of high burnup & fuel enrichment)*
- To determine potential changes to NRC's severe accident analysis code (e.g., MELCOR) to better model those effects.
- Focus on "near-term" designs; however, requested comments on "longer-term" concepts (outside the scope of PIRTs)

---

* Also, established ranks for conventional fuels

Near-Term ATFs

- Advanced stainless steel (FeCrAl) cladding,
- Cr_2O_3 dopant in UO_2 fuels*, and
- Conventional Zr-alloy cladding coated with chromium.

Considering both the impact of high burn-up & high enrichment ($\leq$ 10%) (HALEU).

---

*The ATF concepts evaluated for PIRT do not include the Cr_2O_3 and Al_2O_3 doped or additive ATF technologies also being used in some operating plants (mostly in Europe).

Summary Findings

- FeCrAl-Clad UO_2 Fuel:
  - Exhibits most differences as compared to conventional fuels (i.e., the cladding material is entirely replaced).
  - Limited experimental evidence of FeCrAl degradation at high temperatures, especially when oxidized:
    - Lower initial oxidation rate (prior to clad melting); however, there is potential for significant oxidation (after cladding melts).
    - Oxidation can impact accident progression both during in-vessel and ex-vessel phases

Summary Findings - continued

- FeCrAl-Clad UO_2 Fuel (Cont.):
  - There is significant amount of Al but not Cr (compared to conventional fuels):
    - Al & Cr could (insufficient data) affect speciation & transport of fission products
    - Vapor-phase hydroxides & oxyhydroxides of Al & Cr could form at high steam partial pressures, which impact release & transport of non-radioactive aerosols to containment (e.g., impact of filters, heat exchangers, etc.)
  - Te not expected to sequester by FeCrAl cladding as observed in some experiments for Zr-alloy cladding (which is also uncertain).

Summary Findings - continued

- Cr-Coated Zr-Alloy-Clad UO_2 Fuel:
  - Not very different from conventional fuels (bulk cladding remains conventional & Cr is confined to a thin coating on the outside surface)
  - Considerable quantities of Cr already exist in conventional core structures (i.e., added mass for Cr does not alter progression of severe accidents)
  - Some thermophysical properties are slightly less well known (e.g., thermal conductivity due to thermal resistance at the coating interface is uncertain)

Summary Findings - continued

- Cr-Coated Zr-Alloy-Clad UO_2 Fuel (Cont.):
  - Initial oxidation expected to be lower (prior to exceeding Cr-Zr eutectic temperature) as intended:
    - Coating affects oxidation, etc. (e.g., fuel degradation & relocation due to potential shift in time of rapid oxidation heat input)
    - Cladding burst during a LOCA results in oxidation of interior uncoated cladding surface

Summary Findings - continued

- Cr-Doped UO_2 Fuel:
  - No major differences with conventional fuels
  - Small amount of dopant primarily affects grain size of UO_2 reducing release of volatile radionuclides (e.g., I, Cs, etc.):
    - To the gap (during normal operation), and
    - During early stages of severe accidents.
  - No significant effect on H_2 generation & later stages of severe accidents.
  - Only notable difference with conventional fuels is slightly fewer available test data on fission product speciation & chemistry:
    - Limited information available suggests there might be a significant effect on oxygen potential in the fuel (due to even small quantities of added chromia)

Summary Findings - continued

- High Burnup Fuel:
  - Some thermophysical properties of fuel & cladding (i.e., thermal conductivity & specific heat) affected by higher burnup.
  - Fission product chemistry may be affected by presence of more lower valence atoms in the fuel due to higher burnup (i.e., greater degree of transmutation by fission of U atoms). This affects release of Ru

Summary Findings - continued

- High Burnup Fuel (Cont.):
  - Oxygen potential expected to increase (due to larger concentration of lower valence atoms in fuel), possibly affecting rate of oxidation at cladding inner surface. However, this is buffered by Mo/MoO_2 (Mo inventory may be sufficient to prevent significant excursions of O_2 potential as burnup progresses).
  - Gap inventories of fission products larger in absolute sense, but not clear if they would be larger when expressed as a fraction of the total inventory.

Summary Findings - continued

- High Burnup Fuel (Cont.):
  - Fuel expected to have a different degree of fragmentation or sintering at higher burnup,
    - Can affect fuel behavior during core degradation/relocation & temperature-induced creep rupture (i.e., effect of core debris particle size).
  - Increased cladding embrittlement might be possible at higher burnup (affecting likelihood of core coolability upon reflood). However, this has not been closely examined to date.

Summary Findings - continued

- High Burnup/High Assay Low Enriched Uranium (HALEU) Fuel:
  - No significant qualitative differences in severe accident behavior as compared to just HBU fuels
  - The only noted difference is the greater likelihood of recriticality in some accidents (e.g., accidents involving reflood following core damage, using un-borated water).

Reference*

- "*Review of Accident Tolerant Fuel Concepts with Implications to Severe Accident Progression and Radiological Releases*," Nuclear Regulatory Commission, NUREG/CR-7282 (July 2021).
- "*Phenomena Identification Ranking Tables for Accident Tolerant Fuel Designs Applicable to Severe Accident Conditions*," Nuclear Regulatory Commission, NUREG/CR-7283 (July 2021).

* Pubicly available

PIRT Panel Members

Mohsen Khatib-Rahbar	Chair & Facilitator
Marc Barrachin	IRSN - France
Richard Denning	Consultant - US
Jeff Gabor	Jensen Hughes – US Industry
Randy Gauntt	Consultant (formerly SNL) – US
Luis Herranz	CEMAT – Spain
Richard Hobbins	Consultant – US
Didier Jacquemain	OECD/NEA – France
Yu Maruyama	JAEA – Japan
James Metcalf	Consultant – US Industry
Dana Powers	Consultant (formerly SNL) - US

10TH CONFERENCE ON SEVERE ACCIDENTS RESEARCH
May 16-19, 2022 – Karlsruhe, Germany
ERMSAR 2022

SMR impact on SA research and community

Philippe Dejardin

TRACTEBEL
ENGIE

European Review Meeting on Severe Accident Research, AkademieHotel Karlsruhe, May 2022

Round table: New elements in the SA research domain

IAEA
International Atomic Energy Agency

SNETP
Sustainable Nuclear Energy Technology Platform

NUGENIA TA2
Severe Accidents
Nuclear Generation II&III Alliance

NEA
Nuclear Energy Agency

Table of contents

- **Introduction with some definitions**
  - What are SMR ?
  - What are Severe Accidents for SMR ?



- **Connection/Employment in the Severe Accident Field**
  - What are specific SA issues that can be identified so far for SMR ?



- **Projects and Perspectives**
  - What is known, ongoing and could be expected from my viewpoint ?



- **Key question and messages**
  - Should the SA research community be afraid of SMR impact ?



Introduction – What are SMR ?

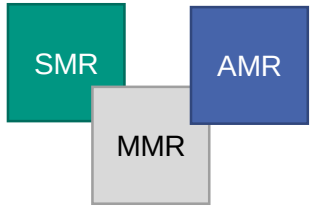

SMR : Small Modular Reactor
AMR : Advanced Modular Reactor
MMR : Micro-Modular Reactor

- Variety of “definitions” proposed
  - Globally common
    - Inherent safety features
    - Modularity
    - Wider range of applications
    - Better economics
  - Some distinctions
    - Maximum power output
    - Between SMR, AMR and MMR
    - Use novel designs features
    - (Large) use of passive systems
- → Harmonization needed

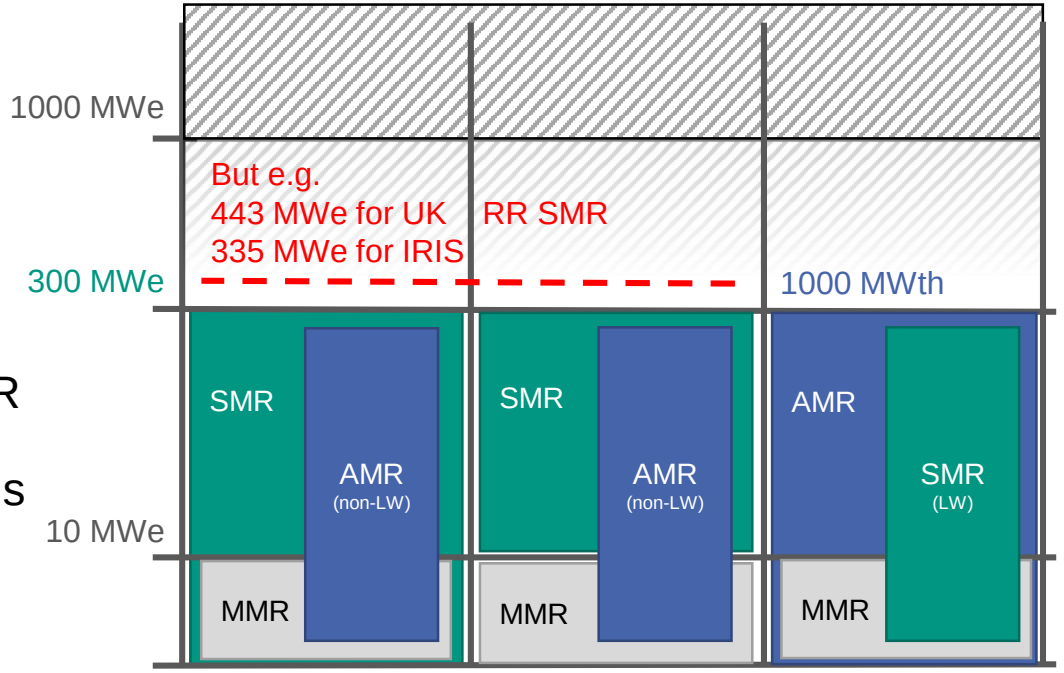

Introduction – What are SMR ?

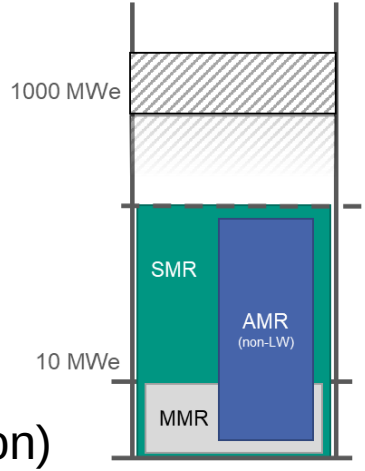

- Tractebel “definition” used for the current presentation

- SMR is a concept embedding
  - Enhanced intrinsic safety, with potential for a better acceptance
  - Modular aspects (multiple modules & design for series production)
  - Variety of usage in a quite disruptive way
  - Smaller footprint (although not absolute)
  - Limited CAPEX to allow deployment by new actors

  - No strict consideration of power output such as < 300 MWe / 1000 MWth
  - No distinction of technology

Introduction – What are Severe Accidents for SMR ?

- IAEA Glossary definition of Severe Accident: *“Accident more severe than a design basis accident and involving* ***significant core degradation****”*

- More specifically for Water-Cooled Reactors (WCR), SA are often referred to as Design Extension Condition (DEC) with **core melting**

- “Conventional” definitions make sense especially for LWSMR but not necessarily for others

  - What would “core degradation” or “core melting” mean for a Molten-Salt SMR ?
  - How should it be understood for TRISO fuels ?

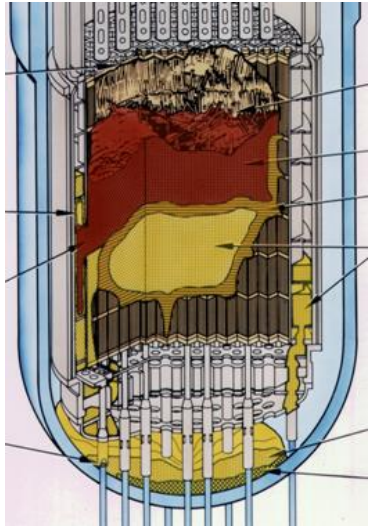

Introduction – What are Severe Accidents for SMR ?

- Understanding of the Severe Accident concept is directly linked to fundamental Safety
  - Defence-in-Depth (DiD)
  - Practical Elimination (PE) of large or early radioactive releases
  - Emergency Planning Zone (EPZ)



- From Tractebel viewpoint:
  - Harmonized definition should envelop all SMR types while maintaining current understanding of SA for LWSMR
  - Considering a graded approach of SA in SMR designs is important

- Not the purpose of today's presentation but point identified as
  - It represents a strong need for clarification and harmonization
  - It will help framing the identification of research needs in SA for SMR

Connection/Employment in the Severe Accident Field

- Hamonized understandings of what are “SMR” and “SA for SMR” should be reached as pre-requisites



- However, do these understandings represent absolute pre-requisites to identify first SMR research needs in SA ?

  - Not from Tractebel point of view as
    - Conventional understanding of SA is applicable to LWSMR
    - LWSMR have a higher Technology Readiness Level (TRL)
    - LWSMR near-term deployment seems achievable to support the needed transition to a low-carbon economy

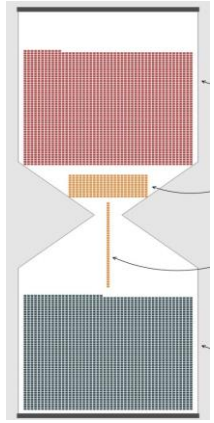

The CO_2 Hourglass
Twitter : @rubenbmathisen

Connection/Employment in the Severe Accident Field

- First SA research needs can therefore be identified in priority for LWSMR
  - From Tractebel knowledge, this is, at least, globally supported within
    - The OECD/NEA Expert Group on SMR (EGSMR)
    - The R&D TG4 on SA (SNETP SMR Partnership Roadmap)
    - The SNETP NUGENIA TA2 (e.g. via the SASPAM-SA proposal)
    - *The IAEA CRP I31033 (Task 2.5)*

- Non-LWSMR should however not be forgotten
  - Second priority set most often on High Temperature Gas-cooled Reactor (HTGR) SMR for industrial heat applications

Connection/Employment in the Severe Accident Field

- What are specific SA issues that can be identified so far for SMR ?

  - As an example, the ongoing R&D TG4 on SA brings some input
    - Not declared exhaustive as other frames exist as well
    - Overview as dedicated presentation at SNETP Forum (2/06/22)

  - 2 High-Level research needs have been identified

    - **Identification of potential or postulated SA scenarios**
      - Combining deterministic and probabilistic tools/methods along with engineering judgment

    - **Identification of specific research needs for these scenarios**

Projects and Perspectives – For LWSMR

- Past/ongoing projects and operating experience from large LWR will be fundamental to
  - Identify LWSMR “research needs” that can be covered by applicability and transfer of large LWR existing knowledge
  - Focus on LWSMR specific research needs (experimental and analytical)
    - **RPV integrity** : IVR mitigation and demonstration, integral design
    - **Containment integrity** : integral design and compaction
    - **EPZ** : objective to limit it to site boundary but might be challenging for existing “conventional” tools/methods

IVR : In-Vessel Retention

Projects and Perspectives – For LWSMR

- **SASPAM-SA** (Safety Analysis of SMR with PAssive Mitigation strategies – Severe Accident):
  - Submitted in the HORIZON-EURATOM2021-NRT-01-0
  - Grant Agreement preparation on-going

  - **Project main objective**: to investigate the applicability and transfer of the operating large-LWR reactor knowledge and know-how to the near-term deployment of integral PWR (iPWR), in the view of SA and EPZ European licensing analyses needs

  - **Expected outcomes**: help speeding up the licensing of iPWRs in Europe, as well as the siting processes of these reactors in light of their possible use near densely populated areas

  - 4 years duration
  - Coordinated by ENEA
  - 23 participating organizations
  - More info : fulvio.mascari@enea.it

Projects and Perspectives – For non-LWSMR

- Need for the hamonized understanding of SA in their case is important
- Difficult to identify the needs for SA research without this pre-requisite
- However, research needs around EPZ assessments and tools would be reinforced, especially for heat applications with shorter distances required
  - District heating
  - Industrial heat relying on HTGR SMR

Projects and Perspectives



- Feelings on impact of SMR on the different “SA research” streams

SA research stream	LWSMR	Non-LWSMR
In-vessel corium and debris coolability	Refined and increased interest to demonstrate low probability / PE of core degradation	
Ex-vessel corium interactions and coolability	Decreased interest providing that core degradation is demonstrated as low probability / PE *(with possible exception for BWR SMR)*	
Severe accident scenarios and uncertainties	Increased interest in relation to HL research need 1	Increased interest with updated SA definition that could lead to different scenarios
Source Term	Constant or decreased interest	Increased interest to understand phenomenology and potential releases
Severe accident modelling and code development	Variable interest (cf. above)	Increased interest as more to develop
Hydrogen and containment related issues	Variable interest (cf. above)	*Not assessed*

Key question and messages

- Should the SA research community be afraid of SMR impact ?
  - Does “inherently safe” mean SA community would be useless in a SMR world ?

- No, as
  - *“The PE concept should not justify omission of a complete DiD level”*
  - SA community has a role to play in demonstrating this inherent safety and challenge SMR designs

- However, SMR will be impactful and require adaptations
  - Technically, with new knowledge and developments
  - Culturally, with even more graded-approach principles
  - From all stakeholders

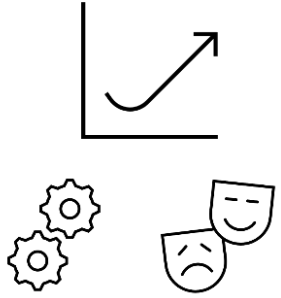

Key question and messages

- Key words and concepts to keep in mind
  - Opportunities, new challenges, adaptation, acceptance



  - Need for strong collaboration between all stakeholders to ease SMR deployment
  - Increase awareness and systematic overview
  - Nuclear safety must certainly be ensured with requirements defined in balance with other major societal risks, firstly the one of climate change



10TH CONFERENCE ON SEVERE ACCIDENTS RESEARCH
May 16-19, 2022 – Karlsruhe, Germany
ERMSAR 2022

Advanced decision support system: JRODOS Application for Ukraine

Wolfgang Raskob
Institute for Thermal Energy Technology and Safety

Karlsruhe Institute of Technology

European Review Meeting on Severe Accident Research, AkademieHotel Karlsruhe, May 2022
Round table: New elements in the SA research domain

IAEA International Atomic Energy Agency

SNETP Sustainable Nuclear Energy Technology Platform

NUGENIA TA2 Severe Accidents Nuclear Generation II&III Alliance

NEA Nuclear Energy Agency

Introduction to the Topic

- Briefly discuss the assessment of contamination of the environment following releases from an NPP – screening calculations for Ukraine
  - Decision Support System JRODOS
  - Application for Ukraine
  - Results with implications to Germany
- Possible common interest with ERMSAR community – final slide

Key features of RODOS
Real-time On-line Decision Support system

- Multi-user operation in national/regional emergency centres for off-site nuclear emergency management
- Provision of information for decision-making
  - on local / national / regional / European scales,
  - in the early and later phases of an accident,
  - for all relevant emergency actions and countermeasures.
- Wide IT applicability - at present Microsoft Windows and Linux

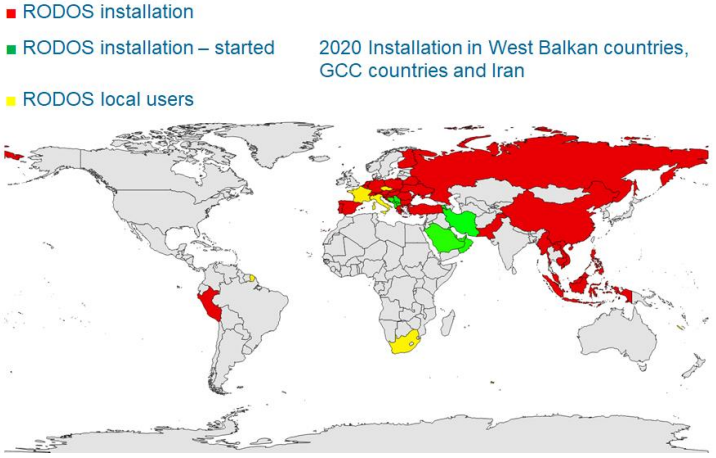

JRodos EMERGENCY chain models

Released activity (Measurement / User)

Meteorological data (Measured / Prognostic / User)

Further data (from JRodos Data bases)

LSMC: Atmospheric dispersion and deposition, local scale (up to several 100 km)

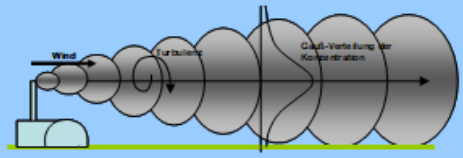

Rimpuff (DEN)

Dipcot (GRE)
Lasat (GER)

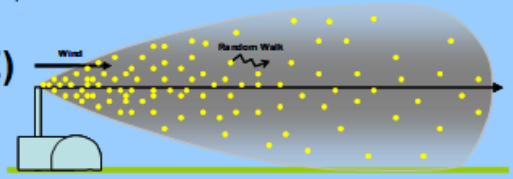

Accident
Release of
52 hours

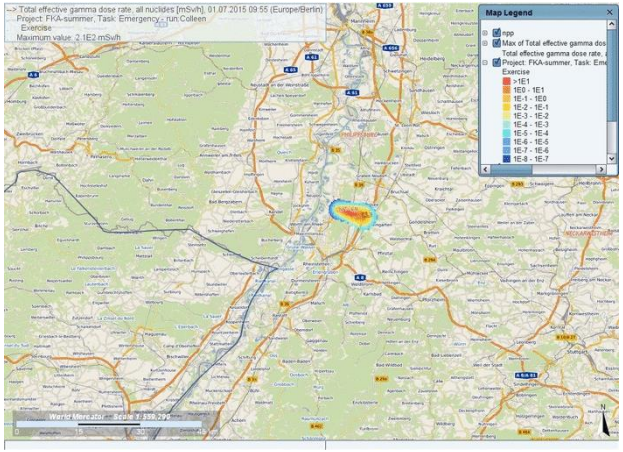

Dose rate calculation,
Early countermeasure simulation,
Health effects and costs

Food chain and dose model, terrestrial FDMT (GER)

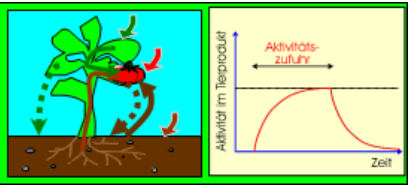

Ukraine NPPs



Questions

- What are the consequences for Germany if there would be an accident in Ukrainian NPPs?
- Is there a risk following the capture of Chernobyl by Russian troops?
- Are there other risks from nuclear installations (e.g. neutron source, research reactors, waste storage sites etc.)?
- Which source term to be applied? ERMSAR community

Preliminary answers

- KIT is working together with Hydromet – the Ukrainian emergency management organisation and SNRIU, the Ukrainian regulator
- Ukrainian NPPs: Yes there is a thread and assessments should be performed. KIT supported Hydromet to set up JRODOS for this purpose
- Chernobyl
  - New Safe Containment: re-critically very unlikely, release of radioactive dust following a damage of the containment would result in local contamination. Forest fires also resulted in local contamination
  - Waste storage sites: Nuclear fuel elements were 20 years old, so no problem, even if water will be not renewed
- Other facilities
  - Neutron source in Kharkov, not active, very small potential source term
  - Other facilities with little potential

Specialised functionalities of JRodos

- Dirty bomb
- Wildfire
- Tornadoes
- Source term reconstruction
- Continuous mode
- Recurrent job launcher
- Ensemble generator
- Web services
- Evaluation tool
- Statistical tool

Use of Recurrent Job Launcher for assessments

Start-up of selection screen

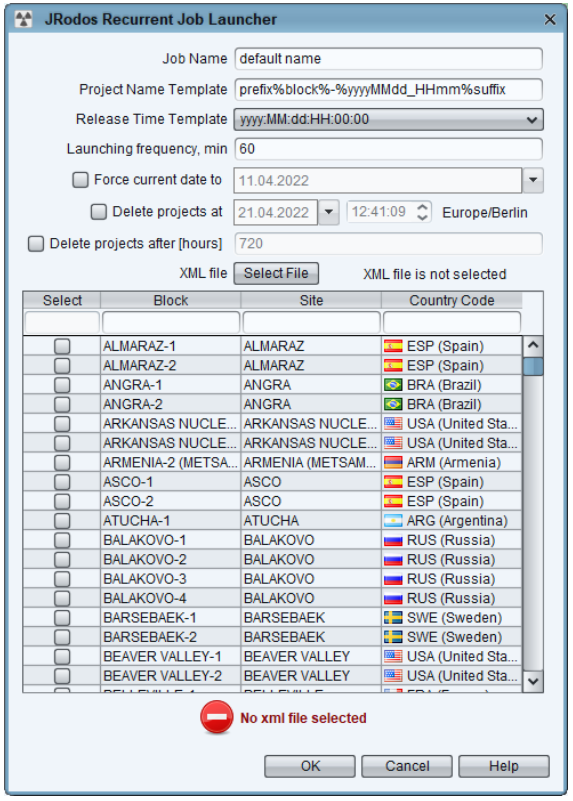

Ukrainian NPPs selected

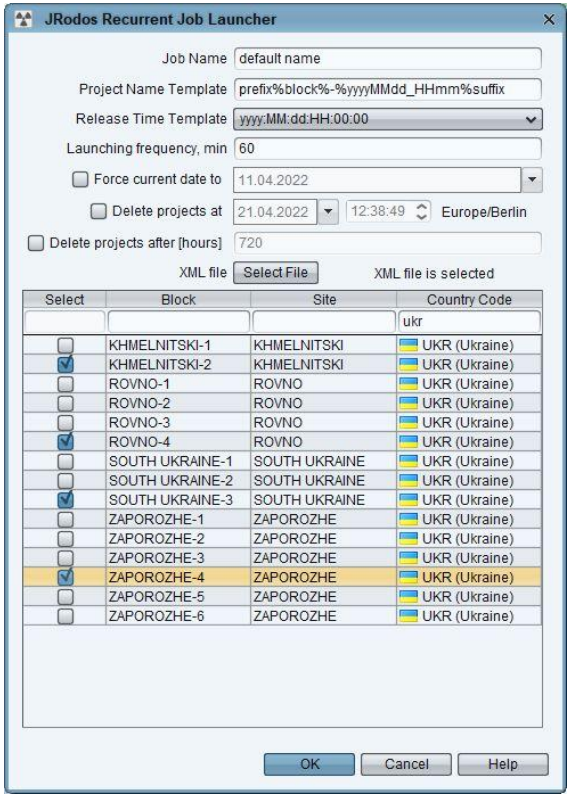

Recurrent Job Launcher cont.

- JRODOS offers a possibility to download numerical weather data from the US weather service
  - Automatic download every 12 hours defined with a prognosis time of 48h
- A source term was defined to be used in the calculations
- Prognosis duration of 36 hours
- Calculations performed every 60 minutes for four NPP locations
  - Rivne, Khmelnitsky, Zaporozhe, South Ukraine
- Important endpoints
  - Arrival time
  - Areas for early countermeasures
  - Dose rates

Result selection

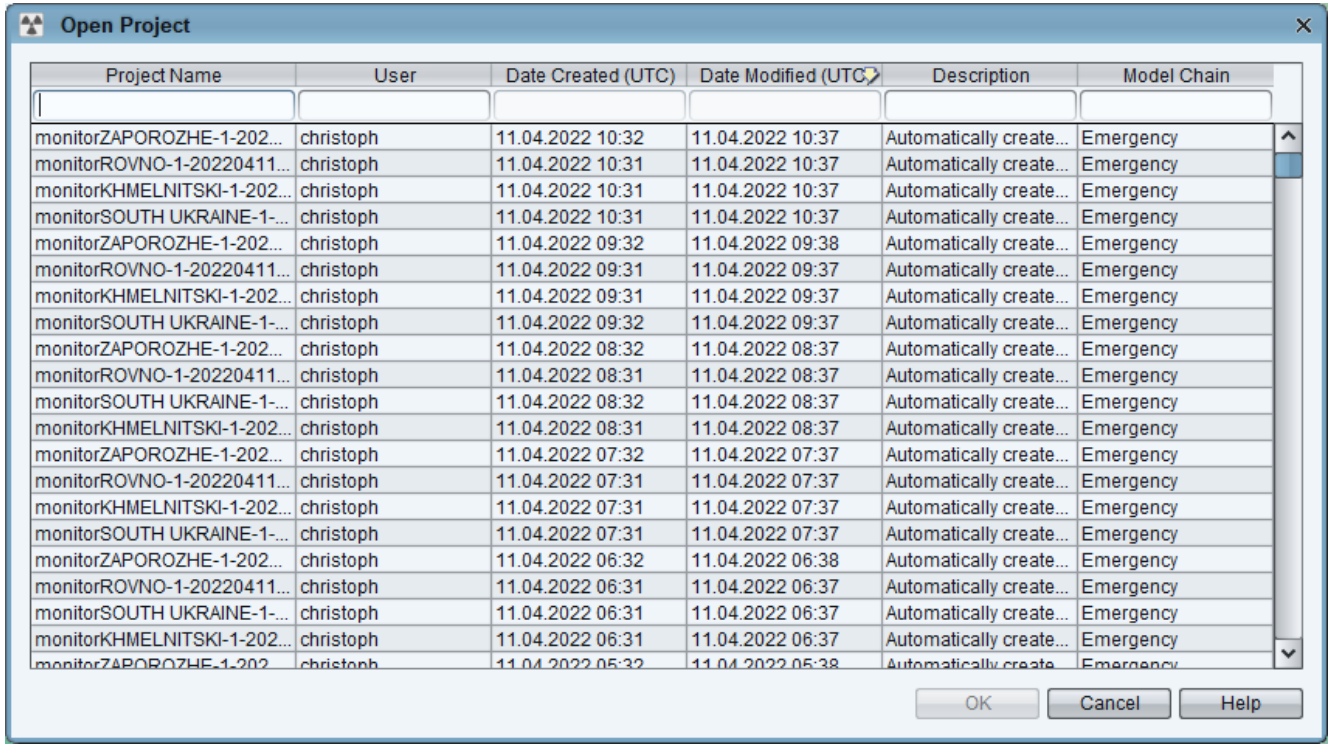

I-131 total deposition, 11.04.22 at 10:00 UTC

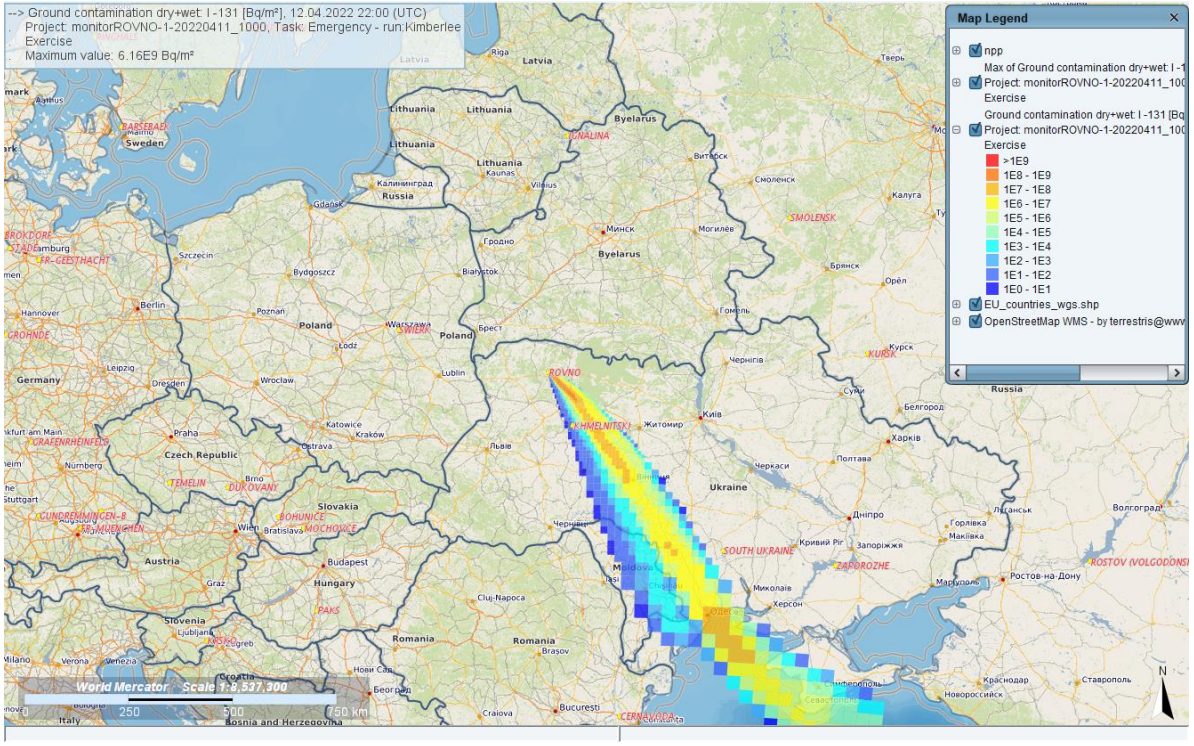

Arrival time, 11.04.22 at 10:00 UTC

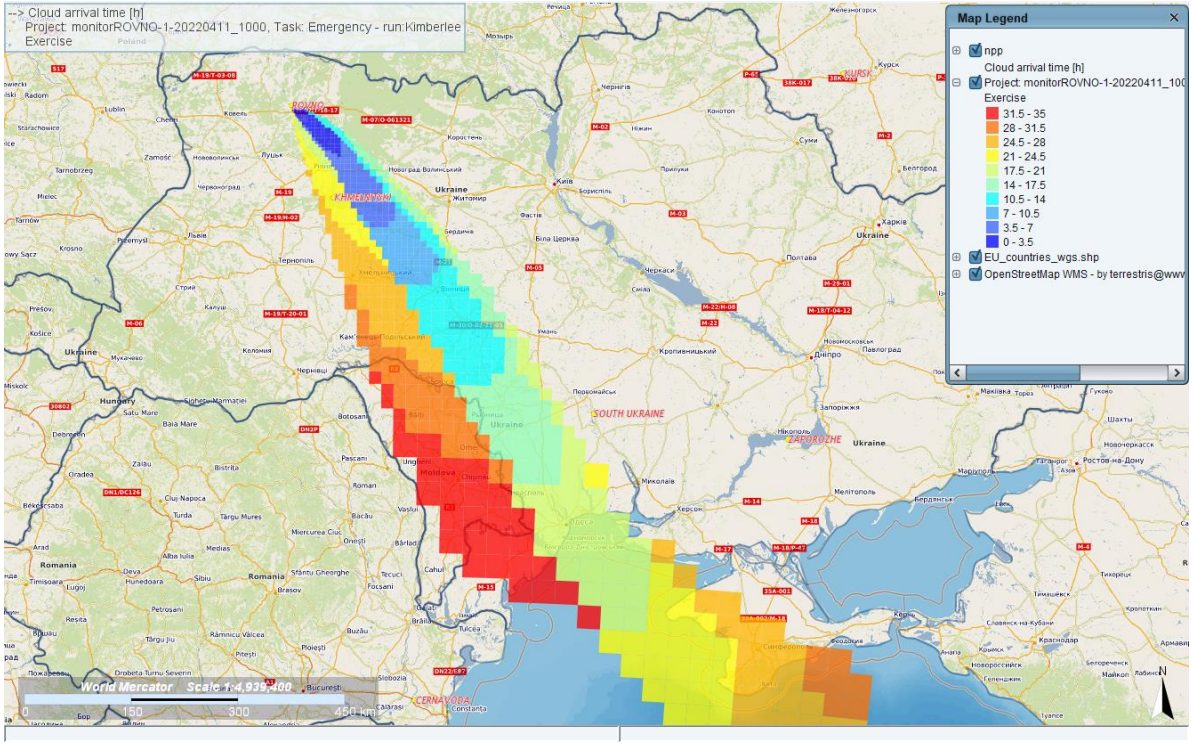

Area for sheltering, 11.04.22 at 10:00 UTC

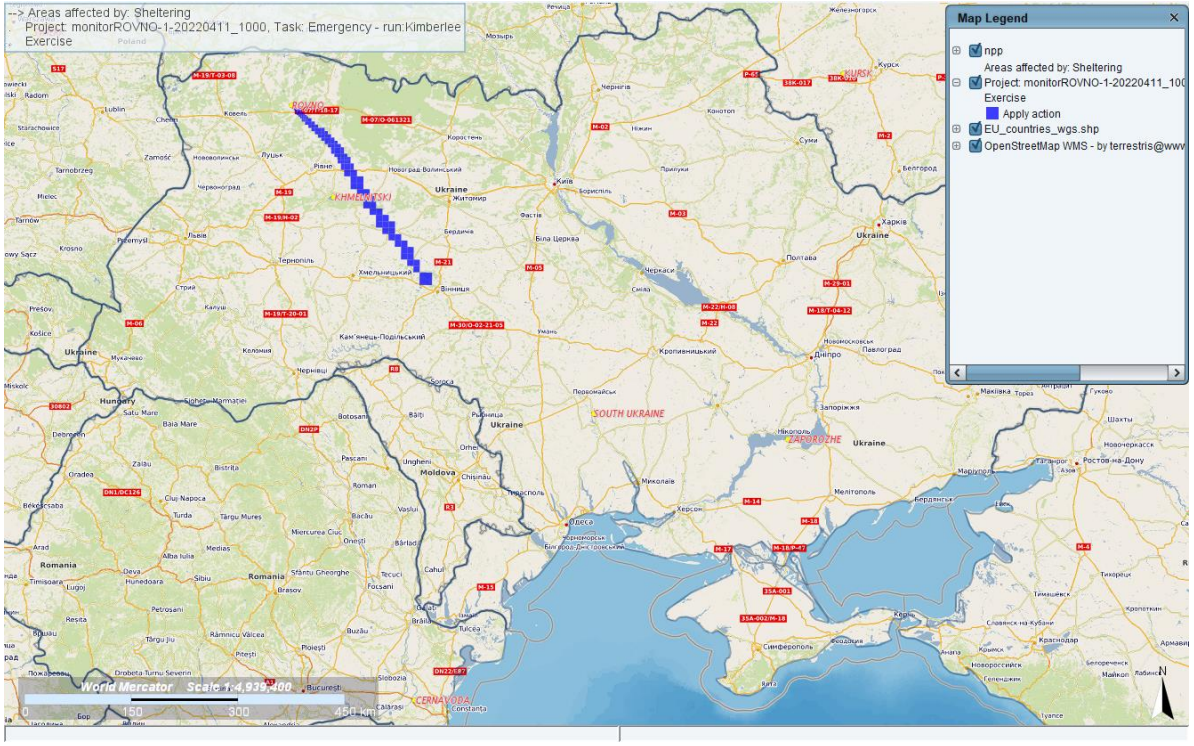

Cloud arrival time, 17.02.2022 at 06:00 UTC

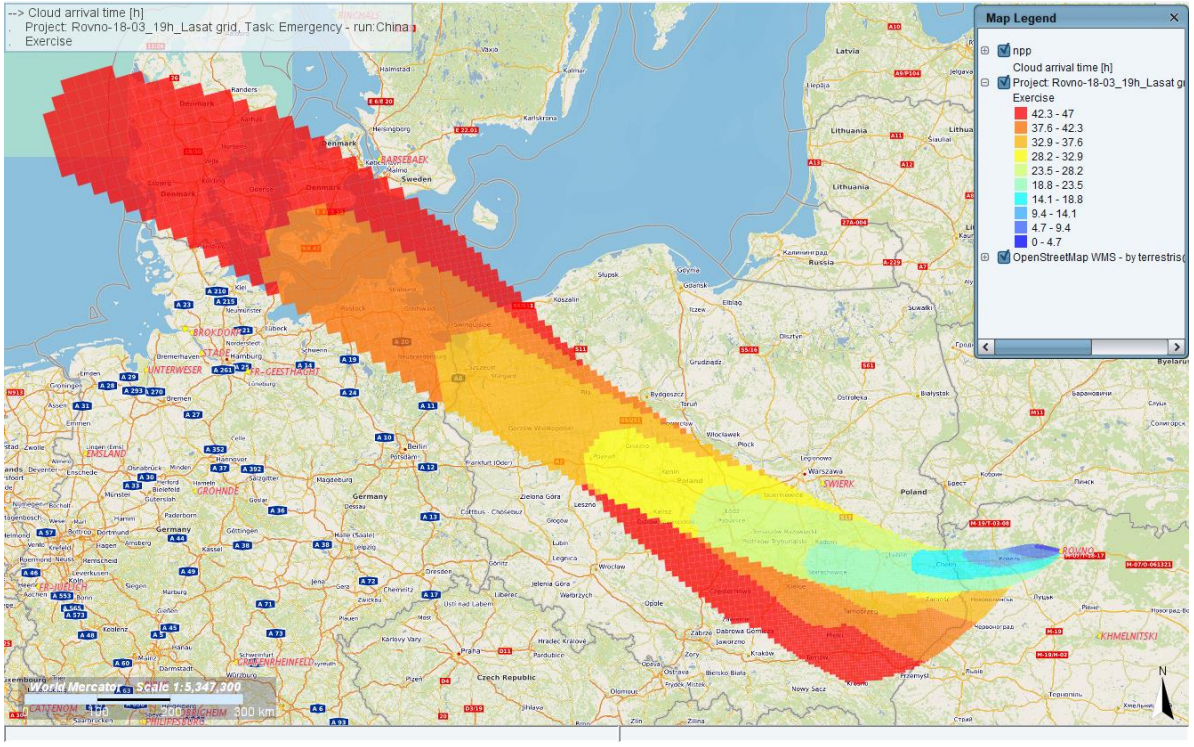

Food restriction areas, 17.02.2022 at 06:00 UTC

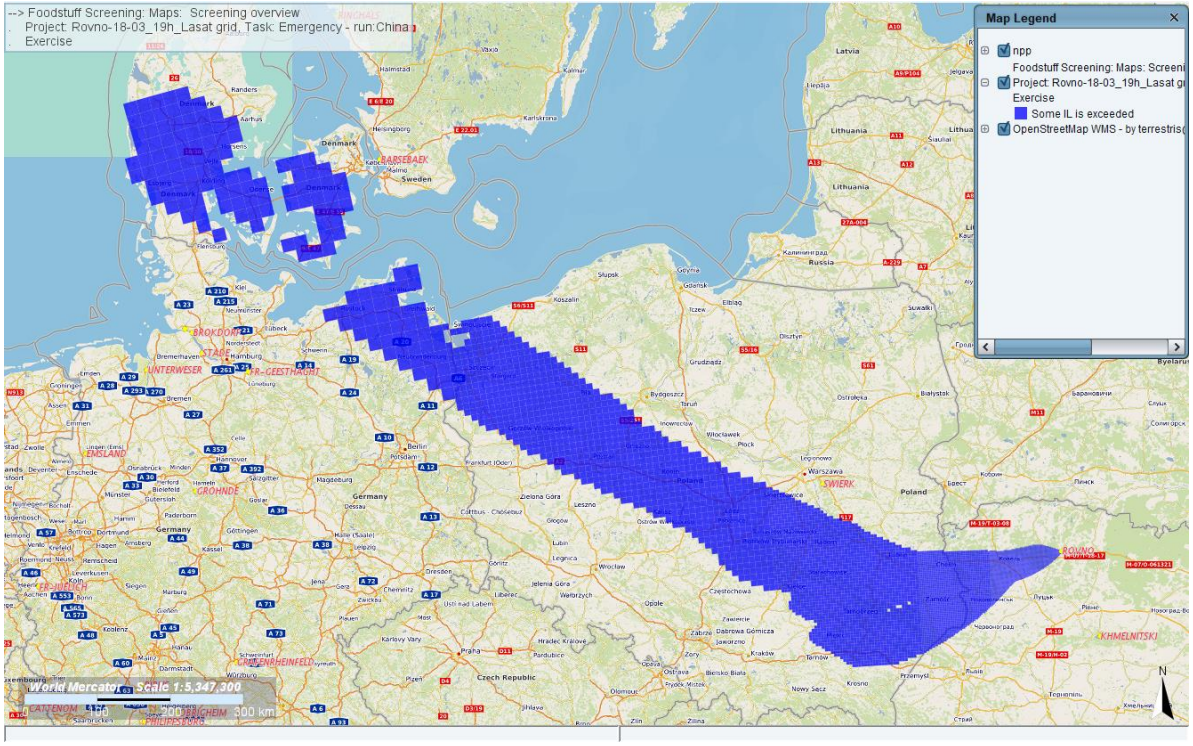

Summary and Perspectives

- Decision Support Systems (DSS) are users of the results of SA research
- The Ukraine war demonstrated the importance of appropriate source terms for consequence assessment
- From a meeting of European research Platforms with NUGENIA representatives in 2020, research ideas were exchanged and the following topics identified as of interest for all participants
  - Source term calculation / estimation from in-plant information and based on off-site gamma dose rate monitors and atmospheric dispersion models – can both approaches be combined?
  - Future of nuclear energy in Europe and how risks, benefits and potentials are seen by stakeholders – social science topic
- Better understanding and modelling of iodine behavior and release pattern
- Direct interfacing of SA codes with a DSS is of high interest

Reference

Thank you for your attention!

https://resy5.iket.kit.edu

Wolfgang Raskob - Head

JRODOS Team

Tel.: +49 721 608-22480
Wolfgang.raskob@kit.edu

Karlsruhe Institute for Technology (KIT)
Institute for Thermal Energy Technology and Safety (ITES)
Hermann-von-Helmholtz Platz 1
76344 Eggenstein-Leopoldshafen, GERMANY

10TH CONFERENCE ON SEVERE ACCIDENTS RESEARCH
May 16-19, 2022 – Karlsruhe, Germany
ERMSAR 2022

Innovation in Modeling

CHAILAN Lionel

IRSN
INSTITUT DE RADIOPROTECTION ET DE SÛRETÉ NUCLÉAIRE

European Review Meeting on Severe Accident Research, AkademieHotel Karlsruhe, May 2022

Round table: New elements in the SA research domain

IAEA
International Atomic Energy Agency

SNETP
Sustainable Nuclear Energy Technology Platform

NUGENIA TA2
Severe Accidents
Nuclear Generation II&III Alliance

NEA
Nuclear Energy Agency

This presentation

Initial scope of the presentation on modelling extended to « innovation » in modelling : some inputs currently investigated for ASTEC to the answers to the following questions:

- How innovation could help solving unresolved issues highlighted by post-Fukushima Daiichi projects?
- How innovation could help broading the type of facilities severe accident codes can be applied to?
- How innovation could help extending the scope of application of severe accident codes?

where the « innovation » can be in the interpretation methods, the modelling approach, the algorithmic or the interfaces.

- **Learning from the post Fukushima Daiichi OECD experiments**
- **New applications of Severe Accident codes**
- **Augmented Severe Accident tools**
- **Conclusion**

Learning from post Fukushima projects

Related to core degradation

- BSAF and crosswalk exercices showed that differences in modeling lead to significant differences for H_2, maximum temperature reached in the vessel, liquid/solid fraction, failure of the vessel and as a consequence the initial conditions for MCCI

- They highlighted the critical role played by Material Interactions
  - In the Lower Plenum more significant in BWR melt progression than in a PWR accident difficult to predict due to the fact that most experiments concerns the PWR
  - Large uncertainties remain on MCCI extent as well as MCCI onset : calculated by most of the codes, no evidence in units 2 and 3

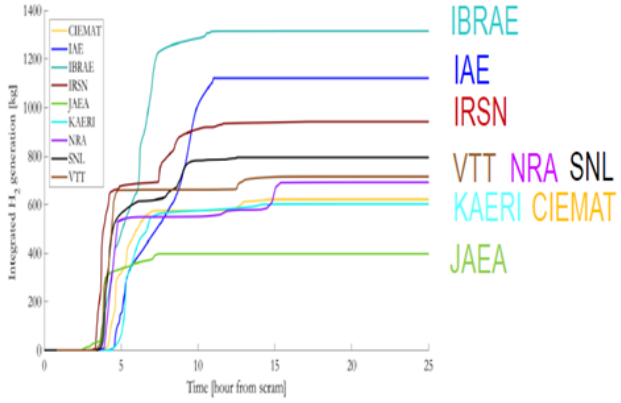

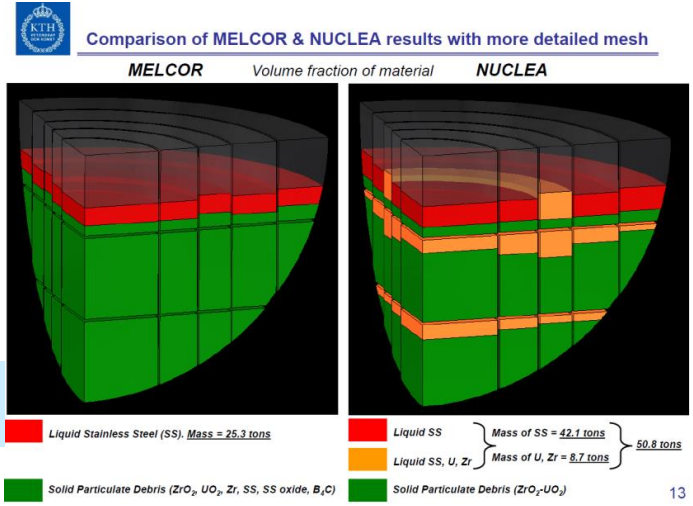

S. Bechta et al., TCOFF Project, Progress Meeting (2018)

Perspective in in-vessel modelling

Improve core degradation modeling

Material interactions are clearly some key phenomena not fully addressed by SA codes. For ASTEC they were already difficult to represent in past experiments as PHEBUS FPT1 and 3 for which the best degradation profile was computed with lowered melting temperatures (but without any particle debris model).

→ **Innovation: re-visit past-integral tests (Phébus FP, PBF SFD 1-4) and accidents (TMI-2) from material science point of view using Post Irradiation Examinations**

More in-depth integration of the material aspects in the degradation process of the core should rely on thermodynamic database knowledge

→ ***Innovation: better integrate thermodynamic databases with SA codes (advanced surrogate model, coupling)***

FPT1 ASTEC reassessment

Lowered Tsol/Tliq, (2500K/2550K) no debris
Good profile

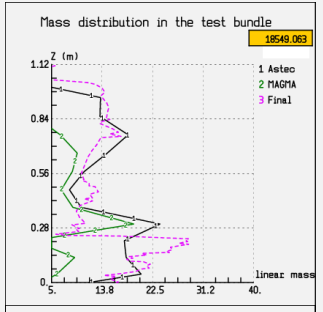

PIE-like Tsol/Tliq, (2700K/2750K) no debris
No sufficient degradation

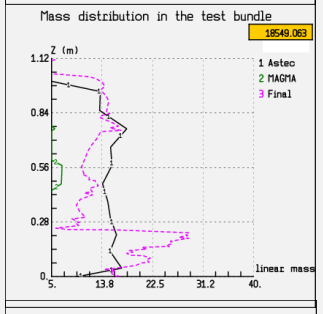

PIE-like Tsol/Tliq, (2700K/2750K) with debris
Degradation is quite good

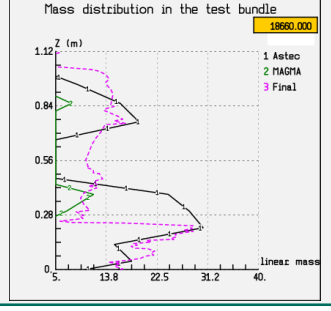

Learning from source term analysis

BSAF major learning : need to develop and validate further models addressing FP remobilization (from pools, building walls and pipe deposits)

- SA codes release calculations for 3 damaged units show reasonable agreement on integral release for Cs and I with other estimates (e.g. see below, Katata 2015, Terada 2012 and Saunier 2015 using extended environmental database and meteorological fields data)
- Kinetics of release phases are not well captured: some major release phases and “chronicles” releases after 6 days are not reflected

Cs integral release (standard ASTEC V2.1 calculation)

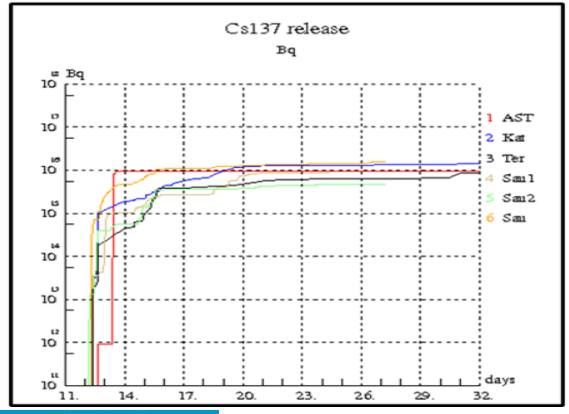

Cs release rate (standard ASTEC V2.1 calculation)

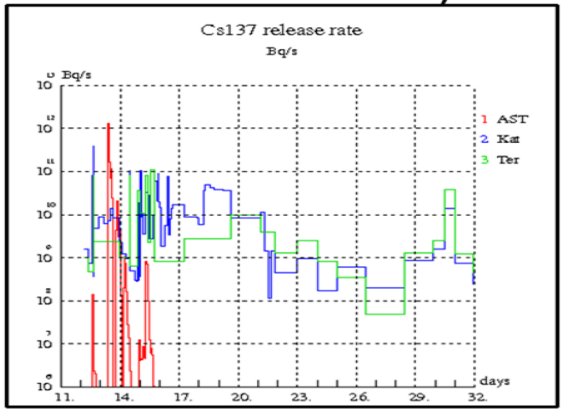

Cs release rate (with Cs remobilization)

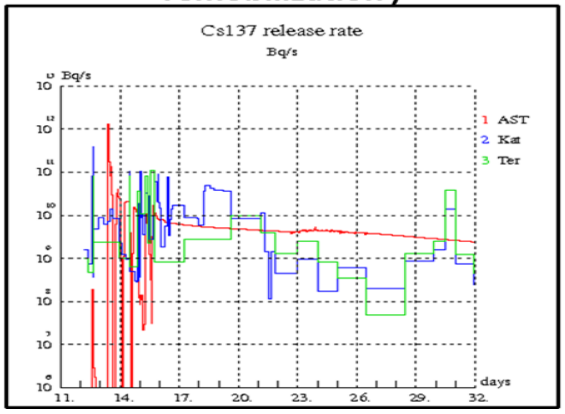

Perspectives for source term modelling

Integrating experimental knowledge gained in dedicated project as

- Cs, Te species remobilization from deposits in RCS and upper core structures: OECD ESTER
- Cs transport and leaching: OECD TCOFF project
- Containment iodine chemistry in WW (pH, impurities incl. organics) and DW (iodine aerosols deposits decomposition, organic iodides formation): OECD/STEM

Some phenomena can benefit from theoretical chemistry (thermo-kinetics models of gas phase reactions)

When the reactional scheme is difficult (impossible) to describe experimentally

→ *Innovation is already on the modelling approaches combining experiments and theoretical chemistry*

Thermodynamic and kinetic constants for main species and reactions of interest

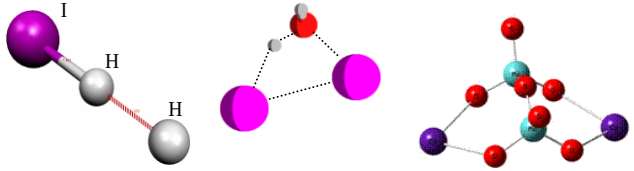

Transition compound

Learning on the SA codes usage

SA codes are mature

Most of the SA codes reach the maturity/stability necessary to run large number of simulations, allowing required sensitivity and uncertainty methodology required by Boundary Conditions knowledge and model uncertainties

But

User effect is considerable: need to improve training, guideline, user experience, tools themselves

Some limitation should be overcome by proper detailed coupling (CFD)

Innovation in risk informed sensitivity and uncertainty analysis

- H2020/MUSA project will contribute to better considering sensitivity and uncertainty analysis
- Ongoing CRP as well: Advancing the State-of-Practice in Uncertainty and Sensitivity Methodologies for Severe Accident Analysis in Water-Cooled Reactors

Are the uncertainties in boundary condition well included?

Innovation in the human and organizational factors impact?



Exporting SA know-how

Knowledge and Know-How developed in the frame of NPP Severe Accident R&D can benefit to other facilities:

- SA codes like MELCOR are currently extended to non water reactors like Fusion reactor, HTGR, SFR, MSR, etc.
- For ASTEC efforts mostly paid on fusion reactor and fuel reprocessing facilities (a nuclear industrial process)
  - Extension of SA tools to nitric acid solution thermal hydraulic phenomena
  - Modelling of FP release from boiling solution with a particular attention on gaseous Ru
  - => Facility assessment through PSA (joined L1&L2 PSA, not separated models) based on a dynamic reliability approach crediting systems repairs and accounting for Material and Human uncertainties but needing a large number of simulation (> million, due to a Monte Carlo approach)
  - Extension to other risks such as red-oils

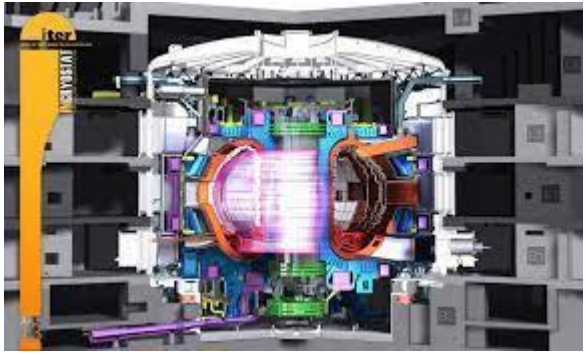



New assessment methodologies will have to be proposed for next generations facilities

It is expected that new facilities (SMR as ex) or new materials (e.g ATF) will likely have to demonstrate a much higher safety level than existing facilities whereas few experiments will be available to validate new models.



Nuward
@ TechnicAtome





ATF
@ USNRC

Evaluation methodologies will so have to evolve drastically

- Increasing uses of methodologies based on multi-scale models *e.g.* by coupling integrated SA codes with detailed codes implying to gain in confidence in multi-physics modelling, validation, uncertainty propagation …
- With few available experimental data, theoretical methods will have to be fully exploited to complete material databases

Augmenting SA tools

Our Integrated severe accident codes have to be continuously renewed

- To improve user experience and to take advantage of recent technologies
- To adapt to new applications and benefit to new usage
- But also to disseminate SA knowledge to next generation
- But no implying necessary to add new knowledge (->augmented codes)

With the help of advanced modeling technics it is possible to better take advantage of existing knowledge capitalized in current codes as well as databases to support new applications:

- Algorithms supporting Artificial Intelligence
- Bayesian network
- Code Coupling
- Multiscale approach

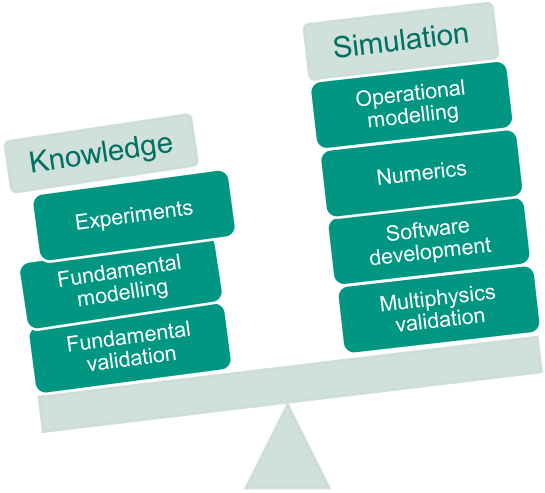

Example of augmented tools currently prototyped at IRSN

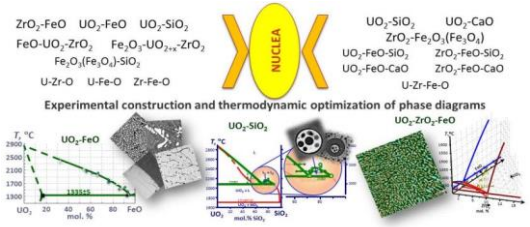

Coupling with thermodynamic databases (in-core and ex-core)

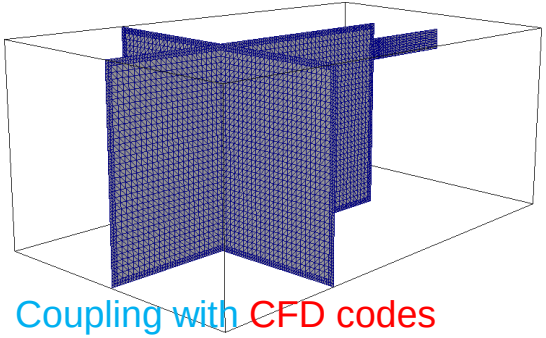

Coupling with CFD codes
Ex: H2 dispersion in SFP acccident



ANACONDA. python™

Coupling with Python allowing

- Improve pre and post treatments
- New features as e.g. multi-cavities MCCI
- New external algorithms



Accelerate to produce fast running tools

- For PSA, crisis, emergency and prepardness purposes
- For education and reducing user effect with simulator
- Expert system (large database require fast calculations)

ASSAS project: an example of augmented SA code initiative

- **“Artificial intelligence for the Simulation of Severe AccidentS”** has been accepted as funded project in Horizon Europe call and will last 4 years
- Its main objective is realizing a Proof Of Concept of a Severe Accident Simulator based on ASTEC
- ASSAS is leaded by IRSN and will gather 14 European partners among Severe Accident R&D Community but Data Scientist Community as well
- It comprises essentially
  - the development of the Graphical User Interface dedicated to the simulation of a generic 1300 Mwe PWR
  - the R&D allowing ASTEC to comply with the performance required in a simulator application following two ways:
    - Classical optimization
    - Artificial Intelligence technics: **the R of R&D**

ASSAS Project – will start 2022/11/01

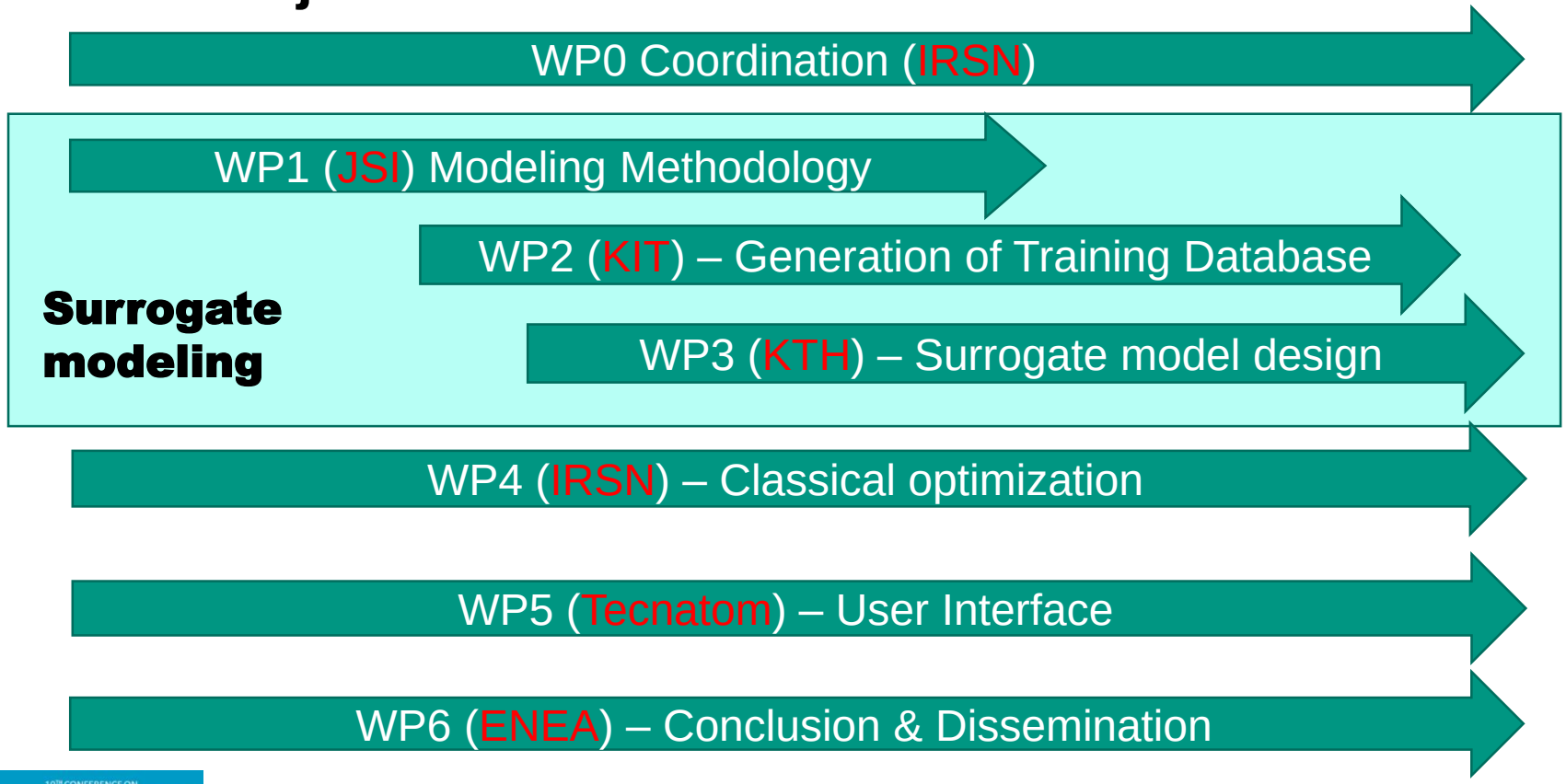

Conclusion: Why innovating?

- **To better solve the « cold cases » (TMI, Phebus) and the current gaps at Fukushima Daiichi**

- **For new applications**
  - Extend SA code application to PSA, EP&R, Simulator, non water-cooled technologie, nuclear industrial facilities
  - Improve the evaluation capabilities for « new nuclear » facilities (less conservative and less uncertain evaluation methods)

- **To maintain skilled and committed teams in Severe Accident Modeling up to the very long term**

Reference

- Benchmark Study of the Accident at the Fukushima Daiichi Nuclear Power Plant Phase II Summary Report October 2019
- IAEA-TECDOC-1872, Status and Evaluation of Severe Accident Simulation Codes for Water Cooled Reactors, INTERNATIONAL ATOMIC ENERGY AGENCY VIENNA, 2019
- TCOFF Project, Final Summary Report
- International OECD/NEA WS on Source Term / 21-22 January 2019, “Current predictive capabilities of Source Term “

Thank you for your attention

Acknowledgment

To ERMSAR committee for invitation

To Marc Barrachin, Eric Delaume, Didier Vola and Nicolas Duflot for support

The 10th European Review Meeting on Severe Accidents Research

Severe Accident Research Eleven Years after the Fukushima Accident

May 16-19, 2022, Karlsruhe, Germany

Technical Session 7-2: Hydrogen and Containment Related issues

Chairs: M. Freitag (Becker Techn.), I. Kljenak (IJS)

ID339	**High combustion risk sequences: Identification and characterization** L. E. Herranz (CIEMAT)	**Paper** **Presentation**
ID312	**Dynamically Prescribed Turbulent Numbers in Containment Atmosphere Mixing Simulations** R. Krpan (IJS)	**Paper** **Presentation**
ID334	**An Analysis of Combustion Regimes for Hydrogen/CO/Air Mixtures in Different Geometries** M. Kuznetsov (KIT)	**Paper** **Presentation**

HIGH COMBUSTION RISK SEQUENCES. IDENTIFICATION AND CHARACTERIZATION

L. E. Herranz, J. Fontanet
CIEMAT
Av. Complutense 40, 28040 Madrid (Spain)
Luisen.herranz@ciemat.es

M. Braun
FRAMATOME

A. Bleyer, A. Bentaib, L. Maas
IRSN

I. Kljenak, M. Leskovar
JSI

M. Müer, J. Hoffrichter, M.K. Koch
RUB

ABSTRACT

The Fukushima accident revived the interest of the nuclear community on severe accident mitigation and, in particular, on optimizing combustible gases management. This paper identifies and characterizes some challenging sequences that could have the potential to jeopardize containment integrity due to large-scale energetic combustion events. Several pressurized water reactor types have been modelled and different Severe Accident (SA) codes and meshing approaches have been used. The selection of the sequences has been based on highly influencing variables, like gas composition and release rates or temperature, as well as on qualitative assessments of the entire scenario.

This project has received funding from the Euratom research and training programme 2019-2020 under Grant Agreement n°945057.

KEYWORDS
Combustible gases, Containment integrity, Severe accident, Modelling

1. INTRODUCTION

Most of currently operating nuclear reactors use fuel claddings made up of different Zr-based alloys, which do have a substantial chemical inertia with respect to cooling water in nominal conditions. During severe accidents (SA), though, the fuel heat-up and the conversion of liquid water into steam (H_2O_v) bring the "chemical system" to a drastically different situation. At temperatures around 1500 K, the reaction between Zr and steam speeds up exponentially, and core temperatures scale up rapidly at the time that hydrogen (H_2) is produced massively. Other in-core materials oxidation, like steel or boron carbide (B_4C), might also contribute, but to a lot less significant extent. In case of Reactor Pressure Vessel (RPV) failure, in-core molten materials at high temperatures might fall into the reactor cavity and interact with concrete (ex-vessel phase of the SA). The resulting H_2O_v and CO_2 from the concrete thermal decomposition would have the

potential to further oxidize remaining metallic materials in the corium pool within the pedestal and, consequently, generate not just more H_2, but also large amounts of carbon monoxide (CO), which is also a combustible gas. In the end, a combustible mixture might form and ignite in non-inerted containments and, depending on the combustion regime, might threaten containment integrity. Evidences of these energetic phenomena occurring in the containment were gathered in TMI-2 [1] and they were also observed in the reactor buildings of Units 1, 3 and 4 of the Fukushima Daiichi NPP [2].

The explosion risk was identified long ago as a priority under different frameworks. It was ranked as a high importance issue in EUROSAFE [3] and, more recently, it was highlighted as a high-priority issue by the NUGENIA association [4]. Consistently with these assessments, the European Stress Tests report underlined the need to consider possible explosion hazards [5] and one of the IAEA requirements for new reactor designs and for upgrading the existing ones refers to the practical elimination of dynamic phenomena leading to the loss of containment integrity [6]. Such a significance has resulted in a number of research projects and expert groups activities, particularly launched after the Fukushima Daiichi accidents, as shortly compiled in [7]. Despite the significant progress achieved, the most recent European project investigating combustion risk under SA conditions (AMHYCO) has noted the need of addressing representative conditions still barely explored so far, particularly during the ex-vessel phase of the accident, and use the findings to feed SA managements guidelines, if necessary.

This paper synthesizes the work done in the AMHYCO frame to identify the most challenging conditions in terms of combustible gas combustion during SA sequences. The performance of both Western (W) and Konvoi (K) PWRs after different initiating events leading to a SA and involvement of diverse engineering safety features has been simulated with different codes and hypotheses, starting from the NPP nodalizations used. The resulting database will provide input for experimental investigations of H_2-CO mixtures recombination and combustion, and will supply initial and boundary conditions to test different approaches of containment modelling (3D vs. LP codes; LP standing for Lumped Parameter).

2. STUDY APPROACH

2.1. Sequence selection

In order to choose accident sequences with the potential to pose a challenge for containment integrity due to gas combustion, a number of factors were identified and set as selection criteria: high molar fractions of combustible gases (H_2 + CO) within flammability limits (the Shapiro diagram [8] serving as a monitor), large amounts of combustible gases, and fast in-containment release rates of H_2 or H_2+CO. Besides, some qualitative analysis might be needed with a broader assessment of the entire scenario. Based on these criteria and the adequate characterization of the challenging conditions either for experimentation and/or analytical modelling a set of variables have been reported (Table 1).

The thresholds set to consider a gas mixture flammable (embedded in the Shapiro diagram) have been:

- $X_{H2} + X_{CO} > 9$ vol.%
- $X_{O2} > 5$ vol.%
- $X_{H2O} < 55$ vol.%

Table 1. Figures of Merit (FOM) for the characterization of challenging combustion conditions.

Figure of Merit	Sequence selection	Initial/Boundary conditions
Gas molar fractions (H_2, CO, H_2O_v, CO_2) in the representative compartment	Yes	Yes
Gas injection/generation rates (H_2, CO, H_2O_v, CO_2, H_2O_l) in each compartment	Yes	Yes
Enthalpy associated to the injection/generation rates into the containment (H_2, CO, H_2O_v, CO_2, H_2O_l) in each compartment	Yes	Yes
Temperature associated to the injection/generation rate into the containment (H_2, CO, H_2O_v, CO_2; H_2O_l)	Yes	Yes
Density of injected gases and water	No	Yes
Pressure difference between volume upwards and downwards of the break	No	Yes
Containment pressure	Yes	Yes
Gas temperature (representative compartment)	Yes	Yes
Heterogeneity index	Yes	No
Breach size	No	Yes
Power sinks/sources due to ESF	No	Yes
Power from CCI due to radiation release to the gas mixture	No	Yes
Initial gas composition (each compartment)	No	Yes
Initial gas temperature (each compartment)	No	Yes
Initial surface, inner and outer, temperature (in each compartment)	No	Yes
Initial containment pressure	No	Yes
Initial amount of water in pools and on surfaces (each compartment)	No	Yes
Inter-compartment gas velocity (representative compartment and time)	No	Yes

2.2. Matrix of sequences

Accident sequences with the potential to evolve in challenging combustion conditions were pooled for different PWR designs: PWR-W (different reactor sizes and variants included) and PWR-K. However, in no case a thorough review of the corresponding level 2 Probabilistic Safety Analysis (PSA) was conducted. Figure 1 displays the complete matrix of sequences simulated; as noted, the VVER ones are not reported as their analysis was not available at the time this paper was written.

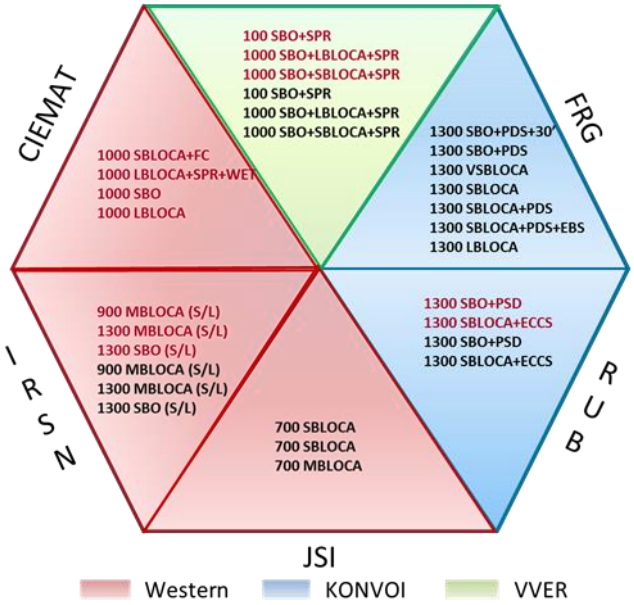

Figure 1. PWR accident sequences modelled.

As for PWR-W, two reactor designs have been modelled: Framatome (900 MWe and 1300 MWe) and Westinghouse (700 MWe and 1000 MWe). However, in the case of PWR-K the same design (by KWU) and size have been simulated.

2.3. Analytical tools and containment model

Table 2 gathers the SA codes used along with the number of nodes used for the modelling, particularly in the containment. Given the relevance of the latter, Figure 2 displays the corresponding containment nodalization schemes of every containment.

Table 2. SA Codes and nodalizations for each reactor type.

Reactor type	Code	Number of plant nodes	Number of containment nodes
PWR-W-900	ASTEC v2.1	~160	14
PWR-W-1300	ASTEC v2.1	~160	18
PWR-W-700	MELCOR v2.2	139	13
PWR-W-1000	MELCOR v2.2	157	19
PWR-K-1300	MELCOR 2.2	69	30
PWR-K-1300	AC^2 2019.1	283	23

Figure 2 gathers the containment noding used in all the cases.

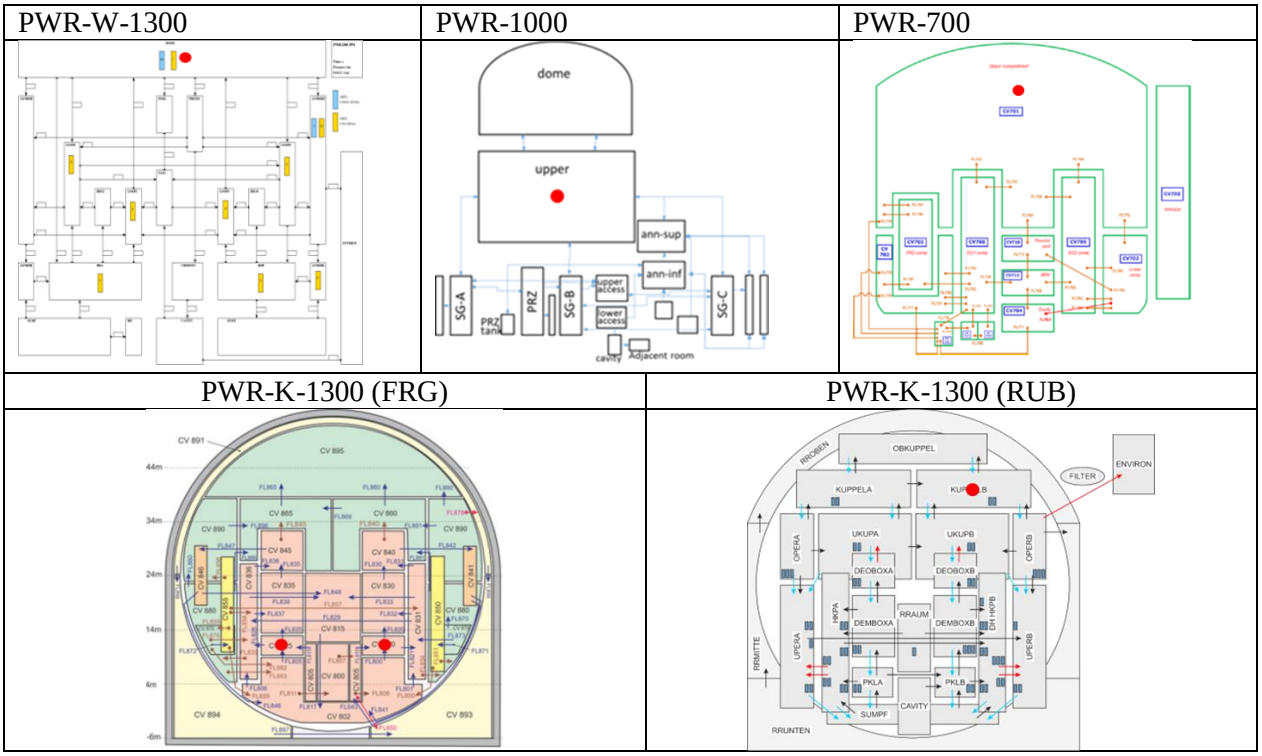

Figure 2. Containment nodalizations

Besides nodalization, hypotheses and approximations were diverse and specific for each plant simulation. Some of the most relevant might be mentioned: in PWR-W 1300/900, containment natural leaks and Passive Auto-catalytic Recombiners (PARs) performance have been considered; in other PWR-W, RCS safety injection is assumed not to be available (except for the accumulators), each RCS loop has been individually modelled; and, a single-layer approach has been considered for CCI (PWR-W-1000); and, finally, for the PWR-K reactor type, the four RCS loops have been aggregated in two loops, one triple weighted and one single loop including the pressurizer and siliceous concrete has been considered.

3. RESULTS & DISCUSSION

3.1. PWR-W

As for the Framatome designs, two SA sequences leading to the RPV failure and subsequent Corium-Concrete Interaction (CCI) have been considered: a 12-inch hot leg LOCA (Loss Of Coolant Accident) and a SBO (Station Black Out); the latter just in the case of PWR-W-1300. Particular emphasis has been placed in the late phase of the accident and, given the effect of concrete composition on H_2 and CO generation, limestone and siliceous concrete have been modelled. In addition, the same sequences have been run with and without PARs to assess their impact on the accident scenario. Hence, a total of 12 sequences have been simulated.

The most challenging conditions (i.e., those where the potential energetic events due to gas combustion are more likely) have been observed to prevail in the 1300 MWe reactor when no PARs are operational and reactor pit floor is made of siliceous concrete. Both the MBLOCA as well as the SBO sequences enter the flammability region in the Shapiro diagrams (Figure 3).

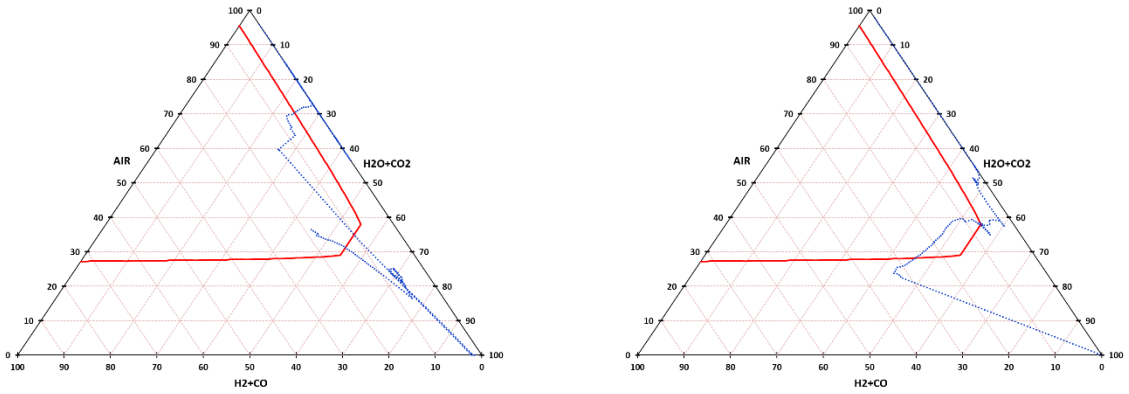

Figure 3. Shapiro diagram for PWR-W-1300 simulations (Left: MBLOCA, Right: SBO)

The concentration evolution over time indicates that those conditions correspond to a very short time at the beginning of the ex-vessel phase and later on in the accident when the containment heat removal is activated right after 24 h of the accident onset, in the case of the MBLOCA. In the case of the SBO, though, the amount of steam decreases along the ex-vessel phase and falls below the inerting threshold (55%) after a few hours of the accident phase onset, while the amount of combustible gases keeps on monotonously increasing. In both cases, H_2 is the majoritarian component of the combustible gas mixture. Figure 4 shows the evolution described.

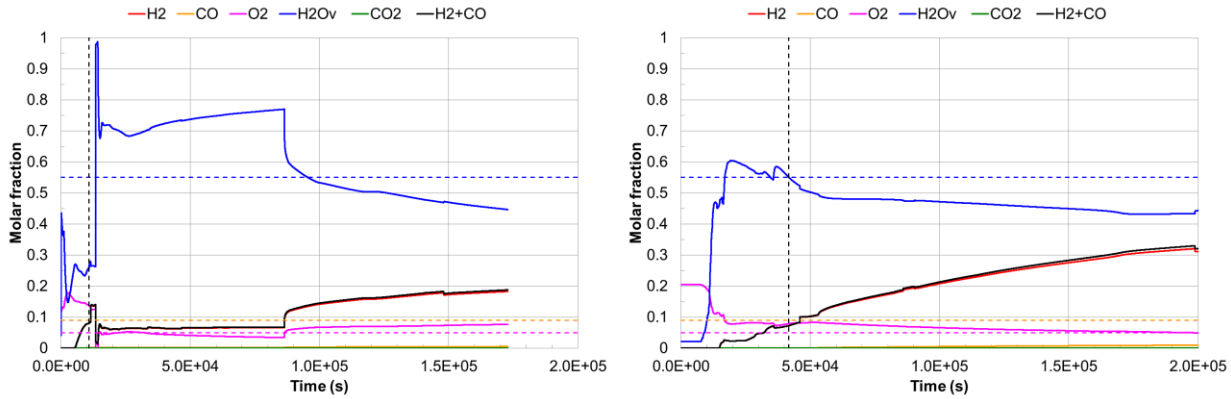

Figure 4. Gas composition in the main compartment of PWR-W-1300 (Left: 12” LOCA, Right: SBO)

As for the Westinghouse designs, two sequence types have been considered (LOCA and SBO) for the larger size PWR (PWR-W-1000). This variability along with the different pipe breach sizes and accident management actions (fan coolers, FC; sprays, cavity flooding), added up to a total of four sequences: 2-inch SBLOCA (fan coolers on); 2-inch SBLOCA (sprays on and cavity flooding implemented); double-ended guillotine LBLOCA (both sprays and fan coolers on); SBO.

In all those sequences with systems capable of condensing steam, a higher fraction of combustible gases has been observed. As a consequence, the two sequences which represent the highest risk associated with combustible gases are the SBLOCA with fan coolers and the LBLOCA. Figure 5 shows the Shapiro diagrams of both of them, where a deeper penetration is noted within the flammability region in the case of LBLOCA.

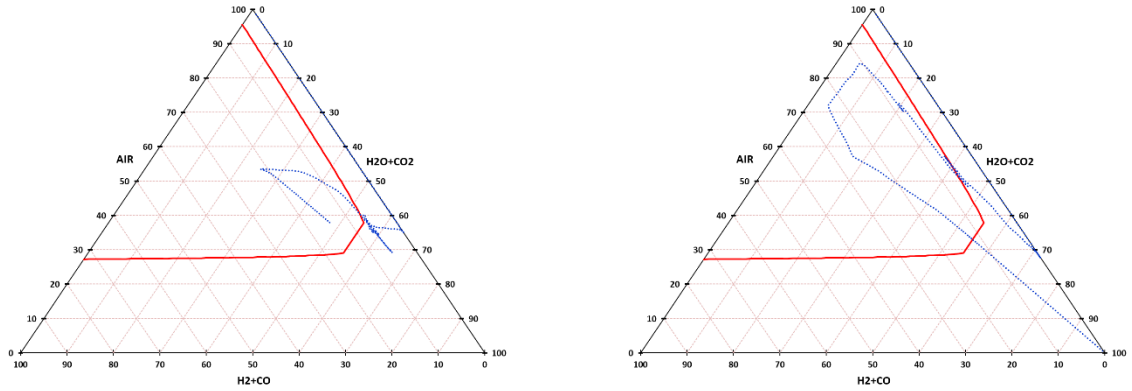

Figure 5. Shapiro diagram of PWR-W-1000 simulations (Left: SBLOCA with FC; Right: LBLOCA)

Both sequences lead to a high steam concentration at the beginning of the accident due to the flashing of the water loss from the RCS (LBLOCA) or to the release of steam directly through the circuit breach (SBLOCA). The sprays operation in the LBLOCA triggers a fast and large drop of steam content. Even though, for a short time the H_2 molar fraction reaches combustion limits set (9%) at the end of the in-vessel phase, it is in the ex-vessel one where further release of H_2 and CO from the CCI together with the efficient condensation of steam, make combustible gas mixture attain concentration over 25% at around 20000 s. The loss of efficiency in condensation due to recirculation mode operation of sprays and the generation of CO_2 results in a progressive dilution of such high combustible gas concentration in the long run of the sequence, but still standing over the combustion limits. For the SBLOCA sequence, the combustible gas mixture does not exceed the combustion threshold till CO is produced in the ex-vessel phase, which together with the effect of FC on steam content, make it grow to higher than 20% at about 30000 s and stay at roughly that high concentration till CO_2 is released in massive amounts to reach higher than 20% of the total gas composition. These evolutions may be observed in Figure 6.

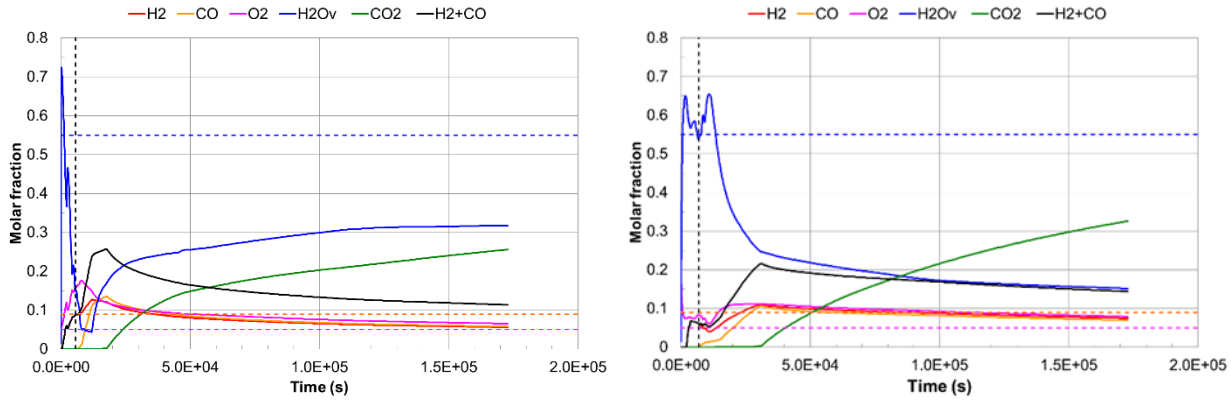

Figure 6. Gas composition in PWR-W-1000 (Left: LBLOCA, Right: SBLOCA)

Finally, for the PWR-W-700 design three SBO, two of them with LOCA sequences (pipe break sizes being 6-inch and 12-inch) were simulated. In all these sequences, containment safety systems were supposed to be unavailable and no safety injection was assumed in the RCS, except for accumulators. Nonetheless, PARs were considered, which resulted in a low combustion risk, as expected (Figure 7 left); additionally, the high steam along most of the sequence kept the containment inerted for the entire ex-vessel phase (Figure 7 right).

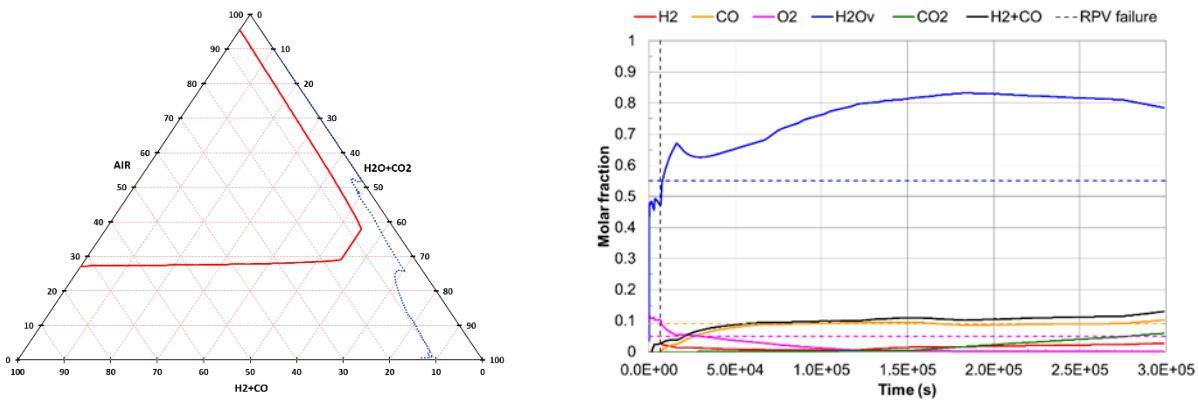

Figure 7. Shapiro diagram (left) and gas composition (right) for the PWR-W-700 SBLOCA

3.2 PWR-K

A number of sequences has been simulated for the Konvoi PWR design. As noted in Table 2, variability is not associated with reactor size, but with the analytical tool and approach used for the modelling: AC^2 and MELCOR. From the pool of sequences that have been run with AC^2, the most challenging ones in terms of combustion risk have been a SBO with Primary Side Depressurization (SBO+PSD) and a SBLOCA (80 cm^2) with a limited water injection by the extra borating system (SBLCAO+ECCS). Both of them were modelled with and without PARs. Even though both sequences enter the flammable region of the Shapiro diagram (Figure 8) when PARs are assumed to fail, SBLOCA+ECCS stays longer and reach higher combustible gas concentration.

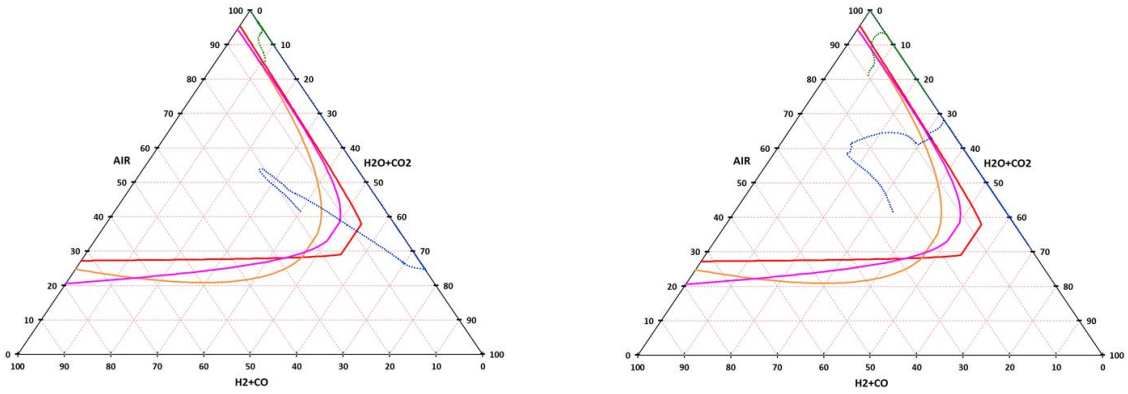

Figure 8. Shapiro diagram for PWR-K (Left: SBO+PSD, Right: SBLOCA+ECCS)

As for atmosphere composition, in the SBO+PSD sequence the steam concentration reaches a value higher than 70 vol.% for nearly 10000 s in the in-vessel phase and progressively falls since the onset of the ex-vessel one, which causes the gas phase to move out of the inert region soon. Combustible gases build a burnable concentration (over 9%) early in the ex-vessel phase and builds up to values around 20%, where they remain for long, despite cavity flooding at around 49000 s rises moderately the steam concentration again to value never exceeding 35%. The evolution of the gas composition is not too different in SBLOCA+ECCS. Steam concentration peaks soon after the accident onset at nearly 70% and decreases progressively, while combustible gases enter the containment a few thousand seconds before RPV fails and build up concentration that get to around 25 vol.% and state steady until the end of the sequence; again, cavity flooding is not massive enough as to bring containment atmosphere into a combustion inert region.

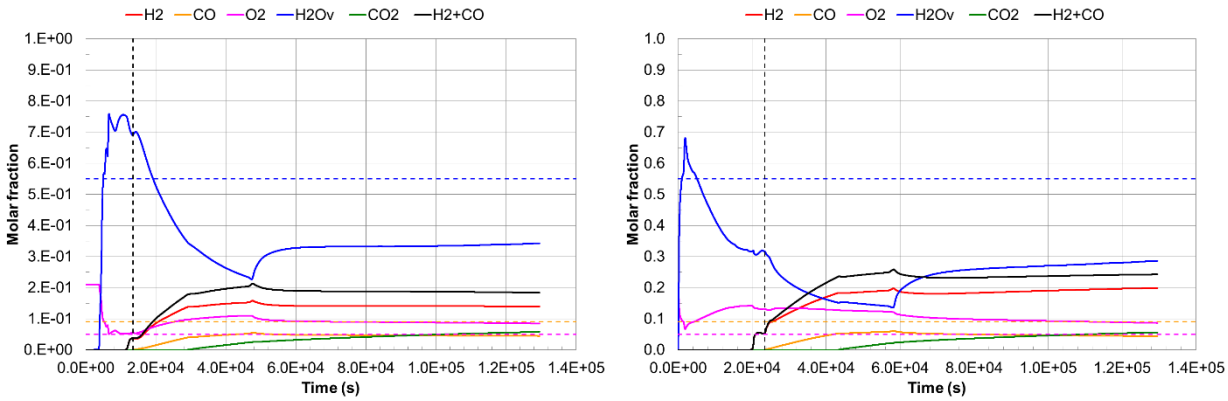

Figure 9. Gas composition in PWR-K sequences (Left: SBO+PSD, Right: SBLOCA+ECCS)

A different pool of sequences were modelled with MELCOR (some of them had certain similarities with those simulated with AC^2): SBO+PDS (at 650ºC core outlet temperature; delayed); SBLOCA with secondary cool-down (5 cm^2; 80 cm^2); SBLOCA 80 cm^2 with (small) and without water injection; LBLOCA (380 cm^2). All of them took into account in-containment PARs performance. From the entire set, those of higher combustion risk were the SBLOCA (80 cm^2) with secondary cool-down and LBLOCA. This said, the presence of PARs (reducing both combustible gas and O_2 concentrations) and the high steam concentration for long times in the ex-vessel phases make gas atmosphere hardly enter the flammable region of the Shapiro diagram (Figure 10).

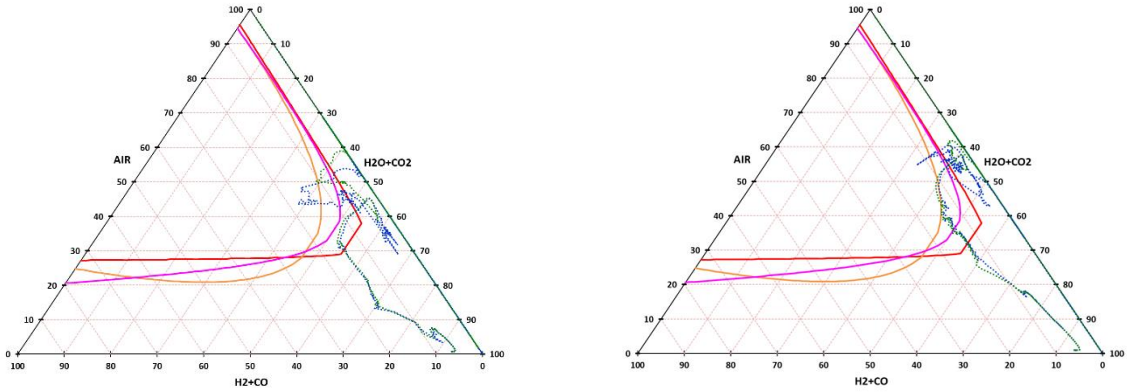

Figure 10. Shapiro diagram for PWR-K (Left: SBLOCA, Right: LBLOCA)

Concerning the SBLOCA sequence, fast H_2 release into the containment during the in-vessel phase peaks over 18% and is rapidly reduced by PARs to concentrations below 9% in large rooms of containment. Once the ex-vessel phase commences, H_2 and CO production makes the combustible gas mixture return to values over 15% with O_2 still holding values over 5%. However, a sharp increase of steam content as a consequence of cavity flooding makes containment atmosphere get over the steam-inerting threshold, and drastically reduces both combustible gases and O_2 concentrations. Even though differences exist, in overall terms LBLOCA evolves similarly to the SBLOCA in terms of gas composition. Figure 11 allows noting so.

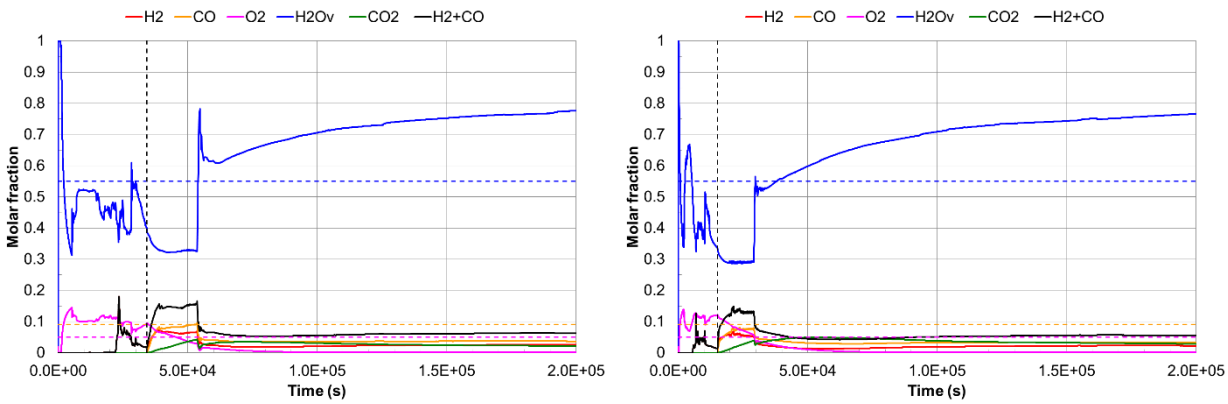

Figure 11. Gas composition for PWR-K (Left: SBLOCA, Right LBLOCA)

3. FINAL REMARKS

Twenty-five PWR SA sequences have been simulated with the purpose of identifying conditions under which combustion events might happen, with particular focus on H_2 and CO combustible mixtures during the ex-vessel phase of the accidents. The main outcomes from the work can be summarized as follows:

- The SA sequences that posed a higher risk of gas combustion (H_2 and CO) have been found to be SBLOCA and LBLOCA, for PWR-W, and MBLOCA (80 cm^2) for PWR-K.
- A key factor heavily conditioning sequence selection is the availability of safety systems capable of condensing steam during the ex-vessel phase since they result in a boost of combustible gas content.
- As expected, the largest gas accumulation (as long as PARs are not modelled) is found in the ex-vessel phase. The composition of the concrete greatly influences the amount of released gas and the CO fraction.
- Whenever PARs are modelled, O_2 starvation in the ex-vessel phase makes gas composition exit the flammable region of the Shapiro diagram, even if combustible gas content is well over 9 vol.%.

The next step of this investigation within AMHYCO, once suitable SA sequences are selected, will be to characterize the most challenging conditions predicted and use them to set up insightful test matrices to investigate PAR performance in presence of combustible gas mixtures and combustion of H_2 and CO mixtures. Additionally, specific studies of in-containment distribution of gas combustible mixtures will be conducted with 3D and lumped parameter approaches to test the effect of some management actions, like venting containment, on the combustion risk.

ACKNOWLEDGMENTS

The work presented in this communication was done under the frame of the AMHYCO project. This project has received funding from the Euratom research and training programme 2019-2020 under Grant Agreement n°945057. The content of this paper reflects only the authors' view. The European Commission is not responsible for any use that may be made of the information it contains.

REFERENCES

[1] B. R. Sehgal, Ed., «Chapter 3 - Early Containment Failure», in *Nuclear Safety in Light Water Reactors*, Boston: Academic Press, 2012, pp. 185-306. doi: 10.1016/B978-0-12-388446-6.00003-4.

[2] Tokyo Electric Power Company, «Evaluation of the Situation of Cores and Containment Vessels of Fukushima Daiichi Nuclear Power Station Units-1 to 3 and Examination into Unsolved Issues in the Accident Progression. Progress Report No. 3», May 2015.
[3] D.Magallon, A. Mailliat, J.M. Seiler, K. Atkhen, H. Sjövall, S. Dickinson, J.Jakab, L. Meyer, M. Buerger, K. Trambauer, L. Fickert, B. Raj Sehgal, Z. Hozer, J. Bagües, F. Martin-Fuertes, R. Zeyen, A. Annunziato, M. El-Shanawany, S. Guentay, C. Tinkler, B. Turland, L. E. Herranz, "European Expert Network on the reduction of uncertainties in severe accident safety sigues??? (EURSAFE)", Nuclear Engineering and Design 235 (2005), 309-346.
[4] D. Manara, D. Jacquemain, J.P. Van Dorsselaere, P.D. Bottomley, M. Adorni, C. Journeau, Y. Pontillon, T. Lind, L.E. Herranz, F. Rocchi, A. Schaffrath, J.C. de la Rosa Blul, S. Bechta, J. Duspiva, I. Kljenak, P. Dejardin, "Severe accident research priority ranking: A new assessment eight years after the Fukushima Daiichi accident", The 9TH European Review Meeting on Severe Accident Research (ERMSAR2019), Prague, Czech Republic, March 18-20, 2019.
[5] ENSREG, «Peer review report. Stress tests performed on European nuclear power plants», 2012.
[6] IAEA, «Considerations on the Application of the IAEA Safety Requirements for the Design of Nuclear Power Plants», IAEA-TECDOC-1791, 2016.
[7] G. Jiménez *et al.*, «AMHYCO Project – Towards an Enhanced Accident Management of the H_2/CO Combustion Risk», presented at The 19th International Topical Meeting on Nuclear Reactor Thermal Hydraulics (NURETH-19), on-line, March 2022.
[8] Z.M.Shapiro. T.R.Moffette, Hydrogen Flammability Data and Application to PWR Loss-of-Coolant Accident, Report WAPD-SC-545, Bettis Plant, Pittsburgh, Pennsylvania, USA, September 1957.

High Combustion Risk Sequences. Identification and Characterization

L. E. Herranz[1], J. Fontanet[1], M. Braun[2], A. Bleyer[3], A. Bentaib[3], L. Maas[3], I. Kljenak[4], M. Leskovar[4], M. Müer[5], J. Hoffrichter[5], M.K. Koch[5]

[1]Centro de Investigaciones Energéticas, Medioambientales y Tecnológicas - CIEMAT (Spain)
[2]Framatome GmgH (Germany)
[3]Institut de Radioprotection et de Sûreté Nucléaire –IRSN (France)
[4]Institut Josez Stefan –JSI (Slovenia)
[5]Ruhr-Universität Bochum (Germany)

Contents

1. *Introduction*
2. *Study approach*
3. *Matrix of sequences*
4. *Results and discussion*
5. *Conclusions*

Introduction

- **Motivation & Framework**
  - Explosion risk has been identified as high priority issue in different frameworks.
  - AMHYCO project devoted to H_2/CO combustion risk management.
- **Objectives**
  - To identify the most challenging conditions in terms of gas combustion.
  - Build-up of a *Scenario Database* to be used in accident management analyses and in experimental research.
- **Scope**
  - Konvoi plant: PWR-KWU
  - Western design: PWR-W (Westinghouse & Framatome)

Study approach: selection criteria

General criteria

- High molar fraction of comb. gases
  (Shapiro diagram)
- Large total masses of comb. gases
- Fast release rates (in-vessel phase)

Practical criteria

- **Flammability boundaries**
  - **$X_{H2} + X_{CO} > 9$ vol.%**
  - **$X_{O2} > 5$ vol.%**
  - **$X_{H2O} < 55$ vol.%**

  } *Shapiro diagram*
- Compartments with big volume
- Sequences w/o PARs

Study approach: Figure of merits

Figure of Merit	Sequence selection	Initial/Boundary conditions
Gas molar fractions & release rates	Yes	Yes
Temperature and Enthalpy associated to the release	Yes	Yes
Density of injected gases and water	No	Yes
Pressure difference between volume in the break	No	Yes
Containment characteristics: pressure & temperature	Yes	Yes
Breach size	No	Yes
Power sinks/sources due to ESF	No	Yes
Heat transfer from cavity	No	Yes
Initial gas composition	No	Yes
Initial pressure and temperature (gas and walls)	No	Yes
Initial amount of water	No	Yes
Inter-compartment gas velocity	No	Yes

- Atmosphere composition
- Gas generation/release characterization
- Initial & boundary conditions
- Other sources/sinks

Matrix of sequences

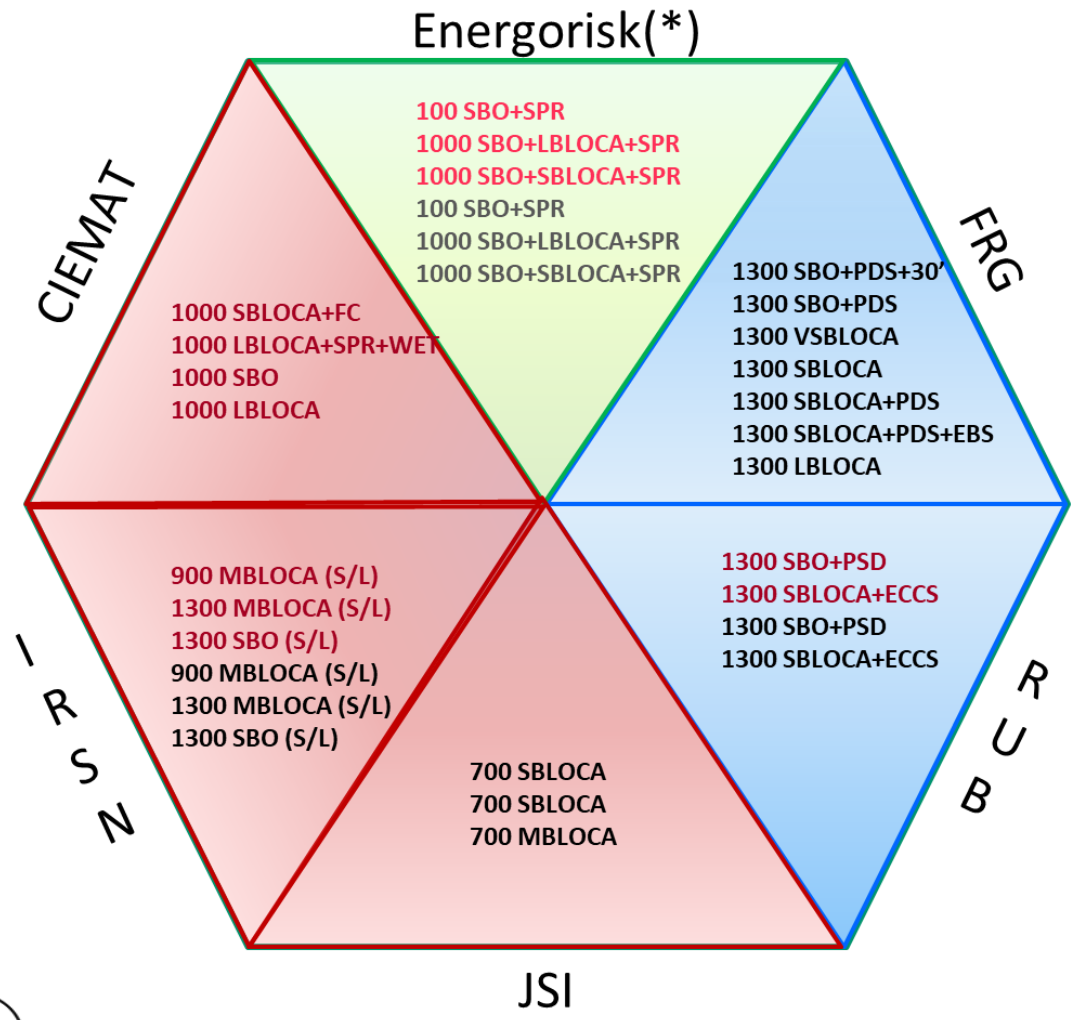

Plant model summary

Reactor type	Code	plant nodes	containment nodes
PWR-W-900	ASTEC v2.1	~160	14
PWR-W-1300	ASTEC v2.1	~160	18
PWR-W-700	MELCOR v2.2	139	13
PWR-W-1000	MELCOR v2.2	157	19
PWR-K-1300	MELCOR v2.2	69	30
PWR-K-1300	AC^2 2019.1	283	23

(*) PWR-VVER results not available at the time of the conference. Results will be added to the Scenario Database

Containment model: PWR-W (framatome)

PWR-900

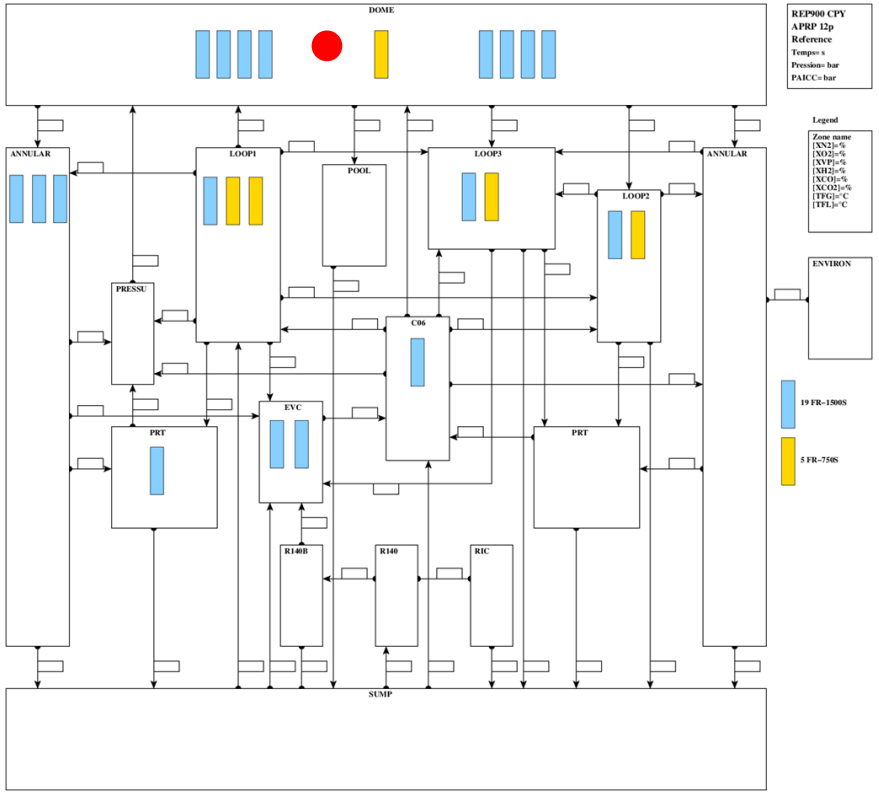

14 nodes

PWR-1300

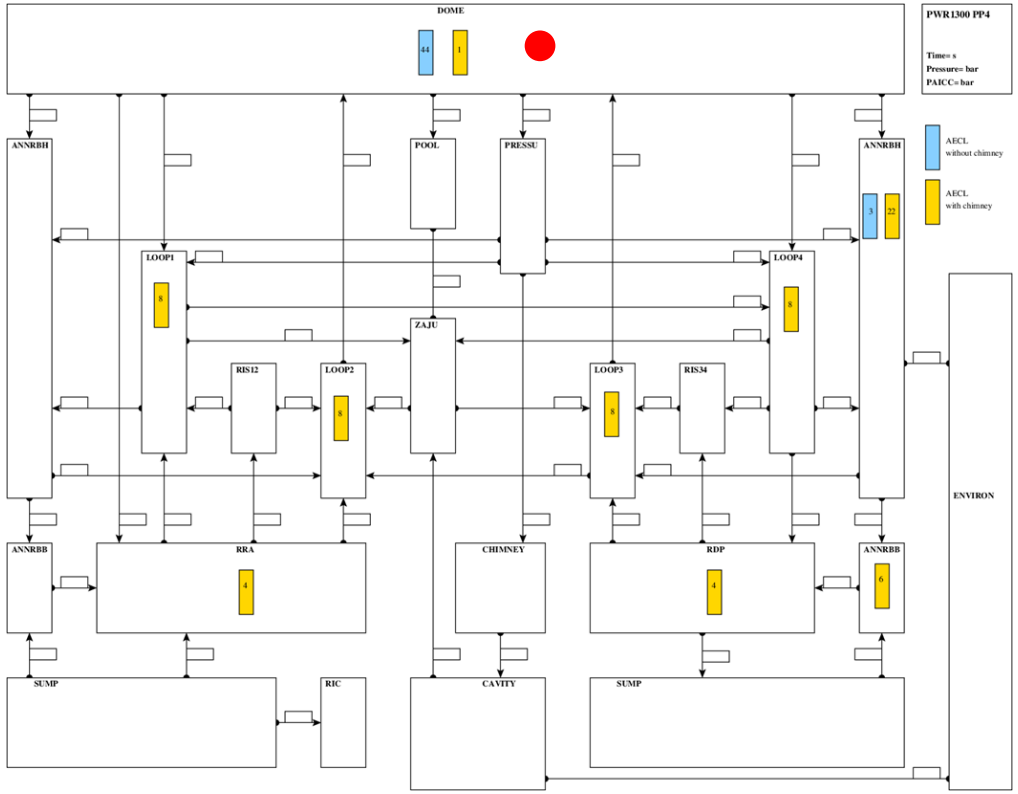

18 nodes

Containment model: PWR-W (Westinghouse)

PWR-700

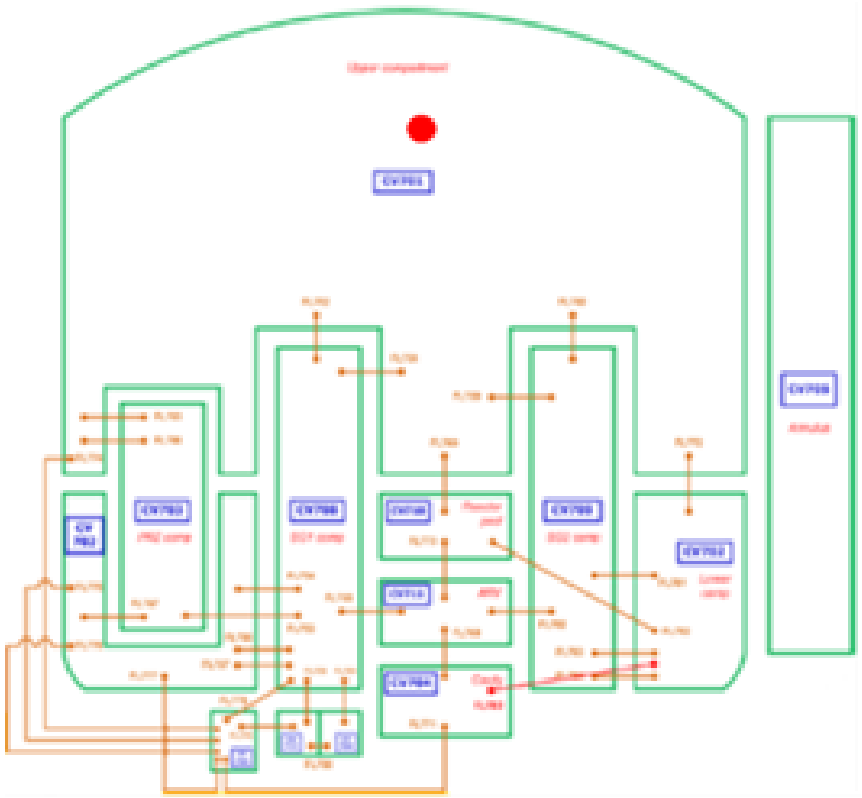

14 nodes

PWR-1000

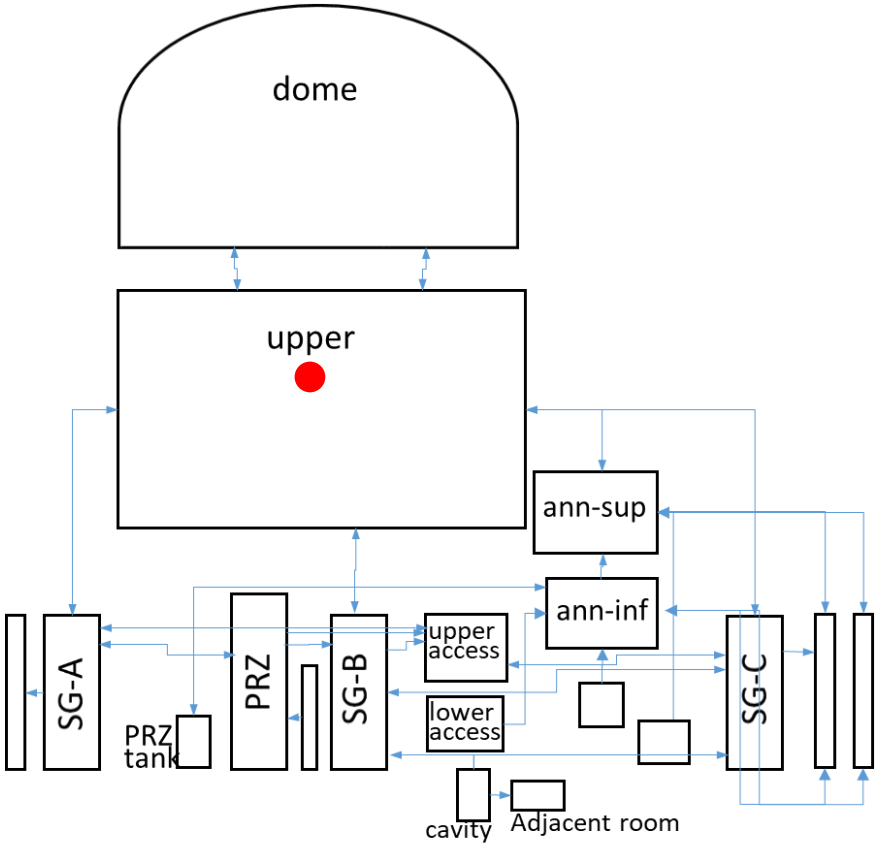

18 nodes

Matrix of sequences

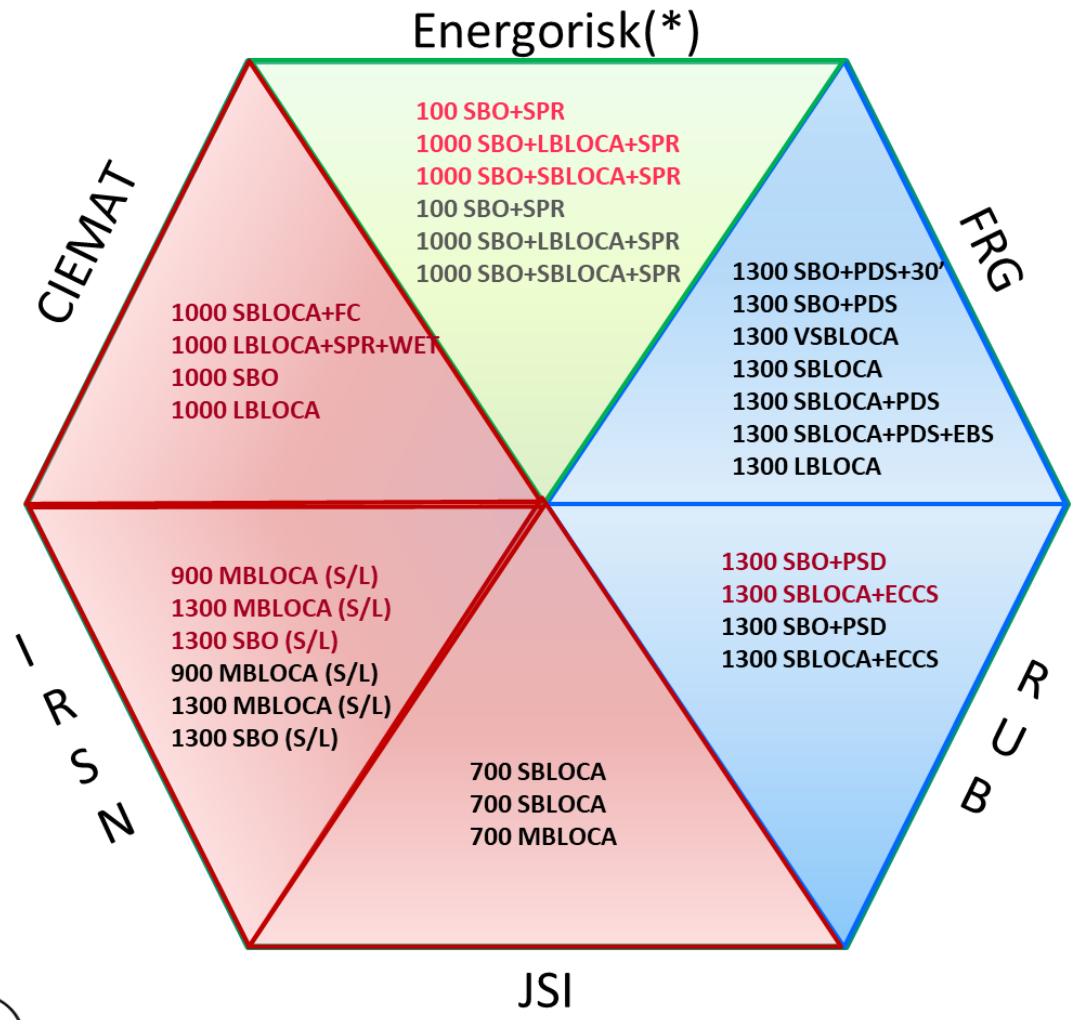

Plant model summary

Reactor type	Code	plant nodes	containment nodes
PWR-W-900	ASTEC v2.1	~160	14
PWR-W-1300	ASTEC v2.1	~160	18
PWR-W-700	MELCOR v2.2	139	13
PWR-W-1000	MELCOR v2.2	157	19
PWR-K-1300	MELCOR v2.2	69	30
PWR-K-1300	AC^2 2019.1	283	23

(*) PWR-VVER results not available at the time of the conference. Results will be added to the Scenario Database

Containment model: PWR-KWU

MELCOR model

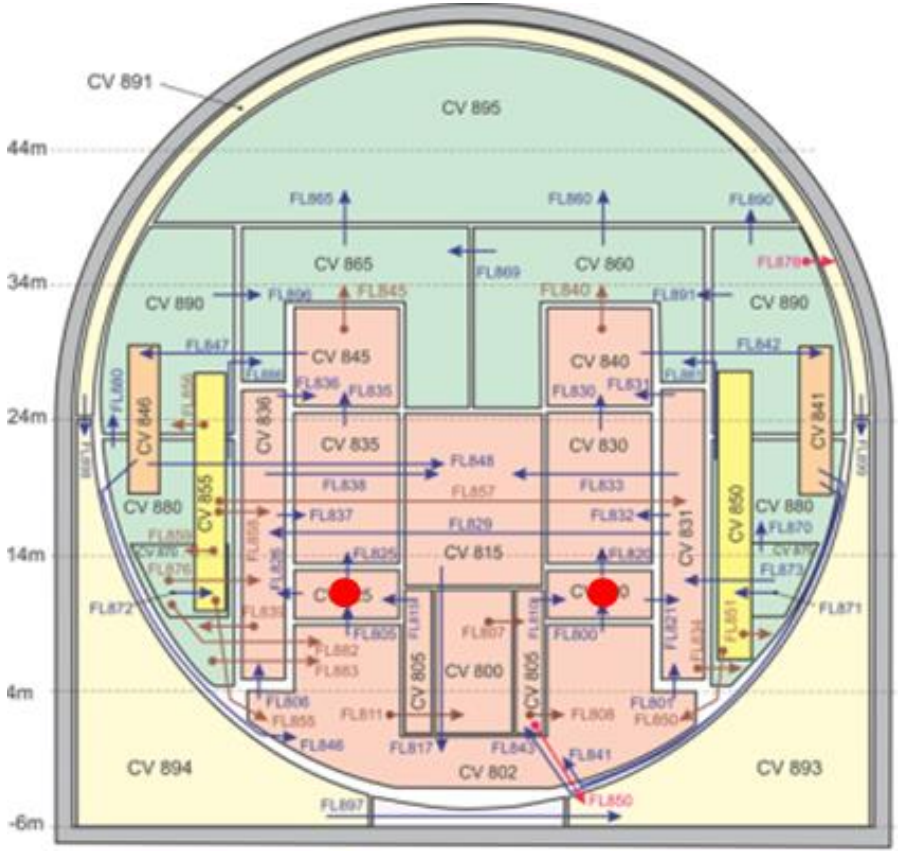

30 nodes

AC² model

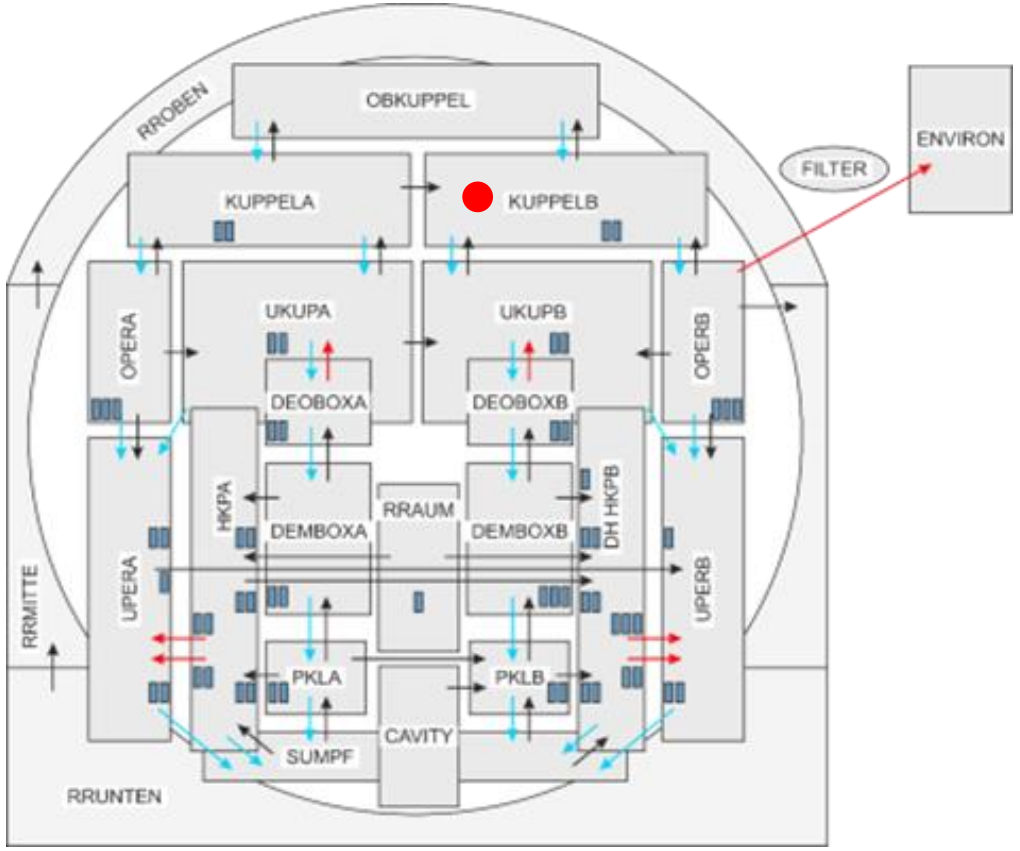

23 nodes

Results and discussion: PWR-W (1)

Westinghouse PWR-1000 SBLOCA

2” Φ (20 cm^2) break in CL
Accumulator’s injection (RCS)
Fan coolers

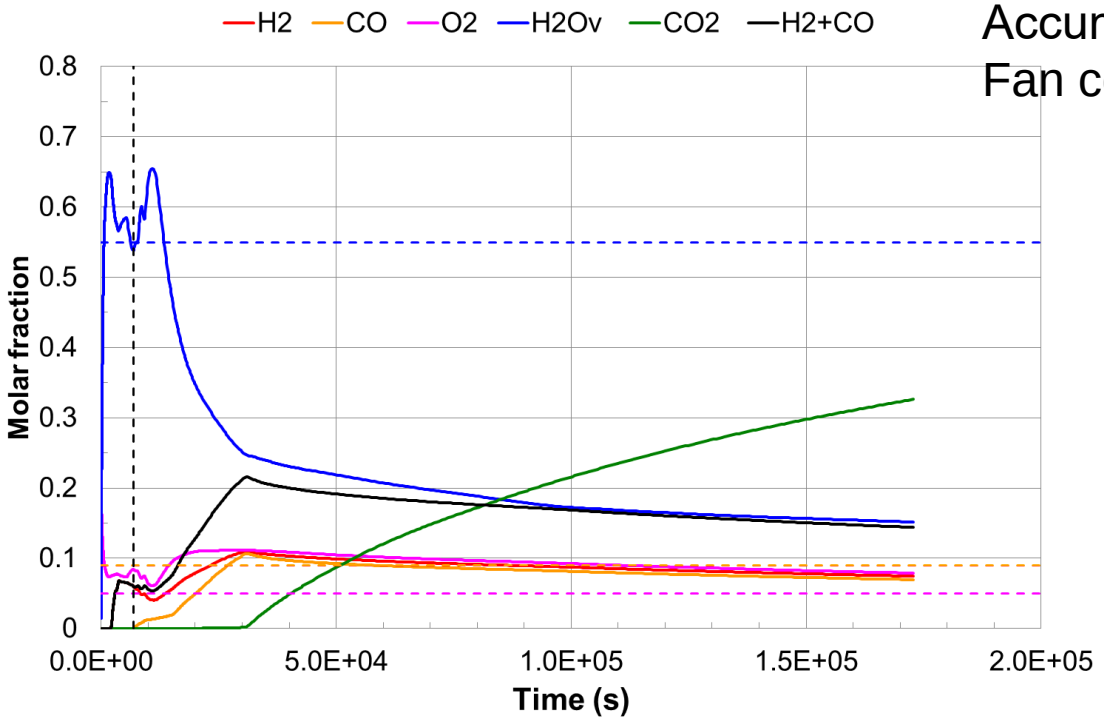

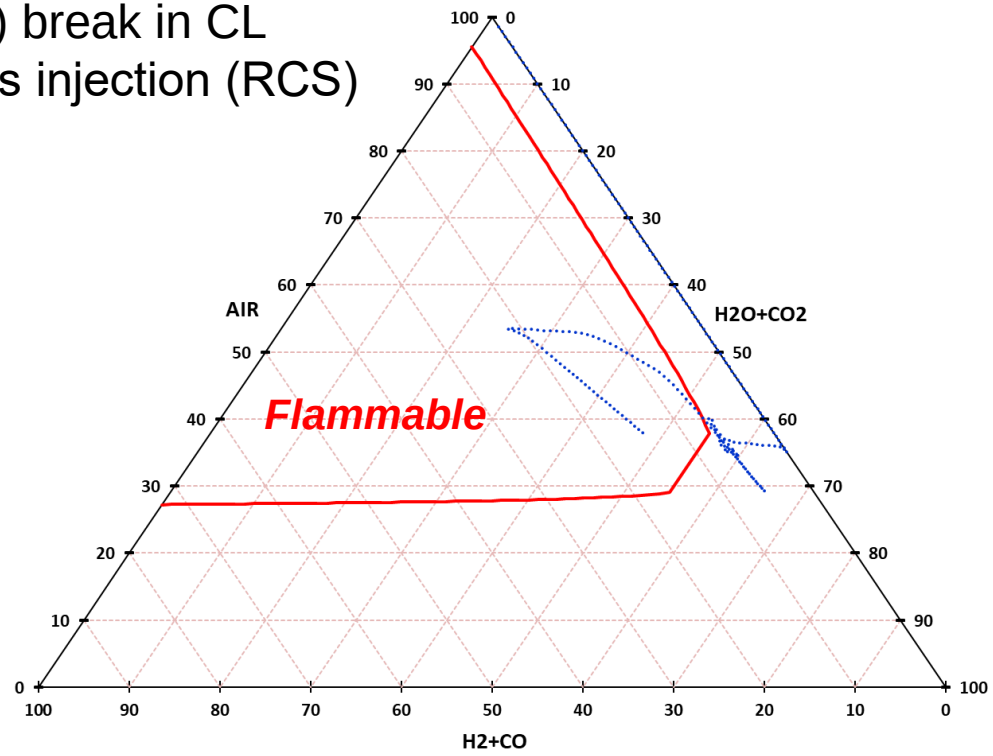

Results and discussion: PWR-W (2)

Westinghouse PWR-1000 LBLOCA

Double-ended guillotine break in HL
Accumulator's injection (RCS)
Fan coolers and sprays

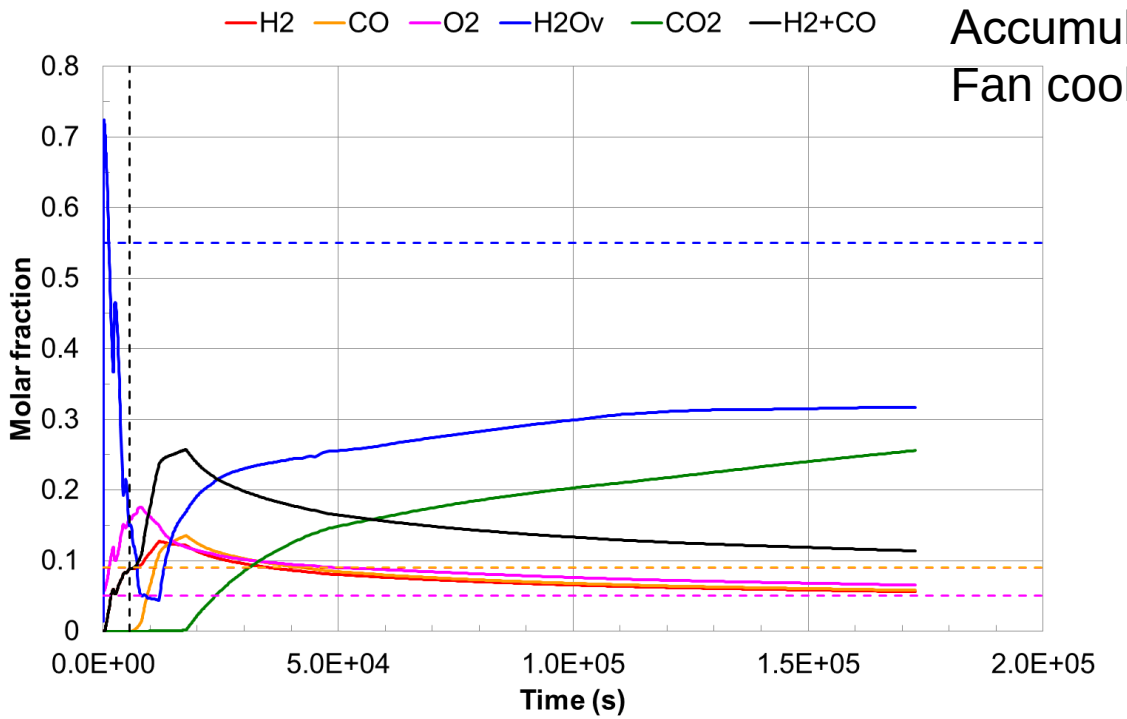

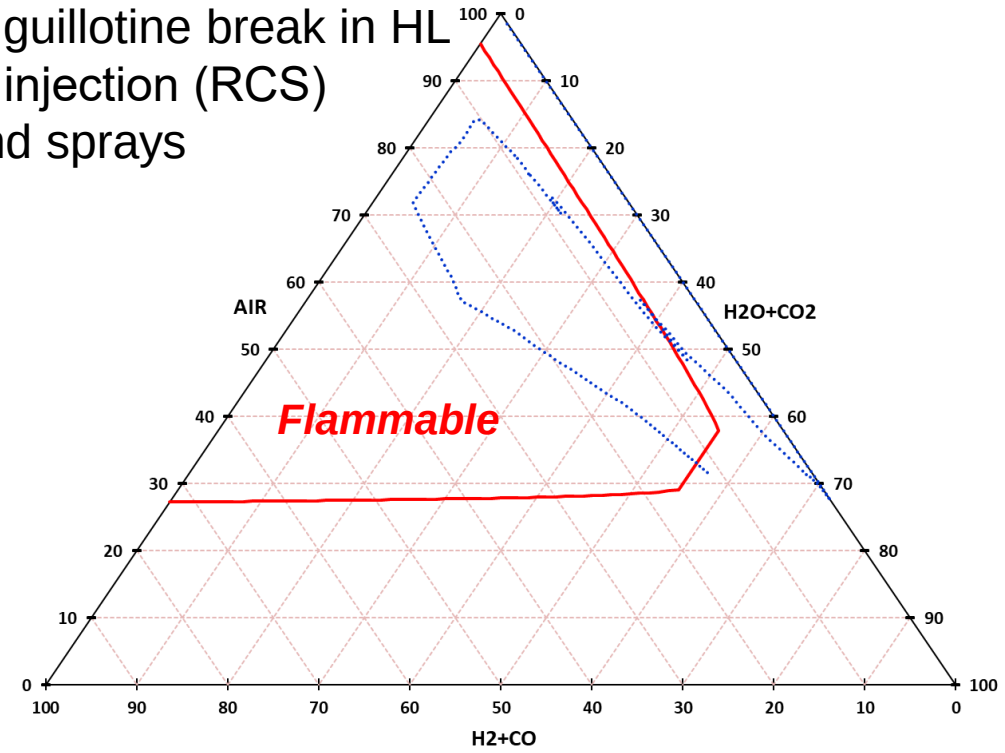

Results and discussion: PWR-W (3)

Framatome PWR-1300 MBLOCA

12” Φ (730 cm^2) break in HL
Accumulator’s injection (RCS)
No containment safety systems

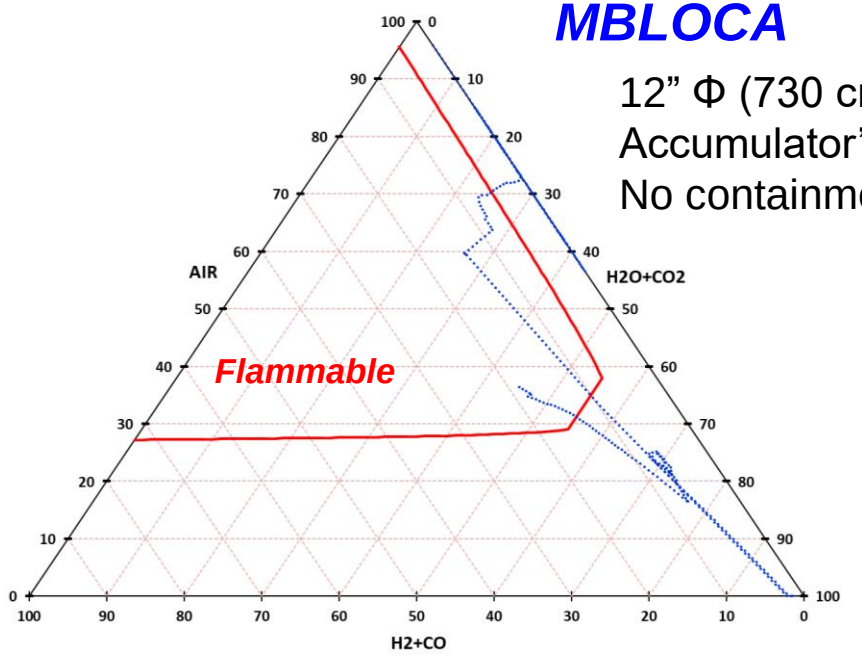

Framatome PWR-1300 SBO

Safety tank discharge
Accumulator’s injection (RCS)
No containment safety systems

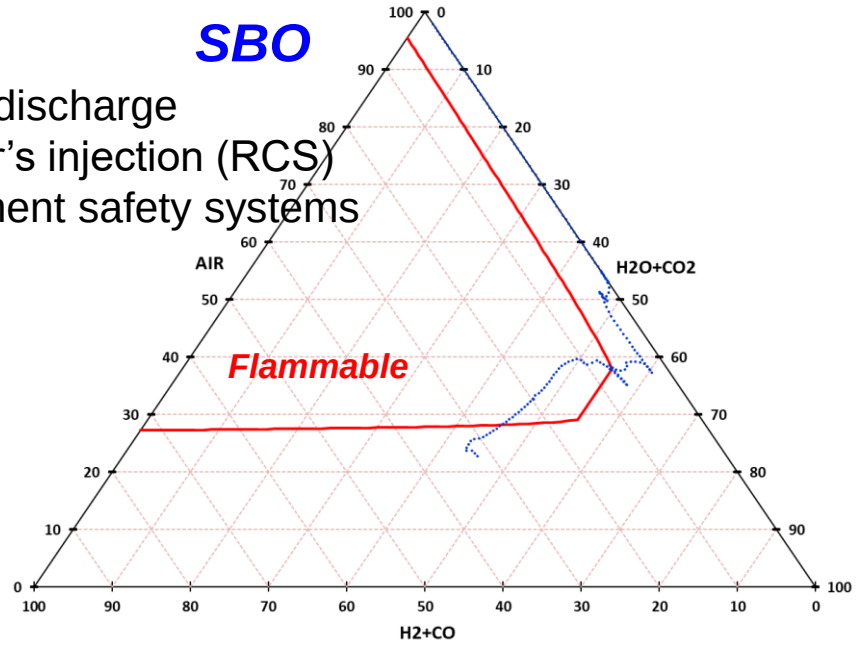

Westinghouse PWR-700 SBLOCA

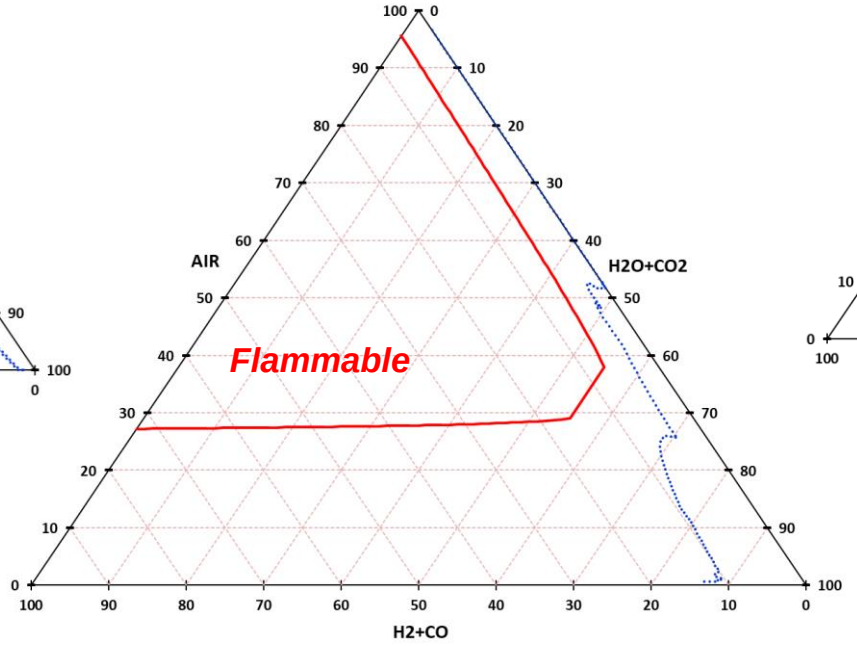

6” Φ (180 cm^2) break in CL
No injection systems (RCS)
No containment safety systems
PARs modelled

Results and discussion: PWR-KWU (1)

Konvoi PWR-1300 SBLOCA

4” Φ (80 cm^2) break in CL
EBS + accumulator injection (RCS)
No containment safety systems

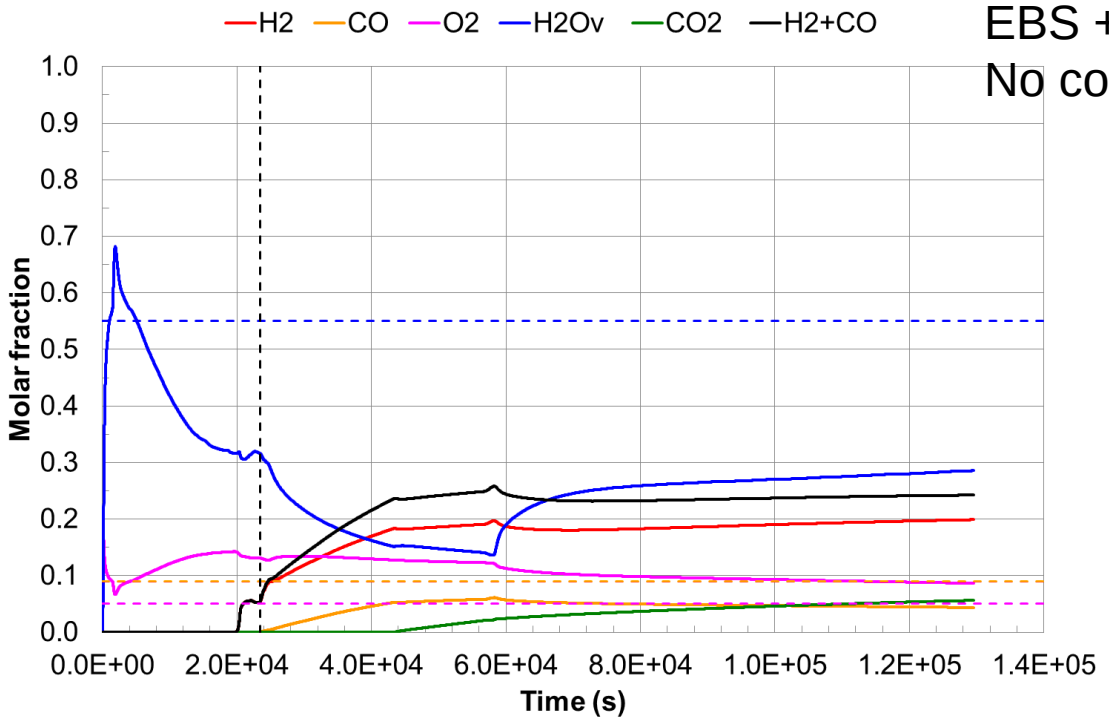

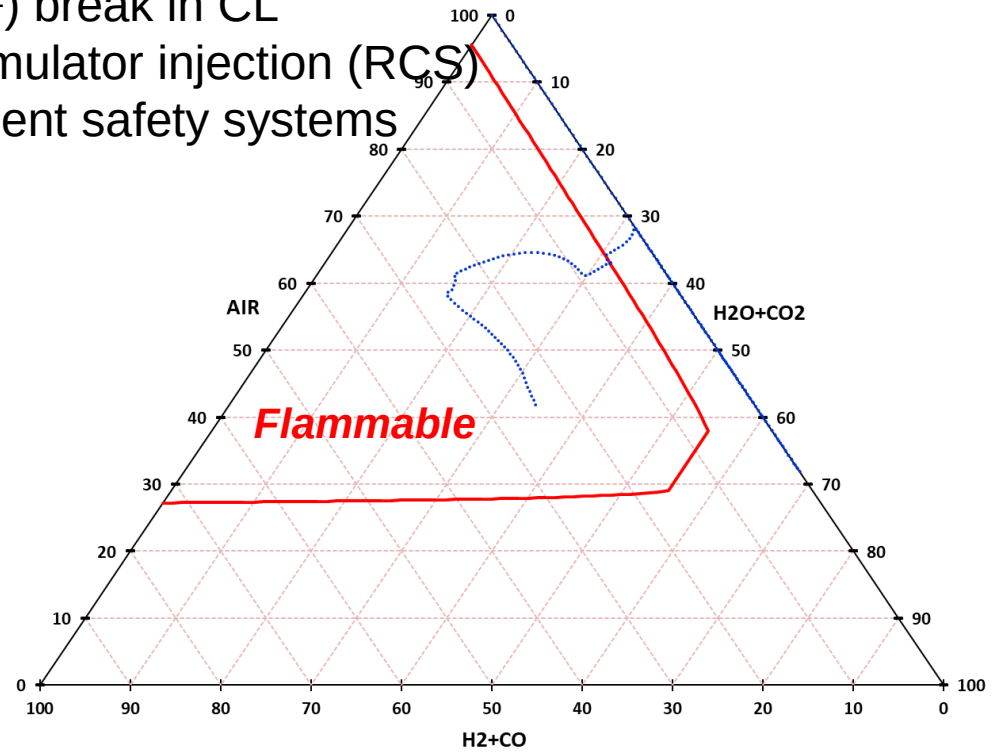

Results and discussion: PWR-KWU (2)

SBO

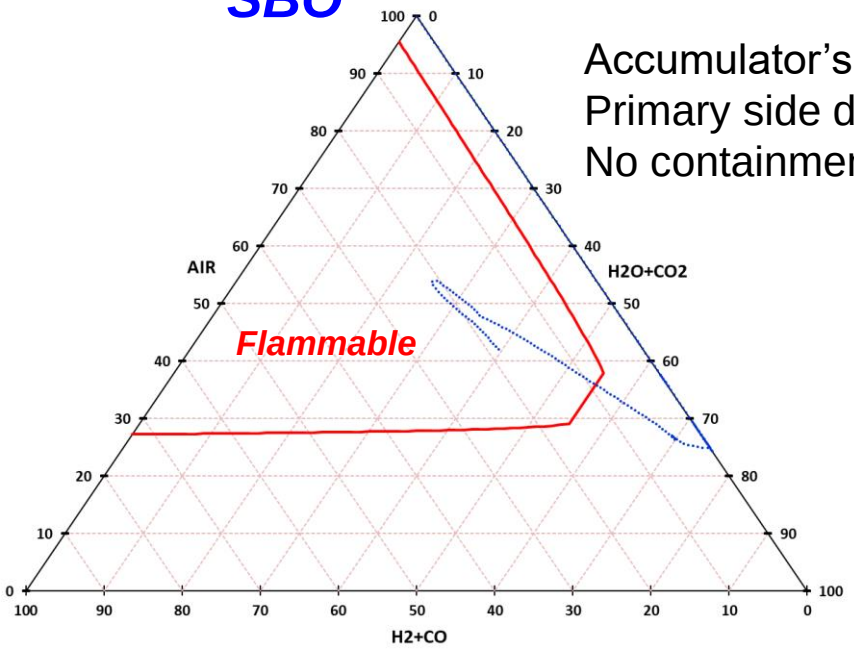

Accumulator's injection (RCS)
Primary side depressurization
No containment safety systems

LBLOCA

8.6" Φ (380 cm^2) break in HL
EBS + accumulator injection (RCS)
No containment safety systems
PARs modelled

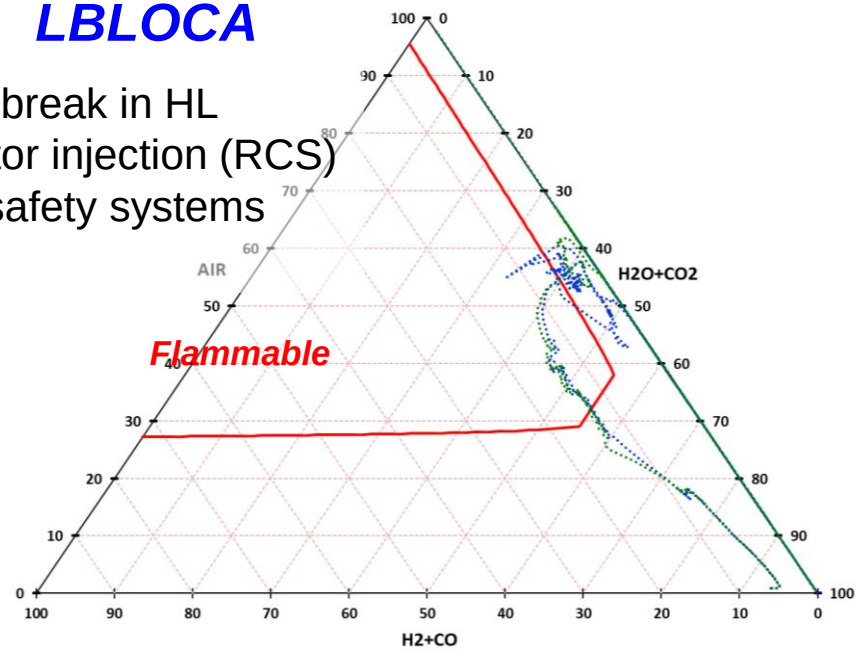

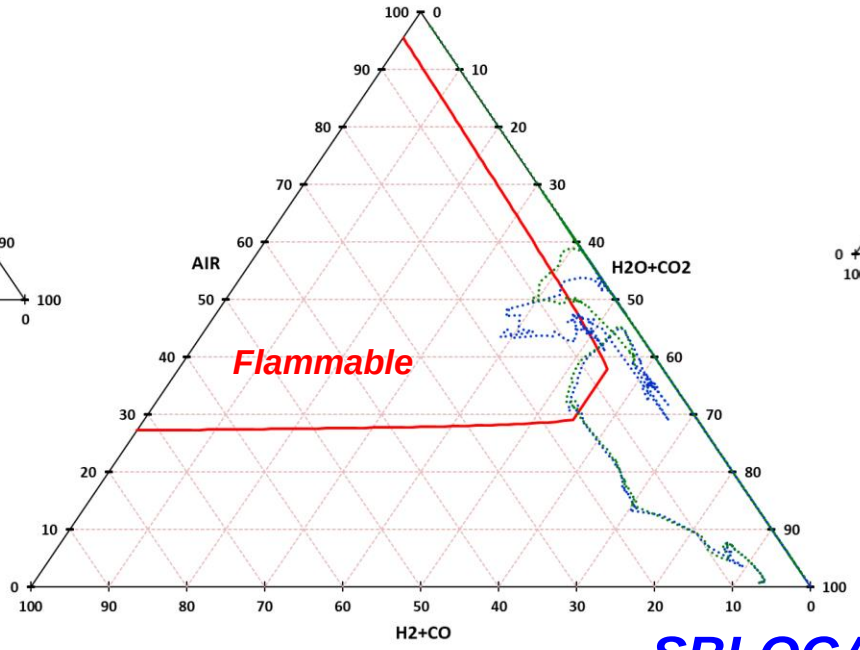

4" Φ (80 cm^2) break in HL
EBS + accumulator injection (RCS)
No containment safety systems
PARs modelled

SBLOCA

Conclusions

- *A scenario database with 30 PWR sequences has been created.*
- *Identified sequences with the largest combustion risk for H_2 & CO mixtures.*
  - *PWR-KWU: **SBLOCA** (80 cm^2).*
  - *PWR-W: **SBLOCA** (20 cm^2) & **LBLOCA** (double-ended guillotine).*
- *Main analysis outcomes:*
  - *Containment safety systems (steam condensing capability) highly condition sequence selection.*
  - *The largest combustible gases accumulation is found in the ex-vessel phase with H_2+CO mixtures.*
  - *If PARs are modelled. O_2 starvation in the ex-vessel phase makes mixture exit the flammable region, even if gas content is over 9 vol.%.*
- *Database will be used in other AMHYCO WPs:*
  - *To set up test conditions for **PAR performance** and **combustion** of H_2 + CO mixtures.*
  - *Test the effect of **accident management actions** by 3D or LP simulations.*

Thanks for your attention

ACKNOWLEDGEMENT

This work has been carried out in the frame of the AMHYCO Project. This project is funded from the **Euratom research and training programme** 2019-2020 under Grant Agreement No. 945057

DYNAMICALLY PRESCRIBED TURBULENT NUMBERS IN CONTAINMENT ATMOSPHERE MIXING SIMULATIONS

Rok Krpan[1,2], Iztok Tiselj[1,2], Ivo Kljenak[1]
[1]Jožef Stefan Institute, Reactor Engineering Division
Jamova cesta 39, SI-1000, Ljubljana, Slovenia
[2]University of Ljubljana, Faculty of Mathematics and Physics
Jadranska ulica 19, SI-1000, Ljubljana, Slovenia
rok.krpan@ijs.si; iztok.tiselj@ijs.si; ivo.kljenak@ijs.si

ABSTRACT

In turbulence modelling, constant values of turbulent Schmidt and Prandtl numbers are usually used. However, when compared to experiments, simulations with constant values do not always provide satisfactory agreement. A new model for prescribing different values of turbulent Schmidt and Prandtl numbers to different flow regions is proposed and validated against three experiments on containment mixing performed in SPARC, PANDA and MiniPanda experimental facilities.

KEYWORDS
stratified atmosphere homogenization, helium layer, vertical jet, Computational Fluid Dynamics

1. INTRODUCTION

During a severe accident in a light water nuclear reactor, hydrogen combustion could threaten the integrity of the nuclear power plant (NPP) containment. The study of hydrogen distribution in the containment is thus important to predict the occurrence of regions with high local hydrogen concentrations and flammable mixture in order to effectively install hydrogen mitigation systems in containments. Various experiments are being performed to simulate atmosphere mixing occurring in containment during severe accidents and results are used to validate models on the local instantaneous scale in order to eventually simulate phenomena in actual power plants [1].

To theoretically investigate atmosphere mixing in a large enclosure representing a NPP containment in the present work, three experiments on homogenization of a stratified atmosphere using a vertical jet are considered. During the tests, the erosion of helium-rich layer in the upper part of the experimental vessels with a vertical axisymmetric air jet was observed. The first experiment considers an isothermal break-up of a helium layer in the SPARC (Spray-Aerosol-Recombiner-Combustion) large-scale test facility, located at Korea Atomic Energy Research Institute (KAERI) in Daejeon (Republic of Korea) [2,3]. The second experiment considered was performed in the PANDA experimental facility at the Paul Scherrer Institute (PSI) in Switzerland [4], and the third experiment was performed in the MiniPanda experimental facility, located at ETH Zürich (Switzerland) [5,6].

The turbulent Schmidt (Sc_t) and Prandtl number (Pr_t) are non-dimensional numbers used in turbulence modelling to describe the turbulent transport of mass and heat, respectively. In modelling on the local instantaneous scale (using CFD), constant values of Sc_t and Pr_t are usually used. Typically, their values are based on comparisons of calculation and experimental results. However, a constant value does not always provide a satisfactory agreement with experiments. In fact, values of these turbulent numbers may be expected to change throughout the flow field and within the boundary layer [7,8].

In the present work, a model to dynamically prescribe Sc_t and Pr_t is proposed. As such, the proposed model is an extension of existing models. The vertical jet in an enclosure is constrained in the streamwise direction and a recirculating flow is eventually generated. The proposed model uses velocity and density gradients to delimit the recirculation zone, and then prescribes different values of Sc_t and Pr_t accordingly. This approach intensifies turbulent mixing outside the recirculation zone, where velocity and its gradients are low and the flow is almost laminar. Consequently, the agreement between measurements and calculation results is improved, especially at isothermal conditions with higher mass inflow.

2. CONSTRAINED VERTICAL JET

In the considered experiments, a vertical axisymmetric jet injected upwards is constrained in the vertical (streamwise) direction, at first with a light gas layer and later with the ceiling of the vessel. Consequently, the jet at some point changes its direction, flows downstream around the main jet and a recirculating flow is generated. Fig. 1 shows the absolute value of instantaneous vertical velocity field in logarithmic scale and streamlines in a typical constrained vertical jet. The velocity field is taken from simulations of experiment performed in SPARC experimental facility at $t = 1000\ s$. Regarding the vertical velocity, the following flow regions can be defined:

A. upward flowing main jet,
B. downward flowing returning jet,
C. quiescent environment.

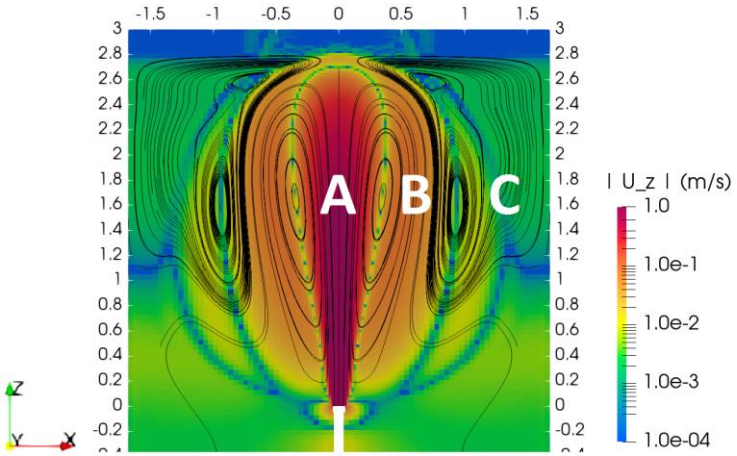

Figure 1. Absolute value of vertical velocity field (logarithmic scale) and streamlines in a constrained vertical jet.

Let us define a Cartesian coordinate system with origin located in the centre of injection and z axis pointing upwards (in the opposite direction of gravity). Fig. 2 (left) shows a vertical velocity radial (x-direction) profile 2 m above the injection, when the flow is already fully-developed. However, the radial profile in a typical fully-developed axisymmetric jet is similar regardless the distance from the injection. The velocity is highest in the axis of the jet. Further away from the axis, the vertical velocity decreases, becomes zero on the boundary between the main jet and the downward flowing returning jet, and reaches its minimum value in the axis of the returning jet. Further on, the vertical velocity increases back to zero in the quiescent environment. Fig. 2 (right) shows the vertical velocity vertical profile in the jet axis. The velocity decreases and when the jet reaches either a layer consisting of light gas or the ceiling, it becomes zero.

Figure 3 (left) shows the vertical velocity gradient in the radial direction ($\partial u_z/\partial x$) multiplied by the x coordinate sign, to preserves the sign across axis crossing. Fig. 3 (right) shows the vertical velocity gradient in the vertical direction ($\partial u_z/\partial z$). Since the jet is assumed to be axisymmetric, the gradient in the y-direction, $\partial u_z/\partial y$, is equal to $\partial u_z/\partial x$. Directly above the injection, in the jet axis, u_z is the highest and thus $\partial u_z/\partial x$ is zero, but this can be only seen on the upper part of the jet. From the axis in the radial direction, $\partial u_z/\partial x$ is negative in the main jet and in the part of the returning jet up to its axis, where it is zero again, then changes its sign and is positive up to the quiescent environment, where it reaches zero. In the jet axis, $\partial u_z/\partial z$ is negative and reaches zero, where the main jet redirects downwards. Above the jet, already in the light gas layer, the gradient is positive. Here, the negative vertical velocity in a generated recirculation zone (Fig. 1) increases to zero.

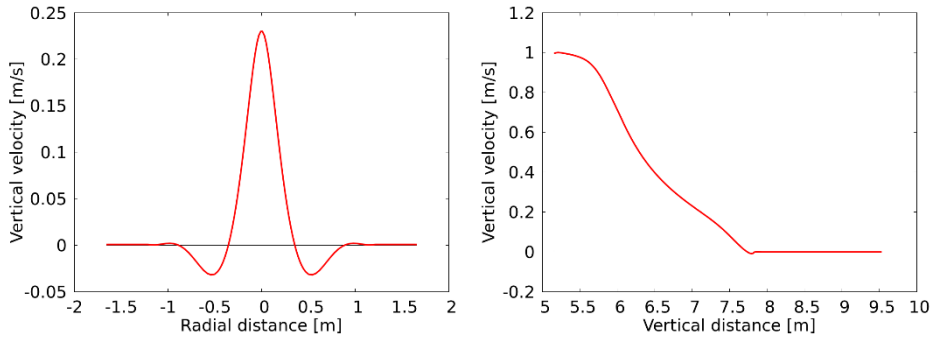

Figure 2. Vertical velocity radial profile (left) and vertical velocity vertical profile (right).

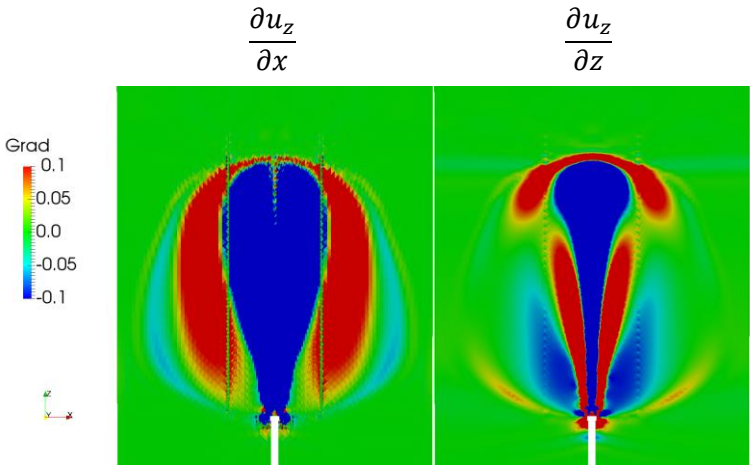

Figure 3. Vertical velocity radial gradient (left) and vertical velocity vertical gradient (right).

3. GOVERNING EQUATIONS

The mixing experiments were simulated using the model implemented in the OpenFOAM CFD code. The atmosphere in the vessel was considered as a compressible mixture of ideal gases. The erosion and mixing processes were modelled (implicitly) as two-component single-phase flows, where single continuity, momentum and total energy equations were solved. The convection-diffusion equation was solved only for a single species, while the other species mass fraction was calculated using $\sum_{i=1,2} Y_i = 1$.

Sc_t and Pr_t numbers are defined as the ratio of momentum eddy diffusivity (ν_t) to mass eddy diffusivity (D_t), and as the ratio of ν_t to thermal eddy diffusivity (α_t), respectively [9]:

$$Sc_t = \frac{\nu_t}{D_t} \tag{1}$$

$$Pr_t = \frac{\nu_t}{\alpha_t} \tag{2}$$

Sc_t takes place in the convection-diffusion equation:

$$\frac{\partial \rho Y_{He}}{\partial t} + \frac{\partial}{\partial x_j}\left(\rho u_j Y_{He}\right) = \frac{\partial}{\partial x_j}\left(\left(\rho D + \frac{\mu_t}{Sc_t}\right)\frac{\partial Y_{He}}{\partial x_j}\right) \tag{3}$$

where $\rho, Y_{He}, t, u_j, D, \mu_t$ and Sc_t are density, helium mass fraction, time, velocity, diffusion coefficient and eddy viscosity, respectively. On the other hand, Pr_t takes place in the total energy equation:

$$\begin{gathered}\frac{\partial \rho h}{\partial t} + \frac{\partial}{\partial x_j}\left(\rho u_j h\right) + \frac{\partial \rho K}{\partial t} + \frac{\partial}{\partial x_j}\left(\rho u_j K\right) - \frac{\partial p}{\partial t} = \\ \frac{\partial}{\partial x_j}\left(\left(\frac{\mu}{Pr} + \frac{\mu_t}{Pr_t}\right)\frac{\partial h}{\partial x_j}\right) - \sum_i \left(\frac{\partial}{\partial x_j}\left(h_i \cdot \left(\rho D + \frac{\mu_t}{Sc_t}\right)\right)\frac{\partial Y_i}{\partial x_j}\right) + \rho g_k u_k\end{gathered} \tag{4}$$

where h, K, p, Pr and h_i are enthalpy, kinetic energy, pressure, Prandtl number and gas species enthalpy, respectively.

More information on numerical settings used in the calculations, generated numerical meshes and mesh convergence study can be found in Krpan et al. [10].

3.1 Dynamic Turbulent Schmidt and Prandtl Number Model

The vertical velocity and its gradients are used to determine the shear flow in the vertical limited jet (i.e. the jet boundary) and to specify the regions with different Sc_t value. The proposed model to prescribe different Sc_t value to different flow regime region is:

$$\mathrm{Sc_t} = \mathrm{Sc_{t,min}} - \frac{1}{2}\left(Sc_{t,max} - Sc_{t,min}\right)\left\{1 + \tanh\left[\mathrm{c}_{k,1}\left(\partial u_g \cdot \partial \rho_n\right) - c_{k,2}\right]\right\} \tag{5}$$

$$\partial u_g = \frac{\partial}{\partial x_i}\left(-\frac{g}{|g|} \cdot \frac{u}{\max(|u|)}\right) \tag{6}$$

$$\partial \rho_n = \frac{1}{\rho}\frac{\partial \rho}{\partial x_i} \tag{7}$$

where $Sc_{t,min}, Sc_{t,max}, c_{k,1}$ and $c_{k,2}$ are minimum and maximum Sc_t values specified by the user, and two model constants, respectively. ∂u_g and $\partial \rho_n$ are normalized vertical velocity gradient and gradient of normalized density, respectively.

The hyperbolic tangent function conveniently maintains the Sc_t number value in the order of unity and limits its upper and lower values, regardless the extreme values of gradients during simulations. This function prescribes lower Sc_t value where function arguments are positive, and vice versa. Furthermore, in

the interval of small arguments around zero, the result of hyperbolic tangent is continuously differentiable, which avoids numerical instabilities. Density and velocity gradients are high in the main and in the returning jet, where changes in density and velocity fields are large (Fig. 3). The constant $c_{k,1}$ adjusts the behaviour of the function regarding the mean flow properties. The constant $c_{k,2}$ decreases the hyperbolic tangent argument and prescribes lower Sc_t (or Pr_t) value in the quiescent environment, where the gradients are low. In the results presented in the next sections, Eq. 5 was also used to dynamically prescribe Pr_t.

4. EXPERIMENTAL FACILITIES AND EXPERIMENTS USED FOR MODEL VALIDATION

The model was validated on three experiments performed in SPARC, PANDA and MiniPanda experimental facilities. The main purpose of these experiments was to observe the interaction of a vertical air jet with a previously established horizontal layer of helium-air mixture in the upper parts of the vessels. The initial and boundary conditions of the tests used for model validation in the present work are listed in Table I. Initial helium volume fraction vertical distribution profiles in the experiments are shown in Fig. 4. On x-axis is relative distance from the injection, $(z - H_{inj})/H_{vessel}$, where z, H_{inj} and H_{vessel} are vertical coordinate, height of the injection and vessel height.

Table I. Boundary and initial conditions for simulated tests.

Experiment	Position of injection	Helium content [vol. %]	Injection flow rate [g/s]	Interaction Froude number
SPARC	Centre	30	28	0.51
PANDA	Near wall	45	15	0.75
MiniPanda	Near wall	100	1.51	1.3

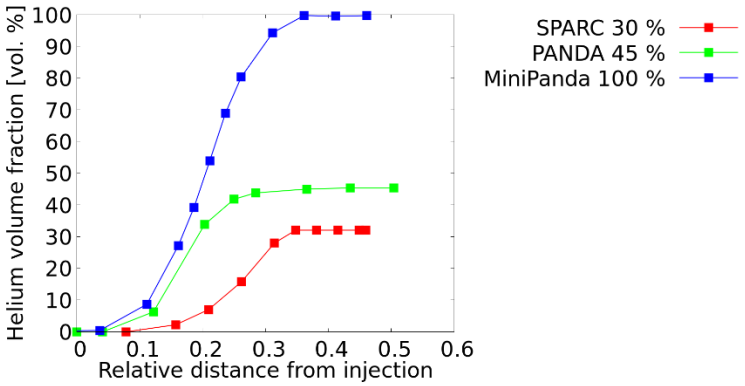

Figure 4: Initial helium distribution profiles for different experiments ([2,4,5])

4.1 SPARC Experimental Facility

The SPARC test facility (Fig. 5) consists of a single cylindrical vessel with a volume of 80 m^3 [2,3]. Before the experiment, a 1.5 m thick layer rich with helium (the rest was air) was established in the upper part of the vessel. The jet with a diameter of 0.1 m was injected at the axis of the vessel at an elevation of 5.15 m and had the same temperature as the previously established atmosphere (25 °C). The experiment was performed at constant pressure of 1 bar [2,3].

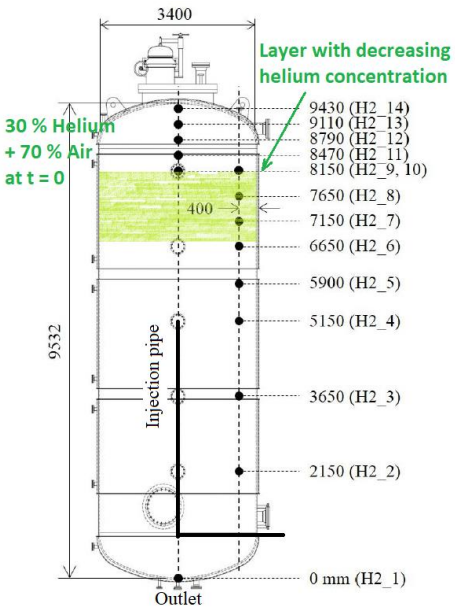

Figure 5. Schematic of SPARC experimental facility and sampling positions [2].

4.2 PANDA Experimental Facility

The PANDA experimental facility consists of two cylindrical vessels and an interconnecting pipe, with a total volume of 183 m^3 (Fig. 6 left). Each vessel has a height of 8.0 m and a diameter of 3.96 m with a volume of 89.9 m^3. The injection pipe is positioned 0.5 m away from the wall and has a diameter of 0.075 m. In the experiment considered in the present work, the initial pressure and temperature in the vessel were 1 bar and 20 °C, respectively.

Before the test, a 2 m thick layer of helium and air was established in the upper part of one of the vessels, as shown in Fig. 6 (left). During the experiment, this layer was eroded with an air jet with a mass flow rate of 15 g/s at a temperature of 30 °C. Fig. 6 (right) shows measuring positions, from which results are compared in this paper [4].

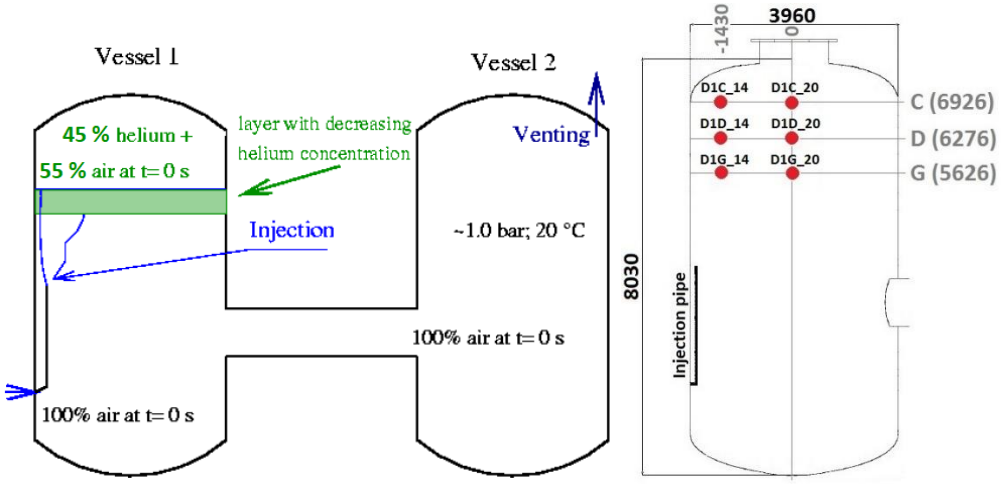

Figure 6. Schematic of PANDA facility and initial conditions (left) and sampling positions (right) [4].

4.3 MiniPanda Experimental Facility

MiniPanda is a 1:4 scaled-down model of the PANDA facility. Each vessel has a height of 2 m and a diameter of 1 m (Fig. 7). The injection pipe with a diameter of 0.018 m is positioned 0.125 m away from the wall. The total volume of the facility is 2.875 m^3 [5].

During the experiment considered in the present work, approximately 0.5 m thick layer of pure helium was eroded with vertical air jet with a temperature of 80 °C. The initial atmosphere temperature was 25 °C. The experiment was performed at constant pressure of 1 bar.

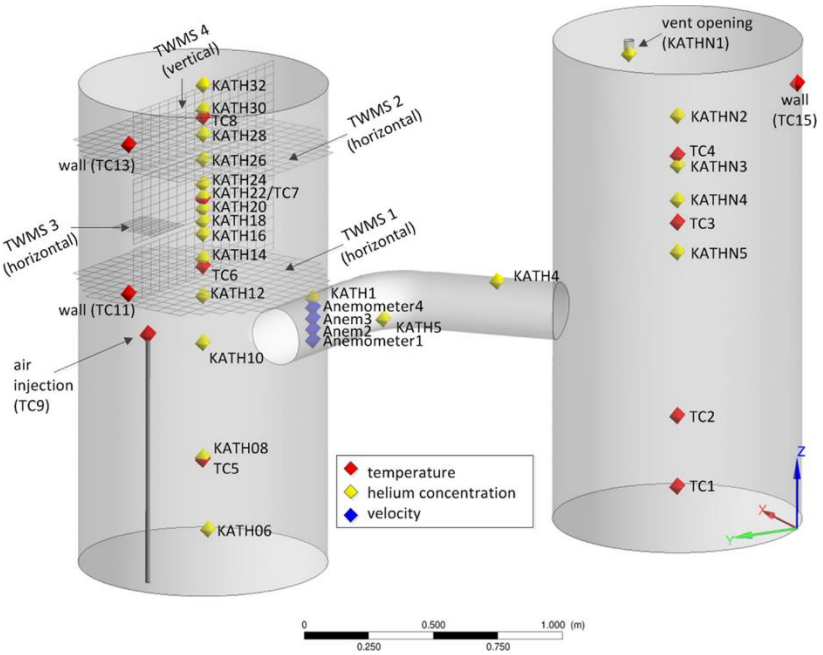

Figure 7. Schematics and sampling positions in MiniPanda facility [6].

5. RESULTS

Figure 8 shows the Sc_t field given by the proposed model (Eq. 5), in a typical constrained vertical jet calculated with parameter values listed in Table II. The values of the constants were set in such manner, that the area, to which higher values of Sc_t and Pr_t, numbers are prescribed, contains the main jet and half of the retuning jet (i.e. most of the main recirculation zone). Sc_t values were selected according to experiments of an inclined jet [11].

Table II. Model constants.

Constant	$Sc_{t,min}$	$Sc_{t,max}$	$c_{k,1}[m^2]$	$c_{k,2}$
Value	0.4	0.9	1000	1

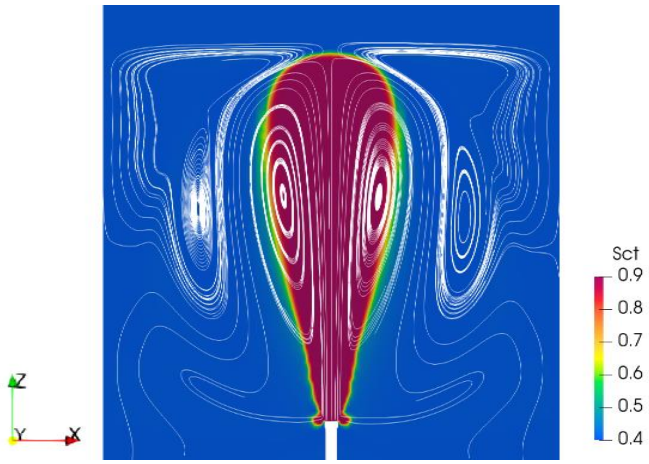

Figure 8. Turbulent Sc number given by proposed model and streamlines in typical vertical jet.

The model prescribes higher Sc_t and Pr_t in the recirculation zone with higher velocity, where turbulence kinetic energy (k) and turbulence kinetic energy dissipation rate (ε) are high (Fig. 9), and lower in the environment, where velocity and its gradients are low and the flow is almost laminar. Due to higher values of terms μ_t/Sc_t in Eq. 3 and μ_t/Pr_t in Eq. 4 in regions with low fluid velocity, turbulent mass diffusion and turbulent heat diffusion rates are increased and the mixing process is intensified.

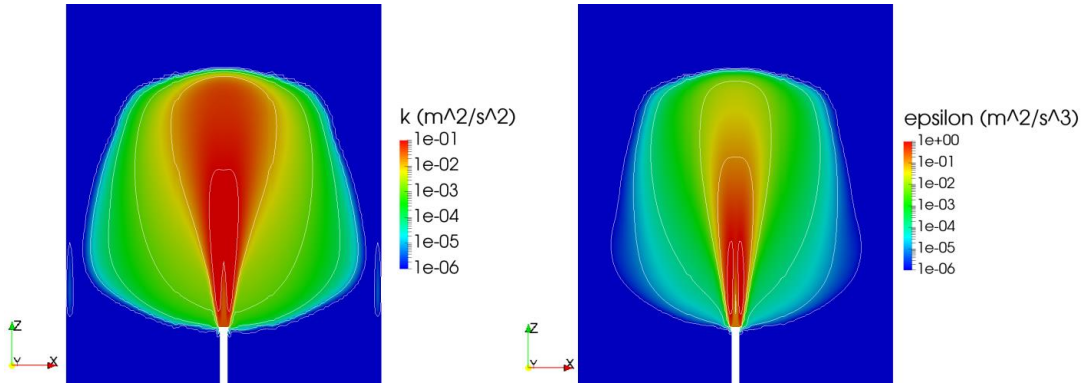

Figure 9. Turbulence kinetic energy (left) and turbulence kinetic energy dissipation rate (right) in a constrained vertical jet.

5.1 SPARC Experiment

On Fig. 10 time-dependent helium volume fractions at several locations in the SPARC facility are compared. The helium concentrations obtained in calculations with constant Sc_t and dynamic Sc_t model in lower measuring positions H2_4, H2_6 (Fig. 10 bottom) and H2_8 (Fig. 10 middle right), match the experimental results. It must be noted, that although the discrepancies in H2_4 and H2_6 seem large, the difference is only 1 vol. %. At the measuring positions directly above the injection H2_10 (Fig. 10 middle left), H2_12 and H2_14 (Fig. 10 top) the experimental concentrations and concentration obtained with constant Sc_t value at first coincide. Later, the rate of concentration decrease is reduced and atmosphere homogenization is reached approximately 1300 s later than observed in the experiment. On the other hand, the results given by the dynamic model are significantly improved, when compared to experimental results.

These results could be interpreted as that the underestimation of μ_t given by the turbulence model is compensated by a smaller value of Sc_t. Namely, smaller Sc_t increases the turbulent mass diffusion and enhances mixing. Similar behaviour were observed in RANS computations also by other authors [12].

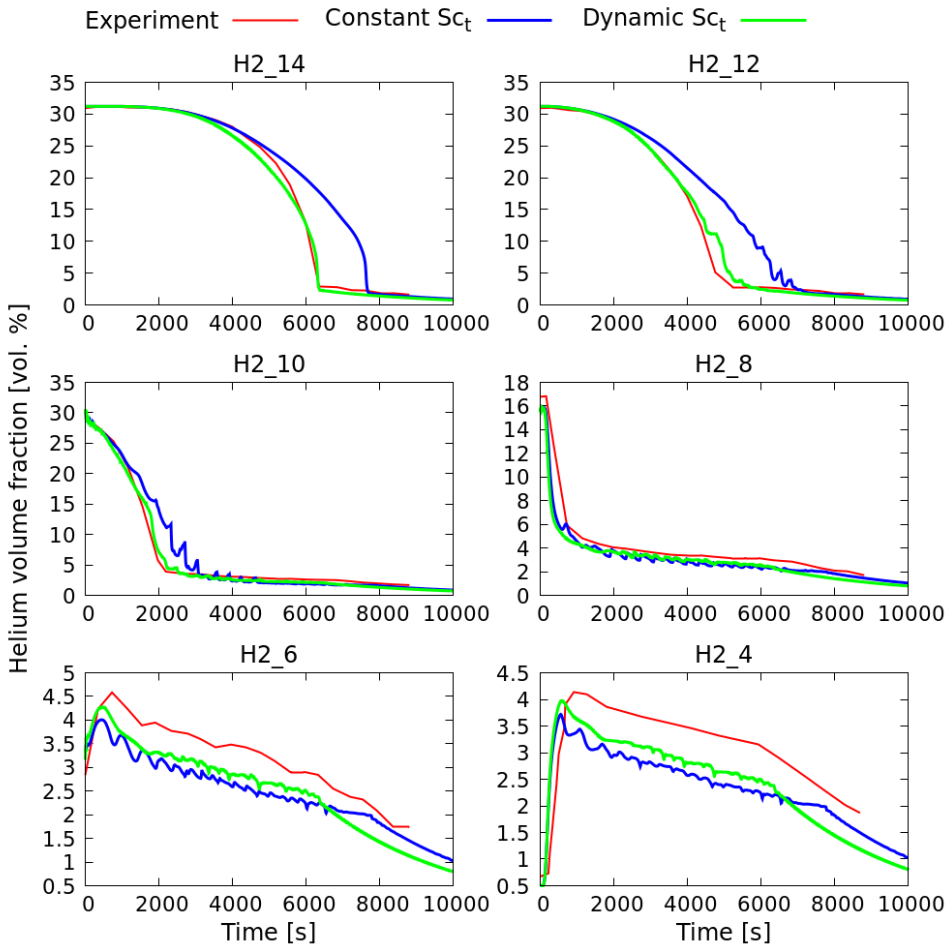

Figure 10. SPARC experiment: helium volume fractions at different measuring locations (for sampling positions see Fig. 5).

5.2 PANDA Experiment

Figure 11 shows time-dependent helium volume fractions at several locations in the PANDA facility, approximately above the injection pipe (figures left) and in the axis of the vessel (figures right). When compared to experiment, helium volume fractions in simulations behave similarly, except that the values in the simulations are approximately 2 vol. % lower. Contrary to what was observed and discussed in the isothermal case in the previous section, there are no major discrepancies in the concentration results obtained with constant values and the dynamic model.

Figure 12 shows time-dependent atmosphere temperatures at different locations approximately above the injection (left) and in the axis of the vessel (right). Some discrepancies can be observed between experimental and simulation results (they may appear large due to the scale on the ordinate axis).

In the upper measuring positions (Fig. 12 top), the temperature in the experiment initially steeply increases, but in the simulations value remains constant. Above the inlet (Fig. 12 left), the sudden temperature increase occurs when the top of the jet reaches measuring positions, which happens simultaneously in the simulations and in the experiment. However, despite generally lower temperatures in the simulations, the maximum temperature values in the axis of the vessel (Fig. 12 right), away from the injection, are higher. Later, when the helium layer is fully eroded (after t ≈ 13,000 s), temperatures are generally underpredicted by 2 °C.

The dynamic Sc_t and Pr_t model increases heat transfer in the quiescent surroundings. Consequently, progress is faster and the temperature values are slightly lower than the values obtained using constant Sc_t and Pr_t values.

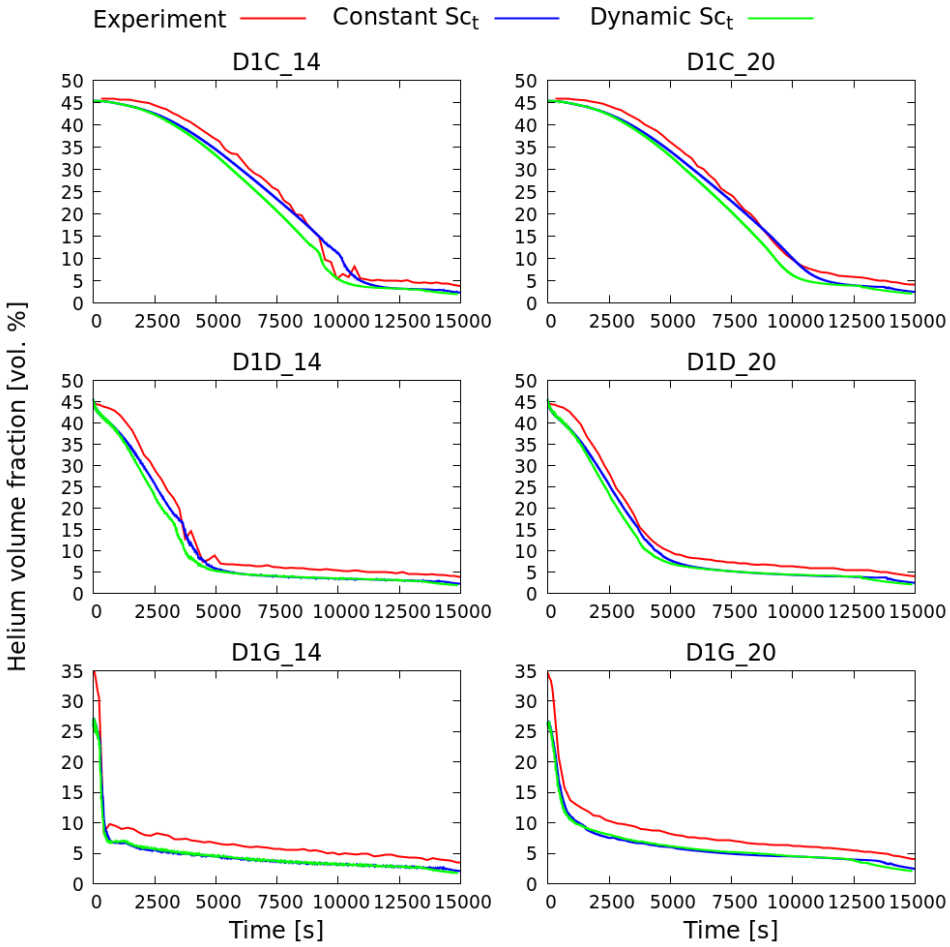

Figure 11. PANDA experiment: helium volume fraction at different elevations and positions (left: above injection, right: axis of the vessel; for sampling positions see Fig. 6 right).

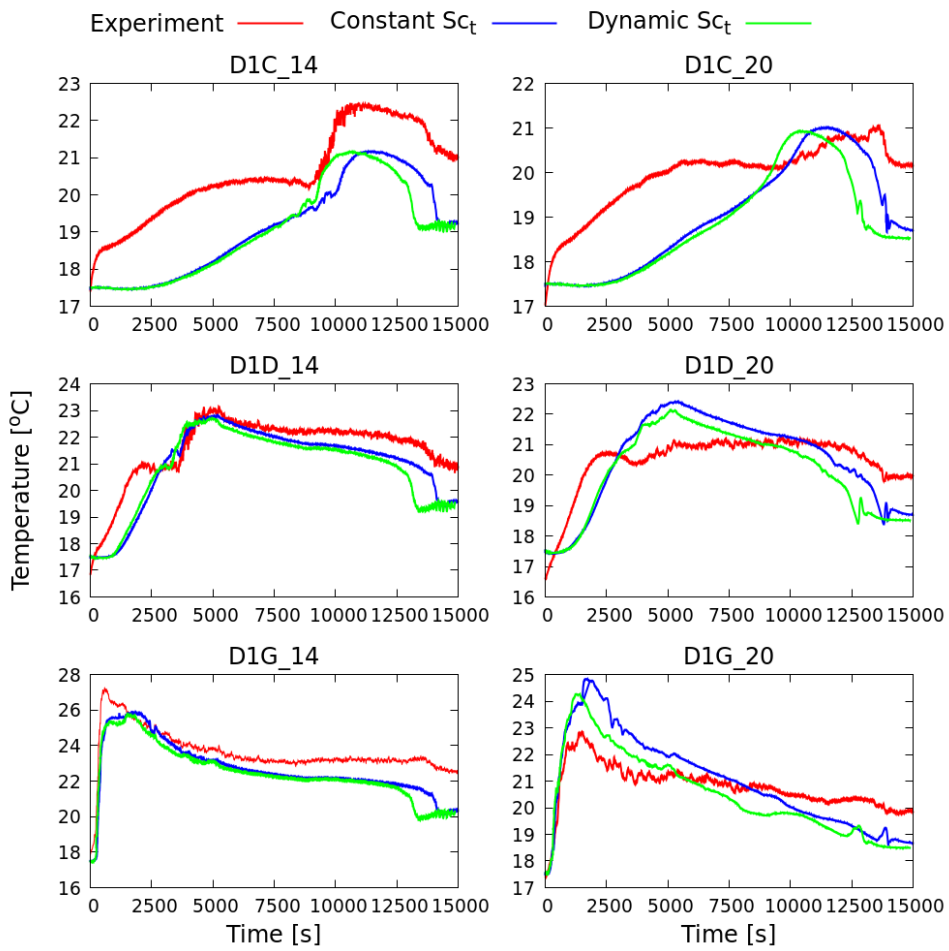

Figure 12. PANDA experiment: atmosphere temperatures at different elevations and positions (left: above injection, right: axis of the vessel; for sampling positions see Fig. 6 right).

5.3 MiniPanda Experiment

Figure 13 shows time-dependent helium volume fractions at several locations in the axis of the vessel in which injection occurred. Although the dynamic model slightly increases the erosion rate, the differences are almost insignificant, and the simulation results obtained with constant Sc_t and Pr_t already agree well with the experimental ones. However, this confirms the basic philosophy of the proposed model, that is, that its results do not differ much from the earlier model where the agreement with the experiment is already satisfactory.

Figure 14 shows time-dependent atmosphere temperatures at different elevations in the axis of the vessel. At earlier times, higher temperature values are obtained in calculations in all sampling positions. Later, when the helium layer is fully eroded, temperatures are 2-3 °C lower than in the experiment. The dynamic Sc_t and Pr_t model increases heat transfer and the temperature values are slightly lower than the values obtained using constant Sc_t and Pr_t.

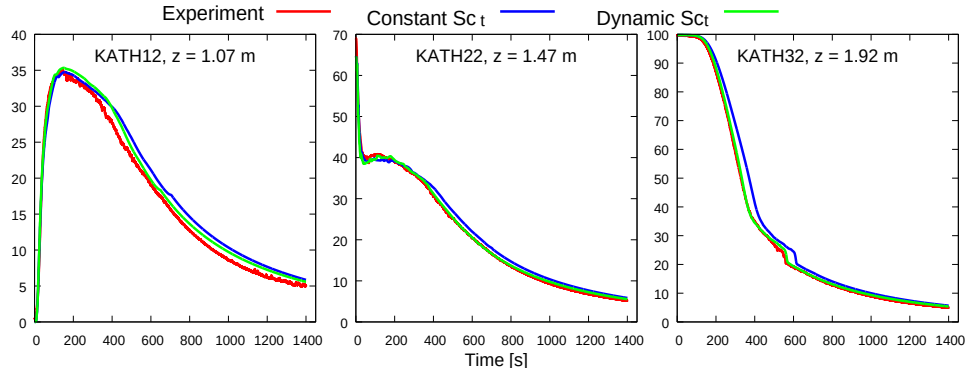

Figure 13. MiniPanda experiment: helium volume fraction at different elevations in vessel axis (for sampling positions see Fig. 7).

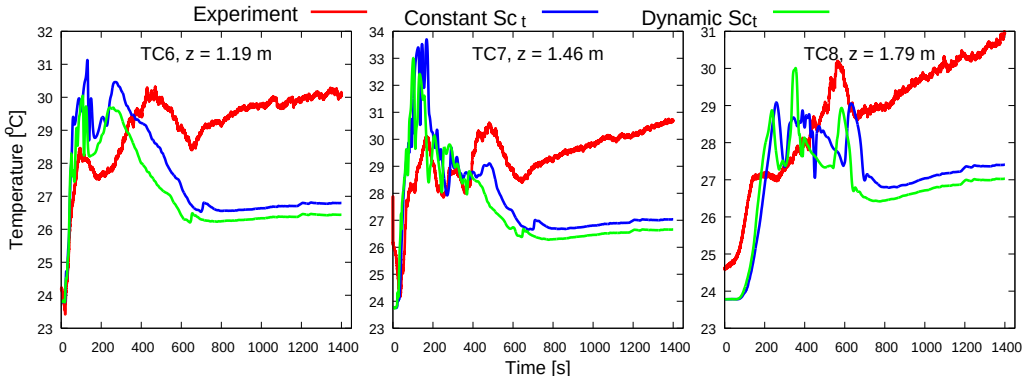

Figure 14. MiniPanda experiment: atmosphere temperatures at different elevations in vessel axis (for sampling positions see Fig. 7).

6. CONCLUSIONS

The successful modelling of breaking-up of atmosphere stratification, induced by vertical injection, was extended to isothermal conditions, by using mean flow properties to define different flow regions with different turbulence intensity and to prescribe different values of turbulent Schmidt and turbulent Prandtl numbers accordingly. The resulting higher turbulent Schmidt number in the quiescent environment enhances the diffusion process. This results in a much better prediction of a light-gas layer erosion, caused by a jet with the same temperature, in the upper regions of a vessel.

In non-isothermal cases, discrepancies between experimental and simulation temperatures are still present. The dynamic turbulent Prandtl model increases heat transfer in the quiescent environment, therefore, heat losses out of the numerical domains are higher and temperature values are slightly lower. However, despite these deficiencies, the proposed model is still a promising advance in the general topic of non-homogeneous atmosphere mixing in large enclosures.

ACKNOWLEDGMENTS

The authors acknowledge the financial support from the Slovenian Research Agency (research core funding No. P2-0026 “Reactor engineering”). The authors acknowledge M. Ritterath, H.-M. Prasser and the

Laboratory of Nuclear Energy Systems at the Federal Institute of Technology Zürich, Switzerland (ETHZ) for providing the experimental data.

REFERENCES

1. I. Kljenak, A. Bentaib and T. Jordan, *Hydrogen Behavior and Control in Severe Accidents*, in: Sehgal, B.R. (Ed.), *Nuclear Safety in Light Water Reactors*, pp. 186-227, Elsevier (2012).
2. Y.S. Na and J. Kim, "Introduction to SPARC test facility for assessment of hydrogen behaviour in severe accident", *12th Int. Topical Meeting on Nuclear Reactor Thermal-Hydraulics, Operation and Safety (NUTHOS-12)*, Qingdao, China (2018).
3. W. Lee, S. Song, Y.S. Na, and J. Kim, "Novel scaling law for long-term interface displacement of a stratified layer by erosion mixing due to turbulent impinging jet applicable to nuclear power plants", *Int. J. Heat Mass Transf.* **141**, pp. 1159-1167 (2019).
4. G. Mignot, R. Kapulla, D. Paladino, N. Erkan, R. Zboray, M. Fehlmann, C. Wellauer and W. Bissels, *OECD/NEA SETH-2, Vertical Fluid Release Test Series Report*, Paul Scherrer Institute, Switzerland (2010).
5. M. Ritterath, *Instrumentation and Mixing Experiments on Safety Relevant Gas Flows in Containments of Nuclear Reactors*, PhD Thesis, ETH Zurich, Switzerland (2012).
6. S. Kelm, M. Ritterath, H.-M. Prasser and H.-J. Allelein, "Application of the MiniPanda test case 'erosion of a stratified layer by a vertical jet' for CFD validation", *Nucl. Eng. Des.* **299**, pp. 124-135, (2016).
7. L. Ishay, U. Bieder, G. Ziskind and A. Rashkovan, "Turbulent jet erosion of a stably stratified gas layer in a nuclear reactor test containment", *Nucl. Eng. Des*. **292**, pp. 133-148 (2015).
8. K. Koeltzsch, "The height dependence of the turbulent Schmidt number within the boundary layer", *Atmos. Environ*. **34**, pp. 1147-1151 (2000).
9. L. Davidson, *Fluid mechanics, turbulent flow and turbulence modelling*, Department of Thermo and Fluid Dynamics, Chalmers University of Technology, Göteborg, Sweden (2019).
10. R. Krpan, I. Tiselj and I. Kljenak, "Simulations of PANDA and SPARC experiments on containment atmosphere mixing caused by vertical gas injection", *Nucl. Eng. Des*. **384**, pp. 111464 (2021).
11. S. Tahmooresi and D. Ahmadyar, "Effects of turbulent Schmidt number on CFD simulation of 45° inclined negatively buoyant jets", *Environ. Fluid Mech*. **21**, pp. 39-62 (2021).
12. Y. Tominaga, A. Mochida, S. Murakami and S. Sawaki, "Comparison of various revised k–ε models and LES applied to flow around a high-rise building model with 1:1:2 shape placed within the surface boundary layer", *J. Wind. Eng. Ind. Aerodyn*. **96**, pp. 389-411 (2008).

Jožef Stefan Institute
R4 Reactor Engineering Division
University of Ljubljana
Faculty of Mathematics and Physics

Dynamically Prescribed Turbulent Numbers in Containment Atmosphere Mixing Simulations

Rok KRPAN, Iztok TISELJ, Ivo KLJENAK
Jožef Stefan Institute (JSI), Slovenia

rok.krpan@ijs.si

10th European Review Meeting on Severe Accident Research (ERMSAR2022)
Karlsruhe, Germany, May 16th – 19th , 2022

May 18th , 2022

Introduction

- Hydrogen combustion during severe accident could threaten containment integrity.
- Hydrogen distribution study important to effectively install hydrogen mitigation systems.
- Experimental results used to validate Computational Fluid Dynamics codes.

- Turbulent Schmidt and turbulent Prandtl numbers are non-dimensional numbers used to describe the turbulent transport of mass and heat, respectively.
- Values of these turbulent numbers may be expected to change throughout the flow field and within the boundary layer.

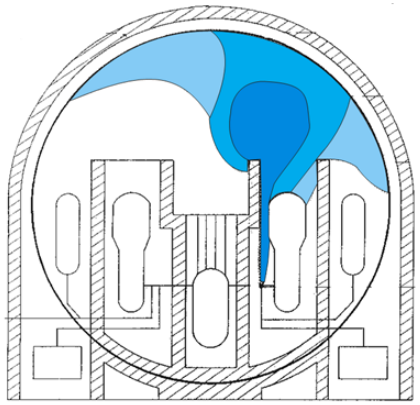

Hydrogen release from RCS



Hydrogen explosions during Fukushima accident

Contents

1) Experiments used for model validation

2) Physical model

3) Results

Experiments

	SPARC	PANDA	MiniPanda
Location	KAERI, Korea	PSI, Switzerland	ETHZ, Switzerland
Geometry	Single cylindrical vessel	Two cylindrical vessels	Two cylindrical vessels
Volume	80 m^3	183 m^3	2.875 m^3
Mass flow rate	28 g/s	15 g/s	1.51 g/s
Atmosphere T	20 °C	20 °C	25 °C
Jet T		30 °C	80 °C

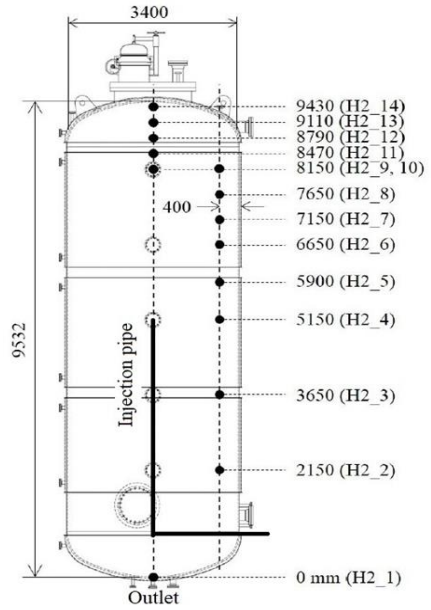

SPARC vessel schematics and sampling positions (Na and Kim, 2018)

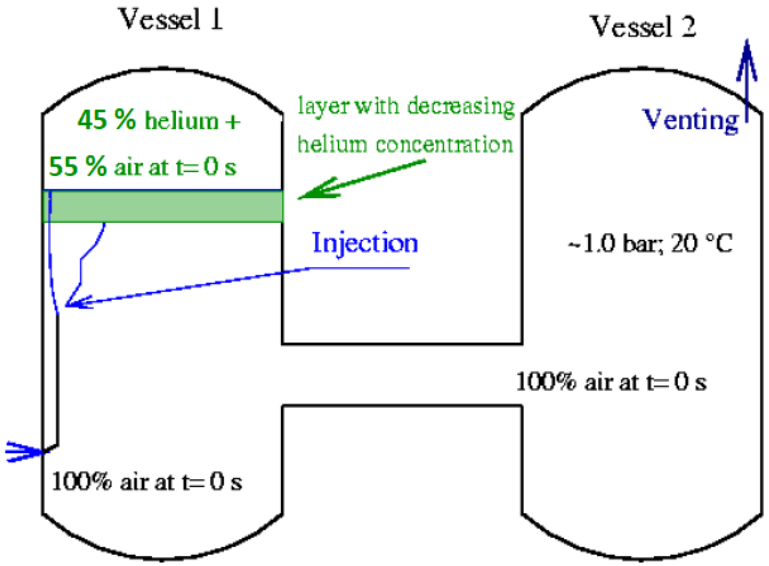

PANDA vessel schematics and sampling positions (Paladino et al. 2008)

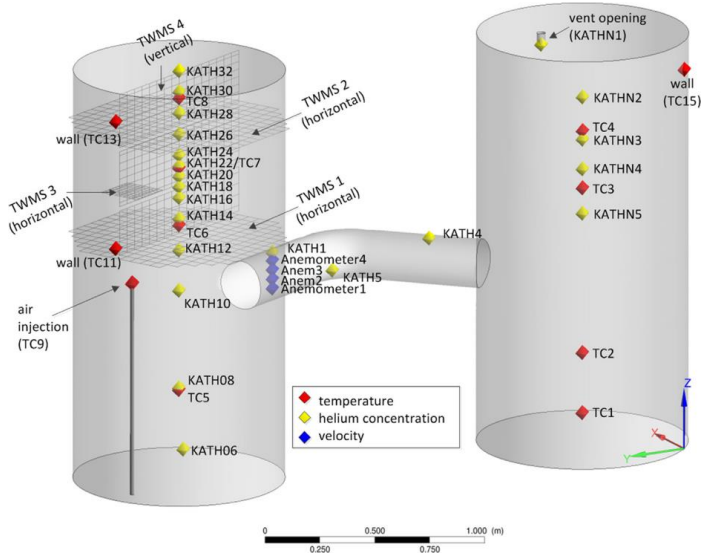

MiniPanda vessel schematics and sampling positions (Kelm et al. 2016)

CFD physical model

- Containment mixing experiments simulated with OpenFOAM CFD code
- Compressible mixture of ideal gases
- Single-phase flow of two-components
- Momentum equation
- Convection-diffusion equation

$$\frac{\partial \rho Y_{He}}{\partial t} + \frac{\partial}{\partial x_j}\left(\rho u_j Y_{He}\right) = \frac{\partial}{\partial x_j}\left(\left(\rho D + \frac{\mu_t}{Sc_t}\right)\frac{\partial Y_{He}}{\partial x_j}\right)$$

- Total energy equation

$$\frac{\partial \rho h}{\partial t} + \frac{\partial}{\partial x_j}\left(\rho u_j h\right) + \frac{\partial \rho K}{\partial t} + \frac{\partial}{\partial x_j}\left(\rho u_j K\right) - \frac{\partial p}{\partial t} =$$

$$\frac{\partial}{\partial x_j}\left(\left(\frac{\mu}{Pr} + \frac{\mu_t}{Pr_t}\right)\frac{\partial h}{\partial x_j}\right) - \sum_i \left(\frac{\partial}{\partial x_j}\left(h_i \cdot \left(\rho D + \frac{\mu_t}{Sc_t}\right)\right)\frac{\partial Y_i}{\partial x_j}\right) + \rho g_k u_k$$

CFD model validation

- PANDA (9 cases)
- MiniPanda (2 cases)
- VIMES (1 case)
- MCTHBF (1 case)
- SPARC (1 case)?

- R. Krpan, I. Tiselj and I. Kljenak, “Simulations of PANDA and SPARC experiments on containment atmosphere mixing caused by vertical gas injection”, Nucl. Eng. Des. 384, 2021.

CFD model validation - SPARC

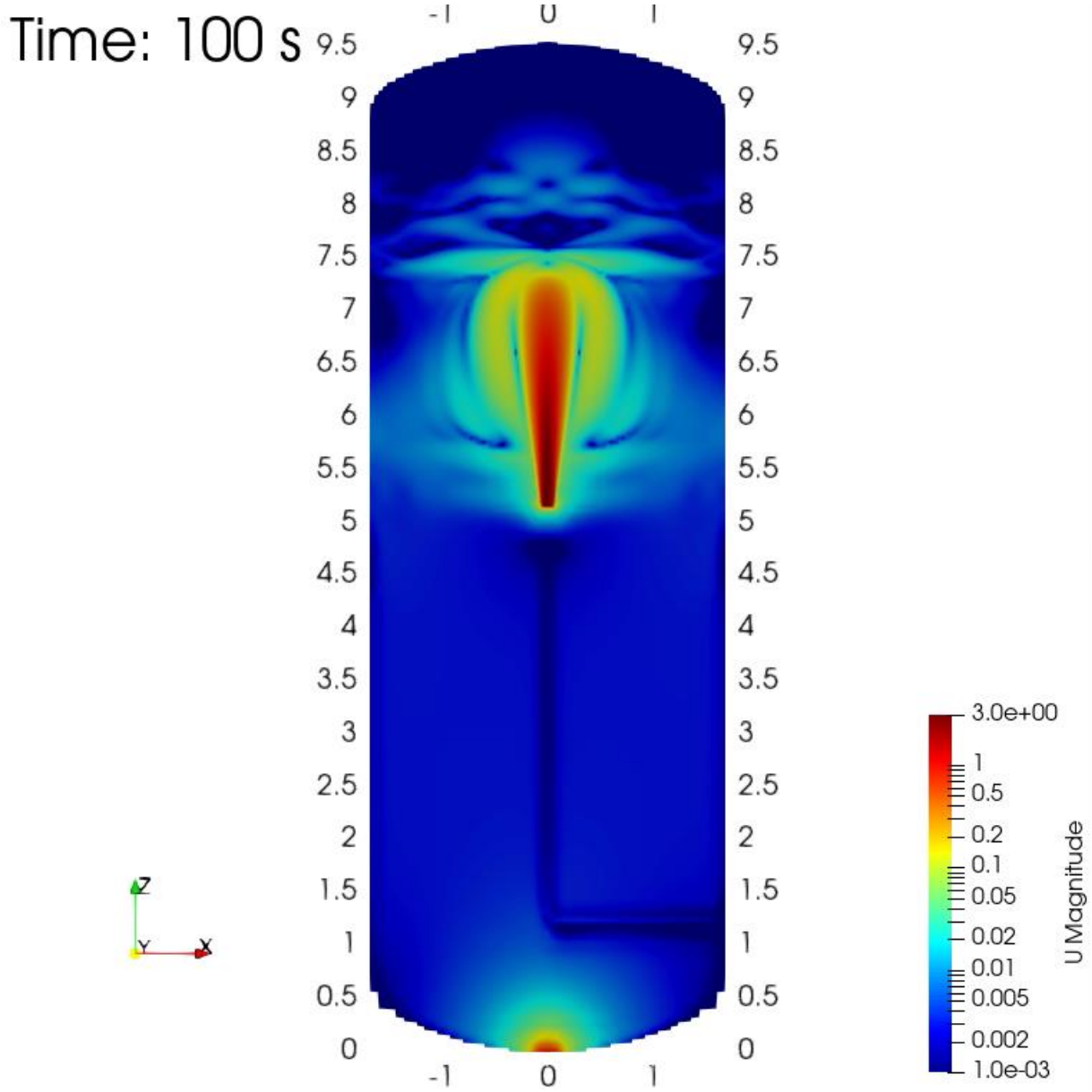

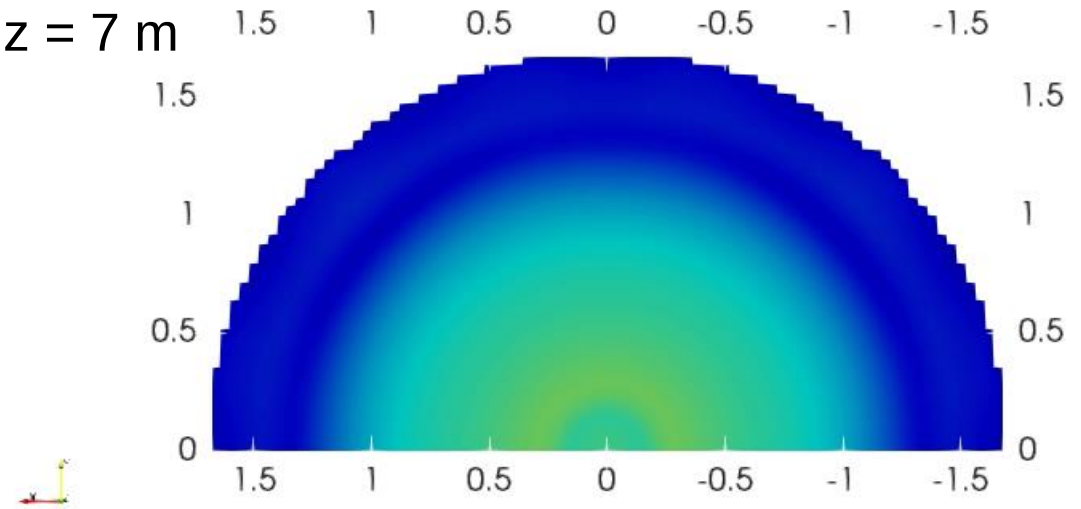

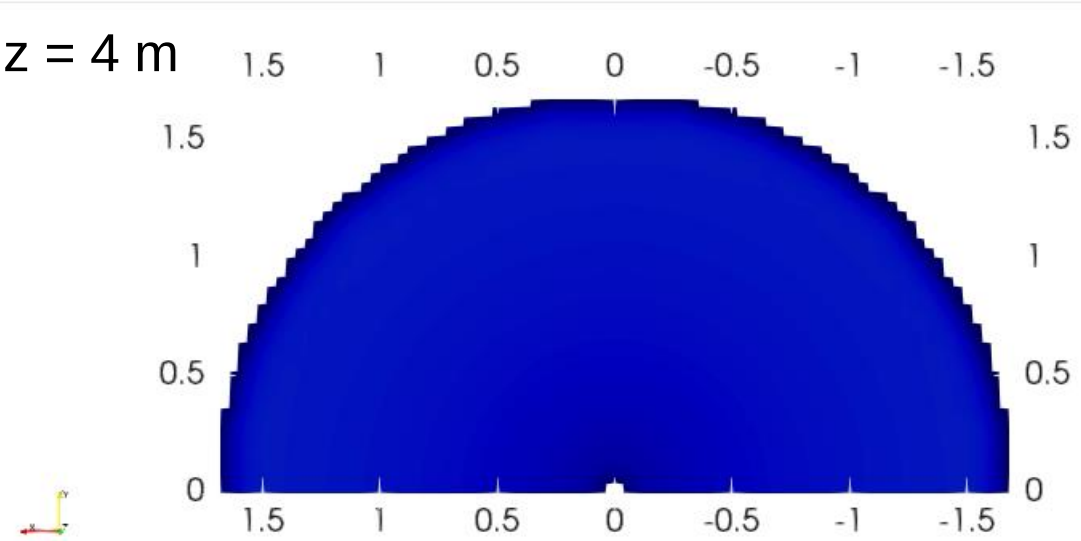

CFD physical model

- Containment mixing experiments simulated with OpenFOAM CFD code
- Compressible mixture of ideal gases
- Single-phase flow of two-components
- Momentum equation
- Convection-diffusion equation

$$\frac{\partial \rho Y_{He}}{\partial t} + \frac{\partial}{\partial x_j}\left(\rho u_j Y_{He}\right) = \frac{\partial}{\partial x_j}\left(\left(\rho D + \frac{\boldsymbol{\mu_t}}{\boldsymbol{Sc_t}}\right)\frac{\partial Y_{He}}{\partial x_j}\right)$$

- Total energy equation

$$\frac{\partial \rho h}{\partial t} + \frac{\partial}{\partial x_j}\left(\rho u_j h\right) + \frac{\partial \rho K}{\partial t} + \frac{\partial}{\partial x_j}\left(\rho u_j K\right) - \frac{\partial p}{\partial t} =$$

$$\frac{\partial}{\partial x_j}\left(\left(\frac{\mu}{Pr} + \frac{\boldsymbol{\mu_t}}{\boldsymbol{Pr_t}}\right)\frac{\partial h}{\partial x_j}\right) - \sum_i \left(\frac{\partial}{\partial x_j}\left(h_i \cdot \left(\rho D + \frac{\boldsymbol{\mu_t}}{\boldsymbol{Sc_t}}\right)\right)\frac{\partial Y_i}{\partial x_j}\right) + \rho g_k u_k$$

Turbulent Schmidt number

$$Sc_t = \frac{\mu_t}{D_t}$$

Turbulent Prandtl number

$$Pr_t = \frac{\mu_t}{\alpha_t}$$

CFD physical model

Dynamic turbulent numbers model

$$\mathrm{Sc_t} = \mathrm{Sc_{t,min}} - \frac{1}{2}\left(Sc_{t,max} - Sc_{t,min}\right)\left\{1 + \tanh\left[c_{k,1}\left(\partial u_g \cdot \partial \rho_n\right) - c_{k,2}\right]\right\}$$

$$\partial u_g = \frac{\partial}{\partial x_i}\left(-\frac{g}{|g|} \cdot \frac{u}{\max(|u|)}\right)$$

$$\partial \rho_n = \frac{1}{\rho}\frac{\partial \rho}{\partial x_i}$$

$$\mathrm{Pr_t} = \mathrm{Sc_t}$$

Constant	$Sc_{t,min}$	$Sc_{t,max}$	$c_{k,1}\ [m^2]$	$c_{k,2}$
Value	0.4	0.9	1000	1

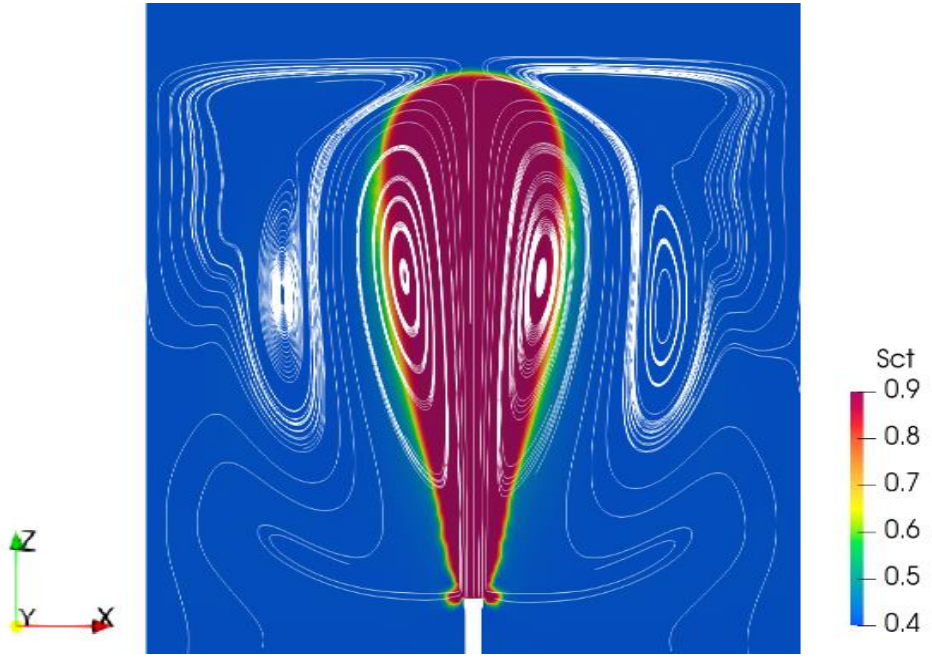

Dynamic turbulent numbers model

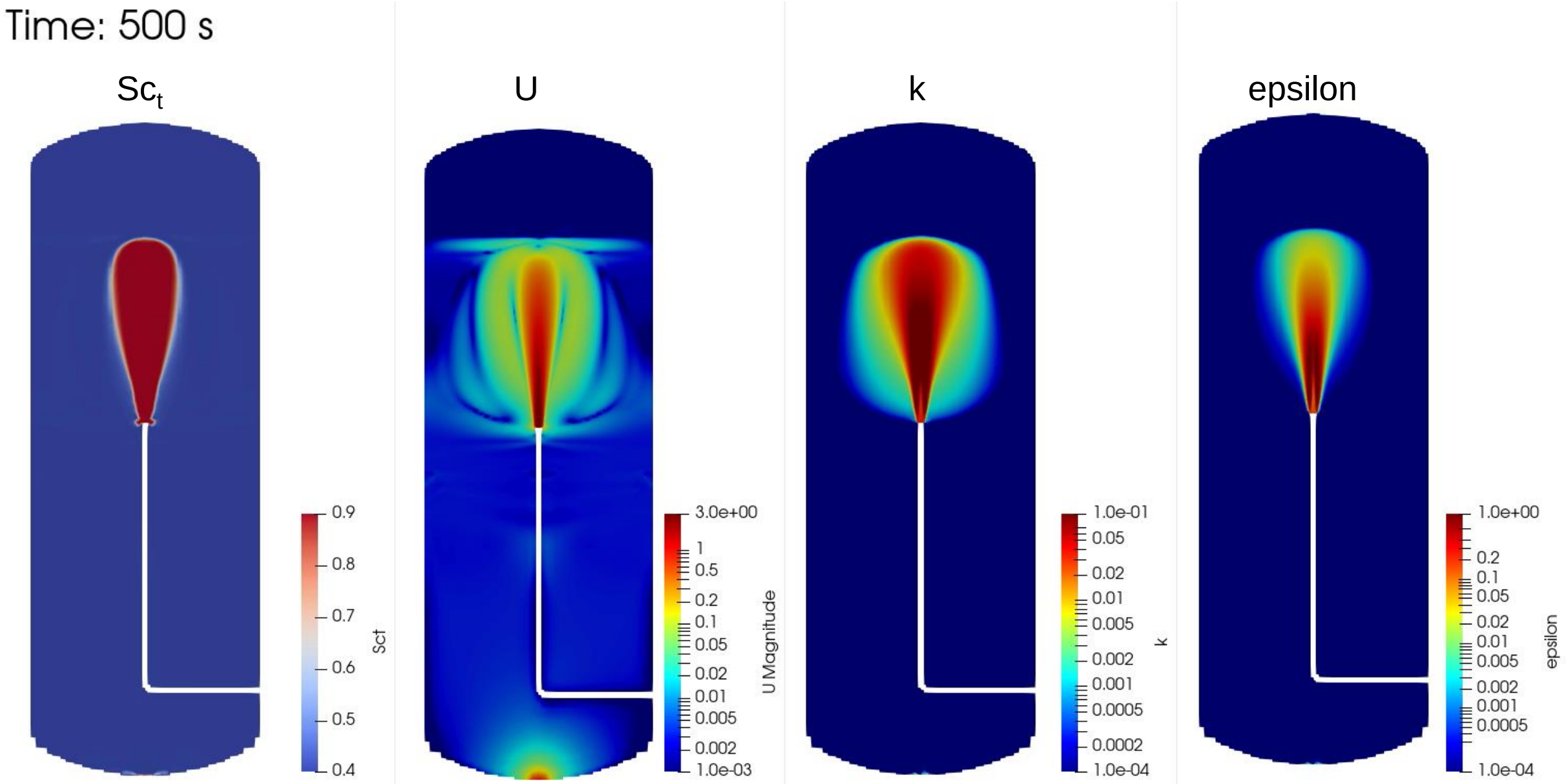

Model validation - SPARC

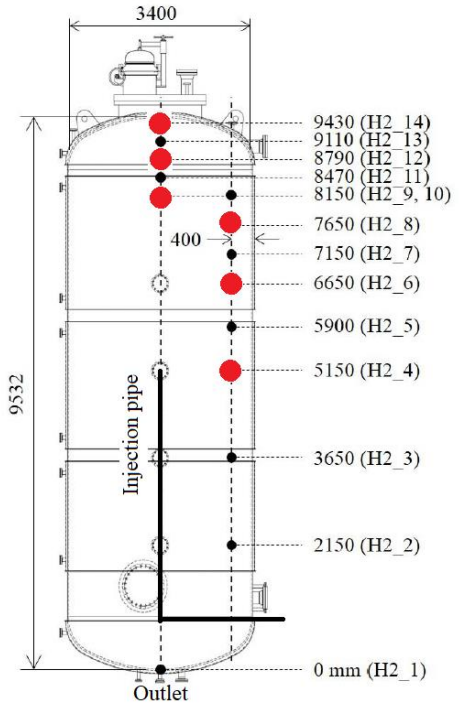

Sampling positions in SPARC facility.

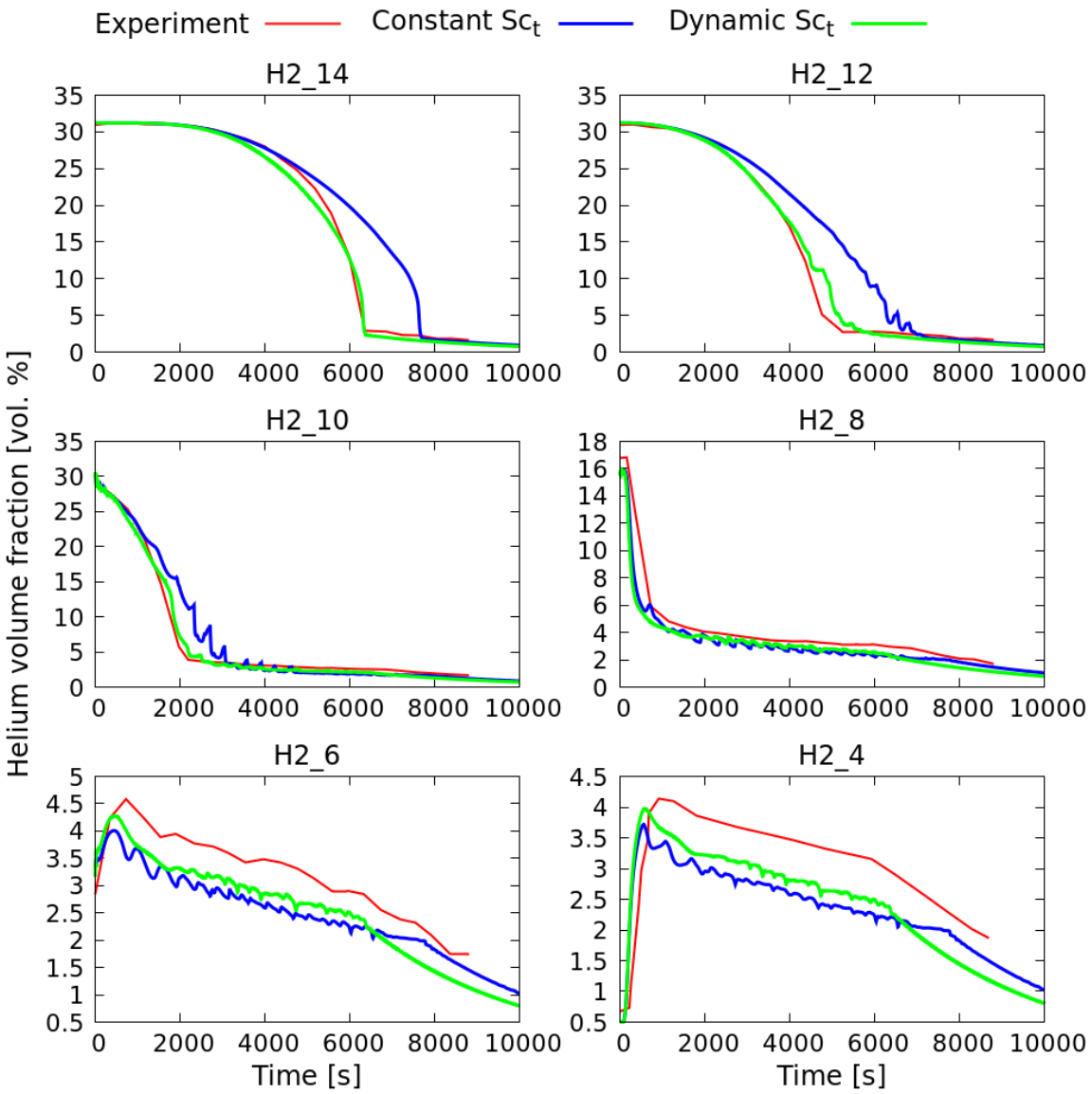

Helium volume fractions at different sampling locations

Model validation - PANDA

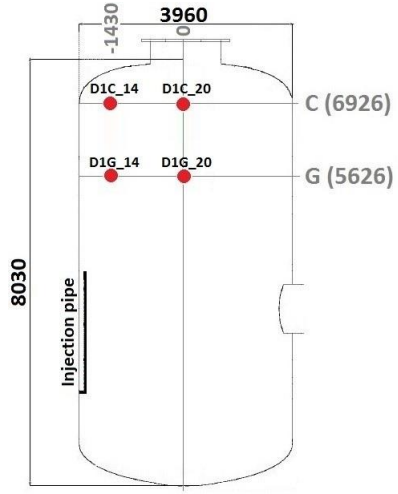

Helium volume fraction [vol.%]

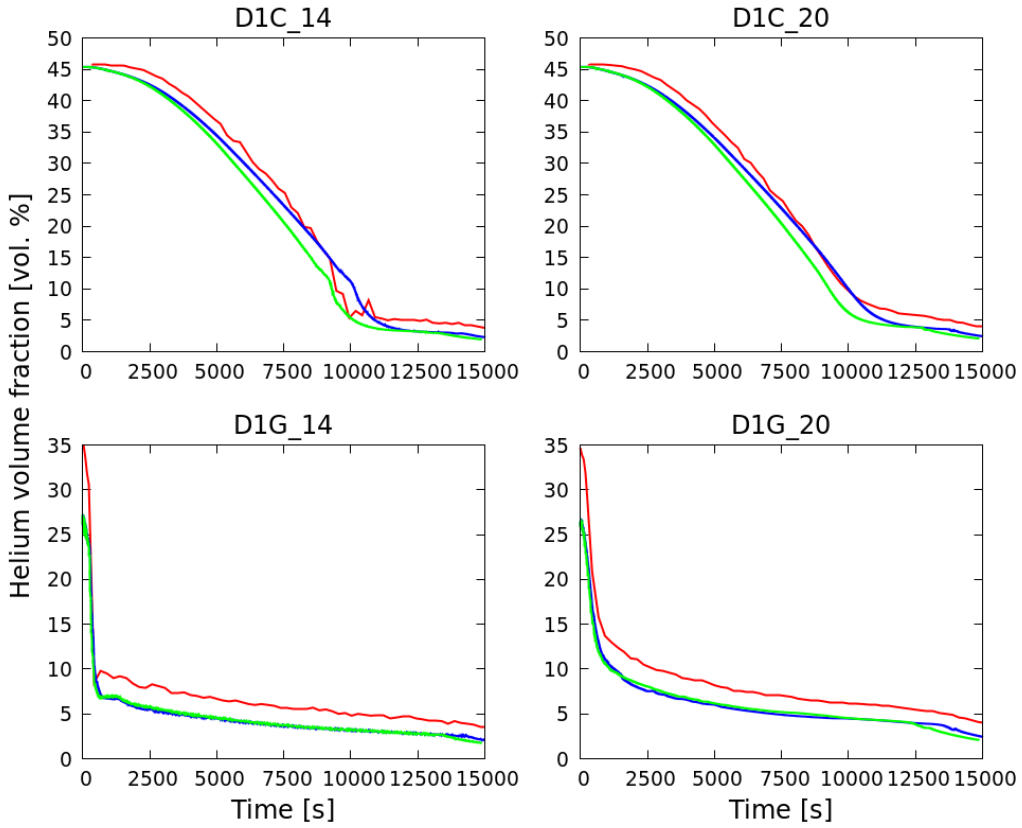

Temperature [°C]

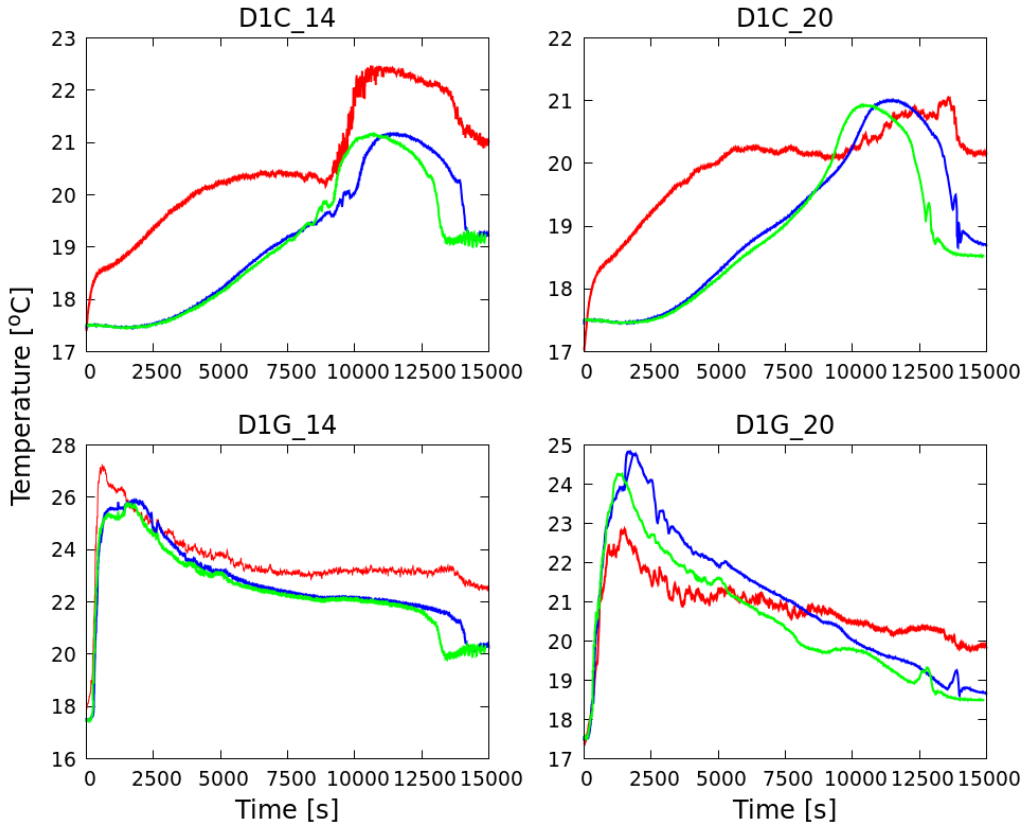

Experiment — Constant — Dynamic

Model validation - MiniPanda

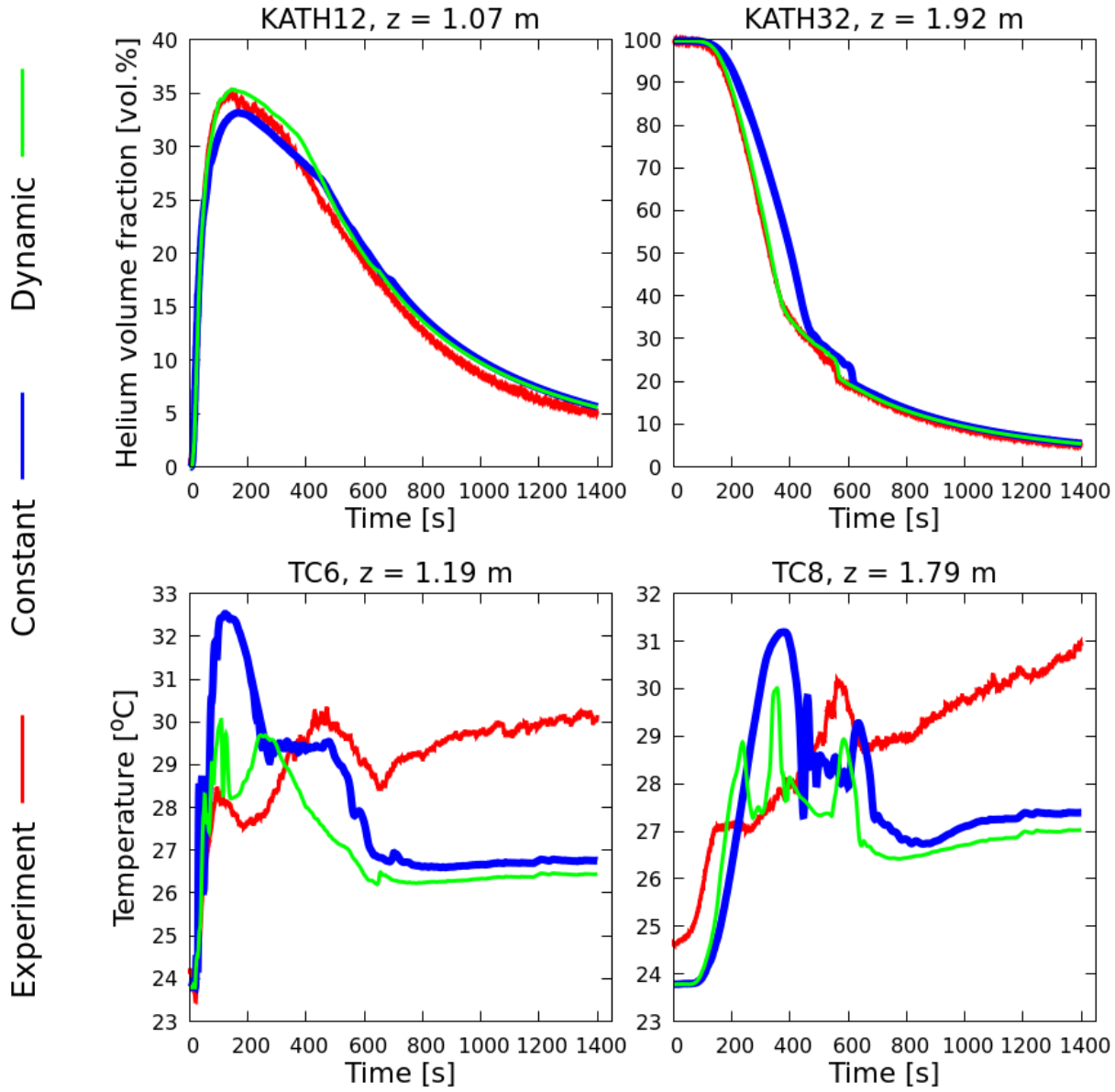

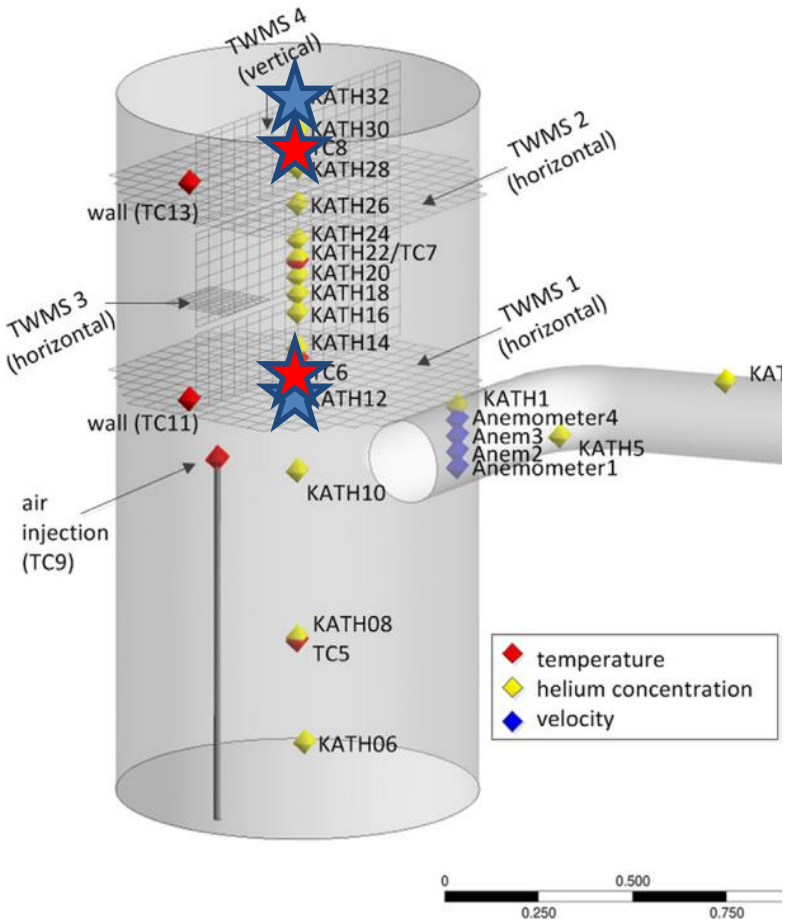

Sampling positions in MiniPanda facility.

Conclusions

- Dynamic turbulent Schmidt and turbulent Prandtl number model proposed.
- Mean flow properties used to prescribe different values of Sc_t and Pr_t.
- Underestimation of μ_t in regions with low velocity is compensated.
- Much better prediction of a light-gas layer erosion performed at isothermal conditions with higher mass inflow.
- In non-isothermal cases, discrepancies still present.

Jožef Stefan Institute
R4 Reactor Engineering Division
University of Ljubljana
Faculty of Mathematics and Physics

Dynamically Prescribed Turbulent Numbers in Containment Atmosphere Mixing Simulations

Rok KRPAN, Iztok TISELJ, Ivo KLJENAK
Jožef Stefan Institute (JSI), Slovenia

rok.krpan@ijs.si

10th European Review Meeting on Severe Accident Research (ERMSAR2022)
Karlsruhe, Germany, May 16th – 19th , 2022

May 18th , 2022

AN ANALYSIS OF COMBUSTION REGIMES FOR HYDROGEN/CO/AIR MIXTURES IN DIFFERENT GEOMETRIES

Kuznetsov M*, Friedrich A, Necker G,
Karlsruhe Institute of Technology
Kaiserstrasse 12, 76131 Karlsruhe, Germany
kuznetsov@kit.edu, andreas.friedrich@kit.edu, gottfried.necker@kit.edu

Veser A, Breitung W
Pro-Science GmbH
76275 Ettlingen, Germany
anke.veser@partner.kit.edu,

ABSTRACT

A number of experiments with H_2-CO mixtures at different ratios H_2:CO in different geometries were performed at the HYKA KIT test site with respect to the safety management of NPP. The first series of experiments with H_2:CO mixtures in the air were performed in a spherical explosion chamber with a volume of 8.2 liters in order to evaluate the lower flammability limits and the laminar burning velocity. Such experimental data allow theoretically predict fundamental properties of combustion and criteria for flame propagation regimes based on critical expansion ratio, σ*. The detonability limits were evaluated using detonation cell size according to 7λ criterion. The second series of middle scale experiments in a tube and in a layer geometries were performed to experimentally confirm the theoretical evaluations of flame acceleration conditions based on critical expansion ratio. First, the experiments were performed in a 7.2-m long tube of 100 mm id with obstacles (blockage ratio was 30%) and second, in a horizontal semi-confined layer with dimensions of 9x3x0.6 m^3 with/without obstacles opened from below. The ratio of H_2:CO in test mixtures with air was varied as 3:1, 1:1, 1:3 to assess the influence of CO on flame propagation regimes. The experiments can be used as benchmark data for numerical code validation.

KEYWORDS
MCCI accident, Hydrogen, Carbon monoxide, Flame acceleration, Detonations

1. INTRODUCTION

Hydrogen release due to the Loss of Cooling Accident (LOCA) and then Molten Corium-Concrete Interaction (MCCI) accidents may lead to the formation of a stratified layer of the hydrogen-air mixture at the top of the reactor building. Its immediate ignition due to operating ignitors or catalytic recombiners results in fame propagation through a gradient of reactivity and establishing of high pressure and temperature in a containment or reactor building. Such a scenario can be the cause of loss of integrity or damage of the structure. Hydrogen explosion followed by an accidental hydrogen release in containment due to a LOCA and MCCI accident was experimentally and numerically analyzed for Fukushima-Daiichi accident in Unit 1 and Unit 3 [1-3].

* corresponding author

One more important aspect of this accident concerns the formation of CO through an extensive melt-concrete interaction (MCCI). The course of the Fukushima accident Unit 1 was extensively simulated by Sandia lab with MELCOR code [4]. As **Figure 1** shows, after the failure of the reactor pressure vessel, in the subsequent ex-vessel phase, MCCI additionally generated several tons of H_2 and CO. The - initially inert - accident atmosphere from H_2, CO, N_2 and steam escaping into surrounding plant rooms mixes with air, the steam condenses to a large extent, and due to the large H_2 and CO inventories inside the reactor building (on the order of several 1000 kg each) can be very reactive gas mixtures arise outside the containment. In the case of the Fukushima accident, this leads to a severe explosion in Unit 1 and Unit 3. The question is how to effectively prevent the H_2-CO explosions and what knowledge of H_2-CO combustion is required in the future based on the analyze of meltdown scenarios of MCCI accident leading to formation of flammable H_2-CO-air mixtures.

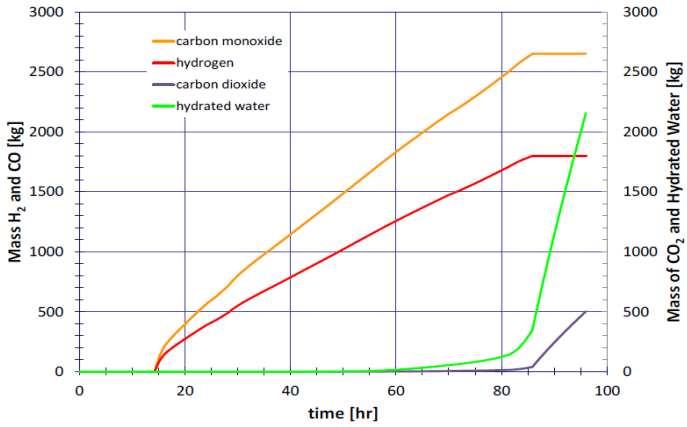

Figure 1. MELCOR predicted reaction products from Core – Concrete Interaction (Unit 1) [4].

In contrast to previous works on H_2-air combustion with different confinement degrees [3, 5-7], there are no corresponding experimental or theoretical studies on H_2-CO-air semi-open layers. The only known OECD report on the simulation of H_2-CO burns in core-destroying accidents [8] deals with basic properties such as flammability limits, ignition temperatures, laminar burning speeds and the calculation of detonation cell sizes. However, the amount of data presented is very limited. With regard to the pressure development in H_2-CO combustion, only theoretically calculated adiabatic P_{AICC} pressures can be evaluated for standard initial conditions by STANJAN or Cantera codes [20-21]. The summary explicitly points out the lack of experimental data in closed and partially opened containers. However, such data are essential for the validation of theoretical models. There is only one measurement of the flame dynamics in H_2-CO combustion in a closed rectangular channel with obstacles [9, 10], but no data for a geometry open at the bottom. Due to the higher temperature and the lower average molecular weight of the emerging accident atmosphere compared to air, a combustible mixture is formed as a stable stratified H_2-CO-air layer. Such layers are delimited at the top by a ceiling but open at the bottom, which is classified as a partial enclosure. To assess the associated risk and as a basis for the design of control measures, the combustion behavior of stratified H_2-CO-air layers with partial confinement must therefore be examined.

The common main goals of the work are:
• Explosion bomb experiments on flammability limits and laminar flame velocities of hydrogen-carbon monoxide mixtures.
• Derivation of scalable criteria for flame acceleration and DDT in stratified H_2-CO-air layers with partial inclusion from the experiment data.
• Experimental data for the combustion of homogeneous and inhomogeneous H_2-CO-air layers (flammability limits, flame speeds, pressures).

2. EXPERIMENTS

2.1. Explosion Bomb

The experiments on the burning behavior of H_2-CO-air mixtures were performed in a spherical stainless steel explosion bomb with an internal diameter of 25 cm (V = 8.2 liter, **Figure 2**, left), for further details see also [11] and [12]. The bomb has optical access via two quartz windows and is equipped with ports for two fast dynamic pressure gauges and two NiCr/Ni thermocouples (type K). Mixtures inside the bomb were ignited using a high voltage (60 kV) high frequency (20 kHz) spark between two electrodes. Due to the design of the facility, the electrodes meet at an angle of 90°, with the gap between them being positioned in the center of the spherical combustion chamber. A gas injection system of the test set-up is depicted in the right part of **Figure 2**. The test mixture was prepared using mass-flow controllers and then, before entering the chamber, additionally monitored by gas-analyzer via by-pass line.

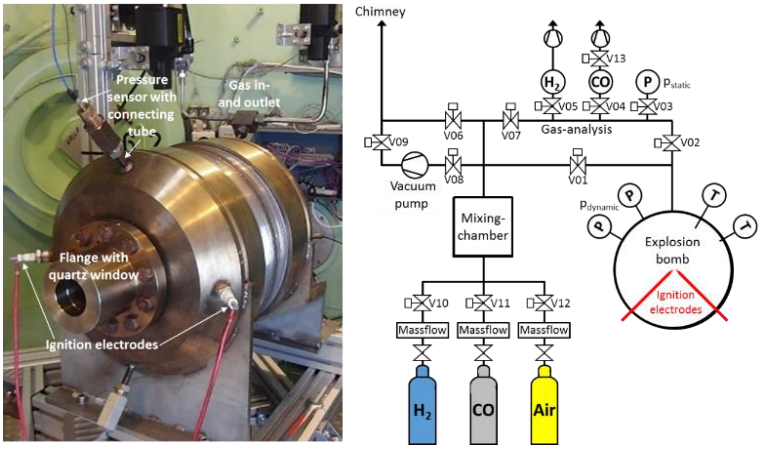

Figure 2. A photo of explosion chamber and a scheme of gas filling system.

2.2. Shock Tube

The experiments were made in a rectangular explosion tube (**Figure 3**) equipped with orifice plate obstacles. The tube was 7.2 m long with an internal tube diameter of 0.1 m. The tube was equipped with an array of obstacles with a blockage ratio BR = 30% and a distance between neighboring obstacles of 0.1 m.



Figure 3. Side view of shock tube for flame acceleration experiments.

The H_2-CO-air mixture experiments have been performed in a range of 9 % to 15% (H_2+CO) fuel gas concentration. The initial temperature was 293 ± 8 K. The instrumentation consisted of photodiodes to measure flame-arrival times and fast pressure transducers (PCB model 113 and 114) to measure transient pressure loads to the tube walls. Photodiode sensors and pressure gauges were mounted pairwise at given

cross sections of the tube. The measuring positions had a distance of 40 cm each from another. A total of 16 photodiodes and 16 pressure transducers were used in the tests.

2.3. Semi-Confined Thin Layer

Homogeneous H_2-CO-air mixtures of various concentrations were ignited in an obstructed horizontal combustion channel with the dimensions 9 m x 3 m x 0.6 m (L x W x H, see **Figure 4**) in the hydrogen test center HYKA at the KIT. The channel, which has an open bottom and rear sides, is mounted into a cylindrical safety vessel with a diameter of approx. 3.5 m, a length of 12 m and two hemispherical ends (total volume approx. 100 m^3) that is designed for a static pressure of 100 bar. The channel is obstructed by 14 equidistant obstacles (spaced by 0.6 m) with a blockage ratio of 50%. Each obstacle is made as a frame fabricated of 5 horizontal bars with a height of 6 cm and a thickness of 4 cm spaced by 6 cm. The mixture was ignited with a linear ignition source in an upper corner of a short side providing a linear flame front from the beginning to simplify flame geometry for easier analysis. The measuring system includes an array of ion probes and photodiodes along and across the channel for monitoring of flame position and a line of pressure sensors to monitor pressure and shock wave dynamics. To have a witness of detonation a smocked foil technique was applied by placing smocked plates at the wall along the channel.

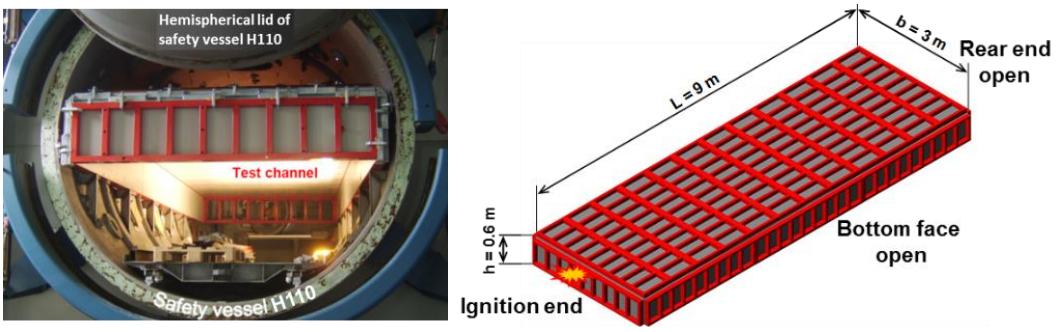

Figure 4. Layered shape combustion channel in the safety vessel A1 at KIT-HYKA (left) and its main dimensions (right).

3. EXPERIMENTS

3.1. Flammability Limits

The ignition event of tested mixtures was determined using the pressure signals and, if available, the high speed video records of the experiments. For comparison, one experiment was performed without fuel to determine the pressure generated by the thermal energy of the ignition source itself. Since the ignition energy was lower than 50 mJ, a pressure increase of 1% of the initial pressure was found to be sufficient as a threshold of ignition – no ignition cases. Of course, it is not a guarantee of complete combustion. This means that at least a part of the mixture in the vicinity of the electric spark will burn out. Most mixtures of higher reactivity were ignited in the first attempt, but with decreasing H_2- or CO-content, it became more and more difficult to ignite the test mixture. Sometimes, it was up to 5 attempts to ignite the mixture. The stochastic character of CO compositions with air very often occurs due to the high sensitivity of the process to water vapor and also due to a very unstable flame surface near the flammability limit. Then the flame may develop further or it can quench. The experiments on flammability limits of H_2-CO-air compositions at ambient conditions are summarized in the left graph of **Figure 5**, where grey dots show that the mixture was ignited while decreasing size indicates that several attempts (number of attempts in brackets) were needed. Black crosses symbolize that no ignition of the mixture was observed.

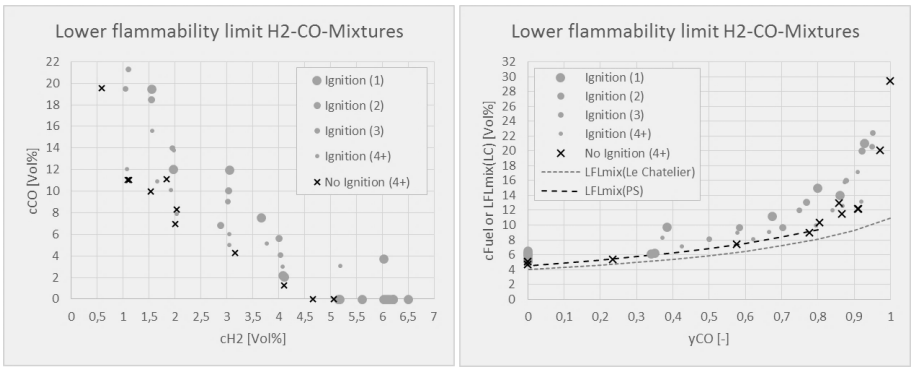

Figure 5. Lower flammability limit for H_2-CO-air mixtures (left) and its comparison with calculations according to Le Chatelier's rule and also literature data (right). Grey dots indicate several attempts (the number in brackets) to ignite the mixture, crosses show no ignition cases [13].

Another series of experiments on flammability limits at 1 bar initial pressure was conducted for H_2-CO-O_2-N_2-H_2O at elevated temperatures 170 ºC and 250 ºC using the same explosion chamber as shown in **Figure 2**. Steam concentration was fixed at [H_2O] = 60% (vol.). All other gases varied in the range [H_2] = 0 - 3% (vol.), [CO] = 0-20% (vol.), [O_2] = 5-20% (vol.), [CO_2] = 0-12% (vol.), [N_2] = 0-12% (vol.). The ratio of [CO_2]/ [N_2] was fixed as [CO_2]/ [N_2] = 1. All data on flammability limit can be summarized as a dependence of the flammable concentration of carbon monoxide [CO] on oxygen concentration [O_2] at different concentrations of hydrogen [H_2] (**Figure 6**). In such presentation, the rest of the summary concentration without total concentration of combustible gases [H_2]+[CO]+[O_2] belongs to inert gases concentration [H_2O]+[CO_2]+[N_2]. All experimental points in **Figure 6** can be presented as a 3-dimensional diagram, called the Shapiro diagram, which shows the effect of integral fuel concentration [H_2]+[CO] on oxygen and inert gas concentrations at flammability limits in multicomponent gas, containing 60% of steam (**Figure 7**). The flammability limit are located down to two asymptotes at 10% of total fuel concentration [H_2]+[CO] and 5% of oxygen concentration [O_2]. The flammability experiments also demonstrate that the maximum combustion pressure is very close to theoretical adiabatic combustion pressure P_{ICC} for fuel concentration [H_2]+[CO] far from the flammability limit. Approaching the flammability, the combustion pressure reduces to 5% of theoretical P_{ICC} pressure at the flammability limit.

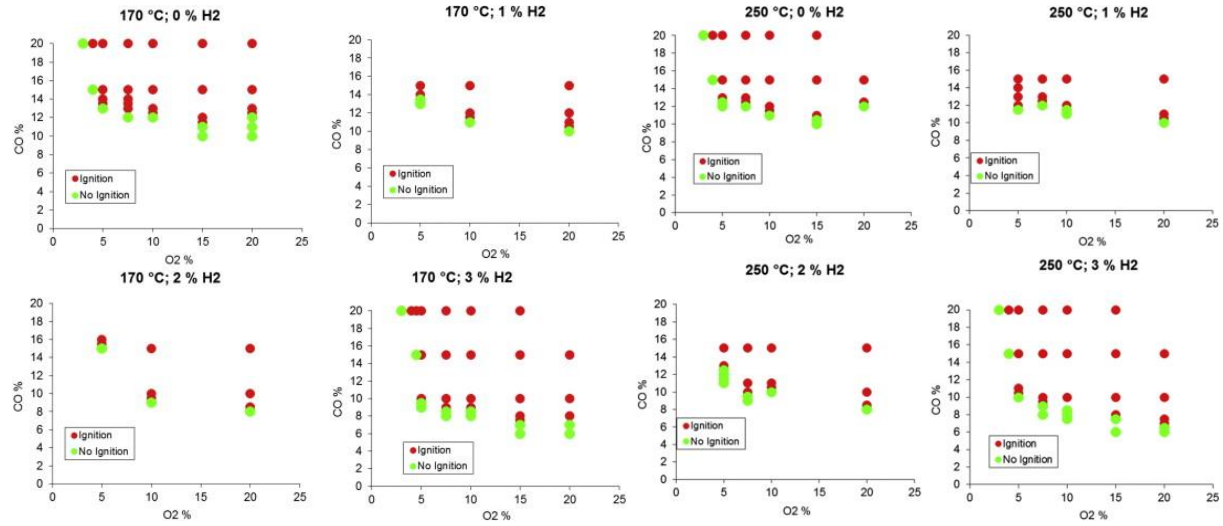

Figure 6. Flammability limits for H_2-CO-O_2-N_2-H_2O mixtures at elevated temperatures 170 ºC and 250 ºC as a function of oxygen concentration [14].

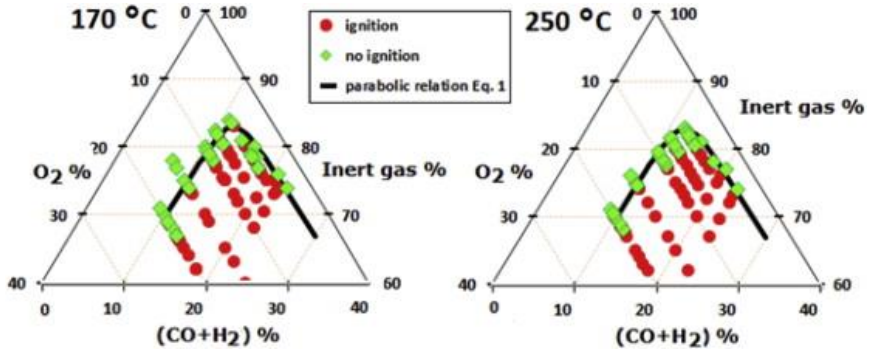

Figure 7. Flammability limits for H_2-CO-O_2-N_2-H_2O mixtures at elevated temperatures 170 °C and 250 °C as a function of oxygen concentration at different inert gas concentration $[H_2]+[CO]+[O_2]$.

3.2. Laminar Flame Velocity

The same explosion chamber (**Figure 2**) was used for laminar flame evaluation of hydrogen-carbon monoxide-air mixtures. The method developed by Andrews and Bradley [12] was already slightly modified and used for the determination of burning velocities on the basis of the experimental pressure records in the paper [11]. Only the initial part of explosion pressure – time history, up to 3-5% of maximum combustion pressure, was used for laminar flame evaluation in an assumption of constant pressure. In such case the pressure can be written as a linear function of time cubed:

$$p(t) = p_0 + B_2 \cdot t^3 . \quad (1)$$

The proportionality coefficient B_2 will then be used in formulas for laminar flame velocity calculations according to paper [11]. The availability of the method is proven by a comparison of our experimental data with published results [15] (**Figure 8**, left). Original experimental data of paper [15] on laminar flame velocity for highly diluted fuel compositions (above 50%CO) are shown in **Figure 8**, right. It shows a significant decrease in laminar flame velocity with stronger fuel dilution with carbon monoxide. The comparison shows that most velocities determined in the current work show good agreement with the literature data [15], larger deviations are solely found for high H_2-fractions of more than 70%.

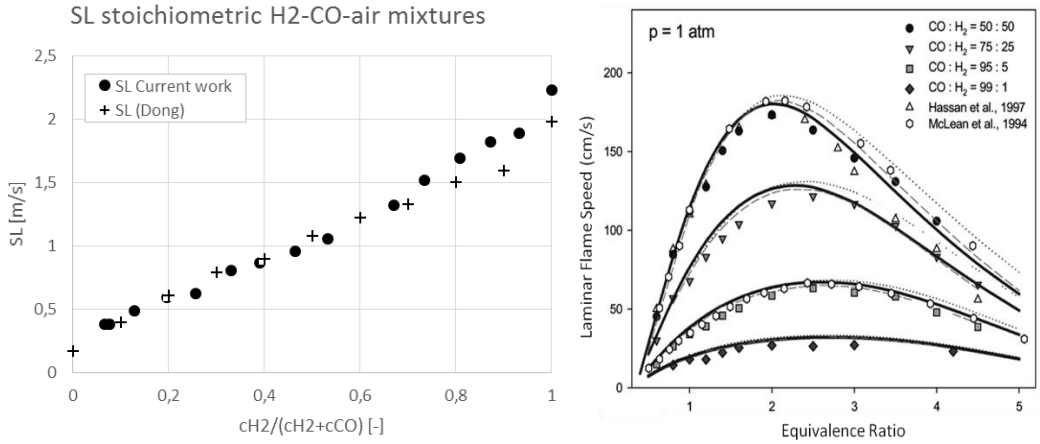

Figure 8. Comparison of measured S_L values for stoichiometric fuel-air-mixtures with various H_2/CO ratios in current work with published data in paper [15] (left); original experimental data and calculations in [15] (right).

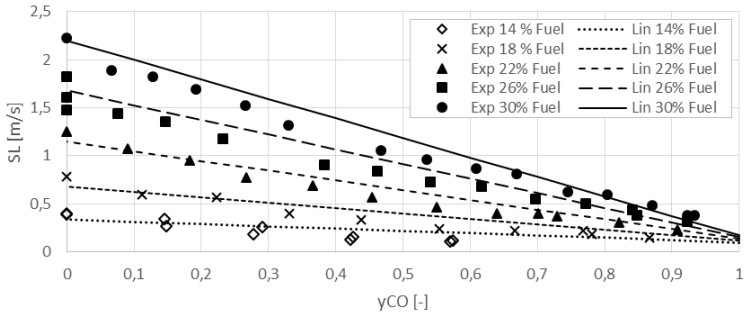

Figure 9. Results of selected experimental series on the laminar burning velocities of H_2-CO-air-mixtures with the same fuel content but different H_2/CO-ratios.

In the current work only selected experimental data series were plotted at the same fuel concentrations. **Figure 9** only shows selected series' which cover the main behavior observed in the tests. As follows from the figure, the laminar flame velocities of the mixtures decrease with increasing CO-fraction in the fuel. Starting from the values for pure H_2-air-mixtures at $y_{CO} = 0$ they decrease almost linearly to the value for pure CO-air-mixtures at $y_{CO} = 1$. A simple linear correlation for such a behavior can be assumed

$$S_{L(mix)} = y_{H2} \cdot S_{L(H2)} + y_{CO} \cdot S_{L(CO)} \,. \tag{2}$$

where S_{Lmix}, S_{LH2} and S_{LCO} are the laminar flame velocities of the mixture and the components H_2 and CO [m/s] and y_{H2} and y_{CO} are the molar fractions of the fuel components H_2 and CO in the mixture [-]. Since only a few values for S_{LCO} were available, Eq. (2) was used even to calculate the values for pure CO-air mixtures. But as mentioned above this formula was derived for CO-concentrations above 22 Vol%. Nevertheless the formula was extrapolated down to concentrations of 12 Vol% CO for this evaluation, which led to increasing deviations of the linear approximation from the experimental values in CO-rich mixtures, especially for fuel concentrations lower than 16 Vol%. For the lowest fuel concentration plotted in the graph (14 Vol%), for instance, an assumed SL-value of 0 m/s would lead to a much better result than the utilization of the calculated value of approx. 0.1 m/s, which seems to be far too high. More accurate values for the laminar burning velocity of pure CO-air mixtures would therefore help to further increase the accuracy of the proposed approximation.

3.3. Flame Acceleration and Critical Expansion Ratio

Shock tube experiments on flame propagation regimes were analyzed for critical conditions for flame acceleration to the speed of sound and detonation (**Figure 3**). Dynamics of the resulting combustion of H_2-CO-air mixtures was recorded with pressure sensors and photodiodes. According to (Breitung, Kuznetsov, 2014), the measured maximum flame velocities v_{max} were normalized by the speed of sound c of the burnt gas and plotted as a function of the expansion ratio σ of the H_2-CO-air mixture for different ratios H_2:CO (**Figure 10**). In the three H_2-CO gas mixtures investigated, the values of the maximum flame velocities characterized by $v_{max}/c = 0.8$ are reached at a certain expansion ratio, which can be regarded as the critical expansion ratio for ultrasonic turbulent deflagration. The experiments show a systematic increase in critical expansion ratio σ* with the CO content of the gas mixture from 3.75 for pure H_2 to 4.0 or 4.3 for two CO-containing mixtures. This means that CO dilution suppresses the mixture reactivity and it needs a more reactive mixture with a higher expansion ratio to accelerate the flame to the speed of sound. **Figure 11** (right) shows an approximation of critical expansion ratio σ* against CO dilution

$$\sigma^* = 3.75 + 1.3[CO] - 0.4[CO]^2 \,. \tag{3}$$

which allows the evaluation of σ* for pure CO-air mixture as σ^*_{CO}=4.65. A significant suppression effect of CO dilution on combustion pressure and flame propagation regime follows from **Figure 11** (left). It shows that at the same fuel concentration (11%), the combustion regime shifts from sonic deflagration with a very high pressure of 7.7 bar for a pure hydrogen-air mixture to slow subsonic flame with the pressure of less than 1 bar for 50% diluted composition. That was a suppressing effect of CO dilution on strength of combustion pressure in an enclosed geometry.

The effect of carbon monoxide on flame propagation regimes was investigated in a semi-confined layer of hydrogen/carbon monoxide/air mixtures of 0.6 m height (**Figure 4**). As follows from **Figure 12**, the critical expansion ratio for flame acceleration to the speed of sound in a semiconfined geometry can be written as a function of CO concentration in H_2-CO fuel:

$$\sigma^* = 4.46 \; + \; 2.3[CO]. \qquad (4)$$

where σ*=4.46 is the critical expansion ratio for combustion of pure hydrogen-air mixture in a layer of 0.6 m height, according to equation [3,7]:

$$\sigma^* = \sigma_0^* \left(1 + K_{H2} \frac{s}{h}\right). \qquad (5)$$

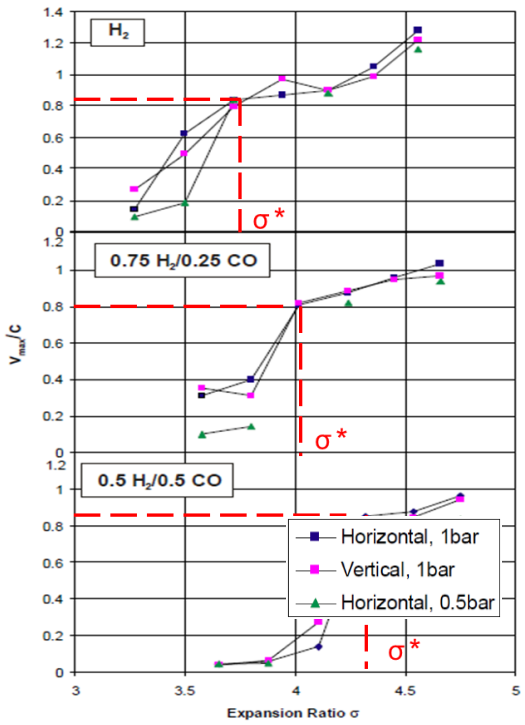

Figure 10. Results of experiments on flame acceleration in a squared obstructed shock tube (BR=30%) with H2-CO-air-mixtures at different H2/CO-ratios.

where σ_0^*=3.75 and K_{H2}=0.175 for hydrogen-air mixtures; s =0.6 m and h =0.6 m are the spacing between obstacles and the height of the channel, respectively. It follows from Eq. (3) and **Figure 12** that the critical expansion ratio for pure CO-air mixture in a layer geometry is σ_{CO}^*=6.76. Assuming the same shape of layer thickness dependence for CO-air composition as for hydrogen, a value of K_{CO} =0.454 can be found. Then, the correlation for critical expansion ratio for H_2-CO compositions can be expressed as a superposition of Eq. 4 – type for hydrogen and carbon monoxide:

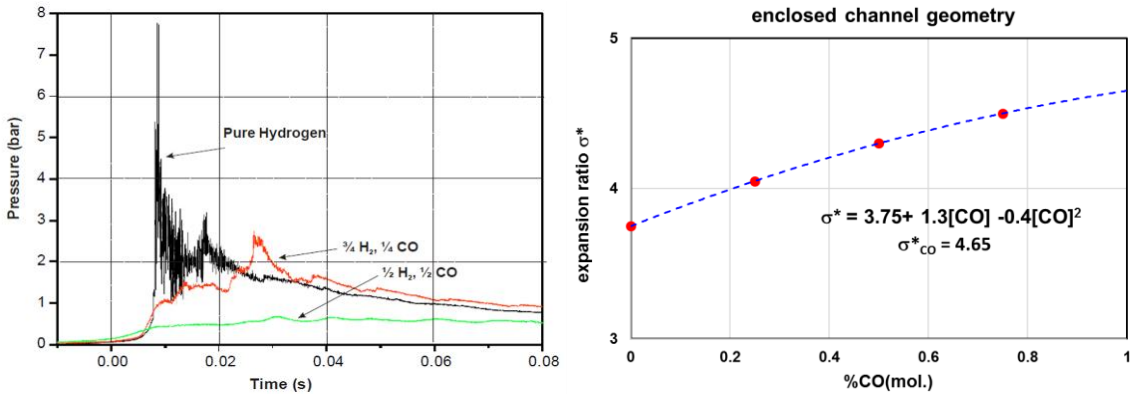

Figure 11. The effect of CO dilution of 11%(H_2+CO) - air composition on combustion pressure (left) and critical expansion ratio in a shock tube experiments for H_2-CO-air-mixtures with different H_2/CO-ratios (BR=30%).

$$\sigma^* = [H_2]\cdot\sigma_0^*(H_2)\cdot\left(1+K_{H2}\frac{s}{h}\right)+[CO]\cdot\sigma_0^*(CO)\cdot\left(1+K_{CO}\frac{s}{h}\right) \quad (6)$$

where $[H_2]$ and $[CO]$ are the mole fraction of hydrogen and CO in fuel; $\sigma_0^*(H_2)$ =3.75 and $\sigma_0^*(CO)$ =4.65 are the critical expansion ratio for pure hydrogen- and CO-air mixtures in closed geometry.

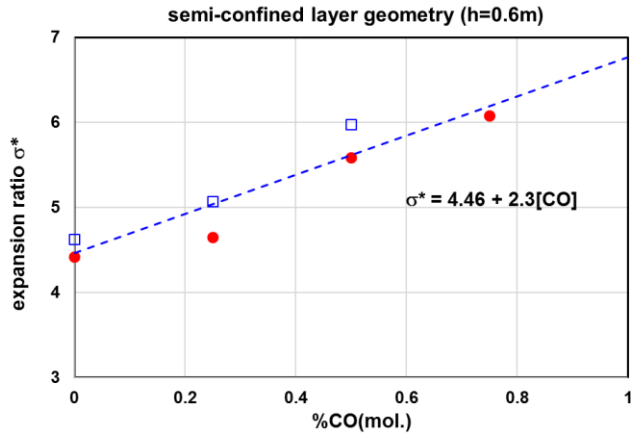

Figure 12. The effect of CO dilution on critical expansion ratio for fuel combustion in a semiconfined layer geometry (left); of 11%(H_2+CO) - air composition on combustion pressure (left) and critical expansion ratio for H_2-CO-air-mixtures for different H_2/CO-ratios (BR=30%).

3.4. Detonability and Detonation Cell Sizes

The measure of detonability of the combustible mixture is the detonation cell size. It takes into account both the chemical reactivity and gas dynamics of the mixture. Since the probability of detonation is evaluated by the dimensionless ratio of characteristic length of the system over the detonation cell size L/λ, the less the detonation cell size is, the higher is the detonability of the mixture. Detonability criteria can be applied depending on geometry and characteristic scale of the system h, L or D [6-7, 17-19]:

$D > \lambda/\pi$ - for detonation propagation in a smooth channel or tube;
$L > 7\lambda$ - for detonation onset in obstructed channel, tube or sequence of rooms;
$D > 13\lambda$ - for critical tube diameter for exit of detonation in a free space;
$h > 13.5\lambda$- for detonation propagation in semiconfined layer of H_2-air mixtures.

The first two conditions are derived for enclosed channels and already approved for hydrocarbon- and CO-diluted fuel compositions. The last two are for open or semi-open systems need additional experiments for H_2-CO-air mixtures. There is an additional problem with detonation cell size measurements for hydrogen-air mixtures diluted with carbon monoxide. As shown in paper [8] for 5 and 10% of CO dilutions all the data collapse into one line being presented as a function of total fuel concentration (H_2+CO), see **Figure 13**, left. Such a representation of detonation cell data for hydrogen-carbon monoxide data with our program CELL_H2 [16] was extended even to 95%CO in the fuel (H_2+CO) see **Figure 13**, right. It is seen that the most deviation from the approximation line takes place for the fuels with more than 80%CO which is not of a practical interest.

A series of experiments on different flame propagation regimes has been conducted in a semi-confined layer geometry of uniform hydrogen-CO-air mixtures as a function of CO dilution (**Figure 4**). When characteristic velocity and pressure approach the Chapman-Jouguet (CJ) values the regime was classified as a detonation (**Figure 14**). It shows almost the same concentration limits for detonation onset for pure hydrogen-air mixtures and for CO-diluted compositions in terms of fuel concentration (H_2+CO). There is only one exception was found for highly CO diluted mixtures, more than CO: H_2= 3:1. The flame did not accelerate to the speed of sound and to detonation at all. It could be due to the same problems as the difficulty under

ignition of H_2+CO compositions with an increase of CO concentration more than 50 % vol. (**Figure 5**). The threshold between "Detonation" and "No detonation" cases kept almost at the same value h/λ = 13.5 as for pure hydrogen-air mixtures, except the highly diluted mixture with more than 50%CO (**Figure 15**).

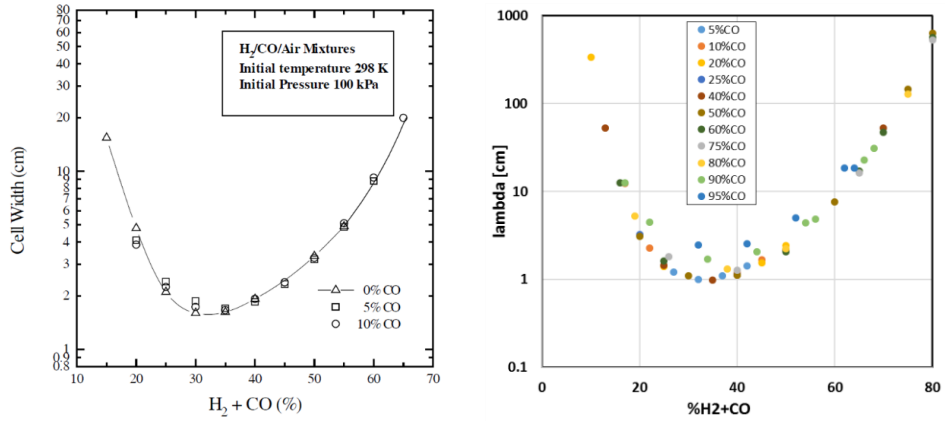

Figure 13. Detonation cell width plotted as a function of total fuel concentration: left - Kumar data [8]; right - theoretical calculations by paper [16].

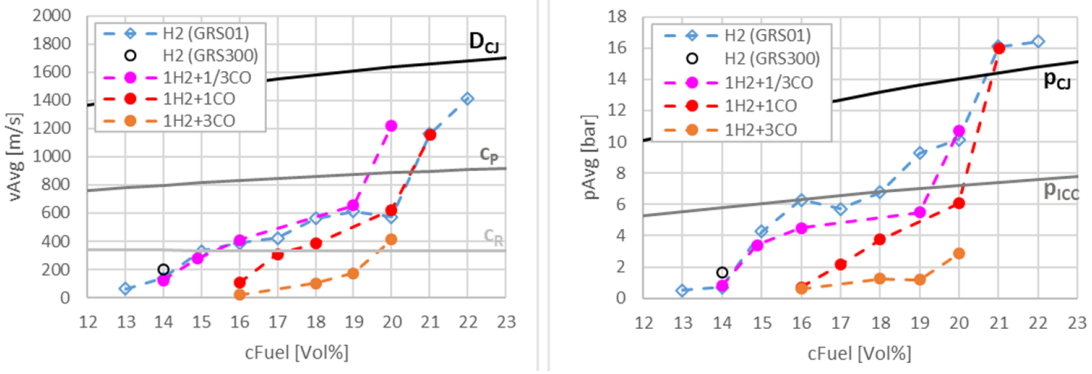

Figure 14. Characteristic flame velocity (left) and combustion pressure for semiconfined layer experiments.

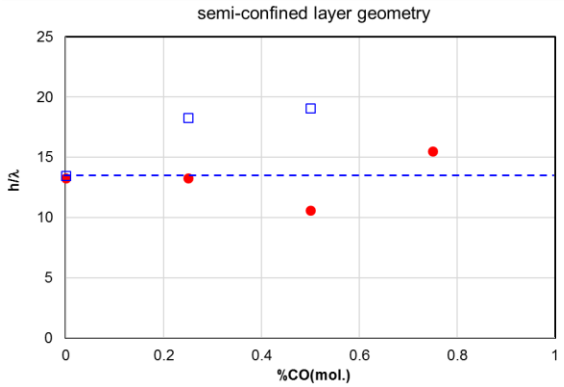

Figure 15. Critical conditions for detonation transition for CO diluted compositions in a layer geometry.

4. CONCLUSIONS

A methodology of explosion safety assessment for H_2-CO-air compositions formed due to MCCI accident is based on the results of small and middle scale experiments conducted at the HYKA test site.
- The experiments include flammability limits of H_2-CO-air compositions with different ratios H_2:CO. Le Chatelier's rule for flammability limits of two component fuel up to 80% CO can be used. Flammability limits for multicomponent composition H_2-CO-O_2-N_2-H_2O(60%) at elevated temperatures 170 ^oC and 250 ^{o} C have been experimentally evaluated.
- Laminar flame velocities for H_2-CO-air compositions were measured at various ratios H_2:CO from 1:20 to 20:1.
- The critical expansion ratio σ^* for H_2-CO-air flame acceleration to the speed of sound was experimentally found for different geometries and enclosure degree as a function of the ratio H_2:CO in binary H_2-CO-fuel. The formula for σ^* evaluation is written as a superposition of two dependencies for a confined and semi-confined geometry proportionally to CO fraction in the fuel.
- Detonation cell sizes for various H_2-CO-air compositions were calculated in the wide range of H_2:CO ratios from 1:20 to 20:1. Then, the different detonability criteria can be applied depending on geometry and characteristic scale h, L or D.
- The same detonability criterion as for pure hydrogen-air mixtures h/λ = 13.5 was for CO diluted compositions in a semi-confined layer geometry.

ACKNOWLEDGMENTS

The authors are very grateful to the German Federal Ministry for Economic Affairs and Energy (BMWi) for funding (Project No. 1501545B) through GRS (Germany), and also to our partners at the Technical University of Munich (TUM) for fruitful discussions and support in the current work.

REFERENCES

1. J. Yanez, M. Kuznetsov, A. Souto-Iglesias, “An analysis of the hydrogen explosion in the Fukushima-Daiichi accident”, *Int. J. Hydr. Energy*, **40**(25), pp. 8261-8280 (2015)
2. J. Xiao, W. Breitung, M. Kuznetsov, H. Zhang, J. R. Travis, R. Redlinger, T. Jordan, “GASFLOW-MPI: A new 3-D parallel all-speed CFD code for turbulent dispersion and combustion simulations Part II: First analysis of the hydrogen explosion in Fukushima Daiichi Unit 1”, *Int. J. Hydr. Energy*, **42**(12), pp. 8369-8381 (2017).
3. M. Kuznetsov, J. Yanez, J. Grune, A. Friedrich, T. Jordan, “Hydrogen Combustion in a Flat Semi-Confined Layer with Respect to the Fukushima Daiichi Accident”, *Nuclear Engineering and Design*, **286**, pp. 36-48 (2015).
4. R. Gauntt et al, “Fukushima Daiichi Accident Study (Status as of April 2012)”, Report SAND2012-6173, 2012, 298 p.
5. Dorofeev, S.B., Kuznetsov, M.S., Alekseev, V.I., Efimenko, A.A., Breitung, W., “Evaluation of limits for effective flame acceleration in hydrogen mixtures”, *J. Loss Prev. Proc. Ind.*, **14**, pp. 583-89 (2001).
6. Dorofeev, S.B., Sidorov, V.P. Kuznetsov, M.S., Matsukov, I.D., Alekseev, V.I., “Effect of scale on the onset of detonations”, *Shock Waves* **10** (2), pp. 137-149 (2000).
7. Grune, J., Sempert, K., Haberstroh, H., Kuznetsov, M., Jordan, T., Experimental Investigation of Hydrogen-Air Deflagrations and Detonations in Semi-Confined Flat Layers, *J. Loss Prev. Proc. Ind.*, **26** (2), pp. 317-323 (2013).
8. Kumar, R.K., Koroll, G.W., Heitsch, M., Studer, E., “Carbon monoxide – hydrogen combustion characteristics in severe accident containment conditions”, OECD Report NEA/CSNI/R(2000)10 (2000).

9. Veser, A., Stern, G.,Grune, J., Breitung ,W., Burgeth, B., "CO-H2-air combustion tests the FZK-7m-tube", Programm Nukleare Sicherheitsforschung. Jahresbericht 2001. Part 1. Report FZKA-6741 pp. 6-14 (2002) http://bibliothek.fzk.de/zb/berichte/FZKA6741.pdf
10. Breitung, W., Kuznetsov, M., "Auswertung von Versuchen zur turbulenten Verbrennung von H2-CO-Gemischen", Interner simaps Bericht, 2014
11. Kuznetsov M., Redlinger R., Breitung W., Grune J., Friedrich A., Ichikawa N., "Laminar burning velocities of hydrogen-oxygen-steam mixtures at elevated temperatures and pressures", *Proceedings of the Combustion Institute*, **33**, (1), pp. 895-903 (2011).
12. Andrews, G.E. and Bradley, D. "Burning velocity of methane-air mixtures". *Combust. Flame*, **18**, pp. 133–153 (2007)
13. Friedrich, A., Necker, G., Veser, A., Grune, J., Kuznetsov, M. Jordan, T., "Experiments on the combustion behaviour of hydrogen-carbon monoxide-air mixtures", *Proc. of the 8th International Conference on Hydrogen Safety (ICHS 8)*, September 24-26, 2019, Adelaide (Australia), paper ID: #229, pp. 1-12
14. J. Grune, W. Breitung, M. Kuznetsov, J. Yanez, W. Jang, W. Shim, Flammability limits and burning characteristics of CO–H2–H2O–CO2–N2 mixtures at elevated temperatures, *International Journal of Hydrogen Energy*, **40** (31), pp. 9838-9846 (2015).
15. Sung C.-J., Law C.K., Fundamental Combustion Properties of H2/CO Mixtures: Ignition and Flame Propagation at Elevated Pressures, *Combustion Science and Technology*, **180** (6), 1097-1116 (2008).
16. A.I Gavrikov, A.A Efimenko, S.B Dorofeev, "A model for detonation cell size prediction from chemical kinetics", *Combustion and Flame*, **120**(1–2), pp. 19-33 (2000).
17. M. Kuznetsov, V. Alekseev, I. Matsukov, S. Dorofeev, "DDT in a smooth tube filled with a hydrogen–oxygen mixture", Shock Waves 14 (2005) 205–215.
18. M. Kuznetsov, V. Alekseev, S. Dorofeev, "Comparison of critical conditions for DDT in regular and irregular cellular detonation systems", Shock Waves 10 (2000) 217–224.
19. J. Lee, R. Knystautas, C. Chan, "Turbulent flame propagation in obstacle-filled tubes", Symposium (International) on Combustion 20 (1) (1985) 1663–1672, Twentieth Symposium (International) on Combustion.
20. W. Reynolds, The element potential method for chemical equilibrium analysis: implementation in the interactive program stanjan, Tech. Rep. Stanford, CA, Stanford University (1980).
21. D. Goodwin, Cantera: An object-oriented software toolkit for chemical kinetics, thermodynamics, and transport processes, Tech. Rep. Pasadena, CA, Caltech (2009).

Karlsruher Institut für Technologie

10TH EUROPEAN REVIEW MEETING
ON SEVERE ACCIDENTS RESEARCH
ERMSAR 2022
MAY 16-19, 2022 — KARLSRUHE, GERMANY

An analysis of combustion regimes for hydrogen/CO/air mixtures in different geometries

M. Kuznetsov[1], A. Friedrich[1], G. Necker[1], A. Veser[2], W. Breitung[2]

[1]Karlsruhe Institute of Technology *[2]Pro-Science GmbH*

INSTITUT FÜR KERN- UND ENERGIETECHNIK

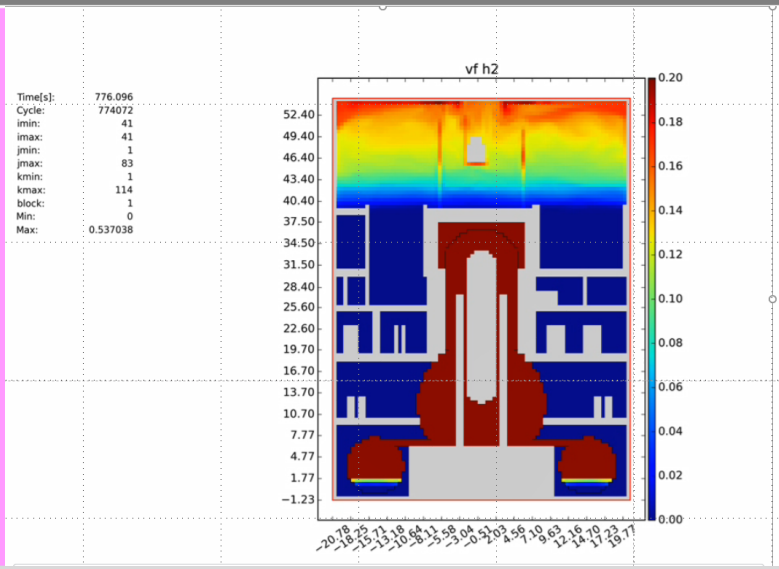

J. Xiao, W. Breitung, M. Kuznetsov, H. Zhang, J. R. Travis, R. Redlinger, T. Jordan, GASFLOW-MPI: A new 3-D parallel all-speed CFD code for turbulent dispersion and combustion simulations Part II: First analysis of the hydrogen explosion in Fukushima Daiichi Unit 1, International Journal of Hydrogen Energy, 42(12), 2017, pp. 8369-8381

Introduction

- Loss of Cooling (LOCA) and MCCI accidents lead to formation of **nonuniform stratified** hydrogen-air or **hydrogen-CO-air** cloud due to the interaction of molten nuclear fuel core with water/concrete and gathering of released hydrogen+CO at the top of containment.
- Such a hydrogen-CO-air cloud can be ignited by external or internal energy source (spark, self-ignition).
- Depending on flame propagation regimes different internal pressure loads may occur. One of the examples is the Fukushima accident when rather strong shock wave at far distance from reactor building with a fireball of combustion products was a result of internal hydrogen-air and hydrogen-CO-air explosion in Unit 1 and Unit 3.
- In order to evaluate hypothetical regimes of flame propagation in a containment of nuclear reactor during LOCA/MCCI accidents **additional experiments on FA and DDT for hydrogen-CO-air mixtures are required**.

CFD numerical simulations of hydrogen distribution

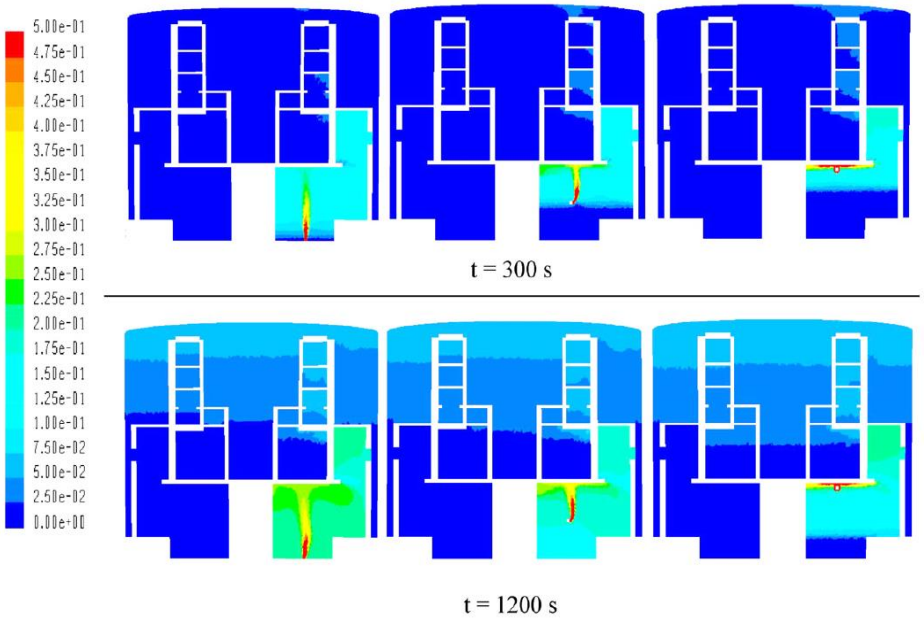

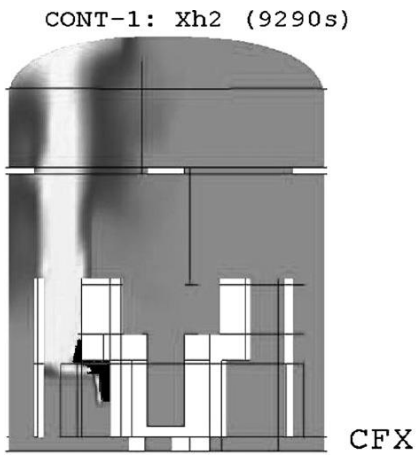

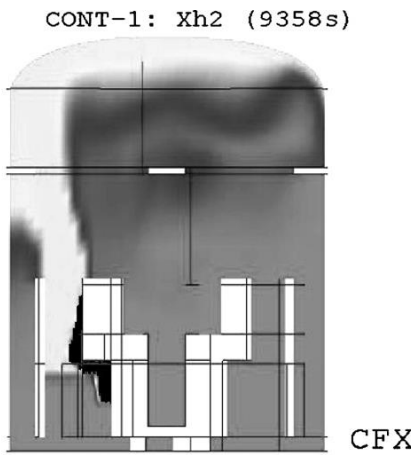

PRABHUDHARWADKAR et al., Simulation of hydrogen distribution in an Indian Nuclear Reactor Containment, *Nuclear Engineering and Design*, 241: 832-842 (2011).

J.M. MARTÍN-VALDEPEÑAS, et al., Improvements in a CFD code for analysis of hydrogen behaviour within containments, *Nuclear Engineering and Design*, 237: 627-647 (2007)

- **A vertical plume geometry or a stratified layer of hydrogen cloud be formed in containment of nuclear reactor depending on room geometry, injection time and hydrogen inventory.**

Gas release during MCCI in Fukushima Unit 1

Gauntt et al, Fukushima Daiichi Accident Study (Status as of April 2012), Report SAND2012-6173, 2012

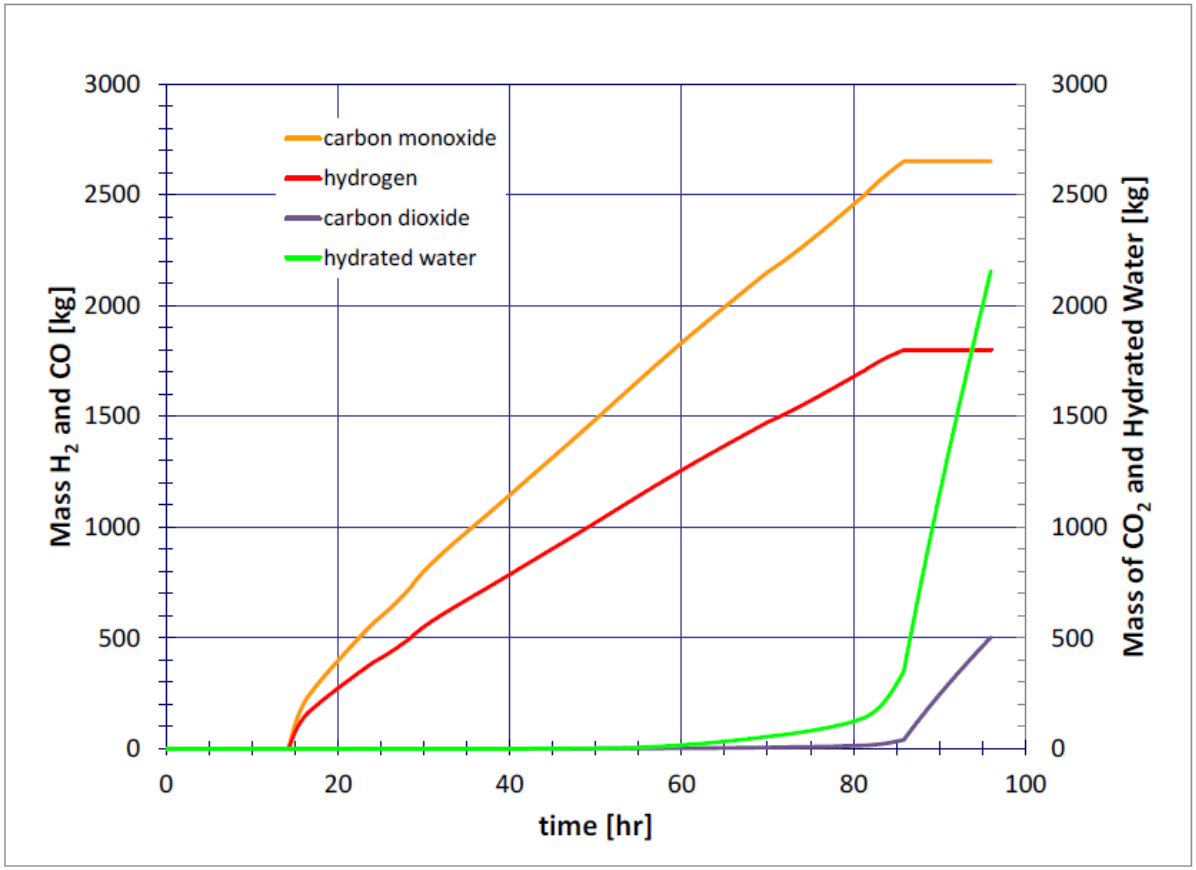

Figure 38. MELCOR Predicted Reaction Products from Core-Concrete Interaction (Unit 1).

GASFLOW-MPI simulation of Fukushima Unit1 accident

Hydrogen release and dispersion

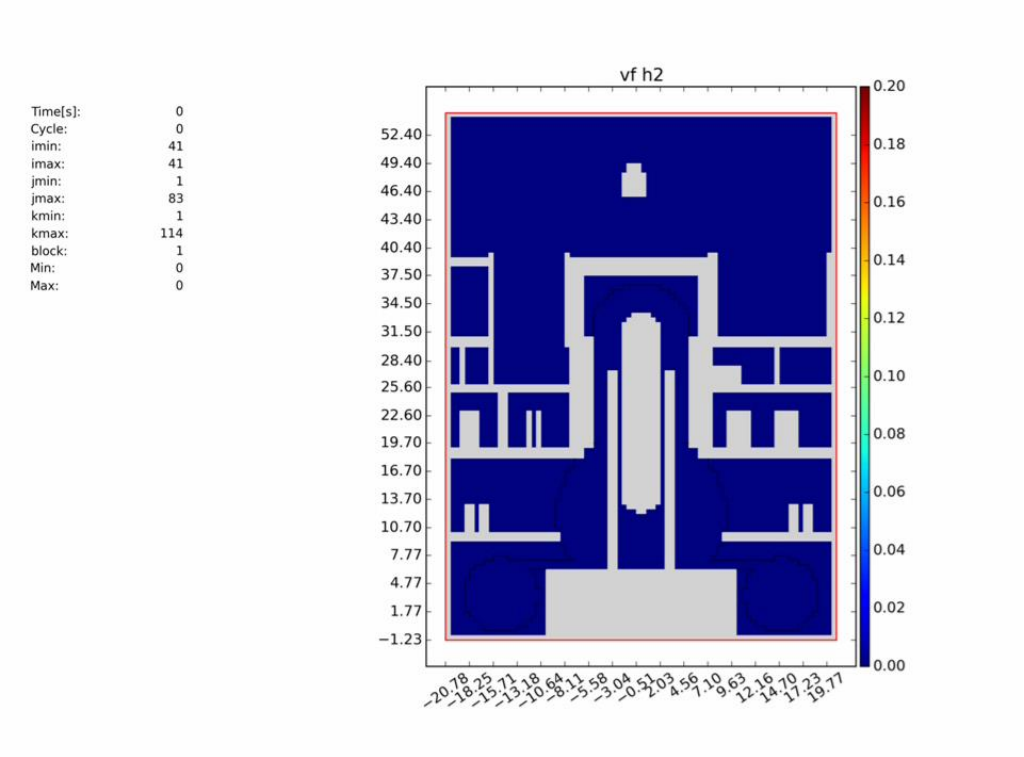

J. Xiao, W. Breitung, M. Kuznetsov, H. Zhang, J. R. Travis, R. Redlinger, T. Jordan, GASFLOW-MPI: A new 3-D parallel all-speed CFD code for turbulent dispersion and combustion simulations Part II: First analysis of the hydrogen explosion in Fukushima Daiichi Unit 1, International Journal of Hydrogen Energy, 42(12), 2017, pp. 8369-8381

- **A stratified layer of hydrogen most probably was formed in Fukushima Unit1. Within 800 s the hydrogen concentration changes from 20 to 0%H2 in air within a layer thickness of 14 m. KIT/PS experiments confirm that the detonation in such an atmosphere may occur.**

GASFLOW simulation of Fukushima Unit1 accident

Internal hydrogen explosion

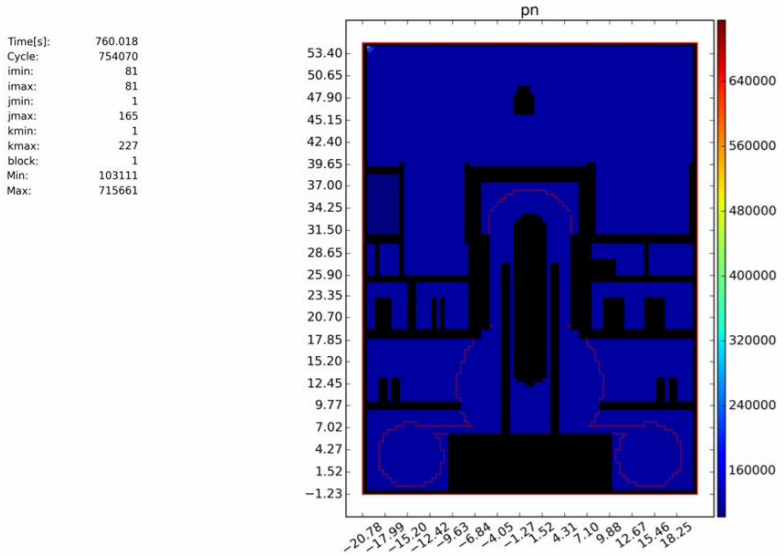

J. Xiao, W. Breitung, M. Kuznetsov, H. Zhang, J. R. Travis, R. Redlinger, T. Jordan, GASFLOW-MPI: A new 3-D parallel all-speed CFD code for turbulent dispersion and combustion simulations Part II: First analysis of the hydrogen explosion in Fukushima Daiichi Unit 1, International Journal of Hydrogen Energy, 42(12), 2017, pp. 8369-8381

J. Yanez, M. Kuznetsov, An analysis of flame instabilities for hydrogen-air mixtures based on Sivashinsky equation, Physics Letters A, 380 (33), 2016, pp. 2549-2560

- Detonation of a stratified hydrogen layer was simulated as the strongest explosive regime leading to demolition of reactor building and formation of rather strong shock wave outdoor.
- Detonation or deflagration of about 200 kg of hydrogen was estimated (K_{TNT} ~ 800 kg)
- Detonation was initiated without a transient flame acceleration and DDT transition. A failure of reactor building was not simulated.

GASFLOW simulation of Fukushima Unit1 accident

- **External blast wave**

J. Xiao, W. Breitung, M. Kuznetsov, H. Zhang, J. R. Travis, R. Redlinger, T. Jordan, GASFLOW-MPI: A new 3-D parallel all-speed CFD code for turbulent dispersion and combustion simulations Part II: First analysis of the hydrogen explosion in Fukushima Daiichi Unit 1, International Journal of Hydrogen Energy, 42(12), 2017, pp. 8369-8381

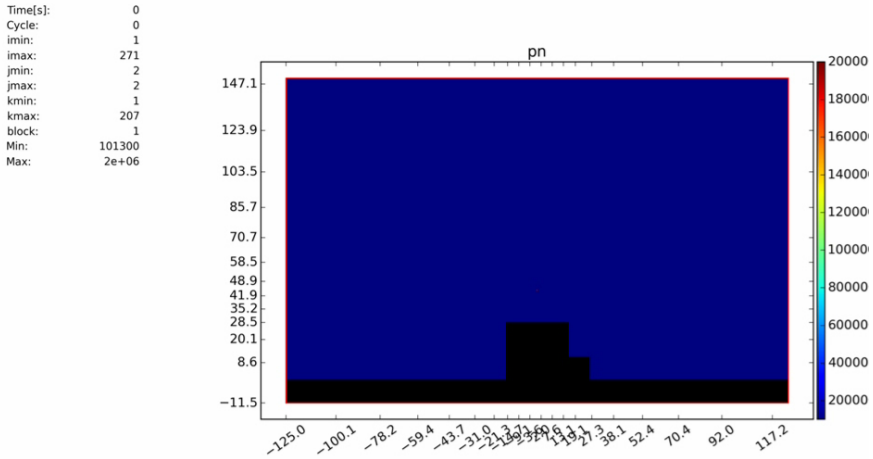

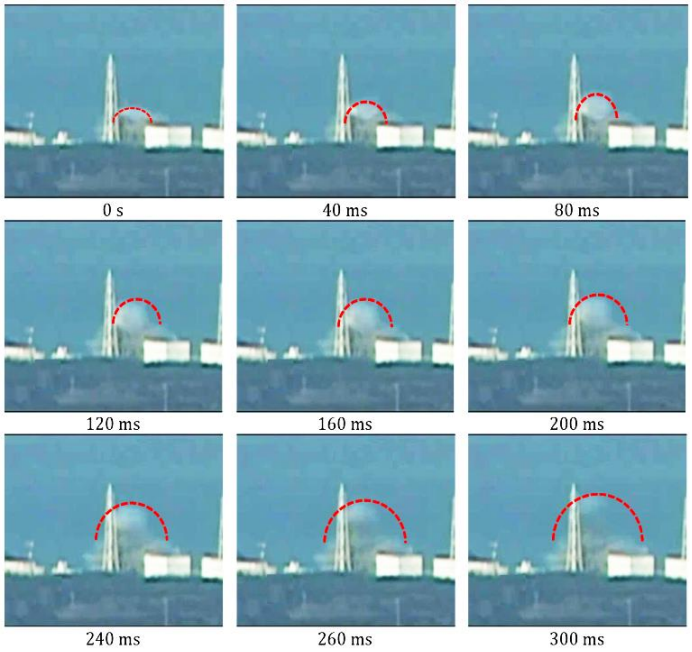

- **A strong blast wave propagation outside of reactor building caused by internal hydrogen explosion was simulated (K_{TNT}~800 kg).**
- **Very similar behavior was registered by outdoor cameras during the Fukushima accident (the right hand side picture).**

Flame propagation regimes. Pressure loads

- **Different combustion regimes are distinguished :**
  - **slow subsonic flame (p = 2-3 bar)**
  - **fast sonic flame (p = 5-8 bar)**
  - **detonation (p =~20 bar)**

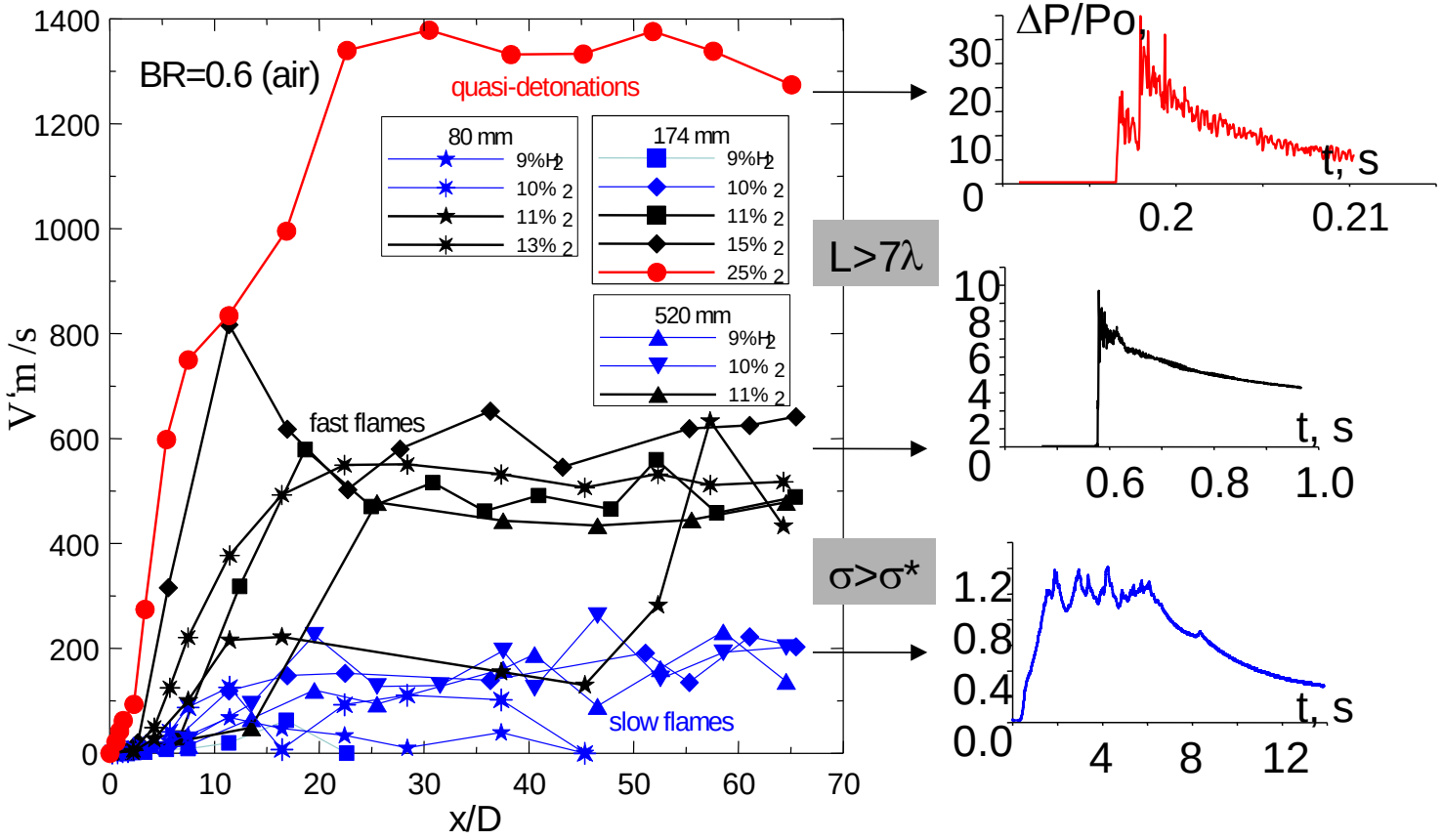

Hazard potential

Characteristic pressure under combustion and explosion in semi-confined flat layer of hydrogen – air mixtures

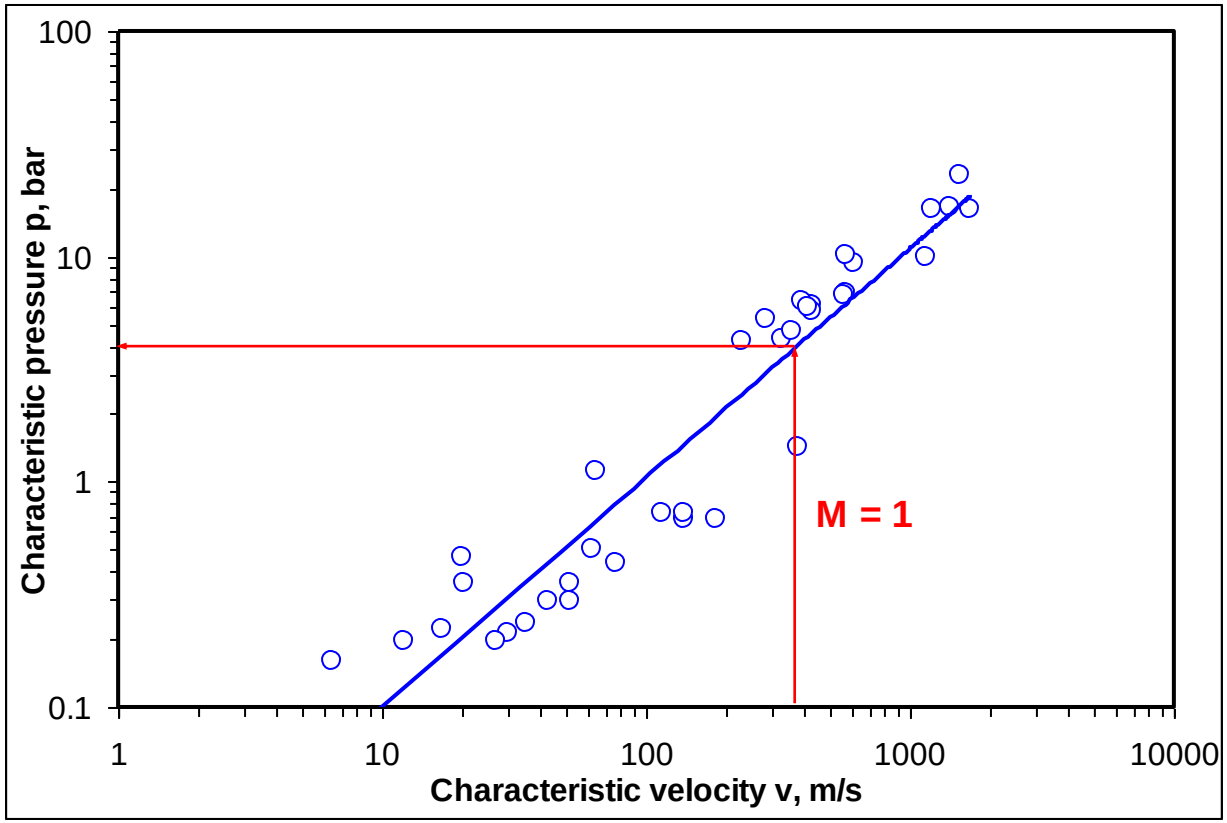

- **Higher combustion velocity leads to a higher pressure load. For fast supersonic flames (M>1) and for detonations the resulting pressure becomes very dangerous and may exceed the design pressure of containment**

Flammability limits for H2-CO-air mixtures

V = 8.2 liter
E_ign<50 mJ

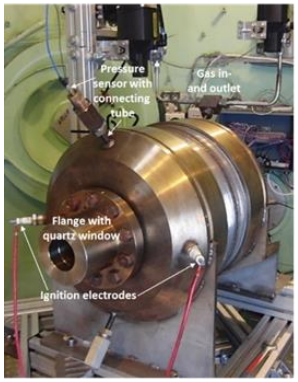

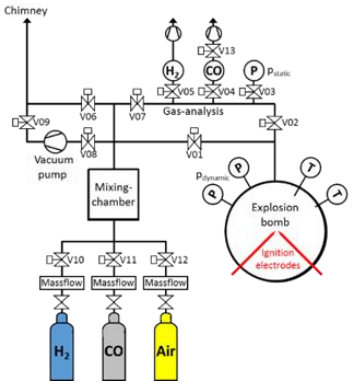

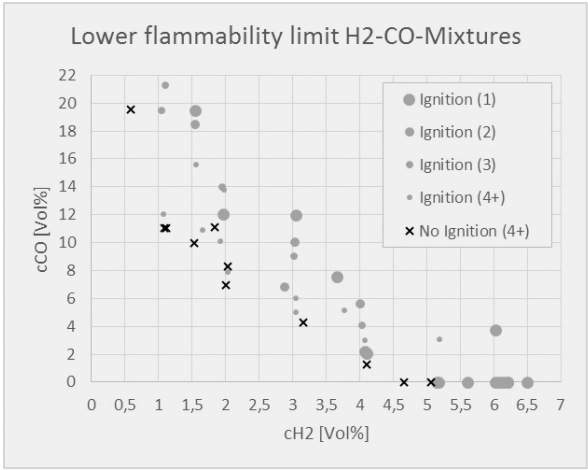

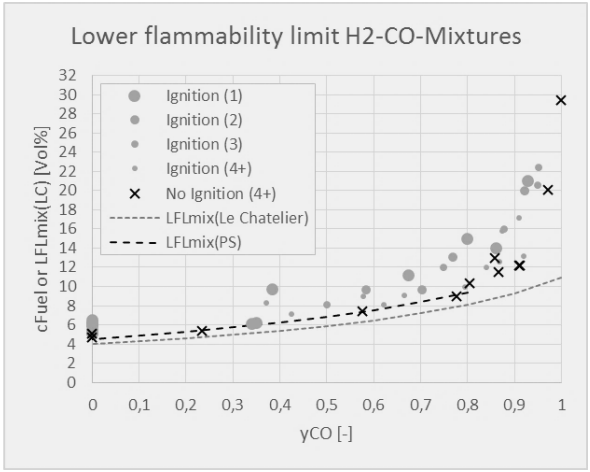

- Stochastic character of ignition depends on water vapor existence (up to 5 attempts!)
- Approaching the pure CO-air compositions there is a difficulty to ignite the mixture and also a higher deviation from Le Chatellier's law.

Flammability limits for H2-CO-O2-N2 mixtures

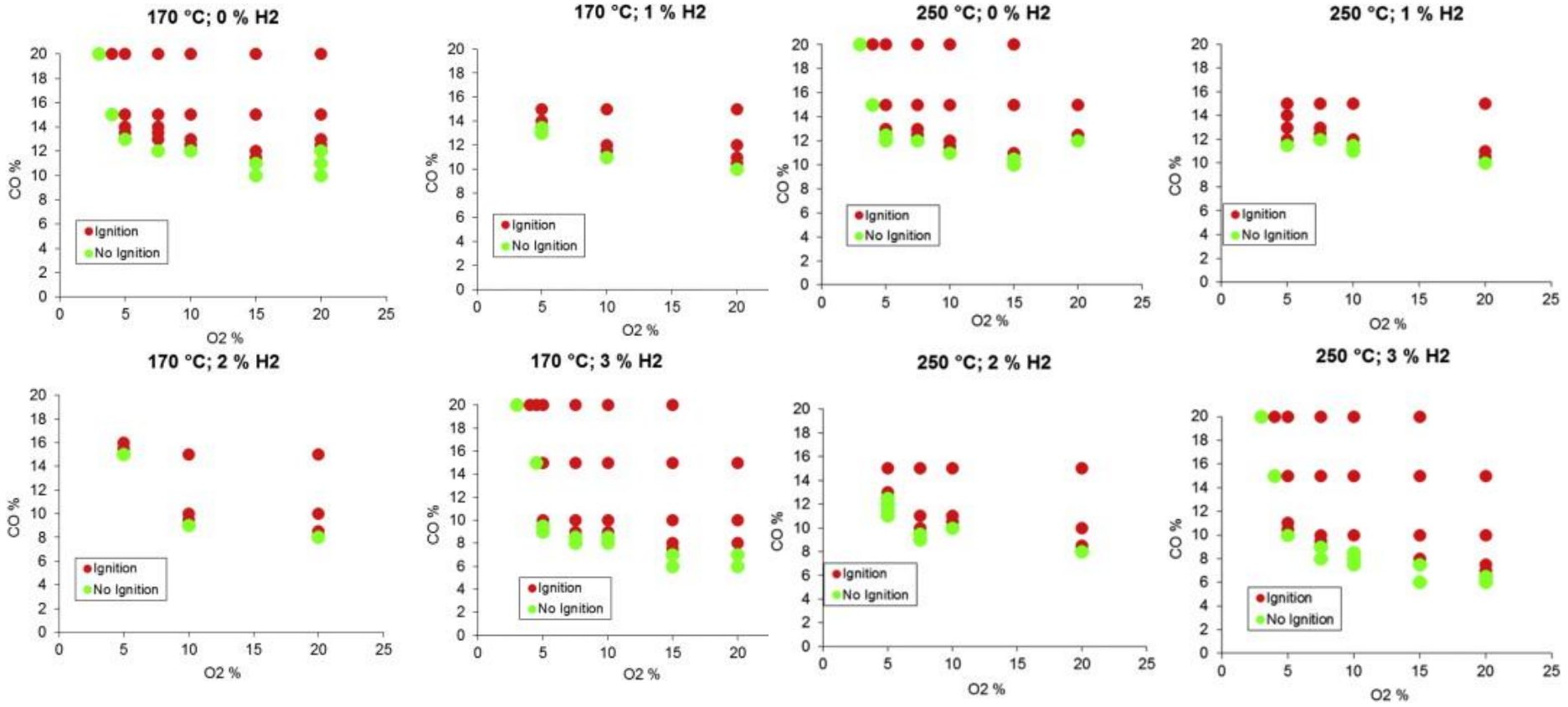

- 1 bar initial pressure
- 60% H2O + remaining small amount of inert gas N2 or CO2
- The integral effect of H2+CO governs the flammability
- Reduced temperature leads to shrinking of flammability limits

Flammability limits for H2-CO-O2-N2 mixtures

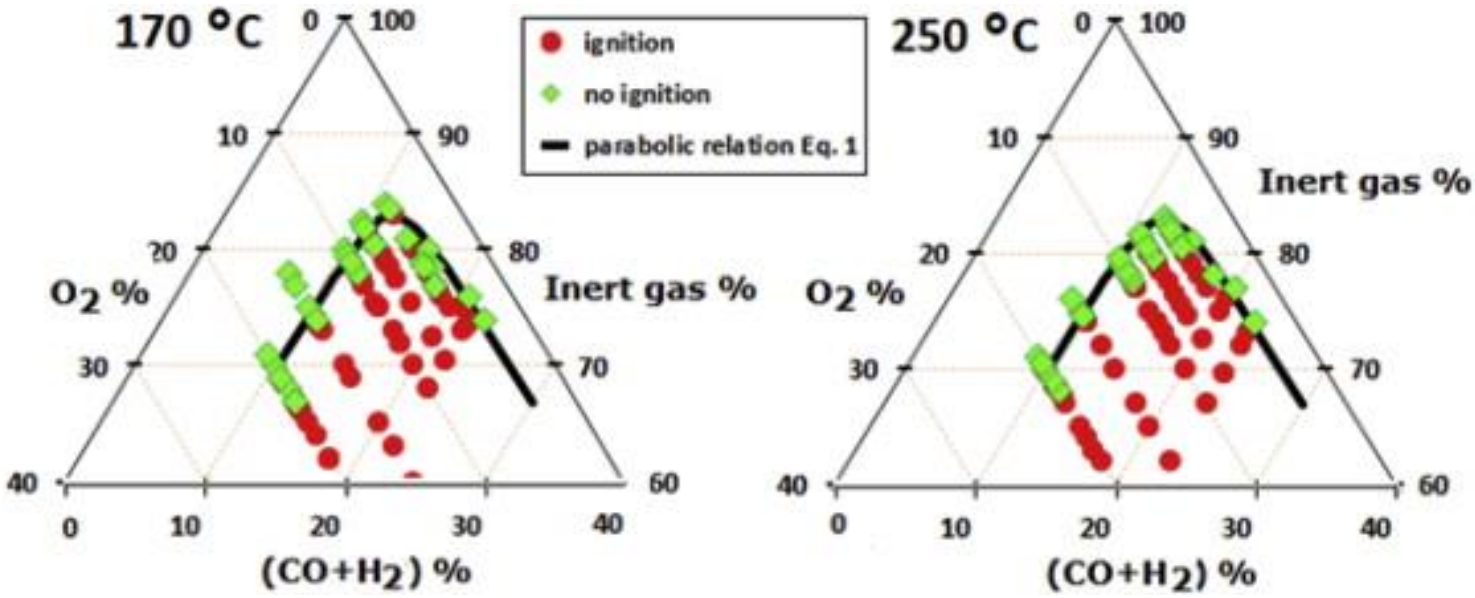

- 1 bar initial pressure
- 60% H2O + remaining small amount of inert gas N2 or CO2
- The integral effect of H2+CO governs the flammability

Flame velocity, maximum combustion pressure
Experiments at ambient conditions

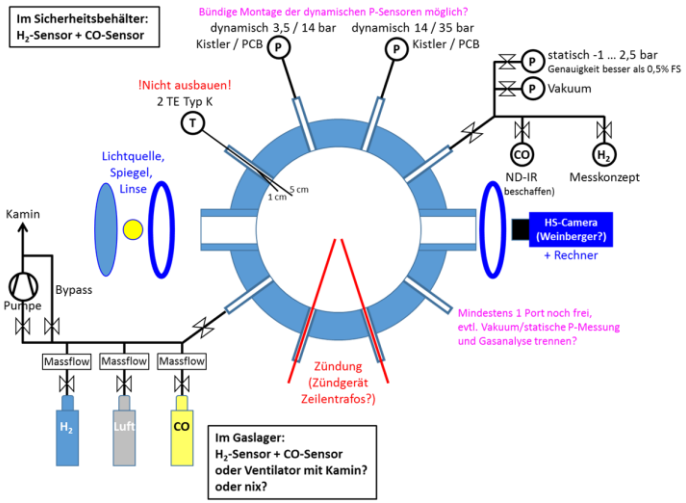

Literature

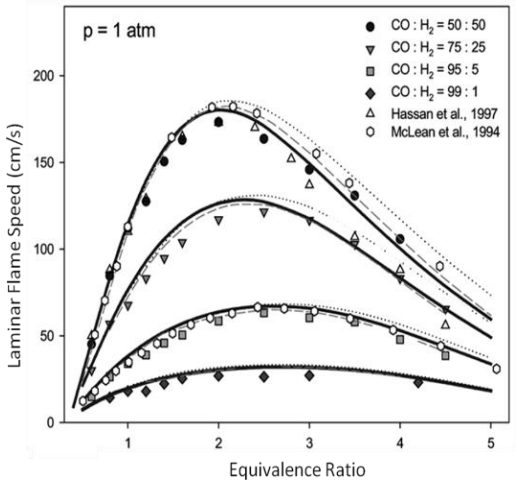

Comparison of literature vs experiments

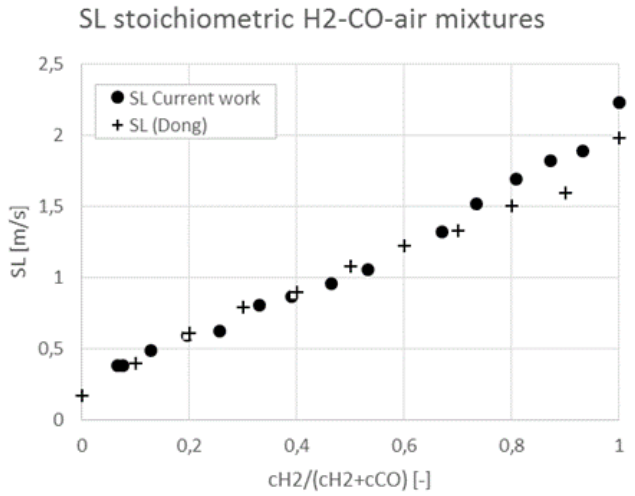

Empirical correlation on the effect of CO

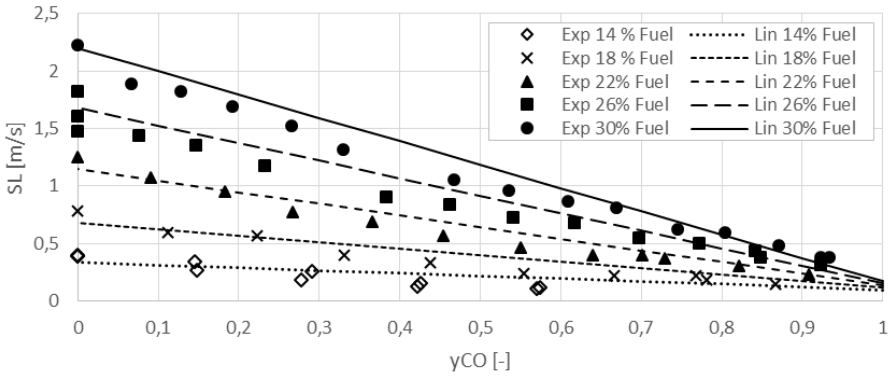

$$S_{L(mix)} = y_{H2} \cdot S_{L(H2)} + y_{CO} \cdot S_{L(CO)}$$

Maximum combustion pressure for H2-CO-O2-N2 mixtures

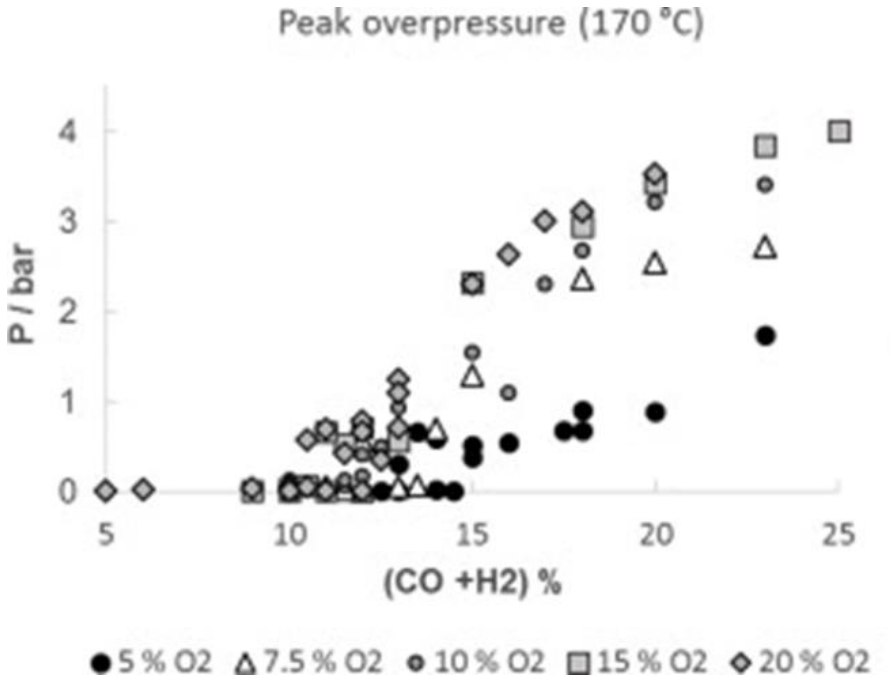

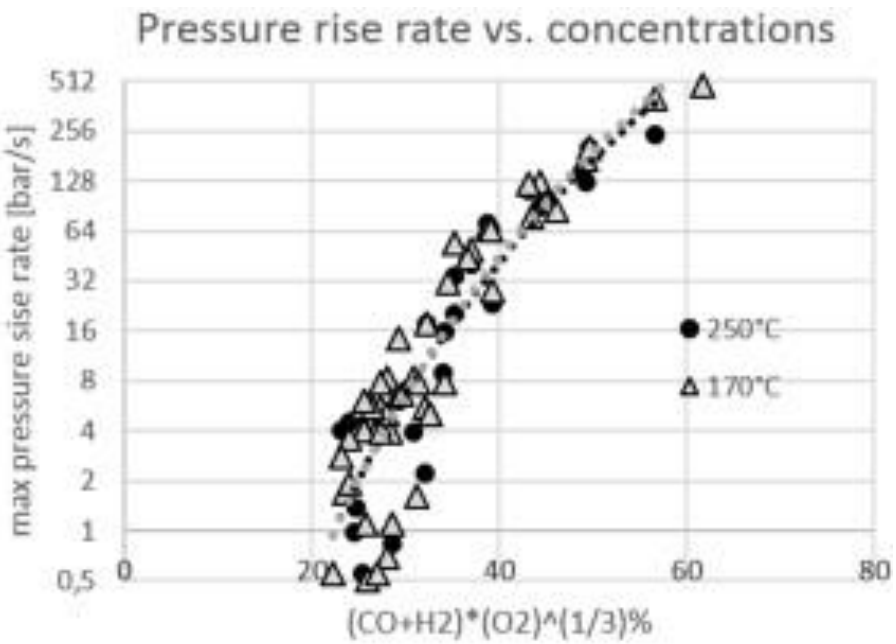

- Maximum combustion pressure increases with fuel concentration increase approaching the theoretical adiabatic combustion pressure Picc
- The reaction rate increases with CO+H2 concentration increase

Flame acceleration experiments
The effect of CO dilution

Shock tube 10 x 10 cm, 7.2-m long
Blockage ratio BR=30%



Pressure records

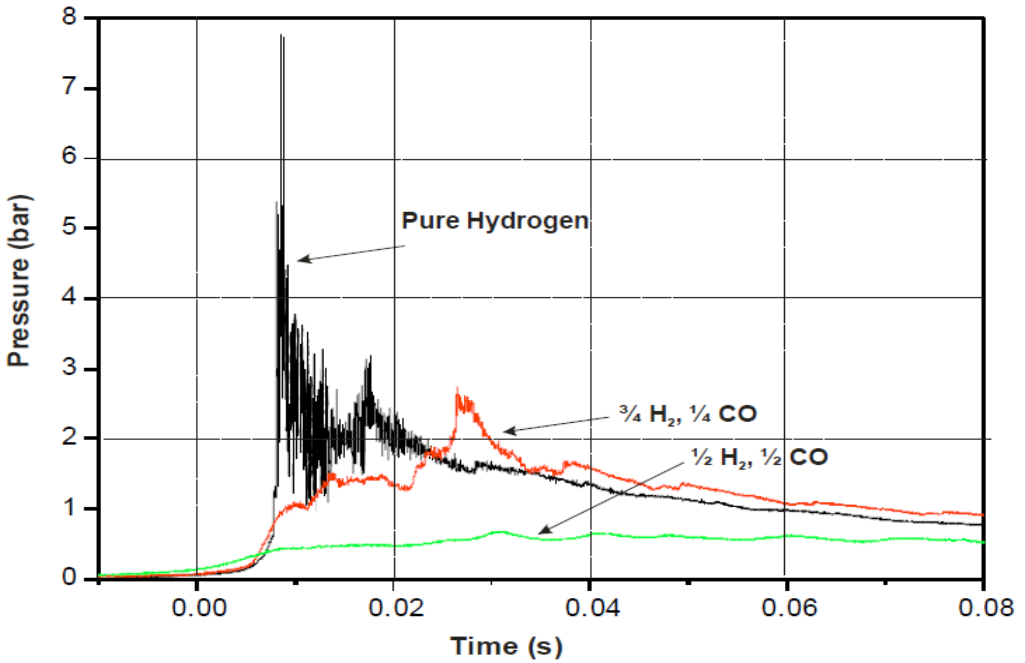

- Total fuel concentration (H2+CO) remains constant 11 vol. %
- Flame acceleration to the speed of sound leads to very high over-pressure of 7.5 bar
- Strong suppressing effect of the CO addition on the combustion pressure and flame velocity. The pressure reduces several times to 1-2.5 bar under subsonic flame velocity.

Effect of CO on flame acceleration in an enclosure

- Interpretation of all measured maximum flame velocities for H2-CO-air mixtures vs expansion ratio of the fuel gas σ shows systematic increase in the critical expansion ratio σ* with increasing CO content, here (H2 + CO) = 9 -15 vol%
- The critical expansion ratio for FA is reached at vmax / c ≈ 0.8, where v_{max} is the maximum flame speed, c is the speed of sound in burned gas
- This is a first indication of the capability of the σ* concept for the determination of criteria for FA and DDT in H2-CO fuel gas mixtures.
- Experimental data are well approximated:

$$\sigma^* = 3.75 + 1.3[CO] - 0.4[CO]^2$$

In particular, **σ*=4.5** for 0.75 CO/0.25H2 and **σ*=4.65** for pure CO is expected

- Further studies are required for the effects of geometry, scale, pressure, temperature and in wider range of CO concentrations

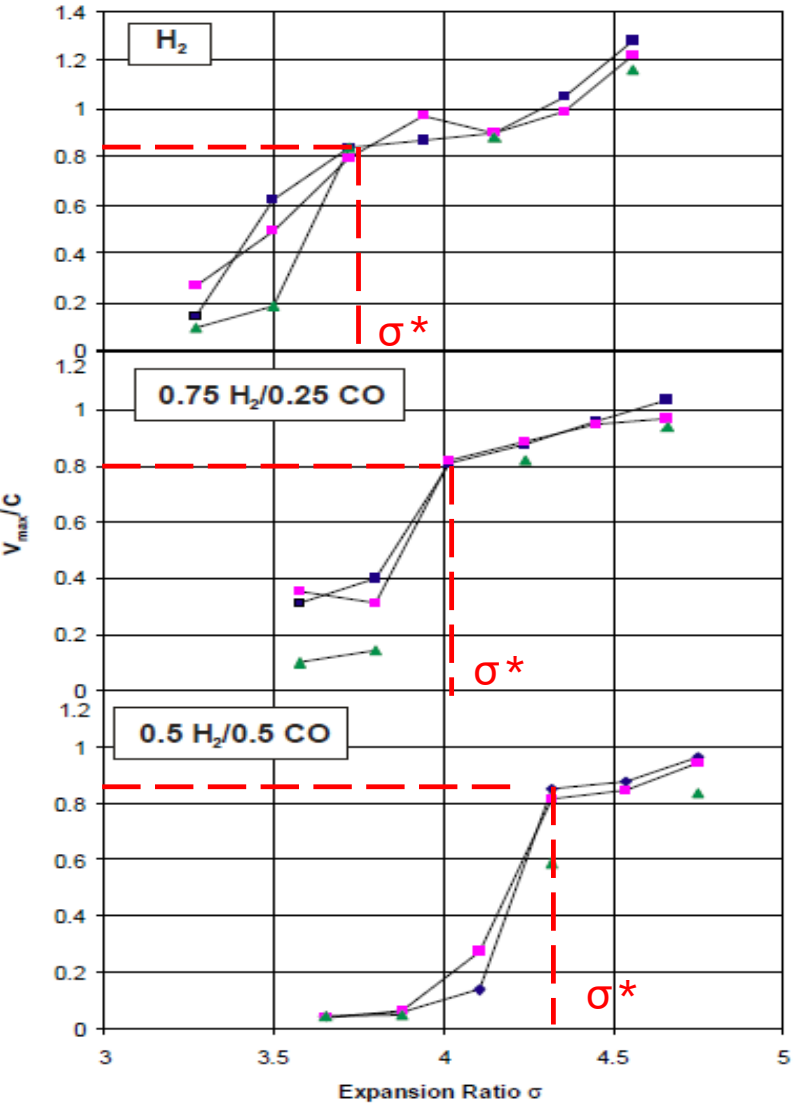

Combustion of uniform semiconfined layer of H2-CO mixture

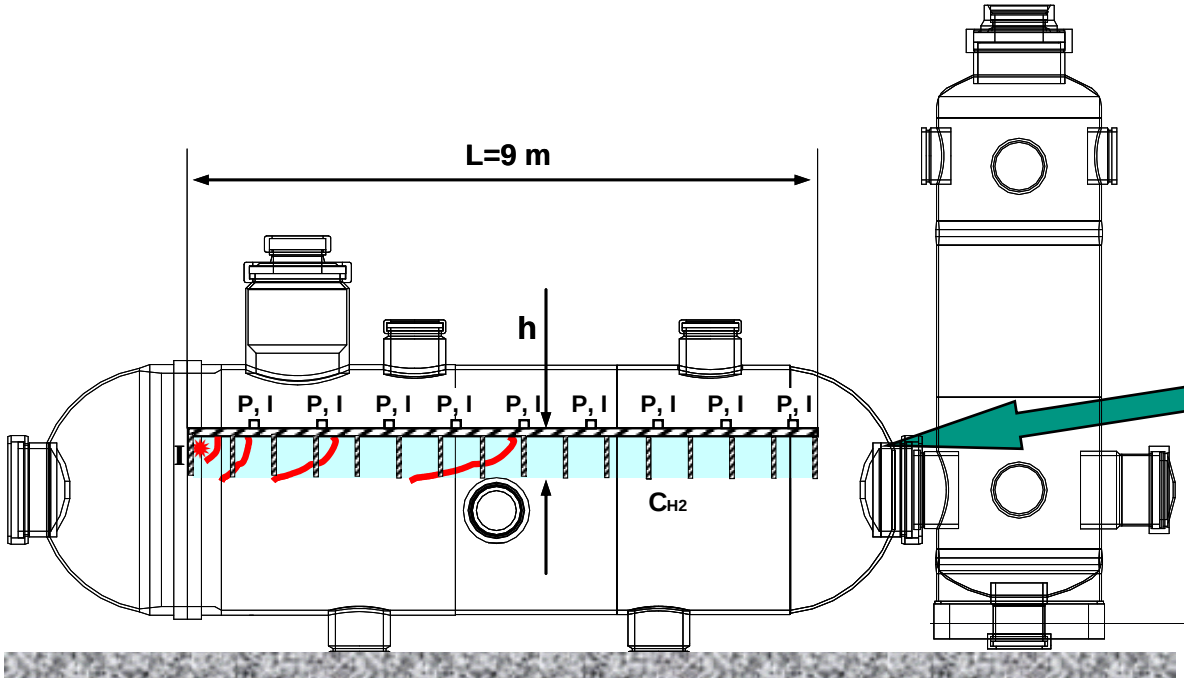

A1 vessel



I – ignition point
P, I – pressure, light and ion probes
L = 12 m – A1 length
D = 3.5 m – A1 diameter
V = 100 m^3– total volume
BR = 0.5 by obstacle grid
h – layer thickness

Geometry of the flat layer

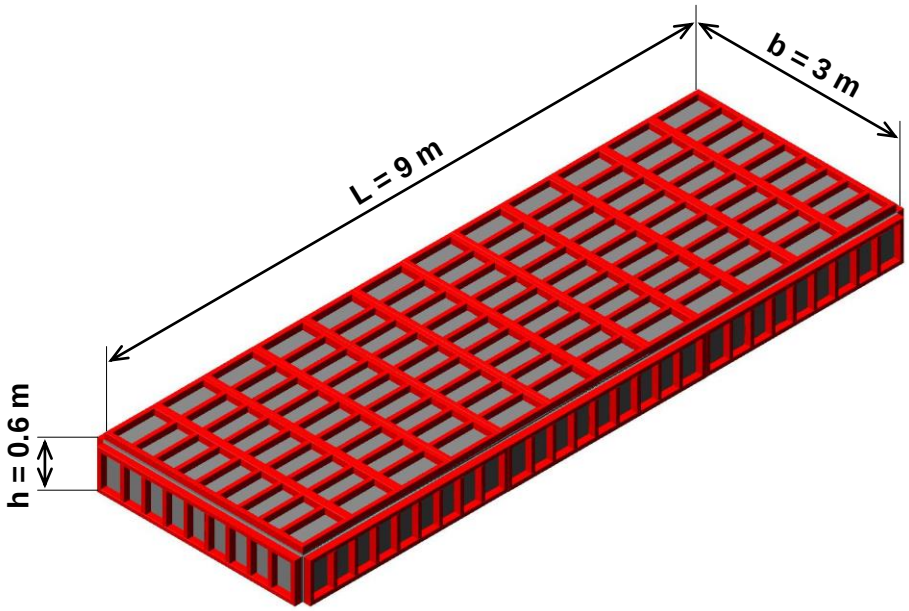

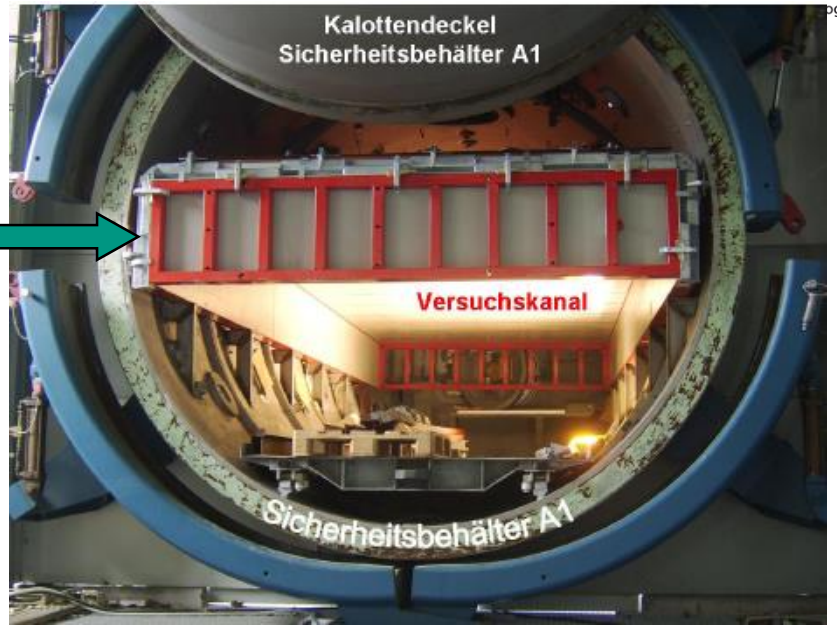

Explosion box (9 x 3 x 0.6 m):
- strong design
- far end is open
- gas filling system for hydrogen gradient formation
- linear ignition source to provide a planar flame surface
- ignition from closed end of the box

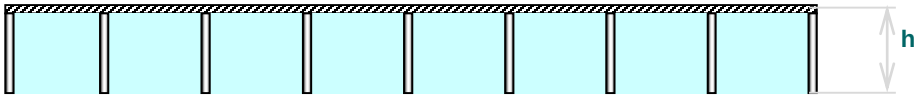



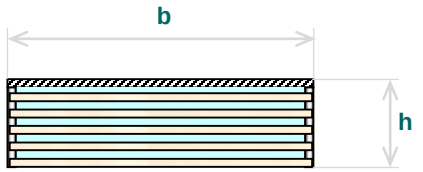

BR = 0.5

Critical conditions for flame acceleration and detonation transition in a semiconfined layer of a pure H2-air mixture

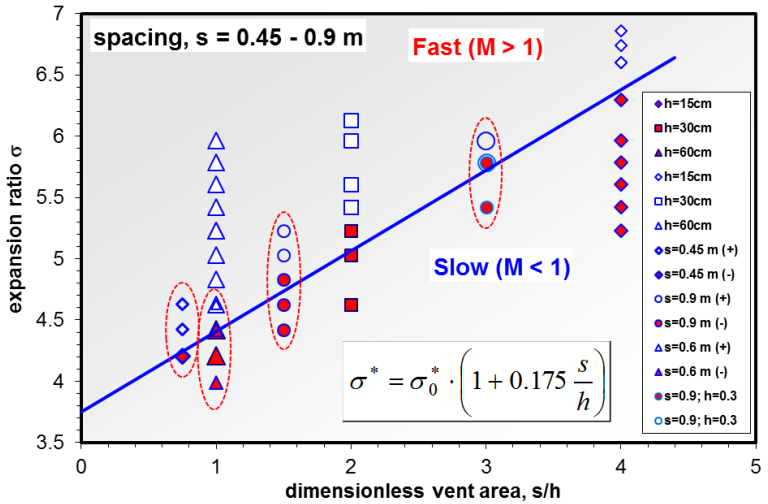

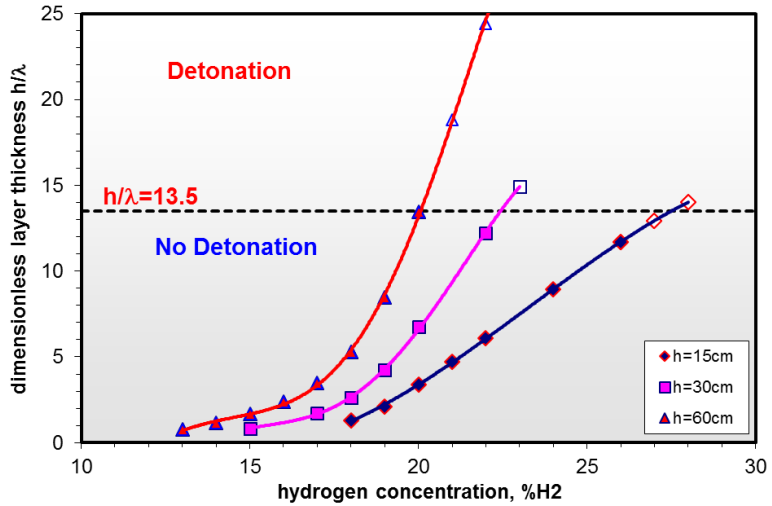

- **A linear correlation for critical expansion ratio σ* of uniform H2-air mixture for fast flame propagation in a flat semi-confined layer :**

$$\sigma^* = \sigma_0^*\left(1+0.175\frac{s}{h}\right) = 3.75\cdot\left(1+0.175\frac{s}{h}\right)$$

where s is the spacing between obstacles; σ_0 = 3.75 is the expansion ratio for hydrogen-air combustion in a closed geometry

- **Detonation can occur if the flame accelerates to the speed of sound (Mach number > 1). Critical layer thickness for detonation onset:**
- **h /λ > (13 – 14)**
- **Detonation is suppressed or fails if an orifice size d/λ < 3 for BR = 0.5**

Flame velocity, maximum combustion pressure

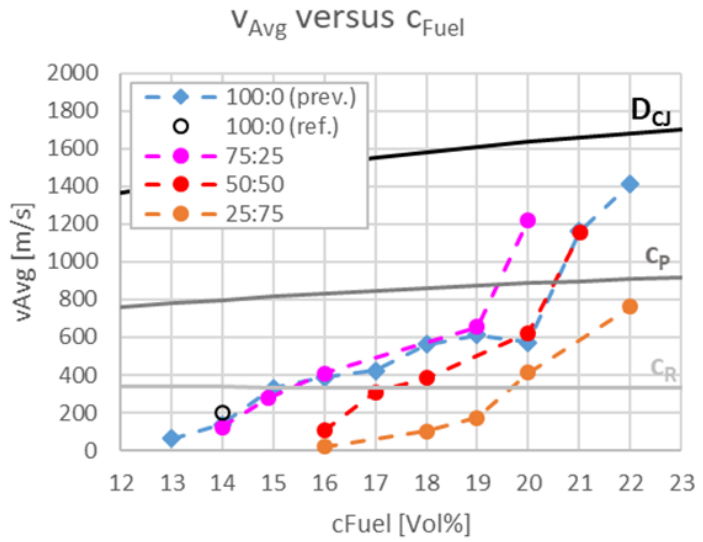

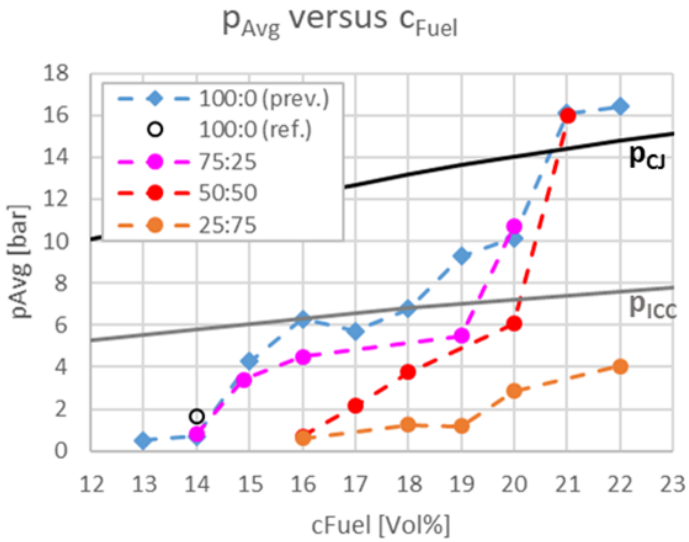

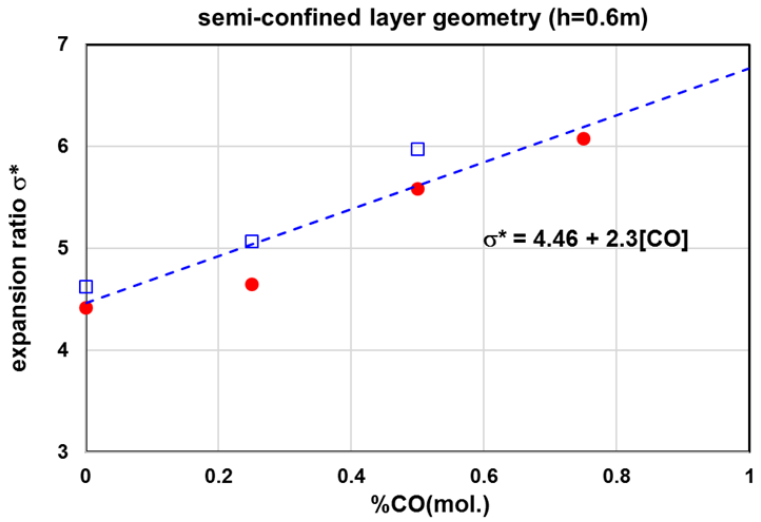

- CO dilution leads to suppression of combustion rate and to increase of critical expansion ratio **σ*** for flame acceleration to the speed of sound
- A linear combination of two correlations for pure hydrogen and carbon monoxide was proposed for a layer geometry

$$\sigma^* = [H_2]\cdot\sigma_0^*(H_2)\cdot\left(1+K_{H2}\frac{s}{h}\right)+[CO]\cdot\sigma_0^*(CO)\cdot\left(1+K_{CO}\frac{s}{h}\right)$$

- The coefficients $\sigma_0^*(H_2)$ =3.75 and $\sigma_0^*(CO)$ =4.65 and K_{H2} =0.175 and K_{CO}=0.454 have been found

Example of CO effect on detonation cell sizes

- The detonation cell size λ of the H2-CO vapor-air gas mixture occurs as a scale for the detonation transition criterion
  At low CO levels as expected in incidents we can calculate λ values for H2-CO mixtures from those of H2-steam-air

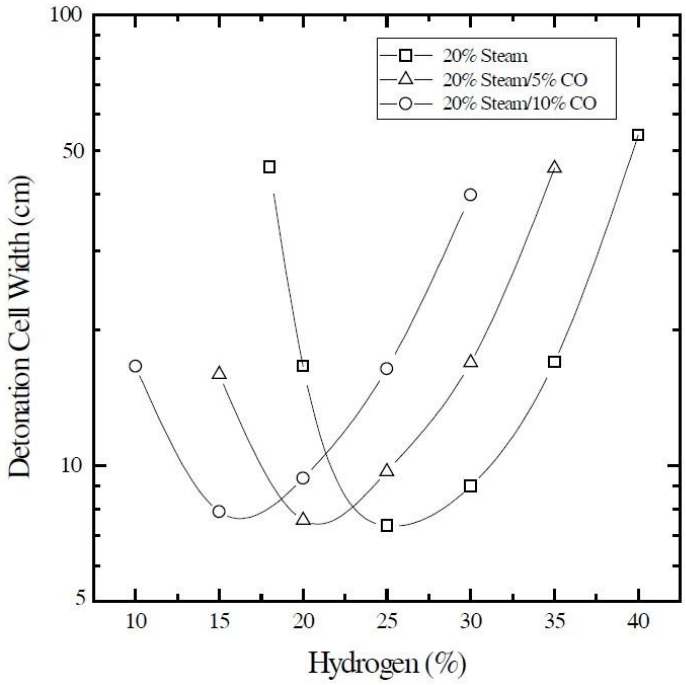

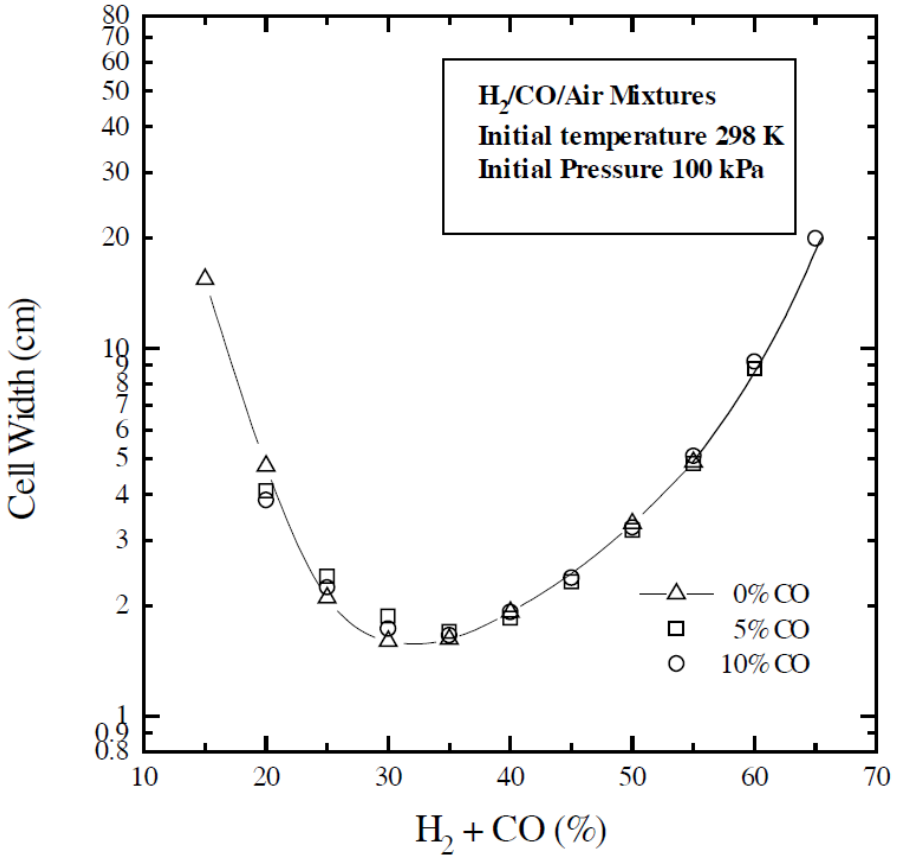

* R.K.Kumar, G.W.Koroll, M.Heitsch, E.Studer, Carbon monoxide – hydrogen combustion characteristics in severe accident containment conditions, report NEA/CSNI/R(2000)10, 10-March-2000

Experimental results
Detonation cell size calculations

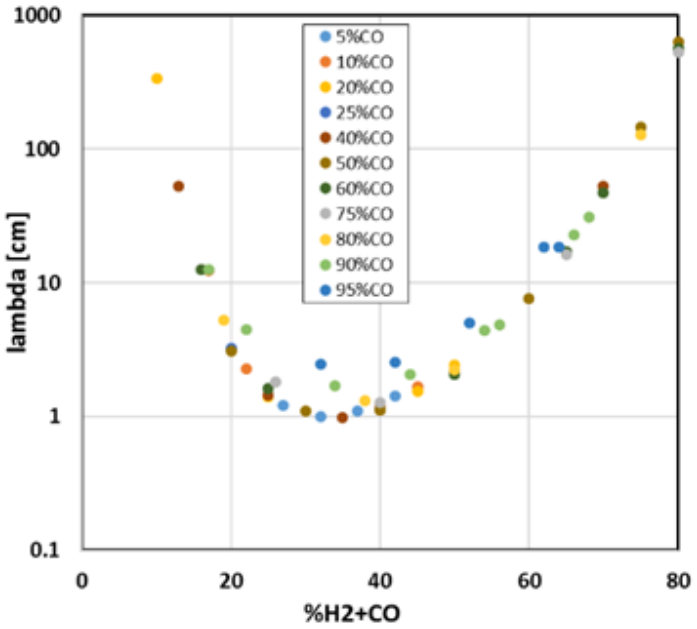

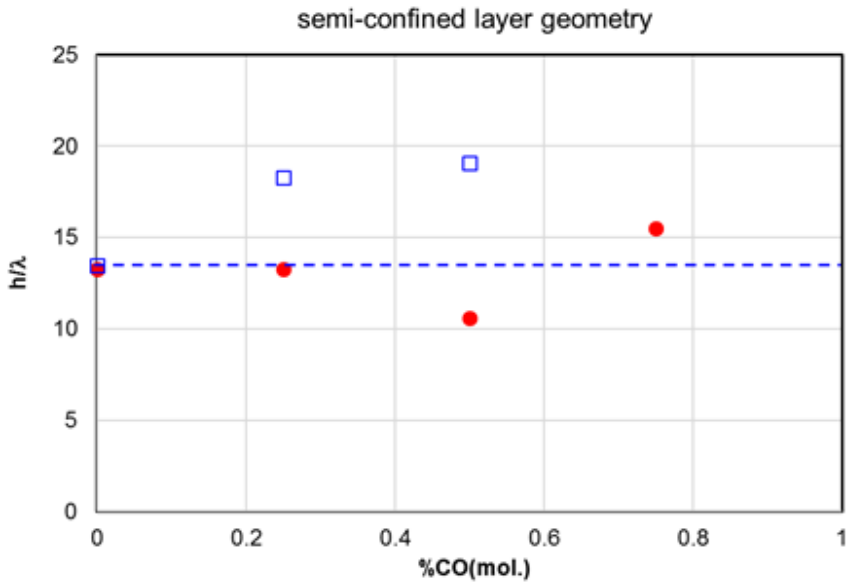

- All curves for detonation cell sizes calculated by CELL_H2 program are overlapping well being plotted vs. H2+CO concentration
- Taking into account characteristic scale of the reactor building as 10 m, the biggest detonation cell size for detonation onset is about 1.4 m according to 7λ criterion.
- It covers the range of concentrations from 11 to 75% H2+CO to be potentially detonated in a containment scale
- The detonability criterion h /λ > (13 – 14) for a layer of hydrogen-air mixture remains valid for H2-CO-air compositions as well

Summary

- A methodology of explosion safety assessment for H_2-CO-air compositions formed due to the MCCI accident is based on the results of small and middle scale experiments conducted at the HYKA test site.
- Experiments on flammability limits at ambient conditions for H_2-CO-air compositions with different ratios of H_2:CO have been conducted. The data show that Le Chatelier's rule for flammability limits for two component fuels up to 80% CO can be applied. Additionally, flammability limits for multicomponent composition H_2-CO-O_2-N_2-H_2O(60%) at elevated temperatures 170 ^oC and 250 ^{o} C have been experimentally evaluated.
- Laminar flame velocities for H_2-CO-air compositions were measured at various ratios H_2:CO from 1:20 to 20:1.
- The critical expansion ratio σ^* for H_2-CO-air flame acceleration to the speed of sound was experimentally found for different geometries and enclosure degree as a function of the ratio H_2:CO in binary H_2-CO-fuel. The formula for σ^* evaluation is written as a superposition of two dependencies for a confined and semi-confined geometry proportionally to CO fraction in the fuel.
- Detonation cell sizes for various H_2-CO-air compositions were calculated in the wide range of H_2:CO ratios from 1:20 to 20:1. Then, the different detonability criteria can be applied depending on geometry and characteristic scale h, L or D.
- The same detonability criterion as for pure hydrogen-air mixtures h/λ = 13.5 was experimentally found for CO diluted compositions in a semi-confined layer geometry.

The 10th European Review Meeting on Severe Accidents Research

Severe Accident Research Eleven Years after the Fukushima Accident

May 16-19, 2022, Karlsruhe, Germany

Technical Session 4-2: Severe Accident Scenarios in Innovative Systems

Chairs: C. Journeau (CEA), F. Rocchi (ENEA)

ID306	**MELCOR Integrated Severe Accident Code Scoping Uncertainty Study of Fluoride-salt-cooled High-Temperature Reactor Accident Progression** D. Luxat (SNL)	**Presentation**
ID272	**MSR Simulation with cGEMS: Fission product release** T. Lind (PSI)	**Paper** **Presentation**
ID323	**Modelling FPs Release from Sodium Pools under DBDA Conditions** L. E. Herranz (CIEMAT)	**Paper** **Presentation**
ID333	**On the Pursuing of Safety Enhancements in Sodium Fast Reactors** S. Perez-Martin (KIT)	**Paper** **Presentation**

10TH CONFERENCE ON SEVERE ACCIDENTS RESEARCH
May 16-19, 2022 – Karlsruhe, Germany
ERMSAR 2022

Sandia National Laboratories

Securing the future of Nuclear Energy

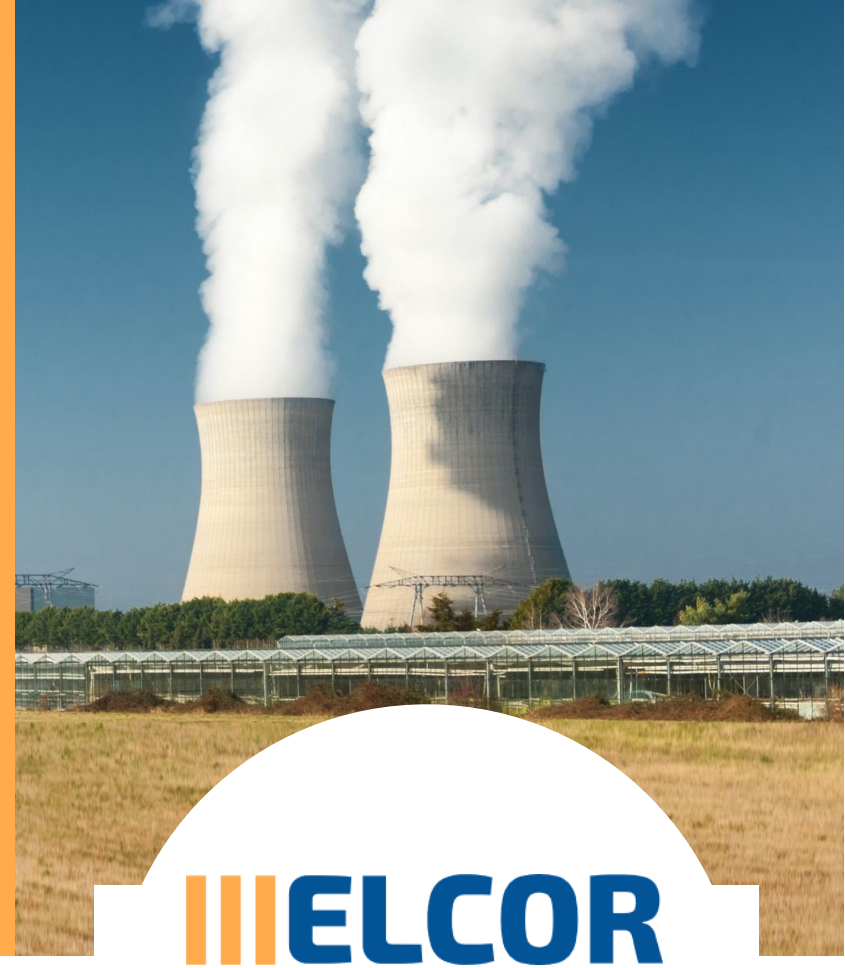

MELCOR

MELCOR Integrated Severe Accident Code Demonstration and Sensitivity Study of FHR Accident Progression

K.C. Wagner, T. Haskin, B. Beeny, F. Gelbard, and D.L. Luxat
Nuclear Energy Safety Modeling and Analysis (8852)

Sandia National Laboratories is a multimission laboratory managed and operated by National Technology and Engineering Solutions of Sandia, LLC., a wholly owned subsidiary of Honeywell International, Inc., for the U.S. Department of Energy's National Nuclear Security Administration under contract DE-NA0003525.

NRC Capability Readiness for non-LWRs

ELCOR

Public Workshop: SCALE/ MELCOR Non LWR Source Term Demonstration Project

Heat pipe reactor – June 29, 2021
Gas cooled reactor – July 20, 2021
Pebble bed molten-salt-cooled reactor – Sept 14, 2021

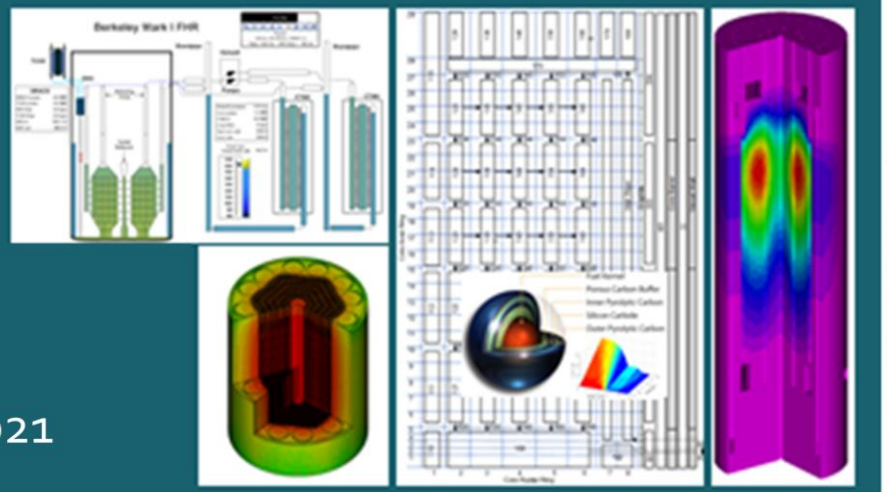

For More Information

Coming in 2022

Molten-salt fueled reactor
Sodium-cooled fast reactor

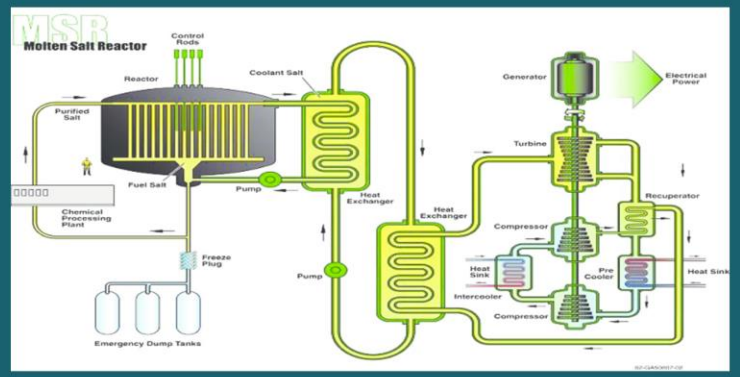

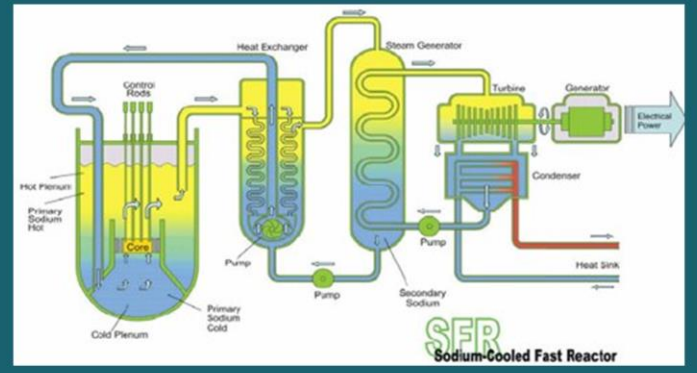

MELCOR Molten Salt Reactor Modeling

MELCOR

Added molten salt as working fluid

Fission product release

- Release from TRISO kernel
- Radionuclide distributions within the layers in the TRISO particle and compact
- Liquid-phase fission product chemistry and transport model

Additional core models

- Graphite oxidation
- Intercell and intracell conduction
- Convection & flow

Fluid point kinetics (liquid-fueled molten salt reactors)

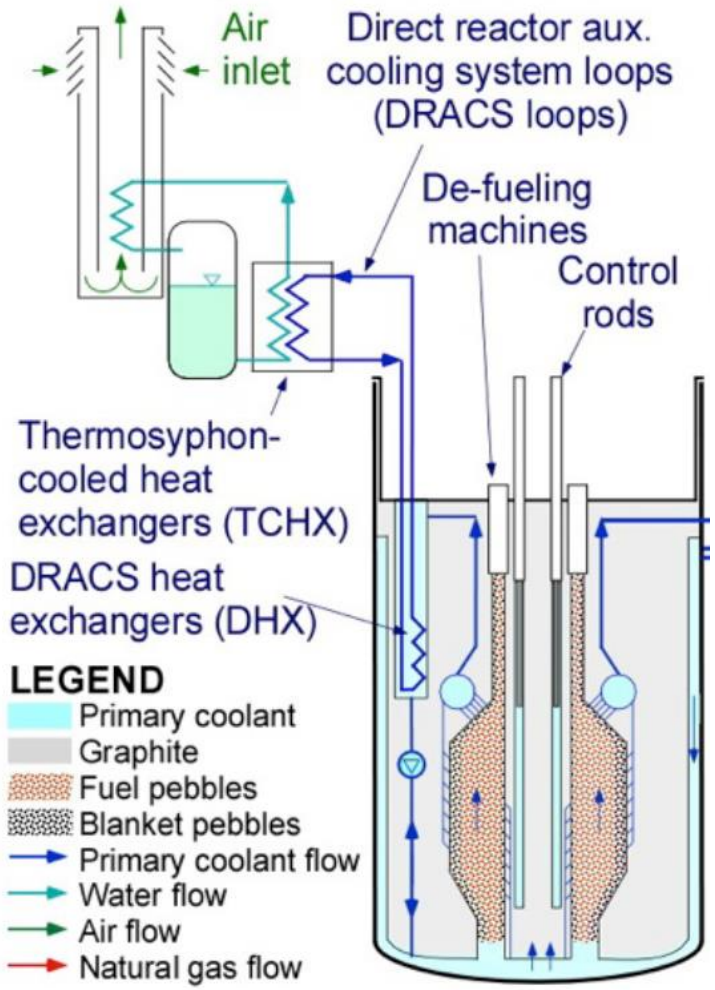

Molten Salt Chemistry and Radionuclide Release

Model Scope

Evaluation of thermochemical state

- Gibbs Energy Minimization with Thermochimica
- Provides solubilities and vapor pressures

Thermodynamic database

- Generalized approach to utilize any thermodynamic database
- An example is the Molten Salt Thermal Database
  - FLiBe-based systems
  - Chloride-based systems

Radionuclides grouped into forms found in the Molten Salt Reactor Experiment

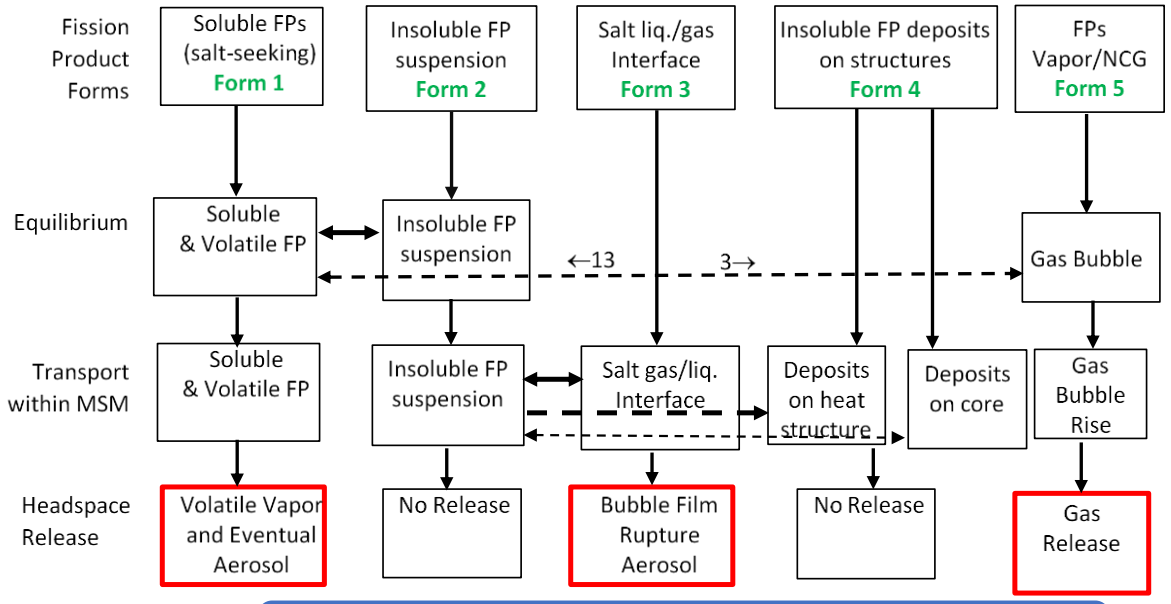

Initial Model Form

Solubility determined from empirical evidence (P. Britt ORNL 2017)

Solubilities mapped to 17 MELCOR fission product classes

Insoluble MELCOR classes are assigned to be colloidal

Core and reactor vessel

Core nodalization – light blue lines

- Assumes azimuthal symmetry
- Subdivided into 11 axial levels and 8 radial rings
- Core cells model molten salt fluid volume, reflector structures, the pebble-bed core, and the pebbles in the defueling chute

Fluid flow nodalization – black boxes

- Molten salt enters through the downcomer and flows into the center reflector and into the bottom of the pebble bed
- Molten salt leaves through the periphery of the core and upwards through the refueling chute
- Unfueled graphite pebbles in box labeled “180”

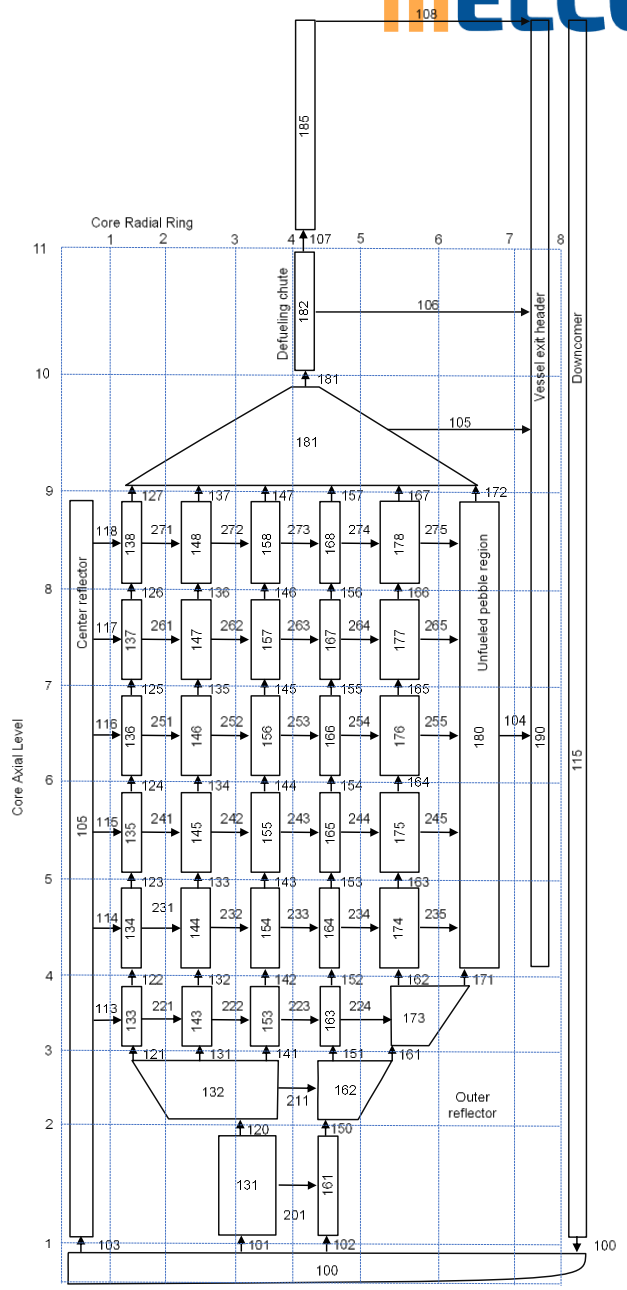

Recirculation loops

Each loop has a pump, a heat exchanger, and a standpipe

Molten salt has free surface in the hotwell and the standpipes

Argon gas above the free surfaces with connection to the cover-gas system

- Over-pressurization relief passes through the cover gas system
- Cover gas enclosure leaks into the containment when over-pressurized

Secondary-side air cools primary-side molten salt

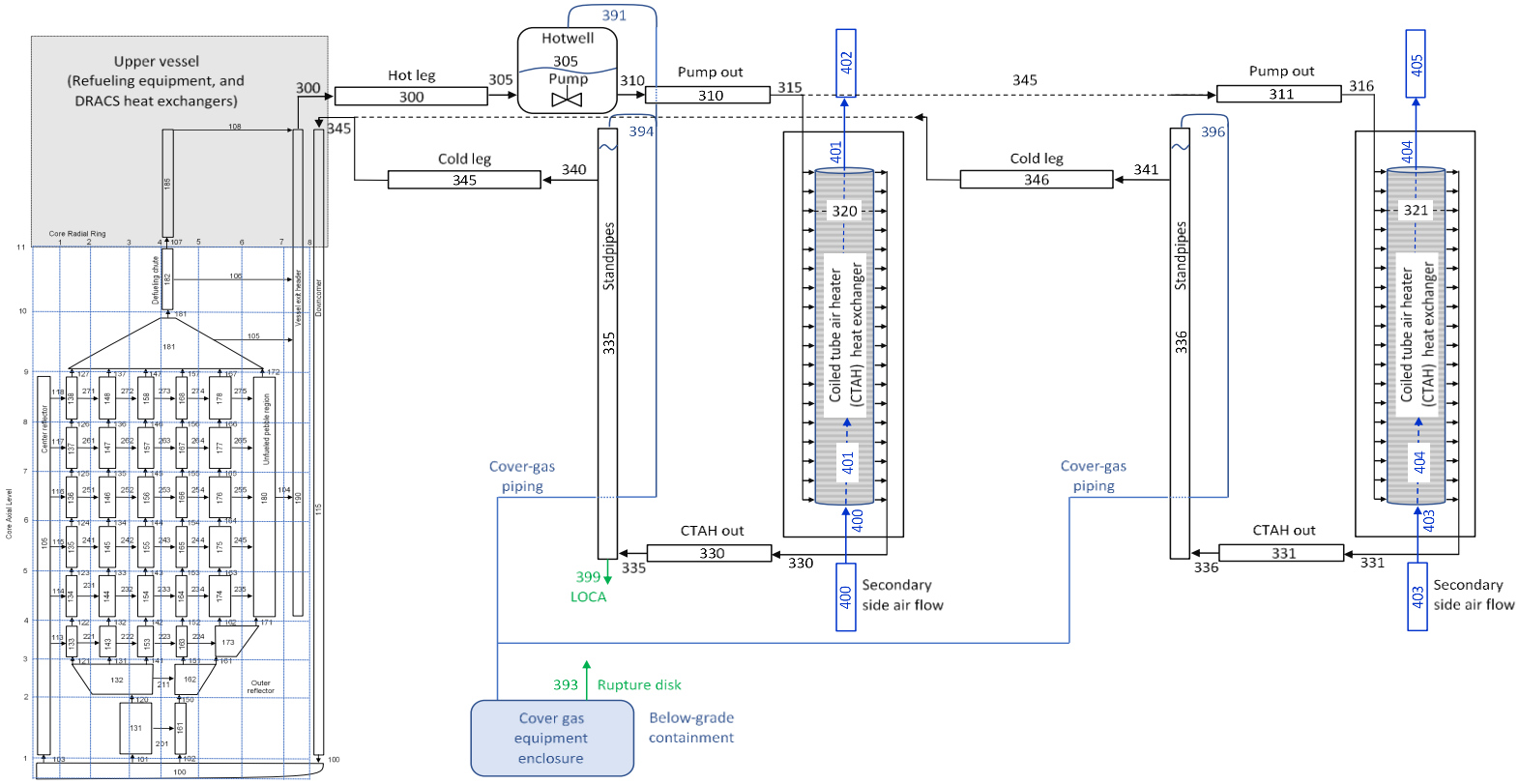

Direct Reactor Auxiliary Cooling System (DRACS)

3 trains – 2.36 MW/train

- 236 MWt reactor

Each train has 4 loops in series

- Primary coolant circulates to DRACS heat exchanger
- Molten-salt loop circulates to the thermosyphon-cooled heat exchangers (TCHX)
- Water circulates adjacent to the secondary salt tube loop in the TCHX
- Natural circulation air circuit cools and condenses steam

Start-up: RCS-pump trip causes ball in valve to drop

Additional system information

- DHXs are in the reactor vessel
- TCHXs are in the shield building



Containment

Shield dome
- Protection against aircraft and natural gas detonations (co-fired turbine concept)
- Contains water for DRACS and RCCS
- DRACS air natural circulation chimneys connected to the shield dome

Reactor cavity
- Fire-brick insulation
- Low free volume
- Low-leakage bellows between reactor cavity and adjacent cavities

Separate compartments for the other RCS components
- Below-grade compartment includes the cover-gas enclosure for reactor cavity over-pressurization

Reactor cavity cooling subsystem in reactor cavity wall
- Water circulation
- Cooling tubes affixed to reactor cavity steel liner
- Cools concrete during normal operation

Leak rate assumed consistent with BWR Mark 1 reactor building
- 100% vol/day at 0.25 psig

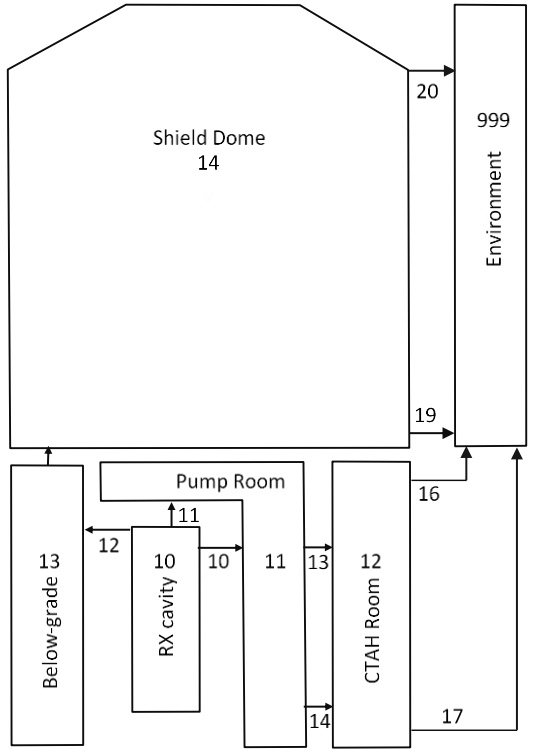

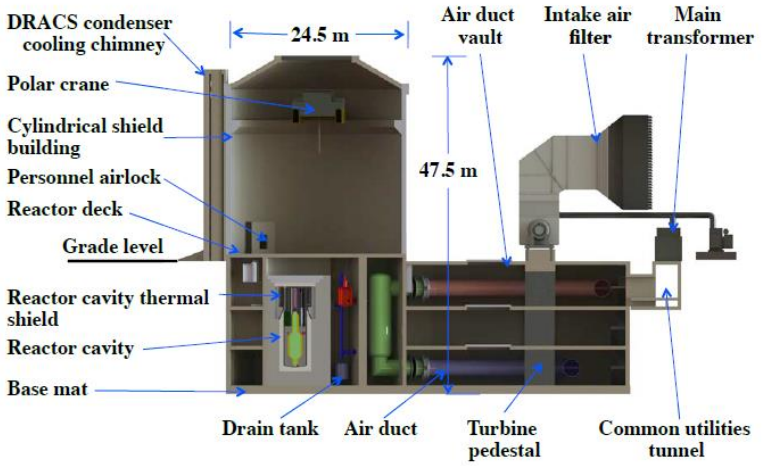

Scenarios

ELCOR

Three scenarios with a loss of secondary heat removal

- ATWS – Anticipated transient without SCRAM
- SBO – Station blackout
- LOCA – Loss-of-coolant accident

Sensitivity calculations included

- DRACS performance
- Alternate cover-gas system interconnections (LOCA only)

ATWS

Loss-of-onsite power with failure to SCRAM

- Salt pumps shut off
- Reactor fails to SCRAM
- Secondary heat removal ends
- 0 to 3 trains of DRACS operating

Includes preliminary analysis with xenon transient

- Guided by ORNL calculations
- Xenon reactivity feedback model being implemented into MELCOR

ATWS with 3xDRACS

Initial fuel heatup has strong negative fuel and moderator feedback that offsets positive reflector feedbacks

Strong negative xenon transient feedback

3xDRACS exceeds core power after 330 s

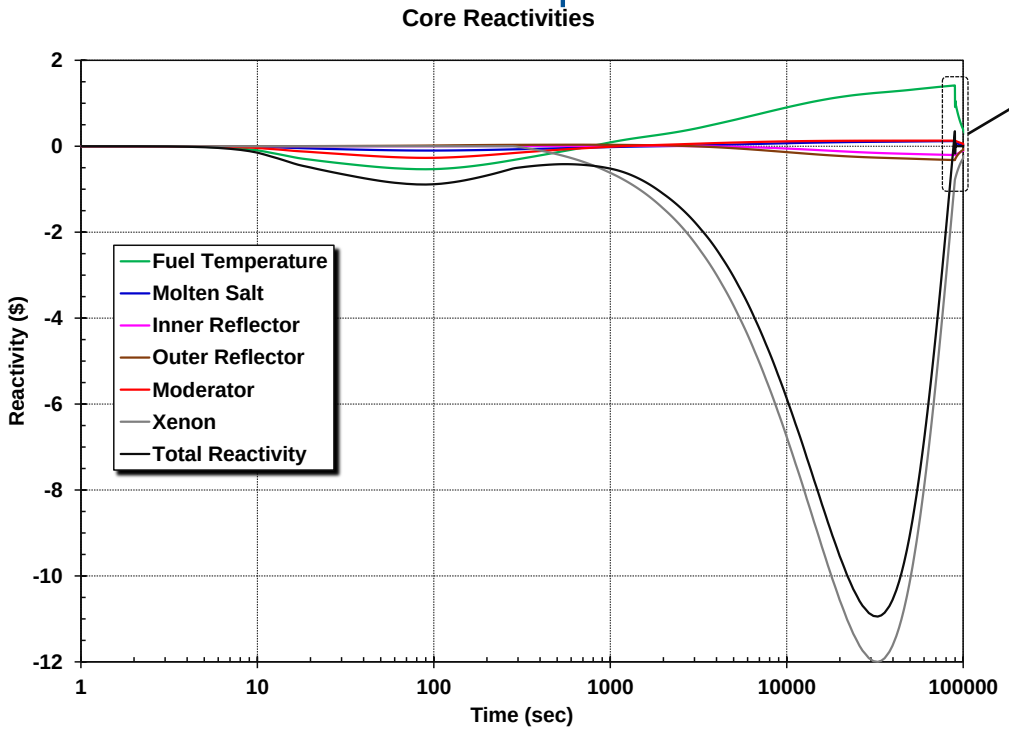

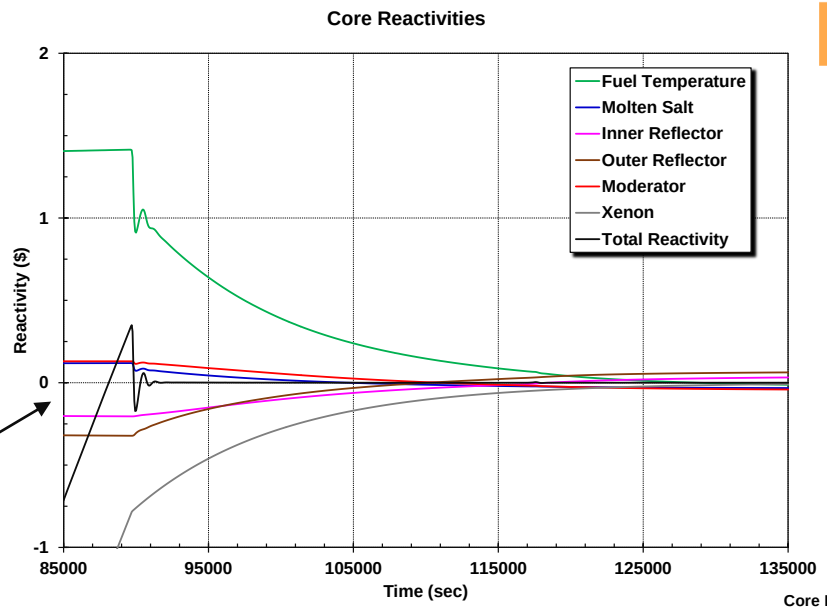

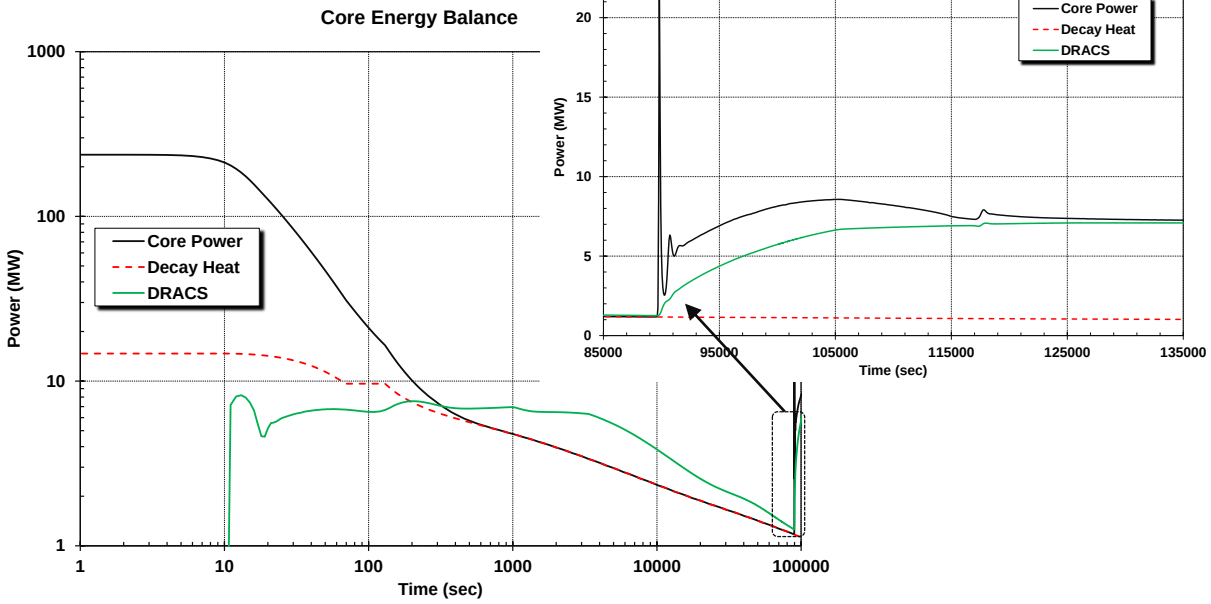

ATWS with variable DRACS (semi-log)

ELCOR

Early power decrease to decay heat level is similar for all cases

- 1xDRACS and 2xDRACS cases exceed decay heat later

Fuel temperatures cool down according to DRACS heat removal rate

- 0xDRACS peak fuel temperature = 990 ºC at 105 s (Tsat~ 1350 ºC)

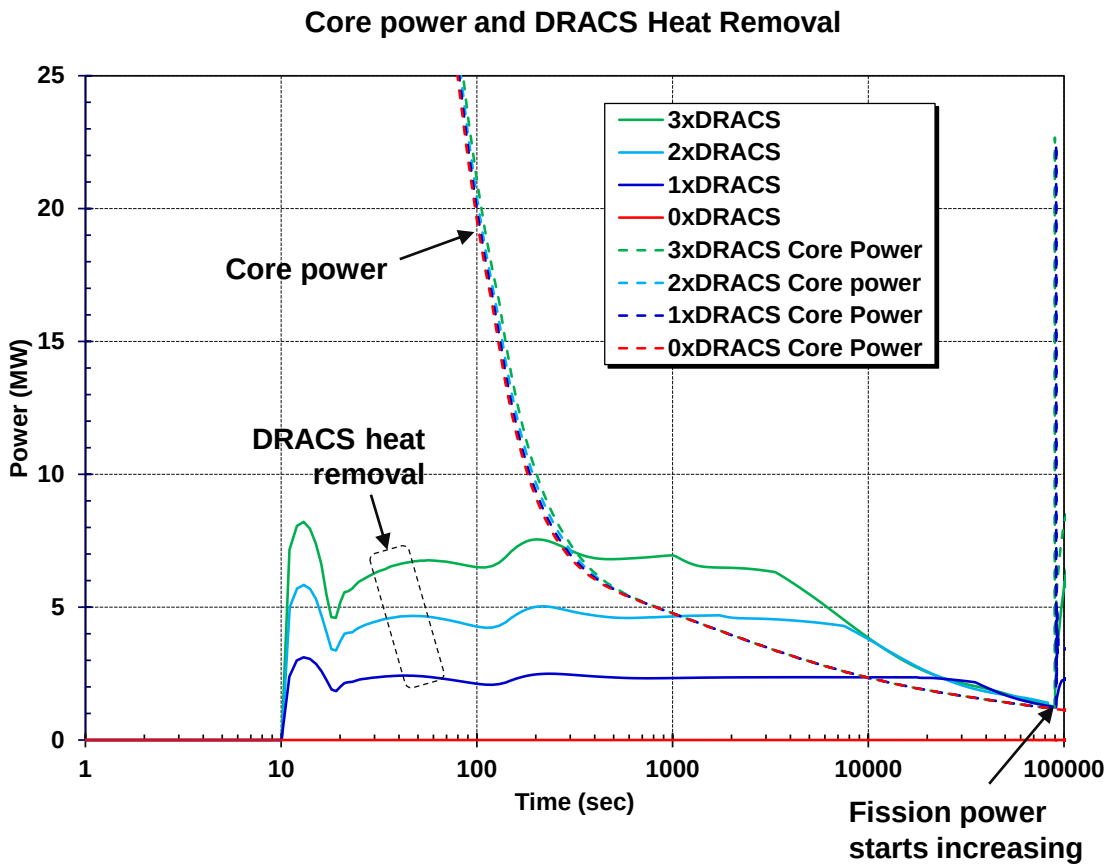

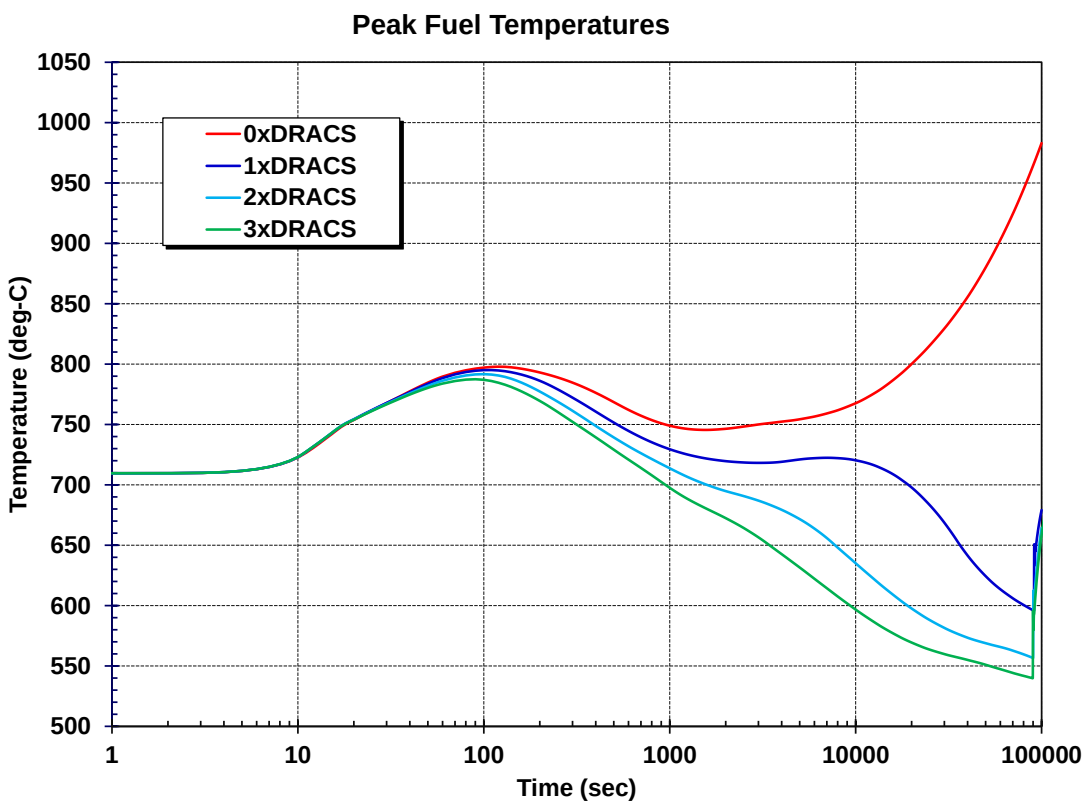

* Xenon transient approximated.

ATWS with variable DRACS – (Linear scale)

When the total reactivity exceeds zero, the core power increases

- Increased power heats the fuel and reduces the positive fuel reactivity
- Core power eventually converges on the DRACS heat removal rate

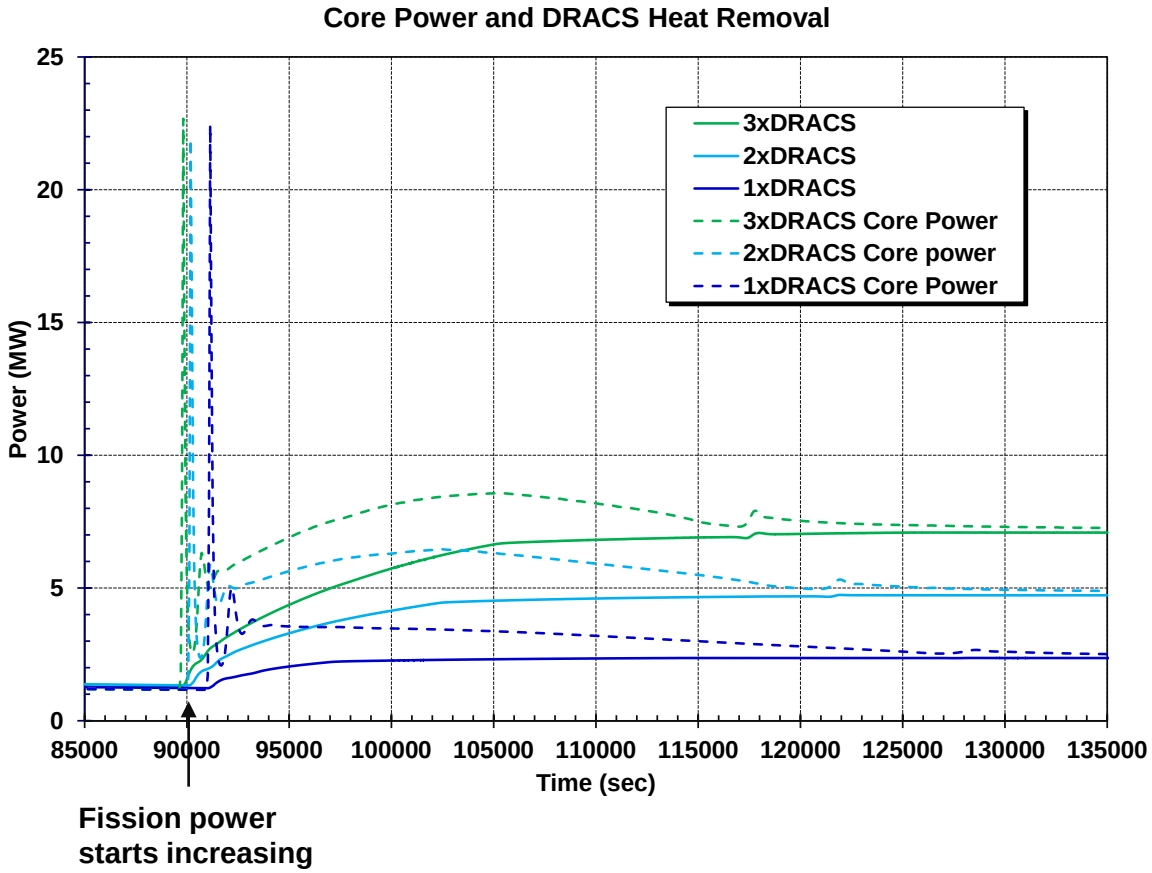

The long-term fuel temperatures increase to offset changes in the xenon feedback

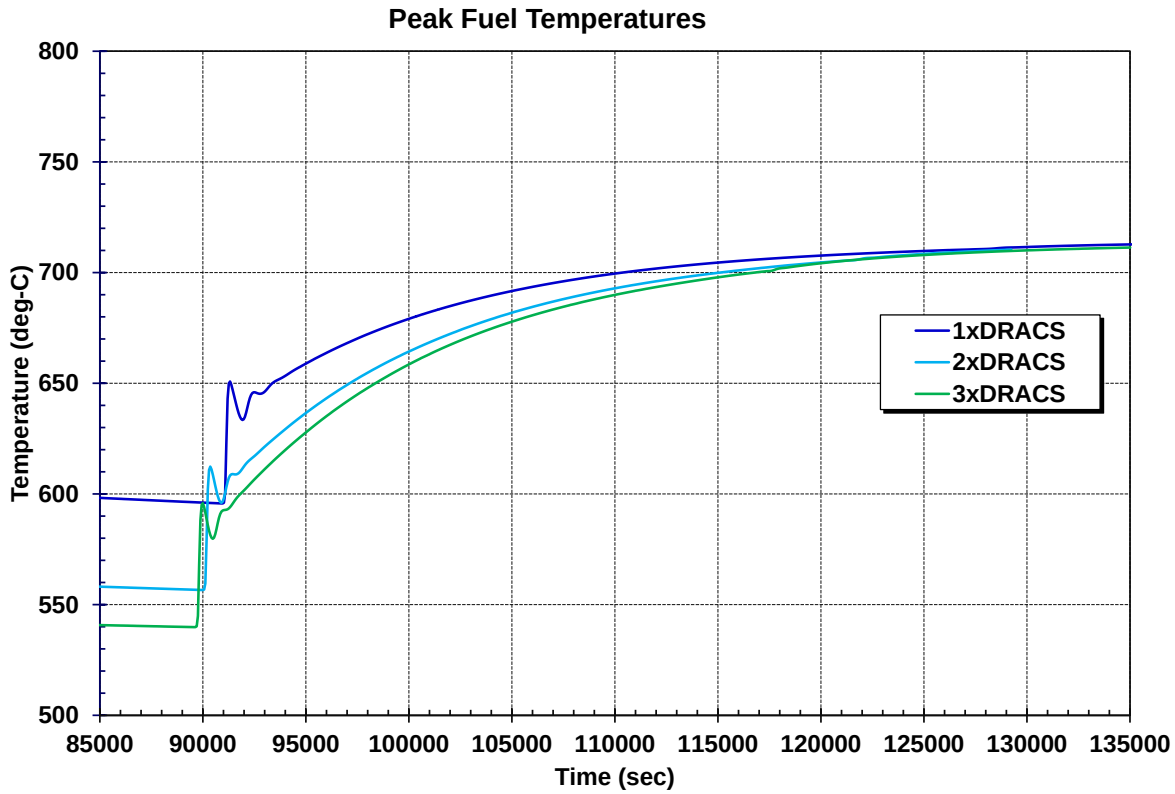

* Xenon transient approximated.

Station Blackout

Loss-of-onsite power with SCRAM

- Salt pumps shut off
- Reactor scrams
- Secondary heat removal ends
- Variable DRACS operating (percentage of 1xDRACS)

Unmitigated sensitivity case

- No DRACS and extended calculation to 7 days

SBO results (1/3)

DRACS cases illustrate degraded response

- Results for fraction of 1xDRACS
- ≥40% of one DRACS stops the temperature rise within 48 hr

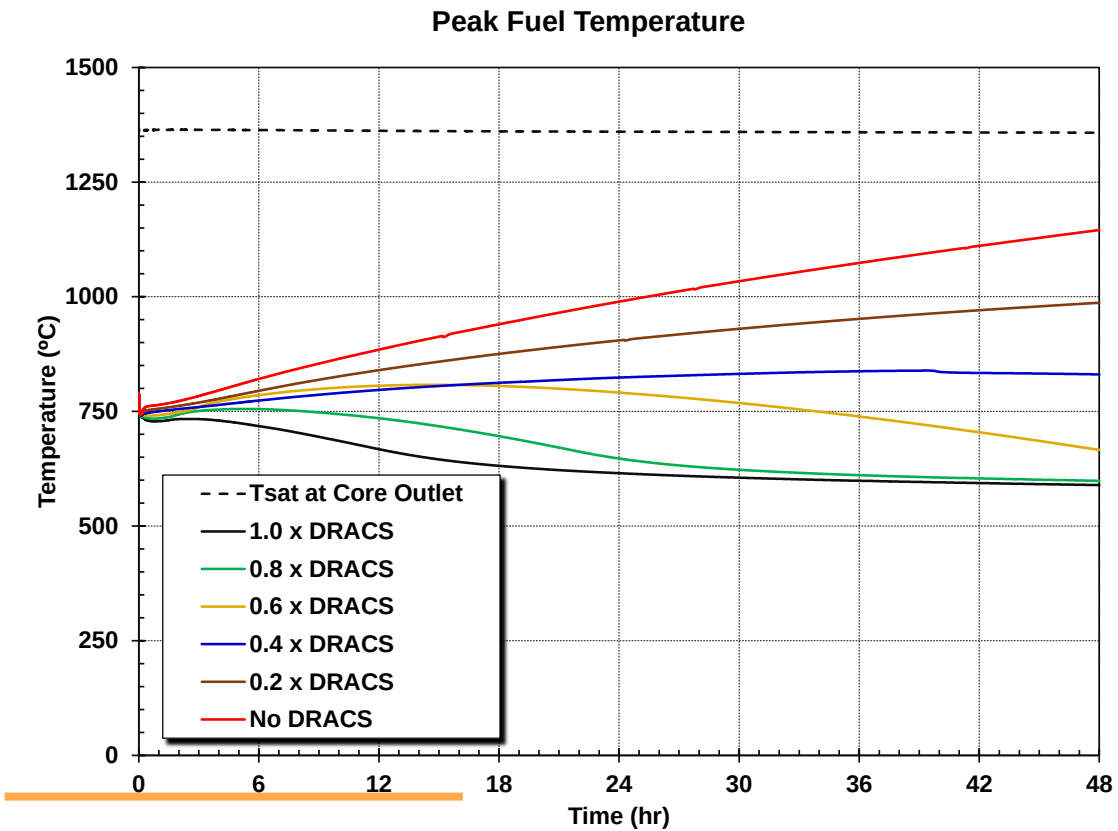

DRACS power follows heat removal requirements

- 1xDRACS exceeds decay heat within 3 hr

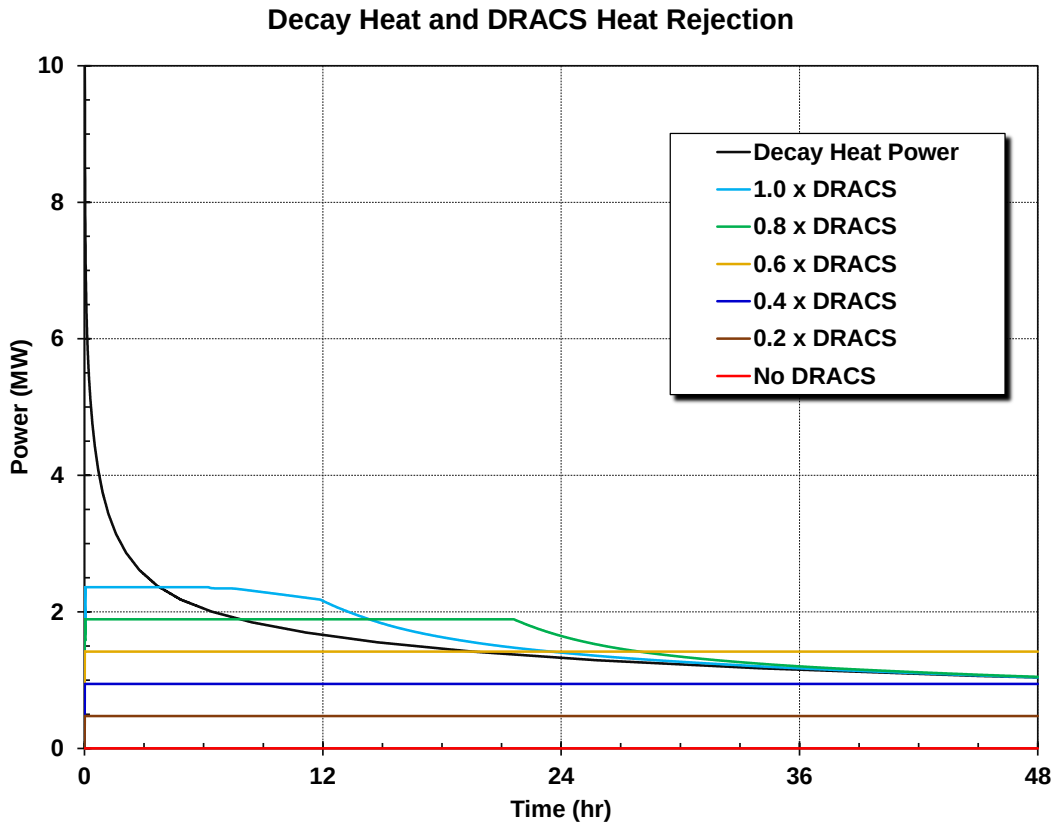

SBO results (2/3)

The TRISO failure fraction remains low ($1x10^{-5}$) in the SBO with one DRACS operating *

- Higher TRISO failures were calculated as the DRACS degrades

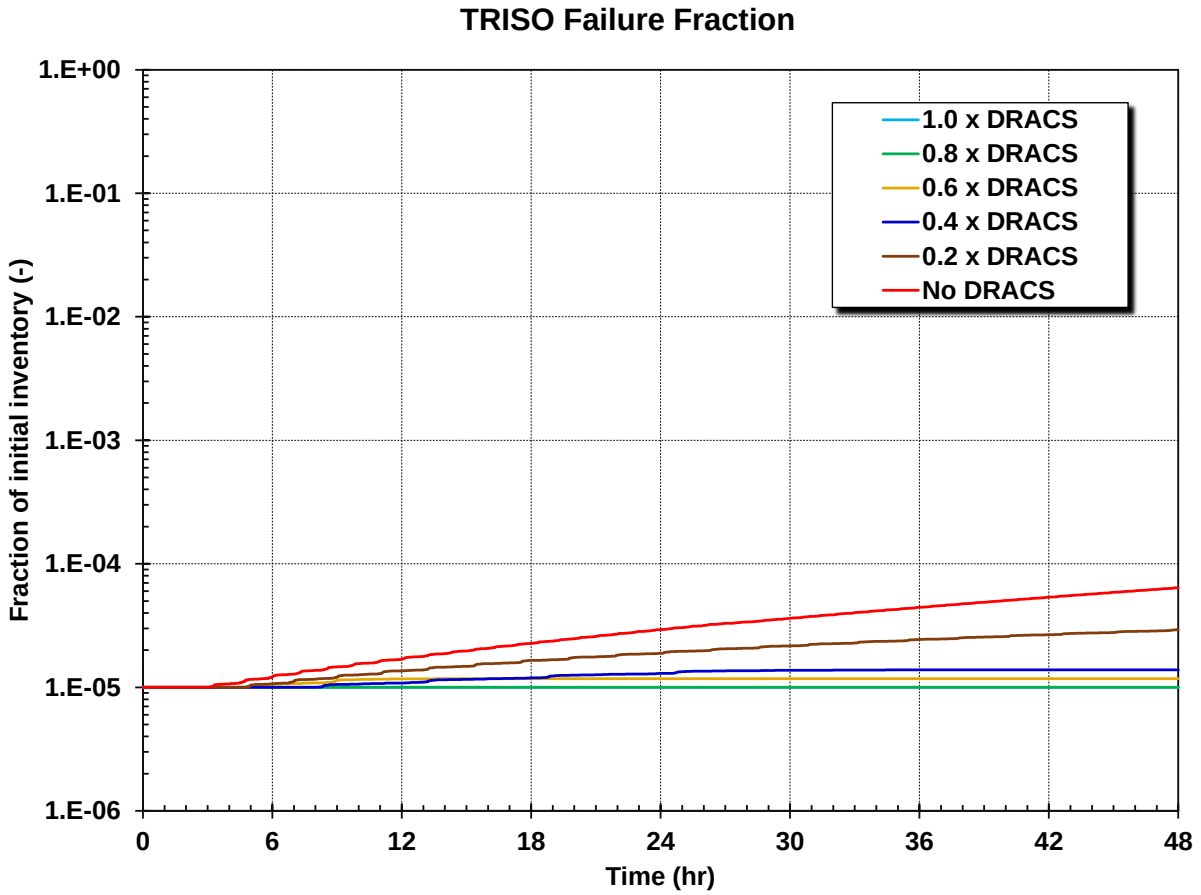

* UCO TRISO thermal failure characteristics were not available, so UO_2 TRISO diffusivity and UO_2 failure data were used. Both are changeable through user input with design-specific data.

SBO results (3/3)

The SBO with no DRACS was extended to 7 days

- No fuel uncovery
- Peak fuel temperature approximately at Tsat (~1350 ºC)

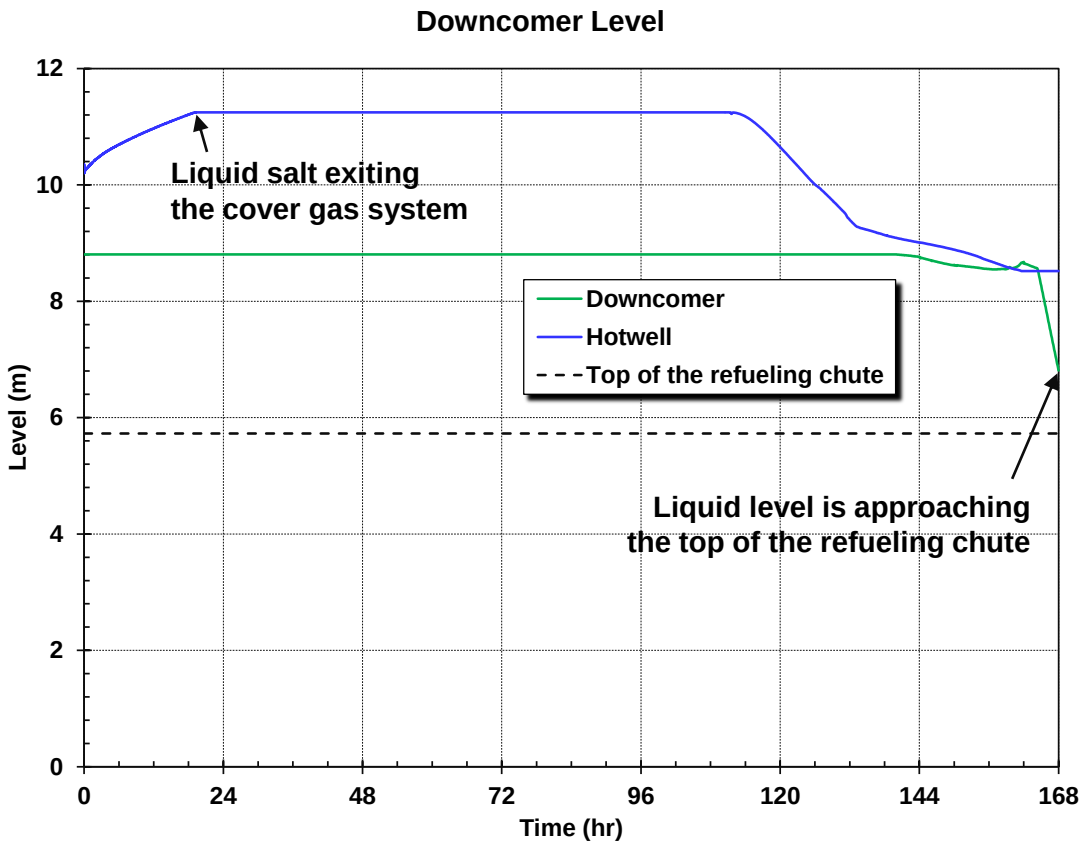

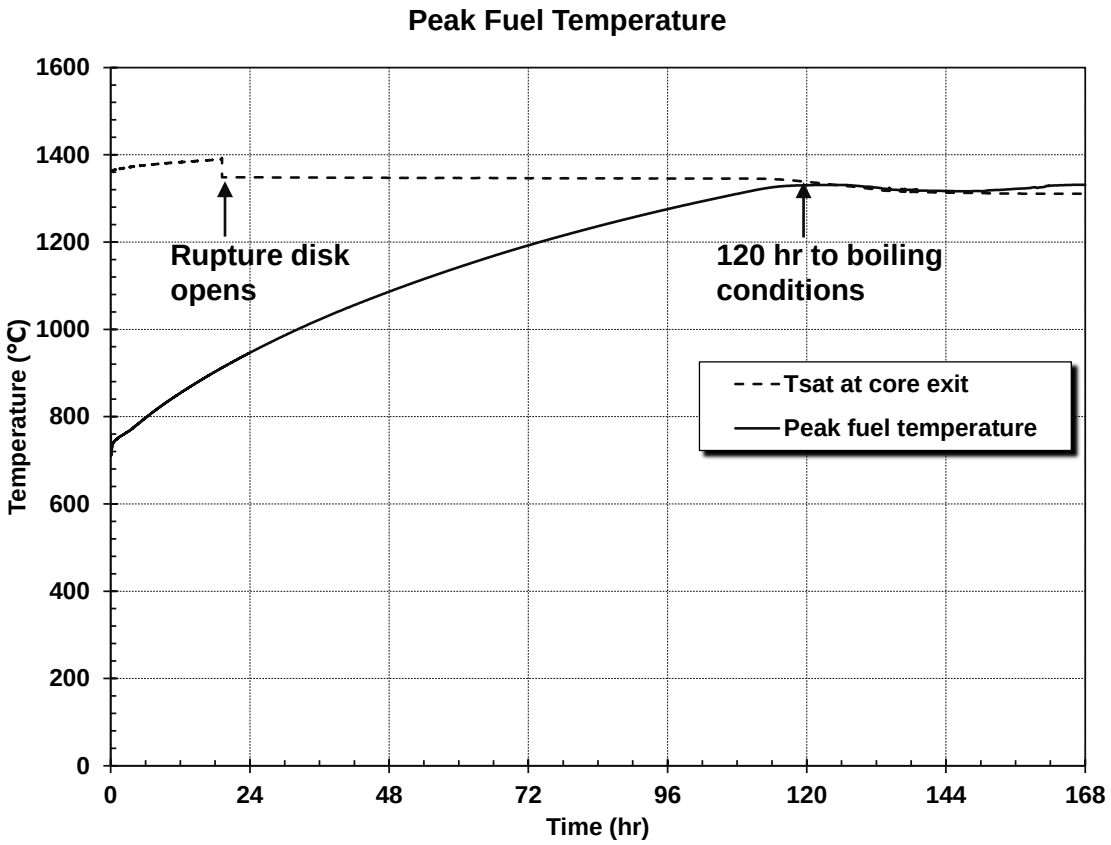

LOCA

Loss-of-onsite power with LOCA

- Variable size leaks of the 3” pipe of the drain tank line
- Salt pumps shut off
- Reactor scrams
- Secondary heat removal ends
- 1 or no trains of DRACS operating
- With or without a cover gas connection path between the hotwell and the standpipes

Unmitigated sensitivity case

- No DRACS case extended to include fuel uncovery

LOCA results (1/6)

10% to 100% LOCA size did not significantly impact vessel boiloff timing

Cover gas connection (+ CG) between hotwell and standpipe prevents siphon

- Stops initial drain down of vessel fluid
- No significant impact on vessel boiloff timing

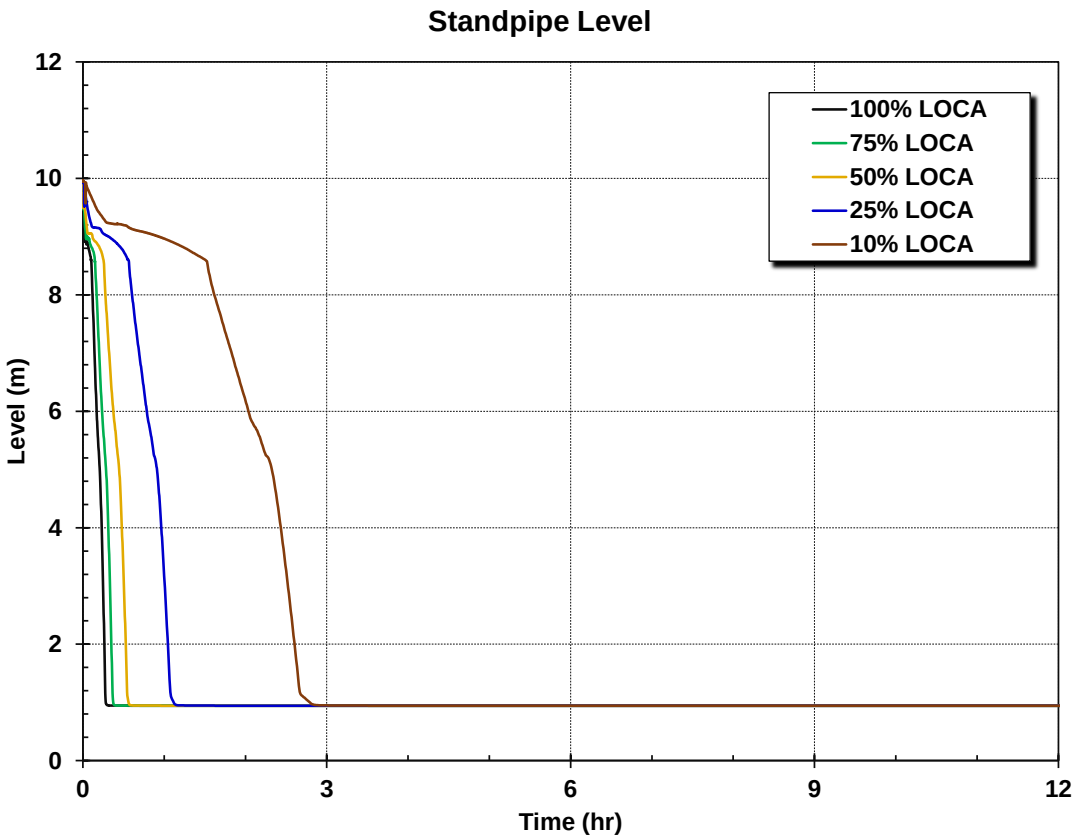

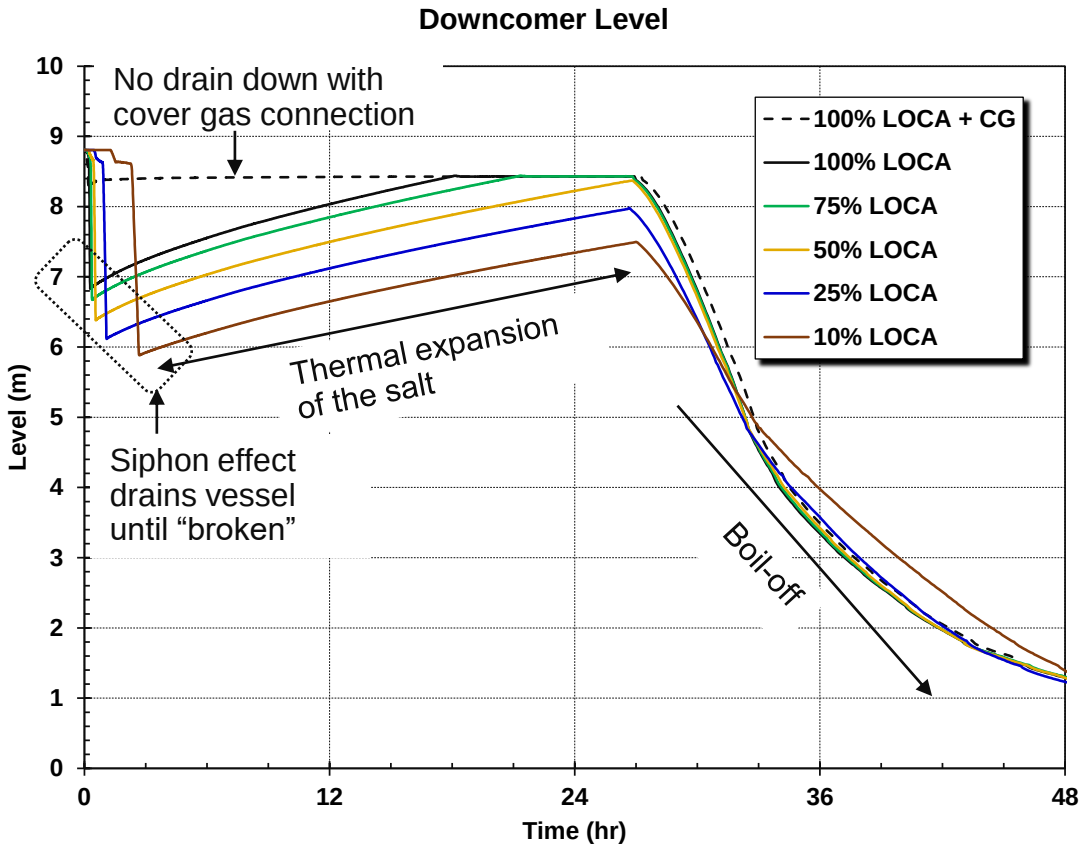

LOCA results (2/6)

Liquid drain down initially creates siphon and then low pressure region

- Causes a level difference between the core and downcomer

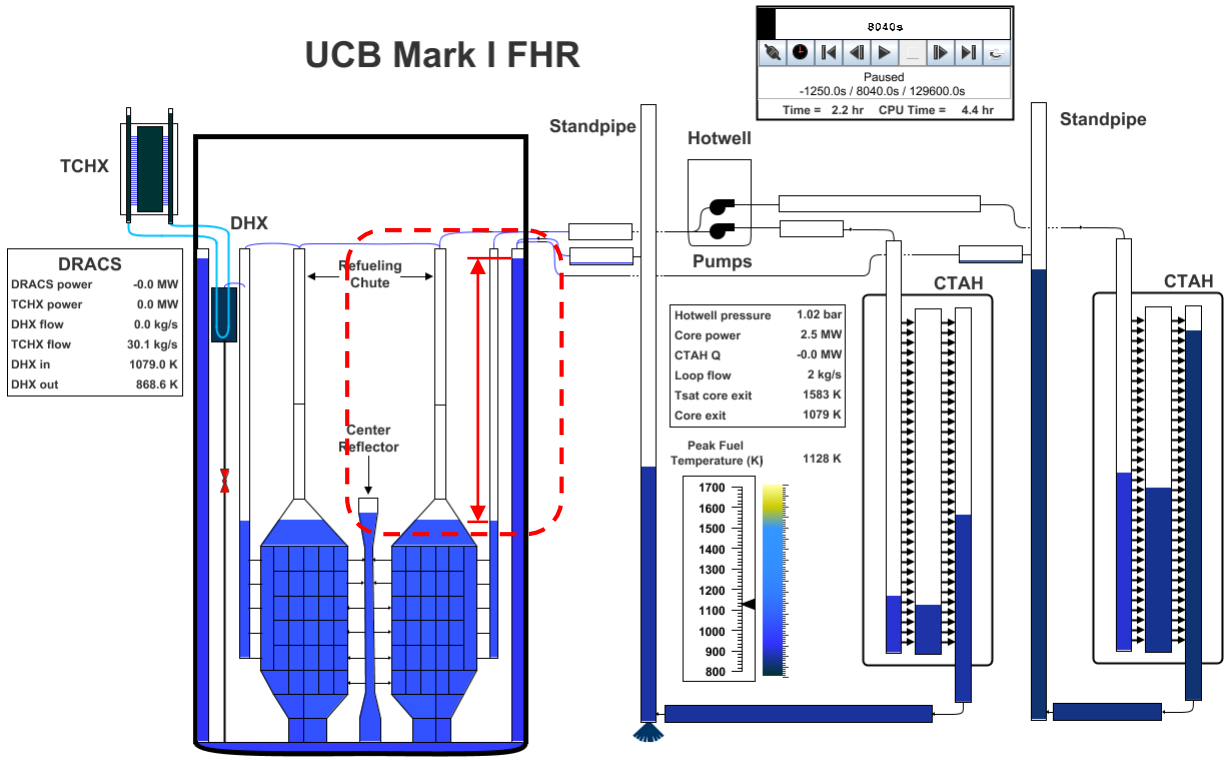

10% LOCA at maximum point in the “siphon”

Core and downcomer levels equilibrate once there is gas flow around the loop

- Standpipe connections to the cover gas system are closed

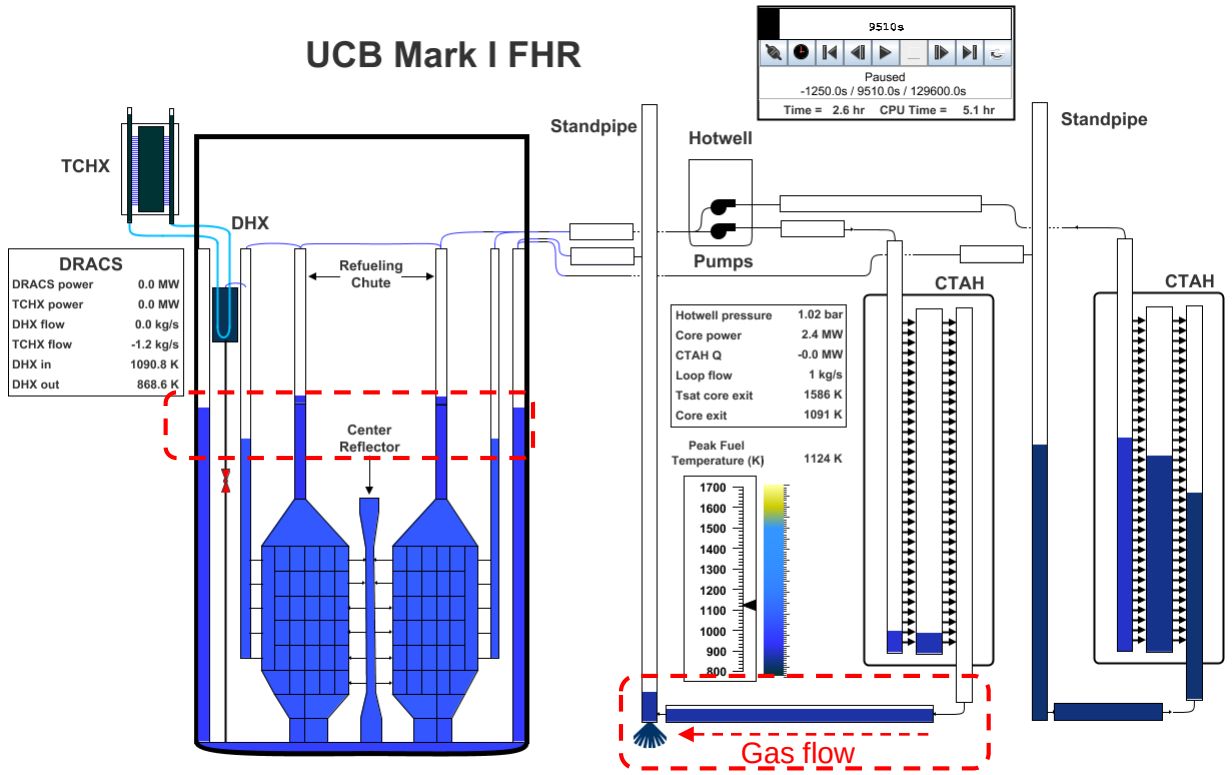

10% LOCA after equilibration

LOCA results (3/6)

LOCA cases without DRACS proceed to fuel uncovery at ~31 hr

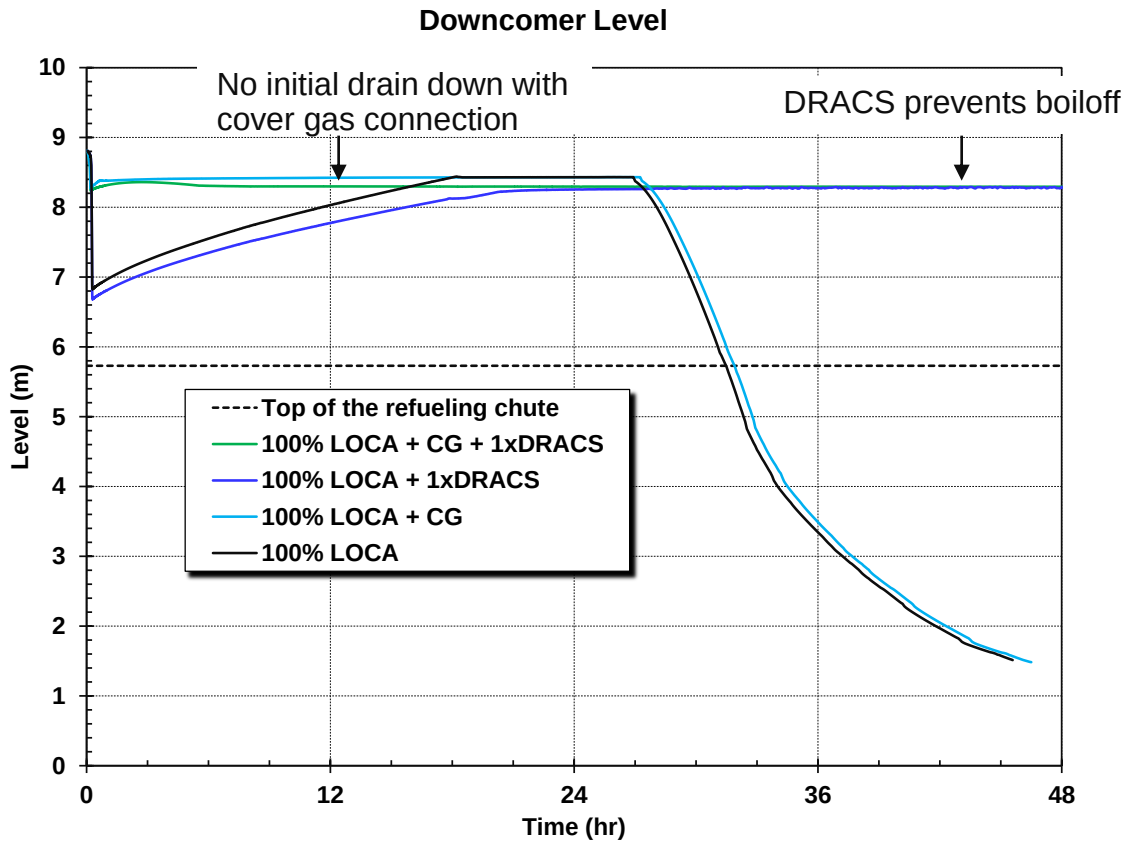

100% LOCA cases

Connection through the cover gas system keeps the DRACS active during the drain down

Without the cover gas connection, the DRACS heat removal is delayed until the salt heats and expands

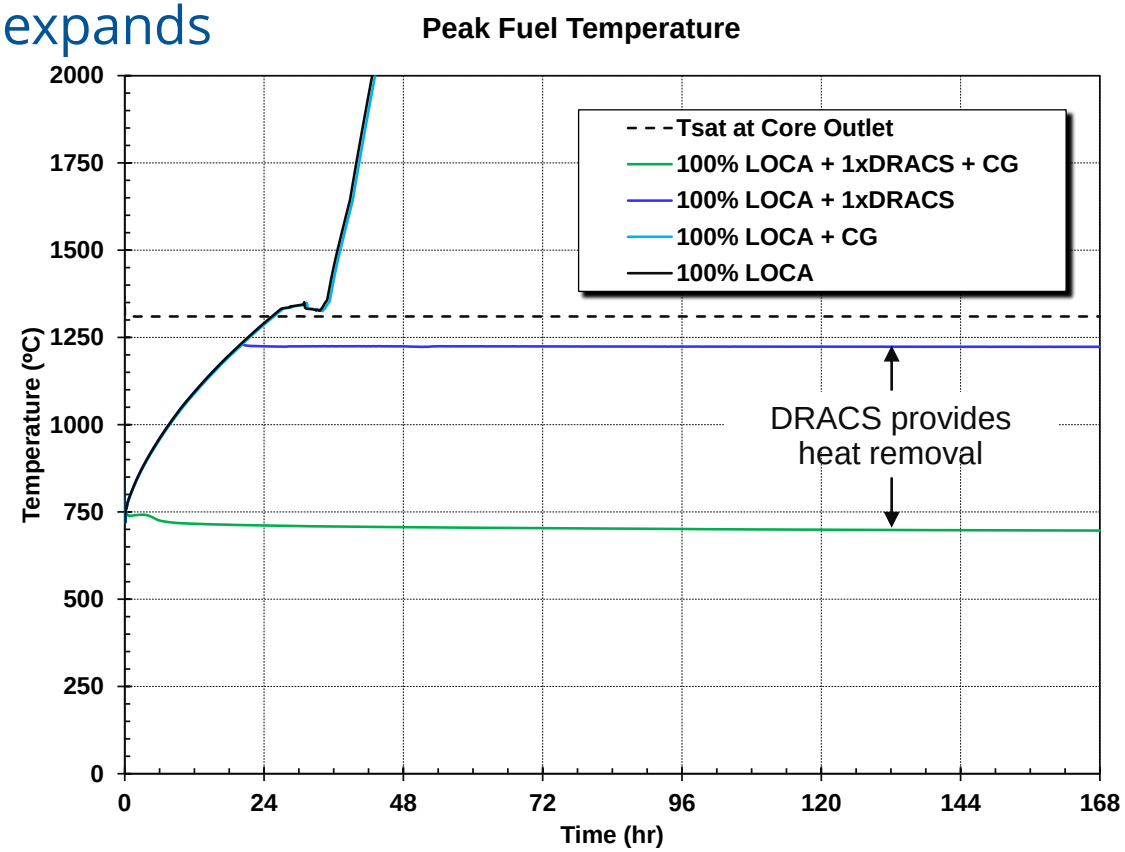

100% LOCA cases

LOCA results (4/6)

We terminated the calculation at ~54 hr peak when the fuel kernel melting starts

- Reactor vessel wall and core barrel below the steel melting temperature
- Residual molten salt keeps the bottom level (level 1) at T_{sat}
- Upper vessel wall cools after downcomer salt level drops
- Pebbles and reflectors below graphite sublimation temperature (3600°C)

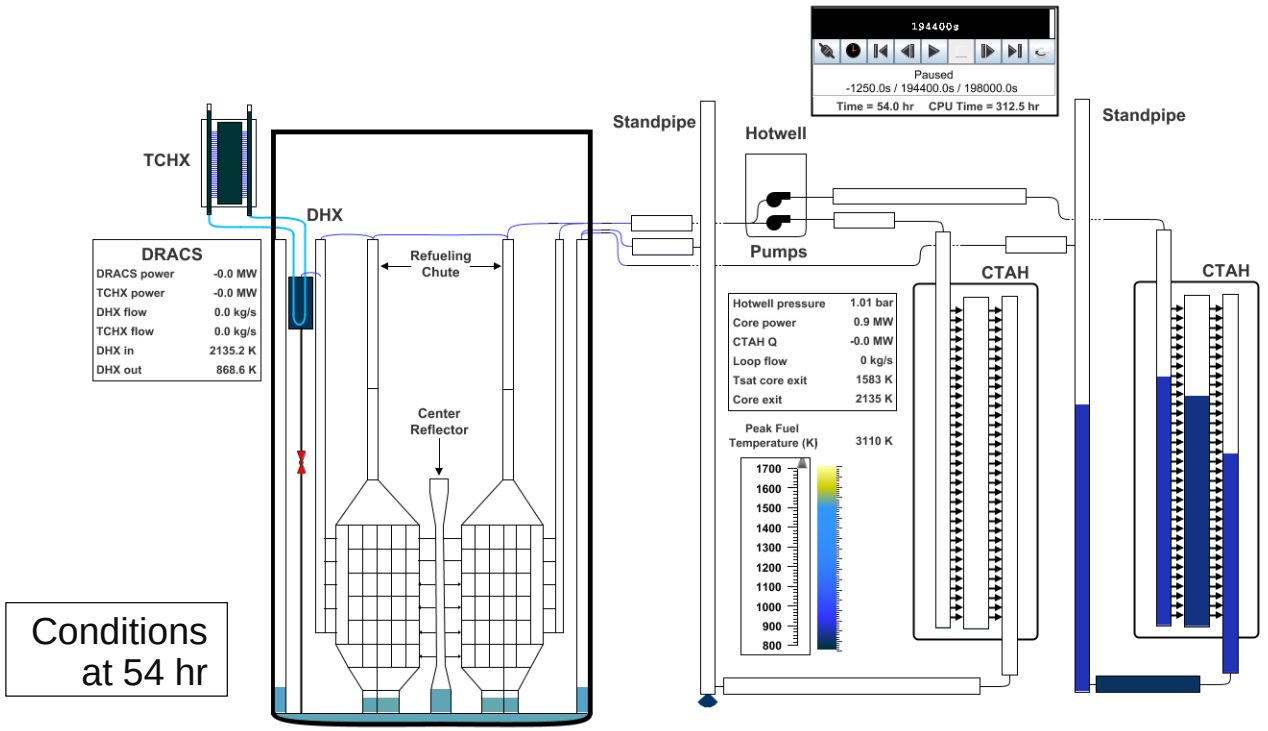

Conditions at 54 hr

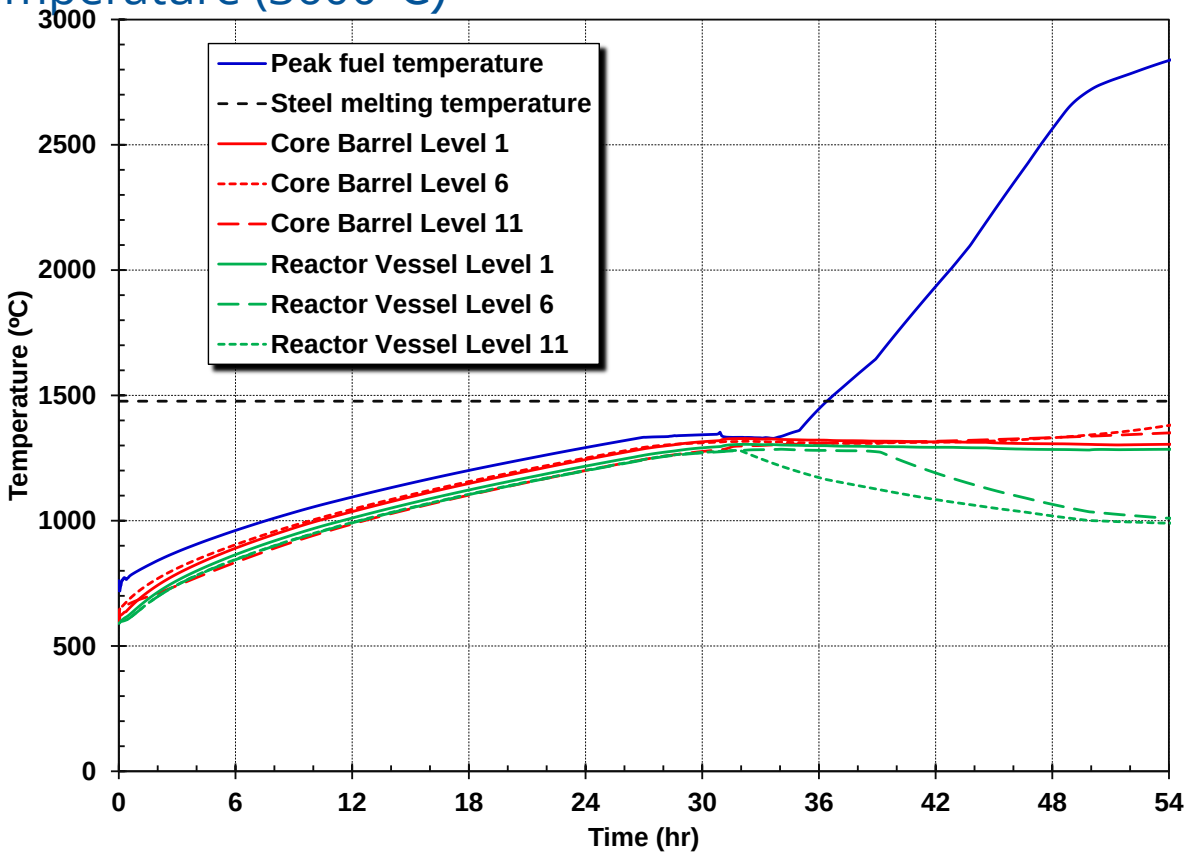

LOCA results (5/6)

TRISO failure rate extrapolated from available UO_2 TRISO data

- Correlation is based on data to 1800°C
- Initial failures set to 10-5 (0.001%)
- 0.017% of the TRISOs failed at 34 hr
- 7.5% of the TRISOs failed at 54 hr

Low failure rate when $<T_{sat}$

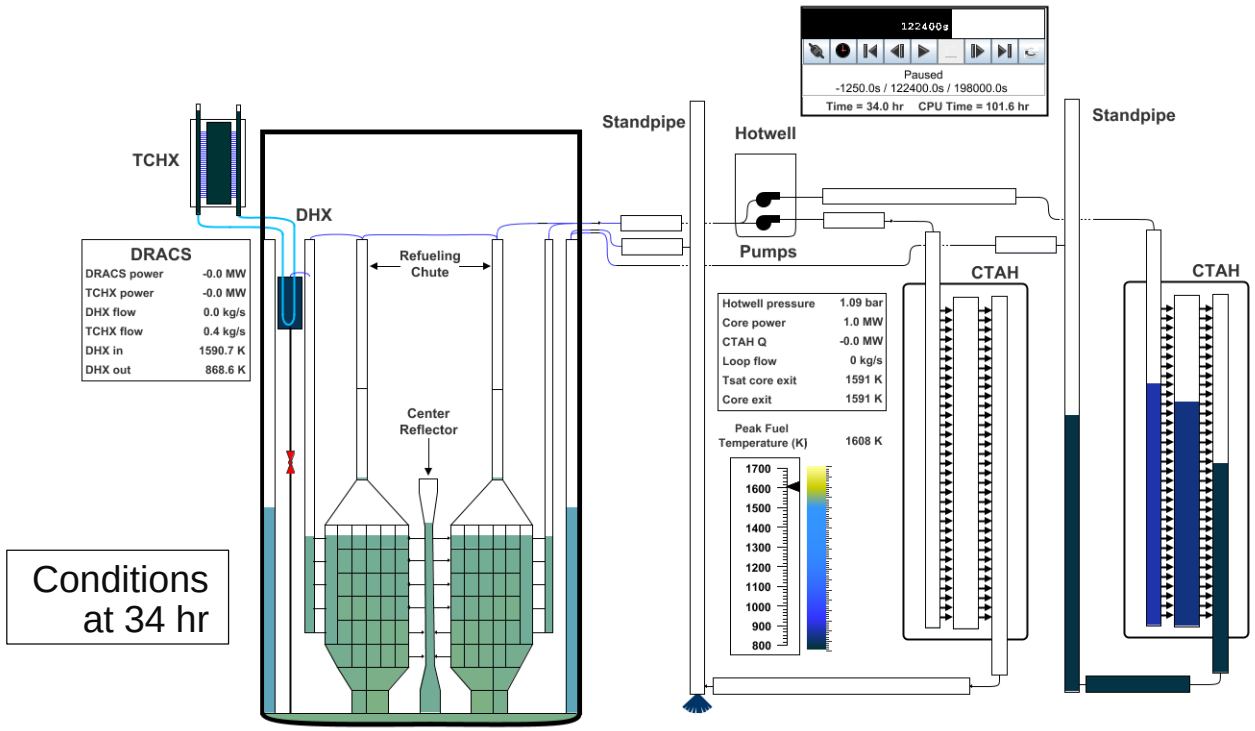

Conditions at 34 hr

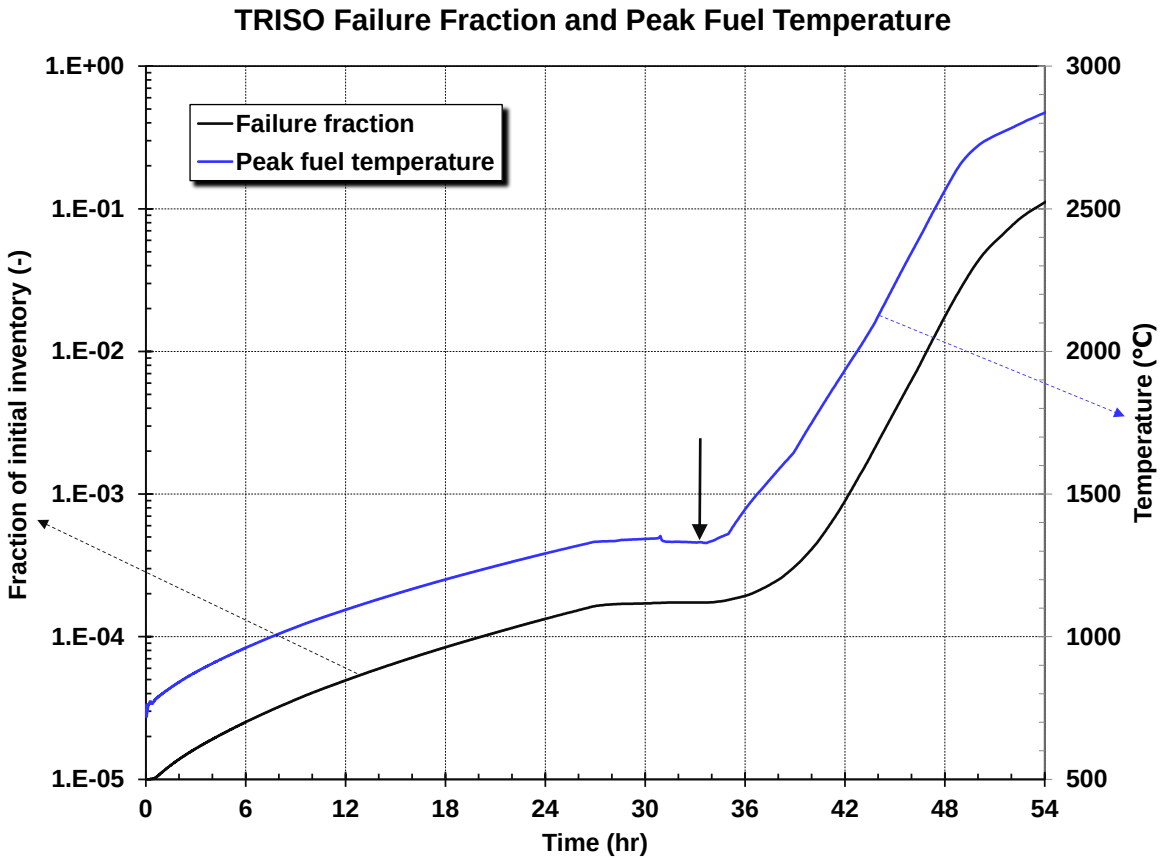

Note:
** Fuel used thermal-physical properties of UO_2.

LOCA results (6/6)

Most of the fission product release from fuel is retained in the containment

- Assumed hole size equivalent to 100% volume per day at 0.25 psig (8.7 in^2)

The radionuclide distribution is affected by the timing of the release from the TRISO

- Cesium release from the pebbles to the liquid molten salt starts earlier at lower fuel temperatures
- Most aerosols leaving the primary system settle in the containment

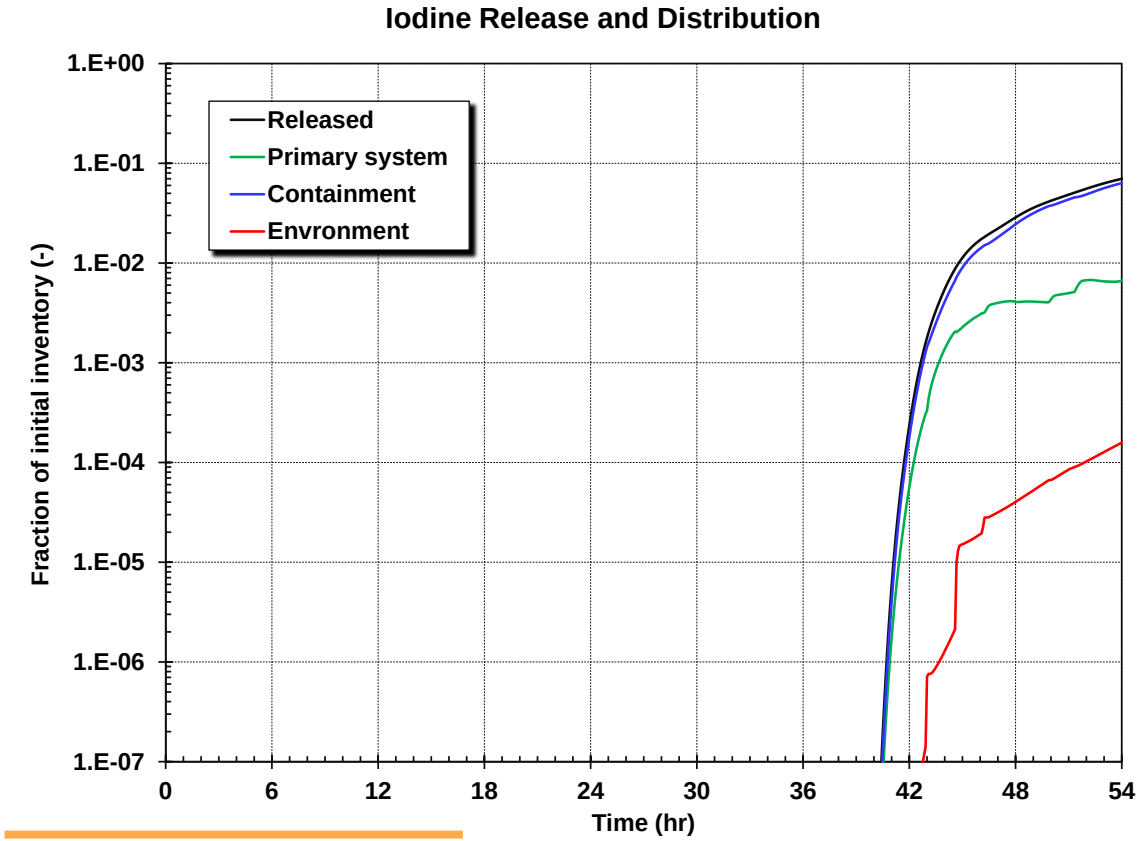

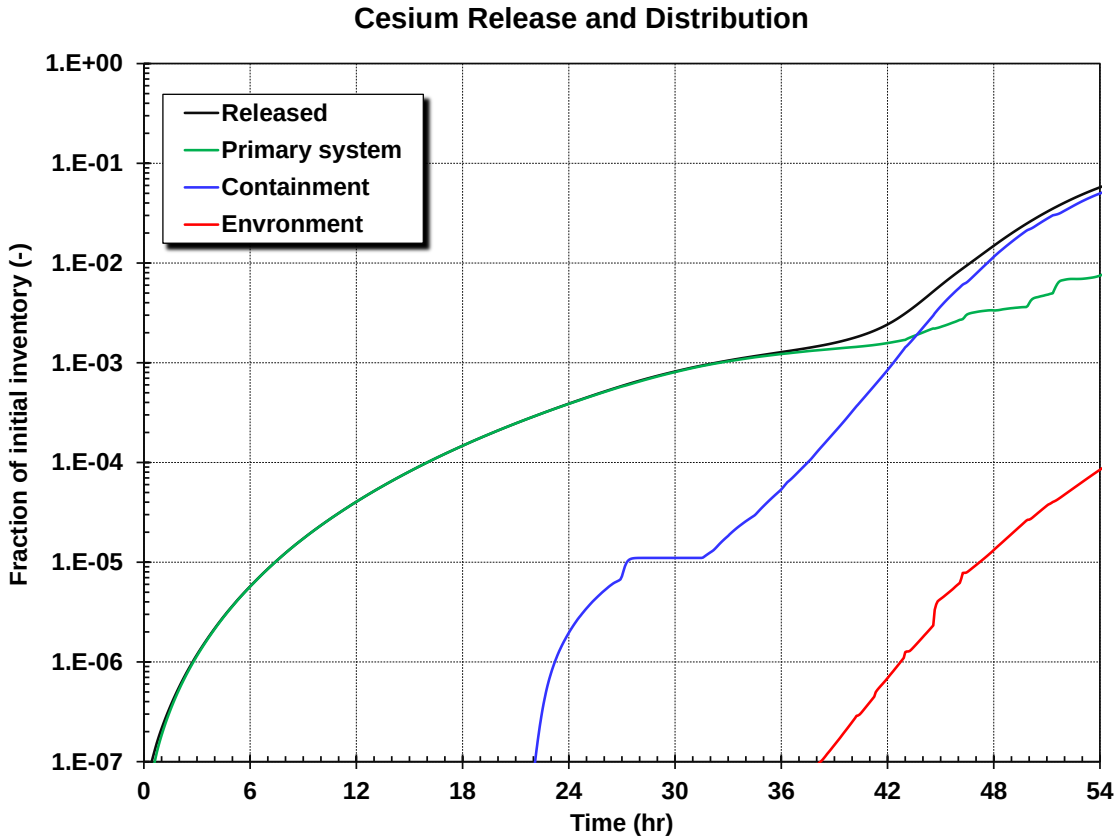

Cesium vaporization from the molten salt

Molten salt chemistry and radionuclide release model calculates cesium and cesium fluoride release to the gas spaces

- Results use OECD/NEA JRC database for Thermochimica *
- Includes vapor phase data for CsF

LOCA sequence

- No accelerated steady state
- No core uncovery through 24 hr
  - Cesium releases are from pebbles → liquid → gas

Model shows Cs/CsF vaporization to gas spaces at higher temperatures

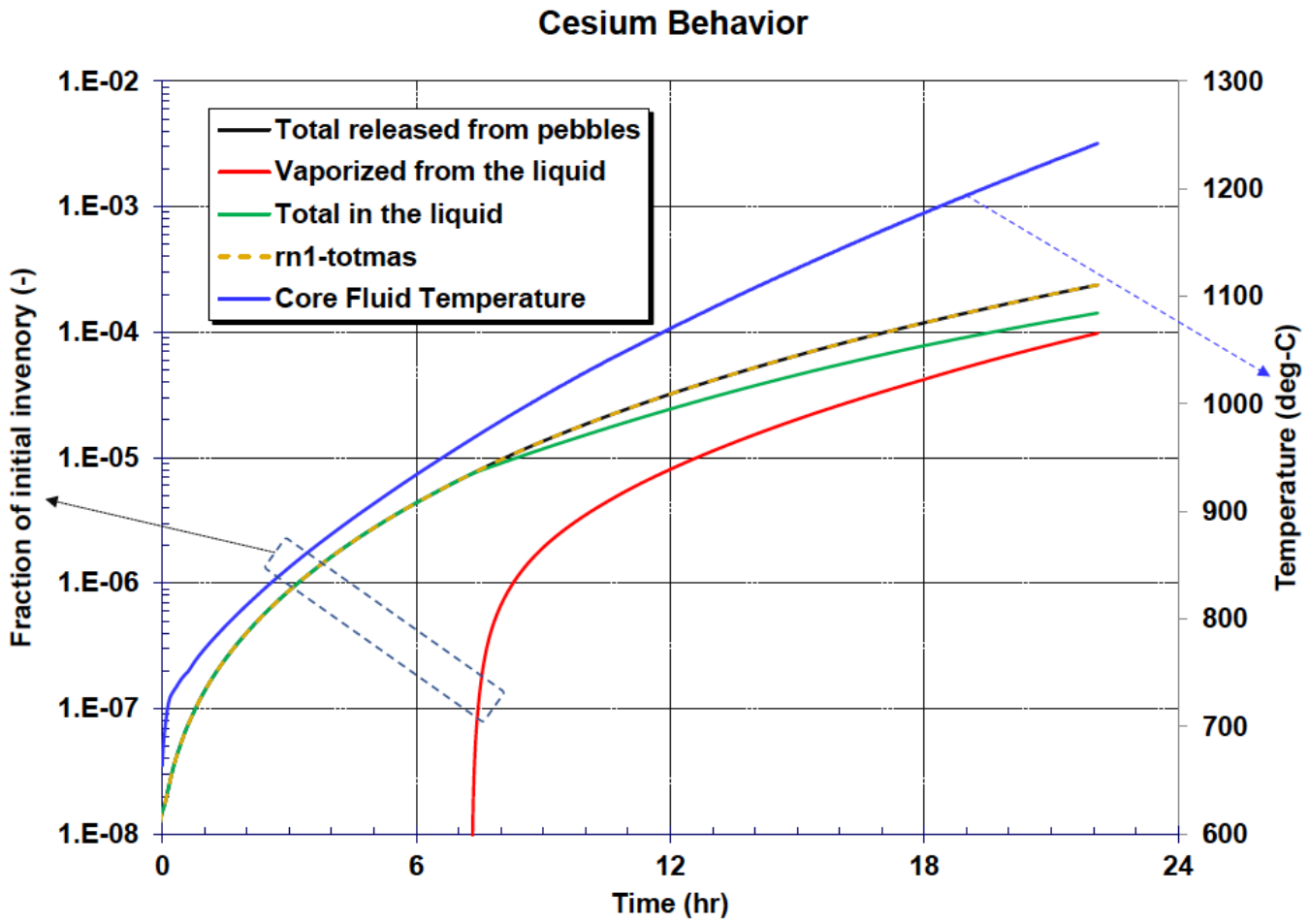

* With modifications by Ontario Tech.

Sandia National Laboratories

Securing the future of Nuclear Energy

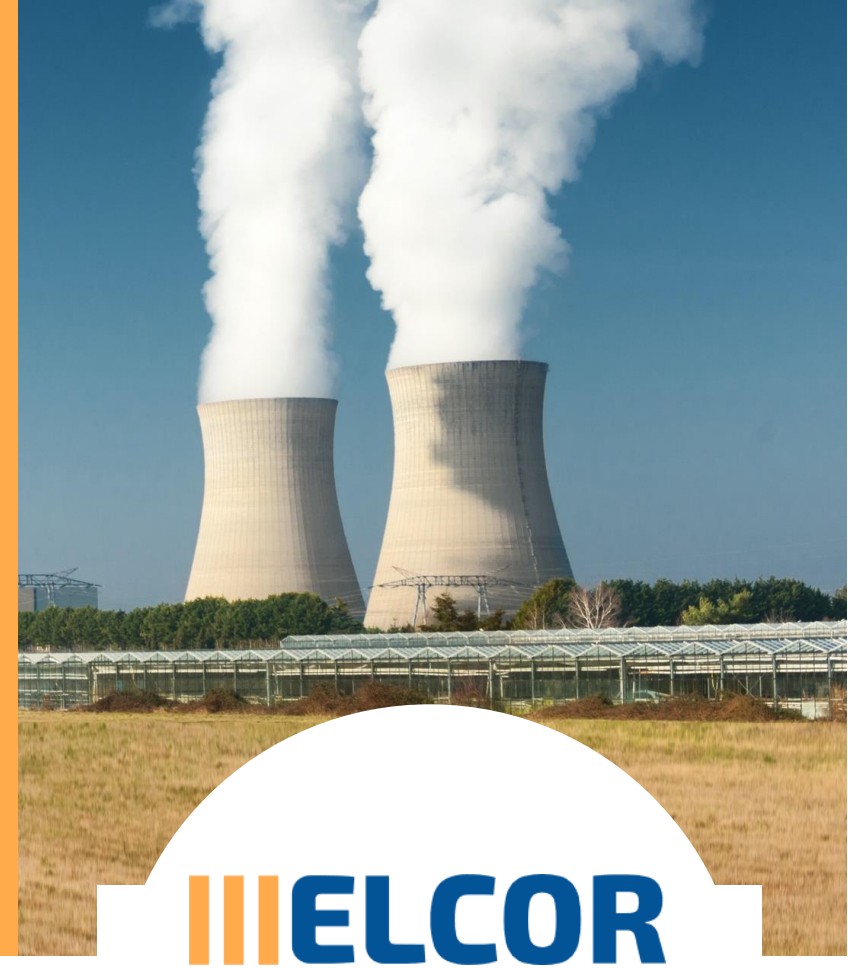

ELCOR

Thanks for your attention!

Sandia National Laboratories is a multimission laboratory managed and operated by National Technology and Engineering Solutions of Sandia, LLC., a wholly owned subsidiary of Honeywell International, Inc., for the U.S. Department of Energy's National Nuclear Security Administration under contract DE-NA0003525.

Transient/Accident Solution Methodology

ELCOR

Stage 0:
Normal Operation
Establish thermal state

Time constant in FHR graphite structures is very large

Reduce heat capacities for structures to reach steady state thermal conditions.

Reset heat capacities after steady state is achieved.

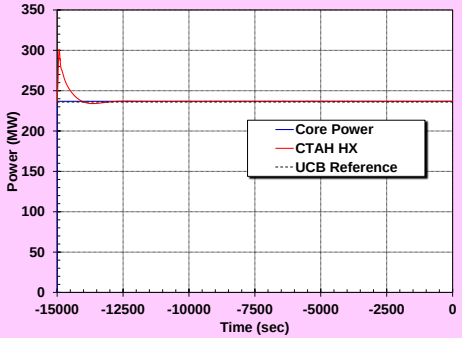

Stage 1:
Normal Operation
Diffusion Calculation

Establish steady state distribution of radionuclides <u>in TRISO particles, and matrix</u>

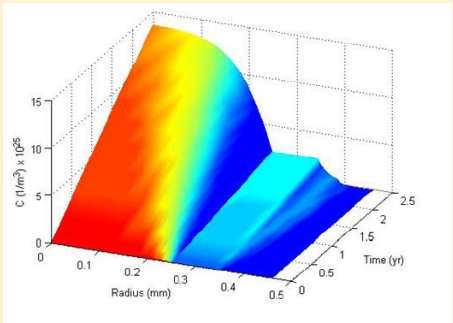

Stage 2:
Normal Operation
Transport Calculation

Calculate steady state distribution of radionuclides <u>into the molten salt</u> (formation of soluble, colloidal fission products, deposition on surfaces, convection through flow paths)

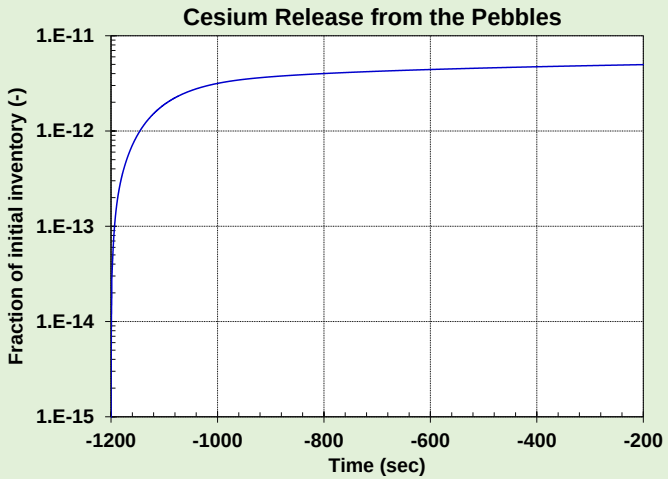

Stage 3:
Accident
Diffusion & Transport calculation

Calculate accident progression and radionuclide release

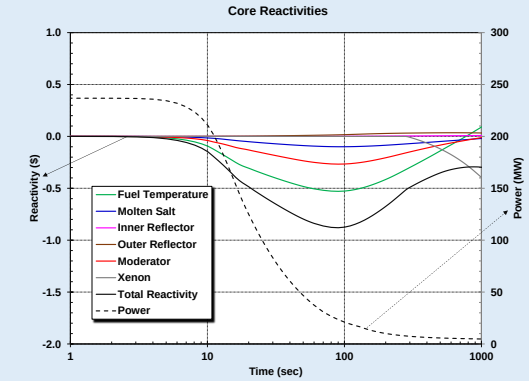

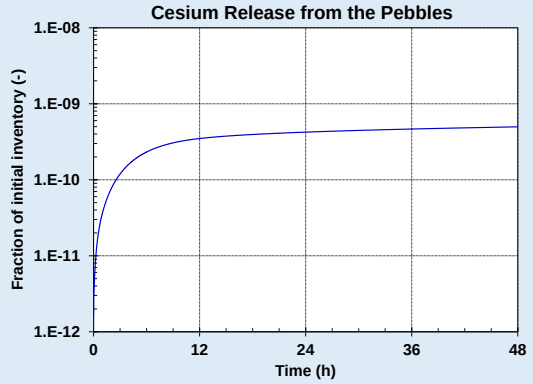

Core components

- Pebble Bed Reactor Fuel/Matrix Components
  - Fueled part of pebble
  - Unfueled shell (matrix) is modeled as separate component
  - Fuel radial temperature profile for sphere

Fueled pebble core

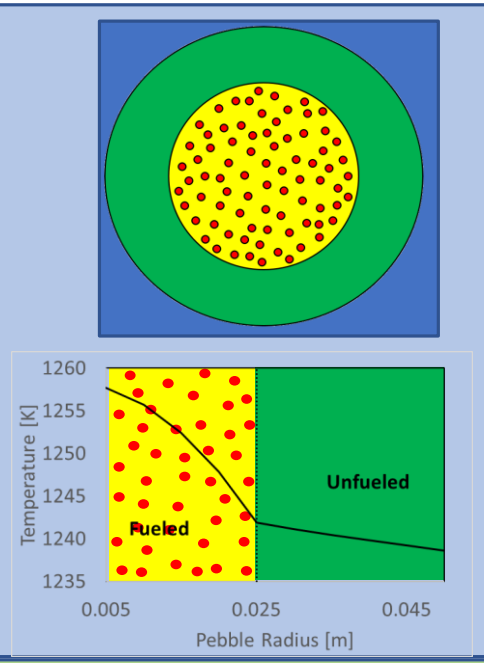

Unfueled pebble core

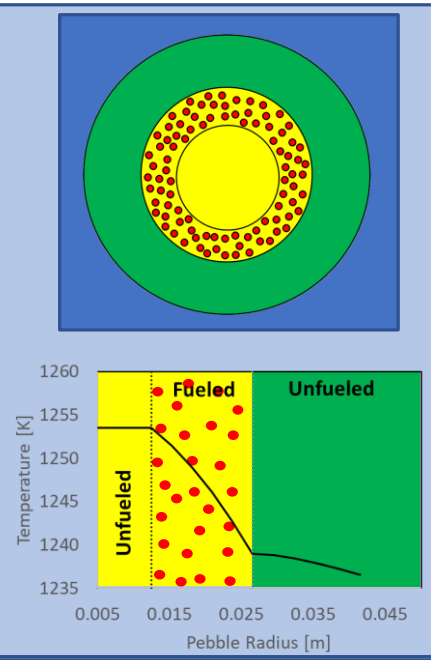

- Prismatic Modular Reactor Fuel/Matrix Components
  - "Rod-like" geometry
  - Part of hex block associated with a fuel channel is matrix component
  - Fuel radial temperature profile for cylinder

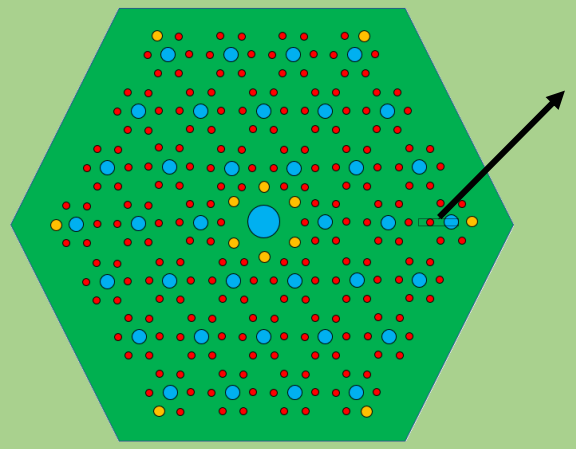

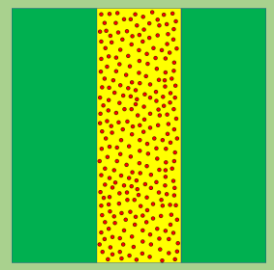

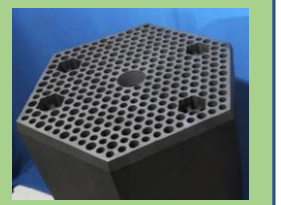

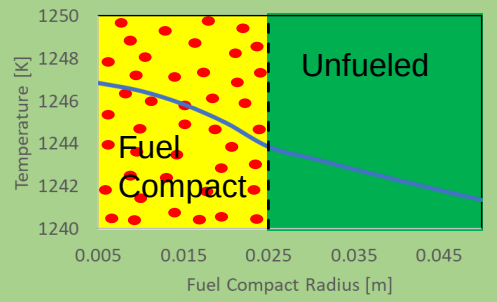

ELCOR

Legend

TRISO
GRAPHITE
Fuel (FU)
GRAPHITE
Matrix (MX)
Fluid B/C

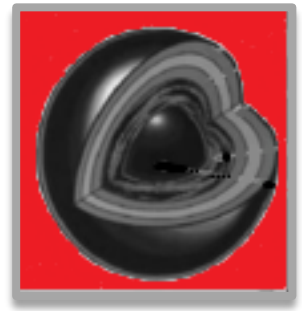

TRISO (FU)

Sub-component model for zonal diffusion of radionuclides through TRISO particle

Radionuclide Release Models

- Recent failures – particles failing within latest time-step (burst release, diffusion release in time-step)
- Previous failures – particles failing on a previous time-step (time history of diffusion release)
- Contamination and recoil

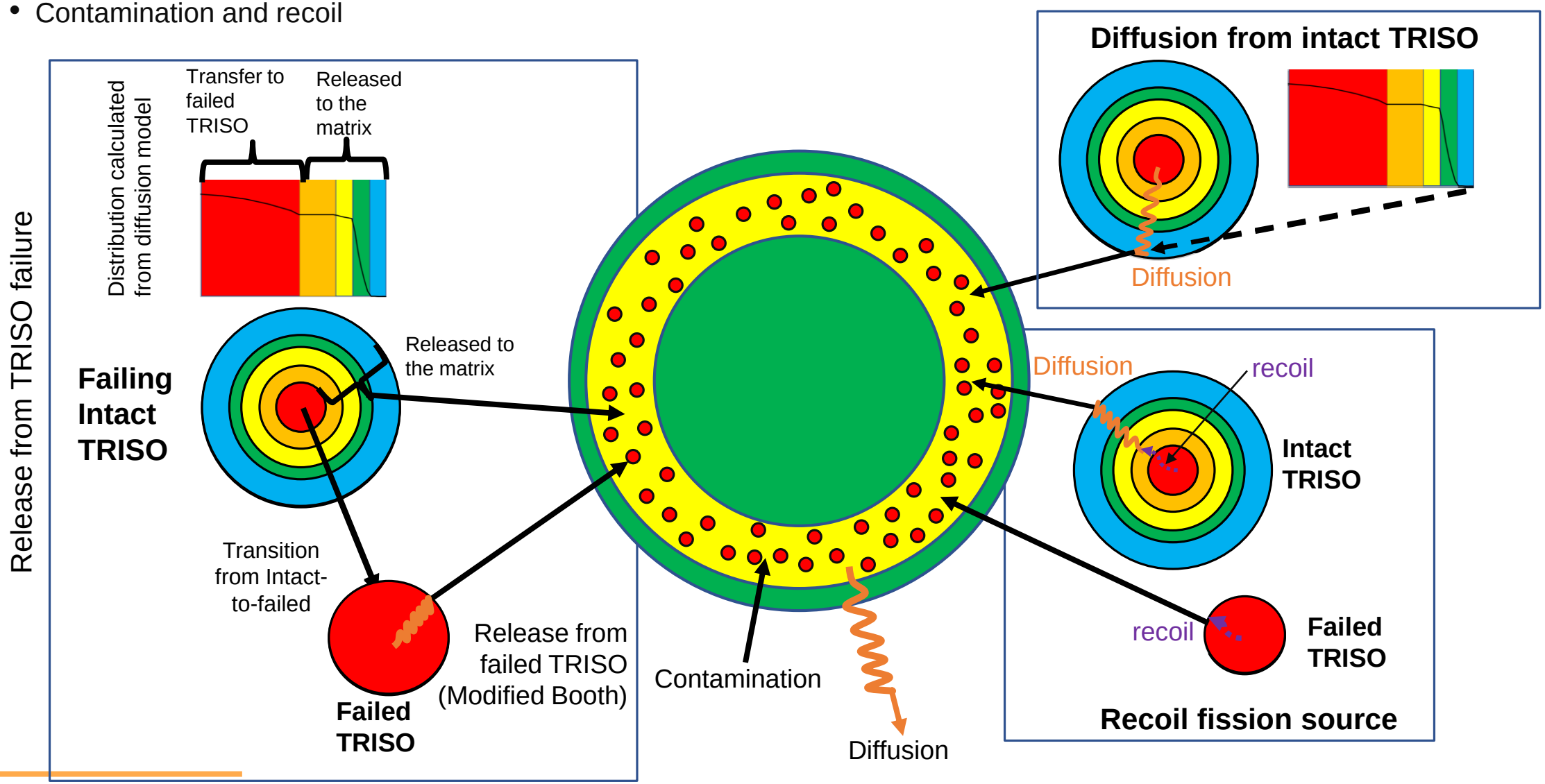

Radionuclide Diffusion Release Model

Intact TRISO Particles

- One-dimensional finite volume diffusion equation solver for multiple zones (materials)
- Temperature-dependent diffusion coefficients (Arrhenius form)

$$\frac{\partial C}{\partial t} = \frac{1}{r^n}\frac{\partial}{\partial r}\left(r^n \boldsymbol{D}\frac{\partial C}{\partial r}\right) - \lambda C + \beta \qquad D(T) = D_0 e^{-\frac{Q}{RT}}$$

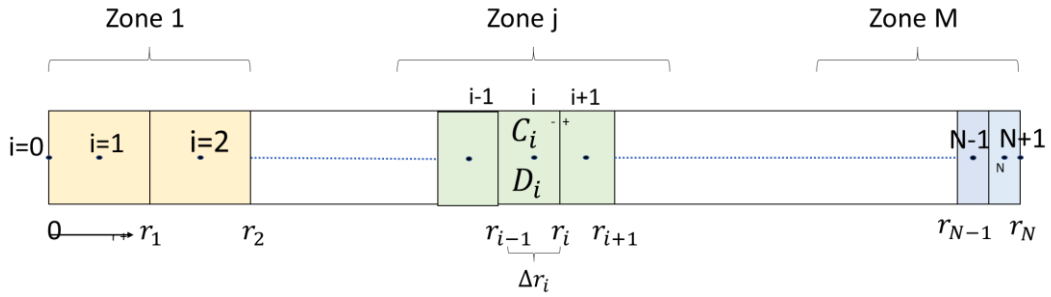

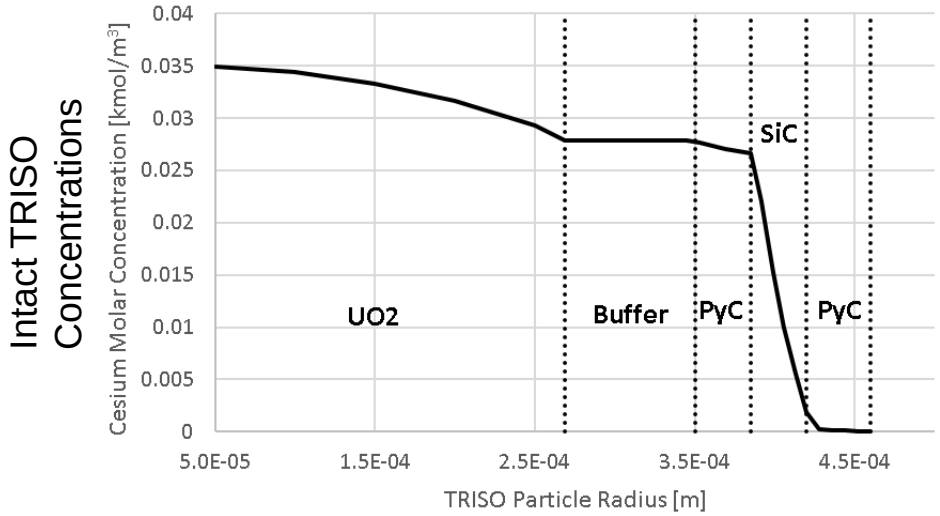

Diffusivity Data Availability

Radionuclide	UO_2	UCO	PyC	Porous Carbon	SiC	Matrix Graphite	TRISO Overall
Ag	Some	Not investigated	Some	Not found	Extensive	Some	Extensive
Cs	Some		Some		Extensive	Some	Some
I	Some		Some		Some	Not found	Not found
Kr	Some		Some		Not found	Some	Some
Sr	Some		Some		Extensive	Some	Some
Xe	Some		Some		Some	Some	Not found

Data used in the demo calculation

[IAEA TECDOC-0978]

	FP Species							
	Kr		Cs		Sr		Ag	
Layer	D (m^2/s)	Q (J/mole)	D (m^2/s)	Q (J/mole)	D (m^2/s)	Q (J/mole)	D (m2/s)	Q (J/mole)
Kernel (normal)	1.3E-12	126000.0	5.6-8	209000.0	2.2E-3	488000.0	6.75E-9	165000.0
Buffer	1.0E-8	0.0	1.0E-8	0.0	1.0E-8	0.0	1.0E-8	0.0
PyC	2.9E-8	291000.0	6.3E-8	222000.0	2.3E-6	197000.0	5.3E-9	154000.0
SiC	3.7E+1	657000.0	7.2E-14	125000.0	1.25E-9	205000.0	3.6E-9	215000.0
Matrix Carbon	6.0E-6	0.0	3.6E-4	189000.0	1.0E-2	303000.0	1.6E00	258000.0
Str. Carbon	6.0E-6	0.0	1.7E-6	149000.0	1.7E-2	268000.0	1.6E00	258000.0

Iodine assumed to behave like Kr

Point Kinetics Modeling

ELCOR

Standard treatment

$$\frac{dP}{dt} = \left(\frac{\rho - \beta}{\Lambda}\right) P + \sum_{i=1}^{6} \lambda_i Y_i + S_0$$

$$\frac{dY_i}{dt} = \left(\frac{\beta_i}{\Lambda}\right) P - \lambda_i C_i, \qquad for\ i = 1 \ldots 6$$

Feedback models

- User-specified external input
- FHR example includes multiple feedbacks
  - Fuel
  - Molten salt around the fuel
  - Inner reflector
  - Outer reflector and unfueled pebbles
  - Moderator (matrix around fueled pebbles)

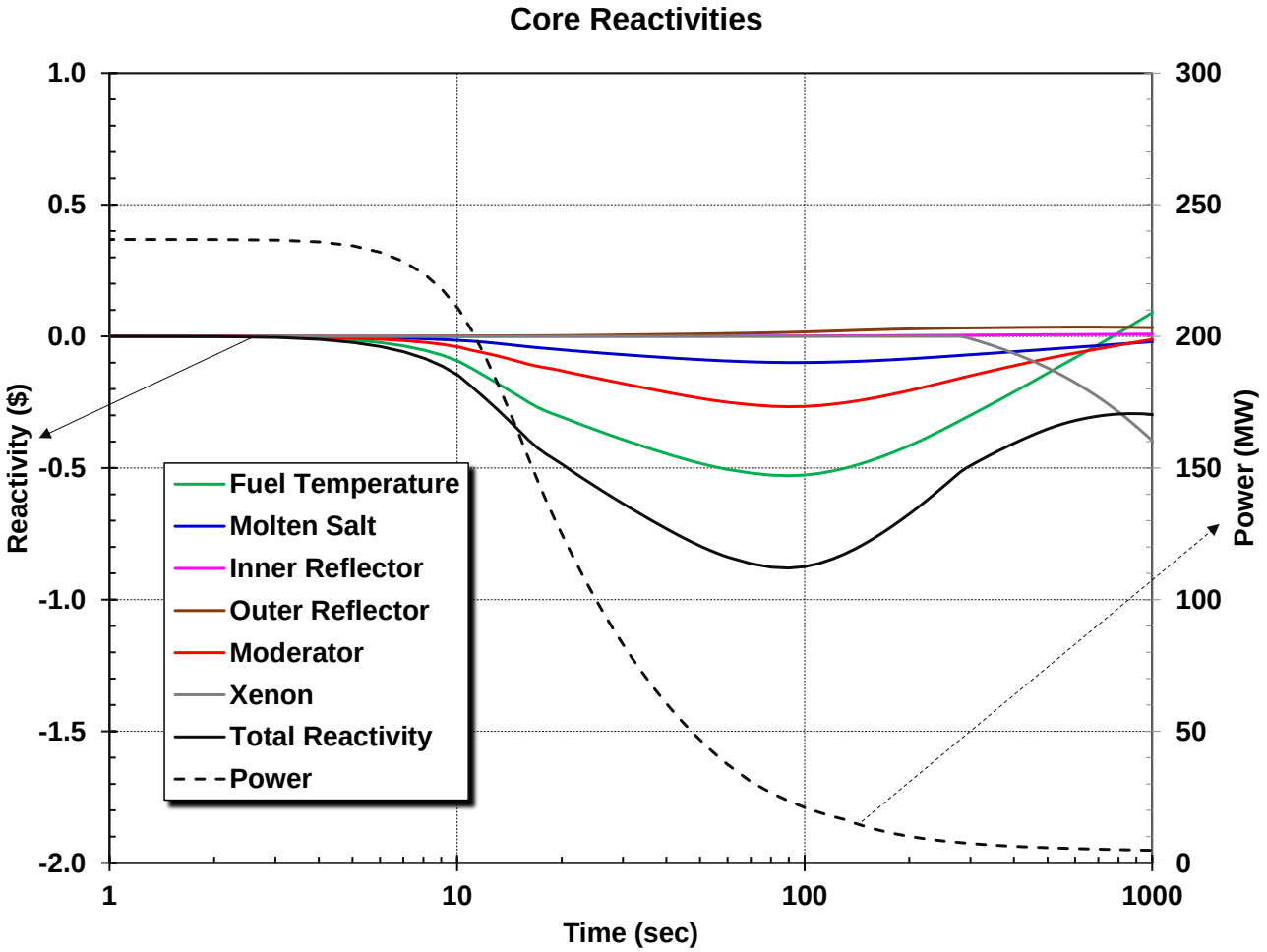

Point Kinetics Modeling (MSR)

Derived from standard PRKEs and solved similarly

$$\frac{dP(t)}{dt} = \left(\frac{\rho(t) - \bar{\beta}(t)}{\Lambda}\right) P(t) + \sum_{i=1}^{6} \lambda_i C_i^C(t) + S_0$$

$$\frac{dC_i^C(t)}{dt} = \left(\frac{\beta_i}{\Lambda}\right) P(t) - \left(\lambda_i + {}^{2}/_{\tau_C}\right) C_i^C(t) + \left(\frac{V_L}{V_C}\right) \left(\lambda_i + {}^{2}/_{\tau_L}\right) C_i^L(t), \qquad i = 1 \ldots 6$$

$$\frac{dC_i^L(t)}{dt} = \left(\frac{V_C}{\tau_C V_L}\right) C_i^C(t) - \left(\lambda_i + {}^{1}/_{\tau_L}\right) C_i^L(t), \qquad i = 1 \ldots 6$$

$$\bar{\beta}(t) = \beta - \beta(t)_{lost} = \beta - \left(\frac{\Lambda}{P(t)}\right) \sum_{i=1}^{6} \lambda_i C_i^L(t)$$

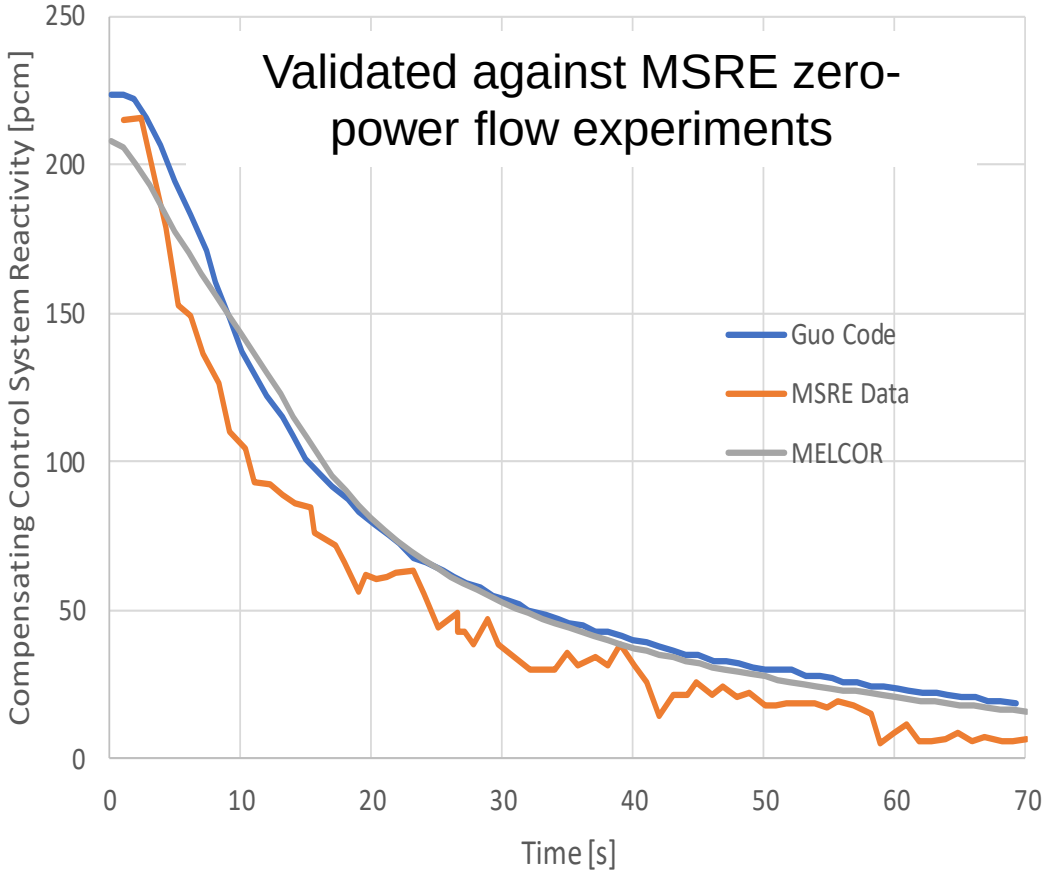

Feedback models

- User-specified external input
- Doppler
- Fuel and moderator density
- Flow reactivity feedback effects integrated into the equation set

Graphite Oxidation

Existing capability introduced with High-Temperature Gas-cooled Reactors (HTGRs)

Steam oxidation

$$R_{OX,steam} = \frac{k_4 P_{H_2O}}{1 + k_5 P_{H_2}^{0.5} + k_6 P_{H_2O}}$$

Reactions

$C + H_2O(g) \rightarrow CO(g) + H_2(g)$
$CO(g) + H_2O(g) \rightarrow CO_2(g) + H_2(g)$

Air oxidation

$$R_{OX} = 1.7804x10^4 \exp\left(-\frac{20129}{T}\right)\left(\frac{P}{0.21228x10^5}\right)^{0.5}$$

Reactions

1. $C + O_2 \rightarrow CO_2(g)$
2. $C + \frac{1}{2}O_2 \rightarrow CO(g)$
3. $CO(g) + \frac{1}{2}O_2(g) \rightarrow CO_2(g)$
4. $C + CO_2(g) \rightarrow 2CO(g)$

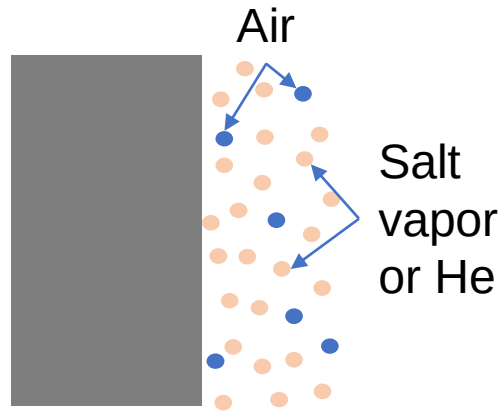

Air diffusion towards oxidation surface is rate limited due to mass transfer limitations in presence of salt vapor

R_{OX} is the rate term in the parabolic oxidation equation [1/s]

Energy Transport between Discrete Core Volumes

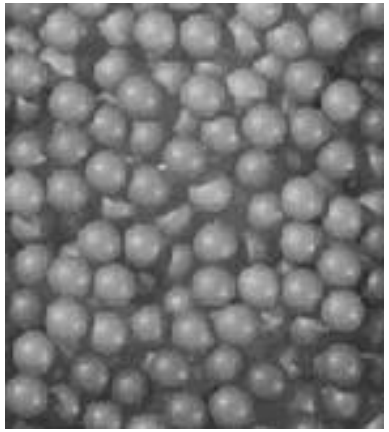

Effective conductivity prescription for pebble bed (bed conductance)

- Zehner-Schlunder-Bauer, without radiation heat transfer

$$k_{eff} = \left(1 - \sqrt{1-\varepsilon}\right)k_f + \left(\sqrt{1-\varepsilon}\right)k_c\left(T, \varepsilon, k_f, k_s\right)$$

where:

ε = Bed porosity [-]

k_f = Fluid (FLiBe) conductivity [W/m/K]

k_c = Effective bed conductivity [W/m/K], used with zero radiative conductivity

k_s = Solid conductivity [W/m/K]

T = Solid temperature [K]

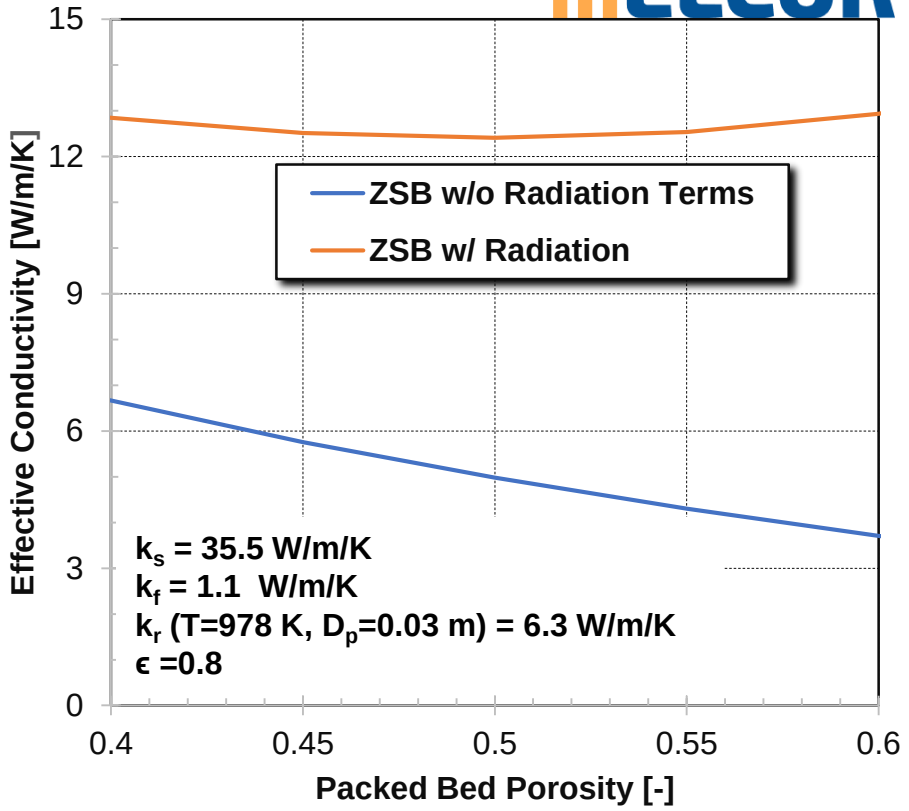

- Effective fluid conductivity combines liquid and vapor contributions according to vapor fraction
- Radiative conductivity is combined by vapor fraction and used in ZSB model with radiation terms

$$k_{eff} = \left(1 - \sqrt{1-\varepsilon}\right)k_r + \left(1 - \sqrt{1-\varepsilon}\right)k_f + \left(\sqrt{1-\varepsilon}\right)k_c\left(T, D_p, \varepsilon, k_f, k_s, k_r\left(X_{Vapor}\right)\right)$$

$$k_r = 4\varepsilon\sigma T^3 D_p X_{Vapor}$$

Interface Between Thermal Hydraulics and Reactor Core Structures

Heat transfer coefficient (Nusselt number) correlations for pebble bed convection:

- Isolated, spherical particles
- Use T_{film} to evaluate non-dimensional numbers, use maximum of forced and free Nu

$$Nu_{Free} = 2.0 + 0.6\, Gr_f^{1/4}\, Pr_f^{1/3} \qquad Nu_{Forced} = 2.0 + 0.6\, Re_f^{1/2} Pr_f^{1/3}$$

- Constants and exponents accessible by sensitivity coefficient

Flow resistance

- Packed bed pressure drop

$$K_L(\varepsilon, Re) = \left[C_1 + C_2 \frac{1-\varepsilon}{Re} + C_3 \left(\frac{1-\varepsilon}{Re}\right)^{C_4}\right] \frac{(1-\varepsilon)}{\varepsilon D_p} L$$

Correlation	C_1	C_2	C_3	C_4
Ergun (original)	3.5	300.	0.0	-
Modified Ergun (smooth)	3.6	360.	0.0	-
Modified Ergun (rough)	8.0	360.	0.0	-
Achenbach	1.75	320.	20.0	0.4

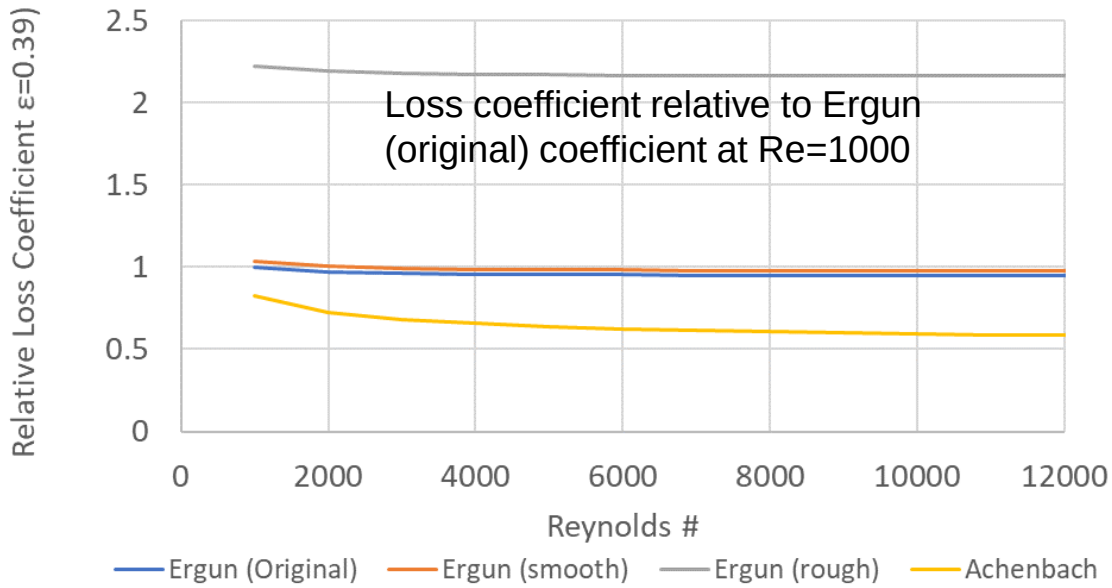

MELCOR model inputs (1/2)

Equilibrium inventory and decay heat from SCALE

Radial and axial power profiles from SCALE

Reactivity feedbacks from SCALE

Cell-to-cell radial and axial heat transfer in the pebble bed and to adjacent reflector structures

- Modified Zehner-Schlunder-Bauer model formulation
- Combined conductive and radiative (when core uncovered) heat transfer depends on the coolant and fuel conductivities, fuel (graphite) emissivity, pebble bed porosity

Pebble bed friction losses – Achenbach pressure drop formulation

- $K_{loss} = 2 + 320\left(\frac{(1-\epsilon)}{Re}\right) + 20\left(\frac{(1-\epsilon)}{Re}\right)^{0.4}$

Pebble to fluid heat transfer within a cell

- Forced convection using Wakao correlation, $Nu = 2 + 1.1\,Re^{0.66}Pr^{0.33}$

MELCOR model inputs (2/2)

Fission product diffusivities through the TRISO and the pebble matrix from IAEA-TECDOC-978, Appendix A

- Primarily based on values from German experiments with UO_2 TRISO pebbles
  - UO_2 data can be easily updated to UCO data*
- Limited data based on nuclides of Xe, Cs, Sr, and Ag
- Iodine assumed to behave like Kr

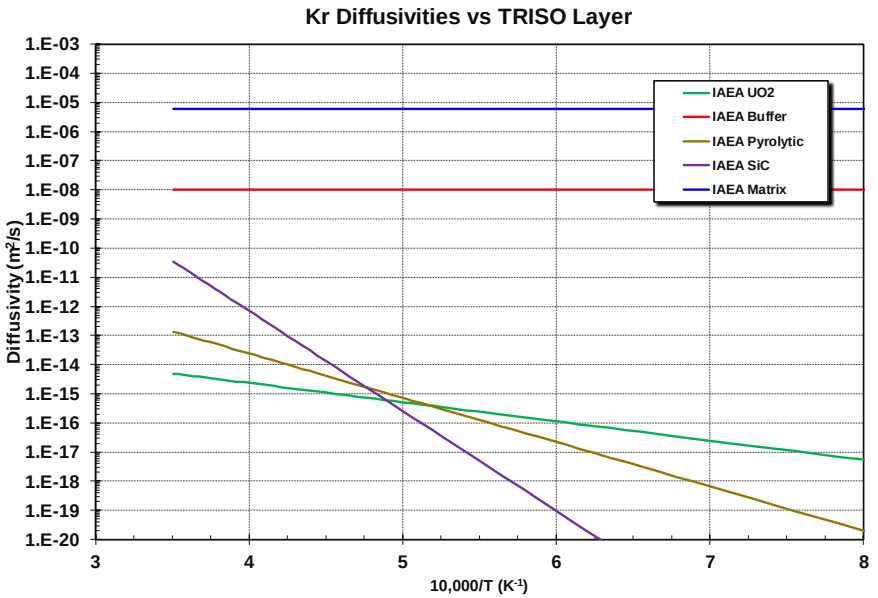

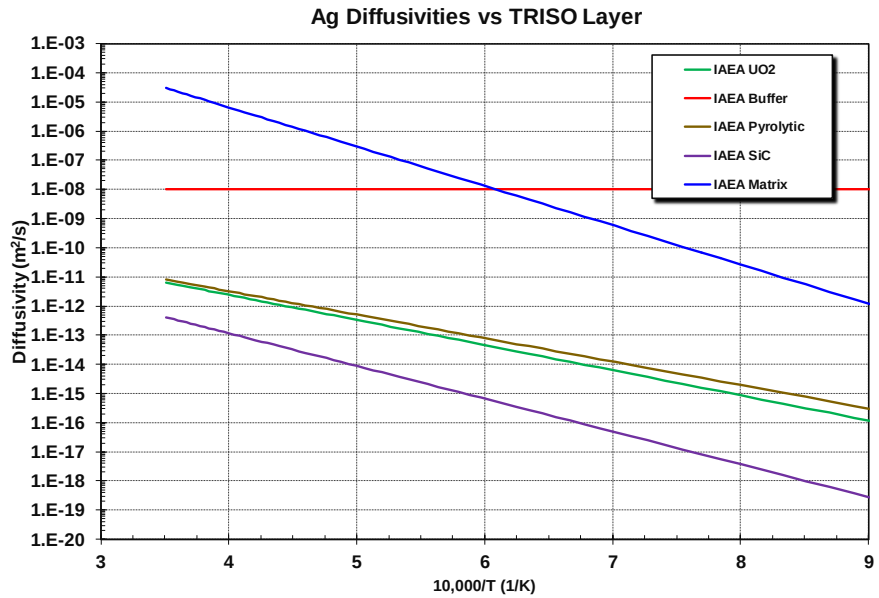

* UCO TRISO thermal failure characteristics were not available, so UO_2 TRISO diffusivity and UO_2 failure data were used. Both are changeable through user input with design-specific data.

MSR SIMULATION WITH CGEMS: SALT AND FISSION PRODUCT EVAPORATION

Terttaliisa Lind, Jarmo Kalilainen, Sergii Nichenko
Paul Scherrer Institute
Forschungsstrasse 111, CH-5232 Villigen, Switzerland
terttaliisa.lind@psi.ch; jarmo.kalilainen@gmail.com; sergii.nichenko@psi.ch;

ABSTRACT

Fission product and fuel materials release from a molten salt reactor (MSR) fuel in an event of a hypothetical accident was investigated. The study was conducted using a coupling between the severe accident code MELCOR and a thermodynamic equilibrium solver GEMS. The coupling, called cGEMS, was developed at PSI. The updated HERACLES database served as a source of thermodynamic information for the simulations. In the beginning of the simulated event, the fuel salt was drained from the reactor to the bottom of a confinement building. The decay heat caused the temperature of the salt to increase, leading to evaporation of the salt components and fission products from the surface of a molten salt pool. A gas-gas heat exchanger encircles the confinement and transfers the heat to the environment. The investigated MSR features a fast neutron spectrum, operation in the thorium cycle, and uses LiF-ThF_4-UF_4 (77.5-20-2.5 mol%) as a fuel salt.

Two chemical systems were investigated in this work. The first system contained the salt components Li, F, Th, and U, as well as the fission products Cs, and I as the main components. The second extended system contained the salt components Li, F, Th, and U, as well as additionally Zr, Np, Pu, Sr, Ba, La, Ce, and Nd. In the first system, the thermodynamic effects, e.g. binary interactions between salt components, on the evaporation behavior were investigated. In the second system, first, the extended salt composition and, second, the release behavior sensitivity to the variations of fluorine in the salt was assessed. This work was carried out within the EU SAMOSAFER project.

KEYWORDS
MSR, fission product, evaporation, severe accident

1. INTRODUCTION

Molten salt reactors (MSR) are characterized by either the coolant, or both coolant and fuel consisting of molten salts, typically fluorides or chlorides. The MSRs differ significantly from the light water reactors from the safety point of view, having many characteristics which limit the usefulness of traditional classification of safety barriers, core damage states and accident sequences when assessing the safety of MSRs. Severe accidents, for example, have been typically characterized as showing a fraction of the core in a molten state or relocated in the reactor pressure vessel. In many MSR designs using a molten fuel, this classification cannot be applied as the fuel is present not only flowing inside the reactor vessel but also outside of the vessel. The absence of fuel cladding, and the presence of a large fraction of radioactive material not only in the core but also in auxiliary systems, such as off-gas system and fuel treatment facility, make MSR distinctly different from light water reactors when regarding the confinement of radioactivity.

The ultimate safety goal, however, remains the same in all nuclear reactors: to ensure reactor operation without the unintended release of radioactivity from the plant to the environment.

The European SAMOFAR project was carried out in years 2015-19 with the grand objective of proving the innovative safety concepts of the MSFR (molten salt fast reactor) by advanced experimental and numerical techniques, to deliver a breakthrough in nuclear safety and optimal waste management, and to create a consortium of stakeholders to demonstrate the MSFR beyond SAMOFAR [1]. The following activities were included in the project: i) To deliver the experimental proof of a concept of the unique safety features of the MSFR, ii) to provide a safety assessment of the MSFR for both the reactor and the chemical plant, iii) to update the conceptual design of the MSFR with all the improvements and recommendations from aforementioned studies incorporated, and iv) to deliver a roadmap for further exploitation of the project results by creating momentum among key stakeholders that can validate and demonstrate the MSFR beyond SAMOFAR. The SAMOFAR project was followed by the project SAMOSAFER in 2019-2023 with the aim of developing and demonstrating new safety barriers for more controlled behavior of MSRs in severe accidents, based on new simulation models and tools validated with experiments. The ultimate goal is for the MSR to be able to comply with all projected regulations in 30 years [2]. To reach this goal, the SAMOSAFER project actively seeks partners among different stake-holders to apply the methods developed in the project. At the end of the project, the results and methods will be evaluated and further steps in the MSR development depicted.

One of the activities in both projects has been to determine the composition of the fuel salt and its fission product concentrations at different phases of the fuel cycle, as well as to assess the potential release of fission products and salt materials during unintended temperature increase of the salt during hypothetical severe accidents. Molten Salt Reactor Experiments [3] showed that minor amounts of fission products were released from the reactor during the operation of the reactor, however, accident conditions were not tested. In the absence of experimental data, analytical tools have been developed to estimate the release of radioactive materials from MSRs under postulated accident conditions [e.g., 4].

In this work, some examples of the PSI work to determine evaporation of fission products and salt compounds during an MSR accident in which the fuel salt is drained from the fuel casing onto the floor of a confinement are given. The confinement is under nitrogen atmosphere, and the fission products and salt material are evaporated from the surface of a molten salt pool which is formed on the confinement floor. The amount of evaporated material and its composition are determined under different assumptions regarding the chemical state of the salt.

2. METHODS

For the analysis of the salt material and fission product evaporation, the integral severe accident analysis code MELCOR [5], together with a thermodynamic solver GEMS [6] using HERACLES database [7] were used.

2.1. cGEMS

The MELCOR and GEMS codes were coupled using a code called cGEMS which was developed at PSI. cGEMS acts as an interface between the GEMS and MELCOR codes, allowing the information to be exchanged between two programs. cGEMS can call both MELCOR and GEMS depending on the situation, and has a controlling function in the simulation process.

MELCOR and GEMS are coupled via an external file system since MELCOR is a commercial product and PSI does not have access to its original source code. This implies that cGEMS sends data to MELCOR

through external input files. In order to transmit the information, cGEMS must restart MELCOR at each time step with a fresh input file containing the updated data. When compared to stand-alone MELCOR computations, a continuous restart of MELCOR with intermediate calculations with GEMS results in longer calculation times. cGEMS, on the other hand, has direct access to the GEMS code via its Application-Programming Interface (API), simplifying data interchange with GEMS.

The general idea of the simulation flow is demonstrated using the diagram in which the process is split into different steps, Fig. 1 [8]:

1. Perform the MELCOR simulation for a predetermined time step (200 s in this study)
2. Collect data containing elemental composition of the fission products in the fuel and the temperature of the fuel salt from MELCOR, and pass it to GEMS for further thermodynamic calculations
3. Perform GEMS thermodynamic calculation
4. Compile the GEMS results, e.g. vapor pressures of the species of interest, into an external input file and pass them to MELCOR for the next simulation step
5. Repeat the cycle

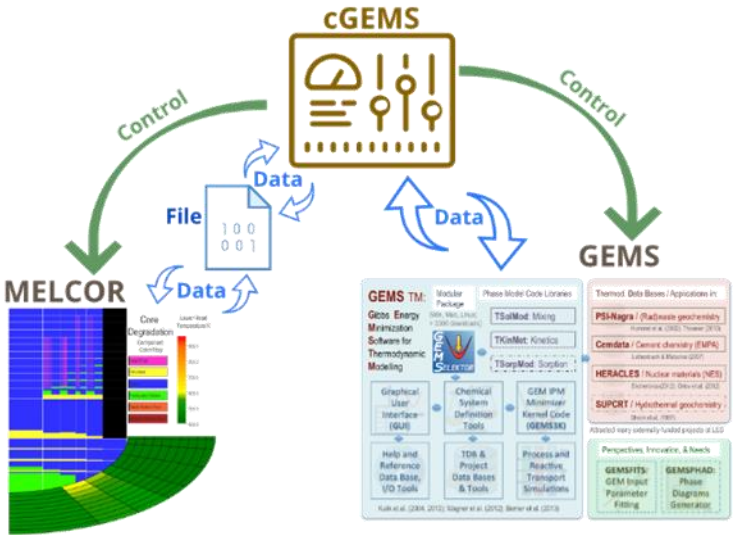

Figure 1. General schematics of the cGEMS [8]

2.2. HERACLES Database

A backbone of any thermodynamic modelling is a reliable database that contains the underlying thermodynamic data for the necessary chemical species as well as parameters for different pair-wise, and higher orders, interactions. These interaction parameters describe deviations of mixing behavior from the ideal, random, mixing in the gaseous, liquid or solid phase. At PSI, a dedicated thermodynamic database, HERACLES, for nuclear field related research has been developed and is being maintained and constantly extended [7]. Originally, the HERACLES database was compiled to support modelling of uranium and fission products speciation during pyro-reprocessing of spent nuclear fuel. For the work in the field of MSR, the HERACLES database was extended with relevant fluoride and chloride species. HERACLES database covers molar thermodynamic properties of solid, liquid (melt) and gaseous compounds of actinides, fission products, and minor actinides in the temperature range of up to 3000 K, covering the majority of the elements of interest. In its current state, the HERACLES database covers metals, actinides, fission products, gases and salts with more than 600 condensed compounds and 400 gaseous species.

For this work, most of the data in the HERACLES database relevant to MSRs were collected from published sources. The data were validated against the melting and boiling points for each particular compound to ensure the accuracy of the underlying thermodynamic data. This involved calculation of the Gibbs energy curves for every phase for a single selected compound and comparing the obtained melting (cross-section of the solid and liquid phases Gibbs energy curves) and boiling (cross-section of the gaseous and liquid phases Gibbs energy curves) points to the available experimental data. In case there was a noticeable deviation of the calculated values from the experimental data, the underlying thermodynamic data were corrected to reproduce the experimental data. The data correction involved the adjustment of the underlying formation enthalpies and standard entropies of the species, as well as, in some cases, heat capacities of the species. All the corrections were performed taking into account available literature information on thermodynamic properties of a particular compound. In the majority of cases, the corrections to the underlying thermodynamic data did not exceed the uncertainty of the original thermodynamic data.

Besides the update of the thermodynamic data of the pure species in the HERACLES database, significant efforts were dedicated to the improvement of the description of the solution phases. This included collection of the available phase equilibria data for a number of binary systems and a fit of the available experimental data with a selected mixing model of interest. The selected model is the Redlich-Kister mixing model. The binary interactions for a liquid phase, as well as all the relevant binary solid solutions, are the following:

- Liquid phase binary interactions: LiF-NaF, CsI-LiF, LiF-KF, CsI-ThF_4, KF-NaF, CsI-PuF_3, LiF-BeF, ThF_4-PuF_3, LiF-ThF_4, LiF-UF_4, LiF-CsF, PuF_3-UF_4, CsI-LiI, CsF-ThF_4, LiF-PuF_3, CsI-ThI_4, CsI-CsF, LiF-LiI, ThF_4-ThI_4, LiI-ThI_4
- Binary solid solutions: LiF-NaF, $Li_7Th_6F_{31}$-$Na_7Th_6F_{31}$, $Li_7U_6F_{31}$-$Na_7U_6F_{31}$, NaF-ThF_4, $Li_7Th_6F_{31}$-$Li_7U_6F_{31}$, $LiTh_4F_{17}$-LiU_4F_{17}, $Na_7Th_6F_{31}$-$Na_7U_6F_{31}$, $Na_3Th_2F_{11}$-$Na_5U_3F_{17}$, $NaTh_2F_9$-NaU_2F_9, PuF_3-ThF_4, UF_4-ThF_4, PuF_3-UF_4

2.3. Evaporation and Fission Product Transport Model

In the input model for this work, the confinement is modeled as a cylindrical container with a salt layer at the bottom surface, Fig. 2. The salt under accident conditions has been drained from the fuel casing, located in the center of the confinement, and is then uniformly dispersed at the bottom of the confinement. A gas-gas heat exchanger encircles the confinement at 15 m above the floor level. The heat exchanger surface area is approximately 235 m^2. The initial confinement atmosphere consists of nitrogen at 0.1 MPa pressure.

The MELCOR model of the confinement is divided into 14 control volumes (CVs) which are connected with flow paths allowing convective heat transfer and transport of the evaporated material, Fig. 2. All confinement boundary heat structures, with the exception of the isothermal heat exchanger and salt surfaces, have adiabatic temperature boundary conditions. Natural convection flow in the container is driven by the hot salt and colder heat exchangers, driving heat and mass transfer. In addition to convection in the MELCOR simulations, the heat conduction and thermal radiation are as well considered. For a more extensive description of the MELCOR input model and the evaporation modelling geometry, please refer to [9].

The salt layer at the bottom of the confinement is also described by a heat structure. At simulation time t = 0 s, the salt surface heating was started at a rate 6 K/min, simulating the salt heat-up due to the decay heat, which is approximately 129 MW immediately after the reactor shut down [9]. At the start of the simulation, the temperature of the salt, all confinement surfaces and the atmosphere were set to 300K and 800 K in the two chemical systems described below, respectively. Due to the slow heating rate the variations in the evaporation process at different fuel temperatures may be easily observed. The heat exchanger temperature was increased from 300 K to 500 K at a rate equivalent to that of the salt, after which it was kept constant.

At each simulation time step, the evaporation rate of FPs and salt components from the salt surface to the bottom CVs 1-3 is calculated using the methodology described in [9].

After the release of the different salt and fission product species from the salt on the confinement floor, their evolution in the confinement atmosphere could be observed. This work will be reported later.

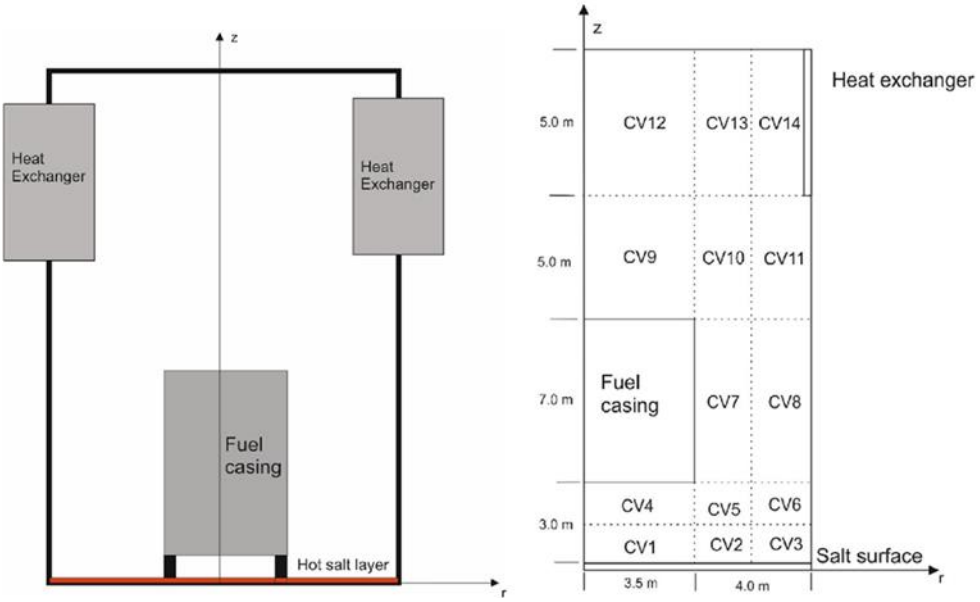

Figure 2. Schematic of the MELCOR model of the confinement [9]

2.4. Simulation matrix

Five different simulation cases are presented in this investigation, Table 1. The elements for each simulation case were selected based on their availability in the updated HERACLES database, their abundance in the fuel salt, and their possible radiotoxicity. Two different chemical systems were considered:

- LiF-ThF_4-UF_4 with Cs and I. In the first elemental system (Kalilainen et al., 2020), the evaporation of Li, Th, U, Cs, I, F was investigated using cGEMS. This corresponded to the system with 78.8% (mol) LiF, 16.9% ThF_4 and 4.2% UF_4. The fission product concentrations were 9.8e-3% Cs and 5.8e-5% I.

- LiF-ThF_4-UF_4 with Zr, Np, Pu, Sr, Ba, La, Ce, and Nd. In the second elemental system, the list of included elements was extended so that the salt components Li, Th, U, and F were complemented with Zr, Np, Pu, Sr, Ba, La, Ce, and Nd. Iodine was not included in the second set of the simulations.

The composition of the salt and the concentrations of the fission products in the first set of simulations were obtained from the EQL0D simulation data, Figure 3, and are given by Hombourger et al. [10].

Table 1. Simulation matrix for evaporation analyses

Simulation case	Elements	Variation
Case 1	Li, Th, U, F Cs, I	Best estimate with salt mixing
Case 2	Li, Th, U, F Cs, I	Pure compound vapor pressures
Base case	Li, Th, U, F Zr, Np, Pu, Sr, Ba, La, Ce, Nd	Base case with salt mixing, extended number of elements, stoichiometric F concentration
Over-fluorinated	Li, Th, U, F Zr, Np, Pu, Sr, Ba, La, Ce, Nd	Fluorine concentration +1%
Under-fluorinated	Li, Th, U, F Zr, Np, Pu, Sr, Ba, La, Ce, Nd	Fluorine concentration -1%

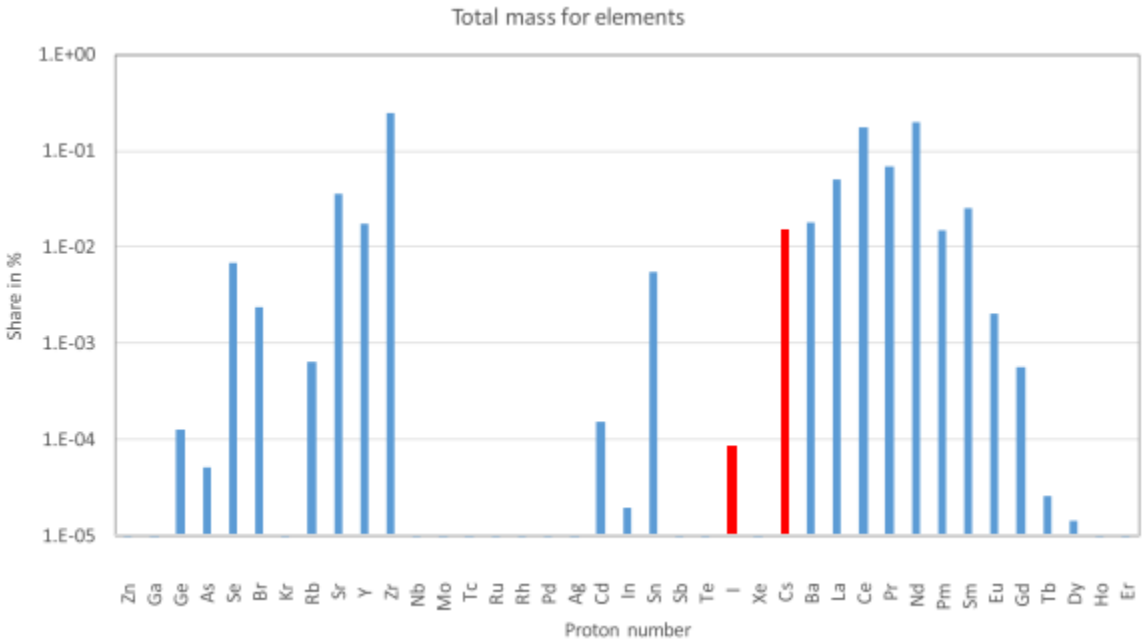

Figure 3. Detailed distribution of fission products in the fuel salt in the first part of the simulations [9]

In the first set of simulations, two cases with the first elemental system (a limited number of elements included) were analyzed:

- **Case 1** represents the best estimate simulation in which GEMS was used to determine the salt mixture vapor pressures during the evaporation calculation.
- **Case 2** in which only MELCOR simulation was performed and the effects of the salt mixing on the evaporation behavior of the FPs and salt compounds were not considered. This simulation used the pure compound vapor pressures.

These simulations were done to demonstrate the influence that different thermodynamic effects in the salt mixtures can have on the release behavior and chemical speciation in the salt. These effects may include entropic contributions to the mixing energies as well as excess Gibbs energy contributions defined by differences in the interaction energies between different pairs of ions in the system.

In the second set of simulations, the extended elemental system (extended list of elements) was used, and three cases were simulated in which the amount of fluorine in the salt varied between cases. This was done because it had been shown that the evaporation behavior of fission products and salt material is highly dependent on the fluorine concentration in the salt [11]. The following simulations were conducted in the second part of the work:

- **Base case** representing the best estimate simulation in which GEMS was used to determine the salt mixture vapor pressures during the evaporation calculation
- **Over-fluorinated case** in which fluorine concentration was increased by 1 mol-% from the stoichiometric value
- **Under-fluorinated case** in which fluorine concentration was decreased by 1 mol-% from the stoichiometric value

3. RESULTS

3.1. Thermal-hydraulic conditions

Thermal-hydraulic conditions were calculated with MELCOR for the hypothetical accident sequence in which the salt is dropped to the confinement floor at time zero. At this time, the salt starts to heat up due to decay heat. Three different temperatures in different elevations CV2, CV7 and CV13, Fig. 4, show that there is very little stratification in the confinement atmosphere due to mixing caused by the natural convective flow induced by the temperature difference between the hot salt surface and the cooler heat exchanger leading to approximately uniform gas temperature in the confinement. Along with the temperature, the pressure in the confinement rises during the salt heat-up phase and reaches its maximum value of 0.385 MPa at approximately 15 000 s after which the pressure stays at around this value until the end of the simulation. Case 4, Fig. 4, shows a simulation in which confinement is depressurized at approximately 5000 s when the confinement pressure reaches 0.1 MPa over-pressure. More details for case 4 simulation can be found in [9]. It should be noted that the thermal-hydraulic conditions are highly dependent on the confinement geometry and design of the safety systems, and thereby the results shown here are valid only for the generic geometry used in this investigation.

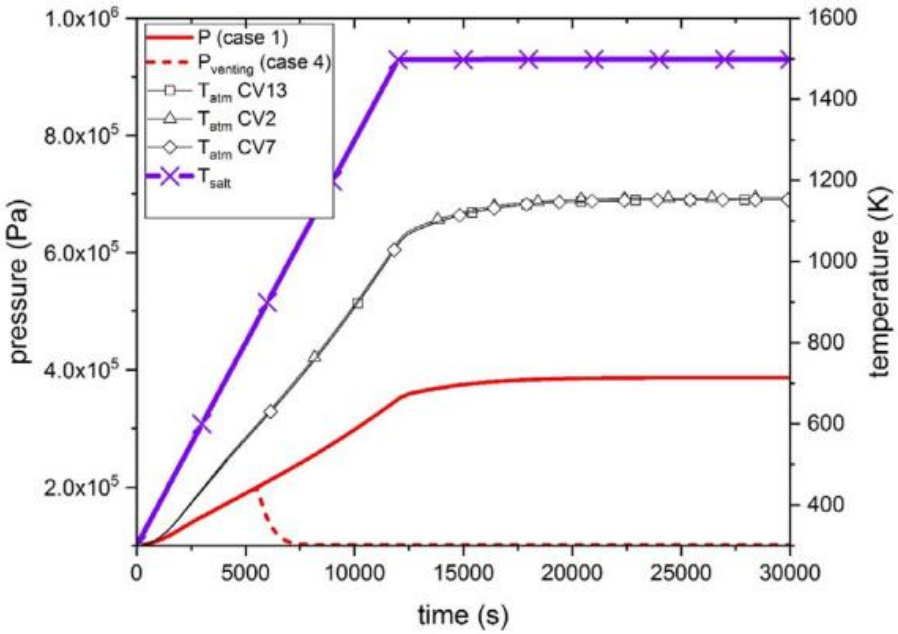

Figure 4. Temperature of the salt and the confinement atmosphere, as well as the confinement pressure in the simulations. Case 4 shows the effect of confinement venting on the pressure, other results for Case 4 can be seen in [9]

3.2. The effect of salt mixing

The influence of the thermodynamic mixing effects in the salt on the evaporation of different compounds from the salt was assessed using the elemental system 1 (limited number of elements). The evaporation of fission products and salt species in case 1 were compared with the evaporation behavior in case 2. In case 1, GEMS was used to calculate the vapor pressures of the compounds whereas in case 2 pure compound vapor pressures were used. The results show that for both cesium and iodine, the retention in the salt is significantly increased when the mixing effects in the salt, in case 1, are considered. This can be seen clearly in Fig. 5, in which the integral release of compounds after 30 000 s simulation time shows that the released mass is consistently higher in case 2 simulations than in case 1. The only exception is iodine which was not released in case 2 simulation. Additionally, it is seen that the total amount of the most non-volatile compounds (Li and UF_3) released during the simulations remained very low in the case 1 in which the mixing effects in the salt were account for whereas the evaporation of these species was relatively high when pure compound vapor pressures were used in case 2.

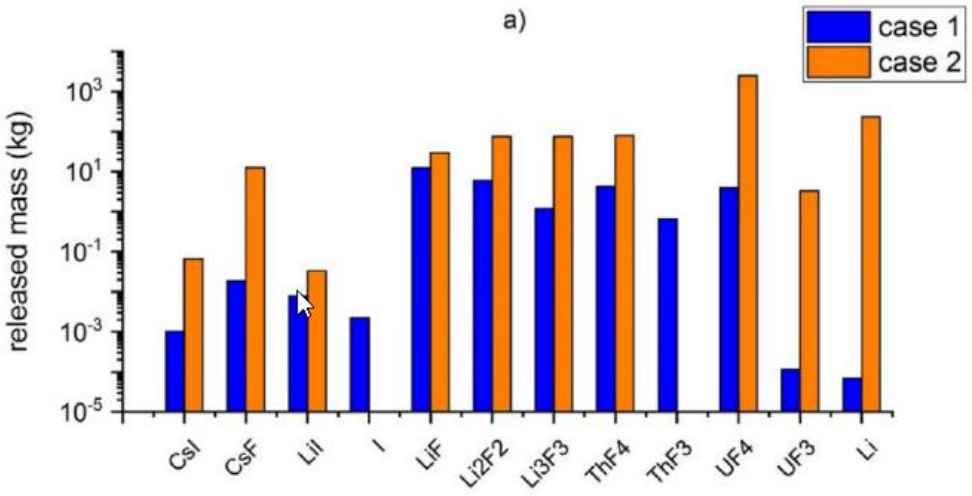

Figure 5. Comparison of integral release from the salt after 30 000 s of simulation for the best estimate case 1 and case 2 with no salt mixing effects [9]

When considering the salt compounds, Fig. 6, it is seen that the overall behavior is similar to the behavior of fission products Cs and I, i.e., almost all the salt species were observed to be retained better in the fuel salt when the mixing effects in the salt were considered and the coupled simulation method was used as compared to the pure compound simulation. This indicates that in addition to the evaporation of the fission products, the mixing effects in the salt are also important when considering the realistic modeling of the evaporation of the actinide compounds.

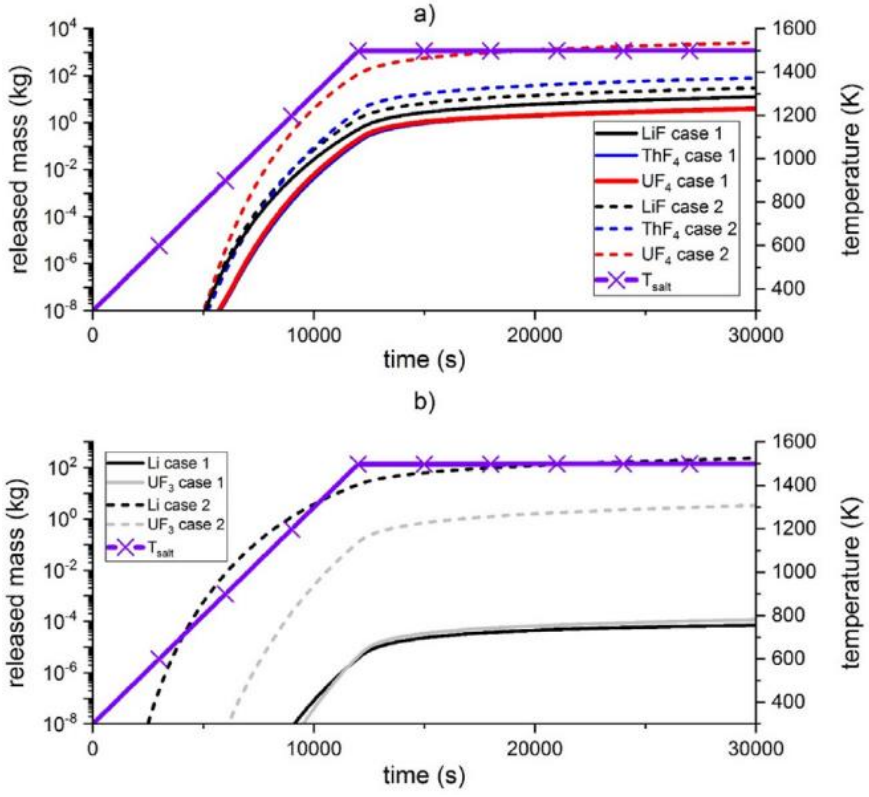

Figure 6. Release of salt species in cases 1 (solid lines) and 2 (dashed lines) [9]

3.3. The effect of fluorine concentration

Three simulation cases were carried out with the elemental system 2 (extended number of elements) to assess the effect of fluorine concentration in the salt on evaporation: a base case, as well as over- and under-fluorinated simulations with +1% and -1% fluorine, respectively. The analyses showed that significant amounts of salt materials and actinide species were released from the salt when the salt was heated up on the confinement floor in all the three simulated cases. In the base case simulation, LiF, UF_4 and ThF_4 were seen to be the most volatile species with more than 10 kg of each released after 15 000 s at 1500 K, Fig. 7 [12]. Additionally, NpF_4 was shown to be relatively volatile with approximately 6 kg released from the salt after 10 000 s. The apparent non-steady increase of the NpF_4, UF_5 and PuF_4 release in the beginning of the simulation was presumably caused by numerical instabilities in the GEMS simulation which did not appear at higher temperatures or in the simulations with different fluorine concentrations, as shown below.

In the over fluorinated case with 1% more fluorine in the salt than the stoichiometric concentration, UF_5, NpF_4 and PuF_4 volatility increased significantly showing the highest releases, as can be seen in Fig. 8 [12]. Especially the high release of UF_5 in the over-fluorinated case is to be noted. On the other hand, in the under-fluorinated case with 1% less fluorine than the stoichiometric concentration, the three compounds showing high release in the over-fluorinated simulation, i.e., UF_5, NpF_4 and PuF_4, are significantly less volatile, and ThF_3 has become the most dominant volatile species, Fig. 9 [12]. The total release in the under-fluorinated case is significantly smaller, about one order of magnitude, than in the over-fluorinated case. These results demonstrate the significant effect of the fluorine concentration on the salt evaporation as only 1% change in the fluorine concentration affects the release of different compounds by orders of magnitude.

The fission product release was seen to be much less sensitive to small changes in the fluorine concentration than the release of salt compounds. In all the simulations, ZrF_4 was the most volatile fission product species with over 100 kg of it being released in all the three simulations.

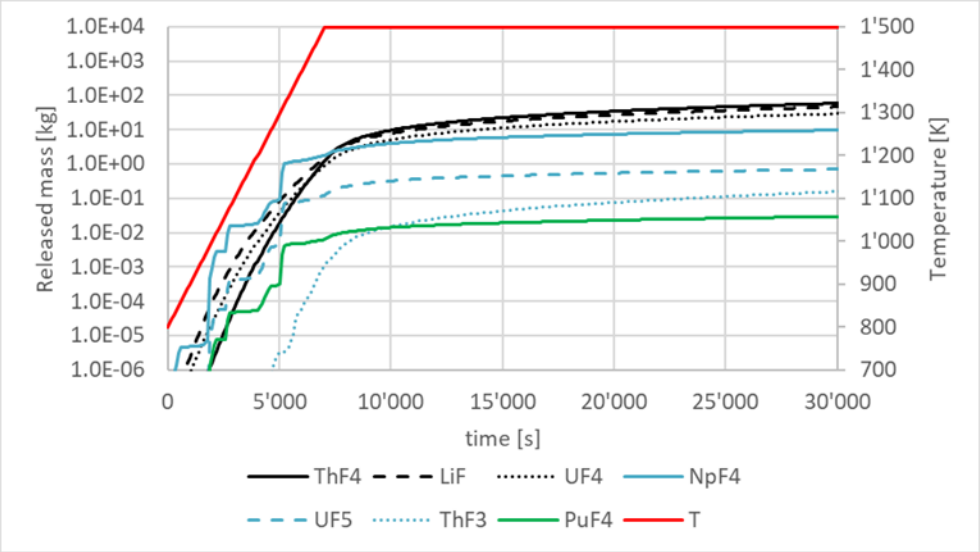

Figure 7. Total amount of salt material and actinides released from the salt in the base case simulation

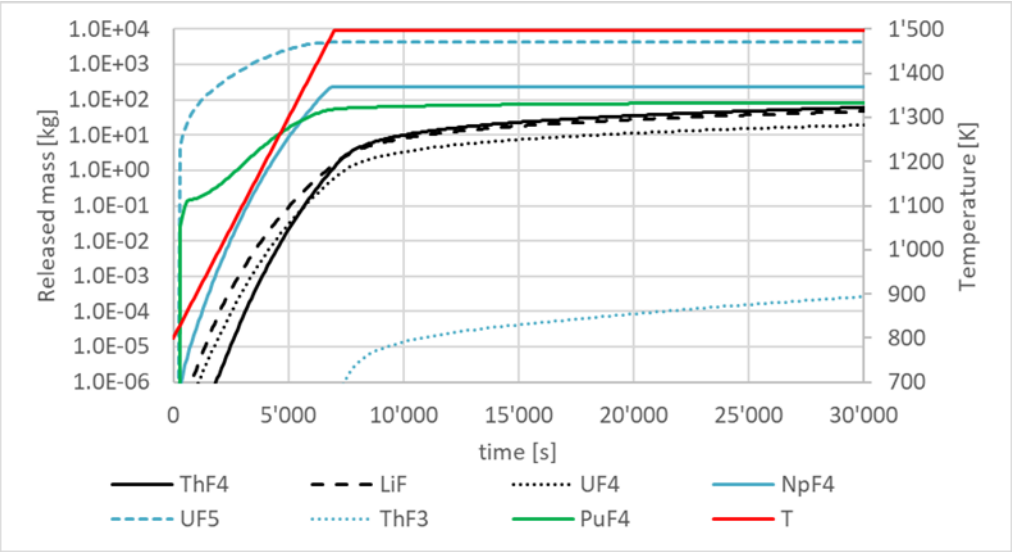

Figure 8. Total amount of salt material and actinides released from the salt in the over-fluorinated (F+1%) simulation

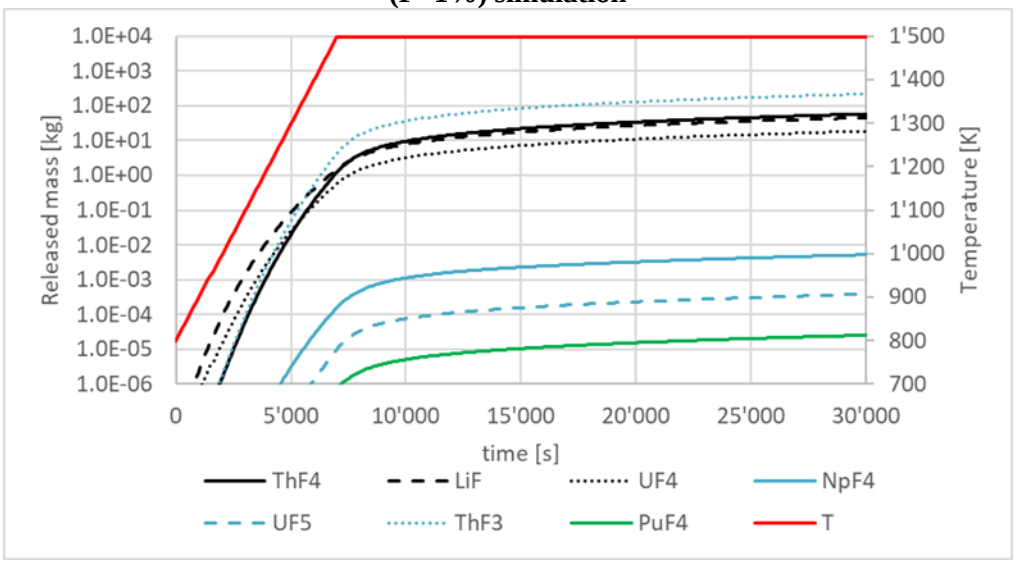

Figure 9. Total amount of salt material and actinides released from the salt in the under-fluorinated (F-1%) simulation

4. CONCLUSIONS

The results obtained in this work indicate that significant amounts of salt materials and fission products may be evaporated from the MSR salt in an accident which postulates that the core is drained to the confinement floor where it heats up by decay heat.

The simulations with the limited number of elements (elemental system 1) demonstrated the importance of accounting for thermodynamic mixing effects in the salt when calculating the evaporation of both salt and fission product compounds. The calculated release of all elements included in the analyses, except iodine, was significantly reduced when the mixing effects in the salt were taken into account using the cGEMS coupling to calculate the vapor pressures of the compounds as compared to simulations using pure compounds vapor pressures.

The simulations with the extended number of elements (elemental system 2) showed the considerable impact of the concentration of fluorine on the evaporation behavior of the salt compounds. With only 1% excess fluorine, the release of UF_5, NpF_4 and PuF_4 increased significantly; particularly, the release of UF_5 increased by more than three orders of magnitude, this compound becoming the most volatile salt compound when fluorine concentration in the salt was +1% of the stoichiometric value. In general, the simulations showed that the release of the salt materials was very sensitive to even small changes in the fluorine content as only 1% deviation from the stoichiometric fluorine concentration resulted in orders of magnitude difference in the release of several major compounds.

ACKNOWLEDGMENTS

This work has received funding from the Euratom research and training program 2014-2018 under grant agreement No. 847527. We would like to thank the SAMOSAFER project partners for fruitful collaboration.

REFERENCES

1. http://samofar.eu/. Accessed 5.1.2022.
2. https://samosafer.eu/. Accessed 5.1.2022.
3. Compere, E.L., Bohlmann, E.G., Kirslis, S.S., Blankenship, F.F., Grimes, W.R., 1975. Fission Product Behavior in the Molten Salt Reactor Experiment. ORNL-4865, Oak Ridge, Tennessee, USA.
4. Thomas, S., Jerden, J., 2020. “Mechanistic Source Term Development for Liquid Fueled MSRs - Model Development Update”. ANL/CFCT-20/16, Argonne, Illinois, USA.
5. L.L. Humphries, B.A. Beeny, F. Gelbard, D.L. Louie, J. Phillips, 2017. MELCOR computer code manuals vol. 2: reference manual. Sandia National Laboratories, United States of America, Albuquerque, NM. Version 2.2.9541.
6. Kulik, D. A., Wagner, T., Dmytrieva, S. V., Kosakowski, G., Hingerl, F. F., Chudnenko, K. V., Berner, U. R., 2013. “GEM-Selektor geochemical modeling package: revised algorithm and GEMS3K numerical kernel for coupled simulation codes”. Computational Geosciences 17, 1–24.
7. Shcherbina, N., Kivel, N., Günther-Leopold, I., Kulik D., Bertsch, J., 2012. HERACLES project and thermodynamic database homepage, [Online]. Available: http://www.psi.ch/heracles/. [Accessed 18. 10. 2019].
8. Nichenko, S., Kalilainen, J., Fernandez Moguel, L., Lind, T., 2021. Modelling of fission product release in VERDON-1 experiment with cGEMS: Coupling of severe accident code MELCOR with GEMS thermodynamic modelling package. Annals of Nuclear Energy 152, 107972.
9. Kalilainen, J., Nichenko, S., Krepel, J., 2020. Evaporation of materials from the molten salt reactor fuel under elevated temperatures. Journal of Nuclear Materials 533, 152134.
10. Hombourger, B., Krepel, J., Pautz, A., 2020. The EQL0D procedure for fuel cycle studies in molten salt reactors and its application to the transition to equilibrium of selected designs. Annals of Nuclear Energy 144, 107504.
11. J. Kalilainen, S. Nichenko, J. Dietz, T. Lind, 2021. “Aerosol formation and filtration in accidental conditions”. Technical report TM-41-21-11, PSI, Villigen, Switzerland.
12. T. Lind, J. Kalilainen, S. Nichenko, 2022. MSR SIMULATION WITH CGEMS: SALT AND FISSION PRODUCT EVAPORATION. 10.5281/zenodo.5969869.

PAUL SCHERRER INSTITUT

PSI



T. Lind, S. Nichenko, J. Kalilainen :: Paul Scherrer Institut

MSR SIMULATION WITH CGEMS: SALT AND FISSION PRODUCT EVAPORATION

10th European Review Meeting on Severe Accident Research, May 16-19, 2022
Karlsruhe, Germany

Laboratory for
Reactor Physics and Thermal-Hydraulics

Contents

- Background: SAMOSAFER project
  - An EU collaboration project 2019-2023
- Methods:
  - MSR design
  - cGEMS
- Results
  - Fission product and salt material evaporation
  - Aerosol formation
- Conclusions and future work

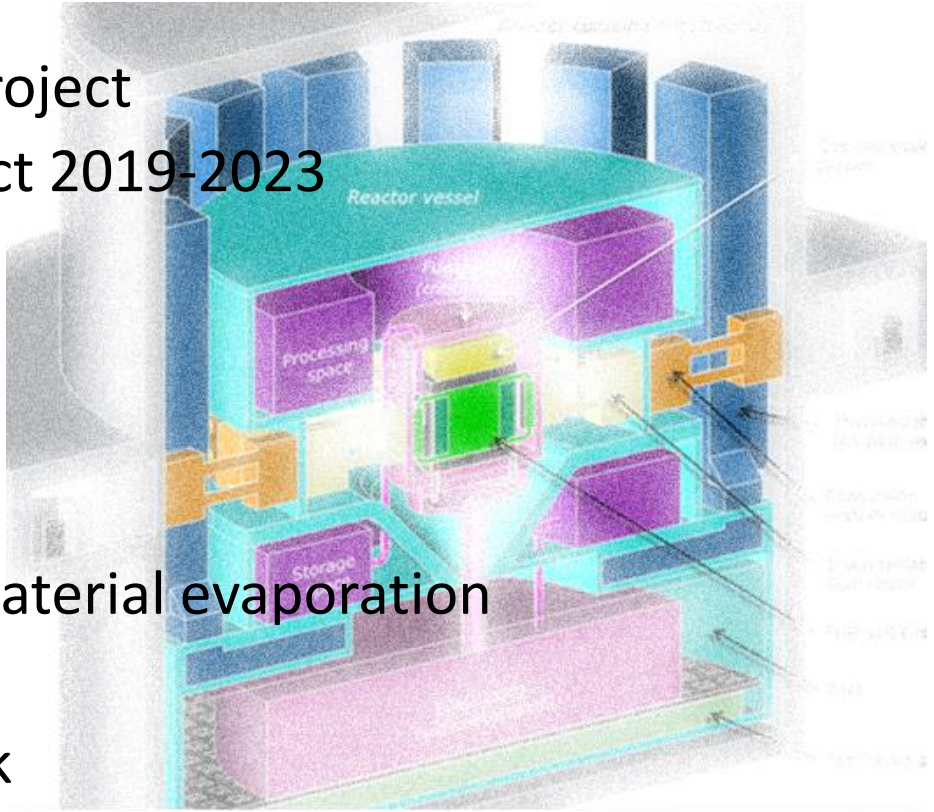

- **SAMOSAFER: "Severe accident modelling and safety assessment for fluid-fuel energy reactors"**
  - Aims to develop and demonstrate new safety barriers for more controlled behavior of Molten Salt Reactors in severe accidents
  - New simulation models and tools validated with experiments
  - The final objective is to ensure that the MSR can comply with **all expected regulations in 30 years' time**

SAMOSAFER


PAUL SCHERRER INSTITUT
PSI

SAM SAFER

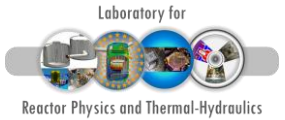
Laboratory for
Reactor Physics and Thermal-Hydraulics


DE LA RECHERCHE À L'INDUSTRIE
cea


cnrs


TU Delft


OntarioTech
UNIVERSITY


IRSN
INSTITUT
DE RADIOPROTECTION
ET DE SÛRETÉ NUCLÉAIRE


NRG


KIT
Karlsruhe Institute of Technology


POLITECNICO
MILANO
POLITECNICO
DI MILANO


eDF


PAUL SCHERRER INSTITUT
PSI


POLITECNICO
DI TORINO


European
Commission


framatome


CVŘ
Centrum
výzkumu Řež

Methods – design #1

- Molten fuel – allows adaptation during operation
- Fast neutron spectrum
- Can be operated in full range from breeder to burner
- Blanket salt containing thorium surrounding the core (red in picture)

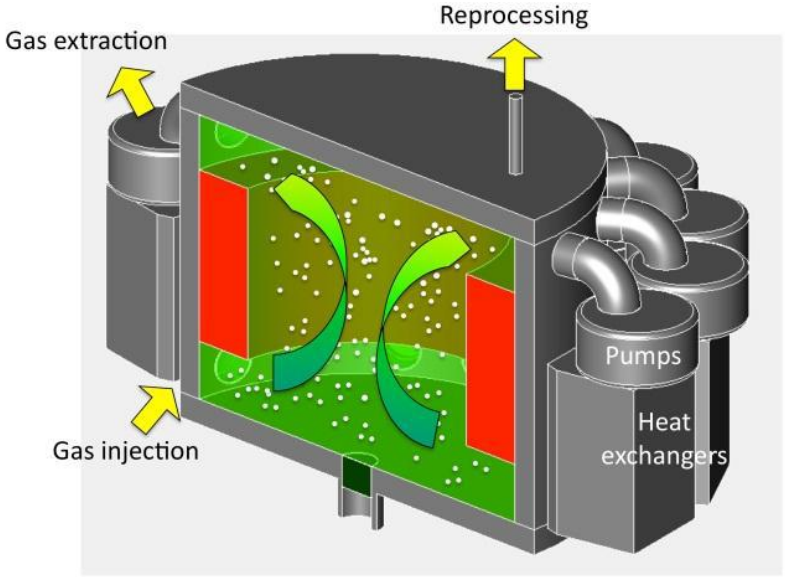

Methods – design #2

- Cylindrical vessel with diameter and height of 2.25 m
- Ambient pressure, T(operation) = 750°C
- 18 m^3 of fuel salt pumped upwards in the core, downwards in the heat exchangers

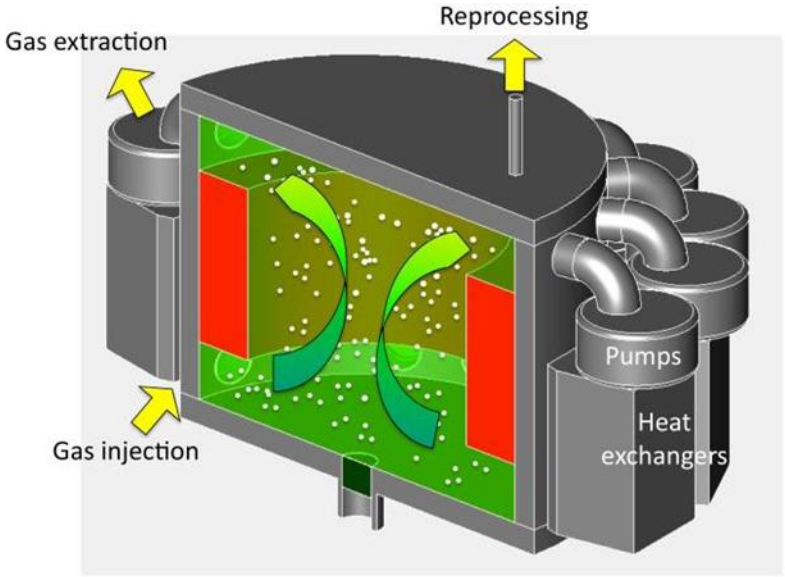

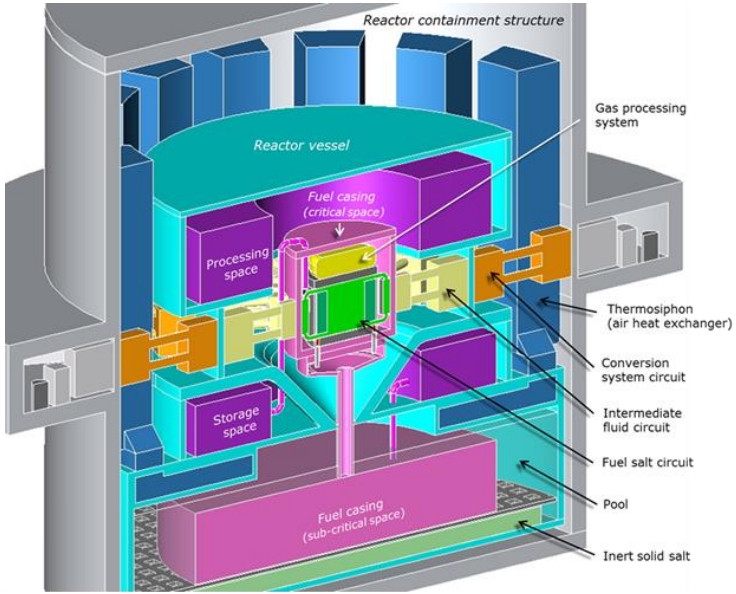

Methods – design #3

- Continuous extraction of salt to fuel salt treatment unit
- Emergency drain system
- Intermediate circuit and energy conversion system

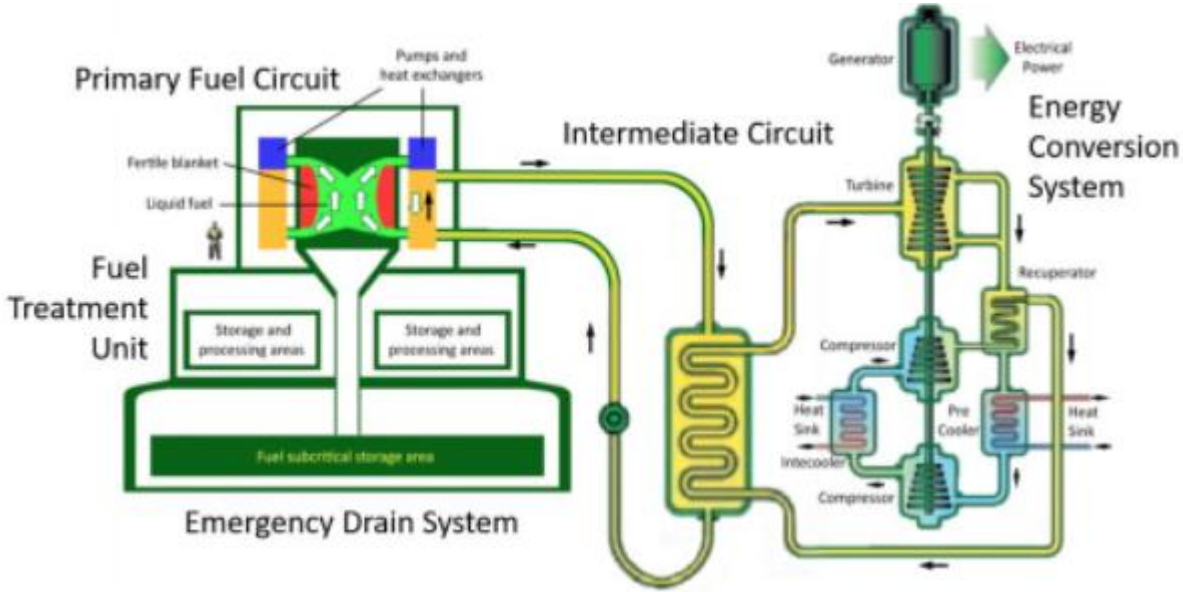

Methods – analysis #1

- **Coupling of a thermodynamic solver GEMS with MELCOR**
  1. Perform the MELCOR simulation for a predetermined time step (200 s in this study)
  2. Collect data containing elemental composition of the fission products in the fuel and the temperature of the fuel salt from MELCOR, and pass it to GEMS for further thermodynamic calculations
  3. Perform GEMS thermodynamic calculation
  4. Compile the GEMS results, e.g. vapor pressures of the species of interest, into an external input file and pass them to MELCOR for the next simulation step
  5. Repeat the cycle

GEMS – MELCOR coupling

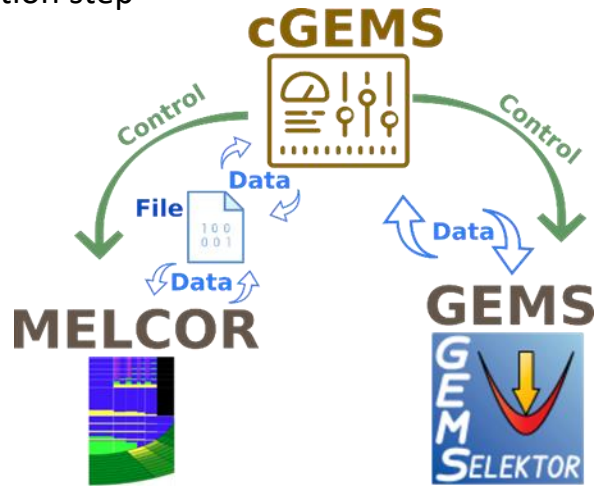

Methods – analysis #2

Schematic overview

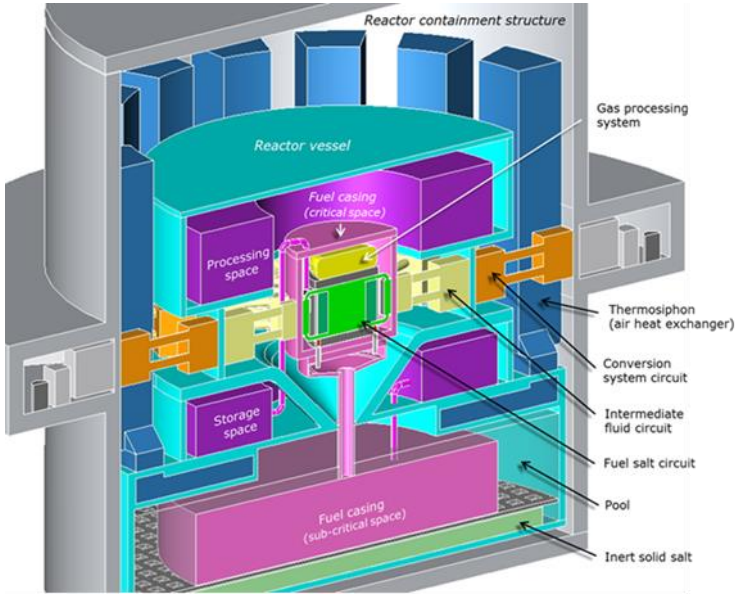

MELCOR model

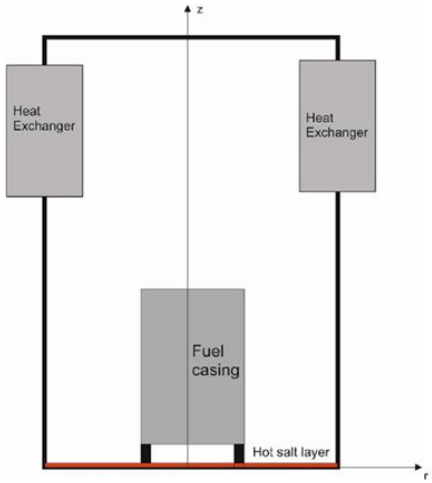

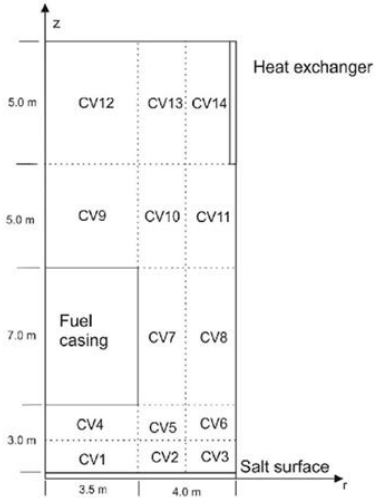

Methods – analysis #3

Schematic overview

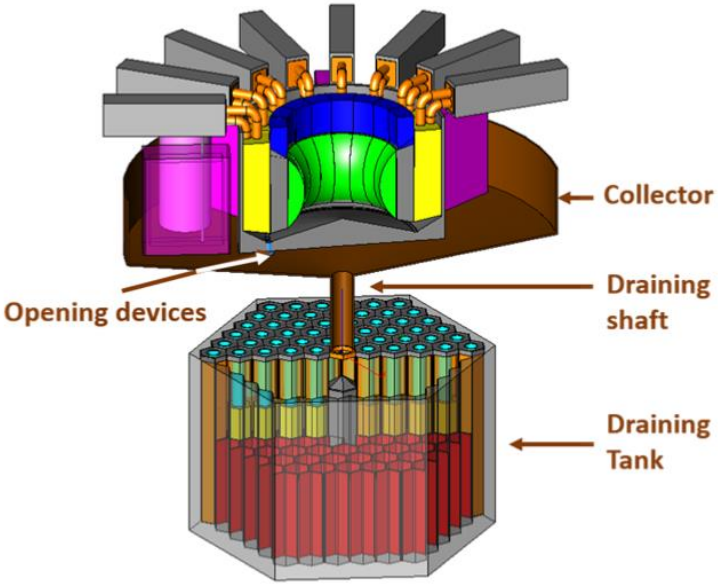

MELCOR model

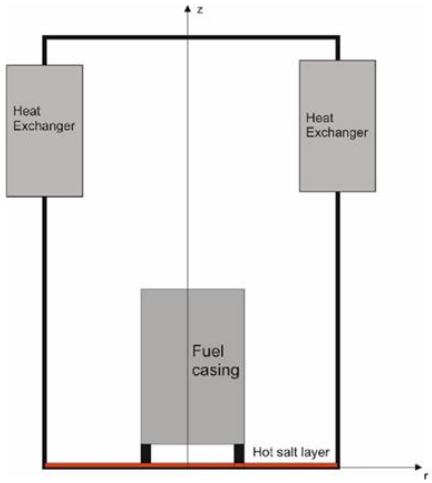

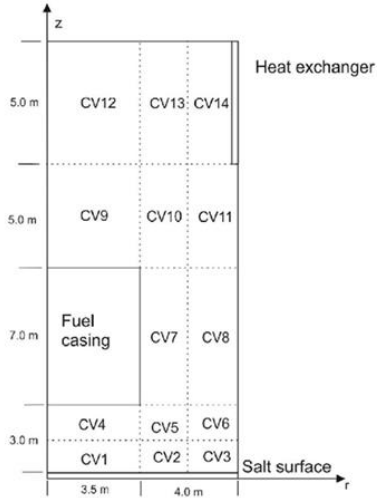

Methods – analysis #4

- Heat exchangers in the confinement
- Decay heat at shut-down 129 MW
- Salt temperature up to 1500 K
- Gas temperature 1150 K

MELCOR model

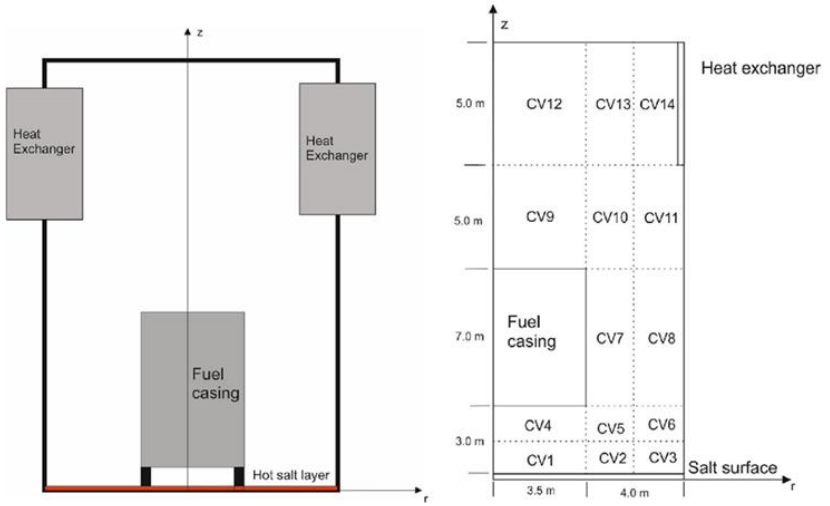

Methods – analyzed species

SYSTEM 1:

LiF-ThF4-UF4

(77.5-20-2.5 mol%)

with Cs and I

SYSTEM 2:

LiF-ThF4-UF4

with Cs, Zr, Np, Pu, Sr, Ba, La, Ce, Nd

Mass and activity calculated by EQL0D

Element	Mass [kg]	Initial activity [PBq]
Th	33 900	85 400
U	8 630	7 500
Li	4 720	0.0
F	26 800	0.0
Cs	11.2	5 500
I	0.063	9 700
Cs	11.2	5 500
Zr	182	22 600
Np	170	2 200
Pu	355	200
Sr	26.5	19 200
Ba	13.4	28 500
La	37.6	30 400
Ce	129	22 900
Nd	170	3 200

Methods – sensitivity cases

SYSTEM 1 and 2:

- Effect of fluorine: + 1% and -1 % fluorine
- Maximum salt temperature: 1300K, 1500K, 1700K
- Pool area: 80%, 90%, 100%

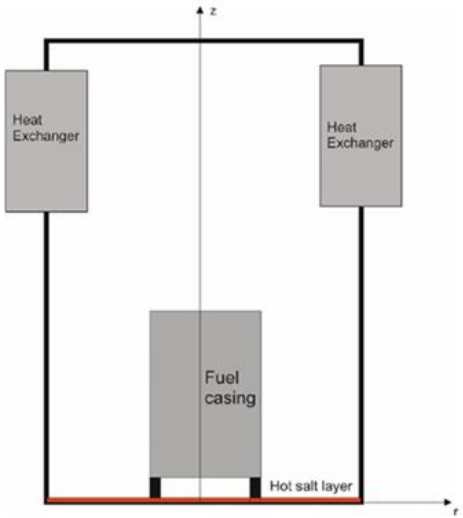

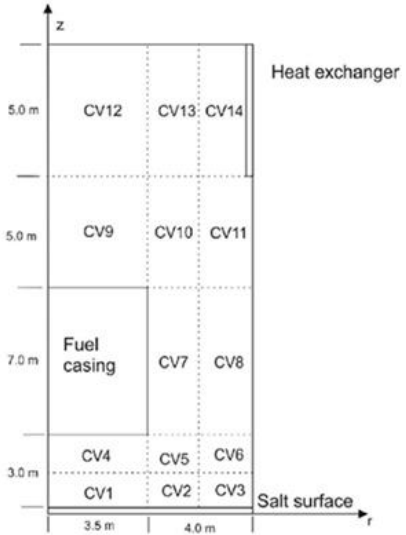

Results – total activity

- Decay of the isotopes considered
- No source from daughter elements from other decay chains considered
- Used to calculate the activity in the aerosols and vapor phase

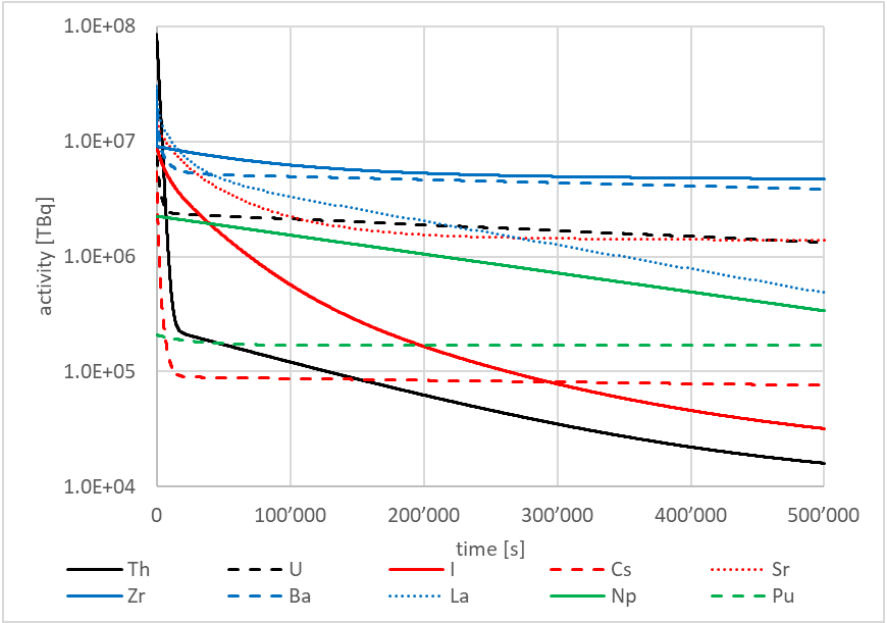

Results – confinement conditions

- Heat exchangers in the confinement
- Decay heat at shut-down 129 MW
- Salt temperature up to 1500 K
- Gas temperature 1150 K
- The whole core dropped to EDS:
  - 75 tons
  - Forms about 8 cm thick layer
  - 250 x 10^{18} Bq (250 000 PBq)

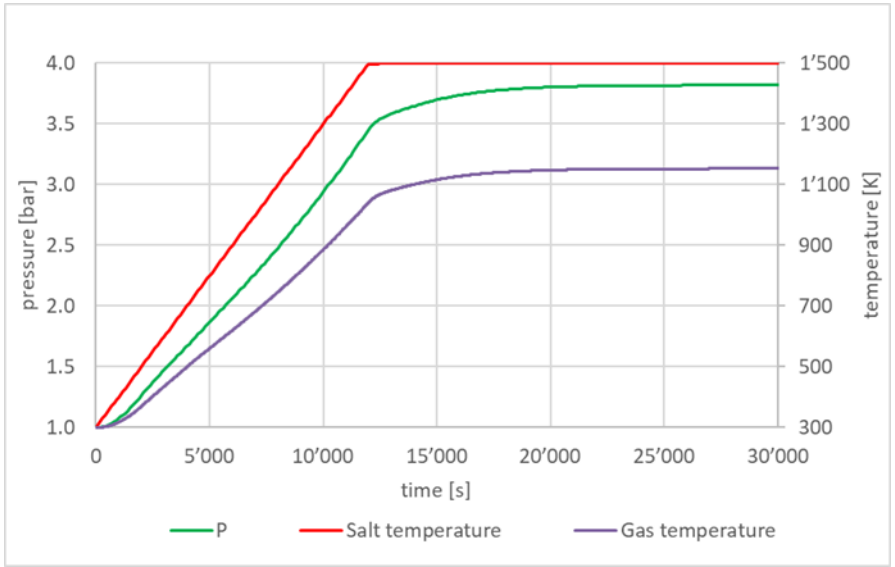

Results – limited system #1

- Release of **salt compounds**

Base case

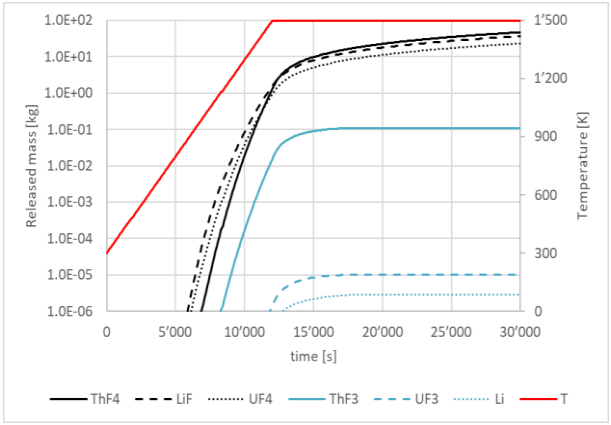

+1 % fluoride

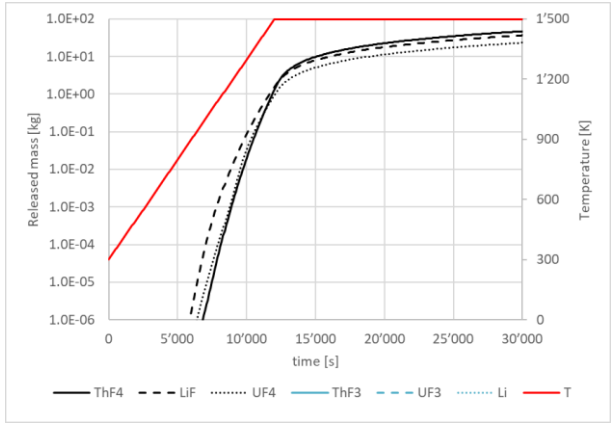

-1 % fluoride

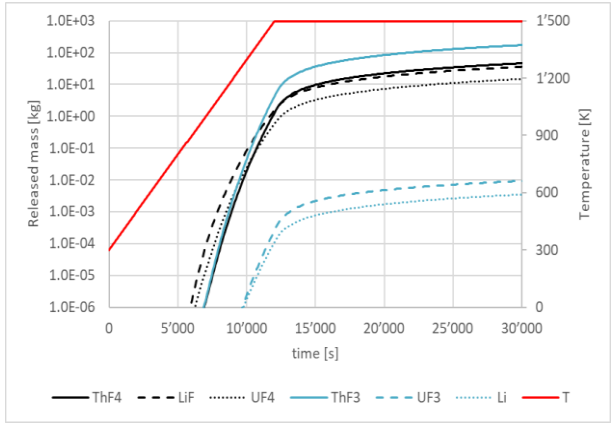

T = salt temperature

Results – limited system #2

- Release of **fission products**

Base case

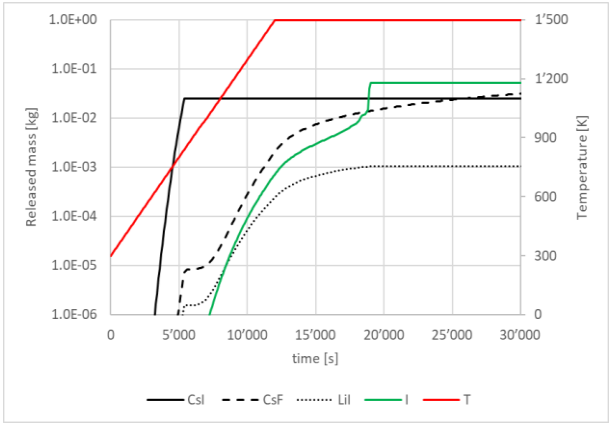

+1 % fluoride

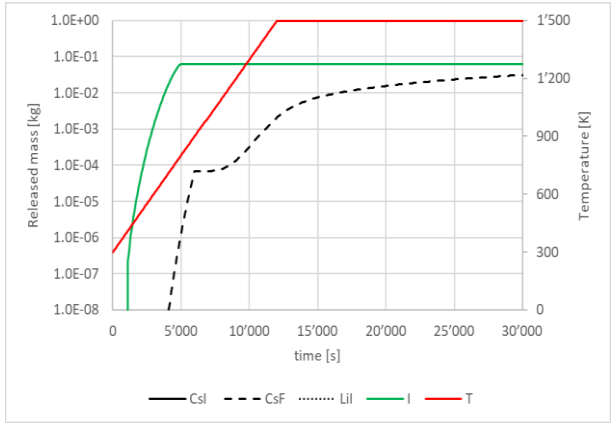

-1 % fluoride

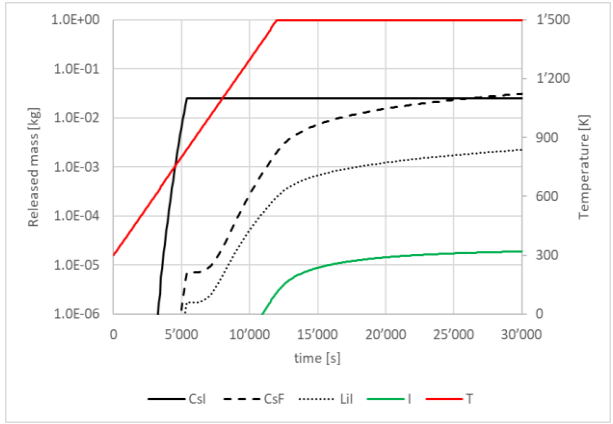

T = salt temperature

Results – limited system #3

- Aerosols and vapors in the confinement – base case

Aerosols

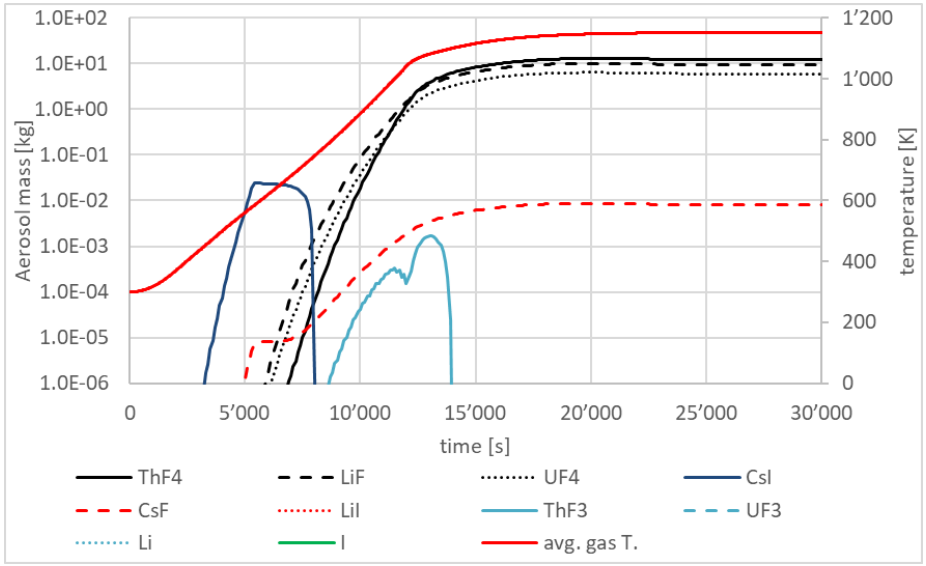

Vapors

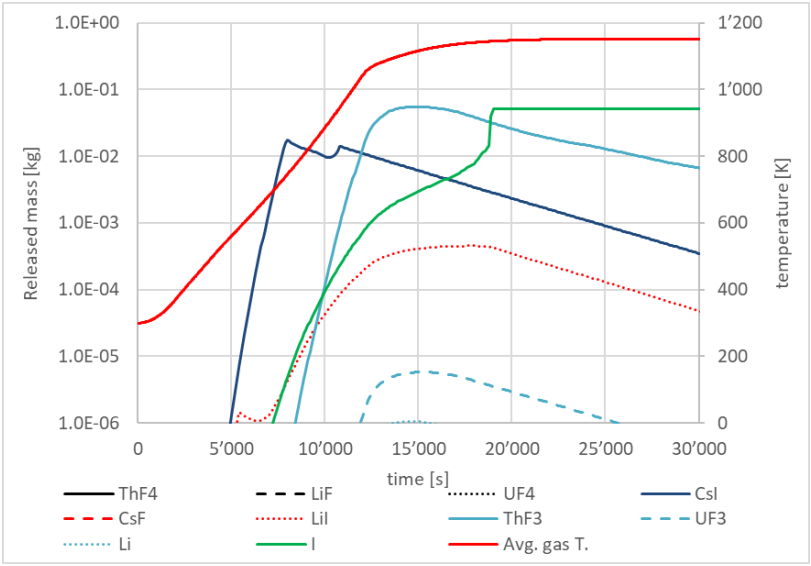

T = gas temperature

Results – extended system #1

- Released **salt and actinide species** – base case

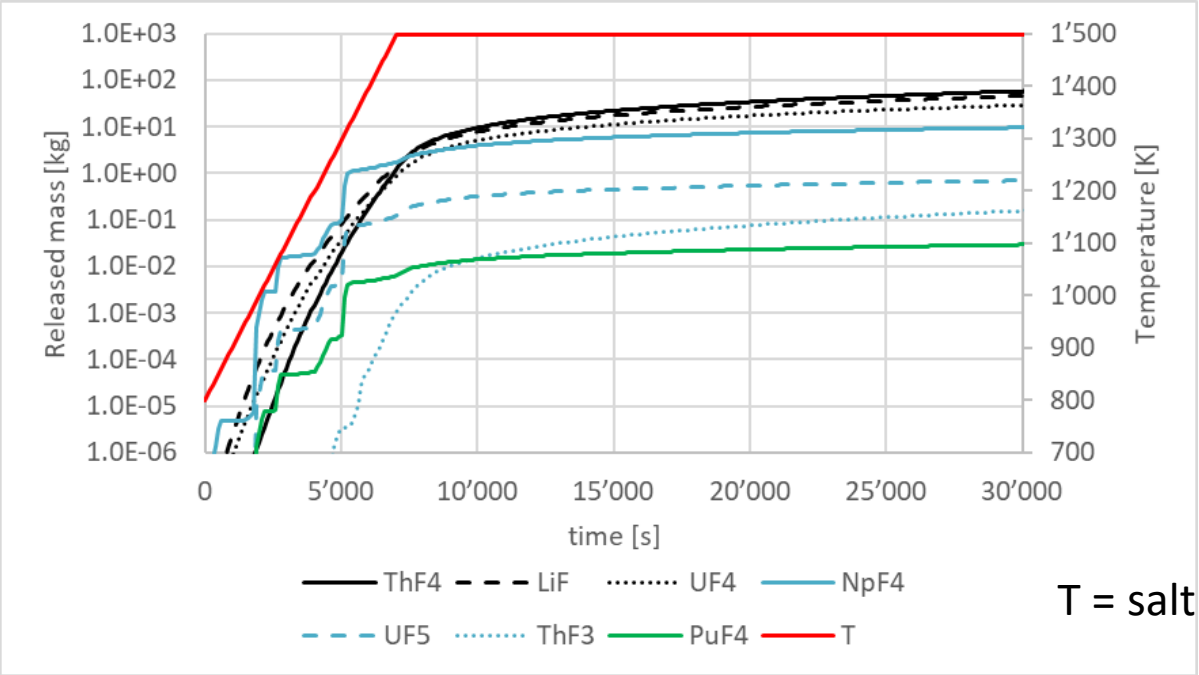

T = salt temperature

Results – extended system #2

- Released **fission products** – base case

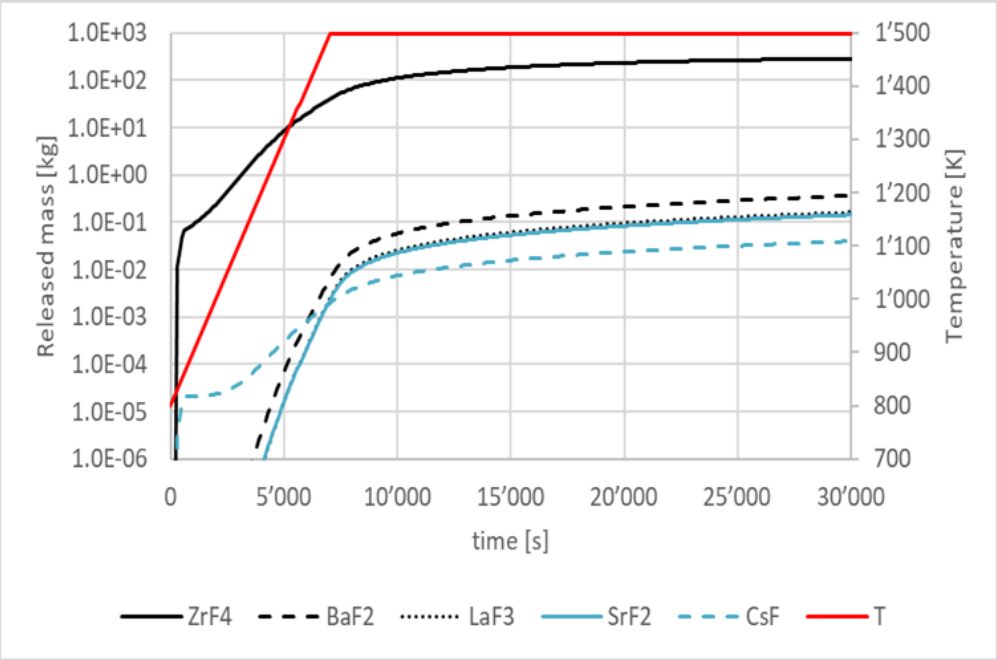

Results – extended system #3

- Aerosols and vapors in the confinement – base case

Aerosols

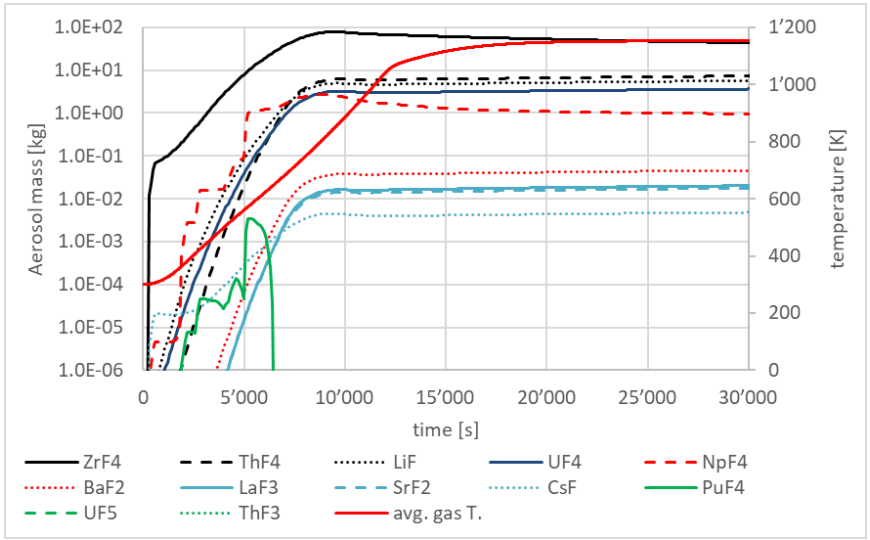

Vapors

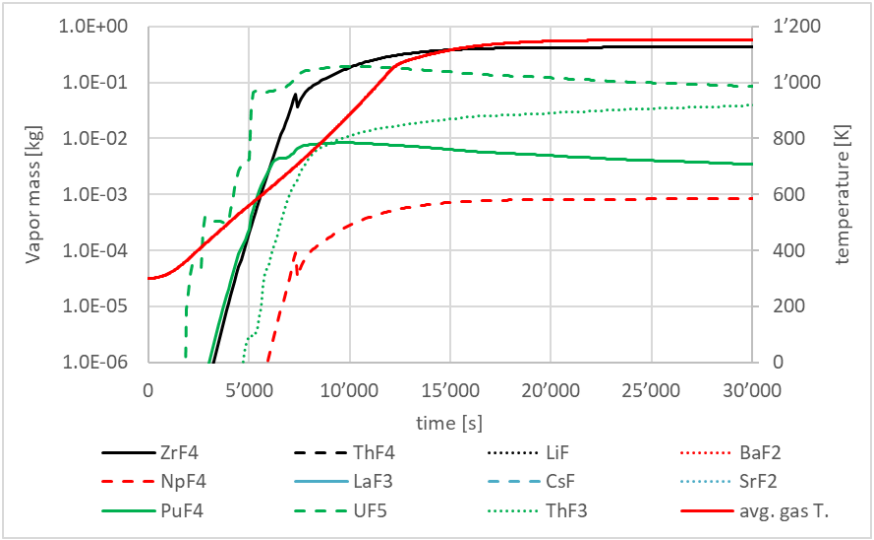

Results – extended system #4

- 330 kg evaporated species
- 26 000 PBq
- The main elements by mass:
  - Th, U, Li, Zr, Np
- The main elements by activity:
  - I, Zr, Ba
- In the **gas phase** in the confinement atmosphere:
  - 25% of iodine; 64% of ThF3 (low activity), 0.1% of Zr
  - 620 PBq iodine, 11 PBq Zr

Summary and future work

- Significant confinement pressure increase due to temperature increase
  - Potentially, need to vent (through a filter)
  - Both aerosols and vapor phase species
- Potentially, considerable **release of salt materials and fission products**
  - Aerosol formation and deposition
  - Deposition mechanisms different from LWR in the absence of steam
- **Evaporation very sensitive to fluoride content in the salt**
- Future work: More chemical data for salt materials and fission products
  - Application of the new data for improved analysis

This work has received funding from the Euratom research and training program 2014-2018 under grant agreement No. 847527. We would like to thank the SAMOSAFER project partners for fruitful collaboration.



MODELLING FPs RELEASE FROM SODIUM POOLS UNDER BDBA CONDITIONS

Monica Garcia and Luis E. Herranz
Unit of Nuclear Safety Research (CIEMAT)
Av. Complutense 40, E-28040 Madrid (Spain)
monica.gmartin@ciemat.es, luisen.herranz@ciemat.es

ABSTRACT

This work studies the release of volatile fission products (NaI) from hot sodium pools. A critical review of a model based on the film theory and its estimates in comparison to data from the NALA experimental program has been conducted. Given the assumptions embedded in the approach, the fitting-to-data transport coefficients derived and some inconsistencies found between its formulation and the estimates reported, an alternate approach including other phenomena anticipated in the scenario is here proposed. Based on diffusive and convective mechanisms in the gas phase, the assumption of the analogy between heat and mass transport (HMT) and the Raoult's law to set the NaI concentration at the Na pool interface, a good agreement has been found with experimental data, which mean a substantial enhancement of qualitative and quantitative predictability and, no less important, at the same time do have a conservative nature.

KEYWORDS
SFRs, Source Term, FPs Release, Mass Transfer Model

1. INTRODUCTION

In the event of a Beyond Design Basis Accident (BDBA) in Sodium-cooled Fast Reactors (SFRs) large amounts of fuel, fission products, and contaminated sodium can enter the containment in case of vessel failure. In addition to the instantaneous or primary source term resulting from the energetic fuel expansion into the coolant to form a bubble and release material from vessel leaks, one must consider the long term release of FPs from contaminated hot pools. In the case of vessel failure, the heated sodium by the decay heat would evaporate in the inertized inner containment with the release of volatile fission products. In this scenario, the estimation of the sodium pool retention capability is of utmost importance.

In the past, analytical models for the prediction of volatile fission products release from the sodium (Na) pool into an inert gas atmosphere were developed. In these models, the release of the volatile fission products is governed by diffusive transport processes. Based on a mass transfer formulation, the retention factor (defined as the ratio between the relative transfer rates of FP with respect to their initial inventories in the pool) of the species of interest is calculated.

This paper synthesizes the results of the work developed by CIEMAT in the frame of the ESFR-SMART project (contract number 754501). A critical review of the earlier work done by [1]–[3] and others on fission products release from hot sodium pools has been done through the comparison of the model results against experimental data from the NALA program [4], [5]. In these works, the film theory was applied for the evaporative release of FPs calculation. With the assumption of a hypothetical stagnant film at the gas/liquid

interface, transport through was assumed to be governed by diffusion. Given the weakness found in the formulation of these works, a more mechanistic approach including other phenomena anticipated in the scenario is proposed and the results are compared and discussed.

2. NALA PROGRAM

NALA is a German (KFK) experimental program that included the investigation of fuel and fission products release from a wide range of sodium pool temperatures, including sodium boiling and sodium aerosol behavior in a closed/open vessel for a variety of geometric and convective conditions and for a representative selection of fission products. All the tests were performed in an inert atmosphere (Ar or N_2). The program consisted of laboratory-scale experiments in a glove box (NALA I), technical-scale experiments (NALA II), and laboratory-scale experiments in a forced convection loop (NALA III). In this work, the focus is on the results derived from the NALA II phase: a sodium aerosol system under natural convection [4], [5].

The main components of the NALA II facility are a 2.2 m^3 heated vessel, a sodium pot of 26 cm inner diameter with external heating devices (acetylene burner) to be flanged to the vessel bottom, inert gas supply, survey instrumentation, and aerosol measurement instrumentation (Fig. 1).

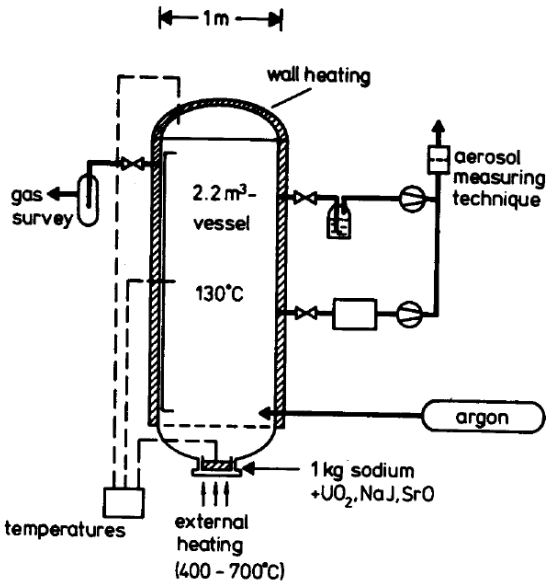

Figure 1. Diagram of the NALA-II facility [4]**.**

The boundary conditions in NALA II experiments were defined according to the SNR 300 core catcher design characteristics: pool temperatures from 600 to 900 K, inert gas temperatures of 400 K, natural convection and admixtures of UO_2, NaI and SrO in the pool [4], [5]. The vessel is filled with argon at normal pressure (1 bar) and heated up to 400 K; this temperature is kept constant during the whole experiment. In the sodium pot, sodium amounts of the order of 1 kg are heated up to the desired pool temperature. By flame regulation, a temperature plateau is approximately achieved during the tests. The duration of the external heating (0.7 to 3 h) is adjusted to the evaporation rate in such a way that ~10% of the sodium evaporates. Temperatures are measured at six different locations in the vessel and at two locations in the sodium pot. During the period of the external heating, all containment gas temperatures were practically the same. The aerosol instrumentation consists of washing bottles, filters and an automatic, continuously measuring device for sodium mass concentration measurements. An Andersen impactor is used for size distribution measurements. In the next table, the main characteristics of NALA II tests are shown (Table I).

Table I. Compilation of some of the available characteristics of NALA II facilities [5]**.**

Geometry	Values
Na pool area (cm^2)	531
Vessel	2.2 m^3 2.30 m high (cylindrical part)
Tests conditions	
Na (kg)	1
Na T (K)	600-900
Atm. gas (K)	400 (Ar)
Contaminants	UO_2, NaI, SrO

The present analysis is focused on the experiments on sodium (Na) and sodium iodine (NaI) vaporization. Table II compiles the experimental data for the tests of interest. As it can be seen, T3, T5 and T7 are exclusively devoted to the Na vaporization estimates. Note that being Na boiling point around 1156 K, the Na vaporization rate is controlled by increasing Na temperature and, in no case, Na pool reached boiling conditions.

Table II. Tests conditions [5]**.**

Exp. Nr.	T (K)	Na amount (g)	NaI amount (g)
T1	835.15	258	1.00
T2	905.15	1100	1.06
T3	754.15	1315	-
T4	769.15	1322	10.00
T5	837.15	1146	-
T6	823.15	1321	0.20
T7	830.15	1007	-

3. THEORETICAL MODELS OVERVIEW

In this section, an overview of the earlier modeling work by other authors is given and the accuracy of their estimates is shown against NALA data. Then, the formulation of a more mechanistic model is thoroughly described. And, finally, additional phenomena are included in the formulation and their effect are assessed against the same database.

3.1. Background

Fission products emission from hot sodium pools was analyzed and compared against experimental data from NALA II program by [1], [4], [6], and later by [2] among others. In all these works, the evaporative release is modeled as governed by diffusive and convective transport processes. Based on the film theory by Nerst (1904) a mass transfer coefficient approach is made: the mass flux of the volatiles is assumed to be controlled by a driving force, i.e. the partial density difference between the gas side of the liquid surface and the atmosphere, and the gas mass transfer coefficient represents the reciprocal resistance of the species against mass transfer [1].

In NALA program [4]–[6], the experimental release of a fission product solute (i) is given with respect to the release of the solvent (liquid sodium) by the Retention Factor (RF):

$$RF = \frac{\left[m_i / m_{solvent} \right]_{pool}}{\left[\phi_i / \phi_{solvent} \right]_{released}} \quad (1)$$

Where m denotes the initial inventory of the FP (i) and solvent (liquid Na) and ϕ the release mass fluxes. In other words, the retention factor is a ratio between the relative transfer rates of Na and FP (relative with respect to their initial inventories in the pool).

Fig. 2 shows the main results obtained by [1] regarding RFs of NaI in the Na pool (black line). In this approach, the gas mass transfer coefficient for sodium vapor has been fitted to the NALA database. Despite this, there is an overestimation in the predictions that in some tests is as high as a factor of 30. An attempt made to reproduce these results is shown (red line). Even by using the same fitted Sherwood number (Eq. 3.10 from [1]) and Na and NaI properties, these estimations are far from [1] ones.

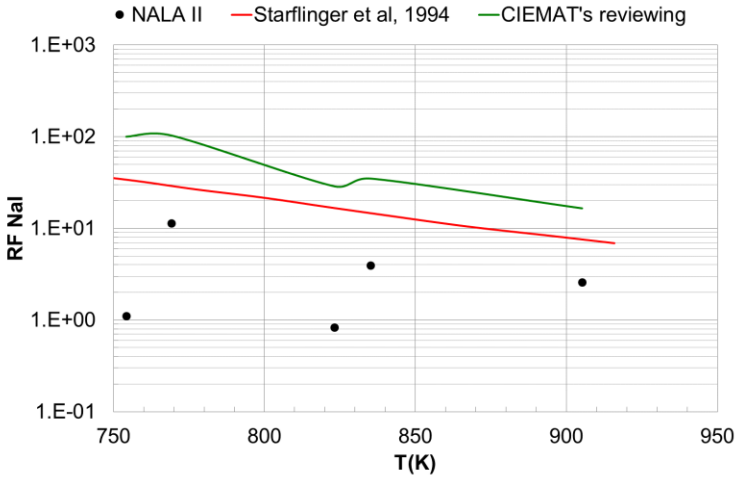

Figure 2. RF of NaI in Na vs. pool temperature.

The correlation given by Eq. 4.29 by [1] in the temperature range of interest (298K ≤ T ≤ 933 K) is as follows:

$$p_{v,NaI} = 10^5 \cdot 10^{\left[7.557 - \frac{10924}{T}\right]} \quad (2)$$

However, results from this equation differ from the experimental data reported by [7]. In the next equation, a correlation of these experimental values [7] for the NaI vapor pressure is presented:

$$p_{v,NaI} = 133.322 \cdot 10^{\left[11.681 - \frac{11028}{T}\right]} \quad (3)$$

By using this correlation, pressure vapors up to one order of magnitude higher than those predicted by Eq. 4.29 [1] are found which would account for the overestimations in RF calculations (Fig. 3):

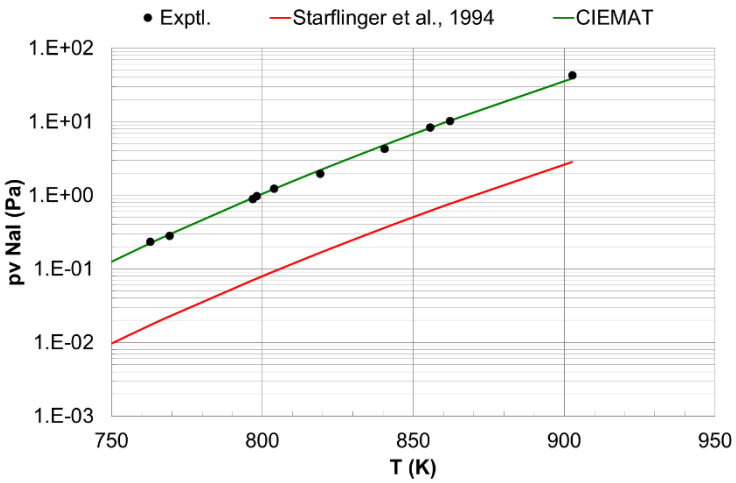

Figure 3. NaI vapor pressure vs. pool temperature.

3.2. Gas mass transfer (GMT) model

Building on the previous works, the gas mass transfer model (GMT) approach is based on the film theory [8]. This theory is a simple conceptualization of the gas-liquid transfer processes in which near the interface there exists a hypothetical stagnant film (bulk liquid is not moving) and transport is governed essentially by molecular diffusion; in the interface, equilibrium is assumed between liquid and gas phases. In this approach and based on estimations of the mass transfer coefficients, only the gas-phase mass transfer is calculated, neglecting the liquid one due to the fact that the resistance to mass transfer in the gas phase is up to four orders of magnitude higher than the liquid mass transfer coefficient [8]. Fig. 4 represents the decrease of the partial density from the gas side of the interface into the gas bulk.

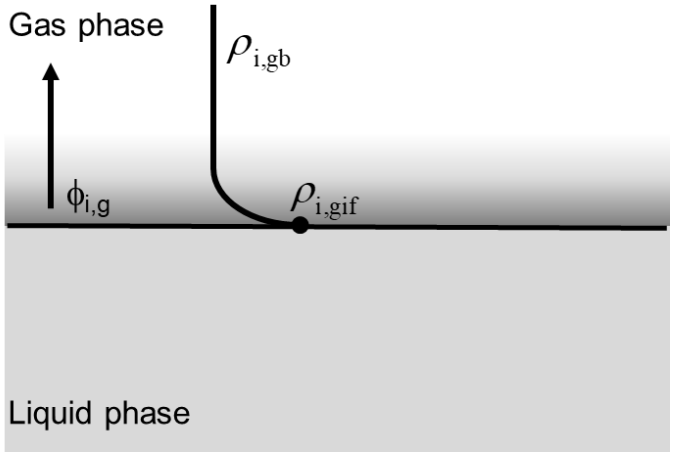

Figure 4. GMT model sketch.

In this approach, the release mass flux (ϕ) of any volatile species (i, FPs and Na) from the liquid phase is controlled by a driving force, i.e. the partial density difference between liquid surface and gas bulk and the reciprocal resistance of the species against mass transfer is taking into account through the gas mass transfer coefficient:

$$\phi_i = k_{i,g} \cdot \Delta\rho_{i,g} \tag{4}$$

Where the mass transfer coefficient ($k_{i,g}$) is derived from the non-dimensional Sherwood number and the ratio between the binary diffusion coefficient of the considered species in the gas phase and the characteristic length of the system:

$$k_{i,g} = Sh_{i,g} \cdot \frac{D_{i,g}}{L} \tag{5}$$

NaI binary diffusion coefficient in Argon ($D_{NaI,Ar}$) has been taken from [9], Na binary diffusion coefficient in Argon ($D_{Na,Ar}$) is taken from [10] and the characteristic length of the system (L) is taken as a quarter of the Na pool diameter (d/4) as recommended by [11]. By applying the HMT analogy (Le~1 in the analyzed scenarios), the convective mass transfer Sherwood number is estimated from suitable heat transfer correlations, according to the prevailing flow regime (as determined through the non-dimensional Ra numbers) [11]:

$$Sh = 0.15 \cdot \left(Gr \cdot Sc\right)^{1/3} \quad (10^7 \le Ra \le 10^{11}, all\ \mathrm{Pr}) \tag{6}$$

The partial density difference in the gas phase between the gas interface (gif) and the gas bulk (gb) is calculated through:

$$\Delta\rho_{i,g} = \rho_{i,gif} - \rho_{i,gb} \tag{7}$$

Where $\rho_{i,gif}$ is estimated from the saturation vapor pressure of the chemical species, which is just correlated with pool temperature [8]. This implicitly entails that the potential interaction between NaI (solute) and Na (solvent) is considered negligible. On these assumptions, $\rho_{i,gif}$ is calculated as

$$\rho_{i,if} = \frac{p_{v,i}(T_{if})}{(R/M_i)\cdot T_{if}} \cdot \gamma_i \cdot x_i \tag{8}$$

With $p_{v,Na}$ from [12] and $p_{v,NaI}$ calculated from Eq. 3, x_i denoting the mole fraction of the species i in the liquid, and γ_i the activity coefficient of the species i. Due to the small amount of fission products solved in the sodium pool, the approximation $x_{Na} = \gamma_{Na} = 1$ is made [1]–[3]. In the case of NaI, γ_{NaI} is calculated through the excess Gibbs free energy of mixing at an infinite solution [13]. The resulting values, larger than 100, indicate the strong tendency of NaI to escape from the Na pool [14]. All gas phase properties involved in the above equations are evaluated at the pool temperature ($T_{if} \approx T_{pool}$). Note that $\rho_{i,gb}$ grows along time due to the incoming NaI flow from the pool over time.

When Na vapor moves away from the pool surface enters in a cooler region where molecules tend to nucleate in the form of tiny primary particles and, depending on conditions, grow by heterogeneous condensation or even coalescence. Beyond the local heat-up this entails in a region close to the pool surface, in terms of mass this means that the growth of gas bulk Na density, $\rho_{Na,gb}$, should be more moderate than initially considered; in other words, Na density difference between interface and gas bulk will be higher and so evaporation rates. To take this effect into account, a correction factor (f_{cond}) is introduced in Eq. 4:

$$\phi_{\mathrm{Na}} = k_{\mathrm{Na,g}} \cdot \Delta\rho_{Na,g} \cdot f_{cond,Na} \tag{9}$$

This correction factor is calculated by the following equation [4], [9] and [13]:

$$f_{\text{cond,Na}} = \frac{\beta_{Na}(T_{if}) \cdot \left(\Delta T \cdot Le^{-n} + \left(\Delta h_{v,Na} \cdot \Delta p \right) / \left(Le \cdot c_{p,gb} \cdot P \right) \right)}{\Delta p \cdot \left(1 + \left(\beta_{Na}(T_{if}) \cdot \Delta h_{v,Na} \right) / \left(Le \cdot c_{p,gb} \cdot P \right) \right)} \quad (10)$$

Where β_{Na} corresponds to the first derivative of the vapor pressure $p_{v,Na}$ to the temperature T at the interface, ΔT and ΔP the temperature and pressure differences in the gas phase, $\Delta T = T_{if} - T_{gb}$ and $\Delta p = p_{Na,gif} - p_{Na,gb}$ respectively, n is the coefficient corresponding to the heat transfer correlation used, $c_{p,gb}$ the specific heat capacity of the gas phase, $\Delta h_{v,Na}$ the latent heat of vaporization of sodium and Le is the dimensionless Lewis number (ratio between the Schmidt and Prandtl numbers).

In the next figure (Fig. 5), a comparison between NALA II experimental data of free convection controlled Na release from a liquid pool into Argon gas atmosphere and the calculated predictions is presented: predictions by [1] (black line) and GMT model estimations (blue dots). At first glance quantitative and qualitative good agreement is obtained by both approaches, specially estimations from [1] where a fitted to data mass transfer coefficient for sodium is used. This quantitative difference points out the sensitivity of the model to the gas transfer coefficient calculation.

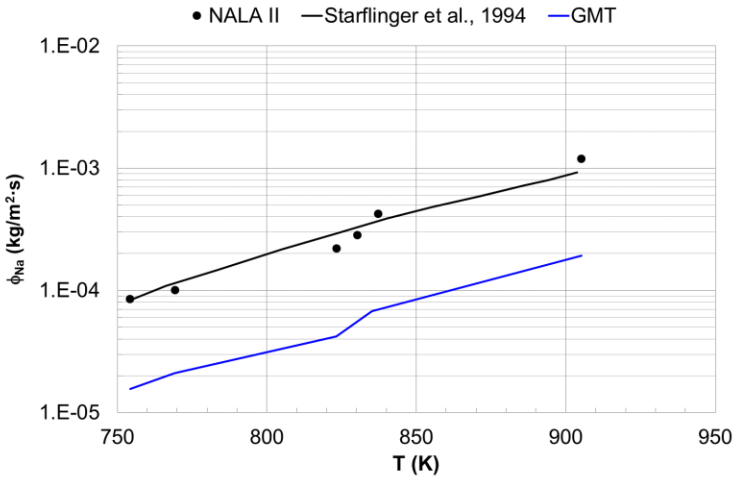

Figure 5. Na mass flux of evaporation vs. pool temperature.

Fig. 6 shows the models-to-data comparison in terms of the RF. In spite of the good estimations for the Na mass flux by [1], a huge overprediction is observed with the lower pool temperatures and as pool temperature increases, the overprediction is reduced. GMT good agreement with experimental data highlights the unnecessary of fitted mass transfer coefficients and the great sensitivity of the model to variables with empirical nature as pressure vapor or binary diffusion coefficients.

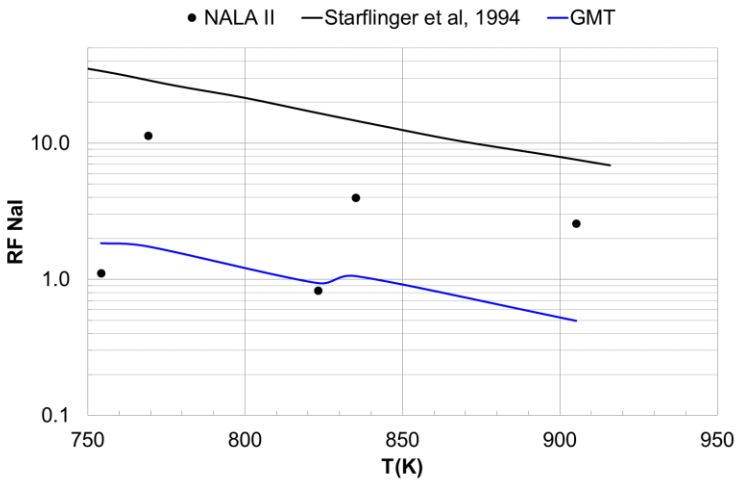

Figure 6. RF of NaI in Na vs. pool temperature.

3.3. Extended gas mass transfer (EGMT) model

Despite the good agreement obtained with GMT approach, the search for a more mechanistic model to include the dragging effect of the Na on the volatile species release leads us to propose an extension of the GMT by adding a term in Eq. 4 to take into account this phenomenon:

$$\phi_i = k_{\mathrm{i,g}} \cdot \Delta\rho_{\mathrm{i,g}} + \frac{\phi_{\mathrm{Na}}}{\rho_{\mathrm{sat,Na}}(T_{\mathrm{pool}})}\rho_{\mathrm{i,gif}} \tag{11}$$

Where ϕ_{Na} is given by Eq. 9 and $\rho_{\mathrm{sat,Na}}$ is the density of sodium vapor above the saturated liquid, calculated from the thermodynamic relation [12]:

$$\rho_{\mathrm{sat,Na}} = \left(\frac{\Delta h_g}{T \cdot \beta_{sat}} + \frac{1}{\rho_l} \right)^{-1} \tag{12}$$

Where Δh_g the enthalpy of vaporization, β_{sat} the temperature derivative of the pressure along the saturation curve and ρ_l the liquid sodium density.

Fig. 7 illustrates the NaI vaporization rates given by GMT and EGMT approaches. In this case, no experimental data are available. From the figure, the effect of Na vapor dragging results in an enhancement of the NaI mass flux by a factor between 4 to 3, the lower the temperature, the higher the dragging impact on the mass flux. Regarding the absence of a clear trend of mass flux with temperature, it can be explained by the scattered initial inventories (Table II) that shield the increasing mass flux trends with pool temperature predicted by the models. As expected, an increasing trend with temperature of NaI mass flux estimations can be observed when looking at the gas mass transfer coefficient (embedded table in Fig. 7).

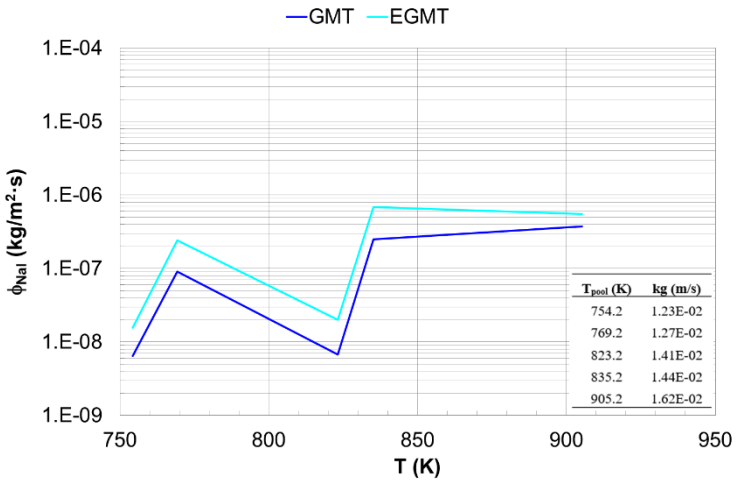

Figure 7. NaI mass flux vs. pool temperature.

RF experimental values are compared against models predictions in the next figure (Fig. 8). As indicated by [1], experimental data of the NaI release under varying conditions of pool temperature and initial inventories (Table II) show a considerable scattering of the retention factor [1]. Differences between GMT and EGMT results indicate an overprediction of the NaI mass flux with the EGMT approach: the dragging effect of Na vapor on the total NaI mass flux seems to be overestimated.

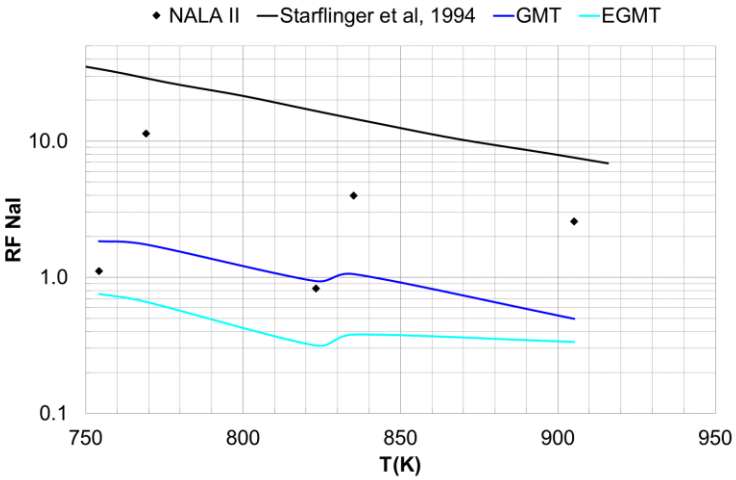

Figure 8. NaI RF vs. pool temperature.

4. CONCLUSIONS

This work studies the release of volatile fission products from hot sodium pools. A critical review of previous works has been done and the main weakness of these approaches identified. A more mechanistic approach including other phenomena anticipated in the scenario is proposed and the results are compared and discussed.

An exhaustive review of previous works based on film theory, besides the assumptions embedded in this approach and some inconsistencies found between its formulation and the estimates reported, reveals the use of fitting-to-data transport coefficients derived from the experimental NALA database, achieving in this manner excellent agreement of Na vapor estimations. However, this is not translated to the RF predictions with a large overprediction of the RF ones that is overcome with a different correlation for the NaI vapor

pressure. Despite the overall good results, the use of an adjusted mass transfer correlation could impair somewhat the validation of these works.

After checking the suitability of the film model for the analyzed scenario through an estimation of the gas/liquid mass transfer coefficients, a mass transfer model based on diffusive and convective mechanisms in the gas phase, the assumption of the analogy between HMT and the Raoult's law to set the NaI concentration at the Na pool interface is build up. Besides, other phenomena anticipated in the scenario are included.

In this approach, the convective mass transfer Sherwood number is estimated from classical heat transfer correlations, according to the prevailing flow regime and the dragging of the Na vapor on the volatile species release is included through a term on the general mass flux equation. From the results, the gas transport coefficient is proved to be the most influencing factor and the results point out the unnecessary of fitted values by means of an adequate Sherwood number choice. Moreover, their formulation has an empirical nature that makes their use restricted to their development range. A good agreement has been found with experimental data, which means a substantial enhancement of qualitative and quantitative predictability and, no less important, at the same time do have a conservative nature.

As future work, the validation of the proposed approach is planned to be extended to NaI and Cs in NALA I conditions, i.e., thermal equilibrium between the liquid pool and atmosphere and forced convection.

ACKNOWLEDGMENTS

The CIEMAT authors wish to thank the funding received from the 7th Framework Programme of the European Commission via the ESFR-SMART project (contract number 754501).



REFERENCES

[1] J. Starflinger, M. Koch, U. Brockmeier, W. Scholtyssek, W. Schütz, and H. Unger, "The release code package REVOLS/RENONS for fission product release from a liquid sodium pool into an inert gas atmosphere," Kernforschungszentrum Karlsruhe G.m.b.H. (Germany, KfK5426, Dec. 1994.

[2] A. Pradeep, P. Mangarjuna Rao, B. K. Nashine, P. Selvaraj, and P. Chellapandi, "Estimation of evaporation rate of cesium from hot sodium pool to inert cover gas of typical SFR," *Annals of Nuclear Energy*, vol. 92, pp. 431–439, Jun. 2016, doi: 10.1016/j.anucene.2016.01.051.

[3] T. Kumada, F. Kasahara, and R. Ishiguro, "Sodium Evaporation into a Forced Argon Flow, (I) Measurements of Evaporation under Condition of Fog Formation," *Journal of Nuclear Science and Technology*, vol. 13, no. 2, pp. 74–80, Feb. 1976, doi: 10.1080/18811248.1976.9733988.

[4] H. Sauter and W. Schütz, "Aerosol release from a hot sodium pool and behavior in sodium vapor atmosphere," presented at the Proceedings of the CSNI Specialist Meeting on Nuclear Aerosols in Reactor Safety, Gatlingburg, Tennessee (USA), Apr. 1980.

[5] H. Sauter and W. Schütz, "Aerosol- und Aktivitaetsfreisetzung aus kontaminierten Natriumlachen in Inertgasatmosphaere," Kernforschungszentrum Karlsruhe G.m.b.H. (Germany, Laboratorium für Aerosolphysik und Filtertechnik, KfK3504, 1983. Accessed: Jan. 31, 2018. [Online]. Available: https://publikationen.bibliothek.kit.edu/270018819

[6] U. Brockmeier, M. Koch, H. Unger, and W. Schütz, "Volatile fission product and sodium release from liquids," *Nuclear Engineering and Design*, vol. 148, no. 2, pp. 499–507, Jul. 1994, doi: 10.1016/0029-5493(94)90129-5.

[7] G. E. Cogin and G. E. Kimball, "The Vapor Pressures of Some Alkali Halides," *J. Chem. Phys.*, vol. 16, no. 11, pp. 1035–1048, Nov. 1948, doi: 10.1063/1.1746720.

[8] D. W. Green and R. H. Perry, *Perry's Chemical Engineers' Handbook, Eighth Edition*. McGraw-Hill: New York, Chicago, San Francisco, Lisbon, London, Madrid, Mexico City, Milan, New Delhi, San Juan, Seoul, Singapore, Sydney, Toronto, 2008. Accessed: Oct. 11, 2019. [Online]. Available: /content/book/9780071422949

[9] S. Tashiro and N. Sagawa, "Diffusion Coefficient Determination of Sodium Iodide Vapor in Rare Gases with Use of Ionization Sensor," *Journal of Nuclear Science and Technology*, vol. 38, no. 7, pp. 551–556, Jul. 2001, doi: 10.1080/18811248.2001.9715066.

[10] A. Pradeep, P. M. Rao, B. K. Nashine, and P. Chellapandi, "Estimation of retention factor of cesium in sodium pool under fuel pin failure scenario in SFR," *Nuclear Engineering and Design*, vol. 243, pp. 102–110, Feb. 2012, doi: 10.1016/j.nucengdes.2011.12.012.

[11] F. P. Incropera and D. P. Dewitt, *Introduction to heat transfer. Sixth Edition*, Jonh Willey&Sons Inc. 2011. Accessed: Jul. 14, 2016. [Online]. Available: http://trove.nla.gov.au/version/206858590

[12] J. K. Fink and L. Leibowitz, "Thermodynamic and transport properties of sodium liquid and vapor," ANL/RE--95/2, 94649, Jan. 1995. Accessed: Jul. 14, 2016. [Online]. Available: http://www.osti.gov/servlets/purl/94649-gXNdLI/webviewable/

[13] A. W. J. Castleman, I. N. Tang, and R. A. Mackay, *Fission Product Behavior in Sodium Systems*. International Atomic Energy Agency (IAEA), 1967. Accessed: Jan. 24, 2018. [Online]. Available: http://inis.iaea.org/Search/search.aspx?orig_q=RN:44072892

[14] K. Haga, Y. Nishizawa, T. Watanabe, S. Miyahara, and Y. Himeno, "Equilibrium and nonequilibrium partition coefficients of volatile fission products between liquid sodium and the gas phase," *Nuclear Technology*, vol. 97, no. 2, pp. 177–185, 1992.

[15] C. F. Clement and P. Hawtin, "Transport of sodium through the cover gas of a sodium cooled fast reactor," International Atomic Energy Agency (IAEA), 1977.

Modelling FPs Release from Sodium Pools under BDBA Conditions

Monica Garcia and Luis E. Herranz

Unit of Nuclear Safety Research
CIEMAT (Spain)

ESFR-SMART Horizon 2020 (contract number 754501)

CONTENTS

- INTRODUCTION
- DATA & MODEL ASSESSMENT
- CIEMAT's MODEL
- RESULTS
- FINAL REMARKS

INTRODUCTION

Gen IV Technology

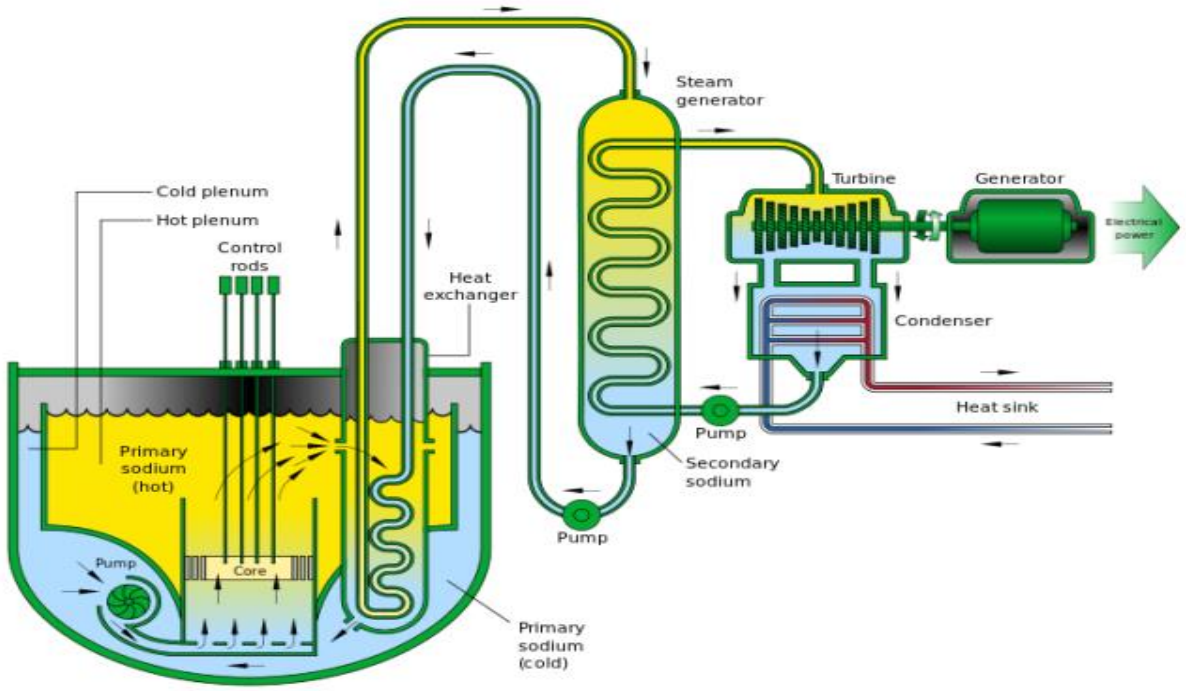

	Name	Type	Country	Thermal power	Criticality	Status
Experimental	CLEMENTINE (Hg)		USA	0.02 MW_{th}	1946	A: 1952
	EBR I (NaK)	Loop	USA	1.4 MW_{th}	1951	A: 1963
	BR 1		USSR	0.03 MW_{th}	1955	A
	BR 2 (Hg)		USSR	0.2 MW_{th}	1956	A: 1957
	BR 5 – BR 10	Loop	USSR	5/10 MW_{th}	1958/1973	A: 2002
	DFR (NaK)	Loop	UK	75 MW_{th}	1959	A: 1977
	LAMPRE		USA	1 MW_{th}	1961	A: 1965
	EBR II	Pool	USA	60 MW_{th}	1963	A: 1994
	RAPSODIE	Loop	France	24/40 MW_{th}	1967/1970	A: 1983
	BOR 60	Loop	USSR	60 MW_{th}	1968	F
	SEFOR	Loop	USA	20 MW_{th}	1969	A: 1972
	KNK I – KNK II	Loop	Germany	60 MW_{th}	1972/1977	A: 1991
	JOYO	Loop	Japan	50 MW_{th}	1977	A: 2007
	FFTF	Loop	USA	400 MW_{th}	1980	A: 1994
	FBTR	Loop	India	40 MW_{th}	1985	F
	PEC	Loop	Italy	120 MW_{th}		A: 1987
	CEFR	Pool	China	60 MW_{th}	2010	F
Demonstrators	FERMI	Loop	USA	100 MW_e	1963	A: 1972
	BN 350	Loop	Kazakhstan	150 MW_e	1972	A: 1998
	PHÉNIX	Pool	France	250 MW_e	1973	A: 2009
	PFR	Pool	UK	250 MW_e	1974	A: 1994
	SNR 300	Loop	Germany	300 MW_e		A: 1992
	MONJU	Loop	Japan	280 MW_e	1992	A: 2010
	CRBR	Loop	USA	350 MW_e		Ab: 1983
	KALIMER	Pool	Korea	150 MW_e	2025	P
Power	BN 600	Pool	USSR	600 MW_e	1980	F
	SUPERPHÉNIX	Pool	France	1200 MW_e	1985	A: 1998
	BN 800	Pool	USSR	800 MW_e	2014	F
	SNR 2	Loop	Germany	1400 MW_e		Ab
	CDFR	Pool	UK	1300 MW_e		Ab
	EFR		Europe	1500 MW_e		Ab
	PRISM	Pool	USA	1245 MW_e		Ab
	JFSR	Loop	Japan	1500 MW_e	2025	P
	KALIMER-600	Pool	Korea	600 MW_e	2025	P
	PFBR	Pool	India	500 MW_e	2010	Constr.

https://www.gen-4.org/gif/jcms/c_59461/generation-iv-systems

A: Shutdown F: Operating P: Project Ab: Abandoned Constr: under construction

Souce Term in BDBAs

Major Sources

$\uparrow T_{fuel}$, $\uparrow P_{rod}$

Core disruption

FCI

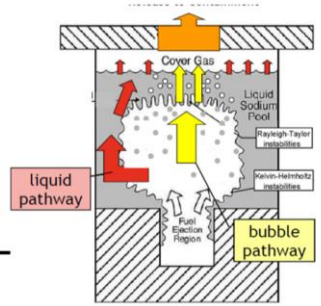

RN in large bubbles

RN absorption in Na

"The bubble pathway"

Na-concrete interaction

Sodium fires

Transfer from hot sodium pools

Database

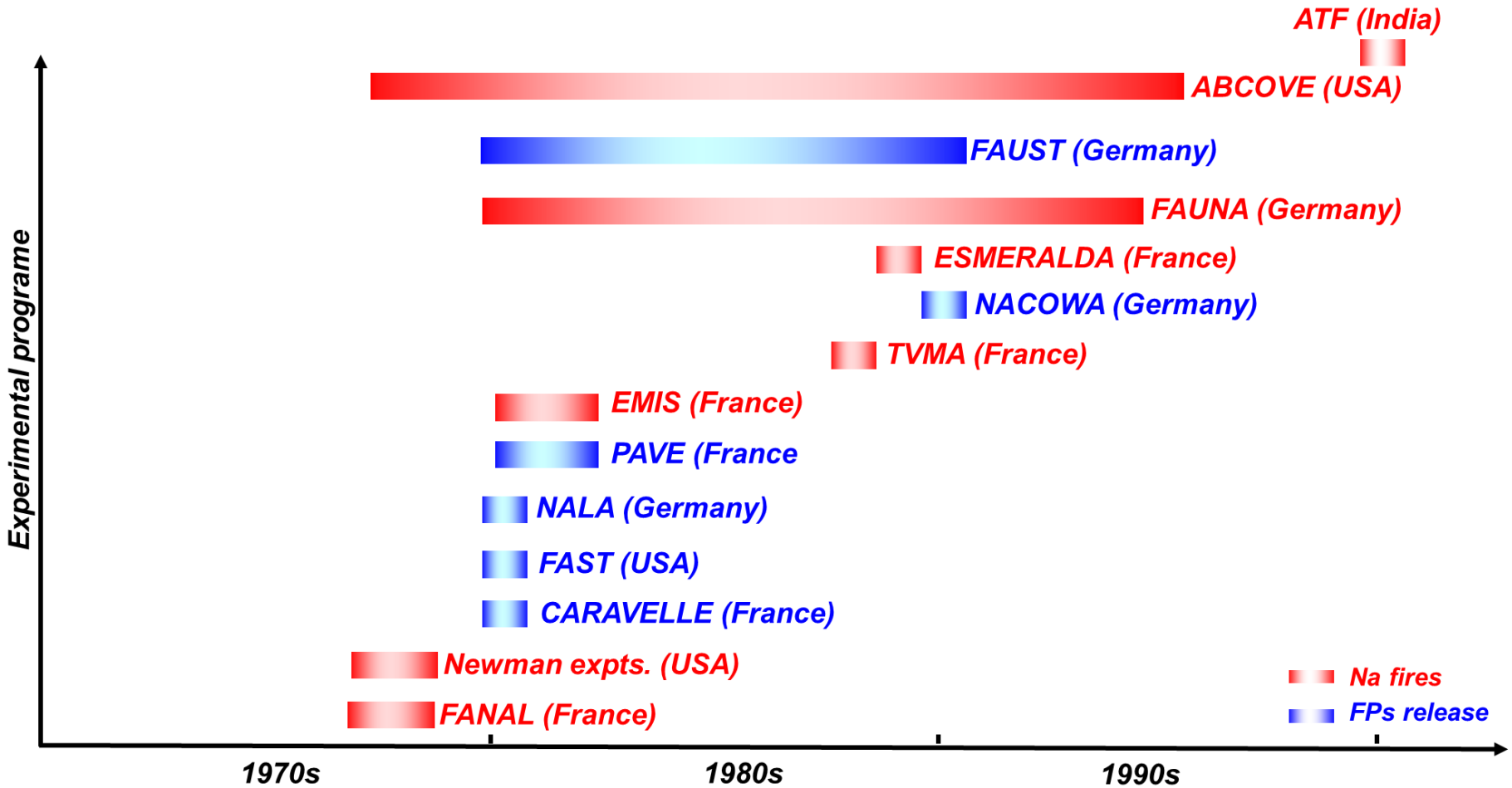
ATF (India)
ABCOVE (USA)
FAUST (Germany)
FAUNA (Germany)
ESMERALDA (France)
NACOWA (Germany)
TVMA (France)
EMIS (France)
PAVE (France
NALA (Germany)
FAST (USA)
CARAVELLE (France)
Newman expts. (USA)
FANAL (France)
Experimental programe
1970s
1980s
1990s
Na fires
FPs release

DATA

&

MODEL ASSESSMENT

NALA Program

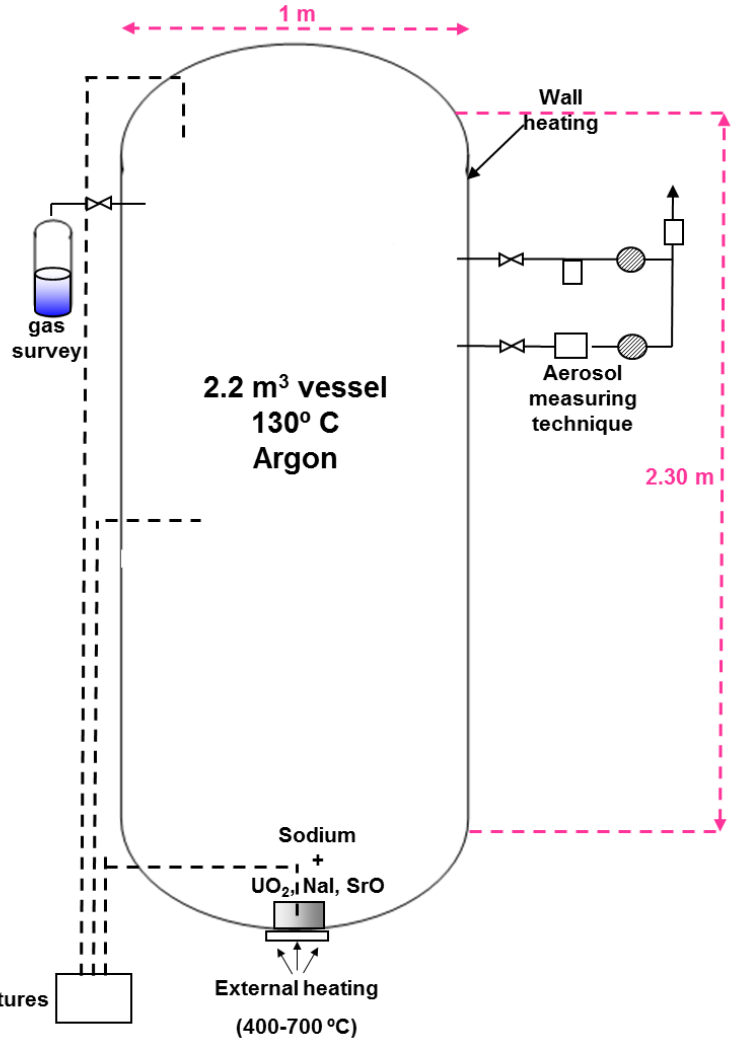

NALA II

Geometry	Values
Na pool area	531 cm^2 (26 cm dia.)
Vessel	2.2 m^3 2.30 m high
Tests conditions	
Na	1 kg
Na T	600-900 K
Atm. gas	400 K (Ar)
Contaminants	UO_2, NaI, SrO

NaI Tests

Exp.	T(K)	Na (g)	NaI (g)
T1	835.15	258	1.00
T2	905.15	1100	1.06
T3	754.15	1315	1.00
T4	769.15	1322	10.00
T5	837.15	1146	-
T6	823.15	1321	0.20
T7	830.15	1007	-

Results & Earlier Modeling

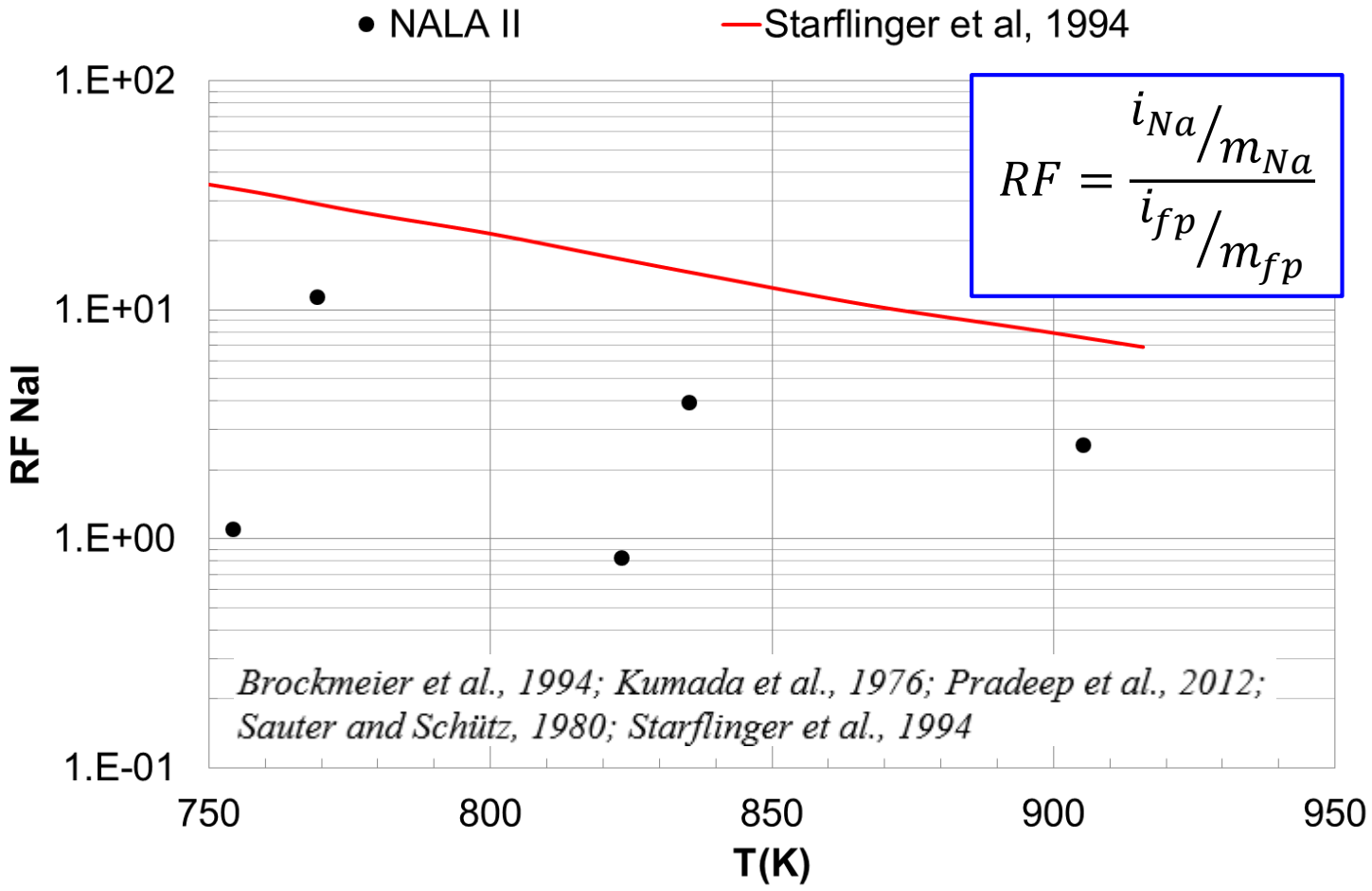

Results & Earlier Modeling

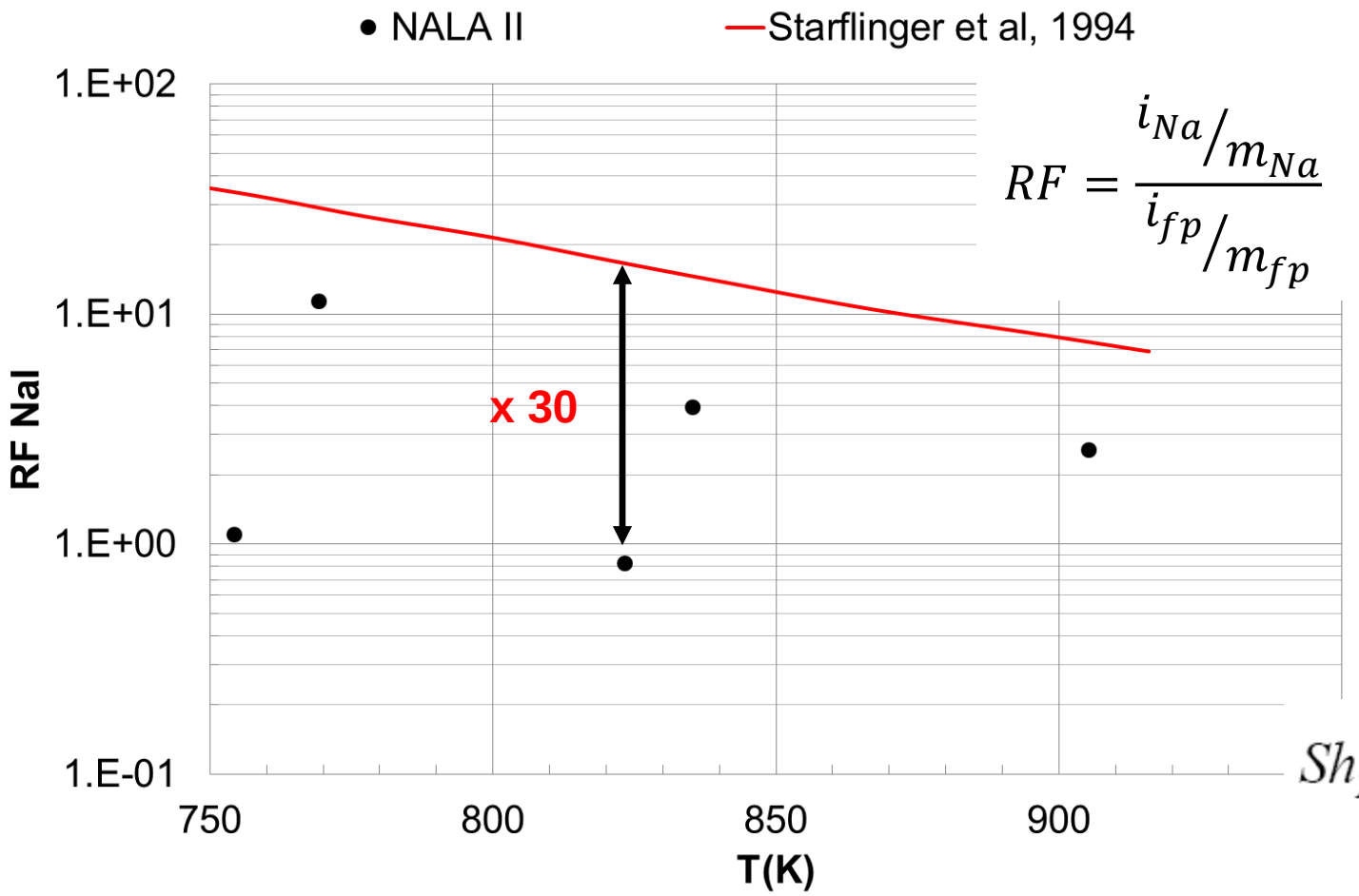

$$RF = \frac{i_{Na}/m_{Na}}{i_{fp}/m_{fp}}$$

Fitted-to-data Sh_{Na}

$$Sh_{Nag,exptl.} = B \cdot \left[Gr_g \cdot Sc_{Ar} \right]^n$$

Model Assessment

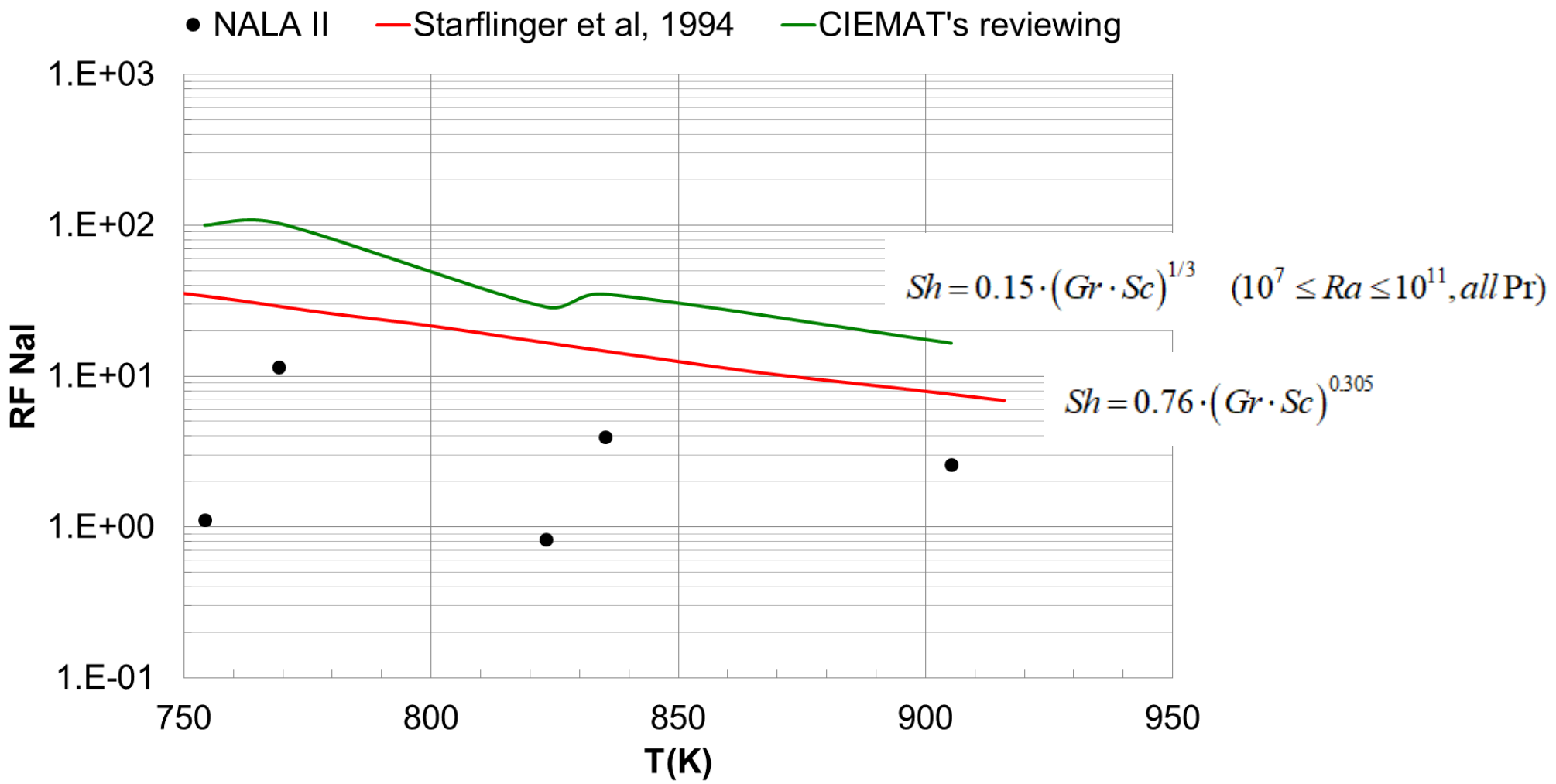

Model Assessment

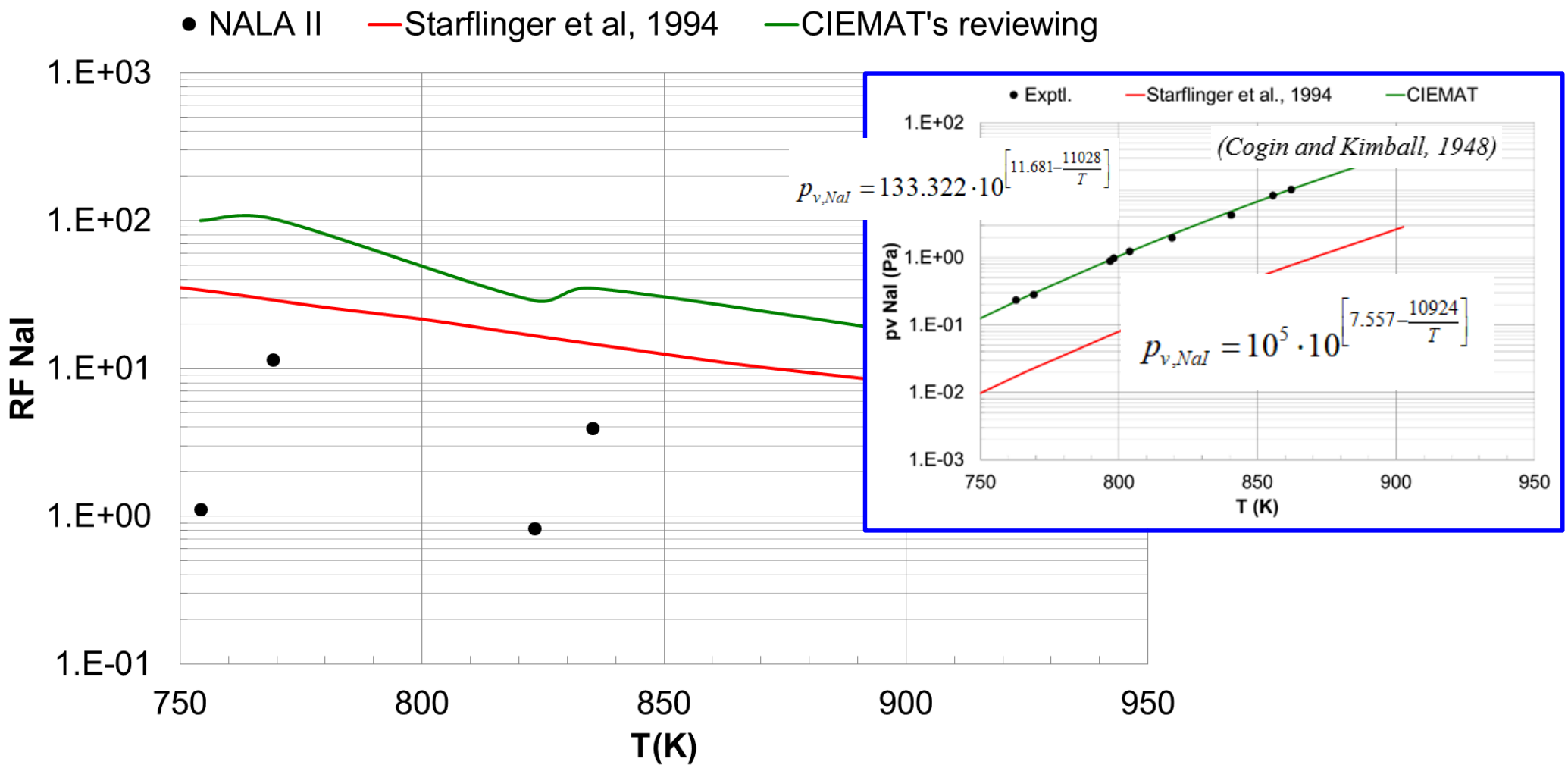

CIEMAT'S MODEL

Gas Mass Transfer model (GMT)

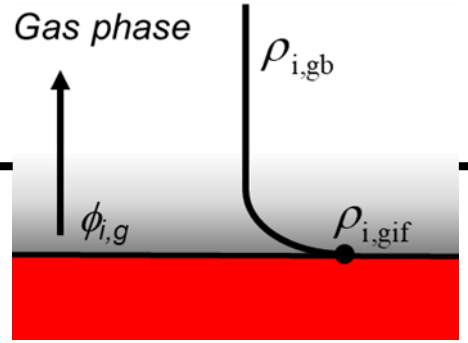

Diffusion — **Entrainment**

$$\phi_{i,g} = Sh_{i,g} \cdot \frac{D_{i,g}}{L} \cdot \Delta\rho_{i,g}$$

HMT analogy

$$Sh = 0.15 \cdot (Gr \cdot Sc)^{1/3}$$

$$(10^7 \le Ra \le 10^{11}, all\ \mathrm{Pr})$$

Raoult's law

$$\Delta\rho_{i,g} = \rho_{i,gif} - \rho_{i,gb}$$

$$\rho_{i,gif} = \frac{p_{v,i}(T_{if})}{(R/M_i) \cdot T_{if}} \cdot \gamma_i \cdot x_i$$

[Nucleation ϕ_{Na}]

$$f_{\mathrm{cond,Na}} = \frac{\beta_{Na}(T_{if}) \cdot \left(\Delta T \cdot Le^{-n} + \left(\Delta h_{v,Na} \cdot \Delta p\right) / \left(Le \cdot c_{p,gb} \cdot P\right)\right)}{\Delta p \cdot \left(1 + \left(\beta_{Na}(T_{if}) \cdot \Delta h_{v,Na}\right) / \left(Le \cdot c_{p,gb} \cdot P\right)\right)}$$

Gas Mass Transfer model (GMT)

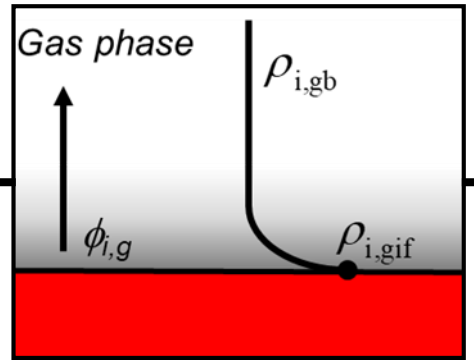

Entrainment — **Diffusion**

$$\phi_{i,g} = Sh_{i,g} \cdot \frac{D_{i,g}}{L} \cdot \Delta\rho_{i,g}$$

HMT analogy

$$Sh = 0.15 \cdot (Gr \cdot Sc)^{1/3}$$

$$(10^7 \le Ra \le 10^{11}, all\ \mathrm{Pr})$$

Raoult's law

$$\Delta\rho_{i,g} = \rho_{i,gif} - \rho_{i,gb}$$

$$\rho_{i,gif} = \frac{p_{v,i}(T_{if})}{(R/M_i) \cdot T_{if}} \cdot \gamma_i \cdot x_i$$

[Nucleation ϕ_{Na}]

$$f_{\mathrm{cond,Na}} = \frac{\beta_{Na}(T_{if}) \cdot \left(\Delta T \cdot Le^{-n} + \left(\Delta h_{v,Na} \cdot \Delta p\right) / \left(Le \cdot c_{p,gb} \cdot P\right)\right)}{\Delta p \cdot \left(1 + \left(\beta_{Na}(T_{if}) \cdot \Delta h_{v,Na}\right) / \left(Le \cdot c_{p,gb} \cdot P\right)\right)}$$

RESULTS

Model Benchmarking

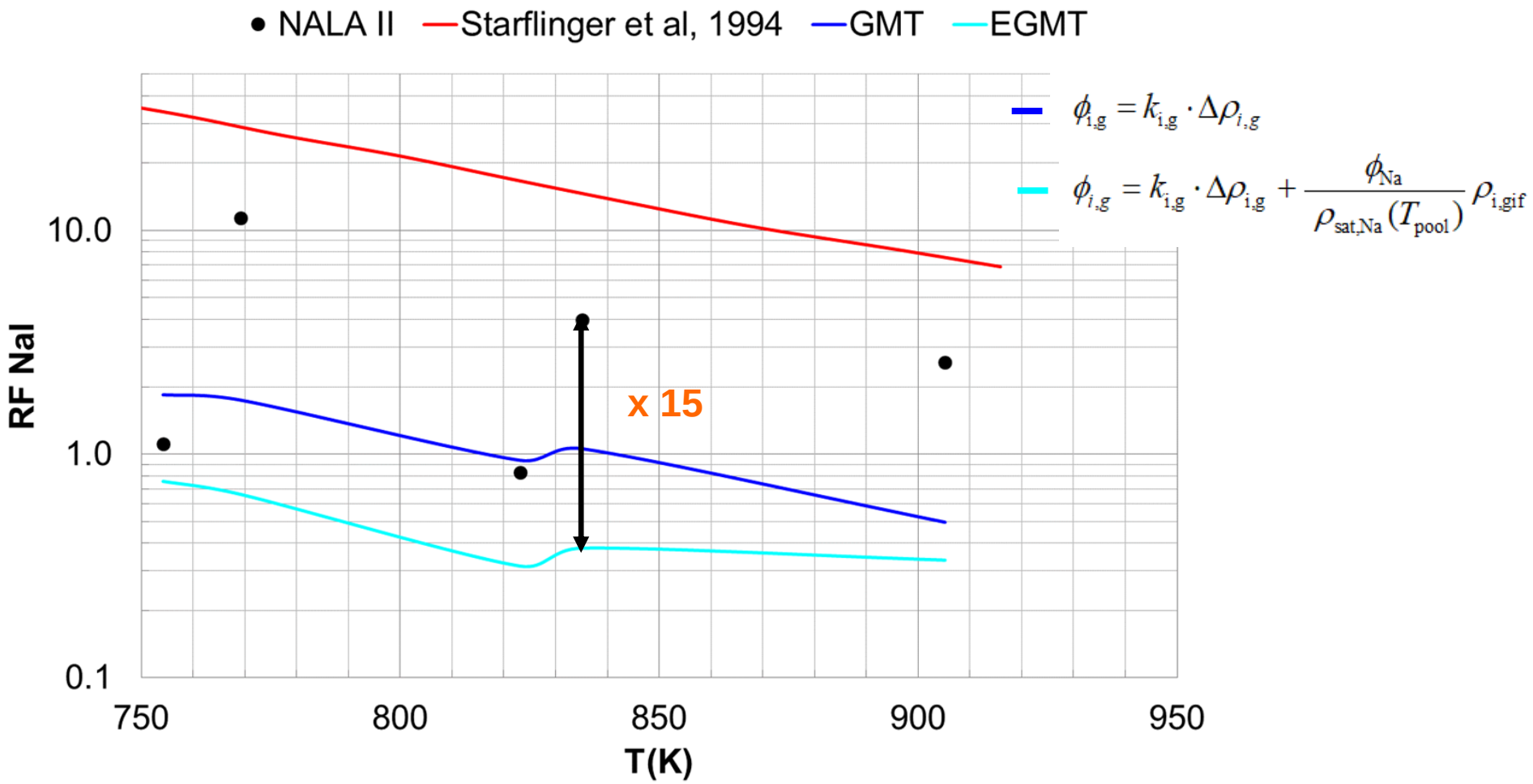

FINAL REMARKS

- *A **Gas Mass Transfer** model for volatile FPs (NaI) release from hot sodium pools has been proposed.*

- ***Enhancement achieved with respect to previous modeling:***

  - *No fitting to data*
  - *Consistency of the fundamentals*
  - *Conservative nature (improvable accuracy)*

- ***Still room for enhancements** (data limited; symptoms-based).*

- ***Extension of validation** to NALA I conditions and other RN (Cs).*

Thank you for your attention!

ON THE PURSUING OF SAFETY ENHANCEMENTS IN SODIUM FAST REACTORS

S. Perez-Martin, E. Bubelis, W. Pfrang, M. Schikorr, W. Hering
Institute for Neutron Physics and Reactor Technology
Karlsruhe Institute of Technology
Hermann-von-Helmholtzplatz, 1
76344 Eggenstein-Leopoldshafen
Germany

sara.perez@kit.edu
evaldas.bubelis@kit.edu
michael.schikorr@kit.edu
wolfgang.hering@kit.edu

ABSTRACT

This paper presents main conclusions extracted from more than one decade of European research in SFRs starting from the CP-ESFR project and ending with the current ESFR-SMART project. Different measures have been considered to reduce the void reactivity effect in large SFR reactors (~ 3000 MWth), namely introducing sodium and boron layers (CP-ESFR Optimized core), a central fertile layer in the inner core region (ESNII+ core), as well as reducing the length of the inner core fissile fuel region (ESFR-SMART core). All these measures together with the passive shut-down rods and the corium discharge tubes have improved the safety response of large SFRs, however they are still not sufficient to avoid a power transient after sodium boiling onset during the ULOF transient.

KEYWORDS
SFR, ULOF, two-phase flow, SAS-SFR code, SIM-SFR code

1 INTRODUCTION

The research on safety features of large Sodium Fast Reactors (SFR) is an international task with more than four decades of efforts. Although the large developmental momentum of 70s and 80s decreased after the cancelation of several Fast Breeder Reactor national programs (USA, Germany, UK, etc.) the know-how acquired during that period has been maintained thanks to several international collaboration projects and those national programs with existing SFRs running beyond 90s (Japan, France, Russia). With the creation of the Gen-IV Forum, SFRs took a leading position as an advanced system with improved safety capabilities and fuel performance. SFRs will therefore become important for future CO_2-free energy systems since they, in particular small, modular SFRs, are robust against power transients.

Thanks to the long lasting international collaboration incorporating more than 400 years of reactor operation, different core designs, structural components and passive safety systems have been developed or further improved. As a result, various numerical simulation computer codes have been also developed and validated to help in the design process of advanced SFR reactors, as well as in the licensing process to demonstrate that their safety functions can be assured under normal and accidental transient conditions. Two of these

codes, SAS-SFR and SIM-SFR can be considered as reference codes in this field that have been developed and supported by the Karlsruhe Institute of Technology. SIM-SFR and SAS-SFR codes simulate core physical phenomena (thermal-hydraulic, neutronic and SFR particular, burnup dependent fuel pin mechanics) involved in two-phase liquid metals dynamic transients. Both code systems have also been validated against experimental data sets from large-scale experiments (i.e. CABRI, Phenix, SPX, KNS-37, TREAT, etc.), (Refs. 1-4) yielding therefore consistent and reliable results.

At the European level, CP-ESFR, ESNII+ and ESFR-SMART projects supported by the EURATOM program have paved the path towards a robust and safer EU-SFR design. They started in 2009 and will continue at least until 2025 with the recently approved ESFR-SIMPLE project. In this paper, the main conclusions of these EU- supported projects are presented focusing on the simulations results obtained with SAS-SFR and SIM-SFR codes. An introduction to the SFR safety analysis is discussed in Section 2. The characteristics of the various SFR reactor designs are presented in Section 3. The core responses to unprotected transients are presented in Section 4. Concerning the positive void reactivity feedback, being the main drawback of 'large' SFRs, a special focus is put on ULOF transients where not only the single-phase coolant flow phase is assessed, but also the transient evolution after boiling onset. The conclusions and future needs are presented in Section 5.

2 SFR SAFETY ANALYSIS

For licensing any reactor design it is needed to demonstrate its capability to accomplish the fundamental safety functions during its entire design lifetime under all normal operating modes (both steady-state and operational transients), as well as under anticipated operational occurrences and accident conditions (Ref. 5). The safety functions include: i) reactor shut-down maintaining safe condition for all operational states or accident conditions; ii) adequate core heat removal after shut-down including accident conditions and iii) retention capabilities for radioactive and hazardous material to minimize its release to the environment (Ref. 6). One of the milestones of the CP-ESFR project (Ref. 8 and 9) back in 2009 was to identify a set of initiating events in Design Basis Conditions (DBC) triggering transients that may challenge the safety characteristics of the plant. Among the many transients considered, two of them were selected to be assessed in detail. The first one was a runaway of a group of control rods in unprotected conditions evolving to rising power levels (Unprotected Transient Over-Power). The second selected transient was assumed initiated by the loss of the active core cooling capability. The Unprotected Loss of Flow (ULOF) accident follows the coast-down of all primary pumps reducing the core mass flow rate to the natural circulation levels. The importance of the ULOF transient relies in its potential to progress into the coolant boiling phase (and eventually into partial or even total core destruction). It requires the detailed consideration of the particular effects of various specific design characteristics (e.g. upper sodium plenum, absorber layers, discharge tubes, etc.) during the progression of the transient under consideration.

The Design Basis Conditions (DBC) cover normal plant operating conditions as well as accidental conditions where the safety functions of the plant shall prevent fuel damage and radioactive material release with certainty or keep it within defined limits in a few exceptional cases. In the CP-ESFR project the initiating events were categorized according to the European practice established in the European Utility Requirements document Revision C (Ref.7). In particular, category DBC4 includes accidents corresponding to initiating events that are not expected to occur during the lifetime of the plant (cumulative frequency is lower than 10^{-4} per reactor-year), namely Unprotected Transients (shutdown system is assumed to fail) and break of LIPOSO (pipelines joining the primary pump with the core diagrid). In this paper, we focus on ULOF transients as were investigated in the various prior EU projects dealing with SFRs.

3 SFR REACTOR DESIGNS IN EU PROJECTS

The reactor designs used in the CP-ESFR (Ref. 8 and 9), ESNII+ (Ref. 10) and ESFR-SMART (Ref. 11) projects are summarized in Table I. During the first part of the CP-ESFR project a reference oxide core reactor with 3600 MWth was studied to improve its performance, particularly in the area of safety and minor actinides management. But in the later stage of the project this first core design was substituted by an optimized core design with a modified core layout in order to decrease the total positive reactivity feedback of the coolant density effect and thus improving its safety characteristics. In the ESNII+ project, the selected SFR design was an ASTRID-like heterogeneous core reactor with 1500 MWth, where the target was to reach negative sodium void worth, when upper parts of the core and upper sodium plenum are voided. This was obtained by adding: i) a large sodium plenum at the top of the core (where neutron leakages are increased), ii) axially heterogeneous fuel pins with a central fertile layer in the inner core (IC) zone (increasing neutron flux in the upper fissile layer), iii) shortening of the fissile zone in the inner core (IC) region(with respect to the outer core), and iv) an absorbing zone in upper shielding (reducing neutron reflection back to the fissile core during voiding) (see Figure 1, where core refers to fissile fuel). ESFR-SMART uses a core similar to the optimized CP-ESFR reactor with 3600 MWth adding new features to reduce further the global void reactivity. As an additional safety measure, the ESFR-SMART core is equipped with 31 corium discharge tubes in order to facilitate the mitigation of severe accidents by preventing recriticality in case of a large pool formation. Figure 1 shows the basic core configurations used in the various SFR projects. The reactivity coefficients, as well as neutron physics and power data for the three reactors studied (including the two CP-ESFR variants) are presented in Table II. The impact of these effects can only be seen in an integral way when they all are involved in the progression of unprotected transients which is presented in next section.

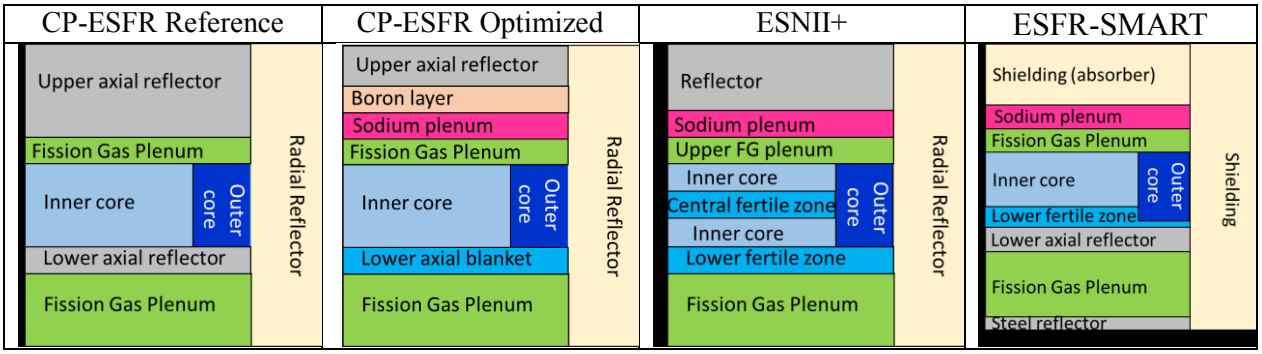

Figure 1 Schematic subassembly configurations used in the various EU SFR projects

Table I. Characteristics of SFR reactors used in CP-ESFR, ESNII+ and ESFR-SMART projects

	CP-ESFR	ESNII+	ESFR-SMART
Reactor power (MWth)	3600	1500	3600
Total number of SA	453	291	504
Number of pins per SA	271	217	271
Core inlet temperature (°C)	395	400	395
Core outlet temperature (°C)	545	550	545
Average core structure temperature (°C)	470	475	470

Table II. Reactivity data for CP-ESFR, ESNII+ and ESFR-SMART projects at EOEC

	CP-ESFR Ref.	CP-ESFR Opt.	ESNII+	ESFR-SMART
Doppler constant (pcm)	-1191	-1169	-626	-761
Fuel exp. (pcm/K)	-0.175	-0.153	-0.21	-0.195
Cladding exp. (pcm/K)	0.1485	0.137	-	0.052
Coolant exp. (pcm/K) (IC/OCI/OCII)	0.40/0.1/0.05	0.14/0.13/0.05	0.042	0.43
Control rod linear worth (pcm/cm)	-8.47	-8.47	-15.8	-47

4 ULOF TRANSIENTS

The unprotected trip of primary pumps is an accident scenario recognized among the loss of flow events (ULOF). It consists of the unintentional simultaneous coast-down of all primary pumps causing a strong reduction in the primary coolant mass flow and the presumed concurrent failure of the reactor shut-down system. No pony motors or other devices maintaining coolant flow are considered. The primary mass flow rate is assumed to decrease according to the typical coast-down characteristics of the primary pumps where the halving time is 10 s, except for ESNII+ case which is 24 s. The evaluation of the transient core behavior was performed under EOEC core conditions in all cases except for the CP-ESFR Optimized ULOF, as it represents the worst-case scenario where the fuel/pin configuration is in degraded thermal and mechanical conditions and all control rods are essentially in the withdrawn position. Additionally to Doppler, fuel cladding and sodium reactivity feedbacks, the effect of the different thermal expansion between the core and the control rods is considered, as well as the control rods driveline thermal expansion.

4.1. Code modelling

The thermal link between fuel and cladding is considered in SAS-SFR and SIM-SFR codes with special, high fidelity fuel pin mechanics models. SIM-SFR used its own dynamic fuel gap model (burn-up dependence of both fuel and cladding material) which is benchmarked to both the SAS-SFR and GERMINAL codes. In SAS-SFR simulation the recommended option based on the URGAP model is used, where the thermomechanical calculations provide a transient gap size and/or a fuel-clad contact pressure, which is used to calculate the axial gap conductance profile according to gas content and composition and surface roughness. All fuel assemblies of the inner and the outer zones of SFR core in SIM-SFR code are modelled with an average power and a peak power fuel assembly in each of the two core zones. Axially, the core is modelled in 16 axial meshes. Apart from the core, the primary, secondary and tertiary cooling circuits, including the intermediate heat exchangers (IHX) and the steam generators (SG), are also modelled. Feedwater supply to the SGs is modelled as a boundary condition, having a fixed feedwater temperature value. The following set of reactivity feedbacks is modelled: Doppler, fuel and cladding axial expansion, diagrid radial expansion, coolant expansion and control rod driveline (CRDL) axial expansion.

The grouping selection of SA to channels in SAS-SFR simulation is based on a case-by-case way depending on similar thermal-hydraulic conditions undergoing the same number of power irradiations. In ESNII+ project it was agreed to use only three channels to represent the core behavior: one average SA for the inner core, one for outer core and a third one representing the hottest SA. For CP-ESFR project, SAS-SFR considered 10 SA-channels, while for ESFR-SMART the core was grouped in 34 SA-channels, where 6 channels are used for the inner core and 28 for the outer core zone. As for the reactivity feedbacks, in SIM-SFR a specifically developed control-rod driveline model was used and appropriately modified, originally

benchmarked to several different SPX1 transient data sets. The reactivity feedback coefficients used in the Point Kinetics models in SAS-SFR were calculated with the modular neutronic code system KANEXT on basis of the JEFF 3.1.1 cross section data library. The different reactivity feedback sets are considered based on a core ring wise approach while the reactivity feedbacks due to control rod driveline expansion and grid plate expansion were adjusted to the data provided in the projects. For the ESFR-SMART project, the reactivity coefficients were calculated by a special task and provided for the benchmarking exercise to the participants so that all simulations use the same set of feedback coefficients.

4.2. Code results

The optimized CP-ESFR core improved the safety response in comparison to the reference design by reducing peak temperatures and enlarging grace times. Nevertheless, the optimization was not sufficient to avoid a power excursion once sodium boiling commenced during a ULOF transient. The newly introduced upper sodium plenum provided a small delay in the boiling onset since the cumulative void effect was dominated by the reactivity increase due to fissile core voiding. It was then concluded that the sodium plenum does not play a decisive role in improving the total void effect during boiling. Even though the total void effect (active core + plenum) was close to zero or even negative, the progression of the ULOF transient went beyond pin and hexcan failure, driven by failure and removal of cladding material from the fissile core zone. Hence the proposed design measures for coming projects were to include other core cooling aspects (e.g. pump flywheel or pony motors) since the optimization of the core neutron physics alone was not sufficient to avoid a power excursion during the ULOF transient.

All the new implemented measures in the ASTRID-like reactor (heterogeneous axial core including an upper sodium plenum) helped in improving the core response thanks to the negative total sodium void reactivity worth, although sodium boiling could not be avoided. This type of core geometrical modifications established a direction to progress for achieving higher safety levels and risk prevention of core meltdown accident.

Since the ESFR-SMART project is the most recent one, an extended discussion of results will be presented hereafter in comparison of CP-ESFR and ESNII+ results. According to SAS-SFR results, under EOEC plant conditions, the gap between fuel and cladding is closed in almost all fuel channels at the Peak Power Node (PPN) with the exception of some channels in the outer core. The level of fission gas release is above 70% in almost all channels in the outer core, and the clad swelling deformation reaches 25-30 μm in channels 23,24,28,29,30 due to the high burn-up levels (11.5 - 14.5 at.%). The highest clad damage occurs in channel 28 with 177 dpa. As a result, the ESFR-SMART reactor cannot avoid early fuel pin break-up during the ULOF transient, eventually followed by a power excursion (see Figure 2). Sodium boiling starts in channel 33 at 46.1 s into the ULOF transient, where the nominal power is 0.61 and the net reactivity is -0.12 $. Other SA channels follow the same events (see blue circles in left part of Figure 2). After boiling onset the next major event is clad motion onset. In channel 33 clad motion onset occurs 30.3 s after boiling onset. This time period is shorter (11.8 s and 11.5 s, 23.0 s and 15.1 s) for the other channels (28, 23, 31 and 15, respectively). Regarding the time period between clad motion onset and pin failure, it varies from 38.3 s to 14.2 s (for channels 33 and 15 respectively). At 114.71 s into the transient, where the nominal power is ~ 45%, the net reactivity surpasses 1.0 $. Although the power axis in Figure 2 (left figure) shows up to 2.0, the maximum power reached during the ULOF is 1874 times the nominal power at 114.7 s. The maximal net reactivity is reached some milliseconds afterwards (at 114.7112 s) with a value of 1.09409 $.

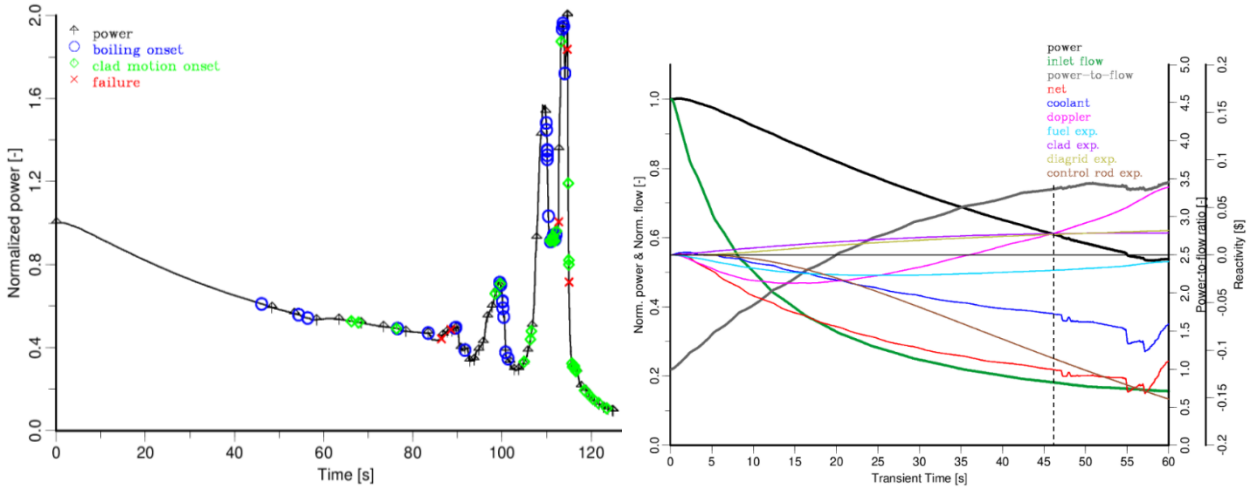

Figure 2 Normalized power behavior (left) and reactivity and coolant flow (right) during the ULOF

The total power and major reactivities affecting the core response during the first 60 s of the transient (see Figure 2 right figure) show an initial decrease of the net reactivity (red curve) thanks mainly to the negative coolant reactivity due to sodium density decrease of the plenum region (dark blue curve) and the control rod expansion reactivity (brown curve). The mismatch between the power (black curve) and the coolant inlet mass flow rate (green curve) largely increases during the first 40 s. The grey curve shows the power-to-flow ratio being stabilized after boiling onset at a value of about 3.5. The fuel expansion, as well as the Doppler reactivity feedback, show a concave shape where the positive trend is related to the reduction of the fuel temperature following a decrease of the core power. The axial boiling extension for the five first channels undergoing boiling is depicted in Figure 3 (left figure, BFC: Bottom of the Fissile Column) together with the corresponding void reactivity associated to that channel (dashed lines) where the black horizontal line represents the Top of the Fissile Column (TFC). A similar trend is seen for all SA channels: once boiling starts at the top of the fissile column, the voiding region spreads both upwards and downwards. Thanks to the negative reactivity feedback coming for the voiding of the upper part of the fuel pin, void reactivity is transiently negative before the boiling region arrives to the midpoint of the fissile region of the core and below.

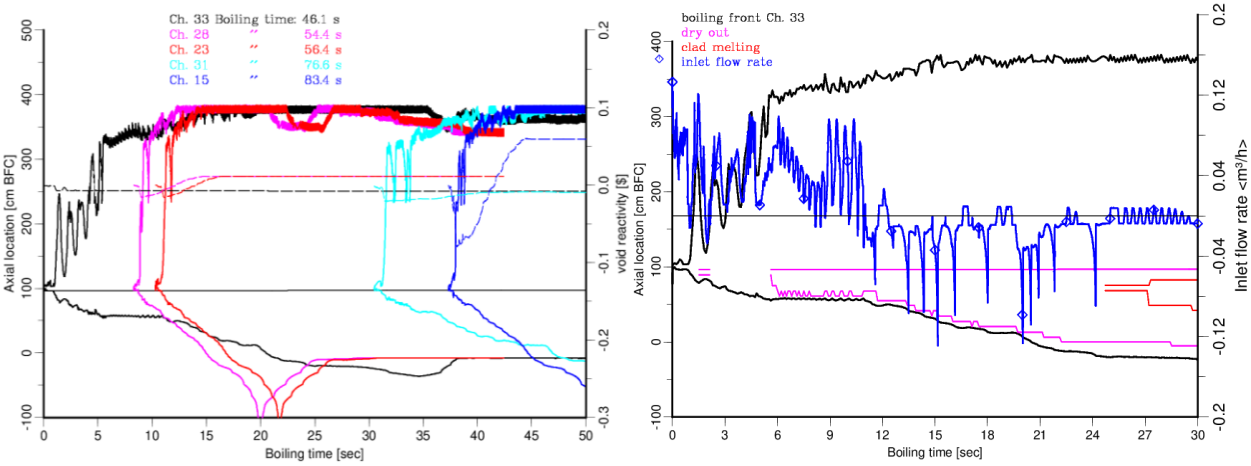

Figure 3 Axial boiling front evolution for the five first channels undergoing boiling (left) and boiling, dry-out and clad melting fronts for channel 33 (local boiling time 46.1 s) (right)

The behavior of the boiling, dry-out and clad melting fronts for channel 33 is depicted in Figure 3 (right figure) together with the inlet flow rate at this channel (the horizontal black line represents zero flow rate). The initial oscillations in the upper boiling front up to 6 s into the boiling are consistent with the inlet flow rate. After 6 s the upper front remains at the upper plenum and no longer decreases. This occurs at the time when clad dry-out is observed permanently (pink line) and evolves till the bottom of the fuel region. Clad motion onset starts 24 s after boiling in the upper region of the fissile fuel region and spreads into the upper region, as well as into the mid-region of the fissile core. The main difference of subsequent boiling channels compared to Channel 33 is the quick voiding of the plenum of the coolant channel with almost no oscillations. The reason for those cases also comes from the inlet flow rate, where for channel 28 at the time of the local boiling (54.4 s) is lower than the corresponding value for channel 33. The explanation of this difference comes from the total power being transferred to the coolant. It is important to note the quicker dry-out and clad motion onset in channel 28 compared to channel 33. Clad relocation has an important role in the evolution of the transient since it provides a positive reactivity insertion due to the reduction of neutron absorptions.

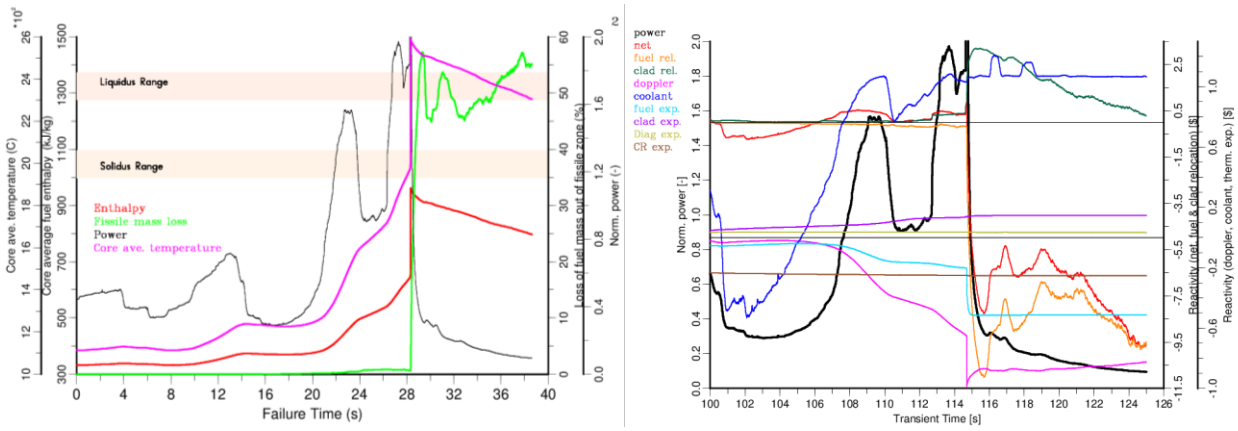

Figure 4 Evolution of fuel enthalpy and temperature after failure (left) and power and reactivities during the ULOF transient (right)

Figure 4 (left figure) shows the fuel enthalpy, fissile mass loss out to the fissile zone, as well as the power and the core fuel average temperature after first fuel pin failure. The solidus and liquidus fuel enthalpy are indicated in clear red rectangles. The fuel bulk enthalpy is just below the solidus range, but locally, for channels 28, 23, 15 etc., fuel melting occurs. The effect can be seen in the loss of fissile mass outside the fissile core zone, which is depicted (clear green curve) as well in Figure 4 (left figure). After the power excursion the net reactivity drops below -4$ driven by the fuel relocation feedback (see Figure 4 right figure). This implies that the ULOF transient is terminated without hexcan damage, therefore the transient does not progress further and following other accidental sequences (i.e. recriticality) are no longer expected. The maximum fuel and cladding temperatures reached during the transient are shown in Figure 5. The fuel pin failure mechanism in this case is pin break-up, meaning that the clad integrity is compromised due to the high clad temperature. The cladding material considered is Oxide Dispersion-Strengthened (ODS) steel, where not only the melting temperature is assumed in the thermal-mechanical model, but also the creep and swelling. These two factors lead to degradation of the cladding integrity. As a conclusion from SAS-SFR results, neither boiling onset nor pin failure is avoided, but hexcan and thus SA integrity is assured.

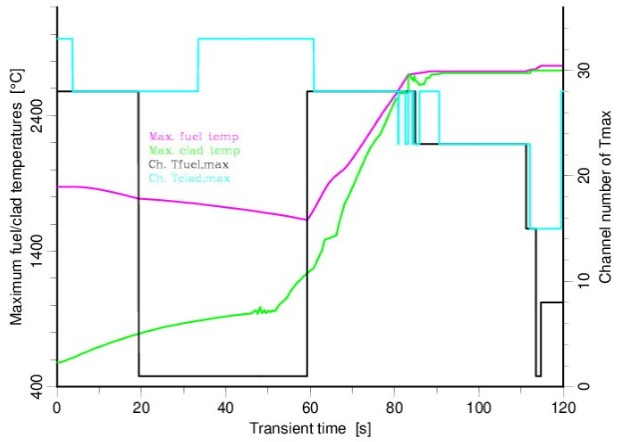

Figure 5 Maximum fuel and cladding temperatures reached during the transient

While running SIM-SFR code, a sensitivity study was conducted to investigate the effect of sodium natural circulation flow reduction in the fuel channels due to sodium boiling in the plenum and the fissile fuel region of the fuel sub-assemblies. Figure 6 shows the evolution of the selected parameters of the primary cooling circuit and the reactor core, while Figure 7 shows evolution of the selected reactivity feedback effects for the ULOF sensitivity cases analyzed. When the primary pumps coast down during ULOF, the sodium flowrate in the fuel channels continuously decreases down to the natural circulation flowrate level, and even below that, depending on the sodium voiding fraction in the fuel channel. The performed sensitivity studies were focused on this parameter, thus calculating different cases, where the natural circulation flowrate level is artificially multiplied by a void fraction dependent factor of 1.0, 0.75, 0.5, 0.3, 0.15 and 0.05, thereby artificially simulating the choking of the flow rate due to sodium boiling within the upper plenum and the fissile region of the fuel sub-assemblies (presuming a uniform, non-oscillatory flow behavior within the SA).

During an ESFR-SMART ULOF transient, sodium starts boiling during pump coast-down at the outlet of the fissile core region for the peak power channel of the outer core zone, then at the outlet of the fissile core region for the average power channels of the outer core zone. Later on, sodium starts boiling at the outlet of the fissile core region for the peak power channel of the inner core zone, then at the outlet of the core for the average power channels of the inner core zone. Sodium boiling sequence – first in the outer core zone, then in the inner core zone – depends on the axial and radial power peaking factors in the ESFR-SMART core, these being much higher for the outer core zone than for the inner core zone. The sodium boiling front usually penetrates first upward into the upper sodium plenum region, thereby inserting negative reactivity into the core and thus depressing reactor power level. Depending on the particular case analyzed, sodium boiling can also propagate downward into the active fissile core region, thereby inserting positive reactivity into the core causing an increase in reactor power level. Reactivity power level decreasing and increasing, supported by the simulated reactivity effects, results in sodium boiling front collapse or intensification in different fuel channels. As a result of that, we observe reactor power fluctuations in time (power chugging, or pulsating within the operational power regime of the reactor) without running into a power excursion for the cases, where natural circulation flowrate level through the core is artificially multiplied (decreased) by a factor of 1.0 to 0.3. For two other cases, where natural circulation flowrate level through the core is artificially multiplied (decreased) by a factor of 0.15 to 0.05, the reactor runs into a power excursion already at 70-80 s into the ULOF transient. In reality, natural circulation flowrate level reduction in the fuel channels is a result of sodium boiling in the fuel channels, where sodium vapor bubbles are formed blocking normal

sodium flow through the boiling channel. As the extent of flow blockage (choking) by the bubble(s) due to boiling sodium is currently not known precisely, the above described sensitivity study was thus performed. For the 100% and 75% natural circulation flow case through the core, the natural convection flowrate stabilizes at ~11-12.5% for both SAs (peak and average power), as no impact of voiding on the flow rate in the channels is presumed. For both average and peak power SAs partial plenum voiding and a part of the upper fissile core region voiding is being observed, thus leading to power cycling (power chugging), as the alternating void reactivities of both plenum and fissile core region for both subassemblies (average and peak power SAs) are changing reactivity levels. The clad temperatures of both SAs remain well below 1400 °C. These core configurations seems to be quasi stable, as observed in the relatively "stable" power cycles.

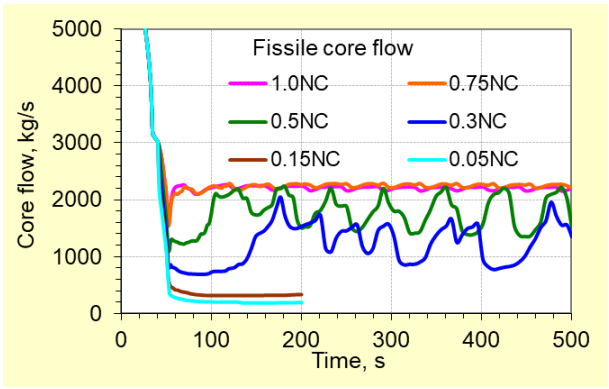

a) Fissile core flow

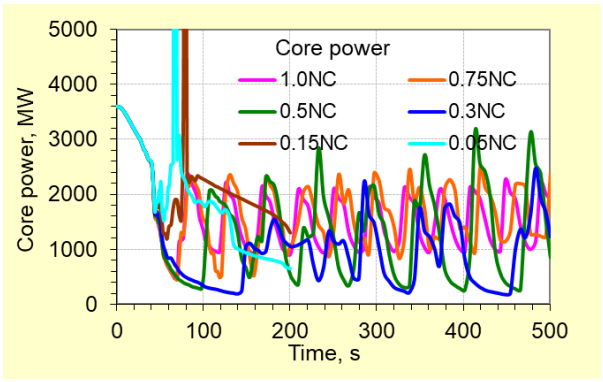

b) Core power

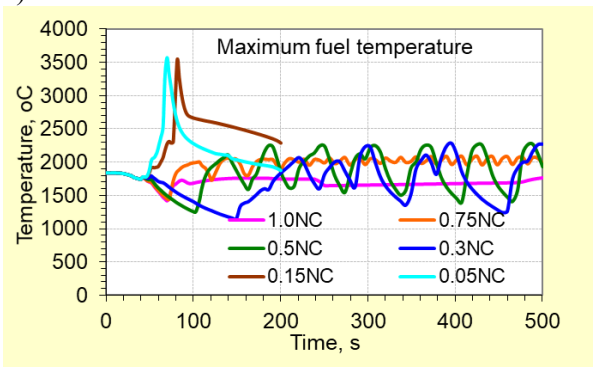

c) Maximum fuel temperature

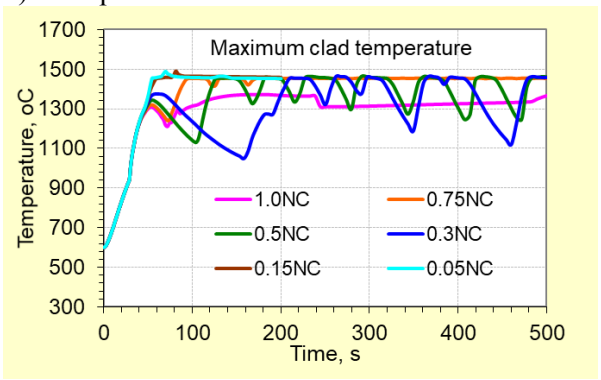

d) Maximum clad temperature

Figure 6 Evolution of the main parameters of the primary cooling circuit and the reactor core for the ULOF sensitivity cases analyzed

For the 50% and 30% natural circulation flow case through the core, hot SA and average power SAs can follow different transient responses. Whereas the hot SA displays a stable, complete plenum voiding with a cyclic penetration into the fissile core region, the average power SAs display a cyclic plenum and a very limited cyclic fissile core voiding front. The corresponding choked flow rates of the hot and average power SAs are thus also different, with the hot SA flow rate remaining at ~4% nominal flow, and the average power SAs displaying a cyclic nominal flow rate of 4-12% following the cycling behavior of the plenum and the core voiding. This leads to larger power cycles, as the changes in the void reactivities (plenum vs core voiding) become larger as the average power SAs are now involved, thus cycling between 10% and 90%, the peak power of the power cycles progressively increasing. However, the clad temperatures of the

hot SA displays a cyclic behavior reaching locally clad melting temperatures with a limited, positive reactivity insertion due to partial (molten) clad material removal from the core region. The clad temperature of the average power SAs remain below 1150°C. These core configurations appear to settle into a cyclic mode, with power swings increasing in amplitude.

For the 15% and 5% natural circulation flow case through the core, the flow rates for both hot and average power SAs are observed to be ~1-2% nominal as significant voiding of both the hot and the average power SAs are now being observed. The average power SAs follow the hot SAs in an almost complete voiding of the core region. The clad temperatures of the hot SA reach melting at ~55-60 s into the transient, closely followed by the clad temperatures of the average power SAs also beginning to melt at ~65-76 s into the transient. Clad melting of the average power SA leads to a large positive reactivity insertion, leading to a power excursion spike at 67-78 s into the transient. Subsequent fuel melting and removing of fuel from the core region shuts down the power spike.

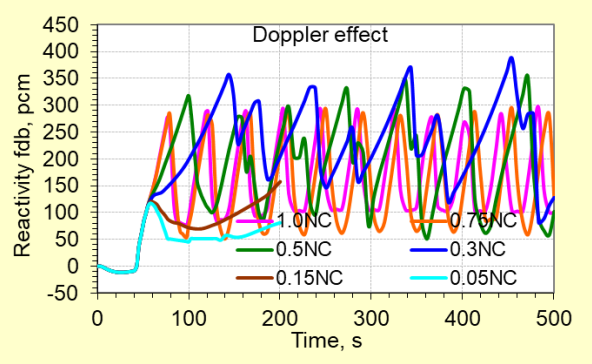

a) Doppler effect

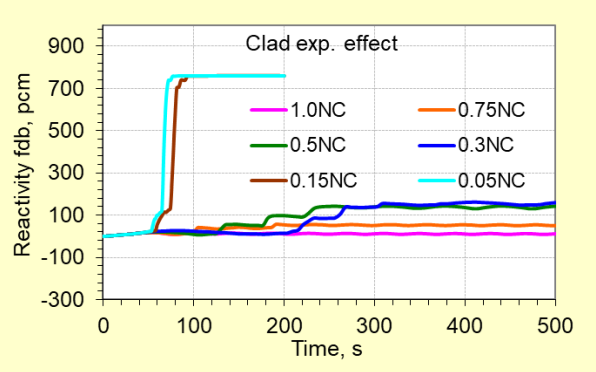

b) Clad expansion effect

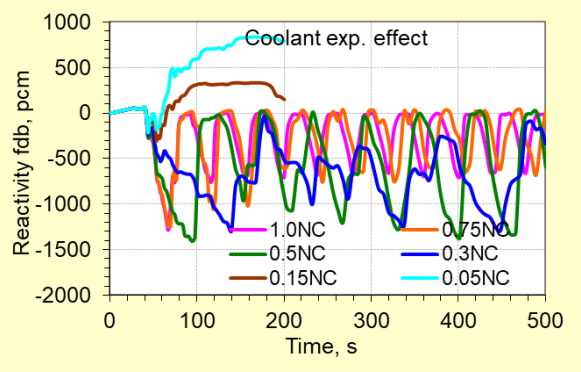

c) Coolant expansion effect

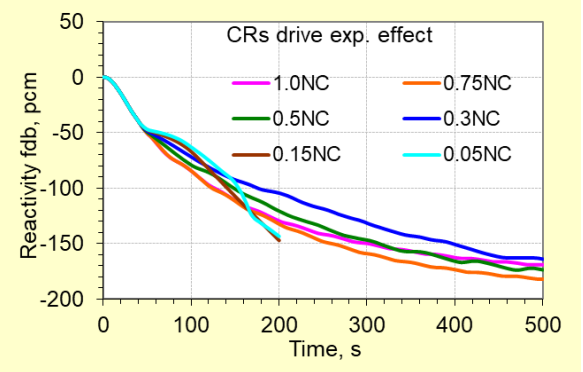

d) Control rods drivelines expansion effect

Figure 7 Evolution of the main reactivity effects for the ULOF sensitivity cases analyzed

As a conclusion for the SIM-SFR results, one can state that depending on the natural circulation flowrate level reduction (choking of flow rate) in the fuel channels as a result of sodium boiling, the outcome of the ULOF transient can be quite different. For the cases, where natural circulation flowrate level through the core is either not reduced at all or reduced down to 30% during the ULOF transient, the ESFR reactor configuration experiences power fluctuations (power chugging) as a function of time (pulsating within the operational regime of the reactor power) without running into a power excursion. The voiding of the ESFR-

SMART plenum thus compensates successfully the positive reactivity contribution due to voiding of the fissile core zone of ESFR-SMART, preventing thereby a power excursion due to sodium boiling within the fissile core zone. Based upon these results, the current ESFR plenum/core design configuration can thus be considered a viable ESFR design. For the cases, where natural circulation flowrate level through the core is choked down to 15%, or even 5% during the ULOF transient, the ESFR reactor configuration runs into a power excursion at around 70-80 s into the transient due to large scale melting of the cladding material leading to a significant positive reactivity insertion that can only be compensated by the removal of molten fuel material from the core zone. The above two cases (15% and 5% flow choking) basically replicate the SAS-SFR ESFR ULOF results documented above.

5 CONCLUSIONS

This paper presents an overview of the main conclusions extracted from the last decade of European research in SFRs. Starting from the CP-ESFR project the assessment of SFR performance under unprotected transients was developed in parallel to the verification and improvement of computational tools able to simulate advanced features of the reactor design. Thanks to the continued development of various dedicated SFR simulation codes, such as e.g., SAS-SFR and SIM-SFR, and their participation in rigorous, EU funded code benchmarking projects, other systems codes, originally devoted to LWR analysis, were adapted to SFRs and also acquired high levels of prediction capabilities up to the point when sodium boiling commences. After initiation of sodium boiling, consistent simulation of two-phase flow is still limited to a few codes, such as SAS-SFR and SIM-SFR. Thus, one of the main issues for the future R&D would be to understand more precisely what happens to the sodium flow rate, when voiding (due to sodium boiling) commences and progresses within the reactor fuel channels by performing a large scale code validation comparisons exercise based on validated experimental data sets. Emphasis should then be placed on the prevention of large scale melting of the cladding material within the fissile core zone, either by adopting appropriate core and/or SA-design measures, or by assuring a minimum flow rate through the core region by active or passive means (i.e. pony motors). The assured minimum flow rate through the core region should be at least ~3% of nominal flow rate in order to assure prevention of large scale clad melting during ULOF.

As for the safety aspect of SFRs, different measures have been considered to reduce the void reactivity effect, namely introducing of a sodium layer and a boron layer below the upper axial reflector (CP-ESFR Optimized core), the insertion of a central fertile layer in the inner core region (ESNII+ core), as well as reducing the length of the inner core fissile fuel region (ESFR-SMART core). All these measures together with the introduction of passive shut-down rods and corium discharge tubes in the ESFR-SMART core have been proved effective in improving the safety response of the core. On one side, it has been demonstrated that all these optimizations (disregarding passive SR e.g. Curie-point triggered) are still not sufficient to avoid a power transient after commencement of sodium boiling during the ULOF transient, but on the other side the grace time for the protection systems to act in order to avoid potentially limiting situations has been enlarged, and more importantly the progression of the transient does not go beyond the melting/rupture of the SA hexcan.

An improvement is needed in convergence of the post coolant boiling phase in the simulations results by improving code models. This was already initiated in the ESFR-SMART project with a dedicated task focusing on code validation using experimental data from sodium tests (Ref. 12) and it is strongly recommended to continue this process using existing experimental data, as well as new experimental tests reflecting the current trends in core designs, since existing experimental data used geometry and characteristics of the previous SFR generation (Superphenix, SNR-300, etc.).

What remains for the future is the assessment of Small Modular Reactors based on Sodium-cooled Fast Reactor technology, where high benefits are expected in terms of safety and flexibility. The topics to be discussed are, among others: i) in which conditions large cores are beneficial versus conditions where medium and small cores due to larger neutron leakage offer larger advancements, ii) the comparison of oxide vs. metal fuel cores with current needs (namely no longer a breeder reactor) and iii) how flexible SFRs can be to accommodate power demand variation from the net. All these aspects will be the target of the coming ESFR-SIMPLE project, which not only will proceed in improving the safety performance of SFRs, but also to make it more attractive to future CO_2-free energy systems.

Finally, it is also recommended to develop code strategies to find the right compromise between computing capabilities (new programming languages, parallelization, etc.), phenomena description (neutronics, thermal-hydraulics, pin thermal-mechanics, corium relocation, etc.) and details of reactor description (pin-by pin level, core level or up to whole plant level). New computing schemes and techniques offer great advantages for the safety analysis of advanced systems, such as machine learning and Digital Twins. Therefore, it is recommended to consider a change of platform from the current typical Fortran-based codes to get benefit from the new methods applying the lessons learnt and know-how acquired during the previous four decades, as well as to offer an attractive field of research to future nuclear engineers and scientist. Being a costly person-intense activity, it will require strong support of both public and private stakeholders.

6 ACKNOWLEDGMENTS

The work presented in this paper was supported by EURATOM under the projects CP-ESFR, ESNII+ and ESFR-SMART. The authors acknowledge the financial support given by the European Commission through the 7th Framework Programme for the CP-ESFR project (FP7-232658) and ESNII+ project (FP7-605172). The research leading to the results obtained within ESFR-SMART project has received funding from the Euratom research and training program 2014-2018 under grant agreement No. 754501.

7 REFERENCES

1. S. Perez-Martin, W. Pfrang. “Analysis of high burn-up annular fuel pin behavior under a CABRI transient over power with the SAS-SFR code”, *Proceedings of the International Congress on Advances in Nuclear Power Plants*, San Francisco (USA), Vol. 1, pp. 371-380 (2016).
2. S. Perez-Martin, W. Pfrang. “Analysis of the E7 CABRI experiment, a structured top transient in restrained conditions with SAS-SFR code”, *Proceedings of the International Conference on Nuclear Engineering*, ICONE, Makuhari Messe Chiba (Japan) (2015).
3. W. M. Schikorr, “Assessment of the kinetic and dynamic transient behavior of sub-critical systems (ADS) in comparison to critical reactor systems”, *Nuclear Engineering and Design* **210**, pp. 95-123, (2001).
4. A. Ponomarev et al. “Superphenix Benchmark Part II: Transient Results” *Journal of Nuclear Engineering and Radiation Science* **8**, pp. 1-20 (2022)
5. L. Ammirabile et al. “SARGEN-IV: Consideration on the possible content of the safety analysis report for innovative ESNII reactors” *Nuclear Engineering and Design* **300** pp. 452–466 (2016).
6. International Atomic Energy Agency, 2004. Format and Content of the Safety Analysis Report for Nuclear Power Plants, IAEA Safety Standards, GS-G-4.1. International Atomic Energy Agency, Vienna.
7. European Utility Requirements for LWR Nuclear Power Plants, 2001. Revision C.

8. A. Lázaro et al. “Code assessment and modelling for Design Basis Accident Analysis of the European sodium fast reactor design. Part I: System description, modelling and benchmarking” N*uclear Engineering and Design* **266** 1– 16 (2014).
9. A. Lazaro et al. Code assessment and modelling for Design Basis Accident analysis of the European Sodium Fast Reactor design. Part II: Optimised core and representative transients analysis. *Nuclear Engineering and Design* **277** 265–276 (2014).
10. E. Bubelis et al. “System codes benchmarking on a low sodium void effect SFR heterogeneous core under ULOF conditions” *Nuclear Engineering and Design* **320** 325–345 (2017).
11. Vademecum data (available only at the ESFR-SMART ECCP website).
12. S. Perez-Martin et al. Evaluation of sodium boiling models using KNS-37 LOF experiments. Journal of Nuclear Engineering and Radiation Science **8** 011310-3 (2022).

ON THE PURSUING OF SAFETY ENHANCEMENTS IN SODIUM FAST REACTORS

S. Perez-Martin, E. Bubelis, W. Pfrang, M. Schikorr, W. Hering

ERMSAR 2022
MAY 16-19, 2022 — KARLSRUHE, GERMANY

Intro & Outline

	1960	1970	1980	1990	2000	2010	2022
FBR National Programs							
FBR National Programs							
International collaborations (e.g. CABRI , …)							
EU funded Projects							

- Outcome of long lasting international collaboration in SFR safety (400+ years of reactor operation):
  - Improved core designs, structural components and passive safety systems.
  - Development of numerical simulation computer codes for design as well as licensing process.
- Assessment of enhanced SFR core designs under ULOF transient

SFR Safety Analysis

- Licensing: demonstration of safety functions under normal operation and accident conditions:
  - i) reactor shut-down maintaining safe condition
  - ii) adequate core heat removal after shut-down
  - iii) retention capabilities for radioactive and hazardous material to minimize its release to the environment.

- CP-ESFR project milestone: identification of initiating events in DBC that may challenge the safety functions.

- Category DBC4: initiating events not expected to occur during plant lifetime (freq.$<10^{-4}$ per reactor-year):
  - Unprotected Transients (shutdown system is assumed to fail)
    - Runaway of control rods: Unprotected Transient Over-Power
    - Loss of the active core cooling capability: Unprotected Loss of Flow
  - Break of LIPOSO (pipelines joining the primary pump with the core diagrid).

- ULOF importance:
  - Potential to progress into the coolant boiling phase (and eventually into partial or even total core destruction).
  - Detailed consideration of the particular effects of various specific design characteristics (e.g. upper sodium plenum, absorber layers, discharge tubes, etc.).

SFR reactor designs in EU projects

	CP-ESFR	ESNII+	ESFR-SMART
Time	2009-2012	2013-2017	2018-2022
Target	SFR	Gen-IV (SFR, LFR, GFR…)	SFR
Reactor power (MWth)	3600	1500	3600
Total number of SA	453	291	504
Number of pins per SA	271	217	271
Core inlet temp. (°C)	395	400	395
Core outlet temp. (°C)	545	550	545
Av. core structure temp. (°C)	470	475	470
Reactor performance	Minor Actinides transmutation	ASTRID	Improved CP-ESFR reactor
Safety measures	decrease sodium void worth	negative sodium void worth	corium discharge tubes passive SR (Curie-point triggered)

SFR reactor designs in EU projects

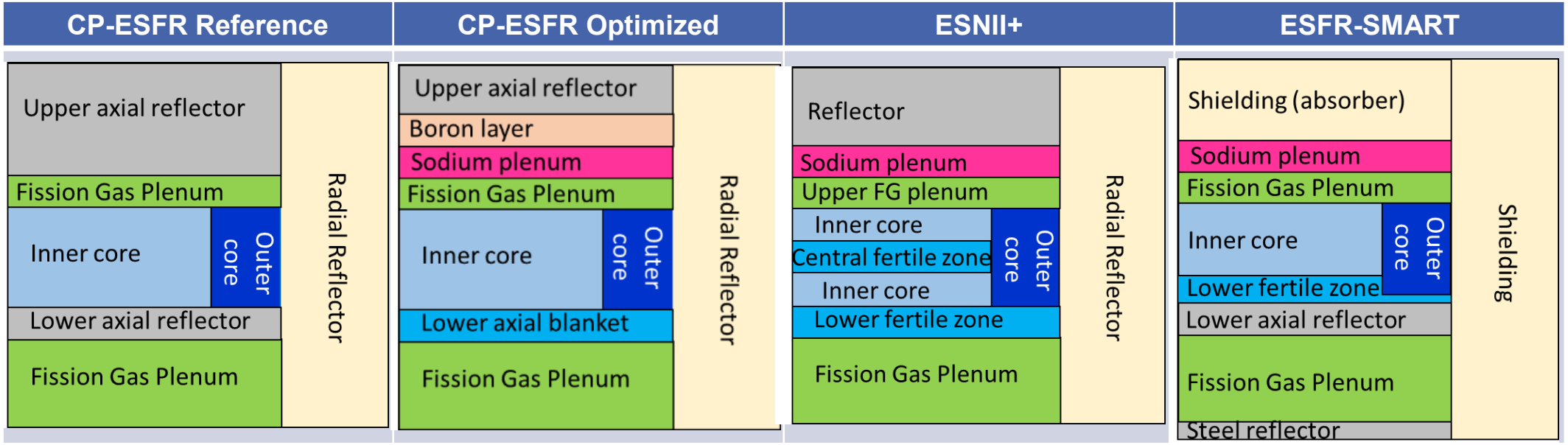

Sodium void (density) reactivity:

- Less neutron capture (positive effect)
- Neutron spectrum hardening (positive effect)
- Larger mean free path: neutron leakage increase (negative effect)

Measures:

- a large sodium plenum at the top of the core (where neutron leakages are increased)
- axially heterogeneous fuel pins with a central fertile layer in IC (increasing neutron flux in the upper fissile layer)
- shortening of the fissile zone in the IC
- absorbing zone in upper shielding (reducing neutron reflection back to the fissile core during voiding)

ULOF transient

- Unintentional simultaneous coast-down of all primary pumps + failure of the reactor shut-down system.
- The primary mass flow rate:

$$\frac{\dot{m}(t)}{\dot{m}_0} = \frac{1}{1 + \frac{t}{\tau}}$$

τ (halving time): 10 s, except for ESNII+ case which is 24 s.

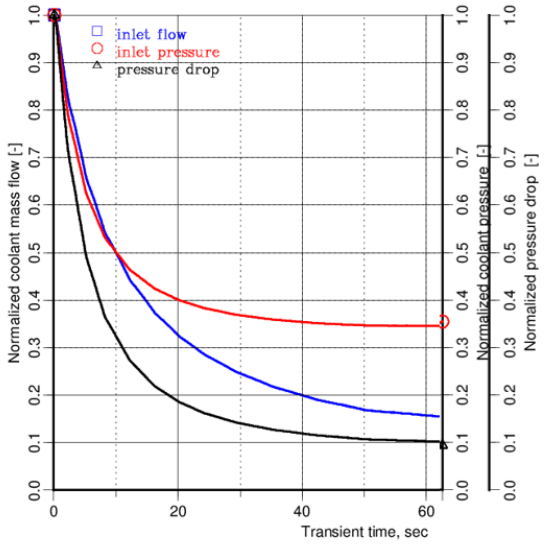

- No pony motors or other devices maintaining coolant
- Evaluation at EOEC core conditions (except for the CP-ESFR Opt. at BOL)
- EOEC represents the worst-case scenario where the fuel/pin configuration is in degraded thermal and mechanical conditions and all control rods are essentially in the withdrawn position.
- Reactivity feedbacks: Doppler, fuel cladding, sodium reactivity, control rods driveline thermal expansion.

SIM-SFR and SAS-SFR codes

- SAS-SFR and SIM-SFR: reference codes in SFR safety evaluations
- Developed and supported by the Karlsruhe Institute of Technology.
- Validated against experimental data from large-scale experiments (i.e. CABRI, SCARABEE, KNS-37, TREAT, Phenix, SPX, etc.).

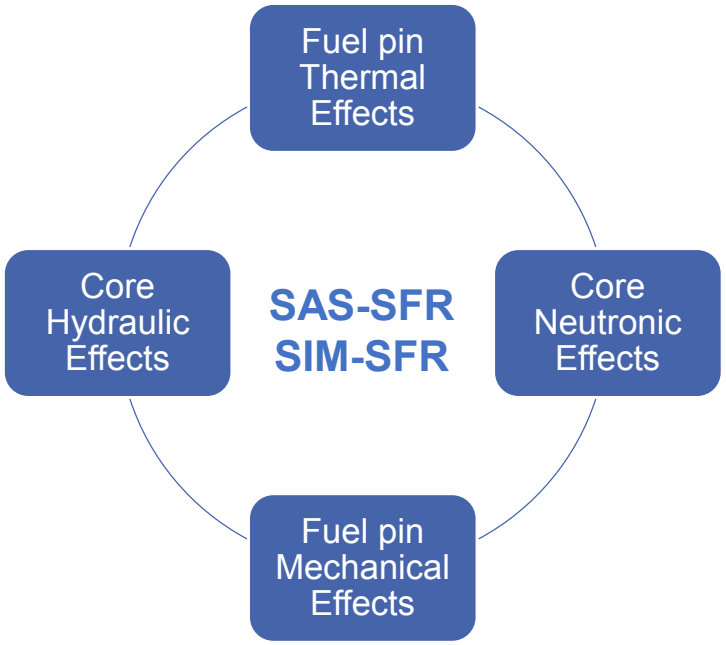

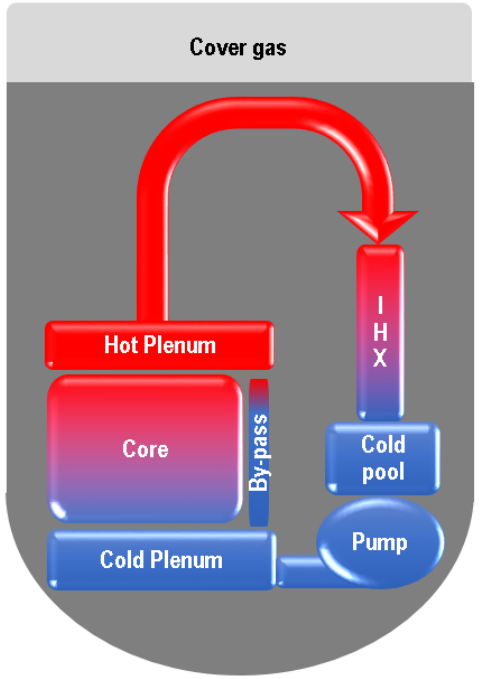

SFR core

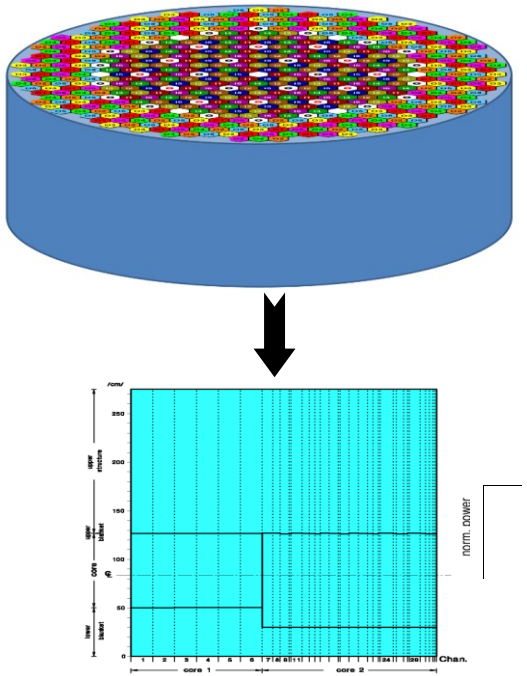

Code representation with SA channels

ULOF Code modelling

- Reactor representation:
  - SIM-SFR: core, the primary, secondary and tertiary cooling circuits, including IHX and SG
  - SAS-SFR: core and primary cooling circuits including IHX
- SA representation:
  - SIM-SFR: average power and a peak power fuel representation for each core zone
  - SAS-SFR: SA grouping based on similar TH conditions undergoing same irradiation (ESFR-SMART 34 SA groups)
- Reactivity feedbacks:
  - SIM-SFR: Doppler, fuel&cladding axial exp. , diagrid radial expansion, coolant expansion and CRDL axial exp.
  - SAS-SFR: Doppler, coolant density, fuel&cladding axial exp., fuel and clad relocation, diagrid radial exp., CRDL ax. exp.
- Gap model: special, high fidelity fuel pin mechanics models.
  - SIM-SFR: dynamic model (burn-up dependence of both fuel and cladding material)
  - SAS-SFR: URGAP model (gap size, fuel-clad contact pressure, gas content and composition and surface roughness)

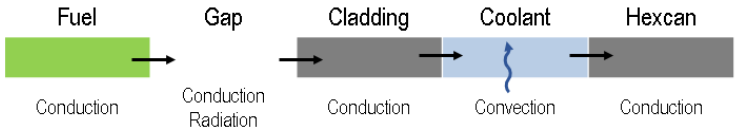

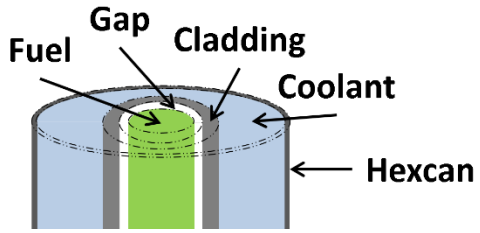

ULOF code results in CP-ESFR and ESNII+

- CP-ESFR:
  - The optimized core improved the safety response by reducing peak temperatures and enlarging grace times.
  - Not sufficient to avoid a power excursion once sodium boiling commenced.
- ESNII+:
  - Upper sodium plenum provided only a small delay in boiling onset (void effect dominated by the fissile core voiding) → sodium plenum does not play a decisive role in improving total void effect
  - Transient progression beyond pin and hexcan failure, driven by cladding failure and relocation from the fissile core zone.
  - Optimization of the core neutron physics alone was not sufficient to avoid a power excursion during the ULOF transient.
- This type of core geometrical modifications established a direction to progress for achieving higher safety levels and risk prevention of core meltdown accident.

SAS-SFR results for ESFR-SMART ULOF

- Sodium boiling starts in ch. 33 (OC) at 46.1 s, nominal power is 0.61, net reactivity is -0.12 $.

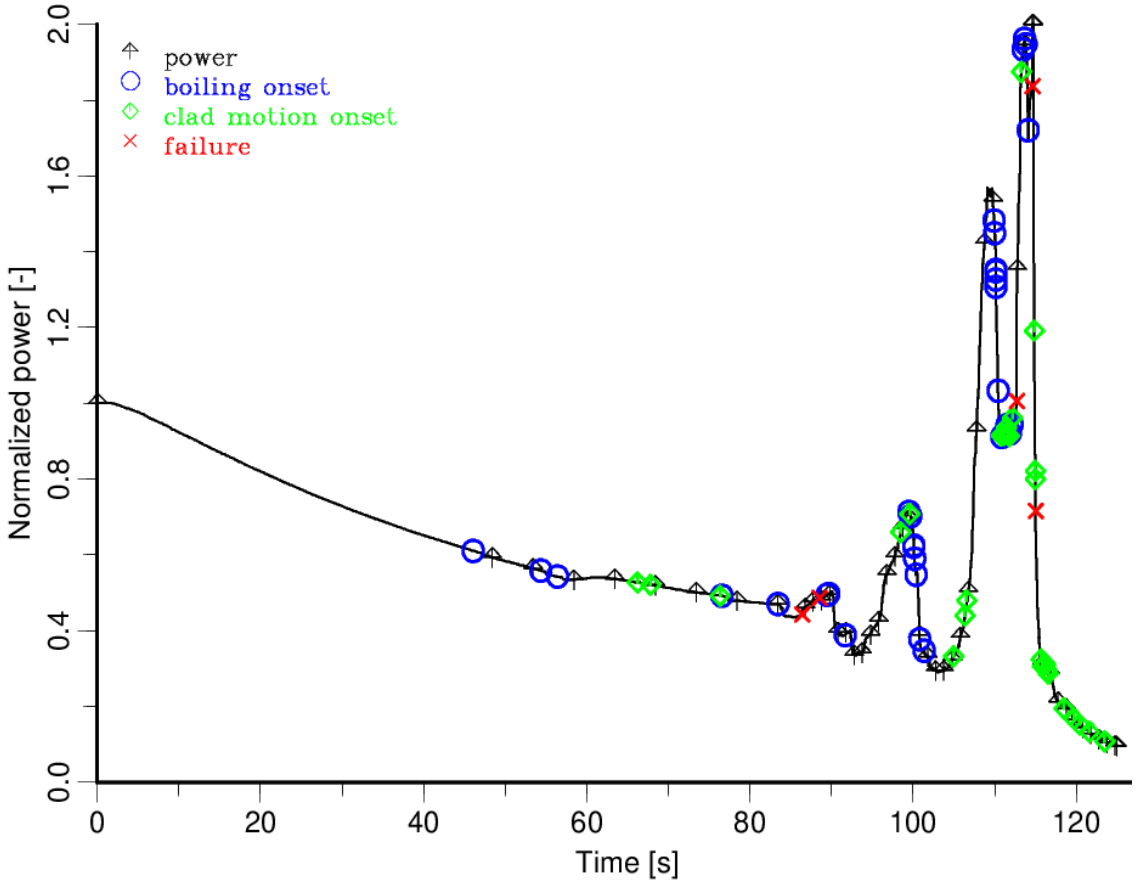

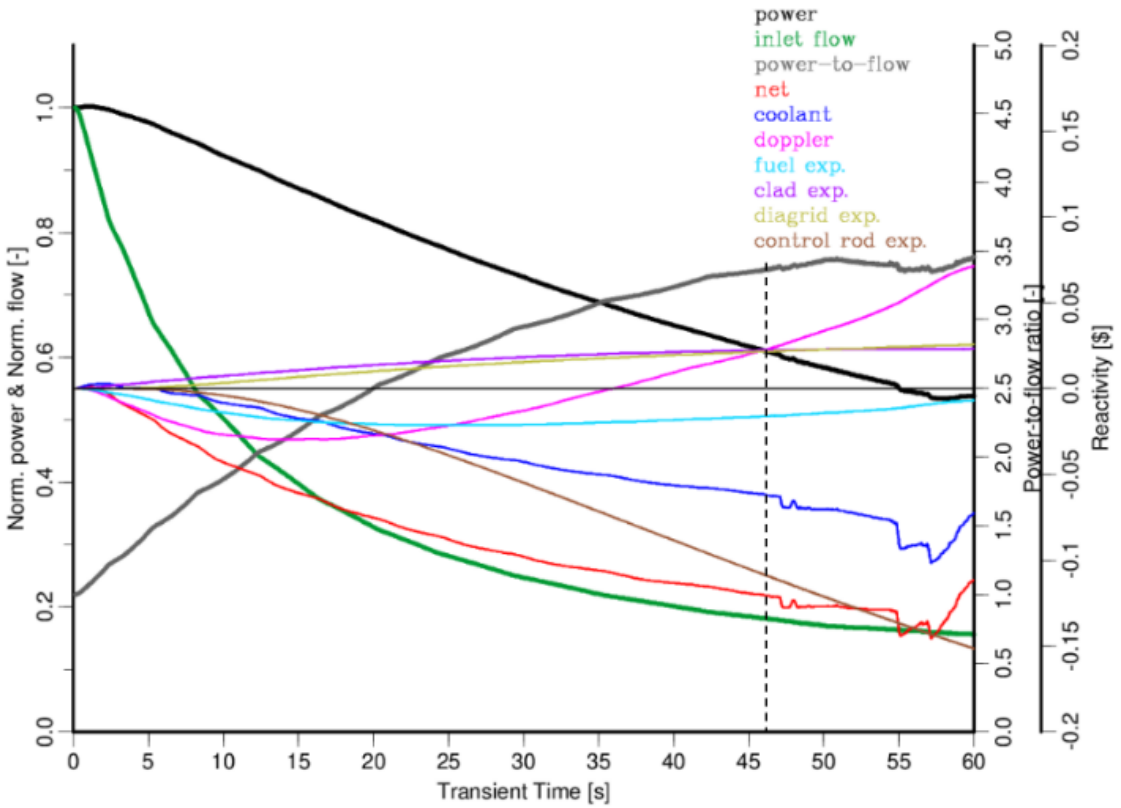

SAS-SFR results for ESFR-SMART ULOF

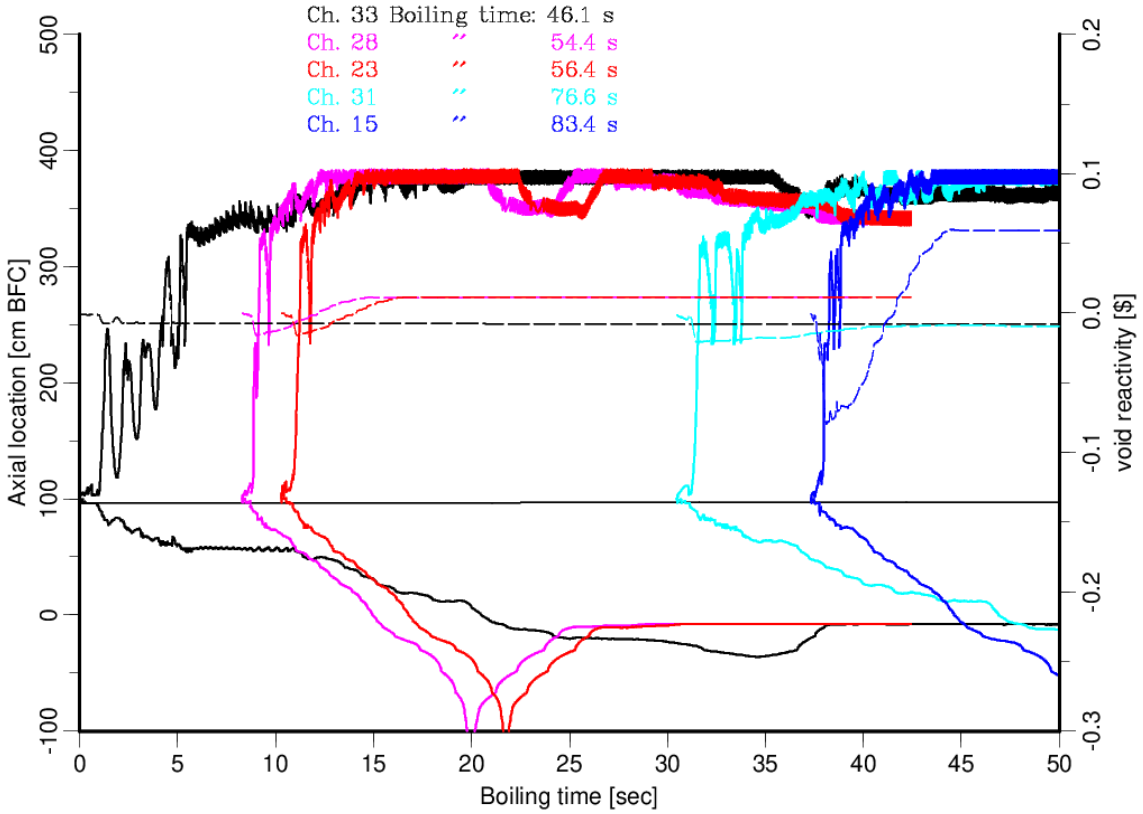

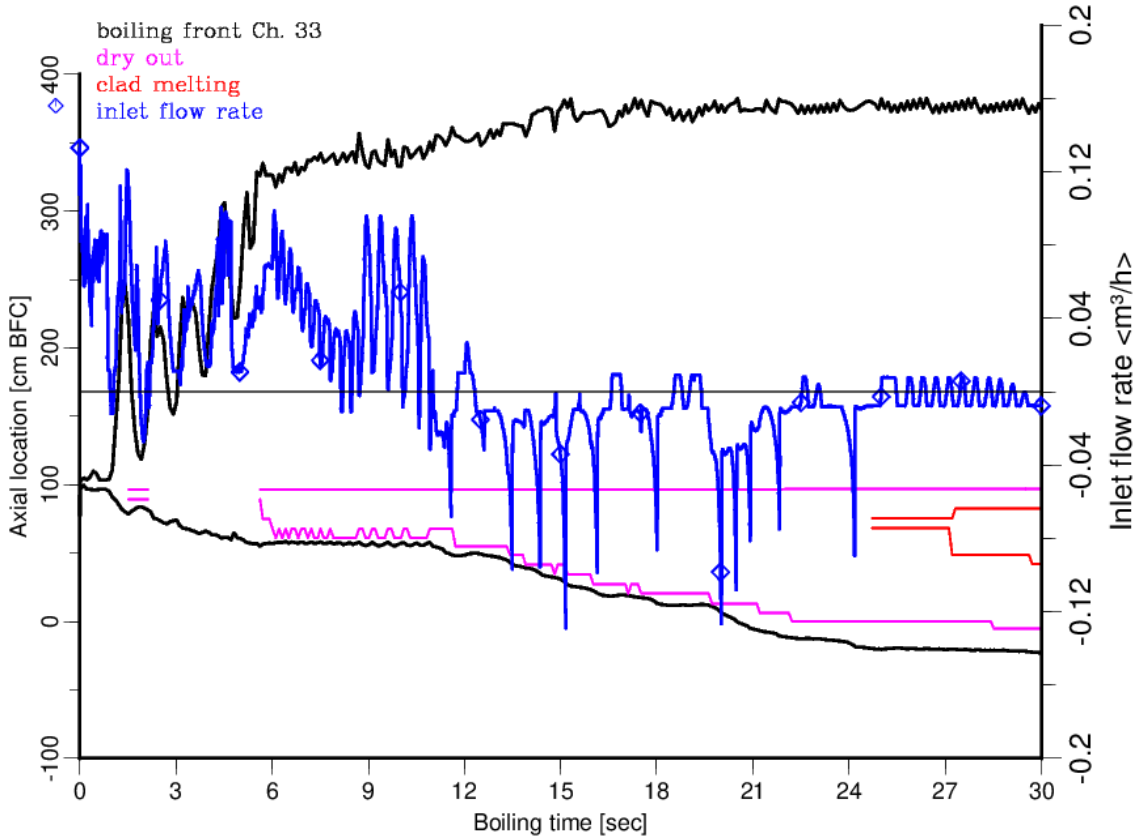

Fuel pin break-up failure mechanism: clad integrity compromised due to the high clad temperature and fuel pellet heat-up exceeds the melting limit and built-up cavity pressures.

ULOF transient period 83-93 s

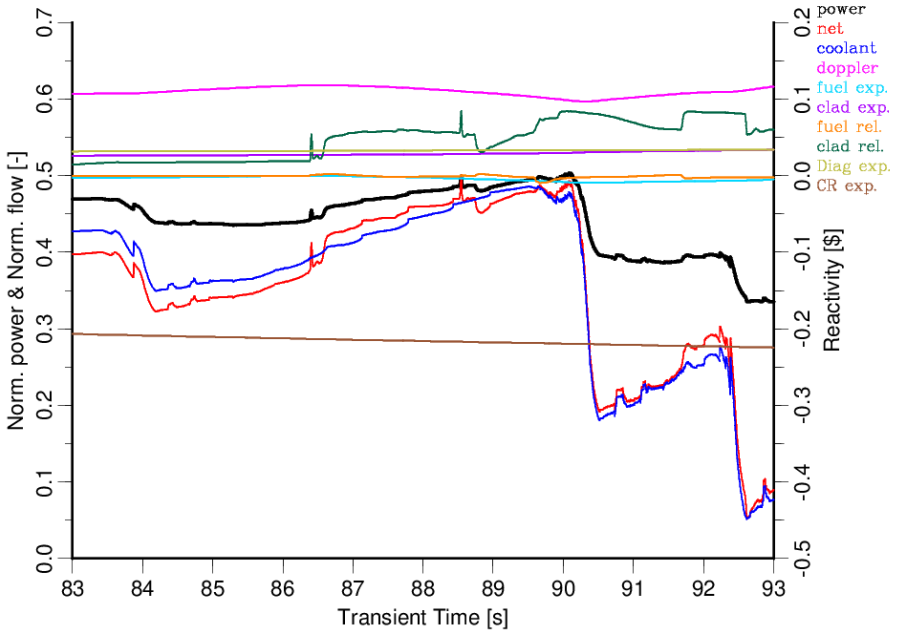

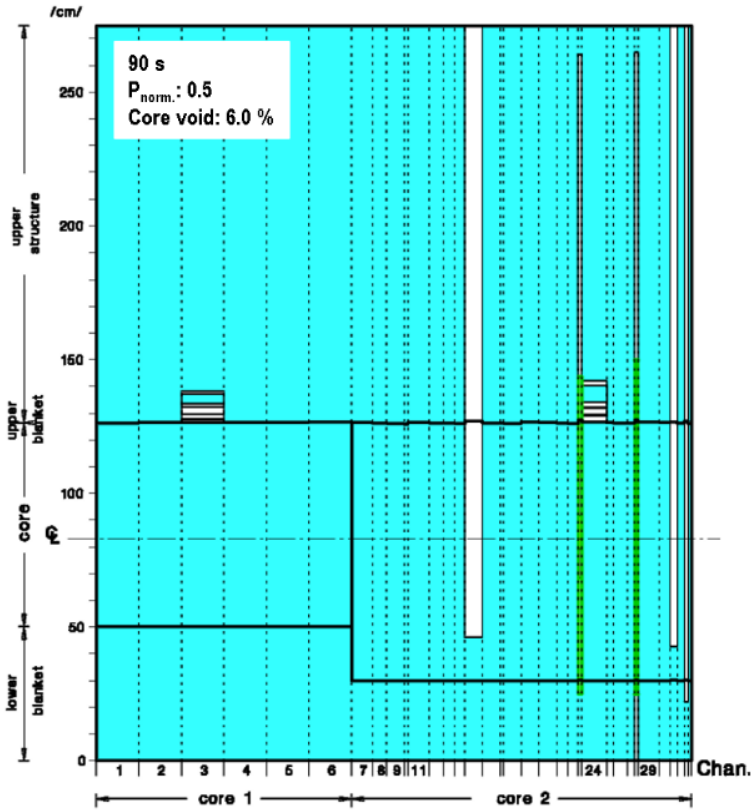

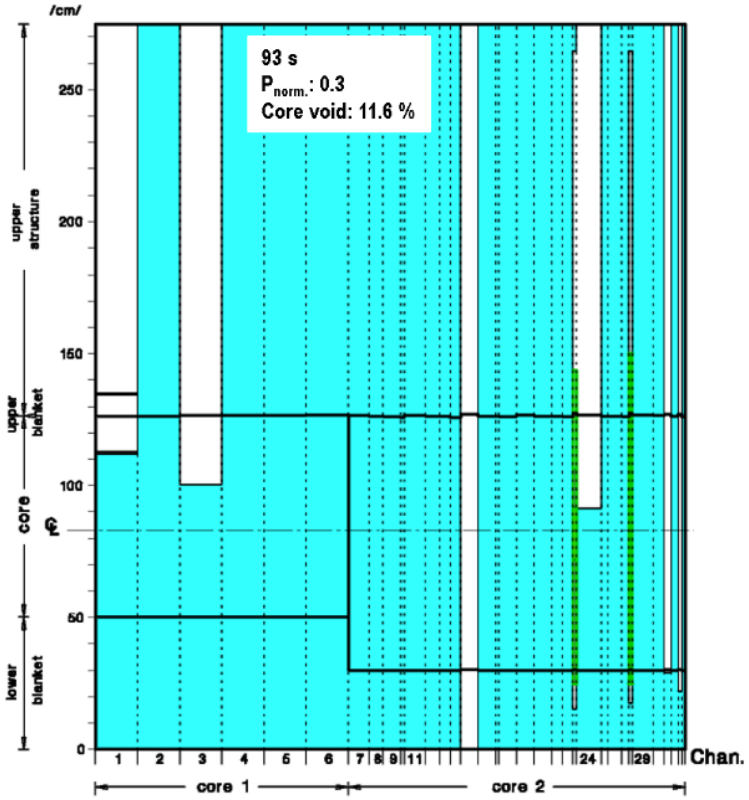

ULOF transient period 90-100 s

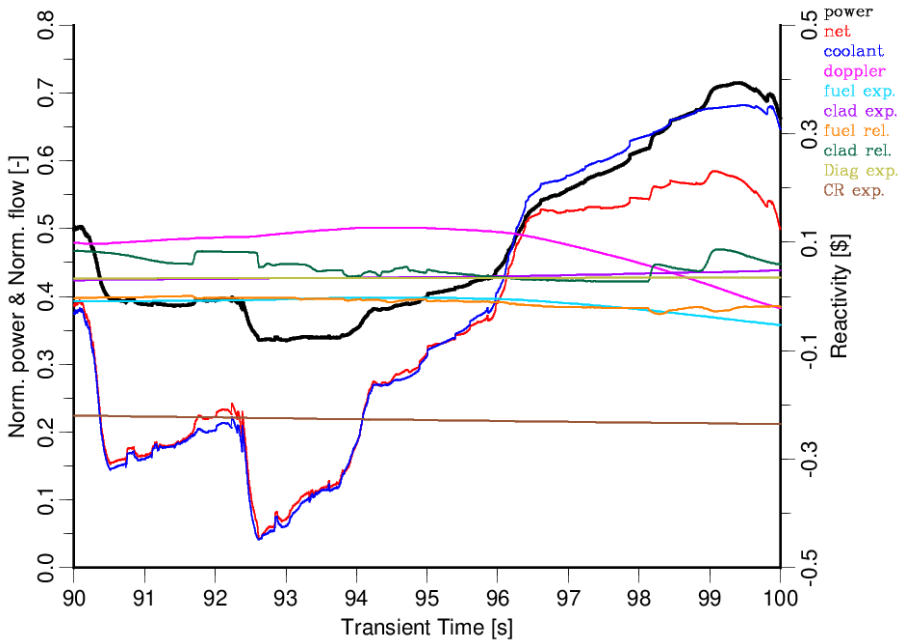

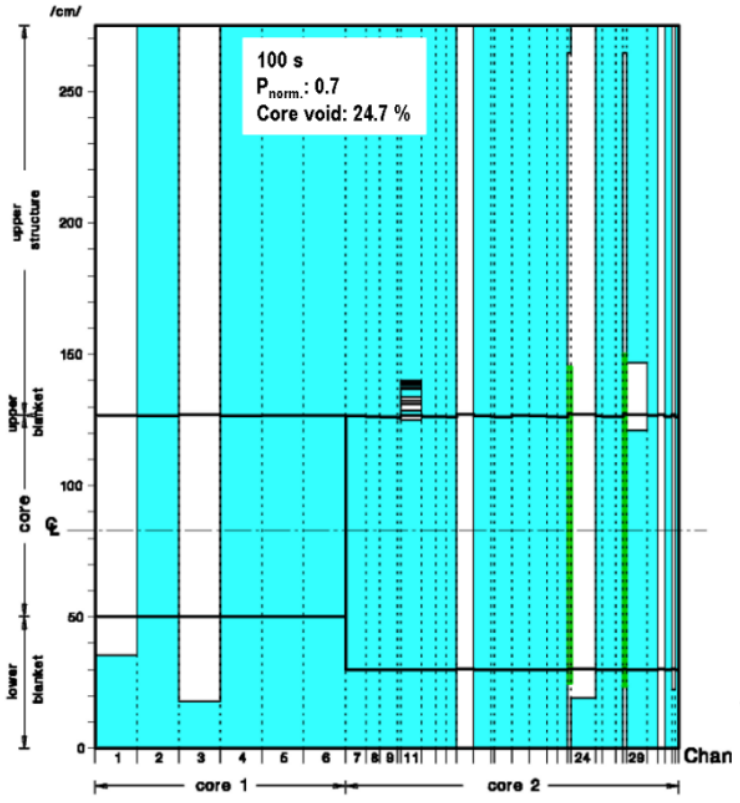

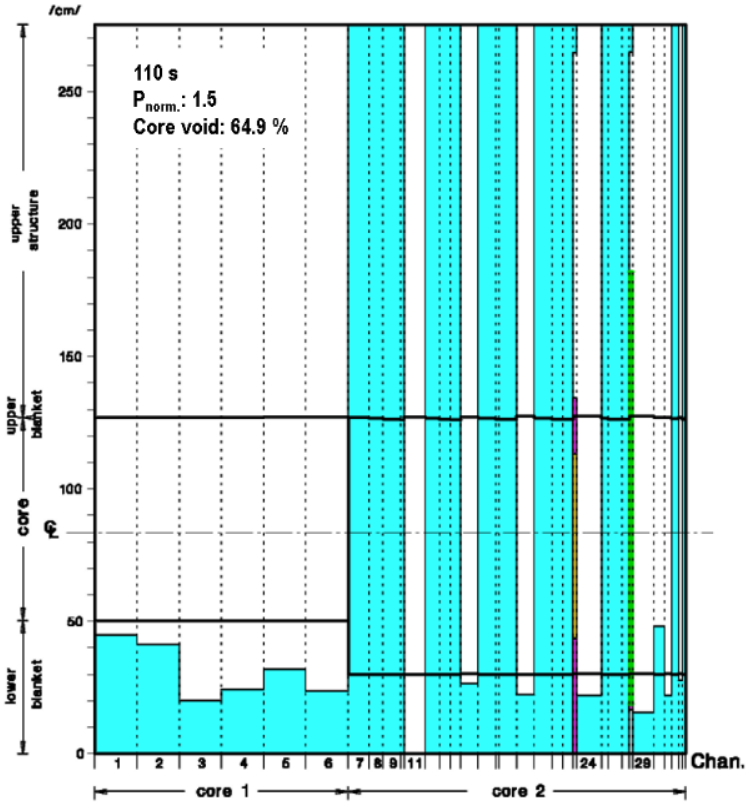

SAS-SFR results for ESFR-SMART ULOF

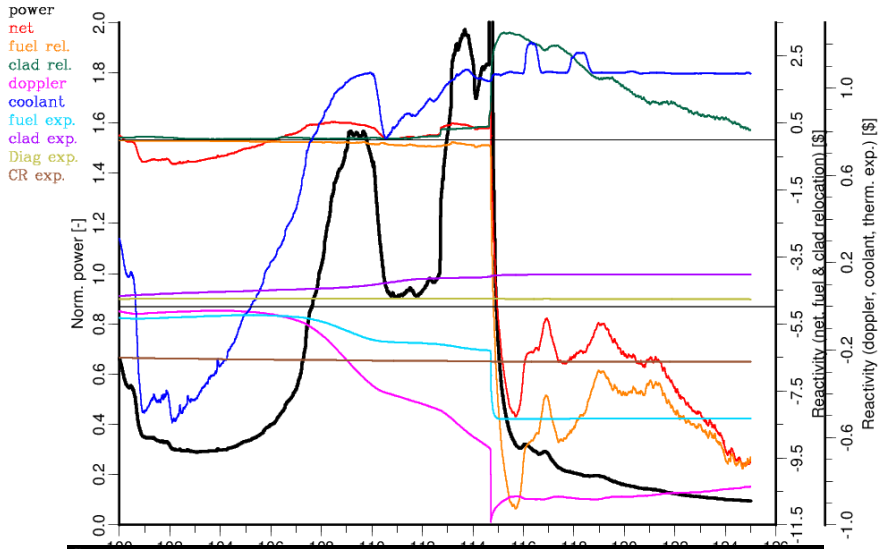

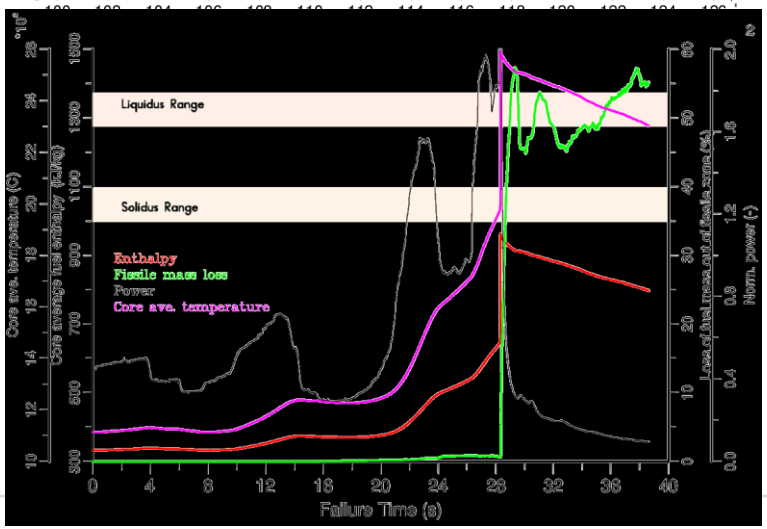

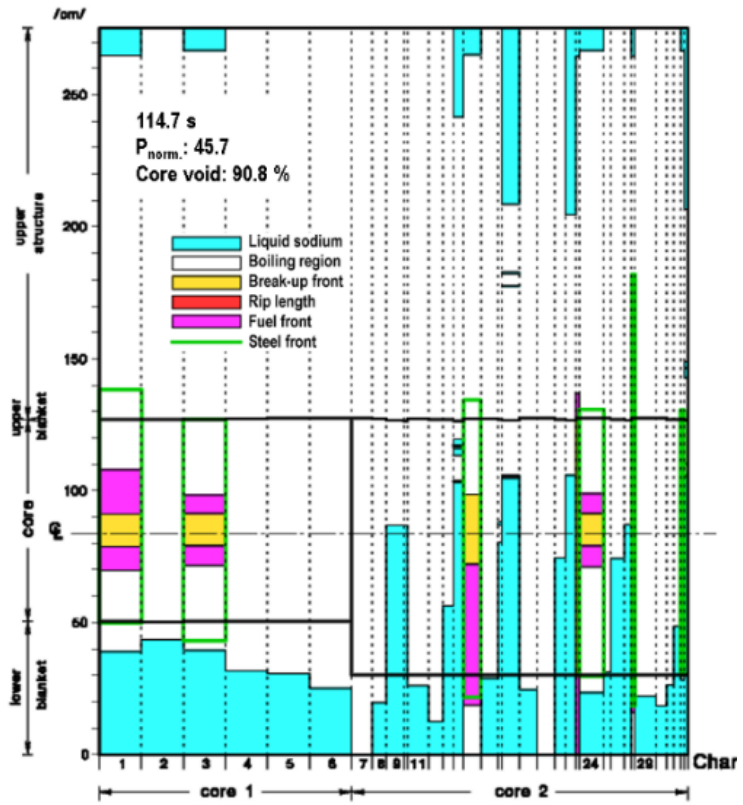

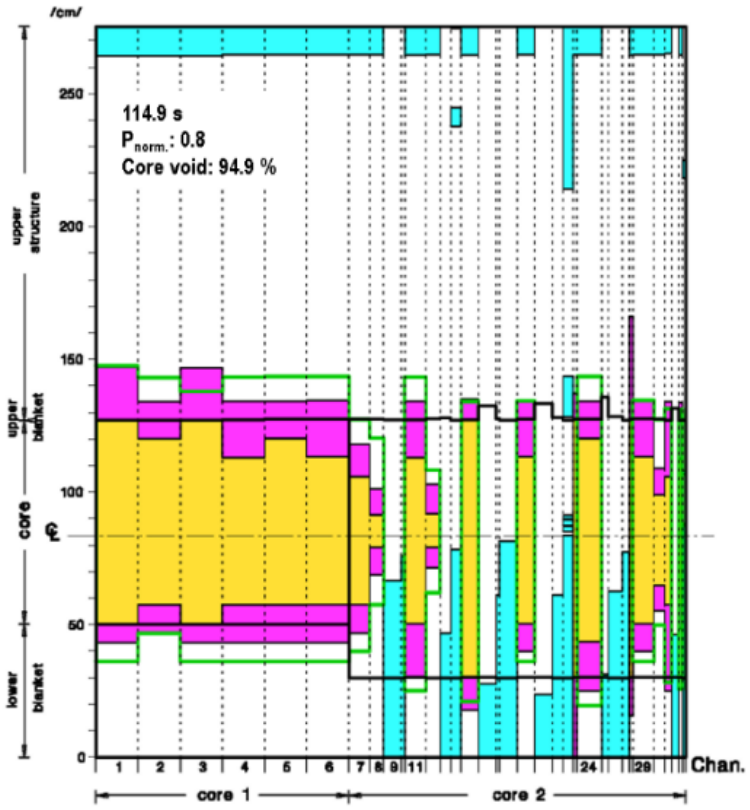

No hexcan damage: transient does not progress further and following accidental sequences (i.e. recriticality) are no longer expected.

SAS-SFR results for ESFR-SMART ULOF

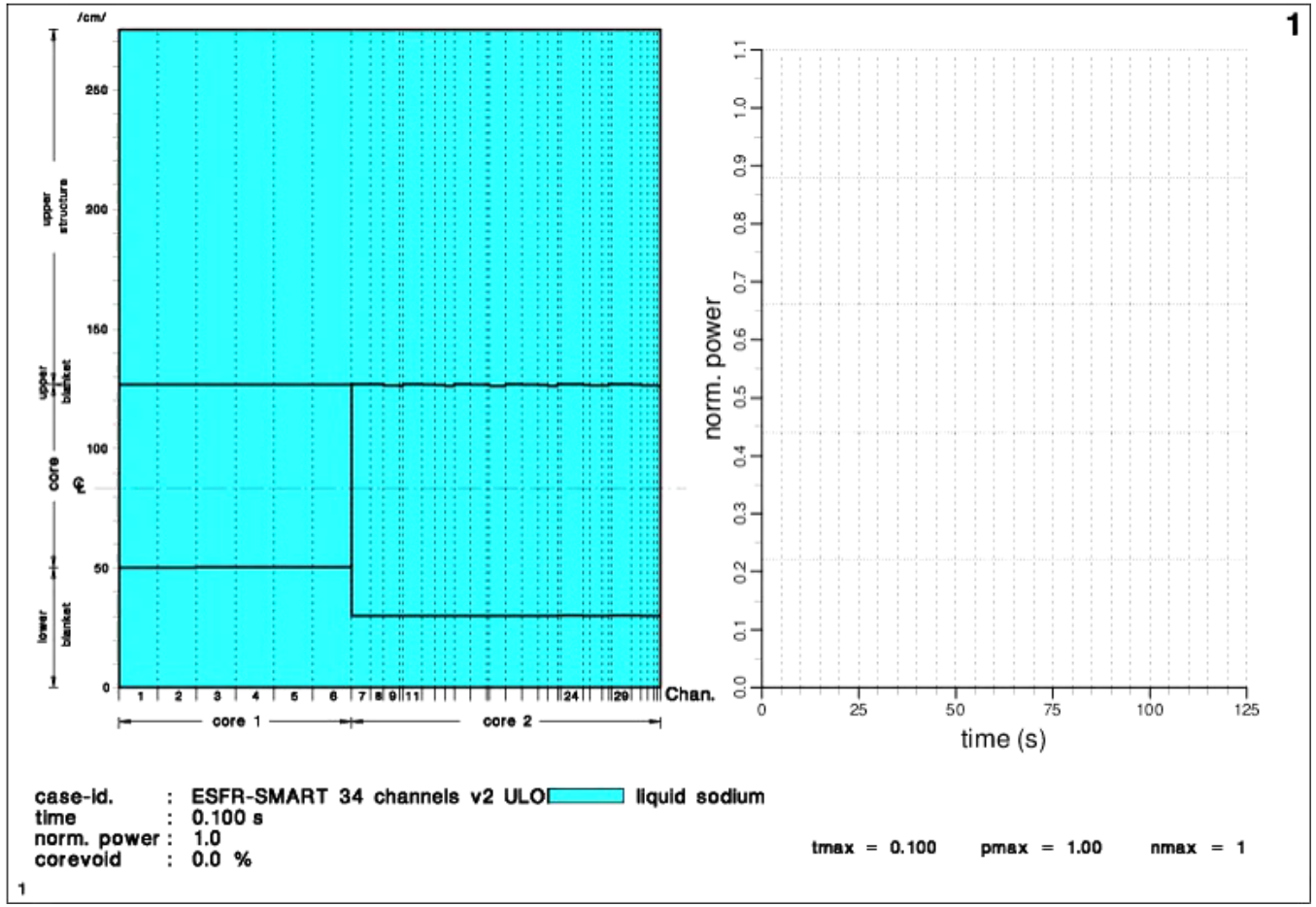

Video

liquid sodium
boiling region
break-up front
rip length
fuel front

504 SAs with 271 pins per SA
Computational running time
- 36 representative pins (6 ch. inner core, 30 ch. outer core)
- Fuel pin irradiation:
  - Real irradiation time: 1800 d
  - Computing time: 38 min. total → ~1 min. per SA
- ULOF transient:
  - Real transient time: 125 s
  - Computing time: ~17 h total → 0.5 h per SA

SIM-SFR results for ESFR-SMART ULOF

- During ULOF sodium flowrate decreases down to natural circulation flowrate and even below depending on sodium voiding.
- Boiling onset sequence (outlet fissile region): i) PP* OC, ii) Av.P** OC, iii) PP IC and iv) Av.P IC.
- Flow blockage due to boiling not known precisely: sensitivity study to investigate the natural circulation flow reduction.

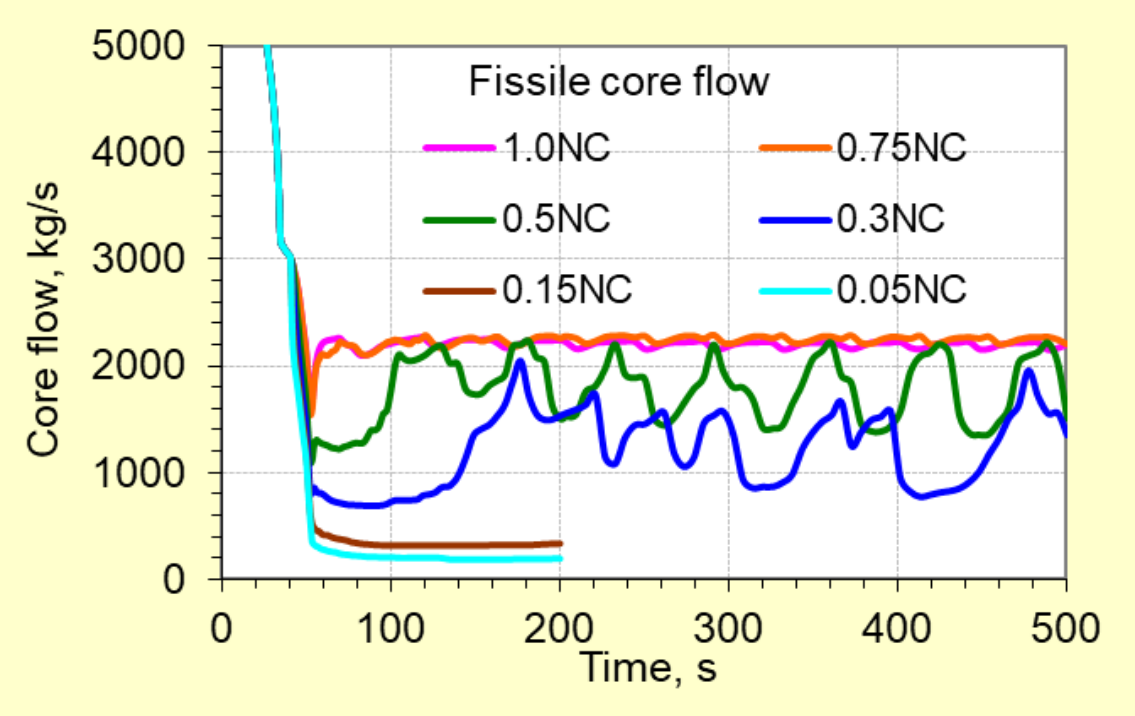

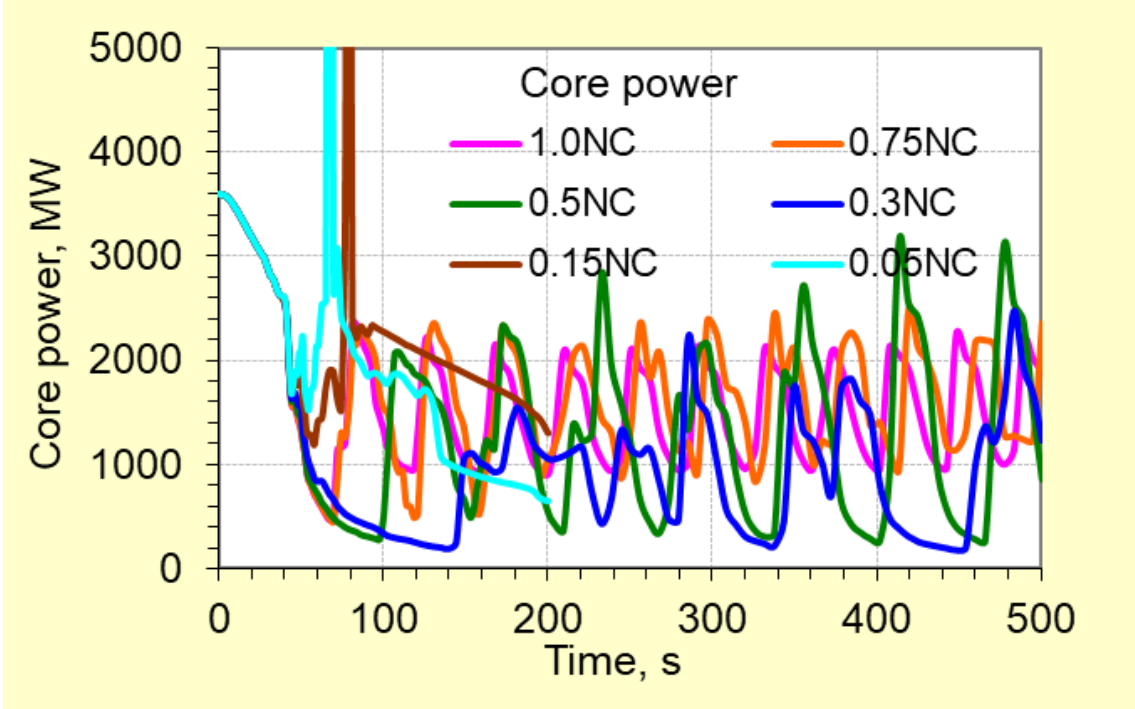

* Peak Power, ** Average Power, IC: Inner Core, OC: Outer Core

SIM-SFR results for ESFR-SMART ULOF

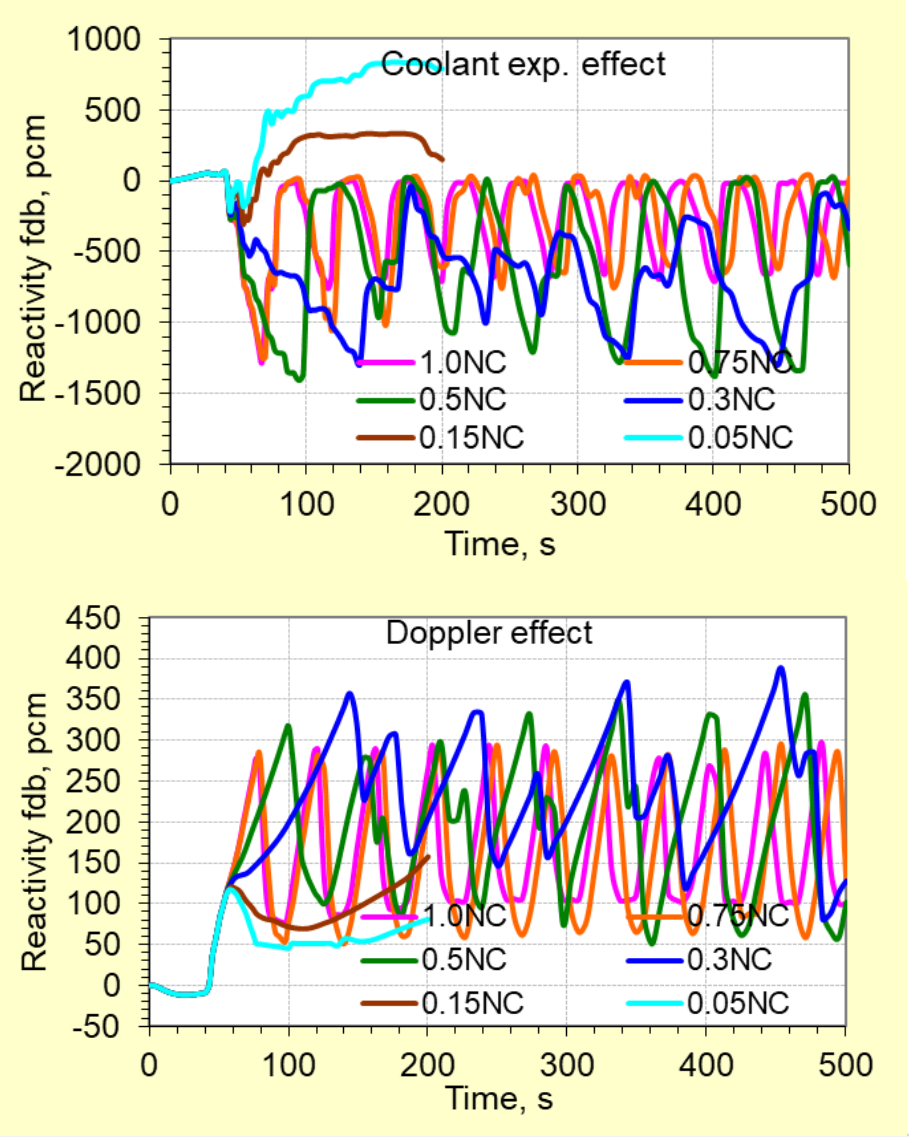

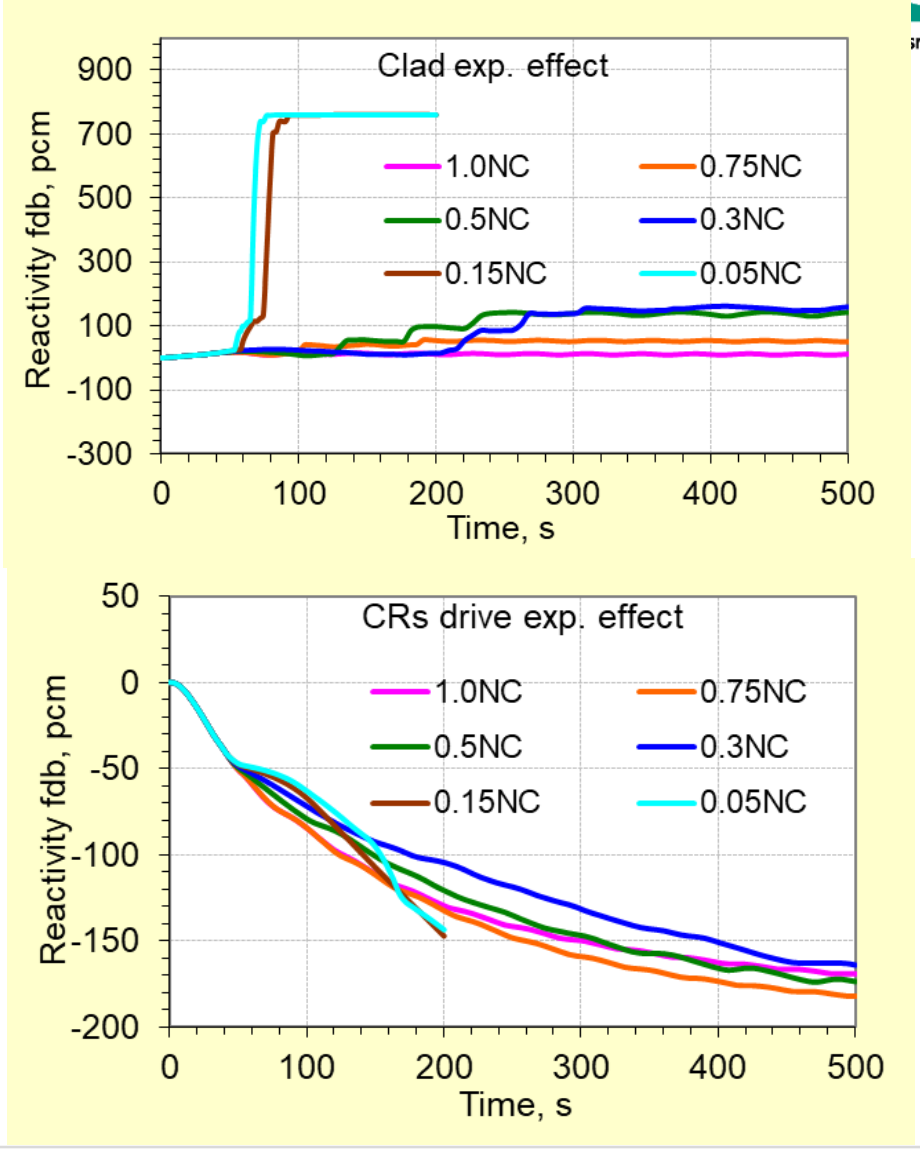

SIM-SFR results for ESFR-SMART ULOF

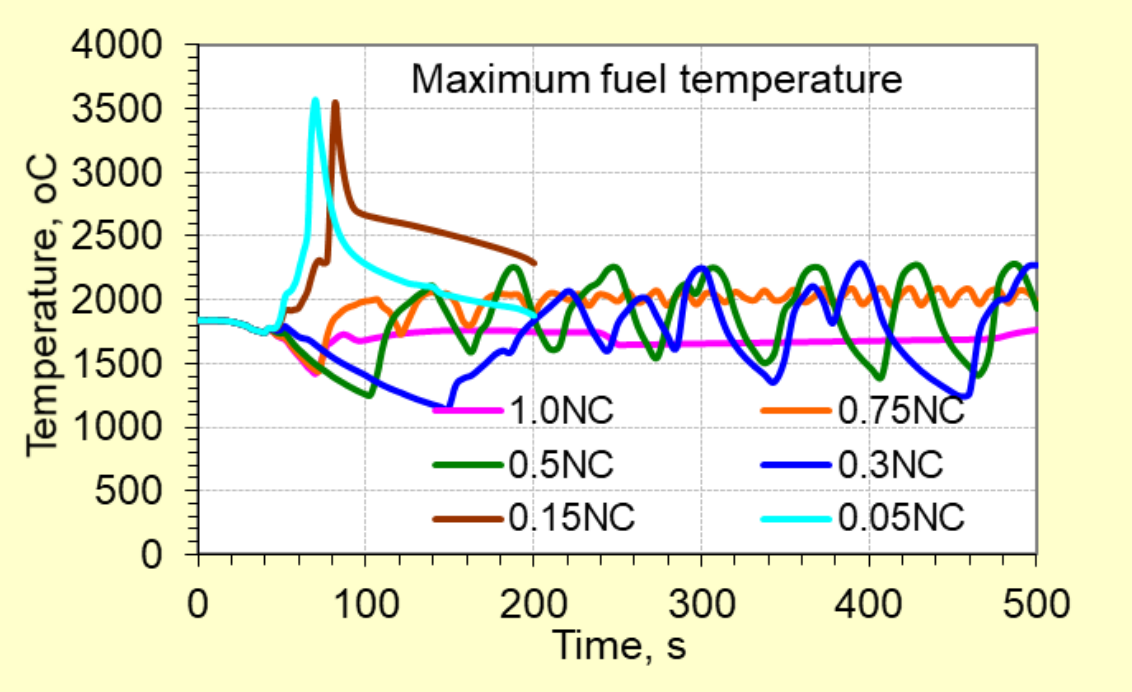

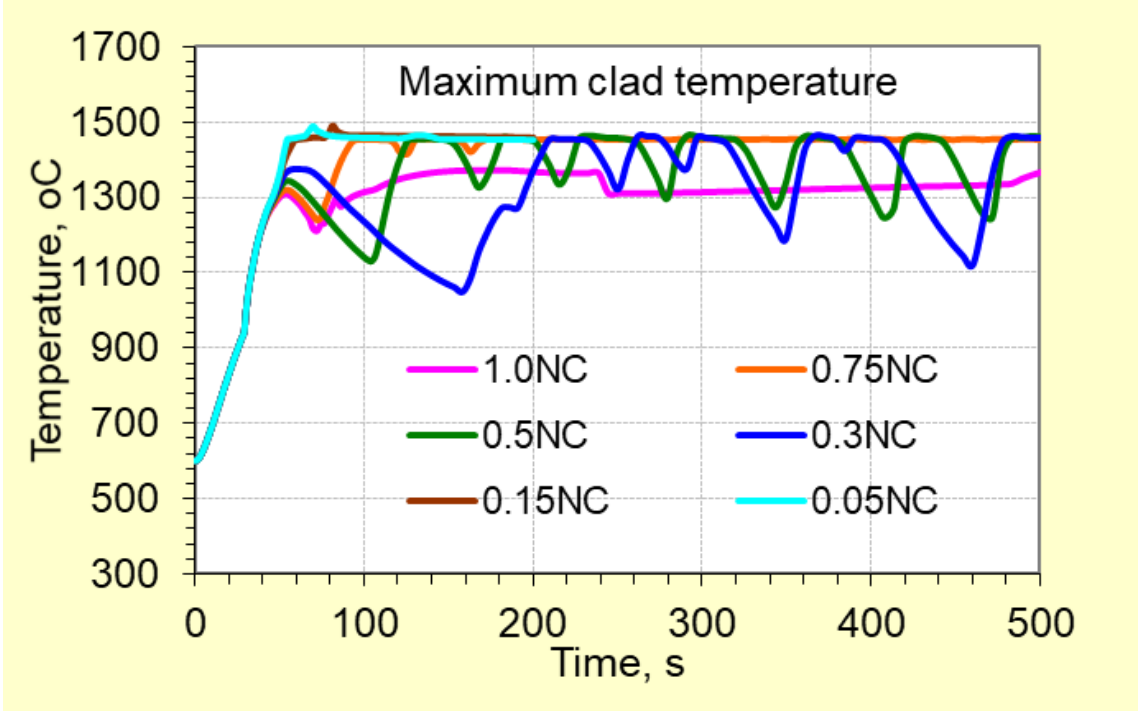

The 15% and 5% flow choking cases basically replicate the SAS-SFR ESFR ULOF results.

CONCLUSIONS

- Assessment of SFR performance + verification & validation of computational tools
- Measures considered to reduce the void reactivity effect in large SFR:
  - Sodium and boron layers (CP-ESFR Optimized core)
  - Central fertile layer in the inner core region (ESNII+ core)
  - Reducing inner core fissile fuel region (ESFR-SMART core).
  - Optimizations not sufficient to avoid a power excursions, though increase grace time, not melting/rupture of the SA hexcan.
- Future R&D:
  - Sodium two-phase flow: large scale code validation comparisons based on experimental data sets (KNS-37 test)
  - New two-phase flow experimental tests reflecting the current trends in core designs.
  - Large scale clad relocation prevention: core and SA-design measures or min. flow rate (active/passive means, pony motor)
  - Assessment of SMRs based on SFR technology, where high benefits are expected in terms of safety and flexibility.
  - New code strategies to find the right compromise between:
    1. computing capabilities (new programming languages, parallelization, etc.)
    2. phenomena description (neutronics, thermal-hydraulics, pin thermal-mechanics, corium relocation, etc.)
    3. details of reactor description (pin-by pin level, core level or up to whole plant level).
    - Advantages for the safety analysis of advanced systems (Machine Learning, Digital Twins) compared to current Fortran-based codes
    - Attractive research to future nuclear engineers/scientist → costly person-intense requiring support of public and private stakeholders.

Acknowledgement

- The work presented in this paper was supported by EURATOM under the projects CP-ESFR, ESNII+ and ESFR-SMART.
  - CP-ESFR project: 7th Framework Programme FP7-232658
  - ESNII+ project: : 7th Framework Programme FP7-605172
  - ESFR-SMART project: H2020 program 2014-2018 grant agreement 754501



ESNII+

ESFR-SMART
sodium fast reactor safety

ESFR-SMART

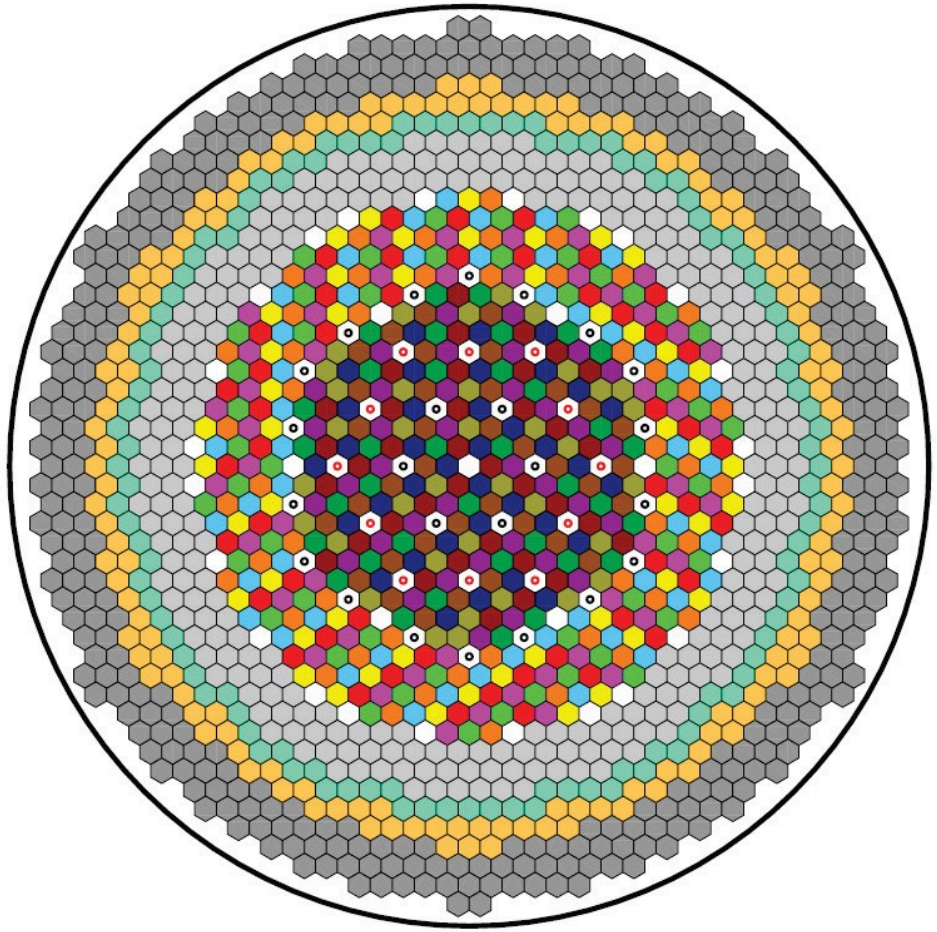

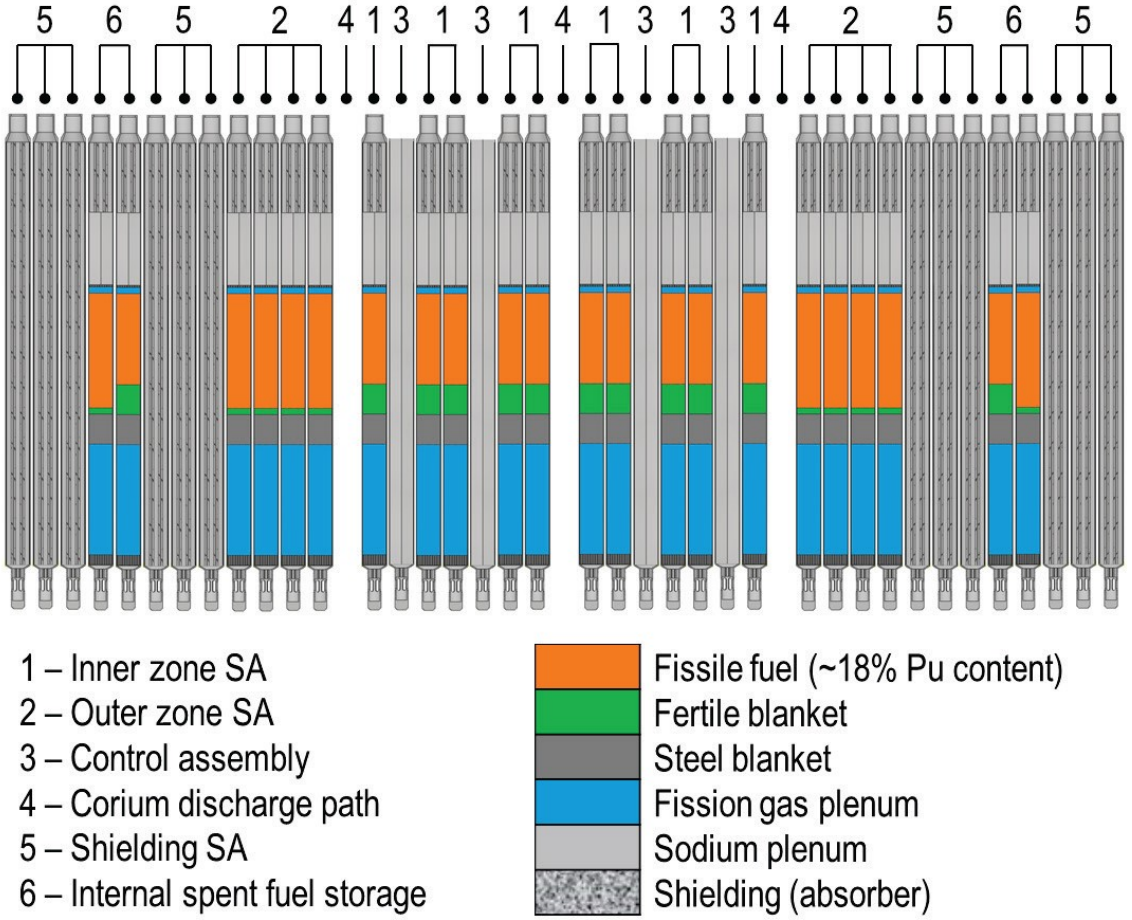
5 6 5 2 4 1 3 1 3 1 4 1 3 1 3 1 4 2 5 6 5
1 – Inner zone SA
2 – Outer zone SA
3 – Control assembly
4 – Corium discharge path
5 – Shielding SA
6 – Internal spent fuel storage
Fissile fuel (~18% Pu content)
Fertile blanket
Steel blanket
Fission gas plenum
Sodium plenum
Shielding (absorber)

ESFR-SMART

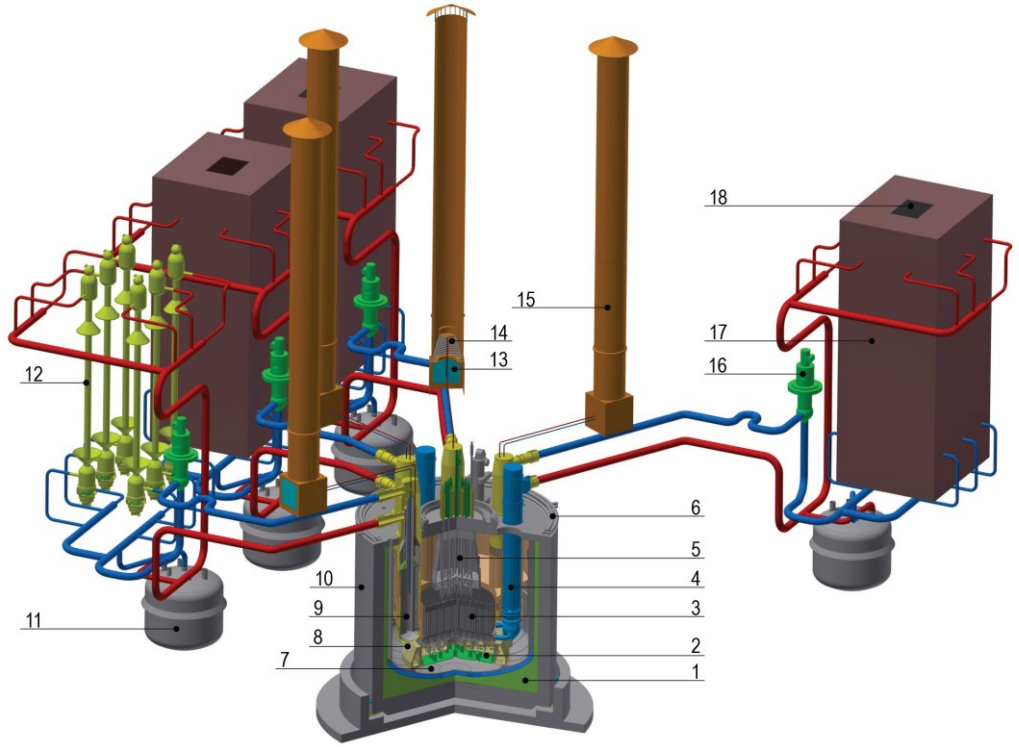

1: Insulation with steel liner
2: Core catcher
3: Core
4: Primary pump
5: Above-core structure
6: Pit cooling system (DHRS-3)
7: Main vessel
8: Strongback
9: IHX
10: Reactor pit
11: Secondary sodium tank
12: Steam generator
13: Window for air circulation (DHRS-1)
14: Sodium-air HX (DHRS-1)
15: Air chimney (DHRS-1)
16: Secondary pump
17: Casing of SGs (DHRS-2)
18: Window for air circulation (DHRS-2)

The 10th European Review Meeting on Severe Accidents Research

Severe Accident Research Eleven Years after the Fukushima Accident

May 16-19, 2022, Karlsruhe, Germany

Technical Session 7-3: Containment Behavior - Recombination

Chairs: A. Bentaib (IRSN), I. Kljenak (IJS)

ID301	**Experimental Investigation on the Effect of Carbon Monoxide on Platinum- and Palladium-based Catalysts for Passive Auto-catalytic Recombiners** G. Nobrega (IRSN)	**Paper** **Presentation**
ID286	**Enhancement of Recombination Rate Correlations for PARs in Oxygen-Lean Conditions** J. Fontanet (CIEMAT)	**Paper** **Presentation**
ID330	**Effectiveness of Hydrogen Recombination by AgX and AgR Zeolites** F. Espegren (PSI)	**Paper** **Presentation**

10TH CONFERENCE ON
SEVERE ACCIDENTS RESEARCH
May 16-19, 2022 – Karlsruhe, Germany
ERMSAR 2022

EXPERIMENTAL INVESTIGATION ON THE CARBON MONOXIDE EFFECT ON PLATINUM- AND PALLADIUM-BASED CATALYSTS FOR PASSIVE AUTO-CATALYTIC RECOMBINERS

Gabriela Nobrega, Ludovic Maas, Ahmed Bentaib
Institut de Radioprotection et de Sûreté Nucléaire
92262 Fontenay-aux-Roses, France
gabriela.senrapessanhariosnobrega@irsn.fr

Ernst-Arnst Reinecke
Forschungszentrum Jülich GmbH
52425 Jülich, Germany

Nabiha Chaumeix
CNRS-INSIS, I.C.A.R.E.
45071 Orléans, France

ABSTRACT

During a severe accident in a nuclear power plant, large amounts of combustible gases (hydrogen and carbon monoxide) can be produced and may form an explosive gas mixture within the containment. In order to mitigate the risk of hydrogen explosions, many containments of water-cooled reactors are nowadays equipped with Passive Autocatalytic Recombiners (PARs). PARs are passive devices designed to convert hydrogen into steam and carbon monoxide into carbon dioxide by exothermic catalytic reactions. Recombiners are assumed to be always fully operational. However, they may be exposed, in normal operation or during the accident, to different airborne substances or atmospheric pollutants that might interfere with the catalytic surface. Catalyst deactivation is a safety concern since it can result in start-up delay and in reduction or loss of recombination capacity. In the framework of the AMHYCO project, specific attention is focused on the effect of carbon monoxide released during molten corium-concrete interaction. In the late phase of a severe accident under the conditions of an oxygen-lean atmosphere, carbon monoxide could act as a potential catalyst poison, preventing hydrogen conversion due to its strong surface adsorption properties. The conversion of carbon monoxide to carbon dioxide is supposed to be promoted at high catalyst temperatures while catalyst deactivation is more likely to take place at lower catalyst temperatures.

In order to enhance the knowledge on the carbon monoxide impact on the catalyst behavior, experiments have been performed at the REKO facilities at Forschungszentrum Juelich. In a first scoping test series, the deactivation conditions of a single catalyst sample have been investigated in the REKO-1 facility. For this purpose, platinum- and palladium-based catalyst samples have been exposed to mixtures of hydrogen, carbon monoxide, air and nitrogen at different temperatures and flow velocities. The experiments reveal that the poisoning can be predicted by the carbon monoxide fraction, the oxygen fraction and the catalyst temperature. Furthermore, the palladium catalyst is by far less affected than the platinum catalyst. The results show that the catalyst temperature in which the platinum is poisoned is independent from the gas temperature, while for the palladium catalyst the gas temperature seems to influence the poisoning temperature. The experimental results provide data for the further enhancement of numerical codes in the framework of the AMHYCO project.

KEYWORDS
Passive auto-catalytic recombiners (PARs), hydrogen, deactivation, carbon monoxide

1. INTRODUCTION

In case of a severe accident in a nuclear power plant (NPP), a large amount of flammable gases can be produced in the course of both the reactor core degradation phase and the molten core-concrete interaction (MCCI). These gases can be released into the containment, and it may lead to explosions that can threaten its integrity as well as result in the failure of safety-relevant systems.

In order to mitigate the risk of hydrogen explosions, passive autocatalytic recombiners (PARs) have been installed in many nuclear power plants worldwide. Recombiners are passive devices that aim to recombine hydrogen through an exothermic catalytic reaction. PARs consist of a vertical channel equipped with catalyst sheets in the lower part. The catalysts usually are platinum and/or palladium-based. The reaction in a recombiner starts spontaneously when the hydrogen molar fraction reaches around 1 to 2% at the recombiner inlet [1].

During normal operation and accident scenarios, PARs can be exposed to various volatile compounds, gases and aerosols present in the containment atmosphere. Some of those products may cause partial or total catalyst deactivation, therefore reducing the efficiency of the recombiner or leading to start-up delays [4].

Carbon monoxide (CO), released during MCCI, is a potential catalyst poison due to its strong adsorption properties. Experimental and analytical studies have studied the impact of CO on PAR operation [2, 4]. It was concluded that CO might poison the catalyst under certain conditions during the late phase of a severe accident (SA).

In the framework of the AMHYCO project, experiments have been performed at the REKO facilities at Forschungszentrum Juelich in order to enhance the knowledge of catalyst deactivation by carbon monoxide. The present paper provides an overview on the outcomes regarding the poisoning conditions.

2. METHODOLOGY

The facility REKO-1 has been used to identify the deactivation conditions on a single catalyst sheet. The facility, shown in **Figure *1***, has been designed to study the reaction kinetics of the catalytic hydrogen recombination under well-defined and steady-state forced flow boundary conditions. It consists of a cylindrical vertical flow channel with a 40 mm inner diameter. The inlet gas composition is set by mass flow controllers for the different gaseous species while the outlet gas composition is determined by means of gas analyzers. The measuring cells are based on different measuring principles: paramagnetic sensor (O_2), heat conductivity sensor (H_2), infrared sensor (CO/CO_2).

Thermocouples are installed in different positions of the channel to obtain the inlet and outlet temperatures. The catalyst temperature is measured by pyrometer through the optical access provided by the glass window. The catalyst sample is located in the center of the flow channel. The catalyst samples used in this test series are thin sheets with a size of 5 x 5 cm² manufactured by Chemical Consulting Dornseiffer company, Aachen/Germany. The supporting material is a thin stainless-steel sheet with a 50 µm thickness. The ceramic washcoat consists of 4 mg/cm² γ-Al_2O_3. The amount of catalytic active material (platinum or palladium) is 1 mg/cm².

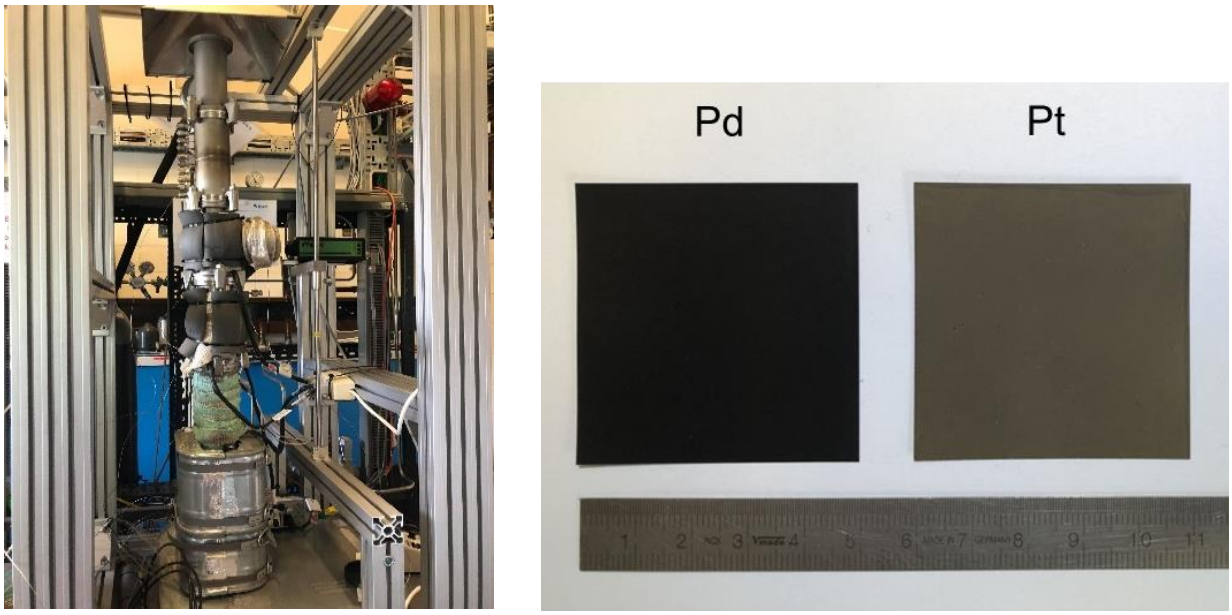

Figure 1. REKO-1 facility (left) and catalyst samples (right).

In the framework of the NUGENIA/SAMHYCO-NET program [4], a review of representative boundary conditions during late phases of severe accident on several NPPs had been performed. ***Table I*** summarizes the lower and upper conditions. The test matrix for the experiments has been defined based on the typical conditions of a severe accident scenario, shown in ***Table I***. The experiments have been performed with hydrogen contents varying from 1 to 7 vol.% and carbon monoxide from 0.5 to 6 vol.%. The oxygen fraction is reduced to 0.7 vol.%. The tests have been carried out at atmospheric pressure and three initial gas temperatures, 20°C, 80°C and 150°C.

A typical test sequence consists of the injection of a continuous hydrogen/air mixture into the reaction channel, followed by the addition of carbon monoxide. After achieving steady-state conditions, the oxygen fraction of the flow is stepwise reduced by replacing part of the air flow with nitrogen until the catalyst is deactivated. The catalyst temperature measured with the pyrometer indicates when the reaction occurs and when the catalyst is deactivated. Since the reaction is exothermic, the temperature increases during hydrogen recombination. A significant decrease in temperature indicates catalyst deactivation.

Table I. Typical conditions during severe accident late phase scenarios [4].

	Lower limit	Upper limit
H_2	0.26 %	8%
O_2	1.2 %	6%
CO	3.5 %	6 %
Temperature	350 K	420 K
Pressure	1.2 bar	6.6 bar

3. RESULTS

Previous experimental data indicate that recombiners operation in the presence of hydrogen and carbon monoxide can be divided into three different regimes [5]:

- Regime I: Undisturbed parallel reaction of hydrogen and carbon monoxide with oxygen.
- Regime II: Constrained parallel reaction of hydrogen and carbon monoxide with oxygen.
- Regime III: Reaction stops due to catalyst deactivation.

The results obtained with the REKO-1 facility confirm these three regimes. The typical behavior of the platinum-based catalyst sample is shown in **Figure 2**. In this case, the gas mixture composition initially introduced in REKO-1 is 2 vol.% H_2, 4 vol.% CO and 7 vol.% O_2 at 0.5 m/s and ambient temperature. It is possible to observe that the catalyst temperature increases to approx. 300°C when hydrogen is injected which means that the catalytic reaction is occurring thus hydrogen is being recombined into steam. Once carbon monoxide is injected into the flow channel, the catalyst temperature increases to almost 500°C, indicating its conversion into carbon dioxide. Finally, oxygen starts being stepwise reduced. Every step takes five minutes in order to achieve steady-state conditions. Down to 4 vol.% O_2, there is no change in the temperature, showing that the catalyst operation is still in the regime I, where there is a parallel reaction of hydrogen and carbon monoxide with oxygen. As soon as the oxygen fraction is decreased to 3.5 vol.%, the temperature also decreases to 452 °C, showing that the reaction is now occurring under oxygen starvation, confirming the regime II. When the oxygen content is reduced to 2.9 vol.%, there is a significant drop in the catalyst temperature followed by a continuous decrease, showing that the reaction is slowly being reduced until total stop, around 4200 s. This last case corresponds to deactivation of the catalyst by carbon monoxide. The catalyst temperature right before the significant temperature decrease, marked by the red dotted line in **Figure *2***, is referred as the poisoning temperature. Later, the injection of carbon monoxide is stopped and the catalyst temperature increases once again to the same temperature as before, indicating that hydrogen is being converted.

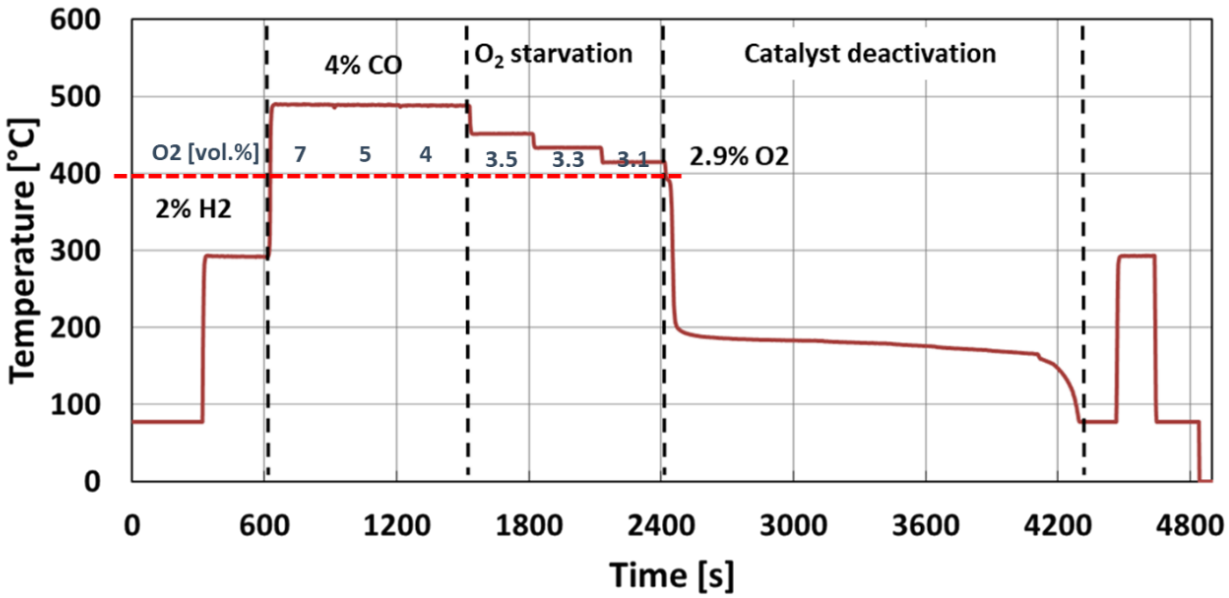

Figure 2. Catalyst temperature measurement during oxygen starvation and poisoning of the platinum catalyst.

Figure 3 shows at which catalyst temperature the poisoning occurs for different carbon monoxide fractions on the platinum catalyst. Each point on the diagram is an individual test where the poisoning was observed. Each symbol represents a different hydrogen fraction. The tests have been performed at 20°C with 0.5 m/s flow rate. For each test, the temperature of the catalyst decreases as the oxygen fraction is reduced, until the point of catalyst deactivation is reached. The catalyst temperature at which deactivation first occurs is referred to as "poisoning temperature". Below this value the reaction does not occur.

The poisoning temperature on platinum seems to be impacted by the carbon monoxide fraction but is independent from the hydrogen fraction. For higher concentrations of carbon monoxide, the poisoning temperature is higher. It is possible to observe that for different hydrogen fractions, the catalyst poisoning temperature is the same for each carbon monoxide fraction, except for 1 vol.% of hydrogen. For this case, showed with the blue filled symbols, the catalyst temperature was not high enough to sustain the reaction and the catalyst was deactivated before oxygen starvation was observed.

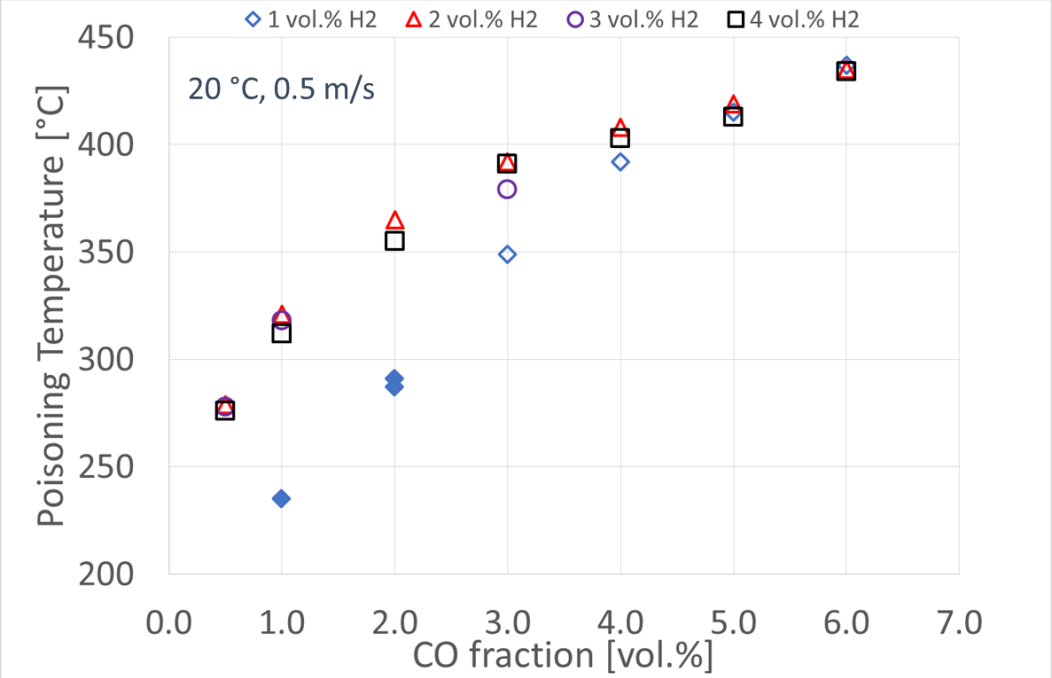

Figure 3. Influence of the hydrogen fraction on the poisoning temperature of the platinum-based catalyst.

The effect of the initial gas temperature is illustrated for the platinum-based catalyst in **Figure 4**. The three initial gas temperatures (20°C, 80°C and 150°C) are represented by different symbols and the tests have been performed with 0.5 m/s flow rate. For the platinum catalyst, the poisoning temperature seems to be independent from the gas temperature. Poisoning seems to occur once the catalyst temperature reaches a threshold value ("poisoning temperature") indicated for each carbon monoxide concentration. The deactivation of the platinum catalyst seems to be a function of the catalyst temperature and the carbon monoxide fraction.

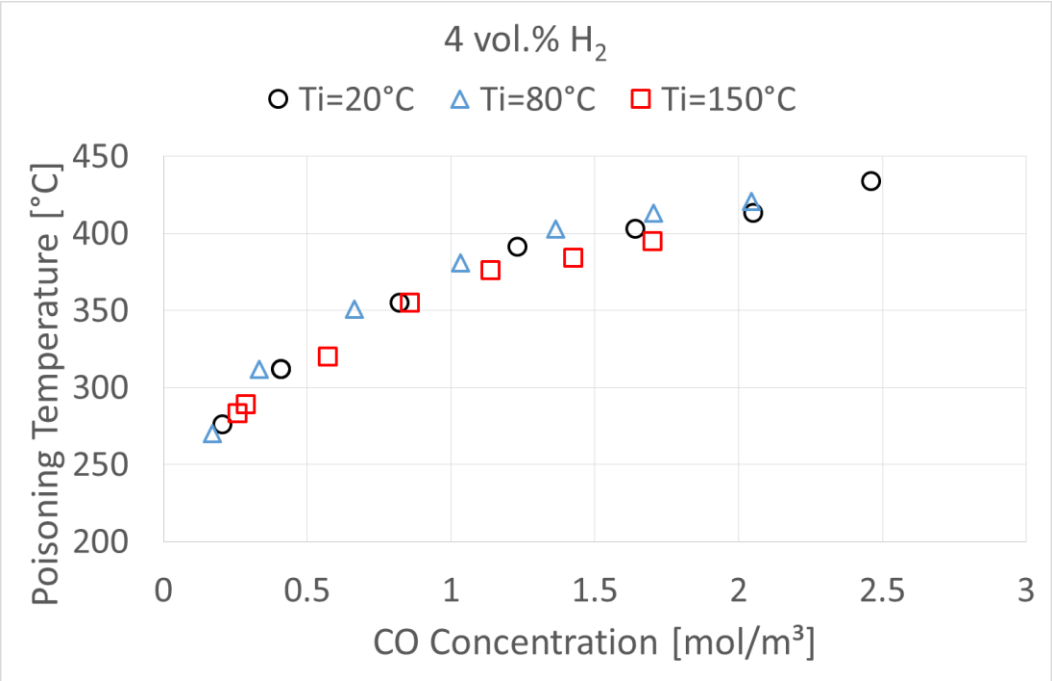

Figure 4. Influence of the gas temperature on the poisoning temperature on the platinum-based catalyst.

Figure 5 shows the effect of the initial gas temperature for a platinum (already shown in **Figure *4***) and a palladium catalyst in order to compare the behaviour of the two different catalysts. The platinum-based catalyst is represented by black symbols and the palladium-based catalyst by red symbols. The results show that poisoning on the palladium catalyst occurs much later than on the platinum-based one. As a consequence, the measured poisoning temperature reaches lower values for the palladium catalyst. Furthermore, the poisoning temperature measured on the platinum catalyst appears to be independent from the gas temperature, while for the palladium catalyst the gas temperature has a significant influence. For the palladium catalyst, in addition to the carbon monoxide fraction and the catalyst temperature the gas temperature needs to be considered when predicting poisoning.

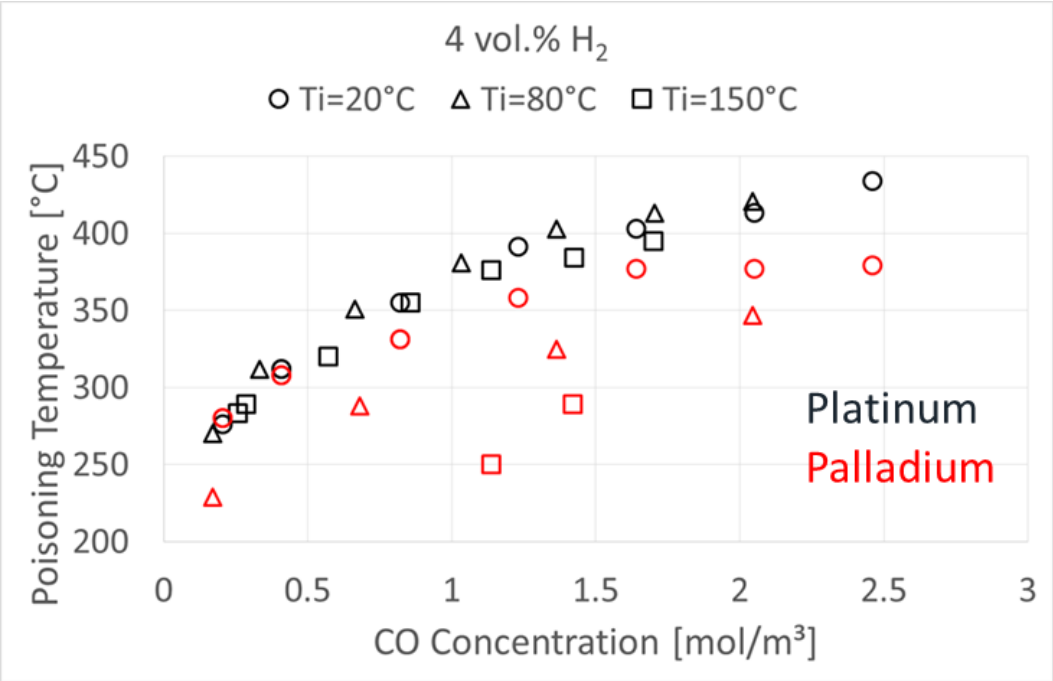

Figure 5. Influence of the gas temperature on the poisoning temperature on platinum and palladium catalysts.

4. CONCLUSIONS

In order to enhance the knowledge on the impact of carbon monoxide on the operation of PARs in the late phase of a severe accident, experiments have been performed at the REKO facilities. In a first scoping test series, the deactivation conditions of a single catalyst sample have been investigated in the REKO-1 facility. For this purpose, platinum- and palladium-based catalyst samples have been exposed to mixtures of hydrogen, carbon monoxide, air, nitrogen and steam at different temperatures and flow velocities.

The experiments reveal that the poisoning can be predicted by the carbon monoxide fraction and the catalyst temperature. Furthermore, the palladium catalyst is deactivated at lower catalyst temperatures than the platinum catalyst, i.e. the palladium catalyst remains active at lower oxygen concentrations than the platinum catalyst. Also, platinum catalyst seems to be significantly more impacted by the poisoning by CO than the palladium one. The results show that the catalyst temperature in which the platinum is poisoned is independent from the gas temperature, while for the palladium catalyst the gas temperature influences the poisoning temperature.

In the next step, the REKO-3 facility will be used to study the effect of carbon monoxide on a section of a recombiner with four full-scale catalyst sheets. These experiments provide data for the improvement of numerical codes in the AMHYCO project. To this end, several benchmarks are planned and will ultimately prepare the study of reactor scale scenarios

ACKNOWLEDGMENTS

AMHYCO has received funding from the Euratom research and training programme 2019-2020 under Grant Agreement n° 945057. The content of this paper reflects only the author's view. The European Commission is not responsible for any use that may be made of the information it contains.

REFERENCES

1. E. Bachellerie, F. Arnould, M. Auglaire, B. de Boeck, O. Braillard, B. Eckardt, F. Ferroni, R. Moffett, "Generic approach for designing and implementing a passive autocatalytic recombiner PAR-system in nuclear power plant containments". *Nuclear Engineering and Design*. **221**: 151-165 (2003).
2. E.-A. Reinecke, H.-J. Allelein, A. Bentaib, A. Chakraborty, N. Chaumeix, D. Heidelberg, S. Kelm, M. Klauck, L. Maas, P.-M. Steffen, "Operating behavior of passive auto-catalytic recombiners under severe accident conditions", *International Severe Accident Management Conference* (ISAMC), Ottawa (Ontario), Canada, October 15-18, 2018.
3. M. Klauck, E.-A. Reinecke, S. Kelm, N. Meynet, A. Bentaib, H. J. Allelein, "Passive auto-catalytic recombiners operation in the presence of hydrogen and carbon monoxide: Experimental study and model development", *Nuclear Engineering and Design*, **266**, pp. 137-147, (2014).
4. A. Bentaib, "International workshop on hydrogen management in NPP-Executive Summary and proceedings", IRSN technical report, 2019-00562.
5. M. Klauck, "Effects of carbon monoxide on the operation of catalytic hydrogen recombiners in light water reactor containments". PhD Thesis, RWTH Aachen University (2019).

RÉPUBLIQUE FRANÇAISE
Liberté
Égalité
Fraternité

JÜLICH Forschungszentrum

cnrs

AMHYCO
Enhancing H_2 & CO Combustion Risk Management

IRSN
INSTITUT DE RADIOPROTECTION ET DE SÛRETÉ NUCLÉAIRE

EXPERIMENTAL INVESTIGATION ON THE CARBON MONOXIDE EFFECT ON PLATINUM- AND PALLADIUM-BASED CATALYSTS FOR PASSIVE AUTO-CATALYTIC RECOMBINERS

ERMSAR 2022 – 19 May 2022 – Karlsruhe, Germany

Gabriela Nobrega, Ernst-Arndt Reinecke, Ahmed Bentaib, Ludovic Maas, Nabiha Chaumeix

IRSN/ERM-296 ind. 06

Outline

- **Context**
  - Hydrogen risk in nuclear power plants
  - Passive Auto-catalytic Recombiners (PARs)
  - Catalyst deactivation
- **Experimental results**
- **Conclusion / outlook**

Hydrogen risk in nuclear power plants and Passive Autocatalytic Recombiners (PARs)

- Hydrogen explosion can threaten the integrity of the containment leading to release of radioactive materials into the environment
- PARs: Hydrogen risk mitigation system in many NPPs worldwide
- Recombiners are assumed to be always fully operational

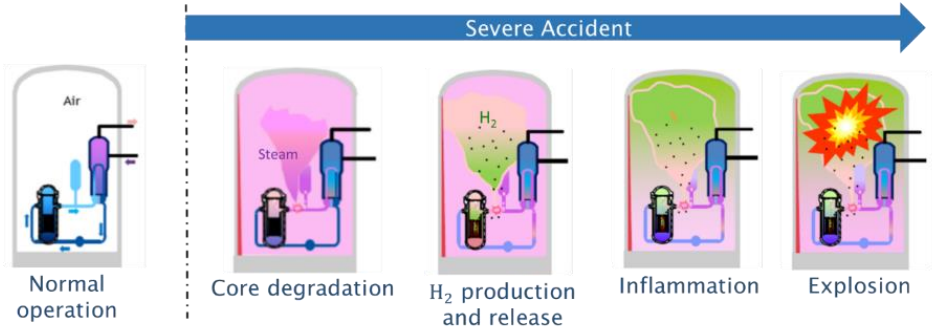

$$H_2 + \frac{1}{2}O_2 \rightarrow H_2O$$

$$CO + \frac{1}{2}O_2 \rightarrow CO_2$$

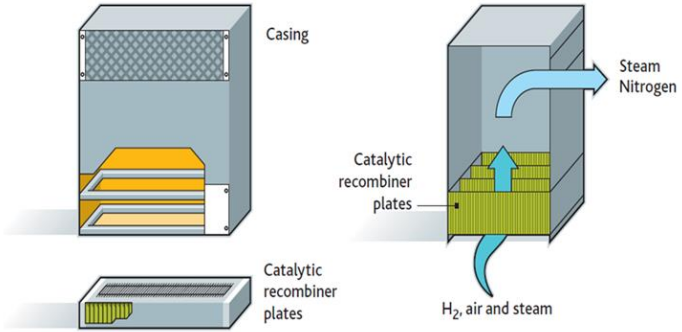

Catalyst deactivation

PARs can be exposed to materials that may negatively affect the catalysts' performance

- **Normal operation**: dust, oil (spray, steam), solvents and paints used during maintenance work, etc.
- **Accidental conditions**: fire products, gases and aerosols from the molten core, MCCI products...

External impact cannot be excluded despite the precautions implemented

- Local catalyst pollution from oil projections from primary pumps (France)
- Corrosion of catalyst sheets from plastic fire (Sweden/Ringhals)
- Catalyst deactivation from burnt diesel products (Germany/Emsland)

SAFETY CONCERN

Catalyst deactivation may affect the recombination start-up (delay up to 30 min)/efficiency and cause unexpected reduction of the hydrogen removal capacity during a severe accident

Catalyst deactivation by carbon monoxide

- Carbon monoxide, released during MCCI, is a potential catalyst poison due to its strong adsorption properties.

- Representative boundary conditions during late phases of severe accident:

	Lower limit	Upper limit
H_2	0.26 %	8%
O_2	1.2 %	6%
CO	3.5 %	6 %
Temperature	350 K	420 K
Pressure	1.2 bar	6.6 bar

A. Bentaib, “International workshop on hydrogen management in NPP-Executive Summary and proceedings”, IRSN technical report, 2019-00562

Experimental facility: REKO-1

- REKO-1: single catalyst sample under well-defined and steady-state forced flow boundary conditions
- 5 x 5 cm² platinum and palladium-based catalyst

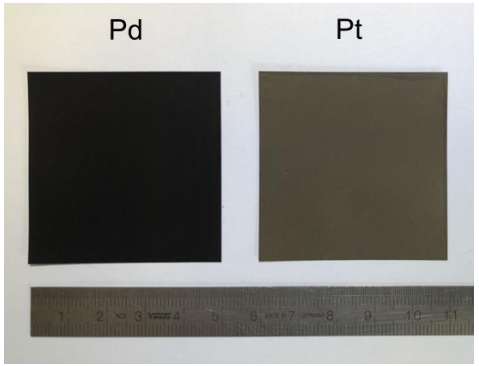

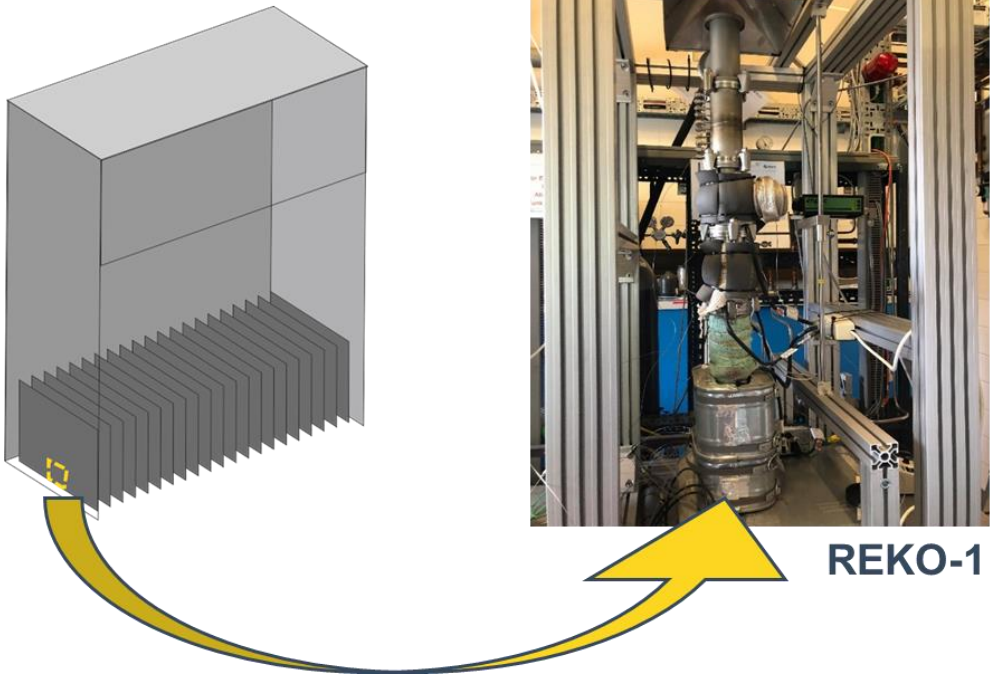

Test procedure

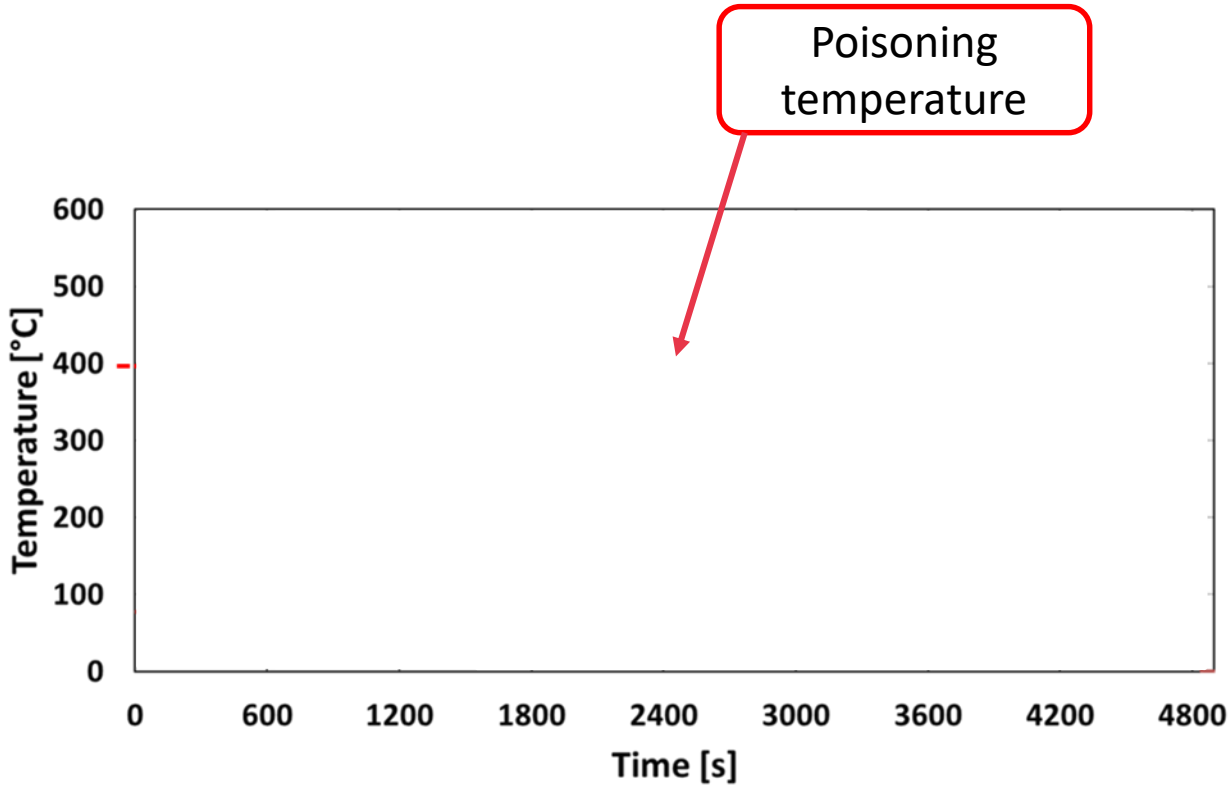

Effect of carbon monoxide

- The catalyst is deactivated at the same temperature for different hydrogen fractions

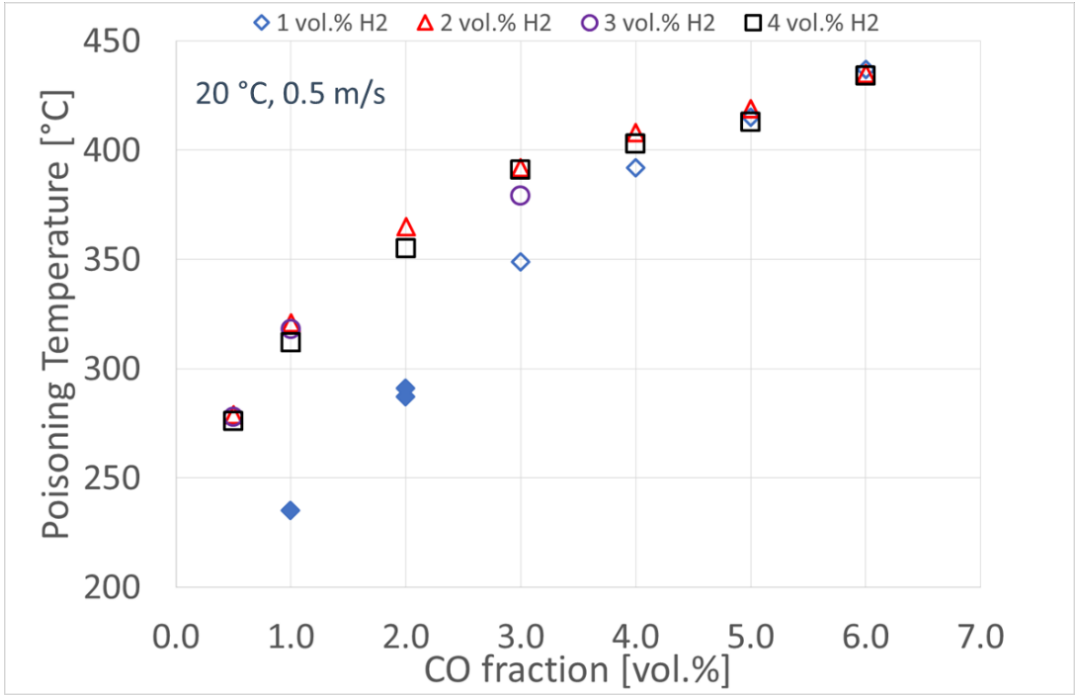

Effect of carbon monoxide

- The catalyst is poisoned when the catalyst temperature is below a threshold defined as poisoning temperature.
- The initial gas temperature seems to have no significant impact on the poisoning temperature for the platinum-based catalyst.

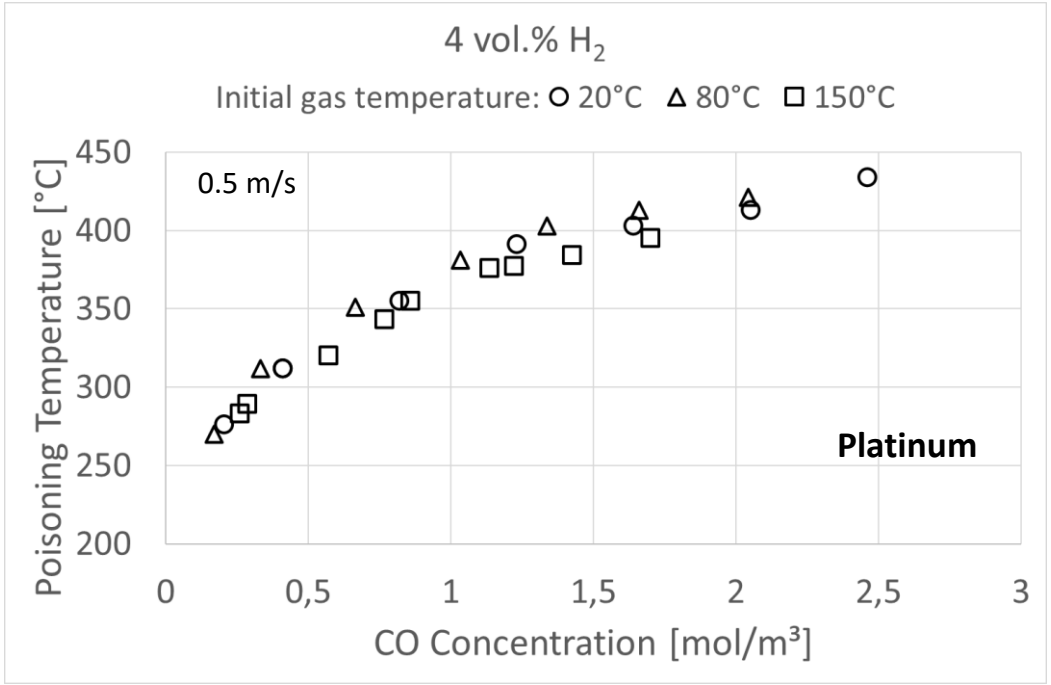

Effect of carbon monoxide

- Initial gas temperature has a higher impact for palladium-based catalyst
- Palladium catalyst seems to be less impacted than the platinum one, especially at elevated gas temperatures.

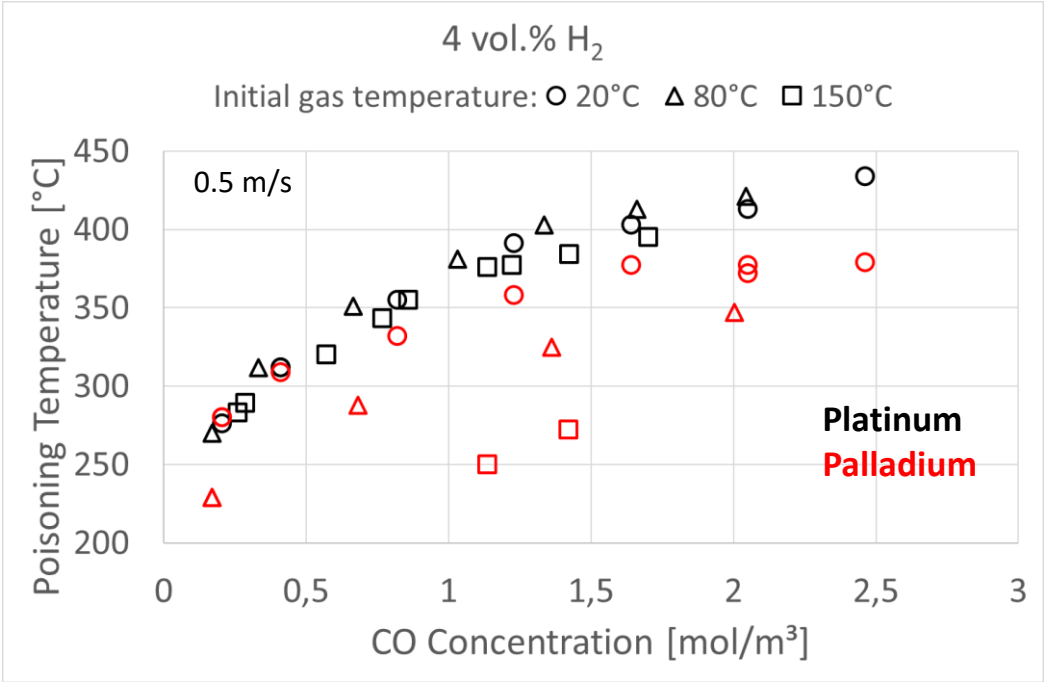

On going work: SPARK code

- SPARK code
  - 2D CFD code dedicated for PARs modeling
  - Complex Chemistry
  - Multi-species transport
- Calculations with CO in progress
  - First results in agreement with the REKO data
- Modifications to predict CO poisoning in progress

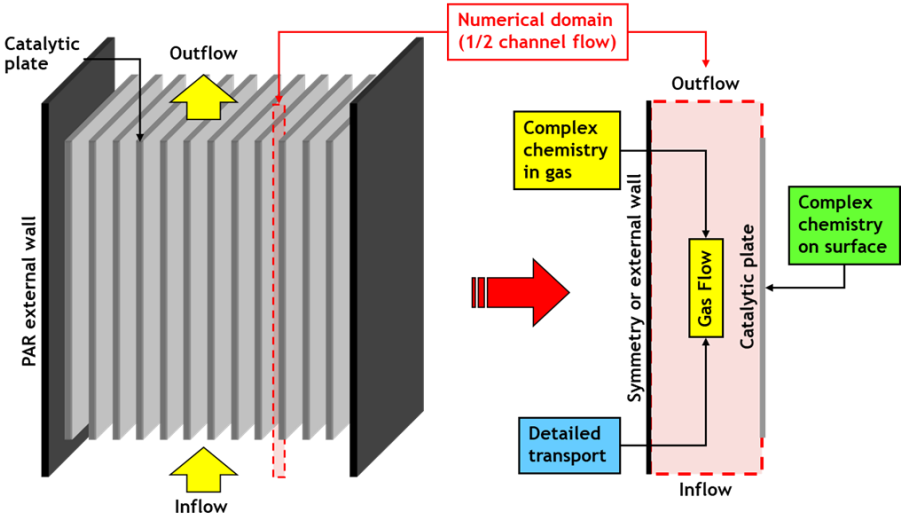

SPARK code calculations

- Catalyst behavior during O_2 reduction for H_2 mixture, without CO.

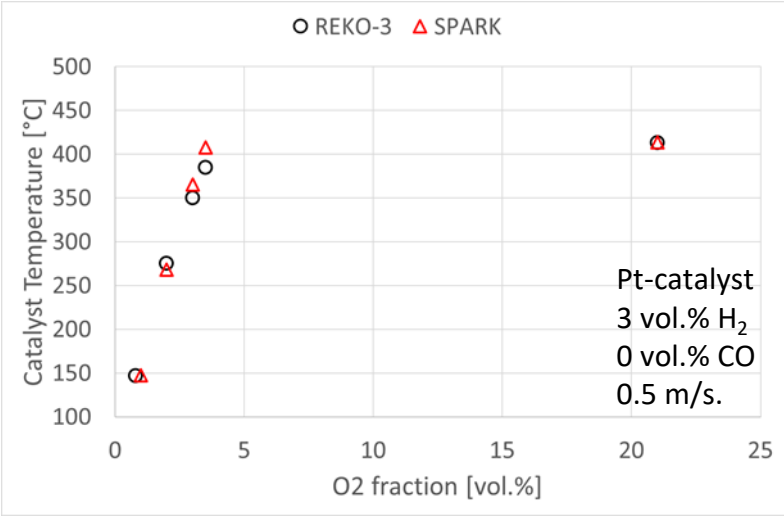

- Catalyst behavior during O_2 reduction for H_2/CO mixture.

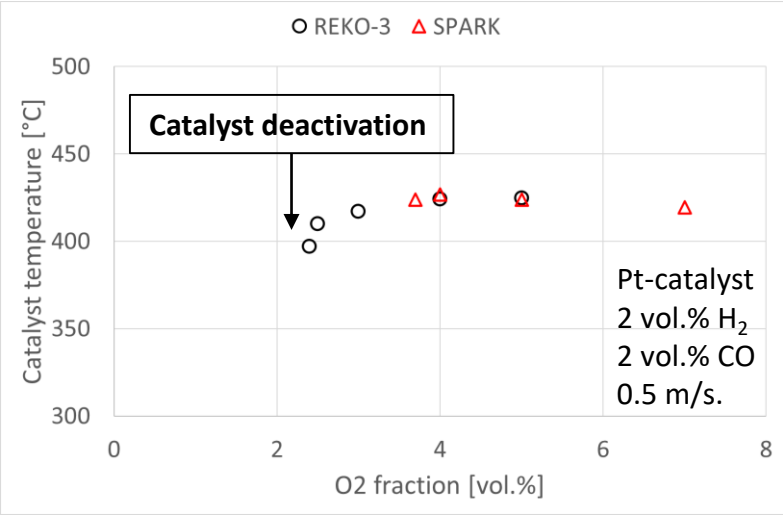

Conclusion / Outlook

- Deactivation can be predicted by the carbon monoxide fraction and the catalyst temperature
- Platinum catalyst seems to be significantly more impacted by the poisoning by CO than the palladium
- Experiments analysis with the SPARK code (on going)
  - Simulations coherent with REKO experiments
- REKO-3 facility will be used to study the effect of carbon monoxide on a section of a recombiner with four full-scale catalyst sheets
- The experiments provide data for the improvement of numerical codes in the AMHYCO project

Thank you for your attention !

SPARK code calculations

- Catalyst temperatures for mixture with 3 vol.% without CO during O_2 reduction.

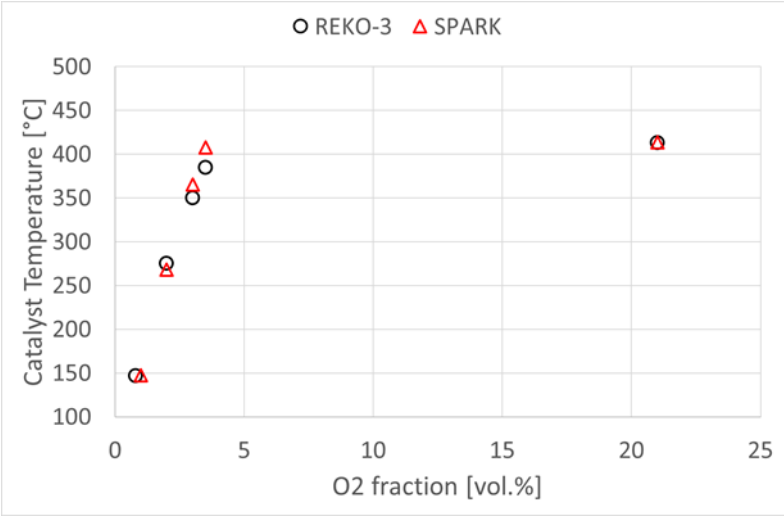

- Catalyst behavior during O_2 reduction for mixture with 2 vol.% H_2 and 2 vol.% CO at 0.5 m/s.

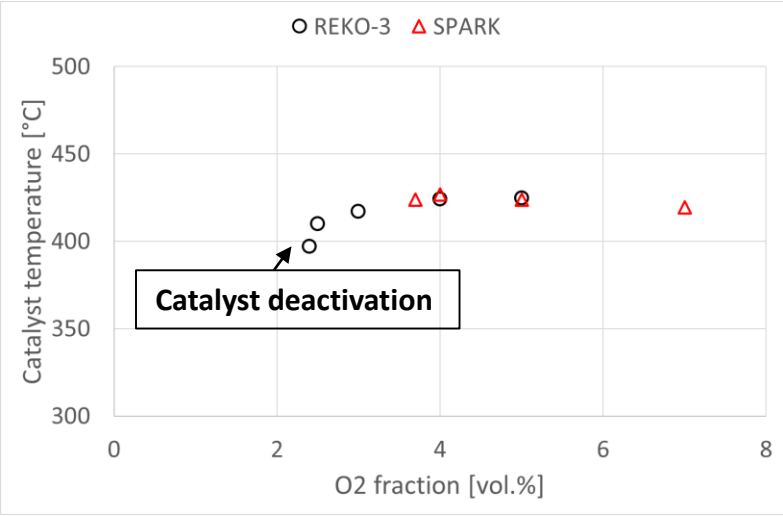

REKO-1 vs REKO-3

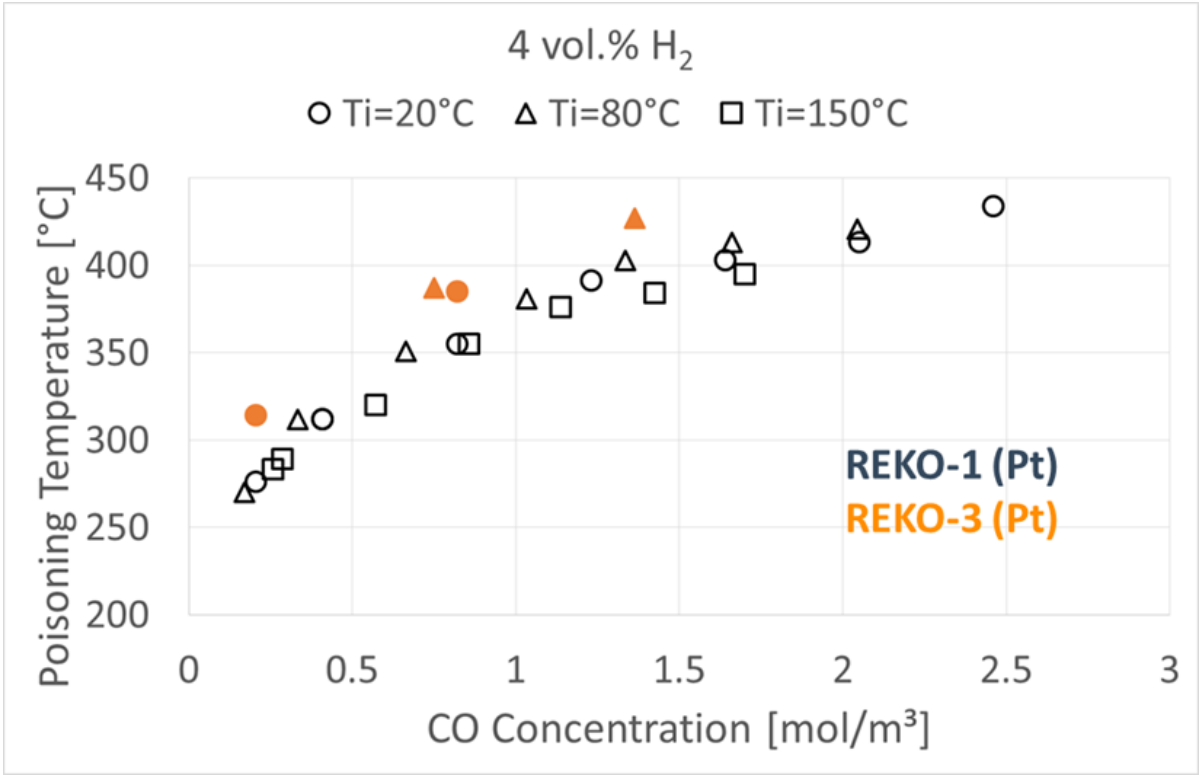

SPARK code calculations – THAI and REKO-3 comparations

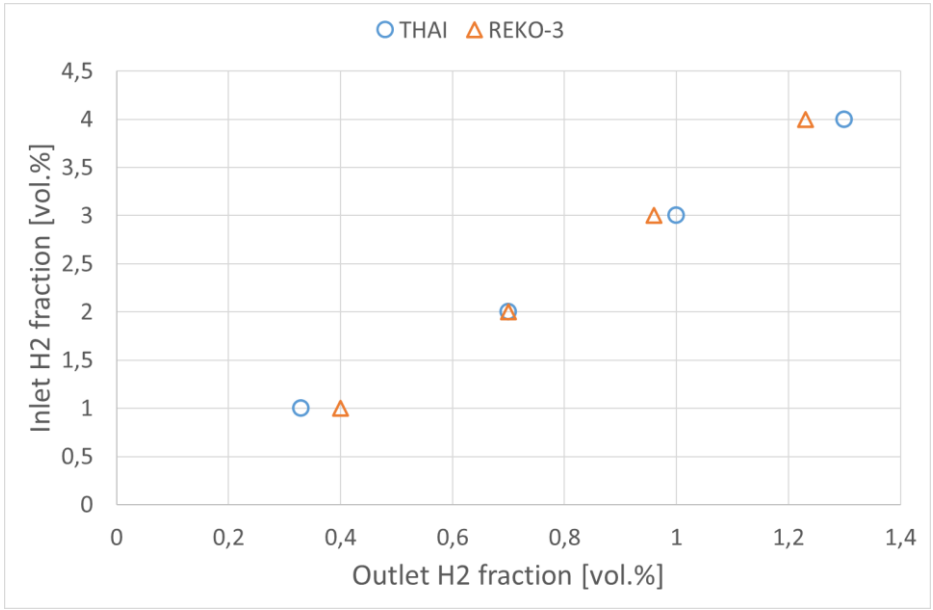

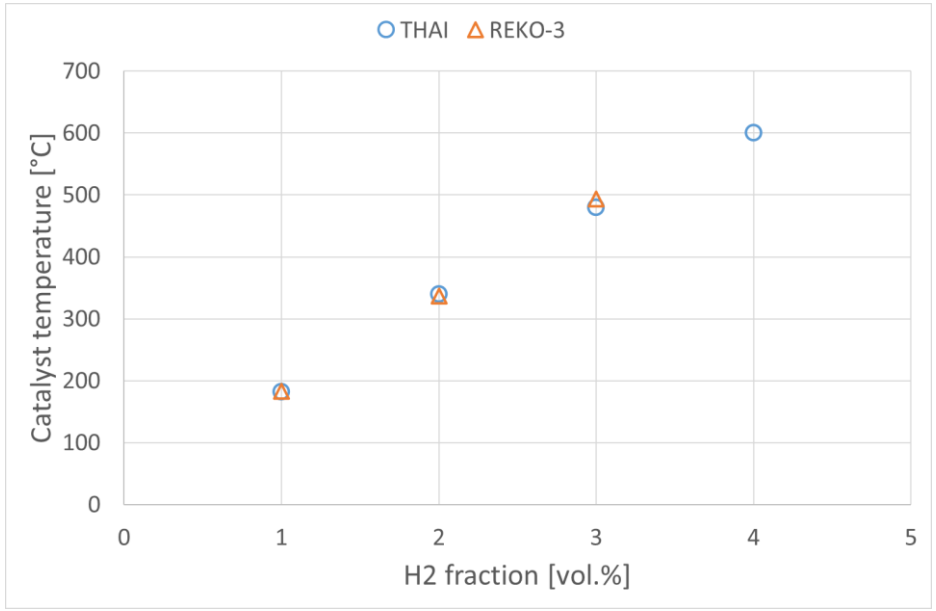

Impact of steam

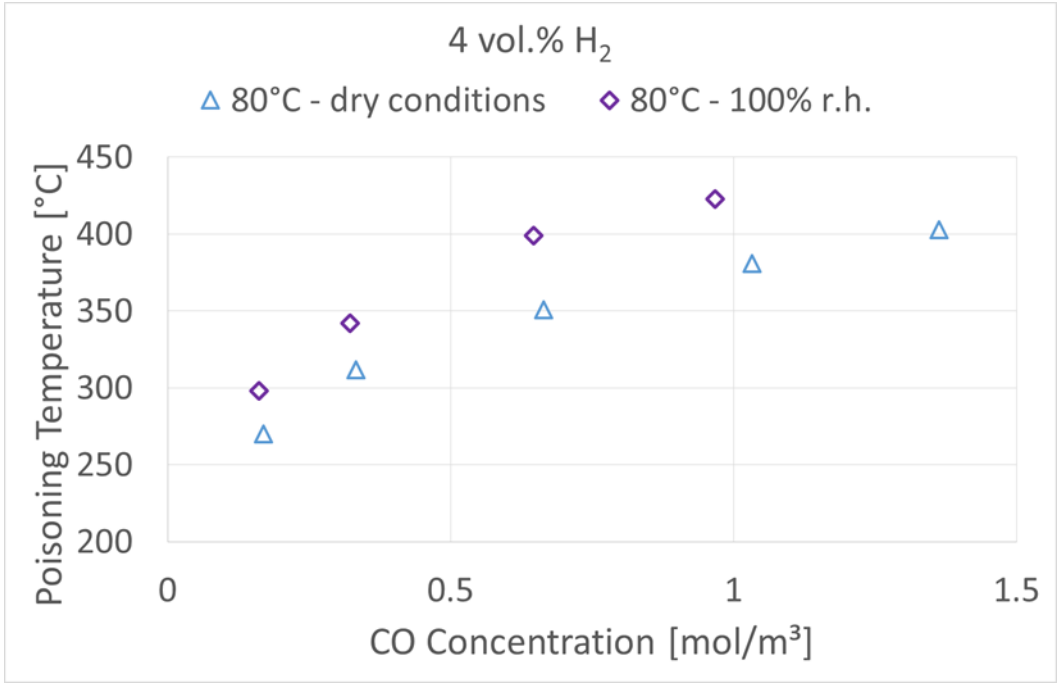

Impact of test procedure

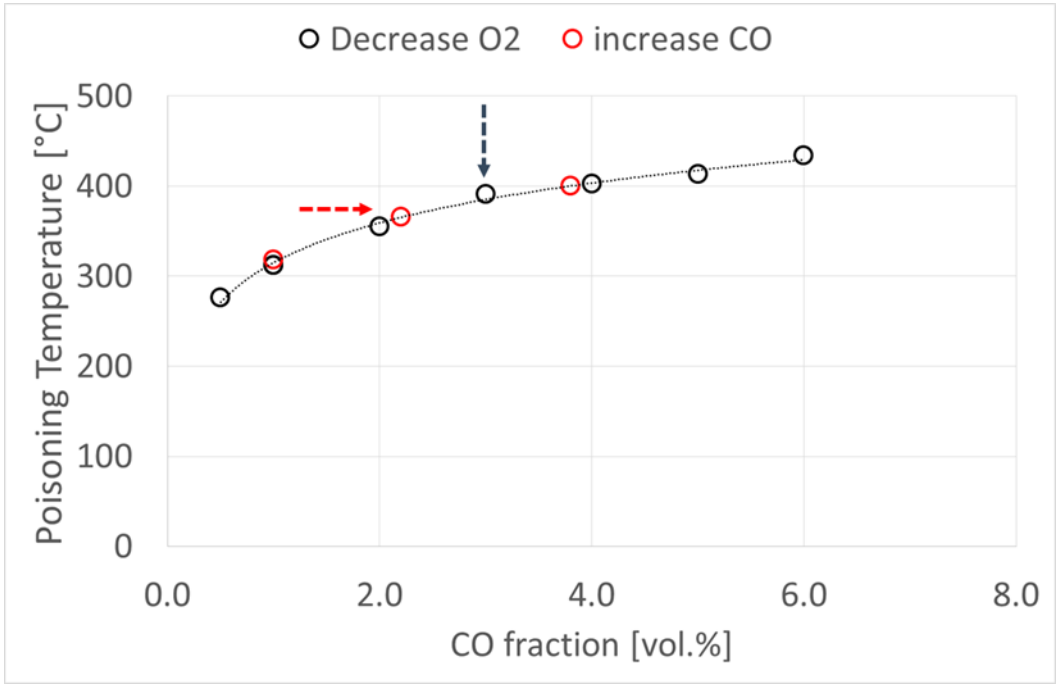

SPARK code calculations

- Catalyst temperature for mixtures without CO.

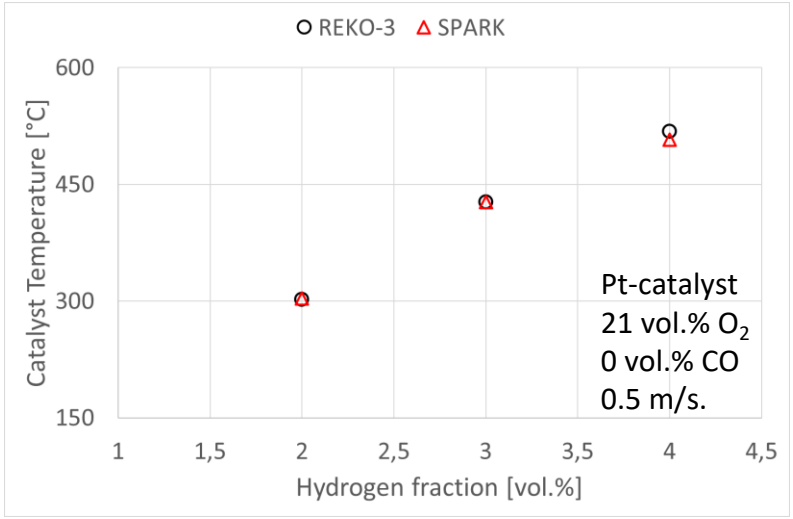

- Catalyst behavior during O_2 reduction for H_2/CO mixture.

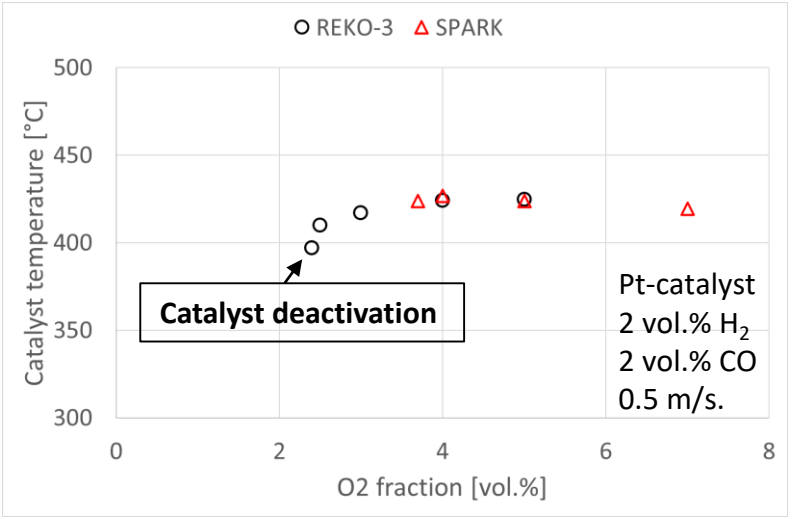

ENHANCEMENT OF RECOMBINATION RATE CORRELATIONS FOR PARS IN OXYGEN-LEAN CONDITIONS

Joan Fontanet, Elena Echevarría, Luis E. Herranz
Unit of Nuclear Safety Research (CIEMAT)
Av. Complutense 40, 28040 Madrid (Spain)
joan.fontanet@ciemat.es

ABSTRACT

Passive Autocatalytic Recombiners are a proven effective mitigation measure of hydrogen combustion risk in severe accidents. In safety analyses, the availability of analytical correlations able to accurately estimate the recombination rate of PARs is of utmost importance. Therefore, estimates of the commonly used correlation describing Framatome type PAR have been compared with test data from the THAI facility in oxygen lean atmosphere conditions, as are anticipated in the long run of some severe accident sequences after a period of PARs operation. Modifications of the equations are proposed to better fit data both during hydrogen injection and in oxygen low concentrations. The integral effect of such enhancements has been investigated through simulating a severe accident with the MELCOR code; despite the better performance under the experimental conditions, a low impact on H_2 concentration estimates has been found in accident calculations.

KEYWORDS
Hydrogen mitigation, PAR, Severe accident, Modelling

1. INTRODUCTION

In a severe accident in Light Water Reactors (LWR), hydrogen is likely to be produced by the exothermic oxidation reaction of the heated fuel cladding, and other internal structures, with steam [1]. This hydrogen finally reaches the containment by, for example, the safety valves or the reactor cooling system break. The hydrogen is then distributed into the containment atmosphere and, depending on the conditions, it can reach flammable concentrations. The accidents in TMI-2 [2] [3] and in Fukushima Daiichi [4] [5] confirmed that large amounts of hydrogen may be generated to the point of deflagrations, which may impair containments and/or reactor buildings or safeguards in the containment.

In order to reduce the deflagration risk due to an accumulation of hydrogen, Passive Autocatalytic Recombiners (PARs) have been installed in nuclear power plants of many countries for combustible gases management [6]. The stress tests performed in Western countries after the Fukushima accident [7] recommended, among other measures, the installation of PARs to enhance safety and to reduce the risk of combustible gases deflagrations.

Different companies have developed their own PAR design (e.g. Framatome/AREVA, NIS, AECL) [8] aimed to operate at significant recombination capacity in all accident conditions and to withstand internal and external risks. With this respect, the availability of an analytical correlation able to estimate the PARs' recombination efficiency in terms of the containment atmosphere conditions is crucial in the analysis of nuclear reactor safety.

The THAI facility [9] [10] (operated by Becker Technologies in Germany) is one of the most representative facilities in this area since it provides data of different commercial sections of a PAR at different conditions of pressure, temperature, steam content, and hydrogen concentrations. Particularly, PARs efficiency is measured at expected conditions in a severe accident which are demanding regarding the PAR performance.

Two research projects have recently been launched to progress in the knowledge of PARs performance in conditions representative of a severe accident: SAMHYCO-Net [11], AMHYCO [12]. In the frame of these projects, this work aims to improve, based on the THAI experiments data, the predictions of the Framatome type PARs under low oxygen conditions. Framatome type PARs are widely used in European nuclear power plants and worldwide. A low oxygen concentration is expected after the operation of PARs for a long period leading to the depletion of oxygen and/or in atmospheres with significant steam fraction. As a result, of the work, a modification of the initial correlation from Framatome is presented and their outcomes are compared with experimental data and the original correlations estimates. Finally, the effect of this modified correlation once introduced in the MELCOR integral code is checked. To do this, a THAI test has been simulated with MELCOR using both correlations (the initial and the modified one) and the simulation results in terms of hydrogen concentration and recombination rate are compared. Additionally, a full-scale plant application with the simulation of a Small Break LOCA sequence has also been analysed.

2. RECOMBINATION RATE CORRELATION

In order to estimate the hydrogen recombination rate, R_{H2}, for the Framatome type PAR, the vendor developed a specific correlation given the composition of the gas mixture and the pressure following the next expression [13], [14]:

$$R_{H2}\left[\frac{g}{s}\right] \propto \tilde{C}_{H2} \cdot tanh(C_{H2} - C_{min}) \cdot \eta \cdot (k_1 \cdot P + k_2) \quad (1)$$

where $\tilde{C}_{H2}$ is the effective H_2 volumetric concentration [vol.%] that considers the limitation of the recombination rate by the oxygen if the oxygen-to-hydrogen ratio is below the stoichiometric ratio of the reaction. It also caps the PAR efficiency at high gas molar fraction (typically, up to 8 vol.%). Therefore, the $\tilde{C}_{H2}$ can be written as:

$$\tilde{C}_{H2} = min(C_{H2}, 2 \cdot C_{O2}, 8) \quad (2)$$

The η coefficient introduces a reduction factor when the oxygen concentration is lower than the hydrogen's. Finally, the factors k_1 and k_2 depend on the dimensions of the PAR [14].

Recombination is supposed to start once the hydrogen volumetric concentration in the mixture reaches a threshold value, set at 2 vol.%. The recombination will stop if hydrogen concentration drops below 0.5 vol.%.

3. THAI HR TESTS

The OECD-THAI project [9] [10] aimed to investigate open questions related to the behaviour of hydrogen, iodine, and aerosols in conditions representative of the containment atmosphere during a severe accident in LWR. Particularly, the HR (Hydrogen Recombination) test series provided relevant data regarding the efficiency of PARs under different conditions. The performance of three PAR designs (Framatome, NIS, and AECL) has been investigated with a focus on the following topics: onset of the recombination, recombination rate, operation under oxygen-lean conditions, and induced ignition. The tests of interest for the present work are restricted to those using the Framatome's PAR unit.

3.1. Facility description and tests configuration

The main component of the THAI facility is a cylindrical stainless-steel vessel of 9.2 m in height and 3.2 m in diameter with a total volume of 60 m^3 (Figure 1). The internal configuration of the vessel allows the establishment of natural convection flow to study heat and mass transport processes in a sufficiently large scale and multi-compartmentalised geometry. The vessel is externally coated with 120-mm rock wool thermal insulation. The cylindrical part of the THAI vessel wall is double-walled and accommodates the wall heating/cooling system.

For the HR test series, a metallic cylinder of 1.4 m diameter is located in the lower region of the vessel and the PAR unit is placed in the annular region left between this inner cylinder and the vessel. The PAR unit consists of a section of a commercial FR-380 PAR provided by Framatome. The capacity of this PAR unit is scaled down to the dimensions of the THAI vessel by reducing the number of the catalyst foils to one-half of the original PAR and by reducing accordingly the active flow cross-section with the help of a vertical partition wall (Figure 2). During the experiment, hydrogen (at ambient temperature) is injected into the vessel at the desired flow rate by a ring distributor at a level below the PAR section.

Different instrumentation is distributed inside the vessel to measure gases composition (H_2, O_2, and steam) and temperature at different positions. The vessel surface temperature is also well characterized during the test. Two strain-gauge-type transducers are installed to measure the vessel pressure. Additionally, extensive instrumentation is installed inside the PAR to measure the temperature in the gas channel and on the catalyst surfaces as well as the flow velocity of the gas passing through the PAR. Gas samplings at the inlet and outlet of the PAR allow measuring the gas mixture composition at both locations.

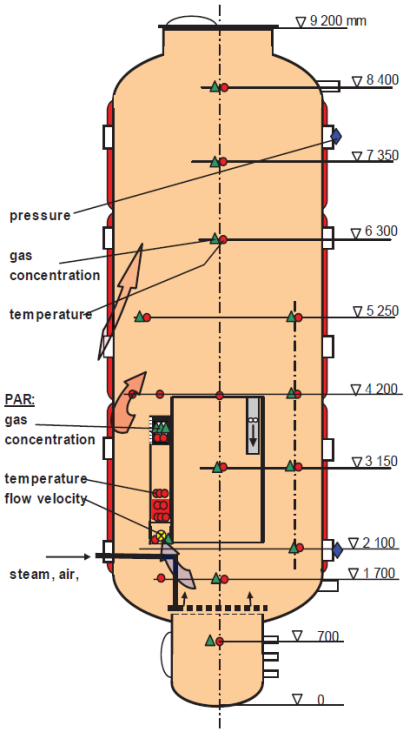

Figure 1. Section of the THAI vessel

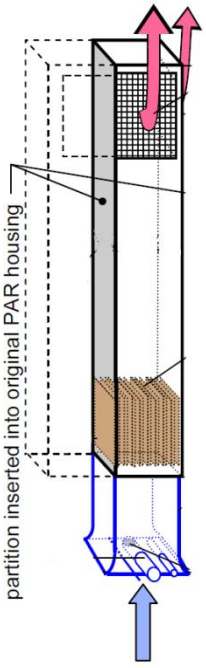

Figure 2. View of the Framatome PAR unit used in the HR tests.

3.2. Test procedure and experimental results

Before each test, the vessel is purged with dry air and then the individual conditions of the test are prepared by feeding the vessel with air and steam. The temperature of the oil circuit in the vessel wall heating/cooling jacket is set to the designed value to regulate the wall temperature during the test.

Once the conditions of the test specification are obtained, the experiment can start. Typically, the standard test procedure is divided into 4 phases:

- Phase 1 begins with the hydrogen injection at a low rate. The H_2 concentration slowly increases until the start of the PAR operation (i.e., the recombination onset). Then, a steep rise in the catalyst temperature and a drop in the H_2 concentration at the PAR outlet are detected. At this time the full H_2 injection rate is switched on to further increase of the H_2 concentration and the recombination rate.
- Phase 2 starts with the interruption of the H_2 injection when a reference value of the H_2 concentration is reached at the inlet of the PAR. The ongoing operation of the PAR leads to the decrease of H_2 concentration. If appropriate, O_2 is replenished to avoid oxygen starvation.
- In Phase 3, the H_2 injection is resumed at full rate. The H_2 concentration and PAR's recombination rate increase again.
- Phase 4 begins with the final stop of hydrogen injection when H_2 concentration reaches the reference value or, depending on the test, once induced ignition occurs. The remaining (not burned) H_2 mass is gradually recombined by the PAR operation.

The recombination rate is calculated experimentally from the difference of the H_2 molar fraction, in the exit and inlet in the PAR unit by the following expression [15]:

$$R_{H2}\left[\frac{kg}{s}\right] = \left(X_{H2,in} - X_{H2,out}\right) \cdot P \cdot v_{in\cdot} \cdot S_{in} \cdot M_{H2}/(R \cdot T_{in}) \quad (3)$$

where X_{H2} is the measured hydrogen molar fraction. P and T are respectively, the pressure and the atmosphere temperature of the test. v is the velocity through the PAR channel with cross section S. The subscripts *in* and *out* stand, respectively, for the PAR inlet and outlet. Finally, M_{H2} is the hydrogen molecular weight and R is the ideal gas constant.

3.3. Test matrix

From the 17 HR tests using the Framatome PAR unit, 4 of them (HR-9, HR-11, HR-12, and HR-13) are especially devoted to investigating PAR behaviour under oxygen lean conditions [10]. Moreover, some other tests, HR-29 and HR-30, have some periods with oxygen concentration below the hydrogen concentration values and they are also used in this study. All these tests have significant steam fractions and cover pressures values from 1 to 3 bar (Table I).

Table I. Test matrix conditions for the THAI-HR tests with low oxygen atmosphere using the Framatome PAR unit.

Experiment	Pressure (bar)	Temperature (ºC)	Steam vol. concentration (%)
HR-9	1.5	90	47
HR-11	1.5	90	60
HR-12	3.0	117	60
HR-13	1.0	86	60
HR-29	1.5	97	60
HR-30	3.0	117	60

4. CORRELATION ASSESSMENT AND ENHANCEMENT

A preliminary assessment of the correlation used for Framatome type PARs was performed in the frame of the SAMHYCO-Net project regarding different conditions representative of a severe accident, including the presence of CO and induced deflagrations [16] [17]. Here, a more detailed analysis is presented focused on the recombination efficiency at low oxygen atmospheres.

Figure 3 to Figure 8 plot the evolution of the tests of interest and compare the experimental recombination rate (Eq. 3) with the estimates given by the correlation (Eq. 1). It is worth noting that correlation estimates are obtained by applying Eq. 1 at the specific conditions of the vessel atmosphere for each available sampling time (every 20 s) and it does not depend on the conditions at an earlier time. The hydrogen concentration (pink dashed line) shows the progression in the different phases of the test (see Section 3.2): rising concentration given by the H_2 injection and depletion phases after the interruption of the injection. The oxygen concentration (green dashed line) decreases due to the recombination reaction in the PAR unit. Some tests (e.g. HR-9, HR-29 & HR-30) have periods of oxygen injection to partially compensate for its depletion.

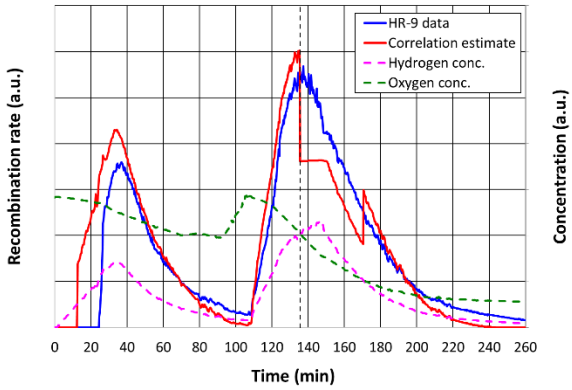

Figure 3. HR-9 test evolution.

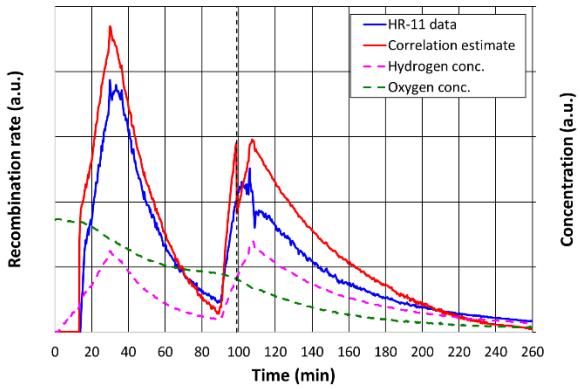

Figure 4. HR-11 test evolution.

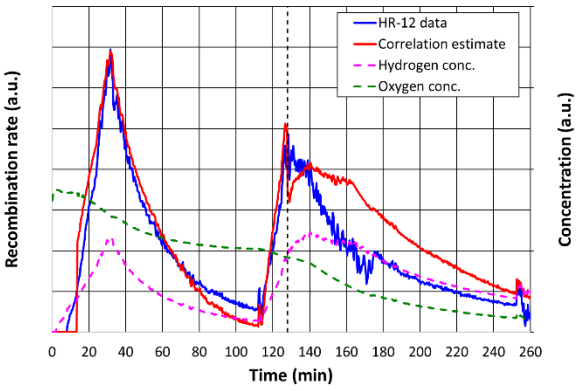

Figure 5. HR-12 test evolution.

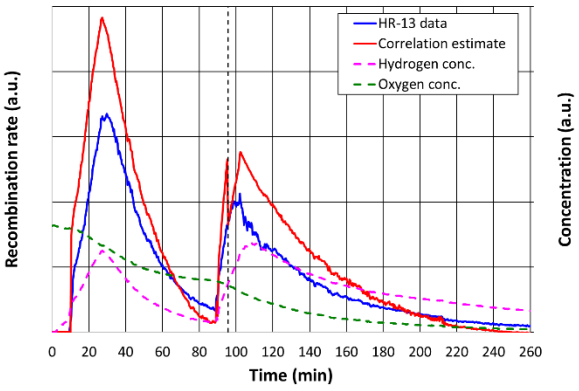

Figure 6. HR-13 test evolution.

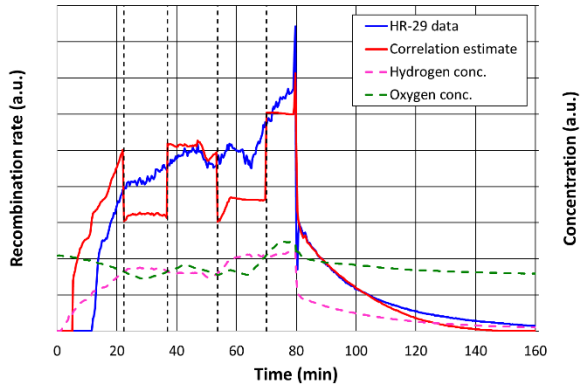

Figure 7. HR-29 test evolution.

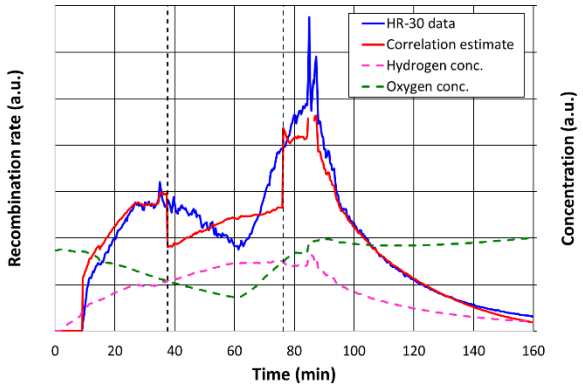

Figure 8. HR-30 test evolution.

From the above figures, several data-to-estimates deviations can be highlighted related to the recombination onset, recombination rate during low oxygen conditions, and hydrogen injection phases as are discussed in the next sections.

4.1. Recombination onset

A first observation from the above figures is that the estimated activation of PARs (recombination onset) is captured for some tests whereas for some others the deviation is significant. The hydrogen concentration necessary to start the recombination in the different tests shows a large scattering. Even experiments with similar conditions (pressure, temperature, and steam content) present significant differences. Therefore, it is not possible to set a relation of the recombination onset with the test conditions and the experimental value is set for the recombination onset of each test.

4.2 Low oxygen concentration

Figure 3 to Figure 8 show how once the PAR is activated, the recombination rate follows the hydrogen concentration evolution as long as the oxygen concentration is high enough. But when the oxygen concentration drops below the hydrogen level the recombination rate changes its tendency and, although the hydrogen concentration continues rising, the recombination rate flattens or even decreases. In other words, the recombination rate detaches from the hydrogen concentration evolution. At this time, the correlation introduces a step-wise drop of the recombination rate (see Section 2). If later in the experiment (e.g. HR-9, HR-29, and HR-30), the oxygen concentration goes over the hydrogen value another discontinuity is estimated but this time to increase the recombination rate. All these discontinuities are not observed experimentally.

In the THAI test analyses performed by Becker Technologies, a deterioration of the recombination efficiency was observed when oxygen surplus (defined as twice the oxygen-to-hydrogen concentration ratio) becomes lower than 2.2 [15]. In that cases, the recombination rate seems to follow the oxygen content evolution. Based on this observation, the $\tilde{C}_{\mathrm{H2}}$ expression in Eq. 2, is modified as follows:

$$\tilde{C}_{\mathrm{H2}} = min(C_{H2}\,, C_{O2}, 8) \tag{4}$$

So that in the modified correlation, it is not the stoichiometric ratio of the reaction which determines the amount of available hydrogen to react but the concentration of the most abundant reactant in the bulk volume surrounding the catalytic sheet. Additionally, the effect of oxygen lean conditions, introduced by

the factor η in the original correlations is no longer considered. Therefore, the value η =1 is assumed for all conditions of the tests.

4.3 Hydrogen injection periods

The estimates of the original correlation (Eq. 1) show significant overprediction for the injection periods. This overestimation in relative terms is high at the beginning of the recombination (in the range of 100 to 500%) and it reduces to 5-20% as the hydrogen concentration increases. For the depletion periods, the correlation provides a better prediction.

Looking at the end of phase-1 of the considered tests, the highest overprediction is obtained at the lowest test pressure and conversely, the better estimates are obtained for the test at the highest pressure. As the initial correlation has a dependency on pressure by a linear function multiplying the expression dependent on gases concentrations, a new function on pressure has been developed to better fit the tests. Figure 9 shows that this function can be fitted by the following expression:

$$f'(P) = 0.0173 \cdot P + 0.0037 \tag{5}$$

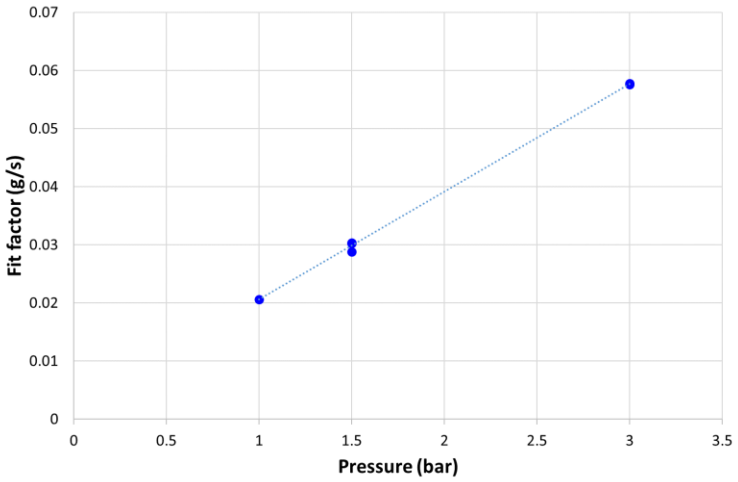

Figure 9. Dependency of recombination rate with the test pressure (referred to phase 1 end).

4.4 Modified correlation

As a result of the modifications described above, the enhanced correlation can be written as:

$$R_{H2}\left[\frac{g}{s}\right] = \min(C_{H2}, C_{O2}, 8) \cdot tanh(C_{H2} - C_{min}) \cdot (k_1' \cdot P + k_2') \tag{6}$$

with k_1'=0.0173 g/s/bar and k_2'=0.0037 g/s.

Figure 10 to Figure 15 show the estimates of the modified correlation (Eq. 6) compared with the experimental data and the original correlations predictions (Eq. 1). Results illustrate how the new correlation better captures the behaviour of data in oxygen lean conditions and provides a better agreement with data in the hydrogen injections periods. Moreover, data-estimates deviation tends to the underprediction of the recombination rate which gives some conservatism to the correlation (i.e., lower recombination rate would imply higher hydrogen concentration in the mixture).

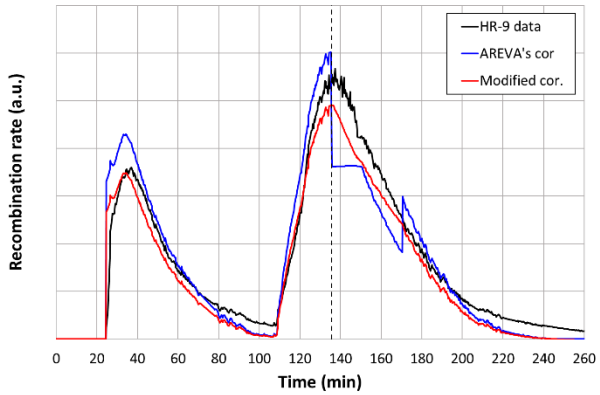

Figure 10. Comparison of initial and modified correlation for HR-9 test.

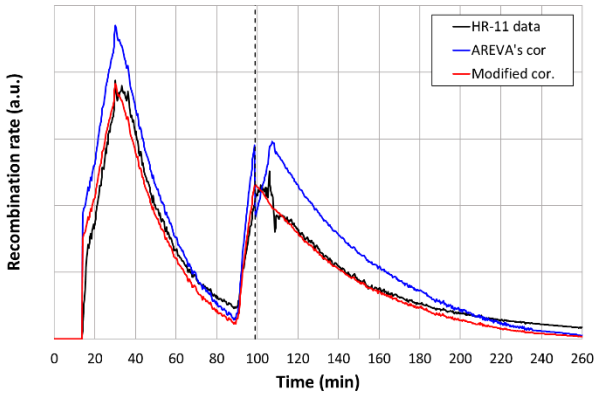

Figure 11. Comparison of initial and modified correlation for HR-11 test.

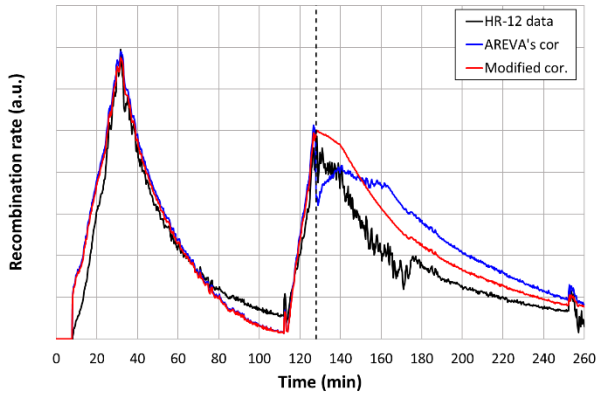

Figure 12. Comparison of initial and modified correlation for HR-12 test.

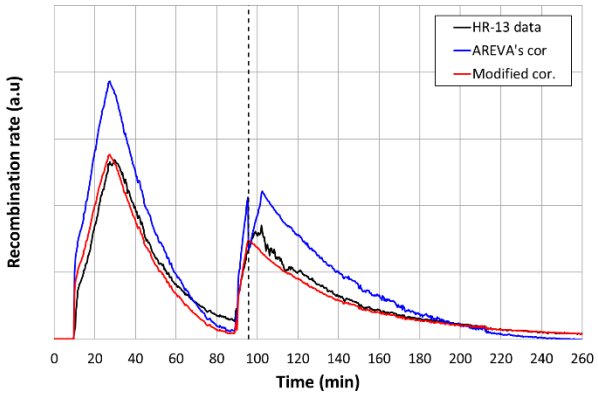

Figure 13. Comparison of initial and modified correlation for HR-13 test

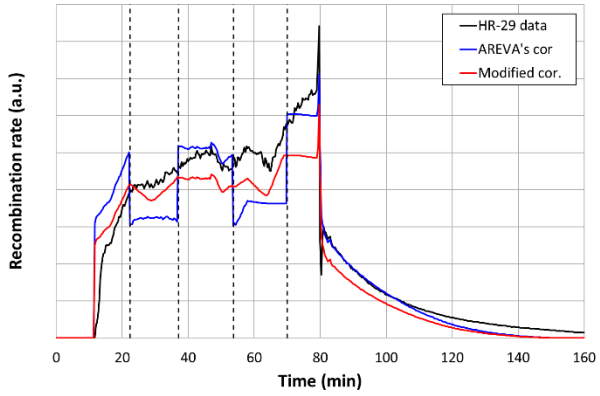

Figure 14. Comparison of initial and modified correlation for HR-29 test.

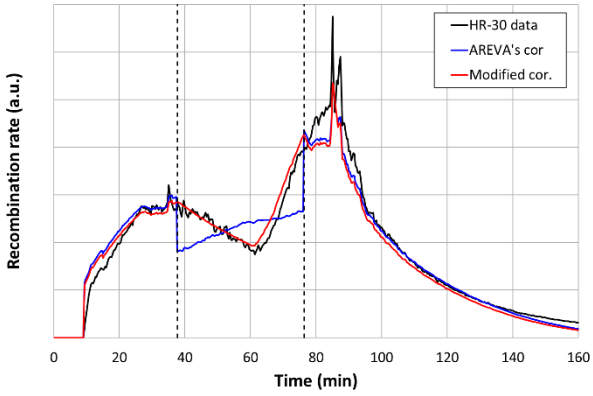

Figure 15. Comparison of initial and modified correlation for HR-30 test.

5. APPLICATION TO ACCIDENT SIMULATION

5.1 THAI experiment simulation

The Framatome's correlation is suitable to be implemented in Lumped Parameter (LP) severe accident codes since it depends on global atmosphere variables (pressure and mixture composition). Therefore, an important point in the assessment of the modifications proposed is to check their effects in the simulation with an integral code, like MELCOR [18].

As an example, the HR-11 test is simulated with MELCOR using a nodalization approach similar to which would be used in a plant application. That is, the geometry and location of internal structures (inner cylinder, PAR unit) determine the number and volume of the different nodes. Thus, the THAI vessel is split into five nodes (Figure 16). The hydrogen is injected into the bottom volume whereas the gases mixture exiting the PAR flows into the upper volume. The different volumes are connected with flow paths to allow convective flows. Their sections and lengths, defined from centre to centre of the node, are derived from the geometry of the vessel.

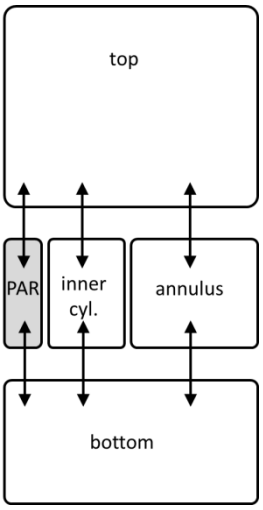

Figure 16. Vessel scheme for the THAI-HR simulation.

Both correlations are coded in the MELCOR's input deck using control functions (CFs) to be evaluated according to the atmosphere composition of the bottom volume (i.e, the condition of the PAR inlet). Besides the sink for hydrogen, a sink for oxygen and a source for steam are also modelled in the PAR node. MELCOR automatically evaluates the effects on pressure and temperature resulting from the new gas composition. The higher temperature of the new gas mixture in the PAR channel induces a flow through the PAR. Friction losses coefficients through the PAR channel are chosen to lead to gas flow rates of the same order as the available data. Heat transfer from the PAR to the annulus volume is modelled through a heat structure wall representing the PAR's housing.

The simulation with MELCOR, and in general with lumped parameter codes, presents limitations in dealing with non-homogeneous atmospheres as it does not model the momentum transport. Besides, uncertainties introduced in the gas flow estimates would propagate to the local gases concentration and consequently in the net recombination rate. Nonetheless, even with the code limitations and the gross scenario modelling, MELCOR is able to follow data trends throughout the test for both the recombination rate and the hydrogen concentration (Figure 17 and Figure 18). It is worth noting that simulations with lumped parameter codes tend to reduce the discrepancies in the correlation behaviour since overestimation

in the recombination rate will imply lower hydrogen concentration and the subsequent reduction of the recombination.

The highest deviation of simulation compared with recombination data is at the beginning of the first and second injection periods. The effect of overestimation due to the original correlation (Eq. 1), as discussed in Section 4, is increased by a higher estimated flow through the PAR that boosts the recombination capacity of the PAR. The modified correlation (Eq. 6) moderately improves this behaviour. Regarding the hydrogen molar fraction (Figure 18), although both correlations provide good estimates, the modified correlation provides a better fit with the data. Moreover, it predicts higher values than the original correlation and therefore it reduces the nonconservatism of the estimations. It is worth noting that as the low oxygen conditions are reached at 97 min of the test, the main difference between both correlations in the first injection-depletion period is due to the new expression of the dependency with the pressure (Section 4.3).

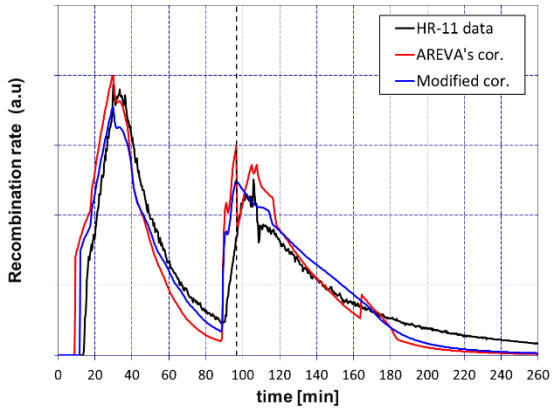

Figure 17. Recombination rate of the HR-11 test.

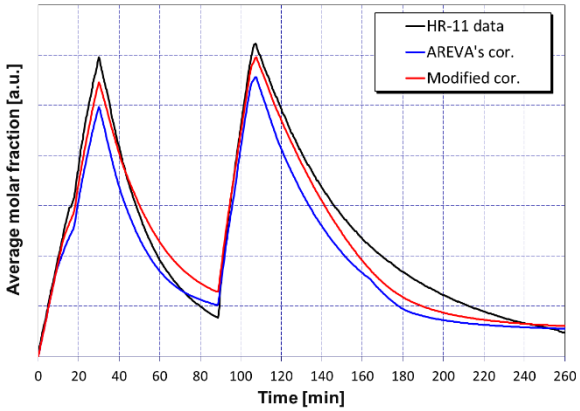

Figure 18. Hydrogen molar fraction of the HR-11 test.

5.2 Plant simulation

The effect of the modification of the correlation in the simulation of an accident sequence, in a pressurized water reactor, has been checked by simulating with the MELCOR code a small break LOCA (SBLOCA). In this sequence, none of the injection systems of the primary circuit is available except for the accumulators. Fan coolers are also available to cool the containment atmosphere. The containment is nodalized with 10 volumes [19]: the cavity pit and its adjacent chamber, the rooms surrounding the three steam generators and the pressurizer, the annular zone, the lower and upper compartments, and the dome.

The progressive uncovering of the core leads to the start of the hydrogen generation at 0.6 h after the beginning of the accident. The degradation of the core and the molten material relocation trigger the failure of the reactor vessel at ~6 h with the subsequent slump of molten material into the cavity pit. The ablation of the cavity concrete produces additional hydrogen and carbon monoxide. The operation of the PARs from the beginning of the hydrogen release reduces its concentration at the same time that depletes oxygen. As a consequence, at around 10 h oxygen concentration decreases below the total combustible gases' concentration. It is worth noting that CO is added to H_2 to determine to availability of oxygen in the catalyst surface. The recombination of CO is also considered but no modification is introduced in the original correlation for the Framatome type PARs.

Since PARs modelled in the sequence (FR-1500) are about 8 times larger than the unit used in THAI tests, the dependency of the correlation with the pressure has not been changed. Therefore, only the

modification with the oxygen concentration behaviour is considered. Figure 19 shows a different qualitative and quantitative evolution of the recombination rate once oxygen concentration becomes lower than H_2+CO concentration (Figure 20). However, the evolution of the cumulative recombined mass, as well as the molar fraction of the combustible gases, are very similar using both correlations. Nonetheless, attention must be paid to these differences since small changes in the gas mixture composition can lead to reaching deflagration limits.

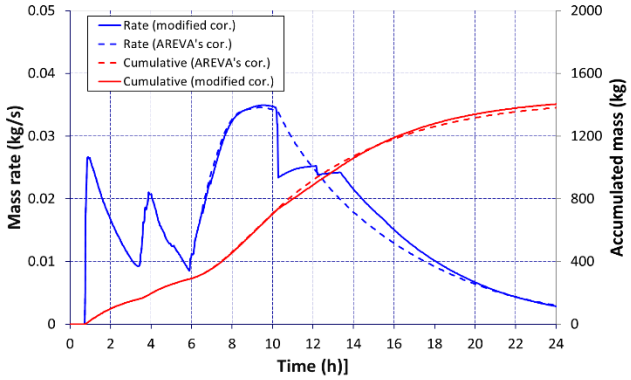

Figure 19. Recombination rate and cumulative recombined mass in the SBLOCA sequence.

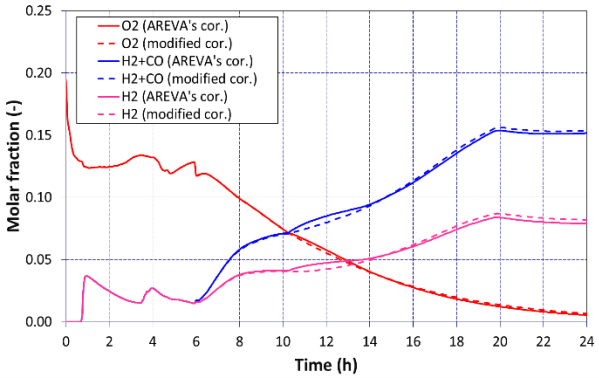

Figure 20. O2 and combustible gases molar fraction in the SBLOCA sequence.

6. CONCLUSIONS

The experimental THAI program has provided useful data to check the performance of the engineering correlation describing Framatome type PARs in oxygen lean conditions. The comparison of experimental data with the estimates of the Framatome's correlation has shown noticeable deviations, particularly for oxygen concentrations lower than hydrogen. Moreover, a significant overprediction of the recombination rate has been observed, especially at the hydrogen injection periods. This fact would tend to underpredict the hydrogen concentration.

The structure of the original correlation, including the dependence on reactant gas concentrations and pressure, can be said to be physically appropriate. However, some significant modifications have been proposed to improve their estimates. The oxygen dependence has been made other than the stoichiometric ratio of the recombination reaction and the simple approach by the η factor has been dropped off from the expression. Finally, the pressure dependent function has been more accurately defined for the THAI tests.

The above enhancements show a very slight effect on the hydrogen concentration when simulating a SBLOCA accident with an integral code. This observation, though, should be extended to other scenarios.

ACKNOWLEDGMENTS

The work presented in this communication is done under the frame of the AMHYCO project. This project has received funding from the Euratom research and training programme 2014-2018 under grant agreement No 945057.

The data for the THAI-HR test, operated by Becker Technologies, were obtained from NEA-OECD database.

REFERENCES

[1] IAEA, "Mitigation of hydrogen hazards in water cooled power reactors", International Atomic Energy Agency, Vienna (Austria), IAEA-TECDOC-1196, 2001.
[2] J. G. Kemeny, "Report of the President's Commission on the Accident at Three Mile Island", 1979.
[3] B. R. Sehgal, Ed., "Chapter 3 - Early Containment Failure", in *Nuclear Safety in Light Water Reactors*, Boston: Academic Press, 2012, pp. 185-306. doi: 10.1016/B978-0-12-388446-6.00003-4.
[4] IAEA, "The Fukushima Daiichi Accident. Technical Volume 1/5: Description and Context of the Accident." International Atomic Energy Agency, Austria, 2015.
[5] TEPCO, "Evaluation of the Situation of Cores and Containment Vessels of Fukushima Daiichi Nuclear Power Station Units-1 to 3 and Examination into Unsolved Issues in the Accident Progression. Progress Report No. 3", May 2015.
[6] NEA/CSNI, "Status Report on Hydrogen Management and Related Computer Codes", NEA/CSNI/R(2014)8, Jun. 2014.
[7] ENSREG, "Peer review report. Stress tests performed on European nuclear power plants", 2012.
[8] F. Arnould *et al.*, "State of Art on Hydrogen Passive Autocatalitic Recombiner", presented at the *International Conference on Nuclear Engineering*, Nice (France), Apr. 2001.
[9] S. Gupta *et al.*, "THAI test facility for experimental research on hydrogen and fission product behaviour in light water reactor containments", *Nuclear Engineering and Design*, **vol. 294**, pp. 183-201, dic. 2015, doi: 10.1016/j.nucengdes.2015.09.013.
[10] T. Kanzleiter *et al.*, "Final Report. Hydrogen and Fission Product Issues Relevant for Containment Safety Assessment under Severe Accident Conditions (Restricted Version)", Becker Technologies (Germany), Reactor safety project 1501326-FR1, Jun. 2010.
[11] L. E. Herranz *et al.*, "NUGENIA/TA2 Achivements in Severe Accidents Research (2015-2020)", Nuclear España, Sep. 2020.
[12] G. Jiménez *et al.*, "AMHYCO Project – Towards an Enhanced Accident Management of the H_2/CO Combustion Risk". *19th International Topical Meeting on Nuclear Reactor Thermal Hydraulics (NURETH-19)*, Bussels (Belgium), Mar. 2022.
[13] E. Bachellerie *et al.*, "Generic approach for designing and implementing a passive autocatalytic recombiner PAR-system in nuclear power plant containments", Nuclear Engineering and Design, **vol. 221**, n.º 1, pp. 151-165, abr. 2003, doi: 10.1016/S0029-5493(02)00330-8.
[14] M. Loeffler, "Correlations for Hydrogen and Carbon Monoxide Recombination by Framatome Passive Autocatalytic Recombiners", Framatome, Framatome technical report D02-ARV-01-143-222, Feb. 2019.
[15] T. Kanzleiter, "Quick look report. Hydrogen recombination test HR-6 to HR-13, HR-29 and HR-30", Becker Technologies GmbH, Germany, Reactor Safety Research Project 150 1326 150 1326-HR-QLR-2, Aug. 2009.
[16] J. Fontanet and L. E. Herranz, "Assessment of the AREVA's Formulation of PARs Recombination Rate", *19th International Topical Meeting on Nuclear Reactor Thermal Hydraulics (NURETH-19)*, Brussels (Belgium), Mar. 2022, p. Log nr.: 35419.
[17] E.-A. Reinecke *et al.*, "PAR Model Development Exercise in the Framework of SAMHYCO-Net", *19th International Topical Meeting on Nuclear Reactor Thermal Hydraulics (NURETH-19)*, Brussels (Belgium), Mar. 2022, p. Log nr.: 36425.
[18] L. L. Humphries, R. K. Cole, D. L. Louie, V. G. Figueroa, and M. F. Young, "MELCOR Computer Code Manuals Vol. 2: Reference Manual", SAND2015-6692 R, Aug. 2015.
[19] J. Fontanet and L. E. Herranz, "Sensitivity of PARs Performance to Accident Modelling in Small Break LOCAs in PWRs", *11th International Topical Meeting on Nuclear Reactor Thermal Hydraulics, Operation and Safety (NUTHOS-11)*, Gyeongju (Korea), oct. 2016, vol. N11P0294.

Enhancement of Recombination Rate Correlation for PARs in Oxygen-lean Conditions

Joan Fontanet and Luis E. Herranz

Unit of Nuclear Safety Research

CIEMAT (Spain)

Introduction

- **Motivation**
  - PARs are installed in many NPP as mitigation system.
  - Availability of validated analytical correlation for PAR's efficiency is crucial for safety analyses.
  - Long operation of PARs will deplete oxygen in the containment atmosphere.
- **Objectives**
  - To improve correlation predictability for mixtures with low O_2 concentration.
  - To review the improved correlation performance in integral code simulations.
- **Scope**
  - Framatome type PAR
  - THAI experimental data with low O_2 conditions

Test description: THAI facility

THAI vessel

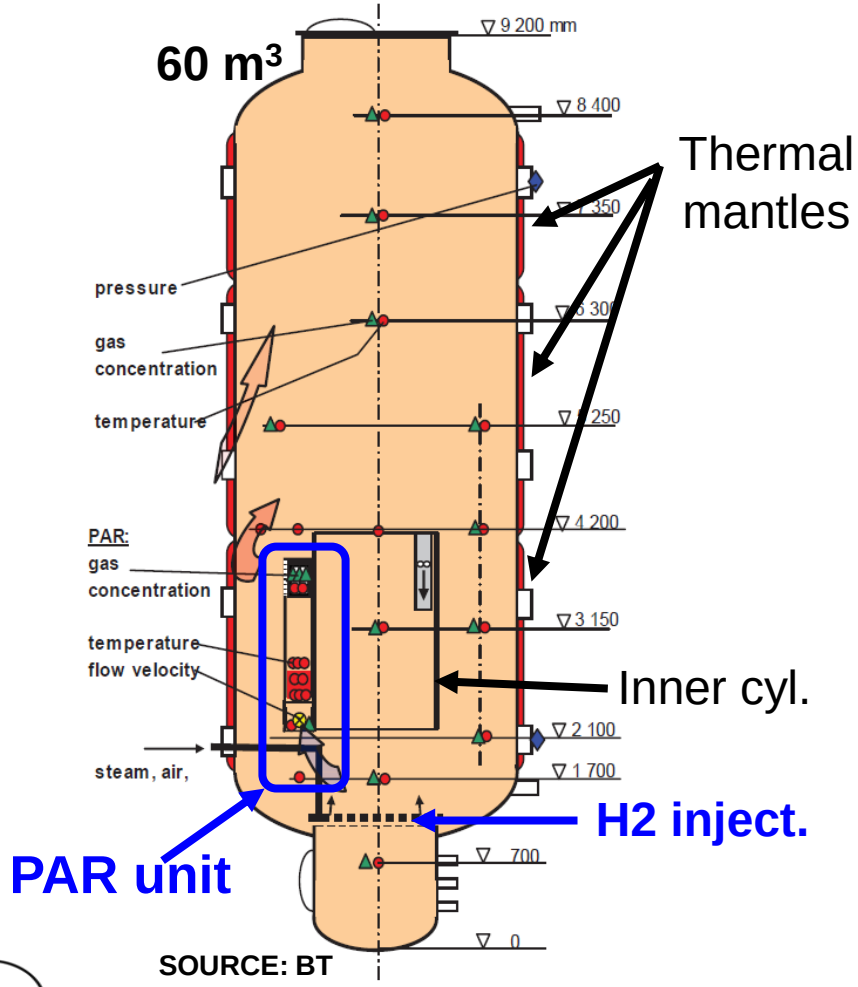

SOURCE: BT

PAR unit (Framatome/AREVA type)

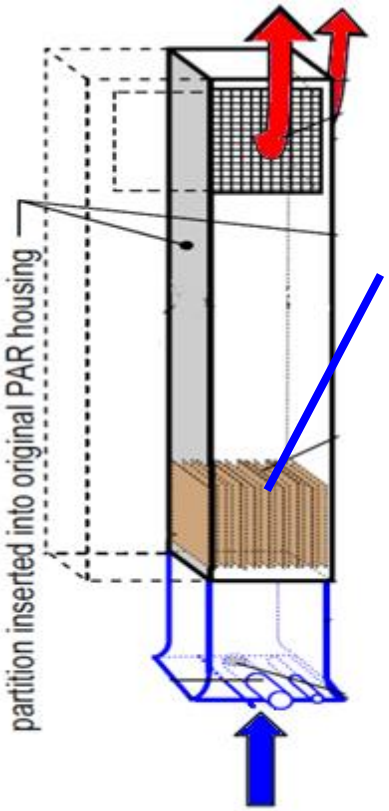

$H_2 + ½\ O_2 \rightarrow H_2O_v$

H_2 + air + steam

Experimental recombination rate:

$$R_{H2}\left[\frac{kg}{s}\right] = \left(X_{H2,in} - X_{H2,out}\right) v_{in.} \cdot S_{in} \cdot \frac{P \cdot M_{H2}}{R \cdot T_{in}}$$

Test description: Experimental matrix

1.0 bar	25 ºC	dry	HR-1 HR-2
	86 ºC	60% steam	**HR-13**
1.5 bar	25 ºC	dry	HR-3 HR-28 HR-27
	74 ºC	25% steam	HR-6 HR-7 HR-8
	90 ºC	47% steam	**HR-9** HR-10
	97 ºC	60% steam	**HR-11 HR-29**
2.2 bar	25 ºC	dry	HR-4
3.0 bar	25 ºC	dry	HR-5
	117 ºC	60% steam	**HR-12 HR-30**

HR-nn: Test with oxygen-lean conditions

Test description: Procedure (HR-11)

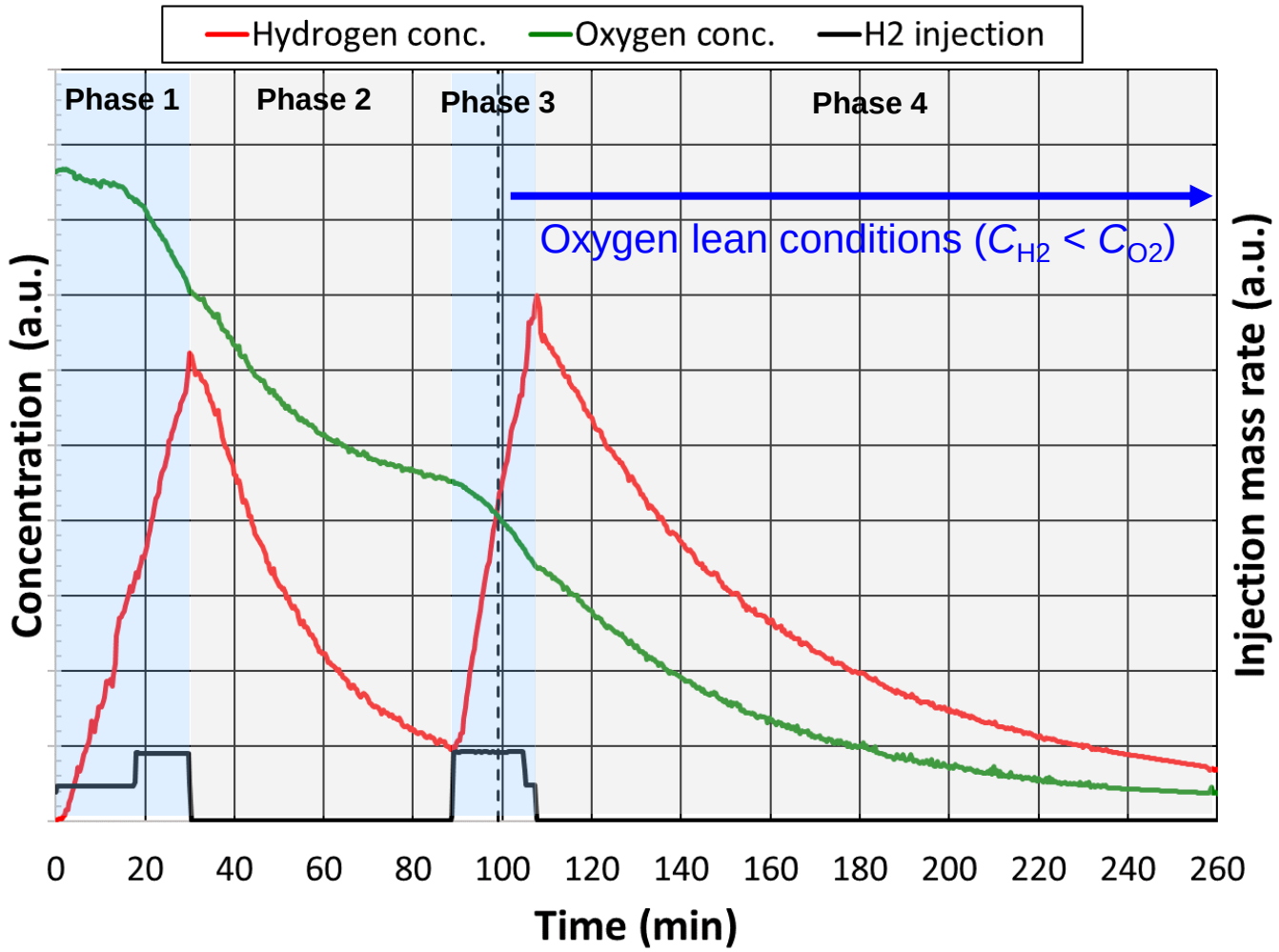

4 phases: succesives **injection** and **depletion** periods

O_2 injection in phase 2 (depending on test)

Analytical correlation: Description

Analytical H_2 recombination rate (Framatome):

$$R_{H2}[kg/s] \propto \tilde{C}_{H2} \cdot tanh(C_{H2} - C_{min}) \cdot \eta \cdot (k_1 \cdot P + k_2)$$

(proprietary correlation)

Effective H_2 conc.
$\tilde{C}_{H2}$ = min (C_{H2}, 2·C_{O2}, C_{lim})

Reduction factor for $C_{O2} < C_{H2}$

k_1 , k_2 depend on the particular dimensions of the PAR

PAR operation condition

Onset	$\tilde{C}_{H2}$ > 2 vol.%
End	$\tilde{C}_{H2}$ < 0.5 vol.%

Analytical correlation: Assessment

THAI HR-11

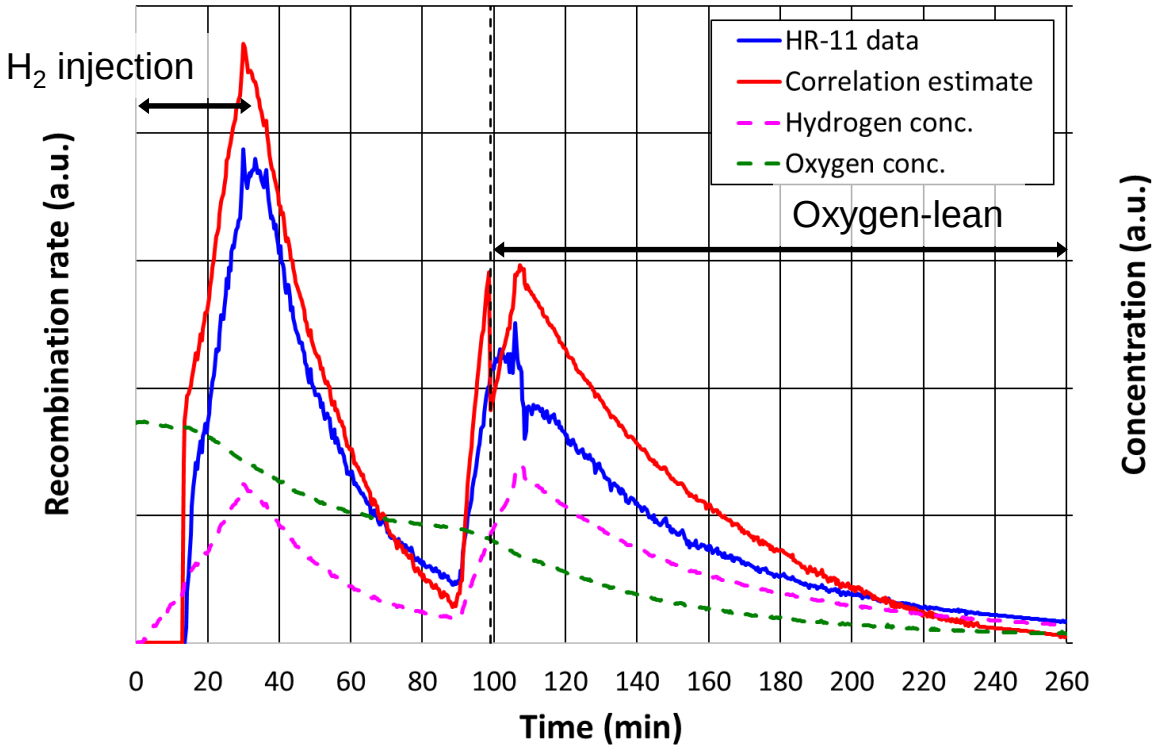

THAI HR-12

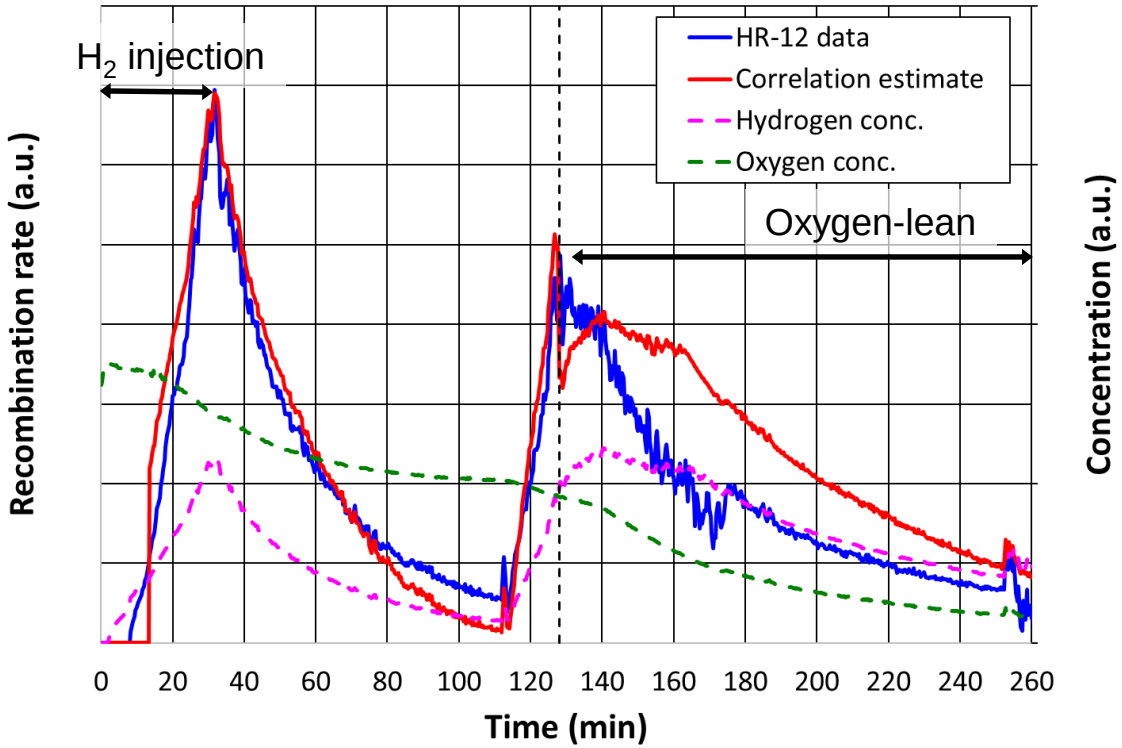

The correlation overpredicts recombination in the injection phases

The correlation does not capture the behaviour in oxygen-lean conditions

Correlation modification (1)

➢ Oxygen-lean condition ($C_{O2} < C_{H2}$)

- No drop in efficiency observed
- Change in tendency: follows O_2 evolution rather than H_2

THAI HR-12

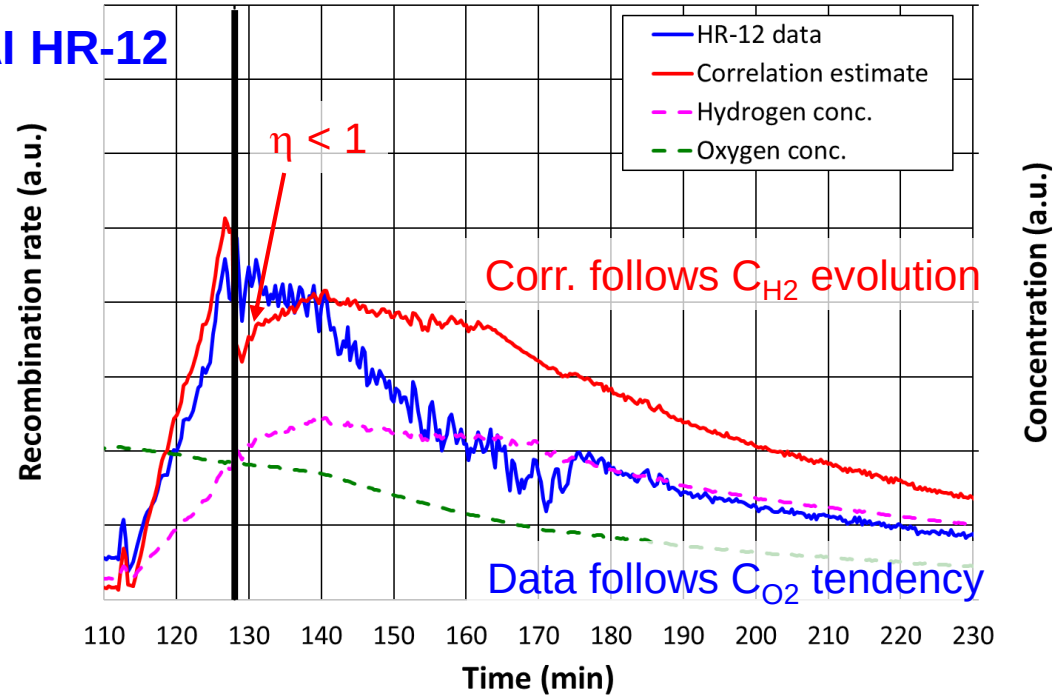

$\tilde{C}_{H2} = \min(C_{H2}, 2 \cdot C_{O2}, C_{lim})$ $\eta < 1$ ($C_{O2} < C_{H2}$)

Proposed modifications

$\tilde{C}_{H2} = \min(C_{H2}, C_{O2}, C_{lim})$ $\eta \equiv 1$

Correlation modification (2)

➢ Hydrogen injection periods

- Clear overestimation for periods with H_2 injection
- Higher overestimation for lower pressure

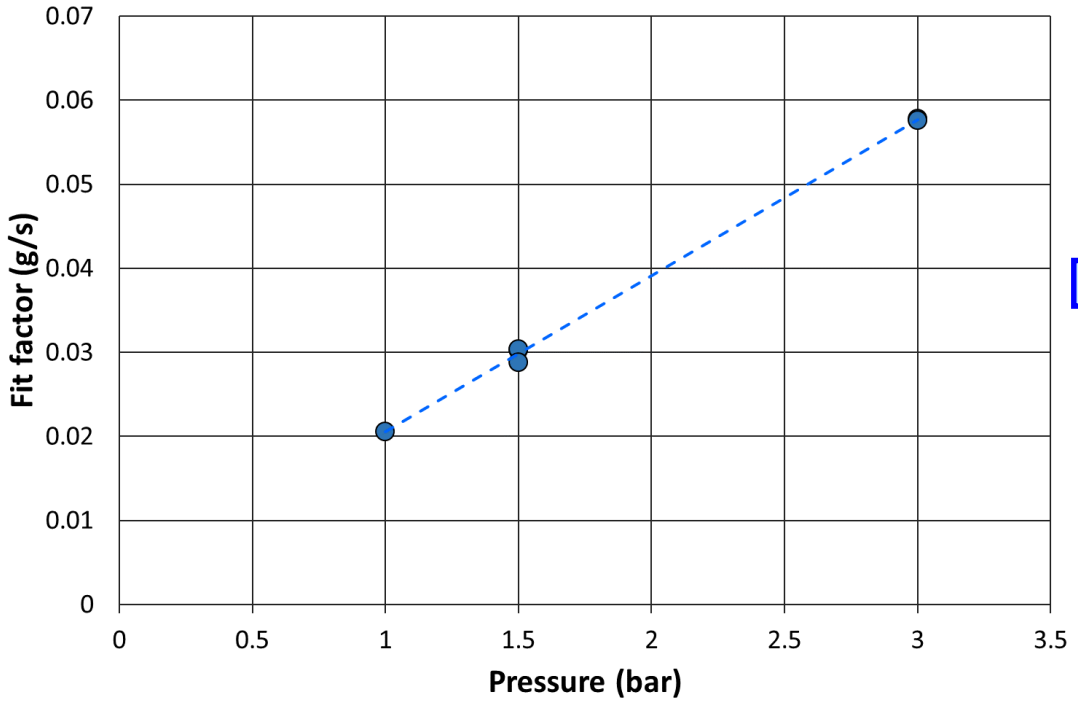

New dependency on pressure:

$$f'(P) = 0.0173 \cdot P + 0.0037$$

Results: THAI tests

THAI HR-9

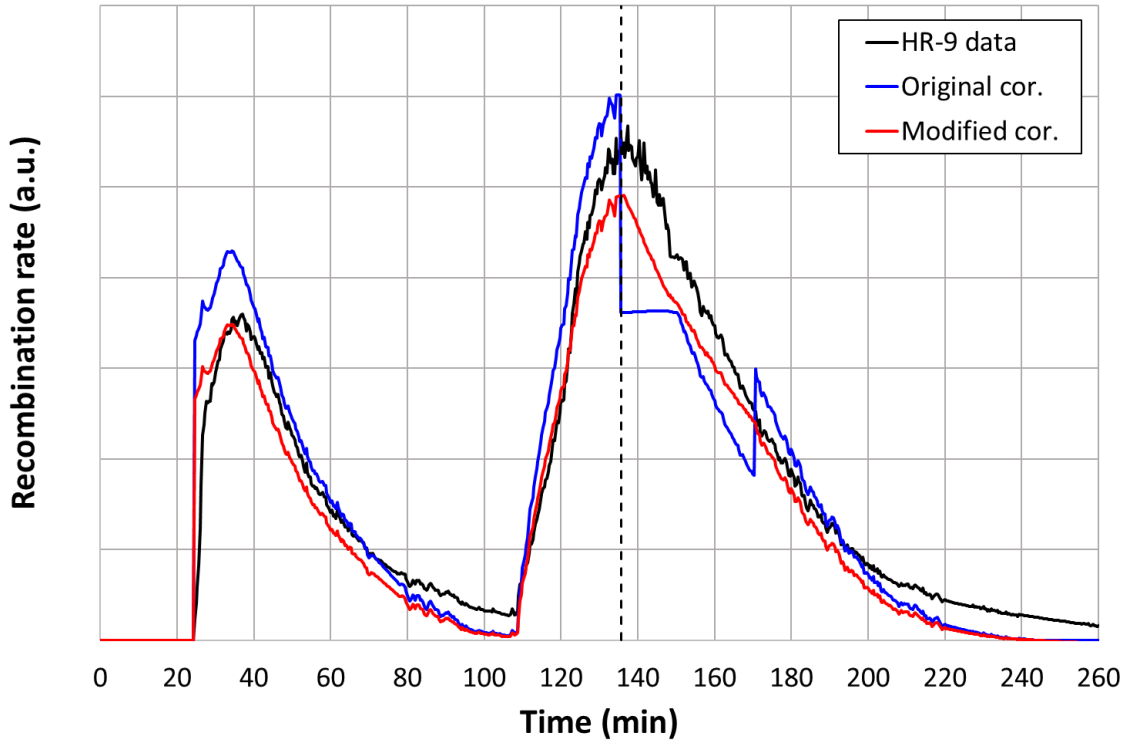

THAI HR-11

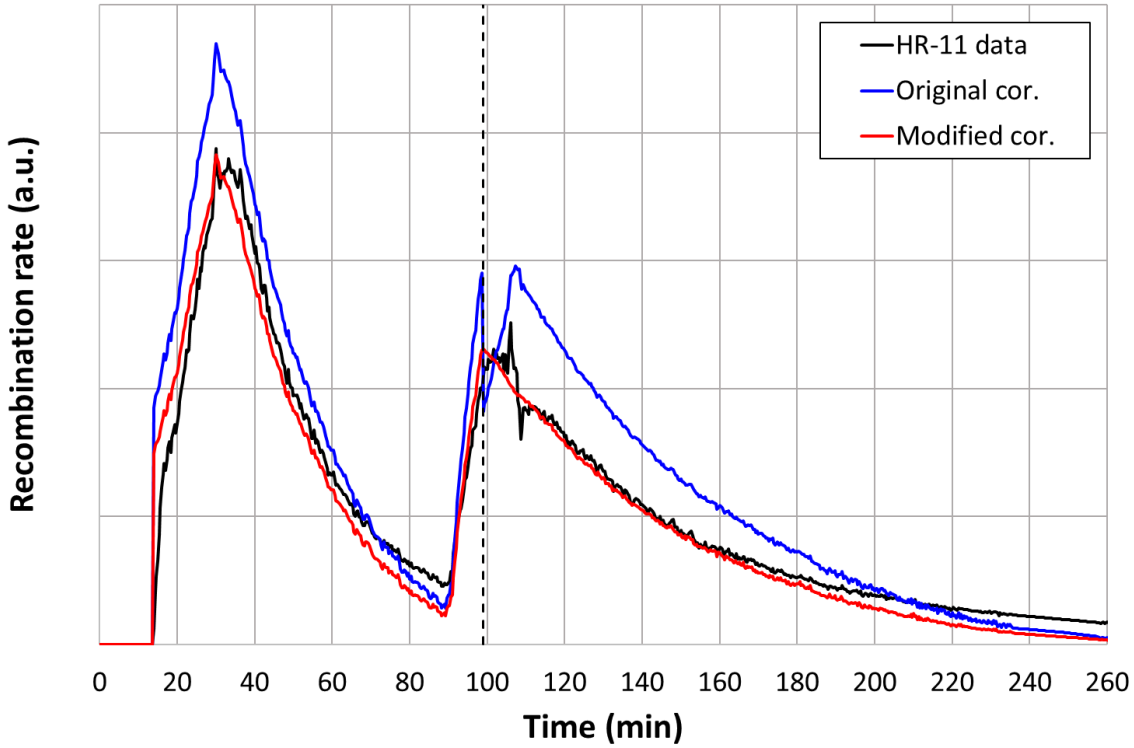

Better capture of data behaviour in oxygen lean conditions

Better agreement with data in injection periods

Application to integral codes: THAI model

THAI vessel model

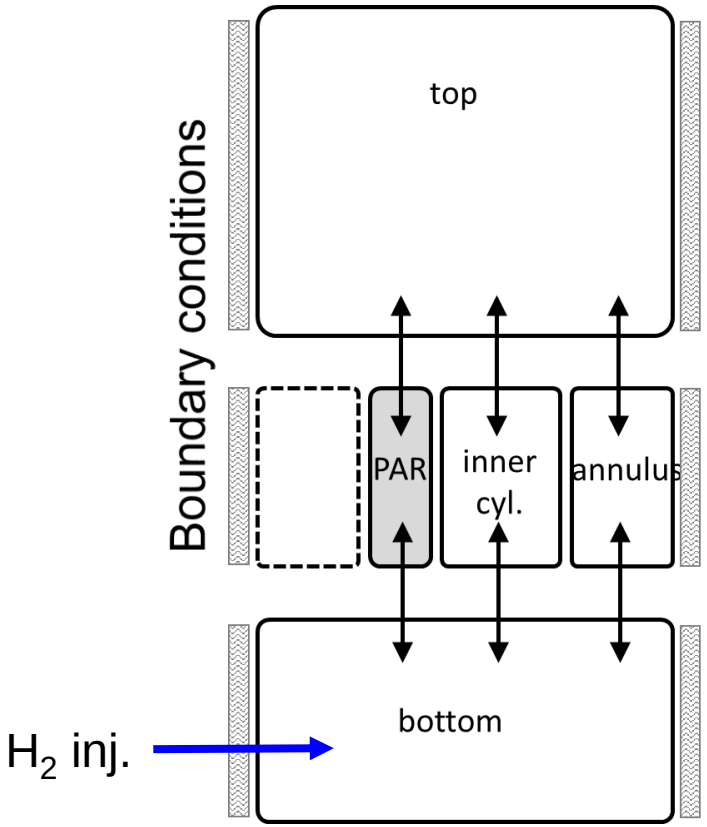

- **MELCOR v2.2 code**
  - Correlation implemented by ‘control functions’ for **sources/sinks of mass and energy.**
  - Vessel geometry and dimensions determine the **number and geometry of nodes** and **flow paths.**
  - **Form loss coefficient** through the PAR volume set to capture the experimental velocity.
- **HR-11 test simulation**
  - Initial and boundary conditions
  - Injection rates

Application to integral codes: THAI results

Recombination rate (HR-11)

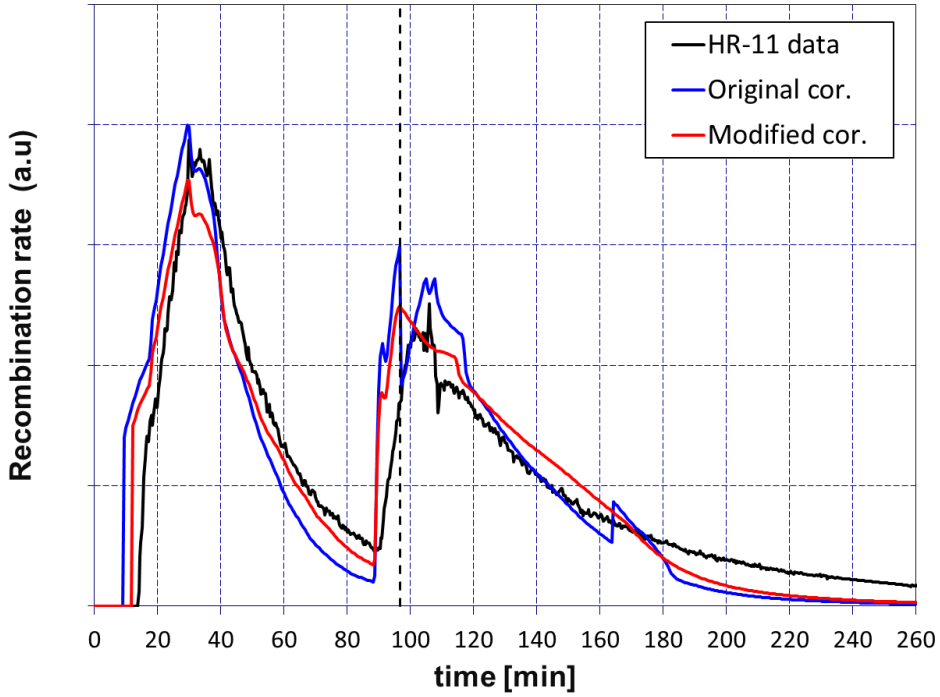

H_2 molar fraction (HR-11)

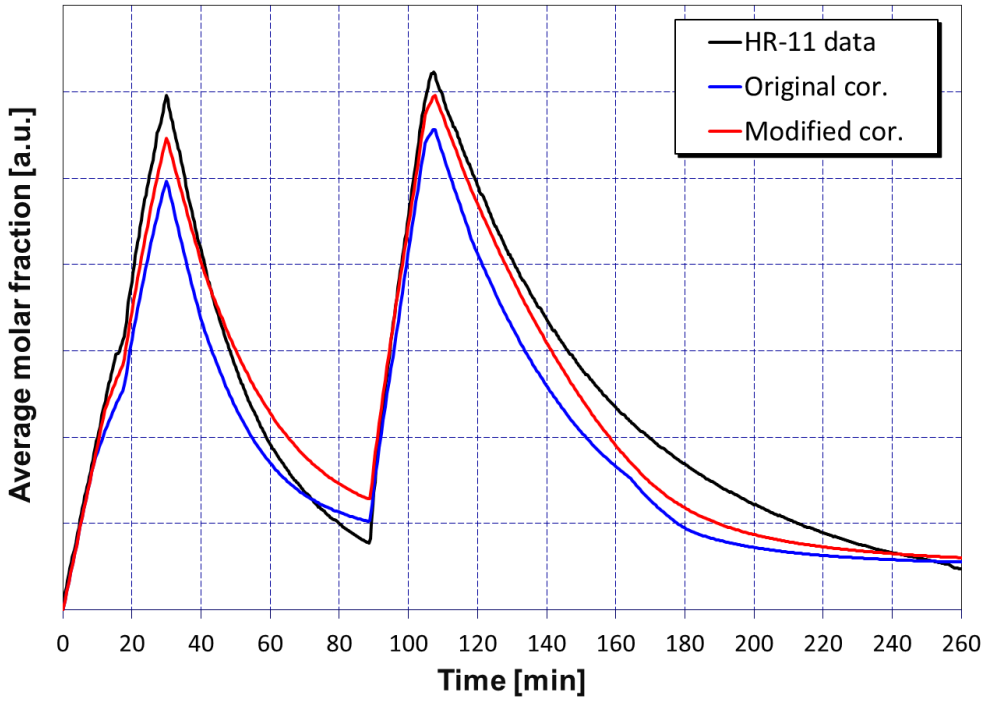

MELCOR is able to follow data trends throughout the test

Modified correlation moderately improve results & reduce non-conservatism of original corr.

Highest discrepancy at beginning of 2nd injection:

Application to integral codes: plant simulation

- ***PWR Containment***

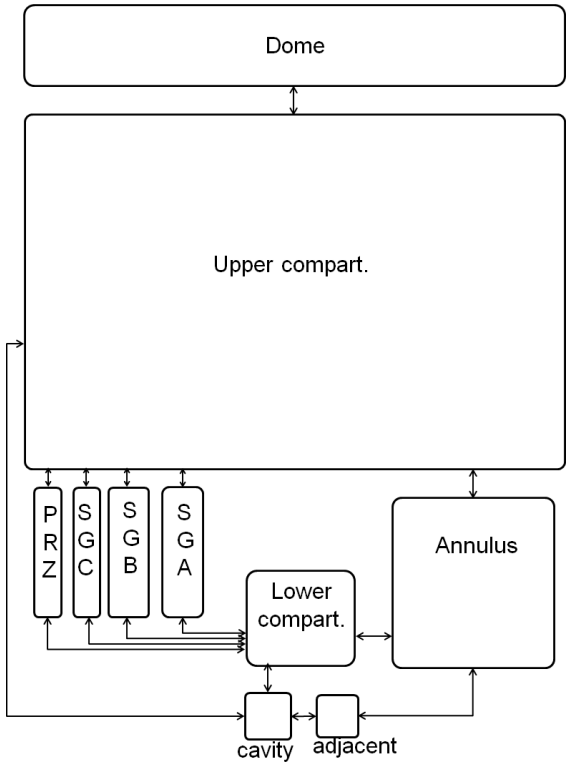

10-node approach

- ***Sequence***

2" LOCA in the cold leg
Accumulator and fan coolers available
H_2 + CO generation

- ***PARs distribution***

Compartment	# of PARs
Cavity	-
Cavity adjacent chamber	1
Lower compartment	1
SGA compartment	1
SGB compartment	1
SGC compartment	1
PRZ compartment	1
Upper compartment	13
Dome	3
Annulus	2

Total: 24 Framatome FR-1500 PARs

Application to integral codes: SBLOCA results

Comb. gases molar fraction

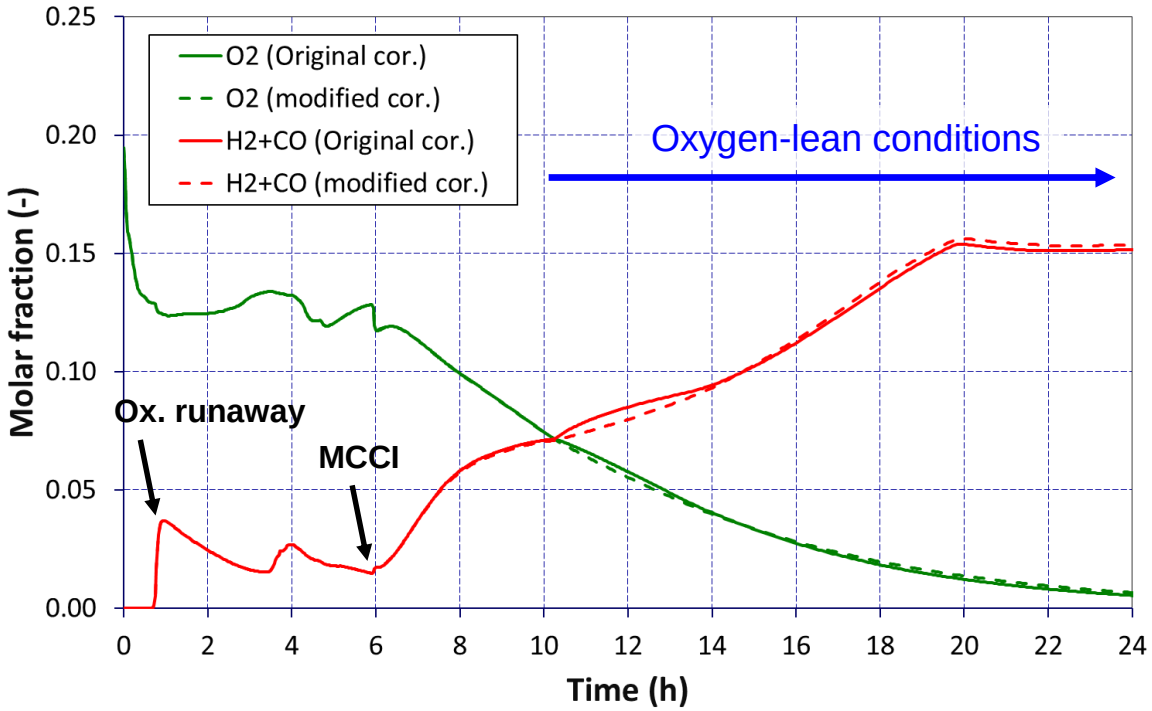

Recombination rate

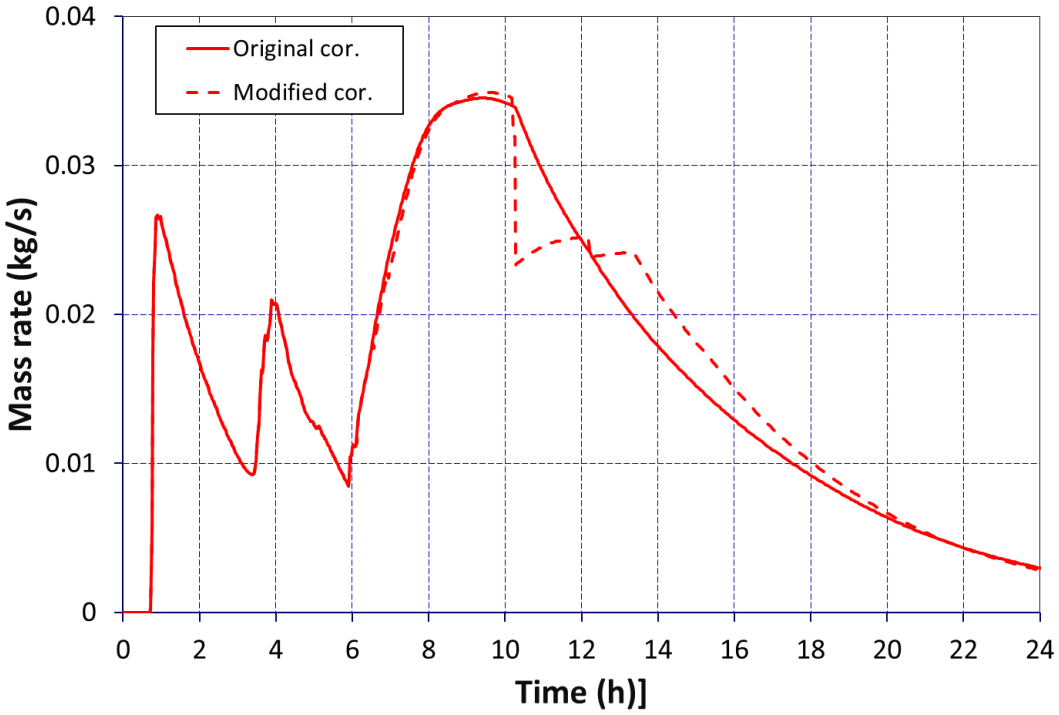

Different qualitative and quantitative recombination rate for $C_{O2} < (C_{H2} + C_{CO})$

Very similar results regarding comb. gases molar fraction

Conclusions

- *The Framatome correlation shows noticeable deviations compared with THAI-HR tests data:*
  - *Oxygen lean atmosphere (**ex-vessel phase**).*
  - *Active gas injection (**oxidation runaways and MCCI**) .*

- *Improvements to the correlation have been proposed to better capture THAI test data:*
  - *Gas concentration dependency with the less abundant reactant in the bulk volume.*
  - *Simple approach with the η factor for O2 lean conditions has been dropped off.*
  - *Pressure dependent function has been more accurately defined for THAI.*

- *Preliminary results with the enhanced correlation leads to a very slight effect on the hydrogen concentration when implemented in a lumped parameter code.*

Thanks for your attention

ACKNOWLEDGEMENT



This work has been carried out in the frame of the AMHYCO Project. This project is funded from the **Euratom research and training programme** 2019-2020 under Grant Agreement No. 945057

The data for the THAI-HR tests, **operated by Becker Technologies**, were obtained from the NEA-OECD database



Correlation assessment

THAI HR-9

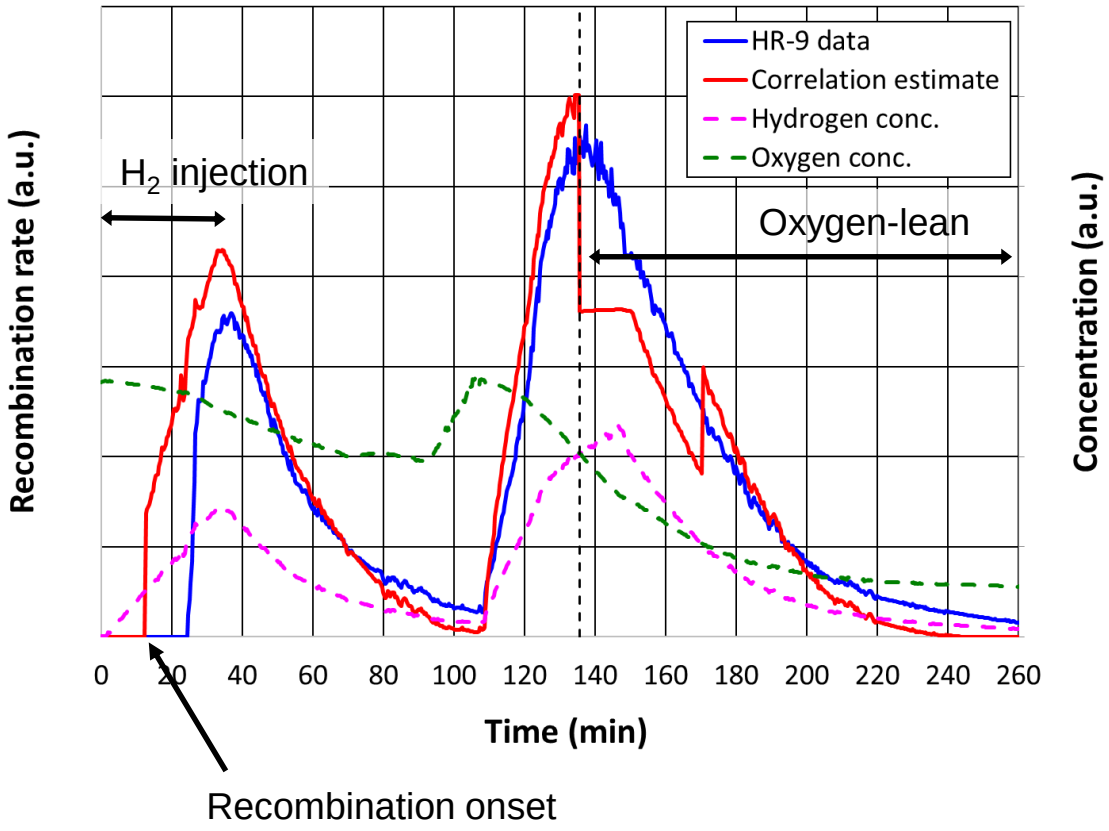

THAI HR-13

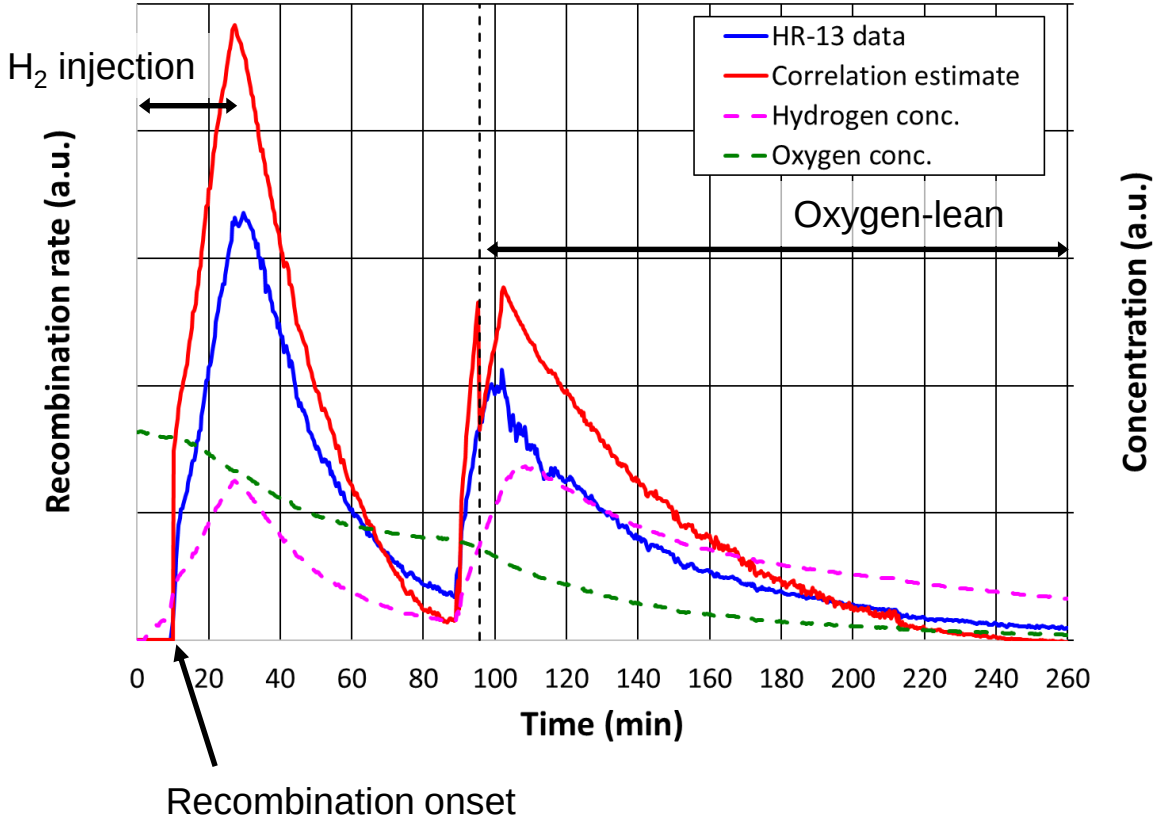

Correlation assessment

THAI HR-29

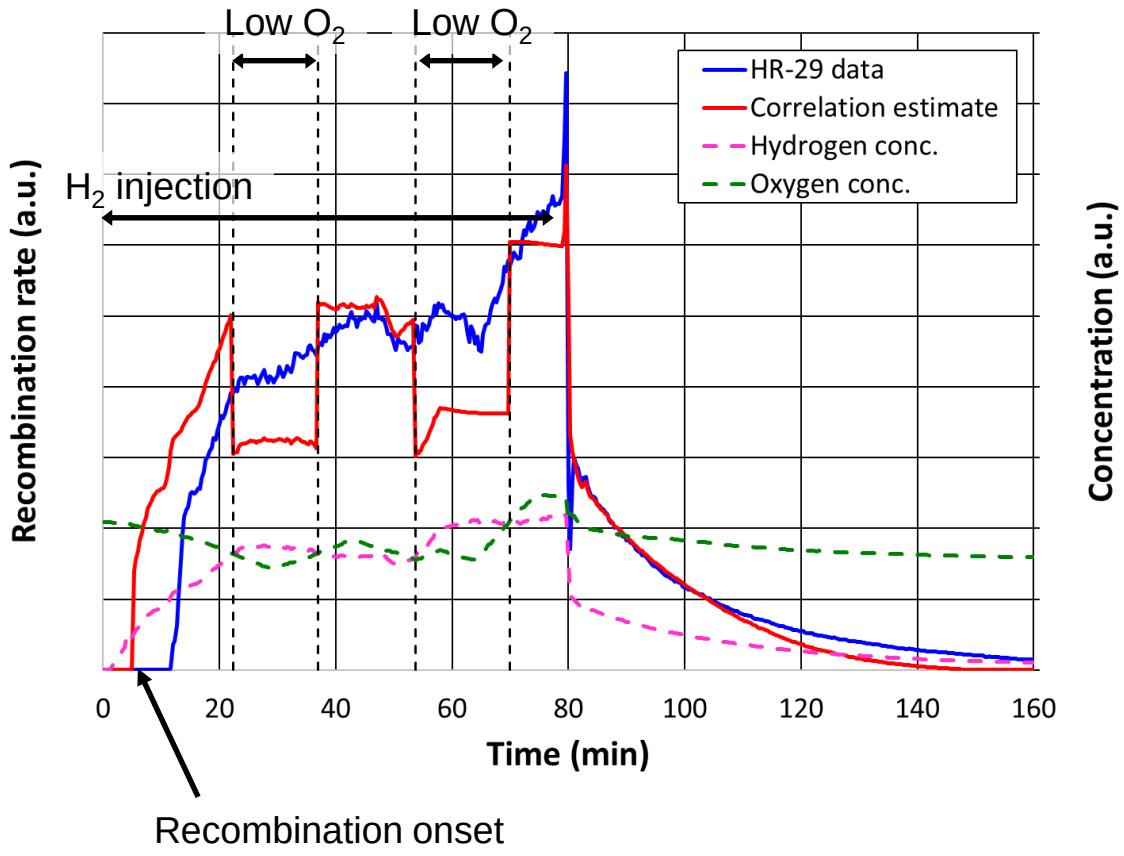

THAI HR-30

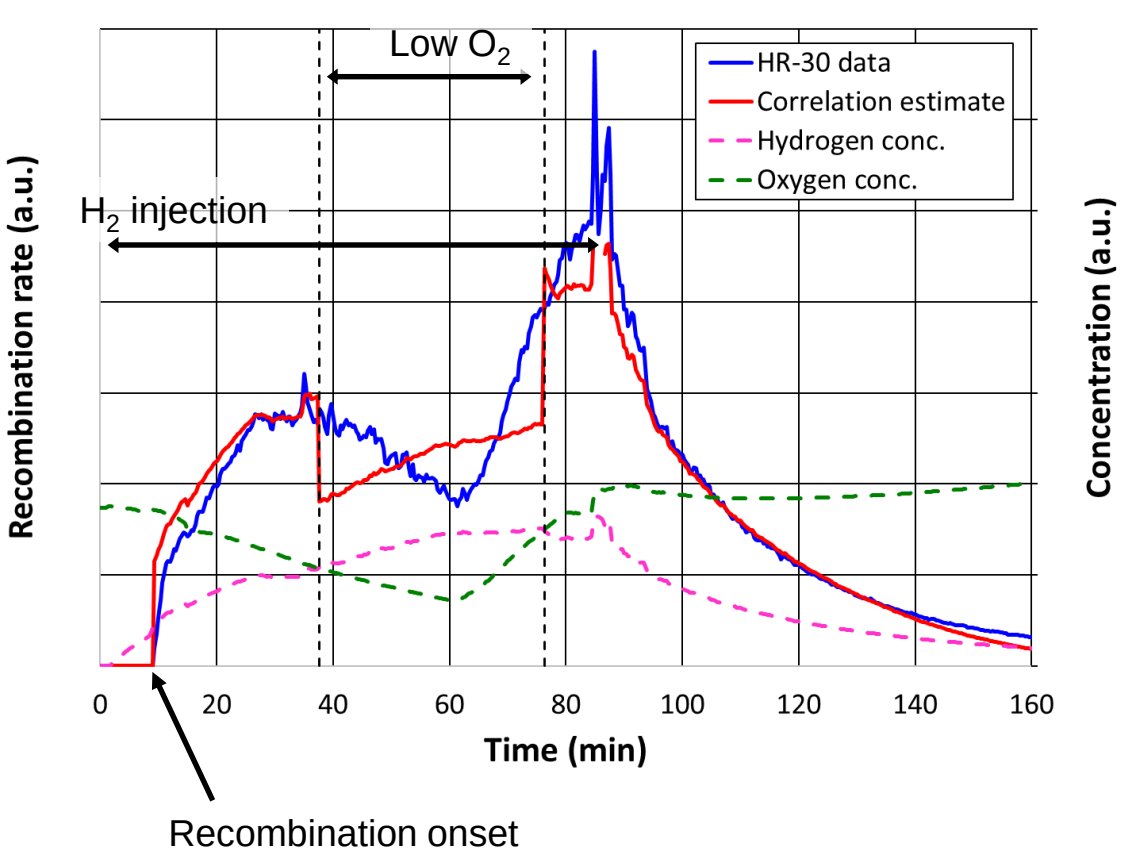

Results: THAI tests

THAI HR-12

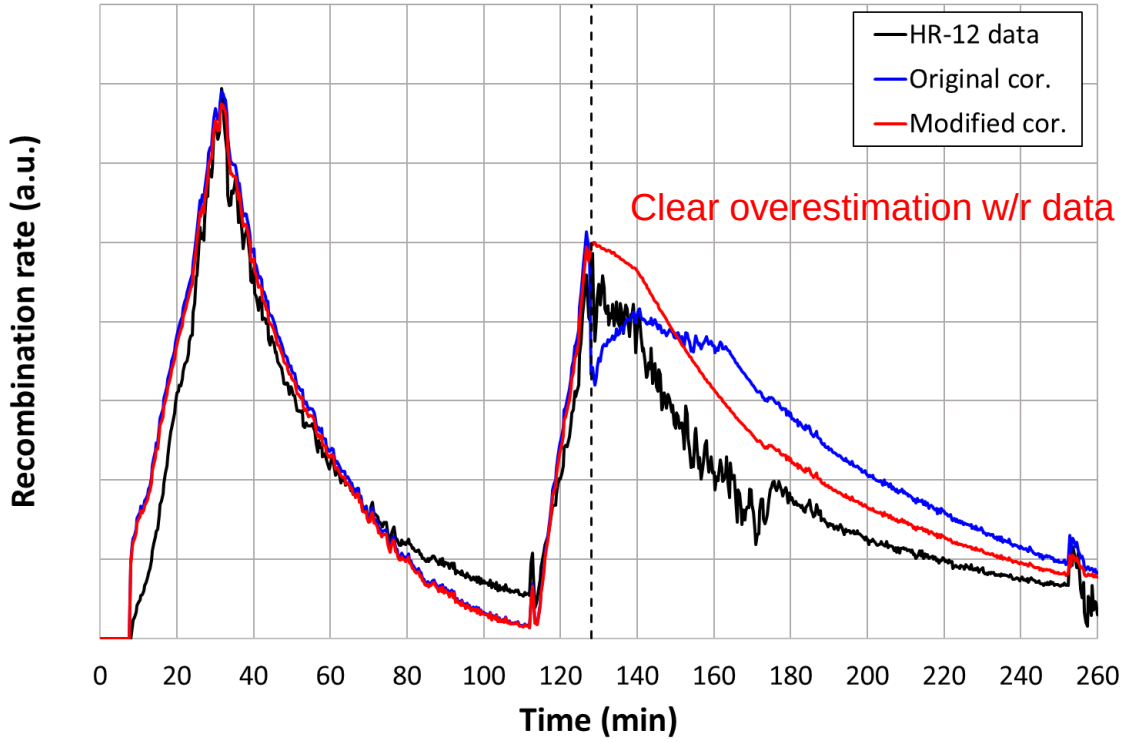

THAI HR-13

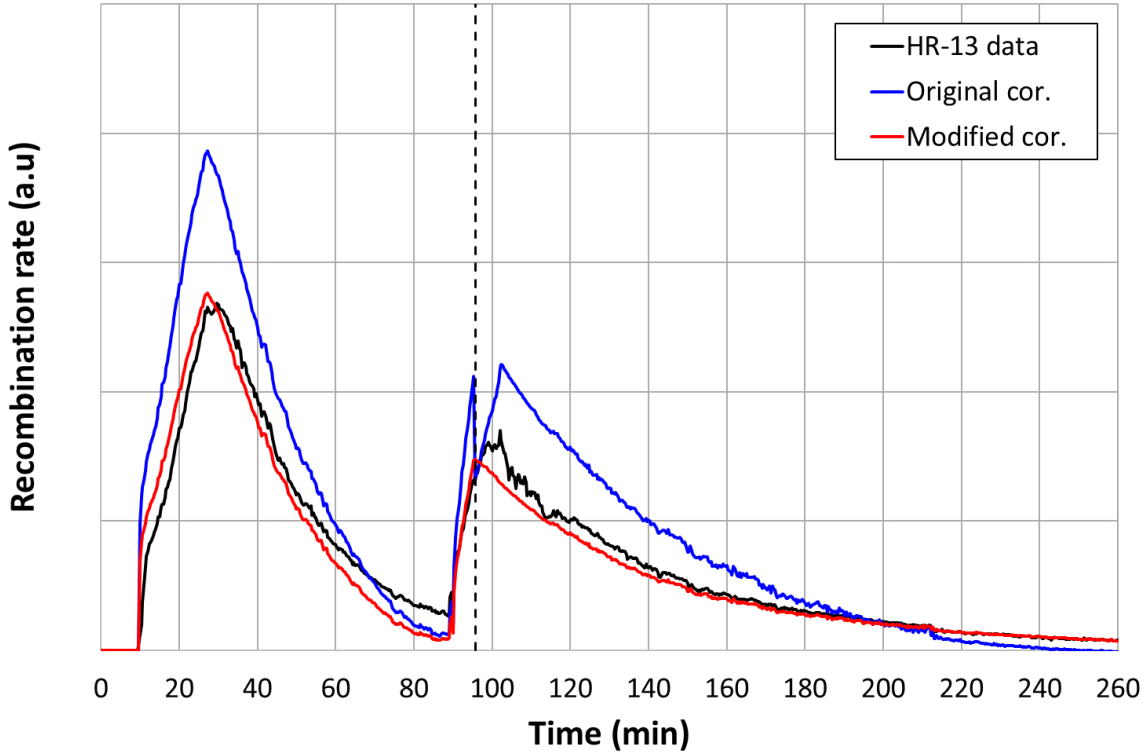

Better capture of data behaviour in oxygen lean conditions

Better agreement with data in injection periods

Results: THAI tests

THAI HR-29

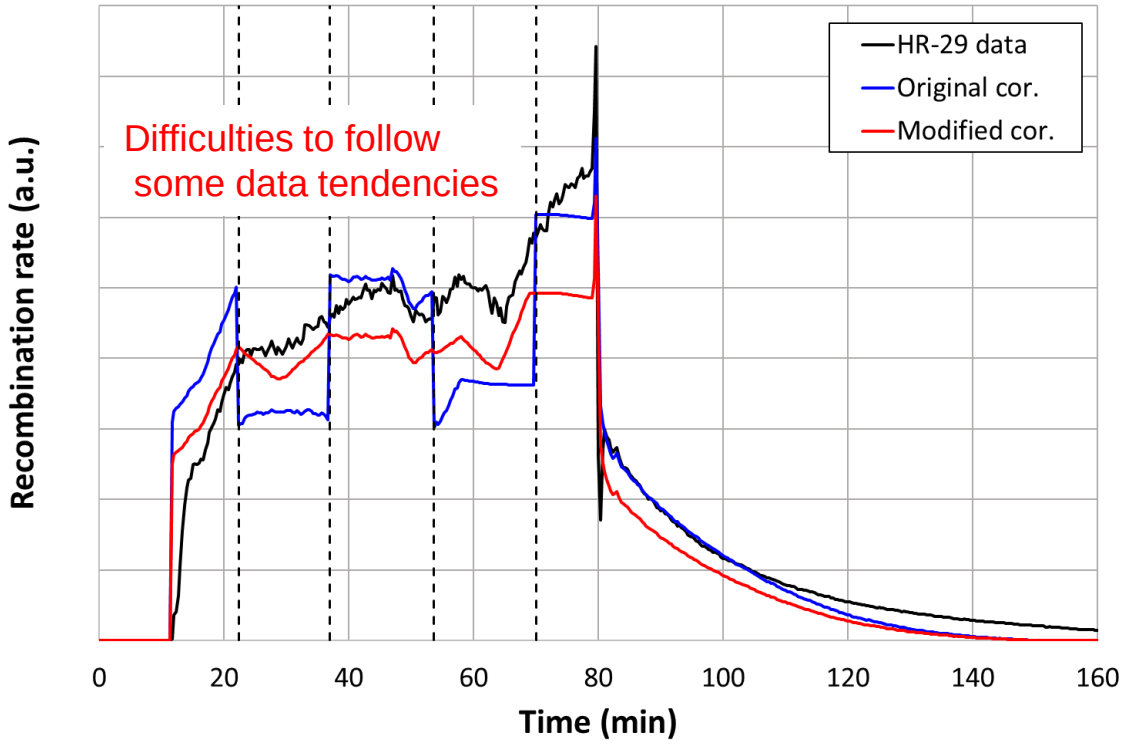

THAI HR-30

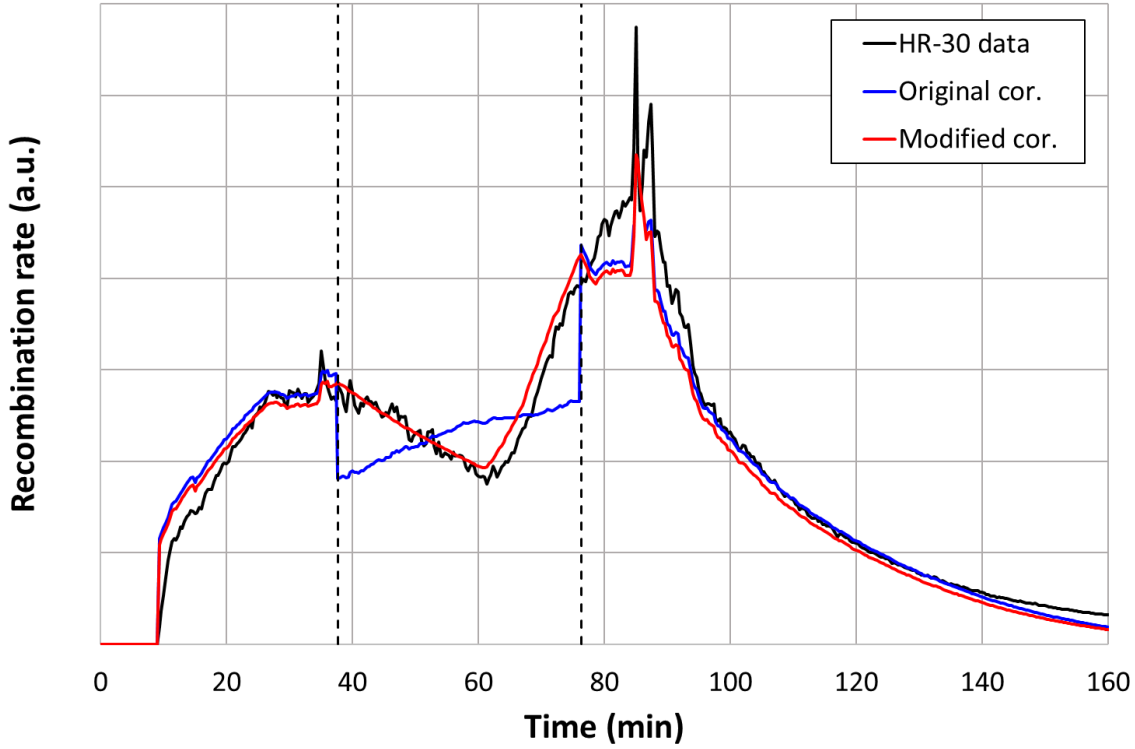

Better capture of data behaviour in oxygen lean conditions

Better agreement with data in injection periods

Effectiveness of Hydrogen Recombination by AgX and AgR Zeolites

F. Espegren, D. Suckow, T. Lind, J. Mantzaras, J. Theile
Paul Scherrer Institute
Forschungsstrasse 111, 5232 Villigen PSI, Switzerland
fredrik.espegren@psi.ch,
detlef.suckow@psi.ch, terttaliisa.lind@psi.ch, ioannis.mantzaras@psi.ch
juergen.theile@psi.ch

Y. Ishikawa, T. Kobayashi, K. Endo
Rasa Industries, Ltd.
Chiyoda-ku, Tokyo, Japan
yoshihiro.ishikawa@rasa.co.jp, toshiki.kobayashi@rasa.co.jp, koji.endo@rasa.co.jp

T. Narabayashi
Tokyo Institute of Technology
Meguro-ku, Tokyo, Japan
tnaraba@zc.iir.titech.ac.jp

S. Kobayashi
Morimura Bros., Inc.
Minato-ku, Tokyo, Japan
s-kobayashi@morimura.co.jp

ABSTRACT
In the event of a severe nuclear accident, one important safety barrier to contain radioactive release to the environment is the containment. To ensure full functionality during an accident, venting of the gas inside may be necessary to avoid reaching critical pressures and accumulation of hydrogen, which both may result in damage to the containment integrity. One solution to mitigate either of these risks is via a filtered containment venting system (FCVS). Such a system is designed to remove different radioactive materials from the vented gas and potentially hydrogen. For the former, iodine is one of the most important fission products needing to be removed and it can exist as e.g., elemental and bound in different organics. In general, elemental iodine can be effectively removed via e.g., a wet scrubber. However, organic iodides are more difficult to retain. One possible solution is Ag-zeolites. After the accident at the Fukushima Daiichi Nuclear Power Plant, Japan installed silver zeolite-based organic iodine filters in all FCVS in order to strengthen mitigation measures against severe accidents. Several tests had already been conducted on the effect of silver zeolite retention of organic iodine, and the test results have been confirmed by the safety review of the Japanese Nuclear Regulatory Authority. In order to improve FCVS, attention should be paid to the reaction of hydrogen and oxygen in the containment vessel and in FCVS for the PWR. When FCVS is started, the scrubber pool water is cold, so the steam in the containment vessel is condensed and the concentration of hydrogen and oxygen increases.

In this study, two Ag-zeolites were experimentally investigated. AgX, which has a catalytic action for hydrogen, is foreseen to be installed in the containment vessel to reduce the hydrogen concentration, and AgR, which does not have a catalytic action for hydrogen, is foreseen to be used for the iodine filter in FCVS. The hydrogen catalysis effect of silver zeolites were compared by experiments.

KEYWORDS
FCVS, Hydrogen, Ag-Zeolites, Severe Nuclear Accidents, Experiments

1. INTRODUCTION

Over the past decades, many measures have been taken to exclude the possibility of a severe accident happening in a nuclear power plant and consequently, the probability of a severe accident in a modern nuclear power plant is very low. Many additional safety systems have been installed in existing power plants, and the new plants are equipped with measures to mitigate any accident that could cause the release of radioactivity to the environment. Examples of improved safety management can be found in Figure 1 and Figure 2.

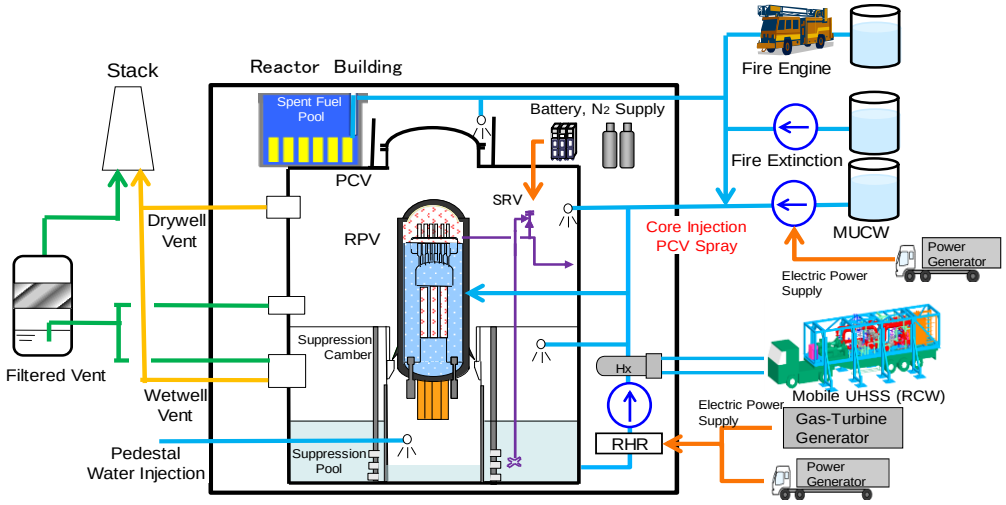

Figure 1. An example of full cooling strategy for station blackout to protect against severe accident for BWR in Japan.

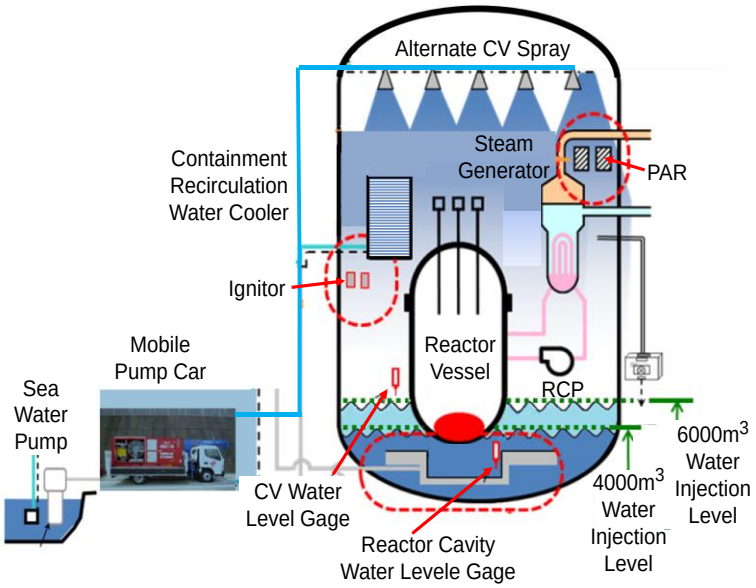

Figure 2. Water injection into containment vessel by alternate spray and core cavity water injection at Ikata NPP unit 3 of Shikoku Electric Power company, Japan.

Although there are many FCVS roles from the early stages of such an accident, including a hypothetical severe accident, the pressure in the containment may increase because of steam generation as well as the generation of hydrogen and other non-condensable gases. To protect the containment integrity as a last

barrier to confine the radioactive material, the pressure in the containment vessel (CV) may need to be decreased during the accident by venting the gas into the environment. In order to prevent the release of radioactivity from the containment during venting, the filtered containment venting systems (FCVS) have been installed in most of NPPs in Europe.

The main purpose of the FCVS is to retain fission products (FPs), which make up the largest fraction of the radioactivity in the event of an accident. One of the most important FPs to retain is iodine [1, 2] as it, via accumulation in the thyroid gland, can result in substantial dose towards people [3]. In the case of the Fukushima Daiichi NPP accident, the prevention of contamination with iodine as well as cesium became a top priority, although there was no significant increase in pediatric thyroid cancer via iodine, presumably due to the restriction of contaminated food immediately after the accident [4, 5]. Nevertheless, iodine could have both short-term and long-term health implications. Therefore, it is critical to avoid releases of iodine during an accident, meaning that efficient filtering stages are needed in the FCVS. Generally, the iodine species considered most relevant for the FCVS are elemental iodine (as I_2) and different organic iodides (generally represented by CH_3I). Of these, the elemental iodine can be removed via wet scrubbers (e.g., Venturi scrubber filter [1, 4]). However, the organic iodides are considerably more difficult to retain, as they are not very water-soluble (e.g., CH_3I is only slightly soluble in water [6]) and therefore would not be efficiently trapped by the scrubber solution [7]. As a means of adsorbing this organic iodine most effectively, an iodine filter using silver zeolite has been adopted in many countries to increase the safety of nuclear power plants in a hypothetical severe accident [1]. In addition to retaining iodine species, some silver zeolites have been shown to not only efficiently absorb organic iodine [8], but also to recombine H_2 at high humidity conditions [9].

After the accidents at Fukushima Daiichi in 2011, new requirements are posed on FCVS [7]. As they were originally designed for venting of the containment during later stages of an accident when containment was pressurized slowly as a result of molten-core concrete interaction, the improved FCVSs are designed for different phases of an accident and are foreseen to be activated, potentially, early on in an accident. Therefore, FCVSs have to provide a flexible operating range, depending on the reactor design (boiling water reactor, BWR, pressure water reactor, PWR), accident type (e.g., air ingress scenario [12]), surrounding parts temperature (i.e., via steam condensation [13]), progression of the accident, and type of undertaken mitigation action (e.g., inertization [14]).

In this study, two types of silver-containing zeolites have been investigated, under conditions that are representative of an FCVS during a venting procedure. These two zeolites are AgR and AgX, which have been designed and proven specifically to be efficient radioactive iodine absorbents by RASA Industries Ltd [1, 9, 15]. For the AgR, the main designed function is based on its new zeolite type with which organic iodide retention is high whereas the catalytic effect for hydrogen recombination has been minimized. Hence, knowing its H_2 recombination efficiency is an important first step in ensuring its performance during an accident. For the AgX zeolite, in addition to having high iodine retention performance, it has been shown to be promising for H_2 recombination [9, 15]. In this work, it is being investigated for its H_2 recombination capability under different conditions.

2. IMPROVEMENTS OF FCVS REGARDING CONTAINMENT INTEGRITY IN JAPAN

In the event of a severe accident, in a PWR where the containment atmosphere is air, it may be necessary to reduce hydrogen concentration in the containment atmosphere to prevent formation of a combustible gas mixture. For this purpose, a PARs (passive autocatalytic recombiner) has been installed in the containment vessels of PWRs. In these PARs, noble metal catalysts such as platinum and palladium are coated on the surface of stainless-steel plates to promote catalytic reactions. As an alternative or in addition to PARs, in this work we investigate hydrogen catalytic activity of Ag-zeolites. A conceptual diagram of the advanced

FCVS using an Ag-zeolite as a pre-stage for removal of hydrogen is shown in Figure 3 and an example of the possible arrangement of filters in the FCVS vessel is shown in Figure 4.

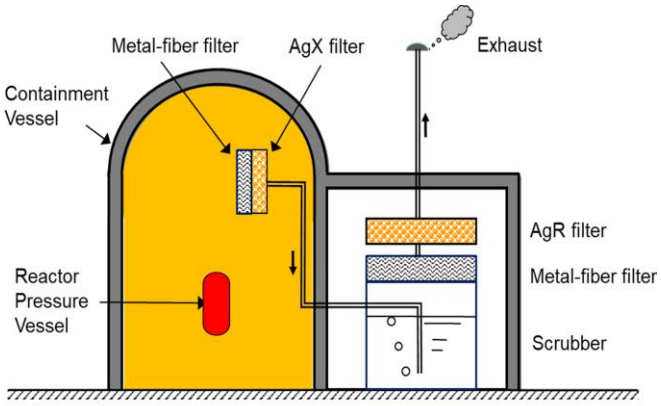

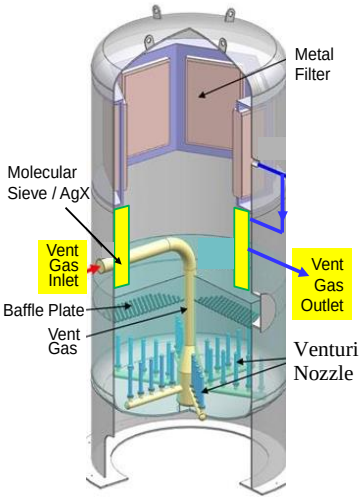

Figure 3. Conceptional schematic of advanced FCVS [9]. **Figure 4. Filter layout in FCVS [1].**

The zeolites are: (a) AgX, which has high iodine (including organic iodine) adsorption performance while reducing hydrogen concentration due to hydrogen catalytic reaction in the containment vessel in the first stage of FCVS, and (b) AgR, which has high iodine (including organic iodine) adsorption performance with very low reaction rate of the catalytic hydrogen reaction in the iodine filter in the second stage. The catalytic and catalytic suppression effects on hydrogen, the temperature of the silver zeolite during the reaction, and the adsorption properties of organic iodine have been measured and characterized using steam and hydrogen concentration as parameters already and exist as shown in Figure 5 and Figure 6. Adsorption efficiencies of CH_3I is shown Tables I and II [9, 15].

Figures 5 and 6 shows the dependence of AgX and AgR temperatures on gas flow time for adsorption behavior at FCVS start venting conditions, simulating PWR.

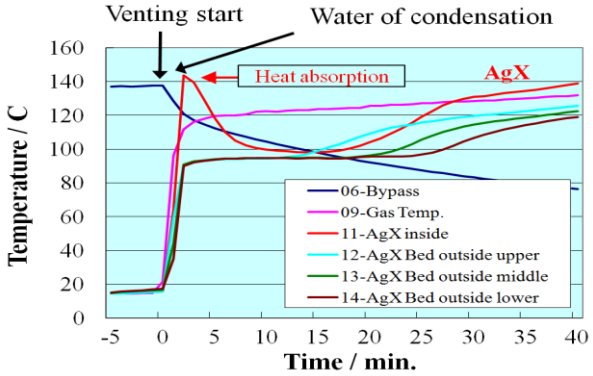

Figure 5. Adsorption test of AgX at initial venting stage: Effectiveness to FCVS (PWR condition).

Table I Adsorption efficiencies of CH_3I on AgX

Time (min.)	Gas composition (Vol. %)			Adsorption efficiency (%)
	H_2	Air	Steam	
0 - 3	2.4	19.0	78.6	99.5
3 - 6	2.4	19.0	78.6	99.3
6 - 9	2.4	19.0	78.6	99.5
15 - 18	2.0	17.0	81.0	> 99.8 (Detection limit)
35 - 38	2.0	16.0	82.0	> 99.8 (Detection limit)

*Temperature of input gas mixtures was fixed at 150°C.
Residence time was between 0.20 and 0.24 second.
The evaluations were performed by Rasa Industries, Ltd.

Figure 6 shows the stable high adsorption efficiency in 10 $_{vol.}$% hydrogen atmosphere. Table II shows adsorption efficiencies of CH_3I on AgR over different periods and gas compositions. Temperature of input

gas mixtures was 120°C, residence time was 0.15 second, and DPD was 37 K. These evaluations were done by Rasa Industries, Ltd [9, 15].

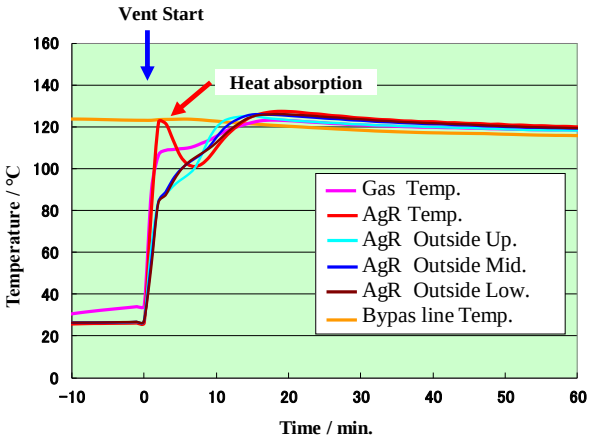

Figure 6. Adsorption test of AgR at initial venting stage: Effectiveness to FCVS (PWR condition).

Table II Adsorption efficiencies of CH_3I on AgR over different periods and gas compositions.

Time (min.)	AgR temperature (°C)	Gas composition (Vol%)	Adsorption efficiency* (%)
0-2	26-122	Steam: 53 % Air: 24 % **H_2: 10 %** N_2: 13 %	99.9
7-9	101-105		> 99.9
15-17	126		> 99.9
30-32	124		> 99.9
60-62	120		> 99.9

3. EXPERIMENTAL AND METHODS AT PSI

This paper aims to determine the recombination efficiency of H_2 (used: 1 $_{vol.}$% and 4 $_{vol.}$%) using the zeolites AgR and AgX under conditions relevant for the FCVS in the case of a nuclear accident. This to show the AgR capability in the FCVS and for the AgX, the outcome is intended as a starting point for its usage in the containment. The two primary conditions used were oxidizing (air) and inert (N_2). As steam is expected to be present under varying concentrations in the containment and in the vent gas depending on the accident progression and FCVS actuation time, two different steam fractions were used, 20 $_{vol.}$% and 90 $_{vol.}$% Moreover, a consistent inlet temperature (150 °C) was chosen and a set at slight lower value for safety reasons, than assessed in literature [15]. For each experimental condition, only one replica was carried out. Two primary methods were employed to monitor the experiments, micro gas chromatography to measure the H_2 content of the exhaust gas, and thermocouples for temperature measurement at various locations along the reactor vessel.

The experiments were performed in a catalytic reactor mounted inside a pressure vessel at PSI (more details of the pressure vessel can be found elsewhere [16]). The test rig consisted of four parts: an initial conical mixing section (L: 240 mm), the main mixing section (Ø: 36 mm, L: 60 mm) containing inert ceramic spheres (Ø: 4 mm), the cylindrical reactor (Ø: 36 mm, L: 100 mm), and the exhaust section (Ø: 36 mm, L: 190 mm). Additionally, fine steel grids (0.5x0.5 mm^2 open mesh size) were located at both ends of the reactor chamber. Moreover, several thermocouples (TC, all K-type) were used to monitor the temperature along the reactor. Of these, the TC located at the end of the main mixing section (TC-3 in Figure 7) was used to control the desired temperature of the experiment. The pressure in all experiments was 1.1 bar. A schematic overview of the reactor is shown in Figure 7 and the schematics of the whole test rig are depicted in Figure 8.

In the upstream conical mixing section, three different flows could be mixed. These flows comprised the main experimental gas, H_2/dilution, and steam. The main gas (either 16 $_{vol.}$%, 74 $_{vol.}$%, 96 $_{vol.}$%, or 98 $_{vol.}$%) was either air (compressed) or N_2 (in-house gas, reported > 99 %) and the volumetric flow was regulated via a mass flow controller (MFC, Bronkhorst F-202AC-Fac-33-V). The H_2 and/or dilution gases were mixed before injection into the conical section (see Figure 7). The H_2 flow (Pangas, 99.995 %) was controlled via an MFC (Brooks, SLA 5859 S1) and the dilution gas (N_2, in-house gas, reported > 99 %) via an MFC (Brooks 5853S). The resulting premixtures comprised either 1 $_{vol.}$% or 4 $_{vol.}$% of H_2. In the experiments involving steam, a steam generator (Cellcraft E-Series) was used to produce the steam from de-ionized water at the desired amounts (either 20 $_{vol.}$% or 90 $_{vol.}$%). In all experiments, the residence time (100 ms) and the temperature (150°C) at the start of the catalyst (TC-3 in Figure 7) were fixed to be representative of venting at containment design pressure. The residence time was determined based on earlier tests which were carried out to measure iodine retention in the Ag-zeolites investigated in this work. The corresponding percentages of each gas component and consequently the operating conditions are summarized in Table III.

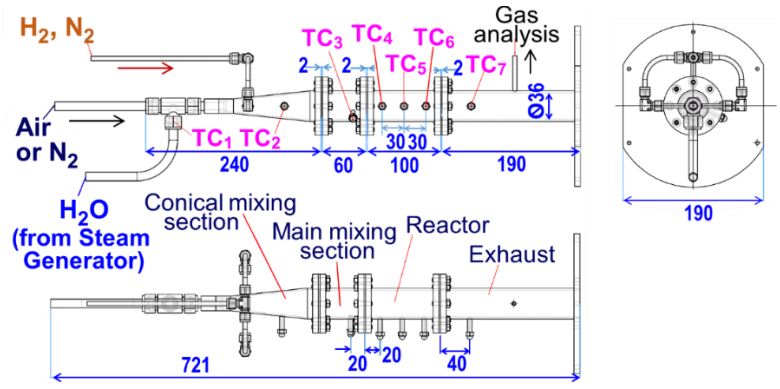

Figure 7. Schematics of the reactor assembly (mm).

Table III. Main parameters of each experiment

Experiment	Main Gas [%vol.]	Hydrogen [%vol.]	Steam [%vol.]
AgR-Ref	96 (Air)	4	-
AgR-1	99 (Air)	1	-
AgR-2	76 (Air)	4	20
AgR-3	6 (Air)	4	90
AgR-4	96 (N_2)	4	-
AgX-1	96 (Air)	2.5	-
AgX-2	92 (Air)	4	20
AgX-3	6 (Air)	4	90

The zeolites (Types: AgR and AgX) used during the experiments were supplied by RASA Industries Ltd. and for each experiment a batch of fresh zeolite was always used. The basic specifications of the zeolites are shown in Table IV. The amount used was always at a level that ensured a full reactor volume. To improve the packing of the zeolite, the side of the reactor was carefully tapped, allowing a better settling of the zeolite in the reactor volume.

Table IV. Specification of the AgR and AgX zeolite

Property	AgR	AgX
Shape	Cylindrical	Spherical
Dimensions (mm)	Ø: 1.1, L: 3.0	Ø: 1.5
Bulk density (g/ml)	1.0	1.2
Silver Content (wt. %)	11	39
Color	Beige	Beige

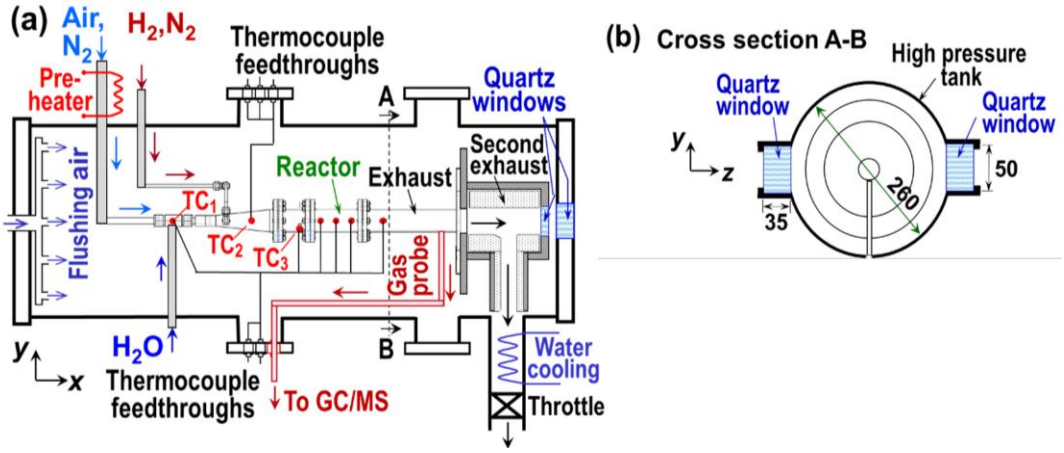

Figure 8. Schematic of the test rig: (a) side view, (b) cross-flow cut (mm).

No specific treatment was carried out before the experiments. However, the system had to be heated to the desired temperature (150°C) at the inlet of the catalyst before injecting the H_2. This heating was done via the preheated main gas, without H_2 being injected and flushed through the zeolite. Moreover, with the highest level of steam, this procedure was not possible, as the electric heater for the main gas could not be used (too low gas flow through it). A different approach was then adopted, where the carrier gas was first used to heat the system. Once the desired inlet temperature was reached and remained stable, steam was injected, the main gas heater was gradually turned off, and the main gas flow was adjusted to the appropriate value. Subsequently, H_2 was injected. If the injection resulted in recombination and hence to an inlet temperature rise, this was compensated by reducing the preheat temperature of the main gas or by lowering the steam being injected. This "pretreatment" was expected to have minimal impact on the results as these were acquired at steady-state conditions. At the exhaust of the vessel, a sampling port was located. This sampling port was used for the dry exhaust gas analysis and was connected directly to the analytical equipment. Hence, the experiments involving steam required a condenser (in-house build) and, in some cases, a dilution step (N_2, 99.95 %) in-between. The latter was controlled by an MFC and set to a constant value. The sampled gas flowrate was in all tests approximately the same.

The main analyzing tool was a micro gas chromatograph (micro-GC, Varian CP 4900 Quad) equipped with four modules of two types, (1) molecular sieve column with a thermal conductivity probe and (2) the PoraPlot U column. The measurements from the first column type were used, as this column was capable of measuring the volumetric percentage of H_2 in the analyzed gas. For it, argon carrier gas was used and the micro-GC was operated isothermally (100ºC). For the calibration of the micro-GC, several gases were used. Their concentrations were chosen to span the possible experimental values. For H_2, the chosen calibration data points were 989.4 ppmv (Pangas), 1.01 $_{vol.}$% (Pangas), and 6.02 $_{vol.}$% (Pangas), which provided the whole range. Additionally, a zero value (compressed air) was also used. The carrier gas was N_2, so as to best mimic the experimental gas. Two calibrations were done, one before the experiments and one after. No significant difference between these calibrations was observed.

As the main goal was to assess the recombined amount of H_2, a comparative approach was used. Essentially, the known amount of H_2 (measured when no zeolite was present; with only H_2) was compared to what was measured during the different experiments. As aforementioned, when steam was used, it had to be condensed before the micro-GC. For the low-content steam experiments, the removed steam was not compensated volumetrically via N_2. Instead, the gas flow was measured directly and then the data was adjusted according to the removed steam. For the high-content steam experiments, this was not possible as the H_2 was well outside the calibration curve. Thus, the dilution step was used. To correct the data, the amount of sample flow needed to get the correct value for the micro-GC was determined beforehand. All

sample values were corrected accordingly. For all the calibration points and experimental data, an average of ten data points were acquired.

For all experiments, the same approach was used and is as follows:

1. Disassemble the facility and remove the reactor vessel to add the zeolite.
2. Assembling the facility and verifying the functionality of all TCs.
3. Heating of the system via the experimental gas.
    a. If steam was included, it was injected at the desired temperature and then the carrier gas electric heater was gradually turned off. The flow of the latter was adjusted to the appropriate value.
4. Hydrogen was injected.
5. The temperature of the TC_3 was monitored.
    a. Either the heater of the carrier gas or the steam amount was adjusted to maintain the desired temperature.
6. Once the temperature was stable, the system was assumed at steady-state.
7. The measurements were acquired during this stage for the H_2-concentrations, and temperatures.
8. Once 10 values from the micro-GC had been obtained (in 5-minute long intervals), the system was shut off and let to cool down under a flow. This flow consisted of only the experimental gas at a volumetric flow much greater than the one used during the experiment.
    a. If steam was used, it was turned off.
    b. H_2 was turned off.
9. When steam was used, the system was always allowed to dry out overnight, as considerable amounts of water accumulated in the system.

4.RESULTS AND DISCUSSION

In this work, the main focus has been on the AgR zeolite performance in the presence of steam and air, with some additional experiments in nitrogen and with the AgX zeolite. The main experimental data, including the recombination rate, come from the micro-GC and the temperature measurements. These results are shown in Table V and Figure 9.

The uncertainties of these experiments are not provided for each experiment. However, they are assumed based on a conservative approached that they are for the dry conditions to be in the range of a few percentage units, for low-steam conditions between 5-10 $_{unit}$%, and finally, and for the high-steam level experiments between 10-15 %$_{units}$. The steam experiments have higher uncertainties due to the steam generator itself and the N_2 dilution step.

The results from the experiments with AgR in only dry air without steam and 4 $_{vol.}$%. H_2 as reference (AgR-Ref) variance in H_2 content (AgR-1), when steam was used (AgR-2, AgR-3), and under dry N_2 (AgR-4) showed clearly that the recombination of H_2 in AgR was low, if any. For the reference case in dry air, the recombination was 3 % (AgR-Ref). When changing the H_2 amount injected from 4 $_{vol.}$% to 1 $_{vol.}$%, the H_2 recombination reached 5.6 % (AgR-1). When steam was added (AgR-2, AgR-3), regardless of the steam level, 0 % recombination were observed. In the cases with N_2, 3 % of the hydrogen was removed (as no oxygen was present, recombination would be unlikely). Finally, only in the two cases with dry air was any temperature increase detectable compared to before the H_2-injection, while for all other cases (i.e., AgR-2, AgR-3, AgR-4) no temperature rise could be detected.

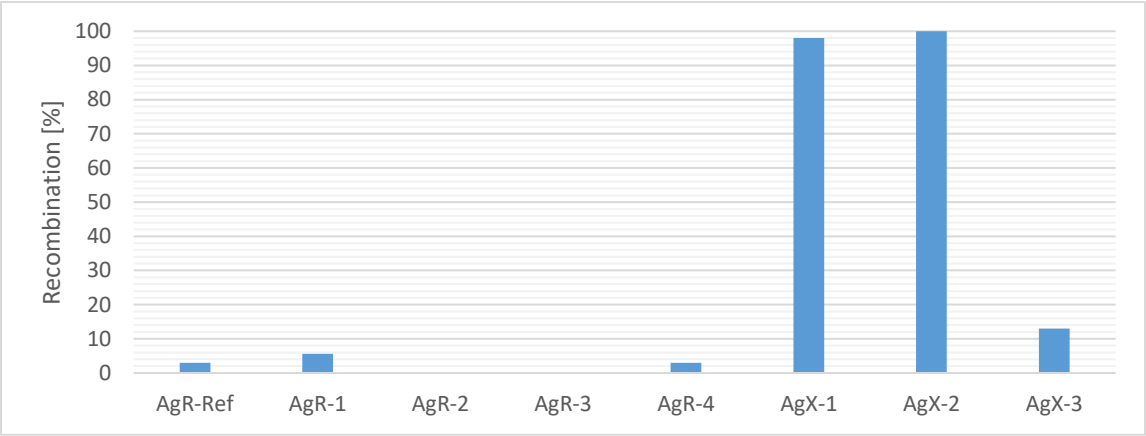

Figure 9. A graphical representation of the experimental outcome from the micro-GC.

In these experiments, it has been demonstrated that the recombination rate of hydrogen in the AgR is very low. In most of the tests, a few % recombination was measured but this was mainly within the uncertainty of the measurements, especially in the tests in which steam was used. Compared to the AgX, it was clearly shown that AgR does not promote hydrogen recombination under the test conditions used in this investigation. This was expected based on the manufacturer's specifications. Lowering the H_2 level in the tests carried out in dry air showed an increase in the H_2 recombination. However, this is quite unexpected as a higher hydrogen concentration would be expected to increase the recombination rate, and the observed result may be within the experimental uncertainty. Additionally, the H_2 recombination was lowered when steam was part of the gas mixture, although the H_2 recombination rate was already low even when no steam was present. Still, this was reasonable as steam is expected to impede H_2 recombination. Additionally, as expected, using N_2 as the experimental gas showed no significant recombination due to the lack of any oxidizer. Despite the absence of an oxidizer, the results showed some removal of H_2. These results might

have been within the uncertainty of the experiments and further tests are needed to confirm the potential removal of hydrogen with only dry nitrogen and hydrogen in the feed gas.

The next stage was to investigate regarding the AgX. For the dry air experiment (AgX-1), the hydrogen recombination reached 98 %. When a low level of steam was used (20 $_{vol.}$%), the H_2 recombination did not change appreciably and potentially increased to 100 % (AgX-2). Increasing the steam level to the highest amount (90 $_{vol.}$%), resulted in a decrease of the H_2 recombination to 13 %. In the dry (AgX-1) and low steam level (AgX-2) experiments, the temperature of the catalyst increased to around 390°C and 480°C respectively, see Table 3. For the high steam level experiment (AgX-3), no noticeable temperature increase was observed.

When changing the zeolite from AgR to AgX, it was found that the H_2 recombination efficiency of AgX was considerably higher than that of AgR, as expected from its higher silver content. Furthermore, the results also show that AgX can reliably and efficiently recombine H_2 even in the presence of low levels of steam in the air. When much higher levels of steam was used, the H_2 recombination was reduced. Likely, due to steam being the mains constitute of the gas phase. Consequently, the oxygen needed for the recombination to occur is significantly reduced. However, it is worth noting that potentially a small amount of H_2 recombination still occurred Considering that the amount of steam was increased to 90%, this would further demonstrates the reliability of AgX in vapor.

When comparing the two zeolites, it is clear that a difference exists in the recombination capability when air was investigated. Observing the main difference between the two zeolites, the silver content, the higher recombination observed for the AgX is reasonable. As higher silver content would enable more hydrogen recombination if enough oxygen is available. This silver content would also explain that the AgX was capable of recombining hydrogen even when low amounts of steam was present.

Table V. Overview of the micro-GC and temperature data for the experiments. Locations of the temperature points: TC_4 – beginning of reactor, TC_5 – middle of the reactor, TC_6 – end of the reactor (see also Figure 7). All experiments with 4 $\%_{vol.}$ H_2 except for AgR-1 and AgX-1, which had 1 and 2.5 $\%_{vol.}$ H_2 respectively.

Experiment	Recombined H_2 [%]	TC_4 [°C]	TC_5 [°C]	TC_6 [°C]	Main parameters
AgR-Ref	3	149	153	173	Dry air
AgR-1	5.6	146	145	144	Dry air, 1 % H_2
AgR-2	0	142	140	136	Low steam air
AgR-3	0	142	135	131	High steam air
AgR-4	0	143	140	136	Dry nitrogen
AgX-1	98	221	389	385	Dry air, 2.5 % H_2
AgX-2	100	484	479	467	Low steam air
AgX-3	13	146	141	143	High steam air

5. CONCLUSIONS

In this work, both the AgR and the AgX have been shown to perform according to the manufacturer's specifications. That is, the AgR has been shown, as designed, to not significantly recombine H_2 under the conditions investigated in this work. Neither in air nor nitrogen was any large amount of H_2 removed even under the reference conditions. Additionally, the addition of steam did not alter the results in any way. The low recombination rate of the AgR shows that the potential of application of AgR in an FCVS for organic iodide removal is feasible.

AgX was seen to efficiently recombine H_2 in the air experiments. Moreover, the addition of a low level of steam had little effect on the recombination capability of the AgX. Moving to a very high steam level in air did noticeably decrease the H_2 recombination. Yet, the fact that the AgX could potentially still recombine H_2 in such high steam level conditions shows its resilience toward steam. Therefore, the combination of this work and those previous carried out on the AgX iodine retention [14, 15] shows that the AgX is a promising candidate for simultaneous hydrogen removal and iodine retention. Hence, further research will be carried out where both the hydrogen and either iodine or organic iodide are included under representative conditions to further test the dual functionality of the AgX. Furthermore, conditions representative of the containment are also planned to demonstrate clearly the idea shown in Figure 5.

The next stage, which is currently underway at PSI, is to investigate the two zeolites under conditions even closer to accident sequence conditions representative of FCVS during severe accidents. The main difference in the test conditions to the current investigation will be the addition of iodine species to the gas phase and higher pressures to investigate the behavior of the zeolites during simultaneous feed of iodine species and hydrogen.

ACKNOWLEDGMENTS

The work was performed under a research contract in cooperation with RASA Industries Ltd. and the Japanese Ministry of Economy, Trade and Industry (METI). Their financial support and good discussions with the RASA team is gratefully acknowledged. We thank Dr. Julian Indlekofer for the help in the micro-GC measurements.

REFERENCES

1. T. Narabayashi and JSME FCVS WG members, “Filter venting System”, ERC Publishing, (2018).
2. E. Cardis, A. Kesminiene, V. Ivanov, I. Malakhova, Y. Shibata, V. Khrouch, V. Drozdovitch, E. Maceika, I. Zvonova, O. Vlassov, A. Bouville, G. Goulko, M. Hoshi, A. Abrosimov, J. Anoshko, L. Astakhova, S. Chekin, E. Demidchik, R. Galanti, M. Ito, E. Korobova, E. Lushnikov, M. Maksioutov, V. Masyakin, Al. Nerovnia, V. Parshin, E. Parshkov, N. Piliptsevich, A. Pinchera, S. Polyakov, N. Shabeka, E. Suonio, V. Tenet, A. Tsyb, S. Yamashita, D. Williams. “Risk of Thyroid Cancer After Exposure to 131 I in Childhood”, *Journal of the National Cancer Institute*, Vol 97 (10) pp.724–732 (2005) https://doi.org/10.1093/jnci/dji129
3. M. Bal, T.T. Reddy, B.C. Meikap, Performance evaluation of venturi scrubber for the removal of iodine in filtered containment venting system, Chemical Engineering Research and Design, Vol. 138, 2018, pp. 158-167, ISSN 0263-8762, https://doi.org/10.1016/j.cherd.2018.08.019.
4. Scientific Annex B: Levels and effects of radiation exposure due to the accident at the Fukushima Daiichi Nuclear Power Station: Implication of information published since the UNSCEAR 2013 Report, UNSCEAR 2020 Report (2020).
5. "Physical Constants of Organic Compounds," in CRC Handbook of Chemistry and Physics, 102nd Edition (Internet Version 2021), John R. Rumble, ed., CRC Press/Taylor & Francis, Boca Raton, FL.
6. Severe Accident Mitigation through Improvements in Filtered Containment Vent Systems and Containment Cooling Strategies for Water Cooled Reactors, IAEA-TECDOC-1812 (2015).
7. H.Oh. Chang., S.K. Eung, C.N. Hee, Z.C. Nam. “Experimental Validation of Stratified Flow Phenomena, Graphite Oxidation, and Mitigation Strategies of Air Ingress Accidents”. United States: N. p.. Web. doi:10.2172/944881. (2008)
8. J. Wang, T. Kobayashi and K. Endo, Adsorption Characteristics of Radioactive Organic Iodine on AgX, NUTHOS-11, Korea, (2016).
9. S. Kobayashi, T. Kobayashi and K. Endo, “AgX and AgR for Organic Iodine Removal”, Top Safe, Vienna, Austria, (2017).
10. Installation of corium shield at Kashiwazaki Kariwa NPS Unit 7, TEPCO HD (2016). https://www.tepco.co.jp/niigata_hq/data/publication/backnumber/pdf/2016/28060902.pdf
11. B. Clement, L. Cantrel, G. Ducros, F. Funke, L. Herranz, A. Rydl, G. Weber, C. Wren. State of the art report on iodine chemistry (NEA-CSNI-R--2007-01). Nuclear Energy Agency of the OECD (2007)
12. D. Jacquemain, S. Guentay, S. Basu, M. Sonnenkalb, L. Lebel, J. Ball, H.J. Allelein, B.L. Martinez, B. Eckardt, N. Losch, L. Ammirabile, D. Gryffroy, L. Sallus, A. Kroes, T. Rensonnet, A. Anden, S. Gyepi-Garbrah, A. Viktorov, J. Duspiva, T. Routamo, S. Guieu, A. Hotta, H. Nakamura, J.H. Song, K.S. Ha, C. Filio, M.V. Kuznetsov, L. Kubisova, T. Nemec, W. Frid, D. Loy, D. Pellini, T. Zieger, L.H. Puebla, A, Amri, M. Kissane. OECD/NEA/CSNI “Status Report on Filtered Containment Venting” Nuclear Energy Agency of the OECD (NEA), NEA-CSNI-R--2014-7, (2014)
13. K. Fernández-Cosials, G. Jiménez, C. Serrano, L. Ibáñez, and Á. Peinado,. "Analysis of Inertization Strategies for the Filtered Containment Venting System in Cofrentes Nuclear Power Plant." *ASME J of Nuclear Rad Sci,* **4**(3): 031016. https://doi.org/10.1115/1.4038595 (2018)
14. O.Y. Golubeva, N.Y. Ternovaya, N.V. Mal'tseva, D. Meyerstein. Catalytic hydrogen oxidation using zeolite rho modified by silver nanoparticles. Glass Physics and Chemistry, **38**(5), pp.455-459. https://doi.org/10.1134/S1087659612050033 (2012)
15. Ph. Dejardin, T. Helman, J. Bulle, J. Dienstbier, L. Oury, L. Sallus, Methodology developed for the definition of the design parameters and associated safety criteria of the Filtered Containment Venting Systems for Belgian NPPs Annals of Nuclear Energy, Vol. 93, pp.58-64 (2016) doi:101016/janucene201512024

16. J. Mantzaras, "Progress in non-intrusive laser-based measurements of gas-phase thermo-scalars and supporting modeling near catalytic interfaces", Prog. Energy Combust. Sci. 70, pp. 169-211 (2019)

PAUL SCHERRER INSTITUT

PSI



Fredrik Espegren :: PostDoc :: Paul Scherrer Institut

Effectiveness of Hydrogen Recombination by AgX and AgR Zeolites

F. Espegren, D. Suckow, T. Lind, J. Mantzaras, J. Theile - Paul Scherrer Institut (Switzerland)
Y. Ishikawa, T. Kobayashi, K. Endo - RASA Industries Ltd. (Japan)
T. Narabayashi - Tokyo Institute of Technology (Japan)
S. Kobayashi - Morimura Bros., Inc. (Japan)

ERMSAR 2022, Karlsruhe, Germany, May 16-19, 2022

Laboratory for

Reactor Physics and Thermal-Hydraulics

PAUL SCHERRER INSTITUT

Outline

Background

Motivation

Experimental

Results and Discussion

Conclusions

Future plan

Background: The Zeolites

The Zeolites

AgX – Hydrogen recombination and iodine retention.

AgR – Organic iodide retention focus, but also iodine retention.
Minimized hydrogen recombination capability.

Planned Application

In FCVS for iodine source term reduction. Moreover, for the AgX, hydrogen management purposes.

Common Features According to the Producer, RASA Ltd.

High performance:

- Under broad operation range, e.g., high temperature, pressure, and relative humidity.
- With condensation of water.
- When hydrogen is present.



Property	AgR	AgX
Shape	Cylindrical	Spherical
Dimensions (mm)	Ø: 1.1, L: 3.0	Ø: 1.5
Bulk density (g/ml)	1.0	1.2
Silver Content (wt. %)	11	39
Color	Beige	Beige

Background: RASA Ltd. Potential Applications

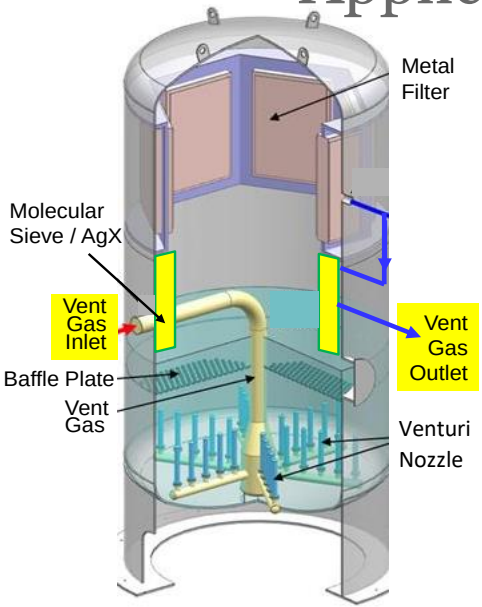

Concept (1)

Single filter stage using AgX,

- Addition to existing FCVS.

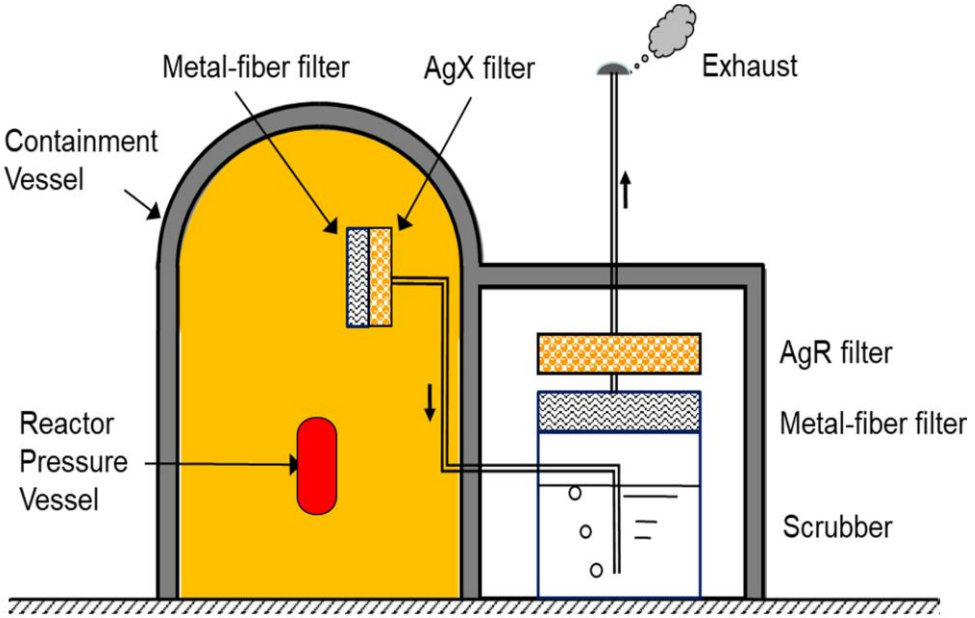

Concept (2)

Dual filter stage using both AgX and AgR zeolite

1. AgX, in the containment for hydrogen recombination and iodine retention.
2. AgR, in the FCVS for iodine retention with the focus on organic iodide.

Motivation

Aims

- Investigate hydrogen removal/recombination by the zeolites AgX and AgR.
- Conditions to be relevant for FCVS.
- To be followed by investigation of the iodine source term reduction. (*future*)

Goals (Current and *future*)

- Hydrogen recombination capability of the AgX and AgR zeolites.
- Stability of the AgX and AgR zeolites
  - under relevant FCVS.
  - under containment conditions. (future)
- The effect of steam at a low and high level.
- The effect of other potential inhibitors. (*future*)
- The iodine and organic iodide retention capacity (*future*)
  - under relevant FCVS.
  - under containment conditions.

Experimental: Facility



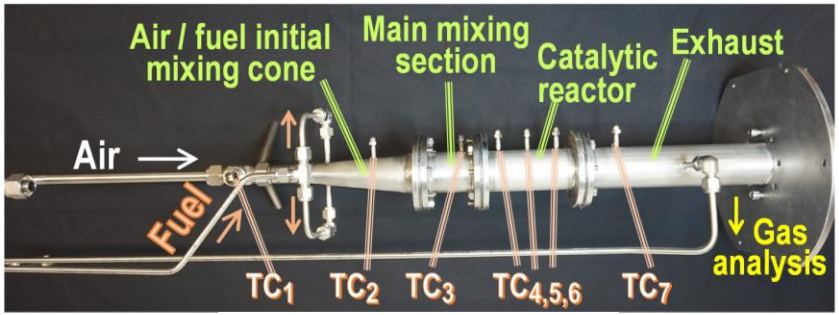

(a) Reactor assembly



(b) Air/H_2 initial mixing conical section

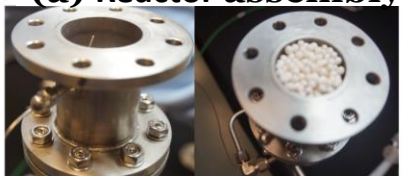

(c) Main mixing section with inert ceramic balls

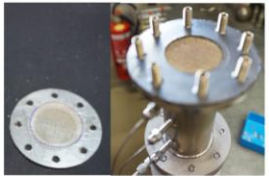

(d) Reactor filled with zeolite particles

Experimental: Details

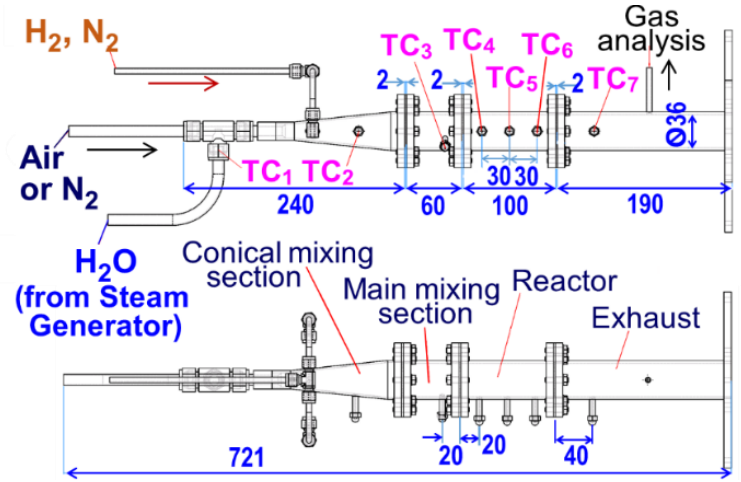

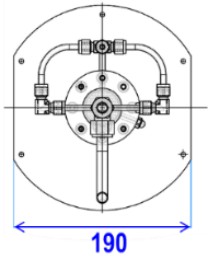

Parameters

Inlet temperature (TC_3)	– 150°C
Residence time	– 100 ms
Experimental gas	– Air or nitrogen
Steam	– 20 $_{vol.}$% or 90 $_{vol.}$%
Hydrogen	– ≈1 $_{vol.}$% or ≈4 $_{vol.}$%
Amounts (approx.)	– 150 g AgX or 110 AgR g
Reactor volume	– 100 cm^3 (Ø: 36 mm, L: 100 mm)
Time at steady-state	– 30 to 60 min (enough to ensure 10 data point at steady state)

Measuring Techniques

Hydrogen content	– Micro-GC (Varian CO 4900 Quad)
Temperature	– Sheathed K-type Thermocouples
Flow control	– Brooks mass flow controllers

Results and Discussion: AgR

Observations: Hydrogen

Lowering the hydrogen

– Slightly higher hydrogen recombination than the reference.

Addition of steam

– Prevented the hydrogen recombination at both levels of steam.

– However, uncertain to what extent steam has an effect. As recombination rate was already low.

Nitrogen

– No hydrogen removal observed.

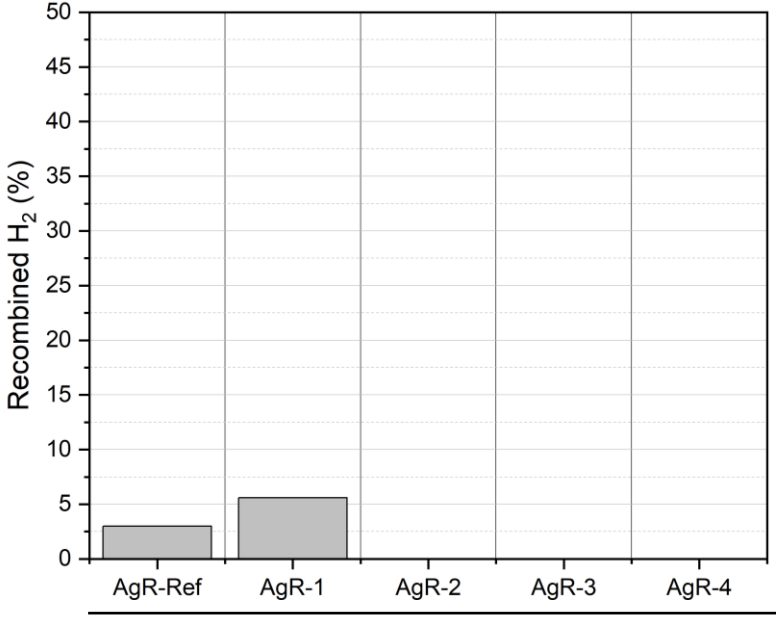

Experiment	Main parameters
AgR-Ref	Dry air, 4 % H_2
AgR-1	Dry air, 1 % H_2
AgR-2	Low steam air (20 $_{vol.}$%)
AgR-3	High steam air (90 $_{vol.}$%)
AgR-4	Dry nitrogen

Results and Discussion: AgR

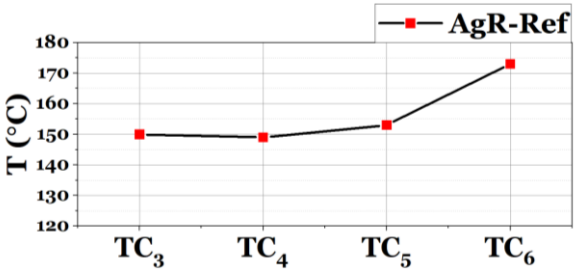

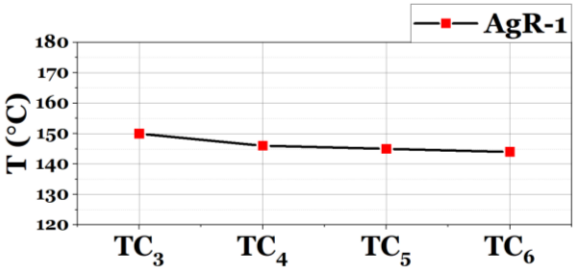

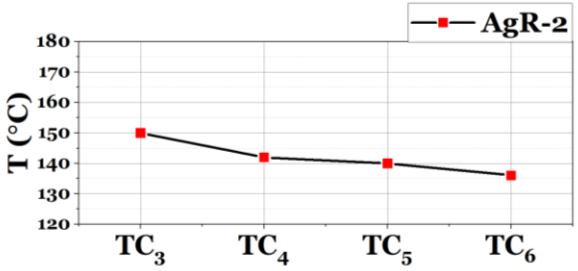

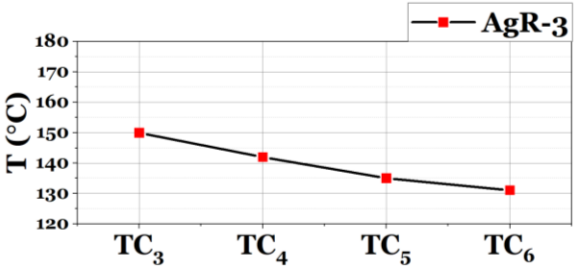

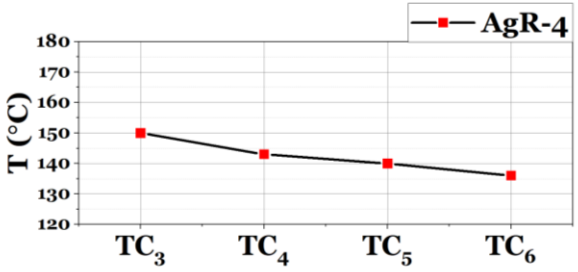

Observations: Temperature

Lowering the hydrogen

– Less temperature increase compared to reference.

Addition of steam

– No significant temperature increase.

Nitrogen

– No significant temperature increase.

Experiment	Main parameters
AgR-Ref	Dry air, 4 % H_2
AgR-1	Dry air, 1 % H_2
AgR-2	Low steam air (20 $_{vol.}$%)
AgR-3	High steam air (90 $_{vol.}$%)
AgR-4	Dry nitrogen

Results and Discussion: AgR

AgR-1

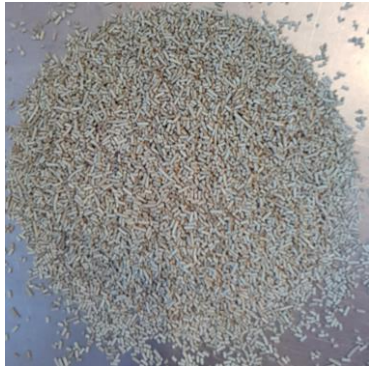

AgR-Ref

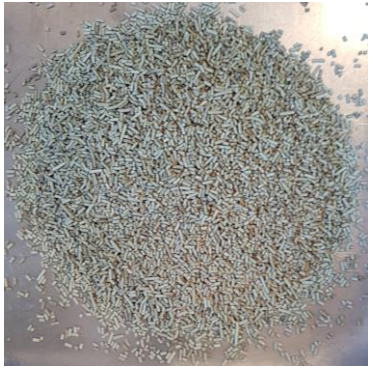

AgR-4



Unused - AgR



Observations: Zeolite

Lowering the hydrogen concentration

– No significant change to the coloration nor location of it.

– No noticeable volume decrease or damage to the zeolite.

Nitrogen atmosphere

– The zeolite turned dark.

– No noticeable volume decrease or damage to the zeolite.

Experiment	Main parameters
AgR-Ref	Dry air, 4 % H_2
AgR-1	Dry air, 1 % H_2
AgR-2	Low steam air (20 $_{vol.}$%)
AgR-3	High steam air (90 $_{vol.}$%)
AgR-4	Dry nitrogen

Results and Discussion: AgR

AgR-Ref



AgR-2



AgR-3



Unused - AgR



Observations: Zeolite

Low steam level

– Slight change in the color, darker beige and brown parts.

– No noticeable volume decrease or damage to the zeolite.

High steam level

– Considerable color change to dark grey. Some part still slightly beige.

– No noticeable volume decrease or damage to the zeolite.

Experiment	Main parameters
AgR-Ref	Dry air, 4 % H_2
AgR-1	Dry air, 1 % H_2
AgR-2	Low steam air (20 $_{vol.}$%)
AgR-3	High steam air (90 $_{vol.}$%)
AgR-4	Dry nitrogen

Results and Discussion: AgX

Observations: Hydrogen

Compared to AgR

– Almost complete hydrogen recombination.

Low level of steam

– No noticeable effect on the recombination rate. Higher temperature, due to higher amount of hydrogen.

High level of steam

– Considerable decrease in the recombination rate. Yet, some recombination did occur. More work needed to confirm this.

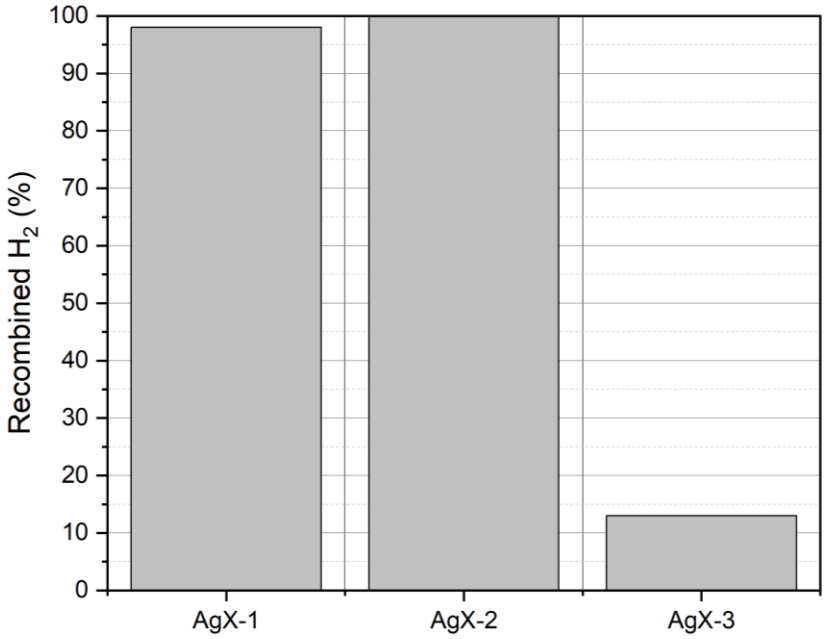

Experiment	Main parameters
AgX-1	Dry air, 2.5 % H_2
AgX-2	Low steam air (20 $_{vol.}$%)
AgX-3	High steam air (90 $_{vol.}$%)

Results and Discussion: AgX

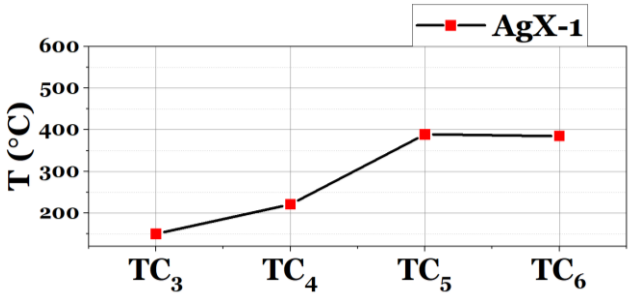

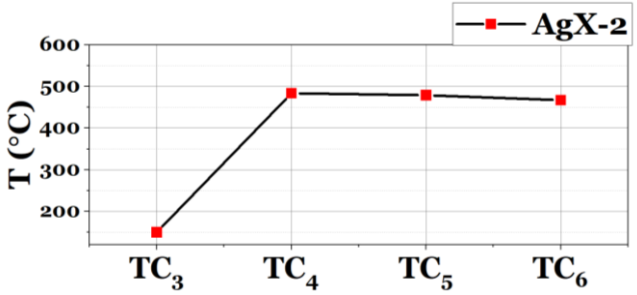

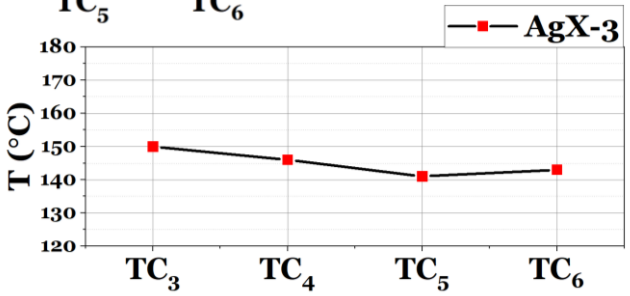

Observations: Temperature

2.5 % H_2

– Large temperature increase.

Using low level steam

– Considerable temperature increase.

Using high level steam

– Little temperature increase, if any

Experiment	Main parameters
AgX-1	Dry air, 2.5 % H_2
AgX-2	Low steam air (20 $_{vol.}$%)
AgX-3	High steam air (90 $_{vol.}$%)

Results and Discussion: AgX

AgX-1

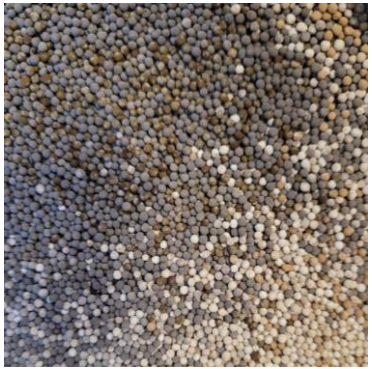

AgX-2



AgX-3



Unused - AgX



Observations: Zeolite

Compared to AgR

– Considerable changes to the coloration, but non-uniformly.

– Minor volume decrease.

Low level of steam

– Similar coloration as the dry experiment, but more variation.

– Minor volume decrease.

High level of steam

– Uniform color of grey, similar to the AgR-4 (nitrogen atmosphere) experiment.

Experiment	Main parameters
AgX-1	Dry air, 2.5 % H_2
AgX-2	Low steam air (20 $_{vol.}$%)
AgX-3	High steam air (90 $_{vol.}$%)

Conclusions

AgR

- No significant hydrogen recombination.
- No conclusion on the effect of steam with either air or nitrogen.
- No sign of significant deterioration during the experimental conditions investigated.
- Considerable color change due to steam.

AgX

- Almost complete hydrogen recombination under conditions with air.
- Low amount of steam had minor effect on the recombination of hydrogen at the level investigated.
- High amount of steam decreased the recombination of hydrogen considerably.

AgX compared to AgR

- AgX considerably higher hydrogen recombination level.
- Similar resulting color during the low steam experiment were observed.

Future Plan

Planned future work

- Scale-up of the reactor (new facility)
- Focus on iodine source term retention
  - Iodine
  - Organic iodide (CH_3I)
- Other containment gases (possibilities: CO, CO_2, N_2O, NO_2)
- The effect of aerosols on zeolite performance
- Parameter changes
  - More FCVS and containment conditions
  - Residence time
  - Inlet temperature
  - Steam content

PAUL SCHERRER INSTITUT

Wir schaffen Wissen – heute für morgen

Thank you for your attention !

Acknowledgement:

The work was performed under a research contract with RASA Industries Ltd. and the Japanese Ministry of Economy, Trade and Industry (METI).

The financial support and discussions with RASA is gratefully acknowledged.



The 10th European Review Meeting on Severe Accidents Research

Severe Accident Research Eleven Years after the Fukushima Accident

May 16-19, 2022, Karlsruhe, Germany

Technical Session 6-2: Severe Accident Modeling and Code Development

Chairs: L. Chailan (IRSN), F. Rocchi (ENEA)

ID320	**Sensitivity Analyses on MELCOR Accumulators Modelling** G. Agnello (ENEA)	**Paper** **Presentation**
ID316	**Experiment Investigation of QUENCH-20 and Simulation with AC2/ATHLET-CD** T. Hollands (GRS)	**Paper** **Presentation**
ID335	**Detection of radionuclides in northern Europe in June 2020: investigations on possible source term location and origin** J.J. Ingremeau (IRSN)	**Paper** **Presentation**
ID293	**RCCS-2021 OECD specialist workshop on "Reactor core and containment cooling systems – long term management and reliability workshop" - Overview on the main outcomes** A. Bentaib (IRSN)	**Paper** **Presentation**

10TH CONFERENCE ON SEVERE ACCIDENTS RESEARCH
May 16-19, 2022 – Karlsruhe, Germany
ERMSAR 2022

SENSITIVITY ANALYSES ON MELCOR ACCUMULATORS MODELLING

G. Agnello, P.A. Di Maio
Università degli Studi di Palermo
Dipartimento di Ingegneria, Viale delle Scienze, Ed. 6, 90128, Palermo, Italy.
giuseppe.agnello04@unipa.it, pietroalessandro.dimaio@unipa.it

J. C. de la Rosa Blul
DG Joint Research Centre – JRC Directorate G – Nuclear Safety & Security
Unit G1.4 Reactor Safety & Emergency Preparedness Westerduinweg 3 1755 LE Petten, The Netherlands
juan-carlos.de-la-rosa-blul@ec.europa.eu

F. Mascari
ENEA
FSN-SICNUC, Via Martiri di Monte Sole 4, 40129, Bologna, Italy.
fulvio.mascari@enea.it

ABSTRACT

In the framework of the Deterministic Safety Analyses (DSAs) of Nuclear Power Plants (NPPs), an unmitigated Small Break Loss Of Coolant Accident (SBLOCA) has been simulated using the Severe Accident (SA) code MELCOR 2.2, developed by Sandia National Laboratories (SNL) for the United States Nuclear Regulatory Commission (USNRC), able to simulate the thermal-hydraulic phenomena in steady-state and transient condition and the main SA phenomena characterizing the Light Water Reactors (LWRs). The postulated transient is initiated by a 2-inch break on the Cold Leg (CL) of a generic PWR-900 MWe three-loops western type. The initiator event has been coupled with the loss of offsite Alternating Current (AC) power and the failure of all diesel generators, considering the accumulators activation the only accident mitigation strategy. To give some insights about the accumulators modelling capabilities of the code and, therefore, analysing the difference in calculations results related to the user effect, a sensitivity analysis on the accumulators modelling has been carried out. The accumulators have been modelled using Control Volumes (CVs) (MELCOR CVH package) for each loop with control functions to set the accumulator opening/closing or the dedicated MELCOR accumulator package (ACC package) that permits to model the accumulators discharge settings the main accumulators' proprieties (e.g. accumulators and surge line geometry, expansion gas model, etc.). The in-vessel phase has been analysed and the effect of the accumulator modelling on the main thermal-hydraulic (e.g. primary system depressurization, accumulator discharge, core heat-up, etc.) and core degradation phenomena (e.g. hydrogen generation, core relocation into the Lower Plenum (LP), etc.) have been investigated analysing the related figure of merits (e.g. cladding temperature, cumulative hydrogen mass produced, etc.).

KEYWORDS
MELCOR, SBLOCA, SEVERE ACCIDENT, ACCUMULATORS, USER-EFFECT

1. INTRODUCTION

Since the last decades, the interest of international nuclear scientific research community involved in Severe Accident (SA) research is focused on the development of new strategies to prevent core loss of integrity, and mitigate possible releases of Fission Products (FPs) to the environment during possible accidental sequences in the view to develop and consolidate Severe Accident Management (SAM) measures. In the framework of Deterministic Safety Analyses (DSAs) of Nuclear Power Plants (NPPs), state-of-art integrated SA codes (e.g. ASTEC, MELCOR., MAAP, etc.) have been developed to simulate the main phenomena taking place during a SA sequence related both to the in-vessel (thermal-hydraulics phase of the transient, core degradation and relocation in the Lower Plenum (LP) and Lower Head (LH) failure) and ex-vessel phase (release of FPs to the containment, Molten Core-Concrete Interaction -MCCI-, etc.). These simulation codes capture the theoretical and experimental knowledge produced in the last four decades. Several SA experimental activities have been conducted [1-5] in order to produce valuable "assessment databases" [6] which permits to validate the models and correlations implemented in the codes.

Despite 30 years of research, there are still uncertainties in the phenomena related to SAs, partly because large scale experiments with prototypical materials are extremely difficult to execute. In addition, transferring the experimental results to the reactor scale is not straightforward [7]. International activities have been organized and are still in progress in order to reduce epistemic uncertainties in SA as the EU-CESAM project [8] and the EU-IVMR project [9,10]. Code-to-code benchmark activities [11,12], involving code developers, have been developed to identify modelling differences affecting the codes and code-to-code involving code users could characterize the user effect on code results prediction [13,14]. The user effect, in fact, could affect the code results [15,16]. Considering the several complex and different phenomena/processes taking place during a SA, code-users require a high-level understanding of the phenomena/processes and need to define several modelling parameters in the use of a SA code.

In this view, a sensitivity analysis on the accumulators modelling on the SA code MELCOR 2.2 [17,18] has been carried out. The modeling of the thermal-hydraulic behavior of the accumulators, providing core cooling at a crucial point during a SA sequence, could influence the SA evolution as underlined in previously studies [19-21]. In [19], studies have been conducted to characterize the effect of coolant injection by accumulators along a SBLOCA event in SA conditions due to the failure of the safety injection systems. A code comparison with the ASTEC and MAAP codes [20] highlights the importance of the user choice on accumulator model parameters (e.g. different polytropic transformation of the nitrogen inside the accumulators). Previous studies on an unmitigated SBLOCA with MELCOR in [21] underline that the accumulator injection flow rate and its modelling have a key role, influencing the core steaming rate and the consequent further cladding oxidation and hydrogen generation. Purpose of this activity is to give some insights about the MELCOR code results discrepancies in terms of some Figure of Merits (FOMs) related to a SA sequence (e.g. hydrogen cumulative production, LH failure time, etc.) attributed to the different modelling approaches of these components and to the user effect in selecting parameters related to the accumulators thermal-hydraulic behavior. The analysis consider different choices that a user can do to model accumulators in MELCOR. The analysis has been carried out considering a generic PWR-900 MWe three-loops western type and an unmitigated Small Break Loss Of Coolant Accident (SBLOCA) as postulated SA scenario.

2. TRANSIENT AND SENSITIVITY ANALYSIS CHARACTERISTICS AND HYPOTHESES

2.1. Transient characteristics and hypotheses

The NPP considered in this analysis is a generic PWR-900 MWe three-loops western type and the SA sequence selected for the presented study is an unmitigated SBLOCA [19-21] in which only the accumulators are considered available. The accident initiator event considered is a 2-inch break of the CL of loop 1 where the pressurizer (PRZ) is located. Before the Start of the Transient (SOT), a steady-state analysis in nominal full power conditions has been conducted. In [13] the steady-state reactor main

parameters are shown. The break event is coupled with the loss of offsite Alternating Current (AC) power and the failure of all the diesel generators determining the unavailability of the following systems: primary pressure control systems (heaters and PRZ spry), Chemical and Volume Control Systems (CVCS), Reactor Coolant Pump (RCP) seal injection, Active safety injection systems (High Pressure Injection System, HPIS, and Low Pressure Injection System, LPIS), Motor-Driven Auxiliary Feedwater (MDAFW) system. The following hypotheses are also considered: reactor SCRAM and Steam Generators (SGs) isolation at SOT, independent failure of the Turbine Driven Auxiliary Feedwater (TDAFW) pump, no RCP seals failure, no primary boundary structures thermal induced degradation phenomena, primary and secondary side Steam Relief Valves (SRVs) availability throughout the accident evolution, Safety Valves of Pressure Compensator (SEBIM) manually stuck open when the core exit temperature reaches 650°C. The transient has been simulated considering the in-vessel phase.

2.2. Sensitivity analysis characteristics and hypotheses

The sensitivity analysis has been carried out considering two different accumulators modelling approaches. In the first one, the accumulators have been modelled using one Control Volume Hydrodynamics (CVH) Control Volume (CV) for each single accumulator and by control functions to set the accumulators opening when the (PCS) pressure falls below a specified set-point. The accumulators CVs have been connected with Heat Structures (HSs) to the containment. An additional sensitivity analysis on the CVH modelling has been carried out: a first model considering the total accumulators discharging of water into the PCS (label: CVH ACC -NO ISOL) and a second model with the isolation of the accumulators (label: CVH ACC -ISOL-) when the CL pressure falls below 15 bar [20] have been considered. This sensitivity has been selected in order to investigate the effect of the accumulators isolation on the SA main phenomena.

In the second modelling approach, the accumulators have been modelled with the dedicated MELCOR ACC Package [17]. Considering previously studies about the effects of different accumulators nitrogen expansions [20], a sensitivity analysis considering the isothermal (label: ACC ISOTH) and the adiabatic (label: ACC ADIAB) expansions. Furthermore, in order to investigate the effects of intermediate polytropic transformations between the isothermal and adiabatic ones, three additional cases, characterized by expansion coefficients of 1.1, 1.2 and 1.3 (labels: ACC C=1.1, ACC C=1.2 and ACC C=1.3), have been considered.

3. MELCOR CODE AND NODALIZATION DESCRIPTION

3.1. MELCOR code description

MELCOR [17,18] (Methods of Estimation of Leakages and Consequences Of Releases) is a fully integrated SA code, developed at Sandia National Laboratories (SNL) for the United States Nuclear Regulatory Commission (USNRC), able to simulate the thermal-hydraulic phenomena in steady state and transient conditions and the main SA phenomena characterizing the Reactor Pressure Vessel (RPV), the Reactor Cavity (RC), the containment, the confinement buildings typical of Light Water Reactors (LWRs). The estimation of the source term is obtained by MELCOR code as well. The code is based on the Control Volume (CV) approach and can be used with the Symbolic Nuclear Analysis Package (SNAP) [22] to develop the nodalization and for the post processing of data by using its animation model capabilities.

MELCOR has a modular structure, and it is based on packages. Each package simulates a different part of the transient phenomenology. In particular the CVH and Flow Paths (FL) packages simulate the mass and energy transfer between CVs, the HS package simulates the thermal response of the heat structure, the Core (COR) package evaluates behavior of the fuel, core and LP structure, including the degradation phenomena, Cavity (CAV) package models the core-concrete interactions, and the Radionuclide (RN) package characterizes the aerosol behavior, transport, dynamics and deposition, and removal by engineering safety

features. It is to underline the role of the CVH/FL packages that provides the boundary conditions for other packages. Among the ESF package (Engineered Safety Features), the ACC Package constitutes a sub package providing a simplified model to calculate liquid injection from a user specified accumulator. The code version used is MELCOR 2.2 18019.

3.2. Generic PWR-900 MWe MELCOR nodalization description

The MELCOR nodalization [12,13,21,23,24] of the generic PWR-900 three-loops western type, shown in Figure 1a, developed by using SNAP, was designed to have a reasonable computational time and realistic prediction of the thermal-hydraulics and core degradation phenomena.

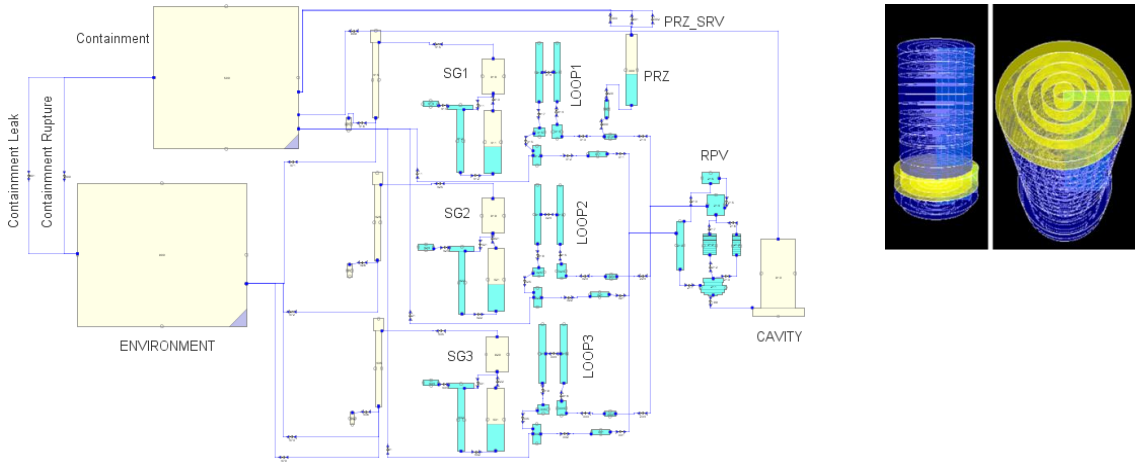

(a) (b)

Figure 1. MELCOR PCS, SCS (a) and core (b) nodalization developed using SNAP.

It has been developed considering the plant information's reported in the 2013 Foucher reports [25,26] and the ASTEC input files provided by IRSN during the EU-CESAM project [8]. The prediction capability of this MELCOR input-deck has been already revised along several projects where ENEA has been involved such as the EU-FASTNET project [27,28] and EU-IVMR project [9,10]. The three loops have been modelled separately. The SG side is composed of three different volumes representing the SG downcomer, the SG riser and the SG cavity. The thermal-hydraulic CVH nodalization of the RPV features different hydraulic regions simulating core, core Bypass (BP), LP, Upper Plenum (UP), and Downcomer (DC). The core is modelled by a single hydraulic region, CVH package, coupled with the correspondent model of the COR package. The core, within the COR package, is modelled with 17 axial regions and 6 radial regions; 5 radial regions are used to model the core region, as shown in Figure 1b. The accumulators have been modelled using two approaches as specified in the previous 2.2 section.

3.3. MELCOR ACC package model description

In the MELCOR ACC Package, accumulators are modelled as a mass and enthalpy sources inside CVs, modelling the reactor CLs, specified by the user, with the total water and nitrogen initial volume. In each loop, the accumulator is considered connected to the CL with a surge line. The main characteristics of the surge line (e.g. length, diameter, etc.) are specified by the user. The accumulator and the CL are separated by two check valves in series that open at the specified pressure [17].

When the pressure in the CL (P_{CVH}) falls below the accumulator pressure (P_{ACC}) [17]:

$$\Delta P = P_{ACC} - P_{CVH} > 0 \tag{1}$$

The accumulator discharge through the surge line the emergency coolant with a certain velocity calculated as defined:

$$u = \sqrt{\frac{2\Delta P}{k_{eff}\rho}}; k_{eff} = k + \frac{4fL}{D} \tag{2}$$

Where:

u = the velocity of pool in surge line [m/s];
L = the surge line length [m];
D = the surge line diameter [m];
f = friction coefficient;
ρ = fluid density [kg/s];
k = form loss coefficient;
k_{eff} = effective loss coefficient.

The mass and enthalpy of the emergency coolant injected into the CL are calculated as below:

$$\Delta V = A_S u \Delta t \tag{3}$$

$$\Delta m = \rho \Delta V \tag{4}$$

$$\Delta H = H_{specific} \Delta m \tag{5}$$

where A_s is the surge line open area. Then, the accumulator water volume inside the accumulator is reduced and the pressure in the accumulator is recalculated.

The thermodynamic expansion of the nitrogen inside the accumulator could be chosen: an adiabatic, an isothermal or a user defined polytropic expansion with a specified expansion coefficient. Based on an adiabatic or an isothermal approximation, the accumulator pressure could be calculated.
Adiabatic approximation for diatomic gas:

$$P_{N_2} V_{N_2}^{7/5} = const = P_{ACC,0} V_{N_2,0}^{7/5} \tag{6}$$

$$P_{N_2} = P_{ACC,0}\left(\frac{V_{N_2}}{V_{N_2,0}}\right)^{-7/5} = P_{ACC,0}\left(\frac{V_{N_2} + \Delta V}{V_{N_2,0}}\right)^{-7/5} = P_{ACC,0}\left(\frac{\Delta V}{V_{N_2,0}} + 1\right)^{-7/5} \tag{7}$$

$$P_{ACC} = P_{N_2} + P_{H_2O} \tag{8}$$

$$P_{H_2O} \ll P_{N_2} \rightarrow P_{ACC} = P_{N_2} = P_{ACC,0}\left(\frac{\Delta V}{V_{N_2,0}} + 1\right)^{-7/5} \tag{9}$$

For the isothermal approximation:

$$P_{N_2}V_{N_2} = const = P_{ACC,0}V_{N_2,0} \tag{10}$$

$$P_{N_2} = P_{ACC,0}\left(\frac{V_{N_2}}{V_{N_2,0}}\right) = P_{ACC,0}\left(\frac{V_{N_2} + \Delta V}{V_{N_2,0}}\right) \tag{11}$$

For the (8):

$$P_{H_2O} \ll P_{N_2} \rightarrow P_{ACC} = P_{N_2} = P_{ACC,0}\left(\frac{\Delta V}{V_{N_2,0}} + 1\right) \tag{12}$$

4. ANALYSIS OF THE RESULTS

4.1. Break opening and first core heat-up

At the SOT (t = 0 s), the SCRAM and the isolation of the SGs take place. With the SCRAM activation, the core power drops from the nominal fission power to the decay power. The break determines the primary coolant leakage to the containment with a consequent RPV blowdown and fast PCS pressure decrease, as shown in Figure 2. In this phase of the transient, part of the core decay power is removed by the coolant discharged through the break and part by the SGs acting as heat sink. Considering the isolation of the SGs, the Secondary Cooling System (SCS) pressure increases, as shown in Figure 2. When the pressure set-point of the SGs Steam Release Valves (SRVs) is reached, the SGs cycling phase starts, the steam is released from the SGs SRVs determining the decrease of secondary coolant mass. After the initial decrease, the PCS pressure stabilizes at the saturation pressure, slightly above the SCS pressure (Figure 2). The loss of primary coolant determines the decrease of the core collapsed coolant level, as shown in Figure 3. The Top of Active Fuel (TAF) is uncovered at about 120 s.

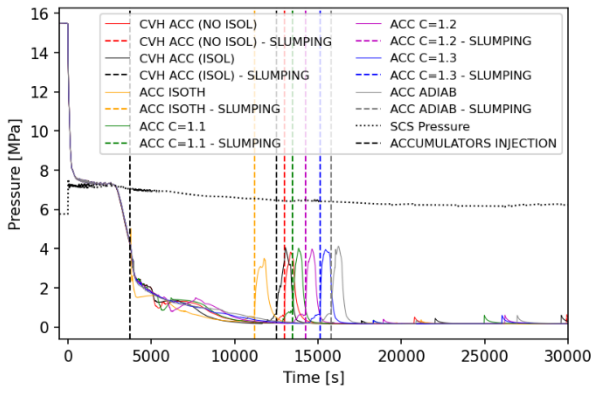

Figure 2. PCS and SCS pressure.

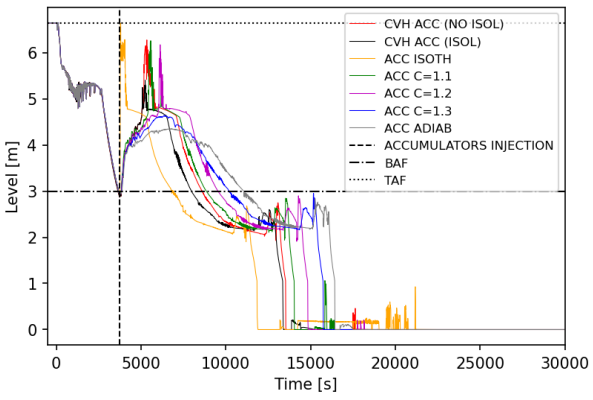

Figure 3. Core and LP collapsed coolant level.

At about 2500 s after the SOT the PCS pressure falls below the SCS pressure. The energy removed from the PCS is less than the decay heat generated in the core, causing the core heat-up with the consequent decrease of core collapsed coolant level (reaching the Bottom of Active Fuel -BAF- at 3687 s after the SOT) and increase of the cladding temperature, as shown in Figure 4 where the maximum cladding temperature is presented. When the cladding temperature reaches 1300 K, at about 3205 s after the SOT, the exothermic oxidation reactions start and hydrogen production begins. The oxidation reactions rate increases considerably when the cladding temperature reaches 1855 K, at about 3480 s after the SOT, as shown in Figure 5.

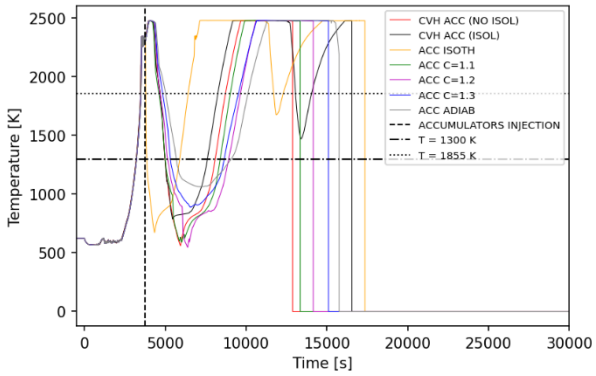

Figure 4. Maximum cladding temperature.

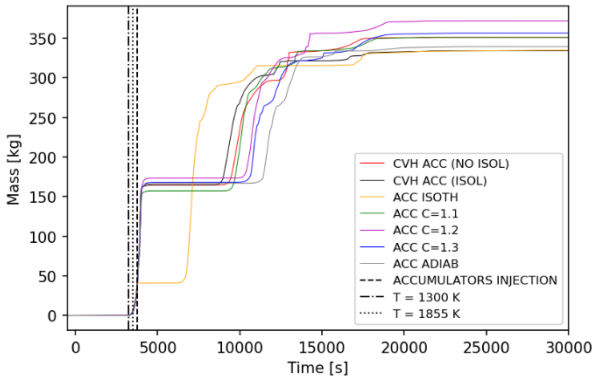

Figure 5. Hydrogen cumulative generation.

4.2. Accumulators discharge and partial core reflooding

When the PCS pressure falls below the selected set-point pressure, at about 3740 s after the SOT, accumulators begin to inject emergency coolant into the PCS as shown in Figure 6, where the total mass of coolant inside the accumulators is shown.

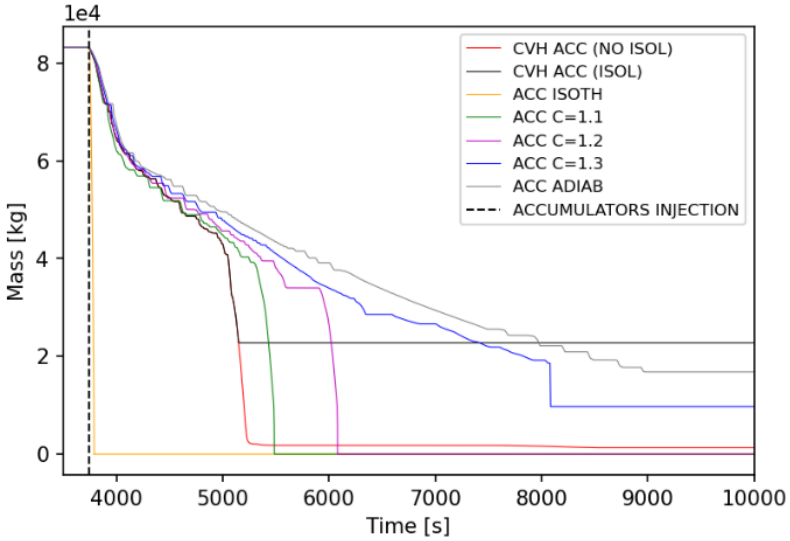

Figure 6. Total accumulators coolant mass.

Before 5000 s after the SOT, the analyses results present a similar trend from a qualitative point of view in terms of coolant discharged mass, except for the ACC ISOTH model. In this one, the accumulators discharge ends after about 40 s by the starting of the injection. Considering the other models, the CVH ACC (ISOL) accumulators are isolated, as hypothesized, from the PCS at about 5150 s after the SOT with the discharging of the 73% of the total accumulators water inventory. In case of CVH ACC (NO ISOL), ACC C=1.1 and C=1.2 discharging is finished respectively at about 5350 s, 5500 s, s and 6050 s after the SOT. In case of CVH ACC (NO ISOL), the accumulators discharge the 98% of the total water inventory. In case of ACC C=1.1 and C=1.2, the accumulators discharge all the water inventory. In case of ACC C=1.3 and ACC ADIAB the water injection continues till about 8000 s and 9000 s, when they stop to inject water into the PCS. The total mass discharged from the accumulators is about the 88% and 80%, respectively, of the total accumulators water inventory. This behaviour, that occurs considering ACC Package with C=1.3 and the adiabatic nitrogen expansion, should be investigate in further studies. A faster accumulators flow rate is underlined for all the sensitivity cases analysed, except for ACC ISOTH, ACC C=1.3 and ACC ADIAB, when the accumulator water mass decrease below half of the total amount of water contained, as shown in Figure 6. This behaviour is caused by the PCS pressure decrease due to the cooling effect of the accumulators. The accumulators water injection, decreasing the cladding oxidation rate and, consequently the steaming rate, determines the decrease of the primary pressure. In a positive feedback process, this phenomena determines an higher accumulator injection flow rate [20].

The differences in terms of accumulators injection determine a different behaviour in terms of core reflooding, cladding temperature and hydrogen cumulative production. As expected, the different phenomenology underlined before for the ACC ISOTH model determines a different behaviour in terms of core reflooding: since the injection is fast, with the total discharging of accumulators in about 40 s, the maximum cladding temperature, after reaching the first peak of about 2300 K, decreases almost instantaneously to 600 K. Considering the others sensitivity studies, the phenomenology presents a good agreement from a qualitative point of view: in CVH ACC (NO ISOL) model the collapsed coolant level reaches a higher level than the CVH ACC (ISOL) model, due to the major water injected. This behaviour determines a less final value of maximum cladding temperature (600 K) than the model with the accumulators isolation (700 K). In relation with ACC C=1.3 and ACC ADIAB, the core coolant level increases slowly due to the slower injection of accumulators and the maximum cladding temperature reaches its minimum value of about 900 K and 1100 K, respectively, at about 7000 s after the SOT. The decrease in terms of cladding temperature determines the end of hydrogen production, as shown in Figure 5. Considering the ACC ISOTH model, the faster water injection determines the stop of oxidation reaction at about 3800 s with a cumulative production of hydrogen of about 40 kg. In the other considered cases, the cumulative production of hydrogen before the accumulators injection is about 160 kg (Figure 5).

4.3. Second core heat-up and core relocation in the LP

After the partial reflooding of the core, the collapsed coolant level in the core decreases again (Figure 3), reaching the BAF first in the ACC ISOTH model at about 7490 s after the SOT. In case of CVH ACC (NO ISOL) model, the BAF is reached at about 9835 s after the SOT. Considering the CVH ACC (ISOL) model the BAF is reached at about 9500 s after the SOT. The BAF is reached at about 12225 s after the SOT in case of ACC ADIAB model considering that the accumulators discharge continues until 9000 s after the SOT. The cladding temperature returns to increase and, consequently, the hydrogen generation starts again. Along this phase, the core degradation and relocation phenomena progress in all cases. The loss of core geometry determines the relocation of core material in the LP (slumping). The slumping occurs first considering the ACC ISOTH model at about 11200 s after the SOT and occurs at about 15780 s after the SOT in case of ACC ADIAB model. This difference is due to the accumulators injection, as seen in Figure 6. The injection up to 9000 s after the SOT in case of ACC ADIAB allows for a longer cooling of the core and delays the total core degradation and consequently the core slumping.

The corium remains in the LP until the failure of the LH that occurs at about 17486 s and 18170 s after the SOT respectively for CVH ACC (NO ISOL) and CVH ACC (ISOL). This difference is due to the quantity of core mass relocated in the LP. In fact, in case of CVH ACC (NO ISOL) the core relocates entirely to the LP during the slumping. In the case of CVH ACC (ISOL) the outer ring does not relocate when the slumping occurs, but relocates after about 4080 s. This is due to the less quantity of water available from accumulator discharge to zircaloy oxidation, determining a retarded total damaging of the core. The LH failure occurs at about 17486 s and 21115 s after the SOT respectively in case of CVH ACC (NO ISOL) and ACC ISOTH. The differences in terms of corium retention in the LP is due to the minor quantity of corium relocated during the slumping due to the less initial damaging of the core caused by the faster accumulators injection in case of ACC ISOTH, as underlined before.

In relation to the hydrogen total production, a maximum quantity of 371 kg and a minimum quantity of 334 kg respectively for the analyses with ACC C=1.2 and ACC ISOTH are underlined. Furthermore, it is underlined a major quantity of about 17 kg of hydrogen produced in case of CVH ACC (NO ISOL) respect the same case with the isolation of accumulators (CVH ACC (ISOL)). This difference is due to the major quantity of steam available for the zircaloy oxidation reactions. In Table I are presented the main relevant phenomenological events predicted by the code along the studied cases with the specific timing.

Table I. Relevant phenomenological events predicted by the code along the sensitivity analyses.

Relevant Phenomenological events [s]	CVH ACC		ACC				
	NO ISOL	ISOL	ISOTH	C = 1.1	C = 1.2	C = 1.3	ADIAB
SOT, SCRAM, SGs isolation	0	0	0	0	0	0	0
SG 1,2,3 cycling inception	25,20,20	25,20,20	25,20,20	25,20,20	25,20,20	25,20,20	25,20,20
Core TAF uncover	115	115	115	115	115	115	115
H_2 generation start	3065	3065	3065	3065	3065	3065	3065
T > 1300 K (before accumulators injection)	3205	3205	3205	3205	3205	3205	3205
T > 1855 K (before accumulators injection)	3480	3480	3480	3480	3480	3480	3480
Core BAF uncover (before accumulators injection)	3687	3687	3687	3687	3687	3687	3687
Start of accumulators discharge	3740	3740	3740	3740	3740	3740	3740
Stop of accumulators discharge	5350	5150	3780	5500	6050	8000	9000
T > 1300 K (after accumulators injection)	8095	7615	5895	8405	8925	8690	9090
T > 1855 K (after accumulators injection)	8725	8250	6415	9025	9655	9525	10110
Core BAF uncover (after accumulators injection)	9835	9500	7490	10174	10670	11500	12225
Core slumping	12980	12530	11200	13490	14270	15150	15780
LH failure	17486	18170	21115	18285	18900	19900	20840

5. CONCLUSIONS

In this present activity, a sensitivity analysis on the accumulators modelling with the SA code MELCOR 2.2 has been conducted considering as SA sequence an unmitigated SBLOCA initiated by a 2-inch break on the CL of a generic PWR-900 MWe three loops western type. The unavailability of all active injection coolant system has been considered and the injection of the accumulators has been assumed as only accident mitigation strategy. The accumulators have been modelled following two approaches. In the first approach they have been modelled as CVH volumes connected with FLs to the CLs. An additional sensitivity considering the isolation of accumulators has been considered. In the second approach the accumulators have been modelled using the dedicated MELCOR ACC Package. The isothermal and adiabatic expansion of the accumulators nitrogen have been considered. In general, the choice about the selection of expansion type of accumulators is function of the loss of coolant rate, namely the size of the LOCA. Without want to give specific guidelines, as generally discussed in [20], an adiabatic expansion is suitable with rapid depressurization such as Large Break LOCA, assuming a constant entropy along the transformation. The isothermal one is more suitable with in case of slowly depressurization as in case of SBLOCA. In order to investigate the effects of intermediate polytropic transformations between the isothermal and adiabatic ones, three additional cases, characterized by expansion coefficients of 1.1, 1.2 and 1.3, have been considered. After the accumulators discharge, occurring at 3740 s after the SOT, all the model considered presents a similar trend in terms of water discharged from a qualitative point of view considering both the modelling with CHV CVs and ACC. An exception is represented by the ACC ISOTH model predicting a fast discharge of all the water inventory in the PCS of the reactor, determining a faster decrease of cladding temperature and, consequently, the stop of hydrogen production. After 5000 s, the models considered presents a different behavior in terms of total mass discharge and mass flow rate influencing the core reflooding, cladding temperature and hydrogen rate production. The slower accumulator water injection in the case of ACC ADIAB determines a delay of the total core damage and the core slumping. The core relocated in the LP first in case of ACC ISOTH and the LH failure occurs first in case of CVH ACC (NO ISOL), probably due to the major quantity of steam available for oxidation reaction, determining a major core damaging. In case of ACC ISOTH the LH failure occurs at about 21115 s after the SOT and a less quantity of corium material relocated along the slumping is underlined. The models considered for the present sensitivity analysis present a similar trend of the FOMs investigated both considering the CVH Package and ACC Package modelling. However, since ACC ISOTH model presents a different phenomenology, further studies will be considered to understand the discrepancies in the view of better evaluate the user effect on accumulators modelling and in general in SA modelling.

NOMENCLATURE

AC: Altenating Current; **ACC**: Accumulator package; **BP**: Bypass; **CAV**: Cavity package; **CL**: Cold Leg; **COR**: Core package; **CV**: Control Volume; **CVCS**: Chemical and Volume Control Systems; **CVH**: Control Volume Hydrodynamics package; **DC**: Downcomer; **DSA**: Deterministic Safety Analyses; **ESF**: Engineered Safety Features; **FL**: Flow Path package; **FOM**: Figure Of Merit; **FP**: Fission Product; **HPIS**: High Pressure Injection System; **HS**: Heat Structure package ; **IRSN** : Institute de Radioprotection et de Sûreté Nucléaire ; **LH** : Lower Head; **LOCA**: Loss Of Coolant Accident; **LP**: Lower Plenum; **LPIS**: Low Pressure Injection System; **LWR**: Light Water Reactor; **MCCI**: Molten Core-Concrete Interaction; **MDAFW**: Motor-Driven Auxiliary Feedwater; **MELCOR**: Methods of Estimation of Leakages and Consequences Of Releases; **NPP**: Nuclear Power Plant; **PRZ**: Pressurizer; **PWR**: Pressurized Water Reactor; **RC**: Reactor Cavity; **RCP**: Reactor Coolant Pump; **RCS**: Reactor Coolant System; **RN**: Radionuclide package; **RPV**: Reactor Pressure Vessel; **SA**: Severe Accident; **SAM**: Severe Accident Management; **SBLOCA**: Small Break Loss Of Coolant Accident; **SCS**: Secondary Cooling System; **SEBIM**: Safety Valves of Pressure Compensator; **SG**: Steam Generator; **SNAP**: Symbolic Nuclear Analysis Package; **SNL**: Sandia National Laboratories;

SOT: Start Of the Transient; **SRV**: Steam Release Valve; **TDAFW**: Turbine Driven Auxiliary Feedwater; **UH**: Upper Head; **UP**: Upper Plenum; **USNRC**: United States Nuclear Regulatory Commission.

REFERENCES

1. Source term uncertainty, recent development in understanding fission product behaviour, NEA/CSNI/R(92)2.
2. SOAR on Containment Thermalhydraulics and Hydrogen Distribution,NEA/CSNI/R(1999)16.
3. In-Vessel Core Degradation Code Validation Matrix, Update 1996-1999, NEA/CSNI/R(2000)21, France, 2001.
4. State-Of-The-Art Report On Nuclear Aerosols, NEA/CSNI/R(2009)5.
5. Containment code validation matrix, NEA/CSNI/R(2014)3.
6. F. Mascari, H. Nakamura, K. Umminger, F. De Rosa, F. D'Auria, "Scaling issues for the experimental characterization of reactor coolant system in Integral Test Facilities and role of system code as extrapolation tool", Proceedings of 16th International Topical Meeting on Nuclear Reactor Thermal Hydraulics (NURETH16) 6, pp. 4921-4934 (2015).
7. J. P. Van Dorsselaere, J. Mustoe, S. Power, M. Adorni, A. Schaffrath, A. Nieminen, "ETSON views on R&D priorities for implementation of the 2014 Euratom Directive on safety of nuclear installations", *Kerntechnik* **81**, Issue 5, pp. 527-534 (2016). DOI: https://doi.org/10.3139/124.110734
8. H. Nowack, P. Chatelard, L. Chailan, S. Hermsmeyer, V. Sanchez, L. Herranz, "CESAM – Code for European severe accident management, EURATOM project on ASTEC improvement", *Annals of Nuclear Energy* **116**, pp. 128-136 (2018). DOI: https://doi.org/10.1016/j.anucene.2018.02.021
9. F. Fichot, L. Carénini, M. Sangiorgi, S. Hermsmeyer, A. Miassoedov, S. Bechta, J. Zdarek, D. Guenadou, "Status of the IVMR Project: First steps Towards a New Methodology to Assess In-Vessel Retention Strategy for High-power Reactors", Proceedings of the 8th European Review Meeting on Severe Accident Research - ERMSAR-2017 Warsaw, Poland, 16-18 May (2017).
10. https://cordis.europa.eu/project/id/662157/it
11. D. Luxat, J. T. Hanophy, D. A. Kalanich, R. O. Gauntt, R. M. Wachowiak, "MAAP-MELCOR Crosswalk Phase 1 Study", Proceedings of 16th International Topical Meeting on Nuclear Reactor Thermal Hydraulics (NURETH16).S. Belon, C. Bouillet, V. Topin, H. Bonneville, N. Andrews, "Insight of core degradation simulation in integral codes throughout ASTEC/MELCOR crosswalk comparisons and ASTEC sensitivity studies", Proceedings of the 8th European Review Meeting on Severe Accident Research ERMSAR-2017, Warsaw, Poland, May 16-18, 2017 (2017).
12. F. Mascari, J. C. De La Rosa Blul, M. Sangiorgi, G. Bandini, "Analysis of an Unmitigated Station Blackout Transient in a Generic PWR-900 with ASTEC, MAAP and MELCOR Codes", NUREG/IA-0515.
13. P. Maccari, F. Mascari, S. Ederli, A. Manservisi, "SBO analysis of a generic PWR-900 with ASTEC and MELCOR codes", *J.Phys.: Conf. Ser.* **1868** 012019 (2021). DOI: https://doi.org/10.1088/1742-6596/1868/1/012019
14. Approaches and Tools for Severe Accident Analysis for Nuclear Power Plants, IAEA Safety Reports Series No. 56, IAEA, Vienna (2008).
15. Good Practices for User Effect Reduction, Status Report, NEA/CSNI/R(98)22,Organisation for Economic Co-operation and Development, Nuclear Energy Agency Committee on The Safety of Nuclear Installation (1998).
16. S. N. Aksan, F. D'Auria, H. Stadtke, "User effects on the thermal-hydraulic transient system code calculations", *Nuclear Engineering and Design*, **145**, pp. 159-174 (1993).
17. MELCOR Computer Code Manuals, Vol.1: Primer and Users' Guide, SAND 2015-6691 R; Vol. 2: Reference Manual, SAND 2015-6692 R; Vol. 3: MELCOR Assessment Problems, SAND 2015-6693 R; Sandia National Laboratories, USA.
18. MELCOR Best Practices as Applied in the State-of-the-Art Reactor Consequence Analyses (SOARCA) Project, NUREG/CR-7008.

19. M. Salehi, M. Shayesteh, "The accumulator effects on in-vessel severe accident progression of a three loop PWR nuclear power plant in a SBLOCA without safety injection system", *Annals of Nuclear Energy*, 107, pp. 1-16 (2017).
20. J. C. De la Rosa Blul, S. Brumm, F. Mascari, S. J. Lee, L. Carenini, "ASTEC-MAAP Comparison of a 2 Inch Cold Leg LOCA until RPV Failure", *Science and Technology of Nuclear Installations*, **2018** (2018). DOI: https://doi.org/10.1155/2018/9189010
21. F. Mascari, A. Guglielmelli, J. C. De la Rosa Blul, "Analysis of a postulated 2-inch Cold Leg LOCA severe accident in a PWR-like 900 MWe with MELCOR code", Proceedings of the International Conference Nuclear Energy for New Europe, NENE 2018, Portorož, Slovenia, September 10-13 (2018).
22. Applied Programming Technology, Inc., Symbolic Nuclear Analysis Package (SNAP) User's Manual (2021).
23. M. Pescarini, F. Mascari, D. Mostacci, F. De Rosa, C. Lombardo, F. Giannetti, "Analysis of unmitigated large break loss of coolant accidents using MELCOR code", *J. Phys.: Conf. Ser*. **923** 012009 (2017). DOI: https://doi.org/10.1088/1742-6596/923/1/012009
24. F. Mascari, S. Ederli S, "Analyses with MELCOR code of an unmitigated SBO scenario with in vessel retention strategy applied to a generic PWR-900 MWe", 18th International Topical Meeting on Nuclear Reactor Thermal Hydraulics, NURETH 2019, pp. 2497-2510 (2019).
25. L. Foucher, ASTEC V20R3 PWR900 Like ASTEC Input Deck, Rapport n° PSNRES/SAG/2013-451.
26. L. Foucher, ASTEC V20R3, PWR900 Like ASTEC Steady State Calculation, Rapport n° PSN-RES/SAG/2013-466.
27. https://cordis.europa.eu/project/id/662284/it
28. F. Mascari et al., "FASTNET scenarios database development and status", Proceedings of the 9TH European Review Meeting on Severe Accident Research (ERMSAR2019), Prague, Czech Republic, March 18-20 (2019).

Italian National Agency for New Technologies, Energy and Sustainable Economic Development

EUROPEAN COMMISSION
JOINT RESEARCH CENTRE
Directorate G - Nuclear Safety and Security
Nuclear Reactor Safety and Emergency Preparedness

UNIVERSITÀ DEGLI STUDI DI PALERMO

SENSITIVITY ANALYSES ON MELCOR ACCUMULATORS MODELLING

G. Agnello[1], P. A. Di Maio[1], J. C. de la Rosa Blul[2], F. Mascari[3]

1 Department of Engineering, University of Palermo, Italy
2 Nuclear Safety & Security Unit, DG Joint Research Centre,
3 FSN-SICNUC, ENEA, C.R. Bologna, Italy

The 10th European Review Meeting on Severe Accident Research (ERMSAR2022), Karlsruhe, Germany, May 16-19, 2022

giuseppe.agnello04@unipa.it

CONTENT

- INTRODUCTION
- CHARACTERISTICS AND HYPOTHESIS OF THE STUDY
- NODALIZATION DESCRIPTION
- ANALYSES OF THE RESULTS
- CONCLUSIONS

INTRODUCTION

- Since the last decades, the interest of international nuclear scientific community involved in Severe Accident (SA) research is focused on the development of new strategies to prevent core loss of integrity and mitigate possible releases of Fission Products (FPs) to the environment in view to develop and consolidate Severe Accident Management (SAM) measures.
- State-of-art integrated codes, capturing the theoretical and experimental knowledge produced in the last four decades, have been developed to simulate the main phenomena taking place during a SA sequence.
- Considering the several complex and different phenomena/processes taking place during a SA, code-users require a high-level understanding of the phenomena/processes and need to define several modelling parameters in the use of a SA code.
- Purpose of this activity is to give some insights about the MELCOR code results discrepancies in terms of some Figure of Merits (FOMs) related to a SA sequence considering different accumulators modelling approaches and user choices in selecting parameters related to the accumulators thermal-hydraulic behavior.

CONTENT

- INTRODUCTION
- CHARACTERISTICS AND HYPOTHESIS OF THE STUDY
- NODALIZATION DESCRIPTION
- ANALYSES OF THE RESULTS
- CONCLUSIONS

CHARACTERISTICS AND HYPOTHESIS OF THE STUDY

- The Nuclear Power Plant (NPP) considered in this analysis is a generic PWR-900 MWe three-loops western type and the SA sequence selected for the present study is an unmitigated Small Break Loss Of Coolant Accident (SBLOCA).
- The initiator event considered is a 2-inch break of the Cold Leg (CL) of Loop 1 where the Pressurizer (PRZ) is located.
- The break event is coupled with the loss of offsite Alternating Current (AC) power and the failure of all the diesel generators. This determines the unavailability of the following systems:
  - Primary pressure control systems,
  - Chemical and Volume Control Systems (CVCS),
  - Reactor Coolant Pump (RCP) seal injection,
  - Active safety injection systems (HPIS and LPIS),
  - Motor-Driven Auxiliary Feedwater (MDAFW).
- Only the accumulators are considered available.

CHARACTERISTICS AND HYPOTHESIS OF THE STUDY

- The following hypotheses have been considered:
  - Reactor SCRAM and Stem Generators (SGs) isolation at SOT,
  - Independent failure of the Turbine Driven Auxiliary Feedwater (TDAFW) pump,
  - No RCPs seals failure,
  - No primary boundary structures thermal induced degradation phenomena,
  - Primary and secondary Steam Relief Valves (SRVs) availability throughout the accident evolution,
  - Safety Vales of Pressure Compensator (SEBIM) manually stuck open when the core exit temperature reaches 650 °C.
- The transient has been simulated considering the in-vessel phase.

CHARACTERISTICS AND HYPOTHESIS OF THE STUDY

- The sensitivity analysis has been carried out considering two different accumulators modelling approaches:
  - Accumulators modelled using MELCOR CVH volumes. An additional sensitivity has been considered:
    - Total discharging of accumulators - CVH ACC (NO ISOL) -
    - Isolation of accumulators when the CL pressure falls below 15 bar - CVH ACC (ISOL) -
  - Accumulators modelled using the dedicated MELCOR ACC Package. An additional sensitivity has been considered related to the nitrogen polytropic expansion:
    - C = 1 (isothermal expansion) - ACC ISOTH -
    - C = 1.1
    - C = 1.2
    - C = 1.3
    - C = 1.4 (adiabatic expansion) - ACC ADIAB -

CONTENT

- INTRODUCTION
- CHARACTERISTICS AND HYPOTHESIS OF THE STUDY
- NODALIZATION DESCRIPTION
- ANALYSES OF THE RESULTS
- CONCLUSIONS

NODALIZATION DESCRIPTION

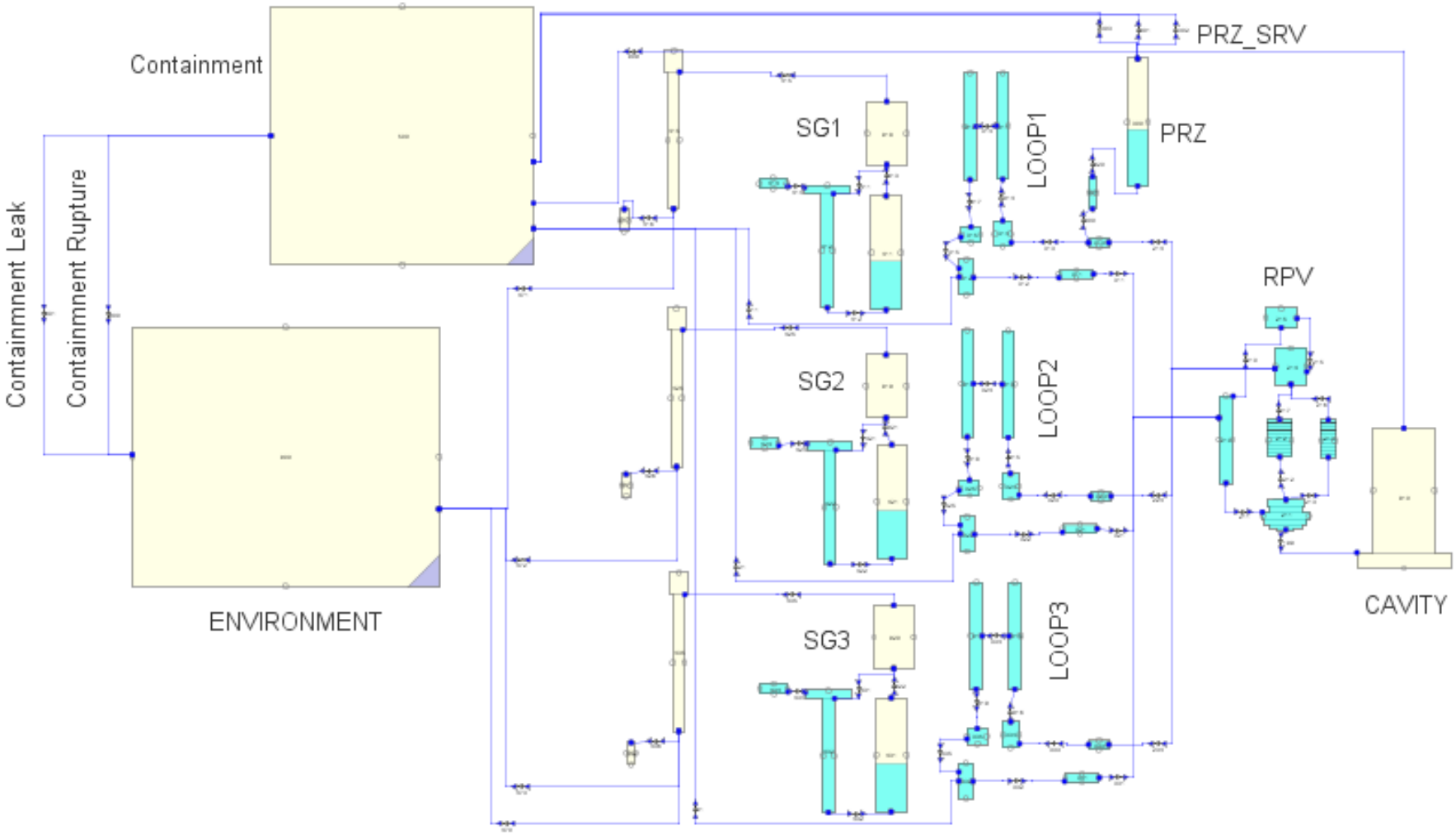

NODALIZATION DESCRIPTION

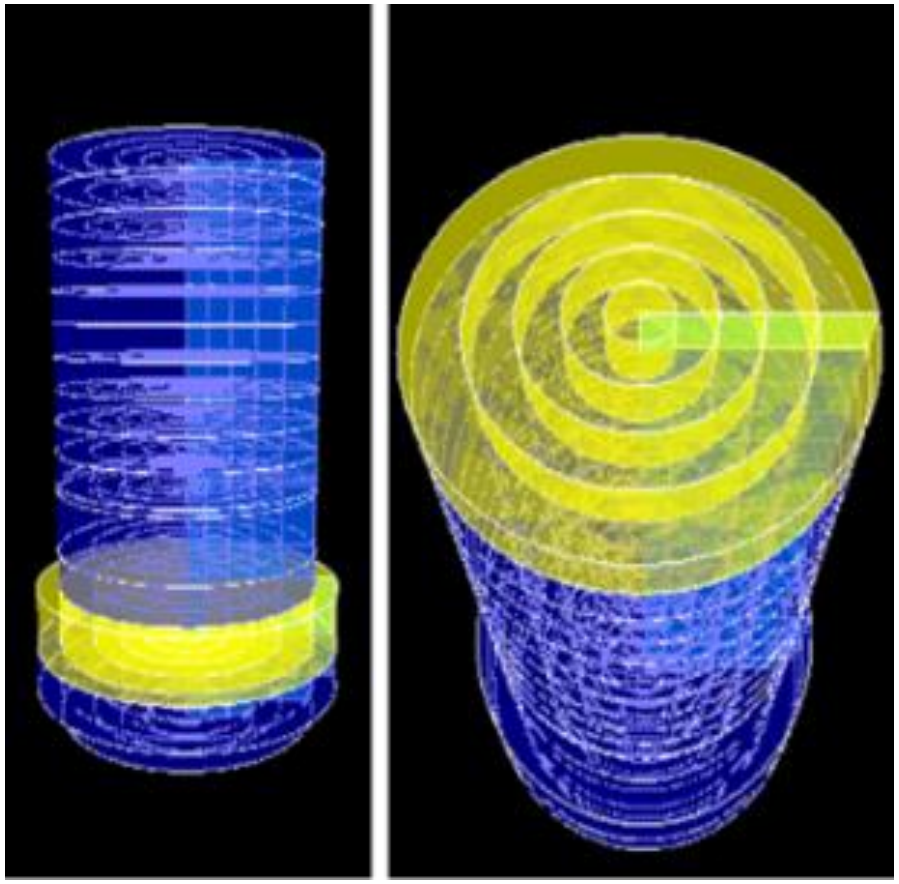

- The MELCOR nodalization of the generic PWR-900 three-loops western type has been developed by using SNAP.
- It has been developed considering the plant information's reported in the 2013 Foucher reports and the ASTEC input files provided by IRSN during the EU-CESAM project.
- The prediction capability of this MELCOR input-deck has been already revised along several project such as the EU-FASTNET project and EU-IVMR project.
- The three loops have been modelled separately.
- The core is modelled by a single hydraulic CVH coupled with the correspondent model of the COR Package.

CONTENT

- INTRODUCTION
- CHARACTERISTICS AND HYPOTHESIS OF THE STUDY
- NODALIZATION DESCRIPTION
- ANALYSES OF THE RESULTS
- CONCLUSIONS

ANALYSES OF THE RESULTS: BREAK OPENING AND FIRST CORE HEAT-UP

- The break determines the primary coolant leakage to the containment with a consequent Reactor Pressure Vessel (RPV) blowdown and fast Primary Coolant System (PCS) pressure decrease.
- At about 2500 s after the SOT, the PCS pressure, from the saturation pressure, falls below the SCS pressure.
- Energy removed from PCS is less than the decay heat in the core, causing the core heat-up with the decrease of the collapsed coolant level and increase of the cladding temperature.

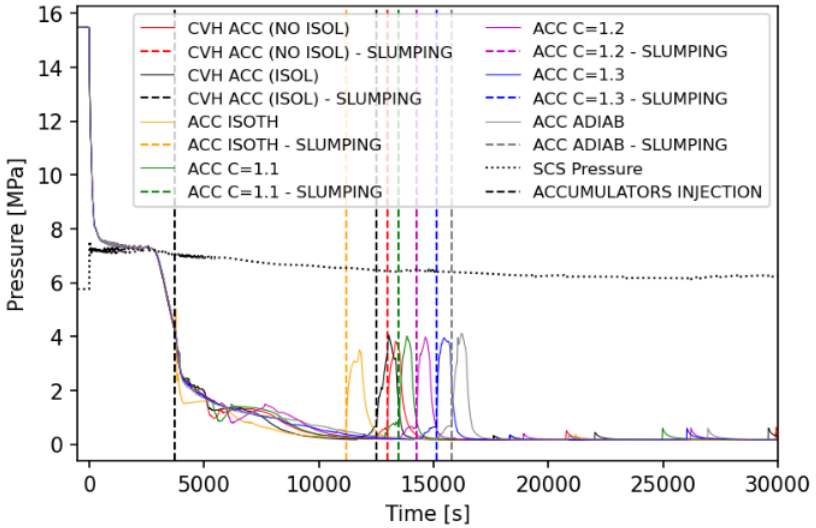

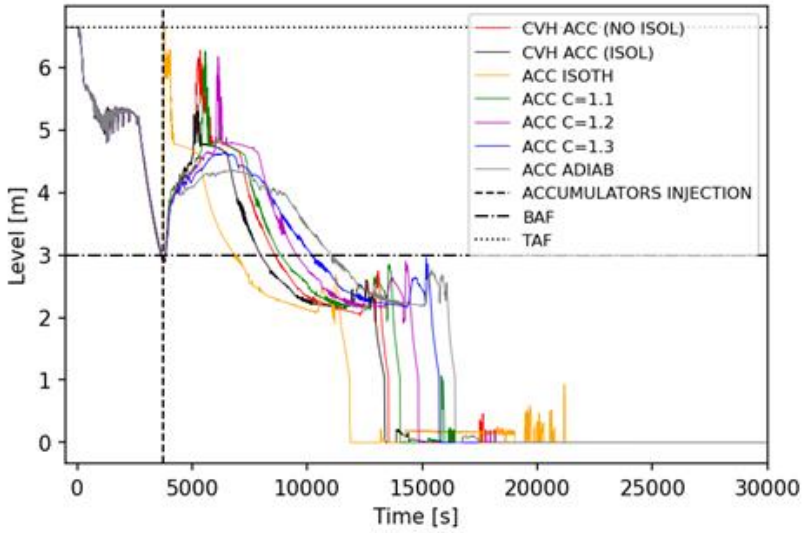

ANALYSES OF THE RESULTS: BREAK OPENING AND FIRST CORE HEAT-UP

- When the cladding temperature reaches 1300 K (3205 s after the SOT), the exothermic oxidation reactions start and hydrogen production begins.
- The oxidation reactions rate increases considerably when the cladding temperature reaches 1855 K (3480 s after the SOT).

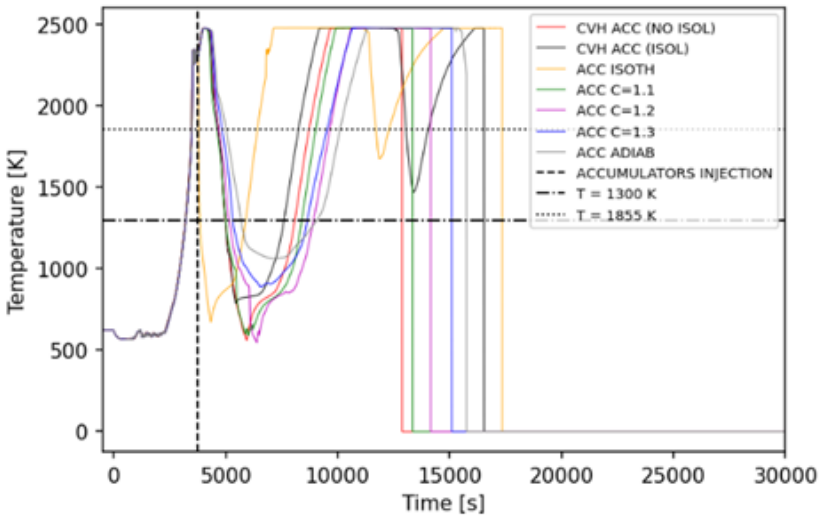

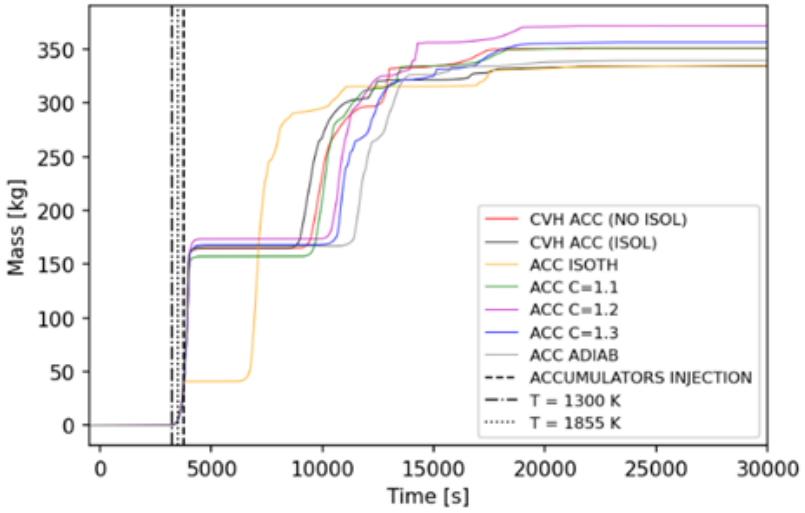

ANALYSES OF THE RESULTS: ACCUMULATORS DISCHARGE AND PARTIAL CORE REFLOODING

- When the PCS pressure falls below the set-point pressure (3740 s after the SOT) accumulators begin to inject into the PCS.
- Until 5000 s after the SOT, the analyses present a similar trend from a qualitative point of view, except for the ACC ISOTH model.
  - In ACC ISOTH the discharge ends after about 40 s by the starting.

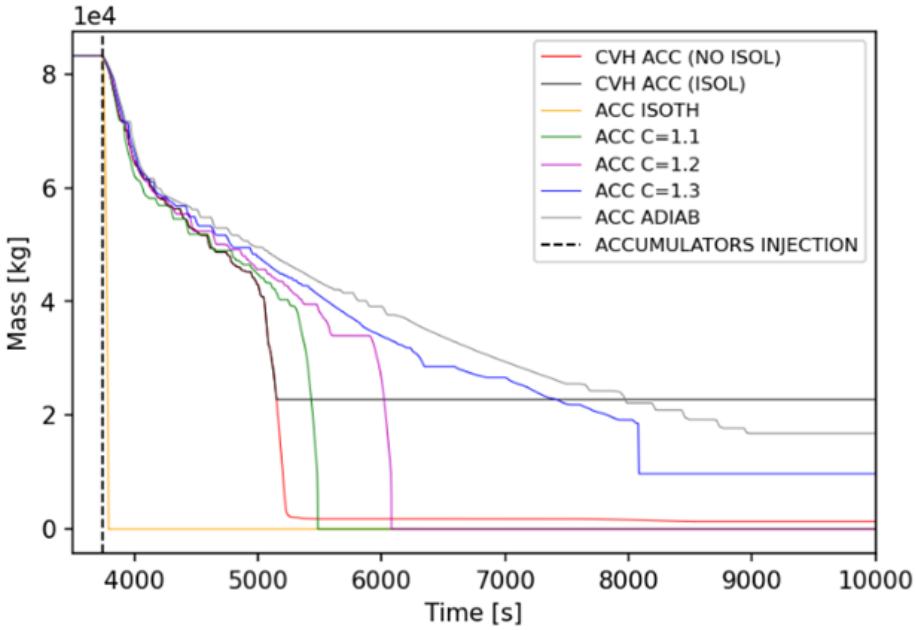

- After 5000 s, the following discrepancies are underlined:
  - In ACC C=1.1, C=1.2 the accumulators discharge all the water inventory. In case of ACC C=1.3 and ACC ADIAB, the accumulators discharge the 88% and 80% of the total inventory.

ANALYSES OF THE RESULTS: BREAK OPENING AND FIRST CORE HEAT-UP

- The differences in terms of accumulators injection determine a different behavior in terms of core reflooding, cladding temperature and hydrogen cumulative production:
  - Different phenomenology in case of ACC ISOTH in terms of core reflooding, cladding temperature and hydrogen production.
  - ACC C=1.3 and ACC ADIAB present a slower increase of collapsed core level determining a higher cladding temperature after the temperature decrease (900 K and 1100 K).

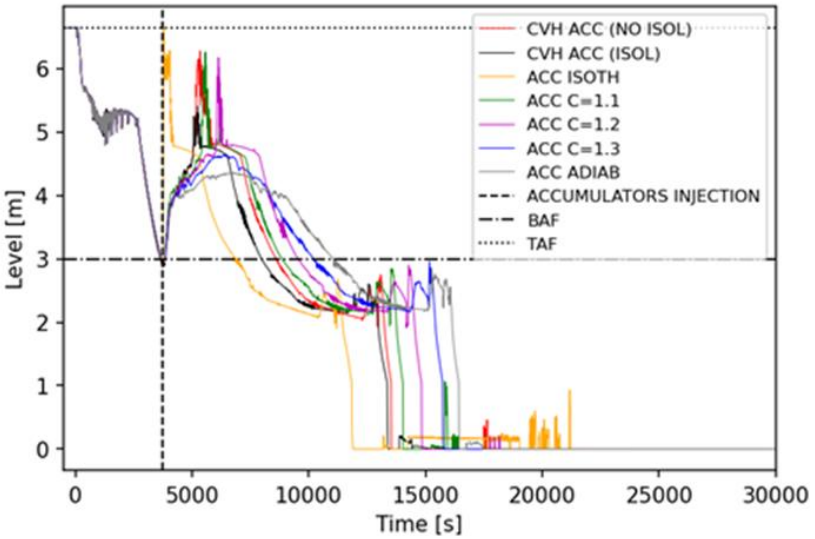

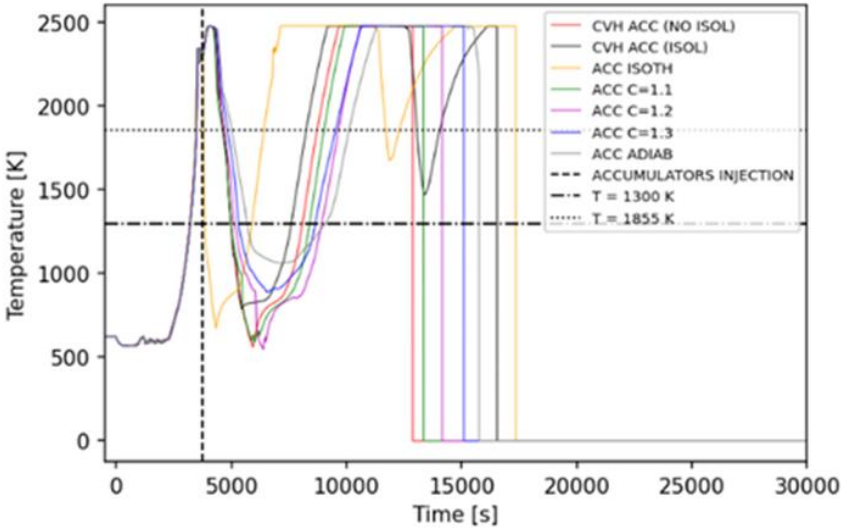

ANALYSES OF THE RESULTS: BREAK OPENING AND FIRST CORE HEAT-UP

- The decrease in terms of cladding temperature determines the stop of hydrogen production.
- Considering the ACC ISOTH model, the faster water injection determines the stop of oxidation reactions at about 3800 s with a cumulative hydrogen production of about 40 kg.
- In the other cases, the cumulative production of hydrogen before the accumulators injection is about 160 kg.

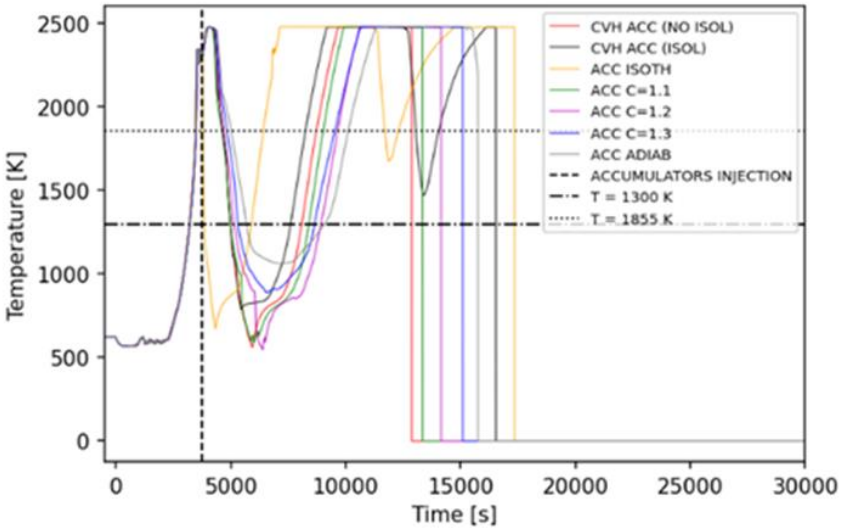

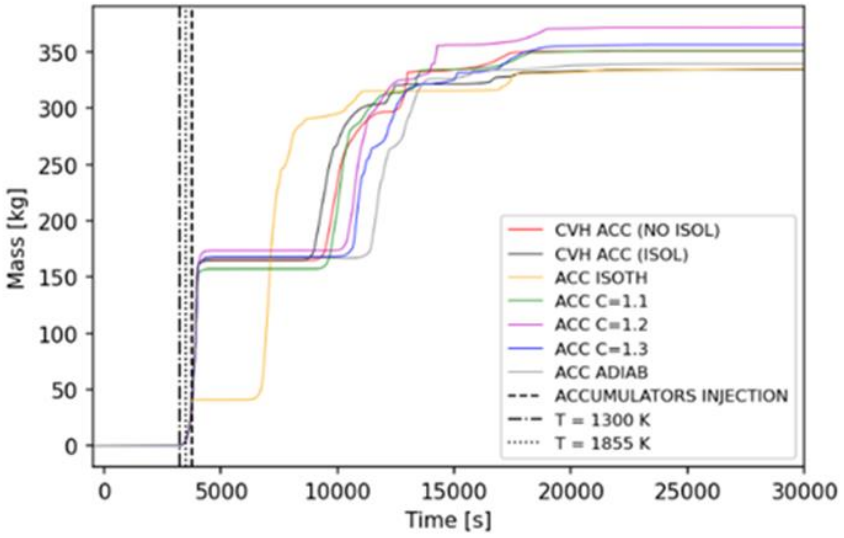

ANALYSES OF THE RESULTS: SECOND CORE HEAT-UP AND CORE RELOCATION IN THE LP

- ❑ After the partial core reflooding, the core collapsed coolant level decreases again.
- ➢ In the ACC ISOTH model, the BAF is reached at 7490 s after the SOT.
- ➢ In the ACC ADIAB model, the BAF is reached at 12225 s after the SOT.
- ❑ The cladding temperature returns to increase and, consequently, the hydrogen generation starts again.

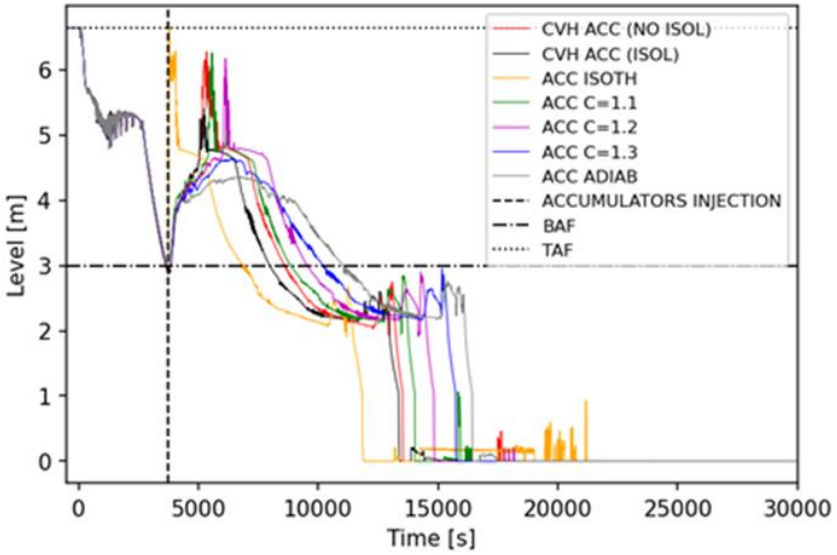

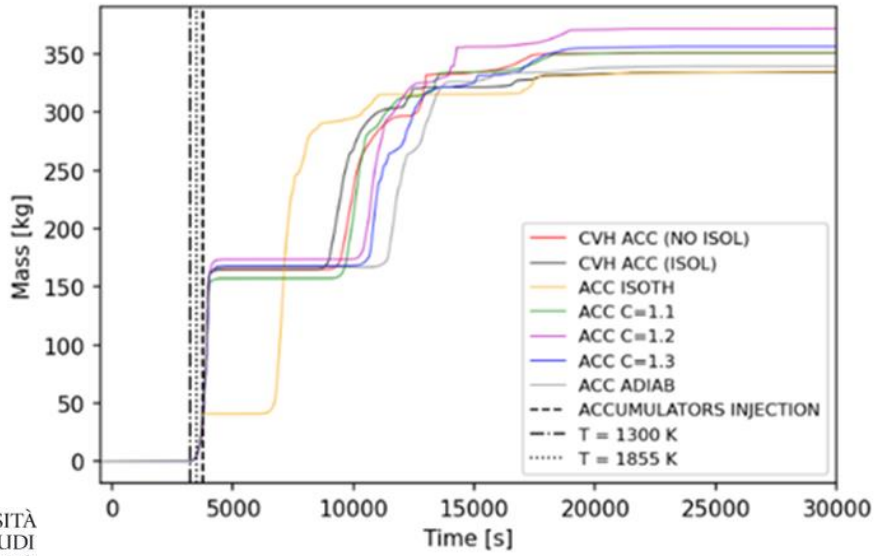

ANALYSES OF THE RESULTS: SECOND CORE HEAT-UP AND CORE RELOCATION IN THE LP

- The loss of core geometry determines the relocation of core material in the LP (slumping).
  - Slumping occurs first considering the ACC ISOTH at about 11200 s after the SOT.
  - Slumping occurs at about 15780 s after the sot for the ACC ADIAB model.
- The injection up to 9000 s after the SOT in case of ACC ADIAB model allows for a longer cooling of the core and delays the total core degradation and, consequently, core slumping.

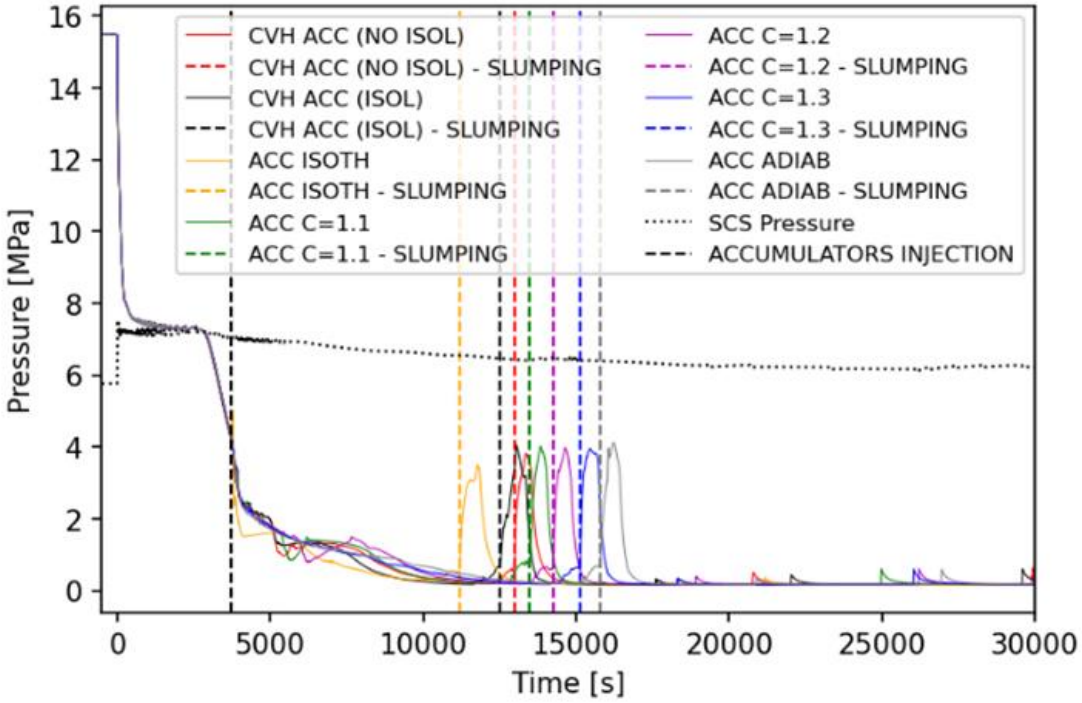

ANALYSES OF THE RESULTS: SECOND CORE HEAT-UP AND CORE RELOCATION IN THE LP

- Corium remains in the LP until the failure of LH occurring at about 17486 s and 18170 s respectively for CVH ACC (NO ISOL) and CVH ACC (ISOL).
- In case of CVH ACC (NO ISOL) the core relocates entirely to the LP during the slumping.
- In case of CVH ACC (ISOL) the core outer ring relocates 4080 s after the slumping.
- This is due to the less quantity of water available from accumulator discharge to zircaloy oxidation, determining a retarded total damaging of the core.

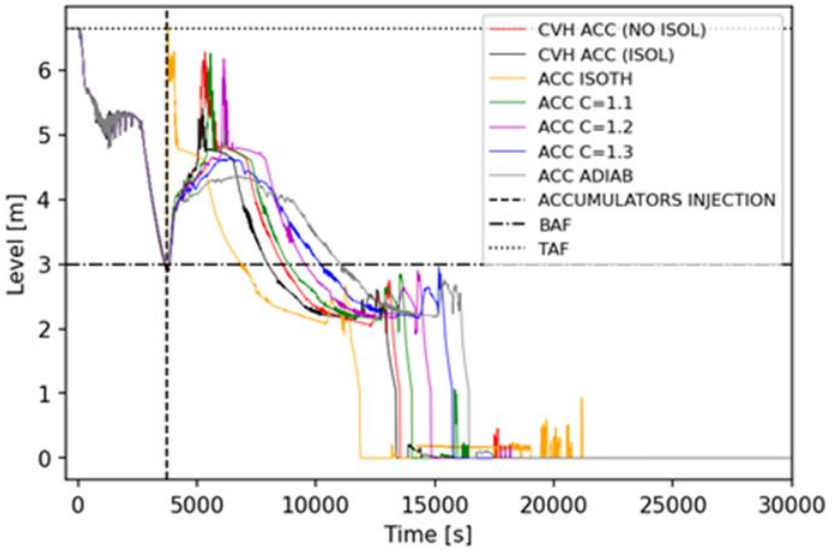

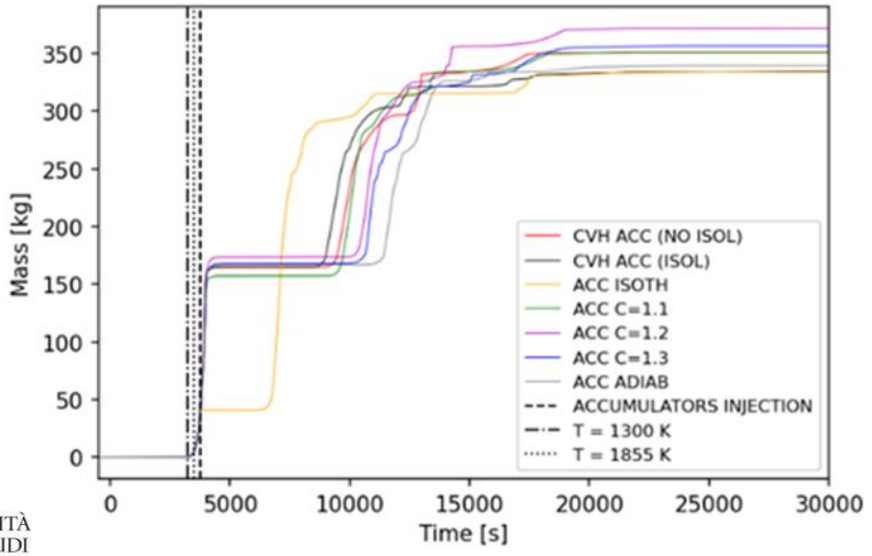

ANALYSES OF THE RESULTS: SECOND CORE HEAT-UP AND CORE RELOCATION IN THE LP

- LH failure occurs at about 17486 s and 21115 s after the SOT, respectively in case of CVH ACC (NO ISOL) and ACC ISOTH.
- Less initial damage of the core in case of ACC ISOTH.
- A maximum quantity of 371 kg and a minimum quantity of 334 kg of hydrogen cumulative mass production for the analyses with ACC C=1.2 and ACC ISOTH are underlined.
- A major quantity of about 17 kg of hydrogen produced in case of CVH ACC (NO ISOL) respect CVH ACC (ISOTH) is underlined.
- Major quantity of steam available for the zircaloy oxidation reactions.

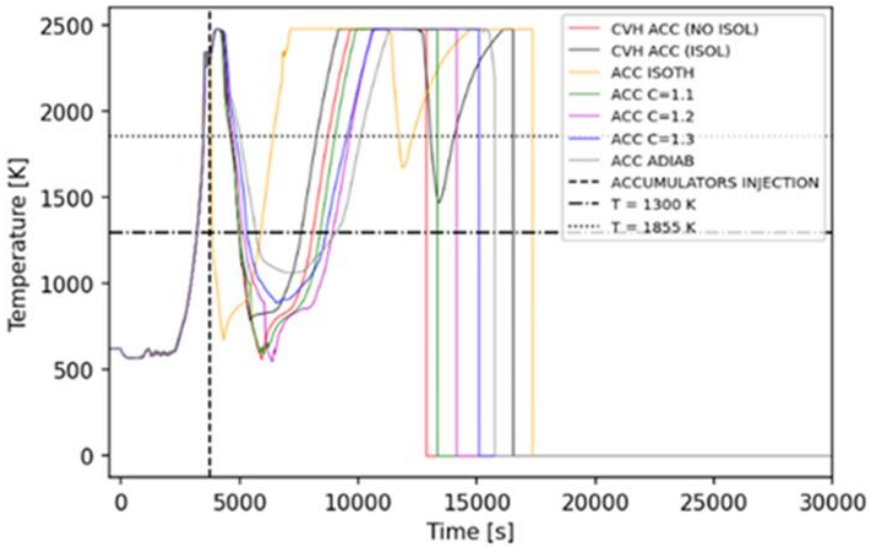

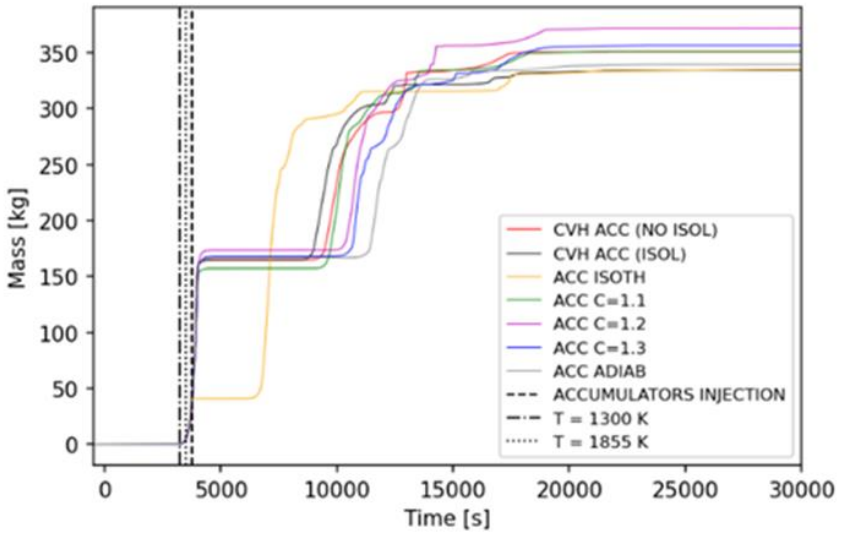

ANALYSES OF THE RESULTS: TIMING OF RELEVANT TRANSIENT PHENOMENA

Relevant Phenomenological events [s]	CVH ACC		ACC				
	NO ISOL	ISOL	ISOTH	C = 1.1	C = 1.2	C = 1.3	ADIAB
SOT, SCRAM, SGs isolation	0	0	0	0	0	0	0
SG 1,2,3 cycling inception	25,20,20	25,20,20	25,20,20	25,20,20	25,20,20	25,20,20	25,20,20
Core TAF uncover	115	115	115	115	115	115	115
H_2 generation start	3065	3065	3065	3065	3065	3065	3065
T > 1300 K (before accumulators injection)	3205	3205	3205	3205	3205	3205	3205
T > 1855 K (before accumulators injection)	3480	3480	3480	3480	3480	3480	3480
Core BAF uncover (before accumulators injection)	3687	3687	3687	3687	3687	3687	3687
Start of accumulators discharge	3740	3740	3740	3740	3740	3740	3740
Stop of accumulators discharge	5350	5150	3780	5500	6050	8000	9000
T > 1300 K (after accumulators injection)	8095	7615	5895	8405	8925	8690	9090
T > 1855 K (after accumulators injection)	8725	8250	6415	9025	9655	9525	10110
Core BAF uncover (after accumulators injection)	9835	9500	7490	10174	10670	11500	12225
Core slumping	12980	12530	11200	13490	14270	15150	15780
LH failure	17486	18170	21115	18285	18900	19900	20840

CONTENT

- INTRODUCTION
- CHARACTERISTICS AND HYPOTHESIS OF THE STUDY
- NODALIZATION DESCRIPTION
- ANALYSES OF THE RESULTS
- CONCLUSIONS

CONCLUSIONS

- A sensitivity analysis on the accumulators modelling with the SA code MELCOR 2.2 has been conducted.
- An unmitigated SBLOCA, initiated by a 2-inch break on the CL of a generic PWR-900 three-loops western type has been selected as postulated transient.
- The accumulators have been modelled considering both CVH volumes, with an additional sensitivity on the effects of accumulators isolation on SA sequence, and the dedicated MELCOR ACC Package, with a sensitivity on the polytropic expansion of the nitrogen inside accumulators.
- The models considered for the present sensitivity analysis present a similar trend of the FOMs investigated both using CVH Package and ACC Package modeling. However, since ACC ISOTH model presents a different phenomenology, further studies will be considered to understand the discrepancies in the view of better evaluate the user effect on accumulators modeling and in general in SA modelling.

GRAZIE PER LA VOSTRA ATTENZIONE

Giuseppe Agnello

giuseppe.agnello04@unipa.it

EUROPEAN COMMISSION
JOINT RESEARCH CENTRE
Directorate G - Nuclear Safety and Security
Nuclear Reactor Safety and Emergency Preparedness

UNIVERSITÀ
DEGLI STUDI
DI PALERMO

EXPERIMENTAL INVESTIAGTION OF QUENCH-20 AND SIMULATION WITH AC²/ATHLET-CD

Thorsten Hollands
Gesellschaft fuer Anlagen- und Reaktorsicherheit (GRS) gGmbH
Boltzmannstrasse 14, 85748 Garching, Germany
thorsten.hollands@grs.de

Juri Stuckert
Karlsruhe Institute of Technology (KIT)
Hermann-von-Helmholtzplatz 1, 76344 Eggenstein-Leopoldshafen, Germany
juri.stuckert@kit.edu

Patrick Isaksson
Swedish Radiation Safety Authority (SSM)
Solna strandväg 96, 171 16 Stockholm, Sweden
patrick.isaksson@ssm.se

Sevostian Bechta
Royal Institute of Technology (Kungliga Tekniska Högskolan - KTH)
AlbaNova University Centre, Roslagstullsbacken 21, S-106 91 Stockholm, Sweden
bechta@kth.se

ABSTRACT

In the frame of the EC funded project SAFEST a QUENCH test with BWR-like mockup composing fuel rods and control blade was proposed by SSM in collaboration with KTH and performed on 9th October 2019 at KIT. QUENCH-20 was the first experiment with a BWR configuration in the QUENCH facility, where only PWR bundle configurations were investigated before. The objective was to understand the effect of B_4C and its prototypic steel cladding on BWR fuel assembly degradation during strong heat-up and subsequent flooding. In contrast to CORA BWR tests performed at KIT earlier in the frame of the CORA test program, the QUENCH-20 bundle represents one quarter of a BWR fuel assembly. The power was increased during heat-up phase to establish a pre-oxidation phase for 4 hours at 960 °C to get a defined oxide layer thickness before the transient phase. During the transient phase the temperatures increased up to 1730 °C due to power increase and oxidation processes. During the subsequent flooding by water a sharp temperature escalation was observed to approximately 2030 °C. In total, 57 g of hydrogen were generated including 10 g from boron carbide oxidation. Additionally, due the B_4C oxidation CO, CO_2 and CH_4 were produced. In addition, post-test simulations were performed by GRS with AC²/ATHLET-CD. The results of the calculations show that the thermal behavior is qualitatively and quantitively predicted in good agreement with the experiment but with some deviations during the reflood and the cooldown phases, which appeared to be slower than in the experiment.

KEYWORDS
QUENCH-20, BWR Configuration, Core Degradation, AC²/ATHLET-CD

1. INTRODUCTION

Between 1988 to 1993 BWR experiments were carried out at the Karlsruhe Institute of Technology (KIT) within the CORA test series, which investigated the behavior of boron carbide absorbers in fuel assembly arrangements typical of boiling water reactors. It was shown that the early melting of the steel absorber box and the subsequent interaction between steel and boron carbide leads to an early redistribution of absorber melt, whereby blockages are formed in the lower bundle area [1], [2]. However, a quantitative determination of the boron carbide oxidation was not possible in these tests, since the quantity of the gases formed (CO, CO_2, CH_4) was not measured. The theme of investigation of BWR phenomena during severe accidents raised up again after the Fukushima Daiichi accident in 2011.
The experiment QUENCH-20 performed at the Karlsruhe Institute of Technology (KIT) in the frame of the EC supported SAFEST project aimed to determine the bundle degradation in a bundle arrangement typical for boiling water reactors (BWR) represented by a ¼-fuel assembly. The canister walls are made of zirconium and the absorber blades were filled with boron carbide in a BWR arrangement which caused an additional energy input due to the exothermic steam reaction at high temperatures. The influence of the absorber degradation on the bundle was investigated and the released gases of the absorber oxidation were used to evaluate this process.
.

2. QUENCH FACILITY AND QUENCH-20 TEST CONDUCT

A short overview of the QUENCH facility and the experiment is given here. In general, the QUENCH facility as well as the test conduct and the experimental results are described and discussed in [3] and [4].

2.1. QUENCH Facility

The general scheme of the test section is given in Figure 1. The test rods were arranged within the QUENCH-20 bundle as shown in the schematic cross section of Figure 2. The test bundle is approximately 2.5 m long and is made up of 24 heated fuel rod simulators. Heating is electric by 5.25 mm diameter tungsten heaters installed in the rod centers, and the bundle section heated by tungsten heaters between bundle elevations 0 and 1024 mm. Molybdenum heaters and copper electrodes are connected to the tungsten heaters at one end and to the cable leading to the DC electrical power supply at the other end. The tungsten heaters are surrounded by annular ZrO_2 pellets simulating UO_2 fuel [4].
The rod cladding of the fuel rod has 9.84 mm outside diameter and 8.63 mm inner diameter. All the test rods were filled with Kr at an overpressure of approximately 0.35 MPa after bundle heating to cladding peak temperature of 900 K. The system pressure maintained at about 0.2 MPa. The fuel rod simulators are held in position by five grid spacers at bundle elevations -200, 50, 550, 1050 and 1410 mm. All five grid spacers were the standard Westinghouse Inconel spacers. Two steel blades with horizontal B_4C absorber pins were filled with helium and inserted between channel box and shroud.
One corner rod was installed in the water channel and was designed to be withdrawn from the bundle to check the amount of oxidation and hydrogen absorption at specific time. This corner rod was withdrawn at the end of pre-oxidation stage.
The test bundle is surrounded by an octagonal shroud of Zr, then by ZrO_2 fiber insulation extending from the bottom to the upper end of the heated zone and a double-walled cooling jacket of Inconel /stainless steel over the entire length. The annulus between shroud and cooling jacket with the fiber insulation is purged and then filled with stagnant argon. The annulus is connected to argon feeding system in order to prevent an access of steam to the annulus after possible shroud failure. The annulus of the cooling jacket is cooled by argon from the upper end of the heated zone to the bottom of the bundle and by water in the upper electrode zone. Both the absence of ZrO_2 insulation above the heated region and the water cooling are to avoid too high temperatures of the bundle in that region.

Beside these, additional information are given in [4].

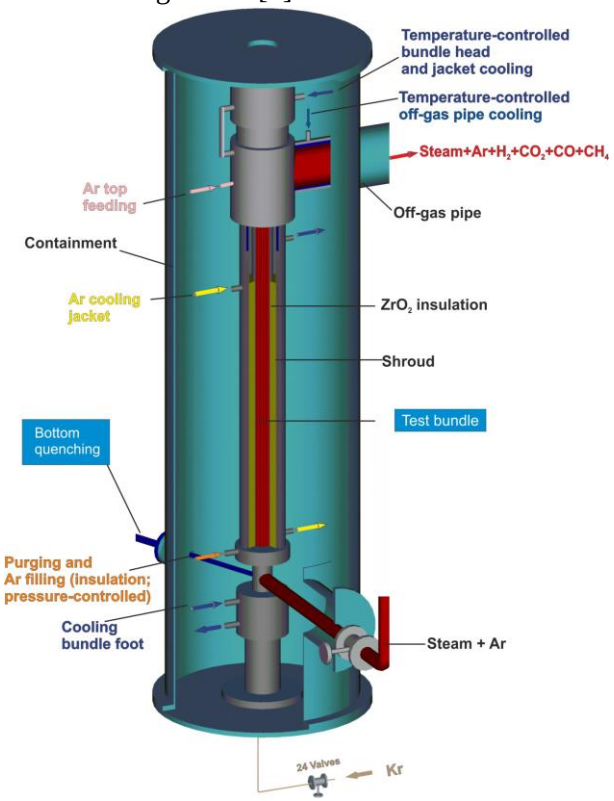

Figure 1. QUENCH Facility [4].

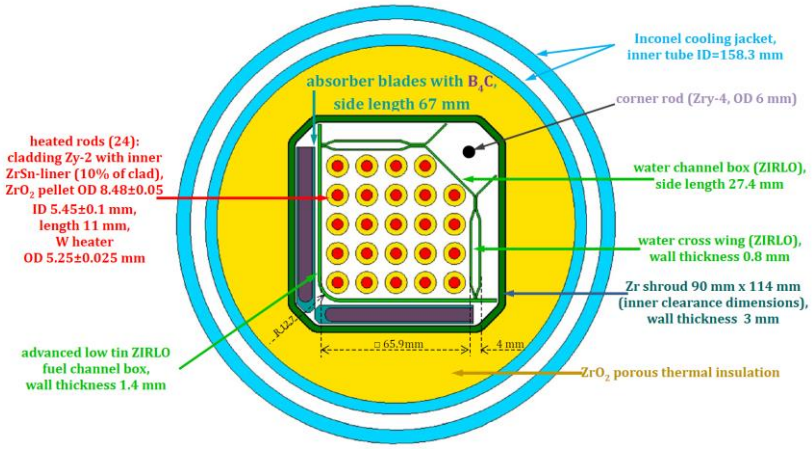

Figure 2. QUENCH-20 Cross-section [4].

2.2. QUENCH-20 Test Conduct

As previous QUENCH experiments the test conduct of QUENCH-20 can be separated in the following phases [4]:

- Pre-oxidation phase 0 – 14416 s,
- Transient phase 14416 – 15882 s,
- Quench 15882 – 16375 s with water flow rate 50 g/s.

Figure 3 show the power evolution during the test as well as some representative temperatures of fuel rod simulator (TFS), shroud (TSH), absorber blades (TBL) as well as the corner rod. After the heat-up the temperature plateau was established at 7200 s for the following pre-oxidation phase. The power needed to be adjusted slightly during the pre-oxidation phase to avoid temperature increase which would lead to faster and thicker oxide layers. The maximum temperature at 950 mm was kept at 1255 K until the transient phase was initiated at 14416 s. The corner rod was withdrawn just before the transient phase to get the degree of oxidation before temperature increase. During the transient phase the electrical power was increased from 7.15 kW and reduced at quench water initiation.

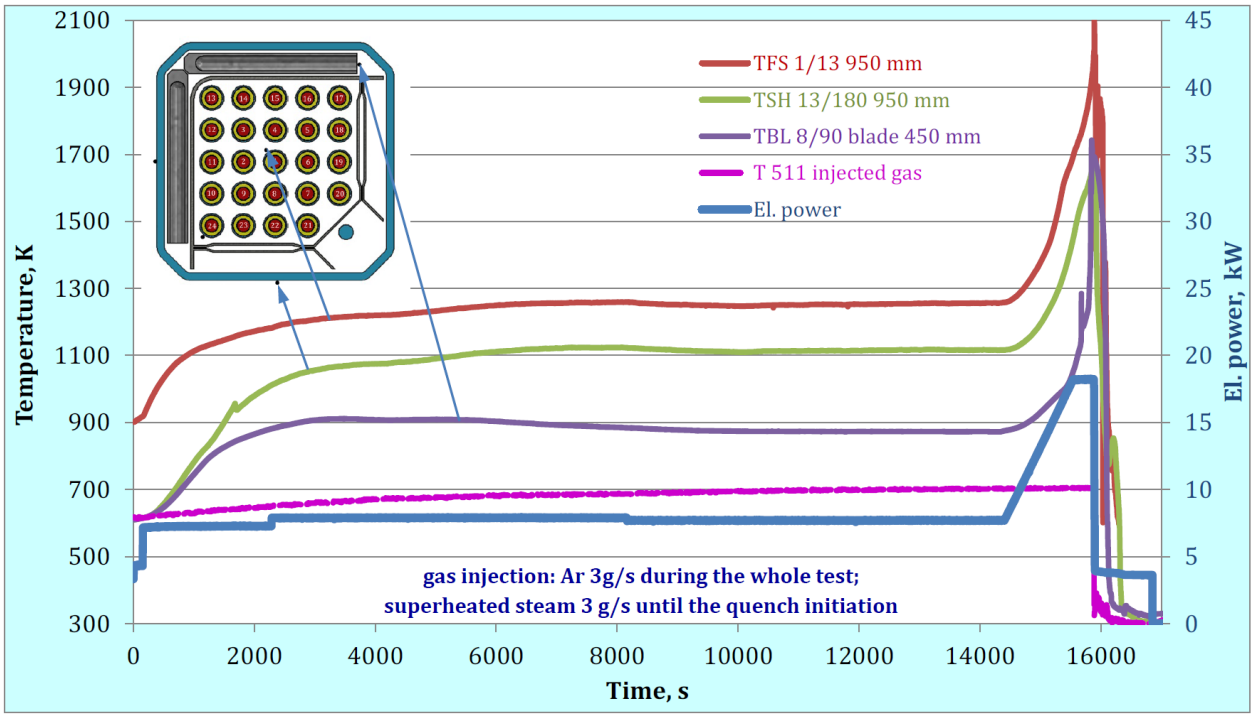

Figure 3. QUENCH-20 Test conduct and results [4].

The hottest elevation of the QUENCH-20 was the level 950 mm similar to most former QUENCH bundle tests.
According to pressure drops, the cladding failures occurred during the transient stage, probably at temperature about 1700 K measured at the failure time point at the elevation 950 mm. Simultaneous release of Kr was registered by mass spectrometer, which shows that seven rod groups failed within about 200 s. The failure sequence from internal to outer rods; this is due to the radial temperature profile, decreasing from the center rod to the shroud. The shroud failure occurred during the cladding failures about 200 s before the quench initiation. The absorber blade failures were registered by He release. The corresponding absorber melt relocations to the elevations of 250 to 450 mm were indicated during the transient stage.

Significant methane formation due to oxidation of B_4C in steam was observed after the quench initiation. The quench water flow rate of 50 g/s was initiated and previously, the bundle foot was filled in about 9 s by fast injection of 4 liters water. The following oscillation readings indicate intensive evaporation of quench water. Finally, the bundle was cooled in about 450 s.
During the quench stage, mass spectrometer registered release of following products of B_4C oxidation by steam: significant amounts of CO (12.6 g), and CO_2 (9.7 g) as well as relatively small mass of CH_4 (0.4 g). The calculations, based on these data, showed that the corresponding mass of reacted B_4C was 38.4 g (4.3% from the total mass of B_4C pins), and additionally to released CO_x and CH_4 gases were formed 96.8 g B_2O_3 and released 10 g hydrogen. The integral hydrogen release during the whole test was 57.4 g, from that 32 g during the quench stage.

3. MODELING OF QUENCH-20 WITH ATHLET-CD

3.1. ATHLET-CD Description

ATHLET-CD (Analysis of THermal-hydraulics of LEaks and Transients with Core Degradation) as part of the code package AC² (developed by GRS) extends the ATHLET code and thus makes use of its models for comprehensive simulation of the thermo-fluid dynamics in the coolant circuit and in the core. ATHLET-CD is activated as a plugin to the ATHLET code. Consequently, ATHLET-CD models are solved using the ATHLET numeric with specific integration schemes depending on whether the modules are strongly coupled or loosely coupled (Figure 4) [5].

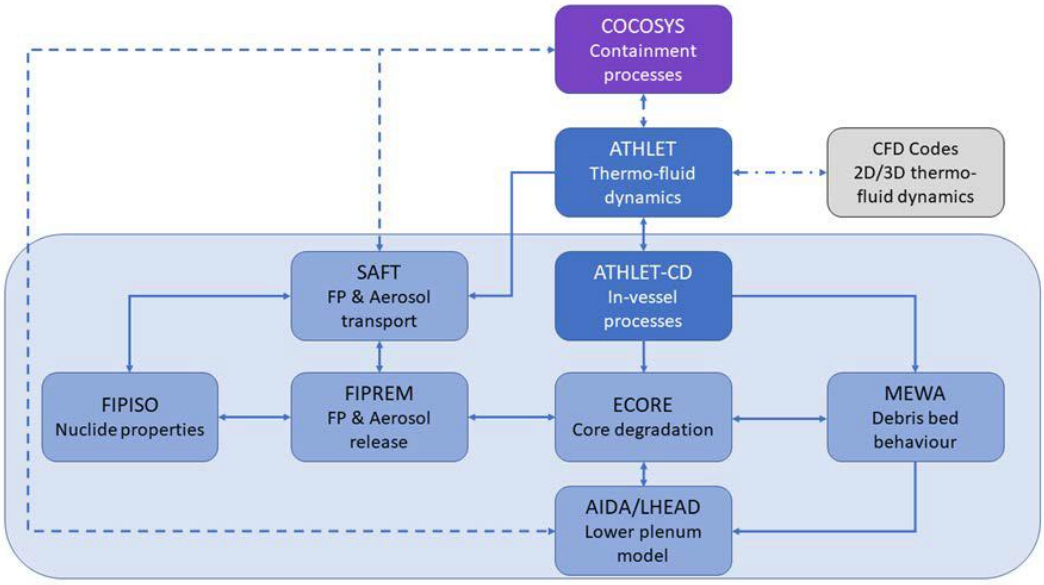

Figure 4. Code structure of ATHLET-CD in AC² [5].

The module ECORE provides models for fuel rod, absorber rod (AIC and B_4C) and the fuel assembly including BWR-canister and -absorber. The module includes models for the mechanical rod behavior (ballooning), an Arrhenius-type rate equation for the oxidation of zirconium and boron carbide, models for Zr-UO_2 dissolution as well as melting of metallic and ceramic components. Melt relocation (candling model) is simulated assuming rivulets with constant velocity and cross section, starting from the node of cladding failure. The model allows oxidation, freezing, re-melting, re-freezing and melt accumulation due to blockage formation.
The feedback to the thermal hydraulics considers steam starvation and blockage formation. In addition to convective heat transfer, energy can also be exchanged by radiation between fuel rods and the surrounding core structures.

The release of fission products is modelled by rate equations or by a diffusion model. The release of aerosols is described by rate equations. The release of control rod material (Ag, In, Cd) is based on temperature functions. The transport and retention of aerosols and fission products in the coolant system are simulated by the SAFT module.
For the simulation of debris bed, a specific model MEWA is implemented with its own fluid dynamic equation system, coupled to the ATHLET thermo-fluid-dynamics on the outer boundaries of the debris bed. The transition of the simulation of the core zones from ECORE to MEWA depends on the degree of degradation in the zone.
The code system ATHLET/ATHLET-CD is coupled to the containment code system COCOSYS with in AC² program package. The AC² codes are supported by the GRS code ATLAS. The ATLAS environment allows not only a graphical visualization of the simulation results but also an interactive control of the calculation.
The code validation is based on integral tests and separate effect tests, as proposed by the CSNI validation matrices with focus on International Standard Problems (ISP) or other benchmarks, and covers thermal-hydraulics, bundle degradation as well as release and transport of fission products and aerosols. They include out-of-pile bundle experiments performed in the CORA and in the QUENCH facility as well as in-pile experiments performed in the PHÉBUS or in the LOFT facility. The TMI-2 accident is used to assess the code for reactor applications [6].

3.2. Nodalisation and Model Options

The nodalisation of QUENCH-20 for the simulation with ATHLET-CD is shown in Figure 5. The main flow path is formed by an inlet (INPIPE), the flow channel with the bundle (BUNDLE) and the outlet (OFFPIPE). The bundle (BUNDLE) is connected via cross-connections (CROSSFLOW) to the outer area of the heated rod bundle (BYPASS), whereby the surface of the BYPASS object covers the free area lying in the area between the canister and the shroud. The length of the test bundle is divided into 17 axial zones, 10 of which are in the heated area. The cross connection between BUNDLE and BYPASS opens after the canister wall fails. The superheated steam, argon as carrier gas and, in the last period of the test, also the quench water flow in at the lower end of the test section via the INPIPE pipe. The steam not consumed during oxidation, argon and the hydrogen produced during the zircon reaction are discharged to the outside at the upper end of the test bundle (OFFPIPE). The inlet and outlet are surrounded by heat conducting structures.
The rod bundle is represented within the ECORE module by an area with 24 heated combustion rod simulators (ROD1). The geometry data of the new arrangement (e.g. free flow areas, hydraulic diameters) were calculated according to the information provided by the experimenters and inserted into the data set. The single corner bar is considered as a HECU object RODA. The pulling of the corner bar is not considered, so it contributes to the oxidation until the end of the simulation.
The 5 spacers (GRID1 to 5) have also been considered as thermal structures, with the HCO's GRID2 to GRID5 being made of zircon and also contributing for oxidation with steam.
The sections of the fuel rod simulators outside the heated length are assumed to be molybdenum and copper electrodes as in previous simulations of the QUENCH experiments.
In addition to the convective heat exchange, the energy transfer due to radiation is also taken into account. In the BWR model, this takes place from the fuel rods to the channel walls and to the absorber blades, but also to the neighboring structure SHROUD and between the structures themselves.

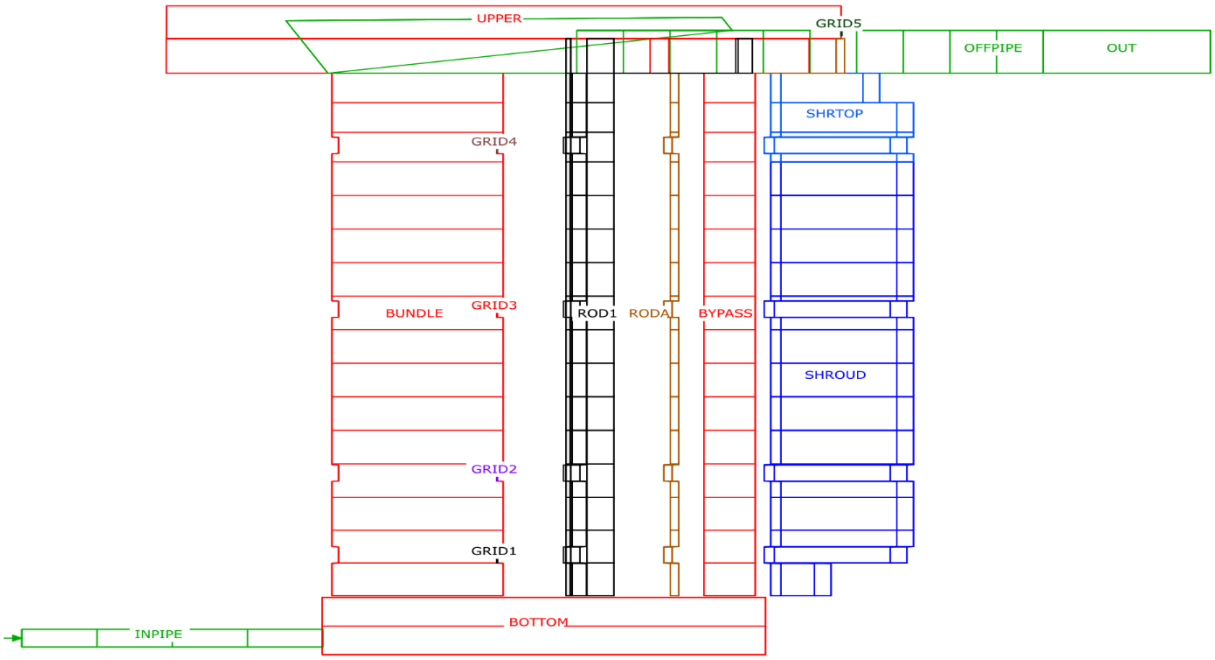

Figure 5. Simplified nodalisation scheme for the simulation with ATHLET-CD.

The BWR main model options relevant for QUENCH-20 are shown in Table 1 based on [4] if available. Additionally, for steam oxidation of cladding, melt and canister walls the correlation of Cathcart and Prater/Courtright is applied [5], [7].

Table I. Main BWR model options for ATHLET-CD

Parameter	Value
Mass of B_4C per absorber blade	0.56 kg/m
Mass of steel per absorber blade	0.985 kg/m
Width of one absorber blade	67 mm
Melt temperature of the eutectic mixture of stainless steel and B_4C	1550 K
Failure temperature of the canister wall	2300 K
Correlation for B_4C oxidation (1. oxidation step)	VERDI-BOX
Correlation for B_2O_3 reaction (2. oxidation step)	BOX-TG
Multiplication factor for surface area due to porosity of B_4C pellet	4.0
Molar mass of CO production	0.525
Molar mass of CO_2 production	0.453
Molar mass of CH_4 production	0.022

4. SIMULATION RESULTS

The results of the simulation in comparison to the experimental data are shown in Figure 6 to Figure 9 for the cladding temperatures, absorber and canister temperatures as well as hydrogen generation and CO, CO_2, CH_4 release.

In general, the predicted cladding temperatures show a qualitative and quantitative good agreement to the measured ones. In Figure 6 the temperatures in the lower and middle elevations are given and show that the calculated temperatures are within the band of experimental values, which is a good result due to the assumption that each single rod in ATHLET-CD has in contrast to the test the same thermal behavior. The measured peak at 550 mm is not captured by the code because the BWR oxidation – canister wall and B_4C oxidation – is underestimated by the code and leads to a lower heat impact. Due to that beside the rod cladding temperature also the absorber and canister wall temperatures in the middle and lower elevations are underestimated (Figure 8). At these elevations the measured absorber blade temperature is higher than the melting temperature of the eutectic mixture of stainless steel and boron carbide, which is not predicted by ATHLET-CD and thus leads to the underestimation of the H_2 generation and corresponding temperatures. In contrast to the experiment the highest absorber temperatures in ATHLET-CD are calculated at higher elevations, but even there the melting temperature is not reached. Due to missing measurement devices a comparison is only possible in the lower elevations where the absorber relocation is assumed based on the findings of the CORA BWR experiments. The calculated cladding temperatures at the higher elevations 750 mm and 950 mm are in good agreement to the measured values and show only a slight overestimation at 950 mm during quenching (Figure 8). The higher cladding temperatures at these elevations are the main driver for the temperature evolution also for the absorber blade and the canister wall, while the B_4C oxidation has only a minor contribution also compared to Zr oxidation of the cladding and the canister wall.

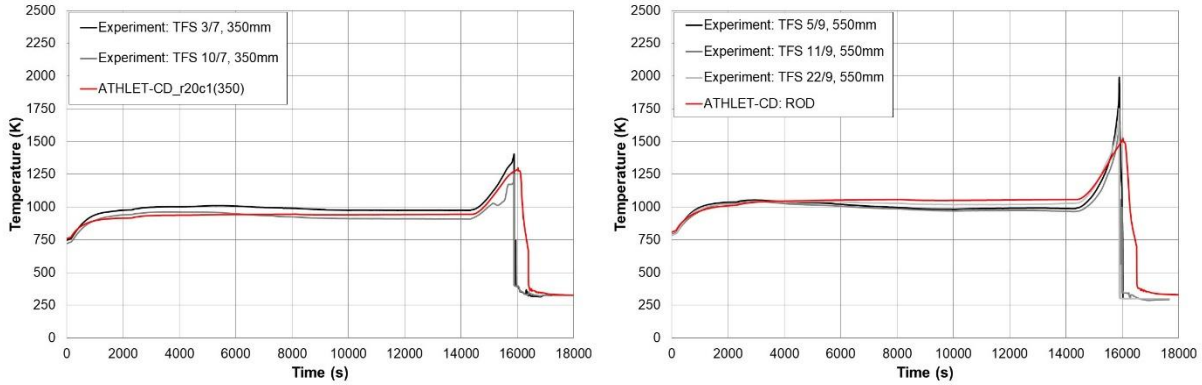

Figure 6. Measured and simulated cladding temperatures at 350 mm (left) and 550 mm (right).

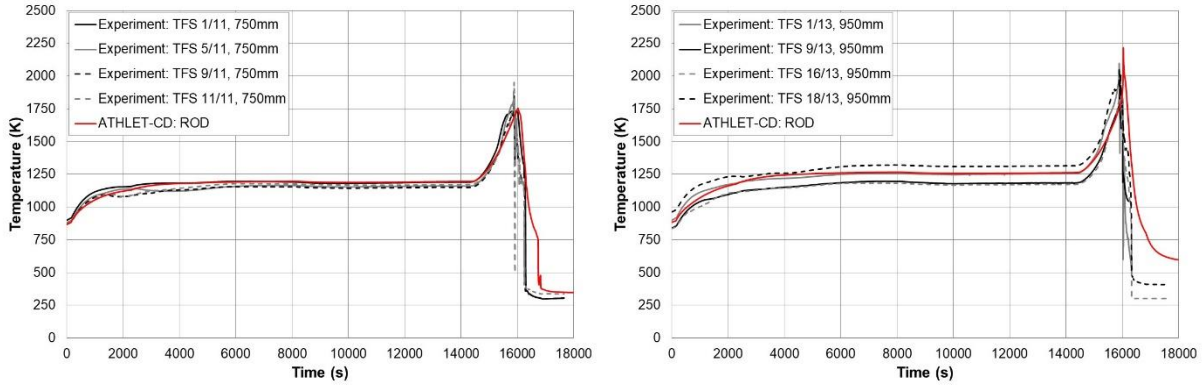

Figure 7. Measured and simulated cladding temperatures at 750 mm (left) and 950 mm (right).

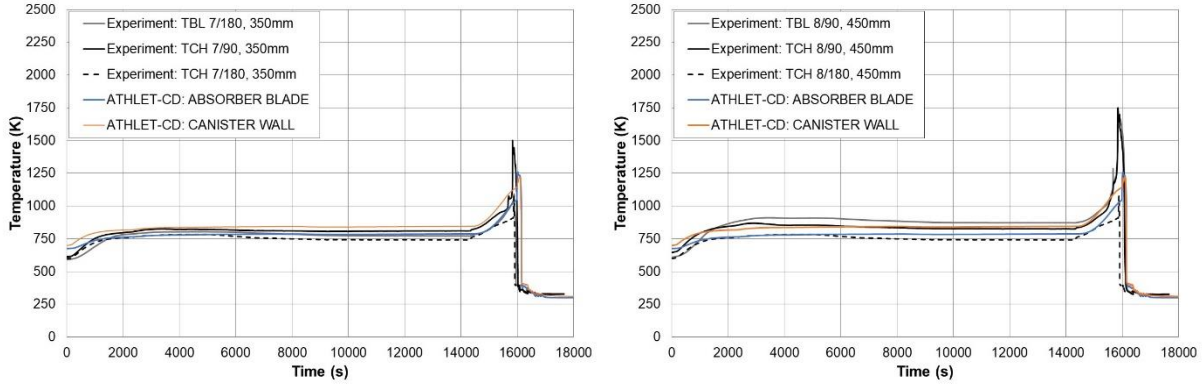

Figure 8. Measured and simulated absorber blade and canister wall temperatures at 350 mm (left) and 450 mm (right).

The total calculated hydrogen generation of all components is close to the experimental value but show an overestimation during the pre-oxidation phase (Figure 9, left), which leads to a higher oxide layer thickness at higher elevations compared to the target of 100 µm. Totally, 44 g H_2 are generated which underestimates the experimental mass (57 g) by 13 g. In the simulation 34 g are caused by rods and BWR structures (11 g) while the shroud and the grids contribute 10 g. By the B_4C oxidation app. 4.2 g H_2 are generated which underestimates the experimental value of 10 g by 58 %, which could be caused by the modeling approach that the BWR oxidation is based on the modelling of PWR B_4C oxidation and the considered surfaces and availability of steam needs to be further investigated. Corresponding to the B_4C oxidation CO, CO_2 and CH_4 are generated and underestimated by the code in the same way as the hydrogen generation (Figure 9, right).

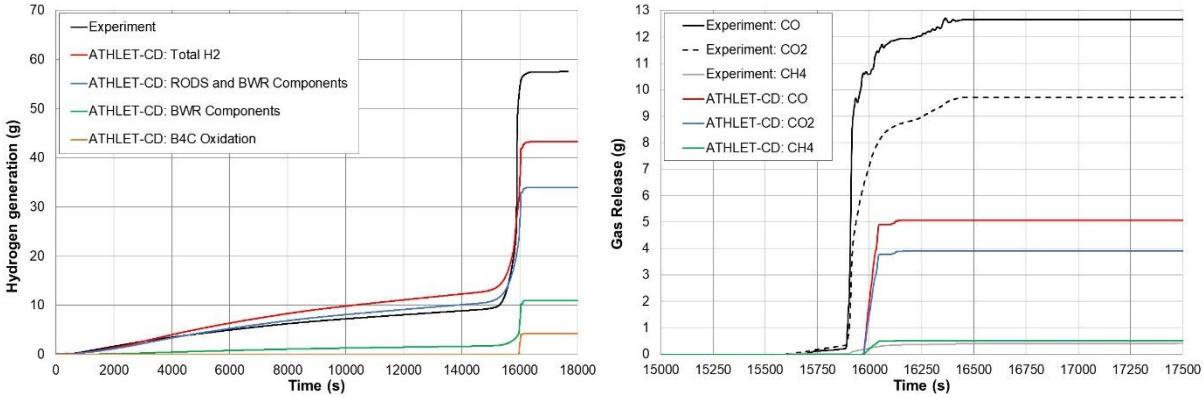

Figure 9. Measured and simulated hydrogen generation (left) and CO, CO_2 and CH_4 release due to B_4C oxidation (right).

5. CONCLUSIONS

The experiment QUENCH-20 was performed at KIT in 2019 in the frame of the EC supported project SAFEST to investigate a BWR bundle under severe accident conditions. This experiment expands the existing BWR test matrix of the CORA test series and was also forced by the accident at Fukushima Daiichi. The results of the experiment show that the cladding reaches the melting point only for a short time at a very high elevation while the absorber blade temperatures in the lower elevations are above the melting temperature. In the pre-oxidation and transient but significantly during quenching hydrogen was generated including a significant mass of 10 g by the oxidation of the B_4C absorber. Post-test examinations are still ongoing with the focus to qualify and quantify the melt evolution and the hydrogen generation by different components.
Pre- and post-test analyses were performed with AC²/ATHLET-CD. The results of the post-test simulations show a good agreement with the experimental observations. The thermal behavior is generally good captured for the cladding, while the BWR components are underestimated especially in the middle and lower bundle heights. This could be caused by the underestimation of the B_4C oxidation which has also an exothermal character with an additional heat impact. Furthermore, melting and relocation of BWR components is not calculated, which could also have an impact on the temperatures in the lower bundle region. Based on post-test examinations the analyses will be continued and a detailed investigation and review of the BWR model including B_4C oxidation is foreseen.

ACKNOWLEDGMENTS

The work of GRS is sponsored by the German Federal Ministry for the Environment, Nature Conservation, Nuclear Safety and Consumer Protection (BMUV).
The Experiment QUENCH-20 was performed in the frame of the EC funded project SAFEST.

REFERENCES

1. S. Hagen et al., “Dry Core BWR Test CORA-33: Test Results“, KfK 5261, Kernforschungszentrum Karlsruhe, Germany, December 1994.
2. L. Sepold et al., “Behavior of BWR-type Fuel Elements with B4C/Steel Absorber Tested under Severe Fuel Damage Conditions in the CORA Facility”, FZKA 7447, Forschungszentrum Karlsruhe, Germany, 2008.
3. J. Stuckert, “First results of the QUENCH-20 experiment with BWR test bundle”, Proceedings of the 25th International QUENCH Workshop, 22-24 October 2019, Karlsruhe Institute of Technology, Karlsruhe, Germany, Editor: Martin Steinbrück, DOI: 10.5445/IR/1000100298.
4. J. Stuckert et al., “Data report on the QUENCH-20 experiment with BWR test bundle”, Scientific Reports NUSAFE 3576-D, Karlsruher Insitut für Technologie, to be published.
5. L. Lovasz et al., “ATHLET-CD 3.3 User's Manual, Input Data Description”, GRS-P-4/Vol. 1 Rev. 8, Gesellschaft für Anlagen- und Reaktorsicherheit (GRS) gGmbH, November 2021.
6. T. Hollands et al., “ATHLET-CD 3.3 Validation”, GRS-P-4/Vol. 3 Rev. 1, Gesellschaft für Anlagen- und Reaktorsicherheit (GRS) gGmbH, November 2021.
7. C. Bals, “Vorausrechnung des Versuchs QUENCH-20 mit ATHLET-CD“, Technische Notiz TN-MIS-19/4, Gesellschaft für Anlagen- und Reaktorsicherheit (GRS) gGmbH, Juli 2019.

EXPERIMENTAL INVESTIAGTION OF QUENCH-20 AND SIMULATION WITH AC²/ATHLET-CD

Thorsten Hollands[1], Juri Stuckert[2], Patrick Isaksson[3], Sevostian Bechta[4]

[1]: GRS gGmbH, Boltzmannstr. 14, 85748 Garching, Germany

[2]: KIT, Hermann-von-Helmholtz-Platz 1, 76344 Eggenstein-Leopoldshafen, Germany

[3]: Swedish Radiation Safety Authority (SSM), Solna Strandväg 96, 171 16 Stockholm, Sweden

[4]: Royal Institute of Technology (Kungliga Tekniska Högskolan - KTH), AlbaNova University Centre, Roslagstullsbacken 21, S-106 91 Stockholm, Sweden

The 10th European Review Meeting on Severe Accident Research (ERMSAR2022)

Akademiehotel, Karlsruhe, Germany

May 16-19, 2022

Content

- Motivation
- QUENCH-20 Experiment
  - Bundle Configuration
  - Test Conduct
- Simulation with AC²/ATHLET-CD
  - Code Overview
  - Nodalisation and Model Options
  - Simulation Results
- Conclusions and Outlook

Motivation

- Between 1988 to 1993 BWR experiments were carried out at the Karlsruhe Institute of Technology (KIT) within the CORA test series, which investigated the behavior of boron carbide absorbers in fuel assembly arrangements typical of boiling water reactors
- It was shown that the early melting of the steel absorber box and the subsequent interaction between steel and boron carbide leads to an early redistribution of absorber melt, whereby blockages are formed in the lower bundle area
- A quantitative determination of the boron carbide oxidation was not possible in these tests, since the quantity of the gases formed (CO, CO_2, CH_4) was not measured
- The theme of investigation of BWR phenomena during severe accidents raised up again after the Fukushima Daiichi accident in 2011

➢ In EU SAFEST project and its call for user access to experimental infrastructure, SSM in collaboration with KIT and KTH suggested QUENCH-20 experiment with a mock-up of BWR core unit cell built with prototypic Westinghouse-made structural materials to study an effect of control blade on fuel assembly degradation

➢ BWR models in severe accident codes needs to be improved and validated

QUENCH-20
– Bundle Configuration –

- Performed at KIT 9th October 2019
- BWR configuration
- Westinghouse bundle parts (clad, channel box, spacer grids, absorber blades, B_4C pins)
- Quadratic Zr shroud
- Bundle configuration:
  - 24 heated rods with tungsten heater
  - ZrO_2 pellets
  - Zy-2 clad with ZrSn inner liner
  - 1 corner rod (withdrawn after pre-oxidation)
  - 5 spacer grids

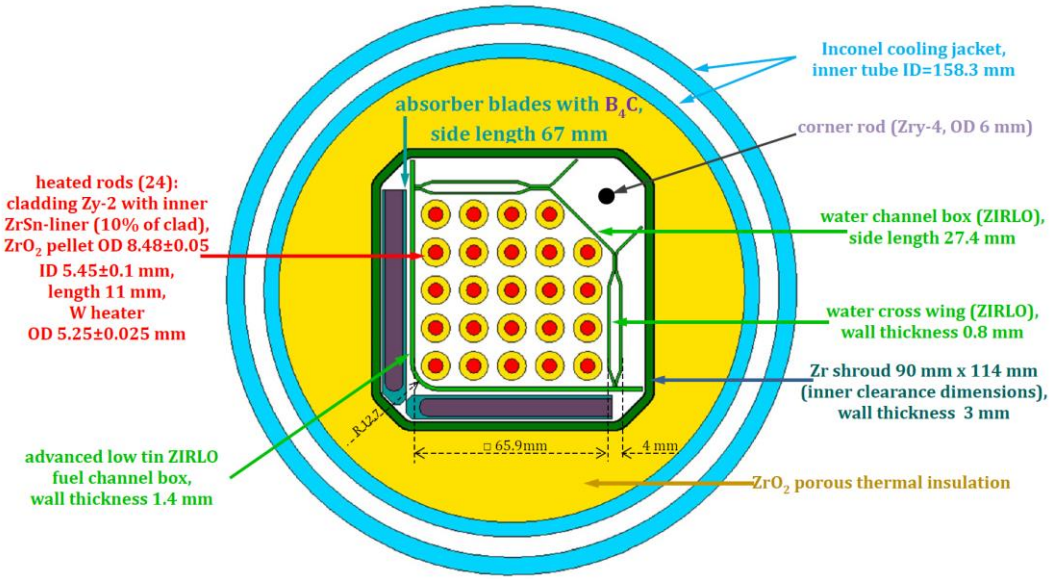

Source: KIT

QUENCH-20
– Test Conduct –

- Pre-Oxidation Phase 0 – 14416 s
- Transient Phase 14416 – 15882 s
- Quench Phase 15882 – 16 375 s

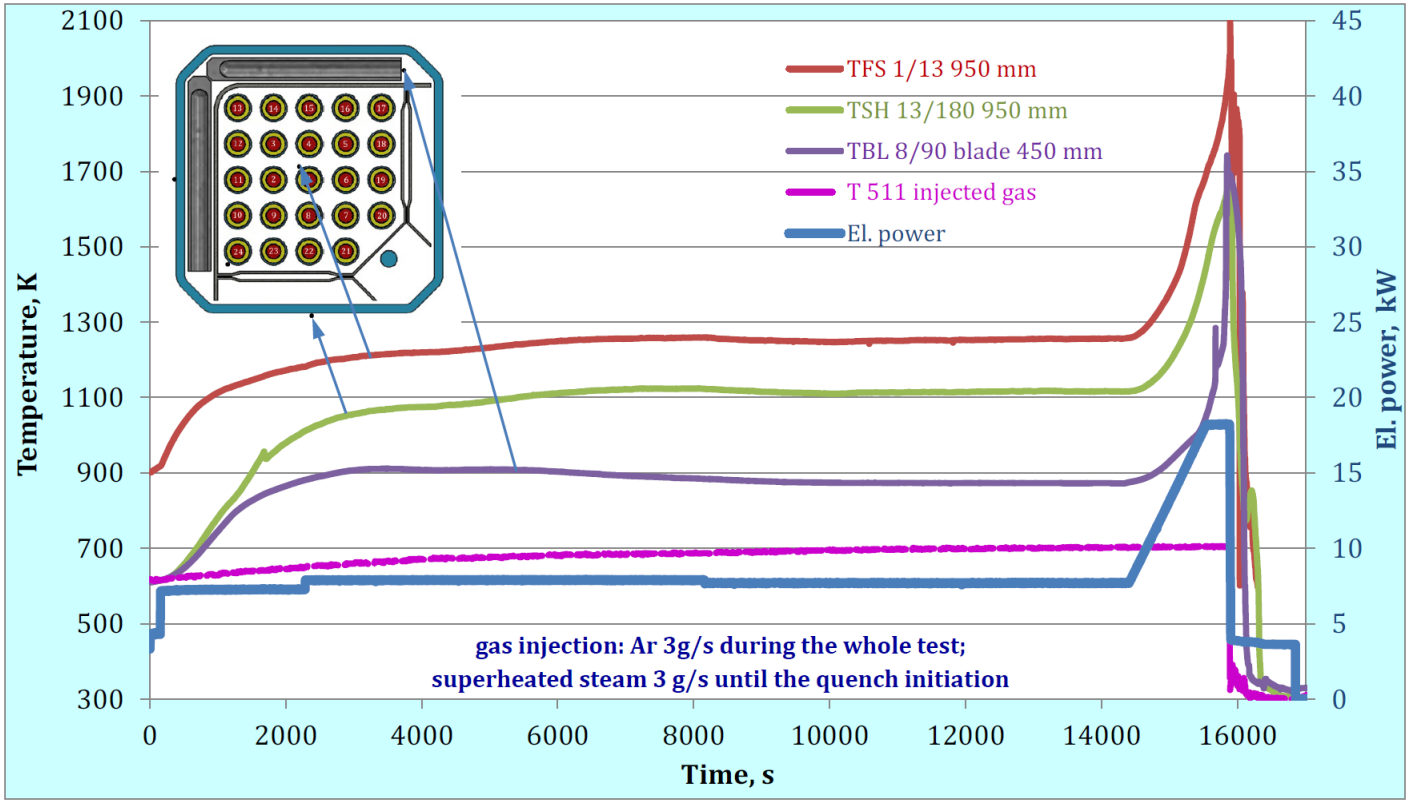

Source: KIT

AC²/ATHLET-CD Code Overview

- The GRS code package AC² consists of
  - ATHLET for the simulation of the thermal hydraulics in the primary circuit,
  - ATHLET-CD for the simulation of core degradation processes and
  - COCOSYS for the simulation of the containment processes for DBA and DEC

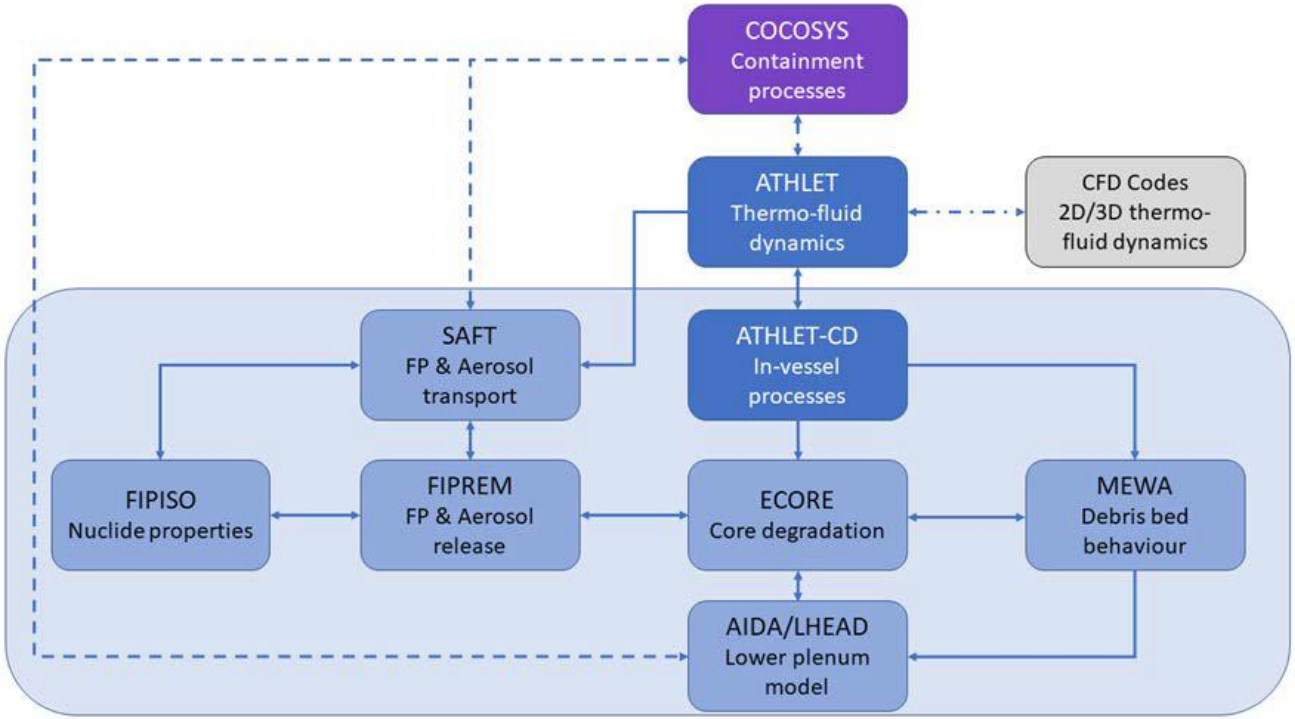

Nodalisation and Model Options

- Standard QUENCH input deck adopted for QUENCH-20 BWR configuration
- Bundle configuration implemented as given by KIT
- Two fluid channels
  - BUNDLE

    53 % within the canister
  - BYPASS

    47 % surrounding the canister
- BWR model for reactor configuration is applied
  - All rods are summed

    up to ROD1
- Corner rod RODA

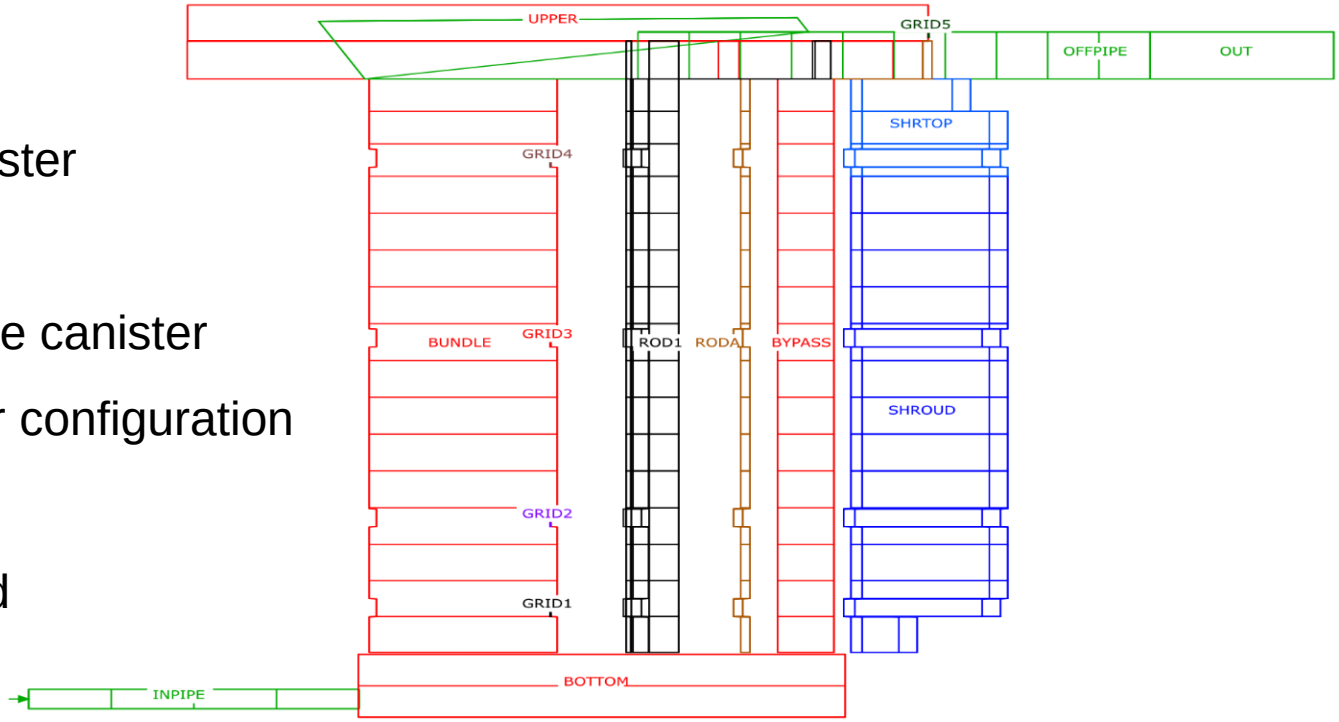

Nodalisation and Model Options

- Cathcart / Prater-Courtright for Zr oxidation
- BWR model options and parameter

Parameter	Value
Mass of B_4C per absorber blade	0.45 kg/m
Mass of steel per absorber blade	1.145 kg/m
Width of one absorber blade	67 mm
Melt temperature of the eutectic mixture of stainless steel and B_4C	1550 K
Failure temperature of the canister wall	2300 K
Correlation for B_4C oxidation (1. oxidation step)	VERDI-BOX
Correlation for B_2O_3 reaction (2. oxidation step)	BOX-TG
Multiplication factor for surface area due to porosity of B_4C pellet	4.0
Molar mass of CO production	0.448
Molar mass of CO_2 production	0.22
Molar mass of CH_4 production	0.025

Simulation Results
– Cladding Temperatures at Lower Elevations –

350 mm

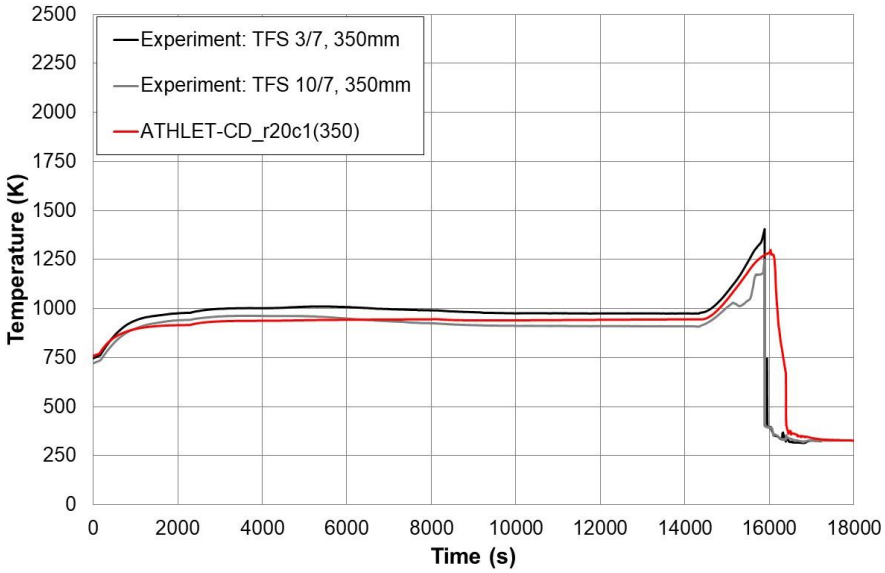

550 mm

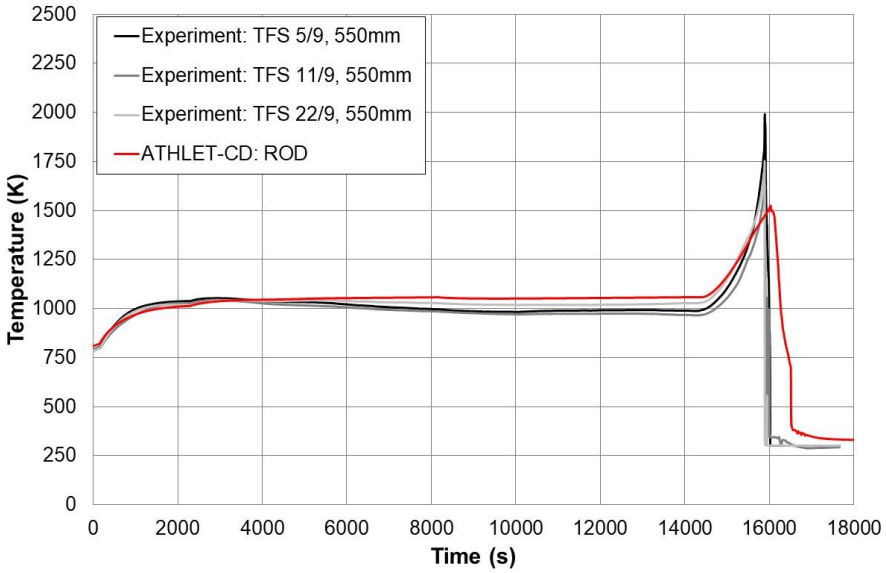

- Good agreement during pre-oxidation
- Underestimation in the middle bundle elevation during transient and quench phases due to underestimation of B_4C oxidation leading which triggers also the temperature escalation of the cladding

Simulation Results
– Absorber/Canister Temperatures at Lower Elevations –

350 mm

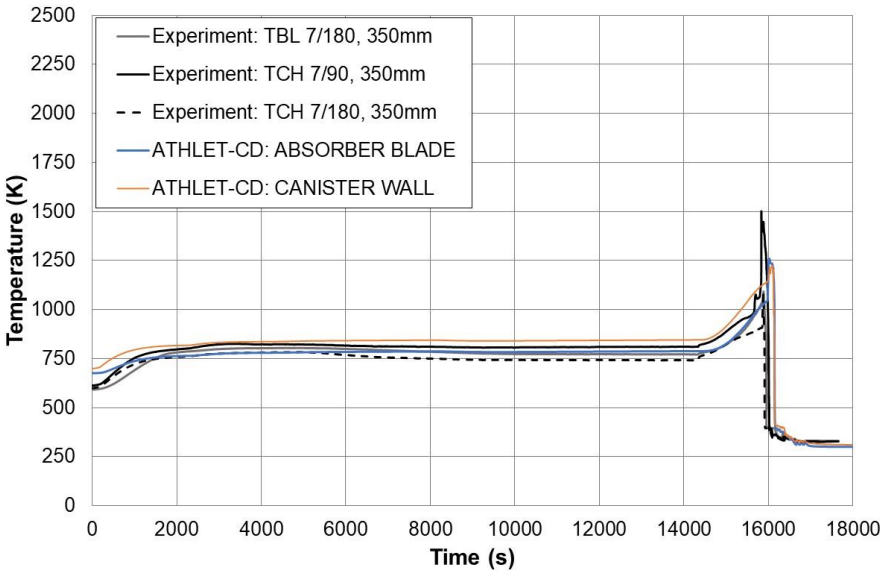

450 mm

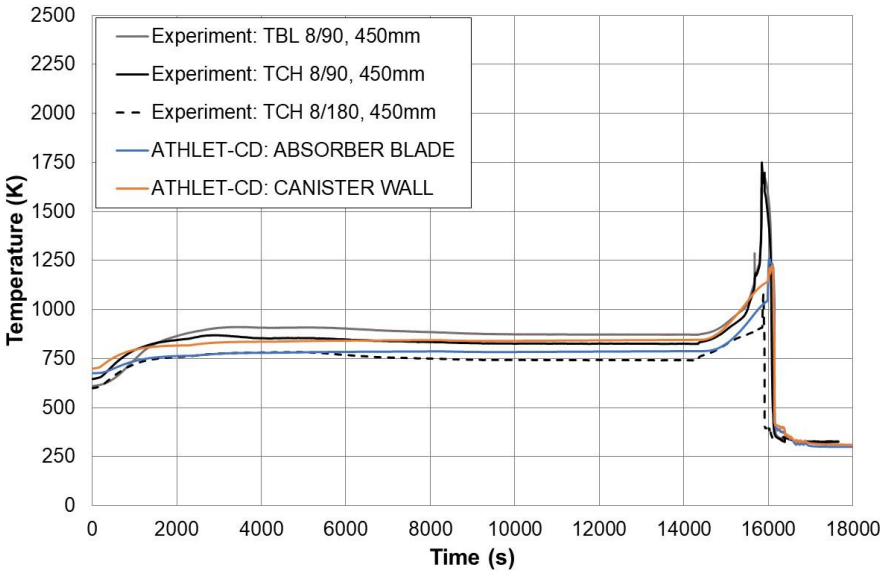

- During the pre-oxidation the numerical results are within the experimental range
- The relocation of absorber material is not calculated which leads – besides the underestimated B_4C oxidation of intact structures – to an underestimation of the oxidation and the corresponding heat impact

Simulation Results
– Cladding Temperatures at Higher Elevations –

750 mm

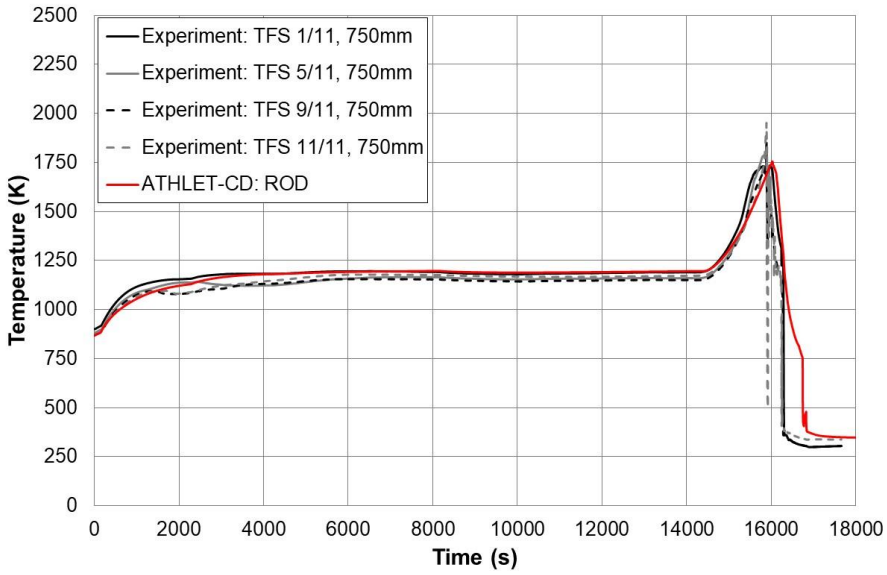

950 mm

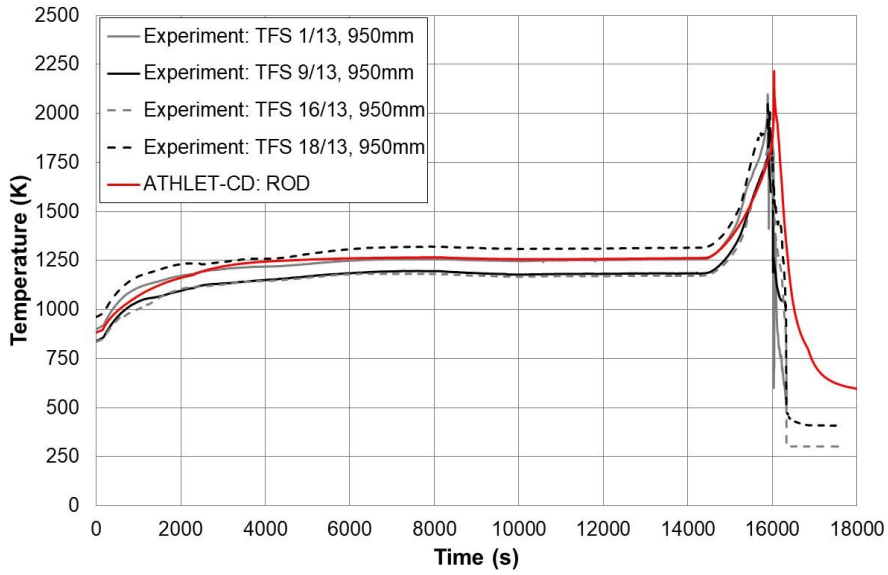

- Simulation results are within the band of measured temperatures
- The observed azimuthal spreading can not be captured by the code due to the assumption that each rod has the same behavior

Simulation Results
– Gas Analysis –

Hydrogen

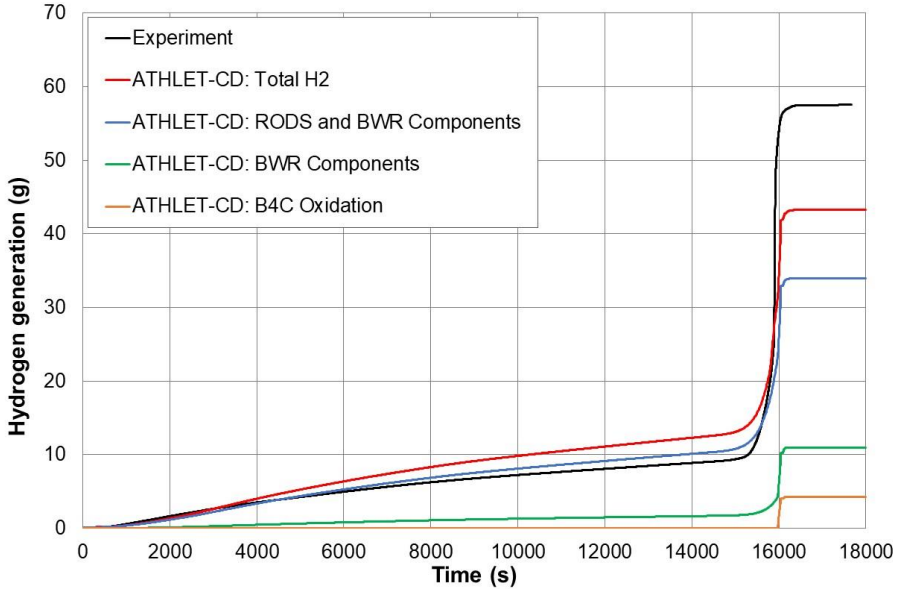

CO, CO_2 and CH_4

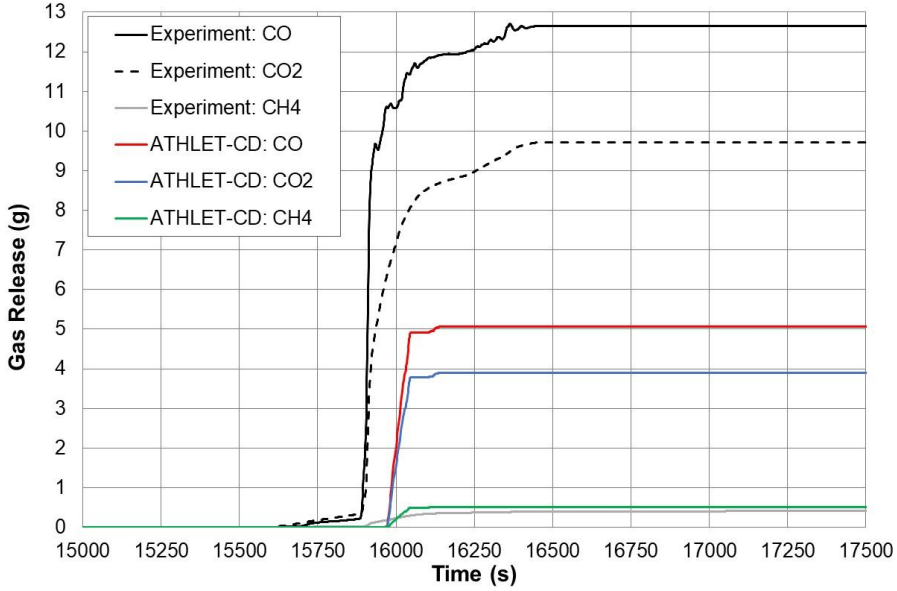

- Total H_2 generation is underpredicted
- B_4C oxidation is underestimated in the simulation by 50 % (10 g H_2 in the experiment), which leads to a comparable underestimation of CO, CO_2 and CH_4
  - Improvement of B_4C oxidation necessary

Conclusions and Outlook (I)

- The experiment QUENCH-20 was performed at KIT in 2019
- The results of the experiment show that the cladding reaches the melting point only for a short time at a very high elevation while the absorber blade temperatures in the lower elevations are above the melting temperature
- In the pre-oxidation and transient but significantly during quenching hydrogen was generated including a significant mass of 10 g by the oxidation of the B4C absorber
- The results of the post-test simulations show a good agreement with the experimental observations
- The thermal behavior is generally good captured for the cladding, while the BWR components are underestimated especially in the middle and lower bundle heights

Conclusions and Outlook (II)

- B_4C oxidation which has also an exothermal character with an additional heat impact is underestimated by the code
- Furthermore, melting and relocation of BWR components is not calculated by ATHLET-CD for QUENCH-20, which could also have an impact on the temperatures in the lower bundle region

- Based on post-test examinations the analyses will be continued and a detailed investigation and review of the BWR model including B_4C oxidation is foreseen

Acknowledgements

- The experiment was performed in the frame of the EC supported project SAFEST
- The work of GRS is sponsored by the German Federal Ministry for the Environment, Nature Conservation, Nuclear Safety and Consumer Protection (BMUV)

Supported by:

Federal Ministry
for the Environment, Nature Conservation,
Nuclear Safety and Consumer Protection

based on a decision of
the German Bundestag

Thank you for your Attention!

Investigation on the detection of radionuclides in North of Europe in June 2020

JJ. Ingremeau, O. Saunier
Institut de Radioprotection et de Sûreté Nucléaire (IRSN)
31 Avenue de la Division Leclerc, 92260, Fontenay-aux-Roses
Jean-jacques.ingremeau@irsn.fr ; Olivier.saunier@irsn.fr

ABSTRACT

During the second half of June 2020, small quantities of artificial radionuclides (^{60}Co, ^{134}Cs, ^{137}Cs, ^{103}Ru, ^{106}Ru, ^{141}Ce, ^{95}Nb, ^{95}Zr) have been detected in northern Europe (Finland, Sweden, Estonia), the source of the release being unknown. The measured values were close to detection limits and didn't represent any health issue. This paper presents the investigations performed at IRSN in order to identify the release location and its origin. Using inverse modelling techniques, the most probable source location has been determined together with an estimation of the release magnitude. Additional investigations have been performed in order to determine from which type and part of a nuclear installation the release could come from. Although no certainty is achievable, the most probable source is a spent primary ion exchange resin. This detection has also been compared to previous similar ones.

KEYWORDS
Atmospheric detection, artificial radionuclides, cobalt, cesium, ruthenium

1. INTRODUCTION

In June 2020, several northern European countries have reported an increase of air concentration levels on aerosol filters sampled at stations belonging to their national monitoring networks. Various artificial radionuclides were indeed detected. The Swedish and Finnish authorities reported that cobalt 60, cesium 134, cesium 137, and ruthenium 103 had been detected by their stations from June 8, 2020. Moreover, the same radionuclides were also detected in Estonia the last week of June. IRSN published an information report on that event [1].

The concentrations levels were very small in the order of several µBq/m3 and do not pose any health or environmental effects. Maximum air concentrations measurements (Figure 1) were reported in Finland at Helsinki, from June 16 to 17, 2020, of the order of ten µBq/m^3 : Cs-137 = 16,4 µBq/m^3 ; Cs-134 = 21,5 µBq/m^3 ; Co-60 : 7,6 µBq/m^3 ; Ru-103 : 4,8 µBq/m^3. The limited number of measurements above detection limits makes it very difficult to pinpoint the geographical origin of the detections.

In Section 2, atmospheric transport modeling combined with measurements was therefore applied to both narrow down the possible locations of the origin of the release and to estimate its magnitude. In Section 3, the characteristics and the estimated magnitude of each isotope are analyzed in order to determine from which type and part of a nuclear installation the release could come from. Section 4 focuses on comparison with previous releases.

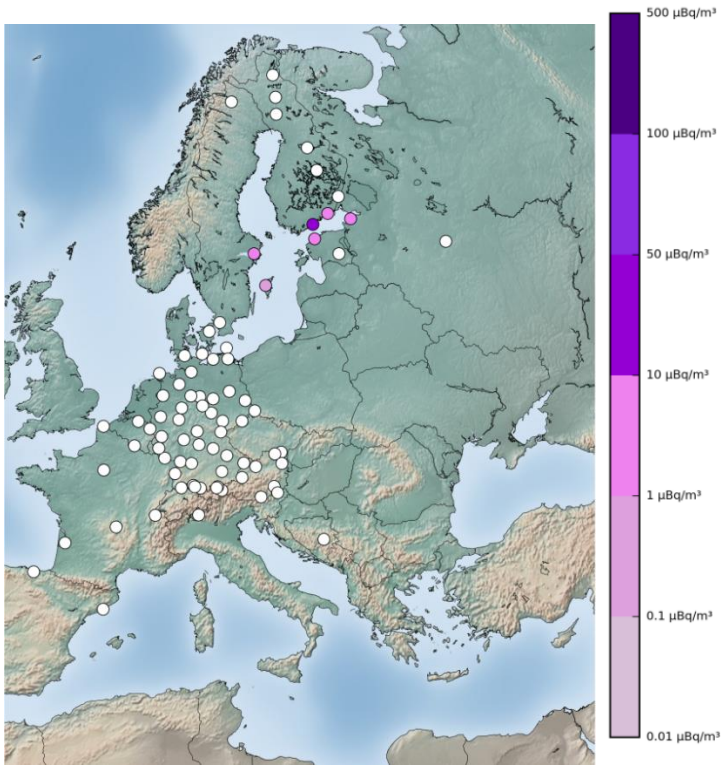

Figure 1. Maximum ^{134}Cs air concentration for each monitoring station (µBq/m3). With dots are air concentration measurements below the detection limit.

2. INVESTIGATIONS ABOUT THE RELEASE LOCATION AND MAGNITUDE

2.1. Source Location

Inverse modelling techniques which combine atmospheric transport model and observations in the environment are applied to reconstruct the source location and its magnitude. 134Cs air concentrations measurements are the most numerous and are therefore exploited for source identification. The approach used is described in detail in [2]. It is first assumed that the release occurred somewhere between Germany and Russian Federation. For computation time reasons, the domain likely to contain the source is divided into a set of 348 grid points. Each centre of cell is then considered to be a potential source of release. Dimensions of the domain including the potential sources are [14E, 42E], [55N, 66N] with 1° × 1° resolution.

For each potential source, a source term is assessed by inverse modelling using a variational approach assuming that the measurement vector can be described as a linear model with a source-receptor matrix and unknown source term vector $\boldsymbol{\sigma}$:

$$\mu = \mathbf{H}\boldsymbol{\sigma} + \boldsymbol{\epsilon} \quad (1)$$

The **H** source-receptor matrix holds modelled ^{134}Cs air concentrations using the ldX atmospheric transport model and in response to a unit source. ldX is used to simulate the ^{134}Cs dispersion over the domain of dimensions [4W, 44E], [40N, 71N], it is part of IRSN's C3X operational platform [3]. It has been applied to deal with massive accidental releases into the environment [4], [5] and minor radionuclide detection events [6]. ldX is fed with hourly meteorological data from ARPEGE model provided by Météo-France. Spatial resolution of the data is 0.1° x 0.1°.

The vector $\boldsymbol{\epsilon}$ represents a combined model-representation-instrumental error. Assuming that the errors $\boldsymbol{\epsilon}$ follow a log-normal disribution, the source term can be assessed by minimizing the cost function $\mathbf{J_{LN}}$ which measures the differences between the model predictions $\mathbf{H\sigma}$ and the real measurements $\boldsymbol{\mu}$:

$$\mathbf{J_{LN}}(\boldsymbol{\sigma}) = \frac{\mathbf{1}}{\mathbf{2}}\big(\mathbf{ln}(\boldsymbol{\mu}) - \mathbf{ln}(\mathbf{H\sigma})\big)^{\mathbf{T}}\mathbf{R^{-1}}\big(\mathbf{ln}(\boldsymbol{\mu}) - \mathbf{ln}(\mathbf{H\sigma})\big) \quad (2)$$

where $\mathbf{R} = \mathbf{E}[\boldsymbol{\epsilon}\boldsymbol{\epsilon}^{\mathbf{T}}]$ is the error covariance matrix associated with the error. It is well known that the source-receptor relationship (1) constitutes an ill-posed inverse problem and its resolution may fail particularly when the number of observations is limited. That is why a background term is usually added in the cost function (2) to stabilize the inverse problem and to ensure the unicity of the solution. This term measures the differences between a priori (or background) source term $\boldsymbol{\sigma_b}$ and the updated source term $\boldsymbol{\sigma}$:

$$\frac{\mathbf{1}}{\mathbf{2}}\big(\mathbf{ln}(\boldsymbol{\mu}) - \mathbf{ln}(\mathbf{H\sigma})\big)^{\mathbf{T}}\mathbf{R^{-1}}\big(\mathbf{ln}(\boldsymbol{\mu}) - \mathbf{ln}(\mathbf{H\sigma})\big) + (\boldsymbol{\sigma} - \boldsymbol{\sigma_b})^{\mathbf{T}}\mathbf{B^{-1}}(\boldsymbol{\sigma} - \boldsymbol{\sigma_b}) \quad (3)$$

In order to mitigate the influence of very small concentration values, a threshold $\boldsymbol{\theta}$ ($\boldsymbol{\theta}$= 1 µBq/m3) is introduced in the cost function:

$$\mathbf{J_{LN}}(\boldsymbol{\sigma}) = \frac{\mathbf{1}}{\mathbf{2}}\big(\mathbf{ln}(\boldsymbol{\mu} + \boldsymbol{\theta}) - \mathbf{ln}(\mathbf{H\sigma} + \boldsymbol{\theta})\big)^{\boldsymbol{T}}\mathbf{R^{-1}}\big(\mathbf{ln}(\boldsymbol{\mu} + \boldsymbol{\theta}) - \mathbf{ln}(\mathbf{H\sigma} + \boldsymbol{\theta})\big) \quad (4)$$

In this study, it is assumed that **R** and **B** are diagonal and the error variance is the same for all diagonal elements of the matrix. The minimization of $\mathbf{J_{LN}}(\boldsymbol{\sigma})$ is therefore equivalent to minimizing:

$$\mathbf{J_{LN}}(\boldsymbol{\sigma}) = \frac{\mathbf{1}}{\mathbf{2}}\big(\mathbf{ln}(\boldsymbol{\mu} + \boldsymbol{\theta}) - \mathbf{ln}(\mathbf{H\sigma} + \boldsymbol{\theta})\big)^{\mathbf{T}}\big(\mathbf{ln}(\boldsymbol{\mu} + \boldsymbol{\theta}) - \mathbf{ln}(\mathbf{H\sigma} + \boldsymbol{\theta})\big) + \boldsymbol{\lambda^2}(\boldsymbol{\sigma} - \boldsymbol{\sigma_b})^2 \quad (5)$$

The cost function (5) is directly minimized using the L-BFGS-B limited-memory quasi-Newton minimizer by enforcing the positivity of the source. The $\boldsymbol{\lambda}$ parameter acts on the magnitude of the source and has to be determined outside the minimization procedure. Usually, when the number of observations used to reconstruct a release event is low, the source term magnitude may be very sensitive to the value of $\boldsymbol{\lambda}$ parameter. In that case, strong values of $\boldsymbol{\lambda}$ lead to source term tempered too much whereas small values of $\boldsymbol{\lambda}$ yield to unrealistic source term in which the norm may tend to infinity. In practice, the choice of the $\boldsymbol{\lambda}$ parameter therefore involves a compromise between reducing the error value related to the cost function and increasing the amount of radionuclides emitted. In this study, the optimal choice of $\boldsymbol{\lambda}$ is determined using L-curve method [7]. It consists in plotting the source term norm versus the norm of the first term of $\mathbf{J}(\boldsymbol{\sigma})$ (residues) obtained after the minimization of (5) for several values of $\boldsymbol{\lambda}$ and to identify the maximum curve point in the graph. For every source term assessment associated with each grid point, an optimal value of $\boldsymbol{\lambda}$ is therefore determined applying the L-curve technique. The initial values are in the range of 10^{-12} to 10^{-3} and the optimal value is reached for inversion performed with $\boldsymbol{\lambda} = 10^{-6}$.

The source reconstruction period is between June 5 and June 28 with daily time intervals. Only ^{134}Cs air concentration measurements have been exploited since they are most numerous. A total of 250 ^{134}Cs air concentration measurements have been taken into account to assess the origin and the magnitude of the release, of which 10 are non-zero measurements and the remaining are non-detections, i.e measurements below the detection limit.

Then, for each inverted source related to each grid point, the agreement between modelled and observed air concentration measurements is assessed using the factor 5 indicator (FAC5). FAC5 is the proportion of the simulated activity concentrations calculated using the reconstructed release that are within a factor of 5 of the observed values.

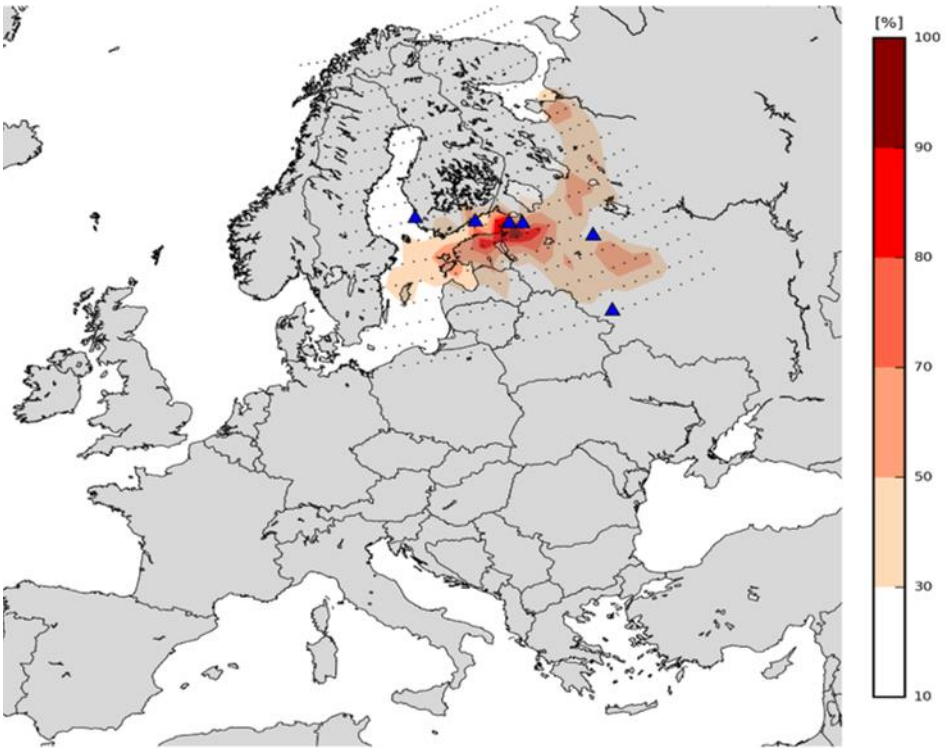

Figure 2. Percent of the simulated air concentrations that is within a factor of 5 of the observed values. Blue triangles are nuclear plants located in the area of interest: Leningrad NPP, Petersburg Nuclear physics Institute (Gatchina), Olkiluhoto NPP, Loviisa NPP and Smolensk NPP

The interpolated values of FAC5 from each grid point are shown in Figure 2. Despite the small number of measurements used to reconstruct each source term, the area where the FAC5 values exceeds 80% is small. This region extends from eastern Estonia to western Russian Federation whereas the FAC5 values reach 100% in an area restricted to the Leningrad region. Moving away from this area, the FAC5 values decrease rapidly indicating that the hypothesis of a release from Western Europe and Scandinavia is unlikely. For the most plausible source location, the released activity of ^{134}Cs is around a few gigabecquerels (GBq). Based on the isotopic ratios obtained from the measurements of radionuclides detected in the environment (^{106}Ru, ^{103}Ru, ^{60}Co, ^{137}Cs), it can be deduced that several tens of gigabecquerels were released during the period considered.

2.2. ^{134}Cs Release Magnitude

In the most plausible release location, we identified two facilities that may be responsible for the emissions namely the Leningrad Nuclear Power Plant and the Gatchina Institute of Nuclear Physics. According to our calculations, due to the proximity of the two nuclear sites, it is not possible to favour one facility over the other.
Nevertheless, considering the source term characteristics the Gatchina location can be excluded. Indeed the Gatchina site had only one nuclear reactor in operation in June 2020, which had only worked at low power at that time. It's impossible that such low power operation can generate such amounts of ^{60}Co. Moreover, it is very unlikely that such reactor leads to the mesured ceasium ratio (§3). Gatchina has also some cyclotrons, that cannot produce this type of source term.

We therefore estimated the source term from the Leningrad Nuclear Power Plant. As the minimization of the cost function $\mathbf{J_{LN}}$ only provides an optimal solution without quantifying the model-representation-instrumental error, we use a Monte-Carlo sensitivity analysis [2] to partially quantify that error. It consists

of generating a set of source terms where, for each sample n, the observation vector μ is perturbed such as $\tilde{\mu}_i = r\mu_i$, $1 \leq i \leq d$, where d is the measurement number and r follows a log-normal law $r \sim \exp(N(0, \zeta^2))$ where ζ is the standard deviation of the related Gaussian law N(0, ζ). Then, for each sample n, an optimal source term $\widehat{\sigma_n}$ is obtained by minimizing the cost function $\mathbf{J_{LN}}(\widehat{\sigma_n})$.$J(\widehat{\sigma_n})$ The Monte-Carlo analysis was performed using n=20,000 samples with a realistic value of the standard deviation ζ=0.8. This analysis indicates that the estimated ^{134}Cs source term for the entire period lies between 2 and 20 GBq. This is a relatively wide range and reflects the uncertainties associated with the source term assessment. Figure 3 shows the temporal evolution of the releases between June 4 and June 28. It can be seen that the first releases started on June 13 and continued until June 22. During this period, the magnitude of the peaks varies significantly and the standard deviation associated with each peak is very large. This emphasizes the uncertainty in our estimates, which may be partially attributed to the use of a limited number of observations. After June 23, the calculations indicate that the occurrence of a release is not consistent with the observations. Indeed, if the release had continued after June 22, the stations would have reported an increase of ^{134}Cs air concentrations. It is therefore likely that the release ended on June 23 or else, it was too small to be detected.

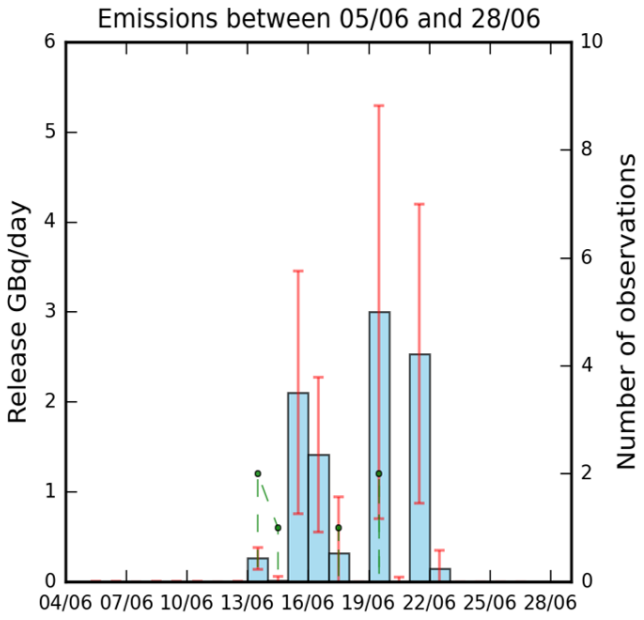

Figure 3. Mean and standard deviation range of the reconstructed source term (blue) using Monte-Carlo sample. Green dots are the number of observations used in the inversion procedure.

2.3. Plume Dispersion Analysis

The ^{134}Cs plume dispersion was performed using the reconstructed source term from Leningrad NPP. The Figure 4 shows the dispersion of the plume at different dates between June 16 and June 25. During the period of the release, it can be seen that the plume mainly affected the northern European countries located between Scandinavia and western Russian Federation. Driven by east to north-east winds, the plume temporarily reached the regions between central Europe and Germany, particularly between June 16 and June 18 then between June 24 and June 26. However, the modelled air concentration levels are extremely low, usually undetectable by the monitoring networks. Nevertheless, the station of Braunschweig in Germany was able to detect tiny traces of ^{60}Co between June 15 and 22, which tends to confirm the results obtained by modelling.

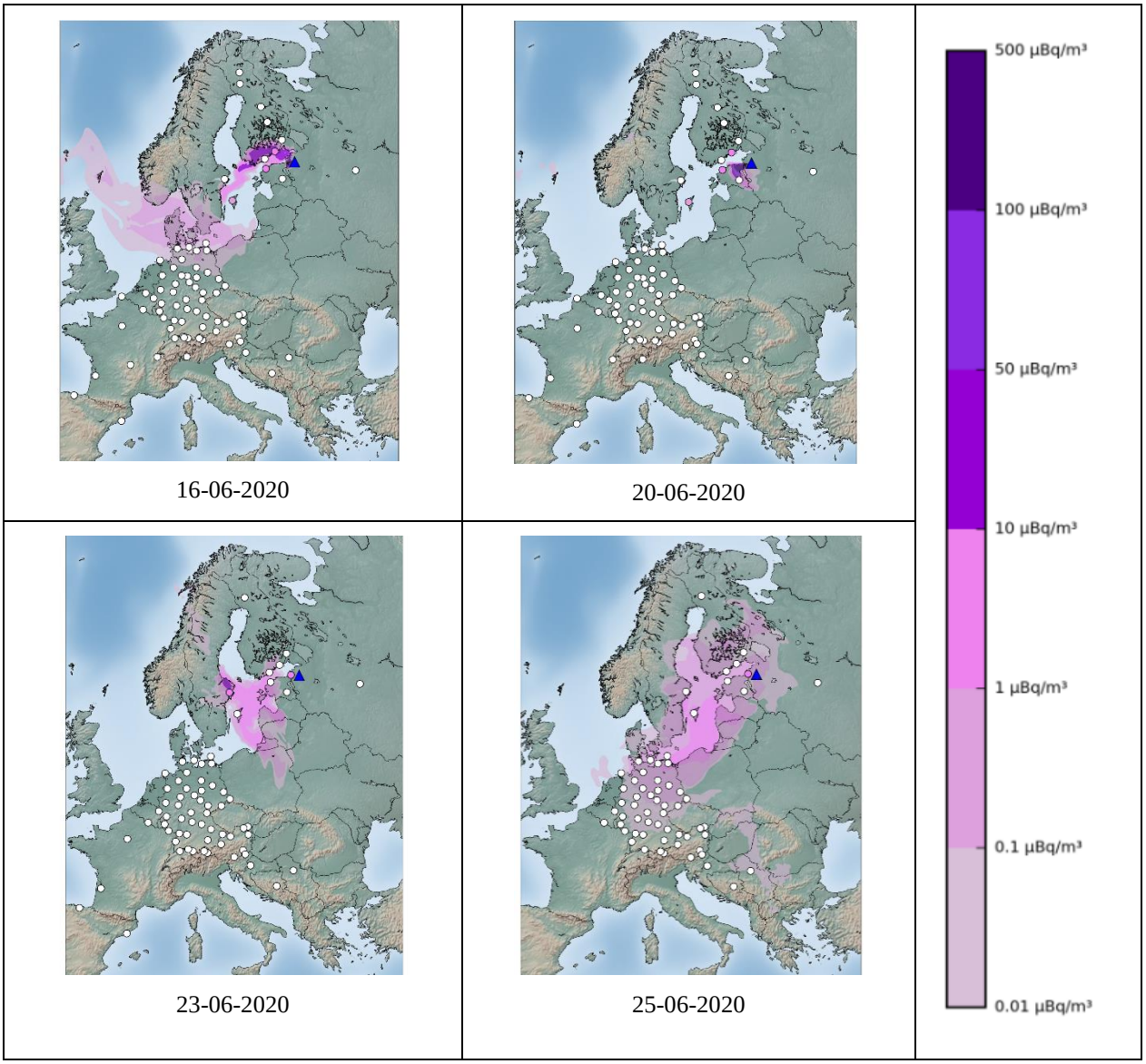

Figure 4. Modelled ^{134}Cs air concentration at different times (UTC) assuming a release location at Leningrad NPP. Blue triangle is Leningrad nuclear power plant. Circles are ^{134}Cs observed air concentrations in µBq/m^3

3. INVESTIGATIONS ABOUT THE SOURCE TERM ORIGIN

The objective of this part is to determine from which type and part of a nuclear installation the release measured in June 2020 could come from. For that purpose, the characteristics and the estimated magnitude of each isotope are analyzed.

3.1. General Information on the Source Term

Considering the ^{134}Cs release magnitude at the most probable release location, and the various activity ratios observed in the different measurements, the order of magnitude of each isotope of the source term has been evaluated and is presented in the Table I.

Table I. Type and estimated order of magnitude of the source term

Isotope	Half-life	Estimated Source Term	Origin
^{60}Co	5,26 y	~ GBq	Activated corrosion product
^{134}Cs	2,07 y	~10 GBq	Volatile fission product
^{137}Cs	30,1 y	~10 GBq	
^{103}Ru	39,2 d	~ GBq	Low-volatile fission product
^{106}Ru	371,8 d	~ GBq	
^{141}Ce	32,5 d	~ 100 MBq	
^{95}Nb	35 d	~ GBq	Low-volatile fission product or / and Activated corrosion product
^{95}Zr	64 d	~ GBq	

Some general comments can be drawn on that source term:

- First, it must be noticed that it doesn't contain any short-lived isotopes (such as iodine). This tends to exclude an event concerning very recently irradiated material (less than a few weeks).
- Second, it contains some "intermediate half-life" isotopes (meaning about a few months) such as ^{103}Ru, ^{141}Ce, ^{95}Nb, ^{95}Zr. This implies that the event concerns relatively recent irradiated materials, with less than a year of decay. The presence of long-lived isotopes (^{60}Co, ^{134}Cs, ^{137}Cs, ^{106}Ru) is coherent with that assumption.
- Third, these isotopes come from various production sources;
    - ^{60}Co is an activated corrosion product,
    - ^{103}Ru, ^{134}Cs are fission products, cesium being volatile, ruthenium being non-volatile.

As a result, the origin of the release must be something mixing activated corrosion products and fission products, with probably a few months of decay.

3.2. ^{60}Co – Presence of Activated Corrosion Product

The evaluated source term contains a few GBq of ^{60}Co. This isotope is an activated corrosion product, produced by neutron capture on ^{60}Ni or ^{59}Co.

Such amount of ^{60}Co is expected to be found in only 4 places:

- **on internal structures (steel) of a nuclear reactor**. But this source can't lead to massively atmospheric release, and as a result is not an option;

- **in the primary water of a nuclear reactor**, due to corrosion of activated steel, or activation of corrosion products due to the neutron flux in the core. That inventory should be partially released into the atmosphere in case of primary water leakage outside of the containment. But, in such a case, a lot of other short-lived isotopes would be expected (such as ^{58}Co or iodine in case of fuel cladding leakage or failure). In addition, the amount of ^{60}Co that could be released into the atmosphere during such event is expected to be a few orders of magnitude too low to explain the measurements. So, this hypothesis isn't consistent with the measured data;
- **in a ^{60}Co gamma radiation source**. In common gamma radiation source, the ^{60}Co activity can vary from a few GBq up to millions of GBq. But, due to the high chemical stability of cobalt, it's very unlikely to release a large part of that activity in the atmosphere, except in case of fire or mechanical cutting in the open air generating fine dust. In addition, in case of an accident on a ^{60}Co source, no other isotope would be expected, in contradiction with the presence of ^{103}Ru or ^{134}Cs. As a result, this hypothesis is not an option;
- **in primary ion exchange resin**. These resins are commonly used to clean the primary water. They accumulate during several years the activated corrosion products of the primary water, and fission products in case of fuel cladding leakage of failure. The typical ^{60}Co inventory in a spent primary resin is about hundreds to thousands of GBq, which is fully compatible with a few GBq atmospheric releases. Some primary filter may also have significant amounts of ^{60}Co in particle form.

In conclusion, the primary ion exchange resin, or other component of the primary loop cleaning system, is the best candidate to explain the presence of such amount of ^{60}Co.

3.3. ^{134}Cs & ^{137}Cs – Presence of Volatile Fission Products

^{134}Cs and ^{137}Cs, which were evaluated to a few tens of GBq each, are volatile fission products[1]. They are expected to be found only in spent nuclear fuel, or in the facilities processing them, except in case of fuel cladding leakage or failure during an operating cycle. In the June 2020 release, the hypothesis of a spent fuel assembly accident, or an event in a spent fuel facility can be excluded, due to the presence of ^{60}Co (not found in such quantities in a fuel assembly), and the presence of intermediate half-life isotopes (such as ^{103}Ru), despite the fact that spent fuel assembly generally decays few years in the spent fuel pool before being evacuated.

In case of fuel cladding leakage or failure in an operating reactor, the cesium isotopes would easily migrate to the primary water. But again, in case of a primary water leakage, the amount of cesium released in the atmosphere would be too low to explain the June 2020 measurements. Besides, in the primary water, they will be cleaned by the primary ion exchange resin and accumulated in it. Typical cesium activities in primary resin in case of fuel leakage or cladding failure during operation are from tens to thousands of GBq. Such amount could explain the June 2020 measurements.

The ^{134}Cs / ^{137}Cs activity ratio is also a good indicator of the type of nuclear fuel involved. It has been measured from 1.2 to 1.7 (Helsinki station). That ratio could be obtained in almost any spent fuel of a Pressurized Water Reactor (PWR) (including WWER) after a few months of decay, depending of the enrichment and burn-up. But this value seems very unlikely to be obtained in a RMBK reactor. Indeed, the typical values at end of cycle are close to 0.5 and decrease after shutdown [8].

As a result, the best hypothesis for the cesium origin in the June 2020 release is a primary resin from a PWR or WWER, with a fuel cladding leakage or failure.

[1] ^{134}Cs is not strictly a fission product as it is mainly produced by the neutron capture on the ^{133}Cs, which is a "direct" fission product. Nevertheless, it is generally associated with the fission products, because it requires fission to be produced.

3.4. ^{103}Ru & ^{106}Ru – Presence of Low Volatile Fission Products

The presence of ^{103}Ru and ^{106}Ru in an atmospheric release is particularly interesting. Indeed, ruthenium is a low volatile fission product, which mainly remains in the fuel pellet. It is very stable and only very small fractions will be released out of the pellet, even in case of fuel cladding failure, except in case of high temperature fire (>2000°C) in very oxidizing conditions. Moreover, the presence of the ^{103}Ru isotope, with a half-life of 39 days, is incompatible with the usual decay of spent fuel in the pool for several years.

Nevertheless, in case of fuel cladding failure, some significant quantities of ^{106}Ru (from tens to thousands of GBq) can be released from the accumulated inventory in the fuel pellets. But, this migration from the UO_2 matrix to the gap is so slow, that the ^{103}Ru decays before reaching the primary water. It is mainly ^{106}Ru which is released by this way.

The only way to get a few GBq of ^{103}Ru outside of a fuel pellet is to have a fuel dispersion in the primary water. Indeed, some fuel cladding failure may lead to the dispersion of small amounts of uranium oxide outside of the pin, in the primary water. Exposed to the neutron flux, that fissile material will fission and release its fission products directly in the primary coolant. Such events are easy to detect by an increase of short-lived isotopes in the coolant, such as ^{135}Xe, ^{138}Xe or ^{134}I **Error! Reference source not found.**. They are quite rare, but considering a fleet of tens of nuclear reactors, they happened time to time. In that case, significant amounts of ruthenium could be released in the primary water and accumulated in the primary resin. It can be estimated that, with respect to the French operating limits, the amount of ^{103}Ru in a resin in such a case can reach hundreds to thousands of GBq. Considering a few months of decay, the inventory will remain of tens to thousands of GBq, consistent with a release of a few GBq.

Similarly to the cesium isotopes, the ^{106}Ru/^{103}Ru ratio can provide some additional information. The Visby (Sweden) measurements, the only one to detect some ^{106}Ru activity, enable to evaluate it to 0,85 – 3,1. Assuming that ruthenium came from fission from dispersed fuel in the primary water (and not from the accumulated inventory in the fuel pellets), it can be evaluated that the decay time of the resin should be in the 4 to 9 months range, which is consistent with the previous conclusions. Nevertheless, considering a part of the ^{106}Ru inventory may come from the pellet inventory (and not the fission in the water), the ruthenium ratio is over-estimated. So, the only reliable information coming from this ratio is that the decay time is less than 9 months.

As a result, the best hypothesis to explain the ^{103}Ru origin of the June 2020 release is a primary resin from a PWR or WWER, after a few months to 9 months of decay, with a fuel cladding failure leading to a fuel dispersion in the primary loop.

3.5. Other Isotopes (^{141}Ce, ^{95}Nb, ^{195}Zr)

The same analysis than for the ^{103}Ru can be drawn for the ^{141}Ce isotope. It is a low volatile fission product, with an intermediate half-life (32 days) and which is not expected to move in significant amount out of the pellet. Its presence also argues to an origin in a primary resin after a cycle with a fuel cladding failure with dispersion in the primary loop.

The couple ^{95}Zr (the father) and ^{95}Nb (the son), can have two main origins:

- Corrosion of activated ^{95}Zr coming from the pin cladding under irradiation (neutron capture on ^{94}Zr);
- Fission of dispersed fuel in the primary water. Indeed, ^{95}Zr is also a low-volatile fission product, which is not expected to move out of the pellet, except in case of fission directly in the water.

In both cases, the ^{95}Zr will accumulate in the primary resin. The measured ^{95}Zr/^{95}Nb ratio is close to 1, consistent with the secular equilibrium expected for this couple after several months of decay. The two types

of production can explain the measurements, but whatever, these isotopes lead to similar conclusions than previous ones.

3.6. Conclusion

The analysis of the origin of each detected isotope, taking into account the cumulated presence of activated corrosion products and fission products indicates that the release measured in June 2020 might be issued from a primary resin after a few months of decay.

No certainty is achievable with so little information, but the most probable hypothesis seems to be of a primary resin, after a few months to 9 months of decay, of a pressurized water reactor with fuel cladding failure and dispersion of fissile material in the primary.

4. COMPARISON WITH PREVIOUS RELEASES

Table II. All comparable detections at Finland border since 2012

Release date	**Activated corrosion product**										**Release localization**
					Fission product						
					Low volatile		Volatile		Low volatile		
	^{60}Co	^{58}Co	^{59}Fe	^{54}Mn	^{95}Nb	^{95}Zr	^{134}Cs	^{137}Cs	^{103}Ru	^{141}Ce	
Half-life	5,3 y	71 d	45 d	0,86 y	35 d	64 d	2 y	30 y	39 d	33 d	
August 2014	X	X	X	X	X	X		*x*			Not evaluated
May 2015	X				X	X	X	*x*	X	X	Compatible with reference
October 2015	X			X			X	X			From the North
May 2017	X		X	X	X	?	X	*x*			Not evaluated
April 2018	X	X	X	X	X	X	X	*x*	X	X	Not evaluated
April 2019	X	X	X	X	X	X		*x*			Not evaluated
July 2019	X		X	X				*x*			Not evaluated
March 2020	X		X	X	X	?		*x*			Not evaluated
June 2020	X				X	X	X	X	X	X	Reference

The June 2020 event is not the only detection of such isotopes in the past decades. At least 9 similar detections have been recorded since 2012 at Finland border. They are provided in Table II. It must be noticed that, due to Chernobyl contamination, a few μBq/m^3 of ^{137}Cs is always detected. So, in the table, the detections compatible with the Chernobyl background are marked with a "*x*" and the larger detections, clearly suggesting a fission products release, are identified with a "X". Besides, in May 2017 and March 2020, no ^{95}Zr has been detected, despite its son, ^{95}Nb, having been recorded. It might be interpreted as the fact that ^{95}Zr was present, but below detection limit.

All these detections can be gathered in four categories, described in Table III.

Table III. Various kind of detection at Finland border since 2012

Release	Composition FP : Fission Products CP&AP : Corrosion Products and Activation Products	Possible origin	Decay before release
May 2015 April 2018 June 2020	CP&AP and low volatile FP Presence of intermediate half-life	Primary resin with fuel cladding failure with fuel dispersion	Few months
May 2017	CP&AP and volatile FP Presence of intermediate half-life	Primary resin with fuel cladding failure without fuel dispersion	Few months
August 2014 April 2019 July 2019 March 2020	CP&AP Presence of intermediate half-life	Primary resin without fuel cladding failure Primary cleaning system filter	Few months
October 2015	CP&AP and volatile FP No intermediaite half-life	Primary resin with fuel cladding failure	Few years

First, three release measurements have the same characteristics than the June 2020 ones. Five additional detections might also be interpreted as primary resin with various fuel cladding failure states (significant failure in May 2017 but without fuel dispersion, limited in the other cases), with a few months of decay. And one last detection that occurred in October 2015, might also be attributed to a primary resin with fuel cladding failure but with years of decay.

As a conclusion, all these detections are consistent with from 3 to 9 atmospheric releases of primary resin inventory at Finland border, since 2012, such event occurring subsequently quite often.

5. CONCLUSIONS

In conclusion, the detection of artificial radionuclides (^{60}Co, ^{134}Cs, ^{137}Cs, ^{103}Ru, ^{106}Ru, ^{141}Ce, ^{95}Nb, ^{95}Zr) in various countries of northern Europe (Finland, Sweden, Estonia), reveals that a release occurred in 2020 from June 13 to June 22. The measured values were close to detection limits and didn't represent any health issue. Using inverse modelling techniques, the most probable release location has been evaluated in a zone

from eastern Estonia to western Russian Federation. An estimation of the release magnitude, at the most probable location, estimates the activity at a few GBq of ^{60}Co and tens of GBq of cesium isotopes.
The analysis of the isotopic composition of the release establishes that its most probable source is a primary ion exchange resin of a pressurized water reactor with fuel cladding failure and dispersion of fissile material in the primary, after a few months to 9 months of decay, even if no certainty is achievable with so little information.

This event is finally quite common since at least three similar events were observed at Finland border in the 2012-2020 period, and potentially up to nine.
Three main phenomena have been investigated in order to imagine what event could explain this release: a resin fire, a thermal decomposition of such resin in a primary loop, or an issue during the resin transfer to the waste management building. Nevertheless, mainly due to the lack of information, no answer has been found.
Finally, the last and most important question, "how the radiological inventory has been released into the atmosphere", remains currently without satisfying answer.

ACKNOWLEDGMENTS

The authors would like to thank all the IRSN colleagues involved in the analysis of that event.

REFERENCES

1. Information Report form IRSN "Detection of an increase in airborne radioactivity levels in Northern Europe – Update of July 22, 2020"
2. O. Saunier O. Saunier, D. Didier, A. Mathieu, O. Masson, J. Dumont Le Brazidec, Atmospheric modeling and source reconstruction of radioactive ruthenium from an undeclared major release in 2017, Proceedings of the National Academy of Science, Volume 116, Issue 50, 2019, Pages 24991-25000; DOI: 10.1073/pnas.1907823116
3. M. Tombette et al., C3X: A software platform for assessing the consequences of an accidental release of radioactivity into the atmosphere, 2014. http://venus.iis.u-tokyo.ac.jp/english/workshop/Poster/3rd%20March/Damien%20Didier.pdf.
4. O. Saunier et al., An inverse modeling method to assess the source term of the Fukushima Nuclear Power Plant accident using gamma dose rate observations. Atmos. Chem. Phys. Volume 13, 2013, Pages 11403–11421.
5. D. Quelo et al., Validation of the Polyphemus platform on the ETEX, Chernobyl and Algeciras cases. Atmos. Environ. Volume 41, 2007, Pages 5300–5315
6. O. Masson et al., Potential source apportionment and meteorological conditions involved in airborne 131I detections in January/February 2017 in Europe. Environ. Sci. Technol. Volume 52, 2018, Pages 8488–8500.
7. C. Hansen, Analysis of discrete ill-posed problems by means of the L-curve, SIAM Revue, Volume 34, Issue 4, 1992, Pages 561-580, https://doi.org/10.1137/1034115
8. V. Remeikis, et al, "Study of the nuclide inventory of operational radioactive waste for the RBMK-1500 reactor" Nuclear Engineering and Design, Volume 239, Issue 4, 2009, Pages 813-818, ISSN 0029-5493, https://doi.org/10.1016/j.nucengdes.2008.11.010.
9. Technical Report of IAEA Nuclear Energy series NF-T-2.1 "Review of Fuel Failures in Water Cooled Reactors"

RÉPUBLIQUE FRANÇAISE
Liberté
Égalité
Fraternité

IRSN
INSTITUT DE RADIOPROTECTION ET DE SÛRETÉ NUCLÉAIRE

INVESTIGATION ON THE DETECTION OF RADIONUCLIDES IN NORTH OF EUROPE IN JUNE 2020

Possible source term origin

Jean-Jacques INGREMEAU, IRSN
Olivier Saunier, IRSN

ERMSAR Conference, 16-19 May 2022, Karlsruhe

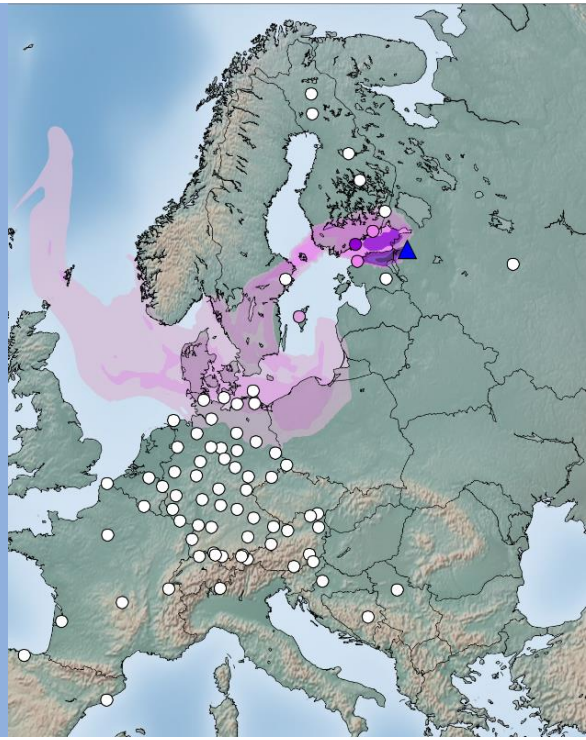

IRSN/ERM-296 ind. 06

Outlines

- Source location? → A suspected area
- Source Term Origin? → A unique consistent answer
  - *From which type and part of a nuclear installation the release came from ?*
- Comparison with previous releases
- What happened?
  - *How the radioisotopes came out of the installation ?*
  - → No Answer



Introduction

Detection of artificial radionucleides in June 2020

- intermediate half-life (~month)
  - ^{103}Ru, ^{106}Ru, ^{141}Ce, ^{95}Nb, ^{95}Zr
- Long term half-life (~year)
  - ^{60}Co, ^{134}Cs, ^{137}Cs
- No short half-life isotopes

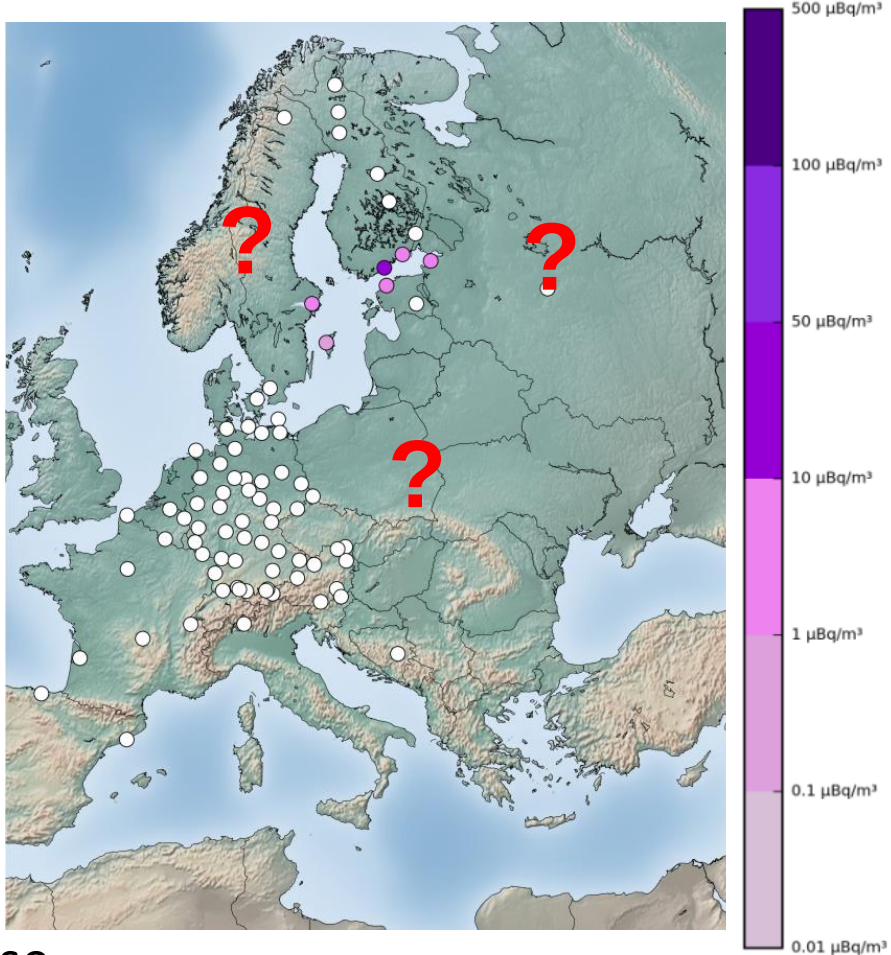

Close to detection limits

- several µBq/m³

No health issue

- Even at a few km far from the release

Release Location

- Use of inverse modelling techniques
  - Use of hourly meteorological data provided by Météo-France
  - Atmospheric Transport Model
  - Grid of potential release locations 1° × 1° resolution

- On the map: Fraction of the simulated air concentrations that are within a factor of 5 of the observed values.

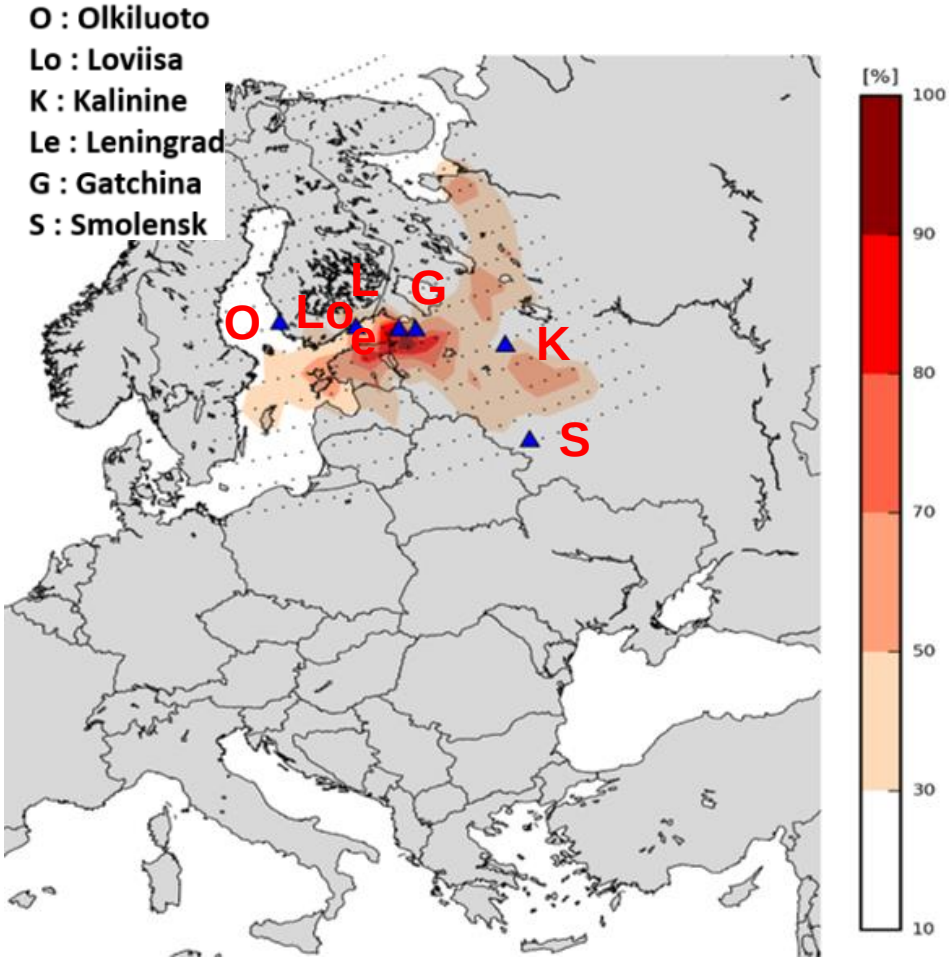

Release Magnitude

- Total source term of tens GBq
- Use of Monte-Carlo sensitivity analysis
  - Large uncertainties
  - From 2 to 20 GBq of ^{134}Cs
- Release from June, 13th to June, 22th

Isotope	Half-life	Estimated source term
^{60}Co	5,26 year	~ GBq
^{134}Cs	2,07 year	~10 GBq
^{137}Cs	30,1 year	~10 GBq
^{103}Ru	39,2 days	~ GBq
^{106}Ru	371,8 days	~ GBq
^{141}Ce	32,5 days	~ 100 MBq
^{95}Nb	35 days	~ GBq
^{95}Zr	64 days	~ GBq

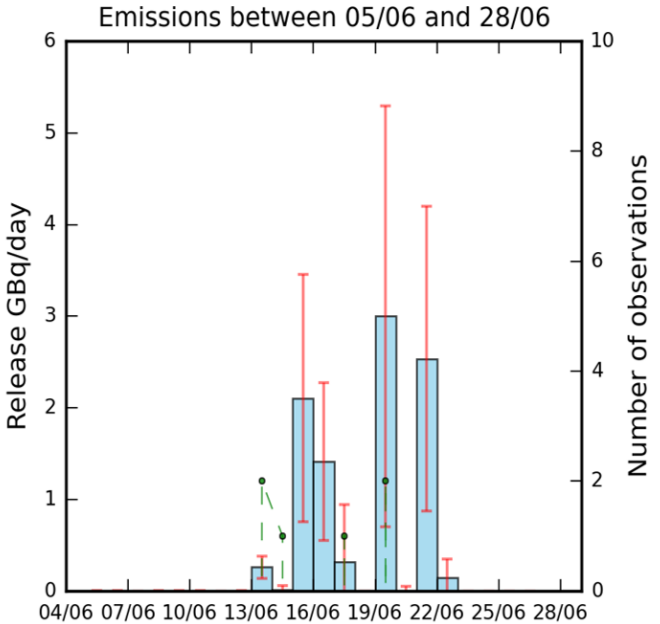

What is the Source Term Origin?



What is the Source Term Origin ?

Isotope	Half-life	Estimated Source Term	Origin
^{60}Co	5,26 y	~ GBq	Activated corrosion product



^{60}Co

- *Produced by neutron capture on ^{60}Ni or ^{59}Co*

Can be found in:

- ^{60}Co gamma source → Can't explain the other isotopes presence
- Reactor primary water
  → Source term too low and can't explain the lack of short-term isotopes
- **Primary ion exchanger resin**
  - → Usual ^{60}Co source term in them ~ 100-1000 GBq
  - Compatible with the estimated release magnitude

What is the Source Term Origin ?

Primary ion exchanger resin

- *Long term accumulation of radionuclides*
  - *Corrosion activated products*
  - *Fission products in case of fuel cladding failure*



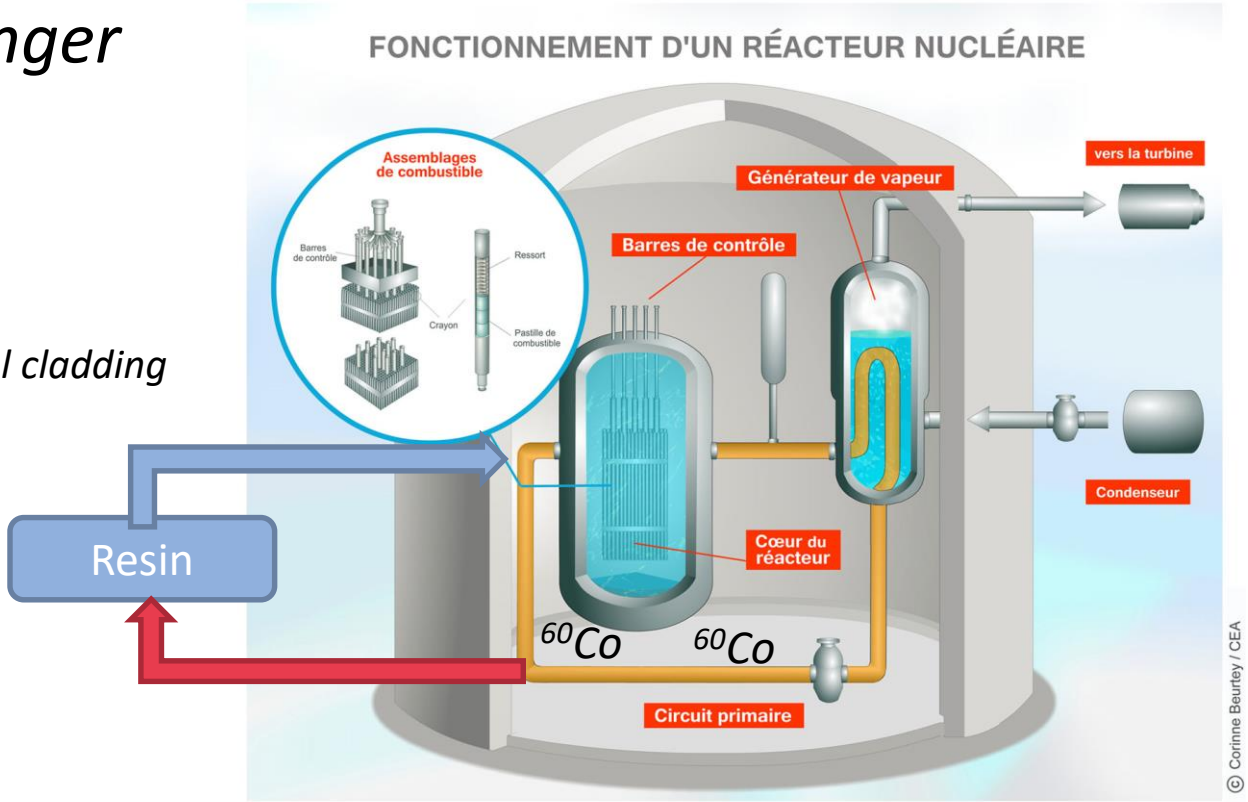

What is the Source Term Origin ?

^{134}Cs & ^{137}Cs

- *"Fission products"*

Isotope	Half-life	Estimated Source Term	Origin
^{134}Cs	2,07 y	~10 GBq	Volatile fission product
^{137}Cs	30,1 y	~10 GBq	

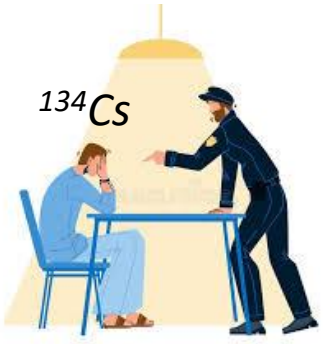

Can be found in :

- Fuel
- Reactor primary water in case of fuel cladding leakage or failure

→ Source term too low and can't explain the lack of short-term isotopes

- **Primary ion exchanger resin in case of cladding leakage or failure**
  - → Usual ^{137}Cs source term ~ 100 GBq

^{134}Cs / ^{137}Cs ratio

- From 1.2 to 1.7 *(Helsinki measures June 17)*

Can be :

- PWR ratio, after a few month of decay

Very unlikely

- RBMK (0.5 at end of cycle)
- Research reactor

What is the Source Term Origin ?

^{103}Ru

- *Low-volatile Fission product*

Isotope	Half-life	Estimated Source Term	Origin
^{103}Ru	39,2 d	~ GBq	Low-volatile fission product
^{106}Ru	371,8 d	~ GBq	
^{141}Ce	32,5 d	~ 100 MBq	



Can be found in :

- Fresh Fuel → Very few can move outside of the fuel, even in case of clad leakage or failure (decay before)

^{103}Ru decay before spent fuel waste management / ^{106}Ru in spent fuel cycle installations

Only 2 ways to get large amount of ^{103}Ru outside of fuel

- Fresh fuel melting → Others short-live isotopes should have been rejected (Iodine)
- Fuel (uranium oxide) dispersed in the primary water (can occur in some specific fuel failure)
  - →Fission products directly produced in the water and migrate to **primary resin**

What is the Source Term Origin ?

Resin

Without fuel failure

With fuel failure

With fuel dissemination

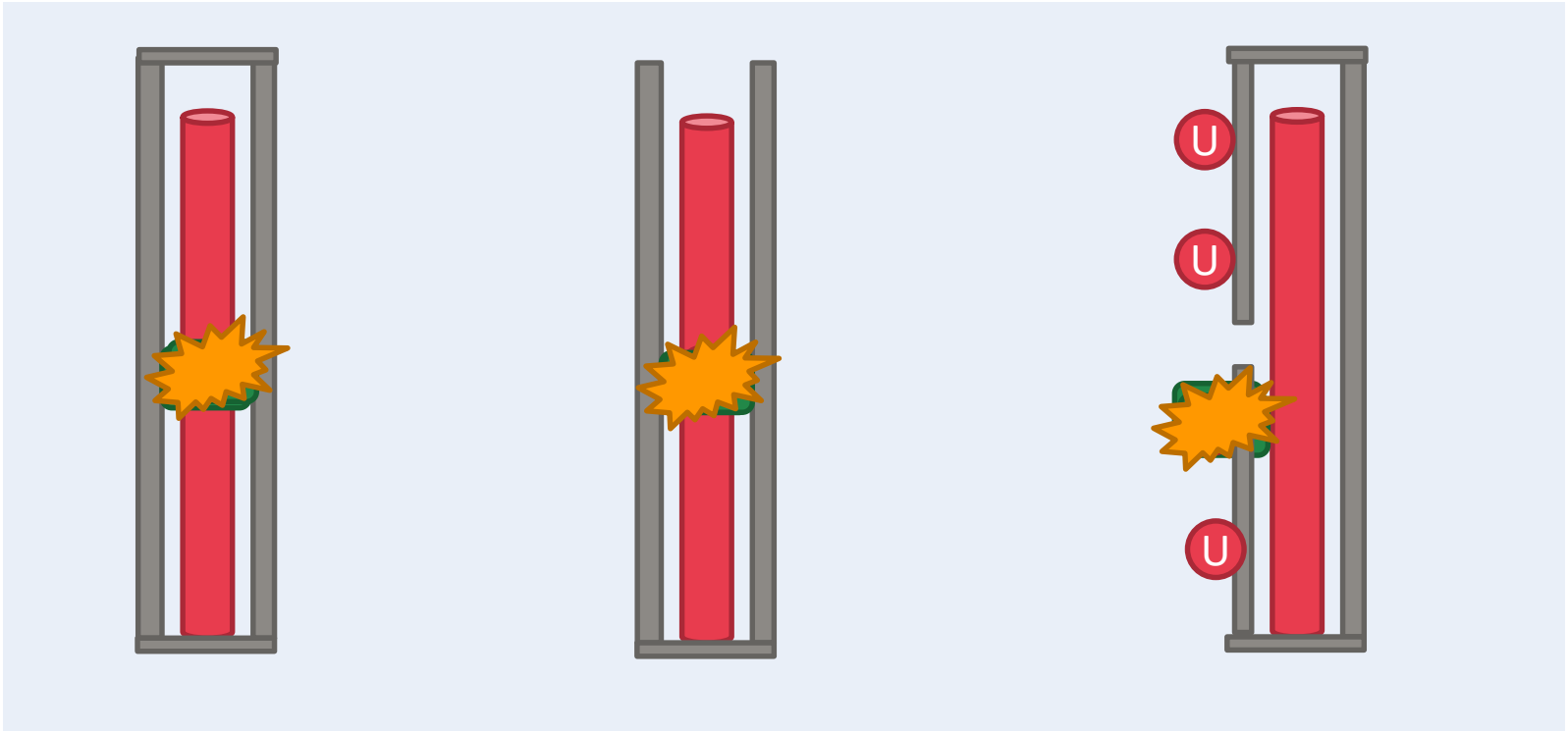

What is the Source Term Origin ?

Isotope	Half-life	Estimated Source Term	Origin
^{103}Ru	39,2 d	~ GBq	Low-volatile fission product
^{106}Ru	371,8 d	~ GBq	
^{141}Ce	32,5 d	~ 100 MBq	



$^{106}Ru/^{103}Ru$

- *Visby (Sweden) measures of June, 22th) → 0.85 – 3.1*

With the hypothesis of Ru coming from dispersed fuel in the primary

- → Decay time between **120 and 270 days (4-9 months)**
- **Compatible** with estimated release magnitude with respect to French radiochemical limits
- Some ^{106}Ru, may come from the fuel pellet inventory : → **Decay time < 9 months**

^{141}Ce → Same than ^{103}Ru

- produced by fission of dispersed fuel in the water and migrate to the resin

What is the Source Term Origin ?



Synthesis

- Amount of ^{60}Co → typical of a fraction of **spent primary ion exchanger resin**
- Amount of ^{137}Cs / ^{134}Cs → typical of a fraction of **spent primary ion exchanger resin** with fuel failure
- Others intermediate-live fission product (^{103}Ru/ ^{141}Ce) → only found in **spent primary ion exchanger resin** with fuel dispersion in the primary (except fresh fuel melting)

All these isotopes being together, the origin of the release is very likely a spent primary ion exchanger resin of a reactor with fuel cladding failure and dispersion of fuel in the primary loop

- With <9 month of decay
- More likely a PWR

Comparison with previous releases



Comparison with previous releases

Release date	Activated corrosion product				Fission product						Release localisation
					Low volatile		Volatile		Low volatile		
	^{60}Co	^{58}Co	^{59}Fe	^{54}Mn	^{95}Nb	^{95}Zr	^{134}Cs	^{137}Cs	^{103}Ru	^{141}Ce	
Half-life	5,3 y	71 d	45 d	0,86 y	35 d	64 d	2 y	30 y	39 d	33 d	
August 2014	X	X	X	X	X	X		x			Not evaluated
May 2015	X				X	X	X	x	X	X	Compatible with reference
October 2015	X			X			X	X			Not from Leningrad, From the North
May 2017	X		X	X	X	?	X	x			Not evaluated
April 2018	X	X	X	X	X	X	X	x	X	X	Not evaluated
April 2019	X	X	X	X	X	X		x			Not evaluated
July 2019	X		X	X				x			Not evaluated
March 2020	X		X	X	X	?		x			Not evaluated
June 2020	X				X	X	X	X	X	X	Reference

- Finland detections since 2012
  - No short-live isotope
  - Often the same isotopes with intermediate-live
  - Mainly in spring or summer

Same isotopes
→ Same analysis
→ Primary resin with fuel dissemination in the primary after months of decay

Comparison with previous releases

Release date	Activated corrosion product				Fission product						Release localisation
					Low volatile		Volatile		Low volatile		
	^{60}Co	^{58}Co	^{59}Fe	^{54}Mn	^{95}Nb	^{95}Zr	^{134}Cs	^{137}Cs	^{103}Ru	^{141}Ce	
Half-life	5,3 y	71 d	45 d	0,86 y	35 d	64 d	2 y	30 y	39 d	33 d	
August 2014	X	X	X	X	X	X		*x*			Not evaluated
May 2015	X				X	X	X	*x*	X	X	Compatible with reference
October 2015	X			X			X	X			Not from Leningrad, From the North
May 2017	X		X	X	X	?	X	*x*			Not evaluated
April 2018	X	X	X	X	X	X	X	*x*	X	X	Not evaluated
April 2019	X	X	X	X	X	X		*x*			Not evaluated
July 2019	X		X	X				*x*			Not evaluated
March 2020	X		X	X	X	?		*x*			Not evaluated
June 2020	X				X	X	X	X	X	X	Reference

Looks like a primary resin after months of decay, with fuel cladding failure **without fuel dissemination** in primary

Comparison with previous releases

Release date	Activated corrosion product				Fission product						Release localisation
					Low volatile		Volatile		Low volatile		
	^{60}Co	^{58}Co	^{59}Fe	^{54}Mn	^{95}Nb	^{95}Zr	^{134}Cs	^{137}Cs	^{103}Ru	^{141}Ce	
Half-life	5,3 y	71 d	45 d	0,86 y	35 d	64 d	2 y	30 y	39 d	33 d	
August 2014	X	X	X	X	X	X		*x*			Not evaluated
May 2015	X				X	X	X	*x*	X	X	Compatible with reference
October 2015	X			X			X	X			Not from Leningrad, From the North
May 2017	X		X	X	X	?	X	*x*			Not evaluated
April 2018	X	X	X	X	X	X	X	*x*	X	X	Not evaluated
April 2019	X	X	X	X	X	X		*x*			Not evaluated
July 2019	X		X	X				*x*			Not evaluated
March 2020	X		X	X	X	?		*x*			Not evaluated
June 2020	X				X	X	X	X	X	X	Reference

Looks like a primary resin after months of decay, **without fuel cladding leakage**

Comparison with previous releases

Release date	Activated corrosion product				Fission product						Release localisation
					Low volatile		Volatile		Low volatile		
	^{60}Co	^{58}Co	^{59}Fe	^{54}Mn	^{95}Nb	^{95}Zr	^{134}Cs	^{137}Cs	^{103}Ru	^{141}Ce	
Half-life	5,3 y	71 d	45 d	0,86 y	35 d	64 d	2 y	30 y	39 d	33 d	
August 2014	X	X	X	X	X	X		*x*			Not evaluated
May 2015	X				X	X	X	*x*	X	X	Compatible with reference
October 2015	X			X			X	X			Not from Leningrad, From the North
May 2017	X		X	X	X	?	X	*x*			Not evaluated
April 2018	X	X	X	X	X	X	X	*x*	X	X	Not evaluated
April 2019	X	X	X	X	X	X		*x*			Not evaluated
July 2019	X		X	X				*x*			Not evaluated
March 2020	X		X	X	X	?		*x*			Not evaluated
June 2020	X				X	X	X	X	X	X	Reference

Looks like a primary resin with fuel cladding failure after **years of decay**

Comparison with previous releases

Synthesis

3 releases with same characteristics than the one observed in June 2020 since 2012

+ 5 other releases compatible with primary ion exchanger resin hypothesis
- With **various fuel cladding failure states**
- With **few month of decay**

+1 release compatible with primary ion exchanger resin hypothesis
- But with **years of decay**

From 3 to 9 primary ion exchanger resin inventory released since 2012 at Finland's border

What happened?



What Happened ?

First: The cycle of life of primary resin

After several reactor cycle (function of their efficiency), they are replaced **during reactor shutdown**

Transferred in the waste management building, dry storage and decay (**several years**)

Then, long term disposal

A dozen of hypothetical events have been considered.

- None explains all the release characteristics
- A few presented here

What Happened ?

Hypothesis: resin fire



What is consistent with this hypothesis

- Release of a large part of activity directly in the atmosphere

What is not consistent with this hypothesis

- If treatment operation
  - → Supposed to be on long decay resin (some years)
- If uncontrolled fire (storage or drying operation)
  - →Shouldn't be so frequent
  - →Release duration too long for June 2020 (9 days) : smouldering fire unlikely



Not enough information to really investigate this hypothesis

What Happened ?

Hypothesis : resin fire

✓	Likely hypothesis	Expected result for this hypothesis
	Possible	No incompatibility with the hypothesis
?	Unlikely hypothesis	Unexpected result for this hypothesis
✗	Excluded hypothesis	This result exclude this hypothesis

Resin fire			Release duration (2-3 weeks)	Présence of ^{103}Ru and ^{141}Ce	Activity Levels	Likelyhood of initiating event / operation	Recurrent nature of the release
Waste treatment installation of Leningradskaya	Deliberate burning of large amount of resin	With smokes filtration	✓	✗	?	?	✓
		Without smokes filtration	✓	✗	✓	?	✓
		Without smokes filtration and with human error leading to short decay resin burning	✓	✓	✓	✗	✓
	Deliberate burning of solid waste contaminated with a resin	With smokes filtration	✓	✓	✗	✓	✓
	Uncontrolled fire during treatment	After long decay	?	✗	✓	?	
		With human error leading to short decay resin treatment	?	✓	✓	?	?
	Uncontrolled fire during resin storage of drying operation		?	?	✓	?	?
Research center of Sosnoviy Bor	Uncontrolled fire during a research experiment		?	?	?		?

What Happened ?

Hypothesis : blocking during a transfer or pipe break

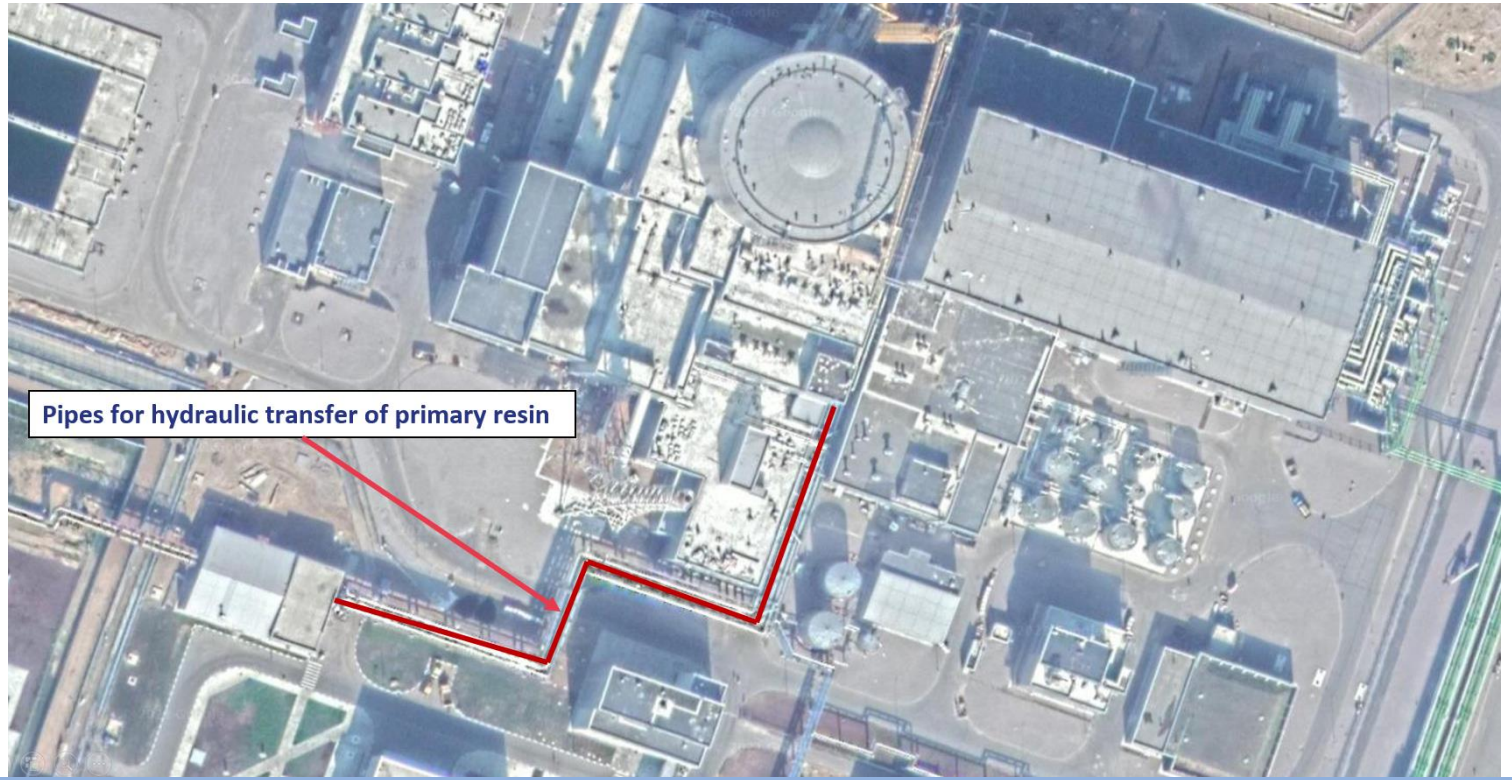

a VVER-1200 reactor

What Happened ?

✓	Likely hypothesis	Expected result for this hypothesis
	Possible	No incompatibility with the hypothesis
?	Unlikely hypothesis	Unexpected result for this hypothesis
✗	Excluded hypothesis	This result exclude this hypothesis

Hypothesis : blocking during a transfer or pipe break

	Release duration (2-3 weeks)	**Isotopes**		**Activity Levels**	**Likelyhood of initiating event / operation**	**Recurrent nature of the release**
		Lack of short-lived isotopes	^{103}Ru, ^{134}Cs, ^{60}Co			
Issue during the resin transfer to the waste management building	?	?	✓	?	✓	✓



Not enough information to really investigate this hypothesis

Conclusion

The most probable release location has been evaluated in a zone from eastern Estonia to western Russian Federation

The radiological source term of June 2020 release, is likely
- **a primary ion exchanger resin**
- with fuel dissemination in the previous cycle

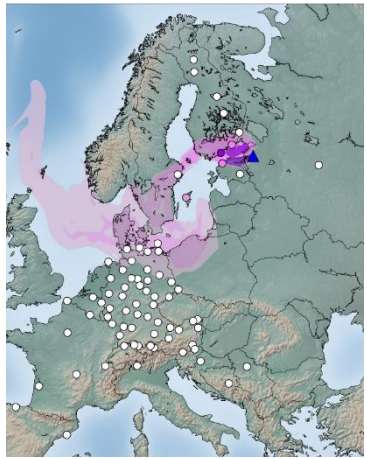

From 3 to 9 similar releases at Finland border since 2012
- May be primary resin: function of the presence of fuel cladding failure with / without dissemination
- Or other sources

No satisfying explanation of what could have happened

THANK YOU FOR YOUR ATTENTION





RCCS-2021 OECD SPECIALIST WORKSHOP ON "REACTOR CORE AND CONTAINMENT COOLING SYSTEMS – LONG TERM MANAGEMENT AND RELIABILITY WORKSHOP" OVERVIEW ON THE MAIN OUTCOMES

Ahmed Bentaib[1], Vicena Ivan[2], Didier Jacquemain[3], Martina Adorni[3], Luis E. Herranz[4], Ali Tehrani[5], Noreddine Mesmous[6], Mohamed Shawkat [6], Lubica Kubisova[7], Bruno Tourniaire[8], Sevostian Bechta[9], Thibaut Van Rompuy[10]

[1]IRSN, 31 avenue de la Division Leclerc, BP 17-92262 Fontenay aux Roses, France
[2] VUEZ, Hviezdoslavova 35, 934 01 Levice Slovakia
[3]OECD/NEA, 46, quai Alphonse le Gallo, 92100 Boulogne-Billancourt, France
[4]CIEMAT, Av. Complutense, 40, 28040 Madrid, Spain
[5]ONR, Office for Nuclear Regulation Building 4 Redgrave Court Merton Road Bootle L20 7HS
[6]CNSC, Canadian Nuclear Safety Commission, 280 Slater Street, P.O. Box 1046, Station B Ottawa, ON K1P 5S9, Canada
[7]UJD SR, Úrad jadrového dozoru SR, Bajkalská 27, P.O.Box 24 820 07 Bratislava, Slovak Republic
[8]EDF, 19 rue Pierre Bourdeix, 69007 Lyon, France
[9] KTH, Kungliga Tekniska Högskolan, SE-100 44 Stockholm, Sweden
[10]BelV, Rue Walcourtstraat 148, Brussels 1070, Belgium

ahmed.bentaib@irsn.fr, vicena.ivan@vuez.sk, didier.jacquemain@oecd-nea.org, martina.adorni@oecd-nea.org, luisen.herranz@ciemat.es, ali.Tehrani@onr.gov.uk, noreddine.mesmous@cnsc-ccsn.gc.ca , mohamed.shawkat@ cnsc-ccsn.gc.ca , lubica.kubisova@ujd.gov.sk, bruno.tourniaire@edf.fr, bechta@kth.se, thibaut.vanrompuy@belv.be

ABSTRACT

Maintaining the reactor core and containment cooling function is of primary importance to limit progression and consequences of accidents. These functions are of particular importance in managing the consequences of severe accident over long periods of time. The need for continued operation of the systems, ensuring the cooling function over long period of time, was highlighted by the accident at the Fukushima Daïchi nuclear power plants. Further, knowledge gaps have been identified on the effect of debris and corrosion products on the long-term reliability of reactor and containment cooling systems.

The reliability of cooling systems in long term accident conditions continue to be the subject of projects and activities performed under the OECD Nuclear Energy Agency (NEA) Committee for the Safety of Nuclear Installations (CSNI). The working group on the long-term management of a severe accident, the task group on sump clogging as well as the ongoing Fukushima-Daiichi-related projects are of note. The RCCS-2021 OECD/NEA/CSNI workshop was developed to promote international exchange of information and practices related to maintaining the cooling function in long-term accidents.

The objective was to bring together international knowledge and expertise on:

- long term effects of accident conditions (e.g. temperature, pressure, dose and chemical environment) on material and components, e.g. potential degradation of material and components and formation of suspensions or debris accumulation that can impair maintaining cooling; and
- robustness of cooling systems regarding clogging issues and effects of corrosion-erosion reactions in sensitive components in the long term.

The workshop discussed the identified gaps with additional experimental research and with consolidation of existing and/or new assessment methods and analytical tools. The workshop covered practical subjects and technologies at existing and advanced new NPPs in four topics areas. These related to the assessment of accident management measures and strategies, new systems and designs, sump clogging issues and debris formation and chemical condition in cooling waters.

The present paper provides an overview of the contents of the workshop and tries to identify lesson learned and recommendations.

KEYWORDS
Clogging, long-term, severe accident, containment cooling and management, debris

1. INTRODUCTION

Core and containment heat removal is a one of fundamental safety functions to be maintained during accident conditions in a nuclear power plant. The Fukushima Daichi accidents highlighted the importance of maintaining the cooling function and the difficulty to manage a large amount of contaminated water, stressing the need of reliable and sustainable recirculation strategy to ensure core and containment heat removal for a long period of time. Similarly, the report (NEA/CSNI/N°7506, 2021) on the long-term management of a severe accident underlined the need to address open issues and technological gaps related to maintaining long-term management actions. These can include maintaining a coolable configuration and containment integrity to ensure the confinement function, managing water wastes, solid wastes and effluents, site clean-up and decontamination, intact and damaged fuel removal from reactors and SFPs and their disposal.

Considering these recommendations and those issued from previous related OECD/NEA activities, as the task group on sump clogging (NEA/CSNI/R(2013)12, 2013) as well as those resulting from the Fukushima-Daiichi-related actions and projects (Akira Nakayoshi, 1 December 2020) (M. Pellegrini, 2020), it was decided to organise the RCCS-2021 workshop, under the OECD/NEA auspices, with the aim to promote international exchange of information and practices related to maintaining the core and containment cooling function in a long-term accident in a nuclear power plant (NPP).

For this purpose, the workshop was to carry out a comprehensive review of the adopted rules and practices to ensure the core and the containment cooling in a long-term accident for both existing and new NPPs design. This was to identify the remaining knowledge gaps linked to the behavior of material, components and systems that are critical for maintaining cooling in the long term after an accident in an NPP and to discuss the best way to address the identified gaps with additional experimental research and with consolidation of existing and/or new assessment methods and analytical tools.

Thus, a small organising committee oversaw the overall workshop arrangements, establishing a time-schedule, technical content and program. The event was announced in April 2020 with the objective to hold the workshop in Levice (Slovakia) in February 2021. A visit of VUEZ experimental facility VIKTORIA was planned to be organised for participants of the workshop, too. Considering the travel restrictions imposed by the COVID pandemic in Europe, the Organizing Committee decided to postpone the RCCS-2021 workshop and to hold it online on October 18th to October 21, 2021.

Accordingly, the workshop agenda was rearranged with short presentations and time for discussion. The workshop featured 7 keynote lectures, 4 sessions and 29 peer reviewed papers addressing the following:

Topic 1 - Review of the Assessment of Accident Managements Measures and Strategies;
Topic 2 - New Systems and Designs;
Topic 3 - Sump Clogging Issue; and
Topic 4 - Debris Formation and Chemical Conditions in Cooling Waters.

A summary session was organised on the last day to present and discuss the preliminary conclusions and to draw comprehensive thoughts and ideas for future research programs.

This virtual workshop attracted over 140 participants representing over 28 countries from the regulatory organisations, reactor designers, operators, consultancies, senior engineers, practitioners and analysts from TSCs/TSOs supporting the regulators and research establishments. The participants reviewed the practices and exchanged information related to maintaining the cooling functions in accident conditions.

2. Overview of the workshop contents

2.1. Invited lectures

The following internationally recognized experts from leading research institutions were invited to present on keys topics on the long-term management of the cooling system for different NPP technologies including lessons learnt from Fukushima Daiichi.

Dr. Jorge LUIS HERNANDEZ from the International Atomic Energy Agency (IAEA)
Dr. Hernandez provided an overview of the updated design safety requirements and recommendations in the IAEA safety standards applicable to new large nuclear power plants equipped with water cooled reactor designs. As the IAEA requirements and the IAEA recommendations on the design, presented in those safety guides, aim at being technology neutral, however they have been influenced by the extensive operating experience of large nuclear power plants equipped with water cooled reactor designs. Among the IAEA recommendations, addressed by Dr. Hernandez, the way to ensure the reactor core residual heat removal by avoiding the clogging of sump strainers and filters and strategies of in vessel melt retention and ex-vessel corium cooling. For large nuclear power plants equipped with water cooled reactor designs currently under construction or in operation, but designed in accordance with former standards, Dr. Hernandez indicated that the application of all the IAEA requirements and all IAEA recommendations on the design, presented in the updated safety guides, might need to be assessed (e.g. though periodic safety reviews, license renewal or design review process) to define which reasonably practicable safety improvements could be made aiming at further enhancing the safe operation of the nuclear power plant. For nuclear power plants equipped with other reactor types, such as non-water-cooled reactor technologies or water cooled small modular reactors, the IAEA requirements and recommendations on the design, might not be fully applicable as they are and further engineering judgement for their interpretation is required. Regarding the long-term severe

accident management, Dr. Hernandez mentionned the IAEA Action Plan on Nuclear Safety to define a comprehensive working programme, including the reinforcement of research and development, particularly in management of severe accidents. Two strategies were identified: in-vessel melt retention and ex-vessel corium cooling/stabilization. For both strategies, Dr. Hernandez highlighted the need of further knowledge of the associated phenomena to reduce the uncertainties concerning their effective implementation.
Dr. Hernandez concluded his talk my mentioning the IAEA safety guides and recommendations related to other long-term strategies, such as the control of combustible gases in the atmosphere of the containment, the control of the pressure inside the containment and the control of radioactive releases. He also mentioned the IAEA recommendations related to the use of portable equipment; their maintenance and inspection; waste management due to long term actions such as water treatment; limits to dose rates to ensure the operator actions and availability of electrical, compressed air or water sources.

- Dr. Bruno Tourniaire from Electricité de France (EDF), France

In his presentation, Dr. Tourniaire provided an overview on the reactor and containment cooling systems already implemented in the French generation 2 (GEN2) fleet and those implemented in the EPR. Both DEC-A and DEC-B situations are covered. Concerning the GEN2, Dr. Tourniaire presented the ongoing upgrade to ensure the core and containment cooling in long term; it includes the ultimate Containment Spray System (CSS) that consists of a pump injecting the water from the Reactor Water Storage Tank (RWST) into the primary circuit and the sumps of the reactor building and then recirculating to the sumps of the latter. It also includes a heat exchanger capable of evacuating the residual power out of the reactor building, with its own mobile ultimate heat sink implemented by the Nuclear Rapid Action Force. It is supplied by an emergency diesel diversified from the main diesels. This system is qualified for severe accident conditions (temperature, irradiation, pressure, debris) and is designed to withstand extreme external hazards. In case of the ultimate CSS failure in long term, the filtered venting system is credited to remove the residual heat power. For GEN3, Dr. Tourniaire indicated that dedicated systems are implemented to evacuate residual power without need of containment venting.

- Mr. Karim Osman from Ontario Power Generation (OPG), Canada

Mr. Osman presented an overview on the adopted strategies by the Canadian utilities along with CANDU Owners Group (COG) to ensure the ability of having sustained core cooling post core degradation. These strategies are developed as guidelines that provide various means of adding water to the core or the shield tank to cool the fuel or corium to maintain In-vessel Retention (IVR). Core cooling after the onset of severe accident conditions can be achieved by making up water to the heat transport system or moderator for in-vessel core cooling and/or the shield tank to maintain ex-vessel cooling. These strategies are designed to provide water flowrates minimizing steaming while cooling the core and preventing pressurization of the reactor building to prevent any radioactive releases. To support the water addition strategies, computational aids were created to estimate the rate of water addition at various times into the event.

- Dr. Pingting. Jiang from CNPRI, China

Dr. Pingting's lecture focused on containment pressure control strategies, with the major subject of how and

when to use the systems properly in long term management strategies. Relevant systems which help to control the containment pressure, like containment heat removal system and containment venting system, were introduced and their effectiveness were assessed based on numerical studies including sensitivity analysis.

- Dr. Randy Bunt form Southern Nuclear, USA

Dr. Bunt presented an overview on the guidance developed by the BWR Owner Group to accomplish reactor core and containment cooling in both design basis events and under severe accident scenarios in BWR. This keynote presentation highlights the features of the BWR design and event response capabilities related to reactor core and containment cooling.

- Dr. Hossein Esmaili from the US-NRC, USA

Dr. Esmaili provided a summary of a number of post-Fukushima severe accident analytical research activities undertaken by NRC to support the regulatory basis for filtered containment venting and hydrogen risk management. Major findings and conclusions drawn therein are described below:

  - A combination of venting and water addition is required to prevent containment failure and to mitigate radiological releases for the BWR Mark I and II containments.
  - Anticipatory venting (before core damage) is beneficial to reduce the containment pressure and delay the radionuclide release to the environment.
  - For BWR Mark I and II containments, containment venting is efficient in purging hydrogen and non-condensable. Water injection is also helpful in maintaining a steam-inerted atmosphere which can preclude energetic hydrogen combustion. The releases to the environment from a BWR Mark II containment are generally comparable to or lower than those from a BWR Mark I containment.
  - For both PWR ice condenser and BWR Mark III containment types, igniters are important for providing adequate containment integrity past the 24-hour performance benchmark. The igniters would delay but not alleviate potential containment overpressure failure.
  - PWR Ice Condenser: Without igniters, containment fails soon after hot leg rupture (~24 hours), while use of igniters can control hydrogen and limit the containment pressure so that a containment failure is not likely within 3 days.
  - BWR Mark-III: Without igniters, the containment fails by overpressure soon after lower head rupture (~18 hours). With the igniters, containment failure by overpressure is significantly delayed (>1 day). Activation of containment sprays at the time of lower head failure further delays the containment overpressure failure.

- ✓ Dr. Shinya Mizokami from TEPCO, Japan

Dr. Mizokami described the reactor and debris cooling systems and alternative approaches used during the Fukushima Daiichi accident. In his presentation, Dr. Mizokami discussed the behavior of each of the used equipment and the differences among the three units. He indicated also that the lessons learned from such extremely severe accidents, compared to the prepared accident management scenarios, help improving the

safety of the existing and future nuclear power plants.

2.2. Contributed papers

The 22 technical presentations were divided into 4 technical sessions dedicated to different topics as shown hereafter:

Topic	Title	Number of contributions
1	**Review of the Assessment of Accident Managements Measures and Strategies**	3
2	**New Systems and Designs**	8
3	**Sump Clogging Issues**	5
4	**Debris formation and chemical conditions in cooling waters**	6

For each topic, a summary session was meant to collect the participants' feedback and impressions on the technical sessions outcomes and to allow thorough discussions on specific topics and issues that may have emerged during the workshop.
In the following, the main outcomes and discussions held during the sessions are summarized.

2.2.1. Topic1: Review of the Assessment of Accident Managements Measures and Strategies

The topic 1 technical session was dedicated to Assessment of Accident Managements Measures and Strategies. The presentations covered a broad range of areas, providing a better understanding of the impact of different parameters and how these will impact accident progression.
Analyses of the reliability of long-term provision of cooling which might be affected by damage caused by DBA or BDBA scenarios were discussed. It was noticed that from the structural integrity perspective, the assessment of long-term cooling requires an analysis of "short-term" ageing due to challenging environmental conditions and failure of the pressure retaining boundary including sealing, with consideration of material properties far from design conditions. Consideration of increased activity in the coolant loops, corrosion effects due to impaired water quality, debris in the coolant and potential clogging of safety systems should be included in the assessment. Moreover, it was highlighted that the remaining challenges concern the materials behavior characterization under long-term accident conditions far from design condition, and the structure mechanical computing tools improvement to allow reliable assessment of component degradation. This also requires a validation of structural simulation approaches for extreme conditions. Additional research is required to enable further consideration of these effects in accident analyses and potential recommendations.

The presentations also highlighted the contributions made by the post-accident analysis of the Fukushima plants which are supported by a number of international initiatives. The presentations have helped to better understanding of some of the key issues and have been informative.

2.2.2. Topic 2: New Systems and Designs

The topic 2 was designated for the new systems and designs introduced to prevent the escalating of design basis accidents to become severe accidents and/or mitigate the consequences of the severe accidents, if occurred, in the NPPs. Topic 2 included 7 presentations from Korea, Czech Republic, Hungary, Germany, and Ukraine. The presentations covered new systems and designs proposed to SMART-100, VVER-440/V213, and VVER-1000 reactors. For the Korean small integral reactor SMART-100 (System-integrated Modular Advanced ReacTor), the main concept used to terminate progression of severe accidents is by preventing reactor vessel rupture using In-Vessel corium Retention through External Reactor Vessel Cooling (IVR-ERVC). The system cools down the outer wall of the reactor vessel to cool the molten core material inside the reactor vessel using Cavity Flooding System (CFS) with In-Containment Refueling Water Storage Tank (IRWST). In addition, SMART-100 incorporates other systems to rapidly depressurize the reactor coolant system to avoid high-pressure melt ejection and hydrogen control systems to mitigate the hazard of hydrogen combustion.

Concerning VVER, technical solutions were proposed and discussed to resolve the concerns regarding integrity of VVER containment due to slow and long-term (more than 3 days) pressurization following severe accidents. All VVER-440/V213 aim at preventing reactor vessel failure by IVR-ERVC, but their containment cooling solutions are different. The new systems performance, added to Dukovany NPP VVER-440/V213, to cope with consequences of severe accidents were discussed based on simulation performed using ASTEC v2.1 code. These systems include IVR-ERVC, PARs, and new depressurization line on pressurizer (the latter currently under implementation). The simulations examined the performance of a new independent containment cooling system (CCS) that utilizes turbo-pump and heat exchanger located inside the containment. These are used to circulate the sump water through sprayers while being driven/cooled by an external cooling circuit. Implementation of the new CCS is under preparation in all 4 units of Dukovany NPP.

In addition, challenges in the design of a long-term containment cooling system for VVER-440/V213 at Paks NPP were discussed and different solutions for dealing with the issue of containment pressurization were investigated based on MAAP4-VVER simulations. Based on the obtained results, it was decided to implement the Severe Accident Spray System (SASS). It allows steam condensation using cooled water droplets injection into the atmosphere of the localization shaft of the containment. The water (condensate and droplets) is collected in the sump and driven by the pumps to be cooled by air cooled heat exchangers located outside the localization shaft (on the roof). Operation of the SASS ensures the conditions for external cooling of the reactor vessel, the leaching of fission products from the containment atmosphere and the reduction of the containment pressure and temperature to achieve a safe state. Adequacy of the selected system design is supported also by the results of L1 and L2 PSA.

Other technical solution, as Containment Cooling Condenser (CCC) and dealing with the containment cooling, was presented by Framatome GmbH. This passive system circulates the water from a back-cooling pool (e.g. shielding/storage pool) into the containment through tilted tube-bundle heat exchanger where steam is condensed on the outer surface of the tubes. The phase-change within the heat exchanger tubes drives a natural 2-phase convection through the tube-bundle. The steam leaving the heat exchanger is then

condensed in a back-cooling pool above. The CCC system was tested at Framatome' experimental facilities and its performance in a VVER-440/V213 containment during severe accident was simulated using MELCOR. The results show that a moderate size system should be sufficient for VVER-440/V213 needs.

Two concepts for long-term containment cooling following severe accidents in VVER-440/V213 with implemented IVR-ERVC were investigated for Rivne NPP Units 1&2. The first concept is fully passive using Containment Cooling Condenser (CCC), similar to what was presented by Framatome GmbH. The second concept is active using turbine driven pumps, heat exchanger and spray nozzles. Both options were analyzed by MELCOR code and preliminary results of their effectiveness in practical application were discussed.

All Ukrainian VVER-1000 reactors are already equipped (or being equipped) with Filtered Containment Venting Systems (FCVS). Operation of FCVS and PARs ensure the containment integrity during SA within 72 hours. IVR-ERVC is not credited/implemented for VVER-1000, due to the high heat fluxes. Therefore in case of severe accident the core is expected to be cooled ex-vessel. Long-Term Containment Cooling System (LTCCS) for VVER-1000 Zaporizhzhya NPP Unit 1 using concept with turbine driven pumps, in-containment heat exchanger and spray nozzles was analyzed using MELCOR code. The obtained results show that the effect of simultaneous filter containment venting system (FCVS) actuation and LTCCS operation on containment behavior should be further investigated to avoid danger of deep negative pressures after loss of non-condensable gases due to FCVS operation.

In addition, a new water turbine driven pump, developed by Westinghouse Electric Germany, to ensure long-term containment cooling was presented and its qualification and testing results summarized. These results suggest that the system allows removing the decay heat of well more than 6.1 MW from the VVER-440 containment during a severe accident with core melt considering In-Vessel Melt Retention (IVMR) availability. The pump is able to operate for prolonged periods of time (over six months). The pump has been designed and tested to be qualified for operation under severe accident conditions together with the pump manufacturer KSB.

2.2.3. Topic 3: Sump Clogging Issues

The topic 3 was dedicated to sump filter clogging issues mostly on the French NPP. Recent experimental programs related to filters sump clogging issue were presented. The conclusions issued from these programs and their use in the framework of the fourth periodic French 900 MWe safety review were presented and discussed illustrating the use of R&D results in the safety assessment process. The experimental approach developed by IRSN is based on both global tests in the VIKTORIA facility (study of sump filtration with representative debris including insulation materials and painting chips) and on separate effect tests performed in the COPIN (Clogging Of sumPs In Nuclear industry) facility. In both cases, conditions representative of the reactor case (either LOCA or severe accidents) are looked for. This includes thermal hydraulic parameters such as temperature, filters design, flow rates, size of the debris and chemical parameters such as water composition of the sumps (boric acid and soda concentrations in water) and chemical compositions of the debris (fibers of materials used in NPP are selected). The global VIKTORIA experiments have shown the influence of several of those parameters on the sumps filters performance and to first order the design of the filter (rectangular cartridges or planar grids types). The separate effects tests aim at better identifying and understanding the chemical phenomena which could be involved in the formation of gels and precipitates that could contribute to the clogging of filters. Since performed in a medium-scale facility, new phenomena such as the effect of radiation leading to the radiolysis of gas and water are planned to be studied in the frame of the analysis of the severe accident case.

The last paper of the session describes a methodology and an application to characterize the sump clogging issue in case of long-term cooling. It is based on the use of the REPAS system developed by ENEA and of the TRACE code (thermal-hydraulic system code) developed by USNRC. The main purpose of the paper is to show that the REPAS system which was developed to study the reliability of passive systems can also be used for active systems. The REPAS system can perform both deterministic and probabilistic analyses. The main question raised from the review of the paper is related to the computation time and thus to the real ability of the systems to perform reactor calculations. If a complete long-term core cooling analysis would require at least 72 hours of simulation time, is that tool really suited to perform probabilistic analyses in which several hundred of calculations may be necessary to limit the uncertainty of the results?

2.1.4. Topic 4: Debris formation and chemical conditions in cooling waters

The topic 4 addressed two items: debris formation and chemical conditions in cooling waters. For the first item, four papers in the session addressed melt jet fragmentation in water (melt from fusion of in-core material), fuel debris formation and coolability mainly during ex-vessel phase of a severe accident. No contribution on other type of debris (e.g. resulting from degradation of in-containment material) which could affect long term cooling was provided for the session.
The first three papers dealt with model development and code validation against available experimental data.
A fourth paper presented application part of severe accident research - modelling results of melt ex-vessel spreading, MCCI and melt solidification in case of hypothetical severe accident in CANDU reactor with unsuccessful in-vessel melt retention and accident progression to the ex-vessel phase.
It was discussed and recognized that significant modelling uncertainties still exist in the prediction of formed debris configurations and debris bed properties due to:

- Uncertainties accumulated during in-vessel accident progression modelling and specifically modelling of RPV failure mode, time and characteristics (vessel vs penetration failure(s), failure location(s), breach area and its time evolution, etc.)
- Variability in melt release scenario, e.g. one or more pours with different locations and melt composition (metal-rich or mostly oxidic), melt pour flow rate, temperature and composition vs time, variability in cavity configurations and system parameters, e.g. possible pressure escalation/oscillations – even if energetic steam explosion does not take place;
- Debris formation and agglomeration models, as well as debris coolability ones, are not completely validated on representative tests reproducing full ranges of major parameter variation in the conditions expected. There is visible lack of experimental data for that;
- Variability and complexity of melt compositions and poor knowledge of properties of liquid and solid corium.

For several important phenomena, experimental data are not covering all needs of model development and code validation. Several new important directions of experimental research are proposed in the papers on model development; some of the suggested experiments are already initiated.
Models and codes developed in different organisations give a good starting for advanced ex-vessel analyses, but it is still challenging to predict cooling or re-melting of accumulated debris and MCCI arrest. The OECD/NEA ROSAU (Basu, June 2020) project should provide new data reducing some of these uncertainties.

Enhancing probabilistic analyses could help in better assessing debris formation and coolability ex-vessel.
Long term aspects of fuel debris bed behaviour and coolability appeared to be novel and quite challenging applications for the models and codes traditionally developed in reactor severe accident research. Regarding long term cooling, no contribution addressed potential effects of the presence of other types of debris and precipitates/sediments in cooling waters which could potentially affect the fuel debris cooling (e.g. by blocking porosities in accumulated fuel debris) but also contribute to blocking/clogging of cooling systems as discussed in session 3.
Addressing the full span of debris/sediments which can be formed under severe accident conditions appears very challenging and further assessment of possible debris sources (e.g. heat insulation material, paints and composite liners, …) and their potential detrimental effects on the long term management of an accident would be needed to prioritize any significant R&D in the field. Explorations inside the containment of the three damaged units at Fukushima-Daiichi (Akira Nakayoshi, 1 December 2020) have evidenced the presence of large amount of non-uniformly distributed structural debris and sediments probably originating from various sources. They do not seem to have posed challenges for the long-term cooling up to now, they may pose a challenge for the fuel debris retrieval operations. The extent, nature and characteristics of debris formed during a severe accident may significantly depend on the accident progression in and ex-vessel and reached conditions (e.g. temperature, irradiation dose, chemical conditions).
Another open question relates to the fuel debris ageing with very high accumulated radiation dose in water/air environment which can result in accelerated leaching of specific elements (including FPs), corrosion damage and degradation of material properties, all contributing into the risk of debris fragmentation, formation of fine particles, and associated secondary Fission Products (FP) releases, but also challenges to predict and to manage debris bed macro- and micro-structure. Some activities on FP leaching studies employing synthetic corium samples produced in the labs and plant samples from Chernobyl are in progress in OECD/NEA TCOFF project, the second phase of which is expected to start soon, but available results mostly cover FP releases during leaching, i.e. with the dissolved species, – not corium ageing and degradation of material properties.

For the second item related to chemical conditions in cooling waters, it was obvious that severe accident chemical conditions are extremely complex to represent in detail. Thus, a key question was raised and concerned the way to prioritize R&D efforts to investigate possible chemical effects on long term cooling in a severe accident as many materials can contribute to formation of sediments/particulates, precipitates and result in clogging, e.g. related to:

- degradation of heat insulation and organic materials (e.g. paints, composite liners, cables), degradation/corrosion of structural material from normal operation/accident conditions, contribution to debris/particulate formation of fuel debris;
- effects of chemical additives in coolant waters;
- effects of some fission products (e.g. iodine) on radio-catalysis of corrosion of structural materials.

In this area, it appears challenging to define what research and chemical models are needed in priority to further assess how chemical conditions can affect precipitate formation and clogging risks during accidents. As earlier discussed, this may also be very much dependent on the accident development and reached conditions in and ex-vessel.

Countermeasures, such as "control" of chemical conditions in cooling waters, have been applied in some NPPs to limit corrosion and precipitation risks. It would be appropriate to share best practice and experience in the field to eventually establish guidance and recommendations.

3. Concluding Remarks

The RCCS-2021 workshop provided a unique opportunity to share experience and practices related to the recent developments covering systems used to maintain the long-term cooling of the core and containment during the accident conditions. The safety assessment methodologies, research development and approaches as well as new system development and implementation of such systems was discussed in detail. The workshop covered accident management measures and strategies, new systems design, debris formation, sump clogging issues and chemical effects in cooling water. Presentations and discussions held after each session allowed the identification of open issues related the system operation and long-term survivability and the effect of debris present in the cooling systems. The discussion highlighted the need to enhance simulation tools dealing with material degradation due the presence of such debris or effects.

ACKNOWLEDGMENTS

The Authors would wish to express their gratitude to the NEA Team supporting the event, to the Scientific committee members, to the key invited speakers, to the presenters and to all the participants who contributed to this event. The authors are thankful to the sponsors for their contribution to the successful organization of the workshop.

REFERENCES

Akira Nakayoshi, J. L. (1 December 2020). Review of Fukushima Daiichi Nuclear Power Station debris endstate location in OECD/NEA preparatory study on analysis of fuel debris (PreADES) project, ,. *Nuclear engineering and design, Volume 369,*.

Basu, S. &. (June 2020). Summary of the Reduction of Severe Accident Uncertainties (ROSAU) Project. *, Transactions of ANS meeting,* , Volume 122(1), pages 497-500.

M. Pellegrini, L. H. (2020). Main Findings, Remaining Uncertainties and Lessons Learned from the OECD/NEA BSAF Project. *Nuclear Technology*.

NEA/CSNI/N°7506. (2021). *Long Term Management and Actions for a Severe Accident in a Nuclear Power Plant, Status report NEA N°7506.*

NEA/CSNI/R(2013)12. (2013). *Updated Knowledge Base for Long Term Core Cooling Reliability, NEA/CSNI/R(2013) 12.*

RÉPUBLIQUE FRANÇAISE
Liberté
Égalité
Fraternité

IRSN
INSTITUT DE RADIOPROTECTION ET DE SÛRETÉ NUCLÉAIRE

RCCS-2021

OECD SPECIALIST WORKSHOP ON "REACTOR CORE AND CONTAINMENT COOLING SYSTEMS – LONG TERM MANAGEMENT AND RELIABILITY WORKSHOP"

OVERVIEW ON THE MAIN OUTCOMES

Ahmed Bentaib[1], Vicena Ivan[2], Didier Jacquemain[3], Martina Adorni[3], Luis E. Herranz[4], Ali Tehrani[5], Noreddine Mesmous[6], Mohamed Shawkat[6], Lubica Kubisova[7], Bruno Tourniaire[8], Sevostian Bechta[9], Thibaut Van Rompuy[10]

[1]IRSN, [2] VUEZ, [3]OECD/NEA, [4]CIEMAT, [5]ONR, [6]CNSC, [7]UJD SR, [8]EDF, [9] KTH,[10]BelV,

IRSN/FRM-296 ind. 06

MEMBRE DE ETSON

IRSN
INSTITUT DE RADIOPROTECTION ET DE SÛRETÉ NUCLÉAIRE

Lessons Learned from Major accidents



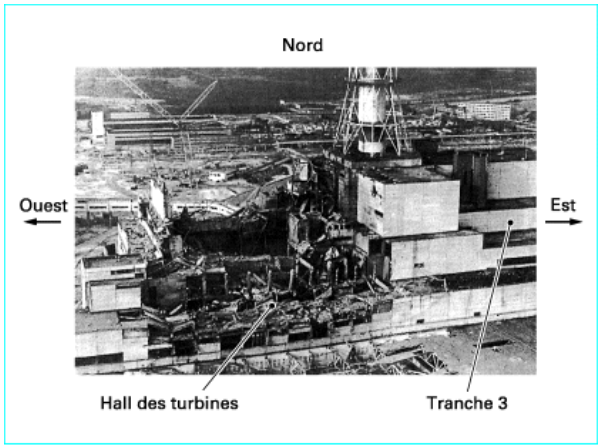

Figure 9







- OECD/NEA *Status report Long-Term Management and Actions for a Severe Accident in a Nuclear Power Plant*
- OECD/NEA *TCOFF, ARC-F and PREADES projects*

Maintaining long-term cooling

Knowledge should be developed on:

- long-term RPV resilience for situations where RPV failure has been prevented;
- long-term reliability of systems and equipment involved in maintaining a coolable configuration to assess failure risks due to induced mechanical weakness (particularly for fixed systems that have withstood challenging SA conditions), due to clogging with debris and due to corrosion-erosion reactions;
- degradation under SA conditions (high dose and temperature) of materials that may form significant amount of debris, posing challenges for the LT cooling.

These recommendations come in addition to recommendations related to implement provisions for replacement of critical systems and equipment for LT cooling (as far as feasible depending on design).

Severe accident long-term phenomena

International sharing and capitalisation of knowledge on phenomena that could affect LTM should be fostered to define appropriate future research on such phenomena.

Appropriate research should be conducted to acquire sufficient knowledge for LTM and related risk evaluation for re-criticality, hydrogen production, phenomena that could induce mechanical failure of safety important components (with consideration of cliff-edge effects) such as corrosion-erosion reactions, sediment formation and clogging of recirculation loops, solidified corium and debris leaching, ageing and fuel dusting and dispersal (in particular during debris retrieval operations).

Such actions should benefit from knowledge sharing between various communities (SA, ageing and waste management experts).

Further development of knowledge on some of these phenomena through investigations on real samples from passed accident should be supported, e.g. debris leaching and ageing from Chernobyl accident (some testing may be performed in the NEA TCOFF project). These investigations should also provide important knowledge for Fukushima Daiichi LTM.

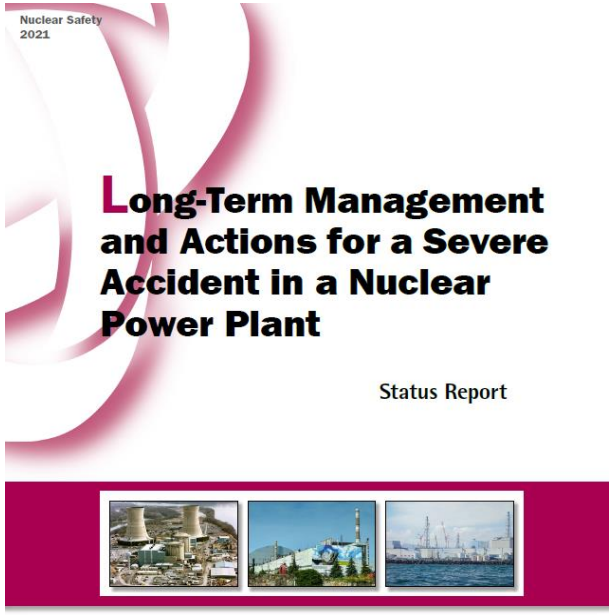

ETSON

IRSN
INSTITUT DE RADIOPROTECTION ET DE SÛRETÉ NUCLÉAIRE

Background

- Since 1992, important work has been performed on sump clogging issue (mainly concerning DBA)
  - NEA/CSNI/R (95)11 Knowledge Base for Emergency Core Cooling System Recirculation Reliability
  - NEA/CSNI/R(2013)12 Update Knowledge Base for Long-term Core Cooling Reliability

- Recent designs of reactors or upgrade of existing reactors rely on recirculating contaminated water strategy to remove decay heat from containment in case of severe accident
  - NEA/CSNI/R(2018)13 Long-Term Management and Actions for a Severe Accident in a Nuclear Power Plant: Status Report

- Fukushima Daïchi accident show the difficulty to manage a large amount of contaminated water, stressing the interest of reliable and sustainable recirculation strategy





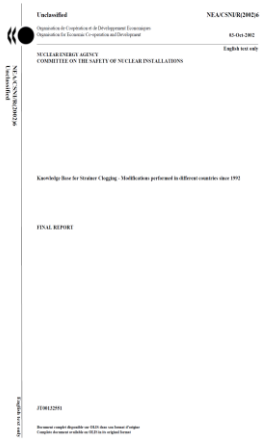

MEMBRE DE ETSON

IRSN
INSTITUT DE RADIOPROTECTION ET DE SÛRETÉ NUCLÉAIRE

WS- Objectives and Topics

Objectives

- To promote international exchange of information and practices related to maintaining the cooling function in a long term accident in a NPP including new design
- To carry out a comprehensive review to identify knowledge gaps linked to the behaviour of material, components and systems that are critical for maintaining cooling in the long term after an accident in a NPP.
- To discuss the best way to address the identified gaps with additional experimental research and with consolidation of existing and/or new assessment methods and analytical tools.

Major Topics of interest

- debris sources and generation – with a focus on SA - and transport characterization
- the filtration systems performance and clogging issues in general
- SA conditions and erosion/corrosion phenomena
- long term accident management measures and strategies

WS structure & Attendance

Considering the travel restrictions imposed by the COVID pandemic in Worldwide, the the RCCS-2021 workshop hold online on October 18th to October 21, 2021.

7 invited lectures:

- **General regulatory aspects (IAEA)**
- **Long term management for different NPP technologies:**
  - Practices for PWR (EDF (France), CNPRI (China))
  - Practices for BWR (Southern Nuclear, USA)
  - Practices for PHWR (Ontario Power Group, Canada)
- **Lessons learnt from the Fukuhisma-Daiichi accident**
  - Post-Fukushima Severe Accident Research Activities (US-NRC, USA)
  - Lessons learned from 1F accident by focusing on the long-term cooling (TEPCO- Japan)

Four technical sessions & 22 papers

Assessment of Accident Managements Measures and Strategies
New Systems and Designs
Sump Clogging Issues
Debris formation and chemical conditions in cooling waters

MEMBRE DE ETSON

IRSN INSTITUT DE RADIOPROTECTION ET DE SÛRETÉ NUCLÉAIRE

Attendance

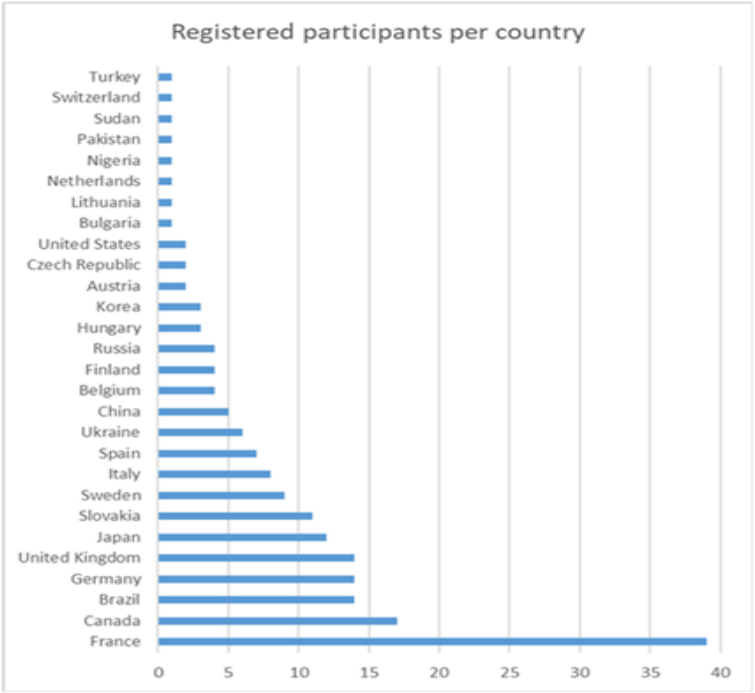

188 participants representing over 28 countries from the regulatory organizations, reactor designers, operators, consultancies, senior engineers, practitioners and analysts from TSCs/TSOs supporting the regulators and research establishments

Outcomes – Current practices

For LOCA conditions, without significant core damage (DEC-A), substantial R&D work has been conducted leading to better understanding of reliability of long-term cooling systems with the development of dedicated experimental facilities.

Establishment of technical bases and the methodology to address long term reliability of cooling systems through:

- the determination of the upstream debris source term, of the sump filtration performance, of chemical effects, and of downstream debris and their potential impact on fuel and core cooling degradation.
- Further, limiting the debris sources (e.g. by reduction or eliminating material inventories such as fiber in containment to limit the level of debris being formed in accident scenarios) and enhancing the filtration capacities have been considered and implemented for a number of plants.

Outcomes – Fukushima lessons learned

Lessons learned from Fukushima Daiichi accident have given meaningful insights into long-term cooling during severe accidents (available time margins before reaching the ultimate limits of the containment strength (for overpressure as well as under-pressure), the coolant inventory, level, etc.).



Safety enhancements and new systems have been added to improve long term core and containment cooling in severe accident scenarios (passive systems and portable equipment).

Outcomes – Identified Gap of knowledge

For Severe Accident conditions: the applicability and sufficiency of the established LOCA technical bases and methodology to address long term reliability of cooling systems need to be assessed.
In particular, debris sources, chemical effects, filtration capacities, erosion-corrosion effects and downstream effects have to be re-evaluated for severe accident conditions and scenarios.

Significant modelling uncertainties still exist in the prediction of formed core material debris configurations and debris bed properties in severe accidents (*limited knowledge of complex corium mixtures properties, Variability on vessel rupture modes and on transfer of core melt and debris from the vessel*)

Outcomes – Identified Gap of knowledge

R&D efforts are needed to investigate possible combined chemical and radiation effects relevant in particular for severe accident conditions..

Knowledge of material, ensuring containment leak tightness (e.g. liners, seals), mechanical response to anticipated prevailing conditions in severe accidents should be extended.

Scaling from sump clogging separate and integral tests to reactor application need to be addressed. Applicability of models developed and/or under development should be demonstrated addressing scaling.

Recommendations to OECD/CSNI

To conduct a ranking exercise in prioritizing the phenomena to investigate, establish research plans in the area with the definition of experimental investigations and assess if the methodology and calculation tools developed for LOCA accidents, without significant core damage, are applicable for severe accidents or need to be completed.

Potential debris sources for severe accidents, e.g. considering degradation of heat insulation and organic materials (e.g. paints, composite liners, cables), degradation/corrosion of structural material from normal operation and accident conditions and the contribution to debris/particle formation of core debris.

Learnings from the Fukushima-Daiichi accident would be valuable though variability of accident scenarios and systems designs

Formation of chemical precipitates from non-metallic insulation debris including thermal effect, buffer composition, pH effect, ionic strength, effect of chemical additives,

Possible combined corrosion, chemical and radiation effects on structural materials and components of cooling systems and possible effect on cooling systems.

Recommendations to OECD/CSNI

To improve sharing internationally data where design specific investigations conducted on a national basis to reduce the need for additional testing requirements.

To improve the containment component degradation assessment using validated structure mechanical computing tools and considering “short-term” ageing due to challenging exposure conditions in severe accidents. It also emphasized the necessity of better assessing the risk of failure of the pressure retaining boundary including sealing, with consideration of material properties far from design conditions.

To improve the connection between ageing and severe accident communities to further assess existing technical bases that can be used to predict the components response in accident and the potential containment leak tightness failures..

Next Steps

Report already reviewed and will be endorsed by CSNI soon

CAPs will be prepared for the PIRT

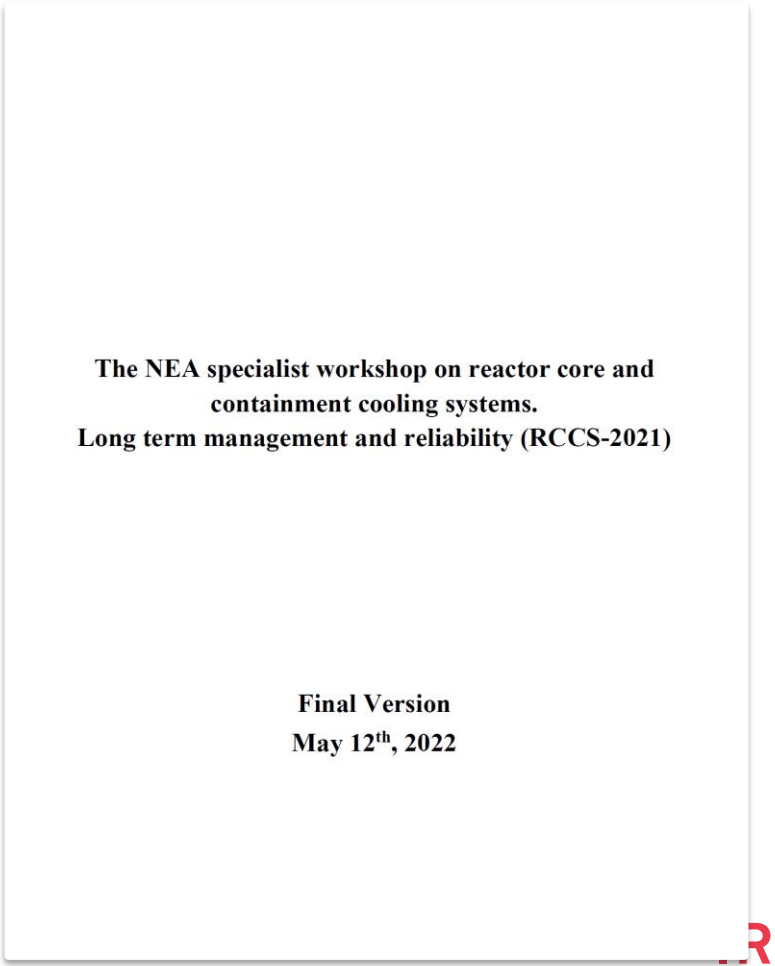

Acknowledgements



Luis E. Herranz	CIEMAT	Spain
Ali Tehrani	ONR	United Kingdom
Noreddine Mesmous	CNSC	Canada
Lubica Kubisova	UJD SR	Slovak Republic
Ivan Vicena	VUEZ	Slovak Republic
Viktoria Valachovicova	VUEZ	Slovak Republic
Juraj Kubica	VUEZ	Slovak Republic
Martina Adorni	NEA	
Didier Jacquemain	NEA	

Thibaut Van Rompuy	BelV	Belgium
Sevostian Bechta	KTH	Sweden
J.-H. Song	KAERI	Republic of Korea
Hossein Esmaili	US NRC	United States of America
Mohamed Shawkat	CNSC	Canada
Martin Sonnenkalb	GRS	Germany
Bruno Tourniaire	EDF	France
Akitoshi Hotta	NRA	Japan
Nadezhda Kozolova	SEC-NRS	Russian Federation
Fudong Liu	NNSA/NSC	China
Kunpeng WANG	NNSA/NSC	China
Vojtech SOLTESZ	VUEZ	Slovak Republic

Christophe Journeau	CEA	France
Marc Barrachin	IRSN	France
Terttaliisa Lind	PSI	Switzerland
Pascal Piluso	CEA	France
Federic Rocchi	ENEA	Italy
Sandro Paci	Unipi	Italy
Ivo Kljenak	IJS	Slovenia

The 10th European Review Meeting on Severe Accidents Research

Severe Accident Research Eleven Years after the Fukushima Accident

May 16-19, 2022, Karlsruhe, Germany

PLENARY SESSION: CLOSING

Chairs: L. E. Herranz (CIEMAT), F. Gabrielli (KIT)

Summary and conclusion of the Session Chairs

Session Chairs

Concluding Remarks and Introduction of ERMSAR2024

A. Bentaib (IRSN), L. E. Herranz (CIEMAT)

Closing Remarks

L. E. Herranz (CIEMAT), F. Gabrielli (KIT)

10TH CONFERENCE ON
SEVERE ACCIDENTS RESEARCH
May 16-19, 2022 – Karlsruhe, Germany
ERMSAR 2022

PLENARY SESSION
International Programs

Luis-Enrique Herranz & Ahmed Bentaib

IAEA
International Atomic Energy Agency

SNETP
Sustainable Nuclear Energy Technology Platform

NUGENIA TA2
Severe Accidents
Nuclear Generation II&III Alliance

NEA
Nuclear Energy Agency

Session overview

- **Presented papers**

  - Euratom projects on Severe Accidents (SA)

    SA have been „steadily“ in the Euratom portfolio in the recent calls for project proposals. There are no signs „a priori“ that this situation is going to change in the near future (2023-2024).

  - OECD/NEA Projects and W

    There are a number of running projects addressing SA. Special mention deserve those addressing the understanding and decommissioning of Fukushima. In addtion, severeal activities are on-going in WGAMA on specific aspects of SA (Wkshps; reports).

  - IAEA axctivities related to SA

    There are ongoing projects on IVMR PIRT and on advanced simulation methods. Some meetings are being called to build some more. Attention is also paid to E&T.

Highlights

- Severe accident research is “alive” and “heartbeat” sounds “healthy”.
- Funding on SA research, though, is NOT raising.
- All the “Agencies” are transparent on their activities.
- Some “agencies” activities overlap, but it looks that to some extent is unavoidable.
- Joint activities among agencies might avoid duplications, though.
- Concern about data preservation, but not a common path on how to proceed.

Further work

- Each platform has its own identity; we (researchers) should do the most „proper use“ of each one.
- Times of the LOFT AND PHEBUS projest are gone. Experiments are expensive and we should properly assess how safety-significant will be the „best“ outcome of any project proposal („safety-enhancement“ driven).
- Times are changing and how „nuclear plays“ in the world too. Researcher awareness of this is indispensable to abandon, if necessary, the BaU approach.
- NUGENIA/TA2 is intending by all means to get all the communities together and plans to insist on it.

10TH CONFERENCE ON
SEVERE ACCIDENTS RESEARCH
May 16-19, 2022 – Karlsruhe, Germany
ERMSAR 2022

PLENARY SESSION
Fukushima: 10 (+1) YEARS AFTER

Ahmed Bentaib & Luis E. Herranz &

IAEA
International Atomic Energy Agency

SNETP
Sustainable Nuclear Energy Technology Platform

NUGENIA TA2
Nuclear Generation II&III Alliance

NEA
Nuclear Energy Agency

Session overview

- **Presented papers**

  - Current understanding of the accident scenarios and major phenomena
    Overview of OECD/NEA projects related to:
    - the analysis of the accidents
    - the decommissioning preparation

  - Current situation of the site
    - New insights on the current status of Unit 2 and Unit 3,
    - Debris collection to perform

  - Accident management & nuclear decommissioning
    - Safety culture improvement: SAMG, education,
    - Ongoing R&D activities to prepare the 1F decommissioning

New advances and results

- Analysis of 1F accidents (BSAF, BSAF2, ARC-F, ..):
  - understanding in accident progress,
  - Code benchmark (degradation, MCCI, H2 explosion, FP distribution..)
- Debris analysis (Preades, TCOFF, ..)
  - Supporting decommissioning
- Data from on site guiding further research
- Safety culture from education and training to decision making
- Fukushima decommissioning: an opportunity for R&D

Further work

- FACE : completion of accident understanding and data preservation
- TCOFF-2: completion in core degradation picture (ATF included)



- Preparation for long term project (SAREF)

10TH CONFERENCE ON
SEVERE ACCIDENTS RESEARCH
May 16-19, 2022 – Karlsruhe, Germany
ERMSAR 2022

Panel Discussion:
New Elements in the Severe Accidents Research Domain

Ivo Kljenak
Jozef Stefan Institute (Slovenia)

IAEA
International Atomic Energy Agency

SNETP
Sustainable Nuclear Energy Technology Platform

NUGENIA TA2
Severe Accidents
Nuclear Generation II&III Alliance

NEA
Nuclear Energy Agency

Panel overview

- **Accident tolerant fuels (M. Khatib-Rahbar)**
  - Overview of main findings from experiments
- **Small modular reactors (P. Dejardin)**
  - Overview of current state and perspectives
- **Interface with environmental impact (W. Raskob)**
  - Need of synergy between research on contaminant dispersion and severe accidents research
- **Innovation in modelling (L. Chailan)**
  - Needs for model developments
  - Use of artificial intelligence

10TH CONFERENCE ON
SEVERE ACCIDENTS RESEARCH
May 16-19, 2022 – Karlsruhe, Germany
ERMSAR 2022

Sessions Summary
1-1 and 1-2 In-vessel Corium and debris coolability

Fabrizio Gabrielli (KIT)
T. Hollands (GRS), S. Massara (IAEA)

IAEA
International Atomic Energy Agency

SNETP
Sustainable Nuclear Energy Technology Platform

NUGENIA TA2
Severe Accidents
Nuclear Generation II&III Alliance

NEA
Nuclear Energy Agency

Sessions overview

- **Total number of papers: 8**

- **Number of papers by subject:**
  - IAEA CRP on PIRT table for IVMR + Benchmark activities: 1
  - Development of models for analysing the pool behaviour: 4
  - Investigations on Corium physio-chemical properties: 1
  - Characterization of Fukushima Daiichi 2 debris : 1
  - Experiments on debris melting behaviour: 1

Sessions overview

The presentations aimed at providing new advancement in the in-vessel–related issues

- Open issues identified in the H2020 IVMR project → need of expanding the experimental matrix, further extensions of the current used models, acceptance criteria → assessment of a IVMR PIRT table for a wide range of technologies
- Development of new models for corium stratification (incl. droplets dynamics), premixed layer in stratified FCI, Turbolent natural convectio in confined cavity.
- CFD analyses for natural convention in IVR and validation against DNS.
- New experiments (transition debris/liquid degradation, LIVE3D), prototypic corium samples Fukushima 2- like (VULCANO), oxidation and dihydrogen phenomena of corium (VITOX).

New advances and results

- New calculation models developed and validated against reference data
- Strong efforts to investigate phenomena affected by large uncertainties or almost unknown
- Experimental investigations on-going and/or planned to tackle open issues in the field
- IAEA as framework to support innovative approaches for different technologies

10TH CONFERENCE ON SEVERE ACCIDENTS RESEARCH
May 16-19, 2022 – Karlsruhe, Germany
ERMSAR 2022

Session summary
2 Severe Accident Scenarios
2-1 SA Scenarios, 2-2 and 2-3 Uncertainties in SA Scenarios

Fabrizio Gabrielli*, Sandro Paci**
*KIT, **UNIPI

IAEA International Atomic Energy Agency
SNETP Sustainable Nuclear Energy Technology Platform
NUGENIA TA2 Severe Accidents Nuclear Generation II&III Alliance
NEA Nuclear Energy Agency

Session overview

- **Total number of papers for Session 2: 11**
  - **2-1** Severe Accident Scenarios: **4** (chair S. Brumm JRC)
  - ***2-2*** Uncertainties in Severe Accident Scenarios: **4** (chair F. Mascari ENEA)
  - **2-3** Uncertainties in Severe Accident Scenarios: **3** (chair O. Coindreau IRSN)

- **Number of papers by subject:**
  - Analysis by ASTEC code of SA sequences for GEN II NPPs : 2
  - Codes platform (KORIGEN/ASTEC/JRODOS) for FP dispersion: 1
  - TH of TMI-2 accident using the CINEMA code: 1
  - Info on IAEA CRP on U&S and K-SOARCA on APR1400: 2
  - Papers on different activities inside the MUSA Project : 5
  - Source term prediction for the KONVOI NPP using ASTEC, the MOCABA algorithm and FSTC tool: 1

Session overview

This Session 2 has been mainly a **presentation on the status of different activities on "SA codes application"**, in particular about the new aspect of UQ in SA scenarios

- The session reflected the continuing effort that helps consolidate the basis of phenomena and reactor modelling
- contributions to development and validation of a single SA code (i.e., ASTEC, CINEMA), tools for estimation of the external source term (i.e., JRODOS, MOCABA) and UQ tools (i.e., FSTC, DAKOTA)
- Presentations about international programmes (IAEA CRP) or project's activities (R2CA, K-SOARCA) on U&S in SA
- Status of different activities undergoing inside the H2020 MUSA project on UQ for SA sequences in a NPP reactor or a SFP

New advances and results

- Emerging the attention towards the **application of UQ methodologies to SA scenarios for a reactor or a SFP,** combining the predictive capability of well known and validated SA analysis codes with the best available/”ad hoc” developed UQ tools
- Development of new coupling strategies (often Phyton based) between SA codes and dedicated external tools
- Confirmation of elevated modelling capabilities of the existing SA codes but also of the limits of the mechanistic approach
- ideas about integrating measurement information into prediction

Comments and conclusions

- Strong international efforts on UQ in SA scenarios
- New needs in this SA area often emerging from the presentations will be challenged by the two future Horizon Europe Projects born inside NUGENIA TA2:
  - ✓ ASSAS for the possible AI use
  - ✓ SEAKNOT for SA knowledges management and preservation
- Key role of SA analyses (as well as U&S applications) for FP dispersion and ST prediction

Further work & research recommendations

- Reduced the computational efforts needed for these analysis (months!)

10TH CONFERENCE ON
SEVERE ACCIDENTS RESEARCH
May 16-19, 2022 – Karlsruhe, Germany
ERMSAR 2022

Sessions Summary
3-1 and 3-2 Ex-vessel Corium interactions and coolability

Pascal Piluso (CEA)
Sevostian Bechta (KTH), Alex Miassoedov (IAEA)

IAEA
International Atomic Energy Agency

SNETP
Sustainable Nuclear Energy Technology Platform

NUGENIA TA2
Severe Accidents
Nuclear Generation II&III Alliance

NEA
Nuclear Energy Agency

Sessions overview

- **Total number of papers: 7**

- **Number of papers by subject:**
  - Mitigation of Fuel Coolant Interaction/Steam explosion: 2
  - PIRT and code development for ex-vessel conditions : 1
  - Assessment of ex-vessel corium coolability for reactor application: 1
  - Debris bed coolability tests and modelling: 1
  - Fukushima-Daiichi Cs-Silica aerosols simulation: 1
  - Behaviour of core catcher to long term conditions: 1

Sessions overview

The presentations aimed at providing new advancement in the ex-vessel–related issues

- New concept of SA management and ex-vessel corium stabilization :water Super Absorbing Polymers (SAP) used in the reactor cavity for prevention or mitigation of **steam explosion**, improvement of melt fragmentation, quenching and coolability of particulate debris bed
- **CASTLE**: a future integral code for severe accident assessment from core degradation till ex-vessel conditions.
- **Ex-vessel corium coolability:** for debris bed, MCCI configuration (melt ejection), application to reactor case
- Design for new experiments to simulate Fukushima Daiichi Conditions and Formation of Cs-Silica aerosols: PLINIUS platform/VITI facility
- Core catcher long term behaviour

New advances and results

- New passive system to mitigate (SAP) ex-vessel steam explosion
- Development of modelling and code for ex-vessel coolability application, CFD approach
- New experimental efforts to simulate Severe Accidents Conditions- Fukushima Daiichi

10TH CONFERENCE ON
SEVERE ACCIDENTS RESEARCH
May 16-19, 2022 – Karlsruhe, Germany
ERMSAR 2022

Session summary

Severe Accident Scenarios in Innovative Systems

Federico Rocchi
ENEA

IAEA
International Atomic Energy Agency

SNETP
Sustainable Nuclear Energy Technology Platform

NUGENIA TA2
Severe Accidents
Nuclear Generation II&III Alliance

NEA
Nuclear Energy Agency

Session overview

- **Total number of papers: 8**
- **Number of papers by subject:**
  - Calculations of PW-SMR sequences: 1
  - SA research (including exp.) for SMRs and other advanced reactors: 1
  - MELCOR applicability demonstration to future, innovative designs: 3
  - SFR: 2
  - MSR: 1

New advances and results

- Calculation of SA sequences for PW-SMRs to test behaviour of codes (ASTEC)
- Initial studies on potential applicability of codes like MELCOR to non-LWR systems through coupling with external codes for chemistry, neutron kinetics, etc.
- New calculation approaches for innovative systems

Comments and conclusions

- Focus on systems: study of near-term technologies and GIV ones (mainly SFR and MSR)
- Focus on design: preliminary SA analyses as a feedback to improve the design
- Focus on codes: use of innovative/advanced concepts to study and investigate calculations/simulation strategies and code applicability
- No papers presented on fusion reactors (too far away in time?)

Further work & research recommendations

- Continue and increase research and investigation of very near-term deployment systems, like PW-SMRs
- Enhance awareness of current code limits for “very innovative” systems and potential ways to overcome some of these limits
- Identify experimental data needs (including chemistry and thermodynamics) in pursuing the aim of studying non-LWR designs and, in the longer term, V&V of codes for the licensing of such systems, in case interest increases (new codes validation matrixes?)

10TH CONFERENCE ON
SEVERE ACCIDENTS RESEARCH
May 16-19, 2022 – Karlsruhe, Germany
ERMSAR 2022

Session summary
Source Term
Session 5.1 (N. Girault) & 5.2 (T. Lind)

Sanjeev Gupta
Becker Technologies GmbH

IAEA
International Atomic Energy Agency

SNETP
Sustainable Nuclear Energy Technology Platform

NUGENIA TA2
Severe Accidents
Nuclear Generation II&III Alliance

NEA
Nuclear Energy Agency

Session overview

- **Total number of papers: 8 (7 in-person, 1 online)**
- **Number of papers by subject:**
  - Overview papers (2) – “consolidated” view on DBA/SA ST research
  - Experimental research (3) – pool hydrodynamics, FPs release & remobilization
  - Analyses, code calculations (2) – reactor application
  - Innovation (1) – SA mitigation

→ ***Papers simulated discussion on application of experimental and analytical outcomes towards reactor application, importance of boundary conditions and the role of uncertainty analyses in source term calculations.***

→ ***Broad range of project frameworks mentioned: National, EC, OECD/NEA, IAEA***

New advances and results

- **Identification**: experimental and modelling research needs

  → E.g. FPs remobilization/delayed releases, FPs release pathways
- **Consolidation**: database for “validation” and “phenomenological understanding”
- **Application**: critical analyses of database towards reactor application, representative BCs, focus on uncertainty analyses, broad range of considered accident scenarios (early-phase, delayed releases etc)
- **R&D status**: continuous focus on SA mitigation – feasibility/development of “new” mitigation measures, Inclusion of other innovation aspects , e.g. artificial intelligence, machine learning

Comments and conclusions

- Reactor analyses for ST calculations

  → *release pathways, nodalization, etc.*

- Validation of safety analyses tools is limited by availability of experimental data, continuous assessment/consolidation/improvement necessary (Experiments ⇌ Modelling)

  → *valid for existing as well as new technologies, e.g. SMRs, ATFs*

- Use of uncertainty analyses in source term calculations → input of UA on assessing impact on SAM measures necessary

  → *new "commonly developed" methodologies will be useful*

Further work & research recommendations

Status update

- Progress in understanding SA issues, e.g. as identified in 2019 OECD(NEA ST workshop (→ ongoing related projects, e.g. MUSA, IPRESCA, THEMIS, ESTER, IAEA/CRP)

(Focused) Continuation

- (Consolidation of „Source Term“ database → ongoing → database update shall be aimed to include from recently conducted and ongoing work, critical analyses of data necessary towards targeted application
- Efforts towards identification of relevant boundary conditions for Source Term calculations: e.g. OECD/BCAPFIS (pool scrubbing) (brorad spectrum of reactor designs !)

Future needs/innovation

- Identification of SA research needs and priority towards new technologies, e.g. SMRs, ATFs & application of AI/machine learning
- Focus on safety-relevant phenomena (“risk informed”)

Further work & Research recommendations

Present status and Future needs

- Assessment of ST experimental infrastructure availability, knowledge management (training and education)

Harmonization

- Streamlining future activities to complete & extend the source term research (*ongoing/planned activities in different frameworks, e.g. National, EC, OECD/NEA, IAEA, others*) → identify complementarity toone another

→ Timely communication among different international originations would be a key to an efficient continuation of ST research, also to ensure streamlining future activities to achieve the common goal of "Enhanced Safety"

10TH CONFERENCE ON
SEVERE ACCIDENTS RESEARCH
May 16-19, 2022 – Karlsruhe, Germany
ERMSAR 2022

Sessions Summary
6-1 and 6-2 Severe Accident Modeling and Code Development

Fabrizio Gabrielli (KIT), F. Rocchi (ENEA)
E.-M. Pauli (Framatome), L. Chailan (IRSN)

IAEA
International Atomic Energy Agency

SNETP
Sustainable Nuclear Energy Technology Platform

NUGENIA TA2
Severe Accidents
Nuclear Generation II&III Alliance

NEA
Nuclear Energy Agency

Sessions overview

- **Total number of papers: 8**

- **Number of papers by subject:**
  - ASTEC v2.2 code and perspectives: 1
  - New model for core catcher in AC^2 (ATHLET/ ATHLET-CD /COCOSYS): 1
  - Development of new SA codes (CORVES, ALCYONE): 2
  - SA modelling choices with MELCOR: 1
  - AC^2 simulation of recent QUENCH-20 test: 1
  - Coupling of measured data, ATM and safety analyses for “hidden emergencies”: 1

Sessions overview

The presentations aimed at providing the status and the new advancements of the integral codes for SA analyses

- ASTEC: continuous validation via weekly regression tests; areas for further improvement identified (i.e. ATF) and extension of the application to innovative systems (i.e. SMRs) also in the frame of the ASCOM project
- AC2 (ATHLET/ATHLET-CD/COCOSYS): further extension of the code applications; new model for core catcher developed; validation planned; application to BWR quenching to take into account effect of absorbers
- New codes under development for analysing specific issues: FP release from fuel (ALCYONE) and in-vessel phase (CORVES)
- Applications to real emissions to the atmosphere

New advances and results

- Efforts to widen the range of applicability of the SA codes both to Gen-IV technologies and to further improve the modelling of specific components in deployed systems (i.e. core catcher in VVER-1200)
- Validation goes on → good agreement with experiments
- Effective methods to couple accident analysis to EP&R for undeclared releases

10TH CONFERENCE ON
SEVERE ACCIDENTS RESEARCH
May 16-19, 2022 – Karlsruhe, Germany
ERMSAR 2022

Session Summary
Hydrogen and Containment Related Issues

Ivo Kljenak
Jozef Stefan Institute (Slovenia)

IAEA
International Atomic Energy Agency

SNETP
Sustainable Nuclear Energy Technology Platform

NUGENIA TA2
Severe Accidents
Nuclear Generation II&III Alliance

NEA
Nuclear Energy Agency

Session overview

- **Total number of papers: 10**
- **Number of papers by subject:**
  - Material phenomena during severe accidents: 3
  - Containment atmosphere behaviour and consequent phenomena: 3
  - Passive Autocatalytic Recombiners: 3
  - Combustion: 1

New advances and results

- **Material phenomena**
  - New experimental results
- **Containment atmosphere behaviour**
  - Experiments in multi-compartment facility
  - Dynamic Sc_t and Pr_t numbers
- **Passive Autocatalytic Recombiners**
  - Experimental investigations of recombination
- **Combustion**
  - Additional data base for flammability limits

Comments and conclusions

- **Material phenomena**
  - Advanced experiments
  - Modelling not based on first principles
- **Containment atmosphere behaviour**
  - Experiments involving mixing and iodine behaviour
  - Modeling as usual: lumped-parameter and CFD
- **Passive Autocatalytic Recombiners**
  - Advanced experiments
  - Correlations for system codes
- **Combustion**
  - Extensive experiments

Further work & research recommendations

- **Material phenomena**
  - Modelling with less empiricism and on a lower scale
- **Containment atmosphere behaviour**
  - Experiments in multi-compartment facilities always useful
  - CFD modelling, but up to a certain point
- **Passive Autocatalytic Recombiners**
  - Simulation of PAR-atmosphere interaction
- **Combustion**
  - Experiments in large-scale facilities

10TH CONFERENCE ON
SEVERE ACCIDENTS RESEARCH
May 16-19, 2022 – Karlsruhe, Germany
ERMSAR 2022

Session Summary
Hydrogen and Containment Related Issues

Ivo Kljenak
Jozef Stefan Institute (Slovenia)

IAEA
International Atomic Energy Agency

SNETP
Sustainable Nuclear Energy Technology Platform

NUGENIA TA2
Severe Accidents
Nuclear Generation II&III Alliance

NEA
Nuclear Energy Agency

ERMSAR 2024: Welcome to Stockholm!

An open city for innovations, different perspectives and new ideas. Home to nearly one million inhabitants and a vibrant destination where innovations in music, design, fashion and technology are born welcomes you spring 2024.







KTH, More than 175 years of excellence

The origins of the Royal Institute of Technology in Stockholm – "Kungliga Tekniska Högskolan", KTH – go back to 1827, as the "Teknologiska Institutet" then began to offer education in technological subjects with a strong professional touch. https://www.kth.se/en





Since its founding, KTH Royal Institute of Technology in Stockholm has grown to become one of Europe's leading technical and engineering universities, as well as a key centre of intellectual talent and innovation. We are Sweden's largest technical research and learning institution and home to students, researchers and faculty from around the world. Our research and education covers a wide area including natural sciences and all branches of engineering, as well as architecture, industrial management, urban planning, history and philosophy

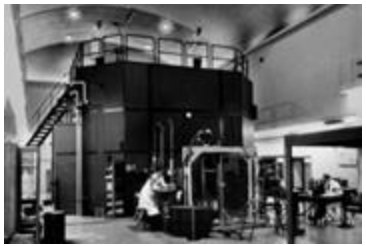

KTH – Campus Valhallavägen was the home of Reactor 1 (R1), the first research reactor of Sweden which was in operation from July 13, 1954 to June 6, 1970



Department of Physics and Division of Nuclear Power Safety

Research at the **Department of Physics** covers a broad range of topics that range from the fundamental to direct applications; from microscopic to astronomical scales; and from few-particle systems to collective phenomena. https://www.physics.kth.se/department-of-physics-1.791524


Nuclear Power Safety


Particle and astroparticle physics


Physics of Medical imaging


Condensed matter theory


Nuclear Engineering


Nuclear Physics

Division of Nuclear Power Safety conducts research on thermal-hydraulics and accident phenomena of risk importance to existing and future nuclear reactors. https://www.physics.kth.se/nps

We perform safety analysis for nuclear power plants, including design basis accident analysis and severe accident analysis.

Our mission is to train future effective leaders in the science and art of Nuclear Power Safety that promote the safe use of nuclear energy in Sweden and worldwide, through quality engineering education, academic excellence and innovative research.

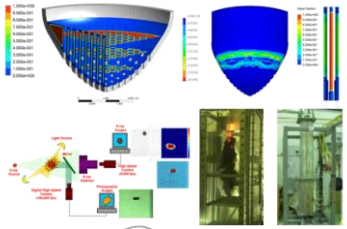



APRI

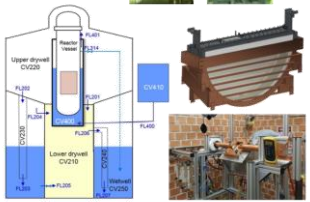

SAFEST

Some examples of premises and rooms

The KTH Campus on Valhallavägen has a large number of premises whose main purposes are teaching and research. These premises offer a variety of solutions for organising conferences and congresses when scheduled educational activities are not being conducted.
More options for room selection are available after June 15



Alfvénsalen, accommodates 467 visitors



F2 is a popular lecture hall with the possibility of mingling in the lobby



Oskar Kleins auditorium, accommodates 265 visitors



U21 with the break-out area and exhibition hall



The Entré hall, ideal for exhibition or reception

See & Do nearby



The Vasa Museum is one of Scandinavia's most visited museums. It is here that you will find in all its glory, the unique and well-preserved warship Vasa from 1628, embellished with hundreds of wooden sculptures.



Stockholm's archipelago is fantastic. from fun excursions, to wonderful beaches, relaxing spa experiences, culture, forts and citadels, as well as art exhibitions, museums, and world-class restaurants.



ABBA The Museum is an interactive museum where you can virtually try on ABBA's costumes, sing, play, mix original music and become the fifth member of ABBA



The Nobel Museum intends to be a "reflecting and forward-looking and spirited memory of Nobel laureates and their achievements, as well as of the Nobel Prize and Alfred Nobel."

Skansen is the world's oldest open-air museum, showcasing the whole of Sweden with houses and farmsteads from every part of the country.



10TH CONFERENCE ON
SEVERE ACCIDENTS RESEARCH
May 16-19, 2022 – Karlsruhe, Germany
ERMSAR 2022

PLENARY SESSION
International Programs

Luis-Enrique Herranz & Ahmed Bentaib

IAEA
International Atomic Energy Agency

SNETP
Sustainable Nuclear Energy Technology Platform

NUGENIA TA2
Severe Accidents
Nuclear Generation II&III Alliance

NEA
Nuclear Energy Agency

Session overview

- **Presented papers**

  - Euratom projects on Severe Accidents (SA)

    SA have been „steadily“ in the Euratom portfolio in the recent calls for project proposals. There are no signs „a priori“ that this situation is going to change in the near future (2023-2024).

  - OECD/NEA Projects and W

    There are a number of running projects addressing SA. Special mention deserve those addressing the understanding and decommissioning of Fukushima. In addtion, severeal activities are on-going in WGAMA on specific aspects of SA (Wkshps; reports).

  - IAEA axctivities related to SA

    There are ongoing projects on IVMR PIRT and on advanced simulation methods. Some meetings are being called to build some more. Attention is also paid to E&T.

Highlights

- Severe accident research is “alive” and “heartbeat” sounds “healthy”.
- Funding on SA research, though, is NOT raising.
- All the “Agencies” are transparent on their activities.
- Some “agencies” activities overlap, but it looks that to some extent is unavoidable.
- Joint activities among agencies might avoid duplications, though.
- Concern about data preservation, but not a common path on how to proceed.

Further work

- Each platform has its own identity; we (researchers) should do the most „proper use“ of each one.
- Times of the LOFT AND PHEBUS projest are gone. Experiments are expensive and we should properly assess how safety-significant will be the „best“ outcome of any project proposal („safety-enhancement“ driven).
- Times are changing and how „nuclear plays“ in the world too. Researcher awareness of this is indispensable to abandon, if necessary, the BaU approach.
- NUGENIA/TA2 is intending by all means to get all the communities together and plans to insist on it.

10TH CONFERENCE ON
SEVERE ACCIDENTS RESEARCH
May 16-19, 2022 – Karlsruhe, Germany
ERMSAR 2022

PLENARY SESSION
Fukushima: 10 (+1) YEARS AFTER

Ahmed Bentaib & Luis E. Herranz &

IAEA
International Atomic Energy Agency

SNETP
Sustainable Nuclear Energy Technology Platform

NUGENIA TA2
Nuclear Generation II&III Alliance

NEA
Nuclear Energy Agency

Session overview

- **Presented papers**

  - Current understanding of the accident scenarios and major phenomena
    Overview of OECD/NEA projects related to:
    - the analysis of the accidents
    - the decommissioning preparation

  - Current situation of the site
    - New insights on the current status of Unit 2 and Unit 3,
    - Debris collection to perform

  - Accident management & nuclear decommissioning
    - Safety culture improvement: SAMG, education,
    - Ongoing R&D activities to prepare the 1F decommissioning

New advances and results

- Analysis of 1F accidents (BSAF, BSAF2, ARC-F, ..):
  - understanding in accident progress,
  - Code benchmark (degradation, MCCI, H2 explosion, FP distribution..)
- Debris analysis (Preades, TCOFF, ..)
  - Supporting decommissioning
- Data from on site guiding further research
- Safety culture from education and training to decision making
- Fukushima decommissioning: an opportunity for R&D

Further work

- FACE : completion of accident understanding and data preservation
- TCOFF-2: completion in core degradation picture (ATF included)



- Preparation for long term project (SAREF)

10TH CONFERENCE ON
SEVERE ACCIDENTS RESEARCH
May 16-19, 2022 – Karlsruhe, Germany
ERMSAR 2022

Panel Discussion:
New Elements in the Severe Accidents Research Domain

Ivo Kljenak
Jozef Stefan Institute (Slovenia)

IAEA
International Atomic Energy Agency

SNETP
Sustainable Nuclear Energy Technology Platform

NUGENIA TA2
Severe Accidents
Nuclear Generation II&III Alliance

NEA
Nuclear Energy Agency

Panel overview

- **Accident tolerant fuels (M. Khatib-Rahbar)**
  - Overview of main findings from experiments
- **Small modular reactors (P. Dejardin)**
  - Overview of current state and perspectives
- **Interface with environmental impact (W. Raskob)**
  - Need of synergy between research on contaminant dispersion and severe accidents research
- **Innovation in modelling (L. Chailan)**
  - Needs for model developments
  - Use of artificial intelligence

10TH CONFERENCE ON
SEVERE ACCIDENTS RESEARCH
May 16-19, 2022 – Karlsruhe, Germany
ERMSAR 2022

Sessions Summary
1-1 and 1-2 In-vessel Corium and debris coolability

Fabrizio Gabrielli (KIT)
T. Hollands (GRS), S. Massara (IAEA)

IAEA
International Atomic Energy Agency

SNETP
Sustainable Nuclear Energy Technology Platform

NUGENIA TA2
Severe Accidents
Nuclear Generation II&III Alliance

NEA
Nuclear Energy Agency

Sessions overview

- **Total number of papers: 8**

- **Number of papers by subject:**
  - IAEA CRP on PIRT table for IVMR + Benchmark activities: 1
  - Development of models for analysing the pool behaviour: 4
  - Investigations on Corium physio-chemical properties: 1
  - Characterization of Fukushima Daiichi 2 debris : 1
  - Experiments on debris melting behaviour: 1

Sessions overview

The presentations aimed at providing new advancement in the in-vessel–related issues

- Open issues identified in the H2020 IVMR project → need of expanding the experimental matrix, further extensions of the current used models, acceptance criteria → assessment of a IVMR PIRT table for a wide range of technologies
- Development of new models for corium stratification (incl. droplets dynamics), premixed layer in stratified FCI, Turbolent natural convectio in confined cavity.
- CFD analyses for natural convention in IVR and validation against DNS.
- New experiments (transition debris/liquid degradation, LIVE3D), prototypic corium samples Fukushima 2- like (VULCANO), oxidation and dihydrogen phenomena of corium (VITOX).

New advances and results

- New calculation models developed and validated against reference data
- Strong efforts to investigate phenomena affected by large uncertainties or almost unknown
- Experimental investigations on-going and/or planned to tackle open issues in the field
- IAEA as framework to support innovative approaches for different technologies

10TH CONFERENCE ON SEVERE ACCIDENTS RESEARCH
May 16-19, 2022 – Karlsruhe, Germany
ERMSAR 2022

Session summary
2 Severe Accident Scenarios
2-1 SA Scenarios, 2-2 and 2-3 Uncertainties in SA Scenarios

Fabrizio Gabrielli*, Sandro Paci**
*KIT, **UNIPI

IAEA International Atomic Energy Agency
SNETP Sustainable Nuclear Energy Technology Platform
NUGENIA TA2 Severe Accidents Nuclear Generation II&III Alliance
NEA Nuclear Energy Agency

Session overview

- **Total number of papers for Session 2: 11**
  - **2-1** Severe Accident Scenarios: **4** (chair S. Brumm JRC)
  - ***2-2*** Uncertainties in Severe Accident Scenarios: **4** (chair F. Mascari ENEA)
  - **2-3** Uncertainties in Severe Accident Scenarios: **3** (chair O. Coindreau IRSN)

- **Number of papers by subject:**
  - Analysis by ASTEC code of SA sequences for GEN II NPPs : 2
  - Codes platform (KORIGEN/ASTEC/JRODOS) for FP dispersion: 1
  - TH of TMI-2 accident using the CINEMA code: 1
  - Info on IAEA CRP on U&S and K-SOARCA on APR1400: 2
  - Papers on different activities inside the MUSA Project : 5
  - Source term prediction for the KONVOI NPP using ASTEC, the MOCABA algorithm and FSTC tool: 1

Session overview

This Session 2 has been mainly a **presentation on the status of different activities on "SA codes application"**, in particular about the new aspect of UQ in SA scenarios

- The session reflected the continuing effort that helps consolidate the basis of phenomena and reactor modelling
- contributions to development and validation of a single SA code (i.e., ASTEC, CINEMA), tools for estimation of the external source term (i.e., JRODOS, MOCABA) and UQ tools (i.e., FSTC, DAKOTA)
- Presentations about international programmes (IAEA CRP) or project's activities (R2CA, K-SOARCA) on U&S in SA
- Status of different activities undergoing inside the H2020 MUSA project on UQ for SA sequences in a NPP reactor or a SFP

New advances and results

- Emerging the attention towards the **application of UQ methodologies to SA scenarios for a reactor or a SFP,** combining the predictive capability of well known and validated SA analysis codes with the best available/”ad hoc” developed UQ tools
- Development of new coupling strategies (often Phyton based) between SA codes and dedicated external tools
- Confirmation of elevated modelling capabilities of the existing SA codes but also of the limits of the mechanistic approach
- ideas about integrating measurement information into prediction

Comments and conclusions

- Strong international efforts on UQ in SA scenarios
- New needs in this SA area often emerging from the presentations will be challenged by the two future Horizon Europe Projects born inside NUGENIA TA2:
  - ✓ ASSAS for the possible AI use
  - ✓ SEAKNOT for SA knowledges management and preservation
- Key role of SA analyses (as well as U&S applications) for FP dispersion and ST prediction

Further work & research recommendations

- Reduced the computational efforts needed for these analysis (months!)

10TH CONFERENCE ON
SEVERE ACCIDENTS RESEARCH
May 16-19, 2022 – Karlsruhe, Germany
ERMSAR 2022

Sessions Summary
3-1 and 3-2 Ex-vessel Corium interactions and coolability

Pascal Piluso (CEA)
Sevostian Bechta (KTH), Alex Miassoedov (IAEA)

IAEA
International Atomic Energy Agency

SNETP
Sustainable Nuclear Energy Technology Platform

NUGENIA TA2
Severe Accidents
Nuclear Generation II&III Alliance

NEA
Nuclear Energy Agency

Sessions overview

- **Total number of papers: 7**

- **Number of papers by subject:**
  - Mitigation of Fuel Coolant Interaction/Steam explosion: 2
  - PIRT and code development for ex-vessel conditions : 1
  - Assessment of ex-vessel corium coolability for reactor application: 1
  - Debris bed coolability tests and modelling: 1
  - Fukushima-Daiichi Cs-Silica aerosols simulation: 1
  - Behaviour of core catcher to long term conditions: 1

Sessions overview

The presentations aimed at providing new advancement in the ex-vessel–related issues

- New concept of SA management and ex-vessel corium stabilization :water Super Absorbing Polymers (SAP) used in the reactor cavity for prevention or mitigation of **steam explosion**, improvement of melt fragmentation, quenching and coolability of particulate debris bed
- **CASTLE**: a future integral code for severe accident assessment from core degradation till ex-vessel conditions.
- **Ex-vessel corium coolability:** for debris bed, MCCI configuration (melt ejection), application to reactor case
- Design for new experiments to simulate Fukushima Daiichi Conditions and Formation of Cs-Silica aerosols: PLINIUS platform/VITI facility
- Core catcher long term behaviour

New advances and results

- New passive system to mitigate (SAP) ex-vessel steam explosion
- Development of modelling and code for ex-vessel coolability application, CFD approach
- New experimental efforts to simulate Severe Accidents Conditions- Fukushima Daiichi

10TH CONFERENCE ON
SEVERE ACCIDENTS RESEARCH
May 16-19, 2022 – Karlsruhe, Germany
ERMSAR 2022

Session summary

Severe Accident Scenarios in Innovative Systems

Federico Rocchi
ENEA

IAEA
International Atomic Energy Agency

SNETP
Sustainable Nuclear Energy Technology Platform

NUGENIA TA2
Severe Accidents
Nuclear Generation II&III Alliance

NEA
Nuclear Energy Agency

Session overview

- **Total number of papers: 8**
- **Number of papers by subject:**
  - Calculations of PW-SMR sequences: 1
  - SA research (including exp.) for SMRs and other advanced reactors: 1
  - MELCOR applicability demonstration to future, innovative designs: 3
  - SFR: 2
  - MSR: 1

New advances and results

- Calculation of SA sequences for PW-SMRs to test behaviour of codes (ASTEC)
- Initial studies on potential applicability of codes like MELCOR to non-LWR systems through coupling with external codes for chemistry, neutron kinetics, etc.
- New calculation approaches for innovative systems

Comments and conclusions

- Focus on systems: study of near-term technologies and GIV ones (mainly SFR and MSR)
- Focus on design: preliminary SA analyses as a feedback to improve the design
- Focus on codes: use of innovative/advanced concepts to study and investigate calculations/simulation strategies and code applicability
- No papers presented on fusion reactors (too far away in time?)

Further work & research recommendations

- Continue and increase research and investigation of very near-term deployment systems, like PW-SMRs
- Enhance awareness of current code limits for “very innovative” systems and potential ways to overcome some of these limits
- Identify experimental data needs (including chemistry and thermodynamics) in pursuing the aim of studying non-LWR designs and, in the longer term, V&V of codes for the licensing of such systems, in case interest increases (new codes validation matrixes?)

10TH CONFERENCE ON
SEVERE ACCIDENTS RESEARCH
May 16-19, 2022 – Karlsruhe, Germany
ERMSAR 2022

Session summary
Source Term
Session 5.1 (N. Girault) & 5.2 (T. Lind)

Sanjeev Gupta
Becker Technologies GmbH

IAEA
International Atomic Energy Agency

SNETP
Sustainable Nuclear Energy Technology Platform

NUGENIA TA2
Severe Accidents
Nuclear Generation II&III Alliance

NEA
Nuclear Energy Agency

Session overview

- **Total number of papers: 8 (7 in-person, 1 online)**
- **Number of papers by subject:**
  - Overview papers (2) – “consolidated” view on DBA/SA ST research
  - Experimental research (3) – pool hydrodynamics, FPs release & remobilization
  - Analyses, code calculations (2) – reactor application
  - Innovation (1) – SA mitigation

→ ***Papers simulated discussion on application of experimental and analytical outcomes towards reactor application, importance of boundary conditions and the role of uncertainty analyses in source term calculations.***

→ ***Broad range of project frameworks mentioned: National, EC, OECD/NEA, IAEA***

New advances and results

- **Identification**: experimental and modelling research needs

  → E.g. FPs remobilization/delayed releases, FPs release pathways
- **Consolidation**: database for “validation” and “phenomenological understanding”
- **Application**: critical analyses of database towards reactor application, representative BCs, focus on uncertainty analyses, broad range of considered accident scenarios (early-phase, delayed releases etc)
- **R&D status**: continuous focus on SA mitigation – feasibility/development of “new” mitigation measures, Inclusion of other innovation aspects , e.g. artificial intelligence, machine learning

Comments and conclusions

- Reactor analyses for ST calculations

  → *release pathways, nodalization, etc.*

- Validation of safety analyses tools is limited by availability of experimental data, continuous assessment/consolidation/improvement necessary (Experiments ⇌ Modelling)

  → *valid for existing as well as new technologies, e.g. SMRs, ATFs*

- Use of uncertainty analyses in source term calculations → input of UA on assessing impact on SAM measures necessary

  → *new "commonly developed" methodologies will be useful*

Further work & research recommendations

Status update

- Progress in understanding SA issues, e.g. as identified in 2019 OECD(NEA ST workshop (→ ongoing related projects, e.g. MUSA, IPRESCA, THEMIS, ESTER, IAEA/CRP)

(Focused) Continuation

- (Consolidation of „Source Term“ database → ongoing → database update shall be aimed to include from recently conducted and ongoing work, critical analyses of data necessary towards targeted application
- Efforts towards identification of relevant boundary conditions for Source Term calculations: e.g. OECD/BCAPFIS (pool scrubbing) (brorad spectrum of reactor designs !)

Future needs/innovation

- Identification of SA research needs and priority towards new technologies, e.g. SMRs, ATFs & application of AI/machine learning
- Focus on safety-relevant phenomena (“risk informed”)

Further work & Research recommendations

Present status and Future needs

- Assessment of ST experimental infrastructure availability, knowledge management (training and education)

Harmonization

- Streamlining future activities to complete & extend the source term research (*ongoing/planned activities in different frameworks, e.g. National, EC, OECD/NEA, IAEA, others*) → identify complementarity toone another

→ Timely communication among different international originations would be a key to an efficient continuation of ST research, also to ensure streamlining future activities to achieve the common goal of "Enhanced Safety"

10TH CONFERENCE ON
SEVERE ACCIDENTS RESEARCH
May 16-19, 2022 – Karlsruhe, Germany
ERMSAR 2022

Sessions Summary
6-1 and 6-2 Severe Accident Modeling and Code Development

Fabrizio Gabrielli (KIT), F. Rocchi (ENEA)
E.-M. Pauli (Framatome), L. Chailan (IRSN)

IAEA
International Atomic Energy Agency

SNETP
Sustainable Nuclear Energy Technology Platform

NUGENIA TA2
Severe Accidents
Nuclear Generation II&III Alliance

NEA
Nuclear Energy Agency

Sessions overview

- **Total number of papers: 8**

- **Number of papers by subject:**
  - ASTEC v2.2 code and perspectives: 1
  - New model for core catcher in AC^2 (ATHLET/ ATHLET-CD /COCOSYS): 1
  - Development of new SA codes (CORVES, ALCYONE): 2
  - SA modelling choices with MELCOR: 1
  - AC^2 simulation of recent QUENCH-20 test: 1
  - Coupling of measured data, ATM and safety analyses for “hidden emergencies”: 1

Sessions overview

The presentations aimed at providing the status and the new advancements of the integral codes for SA analyses

- ASTEC: continuous validation via weekly regression tests; areas for further improvement identified (i.e. ATF) and extension of the application to innovative systems (i.e. SMRs) also in the frame of the ASCOM project
- AC2 (ATHLET/ATHLET-CD/COCOSYS): further extension of the code applications; new model for core catcher developed; validation planned; application to BWR quenching to take into account effect of absorbers
- New codes under development for analysing specific issues: FP release from fuel (ALCYONE) and in-vessel phase (CORVES)
- Applications to real emissions to the atmosphere

New advances and results

- Efforts to widen the range of applicability of the SA codes both to Gen-IV technologies and to further improve the modelling of specific components in deployed systems (i.e. core catcher in VVER-1200)
- Validation goes on → good agreement with experiments
- Effective methods to couple accident analysis to EP&R for undeclared releases

10TH CONFERENCE ON
SEVERE ACCIDENTS RESEARCH
May 16-19, 2022 – Karlsruhe, Germany
ERMSAR 2022

Session Summary
Hydrogen and Containment Related Issues

Ivo Kljenak
Jozef Stefan Institute (Slovenia)

IAEA
International Atomic Energy Agency

SNETP
Sustainable Nuclear Energy Technology Platform

NUGENIA TA2
Severe Accidents
Nuclear Generation II&III Alliance

NEA
Nuclear Energy Agency

Session overview

- **Total number of papers: 10**
- **Number of papers by subject:**
  - Material phenomena during severe accidents: 3
  - Containment atmosphere behaviour and consequent phenomena: 3
  - Passive Autocatalytic Recombiners: 3
  - Combustion: 1

New advances and results

- **Material phenomena**
  - New experimental results
- **Containment atmosphere behaviour**
  - Experiments in multi-compartment facility
  - Dynamic Sc_t and Pr_t numbers
- **Passive Autocatalytic Recombiners**
  - Experimental investigations of recombination
- **Combustion**
  - Additional data base for flammability limits

Comments and conclusions

- **Material phenomena**
  - Advanced experiments
  - Modelling not based on first principles
- **Containment atmosphere behaviour**
  - Experiments involving mixing and iodine behaviour
  - Modeling as usual: lumped-parameter and CFD
- **Passive Autocatalytic Recombiners**
  - Advanced experiments
  - Correlations for system codes
- **Combustion**
  - Extensive experiments

Further work & research recommendations

- **Material phenomena**
  - Modelling with less empiricism and on a lower scale
- **Containment atmosphere behaviour**
  - Experiments in multi-compartment facilities always useful
  - CFD modelling, but up to a certain point
- **Passive Autocatalytic Recombiners**
  - Simulation of PAR-atmosphere interaction
- **Combustion**
  - Experiments in large-scale facilities

10TH CONFERENCE ON
SEVERE ACCIDENTS RESEARCH
May 16-19, 2022 – Karlsruhe, Germany
ERMSAR 2022

Session Summary
Hydrogen and Containment Related Issues

Ivo Kljenak
Jozef Stefan Institute (Slovenia)

IAEA
International Atomic Energy Agency

SNETP
Sustainable Nuclear Energy Technology Platform

NUGENIA TA2
Severe Accidents
Nuclear Generation II&III Alliance

NEA
Nuclear Energy Agency

ERMSAR 2024: Welcome to Stockholm!

An open city for innovations, different perspectives and new ideas. Home to nearly one million inhabitants and a vibrant destination where innovations in music, design, fashion and technology are born welcomes you spring 2024.







KTH, More than 175 years of excellence

The origins of the Royal Institute of Technology in Stockholm – "Kungliga Tekniska Högskolan", KTH – go back to 1827, as the "Teknologiska Institutet" then began to offer education in technological subjects with a strong professional touch. https://www.kth.se/en





Since its founding, KTH Royal Institute of Technology in Stockholm has grown to become one of Europe's leading technical and engineering universities, as well as a key centre of intellectual talent and innovation. We are Sweden's largest technical research and learning institution and home to students, researchers and faculty from around the world. Our research and education covers a wide area including natural sciences and all branches of engineering, as well as architecture, industrial management, urban planning, history and philosophy

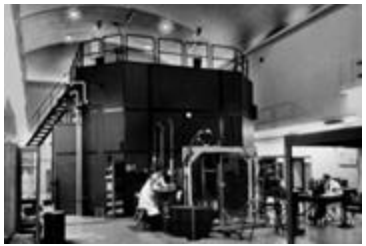

KTH – Campus Valhallavägen was the home of Reactor 1 (R1), the first research reactor of Sweden which was in operation from July 13, 1954 to June 6, 1970



Department of Physics and Division of Nuclear Power Safety

Research at the **Department of Physics** covers a broad range of topics that range from the fundamental to direct applications; from microscopic to astronomical scales; and from few-particle systems to collective phenomena. https://www.physics.kth.se/department-of-physics-1.791524


Nuclear Power Safety


Particle and astroparticle physics


Physics of Medical imaging


Condensed matter theory


Nuclear Engineering


Nuclear Physics

Division of Nuclear Power Safety conducts research on thermal-hydraulics and accident phenomena of risk importance to existing and future nuclear reactors. https://www.physics.kth.se/nps

We perform safety analysis for nuclear power plants, including design basis accident analysis and severe accident analysis.

Our mission is to train future effective leaders in the science and art of Nuclear Power Safety that promote the safe use of nuclear energy in Sweden and worldwide, through quality engineering education, academic excellence and innovative research.

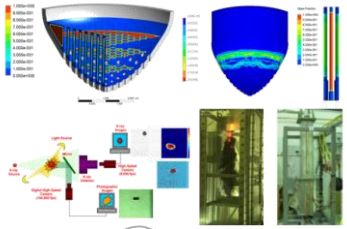



APRI

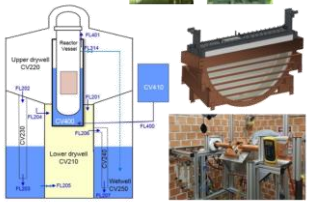

SAFEST

Some examples of premises and rooms

The KTH Campus on Valhallavägen has a large number of premises whose main purposes are teaching and research. These premises offer a variety of solutions for organising conferences and congresses when scheduled educational activities are not being conducted.
More options for room selection are available after June 15



Alfvénsalen, accommodates 467 visitors



F2 is a popular lecture hall with the possibility of mingling in the lobby



Oskar Kleins auditorium, accommodates 265 visitors



U21 with the break-out area and exhibition hall



The Entré hall, ideal for exhibition or reception

See & Do nearby



The Vasa Museum is one of Scandinavia's most visited museums. It is here that you will find in all its glory, the unique and well-preserved warship Vasa from 1628, embellished with hundreds of wooden sculptures.



Stockholm's archipelago is fantastic. from fun excursions, to wonderful beaches, relaxing spa experiences, culture, forts and citadels, as well as art exhibitions, museums, and world-class restaurants.



ABBA The Museum is an interactive museum where you can virtually try on ABBA's costumes, sing, play, mix original music and become the fifth member of ABBA



The Nobel Museum intends to be a "reflecting and forward-looking and spirited memory of Nobel laureates and their achievements, as well as of the Nobel Prize and Alfred Nobel."

Skansen is the world's oldest open-air museum, showcasing the whole of Sweden with houses and farmsteads from every part of the country.

